AD-A152 757 COST REDUCTION IN VERTICALLY RELATED INDUSTRIES: INTEGRATION VERSUS NONLINEAR PRICING(U) RAND CORP SANTA MONICA CA H C QUIRMBACH MAY 83 RAND/P-6839 1/9

UNCLASSIFIED F/G 5/1 NL

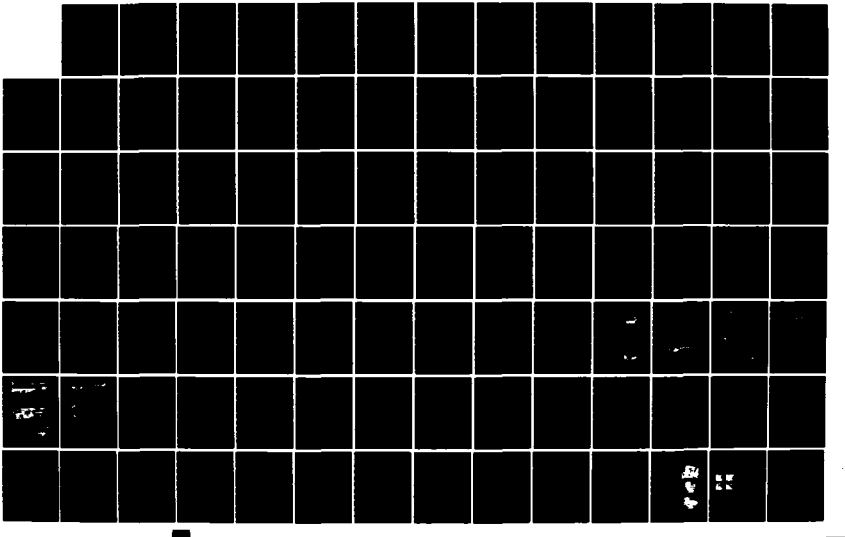

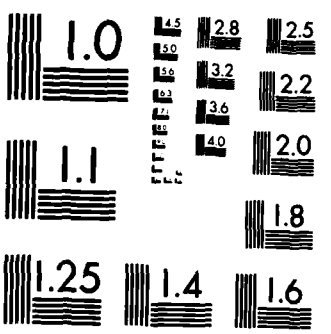

MICROCOPY RESOLUTION TEST CHART
NATIONAL BUREAU OF STANDARDS-1963-A

AD-A152 757

(2)

COST REDUCTION IN VERTICALLY RELATED INDUSTRIES: INTEGRATION VERSUS NONLINEAR PRICING

Herman C. Quirmbach

December 1982, Revised May 1983

DTIC FILE COPY

DTIC
ELECTE
APR 25 1985
S D
D

DISTRIBUTION STATEMENT A
Approved for public release;
Distribution Unlimited

P-6839

85

COST REDUCTION IN VERTICALLY RELATED INDUSTRIES: INTEGRATION VERSUS NONLINEAR PRICING

Herman C. Quirmbach

December 1982, Revised May 1983

DDC
QUALITY INSPECTED
1

Accession For
NTIS GRA&I ☒
DTIC TAB ☐
Unannounced ☐
Justification
By
Distribution/
Availability Codes
Dist | Avail and/or Special
A-1

ACKNOWLEDGMENTS

This paper has benefited from the comments and advice of William J. Baumol, Avinash K. Dixit, and Robert D. Willig. Part of the author's time was funded by a grant from the Sloan Foundation to the Economics Department at Princeton University. Technical support was provided by The Rand Corporation and in particular, by Janet D'Amore, Gloria Lenaris, Helen Loesch, and Connie Moreno. The author thanks all for their efforts but retains sole responsibility for the results.

PREVIOUS PAGE IS BLANK

CONTENTS

ACKNOWLEDGMENTS iii

Section

I. INTRODUCTION 1

II. INTERMEDIATE GOOD PRICES AND INDUSTRY PRODUCTION COSTS 6

III. ROYALTY SCHEMES, TWO-PART TARIFFS, AND INDUSTRY COSTS 15

IV. NONLINEAR PRICING SCHEMES AND VERTICAL INTEGRATION 32

V. CONCLUSIONS 43

REFERENCES 46

PREVIOUS PAGE IS BLANK

I. INTRODUCTION

A continuing concern in the study of vertical integration is whether ownership integration is necessary or sufficient to achieve all possible cost savings in the operation of a vertically related sequence of production processes. Integration--or any other mechanism for controlling intermediate markets--must accomplish two functions: to coordinate production and to divide revenues among the various levels. The analysis here compares integration and several other revenue division mechanisms in terms of the production efficiency they induce. As Flaherty {6} has pointed out, ownership integration may not always provide the best institutional arrangement for balancing these functions.

The intermediate market control mechanisms compared are simple (linear) pricing; two forms of nonlinear pricing, a royalty scheme and a two-part tariff; and vertical integration. Under a royalty scheme, the purchaser of an intermediate good pays a price per unit of intermediate good bought plus a royalty fee for each unit of final good produced. Under a two-part tariff, the intermediate good buyer pays a lump-sum access charge in addition to the per-unit price. → p. 43

The market setting for the comparisons is a two-stage production process involving a single intermediate good and a single final good. Throughout, the upstream production of the intermediate good is assumed to be monopolized. The upstream monopolist, it is further assumed, chooses the control mechanism for the intermediate market. We will consider both a profit maximizing monopolist and a monopoly controlled by a welfare (profit plus consumer surplus) maximizing social planner. In the latter case (and only then), it is assumed that the upstream firm exhibits scale economies and must cover its costs, so that marginal cost simple pricing is ruled out.

Firms in the downstream industry combine the intermediate good with other exogenously supplied inputs under a U-shaped average cost technology. The downstream industry will be characterized by free entry and no sunk costs.[1] Free entry will force downstream firms to sell

their output at minimum average cost. Thus, under each of the control mechanisms, the downstream industry will be allocated just enough revenue to cover its expenditures.

In order to determine which of two control mechanisms induces the lower industry cost, one must hold the industry final good output constant. But, final good demand is, of course, an *endogenous* variable: it is determined by the independent downstream firms' minimum value of average costs, which in turn depends on the terms of intermediate good sale. Thus, care must be taken that the mechanisms compared each induce the same level of minimum average cost and thereby the same final good demand.

Why compare industry costs rather than welfare or the monopolist's profit? First, production efficiency is in itself an interesting issue. Baumol, Panzar and Willig {2} have shown that a horizontal contestable market will minimize industry costs. However, as I have shown elsewhere {9}, a vertically related pair of industries with technologies as are considered here will generally fail to minimize costs when the upstream industry (contestable or otherwise) is monopolized and simple pricing is used. Cost minimization fails even when (partial) forward integration is allowed. Full forward integration may not be efficient either. The question then arises of whether a nonlinear pricing scheme can achieve efficient production.

Second, under the specified comparison conditions--namely that two mechanisms elicit the same final good demand--one mechanism's superior production efficiency is sufficient for both superior welfare and profit performance. Inducing the same final good implies that both consumer surplus and industry revenue will be the same. With revenue the same, any industry cost savings must show up in higher industry profit. Since free entry keeps independent downstream profits at zero, industry cost savings translate dollar for dollar into higher profits for the upstream monopolist. And, with the same consumer surplus, profit gains are dollar for dollar welfare gains.

Third, not only are cost savings sufficient for one mechanism to be

---

[1]A market characterized by free entry and no sunk costs is "contestable." That a contestable market may have *fixed* costs and therefore scale economies is not a contradiction. See Baumol, Panzar, and Willig {2} for more on the distinction between sunk and fixed costs.

preferred on profit and welfare grounds, but it turns out that "locally" they are also necessary. That is, to the extent that switching from one mechanism to another can be characterized in terms of local parameter changes, a profit- (or profit-constrained welfare-) maximizing monopolist will gain by switching if and only if there are cost savings.

The comparison results below differ sharply from those of Blair and Kaserman {3} who compare integration, royalty, and two-part tariff mechanisms in the case where the downstream technology has constant returns to scale.[2] They conclude that all three produce identical results in terms of production efficiency and profits to the upstream monopolist. Implicitly, they find each is superior to a simple pricing scheme except when the downstream technology uses the intermediate good in fixed proportions to final output. Though they do not directly address the issue, it is also true of their model that vertical integration eliminates the incentive to impose a nonlinear pricing scheme, and vice versa.

When the downstream technology has U-shaped average costs, the conclusions are different in a number of respects. While a royalty scheme again yields lower industry costs than does a simple pricing system (with a fixed proportions exception), a royalty scheme here is also preferable to a two-part tariff (with one exception where the two are equivalent). Furthermore, a two-part tariff need *not* be preferable to a simple pricing scheme: when the intermediate good is used in fixed proportions to final output, a non-trivial[3] two-part tariff is inferior to a simple price. Sufficient conditions are given for a two-part tariff to reduce costs.[4]

---

[2]The research on which this paper is based was completed independently of both Blair and Kaserman {3} and of the Ordover and Panzar {8} paper cited below. In writing this paper, I have tried to minimize the inevitable overlap, focusing as far as possible on how my results add to or contrast with their findings.

[3]A "non-trivial" two-part tariff has a strictly positive access charge. Since a simple price is a two-part tariff with a zero access charge, the general class of two-part tariffs are weakly superior to simple prices. In what follows, however, a "two-part tariff" will always refer to the non-trivial variety.

[4]Ordover and Panzar {8} compare simple pricing and a two-part tariff directly on profit and welfare rather than cost grounds. Two of the results they have established are quite similar to those just mentioned. The results below correct their findings slightly and, more

Other differences appear when the cost reducing potential of vertical integration is considered. While the use of a royalty scheme again eliminates the cost reduction incentive to integrate, the reverse is no longer true: in most circumstances, a vertically integrated upstream monopolist could reduce costs still further by imposing a royalty scheme. Thus, a royalty scheme generally induces lower costs than vertical integration. Imposing a two-part tariff, on the other hand, does not generally eliminate the cost incentive to integrate, nor vice versa. Thus both vertical integration and a two-part tariff are imperfect coordination devices; that each may add to the cost reductions of the other indicates the nature of their imperfections are not identical.

The key to these various results is the catalogue of distortions that can be induced in the downstream firms' input and output choices. For a constant returns downstream industry, the upstream firm wishes to control the downstream input mix and the final good price. When, under simple pricing, the intermediate good is priced above its marginal cost (to induce a higher final good price), downstream firms tend (inefficiently) to substitute away from the intermediate good. Partial integration solves only the integrated firm's subsidiary's input mix problem; the independent firms' input mix and the final good price both still depend on the intermediate good price offered to those firms. That price will generally be above marginal cost. Under constant returns, however, there are several efficient ways to fix this problem: simply sell the intermediate good at its marginal cost and use either an access charge or a royalty fee or full forward integration to control final good price. Since there is no one efficient downstream scale, all three are equally effective.

The results are different for the U-shaped downstream average cost case precisely because the upstream firm now needs to control the scale of the downstream operations in addition to the input mix and the final good price. A simple intermediate good price above marginal cost may

---

importantly, show that the source of the profit/welfare gains is improved coordination of production between the two levels. I refer the reader to their presentation for several additional interesting results.

distort the scale of each downstream firm as well as its input mix. Partial integration again fails to be fully efficient for the same reason as before: the intermediate good price to the remaining downstream firms will exceed marginal cost. Differences appear now among full forward integration, a two-part tariff, and a royalty scheme, since each has a different effect on the scale of downstream operations. Since generally the royalty fee is the only mechanism that does not alter scale, it is the only one that is fully efficient.

The paper is organized as follows: Section II develops the general relationship between intermediate good prices and industry costs. The coordination potential (and problems) of the nonlinear pricing schemes can be understood better by characterizing the "nonlinear" parts (i.e., the access charge and royalty fee) as payments for "pseudo-inputs". To do this requires a multiple intermediate good approach in Sec. II. Section III applies the results to compare industry costs under the linear and nonlinear pricing schemes. Section IV then introduces vertical integration into the cost analysis. Costs are compared with and without integration for a given nonlinear pricing arrangement, and with and without each nonlinear scheme, given integration. The relative advantages of integration and the nonlinear schemes are thereby determined. Section V provides a conclusion.

II. INTERMEDIATE GOOD PRICES AND INDUSTRY PRODUCTION COSTS

Let us begin by exploring in a general way the effect of intermediate good prices on total industry production costs. In the next section, I will use the results derived here to compare industry costs under the two nonlinear schemes and under a simple pricing arrangement. While there is only one intermediate good actually traded in this model, the representation here must allow for multiple intermediate goods so that the access charge and royalty fee can be treated below as payments for pseudo-inputs.

The total cost incurred in producing Q total units of final output[1] is the sum of upstream production costs plus downstream production costs. The upstream monopoly's costs are captured by the upstream cost function $C^U(Y)$, where Y is the vector of total intermediate outputs.[2] For simplicity, I assume all of Y is sold to the downstream industry in question. The case of multiple downstream industries is an easy generalization.

Downstream production costs are the sum of the costs of the N independent downstream firms (where N is endogenous) plus, when the upstream monopoly is integrated forward, the cost of the integrated firm's downstream subsidiary. I assume that each downstream firm, independent or otherwise, uses a technology whose cost function is $C^D(z,p)$, where z is the firm's output and p the vector of intermediate good prices. I allow (z,p) to be different for the integrated firm's subsidiary than for the independent downstream firms. Let (z^I,p^I) be the final output and intermediate good prices for the subsidiary, and let p^* be the intermediate good prices for the independent sector.[3] Given free entry and U-shaped average costs downstream, each independent

---

[1] In the definition of industry production costs, Q should be considered fixed. Final demand will be treated endogenously in the analysis in later sections.

[2] The costs associated with producing pseudo-inputs are, of course, zero. Also, I will assume throughout that inputs exogenous to the model are perfectly elastically supplied at their social marginal costs.

[3] Below I refer to p_j^*, the price on external sales of the jth intermediate good as the jth "external price," and similarly

downstream firm will operate at the output z^* which minimizes downstream average costs Since downstream average costs depend on p^*, so will z^*. Then, downstream production costs are:

$$(2.1) \qquad C^D(z^I,p^I) + N \cdot C^D(z^*(p^*),p^*).$$

Note that N is treated as a continuous variable given by

$$(2.2) \qquad N \equiv (Q-z^I)/z^*,$$

and that N implicitly adjusts if z^I or z^* changes.

Putting the pieces together, let us define the industry cost function as follows:

$$(2.3) \qquad IC(Q,p^I,z^I,p^*) \equiv C^U(Y) + C^D(z^I,p^I) + N \cdot C^D(z^*,p^*) - p^I \cdot y^I - Np^* \cdot y^*,$$

where

$$(2.4) \qquad y(z,p) \equiv \text{downstream firm's vector of intermediate good demands}$$

$$y^I \equiv y(z^I,p^I),$$

$$y^* \equiv y(z^*,p^*), \text{ and}$$

$$Y \equiv y^I + Ny^*.$$

The two subtraction terms in Eq.(2.3) are the payments to the

---

p_j^I as the jth "internal price." Allowing p^I to be different from p^* is only a matter of notational convenience. The results do not depend on discrimination in the prices actually paid, but rather on the signals which the various downstream firms use for input allocation and output choice (including entry/exit). The integrated firm's downstream subsidiary might actually pay p^*; the results require only that it use

upstream firm for intermediate goods sold between the two levels. Since the costs of these goods are already captured in C^U, the subtractions must be made to avoid double counting. Note also that, since z^* is completely determined by p^*, it is not separately an argument of IC.

The following regularity conditions will be assumed throughout.[4]

R1) *Differentiability.* The downstream cost function $C^D(z,p)$ is twice continuously differentiable in all arguments. Upstream marginal costs are finite and well defined for all positive outputs.

R2) *Existence of a minimum.* For each Q and z^I, the IC function assumes a minimum for some finite vector of prices (p^I, p^*).

R3) *Uniqueness.* For any given values of the other variables, the downstream industry's demand for intermediate good i, as a function of its price, crosses the corresponding upstream marginal cost curve once from above.

Several assumptions about the technology available to an integrated firm are implicit in Eq.(2.3). First, the integrated firm's costs are assumed to be additively separable between the upstream monopoly and its downstream subsidiary. As I have shown in {9}, this is equivalent to assuming that the technology set of the integrated firm is the set sum of the upstream technology set and the downstream set; that is, that the integrated firm's technology is a simple concatenation of the upstream and downstream production processes. What this assumption rules out are direct savings in raw materials achievable only through integration. The classic example of such savings is the savings in reheating costs achieved by integrating the production of steel ingots with the process of rolling ingots into sheets. When the integrated firm's technology

---

p^I as a shadow price.

[4]Note that I have not assumed that the intermediate good is essential to the downstream process. If it were not--that is, if, using none of the intermediate good, the final good could be produced by some backstop technology at a minimum average cost of AC_0--then to be used at all the intermediate good would have to be offered at such terms of sale that the final good could be produced at an average cost below AC_0. The comparisons below adjust the sale terms so that downstream average cost (i.e., the final good price) is held the same for each mechanism. It should be assumed that the level at which it is held constant is below AC_0. Of course, it may be that for some (inefficient) mechanisms downstream average cost cannot be held below AC_0. In that case, the mechanism's problem of production inefficiency is superceded by its lack of commercial viability. In that case, the intermediate good could only be offered under a "more efficient" mechanism.

does allow for such savings, integration can always reduce costs, regardless of any intermediate good pricing arrangement that might be used. We set aside the possibility of a superior integrated technology in order to focus on the issue of coordination mechanisms.

A second assumption implicit in Eq.(2.3) is that the upstream monopoly, if it integrates, is--in effect--limited to a single downstream subsidiary. There are two ways this may arise. The first is that no matter how many subsidiaries are set up on paper, the downstream technology is the same as if there were only one. Specifically, the (eventually) decreasing returns of the downstream U-shaped average cost technology cannot be avoided by simply replicating plants. Such decreasing returns may, for instance, result from congestion of the management of the downstream operation. The second way in which a limit may arise on the number of downstream subsidiaries is if it is imposed exogenously through the actions (actual or feared) of the antitrust authorities. For simplicity, I assume in this latter scenario that downstream acquisitions are limited to one. The results are different in no important respect if the upstream monopolist can acquire several downstream subsidiaries before risking antitrust action.

The effect of an intermediate good price on industry costs is found by differentiating Eq.(2.3). For the i external price,[5]

$$(2.5) \qquad \partial IC/\partial p_i^* = \Sigma(\partial C^U/\partial Y_j - p_j^*)(\partial Ny_j^*/\partial p_i^*) + Ny_i^* - Ny_i^* + (Q-z^I)(\partial AC^D/\partial z)(dz^*/dp_i^*)$$

$$= \Sigma(\partial C^U/\partial Y_j - p_j^*)(\partial Ny_j^*/\partial p_i^*),$$

where the summations are taken over all the intermediate goods and where AC^D (downstream average cost) is evaluated at z^*. Equation (2.5) uses Shephard's Lemma,[6] which implies

[5]To achieve production efficiency, internal prices, it is easy to show, must be set equal to upstream marginal costs if the downstream technology allows any substitution possibilities. Since it is always in the interest of an integrated firm to minimize its costs, we will assume throughout that internal prices are set at marginal cost.

[6]See Varian (12), p. 32.

$$(2.6) \qquad \partial C^D(z^*,p^*)/\partial p_i^* = y_i^*,$$

and also uses the fact that $N \cdot C^D(z^*,p^*) = (Q-z^I) \cdot AC^D(z^*,p^*)$. The simplification uses the fact that

$$(2.7) \qquad \partial AC^D/\partial z = 0,$$

since the average cost curve is flat at z^* by definition.

For the industry to achieve the least cost means of producing Q, Eq.(2.5) must be zero for all i. Clearly, marginal cost pricing of all intermediate goods would satisfy these necessary conditions. This is an unlikely result for a profit-maximizing upstream monopolist or for a welfare-maximizing planner when there are scale economies upstream and each firm must cover its costs. Absent marginal cost pricing, the achievement of (or divergence from) industry production efficiency will depend on the price responsiveness of the independent downstream sector's intermediate good demands.

The total external sales of the j intermediate good, Ny_j^*, depends on the i external price as follows:

$$\begin{aligned} \partial(Ny_j^*)/\partial p_i^* &= (Q-z^I)(\partial(y^*_j/z^*)/\partial p_i^*) \\ (2.8) \qquad &= ((Q-z^I)/z^*) \cdot [(\partial y_j^*/\partial p_i^*) \\ &\qquad + (\partial y_j^*/\partial z - y_j^*/z^*)(dz^*/dp_i^*)], \end{aligned}$$

where the first line uses Eq. (2.2). Equation (2.8) can be simplified further by using a result of Bassett and Borcherding {1}:

$$(2.9) \qquad dz^*/dp_j = (y_j^*/z^*)(1-e_{jz})/C^D_{zz},$$

where

$e_{jz} \equiv$ output elasticity of the jth input demand at efficiency scale

$= (z^*/y^*_j)(\partial y_j^*/\partial z)$, and

$C^D_{zz} \equiv \partial^2 C^D(z^*)/\partial z^2$.

We know C^D_{zz} is positive since marginal costs are upward sloping at the bottom of a U-shaped average cost curve. Using Eqs.(2.9) and (2.2), we can rearrange Eq.(2.8) to give

$$(2.10) \qquad \partial(Ny_j^*)/\partial p_i^* = N(\partial y_j^*/\partial p_i^* - C^D_{zz}\cdot(dz^*/dp_j^*)(dz^*/dp_i^*))$$

To illustrate the types of production inefficiencies--or "cost distortions"--that might arise because of a failure to price at marginal cost, consider the case where all intermediate goods save one are priced at marginal costs. If the exception is input i, then

$$(2.11) \qquad \partial IC/\partial p_i^* = (\partial C^U/\partial Y_i - p_i^*)N[\partial y_i^*/\partial p_i^* - C^D_{zz}(dz^*/dp_i^*)^2]$$

As is well known {12,p.33}, a firm's derived demand for input i is downward sloping in the price of the input:

$$(2.12) \qquad \partial y_i/\partial p_i < 0 \quad \text{for any } i$$

Thus, both parts of the square-bracketed term in Eq. (2.11) are non-positive. Then, Eq. (2.11) is non-negative if input i is priced above marginal costs.

Pricing input i above its marginal cost increases industry costs if either $\partial y_i^*/\partial p_i^*$ or dz^*/dp_i is non-zero. If the former is negative, the independent downstream firms inefficiently substitute away from input i at z^*. The resulting cost increase I will refer to as a "substitution distortion." If dz^*/dp_i^* is non-zero, then z^* diverges from the socially optimal scale when p^*_i is above marginal costs. The independent downstream firms are then induced to produce at the "wrong" output levels. I refer to this kind of inefficiency as a "scale distortion."

The identification of substitution and scale distortions leads naturally to a definition of input types:

Definition 2.1. Input i is a *variable proportions input* if Eq.(2.11) holds strictly.

Definition 2.2. Input i is a *fixed schedule input* if Eq. (2.11) holds with equality.

Definition 2.3. A *fixed proportions input* is a fixed schedule input whose firm level input demand is linear in the firm's output.

If the ith input demand is linear in output, then $e_{iz} = 1$ and, by Eq.(2.9), $dz^*/dp_i = 0$.

As is clear from the definitions and foregoing discussion, substitution distortions do not occur when a fixed schedule input is priced above its marginal cost. Further, scale distortions are absent when an input whose demand is linear in output is priced above marginal cost. Finally, pricing a fixed proportions input above its marginal cost does not result in either substitution or scale distortions. Thus, for i=j, Eq. (2.10) simplifies for a fixed schedule input to

$$(2.13) \qquad \partial(Ny_i^*)/\partial p_i^* = - N \cdot C^D_{zz} \cdot (dz^*/dp^*_i)^2,$$

and for a fixed proportions input to

$$(2.14) \qquad \partial(Ny_i^*)/\partial p_i^* = 0.$$

These findings generalize to the effects of a fixed schedule/proportions input's price on the demands for other inputs and of the prices of other inputs on the demand for a fixed schedule/proportions input via the following lemma.

Lemma 2.1 At a given output level, suppose that the cost function of a firm is twice continuously differentiable in input prices. Then, at that output, the demand for any fixed schedule input is insensitive to all input prices. Further, the demand for any other input is insensitive to the price of the fixed schedule input.

Proof: From standard micro theory {12,p.28}, we know the cost function is concave in input prices. Thus, the determinant of any second order principal minor of the cost function's input price Hessian must be non-negative. That is,

$$(2.15) \qquad (\partial^2 C^D/\partial p_i^{\,2})(\partial^2 C^D/\partial p_j^{\,2}) - (\partial^2 C^D/\partial p_i \partial p_j)^2 > 0,$$

for any inputs i,j, with i≠j. Suppose input i is a fixed schedule input. Then, from Shephard's Lemma and Def. 2.2,

$$(2.16) \qquad \partial^2 C^D/\partial p_i^{\,2} = \partial y_i/\partial p_i = 0.$$

But then Eq. (2.15) implies $\partial^2 C^D/\partial p_i \partial p_j = 0$. Differentiating Shephard's Lemma also yields

$$(2.17) \qquad \partial^2 C^D/\partial p_i \partial p_j = \partial y_i/\partial p_j = \partial y_j/\partial p_i,$$

where the second equality is based on reversing the order of the derivatives of the cost function. The two conclusions of the lemma follow immediately.

E.O.P.

Using Lemma 2.1 and Eq. (2.10), we see that

$$(2.18) \qquad \partial(Ny_j^*)/\partial p_i^* = - N \cdot C^D_{zz} \cdot (dz^*/dp_i^*)(dz^*/dp_j^*)$$

if *either* input i or input j is a fixed schedule input. If either i or j is a fixed proportions input,

$$(2.19) \qquad \partial(Ny_j^*)/\partial p_i^* = 0.$$

It follows that if i is a fixed schedule input, taking the sum over all inputs j,

$$(2.20) \qquad \partial IC/\partial p_i^* = N \bullet C^D_{zz}(dz^*/dp_i^*)\{\Sigma(p_j^* - \partial C^U/\partial Y_j)(dz^*/dp_i^*)\}$$

If i is a fixed proportions input,

$$(2.21) \qquad \partial IC/\partial p_i^* = 0.$$

III. ROYALTY SCHEMES, TWO-PART TARIFFS, AND INDUSTRY COSTS

Having established the relationship between industry costs and intermediate good prices, we can use these results to compare the production costs when an intermediate good is sold at a simple price with the industry costs under a royalty scheme and under a two-part tariff. Of course, to make such a cost comparison valid, we must make sure that both of the schemes compared induce the same level of final good demand. For each of the comparisons with a simple price, I then go on to show that cost reductions (keeping final output fixed) are a necessary (not just sufficient) part of broader profit or welfare superiority.

The analysis below characterizes the royalty fee and the two-part tariff's access charge as payments for "pseudo-inputs". The royalty fee can be thought of as the price of an input one and only one unit of which is used for each unit of final output. This pseudo-input is clearly a fixed proportions input. The two-part tariff's access charge, on the other hand, can be represented as payment for an input only one unit of which is used by each downstream firm regardless of the firm's output. This pseudo-input is a fixed schedule input with zero output elasticity (i.e., $e_{jz} = 0$).[2] Both pseudo-inputs of course have zero marginal costs.

To adapt Sec. II's general notation to our purposes here, let good "one" be the true intermediate good sold to independent downstream firms at price p_1^*. Let R represent the royalty fee per unit of final good, and, for a two-part tariff, let A be the access charge per firm. The demand for the royalty pseudo-input is then Q, the total final output

---

[1]Vertical integration considerations are deferred until the next section: here we consider only the nonintegrated case (i.e., where $z^I = 0$).

[2]If, for example, the real intermediate good is Hershey's chocolate and the final good is chocolate cake, then the royalty fee could be the price of a "label" to go on each cake box proclaiming "This cake made with Hershey's chocolate." The access charge could be the price of a "sign" at each bakery saying "Our cakes use Hershey's chocolate."

(held fixed here), whereas the demand for the access input is N, the number of downstream firms. Further, let $AC^* = AC^D(z^*(p_1^*,R,A),p_1^*,R,A)$. Free entry downstream causes this to be the price of the final good to consumers.

From Eq. (2.21) and the above discussion, it follows that

$$(3.1) \qquad \partial IC/\partial R = 0$$

and from Eq. (2.20) that

$$(3.2) \qquad \partial IC/\partial A = NC^D_{zz}(dz^*/dA)\{(p_1^* - \partial C^U/\partial Y_1)(dz^*/dp_1^*) + A(dz^*/dA)\}$$

Further, from Eq. (2.9) and the above observation that a firm's demand for "access" (under a two-part tariff) is completely inelastic with respect to the firm's output, we see that

$$(3.3) \qquad dz^*/dA = 1/(z^* \cdot C^D_{zz}) > 0$$

and also that

$$(3.4) \qquad dz^*/dp_1^* = y_1^*(1 - e_{1z})(dz^*/dA)$$

Finally, we will use the fact that

$$(3.5) \qquad dAC^*/dp_1^* = \partial AC^*/\partial p_1^* + (\partial AC^D/\partial z)(dz^*/dp_1) = y_1^*/z^*,$$

where the simplification uses both Eq. (2.7) and Shephard's Lemma. Similarly,

$$(3.6) \qquad dAC^*/dA = 1/z^*,$$

while

$$(3.7) \qquad dAC^*/dR = z^*/z^* = 1$$

With these preliminaries established we can now compare pricing schemes.

III.A. Royalty vs. Simple Pricing

The first comparison is between a royalty scheme and simple pricing. The result is that a royalty scheme generally induces lower industry costs. To show this, we start from the "optimal" simple price and determine when costs can be lowered by introducing a royalty scheme. Whether it is a social planner who must cover the costs of an increasing returns upstream production process or an upstream monopolist who wishes to maximize profits, the "optimal" simple price will be above upstream marginal cost. This is the only characteristic of the simple price needed to demonstrate the claimed result.[3]

> *Proposition 3.1:* Suppose that the intermediate good is sold at a simple price above its marginal cost. Then, except when the intermediate good is a fixed proportions input downstream, there exists a royalty scheme with positive royalty payment and per-unit price equal to upstream marginal cost that will induce the same level of final good output to be demanded at a lower industry cost. For a fixed proportions input, the costs are the same under either scheme.

Proof: Suppose the simple price of the intermediate good is $p_1^0 > \partial C^U/\partial Y_1$. Then let us introduce a royalty scheme by simultaneously reducing the per-unit price (toward upstream marginal cost) and raising R (from zero) so as to keep the price of the final output, AC*, constant. That is, the rate of change of p_1^* and R must satisfy

[3] In fact, *any* simple price not equal to marginal cost is generally inferior to an appropriately chosen royalty scheme. However, if the price is below marginal cost, then inducing the same level of final demand while reducing costs will require the royalty fee to be negative--i.e., a rebate to the final consumers.

If the upstream process exhibits constant or decreasing returns, then a social planner can cover upstream costs by pricing at marginal cost and will have no need of either nonlinear scheme.

$$(3.8) \qquad (dAC^*/dp_1^*)dp_1^* + (dAC^*/dR)dR = 0$$

or

$$(3.9) \qquad dR/dp_1^* = -y_1^*/z^* \ .$$

Then, along this (p_1^*,R) path, final good demand is constant, and

$$(3.10) \qquad dIC/dp_1^* = (\partial IC/\partial p_1^*) + (\partial IC/\partial R)(dR/dp_1^*)$$

$$= \partial IC/\partial p_1^* - 0 \cdot y_1^*/z^*$$

$$= (\partial C^U/\partial Y_1 - p_1^*)N\{\partial y_1^*/\partial p_1^* - C^D_{zz}(dz^*/dp_1^*)^2\}$$

$$\geq 0$$

The first simplification uses Eq. (3.1), and the second Eqs. (2.5), (2.10), and (2.19). The sign of the derivative holds until p_1^* falls to upstream marginal costs. Along the path, Eq. (3.10) is zero only when the curved bracketed term is zero, and that occurs only when the intermediate good is a (locally) fixed proportions input downstream. Thus, in adjusting from the simple pricing scheme to a royalty scheme with positive royalty payment and marginal cost per-unit price, industry costs fall except in the fixed proportions case where they are unchanged.

E.O.P.

The reason a royalty scheme is preferable to simple pricing lies in the fixed proportions nature of the royalty pseudo-input. Pricing a non-fixed proportions (true) input above its marginal cost under simple pricing causes scale or substitution distortions or both. Under a royalty scheme, however, such distortions are avoided by pricing the true input at its marginal cost while using the royalty payment to carry the mark-up. Since the royalty payment acts as payment for a fixed proportions pseudo-input, no cost distortions are created by pricing that input above its zero marginal cost. Of course, if the true input

is also used in fixed proportions, then neither scheme creates distortions.[4]

A royalty scheme's ability to induce lower costs at the same output is not only sufficient for welfare and/or profit superiority over a simple price, it is also locally necessary.

Proposition 3.2. Starting from the profit maximizing simple price, suppose a "small" royalty fee is introduced and final output is allowed to vary. Then, to a first order approximation, profits will increase if and only if a royalty fee could lower costs in the output-constant comparison. The same can be said of increasing welfare, starting from the profit-constrained welfare-optimal simple price.

Proof: For the profit-maximizing case, consider the change in profits Π if R is raised from zero *and* p_1^* is adjusted along the constant-output path given by Eq. (3.8). Along that (p_1^*,R) path,

$$d\Pi/dR = \partial\Pi/\partial R + (\partial\Pi/\partial p_i^*)(dp_i^*/dR).$$

Evaluated at R=0 (i.e., at the profit-maximizing price), the second term is zero. Thus, the output-constant and the output-free profit changes are there equal. But, profit change is the difference between industry revenue change and industry cost change, and the former is zero along the constant output path. Thus, at R=0,

---

[4]The result here is reminiscent of Diamond and Mirrlees's optimal taxation results. They argue (e.g., { ,p.24} that it is not optimal to levy taxes on an intermediate good but rather to maintain production efficiency and raise any needed revenue by taxing final goods. One could consider the simple price mark-up above marginal cost as an intermediate good "tax" and the royalty payment as a final good "tax". That raising the revenue to cover upstream fixed costs is better accomplished by a royalty scheme than by simple pricing is a finding analogous to their conclusion. Note, however, that their downstream technology is constant returns. (I am indebted to Robert Willig for pointing out the analogy.)

Along the same line, one could consider the access charge of a two-part tariff as a lump sum tax on downstream firms. That a two-part tariff will not turn out to be optimal (in general) seems to contradict the usual optimality of head taxes. The reason for the difference is that, unlike the number of consumers, the number of firms is here endogenous.

$$\partial\Pi/\partial R = d\Pi/dR = -dIC/dR,$$

where the left-most expression allows total output to vary and the right-most is evaluated along the constant output path. Thus, a local increase in R (from zero) increases profit (output free) if and only if it reduces costs (output constant), to a first order approximation.

The same argument works for the profit-constrained welfare-maximing case when the Lagrangean from that maximization is substituted for Π.

E.O.P

III.B. Two-Part Tariff vs. Simple Pricing

The next comparison is between a simple price and a two-part tariff. Again, we begin the comparison from the "optimal" simple price--a price taken to be above upstream marginal cost.[5] Since a simple price is a degenerate two-part tariff--i.e., one with a zero access charge--a two-part tariff will be superior if costs can be reduced by increasing the access charge in the neighborhood of zero. As before, the per-unit price of the intermediate good is simultaneously adjusted to keep the final good price and demand constant.

As described above, the access charge pseudo-input is a fixed schedule input with zero output elasticity. Thus, while not causing a substitution distortion, a positive access charge does distort downstream scale, namely by increasing it, per Eq. (3.3). Therefore, unlike a royalty scheme, a two-part tariff will not generally allow all distortions to be eliminated. The attractiveness (or lack thereof) of a two-part tariff depends on the relative balance of distortions caused by the access charge and by non-marginal cost pricing of the intermediate good.[6], [7]

---

[5]See the discussion in the preceding subsection.

[6]Blair and Kaserman {3} have noted in a brief discussion of the U-shaped average cost case the fact that an access charge tends to increase downstream scale. However, their Fig. 2 (p. 1126) seems to indicate that the intermediate good would be priced at marginal cost under a two-part tariff. This is not generally optimal. They specifically seem to be unaware that if the intermediate good is a fixed schedule input, the scale distortion caused by an access charge may exactly offset the existing distortion. This case will be discussed in the next subsection.

[7]Note, however, that in other situations, a "scale" distortion may

A sufficient condition for industry costs to fall is that the scale distortion caused by the access charge be opposite to--and therefore tend to offset--a scale distortion caused by pricing the intermediate good above marginal cost. An alternative sufficient condition is that, should both scale distortions go in the same direction, the access charge's distortion be (in a certain sense) less severe. This condition implies that, as the access charge is raised and the intermediate good price simultaneously lowered, the net effect on downstream scale is to reduce the existing distortion. If the intermediate good is subject also to a substitution distortion, then in either of these cases a two-part tariff is even more attractive and becomes advantageous even if there is no existing scale distortion. However, if there are no existing distortions of either kind--that is, if the intermediate good is a fixed proportions input--then a non-trivial two-part tariff (i.e., one with a positive access charge) is always *inferior* to a simple price.

These results are captured in a formal proposition and a corollary.

Proposition 3.3: Suppose that the intermediate good is sold at a simple price above its marginal cost. Then, there exists a two-part tariff that induces the production of the same final good demand at lower industry cost if *either* of the following conditions is satisfied:

i) If downstream scale falls as the intermediate good price rises (i.e., $dz^*/dp_1^* < 0$). (This is the case in which the two scale distortions go in opposite directions.) An equivalent condition is that the intermediate good is a "luxury" input downstream (i.e., $e_{1z} > 1$).

---

be beneficial. Suppose the downstream industry were monopolistically competitive, and suppose the market equilibrium under a simple price involved "too many" firms (i.e., too many varieties and too little output of each, as measured by a profit or welfare criterion). Then an access charge, by forcing downstream firms to increase volume (or price or both), may crowd enough firms out of that market that the social (or profit) optimum is achieved. Whether such possibilities actually arise depend, of course, on the model used. Two papers which have explored the subject are Dixit (5) and Mathewson and Winter (7).

ii) If downstream scale rises with a rise in the intermediate good price and rises faster per unit of input than it rises with increase in the access charge; i.e.,

$$(3.11) \qquad (1/y_1^*)(dz^*/dp_1^*) > dz^*/dA > 0.$$

(This is the case in which the scale distortions go in the same direction but access charge distortion is less severe.) An equivalent condition is that $e_{1z} < 0$.

The strong inequalities in either i) or ii) can be replaced with weak inequalities if the intermediate good is subject to substitution distortions.

Proof: As with Prop. 3.1, let us adjust the access charge A and the per-unit price p_1^* in such a way as to leave average downstream costs AC* unchanged. From Eqs. (3.5) and (3.6), this requires

$$(3.12) \qquad dp_1^*/dA = -1/y_1^*.$$

The change in industry costs induced by such pricing changes is given by

$$\begin{aligned} dIC/dA &= (\partial IC/\partial A) + (\partial IC/\partial p_1^*)(dp_1^*/dA) \\ &= N \cdot C^D_{zz}(dz^*/dA)[(p_1^* - \partial C^U/\partial Y_1)(dz^*/dp_1^*) \\ &\quad + A(dz^*/dA)] + (1/y_1^*)[(p_1^* - \partial C^U/\partial Y_1) \\ &\quad (\partial N y_1^*/\partial p_1^*) + A(\partial N/\partial p_1^*)], \end{aligned} \qquad (3.13)$$

where use is made of Eqs. (2.5) and (3.2). Evaluating Eq. (3.13) at the initial simple price p_1^0 ($> \partial C^U/\partial Y_1$) and at A = 0, we get

$$\left.\frac{dIC}{dA}\right|_{\substack{p_1^*=p_1^0 \\ A=0}} = (p_1^0 - \partial C^U/\partial Y_1)[(1/y_1^*)(\partial N y_1^*/\partial p_1^*) + NC^D_{zz}(dz^*/dA)(dz^*/dp_1^*)]$$

$$= (p_1^0 - \partial C^U/\partial Y_1)(1/y_1^*)N(\partial y_1^*/\partial p_1^*) + \{(p_1^0 - \partial C^U/\partial Y_1) \cdot N \cdot C^D_{zz}(dz^*/dp_1^*) \cdot [-(1/y_1^*)(dz^*/dp_1^*) + (dz^*/dA)]\}, \tag{3.14}$$

where the second line uses Eq. (2.10) and collects terms.

If Eq. (3.14) is negative, then a small positive access charge will result in lower industry costs for the same final demand. Under the assumptions, the term involving $(\partial y_1^*/\partial p_1^*)$ is non-positive. Thus, Eq. (3.14) will surely be negative if the curly bracketed term is negative. Since dz^*/dA is positive, the curly bracketed term will be negative if $dz^*/dp_1 < 0$ or, equivalently, if $e_{1z} > 1$. This establishes sufficient condition i).

Sufficient condition ii) is established by noting that Eq. (3.11) implies both that $dz^*/dp_1 > 0$ and that

$$[-(1/y_1^*)(dz^*/dp_1^*) + (dz^*/dA)] < 0, \tag{3.15}$$

again making the curly bracketed term in Eq. (3.14) negative. Note that Eq (3.15) implies that downstream scale on net falls as A and p_1^* are changed along the path given by Eq. (3.12) This reduces the scale distortion caused by $dz^*/dp_1^* > 0$. From Eq. (3.4), one can see that Eq. (3.11) is equivalent to $e_{1z} < 0$.

Finally, if the intermediate good is subject to substitution distortions--i.e., if it is not a fixed schedule input--the term involving $\partial y_1^*/\partial p_1^*$ in Eq. (3.14) is negative. Then, it suffices for Eq. (3.14) to be negative that the curly bracketed term is non-positive. Said term is zero if the above strict inequalities are weakened; that is, if e_{1z} is one (implying $dz^*/dp_1^* = 0$) or zero (implying Eq. (3.15) is zero). This establishes the last part of the theorem.

E.O.P.

The weakened version of condition i) indicates that even if there are no existing scale distortions (i.e., if $dz^*/dp_1^* = 0$) it is optimal to incur some distortion in scale if by doing so one can reduce a substitution distortion (i.e., if $\partial y_1^*/\partial p_1^* < 0$). The weakened version of ii) indicates a gain from reducing the substitution distortion even if the net effect on scale (given by Eq. (3.15)) is zero.[8]

---

[8]Ordover and Panzar {8} compare simple pricing with a two-part tariff directly on welfare and profit grounds, rather than on cost grounds. (See their propositions 3 and 4, {8, pp. 665-666}.) Their proposition 3 establishes that a simple price can be preferable only if $0 < e_{1z} \leq 1$. My Proposition 3.2, interpreted contrapositively, establishes that a simple price can be preferable only if $0 \leq e_{1z} \leq 1$ and, if there is a substitution distortion, only if $0 < e_{1z} < 1$. Since, for purposes of their proposition 3, Ordover and Panzar assume $\partial y_1^*/\partial p_1^* < 0$ (see {8, p. 661}), the discrepancy here concerns the case where $e_{1z} = 1$.

O & P examine this case separately in their proposition 4. There, they do not assume a substitution distortion directly. Rather, they assume the production function is "strongly quasiconcave." I interpret this term to mean that the downstream technology requirement sets $A(z) = \{(x,y) : f(x,y) \geq z$, where $f(\ ,\ )$ is the downstream production function$\}$ are strictly convex. Unfortunately, this condition does *not* guarantee a substitution distortion, and therefore their proposition is not proved.

To see that strong quasiconcavity does not guarantee a substitution distortion, suppose, for a two-input technology, the unit isoquant (i.e., $z = 1$) is given by $\{(x,y) : x(y + 1) = 1$ if $y \geq x$ and $y(x + 1) = 1$ if $x \geq y\}$. Assuming monotonicity, one can see the corresponding requirement set is strictly convex. Then, using x as the numeraire and p as the price of y, it is easy to show that $\partial y/\partial p = 0$ for any p satisfying $p + p^{1/2} > 1 > p - p^{1/2}$. Graphically, this is like clipping out a piece of a nice Cobb-Douglas isoquant on either side of the 45° line and pasting the remaining pieces together. They do not match up "smoothly" in terms of slope, and the isocost line "teeters" at the joint. (Satisfying Ordover and Panzar's other hypothesis, namely, homotheticity, merely requires that the other isoquants be constructed from the unit isoquant by imposing linear expansion paths.)

O & P's proof of their proposition 4 rests on a result attributed to Silberberg {11}. However, I have been unable to find a theorem in the Silberberg article cited which uses strong quasiconcavity. The closest result is the corollary to Silberberg's Theorem 5 {11,p. 739}.

Proposition 3.3 covers the case where the initial price exceeds upstream marginal cost and only a positive access charge is allowed. If, on the other hand, the initial price were for some reason below marginal cost, a sufficient condition for a positive access charge to be optimal (i.e., for Eq. (3.14) to be negative) would be that $\partial y_1^*/\partial p_1^* = 0$ and $0 < e_{1z} < 1$, since then dz^*/dp_1^* and Eq. (3.15) are both positive. Note that if a negative access charge (e.g., a lump sum kickback to retailers) is also permitted, then a two-part tariff is optimal any time Eq. (3.14) is non-zero.

One case in which a simple price is definitely superior is given by the following.[9]

Corollary 3.4. A two-part tariff (with a positive access charge) always induces higher costs if the intermediate good is a fixed proportions input.

Proof. If the intermediate good is a fixed proportions input, then Eqs. (2.9) and (2.19) indicate that

$$(3.16) \qquad dz^*/dp_1^* = \partial N y_1^*/\partial p_1^* = \partial N/\partial p_1^* = 0.$$

Then, Eq. (3.13) is clearly positive for any positive A, and increasing the access charge from zero increases industry costs.

However, said corollary rests not on strong quasiconcavity, but rather on "sufficient regularity of the production function" {11, footnote 10, pp. 736-7}. In Silberberg's context--see, for instance, his equation (11), p. 737--absent a scale distortion (as is the case when $e_{1z} = 1$), this requires a substitution distortion, not merely strong quasiconcavity. Strong quasiconcavity paired with a continuously differentiable production function suffices for a substitution distortion.

These minor differences notwithstanding, the major contributions of Prop.3.2 to O & P's results are to show that the profit and welfare advantages of a two-part tariff (when they arise) are based on a superior ability to control industry costs and to show the nature of the distortions which give rise to the advantages.

[9]This is the "cost" version of Ordover and Panzar's proposition 5 {8, p.13}.

E.O.P.

As with a royalty scheme, cost savings from introducing a two-part tariff (output constant) are both sufficient *and* necessary for profit or welfare gains (output variable). The following proposition formalizes the comparison with Ordover and Panzar's results.

> *Proposition 3.5* Starting from the profit-maximizing simple price, suppose a "small" access charge is introduced and final output is allowed to vary. Then, to a first order approximation, profits will increase if and only if a two-part tariff that holds output constant can lower costs. The same can be said of increasing welfare, starting from the profit-constrained welfare-optimal simple price.

Proof: The proof is identical to that of Prop. 3.2, replacing R with A.

E.O.P.

III.C. Royalty vs. Two-Part Tariff

The final comparison of the section is between a royalty scheme and a two-part tariff. Since the royalty fee is non-distorting, one would anticipate that a royalty scheme with marginal cost pricing of the intermediate good would induce the lowest possible industry costs. This is in fact the case. Thus, a royalty scheme will generally be at least as good as a two-part tariff.[10]

The interesting finding here is that, in some cases, a two-part tariff will be as good as a royalty scheme. Least cost production can in such cases be achieved, provided that the scale distortion caused by the access charge exactly offsets a scale distortion caused by the intermediate good price and that there are no substitution distortions. This in turn requires that the intermediate good be a fixed schedule (but not fixed proportions) input downstream.

---

[10]The cost comparison below between nonlinear schemes is "non-local" and thus does not lend itself to the type of argument used above to establish the necessity of cost savings to profit or welfare improvement. The author has been unable to date to find another means of argument to demonstrate necessity.

The comparison is made by starting from a given two-part tariff, showing under what conditions it fails to minimize industry costs, and then constructing a royalty scheme that does minimize costs. If a negative royalty fee is allowed (e.g., a rebate to final consumers), then the results claimed hold for any initial two-part tariff. For the results to hold with a strictly positive royalty fee, the results hold only for a restricted set of initial two-part tariffs. Fortunately, the restriction, contained in the following condition, does not significantly limit the two-part tariffs considered.

Condition 3.6. Suppose that an upstream firm uses a two-part tariff with access charge A and per-unit price p_1^*. Suppose further that the resulting final good demand is Q. Let the upstream profits thus earned be $\Pi^U(Q,p_1^*,A)$. Now suppose that the intermediate good were sold at a simple, marginal cost price and that the output of the final good were somehow restricted to Q (e.g., if the final good demand were totally inelastic). Let the resulting upstream profits be $\Pi^U(Q,\partial C^U/\partial Y_1,0)$. Then the desired condition is that

$$(3.17) \qquad \Pi^U(Q,p_1^*,A) \geq \Pi^U(Q,\partial C^U/\partial Y_1,0).$$

The optimal two-part tariffs of both the social planner and the profit-maximizer certainly satisfy Condition 3.6 when there are scale economies upstream: under both tariffs the monopoly at least breaks even, whereas with scale economies it would run a loss if it is priced at marginal cost. The condition would also hold for the profit-maximizing (p_1^*,A) regardless of upstream technology if final output were allowed to adjust to the true final demand curve instead of being artificially restricted to Q. Indeed, I have been unable to derive a plausible circumstance under which it would not hold at an "optimal" two-part tariff.[11]

[11]Note that an alternative for Condition 3.6 that comes to mind is to consider only two-part tariffs with p_1^* at or above marginal cost. However, this would impose a significant restriction: if e_{1z} is negative, it can be shown that the profit-maximizing two-part tariff involves a p_1^* *below* marginal cost.

Proposition 3.7. Suppose the upstream monopoly employs a two-part tariff with a positive access charge and that the tariff satisfies Condition 3.6. Then, with one exception, the monopoly can always find a royalty scheme with a positive royalty payment which lowers industry costs while inducing the same level of final good demand. The exception may arise when the intermediate good is used as a fixed schedule (but *not* fixed proportions) input downstream.

Proof. The proof proceeds by considering the industry costs that would be induced if the monopolist could simultaneously levy an access charge and a royalty fee. That is, IC is considered as a function of (p_1*, A,R). It is shown that, except when the intermediate good is a fixed schedule input, the IC-minimizing triple must be of the form ($\partial C^U/\partial Y_1$, 0,R), with R being a free variable. In other words, with one exception minimizing IC requires a zero access charge and a marginal cost per-unit price but imposes no restriction on R. Thus, the industry costs of any (but the excepted) positive access charage two-part tariff can be bettered by some royalty scheme with a marginal cost per-unit price. Finally, it is shown that, if Condition 3.6 is satisfied by a particular two-part tariff, a royalty scheme can be constructed with a positive R that not only reduces costs but also induces the same final good demand.

Since regularity condition R2) assumes IC has a minimum for some finite (p_1*,A,R), the necessary conditions for that minimum are that the partial derivatives of IC with respect to those variables are all zero. Equation (3.1) indicates that $\partial IC/\partial R$ is always zero; thus, R can indeed be chosen freely to generate the proper final good demand without affecting costs.

The next first order condition is that

$$
\begin{aligned}
\partial IC/\partial p_1^* &= -(p_1^* - \partial C^U/\partial Y_1)(\partial N y_1^*/\partial p_1^*) - A(\partial N/\partial p_1^*) \\
&= -(p_1^* - \partial C^U/\partial Y_1)N(\partial y_1^*/\partial p_1^*) \\
&\quad + (p_1^* - \partial C^U/\partial Y_1)NC^D_{zz}(dz^*/dp_1^*)^2 \\
&\quad + A \cdot N \cdot C^D_{zz}(dz^*/dp_1^*)(dz^*/dA) \qquad (3.19) \\
&= -(p_1^* - \partial C^U/\partial Y_1)N(\partial y_1^*/\partial p_1^*) + y_1^*(1-e_{1z}) \\
&\quad \cdot NC^D_{zz}(dz^*/dA)[(p_1^* - \partial C^U/\partial Y_1)(dz^*/dp_1^*) \\
&\quad + A(dz^*/dA)] \\
&= -(p_1^* - \partial C^U/\partial Y_1)N(\partial y_1^*/\partial p_1^*) + y_1^*(1-e_{1z})(\partial IC/\partial A) \\
&= 0,
\end{aligned}
$$

where the first equation is based on Eq. (2.5), the second on Eqs. (2.10) and (2.18), the third on collecting terms and substituting for dz^*/dp_1^* from Eq. (3.4), and the fourth on Eq. (3.2). Clearly, if $\partial IC/\partial A = 0$ to satisfy the other first order condition, Eq. (3.19) requires the per-unit price to be marginal cost unless the intermediate good is a fixed schedule input (i.e., unless $\partial y_1^*/\partial p_1^*=0$). But, if the per-unit price is marginal cost, then setting $\partial IC/\partial A$ to zero requires $A=0$ by Eq. (3.2). Thus, except for a fixed schedule input, the IC-minimizing (p_1^*,A,R) must be of the form $(\partial C^U/\partial Y_1, 0, R)$. That such a solution exists is assured by R2).

(Note that if the intermediate good is a fixed proportions input, then $dz^*/dp_1^*=0$ and, consequently, A must again be zero by Eq. (3.2). Thus, a non-trivial two-part tariff may be able to attain minimum costs only when the intermediate good is a fixed schedule, non-fixed proportions input.)

All that remains is to show that a positive royalty fee can be chosen so as to induce the same level of final good demand as under the initial two-part tariff. To do this, note first that (absent vertical integration) the expression for industry costs given in Eq. (2.3) can be rearranged to yield

$$(3.20) \qquad IC(Q,p_1^*,R,A) = Q \cdot AC^*(p_1^*,R,A) - \Pi^U(Q,p_1^*,A),$$

where Π^U is defined in Condition 3.6 and use is made of Eq. (2.2). If industry costs are not minimized by the two-part tariff being considered and since costs are minimized when the intermediate good is priced at marginal cost (with R = A = 0), we find

$$(3.21) \qquad IC(Q,p_1^*,R,A) > IC(Q,\partial C^U/\partial Y_1,0,0),$$

or

$$Q \cdot AC^*(p_1^*,0,A) - \Pi^U(Q,p_1^*,A) > Q \cdot AC^*(\partial C^U/\partial Y_1,0,0) - \Pi^U(Q,\partial C^U/\partial Y_1,0).$$

Since the two-part tariff being considered satisfies Condition 3.6, Eq. (3.21) implies

$$(3.22) \qquad AC^*(p_1^*,0,A) > AC^*(\partial C^U/\partial Y_1,0,0).$$

Thus, the marginal cost per-unit price must be supplemented with a positive royalty fee in order to get the final good price (and demand) back to its original level.

E.O.P.

As a final note, let us determine under what conditions we can construct a non-distorting two-part tariff. As Eq. (3.19) demonstrates, a two-part tariff can be non-distorting only when the intermediate good is a fixed schedule input. Then, one begins with a given final output Q and a simple price p_1^* equal to marginal cost. The given final output Q will then be produced at least industry cost, as established above. If one then simultaneously raises A from zero and adjusts p_1^* according to

$$(3.23) \qquad dp_1^*/dA = -1/(y_1^*(1 - e_{1z})),$$

it is easy to see from Eq. (3.19) that industry costs will remain unchanged. The final good price will generally change, however. When

(and if) the final good price changes so that final demand just equals Q, the resulting two-part tariff will clear the market while achieving minimum industry costs.

IV. NONLINEAR PRICING SCHEMES AND VERTICAL INTEGRATION

This section compares the coordination potential of royalty and two-part tariff schemes with that of vertical integration. As I have shown elsewhere {9}, vertical integration can reduce costs relative to simple pricing whenever there are substitution or scale distributions.[1] Here I determine whether vertical integration achieves full cost minimization or whether a nonlinear scheme may achieve further savings even after integration. Conversely, I determine whether cost savings achieved by a nonlinear scheme in an unintegrated setting can be supplemented by further savings through integration. As before, cost savings are shown to be necessary as well as sufficient for broader profit or welfare gains.

As I have shown in {9}, when an integrated firm's downstream subsidiary is limited to the same U-shaped average cost technology as the independent downstream firms[2], vertical integration may lead either to partial or full forward integration. This is true whether the objective is maximizing profit or welfare. Which degree of integration occurs depends on how quickly downstream unit costs rise with output, relative to final good demand: the deeper final good demand and the more sharply downstream average costs rise, the less profitable (or efficient) it will be to have the integrated firm produce the entire final good output. When partial integration is the result, it is important to note that the intermediate good price to the independent downstream firms (the "external" price) is above marginal cost.[3]

---

[1]Specifically, what is shown in {9} is that, if the upstream firm were to buy up a single downstream firm, it could increase its profits by changing the intermediate good price to or the output of the downstream subsidiary, provided there were, respectively, a substitution or a scale distortion. Since neither of these variables affects the final good price to consumers, the increased profit comes from industry cost savings.

[2]See the technology discussion in Sec. II above. Though the subsidiary and its independent rivals share the same downstream technology, they need not (and generally will not) face the same intermediate good price.

[3]Recall that, in the welfare maximization case, we are assuming scale economies upstream.

How one determines whether a nonlinear pricing scheme can produce further cost savings after integration depends on the degree of integration. For partial integration, the question is of imposing a nonlinear scheme on the independent downstream firms and is approached in the same way as in Sec. III (with identical results). For full integration, the question is whether to spin off an independent downstream firm which would purchase the intermediate good under a nonlinear pricing scheme.

As for the converse question of whether integration is beneficial even after a nonlinear scheme has been imposed, the answer can be determined by allowing the upstream firm to acquire a single downstream firm. The acquisition by itself--i.e., absent any price or output changes--does not alter the industry's costs. However, the integrated firm may now be able to reduce costs by changing either the output of or the terms of intermediate good sale to its new subsidiary. If so, then the nonlinear scheme alone will not have achieved the optimal coordination.

Let us turn first to the royalty-vs.-integration comparison, reserving the two-part tariff-vs.-integration comparison for later.

IV.A. Vertical Integration and a Royalty Scheme

The non-distorting nature of a royalty scheme guides the results here. Specifically, imposing a royalty scheme eliminates the incentive to integrate but not vice versa (in general). Cost savings are again locally necessary for profit or welfare gains. These results are contained in the following propositions.

Proposition 4.1. Suppose the upstream monopolist is optimally (in terms of welfare or profit) integrated into the downstream industry. Then, except when the intermediate good is a fixed proportions input downstream, a partially integrated monopolist can further reduce industry costs by imposing a royalty scheme. A fully integrated monopolist will always be able to reduce costs by using a royalty scheme with per-unit price set at upstream marginal cost, provided the final goods market is large enough to support more than one downstream firm operating at efficient scale.

Proof. For a partially integrated monopolist, the external price is optimally above upstream marginal cost, as described above. Then, if a royalty scheme were imposed on the independent downstream firms along the lines described in Proposition 3.1, industry costs would fall. The proof is identical to that of Proposition 3.1, since that proof depends in no way on z^I being zero. The exception there also applies here: costs are unaffected if the intermediate good is a fixed proportions input.

If the monopolist is fully integrated, we must look at the cost effects of lowering z^I below the total final output Q. The downstream slack will be picked up by an independent firm operating under a royalty scheme. Let the royalty scheme's per-unit price p_1^* be upstream marginal cost and the royalty fee R be just high enough to make $AC^*(p_1^*,R)$ equal to the going final good price. Then the effect on industry cost of reducing z^I is given by:

$$\begin{aligned} \partial IC/\partial z^I &= (\partial C^U/\partial Y_1 - p_1^I)(\partial y_1^I/\partial z^I) \\ &\quad - (\partial C^U/\partial Y_1 - p_1^*)(y_1^*/z^*) + \partial C^D(z^I,p_1^I)/\partial z \\ &\quad - C^D(z^*,p_1^*,R)/z^* + R \\ &= \partial C^D(z^I,p^I)/\partial z^I - AC^*(p_1^*,R) + R. \end{aligned} \tag{4.1}$$

Equation (4.1) is derived from Eq. (2.3), using Eq. (2.2) and the fact that the internal price p_1^I is always (optimally) set at upstream marginal cost. Since the royalty fee does not affect the independent downstream firm's choice of output or inputs, the fee's effect on downstream unit costs is strictly additive; that is,

$$AC^*(p_1^*,R) = AC^*(p_1^*,0) + R. \tag{4.2}$$

Thus, evaluating Eq. (4.1) at $z^I = Q$,

$$(4.3) \qquad \partial IC/\partial z^I = \partial C^D(Q,p_1^I)/\partial z^I - AC^D(z^*,p_1^*,0).$$

Since the hypothesized royalty scheme has p_1^* equal to p_1^I, the marginal and average cost functions in Eq. (4.3) are as if for the same firm. By assumption, the final goods market is large enough to support more than one firm at efficient scale. Thus, Q is greater than z^*. That downstream average costs are U-shaped then implies Eq. (4.3) is positive, and lowering z^I lowers industry costs.

E.O.P.

Proposition 4.2. Suppose the upstream monopolist is using a royalty scheme with a per-unit price equal to upstream marginal cost. Then there are no local cost reducing incentives to partially integrate.

Proof. Let the monopolist acquire a downstream firm (i.e., set $z^I = z^*$), leaving all prices initially the same. Industry costs are initially unchanged. Then, the monopolist may adjust four variables to try to lower costs: the internal price p_1^I, z^I, the external price p_1^*, and the royalty fee R, with adjustments in the latter two paired so as to keep AC^* constant. However, as Eq. (3.10) indicates, there is no incentive to change p_1^* and R when the former is already set at upstream marginal cost. As for adjusting p_1^I, note that (using Eq. (2.3) and Shephard's lemma):

$$(4.4) \qquad \partial IC/\partial p_1^I = (\partial C^U/\partial Y_1 - p_1^I)(\partial y_1^I/\partial p_1^I) + y_1^I - y_1^I$$

$$= 0$$

for the immediate post-integration values of the variables (i.e., for $p_1^I = p_1^* = \partial C^U/\partial Y_1$). Finally, the incentive to change z^I is found by evaluating Eq. (4.1) at $z^I = z^*$ and $p_1^* = p_1^I = \partial C^U/\partial Y_1$. In view of Eq. (4.2), this derivative is also zero.

E.O.P.

Proposition 4.3. Suppose the upstream monopolist is optimally integrated, in a profit (or profit-constrained welfare) sense, into a downstream industry large enough to support more than one producer at efficient scale. Then the monopolist has a local incentive to impose a royalty scheme (allowing final output to vary) if and only if there would be a cost saving from a royalty scheme which held output fixed.

Proof: Certainly the "if" holds, as already argued. The "only if" will be argued in the contrapositive. That is, it will be shown that the absence of a cost-saving, constant-output royalty scheme implies the lack of a profit-increasing (or profit-constrained welfare-increasing) increasing) royalty, even if output is allowed to vary.

Under the conditions stated, a fully integrated monopolist can always find a cost-reducing royalty scheme. (See Prop. 4.1.) The only case in which a partially integrated monopolist cannot reduce costs with a royalty is if the intermediate good is a fixed proportions input downstream.

Suppose the intermediate good is a fixed proportions input. Consider the profit-maximization case. The monopolist's profits are

$$(4.5) \qquad \Pi(z^I, p_1^*, R) = AC^* \cdot Q(AC^*) - IC(Q(AC^*), z^I, p_1^*, R)$$

suppressing the dependence of AC^* on p_1^* and R and of IC on p^I. Absent a royalty fee, the profit-maximizing p_1^* satisfies

$$(4.6) \qquad \partial\Pi/\partial p_i^* = (MR - \partial IC/\partial Q)\cdot Q'\cdot(y^*/z^*) - \partial IC/\partial p_1^*$$

$$= (MR - \partial IC/\partial Q)\cdot Q'\cdot(y^*/z^*)$$

$$= 0,$$

using Eqs. (3.5) and (2.21) and where MR is final good marginal revenue. The local incentive to raise R from zero is given by

$$(4.7) \qquad \partial\Pi/\partial R = (MR - \partial IC/\partial Q)\ Q'\cdot\ (1/z^*) - \partial IC/\partial R.$$

From Eqs. (3.1) and (4.6), we see this must be zero. Thus, absent a locally cost-saving royalty scheme, there is no locally profit-increasing one either. (The proof for the profit-constrained welfare-maximizing case is similar.)

E.O.P.

Proposition 4.4. Suppose the monopolist is using the profit-maximizing (or profit-constrained welfare-maximizing) royalty scheme. Then, there is a local profit (or welfare) incentive for partial integration only if there is a local cost incentive.

Proof: For partial integration, changes in z^I and p_1^I affect profits (or welfare) only through IC, since neither affects AC*. The theorem is true then if partial integration never permits a profit (or welfare) improving local readjustment of R or p_1*.

Consider the profit-maximizing case. There, the pre-integration profit-optimal R must set Eq. (4.7) to zero, where IC is evaluated at $z^I = 0$. The question is whether Eq. (4.7) is still zero when z^I becomes positive. It is easy to show that the profit-maximizing p_1* is marginal cost and that at that value $\partial IC/\partial Q = AC^*$ is independent of z^I. Since $\partial IC/\partial R = 0$ everywhere by Eq. (3.1), Eq. (4.7) is still zero after integration. The derivative of profit with respect to p_1* can be shown to be zero at the profit-optimal p_1*, both before and after integration, by a similar argument.

The profit-constrained welfare-maximizing case is argued similarly.

E.O.P

IV.B. Vertical Integration and a Two-Part Tariff

Whether vertical integration or a two-part tariff is more effective in reducing costs is less clear than in the comparison between integration and a royalty scheme. Since, after partial integration, the external price is above marginal cost, distortions may persist among the independent downstream firms. In that case, a two-part tariff may lower costs further by reducing these distortions. Sufficient conditions for it to do so are exactly the same conditions under which a two-part tariff is effective in reducing these distortions absent integration. If full forward integration is the case, a two-part tariff can then lower costs if a tariff can be designed so as to induce downstream independents to produce the final good at a unit (social) cost that is

lower than the marginal cost of the integrated firm's downstream subsidiary. If so, then the cost savings are had by *lowering* the latter's output. Further, with a two-part tariff already in place, vertical integration will still lower costs unless the two-part tariff satisfies the first order conditions for industry cost minimization; that is, if the tariff causes no substitution distortion and if the scale distortions are offsetting. Finally, cost gains are locally necessary for profit or welfare improvements.

> *Proposition 4.5.* Suppose the upstream monopolist is partially integrated and optimally so (in profit or welfare terms). Consider the conditions which in Proposition 3.3 guarantee the existence of a cost-reducing two-part tariff in the absence of integration. If any of these conditions are satisfied in the partially integrated case, then too a two-part tariff can be constructed which will lower industry costs.

Proof. Recall that optimal partial integration results in an external price above upstream marginal cost. Let a two-part tariff be introduced along the lines specified in Proposition 3.3. The proof that costs will be lowered here under the stated conditions is identical to the proof of Proposition 3.3, since the latter depends in no way on z^I being zero.

E.O.P.

Now consider the case where full integration is initially optimal. Suppose that a two-part tariff (p_1^*, A) would induce an independent downstream firm's unit costs AC* to be just equal to the post-integration final good price. Under such a two-part tariff, industry costs as a function of the integrated firm's final output vary according to

$$
\begin{aligned}
\partial IC/\partial z^I &= (\partial C^U/\partial Y_1 - p_1{}^I)(\partial y_1{}^I/\partial z^I) \\
&\quad + (p_1{}^* - \partial C^U/\partial Y_1)(y^*/z^*) \\
&\quad + \partial C^D(z^I, p_1{}^I)/\partial z - AC^*(p_1{}^*, A) + A/z^* \\
&= \partial C^D(z^I, p_1{}^I)/\partial z \\
&\quad - [AC^*(p_1{}^*, A) - A/z^* - (p_1{}^* - \partial C^U/\partial Y_1)(y^*/z^*)]
\end{aligned}
\tag{4.8}
$$

Equation (4.8) is derived from Eq. (2.3), and the simplification uses the fact that the internal price is always set at marginal cost.

The square bracketed term in Eq. (4.8) represents the social unit cost of independent downstream production; that is, an independent firm's private unit costs minus the mark-ups charged under the two-part tariff. If, at $z^I = Q$, this social unit cost is less than the integrated firm's marginal downstream cost, then Eq. (4.8) is positive. This implies industry costs would be lowered if the integrated firm gave up part of the downstream market to an independent firm subject to said tariff.

Thus, the potential for a two-part tariff to generate further cost savings in the full integration case depends on whether a tariff can be found to make Eq. (4.8) positive. One case in which such a tariff could be found is the case where there is no substitution distortion [4] and the scale distortions caused by the two parts of the tariff are exactly offsetting. Then the square bracketed term in Eq. (4.8) represents the minimum social unit cost. If the final goods market will support more than one efficient-sized downstream firm (i.e., if $z^I = Q > z^*(p_1{}^*, A)$), then Eq. (4.8) is certainly positive.

That vertical integration can generally add to the cost savings already achieved by a two-part tariff is shown in the following proposition.

Proposition 4.6. Suppose that a two-part tariff $(p_1{}^*, A)$ is imposed on a non-integrated downstream industry. Then, the upstream monopolist can further lower costs by integrating unless $(p_1{}^*, A)$ already satisfies the first order conditions for industry cost minimization.

[4] I.e., the intermediate good is a fixed schedule input downstream.

Proof. As with Proposition 4.2, the proof begins by supposing the monopolist acquires a downstream firm (i.e., sets $z^I = z^*$). Before any changes are made in the output of the new subsidiary or in the terms of intermediate good sales (internal or external), industry costs have not changed. Now the monopolist has four variables to change to try to reduce costs: the external price, the access charge for the independent firms[5], the internal price, and the downstream subsidiary's output.

The effect of changing z^I on industry costs is given by

$$\begin{aligned} \partial IC/\partial z^I &= (\partial C^U/\partial Y_1)(\partial y_1{}^I/\partial z^I - y_1^*/z^*) \\ &\quad - p^I(\partial y_1{}^I/\partial z^I) + p_1^*(y_1^*/z^*) \\ &\quad - AC^*(p_1^*,A) + \partial C^D(z^I,p_1{}^I)/\partial z + A/z^* \\ &= (p_1^* - \partial C^U/\partial Y_1)(y_1^*/z^* - \partial y_1{}^I/\partial z^I) + A/z^*, \end{aligned} \tag{4.9}$$

where the equation is evaluated at $p_1{}^I = p_1^*$ and $z^I = z^*(p_1^*,A)$ and where use is made of the fact that, at those prices and outputs, the marginal cost of the subsidiary equals the marginal (and thus average) cost of an independent downstream firm. Equation (4.9) can be further simplified using the fact that, at the values in question, $\partial y_1{}^I/\partial z^I = \partial y_1^*/\partial z^*$ and by using Eqs. (2.9) and (3.3):

$$\partial IC/\partial z^I = [(p_1^* - \partial C^U/\partial Y_1)(dz^*/dp_1^*) + A(dz^*/dA)]C^D{}_{zz} \tag{4.10}$$

If Eq. (4.10) is non-zero, then integration can further lower industry costs. Referring to Eq. (3.2), one can see that Eq. (4.10) equals zero if and only if $\partial IC/\partial A = 0$; i.e., if and only if the initial two-part tariff satisfies one of the industry cost minimization necessary conditions. (Note that this cannot happen if p_1^* is set at marginal cost.)

---

[5]The access charge made to its own subsidiary no longer affects the subsidiary's output, since the latter is now chosen directly. Thus, the internal access charge is a pure transfer and does not affect industry costs.

Consider next the effect of changing the internal price, p_1^I:

$$(4.11) \qquad \partial IC/\partial p_1^I = (\partial C^U/\partial Y_1 - p_1^I)(\partial y_1^I/\partial p_1^I),$$

where the equation is evaluated at $p_1^I = p_1^*$. If Eq.(4.11) is not zero, then costs may be lowered by adjusting p_1^I in the appropriate direction. (If p_1^* is set at marginal cost, then costs may be reduced by adjusting z^I, as above.) Thus, costs can be lowered through integration unless there are no substitution distortions.

So far, we have established that costs may be reduced through integration unless $\partial IC/\partial A = 0$ *and* there are no substitution distortions. From Eq. (3.17), we see that this is equivalent to $\partial IC/\partial p_1^* = 0$. This completes the proof.[6]

E.O.P.

Proposition 4.7. Suppose that the upstream monopolist is partially integrated and optimally so, in a profit (or profit-constrained welfare) sense. Then, to a first order approximation he will have a profit (or welfare) incentive to introduce a "small" access charge (allowing output to vary) if and only if a constant-output two-part tariff could locally reduce costs.

Proof: The proof is identical to that of Prop. 3.5, since that depended in no way on z^I being zero.

E.O.P.

Proposition 4.8. Suppose that the non-integrated upstream monopolist is imposing a profit-maximizing (or profit-constrained, welfare-maximizing) two-part tariff. Then, local profit (or welfare) incentives for partial integration arise only if such integration could save costs locally.

Proof: As with Prop. 4.4, changes in z^I and p^I do not affect AC* and

[6]Note that changing the two-part tariff (while maintaining the same value of AC*) presents no cost reduction possibilities if neither p_1^I nor z^I do. Refer to Eq. (3.13).

thus affect profit (or welfare) only through IC. The question again is whether integration allows profit (or welfare) improving adjustments in the two-part tariff. Using Eqs. (3.2) and (3.10), it can be shown, in the profit-maximizing case, that after integtation

$$(4.12) \qquad \partial\Pi/\partial A = - (z^I/Q)\cdot\partial IC/\partial A, \text{ and}$$

$$(4.13) \qquad \partial\Pi/\partial p_1^* = - (z^I/Q)\cdot\partial IC/\partial p_1^*,$$

where both are evaluated at the pre-integration two-part tariff. Thus, profit increasing adjustments may be made unless the original two-part tariff satisfied the cost-minimization first order conditions. By Prop. 4.6, this implies integration can save costs. (The welfare case is argued similarly.)

E.O.P.

Proposition 4.7. Suppose that the upstream monopolist is partially integrated, and optimally so, in a profit (or profit-constrained welfare) sense. Then, he will have a profit (or welfare) incentive to introduce a "small" access charge (allowing output to vary) if and only if a constant-output two-part tariff could locally reduce costs.

Proof: The proof is identical to that of Prop. 3.5, since that depended in no way on z^I being zero.

E.O.P.

V. CONCLUSIONS

The theme of this paper has been to explore the means by which an upstream monopolist can control a downstream industry so as to reduce overall industry costs. Such cost reduction serves the monopolist's interests whether his goal is to maximize profits or welfare. Pricing the intermediate good at marginal cost may either not be feasible (e.g., because of a need to cover the costs of an increasing returns upstream production process) or may not be desirable (e.g., under profit maximization). When the intermediate good is priced above marginal cost, excess industry costs may occur because the downstream firms choose either the wrong input mix or (when downstream firms have U-shaped average costs) the wrong output level or both. When this occurs, the monopolist may consider more elaborate instruments for controlling the downstream industry. The three considered here are royalty and two-part tariff nonlinear pricing schemes and vertical integration.

The issue of cost savings is interesting partly in its own right and partly because cost savings at a constant final output level are sufficient for profit or welfare gains. The analysis has also demonstrated a third reason: for the cases where results were achieved, cost savings at a constant output are also necessary ("locally") for one mechanism to be profit or welfare preferred to another.

The downstream industry modeled here is characterized by free entry and U-shaped average costs. Previous work by Blair and Kaserman (3) examined similar issues when the downstream technology is linearly homogeneous. They found that full integration[1] and each of the nonlinear schemes are equally effective in achieving minimum industry costs. The reason is that, with constant returns, there are no scale distortions. Thus, the means for raising upstream revenue does not matter as long as the per-unit price of the intermediate good is set at marginal cost.

---

[1]Partial integration is never optimal with constant returns downstream. See Schmalensee (10).

The results are different when downstream average costs are U-shaped, since downstream scale then matters and the three control mechanisms may have different effects on downstream scale. Full vertical integration may not then be optimal precisely for scale-related reasons, and partial integration fails to minimize industry costs, since the external price is still set above marginal cost. Even when full integration is optimal, costs will not be minimized if the downstream subsidiary operates above the socially efficient scale. Thus, the upstream monopolist has reason to look beyond integration for other ways to cut costs.

The royalty scheme turns out to be the most effective at reducing costs. The reason is that a royalty scheme effectively creates a fixed proportions pseudo-input to the downstream process, the price of which is the royalty fee. Since the price of a fixed proportions input distorts neither the scale nor the input mix of the downstream firms, a positive royalty fee allows the monopolist to raise revenue without distorting industry costs. He can then afford to set the price of the actual intermediate good at its marginal cost.

A royalty scheme thus allows the monopolist to avoid the scale and/or substitution distortions caused by a (non-marginal cost) simple price. Furthermore, it allows the monopolist to avoid the cost distortions which remain after partial vertical integration as a result of the external price remaining above marginal cost. A royalty scheme also renders full integration undesirable when the downstream subsidiary would have to produce beyond the socially efficient scale. Indeed, a royalty scheme eliminates the cost reducing advantages of vertical integration completely.[2] Finally, a royalty scheme (weakly) dominates a two-part tariff.

A two-part tariff is not generally as effective as a royalty scheme in reducing costs, since it carries its own source of distortions: the access charge tends to raise the scale of the downstream firms. This occurs because the access charge is in effect a payment for a fixed schedule pseudo-input with zero output elasticity. Except when there

[2]That is, for a technology (studied here) where upstream and downstream costs are additively separable.

are no substitution distortions and the access charge and per-unit price cause exactly offsetting scale distortions, a two-part tariff fails to induce the efficient input and output choices downstream.

Thus, the comparisons of a two-part tariff to simple pricing and to vertical integration are comparisons of "second bests." A two-part tariff will reduce simple prices distortions when the access charge's scale distortion alone offsets an existing scale distortion. A two-part tariff will also produce lower costs than a simple price when simultaneously adjusting the access charge and per-unit price to induce the same level of final demand produces a net reduction of a scale distortion. When an industry is already partially integrated, imposing a two-part tariff can reduce costs further, provided the same sort of scale distortion corrections can be achieved for the independent downstream firms. However, the converse is also generally true: despite an existing two-part tariff, vertical integration still will reduce costs except when the absence of substitution distortions and the presence of offsetting scale distortions allow the two-part tariff to induce exactly the correct downstream input and output choices.

Finally, none of the above has considered the implementation costs of the three control mechanisms: the costs of preventing resale by customers to other customers wishing to avoid an access charge; the costs of monitoring final good output levels to collect royalty payments; or the costs of acquiring a downstream subsidiary. Each of these costs may be significant and may alter the choice of control strategy. The point to be emphasized when the downstream industry has U-shaped average costs is that, unlike the constant returns case, the nonlinear pricing schemes and vertical integration do not differ on these implementation costs alone.

REFERENCES

1. Bassett, L. R., and B. Borcherding, "The Relationship between Firm Size and Factor Price," *Quarterly Journal of Economics,* August 1970, *84,* pp. 518-522.

2. Baumol, W. J., J. C. Panzar, and R. D. Willig, *Contestable Markets and the Theory of Industry Structure,* San Diego, Harcourt Brace Jovanovich, 1982.

3. Blair, R. D., and D. L. Kaserman, "Vertical Control with Variable Proportions: Ownership Integration and Contractual Equivalents," *Southern Economic Journal,* April 1980, *46,* pp. 1118-1128.

4. Diamond, P. A., and J. A. Mirrless, "Optimal Taxation and Public Production: I-Production Efficiency," *American Economic Review,* March 1971, *61,* pp. 8-27.

5. Dixit, A. K., "Vertical Integration in a Monopolistically Competitive Industry," *International Journal of Industrial Organization,* March 1983, *I*, pp. 63-78.

6. Flaherty, M. T., "Prices versus Quantities and Vertical Financial Integration," *Bell Journal of Economics,* Autumn 1981, *12,* pp. 507-525.

7. Mathewson, G. F., and R. A. Winter, "An Economic Theory of Vertical Restraints," unpublished, April 1982, Institute for Policy Analysis, University of Toronto.

8. Ordover, J. A., and J. C. Panzar, "On the Nonlinear Pricing of Inputs," *International Economic Review,* October 1982, *23*, pp. 659-676.

9. Quirmbach, H. C., "Vertical Integration, Contestable Markets, and the Misfortunes of the Misshaped U," The Rand Corporation, P-6782, December 1981.

10. Schmalensee, R., "A Note on the Theory of Vertical Integration," *Journal of Political Economy,* March/April 1973, *81,* pp. 442-9.

11. Silberberg, E., "The Theory of the Firm in 'Long-Run' Equilibrium," *African Economic Review,* September 1974, *64,* pp. 734-741.

12. Varian, H. R., *Microeconomic Analysis,* W. W. Norton, New York, 1978.

AFAPL-TR-78-52

AD-A059 784

THE AEROTHERMODYNAMICS OF AIRCRAFT GAS TURBINE ENGINES

Gordon C. Oates, Editor

AIR FORCE AERO PROPULSION LABORATORY
AIR FORCE WRIGHT AERONAUTICAL LABORATORIES
AIR FORCE SYSTEMS COMMAND
WRIGHT-PATTERSON AIR FORCE BASE, OHIO 45433

REPRODUCED BY
NATIONAL TECHNICAL
INFORMATION SERVICE
U.S. DEPARTMENT OF COMMERCE
SPRINGFIELD, VA 22161

NOTICE

When Government drawings, specifications, or other data are used for any purpose other than in connection with a definitely related Government procurement operation, the United States Government thereby incurs no responsibility nor any obligation whatsoever; and the fact that the government may have formulated, furnished, or in any way supplied the said drawings, specifications, or other data, is not to be regarded by implication or otherwise as in any manner licensing the holder or any other person or corporation, or conveying any rights or permission to manufacture, use, or sell any patented invention that may in any way be related thereto.

This report has been reviewed by the Information Office (OI) and is releasable to the National Technical Information Service (NTIS). At NTIS, it will be available to the general public, including foreign nations.

This technical report has been reviewed and is approved for publication.

FRANCIS R. OSTDIEK
Chief, Test Group
Technology Branch

WALKER H. MITCHELL
Chief, Technology Branch
Turbine Engine Division

FOR THE COMMANDER

ERNEST C. SIMPSON
Director, Turbine Engine Division
AF Aero Propulsion Laboratory

"If your address has changed, if you wish to be removed from our mailing list, or if the addressee is no longer employed by your organization please notify AFAPL/TBX *,W-PAFB, OH 45433 to help us maintain a current mailing list".*

Copies of this report should not be returned unless return is required by security considerations, contractual obligations, or notice on a specific document.

Unclassified

SECURITY CLASSIFICATION OF THIS PAGE (When Data Entered)

REPORT DOCUMENTATION PAGE		READ INSTRUCTIONS BEFORE COMPLETING FORM
1. REPORT NUMBER AFAPL TR 78-52	2. GOVT ACCESSION NO.	3. RECIPIENT'S CATALOG NUMBER
4. TITLE (and Subtitle) The Aerothermodynamics of Aircraft Gas Turbine Engines		5. TYPE OF REPORT & PERIOD COVERED Final Report 1975-1978
		6. PERFORMING ORG. REPORT NUMBER
7. AUTHOR(s) Gordon C. Oates, Editor, University of Washington Many Authors		8. CONTRACT OR GRANT NUMBER(s) AFOSR-75-2783
PERFORMING ORGANIZATION NAME AND ADDRESS University of Washington Seattle, Washington 98195		10. PROGRAM ELEMENT, PROJECT, TASK AREA & WORK UNIT NUMBERS 30660421
11. CONTROLLING OFFICE NAME AND ADDRESS Francis R. Ostdiek AFAPL/TBX WPAFB OH 45433		12. REPORT DATE July 1978 13. NUMBER OF PAGES 780
14. MONITORING AGENCY NAME & ADDRESS(if different from Controlling Office)		15. SECURITY CLASS. (of this report) Unclassified 15a. DECLASSIFICATION/DOWNGRADING SCHEDULE

16. DISTRIBUTION STATEMENT (of this Report)

Approved for public release; distribution unlimited.

17. DISTRIBUTION STATEMENT (of the abstract entered in Block 20, if different from Report)

Same

18. SUPPLEMENTARY NOTES

REPRODUCED BY
NATIONAL TECHNICAL
INFORMATION SERVICE
U. S. DEPARTMENT OF COMMERCE
SPRINGFIELD, VA. 22161

19. KEY WORDS (Continue on reverse side if necessary and identify by block number)

Turbomachinery, Turbine Engine, Propulsion, Aerodynamics, Aerothermodynamics, Aircraft Gas Turbine

20. ABSTRACT (Continue on reverse side if necessary and identify by block number)

An extensive study of many aspects of the aerothermodynamics of aircraft gas turbine engines is presented. The study consists of twenty-six chapters written by a total of twenty-four authors. After an initial comprehensive introductory chapter, the report provides a review of thermodynamics and gas dynamics and of laminar and turbulent flows. The cycle analysis of ideal engines is then considered, followed by the description of component losses and then the cycle analysis of non-ideal engines. Engine off-design performance is then considered followed by the description of engine/airplane

DD FORM 1 JAN 73 1473 EDITION OF 1 NOV 65 IS OBSOLETE

Unclassified

SECURITY CLASSIFICATION

matching. Succeeding chapters consider the behavior of the various components in detail. Major problem areas such as computation of turbomachinery boundary layers, aeroelasticity and unsteady aerodynamics, engine stability, engine noise, jet noise and finally the system aspects of engine installation are considered in detail. The document is intended to serve many purposes, including those of text, design manual, research reference and comprehensive overview of the aerothermodyns of aircraft gas turbine engines.

NOTICE

THIS DOCUMENT HAS BEEN REPRODUCED FROM THE BEST COPY FURNISHED US BY THE SPONSORING AGENCY. ALTHOUGH IT IS RECOGNIZED THAT CERTAIN PORTIONS ARE ILLEGIBLE, IT IS BEING RELEASED IN THE INTEREST OF MAKING AVAILABLE AS MUCH INFORMATION AS POSSIBLE.

THE AEROTHERMODYNAMICS OF AIRCRAFT GAS TURBINE ENGINES

TABLE OF CONTENTS

CHAPTER 1 - INTRODUCTION

R. O. Bullock
Airesearch Manufacturing Company of Arizona
402 S. 36th Street
Phoenix, Arizona 85034

CHAPTER 2 - THERMODYNAMICS AND QUASI-ONE-DIMENSIONAL FLUID FLOWS

Gordon C. Oates
Department of Aeronautics and Astronautics, FS-10
University of Washington
Seattle, Washington 98195

CHAPTER 3 - LAMINAR VISCOUS FLOWS

Gordon C. Oates
Department of Aeronautics and Astronautics, FS-10
University of Washington
Seattle, Washington 98195

CHAPTER 4 - TURBULENT FLOWS

Gordon C. Oates
Department of Aeronautics and Astronautics, FS-10
University of Washington
Seattle, Washington 98195

CHAPTER 5 - IDEAL CYCLE ANALYSIS

Gordon C. Oates
Department of Aeronautics and Astronautics, FS-10
University of Washington
Seattle, Washington 98195

CHAPTER 6 - COMPONENT PERFORMANCE

Gordon C. Oates
Department of Aeronautics and Astronautics, FS-10
University of Washington
Seattle, Washington 98195

CHAPTER 7 - NON-IDEAL CYCLE ANALYSIS

Gordon C. Oates
Department of Aeronautics and Astronautics, FS-10
University of Washington
Seattle, Washington 98195

CHAPTER 8 - ENGINE OFF-DESIGN PERFORMANCE

Gordon C. Oates
Department of Aeronautics and Astronautics
FS-10
University of Washington
Seattle, Washington 98195

CHAPTER 9 - ENGINE/AIRPLANE PERFORMANCE MATCHING

D. B. Morden
Propulsion Staff
The Boeing Company
P. O. Box 3999
Seattle, Washington 98124

CHAPTER 10 - ELEMENTARY THEORY OF BLADE AERODYNAMICS

Gordon C. Oates
Department of Aeronautics and Astronautics, FS-10
University of Washington
Seattle, Washington 98195

CHAPTER 11 - THROUGHFLOW THEORY

Gordon C. Oates
Department of Aeronautics and Astronautics, FS-10
University of Washington
Seattle, Washington 98195

CHAPTER 12 - CASCADE FLOWS

Gordon C. Oates
Department of Aeronautics and Astronautics
FS-10
University of Washington
Seattle, Washington 98195

CHAPTER 13 - INLETS AND INLET ENGINE INTEGRATION

D. L. Paul
J. L. Younghans
Aircraft Engine Group
General Electric Company
Evandale, Ohio 45215

CHAPTER 14 - VARIABLE CONVERGENT-DIVERGENT NOZZLE AERODYNAMICS

A. P. Kuchar
Aircraft Engine Group
General Electric Company
Evandale, Ohio 45215

CHAPTER 15 - FUNDAMENTALS OF COMBUSTION

W. S. Blazowski
A. F. Aero Propulsion Laboratory
A. F. Wright Aeronautical Laboratories
Wright-Patterson AFB, Ohio 45433

Currently at
Exxon Research and Engineering Company
Linden, New Jersey 07036

TABLE OF CONTENTS

CHAPTER 16 - COMPUTATION OF TURBOMACHINERY BOUNDARY LAYERS

H. McDonald
United Technologies Research Center
Silver Lane
East Hartford, Connecticut 06108

Currently at
Scientific Research Associates, Inc.
P. O. Box 498
Glastonberry, Connecticut 06033

CHAPTER 17 - AXIAL COMPRESSOR AERODYNAMICS

G. K. Serovy
Department of Mechanical Engineering
Iowa State University
Ames, Iowa 50010

CHAPTER 18 - TURBINE AERODYNAMICS

R. P. Dring
United Technologies Research Center
Silver Lane
East Hartford, Connecticut 06108

W. H. Heiser
Arnold Engineering Development Center
Arnold Air Force Station
Tennessee 37389

CHAPTER 19 - TURBINE COOLING

M. Suo
United Technologies Research Center
Silver Lane
East Hartford, Connecticut 06108

CHAPTER 20 - TURBOPROPULSION COMBUSTION TECHNOLOGY

R. E. Henderson
W. S. Blazowski*
A. F. Aero Propulsion Laboratory
A. F. Wright Aeronautical Laboratories
Wright-Patterson AFB, Ohio 45433

*Currently at
Exxon Research and Engineering Company
Linden, New Jersey 07036

CHAPTER 21 - AFTERBURNERS

E. Zukoski
California Institute of Technology
Pasadena, California 91109

CHAPTER 22 - AEROELASTICITY AND UNSTEADY AERODYNAMICS

F. O. Carta
United Technologies Research Center
Silver Lane
East Hartford, Connecticut 06108

CHAPTER 23 - ENGINE STABILITY

T. P. Collins
Aircraft Engine Group
General Electric Company
Evandale, Ohio 45215

CHAPTER 24 - ENGINE NOISE

N. A. Cumpsty
The Whittle Laboratory
University Engineering Department
Madingley Road
Cambridge CB3 OEL
England

CHAPTER 25 - JET NOISE

R. Mani
General Electric Company
Corporate Research and Development
Schenectady, New York 12301

CHAPTER 26 - SYSTEM ASPECTS OF ENGINE INSTALLATION

R. Decher
W. Gillette
J. Koncsek
F. Marshall
R. Ridgeway
V. Salemann

Propulsion Staff
The Boeing Company
P. O. Box 3999
Seattle, Washington 98124

FORWARD

This book has been prepared with AF assistance in order to have a much more complete technical book than those available. The last effort edited by Dr. Hsue-Shen Tsien (now a high official in the Government of the People's Republic of China) was well-received and broadly used by industry over thirty years ago.

The gas turbine has been evolving as a practical device since 1902 or before. Concepts of utilizing the gas turbine principle as prime mover for aircraft were proposed and investigated in many countries including France, USA, Sweden, England, and Germany. Two actual developments of specific jet gas turbines for aircraft propulsion began in the mid 30s independently from each other, in Germany by Hans von Ohain and in England by Sir Frank Whittle. The resulting engines powered the Heinkel He-178, first flown in August 1939 and the Gloster 28/39, first flown in May 1941. The aircraft gas turbine has one similarity to the nuclear bomb in that the most sensitive piece of information is the fact that it works. Knowing this, you are positive that with enough effort you too can make it work. The first builder is, therefore, by necessity, the most determined, most clever, and most vulnerable of the chain. The main reason no book exists compiling much of today's state-of-the-art is that the gas turbine has evolved so rapidly and so greatly that such a document could not be prepared and published before it was obsolete and this will no doubt be true for large sections of this volume.

Since the first gas turbine flew, the weight characteristics have improved by a factor of four and the fuel consumption by a factor of 2.5 and life by a factor of 400. It is, when performing its design job, operating at an efficiency competitive with a stationary steam plant. This device is remarkable in many ways and its usage will expand greatly in the near future.

This book is exceptionally complete but does not address controls and diagnostics, production means and structure and perhaps your own favorite element. The structural aspects and technology are expanding rapidly but since this device is one of the few which operate in a regime where plastic deformation happens continuously, structure is most difficult. This book is not a Bible but will provide a tremendous amount of guidance to those in the aircraft propulsion business. I commend it to your attention.

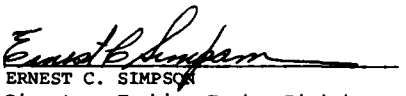

ERNEST C. SIMPSON
Director, Turbine Engine Division
AF Aero Propulsion Laboratory

THE AEROTHERMODYNAMICS OF AIRCRAFT GAS TURBINE ENGINES

GORDON C. OATES - EDITOR

PREFACE

This report has been sponsored jointly by the Air Force Office of Scientific Research (AFOSR) and by the Air Force Aero-Propulsion Laboratory (AFAPL). The Study was conducted in response to a perceived need to create a comprehensive and up to date description of the aerothermodynamics of aircraft gas turbine engines. It is hoped that the report will both provide understanding and stimulate interest in a most profound and demanding engineering discipline.

In its original concept, the report was planned as a comprehensive description of gas turbine theory and technology. It was soon evident, however, that such a breadth of subject matter was far too great for a single document, and it was decided instead to restrict the effort to the description of some of the aspects of the aerothermodynamics of aircraft gas turbine engines. Many experts from universities, industry and government and industrial research laboratories have contributed to the report. However, it was decided early in the planning of the report that the authors should contribute only in those areas of their prime expertise, rather than attempting a completely comprehensive description of their subject matter. As a result, some important areas of interest to aircraft engine practioners are only scantily outlined. In many such cases, it was felt that suitable literature was already available, and much of the present document is devoted to the description of presently emerging fields of emphasis.

It will be evident to the reader that the many authors who contributed to this document represent a wide profile of those active in the aircraft gas turbine industry. As a result, the "audience" to which the separate chapters are directed varies somewhat because of the author's own prime interest. Thus, some authors present a comprehensive overview of their area of expertise, with emphasis and attention to detail appropriate to aid the young practising engineer in attaining an understanding and overview of the particular subject matter. It is expected that such practically-oriented chapters will also be of direct value to the more mature engineer in a management role who, it is hoped, will be aided in perceiving some of the developing techniques and more intricate problems of the given subject area.

Several of the chapters are submitted by practising researchers, who describe not only an overview of the state of their research specialties, but describe also the development of their own advanced theories and techniques from their fundamental foundations. It is expected that these contributions will be of value not only to practising researchers and engineers, but also to the university community as graduate course references and graduate research references.

The editor authored ten of the chapters (2-8, 10-12) with a twofold intent. It is hoped that these ten chapters in concert with other early chapters will be suitable for use as an advanced undergraduate and graduate text. Considerable emphasis has been placed upon description of the very interactive nature of the component behaviors, and it is hoped that the treatment of the subject will also aid practising specialists to easily acquire a comprehensive understanding of the overall engine behavior. It will be noted that, except for a very few reference examples, all analytically obtained curves displayed in these chapters have been calculated directly from equations obtained within the text. To facilitate such calculations, the more complex sets of equations are summarized in a form suitable for straightforward calculation in a section following their development. The fairly recent advent of programmable calculators makes such calculation a simple task, and the reader is urged to conduct such analytical investigations himself to investigate the many parametric variations possible.

With regard to the use of the report as a text, the introductory chapter provided by Robert O. Bullock should provide a most useful overview of both this report and the entire field of aircraft gas turbine engines. This writer has found that the content of Chapter 2 forms a suitable review for most engineering students of the required fluid mechanics and thermodynamics. Because of the ensuing subject matter, emphasis is placed on the behavior of internal flows, with particular emphasis on the behavior of the stagnation properties. This emphasis is stressed, of course, because of the great significance of the stagnation property variations on the component and overall engine performance behaviors. Chapters 3 and 4 contain material of conceptual importance to the understanding of the limiting behavior of many of the components, but the instructor may find, because of time limitations, that the material need not be included for other than reference material in the typical aero-engine course.

Chapters 5-8 provide the necessary understanding of the performance and design aspects of the engine alone, and of the requirement to understand the mission before attempting to design the engine. Chapter 9 provides an appropriate insight into engine-airframe interactions, and should be of particular use to those students wishing to pursue engine-airframe design in depth. Chapter 26, which considers the airframe-engine interaction and design methodology of the combined system should also be of direct utility to the serious design student.

The description of the flow in the major engine components (inlet-compressor-combustion-turbine-nozzle) is considered in Chapters 10 through 15, with more advanced treatments of many of the subject areas covered in later chapters. It is expected that most instructors would prefer to select the subject matter and order of the subject matter to best suit their own preferences and specialties. This, of course, will also be true for the more advanced later chapters, some of which may form a suitable core for an entire course by themselves.

In conclusion, it is hoped that this report will serve many purposes, including those of text, design manual, research reference and comprehensive overview of the aerothermodynamics of aircraft gas turbine engines. In a work of this magnitude it is inevitable that many minor errors will persist in spite of the best efforts of all concerned. In view of the fact that there may be later updated versions of this report, it would hence be greatly appreciated if interested readers would report such errors to the editor so that ensuing versions of the report will be of increased accuracy.

ACKNOWLEDGEMENTS

The writing of this report would not have been possible without the support of both the Air Force Office of Scientific Research (AFOSR) and the Air Force Aero-Propulsion Laboratory (AFAPL). My thanks are especially directed to Lt. Col. Robert C. Smith of AFOSR and Dr. Francis R. Ostdiek of AFAPL whose spirits of cooperation, encouragement and direct assistance are so greatly appreciated.

To the many authors who contributed such extensive effort I am most appreciative, as I am also to the parent organizations of those authors from industry for the organizational support and encouragement so generously given.

I want to especially thank Miss Nancy L. Huff who typed all ten of the editors' chapters with great skill and patience.

There are many people who have greatly affected my career and interest in the aircraft gas turbine field, whose influences will be apparent in my writings. Most importantly, in this respect I must acknowledge the great influence Professor Frank E. Marble of the California Institute of Technology has had upon my interests and these writings. My thanks are also due to my colleagues at Pratt and Whitney, who have presented me with so many challenging problems in my years of association with them, as well as to the several members of the Department of Aeronautics at the USAF Academy for their encouragement and helpful comments upon the writing of the text.

Finally, my great thanks to my wife Joan for her enthusiastic encouragement and never-ending patience.

Chapter 1

INTRODUCTION

Robert O. Bullock

AiResearch Manufacturing Co. of Arizona

TABLE OF CONTENTS

	Page
CHAPTER 1	
1.0 INTRODUCTION	
1.1 PRELIMINARY REMARKS	1-1
1.1.1 History	1-1
1.1.2 Some Examples of Engines and Engine Installations	1-2
1.1.3 Purpose of this Report	1-6
1.1.4 Plan of Publication	1-7
1.2 FACTORS INFLUENCING PROPULSION ENGINE DESIGN	1-7
1.2.1 Effects of Engine Performance on Airplane Capabilities	1-7
1.2.1.1 Factors Determining Engine Size	1-7
1.2.1.2 Figures of Merit for Thrust, Size and Weight	1-8
1.2.2 Engine Power and Thermal Efficiency	1-9
1.2.2.1 Thermodynamic Determination of Power and Efficiency of Simple Engines	1-9
1.2.2.2 Some Effects of Afterburning	1-10
1.2.2.3 Thermodynamic Effects of Flight Speed	1-11
1.2.2.4 Basic Concepts Derived from Thermodynamic Analysis	1-11
1.2.3 Conversion of Engine Power to Propulsive Power	1-12
1.2.3.1 Propulsion Mechanics	1-12
1.2.3.2 Direct Coupling of Engines with Propulsive Devices	1-13
1.2.3.3 Coupling with a Secondary Jet	1-13
1.3 OFF-DESIGN ANALYSIS AND RELATED PROBLEMS	1-17
1.3.1 Steady-State Analysis	1-18
1.3.1.1 Typical Input Data for Steady-State Analysis	1-18
1.3.1.2 Typical Problem	1-19
1.3.1.3 A Sample Technique	1-19
1.3.1.4 Typical Information Derived from Analysis	1-20
1.3.1.5 Simplified Appraisals of Steady State Operation	1-21
1.3.2 Variable Geometry	1-25
1.3.2.1 Variable Compressor Stators	1-25
1.3.2.2 Variable Turbine Stators	1-25
1.3.2.3 Variable Exhaust Nozzles	1-25
1.3.2.4 Variable Inlets	1-25
1.3.2.5 Variable Rotors for Fans and Compressors	1-26
1.3.3 Transient Analysis	1-27

TABLE OF CONTENTS (CONTD)

	Page
1.3.3.1 Computation of Transient Response	1-27
1.3.3.2 Effects of Response Time of Variable Components	1-28
1.3.3.3 Delays in Time Response Due to Aerodynamic Phenomena	1-28
1.3.3.4 Information Delivered from Transient Analysis	1-29
1.3.3.5 Airplane Acceleration	1-29
1.4 CHARACTERISTICS OF FLOW IN AN ENGINE	1-29
1.4.1 Genesis of Losses	1-29
1.4.1.1 Ideal Shock Losses	1-29
1.4.1.2 Friction Losses	1-30
1.4.2 Amplification of Friction Losses	1-30
1.4.2.1 Qualitative Observations	1-30
1.4.2.2 Mixing Losses	1-31
1.4.2.3 All Compression in Engines Requires a Diffusion Process	1-33
1.4.3 Effects in Curved Flow	1-33
1.4.3.1 Unstable and Stable Flow	1-33
1.4.3.2 Secondary Flows	1-33
1.4.4 Special Losses in Centrifugal Compressors	1-34
1.4.4.1 Impellers	1-35
1.4.4.2 Diffusers	1-36
1.4.4.3 Possibilities for Future Developments of Centrifugal Compressors	1-36
1.4.5 Flow About Blade Ends of Axial Turbomachines	1-37
1.4.6 Summary of Loss Problems	1-38
1.5 INTERRELATIONSHIP OF AEROTHERMODYNAMIC COMPONENTS	1-38
1.5.1 Inlets	1-38
1.5.2 Compressors	1-38
1.5.3 Combustors	1-40
1.5.4 Turbines	1-40
1.5.5 Afterburners	1-41
1.5.6 Nozzles	1-41
1.5.7 Summary	1-41
1.6 INTERACTIONS WITH OTHER SPECIALTIES	1-41
1.6.1 Dimensional Integrity	1-42
1.6.2 Experimental Testing	1-42
1.6.3 Flow Blockage by Struts and Accessory Drive Shafts	1-42
1.6.4 Foreign Object Damage	1-43
1.6.5 Effects of Advanced Aerodynamic Technology	1-43
1.6.6 Ceramic Turbine Blades and Vanes	1-43
1.6.7 Environmental Problems	1-44
1.7 REMARKS ON ADVANCED FLOW CALCULATIONS	1-44
1.8 A BRIEF BIOGRAPHY OF A TYPICAL ENGINE	1-45

LIST OF FIGURES

		Page
Figure 1.1-1	Cutaway View of the Heinkel He-S 3B Turbojet Engine -- The First Jet Engine to Make a Successfull Flight	1-1
Figure 1.1-2	Heinkel He 178--the First Airplane to Fly with a Turbojet Engine	1-1
Figure 1.1-3	Cutaway View of a Jet Engine with Afterburner	1-2
Figure 1.1-4	Cutaway of the Model T56-A-15 Turboprop Engine	1-3
1.1-5	Model T56-A-15 Turboprop Engine. This is the Way the Engine Pictured in Figure 1.1-4 Actually Appears. Note the Numerous Accessories, Wires, and Tubing for Oil and Fuel	1-3
1.1-6	USAF AC-130	1-3
1.1-7	Cutaway of the CF6 Turbofan Engine	1-4
1.1-8	USAF E-4 Aircraft	1-4
1.1-9	Cutaway of the TF30 Engine	1-5
1.1-10	Cutaway View of the F100 Engine. (See Remarks on Figure 1.1-9.)	1-5
1.1-11	USAF B-1 Bomber Just After Takeoff	1-5
1.1-12	USAF F-16 Just After Takeoff	1-6
1.1-13	USAF F-16 in Flight	1-6
1.1-14	USAF F-15 in Flight	1-6
1.1-15	USAF F-111 in Flight	1-6
1.1-16	USAF F5E in Flight	1-6
1.2-1	Characteristic Variation of Drag with Mach Number. (Taken from Figure 26.1.2-3, Chapter 26.)	1-8
1.2-2	Effect of λ on Thrust Produced and Propulsive Efficiency	1-12
1.3-1	Example of Compressor Map	1-18
1.3-2	Example of Turbine Map	1-18
1.3-3	Typical Compressor Map and Its Engine Operating Line	1-21
1.3-4	Variation of Compressor Temperature Rise Coefficient with Engine Temperature Ratio	1-22
1.3-5	Typical Variation of $\dot{m}\sqrt{\theta}/\delta$ of a Nozzle with Pressure Ratio	1-23

LIST OF FIGURES (CONTD)

		Page
1.3-6	Relationship Between Pressure Ratio of Second Unit and Mass Flow Through It	1-23
1.3-7	Variation of Mass Flow Through First Turbine with Overall Pressure Ratio 23	1-23
1.3-8	Variation of Pressure Ratio Across First Turbine with Overall Pressure Ratio	1-24
1.3-9	Relationship Between Flight Mach Number and Compressor Speed and Airflow	1-26
1.3-10	Inlet Flow Shapes with Stovepipe Inlet	1-26
1.3-11	Effect of Step Change in Combustor Outlet Temperature	1-27
1.3-12	Compressor Map Showing Boundaries for Four Types of Blade Flutter (See Chapter 22)	1-27
1.4-1	Separation Static-Pressure-Ratio Versus Mach Number -- Single Shock, Straight Surface	1-29
1.4-2	The Drag Experienced by this Airfoil and the Wire is the Same	1-30
1.4-3	Examples of Flow about Isolated Bodies	1-30
1.4-4	Development of Separation of Flow about a Circular Cylinder	1-31
1.4-5	Flow Passage with Sudden Change in Flow Area	1-32
1.4-6	Two-Dimensional Curved Duct Illustrating Secondary Flows	1-33
1.4-7	An Effect of Passage Shape on Secondary Flows	1-34
1.4-8	Centrifugal Compressor and Diffuser	1-34
1.4-9	Performance of Compressor Shown in Figure 1.4-8	1-35
1.4-10	Velocity Diagram at Rotor Exit	1-35
1.5-1	Schematic Development of Three Blade Rows of Axial Flow Compressor	1-39
1.5-2	Representative Compressor Map	1-39

CHAPTER 1

1.0 INTRODUCTION

1.1 PRELIMINARY REMARKS

Developing a competitive aircraft gas turbine engine design is one of the most challenging tasks in engineering. Airplane performance is so responsive to reductions in the size, weight and fuel consumption of its engine that maximum effectiveness must be demanded of each engine part. On the other hand, the aerodynamic and mechanical capacity of any part dare not be exceeded because the potential consequences can be disastrous. Engineering design development must, therefore, be based on the following criteria:

- The presently available maximum aerodynamic and mechanical effectiveness and capacity of each part of an aircraft gas turbine engine must be known.
- How to design precisely up to the presently available maximum aerodynamic and mechanical effectivenesses and capacities without exceeding them must be known.
- The research necessary to extend the maximum effectiveness and capacity of each part must be recognized.

Engineering specialties required to ascertain and extend these limits include aerodynamics, thermodynamics, controls, stress analysis, vibration and acoustics, combustion, heat transfer, lubrication, instrumentation, manufacturing, and inspection. All of these specialties must work together if the design goals are to be realized.

It is generally recognized that a gas turbine engine derives its useful power from a thermodynamic cycle. Demands for improved engine power as well as fuel consumption are therefore met by increases in:

- Cycle efficiencies
- Peak cycle temperature.

Increasing these quantities without sacrificing reliability have been, and will continue to be, two of the major goals of gas turbine engineering.

1.1.1 History

The potential simplicity of a gas turbine had enticed inventive minds for over a century. What could be less complicated than mounting a rotating compressor and turbine on the same shaft and inserting a source of heat (combustion chamber) between them as illustrated in Figure 1.1-1? Unfortunately, the aerodynamic and material technologies of that time were not sufficiently developed for the construction of a useful engine; component efficiencies were too low, and the allowable peak cycle temperature (that of the gas at the turbine inlet) was excessively restricted by the strength of available turbine materials at elevated temperatures.

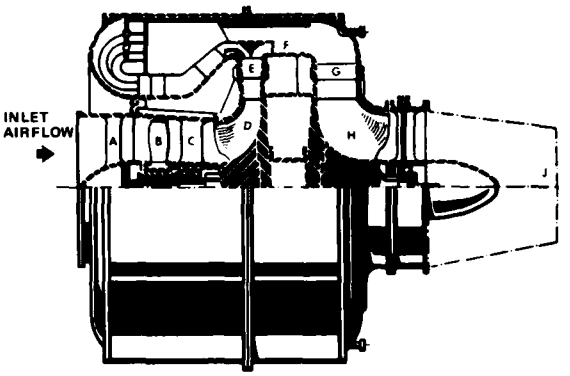

A	INLET GUIDE VANE	F	COMBUSTOR
B	AXIAL COMPRESSOR ROTOR	G	RADIAL TURBINE NOZZLE
C	AXIAL COMPRESSOR STATOR	H	RADIAL TURBINE IMPELLER
D	CENTRIFUGAL COMPRESSOR ROTOR	J	EXHAUST NOZZLE
E	CENTRIFUGAL COMPRESSOR DIFFUSER		

THE INLET AIRFLOW IS COMPRESSED FIRST BY A SINGLE-STAGE AXIAL COMPRESSOR, THEN BY A CENTRIFUGAL COMPRESSOR. HEATING OF THE WORKING FLUID TAKES PLACE IN THE COMBUSTOR. THE GAS IS THEN EXPANDED, FIRST THROUGH A TURBINE AND THEN THROUGH AN EXHAUST NOZZLE. THE TURBINE DRIVES THE COMPRESSOR, AND FURNISHES OTHER AUXILIARY POWER. THE EXPANSION THROUGH THE NOZZLE RESULTS IN THE EXHAUST JET.

Figure 1.1-1. Cutaway View of the Heinkel He-S 3B Turbojet Engine -- The First Jet Engine to Make a Successful Flight.

Persistent work in these areas, however, gradually paved the way for the first successful flight of a turbojet engine on August 27, 1939. The engine, invented and developed by Hans von Ohain, in Germany, was the He-S 3B and is shown in Fig 1.1-1. It developed about 900 pounds of thrust and powered the He 178 airplane shown in Fig 1.1-2

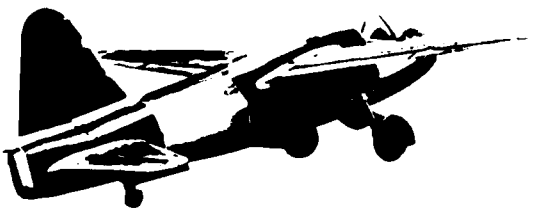

Figure 1.1-2. Heinkel He 178--the First Airplane to Fly with a Turbojet Engine.

The development of a jet engine was also undertaken by Sir Frank Whittle in England. His 1930 patent anticipated most of the essential elements of a workable engine. His W.1 engine, which produced 860 pounds of thrust, powered the Gloster Aircraft E28/39 on its maiden flight on May 14, 1941. (Unfortunately, photographs of the engine were not available for this publication). This flight undoubtedly could have been made years earlier if proper financial support had been given to the enterprise. (There is a plausible reason for this delay, however, which is offered in 1.2.3.2. In a nutshell, jet airplanes want to fly at high speeds, and external aerodynamic technology was not ready for even moderately high speeds until the late 1930's).

National defense was the first area in which the impact of turbojet engines was felt. Turbojet engine weight was markedly reduced from reciprocating engine weight and the propeller was eliminated. The resulting airplanes could fly so much faster than their predecessors that local air superiority was practically guaranteed. Governments were thus strongly motivated to invest in the development of the technologies for gas turbine engines and high speed aircraft. Maintaining competitive postures compelled industry also to make large investments in these technologies. Notable improvements in gas turbines were inevitable as a result of increased component efficiencies and elevated turbine inlet temperatures. Further improvements resulted from additional reductions in engine size and weight per unit of thrust. These reductions were derived from advances in stress and vibration analysis, which in turn provided better structural efficiency. The development of materials having higher stress-to-weight ratios was also gradually introduced in various engine components to obtain further weight reductions.

In addition to improved turbojet engines, efficient turboprop and turbofan engines also evolved. Long range and supersonic aircraft designs with afterburning followed the improved engine and airframe technologies. A by-product of this evolution was a revolution in commercial air travel. Many areas of the world were made accessible by overnight flights.

1.1.2 Some Examples of Engines and Engine Installations

Some examples of engines and aircraft produced for defense purposes are presented in Figures 1.1-3 through 1.1-16. Statements in both the following text and the footnotes in the pictures will be justified in later paragraphs of this chapter.

Figure 1.1-3 presents a cutaway view of a single-shaft turbojet engine with an afterburner. It is the J85-21 made by the General Electric Company. This engine represents an intermediate design prior to the widespread introduction of turbofan engines.

Figure 1.1-4 presents a cutaway view of a Detroit Diesel Allison turboprop engine. Engines of this type appeared when their weight and efficiency made them more economical than reciprocating engines. This engine also represents an intermediate design which preceded the technology available at this writing. A view of the complete engine with all its necessary accessories is shown in Figure 1.1-5. An example of the way these engines

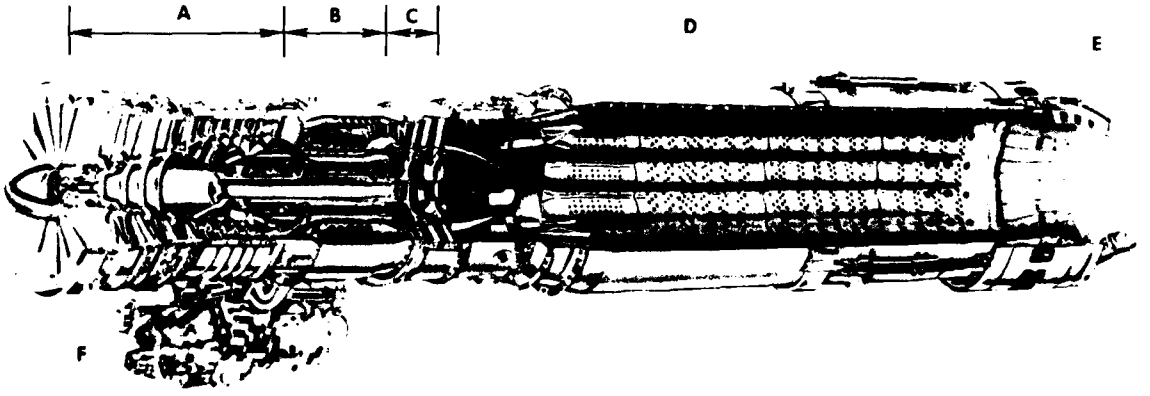

A MULTISTAGE AXIAL FLOW COMPRESSOR
B COMBUSTOR
C MULTISTAGE TURBINE
D AFTERBURNER
E VARIABLE EXHAUST NOZZLE
F ACCESSORIES

MULTISTAGE COMPRESSOR FURNISHES PRESSURE RATIO DESIRED BASED ON TURBINE INLET TEMPERATURE, ENGINE SIZE AND WEIGHT, FLIGHT SPEED, AND AIRCRAFT MISSION. AFTERBURNER HEATS EXHAUST GAS TO RAISE ITS TEMPERATURE. THIS PROVIDES EXTRA THRUST FOR SHORT PERIODS OF TIME. EXHAUST NOZZLE AREA FOR AFTERBURNING IS GREATER THAN FOR NONAFTERBURNING.

Figure 1.1-3. Cutaway View of a Jet Engine with Afterburner.

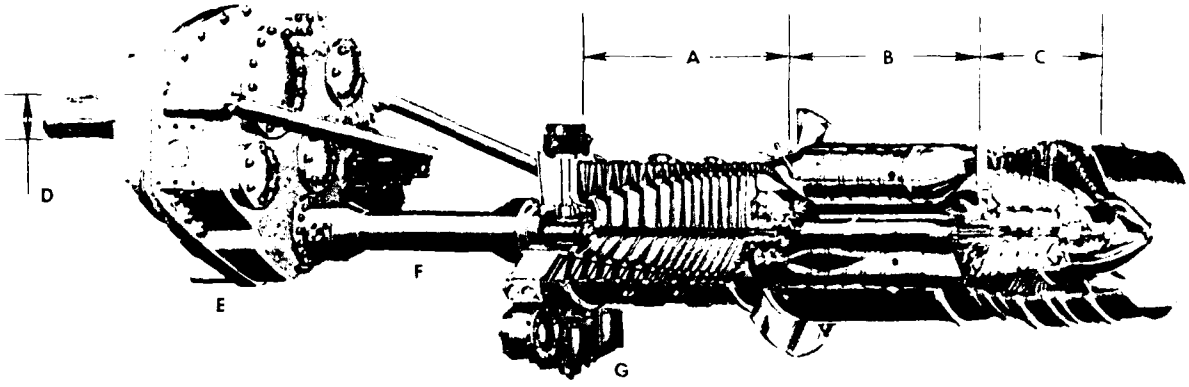

A MULTI-STAGE AXIAL COMPRESSOR
B COMBUSTOR
C MULTISTAGE TURBINE
D PROPELLER SHAFT
E GEARBOX
F DRIVE SHAFT
G PROVISIONS FOR MOUNTING ACCESSORIES

THE TURBINE ABSORBS MOST OF THE AVAILABLE ENERGY AFTER COMBUSTION. THE EXTRA ENERGY REMAINING AFTER THE COMPRESSOR IS DRIVEN IS USED TO DRIVE A PROPELLER ATTACHED TO THE PROPELLER SHAFT. SINCE THE PROPELLER TURNS AT A MUCH LOWER SPEED THAN THE ENGINE, A GEARBOX IS NECESSARY. THE LENGTH OF THE DRIVE SHAFT IS DECIDED BY THE INSTALLATION, FIGURE 1.1-6.

Figure 1.1-4. Cutaway of the Model T56-A-15 Turboprop Engine.

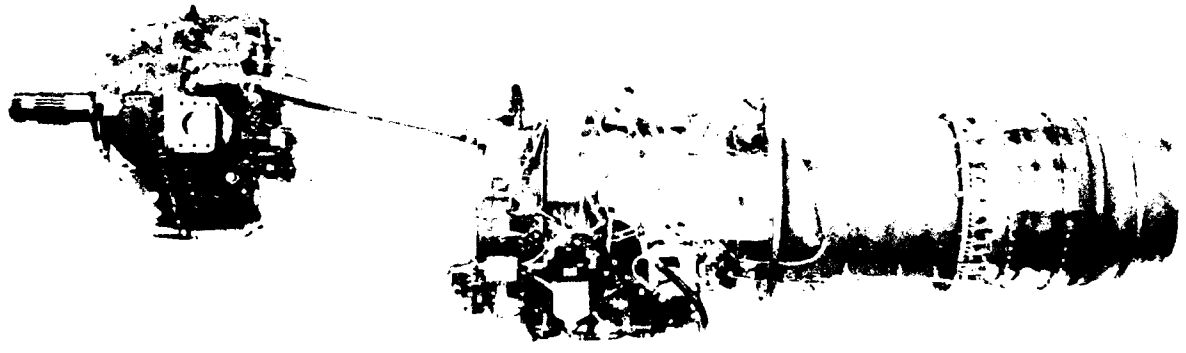

Figure 1.1-5. Model T56-A-15 Turboprop Engine. This is the Way the Engine Pictured in Figure 1.1-4 Actually Appears. Note the Numerous Accessories, Wires, and Tubing for Oil and Fuel.

are installed on an airplane is illustrated in Figure 1.1-6. Observe that the engine installation certainly disturbs the flow over the wings. The importance of minimizing engine diameter may be intuitively recognized from this picture.

A high bypass turbofan engine, the General Electric CF6, which is specifically designed for flights at high subsonic flight Mach numbers, is shown in Figure 1.1-7. This engine is a dual shaft unit and is representative of modern technology. A study of Figure 1.1-7 reveals the design care exercised to achieve compactness and the prolific use of expensive features which enable satisfactory structural rigidity to be achieved with relatively light weight. Although the mechanism is not obvious, provisions were made to cool the turbines with air bled from

THIS AIRPLANE IS POWERED BY T56 TURBOPROP ENGINES. THESE AIRPLANES FLY AT LOWER SPEEDS THAN TURBOJET ENGINES, BUT THEY CAN PRODUCE LARGE THRUSTS WITH GOOD OVERALL EFFICIENCY.

Figure 1.1-6. USAF A-10A.

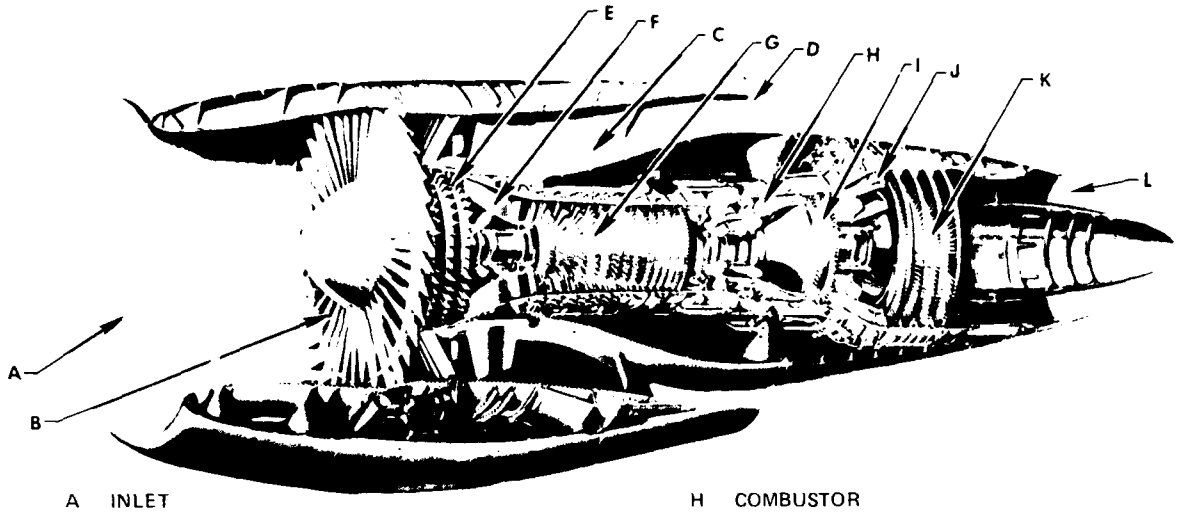

A INLET

B FAN

C OUTLET DUCT FOR BYPASS FLOW

D NOZZLE FOR BYPASS FLOW

E MULTISTAGE COMPRESSORS ON SAME SHAFT AS FAN ("LOW PRESSURE" COMPRESSOR)

F TRANSITION DUCT

G MULTISTAGE COMPRESSOR ("HIGH PRESSURE" COMPRESSOR ON SEPARATE SHAFT)

H COMBUSTOR

I MULTISTAGE "HIGH PRESSURE" TURBINE, DRIVES HIGH-PRESSURE COMPRESSOR

J TRANSITION DUCT

K MULTISTAGE "LOW PRESSURE" TURBINE, DRIVES LOW-PRESSURE COMPRESSOR AND FAN

L EXHAUST NOZZLE FOR ENGINE AIRFLOW

THIS ENGINE REPRESENTS A CROSS BETWEEN TURBOJET AND TURBOPROP ENGINES. AFTER THE FLOW IS COMPRESSED BY THE FAN, MOST OF IT IS DISCHARGED THROUGH THE FAN NOZZLE. THE REST OF THE FLOW IS COMPRESSED FURTHER. THE COMPRESSION IS DONE BY TWO SEPARATELY DRIVEN COMPRESSORS IN SERIES. THE EXPANSION ACROSS THE TURBINES IS PROPORTIONALLY LESS THAN THAT OF THE ENGINE SHOWN IN FIGURE 1.1-4.

Figure 1.1-7. Cutaway of the CF6 Turbofan Engine.

the compressors. High turbine inlet temperatures are thus realized. A typical installation of a high-bypass engine in an airplane is shown in Figure 1.1-8. The inlets are located upstream of the wings to get uniform airflow into the engines. The curvature of the leading edge of the inlet is generous to permit some misalignment of the incoming flow with the inlet axis.

The next two figures (1.1-9 and 1.1-10) show two turbofan engines, of the type needed for combined supersonic and subsonic flights. These engines are also representative of modern engine technology. Turbine cooling is again used. Identification of all engine parts is not provided since only one new part is introduced. This part is a flow mixer designed to efficiently mix the bypass flow with the flow through the engine. Observe again the compactness of the turbomachinery and main combustor. Note that the accessories and plumbing constitute an appreciable portion of the total engine volume. The afterburner space might seem to be disportionately large. However, this is beneficial for achieving good combustion efficiency and mixing without impairing performance excessively.

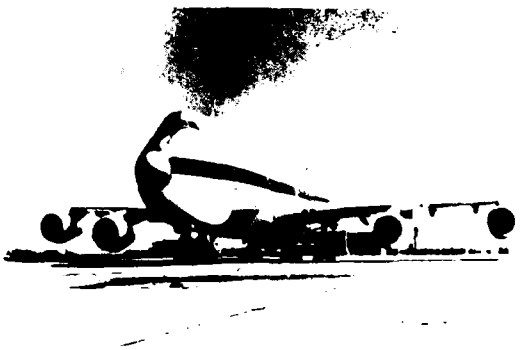

THIS AIRPLANE REPRESENTS A TYPICAL INSTALLATION OF A HIGH BYPASS TURBOFAN ENGINE. AIRPLANES SUCH AS THESE CAN FLY AT MACH NUMBERS ABOVE 0.8 AND STILL STAY IN THE AIR FOR MANY HOURS. NOTE HOW THE ENGINES ARE ATTACHED TO THE WINGS. THE IDEA IS TO MINIMIZE THE DISTURBING EFFECTS OF THE ENGINES. NOTE ALSO THAT LARGER BYPASS RATIOS WOULD REQUIRE BIGGER LANDING GEAR TO MAINTAIN GROUND CLEARANCE FOR THE ENGINES. THE RESULTING INCREASE IN LANDING GEAR WEIGHT WOULD OFFSET THE CARE IN ENGINE DESIGN. THIS IS ONE OF MANY INSTANCES THAT SHOW THAT FEW ITEMS IN ENGINE DESIGN CAN BE DIVORCED FROM THE AIRPLANE OBJECTIVES.

Figure 1.1-8. USAF F-4 Aircraft.

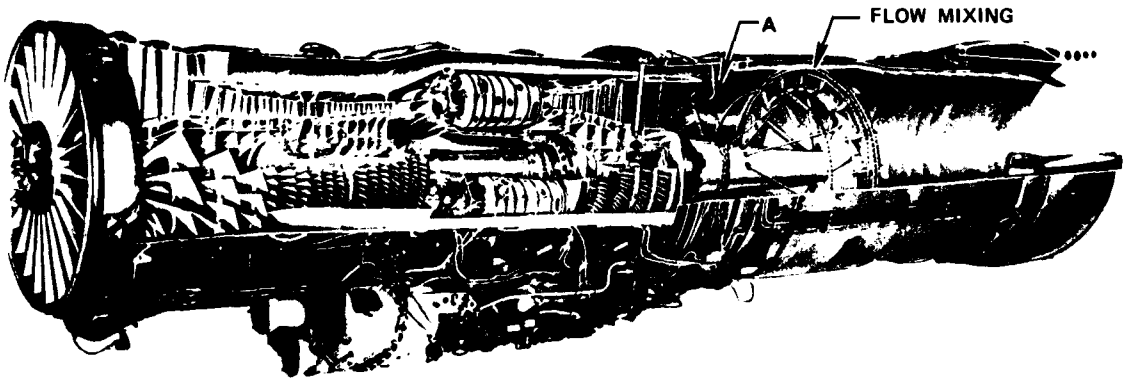

THE GREATER NUMBER OF STAGES IN THE FAN PROVIDES THE HIGHER PRESSURE RATIOS NEEDED FOR EFFICIENT OPERATION AT SUPERSONIC FLIGHT. AFTERBURNING IS APPLIED TO BOTH THE FAN FLOW AND THE ENGINE FLOW. THE DESIGN PRESSURE MUST BE CAREFULLY BALANCED AT A, WHERE THE TWO FLOWS UNITE.

Figure 1.1-9. Cutaway of the TF30 Engine.

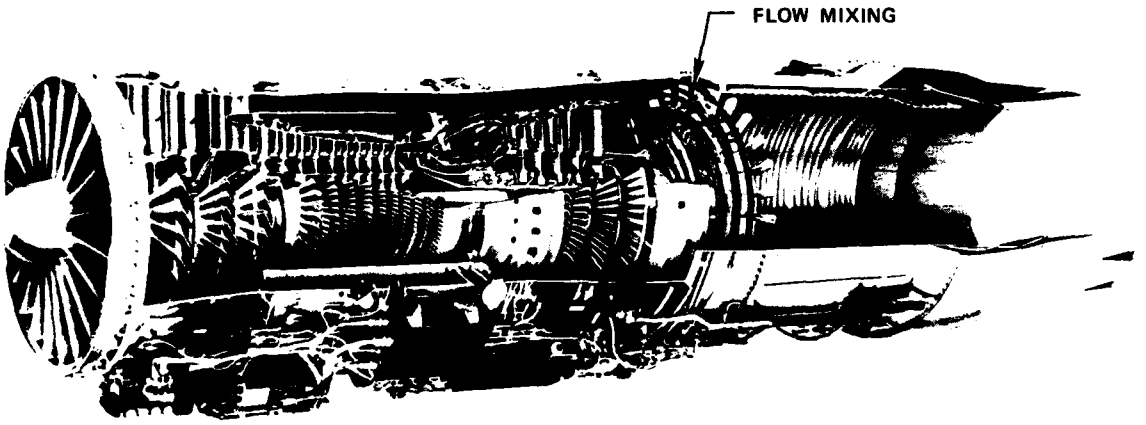

Figure 1.1-10. Cutaway View of the F100 Engine. (See Remarks on Figure 1.1-9.)

Figures 1.1-11 through 1.1-16 show selected airplanes with supersonic capabilities at various flight conditions. In contrast to the engine installations pictured in Figures 1.1-6 and 1.1-8, the engines for supersonic aircraft must nestle close to the airframe. The air displaced by the engine installation has to systematically blend with the air displaced by the rest of the airframe, otherwise supersonic drag is untenable.

Figures 1.1-11 and 1.1-12 show typical aircraft attitudes during takeoff and climb. An excessive angle of attack for the inlet or angle of yaw could cause the engine inlet air to flow over a sharp edge. This could create havoc with finely tuned compact engines. Great care must be exercised in the design and location of inlets.

Figure 1.1-11. USAF B-1 Bomber Just After Takeoff.

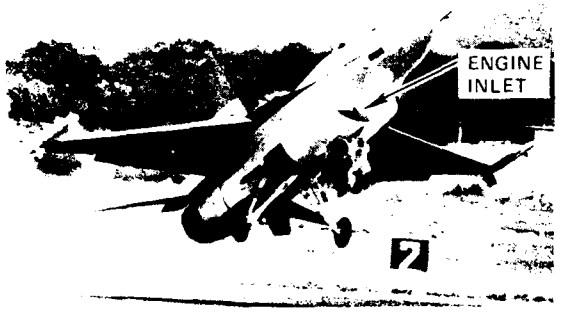

Figure 1.1-12. USAF F-16 Just After Takeoff.

Figures 1.1-13 and 1.1-14 show two other views of airplanes with the engine inlets installed beneath the aircraft.

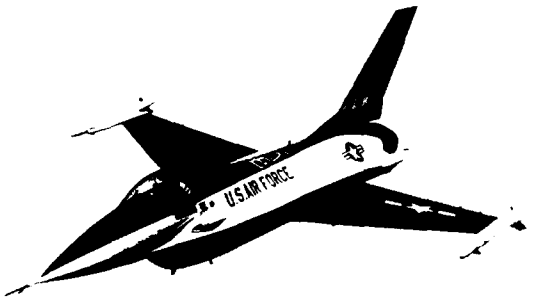

Figure 1.1-13. USAF F-16 in Flight.

Figure 1.1-14. USAF F-15 in Flight.

Figures 1.1-15 and 1.1-16 show the engines mounted at the sides of the fuselage. No matter how the engines are mounted and sized, it is impossible, at the present time, to obtain good flow either into or around them over the entire range of flight speeds and altitudes. Coping with this problem is not the least of the many confronting designers.

Although gas turbine propulsion engines have come a long way, many problems remain to be solved and numerous improvements remain to be incorporated. Advancements will be achieved by engine developers who understand the mathematics and physics of their own field, together with those of peripheral fields.

Figure 1.1-15. USAF F-111 in Flight.

Figure 1.1-16. USAF F5E in Flight.

1.1.3 Purpose of this Report

As noted previously, the successful development of gas turbine engines has resulted from dramatic advancements in many engineering specialties. Prominent among these specialties are the activities of aerothermodynamic groups. This is the area where engine concepts begin and engine efficiency is established. The experiences gained (and sometimes suffered) by aerothermodynamicists are the foundations for new design approaches. They also provide guidance for future areas of gas turbine research.

This publication reviews the development of aerothermodynamics in aircraft gas turbines and has been prepared by experts who have participated in and contributed to advancements in technology. The publication has the following objectives:

- Provide a graduate-level text that treats the basic aerothermodynamics of the engine
- Review the state-of-the-art, component problems, and design approaches
- Be a useful guide for the management of gas turbine research
- Guide new engineers in the industry along the paths of needed research
- Reflect the general design and development philosophies of the turbine engine community
- Enjoy a wide circulation as a useful government technical publication

1.1.4 Plan of Publication

Chapters 2 through 26 present a comprehensive treatise on the function of aircraft gas turbines, what the important aerothermodynamic problems are, and how these problems have been attacked. These chapters fulfill the basic objectives of this effort. In addition to the material presented in those chapters, the reader should also be acquainted with the following subjects:

- Basic factors influencing the objectives and directions of gas turbine engine design
- The interrelationship of gas turbine components
- The interdependence of aerothermodynamics with the other engineering specialities involved in the manufacture of gas turbines

These subjects are addressed in this chapter, which complements the rest of the publication by indicating, in advance, the many considerations underlying the design of gas turbine engines. Although introductory in nature, some comments in this chapter may have more meaning if they are also read in conjunction with appropriate succeeding chapters.

1.2 FACTORS INFLUENCING PROPULSION ENGINE DESIGN

This topic is introduced here to prepare the reader for subsequent statements in this chapter and to supplement important material contained in later chapters. It is divided into three sections. The first section shows how two critical variables--(a) thrust of the propulsion system per unit of weight, and (b) efficiency or thrust specific fuel consumption--govern the usefulness of an engine. The second section briefly discusses the thermodynamic factors that control the power and thermal efficiency of an engine. The third section discusses the options for converting engine power to propulsive power.

1.2.1 Effects of Engine Performance on Airplane Capabilities

Every airplane requires an economic reason for its existence, since enough people must be willing to pay whatever is necessary for the particular service it offers. The design of an engine is therefore greatly influenced by its own contribution to the cost of the service.

By definition, an airplane must carry a given payload a prescribed distance along a flight path in which the speed and altitude are stipulated at every point. In order to transport a payload, an airplane must also carry a propulsion system and sufficient fuel to complete its mission. Unfortunately, the weight of the propulsion system is frequently comparable to that of the payload, while the fuel weight may exceed the payload several-fold. Propulsion system and fuel weights, together with engine efficiency, are thus important factors in determining the economic value of any airplane. The relative importance of these quantities varies with many factors. Prominent among them are the cost and availability of fuel, and the nature of the fuel.

1.2.1.1 Factors Determining Engine Size

In a well designed airplane, there are always one or more flight conditions where the maximum effective thrust-producing capability of the propulsion system is demanded. This requirement dictates the size and weight of the propulsion system. At any point in its mission, thrust is determined by the expression

$$\tau_e = \text{Drag} + M_g \times \alpha$$

Drag = force of aerodynamic drag

M_g = mass of the airplane

α = acceleration (that of airplane and the appropriate component of gravity)

τ_e = effective thrust

The acceleration term is dominant in airplanes that require vertical takeoff capability, short takeoff distances, or great maneuverability. These requirements then decide the maximum effective thrust and consequently the size and weight of the propulsion system. An engine-out requirement during takeoff and climb of a multi-engined aircraft may also be decisive in determining size. Both acceleration and drag forces are then involved. High altitude cruise can be another determinant.

In other cases, the drag during cruise at high altitude or at transonic and supersonic flight speeds may fix the thrust that determines propulsion system size. When acceleration forces are not involved, one may write

$$\tau_e = 1/2\ \rho_o V_o^2 S C_D$$

ρ_o = ambient air density

V_o = flight speed

S = a constant associated with the surface area of the airplane

C_D = drag coefficient of the airplane

Representative graphs of the variation of C_D with Mach number are shown in Figure 1.2-1. Because of the relatively high drag observed during transition from subsonic to supersonic speeds with fixed wing aircraft, it is usually very desirable to accelerate an airplane through this regime rapidly. The thrust demanded then exceeds

that determined by C_D alone. An objective of propulsion system design is to produce this thrust with minimum system weight and fuel consumption, as long as other important qualities and drag due to the system installation are not prejudiced.

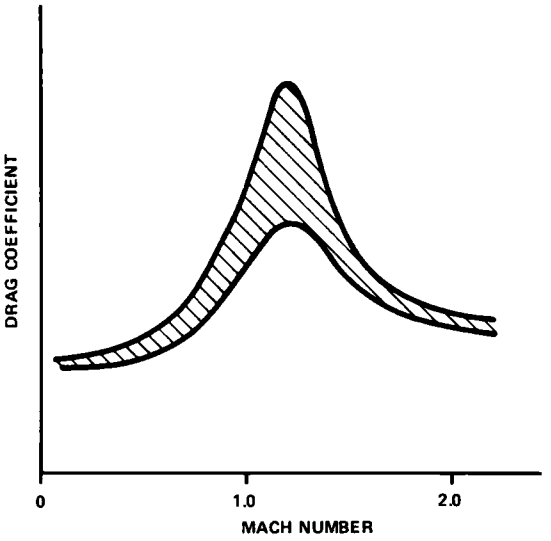

Figure 1.2-1. Characteristic Variation of Drag with Mach Number. (Taken from Figure 26.1.2-3, Chapter 26.)

In this connection, the effective thrust of a propulsion system is that thrust produced by aerothermodynamic forces within it minus drag due to:

- The flow of air over the external surfaces of the propulsion system
- The interference of flow about the airframe caused by the presence of the propulsion system and the flow of gases into and out of it
- The extra weight that must be added to the airframe in order to accommodate the propulsion system.

Establishing the most suitable propulsion system for a given mission requires extensive system and airplane studies such as those described in Chapter 9. Some of the ancillary installation problems are also presented in Chapters 13, 14, and 26.

Although no simple evaluation criteria are completely adequate, quantities for distinguishing good aerothermodynamic qualities of an engine from undesirable qualities can be identified. The quantities chosen must be related to size, and fuel consumption. Those selected for this section are described in the following paragraphs.

1.2.1.2 Figures of Merit for Thrust, Size and Weight

The dimensionless quantity $\tau/(\dot{m} V_o)$ can be used as a simple figure of merit for gauging the effective interrelations among thrust, size, and weight of a propulsion system. (At negligible flight speeds or at a given value of V_o, $\tau/\dot{m}$ is obviously appropriate.)

τ = thrust created by aerothermodynamic forces within the propulsion system

$\dot{m}$ = mass flow in the propulsion system

V_o = velocity of flight

There are several important factors exposed by this quantity. In level flight, $\tau/(\dot{m} V_o)$ is proportional to the drag coefficient of the airplane. It can be shown that

$$\frac{\tau}{\dot{m} V_o} = \frac{1}{2} \frac{S}{A_o} C_D \qquad (1.2.1)$$

$$A_o = \frac{\dot{m}}{\rho_o V_o} = \text{area required}$$

for the air approaching and entering the propulsion system. A_o is thus a measure of the size of the propulsion system.

When the maximum value of aerodynamic drag is the principal determinant of the size of an engine, the size varies inversely with the value of $\tau/(\dot{m} V_o)$ developed by the engine. Moreover, for a defined type of propulsion system, the weight of the engine and its installation tends to increase with A_o. Thus, the ability to develop high values of $\tau/(\dot{m} V_o)$ suggests relatively low weight and installation drag for the propulsion system. In many instances, the term $\tau/\dot{m} V_o$ may then be considered more or less proportional to $\tau_e/\dot{m} V_o$.

1.2.1.3 Figure of Merit for Fuel Consumption

Fuel weight is closely associated with the magnitude of η_o, the overall propulsion system efficiency. The familiar Breguet equation for range is:

$$R_N = -H_f \bar{\eta}_o (\overline{L/D}) \ln (1 - M_f/M_g)$$

H_f = lower heating value of fuel

$(\overline{L/D})$ = average lift-drag ratio of the aircraft during its mission

M_f = fuel weight at takeoff

M_g = takeoff gross weight of airplane

$\bar{\eta}_o$ = average overall efficiency of propulsion system

This equation clearly indicates that high values of η_o are necessary to enjoy relatively low values of fuel weight. Thrust specific fuel consumption is related to η_o by the equation $SFC_T = 4.63\ V_o/H_f\eta_o$.

1.2.2 Engine Power and Thermal Efficiency

The word "engine" in this section refers to the prime mover that transforms thermal energy to useful mechanical energy. In the subsequent section, the term "propulsion device" indicates the unit that converts this useful energy into thrust. A complete assembly is called the "propulsion system". This terminology has been adopted for Sections 1.2.2 and 1.2.3. It is employed to separate and clarify the various functions of the propulsion system. Throughout the rest of this chapter, however, the word "engine" will refer to the entire system, as it normally does.

The size of an engine decreases as the mass flow of gas passing through it is reduced. It is manifest that the interests of light engine weight and low installation drag are served when the ratio of engine power to engine mass flow ($P_{WRE}/\dot{m}_e$) is high.

The fuel weight required for a given mission depends upon the thermal efficiency, η_{TH}; this is true since it can be shown that $\eta_o = \eta_{TH} \times \eta_{PR}$. ($\eta_{PR}$ is the efficiency of the propulsion device.) Engine specific fuel consumption is related to η_{TH} by the equation $SFC_E = 2545/H_f\ \eta_{TH}$. High thermal efficiencies or low engine fuel consumptions are therefore desirable.

Both $P_{WRE}/\dot{m}_e$ and η_{TH} are included in the subjects presented in Chapters 5, 6 and 7. In order to preserve continuity in this chapter, however, and also establish a base for subsequent discussions, the following development is made. The approach is unorthodox, but it has the merit of clearly delineating cause and effect. For the purpose of this study, the assumption of a perfect gas (see Chapter 2) is adequate.

1.2.2.1 Thermodynamic Determination of Power and Efficiency of Simple Engines

The following identity is readily derived; see Chapter 2.

$$\left(\frac{p_u}{p_d}\right)^{\frac{\gamma-1}{\gamma}} = \left(\frac{t_u}{t_d}\right) e^{\sigma}$$

p = static pressure

t = static temperature

$\gamma = C_p/C_v$

C_p = specific heat at constant pressure

C_v = specific heat at constant volume

$\sigma = \Sigma\Delta S/C_p$

ΔS = total increase in entropy between any two stations within an engine

Σ designates summation sign

u designates condition of air at any upstream station

d designates condition of air at any station downstream of u

Consider an airplane engine similar to the engines in Figures 1.1-3 and 1.1-4.

Since the static pressures upstream and downstream of an engine are equal

$$\left(\frac{p_i}{p_e}\right)^{\frac{\gamma-1}{\gamma}} = 1 = \left(\frac{t_i}{t_e}\right) e^{\sigma}$$

i designates condition of engine air ahead of the inlet

e designates condition of engine gas after it is discharged into the atmosphere

For simplicity, let the mass flow be constant throughout the engine. The previous equation may then be written as:

$$(t_e - T_e) - (T_y - T_e) - (T_{ti} - T_y) + (T_{ti} - T_{co}) + (T_{co} - T_i) + (T_i - t_i) = t_i\ (e^{\sigma} - 1)$$

T_{ti} = turbine inlet total temperature

T_{co} = compressor outlet total temperature

T_y = total temperature downstream of the turbine driving the compressor and upstream of a turbine, or the part of a turbine, producing useful power ($T_y = T_e$ in Figure 1.1-3, but $T_y > T_e$ in Figure 1.1-4).

Assume now that

$$C_p\ (T_{ti} - T_y) = C_p\ (T_{co} - T_i)$$

This approximately accounts for the specific energy provided to the compressor by the turbine driving it. If the air after the power turbine is allowed to expand to the atmosphere, then

$$JC_p\ (T_e - t_e) = \frac{1}{2} V_{ex}^2 \qquad (1.2.2)$$

Note also that

$$JC_p\ (T_i - t_i) = \frac{1}{2} V_o^2$$

or

$$\frac{T_i}{t_i} = 1 + \frac{V_o^2}{2JC_p t_1} = 1 + \frac{\gamma-1}{2} M_o^2 \qquad (1.2.3)$$

furthermore

$$C_p (T_{ti} - T_{co}) = \Delta H_I$$

J = ratio of mechanical to thermal energy units

V_{ex} = speed of gas flow leaving the engine relative to the engine

V_o = flight speed

M_o = flight Mach number

ΔH_I = specific energy (per unit of mass) delivered to the cycle

The equation now becomes

$$JC_p (T_y - T_e) + \frac{1}{2} (V_{ex}^2 - V_o^2) = J\Delta H_I - JC_p t_i (e^{\sigma} - 1)$$

Observe that if the only change in entropy came about from the addition of ΔH_I to the flow, then

$$\frac{P_{co}}{P_{ti}} = 1 = \frac{T_{co}}{T_{ti}} e^{(\Delta S/C_p)_c}$$

P = total pressure

c identifies the entropy increase accompanying the heat added in the combustor

and

$$JC_p(T_y - T_e) + \frac{1}{2} (V_{ex}^2 - V_o^2) = J\Delta H_I - JC_p t_i \left(\frac{T_{ti}}{T_{co}} - 1\right) = J\Delta H_I \left(1 - \frac{t_i}{T_{co}}\right)$$

The quantity $[JC_p (T_y - T_e) + \frac{1}{2} (V_{ex}^2 - V_o^2)]$ represents the total power that can be developed by the engine per unit of engine mass flow. For this idealized condition, the efficiency with which ΔH_I is utilized is obviously $(1 - t_i/T_{co})$. The quantity $t_i (T_{ti}/T_{co} - 1)$ represents the tax that nature demands for the privilege of converting heat energy to useful energy.

When energy degradation by effects such as friction is also recognized, the term e^{σ} can be written as

$$e^{\sigma} = e^{\Sigma\Delta S/C_p} = e^{[(\Delta S/C_p)_c + \Sigma(\Delta S/C_p)_D]} = \frac{T_{ti}}{T_{co}} e^{\sigma_D}$$

The term e^{σ_D} then embraces all entropy changes resulting from the degradation of mechanical energy. That entropy change deliberately introduced by heat transfer through combustion is replaced by a temperature ratio. The power output per unit mass can now be expressed by

$$\frac{P_{WRE}}{\dot{m}_E} = J\Delta H_I \left(1 - \frac{t_i}{T_{co}}\right) - J_{cp} T_{ti} \frac{t_i}{T_{co}} (e^{\sigma_D} - 1)$$

$$= J_{cp} T_{ti} \left[\left(1 - \frac{T_{co}}{T_{ti}}\right)\left(1 - \frac{t_i}{T_{co}}\right) - \frac{t_i}{T_{co}} (e^{\sigma_D} - 1)\right] \qquad (1.2.4)$$

The last term is the surtax imposed for ineptness in converting heat to useful energy. The thermal efficiency is now expressed by:

$$\eta_{TH} = \left(1 - \frac{t_i}{T_{co}}\right) - \left[\frac{t_i}{T_{co}}(e^{\sigma_D} - 1)\right] / \left[1 - \frac{T_{co}}{T_{ti}}\right] \qquad (1.2.5)$$

Observe that temperatures have been used as variables. These fundamental variables of thermodynamics provide the best illumination of the subject. In 1.3, pressures are introduced, since they are more useful in industry.

1.2.2.2 Some Effects of Afterburning

The relatively small engine diameters associated with high values of $P_{WRE}/\dot{m}_E$ are particularly needed for transonic and supersonic flight, where anything that gets in the way of the airstream produces important increments in drag. In these cases, $P_{WRE}/\dot{m}_E$ is raised by afterburning or reheat. (An afterburner in an engine is shown in Figure 1.1-3). The foregoing equation for power may then be readily extended to read

$$P_{WRT}/\dot{m}_E = JC_p \{(T_{ti} - T_{co}) + (T_{ab} - T_{to}) - t_i \left[\frac{T_{ti}}{T_{co}} \frac{T_{ab}}{T_{to}} - 1\right] - t_i \left[\frac{T_{ti}}{T_{co}} \frac{T_{ab}}{T_{to}}\right] [e^{\sigma_{DA}} - 1]\} \qquad (1.2.6)$$

T_{to} = turbine discharge total temperature

T_{ab} = afterburner discharge total temperature

$\sigma_{DA} = \Sigma\Delta S_{DA}/C_p$ for all components including the afterburner

The efficiency of the afterburning process can be determined as follows: Divide the gain in power due to afterburning by the extra energy added by combustion in the afterburner. For ideal conditions

$$\eta_{abi} = 1 - \frac{t_i}{T_{co}} \frac{T_{ti}}{T_{to}} \qquad (1.2.7)$$

η_{abi} = ideal efficiency of the afterburning process itself.

The difference between this and the non-afterburning efficiency is $[\frac{T_{ti}}{T_{to}} - 1]$. This extra loss is analagous to a late-charge tax exacted by the IRS. The corresponding equation with the entropy terms can also be derived, and it may be determined that these entropy terms greatly augment this loss in efficiency. The trade-off between the increase in P_{WRE} and the loss in η_{TH} depends on the airplane mission. It might be expected, however, that the desire for high values of $P_{WRE}/\dot{m}$ often predisposes the trade-off in favor of afterburning.

1.2.2.3 Thermodynamic Effects of Flight Speed

Recall that T_{co}/t_i is the result of two processes -- the temperature rise due to the speed of the airplane, Equation (1.2.3), and the temperature rise in the compressor(s).

$$\frac{T_{co}}{t_i} = \frac{T_i}{t_i} + \frac{(T_{co}-T_i)}{t_i} = (1 + \frac{\gamma-1}{2} M_o^2) + \frac{\Delta T_c}{t_i} \qquad (1.2.8)$$

A given temperature rise is usually produced with less entropy increase in an inlet than that in a compressor. The magnitudes of $P_{WRE}/\dot{m}_E$ and η_{TH} attainable in high speed aircraft are therefore significantly greater than those available from a stationary engine.

1.2.2.4 Basic Concepts Derived from Thermodynamic Analysis

The following deductions and observations are noteworthy.

1.2.2.4.1 Turbine Inlet Temperature

If σ_D were independent of T_{ti}, both P_{WRE} and η_{TH} would increase with T_{ti}, providing the right side of Equation (1.2.4) is positive. In many current designs, however, σ_D increases with T_{ti} because the turbine blades are cooled by air withdrawn from the main engine flow during the compression process (see Chapter 19). (The cooling is necessary to keep the turbine and other metal temperatures below T_{ti}. Otherwise, the loss in both the strength and corrosion resistance of the metal would be intolerable.) As the turbine inlet temperature increases, more cooling air is required. The resulting loss in available power after the compressor is equivalent to an increase in entropy. When an appreciable amount of air is required to achieve the necessary cooling, the growth of σ_D can offset the potential benefits of elevated turbine inlet temperatures. An upper limit of T_{ti} is eventually imposed. Methods for improving and protecting materials, and reducing losses due to blade cooling are consequently continually being pursued to improve both $P_{WRE}/\dot{m}_E$ and η_{TH}.

When an engine is being started, high values of σ_D and low values of T_{co}/t_i make the entropy term decisive. This causes the right hand side of Equation (1.2.3) to be negative. Excessive values of T_{ti} can increase the mechanical power demanded of the starter. The fuel flow must therefore be carefully controlled in this operating regime.

1.2.2.4.2 Effects of T_{co}/t_i

As T_{co}/t_i is raised from unity, both $P_{WRE}/\dot{m}_E$ and η_{TH} are initially increased. A value of T_{co}/t_i is eventually reached which makes $P_{WRE}/\dot{m}_E$ a maximum. Differentiating Equation (1.2.4) with respect to T_{co}/t_i would identify this condition when σ_D is known as a function of T_{co}/t_i. However, the relation given in Chapter 5

$$T_{co}/t_i = \sqrt{T_{ti}/t_i}$$

provides a good basis for discussion. A design for maximum power requires T_{co}/t_i to increase as the permissible value of T_{ti} is raised. Further increases in T_{co}/t_i, beyond that for maximum power, cause the efficiency to continue to increase until it too reaches a maximum. The higher the value of σ_D, the closer the value of T_{co}/t_i for maximum power approaches the value of T_{co}/t_i for maximum efficiency. In any event, a quest for high engine efficiency also requires T_{co}/t_i to increase as T_{ti} is raised.

For a given flight condition, however, engine weight also increases with T_{co}/t_i because larger compressors and turbines are required to supply the increased load imposed on them. The compressors and turbines of modern engines such as those shown in Figures 1.1-7,

1.1-9, and 1.1-10 are made as compactly as possible to minimize this trend. However, the value of T_{co}/t_i usually selected is less than that for maximum η_{TH}. The optimum value of T_{co}/t_i depends upon this discussion and the relation expressed in Equation (1.2.8).

1.2.2.4.3 Effects of σ_D

Low values of σ_D enhance both $P_{WRE}/\dot{m}_E$ and η_{TH}. High component efficiencies and low flow losses in transition ducts are major design objectives. If entropy losses were constant, their effect would diminish as T_{co}/t_i increases. Unfortunately, the losses in compressors and turbines (and even engine inlets and outlets) increase in such a manner that $(e^{\sigma_D}-1)$ increases with $\frac{T_{co}}{t_i}$. (As a matter of interest, a simple expression may be derived to relate the entropy increase in compressors and turbines to their temperature ratios and their polytropic efficiencies, defined in Chapter 6.) Besides offering reduced losses, increased component efficiencies permit higher values of T_{co}/t_i to be selected; this offers additional improvements. Since T_{co}/t_i naturally increases with flight Mach number when $(T_{co}-T_i)$ is fixed, a condition that is usually approximated in a real engine, the values of $P_{WRE}/\dot{m}_E$ and η_{TH} also increase with flight Mach number until either T_{co}/t_i reaches its value for maximum power, or σ_D become too high because of inlet losses.

1.2.2.4.4 Afterburning

Afterburning increases $P_{WRE}/\dot{m}$ at the expense of η_{TH}.

1.2.3 Conversion of Engine Power to Propulsive Power

Thrust is produced by coupling the engines of the previous section to a propulsive device. A brief study of the mechanics of propulsion is now appropriate. The problem is similar to one of impedance matching.

1.2.3.1 Propulsion Mechanics

The thrust produced by any aircraft propulsive device causes a change in the momentum of the gas passing through it (see Chapters 2 and 5). The air discharged from a propulsive device is called the jet, and the magnitude of thrust is:

$\tau = C_F \dot{m}_j (V_j - V_o)$

$\dot{m}_j$ = mass flow of gas in the jet

V_j = speed of jet

C_F = thrust coefficient. For convenience, this term will be disregarded in the following discussions, since its magnitude is usually only slightly less than unity. Consult Chapters 9, 14, and 26.

The power required to produce the jet is:

$$P_{WRj} = \frac{1}{2} \dot{m}_j (V_j^2 - V_o^2)$$

Thrust and jet power are thus related by

$$\tau = \dot{m}_j \left[\sqrt{\frac{2P_{WRj}}{\dot{m}_j} + V_o^2} - V_o\right]$$

or

$$\frac{\tau}{\dot{m}_j V_o} = \sqrt{2\Lambda_j + 1} - 1$$

$$\Lambda_j = \frac{P_{WRj}}{\dot{m}_j V_o^2} \qquad (1.2.9)$$

Thrust increases with $\dot{m}_j$ and P_{WRj}, however it asymtotically approaches the value of $\tau_{MAX} = P_{WRE}/V_o$ as $\dot{m}_j$ increases indefinitely. Note that

$$\frac{\tau}{\tau_{MAX}} = \frac{1}{\Lambda_j} \left[\sqrt{2\Lambda_j + 1} - 1\right]$$

Since the useful power developed by the thrust is τV_o, the propulsive efficiency of the jet is

$$\eta_{PR} = \frac{\tau V_o}{P_{WRJ}} = \frac{1}{\Lambda} \left[\sqrt{2\Lambda_j + 1} - 1\right] = \frac{\tau}{\tau_{MAX}} \qquad (1.2.11)$$

An important relation between thrust and power may now be written

$$\frac{\tau}{\dot{m}_j V_o} = \eta_{PR} \Lambda_j \qquad (1.2.12)$$

Figure 1.2-2 presents η_{PR} (or τ/T_{MAX}) plotted against $1/\Lambda_j$. (The reciprocal of Λ_j is used for convenience.)

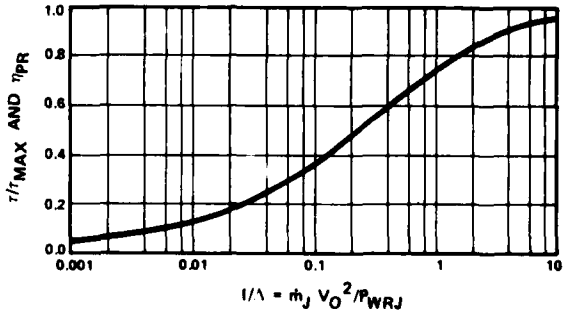

Figure 1.2-2. Effect of λ on Thrust Produced and Propulsive Efficiency.

1.2.3.2 Direct Coupling of Engines with Propulsive Devices

The power of the jet flow (which is related to propulsive force) must ultimately come from the engine. The simplest way of coupling an engine to a jet is to put a nozzle behind the engine, as in Figures 1.1-1 and 1.1-3, and then expand the flow to ambient pressure. This action forms the jet from the engine airflow ($\Lambda_j = \Lambda_e$ and $\dot{m}_E = \dot{m}_j$). It is of interest to investigate the aerothermodynamic behavior of this and other couplings with the aid of engine characteristics that partially represent current technology. Pertinent information from such an engine with direct coupling is given in Table 1.2-1.

TABLE 1.2-1

M_N	Λ_e	η_{TH}	$\frac{\tau}{\dot{m}_e V_o}$	η_{PR}	η_o*
0.8	10.5	0.48	3.7	0.35	0.17
0.8**	18.1	0.43	5.1	0.28	0.12
2	1.7	0.57	1.1	0.65	0.37
2**	3.1	0.50	1.7	0.54	0.27
3	0.57	0.57	0.5	0.81	0.46
3**	1.3	0.55	0.9	0.69	0.38

*η_o = overall efficiency = $\eta_{TH} \times \eta_{PR}$

**Afterburning to 3500°R

The values of Λ_e and η_e reflect the level of engine technology used in this example. As flight Mach number increases, Λ_e decreases and η_{TH} increases. The latter trend occurs because T_i/t_i rises [Equation (1.2.3)] and this causes T_{co}/t_i to increase also. The increase in η_{TH} is then expected from Equation (1.2.5). The value of $P_{WRE}/\dot{m}_e$ can and does increase also, [see Equation (1.2.4)] but V_o^2 increases much faster. Afterburning increases Λ_e at the expense of η_{TH}, as expected.

The relatively high values of Λ_e at 0.8 Mach number cause the associated values of η_{PR} to be low. The utilization of power for thrust is poor and the overall efficiency, η_o, is atrocious. Better propulsive efficiency could be obtained at this Mach number by reducing $P_{WRE}/\dot{m}_E$ and, hence, Λ_j. This is readily accomplished by lowering T_{ti} [see Equation (1.2.4)]. The resulting increase in T_{co}/T_{ti} may even increase η_{TH}. Overall efficiency would thus further improve. As previously emphasized, analysis similar to that discussed in Chapter 9 is ultimately necessary to make the proper decision.

It is worth noting that even the early concepts of jet engines (with their low pressure ratios, turbine inlet temperatures, and thermal efficiencies) still provided such high values of Λ_j to the jet that flight speeds greater than the capability of contemporary aircraft were necessary for tolerable propulsive efficiency. This situation was, for a while, a deterrent to the investment of money in jet engine technology.

The value of engine efficiency at supersonic Mach numbers exceeds that which can be obtained by any prime mover at sea level. At a Mach No. of 3.0, the overall efficiency at least approaches anything that can be offered at sea level. Unfortunately, the magnitude of $\tau/\dot{m}V_o$ is low while the drag is high, contrary to the demands of Equation (1.2.1).

Although the direct coupling just discussed is simple and contributes minimally to the size and weight of the propulsion system, it does not provide the necessarily high values of η_{PR} and large values of $\tau/\dot{m}\ V_o$ simultaneously. Part of this problem of achieving the desired thrust with high overall efficiency and light engines is avoided by using part of the engine power to drive a separate air-moving device such as a propeller or fan. This feature is discussed in the following section.

1.2.3.3 Coupling with a Secondary Jet

Systems using this coupling are commonly called turboprops or turbofans, see Figures 1.1-4 and 1.1-7. The idea is to divert a portion of the power developed by the engine to create another or secondary jet with a lightweight device.

1.2.3.3.1 Thermodynamic Behavior of Secondary Propulsion Device

The thermodynamic and propulsive characteristics of the secondary propulsive device are readily derived by the same method as that used in 1.2.2. The power ΔP_{WRE} is abstracted from the engine to increase the temperature (or pressure ratio) of the secondary airstream. A fan (or a propeller) is the instrument that adds most of this energy to the secondary flow. In addition, heat may be transferred to this stream by combustion as illustrated in Figure 1.1-9. Following the scheme devised in 1.2.2, it follows that

$$(t_e' - T_e') + (T_e' - T_f) + (T_f - T_i)$$

$$+ (T_i - t_i) = t_i \left[\frac{T_e'}{T_f} e^{\sigma_{DS}} - 1\right]$$

T_f = total temperature aft of a fan or propeller

T_e' = total temperature of the flow discharged from the secondary propulsive device. Combustion takes place in the device when $T_e' > T_f$.

σ_{DS} = entropy rise due to degradation of useful energy associated with the secondary device

The power per unit of mass flow in the secondary jet is

$$\frac{P_{WRSJ}}{\dot{m}_s} = JC_p \left[(T_f - T_i) + (T_e' - T_f) - t_i \left(\frac{T_e'}{T_f} e^{\sigma_{DS}} - 1\right)\right]$$

P_{WRSJ} = total power available for thrust in the secondary propulsive device

$\dot{m}_s$ = mass flow through secondary device

A not inconsiderable part of σ_{DS} is associated with $(T_f - T_i)$. Moreover, σ_{DS} increases with T_f at a fixed value of T_i. A positive maximum for $P_{WRSJ}/\dot{m}_s$ can thus be anticipated.

Observe that the power $\dot{m}_s JC_p (T_f - T_i)$ is derived from the engine and can be expressed by

$$\dot{m}_s JC_p (T_f - T_i) = \Delta P_{WRE} - \zeta_T \dot{m}_S$$

ΔP_{WRE} = power abstracted from the engine for the secondary propulsion device

ζ_T = losses in available energy per unit mass in the secondary device due to the transmission system including losses in the turbine driving the fan or propeller.

Hence

$$\frac{P_{WRSJ}}{\dot{m}_s} = \frac{\Delta P_{WRE}}{\dot{m}_s} - \zeta_T + JC_p \left[(T_e' - T_f) - t_i \left(\frac{T_e'}{T_f} e^{\sigma_{DS}} - 1\right)\right]$$

It is also convenient to write this equation as

$$\frac{P_{WRSJ}}{\dot{m}_s} = \frac{\Delta P_{WRE}}{\dot{m}_s} - \zeta_T - \zeta_F - \zeta_C + \frac{\Delta P_{WRSC}}{\dot{m}_S} \qquad (1.2.13)$$

ζ_F = the portion of energy input by the fan that is degraded in the secondary device.

$$\zeta_C = JC_p\, t_i \frac{T_e'}{T_f}(e^{\sigma_{DS}} - 1) - \zeta_F = \frac{\frac{T_e'}{T_f}(e^{\sigma_{DS}} - 1)\, V_o^2}{(\gamma - 1)\, M_o^2} - \zeta_F$$

$$\Delta P_{WRSC} = JC_p\, (T_e' - T_f)\left(1 - \frac{t_i}{T_f}\right) \dot{m}_S$$

Note that $\left(1 - \frac{t_i}{T_f}\right)$ is the ideal efficiency with which the additional thermal energy of combustion is converted into useful energy. The real efficiency must include the increases in entropy caused by energy degradation.

1.2.3.3.2 Propulsion Mechanics of Combined Primary and Secondary Thrust Devices

Equation (1.2.13) may be written as

$$\Lambda_S = \Delta\Lambda_E/B + \Delta\Lambda_{SC} - \frac{\zeta_T + \zeta_F + \zeta_C}{V_o^2}$$

$$\Lambda_S = \frac{P_{WRSJ}}{\dot{m}_S V_o^2}$$

$$\Delta\Lambda_E = \frac{\Delta P_{WRE}}{\dot{m}_E V_o^2} \qquad (1.2.14)$$

$$\Delta\Lambda_{SC} = \frac{\Delta P_{WRSC}}{\dot{m}_S V_o^2} = \frac{\left(\frac{T_e'}{T_f} - 1\right)\left(\frac{T_f}{t_i} - 1\right)}{(\gamma - 1)\, M_o^2}$$

$B = \frac{\dot{m}_S}{\dot{m}_e}$, commonly called the bypass ratio

M_o = flight Mach number

The effective thrust and propulsive efficiency of the secondary jet must include the drag of the secondary device [see Equation (1.2.1)].

$$\frac{\tau_s}{\dot{m}_s V_o} = \sqrt{2\Lambda_S + 1} - 1 - X_D C_{DS}$$

C_{DS} = coefficient to recognize added drag charged to the secondary device.

X_D = a factor equivalent to $\frac{1}{2}\frac{S}{A_o}$ in Equation (1.2.1)

$$\eta_{PRS} = \frac{1}{\Lambda_S}\left[\sqrt{2\Lambda_S + 1} - 1 - X_D C_{DS}\right]$$

The power available in the jet formed by the engine airflow is expressed as

$$\frac{P_{WREJ}}{\dot{m}_e V_o^2} = \frac{P_{WRE}}{\dot{m}_e V_o^2} - \frac{\Delta P_{WRE}}{\dot{m}_e V_o^2}$$

The thrust and efficiency of the primary jet are now given by

$$\frac{\tau_E}{\dot{m}_e V_o} = \sqrt{2\Lambda_E' + 1} - 1$$

$$\eta_{PRE} = \frac{1}{\Lambda_E'}\left[\sqrt{2\Lambda_E' + 1} - 1\right]$$

$$\Lambda_E' = \frac{P_{WREJ}}{\dot{m}_E V_o^2} = \Lambda_E - \Delta\Lambda_E \qquad (1.2.15)$$

The overall thrust is expressed by

$$\frac{\tau}{\dot{m}_e V_o} = B\left[\sqrt{2\Lambda_S + 1} - 1 - X_D C_{DS}\right] + \sqrt{2\Lambda_E' + 1} - 1$$

$$= B\left[\sqrt{2\left(\frac{\Delta\Lambda_E}{B} + \Delta\Lambda_{SC} - \frac{\zeta_T + \zeta_F + \zeta_C}{V_o^2}\right) + 1} - 1 - X_D C_{DS}\right] + \sqrt{2(\Lambda_E - \Delta\Lambda_E) + 1} - 1 \qquad (1.2.16)$$

Two important variables affecting the thrust are B and $\Delta\Lambda_E$. From the appearance of the equation, it is of interest to inquire if there are conditions that might make $\tau/(\dot{m}_E V_o)$ a maximum. To simplify the approach, make the substitution $B = \Delta\Lambda_E/\Delta\Lambda_{SX}$. Consider $\Delta\Lambda_{SX}$ and $\Delta\Lambda_E$ to be the independent variables and let Λ_E be constant. When this is done, it can be shown that $\tau/(\dot{m}_E V_o)$ is a maximum when the value of $\Delta\Lambda_S$ is such that

$$\frac{\sqrt{2\left(\Delta\Lambda_{SX} + \Delta\Lambda_{SC} - \frac{\zeta_T + \zeta_F + \zeta_C}{V_o^2}\right) + 1} - 1 - X_D C_{DS}}{\Delta\Lambda_{SX}} = \text{Maximum Value} \qquad (1.2.17)$$

The variable $\Delta\Lambda_{SX}$ is really $\Delta P_{WRE}/(\dot{m}_S V_o^2)$. It appears that its optimum value occurs when the ratio of the secondary thrust to $\Delta P_{WRE}/(\dot{m}_S V_o^2)$ itself is a maximum. The optimum secondary device thus seems to depend only on its own aerodynamic properties.

If $\Delta\Lambda_{SC}$ and ζ_C were zero, this optimum value of $\Delta\Lambda_{SX}$ would decrease with ζ_T, ζ_F, and $X_D C_{DS}$. In fact, $\Delta\Lambda_{SX}$ would be zero if these quantities were also zero. When $\Delta\Lambda_{SC}$ is large in comparison to the other variables of this equation, the optimum value of $\Delta\Lambda_{SX}$ is also governed by its influence on T_f/t_i, which determines the efficiency with which thermal energy is converted into mechanical energy. Refer to notes concerning Equations (1.2.13) and (1.2.14).

The overall propulsion efficiency of the secondary device is approximately given by

$$\eta_{PROS} = \frac{\tau_S/\dot{m}_S V_o}{\Delta\Lambda_{SX} + \Delta\Lambda_{SC}}$$

When $\Delta\Lambda_{SC}$ is zero, the condition for maximum thrust is tantamount to the condition for maximum propulsive efficiency of the secondary device. The adverse effect of $\Delta\Lambda_{SC}$ is reduced by reserving secondary combustion to supersonic flight velocities so that $\Delta\Lambda_{SC}$ is moderate.

Another interesting relationship can be found by letting $\Delta\Lambda_E = \Delta\Lambda_{SX} B$, differentiating the resulting equation for $\tau/\dot{m}_e V_o$ with respect to $\Delta\Lambda_{SX}$, and equating the result to zero. The following relation is provided.

$$\left[1 - \frac{\partial}{\partial(\Delta\Lambda_{SX})}\left(\frac{\zeta_T + \zeta_F + \zeta_C}{V_o^2}\right)\right]\sqrt{2(\Lambda_E - \Delta\Lambda_E) + 1} = \sqrt{2\left(\Delta\Lambda_{SX} + \Delta\Lambda_{SC} - \frac{\zeta_T + \zeta_F + \zeta_C}{V_o^2}\right) + 1}$$

By recalling the discussion leading to Equation (1.2.9), it appears that the second requirement for optimization of

η_{PR} or $(\tau/\dot{m}_E V_o)$ is met when

$$\left[1 - \frac{\partial}{\partial\Lambda_{SX}}\left(\frac{\zeta_T + \zeta_F + \zeta_C}{V_o^2}\right)\right]\left(\frac{V_{JE}}{V_o}\right)^2 = \left(\frac{V_{JS}}{V_o}\right)^2 \qquad (1.2.18)$$

V_{JE} = speed of jet of engine flow

V_{JS} = speed of jet of secondary flow

The energy in the secondary jet should equal that of the primary jet minus a factor that is proportional to the rate of change of losses with the ratio $\Delta P_{WRE}/(\dot{m}_S V_o^2)$. The magnitude of B is a

function of the relations expressed by Equations (1.2.17) and (1.2.18).

Although this exercise vastly oversimplifies the events involved, the trends that can be derived provide background for discussing why various propulsion systems are designed the way they are.

1.2.3.3.3 Engines for Low Flight Speeds

When an airplane is intended for cruising at 0.4 Mach No. or lower, values of Λ_E that exceed 40 can be encountered (see Table 1.2-1). A propulsive efficiency of about 20 percent is achieved by direct coupling, whereas efficiencies of at least 70 percent should be sought; thus, values of about 1.25 are needed for both Λ_S and Λ_E' (see Figure 1.2-2). Equations (1.2.14) and (1.2.15) suggest that almost the entire output of the engine should be offered to the secondary propulsive device. Adding thermal energy to the secondary system is too inefficient to be considered at this flight speed. (See Equations (1.2.13), (1.2.14), and the associated text.)

In this situation, the use of a propeller is a good solution. Figures 1.1-4 and 1.1-6 illustrate the engine concept and its installation on an airplane. Consider, for example, that the prime mover includes the main compression system, the turbine driving it, and the combustor. At the present time, the dense materials needed in the turbine, combustor, and supporting structures tend to concentrate much of the weight of the propulsion system in the engine. The weight of the secondary device consists of the propeller, the turbine driving it, and the gearbox and structure connecting them. These can be relatively light in comparison to the extra thrust they produce. At a flight Mach number of approximately 0.4, propulsion efficiencies in the neighborhood of 80 percent and higher are realized by a properly designed propeller. If the combined efficiency of the turbine and gearbox are slightly under 90 percent, the net propulsive efficiency can be over 70 percent (or about 70 percent of the maximum theoretical thrust).

In order to get a propulsive efficiency of 70 percent with direct coupling, the engine alone would need the value of Λ to be 1.25, and its mass flow would have to be increased by a factor of 30. The resulting weight and installation drag would be ridiculous. By comparison, the added weight and drag involved in the propeller, gearbox, and turbine are clearly much more attractive.

The secondary flow device with the propeller would certainly be a good investment in this case. The actual selection of the propeller and the power delivered to it depends on the factors suggested by Equations (1.2.17) and (1.2.18). The energy imparted to each unit of mass comprising the secondary flow should be about what is necessary to compensate for the losses and installation drag of the propeller and the transmission losses. The mechanical energy of the engine jet should be higher than that in the secondary jet because of these losses. In the final analysis, however, the design of the propeller and the engine installation should be decided only after thorough analysis of the airplane and propulsion system with respect to the expected mission(s). This statement refers again to the important concepts presented in Chapter 9. The resulting overall propulsive efficiency at cruise could be higher or lower than 0.7.

1.2.3.3.4 Engines for High Subsonic Speeds

Until recently there has been no evidence that useable propeller efficiency could be achieved at the high subsonic Mach numbers where airplane drag coefficients are still low. Some encouraging results with new propeller designs have been observed recently, but the combined effects of propulsion efficiency and installation drag still need to be evaluated. It follows from the discussion of Equation (1.2.17) that augmented installation losses increase the optimum value of $\Delta\Lambda_{SX}$. This would lower the propulsive efficiency of both the propeller and the jet from the primary flow.

The propulsive efficiency in this regime has been enhanced by turbofan engines. Figures 1.1-7 and 1.1-8 show details of the configuration and the installation of propulsion systems designed for this kind of flight.

If a propulsion efficiency of 0.7 for the secondary device is tentatively pursued, the value of Λ_S (in the secondary system) would be about 1.25 and the magnitude of Λ_E' would be higher. In this case, (referring to Table I) $B = (10.5\text{-}1.25)/1.25 = 7.4$. In general, energy degradations and installation drag would reduce this B value. Note that adding heat in the secondary stream would also be an inefficient use of energy at this Mach number. Whether a 70 percent propulsive efficiency is reasonable or not depends upon the principles enunciated by Equations (1.2.17) and (1.2.18). High transmission losses, and large installation drag require relatively high values of $\Delta\Lambda_{SX}$, as noted by the discussion associated with Equation (1.2.17). The value of Λ_S would, of course, then be too high to achieve a value of 0.7 for η_{PRS}. Maximum overall efficiency would require the propulsive efficiency of the primary jet to be even lower [see Equation (1.2.18)].

An important point to note is that lowering the installation drag and the losses is not only directly beneficial, but it permits the system to be rematched for lower jet speeds and higher bypass ratios. Additional benefits may thus be accrued. Double benefits of this type are often encountered. Achieving them is an important objective in detailed airplane/propulsion system analysis and research.

1.2.3.3.5 Acceleration at Transonic Speeds

The transonic flight speeds that embrace the high drag regions of Figure 1.2-1 are no place to linger. The goal of fixed wing supersonic aircraft is to accelerate from subsonic speed to supersonic speed as quickly as a reasonable propulsion system will allow. Propulsion system inefficiencies can be tolerated for a brief period if the added thrust sufficiently reduces the time and fuel spent in the high drag regime.

1.2.3.3.6 Supersonic Flight Speeds

As shown previously, high efficiencies are available from a simple engine at supersonic flight speeds. The thrust per unit of mass flow is low, however. To make matters worse, the air swallowing capacity is reduced and the airplane drag is not low. These phenomena are discussed further in Chapters 9, 13, and 26. All of these events combine to enlarge the size and weight of the engines required for supersonic propulsion. High turbine inlet temperatures, lightweight engine materials, high component efficiencies with reliable compact engines having excellent structural efficiency are sought avidly.

The use of bypass propulsion systems is advantageous because they offer reductions in the thrust-to-weight ratio of propulsion systems. That is, a significant improvement in thrust-minus-drag can be achieved with a relatively small addition of weight or volume: $\tau_e/\dot{m}\ V_o$ improves even though $\tau/\dot{m}\ V_o$ may be slightly reduced. Combustion in the secondary flow is valuable because the ideal thermal efficiency is fundamentally high at elevated Mach numbers. The magnitude of T_i/t_i is large by virtue of the relations given in Equation (1.2.3) and the ideal value of T_f/t_i should be higher than the value required for subsonic flight. Note that Λ_s is about maximum when $T_f/t_i = \sqrt{T_e'/t_i}$. Compare with 1.2.2.4.2.

One more point to note is that often there are good reasons for requiring an airplane to cruise at subsonic speeds and still have the ability to fly at high Mach numbers for short periods of time. Bypass propulsion systems with provisions for afterburning provide another degree of design freedom for attacking this problem. Subsonic speeds would be negotiated without afterburning in either flow path; afterburning would then be used for transonic acceleration and supersonic flight.

Both aircraft and engines represent a compromise. Engineering has the responsibility of minimizing the penalties associated with the compromises. Exhaustive studies of various combinations of aircraft and engine designs must always be made to define a competitive airplane. Even so, these studies rarely completely solve or anticipate all of the important options that must be selected or the problems that must be solved. Some of the resulting activities associated with engine design and development are described in the last section of this chapter.

1.3 OFF-DESIGN ANALYSIS AND RELATED PROBLEMS

The effort spent in the study of off-design performance and in finding solutions to the problems uncovered, consumes a large percentage of the total aerothermodynamic engineering devoted to the design and development of an engine. Several volumes would be required to treat this subject adequately. The present publication is limited to familiarizing the reader with the principal problems and suggesting how he might estimate the magnitude of some aerothermodynamic states under defined off-design conditions. Chapters 7 and 8 provide tools that are valuable for making approximate numerical estimates of these states. Studying off-design performance with use of the methods presented in Chapter 8 will permit the reader to appreciate the variations in flow that engine components must tolerate. This is a necessary prerequisite for approaching any design or development activity. Chapters 13 and 14 present other features of off-design performance and follow through with ideas for varying the shape of some critical engine parts while the engine is running in order to cope with some of the problems encountered.

In actual practice, the configuration of a number of engine components can be changed almost continuously during engine operation. The conception, design, and development of the complete engine requires the use of analytical tools which can quickly translate conceived changes in component configuration into predicted changes in performance of the real or proposed component. Additional tools are then required to compute the resulting engine performance for prescribed operating conditions. Both steady-state and transient analyses are necessary.

1.3.1 Steady-State Analysis

An example of a technique employed by industry and others for using high speed computers to compute the performance of engines is described below. Methods such as this are used extensively to examine the value of a presumed advance in aerothermodynamics. However, the procedures are useful only for evaluation purposes; they do not originate or contribute new ideas by themselves.

New ideas, on the other hand, are developed from an engineer's mental picture of the interaction of components and subcomponents of an engine. This understanding comes primarily from experience, but it can be aided by primitive concepts based on assumptions that are tolerably reasonable. The later part of this section is devoted to developing some of this background. Besides providing a useful understanding of engine operation, this section supports and enlarges the design objectives of the components discussed in subsequent chapters.

1.3.1.1 Typical Input Data for Steady-State Analysis

Large high-speed digital computers are employed for all performance analysis. Data are stored in the computers together with appropriate interpolation routines either in the form of tables or as coefficients of polynomials. Data necessary to determine the following information are stored.

- Thermodynamic and aerodynamic properties of dry air as a function of temperature
- Similar properties for water vapor in order to account for humidity or the effects of injecting water into the engine for power augmentation
- Similar properties for the products of combustion of the fuels to be used
- The aerothermodynamic performance of all the engine components as functions of their principal controlling independent variables. These components are discussed in appropriate succeeding chapters. Examples of compressor and turbine performance maps are illustrated in Figures 1.3-1 and 1.3-2, respectively. The effect of changing the orientation of the components on the shape of the maps is also stored. The shape of the map can be

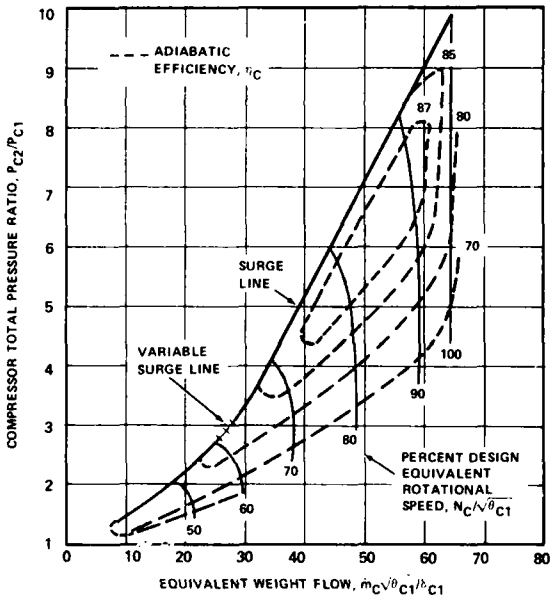

θ_{C1} = INLET TOTAL TEMP./STANDARD SEA-LEVEL TEMP
δ_{C1} = INLET TOTAL PRESS./STANDARD SEA-LEVEL PRESS.
P_{C1} = INLET TOTAL PRESSURE
P_{C2} = OUTLET TOTAL PRESSURE
N_C = SPEED OF ROTATION
$\dot{m}_C$ = MASS FLOW
SUBSCRIPT C REFERS VALUES TO COMPRESSOR

WHEN $\dot{m}_C\sqrt{\theta_{C1}}/\delta_{C1}$ AND $N_C/\sqrt{\theta_{C1}}$ ARE GIVEN, BOTH PRESSURE RATIO AND EFFICIENCY CAN BE ESTIMATED BY AN INTERPOLATION ROUTINE. THE CORRESPONDING CHANGE IN TEMPERATURE AND ENTHALPY CAN BE FOUND FROM THE DEFINITIONS IN CHAPTER 6.

Figure 1.3-1. Example of Compressor Map.

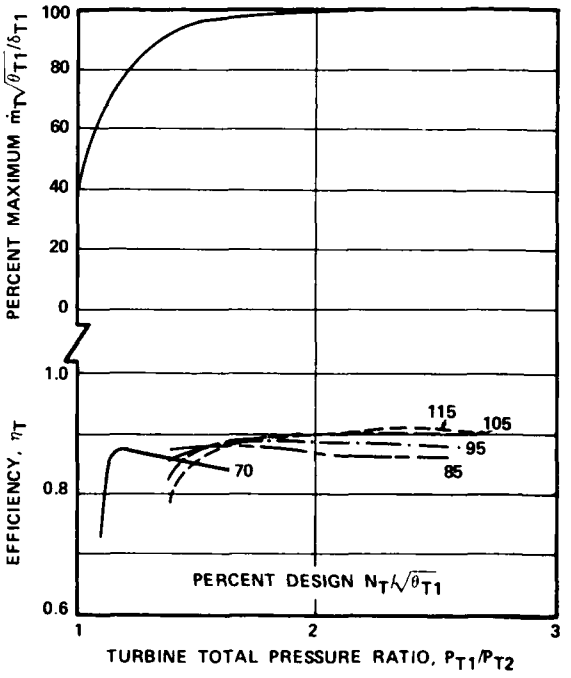

WHEN P_{T1}/P_{T2} AND $N_T/\sqrt{\theta_{T1}}$, ARE GIVEN, BOTH $\dot{m}_T\sqrt{\theta_{T1}}/\delta_{T1}$ AND η_T CAN BE ESTIMATED BY INTERPOLATION. THE CORRESPONDING CHANGES IN TEMPERATURE AND ENTHALPY CAN BE FOUND BY THE DEFINITIONS IN CHAPTER 6.

Figure 1.3-2. Example of Turbine Map.

deliberately changed by variable geometry (see 1.3.2) or it can vary as a function of Reynolds number effect or by nonuniform inlet flow. Figure 1.3-2 happens to show $(\dot{m}_T\sqrt{\theta_{T1}}/\delta_{T1})$ to be independent of $(N/\sqrt{\theta_{T1}})$. Some turbines experience small decreases in $(\dot{m}_T\sqrt{\theta_{T1}}/\zeta_{T1})$ as $(N\sqrt{\theta_{T1}})$ increases. The general shape of the curve for each speed is similar to Figure 1.3-2, however.

- Power lost by friction and absorbed by auxiliary units such as pumps and generators.
- Power lost because part of the air compressed by the compressors does not go through the turbines, but is used instead for pneumatic power, cabin air conditioning, and cooling turbines and other hot metal parts.
- The effective loss of power due to leakage of compressed air through flanges and seals that separate cavities having different pressure levels within the engine.

Some programs store additional data to account for such things as changes in component performance due to blade and vane heights and clearances, and heat loss.

1.3.1.2 Typical Problem

A typical problem is to determine all pertinent performance data when the inlet pressure and temperature, flight speed, component performance maps, and fuel flow are given. If it is possible to vary the geometrical shape of the components, the data necessary to account for performance changes associated with each geometrical shape desired are also given. Strict accounting of the gas flow is required. The difference between the gas flow leaving one part of an engine and that entering any part downstream must either equal the scheduled leakage or equal the addition of fuel or water to the mass flow. Two mechanically connected rotating components must rotate at a constant speed ratio. The power delivered by the turbine must equal that required by the compressor, fan, or propeller that it is driving plus the power necessary to drive attached accessories and overcome friction. Finally, the net change in pressure through the engine must eventually be zero. The computer is asked to set up and solve several non-linear simultaneous equations.

1.3.1.3 A Sample Technique

A simplified illustration is given to illustrate a procedure, which is necessarily iterative. Assume that there is one compressor which is driven by a turbine with no leakage or other loss of air. Assume further that the flow enters the compressor through an inlet and is eventually returned to the atmosphere through a nozzle at the rear of the engine. A computing procedure for the problem posed in the previous paragraph would be as follows:

(a) Use the given flight speed to calculate the total pressure and temperature ahead of the engine inlet. This provides the values of P_i and T_i.

(b) Assume the mass flow, $\dot{m}_1$, of air entering the engine.

(c) "Look up" the inlet performance characteristics and calculate the total pressure loss. The total pressure and temperature (P_{c1} and T_{c1} respectively) are thus known.

(d) Assume a compressor and turbine speed (N).

(e) Use (b), (c), and (d) to "look up" compressor performance (e.g., use Figure 1.3-1 and interpolate) and thus determine the total pressure (P_{co}) and total temperature (T_{co}) it would develop. Also, calculate the power, P_{WRC}, required to drive the compressor, the accessories, and to overcome friction (gears, bearings, and seals). It is appropriate to note here that the compressor power for real gasses is approximated with the aid of the thermodynamic tables. However, the result is approximated by the equation.

$$P_{WRC} = \frac{J\bar{C}_p\, T_{c1}\left[\left(\frac{P_{co}}{P_{c1}}\right)^{\frac{\bar{\gamma}-1}{\bar{\gamma}}} - 1\right]\dot{m}_1}{\eta_{cp}}$$

$\bar{C}_p$ = average specific heat during the compression process

$\bar{\gamma}$ = average ratio of specific heats during the compression process

η_{cp} = compressor efficiency

(f) Use (b) and (e) together with given fuel flow and interpolated combustor characteristics to calculate the combustor discharge temperature (T_{t1}) and total gas flow $\dot{m}_2$ at the combustor discharge.

(g) Use (b), (e) and (f) together with interpolated combustor characteristics to calculate combustor discharge pressure (P_{t1}).

(h) Assume turbine pressure ratio $[(P/P)_T \leq (P_{T1}/P_e)]$.

(i) "Look up" turbine performance (e.g., Figure 1.3-2) and interpolate to determine the total temperature ratio, mass flow $\dot{m}_3$ passing through it, and the power, P_{WRT}, delivered by the turbine. Turbine power is estimated with the aid of the thermodynamic tables. Similar to compressors, the result is approximated by

$$P_{WRT} = J\bar{C}_p T_{T1} \left[1-(P/P)_T^{\frac{\bar{\gamma}-1}{\bar{\gamma}}}\right]\eta_T \dot{m}_3$$

η_T = turbine efficiency

$\bar{C}_p$ and $\bar{\gamma}$ now refer to the average during the expansion process in the turbine. The value of T_{to} is also obtained.

(j) Use (g), (h), and (i), plus ambient pressure together with an interpolated nozzle performance, to calculate flow, $\dot{m}_4$, through the nozzle.

(k) Unless the first estimates are extremely lucky, the power calculated in (i) will not equal that of (e). Subtract the power of (i) from that of (e). Call the result ΔP_{ro}.

(l) Similarly, the mass flows, $\dot{m}_2$ and $\dot{m}_3$, will not equal either each other or $\dot{m}_4$. Call the errors $\Delta\dot{m}_{ao}$ and $\Delta\dot{m}_{bo}$ respectively.

(m) These errors are the result of bad estimates for $\dot{m}_1$, N, and $(P/P)_T$. Change $\dot{m}_1$ to $\dot{m}_1+\Delta\dot{m}_1$. Repeat Steps (b) through (l). Identify the new errors by ΔP_{r1}, Δm_{a1}, and $\Delta\dot{m}_{b1}$. Make the approximation:

$$\frac{\partial\Delta P_r}{\partial\dot{m}_1} = \frac{\Delta P_{r1} - \Delta P_{ro}}{\Delta\dot{m}_1}$$

Approximations for $\frac{\partial\Delta\dot{m}_a}{\partial\dot{m}_1}$ and $\frac{\partial\Delta\dot{m}_b}{\partial\dot{m}_1}$ are also made.

(n) Repeat Steps (b) through (m) twice, but instead of changing $\dot{m}_1$, successively change N to $N_1 + \Delta N$ and then $(P/P)_T$ to $(P/P)_T + \Delta(P/P_T)$. The terms,

$$\frac{\partial\Delta P_R}{\partial N}, \frac{\partial\Delta\dot{m}_a}{\partial N}, \frac{\partial\Delta\dot{m}_b}{\partial N}, \frac{\partial\Delta P_R}{\partial(P/P)_T}, \frac{\partial\Delta\dot{m}_a}{\partial(P/P)_T}, \frac{\partial\Delta\dot{m}_b}{\partial(P/P)_T}$$

are thus approximated.

(o) A better estimate for $\dot{m}_1$, N, and $(P/P)_T$ may now be found by an extension of Newton's method. This procedure consists of finding $\dot{m}_W$, N_W, and $(P/P)_{TW}$ from three equations. One equation is:

$$\Delta P_r = \frac{\partial P_r}{\partial\dot{m}_1}(\dot{m}_1 - m_W) + \frac{\partial P_r}{\partial N}(N_1 - N_W) + \frac{\partial P_r}{\partial(P/P)_T}\left[(P/P)_T - (P/P)_{TW}\right]$$

The others are similar and involve $\Delta\dot{m}_a$ and $\Delta\dot{m}_b$ instead of ΔP_R.

(p) Set $\dot{m}_1 = \dot{m}_W$, $N = N_W$, $(P/P)_T = (P/P)_{TW}$ and repeat the process from (b) until the errors involving $\dot{m}_1$, N, and $(P/P)_T$ fall within some prescribed limit.

It must be noted that mathematicians would regard this procedure for computing $\dot{m}_1$, N, and $(P/P)_T$ as risky because there are many theoretical ways in which convergence to a true solution will fail. For this reason, more elaborate methods of solution have been devised at times. The technique outlined above, however, does work well enough in engine analysis--particularly when small deviations from known solutions are sought. The main reason for outlining the above procedure is to make the reader aware of the elaborate efforts that have been devised to assure the necessary accuracy and completeness required by the whole aviation industry.

1.3.1.4 Typical Information Derived from Analysis

With use of the procedure outlined above, the flow rate, pressure, and temperature at any point in the engine can be defined. The calculation of overall engine performance is routine. In addition, steady-state pressure forces on the stationary and rotating parts of real or tentative designs can be determined. Data for estimating heat transfer coefficients at any internal surface of the engine can also be supplied. This knowledge permits the steady-state temperature of all engine parts to be assessed.

The approximate thermal growth of any part can then be computed. The resulting thermal stresses due to unequal temperatures in different regions of a solid part may then be estimated. Of equal importance, the changes in the clearances between rotating and stationary parts can be approximated. The possibilities of dangerous rubbing or of excessive gas leakage (and performance deterioration) can be anticipated and controlled. These are a few of the pertinent data than can be made available to a wide variety of specialists.

Of equal importance, is the inverse use of performance analysis. During engine development, overall performance speeds and several critical pressures and temperatures are measured. If these are not reasonably in accord with the values anticipated, something is wrong with either the performance assumptions, one or more parts, or the assembly of the engine itself. Engine data over a range of speeds permits an analyst to quickly review the assumptions and vary them until he can approximate the measured engine data over the same speed range. The identification of the assumptions that had to be changed provides a valuable tool for resolving the offending problems. The division of flow between a core engine and the bypass device is a particularly sensitive area that can be thus revealed.

More complicated engines require the same basic analytical procedures, except that more variables and equations must be used. Although the procedure appears to be tedious, the operating state of a very complicated engine can be found in a matter of seconds.

1.3.1.5 Simplified Appraisals of Steady State Operation

1.3.1.5.1 Compressor Map and Equilibrium Operating Line

An important concept for acquiring a good appreciation for off-design analysis is the equilibrium operating line, as displayed on the compressor map shown in Figure 1.3-3. The map should reflect the airplane operating regime since flow, pressure ratio, and efficiency are affected by Reynolds number and inlet flow distortions.

A quick glance will show the designer the proximity of the surge line to the equilibrium line. The relative position of these two lines is a matter of major concern.

Some problems associated with the surge line are discussed in Chapters 9 and 13. It is important to note that operation at or to the left of the surge line can invite engine failure unless the overall pressure ratio is very low. Even under the best of conditions, the surge line can be multi-valued in the neighborhood of the region denoted by "variable surge line". The shape and

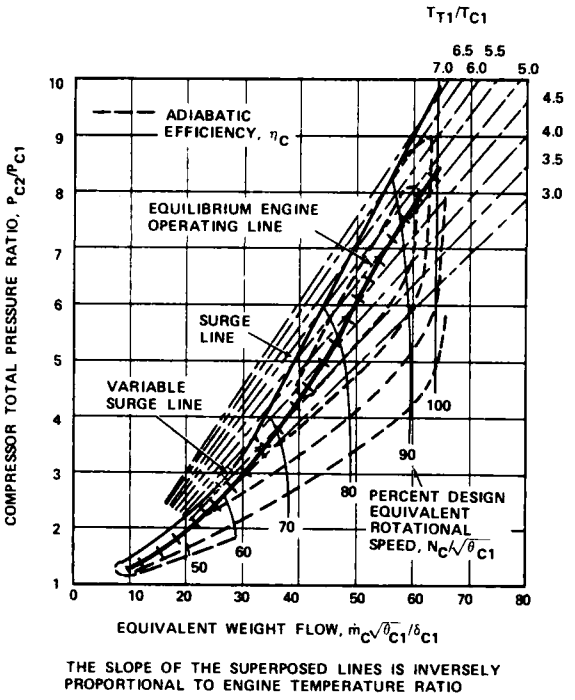

Figure 1.3-3. Typical Compressor Map and Its Engine Operating Line.

position of surge lines in this domain are often different, even in compressors of the same design. The differences may be attributed to many factors, including the necessary tolerances in manufacturing and assembly. As previously suggested, such events as operation at low flight Reynolds numbers, or flying under conditions that cause significant portions of the inlet flow to have nonuniform total pressures or temperatures (categorized as flow distortions) always cause the surge line to move to the right and down. Military aircraft are expected to fly through hot turbulent wakes caused by gun fire, rocket fire, and other aircraft. These transients not only produce step changes in the operating line, but they further depress the surge line. Extra surge margin is thus required by compressors on some military aircraft engines. The relative positions of the surge line and the equilibrium operating line thus plainly exhibit possible problems associated with surge. The line shown in Figure 1.3-3 indicates that surge problems would probably afflict some production versions of this compressor at rotative speeds in the vicinity of 60-percent design equivalent speed.

1.3.1.5.2 Locus of Lines for Constant Ratio of Turbine Inlet to Compressor Inlet Temperatures

When a compressor is directly coupled to the turbine immediately downstream of the combustor, lines indicating a constant ratio of turbine inlet temperature to compressor inlet temperature can

be approximated. These lines are shown in Figure 1.3-3 also. They represent the identity:

$$\frac{\dot{m}_C\sqrt{\theta_{C1}}}{\delta_{C1}} = \left[\left(\frac{\dot{m}_T\sqrt{\theta_{T1}}}{\delta_{T1}}\right)\left(\frac{\dot{m}_C}{\dot{m}_T}\right)\left(\frac{P_{T1}}{P_{C2}}\right)\right]\left(\frac{P_{C2}}{P_{C1}}\right)\sqrt{\frac{T_{C1}}{T_{T1}}} \qquad (1.3.3)$$

It is reasonable to assume that $\dot{m}_C/\dot{m}_T$ is a constant that is nearly unity. The same thing may be said about P_{T1}/P_{C2}. An argument will be presented later to show that $(\dot{m}_T\sqrt{\theta_{T1}}/\delta_{T1})$ can be practically constant over a wide range of operating conditions. It is then possible to plot P_{C2}/P_{C1} against $\dot{m}_C\sqrt{\theta_{C1}}/\delta_{C1})$ with T_{T1}/T_{C1} as the parameter. The slope of the resulting lines is proportional to $\sqrt{T_{T1}/T_{C1}}$. Typical lines are shown in Figure 1.3-3 for an arbitrary value of the bracketed quantity in Equation (1.3.3).

1.3.1.5.3 Approximate Correlation of Work of High-Pressure Compressor and Turbine (Fixed Geometry)

An interesting property of many operating lines can be demonstrated by noting compressor performance at the intersection of the constant $N/\sqrt{\theta_{C1}}$ curves with the constant T_{T1}/T_{C1} lines. Let ΔT_C = temperature rise in the compressor at any operating point. Values of $\Delta T_C/N^2$ (a temperature rise coefficient) can be calculated for these points and then plotted against T_{T1}/T_{C1}, with $N/\sqrt{\theta_{C1}}$ as a parameter. This plot is shown in Figure 1.3-4. The equilibrium operating line for this coordinate system can be superposed as shown.

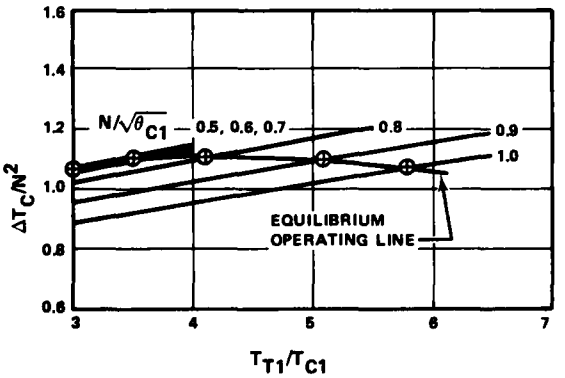

Figure 1.3-4. Variation of Compressor Temperature Rise Coefficient with Engine Temperature Ratio.

Note that as a first approximation, $\Delta T_C/N^2$ can be assumed to be approximately constant along the operating line of a high-pressure compressor such as those indicated in Figures 1.1-7, 1.1-9 and 1.1-10. The work demanded of a high-pressure turbine is then almost proportional to the square of its rotating speed. This trend is true for many gas turbine engines when the compressor and turbine geometries are fixed. For the purpose of visualizing trends, it may be assumed that:

$$\frac{\Delta H_{HPC}}{N^2} = \frac{\Delta H_{HPT}}{N^2} = \text{constant} \qquad (1.3.4)$$

HPC refers to high-pressure compressor
HPT refers to high-pressure turbine
ΔH = enthalpy change in component

1.3.1.5.4 Approximate Correlation of Mass Flow Through High-Pressure Turbines

A detailed examination will now be made of the variation of turbine mass flow, $\dot{m}_T\sqrt{\theta_{T1}}/\delta_{T1}$, with the total pressure ratio across the turbines and the exhaust nozzle. Observe that the quantity $(\dot{m}\sqrt{\theta}/\delta)$ is really proportional to a dimensionless variable and a flow area. This is shown by the one-dimensional equation (see Chapter 2).

$$\frac{\dot{m}\sqrt{\theta}}{\delta} = \frac{P_{SL}}{\sqrt{T_{SL}}}\sqrt{\frac{\gamma}{R}}\,A\,\frac{M}{\left[1+\frac{\gamma-1}{2}M^2\right]^{\frac{1}{2}\frac{\gamma+1}{\gamma-1}}} \qquad (1.3.5)$$

Note also that

$$\frac{\dot{m}\sqrt{\theta}}{\delta A} = \frac{P_{SL}}{\sqrt{T_{SL}}}\sqrt{\frac{\gamma}{R}}\left(\frac{2}{\gamma+1}\right)^{\frac{1}{2}\frac{\gamma+1}{\gamma-1}}\frac{A^*}{A}$$

and $$\frac{P}{p} = \left(1+\frac{\gamma-1}{2}M^2\right)^{\frac{\gamma}{\gamma-1}}$$

M = Mach number where passage flow area is A
P_{SL} = standard sea-level pressure
T_{SL} = standard sea-level temperature
A = area of flow passage
A* = area of a flow passage where M = 1.0
P/p = total-to-static pressure ratio

When a pressure ratio is applied across any flow device, a stream of fluid is set into motion. As the pressure ratio is increased, $(\dot{m}\sqrt{\theta}/\delta)$ increases at the inlet until the average Mach number is unity at the minimum flow area of the device. The overall pressure ratio at this condition is called the critical pressure ratio, and the corresponding inlet value of $\dot{m}\sqrt{\theta}/\delta$ is the maximum that the device can handle. Further increases in pressure ratio may increase the Mach number at points further downstream of the minimum area, but the inlet value of $\dot{m}\sqrt{\theta}/\delta$ is unaffected. This trend is exhibited in Figure 1.3-5, where the critical pressure ratio is noted.

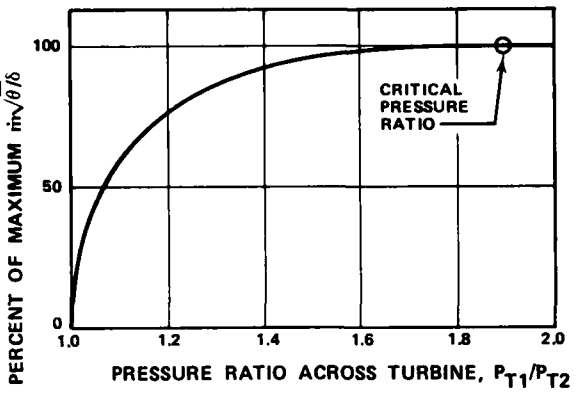

Figure 1.3-5. Typical Variation of $\dot{m}\sqrt{\theta}/\delta$ of a Nozzle with Pressure Ratio.

The variation of mass flows through turbines and nozzles follows the same trend. (Total-to-total pressure ratios are usually used for turbines and total-to-static ratios for nozzles.) The critical pressure ratio, however, is not a unique value for all turbines. That of Figure 1.3-2, for example, is about 2.3.

Suppose that a second unit having the flow characteristics of Figure 1.3-6 is placed downstream of the turbine having the performance maps of Figure 1.3-2. The value of $\dot{m}_T\sqrt{\theta_{T2}}/\delta_{T2}$ of Figure 1.3-6 is related to $\dot{m}_T\sqrt{\theta_{T1}}/\delta_{T1}$ of Figure 1.3-2 by the equation:

$$\frac{\dot{m}_T\sqrt{\theta_{T2}}}{\delta_{T2}} = \frac{\dot{m}_T\sqrt{\theta_{T1}}}{\delta_{T1}} \frac{P_{T1}}{P_{T2}} \sqrt{\frac{T_{T2}}{T_{T1}}}$$

If a value of P_{T1}/P_{T2} is assumed, $\dot{m}_T\sqrt{\theta_{T1}}/\delta_{T1}$ is determined from Figure 1.3-2. The magnitude of T_{T2}/T_{T1} is obtained from the efficiency curves and the definition of efficiency (Refer to Chapter 5). Inasmuch as $\sqrt{T_2/T_1}$ is a weak function of efficiency, no great truth is violated if $\sqrt{T_2/T_1}$ is assumed to be a function of P_{T1}/P_{T2} only, if the turbine equivalent speeds in Figure 1.3-2 are 85 percent of the design value or higher.

With the aid of this assumption, $\dot{m}_T\sqrt{\theta_{T2}}/\delta_{T2}$ of Figure 1.3-6 can be calculated from the assumed value of P_{T1}/P_{T2}. The pressure ratio across the second unit, up to the critical pressure ratio, is uniquely determined by Figure 1.3-6. The product of this pressure ratio with P_{T1}/P_{T2} is the overall pressure ratio across both units. Figure 1.3-7 illustrates the result.

The equivalent mass flow of this figure is that of Figure 1.3-2. Notice that this procedure can be extended to include any additional downstream units. It can thus be shown the value of $\dot{m}\sqrt{\theta_{T1}}/\delta_{T1}$ maintains its nearly maximum value down to low fractions of the design overall pressure ratio of high pressure ratio engines. The corresponding pressure across the first turbine is shown in Figure 1.3-8.

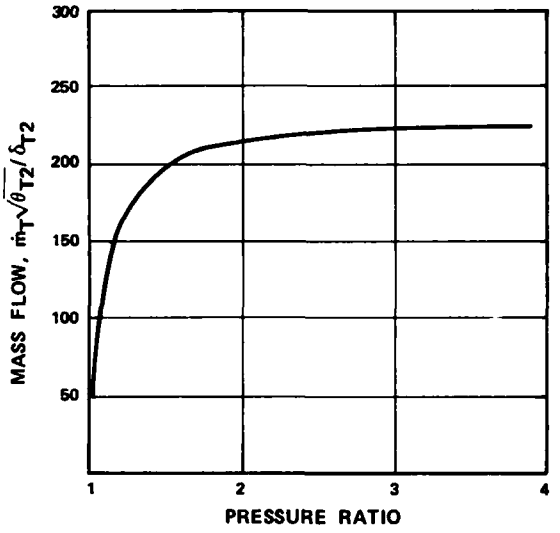

Figure 1.3-6. Relationship Between Pressure Ratio of Second Unit and Mass Flow Through It.

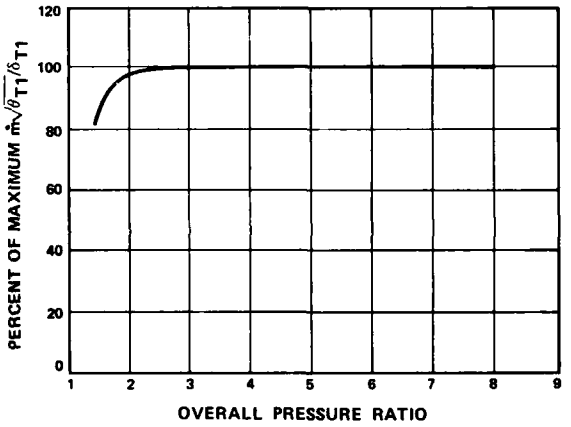

Figure 1.3-7. Variation of Mass Flow Through First Turbine with Overall Pressure Ratio.

1.3.1.5.5 Approximate Pressure Ratio Across High-Pressure Turbine

The assumption that $(\dot{m}_T\sqrt{\theta_{T1}}/\delta_{T1})$, in Equation (1.3.3), is constant over a wide range of operating conditions is justified in Figure 1.3-7. Meanwhile, Figure 1.3-8 shows a second approximation for simplifying the understanding of off-design operation of an engine with fixed geometry--the pressure ratio across the high-pressure turbine of such an engine may be assumed approximately constant over a wide range of operating conditions along an engine operating line.

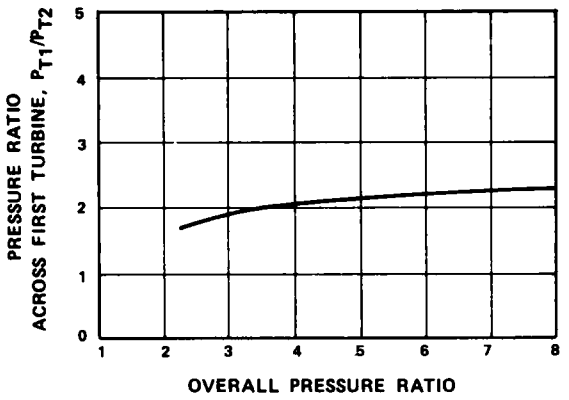

Figure 1.3-8. Variation of Pressure Ratio Across First Turbine with Overall Pressure Ratio.

1.3.1.5.6 Approximate Energy Rise Across High-Pressure Compressor

It can be shown that if Equation (1.3.4) is valid, and if the turbine pressure ratio is constant, then the turbine operating point is unchanged and $N/\sqrt{\theta_T}$ is constant. This deduction is approximately true for most high pressure components of fixed geometry engines. Observe that $\Delta H_{HPC}/\theta_{T1}$ is then also about fixed, according to Equation (1.3.4). At a given value of turbine inlet temperature, one may consider that the specific energy added to the air by the high-pressure compressor is constant along the operating line over the range of compressor inlet temperatures required for cruise and high speed flight.

1.3.1.5.7 Hierarchy of Pressure Ratios

Recall the history of flow through an engine. After the gas has been compressed and heated, it is expanded through one or more turbines and a nozzle. The first turbine after the combustor has the first mortgage on the pressure ratio. Figure 1.3-8, together with 1.3-3 shows that this turbine receives an almost constant pressure ratio over a wide range of combustor discharge temperatures. Its speed is about proportional to the square root of this temperature. The nozzle, which is last in line, has a smaller claim; it must immediately respond to changes in combustor discharge temperatures. Intermediate turbines have only fairly secure claims. They can however, maintain their pressure ratios as combustor discharge temperatures are diminished over a short range from their design value. They must then react to temperature changes. When the combustor discharge temperature is very low, even the speed of the high-pressure turbine finally falls. Because of this hierarchy in pressure ratio, the off-design behavior of turboprop and turbofan engines depends upon the sequence in which the rotating components are coupled. Two turboprop examples will be touched upon here. Other examples can be readily imagined by the reader.

In one turboprop version, the turbine driving the compressor is directly downstream of the combustor. The turbine driving the propeller is further downstream, and has a lower priority on pressure ratio. The speed of the compressor and its turbine with this arrangement is approximately proportional to the square root of the combustor discharge temperature in the normal operating range. A reduction in fuel flow reduces the power in two ways:

- o A moderate reduction in temperature reduces power directly [Equation (1.2.4)]
- o The consequent reduction in turbine and compressor speed reduces both the mass flow of air and the pressure ratio. This change in flow also lowers the power. The reduction in pressure ratio will contribute to a further lowering of power when the pressure ratio is below that for optimum power, (see 1.2.2.4.2). Because the drop in compressor speed reduces the flow without large increases in entropy, the compressor might be called an isentropic throttle.

Suppose that a change in design now enables a propeller to be driven by the turbine immediately downstream of the combustor. The pressure ratio across the turbine driving the compressor is no longer about constant since it no longer has a priority. This loss in turbine pressure ratio causes the compressor speed, pressure ratio, and mass flow to decrease more rapidly with combustor outlet temperature than the previous arrangement. The isentropic throttling action of the compressor is more effective, and the power output is far more responsive to small changes in turbine inlet temperature. Such an arrangement may yield better part load specific fuel consumption. The temperature ratio lines of Figure 1.3-3 are still valid however, and surge problems at part load are aggravated.

Note that the turboprop engine shown in Figure 1.1-4 has only one shaft for the compressor and turbines. This is a common arrangement. The controls are relatively simple and the propeller can serve as a dive brake by feeding power back into the compressor at low turbine inlet temperatures.

Rearranging the coupling between compressors and turbines can offer a degree of design freedom which may be useful for various applications. This opportunity is always worth an inquiry.

1.3.2 Variable Geometry

1.3.2.1 Variable Compressor Stators

Even more degrees of freedom are offered by "variable geometry" devices. As noted previously, Chapters 13 and 14 describe some variable-geometry devices associated with engine inlets and jet nozzles.

Many engine compressors are designed with variable stators. By rotating the stators about their nominal setting, the compressor map can be noticeably changed. This technique is used to evade surge problems at low values of $N/\sqrt{\theta}$, without significantly impairing efficiency at higher speeds. Improved performance can also be obtained at other important off-design conditions.

Variable compressor stators do not affect the hierchy of turbine pressure ratios, however. When the change in stator setting reduces the work done by the compressor, its speed increases because its turbine wants to keep its pressure ratio and do about the same work. This fact must be recognized from the beginning of any variable-compressor-stator proposal.

1.3.2.2 Variable Turbine Stators

Variable turbine stators have also been used. Because of high temperatures and associated material problems, their use until very recently has been confined to the low pressure (and temperature) turbine stages. Adjusting these stators changes the distribution of pressure across both the turbines and exhaust nozzle. This outside intervention overturns the hierchy of turbine pressure ratios. When the stators are closed, not only is the flow area reduced, but the pressure ratio across that turbine itself increases and it can do more work per unit of mass flow. If the turbine drives a compressor, its speed, pressure ratio and possibly its through-flow will increase. (The higher pressure encourages the higher flow in spite of the reduced flow area.) When the downstream stators are closed far enough, the pressure ratio across the upstream turbine is reduced, as is the work it can do. Its speed decreases together with the flow and pressure ratio of the high pressure compressor.

Opening the stators has the opposite effect. (The range of effectiveness is limited however, because the rotor area begins to control the flow when the stator areas becomes large enough.) This area flexibility is another valuable tool for modifying part-load operating characteristics.

Closing the area of high pressure turbine stators increases the pressure ratio across them at the expense of downstream units. The speed and flow of the low-pressure compressor decreases because of this reduced pressure ratio. In fact, this compressor can be quite sensitive to changes in high pressure stator area.

It is expected that more turbine stators will be made variable in the near future. The resulting possibilities of changing the relative position of the operating line on the compressor map are obvious.

1.3.2.3 Variable Exhaust Nozzles

Variable exhaust nozzles offer the same, but less effective, type of control of the pressure ratio hiearchy. They are absolutely necessary, however, in afterburning engines. Notice that if the available pressure ratio for the nozzle remains unchanged, the Mach number is also unchanged. The value of $\frac{\dot{m}\sqrt{\theta}}{\delta A_N}$ is then constant. (A_N is the nozzle area.) The nozzle area should thus be proportional to the square root of θ, or the square root of total temperature of the jet. This subject is thoroughly reviewed in Chapters 14 and 26. See 1.3.3.3 also.

1.3.2.4 Variable Inlets

The following discussion is presented to pave the way for Chapters 9 and 26, and to introduce the discussion of inlet-compressor interactions in 1.3.2.5 and 1.5.1. Only the most simple concepts are used for identifying the factors involved.

Variable inlets are necessary for two reasons. The first concerns matching the inlet flow with the flow that the engine demands. Recall Equation (1.2.8) and the discussion in 1.3.1.5.6. These concepts show that the total temperature at the compressor inlet increases with flight Mach number, and that this trend causes $N/\sqrt{\theta_1}$ to decrease, as shown in Curve D, Figure 1.3-9. An example of the corresponding change of flow along the equilibrium operating line of Figure 1.3-3 is indicated by Curve A in Figure 1.3-9. Special note should be made of the fact that this operating line flirts with the surge line at the higher Mach numbers even though T_{T1}/T_{C1} also decreases, Figure 1.3-3.

The other curves in Figure 1.3-9 concern the net flow capacities of the inlet and engine. Suppose, for simplicity, that the inlet looks like a stovepipe. Let the area of the inlet be arbitrarily sized so that the flow goes straight into it when the Mach number is 0.6. The resulting inlet flow lines are sketched in Figure 1.3-10a.

If the flow could continue straight into the inlet over a range of flight Mach numbers, the flow through the engine would have to vary, as shown by Curve B in Figure 1.3-9. This trend is explained by Equation (1.3.5). (Distinguished indeed would be the engine designer who could provide an engine with this characteristic.)

However, at Mach numbers greater than 0.6 and less than 1.0, the compressor cannot swallow all of the flow that the inlet could deliver. The inlet streamlines look like those shown in Figure 1.3-10b. When the flow velocity is sonic or higher, the

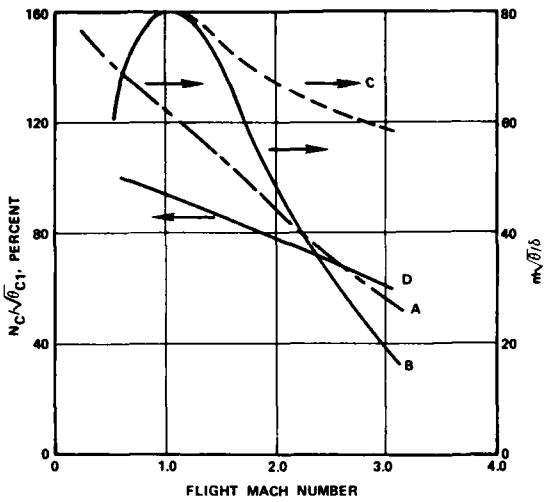

A EQUILIBRIUM OPERATING LINE

B IDEAL FLOW FOR FIXED INLET AREA

C NORMAL SHOCK FOR FIXED INLET AREA

D VARIATION OF $N_C/\sqrt{\theta_{C1}}$ AT CONSTANT N

Figure 1.3-9. Relationship Between Flight Mach Number and Compressor Speed and Airflow.

approaching flow does not know the inlet is coming. The air cannot adjust far upstream to prepare for the difference between what the compressor can handle and what the inlet can deliver. Normal and oblique shocks, Figure 1.3-10c, provide the mechanism necessary to push the excess flow (the difference between a curve similar to Curve C and Curve A of Figure 1.3-9) around the inlet. (The subsonic flow behind the shock then anticipates the inlet.) The pressure loss through the shock lowers the value of δ_{C1} and Curve C of Figure 1.3-9 shows an effect of this decrease.

These shock losses increase so rapidly with Mach number that they can be tolerated only at low supersonic Mach numbers. It is shown in Chapters 14 and 26 that a properly designed variable inlet having a shape such as that schematically shown in Figure 1.3-10c can drop the losses well below those of a normal shock at high flight Mach numbers. (Providing this benefit is the second reason for variable inlets.) A curve for such an inlet would lie between B and C of Figure 1.3-9.

At flight Mach numbers below 0.6, the flow lines would now assume the form suggested by Figure 1.3-10e. The flow entering the edges of this inlet might separate and impair the flow within the inlet as discussed in 1.4. Whenever possible, inlet leading edges are shaped to minimize this problem, but potential internal flow losses always exist for low flow situations.

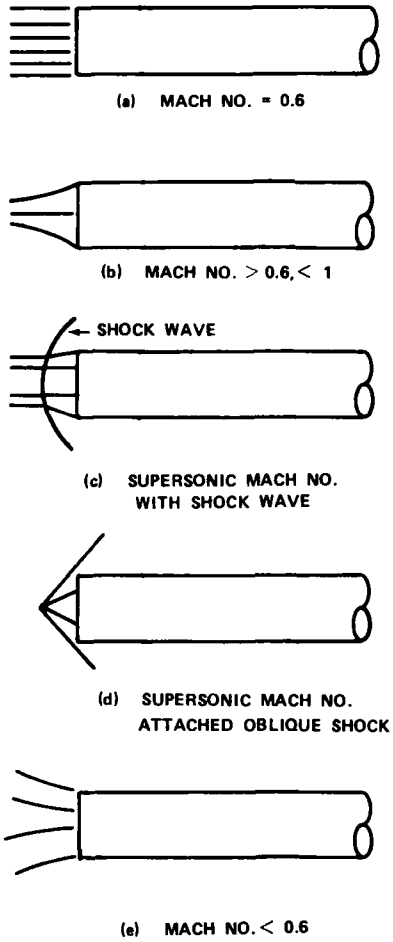

Figure 1.3-10. Inlet Flow Shapes with Stovepipe Inlet.

1.3.2.5 Variable Rotors for Fans and Compressors

Variable rotors, in the form of variable pitch propellers, have been an invaluable aid to aircraft for many years. They permit better matching of an engine with the propeller over a range of flight conditions. They also permit a high level of reverse thrust -- a valuable aid during landing. The rotor blades of helicopters, of course, are not only variable, but they vary over a given range each time the rotor makes one revolution.

There have been occasional applications of variable rotor vanes on fans. One of the goals of these efforts is reverse thrust. The fan blades have to be far enough apart to permit the necessary movement. This limits the solidity and hence, the pressure ratio, as indicated in Chapter 17. Because of centrifugal force on the mechanisms attaching the blades to their rotating disks, the speed of the resulting fan is lower than normal. This further limits the pressure ratio.

As materials, stress and vibration analysis, and manufacturing processes improve, variable rotors will probably become a reality. Together with other variable components, they will improve engines and extend their useful range. Variable rotors, together with other variable geometry, should eventually permit the engine airflow of Curve A in Figure 1.3-9 to approximately match Curve B.

In order to identify and develop what is needed, the engineer must continuously ask "what must we do to get what we need", rather than "how can we live with what we have?". It is recognized, however, that answers to the latter question are often necessary as temporary measures.

1.3.3 Transient Analysis

Transient analysis is used to determine the sequence of events that occur when engine operation is changed from one steady-state point to another. In many respects, the information derived from transient analysis is as valuable as steady-state information. The following is a simple problem in transient analysis. Figure 1.3-11 illustrates the sequence of events described. Let fuel be suddenly added to the engine while it is operating at Point A. The sudden addition of fuel causes the operating point of the compressor to move along the constant equivalent speed curve to Point B. The turbine power temporarily exceeds the compressor power, and the engine speed increases until equilibrium is eventually restored at Point C. To cope with the effects of the changing conditions, the engineer needs to know how all aerothermodynamic states within an engine vary with time.

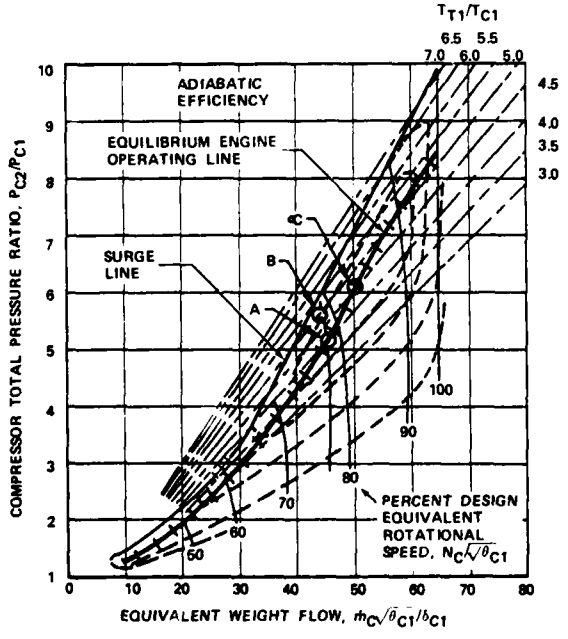

Figure 1.3-11. Effect of Step Change in Combustor Outlet Temperature.

Other transients result from flight conditions. Flying through a hot jet plume suddenly lowers T_{T1}/T_{C1}. An upstream blast suddenly changes overall engine pressure ratio.

In actual applications, all changes in engine operation are governed by automatic controls. (Of course provisions are included for manual controls to override some of the automatic ones during emergencies.)

1.3.3.1 Computation of Transient Response

Note that the sequence of events involved in starting an engine is controlled from the moment that starting is initiated. The engine starter is automatically engaged, and fuel flow automatically begins at a stipulated rate when prescribed engine operating conditions are reached. After the engine is more than self-sustaining [Equation (1.2.4) is positive], the starter is automatically disengaged. The engine runs up to idle speed and stays there until further instructions are received. If the engine is equipped with variable compressor or turbine stators, these too are automatically adjusted as functions of the engine operating states. The controls are designed to accelerate the engine as quickly as possible to idle speed without exposing the engine to hazardous vibrations associated with the surge line and without overheating the combustor or the components downstream of it. (Overheating is easy to do. The airflow is so low that several extra drops of fuel are a liability.)

When higher speed is demanded, the fuel and other controls quickly guide the engine to design speed while avoiding surge, overheating, and dangerous vibration areas such as those indicated in Figure 1.3-12. Other changes in operating conditions, including decelerations are similarly controlled.

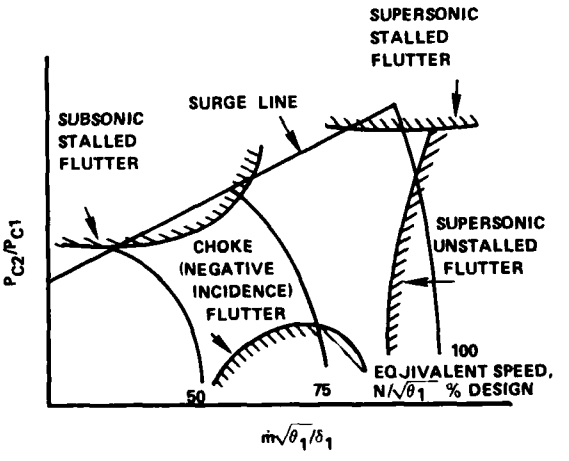

Figure 1.3-12. Compressor Map Showing Boundaries for Four Types of Blade Flutter (See Chapter 22).

Computer programs are used to predict and analyze all transient processes. The anticipated response of the controls to their independent variables can be stored in the computer. The effective polar moments of inertia associated with each rotating shaft are also stored as input data. In addition, a small time interval, Δt, is selected. The rest of the input data are the same as those outlined in 1.3.1.1. The calculations begin at a known equilibrium point. Assume that a new equilibrium condition is given as additional input. The original equilibrium point determines the configuration of the engine and the increment of fuel flow to be added initially. The sequence of calculations in 1.3.1.1 are repeated only to the extent necessary for establishing compatibility of airflow and shaft speeds. The differences between the torques of the turbines and those of the driven elements of each shaft are then computed. Dividing each excess torque by the effective polar moment of inertia of the corresponding shaft and rotor, provides the angular accelerations. New shaft speeds can then be estimated at the end of the time interval Δt. The new speeds and airflows must meet the compatibility requirements of 1.3.1.1 except power balances. The procedure is then repeated. Compatibility of power ($\Delta P_{ro} = 0$), is required only at the initial and final conditions. The thermodynamic program of 1.3.1.2 is now a subroutine of a numerical integration program.

1.3.3.2 Effects of Response Time of Variable Components

So far, only polar moment of inertia has been identified as a factor that causes a time delay between stimulus and response. Other factors may also become involved. Any variable-geometry component that has the equivalence of inertia, spring rate, or hysteresis may have a role in the transient response of an engine. Response rate, control element weight, control actuator weight, and control reliability become new factors to consider in engine design. For instance, variable inlets and outlets make contributions to engine weight that cannot be ignored. A finite interval of time is required for them to move from one position to another. The controls governing these elements must have the correct timing with the other control elements to avoid instabilities or even catastrophe. Transient inlet conditions also require special treatment.

1.3.3.3 Delays in Time Response Due to Aerodynamic Phenomena

Two phenomena involving aerodynamics may be important. One involves the equation of state noted in Chapter 2. It provides the following relationship:

$$pv = mRt$$

- v = a given volume
- p = average static pressure in v
- t = average static temperature in v
- m = mass of gas in v
- R = gas constant

This equation can be expressed in differential form as:

$$\frac{1}{m}\frac{dm}{d\tau} = \frac{1}{p}\frac{dp}{d\tau} - \frac{1}{t}\frac{dt}{d\tau} = \frac{1}{m}(\dot{m}_1 - \dot{m}_2)$$

- τ = time
- $\dot{m}_1$ = mass flow entering v
- $\dot{m}_2$ = mass flow leaving v

The discussion associated with Figure 1.3-11 really assumed that m, and hence v, was so small that p responded much faster than engine speed to a change in t. This assumption always needs to be at least qualitatively examined.

The other phenomenon involves the momentum equation which is also derived in Chapter 2. Consider again the finite volume v. The equation for momentum balance is

$$F_x + p_1A_1 + \rho_1V_1^2A_1 - p_2A_2 - \rho_2V_2^2A_2 = \frac{d}{d\tau}(mV)$$

- p_1 = static pressure of gas entering volume
- p_2 = static pressure of gas leaving volume
- ρ_1 = density of gas entering volume
- ρ_2 = density of gas leaving volume
- A_1 = area of flow entering volume
- A_2 = area of flow leaving volume
- V_1 = speed of gas entering volume
- V_2 = speed of air leaving volume
- V = average speed of gas within volume
- m = mass of fluid in volume
- F_x = component, in the direction of flow, of pressure forces on internal surfaces of volume.

Large rates of change of velocity or mass within a volume are accompanied by changes in pressure, velocity, and mass flow at both inlet and outlet. The magnitude of the effects of this equation must also be examined, at least qualitatively, during transient analysis if v is large.

The equations in this section are directly involved in the phenomena of surging. They are also involved when the pressure and temperature of the flow into an inlet or about an exit is suddenly disturbed, say by a nearby blast or rocket fire. Understanding the chain of reactions

requires a study of each elemental component of an engine. In this case, the change in total momentum or F_x, effected by each element must be known as a function of $(\dot{m}\sqrt{\theta}/\delta)$ and $(N/\sqrt{\theta})$.

1.3.3.4 Information Delivered from Transient Analysis

In addition to determining the operating regime of the components and the efficacy of the controls, the information of the type noted in 1.3.1.4 is available from transient analysis. Thermal stresses during transients are extremely important because thin sections or thin parts tend to change their temperature and length faster than thick parts. Thermal strains can be severe if necessary precautions are not provided. (Repetitious thermal strains can cause low-cycle fatigue.) Information about transient airflows for estimating local heat transfer coefficients is thus needed. Differences of temperature between stationary and rotating parts and hence, their distance apart also depends on the magnitude and the direction of a temperature transient.

The relative thermal inertia of the aerodynamic parts can play an important role. Certainly, the clearances between stationary and rotating parts must be large enough to avoid rubbing under the worst conceivable conditions. This can also have an unfavorable affect on surging, inasmuch as surge margin usually decreases as clearance increases (1.4.1.6 and Chapter 17).

Suppose, for example, that an engine is decelerated from full power to idle. Thin blades will cool more rapidly than a relatively thick casing. The blade clearances will then momentarily exceed those at normal idle conditions. A performance curve with these larger clearances would show a depressed surge line. Thus, if an engine is rapidly decelerated to idle and then immediately reaccelerated, it may surge, even though it behaves perfectly during normal accelerations from a cool idle condition. The problem then is to avoid this surging without excessively depreciating engine performance.

1.3.3.5 Airplane Acceleration

Observe that airplane acceleration has not been mentioned. This subject has been avoided because it would entail a large treatise on airplane performance. Such an endeavor is far beyond the scope of this publication.

1.4 CHARACTERISTICS OF FLOW IN AN ENGINE

The flow of gas through an engine has an economic similarity to the flow of merchandise along ancient trade routes. Each component along the way exerts a tax in the form of useful energy, for the privilege of allowing the gas to pass through (Section 1.2). Some of the tax is inevitable, some is due to inadvertent mismanagement of the gas flow within a component, and some is due to the lack of appreciation of how one component affects another. Creating an awareness of the principal causes of energy degradation, or losses prior to Chapters 3 and 4 is the object of this discussion. The genesis and growth of losses in available energy are first described. Secondary effects of those losses will then be noted. Finally, interactions between components will be considered. Some are obvious, while others are rather insidious.

1.4.1 Genesis of Losses

Much of this material is a narrated account of some of the material in Chapters 3, 4, and 10.

1.4.1.1 Ideal Shock Losses

These losses are unique because they can be predicted by the ideal equations for the conservation of mass, momentum, and energy. Even though thermal conductivity and viscosity are involved in the mechanism of the losses, these properties do not determine the magnitude of the ideal losses. Adequate discussions of this subject can be found in any text on gas dynamics.

Experiments on flat surfaces have shown that as long as the relationship between static pressure rise through a shock and the upstream Mach number is below that shown in Figure 1.4.1, the observed losses are approximately equal to the ideal losses. When the surface is curved, a maximum static pressure ratio of 1.4 across the shock is a better guide. Additional losses arise due to shock-boundary layer interactions when higher static pressure ratios are encountered. The higher losses properly belong in the cagetory of the diffusion losses discussed in 1.4.1.3.

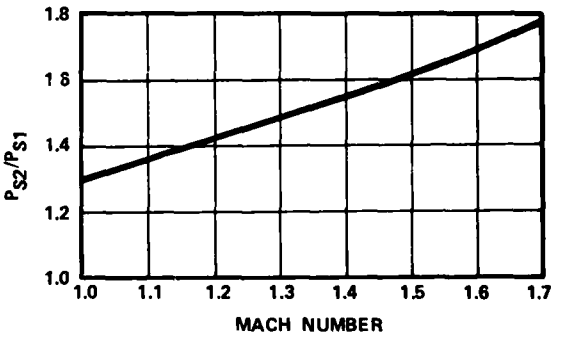

Figure 1.4-1. Separation Static-Pressure-Ratio Versus Mach Number -- Single Shock, Straight Surface.

1.4.1.2 Friction Losses

Most other losses have their origin in viscosity. Viscosity exerts a shear stress on a fluid. The magnitude of the stress is:

$$\tau = \mu' \frac{du}{dn} \qquad (1.4.1)$$

τ = shear stress on an elemental plane parallel to the flow of the fluid, it includes Reynolds stresses (see Chapter 4)

μ' = coefficient of viscosity, includes the virtual viscosity due to turbulent momentum interchange. Consult Chapter 4

u = magnitude of fluid velocity

n = distance measured perpendicular to an elemental plane of the flow.

At any solid boundary of a fluid (e.g., the inner wall of a pipe), the relative velocity at the boundary of the fluid must be zero. Viscous forces are brought into play when finite relative motion exists elsewhere in the flow, since du/dn must then be finite over at least some interval of the flow.

The losses directly due to the friction stresses just defined are only a small portion of the total losses found in turbomachinery. Friction forces, however, do initiate sequences of events which result in losses that are orders of magnitude greater than those directly due to friction forces themselves.

1.4.2 Amplification of Friction Losses

1.4.2.1 Qualitative Observations

Figure 1.4-2 vividly illustrates this subject. The shape of the airfoil shown resulted from many years of study and tests. Air flows about it very smoothly. Nearly all of the drag on the airfoil is the result of the friction forces described in Equation (1.4.1). (Moreover, the turbulence components of μ' are low.)

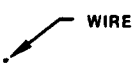

Figure 1.4-2. The Drag Experienced by this Airfoil and the Wire is the Same.

A visual contrast between flow around a good airfoil and that about a cylinder is shown in the photographs of Figures 1.4-3a and 1.4-3b. Figure 1.4-3c is included in the series to show that a good airfoil can be misused. Figures 1.4-3b and c were made by Prandtl, while 1.4-3a was done by Prandtl/Tietjens. In Figures 1.4-3a and -3c, the flow path markedly departs from some sections of the surface of the body. This condition is known as flow separation.

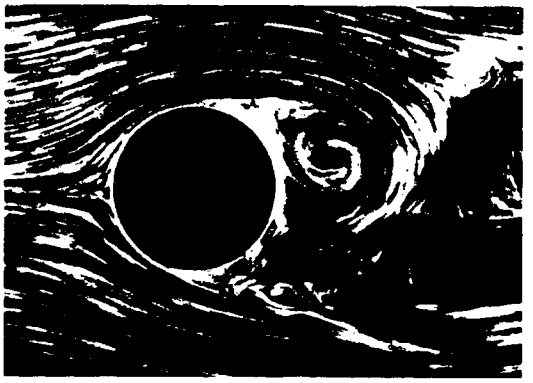

(a) FLOW ABOUT A CYLINDER

(b) SMOOTH FLOW ABOUT AN AIRFOIL

AN AIRFOIL

Figure 1.4-3. Examples of Flow about Isolated Bodies.

Flow separation results from a sequence of events illustrated in Figure 1.4-4 (also from Prandtl and Tietjens). Figure 1.4-4a shows the distribution of flow immediately after it was almost instantly started from rest. Notice that with incompressible flow, the theoretical maximum velocity occurs at the top and bottom of the cylinder. Its value is twice that of the velocity far upstream and downstream. The ideal minimum velocity is +90° away from the top and bottom; its theoretical magnitude is zero. Between the top of the cylinder and its downstream surface element, the flow theoretically encounters a static pressure rise equal to

$$\Delta p = \frac{1}{2} \rho (2V_o)^2 = 2 \rho V_o^2 \qquad (1.4.2)$$

ρ = density

V_o = velocity far upstream

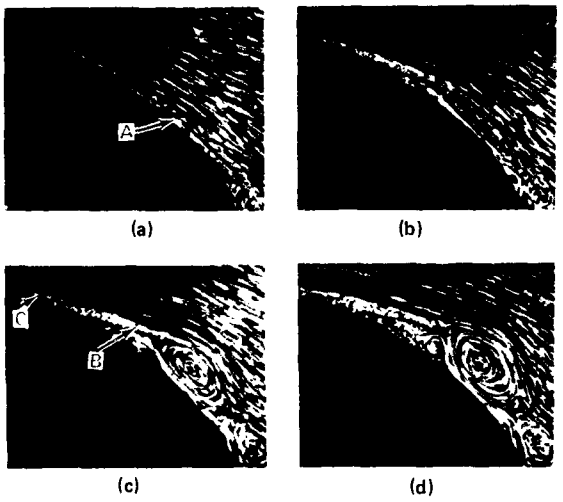

Figure 1.4-4. Development of Separation of Flow about a Circular Cylinder.

The shear forces of friction retard the flow at the surface, but they require a finite time interval to develop. The friction forces in Figure 1.4-4a were small, and velocities near but not adjacent to the surface were almost equal to the ideal. The average available velocity very close to the surface, however, was not quite sufficient to negotiate all the pressure rise required by Equation 1.4.2. Consequently, the flow came to rest near the point indicated by A.

Figures 1.4-4b and -4c were taken successively as the flow developed with time. The latter picture clearly shows a "separation eddy". Such a vortex would cause even viscous-free flow to stagnate at Point B. The resulting change in the pressure field is communicated upstream, and this causes the retarded flow to come to a halt near Point C. This situation is a typical point in a chain of events that causes the eddy to continuously advance upstream.

Figure 1.4-4d was taken a short time later. The disturbed flow in this view had just about reached the top of the cylinder. Right after this point in time, the eddy was washed downstream by the surrounding flow. The process was then more or less repeated over and over again. In general, the opposite sides of a cylinder take turns in generating and discarding eddies. The periodic shedding of vortices subjects the cylinder to an oscillating force. The flow is unsteady for a short distance downstream, particularly in the neighborhood of the cylinder.

The time-averaged vorticity shed from the cylinder must be zero, however. This means that far downstream, after all the disturbed flow is mixed together, the mixture can have no angular momentum. If this condition did not prevail, the cylinder would experience an average force perpendicular to the flow.

The separated flow in Figure 1.4-3c is one sided, but a finite time was also required to develop it. Immediately after the flow is started, a small eddy appears near the trailing edge. A stagnation point then forms at the leading edge of the eddy. This local high pressure causes the flow upstream of the eddy to leave the airfoil surface and join the existing eddy. Thus, as in Figure 1.4-4, the eddy continues to move upstream until it is very close to the leading edge, as shown in Figure 1.4-3c. The separation eddy caused by the retarded surface fluid induces an opposite vortex to form immediately downstream. From time to time, parts of both eddies are washed away. Again, the time-average of the shed vorticity must be zero. At any instant, however, the vorticity shed by one vortex may exceed that of the other. The airfoil then experiences both fluctuating lift and drag forces. The previous discourse illustrates the following points:

- When an attempt is made to convert part of the kinetic energy of a flow into static pressure, the flow may separate.
- Separated flow almost invariably causes the downstream flow to be time-unsteady.
- Because flow separation requires a finite time to develop, its behavior in an imposed unsteady flow can be different than that in steady flow.
- Separated flow can produce fluctuating forces on a body
- Severely separated flow produces high drag or losses.

1.4.2.2 Mixing Losses

The first four of these ideas were previously noted. The fifth can be inferred from Figure 1.4-2. A simple classic analysis, found in most standard texts on fluid mechanics, is a useful analogue to show what happens when random flow velocities are allowed to mix freely.

Consider the flow in a conduit in which the area suddenly expands as shown in Figure 1.4-5.

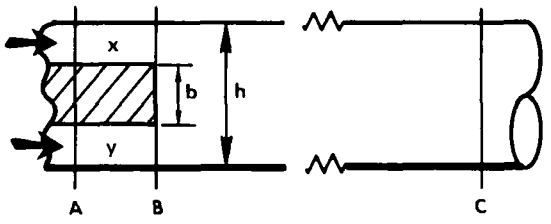

Figure 1.4-5. Flow Passage with Sudden Change in Flow Area.

Stations B and C are sufficiently far apart that the flow at C is ideally uniform. A solid inner body is represented by Surfaces x and y. By assuming constant static pressure at B, the requirements of conservation of mass flow and momentum (see Chapter 2) demand a loss in total pressure between B and C. The loss for an incompressible fluid amounts to:

$$\Delta P = \frac{1}{2} \rho V_B^2 \left(1 - \frac{A_B}{A_C}\right)^2 \qquad (1.4.3)$$

ρ = density

$A_A = A_B$ = area of small passage

A_C = area of large passage

$V_A = V_B$ = fluid speed in small passage

The overall drag force could be found by subtracting the total flow momentum $[(p + \rho V^2)A]$ at C from that at A.

p = static pressure

This idea is easily generalized. Assume that there are no surface forces in the direction of flow and that the flow at B is irregular and compressible. Assume also that the flow at Station C is uniform. The mixing losses may then be estimated by observing the equation of state and noting that the flow between Stations B and C must also satisfy the laws of conservation of mass flow, momentum, and energy.

$$p_C = R \rho_C t_C$$

$$\dot{m}_B = \int \rho_B V_B dA_B = \rho_C V_C A_C$$

$$\mu_B = \int p_B dA_B + \int \rho_B V_B^2 dA_B$$
$$= p_C A_C + \rho_C V_C^2 A_C$$

$$\frac{\gamma}{\gamma-1} R\bar{T}_B = \frac{1}{\dot{m}_B} \int \left[\frac{\gamma}{\gamma-1} Rt_B + \frac{1}{2} V_B^2\right] \rho V_B dA_B$$
$$= \frac{\gamma}{\gamma-1} Rt_C + \frac{1}{2} V_C^2$$

μ = total momentum

γ = ratio of specific heats

R = gas constant

$\bar{T}$ = average total temperature

t = local static temperature

Two equations may be combined to get:

$$\frac{\mu_B}{\dot{m}_B} = \frac{Rt_C}{V_C} + V_C$$

This, and the energy equation, are now available for determining V_C and t_C when $\dot{m}_B$, μ_B, and $\bar{T}_B$ are known, say by measurements. The value of ρ_C can then be found from the equation for $\dot{m}_B$, and p_C is finally determined from the equation of state. The total pressure at C is then given by

$$P_C = p_C \left(\frac{\bar{T}_B}{t_C}\right)^{\frac{\gamma}{\gamma-1}}$$

Inasmuch as pressure is energy per unit of volume, the comparable average total pressure at B is given by,

$$P_B \int V_B \, dA = \int p_B \left[1 + \frac{\gamma-1}{\gamma} M_B^2\right]^{\frac{\gamma}{\gamma-1}} V_B \, dA$$

M_B = local Mach number

The difference between P_B and P_C increases as the flow irregularity at B increases. Incidentally, although additional losses in total pressure occur between Stations B and C, the static pressure at C is higher than that at B. Note that entropy could be used instead of total pressure to indicate loss. In this case however, the relative entropy, S, at B is given by $\int S d\dot{m}$.

Besides indicating a principle, this procedure is a valuable tool for estimating losses or for interpreting measured data. A mathematical flow model may be used instead of a uniform one at C. This will alter the coefficients of V in the initial equations.

If another flow device is required downstream of Station B, the mixing losses can often be mitigated. Favorable pressure forces on a bounding surface can be used to make the momentum more uniform. The nozzle discussed in Subsection 1.5.6 performs this function. If the bounding surface is rotating, the proper pressure forces can also redistribute the energy and momentum distributions. The best way to use this possibility depends upon each individual case.

This idea also applies to badly separated flow. If the separated flow can be confined with minimum mixing, the losses are small. This is analogous to the idea that falling 100 feet doesn't hurt anyone; it's the sudden stop that causes the damage.

AD-A152 757 COST REDUCTION IN VERTICALLY RELATED INDUSTRIES: INTEGRATION VERSUS NONLINEAR PRICING(U) RAND CORP SANTA MONICA CA H C QUIRMBACH MAY 83 RAND/P-6839 2/9

UNCLASSIFIED F/G 5/1 NL

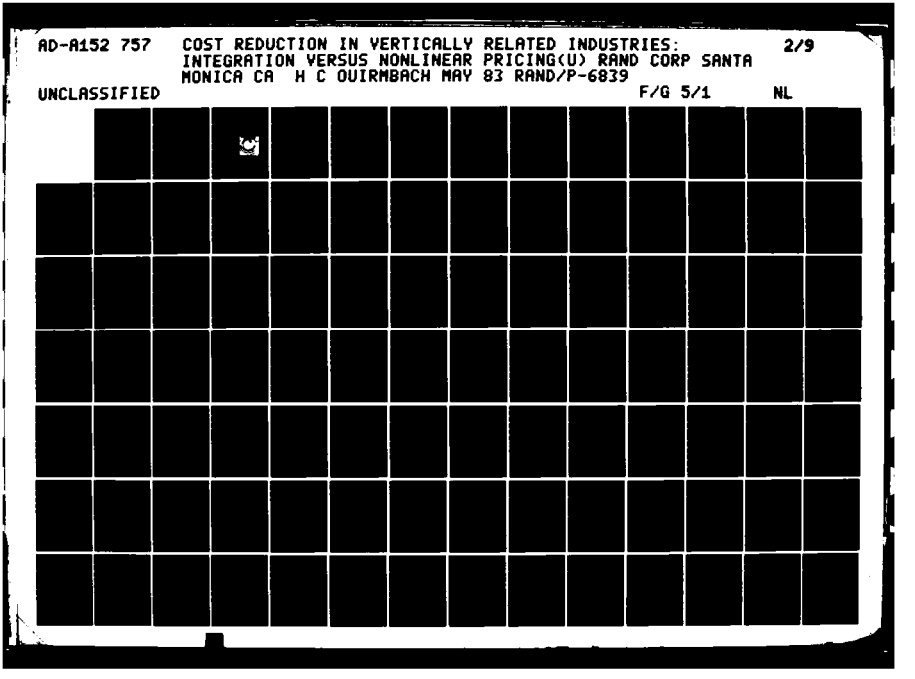

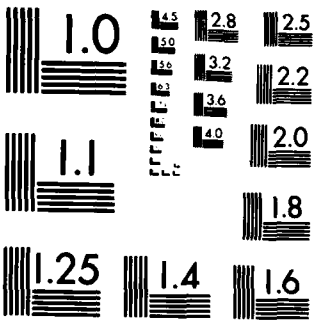

MICROCOPY RESOLUTION TEST CHART
NATIONAL BUREAU OF STANDARDS-1963-A

1.4.2.3 All Compression in Engines Requires a Diffusion Process

Recall that the air in all propulsion gas turbines must be compressed. This is almost always achieved by converting some of the kinetic energy of the relative motion of the air into static pressure. In most propulsion engines, much of the compression of air occurs in axial compressors, discussed in Chapter 17. These essentially consist of a series of rotating and stationary diffusers. (Centrifugal compressors are sometimes used. Although part of their pressure rise is accomplished by centrifugal force, an additional diffusion tax paid for this aid consumes much of this advantage. Moreover, even these compressors have diffusers -- see 1.4.4). A separate diffuser just ahead of the combustor provides the final compression for most engines.

Unfortunately, the most efficient diffusion processes usually occur when the flow in the diffuser is on the verge of separation. A more conservative design suffers from excessive friction losses. A less conservative design invites the separation losses just discussed. The designer thus must walk a tightrope.

1.4.3 Effects in Curved Flow

Strongly curved flow creates both beneficial and penalizing conditions. No rigorous rules are yet known, but the following qualitative information is valid.

1.4.3.1 Unstable and Stable Flow

One problem arises because flow direction must be changed in turbomachinery (Chapter 10), and flow changes direction only when a static pressure gradient is imposed perpendicular to the flow. It can be shown that if this static pressure gradient is in the same direction as a local entropy gradient, the flow is unstable. The degree of instability is proportional to the product of the gradients.

Unstable flow encourages the interchange of momentum between the main stream and the retarded flow near the flow boundaries. The value of $\frac{du}{dn}$ in Equation 1.4.1 is high. The friction forces are also relatively high, and heat transfer rates are enhanced. This type of flow can postpone flow separation. An overhanging cold front with its accompanying strong surface winds, including tornadoes, is an example of instability.

Stable flow has the opposite characteristics. Momentum interchange is discouraged. Friction and heat transfer are reduced. Flow separation is less easily averted. An atmospheric inversion with its associated calm smoggy air is an example of stability.

1.4.3.2 Secondary Flows

Consider the flow in the curved duct shown in Figure 1.4-6. Let the flow be in the direction indicated. If the mean effective velocity of the main flow is V_n, a static pressure gradient V_n^2/R_c, (R_c is the radius of curvature of the effective velocity) will be produced that is perpendicular to V_n. The pressure on the surface indicated by H is greater than that at L.

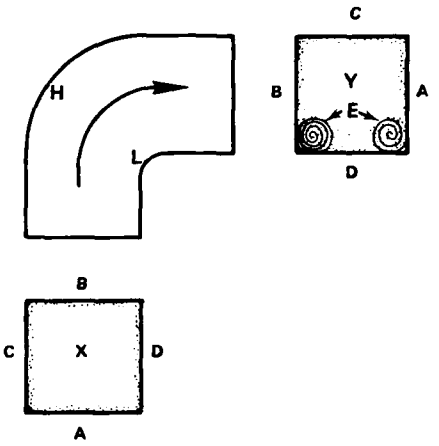

Figure 1.4-6. Two-Dimensional Curved Duct Illustrating Secondary Flows.

The shading in the sketches of the inlet and outlet flow passages (X and Y) schematically indicates retarded flow. The retarded flow at the inlet is assumed to have uniform circumferential distribution.

Observe first that the previous remarks about flow stability suggest that the retarded flow along H will mix with the main flow. Except for a narrow region along H where entropy increases in the direction of flow because of friction, any entropy gradients will be perpendicular to the flow in the direction of H to L. Retarded flow thus "floats" from H to L. Meanwhile, the difference in pressure gradients between the main and retarded flows along surfaces A and B causes this retarded flow to be swept towards L. This flow is known as secondary flow. Experimental evidence on two-dimensional bends shows that the swept flow tends to roll up into vortices denoted by E at the corners. The retarded flow at the outlet of Figure 1.4-6 is exaggerated to emphasize trends. The gradients of entropy and static pressure within these vortices have opposite directions. They are therefore, very stable, and resist any interchange of momentum with the main flow, and thus, they interfere with subsequent attempts to diffuse the flow. The rest of the retarded flow along L is also stable. If the area of the duct is constant, the main flow near L must first accelerate and then decelerate.

Inasmuch as the stable boundary layer and vortices cannot be supplied with the necessary momentum to combat the rising static pressure, the flow will separate and generate mixing losses.

Secondary flow occurs whenever there is a pressure gradient normal to the main stream in either the main or retarded flow. When the bounding surface itself is rotating, secondary flow adjacent to the boundaries will move outwards, provided that the rotational speed of the retarded flow exceeds that of the mainstream. Otherwise, the motion is inwards. The normal pressure gradients in turbomachinery are complex and they produce complex secondary flow patterns. Some additional comments are presented in Chapter 10. The ideas suggested in Section 1.7 and Chapter 18 offer promise for coping with these phenomena.

The shape of the flow passage indicated by X and Y plays an important role in deciding the magnitude of the disturbing influence of secondary flows. Consider the shape shown in Figure 1.4-7. This shape has half the flow area as Figure 1.4-6, and a lower hydraulic diameter, 2(HXB)/(H+B). It therefore suffers comparatively higher friction losses and the Surfaces A and B of Figure 1.4-7 provide most of these losses. Thicker regions of retarded flow will accumulate at L because the volume of the retarded flow is comparable to that in Figure 1.4-6, while L is only half as long.

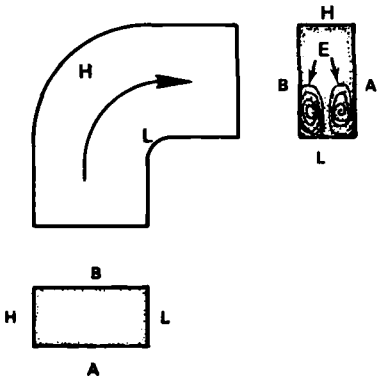

Figure 1.4-7. An Effect of Passage Shape on Secondary Flows.

Shapes of this type are deemed to have low aspect ratios. An attempt to diffuse this flow will cause the retarded flow area to grow rapidly, because it resists being energized. The potential mixing losses exceed those of Figure 1.4-6. Shapes having high aspect ratios (H>A) reduce secondary flow losses. They are generally preferred as long as the friction losses are smaller than the mixing losses.

1.4.4 Special Losses in Centrifugal Compressors

Axial turbomachinery has been emphasized thus far. They have been the mainstay of most of the recent propulsion engines. However, there are reasons for believing that centrifugal compressors will play an increasingly important role in turboprop and turbofan engines of the future. Since no Chapter in this publication has been appointed for this subject, some relevant remarks are made here because flow stability and secondary flows are the principal items that distinguish the behavior of centrifugal compressors.

Centrifugal compressors are potentially capable of efficiently generating a high-pressure-ratio in a short single stage. Their diameters need to exceed those of an equivalent axial compressor, but they can be smaller than those of other engine components -- a fan, for example. Figure 1.4-8 shows a centrifugal compressor that has been in production for a number of years at the Garrett Corporation. Its principal parts are identified in the photograph. The pressure ratios and efficiencies produced by this unit are shown in Figure 1.4-9. The blades in this impeller are curved at the outlet. Because of the direction of curvature, this is known as a "backward curved impeller". Many other impellers have straight radial blades at the outlet.

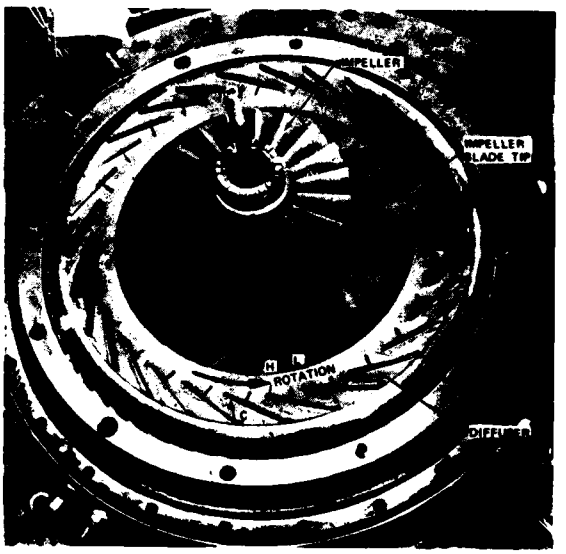

Figure 1.4-8. Centrifugal Compressor and Diffuser.

The flow in the impeller and diffuser are subject to the same aerodynamic laws that govern the flow in axial compressors. The same type of aerodynamic calculations are applicable. There is a difficulty, however, in obtaining favorable aspect ratios near the inlet and exit of the rotor and in the diffuser. The reasons are given in the following paragraphs.

One of the principal virtues of centrifugal compressors has been their simplicity. One continuous set of blades often comprises the rotor. Another continuous set frequently forms the stator or diffuser. The number of blades of the

rotor and stator are limited by the area required at their inlets. (The allowable height of the inlet blades of the rotor is determined by Mach number limits and stress.) If too many blades are used at the inlets, the compressor will not move the required amount of air. Two potential adverse consequences result from these restrictions.

1.4.4.1 Impellers

Since both the static pressure and density increase in impellers, much smaller flow areas are needed at their outlets, where the radius is large, than at the inlet where the radius is small. Observe that the distance between the blades increases with the radius, while the flow area is about equal to the product of this distance by the blade height. The height of the blades must therefore diminish rapidly with radius. Figure 1.4-8 illustrates these characteristics. The aspect ratio of the impeller flow passage becomes very small. The aspect ratio at the exit further decreases as the design pressure ratio increases, since smaller flow areas are required because of the higher gas density.

High impeller blade loading is a consequence of a low number of blades, although considerable control of blade loading may be obtained by the judicious use of blade curvature. Even in the impeller shown in Figure 1.4-8 however, the blade loading is pushed to the limit because the air is accelerated from zero to about 1800 feet per second. Achieving this acceleration requires high pressure on one side of a flow passage (H), and a low pressure on the other side (L). The main tangential accelerating force is that due to the Coriolis acceleration, which is $2\omega V_r$ (ω is the angular velocity and V_r is the radial component of velocity). This force is tempered however, by the backward curvature. Recall that the product of the tangential acceleration by the fluid density equals the tangential pressure gradient. (See Chapter 2.) The difference between the pressures at L and H is thus proportional to the tangential acceleration and the spacing of the blades. The net effect of this acceleration can be many times the effect V_n^2/R_c with blade spacing found in axial flow compressors or other familiar flow devices. Differences in the pressures between L and H are sometimes comparatively enormous. To achieve these large pressure differences, high velocities must theoretically exist near the surface L if those at surface H are to have real finite values.

Any retarded flow originating or developing along H is scoured from that surface and deposited on L. The low aspect ratio of the passage causes the retarded flow along L to become thick while the large tangential accelerations and the entropy gradients make it extremely stable. The difference in pressure between H and L, however, must vanish at the blade tips. Rapid diffusion is attempted near the side marked L. Extensive flow separation and mixing losses can then occur near the outer part of a highly loaded rotor. Relieving this situation has continued to be an objective of research.

Consider now, the main relative flow between the rotor blades. When this flow escapes from the rotor, the absolute flow becomes pertinent. The illustration in Figure 1.4-10 distinguishes absolute and relative flows. They are described more completely in Chapter 10. The vector OA represents the highest relative velocity of the main flow leaving the rotor. This is the highest velocity that would be observed if one could sit on this rotating unit. The vectors OB and BA are the axial and tangential components of OA. The vector AC represents the tangential velocity of the rotor at its maximum radius. By vectorially adding AC to OA, the absolute velocity, vector OC, is obtained. This is the velocity that a stationary observer would see. It is also the velocity that determines the behavior of the flow after it leaves the rotor.

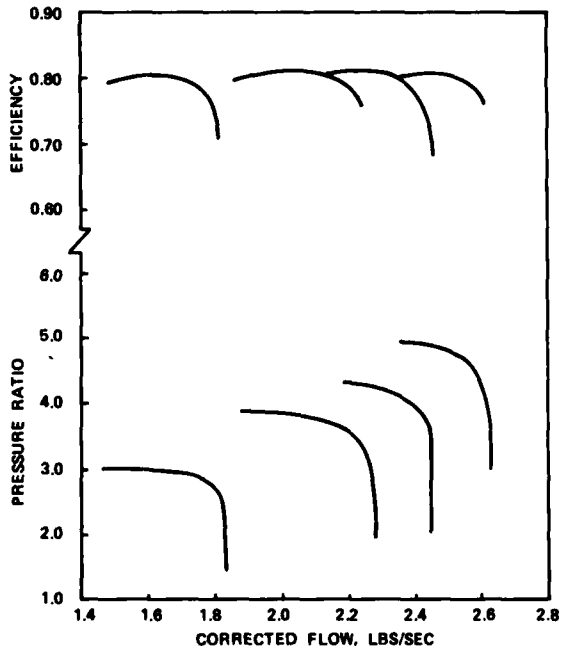

Figure 1.4-9. Performance of Compressor Shown in Figure 1.4-8.

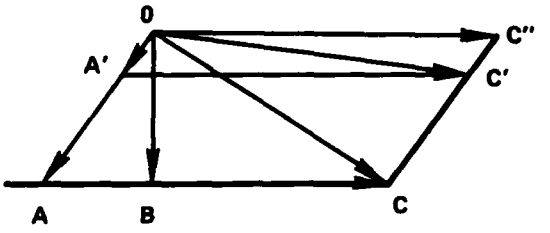

Figure 1.4-10. Velocity Diagram at Rotor Exit.

Now let OA' represent the relative velocity vector for a portion of the retarded flow along L. The rotor velocity vector AC is now represented by A'C'. The corresponding absolute velocity vector OC' is greater than OC in this case. As noted in Figure 1.4-10, the absolute velocities leaving the rotor may vary from OC to OC". This variation is time-unsteady with respect to a stationary observer.

The mixing of this type of velocity spectrum in a free field is complex because the flow is unsteady and two types of momentum must be conserved instead of one (momentum in the radial direction as well as angular momentum). In comparison to the variation of the relative velocities, the ratio of the minimum to the maximum absolute velocity of the unsteady flow is small in this illustration.

The disparity in the energy of the flow leaving the rotor of the type shown in Figure 1.4-8 can be large. It is shown in Chapter 10 that the energy added to the air by a rotor having no preswirl is proportional to the absolute tangential component of velocity. (This does not include the extra thermal energy added by recirculations.) In Figure 1.4-10, the range of the mechanical energy addition is represented by the differences in the lengths of BC and OC". This variation also augments the mixing losses.

The previous discussion has been devoted to the bulk of the flow between the blades. The flow adjacent to the rotating surface between the blades is retarded with respect to that surface, but it really has a high tangential velocity. The other velocity components of this retarded flow are low. There is, however, a radial clearance between the rotating surface and its companion surface in the diffuser. (See Figure 1.4-8.) Flow can enter and leave a cavity behind the impeller through this clearance. Within this cavity the flow rotates at a mean velocity that is about one-half that of the impeller. The tangential velocity of the actual flow leaving the impeller is thus depressed immediately beyond the rotating surface because of recirculation into and out of the cavity, and because of friction.

The outer portion of the rotor flow passages is usually formed by a stationary surface known as a shroud. A small clearance is maintained between the shroud and the adjacent blade ends. Both the through flow and tangential velocity component next to this surface are retarded. The tangential velocity is further retarded by the flow, over the blade ends, from the high to the low pressure sides. The tangential component is somewhat enhanced, however, by secondary flow between the blades and by the turbulence created by the flow over the ends of the blades.

The low tangential flow along the shroud invites additional secondary flows which move radially inward along the stationary surface. The physics of this flow are imperfectly understood also. The inward flow eventually reenters the impeller and moves outwards. All recirculating flows of this type represent an additional dissipation of useful energy and require the expenditure of additional mechanical energy.

The important points to note are that the flow next to the low-pressure surfaces of the blades, the flow next to the rotating surfaces between the blades, and the flow next to the shroud create situations that can cause separated flow and loss amplification within an impeller. The diffuser can be thus presented with time-unsteady flows having large gradients in energy, momentum, and direction. This situation again emphasizes the possibilities for advanced rotor design concepts.

1.4.4.2 Diffusers

Although the diffusers shown in Figure 1.4-8 appear to be straight, they do reduce the angular momentum of the air and thus produce a tangential force that is greater in the main flow than in the retarded flow near the bounding surfaces. However, the tangential velocity of the main flow also produces a centrifugal force that is not in equilibrium with that of the retarded flow. The net effect produces a secondary flow more or less in the direction indicated by the arrow at C. The increase in radius between the inlet and outlet increases the distance between diffuser blades also. This trend causes even lower aspect ratios. Stable stagnant air accumulates along most of the surface indicated by the point of the arrow and the amount of diffusion that can be efficiently obtained, even with uniform inlet conditions, is thus limited. Note that rotating diffusers would help the aerodynamic problem at the expense of mechanical complexity.

1.4.4.3 Possibilities for Future Developments of Centrifugal Compressors

Improved materials and stress analysis will enable the number of blades and vanes to be increased at intervals between the inlet and outlet. For example: ten blades may be used at the impeller inlet, an additional ten added when the flow is sufficiently compressed, and another twenty added near the outlet. Similar ideas may be applied to the diffuser. This will partially relieve the diffusion and aspect ratio problems in both the impeller and diffuser. Meanwhile, improved aerodynamic

analysis indicated in 1.7 is expected to be more potent in the near future. This will enable the blade shapes to be designed to provide high pressure ratios with greatly improved efficiency. There is reason to hope that mixing losses may be subdued by designing diffusers to apply pressure distributions that minimize the mixing losses. This goal is being pursued.

An aspect ratio problem that is frequently overlooked in centrifugal impeller rotors arises from turning the air from an axial to a radial direction. High flow units in particular require blades in which the distance from hub to shroud at the inlet is much greater than the corresponding average distance between the blades. A low aspect ratio bend is thus formed. The secondary flows due to the turning combine with the effects of centrifugal force on the retarded flow relative to the blades to accumulate retarded flow along the surface of the shroud near the inlet. This part of the flow then has increased difficulty in negotiating the subsequent pressure rise derived from the main flow.

This type of secondary flow has been alleviated by using mixed-flow impellers. Such units discharge the flow with both axial and radial components of velocity. The curvature of the turn toward the radial direction is thus reduced. The weight of mixed flow rotors can be undesireably high however, because of the added length. Problems in critical shaft speeds can also be augmented.

Some thought has been given to forming mixed-flow impellers from three or more disks, each similar to an axial-flow rotor and each carrying a different number of blades. A few long blades would be used at the inlet while many short blades would be used at the outlet. The aspect ratios presented to the flow would improve and the impeller weight would be reduced.

A final comment is pertinent. When one reviews all the possible sources of losses, he has to wonder why centrifugal compressors achieve the good performance that they deliver. The principal unknown quantities are the effects of the complicated mixing process in the presence of diffuser vanes, and the effects of large unsteady components of flow. (Recall the discussion near the end of 1.4.1.3.1.) Possible latent benefits of these phenomena deserve future attention.

1.4.5 Flow About Blade Ends of Axial Turbomachines.

Examination of the cutaway views of the engines in 1.1 reveals that the outer end of a rotor blade is near a stationary surface while the inner end of a stationary vane is near a rotating surface. Some clearance between stationary and rotating surfaces is always necessary to avoid damage. Flow squirts from high to low pressure through this clearance and kinetic energy is converted into heat. Gas flowing backwards over rotor tips of compressors reenters the flow at lower useful energy levels. The retarded flow tends to thicken and the entropy is increased. Moreover, additional thermal energy is thus added to this flow. Clearance flow also makes its own contribution to secondary flow eddies. The resulting losses have several adverse affects on turbomachinery performance: The attainable pressure ratio is reduced, the entropy rise increased, and the surge-free margin of the compressor eroded. Flow over blade ends, together with secondary flow has been the subject of much inquiry, but many important quantitative aspects are not clearly understood.

In order to avoid clearance losses, the outer ends of rotor blades are often attached to co-rotating rings known as shrouds. Stator vanes may be shrouded also. In this case, the rings are attached to the inner ends of the vanes. Circumferential seals adjacent to a shroud then limit the amount of flow from the high to the low pressure side of a blade or vane. Many varieties of shrouds and seals have been made.

Shrouds are known to be aerodynamically beneficial in many turbine blade designs where the useful energy of the clearance flow is irrevocably lost and the secondary flow sets up eddies that rotate in about the same direction as the clearance flow. The general aerodynamic value of shrouds in compressors still has to be decided. All experimental data do not agree, possible because clearance flow vortices oppose those from the secondary flow.

Shrouds are often necessary on compressor stators, however. An accidental rub by a stator heats and expands both the stator and its adjacent rotating hub. As a result, they move towards each other. Rubbing is then intensified, sometimes with disastrous results. The clearance required to eliminate this possibility can be so great that the resulting clearance flows severely reduce performance. In this case, any adverse effects of the shrouds are more than compensated by eliminating the flow about the blade ends. Blade and vane vibrations can supply another motive for using shrouds. Ingestion of large birds (1.6.4) may also require the use of shrouds, particularly on the rotor. "Part span" shrouds may be used. These are placed between the hub and the shrouds of rotors at radii where they can be most effective mechanically.

Shrouds have sometimes been used on rotor blades of axial compressors (some have also been employed on centrifugal rotors with no obvious advantage, with the possible exception of those with very small blade heights). The stationary surface next to the rotor blades however, can be designed to move away from the blades during rubbing. Closer operating clearances can thus be tolerated. Losses due to blade clearances can probably be reduced by changing the shape of the blade

ends when more is known about the flow there. The magnitude of some of these losses as well as the losses due to leakages through seals depends frequently upon controlling the relative movements of the rotating and stationary units, thus evading some of the flow problems. This demands the recognition of problems that are germane to other disciplines rather than upon aerodynamic expertise. This important area also is discussed in 1.6.

1.4.6 Summary of Loss Problems

The losses arising from nonuniform velocity distributions are the principal losses that concern the aerodynamicist. These adverse distributions are brought about by the necessary diffusion during the compression process, by changing the direction of the flow, and by leakage around the ends of blades and vanes.

Losses in nonuniform flow are aggravated by decelerating the flow. Remember also that the retarded flow is urged forward by an interchange of the momentum of slowly moving fluid particles with that of faster moving particles. Numerous experimental studies of jets and diffusers have shown that the rate of this interchange is limited and that it depends upon the passage shape. The rate of momentum exchange is obviously hastened in unstable flows and delayed in stable ones.

Probably the greatest sources of losses result from the necessary diffusion of partially stabilized flow. Such flow frequently rolls up into a localized vortex. The entropy gradient in the vortex is in the opposite direction from its pressure gradient. The flow is stable and momentum interchange with the rest of the flow is resisted. Attempting to diffuse the resulting flow aggravates nonuniform velocity distributions. Subsequent mixing amplifies the losses.

Until recently, this situation had to be reluctantly accepted, particularly where compactness was required. Emerging techniques for numerical aerodynamic analysis are demonstrating, however, that designs can be made that will alleviate the accumulation of stable impregnable regions of retarded flows. Special types of tangential, axial, and radial pressure fields have been created by stator vanes. These fields minimize transverse movements of retarded flows. An exciting improvement in a turbine has been obtained. Even greater accomplishments are expected in the near future by alert students of this work. This subject is briefly elaborated again in 1.7.

1.5 INTERRELATIONSHIP OF AEROTHERMODYNAMIC COMPONENTS

Most of the problems in this category were anticipated in the discussions of the previous sections. Any component that delivers a nonuniform distribution to a component downstream contributes losses and other problems to the downstream component. Conversely, events in a downstream component may affect an upstream one. Because of component interactions, potentially beneficial concepts for one component sometimes have to be deferred to help another in an engine design.

1.5.1 Inlets

The subject of inlets is thoroughly covered in Chapters 9, 13, and 26. Subsonic inlets rarely impose formidable problems. When airplane speeds are low, the flow configuration may cause some extra internal losses and flow distortions as suggested in the sketch in Figure 1.3-10e. Rounded inlet leading edges make any accompanying compressor problem far less severe than that which might be suggested in this sketch. This flow situation usually lasts only for a short time and may be considered to be under control in most subsonic airplanes.

Inlets for supersonic flight speeds are more difficult to design. Their leading edges must be relatively sharp and their flow mismatch with engines often creates unsteady and nonuniform flow distributions that penalize the compressor. Present knowledge really permits us only to install devices in the inlet that serve as bandaids for the problem. What is really needed is variable-geometry that enables the engine to efficiently inhale air with the schedule shown in Figure 1.3-9, Curve B.

1.5.2 *Compressors*

Other parts of this chapter have at least hinted that compressors prefer time-steady and uniform flow. If they don't receive flow that reasonably meets these specifications, they respond by surging or by reduced performance. At the present time, compressors are prima donnas because they are essentially diffusers and the best diffusion processes occur just before flow separation (or stall) is encountered. When questionable inlet flow is expected, compressors must be given ample stall margin, even at the expense of efficiency. The amount and rate of static pressure rise asked of the critical stages is then reduced. One objective of future research should be aimed at identifying appropriate variable engine geometry together with controls that are capable of coping with the temperamental nature of a compressor.

Compact transition ducts between compressors, such as that shown in Figure 1.1-7 can be a further source of nonuniform flow. Curved surfaces just ahead or just behind the blades or vanes alter the radial distribution of the flow. The performance of the compressor is then affected unless this radial distribution is anticipated. If these ducts also have significant localized total pressure losses, they impair the performance of the following compressor and increase its design problems. Careful planning is essential in the layout of the flow path.

A compressor can cause problems for itself and other components. One important problem stems from the ability of a compressor to trap an anomaly in the flow. This phenomenon may be visualized with the aid of Figure 1.5-1. This sketch is a partial two-dimensional development of three stages of an axial flow compressor.

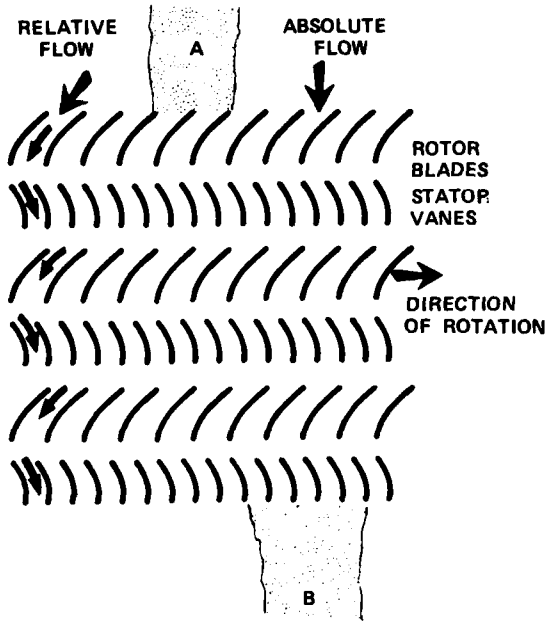

Figure 1.5-1. Schematic Development of Three Blade Rows of Axial Flow Compressor.

Observe that the close spacing of the blades and vanes in this development limits the horizontal spread of the flow. Suppose we inject a plume of smoke such as that indicated by A into this compressor. The smoke will be confined by a group of the first row of rotor blades and will move towards the right. A little bit of the smoke may escape between the rotor and stator, but most of it will be captured by a few passages in the next row of stator blades. The continuation of these events through each stage eventually will cause the smoke to emerge from the three stages at Position B. It is displaced in the direction of rotation and its circumferential extent is somewhat expanded.

This trapping of the flow is responsible for some important interactions between a compressor and the rest of an engine. If the flow entering the compressor is not uniform, the compressor almost behaves as if it were a number of independent compressors, each having different inlet conditions. Each path then, would have the same map, such as that sketched in Figure 1.5-2. The processes actually involved with nonuniform entering flows are complex and some of them are imperfectly

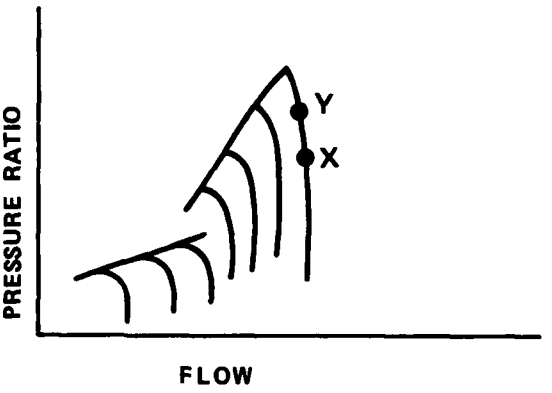

Figure 1.5-2. Representative Compressor Map.

understood. This statement is supported by the material in Chapter 17. The trapped flow concept does help to explain some important observations, however.

Suppose that the flow in Region A of Figure 1.5-1 has relatively low total pressure due to a flow obstruction upstream. Suppose further that the compressor would normally operate at Point X of Figure 1.5-2 if the flow were uniform. The compressor apparently manages the flow through A as if the operating point were at a point of higher pressure ratio, say at Y. If Region A is large enough, and if its total pressure is sufficiently depressed, the compressor will surge. (Point Y would cross the surge line.) If the low total pressure in Region A is the result of flow separation in the inlet, the magnitude and extent of the losses probably varies with time. If the losses are large enough and persist long enough, compressor surging can be expected. The discussion in 1.3.3.3 is applicable to this situation also.

Figures 1.3-3 and 1.3-4 show the low pressure of the flow approaching Region A will also cause the temperature rise in the compressor to be higher at Y than at X. This higher temperature rise is transmitted through the combustor into the turbine. A local area in the turbine flow would then be hotter than the average. The combustor exit temperature must be tempered if compressor inlet distortions occupying a fixed region in space and lasting a considerable length of time are anticipated. This necessary compromise would impair the thrust and efficiency of an engine.

It is worth noting that the discussion associated with Figure 1.4-10 is applicable to all turbomachinery, although the amount of retarded flow in axial compressors is usually less than in centrifugal compressors. Note from Figure 1.5-1 that the air leaving the rotor with the largest absolute tangential velocity may impinge on the concave side of each of the following stator vanes and remain there. The

temperature of this air is higher than average. It has also been shown that the concave side of a rotor blade will capture retarded air from the stator. The details depend upon rotor speed, airspeed, and the orientation of the blades and vanes. Repetition of this phenomenon leads to circumferentially varying temperatures throughout the compressor exit flow. Their disposition in space depends upon the aspect ratio of the blades and vanes, and the magnitude of their loading. This may continue through the engine. Because of the heavily loaded vanes and blades and the consequently thicker regions of retarded flow, centrifugal compressors are potentially the worst offenders.

The trapped flow illustrated in Figure 1.5-1 also works backwards. A strut or other obstacle placed in a flow creates a high static pressure field near its leading edge. Ordinarily, the pressure of such a field decreases rapidly with distance. If the strut is placed close enough to a row of vanes, however, the local increase in pressure will retard the flow through one or more of these vanes. Because of the trapped-flow principle, this retardation is propagated through a limited circumferential extent upstream. The strut will thus cause a small portion of the compressor to assume the operating point symbolized by Y in Figure 1.5-2 while the rest of the compressor operates at Point X. This behavior rarely produces surging problems, but it does cause local zones of high temperature and low airflow. The consequenses previously noted must be recognized. Inasmuch as the rotor blades passing through a trapped-flow region experience a variation in force, blade vibrations can be induced at a considerable distance upstream or downstream of a disturbing device.

In order to control mixing losses at the ends of the blades and vanes of a compressor, and preserve a reasonably uniform axial component of velocity through it, extra energy is usually deliberately added to the air near the blade ends to compensate for momentum deficiencies there. (Additional discussion of compressor flow control is given in Chapter 17.) This extra energy produces radial temperature and entropy gradients at the compressor exit, but these properties are approximately axisymmetric if the rotor and stator clearances are uniform. As discussed in 1.6, circumferential clearance variations must be expected. The net result can be additional uneveness in the flow, pressure and temperature distributions leaving the compressor.

1.5.3 Combustors

The relationship between the combustor and its adjacent components is thoroughly discussed in Chapter 20. The remarks presented here are included to preserve the continuity of this section.

The temperature distributions of the gasses within and leaving a combustor depend upon the distributions of the magnitude and temperature of the approaching airflow as well as the distribution of fuel and airflow into the combustor itself. Local deficiencies in approaching airflow or excesses in inlet air temperature cause local hot spots within and downstream of a combustor. Minimizing these hot spots is a goal of engine (not just combustor) design.

One should be aware that compact compressors must be designed so that their discharge velocity is greater than the velocity that combustors can tolerate. A diffuser must be placed, therefore, between the compressor and the combustor even though part of the combustor can be used to aid diffusion. Some of the discussions presented in 1.4.1.3 apply to this diffuser. If the compressor dispenses nonuniform flow, the diffuser problem can become very difficult. The unevenness in the flow is amplified by the diffuser and the flow can even become time unsteady. Such a situation must be rectified before an efficient combustor furnishing acceptable discharge conditions can be designed.

1.5.4 Turbines

The temperature of the gas entering a turbine should be as circumferentially uniform as possible. There is a maximum temperature that any portion of turbine stator can withstand before it loses strength or is corroded by chemical processes. The maximum temperature of the flow from the combustor is thus determined. However, the output from the turbine depends on the average temperature. The need for circumferential uniformity is obvious.

On the other hand, there is always an optimum but nonuniform radial temperature distribution that yields the best power with a minimum expenditure of cooling air, and still subjects the rotors to the same mechanical duress at all radii. Ample discussions of this subject are included in Chapters 18 and 19.

Any flow disturbance that inhibits uniform circumferential temperatures or proper radial temperature distribution imposes a penalty on engine performance. Close cooperation is required, therefore, between the designers of inlets, compressors, and combustors so that any necessary compromises are consistent with the objectives of the engine. This is another example where specialists should be familiar with peripheral disciplines.

A large change in flow direction is required in the vanes and blades of many turbines. This is particularly true near a turbine hub. Large secondary flow vortices (1.4.3.2) are often generated there. The extent of these vortices depends upon the quality of the flow entering the turbine. They can be partially controlled by adjusting the radial gradients of the energy abstracted from a turbine.

The statements made in connection with Figure 1.4-10 can be extended, with some modification, to turbines (see Chapter 10). It can be shown that retarded flow leaving a turbine stator elevates the effective temperature of the corresponding flow about the rotor. Unexpected damage near rotor blade ends can be traced to this phenomenon. The need for achieving proper flow distributions at the turbine inlet is thus emphasized.

In many engines, the flow immediately behind the last turbine is decelerated. The stable flow within the secondary flow vortices at the hub usually causes flow separation along the inner surface behind the turbine. (Such surfaces are shown in the cutaway views of engines shown in 1.1.)

Since the average entropy and static pressure gradients near the tips are in the same direction, the flow there is unstable. The flow in this region can usually be decelerated efficiently. The radial distribution of static pressure in the flow leaving the turbine can then often be controlled so that, although there is no subsequent deceleration at the hub, an average deceleration of the flow can be efficiently accomplished behind a turbine. In this connection, it is noteworthy that the shape of the flow passage behind a turbine can strongly influence its performance.

Emerging techniques for calculating flow distributions (see 1.7) will make it possible to diminish many unwanted flow effects. More freedom will then be available to a turbine designer.

1.5.5 Afterburners

Three interrelationships may be anticipated with afterburners. One is associated with presenting an afterburner with a flow in which the velocity is so low that the flame won't be blown out. This is a function of the turbine diffuser. The second was intimated in 1.3.3.2 and 1.3.3.3. When afterburning begins, the rate of temperature increase in the chamber must be carefully synchronized with the opening rate of the nozzle area. If the temperature rise is too fast, the corresponding rapid increase in pressure may cause the compressor, and especially the fan, to surge. This synchronization is a function of the controls. The third interaction is that of presenting the nozzle with a flow that has reasonably uniform momentum. This is mentioned in 1.5.6. Other important and unique features of an afterburner are discussed in Chapter 21.

1.5.6 Nozzles

The average total pressure of the gas immediately upstream of a nozzle exceeds the static pressure in the vicinity of the nozzle exit. It is the function of the nozzle to convert this pressure difference into velocity as effectively as possible. Although the momentum of the flow leaving the nozzle has been used to calculate the thrust, this momentum is only the reaction to the static pressure forces within the engine. It is these pressure forces that actually produce the thrust.

The mass flow, thermal energy, and mechanical energy of the flow upstream of a nozzle are established by the other components of the engine. Recall from 1.4.2.4 that the magnitude of the static pressure depends on the uniformity of the flow. Low static pressures due to nonuniform velocities ahead of the nozzle do reduce the thrust. The thrust developed is thus, not only dependent on the losses in all the components upstream, but upon the uniformity of the velocity presented to the nozzle. The acceleration of the flow through the nozzle does improve the distribution and reduces the potential losses, however. This is effected by the distributions of static pressure over the inner surface of the nozzle. The adverse effects of a maldistribution can never be completely overcome, however.

Note that swirling flow into the nozzle contributes nothing to the momentum from a nozzle. Such a flow represents wasted energy, although some swirl may be acceptable if it sufficiently improves the efficiency of the turbine and hence, the useful energy available to the jet.

The effects of nonuniform velocities and temperatures are usually reconciled during cycle analysis by using some average value for each together with an appropriate flow and thrust coefficients for the nozzle (See Chapters 6 and 14.) Care must be taken in the choice of averaging and the choice of these coefficients if contributions to performance (or performance defects) are to be correctly identified.

Care must also be taken to ensure that the static pressure at a nozzle exit is the one assumed. Pressure fields created by the airframe, or by curvature of the flow from or about the nozzle itself may alter the effective value of this pressure.

1.5.7 Summary

Besides the obvious effect of a mismatch in the flow capabity and efficiency of the engine components, the main source of unfavorable interaction comes from nonuniform flows and unsteady flows. Some deliberate distortions of flow may make a component look good at the expense of its neighbors. Such an endeavor may or may not be satisfactory. The overall effect on the engine must be considered to determine a components worth. Again, recall that each component exists for the engine and not vice-versa. There is nearly always a need to compromise.

1.6 INTERACTIONS WITH OTHER SPECIALTIES

It cannot be mentioned too often that there are many disciplines associated with designing, developing, and manufacturing an engine. How well one

discipline understands the problems and technology of other disciplines plays an important role in determining costs as well as the elapsed time between the initiation of design and the delivery of an approved product.

An aerodynamicist's lack of appreciation of stress and material technology may require him to design and redesign a blade a number of times before the aerodynamic and endurance requirements are satisfied. If manufacturing technology is ignored, an unnecessarily expensive process may have to be devised to make and inspect the blade. It is especially noteworthy that a part that can be thoroughly inspected is often preferred to a potentially superior part that does not lend itself to inspection. Frequently, the potentially superior part turns out to be inferior because it doesn't conform to design requirements. Simple design changes that improve the ability to reproduce a product, perhaps with a slight penalty in abeyant performance, should always be in the thoughts of an aerodynamic designer. This brings up the requirement for the designer to understand the real needs of the customer.

As mentioned in 1.1, the purpose of an airplane is to render a service that enough people want and can afford. The costs to the eventual customer include his share of the costs associated with the initial design and development, manufacturing, maintenance, and reliability. (Reliability signifies, among other connotations, whether nine or ten engines must be purchased to be sure that at least eight are available when needed.) By understanding the total picture, an honest evaluation can be made about whether the added cost of a supposedly more efficient part is worth its latent contribution to reduced fuel consumption, reduced weight or increased thrust. This knowledge, of course, cannot be acquired instantly. The successful aerodynamic designer will always be alert to opportunities that will improve his understanding of these interrelationships.

Besides adopting this long range philosophy, there are many areas where a good understanding of peripheral technology should be sought almost immediately. A few subjects and problem areas have been selected to illustrate the need for the aerodynamicist to be involved in many activities. The important subject of controls is not covered here since attention was directed to them earlier.

1.6.1 Dimensional Integrity

Notice was taken in previous sections of some effects of dimensional changes that accompany temperature variations throughout an engine. The existence of variations in temperature and dimensional changes along the length of the engine during steady-state operation should be readily appreciated. The effects of transient operation on changing these variations of temperature and dimensions with time should also be recognized.

Circumferential variations in temperature near an outer casing can cause local bulges in the casing, with a resulting local increase in clearance. Simple calculations can indicate how easily noticeable increases in local clearance are achieved.

It is practically impossible to keep uniform clearance between stationary and rotating parts at all times. There is, however, always some operating condition and one or more areas of an engine where the clearance is a minimum. The circumstances depend upon the temperatures and the vibrations, noted in 1.6.3. Airplane maneuvers are also involved. The requirement of mechanical integrity sets the magnitude of the minimum clearances. The clearances at other operating conditions are then automatically defined.

The relative growth of the rotating and stationary parts depends to some extent on the aerothermodynamic design. Heat transfer rates, blade shapes, and factors discussed in 1.6.3 are involved.

Changes in the area of turbine stators and exhaust nozzles with temperature are also pertinent items. If these areas are even moderately different than the design intent, the engine will be mismatched. Improper pressure ratios will be imposed upon the turbine and the engine exhaust nozzle. The bypass ratio will be affected and the thrust of a well designed engine will deteriorate.

1.6.2 Experimental Testing

It is easy to fall into the organizational trap of four isolated groups. One group does the design of a component, another group supervises its manufacture and assembly, a third group tests it in the laboratory, while a fourth group interprets the data. If the performance is lower than anticipated, the resulting discussions, while stimulating, do not hasten the delivery of a product nor lower its cost. Was the design bad? Was it poorly made or assembled? Are the test data bad? Are the interpretations inadequate?

The four activities stated above constitute the source of nearly all pertinent aerothermodynamic data. The elements in each process should be carefully monitored and understood by the aerothermodynamic designer. Ideas for changing and improving procedures will always be uncovered. More valuable information has often been learned by watching or participating in an assembly or a test than by looking at an inspection report or examining performance curves.

1.6.3 Flow Blockage by Struts and Accessory Drive Shafts

The rotating parts of an engine require bearings that must be supported by the external casing. The mechanical support is provided by struts that pass through the flow passages of an engine. At first blush, an aerodynamicist prefers the struts to be thin, few in number, and

remotely located from any blade or vane rows. One reason for this was noted in 1.4 where "flow trapping" was discussed.

Unfortunately, this "ideal" aerodynamic arrangement doesn't work. When an airplane executes some required, but violent, maneuvers, the struts must be strong enough to resist the inertial (including the gyroscopic) reactions of the rotor with minimal deflections. Excessive deflections would require blade and vane end clearances that would consume more efficiency than would the mechanically appropriate struts.

Designers must also anticipate the loss of one or more blades due to unanticipated blade vibrations or to foreign object damage. Rotor vibrations thus created are greater than those normally accepted by even self-adjusting bearings. The choice of strong struts is again preferable to excessive blade and vane clearances.

Supplying and scavenging oil from the bearings requires struts having adequate cross-sectional area. These struts also pass through engine flow passages. The use of thick struts is frequently necessary, but they should not be placed in sensitive aerodynamic areas. A mutual understanding of the problem by specialists in aerodynamics, stress and vibration analysis, lubrication, bearings, and weight control is the key for arriving at the proper trade-offs between clearances, blockage, and assembly.

It is noted in passing that some struts may be aerodynamically useful. For instance, they can be shaped and located to remove part of the swirl from the flow leaving a turbine. Refer to remarks in 1.5.6.

Similar problems arise when mounting accessories such as oil pumps, fuel pumps, starters, generators, and other rotating accessories along the external side of the engine casing. Some of these are shown in the engine photographs of 1.1. A so-called tower shaft must then pass through the airstream to connect the accessories to an engine shaft. When there are high- and low-pressure compressors and turbines, most connections are made to the high-pressure shaft because its speed usually varies less than that of any other shaft during flight. Moreover, this is the logical unit to be attached to the starter. The tower shaft is then mounted radially between compressors. (Putting it between turbines invites additional problems due to high local temperatures.) The tower shaft must be contained within a housing which also supplies oil to and from the internal gears.

Because of the need for compactness, there are often strong motives for placing the tower shaft close enough to the stators of the first compressor to introduce the trapping problem discussed in 1.5. Determining the best location and the shape of its housing, is another problem that requires intelligent compromises by all the specialties concerned with the design.

1.6.4 Foreign Object Damage

There are many causes of foreign object damage (FOD). When some airplanes begin their takeoff run, a veritable tornado often develops between the engine inlet and the runway. Loose objects are picked up and sucked into the inlet where they impact the rapidly moving compressor blades. Rags, tools, and other materials are sometimes carelessly left in the inlet by maintenance attendants. These materials hit the blades when the engine is started. Birds can be sucked into the inlet while the airplane is in flight. Special provisions must be made for large birds, or the devastation can be catastrophic.

Engines must pass certain tests prescribed either by law or by contract to prove their ability to withstand particular types of foreign object ingestion. Some of the tests are so severe that aerodynamic performance of the fan or the first-stage compressor may have to be sacrificed to meet the requirements. A mutual problem of the aerodynamicist and the stress analyst is to minimize this sacrifice. Unless each understands the other's field to some extent, intelligent dialogue is difficult and the probability of finding an optimum solution becomes remote.

In order to make intelligent decisions from the beginning, the stress, aerodynamic, and performance analysts must anticipate critical problems and their solution before the engine specifications are solidified. A great deal of time and money is otherwise spent overcoming unexpected obstacles.

1.6.5 Effects of Advanced Aerodynamic Technology

Initial efforts with advanced computational techniques, summarized in 1.7, have already shown that marked departures from conventional vane shapes will produce improvements in efficiency that have great financial value, particularly when fuel availability is decisive. A logical extrapolation of this result indicates that the vane and blade shapes of future engines will have different shapes than the ones now in use. The first reaction of stress analysts and manufacturers will probably reflect a complete lack of enthusiasm. Acceptance and use of new and improved ideas will come only when the three specialties share sufficient information to permit them to mutually overcome the apparent difficulties. The effectiveness of the aerodynamicist is again enhanced by his growing ability to contribute to solutions of the problems that stand between his good ideas and their ultimate use in engines.

1.6.6 Ceramic Turbine Blades and Vanes

The high turbine inlet temperatures of newer engines are obtained through the use of cooled turbines in which the principal material is nickel. This situation

has certain disadvantages. Nickel is not native to the United States, and the supply could be curtailed by the whims of another nation. Moreover, the total known supply is not inexhaustable and there are competing demands for it. Nickel is heavy and expensive. The turbine cooling process limits the advantage of elevated temperatures because it lowers turbine efficiency and a good first approximation to a turbine's value is the product:

(Turbine Efficiency)
X (Turbine Inlet Temperature)

(Refer to Chapter 7)

For these reasons, a great deal of time and money has been spent on the search for cheap and readily available materials that do not require cooling. Two ceramics, silicon carbide and silicon nitride, have been identified as promising candidates at this writing.

These materials are extremely brittle in comparison with presently used turbine materials which are already brittle to a troublesome degree. Extreme care must be taken in mechanical design. Even so, reductions in the allowable tensile stresses must be contemplated. These reductions can be accomplished by reducing the centrifugal forces on the blades, and by minimizing bending stresses due to centrifugal and aerodynamic forces.

Either scheme offers a threat to turbine efficiency. Large aerodynamic blade loadings may be necessary because comparatively low blade speeds would be required to reduce centrifugal forces. In addition, the radial distribution of the axial and circumferential components of flow entering and leaving the blades and vanes may differ from that encompassed by our present experience in order to reduce bending stresses. The need for new blade shapes must therefore, be anticipated. The development of new turbine aerodynamic technology to keep the efficiency within tolerable levels thus becomes a challenge to the aerodynamicist. Emerging computation techniques may enable this development to be realized at an affordable price. An alert appraisal of such opportunities is a continuing requisite.

There is a question whether these particular ceramic materials are the answer. Even better materials can certainly be expected. The law of the "perversity of nature" probably applies however, and increases in brittleness seem to be an inevitable accompanyment to increases in allowable material temperatures. An aerodynamicist should understand the interaction between his blade designs, the corresponding stresses, and their effect on forthcoming materials. He is then prepared to pursue the courses necessary to extend his degrees of freedom for the design of efficient high temperature turbines. Remember however, that a small reduction in the basic aerodynamic efficiency can be an almost trivial ransom for retrieving power that would otherwise be lost to cooling at very high turbine inlet temperatures.

1.6.7 Environmental Problems

The design freedom in propulsion engines has recently been restricted by laws and regulations enacted to protect our environment. One area of protection limits the allowable noise that various types of aircraft can generate. The other concerns certain polluting compounds that are generated in a combustor and then discharged in the exhaust.

Noise is the subject of Chapters 24 and 25. A section on the subject of emissions is contained in Chapter 20. Background information is presented in Chapter 15. The noise considerations described below illustrate one of the conflicts of interest in this area.

Acousticians and vibration analysts would like to see successive blade rows placed far apart. Time-steady flow in a rotor produces time-unsteady flow in a stator, and vice-versa. The closer the two elements are to each other, the greater becomes the forces causing vibration and noise.

The aerodynamicist and the weight analyst, on the other hand, prefer to have them close together. The effect on engine weight is obvious. As far as aerodynamics is concerned, there is experimental evidence that placing rotors and stators close together benefits performance. The optimum solution is found when all four specialties share their expertise to meet all of the objectives of the engine. A new interface is thus introduced by environmental considerations.

As a general note, proposed regulations are published, and comments by the affected parties are invited. The participants in these areas should have a thorough understanding of existing regulations, and be constantly alert to proposed changes. They must also be aware of the attitudes of key people involved in offering and adopting regulations, so that improvements in technical competence can be directed to those areas where problems are anticipated.

1.7 REMARKS ON ADVANCED FLOW CALCULATIONS

The art of flow calculations is burgeoning at an enormous rate. Until very recently, the methods in Chapters 4 and 10 were the standard repertoire of aerodynamic designers of turbomachinery. The revolution in digital computers has inspired an accompanying revolution in the art of numerical analysis. Even a lengthy treatise at this point would do an injustice to this subject. Just enough information will be given to describe what lies behind some of the ongoing activities.

Most of the new procedures embody some form of the Navier-Stokes equations including the Reynolds turbulence stresses.

This equation is developed in Chapter 4. Some model for estimating the distribution of turbulence is also required. Available models are approximate and subject to opinions and improvements. Nevertheless, some very useful advances have been made with the crude turbulence models now existing. Several methods of calculating a flow field can be developed from this base. Some procedures use the concept of boundary layer, introduced in Chapter 4 and expanded in Chapter 18.

Another technique that was recently introduced borrows an idea from electromagnetic theory. The flow vector is divided into two components--one of which has no curl, and one of which has no divergence. The latter vector describes all the vorticity in the flow. In some respects it is really a generalization of the boundary layer concept. Compatibility conditions between the two vector fields are required. The first field is mixed elliptic-hyperbolic, and can be solved by known "relaxation" procedures. The second field is essentially parabolic, and is solved by "marching methods". (The upstream vector doesn't know what the downstream vector is doing.)

Two classes of computational techniques are being pursued. One class begins by assuming the flow to be at rest, and imposes the boundary conditions. The time-unsteady equations of motion then estimate the acceleration of the flow until it reaches equilibrium.

The other class uses finite difference or finite element methods. Transformation of coordinates as a function of the local Mach number and the location of the point of interest in the flow field may be used. Methods of taking the finite differences or of describing the finite elements also vary with both the local Mach number and the point in the field.

All the programs are very involved, and their preparation presently requires an outstanding ability in computer programming, numerical analysis, and fluid mechanics. Because of the enormity of the problem, existing programs must be considered to be only partially developed. Even in this crude state, their use has, for example, indicated ways of designing turbine vanes so that the secondary-flow losses are reduced. The experimental test of the resulting turbine was more than gratifying.

This field is moving forward at a rapid rate. Useful new concepts are continually being disclosed. As a result, the ability to accurately analyze complex flows in detail is noticeably improving from year to year. Close attention must be paid to this activity.

The pursuit of advanced three-dimensional analysis will bring about step improvements in turbomachinery performance. Side benefits will be the reduction of expensive testing and the delineation of forcing functions that affect blade vibration.

1.8 A BRIEF BIOGRAPHY OF A TYPICAL ENGINE

The final section of this chapter is presented to show that all specialties have a long way to go before we can truly say that engines can be accurately designed. A lot of development work needs to be done in order to produce a successful engine. Most of it has to be performed by "greasy-fingered" engineers, who are often forced to work with trial and error methods. They need all the useful help they can get from the various specialties for reducing weight, improving fuel consumption, and increasing both reliability and component life.

With respect to the biography, observe first that research is continually being directed toward improving the capabilities of aircraft and engines. General analyses of these results are periodically made to examine the feasibility of improving existing airplanes, of making an airplane that will either perform a useful service more economically, or of providing one that was hitherto unavailable.

When the feasibility of an improved engine/airframe system is determined, an analysis similar to that presented in Chapter 3 is initiated. Engines and airplanes having the proposed advanced concepts are simulated on large digital computers. Estimates are made of the properties and behavior of every significant part of the engine and aircraft. Interfaces such as those discussed in Chapters 13, 14, and 26 are carefully considered. The vital features of the synthesized airplane are calculated along its proposed flight paths. Numerous modifications of the synthesized engines and aircraft are examined until the calculated optimum reliable airframe/engine combination for the proposed mission is found.

The results are then reviewed to determine the worthiness of the airplane. This review includes an estimate of the cost of designing and developing the engine and airplane, the cost of manufacturing the desired number, and the cost of operating and maintaining them over their expected life. These economic evaluations (which are often identified by the words "cost of ownership", "life-cycle-costs", or "return on investment") are repeated throughout the life of the enterprise.

If a decision is made to proceed with the design and development of an engine, the inital specifications are provided by the preceding studies. Tests are begun on the various components to evaluate their effectiveness; i.e., how does the performance compare to that expected? Several design modifications are frequently required to realize the initial expectations.

After the components are functioning reasonably well, they are assembled into an engine to evaluate overall performance and reliability. Parts of new engines usually operate in more hostile environments than any of their predecessors, and

unanticipated interactions among the parts (both aerothermodynamic and mechanical) are occasionally encountered. Many events can and do happen. Some problems can be rectified by minor changes in engine design. Others may require major redesigns that need to be reevaluated on component rigs. In some instances, added required costs of time and money can put the project in jeopardy.

When the engine performs its functions on a test stand with sufficient reliability, it is ready for flight tests. New interactions between the airframe and the engine introduce additional problems. This is particularly true when there is no previous experience with the maneuvers and flight regimes demanded of the airplane. Expedited rebirth and development of critical engine components has been necessary even at this late phase of development. Dedicated and competent engineering teamwork usually solves the problems, and an airplane that meets its specifications is finally derived.

After an engine has been certified by a government bureau, it enters its intended service. When many hours of flight have elapsed, new major problems have suddenly appeared. Although most of these are mechanical and related to low-cycle fatigue, they probably represent a poor trade-off, initially made with incomplete data, between aerodynamics and stress. New evaluations and new designs have to be made and developed in a hurry to solve the problems. Again, it is the teamwork of many talents that overcome the difficulties.

Eventually, even better performance is wanted and advanced development begins. The engine is gradually and continually improved by new technology. This phase may last 20 years or more. Weak parts are strengthened to increase the time between overhauls (TBO). The weights of other parts are decreased by improved design or by material substitution. Superior aerothermodynamics are developed that can, for instance, raise the output without objectionable increases, or even reductions, in fuel consumption. By the time the engine is eventually superseded by one from a new generation, its output may have been increased 100 percent with only small increases in size and weight, and little, if any, increase in specific fuel consumption.

The events described in this review are not atypical. Including them is not meant to disparage any work of the past, or discourage bold ventures in the future. Rather, it is intended to emphasize the need for recognizing problems as early as possible during design and development. It also points out the value of individuals having the wide scientific background necessary for recognizing the source of a variety of interrelated problems and solving them.

Of equal importance, it emphasizes the need of basic research for anticipating and solving problems on inexpensive rigs rather than expensive engines. Most of this research is not glamorous and does not provide headlines. Its ultimate financial value cannot, however, be overemphasized.

Chapter 2

THERMODYNAMICS AND QUASI-ONE-DIMENSIONAL FLUID FLOWS

Gordon C. Oates

University of Washington

TABLE OF CONTENTS

CHAPTER 2 THERMODYNAMICS AND QUASI-ONE-DIMENSIONAL FLUID FLOWS

		Page
2.0	Introduction	2-1
2.1	Definitions	2-1
2.2	The Laws of Thermodynamics	2-1
2.3	The Zeroth Law of Thermodynamics	2-1
2.4	The First Law of Thermodynamics	2-2
2.5	The Reversible Process	2-2
2.6	Derived Properties - Enthalpy and Specific Heats	2-2
2.7	The Second Law of Thermodynamics	2-3
2.8	The Gibbs Equation	2-3
2.9	The Gibbs Function and the Helmholtz Function	2-3
2.10	Maxwell's Relations	2-4
2.11	General Relationships Between Properties	2-4
2.12	The Perfect Gas	2-5
2.13	Quasi-One-Dimensional Fluid Flows	2-6
2.14	The First Law for a Flowing System-- The Control Volume	2-7
2.15	The Channel Flow Equations	2-9
2.16	Stagnation Properties	2-10
2.17	Property Variations in Channels	2-11
2.17.1	Adiabatic Flow of a Perfect Gas	2-11
2.17.2	Non-Adiabatic Flow of a Perfect Gas	2-12
2.17.3	Constant Area Heat Interaction	2-13
2.17.4	Ideal Constant Area Heat Interaction - Thermal Choking	2-13
2.17.5	Adiabatic Constant Area Flow - Viscous Choking	2-14
2.18	The Nozzle Flow Equations	2-15

LIST OF FIGURES

		Page
Figure 2.13.1	Control Volume and Control Mass.	2-7
Figure 2.14.1	Adiabatic Nozzle	2-8
Figure 2.14.2	Fluid Container	2-8
Figure 2.14.3	Container and Nozzle	2-9
Figure 2.15.1	Element of Fluid in Duct	2-9
Figure 2.16.1	Duct and Imaginary Duct for Stagnation Condition	2-10
Figure 2.16.2	Stagnation Conditions at Two Axial Locations	2-11
Figure 2.17.1	Element of Channel	2-12
Figure 2.17.2	$f(M^2)$ vs M, Ideal Constant Area Heat Interaction	2-13
Figure 2.17.3	Mach Number and Stagnation Pressure Ratio vs $\Delta q/C_p T_{t1}$ for Ideal Constant Area Heat Interaction	2-14
Figure 2.17.4	Variation of Static Pressure, Stagnation Pressure and Mach Number with Axial Position, Adiabatic Constant Area Flow	2-15
Figure 2.18.1	Pressure Ratio and Mach Number Versus Area Ratio for Isentropic Nozzle Flow	2-15

CHAPTER 2

LIST OF SYMBOLS

The symbols are listed in alphabetical order, first in the English alphabet, then in the Greek alphabet. Subscripts and superscripts are then given. The equation, figure or section in which the symbols are first introduced is indicated in parentheses. Often the symbol will be defined in the text just preceding or just following the equation or figure.

A - Cross sectional area (Eq. 2.14.2)

a - Speed of sound (Eq. 2.16.3)

C - Specific heat (Eq. 2.6.2)

c - Circumference (Eq. 2.15.5)

- Characteristic velocity (Eq. 2.18.3)

D - Diameter (Eq. 2.17.9)

$\bar{d}Q$ - Incremental heat interaction (Eq. 2.4.1)

$\bar{d}q$ - Incremental heat interaction/mass (Eq. 2.6.1)

$\bar{d}W$ - Incremental work interaction (Eq. 2.4.1)

E - Energy (Eq. 2.4.1)

F - Helmholtz function (Eq. 2.9.2)

f - Mathematical function (Eq. 2.17.21, 2.17.25)

G - Gibbs function (Eq. 2.9.1)

h - Specific enthalpy (Eq. 2.6.1)

- Heat transfer coefficient (Eq. 2.17.11)

M - Mathematical function (Eq. 2.10.1)

- Mach number (Eq. 2.16.3)

m - Mass (Eq. 2.14.8)

$\dot{m}$ - Mass flow rate (Eq. 2.14.4)

N - Mathematical function (Eq. 2.10.1)

N_{ST} - Stanton number (Eq. 2.17.12)

p - pressure (Eq. 2.5.1)

P.E. - Potential energy (Eq. 2.14.3)

R - Gas constant (Eq. 2.12.1)

s - Specific entropy (Eq. 2.7.1)

T - Temperature (Eq. 2.6.2)

t - Time (Eq. 2.14.2)

U - Internal energy (Eq. 2.5.1)

u - Specific internal energy (Eq. 2.6.3)

- Velocity (Eq. 2.15.1)

V - Volume (Eq. 2.5.1)

- Velocity (Fig. 2.14.3)

v - Specific volume (Eq. 2.6.1)

x - Independent variable (Eq. 2.10.1)

- Axial co-ordinate (Eq. 2.15.5)

y - Independent variable (Eq. 2.10.1)

z - Dependent variable (Eq. 2.10.1)

γ - Ratio of specific heats (Eq. 2.6.4)

Δ - Mathematical function (Eq. 2.17.21)

- (also used for increment in quantity)

δ - Small increment in quantity (Eq. 2.6.2)

θ - Angle of wall (Fig. 2.15.1)

ρ - Density (Eq. 2.11.18)

τ - Shear stress (Eq. 2.15.5)

χ - Nondimensional axial coordinate (Eq. 2.17.25)

Subscripts

c - Chamber (Eq. 2.14.8)

C.M. - Control mass (Eq. 2.14.1)

C.V. - Control volume (Eq. 2.14.3)

e - Exit (Eq. 2.14.4)

f - Skin friction (Eq. 2.17.8)

i - Inlet (Eq. 2.14.4)

M - Mechanical (Eq. 2.14.4)

p - At constant pressure (Eq. 2.6.2)

R - Radiative transfer (Eq. 2.17.14)

r - Reversible (Eq. 2.4.1)

T - Total (Eq. 2.14.1)

- Convective transfer (Eq. 2.17.13)

t - Stagnation (Eq. 2.16.1)

u - Universal (Eq. 2.12.2)

v - At constant volume (Eq. 2.6.2)

w - Wall (Eq. 2.17.11)

1 - reference state (Eq. 2.4.1)

- Condition at entry to control volume (Eq. 2.14.2)

Superscripts

* - Conditions at the throat (Eq. 2.18.3)

2 - Condition at exit to control volume (Eq. 2.14.2)

CHAPTER TWO
THERMODYNAMICS AND QUASI-ONE-DIMENSIONAL FLUID FLOWS

2.0 INTRODUCTION

This chapter will be limited to a very brief review of the concepts and laws of thermodynamics and to the description of quasi-one-dimensional flows. It is important to understand that the subject of thermodynamics itself is restricted to the study of substances in equilibrium; including thermal, mechanical and chemical equilibrium, and hence is more nearly analogous to statics than to dynamics. This restriction might seem to be hopelessly restrictive to an engineer because an engineer is most often concerned with flow processes, and the substances involved in flow processes are not, strictly speaking, in equilibrium. In fact, however, in most cases of interest to the engineer, such substances may be considered to be in "quasi-equilibrium" such that we may consider local values of the thermodynamic properties to be defined.

Flow processes have losses associated with them that can be identified with the lack of equilibrium, and it should be realized that the quantitative prediction of such losses is beyond the scope of thermodynamics. The "theory of transport phenomena" must be applied in order to quantitatively estimate such losses, and the prediction of the various "transport coefficients" must rely upon the techniques of kinetic theory.

The complicated transport mechanism known as turbulence is an essentially macroscopic phenomenon. The accurate description of losses in turbomachines relies very heavily upon the accurate description of turbulent processes because the turbulent transport mechanisms contribute the dominant portion of the losses in virtually all turbomachine components. Chapters 4 and 16 deal specifically with the methods of estimating turbulent transport effects.

2.1 DEFINITIONS

It is important to be precise in the definition of terms intended for use in the context of thermodynamics so that possible confusion with the colloquial usage of a term may be avoided. A very abbreviated list of definitions as will be utilized herein follows.

PROPERTY - A property is a characteristic (of a system) that can in principle be quantitatively evaluated. Properties are macroscopic quantities that involve no special assumptions regarding the structure of matter. (Ex.: temperature, pressure, volume, entropy, internal energy, etc.)

Properties are grouped into two classes:

Extensive properties - Properties which are proportional to the mass of the system.

Intensive properties - Properties which are independent of the mass of the system. Any extensive property can be made an intensive property simply by dividing by the mass of the system.

THERMODYNAMIC STATE - The state of a system is its condition as described by a list of the values of its properties.

THERMODYNAMIC PROCESS - In the limiting case when a change in the properties of a thermodynamic system takes place very slowly, with the system at all times very close to equilibrium the "in-between" states can be described in terms of properties. A change under such conditions is called a thermodynamic process.

WORK - The concept of work is a familiar one from mechanics. Work is said to be done by a system when the boundary of the system undergoes a displacement under the action of a force. The amount of work is defined as the product of the force and the component of the displacement in the direction of the force. Work is so defined as to be positive when the system does work on the surroundings. It should be noted that work can by no means be considered a property, but rather is identified with the transitory process. In order to avoid possible confusion, the term "work interaction" will often be used when a system is undergoing a "work process." Thus, a positive work interaction occurs when the system does work on its surroundings and a negative work interaction occurs when the surroundings do work on the system.

HEAT - In analogy to the work interaction defined above, we also define a heat interaction. Thus, when a hot body is brought into contact with a cold body, the temperature of each changes, and we say that the cold body experiences a positive heat interaction. Similarly, the hot body simultaneously experiences a negative heat interaction. In order to define the heat interaction of a body quantitatively, the change in one or more properties (usually the temperature) of a standard system is measured when the standard system and the body reach equilibrium after being placed in contact. Like the work interaction, the heat interaction is used only in connection with the transitory process.

2.2 THE LAWS OF THERMODYNAMICS

In the following sections, the first three laws of thermodynamics will be discussed. Because thermodynamics is primarily concerned with heat and work interactions, the experiments leading to the formulation of the laws are in all cases considered to deal with macroscopically stationary materials. That is, though the material boundaries may be movable, there is no contribution to the interchanges of energy, etc., due to a change in potential energy or kinetic energy of the macroscopic sample. It is to be understood that when such contributions are of importance in an interaction (as they obviously are in most processes in turbomachinery), they may be included later in a straightforward manner by applying the laws of mechanics. The interaction of thermodynamic and overall mechanical energy effects is considered in sections 2.13-2.15.

2.3 THE ZEROTH LAW OF THERMODYNAMICS

This law is so fundamental in classical thermodynamics that it was at first accepted as being self-evident and was not formally denoted a law till after the "First Law" and "Second Law" had become established. It is now recognized that it is of fundamental importance to the foundation of classical thermodynamics, however.

Experience has shown that if a hot body is brought into contact with a cold body, changes take place till eventually the hot body stops getting colder and the cold body stops getting hotter. At this point we say the bodies are in thermal equilibrium. The Zeroth law states:

> If two bodies are separately in thermal equilibrium with a third body, they are in thermal equilibrium with each other.

It is evident that bodies in thermal equilibrium have some property in common and we call this property the temperature. Thus, if we so pleased, we could use any reference temperature scale (a mercury thermometer for example) to determine the temperature of an object; but it can be shown that the second law allows the definition of a temperature scale independent of the properties of the reference substance.

We see then that the Zeroth law allows definition of the property temperature, though it does not lead to the definition of any particular reference scale for temperature. The restriction of thermodynamics to the study of equilibrium conditions is very evident here; because temperature could be defined as that property the bodies had in common, only if the bodies were allowed to reach equilibrium.

2.4 THE FIRST LAW OF THERMODYNAMICS

Joule, in 1840, conducted his famous experiment to establish the equivalence of a heat interaction and a work interaction. His result, available in many texts, allowed the definition of a new property, the energy E. Thus, denoting $đQ$ as an incremental heat interaction and $đW$ as an incremental work interaction, we have

$$E - E_1 = \int_1 (đQ - đW) \qquad (2.4.1)$$

Here we note:

(1) The energy can be defined in terms of the system properties only when the end states are equilibrium states, though the intervening states on the path need not be in equilibrium.

(2) The energy is given as a difference in magnitude between the two states and is not defined in absolute value.

The definition of a simple system states that such a system is completely defined in terms of any two intensive properties, and the energy in such a restrictive case is usually termed the internal energy and denoted by U. Usually any two of the three properties--temperature (defined from the zeroth law), pressure (defined from mechanics), or volume per unit mass (defined from geometry)--are used as the independent properties. It is apparent also that the internal energy of a system can be "tapped" so that we can obtain a net outflow of energy in the form of either a heat or work interaction. Any observant person, however, can sense that there must be some restriction on the form in which this outflow of energy can occur because of the comparative ease of obtaining a negative heat interaction from a system as compared to that of obtaining a positive work interaction. This restriction is formalized in the statement of the second law of thermodynamics.

We may note the differential form of the first law may be written

$$đQ = dE + đW \qquad (2.4.2)$$

2.5 THE REVERSIBLE PROCESS

A very useful reference process in thermodynamics is that of the reversible process. A thermodynamic process is defined as a process in which changes take place so slowly that the "in-between" states of the system are at all times close to equilibrium so that the intermediate states can be described in terms of properties. In the case where, in addition, all external constraints vary only infinitesimally from equilibrium, the process is said to be "reversible." The terminology is obvious here in that if there is an infinitesimal change in the properties of the system or its surroundings, the process can be reversed and the system returned to its initial conditions.

Our interest in this study is in gases, which are very close to ideal "simple systems," in that their thermodynamic state is (very nearly) completely determined by any two thermodynamic properties. For such a substance the element of work done in a reversible process is simply $đW = pdV$, in which, by the definition of a reversible process, the pressure must be defined at all times throughout the process. We see then that the first law for a gas undergoing a reversible process may be written

$$đQ_r = dU + pdV \qquad (2.5.1)$$

2.6 DERIVED PROPERTIES - ENTHALPY AND SPECIFIC HEATS

So far in our discussion of thermodynamics, we have defined and used only four properties--specific volume, pressure, temperature, and internal energy (v, p, T, and U). These properties are defined very fundamentally, but we will find that there is great utility of notation allowed if certain properties derived from these fundamental properties are defined. It should be noted, of course, that any combination of properties is itself a property.

One group of properties that occurs frequently for gas dynamicists is u + pv, and this group is given the symbol h and the name specific enthalpy. We may write the first law in terms of enthalpy for a gas undergoing a reversible process as: (henceforth, for convenience, we shall refer to [specific] quantities)

$$đq_r = dh - vdp \qquad (2.6.1)$$

Two further useful derived properties are the specific heat at constant pressure and the specific heat at constant volume. These specific heats (or specific heat capacities) are defined as the (differential) heat interaction (at constant pressure; volume) occurring in a reversible process, divided by the resultant (differential) temperature change. That is,

$$C_p = \frac{(\delta q_r)}{\delta T} \qquad p = \text{Const}$$

$$C_v = \frac{(\delta q_r)}{\delta T} \qquad v = \text{Const} \qquad (2.6.2)$$

The two forms of the first law given above show that these terms are in fact properties, and that they may be written

$$C_p = \left(\frac{\partial h}{\partial T}\right)_p$$

$$C_v = \left(\frac{\partial u}{\partial T}\right)_v \qquad (2.6.3)$$

The ratio of the specific heats is also often used and is given the symbol γ, where

$$\gamma \equiv \frac{C_p}{C_v} \qquad (2.6.4)$$

2.7 THE SECOND LAW OF THERMODYNAMICS

Joules experiment which led to the establishment of the First Law of Thermodynamics involved a negative work interaction with a system and the consequent increase of internal energy of the system, rather than the reverse process of a positive work interaction at the expense of the internal energy of the system. The engineer is usually concerned with this latter procedure, and it is clear that a very desirable type of engine--that would not violate the first law--would be one which used a very large reservoir of internal energy (the ocean for example) and converted the energy drawn from the reservoir entirely into a work interaction. Even though, wittingly or unwittingly, inventors still attempt to obtain patents for devices capable of performing in the manner described above, no working model of such a device has ever been constructed, and the very long history of failures to do so has long since led to the belief that it is impossible. This restriction on the first law has been formalized in the Second Law of Thermodynamics which may be stated:

> It is impossible for any engine, working in a cyclic process, to draw heat from a single reservoir and convert it to work.

This statement (or any of its equivalent forms) when combined with the zeroth and first laws allows many remarkable deductions to be drawn concerning the thermodynamic behavior of matter.

These deductions are usually presented as theorems, and include amongst them the definition of a new intensive property, the entropy, s. Thus,

$$s - s_1 = \int_1 \frac{\delta q_r}{T} \qquad (2.7.1)$$

We also note the differential form

$$Tds = \delta q_r \qquad (2.7.2)$$

Here we note:

(1) The entropy, like the internal energy, is given as a difference in magnitude between the two states and is not defined in absolute value.

(2) It is very important to note that the definition of entropy in no way requires that the state to be described be reached reversibly from some reference state. The integral relation given above simply gives a procedure for calculating the entropy difference between specified end states. The value of entropy itself, like temperature, pressure, or any other thermodynamic property, depends only on the (equilibrium) conditions at the specified state and in no way depends on the "history" of the processes leading to that state. As stated previously, the assignment of any two thermodynamic properties completely defines all further thermodynamic properties for a simple system; and, hence for example, if the pressure and temperature of the air in a given room are specified, so too is the entropy. Conversely, of course, if the temperature and entropy are specified, so too is the pressure.

A further theorem of enormous consequence is that the entropy of an isolated system cannot decrease. This theorem has great utility in investigating the possibility or impossibility of an assumed process.

2.8 THE GIBBS EQUATION

An equation relating the five fundamental properties of thermodynamics--specific volume, v (defined from geometry), pressure, p (defined from mechanics), absolute temperature, T (defined from the zeroth and second laws), internal energy, u (defined from the first law), and entropy, s (defined from the second law)--follows directly by combining Eqs. (2.5.1) and (2.7.2). Thus,

$$Tds = du + pdv \qquad (2.8.1)$$

This equation is known as the Gibbs equation, and as stated, relates the five fundamental properties of thermodynamics. We note that a similar equation is obtained in terms of the derived property, enthalpy, by combining Eqs. (2.6.1) and (2.7.2) to give

$$Tds = dh - vdp \qquad (2.8.2)$$

2.9 THE GIBBS FUNCTION AND THE HELMHOLTZ FUNCTION

Two further derived properties are defined by the relationships

$$G = h - Ts \qquad G \equiv \text{Gibbs function} \qquad (2.9.1)$$

$$F = u - Ts \qquad F \equiv \text{Helmholtz function} \qquad (2.9.2)$$

In some applications, particularly applications involving determination of chemical equilibrium, these newly defined properties have important physical interpretations. For our purposes, however, we simply note that we may obtain expressions for differential changes in G and F which may be promptly utilized to obtain a very useful set of relationships known as Maxwell's Relations.

2.10 MAXWELL'S RELATIONS

By definition, when a simple thermodynamic system is considered, specification of any two (intensive) properties completely defines the thermodynamic state (and hence all properties) of the system. Thus, if the differential change dz in a property z is given in the form

$$dz = M(x,y)dx + N(x,y)dy \qquad (2.10.1)$$

the condition for exactness gives

$$\left[\frac{\partial M}{\partial y}\right]_x = \left[\frac{\partial N}{\partial x}\right]_y \qquad (2.10.2)$$

In addition, we note

$$M = \left[\frac{\partial z}{\partial x}\right]_y , \quad N = \left[\frac{\partial z}{\partial y}\right]_x \qquad (2.10.3)$$

Before utilizing these equations to generate Maxwell's Relations, we should reflect upon the necessity of utilizing the partial differential notation in which the variable being held constant is explicitly indicated. This notation is required in thermodynamics because though (for a simple system) only two properties may be separately specified, there is a wide choice of which two properties may be selected. Thus, for example, the rate of change of pressure with density with the entropy held constant is not equal to the rate of change of pressure with density with the temperature held constant. Hence, of course, we must provide a notation that clarifies which partial derivative is intended.

Combination of Eqs. (2.8.1-2.9.2) leads to:

$$du = Tds - pdv \qquad (2.10.4)$$

$$dh = Tds + vdp \qquad (2.10.5)$$

$$dG = - sdT + vdp \qquad (2.10.6)$$

$$dF = - sdT - pdv \qquad (2.10.7)$$

Systematic application of Eqs. (2.10.2) and (2.10.3) then leads to:

$$\left(\frac{\partial u}{\partial s}\right)_v = T = \left(\frac{\partial h}{\partial s}\right)_p \qquad (2.10.8)$$

$$\left(\frac{\partial u}{\partial v}\right)_s = - p = \left(\frac{\partial F}{\partial v}\right)_T \qquad (2.10.9)$$

$$\left(\frac{\partial h}{\partial p}\right)_s = v = \left(\frac{\partial G}{\partial p}\right)_T \qquad (2.10.10)$$

$$\left(\frac{\partial G}{\partial T}\right)_p = - s = \left(\frac{\partial F}{\partial T}\right)_v \qquad (2.10.11)$$

$$\left(\frac{\partial T}{\partial v}\right)_s = - \left(\frac{\partial p}{\partial s}\right)_v \qquad (2.10.12)$$

$$\left(\frac{\partial T}{\partial p}\right)_s = \left(\frac{\partial v}{\partial s}\right)_p \qquad (2.10.13)$$

$$\left(\frac{\partial s}{\partial p}\right)_T = - \left(\frac{\partial v}{\partial T}\right)_p \qquad (2.10.14)$$

$$\left(\frac{\partial s}{\partial v}\right)_T = \left(\frac{\partial p}{\partial T}\right)_v \qquad (2.10.15)$$

This set of equations is known as Maxwell's Relations. One of the prime utilizations of these relations is found when we wish to obtain the behavior of certain properties in terms of the "properties of state," p, v, or T. Usually a substance is described by its equation of state relating the three variables, p, v, and T, and by manipulating the Maxwell's Relations appropriately, the behavior of other properties may be deduced. We note, of course, that the equation of state may not be available in analytic form, but rather in the form of tables or graphs. However, in turbomachinery we are most often interested in gases which may be considered perfect. Special forms of the several following relationships, valid for perfect gases, are given in section 2.12.

2.11 GENERAL RELATIONSHIPS BETWEEN PROPERTIES

We begin by writing an expression for a differential change in entropy, with the entropy considered to be a function of temperature and specific volume. Thus,

$$ds = \left(\frac{\partial s}{\partial T}\right)_v dT + \left(\frac{\partial s}{\partial v}\right)_T dv = \frac{\left(\frac{\partial u}{\partial T}\right)_v}{\left(\frac{\partial u}{\partial s}\right)_v} dT + \left(\frac{\partial s}{\partial v}\right)_T dv$$

With Eqs. (2.6.3), (2.10.8), and (2.10.15) we then obtain

$$Tds = C_v dT + T \left(\frac{\partial p}{\partial T}\right)_v dv \qquad (2.11.1)$$

Similarly, we consider the entropy to be a function of temperature and pressure to give

$$ds = \left(\frac{\partial s}{\partial T}\right)_p dT + \left(\frac{\partial s}{\partial p}\right)_T dp = \frac{\left(\frac{\partial h}{\partial T}\right)_p}{\left(\frac{\partial h}{\partial s}\right)_p} dT + \left(\frac{\partial s}{\partial p}\right)_T dp$$

With Eqs. (2.6.3), (2.10.8), and (2.10.14) we then obtain

$$Tds = C_p dT - T \left(\frac{\partial v}{\partial T}\right)_p dp \qquad (2.11.2)$$

Applying the condition for exactness to the expressions for ds given by Eqs. (2.11.1) and (2.11.2) gives

$$\left(\frac{\partial C_v}{\partial v}\right)_T = T \left(\frac{\partial^2 p}{\partial T^2}\right)_v \qquad (2.11.3)$$

$$\left(\frac{\partial C_p}{\partial p}\right)_T = -T \left(\frac{\partial^2 v}{\partial T^2}\right)_p \qquad (2.11.4)$$

An expression for the difference of specific heats is obtained by subtracting Eq. (2.11.1) from (2.11.2) and in addition noting that the ratio

$\frac{dp}{dT}$ corresponds to $(\frac{\partial p}{\partial T})_v$ for the case where dv = 0. Thus, we obtain

$$C_p - C_v = T\,(\frac{\partial p}{\partial T})_v\,(\frac{\partial v}{\partial T})_p \qquad (2.11.5)$$

Combination of Eqs. (2.8.1) and (2.11.1) gives an expression for the differential change in internal energy,

$$du = C_v dT + [T\,(\frac{\partial p}{\partial T})_v - p]\,dv \qquad (2.11.6)$$

and combination of Eqs. (2.8.2) and (2.11.2) gives an expression for the differential change in enthalpy,

$$dh = C_p dT + [v - T\,(\frac{\partial v}{\partial T})_p]\,dp \qquad (2.11.7)$$

As a final example we obtain an expression for the rate of change of pressure with density at constant entropy. This ratio is of particular importance in fluid mechanics because (as follows from momentum considerations) it is equal to the square of the speed of small disturbances relative to the local fluid velocity. We begin by writing

$$(\frac{\partial p}{\partial \rho})_s = \frac{(\frac{\partial p}{\partial \rho})_s}{(\frac{\partial p}{\partial \rho})_T}\,(\frac{\partial p}{\partial \rho})_T = \frac{(\frac{\partial p}{\partial v})_s}{(\frac{\partial p}{\partial v})_T}\,(\frac{\partial p}{\partial \rho})_T$$

Applying the chain rule of calculus we have

$$\frac{(\frac{\partial p}{\partial v})_s}{(\frac{\partial p}{\partial v})_T} = \frac{-(\frac{\partial T}{\partial v})_s(\frac{\partial v}{\partial s})_T}{-(\frac{\partial T}{\partial p})_s(\frac{\partial p}{\partial s})_T} = \frac{(\frac{\partial s}{\partial T})_p}{(\frac{\partial s}{\partial T})_v} = \frac{T(\frac{\partial s}{\partial T})_p}{T(\frac{\partial s}{\partial T})_v} = \frac{(\frac{\partial h}{\partial s})_p(\frac{\partial s}{\partial T})_p}{(\frac{\partial u}{\partial s})_v(\frac{\partial s}{\partial T})_v}$$

The latter result follows from Eq. (2.10.8). Finally, combining the derivatives in the numerator and denominator of this latter expression, and noting Eq. (2.6.3), we obtain

$$(\frac{\partial p}{\partial \rho})_s = \frac{C_p}{C_v}\,(\frac{\partial p}{\partial \rho})_T \equiv \gamma\,(\frac{\partial p}{\partial \rho})_T \qquad (2.11.8)$$

It is important to note that in the development of this latter equation, no assumption was made regarding the equation of state. The expression is hence valid for situations in which the ratio of specific heats may vary substantially.

2.12 THE PERFECT GAS

A perfect gas is defined as a substance with equation of state given by

$$pv = RT \qquad (2.12.1)$$

In this expression, R is a constant termed the gas constant.

If, in addition to satisfying Eq. (2.12.1), the gas has a constant ratio of specific heats, it is termed a "Calorically Perfect" gas.

It should be noted that the gas constant R is given in terms of the "Universal Gas Constant," R_u by

$$R = \frac{R_u}{M},\ M \equiv \text{Molecular weight} \qquad (2.12.2)$$

The value of R_u in several systems is

$$R_u = 1545\ (\frac{\text{lbf}\ \frac{\text{sec}^2}{\text{ft}}}{\text{lbm}})\ \frac{\text{ft}^2}{\text{sec}^2}\ \frac{\text{lbm}}{\text{lbm-mole}^{\circ}\text{R}}$$

$$= 49{,}700\ \frac{\text{ft}^2}{\text{sec}^2}\ \frac{\text{lbm}}{\text{lbm-mole}^{\circ}\text{R}}$$

$$= 8{,}317\ \frac{\text{m}^2}{\text{sec}^2}\ \frac{\text{Kg}}{\text{Kg-mole}^{\circ}\text{K}} \qquad (2.12.3)$$

We note that for air of molecular weight (approx.) 29, we have

$$R = 53.3\ (\frac{\text{lbf sec}^2}{\text{lbm ft}})(\frac{\text{ft}}{\text{sec}})^2\ \frac{1}{^{\circ}\text{R}}$$

$$= 1714\ (\frac{\text{ft}}{\text{sec}})^2\ \frac{1}{^{\circ}\text{R}}$$

$$= 286.8\ (\frac{\text{m}}{\text{sec}})^2\ \frac{1}{^{\circ}\text{K}} \qquad (2.12.4)$$

It should be noted from Eq. (2.12.2) that when a gas is in a regime where dissociation is occurring, it is not strictly speaking, a perfect gas. This is because dissociation changes the value of M, and hence of R. We note, however, that if no dissociation occurs, but substantial vibrational excitation occurs, then the gas would be perfect, but not calorically perfect.

The behavior of a perfect gas may be illuminated by applying the relationships of section 2.11. Thus, with Eq. (2.12.1) and Eqs. (2.11.3) and (2.11.4) we find

$$(\frac{\partial C_v}{\partial v})_T = 0 \qquad (2.12.5)$$

hence C_v = function of temperature only

$$(\frac{\partial C_p}{\partial p})_T = 0 \qquad (2.12.6)$$

hence C_p = function of temperature only

From Eqs. (2.11.6) and (2.11.7)

$$du = C_v dT \qquad (2.12.7)$$

$$dh = C_p dT \qquad (2.12.8)$$

Thus, we note with Eqs. (2.12.5) and (2.12.6) that both the internal energy and the enthalpy are functions of temperature only. From Eq. (2.11.5) we find

$$C_p - C_v = R \qquad (2.12.9)$$

and from Eq. (2.11.8)

$$\left(\frac{\partial p}{\partial \rho}\right)_s = \gamma RT \qquad (2.12.10)$$

Thus, the many familiar relationships peculiar to a perfect gas follow directly from the equation of state and Maxwell's Relations. Note particularly that Eqs. (2.12.9) and (2.12.10) are valid whether or not the ratio of specific heats, γ, varies.

2.13 QUASI-ONE-DIMENSIONAL FLUID FLOWS

A quasi-one-dimensional flow is defined as a flow in which the fluid properties can be described in terms of a single spatial coordinate (the axial dimension), the specified axial area variation of the containing tube or channel, and (if the flow is time dependent) the time. The simplicity introduced by utilizing such an approximate description of the flow in a channel is clearly a virtue, but it is equally clear that the regimes of validity of any analysis incorporating such an approximation should be thoroughly investigated.

Before investigating the expected regimes of validity of the quasi-one-dimensional approximation, let us note that the approximation is of particular utility in the study of aircraft gas turbine engines. In the first order analysis of the various components of a turbomachine, it is customary to refer to the "inlet and outlet" conditions of each component. It is quite obvious that the conditions at inlet and outlet of any component are not, in fact, uniform, and hence any single quantity chosen to represent a given property must be a properly chosen average quantity. When properly chosen, these average quantities may be utilized with ease in a cycle analysis to predict the overall performance of a given engine in terms of the performance of its individual components.

In many situations, however, it is the effect of the non-one-dimensionality that is at the core of the problem considered. Thus, for example, when describing the performance of ejectors, careful distinction must be made between the use of such averaging methods as area weighted, mass weighted and mixed out. Another example of the importance of the non-one-dimensionality of a flow appears in the study of inlet distortion, where inlet distortion by its definition involves the study of the variation of the stagnation temperature and stagnation pressure about their appropriately chosen averages.

It is clear that if we consider a channel with solid walls in which a flow exists that severe property variations will occur across the channel. To make this statement clear we can consider the example of the behavior of the velocity which we know must have a value of zero on the wall and be finite in the channel center. If the walls are heat conducting (or if the Mach number at the channel center is large), we would expect to find large variations in temperature across the channel. In such cases we recognize that the "temperature" or "velocity" that appear in the quasi-one-dimensional equations would in fact be an appropriately chosen average of the values found across the channel. The definition of this "average" would depend somewhat upon the particular problem to be investigated, but it can be seen that if the "shape" of the cross-channel property variation changes radically with axial position, whatever averaging process is chosen will have to be modified with axial position in order to obtain meaningful results from the analysis. Since the suitable averaging procedures would not be known "a priori," such a procedure is tantamount to conducting a full two-dimensional investigation.

Conversely, however, we see that there are two limits in which we could expect a quasi-one-dimensional assumption to be of use. The first is the so-called "fully developed flow" in which, in fact, the shape of the cross-channel property variations varies only slowly with axial position. In this case, the quasi-one-dimensional assumption leads to an accurate description of the behavior of the average fluid properties. The other limit of channel flow behavior that allows an accurate analysis under the restrictions of the approximation is that limit where a dominant portion of the flow in the channel satisfies the assumption of very nearly uniform cross-channel conditions, and only a small portion, "the boundary layer," has rapidly varying properties in the cross-channel direction. In this latter case it is tacitly assumed that the boundary layer entrains such a small portion of the flow that the average quantities are not affected by excluding the effects of the boundary layer.

It would be well to mention here that a technique commonly used to extend the quasi-one-dimensional solution utilizes the results of the quasi-one-dimensional solution and applies these results as the boundary conditions ("free stream conditions") to be applied to the solution of the behavior of the (two-dimensional) boundary layer equations.

The effect of the curvature of the channel must be considered carefully, because it is evident that channel curvature introduces cross-channel pressure gradients which, in turn, introduce cross-channel gradients in other fluid properties. In general, we might expect that if the radius of curvature of the channel centerline is large compared to the channel dimension in the radial direction that we would expect the effects of the induced radial pressure fields to be small. This observation can be extended to indicate that the flow in individual stream tubes of a general three-dimensional flow can be expected to be described by the quasi-one-dimensional flow equations, though the determination of the behavior of the stream tube itself (through the pressure fields induced by other stream tubes) will rely upon solution of the complete equations.

In what follows we shall first extend the first law of thermodynamics to include the effects of the kinetic energy, and potential energy of the flowing fluid, in a form suitable to adapt for use in the quasi-one-dimensional equations. In this derivation the very useful concept of the "control volume" will be introduced, and the concept of the control volume will be employed later in the derivation of the quasi-one-dimensional equations.

2.14 THE FIRST LAW FOR A FLOWING SYSTEM--THE CONTROL VOLUME

An important application of the first law of thermodynamics is to be found in the analysis of a flowing system. A very convenient and often used concept is that of a "Control Volume," defined simply as a given region in space. This region in space may be moving, changing shape, etc., but most often if we wish to analyze material behavior using the control volume technique, we select a simple control volume of fixed size, shape and position. The selection of the most suitable control volume will depend upon the problem at hand, but it can be stated in general that most often we attempt to select a control volume such that the material at entrance and exit is in local thermodynamic equilibrium and in addition may have its behavior closely approximated by assuming that all properties at the entrance or exit are the average properties at the entrance or exit. This latter requirement is equivalent to stating that conditions at the entrance and exit are "quasi-one-dimensional." As will be seen shortly, we will also require some information concerning the heat and work interactions at the boundaries of the control volume, but it should be noted carefully that no requirement of reversibility or one dimensionality for the processes within the control volume will be imposed.

An important point to recognize is that in the preceding sections on thermodynamics we wrote the first law as it pertained to a given mass of material (the thermodynamic system), and we now focus our attention on a given volume in space through which material passes. It will be recalled that we did not consider that portion of work, kinetic energy or potential energy identified with the bulk motion of the thermodynamic system, simply because such behavior was considered to be already known from the laws of mechanics. Now that we are to consider a control volume, through which fluid enters and leaves, however, the energy identified with the bulk motion of the fluid must be included in order to account for any such bulk motion energy changes experienced by the fluid between entrance and exit.

Our method for extending the first law for a thermodynamic system to a control volume will be to first write the first law for that mass contained within the control volume at time t. We then follow the mass till time t + dt and apply the first law of thermodynamics to the change experienced by the mass. These changes may then be related to the changes experienced by the material passing through the control volume.

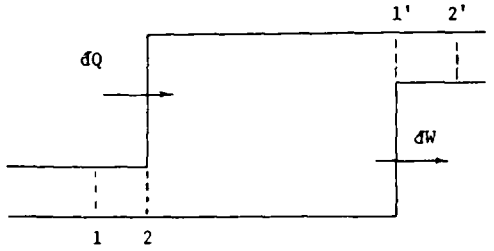

Figure 2.13.1. Control Volume and Control Mass

We consider a control mass which at time t occupies the volume bounded by the two dotted lines 1 and 1' and the solid walls of the container. At time t + dt the control mass occupies the volume bounded by the two dotted lines 2 and 2' and the solid walls of the container. The control volume will be considered to be the volume bounded by the container and lines 2 and 1'.

The change in "total energy" (i.e., internal plus kinetic plus potential energy) of the control mass is given by

$$dE_{C.M.} = đQ - đW_T \qquad (2.14.1)$$

Here we have written $đW_T$ to indicate the total work interaction of the control mass in the time dt. This work interaction can be considered to be of two parts.

(1) The work interaction with mechanical contrivances ($đW_M$) such as shafts, etc.

(2) The net work interaction of the fluid in the control mass with the fluid external to the control mass by the moving interfaces at entrance and exit. This form of work interaction, sometimes called the flow work, is equal to $F_2V_2dt - F_1V_1dt$ in which F_1 and F_2 are the forces on the interfaces at entrance and exit to the control volume, respectively. With the assumptions of local thermodynamic equilibrium and quasi-one-dimensionality, these forces can be written as the product of the pressure times the area so that the flow work may be written

$$p_2A_2V_2dt - p_1A_1V_1dt$$

The expression for the change in energy of the control mass may then be written

$$dE_{C.M.} = đQ - đW_M - (p_2A_2V_2 - p_1A_1V_1)\,dt \qquad (2.14.2)$$

The energy within the control volume is related to that within the control mass at times t and t + dt by

$$E_{C.V.}(t) = E_{C.M.}(t) - (A_1V_1dt)\rho_1\left(u_1 + \frac{V_1^2}{2} + P.E._1\right)$$

$$E_{C.V.}(t+dt) = E_{C.M.}(t+dt) - (A_2V_2dt)\rho_2\left(u_2 + \frac{V_2^2}{2} + P.E._2\right)$$

Thus

$$dE_{C.V.} = dE_{C.M.} + A_1V_1dt\rho_1\left(u_1 + \frac{V_1^2}{2} + P.E._1\right) - A_2V_2dt\rho_2\left(u_2 + \frac{V_1^2}{2} + P.E._2\right) \qquad (2.14.3)$$

But $A\rho V = \dot{m}$, the mass transfer per second through the boundary. By equating the expressions for $dE_{C.M.}$, dividing by dt and writing $u + p/\rho$ as the enthalpy, h, there is obtained

$$\left(\frac{dE}{dt}\right)_{C.V.} = \left[\dot{m}\left(h + \frac{V^2}{2} + P.E.\right)\right]_i - \left[\dot{m}\left(h + \frac{V^2}{2} + P.E.\right)\right]_e - \frac{đW_M}{dt} + \frac{đQ}{dt} \qquad (2.14.4)$$

EXAMPLE 2.14.1 Flow in an adiabatic nozzle.

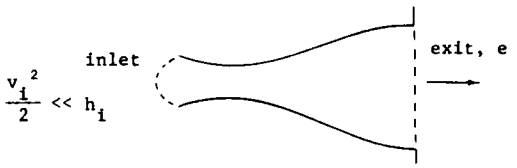

Figure 2.14.1 Adiabatic Nozzle

As a very simple example, let us consider the adiabatic, steady flow of a fluid in a nozzle. We shall consider the control volume to be that volume bounded by the solid walls of the nozzle and the dotted lines shown in the sketch. The assumption of steady flow allows us to write $(\frac{dE}{dt})_{C.V.} = 0$ and $\dot{m}_i = \dot{m}_o$, the assumption of adiabatic flow requires $\frac{\delta Q}{dt} = 0$, and because the nozzle has no work interaction with mechanical contrivances, we have $\frac{\delta W}{dt}_m = 0$. We may also assume very little, if any, change in potential energy across the nozzle so that the control volume form of the energy equation gives

$$(h + \frac{V^2}{2})_i = (h + \frac{V^2}{2})_e \qquad (2.14.5)$$

If, as indicated in the sketch, the inlet surface is so chosen that the kinetic energy per unit mass of the fluid is very small compared to the enthalpy of the fluid, we find

$$V_e = \sqrt{2(h_i - h_e)} \qquad (2.14.6)$$

We may interpret this simple and convenient result in the following way. The function of the nozzle is to take the random thermal velocities of the fluid in the reservoir and to direct such velocities so as to give a directed kinetic energy to the expelled fluid. In addition, the pressure within the chamber also supplies "flow work" which adds further to the directed energy. We should note that the flow work so supplied must be supplied by a compressor or similar device if the reservoir conditions are not to change with time. We may note also that without further specifying the process we cannot state what the conditions should be at a particular point on the nozzle. Thus, a very rough nozzle might cause the process to be highly irreversible with the result that even if the pressure drops the same amount as it does in another smoother nozzle, the velocity at that point in the nozzle would be less than that in the smooth nozzle. The sum of the kinetic energy and enthalpy would be the same, however, indicating that the roughness has had the effect of slowing down the fluid and returning the directed velocity to the random thermal velocities we identify with the temperature (and enthalpy).

EXAMPLE 2.14.2

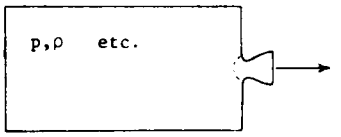

Figure 2.14.2 Fluid Container

As a further example, consider the "blowdown" of a calorically perfect gas from a vessel through a nozzle. We desire the relationship between the pressure, temperature and density of the fluid in the container as mass is expelled. Again assume the container to be adiabatic. In this case, of course, the conditions in the control volume change with time and the control volume form of the energy equation hence gives

$$(\frac{dE}{dt})_{C.V.} = -\dot{m}_o [h + \frac{V^2}{2}]_o \qquad (2.14.7)$$

Now $\dot{m}_o$ is the mass flow <u>out</u> of the container, and may be written - dm/dt where m is the mass within the container. For simplicity we select the "exit portion" of the control volume to be the dotted line shown which by assumption exists where $h = h_c >> \frac{V^2}{2}$. In this case the energy, E, within the control volume consists of internal energy only, so that $E = mC_vT_c$ and there is obtained

$$C_v \frac{dmT_c}{dt} = \frac{dm}{dt} h_c = \frac{dm}{dt} C_pT_c$$

Expanding the derivative on the left side, cancelling the differential of time and rearranging, it follows that

$$\frac{dT_c}{T_c} = (\gamma - 1) \frac{dm}{m}$$

This then integrates to give

$$\frac{T_{c_1}}{T_{c_2}} = (\frac{m_1}{m_2})^{\gamma-1} = (\frac{\rho_{c_1}}{\rho_{c_2}})^{\gamma-1} \qquad (2.14.8)$$

It has been emphasized to this point that the assumptions leading to the control volume form of the first law did not require the presence of reversibility. We know also that if an adiabatic process is reversible, no entropy change occurs. Let us hence calculate the entropy change occurring in this process. From the Gibbs' equation for a calorically perfect gas we obtain

$$ds = C_v \frac{dT}{T} + R \frac{d(1/\rho)}{1/\rho}$$

hence

$$s_{c_2} - s_{c_1} = C_v \ln \frac{T_{c_2}}{T_{c_1}} + R \ln \frac{\rho_{c_1}}{\rho_{c_2}} \qquad (2.14.9)$$

Thus, in this case

$$s_{c_2} - s_{c_1} = -C_v(\gamma-1)\ln\frac{\rho_{c_1}}{\rho_{c_2}} + R\ln\frac{\rho_{c_1}}{\rho_{c_2}} = 0$$

It thus seems we have encountered a paradox, because no explicit statement was made to introduce the assumption of reversibility, yet the result indicates that the process described must have been reversible. It is apparent that an assumption of reversibility must have been made implicitly. A little thought indicates that by assuming the enthalpy at the exit was that of the entire container, or more particularly by assuming the pressure at the exit was that of the entire chamber, we in fact assumed no "viscous drop" for the pressure and hence that the process within the chamber was reversible. If the expulsion of the fluid had been particularly rapid or the fluid particularly viscous, we might have expected a pressure drop across the chamber, and hence would have been in error assuming the pressure at exit and chamber pressure to be identical.

EXAMPLE 2.14.3

An example that will hopefully clarify the method and utility of utilizing the control volume or control mass method of "bookkeeping" the equation for the first law of thermodynamics follows by considering the combined behavior of examples 2.14.1 and 2.14.2.

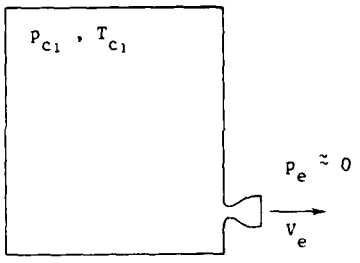

Figure 2.14.3 Container and Nozzle

We thus consider the "blowdown" of a calorically perfect gas from a large container through a nozzle to an (approximately) zero exit pressure. We consider the behavior of the gas in the chamber and across the nozzle to be that previously derived in examples 2.14.1 and 2.14.2. Utilizing the control volume approach we are to find the directed kinetic energy per mass at the nozzle exit, and to integrate this energy over the entire mass outflow to determine the total directed kinetic energy in the departing fluid. We then will check this latter result by utilizing the control mass form of the first law.

We first note from the Gibbs equation for a calorically perfect gas that

$$ds = C_p\frac{dT}{T} - R\frac{dp}{p}$$

so that

$$\frac{p_2}{p_1} = \left(\frac{T_2}{T_1}\right)^{\frac{\gamma}{\gamma-1}} e^{-\frac{s_2 - s_1}{R}} \qquad (2.14.10)$$

Thus, for this case of expansion to zero exit pressure, the exit temperature and hence exit internal energy and enthalpy are zero. Equation (2.14.6) thus gives

$$\text{Directed kinetic energy/mass} = \frac{Ve^2}{2} = C_pT_c$$

At first this result might appear incongruous because the energy/mass escaping the container is larger (by a factor of γ) than the energy/mass within the container. Clearly, however, the additional energy is being transmitted to the escaping mass by the "flow work" of the internal fluid. This flow work is supplied by the expanding gas within the container which, as a result of its expansion (and hence work interaction), has its own internal energy and hence temperature reduced. The total outflow of energy from the nozzle is given by

$$\text{Total energy} = \int_0^{m_{c_1}} \frac{Ve^2}{2}\,dm = \int_0^{m_{c_1}} C_pT_c\,dm$$

$$= m_{c_1}T_{c_1}C_p\int_0^1 \frac{T_c}{T_{c_1}}\,d\frac{m}{m_{c_1}}$$

With equation (2.14.8) we have

$$\text{Total energy} = m_{c_1}T_{c_1}C_p\int_0^1 \left(\frac{m}{m_1}\right)^{\gamma-1} d\frac{m}{m_{c_1}}$$

$$= m_{c_1}T_{c_1}C_v$$

This latter result follows immediately when the control mass form of the first law is considered, because the control mass statement would simply be that all the energy originally contained in the vessel ($m_1C_vT_{c_1}$) must be equal to all the energy in the exhausted gas (namely all the directed kinetic energy).

2.15 THE CHANNEL FLOW EQUATIONS

We now consider the steady flow of fluid in channels with rigid walls. Quasi-one-dimensionality will be assumed, the effects of potential energy changes will be ignored and, in addition, the wall slope, and hence rate of change of cross-sectional area, will be assumed to be small. The effect of this latter assumption is that the cosine of the wall angle, θ, may be considered to be unity.

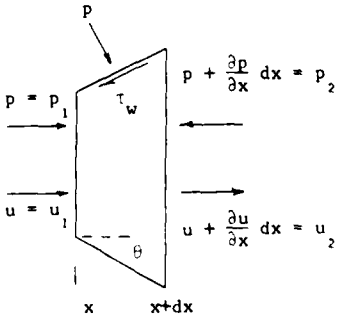

Figure 2.15.1 Element of Fluid in Duct

We develop the conservation equations by considering the conditions across a small axial segment of the duct, as indicated in the sketch. The conservation of mass gives immediately

$$\rho u A = \text{Const}$$

or

$$\frac{d\rho}{\rho} + \frac{du}{u} + \frac{dA}{A} = 0 \quad \text{Continuity} \quad (2.15.1)$$

The first law of thermodynamics follows directly from Eq. (2.14.4) as applied across the element. Thus, noting $\dot{m}_1 = \dot{m}_0$, and that $\frac{1}{\dot{m}} \frac{\delta Q}{dt} = \delta q$, the heat interaction per unit mass, we obtain

$$dh + udu = \delta q \qquad \text{FIRST LAW} \qquad (2.15.2)$$

The Gibbs Equation may be applied directly,

$$Tds = dh - \frac{1}{\rho} dp \qquad \text{GIBBS EQUATION} \qquad (2.15.3)$$

and the First Law and Gibbs Equation may be combined to give

$$\frac{1}{\rho} dp + udu = \delta q - Tds \qquad (2.15.4)$$

We now obtain the momentum equation by writing Newton's Law in a form appropriate for use with a control volume, namely

Sum of the forces = rate of production of momentum

or

Pressure forces + viscous forces = momentum convected out through surface 2 per second - momentum convected in through surface 1 per second

In symbols we thus obtain

$$p_1 A_1 + \int_{\text{side}} p dA - p_2 A_2 - \int \tau c \, dx = (\rho u^2 A)_2 - (\rho u^2 A)_1$$

In this expression we have introduced the shear stress, τ, and the circumference, c. Retaining terms only to the first order, then, we have, utilizing the continuity equation, Eq. (2.15.1)

$$-d(pA) + pdA - \tau c dx = \rho u A du$$

or

$$\frac{1}{\rho} dp + udu = -\frac{\tau c}{\rho A} dx \quad \text{Momentum Equation} \quad (2.15.5)$$

It may be noted that this equation closely resembles the familiar Bernoulli Equation of elementary ideal fluid mechanics. The only addition to the ideal form of the equation arises from the viscous shear stress contribution. An equation for the entropy variation follows by combining Eqs. (2.15.4) and (2.15.5) to give

$$Tds = \delta q + \frac{\tau c}{\rho A} dx \qquad (2.15.6)$$

It is apparent in this relationship that for an ideal process, in which the shear stress is zero, the entropy variation corresponds to that for reversible heat interaction, as already given in Eq. (2.7.2). The irreversibility of the viscous terms is apparent in its contribution to the increase in entropy.

2.16 STAGNATION PROPERTIES

A stagnation property is defined as that value of the property that would exist if the fluid was extracted and brought isentropically to rest. The process may be imagined to be that shown in the sketch wherein the fluid flows isentropically through a duct from condition 1 to condition t_1.

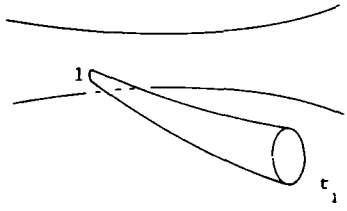

Figure 2.16.1 Duct and Imaginary Duct for Stagnation Condition

Application of Eq. (2.15.2) gives an expression for the stagnation enthalpy. Thus, noting $\delta q = 0$ and integrating, we find

$$h_{t_1} = h_1 + \frac{u_1^2}{2} \qquad (2.16.1)$$

Obviously the location of point 1 in the duct in which the flow actually occurs is arbitrary, so in the following relationships between properties and their related stagnation values, the subscript 1 will be omitted.

The equations take on particularly simple forms when a calorically perfect gas is considered. Thus, Eq. (2.16.1) becomes

$$C_p T_t = C_p T + \frac{u^2}{2} \qquad (2.16.2)$$

Further manipulation leads to

$$\frac{T_t}{T} = 1 + \frac{\gamma R}{2C_p} \frac{u^2}{\gamma RT} = 1 + \frac{\gamma - 1}{2} M^2 \qquad (2.16.3)$$

Here we have introduced the Mach number, defined as $M = u/a$. The speed of sound, a, as stated in section 2.11, is equal to $\left(\frac{\partial p}{\partial \rho}\right)_s^{1/2}$, which combined with Eq. (2.12.10) gives $a^2 = \gamma RT$. Eq. (2.12.9) was utilized to give $\frac{\gamma R}{C_p} = \gamma - 1$.

Equation (2.14.10) may be applied directly (with $s_2 = s_1$) to give

$$\frac{p_t}{p} = \left(\frac{T_t}{T}\right)^{\frac{\gamma}{\gamma-1}} = \left(1 + \frac{\gamma-1}{2} M^2\right)^{\frac{\gamma}{\gamma-1}} \qquad (2.16.4)$$

Then, also

$$\frac{\rho_t}{\rho} = \frac{p_t}{p}\frac{T}{T_t} = \left(1 + \frac{\gamma-1}{2} M^2\right)^{\frac{1}{\gamma-1}} \qquad (2.16.5)$$

Some important behaviors concerning the variation of stagnation properties in ducts can be illuminated by applying Eq. (2.14.10) directly to the conditions at t_1 and t_2. Thus,

$$\frac{p_{t_2}}{p_{t_1}} = \left(\frac{T_{t_2}}{T_{t_1}}\right)^{\frac{\gamma}{\gamma-1}} e^{-\frac{s_2 - s_1}{R}} \qquad (2.16.6)$$

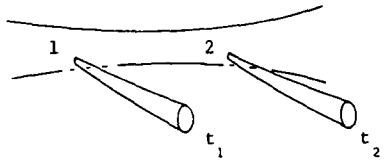

Figure 2.16.2 Stagnation Conditions at Two Axial Locations

Here we note that by definition $s_1 = s_{t_1}$ and $s_2 = s_{t_2}$.

In the special case of adiabatic flow in the duct, we note from Eqs. (2.15.2) and (2.16.2) that $T_{t_2} = T_{t_1}$. Then

$$\frac{p_{t_2}}{p_{t_1}} = e^{-\frac{s_2 - s_1}{R}} \qquad (2.16.7)$$

We saw from the second law, or equivalently from Eq. (2.15.6) that when shear exists in an adiabatic flow, $s_2 > s_1$. Thus,

$$\frac{p_{t_2}}{p_{t_1}} = \frac{\rho_{t_2}}{\rho_{t_1}} < 1 \text{ for adiabatic flow} \qquad (2.16.8)$$

This result has important consequences in turbomachinery, because the high performance of turbomachinery is dependent upon the efficient attainment of high stagnation pressures. It is clear from this application of the second law that nature naturally tends to erode the attained stagnation pressure.

2.17 PROPERTY VARIATIONS IN CHANNELS

Several important relationships may be obtained in a fairly general form by combining the conservation equations of section 2.14. In so doing it will be appropriate to express the change in pressure in terms of corresponding changes in density and entropy. We thus utilize Eq. (2.10.12) to obtain

$$dp = \left(\frac{\partial p}{\partial \rho}\right)_s d\rho + \left(\frac{\partial p}{\partial s}\right)_\rho ds$$

$$= \left(\frac{\partial p}{\partial \rho}\right)_s d\rho + \rho^2 \left(\frac{\partial T}{\partial \rho}\right)_s ds \qquad (2.17.1)$$

Then note that $dT = \left(\frac{\partial T}{\partial \rho}\right)_p d\rho + \left(\frac{\partial T}{\partial p}\right)_\rho dp$ gives

$$\left(\frac{\partial T}{\partial \rho}\right)_s = \left(\frac{\partial T}{\partial \rho}\right)_p + \left(\frac{\partial T}{\partial p}\right)_\rho \left(\frac{\partial p}{\partial \rho}\right)_s \qquad (2.17.2)$$

Thus, utilizing Eq. (2.11.8) and the relationship

$$\left(\frac{\partial T}{\partial p}\right)_\rho \left(\frac{\partial p}{\partial \rho}\right)_T = -\left(\frac{\partial T}{\partial \rho}\right)_p$$

Eqs. (2.17.1) and (2.17.2) may be combined to give

$$dp = \left(\frac{\partial p}{\partial \rho}\right)_s d\rho - \rho^2 (\gamma-1)\left(\frac{\partial T}{\partial \rho}\right)_p ds \qquad (2.17.3)$$

This expression for the pressure increment may now be substituted into Eq. (2.15.4), whereupon by utilizing the continuity equation, Eq. (2.15.1) together with $\left(\frac{\partial p}{\partial \rho}\right)_s = a^2$ and $M^2 = \frac{u^2}{a^2}$,

$$\frac{dA}{A} + (1-M^2)\frac{du}{u} = \frac{1}{a^2}\left[\left\{T - (\gamma-1)\rho\left(\frac{\partial T}{\partial \rho}\right)_p\right\} ds - \bar{d}q\right] \qquad (2.17.4)$$

It will be recognized that this equation implies the requirement of the famous convergent-divergent duct shape if an adiabatic perfect flow ($\bar{d}q = ds = 0$) is to be accelerated from a Mach number less than unity to a Mach number greater than unity. When a perfect gas is considered the equation reduces to

$$\frac{dA}{A} + (1-M^2)\frac{du}{u} = \frac{1}{\gamma RT}\left[\gamma T ds - \bar{d}q\right] \quad \text{perfect gas} \qquad (2.17.5)$$

2.17.1 ADIABATIC FLOW OF A PERFECT GAS

When no heat interaction occurs, Eq. (2.17.5) further reduces to

$$\frac{dA}{A} + (1-M^2)\frac{du}{u} = \frac{ds}{R} \qquad (2.17.6)$$

(perfect gas, adiabatic flow)

In an accelerating flow (i.e., in a nozzle), du is positive. In an adiabatic (real) flow, ds is positive. Thus, at the throat of a nozzle ($dA = 0$) we must have $M^2 < 1$. A method of estimating how much less than unity M^2 is, at a nozzle throat, will be developed shortly, but it is of interest at this point to relate this quasi-one-dimensional description to the two dimensional description of a free stream interacting with a (growing) boundary layer. In the latter case, it

is imagined that the growing boundary layer causes the effective throat of the nozzle (as "seen by the free stream") to shift slightly downstream, so that the Mach number at the geometrical throat remains less than unity. It can be seen that the two descriptions are not in opposition to each other.

To estimate the effect of shear upon the Mach number at the throat in an adiabatic nozzle ($dA = 0$, $\bar{d}q = 0$), we combine Eqs. (2.15.5), (2.15.6), and (2.17.6) to give

$$M^2_{throat} = 1 + \frac{\gamma \frac{\tau c dx}{Adp}}{1-(\gamma-1)\frac{\tau c dx}{Adp}} \qquad (2.17.7)$$

It can be seen that the group $\frac{\tau c dx}{Adp}$ is just the ratio of the shear force acting on the edges of an elemental volume of length dx to the pressure forces acting upon the cross-section of the same volume. In order to further estimate the magnitude of this number, we introduce the skin friction coefficient, C_f, defined by

$$C_f = \frac{\tau}{\frac{1}{2}\rho u^2} \qquad (2.17.8)$$

Then, considering a circular throat of diameter, D, we have

$$\frac{\tau c dx}{Adp} = \frac{2\gamma M^2 C_f}{\frac{D}{p}\frac{dp}{dx}} \qquad (2.17.9)$$

As a rough approximation we may approximate the denominator of this expression as unity with the assumption that the very rapid pressure changes found at a throat correspond to the pressure changing on the order of magnitude of its own value within one nozzle diameter. Such a coarse approximation is not wildly distant from the truth for typical nozzles. A typical value for C_f would be approximately 0.005, so that Eq. (2.17.7) yields $M_{Throat} \approx .995$. (Note dp/dx is negative.) This somewhat justifies the almost universally used approximation that $M_{Throat} = 1$.

2.17.2 NON-ADIABATIC FLOW OF A PERFECT GAS

As will be evident in Chapter 7, the behavior (and preservation) of the stagnation pressure has a vital effect upon the performance of gas turbine engines. The effects upon stagnation pressure of heat transfer and shear may be obtained by combining Eqs. (2.15.2) and (2.16.2), together with (2.15.6) and (2.14.10). These may be written

$$C_p dT_t = \bar{d}q$$

$$ds = \frac{\bar{d}q}{T} + \frac{\tau c}{\rho TA} dx$$

$$ds_t = ds = C_p \frac{dT_t}{T_t} - R\frac{dp_t}{p_t}$$

Combination of these three equations and Eq. (2.17.8) leads to

$$\frac{dp_t}{p_t} = -\frac{\gamma M^2}{2}\left[\frac{\bar{d}q}{C_p T_t} + C_f \frac{c}{A} dx\right] \qquad (2.17.10)$$

This expression makes it clear that both heat interaction and frictional effects cause a degradation in stagnation pressure when the Mach number is other than zero. The source of this degradation becomes clear when Eq. (2.16.6) is considered along with the above equations. Thus, from Eq. (2.16.6) it follows that for a given stagnation temperature the stagnation pressure decreases with increasing entropy. If a positive heat interaction is to occur, and the entropy increase kept to a minimum, the (static) temperature at which the heat interaction takes place must be kept as high as possible. Clearly, when a flow of given stagnation temperature exists at finite Mach number, the static temperature is reduced, leading to a lower stagnation pressure than that attainable for zero Mach number heat addition.

This effect upon the stagnation pressure becomes of paramount importance in both the combustion chamber and afterburner of an aircraft gas turbine engine. In some modern, high performance aircraft, the maximum engine cross-section is determined by the requirement to keep the Mach number at entrance to the afterburner at an acceptably low value.

It would appear at first glance that Eq. (2.17.10) implies that in the case of a negative heat interaction, the stagnation pressure of the fluid could be increased. To investigate this concept we assume that the heat interaction may occur, by either convective heat transfer ($\bar{d}q_T$), or radiative heat transfer ($\bar{d}q_R$).

Introducing the heat transfer coefficient, h, we have

(by definition of h)

$$\dot{m}\bar{d}q_T = h\,(T_w - T_t)\,c\,dx \qquad (2.17.11)$$

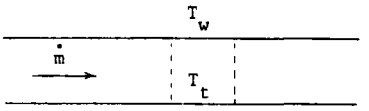

Figure 2.17.1 Element of Channel

The Stanton number, N_{ST}, is defined by

$$N_{ST} = \frac{hA}{\dot{m}C_p} \qquad (2.17.12)$$

We may thus write

$$\frac{\bar{d}q_T}{C_p T_t} = N_{ST}\frac{T_w - T_t}{T_t}\frac{c}{A} dx \qquad (2.17.13)$$

Hence Eq. (2.17.10) becomes

$$\frac{dp_t}{p_t} = -\frac{\gamma M^2}{2}\frac{c}{A}dx\left[\frac{T_w - T_t}{T_t}N_{ST} + C_f\right] - \frac{\gamma M^2}{2}\frac{\bar{dq}_R}{C_p T_t} \qquad (2.17.14)$$

A remarkable relationship termed "Reynolds Analogy" relates the skin friction coefficient and Stanton number over a wide range of flow conditions:

$$N_{ST} \approx \frac{C_f}{2} \qquad \text{Reynolds Analogy} \qquad (2.17.15)$$

Incorporating this relationship in Eq. (2.17.14), we obtain

$$\frac{dp_t}{p_t} \approx -\frac{\gamma M^2}{4}\frac{c}{A}C_f dx\left[\frac{T_w + T_t}{T_t}\right] - \frac{\gamma M^2}{2}\frac{\bar{dq}_R}{C_p T_t} \qquad (2.17.16)$$

This latter result indicates that (assuming Reynolds Analogy is approximately valid) no matter how far the wall temperature is reduced, the stagnation pressure cannot be increased through convective transfer effects. The possibility remains, however, that extreme radiative transfer (as might occur in a high powered gas laser) might contribute to a stagnation pressure increase. Similarly, if evaporation occurs, the heat transfer is not limited by Reynolds analogy and the stagnation pressure can increase.

2.17.3 CONSTANT AREA HEAT INTERACTION

Combination of the continuity equation (with dA = 0), Eq. (2.15.1), the momentum equation, Eq. (2.15.5) and Eq. (2.17.8) yields

$$d(p + \rho u^2) = -\tfrac{1}{2}\rho u^2 C_f \frac{c}{A}dx$$

Then, noting $M^2 = \frac{\rho u^2}{\gamma p}$, this expression may be manipulated to give

$$\frac{dp}{p} + \frac{\gamma\, dM^2}{1+\gamma M^2} = -\frac{\gamma}{2}\frac{c}{A}C_f\frac{M^2}{1+\gamma M^2}dx \qquad (2.17.17)$$

The logarithmic derivative of Eq. (2.16.4) gives

$$\frac{dp_t}{p_t} = \frac{dp}{p} + \frac{\frac{\gamma}{2}dM^2}{1 + \frac{\gamma-1}{2}M^2} \qquad (2.17.18)$$

Thus, noting that $C_p dT_t = \bar{dq}$, Eqs. (2.17.10), (2.17.17) and (2.17.18) may be combined to yield

$$\frac{dT_t}{T_t} = -C_f\frac{c}{A}\frac{\gamma M^2}{1+\gamma M^2}dx + \frac{2dM^2}{M^2(1+\gamma M^2)} - \frac{dM^2}{M^2\left(1+\frac{\gamma-1}{2}M^2\right)} \qquad (2.17.19)$$

If the heat interaction rate is known, this equation may be numerically integrated to give M versus x. Two special cases are considered in the following sections.

2.17.4 IDEAL CONSTANT AREA HEAT INTERACTION - THERMAL CHOKING

In the limit where the flow may be considered to be ideal ($C_f = 0$), Eq. (2.17.19) may be integrated directly to give

$$\frac{T_{t_2}}{T_{t_1}} = 1 + \frac{\Delta q_{1\text{-}2}}{C_p T_{t_1}} = \frac{f(M_2^2)}{f(M_1^2)} \qquad (2.17.20)$$

here

$$f(M^2) \equiv \frac{1 + \frac{\gamma-1}{2}M^2}{(1+\gamma M^2)^2}M^2$$

Clearly, when the stagnation temperature increases, $f(M_2^2)$ must be larger than $f(M_1^2)$. It is hence of interest to investigate the form of the function $f(M^2)$ to see if it is always possible to increase the stagnation temperature. Straightforward differentiation shows that $\frac{\partial f(M^2)}{\partial M} = 0$ at M = 1, so noting also that f(0) = 0, $f(1) = \frac{1}{2(\gamma+1)}$ and $f(\infty) = \frac{\gamma-1}{2\gamma^2}$, we obtain a graph of $f(M^2)$ versus M as indicated in Fig. 2.17.2.

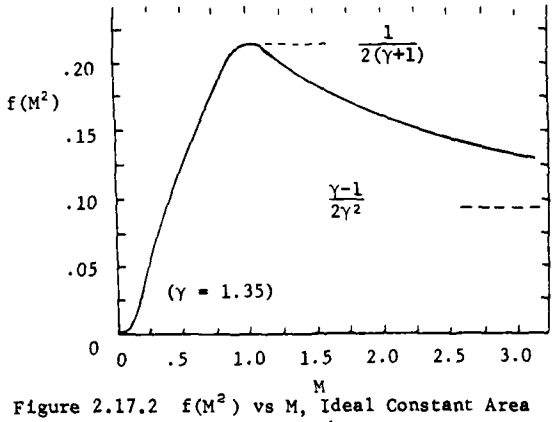

Figure 2.17.2 $f(M^2)$ vs M, Ideal Constant Area Heat Interaction

This figure aids in the prediction of certain famous characteristics of heat addition at constant area. Thus, we see from Eq. (2.17.20) that if the stagnation temperature increases, $f(M_2^2)$ must be larger than $f(M_1^2)$. The figure indicates that it must then be true that whether M_1 was greater than or less than unity, M_2 must be closer to unity than M_1.

A further result, at first appearing to be a paradox, occurs when a heat interaction sufficient to require $f(M_2^2)$ to be greater than $1/2(\gamma+1)$ is imposed. Since this requirement is impossible to satisfy, it appears that the analysis flies in the face of reality, because it is apparent that we will not be limited experimentally in the amount of heat interaction we may impose. It must be recalled, however, that $\Delta q_{1\text{-}2}$ is the heat interaction per unit mass, and the condition of

$M_2 = 1$ represents that state when the maximum mass flow per unit area exists for the given p_{t_2} and T_{t_2}. Thus, if in an experiment this condition, termed "thermal choking" is reached, and it is attempted to cause a further heat interaction, the upstream conditions must change (usually the stagnation pressure must increase) if the mass flow is to be passed. It can be recognized that this phenomenon of thermal choking can be of vital importance in determining the maximum allowable heat interaction in a ramjet, in an afterburner, or even in a conventional combustor.

Equation (2.17.20) is a quadratic equation in M_2^2, which may be solved and manipulated to yield

$$M_2^2 = 1 - \frac{\Delta[1+\Delta]}{1-2\gamma f+\Delta}$$

where

$$\Delta = \pm \{1 - 2(\gamma+1) f\}^{\frac{1}{2}} \qquad (2.17.21)$$

$$f = M_1^2 \frac{1+\frac{\gamma-1}{2} M_1^2}{(1+\gamma M_1^2)^2} \left[1 + \frac{\Delta q_{1-2}}{C_p T_{t_1}}\right]$$

and the + sign corresponds to subsonic flow;
the - sign corresponds to supersonic flow.

The stagnation temperature follows immediately from Eq. (2.17.20), and combination of the continuity equation and momentum equation for constant area flow gives

$$p_1 + \rho_1 u_1^2 = p_2 + \rho_2 u_2^2$$

or (2.17.22)

$$\frac{p_2}{p_1} = \frac{1+\gamma M_1^2}{1+\gamma M_2^2}$$

Then

$$\frac{p_{t_2}}{p_{t_1}} = \frac{1+\gamma M_1^2}{1+\gamma M_2^2} \left\{\frac{1+\frac{\gamma-1}{2} M_2^2}{1+\frac{\gamma-1}{2} M_1^2}\right\}^{\frac{\gamma}{\gamma-1}} \qquad (2.17.23)$$

Example results are shown in Fig. 2.17.3.

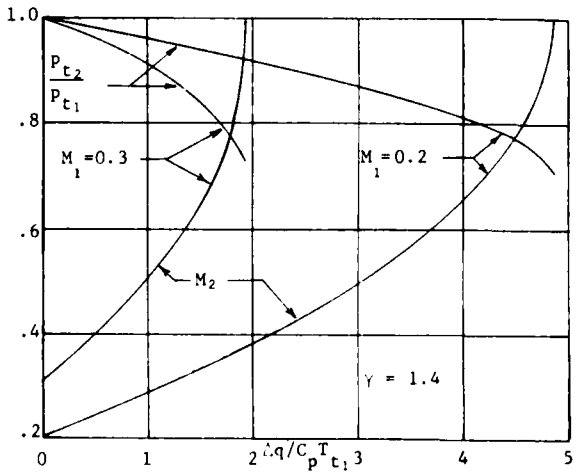

Figure 2.17.3 Mach Number and Stagnation Pressure Ratio vs $\Delta q/C_p T_{t_1}$ for Ideal Constant Area Heat Interaction

2.17.5 ADIABATIC CONSTANT AREA FLOW - VISCOUS CHOKING

When adiabatic flow is considered no change in stagnation temperature occurs, so Eq. (2.17.19) yields

$$\gamma C_f \frac{c}{A} dx = \frac{1-M^2}{M^4\{1+\frac{\gamma-1}{2} M^2\}} dM^2 \qquad (2.17.24)$$

It is apparent that $\frac{dM^2}{dx}$ is positive for $M < 1$ and negative for $M > 1$. Thus, as with thermal choking, the effect of viscosity is to drive the flow to Mach one. This effect is termed viscous choking. As in the case of thermal choking, the condition represents that state where maximum flow per unit area has been achieved for the given local values of stagnation pressure and temperature. If more flow is to be passed, the upstream conditions must change.

Equation (2.17.24) may be integrated in a straightforward manner to yield

$$\chi_2 - \chi_1 = f(M_2^2) - f(M_1^2)$$

here

$$f(M) = \frac{\gamma+1}{2} \ln \left(\frac{1+\frac{\gamma-1}{2} M^2}{M^2}\right) - \frac{1}{M^2} \qquad (2.17.25)$$

and

$$\chi_2 - \chi_1 = \int_1^2 \gamma C_f \frac{c}{A} dx \equiv \int_1^2 d\chi$$

Combination of Eqs. (2.17.17) and (2.17.24) gives

$$\frac{dp}{p} = -\frac{1}{2}\left[\frac{1}{M^2} + \frac{\frac{\gamma-1}{2}}{1+\frac{\gamma-1}{2} M^2}\right] dM^2$$

from which

$$\frac{p_2}{p_1} = \frac{M_1}{M_2} \left(\frac{1+\frac{\gamma-1}{2} M_1^2}{1+\frac{\gamma-1}{2} M_2^2}\right)^{\frac{1}{2}} \qquad (2.17.26)$$

and

$$\frac{p_{t_2}}{p_{t_1}} = \frac{M_1}{M_2} \left(\frac{1+\frac{\gamma-1}{2} M_2^2}{1+\frac{\gamma-1}{2} M_1^2}\right)^{\frac{\gamma+1}{2(\gamma-1)}} \qquad (2.17.27)$$

Example results are indicated in Fig. 2.17.4.

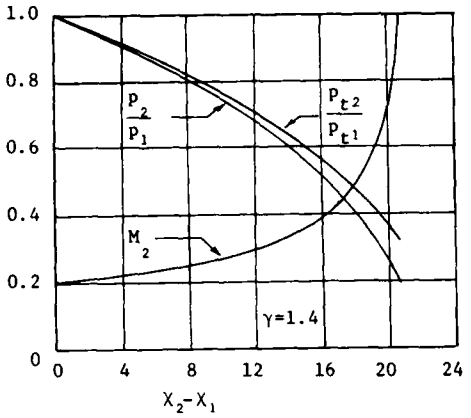

Figure 2.17.4 Variation of Static Pressure, Stagnation Pressure and Mach Number with Axial Position, Adiabatic Constant Area Flow

2.18 THE NOZZLE FLOW EQUATIONS

We now consider the adiabatic flow of a calorically perfect gas in a channel of varying cross section. The mass flow rate, $\dot{m}$, may be obtained in terms of the local area, Mach number and stagnation properties directly from the continuity equation and Eqs. (2.16.4), (2.16.5), and $a^2 = \gamma RT$ as follows:

$$\dot{m} = \rho u A = \rho_t a_t A \frac{\rho}{\rho_t} \frac{a}{a_t} \frac{u}{a}$$

$$= \frac{A p_t}{\sqrt{T_t}} \sqrt{\frac{\gamma}{R}} \left[1 + \frac{\gamma-1}{2} M^2\right]^{-\frac{\gamma+1}{2(\gamma-1)}} M \qquad (2.18.1)$$

Alternatively, this expression may be written in terms of the local static pressure by utilizing Eq. (2.16.4) to give

$$\dot{m} = \frac{A p_t}{\sqrt{T_t}} \left(\frac{p}{p_t}\right)^{1/\gamma} \left[\frac{2}{R} \frac{\gamma}{\gamma-1} \left\{1 - \left(\frac{p}{p_t}\right)^{\frac{\gamma-1}{\gamma}}\right\}\right]^{\frac{1}{2}} \qquad (2.18.2)$$

It is common, also, to reference conditions to conditions at the throat, which we will here denote by an asterisk. In section 2.16.1 it was shown that the Mach number at the throat can be expected to be very close to unity, and it is usual to include this approximation. We may then write

$$\dot{m} = \frac{A^* p_t^*}{C^*} \qquad (2.18.3)$$

where by definition C* is the characteristic velocity

$$C^* \equiv \left(\frac{\gamma+1}{2}\right)^{\frac{\gamma+1}{2(\gamma-1)}} \sqrt{\frac{RT_t}{\gamma}}$$

Note that by the assumption of adiabatic flow $T_t = T_t^*$ everywhere. It should be pointed out here that it is not inconsistent to consider the Mach number to be unity at the throat, but to not insist that $p_t = p_t^*$ throughout. Thus, $M^* = 1$ is an approximation that is numerically quite accurate, it does not imply the assumption that viscous effects are absent. It is possible to have the accumulated effects of viscosity upon the stagnation pressure be quite significant, but to still have the local viscous effect at the throat be very small.

Expressions for the area variation with Mach number and static pressure can be obtained directly by dividing Eq. (2.18.3) into Eqs. (2.18.1) and (2.18.2), respectively, to give

$$\frac{A}{A^*} = \frac{p_t^*}{p_t} \left[\frac{2}{\gamma+1} \left(1 + \frac{\gamma-1}{2} M^2\right)\right]^{\frac{\gamma+1}{2(\gamma-1)}} \frac{1}{M} \qquad (2.18.4)$$

$$\frac{A}{A^*} = \sqrt{\frac{\gamma-1}{2}} \left(\frac{2}{\gamma+1}\right)^{\frac{\gamma+1}{2(\gamma-1)}} \frac{p_t^*}{p_t} \left(\frac{p_t}{p}\right)^{\frac{1}{\gamma}} \left\{1 - \left(\frac{p}{p_t}\right)^{\frac{\gamma-1}{\gamma}}\right\}^{-\frac{1}{2}} \qquad (2.18.5)$$

Example results for isentropic flow ($p_t = p_t^*$) are shown in Fig. 2.18.1.

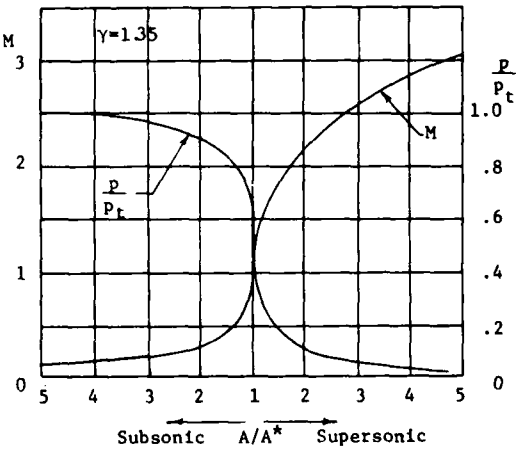

Figure 2.18.1 Pressure Ratio and Mach Number Versus Area Ratio for Isentropic Nozzle Flow

Chapter 3

LAMINAR VISCOUS FLOWS

Gordon C. Oates

University of Washington

TABLE OF CONTENTS

CHAPTER 3 LAMINAR VISCOUS FLOWS

		Page
3.0	Introduction	3-1
3.1	Couette Flow - Incompressible Fluid	3-1
3.1.1	The Coefficient of Viscosity	3-1
3.1.2	Behavior of the Velocity	3-1
3.1.3	The Coefficient of Heat Transfer	3-2
3.1.4	Thermal Effects in Couette Flows	3-2
3.1.5	Temperature Distribution - Upper and Lower Walls Thermally Conducting	3-3
3.1.6	Temperature Distribution - Lower Wall Thermally Insulated	3-4
3.1.7	Relationship Between the Heat Transfer and Wall Friction	3-4
3.2	The Relative Effects of Viscous Forces and Inertial Forces	3-5
3.3	The Boundary Layer	3-6
3.4	Separation	3-6
3.5.1	References	3-7

LIST OF FIGURES

		Page
Figure 3.1.1	Couette Flow	3-1
Figure 3.1.2	Forces on Fluid Element	3-1
Figure 3.1.3	Couette Velocity Profiles	3-2
Figure 3.1.4	Heat and Work Interactions	3-2
Figure 3.1.5	Temperature Perturbations Due to Dissipation x $1/\beta$ (Lower Wall Conducting)	3-3
Figure 3.1.6	Temperature Perturbations Due to Dissipation x $1/\beta$ (Lower Wall Insulated) $\Delta\theta/\beta = 1/6[3(1+P)^2 (1-\eta^2)-4P(1+P)(1-\eta^3)+2P(1-\eta^4)]$	3-4
Figure 3.3.1	The Boundary Layer	3-6
Figure 3.4.1	Airfoil with Separated Flow	3-6
Figure 3.4.2	Simple "Non-Viscous-Boundary Layer"	3-7

CHAPTER 3

LIST OF SYMBOLS

The symbols are listed in alphabetical order, first in the English alphabet, then in the Greek alphabet. Subscripts and superscripts are then given. The equation, figure or section in which the symbols are first introduced is indicated in parentheses. Often the symbol will be defined in the text just preceding or just following the equation or figure.

e - Unit vector (Eq. 3.2.2)

h - Height (Fig. 3.1.1)

k - Heat transfer coefficient (Eq. 3.1.8)

L - Reference length (Eq. 3.2.2)

M - Mach number (Eq. 3.1.24)

N_{ST} - Stanton number (Eq. 3.1.33)

P - Pressure gradient parameter (Eq. 3.1.6)

Pr - Prandtl number (Eq. 3.1.23)

p - Pressure (Eq. 3.1.3)

q - Heat transfer per area (Eq. 3.1.8)

R_e - Reynolds number (Eq. 3.2.3)

r - Recovery factor (Eq. 3.1.26)

T - Temperature (Eq. 3.1.8)

U - Wall velocity (Fig. 3.1.1)

u - Velocity (Fig. 3.1.1)

- Also x-component of velocity (Eq. 3.1.15)

$\bar{u}$ - Vector velocity (Eq. 3.2.1)

v - y-component of velocity (Eq. 3.1.15)

w - z-component of velocity (Eq. 3.1.15)

x - Co-ordinate (Fig. 3.1.1)

y - Co-ordinate (Fig. 3.1.1)

z - Co-ordinate (Eq. 3.1.3)

β - Dimensionless group (Eq. 3.1.14)

γ - Ratio of specific heats (Eq. 3.1.24)

δ - Boundary layer thickness (Fig. 3.3.1)

η - Dimensionless co-ordinate (Eq. 3.1.7)

θ - Dimensionless temperature (Eq. 3.1.12)

μ - Coefficient of viscosity (Eq. 3.1.2)

ρ - Density (Eq. 3.2.1)

τ - Shear stress (Eq. 3.1.2)

Φ - Dissipation function (Eq. 3.1.15)

Subscripts

h - Condition at $y = h$ or $\eta = 1$ (Eq. 3.1.22)

L - "Lower" velocity (Fig. 3.4.2)

u - "Upper" velocity (Fig. 3.4.2)

w - Value at the wall at $\eta = 0$ (Eq. 3.1.27)

o - Condition at y or $\eta = 0$ (Eq. 3.1.14)

- Also condition at $y = 0$ when lower wall insulated. (Eqs. 3.1.22, 3.1.31)

- Also upstream reference value (Eq. 3.2.2)

1 - Upstream condition (Eq. 3.4.1)

2 - Downstream condition (Eq. 3.4.1)

Superscripts

' - Dimensionless quantity (Eq. 3.2.2)

" - Quantities made dimensionless with respect to δ (Eq. 3.3.1)

CHAPTER THREE
LAMINAR VISCOUS FLOWS

3.0 INTRODUCTION

In this chapter we will seek to investigate the behavior of fluids under flow conditions in which the molecular transport of momentum or energy has a determining effect. We will exclude consideration of the phenomenon of turbulence (to be considered in Chapters 4 and 16), and restrict our attention to laminar flows. A laminar flow is defined simply as a flow in which adjacent layers of fluid slide smoothly over each other. The transfer of normal and tangential momentum, as well as energy, is due to molecular transport only.

In what follows selected simple examples of laminar flows will be considered, the intent being to illuminate several fundamental physical interactions that affect the limiting performance of turbomachines. Principal among such effects is the phenomenon of separation, wherein the combination of viscous effects and imposed pressure gradient causes a region of reversed (separated) flow to form. Such separated flow regions lead to large drag losses, and in the case of airfoils can lead also to loss of lift.

3.1 COUETTE FLOW - INCOMPRESSIBLE FLUID

A very simple conceptual experiment is that wherein flow occurs between two parallel flat walls, one of which is at rest, the other moving with velocity U. We consider a pressure gradient to exist, but note that because of the assumption of incompressibility of the fluid, together with the assumption of very large walls, no *streamwise* variations in pressure gradient or fluid velocity will exist. This type of flow, Couette flow, hence allows us to consider the interaction of the pressure and shear stresses without the additional complication of including the fluid inertial reaction. A similar analysis to the following can be carried out considering compressible flow (Reference 3.1). It is necessary in the compressible flow case to restrict attention to flows with no axial pressure gradient, however, in order to exclude the presence of axial variation of the fluid properties.

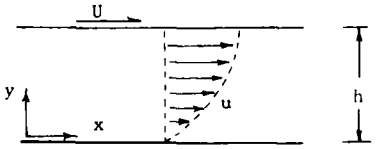

Figure 3.1.1 Couette Flow

3.1.1 THE COEFFICIENT OF VISCOSITY

In the special case of Couette flow in which no pressure gradient exists, experiment shows that for gases and most liquids, a linear velocity profile exists between the plates such that

$$\frac{u}{U} = \frac{y}{h} \qquad (3.1.1)$$

In addition, it is found that the shear stress, τ, at the wall is proportional to the (linear) velocity gradient. The proportionality constant is termed the coefficient of viscosity, μ, so that we obtain

$$\tau = \mu \frac{\partial u}{\partial y} \qquad (3.1.2)$$

Note that a simple force balance indicates that τ is constant throughout the fluid. (Fluids that (closely) follow a relationship of the form given in Eq. (3.1.2) are termed Newtonian fluids.) In flows of a more complicated nature than the very simple uniformly deforming flow considered above, the coefficient of viscosity plays essentially the same role as that described above. The primary additional complication in a more general flow arises because i) there will be a stress component present on all the faces of a fluid element, and ii) normal stresses will exist because of the rate of change of fluid properties in the fluid flow direction. The required relationships involve the use of tensor concepts, and are developed in many books on fluid mechanics (Ref. (3.2)).

3.1.2 BEHAVIOR OF THE VELOCITY

We now consider a force balance on a fluid element and note that because there is no acceleration of the fluid, the statement of the equation

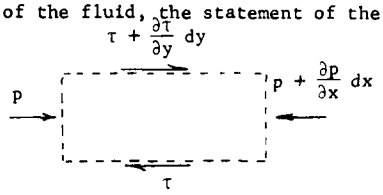

Figure 3.1.2 Forces on Fluid Element

of motion becomes simply that the pressure forces must be equal and opposite to the viscous forces. That is,

$$\left(\tau + \frac{\partial \tau}{\partial y} dy\right) dxdz - \tau dxdz = \left(p + \frac{\partial p}{\partial x} dx\right) dydz - dydz$$

or

$$\frac{\partial p}{\partial x} = \frac{\partial \tau}{\partial y} \qquad (3.1.3)$$

For simplicity we restrict our attention to flows in which the coefficient of viscosity is constant throughout the fluid. Then noting that $\frac{\partial p}{\partial x} = \frac{dp}{dx}$ must be constant throughout the fluid, that $\frac{\partial \tau}{\partial y} = \frac{d\tau}{dy}$, and incorporating Eq. (3.1.1), there is obtained

$$\frac{dp}{dx} = \mu \frac{d^2 u}{dy^2} \qquad (3.1.4)$$

This equation may be integrated directly, and utilizing the boundary conditions y = 0, u = 0; y = h, u = U it follows that

$$\frac{u}{U} = \frac{y}{h} + \frac{h^2}{2\mu U}\left(-\frac{dp}{dx}\right)\frac{y}{h}\left(1 - \frac{y}{h}\right) \qquad (3.1.5)$$

The velocity profile is thus the sum of a linear part which exists for no pressure gradient and a parabolic part that exists as a result of the pressure gradient.

The dimensionless group $P \equiv \frac{h^2}{2\mu U}\left(-\frac{dp}{dx}\right)$ may be considered a pressure gradient parameter. (The negative sign is included with the derivative for convenience, because P is then positive for a "favorable pressure gradient." That is, a pressure gradient that tends to accelerate the flow downstream.) For interpretive purposes we note that by regrouping the terms

$$P = \frac{(-dp)\ (hdz)}{2\mu\ \frac{U}{h}\ (dxdz)} = \frac{(-dp)(hdz)}{2\tau_o(dxdz)} \qquad (3.1.6)$$

$$= \frac{1}{2}\ \frac{\text{Net pressure force on fluid element}}{\text{Shear force existing on one surface of fluid element in the absence of a pressure gradient}}$$

Introducing the further dimensionless groups, $\eta \equiv \frac{y}{h}$, $v = \frac{u}{U}$, Eq. (3.1.5) may be written as

$$v = \eta + P\eta\,(1 - \eta) \qquad (3.1.7)$$

Velocity profiles for several values of P are indicated in the sketch. These results, though obtained for a highly simplified example flow, indicate tendencies of great significance.

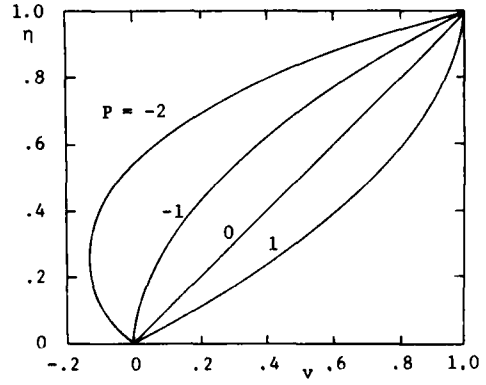

Figure 3.1.3 Couette Velocity Profiles

Thus, for example, it can be seen that the movement of the upper plate tends, through viscous momentum transfer, to transfer momentum to the lower fluid laminae. When an "adverse pressure gradient" (P negative) is imposed, such a gradient tends to remove the momentum present in the fluid. It can be seen that, in this case of Couette flow, when P reaches a value of minus one, the onset of reverse flow is imminent. Note that in this case $\frac{\partial v}{\partial \eta} = 0$ at the lower wall. For larger negative values of P, a portion of the flow exists in which the velocity is directed "upstream."

This situation has a close analog in some cases of flow in turbomachinery. Thus, for example, the condition can exist where the flow over a compressor blade will encounter a region of strong adverse pressure gradient. As in the above example, the flow near the blade surface will have a lower momentum than that further away (in the "free stream"), and if the pressure gradient is sufficient to overcome the effects of the inwardly convected momentum, flow reversal can occur. This condition is referred to as "separation," and in most cases in turbomachinery it is the onset of separation that establishes the limiting performance of the machine.

3.1.3 THE COEFFICIENT OF HEAT TRANSFER

A coefficient of heat transfer, k, can be defined in a manner quite analogous to the definition of the coefficient of viscosity already considered in section 3.1.1. Thus, if a temperature gradient is imposed on a material, it is found that the heat transfer per unit area, q, is proportional to the negative of the temperature gradient. Thus, in the simple case of a temperature gradient existing in the y direction only, we would have

$$q = -k\frac{dT}{dy} \qquad (3.1.8)$$

In the more general case of an arbitrarily imposed temperature field, the expression would be written

$$\bar{q} = -k\nabla T \qquad (3.1.9)$$

3.1.4 THERMAL EFFECTS IN COUETTE FLOWS

We again restrict ourselves to the simple Couette geometry considered in section 3.1. We shall consider the effects of heat transfer upon the flow, and again consider only cases where no axial variations in fluid properties occur. It may be noted that this latter assumption excludes from consideration the case where both of the channel walls are thermally insulated. If the walls were thermally insulated, the viscous dissipation within the fluid would cause a continual temperature increase in the axial direction, thereby violating the assumed axial invariance of the fluid properties.

To analyze the temperature distribution in the fluid, we apply the first law of thermodynamics to a fluid element.

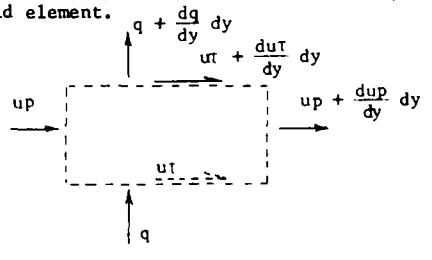

Figure 3.1.4 Heat and Work Interactions

The energy balance is indicated schematically in the figure, and may be written in words as:

Heat transfer from upper face - Heat transfer into lower face = Viscous work interaction with upper face - Viscous work interaction with lower face + Pressure work interaction with left face - Pressure work interaction with right face

This leads to

$$\frac{dq}{dy} = \frac{du\tau}{dy} - \frac{dup}{dx} \qquad (3.1.10)$$

Noting that $\frac{du}{dx} = 0$, and utilizing Eqs. (3.1.2), (3.1.3), and (3.1.8), it follows that

$$\frac{d}{dy}\left(k\frac{dT}{dy}\right) = -\mu\left(\frac{du}{dy}\right)^2 \qquad (3.1.11)$$

Again, for simplicity we assume the transport coefficients k and μ are constant. Then utilizing the previously defined dimensionless variables and introducing β and θ such that

$$\eta = \frac{y}{h},\ v = \frac{u}{U},\ P = -\frac{h^2}{2\mu U}\frac{dp}{dx}$$

$$\theta = \frac{T}{T_h},\ \beta = \frac{\mu U^2}{kT_h} \qquad (3.1.12)$$

Equation (3.1.11) may be written

$$\frac{d^2\theta}{d\eta^2} = -\beta\left(\frac{dv}{d\eta}\right)^2 \qquad (3.1.13)$$

In Eq. (3.1.12) T_h refers to the temperature of the upper wall which will be considered constant in the example solutions to follow. It is to be noted that the thermal effects considered here in no way affect the previously obtained solution for the velocity distribution. This is because of the assumed constant density and coefficient of viscosity.

The dimensionless group β gives a measure of the relative effects of the viscous dissipation and the heat transfer. Thus, we note

$$\beta = \frac{\mu U^2}{kT_h} = \frac{(\mu\frac{U}{h})U}{k\left(\frac{T_h}{h}\right)} = \frac{\text{Viscous work interaction}}{\text{Heat transfer}} \qquad (3.1.14)$$

Before obtaining explicit example solutions, it is of interest to note that any difference in the heat convected out the upper wall $\left(\sim -\left(\frac{d\theta}{d\eta}\right)_h\right)$ as compared to that convected in the lower wall $\left(\sim -\left(\frac{d\theta}{d\eta}\right)_o\right)$ must arise from the effects of viscous dissipation within the fluid. A direct first integral of Eq. (3.1.13) gives

$$-\left(\frac{d\theta}{d\eta}\right)_h + \left(\frac{d\theta}{d\eta}\right)_o = \beta\int_o^h \left(\frac{dv}{d\eta}\right)^2 d\eta \qquad (3.1.14)$$

The integrand $\left(\frac{dv}{d\eta}\right)^2$ is thus proportional to the viscous dissipation occurring at the location η. This is a very simple form of the more general "dissipation function" Φ; defined by (Ref. (3.3)):

$$\Phi \equiv 2\left[\left(\frac{\partial u}{\partial x}\right)^2 + \left(\frac{\partial v}{\partial y}\right)^2 + \left(\frac{\partial w}{\partial z}\right)^2\right] + \left(\frac{\partial v}{\partial x} + \frac{\partial u}{\partial y}\right)^2 + \left(\frac{\partial w}{\partial y} + \frac{\partial v}{\partial z}\right)^2 + \left(\frac{\partial u}{\partial z} + \frac{\partial w}{\partial x}\right)^2 - \frac{2}{3}\left(\frac{\partial u}{\partial x} + \frac{\partial v}{\partial y} + \frac{\partial w}{\partial z}\right)^2 \qquad (3.1.15)$$

3.1.5 TEMPERATURE DISTRIBUTION - UPPER AND LOWER WALLS THERMALLY CONDUCTING

An equation for the temperature ratio, θ, in terms of position, η, is obtained by combining Eqs. (3.1.7) and (3.1.13). Thus,

$$\frac{d^2\theta}{d\eta^2} = -\beta\left[1 + 2P + P^2 - 4\eta(1+P) + 4\eta^2P^2\right] \qquad (3.1.16)$$

Straightforward integration of this equation subject to the boundary conditions $\theta = \theta_o$ on $\eta = 0$, $\theta = 1$ on $\eta = 1$ gives, after some simple manipulation,

$$\theta = \theta_o(1-\eta) + \eta + \frac{\beta\eta(1-\eta)}{6}\left[3 + 2P + P^2 - 2P(2+P)\eta + 2P^2\eta^2\right] \qquad (3.1.17)$$

Several example temperature distributions are shown in Figure 3.1.5.

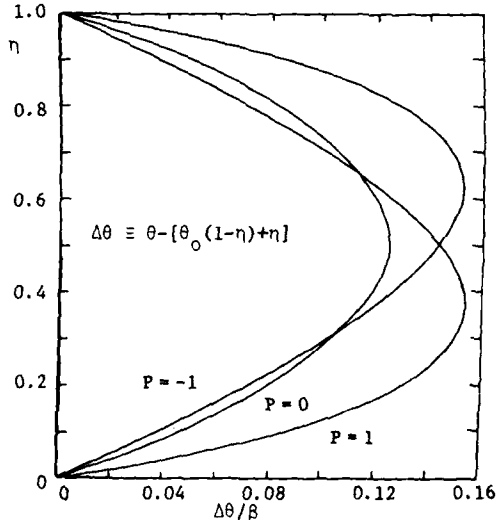

Figure 3.1.5 Temperature Perturbations Due to *Dissipation* x $1/\beta$ (Lower Wall Conducting)

The heat transfer rate is proportional to $\frac{\partial\theta}{\partial\eta}$, as is evident from Eqs. (3.1.8) and (3.1.12). From Eq. (3.1.17) we note that

$$\frac{\partial\theta}{\partial\eta} = 1 - \theta_o + \frac{\beta}{6}\left[(1-2\eta)(3+2P+P^2)\right.$$

$$\left.-2P(2+P)(2\eta-3\eta^2)+2P^2(3\eta^2-4\eta^3)\right] \quad (3.1.18)$$

We may now determine when the minimum in heat transfer rate occurs at a given value of η as a function of P. Thus, we note

$$\frac{\partial}{\partial P}\left(\frac{\partial\theta}{\partial\eta}\right) = \frac{\beta}{3}\left[(1-2\eta)(1+P)-2(1+P)(2\eta-3\eta^2)\right.$$

$$\left.+2P(3\eta^2-4\eta^3)\right] \quad (3.1.19)$$

The minimum value of $\frac{\partial\theta}{\partial\eta}$ at each wall hence occurs at $P = -1$ for $\eta = 0$ and $P = +1$ for $\eta = 1$. It will be noted that each of these values corresponds to the case where $\frac{dv}{d\eta} = 0$, which in turn corresponds to the case where the local value of the dissipation function is zero.

3.1.6 TEMPERATURE DISTRIBUTION - LOWER WALL THERMALLY INSULATED

When the lower wall is considered to be insulated, the boundary condition at $\eta = 0$ becomes $\frac{d\theta}{d\eta} = 0$. With this boundary condition, as well as $\theta = 1$ on $\eta = 1$, Eq. (3.1.16) yields

$$\theta = 1 + \frac{\beta}{6}\left[3(1+P)^2(1-\eta^2)-4P(1+P)(1-\eta^3)\right.$$

$$\left.+ 2P(1-\eta^4)\right] \quad (3.1.20)$$

Several example temperature profiles are shown in Fig. 3.1.6.

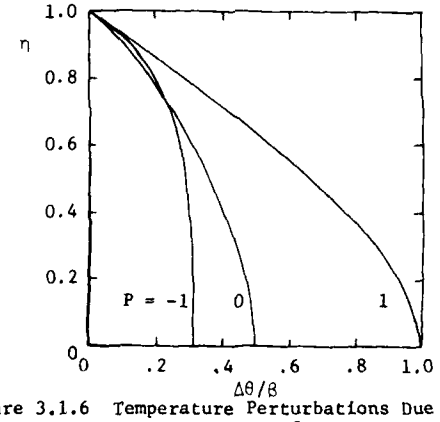

Figure 3.1.6 Temperature Perturbations Due to Dissipation x $1/\beta$ (Lower Wall Insulated) $\Delta\theta/\beta = 1/6[3(1+P)^2(1-\eta^2) -4P(1+P)(1-\eta^3)+2P(1-\eta^4)]$

It is of interest to note the behavior of the temperature at the lower wall. Thus, we see from Eq. (3.1.20) with $\eta = 0$:

$$\theta_o = 1 + \frac{\beta}{6}\left[3+2P+P^2\right] \quad (3.1.21)$$

This is more easily interpreted in terms of the original dimensional variables, for which we obtain

$$T_o = T_h + \frac{\mu}{k}\frac{U^2}{6}\left[3+2P+P^2\right] \quad (3.1.22)$$

We now introduce the Prandtl number, Pr, defined by

$$Pr = \frac{\mu C_p}{k} \quad (3.1.23)$$

Then, assuming that the fluid is a perfect gas, so that we may write

$$\frac{U^2}{C_p T_h} = \frac{\gamma R}{C_p}\frac{U^2}{\gamma R T_h} = (\gamma-1)\,M_h^2$$

Eq. (3.1.22) may be written

$$T_o = T_h\left[1 + Pr\left\{\frac{3+2P+P^2}{3}\right\}\frac{\gamma-1}{2}M_h^2\right] \quad (3.1.24)$$

Or in the special case of zero pressure gradient,

$$T_o = T_h\left[1 + Pr\,\frac{\gamma-1}{2}M_h^2\right] \quad (3.1.25)$$

We note that the development here applies strictly only to flows in which the Mach number is very low. This is because we have assumed the flow to be incompressible. A development allowing compressibility leads, however, to the same result as Eq. (3.1.25) provided that the pressure gradient is zero (Ref. (3.1)).

For gases the Prandtl number is not far from unity (for air $Pr \approx 0.73$). Thus, the temperature attained at the adiabatic wall, termed the recovery temperature, is not far from the stagnation temperature of the fluid at the moving surface. The recovery factor, r, is defined by

$$r = \frac{T_o - T_h}{T_{t_h} - T_h} \quad (3.1.26)$$

and in this case of Couette flow of a perfect gas is seen to be equal to Pr.

When a boundary layer exists on an adiabatic wall, the situation is similar to that described above, conditions in the "free stream" becoming analagous to those at the upper wall in Couette flow. In the boundary layer case, except under conditions of extreme acceleration, the equivalent pressure gradient parameter is very small. This is because the height, h, in the expression for P (Eq. (3.1.12)) is very small. Obviously the recovery temperature is that value of wall temperature for which the heat transfer is zero.

3.1.7 RELATIONSHIP BETWEEN THE HEAT TRANSFER AND WALL FRICTION

In the special case of zero pressure gradient an expression relating the wall heat transfer and skin friction is easily obtained. Thus, integration of Eq. (3.1.10) from y = 0 to y = y gives

$$-q + u\tau = -q_w \quad (3.1.27)$$

Eqs. (3.1.2) and (3.1.8) then give

$$k\frac{dT}{dy} + \mu u\frac{du}{dy} = -q_w = \mu\left[\frac{C_p}{Pr}\frac{dT}{dy} + \frac{d\frac{u^2}{2}}{dy}\right] \tag{3.1.28}$$

The Prandtl number is usually very nearly constant, and if, in addition, C_p can be considered constant, we obtain

$$\frac{1}{Pr}C_p(T - T_w) + \tfrac{1}{2}u^2 = -q_w\int_o^y \frac{dy}{\mu} \tag{3.1.29}$$

Eq. (3.1.3) indicates that the shear, τ, is a constant when the pressure gradient is equal to zero. Eq. (3.1.2) may then be integrated directly and substituted into Eq. (3.1.29), to give

$$C_pT_w = C_pT_h + Pr\left(\frac{U^2}{2} + \frac{q_w}{\tau_w}U\right) \tag{3.1.30}$$

It can be recognized that this expression reduces to Eqs. (3.1.22) or (3.1.25) in the case $P = 0$ and $q_w = 0$. Utilizing Eq. (3.1.22) with $P = 0$ we then obtain

$$q_w = (T_w - T_o)\frac{\tau_w}{U}\frac{C_p}{Pr} \tag{3.1.31}$$

This form emphasizes the requirement that $T_w > T_o$ for heat transfer into the stream to occur. In section 2.17.2 we introduced the heat transfer coefficient h in a form valid for the case where $Pr = 1$ (Eq. (2.17.11)). The Stanton number, N_{ST}, and skin friction coefficient, C_f, were also introduced in Chapter 2 (Eqs. (2.17.8) and (2.17.12)). In a form appropriate for $Pr \neq 1$, these may be written

$$h = \frac{q_w}{T_w - T_o},\quad N_{ST} = \frac{h}{\rho U C_p},\quad C_f = \frac{\tau_w}{\frac{1}{2}\rho U^2} \tag{3.1.32}$$

Substitution of these relationships into Eq. (3.1.31) gives

$$N_{ST} = \frac{C_f}{2Pr} \tag{3.1.33}$$

Thus, we see that in the case of Couette flow at constant pressure, "Reynolds Analogy" relates the Stanton number to the skin friction coefficient. In the case where $Pr \approx 1$, the expression reduces to the form assumed in Chapter 2.

3.2 THE RELATIVE EFFECTS OF VISCOUS FORCES AND INERTIAL FORCES

In section 3.1 we considered the behavior of a fluid in which the effects of the inertia of the fluid were zero, because the fluid underwent no acceleration. In general, it is of interest to consider flow fields with acceleration, however, and in such cases it is necessary to estimate the relative effects of the inertial and viscous terms. To this end we shall consider the three dimensional equations of motion, again restricting our attention to a constant density fluid with constant transport properties.

In the case of steady flow, the momentum equation may be written in vector form as:*

$$\rho(\bar{u}\cdot\nabla)\,\bar{u} + \nabla p = \mu\nabla^2\bar{u} \tag{3.2.1}$$

This expression gives the relationship between the inertial, pressure and viscous terms, respectively. It is of use to compare the expected magnitudes of each of these separate terms, and to do so we first non-dimensionalize the equation.

The operator $(\bar{u}\cdot\nabla)$ expresses the rate of change along streamlines. We thus imagine a characteristic length, L, over which the quantity being operated upon will change of the order of its own reference value. For example, we may consider the flow of a fluid about a cylinder. We know in this case the velocity changes from the oncoming velocity, u_o, to a value of $2u_o$ at the upper surface of the cylinder in a length of "about" the diameter of the cylinder. In such a case the diameter would be considered the characteristic length, L, and the distant velocity, u_o, the characteristic velocity. Introducing the dimensionless quantities

$$\bar{u}' = \frac{\bar{u}}{u_o};\quad x', y', z' = \frac{x}{L}, \frac{y}{L}, \frac{z}{L};$$

$$\nabla' \sim \frac{\partial}{\partial x'}\bar{e}_x + \frac{\partial}{\partial y'}\bar{e}_y + \frac{\partial}{\partial z'}\bar{e}_z \tag{3.2.2}$$

we would thus expect that the term $(\bar{u}'\cdot\nabla')\bar{u}'$ would be expected to have a value of about unity in the region of flow of interest (i.e., near the obstacle). With the additional definitions

$$p' = \frac{p}{\rho u_o^2};\quad Re = \frac{\rho u_o L}{\mu} = \text{Reynolds number} \tag{3.2.3}$$

Eq. (3.2.1) becomes:

$$(\bar{u}'\cdot\nabla')\bar{u}' + \nabla'p' = \frac{1}{Re}\nabla'^2\bar{u}' \tag{3.2.4}$$

It is evident from Bernoulli's equation that if $\bar{u}' = \frac{\bar{u}}{u_o}$ changes by a sizeable fraction, that we would expect p' to change by a fraction of corresponding magnitude. It would hence seem that the magnitude of the viscous contribution to the momentum equation is of the order of 1/Re times the inertial and pressure contributions.

---

*Note that $\nabla^2\bar{u}$ in fact requires tensor concepts to be expanded in other than Cartesian coordinates. However, vector notation can be retained if we define $\nabla^2\bar{F}$ with $\bar{F}$ a vector, by the relationship $\nabla^2\bar{F} = \nabla(\nabla\cdot\bar{F}) - \nabla\times(\nabla\times\bar{F})$.

For instructive purposes it is useful to write the Reynolds number as $Re = \frac{\rho u_o^2}{\mu u_{o/L}}$. When written in this form it is obvious that Re is the ratio of inertial stresses to viscous stresses that would exist in a fluid with velocity gradient $\frac{\partial u}{\partial y} \sim \frac{\partial u}{\partial x} \sim \frac{u_o}{L}$. Without postulating the existence of such a thing as a boundary layer, we find that solutions to the "perfect fluid" equations (i.e., no viscosity) do indicate that the velocity gradients found are of the order u_o/L. With this being the case we can then check to find the approximate ratio of the inertial effects to viscous effects to be expected in flow fields predicted by the perfect fluid equations.

As an example, let us consider air at about room temperature (15°C) flowing past an object of characteristic dimension one meter at a velocity of fifty meters per second. The appropriate parameters for these conditions are approximately $\mu = 180(10^{-6})\ \frac{\text{Newt-sec}}{\text{m}^2}$, $\rho = 1.3\ \text{Kg/m}^3$, $u_o \approx 50\ \frac{\text{m}}{\text{sec}}$, $L = 1\text{m}$. Hence $Re \approx 3.6(10^6)$.

Thus, we estimate in this case that the inertial terms are more than a million times larger than the viscous terms! It is small wonder that early investigators in the field of fluid mechanics felt justified in excluding the viscous terms. It is clear, however, that in a real flow the fluid velocity at the wall must be zero. (Here we exclude rarefied gas effects that allow "wall slip.") And it is apparent that at least near the wall the viscous effects must be comparable to the inertial effects. This region in the vicinity of the wall, the boundary layer, is discussed in the next section.

3.3 THE BOUNDARY LAYER

Let us now hypothesize the existence of a thin layer adjacent to the fixed boundary. This layer will be defined as the layer within which the viscous forces are "about" as large or larger than the inertial forces. We note that within the boundary layer the largest rates of change will be across the fluid laminae. Thus, the rates

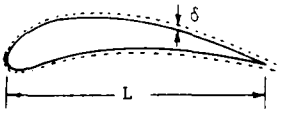

Figure 3.3.1 The Boundary Layer

of change in the inertial terms (which occur along the streamline direction) remain of the same order as discussed in section 3.2, whereas we now expect the fluid velocity to change from of order u_o to zero across the laminae in a distance δ. Defining

$$x'', y'', z'' = \frac{x}{\delta}, \frac{y}{\delta}, \frac{z}{\delta} \quad \text{and}$$

$$\nabla'' = \frac{\partial}{\partial x''} + \text{etc.} \qquad (3.3.1)$$

We would expect the group $\nabla''^2\bar{u}'$ to be of order unity. The entire viscous term of Eq. (3.2.4) then becomes $\frac{1}{Re}\left(\frac{L}{\delta}\right)^2\nabla''^2\bar{u}'$. Now since by hypothesis δ is the width of the layer within which the viscous forces are about as large as the inertial forces, we must have $\frac{1}{Re}\left(\frac{L}{\delta}\right)^2 \sim 1$.

The estimate for the thickness of the boundary layer is thus

$$\frac{\delta}{L} \sim \frac{1}{\sqrt{Re}} = \frac{1}{\sqrt{\frac{\rho u_o L}{\mu}}} \qquad (3.3.2)$$

If L is considered to be the length from the leading edge of the obstacle we see in this case of laminar flow that the boundary layer thickness grows as $L^{\frac{1}{2}}$. Note that for the example of section 3.2 the ratio of δ to L would be approximately $\frac{1}{1000}$. This helps to illustrate why we may often calculate the "inviscid flow field" ignoring the effect of the boundary layer, and then later calculate the conditions within the boundary layer using the results of the inviscid flow field calculations as the boundary conditions (or "free stream" conditions) for the boundary layer calculations.

3.4 SEPARATION

An often observed phenomenon is that of fluid "separation" from the boundary.

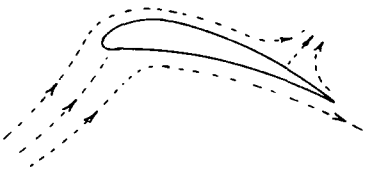

Figure 3.4.1 Airfoil with Separated Flow

By separation, we mean that the flow divides from the boundary and has a region of reverse flow. Clearly, if such an event occurs we can no longer assume that the "boundary layer" is thin. It is equally clear that we can no longer calculate the inviscid flow field assuming that the apparent fluid boundary is very nearly that of the physical boundary.

The phenomenon of separation is of great engineering interest, because of its effect on such things as the performance of airfoils, the performance of gas turbine compressors and the off design performance of (over expanded) rocket nozzles. In many cases the conditions under which separation will just occur can be estimated by finding where the derivative of the fluid velocity, in the normal direction, goes to zero. The calculations leading to the estimate of such a position are rather complex, but we can gain some insight by considering the qualitative effects of the momentum influx from the free stream and of the externally imposed pressure gradient.

The velocity at a given elevation in the boundary layer is partly determined by the balance between incoming momentum from the upper layers, and outgoing momentum to the lower layers (and wall). It is this transmission of momentum to the wall that results in the skin friction, τ_w, at the wall. Thus, if we have a turbulent boundary layer in which a great deal of "macroscopic" interchanging of fluid "packets" occurs, and consequently a great deal of interchanging of fluid momentum occurs, we would expect the transmission of momentum inward to resist the effects of the (adverse) pressure gradient and consequently, separation to be delayed. The result then is that the increased inward flux of momentum helps to resist the formation of a flow reversal region.

The effects of the pressure gradient on the boundary layer have already been somewhat foreshadowed in section 3.1.2. There we noticed that reverse flow occurred for values of the pressure gradient parameter P more negative than minus one. This reversal occurs even though the upper wall attempts to drag all the fluid forward.

In the case of boundary layers, an important mathematical approximation (introduced by Prandtl) is that any effect of the normal pressure gradient is negligible. This result occurs because the boundary condition on the vertical velocity component at both edges of the boundary layer is that it be zero, and the additional fact that the boundary layer is very thin ensures that no sizeable vertical velocity component can be attained. The result then is that no sizeable inertial effects are present in the normal direction to lead to sizeable pressure gradients. This extremely useful approximation then allows us to state that the pressure at the outer edge of the boundary layer is the same as that at the inner edge, or in more mathematical phrasing $p = p(x)$.

Insight into the effects of an axial pressure gradient can be gained by considering the behavior of a very simple "non-viscous boundary layer." That is, suppose for now that a boundary layer of the form sketched in Fig.3.4.2 has been formed, and then the viscosity "turned off." (This example is not as far removed from reality as might at first be suspected, because near separation $\frac{\partial u}{\partial y}$ is very nearly zero near the wall and hence the effects of viscous stresses are very small indeed.)

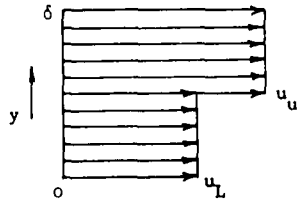

Figure 3.4.2 Simple "Non-Viscous-Boundary Layer"

Now, because there are no viscous stresses on the fluid streams, if the pressure changes from p_1 to p_2, the corresponding changes in the velocities u_L and u_u follow from Bernoulli's equation and may be written

$$u_{u_2}^2 - u_{u_1}^2 = -\frac{2}{\rho}(p_2 - p_1) \qquad (3.4.1)$$

$$u_{L_2}^2 - u_{L_1}^2 = -\frac{2}{\rho}(p_2 - p_1) \qquad (3.4.2)$$

and

$$\frac{u_{u2}-u_{L2}}{u_{u1}-u_{L1}} = \frac{u_{u1}+u_{L1}}{u_{u2}+u_{L2}} \qquad (3.4.3)$$

We thus see what is intuitively obvious. If the fluid is forced to negotiate a pressure rise ($p_2 - p_1$ positive) a point is reached (at $\frac{2}{\rho}(p_2 - p_1) = u_{L_1}^2$) after which the initial momentum of the lower stream is no longer capable of negotiating a further pressure rise. We note also from equation (3.4.3) that the difference between the upper and lower velocities increases for a pressure rise ($[u_{u_2} + u_{L_2}] < [u_{u_1} + u_{L_1}]$) and decreases for a pressure reduction ($[u_{u_2} + u_{L_2}] > [u_{u_1} + u_{L_1}]$). Thus, an adverse pressure gradient (i.e., a positive pressure gradient) leads to separation, while separation cannot occur in a favorable pressure gradient.

3.5.1 REFERENCES

(3.1) Liepman, H.W. and Roshko, A., Elements of Gasdynamics (Wiley, New York, 1957), pp. 306-313.

(3.2) Batchelor, G.H., An Introduction to Fluid Dynamics, (Cambridge, 1967), pp. 141-151.

(3.3) Schlicting, H., Boundary Layer Theory (McGraw-Hill, 1960), p. 291.

Chapter 4

TURBULENT FLOWS

Gordon C. Oates

University of Washington

TABLE OF CONTENTS

CHAPTER 4 TURBULENT FLOWS

		Page
4.0	Introduction	4-1
4.1	Some Experimental Results	4-1
4.2	The Momentum Equation Including Turbulence - Reynolds Stresses	4-2
4.3	The Balance of Forces within the Boundary Layer - Estimation of the Equilibrium Length	4-3
4.4	Creation and Destruction of Turbulence within the Boundary Layer	4-4
4.5	Regimes of the Boundary Layer	4-5
4.5.1	The Inner Layer.	4-5
4.5.1.1	The Sublayer	4-6
4.5.1.2	The Blending Region	4-6
4.5.1.3	The Equilibrium Layer - The Law of the Wall	4-6
4.5.2	The Outer Layer - The Law of the Wake.	4-8
4.6.1	References	4-10

LIST OF FIGURES

		Page
Figure 4.1.1	Flow About a Sphere	4-1
Figure 4.1.2	Drag Coefficient for Spheres Versus Reynolds Number	4-1
Figure 4.1.3	Flow About a Sphere at Moderate Reynolds Number	4-2
Figure 4.1.4	Flows About a Sphere Near Re_{CRIT}	4-2
Figure 4.3.1	Portion of Boundary Layer	4-3
Figure 4.4.1	Fluid Element in Turbulent Flow	4-4
Figure 4.4.2	Normalized Turbulent Energy Production Rate Per Unit Volume in a Typical Turbulent Boundary Layer.	4-4
Figure 4.5.1	Forces on a Fluid Element	4-5
Figure 4.5.2	Fully Developed Pipe Flow	4-6
Figure 4.5.3	Annular Fluid Element	4-7
Figure 4.5.4	Turbulent Boundary Layer Regimes	4-8
Figure 4.5.5	The Wake Function	4-9

CHAPTER 4

LIST OF SYMBOLS

The symbols are listed in alphabetical order, first in the English alphabet, then in the Greek alphabet. Subscripts and superscripts are then given. The equation, figure or section in which the symbols are first introduced is indicated in parentheses. Often the symbol will be defined in the text just preceding or just following the equation or figure.

A - Cross sectional area (Eq. 4.1.1)

- Constant (Eq. 4.5.18)

$\bar{A}$ - Arbitrary vector (Eq. 4.2.3)

a - Constant (Eq. 4.5.21)

$\bar{B}$ - Arbitrary vector (Eq. 4.2.3)

b - Constant (Eq. 4.5.21)

C_D - Drag coefficient (Eq. 4.1.1)

D - Drag (Eq. 4.1.1)

d - Diameter (Eq. 4.1.1)

E - Rate of energy input/axial length (Eq. 4.5.10)

F - Force (Eq. 4.3.1)

- Function (Eq. 4.5.2, 4.5.23)

f - Function (Eq. 4.5.1, 4.5.22)

g - Function (Eq. 4.5.26)

h - Function (Eq. 4.5.22)

K - Constant (Eq. 4.5.16)

K.E. - Kinetic energy (Eq. 4.3.2)

K_τ - Acceleration parameter (Eq. 4.5.4)

L - Characteristic length (Eq. 4.3.3)

p - Pressure (Eq. 4.2.1)

R - Pipe radius (Fig. 4.5.2)

R_e - Reynolds number (Eq. 4.1.1)

r - Radius (Eq. 4.5.6)

t - Time (Eq. 4.2.1)

U - Reference velocity (Eq. 4.1.1)

u - x-velocity component (Fig. 4.3.1)

$\bar{u}$ - Vector velocity (Eq. 4.2.1)

v - y-velocity component (Fig. 4.4.2)

w - Wake function (Eq. 4.5.26)

x - Co-ordinate (Eq. 4.3.1)

y - Co-ordinate (Fig. 4.4.1)

δ - Boundary layer thickness (Fig. 4.3.1)

ϵ - Dissipation rate (Eq. 4.5.16)

θ - Angle (Fig. 4.1.3)

μ - Coefficient of viscosity (Eq. 4.1.1)

π - Pressure gradient parameter (Eq. 4.5.23)

ρ - Density (Eq. 4.1.1)

τ - Shear stress (Eq. 4.2.11, Fig. 4.3.1)

Subscripts

i - Tensor suffix (Eq. 4.2.4)

(i) - Radius just outside region of large velocity gradients (Fig. 4.5.2)

j - Tensor suffix (Eq. 4.2.4)

- Vector suffix (Eq. 4.2.11)

L - Laminar (Eq. 4.2.11)

t - Turbulent (Eq. 4.2.12)

w - Wall value (Eq. 4.3.1)

B.L. - Boundary layer (Eq. 4.3.4)

CRIT - Critical (Fig. 4.1.2)

net - Net (Eq. 4.3.1)

$\bar{}$ - Average (Eq. 4.2.8)

$\tilde{}$ - Tensor quantity (Eq. 4.2.11)

o - Freestream (Fig. 4.3.1)

τ - Friction (Eq. 4.5.2)

Superscripts

$'$ - Perturbation (Eq. 4.2.8)

$*$ - Dimensionless (y co-ordinate) (Eq. 4.5.2)

- Displacement thickness (Eq. 4.5.28)

CHAPTER FOUR
TURBULENT FLOWS

4.0 INTRODUCTION

A turbulent flow is a flow in which the momentum, energy, and other properties of the fluid are transported across "streamlines" by the random movement of "macroscopic eddies", rather than (solely) by the molecular movement. Turbulent mechanisms have a profound effect upon the nature of flow within turbomachines, and as a result are crucial in determining the operating limits of many of the turbomachine components. For the engineer, it is important to attempt to understand the physics of turbulent flows so that design pitfalls may be avoided, and possible benefits of turbulence exploited. It is important, also, to develop computational techniques so that the loss mechanisms identified with turbulence effects may be accurately estimated. Such accurate estimates would not only allow suitable estimates of component efficiencies to be obtained for use in cycle analysis (Chapter 7), but could also allow competing designs to be compared analytically.

In this chapter an attempt is made to describe the physics of turbulent flows. Particular emphasis is placed upon the description of turbulent boundary layers because of their great importance in turbomachinery. Chapter 16 presents an exhaustive study of computational techniques and turbulence modeling for turbulent boundary layers.

4.1 SOME EXPERIMENTAL RESULTS

Perhaps the most famous series of experiments illuminating the nature of drag are those experiments taken on circular cylinders or spheres. Simple dimensional arguements indicate that in incompressible, time independent flows, the drag coefficient can be a function of the Reynolds number only.

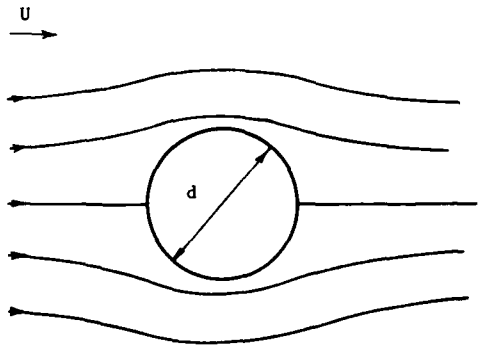

Figure 4.1.1 Flow About a Sphere

Note we define the symbols

D = Drag

ρ = Density

U = Far upstream flow speed

A = cross sectional area

d = Diameter

μ = Viscosity

$$C_D = \text{Drag coefficient} = \frac{D}{1/2\ \rho U^2 A}$$

$$R_e = \text{Reynolds number} = \frac{\rho U d}{\mu} \qquad (4.1.1)$$

The results of many investigators who studied incompressible flow about a sphere led to the relationship indicated in Figure 4.1.2.

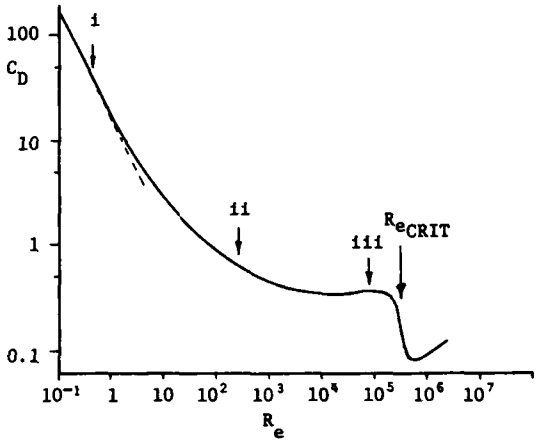

Figure 4.1.2 Drag Coefficient for Spheres Versus Reynolds Number

Figure 4.1.2 indicates that the drag coefficient becomes very large at very low Reynolds numbers. As a matter of fact, when the Reynolds number is less than unity (point i, Fig. 4.1.2) the experimental results approach the analytical result obtained by Stokes in 1851 (Ref. 4.1) which may be written

$$C_D = \frac{24}{R_e} \qquad \text{Stokes' Equation} \qquad (4.1.2)$$

It is interesting to note that in the analytical result obtained by Stokes, the streamline patterns approaching and departing the sphere are symmetric. Also, one third of the drag arises because the pressure on the downstream side is less than the pressure on the upstream side, and the remaining two thirds of the drag arises from the surface shearing stresses. In this case, then, we would say that one third of the drag is profile drag, and two thirds of the drag is skin drag.

As the Reynolds number is increased, the inertial stresses within the fluid increase more rapidly than do the (molecular) viscous stresses. Soon the situation is reached (point ii, Fig. 4.1.2) where the inertial stresses are sufficiently large that a substantial pressure rise is identified with the retarding of the flow from point A to point B of Figure 4.1.3.

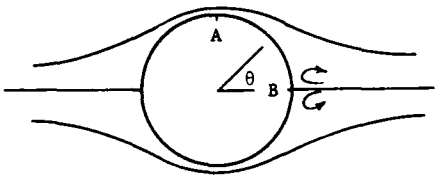

Figure 4.1.3 Flow About a Sphere at Moderate Reynolds Number

At this condition, it happens that the fluid near the sphere surface (in the "boundary layer") has insufficient momentum to surmount the imposed adverse pressure gradient and a small separated region of flow exists. The presence of the separated region, itself, prevents the attainment of the higher static pressure on the aft end of the sphere, and as a result the form drag increases in comparison to what it would be if separation did not occur. Thus, the drag coefficient increases over what it would be if Stokes flow were still present. ($C_D \Rightarrow 24/R_e$)

With further increase in Reynolds number (point iii, Fig. 4.1.2) this separated region spreads until the separation point actually moves ahead of the $\theta = 90°$ point of the sphere. In this condition the skin drag is very low and the form drag very large. It is interesting to note, as an aside, that such a flow field would never even be approximated by the "classical" method of first calculating the free stream and then determining the boundary layer behavior under the influence of the pressure field imposed by the free stream. The classical method would predict a favorable pressure gradient up to the $\theta = 90°$ point, whereas it is apparent from the experimental results that the effect upon the external flow field of the aft end separation is so enormous that the imposed pressure gradient must in fact be adverse well ahead of the $\theta = 90°$ point.

With still further increases in Reynolds number a dramatic reduction in drag coefficient occurs. This, at first surprising result, occurs because the boundary layer becomes turbulent over a substantial portion of its length. As a result the increased transfer of momentum from the outer streamlines to the inner streamlines enables the boundary layer to remain attached to a much more rearward position, leading in turn to a great reduction in form drag with only a slight increase in skin friction. Figure 4.1.4 shows the related flow fields for flows with Reynolds numbers above and below this critical value. ($R_{e_{CRIT}}$)

Beyond $R_e = R_{e_{CRIT}}$ the drag coefficient continues to rise as the separated region again enlarges. This classic experiment illustrates how drag may be considered to be of two parts, skin drag and profile drag, and how each may be somewhat controlled to affect the other. Thus, for example, as in Prandtl's famous experiment, a "trip ring" may be attached to the sphere to hasten the onset of turbulence in the boundary layer. At the appropriate Reynolds number this slightly increases the skin drag but greatly decreases the form drag.

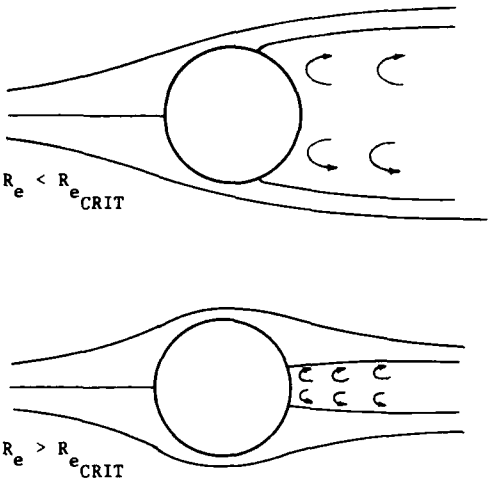

Figure 4.1.4 Flows about a Sphere Near $R_{e_{CRIT}}$

Such tradeoffs between skin drag and form drag occur in many engineering applications. An example is that of an inlet diffuser equipped with vortex generators. The vortex generators act somewhat as turbulence generators by causing the external high momentum air to be transported into the boundary layer where the added momentum delays the onset of separation. Similarly, vortex generators can be placed on upper wing surfaces to delay separation at high angles of attack. In the latter case, however, the increased skin drag can cause a substantial drag penalty when the aircraft is in the cruise condition, and when in fact the vortex generators are not required.

4.2 THE MOMENTUM EQUATION INCLUDING TURBULENCE - REYNOLDS STRESSES

The momentum equation may be written in the form (Ref. 4.2)

$$\rho \frac{\partial \bar{u}}{\partial t} + (\rho\bar{u}\cdot\nabla)\bar{u} = -\nabla p + \mu\nabla^2\bar{u} + \frac{\mu}{3}\nabla(\nabla\cdot\bar{u}) + 2[(\nabla\mu)\cdot\nabla]\bar{u}$$

$$+\nabla\mu\times(\nabla\times\bar{u}) - \frac{2}{3}\nabla\mu(\nabla\cdot\bar{u}) \qquad (4.2.1)$$

Our principal concern in this chapter is to investigate the effects of turbulence, so for simplicity we will restrict our attention to flows in which the effects of the spatial variation of viscosity are negligible. In this case, the last three terms of Eq. (4.2.1) vanish, so that upon adding the vector velocity times the continuity equation [$\bar{u}(\partial\rho/\partial t + \nabla\cdot\rho\bar{u}) = 0$] to Eq. (4.2.1) there is obtained

$$\frac{\partial\rho\bar{u}}{\partial t} + (\rho\bar{u}\cdot\nabla)\bar{u} + \bar{u}(\nabla\cdot\rho\bar{u}) = -\nabla p + \mu\nabla^2\bar{u} + \frac{\mu}{3}\nabla(\nabla\cdot\bar{u})$$

$$(\mu = \text{const}) \qquad (4.2.2)$$

It is of convenience to introduce the dyadic operator $(\bar{A}o\bar{B})$, where $(\bar{A}o\bar{B})$ is the special tensor defined by the property

$$(\bar{A}o\bar{B})\bar{C} = \bar{A}(\bar{B}\cdot\bar{C}) \qquad (4.2.3)$$

Direct expansion shows that the tensor $(\bar{A}o\bar{B})$ is symmetric with elements given by

$$A_{ij} = A_i B_j \tag{4.2.4}$$

Direct expansion further shows (Ref. 4.2) that

$$\nabla\cdot(\bar{A}o\bar{B}) = \bar{B}(\nabla\cdot\bar{A}) + (\bar{A}\cdot\nabla)\bar{B} \tag{4.2.5}$$

Utilizing Eq. (4.2.5), Eq. (4.2.2) may be written in the compact form

$$\frac{\partial\rho\bar{u}}{\partial t} + \nabla\cdot(\rho\bar{u}o\bar{u}) = -\nabla p + \mu\nabla^2\bar{u} + \frac{\mu}{3}\nabla(\nabla\cdot\bar{u}) \qquad (\mu = \text{const}) \tag{4.2.6}$$

In order to most easily illuminate the major effects of turbulence we now restrict our attention to incompressible fluids, so that the momentum equation reduces to

$$\rho\left[\frac{\partial u}{\partial t} + \nabla\cdot(\bar{u}o\bar{u})\right] = -\nabla p + \mu\nabla^2\bar{u} \quad (\mu = \text{const},\ \rho = \text{const}) \tag{4.2.7}$$

We now postulate the possible presence of velocity fluctuations due to turbulence within the fluid. Virtually by definition such fluctuations are random, so that a general solution of an equation as complicated as Eq. (4.2.7) would seem to be impossible. Thus, rather than seek a general time varying solution to Eq. (4.2.7), we attempt to obtain solutions to the velocity field averaged over a time long compared to the time of a "typical" turbulent fluctuation. We thus introduce the perturbation velocity $\bar{u}'$ defined by

$$\bar{u} = \underline{\bar{u}} + \bar{u}' \tag{4.2.8}$$

here $\underline{\bar{u}}$ is the time averaged value of $\bar{u}$

Denoting a time average by the symbol < >, we see that

$$\langle\bar{u}\rangle \equiv \underline{\bar{u}}\ ,\ \langle\bar{u}'\rangle = 0 \tag{4.2.9}$$

Note that the time scale of the averaging process of the turbulence quantities may be much less than the time scale of the variation of the mean quantities, so that $\partial\underline{\bar{u}}/\partial t$ need not necessarily be zero.

Equation (4.2.8) is now substituted into Eq. (4.2.7) and the time average taken to give:

$$\rho\left[\frac{\partial\underline{\bar{u}}}{\partial t} + \nabla\cdot(\underline{\bar{u}}o\underline{\bar{u}})\right] = -\nabla p + \mu\nabla^2\underline{\bar{u}} - \nabla\cdot(\rho\langle\bar{u}'o\bar{u}'\rangle) \tag{4.2.10}$$

It can be seen that the effect of the fluctuating velocities is to introduce "apparent stresses" on the right side of the equation. It is evident that these apparent stresses or "Reynolds stresses" do, in fact, represent the effects of the flow of momentum across fluid element surfaces, and in that sense are analagous to the molecular viscosity brought about by the flux of molecules across element surfaces.

Introducing the molecular (or laminar) stress tensor $\underline{\underline{I}}_L$, and the turbulent stress tensor $\underline{\underline{I}}_t$, it follows (utilizing $\nabla^2\underline{\bar{u}} = -\nabla\times(\nabla\times\underline{\bar{u}})$, Sec. 3.2) that

$$(\underline{\underline{I}}_L)_{ij} = \mu\left\{\frac{\partial\underline{u}_i}{\partial x_j} + \frac{\partial\underline{u}_j}{\partial x_i}\right\} \tag{4.2.11}$$

and $$(\underline{\underline{I}}_t)_{ij} = -\rho\langle u_i' u_j'\rangle \tag{4.2.12}$$

The momentum equation may then be written

$$\rho\left[\frac{\partial\underline{\bar{u}}}{\partial t} + (\underline{\bar{u}}\cdot\nabla)\underline{\bar{u}}\right] = -\nabla p + \nabla\cdot\underline{\underline{I}}_L + \nabla\cdot\underline{\underline{I}}_t \tag{4.2.13}$$

The stress terms defined by Eq. (4.2.12) are termed the Reynolds stresses.

4.3 THE BALANCE OF FORCES WITHIN THE BOUNDARY LAYER - ESTIMATION OF THE EQUILIBRIUM LENGTH

Often boundary layers experience sudden changes in environment, as for example, when they pass from a rough surface to a smooth one. It would be expected that the behavior of the boundary layer with regard to such things as its energy content, etc., would begin to change, and it is of interest to attempt to estimate over what kind of distance one might expect the "upstream history" of the layer to persist. To make such an estimate we consider a portion of a fixed wall, Δx in length and of unit width, as shown in Figure 4.3.1.

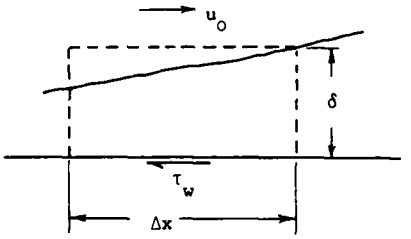

Figure 4.3.1 Portion of Boundary Layer

Note as indicated in Figure 4.3.1 we will hereafter refer to the time averaged velocities and velocity components without the use of the underbars.

The net force acting in the negative x-direction is

$$F_{net} = \tau_w\Delta x + \frac{\partial p}{\partial x}\Delta x\delta = \tau_w\Delta x\left(1 + \frac{\delta}{\tau_w}\frac{\partial p}{\partial x}\right) \tag{4.3.1}$$

The kinetic energy (K.E.) within the boundary layer is

$$\text{K.E.} = \frac{1}{2}\rho\int_o^{\Delta x}\int_o^{\delta} u^2 dy dx \sim \frac{\rho u_o^2}{2}\delta\Delta x \tag{4.3.2}$$

Again defining, as in Sec. (3.3), that the edge of the boundary layer is "about" where the viscous stresses are of the order of the inertial stresses, we obtain the approximate relationships

$$\frac{\partial \tau}{\partial y} \approx \rho u \frac{\partial u}{\partial x} \quad \text{or} \quad \tau_w \sim \rho u_o^2 \frac{\delta}{L} \qquad (4.3.3)$$

here L is a characteristic length of the body

The ratio of the kinetic energy to the net force gives us an estimate of the length ($L_{B.L.}$) over which we would expect sizeable changes in the conditions in the boundary layer to occur. It follows from Eq. (4.3.1-4.3.3) that

$$L_{B.L.} \sim \frac{K.E.}{F_{net}} \sim \frac{L}{2\left(1 + \frac{\delta}{\tau_w}\frac{\partial p}{\partial x}\right)} \qquad (4.3.4)$$

Thus, the "boundary layer interaction length" is of the order of the length of the object itself. This implies a very large distance in terms of the number of boundary layer thicknesses that the boundary layer must travel after encountering a disturbance before it comes to "equilibrium". This result serves to emphasize that the previous history of a boundary layer is very important in determining its behavior.

It can be suspected, also, that boundary layers with a constant ratio of net pressure force to wall shear force (that is with $\frac{\delta}{\tau_w}\frac{\partial p}{\partial x}$ = const) will have especially simple behaviors. This class of boundary layer, the "equilibrium" boundary layer, is described in the classic work of Ref. (4.3).

4.4 CREATION AND DESTRUCTION OF TURBULENCE WITHIN THE BOUNDARY LAYER

We now restrict our attention to flows which on the average are two dimensional, incompressible and steady. It is desired to relate the fluid velocity profile and turbulence levels to the volumetric rate of production of turbulence, and to the interaction of the turbulence shear stresses with the mean velocity profiles. An example fluid element is illustrated in Figure 4.4.1.

$$u\tau_{xy} + \frac{\partial u\tau_{xy}}{\partial y} dy = u\tau_{xy} + u\frac{\partial \tau_{xy}}{\partial y} dy + \tau_{xy}\frac{\partial u}{\partial y} dy$$

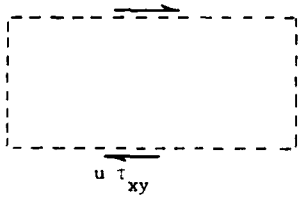

Figure 4.4.1 Fluid Element in Turbulent Flow

It is evident from Figure 4.4.1 that the shear interaction with the flow field can be considered to be of three parts:

$u\tau_{xy}$ - This is the shear work interaction rate per area which is transmitted through the element to the next element.

$u\frac{\partial \tau_{xy}}{\partial y} dy$ - This term represents the effect of the unbalanced forces upon the fluid element and leads to acceleration of the mean flow. Note that in this simplified case, utilizing Eq. (4.2.12), we may write for the turbulent portion

$$u\frac{\partial \tau_{xy}}{\partial y} dy = -\rho u \frac{\partial \langle u'v' \rangle}{\partial y} dy .$$

$\tau_{xy}\frac{\partial u}{\partial y} dy$ - This term represents a net work interaction of the stresses with the fluid element. This term does not involve any unbalanced forces, so the work interaction goes directly to the element and immediately appears as turbulent energy. Note that in this simplified case, utilizing Eq. (4.2.12), we may write for the turbulent portion

$$\tau_{xy}\frac{\partial u}{\partial y} dy = -\rho \langle u'v' \rangle \frac{\partial u}{\partial y} dy .$$

The measurements of Klebanoff (Ref. 4.4) reported in 1954 and illustrated in Figure 4.4.2 support the hypothesis that large eddies are "born" deep within the shear layer. Such eddies are ejected outward where initially the mean flow velocity gradient is very large. As a result, the eddy grows rapidly in energy, leading to still larger values of $\langle u'v' \rangle$. As the eddy approaches the boundary layer edge, however, its growth rate diminishes because of the ever decreasing velocity gradient $\partial u/\partial y$.

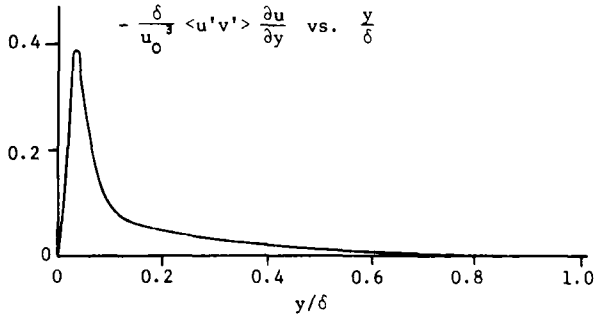

Figure 4.4.2 Normalized Turbulent Energy Production Rate Per Unit Volume in a Typical Turbulent Boundary Layer

The axial distance for the entire process of eddy birth, growth, interaction with the fluid near the outer edge of the boundary layer and decay, can be roughly estimated utilizing a simple model. Most of the change in fluid velocity in a turbulent boundary layer occurs very close to the wall so we may assume that the axial speed of the eddy through most of its life is approximately the free stream velocity, u_o. The axial distance over which the eddy will be convected while traveling to the boundary layer edge will hence be approximately $\frac{\delta}{v/u_o}$. In most cases v/u_o is considerably less

than one-tenth, so we would expect a "turbulence upstream history" to date from at least 10δ upstream of a given axial location.

The models postulated in the preceding paragraphs lead to the "picture" of turbulence interaction given in Figure 4.4.3 (Ref. 4.5).

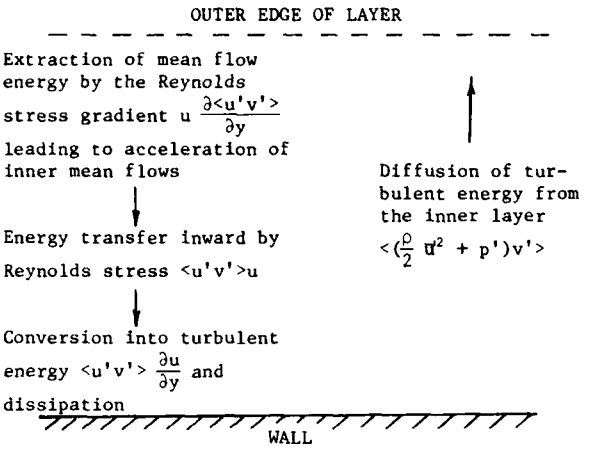

Figure 4.4.3 Turbulent Processes in the Boundary Layer

The essence of the problem in calculating turbulent shear flows is to obtain a valid representation of the Reynolds stresses. Calculation procedures rely upon empirical representation of these stresses, and the success of utilizing such procedures beyond the range of the data used to supply the empiricism is usually directly related to how physically plausible the model was that was used to represent the stresses. In formulating such models, particularly in attempting to describe typical flows in turbomachinery where large rates of change of imposed pressure gradients often occur, particular care must be directed to the description of the turbulence history effects. (Chapter 16)

4.5 REGIMES OF THE BOUNDARY LAYER

The simplified model of a turbulent boundary layer represented by Figure 4.4.3 allows us to postulate the dominance of certain mechanisms within the boundary layer. By so doing, we are able to postulate the existence of an "inner layer" where conditions depend only on the distance from the surface and conditions at the surface, and an "outer layer" where conditions depend somewhat on the history of the diffusion of turbulence energy into the outer layer from the inner layer, and also on the transverse mean velocities and their gradients. These latter two effects of the transverse velocities in the outer layer owe their importance to the fact that such effects may modify considerably the course of development of the large eddies that control the entrainment of the non-turbulent fluid.

4.5.1 THE INNER LAYER

We postulate that very close to the surface the flow should depend only on conditions at the surface and the distance from the wall. Thus we expect a functional relationship of the form

$$u = f(\tau_w, \rho, \mu, y, \frac{dp}{dx}) \qquad (4.5.1)$$

It should be noted that this functional form does not exclude the effects of external conditions, because the external conditions affect τ_w. The six terms of the functional equation, Eq. (4.5.1), give rise to three dimensionless groups, giving in turn a functional relationship of the form

$$\frac{u}{u_\tau} = F(y^*, K_\tau) \qquad (4.5.2)$$

Here there has been introduced

$$u_\tau = (\frac{\tau_w}{\rho})^{1/2} \equiv \text{"the friction velocity"}$$

$$y^* = \frac{\rho u_\tau y}{\mu}$$

$$K_\tau = -\frac{\mu}{\rho^2 u_\tau^3} \frac{dp}{dx}$$

The dimensionless acceleration parameter, K_τ, can be interpreted in a physical way. Thus, we consider the ratio of the wall shear force to (minus) the pressure force for an element of fluid as indicated in Figure 4.5.1.

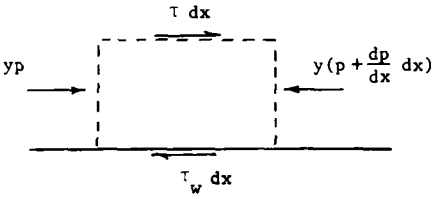

Figure 4.5.1 Forces on a Fluid Element

The ratio of net pressure force to wall shear force is

$$\text{Ratio} = -\frac{ydp}{\tau_w dx}$$

However we may write

$$K_\tau = -\frac{\mu}{\rho^2 u_\tau^3} \frac{dp}{dx} = -\frac{1}{y^*} \frac{ydp}{\tau_w dx}$$

Thus the acceleration parameter, K_τ, is equal to the ratio of net pressure force to shear force acting on a fluid element of height $y = \mu/\rho u_\tau$. (That is of height y such that $y^* = 1$). This height is in fact very small indeed, and it is only under conditions of very extreme acceleration that K_τ assumes values of the order of unity.

A relationship of the form of Eq. (4.5.2) can be very useful in itself, but it is possible to consider the inner layer to itself be composed of three separate layers, the sublayer, the blending region and the equilibrium layer. These layers are separately considered in the following sections.

4.5.1.1 THE SUBLAYER

This layer is considered to be very close to the wall, so close in fact that the inertial terms of the momentum equation are very small. The presence of the wall also prevents the attainment of substantial turbulent perturbation velocities so that the Reynolds stresses are also very small. Considering a steady two-dimensional flow, and ignoring the inertial terms and Reynolds stresses, Eq. (4.2.13) reduces to the very simple form

$$\frac{\partial^2 u}{\partial y^2} = \frac{1}{\mu}\frac{dp}{dx} \tag{4.5.3}$$

Note in this expression that the boundary layer approximation $\partial p/\partial x = dp/dx$ has been employed, where p is the pressure imposed by the free stream. In terms of the dimensionless variables of Eq. (4.5.2), Eq. (4.5.3) may be written

$$\frac{\partial^2 u/u_\tau}{\partial y^{*2}} = -K_\tau \tag{4.5.4}$$

The boundary conditions are $\frac{u}{u_\tau} = 0$ at $y^* = 0$, and from $\tau_w = \mu \left.\frac{\partial u}{\partial y}\right|_{y=0}$, we find $\left.\frac{\partial u/u_\tau}{\partial y^*}\right|_{y^*=0} = 1$. With these boundary conditions, Eq. (4.5.4) integrates immediately to give

$$\frac{u}{u_\tau} = y^* - \frac{1}{2}K_\tau\, y^{*2} \tag{4.5.5}$$

It can be noted that this latter form is a very simple example of the general form of Eq. (4.5.2). Often, even in flows with a pressure gradient, the term in y^{*2} is excluded because it is usually quite small. This is not always the case, however, and considering its simplicity it would be wise to include its effects. Note, however, that if, in an experiment, it is attempted to estimate the wall shear stress τ_w by obtaining the slope $\frac{\partial u}{\partial y}$ and then writing $\tau_w = \mu \frac{\partial u}{\partial y}$ (not usually a recommended procedure), then the pressure gradient term does not affect the expression for the slope $\frac{\partial u}{\partial y}$ as $y \to 0$.

It is to be noted that in a typical turbulent boundary layer the sublayer may be considered to extend out to approximately $y^* = 10$. In this distance the velocity may reach approximately 40% of its free stream value. Typically the physical height corresponding to $y^* = 1$ is only one or two-tenths of a percent of the boundary layer height so we see that the velocity reaches about 40% of its free stream value in only one or two percent of the boundary layer height!

4.5.1.2 THE BLENDING REGION

With increased distance from the wall, the assumption of very low Reynolds stresses and inertial terms, fails, and a region is entered where the contributions of the inertial terms, and molecular and turbulent transport terms are all comparable. This region is termed the blending region, and its description requires the full functional form of Eq. (4.5.2). This functional relationship is obtained from experiment.

4.5.1.3 THE EQUILIBRIUM LAYER - THE LAW OF THE WALL

It can be seen that within the sublayer, except for conditions with extreme pressure gradients, the shear stress remains constant with y. This is a direct result of the assumption that the inertial terms were assumed to be small, so that the remaining forces on a fluid element, the shear forces, had to balance. This so called "constant stress layer" exists to some extent in any flow near a wall. As a simple example of such a flow, and to observe some of the consequences, consider fully developed flow in a circular pipe.

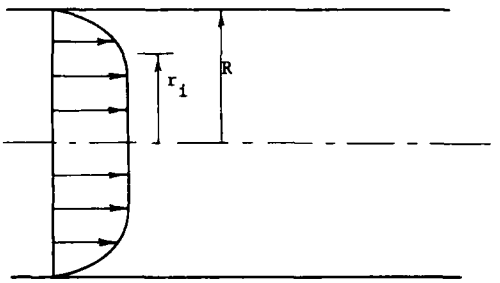

Figure 4.5.2 Fully Developed Pipe Flow

Fully developed pipe flow offers some special simplifications, because though analagous regimes to all the regimes of the turbulent boundary layer are present, conditions are invariant with axial positions so that $\frac{dp}{dx}$ is constant, and no inertial terms are present. A simple force balance on a tube of fluid of radius r and length dx gives

$$2\pi r dx\tau = \pi r^2 dx \frac{dp}{dx} \quad \text{or} \quad \tau = \frac{r}{2}\frac{dp}{dx} \tag{4.5.6}$$

In terms of the shear stress at the wall, we may hence write

$$\frac{\tau}{\tau_w} = \frac{r}{R} = 1 - \frac{(R-r)}{R} \tag{4.5.7}$$

Measurements indicate that in turbulent flows at moderately large Reynolds numbers, the fluid velocity will be about 80% of the value in the center of the pipe within a distance $\frac{R-r}{R} \leq 0.1$. Thus, the shear will change by only about 10% across a layer in which the fluid velocity reaches 80% of its maximum value.

We can now estimate the total rate of energy input to the flow from the centerline to a radius r_i, where r_i is just outside the layer of large velocity gradient. (Fig. 4.5.2) We consider first an annular element of length dx, thickness dr and inner radius r, as in Figure 4.5.3.

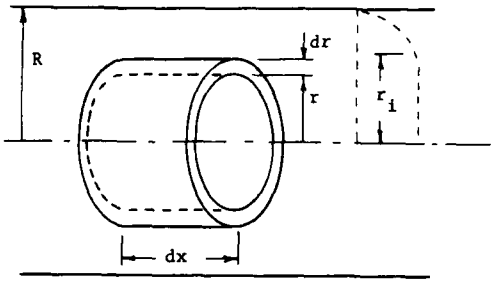

Figure 4.5.3 Annular Fluid Element

The total rate of input of energy to the element by shear and pressure forces may be written

$$\tau u(2\pi r dx) + \frac{\partial \tau u(2\pi r dx)}{\partial r} dr - \tau u(2\pi r dx)$$

$$+ pu(2\pi r dr) - \{pu(2\pi r dr) + \frac{\partial pu(2\pi r dr)}{\partial x} dx\} \quad \text{or}$$

$$2\pi dx dr[\frac{\partial \tau u r}{\partial r} - ur \frac{\partial p}{\partial x}] \quad \text{—rate of energy input to element} \qquad (4.5.8)$$

With Eq. (4.5.6) this expression may be reduced to

$$2\pi r\tau \frac{\partial u}{\partial r} dx dr \quad \text{—rate of energy input to element} \qquad (4.5.9)$$

The rate of energy input, per axial length, to the entire flow from r_i to the axis, $E(r_i)$ is hence given by

$$E(r_i) = \int_{r_i}^{0} 2\pi r \tau \frac{\partial u}{\partial r} dr = -2\pi [r\tau u]_0^{r_i} + \int_0^{r_i} 2\pi u d\tau r$$

Utilizing Eq. (4.5.7) it follows that

$$E(r_i) = -2\pi\tau_w \frac{r_i^2}{R} u_i + 4\pi\tau_w \int_0^{r_i} u \frac{r}{R} dr \qquad (4.5.10)$$

The latter integral is now approximated as $\int_0^{r_i} u \frac{r}{R} dr = \frac{u_o + u_i}{2} \frac{r_i^2}{2R}$ to give

$$E(r_i) \approx \tau_w \frac{r_i^2}{R} u_o [1 - \frac{u_i}{u_o}] \qquad (4.5.11)$$

This rate of energy input into the fluid inside the radius r_i may be compared to the rate of energy input into the fluid inside the radius R. We thus have, with r_i replaced by R and u_i replaced by zero in Eq. (4.5.10),

$$E(R) = \int_0^R \tau \frac{\partial u}{\partial r} dr = 4\pi\tau_w \int_0^R u \frac{r}{R} dr$$

Thus, making the quite rough approximation that $u \approx u_o$ we obtain the estimate

$$E(R) \approx 2\pi\tau_w u_o R \qquad (4.5.12)$$

and hence

$$\frac{E(r_i)}{E(R)} \approx \frac{1}{2} (\frac{r_i}{R})^2 [1 - \frac{u_i}{u_o}] \qquad (4.5.13)$$

Thus, in a typical wall layer where $\frac{u_i}{u_o} \approx 0.8$, $\frac{r_i}{R} \approx 0.9$ we find

$$\frac{E(r_i)}{E(R)} \approx 0.1 \qquad (4.5.14)$$

That is, about 90% of the entire turbulent energy production occurs in a layer over which the shear changes by only about 10%. Very similar arguements lead to the same result for boundary layer flow, because we may argue that the inertial terms and pressure gradient terms (usually) have little effect on the thin inner layer.

This enormous production of energy within the constant stress layer leads us to the "equilibrium hypothesis" that within the constant stress layer the rate of production of turbulent energy is equal to the rate of dissipation of turbulent energy. This hypothesis is equivalent to the statement that the transport of turbulent energy from the layer, and rate of work interaction from the pressure gradient are very small. Careful measurements (Ref. 4.6 for example) have verified the assumption that the energy transfer in the constant stress layer is negligible compared to the production and decay terms. Furthermore, measurements have indicated that for moderately large Reynolds numbers in flows without extreme pressure gradients, the constant shear region includes both the sub-layer and a considerable portion of the turbulent region. This allows us to hypothesize a region of flow of (almost) constant shear in which the major contribution to the stress is the turbulent contribution.

The rate of production of turbulent energy (per mass/sec) by extraction of energy from the mean flow is $\frac{\tau}{\rho} \frac{\partial u}{\partial y}$ (Sec. 4.4). This turbulent energy appears dominantly in the large eddies thrown up from the sub-layer and blending region. It is important, now, to realize that the dissipation of energy from these large "energy containing eddies" can be viewed as a two-step process. The actual degradation of the mechanical energy of an eddy to "viscous heating" through molecular viscosity is dependent upon the square of the frequency of movement of the eddy. The large eddies in fact have low frequencies and consequently low dissipation rates. Thus the energy is extracted from the energy containing eddies by their first dispersing their energy to higher frequency, smaller eddies, and then the subsequent dissipation of the small high frequency eddies. It is the process of dispersion (by the mechanical process of the "collisions" of the eddies) that forms the rate limiting step in the overall process of dissipation. This observation is of importance because the process of dispersion is dependent only on the collision rate of the eddies and not on the molecular

viscosity of the fluid. We thus have the perhaps surprising result that processes within the equilibrium layer are independent of the Reynolds number!

The net dissipation rate, ε, can hence only depend upon the parameters ρ and τ, so that dimensional analysis reveals that a functional relationship of the form

$$f\left(\frac{\varepsilon y}{u_\tau^3}\right) = 0 \qquad (4.5.15)$$

must exist. Equivalently this means

$$\varepsilon = \frac{u_\tau^3}{Ky} \quad , \quad K = \text{const} \qquad (4.5.16)$$

We now invoke the equilibrium hypothesis and equate the production and dissipation terms to find

$$\frac{\partial u}{\partial y} = \frac{u_\tau}{Ky} \quad , \text{ or } \quad \frac{\partial u/u_\tau}{\partial y^*} = \frac{1}{Ky^*} \qquad (4.5.17)$$

Direct integration then gives

$$\frac{u}{u_\tau} = \frac{1}{K} \ell n\, y^* + A \quad \text{The law of the wall} \qquad (4.5.18)$$

This is the famous expression known as the law of the wall. It is apparent from the development leading to it that the expression should be valid in the regime where $\tau_t >> \tau_L$, and where τ_t is approximately constant in y. This latter requirement implies, also, that strong pressure gradients are not present.

Experimental values have been obtained for the constants K and A, and they are found to have values of approximately

$$K = 0.4 \quad , \quad A = 5.1 \qquad (4.5.19)$$

As stated above, we expect Eq. (4.5.18) to be valid when $\tau_t >> \tau_L$, or when, say

$$10 < \frac{\tau_t}{\mu \frac{\partial u}{\partial y}} = \frac{\rho u_\tau^2}{\mu u_\tau} Ky = Ky^* \qquad (4.5.20)$$

Thus, we would expect Eq. (4.5.18) to be valid for y^* greater than about 25. Typical experimental results are indicated in Figure 4.5.4.

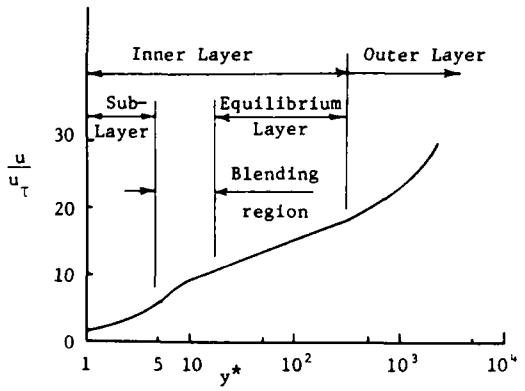

Figure 4.5.4 Turbulent Boundary Layer Regimes

It can be noted here, that in practice Eq. (4.5.18) provides an implicit relationship for the wall skin friction. Thus, if actual data is fitted (in the law of the wall regime) by a formula of the form

$$u = a\, \ell n\, y + b \qquad (4.5.21)$$

then by equating Eqs. (4.5.18) and (4.5.21), a single equation for the unknown value of the skin friction velocity, u_τ results. This process can be simplified by utilizing graphical procedures. (Refs. 4.3, 4.7)

4.5.2 THE OUTER LAYER - THE LAW OF THE WAKE

We have seen that the inner region of the boundary layer flow may be subdivided into three layers, the sub-layer, the blending region and the logarithmic region. We now consider the outer portion of the boundary layer (approximately the outer 80%) which for reasons that will become apparent is termed the wake region.

The success of the inner layer theories in matching the empirical results would support the notion that we might gainfully write the general equation for the velocity profile in the form (Ref. 4.8)

$$\frac{u}{u_\tau} = f(y^*) + h(x,y) \qquad (4.5.22)$$

here

$f(y^*) = y^*$ in the sublayer (small pressure gradient)

$f(y^*) = \frac{1}{K} \ell n\, y^* + A$ in the logarithmic region

$h(x,y)$ is a general function that must have the property that it be negligibly small close to the wall

The problem of the outer flow is to determine the form of $h(x,y)$. The experiments of Ref. 4.3 indicated that at least in the case of equilibrium profiles (Sec. 4.3,-to be more carefully defined in the following), the velocity defect $u_o - u$ could be plotted versus y/δ in the form

$$\frac{u_o - u}{u_\tau} = F(\pi, y/\delta) \qquad (4.5.23)$$

Here π is a pressure gradient parameter which is a constant for a given equilibrium flow. This form of velocity defect profile was found to be valid outside the laminar sub-layer and blending region, provided the pressure gradient was moderate.

The behavior of $h(x,y)$ can be inferred from this result (for the case of equilibrium flows) by writing

$$\frac{u_o}{u_\tau} = \frac{1}{K} \ell n \frac{\delta u_\tau \rho}{\mu} + A + h(x,\delta)$$

$$\frac{u}{u_\tau} = \frac{1}{K} \ell n \frac{y u_\tau \rho}{\mu} + A + h(x,y)$$

hence with Eq. (4.5.23)

$$h(x,y) = h(x,\delta) + \frac{1}{K} \ln \frac{\delta}{y} - F(\pi, \frac{y}{\delta}) \qquad (4.5.24)$$

Thus, the function $h(x,y)$ can be written as a function of π and y/δ for equilibrium boundary layers. That is:

$$h(x,y) = g(\pi, \frac{y}{\delta}) \qquad (4.5.25)$$

It was found in reference 4.8 that in a wide variety of conditions the function $g(\pi, y/\delta)$ would be well represented by

$$g(\pi, \frac{y}{\delta}) = \frac{\pi(x)}{K} w(\frac{y}{\delta}) \qquad (4.5.26)$$

The equation for the velocity, Eq. (4.5.22), then becomes

$$\frac{u}{u_\tau} = f(y^*) + \frac{\pi(x)}{K} w(\frac{y}{\delta}) \qquad (4.5.27)$$

This equation is known as the law of the wake, and the function $w(y/\delta)$ is termed the wake function. It is obvious that we can absorb any constants of proportionality in the as yet undefined function $\pi(x)$, so we look for a convenient form of $w(y/\delta)$. The displacement thickness, δ^*, is an often used quantity. This distance is defined as the thickness through which the external streamlines are shifted owing to the formation of the boundary layer. For an incompressible boundary layer we hence find

$$u_o \delta^* = \int_c^\delta (u_o - u)dy \quad \text{or} \quad \frac{\delta^*}{\delta} = \int_o^1 (1 - \frac{u}{u_o})\, d(\frac{y}{\delta}) \qquad (4.5.28)$$

We now utilize Eq. (4.5.27) to obtain the ratio δ^*/δ. The answer is simplified considerably if we ignore the presence of the sub-layer and blending region and assume the logarithmic region extends to the wall. This is in fact a good approximation (numerically) because the sub-layer and blending region are in fact very thin. We thus obtain:

$$\delta^*/\delta = \int_o^1 [1 - \frac{u_\tau}{u_o} \{\frac{1}{K} \ln \frac{y u_\tau \rho}{\mu} + A + \frac{\pi}{K} w(\frac{y}{\delta})\}] d \frac{y}{\delta}$$

$$= 1 - \frac{u_\tau}{u_o} \{\frac{1}{K} (\frac{y}{\delta} \ln \frac{y}{\delta} - \frac{y}{\delta} + \frac{y}{\delta} \ln \frac{\delta u_\tau \rho}{\mu})$$

$$+ A \frac{y}{\delta} + \frac{\pi}{K} \frac{y}{\delta} w(\frac{y}{\delta})\}_o^1 + \frac{u_\tau}{u_o} \frac{\pi}{K} \int_o^{w_o} \frac{y}{\delta}\, dw$$

$$= \frac{u_\tau}{u_o} [\frac{u_o}{u_\tau} - \{\frac{1}{K} \ln \frac{\delta u_\tau \rho}{\mu} + A + \frac{\pi}{K} w_o\} + \frac{1}{K} + \frac{\pi}{K} \int_o^{w_o} \frac{y}{\delta}\, dw]$$

or

$$\frac{\delta^*}{\delta} = \frac{1}{K} \frac{u_\tau}{u_o} [1 + \pi \int_o^{w_o} \frac{y}{\delta}\, dw] \qquad (4.5.29)$$

For convenience then, Coles (Ref. 4.8) chose

$$\int_o^{w_o} \frac{y}{\delta}\, dw = 1 \qquad (4.5.30)$$

Then

$$\frac{\delta^*}{\delta} = \frac{1}{K} \frac{u_\tau}{u_o} [1 + \pi] \qquad (4.5.31)$$

A second condition on the wake function, w, came from the experimentally observed very near asymmetry of the function (Fig. 4.5.5). As a result we may write

$$\int_o^1 w\, d \frac{y}{\delta} \approx \frac{w_o}{2} = [w(\frac{y}{\delta})]_o^1 - \int_o^{w_o} \frac{y}{\delta}\, dw$$

$$= w_o - 1 \qquad (4.5.32)$$

Hence $w_o = 2$

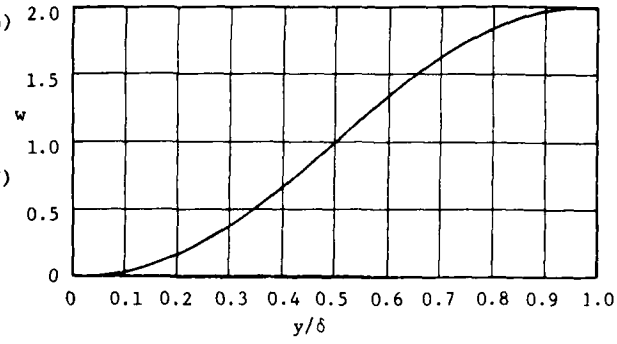

Figure 4.5.5 The Wake Function

Coles (Ref. 4.8) determined the values of the wake function empirically to be those of Table 4.5.1.

$\frac{y}{\delta}$	0	0.05	0.10	0.15	0.20	0.25	0.30
$w(\frac{y}{\delta})$	0	0.004	0.029	0.084	0.168	0.272	0.396
$\frac{y}{\delta}$	0.35	0.40	0.45	0.50	0.55	0.60	0.65
$w(\frac{y}{\delta})$	0.535	0.685	0.838	0.994	1.152	1.307	1.458
$\frac{y}{\delta}$	0.70	0.75	0.80	0.85	0.90	0.95	1.00
$w(\frac{y}{\delta})$	1.600	1.729	1.840	1.926	1.980	1.999	2.00

Table 4.5.1 The Wake Function

This experimental determination of the actual wake function is often approximated by convenient antisymmetrical analytic approximations. Two examples are:

$$w(\frac{y}{\delta}) = 1 + \sin [\frac{(2 \frac{y}{\delta} - 1)\pi}{2}] \quad \text{(Ref. 4.8)} \qquad (4.5.33)$$

$$w(\frac{y}{\delta}) = 2(\frac{y}{\delta})^2 (3 - 2 \frac{y}{\delta}) \quad \text{(Ref. 4.9)} \qquad (4.5.34)$$

Interpretation of w as a Wake Function

The "wake-like" aspect of the function $w(y/\delta)$ can be inferred from several empirical observations. For example, by representing the function $h(x,y)$ as $\pi/K\, w(y/\delta)$, it is apparent that the outer region of the boundary layer is similar. Many studies of (fully developed) wakes have indicated their similarity.

Another result of interest follows by considering the boundary layer in the case where the boundary layer approaches separation. At separation the skin friction, and hence u_τ, goes to zero. The expression for the velocity profile is then written in terms of u/u_o. We note then, utilizing Eq. (4.5.31)

$$\frac{u}{u_o} = \frac{u}{u_\tau}\frac{u_\tau}{u_o} = \frac{u_\tau}{Ku_o}\ln\frac{\rho y u_\tau}{\mu} + A\frac{u_\tau}{u_o} + \left(\frac{\delta^*}{\delta} - \frac{1}{K}\frac{u_\tau}{u_o}\right) w\left(\frac{y}{\delta}\right) \tag{4.5.35}$$

Then noting $u_\tau \to 0$ as the boundary layer approaches separation, we find

$$\frac{u}{u_o} \to \frac{\delta^*}{\delta} w\left(\frac{y}{\delta}\right) \quad \text{(at separation)} \tag{4.5.36}$$

We note also

$$\frac{\delta^*}{\delta} = \int_o^1 \left(1 - \frac{u}{u_o}\right) d\left(\frac{y}{\delta}\right) = 1 - \frac{\delta^*}{\delta}\int_o^1 w\left(\frac{y}{\delta}\right) d\left(\frac{y}{\delta}\right)$$

or $$\frac{\delta^*}{\delta} = \frac{1}{2} \quad \text{at separation} \tag{4.5.37}$$

Thus $$\frac{u}{u_o} = \frac{1}{2} w\left(\frac{y}{\delta}\right) \quad \text{at separation} \tag{4.5.38}$$

It can be seen that at separation the entire velocity profile is that corresponding to the wake function, $w(y/\delta)$. At separation the effects of the wall shear are zero, so the boundary layer processes, in this condition, can be interpreted as a large scale mixing process, as in a wake. In non-separated flow the "wall effect" penetrates the "wake effect" to varying degrees.

The Pressure Gradient Parameter, π

We have from Eqs. (4.5.22) and (4.5.27) that outside the sub-layer and blending region

$$\frac{u_o - u}{u_\tau} = \frac{\pi}{K}\left(2 - w\left(\frac{y}{\delta}\right)\right) + \frac{1}{K}\ln\frac{\delta}{y} \tag{4.5.39}$$

Equilibrium flows (Ref. 4.3) are experimentally obtained by adjusting the pressure distribution in the test section so that the given value of $\frac{u_o - u}{u_\tau}$ found at entry is held constant throughout the test section. Obviously for such a pressure distribution the parameter π remains constant in x, and hence the term pressure gradient parameter.

In summary, it is hoped that the underlying physics of turbulent boundary layers has been reasonably revealed in this chapter. Many numerical techniques exploit the analytical forms presented for the several regimes in the boundary layer, and extend their areas of validity beyond those strictly implied in the foregoing derivations by allowing some of the parameters fairly wide functional variation. Such techniques are thoroughly considered in Chapter 16, but it should be remembered that almost always the most successful analytical techniques arise from the most physically plausible models for the phenomenon studied.

4.6.1 REFERENCES

(4.1) Stokes, G. G., "On the Effect of the Internal Friction of Fluids on the Motion of Pendulums." Cambr. Phil. Trans. IX (1851).

(4.2) Milne-Thomson, L. M., "Theoretical Hydrodynamics." The Macmillan Company, New York.

(4.3) Clauser, F. H., "Turbulent Boundary Layers in Adverse Pressure Gradients." Jour. Aero. Sci., Vol. 21, 1954, pp. 91-108.

(4.4) Klebanoff, P.S., NACA TN No. 3178, 1954.

(4.5) Townsend, A. A., "The Structure of Turbulent Shear Flow." Cambridge 1956.

(4.6) Laufer, J., "The Structure of Turbulence in Fully Developed Pipe Flow." NACA Rept. No. 1174.

(4.7) Kline, S. J., Reynolds, W. C., Schraub, F. A., and Rundstadler, P. W., "The Structure of Turbulent Boundary Layers." J. Fluid Mech., Vol. 30, Part 4, 1967, pp. 741-773.

(4.8) Coles, D., "The Law of the Wake in the Turbulent Boundary Layer." J. Fluid Mech., Vol. 1, 1956, pp. 191-226.

(4.9) Moses, H. L., "The Behavior of Turbulent Boundary Layers in Adverse Pressure Gradients." Gas Turbine Laboratory Rept. No. 73, Massachusetts Institute of Technology, 1964.

Chapter 5

IDEAL CYCLE ANALYSIS

Gordon C. Oates

University of Washington

TABLE OF CONTENTS

CHAPTER 5 IDEAL CYCLE ANALYSIS

		Page
5.0	Introduction	5-1
5.1	Notation	5-1
5.2	Ideal Component Behaviors	5-2
5.2.1	Diffuser	5-2
5.2.2	Compressor or Fan	5-2
5.2.3	Combustor or Afterburner	5-2
5.2.4	Turbine	5-2
5.2.5	Nozzle	5-2
5.3	The Ideal Thermodynamic Cycle	5-2
5.4	The Propulsive Efficiency, η_p	5-3
5.5	Systems of Units	5 4
5.6	The Ideal Turbojet	5-5
5.6.1	Methodology of Cycle Analysis	5-5
5.6.2	Cycle Analysis of the Ideal Turbojet	5-5
5.7	Summary of the Equations, Ideal Turbojet (or Ramjet)	5-6
5.8	Example Results, Ideal Turbojet and Ramjet.	5-7
5.9	Interpretation of the Behavior of the Specific Fuel Consumption	5-8
5.10	The Maximum Thrust Turbojet	5-9
5.10.1	Temperature Relationships at Maximum Thrust	5-9
5.10.2	Example Results - Max Thrust Turbojet.	5-10
5.11	The Ideal Turbojet with Afterburning	5-10
5.11.1	Cycle Analysis of the Ideal Afterburning Turbojet	5-11
5.12	Summary of the Equations, Ideal Turbojet with Afterburning	5-11
5.13	Example Results, Ideal Turbojet with Afterburning	5-12
5.14	The Turbofan with Separate Exhaust Streams	5-12
5.14.1	Cycle Analysis of the Ideal Turbofan with Separate Exhaust Streams	5-12
5.14.2	Summary of the Equations, Ideal Turbofan, By-Pass Ratio Prescribed	5-13
5.14.3	By-Pass Ratio for Minimum Specific Fuel Consumption	5-14
5.14.4	Summary of the Equations, Ideal Turbofan By-Pass Ratio Optimized	5-14
5.14.5	Example Results - Ideal Turbofan with Separate Exhaust Streams	5-15
5.15	The Ideal Turbofan with Mixed Exhaust Streams	5-16
5.15.1	Cycle Analysis of the Ideal Turbofan with Mixed Exhaust Streams	5-16
5.15.2	The Ideal Constant Area Mixer	5-17
5.15.3	Summary of the Equations - Ideal Constant Area Mixer	5-17
5.14.4	Summary of the Equations - Ideal Turbofan with Mixed Exhaust Streams	5-18
5.15.5	Example Results - Ideal Constant Area Mixer	5-18
5.15.6	Example Results - Ideal Turbofan with Mixed Exhaust Streams	5-19
5.16	The Ideal Turbofan with Afterburning.	5-20
5.16.1	Cycle Analysis of the Ideal Turbofan with Afterburning	5-20
5.16.2	Summary of the Equations, Ideal Turbofan with Afterburning	5-21
5.16.3	Example Results - Ideal Turbofan with	

LIST OF FIGURES

CHAPTER 5 IDEAL CYCLE ANALYSIS

		Page
Figure 5.1.1	Station Numbering	5-1
Figure 5.3.1	Ideal Turbojet	5-3
Figure 5.3.2	Pressure-Specific Volume Diagram	5-3
Figure 5.3.3	Temperature-Entropy Diagram	5-3
Figure 5.8.1	Effect of Compressor Pressure Ratio on Performance, Ideal Turbojet	5-7
Figure 5.8.2	Specific Thrust Versus Mach Number, Ideal Turbojets and Ramjet	5-7
Figure 5.8.3	Specific Fuel Consumption Versus Mach Number, Ideal Turbojets and Ramjet	5-7
Figure 5.8.4	Specific Fuel Consumption and Specific Thrust Versus τ_λ, Ideal Turbojet	5-8
Figure 5.9.1	Thermal and Propulsive Efficiencies	5-9
Figure 5.10.1	Temperature Entropy Diagram for Max Thrust Turbojet	5-10
Figure 5.10.2	Specific Thrust Versus Flight Mach Number - Max Thrust Turbojet	5-10
Figure 5.10.3	Compressor Pressure Ratio for Maximum Thrust	5-10
Figure 5.11.1	The Turbojet with Afterburning.	5-10
Figure 5.11.2	Pressure-Volume Diagram, Ideal Afterburning Turbojet	5-11
Figure 5.11.3	Temperature-Entropy Diagram, Ideal Afterburning Turbojet	5-11
Figure 5.13.1	Effect of Compressor Pressure Ratio on Performance, Ideal Turbojet with Afterburner	5-12
Figure 5.14.1	Optimal By-Pass Ratio Versus By-Pass Pressure Ratio	5-15
Figure 5.14.2	Specific Thrust and Specific Fuel Consumption Versus By-Pass Pressure Ratio	5-15
Figure 5.14.3	Optimal By-Pass Ratio Versus Flight Mach Number	5-15
Figure 5.14.4	Specific Thrust and Specific Fuel Consumption Versus Flight Mach Number	5-15
Figure 5.14.5	Optimal By-Pass Ratio Versus τ_λ	5-15
Figure 5.14.6	Specific Thrust and Specific Fuel Consumption Versus τ_λ	5-15
Figure 5.14.7	Specific Thrust and Specific Fuel Consumption Versus By-Pass Ratio	5-16
Figure 5.15.1	The Ideal Turbofan with Mixed Exhaust Stream	5-16
Figure 5.15.2	The Constant Area Mixer	5-17
Figure 5.15.3	Effect of Variation in Stream Pressure Ratio, Ideal Constant Area Mixer	5-19
Figure 5.15.4	Effect of Variation in Stream Temperature Ratio and Exit Pressure Ratio, Ideal Constant Area Mixer	5-19
Figure 5.15.5	Effect of Variation in Inlet Mach Number, Ideal Constant Area Mixer	5-19
Figure 5.16.1	Specific Thrust and Specific Fuel Consumption Versus By-Pass Ratio, Duct Burning Turbofan	5-21

CHAPTER 5

LIST OF SYMBOLS

The symbols are listed in alphabetical order, first in the English alphabet, then in the Greek alphabet. Subscripts and superscripts are then given. The equation, figure or section in which the symbols are first introduced is indicated in parentheses. Often the symbol will be defined in the text just preceding or just following the equation or figure.

A - Cross sectional area (Fig. 5.15.2)

a - Speed of sound (Eq. 5.6.1)

C - Specific heat (Eq. 5.1.2)

F - Thrust (Eq. 5.4.1)

f - Fuel to air ratio (Eq. 5.6.14)

- Function (Eq. 5.15.20)

g_o - Gravitational constant (Table 5.5.1)

HP - Horsepower (Table 5.5.1)

h - Heating value (Eq. 5.6.14)

J - Joule (Table 5.5.1)

kg - Kilogram (Table 5.5.1)

M - Mach number (Eq. 5.1.1)

$\dot{m}$ - Mass flow rate (Eq. 5.4.1)

N - Newton (Table 5.5.1)

p - Pressure (Eq. 5.1.1)

R - Gas constant (Eq. 5.6.1)

S - Specific fuel consumption (Eq. 5.6.15)

s - Entropy (Fig. 5.3.3)

T - Temperature (Eq. 5.1.1)

u - Velocity (Eq. 5.4.1)

α - By-pass ratio (Eq. 5.14.1)

γ - Ratio of specific heats (Eq. 5.6.2)

Δ - Function (Eq. 5.15.20)

η - Efficiency (Eq. 5.3.1)

π - Pressure ratio (Sect. 5.1)

ρ - Density (Fig. 5.3.2)

τ - Temperature ratio (Sect. 5.1)

Subscripts

0-9 - Station numbers (Fig. 5.1.1)

1 - Primary stream (Eq. 5.14.1)

2 - Secondary stream (Eq. 5.14.1)

AB - Afterburner (Sect. 5.1)

b - Burner (Sect. 5.1)

c - Compressor (Sect. 5.1)

d - Diffuser (Sect. 5.1)

n - Nozzle (Sect. 5.1)

p - Constant pressure (Eq. 5.1.2)

- Propulsive (Sect. 5.4)

r - "Recovery" (Eq. 5.1.1)

t - Turbine (Sect. 5.1)

- Also stagnation quantity (Sec. 5.1)

th - Thermal (Eq. 5.3.1)

λ - Refers to enthalpy ratios (Eq. 5.1.2, Table 5.1.1)

TOT - Total (Eq. 5.11.8)

UN - Unmixed (Eq. 5.15.34)

MIX - Mixed (Eq. 5.15.35)

Superscripts

' - Refers to by-pass stream (Fig. 5.1.1)

* - Value leading to minimum specific fuel consumption (Eq. 5.14.23)

CHAPTER FIVE
IDEAL CYCLE ANALYSIS

5.0 INTRODUCTION

In this chapter we will apply the systematic process termed "cycle analysis" to several different engine types. The object of cycle analysis is to obtain estimates of the performance parameters (primarily thrust and specific fuel consumption) in terms of design limitations (such as the maximum allowable turbine temperature), the flight conditions (the ambient pressure and temperature and the Mach number) and design choices (such as the compressor pressure ratio, fan pressure ratio, by-pass ratio, etc.). In this chapter we will consider all components to be ideal, with the result that the various algebraic manipulations will be quite simplified and hopefully as a result, the methodology of the analysis will be comparatively transparent. The analytical results will, of course, be far more optimistic than would be the case if component losses were included, but many of the general trends will be valid. The effects of component losses will be quite thoroughly investigated in Chapter Seven.

5.1 NOTATION

We here introduce a systematic notation in order to facilitate simple manipulation of the equations to follow. Throughout this document we will refer to the station numbers indicated in Figure 5.1.1.

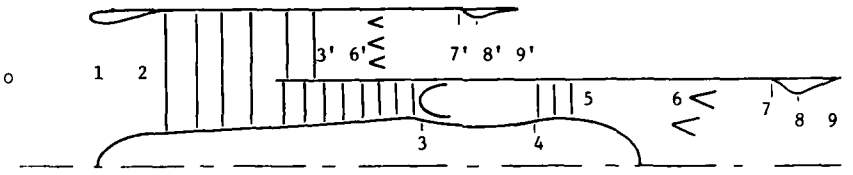

Figure 5.1.1 Station Numbering

The locations indicated in Figure 5.1.1 are:

0	Far upstream	6	Afterburner entry
1	Inlet entry	6'	Duct afterburner entry
2	Compressor face	7	Primary nozzle entry
3	Compressor exit	7'	Secondary nozzle entry
3'	Fan exit	8	Primary nozzle throat
4	Turbine entry	8'	Secondary nozzle throat
5	Turbine exit	9	Primary nozzle exit
		9'	Secondary nozzle exit

We introduce the ratio of stagnation pressures, π, and ratio of stagnation temperatures, τ, where

$$\pi = \frac{\text{Stagnation pressure leaving component}}{\text{Stagnation pressure entering component}}$$

$$\tau = \frac{\text{Stagnation temperature leaving component}}{\text{Stagnation temperature entering component}}$$

Examples

τ_c, π_c ≡ Compressor stagnation temperature, pressure ratio

τ_b, π_b ≡ Burner stagnation temperature, pressure ratio, etc.

Exceptions

We define τ_r and π_r by

$$\tau_r = 1 + \frac{\gamma-1}{2} M_o^2 = \frac{T_{t_o}}{T_o} \qquad (5.1.1)$$

$$\pi_r = \{1 + \frac{\gamma-1}{2} M_o^2\}^{\frac{\gamma}{\gamma-1}} = \frac{P_{t_o}}{P_o}$$

Thus, free stream stagnation temperature $T_{t_o} = T_o\tau_r$; free stream stagnation pressure $P_{t_o} = P_o\pi_r$. It should be noted that τ_r and π_r represent the effects of the flight Mach number, M_o.

Further exceptions

It is often appropriate to introduce the effect of a design limitation such as the maximum allowable turbine inlet stagnation enthalpy, $C_{p_t}T_{t_4}$. We thus introduce the term τ_λ, where τ_λ is defined by

$$\tau_\lambda \equiv \frac{C_{p_t}T_{t_4}}{C_{p_c}T_o} \qquad (5.1.2)$$

Similarly, $\tau_{\lambda_{AB}}$ and $\tau_{\lambda_{AB'}}$ will be used where the maximum stagnation enthalpy referred to will be the stagnation enthalpy following the primary stream afterburner or duct afterburner respectively.

Components

Each component will be identified by a subscript as follows:

d - diffuser (or "inlet")
c - compressor
c' - fan
b - burner
t - turbine
AB - afterburner (primary stream)
AB' - afterburner (secondary stream)
n - nozzle (primary stream)
n' - nozzle (secondary stream)

Table 5.1.1 gives the relationships between all defined π's and τ's and the corresponding temperatures, pressures and Mach numbers.

Table 5.1.1 Temperature and pressure relationships for all τ's and π's

$$\tau_r = 1 + \frac{\gamma-1}{2} M_o^2 \qquad \pi_r = \left(1 + \frac{\gamma-1}{2} M_o^2\right)^{\frac{\gamma}{\gamma-1}}$$

$$\tau_\lambda = \frac{C_{p_t}}{C_{p_c}} \frac{T_{t_4}}{T_o}$$

$$\tau_{\lambda_{AB}} = \frac{C_{p_{AB}}}{C_{p_c}} \frac{T_{t_8}}{T_o}$$

$$\tau_{\lambda_{AB'}} = \frac{C_{p_{AB'}}}{C_{p_c}} \frac{T_{t_8'}}{T_o}$$

$$\tau_d = \frac{T_{t_2}}{T_{t_o}} \qquad \pi_d = \frac{p_{t_2}}{p_{t_o}}$$

$$\tau_c = \frac{T_{t_3}}{T_{t_2}} \qquad \pi_c = \frac{p_{t_3}}{p_{t_2}}$$

$$\tau_{c'} = \frac{T_{t_3'}}{T_{t_2}} \qquad \pi_{c'} = \frac{p_{t_3'}}{p_{t_2}}$$

$$\tau_b = \frac{T_{t_4}}{T_{t_3}} \qquad \pi_b = \frac{p_{t_4}}{p_{t_3}}$$

$$\tau_t = \frac{T_{t_5}}{T_{t_4}} \qquad \pi_t = \frac{p_{t_5}}{p_{t_4}}$$

$$\tau_{AB} = \frac{T_{t_8}}{T_{t_5}} \qquad \pi_{AB} = \frac{p_{t_8}}{p_{t_5}}$$

$$\tau_{AB'} = \frac{T_{t_8'}}{T_{t_3'}} \qquad \pi_{AB'} = \frac{p_{t_8'}}{p_{t_3'}}$$

$$\tau_n = \frac{T_{t_9}}{T_{t_5}} \qquad \pi_n = \frac{p_{t_9}}{p_{t_5}}$$

$$\tau_{n'} = \frac{T_{t_9'}}{T_{t_3'}} \qquad \pi_{n'} = \frac{p_{t_9'}}{p_{t_3'}}$$

5.2 IDEAL COMPONENT BEHAVIORS

In the analysis to follow in this chapter, ideal performance of all components will be assumed. In addition, we will assume that the gas is calorically perfect throughout, with γ and C_p constant throughout, and that the fuel mass flow is so small that the fuel to air ratio may be ignored in comparison to unity. Under these circumstances the following relationships for the components are valid.

5.2.1 DIFFUSER

To a very high degree of approximation the flow through the diffuser may be considered to be adiabatic. When, in addition, the flow is ideal it may also be considered to be isentropic. We thus have, with Eq. (2.14.10),

$$\tau_d = 1 \quad \text{and} \quad \pi_d = \tau_d^{\frac{\gamma}{\gamma-1}} = 1 \qquad (5.2.1)$$

5.2.2 COMPRESSOR OR FAN

The compressor or fan pressure ratio is usually selected as a design choice and hence may be considered prescribed. For an ideal process, the process will be isentropic, so we have (again utilizing Eq. (2.14.10))

$$\tau_c = \pi_c^{\frac{\gamma-1}{\gamma}} \quad \text{and} \quad \tau_{c'} = \pi_{c'}^{\frac{\gamma-1}{\gamma}} \qquad (5.2.2)$$

5.2.3 COMBUSTOR OR AFTERBURNER

For an ideal burner the stagnation pressure remains constant. It may be noted, as shown in section 2.17.2, that this assumption implies burning at very low Mach number. We have then

$$\pi_b = 1 \qquad (5.2.3)$$

5.2.4 TURBINE

Here, as with the compressor, the ideal process is an isentropic process so that we have

$$\tau_t = \pi_t^{\frac{\gamma-1}{\gamma}} \qquad (5.2.4)$$

5.2.5 NOZZLE

As with the diffuser, the flow through nozzles is very nearly adiabatic and is ideally isentropic. Thus,

$$\tau_n = 1, \quad \pi_n = \tau_n^{\frac{\gamma}{\gamma-1}} = 1 \qquad (5.2.5)$$

5.3 THE IDEAL THERMODYNAMIC CYCLE

We now consider an ideal turbojet and investigate its behavior as a heat engine.

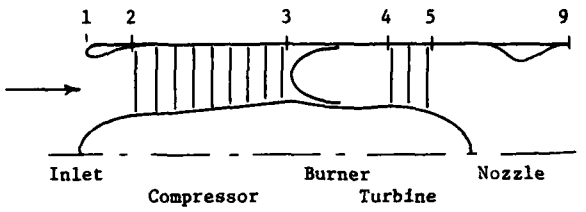

Figure 5.3.1 Ideal Turbojet

The pressure-specific volume and temperature-entropy diagrams for this ideal engine are indicated in Figures 5.3.2 and 5.3.3.

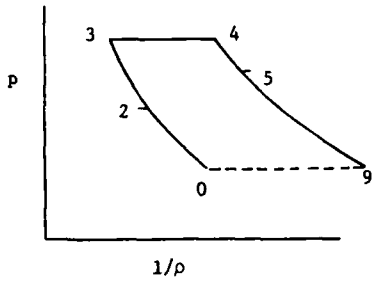

Figure 5.3.2 Pressure-Specific Volume Diagram

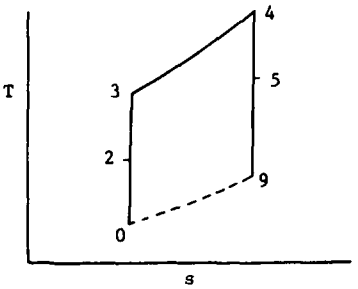

Figure 5.3.3 Temperature-Entropy Diagram

These diagrams represent the "Brayton Cycle," which consists of

- 0 → 3 Isentropic compression
- 3 → 4 Constant pressure combustion (equivalent to a constant pressure heat interaction)
- 4 → 9 Isentropic expansion
- 9 → 0 Constant pressure "heat rejection"

When viewed as a thermal engine, the "work" of the engine, in the thermodynamic sense, appears as the change in kinetic energy between the incoming and outgoing fluid. It can be noted, for example, that if the engine was to be utilized for ground power, the kinetic energy of the jet could be extracted by a further turbine which in turn would supply a mechanical work interaction. Not all of the work of the turbojet engine appears as useful work (supplied to the aircraft), however, because the force from the engine provides work to the airoraft in an amount proportional to the flight speed.

Performance parameters of direct utility to the aircraft designer are the thrust, F, and specific fuel consumption, S. The specific fuel consumption is measured as the kilograms of fuel flow per second divided by the thrust in Newtons (or alternatively $S = \frac{\text{lbm fuel/hr}}{\text{lbf thrust}}$). Clearly S is, in some sense, the inverse of the overall engine efficiency, and both the thermodynamic efficiency of the engine and the efficiency of transmitting the work of the engine into work on the aircraft (or equivalently of the "propulsive efficiency" (section 5.4)), are of importance.

The thermal efficiency, η_{th} of this ideal engine may be obtained directly by writing

$$\eta_{th} = 1 - \frac{C_p(T_9 - T_o)}{C_p(T_{t_4} - T_{t_3})} = 1 - \frac{T_o}{T_{t_3}} \frac{(\frac{T_9}{T_o} - 1)}{(\frac{T_{t_4}}{T_{t_3}} - 1)}$$

We note, however,

$$(\frac{T_{t_3}}{T_o})^{\frac{\gamma}{\gamma-1}} = \frac{p_{t_3}}{p_o} = \frac{p_{t_4}}{p_9} = (\frac{T_{t_4}}{T_9})^{\frac{\gamma}{\gamma-1}}$$

thus

$$\frac{T_{t_3}}{T_o} = \frac{T_{t_4}}{T_9}$$

and hence

$$\frac{T_9}{T_o} = \frac{T_{t_4}}{T_{t_3}}$$

Thus with $\frac{T_{t_3}}{T_o} = \tau_r\tau_c$ we obtain

$$\eta_{th} = 1 - \frac{1}{\tau_r\tau_c} \qquad (5.3.1)$$

Thus, it is apparent that the thermal efficiency of the ideal engine increases as the flight Mach number increases (τ_r increases), and as the compressor pressure ratio increases (τ_c increases).

5.4 THE PROPULSIVE EFFICIENCY, η_p

The propulsive efficiency is a measure of how well the power produced by the engine is utilized in propelling the vehicle. It is defined by

$$\eta_p = \frac{\text{Power delivered to vehicle}}{\text{Net (mechanical) power in the exhaust}}$$

$$= \frac{\text{Thrust x vehicle flight speed}}{\text{Power produced by the engine}}$$

An ideal engine has the nozzle exit pressure equal to the ambient pressure, so the thrust is simply equal to the rate of momentum production of the engine. Thus,

$$F = \dot{m}_9 u_9 - \dot{m}_o u_o = \dot{m}(u_9 - u_o) \qquad (5.4.1)$$

The power produced by the engine is $\frac{\dot{m}}{2}(u_9^2 - u_o^2)$, so we obtain for this ideal engine

$$\eta_p = \frac{2u_o}{u_9 + u_o} \qquad (5.4.2)$$

In order to increase the propulsive efficiency we should reduce the exit velocity, u_9. This, of course, will come with a penalty in thrust if the mass flow is not increased. An obvious way to obtain good propulsive efficiency is to utilize a large diameter propeller in order to move a very large mass. Turbo-prop engines are, in fact, highly efficient engines, but have encountered two major problems in the past. The large gearbox necessary to reduce the propeller speed has often caused weight and reliability problems, and the onset of high Mach numbers at the propeller tips (as the aircraft speed increases) has led to unacceptably low propeller efficiencies.

Lately, a resurgence of interest has occurred in "very high bypass ratio turbofans," however. Thus, engines with up to eight relatively small radius propeller blades are envisioned. These blades will be swept backwards (in the relative flow) in order to forestall the onset of high Mach number effects, and because of the relatively small radius of the blades, the amount of gear reduction required will be much reduced as compared to conventional turboprops.

By ducting the "propeller" or fan, the tip Mach number problems can be avoided by diffusing the flow prior to the fan. An additional benefit occurs because the blades may be highly loaded, aerodynamically, right out to the blade tips because the cowl much reduces tip flow. Such ducted fan engines, termed turbofan engines, have been very successful when utilized for high subsonic or low supersonic flight regimes. Present turbofans used for subsonic flight have "by-pass ratios" (the ratio of air passing through the outer duct to that passing through the core engine) of about five or six, whereas it is imagined that the very high by-pass engines discussed in the preceding paragraph will have (equivalent) by-pass ratios of twenty five to fifty. (A turboprop has a "by-pass ratio" of about 100.) A cowl for an engine with such a huge by-pass ratio would not only be large and heavy, but would also present a large wetted area and projected area, with consequent large drag penalty.

The various "trade-offs" for such engine choices are best determined by a systematic use of cycle analysis.

5.5 SYSTEMS OF UNITS

In the following sections, the various dimensionless quantities will be calculated in the SI system of units. However, because of the greater familiarity to some readers of the British system of units (or of the British gravitational system of units), the various formulae will also be presented in these alternate systems. Table 5.5.1 gives a brief list of pertinent terms for use in propulsion, together with appropriate conversion factors.

Table 5.5.1 Units and Conversion Factors British System, SI

Item	Units British System	Units SI	Conversion Factor (Multiply British System to get SI Value)
Length	ft	m	0.30480
Mass	slug, lbm	kg	14.594, 0.45359
Rotational Speed	rpm	rad/sec	$\frac{2\pi}{60} = 0.10472$
Power	HP	w	745.70
Fuel Heating Value, h	$\frac{BTU}{lbm}$	J/kg	2326.0
Specific Heat, C_p	$\frac{BTU}{lbm\ ^oR}$	J/(kg k)	4180.8
Gas Constant, R	$\frac{ft^2}{sec^2\ ^oR}$	$m^2/s^2 k$	0.16723
Specific Fuel Consumption S	$\frac{lbm\ fuel/hr}{lbf\ thrust} = \frac{lbm}{lbf\ hr}$	$\frac{kg\ fuel/sec}{newtons\ thrust} = kg/Ns = s/m$	$2.8325(10^{-6})$
Power Specific Fuel Consumption S_p	$\frac{lbm\ fuel/hr}{HP}$	$\frac{kg/sec}{watt} = kg/ws$	$1.6897(10^{-7})$
Specific Thrust	$\frac{F}{g_o\dot{m}} = \frac{lbf}{lbm/sec}$	$\frac{F}{\dot{m}} = Ns/kg = m/s$	9.8067

British System - Gravitational Constant $g_o = 32.174\ \frac{lbm}{lbf}\ \frac{ft}{sec^2}$

SI - Acceleration of Gravity 9.8067 m/s^2

5.6 THE IDEAL TURBOJET

5.6.1 METHODOLOGY OF CYCLE ANALYSIS

We will now manipulate the pertinent conservation equations to obtain the performance variables specific thrust and specific fuel consumption in terms of assumed design variables, ambient conditions and design limitations. The methodology for all cycles to be considered will be the same. Thus, we will find (even in the cases where losses are included) that to obtain the specific thrust we will require both the ratio of temperature at nozzle exit to ambient temperature, and the ratio of Mach number at nozzle exit to flight Mach number. By then writing the ratio of stagnation to static temperature, T_{t_9}/T_9, at exit as a function of exit Mach number, and then further writing the stagnation temperature at exit in terms of the products of all the component temperature ratios, an expression for the ratio T_9/T_0 will be obtained in terms of M_9 and all stagnation temperature ratios. A second equation for M_9 in terms of all the component pressure ratios (and imposed exit pressure ratio p_9/p_0) is similarly obtained by writing the ratio of stagnation to static pressure, p_{t_9}/p_9, at exit as a function of exit Mach number. The component relationships of Secs. (5.2.1) to (5.2.5)(or their non-ideal equivalents) then allow description of the engine specific thrust in terms of the component performances and design choices.

Not all component performances are independent, however, because, for example, the turbine and compressor work interaction rates must be equated. Such a power balance will lead to evaluation of the turbine temperature ratio and pressure ratio in terms of the chosen compressor pressure ratio and other parameters.

Finally, the specific fuel consumption is evaluated by considering an enthalpy balance across the combustor. Several example cycles are evaluated in the following sections as well as in Chapter Seven, and it will be seen that the methodology described in this section is systematically applied throughout.

5.6.2 CYCLE ANALYSIS OF THE IDEAL TURBOJET

We assume ideal behavior so that the component relationships are as in sections 5.2.1-5.2.5. Additionally, the gas is assumed to be calorically perfect throughout, the pressure at exit is assumed equal to the ambient pressure and the fuel to air ratio, $\dot{m}_f/\dot{m}_0 \equiv f$, is assumed to be much less than unity. With these assumptions we have (referencing Figure 5.3.1)

$$F = \dot{m}\,(u_9 - u_0)$$

or

$$\text{Specific thrust} = \frac{F}{\dot{m}} = u_0\left(\frac{u_9}{u_0} - 1\right) = a_0 M_0\left(\frac{u_9}{u_0} - 1\right) \tag{5.6.1}$$

We may write

$$\left(\frac{u_9}{u_0}\right)^2 = \frac{\gamma_9 R_9 T_9}{\gamma_0 R_0 T_0}\left(\frac{M_9}{M_0}\right)^2 = \frac{T_9}{T_0}\left(\frac{M_9}{M_0}\right)^2 \tag{5.6.2}$$

(Note $\gamma_9 = \gamma_0 = \gamma$, $R_9 = R_0 = R$.)

Now note

$$T_{t_9} = T_9\left(1 + \frac{\gamma-1}{2} M_9^2\right) = T_0 \frac{T_{t_4}}{T_0}\frac{T_{t_5}}{T_{t_4}}\frac{T_{t_9}}{T_{t_5}}$$

or

$$T_{t_9} = T_0\tau_\lambda\tau_t\tau_n = T_0\tau_\lambda\tau_t = T_9\left(1 + \frac{\gamma-1}{2} M_9^2\right) \tag{5.6.3}$$

Here we have put $\tau_n = 1$ which follows from Eq. (5.2.5). We should also note

$$\tau_\lambda = \frac{T_{t_4}}{T_0} = \frac{T_{t_0}}{T_0}\frac{T_{t_2}}{T_{t_0}}\frac{T_{t_3}}{T_{t_2}}\frac{T_{t_4}}{T_{t_3}} = \tau_r\tau_d\tau_c\tau_b$$

Hence with Eq. (5.2.1)

$$\tau_\lambda = \tau_r\tau_c\tau_b \tag{5.6.4}$$

Thus, we note that the minimum conceivable τ_λ, which corresponds to no burning in the combustor, is

$$(\tau_\lambda)_{min} = \tau_r\tau_c \tag{5.6.5}$$

We may write for the pressures

$$p_{t_9} = p_9\left\{1 + \frac{\gamma-1}{2} M_9^2\right\}^{\frac{\gamma}{\gamma-1}}$$

$$= p_0 \frac{p_{t_0}}{p_0}\frac{p_{t_2}}{p_{t_0}}\frac{p_{t_3}}{p_{t_2}}\frac{p_{t_4}}{p_{t_3}}\frac{p_{t_5}}{p_{t_4}}\frac{p_{t_9}}{p_{t_5}} = p_0\pi_r\pi_d\pi_c\pi_b\pi_t\pi_n \tag{5.6.6}$$

or noting $p_9 = p_0$ and from Eqs. (5.1.1) and (5.2.1-5.2.5), $\pi_d = \pi_b = \pi_n = 1$ and $\pi_r^{\frac{\gamma-1}{\gamma}} = \tau_r$, $\pi_c^{\frac{\gamma-1}{\gamma}} = \tau_c$, $\pi_t^{\frac{\gamma-1}{\gamma}} = \tau_t$, we obtain from Eq. (5.6.6)

$$1 + \frac{\gamma-1}{2} M_9^2 = \tau_r\tau_c\tau_t \tag{5.6.7}$$

Combination of Eqs. (5.1.1), (5.6.3) and (5.6.7) then gives

$$\frac{T_9}{T_0} = \frac{\tau_\lambda}{\tau_r\tau_c} \tag{5.6.8}$$

and

$$\left(\frac{M_9}{M_0}\right)^2 = \frac{\tau_r\tau_c\tau_t - 1}{\tau_r - 1} = \frac{2}{\gamma-1}\frac{1}{M_0^2}\left(\tau_r\tau_c\tau_t - 1\right) \tag{5.6.9}$$

The specific thrust then follows by combining Eqs. (5.6.1), (5.6.2), (5.6.8), and (5.6.9) to give

$$\frac{F}{\dot{m}} = a_o\left[\left\{\frac{2}{\gamma-1}\frac{\tau_\lambda}{\tau_r\tau_c}(\tau_r\tau_c\tau_t - 1)\right\}^{\frac{1}{2}} - M_o\right] \quad (5.6.10)$$

The Power Balance

We now utilize a power balance between the compressor and turbine to relate the turbine temperature ratio, τ_t, to other variables. It follows from the first law applied to a control volume (section 2.14) that for steady state conditions the mechanical work interaction per mass is equal to the negative of the change in stagnation enthalpies across the control volume. The turbine work output must be equal to the compressor work input, so applying the first law we have

$$(\dot{m}+\dot{m}_f)\,C_{p_t}(T_{t_4} - T_{t_5}) = \dot{m}C_{p_c}(T_{t_3} - T_{t_2})$$

or

$$(1+f)\frac{C_{p_t}T_{t_4}}{C_{p_c}T_o}\left(1 - \frac{T_{t_5}}{T_{t_4}}\right) = \frac{T_{t_o}}{T_o}\frac{T_{t_2}}{T_{t_o}}\left(\frac{T_{t_3}}{T_{t_2}} - 1\right)$$

or

$$(1+f)\tau_\lambda(1-\tau_t) = \tau_r\tau_d(\tau_c - 1)$$

But here $f \ll 1$, $\tau_d = 1$ (also $C_{p_t} = C_{p_c} = C_p$) so that we obtain

$$\tau_t = 1 - \frac{\tau_r}{\tau_\lambda}(\tau_c - 1) \quad (5.6.11)$$

Eq. (5.6.11) can now be substituted into Eq. (5.6.10) to give after some manipulation

$$\frac{F}{\dot{m}} = a_o\left[\left\{\frac{2\tau_r}{\gamma-1}\left(\frac{\tau_\lambda}{\tau_r\tau_c} - 1\right)(\tau_c - 1) + \frac{\tau_\lambda}{\tau_r\tau_c}M_o^2\right\}^{\frac{1}{2}} - M_o\right] \quad (5.6.12)$$

We may note here that when a ramjet is considered (no compressor so $\tau_c = 1$), the equation for the specific thrust reduces to the very simple form

$$\frac{F}{\dot{m}} = a_o M_o\left[\sqrt{\frac{\tau_\lambda}{\tau_r\tau_c}} - 1\right] \text{(IDEAL RAMJET)} \quad (5.6.13)$$

We can also note from Eq. (5.6.12) that the thrust goes to zero (of course) for no combustion in the burner ($\tau_b = \frac{\tau_\lambda}{\tau_r\tau_c} = 1$).

Specific Fuel Consumption

From the enthalpy balance across the combustor we may write

$$(\dot{m}+\dot{m}_f)\,C_pT_{t_4} - \dot{m}\,C_pT_{t_3} = \dot{m}_f h$$

Here, h is the "heating value of the fuel."

Thus, again taking $f \ll 1$, we obtain

$$f = \frac{C_pT_o}{h}(\tau_\lambda - \tau_r\tau_c) \quad (5.6.14)$$

The specific fuel consumption may hence be written

$$S = \frac{\text{kg fuel/sec}}{\text{Newtons thrust}} = \frac{\dot{m}_f}{F} = \frac{f}{F/\dot{m}} \quad (5.6.15)$$

5.7 SUMMARY OF THE EQUATIONS, IDEAL TURBOJET (OR RAMJET)

We here summarize the equations in a form suitable for calculation. The pertinent equations and terms for the British system of units will be included in brackets ([ ]).

Inputs: T_o(K)[°R], γ, h(J/kg)[$\frac{\text{BTU}}{\text{lbm}}$],

C_p(J/kg K)[$\frac{\text{BTU}}{\text{lbm °R}}$], τ_λ, π_c, M_o

Outputs: $\frac{F}{\dot{m}}$ (Ns/kg)[$\frac{F}{g_o\dot{m}}$, $\frac{\text{lbf}}{\text{lbm/sec}}$],

S (kg/Ns)[$\frac{\text{lbm fuel/hr}}{\text{lbf thrust}}$],

f ($\frac{\text{kg fuel/sec}}{\text{kg air/sec}}$)[$\frac{\text{lbm fuel/sec}}{\text{lbm air/sec}}$]

Equations:

$$R = \frac{\gamma-1}{\gamma}C_p \text{ m}^2/\text{s}^2\text{k}\left[R = \frac{\gamma-1}{\gamma}C_p(2.505)(10^4)\frac{\text{ft}^2}{\text{sec}^2\,^\circ\text{R}}\right] \quad (5.7.1)$$

$$a_o = \sqrt{\gamma RT_o}\ \text{m/s [ft/sec]} \quad (5.7.2)$$

$$\tau_r = 1 + \frac{\gamma-1}{2}M_o^2 \quad (5.7.3)$$

$$\tau_c = \pi_c^{\frac{\gamma-1}{\gamma}} \quad (5.7.4)$$

$$\frac{F}{\dot{m}} = a_o\left[\left\{\frac{2\tau_r}{\gamma-1}\left(\frac{\tau_\lambda}{\tau_r\tau_c} - 1\right)(\tau_c - 1) + \frac{\tau_\lambda}{\tau_r\tau_c}M_o^2\right\}^{\frac{1}{2}} - M_o\right]$$

$$\left[\frac{F}{g_o\dot{m}} = \frac{a_o}{32.174}\left[\left\{\frac{2\tau_r}{\gamma-1}\left(\frac{\tau_\lambda}{\tau_r\tau_c} - 1\right)(\tau_c - 1) + \frac{\tau_\lambda}{\tau_r\tau_c}M_o^2\right\}^{\frac{1}{2}} - M_o\right]\right] \quad (5.7.5)$$

$$f = \frac{C_pT_o}{h}(\tau_\lambda - \tau_r\tau_c) \quad (5.7.6)$$

$$S = \frac{f}{F/\dot{m}}\left[S = \frac{3600\,f}{F/g_o\dot{m}}\right] \quad (5.7.7)$$

5.8 EXAMPLE RESULTS, IDEAL TURBOJET AND RAMJET

As an example of the use of the performance equations, consider the problem of selecting an appropriate compressor pressure ratio for a given flight condition. We consider a turbojet to fly at $M_o = 2$ with the conditions $\gamma = 1.4$, $T_o = 222.2$ K [400°R], $h = 4.4194(10^7)$ J/kg [19,000 BTU/lbm], $C_p = 1004.9$ J/kg K [0.24 BTU/lbm °R], $\tau_\lambda = 7$. Figure 5.8.1 indicates the results.

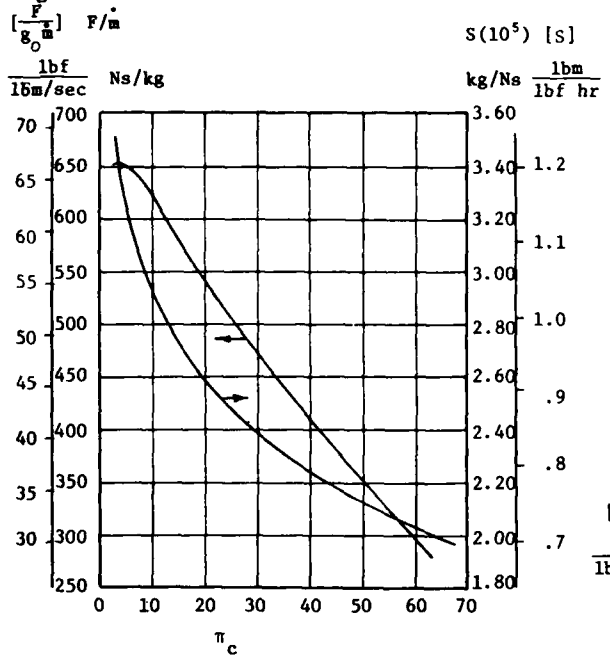

Figure 5.8.1 Effect of Compressor Pressure Ratio on Performance, Ideal Turbojet

It can be seen from the figure that even with the assumption of ideal engine behavior some important design trends become evident. Thus, this ideal analysis indicates that the specific fuel consumption tends to decrease as the compressor pressure ratio increases. (This trend is true also when the losses are included over a large pressure ratio range, but not out to extreme pressure ratios.) The specific thrust, however, maximizes at quite low values of the compressor pressure ratio. (Note that as the compressor pressure ratio increases, the stagnation temperature at entry to the burner increases with the consequence that the allowable fuel addition is reduced because of the restricted τ_λ.) It is hence evident that (ignoring afterburning effects for the moment) if a designer wanted a high thrust lightweight engine for use in an interceptor, he would favor a low compression ratio engine, whereas if the engine was to be used for transport purposes where fuel consumption is of paramount importance, a heavier higher compression ratio but more efficient engine would be appropriate.

Figures 5.8.2 and 5.8.3 show the expected performance of engines over a range of flight Mach numbers.

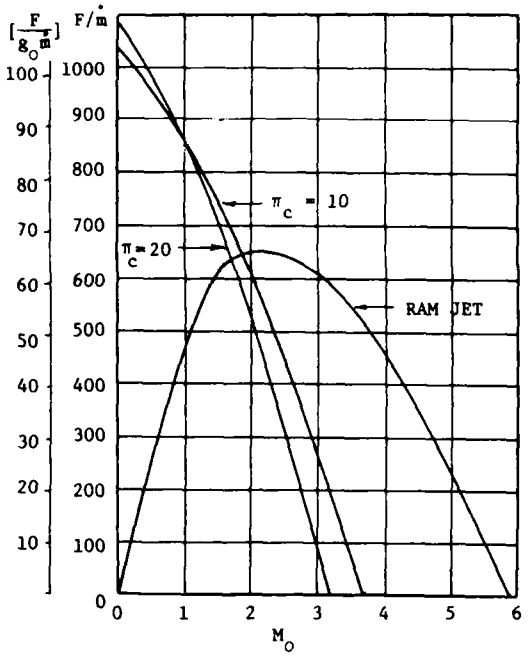

Figure 5.8.2 Specific Thrust Versus Mach Number, Ideal Turbojets and Ramjet

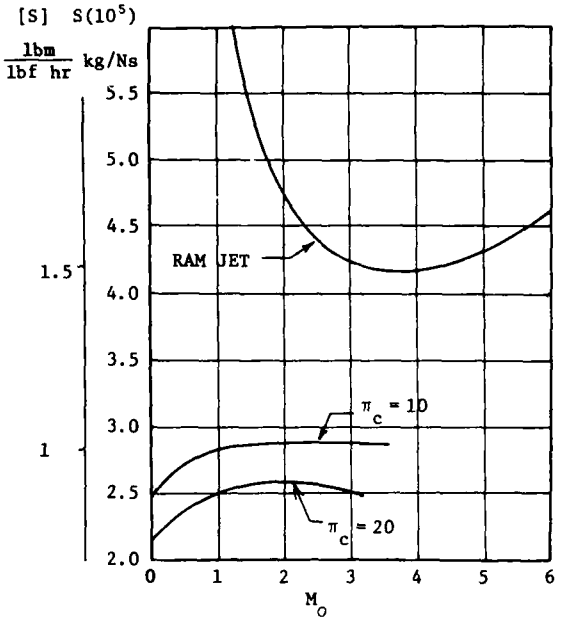

Figure 5.8.3 Specific Fuel Consumption Versus Mach Number, Ideal Turbojets and Ramjet

The conditions assumed for these examples are identical to those in the preceding example except that τ_λ was taken to be equal to eight for the ramjet. It is important to note that these examples illustrate the behavior of what would be a series of engines designed to fly at the illustrated Mach number at the indicated pressure ratio. In other words, the graphs represent the behavior

of a family of engines all with the same compressor pressure ratio but flying at various design Mach numbers. If an engine designed for a certain Mach number and pressure ratio is flown off-design (at a different Mach number), its compressor pressure ratio will change. These effects are analyzed in section 8.1.

It is apparent in Figure 5.8.2 that in the case of the turbojets, as the flight Mach number increases the resultant increase in compressor outlet temperature restricts the allowable fuel addition causing a reduction in specific thrust. (Note that in an actual engine the airflow would increase as M_o increased causing the thrust (but not specific thrust) to initially increase.) In the case of the ramjet, the thermal efficiency of the engine is so low at low Mach numbers that the specific thrust at first increases with increasing Mach numbers before eventually decreasing due to the limitation on fuel addition.

Figure 5.8.3 indicates that the turbojet specific fuel consumption at first increases with increase in M_o. This is because the energy required for a given velocity change from inlet to exit (and hence thrust production) increases as the flight speed increases. At very low thrusts the specific fuel consumption decreases (for this ideal engine) because the propulsive and thermal efficiencies increase. For the ramjet, the initial sharp drop in S reflects the increasing thermal efficiency. Later, the effect of the extra required energy for a given velocity change causes S to increase.

As a final example calculation, we again consider a family of turbojets with $M_o = 2$ and with $\pi_c = 20$. We then consider the effect of varying the turbine inlet temperature, or equivalently of varying τ_λ. Figure 5.8.4 indicates the results.

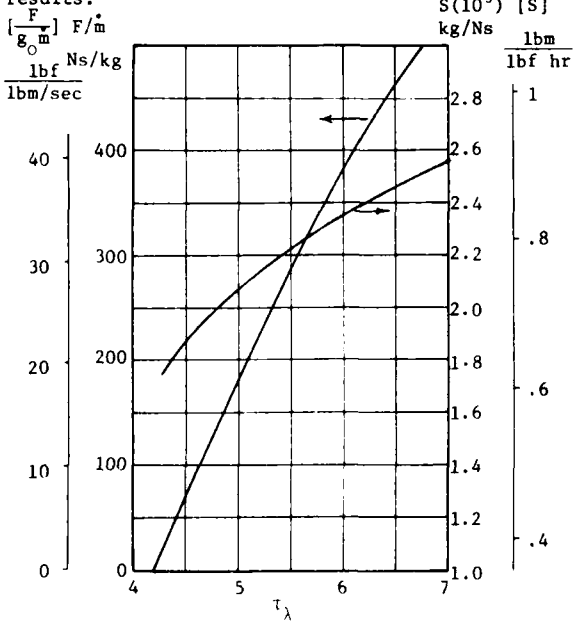

Figure 5.8.4 Specific Fuel Consumption and Specific Thrust Versus τ_λ, Ideal Turbojet

Figure 5.8.4 indicates how the specific fuel consumption decreases as the turbine inlet temperature decreases because of the increasing propulsive efficiency. However, if component losses were present, a finite fuel flow would be required as the thrust approached zero with the result that the specific fuel consumption would increase dramatically.

5.9 INTERPRETATION OF THE BEHAVIOR OF THE SPECIFIC FUEL CONSUMPTION

In the preceding sections the equations for S and $F/\dot{m}$ were deliberately formulated in a manner that led to easy algebraic manipulation and calculation. For interpretive purposes we may write S in the alternate form

$$S = \frac{\dot{m}_f}{F} = \frac{(h\dot{m}_f)\,\frac{u_o}{h}}{u_o F}$$

or

$$S = \frac{u_o}{h}\,\frac{1}{\left\{\frac{u_o F}{\frac{\dot{m}}{2}(u_9^2 - u_o^2)}\right\}\left\{\frac{\frac{\dot{m}}{2}(u_9^2 - u_o^2)}{h\dot{m}_f}\right\}} \qquad (5.9.1)$$

From sections 5.3 and 5.4 it can be seen that the expressions in parentheses are just the propulsive and thermal efficiencies. That is,

$$\eta_p = \frac{u_o F}{\frac{\dot{m}}{2}(u_9^2 - u_o^2)}$$

and

$$\eta_{th} = \frac{\frac{\dot{m}}{2}(u_9^2 - u_o^2)}{h\dot{m}_f} \qquad (5.9.2)$$

Hence we may write

$$S = \frac{a_o M_o}{h}\,\frac{1}{\eta_p\,\eta_{th}} \qquad (5.9.3)$$

Equation (5.3.1) related the thermal efficiency to the thermodynamic variables by

$$\eta_{th} = 1 - \frac{1}{\tau_r \tau_c} = 1 - \frac{1}{(\pi_r \pi_c)^{\frac{\gamma-1}{\gamma}}}$$

and we may obtain an expression for the propulsive efficiency by combining Eq. (5.4.2), (5.6.1) and (5.7.5) to give

$$\eta_p = \frac{2M_o}{\left\{\frac{2\tau_r}{\gamma-1}\left(\frac{\tau_\lambda}{\tau_r\tau_c} - 1\right)(\tau_c - 1) + \frac{\tau_\lambda}{\tau_r\tau_c} M_o^2\right\}^{\frac{1}{2}} + M_o} \qquad (5.9.4)$$

Equation (5.9.3) indicates that we may interpret the behavior of the specific fuel consumption as a combination of three influences. Thus, as the flight Mach number increases, the required increase in energy requirement appears in the factor M_o. This effect is somewhat compensated for by the increases in η_p and η_{th} that occur for increases in M_o for the ideal engine case. Figure 5.9.1 illustrates the variation in behavior of the thermal and propulsive efficiencies for the ideal turbojets and ramjets previously considered.

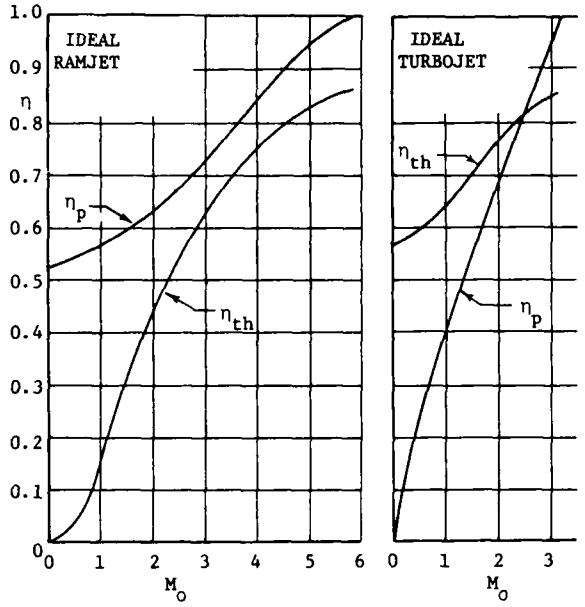

Figure 5.9.1 Thermal and Propulsive Efficiencies

It can be seen that the trends support the comments made in the previous section in that the low thermal efficiency dominates the ramjet performance at low M_o whereas the rapidly increasing propulsive efficiency leads to the reduced specific fuel consumption at high Mach numbers for the turbojet.

As a final observation upon the behavior of the specific fuel consumption, it can be noted that for given M_o (τ_r) and compressor pressure ratio, π_c (hence τ_c), the thermal efficiency of the ideal engine is independent of turbine inlet temperature. Thus, the observed decrease in S with τ_λ seen in Figure 5.8.4 results solely from the increase in propulsive efficiency that occurs with decrease in τ_λ.

5.10 THE MAXIMUM THRUST TURBOJET

In Figure 5.8.1 it is evident that a maximum specific thrust occurs for a specific value of compressor pressure ratio. This specific value of compressor pressure ratio can be directly obtained from Eq. (5.7.5) by equating the derivative of the specific thrust with τ_c to zero. Noting that at fixed flight conditions and turbine inlet temperature, a_o, τ_r, M_o and τ_λ are all constant, it is evident that $F/\dot{m}$ will be a maximum when

$$\frac{\partial}{\partial \tau_c}\left\{\frac{2\tau_r}{\gamma-1}\left(\frac{\tau_\lambda}{\tau_r\tau_c}-1\right)(\tau_c-1)+\frac{\tau_\lambda}{\tau_r\tau_c}M_o^2\right\}=0$$

or when

$$\frac{2\tau_r}{\gamma-1}\left(-1+\frac{\tau_\lambda}{\tau_r\tau_c^2}\right)-\frac{\tau_\lambda}{\tau_r\tau_c^2}M_o^2=0$$

Hence

$$\tau_c=\frac{\sqrt{\tau_\lambda}}{\tau_r} \qquad (5.10.1)$$

when $F/\dot{m}$ is a maximum. The expression for the specific thrust in this special case is hence

$$\left(\frac{F}{\dot{m}}\right)_{max}=a_o\left[\left[\left(\frac{2}{\gamma-1}\right)\left(\sqrt{\tau_\lambda}-1\right)^2+M_o^2\right)\right]^{\frac{1}{2}}-M_o\right] \qquad (5.10.2)$$

Also, it follows from Eqs. (5.10.1) and (5.7.6) that

$$f=\frac{C_p T_o}{h}\sqrt{\tau_\lambda}\left(\sqrt{\tau_\lambda}-1\right) \qquad (5.10.3)$$

5.10.1 TEMPERATURE RELATIONSHIPS AT MAXIMUM THRUST

The relationship of Eq. (5.10.1) leads to the result that the stagnation temperature following the compressor is equal to the static temperature at nozzle exit. This can be shown as follows:

$$\frac{T_{t_3}}{T_o}=\tau_c\tau_r=(\pi_c\pi_r)^{\frac{\gamma-1}{\gamma}}=\left(\frac{p_{t_3}}{p_o}\right)^{\frac{\gamma-1}{\gamma}}$$

But $p_o=p_9$ and $p_{t_3}=p_{t_4}$ so that with

$$\left(\frac{p_{t_3}}{p_o}\right)^{\frac{\gamma-1}{\gamma}}=\left(\frac{p_{t_4}}{p_9}\right)^{\frac{\gamma-1}{\gamma}}=\frac{T_{t_4}}{T_9}$$

We may write

$$\frac{T_{t_3}}{T_o}=\tau_c\tau_r=\frac{T_{t_4}}{T_9}=\sqrt{\tau_\lambda}$$

or

$$\left(\frac{T_{t_3}}{T_o}\right)^2=\frac{T_{t_4}}{T_o}=\left(\frac{T_{t_4}}{T_9}\right)^2$$

Thus

$$T_{t_3}=\sqrt{T_{t_4}T_o}=T_9 \quad \text{Q.E.D.} \qquad (5.10.4)$$

The temperature entropy diagram is then as indicated in Figure 5.10.1. Note that the T-s diagram is very "full" for the condition $T_{t_3}=T_9$.

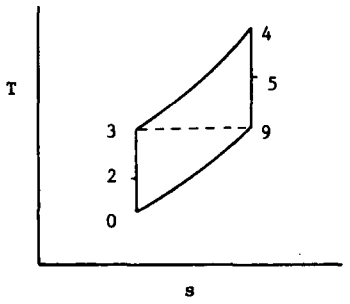

Figure 5.10.1 Temperature Entropy Diagram for Max Thrust Turbojet

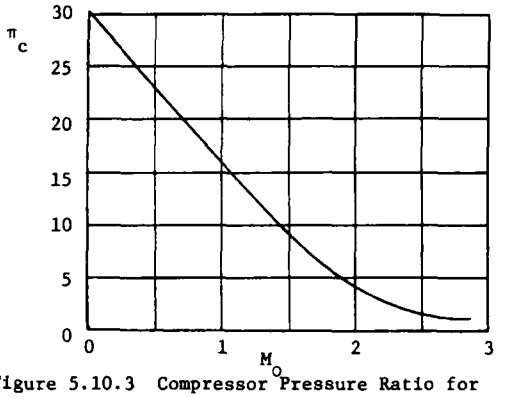

Figure 5.10.3 Compressor Pressure Ratio for Maximum Thrust

5.10.2 EXAMPLE RESULTS - MAX THRUST TURBOJET

The performance of a max thrust turbojet may be plotted in a similar manner to the conventional turbojet and ramjet. Figure 5.10.2 shows the specific thrust versus flight Mach number for a family of max thrust turbojets. Shown for comparison is the equivalent performance of a family of turbojets with a compressor pressure ratio of twenty. Conditions are as in Figures 5.8.1-5.8.3, namely $\gamma = 1.4$, $T_o = 222.2$ K, $h = 4.4194(10^7)$J/kg, $C_p = 1004.9$ J/kg K, $\tau_\lambda = 7$.

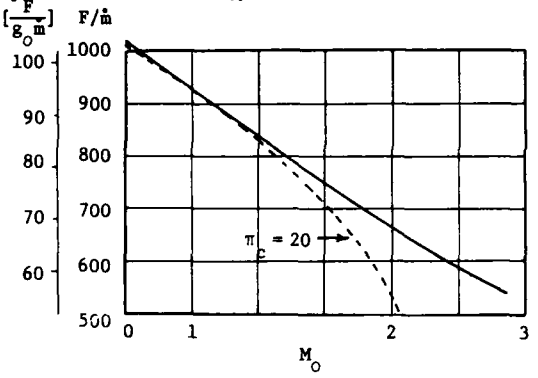

Figure 5.10.2 Specific Thrust Versus Flight Mach Number - Max Thrust Turbojet

The related compressor pressure ratio giving maximum thrust is shown in Figure 5.10.3. Note that each max thrust turbojet graph must terminate where $\pi_c = 1$. This occurs when $\tau_c = 1$ giving from Eq. (5.10.1) $\tau_r = \sqrt{\tau_\lambda}$. Hence

$$(M_o)_{max} = \{\frac{2}{\gamma-1}(\sqrt{\tau_\lambda} - 1)\}^{\frac{1}{2}} \qquad (5.10.5)$$

5.11 THE IDEAL TURBOJET WITH AFTERBURNING

A well established and relatively simple method of increasing the thrust level of a turbojet is to "afterburn" in the duct following the turbine outlet. The additional enthalpy addition coupled with the nozzle pressure ratio provides a substantial thrust augmentation, though at the expense of an increase in specific fuel consumption. The mechanical arrangement and related station numbering are indicated in Fig. 5.11.1

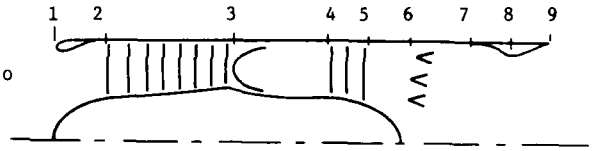

Figure 5.11.1 The Turbojet with Afterburning

When the entire cycle is considered ideal, all the component relationships of Sec. (5.2) remain true and in addition we note $\pi_{AB} = 1$. Usually the maximum temperature attainable in the afterburner is substantially higher than that attainable in the primary combustor because of the restriction placed upon the attainable temperature in the primary combustor by the presence of the turbine. Figures 5.11.2 and 5.11.3 indicate the thermodynamic cycles appropriate for the ideal afterburning turbojet.

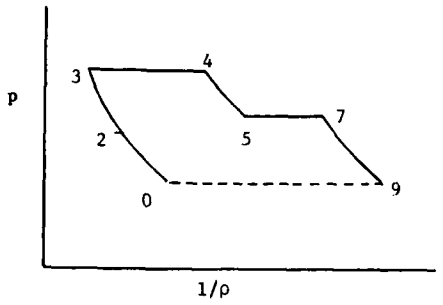

Figure 5.11.2 Pressure-Volume Diagram, Ideal Afterburning Turbojet

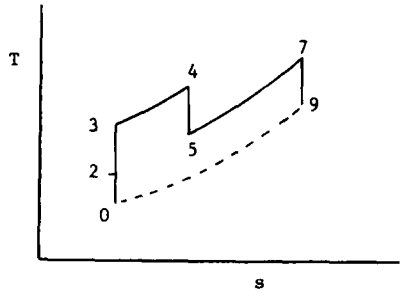

Figure 5.11.3 Temperature-Entropy Diagram, Ideal Afterburning Turbojet

5.11.1 CYCLE ANALYSIS OF THE IDEAL AFTERBURNING TURBOJET

Again assuming, as in Sec. (5.6.2), that all component efficiencies are perfect, that the gas is calorically perfect, that the exit static pressure is equal to the ambient pressure and that the fuel to air ratio in both primary combustor and afterburner is much less than unity, we have:

$$\text{Specific thrust} = \frac{F}{\dot{m}} = a_o M_o \left(\frac{u_9}{u_o} - 1\right) \qquad (5.11.1)$$

Where as before,

$$\left(\frac{u_9}{u_o}\right)^2 = \frac{T_9}{T_o}\left(\frac{M_9}{M_o}\right)^2 \qquad (5.11.2)$$

We now write

$$T_{t_9} = T_9\left(1 + \frac{\gamma-1}{2} M_9^2\right) = T_o\, \tau_{\lambda AB} \qquad (5.11.3)$$

$$p_{t_9} = p_9\left(1 + \frac{\gamma-1}{2} M_9^2\right)^{\frac{\gamma}{\gamma-1}} = p_o \pi_r \pi_c \pi_t \qquad (5.11.4)$$

Hence with Eqs. (5.1.1), (5.2.2), (5.2.4) and (5.11.4)

$$1 + \frac{\gamma-1}{2} M_9^2 = \tau_r \tau_c \tau_t \qquad (5.11.5)$$

Equations (5.11.1) to (5.11.5) may now be combined to give

$$\frac{F}{\dot{m}} = a_o\left[\left\{\frac{2}{\gamma-1}\frac{\tau_{\lambda AB}}{\tau_r\tau_c\tau_t}(\tau_r\tau_c\tau_t - 1)\right\}^{1/2} - M_o\right] \qquad (5.11.6)$$

The similarity between this expression and that obtained for the turbojet without afterburning (Eq. 5.6.10) is evident when it is noted that the minimum value for $\tau_{\lambda AB}$ that occurs for no afterburning is $(\tau_{\lambda AB})_{min} = \tau_\lambda \tau_t$. With this substitution Eq. (5.11.6) reduces immediately to Eq. (5.6.10).

The power balance between compressor and turbine remains unchanged, so that Eq. (5.6.11) remains valid, namely:

$$\tau_t = 1 - \frac{\tau_r}{\tau_\lambda}(\tau_c - 1)$$

The expression for the fuel to air ratio in the primary burner also remains as before (Eq. 5.6.14). The fuel to air ratio for the afterburner is obtained from an enthalpy balance across the burner to give

$$\dot{m}_{fAB}\, h = (\dot{m} + \dot{m}_f + \dot{m}_{fAB})C_p T_{t_8} - (\dot{m} + \dot{m}_f)C_p T_{t_5}$$

$$\text{or} \qquad f_{AB} = \frac{\dot{m}_{fAB}}{\dot{m}} \simeq \frac{C_p T_o}{h}(\tau_{\lambda AB} - \tau_\lambda \tau_t) \qquad (5.11.7)$$

Combining Eqs. (5.6.11), (5.6.14) and (5.11.7) then gives

$$f_{TOT} = \frac{\dot{m}_f + \dot{m}_{fAB}}{\dot{m}} = \frac{C_p T_o}{h}(\tau_{\lambda AB} - \tau_r) \qquad (5.11.8)$$

5.12 SUMMARY OF THE EQUATIONS, IDEAL TURBOJET WITH AFTERBURNING

Inputs: T_o(K)[°R], γ, h(J/kg) [$\frac{BTU}{lbm}$], C_p(J/kgK)[$\frac{BTU}{lbm\,°R}$], τ_λ, $\tau_{\lambda AB}$, π_c, M_o

Outputs: $\frac{F}{\dot{m}}$ (Ns/kg)[$\frac{F}{g_o\dot{m}}$, $\frac{lbf}{lbm/sec}$], S(kg/Ns)[$\frac{lbm\ fuel/hr}{lbf\ thrust}$], f_{TOT} ($\frac{kg\ fuel/sec}{kg\ air/sec}$)[$\frac{lbm\ fuel/sec}{lbm\ air/sec}$]

Equations:

$$R = \frac{\gamma-1}{\gamma} C_p \ \text{m}^2/\text{s}^2\text{k} \quad \left[R = \frac{\gamma-1}{\gamma} C_p (2.505)(10^4)\frac{ft^2}{sec^2\,°R}\right] \qquad (5.12.1)$$

$$a_o = \sqrt{\gamma R T_o}\ \text{m/s [ft/sec]} \qquad (5.12.2)$$

$$\tau_r = 1 + \frac{\gamma-1}{2} M_o^2 \qquad (5.12.3)$$

$$\tau_c = \pi_c^{\frac{\gamma-1}{\gamma}} \qquad (5.12.4)$$

$$\tau_t = 1 - \frac{\tau_r}{\tau_\lambda}(\tau_c - 1) \qquad (5.12.5)$$

$$\frac{F}{\dot{m}} = a_o\left[\left\{\frac{2}{\gamma-1}\frac{\tau_{\lambda AB}}{\tau_r\tau_c\tau_t}(\tau_r\tau_c\tau_t - 1)\right\}^{1/2} - M_o\right]$$

$$\left[\frac{F}{\dot{m}g_o} = \frac{a_o}{32.174}\left[\left\{\frac{2}{\gamma-1}\frac{\tau_{\lambda AB}}{\tau_r\tau_c\tau_t}(\tau_r\tau_c\tau_t - 1)\right\}^{1/2} - M_o\right]\right] \qquad (5.12.6)$$

NOTE: The minimum allowable value for $\tau_{\lambda AB}$ is $\tau_{\lambda AB} = \tau_\lambda \tau_t$.

$$f_{TOT} = \frac{C_p T_o}{h} (\tau_{\lambda AB} - \tau_r) \qquad (5.12.7)$$

$$S = \frac{f}{F/\dot{m}} \quad \left[S = \frac{3600F}{F/g_o \dot{m}}\right] \qquad (5.12.8)$$

5.13 EXAMPLE RESULTS, IDEAL TURBOJET WITH AFTERBURNING

We consider a turbojet to fly at a flight Mach number of two, with the conditions $\gamma = 1.4$, $T_o = 233.3$ [420°R], $h = 4.5357(10^7)$J/kg[19,500 $\frac{BTU}{lbm}$], $C_p = 1004.9$ J/kgK[0.24 BTU/lbm°R], $\tau_\lambda = 7$, $\tau_{\lambda AB} = 8$. Figure 5.13.1 compares the performance of the turbojet over a range of compressor pressure ratios operating with and without afterburner.

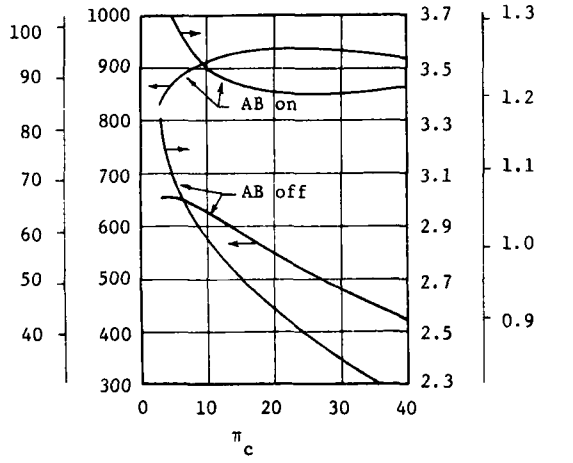

Figure 5.13.1 Effect of Compressor Pressure Ratio on Performance, Ideal Turbojet with Afterburner

As predicted, the addition of afterburning leads to an increase of specific thrust at the expense of an increase in specific fuel consumption. It is of interest to note the location of the maximum in the specific thrust when afterburning is present. By formally taking the derivative of the specific thrust with τ_c (Eq. 5.12.6), it is evident that the maximum occurs when the product $\tau_r \tau_c \tau_t$ reaches a maximum. Such a maximum occurs when $\pi_r \tau_c \tau_t = p_{t_5}/p_o = p_{t_5}/p_9$ reaches a maximum and it is evident (and obvious) that the maximum thrust occurs when the nozzle pressure ratio reaches a maximum. We note also that because f_{TOT} is a function of $\tau_{\lambda AB}$ and τ_r (and $C_p T_o/h$) only, the maximum in thrust corresponds to the minimum in specific fuel consumption!

We may obtain the analytical expression for the compressor pressure ratio giving maximum thrust by noting with Eq. (5.12.5),

$$\frac{\partial \tau_c \tau_t}{\partial \tau_c} = \frac{\partial}{\partial \tau_c} \{\tau_c - \frac{\tau_r}{\tau_\lambda} (\tau_c^2 - \tau_c)\}$$

Hence at the maximum

$$1 - \frac{\tau_r}{\tau_\lambda} (2\tau_c - 1) = 0 \quad \text{or} \quad (\tau_c)_{\text{max thrust}} = \frac{\tau_\lambda + \tau_r}{2\tau_r}$$

and

$$\pi_{c\,\text{max thrust}} = \left\{\frac{\tau_\lambda + \tau_r}{2\tau_r}\right\}^{\frac{\gamma}{\gamma-1}} \qquad (5.13.1)$$

In the example given above we obtain

$$\pi_{c\,\text{max thrust}} = \left(\frac{7+1.8}{3.6}\right)^{3.5} = 22.84$$

It would appear then that such a value for compressor pressure ratio would be near a suitable compromise for an aircraft that was to cruise efficiently with no afterburning, but was to engage in combat with high thrust and relatively efficient afterburning fuel consumption.

5.14 THE TURBOFAN WITH SEPARATE EXHAUST STREAMS

5.14.1 CYCLE ANALYSIS OF THE IDEAL TURBOFAN WITH SEPARATE EXHAUST STREAMS

The methodology of cycle analysis, as described in Sec. (5.6.1), will again be applied. When applying the cycle analysis, we must now account for the thrust of both the primary (core engine) and secondary (fan) streams, and must note that the turbine power output will now be equated to the power input to both fan and compressor. We again assume that all component efficiencies are perfect, that the gas is calorically perfect, that the fuel to air ratio in the combustor is much less than unity and that the exit static pressures of both primary and secondary streams are equal to the abmient pressure. The nomenclature and notation are as in Fig. 5.1.1 and Sec. (5.1).

The total thrust may be written as the sum of the thrust contributions of the two streams to give

$$F = \dot{m}_1 (u_9 - u_o) + \dot{m}_2 (u_{9'} - u_o)$$

$$\text{or} \quad \frac{F}{\dot{m}_1 + \dot{m}_2} = \frac{a_o M_o}{1+\alpha} \left[\left(\frac{u_9}{u_o} - 1\right) + \alpha \left(\frac{u_{9'}}{u_o} - 1\right)\right] \qquad (5.14.1)$$

Here we have introduced

$\dot{m}_1$ = Mass flow rate of the primary stream

$\dot{m}_2$ = Mass flow rate of the secondary stream

$\alpha = \frac{\dot{m}_2}{\dot{m}_1}$ = By-pass ratio

SECONDARY STREAM

We again have $\left(\frac{u_9'}{u_O}\right)^2 = \frac{T_9'}{T_O}\left(\frac{M_9'}{M_O}\right)^2$ (5.14.2)

Now write

$$T_{t_9}' = T_9'\left(1 + \frac{\gamma-1}{2} M_9'^2\right) = T_O \tau_r \tau_c' \quad (5.14.3)$$

$$p_{t_9}' = p_9'\left(1 + \frac{\gamma-1}{2} M_9'^2\right)^{\frac{\gamma}{\gamma-1}} = p_O \pi_r \pi_c' \quad (5.14.4)$$

With Eqs. (5.1.1), (5.2.2), and (5.14.4)

$$1 + \frac{\gamma-1}{2} M_9'^2 = \tau_r \tau_c' \quad (5.14.5)$$

So that

$$T_9' = T_O \quad (5.14.6)$$

We might note here that this result could have been obtained more directly by noting $p_9' = p_O$ and $s_9' = s_O$, hence $T_9' = T_O$. Equations (5.14.2), (5.14.5), and (5.14.6) then give

$$M_O\left(\frac{u_9'}{u_O} - 1\right) = \left\{\frac{2}{\gamma-1}(\tau_r\tau_c' - 1)\right\}^{1/2} - M_O \quad (5.14.7)$$

PRIMARY STREAM

The relationships for temperatures and pressures, here, are exactly as previously obtained for the turbojet (Sec. 5.6.2), so we may write

$$M_O\left(\frac{u_9}{u_O} - 1\right) = \left\{\frac{2}{\gamma-1}\frac{\tau_\lambda}{\tau_r\tau_c}(\tau_r\tau_c\tau_t - 1)\right\}^{1/2} - M_O \quad (5.14.8)$$

POWER BALANCE

For this ideal cycle the power output from the turbine will just equal the power input to the fan and compressor. We hence obtain

$$\dot{m}_1 C_p(T_{t_4} - T_{t_5}) = \dot{m}_1 C_p(T_{t_3} - T_{t_2}) + \dot{m}_2 C_p(T_{t_3'} - T_{t_2})$$

or $\tau_\lambda(1-\tau_t) = \tau_r(\tau_c - 1) + \alpha\tau_r(\tau_c' - 1)$

hence $$\tau_t = 1 - \frac{\tau_r}{\tau_\lambda}[(\tau_c - 1) + \alpha(\tau_c' - 1)] \quad (5.14.9)$$

SPECIFIC FUEL CONSUMPTION

An enthalpy balance across the combustor gives

$$\dot{m}_f h = \dot{m}_1 C_p(T_{t_4} - T_{t_3})$$

or $$f = \frac{\dot{m}_f}{\dot{m}_1} = \frac{C_p T_O}{h}(\tau_\lambda - \tau_r\tau_c) \quad (5.14.10)$$

The specific fuel consumption then follows from

$$S = \frac{\dot{m}_f}{F} = \frac{\dot{m}_f}{\dot{m}_1}\frac{1}{\left(\frac{\dot{m}_1+\dot{m}_2}{\dot{m}_1}\right)}\frac{1}{\left(\frac{F}{\dot{m}_1+\dot{m}_2}\right)}$$

or $$S = \frac{f}{(1+\alpha)\left(\frac{F}{\dot{m}_1+\dot{m}_2}\right)} \quad (5.14.11)$$

Combination of Eqs. (5.14.1) and (5.14.7)-(5.14.11) then gives the following summary of equations.

5.14.2 SUMMARY OF THE EQUATIONS, IDEAL TURBOFAN, BY-PASS RATIO PRESCRIBED

Inputs: T_O(K)[°R], γ, h(J/kg) $\left[\frac{BTU}{lbm}\right]$,

C_p(J/kgK) $\left[\frac{BTU}{lbm°R}\right]$, τ_λ, π_c, π_c', M_O, α

Outputs: $\frac{F}{\dot{m}_1+\dot{m}_2}$ (Ns/kg) $\left[\frac{F}{g_O(\dot{m}_1+\dot{m}_2)}, \frac{lbf}{lbm/sec}\right]$,

S(kg/Ns) $\left[\frac{lbm\ fuel/hr}{lbf\ thrust}\right]$,

f $\frac{kg\ fuel/sec}{kg\ primary\ air/sec}$

Equations:

$$R = \frac{\gamma-1}{\gamma} C_p \ m^2/s^2K \quad \left[R = \frac{\gamma-1}{\gamma} C_p (2.505)(10^4)\ \frac{ft}{sec^2°R}\right] \quad (5.14.12)$$

$$a_O = \sqrt{\gamma R T_O}\ \ m/s\ \ [ft/sec] \quad (5.14.13)$$

$$\tau_r = 1 + \frac{\gamma-1}{2} M_O^2 \quad (5.14.14)$$

$$\tau_c = \pi_c^{\frac{\gamma-1}{\gamma}} \quad (5.14.15)$$

$$\tau_c' = \pi_c'^{\frac{\gamma-1}{\gamma}} \quad (5.14.16)$$

$$\tau_t = 1 - \frac{\tau_r}{\tau_\lambda}[(\tau_c - 1) + \alpha(\tau_c' - 1)] \quad (5.14.17)$$

$$\frac{F}{\dot{m}_1+\dot{m}_2} = \frac{a_O}{1+\alpha}\left[\left\{\frac{2}{\gamma-1}\frac{\tau_\lambda}{\tau_r\tau_c}(\tau_r\tau_c\tau_t - 1)\right\}^{1/2} - M_O + \alpha\left[\left\{\frac{2}{\gamma-1}(\tau_r\tau_c' - 1)\right\}^{1/2} - M_O\right]\right] \quad (5.14.18)$$

(To obtain British units of $\frac{lbf}{lbm/sec}$, a_O in meters/sec would be replaced by $\frac{a_O}{32.174}$ where a_O should be given in ft/sec)

$$f = \frac{C_p T_O}{h}(\tau_\lambda - \tau_r\tau_c) \quad (5.14.19)$$

$$S = \frac{f}{(1+\alpha)\left(\frac{F}{\dot{m}_1+\dot{m}_2}\right)} \quad \left[S = \frac{3600f}{(1+\alpha)\left(\frac{F}{g_O(\dot{m}_1+\dot{m}_2)}\right)}\right] \quad (5.14.20)$$

5.14.3 BY-PASS RATIO FOR MINIMUM SPECIFIC FUEL CONSUMPTION

It would be desirable to select the by-pass ratio α, to give the minimum specific fuel consumption possible for given prescribed operating conditions (T_o, M_o), design limits (τ_λ) and design choices (π_c, π_c'). It is evident from Eqs. (5.14.18) - (5.14.20) that the minimum value for S will occur at the maximum value of the expression

$$\{\frac{2}{\gamma-1}\frac{\tau_\lambda}{\tau_r\tau_c}(\tau_r\tau_c\tau_t-1)\}^{1/2}-M_o+\alpha[\{\frac{2}{\gamma-1}(\tau_r\tau_c'-1)\}^{1/2}-M_o]$$

Taking the derivative of this expression with α we obtain

$$\frac{(\frac{1}{\gamma-1})\tau_\lambda\frac{\partial\tau_t}{\partial\alpha}}{\{\frac{2}{\gamma-1}\frac{\tau_\lambda}{\tau_r\tau_c}(\tau_r\tau_c\tau_t-1)\}^{1/2}}+[\{\frac{2}{\gamma-1}(\tau_r\tau_c'-1)\}^{1/2}-M_o]$$

$$= 0 \quad \text{at minimum} \quad S \tag{5.14.21}$$

From Eq. (5.14.17) we find

$$\frac{\partial\tau_t}{\partial\alpha} = -\frac{\tau_r}{\tau_\lambda}(\tau_c'-1) \tag{5.14.22}$$

Equations (5.14.21) and (5.14.22) give an equation for that value of τ_t identified with the minimum specific fuel consumption. Thus, denoting by an asterisk the particular value of the property leading to minimum specific fuel consumption we find

$$\tau_t^* = \frac{1}{\tau_r\tau_c}+\frac{1}{2(\gamma-1)\tau_\lambda}\left[\frac{\tau_r(\tau_c'-1)}{\{\frac{2}{\gamma-1}(\tau_r\tau_c'-1)\}^{1/2}-M_o}\right]^2 \tag{5.14.23}$$

Utilizing this value of τ_t^*, we then find

$$\{\frac{2}{\gamma-1}\frac{\tau_\lambda}{\tau_r\tau_c}(\tau_r\tau_c\tau_t^*-1)\}^{1/2}-M_o =$$

$$\frac{\frac{1}{\gamma-1}\tau_r(\tau_c'-1)}{[\{\frac{2}{\gamma-1}(\tau_r\tau_c'-1)\}^{1/2}-M_o]} - M_o =$$

$$\frac{\frac{1}{\gamma-1}(\tau_r\tau_c'-1)-\frac{1}{\gamma-1}(\tau_r-1)-M_o\{\frac{2}{\gamma-1}(\tau_r\tau_c'-1)\}^{1/2}+M_o^2}{[\{\frac{2}{\gamma-1}(\tau_r\tau_c'-1)\}^{1/2}-M_o]} =$$

$$\frac{\frac{1}{2}[\frac{2}{\gamma-1}(\tau_r\tau_c'-1)+M_o^2-2M_o\{\frac{2}{\gamma-1}(\tau_r\tau_c'-1)\}^{1/2}]}{[\{\frac{2}{\gamma-1}(\tau_r\tau_c'-1)\}^{1/2}-M_o]}$$

or

$$\{\frac{2}{\gamma-1}\frac{\tau_\lambda}{\tau_r\tau_c}(\tau_r\tau_c\tau_t^*-1)\}^{1/2}-M_o] = \frac{1}{2}[\{\frac{2}{\gamma-1}(\tau_r\tau_c'-1)\}^{1/2}-M_o] \tag{5.14.24}$$

It can be seen from Eq. (5.14.18) that this relationship shows that when the by-pass ratio is such as to give minimum specific fuel consumption (for the ideal engine) the thrust per mass per second of the primary stream is one-half of the thrust per mass per second of the secondary stream. This somewhat surprising result follows primarily because when the efficiency of energy transmission between the two streams is very high, the propulsive efficiency of the engine is improved by expending most of the energy in providing momentum to the denser (cooler) secondary stream. It should be noted that when component losses are present, the optimal thrust per mass per second of the primary stream is a much higher fraction of that of the secondary stream. (Usually larger than unity.)

The optimal by-pass ratio may be obtained from Eq. (5.14.17) to give

$$\alpha^* = \frac{\tau_\lambda}{\tau_r}\frac{1-\tau_t^*}{\tau_c'-1}-\frac{\tau_c-1}{\tau_c'-1} \tag{5.14.25}$$

The expression for the thrust, Eq. (5.14.18) may be simplified with Eq. (5.14.24) to give

$$\frac{F^*}{\dot m_1+\dot m_2} = a_o\frac{1+2\alpha^*}{2(1+\alpha^*)}[\{\frac{2}{\gamma-1}(\tau_r\tau_c'-1)\}^{1/2}-M_o] \tag{5.14.26}$$

These equations are summarized in the next section.

5.14.4 SUMMARY OF THE EQUATIONS, IDEAL TURBOFAN, BY-PASS RATIO OPTIMIZED

Inputs: $T_o(K)[°R]$, γ, h J/kg, $[\frac{BTU}{lbm}]$,

C_p(J/kgK) $[\frac{BTU}{lbm\,°R}]$, τ_λ, π_c, π_c', M_o

Outputs: $\frac{F^*}{\dot m_1+\dot m_2}$ (Ns/kg) $[\frac{F^*}{g_o(\dot m_1+\dot m_2)}\frac{lbf}{lbm/sec}]$,

S^*(kg/Ns)$[\frac{lbm\ fuel/hr}{lbf\ \ thrust}]$,

$f\ \frac{kg\ fuel/sec}{kg\ primary\ air/sec}$, α^*

Equations:

The first five equations are identical to Eqs. (5.14.12-5.14.16), then

$$\tau_t^* = \frac{1}{\tau_r\tau_c}+\frac{\gamma-1}{2\tau_\lambda}\left[\frac{\frac{1}{\gamma-1}\tau_r(\tau_c'-1)}{\{\frac{2}{\gamma-1}(\tau_r\tau_c'-1)\}^{1/2}-M_o}\right]^2 \tag{5.14.27}$$

$$\alpha^* = \frac{\tau_\lambda}{\tau_r}\frac{1-\tau_t^*}{\tau_c'-1}-\frac{\tau_c-1}{\tau_c'-1} \tag{5.14.28}$$

$$\frac{F^*}{\dot m_1+\dot m_2} = a_o\frac{1+2\alpha^*}{2(1+\alpha^*)}[\{\frac{2}{\gamma-1}(\tau_r\tau_c'-1)^{1/2}-M_o] \tag{5.14.29}$$

(To obtain British units of $\frac{lbf}{lbm/sec}$, a_o in meters/sec would be replaced by $\frac{a_o}{32.174}$ where a_o should be given in ft/sec .)

$$f = \frac{C_p T_o}{h}(\tau_\lambda - \tau_r \tau_c) \qquad (5.14.30)$$

$$S^* = \frac{f}{(1+\alpha^*)\left(\frac{F^*}{\dot{m}_1 + \dot{m}_2}\right)} \quad \left[S = \frac{3600 f}{(1+\alpha^*)\left\{\frac{F^*}{g_o(\dot{m}_1 + \dot{m}_2)}\right\}}\right] \qquad (5.14.31)$$

5.14.5 EXAMPLE RESULTS - IDEAL TURBOFAN WITH SEPARATE EXHAUST STREAMS

As an example of the use of the performance equations we consider the effect upon the performance parameters and the optimal by-pass ratio of variations in the by-pass pressure ratio.

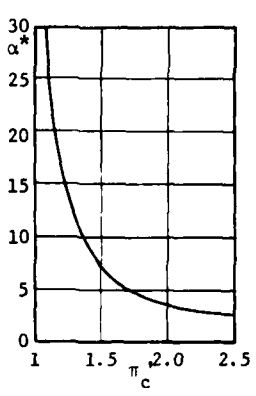

Figure 5.14.1 Optimal *By-Pass Ratio Versus* By-Pass Pressure Ratio

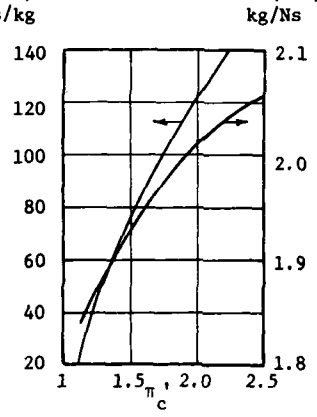

Figure 5.14.2 Specific *Thrust and Specific Fuel* Consumption Versus By-Pass Pressure Ratio

Conditions assumed for these calculations were $\gamma = 1.4$, $T_o = 233.3°K[420°R]$, $h = 4.4194(10^7)J/kg$ [19,000 BTU/lbm], $C_p = 1004.9$ J/kgK[0.24 BTU/lbm°R], $\pi_c = 20$, $\tau_\lambda = 6.5$, $M_o = 2$. It is apparent that a trade-off between high thrust per frontal area and low specific fuel consumption occurs. This clearly reflects the increase of propulsive efficiency with a decrease in fan exit velocity (low π_c'). The enormous optimal by-pass ratios occurring for the very low by-pass pressure ratios do not in fact occur when losses are considered (Chapt. 7). The effect of losses is to much reduce the optimal fraction of energy to be supplied to the by-pass stream.

The variations of α^*, S^* and $\frac{F^*}{\dot{m}_1 + \dot{m}_2}$ with flight Mach number are shown in Figs. 5.14.3 and 5.14.4. The conditions assumed are as above with the additional value $\pi_c' = 2.0$.

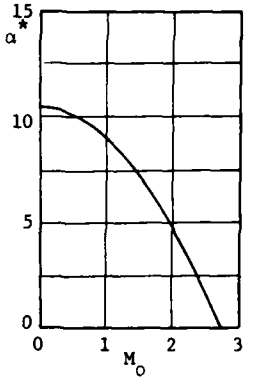

Figure 5.14.3 Optimal By-Pass Ratio Versus Flight Mach Number

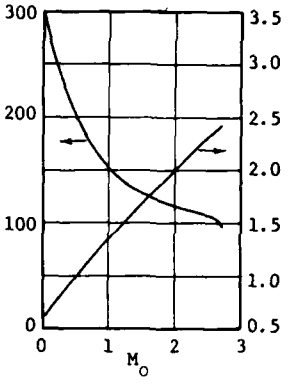

Figure 5.14.4 Specific Thrust and Specific Fuel Consumption Versus Flight Mach Number

The strong effect of flight at increasing Mach numbers is very evident in these curves. Thus, even though the optimal by-pass ratio reduces sharply, the much reduced power capability of the turbine causes a reduction in the specific thrust. It can be seen that it is most important that a designer be aware of the intended flight regime if he is to be able to properly choose his design variables.

Figures 5.14.5 and 5.14.6 indicate that increasing τ_λ has a similar effect upon the optimal by-pass ratio and specific thrust as does reducing the flight Mach number. (Conditions assumed are as above with $M_o = 2$). This is true, of course, because an increase in τ_λ gives an increase in turbine power capability. The slight increase in specific fuel consumption with τ_λ would appear to negate the thrust advantages of going to higher turbine temperatures. However, it should be noted that not only would the engine be smaller (particularly the core engine), but the specific fuel consumption will actually tend to decrease with increasing τ_λ when component losses are included.

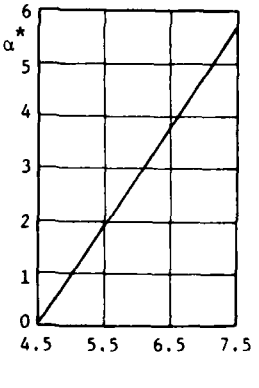

Figure 5.14.5 Optimal By-Pass Ratio Versus τ_λ

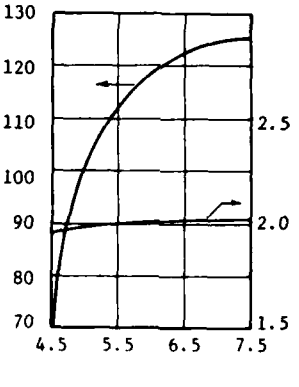

Figure 5.14.6 Specific Thrust and Specific Fuel Consumption Versus τ_λ

As a final example of the ideal turbofan with separate exhaust streams we consider the effects of varying the by-pass ratio from the optimum value. Conditions are as assumed in the above examples, and the results are illustrated in Figure 5.14.7.

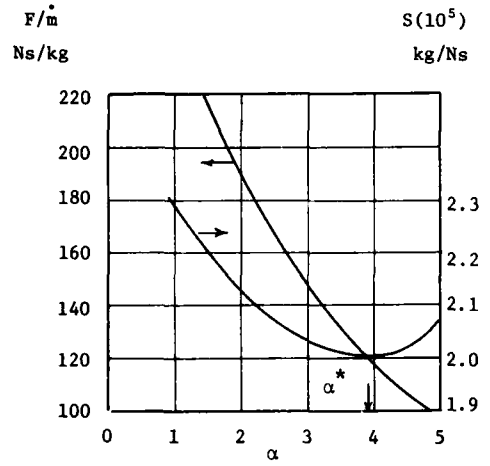

Figure 5.14.7 Specific Thrust and Specific Fuel Consumption Versus By-Pass Ratio

This figure illustrates that a truly optimal choice of by-pass ratio might be other than that leading to the minimum specific fuel consumption. Thus for example note that by selecting $\alpha = 3$ rather than $\alpha^* = 3.91$, a 21% increase in specific thrust can be obtained at a penalty of a 1.5% increase in specific fuel consumption. When the engine size, weight and cowl diameter are all considered for the installation effects, it is probable that a by-pass ratio lower than that corresponding to α^* would be selected.

5.15 THE IDEAL TURBOFAN WITH MIXED EXHAUST STREAMS

In many installations, particularly in aircraft with body mounted engines, it is suitable and convenient to duct the primary and secondary streams through a common exit nozzle. In the event that little mixing of the streams occurs the analysis of the preceding section would remain valid. In many applications, however, "forced mixers" are used to greatly enhance the mixing of the streams. Several benefits may accrue from mixing the streams, such as improvements in the performance parameters and reductions in the exhaust jet noise.

In order to analyze the behavior of a turbofan with ideal stream mixing, we will assume the presence of an "ideal constant area mixer". An ideal constant area mixer is defined as a constant area mixer with no sidewall friction. Analysis of such a device provides us with the outlet stagnation conditions as a function of the two sets of inlet conditions. When the outlet conditions are known the performance of the engine can be determined.

5.15.1 CYCLE ANALYSIS OF THE IDEAL TURBOFAN WITH MIXED EXHAUST STREAMS

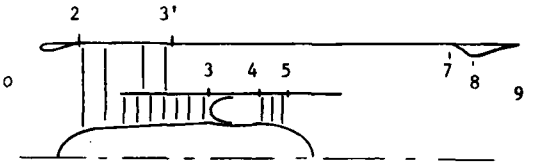

Figure 5.15.1 The Ideal Turbofan with Mixed Exhaust Streams

We again assume all efficiencies perfect, nozzle exit pressure equal to the ambient pressure, that the gas is calorically perfect and that the combustor fuel to air ratio is much less than unity. The specific thrust may hence be written

$$\frac{F}{\dot{m}_1+\dot{m}_2} = a_0 M_0 \left(\frac{u_9}{u_0} - 1\right) \tag{5.15.1}$$

We again have

$$\left(\frac{u_9}{u_0}\right)^2 = \frac{T_9}{T_0}\left(\frac{M_9}{M_0}\right)^2 \tag{5.15.2}$$

and may write

$$T_{t_9} = T_9\left(1 + \frac{\gamma-1}{2} M_9^2\right) \tag{5.15.3}$$

$$p_{t_9} = p_9\left(1 + \frac{\gamma-1}{2} M_9^2\right)^{\frac{\gamma}{\gamma-1}} = p_0 \pi_r \pi_c' \frac{p_{t_9}}{p_{t_3'}} \tag{5.15.4}$$

An enthalpy balance gives

$$\dot{m}_1 C_p T_{t_5} + \dot{m}_2 C_p T_{t_3'} = (\dot{m}_1 + \dot{m}_2) C_p T_{t_9}$$

or

$$\frac{T_{t_9}}{T_0} = \frac{1}{1+\alpha}\left\{\tau_\lambda \tau_t + \alpha \tau_r \tau_c'\right\} \tag{5.15.5}$$

Combination of Eqs. (5.15.1-5.15.5) then gives

$$\frac{F}{\dot{m}_1+\dot{m}_2} = a_0\left[\left\{\frac{\left(\frac{2}{\gamma-1}\right)}{1+\alpha}\left(1 - \frac{1}{\tau_r \tau_c' \left(\frac{p_{t_9}}{p_{t_3'}}\right)^{\frac{\gamma-1}{\gamma}}}\right)\left(\tau_\lambda \tau_t + \alpha \tau_r \tau_c'\right)\right\}^{1/2} - M_0\right] \tag{5.15.6}$$

The power balance between compressor, fan and turbine remains unchanged, so τ_t is still given from Eq. (5.14.9). In Sec. (5.15.2) we will obtain the ratio p_{t_9}/p_{t_5}, so note here

$$\frac{p_{t_9}}{p_{t_3'}} = \frac{p_{t_9}}{p_{t_5}} \frac{p_{t_5}}{p_{t_3'}} = \frac{p_{t_9}}{p_{t_5}} \frac{\pi_c \pi_t}{\pi_c'} \tag{5.15.7}$$

The expressions for f and S remain as in Eqs. (5.14.10) and (5.14.11). These equations will be summarized in Sec. (5.15.4).

5.15.2 THE IDEAL CONSTANT AREA MIXER

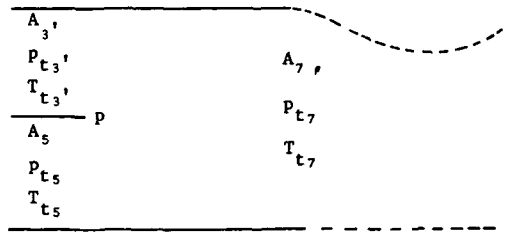

Figure 5.15.2 The Constant Area Mixer

We may consider p_{t_5}, T_{t_5}, M_5, $p_{t_3'}$, $T_{t_3'}$, and α to be prescribed. The common static pressure at the splitter, p, can then be obtained directly from

$$\frac{p_{t_5}}{p} = \{1 + \frac{\gamma-1}{2} M_5^2\}^{\frac{\gamma}{\gamma-1}} \tag{5.15.8}$$

from which we obtain

$$M_{3'}^2 = \frac{2}{\gamma-1}\left[\left(\frac{p_{t_3'}}{p}\right)^{\frac{\gamma-1}{\gamma}} - 1\right] = \frac{2}{\gamma-1}\left[\left(\frac{p_{t_3'}}{p_{t_5}}\right)^{\frac{\gamma-1}{\gamma}} \left(1 + \frac{\gamma-1}{2} M_5^2\right) - 1\right] \tag{5.15.9}$$

Equation (2.18.1) for the mass flows may be utilized to give

$$\frac{A_{3'}}{A_5} = \alpha \sqrt{\frac{T_{t_3'}}{T_{t_5}}} \frac{M_5}{M_{3'}} \left(\frac{p_{t_3'}}{p_{t_5}}\right)^{-\left(\frac{\gamma-1}{2\gamma}\right)} \tag{5.15.10}$$

The momentum equation may be written as

$$A_5(p_5 + \rho_5 u_5^2) + A_{3'}(p_{3'} + \rho_{3'} u_{3'}^2) = A_7(p_7 + \rho_7 u_7^2)$$

or

$$A_5 p_5(1 + \gamma M_5^2) + A_{3'} p_{3'}(1 + \gamma M_{3'}^2) = A_7 p_7 (1 + \gamma M_7^2) \tag{5.15.11}$$

The equation for the mass flow, Eq. (2.18.1), may be written in the form

$$p_i A_i = \sqrt{\frac{R}{\gamma}} \sqrt{T_{t_i}} \frac{1}{M_i} \left(1 + \frac{\gamma-1}{2} M_i^2\right)^{-1/2} \dot{m}_i \quad (i = 3', 5 \text{ or } 7) \tag{5.15.12}$$

Noting from the enthalpy balance that

$$\frac{T_{t_7}}{T_{t_5}} = \frac{1 + \alpha \frac{T_{t_3'}}{T_{t_5}}}{1 + \alpha} \tag{5.15.13}$$

an equation for M_7 can be obtained by combining Eqs. (5.15.11 - 5.15.13), and may be written in the form

$$f = f(M_7) = \frac{(1+\alpha)(1 + \alpha \frac{T_{t_3'}}{T_{t_5}})}{\left[\frac{1}{\sqrt{f(M_5)}} + \frac{\alpha\sqrt{\frac{T_{t_3'}}{T_{t_5}}}}{\sqrt{f(M_{3'})}}\right]^2}$$

where

$$f(M) \equiv \frac{M^2(1 + \frac{\gamma-1}{2} M^2)}{(1 + \gamma M^2)^2} \tag{5.15.14}$$

This is once again of the same functional form for the Mach number as occurred in the solution for the heat interaction at constant area, Sec. (2.17.4), so we may write

$$M_7^2 = 1 - \frac{\Delta[1+\Delta]}{1-2\gamma f+\Delta}$$

where $\Delta = \sqrt{1-2(\gamma+1)f}$ (5.15.15)

Following solution for M_7, the other downstream variables follow directly. Thus, Eqs. (5.15.12) and (5.15.13) may be combined to give

$$\frac{p_{t_7}}{p_{t_5}} = \{(1+\alpha)(1+\alpha \frac{T_{t_3'}}{T_{t_5}})\}^{1/2} \left[\frac{1 + \frac{\gamma-1}{2} M_7^2}{1 + \frac{\gamma-1}{2} M_5^2}\right]^{\frac{\gamma+1}{2(\gamma-1)}} \frac{M_5}{M_7} \frac{1}{1 + A_{3'}/A_5} \tag{5.15.16}$$

The equations of this section are summarized in Sec. (5.15.3).

5.15.3 SUMMARY OF THE EQUATIONS - IDEAL CONSTANT AREA MIXER

Inputs: $\frac{p_{t_3'}}{p_{t_5}}$, $\frac{T_{t_3'}}{T_{t_5}}$, M_5, α

Outputs: $\frac{p_{t_7}}{p_{t_5}}$, M_7

Equations:

$$M_{3'}^2 = \frac{2}{\gamma-1}\left[\left(\frac{p_{t_3'}}{p_{t_5}}\right)^{\frac{\gamma-1}{\gamma}} \{1 + \frac{\gamma-1}{2} M_5^2\} - 1\right] \tag{5.15.17}$$

$$\frac{A_3'}{A_5} = \alpha\sqrt{\frac{T_{t_3}'}{T_{t_5}}}\frac{M_5}{M_3'}\left(\frac{p_{t_3}'}{p_{t_5}}\right)^{-\left(\frac{\gamma-1}{2\gamma}\right)} \tag{5.15.18}$$

$$f = \frac{(1+\alpha)\left(1+\alpha\dfrac{T_{t_3}'}{T_{t_5}}\right)}{\left[\dfrac{1}{\sqrt{f(M_5)}} + \dfrac{\alpha\sqrt{\dfrac{T_{t_3}'}{T_{t_5}}}}{\sqrt{f(M_3')}}\right]^2} \tag{5.15.19}$$

here $$f(M) \equiv \frac{M^2\left(1+\frac{\gamma-1}{2}M^2\right)}{(1+\gamma M^2)^2}$$

$$\Delta = \sqrt{1-2(\gamma+1)f} \tag{5.15.20}$$

$$M_7 = \left[1 - \frac{\Delta(1+\Delta)}{1-2\gamma f+\Delta}\right]^{1/2} \tag{5.15.21}$$

$$\frac{p_{t_7}}{p_{t_5}} = \frac{\left\{(1+\alpha)\left(1+\alpha\dfrac{T_{t_3}'}{T_{t_5}}\right)\right\}^{1/2}}{1+\dfrac{A_3'}{A_5}}\frac{M_5}{M_7}\left[\frac{1+\frac{\gamma-1}{2}M_7^2}{1+\frac{\gamma-1}{2}M_5^2}\right]^{\frac{\gamma+1}{2(\gamma-1)}} \tag{5.15.22}$$

5.15.4 SUMMARY OF THE EQUATIONS - IDEAL TURBOFAN WITH MIXED EXHAUST STREAMS

Inputs: $T_o(K)[°R]$, γ, $h(J/kg)[\frac{BTU}{lbm}]$,

$C_p(J/kgK)[\frac{BTU}{lbm°R}]$, τ_λ, π_c, π_c', M_o, α, M_5

Outputs: $\frac{F}{\dot m_1+\dot m_2}$ $(Ns/kg)[\frac{F}{g_o(\dot m_1+\dot m_2)}, \frac{lbf}{lbm/sec}]$,

$S(kg/Ns)[\frac{lbm\ fuel/hr}{lbf\ \ thrust}]$, $f\ \frac{kg\ fuel/sec}{kg\ primary\ air/sec}$

Equations:

$$R = \frac{\gamma-1}{\gamma}C_p \ m^2/s^2K \quad \left[R = \frac{\gamma-1}{\gamma}C_p(2.505)(10^4)\ \frac{ft^2}{sec^2°R}\right] \tag{5.15.23}$$

$$a_o = \sqrt{\gamma R T_o}\ m/s \quad [ft/sec] \tag{5.15.24}$$

$$\tau_r = 1 + \frac{\gamma-1}{2}M_o^2 \tag{5.15.25}$$

$$\tau_c = \pi_c^{\frac{\gamma-1}{\gamma}} \tag{5.15.26}$$

$$\tau_c' = \pi_c'^{\frac{\gamma-1}{\gamma}} \tag{5.15.27}$$

$$\tau_t = 1 - \frac{\tau_r}{\tau_\lambda}\left[(\tau_c-1)+\alpha(\tau_c'-1)\right] \tag{5.15.28}$$

$$\pi_t = \tau_t^{\frac{\gamma}{\gamma-1}} \tag{5.15.29}$$

$\left\{\frac{p_{t_9}}{p_{t_5}}\right.$ is then obtained from the equations for the ideal constant area mixer, Sec. (5.15.3). Note $p_{t_9} = p_{t_7}$ and $\frac{p_{t_3}'}{p_{t_5}} = \frac{\pi_c'}{\pi_c\pi_t}$, $\frac{T_{t_3}'}{T_{t_5}} = \left.\frac{\tau_r\tau_c'}{\tau_\lambda\tau_t}\right\}$

$$\frac{p_{t_9}}{p_{t_3}'} = \frac{p_{t_9}}{p_{t_5}}\frac{\pi_c\pi_t}{\pi_c'} \tag{5.15.30}$$

$$\frac{F}{\dot m_1+\dot m_2} =$$

$$a_o\left[\left\{\frac{2}{\gamma-1}\left(1-\frac{1}{\tau_r\tau_c'\left(\frac{p_{t_9}}{p_{t_3}'}\right)^{\frac{\gamma-1}{\gamma}}}\right)(\tau_\lambda\tau_t+\alpha\tau_r\tau_c')\right\}^{1/2} - M_o\right] \tag{5.15.31}$$

(To obtain British units of $\frac{lbf}{lbm/sec}$, a_o in meters/sec would be replaced by $\frac{a_o}{32.174}$ where a_o should be given in ft/sec .)

$$f = \frac{C_{p_o}T_o}{h}(\tau_\lambda - \tau_r\tau_c) \tag{5.15.32}$$

$$S = \frac{f}{(1+\alpha)\left(\frac{F}{\dot m_1+\dot m_2}\right)} \quad \left[S = \frac{3600f}{(1+\alpha)\left\{\frac{F}{g_o(\dot m_1+\dot m_2)}\right\}}\right] \tag{5.15.33}$$

5.15.5 EXAMPLE RESULTS - IDEAL CONSTANT AREA MIXER

In order to compare the performance of fully mixed streams and separate streams, we will consider the "gross thrust" capability of the two cases. By gross thrust we mean that thrust that would occur if all the momentum of the exit streams contributed entirely to thrust. We thus write

$$F_{UN} = \dot m_1 u_{e_1} + \dot m_2 u_{e_2} \quad \text{for unmixed streams} \tag{5.15.34}$$

$$F_{MIX} = (\dot m_1+\dot m_2)u_e \quad \text{for mixed streams} \tag{5.15.35}$$

Noting that for all cases (Sec. 2.14)

$$u_e^2 = \frac{2\gamma}{\gamma-1}RT_t\left[1-\left(\frac{p_e}{p_t}\right)^{\frac{\gamma-1}{\gamma}}\right] \tag{5.15.36}$$

it follows immediately that

$$\frac{F_{UN}}{F_{MIX}} = \frac{\left\{1-\left(\frac{p_e}{p_{t_5}}\right)^{\frac{\gamma-1}{\gamma}}\right\}^{1/2} + \alpha\sqrt{\frac{T_{t_3}'}{T_{t_5}}}\left\{1-\left(\frac{p_e}{p_{t_3}'}\right)^{\frac{\gamma-1}{\gamma}}\right\}^{1/2}}{\left\{(1+\alpha)\left(1+\alpha\frac{T_{t_3}'}{T_{t_5}}\right)\left[1-\left(\frac{p_e}{p_{t_7}}\right)^{\frac{\gamma-1}{\gamma}}\right]\right\}^{1/2}} \tag{5.15.37}$$

Equations (5.15.17 - 5.15.22) and (5.15.37) allow direct calculation and comparison of the ideal constant area mixer performance with non-mixed stream performance. As an example we consider a mixer with $\alpha = 2$, $M_5 = 0.5$ and $\gamma = 1.4$, and investigate the effects of varying the temperature ratio $\frac{T_{t_3}'}{T_{t_5}}$, stream pressure ratio $\frac{p_{t_3}'}{p_{t_5}}$ and exit pressure ratio $\frac{p_e}{p_{t_5}}$.

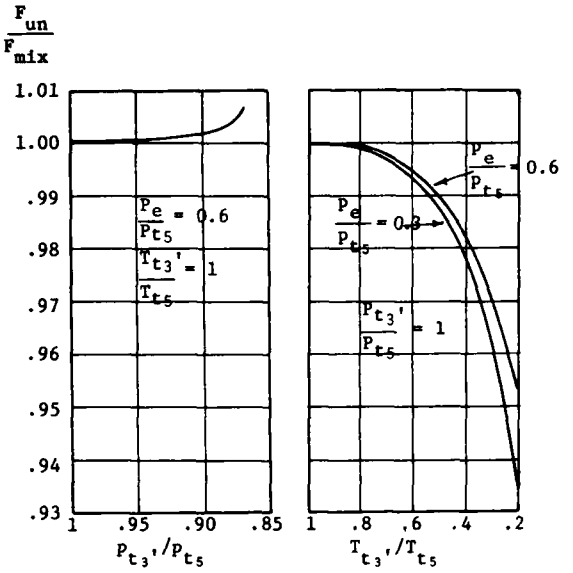

Figure 5.15.3 Effect of Variation in Stream Pressure Ratio, Ideal Constant Area Mixer

Figure 5.15.4 Effect of Variation in Stream Temperature Ratio and Exit Pressure Ratio, Ideal Constant Area Mixer

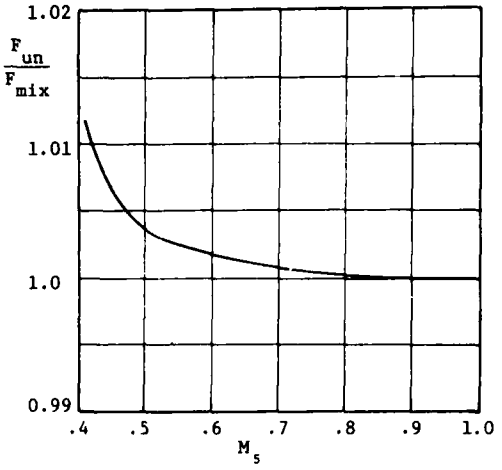

Figure 5.15.5 Effect of Variation in Inlet Mach Number, Ideal Constant Area Mixer

Several trends are evident in Figs. 5.15.3 and 5.15.4. Thus note that a mixing benefit occurs only when there is a difference in stagnation temperatures in the streams. This is because the stagnation pressure losses identified with mixing will cause a decrease in thrust unless one of the streams has a higher stagnation enthalpy, with consequent possible benefit of equalizing the enthalpies. It is to be noted also, that when the exit pressure is further reduced, the penalty identified with stagnation pressure loss in mixing is reduced, because the overall pressure ratio is so large.

It can be surmised then, that real mixers (including viscous losses) may show signs of performance gains when used with nozzles with large expansion ratios and in which substantial temperature differences between the two streams exist. It should be noted that "forced mixers" are being considered very much for transport aircraft, where the promise of performance benefits is not substantial. In such cases the prime motivation for the use of mixers arises from the hope of substantially reducing the jet noise.

As a final example we note the effect of varying the inlet Mach numbers of the mixing streams. We consider the case $\alpha = 2$, $\frac{T_{t_3'}}{T_{t_5}} = 1$, $\frac{P_{t_3'}}{P_{t_5}} = 0.9$, $\frac{P_e}{P_{t_5}} = 0.5$.

We note here that increasing the Mach number at entry to the mixer reduces the losses. This might at first appear anomalous because one might expect interactions at low Mach number to be less vigorous. It is apparent, however, that as the Mach number M_5 decreases, the pressure at the splitter plate increases, leading to a lower value of $M_{3'}$. Thus the relative velocity difference increases as M_5 decreases, leading to the greater mixing losses predicted by the ideal analysis. It should be noted that when skin friction losses are included, there will be an opposing effect because of the Mach number squared dependence of the skin friction losses. (Secs. 2.16 and 2.17) The design of a real mixer will involve the optimal choice of the design parameters including not only the effects just discussed, but including also consideration of the many installation effects.

5.15.6 EXAMPLE RESULTS - IDEAL TURBOFAN WITH MIXED EXHAUST STREAMS

To compare the performance of turbofans with and without mixing, we consider a turbofan with by-pass ratio, α , equal to two. Other conditions will be as those given for Fig. 5.14.7, that is:

$\gamma = 1.4$, $T_0 = 233.3°K[420°R]$, $h = 4.4194(10^7)$ J/kg [19,000 BTU/lbm], $C_p = 1004.9$ J/kgK$[0.24 \frac{BTU}{lbm°R}]$, $\pi_c = 20$, $\pi_c' = 2$, $\tau_\lambda = 6.5$, $M_0 = 2$.

The analysis utilized to obtain Fig. 5.14.7 yielded $\tau_r = 1.8$, $\tau_c = 2.3535$, $\tau_c' = 1.2190$, $\tau_t = 0.50387$, and $\pi_t = 0.090807$. These values utilized with the equations of (5.15.3) and (5.15.4) then give $\frac{P_{t_7}}{P_{t_5}} = 1.0564$. Finally Eqs. (5.15.30) - (5.15.33) yielded for the turbofan with mixed streams

$$S = 2.10(10^{-5})\text{kg/Ns}\ \left[.741\ \frac{\text{lbm/hr}}{\text{lbf}}\right]$$

$$\frac{F}{\dot{m}_1+\dot{m}_2} = 190.8\ \text{Ns/kg}\ \left[\frac{F}{g_o(\dot{m}_1+\dot{m}_2)} = 19.46\ \frac{\text{lbf}}{\text{lbm/sec}}\right]$$

These values are to be compared with the following values for the unmixed case

$$S = 2.14(10^{-5})\text{kg/Ns}\ \left[.754\ \frac{\text{lbm/hr}}{\text{lbf}}\right]$$

$$\frac{F}{\dot{m}_1+\dot{m}_2} = 187.5\ \text{Ns/kg}\ \left[\frac{F}{g_o(\dot{m}_1+\dot{m}_2)} = 19.12\ \frac{\text{lbf}}{\text{lbm/sec}}\right]$$

Thus the ideal mixer, in this case, provides a thrust and specific fuel consumption improvement of almost two percent.

5.16 THE IDEAL TURBOFAN WITH AFTERBURNING

A cycle that somewhat combines the high thrust per frontal area of a turbojet at high Mach number while providing respectable specific fuel consumption for subsonic cruise conditions is the turbofan with duct burning. The turbofan would utilize duct burning (burning in the secondary stream) for supersonic cruise, but would cruise subsonically without duct burning. In many cycles, the fan and compressor require so much power extraction from the primary stream that the turbine outlet pressure is greatly reduced. The resulting low primary nozzle pressure ratio renders primary stream afterburning unattractive. In the following analysis, however, the possibility of primary stream afterburning as well as secondary stream afterburning will be included.

5.16.1 CYCLE ANALYSIS OF THE IDEAL TURBOFAN WITH AFTERBURNING

It is again assumed that all component efficiencies are perfect, that the gas is calorically perfect, that the fuel to air ratio in all combustors is much less than unity and that the exit static pressures of both primary and secondary streams are equal to the ambient pressure. The nomenclature and notation are as in Fig. 5.1.1 and Sec. (5.1).

The expression for the total thrust remains as given by Eq. (5.14.1), thus:

$$\frac{F}{\dot{m}_1+\dot{m}_2} = \frac{a_o M_o}{1+\alpha}\left[\left(\frac{u_9}{u_o}-1\right)+\alpha\left(\frac{u_{9'}}{u_o}-1\right)\right] \qquad (5.16.1)$$

Secondary Stream

We again have

$$\left(\frac{u_{9'}}{u_o}\right) = \frac{T_{9'}}{T_o}\left(\frac{M_{9'}^2}{M_o}\right) \qquad (5.16.2)$$

Now write

$$T_{t_{9'}} = T_{9'}\left(1+\frac{\gamma-1}{2}M_{9'}^2\right) = T_o\,\tau_{\lambda AB'} \qquad (5.16.3)$$

$$p_{t_{9'}} = p_{9'}\left(1+\frac{\gamma-1}{2}M_{9'}^2\right)^{\frac{\gamma}{\gamma-1}} = p_o\pi_r\pi_c' \qquad (5.16.4)$$

With Eqs. (5.1.1), (5.2.2), and (5.16.4)

$$1+\frac{\gamma-1}{2}M_{9'}^2 = \tau_r\tau_c' \qquad (5.16.5)$$

Combining Eqs. (5.16.3) and (5.16.5) gives

$$\frac{T_{9'}}{T} = \frac{\tau_{\lambda AB'}}{\tau_r\tau_c'} \qquad (5.16.6)$$

so that with Eqs. (5.16.2), (5.16.5) and (5.16.6) we obtain

$$M_o\left(\frac{u_{9'}}{u_o}-1\right) = \left\{\frac{2}{\gamma-1}\frac{\tau_{\lambda AB'}}{\tau_r\tau_c'}(\tau_r\tau_c'-1)\right\}^{1/2}-M_o \qquad (5.16.7)$$

Primary Stream

The relationships for temperatures and pressures, here, are exactly as previously obtained for the turbojet with afterburning (Sec. 5.11.1), so we may write

$$M_o\left(\frac{u_9}{u_o}-1\right) = \left\{\frac{2}{\gamma-1}\frac{\tau_{\lambda AB}}{\tau_r\tau_c\tau_t}(\tau_r\tau_c\tau_t-1)\right\}^{1/2}-M_o \qquad (5.16.8)$$

Power Balance

The power balance between fan, compressor and turbine remains as for the turbofan without afterburning, (Eq. 5.14.9) so we may write

$$\tau_t = 1-\frac{\tau_r}{\tau_\lambda}\left[(\tau_c-1)+\alpha(\tau_c'-1)\right] \qquad (5.16.9)$$

Specific Fuel Consumption

The specific fuel consumption could be obtained by writing an enthalpy balance for each burner separately and then summing the separate fuel consumptions. It is more direct, however, to write an enthalpy balance across the entire system and to equate the energy addition in the burners to the overall enthalpy change. Thus

$$(\dot{m}_f+\dot{m}_{fAB}+\dot{m}_{fAB'})h = \dot{m}_1 C_p T_{t_9}+\dot{m}_2 C_p T_{t_{9'}}-(\dot{m}_1+\dot{m}_2)C_p T_{t_2}$$

or

$$f_{TOT} \equiv \frac{\dot{m}_f+\dot{m}_{fAB}+\dot{m}_{fAB'}}{\dot{m}} = \frac{C_p T_o}{h}\left[\tau_{\lambda AB}+\alpha\tau_{\lambda AB'}-(1+\alpha)\tau_r\right] \qquad (5.16.10)$$

The specific fuel consumption then follows from

$$S = \frac{\dot{m}_f+\dot{m}_{fAB}+\dot{m}_{fAB'}}{F} = \frac{f_{TOT}}{(1+\alpha)\left(\frac{F}{\dot{m}_1+\dot{m}_2}\right)} \qquad 5.16.11)$$

These equations can then be summarized as in Sec. (5.16.2). It can be noted here, however, that in fact this analysis contains most of the preceding analyses of this chapter as special cases. Thus note that if a duct burning turbofan with no primary stream burning is to be considered, $\tau_{\lambda AB}$ need only be replaced by its minimum value,

$$(\tau_{\lambda AB})_{min} = \tau_\lambda\tau_t \qquad (5.16.12)$$

If no duct burning is present, $\tau_{\lambda AB'}$ must be replaced by its minimum value,

$$(\tau_{\lambda AB'})_{min} = \tau_r \tau_c' \qquad (5.16.13)$$

If a turbojet is to be considered (with or without afterburning) the by-pass ratio, α, must be put equal to zero, and finally if a ramjet is to be considered, α must be put equal to zero and also π_c (or τ_c) must be put equal to unity.

5.16.2 SUMMARY OF THE EQUATIONS, IDEAL TURBOFAN WITH AFTERBURNING

Inputs: T_o(K)[°R], γ, h(J/kg)[$\frac{BTU}{lbm}$],

C_p(J/kgK)[$\frac{BTU}{lbm°R}$], τ_λ, $\tau_{\lambda AB}$, $\tau_{\lambda AB'}$,

π_c, π_c', M_o, α

Outputs: $\frac{F}{\dot{m}_1+\dot{m}_2}$ (Ns/kg) [$\frac{F}{g_o(\dot{m}_1+\dot{m}_2)}$, $\frac{lbf}{lbm/sec}$],

S(kg/NS)[$\frac{lbm\ fuel/hr}{lbf\ \ thrust}$],

f_{TOT} $\frac{kg\ fuel/sec}{kg\ primary\ air/sec}$

Equations:

The first six equations are identical to Eqs. (5.14.12-5.14.17), then:

$$\frac{F}{\dot{m}_1+\dot{m}_2} = \frac{a_o}{1+\alpha}\left[\left\{\frac{2}{\gamma-1}\frac{\tau_{\lambda AB}}{\tau_r\tau_c\tau_t}(\tau_r\tau_c\tau_t-1)\right\}^{1/2}-M_o + \alpha\left[\left\{\frac{2}{\gamma-1}\frac{\tau_{\lambda AB'}}{\tau_r\tau_c'}(\tau_r\tau_c'-1)\right\}^{1/2}-M_o\right]\right] \qquad (5.16.14)$$

(To obtain British units of $\frac{lbf}{lbm/sec}$, a_o in meters per second would be replaced by $\frac{a_o}{32.174}$ where a_o should be given in ft/sec.)

$$f_{TOT} = \frac{C_p T_o}{h}\left[\tau_{\lambda AB}+\alpha\tau_{\lambda AB'}-(1+\alpha)\tau_r\right] \qquad (5.16.15)$$

$$S = \frac{f_{TOT}}{(1+\alpha)\left(\frac{F}{\dot{m}_1+\dot{m}_2}\right)} \qquad (5.16.16)$$

NOTE: In these equations the minimum values of $\tau_{\lambda AB}$ and $\tau_{\lambda AB'}$ to be considered are

$$(\tau_{\lambda AB})_{min} = \tau_\lambda \tau_t \qquad (5.16.17)$$

$$(\tau_{\lambda AB'})_{min} = \tau_r \tau_c' \qquad (5.15.18)$$

If either of these minimum values is used, the calculation corresponds to the case where burning is not present in the respective afterburner.

5.16.3 EXAMPLE RESULTS - IDEAL TURBOFAN WITH AFTERBURNING

As an example of the effect of afterburning, we consider the family of turbofan engines considered in Sec. (5.14.5) that gave the results of Fig. 5.14.7. Here, we again consider the addition of burning in the secondary stream such that $\tau_{\lambda AB'} = 7.5$. Conditions are hence $\gamma = 1.4$, $T_o = 233.3°K[420°R]$, $h = 4.4194(10^7)J/kg[19{,}000BTU/lbm]$, $C_p = 1004.9J/kgK[0.24\ BTU/lbm°R]$, $\pi_c = 20$, $\tau_\lambda = 6.5$, $M_o = 2$ and $\pi_c' = 2$. The results are indicated in Fig. 5.16.1.

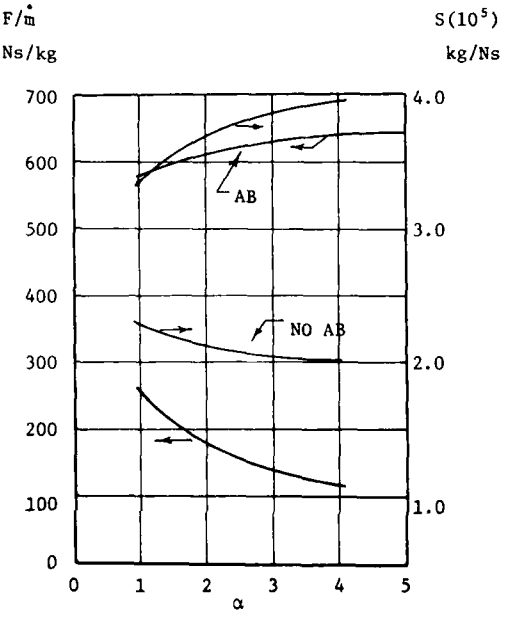

Figure 5.16.1 Specific Thrust and Specific Fuel Consumption Versus By-Pass Ratio, Duct Burning Turbofan

The figure illustrates the very substantial increases in specific thrust that can be obtained by the use of duct burning. The results suggest, also, that if high thrust levels are to be attained for given flight conditions, whereas efficient cruising is desired for other (lower thrust) flight conditions, the duct burning turbofan shows promise of affecting a reasonable compromise.

Chapter 6

COMPONENT PERFORMANCE

Gordon C. Oates

University of Washington

TABLE OF CONTENTS

CHAPTER 6 COMPONENT PERFORMANCE

		Page
6.0	Introduction	6-1
6.1	The Thrust Equation	6-1
6.1.1	Interpretation of the Terms Appearing in the Thrust Equation	6-2
6.1.2	One-Dimensional Calculation of the Additive Drag	6-3
6.1.3	Some Realities of the Determination of Inlet Drag	6-4
6.2	The Inlet	6-5
6.3	The Compressor	6-5
6.3.1	The Compressor Efficiency, η_c	6-6
6.3.2	The Compressor Polytropic Efficiency, e_c	6-6
6.3.3	The Compressor Stage Efficiency	6-6
6.3.4	Relationship Between the Compressor, Stage and Polytropic Efficiencies.	6-7
6.4	The Burner	6-8
6.4.1	The Behavior of the Thermodynamic Properties Across the Combustor	6-8
6.4.2	One-Dimensional Estimation of the Burner Stagnation Pressure Ratio	6-8
6.5	The Turbine	6-9
6.5.1	The Turbine Efficiency, η_t	6-9
6.5.2	The Turbine Polytropic Efficiency, e_t	6-10
6.5.3	The Turbine Stage Efficiency	6-10
6.6	The Nozzle	6-10
6.7	Summary of Component Figures of Merit.	6-11
6.8.1	References	6-11

LIST OF FIGURES

		Page
Figure 6.1.1	General Control Volume	6-1
Figure 6.1.2	Pressure and Viscous Stresses on Engine	6-1
Figure 6.1.3	Control Volume for Approaching Flow	6-2
Figure 6.1.4	External Fluid Control Volume	6-2
Figure 6.1.5	Flow into Inlets	6-3
Figure 6.1.6	Additive Drag Coefficient Versus Flight Mach Number	6-4
Figure 6.1.7	Instrumented Cowl and Stagnation Streamline	6-4
Figure 6.1.8	Wind Tunnel Test of Inlet Model.	6-5
Figure 6.2.1	Internal Losses in an Inlet	6-5
Figure 6.3.1	Compressor Design Efficiency Versus Pressure Ratio	6-6
Figure 6.4.1	Constant Area Combustion Chamber	6-8
Figure 6.4.2	Combustor Stagnation Pressure Ratio and Exit Mach Number	6-9
Figure 6.5.1	Turbine Design Efficiency Versus Pressure Ratio	6-10

CHAPTER 6

LIST OF SYMBOLS

The symbols are listed in alphabetical order, first in the English alphabet, then in the Greek alphabet. Subscripts and superscripts are then given. The equation, figure or section in which the symbols are first introduced is indicated in parentheses. Often the symbol will be defined in the text just preceding or just following the equation or figure.

Where appropriate, the location of the introduction of the symbols is referred to in previous chapters.

A - Cross-sectional area (Eq. 6.1.3)

C - Specific heat (Sect. 2.6)

$d\bar{s}$ - Area element (Fig. 6.1.1)

dv - Volume element (Fig. 6.1.1)

e - Polytropic efficiency (Eq. 6.3.2)

F - Force (Eq. 6.1.1)

H - Force defined in Fig. 6.1.8

h - Enthalpy (Sect. 2.6)

- Heating value (Eq. 6.4.1)

M - Mach number (Eq. 6.1.19)

- Molecular weight (Eq. 6.4.3)

$\dot{m}$ - Mass flow rate (Eq. 6.1.5)

N - Number of stages (Eq. 6.3.7)

p - Pressure (Eq. 6.1.1)

R - Gas constant (Eq. 6.4.3)

s - Entropy (Sect. 2.7)

T - Temperature (Eq. 6.1.19)

t - Time (Eq. 6.1.1)

u - x-component of velocity (Eq. 6.1.4)

$\bar{u}$ - Vector velocity (Eq. 6.1.1)

V - Velocity (Fig. 6.1.8)

γ - Ratio of specific heats (Sect. 2.6)

Δ - Function (Eq. 6.4.9)

Δq - Heat interaction (Fig. 6.4.1)

Δw - Work interaction (Table 6.7.1)

η - Efficiency (Eq. 6.3.1)

Π - Product (Eq. 6.3.9)

τ - Ratio of pressures (Sect. 5.1)

ρ - Density (Eq. 6.1.1)

τ - Ratio of temperatures (Sect. 5.1)

χ - Function (Eq. 6.4.8)

Subscripts

A - Uninstalled (Eq. 6.1.8)

D - Drag (Eq. 6.4.5)

e - Exit (Fig. 6.1.2)

f - Fuel (Eq. 6.4.1)

i - Inlet (Fig. 6.1.2)

- Also ideal (Sect. 6.3.1)

j - Stage number (Eq. 6.3.7)

m - Mechanical (Table 6.7.1)

p - Installed (Eqs. 6.1.3, 6.1.11)

- constant pressure (Sect. 2.6)

s - Stage (Eq. 6.3.11)

t - Stagnation quantity (Sect. 2.16)

u - Universal (Eq. 6.4.3)

v - Viscous (Eq. 6.1.1)

o - Far upstream (or ambient) (Eq. 6.1.3)

∞ - Far downstream (Fig. 6.1.4)

add - Additive (Eq. 6.1.9)

ext - External (Fig. 6.1.2)

int - Internal (Fig. 6.1.2)

CB - Centerbody (Fig. 6.1.2)

DA - Additive drag (Eq. 6.1.18)

Special symbols defined in Fig. 6.1.8

∞, c, L, n, s

Subscripts previously defined in Sect. 5.1

b, c, d, n, r, t

0-9 Station numbers (Fig. 5.1.1)

CHAPTER SIX
COMPONENT PERFORMANCE

In this chapter the behavior of the engine components including the non-ideal effects will be described. The performance of the various components will be described in terms of "figures of merit", which will allow cycle analyses including losses to be efficiently carried out. It should be noted, however, that both the accurate quantitative estimation of such figures of merit, and the design of the components to reduce the losses, are very demanding processes and absorb much of the industry effort. Prior to considering each individual component, we first consider the expression for the overall thrust of the engine when losses are present. It will be found that both internal and external losses will be present, and an optimal design would be such as to minimize the combination of all losses.

6.1 THE THRUST EQUATION

General Momentum Equation

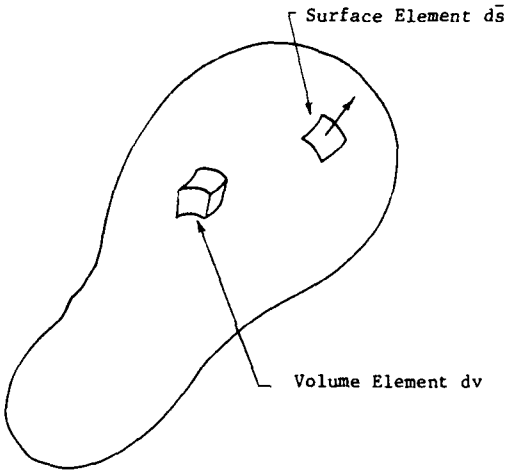

Figure 6.1.1 General Control Volume

The momentum equation for a control volume may be written in the form:

Force on volume of fluid =

Rate of production of momentum

or

Pressure force + viscous force =

Rate of accumulation of momentum

+ Rate of convection of momentum through boundaries

Each of these terms may be represented by an appropriate area or volume integral, but for simplicity of presentation we will write the viscous force simply as F_v. The above word equation can then be written:

$$-\iint p d\bar{s} + F_v = \frac{\partial}{\partial t}\iiint \rho \bar{u} dv + \iint \rho \bar{u}\bar{u}\cdot d\bar{s} \qquad (6.1.1)$$

It should be noted here that the vector area element, $d\bar{s}$, is defined to be positive when directed outwardly. Thus, the pressure force from the surface onto the fluid must have the negative sign identified with it. We will be considering the engine operating in steady-state conditions (or "quasi-steady-state"), so the integral denoting the volumetric accumulation of momentum with time will be zero.

The thrust equation may then be written

$$F_v - \iint p d\bar{s} = \iint \rho \bar{u}\bar{u}\cdot d\bar{s} \qquad (6.1.2)$$

Application to Engine

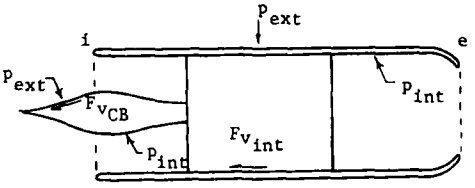

Figure 6.1.2 Pressure and Viscous Stresses on Engine

It has been agreed to define the thrust of the engine as the net force resulting from all the pressure and viscous stresses, less the external viscous drag. This means that the external viscous forces will be considered to be drag and will be included in the airplane drag as far as "accounting" goes.

We desire the axial component of force only, so define dA as the axial projection of an area element. The thrust, F_p, is defined as being positive in the negative x-direction, so that applying Eq. (6.1.2), and referencing Fig. 6.1.2 we obtain for F_p

$$F_p = \int_{i_{int}}^{e} (p_{int}-p_o)dA - F_{v_{int}} - \int_{ext\ CB} (p_{ext}-p_o)dA - F_{v\ CB}$$

$$- \int_{i_{ext}}^{e} (p_{ext}-p_o)dA \qquad (6.1.3)$$

here int refers to surfaces wetted by fluid passing through the engine

ext refers to surfaces wetted by fluid passing outside the engine

ext CB refers to that portion of the centerbody protruding forward of the inlet plane

It is clear that direct evaluation of the internal viscous and pressure forces would be hopeless, so we relate the internal forces to the changes in fluid properties occurring from inlet to exit of the engine. To do this we consider the effects of the internal forces acting inward on the fluid. The forces acting on the fluid between inlet and exit will now include the pressure and viscous forces acting on the interior engine parts. Thus, again applying Eq. (6.1.2) we obtain

$$-F_{v_{int}} + \int_{i_{int}}^{e} (p_{int}-p_o)dA + \int_i (p_i-p_o)dA - \int_e (p_e-p_o)dA = -\int_i \rho u^2 dA + \int_e \rho u^2 dA \qquad (6.1.4)$$

We note here that the first two terms are identical to the same pair of terms appearing in Eq. (6.1.3). The effect of the minus sign that would appear because of the difference in direction of the outwardly directed area element is cancelled because F_p was defined to be positive in the negative x-direction. For simplicity in writing the equations we assume conditions are one-dimensional at entrance and exit to obtain, by combining Eqs. (6.1.3) and (6.1.4)

$$F_p = \dot{m}_e u_e - \dot{m}_i u_i + (p_e-p_o)A_e - (p_i-p_o)A_i - \int_{ext\,CB} (p_{ext}-p_o)dA - F_{v_{CB}} - \int_{i_{ext}}^{e} (p_{ext}-p_o)dA \qquad (6.1.5)$$

This form is not particularly useful, because not only is it difficult to determine u_i without quite detailed engine information, but u_i and hence the pressure integrals over the centerbody and exterior change with a change in design of the inlet. It would be better to relate F_p to the flow conditions far upstream, and to do this we consider the control volume shown in Fig. 6.1.3.

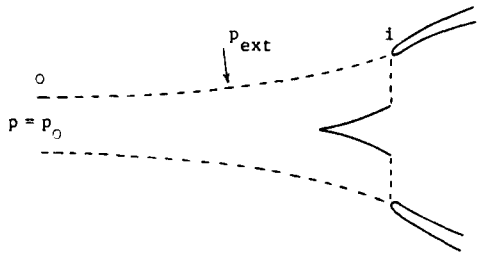

Figure 6.1.3 Control Volume for Approaching Flow

Again assuming one-dimensional conditions at entrance (and far upstream), we find with application of Eq. (6.1.2)

$$\dot{m}_i u_i + (p_i-p_o)A_i + \int_{ext\,CB} (p_{ext}-p_o)dA + F_{v_{CB}} = +\dot{m}_o u_o + \int_o^i (p_{ext}-p_o)dA \qquad (6.1.6)$$

and hence with Eq. (6.1.5)

$$F_p = \dot{m}_e u_e - \dot{m}_o u_o + (p_e-p_o)A_e - \int_o^i (p_{ext}-p_o)dA - \int_{i_{ext}}^{e} (p_{ext}-p_o)dA \qquad (6.1.7)$$

We now write

$$F_A = \dot{m}_e u_e - \dot{m}_o u_o + (p_e-p_o)A_e \qquad (6.1.8)$$

$$D_{add} = \int_o^i (p_{ext}-p_o)dA \equiv \text{additive drag} \qquad (6.1.9)$$

$$D_{ext} = \int_{i_{ext}}^{e} (p_{ext}-p_o)dA \equiv \text{external drag} \qquad (6.1.10)$$

then

$$F_p = F_A - D_{add} - D_{ext} \qquad (6.1.11)$$

It is usual to term F_A the uninstalled thrust and F_p the installed thrust.

6.1.1 INTERPRETATION OF THE TERMS APPEARING IN THE THRUST EQUATION

Equations (6.1.8-6.1.11) are in a suitable form for design purposes, but they are at first difficult to interpret. Thus, for example, it at first seems peculiar that a pressure integral over surfaces external to the engine (0-i) could have anything to do with the forces on the engine. The additive drag term and external drag term are interdependent, however, and we can learn something about this interdependence by considering a "perfect engine", that is an engine with no external viscous drag or form drag.

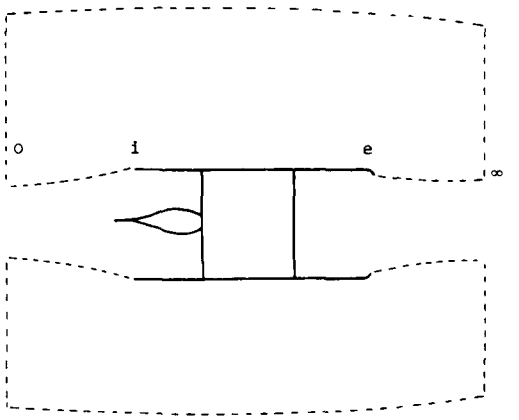

Figure 6.1.4 External Fluid Control Volume

We now consider the momentum equation for all the fluid flowing external to the engine. Because the flow is perfect (no shocks, no boundary layers) the fluid conditions externally are identical at 0 and ∞. The pressure is p_o around the external contour, and we choose the contour to be a streamline so that no momentum is convected through the

perimeter. The momentum fluxes through the ends of the control volume are equal because the velocities are equal, so that the momentum equation reduces to the simple statement that the sum of the pressure integrals over all the internal surfaces must be zero. Thus

$$D_{add} + D_{ext} + \int_e^\infty (p_{ext}-p_o)dA = 0 \quad \text{(perfect flow)} \tag{6.1.12}$$

It can be seen then that for a correctly expanded nozzle ($p_e = p_o$, jet parallel to the main stream) and for perfect external flow

$$D_{ext} = - D_{add} \tag{6.1.13}$$

and $$(F_p)_{perfect} = F_A \tag{6.1.14}$$

It is evident from Eq. (6.1.13) that when evaluating the drag terms for a real inlet the additive drag and external drag must be evaluated most carefully, because the net drag can be the difference between two quite large terms. (Note, of course, that in such a case the external "drag" would be negative.)

It is common practice to break the external drag into two components, D_w, the drag associated with the "front end" of the engine, and D_b, the drag associated with the back end. This is usually a reasonable approach because often lip separation dominates near the inlet and boat-tail drag near the exit. Assuming this division is meaningful we can interpret the terms by considering the engine to be very long and parallel in the middle. In this case, perfect flow would give us p_o etc., at the middle, and the same argument as led to Eq. (6.1.12) would lead to

$$D_{add} + D_w = 0 \quad \text{(perfect flow)} \tag{6.1.15}$$

and

$$D_b + \int_e^\infty (p_{ext}-p_o)dA = 0 \quad \text{(perfect flow)} \tag{6.1.16}$$

The negative forebody drag required to cancel the additive drag arises from the suction near the leading edge of the inlet. This is why supersonic inlets, with their sharp leading edges, have a large "additive drag penalty" when operated at mass flows other than their design mass flows because their sharp leading edge prevents the suction from occurring (Fig. 6.1.5). Note that the additive drag penalty for the supersonic inlet is much more severe than that for the subsonic inlet, even though the additive drags (in the figure) are identical.

Similarly, separation from the trailing body of the engine prevents the diffusion that would lead to large "forward thrusts", giving boat-tail drag.

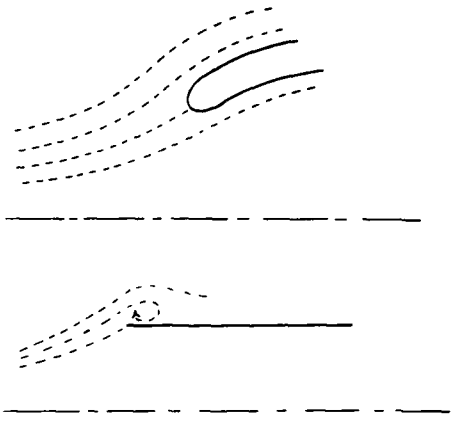

Figure 6.1.5 Flow into Inlets

6.1.2 ONE-DIMENSIONAL CALCULATION OF THE ADDITIVE DRAG

For simplicity, we consider an inlet without external centerbody, so obtain from Eqs. (6.1.6) and (6.1.9),

$$D_{add} = \dot{m}_i u_i - \dot{m}_o u_o + (p_i - p_o)A_i \tag{6.1.17}$$

An additive drag coefficient C_{DA} can be defined in terms of the inlet area A_i by:

$$C_{DA} = \frac{D_{add}}{1/2\ \rho_o u_o^2 A_i} \tag{6.1.18}$$

Noting that $\dot{m}_i = \dot{m}_o = \rho_o u_o A_o$ we obtain from Eqs. (6.1.17-6.1.18)

$$C_{DA} = 2\frac{A_o}{A_i}\left[\frac{u_i}{u_o} - 1 + \frac{(p_i-p_o)A_i}{\dot{m}_i u_o}\right]$$

$$= 2\frac{A_o}{A_i}\left[\frac{u_i}{u_o} - 1 + \frac{u_o}{u_i}\frac{\gamma p_o/\rho_o}{u_o^2}\frac{1}{\gamma}\frac{\rho_o}{\rho_i}\frac{p_i}{p_o}\left(1 - \frac{p_o}{p_i}\right)\right]$$

or

$$C_{DA} = 2\frac{A_o}{A_i}\left[\frac{u_i}{u_o} - 1 + \frac{1}{u_i/u_o}\frac{1}{\gamma M_o^2}\frac{T_i}{T_o}\left(1 - \frac{p_o}{p_i}\right)\right] \tag{6.1.19}$$

The flow from far upstream to the inlet may be considered to be isentropic, so that the separate terms of Eq. (6.1.19) may be evaluated as follows:

From Eq. (2.18.1)

$$\frac{A_o}{A_i} = \frac{M_i}{M_o}\left[\frac{1 + \frac{\gamma-1}{2}M_o^2}{1 + \frac{\gamma-1}{2}M_i^2}\right]^{\frac{\gamma+1}{2(\gamma-1)}} \tag{6.1.20}$$

$$\frac{T_i}{T_o} = \frac{1 + \frac{\gamma-1}{2}M_o^2}{1 + \frac{\gamma-1}{2}M_i^2} \tag{6.1.21}$$

$$\frac{u_i}{u_o} = \left\{\frac{T_i}{T_o}\frac{M_i^2}{M_o^2}\right\}^{1/2} = \left\{\frac{1+\frac{\gamma-1}{2}M_o^2}{1+\frac{\gamma-1}{2}M_i^2}\right\}^{1/2}\frac{M_i}{M_o} \qquad (6.1.22)$$

$$\frac{p_o}{p_i} = \left\{\frac{1+\frac{\gamma-1}{2}M_i^2}{1+\frac{\gamma-1}{2}M_o^2}\right\}^{\frac{\gamma}{\gamma-1}} \qquad (6.1.23)$$

Thus, when the "design Mach number" (that Mach number existing at the inlet plane for the given engine setting) is known, the drag coefficient can be obtained as a function of the flight Mach number. We may note that when the flight Mach number is equal to the design Mach number the inlet just swallows its projected image. As a result no curvature exists in the entering streamtube and the additive drag is zero. Figure 6.1.6 shows the behavior of the additive drag coefficient with flight Mach number for an inlet with design Mach number, M_i, equal to 0.6 (γ = 1.4).

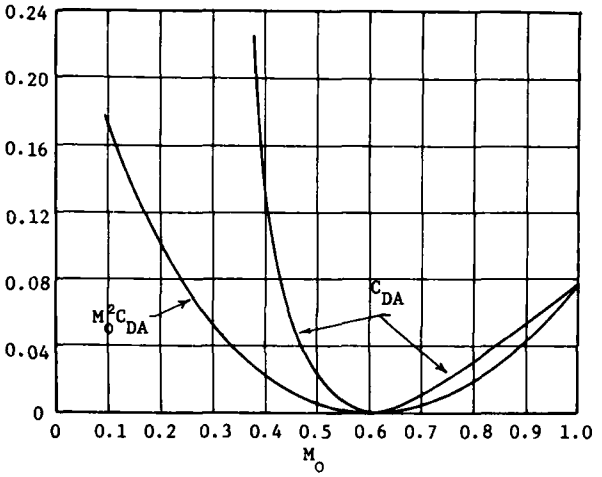

Figure 6.1.6 Additive Drag Coefficient Versus Flight Mach Number

It should be noted here that the very large drag coefficients occurring for low Mach numbers do not, in fact, correspond to extremely large drag forces, because the reference dynamic pressure, $1/2\ \rho_o u_o^2$, is itself rapidly decreasing as the flight Mach number decreases. For a given reference pressure p_o, the drag force will be proportional to $M_o^2 C_{DA}$, and as can be seen the drag force does not increase as severely at small Mach numbers as does the drag coefficient. The results do serve to emphasize, however, that the additive drag itself may be quite large, whereas the net drag of the inlet could be very small.

6.1.3 SOME REALITIES OF THE DETERMINATION OF INLET DRAG

It has been emphasized in the preceding section that inlet drag must, in some cases, be determined as the difference between two large quantities, the additive drag and the external pressure drag. If various cowl shapes are to be compared for their drag characteristics, we must in some way obtain the (net) inlet drag accurately. One method of determining inlet drag is to heavily instrument a given cowl with static pressure taps, and then to integrate the axial force implied by such measurements.

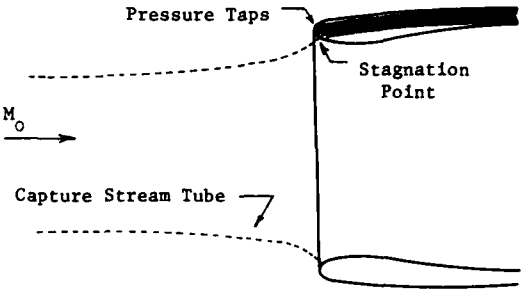

Figure 6.1.7 Instrumented Cowl and Stagnation Streamline

The internal flow must also be simulated accurately in such a technique in order to give the proper additive drag and correct boat-tail-jet interactions. Even assuming correct internal flow simulation the location of the contact point of the stagnation streamline must be very accurately determined, and the upstream shape of the streamline and pressure at each location accurately estimated through the use of a compressible flow calculation (Ref. 6.1).

It is evident that the one-dimensional approximation for the additive drag will have serious shortcomings in accuracy for several reasons. Firstly, as is evident from Fig. 6.1.7, the projected area of the stagnation streamtube increases abruptly in the immediate neighborhood of the cowl. It is in this regime that the one-dimensional estimate of the static pressure is poorest, because the local static pressure is approaching stagnation pressure whereas the one-dimensional estimate of the static pressure will be that corresponding to the Mach number for one-dimensional flow through the area A_i. The location of the area, A_i, itself is not precisely determined, because in the one-dimensional approximation it is consistent to assume A_i is the minimum area of the inlet, whereas in a two-dimensional calculation A_i would be that area within the locus of stagnation points, and would change with operating condition.

Several methods have been devised for simulating the internal flow behavior in order to determine nacelle drag. Reference (6.2) describes a method suitable for directly measuring the net nacelle drag of the front portion of the cowl. (The lip)

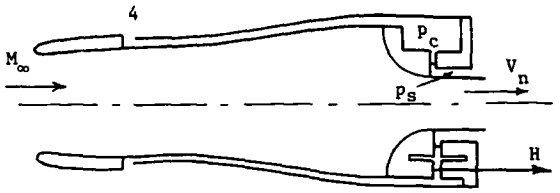

Figure 6.1.8 Wind Tunnel Test of Inlet Model

The authors show by utilizing a force balance similar in nature to those considered in Secs. (6.1) and (6.1.1) that the lip drag D_L' is given in terms of the directly measureable quantities indicated in Fig. 6.1.8 by

$$D_L' = m_\infty(v_n-v_\infty)+A_n(p_n-p_s)+A_4(p_c-p_\infty)+A_s'(p_s-p_c)-H \qquad (6.1.24)$$

This method has the advantage of simple data reduction but has several disadvantages. Each separate measurement must be made with extreme accuracy because, once again, the desired term, the lip drag, can be very small compared to the individual measured terms. The method also includes the lip skin drag, so strictly speaking does not directly obtain the desired additive drag plus profile drag, only. Finally, the lack of jet simulation precludes the measurement of the complete cowl drag.

A device that has been utilized extensively to determine cowl drag is the "Powered Nacelle" (Ref. 6.3). This device utilizes an air driven turbine to power a fan, and as a result succeeds in simulating the internal flow quite well. Data reduction usually is carried out by utilizing many surface static pressure taps and computing the additive drag from a two-dimensional computer program. Sometimes the changes in drag for different inlets have been measured by utilizing a thrust balance. In such cases great care must be taken to exactly match the powered fan settings from test to test in order to duplicate the thrust contributions. Use of the thrust balance also includes the external skin friction drag which can confuse measurement of the profile drag.

In common with all subscale models, the powered nacelle has problems with correct Reynolds number simulation. The problem is particularly aggravated with inlet testing, because the only phenomenae that lead to net drag are the presence of shock waves or regions of separation. (Remember the skin drag is excluded.) It is easily possible, particularly for a relatively sharp edged inlet, for a small scale model to have a laminar separation bubble occur in the regime of rapid recompression following the acceleration around the lip, whereas in the full scale inlet the boundary layer could be turbulent with no separation present. Similarly the aft end separation characteristics could change markedly from subscale to fullscale testing.

It is hoped that the comments of this section will sound a warning that when the great accuracy required in practice is to be obtained, much attention to detail and subtlety of thought is required!

6.2 THE INLET

We now concern ourselves with the internal behavior of the engine, and consider first the inlet.

Figure 6.2.1 Internal Losses in an Inlet

Inlet losses arise because of the presence of wall friction, shock waves and regimes of separated flow. All of these loss mechanisms result in a reduction in stagnation pressure so that

$$\pi_d < 1 \qquad (6.2.1)$$

Virtually all inlets are adiabatic to a very high degree of approximation, so we have

$$\tau_d = 1 \qquad (6.2.2)$$

It is important to note that a major problem with inlets centers about the lack of one-dimensionality of the flow. The shock system and wall friction lead to areas of reduced stagnation pressure at exit from the diffuser. The static pressure is very nearly constant across the diffuser exit, so a reduced stagnation pressure corresponds to a reduced axial velocity. Such a reduced velocity will cause the rotor blade to encounter a sudden increase in angle of attack with consequent possibility of blade stall. In addition, the shock system is unstable and produces time varying fluctuations in stagnation pressure. These non one-dimensional effects are thoroughly discussed in Chapter 13.

6.3 THE COMPRESSOR

Compressors are, to a high degree of approximation, adiabatic, so that the work interaction across the compressor per mass is just equal to the change in stagnation enthalpy per mass. We will assume that the gas is calorically perfect across the compressor, and will consequently be easily able to relate the temperature change to the desired pressure change. There are in fact three related definitions of efficiency of use in describing compressor behavior, each of which is described in the following sections.

6.3.1 THE COMPRESSOR EFFICIENCY, η_c

The compressor efficiency is defined by

$$\eta_c = \frac{\text{ideal work interaction for a given pressure ratio}}{\text{actual work interaction for a given pressure ratio}} = \frac{C_p(T_{t_3 i} - T_{t_2})}{C_p(T_{t_3} - T_{t_2})} = \frac{\left(\frac{T_{t_3 i}}{T_{t_2}} - 1\right)}{\left(\frac{T_{t_3}}{T_{t_2}} - 1\right)} \equiv \frac{\tau_{ci} - 1}{\tau_c - 1}$$

The ideal process is an isentropic process so that from Eq. (2.14.10)

$$\frac{T_{t_3 i}}{T_{t_2}} = \left(\frac{p_{t_3}}{p_{t_2}}\right)^{\frac{\gamma_c - 1}{\gamma_c}} \equiv \pi_c^{\frac{\gamma_c - 1}{\gamma_c}}$$

hence

$$\eta_c = \frac{\pi_c^{\frac{\gamma_c - 1}{\gamma_c}} - 1}{\tau_c - 1} \tag{6.3.1}$$

Thus, for example, if the desired pressure ratio is given and the compressor efficiency estimated, the stagnation temperature ratio and hence required work interaction may be obtained.

6.3.2 THE COMPRESSOR POLYTROPIC EFFICIENCY, e_c

This efficiency, which is related to the compressor efficiency, is defined by

$$e_c = \frac{\text{ideal work interaction for a given differential pressure change}}{\text{actual work interaction for a given differential pressure change}}$$

The concept embodied in the use of the polytropic efficiency is that if we may assume that the stage efficiencies are constant throughout a given compressor, (it will be shown shortly that the stage efficiency is very nearly the polytropic efficiency) then by assuming e_c is a constant, the effect of increasing the compressor pressure ratio (by adding stages) upon the compressor efficiency may be estimated. Thus, when conducting a cycle analysis the most appropriate compressor pressure ratio may be selected.

We may write

$$e_c = \frac{dh_{ti}}{dh_t} \tag{6.3.2}$$

The Gibbs Equation, Eq. (2.8.2) gives

$$T_t ds_t = dh_t - \frac{1}{\rho_t} dp_t$$

but for the ideal process $ds_{ti} = 0$ so that we obtain

$$dh_{ti} = \frac{1}{\rho_t} dp_t \tag{6.3.3}$$

Thus, writing $dh_t = C_p dT_t$ we obtain from Eqs. (6.3.2) and (6.3.3) together with the equation of state

$$e_c = \frac{dp_t}{\rho_t C_p dT_t} = \frac{R}{C_p} \frac{dp_t/p_t}{dT_t/T_t}$$

hence

$$\frac{dT_t}{T_t} = \frac{\gamma_c - 1}{\gamma_c e_c} \frac{dp_t}{p_t} \tag{6.3.4}$$

If we may now assume that e_c is constant over the range of interest (this is similar to assuming that each stage efficiency is the same), Eq. (6.3.4) may be integrated immediately to give

$$\frac{T_{t_3}}{T_{t_2}} = \left(\frac{p_{t_3}}{p_{t_2}}\right)^{\frac{\gamma_c - 1}{\gamma_c e_c}}, \text{ or } \tau_c = \pi_c^{\frac{\gamma_c - 1}{\gamma_c e_c}} \tag{6.3.5}$$

Equations (6.3.1) and (6.3.5) then give an equation relating η_c, e_c and the compressor pressure ratio, π_c.

$$\eta_c = \frac{\pi_c^{\frac{\gamma_c - 1}{\gamma_c}} - 1}{\pi_c^{\frac{\gamma_c - 1}{\gamma_c e_c}} - 1} \tag{6.3.6}$$

This relationship is plotted in Figure 6.3.1

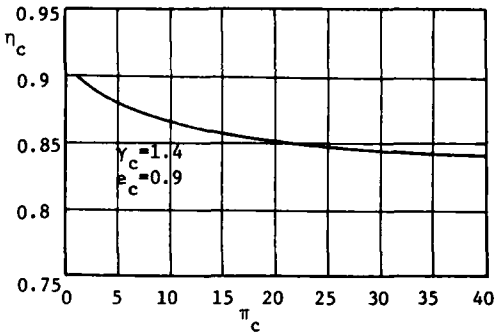

Figure 6.3.1 Compressor Design Efficiency Versus Pressure Ratio

It can be seen that the compressor efficiency goes down with increase in compressor pressure ratio for a given fixed value of e_c. It must be emphasized here that this behavior of compressor efficiency with pressure ratio reflects the estimated behavior of a family of compressors designed to different pressure ratios (and hence incorporating different numbers of stages). Such a curve in no way reflects the expected behavior for a given compressor operating off-design.

6.3.3 THE COMPRESSOR STAGE EFFICIENCY

The compressor stage efficiency is defined in a completely analagous manner to the compressor efficiency, Sec. (6.3.1), except that the reference pressure ratio is that of the stage itself. Thus

$$\eta_{c_j} = \frac{(\pi_{c_j})^{\frac{\gamma_c-1}{\gamma_c}} - 1}{\tau_{c_j} - 1} \qquad (6.3.7)$$

Here the subscript j refers to the j^{th} stage of N total stages.

To relate the stage efficiencies to the compressor efficiency we note

$$\frac{T_{t_j}}{T_{t_{j-1}}} = \tau_{c_j} = 1 + \frac{1}{\eta_{c_j}} \{(\pi_{c_j})^{\frac{\gamma_c-1}{\gamma_c}} - 1\}$$

and hence

$$\tau_c = \frac{T_{tN}}{(T_t)_o} = \prod_{j=1}^{N} \tau_{c_j} = \prod_{j=1}^{N} [1 + \frac{1}{\eta_{c_j}} \{(\pi_{c_j})^{\frac{\gamma_c-1}{\gamma_c}} - 1\}] \qquad (6.3.8)$$

Thus

$$\eta_c = \frac{\pi_c^{\frac{\gamma_c-1}{\gamma_c}} - 1}{\prod_{j=1}^{N} [1 + \frac{1}{\eta_{c_j}} \{(\pi_{c_j})^{\frac{\gamma_c-1}{\gamma_c}} - 1\}] - 1} \qquad (6.3.9)$$

Equation (6.3.9) gives a method of predicting the efficiency of a compressor from the (possibly measured) efficiencies of the individual stages. Note of course that

$$\pi_c = \prod_{j=1}^{N} \pi_{c_j} \qquad (6.3.10)$$

In the special case where all stage efficiencies (η_s), and stage pressure ratios are equal, Eq. (6.3.9) reduces to the special form

$$\eta_c = \frac{\pi_c^{\frac{\gamma_c-1}{\gamma_c}} - 1}{[1 + \frac{1}{\eta_s} \{\pi_c^{\frac{\gamma_c-1}{\gamma_c N}} - 1\}]^N - 1} \qquad (6.3.11)$$

6.3.4 RELATIONSHIP BETWEEN THE COMPRESSOR, STAGE AND POLYTROPIC EFFICIENCIES

Equations (6.3.6), (6.3.9), and (6.3.11) give analytical relationships between the various definitions of efficiency, but it should be of interest to see if η_s formally approaches e_c as we let the number of stages, for a given pressure ratio, get very large. (That is the pressure ratio per stage approaches a differential pressure ratio per stage.)

First note the relationship that if

$$1-\chi^{1/N} = \frac{y}{N} \text{ , then } \chi = (1 - \frac{y}{N})^N$$

thus, noting $\frac{y}{N} \ll 1$ for N very large

$$\ln \chi = N \ln(1-\frac{y}{N}) \Rightarrow N(-\frac{y}{N} + \ldots)$$

hence in the limit of large N

$$y = -\ln \chi$$

We now consider

$$[1 + \frac{1}{\eta_s} \{\pi_c^{\frac{\gamma_c-1}{\gamma N}} - 1\}]^N = [1 - \frac{1}{\eta_s} \{1-\pi_c^{\frac{\gamma_c-1}{\gamma_c N}}\}]^N$$

Thus as N becomes large we have

$$[1 - \frac{1}{\eta_s} \{1-\pi_c^{\frac{\gamma_c-1}{\gamma_c N}}\}]^N \to [1 - \frac{1}{\eta_s} \{-\frac{\ln \pi_c^{\frac{\gamma_c-1}{\gamma_c}}}{N}\}]^N$$

$$= [1 + \frac{1}{N} \ln \pi_c^{\frac{\gamma_c-1}{\gamma_c \eta_s}}]^N$$

$$\to e^{\ln \pi_c^{\frac{\gamma_c-1}{\gamma_c \eta_s}}} = \pi_c^{\frac{\gamma_c-1}{\gamma_c \eta_s}}$$

Hence for N large, Eq. (6.3.11) approaches

$$\eta_c = \frac{\pi_c^{\frac{\gamma_c-1}{\gamma_c}} - 1}{\pi_c^{\frac{\gamma_c-1}{\gamma_c \eta_s}} - 1} \qquad (6.3.12)$$

But this expression is identical to that obtained for η_c versus e_c, Eq. (6.3.6) indicating that $\eta_s \to e_c$ as N becomes large.

As an example calculation, say a sixteen stage compressor of $\pi_c = 25$ is to be constructed. We wish to estimate the compressor efficiency from the measured stage efficiency η_s. We have $\pi_s = 25^{1/16} = 1.223$, and say η_s is measured at 0.93. Then from

$$\eta_s = \frac{\pi_s^{\frac{\gamma_c-1}{\gamma_c}} - 1}{\pi_s^{\frac{\gamma_c-1}{\gamma_c e_c}} - 1}$$

we have $e_c = \dfrac{\frac{\gamma_c-1}{\gamma_c} \ln \pi_s}{\ln[1 + \frac{1}{\eta_s} \{\pi_s^{\frac{\gamma_c-1}{\gamma_c}} - 1\}]} = 0.932$ here.

We get two estimates for η_c from Eqs. (6.3.6) and (6.3.11), to give $\eta_c = .897$ or $.896$ respectively. It can be noted that if we simply assumed e_c was equal to the measured η_s and utilized Eq. (6.3.6), we would have found $\eta_c = .895$.

The point of these manipulations is that use of the polytropic efficiency allows rapid estimation of the compressor efficiency. In addition, for very rapid preliminary estimates it is sufficient to assume the polytropic efficiency is equal to the stage efficiency and then to utilize Eq. (6.3.6) to estimate η_c.

6.4 THE BURNER

The burner is usually approximated as having adiabatic combustion because no heat transfer is assumed at the boundaries. There are two measures of the burner performance, incomplete combustion and stagnation pressure loss. The burner efficiency, η_b, is defined as

$$\eta_b = \frac{1}{\dot{m}_f h}\left[(\dot{m}+\dot{m}_f)h_{t_4} - \dot{m}h_{t_3}\right] =$$

$$\frac{1}{\dot{m}_f h}\left[(\dot{m}+\dot{m}_f)C_{p_t}T_{t_4} - \dot{m}C_{p_c}T_{t_3}\right] \qquad (6.4.1)$$

where h = "heating value" of the fuel

h_t = stagnation enthalpy = $C_p T_t$

$\dot{m}_f$ = fuel mass flow rate

The stagnation pressure loss arises from two effects, the viscous losses in the combustion chamber and the stagnation pressure losses due to enthalpy addition at finite Mach number. These effects are combined for the purposes of performance analysis in the burner stagnation pressure ratio π_b, where

$$\pi_b = \frac{p_{t_4}}{p_{t_3}} < 1 \qquad (6.4.2)$$

As with the inlet there are many important limitations brought about by the lack of one-dimensionality of the flow (hot spots). These effects, which are thoroughly discussed in Chapter 20 appear in the preliminary cycle analysis only indirectly through the required reduction in average combustor outlet temperature, T_{t_4}.

6.4.1 THE BEHAVIOR OF THE THERMODYNAMIC PROPERTIES ACROSS THE COMBUSTOR

In the cycle analysis to follow in Chapter 7, it will be assumed that the gas prior to the combustor is calorically perfect with properties C_{p_c}, γ_c etc. Similarly the gas following the combustor will be assumed calorically perfect with properties C_{p_t}, γ_t etc. In very high temperature engines this latter assumption is not highly accurate, and it should be understood that if highly accurate results are required, resort should be made to the use of real gas tables. The tendencies, and even magnitudes (provided γ_t is selected in the appropriate range) of the relatively simple calculations to follow, are quite suitable for preliminary cycle analysis.

When considering changes in the thermodynamic properties C_p and γ, it should be remembered that these two properties are related. Thus we note

$$C_p = \frac{\gamma}{\gamma-1}R = \frac{\gamma}{\gamma-1}\frac{R_u}{M} \qquad (6.4.3)$$

here R_u = universal gas constant

M = molecular "weight"

Thus, if the chemical reaction in the combustion chamber causes the vibrational modes to be excited but does not cause appreciable dissociation, and if in addition the rather small percentage of fuel addition does not significantly change the molecular weight, then M would be approximately constant. In this case, a reduction in γ_t is directly related to an increase in C_{p_t} by the formula

$$\frac{C_{p_t}}{C_{p_c}} = \frac{\gamma_t}{\gamma_c}\frac{\gamma_c-1}{\gamma_t-1} \qquad (6.4.4)$$

This approximation will be used throughout Chapters 7 and 8.

6.4.2 ONE-DIMENSIONAL ESTIMATION OF THE BURNER STAGNATION PRESSURE RATIO

We now consider the effect of flameholder drag and enthalpy increase at finite Mach number on the stagnation properties in a combustion chamber. For simplicity we consider a constant area duct and assume that the drag may be estimated by relating the drag loss to the incoming dynamic pressure. (Such an analysis tends to be most suitable to the description of flow in a constant area afterburner.)

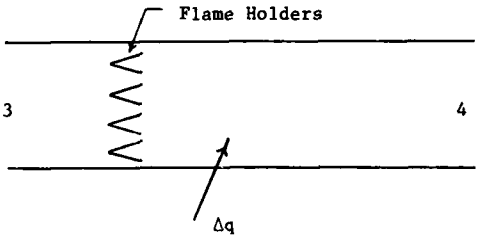

Figure 6.4.1 Constant Area Combustion Chamber

To simply analyze the combustion chamber behavior, we assume the gases to be calorically perfect at entrance and exit to the chamber, and in addition assume that the mass addition of fuel is extremely small compared to the air mass flow. The momentum equation may then be written

$$p_3 + \rho_3 u_3^2 = p_4 + \rho_4 u_4^2 + (\tfrac{1}{2}\rho_3 u_3^2)C_D$$

from which

$$p_3\left[1 + \frac{\rho_3 u_3^2}{p_3}\left(1 - \frac{C_D}{2}\right)\right] = p_4\left[1 + \frac{\rho_4 u_4^2}{p_4}\right]$$

$$\text{or} \quad \frac{p_4}{p_3} = \frac{1 + \gamma_c M_3^2\left(1 - \frac{C_D}{2}\right)}{1 + \gamma_t M_4^2} \tag{6.4.5}$$

The state equation and continuity equation ($\rho_3 u_3 = \rho_4 u_4$) may be combined to give

$$\left(\frac{T_4}{T_3}\right) = \left(\frac{\rho_3}{\rho_4}\frac{p_4}{p_3}\right)^2 = \left(\frac{u_4}{u_3}\right)^2\left(\frac{p_4}{p_3}\right)^2$$

hence

$$\frac{T_4}{T_3} = \frac{u_4^2}{\gamma_t R T_4}\frac{1}{u_3^2/(\gamma_c R T_3)}\left(\frac{p_4}{p_3}\right)^2\frac{\gamma_t}{\gamma_c} = \frac{\gamma_t}{\gamma_c}\frac{M_4^2}{M_3^2}\left(\frac{p_4}{p_3}\right)^2 \tag{6.4.6}$$

We also have

$$\frac{T_{t4}}{T_{t3}} = \frac{T_4}{T_3}\frac{1 + \frac{\gamma_t - 1}{2}M_4^2}{1 + \frac{\gamma_c - 1}{2}M_3^2} \tag{6.4.7}$$

Combining Eqs. (6.4.5-6.4.7) then gives

$$\frac{M_4^2\left(1 + \frac{\gamma_t - 1}{2}M_4^2\right)}{\left(1 + \gamma_t M_4^2\right)^2} = \frac{\gamma_c}{\gamma_t}\frac{M_3^2\left(1 + \frac{\gamma_c - 1}{2}M_3^2\right)}{\left[1 + \gamma_c M_3^2\left(1 - \frac{C_D}{2}\right)\right]^2}\frac{T_{t4}}{T_{t3}} \equiv \chi \tag{6.4.8}$$

This is an equation for M_4 in terms of the upstream variables and prescribed stagnation temperature ratio T_{t4}/T_{t3}. This is once again of the same functional form for the Mach number as occurred in the solution for the heat interaction at constant area, Sec. (2.17.4), so we may write

$$M_4^2 = 1 - \frac{\Delta[1+\Delta]}{1 - 2\gamma_t\chi + \Delta}$$

where $$\Delta = \sqrt{1 - 2(\gamma_t + 1)\chi} \tag{6.4.9}$$

Following solution for M_4, the desired stagnation pressure ratio, π_b, is then given by

$$\frac{p_{t4}}{p_{t3}} \equiv \pi_b = \frac{\left\{1 + \frac{\gamma_t - 1}{2}M_4^2\right\}^{\frac{\gamma_t}{\gamma_t - 1}}}{\left\{1 + \frac{\gamma_c - 1}{2}M_3^2\right\}^{\frac{\gamma_c}{\gamma_c - 1}}}\frac{p_4}{p_3} \tag{6.4.10}$$

where p_4/p_3 is given by Eq. (6.4.5).

As an example calculation we consider an aircraft flying at Mach number 0.8 with compressor pressure ratio $\pi_c = 15$. We are given $T_{t4}/T_0 = 7$, $\gamma_c = 1.4$, $\gamma_t = 1.3$, $e_c = .905$ and $C_D = 1.5$, so obtain

$$\frac{T_{t4}}{T_{t3}} = \frac{\frac{T_{t4}}{T_0}}{\frac{T_{t3}}{T_{t2}}\frac{T_{t2}}{T_0}} = \frac{\frac{T_{t4}}{T_0}}{\tau_c\,\tau_r}$$

Here $\tau_r = 1.128$, and $\tau_c = (15)^{\frac{1}{(3.5)(.905)}} = 2.354$, so $T_{t4}/T_{t3} = 2.637$. Direct calculation then yields the results of Figure 6.4.2.

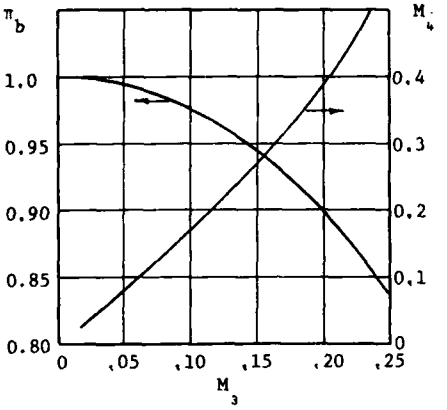

Figure 6.4.2 Combustor Stagnation Pressure Ratio and Exit Mach Number

It is evident from Figure 6.4.2, that for these conditions the inlet Mach number must be restricted to a value of 0.15 or less if the combustor pressure loss is not to become excessive. This restriction to low required Mach numbers, particularly in afterburners, can lead to design limitations upon the required burner cross-sectional area.

6.5 THE TURBINE

Unlike compressors, modern turbines are almost always cooled, at least in the first several high pressure stages. Cooling is accomplished by passing air directly from the compressor to the turbine blades where any one of several cooling methods may be employed. (See Chapter 19.) The "accounting" of cooling losses is best carried out by considering the cooling air and mainstream air to be a combined multiple stream adiabatic flow. This method of accounting for cooling losses is described in detail in Chapter 18. In this section the so-called adiabatic efficiencies will be described, and estimation of the effect of cooling will be considered to be separately determined.

6.5.1 THE TURBINE EFFICIENCY, η_t

The turbine efficiency is defined in a manner analogous to that of the compressor efficiency to give

$$\eta_t = \frac{\text{actual work interaction for a given pressure ratio}}{\text{ideal work interaction for a given pressure ratio}}$$

$$= \frac{C_p(T_{t_4} - T_{t_5})}{C_p(T_{t_4} - T_{t_{5_i}})} = \frac{1-\tau_t}{1-\tau_{t_i}}$$

The ideal process is isentropic so we obtain

$$\eta_t = \frac{1-\tau_t}{1-(\pi_t)^{\frac{\gamma_t-1}{\gamma_t}}} \qquad (6.5.1)$$

6.5.2 THE TURBINE POLYTROPIC EFFICIENCY, e_t

Again, analogous to the compressor polytropic efficiency we define

$$e_t = \frac{\text{actual work interaction for a given differential pressure change}}{\text{ideal work interaction for a given differential pressure change}}$$

Thus we write

$$e_t = \frac{dh_t}{dh_{t_i}} = \frac{C_p\, dT_t}{\frac{1}{\rho_t} dp_t}$$

or $$e_t = \frac{\gamma_t}{\gamma_t - 1} \frac{dT_t/T_t}{dp_t/p_t}$$

Hence if we may assume e_t to be approximately constant, integration gives

$$\frac{T_{t5}}{T_{t4}} = \left(\frac{p_{t5}}{p_{t4}}\right)^{\frac{e_t(\gamma_t-1)}{\gamma_t}} \quad \text{or} \quad \tau_t = \pi_t^{\frac{e_t(\gamma_t-1)}{\gamma_t}} \qquad (6.5.2)$$

Equations (6.5.1) and (6.5.2) then give

$$\eta_t = \frac{1-\pi_t^{\frac{e_t(\gamma_t-1)}{\gamma_t}}}{1-\pi_t^{\frac{\gamma_t-1}{\gamma_t}}} = \frac{1-\tau_t}{1-\tau_t^{1/e_t}} \qquad (6.5.3)$$

This relationship is plotted in Figure 6.5.1.

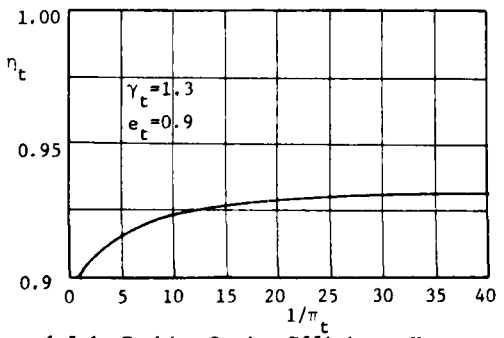

Figure 6.5.1 Turbine Design Efficiency Versus Pressure Ratio

It can be seen that the turbine efficiency increases as the turbine design expansion ratio $(1/\pi_t)$ increases. This occurs because that energy that is not extracted in a given stage because of inefficiencies remains partly available to the succeeding stages.

6.5.3 THE TURBINE STAGE EFFICIENCY

The turbine stage efficiency is defined in a completely analogous manner to the turbine efficiency, Sec. (6.5.1), to give

$$\eta_{t_j} = \frac{1-\tau_{tj}}{1-(\pi_{t_j})^{\frac{\gamma_t-1}{\gamma_t}}} \qquad (6.5.4)$$

Noting $$\tau_{t_j} = 1-\eta_{t_j}\{1-(\pi_{t_j})^{\frac{\gamma_t-1}{\gamma_t}}\} \text{ and } \tau_t = \prod_{j=1}^{N} \tau_{t_j}$$

we obtain

$$\eta_t = \frac{1-\prod_{j=1}^{N}[1-\eta_{t_j}\{1-(\pi_{t_j})^{\frac{\gamma_t-1}{\gamma_t}}\}]}{1-\pi_t^{\frac{\gamma_t-1}{\gamma_t}}} \qquad (6.5.5)$$

In the special case when all stage efficiencies (η_s) and stage pressure ratios are equal, Eq. (6.5.5) reduces to

$$\eta_t = \frac{1-[1-\eta_s\{1-(\pi_t)^{\frac{\gamma_t-1}{\gamma_t N}}\}]^N}{1-\pi_t^{\frac{\gamma_t-1}{\gamma_t}}} \qquad (6.5.6)$$

6.6 THE NOZZLE

The major loss mechanisms of a nozzle are usually identified with the pressure imbalance at exit caused by over or underexpansion. The degree of over or under expansion is often selected for the best balance of internal (exit pressure) and external (boat-tail drag) losses. In any case, the boat-tail losses are separately accounted for when the cowl drag is determined and the effect of exit pressure imbalance is included in the expression for F_A, Eq. (6.1.8).

For convenience we include in the nozzle stagnation pressure losses, all those losses occurring from the turbine exit to nozzle exit. Thus we write

$$\pi_n = \frac{p_{t_9}}{p_{t_5}} < 1 \qquad (6.6.1)$$

For engines without afterburners π_n is usually very nearly unity (0.99 or larger), but when the flameholder ducts are present π_n can be

much lower ($\sim$ 0.97). When afterburning is present π_n can be estimated by the analysis of Sec. (6.4.2).

Usually nozzles are very nearly adiabatic, so we will assume

$$\tau_n = 1 \qquad (6.6.2)$$

In some cases of afterburning the nozzle may be cooled with compressor air, in which case it would be necessary to consider a two stream analysis. Such an analysis is straightforward conceptually, though somewhat tedious algebraically, and will not be included in this document.

6.7 SUMMARY OF COMPONENT FIGURES OF MERIT

The loss mechanisms and their measures considered in the preceding sections may be summarized as in Table 6.7.1.

COMPONENT	IDEAL BEHAVIOR	ACTUAL BEHAVIOR	"FIGURES OF MERIT"
INLET	ISENTROPIC, HENCE $\tau_d = 1,\ \pi_d = 1$	ADIABATIC, NOT ISENTROPIC, HENCE $\tau_d = 1,\ \pi_d \neq 1$	π_d
COMPRESSOR	ISENTROPIC, HENCE $-\Delta w_m = C_{p_c} T_{t_2} (\tau_c - 1)$ $\pi_c = \tau_c^{\gamma_c/(\gamma_c-1)}$	ADIABATIC, NOT ISENTROPIC $-\Delta w_m = C_{p_c} T_{t_2} (\tau_c - 1)$ $\pi_c = [1+\eta_c(\tau_c-1)]^{\gamma_c/(\gamma_c-1)}$ $\tau_c = 1 + \frac{1}{\eta_c}[\pi_c^{(\gamma_c-1)/\gamma_c} - 1]$	$\eta_c = \frac{\pi_c^{(\gamma_c-1)/\gamma_c} - 1}{\tau_c - 1}$ $\eta_c = \frac{\pi_c^{(\gamma_c-1)/\gamma_c} - 1}{\pi_c^{(\gamma_c-1)/\gamma_c e_c} - 1}$
BURNER	NO STAGNATION PRESSURE LOSS, COMPLETE COMB $\pi_b = 1$ $(\dot{m}+\dot{m}_f) C_{p_4} T_{t_4} - \dot{m} C_{p_3} T_{t_3} = \dot{m}_f h$	STAGNATION PRESSURE LOSS, INCOMPLETE COMB $\pi_b \neq 1$ $(\dot{m}+\dot{m}_f) C_{p_t} T_{t_4} = \dot{m} C_{p_c} T_{t_3} + \eta_b \dot{m}_f h$	π_b $\eta_b = \frac{(\dot{m}+\dot{m}_f) C_{p_t} T_{t_4} - \dot{m} C_{p_c} T_{t_3}}{\dot{m}_f h}$
TURBINE	ISENTROPIC $\Delta w = C_{p_t} T_{t_4} (1-\tau_t)$ $\pi_t = \tau_t^{\gamma_t/(\gamma_t-1)}$	ADIABATIC, NOT ISENTROPIC $\Delta w_m = C_{p_t} T_{t_4} (1-\tau_t)$ $\pi_t = [1 - \frac{1}{\eta_t}(1-\tau_t)]^{\gamma_t/(\gamma_t-1)}$ $\tau_t = [1-\eta_t(1-\pi_t^{(\gamma_t-1)/\gamma_t})]$ Note: Cooling to be considered separately	$\eta_t = \frac{1-\tau_t}{1-\pi_t^{(\gamma_t-1)/\gamma_t}}$ $\eta_t = \frac{1-\tau_t}{1-\tau_t^{1/e_t}}$
NOZZLE	ISENTROPIC $\tau_n = 1,\ \pi_n = 1$	ADIABATIC $\tau_n = 1,\ \pi_n \neq 1$	π_n

Table 6.7.1 Component Figures of Merit

6.8.1 REFERENCES

(6.1) Bober, J. L., "Use of Potential Flow Theory to Evaluate Subsonic Inlet Data from a Simulator-Powered Nacelle at Cruise Conditions." NASA TN D-7850. December 1974.

(6.2) Holdhusen, J. S., "A Model Testing Technique for Determining Inlet Spillage Drag." 16th Meeting of AIAA Turbine Engine Testing Working Group on Subscale Test and Simulation. St. Louis, Missouri. May 13-14, 1976.

(6.3) Motycka, D. L., Di Sabato, V. J., and Andersen, L. Q., "The Use of a Powered Model for Subsonic Nacelle Optimization." ASME Paper No. 72-GT-14. March 1972.

Chapter 7

NON-IDEAL CYCLE ANALYSIS

Gordon C. Oates

University of Washington

AD-A152 757 COST REDUCTION IN VERTICALLY RELATED INDUSTRIES: INTEGRATION VERSUS NONLINEAR PRICING(U) RAND CORP SANTA MONICA CA H C QUIRMBACH MAY 83 RAND/P-6839 3/9

UNCLASSIFIED F/G 5/1 NL

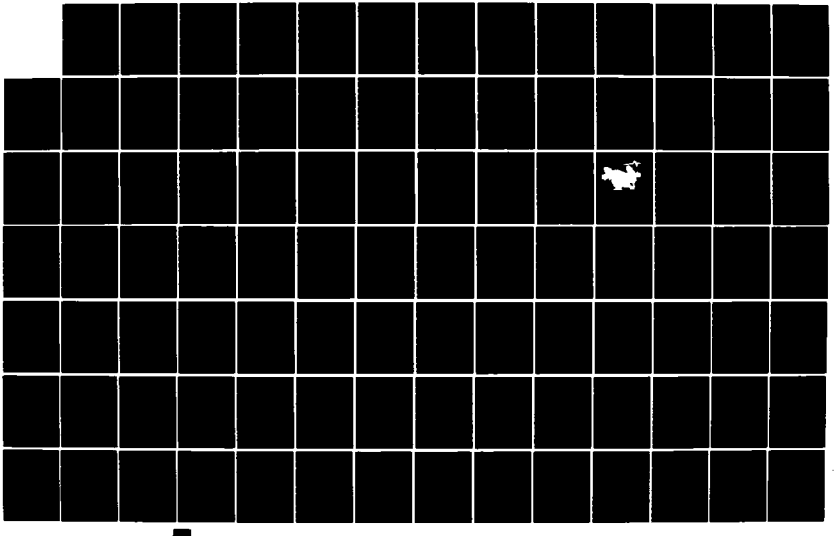

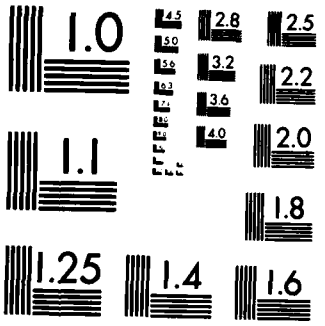

MICROCOPY RESOLUTION TEST CHART
NATIONAL BUREAU OF STANDARDS-1963-A

TABLE OF CONTENTS

CHAPTER 7 NON-IDEAL CYCLE ANALYSIS

		Page
7.0	Introduction	7-1
7.1	Numerical Solution of Equations	7-1
7.1.1	Newtonian Iteration	7-1
7.1.2	Functional Iteration	7-1
7.2	The Turbojet	7-1
7.2.1	Cycle Analysis of the Turbojet with Losses	7-2
7.2.2	Summary of the Equations, Turbojet with Losses	7-3
7.2.3	Example Results - Turbojet with Losses	7-3
7.3	The Turbofan	7-5
7.3.1	Cycle Analysis of the Turbofan with Losses	7-5
7.3.2	Summary of the Equations, Turbofan with Losses, By-Pass Ratio Prescribed	7-6
7.3.3	Operation with Convergent Exit Nozzles	7-6
7.3.4	By-Pass Ratio for Minimum Specific Fuel Consumption	7-7
7.3.5	Summary of the Equations, Turbofan with Losses, No Afterburning, Exit Pressures Matched, and By-Pass Ratio Optimized	7-7
7.3.6	Example Results - Turbofan with Losses	7-8
7.4	The Turboprop or Prop Fan	7-9
7.4.1	Cycle Analysis of the Turboprop	7-10
7.4.2	Summary of the Equations, Turboprop with Optimal Work Distribution	7-11
7.4.3	Example Results - Turboprop	7-12
7.5	Summary and Conclusions for Cycle Analysis	7-13

LIST OF FIGURES

		Page
Figure 7.2.1	Turbojet Reference Station	7-2
Figure 7.2.2	Effect of Compressor Pressure Ratio and Efficiency on Performance, Turbojet with Losses	7-4
Figure 7.2.3	Effect of Exit Pressure Variations on Specific Fuel Consumption	7-4
Figure 7.2.4	Performance of Turbojet with Afterburning	7-4
Figure 7.3.1	Turbofan Reference Stations	7-5
Figure 7.3.2	Optimal By-Pass Ratio Versus By-Pass Pressure Ratio	7-8
Figure 7.3.3	Turbofan Performance	7-9
Figure 7.3.4	Variation of Specific Fuel Consumption with By-Pass Pressure Ratio and Compressor Pressure Ratio	7-9
Figure 7.4.1	Turboprop Reference Stations	7-10
Figure 7.4.2	Specific Thrust and Specific Fuel Consumption Versus Compressor Pressure Ratio for Turboprop with Optimum Turbine Temperature Ratio	7-12

CHAPTER 7

LIST OF SYMBOLS

The symbols are listed in alphabetical order, first in the English alphabet, then in the Greek alphabet. Subscripts and superscripts are then given. The equation, figure or section in which the symbols are first introduced is indicated in parentheses. Often the symbol will be defined in the text just preceding or just following the equation or figure.

Where appropriate, the location of the introduction of the symbol is referred to in previous chapters.

A - Cross-sectional area (Eq. 7.2.1)

a - Speed of sound (Eq. 7.2.4)

C - Specific heat (Sect. 2.6)

- Work interaction coefficient (Eq. 7.4.3)

F - Thrust (Eq. 7.2.1)

f - Fuel to air ratio (Eq. 7.2.2)

g_o - Gravitational constant (Sect. 7.2.2)

h - Heating value (Eq. 7.2.13)

M - Mach number (Eq. 7.2.3)

$\dot{m}$ - Mass flow rate (Eq. 7.2.1)

p - Pressure (Eq. 7.2.1)

R - Gas constant (Sect. 2.12)

S - Specific fuel consumption (Eq. 7.2.15)

T - Temperature (Eq. 7.2.3)

u - Velocity (Eq. 7.2.1)

α - By-pass ratio (Eq. 7.3.2)

γ - Ratio of specific heats (Sect. 2.6)

η - Efficiency (Eq. 7.2.11)

Π - Group defined in Eq. 7.3.35

π - Ratio of pressures (Sect. 5.1)

ρ - Density (Eq. 7.2.3)

τ - Ratio of temperatures or enthalpies (Sect. 5.1)

A - Uninstalled (Eq. 7.2.1)

c - Core (Eq. 8.4.10)

f - Fuel (Eq. 7.2.2)

g - Gearbox (Eq. 7.4.11)

m - Mechanical (Eq. 7.2.11)

p - Constant pressure (Sect. 2.6)

- Power (Eq. 7.4.18)

t - Stagnation quantity (Sect. 2.16)

core - Core engine (Eq. 7.4.9)

PROP - Propeller (Eq. 7.4.12)

1 - Core stream (Eq. 7.3.1)

2 - Fan stream (Eq. 7.3.1)

Subscripts previously defined in Sect. 5.1

AB, b, c, d, n, r, t, λ

0-9 Station numbers (Figs. 5.1.1, 7.2.1)

Superscripts'

' - Fan stream (Fig. 7.3.1)

* - Conditions at minimum specific fuel consumption (Eq. 7.3.33)

CHAPTER SEVEN
NON-IDEAL CYCLE ANALYSIS

7.0 INTRODUCTION

In this chapter we again apply cycle analysis to several example engine types. The methodology will remain as in Sec. (5.6.1), the only difference between the results of this chapter and Chapter 5 arising because of the non-ideal component processes assumed, and because of the use of different thermodynamic properties following the primary burner and afterburners. The notation will be that already introduced in Sec. (5.1).

7.1 NUMERICAL SOLUTION OF EQUATIONS

In several of the examples to follow, desired variables appear in transcendental equations. Many iterative techniques are available for the solution of such equations. The numerical complications of such techniques have been greatly reduced with the advent of small computers with branching and looping capability, so that graphical techniques, etc. are no longer necessary. In the following, two well known techniques are described.

7.1.1 NEWTONIAN ITERATION

We consider a transcendental equation of the form

$$F(x) = 0 \tag{7.1.1}$$

Now we consider a j^{th} estimate of x to be x_j, and desire a method of estimating a next (closer) estimate, x_{j+1}. The function $F(x_{j+1})$ is expanded in a Taylor's series to give

$$F(x_{j+1}) = F(x_j) + (x_{j+1}-x_j)\, F'(x_j) + \ldots \tag{7.1.2}$$

Here $F'(x_j)$ means the derivative of the function $F(x)$ by x, evaluated at the value x_j. Now if x_{j+1} is to be close to the solution of $F(x) = 0$, we may approximate $F(x_{j+1})$ as being zero. Also, if x_j is not far from x_{j+1} we may ignore the higher order terms in the series to give

$$x_{j+1} = x_j - \frac{F(x_j)}{F'(x_j)} \quad \text{Newtonian Iteration} \tag{7.1.3}$$

Equation (7.1.3) gives a method for obtaining the next estimate for the solution to the equation, x_{j+1}, in terms of the previous approximation. In practice the process would be continued till $(x_{j+1}-x_j)$ was less than the desired accuracy.

It is sometimes convenient to approximate the derivative of the function by a finite difference form, say

$$F'(x_j) \approx \frac{F(x_j+\delta)-F(x_j-\delta)}{2\delta} \tag{7.1.4}$$

here δ would be a suitably small quantity. The advantage of utilizing such an approximation is that if a computer is to be programmed to utilize Newtonian Iteration, only a sub-routine to calculate the function $F(x)$ itself need be supplied, it not being necessary to provide a separate subroutine to calculate the derivative.

Newtonian iteration is sometimes unstable, but it is fortunate in the examples to follow, that provided a suitable first guess for the desired variable is made, Newtonian iteration, or the simpler functional iteration, (next section) is stable in all examples considered herein.

7.1.2 FUNCTIONAL ITERATION

A simple form of iteration related to Newtonian iteration is functional iteration. We now assume we have a transcendental equation of the form

$$x = f(x) \tag{7.1.5}$$

This may be formally converted to a form suitable for solution by Newtonian iteration by defining

$$F(x) = x - f(x)$$

hence from Eq. (7.1.3)

$$x_{j+1} = x_j - \frac{F(x_j)}{F'(x_j)} = x_j - \frac{x_j - f(x_j)}{1-f'(x_j)} \tag{7.1.6}$$

Now, if the function $f(x)$ is slowly varying in x, then $f'(x_j)$ may be ignored compared to unity. In that case Eq. (7.1.6) reduces to

$$x_{j+1} = f(x_j) \quad \text{Functional Iteration} \tag{7.1.7}$$

This extremely simple form would then be iterated till $(x_{j+1}-x_j)$ is less than the desired accuracy. This form is very simple and convenient, but is suitable only when $|f'(x_j)| \ll 1$.

7.2 THE TURBOJET

We will now develop the performance equations for the turbojet. It will be assumed that the gas is calorically perfect up to the compressor outlet, with properties γ_c, C_{p_c} etc. The gas will also be assumed calorically perfect following the burner with properties γ_t, C_{p_t} etc. If an afterburner is in operation, the gas following the afterburner will again be assumed calorically perfect with properties γ_{AB}, $C_{p_{AB}}$ etc. It will be assumed that the gas constant remains unchanged throughout so that Eq. (6.4.4) (or equivalent for $C_{p_{AB}}$ and γ_{AB}) remains valid. All components will be considered to be adiabatic (no turbine cooling) and the efficiencies of compressor and turbine will be described through the use of constant polytropic efficiencies. Finally, the effects of gas leakage and the use of drawn-off air for auxilliary power will not be included. The reference stations are indicated in Fig. 7.2.1.

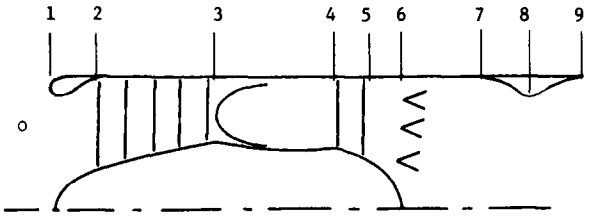

Figure 7.2.1 Turbojet Reference Stations

The analysis to follow will be developed in a form suitable for use whether or not an afterburner is present or in operation.

7.2.1 CYCLE ANALYSIS OF THE TURBOJET WITH LOSSES

The expression for the uninstalled thrust is as given by Eq. (6.1.8). That is with the station numbering of Figure 7.2.1.

$$F_A = \dot{m}_9 u_9 - \dot{m}_o u_o + (p_9 - p_o)A_9 \qquad (7.2.1)$$

Because gas leakage and the use of auxilliary air is being ignored, we may write

$$\dot{m}_9 = \dot{m}_o + \dot{m}_f + \dot{m}_{fAB} = \dot{m}_o(1+f+f_{AB}) \qquad (7.2.2)$$

Also note

$$\frac{1}{\dot{m}_o}(p_9 - p_o)A_9 = (1+f+f_{AB})\frac{A_9 p_9}{\rho_9 u_9 A_9}\left(1 - \frac{p_o}{p_9}\right)$$

$$= \frac{(1+f+f_{AB})}{u_9/u_o}\frac{u_o}{u_o^2/(\gamma_c R_c T_o)}\frac{R_9 T_9}{\gamma_c R_c T_o}\left(1 - \frac{p_o}{p_9}\right)$$

or

$$\frac{1}{\dot{m}_o}(p_9 - p_o)A_9 = (1+f+f_{AB})\frac{u_o}{\gamma_c M_o^2}\frac{1}{u_9/u_o}\left(1 - \frac{p_o}{p_9}\right)\frac{T_9}{T_o} \qquad (7.2.3)$$

In this last expression we have utilized $R_9 = R_c$. Equations (7.2.1-7.2.3) then give

$$\frac{F_A}{\dot{m}_o} = a_o\left[(1+f+f_{AB})\left(M_o\frac{u_9}{u_o}\right) - M_o + (1+f+f_{AB})\frac{1}{\gamma_c\left(M_o\frac{u_9}{u_o}\right)}\frac{T_9}{T_o}\right.$$

$$\left. \times \left(1 - \frac{p_o}{p_9}\right)\right] \qquad (7.2.4)$$

$$M_o^2\left(\frac{u_9}{u_o}\right)^2 = \frac{\gamma_{AB}R_{AB}}{\gamma_c R_c}\frac{T_9}{T_o}M_9^2 \qquad (7.2.5)$$

Then noting

$$T_{t_9} = T_9\left\{1 + \frac{\gamma_{AB}-1}{2}M_9^2\right\} = T_o\frac{C_{pc}}{C_{pAB}}\tau_{\lambda AB} \qquad (7.2.6)$$

and

$$p_{t_9} = p_9\left\{1 + \frac{\gamma_{AB}-1}{2}M_9^2\right\}^{\frac{\gamma_{AB}}{\gamma_{AB}-1}} = p_o\pi_r\pi_d\pi_c\pi_b\pi_t\pi_n \qquad (7.2.7)$$

we may write

$$M_9^2 = \frac{2}{\gamma_{AB}-1}\left\{\left(\frac{p_{t_9}}{p_9}\right)^{\frac{\gamma_{AB}-1}{\gamma_{AB}}} - 1\right\} \qquad (7.2.8)$$

and

$$M_o^2\left(\frac{u_9}{u_o}\right)^2 = \frac{\gamma_{AB}R_{AB}}{\gamma_c R_c}\frac{C_{pc}}{C_{pAB}}\frac{2}{\gamma_{AB}-1}\tau_{\lambda AB}\left\{1 - \left(\frac{p_{t_9}}{p_9}\right)^{-\left(\frac{\gamma_{AB}-1}{\gamma_{AB}}\right)}\right\}$$

or

$$M_o^2\left(\frac{u_9}{u_o}\right)^2 = \frac{2}{\gamma_c - 1}\tau_{\lambda AB}\left\{1 - \left(\frac{p_{t_9}}{p_9}\right)^{-\left(\frac{\gamma_{AB}-1}{\gamma_{AB}}\right)}\right\} \qquad (7.2.9)$$

Also note

$$\frac{T_9}{T_o} = \frac{\frac{C_{pc}}{C_{pAB}}\tau_{\lambda AB}}{\left(\frac{p_{t_9}}{p_9}\right)^{\left(\frac{\gamma_{AB}-1}{\gamma_{AB}}\right)}} \qquad (7.2.10)$$

Equations (7.2.9) and (7.2.10) allow determination of the principal terms in the expression for the specific thrust, except that the turbine pressure ratio, π_t, must be obtained from the power balance between turbine and compressor. We thus write:

$$\dot{m}_o C_{pc}(T_{t_3} - T_{t_2}) = (\dot{m}_o + \dot{m}_f)C_{pt}\eta_m(T_{t_4} - T_{t_5})$$

Dividing by $\dot{m}_o C_{pc} T_o$, and rearranging we obtain

$$\tau_t = 1 - \frac{1}{\eta_m(1+f)}\frac{\tau_r}{\tau_\lambda}(\tau_c - 1) \qquad (7.2.11)$$

and then

$$\pi_t = \tau_t^{\frac{\gamma_t}{(\gamma_t - 1)e_t}} \qquad (7.2.12)$$

It should be noted here that the mechanical efficiency, η_m, will normally be very high (approximately unity) for most gas turbine engines. However, by retaining η_m in the equation we provide a convenient method of accounting for auxilliary power take-off.

Finally, expressions are obtained for the fuel to air ratios from the enthalpy balances across the appropriate burners. Thus,

PRIMARY BURNER

$$\dot{m}_o C_{pc} T_{t_3} + \eta_b \dot{m}_f h = (\dot{m}_o + \dot{m}_f)C_{pt}T_{t_4}$$

Dividing by $\dot{m}_o C_{pc} T_o$ and rearranging, there is obtained

$$f = \frac{\tau_\lambda - \tau_r\tau_c}{\frac{h\eta_b}{C_{pc}T_o} - \tau_\lambda} \qquad (7.2.13)$$

AFTERBURNER

$$(\dot{m}_o+\dot{m}_f)C_{p_t}T_{t_5}+\eta_{AB}\dot{m}_{fAB}h = (\dot{m}_o+\dot{m}_f+\dot{m}_{fAB})C_{p_{AB}}T_{t_8}$$

Dividing by $\dot{m}_o C_{p_c} T_o$ and rearranging, there is obtained

$$f_{AB} = (1+f)\frac{\tau_{\lambda AB} - \tau_\lambda \tau_t}{\frac{h\eta_{AB}}{C_{p_c}T_o} - \tau_{\lambda AB}} \qquad (7.2.14)$$

The specific fuel consumption may then be written

$$S = \frac{\dot{m}_f+\dot{m}_{fAB}}{F_A} = \frac{f+f_{AB}}{F_A/\dot{m}_o} \qquad (7.2.15)$$

Equations (7.2.1) to (7.2.15) may now be arranged in an order to allow direct calculation of the desired performance variables in terms of the imposed flight conditions, design limits, design choices and component efficiencies. The equations are summarized in the next section.

7.2.2 SUMMARY OF THE EQUATIONS, TURBOJET WITH LOSSES

Inputs: T_o(K)[°R], γ_c, γ_t, γ_{AB}, C_{p_c}, C_{p_t}, $C_{p_{AB}}$(J/kg K) [$\frac{BTU}{lbm°R}$], h(J/kg) [$\frac{BTU}{lbm}$], π_d, π_b, π_n, η_b, η_{AB}, η_m, e_c, e_t, $\frac{p_9}{p_o}$, τ_λ, $\tau_{\lambda AB}$, π_c, M_o

Outputs: $\frac{F_A}{\dot{m}_o}$ (Ns/kg) [$\frac{F_A}{g_o\dot{m}_o}$, $\frac{lbf}{lbm/sec}$]

S(kg/Ns) [$\frac{lbm\ fuel/hr}{lbf\ thrust}$], f, f_{AB} etc.

Equations:

$$R_c = \frac{\gamma_c-1}{\gamma_c} C_{p_c}\ m^2/s^2K \quad [R_c = \frac{\gamma_c-1}{\gamma_c} C_{p_c}(2.505)(10^4) \times \frac{ft^2}{sec\ °R}] \qquad (7.2.16)$$

$$a_o = \sqrt{\gamma_c R_c T_o}\ m/s\ [ft/sec] \qquad (7.2.17)$$

$$\tau_r = 1 + \frac{\gamma_c-1}{2} M_o^2 \qquad (7.2.18)$$

$$\pi_r = \tau_r^{\frac{\gamma_c}{\gamma_c-1}} \qquad (7.2.19)$$

$$\tau_c = \pi_c^{\frac{\gamma_c-1}{\gamma_c e_c}} \qquad (7.2.20)$$

$$f = \frac{\tau_\lambda - \tau_r\tau_c}{\frac{h\eta_b}{C_{p_c}T_o} - \tau_\lambda} \qquad (7.2.21)$$

$$\tau_t = 1 - \frac{1}{\eta_m(1+f)}\frac{\tau_r}{\tau_\lambda}(\tau_c-1) \qquad (7.2.22)$$

$$\pi_t = \tau_t^{\frac{\gamma_t}{(\gamma_t-1)e_t}} \qquad (7.2.23)$$

$$\frac{p_{t_9}}{p_9} = \frac{p_o}{p_9}\pi_r\pi_d\pi_c\pi_b\pi_t\pi_n \qquad (7.2.24)$$

$$\frac{T_9}{T_o} = \frac{\frac{C_{p_c}}{C_{p_{AB}}}\tau_{\lambda AB}}{(\frac{p_{t_9}}{p_9})^{\frac{\gamma_{AB}-1}{\gamma_{AB}}}} \qquad (7.2.25)$$

NOTE: If no afterburning is present, then $\tau_{\lambda AB}$ should be put equal to $\tau_\lambda\tau_t$. Also, $C_{p_{AB}}$ and γ_{AB} would be put equal to C_{p_t}, and γ_t.

$$f_{AB} = (1+f)\frac{\tau_{\lambda AB} - \tau_\lambda\tau_t}{\frac{h\eta_{AB}}{C_{p_c}T_o} - \tau_{\lambda AB}} \qquad (7.2.26)$$

$$M_o\frac{u_9}{u_o} = [\frac{2}{\gamma_c-1}\tau_{\lambda AB}\{1 - (\frac{p_{t_9}}{p_9})^{-(\frac{\gamma_{AB}-1}{\gamma_{AB}})}\}]^{1/2} \qquad (7.2.27)$$

$$\frac{F_A}{\dot{m}_o} = a_o[(1+f+f_{AB})(M_o\frac{u_9}{u_o}) - M_o + \frac{(1+f+f_{AB})\frac{T_9}{T_o}}{\gamma_c(M_o\frac{u_9}{u_o})}(1-\frac{p_o}{p_9})] \qquad (7.2.28)$$

(To obtain British units of $\frac{lbf}{lbm/sec}$, a_o in meters/sec would be replaced by $\frac{a_o}{32.174}$ where a_o should be given in ft/sec.)

$$S = \frac{f+f_{AB}}{F_A/\dot{m}_o}\ [s = \frac{3600(f+f_{AB})}{F_A/g_o\dot{m}_o}] \qquad (7.2.29)$$

7.2.3 EXAMPLE RESULTS - TURBOJET WITH LOSSES

As a first example we consider a turbojet to be designed for flight at Mach two without afterburner. A range of possible pressure ratios is considered, and the following characteristics were assumed.

T_o = 233.3°K[420°R]
γ_c = 1.4
C_{p_c} = 996.5 J/kgK[0.238 BTU/lbm°R]
γ_t = 1.35
C_{p_t} = 1098.2 J/kgK[0.262 BTU/lbm°R]
π_d = .9425
π_b = .98
π_n = .99
η_b = .97
η_m = .99 p_9/p_o = 1
e_c = .92, .89 h = 4.5357(10^7)J/kg[19,500 BTU/lbm]
e_t = .91 τ_λ = 7.7

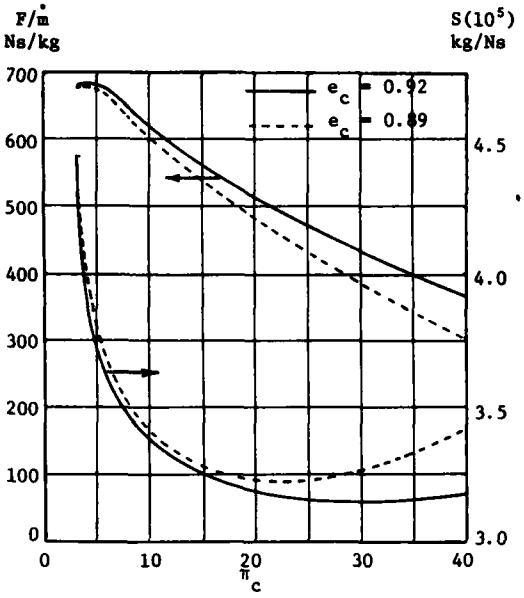

Figure 7.2.2 Effect of Compressor Pressure Ratio and Efficiency on Performance, Turbojet with Losses

Figure 7.2.2 indicates that the general trend of the performance of the turbojet with losses is quite similar to that of the ideal turbojet depicted in Fig. 5.8.1. The most notable difference in trend is that when losses are present a minimum exists in the specific fuel consumption, whereas in the ideal case the specific fuel consumption continues to decrease with increasing compressor pressure ratio.

If the engine was to be used without afterburning, the designer would again be faced with the choice of selecting a low thrust, large pressure ratio, low specific fuel consumption engine as compared to a high thrust, low pressure ratio high specific fuel consumption engine. Another aspect of the designers dilemma becomes apparent when comparing the curves obtained for the two different compressor efficiencies. Thus, for example, if a designer chose a compression ratio of 30 for use in a supersonic transport because his compressor design group had promised a compressor with $e_c = 0.92$, and then the group delivered a compressor with $e_c = 0.89$, it can be seen that the choice of $\pi_c = 30$ would be quite inappropriate. That is, such a compressor would be of a higher pressure ratio than that leading to minimum fuel consumption. Thus, the designer would have a compressor that was heavier (and more expensive) than that leading to a minimum specific fuel consumption, he would also have lower thrust per frontal area, and finally he would have an acute need to change his location of employment.

The effects of nozzle off-design can be investigated by considering the engine to have the same parameters as those indicated above, but to have various values of p_9/p_0. Figure 7.2.3 shows the effect upon specific fuel consumption of varying the exit pressure for an engine with $\pi_c = 16$, $e_c = 0.92$ and other parameters as given above.

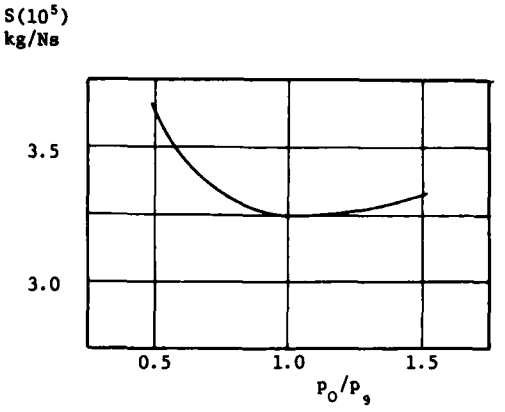

Figure 7.2.3 Effect of Exit Pressure Variations on Specific Fuel Consumption

It is apparent from Fig. 7.2.3 that variations in the pressure ratio p_9/p_0 in the neighborhood of $p_9/p_0 = 1$ do not strongly affect the specific fuel consumption. It is hence of great importance to consider this mild sensitivity of S to p_9/p_0 when designing a nozzle so as to select that nozzle giving the best combination of internal and external performance.

In order to assess the effects of afterburning, an engine was considered with the same characteristics as that considered above but with the addition that $e_c = 0.92$, $\eta_{AB} = 0.96$, $\pi_n = 0.96$ burner on, $= 0.98$ burner off, $\tau_{\lambda AB} = 8.8$, and $\gamma_{AB} = \gamma_t$. Figure 7.2.4 shows the results.

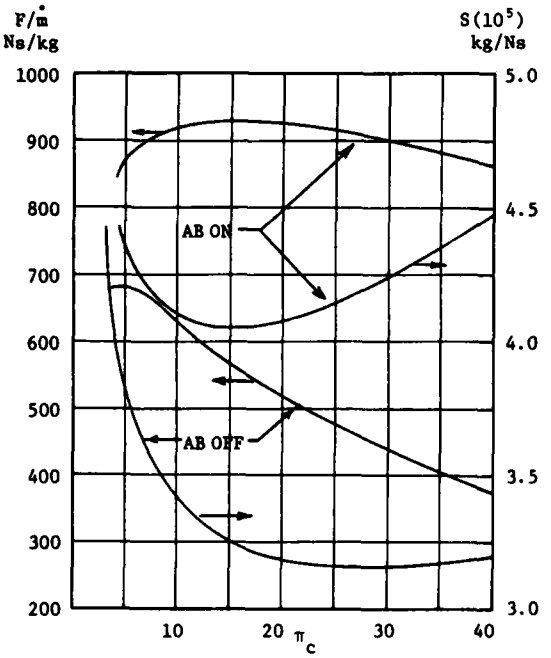

Figure 7.2.4 Performance of Turbojet with Afterburning

7.3 THE TURBOFAN

The performance equations for the turbofan will be developed with the same, or equivalent, assumptions as utilized for the analysis of the turbojet, Sec. (7.2). The equations will be developed to allow for both primary stream afterburning and/or secondary stream afterburning. Only the case of separate exhaust streams will be considered here, as it is hoped that the techniques of cycle analysis as developed herein together with the results of Sec. (5.15.1) will enable the interested reader to rapidly generate an analysis for the mixed stream case if so desired.

7.3.1 CYCLE ANALYSIS OF THE TURBOFAN WITH LOSSES

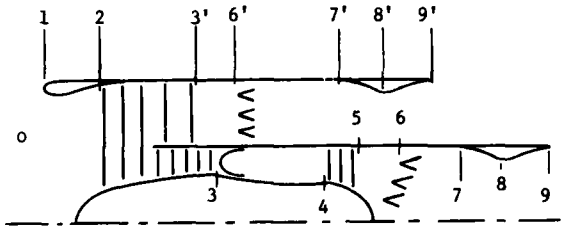

Figure 7.3.1 Turbofan Reference Stations

The expression for the uninstalled thrust can be written as the direct sum of the primary stream and secondary stream thrust contributions to give

$$F_A = (\dot{m}_1+\dot{m}_f+\dot{m}_{fAB})u_9 - \dot{m}_1 u_0 + (p_9-p_0)A_9 + (\dot{m}_2+\dot{m}_{fAB'})u_{9'} - \dot{m}_2 u_0 + (p_{9'}-p_0)A_{9'} \quad (7.3.1)$$

This expression can then be manipulated in a manner completely analogous to that of Sec. (7.2.1) to give

$$\frac{F_A}{\dot{m}_1+\dot{m}_2} = \frac{a_0}{1+\alpha}\left\{(1+f+f_{AB})\left(M_0\frac{u_9}{u_0}\right)-M_0+(1+f+f_{AB})\frac{1}{\gamma_c\left(M_0\frac{u_9}{u_0}\right)}\times\frac{T_9}{T_0}\left(1-\frac{p_0}{p_9}\right)+\alpha\left[(1+f_{AB'})\left(M_0\frac{u_{9'}}{u_0}\right)-M_0+(1+f_{AB'})\frac{1}{\gamma_c\left(M_0\frac{u_{9'}}{u_0}\right)}\frac{T_{9'}}{T_0}\left(1-\frac{p_0}{p_{9'}}\right)\right]\right\} \quad (7.3.2)$$

SECONDARY STREAM

The temperature and pressure relationships for the secondary stream may be written

$$T_{t9'} = T_{9'}\left(1+\frac{\gamma_{AB'}-1}{2}M_{9'}^2\right) = T_0\frac{C_{p_c}}{C_{p_{AB'}}}\tau_{\lambda AB'} \quad (7.3.3)$$

$$p_{t9'} = p_{9'}\left(1+\frac{\gamma_{AB'}-1}{2}M_{9'}^2\right)^{\frac{\gamma_{AB'}}{\gamma_{AB'}-1}} \quad (7.3.4)$$

here $$\frac{p_{t9'}}{p_{9'}} = \frac{p_0}{p_{9'}}\pi_r\pi_d\pi_{c'}\pi_n, \quad (7.3.5)$$

Hence noting $M_0^2\left(\frac{u_{9'}}{u_0}\right)^2 = \frac{\gamma_{AB'}R_{AB'}T_{9'}}{\gamma_c R_c T_0}M_{9'}^2$, there is obtained

$$M_0^2\left(\frac{u_{9'}}{u_0}\right)^2 = \frac{2}{\gamma_c-1}\tau_{\lambda AB'}\left[1-\left(\frac{p_{t9'}}{p_{9'}}\right)^{-\left(\frac{\gamma_{AB'}-1}{\gamma_{AB'}}\right)}\right] \quad (7.3.6)$$

PRIMARY STREAM

The relationships of Sec. (7.2.1) leading to Eqs. (7.2.9) and (7.2.10) remain identical for use in the description of the turbofan primary stream. The expression for the turbine temperature ratio must be modified, however, to include the effect of power extraction by the fan. We thus write for the power balance of fan compressor and turbine

$$\dot{m}_1 C_{p_c}(T_{t_3}-T_{t_2})+\dot{m}_2 C_{p_c}(T_{t_{3'}}-T_{t_2}) = \eta_m(\dot{m}_1+\dot{m}_f)C_{p_t}(T_{t_4}-T_{t_5})$$

Dividing this expression by $\dot{m}_1 C_{p_c} T_0$, and rearranging, there is obtained

$$\tau_t = 1-\frac{1}{\eta_m(1+f)}\frac{\tau_r}{\tau_\lambda}\left[(\tau_c-1)+\alpha(\tau_{c'}-1)\right] \quad (7.3.7)$$

also, $$\pi_t = \tau_t^{\frac{\gamma_t}{(\gamma_t-1)e_t}} \quad (7.3.8)$$

Expressions for the fuel to air ratios are obtained by considering enthalpy balances across each of the burners. The expressions for the primary burner and afterburner remain exactly as given by Eqs. (7.2.13) and (7.2.14). For the secondary afterburner we obtain

$$\dot{m}_2 C_{p_c}T_{t_{3'}}+\dot{m}_{fAB'}\eta_{AB'}h = (\dot{m}_2+\dot{m}_{fAB'})C_{p_{AB'}}T_{t_8},$$

Hence, dividing by $\dot{m}_2 C_{p_c} T_0$ and rearranging, we obtain

$$f_{AB'} = \frac{\tau_{\lambda AB'}-\tau_r\tau_{c'}}{\frac{\eta_{AB'}h}{C_{p_c}T_0}-\tau_{\lambda AB'}} \quad (7.3.9)$$

Finally, the specific fuel consumption is obtained from

$$S = \frac{\dot{m}_f+\dot{m}_{fAB}+\dot{m}_{fAB'}}{F_A} = \frac{f+f_{AB}+\alpha f_{AB'}}{(1+\alpha)\left(\frac{F_A}{\dot{m}_1+\dot{m}_2}\right)} \quad (7.3.10)$$

Equations (7.3.1-7.3.10), (7.2.9), (7.2.10), (7.2.13) and (7.2.14) completely describe the desired performance behavior of the turbofan. The equations are summarized in a form suitable for calculation in Sec. (7.3.2).

7.3.2 SUMMARY OF THE EQUATIONS, TURBOFAN WITH LOSSES, BY-PASS RATIO PRESCRIBED

Inputs: $T_o(K)[°R]$, γ_c, γ_t, γ_{AB}, γ_{AB}', C_{p_c}, C_{p_t}, $C_{p_{AB}}$,

$C_{p_{AB}}'(J/kgK)[\frac{BTU}{lbm°R}]$, $h(J/kg)[\frac{BTU}{lbm}]$,

π_d, π_b, π_n, π_n', η_b, η_{AB}, η_{AB}', η_m,

e_c, e_c', e_t, $\frac{p_9}{p_o}$, $\frac{p_9'}{p_o}$, τ_λ, $\tau_{\lambda AB}$, $\tau_{\lambda AB}'$,

π_c, π_c', M_o, α

Outputs: $\frac{F_A}{\dot m_1+\dot m_2}$ (Ns/kg) $[\frac{F_A}{g_o(\dot m_1+\dot m_2)}\ \frac{lbf}{lbm/sec}]$,

$S(kg/Ns)\ [\frac{lbm\ fuel/hr}{lbf\ \ thrust}]$, f, f_{AB}, f_{AB}', etc.

Equations:

$$R_c = \frac{\gamma_c-1}{\gamma_c} C_{p_c}\ m^2/s^2K$$

$$[R_c = \frac{\gamma_c-1}{\gamma_c} C_{p_c}(2.505)(10^4)\ \frac{ft^2}{sec^2°R}] \qquad (7.3.11)$$

$$a_o = \sqrt{\gamma_c R_c T_o}\ \ m/s\ \ [ft/sec] \qquad (7.3.12)$$

$$\tau_r = 1 + \frac{\gamma_c-1}{2} M_o^2 \qquad (7.3.13)$$

$$\pi_r = \tau_r^{\frac{\gamma_c}{\gamma_c-1}} \qquad (7.3.14)$$

$$\tau_c = \pi_c^{\frac{\gamma_c-1}{\gamma_c e_c}} \qquad (7.3.15)$$

$$\tau_c' = (\pi_c')^{\frac{\gamma_c-1}{\gamma_c e_c'}} \qquad (7.3.16)$$

$$f = \frac{\tau_\lambda - \tau_r\tau_c}{\frac{h\eta_b}{C_{p_c}T_o} - \tau_\lambda} \qquad (7.3.17)$$

$$\tau_t = 1 - \frac{1}{\eta_m(1+f)} \frac{\tau_r}{\tau_\lambda} [(\tau_c-1)+\alpha(\tau_c'-1)] \qquad (7.3.18)$$

$$\pi_t = \tau_t^{\frac{\gamma_t}{(\gamma_t-1)e_t}} \qquad (7.3.19)$$

$$\frac{P_{t_9}}{p_9} = \frac{p_o}{p_9}\pi_r\pi_d\pi_c\pi_b\pi_t\pi_n \qquad (7.3.20)$$

$$\frac{T_9}{T_o} = \frac{\frac{C_{p_c}}{C_{p_{AB}}}\tau_{\lambda AB}}{(\frac{p_{t_9}}{p_9})^{(\frac{\gamma_{AB}-1}{\gamma_{AB}})}} \qquad (7.3.21)$$

NOTE: If no primary stream afterburning is present, then $\tau_{\lambda AB}$ should be put equal to $\tau_\lambda\tau_t$. Also, C_{PAB} and γ_{AB} would be put equal to C_{pt} and γ_t.

$$M_o\frac{u_9}{u_o} = [\frac{2}{\gamma_c-1}\tau_{\lambda AB}\{1-(\frac{p_{t_9}}{p_9})^{-(\frac{\gamma_{AB}-1}{\gamma_{AB}})}\}]^{1/2} \qquad (7.3.22)$$

$$\frac{p_{t_9}'}{p_9'} = \frac{p_o}{p_9'}\pi_r\pi_d\pi_c'\pi_n' \qquad (7.3.23)$$

$$\frac{T_9'}{T_o} = \frac{\frac{C_{p_c}}{C_{p_{AB}}'}\tau_{\lambda AB}'}{(\frac{p_{t_9}'}{p_9'})^{(\frac{\gamma_{AB}'-1}{\gamma_{AB}'})}} \qquad (7.3.24)$$

NOTE: If no secondary stream afterburning is present, then $\tau_{\lambda AB}'$ should be put equal to $\tau_r\tau_c'$. Also, $C_{p_{AB}}'$ and γ_{AB}' would be put equal to C_{p_c} and γ_c.

$$M_o\frac{u_9'}{u_o} = [\frac{2}{\gamma_c-1}\tau_{\lambda AB}'\{1-(\frac{p_{t_9}'}{p_9'})^{-(\frac{\gamma_{AB}'-1}{\gamma_{AB}'})}\}]^{1/2} \qquad (7.3.25)$$

$$f_{Aj} = (1+f)\frac{\tau_{\lambda AB}-\tau_\lambda\tau_t}{\frac{h\eta_{AB}}{C_{p_c}T_o}-\tau_{\lambda AB}} \qquad (7.3.26)$$

$$f_{AB}' = \frac{\tau_{\lambda AB}'-\tau_r\tau_c'}{\frac{h\eta_{AB}'}{C_{p_c}T_o}-\tau_{\lambda AB}'} \qquad (7.3.27)$$

$$\frac{F_A}{\dot m_1+\dot m_2} = \frac{a_o}{1+\alpha}\{(1+f+f_{AB})(M_o\frac{u_9}{u_o}) - M_o + (1+f+f_{AB})$$

$$\times \frac{1}{\gamma_c(M_o\frac{u_9}{u_o})}\frac{T_9}{T_o}(1-\frac{p_o}{p_9}) + \alpha[(1+f_{AB}')(M_o\frac{u_9'}{u_o})$$

$$- M_o + (1+f_{AB}')\frac{1}{\gamma_c(M_o\frac{u_9'}{u_o})}\frac{T_9'}{T_o}(1-\frac{p_o}{p_9'})]\} \qquad (7.3.28)$$

(To obtain British units of $\frac{lbf}{lbm/sec}$, a_o in meters/sec would be replaced by $\frac{a_o}{32.174}$ where a_o should be given in ft/sec .)

$$S = \frac{f+f_{AB}+\alpha f_{AB}'}{(1+\alpha)(\frac{F_A}{\dot m_1+\dot m_2})}\ \ [S = \frac{3600(f+f_{AB}+\alpha f_{AB}')}{(1+\alpha)(\frac{F_A}{g_o(\dot m_1+\dot m_2)})}] \qquad (7.3.29)$$

7.3.3 OPERATION WITH CONVERGENT EXIT NOZZLES

In the usual subsonic transport application of separate stream turbofan engines, no afterburning is utilized and the pressure ratio across both the primary and secondary nozzles is not very large. It is usual therefore to employ convergent, only, nozzles. In such cases, if the nozzles are choked, we have:

$$\frac{p_{t_9'}}{p_{9'}} = \left(\frac{\gamma_c+1}{2}\right)^{\frac{\gamma_c}{\gamma_c-1}} \quad \text{and} \quad \frac{p_{t_9}}{p_9} = \left(\frac{\gamma_t+1}{2}\right)^{\frac{\gamma_t}{\gamma_t-1}} \tag{7.3.30}$$

Thus

$$\frac{p_o}{p_{9'}} = \frac{p_{t_9'}/p_{9'}}{p_{t_9'}/p_o} = \frac{\left(\frac{\gamma_c+1}{2}\right)^{\frac{\gamma_c}{\gamma_c-1}}}{\pi_r\pi_d\pi_{c'}\pi_n} \tag{7.3.31}$$

and

$$\frac{p_o}{p_9} = \frac{p_{t_9}/p_9}{p_{t_9}/p_o} = \frac{\left(\frac{\gamma_t+1}{2}\right)^{\frac{\gamma_t}{\gamma_t-1}}}{\pi_r\pi_d\pi_c\pi_b\pi_t\pi_n} \tag{7.3.32}$$

Equations (7.3.31) and (7.3.32) would then be utilized in Eq. (7.3.28) to give the specific thrust. Note that the expressions are valid for a convergent nozzle only when p_9 and/or $p_{9'}$ are larger than p_o. If Eqs. (7.3.31) and (7.3.32) predict that p_o is larger than p_9 or $p_{9'}$, the given nozzle will not be choked, and in such a case the exit pressure should be taken equal to p_o.

7.3.4 BY-PASS RATIO FOR MINIMUM SPECIFIC FUEL CONSUMPTION

Particularly with engines for transport aircraft, it is appropriate to select the by-pass ratio to give the minimum specific fuel consumption possible for given prescribed operating conditions, design limits, design choices and component efficiencies. We thus consider a non-afterburning turbofan engine with nozzle exit pressures matched to the ambient static pressure, and note from Eqs. (7.3.29) and (7.3.17) that the minimum specific fuel consumption will occur where $(1+\alpha)(F_A/(\dot{m}_1+\dot{m}_2))$ reaches a maximum. Equivalently (from Eq. 7.3.28) we take

$$\frac{\partial}{\partial\alpha}\left[(1+f)\sqrt{\left(M_o\frac{u_9}{u_o}\right)^2} - M_o + \alpha\left\{M_o\frac{u_{9'}}{u_o} - M_o\right\}\right]$$

Taking the derivative, and rearranging slightly, there is obtained

$$\left(M_o\frac{u_9}{u_o}\right)^2 = \left[\frac{1+f}{2}\,\frac{1}{M_o\frac{u_{9'}}{u_o} - M_o}\,\frac{\partial\left(M_o\frac{u_9}{u_o}\right)}{\partial\alpha}\right]^2 \text{ at } S = S^* \tag{7.3.33}$$

Here the asterisk will be used to denote quantities with values appropriate to give the minimum specific fuel consumption, S^*.

We note from Eqs. (7.3.18-7.3.20) and (7.3.22), with $\tau_{\lambda AB} = \tau_\lambda\tau_t$, $\gamma_{AB} = \gamma_t$ and $p_o = p_9$ that we may write

$$\left(M_o\frac{u_9}{u_o}\right)^2 = \frac{2\tau_\lambda}{\gamma_c-1}\left[\tau_t - \frac{1}{\Pi}\tau_t^{-\left(\frac{1-e_t}{e_t}\right)}\right] \tag{7.3.34}$$

Here we have defined for convenience

$$\Pi \equiv (\pi_r\pi_d\pi_c\pi_b\pi_n)^{\frac{\gamma_t-1}{\gamma_t}} \tag{7.3.35}$$

It then follows that

$$\frac{\partial\left(M_o\frac{u_9}{u_o}\right)^2}{\partial\alpha} = \frac{\partial\left(M_o\frac{u_9}{u_o}\right)^2}{\partial\tau_t}\,\frac{\partial\tau_t}{\partial\alpha}$$

Thus with Equations (7.3.35) and (7.3.18) it follows directly that

$$\frac{\partial\left(M_o\frac{u_9}{u_o}\right)^2}{\partial\alpha} = \frac{-2\tau_r(\tau_{c'}-1)}{\eta_m(1+f)(\gamma_c-1)}\left[1+\left(\frac{1-e_t}{e_t}\right)\frac{1}{\Pi}\tau_t^{-1/e_t}\right] \tag{7.3.36}$$

Equations (7.3.33-7.3.35) and (7.3.36) may then be combined to give a single equation for the turbine temperature, ratio, τ_t^*, leading to minimum specific fuel consumption.

$$\tau_{t^*} = \frac{1}{\Pi}\tau_{t^*}^{-\left(\frac{1-e_t}{e_t}\right)} + \frac{1}{2(\gamma_c-1)\tau_\lambda}\left[\frac{\tau_r(\tau_{c'}-1)}{\eta_m\left(M_o\frac{u_{9'}}{u_o} - M_o\right)}\right.$$

$$\left.\times\left\{1+\left(\frac{1-e_t}{e_t}\right)\frac{1}{\Pi}\tau_{t^*}^{-1/e_t}\right\}\right]^2 \tag{7.3.37}$$

It can be noted here that when the ideal conditions assumed in Chapter 5 are inserted in the expression, the equation reduces to that given by Eq. (5.14.23). In fact, the right side of Eq. (7.3.37) varies quite slowly with τ_{t^*}, and as a result the equation can be solved very simply by utilizing functional iteration, Sec. (7.1.2). A suitable starting guess for the iteration is obtained by taking $e_t = 1$ to give

$$\tau_{t_o^*} = \frac{1}{\Pi} + \frac{1}{2(\gamma_c-1)\tau_\lambda}\left[\frac{\tau_r(\tau_{c'}-1)}{\eta_m\left(M_o\frac{u_{9'}}{u_o} - M_o\right)}\right]^2 \tag{7.3.38}$$

Following solution for τ_{t^*}, the related by-pass ratio, α^*, follows directly from Eq. (7.3.7) to give

$$\alpha^* = \frac{\eta_m(1+f)(1-\tau_{t^*})}{(\tau_{c'}-1)}\,\frac{\tau_\lambda}{\tau_r} - \frac{\tau_c-1}{\tau_{c'}-1} \tag{7.3.39}$$

The equations may be summarized in a form suitable for calculation as in the next section.

7.3.5 SUMMARY OF THE EQUATIONS, TURBOFAN WITH LOSSES, NO AFTERBURNING, EXIT PRESSURES MATCHED, AND BY-PASS RATIO OPTIMIZED

Inputs: $T_o(K)[^\circ R]$, γ_c, γ_t, C_{p_c},

$C_{p_t}(J/kgK)[\frac{BTU}{lbm\,^\circ R}]$, $h(J/kg)$ $[\frac{BTU}{lbm}]$,

π_d, π_b, π_n, $\pi_{n'}$, η_b, η_m, e_c, $e_{c'}$, e_t,

π_c, $\pi_{c'}$, M_o, τ_λ

Outputs: $\frac{F_A}{\dot{m}_1+\dot{m}_2}$ (Ns/kg) $[\frac{F_A}{g_o(\dot{m}_1+\dot{m}_2)}\ \frac{\text{lbf}}{\text{lbm/sec}}]$,

S(kg/Ns) $[\frac{\text{lbm fuel/hr}}{\text{lbf thrust}}]$, α^*, f etc.

Equations:

The first seven equations are identical to Eqs. (7.3.11-7.3.17), then:

$$\Pi = (\pi_r\pi_d\pi_c\pi_b\pi_n)^{\frac{\gamma_t-1}{\gamma_t}} \tag{7.3.40}$$

$$\frac{p_{t_9'}}{p_{9'}} = \pi_r\pi_d\pi_{c'}\pi_{n'} \tag{7.3.41}$$

$$M_o\frac{u_{9'}}{u_o} = [\frac{2\tau_r\tau_{c'}}{\gamma_c-1}\{1-(\frac{p_{t_9'}}{p_{9'}})^{-(\frac{\gamma_c-1}{\gamma_c})}\}]^{1/2} \tag{7.3.42}$$

$$\tau_{to^*} = \frac{1}{\Pi} + \frac{1}{2(\gamma_{c-1})\tau_\lambda}[\frac{\tau_r(\tau_{c'}-1)}{\eta_m(M_o\frac{u_{9'}}{u_o}-M_o)}]^2 \tag{7.3.43}$$

$$\tau_{t^*} = \frac{1}{\Pi}\tau_{t^*}^{-(\frac{1-e_t}{e_t})} + \frac{1}{2(\gamma_{c-1})\tau_\lambda}[\frac{\tau_r(\tau_{c'}-1)}{\eta_m(M_o\frac{u_{9'}}{u_o}-M_o)} \times \{1+(\frac{1-e_t}{e_t})\frac{1}{\Pi}\tau_{t^*}^{-1/e_t}\}]^2 \tag{7.3.44}$$

This equation requires iteration to determine τ_{t^*} (utilizing $\tau_{t_o^*}$ as the first guess), then:

$$\alpha^* = \frac{\eta_m(1+f)(1-\tau_{t^*})}{(\tau_{c'}-1)}\frac{\tau_\lambda}{\tau_r} - \frac{\tau_c-1}{\tau_{c'}-1} \tag{7.3.45}$$

$$M_o\frac{u_9}{u_o} = \{\frac{2\tau_\lambda}{\gamma_c-1}[\tau_{t^*} - \frac{1}{\Pi}\tau_{t^*}^{-(\frac{1-e_t}{e_t})}]\}^{1/2} \tag{7.3.46}$$

$$\frac{F_A}{\dot{m}_1+\dot{m}_2} = \frac{a_o}{1+\alpha^*}[(1+f)M_o\frac{u_9}{u_o} - M_o + \alpha^*(M_o\frac{u_{9'}}{u_o}-M_o)] \tag{7.3.47}$$

(To obtain British units of $\frac{\text{lbf}}{\text{lbm/sec}}$, a_o in meters/sec would be replaced by $\frac{a_o}{32.174}$ where a_o should be given in ft/sec .)

$$S = \frac{f}{(1+\alpha^*)(\frac{F_A}{\dot{m}_1+\dot{m}_2})} \quad [S = \frac{3600\ f}{(1+\alpha^*)(\frac{F_A}{g_o(\dot{m}_1+\dot{m}_2)})}] \tag{7.3.48}$$

7.3.6 EXAMPLE RESULTS - TURBOFAN WITH LOSSES

As an example study we consider a "core engine" with $\pi_c = 25$, and investigate the effect of variation in by-pass pressure ratio on the optimum by-pass ratio and on the performance parameters. In order to emphasize the effects upon the design configuration of changes in component efficiencies, three engines are considered, (1) a perfect engine, (2) an engine with high component efficiencies, and (3) an engine with low component efficiencies. Flight Mach number was taken to be $M_o = 0.9$, and the component efficiencies for the three engines taken to be

	π_n	$\pi_{n'}$	π_d	π_b	η_b	η_m	e_c	$e_{c'}$	e_t
1	1	1	1	1	1	1	1	1	1
2	.99	.99	.98	.98	.98	1	.93	.93	.92
3	.96	.96	.95	.95	.96	.98	.87	.86	.86

In addition it was assumed that the exit pressures are matched ($p_{9'} = p_9 = p_o$), and that $h = 4.4194(10^7)$J/kg[19,000 BTU/lbm], $C_{p_c} = 1004.9$ J/kgK [$0.24\frac{\text{BTU}}{\text{lbm°R}}$], $T_o = 233.3$°K[420°R], $\tau_\lambda = 7.71$ and $\gamma_t = 1.35$.

The resulting values for optimal by-pass ratio α^*, versus the by-pass pressure ratio, $\pi_{c'}$, are shown in Fig. 7.3.2.

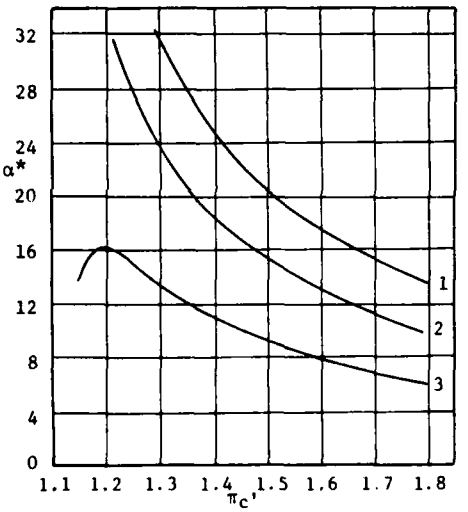

Figure 7.3.2 Optimal By-Pass Ratio Versus By-Pass Pressure Ratio

Several tendencies are immediately notable. It is clear that the optimum by-pass ratio for a given π_c, can change dramatically with changes in component performance, particularly at low values of fan pressure ratio. This again emphasizes the designers problem in that he must have accurate component performance estimates in order to correctly select his engine configuration. The very large by-pass ratio indicated to be optimum (as compared to present day practice) result because of the very high turbine temperature capability assumed, and further because the turbine cooling air penalty has not been included.

Even when the by-pass ratio is selected to be optimal for the given component efficiencies, the penalties in performance for the component inefficiencies are substantial as is evident in Fig. 7.3.3.

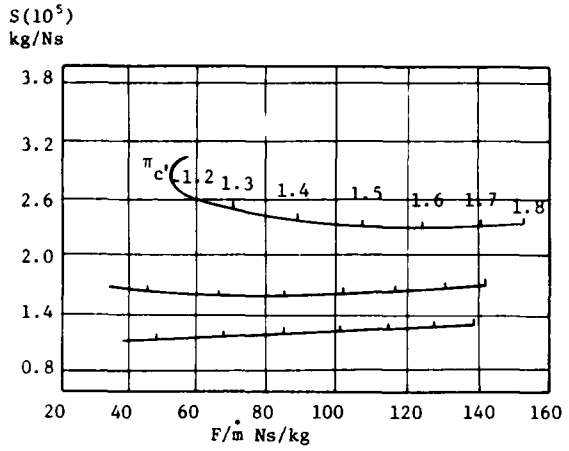

Figure 7.3.3 Turbofan Performance

Similar results for higher Mach number flight are easily attainable, though of course, the optimal by-pass ratios are lower and appropriate fan pressure ratios higher.

The selection of appropriate compressor pressure ratios and fan pressure ratios is aided by a figure of the form of Fig. 7.3.4. Clearly, if specific fuel consumption was the dominant concern, the appropriate values would be $\pi_c = 40$ (or greater) and $\pi_{c'} = 1.3$ (or less). However, we note that at $\pi_c = 40$, the specific thrust is 68, 86, and 102 (Ns/kg) for $\pi_{c'} = 1.3$, 1.4, and 1.5 respectively. The very low specific thrust identified with the low fan pressure ratio could dictate a choice of higher $\pi_{c'}$.

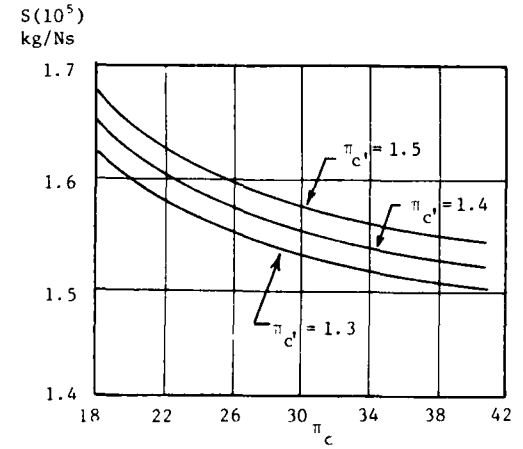

Figure 7.3.4 Variation of Specific Fuel Consumption with By-Pass Pressure Ratio and Compressor Pressure Ratio

7.4 THE TURBO-PROP OR PROP FAN

In recent years renewed interest in highly efficient flight transportation has spurred investigation into "very high by-pass ratio fans." Cycle analysis indicates that such by-pass ratios (for subsonic flight) could approach those corresponding to the "old" turboprop engines (approx. 100/1).

There are several reasons why the turbofan engines became much more popular than the turboprop engines, and it is wise to review such reasons so that we can comprehend why similar concepts are again gaining in popularity. A major reason for the success of the turbofan was its high (subsonic) Mach number capability. In a turboprop, the propeller tip Mach numbers become very large whe. the flight Mach number approaches about 0.7, and the resultant loss in propeller efficiency limits the turboprop use to $M_o < 0.7$. With a turbofan, the onset of high Mach number effects is reduced by the diffusion within the inlet duct. In addition, the individual blade loading can be much reduced by utilizing many blades, and the cowl much reduces blade tip losses.

A further important benefit of conventional turbofans is that they require no gearbox to reduce the tip speeds of their relatively short blades. (Note, of course, that usually a turbofan engine has multiple spools.) Turboprop gearboxes have to date been heavy and subject to reliability problems.

Finally, the high tip speed of the turboprops led to high noise levels, both in the airport vicinity and within the aircraft at flight speeds.

Recent studies of the very high by-pass ratio engines have, however, suggested some compromise designs that show high promise. Thus, if a by-pass ratio of (say) 25 is selected, the corresponding cowl could have identified with it weight penalties and drag penalties that do not compensate for the benefits of the inlet diffusion and of the reduction in tip losses. By considering this "in between" by-pass ratio, (sometimes termed a "prop-fan"), the required shaft speed reduction will be reduced with the result that a lighter and simpler gear box may be utilized. Finally, the effects of tip losses and noise production may be somewhat curtailed by utilizing many (about eight) of the smaller diameter blades, and by sweeping the blades to reduce the relative Mach numbers. An additional benefit is available in that the blades may be made variable pitch which will allow high propeller efficiencies to be maintained over a wide operating range.

It will be recalled (Sec. 5.4) that the propulsive efficiency of a thruster was

$$\eta_p = \frac{2u_o}{u_9+u_o}$$

where u_o = flight speed and u_9 = "jet speed".

This expression is appropriate for a propeller, also, and serves to emphasize that we want a large propeller (to reduce u_9 for a given thrust $F = \dot{m}(u_9 - u_o)$) if the propulsive efficiency is to be high. The propulsive efficiency, η_p , represents the ideal limit of the propeller efficiency defined by

$$\eta_{PROP} = \frac{\text{power to vehicle}}{\text{power to propeller}} \qquad (7.4.1)$$

Thus,

$$\eta_{PROP} = \frac{Fu_o}{W_{PROP}} = \frac{\dot{m}(u_9 - u_o)u_o}{\frac{1}{2}\dot{m}(u_9^2 - u_o^2)} \frac{\frac{1}{2}\dot{m}(u_9^2 - u_o^2)}{W_{PROP}} \equiv \eta_p \eta_L \qquad (7.4.2)$$

Here W_{PROP} is the propeller power input

and $$\eta_L = \frac{\frac{1}{2}\dot{m}(u_9^2 - u_0^2)}{W_{PROP}}$$

η_L represents the power output of the propeller to the fluid stream (in the "axial" direction) divided by the power input to the propeller.

Thus we expect the propeller efficiency to increase with propeller size simply because the ideal propeller efficiency (that is, the propulsive efficiency) increases as more mass is handled. This, of course, relates the propeller efficiency and the "by-pass ratio". It should be noted that if the propeller size is increased to the extreme, η_L will begin to decrease because of high Mach number losses in the outer portion of the blades.

7.4.1 CYCLE ANALYSIS OF THE TURBOPROP

It is appropriate in analyzing the turboprop class of engine to consider the work interaction with the vehicle, rather than the thrust. To facilitate this we introduce the "work interaction coefficient," C, defined by

$$C = \frac{\text{total work interaction with the vehicle/ mass of air through core engine}}{C_{p_c} T_0} \qquad (7.4.3)$$

It is usual with turboprop engines to have the core stream exit nozzle unchoked, so the pressure imbalance term will not be included in the expression for the thrust. We consider the numbering stations indicated in Fig. 7.4.1, and proceed with the analysis in much the same way as with the previously considered engine types.

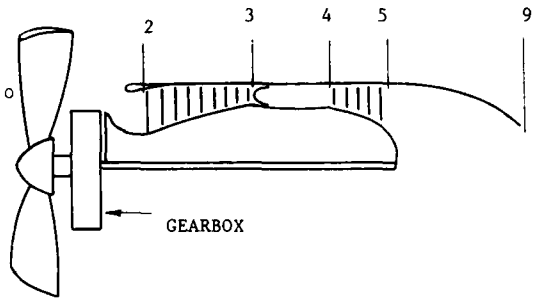

Figure 7.4.1 Turboprop Reference Stations

We will want to select the turbine expansion ratio to give optimal performance, so again utilize the concept of polytropic efficiency. Thus we have

$$\pi_t^{\frac{\gamma_t - 1}{\gamma_t}} = \tau_t^{1/e_t} \qquad (7.4.4)$$

CORE ENGINE

We have $$p_{t_9} = p_9\left(1 + \frac{\gamma_t - 1}{2} M_9^2\right)^{\frac{\gamma_t}{\gamma_t - 1}} = p_0 \pi_r \pi_d \pi_c \pi_b \pi_t \pi_n \qquad (7.4.5)$$

and $$T_{t_9} = T_9\left(1 + \frac{\gamma_t - 1}{2} M_9^2\right) = T_0 \tau_\lambda \tau_t \qquad (7.4.6)$$

Then with $p_0 = p_9$ and again defining

$$\Pi = (\pi_r \pi_d \pi_c \pi_b \pi_n)^{\frac{\gamma_t - 1}{\gamma_t}} \qquad (7.4.7)$$

it follows directly (just as for Eq. 7.3.34) that

$$\left(M_0 \frac{u_9}{u_0}\right)^2 = \frac{2\tau_\lambda}{\gamma_c - 1}\left[\tau_t - \frac{1}{\Pi}\tau_t^{-\left(\frac{1-e_t}{e_t}\right)}\right] \qquad (7.4.8)$$

Thus

$$\frac{F_{core}}{\dot{m}_1} = a_0[(1+f) M_0 \frac{u_9}{u_0} - M_0] \qquad (7.4.9)$$

The work interaction coefficient for the core, C_c, is then given by

$$C_c = \frac{u_0}{C_{p_c} T_0} \frac{F_{core}}{\dot{m}_1} = \frac{a_0^2 M_0}{\gamma_c R_c T_0} \frac{\gamma_c R_c}{C_{p_c}} [1+f) M_0 \frac{u_9}{u_0} - M_0]$$

or $$C_c = (\gamma_{c-1}) M_0 [(1+f) M_0 \frac{u_9}{u_0} - M_0] \qquad (7.4.10)$$

It may be noted here, also, that f is still given by Eq. (7.2.13).

PROPELLER OUTPUT

The net work interaction of the turbine with the gearbox input shaft per mass of core engine air, may be written

$$(1+f)\eta_m C_{p_t}(T_{t_4} - T_{t_5}) - C_{p_c}(T_{t_3} - T_{t_2})$$

Hence the work interaction with the propeller per mass of core engine air is

$$C_{p_c} T_0 \eta_g [\eta_m (1+f)\tau_\lambda (1 - \tau_t) - \tau_r (\tau_c - 1)] \qquad (7.4.11)$$

here η_g = efficiency of the gearbox

The work interaction coefficient for the propeller, C_{PROP}, is then given by

$$C_{PROP} = \eta_{PROP} \eta_g [\eta_m (1+f)\tau_\lambda (1 - \tau_t) - \tau_r (\tau_c - 1)] \qquad (7.4.12)$$

The total work interaction coefficient, C is simply the sum of the core and propeller work interaction coefficients, hence

$$C = C_{PROP} + C_c \qquad (7.4.13)$$

The work interaction coefficient can then be determined when the "work split" between core engine and propeller is decided upon. (This will determine τ_t.) Analogously to the case with the turbofan engine, we may determine an optimum value of τ_t that corresponds to minimum specific fuel consumption, but before doing so, it will be useful to relate the work interaction coefficient to more familiar quantities. Thus we note that the work interaction per second with the flight vehicle is given by the two expressions Fu_o and $C_{p_c}T_o\dot{m}_1 C$. Hence equating these expressions,

$$\text{Specific thrust} = \frac{F}{\dot{m}_1} = C_{p_c} T_o \frac{C}{u_o} \qquad (7.4.14)$$

Similarly, the specific fuel consumption follows from

$$S = \frac{f}{F/\dot{m}} = \frac{f u_o}{C_{p_c} T_o C} \qquad (7.4.15)$$

In British units these expressions become

$$\frac{F}{g_o \dot{m}_1} = 778\ C_{p_c} T_o \frac{C}{u_o}$$

$$\left(778 = \frac{\text{ft lbf}}{\text{BTU}},\ C_{p_c}T_o = \frac{\text{BTU}}{\text{lbm}}\ \text{etc.}\right) \qquad (7.4.16)$$

$$S = \frac{3600}{778} \frac{f u_o}{C_{p_c} T_o C} \frac{\text{lbm fuel/hr}}{\text{lbf thrust}} \qquad (7.4.17)$$

A further parameter often used in describing the performance of propeller engines is the power specific fuel consumption, S_p, where

$$S_p = \frac{\text{kg fuel/sec}}{\text{watts to vehicle}} = \frac{f}{C_{p_c} T_o C} \qquad (7.4.18)$$

In the British system S_p is defined by

$$S_p = \frac{\text{lbm fuel/hr}}{\text{horsepower to vehicle}} = \frac{2545\ f}{C_{p_c} T_o C} \qquad (7.4.19)$$

SELECTION OF THE OPTIMAL TURBINE TEMPERATURE RATIO

Turbopropeller or prop-fan engines will be designed primarily to be low specific fuel consumption engines. Thus, we select τ_t to make S a minimum, or equivalently we locate the maximum of C. Thus, from Eqs. (7.4.10), (7.4.12), and (7.4.13) we obtain

$$\frac{\partial C}{\partial \tau_t} = \frac{\partial}{\partial \tau_t}\left[\eta_{PROP}\eta_g\left\{\eta_m(1+f)\tau_\lambda(1-\tau_t)-\tau_r(\tau_c-1)\right\}\right.$$
$$\left. + (\gamma_c-1)M_o\left\{(1+f)\sqrt{\left(M_o \frac{u_9^2}{u_o}\right)} - M_o\right\}\right]$$
$$= (1+f)\left[-\eta_{PROP}\eta_g\eta_m\tau_\lambda + \frac{(\gamma_c-1)M_o}{2M_o\, u_9/u_o}\frac{\partial (M_o\, u_9/u_o)^2}{\partial \tau_t}\right]$$
$$= 0 \quad \text{when} \quad \tau_t = \tau_{t*} \qquad (7.4.20)$$

The equation for τ_{t*} may then be written in the form

$$\left(M_o \frac{u_9^2}{u_o}\right) = \left[\frac{(\gamma_c-1)M_o}{2\eta_{PROP}\eta_g\eta_m\tau_\lambda}\frac{\partial\left(M_o \frac{u_9^2}{u_o}\right)}{\partial \tau_t}\right]^2 \qquad (7.4.21)$$

An equation for τ_{t*} follows by combining Eqs. (7.4.8) and (7.4.21) to give after some manipulation

$$\tau_{t*} = \frac{1}{\Pi}\tau_{t*}^{-\left(\frac{1-e_t}{e_t}\right)} + \frac{\gamma_c-1}{2}\frac{M_o^2}{\tau_\lambda(\eta_{PROP}\eta_g\eta_m)^2}$$
$$\times \left[1 + \left(\frac{1-e_t}{e_t}\right)\frac{1}{\Pi}\tau_{t*}^{-1/e_t}\right]^2 \qquad (7.4.22)$$

This equation is very similar in form to the equivalent equation for the turbofan, Eq. (7.3.44), and is also easily solved using functional iteration. A suitable starting guess is obtained by taking $e_t = 1$, to give

$$\tau_{t_o*} = \frac{1}{\Pi} + \frac{\gamma_c-1}{2}\frac{M_o^2}{\tau_\lambda(\eta_{PROP}\eta_g\eta_m)^2} \qquad (7.4.23)$$

It might be noted here that the by-pass ratio does not appear in these calculations. This is because the propeller size (and hence by-pass ratio) will be determined once τ_{t*} and hence the work interaction coefficient, C_{PROP}, is obtained. The propeller will be sized to give the desired propeller efficiency.

7.4.2 *SUMMARY OF THE EQUATIONS, TURBOPROP WITH OPTIMAL WORK DISTRIBUTION*

Inputs: $T_o(K)[°R]$, γ_c, γ_t, C_{p_c}, $C_{p_t}(J/kgK)[\frac{BTU}{lbm°R}]$, $h(J/kg)[\frac{BTU}{lbm}]$, π_d, π_b, π_n, η_b, η_m, η_{PROP}, η_g, e_c, e_t, π_c, τ_λ, M_o

Outputs: $\frac{F}{\dot{m}_1}(Ns/kg)[\frac{F}{g_o\dot{m}_1}\frac{lbf}{lbm/sec}]$, $S(kg/Ns)\ [\frac{lbm\ fuel/hr}{lbf\ \ thrust}]$, $S_p(kg/Ws)[\frac{lbm/hr}{HP}]$, C, C_c, C_{PROP}, f etc.

Equations:

$$R_c = \frac{\gamma_c-1}{\gamma_c} C_{p_c}\ m^2/s^2K$$
$$\left[R_c = \frac{\gamma_c-1}{\gamma_c} C_{p_c}(2.505)(10^4)\ \frac{ft^2}{sec^2°R}\right] \qquad (7.4.24)$$

$$a_o \quad \sqrt{\gamma_c R_c T_o}\ \ m/s\ \ [ft/sec] \qquad (7.4.25)$$

$$\tau_r = 1 + \frac{\gamma_c-1}{2} M_o^2 \qquad (7.4.26)$$

$$\pi_r = \tau_r^{\frac{\gamma_c}{\gamma_c-1}} \qquad (7.4.27)$$

$$\tau_c = \pi_c^{\frac{\gamma_c - 1}{\gamma_c e_c}} \tag{7.4.28}$$

$$\Pi = (\pi_r \pi_d \pi_c \pi_b \pi_n)^{\frac{\gamma_t - 1}{\gamma_t}} \tag{7.4.29}$$

$$\tau_{t_o}^* = \frac{1}{\Pi} + \frac{\gamma_c - 1}{2} \frac{M_o^2}{\tau_\lambda (\eta_{PROP} \eta_g \eta_m)^2} \tag{7.4.30}$$

$$\tau_{t^*} = \frac{1}{\Pi} \tau_{t^*}^{-(\frac{1-e_t}{e_t})} + \frac{\gamma_c - 1}{2} \frac{M_o^2}{\tau_\lambda (\eta_{PROP} \eta_g \eta_m)} \times [1 + (\frac{1-e_t}{e_t}) \frac{1}{\Pi} \tau_{t^*}^{-1/e_t}]^2 \tag{7.4.31}$$

This equation requires iteration to determine τ_{t^*} (utilizing $\tau_{t_o}^*$ as the first guess), then:

$$(M_o \frac{u_9}{u_o}) = \{\frac{2\tau_\lambda}{\gamma_c - 1} [\tau_{t^*} - \frac{1}{\Pi} \tau_{t^*}^{-(\frac{1-e_t}{e_t})}]\}^{\frac{1}{2}} \tag{7.4.32}$$

$$f = \frac{\tau_\lambda - \tau_r \tau_c}{\frac{h \eta_b}{C_{p_c} T_o} - \tau_\lambda} \tag{7.4.33}$$

$$C_{PROP} = \eta_{PROP} \eta_g [\eta_m (1+f) \tau_\lambda (1 - \tau_{t^*}) - \tau_r (\tau_{c-1})] \tag{7.4.34}$$

$$C_c = (\gamma_{c-1}) M_o [(1+f)(M_o \frac{u_9}{u_o}) - M_o] \tag{7.4.35}$$

$$C = C_{PROP} + C_c \tag{7.4.36}$$

$$\frac{F}{\dot{m}} = \frac{C_{p_c} T_o}{a_o M_o} C \quad , \quad [\frac{F}{g_o \dot{m}} = 778 \frac{C_{p_c} T_o}{a_o M_o} C] \tag{7.4.37}$$

$$S = \frac{a_o M_o}{C_{p_c} T_o} \frac{f}{C} \quad [S = \frac{3600}{778} \frac{a_o M_o}{C_{p_c} T_o} \frac{f}{C}] \tag{7.4.38}$$

$$S_p = \frac{f}{C_{p_c} T_o C} \quad [S_p = \frac{2545\ f}{C_{p_c} T_o C}] \tag{7.4.39}$$

7.4.3 EXAMPLE RESULTS - TURBOPROP

An engine suitable for use in an eight to ten passenger business aircraft was considered. The parameters assumed were those listed in Table 7.4.1, and the values reflect the somewhat modest values it is reasonable to assume for such small, high reliability engines. The relatively high propeller efficiency has been taken from estimated propeller performance when modern transonic techniques are used in the blade design.

T_o	238.9 K [430°R]
γ_c	1.4
γ_t	1.35
C_{p_c}	996.5 J/kgK [0.238 BTU/lbm°R]
C_{p_t}	1098.2 J/kgK [0.262 BTU/lbm°R]
h	$4.5357(10^7)$ J/kgK [19,500 BTU/lbm]
π_d	0.97
π_b	.98
π_n	0.99
η_b	0.98
η_m	0.95 (power take-off assumed)
η_{PROP}	0.83
η_g	0.99
e_c	0.90
e_t	0.90
τ_λ	6.05
M_o	0.8

Table 7.4.1 Parameters Assumed for Turboprop Example

With the values assumed in the table, a range of compressor pressur ratios was considered, and the thrust and specific fuel consumption corresponding to the minimum fuel consumption at each value of the pressure ratio obtained. Figure 7.4.2 indicates the results. It is interesting to note, also, that at the minimum specific fuel consumption (π_c = 24.5), the ratio of propeller thrust to core thrust was 8.04.

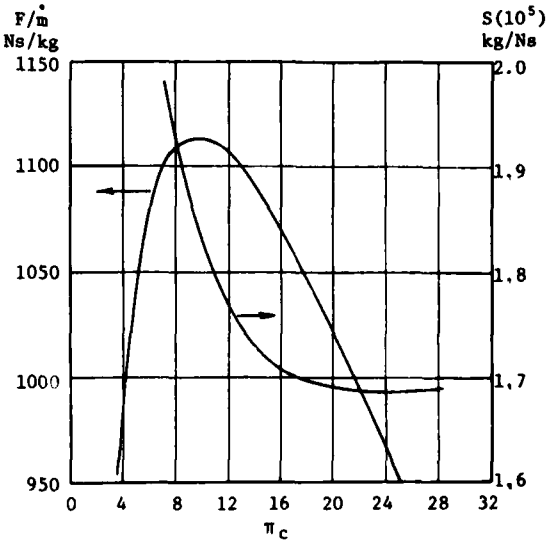

Figure 7.4.2 Specific Thrust and Specific Fuel Consumption Versus Compressor Pressure Ratio for Turboprop with Optimum Turbine Temperature Ratio.

It is of interest to note that when the turboprop of the above example is compared to a turbofan also optimized to minimum specific fuel consumption (with $\pi_{c'} = 1.4$), and with the same parameters where appropriate, the turboprop shows an approximately 13% improvement in specific fuel consumption.

7.5 SUMMARY AND CONCLUSIONS FOR CYCLE ANALYSIS

In the preceding sections, equations capable of describing the expected on design behavior of several different engine types were developed. The intent was twofold in the sense that it is hoped the reader will have gained an understanding of the methodology of cycle analysis, as well as an appreciation for the actual behavior of the several engine types considered. The very simple examples of the analyses considered in this chapter are quite suitable for preliminary design purposes, but it should be realized that more exacting analyses should be utilized if further accuracy is desired. The principal limitations of the analyses considered here arise because of the restriction to calorically perfect gases, because of the lack of inclusion of the penalty paid for utilizing cooling air (see Chapt. 19), and because of the lack of inclusion of the effects of power and air take-offs to operate auxiliary systems. All these effects can be included in a straightforward manner utilizing the same conceptual approaches as already utilized in this chapter, but at the cost of considerably more algebraic complexity.

The very large number of possible input variables in the several example summaries make it difficult indeed to even attempt a comprehensive presentation of the effects of parameter variations. It is of interest, however, to note some of the design trends observable today, the reasons for which are easily shown by utilizing the preceding analyses. It is evident that the industry is spending considerable effort attempting to increase the turbine inlet temperature. The prime benefit for a turbojet that arises from such an increase is in the increased specific thrust.. The turbofan engine also benefits from an increase in turbine inlet temperature because the increased work capability of the turbine causes the optimal by-pass ratio (for minimum S) to increase (giving better propulsive efficiency).

Important related changes in the design of other components also occur when an increase in turbine inlet temperature is attained. Thus, generally a higher compressor pressure ratio will be utilized, to give higher thermal efficiencies. The burner will usually have to be increased in cross-section because the increased burner outlet temperature will cause increased losses in stagnation pressure unless the burner inlet Mach number is reduced. As a result of these combined effects, we find the later stages of even large compressors becoming excessively small, and the burners themselves becoming excessively large. Because of this discrepancy, some modern designs incorporate a single stage centrifugal compressor following an axial compressor. The centrifugal compressor has the advantage of being rugged and not so subject to such things as tip losses as the several stages of axial compressor it replaces. The traditional disadvantage of a centrifugal compressor (large cross-sectional area compared to inlet capture are) is now not significant because the compressor is handling high density air (and hence is relatively small), and is located in front of the necessarily large combustion chambers.

The design of other components is also affected. Thus, if the inlet efficiency is high as well as the turbine inlet temperature, preliminary cycle analysis indicates that the "optimal" by-pass ratio will be very large. (With a low by-pass pressure ratio) Though such large by-pass ratio engines look attractive from the point of view of low noise and high propulsive efficiency, the aircraft can be penalized by the requirement of enormous landing gear to accommodate the very large diameter engines.

These and similar design interactions must all be considered in a successful aircraft design (Chapter 9), and if the design is to be successful, accurate estimates of the component efficiencies and an accurate description of the aircraft flight requirements must be available early in the design process.

Chapter 8

ENGINE OFF-DESIGN PERFORMANCE

Gordon C. Oates

University of Washington

TABLE OF CONTENTS

CHAPTER 8 ENGINE OFF-DESIGN PERFORMANCE

		Page
8.0	Introduction	8-1
8.1	Off-Design Analysis of the Turbojet	8-1
8.1.1	Summary of the Equations, Off-Design Turbojet (Non-Afterburning)	8-3
8.1.2	The Fixed Area Turbojet (FAT)	8-3
8.1.3	The Variable Area Turbojet (VAT)	8-5
8.1.4	Installation Effects	8-8
8.2	The Turbofan Off-Design	8-9
8.3	Off-Design Analysis of the Turboprop	8-9
8.4	The Use of Component Characteristics	8-11
8.4.1	The Compressor Characteristics	8-11
8.4.2	Compressor Behavior During Starting	8-13
8.4.3	The Turbine Characteristics	8-13
8.4.4	The Pumping Characteristics	8-14
8.4.5	Gas Generator - Nozzle Matching	8-15
8.4.6	Performance Prediction with Pumping Characteristics	8-16
8.5	Limitations on the Accuracy of Component Characteristics	8-16
8.6.1	References	8-17

LIST OF FIGURES

		Page
Figure 8.1.1	The Turbojet	8-1
Figure 8.1.2	Compressor Operating Line	8-2
Figure 8.1.3	S/S_R versus F/F_R for a Fixed Area Turbojet	8-4
Figure 8.1.4	Compressor Characteristic, Fixed Area Turbojet	8-5
Figure 8.1.5	Exit Area Variation, Fixed Area Turbojet	8-5
Figure 8.1.6	Variable Area Turbine Nozzles	8-6
Figure 8.1.7	S/S_R versus F/F_R for a VAT and for a FAT	8-7
Figure 8.1.8	A_4/A_{4_R}, A_8/A_{8_R} and A_9/A_{9_R} versus F/F_R, VAT	8-7
Figure 8.1.9	Variation in Turbine Expansion Ratio	8-7
Figure 8.1.10	Annulus Inverting Valve	8-8
Figure 8.1.11	Variable By-Pass Ratio Engine	8-8
Figure 8.3.1	Turboprop Station Numbering	8-9
Figure 8.3.2	Assumed Propeller Efficiency	8-11
Figure 8.3.3	S/S_R and F/F_R versus M_O for a Turboprop	8-11
Figure 8.4.1	Compressor Test Facility	8-12
Figure 8.4.2	Compressor Characteristics	8-12
Figure 8.4.3	Rotating Stall Packet	8-12
Figure 8.4.4	Compressor Section	8-13
Figure 8.4.5	Multiple Spool Compressor	8-13
Figure 8.4.6	Turbine Characteristics	8-14
Figure 8.4.7	Alternate Form Turbine Characteristics	8-14
Figure 8.4.8	Compressor Performance Map	8-14
Figure 8.4.9	Turbine Performance Map	8-15
Figure 8.4.10	The Pumping Characteristics	8-15
Figure 8.4.11	The Fuel Air Ratio	8-15
Figure 8.4.12	Area Variation	8-15
Figure 8.4.13	Gas Generator-Nozzle, Pumping Characteristics	8-16

CHAPTER 8

LIST OF SYMBOLS

The symbols are listed in alphabetical order, first in the English alphabet, then in the Greek alphabet. Subscripts and superscripts are then given. The equation, figure or section in which the symbols are first introduced is indicated in parentheses. Often the symbol will be defined in the text just preceding or just following the equation or figure.

Where appropriate, the location of the introduction of the symbol is referred to in previous chapters.

A - Cross-sectional area (Eq. 8.1.1)

a - Speed of sound (Eq. 8.1.10)

C - Specific heat (Sect. 2.6)

F - Thrust (Eq. 8.1.10)

FAT - Fixed area turbojet (Sect. 8.1.2)

f - Fuel to air ratio (Eq. 8.1.12)

h - Heating value (Eq. 8.1.12)

M - Mach number (Eq. 8.1.10)

$\dot{m}$ - Mass flow rate (Eq. 8.1.1)

N - Rotational speed (Eq. 8.4.1)

p - Pressure (Eq. 8.1.1)

R - Gas constant (Sect. 2.12)

S - Specific fuel consumption (Eq. 8.1.13)

T - Temperature (Eq. 8.1.1)

u - Velocity (Eq. 8.1.9)

VAT - Variable area turbojet (Sect. 8.1.3)

α - By-pass ratio (Eq. 8.2.3)

Γ - Group defined in Eq. 8.1.1

γ - Ratio of specific heats (Sect. 2.6)

δ - Ratio of pressures (Eq. 8.1.6)

η - Efficiency (Eq. 8.1.12)

θ - Ratio of temperatures (Eq. 8.1.6)

π - Ratio of pressures (Sect. 5.1)

τ - Ratio of temperatures or enthalpies (Sect. 5.1)

Subscripts

c - Corrected (Eq. 8.1.5)

- Core (Eq. 7.4.10)

m - Mechanical (Eq. 8.1.3)

p - Constant pressure (Sect. 2.6)

R - Reference (Eq. 8.1.7)

t - Stagnation quantity (Sect. 2.16)

PROP - Propeller (Eq. 7.4.12)

STP - Standard temperature and pressure (Eq. 8.1.6)

1 - Core stream (Eq. 8.2.1)

2 - Fan stream (Eq. 8.2.2)

Subscripts previously defined in Sect. 5.1

AB, b, c, d, n, r, t, λ

0-9 Station numbers (Figs. 5.1.1, 8.1.1)

CHAPTER EIGHT
ENGINE OFF-DESIGN PERFORMANCE

8.0 INTRODUCTION

In the previous chapter, cycle analysis was applied to several example engine types in order to predict the expected performance of such engines as a function of design choices, design limitations or environmental conditions. The various results obtained are hence to be interpreted as the expected behavior of a family of engines as it would behave under the various imposed conditions. In this chapter, we consider the related problem of how a given engine (designed for certain prescribed conditions) will behave at conditions other than that for which it was designed.

Off-design performance analysis can be considered to be of two classes, the first being that where no component performances are available so that the component efficiencies as functions of operating conditions must be estimated, and the second class being that where the components have been developed and tested so that the component characteristics are available. The former class of analysis is used in preliminary estimates of engine off-design performance, whereas the second class is used for more exact estimates of the expected performance of an engine that is approaching completion of construction. Both classes of analysis will be considered in the following.

8.1 OFF-DESIGN ANALYSIS OF THE TURBOJET

We now consider the simple case where both the turbine entrance nozzle and primary nozzle are choked. This puts algebraically simple restrictions on the various relationships, and is in fact true over a wide operating range for modern turbojets. Further simplifying assumptions consistent with those of Chapter 7 will be made. Thus, the gases will be assumed to be calorically perfect both upstream and downstream of the burner, turbine cooling will be ignored and no power take-off or air take-off will be considered. In addition, we will here ignore the fuel to air ratio, f, compared to unity, and will ignore the variation of γ_t and C_{p_t} with power setting. These additional assumptions introduce little inaccuracy because we will in fact be looking for the ratios of desired quantities to their design values, rather than for their absolute values.

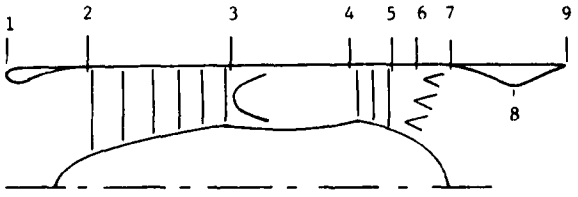

Figure 8.1.1 The Turbojet

The station numbering is indicated in Fig. 8.1.1, and we again utilize the notation introduced in Sec. 5.1 and utilized throughout Chapters 5-7. Equation (2.18.1), together with the assumption of choked flow at stations 4 and 8 allows us to write

$$\dot{m}_4 = \frac{\Gamma_t}{\sqrt{R}} \frac{A_4 p_{t_4}}{\sqrt{T_{t_4}}} \quad \text{and} \quad \dot{m}_8 = \frac{\Gamma_t}{\sqrt{R}} \frac{A_8 p_{t_8}}{\sqrt{T_{t_8}}} \tag{8.1.1}$$

here

$$\Gamma \equiv \sqrt{\gamma} \left(\frac{2}{\gamma+1}\right)^{\frac{\gamma+1}{2(\gamma-1)}}$$

By equating $\dot{m}_4$ and $\dot{m}_8$ there is then obtained

$$\frac{\tau_t^{1/2}}{\pi_t} = \frac{A_8}{A_4} \frac{\pi_{AB}}{\sqrt{\tau_{AB}}} \tag{8.1.2}$$

We may note at this point that the area ratio A_8/A_4 will be prescribed (by the control system), and τ_{AB} will be prescribed by the afterburner setting. π_{AB} will change relatively little, so the area ratio setting and afterburner setting determine the ratio $\tau_t^{1/2}/\pi_t$. We note from Eq. (6.5.1), π_t is a unique function of τ_t and the turbine efficiency, so if the turbine efficiency does not change much over the operating range, Eq. (8.1.2) becomes a single equation for τ_t and hence π_t. As an example we note that for a conventional turbojet without afterburning, A_8 and A_4 remain fixed. (When afterburning is present A_8 is varied so that $A_8 \frac{\pi_{AB}}{\sqrt{\tau_{AB}}}$ remains constant.) For the conventional turbojet, then, the turbine expansion ratio remains very nearly constant over the entire operating range! (The only change in π_t arises because of changes in η_t.)

With τ_t determined from Eq. (8 1.2), τ_c may be obtained from the expression for the power balance, Eq. (7.2.11)

$$\tau_c = 1 + \eta_m \frac{\tau_\lambda}{\tau_r} (1-\tau_t) \tag{8.1.3}$$

We note here that τ_λ is not now the design limit turbine inlet enthalpy divided by the ambient enthalpy, but rather is the selected turbine inlet enthalpy divided by the ambient enthalpy. Thus τ_c (and hence π_c) is determined by the throttle setting (T_{t_4}), environment (T_0), and flight condition (τ_r).

THE MASS FLOW

It will be necessary to determine the variation in mass flow rate in order to determine the variation in thrust. We thus write (with the assumption $f << 1$)

$$\dot{m}_2 = \dot{m}_4 = \frac{\Gamma_t}{\sqrt{R}} \frac{A_4 p_{t_4}}{\sqrt{T_{t_4}}}$$

$$\text{or} \quad \dot{m}_2 = \left[\frac{\Gamma_t}{\sqrt{R}} \sqrt{\frac{c_{p_t}}{c_{p_c}}}\right] \pi_d \pi_b \pi_r \pi_c \frac{p_o}{\sqrt{T_o}} \frac{A_4}{\sqrt{\tau_\lambda}} \qquad (8.1.4)$$

THE CORRECTED MASS FLOW

The corrected mass flow, $\dot{m}_c$, is defined as the group

$$\dot{m}_c \equiv \frac{\dot{m}\sqrt{\theta}}{\delta} \qquad (8.1.5)$$

where $\dot{m}$ = actual mass flow at the plane of interest

$$\theta = \frac{T_t}{T_{STP}}$$

$$\delta = \frac{p_t}{p_{STP}}$$

here STP refers to Standard Temperature and pressure so that

$$T_{STP} = 288.33 \text{ K } [519°R],$$

$$p_{STP} = 1.013(10^5) \text{ N/m}^2 [14.69 \text{ lbf/in}^2]$$

It can be noted from Eq. (2.18.1), that a given value of corrected mass flow corresponds to a particular value of the Mach number at a given reference area. Thus a particular corrected mass flow corresponds to a particular engine face Mach number for a given engine.

With Eq. (8.1.4) we obtain

$$\dot{m}_c = \frac{\dot{m}_2\sqrt{\theta_2}}{\delta_2} = [p_{STP}\Gamma_t\left(\frac{c_{p_t}}{Rc_{p_c}T_{STP}}\right)^{1/2}] \pi_b \pi_c A_4 \left(\frac{\tau_r}{\tau_\lambda}\right)^{1/2} \qquad (8.1.6)$$

It is to be noted, that when the "schedule" of A_8/A_4 is known, τ_t is fixed by Eq. (8.1.2) (assuming no afterburning is present). The chosen area ratio A_8/A_4 and τ_c (hence π_c) thus fully determine τ_λ/τ_r as is apparent from Eq. (8.1.3). It is then apparent from Eq. (8.1.6) that the corrected mass flow is a unique function of the compressor pressure ratio and the chosen area scheduling. If the area scheduling is related directly to the compressor pressure ratio then a unique relationship exists between $\dot{m}_c$ and π_c. (The most obvious example is that occurring in a conventional engine where A_4 and A_8 are fixed.) When the locus of the points of such an $\dot{m}_c$ vs π_c relationship is plotted on a graph, the resulting line is termed the compressor operating line, Fig. 8.1.2.

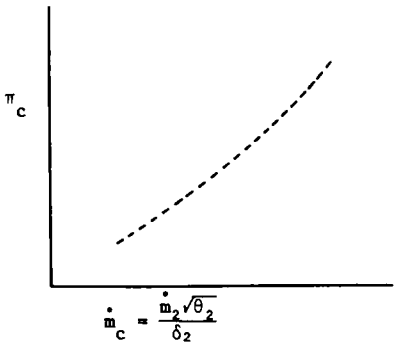

Figure 8.1.2 Compressor Operating Line

It is usually most convenient to obtain the off-design behaviors in terms of the ratio of the desired parameter to the value of the parameter at on design. Denoting the reference, or on design, quantities by a subscript R, we obtain from Eq. (8.1.6)

$$\frac{\dot{m}_c}{\dot{m}_{cR}} = \frac{\pi_b \pi_c}{\pi_{bR}\pi_{cR}} \frac{A_4}{A_{4R}} \left(\frac{\tau_{\lambda R}}{\tau_\lambda} \frac{\tau_r}{\tau_{rR}}\right)^{1/2} \qquad (8.1.7)$$

PERFORMANCE PARAMETERS

We now consider the behavior of the performance parameters when the engine is operated off-design In order to simplify the equations algebraically we will assume that the nozzle exit area is varied so as to keep $p_9 = p_o$, and in addition we continue to assume $f << 1$. We also restrict our attention to non-afterburning turbojets so that with $\tau_{\lambda AB} = \tau_\lambda \tau_t$ we obtain from Eqs. (7.2.24) and (7.2.27)

$$\frac{p_{t_9}}{p_9} = \pi_r \pi_d \pi_c \pi_b \pi_n \pi_t \qquad (8.1.8)$$

$$M_o \frac{u_9}{u_o} = \left[\frac{2}{\gamma_c - 1} \tau_\lambda \tau_t \{1 - \left(\frac{p_{t_9}}{p_9}\right)^{-\left(\frac{\gamma_t - 1}{\gamma_t}\right)}\}\right]^{1/2} \qquad (8.1.9)$$

The equation for the thrust becomes

$$F = \dot{m}(u_9 - u_o) = \dot{m}a_o\left(M_o \frac{u_9}{u_o} - M_o\right) \qquad (8.1.10)$$

from which, with Eq. (8.1.4)

$$\frac{F}{F_R} = \frac{\pi_d \pi_b \pi_r \pi_c}{(\pi_d \pi_b \pi_r \pi_c)_R} \frac{p_o}{p_{oR}} \frac{A_4}{A_{4R}} \left(\frac{\tau_{\lambda R}}{\tau_\lambda}\right)^{1/2} \frac{\left(M_o \frac{u_9}{u_o} - M_o\right)}{\left(M_o \frac{u_9}{u_o} - M_o\right)_R} \qquad (8.1.11)$$

With the assumption that $f \ll 1$, or equivalently that $\frac{h\eta_b}{c_{p_c}T_o} \gg \tau_\lambda$, we have from Eq. (7.2.21)

$$f = \frac{c_{p_c}T_o}{h\eta_b}(\tau_\lambda - \tau_r\tau_c) \tag{8.1.12}$$

Then we obtain from $S = \frac{f}{F/\dot{m}}$, and Eqs. (8.1.10) and (8.1.12)

$$\frac{S}{S_R} = \left(\frac{T_o}{T_{oR}}\right)^{1/2} \frac{\left(M_o \frac{u_9}{u_o} - M_o\right)_R}{\left(M_o \frac{u_9}{u_o} - M_o\right)} \frac{(\tau_\lambda - \tau_r\tau_c)}{(\tau_\lambda - \tau_r\tau_c)_R} \tag{8.1.13}$$

EXIT AREA VARIATION

It has been assumed that the nozzle exit area will be varied in a manner to keep $p_9 = p_o$. As discussed in Sec. (6.1), it is important to know the exit area variation so that installation penalties (boat-tail drag) can be estimated. We may thus write, utilizing Eq. (2.18.5)

$$\frac{A_9}{A_8} = \Gamma_t\left(\frac{\gamma_t - 1}{2\gamma_t}\right)^{1/2} \frac{\left(\frac{p_{t_9}}{p_o}\right)^{\frac{\gamma_t+1}{2\gamma_t}}}{\left\{\left(\frac{p_{t_9}}{p_o}\right)^{\frac{\gamma_t-1}{\gamma_t}} - 1\right\}^{1/2}} \frac{\pi_{AB}}{\pi_n} \tag{8.1.14}$$

The schedule of A_8 variation is separately prescribed, so that the exit area variation may be obtained from

$$\frac{A_9}{A_{9R}} = \frac{A_9/A_8}{(A_9/A_8)_R} \frac{A_8}{A_{8R}} \tag{8.1.15}$$

These equations and appropriate subsidiary equations are summarized in a manner suitable for sequential solution in Sec. (8.1.1). Following Sec. (8.1.1) several example cases are considered.

8.1.1 SUMMARY OF THE EQUATIONS, OFF-DESIGN TURBOJET (Non-Afterburning)

Inputs: γ_c, γ_t, $\frac{A_8}{A_{8_R}}$, $\frac{p_o}{p_{oR}}$, $\frac{T_o}{T_{oR}}$, π_{cR}, and both the reference values and off-design values of $\frac{A_8}{A_4}$, M_o, π_d, π_b, π_{AB}, π_n, τ_λ, η_m, η_c, η_t

Outputs: $\frac{F}{F_R}$, $\frac{S}{S_R}$, $\frac{A_9}{A_{9R}}$, $\frac{\dot{m}_c}{\dot{m}_{cR}}$, $\frac{\pi_c}{\pi_{cR}}$, $\frac{\pi_t}{\pi_{tR}}$

Equations: (where appropriate, valid for both design and off-design cases)

$$\frac{\tau_t^{1/2}}{\left[1 - \frac{1}{\eta_t}(1-\tau_t)\right]^{\gamma_t/(\gamma_t-1)}} = \frac{A_8}{A_4}\pi_{AB} \tag{8.1.16}$$

$$\pi_t = \left[1 - \frac{1}{\eta_t}(1-\tau_t)\right]^{\gamma_t/(\gamma_t-1)} \tag{8.1.17}$$

$$\tau_r = 1 + \frac{\gamma_c - 1}{2} M_o^2 \tag{8.1.18}$$

$$\pi_r = \tau_r^{\gamma_c/(\gamma_c-1)} \tag{8.1.19}$$

$$\tau_c = 1 + \eta_m \frac{\tau_\lambda}{\tau_r}(1 - \tau_t) \tag{8.1.20}$$

$$\pi_c = \left[1 + \eta_c(\tau_c - 1)\right]^{\gamma_c/(\gamma_c-1)} \tag{8.1.21}$$

$$\frac{p_{t_9}}{p_o} = \frac{p_{t_9}}{p_9} = \pi_r\pi_d\pi_c\pi_b\pi_n\pi_t \tag{8.1.22}$$

$$M_o \frac{u_9}{u_o} = \left\{\frac{2}{\gamma_c - 1}\tau_\lambda\tau_t\left[1 - \left(\frac{p_{t_9}}{p_9}\right)^{-(\gamma_t-1)/\gamma_t}\right]\right\}^{1/2} \tag{8.1.23}$$

$$\frac{F}{F_R} = \frac{\pi_d\pi_b\pi_r\pi_c}{(\pi_d\pi_b\pi_r\pi_c)_R}\left(\frac{p_o}{p_{oR}}\right)\frac{A_4}{A_{4R}}\left(\frac{\tau_{\lambda R}}{\tau_\lambda}\right)^{1/2}\frac{\left(M_o \frac{u_9}{u_o} - M_o\right)}{\left(M_o \frac{u_9}{u_o} - M_o\right)_R} \tag{8.1.24}$$

$$\frac{S}{S_R} = \left(\frac{T_o}{T_{oR}}\right)^{1/2} \frac{\left(M_o \frac{u_9}{u_o} - M_o\right)_R}{\left(M_o \frac{u_9}{u_o} - M_o\right)} \frac{(\tau_\lambda - \tau_r\tau_c)}{(\tau_\lambda - \tau_r\tau_c)_R} \tag{8.1.25}$$

$$\frac{A_9}{A_8} = \Gamma_t\left(\frac{\gamma_t - 1}{2\gamma_t}\right)^{1/2} \frac{\left(\frac{p_{t_9}}{p_o}\right)^{\frac{\gamma_t+1}{2\gamma_t}}}{\left\{\left(\frac{p_{t_9}}{p_o}\right)^{(\gamma_t-1)/\gamma_t} - 1\right\}^{1/2}} \frac{\pi_{AB}}{\pi_n} \tag{8.1.26}$$

$$\frac{A_9}{A_{9R}} = \frac{A_9/A_8}{(A_9/A_8)_R} \frac{A_8}{A_{8R}} \tag{8.1.27}$$

$$\frac{\dot{m}_c}{\dot{m}_{cR}} = \frac{\pi_b\pi_c A_4}{(\pi_b\pi_c A_4)_R}\left(\frac{\tau_{\lambda R}}{\tau_\lambda}\frac{\tau_r}{\tau_{rR}}\right)^{1/2} \tag{8.1.28}$$

8.1.2 THE FIXED AREA TURBOJET (FAT)

To date, no main propulsion turbines have been used that incorporate a variable turbine inlet area (A_4). Such "conventional" turbines are also usually coupled with a nozzle of fixed area, A_8, except when an afterburner is utilized. However, it is customary to design a primary nozzle variable throat so that when the afterburner is in operation A_8 is varied just such as to keep the engine operating at its original setting. It can be seen from Eq. (8.1.2) that this would require

$A_8 \frac{\pi_{AB}}{\sqrt{\tau_{AB}}}$ to remain constant. We now utilize the results of Secs. (8.1.4) and (8.1.1) to estimate the off-design behavior of a fixed area turbojet (FAT) operating without afterburner.

The equations of the preceding sections can be simplified considerably in this special case, for we see from Eq. (8.1.2) that

$$\frac{\tau_t^{1/2}}{\pi_t} = \text{const.} \tag{8.1.29}$$

We now make the further assumption that (many of) the component efficiencies remain constant in the regime of parameter variation we are to consider. This is a very convenient numerical approximation for illustrative purposes, and the results obtained utilizing this simplification still reveal the principal effects of the off-design behavior which result primarily from the changes in propulsive efficiency and thermal efficiency, rather than from changes in component efficiencies. If greater accuracy is desired, the more complete equations of Secs. (8.1.1) may be utilized.

With the assumption of constant turbine efficiency, we find that the turbine expansion ratio remains fixed. We may write from Eq. (8.1.3) then, that

$$\tau_c = 1 + (\tau_{cR}-1)\frac{\tau_\lambda}{\tau_{\lambda R}}\frac{\tau_{rR}}{\tau_r} \tag{8.1.30}$$

Utilizing this relationship, and further assuming that η_m, η_c, η_t, π_n, π_{AB}, and π_b remain constant, the equations of Sec. (8.1.1) may be simplified and re-ordered to give the following summary.

SUMMARY OF THE EQUATIONS, OFF-DESIGN FAT

Inputs: γ_c, γ_t, $\frac{p_O}{p_{OR}}$, $\frac{T_O}{T_{OR}}$, η_m, η_c, η_t, π_{cR}, π_{dR}, $\tau_{\lambda R}$, M_{OR}, π_d, τ_λ, M_O

Outputs: $\frac{F}{F_R}$, $\frac{S}{S_R}$, $\frac{A_9}{A_{9R}}$, $\frac{\dot m_c}{\dot m_{cR}}$, $\frac{\pi_c}{\pi_{cR}}$

Equations:

$$\tau_{rR} = 1 + \frac{\gamma_c-1}{2}M_{OR}^2\ ,\ \pi_{rR} = \tau_{rR}^{\gamma_c/(\gamma_c-1)} \tag{8.1.31}$$

$$\tau_r = 1 + \frac{\gamma_c-1}{2}M_O^2\ ,\ \pi_r = \tau_r^{\gamma_c/(\gamma_c-1)} \tag{8.1.32}$$

$$\tau_{cR} = 1 + \frac{1}{\eta_c}\{\pi_{cR}^{(\gamma_c-1)/\gamma_c}-1\} \tag{8.1.33}$$

$$\tau_c = 1+(\tau_{cR}-1)\frac{\tau_\lambda}{\tau_{\lambda R}}\frac{\tau_{rR}}{\tau_r}\ ,$$

$$\pi_c = [1+\eta_c(\tau_c-1)]^{\gamma_c/(\gamma_c-1)} \tag{8.1.34}$$

$$\tau_{tR} = 1-\frac{1}{\eta_m}\frac{\tau_{rR}}{\tau_{\lambda R}}(\tau_{cR}-1)\ ,\ \tau_t = \tau_{tR} \tag{8.1.35}$$

$$\pi_{tR} = [1-\frac{1}{\eta_t}(1-\tau_{tR})]^{\gamma_t/(\gamma_t-1)}\ ,\ \pi_t = \pi_{tR} \tag{8.1.36}$$

$$\left(\frac{p_{t_9}}{p_9}\right)_R = \pi_b\pi_t\pi_n(\pi_r\pi_d\pi_c)_R \tag{8.1.37}$$

$$\frac{p_{t_9}}{p_9} = \left(\frac{p_{t_9}}{p_O}\right)_R\frac{\pi_r\pi_d\pi_c}{(\pi_r\pi_d\pi_c)_R} \tag{8.1.38}$$

$$M_O\frac{u_9}{u_O} = \left[\frac{2}{\gamma_c-1}\tau_\lambda\tau_t\left\{1-\left(\frac{p_{t_9}}{p_9}\right)^{-(\gamma_t-1)/\gamma_t}\right\}\right]^{1/2} \tag{8.1.39}$$

(Note the formula for $\left(M_O\frac{u_9}{u_O}\right)$ is identical, but R quantities to be used)

$$\frac{F}{F_R} = \frac{\pi_r\pi_d\pi_c}{(\pi_r\pi_d\pi_c)_R}\frac{p_O}{p_{OR}}\left(\frac{\tau_{\lambda R}}{\tau_\lambda}\right)^{1/2}\frac{\left(M_O\frac{u_9}{u_O}-M_O\right)}{\left(M_O\frac{u_9}{u_O}-M_O\right)_R} \tag{8.1.40}$$

$$\frac{S}{S_R} = \left(\frac{T_O}{T_{OR}}\right)^{1/2}\frac{\left(M_O\frac{u_9}{u_O}-M_O\right)_R}{\left(M_O\frac{u_9}{u_O}-M_O\right)}\frac{(\tau_\lambda-\tau_r\tau_c)}{(\tau_\lambda-\tau_r\tau_c)_R} \tag{8.1.41}$$

$$\frac{A_9}{A_{9R}} = \left[\frac{p_{t_9}/p_O}{(p_{t_9}/p_O)_R}\right]^{(\gamma_t+1)/2\gamma_t}\left[\frac{(p_{t_9}/p_O)_R^{(\gamma_t-1)/\gamma_t}-1}{(p_{t_9}/p_O)^{(\gamma_t-1)/\gamma_t}-1}\right]^{1/2} \tag{8.1.42}$$

$$\frac{\dot m_c}{\dot m_{cR}} = \frac{\pi_c}{\pi_{c_R}}\left(\frac{\tau_{cR}-1}{\tau_c-1}\right)^{1/2} \tag{8.1.43}$$

As an example calculation, we consider an engine held at fixed altitude and Mach number. Parameters assumed are $\gamma_c = 1.4$, $\gamma_t = 1.3$, $\eta_m = 1$, $\eta_c = 0.88$, $\eta_t = 0.9$, $\pi_b = 0.98$, $\pi_n = 0.99$, $\pi_d = 0.97$, $\pi_{cR} = 20$, $\tau_{\lambda R} = 7$, $M_O = 0.8$. Figure 8.1.3 shows the resulting variation in specific fuel consumption versus thrust.

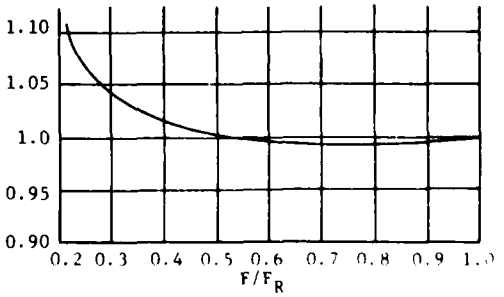

Figure 8.1.3 $\frac{S}{S_R}$ versus $\frac{F}{F_R}$ for a fixed area turbojet.

It is evident that the specific fuel consumption at first decreases with decrease in thrust, but later increases at very reduced thrust levels. This behavior is of enormous importance in determining the proper sizing of an engine for use in such things as a high performance fighter. It is often desirable to have such a fighter have a subsonic "ferry" capability, and in such a case the engine could be required to operate at very low thrust levels. If the engine is very large, such low thrust levels could be well on the "back side of the SFC bucket".

It should be noted that it is the increase in propulsive efficiency that causes the original reduction in specific fuel consumption. At lower thrust levels, however, the decreasing thermal efficiency (caused by decreasing π_c), coupled with the small output compared to the component losses, causes the specific fuel consumption to rise. Figure 8.1.4 shows the related compressor characteristic as the thrust is decreased.

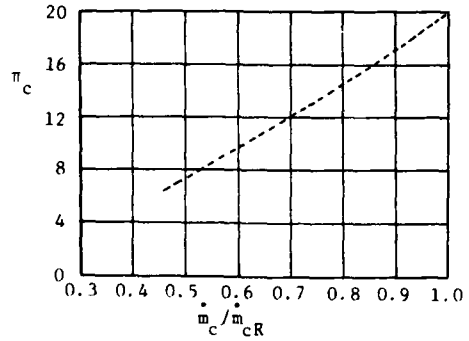

Figure 8.1.4 Compressor Characteristic, Fixed Area Turbojet

Finally, the substantial contraction required of the exit nozzle to keep the exit pressure balanced is shown in Fig. 8.1.5.

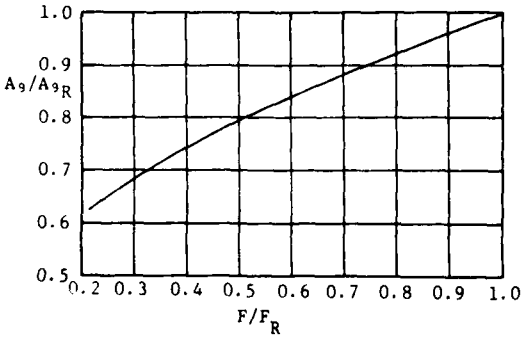

Figure 8.1.5 Exit Area Variation, Fixed Area Turbojet

A second example of some interest is that wherein an aircraft flys at the same Mach number but at two different altitudes. We consider the case where the turbine inlet temperature is held the same so that

$$\frac{\tau_\lambda}{\tau_{\lambda R}} = \frac{T_{OR}}{T_O} .$$

We consider the case where $T_O/T_{OR} = 0.759$ and $p_O/p_{OR} = 0.162$ and take all other values as given in the preceding example. (Note these ratios of T_O/T_{OR} and p_O/p_{OR} correspond approximately to the changes experienced in going from sea level to 40,000 ft. altitude.) Straightforward calculation yields $F/F_R = .345$, $S/S_R = .900$, $\dot{m}_c/\dot{m}_{cR} = 1.57$, $\pi_c/\pi_{cR} = 1.80$, $A_9/A_{9R} = 1.42$.

It is at first surprising that the thrust decreases as little as indicated, particularly when the large reduction in pressure is considered. The prime reason for the relatively small decrease in thrust is that the reduced compressor inlet temperature reduces the compressor power requirement to sustain a given pressure ratio. Thus, because the turbine inlet temperature is fixed, the turbine has the power capability of providing much higher compression, with consequent increase in corrected mass flow and hence thrust. There is some question whether, in fact, the compressor could be operated at 1.8 times the sea level value of compressor ratio, and it is possible that the engine would have to be throttled back at altitude. It is, of course, the high compression ratio that is primarily responsible for reducing the specific fuel consumption, even though the propulsive efficiency has decreased.

As a final example of off-design performance of a fixed area turbojet, consider the problem of designing an engine for an aircraft capable of flying at Mach number three that is to be able to take-off under its own power. Thus we consider an engine with $\pi_{cR} = 9$, at $M_{OR} = 0$, and with $T_O/T_{OR} = 0.759$, $p_O/p_{OR} = 0.162$ and $M_O = 3$. Other conditions are as in the preceding examples. Straightforward calculation then gives $\pi_c = 3.34$, $\dot{m}_c/\dot{m}_{cR} = .541$, $F/F_R = 0.841$, $S/S_R = 1.15$, and $A_9/A_{9R} = 5.04$ (!)

It can be seen that when an engine is to be used in an aircraft with such an extreme operating range, the restriction to fixed A_4 and A_8 presents a very serious design problem. Thus it is hard to imagine how such a huge exit area variation could be accomplished, and it is probable that the engine would have to be operated with substantial overexpansion in the nozzle at take-off and substantial underexpansion at cruise. The large reduction in compressor pressure ratio, with corresponding reduction in corrected mass flow, would be difficult to achieve, and would probably imply the use of compressor bleed at the cruise condition. (Sec. 8.4.2)

These simple calculations serve to emphasize that the difficult task of designing an engine is further complicated when the engine must operate at more than one "design point" for a substantial time. Some of the restrictions are so severe, that competing concepts to conventional engines have gained interest as the demand for multiple mission aircraft has grown. An example of such a concept is considered in the next section.

8.1.3 THE VARIABLE AREA TURBOJET (VAT)

A concept of considerable interest to the industry today is that of the variable area turbojet, or VAT. It is planned with such a machine to make both the turbine inlet area variable (by

having movable turbine nozzles for example Fig. 8.1.6), and the primary nozzle variable.

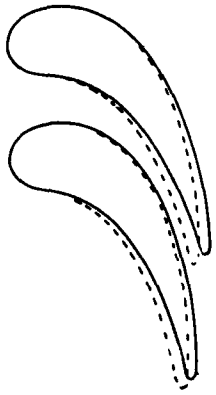

Figure 8.1.6 Variable Area Turbine Nozzles

In spite of the enormous complexity and difficulty of developing such a concept, the possible performance benefits are sufficiently substantial that considerable research and development effort is presently being devoted to such concepts. To investigate the possible performance benefits, let us again consider the first example of Sec. (8.1.2). In Sec. (8.1.2) the behavior of an engine at fixed Mach number and altitude was considered. It was found that the specific fuel consumption rose at low thrust levels, primarily because the compressor pressure ratio decreased with thrust.

We now consider a competitive engine in which the turbine and primary nozzle areas are varied in a manner to keep the compressor pressure ratio and corrected mass flow constant. We note that by so doing, not only will the thermodynamic efficiency of the engine be maintained, but the inlet airflow will also be maintained, thereby preventing excessive inlet spillage drag. The required relationship for the area variation follows directly from Eq. (8.1.7) to give

$$\frac{A_4}{A_{4R}} = \left(\frac{\tau_\lambda}{\tau_{\lambda R}}\right)^{1/2} \tag{8.1.44}$$

Equation (8.1.3) also gives directly

$$\tau_t = 1 - (1 - \tau_{tR}) \frac{\tau_{\lambda R}}{\tau_\lambda} \tag{8.1.45}$$

We thus find that this VAT is quite the opposite to the FAT, in that the VAT has a variable turbine expansion ratio but fixed compressor pressure ratio, whereas the FAT has a variable compressor pressure ratio but fixed turbine expansion ratio.

The required primary nozzle area variation follows from Eq. (8.1.2) to give

$$\frac{A_8}{A_{8R}} = \frac{A_4}{A_{4R}} \left(\frac{\tau_t}{\tau_{tR}}\right)^{1/2} \frac{\pi_{tR}}{\pi_t} = \left(\frac{\tau_\lambda \tau_t}{\tau_{\lambda R} \tau_{tR}}\right)^{1/2} \frac{\pi_{tR}}{\pi_t} \tag{8.1.46}$$

The remaining equations follow directly from Eqs. (8.1.16)-(8.1.28). In the special case of flight at fixed Mach number and fixed altitude (i.e., fixed M_o, T_o, p_o), for example, the necessary equations may be summarized as follows.

SUMMARY OF THE EQUATIONS, OFF-DESIGN VAT (Fixed π_c, M_o, T_o, p_o and component efficiencies)

Inputs: γ_c, γ_t, η_c, η_t, η_m, π_b, π_d, π_n, π_c, $\tau_{\lambda R}$, M_o, τ_λ

Outputs: $\frac{F}{F_R}$, $\frac{S}{S_R}$, $\frac{A_4}{A_{4R}}$, $\frac{A_9}{A_{9R}}$, $\frac{1/\pi_t}{1/\pi_{tR}}$, $\frac{A_8}{A_{8R}}$

Equations:

$$\tau_r = 1 + \frac{\gamma_c - 1}{2} M_o^2, \quad \pi_r = \tau_r^{\gamma_c/(\gamma_c - 1)} \tag{8.1.47}$$

$$\tau_c = 1 + \frac{1}{\eta_c} \{\pi_c^{(\gamma_c - 1)/\gamma_c} - 1\} \tag{8.1.48}$$

$$\tau_{tR} = 1 - \frac{1}{\eta_m} \frac{\tau_r}{\tau_{\lambda R}} (\tau_c - 1), \quad \pi_{tR} = \left[1 - \frac{1}{\eta_t} (1 - \tau_{tR})\right]^{\gamma_t/(\gamma_t - 1)} \tag{8.1.49}$$

$$\tau_t = 1 - (1 - \tau_{tR}) \frac{\tau_{\lambda R}}{\tau_\lambda}, \quad \pi_t = \left[1 - \frac{1}{\eta_t} (1 - \tau_t)\right]^{\gamma_t/(\gamma_t - 1)} \tag{8.1.50}$$

$$\left(\frac{p_{t_9}}{p_9}\right)_R = \pi_b \pi_c \pi_n \pi_r \pi_d \pi_{tR}, \quad \frac{p_{t_9}}{p_9} = \left(\frac{p_{t_9}}{p_9}\right)_R \frac{\pi_t}{\pi_{tR}} \tag{8.1.51}$$

$$M_o \frac{u_9}{u_o} = \left[\frac{2}{\gamma_c - 1} \tau_\lambda \tau_t \left\{1 - \left(\frac{p_{t_9}}{p_9}\right)^{-(\gamma_t - 1)/\gamma_t}\right\}\right]^{1/2} \tag{8.1.52}$$

(Note the formula for $\left(M_o \frac{u_9}{u_o}\right)_R$ is identical but R quantities to be used.)

$$\frac{F}{F_R} = \frac{M_o \frac{u_9}{u_o} - M_o}{\left(M_o \frac{u_9}{u_o} - M_o\right)_R} \tag{8.1.53}$$

$$\frac{S}{S_R} = \frac{\tau_\lambda - \tau_r \tau_c}{(\tau_\lambda - \tau_r \tau_c)_R} \frac{1}{F/F_R} \tag{8.1.54}$$

$$\frac{A_4}{A_{4R}} = \left(\frac{\tau_\lambda}{\tau_{\lambda R}}\right)^{1/2} \tag{8.1.55}$$

$$\frac{A_8}{A_{8R}} = \left(\frac{\tau_\lambda \tau_t}{\tau_{\lambda R} \tau_{tR}}\right)^{1/2} \frac{\pi_{tR}}{\pi_t} \tag{8.1.56}$$

$$\frac{A_9/A_8}{(A_9/A_8)_R} = \left\{\frac{p_{t9}/p_9}{p_{t9}/p_9)_R}\right\}^{(\gamma_t+1)/2\gamma_t} \left[\frac{(\frac{p_{t9}}{p_9})^{(\gamma_t-1)/\gamma_t} - 1}{(\frac{p_{t9}}{p_9})_R^{(\gamma_t-1)/\gamma_t} - 1}\right]^{1/2} \tag{8.1.57}$$

$$\frac{A_9}{A_{9R}} = \frac{A_9/A_8}{(A_9/A_8)_R}\frac{A_8}{A_{8R}} \tag{8.1.58}$$

As an example calculation, we consider an engine with the same on-design characteristics as the engine considered in the first example of Sec. (8.1.2). Thus we take $\gamma_c = 1.4$, $\gamma_t = 1.3$, $\eta_m = 1$, $\eta_c = 0.88$, $\eta_t = 0.9$, $\pi_b = 0.98$, $\pi_n = 0.99$, $\pi_d = 0.97$, $\pi_c = 20$, $\tau_{\lambda R} = 7$, and $M_o = 0.8$. Figure 8.1.7 shows the resulting variation in specific fuel consumption versus thrust. Included for comparison is the FAT result (Fig. 8.1.3) and also the related turbine enthalpy ratio τ_λ.

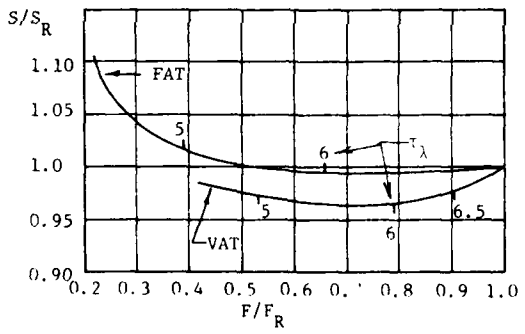

Figure 8.1.7 S/S_R versus F/F_R for a VAT and for a FAT

The potential operating advantage for a VAT is evident here in that the superior thermal efficiency and propulsive efficiency of the VAT at part thrust operation leads to substantial benefits in reduced specific fuel consumption. A further benefit is implied by the behavior of the turbine inlet enthalpy. Thus the more rapid fall-off with thrust of the turbine inlet temperature for the VAT indicates the possibility that less cooling air will be required from a VAT during part throttle operation than will be required for a FAT.

The required area variations for the VAT are shown in Fig. 8.1.8.

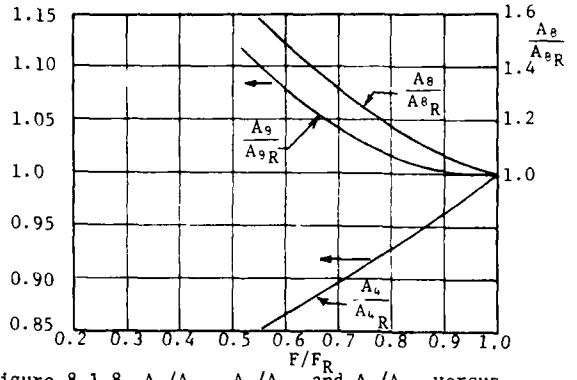

Figure 8.1.8 A_4/A_{4R}, A_8/A_{8R} and A_9/A_{9R} versus F/F_R, VAT

It is evident that substantial variations in A_4 and A_8 are required, and there is some question as to whether the more extreme variations could be attained in a working design. We note, however, the very much reduced area variation required of the exit nozzle. (Note this particular VAT requires an area increase, in contrast to the severe decrease required for the FAT.) As discussed in Sec. (8.1.4) this reduced exit area variation could lead to substantial benefits in reduced installation losses.

The required variation in turbine expansion ratio is indicated in Fig. 8.1.9.

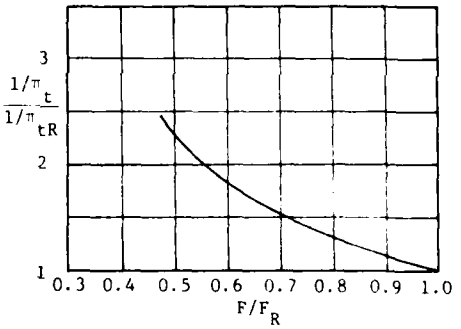

Figure 8.1.9 Variation in Turbine Expansion Ratio

It is clear that at very low thrust levels the turbine expansion ratio compared to that required at the on design point is very large. This required variation of expansion ratio would seem to imply the need for substantial research and development to extend the capabilities of present day turbines. It would also seem to imply the use of a turbine with several more stages than would be required for operation at high thrust levels, so that the turbine would be capable of supporting the required large expansion ratios at low thrust levels.

Further potential operating benefits of a VAT become apparent when flight at various altitudes, various Mach numbers etc. are considered. It is these possible benefits that have stimulated industry interest in the VAT as well as other variable geometry engines, such as the variable by-pass ratio turbofan.

Though the analysis of other variable geometry engines will not be included here, a brief description of some possible engine types will be given to illustrate the extent of creative thought that has been directed to the problem of developing engines with efficient multi-mission capability. In Ref. (8.1) the annulus inverting valve (AIV) is described, and many possible cycles utilizing the value are considered. The valve has the capability of switching half the flow it encounters from the inside of an annulus to the outside, and vice-versa. Alternatively it can be operated so that the flow passes straight through the valve. This capability offers the opportunity of varying the cycle by-pass ratio and by-pass pressure ratio to better suit the required operating point. The valve in its most simple utilization is illustrated in Fig. 8.1.10.

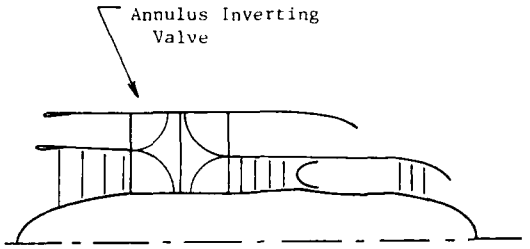

Figure 8.1.10 Annulus Inverting Valve

It is evident from Fig. 8.1.10 that the AIV allows operation of the engine as a turbofan engine with low compressor pressure ratio, or as a turbojet engine with high compressor pressure ratio. (In the latter mode, half the inlet air is by-passed.) The design calculations of Chapter 7 indicated that flight at low Mach numbers is best served by a turbofan, whereas flight at high Mach numbers is best served by a turbojet. Thus, the AIV offers the opportunity of substantially extending an engine's efficient flight envelope.

Many other variable geometry concepts are possible, as for example the variable by-pass ratio engine illustrated in Fig. 8.1.11.

In an engine such as that shown in Fig. 8.1.11, a relatively simple diverting valve would be utilized to vary the amount of air by-passed. The required adjustments for power split between fan and compressor would be supplied through the use of a variable area turbine nozzle at entrance to the low pressure turbine. This latter configuration would have the added advantage that the variable area nozzles would be operating in a temperature regime such that cooling would not be required, and hence the required mechanical complexity of the movable nozzles would be greatly reduced.

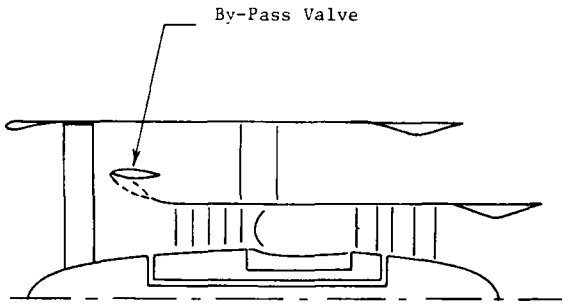

Figure 8.1.11 Variable By-Pass Ratio Engine

The examples of variable geometry engines cited in this section represent only a few of the very large possible number of engine concepts that deserve consideration, and the future should see extensive study of such advanced concepts. The eventual development and production of such engines will depend upon the many technical trade-offs obviously present, as well as the enormous economic trade-offs required.

8.1.4 INSTALLATION EFFECTS

The example calculations of the preceding two sections illustrated the variation of parameters with the "uninstalled" thrust, and the specific fuel consumption based upon this value of thrust. Many of the major benefits of variable geometry engines are identified with the reduction of installation effects, however.

When a high Mach number aircraft is flown at low Mach number, the mass of air per second swallowed by the projection of the inlet area decreases, but not in fact as rapidly as the engine demand for air decreases. Thus, at low flight Mach numbers the inlet must spill air, and in the case of a sharp edged supersonic inlet, substantial spillage losses occur. It can be seen then that the VAT, by maintaining a high airflow demand, will much reduce such spillage losses at low thrust levels.

A further installation benefit arises for the VAT, because of the small required exit area variation as thrust is reduced. Usually, the exit area when no afterburning is present, even with full thrust, is substantially less than the main engine cross sectional area. This projected area can lead to serious drag penalties and it is important to design the engine aft end so that substantial separation does not occur. When a conventional engine (FAT) is operated at very low thrust levels, the required exit area closure is so substantial that the prevention of separation is usually impossible, and as a result large boat-tail drag penalties are incurred. The VAT, because of its continued handling of a large mass flow rate which is delivered at ever decreasing exit velocity, leads to a requirement of very little area change. As a result the VAT shows

promise of leading to much reduced aft end installation losses as well as reduced inlet losses.

In conclusion, it should be pointed out that the effects upon installation losses for a VAT are comparable to the effects upon uninstalled performance. Thus, the VAT like all competing concepts should be evaluated in terms of the installed behavior. This, of course, requires knowledge of the inlet and aft end losses which must generally be obtained from experiment. (Chaps. 9 and 26)

8.2 THE TURBOFAN OFF-DESIGN

When the off-design performance of a turbofan is considered, a slight additional complication arises in that the variation in performance of each separate stream must be determined. In order to determine these separate variations in performance, additional information must be provided to describe the "work split" between the two streams of the turbine output. To illustrate such a procedure we consider a turbofan in which the fan is driven by its own low pressure turbine, and the high pressure compressor is driven by the high pressure turbine. We introduce the intermediate location between the two turbines as station 4a, and introduce the obvious definitions

$$\tau_{ch} = \frac{T_{t3}}{T_{t3'}} = \frac{\tau_c}{\tau_{c'}},\quad \pi_{ch} = \frac{p_{t3}}{p_{t3'}} = \frac{\pi_c}{\pi_{c'}},\quad \tau_{th} = \frac{T_{t4a}}{T_{t4}},$$

$$\pi_{th} = \frac{p_{t4a}}{p_{t4}},\quad \tau_{tL} = \frac{T_{t5}}{T_{t4a}},\quad \pi_{tL} = \frac{p_{t5}}{p_{t4a}} \qquad (8.2.1)$$

The off-design analysis of the turbofan is much simplified algebraically if, analagously to the assumptions already utilized for description of the off-design performance of the turbojet, we may assume the two exit nozzles to be choked, and both turbine entrances to be choked. These assumptions are valid over a fairly wide operating range for flight at high Mach number, but the exit nozzles will tend to unchoke at only slightly reduced power settings at low Mach numbers. An algebraic method of handling the unchoked nozzle problem is illustrated in Sect. 8.3.

For simplicity of presentation we consider the example of fixed turbine inlet and fixed nozzle exit areas. Analagously to the result of Sect. 8.1.2 it then follows that τ_{th}, π_{th}, τ_{tL}, π_{tL} are all constant. A power balance between high pressure compressor and high pressure turbine then leads to

$$\tau_{c'}(\tau_{ch}-1) = \tau_{c'R}(\tau_{ch}-1)_R \frac{\tau_\lambda/\tau_r}{(\tau_\lambda/\tau_r)_R} \qquad (8.2.2)$$

Similarly a power balance between fan and low pressure turbine gives

$$(\tau_{c'}-1)(\alpha+1) = (\tau_{c'}-1)_R(\alpha+1)_R \frac{\tau_\lambda/\tau_r}{(\tau_\lambda/\tau_r)_R} \qquad (8.2.3)$$

Finally, utilizing the mass flow equation in both streams (as in Eq. 8.1.4) leads to

$$\frac{\alpha}{\alpha_R} = \frac{\pi_{chR}}{\pi_{ch}}\left[\frac{\tau_{c'R}}{\tau_{c'}}\frac{\tau_\lambda/\tau_r}{(\tau_\lambda/\tau_r)_R}\right]^{1/2} \qquad (8.2.4)$$

These three equations (and appropriate intermediate equations for the temperature and pressure ratio in terms of efficiencies) can be iterated rapidly to determine the desired values. Thus, for example, the iteration may be started by assuming $\tau_{c'} = \tau_{c'R}$ in eq. 8.2.2 to give a first estimate of τ_{ch}. This value is used in eq. 8.2.4 to estimate α, and an updated value of $\tau_{c'}$ is then obtained from eq. 8.2.3. This process is repeated until appropriate accuracy is attained. Following solution for these three variables, the remaining performance variables follow in a straightforward manner.

As an example we consider an engine with design conditions Mo=2, $\pi_{c'}$=1.5, π_c=15, α=1, τ_λ=7.2. Calculation then gives

Mo	1.0	1.4	1.8	2.2	2.6	3.0
$\pi_{c'}$	2.02	1.78	1.58	1.43	1.32	1.24
π_c	34.7	25.6	17.9	12.6	9.20	6.94
α	.661	.772	.916	1.09	1.28	1.48

These results indicate that variable geometry should also be considered for use with turbofans. Thus, it is evident that, for example, the by-pass ratio increases with increase in flight Mach number. This tendency is opposite to the tendency indicated for on design behavior. The variable geometry engine already exhibited in Fig. 8.1.11 shows promise to alleviate many of these problems.

8.3 OFF-DESIGN ANALYSIS OF THE TURBOPROP

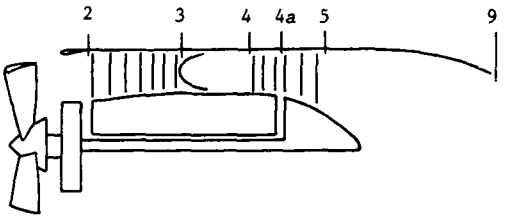

Figure 8.3.1 Turboprop Station Numbering

We begin the analysis of the off-design performance of the turboprop by again assuming that the entrance areas to both turbines are choked, and that the turbine entrance areas and the nozzle exit area are fixed. The power balance between compressor and high pressure turbine then gives immediately

$$\tau_c - 1 = (\tau_c - 1)_R \frac{\tau_\lambda/\tau_r}{(\tau_\lambda/\tau_r)_R} \qquad (8.3.1)$$

In virtually all operating conditions of a turboprop the exit nozzle will not be choked, and we thus write from Eq. (2.18.1)

$$\dot{m}_4 = \frac{A_4 p_{t4}}{\sqrt{T_{t4}}}\sqrt{\frac{\gamma_t}{R}}\left(\frac{2}{\gamma_t+1}\right)^{(\gamma_t+1)/2(\gamma_t-1)} \qquad (8.3.2)$$

$$\dot{m}_9 = \frac{A_9 p_{t9}}{\sqrt{T_{t9}}}\sqrt{\frac{\gamma_t}{R}}\,M_9\left[1+\frac{\gamma_t-1}{2}M_9^2\right]^{-(\gamma_t+1)/2(\gamma_t-1)} \qquad (8.3.3)$$

Equating these two expressions and rearranging slightly there follows

$$M_9 = \frac{A_4}{A_9}\frac{1}{\tau_n\pi_t}\frac{\sqrt{\tau_t}}{\frac{2}{\gamma_t+1}\left(1+\frac{\gamma_t-1}{2}M_9^2\right)^{(\gamma_t+1)/2(\gamma_t-1)}} \tag{8.3.4}$$

We have also

$$\left[1+\frac{\gamma_t-1}{2}M_9^2\right]^{\gamma_t/(\gamma_t-1)} = \frac{p_{t9}}{p_9} = \frac{p_0}{p_9}\pi_r\pi_d\pi_c\pi_b\pi_t\pi_n \tag{8.3.5}$$

Thus noting that $\frac{p_0}{p_9} = 1$ because the exit is unchoked, we have,

$$\tau_t = \frac{1}{\pi_r\pi_d\pi_c\pi_b\pi_n}\left[1+\frac{\gamma_t-1}{2}M_9^2\right]^{\gamma_t/(\gamma_t-1)} \tag{8.3.6}$$

Equations 8.3.4 and 8.3.6, together with the intermediate equation relating π_t and τ_t (Eq. 6.5.1) may be easily solved by functional iteration. With the thus determined values of M_9, π_t and τ_t, the performance variables follow directly. Utilizing the results of the summary of Sec. (7.4.2), with Eqs. (7.3.22) and (8.1.4) the results of the following summary are obtained.

SUMMARY OF THE EQUATIONS, OFF-DESIGN TURBOPROP

Inputs: γ_c, γ_t, η_{PROP}, η_g, η_m, η_c, η_t, η_b, π_d, π_b, π_{cR}, $\tau_{\lambda R}$, M_{oR}, τ_λ, M_o

Outputs: $\frac{F}{F_R}$, $\frac{S}{S_R}$, $\frac{\dot m}{\dot m_R}$, $\frac{\dot m_c}{\dot m_{c_R}}$, π_c

Equations:

$$\tau_{cR} = 1 + \frac{1}{\eta_c}\left(\pi_{cR}^{\frac{\gamma_c-1}{\gamma_c}} - 1\right) \tag{8.3.7}$$

$$\tau_c = 1 + (\tau_{cR}-1)\frac{\tau_\lambda/\tau_r}{(\tau_\lambda/\tau_r)_R} \tag{8.3.8}$$

$$\pi_c = [1 + \eta_c(\tau_c-1)]^{\gamma_c/(\gamma_c-1)} \tag{8.3.9}$$

$$\tau_t = \frac{1}{\pi_r\pi_d\pi_c\pi_b\pi_n}\left[1+\frac{\gamma_t-1}{2}M_9^2\right]^{\gamma_t/(\gamma_t-1)} \tag{8.3.10}$$

$$\tau_t = 1-\eta_t\left[1-\pi_t^{(\gamma_t-1)/\gamma_t}\right] \tag{8.3.11}$$

$$M_9 = M_{oR}\left[\frac{\tau_t}{\tau_{tR}}\right]^{\frac{1}{2}}\frac{\tau_{tR}}{\tau_t}\left[\frac{1+\frac{\gamma_t-1}{2}M_9^2}{1+\frac{\gamma_t-1}{2}M_{oR}^2}\right]^{(\gamma_t+1)/2(\gamma_t-1)} \tag{8.3.12}$$

Eqs. 8.3.10 - 8.3.12 may be solved by functional iteration. Thus, assume M_9, calculate π_t, τ_t and then a new value of M_9 from Eq. 8.3.12. Continue till the desired accuracy is obtained.

Alternatively, Eqs. 8.3.10 and 8.3.11 may be substituted directly into Eq. 8.3.12 to give a quadratic expression for M_9^2. The resulting equation is very messy, however, and in view of the fact that the given three equations converge very rapidly to appropriate accuracy (usually within two iterations), it would seem simpler to use the above forms.

$$\left(M_o\frac{u_9}{u_o}\right)^2 = \frac{2}{\gamma_c-1}\tau_\lambda\tau_t\left[1-(\pi_r\pi_d\pi_c\pi_b\pi_t\pi_n)^{-(\gamma_t-1)/\gamma_t}\right] \tag{8.3.13}$$

$$f = \frac{C_{pc}T_o}{h\eta_b}(\tau_\lambda-\tau_r\tau_c) \tag{8.3.14}$$

$$C_{PROP} = \eta_{PROP}\eta_g[\eta_m\tau_\lambda(1-\tau_t)-\tau_r(\tau_c-1)] \tag{8.3.15}$$

$$C_c = (\gamma_c-1)M_o\left[M_o\frac{u_9}{u_o} - M_o\right] \tag{8.3.16}$$

$$C = C_{PROP} + C_c \tag{8.3.17}$$

$$\frac{F}{\dot m} = \frac{C_{pc}T_o}{a_oM_o}C \tag{8.3.18}$$

$$S = \frac{a_oM_o}{C_{pc}T_o}\frac{f}{C} \tag{8.3.19}$$

$$\frac{\dot m}{\dot m_R} = \frac{\pi_d\pi_b\pi_r\pi_c}{(\pi_d\pi_b\pi_r\pi_c)_R}\frac{p_o/\sqrt{T_o}}{(p_o/\sqrt{T_o})_R}\left[\frac{\tau_{\lambda R}}{\tau_\lambda}\right]^{\frac{1}{2}} \tag{8.3.20}$$

$$\frac{\dot m_c}{\dot m_{cR}} = \frac{\pi_b\pi_c}{(\pi_b\pi_c)_R}\left[\frac{(\tau_\lambda/\tau_r)_R}{\tau_\lambda/\tau_r}\right]^{\frac{1}{2}} \tag{8.3.21}$$

$$\frac{F}{F_R} = \frac{F/\dot m}{(F/\dot m)_R}\frac{\dot m}{\dot m_R} \tag{8.3.22}$$

As an example calculation we consider the off-design performance of the engine considered in Sec. (7.4.3). The engine on-design parameters are listed in Table 7.4.1. We assume the engine is operated at fixed altitude with fixed turbine inlet temperature and wish to obtain the variation of thrust and specific fuel consumption with flight Mach number. As a simple approximation to real propeller efficiency variation with Mach number, η_{PROP} is assumed to vary as in Fig. 8.3.2.

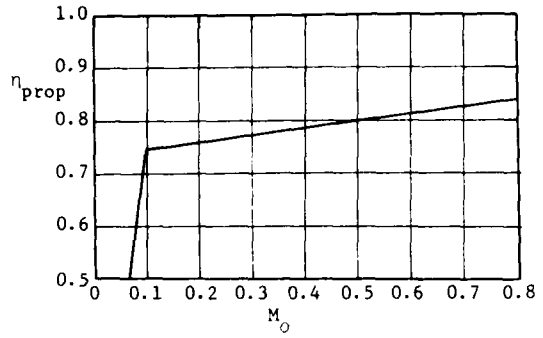

Figure 8.3.2 Assumed Propeller Efficiency

The results of the calculation are shown in Fig. 8.3.3.

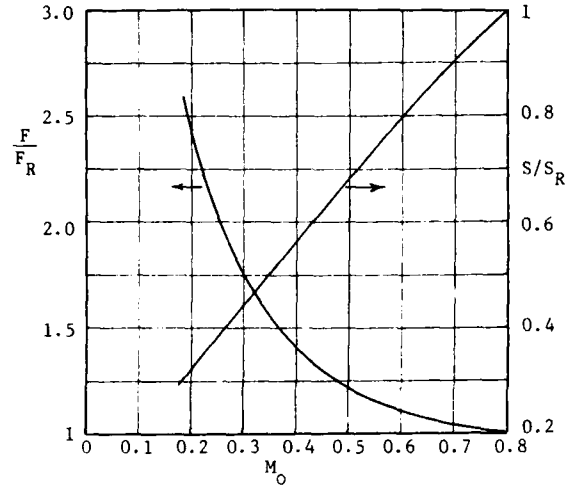

Figure 8.3.3 $\frac{S}{S_R}$ and $\frac{F}{F_R}$ versus M_o for a Turboprop

The results indicate that the prop-fan (or turboprop) represents a very desirable engine for use in low Mach number aircraft, ($M_o < 0.8$) provided that the high propeller efficiencies indicated in Fig. 8.3.2 (particularly at the higher Mach numbers) can be attained. Thus, as was shown in Sec. (7.4.3), the prop-fan gave substantially improved behavior at the design condition, compared to a turbofan engine, and it can be seen from Fig. 8.3.3 that the high propulsive efficiency of a prop-fan engine leads to very high thrusts and low fuel consumptions when operated at low Mach numbers. These results further explain the renewed interest in the development of advanced turboprop engines.

8.4 THE USE OF COMPONENT CHARACTERISTICS

When the performance characteristics of the various components are available, the combined performance of the compressor, burner and turbine can be predicted. These combined characteristics, termed the pumping characteristics, can then be utilized to predict the overall engine performance. Once a schedule of turbine area variation and primary nozzle area variation is selected, a unique operating characteristic may be determined.

In what follows, the individual component characteristics will be described, and the method of combining these characteristics to obtain the pumping characteristics and then operating characteristic will be developed.

8.4.1 THE COMPRESSOR CHARACTERISTICS

When a new compressor has been developed, it will be subjected to a compressor rig test to determine its performance capability. It is most efficient to present the results of such a test in terms of dimensionless or pseudo-dimensionless variables. Routine dimensional analysis reveals that we could expect the compressor pressure ratio p_{t_3}/p_{t_2}, to be a function of four dimensionless parameters which could be taken to be the ratio of specific heats, γ_c, the Reynolds number R_e, the Mach number at the engine face and the ratio of blade (tip) speed to speed of sound.

Experience has shown that variations in both γ_c and R_e have relatively little effect over much of the operating range of the typical compressor, so it is usual to present the performance in terms of the other dimensionless variables and to provide γ_c and R_e corrections when necessary. (Sec. 8.5) It is usual also, to utilize variables related to the engine face Mach number and "blade" Mach number, rather than to use those variables directly. Thus, as was shown in Sec. (8.1), a unique value of engine face Mach number corresponds directly to a unique value of corrected mass flow, $\dot{m}_c$, and it is usual to utilize $\dot{m}_c$ as a "pseudo-dimensionless" variable.

When a specific compressor (i.e., given geometry) is to be tested, it is apparent also that a given blade speed occurs for a specific value of rotational frequency, and that the reference speed of sound can be taken to be proportional to the square root of the incoming stagnation temperature, T_{t_2}. Thus, it is customary to utilize the corrected speed, N_c, as the second pseudo-dimensionless variable, where N_c is defined by

$$N_c = \frac{N}{\sqrt{\theta}} \tag{8.4.1}$$

here N is the actual rotational speed (in radians/sec for the SI system of units, in RPM for the British system). θ is the dimensionless temperature as already defined in Eq. (8.1.5).

The method of obtaining a "map" of the compressor characteristics is thus to set a given corrected speed for the compressor (on a separately driven motor), and to vary the corrected mass flow over the desired range by varying the exit valve opening. By operating at an appropriate number of corrected speed settings, and over an appropriate range of corrected mass flows, the operating behavior of the compressor over its entire range may be determined.

A schematic diagram of a typical compressor test facility is shown in Fig. 8.4.1, and typical results are indicated in Fig. 8.4.2.

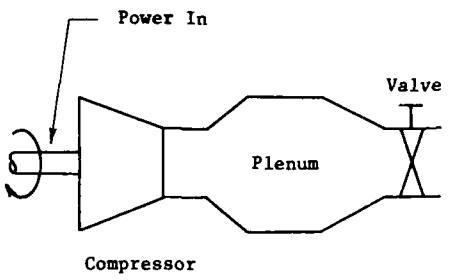

Figure 8.4.1 Compressor Test Facility

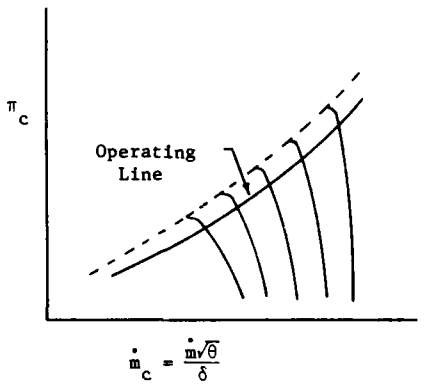

Figure 8.4.2 Compressor Characteristics

The dotted line indicated in Fig. 8.4.2 represents the limit of pressure ratio that can be obtained for the given corrected speed. This limit occurs when the pressure rise across the compressor is so extreme that the blade loadings reach levels that cause boundary layer separation over substantial portions of the blades. In this condition several forms of flow instability can occur, principal among which are rotating stall and compressor surge. These instabilities, which are thoroughly described in Chapter 23, effectively limit the attainable pressure ratio.

The mechanism of rotating stall is complicated indeed, but some understanding of the phenomenon can be attained from a relatively simple model, as depicted in Fig. 8.4.3.

Figure 8.4.3 Rotating Stall Packet

Figure 8.4.3 depicts a packet of fluid which, because of the large imposed pressure gradient, has undergone a severe flow reversal. To the surrounding fluid such a reversal region appears to be a blockage area, and the fluid divides to by-pass the area. It can be seen in the figure that the blades on the lower side of the stall packet are thus confronted with a flow of reduced angle of attack whereas the blades on the upper side of the stall packet are confronted with a flow at increased angle of attack. The result then is that the lower blades tend to unstall and the upper blades tend to go into stall, leading to a net movement (or rotation) of the stall packet.

Rotating stall, and its inception, are of enormous importance to the industry, because not only does rotating stall cause the onset of limiting attainable pressure ratio in some portions of the compressor characteristics, but the vibratory stresses set up in the blades can lead to very rapid and catastrophic failure of the compressor.

Surge is that phenomenon where a substantial fraction of the compressor blades simultaneously reach their limit of load carrying ability. As a result, flow breakdown occurs and the entire compressor looses its capability of supporting the overall pressure rise and massive flow reversal occurs. The frequency of such reversals is quite obviously related to the storage volume following the compressor as well as to the compressor behavior itself. Compressor surge represents a very serious design limit, because when it occurs in an operating engine, very often engine flame out occurs.

The distance between the operating line and surge line, shown in Fig. 8.4.2, is referred to as the surge margin. It usually happens that the best engine performance occurs when the compressor operates near the surge line. This introduces a difficult design problem in that "appropriate" precautions must be taken to prevent engine surge due to such things as severe inlet flow distortions occurring (due, for example, to operation at extreme angle of attack), to ingestion of combustibles from gun rocket firing (leading to added combustion in the burner with consequent pressure rise), to burner over pressuring from

fuel surges during acceleration, etc. A careful balance must be chosen between selecting an overly large surge margin with poor steady state performance, and selecting too small a surge margin with inherent low engine safety.

8.4.2 COMPRESSOR BEHAVIOR DURING STARTING

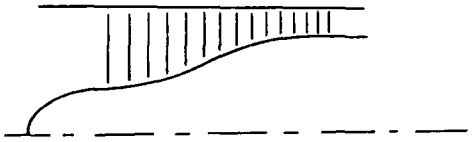

Figure 8.4.4 Compressor Section

Figure 8.4.4 depicts a typical compressor section. It is apparent that the overall contraction in annulus area will be selected so that when the compressor is on its design point the axial velocity throughout will be appropriate to match the design angles of the many blades. When the compressor is operated at a pressure ratio other than the design pressure ratio, then, the ratio of exit axial velocity to entrance axial velocity will not be the same as when the compressor is on design because the density ratio will be dependent on the pressure ratio.

When the compressor is running at very low rotational speed, as during starting, the first stage will tend to induce a flow at an appropriate angle of attack to the first stage blades. As the flow proceeds through the compressor it will then tend to accelerate because the low stage compression ratios identified with the low rotational speed will not introduce a sufficient increase in density to compensate for the annulus area contraction. As a result, the axial velocity can become very large near the back of a high compression ratio compressor leading to "windmilling" of the rear stages, and in severe cases leading to choking of the flow. The net result is that during starting the early blade rows operate at high angle of attack (hence tending to stall), the mid-blade rows operate approximately on design, and the rearmost blade rows operate at low angle of attack (hence tending to windmill).

There are several design techniques available to relieve these starting problems, some or all of them being utilized in all modern high compression ratio compressors. The first technique is to utilize bleed valves. Bleed valves operate by releasing air from an appropriate stage in order to reduce the axial velocity and thereby reduce the tendency to windmill the rear stages.

A second technique to reduce the starting problem is to utilize variable angle stators. By varying the angle of the stators the angle of attack to the rotor can be changed to more closely approach the design angle, and because of this the compression per stage can be improved. The effect of variable stators is hence to both reduce the tendency of the front blades to stall and to reduce the tendency of the rear blades to windmill.

The third technique to reduce the starting problem is to drive the compressor with multiple spools. Thus, the low pressure portion of the compressor will be connected directly to the low pressure portion of the turbine and the high pressure portion of compressor and turbine will be directly connected on another "spool".

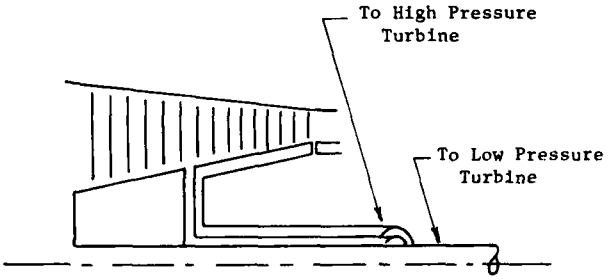

Figure 8.4.5 Multiple Spool Compressor

It can be noted that the same argument used to explain the stalling and windmilling behavior of the compressor can be used to explain the turbine starting problem. Thus, by providing separate spools, the (for example) high pressure portion of the compressor will be allowed to match with the high pressure portion of the turbine, both components in fact operating closer to their design point if allowed to speed up.

It is obvious that the requirement for these additional complexities increases as the design pressure ratio of the compressor increases which tends to explain why modern engines usually utilize all three techniques described above. Aircraft designed for operation over a wide Mach number range (as considered in the example of Sec. 8.1.2) are also required to fly with widely different compressor pressure ratios at their various flight conditions, and as a result may even be forced to fly with compressor bleed when cruising at a "design" flight Mach number. These complexities, and the demands that cause them, again serve to emphasize the need for design ingenuity in the development of modern engines.

8.4.3 THE TURBINE CHARACTERISTICS

The same reasoning that lead to the use of the parameters corrected mass flow and corrected speed for the compressor, suggests that we plot the turbine performance characteristics the same way with the simple exception that the reference inlet and exit quantities are now those at stations 4 and 5. Utilizing this procedure, the results of a turbine rig test would appear, typically, as those shown in Fig. 8.4.6.

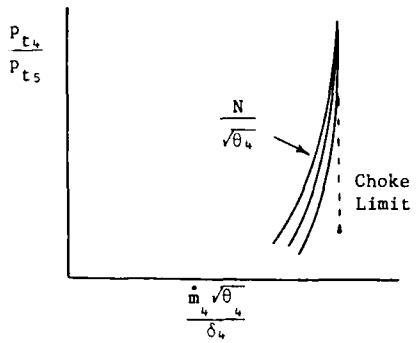

Figure 8.4.6 Turbine Characteristics

It is evident from Fig. 8.4.6, that in the case of the turbine, an alternative presentation format is desirable because so much of the desired information collapses on the choke limit line, where in fact the turbines most usually operate. A simple method for displaying the desired information is to multiply the corrected mass flow by the corrected speed. This has the effect of moving apart the separate corrected speed lines so that the efficiency contours, etc. may be discerned. (Fig. 8.4.7)

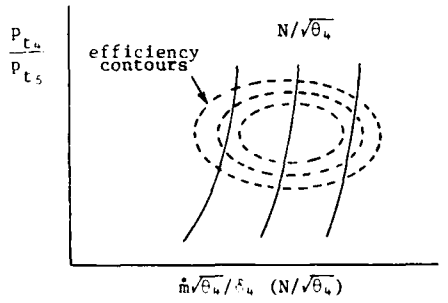

Figure 8.4.7 Alternate Form Turbine Characteristics

8.4.4 THE PUMPING CHARACTERISTICS

The group of the three components, the compressor, burner and turbine is termed the gas generator, and the performance of the gas generator is represented by the "pumping characteristics". The pumping characteristics simply give the output variables (station 5) in terms of the input variables (station 2).

To obtain the pumping characteristics from the individual component characteristics, we utilize the matching of mass flow, shaft speeds, stagnation pressures and power requirements. For simplicity we will consider the simple example of a non-afterburning, single spool turbojet. We then have:

$$N_t = N_c = N \tag{8.4.2}$$

$$\dot{m}_4 = (1+f)\dot{m}_2 \tag{8.4.3}$$

$$p_{t_4} = p_{t_2}\,\pi_c\,\pi_b \tag{8.4.4}$$

$$C_{p_c}\,(T_{t_3}-T_{t_2}) = \eta_m(1+f)C_{p_t}\,(T_{t_4}-T_{t_5}) \tag{8.4.5}$$

From Eq. (8.4.3) we obtain (with $\dot{m}_c = \dot{m}\sqrt{\theta}/\delta$)

$$\dot{m}_{c_2} = \frac{1}{1+f}\,\dot{m}_{c_4}\,\frac{p_{t_4}}{p_{t_2}}\,\left(\frac{T_{t_4}}{T_{t_2}}\right)^{-1/2} = \frac{\dot{m}_{c_4}}{1+f}\,\pi_c\,\pi_b\,\left(\frac{T_{t_4}}{T_{t_2}}\right)^{-1/2} \tag{8.4.6}$$

In the case where the turbine is choked, the corrected mass flow $\dot{m}_{c_4}$ will be a constant (or proportional to A_4 for a variable area turbine), and for simplicity we now assume that this is the case. (Note that if this is not true it is simply required to iterate to determine the value of $\dot{m}_{c_4}$.) The burner characteristics will give π_b as a function of $\dot{m}_{c_2}$ and the fuel to air ratio f. Thus, if T_{t_4}/T_{t_2} is specified, $\dot{m}_{c_2}$ is specified as a function of π_c. (Note that the effect of f is small, but to be exact we would iterate upon its value when we later determine more exactly what value f actually has.) The relationship between T_{t_4}/T_{t_2}, π_c and $\dot{m}_{c_2}$ may be indicated on the compressor performance map as in Fig. 8.4.8.

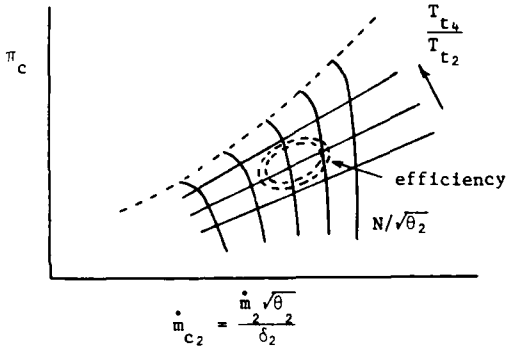

Figure 8.4.8 Compressor Performance Map

Once the compressor performance map has been obtained in the manner indicated in Fig. 8.4.8, the graph may be utilized to obtain π_c and $\dot{m}_{c_2}$ when $N/\sqrt{\theta_2}$ and T_{t_4}/T_{t_2} are prescribed. We note also that τ_c may be obtained for a given location on the map because both π_c and η_c are provided.

The equation for the power balance, Eq. (8.4.5) may be rearranged to give

$$\tau_t = 1 - \frac{1}{\eta_m(1+f)}\,\frac{C_{p_c}}{C_{p_t}}\,\left(\frac{T_{t_4}}{T_{t_2}}\right)^{-1}(\tau_c - 1) \tag{8.4.7}$$

When T_{t_4}/T_{t_2} and $N/\sqrt{\theta_2}$ are prescribed we may obtain π_c, $\dot{m}_{c_2}$, η_c and hence τ_c from Fig. 8.4.8. We then obtain τ_t from Eq. (8.4.7) and $N/\sqrt{\theta_4}$ from $N/\sqrt{\theta_4} = N/\sqrt{\theta_2}\,\left(\frac{T_{t_4}}{T_{t_2}}\right)^{-1/2}$. This allows us to locate our position on the turbine performance map (Fig. 8.4.9), which in turn provides us with the corresponding value of π_t.

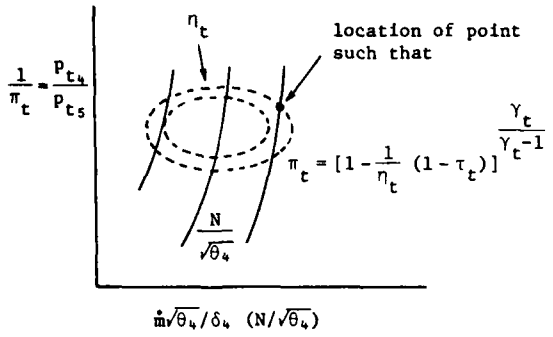

Figure 8.4.9 Turbine Performance Map

The pumping characteristics then follow by noting

$$\frac{p_{t_5}}{p_{t_2}} = \pi_t \pi_b \pi_c \quad \text{and} \quad \frac{T_{t_5}}{T_{t_2}} = \tau_t \frac{T_{t_4}}{T_{t_2}}$$

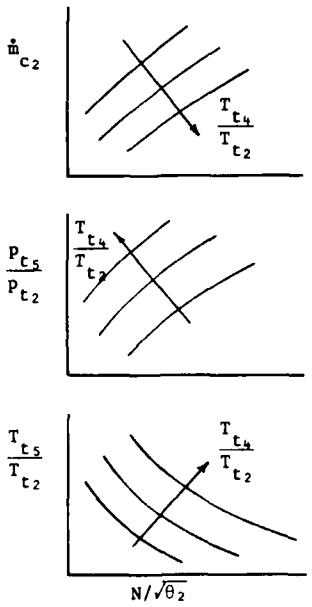

Figure 8.4.10 The Pumping Characteristics

Finally, the fuel to air ratio is determined from an enthalpy balance across the combustor to give:

$$\dot{m}_2 \, C_{p_c} \, T_{t_3} + \eta_b \, h \, \dot{m}_f = \dot{m}_2 (1+f) \, C_{p_t} \, T_{t_4}$$

hence

$$f = \frac{\frac{C_{p_t}}{C_{p_c}} \frac{T_{t_4}}{T_{t_2}} - \tau_c}{\frac{\eta_b \, h}{C_{p_c} \, T_{t_2}} - \frac{C_{p_t}}{C_{p_c}} \frac{T_{t_4}}{T_{t_2}}} \qquad (8.4.8)$$

Thus a relationship of the form of Fig. 8.4.11 may be obtained.

Note that unlike the results of Fig. 8.4.10, the results of Fig. 8.4.11 are valid for only a single specified value of T_{t_2}.

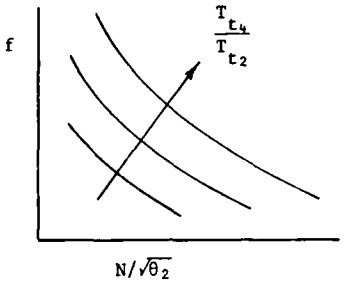

Figure 8.4.11 The Fuel Air Ratio

8.4.5 GAS GENERATOR - NOZZLE MATCHING

The pumping characteristics allow determination of conditions at station 5 in terms of those at station 2 when the corrected speed and the ratio T_{t_4}/T_{t_2} are prescribed. When the gas generator is coupled with a nozzle of prescribed throat variation however, $N/\sqrt{\theta_2}$ and T_{t_4}/T_{t_2} are not separately prescribable. (Recall the results of Sec. 8.1 where it was shown that by prescribing the ratio A_4/A_8, a unique compressor operating line will be determined.) For simplicity we again consider the case where the primary nozzle is choked, so that the group $\dot{m}_8\sqrt{\theta_8}/A_8\delta_8$ is a constant. Mass flow continuity then gives

$$\frac{A_8}{A_2} = \left(\frac{\dot{m}_2\sqrt{\theta_2}}{A_2\delta_2}\right)\left(\frac{\dot{m}_8\sqrt{\theta_8}}{A_8\delta_8}\right)^{-1} (1+f) \left(\frac{T_{t_8}}{T_{t_2}}\right)^{1/2} \frac{p_{t_2}}{p_{t_8}} \qquad (8.4.9)$$

Noting that for the non-afterburning case, $T_{t_8} = T_{t_5}$ and also that $p_{t_8}/p_{t_2} = p_{t_5}/p_{t_2} \, \pi_n$, this expression may be written

$$\frac{A_8}{A_2} = \left(\frac{T_{t_5}}{T_{t_2}}\right)^{1/2} \left(\frac{p_{t_5}}{p_{t_2}}\right)^{-1} \frac{(1+f)}{\pi_n} \left(\frac{\dot{m}_2\sqrt{\theta_2}}{A_2\delta_2}\right)\left(\frac{\dot{m}_8\sqrt{\theta_8}}{A_8\delta_8}\right)^{-1} \qquad (8.4.10)$$

π_n will be known as a function of the corrected mass flow rate through the tail pipe and nozzle, so that if we prescribe T_{t_4}/T_{t_2} and $N/\sqrt{\theta_2}$ then, $\dot{m}_2\sqrt{\theta_2}/\delta_2$, p_{t_5}/p_{t_2}, T_{t_5}/T_{t_2} and f will all be determined from the pumping characteristics. Thus A_8/A_2 will also be prescribed and a graph of the form of Fig. 8.4.12 obtained.

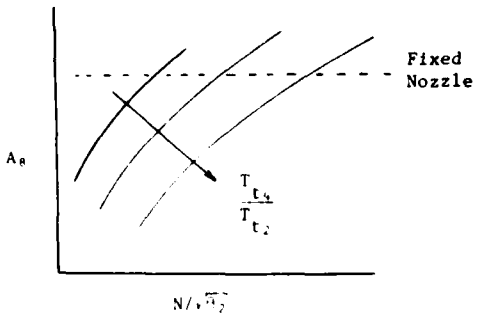

Figure 8.4.12 Area Variation

When the desired schedule for the nozzle area, A_8, is prescribed a unique T_{t_4}/T_{t_2} versus $N/\sqrt{\theta_2}$ curve is established. This allows determination of a unique set of gas-generator, nozzle, pumping characteristics as indicated in Fig. 8.4.13.

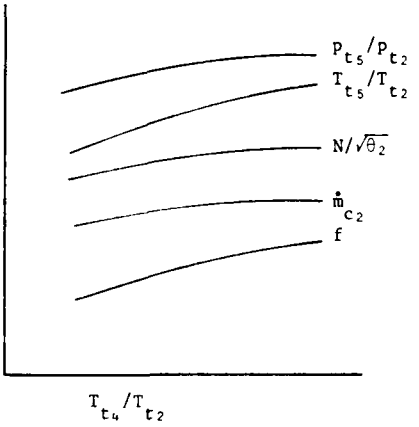

Figure 8.4.13 Gas Generator-Nozzle, Pumping Characteristics

8..6 PERFORMANCE PREDICTION WITH PUMPING CHARACTERISTICS

Once the gas generator-nozzle, pumping characteristics are available, the performance parameters follow very directly from the equations for the performance variables. Thus, with reference to the summary of Sec. 7.2.2, the performance variables may be obtained from the pumping characteristic variables from the following equations. (Note that T_{t_4}/T_{t_2} would be assumed and the flight conditions etc. would be known.)

$$\frac{P_{t_9}}{P_9} = \{\pi_r \pi_d \pi_n \frac{P_O}{P_9}\} \frac{P_{t_5}}{P_{t_2}} \tag{8.4.11}$$

$$\frac{T_9}{T_O} = \tau_r \frac{T_{t_5}}{T_{t_2}} \left(\frac{P_{t_9}}{P_9}\right)^{-(\gamma_t-1)/\gamma_t} \tag{8.4.12}$$

$$M_O \frac{u_9}{u_O} = \left[\frac{2}{\gamma_c-1} \frac{C_{p_t}}{C_{p_c}} \tau_r \frac{T_{t_5}}{T_{t_2}} \left\{1 - \left(\frac{P_{t_9}}{P_9}\right)^{-(\gamma_t-1)/\gamma_t}\right\}\right]^{1/2} \tag{8.4.13}$$

$$f = \frac{\tau_r \left(\frac{T_{t_4}}{T_{t_2}} - \tau_c\right)}{\frac{h\eta_b}{C_{p_c} T_O} - \tau_r \frac{T_{t_4}}{T_{t_2}}} \tag{8.4.14}$$

$$\frac{F}{\dot{m}} = a_O \left[(1+f)\left(M_O \frac{u_9}{u_O}\right) - M_O + \frac{(1+f)}{\gamma_c \left(M_O \frac{u_9}{u_O}\right)} \frac{T_9}{T_O} \left(1 - \frac{P_O}{P_9}\right)\right] \tag{8.4.15}$$

$$S = \frac{f}{F/\dot{m}} \tag{8.4.16}$$

8.5 LIMITATIONS ON THE ACCURACY OF COMPONENT CHARACTERISTICS

It is important when utilizing component characteristics to generate pumping characteristics, to be aware of any accuracy limitations. The most obvious accuracy limitations will occur because of the inevitable instrumentation and recording inaccuracies present in any test procedure and, of course, every effort must be made to minimize such sources of error. Other sources of error, however, arise when the effects of ignoring changes in Reynolds number and the ratio of specific heats are not included.

In many large engines, the effect of Reynolds number variations are, in fact, very small over virtually the entire operating range of the engine. It can happen, however, particularly in small business-jet engines, that Reynolds number effects can become substantial for flight at extreme altitudes. In the compressor, for example, it is entirely possible that the flow over the first blade row will become largely laminar with consequent onset of early (laminar) separation. Aside from reducing the performance of the first blade row, such separation causes velocity miss-matches at all succeeding rows with consequent substantial change in compressor performance.

In a similar way, operation at extreme altitudes can lead to very low Reynolds numbers at the later turbine stages with consequent deterioration in performance. (Unless the blades had been designed "oversize" originally to prevent such deterioration.) The point, then, is that if operation over extreme Reynolds number ranges is to be expected, appropriate investigations of the effects of the Reynolds number variations should be included in the engine test program.

An entirely different phenomenon arises when operation at very high humidity is carried out. Several effects arise when large amounts of water vapor are present in the flow, including changing the ratio of specific heats (so that the value of corrected mass flow at a choke condition changes, as does the reference speed of sound in the corrected speed). When condensation (and later evaporation) occurs, substantial effects arise because of the release or absorption of the latent enthalpy of evaporation.

As an example, if an inlet is considered, the presence of water vapor causes three major effects to occur:

1. Mass Continuity - The specific density of water is so high that any droplets that form (due to the lowered static temperature as the air accelerates into the inlet) occupy effectively zero volume. The result is that this aspect of condensation allows the inlet to pass a larger mass flow than it can without condensation.

2. Stagnation Enthalpy Increase - When droplets form, their latent enthalpy of vaporization is released to the surrounding gas thereby increasing the stagnation temperature of the gas. This tends to reduce the mass flow handling capability of the inlet. (Recall $\dot{m} \propto 1/\sqrt{T_t}$)

3. Stagnation Pressure Decrease - The latent enthalpy of vaporization, released upon formation of droplets, reduces the stagnation pressure, as was pointed out in the analysis of Sec. 2.17.2.

This reduction in stagnation pressure tends to reduce the mass flow handling capability of the inlet. (Recall $\dot{m} \alpha p_t$)

The net effect of 1, 2 and 3 is that when condensation occurs, less mass flow can be handled by the inlet than could be when no condensation occurs. Thus inlet testing (and engine testing) at ground level on hot humid days can lead to substantial variations in performance (greater than 1% mass flow rate changes) and great care should be exercised in applying data correction procedures.

8.6.1 REFERENCES

8.1 Klees, G. W. and Welliver, A. D., "Variable-Cycle Engines for the Second Generation SST," Society of Automotive Engineers, Paper No. 750630. (Presented at Air Transportation Meeting, Hartford, Connecticut, May 6-8, 1975.)

Chapter 9

ENGINE/AIRPLANE PERFORMANCE MATCHING

D.B. Morden

The Boeing Company

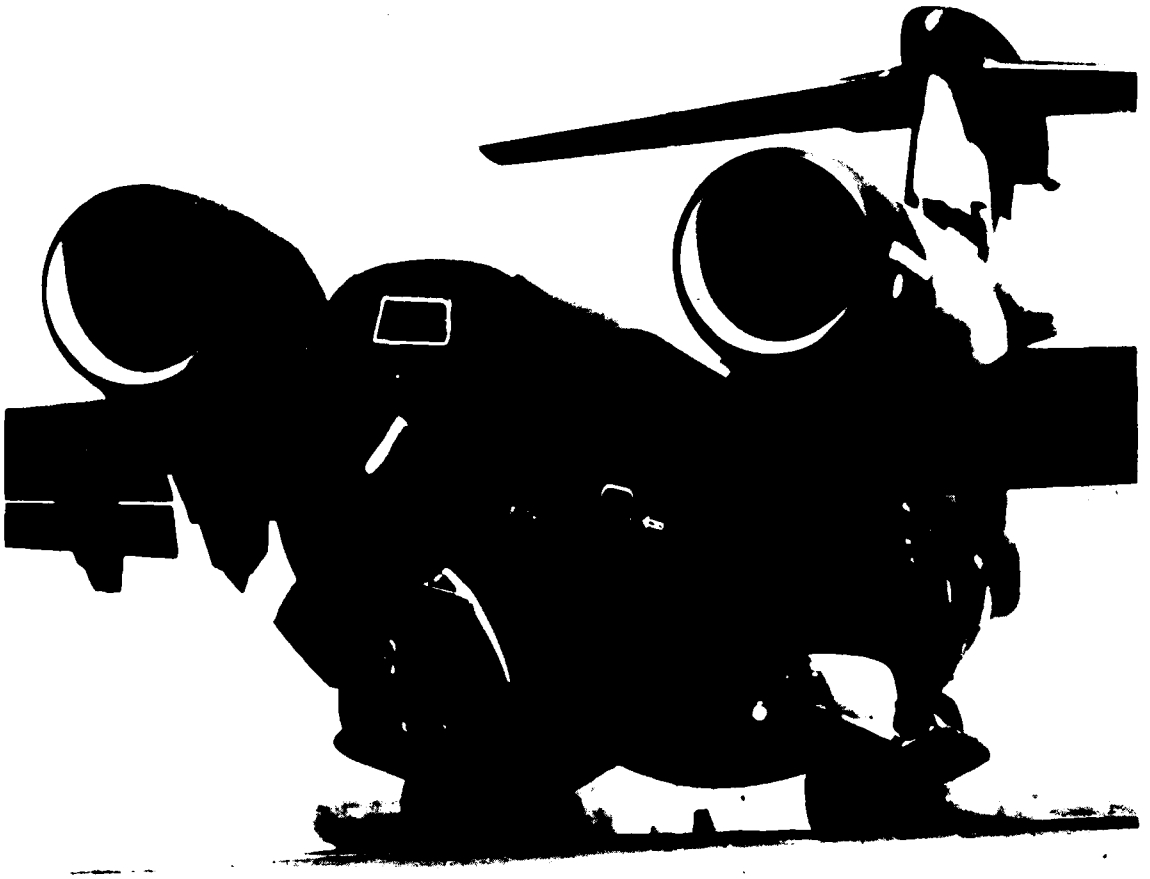

9. ENGINE/AIRPLANE PERFORMANCE MATCHING

D. B. Morden

This chapter is the work of the propulsion staff of The Boeing Company. The author expresses appreciation to the many contributors including R. Decher, E. Tjonneland, A. D. Welliver, W. C. Swan, G. C. Oates, F. F. Tolle, and S. G. Kyle.

9. ENGINE/AIRPLANE PERFORMANCE MATCHING

9.0.1 TABLE OF CONTENTS

9.0.2 NOMENCLATURE

9.0.3 INTRODUCTION

9.1 MISSION ANALYSIS

9.1.1 Philosophy and Logic

a) Fixed Missions, Variable Airplane Size
b) Fixed Airplane Size, Variable Mission

9.1.2 Overview of Aerodynamic Force Determination

a) Lift and Drag
b) Drag Polar Buildup
c) Use of the Drag Polar for Mission Analysis

9.1.3 Mission Segments and Thrust Requirements

a) Introduction
b) Warm-up and Takeoff
c) Thrust Available and Required
d) Climb, Acceleration and Descent
e) Cruise
f) Endurance or Loiter
g) Combat
h) Refuel or Munition Drop
i) Landing
j) Reserves

9.1.4 Engine Performance Representation
9.1.5 Propulsion System Installation
9.1.6 Results of Mission Analysis

9.2 OPTIMIZATION OF ENGINE/AIRPLANE MATCH

9.2.1 Introduction
9.2.2 Figures of Merit
9.2.3 Methods of Optimization
9.2.4 Dependent and Independent Variables
9.2.5 Minimizing Required Combinations of Independent Variable Values
9.2.6 Boundary Values for Independent Variables
9.2.7 Reexamination and Validation
9.2.8 Example Mission

9.3 SENSITIVITY AND INFLUENCE COEFFICIENTS

9.3.1 General
9.3.2 Importance of the Choice of Independent Variables

9.4 COMPUTER SIMULATION OF GAS TURBINE ENGINES

9.4.1 Introduction
9.4.2 Method of Performance Simulation
9.4.3 Design Point Simulation
9.4.4 Off-design
9.4.5 Newton-Raphson Iteration
9.4.6 The Generalized Engine and Mechanical Design Simulation

9.5 REFERENCES

9.0.2 NOMENCLATURE

Throughout Chapter 9 the symbols are defined in the text where they are used. Commonly accepted symbols are used whenever possible.

9.0.3 INTRODUCTION

The preceding chapters have emphasized the development of analytical methods to describe engine performance both on and off design. It has been pointed out that the "installation effects" could be of paramount importance, and that any engine design must include consideration of the interactions between engine and airframe. When engine cycles and airframe concepts are analytically integrated to define an airplane system, the engine and airframe subsystems interact with one another. Engine physical characteristics affect the size, shape, weight and balance of the airframe. Airframe characteristics affect the installed performance of the propulsion system. The "best" engines for a given airplane can NOT be identified until the required installed thrust has been established for the desired mission. Analytical and empirical tools can be used to estimate the required engine size and airplane size to perform any desired mission. Further, the calculation can be used to optimize the engine cycles and the aircraft geometry for a mission and thus provide a quantitative measure of the sensitivity of the system's performance to any changes in engine, airplane, or mission description.

System matching requires that the installed engine/airframe performance be evaluated over the entire operating range of Mach numbers and altitudes. The specified flight path elements and the corresponding performance requirements for the aircraft are referred to as the design mission. Mission analysis is introduced to evaluate engine/airframe performance by summing the increments in fuel consumed and/or distance covered for the specified mission segments or legs. The performance is also computed at constraint points where, for example, a particular acceleration, maneuverability or noise level is required. If the design objectives are not met, the candidate engine cycle and airframe are resized and the process is repeated. Several iterations are usually necessary to size a candidate engine and airplane to meet the mission. The objective of the design process, referred to as optimization, is to compare satisfactory candidate configurations and identify the one which best satisfies the mission requirements. The digital computer provides the means of quickly and efficiently assessing large numbers of configurations. While the computer is a powerful tool, the quality of the final airplane is dependent on the engineering judgment applied in choosing candidates and by the accuracy of the analytical methods and the empirical expressions used to describe the engine and airframe.

Over a period of years, airframe and engine manufacturers have compiled a large inventory of experience which has been used to carry out these simulations. Routines vary within industry, and on-going efforts keep changing the program formats and complexity in a continual quest for more accurate and less costly computation techniques. It is not the purpose of this text to describe specific current programs. Rather, this chapter presents some examples of the basic procedures that are fundamental to computer simulations of mission analysis, design optimization and sensitivity, and gas generator performance calculation.

9.1 MISSION ANALYSIS

9.1.1 Philosophy and Logic

The mission which an aircraft is designed to perform consists of a flight path with several

distinct segments where specific performance requirements must be met. Each of the mission segments can be analyzed using Newton's laws of motion. The final condition resulting from calculation of one segment becomes the initial condition for the next segment. By combining the various segments into an appropriate sequence, any mission can be described. Relationships must be provided to describe the following for each segment:

1) Lift and drag for the airframe
2) Engine cycle characteristics
3) Weight build-up and scaling rules
4) Inlet and nozzle performance
5) Interaction or installation effects

To begin the analysis, an initial airplane configuration must be specified. Customarily, the various disciplines contributing components to the airplane supply initial weight and volume requirements. A configuration is produced which incorporates the various constraints into an aerodynamic shape. This stage relies very heavily on past experience and perceived benefits. The result constitutes the "candidate airplane." The wetted area, volume distribution, weight, and drag are then estimated. The design point for the engine cycle usually corresponds to the most demanding performance point or segment in a mission. The engine operation is simulated for appropriate altitude and Mach number conditions characteristic of the mission with engine size (i.e., airflow rate) determined from the required thrust. The engine can then be resized if necessary by comparing the thrust obtained to thrust required at other operating conditions. Thus, the mission analysis also requires scaling rules for changes in engine dimensions and weight as a function of airflow.

Mission analysis is used to iterate on engine and airplane size to satisfy mission requirements for a fixed payload or to iterate on range with trades in fuel and payload for a fixed airplane size. Normally, the most demanding mission or the mission which results in the largest takeoff gross weight (TOGW) is referred to as the design mission. Once an engine and airplane are matched for the design mission, off design missions can be run using the fixed airplane to establish performance or payload on other missions of interest. The designer will usually choose an efficient computer program which uses a minimum number of inputs to simulate the aircraft system to the desired accuracy. The required accuracy and complication in system description increases as an airplane concept proceeds from initial concept evaluation through final design.

The fundamentals of the process of combining subsystems and assessment of the resulting systems are the subject of the remainder of this section. Increases in accuracy do not change the basic approach, but only increase the complexity of the component and interaction descriptions.

a) *Fixed Missions, Variable Airplane Size*

Missions may be specified partially or completely; i.e., while the sequence of mission segments is always specified, either the distance traveled or the elapsed time may be taken as a variable determined by the amount of fuel available. For a given set of performance requirements, an aircraft can be sized to fly any desired distance, up to the point of design divergence (zero payload) if all major components (including the engine) are appropriately scaled. A mission is said to be fixed when distance and altitude/Mach number requirements together with either distance or time are specified for all segments.

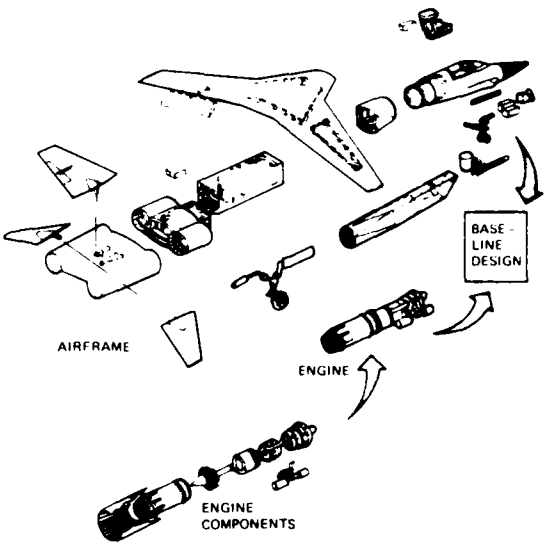

Figure 9.1.1-1. Multitechnology Computer Program Design Representation

The weight of the airplane is the sum of all the component weights, including payload and fuel, as represented by Figure 9.1.1-1. The takeoff gross weight is initially estimated for the airplane. The engine is initially sized to produce the required thrust to weight ratio at each of several points where a specific level of performance is required. Typical engine sizing points include: maximum Mach number at specified (or best) altitude, maximum speed at sea level, takeoff field length, landing distance, excess power, and acceleration. The airframe size and weight must be chosen to provide necessary lift, maneuverability and fuel. Starting with this initial engine and airplane weight estimate the fixed mission is "flown" to see if the performance requirements are met and to compute the amount of fuel consumed. An iterative process is then used until the airplane gross takeoff weight is appropriate for the entire mission, consuming all the fuel except for specified reserves.

b) Fixed Airplane Size, Variable Mission

In this mode of operation, the airplane size and weight are held constant while trading fuel and payload weight. Usually, the capability of the airplane is evaluated on several different missions with different payloads to develop a payload-range curve. This approach is used to evaluate candidate engines using the criteria of best range or largest payload. Occasionally, this form of mission analysis is also used to evaluate new or modified airframes using existing engines.

9.1.2 *Overview of Aerodynamic Force Determination*

Engines must produce enough thrust to overcome drag and the additional thrust to provide the desired acceleration at each point in a mission. Traditionally, the aircraft industry employs separate staffs to evaluate the propulsion system and the aerodynamics of the airplane. Though it is seldom necessary for the propulsion engineer to become involved in the detailed analysis of the airplane aerodynamics, it is important that he understand the principal drag sources. This is becoming increasingly important with the advent of multi-mission aircraft, fighters, and supersonic

transports because of the substantial interactions between the propulsion system and airframe.

This section presents a brief overview of airplane lift and drag and shows how to build-up the drag polar which will be used to relate the airplane weight and thrust requirements.

a) Lift and Drag

Dimensional analysis can be conveniently exploited to show that the dimensionless force, C_F, acting on a body immersed in a fluid can be expressed as a function of three dimensionless parameters, the Reynolds number, R_e, the Mach number, M, and the ratio of specific heats of the fluid, γ. We consider here only bodies interacting with air, so γ remains approximately constant. Thus, if geometrically similar bodies are considered, the force relationship may be written in the form

$$C_F = f(R_e, M) \qquad 9.1.1$$

where

$C_F = \frac{F}{qA}$ = force coefficient

F = force (component)

q = dynamic pressure = $\frac{1}{2}\rho V^2$

A = representative area, usually the wing area

$R_e = \frac{\rho V \ell}{\mu}$ = Reynolds number

ℓ = representative length, often the mean wing chord

The most commonly used forms of eq. 9.1.1 are those in which the forces considered are lift and drag. In these cases the coefficients are denoted C_L and C_D, respectively. Experiments demonstrate that Mach number has much more influence on C_F than does the Reynolds number in the cruise flight regime of both subsonic and supersonic aircraft.

The vector integral of the static pressure distribution over a surface is the net pressure force. It is convenient to express this force as acting at a point about which moments generated by the force are zero (referred to as the center of pressure). Figure 9.1.2-1 shows the pressure distribution and net pressure force for a typical airfoil section. The force is resolved into lift and drag components which are perpendicular and parallel to the flight velocity vector.

Airfoils usually show a linear variation of lift coefficient within a range of angle of attack,

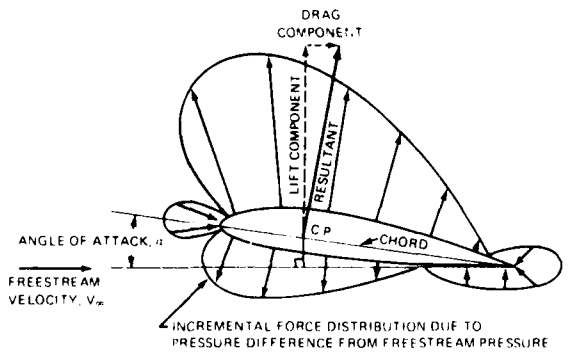

Figure 9.1.2-1. Airfoil Section Pressure Distribution and Nomenclature Definition

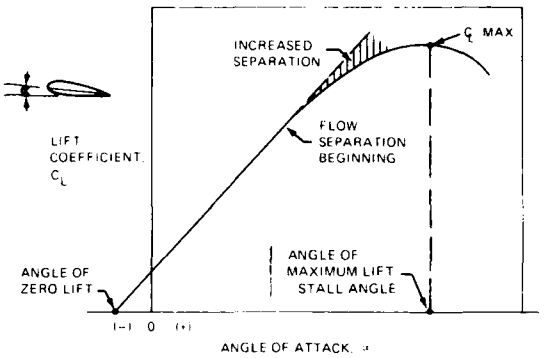

Figure 9.1.2-2. Variation of Lift Coefficient With Angle of Attack for a Typical Array

α. At large α, airflow separation is experienced and the lift curve becomes nonlinear (see Figure 9.1.2-2) until a maximum lift coefficient value is reached, at $C_{L_{max}}$. Beyond this point C_L decreases, either abruptly or gradually, depending on the particular airfoil. This phenomenon is called "stalling," and the angle corresponding to $C_{L_{max}}$ is called the stall angle. The angle of attack resulting in zero lift is zero for airfoils with symmetrical cross-sections and negative for typical wing cross-sections which have camber.

For most airfoils, the relationship between the drag coefficient and lift coefficient is approximately parabolic in shape, up to $C_{L_{max}}$, and the plot of C_L vs. C_D is called a drag polar (Figure 9.1.2-3). The angle of attack associated with such a curve increases as C_L increases below stall; and for wings with camber, the minimum C_D value does not occur at zero C_L. The drag polar for a complete airplane has a similar shape to that of the wing alone.

From the definitions of C_L and C_D

$$\frac{L}{D} = \frac{C_L qS}{C_D qS} = \frac{C_L}{C_D} \qquad 9.1.2$$

A tangent line through the origin on Figure 9.1.2-3 defines the C_L and C_D values for the maximum lift to drag ratio. The tangent point locates the angle of attack which produces the most lift for the least drag.

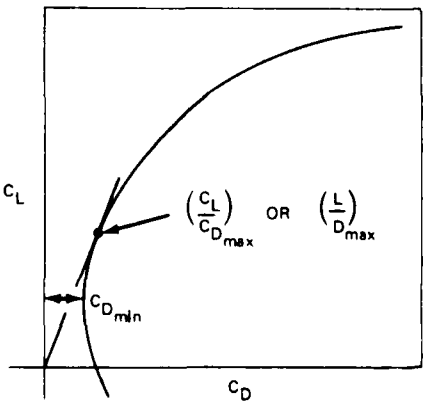

Figure 9.1.2-3. Typical Wing Drag Polar Showing Points of Minimum Drag and Maximum L/D

By extending the idea of a drag polar to represent the entire airplane, the relationship between lift and drag combined with the equation of motion for each flight segment is sufficient for computing the thrust requirement for each increment of a mission.

b) Drag Polar Buildup

The thrust which the engines must produce for each increment of a given mission is dependent on the following factors:

Atmospheric conditions: Altitude and temperature,
Flight Mach number (M),
Average gross weight during the increment (GW),
Type of segment.

These conditions, together with the aircraft drag polar are sufficient for mission analysis.

A drag polar for the entire airplane can be developed using the lift/drag relationships for each of the components including the components' interactions. In an effort to understand drag and produce equations suitable for determining drag polars, a methodology has been developed which combines theoretical and empirical drag contributions into a drag "build-up." Traditionally, subsonic drag is represented as the sum of parasite (friction), induced (drag due to lift), and compressibility drag terms.

The parasite drag term includes the skin friction drag on the entire wetted area of the airplane and the profile or form drag due to the net force in the drag direction arising from the zero lift pressure distribution on the wing, body and appendages. Another factor traditionally grouped with the parasite drag, is interference drag due to the changes in flow pattern that accompanies placing two bodies in close proximity. (The total drag on the two bodies generally differs from the sum of the isolated drags on each body. Depending on the configuration the inferred interference force can act in the thrust or drag direction. The parasite drag, C_{D_P} is, by convention, defined as the minimum drag experienced by an airplane.) Some changes in drag also occur as a result of the change of the aircraft's geometrical orientation in the flow field due to changes in angle of attack. Such (small) changes as are not attributable to the changes induced in the flow field due to lift are traditionally accounted for as an attitude dependent term ΔC_{D_P} and are usually obtained from wind tunnel tests. As defined for any given configuration C_{D_P} is a constant which does not depend on lift or Mach number. C_{D_P} changes only with Reynolds number and alterations to the configuration such as landing gear, flaps, and changes in external stores.

The portion of drag resulting from lift is referred to as induced drag. In practice, induced drag from components other than the wing is usually small and is lumped into the ΔC_{D_P}. A physical feeling for induced drag may be obtained by considering the flow over a wing with positive lift in subsonic flow. For this condition, the air pressure on the upper surface is less than the air pressure on the lower surface. This pressure differential causes air to flow toward the area above the wing and thus form vortices which concentrate near the wing tips. The net effect of this vortex system is to create a downward inclination to the air behind the wing. The influence of the transverse flow on the wing depends primarily on its aspect ratio (AR=wing span^2/wing planform area). In the limit of infinite aspect ratio the transverse flow would be absent. For a finite aspect ratio, the average downwash angle is finite. It can be shown that the effective angle of attack is reduced by half the average downwash angle (see ref. 9.1.2-1). This angle of the incoming flow results in an additional component in the drag direction referred to as induced drag. The planform of the wing also influences the induced drag because of its effect on the average downwash angle. An elliptical lift distribution results in the theoretical minimum of induced drag (ref. 9.1.2-2). This distribution can be obtained by 1) varying airfoil sections along the span, 2) using the same airfoil section and an elliptical planform, 3) twisting the wing to vary the geometric angle of attack along the span, or 4) using a combination of these on a tapered planform. The effect of the non-elliptical loading is accounted for with a span efficiency factor, e ($\leq$1.0) which should be maximized within structural and design constraints.

The relationship between lift and induced drag is

$$C_{D_{induced}} \quad C_{D_L} = \frac{(C_L - C_{L_{min}})^2}{\pi \cdot AR \cdot e} \qquad 9.1.3$$

where $C_{L_{min}}$ is the value of the lift coefficient when the induced drag equals zero. The induced drag is assumed to be independent of Reynolds number.

The sum of the parasite and induced drag completely accounts for the drag in low speed flight. A typical low speed polar is shown in Figure 9.1.2-4. Notice that the parabolic form of the drag polar is primarily due to the induced drag term. Transport airplanes are usually designed so that the minimum value of C_D corresponds to the required C_L for a cruise condition.

As flight speed increases, compressibility effects become significant when local sonic speeds are reached by the air. The sudden rise in pressure through the resulting shock waves necessary for recompressing the high speed flow cause boundary layer thickening and possibly separation resulting in a general degradation of lift and an increase in drag. A typical C_L vs. Mach number curve is shown in Figure 9.1.2-5. An associated compressibility drag curve, Figure 9.1.2-6, shows the onset of "drag rise" associated with shock induced separation.

The compressibility drag (C_{D_M}) onset may be delayed by sweeping the wing. If the critical or initial drag rise Mach number, M_{DR}, is defined as the Mach number at which the C_D increases by .002 above the low speed value, the effect of sweep angle, Λ on drag rise Mach number for a typical family of wings can be seen from Table 9.1.2-1.

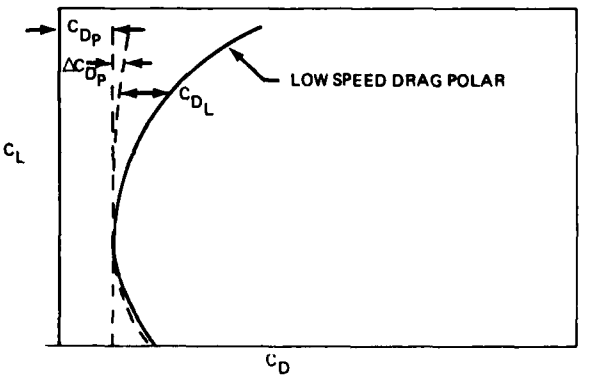

Figure 9.1.2-4. Low Speed Drag Polar Components

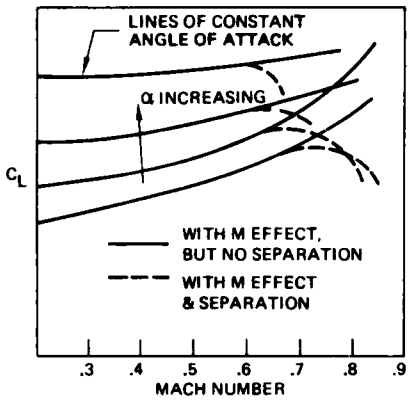

Figure 9.1.2-5. Lift Coefficient Variation With Mach Number

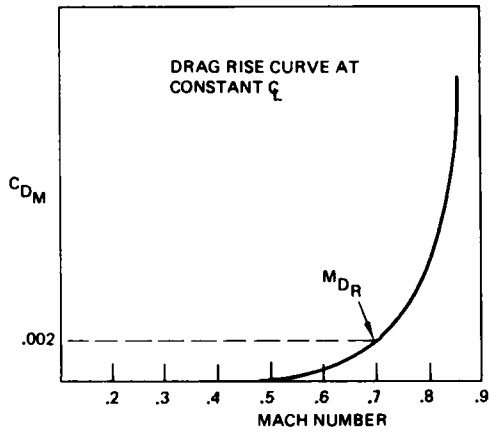

Figure 9.1.2-6. Compressibility Drag Associated With Increasing Mach Number for a Constant Lift Coefficient

Table 9.1.2-1. Drag Rise Mach Number Vs. Sweep Angle

Sweep angle measured ¼ distance between leading and trailing edge (quarter chord) Λ	Drag Rise Mach No. M_{DR}
0° ≤ Λ ≤ 25°	.55
25° ≤ Λ ≤ 30°	.60
30° ≤ Λ ≤ 35°	.65
35° ≤ Λ ≤ 40°	.70
40° ≤ Λ	.75 (max)

The compressibility drag is affected to a small extent by the airfoil's thickness to chord ratio and C_L value. An empirical equation which gives approximate compressibility drag for subsonic airplanes has the form

$$C_{D_M} = K_1(M-M_{DR})^8 + K_2(M-M_{DR})^2(C_L-C_{L_{Min}})^3 \qquad 9.1.3$$

where K_1 and K_2 are constants which depend on the configuration (thickness to chord, sweep angle, etc.).

Combining the various drag terms gives an equation from which subsonic drag polar can be plotted.

$$C_D = C_{D_P} + \Delta C_{D_P} + \frac{(C_L-C_{L_{min}})^2}{\pi ARe} + K_1(M-M_{DR})^8 + K_2(M-M_{DR})^2(C_L-C_{L_{min}})^3 \qquad 9.1.4$$

A typical subsonic drag polar is shown in Figure 9.1.2-7.

The drag rise in high subsonic flow continues through transonic flow. Depending on the configuration, a maximum drag coefficient is observed in the transonic or low supersonic Mach number region.

An additional term, wave drag, is required in supersonic flow. Wave drag replaces the subsonic terms of profile and compressibility drag. Approximate equations describing the wave drag on bodies and planar surfaces are shown below

1) Bodies: 9.1.5

$$C_{D_W} \approx .7\left(\frac{\text{Length}}{\text{maximum equivalent diameter}}\right)^{5/3}$$

2) Plannar Surfaces: 9.1.6

$$C_{D_W} \approx 3.05\left(\frac{\text{thickness}}{\text{chord}}\right)^{5/3}\cos^{3/2}(\Lambda \text{ leading edge})$$

Notice that these approximations are not Mach number dependent. The drag coefficient vs. Mach number for a typical supersonic aircraft in level flight is as shown in Figure 9.1.2-8.

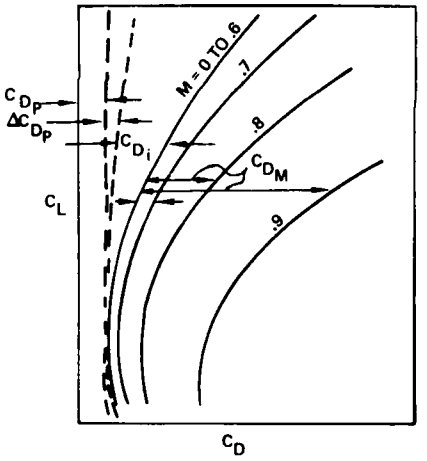

Figure 9.1.2-7. Drag Polar of a Subsonic Airplane Showing Contribution Due to Compressibility Effects

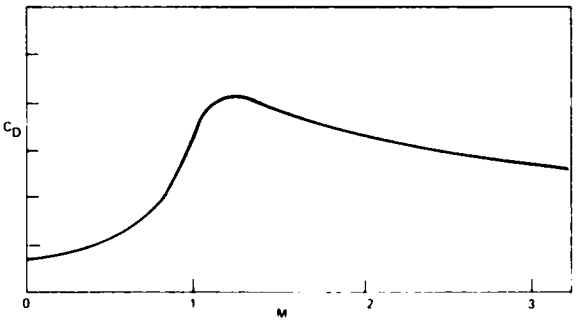

Figure 9.1.2-8. Representative Drag Coefficient Variation for a Supersonic Airplane in Level Flight

More detailed analyses of high speed flight indicate that C_D at M = 3 can be below the maximum value by as much as 25% depending on the configuration.

The aerodynamicist depends largely on three sources for information pertaining to the drag polar: similar existing airplanes, aerodynamic component test, and scale wind tunnel tests. Wind tunnel models are used to verify analytic estimates and to investigate certain design features for which no data is available. The basic drag polar is usually obtained for the complete airplane from wind tunnel tests, although the drag so obtained is not used directly because of the differences in scale. While the shape and spacing of the curves relative to each other are used directly, the intersection of the low Mach number polar with the C_D axis is obtained by other means. Experience has shown that wind tunnel data will accurately predict the polar shape and drag rise characteristics but will not predict the basic drag level. Two major reasons for this are Reynolds number effects and the difficulty in accurately separating out the drag and interference effects of the model suspension system.

The equations shown above, with appropriate coefficients, are sufficiently accurate for most preliminary design work and initial engine cycle selection studies. As more detail is desired the descriptive equations are improved through the use of additional terms and modified coefficients. Provision for the more accurate equations is usually the responsibility of the aerodynamicist and the propulsion designer need only assure himself that accuracy of the polar is compatible with that required for his study.

Because the interactions between the engine and airframe are very strong, particularly in fighter aircraft, detailed thrust/drag bookkeeping is a substantial problem. Chapter 26 considers thrust/drag bookkeeping in detail. The present section avoids bookkeeping details in order to provide insight into the method of mission analysis.

c) Use of the Drag Polar for Mission Analysis

In order to clarify the use of the drag polar for mission analysis, a routine airlift mission will be considered. It is common in this case to consider altitude changes within cruise mission segments to be negligible, to assume that the engine propulsive force and the drag act along the same line, and to note that the lift acts at right angle to the drag and to the aircraft's instantaneous velocity. As a result, in non-accelerating level flight the lift is equal to the weight. When the airplane is accelerating in the lift direction (as would occur when pulling out of a dive, for example) the lift must, of course, be greater than the aircraft weight. If the total lift is expressed as a fraction of standard gravity, N, then the equation for the lift coefficient can be generalized,

$$C_L = \frac{L}{qS} = \frac{W \cdot N}{qS} \qquad 9.1.8$$

Mission analysis is an incremental progression through the following steps for the number of segments into which the mission has been divided:

1) The weight, reference area, and flight conditions, are used to compute the required C_L for the first mission segment.

2) The drag polar and Mach number are then used to determine the drag coefficient, C_D.

3) The calculated C_D, the flight condition, and reference area, permit the airplane drag to be computed.

4) The net thrust is calculated to be the drag plus additional thrust to provide linear acceleration requirements for the flight segment.

5) The weight of fuel consumed by the engine to produce the net thrust during the increment is computed and the weight of the aircraft diminished by that amount. (This is done for each increment that the segment has been divided into.)

6) The procedure is repeated by returning to step 1, with the newly computed weight and flight conditions for the next mission segment.

7) This incremental process is continued until all fuel is used or the mission is completed. If the fuel aboard does not match the fuel required for the mission (including reserves) the airplane is resized and the computation repeated.

8) If the engine size (usually estimated initially from a thrust to takeoff gross weight ratio) does not exactly provide the required thrust at the most demanding point of the segment, the engine size is altered and the entire computation is repeated.

The unknowns remaining in the above procedure are the characteristics of the mission segments and thrust required for each. These will be discussed for the eight segments which commonly provide the building blocks for a mission.

9.1.3 Mission Segments and Thrust Requirements

a) Introduction

Mission segments can be combined to define any desired flight profile. A typical combat mission profile is shown in Figure 9.1.3-1. The following subsections provide a brief description of each segment, standard assumption, and the appropriate equations for use in mission analysis. For further details see References 9.1.2-1 and 9.1.3-1.

Computer programs for mission analysis break each major segment of the mission into increments. At each step the program calculates the airplane weight change due to fuel consumption, refueling, and payload expenditure.

All of the methods of mission performance analysis are based on the same fundamental laws of

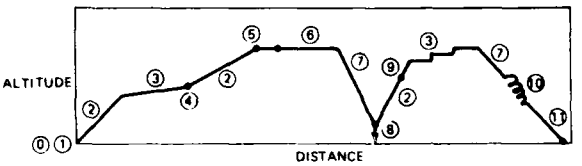

SEGMENTS

0	WARM UP	7	DESCENT
1	TAKEOFF	8	MUNITION OR PAYLOAD DROP
2	CLIMB	9	COMBAT
3	SUBSONIC CRUISE	10	LOITER
4	REFUEL	11	LANDING AND THRUST REVERSE
5	ACCELERATE	RESERVES	
6	CRUISE SUPERSONIC		

Figure 9.1.3-1. Example Mission Profile

motion and flight mechanics; however, one technique (Reference 9.1.3-2) is particularly well suited for the purpose of engine/airplane matching. This method will be emphasized in the following sections.

During mission analysis the range is not known a priori when calculating climb and descent segments. During cruise required range may be specified, or maximized by assuming exhaustion of fuel allotted for the segment. During loiter conditions, no range is credited, and fuel consumption is computed from maximum endurance considerations (safe flight speed, minimum fuel consumption.) The range for any other kind of segment cannot be specified (or independently varied) because range for other segments depend upon the flight path conditions specified.

This flexibility allows the representation of virtually any mission profile. In addition, at any point in the mission and for any segment, performance requirements and constraints can be specified. Typical examples of these requirements include: payload may be added or subtracted, external stores or tanks or weapons may be released, the "g" loading experienced by the airplane can be changed to any desired level (to simulate combat conditions), the thrust of any number of engines can be omitted to simulate engine-out, the wing sweep may be varied, the specific excess power required for acceleration and climb can be specified and maximum noise levels can be prescribed.

Although several engine sizing criteria must be specified in one mission, the most demanding condition must be identified and used. Once the size of the engine has been established, most portions of the mission will require only part power. The fuel consumption is then deduced as a function of thrust for each altitude and Mach number specified in the mission analysis program as is discussed in Section 9.1.4.

b) Warm-up and Takeoff

Ground taxiing and holding before takeoff consumes fuel in an amount which can be calculated from the power settings and time requirements specified. Since the fuel consumed and resulting weight changes do not contribute to the flight portion of the mission, the required fuel weight is added to the takeoff gross weight of the airplane. The additional fuel tank volume must be allowed for in the aircraft size and shape.

The takeoff segment of the mission includes the ground run, rotation, and a climb to a standard height of 35 feet. The analysis of the takeoff segment yields an estimate of the fuel used during takeoff, and the size of the engine to provide takeoff within the desired takeoff distance.

For the ground roll the relationship between acceleration, a, velocity, V, distance, s, and time, t, is of course ds = Vdt and a = dV/dt. Thus

$$ds = \frac{VdV}{a} \qquad 9.1.9$$

If a steady headwind velocity of V_W exists, the ground roll distance, S_G, may be obtained as an integral over the velocity relative to the airplane, V_r, by noting $V_r = V + V_W$. Then

$$S_G = \int_{V_W}^{V_{LO}} \frac{V_r - V_W}{a}\, dV_r \qquad 9.1.10$$

where V_{LO} is the required relative velocity for lift off.

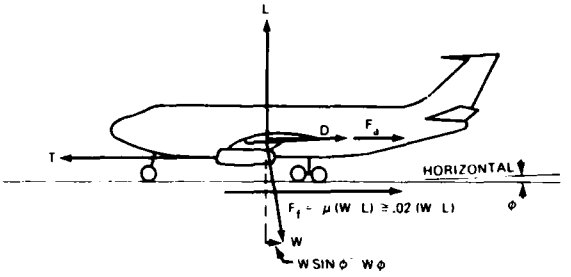

Figure 9.1.3-2. Forces on Airplane During Ground Run

The acceleration can be evaluated using Newton's law of motion ($\Sigma F = Ma = \frac{W}{g} a$) and Figure 9.1.3-2.

Solving for a and substituting into equation 9.1.10 yields an expression for the takeoff distance with the symbols defined as in the figure:

$$S_G = \int_{V_W}^{V_{LO}} \frac{W}{g} \cdot \frac{(V_r - V_W)\, dV_r}{[(T-\mu W)-(C_D-\mu C_L)qS-W\Phi]} \qquad 9.1.11$$

In order to carry out the integration the variation of thrust, weight, drag and lift with velocity must be determined. In general, thrust is a function of velocity, air temperature and pressure; weight is nearly constant for the ground run; drag and lift are functions of velocity and air density, as discussed in section 9.1.2.2.

With a tricycle landing gear, the airplane attitude (i.e. α) will remain constant during the ground operation, and C_L and C_D will also remain constant. Figure 9.1.3-3 shows the approximate order of magnitude of the forces acting during a takeoff run.

The time required for the ground run is

$$t = \int_{V_W}^{V_{LO}} \frac{W}{g} \cdot \frac{dV_r}{(T-\mu W)-(C_D-\mu C_L)Sq-W\Phi} \qquad 9.1.12$$

Equations 9.1.11 and 9.1.12 can be solved by stepwise integration.

In preliminary design the above degree of accuracy is not usually necessary and approximate values are often used. Wind speed is ignored and equation 9.1.10 is integrated to give

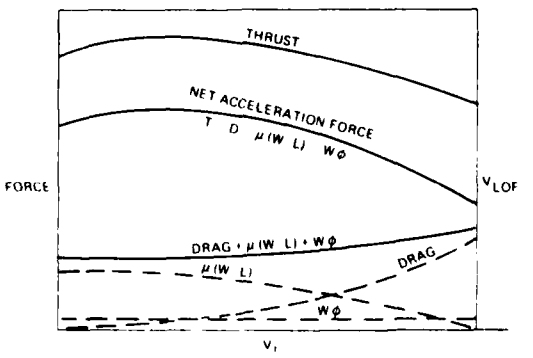

Figure 9.1.3-3. Relative Magnitude of Forces During Ground Roll

$$S_G = \frac{V_{LO}^2}{2\bar{a}} \qquad 9.1.13$$

where $\bar{a}$ is a representative constant acceleration. With the assumption of a horizontal runway and negligible aerodynamic drag during ground roll, an appropriate value for $\bar{a}$ is

$$\bar{a} = \frac{(FN - 0.02\ W_o)}{W_o} \cdot g \qquad 9.1.14$$

where W_o is the initial brake release weight (and usually equals takeoff gross weight, in mission analysis) of the airplane and FN is the net thrust of the propulsion system at .707 V_{LO}. The time required is approximately $V_{LO}/\bar{a}$. (Note: The thrust, T, is the net thrust of the propulsion system and is interchangeable with FN. T is commonly used by aerodynamicist to mean the net thrust required for the airplane, while FN is used by the propulsion specialist to mean either the net thrust per engine or total net thrust.)

Several rules governing speed requirements for airplane control and engine out operation govern the lift off velocity in actual practice. For preliminary design, a lift-off speed of 1.2 times the stall speed is a reasonable approximation. When conducting precise mission analysis the appropriate military or FAA rules should be used.

Various field length definitions are in common usage. When field length is a critical segment in the airplane analysis, a consistent definition of that length must be used. For example, one criterion for evaluating a multiple engine commercial aircraft is the balanced field length: a takeoff calculated according to Civil Air Regulations, SR-422, provides for a field length that satisfies both the takeoff and accelerate-stop requirements. If it is assumed that an engine failure occurs at a speed such that the distance to continue takeoff and climb to a stipulated height is equal to the distance required to stop, the total field length is termed "balanced". SR-422B and FAR part 25 stipulate using a field length which is the greatest of either the accelerate and go distance, the accelerate-and-stop distance, or 115% times the all-engine-operating distance to a 35-ft. height.

Detailed takeoff calculations are generally performed in discrete segments which define the distinct parts of the takeoff as shown in Figure 9.1.3-4.

The drag polar used to compute the increment in time and distance required to clear the 35 foot obstacle is often different from that used for the majority of the mission. The appropriate polar must include the drag penalty and lift benefits due to flaps or other lift augmentation devices, as well as landing gear drag. Detailed calculations require estimating the effects of wind, flap setting, altitude, temperature, desired climbout rate, and lift-off gross weight. Preliminary mission studies use a nominal drag polar penalty and account for the temperature and altitude effects on engine performance, computed as changes from standard day (unless the engine is "flat rated" to the desired temperature in which case the throttle is advanced until standard day thrust is produced).

The weight of fuel consumed during takeoff is computed, knowing the takeoff power setting, TSFC, and the time duration.

c) Thrust Available and Required

For an airplane in level unaccelerated flight, the net thrust (F_N) must equal drag (D) and the lift must equal weight (W). The lift and drag

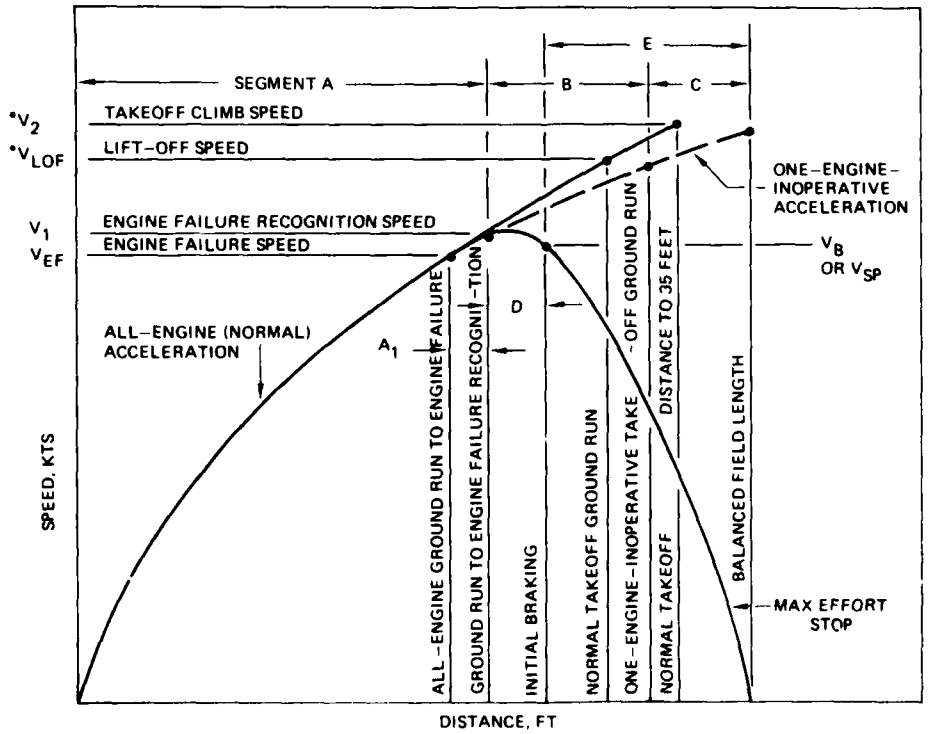

*ONE-ENGINE-INOPERATIVE V_2 AND V_{LOF} SPEEDS WILL BE SLIGHTLY LOWER THAN THE ALL-ENGINES-OPERATING V_2 AND V_{LOF} SPEEDS FOR THE SAME ROTATION SPEED, V_R

Figure 9.1.3-4. Balanced Field Length and Performance Segments

coefficient equations can be rewritten for this flight condition as

$$\frac{D}{\delta} = \frac{\gamma}{2} p_{STD} C_D M^2 S \qquad 9.1.15$$

$$\frac{W}{\delta} = \frac{\gamma}{2} p_{STD} C_L M^2 S \qquad 9.1.16$$

$$\frac{FN}{\delta} = \frac{D}{\delta} \qquad 9.1.17$$

where δ is here defined as the local freestream static pressure divided by the standard reference pressure ($p_{STD} = 1.013X(10^5)$ N/m^2 or 2116 lb$_f$/ft^2).

The equations describing the off design performance of various engines were developed in Chapter 8. It was shown (see summary of equations in Section 8.1.1, for example) that F/δ is independent of altitude if the ambient temperature, flight speed, and the engine setting (turbine inlet temperature) remain constant. F/δ is hence a convenient thrust parameter, and the ratio W/δ is used for consistency.

The above equations are applied to performance computations as follows. The value of C_L at a given W/δ and Mach number is computed from equation 9.1.16. The C_L and Mach number are used to find the appropriate C_D from the drag polar which is then substituted into equation 9.1.17 to establish the required net thrust.

Selecting a range of Mach numbers for a given W/δ results in a series of points defining a curve which may be plotted on axes of FN/δ and Mach number. By selecting several values of W/δ, a family of curves may be obtained as in Figure 9.1.3-5. These curves define the T/δ which must be provided by the engines to sustain level unaccelerated flight. Typical net thrust/δ available curves from jet engines are superimposed on Figure 9.1.3-5. The intersections show the maximum Mach number that can be maintained in level flight for each weight and altitude.

For well designed high speed aircraft, the decrease in dynamic pressure with altitude increases more than compensates for the increase in drag coefficient with Mach number; resulting in less drag at altitude for transonic and supersonic speeds than for high subsonic speeds flown at sea level.

At Mach numbers below the intersections on Figure 9.1.3-5 the available net thrust exceeds that required for level unaccelerated flight and either the throttle setting must be reduced or the

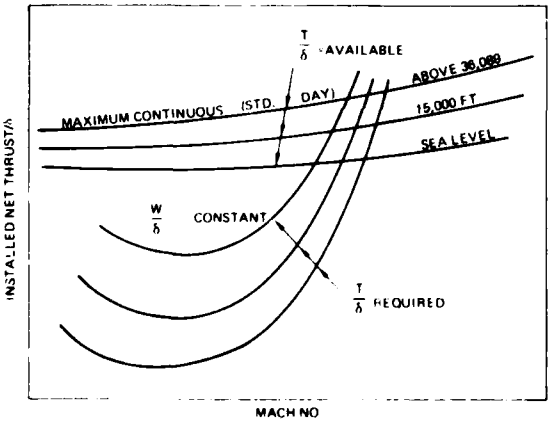

Figure 9.1.3-5. Thrust Required and Available for Level Unaccelerated Flight

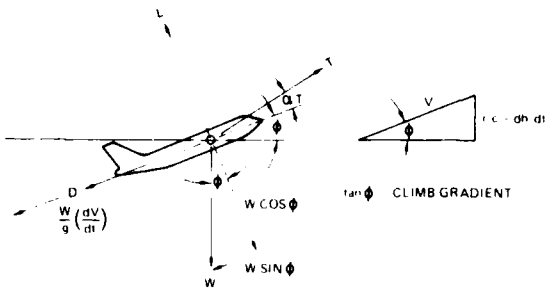

Figure 9.1.3-6. Freebody Diagram of Airplane With Acceleration and Climb

excess thrust will result in acceleration and/or climb.

d) Climb, Acceleration and Descent

If excess thrust is available, it can be used for climb and/or acceleration. Newton's laws of motion can be applied to this situation with the aid of Figure 9.1.3-6.

The gravitational force is resolved into components perpendicular and parallel to the flight path. The inclination of the flight path to the horizontal is γ and the thrust vector is at an angle α_T to the flight path. The following analysis presumes that α_T is small enough (<15°) to assume that $T \cdot \sin\alpha_T = 0$ and $T \cdot \cos\alpha_T = T$. The small angle assumption is adequate for the majority of missions. (In configurations using vectored thrust or at high angle of attack these contributions must be included.)

Resolving the forces along the flight path yields

$$T - D - W \cdot \sin\gamma = \frac{W}{g}\frac{dV}{dt} \qquad 9.1.18$$

Perpendicular to the flight path, the sum of the forces is equal to the centripetal force necessary to change the flight path angle at a rate $d\gamma/dt$

$$L - W\cos\gamma = \frac{W}{g} V \frac{d\gamma}{dt} \qquad 9.1.19$$

In a climb $d\gamma/dt$ is essentially zero and thus

$$L = W\cos\gamma \qquad 9.1.20$$

This equation shows that in a climb, the lift will be less than the weight (and thus the level flight lift) by the factor $\cos\gamma$; the balance of the weight is supported by a thrust vector component. This means that at a particular speed, the induced drag will be less than at the same speed in level flight. The reduction in lift (and therefore drag) will be greater for larger climb angles. For transport airplanes, under most conditions, the climb angles are small so that $\cos\gamma$ is very close to unity. Thus, the lift and drag during climb are practically identical to those existing under level flight conditions, and the level flight drag polar data for the airplane can be used. It is consistent for this approximation to use

$$C_L = \frac{W}{qS}$$

For fighter type aircraft missions with segments calling for climb angles greater than 15°, the effect of climb angle on weight and hence drag must

be considered. Occasionally, fighter and aerobatic type aircraft missions will include segments where $d\phi/dt$ is large and equation 9.1.19 must be used without simplification.

Equation 9.1.18 can be rewritten as

$$\sin\phi = \frac{1}{W}\left[T-D-\frac{W}{g}\frac{dV}{dt}\right] = \frac{T-D}{W} - \frac{1}{g}\frac{dV}{dt} \qquad 9.1.21$$

The rate of climb, dh/dt, is equal to the vertical component of the flight velocity.

$$\frac{dh}{dt} = V\sin\phi \qquad 9.1.22$$

$$\text{or,}\quad \frac{dh}{dt} = \frac{(T-D)V}{W} - \frac{V}{g}\frac{dV}{dt} \qquad 9.1.23$$

and noting that $\frac{dV}{dt} = \frac{dV}{dh}\frac{dh}{dt}$, it follows that

$$\frac{dh}{dt}\left(1 + \frac{V}{g}\frac{dV}{dh}\right) = \frac{(T-D)V}{W} \qquad 9.1.24$$

The right side of the equation is the excess thrust times velocity (excess power) divided by the weight and is defined as the specific excess power, P_S. The dimensionless term $\frac{V}{g}\frac{dV}{dh}$ is an acceleration factor. When a climb is executed at a constant true airspeed the acceleration factor is zero and equation 9.1.24 becomes:

$$\text{Rate of unaccelerated climb} = \frac{(T-D)V}{W} \qquad 9.1.25$$

The specific excess power is one of the criteria by which fighter aircraft are evaluated and mission constraints usually specify a minimum level. Commercial transport analysis on the other hand, follows a rule of thumb that if the candidate airplane can climb at greater than 1500 feet/minute (average), the engines are oversized and the configuration is likely to have excessively high direct operating costs.

For slow acceleration rates the rate of climb can be obtained in terms of Mach number by rewriting equation 9.1.24 as

$$\frac{dh}{dt} = a_o M\sqrt{\theta}\left(\frac{T/\delta - D/\delta}{W/\delta}\right) \qquad 9.1.26$$

where a_o is the speed of sound at standard condition, and $\theta = T/To$, the ratio of temperature to standard temperature.

Maximum rate of climb for a given weight and altitude will occur at the speed where $\frac{T-D}{\delta}$ multiplied by the Mach number is greatest. This will be at a speed slightly higher than that for $\left(\frac{T-D}{\delta}\right)_{max}$. The true airspeed at the maximum-rate-of-climb increases with altitude; therefore, the airplane must accelerate along the flight path to maintain the maximum rate of climb. If the thrust rating cannot be increased, the rate of climb will be reduced to account for this lack of acceleration, as seen from equation 9.1.26.

Figure 9.1.3-6 shows that the sine of the climb angle is equal to rate of climb divided by the climb velocity, V. The climb gradient is defined as the tangent of the climb angle. For small angles, the sine of an angle is approximately equal to the tangent of the angle; therefore,

$$\text{climb gradient} = \tan\phi = \sin\phi = \frac{dh/dt}{V} \qquad 9.1.27$$

Substituting equation 9.1.25 into equation 9.1.27, and noting that

$$\frac{D}{W} = \frac{C_D}{C_L}$$

results in the climb gradient for unaccelerated climb,

$$(\tan\phi)_{V=CONST} = \frac{T}{W} - \frac{C_D}{C_L} \qquad 9.1.28$$

Substituting equation 9.1.24 into equation 9.1.27 results in the climb gradient for accelerated climb,

$$\tan\phi = \frac{\frac{T}{W} - \frac{C_D}{C_L}}{1 + \frac{V}{g}\frac{dV}{dh}} \qquad 9.1.29$$

Climb gradients are often expressed in percent.

For level accelerated flight the equation of motion becomes

$$T-D = \frac{W}{g}a \qquad 9.1.30$$

or

$$\frac{T}{W} - \frac{C_D}{C_L} = \frac{a}{g} \qquad 9.1.31$$

where $\frac{a}{g}$ is the acceleration gradient for level flight.

Equations 9.1.28, 9.1.29 and 9.1.31 show that the quantity

$$\frac{T}{W} - \frac{C_D}{C_L}$$

can be used to measure climb or acceleration performance.

In practice the climb gradients for commercial transports are specified by rules (ex. SR-422 and FAR part 25) which state percentages of climb gradients required for 2, 3 or 4 engine transports during climb, approach (descent) and landing.

If the horizontal velocity, V_H, is plotted against the vertical velocity, V_V, a hodograph plot

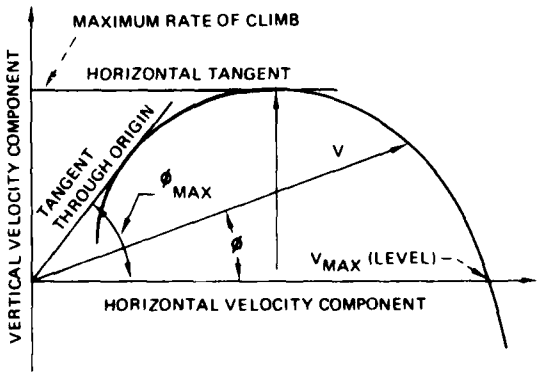

Figure 9.1.3-7. Climb Hodograph Showing Locations of Maximum Climb Angle and Rate

results. The radius vector from the origin to any point on the curve is proportional to the flight path speed and the angle from the horizontal is equal to the climb angle, ϕ. Figure 9.1.3-7 shows a hodograph typical of full power performance where the distinction between maximum climb angle (ϕ_{max}) and maximum rate of climb are delineated. Figure 9.1.3-8 (which is not a hodograph) displays the speed for best climb angle and speed for best rate of climb.

Altitude affects both the velocity and the maximum rate of climb as illustrated on Figure 9.1.3-9. (The assumption of constant weight is appropriate for long range subsonic transports which burn only about 3% of their total fuel during climb.) Figure 9.1.3-10 depicts the true airspeed variation with altitude necessary to fly at either constant indicated airspeed or at the speed for maximum rate of climb. Above 36089 feet jet aircraft obtain the maximum rate of climb at a constant true airspeed and hence constant Mach number.

The T/δ available for climb decreases with increasing temperature. On a hot day the rate of climb decreases and the time to climb, range and fuel flow increase.

Excess power decreases as altitude increases. The altitudes at which the unaccelerated rates of climb are 100 ft/min and zero are referred to as the service ceiling and absolute ceiling, respectively.

The time required to climb to desired altitude, h_1, is

$$t = \int_0^{h_1} \frac{dh}{dh/dt} \qquad 9.1.33$$

where dh/dt is a function of h as shown in Figure 9.1.3-9. Computer programs conveniently obtain the time as a summation of small increments using the average rate of climb within the increment.

$$\Delta t = t_2 - t_1 = \frac{h_2 - h_1}{(dh/dt)_{average}} \qquad 9.1.34$$

For precise computations care must be taken to distinguish between pressure altitude and actual altitude on non-standard days.

The range during climb is the summation of the incremental values of $V\cos\phi$ multiplied by time.

During the climb segment of a mission the engine is sized to produce or exceed the desired rate of climb at the engine power setting provided for climb.

An example mission analysis computer approximation for climb is shown in Figure 9.1.3-11. Thrust, fuel flow, and drag are determined at the midpoint of each increment (i) and applied over the increment to approximate time, fuel weight (WF) and range (R). Five to ten increments usually provide sufficient accuracy.

Descent calculation is identical to climb except the power required is less than the power required for level unaccelerated flight. To avoid acceleration during descent low power settings are used and the drag polar is often changed to represent the increase in drag and decrease in lift made possible from spoilers or dive brakes. If the descent angle is less than 15°, the rate of sink is approximated as

$$\text{rate of sink} = \frac{V}{W}\left(T_{average} - \frac{\rho V^2 C_D S}{2\cos\alpha_T}\right) \qquad 9.1.35$$

For commercial aircraft the descent rate is specified for air traffic control convenience. In general, descent analysis can be computed using the technique of Figure 9.1.3-11, but with the altitude and Mach number path calculated in descending order. Because the power setting must be very low, in cases where descent is either a small portion of the total range or the descent is flown in a spiral, preliminary mission analysis often credits zero range and zero fuel expenditure to the descent segment.

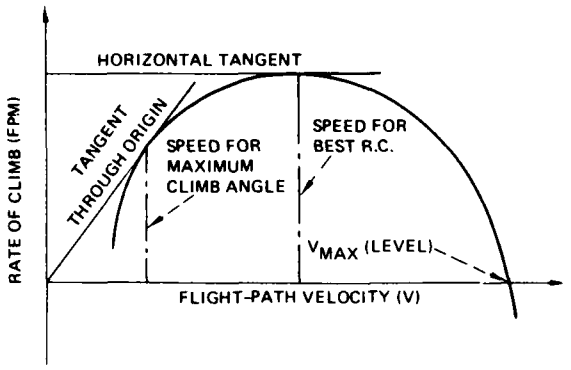

Figure 9.1.3-8. Speed for Maximum Rate of Climb and Speed for Maximum Climb Angle

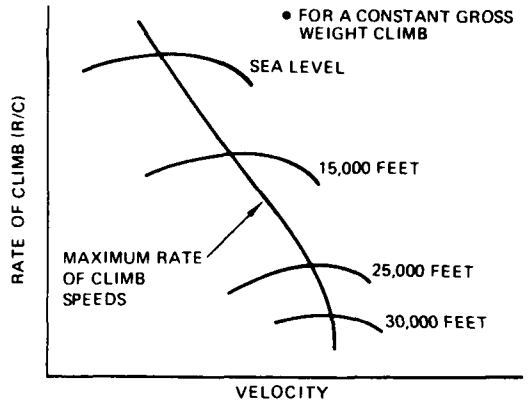

Figure 9.1.3-9. Altitude Effects on Climb

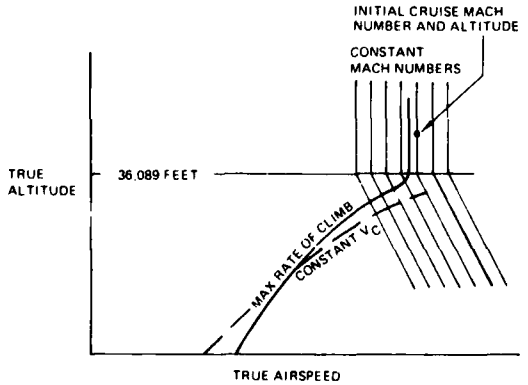

Figure 9.1.3-10. True Airspeed Versus Altitude for Climb

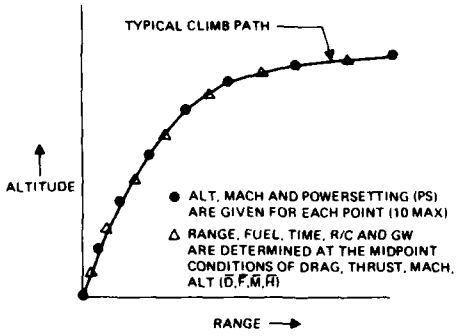

$$\Delta t_i = \frac{GW_i\left(\frac{\Delta V_i}{S} + \frac{\Delta H_i}{V_i}\right)}{(F_i - D_i)}$$ Time for any increment where GW_i is found by iteration with $\overline{GW}_i = GW_i - \frac{\Delta WF_i}{2}$

$$\Delta WF_i = \overline{SFC}_i \times \Delta t_i \times \bar{F}_i$$ Fuel used in any increment

$$\Delta R_i = \bar{V}_i \times \Delta t_i$$ Range for any increment

$$\left(\frac{dh}{dt}\right)_i = \frac{(F_i - D_i)}{GW_i} \cdot \frac{1}{\left(\frac{1}{\bar{V}_i} + \frac{\Delta V_i}{g\Delta H_i}\right)}$$ Rate of climb for any increment

$$WF = \sum_{i=1}^{N} (\Delta WF_i)$$ Total fuel

$$t = \sum_{i=1}^{N} (\Delta t_i)$$ Total time (Ref. 9.1.3-2)

$$R = \sum_{i=1}^{N} (\Delta R_i)$$ Total range

● Descent is calculated with the same procedure except that the altitude and mach number variation are decreasing.

Figure 9.1.3-11. Method of Climb (and Descent) Fuel, Range, and Time Calculation

Deceleration at constant altitude can be represented with a descent segment. This can be done by specifying a minimal descent of say one foot per increment. When using an incremental technique for any segment it is safest to require monotonic increases or decreases in altitude/Mach number to prevent division by zero.

Figure 9.1.3-12 illustrates the use of increments to calculate the time, range, and fuel consumed during acceleration in level flight. To accurately estimate acceleration small increments of Mach number (0.05 to 0.10) should be used. In the transonic region where the aircraft drag changes rapidly very small increments should be used.

An acceleration segment can be used at any point in the mission to meet constraints which may size the engine or airframe but are not necessarily a part of the design mission. If the aircraft, as defined when it enters the acceleration constraint segment, is incapable of fulfilling the constraint, the program will automatically resize the engine and initiate computation from the original mission start condition. When the constraint is satisfied the analysis proceeds with the aircraft in a new configuration. Because the design mission does not include the requirement that the aircraft actually fly this segment, but rather only be capable of flying it if the need arises, the total mission is credited with zero distance and zero time for the constraint mission. (It is assumed that should the constraint segment actually be flown by the aircraft the aircraft will not proceed along the design mission because of fuel constraint.) For example, an airplane may be required to accelerate to a high Mach number if an intercept is necessary. If the design mission for the aircraft is to penetrate enemy territory without making an intercept, the intercept capability may be the most stringent engine sizing criteria. To insure that the intercept could be made, if necessary, an acceleration to the high Mach number, intercept and return to base must be verified, but will not contribute to flying the full mission requirement.

e) Cruise

The fuel consumption is usually stipulated in terms of fuel flow per unit thrust, commonly called specific fuel consumption, SFC. The SFC of an engine at constant flight Mach number decreases with altitude up to a particular altitude (usually between 30,000 and 40,000 feet depending on design) and then begins to increase with altitude. The best cruise condition produces the most range for the least fuel consumption. Over a small increment of range, ΔR, an airplane consumes ΔW pounds of fuel. The mileage per pound of fuel, S, is

$$S = -\frac{\Delta R}{\Delta W} \qquad 9.1.36$$

(Note ΔW is negative.) In the limit as the increment becomes small

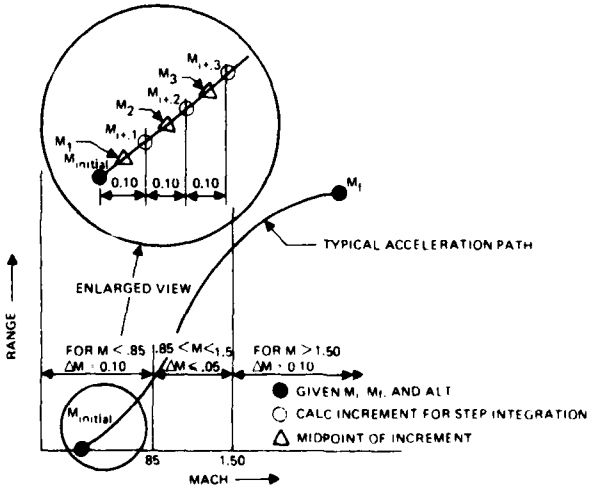

$$M_i = M_{initial} + \sum_{1}^{N} \Delta M_i - \frac{\Delta M_i}{2}$$ ΔM: 0.10 or 0.05 depending on M_i ($i \rightarrow$ any increment) ($N \rightarrow$ number of increments)

$$GW_i = GW_{initial} - \sum_{1}^{N-1} (\Delta WF_i)$$ Note that the GW at the start of each increment is used in Δt_i Eq below

$$\Delta t_i = \frac{V_i \times GW_i}{\bar{F}_i - \bar{D}_i}$$ Time for increment

$$\Delta WF_i = \overline{SFC}_i \times \bar{F}_i$$ Fuel for increment

$$\Delta R_i = V_i \times \Delta t_i$$ Range for increment

$$\frac{(F-D)_i}{D_i} = \frac{F_i - D_i}{D_i}$$ Acceleration thrust margin

$$W_F = \sum_{1}^{N} (\Delta WF_i)$$ Total fuel (Ref. 9.1.3-2)

$$t = \sum_{1}^{N} (\Delta t_i)$$ Total time

$$R = \sum_{1}^{N} (\Delta R_i)$$ Total range

Figure 9.1.3-12. Method of Accleration Fuel, Range and Time Calculation

$$dR = - S \cdot dW = - (W \cdot S \cdot \frac{dW}{W}) \qquad 9.1.37$$

where the quantity W • S is referred to as the range factor.

If the range factor for any increment of a cruise segment can be considered constant, equation 9.1.37 can be integrated and evaluated between the initial weight, W_1, and the final weight, W_2, yielding

$$R = W \cdot S \cdot \ln \frac{W_1}{W_2} \qquad 9.1.38$$

By noting that

$$S \quad \frac{\text{miles}}{\text{lb.}} = \frac{\text{miles}}{\text{hour}} \cdot \frac{\text{hours}}{\text{lb.}} , \qquad 9.1.39$$

the range factor can be rewritten in the more useful, form

$$W \cdot S = W \cdot V \cdot \frac{1}{T \cdot SFC} \qquad 9.1.39$$

For level unaccelerated flight: the net thrust is equal to the total airplane drag and the thrust term, T, in equation (9.1.39) may be replaced by the drag, D; the numerator may be multiplied by L, the airplane lift, and the denominator by W, the airplane weight, since the lift and weight are equal in this flight condition. Thus, an alternate form for the range factor is obtained:

$$W \cdot S = W \cdot \frac{V}{SFC} \cdot \frac{L}{D} \cdot \frac{1}{W} = \frac{V}{SFC} \cdot \frac{L}{D} = \frac{V}{SFC} \cdot \frac{C_L}{C_D}$$

9.1.40

Substituting 9.1.40 into 9.1.38 produces the Breguet range equation

$$R = \frac{V}{SFC} \cdot \frac{L}{D} \cdot \ln \frac{W_1}{W_2}$$

If the SFC is nearly constant, then the airplane will achieve the greatest level unaccelerated range if V•L/D (or M•L/D) is maximized.

Figure 9.1.3-13 shows a C_L versus C_D polar on which lines have been drawn from the origin tangent to the polars at various Mach numbers. The points of tangency define the maximum L/D for that Mach number. By plotting the identified M•(L/D) vs. Mach number (Figure 9.1.3-13), the Mach number producing the maximum M•(L/D) can be found. The maximum M•(L/D) will occur at a slightly higher Mach number than that associated with the highest possible L/D. For subsonic cruise, it is found that maximum range occurs at conditions where compressibility phenomena are important; that is, where the airplane experiences transonic drag rise.

The airspeed for optimum range occurs at the airspeed corresponding to maximum $C_L^{1/2}/C_D$. Because maximum T/δ is indepedent of altitude (at high altitude and fixed engine setting), the range factor will remain constant if flight Mach number and W/δ are held constant. As the weight is reduced by fuel burnoff the altitude must increase to keep W/δ constant. Thus to maximize range, as the weight decreases due to fuel consumption the altitude must increase to maintain a constant value of W/δ. Air traffic control requirements prevent gradual change of altitude (except on some very low density routes), so in practice the desired gradual altitude increase is approximated by changing altitude in discrete climbing steps. This non-optimal procedure can cause a fuel consumption penalty on the order of 3% in total fuel consumption for a long-range subsonic jet transport.

Examination of equation 9.1.41 shows that supersonic cruise airplanes can be designed for long-range operation because the high velocity can offset high SFC and drag.

Figure 9.1.3-14 illustrates methods of representing the cruise segment for computer mission analysis.

If the range is specified the calculations give time and fuel consumption. Alternatively, if fuel burned is specified, the corresponding cruise distance and time can be computed.

f) Endurance or Loiter

Maximum endurance implies staying in the air for the maximum amount of time using the specified amount of fuel. Maximum endurance occurs at the flight conditions corresponding to the best C_L/C_D (i.e., the tangent to the drag polar which passes through the origin). Maximum endurance is used for hold or loiter (for example, surveillance). The endurance portion of a mission is not considered to contribute to the total mission range.

g) Combat

A combat segment is often pictured as consisting of a series of turning maneuvers. The assumed battle scenario leads to a specification of combat Mach number, altitude, power setting, and time

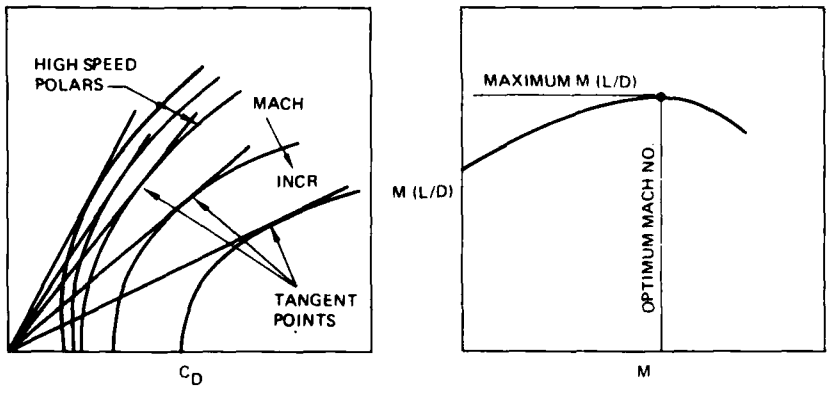

Figure 9.1.3-13. Determination of Maximum M(L/D)

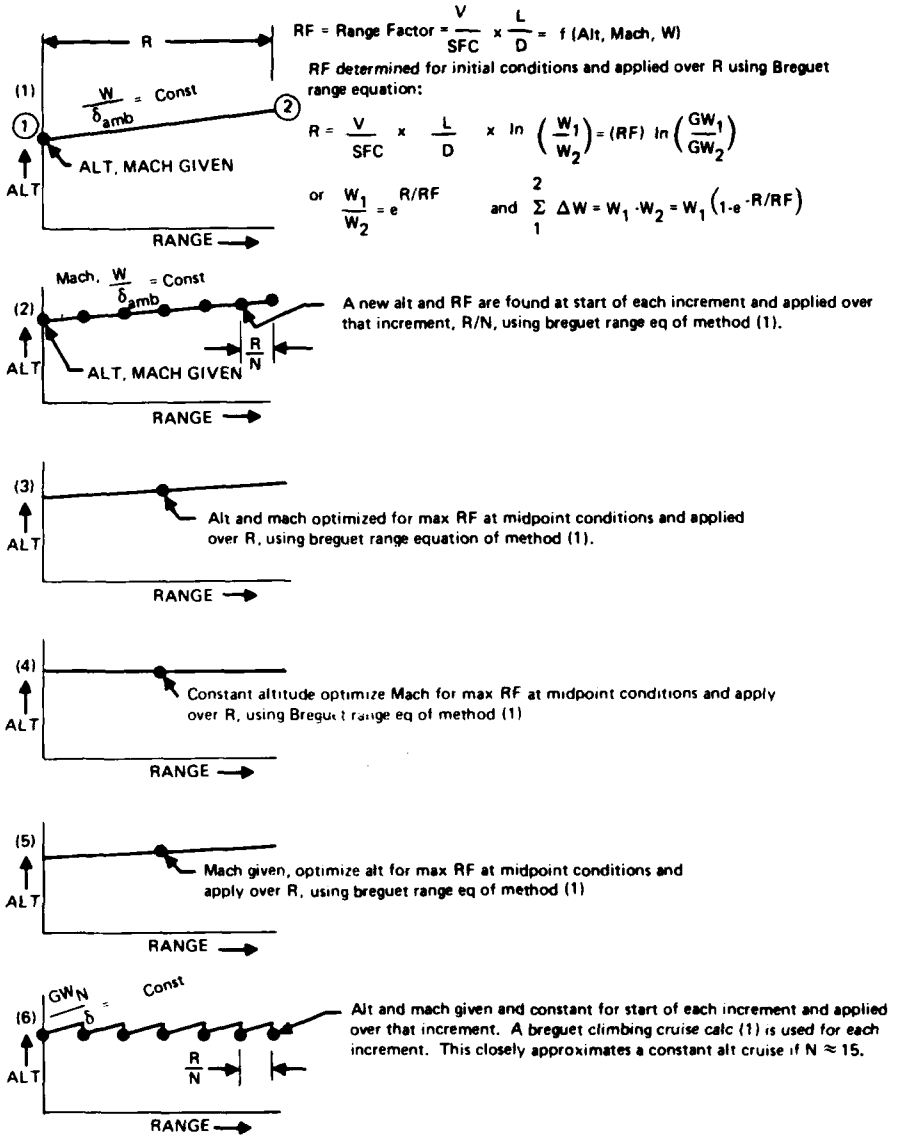

Figure 9.1.3-14. Cruise Methods

duration. No range credit is taken. The mission analysis computes the fuel consumed over the time duration taking into account changes in weight. Since the power setting is specified, the fuel consumption can be calculated directly for the time of combat. The engine may be sized by the combat condition if a specific excess power, P_s, is specified.

h) Refuel or Munitions Drop

Refueling, weapon expenditures and fuel tank release are treated as weight changes which sometimes affect the airplane drag polar.

i) Landing

The problem of determining landing performance is in most respects similar to the takeoff calculation, varying only in the treatment of the approach and flare and in the consideration of auxiliary stopping devices such as the speed brakes or in-flight thrust reversers. Detailed analysis and derivation of equations are omitted because of the similarity of the calculation procedure for the landing segment to the procedure for the takeoff segment already discussed.

j) Reserves

Reserves are simply treated as an additional increment of takeoff gross weight or as a fraction of the full fuel load which is not expendable in the normal mission analysis.

9.1.4 Engine Performance Representation

Engine performance is usually specified in terms of thrust, fuel consumption and airflow rate. Each of these variables may be used in a variety of corrected forms (Table 9.1.4-1). δ_2 and θ_2 are compressor face total pressure and temperature divided by reference values (2116 lbs/ft^2 and 519.7°R, respectively); while δ_{amb} and θ_{amb} are ambient static pressure and temperature at altitude, divided by the reference sea level standard values.

Table 9.1.4-1. Variables Used for Engine Performance Representation

THRUST	$F_N \boxed{F_N \delta_2}$	$F_N \delta_{amb}$	$(F_N \delta_{amb})_{ref}$
FUEL FLOW RATE	$W_F \cdot \boxed{W_F/\delta\sqrt{\theta_2}\,\delta_2}$	$SFC\sqrt{\theta_{amb}}$	$W_F\,\delta/\theta\,\delta_{amb}$
AIR FLOW RATE	$W_O \cdot \boxed{W_O\sqrt{\theta_2}\,\delta_2}$		$W_O\sqrt{\theta_{amb}}\,\delta_{amb}$

Of these choices the quantities boxed in the table give the most nearly linear relationship with Mach number and altitude. Thus their use is desirable because it allows more accurate interpolation or extrapolation between specified conditions.

The calculation of engine performance at representative flight conditions independent of the mission, is shown schematically in Figure 9.1.4-1. At each of the selected flight conditions, a complete power line is obtained for an engine with a reference design airflow size. For this engine the corrected fuel and airflow can then be computed for any desired corrected thrust. Using

$$W_o = \frac{FN}{FN_{ref}} \cdot W_{o_{ref}}, \qquad 9.1.42$$

the required engine airflow size can be scaled from the reference airflow value so that the required thrust at the most demanding flight condition equals the maximum thrust available. At this new airflow size, the power lines of all other flight conditions can be scaled by the same amount, and the part power fuel flow rate necessary to produce the required thrust at any flight condition can be calculated.

Linear interpolation is used whenever the flight condition being evaluated falls between two or four given points. For example, assume the increment of a mission segment being considered is at conditions represented by the point "g" on the Mach number and altitude map shown in Figure 9.1.4-1 . The type of mission segment being flown combined with the airplane drag polar determine the required net thrust for the flight condition. The fuel flow at "g" is found from interpolating the fuel flow required to produce the same thrust at points "e" and "f" where the altitude is different from "g" and the Mach number is the same. Similarly performance at points "e" and "f" are obtained from fuel flow rate at the required thrust interpolated between given power lines at flight conditions "a" and "b", and "c" and "d", respectively.

9.1.5 Propulsion System Installation

Engine/airplane matching requires an accurate evaluation of the interactions between the propulsion system and the airframe. The evaluation is traditionally broken into inlet effects (Chapters 13 & 26) and nozzle/aftbody effects (Chapters 14 & 26).

Depending upon the accuracy desired from the mission analysis, different techniques are used to evaluate the installation effects. For conceptual and preliminary design evaluations, estimates are usually based on past experience and limited computations.

As the complexity of the analysis and the need for accuracy increase, wind tunnel tests may be required. Typically, a complete airplane model is tested and the drag information is used as a baseline or reference value. The inlet (and forward portion of the aircraft, if necessary) is then tested in detail and changes in drag which result from changes in configuration or engine power setting are tabulated as drag increments relative to the reference configuration. Similarly, detailed models of the afthody (usually from the maximum diameter aft) are used to evaluate incremental changes in thrust minus drag due to change in configuration or power setting.

Although much of this chapter discusses computer simulations, the importance of experimental evaluation of the interaction effects on engine/airplane matching process cannot be overemphasized. Wind tunnel and/or scale model remotely piloted free flight testing is a very expensive portion of the aircraft system development process. Useful results depend on comprehensive planning and careful and accurate execution of tests. As the engine/airplane matching process continues toward the identification of optimum aircraft, the validity of the estimation of the interaction effects must be constantly reevaluated and updated.

9.1.6 Results of Mission Analysis

The mission analysis requirements, discussed in the preceding sections, form the starting point for a computer program with the logic shown in

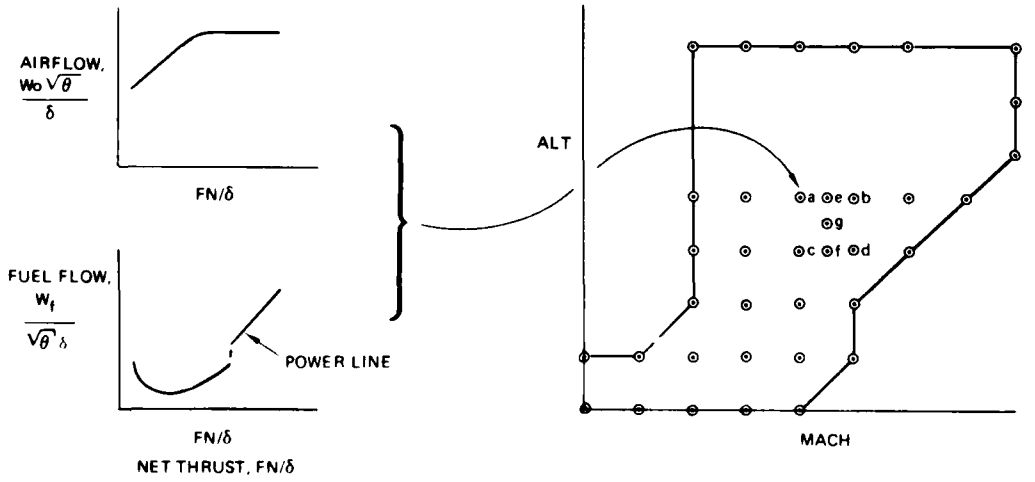

Figure 9.1.4-1. Engine Performance Representation

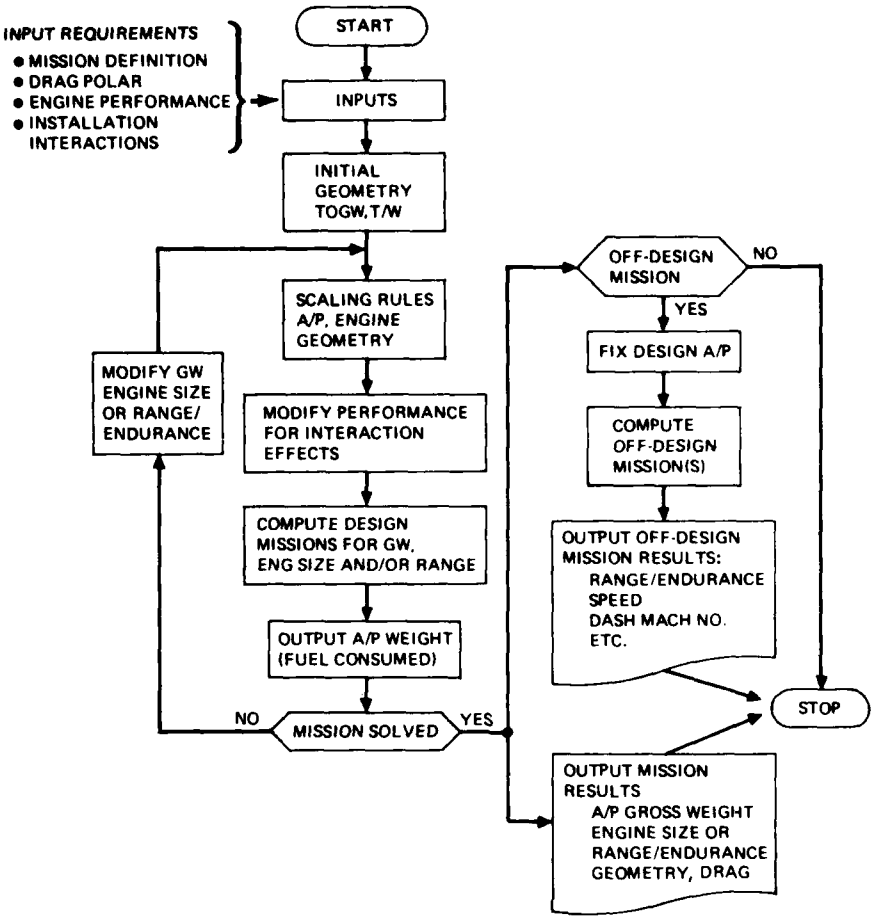

Figure 9.1.6-1. Mission Analysis Process

Figure 9.1.6-1. As indicated, the iterative process uses the specified drag polar, engine cycle, and scaling rules to define an engine/airplane match which satisfies the mission. This integrated engine/airplane system represents the combination which simultaneously meets the conditions of appropriate engine airflow size and airplane gross takeoff weight or maximum range (or endurance).

The engine is sized by the airflow required to produce the net thrust for the most demanding point of the mission in the following way. The engine performance relates the thrust per unit (or reference) airflow size for each Mach, altitude, and temperature used in the mission. The inlet and nozzle losses and the installation-interaction effects account for the difference between installed and uninstalled thrust. The maximum thrust available from an engine varies with the flight segment. The highest power setting is usually takeoff power, which can be used for 2 to 5 minutes. Slightly lower power settings are allowed for continuous operation and a continuum of part power settings exist down to an idle setting usually determined by minimum air flow, fuel flow, or engine PRM acceleration requirements. Thus, when combined with the scaling rules, the net thrust required at the most demanding condition in the mission defines the required airflow size which, in turn, fixes the engine weight, dimensions, and full power fuel consumption. With the engine size fixed to meet this condition, all other points in the mission are calculated with the engine operating at part power. The fuel consumption is determined from the specific fuel consumption at the appropriate part power setting. When afterburning or variable cycle engines are used the iterative process must account for the complexity of additional parameters in the thrust-fuel-flow relationship.

The computation of airplane takeoff gross weight results from a fixed range mission analysis. Simulation of a specified mission with a given engine cycle and size requires a specific fuel quantity for a given airplane size. Since the weight of the airplane is the sum of all the component weights, payload, and fuel, there exists a unique size of scaled candidate airframe which will carry enough fuel to be able to fly the required mission range.

As the airplane size changes so does the lift and drag, which implies a changing reference area (if polars are similar). The change in drag results in a change in thrust that must be supplied and hence a different engine size and fuel consumption. The change in fuel consumption requires a change in airframe size and the iterative loop required to find the unique size of the candidate engine and airplane continues until a match is found to the desired degree of accuracy.

If the final airplane is substantially different in size from the first guess the scaling laws should be reexamined. The installation of the engine should be reexamined to see that the engine size has not so altered the airframe as to change the drag polar. Finally, the interaction effects must be reexamined.

Once the appropriate airplane weight and engine size have been established the characteristics of the fixed configuration can be evaluated on alternative (off-design) missions. These missions typically leave the distance or time of one leg unspecified and the range or endurance of the fixed aircraft is computed for the alternate operating conditions. Off-design missions can also be used to evaluate configuration changes, such as external munitions, in which case the drag polar should be altered.

The end result of a design mission analysis is the airplane weight and engine size. Off-design computation provides additional information about range, endurance, dash capability, etc. These results can be used to reevaluate the inputs but the final result is one engine and airplane combination which can fly the specified mission. The analysis indicates nothing of the quality of the choice of engine cycle and airframe geometry. Optimizing the choice of cycle and airplane parameters is the principal task of the preliminary design process which is discussed in the next section. In preliminary design, mission analysis is used repeatedly in order to identify the region of optimum cycle and geometry characteristics. Following the identification of these characteristics, mission analysis is again used during system development. In the latter application, the output is used to refine the airplane and engine characteristics to the next level of development which carries requirements for increased accuracy.

9.2 OPTIMIZATION OF ENGINE/AIRPLANE MATCH

9.2.1 Introduction

Having discussed the process of sizing a candidate engine cycle and "weighing" a given airplane geometry to meet the requirements of a specified mission, we are now in a position to ask if this was a good choice or if a different engine cycle and airplane geometry could do the mission better. This section describes a process for obtaining the best engine/airplane match for a specified mission. Before the optimum can be chosen it is necessary to decide by what criteria "best" can be defined.

9.2.2 Figures of Merit

While it is obvious that the best airplane can only be chosen once a criteria for its goodness has been established, the commonly used selection criteria, or figures of merit, are not all that obvious and are often difficult to define quantitatively during a preliminary design study.

Airplane selection procedures seldom seek the aircraft which flies the mission best without any regard for cost. The desired mission performance and constraints must be weighed against the cost of ownership. The total cost of purchasing, operating, and maintaining the aircraft during the entire period of ownership, less the final resale value is referred to as the life cycle cost (LCC). Equally obvious, a low cost system may lack mission effectiveness--that is, it might take too long to fly a mission (low productivity), or it may lack flexibility to fly off-design missions. This has caused the Department of Defense to choose an optimization criterion called cost effectiveness, a blend of cost and mission effectiveness which must be formulated for each system, often using judgemental factors. Defense budget constraints have forced the military to balance the aircraft system effectiveness against estimated life cycle costs. Due to the requirement for "crystal ball" estimates needed for accurate life cycle costing, it is more appropriate to say that life cycle cost as a figure of merit is a goal toward which evaluation techniques are evolving.

Aircraft utilization has a significant impact on the cost of ownership. A typical commercial aircraft will have an annual utilization of 3500 hours while a military fighter will fly less than 350 hours per year. The research, development and acquisition costs of a military aircraft are analogous to the depreciation costs of a commercial transport. The high utilization of the commercial airplane de-emphasizes this cost relative to the direct operating costs (DOC). For this reason DOC is usually used as a figure of merit in commercial aircraft and fuel costs are a dominant contributor. The best commercial aircraft is therefore the one that flies the desired mission using the least fuel or providing the most range (per passenger seat mile) while simultaneously meeting the noise and emission constraints and having acceptable reliability and maintainability.

Even though LCC or DOC are important figures-of-merit, they do not easily lend themselves to engineering analysis. Therefore, engine/airplane systems are usually optimized to some performance figure of merit and the cost optimization is inferred indirectly. For example, takeoff gross weight is used as a performance figure of merit because a smaller airplane should cost less to build and operate. This perceived, or inferred, minimum cost is only valid if the optimization procedure uses consistent technology levels throughout. Traditionally, minimum engine takeoff thrust-to-weight ratio was assumed to be a measure of goodness. Recent analyses have shown, however, that in some cases overall system performance and cost need not meet this requirement. The high throttle ratio engine

concept, for example, sacrifices takeoff thrust in favor of optimizing cycle characteristics in supersonic cruise as will be demonstrated by the example in Section 9.2.8.

The propulsion system has both direct and indirect impact on system costs. The direct cost is due to engine development, procurement and support costs. Indirect costs include the performance and installation characteristics which affect the airplane size, takeoff gross weight and mission fuel. The operating cost benefit of a better matched, newer technology engine must be weighed against the cost of development for a new engine. The decision to develop a new engine or use an existing one for a new airplane requires that the direct and indirect operating costs be considered along with the system effectiveness.

The date of initial operational capability (IOC) and mission requirements define the level of technology and thus the component efficiencies and weights available to reduce the cost of ownership and improve system effectiveness. Occasionally engine/airplane matching has been used to identify and prioritize advanced technology efforts.

Other figures of merit used in the military arena are survivability/vulnerability, and operationally ready rates. Airplane systems evaluations often optimize to a combination of factors over the most probable mission mix.

The following section shows a procedure for optimizing the engine/airplane match based on performance figures of merit which can be evaluated by computer. These figures of merit become dependent variables in the computer solution. The more subjective figures of merit are not treated further.

9.2.3 Methods of Optimization

Historically the selection of an optimum engine and airplane combination was made on the basis of experience. Mission analysis was conducted on selected engine cycles and aircraft geometries and the best airplane selected as the combination that best satisfies the figure of merit. For missions that are similar to ones already being flown it is possible for experienced designers to consider good candidate configurations. Historically, airplanes have been designed in this manner. Two weaknesses of this approach are 1) the reliance on the insight required by the designers and 2) the tendency to perpetuate design philosophies without due consideration for alternatives that new technology may have made available.

The advent of computer assistance to the designer made it possible to consider many more design alternatives, and has created a new preliminary design approach throughout the aerospace industry. To provide insight into the nature of computer optimization the philosophy is presented for one method, currently used in industry as an operational preliminary design tool.

The procedure applies statistics to independent cycle and airframe variables to determine a minimum number of mission analysis cases that must be run to create parametric equations for the solutions for all variables and constraints under consideration. These equations can be considered to form multivariant surfaces as a function of the independent variables. An optimum can then be obtained on any solution surface by standard methods, although the solution of a non-linear equation may be required.

For any two independent variables, for example compressor pressure ratio (CPR) and bypass ratio (BPR), the performance of a dependent variable, say takeoff gross weight (TOGW) can be determined. By computing TOGW for many combinations of CPR and BPR an equation could be fitted to the points to represent TOGW as a continuous function of BPR and CPR; the equation so obtained can be represented as a surface (Figure 9.2.3-1). The form of the equation is found by regression techniques using the computed points to obtain coefficients for polynominal equations representing the surface. A second order equation for this example would have the form

$$TOGW = C_o + C_1(BPR) + C_2(CPR) + C_3(BPR)^2 +$$

where C_0, C_1.....C_5 are constants to be determined.

A regression analysis could be used to compute the coefficients C_i using a least squares fit to the data points; goodness-of-fit statistics are also calculated by which suitability of the form of the regression equation can be judged.

Once the surface is established, the surface fit polynomials are interrogated by non-linear optimization methods which use gradient vectors to search for maximum or minimum dependent variable (TOGW) values within the specified boundaries of each independent variable. Conceptually this amounts to plotting contour lines on the surface of Figure 9.2.3-1 as shown in Figure 9.2.3-2, and identifying the extreme values. In this case, the resulting minimum TOGW is referred to as an uncon-

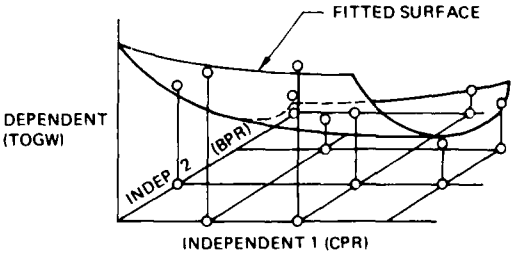

Figure 9.2.3-1. Surface Fit Using Least Squares

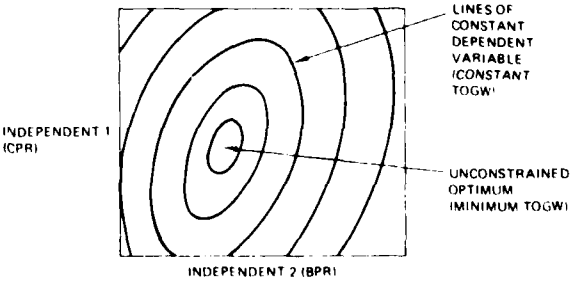

Figure 9.2.3-2. Lines of Constant Dependent Variable

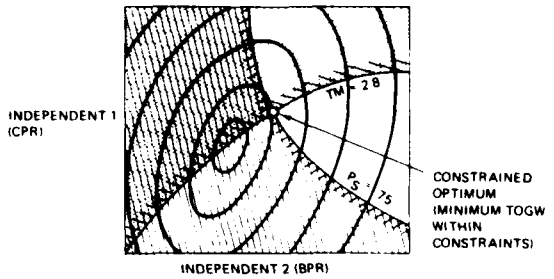

Figure 9.2.3-3. Constrained Optimum

strained optimum, or the optimum combination of BPR and CPR for the desired mission. Constraints such as minimum specific excess power (P_S) or thrust margin (TM) can be superimposed on the contour maps after the unconstrained optimum is obtained. Figure 9.2.3-3 shows the choice of CPR and BPR which provide optimum TOGW when design constraints include P_S=75 and TM=2.8. An advantage of this technique is that since the constraints are placed on the system after the regression analysis is completed, the constraints can be changed without recomputating the optimization. This simple example, drawn from Ref. 9.2.3-1, shows the optimization process for two independent variables. The actual optimization program uses the same procedure, solving for the optimum as a function of a larger number (10-20) of independent variables. Conceptually, this amounts to a process of determining a quadratic surface fit and contour mapping in multi-dimensional space. The solution is not difficult on a large modern computer, provided the number of input values for each of the independent variable can be restricted.

9.2.4 Dependent and Independent Variables

Independent variables of most significance for engines/airplane matching are shown in Table 9.2.4-1. The engine variables identified as secondary in the table are not commonly used except in exercises concentrating on engine size and weight. Table 9.2.4-2 displays dependent variables commonly used as the performance figures of merit to be optimized. In a given study, a surface fit and contour mapping is computed for each dependent variable. The contour line values of one variable can be constrained to a specific value and cross plotted. For example, the line of P_S=75 on Figure 9.2.3-3 was obtained from a contour map of P_S as a function of CPR and BPR (Figure 9.2.4-1). By selecting the appropriate contour line on the P_S map any value of P_S can be used as a constraint on TOGW.

9.2.5 Minimizing Required Combinations of Independent Variable Values

The number of mission analyses necessary to define an equation grows very rapidly with the number of independent variables. If each of ten independent variables is allowed to take on four values to define the surface shape, a total of 1,048,580 missions would have to be calculated! Fortunately, statistical methods can be used to reduce this number of combinations without jeopardizing the validity of the results.

Table 9.2.4-1. Typical Independent Variables

Typical independent variables	
Engine	
	Fan pressure ratio
	Bypass ratio
	Overall pressure ratio
	T_4
	Turbine nozzle area variation
	Throttle ratio
	Exhaust nozzle area ratio
Secondary variables	Number of spools
	Number of stages
	Afterburning
	Stage loading
	Hub/tip ratio
Airframe	
	Takeoff gross weight
	Thrust/weight
	Wing loading
	Aspect ratio
	Sweep angle
	Wing thickness ratio
	Wing taper ratio
	Operating weight increment
	Mission radius

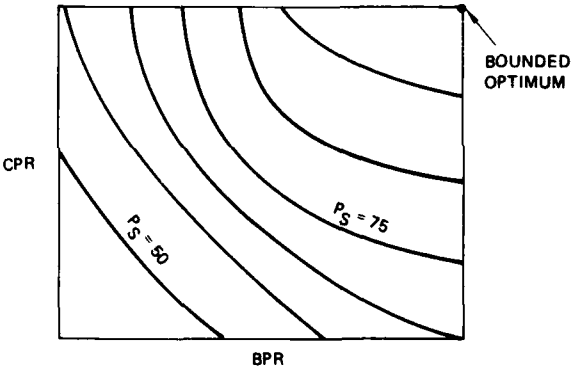

Figure 9.2.4-1. Bounded (Box Limited) Optimum

Table 9.2.4-2. Typical Dependent Variables

Typical dependent variables
Takeoff gross weight
Cruise range factor
Loiter factor
Fuel weight
Dash time required
Rate of climb or climb gradient
Cruise mach/altitude engine out performance
Specific excess power
Thrust margin
Takeoff roll distance
Service ceiling
Spotting factor (airplane size for carrier handling)

One such technique is known as Orthagonal Latin Squares (OLS). OLS is used to select the values of each independent variable to provide a sparse but uniformly distributed set of data points to which the curve fitting routines can be applied. Reference 9.2.3-1 discusses the theory of OLS in some detail. Here, it is sufficient to note that by applying OLS, the number of missions that must be analyzed is reduced to N^2, where N is the smallest prime number (or power of a prime number) larger than the number of independent variables being considered. For example when ten independent variables are being analyzed, 121 (11^2) missions must be calculated. Regression methods produce quadratic equations for each dependent variable as a function of the independent variables. For ten independent variables each equation requires 66 coefficients. Experience has shown that some dependent variables are not a strong function of all independent variables and the corresponding coefficients may be insignificant. A least square fit of the data to ten independent variables can usually be done adequately with less than twenty-five coefficients and still define the proper optimum engine/airplane combination. The logic flow for finding the optimum is reviewed in Figure 9.2.5-1.

9.2.6 Boundary Values for Independent Variables

The computer optimization technique selects the combination of values for the independent variables which represent the best engine/airplane system combination measured in terms of a specified figure of merit for the mission. If the optimum of any independent variable equals its boundary value, this value can be changed and the optimization rerun to see the relevance of this possibly arbitrary constraint. Suppose, for example, fan pressure ratio (FPR) is an independent variable and the range of values selected was FPR = 2.5-4.5. If the optimization program selected a best configuration with FPR = 2.5, it is not possible to ascertain if this FPR is really optimum or if FPR was constrained by the boundary value initially specified. New limits for FPR of say 1.5 - 3.0 can be specified and after the optimization program is rerun, the true optimum FPR may turn out to be 2.15. This feature of the technique leads the engineer to an optimum even if he is not experienced enough to guess the limits for each variable appropriately. Whenever the limits are changed, the mission analyses program should be reexamined to insure that the geometry, scaling, and interaction relationships remain valid.

Thus the boundary conditions on each independent variable are self correcting, but the designer does not know if he has selected the most important independent variables!

9.2.7 Reexamination and Validation

The validity of the airplane configuration identified by the computer optimization must be established since the real optimum configuration rarely corresponds to one of the 121 configurations computed through actual mission analysis. Therefore the values of each of the independent variables specified by the optimum are used as input values to a mission analysis. If the value of the figure of merit for single mission analyses agrees with that obtained from optimization, then some confidence in the optimum is justified. Because the surface (equation) is a least squares quadradic fit, the values of the single mission analysis may not be on the surface, particularly if the true

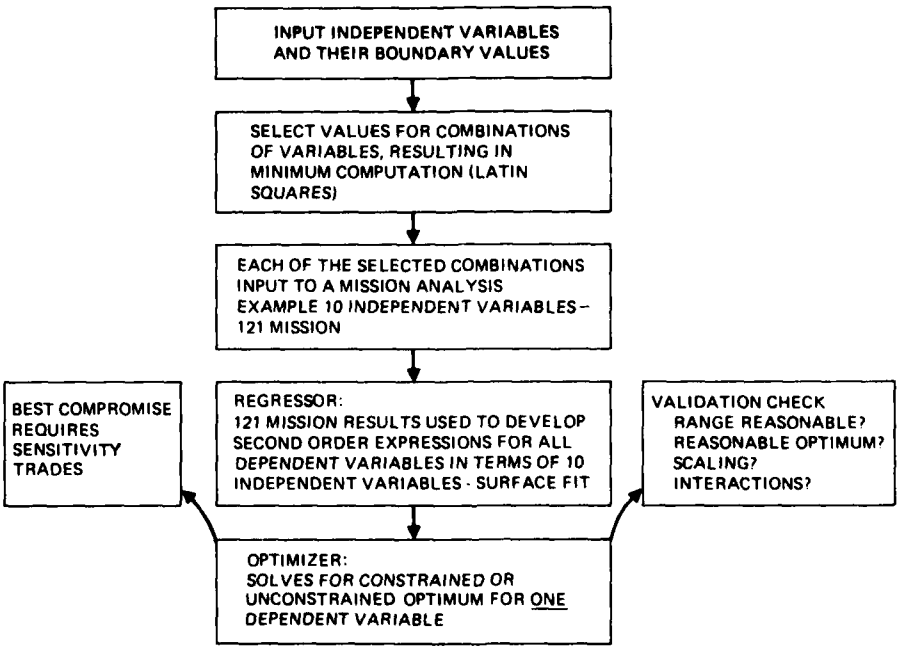

Figure 9.2.5-1. Optimization Logic

surface is a higher order polynomial or is discontinuous. Fortunately, most configurations analyzed match reasonably well near the optimum.

Computer optimization is a preliminary design tool whose main value is to quickly obtain an unbiased estimate of the "neighborhood" in which the real optimum configuration can be expected. The solution is unbiased only to the extent that the engine/airplane combinations in the mission analysis are realistic. Thus the mission analysis should be reexecuted to assure that scaling, interactions, and geometries were appropriate, and that the optimum is not artificially constrained by the range of one or more independent variable. Finally, it should be emphasized that the optimum can only be defined for one independent performance figure of merit. That is, the optimum engine/airplane combination can be found using either takeoff gross weight or specific excess power as the unconstrained figure of merit. Alternately, a constrained optimum can be obtained for either figure of merit with the other constrained, but it is not possible to use this technique to find the configuration which simultaneously optimizes both figures of merit.

9.2.8 Example Mission

To illustrate the results of mission analysis, engine/airplane optimization, and the impact of mission constraints, an example is presented for a military airplane designed to perform a medium range ground attack mission*. The design mission is shown in Figure 9.2.8-1 and consists of 1) takeoff from a fixed maximum field length, 2) climb to altitude for maximum subsonic cruise range (during the fixed range subsonic cruise leg the aircraft is required to perform evasive maneuvers of substantial "g" force), 3) using afterburning (A/B) accelerate and climb to supersonic cruise altitude in minimum time, 4) level off at the supersonic cruise design Mach number, cruise into hostile territory (with or without A/B) and perform the radius mission, 5) returning from hostile territory decelerate to subsonic cruise, 6) loiter for a fixed period of time and 7) land.

Five distinct engine cycle concepts were analyzed to show how they affect the geometry of a fixed weight airplane and how the optimum aircraft compared (with and without various mission constraints). The mission includes a relatively long subsonic leg of fixed distance but does not fix the length of the supersonic range (twice the supersonic radius). Supersonic range was the

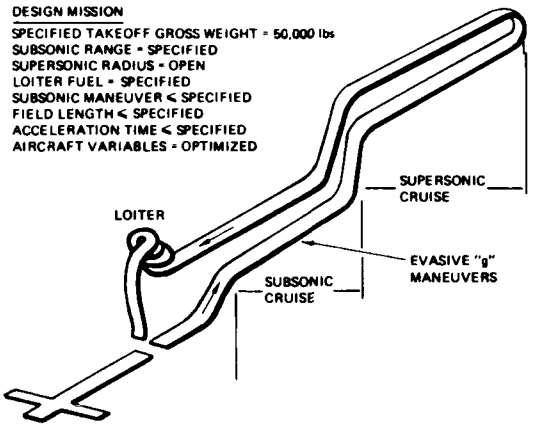

Figure 9.2.8-1. Medium Range Ground Attack Mission

figure of merit to be optimized for a fixed gross weight airplane. For each engine type an optimization was conducted using airplane polars and configurations which properly accounted for scale and installation effects. (If flight to a specific target at known range had been desired, takeoff gross weight would have been the optimization variable.)

For the five engine types under investigation, the design bypass ratio, pressure ratio, and cruise throttle ratios are presented in Figure 9.2.8-2; a complete study would include these as independent variables. The technology level, combustor exit temperature, and cooling air requirements, for all engines were held constant. The fixed values shown in the figure were chosen as representative for each engine type. The lapse in thrust as a function of Mach number for the chosen engines is shown in Figure 9.2.8-3. Figure 9.2.8-4 shows the relative dimensions of the engines which produce the same takeoff thrust.

These five fixed cycles affect the optimum geometry of the airplane designed for maximum supersonic cruise. For each independent engine cycle study, five airplane variables were analyzed

*Specific numbers are not shown in the example. the results are from an actual mission analysis and all characteristics and constraints are respresentative of current state-of-the-art in military airplane design. (Reference 9.28-1).

	BYPASS RATIO	OVERALL PRESSURE RATIO	MAXIMUM COMBUSTOR EXIT TEMP, CET	THROTTLE RATIO*	AUGMENTOR TYPE
LOW THROTTLE RATIO* TURBOJET (LTR)	.20	15	↑	1.05	AFTERBURNER
HIGH THROTTLE RATIO TURBOJET (HTR)	.20	15	↑	1.31	AFTERBURNER
VARIABLE GEOMETRY TURBINE (VGT) TURBOJET		15	CONSTANT TECHNOLOGY	1.00	AFTERBURNER
MIXED FLOW TURBOFAN (AB FAN)	1.30	20	↓	1.15	AFTERBURNER
SEPARATE FLOW TURBOFAN (DB FAN) WITH FAN DUCT BURNER	1.30	20	↓	1.17	DUCT BURNER

*THROTTLE RATIO $\frac{CET_{CRUISE}}{CET_{TAKEOFF}}$

Figure 9.2.8-2. Selected Engine Cycle Definition

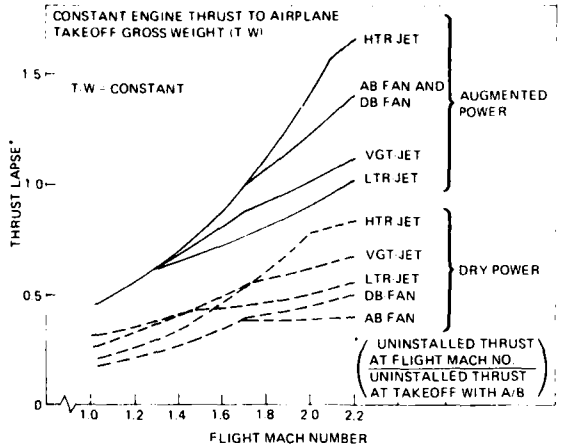

Figure 9.2.8-3. Comparative Thrust Lapse

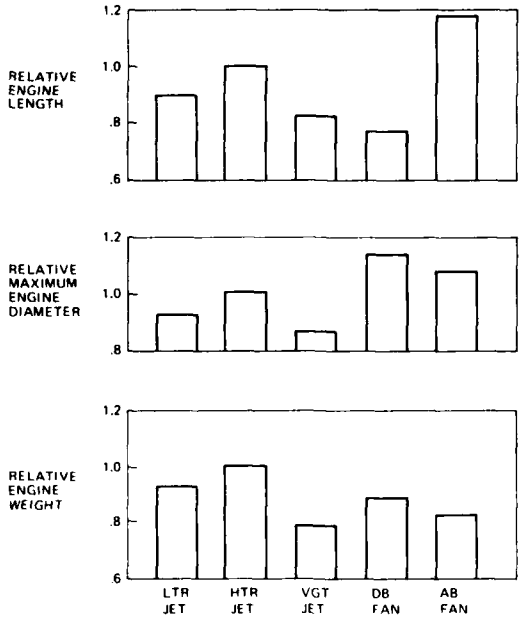

Figure 9.2.8-4. Engine Dimension and Weight Comparison at Equal Sea Level Static Maximum Thrust (A/B)

INDEPENDENT VARIABLES	RANGE OF INTEREST
WING ASPECT RATIO	1.3-4.3
WING LOADING	50-150 lb/ft^2
WING THICKNESS TO CHORD	.030-.060
WING LEADING EDGE SWEEP	34^o-74^o
AIRPLANE THRUST TO WEIGHT	.70-1.40
DEPENDENT VARIABLE TO BE OPTIMIZED	SUPERSONIC RANGE

Figure 9.2.8-5. Airframe Variables

MAXIMUM SUPERSONIC RADIUS FOR 45,000 lb THRUST ENGINES WITH NO PERFORMANCE CONSTRAINTS

		LTR JET	HTR JET	VGT JET	DB FAN	AB FAN
AIRPLANE	AR	4.3	4.2	4.3	4.3	4.3
	T/C	.030	.030	.030	.030	.030
	W/S	120	120	135	115	120
	SWEEP	40°	45°	52°	34°	43°
SUPERSONIC	PS	AUG	DRY	DRY	AUG	AUG
	SFC	1.87	1.37	1.49	1.44	2.08
	L/D	3.7	4.9	4.9	4.6	4.8
SUBSONIC	PS	.42	.62	.44	.70	.71
	SFC	1.25	1.15	1.49	.94	1.04
	L/D	11.1	10.2	9.9	10.5	10.7

Figure 9.2.8.6 Airplane Optimization Results

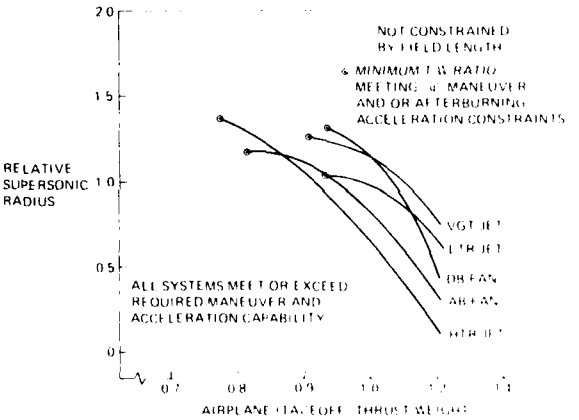

Figure 9.2.8-7. Maximum Supersonic Radius

to give the optimum supersonic range. The independent variables and their boundary values are shown on Figure 9.2.8-5. As described in Section 9.2, 49 mission analyses (the square of the prime number greater than the number of independent variables) were run for each engine. Each of the 49 had a different combination of values for the independent variables as prescribed by the Latin Square technique. A surface fit (regression analysis) then provides the unconstrained optimum range and "contour lines" of configurations producing constant values of range. These results can be used to evaluate the effects of changing mission constraints without rerunning the mission analysis.

Figure 9.2.8-6 shows the resulting optimum airplane for each engine type. The optimum is constrained only by a constant thrust to weight ratio. The optima were not constrained by field length nor acceleration requirements. Notice that each engine cycle requires a substantially different optimum airframe geometry. The wing loading varies from 115 to 135 lbs/ft^2 and the wing sweep varies from 34° to 52°. Thus it is evident that it is not appropriate to evaluate the merits of various engine concepts installed in an airplane of fixed geometry.

Figure 9.2.8-7 shows the relative supersonic range as a function of airplane takeoff thrust to weight ratio. At each T/W the airplane variables are optimized to produce curves which represent the loci of constrained optima (constrained by T/W). For each curve, a minimum T/W is obtained where the constrained optimum engine/airframe match can no longer meet the selected "g" maneuver or A/B acceleration time as indicated by the solid dots on Figure 9.2.8-7. Figure 9.2.8-8 is a comparison of constrained optima (dots).

From Figure 9.2.8-8 the optimum aircraft appears to be a high throttle ratio (HTR) turbojet which yields the lowest T/W and longest range while meeting the acceleration and maneuver requirements. In this case the field length is not restricted.

If short field lengths are important, higher takeoff T/W ratios are necessary. Airplanes with T/W = .9 produce takeoff field lengths representative of medium range attack aircraft. As shown in

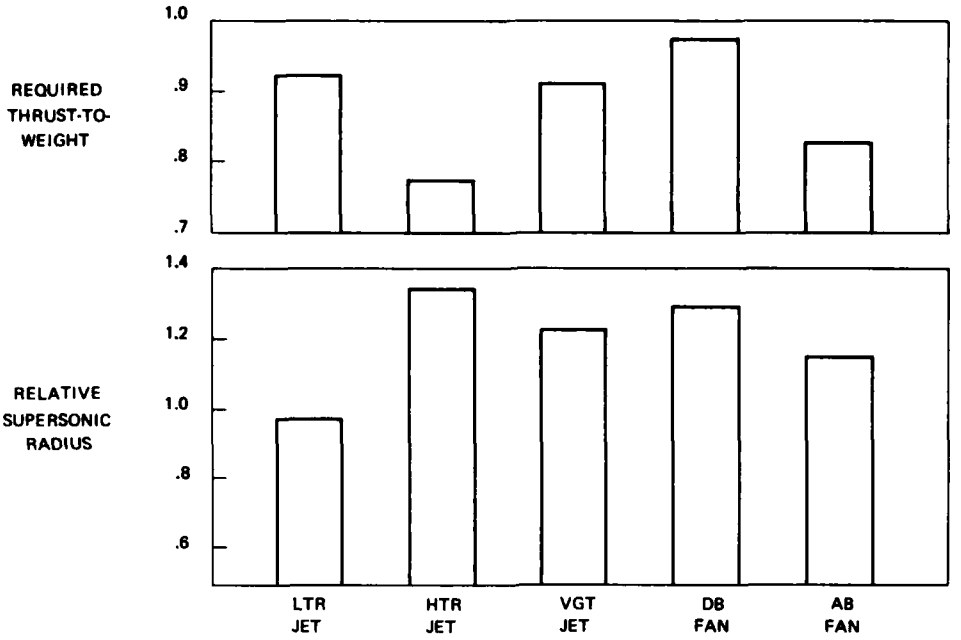

Figure 9.2.8-8. Optimum System Performance at Constant Acceleration and Maneuver Requirement

Figure 9.2.8-9, the required T/W ratios, necessary to produce reasonable takeoff distance, result in a different engine providing the best supersonic radius. The HTR concept has moved from the best choice to worst choice, because of the field length restriction. This result is to be expected because the concept of HTR engines is to design the engine for supersonic cruise using a constant corrected engine weight flow. The resulting engine produces the required cruise thrust from an engine that is smaller in length, diameter, and air flow rate at low Mach number. As a result the takeoff thrust is relatively low. This deficiency can be somewhat offset by incorporating variable turbine geometry, or variable burner by-pass which was not included in this study.

If a fixed airplane geometry is chosen and the engines are sized to meet given maneuver and acceleration time requirements, the relative engine performance shifts and the duct burning turbofan which was best for supersonic range becomes the worst (Figure 9.2.8-10).

In the considerations thus far, the amount of afterburning has been allowed to vary. Flying supersonic missions with turbofan cycles requires more A/B than with turbojets. If the infrared (IR) signature of the aircraft over hostile territory is considered the engines may be constrained to dry (non A/B) operations. Such a requirement applied to the aircraft discussed in Figure 9.2.8-10 results in the characteristics shown in Figure 9.2.8-11. The fan engines cannot even perform the desired mission under this constraint.

This example has illustrated that the engine designer cannot work alone. Optimum engine/airplane matching cannot be accomplished unless an array of both engine and airframe variables are considered together with mission rules and constraints. The next section will consider ways to evaluate the sensitivity of the mission and aircraft to changes in the variables and constraints.

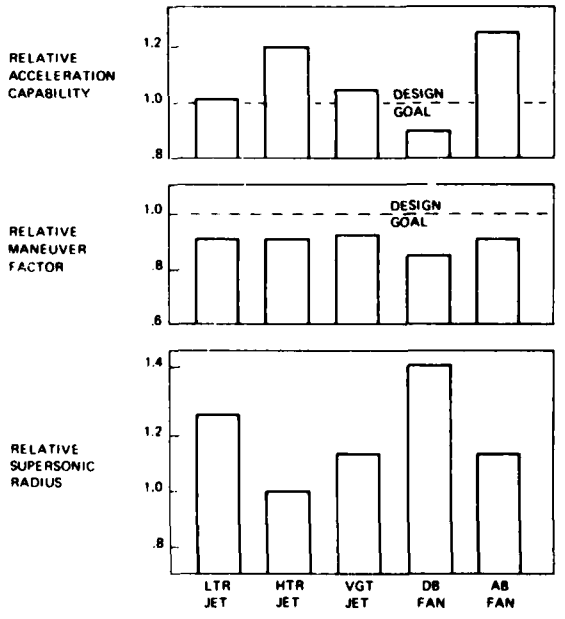

Figure 9.2.8-9. Performance Comparison at T/W = 0.90 (Constraint: Fixed Airplane Design and Equal, Reasonable, Field Length)

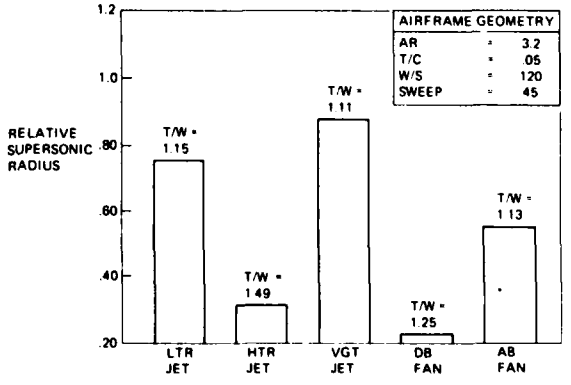

Figure 9.2.8-10. Supersonic Radius With Required Maneuver and Acceleration Capability (Fixed Airplane Design)

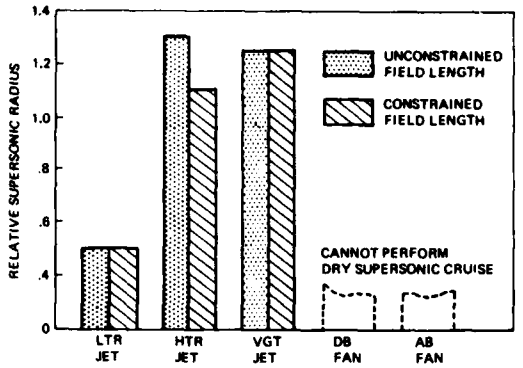

Figure 9.2.8-11. Optimum Systems for Dry Supersonic Cruise

9.3 SENSITIVITY AND INFLUENCE COEFFICIENTS

9.3.1 General

Sensitivity studies use influence coefficients to measure the change of a dependent variable (y) due to the change of a single variable (x) of several independent variables. Influence coefficients therefore involve the use of partial derivatives:

$$I_{y,x} = \frac{x}{y}\frac{\partial y}{\partial x} = \frac{\partial \ell n y}{\partial \ell n x} \quad \text{or} \quad I_{y,x} = \frac{\partial y}{\partial x}$$

Dependent variables may be performance or cost figures of merit, while independent variables are usually the design parameters. Examples of sensitivity studies commonly conducted during engine/airplane matching include:

a) The sensitivity of a configuration to the proximity of the optimum.
b) The sensitivity to relaxation of a mission constraint.
c) The influence of changing the level of technology.

Item "a" is a logical extension of the optimization program. Using the optimum value of each of the independent variables as a central configuration, a careful analysis is usually conducted on designs lying in a neighborhood near the optimum. Mission analyses are conducted on each combination of independent variables in order to more closely approximate the surface fit polynomials near the optimum. Once the polynomials fit the mission analysis results with the desired certainty, a comprehensive sensitivity study can be done by partial differentiation of the polynomial. Using the simple example introduced in Section 9.2, the influence on takeoff gross weight due to changing bypass ratio or compressor pressure ratio can be evaluated, i.e.,

$$\left.\frac{\partial(\text{TOGW})}{\partial(\text{BPR})}\right|_{\text{CPR = CONSTANT}} \quad \text{or} \quad \left.\frac{\partial(\text{TOGW})}{\partial(\text{CPR})}\right|_{\text{BPR = CONSTANT}}$$

The resulting values may be nondimensionalized and ranked according to their importance (influence) on performance or cost. As a result of ranking the independent variables and establishing the cost of changing any of them the engine and airframe companies identify the areas where improvements will be most beneficial. The customer or systems integrator can also weigh the cost versus performance to see if moving away from the specified optimum will decrease cost sufficiently to justify reduced performance.

If the optimum engine/airframe combination is constrained by a customer, the penalties associated with the constraint may be identified. In preliminary design the sensitivity of the aircraft system to mission constraints is of paramount importance in the interaction between the engine and airframe designers and the customer. For military applications the results of sensitivity studies provide a quantitative guide allowing the customer to establish the trade between the mission requirements he foresees as important and the benefits of relaxing one or more constraints.

The other important use of sensitivity is to establish the priorities in technology development. It can be a very costly decision to increase the performance of an engine component. Similar commitments are necessary from structures, aerodynamics, and production groups in the airframe companies. Budget constraints necessitate that the performance of only some of the components may be advanced at the same rate. Priorities are established within industry and government in an effort to find those components whose development will produce the largest benefit to the system in the given time period with the available funding. Such decisions are best made when a priority of the independent variables is established and the performance level available for a given expenditure has been estimated.

9.3.2 Importance of the Choice of Independent Variables

Section 9.2 demonstrated that the optimum engine/airplane combination could be selected for a given set of independent variables and that the boundary values selected for the variables were self correcting. Section 9.3.1 indicated that required levels of component technology and trades between performance and cost could be established by analysis of the surface fit polynomial which is obtained as a function of the chosen independent variables. As a result, independent variables could be ranked so that those having the most influence could be emphasized. The choice of independent variables, based on intuition, new evidence, or past experience, must be made prior to optimization and sensitivity studies. Unfortunately, there is no method of guaranteeing that an important independent variable has not been overlooked. The most important variables, identified through experience, were shown on Table 9.2.4-1. The occasional importance of other variables is usually realized during component design or mission analysis. If a very strong variable has been ignored its influence will be obvious if that variable is changed for the "optimum" aircraft design. Sometimes variables can significantly influence the true optimum aircraft design even though they do not show up as important when the optimum (chosen using fixed values for these elements) is perturbed. Consider the following example.

For a specified mission the optimum configuration of a variable sweep wing strategic bomber was desired. The mission included both subsonic and supersonic segments. During the subsonic flight the aircraft used a low altitude, terrain following path which imposed a q loading constraint; a 2400 mile supersonic range and a fixed payload were specified. Three engine variables (fan pressure ratio, overall pressure ratio, and turbine inlet temperature) and five airframe variables (takeoff gross weight, takeoff thrust/takeoff gross weight,

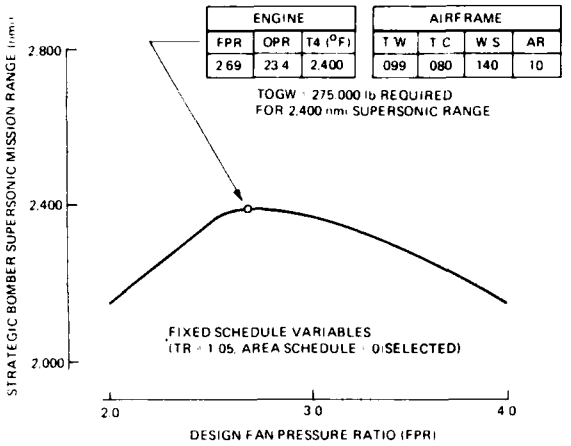

Figure 9.3.2-1. Optimum Bomber Configuration Using Eight Independent Variables

wing loading, wing thickness to chord ratio, and aspect ratio) were chosen. The selected figure-of-merit was the takeoff gross weight which the analysis showed to be minimum at 275,000 pounds TOGW. The table in Figure 9.3.2-1 shows the values of the independent variables at that weight.

Suppose one would like to know the sensitivity of supersonic range to changes in design or fan pressure ratio. Recall from the mission analysis that either the TOGW is evaluated for a given range or the range is evaluated for a fixed TOGW. Therefore for the sensitivity study TOGW was fixed to the optimum value, and design FPR was calculated away from the optimum while the other six independent variables were allowed to reoptimize. The resulting variation of range for the constrained optimum airplane is plotted as a function of design fan pressure ratio in Figure 9.3.2-1. For each value of FPR, the range shown is the best that can be obtained from a 275,000 lb. airplane and the values of each of the other six independent variables may vary accordingly. Therefore a different aircraft configuration is implied by each point on the curve. Each point is just the constrained optimum range value (found by the optimization process of Section 9.2) for constraints of TOGW and FPR. Looking at the curve of Figure 9.3.2-1 one would conclude that range is sensitive to fan pressure ratio and that the influence becomes strongest as FPR moves away from optimum toward lower fan pressure ratio.

Now consider the importance of the nozzle throat area schedule or the throttle ratio. Since neither of these were considered as independent variables, the sensitivity of range to either of these must be evaluated externally to the optimization process. This is done by fixing the optimum aircraft (from Table in Figure 9.3.2-1) as a reference configuration; then, using mission analysis on the fixed aircraft, establish the effect of variations in nozzle area schedule and throttle ratio on range. Figure 9.3.2-2 shows the results. The throttle ratio extremes were chosen to represent the available range consistent with expected engine technology levels. The nozzle schedule represents the maximum dry nozzle throat area increase beyond that used in the original optimum (nondimensionalized to fall between -1 and +1). The values of nozzle schedule are not important, per se, but the results show that changing the nozzle throat area can produce slightly more range (0.5 - 0.8%) and that throttle ratio has less effect than the area schedule.

Three questions arise at this point;

a) Is the airplane specified by the Table in Figure 9.3.2-1 but with area schedule = .22 and throttle ratio = 1.15 (point "A" in Figure 9.3.2-2) the true optimum airplane?
b) Is the sensitivity of range to throttle ratio and nozzle area schedule sufficient to imply that the two variables have a strong enough influence that they should have been included as independent variables?

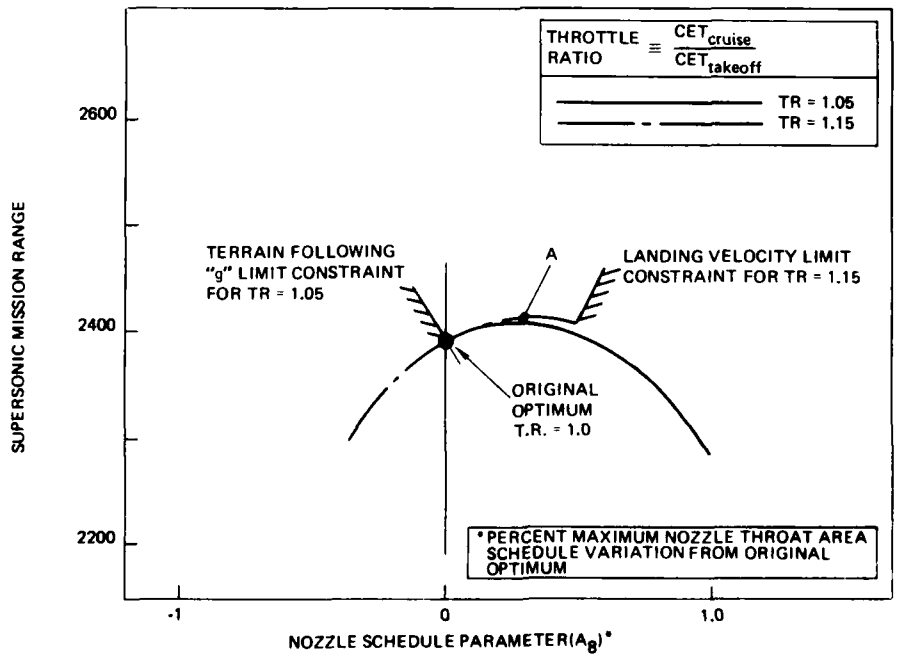

Figure 9.3.2-2. Effect of Additional Independent Variables

c) If they had been included as independent variables what would have been the configuration of the optimum aircraft?

When the best airplane is selected by the optimization technique all independent variables must be optimized at the same time. The airplane described in question 1 is *therefore not* necessarily the best because eight of the variables were fixed before the other two were introduced. Only a new optimization using ten variables will establish how the other variables change.

Based on the results shown in Figure 9.3.2-2 the 0.8% increase in range is not usually sufficient to justify the time and expense of running a new optimization with ten variables. However, if the ten variable optimization is run the following results are obtained. As can be seen on Figure 9.3.2-2 the throttle ratio = 1.05 (original optimum) aircraft was very near the limit imposed by subsonic "g" loading for terrain following, while the throttle ratio = 1.15 is not affected by this limit. The results of the ten variable analysis are shown on Figure 9.3.2-3 with the results of the original eight variable optimization repeated for comparison. If the FPR and TOGW are constrained to the same values as for Figure 9.3.2-1, a new set of constrained optimum airplanes is produced which have more range than those with fixed throttle ratio and nozzle area schedules over the entire range of fan pressure ratios. The new optimum airplane has 4% more range, but more significantly, the engine and airframe changed substantially. Note the change in the fan pressure ratio and wing aspect ratio.

The advantage of using an optimization process over merely comparing mission analysis results can be appreciated when one considers the experience necessary to realize that "g" loading and nozzle area schedule profoundly affect the optimum values for wing aspect ratio and fan pressure ratio. For these reasons it is recommended that the maximum numbers of independent variables allowed by time, cost, and simulation technique be used whenever a preliminary design study for a new mission is being conducted.

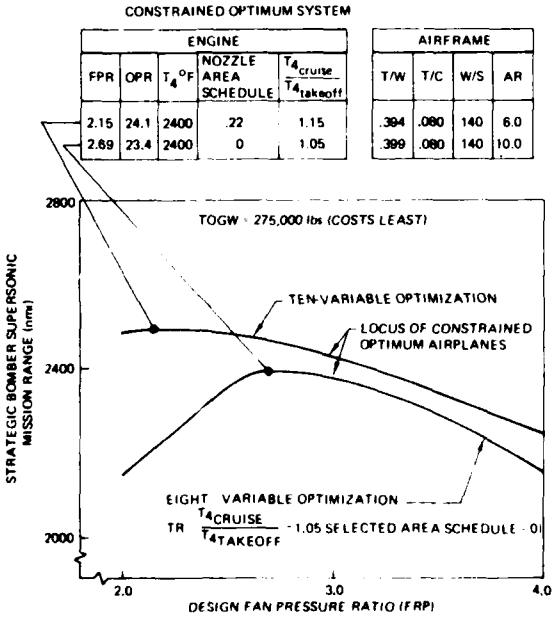

Figure 9.3.2-3. Comparison of Optimum Aircraft Resulting From 8 and 10 Variable Optimization

A final point this example illustrates is the impact of technology level. The turbine inlet temperature for both optimizations was 2400°F which was the maximum value felt to be reasonable. One might conclude from a sensitivity study on turbine temperature that increasing T_4 is very worthwhile. If the metal temperature in the turbine is as high as possible for the method of cooling chosen, then the only way to increase turbine temperature is to increase the amount of compressor bleed air used for cooling. The requirements for additional bleed air which affect engine size, weight and performance may well mean that increasing T_4 is not beneficial. This trade between turbine temperature and bleed air requirement to maintain metal temperature limits is critical for missions requiring long endurance at part power. These missions frequently optimize at relatively low turbine temperature for these reasons. (This problem could be alleviated by using a cooling system with throttling capability.)

9.4 COMPUTER SIMULATION OF GAS TURBINE ENGINES

9.4.1 Introduction

Engine/airplane matching has been shown to require inputs from many disciplines as shown schematically in Figure 9.4.1-1. Figure 9.4.1-2 displays a breakdown for the performance and weight contributions to the matching process. The figure indicates that mission analysis and optimization programs require inputs from aerodynamics and structures, as well as propulsion. The propulsion contribution includes performance and weight analysis for the gas generator, inlet, exhaust, and their interactions. The previous chapters have discussed the aerothermodynamics of engines in general. The chapters that follow will develop the details of individual components. This section demonstrates the usefulness of the computer in combining the results of detailed component design with basic cycle analysis to accurately simulate the performance of gas turbine engines.

The computer simulation to be described assumes a quasi-steady state situation where the rates of change of Mach numbers, altitude, engine RPM, and power setting are assumed small. While this assumption is sufficient for mission analysis, where the flight profile is broken into a series of quasi-steady conditions, it must be acknowledged that the

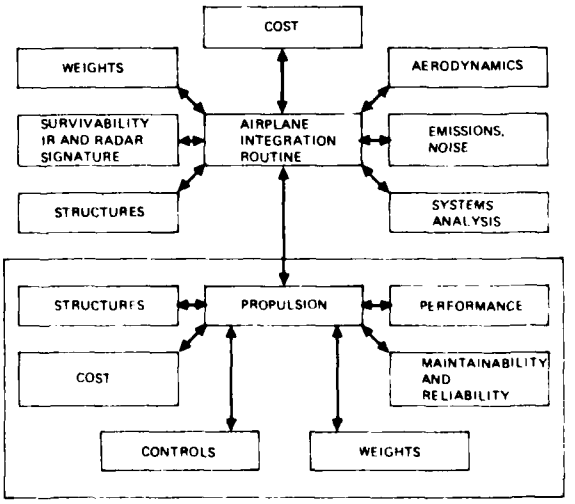

Figure 9.4.1-1. Engine/Airplane Matching Disciplines

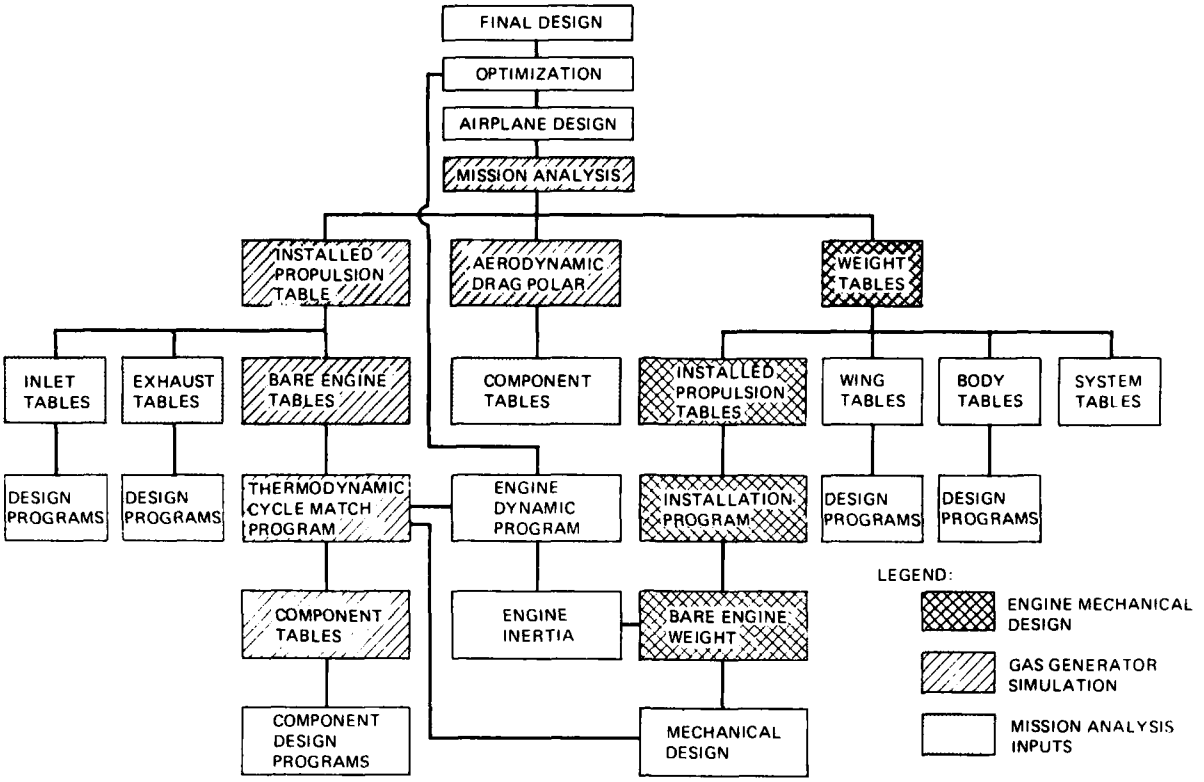

Figure 9.4.1-2. Engine/Airplane Matching (Summary of Considerations for Engine Performance and Weight)

performance of the final aircraft will also depend on the engine dynamics and controls, which are beyond the scope of the present text.

9.4.2 Method of Performance Simulation

The computer simulates gas turbine engine performance by an appropriate matching of components. Two philosophies are common in engine simulation programs. One incorporates a "generalized" engine, say a three spool duct burning afterburning turbofan engine, and provides a technique for elimination of unneeded components. The other philosophy used by industry and government for more than a decade, allows the interconnection of components in a building block manner to simulate any conceivable combination of engine components. The latter technique is considered in detail. The generalized engine will be shown to be a particular preprogrammed version of the building block technique which simplifies the work required by the user in order to simulate most engines (Sec. 9.4.6).

For any arbitrary choice of engine components, power and airflow paths through the engine can be drawn connecting the output of one component to the input of the next component. The output/input connection points are referred to as nodes. The nodes do not have to connect physically adjoining elements. For example the airflow path of a simple turbojet has a node connecting the compressor and burner and another connecting the burner and turbine while the power path of the same engine has a single node connecting the compressor and turbine. Either design or off-design engine performance calculations are performed on each component based on flight conditions input to the node in front of the engine and information given the input node to each component. As each component calculation is completed, all output flow properties and other characteristics of that component are transmitted to the next node. Connecting components are therefore related to one another as functions of the program inputs, system variables, and specified component characteristics (equations and component maps). The component calculations produce a system of coupled algebraic transcendental and partial differential equations to be solved.

One method is illustrated by calculating design and off-design performance of a single spool turbojet engine.

9.4.3 Design Point Simulation

The simulation of engine design point performance is a direct computation requiring that the efficiency of each component be known. The design flight conditions (Mach number, altitude, and temperature) and inlet mass flow are specified at a node in front of the engine. The schematic for a single spool turbojet is shown in Figure 9.4.3-1. The primary airflow path is through nodes 1-2-3-4-5 and 6. The power demand path connects the compressor to the turbine through nodes 7 and 8. The transmission represents either gears or a shaft. Compressor bleed is supplied to the turbine through node 9 if the air becomes working fluid in the turbine and through node 10 if bleed re-enters the airstream from the trailing edge of the last turbine stage. More complex cooling bleed paths can be specified if a detailed stage by stage study is being performed. Bleed air can be taken from intermediate compressor stages and reintroduced through the leading and trailing edges of turbine vanes and rotors, as desired. Node 11 can be used to account for leakage through seals (similar nodes

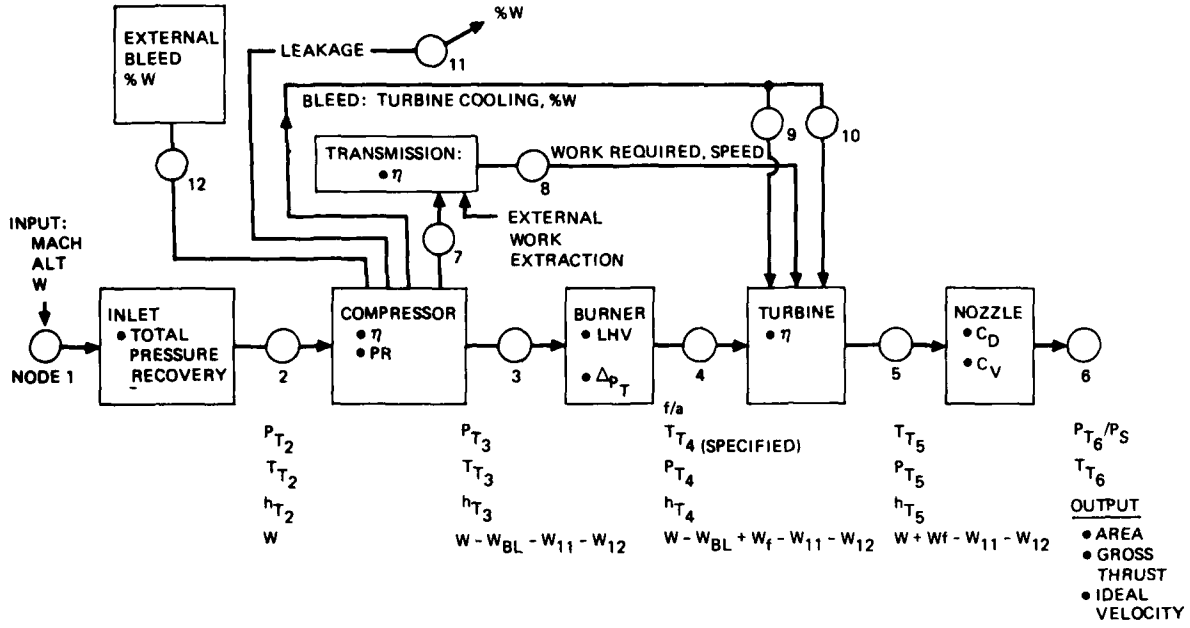

Figure 9.4.3-1. Design-Point Engine Performance Setup

could be established to account for leakage from any other component). In the example, the leakage is assumed to be lost overboard without producing a thrust or drag increment.

Bleed for air conditioning, anti-icing, avionics cooling, etc., is removed from the engine through node 12 as a percent of the inlet weight flow. Power extraction from the engine to operate pumps and generators can be treated as a horsepower addition to the work demanded by the compressor from the turbine. At times it is convenient to specify the external work requirement as a constant percent of the turbine work available by subtracting it from the transmission efficiency.

The input node values and inlet total pressure recovery are sufficient to establish total pressure, P_T, total temperature, T_T, total enthalpy, h_T, and weight flow, W, at node 2. These properties at node 2, plus the compressor pressure ratio (PR), adiabatic efficiency, and the bleed fraction

$$\text{Bleed Fraction} = \frac{W_9 + W_{10} + W_{11} + W_{12}}{W_1}$$

are sufficient to determine the compressor outlet properties (P_T,T_T,h_T, and $W_{air\ remaining}$) at node 3.

Burner outlet properties at node 4 are determined from specified values of combustor exit temperature (T_4), fuel to air ratio (f/a), fuel lower heating value (LHV), and the total pressure drop (ΔP_T). Alternatively the rotor inlet temperature (RIT) may be specified and a short iteration loop set up to establish the T_4 which together with turbine nozzle cooling air will produce the desired RIT.

The turbine exit properties at node 5 are calculated using the properties of node 4, the cooling air from nodes 9 and 10, the work to supply the compressor and extraneous work requirements, and the turbine adiabatic efficiency. The conditions at node 5 plus the nozzle discharge coefficient (C_D) and nozzle pressure ratio (P_{T5}/P_∞) are used to size the nozzle throat area. Following the calculation of the nozzle throat conditions, the gross thrust, ideal exit velocity, and nozzle exit area are computed. The design point solution for the engine cycle performance is thus complete and requires no iteration. The design point establishes the thermodynamic cyle and sizes the flow passages through the engine.

9.4.4 Off-Design*

For off-design cycle calculations the nozzle throat area computed from the design case is assumed unless a new value (simulating variable nozzle area) is specified. The turbine temperature, T_4, must be supplied along with flight conditions. Off-design cycle calculations are iterative processes requiring several guesses before all component properties can be established.

Using the example turbojet, Figure 9.4.3-1, the flight conditions, inlet recovery, and an initial guess of inlet mass flow (W_{inl}) are necessary to establish the properties at node 2. Compressor data ($W\sqrt{T}/P$, PR, and η) can be determined from the compressor map (illustrated in Figure 9.4.4-1) using values from node 2, and a guess at speed (N) and compressor grid line (R). The corrected mass flow ($W\sqrt{T}/P$) is obtained at the intersection of the "R" grid line and the guessed value of corrected speed line ($N/\sqrt{\ }$). The mass flow (W_{map}) is calculated using the corrected mass flow from the map and T_t and P_t at the compressor inlet (node 2). Discrepancies in mass flow rate are merely noted at this point for later iterative correction. Map properties η and PR are used to calculate the compressor outlet properties at node 3.

The inputs to the burner (LHV, ΔP_T, f/a), the T_4 estimate and the properties from node 3 are sufficient to define the fuel flow required and all other burner outlet properties at node 4.

The turbine speed is known (from the guess of N) and the turbine work requirement (HP) is obtained from a power balance between turbine and compressor

*Adapted from the unpublished work of A. T. Yamagiwa, and S. C. Rayl, Boeing Document D6-41915-1, Oct. 1969.

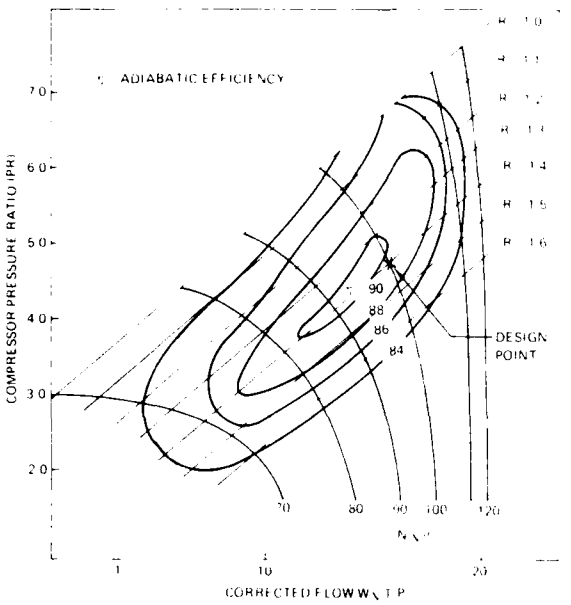

Figure 9.4.4-1. Typical Compressor Map

and external power requirements. The turbine pressure ratio (PR) is found by an iterative method. A first guess is made for the turbine isentropic discharge temperature (T_{ti}) to determine the corresponding pressure ratio (PR) from T_{inl} to T_{ti}. The PR from this calculation is used with the turbine map (lower part of Figure 9.4.4-2) to find the turbine efficiency (η). A calculated value for h_{ti} (exit) is found by the equation: $h_{ti} = (h_{tinl} - \Delta H/\eta)$. This calculated h_{ti} is converted to T_{ti} (function of the f/a and h_{ti}) compared with the guess for T_{ti}. When the guess and calculated T_{ti} values agree, the PR value from the last iteration is used with Figure 9.4.4-2 (upper plot) to obtain the corrected mass flow ($W\sqrt{\theta}/P$) at the turbine inlet (at the intersection of PR and $N/\sqrt{\theta}$). The turbine inlet mass flow (W_{map}) is determined from the corrected mass flow from the map and T_t and P_t at the turbine inlet (node 4). The mass flow residual at the turbine inlet is: $\Delta W_T = [W_{map} - W_{node\ 4}]$. The flow properties at node 4, the turbine work requirement (ΔH), and the turbine pressure drop define the turbine outlet properties at node 5.

The throat area and discharge coefficient are specified for the nozzle. The pressure ratio across the nozzle is determined from $\Delta W_{noz} = [W_{cal} - W_{node\ 5}]$, where W_{cal} is determined at the throat. The first pass through the engine is thus complete. The quality of off-design cycle simulation computer programs is often determined by the efficiency with which they converge to a solution. The Newton-Raphson technique described in the following section is an example of a convergence method. In practice, highly sophisticated iteration techniques have been developed, and are described in the literature on numerical analysis.

9.4.5 Newton-Raphson Iteration

The off-design simulation of gas turbine engine performance required an initial guess for the inlet weight flow W_{inl}, RPM, N, (if a geared transmission is used the gear ratio must be specified a priori), and compressor grid line, R. These guesses must next be improved through iteration to converge to their correct values. The method of iterative solution illustrated is the matrix residuals technique of Newton-Raphson. The guessed variables W_{inl}, N, and R and the mass flow residuals ΔW_C for the compressor, ΔW_T for the turbine, and ΔW_{noz} for the nozzle are used to form a set of equations of the following form. [The mass residual is the difference between the calculated outlet mass flow (from maps and equations) and the inlet mass flow (arriving from an upstream component)].

$$\Delta(\Delta W_C) = \frac{\partial(\Delta W_C)}{\partial W_{inl}}\Delta W_{inl} + \frac{\partial(\Delta W_C)}{\partial N}\Delta N + \frac{\partial(\Delta W_C)}{\partial R}\Delta R$$

$$\Delta(\Delta W_T) = \frac{\partial(\Delta W_T)}{\partial W_{inl}}\Delta W_{inl} + \frac{\partial(\Delta W_T)}{\partial N}\Delta N + \frac{\partial(\Delta W_T)}{\partial R}\Delta R$$

$$\Delta(\Delta W_N) = \frac{\partial(\Delta W_N)}{\partial W_{inl}}\Delta W_{inl} + \frac{\partial(\Delta W_N)}{\partial N}\Delta N - \frac{\partial(\Delta W_N)}{\partial R}\Delta R$$

or in matrix form

$$\begin{vmatrix} \Delta(\Delta W_C) \\ \Delta(\Delta W_T) \\ \Delta(\Delta W_N) \end{vmatrix} = \begin{vmatrix} \frac{\partial(\Delta W_C)}{\partial W_{inl}} & \frac{\partial(\Delta W_C)}{\partial N} & \frac{\partial(\Delta W_C)}{\partial R} \\ \frac{\partial(\Delta W_T)}{\partial W_{inl}} & \frac{\partial(\Delta W_T)}{\partial N} & \frac{\partial(\Delta W_T)}{\partial R} \\ \frac{\partial(\Delta W_N)}{\partial W_{inl}} & \frac{\partial(\Delta W_N)}{\partial N} & \frac{\partial(\Delta W_N)}{\partial R} \end{vmatrix} \begin{vmatrix} \Delta W_{inl} \\ \Delta N \\ \Delta R \end{vmatrix}$$

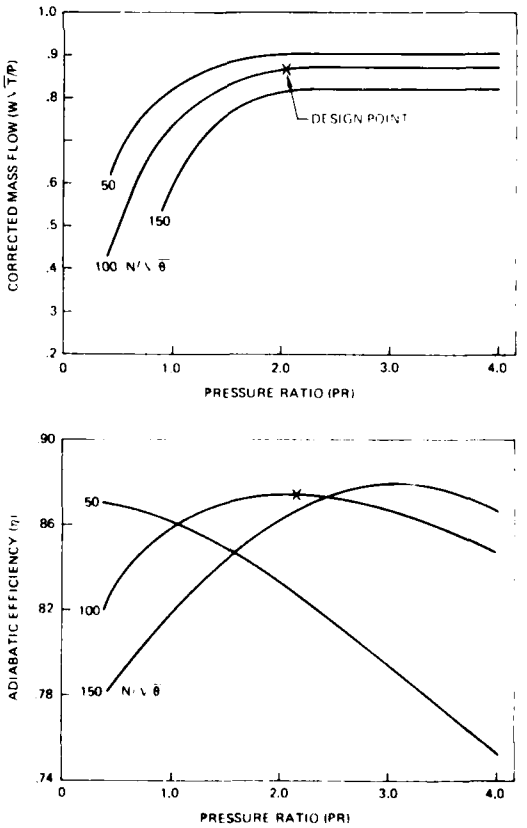

Figure 9.4.4-2. Turbine Map Format

The matrix partial derivatives

$$\frac{\partial(\ )}{\partial W_{inl}}\ ,\ \frac{\partial(\ )}{\partial N}\ ,\ \text{and}\ \frac{\partial(\ )}{\partial R}$$

represent the first term approximation of a Taylor's series expansion, and are determined numerically in successive passes through the engine cycle off-design equations. The first pass through the cycle is used as a base case (the off-design case just discussed). These initial guesses can literally be guesses, or the values from the design case can be used as a first guess. Succeeding passes (three are needed for this matrix) are used to determine the mass flow residual changes associated with small changes in each of the guessed variables. For example, the quantities

$$\frac{\partial(\Delta W_C)}{\partial N}\ ,\ \frac{\partial(\Delta W_T)}{\partial N}\ ,\ \text{and}\ \frac{\partial(\Delta W_N)}{\partial N}$$

(in the second column of the matrix) are obtained by perturbing N by a small amount, ΔN, to give

$$\frac{\partial \Delta W_C}{\partial N} = \frac{(\Delta W_C)_2 - (\Delta W_C)_1}{\Delta N}\ ,\ \frac{\partial \Delta W_T}{\partial N} = \frac{(\Delta W_T)_2 - (\Delta W_T)_1}{\Delta N}\ ,$$

and $$\frac{\partial \Delta W_N}{\partial N} = \frac{(\Delta W_N)_2 - (\Delta W_N)_1}{\Delta N}$$

calculated at the compressor, turbine and nozzle, respectively. Other partial derivatives are similarly developed with respect to the variables W_{inl} and compressor grid line R. The values $\Delta(\Delta W_C)$, $\Delta(\Delta W_T)$, and $\Delta(\Delta W_N)$ are obtained from the base case. The matrix is then solved for ΔW_{inl}, ΔN, and ΔR, and the initial guesses for W_{inl}, N, and R are revised. These revised values are used in the next iteration until the residuals (ΔW_C, ΔW_T, ΔW_N) satisfy the convergence criteria.

As demonstrated, the number of guessed variables must equal the number of residuals in an off-design calculation.

In general, the variables in the calculation are those which must be estimated (guessed) to initiate calculation. Common examples are inlet mass flow, rotational speed, bypass ratio, burner outlet temperature, work split relationships, etc. Once input variable values are guessed, residuals are calculated at those components which must satisfy a mass balance (compressors, turbines and nozzles) or speed balance (transmission).

Returning to the original off-design problem, the off-design thrust can be calculated, compared to the required value, and an iteration on T_4 commenced.

9.4.6 The Generalized Engine and Mechanical Design Simulation

Any conceivable combination of components can be simulated in a building block fashion using nodes to connect airflow and power transmission paths. Given the equations governing their behavior, uncommon components (regenerators, air inverter valves, etc.), can be placed at any location within the engine. While this total flexibility is desirable in some situations, a great deal of time is consumed if the geometry has to be generated anew each time an engine simulation is desired. The vast majority of aircraft engines are relatively similar and a single geometry can represent them.

Consider the "generalized" engine shown in Figure 9.4.6-1. The figure represents a three-spool, duct burning, afterburning turbofan, which incorporates features common to a wide variety of engines. By creating a computer program capable of describing such a "general engine," but including the capability of excluding undesired components, considerable savings in set-up time can be realized. The effective removal of unwanted compressor or turbine components can be accomplished simply by setting their pressure ratio and efficiency equal to 1. The entire fan stream can be ignored by specifying a bypass ratio of zero. Ducts have no effect if they have zero length and zero pressure loss. Augmentors and duct burners can be eliminated by specifying no fuel flow and zero pressure drop. Often a program uses default values so that the output temperature is set equal to the input temperature for burners and augmentors when the temperature of the downstream node is specified as a lower number than the incoming temperature.

Thus the simple turbojet of Figure 9.4.3-1 can be simulated by the generalized engine by setting the following conditions: Bypass ratio = 0; pressure ratio and efficiency =1 for LPC, IPC, IPT and LPT; dummy nozzle length equals zero and area ratio =1; and augmentor exit temperature $= T_4$.

The concept of generalized engines can provide further savings in the time required to set up an engine simulation. For preliminary design studies, non-dimensionalized maps can be prespecified for each component to represent a given technology level. For the representative state of the art, default values can also be preprogrammed for component efficiencies and cooling bleed requirements. As the desired precision increases from preliminary design to the simulation of actual hardware, the default component maps, design efficiencies, bleed

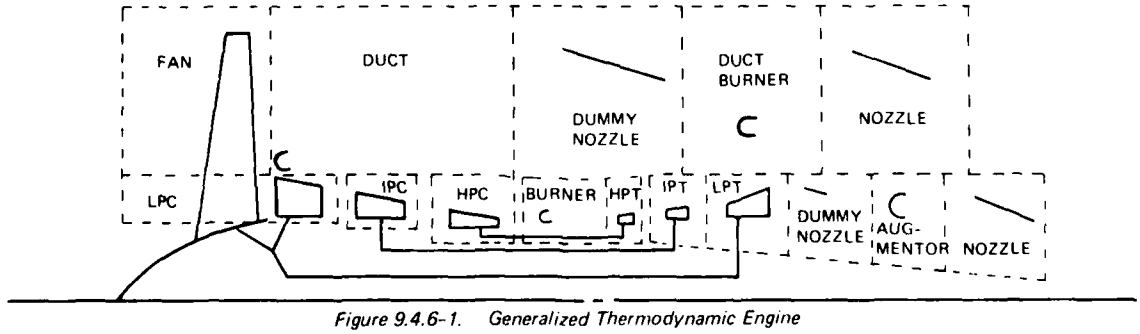

Figure 9.4.6-1. Generalized Thermodynamic Engine

requirements and leakages can be replaced with values from test results without having to alter the simulation program.

In addition to the thermodynamic analysis, engine evaluation requires consideration of the dimensions and weight. In one approach, a configurator will draw out the entire engine. This "paper" engine can be measured and the weight can be obtained as the sum of the historical weights of components similar to those used for the design. Alternatively, a computer program can be used to "weigh" and "measure" an engine using the thermodynamic cycle results and a mix of empirical values, stress analysis and material characteristics. Figure 9.4.6-2 shows a schematic of a weight prediction procedure for a compressor. Though the details of mechanical design programs are beyond the scope of this text, some general comments are in order.

The gas generator maximum diameter can be established if the maximum airflow, compressor (or fan) hub-to-tip ratio, and compressor face Mach number are known. Precise values of these vary from configuration to configuration. Approximate preliminary design values can be defaulted because each engine company tends to use hub/tip ratios and flow per unit area values that are consistent within the desired technology level and major types of application. Compressor face Mach numbers are typically near M = 0.6. With the addition of an historically derived case and flange thickness, the maximum diameter can be estimated.

The length of the engine depends on the engine type, technology level, the number of stages in each component, the ducts required to connect the flow paths between components, and the burner length. The number of stages is determined by specifying the work per stage that can be done by the component within the specified state of the art. The work per stage, which can use a default value for preliminary studies, is divided into the total work for the component (as computed by the thermodynamic cycle program) to arrive at the number of stages. The length of each stage is found from empirical correlations based on diameter, loading, temperature, and stresses.

Duct lengths are computed from empirical values for acceptable turning and diffusion rates and the radius changes necessary to connect the

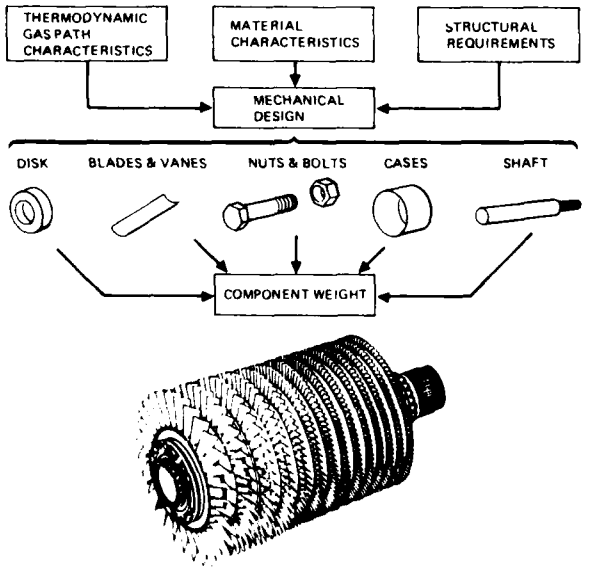

Figure 9.4.6-2. Schematic of Compressor Weight Prediction

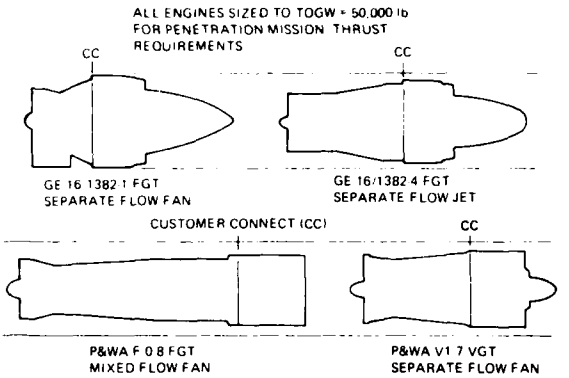

Figure 9.4.6-3. Shape Variation of Some Study Engines

components. Burner length is again empirical but is governed primarily by burner type and the length necessary to provide the needed residence time for flame front propagation.

Complete mechanical design requires many inputs including: thermodynamic inputs, work/stage, hub/tip dimensions, blade pull stress, disc burst stress, blade aspect ratio, temperature gradients, load paths, etc. As a program incorporates more actual design and stress methods instead of empirical correlations, the program complexity and, hopefully, the simulation accuracy increase. While industry and Government are continually working to increase the accuracy of the predictions, the combination of a large empirical data base and well chosen correlation parameters provide useful data for preliminary design work. The generalized engine concept, Figure 9.4.6-1, applies very well to mechanical design. For a desired technology level, default values for correlation functions for each component can be preprogrammed. The mechanical design subroutines can thus be connected directly to the thermodynamic cycle analysis. One such program, used in industry, predicts the weight of a wide variety of engines to within +10% (Reference: 9.4.6-2)

The computer simulation of engine aerothermodynamic performance discussed in Section 9.4.5 specify nothing about the gas generator dimensions or weight. The engine/airplane matching process depends on the physical properties of the engine as well as the performance, as shown in Figure 9.4.1-2. Airplane weight and drag are influenced by the engine dimensions, external shape, weight, and center of gravity location. Consider, as a final example, a Mach 2.7 fighter-type aircraft flying a penetration mission (Reference 9.1.3-1). The shape differences between candidate engines producing the required thrust are shown in Figure 9.4.6-3. The effect of engine weight and dimensions on the take-off gross weight required to fly a mission of specified range is summarized in Table 9.4.6-1.

Table 9.4.6-1 Change in Required TOGW Due to Changes in Engine Physical Characteristics

Physical Characteristics (Independent Variable)	Change in Engine Characteristics	Resulting Change in Airplane TOGW Required to Fly Mission
Engine Diameter (Max)	10%	5%
Engine Length	10%	0.02%
Engine Weight	10%	6%

9.5 REFERENCES

9.1.2-1 Perkins, C. D. and R. E. Hage, Airplane Performance Stability and Control, John Wiley and Son, 1967

9.1.2-2 Hoerner, S., Fluid Dynamic Drag, 1965

9.1.3-1 Dommasch, D. O, S. S. Sherby, and T. F. Connolly, Airplane Aerodynamics

9.1.3-2 "Exhaust System Interaction Program (ESIP)," USAF Aero Propulsion Lab., D162-10467, Wright-Patterson AFB, Ohio, April, 1973

9.2.2-1 Zavatkay, W. F., "Engine Cycle Selection Considerations in the Aircraft Design Process," presented at Aircraft Design Short Course, University of Dayton, July, 1976.

9.2.3-1 Healy, M. J., J. S. Kowalik, and J. W. Ramsay, "Airplane Engine Selection by Optimization on Surface Fit Approximations," Journal of Aircraft, Vol. 12, No. 7, July, 1975, pp. 593-599

9.2.8-1 Swan, W. C., A. D. Welliver, G. W. Klees, and S. G. Kyle, "Opportunities for Variable Geometry Engines in Military Aircraft," presented at 48th AGARD Propulsion and Energetics Panl, Paris, France, September, 1976

9.4.6-1 Jaeger, D. L., "Engine Performance Analysis through Computerized Design and Integration," ASME Gas Turbine Conference, New Orleans, November, 1975

9.4.6-2 Pera, R. J., E. Onat, G. W. Klees, and E. Tjonneland, "A Method to Estimate Weight and Dimensions of Aircraft Gas Turbine Engines," CR 135170, NASA-Lewis Research Center, Ohio, May, 1977

Chapter 10

ELEMENTARY THEORY OF BLADE AERODYNAMICS

Gordon C. Oates

University of Washington

TABLE OF CONTENTS

CHAPTER 10 ELEMENTARY THEORY OF BLADE AERODYNAMICS

		Page
10.0	Introduction	10-1
10.1	Two-Dimensional Incompressible Flow Through Blade Rows	10-2
10.1.1	The Euler Equation	10-3
10.1.2	Velocity Triangles	10-4
10.1.3	Pressure Relationships Across Blade Rows - the Degree of Reaction and the Diffusion Factor	10-5
10.1.4	Relationships in Terms of Flow Angles.	10-7
10.2	Free Vortex Flow	10-8
10.2.1	Example Free Vortex Calculation	10-9
10.3	Radial Equilibrium Flows	10-11
10.3.1	The Stream Function	10-11
10.3.2	The Equations for Radial Equilibrium Flows	10-12
10.3.3	Solution of the Radial Equilibrium Equations	10-12
10.3.4	Example Radial Equilibrium Calculation	10-14
10.4	The Effects of Compressibility	10-15
10.4.1	Turbine Aerodynamics	10-16
10.4.2	The Impulse Turbine	10-18
10.4.3	The Reaction Turbine	10-18
10.4.4	Comparison of the Impulse Turbine and "50%" Reaction Turbine	10-19

LIST OF FIGURES

		Page
Figure 10.0.1	Coordinate System and Through-flow Representation	10-1
Figure 10.0.2	Typical Axial Velocity Profiles	10-1
Figure 10.0.3	Typical Streamsurface	10-1
Figure 10.0.4	Meridional Projections of Blade Profiles	10-2
Figure 10.0.5	Secondary Flows Within a Stator Row	10-2
Figure 10.1.1	Streamtube Geometry and Nomenclature	10-3
Figure 10.1.2	Blade Rows and Station Numbering	10-4
Figure 10.1.3	Flow Past an Inlet Guide Vane Row	10-4
Figure 10.1.4	Flow Past a Rotor Row	10-5
Figure 10.1.5	Rotor Row Composite Diagram	10-5
Figure 10.1.6	Flow Past a Stator Row	10-5
Figure 10.1.7	Geometry and Velocity Changes Across Blade Row	10-7
Figure 10.1.8	Recirculating Flow Region	10-8
Figure 10.3.1	Parallel Walled Annulus	10-11
Figure 10.3.2	Flow in an Annulus	10-11
Figure 10.3.3	Nomenclature for Radial Equilibrium	10-12
Figure 10.3.4	Radial Equilibrium Velocity Profiles	10-15
Figure 10.4.1	Turbine Nozzle Row	10-16
Figure 10.4.2	Maximum Swirl Kinetic Energy	10-17
Figure 10.4.3	Stage Pressure Ratio Versus Axial Mach Number	10-17
Figure 10.4.4	Enthalpy Ratio and Maximum Swirl Velocity Versus Area Ratio	10-18
Figure 10.4.5	Velocity Diagram for an Impulse Turbine Stage	10-18
Figure 10.4.6	Velocity Diagram for a Reaction Turbine Stage	10-19

CHAPTER 10

LIST OF SYMBOLS

The symbols are listed in alphabetical order, first in the English alphabet, then in the Greek alphabet. Subscripts and superscripts are then given. The equation, figure or section in which the symbols are first introduced is indicated in parentheses. Often the symbol will be defined in the text just preceding or just following the equation or figure.

Where appropriate, the location of the introduction of the symbol is referred to in previous chapters.

A - Constant defined in Eq. 10.3.16

- Cross-sectional area (Eq. 10.4.5)

a - Speed of sound (Eq. 10.4.9)

C - Specific heat (Sect. 2.6)

c - Chord (Fig. 10.1.7)

D - Diffusion factor (Eq. 10.1.23)

H - Dimensionless stagnation enthalpy (Eq. 10.3.11)

h - Enthalpy (Eq. 10.1.1)

I.G.V. - Inlet guide vane (Fig. 10.1.2)

J_i - Bessel function of first kind, order i (Eq. 10.3.20)

M - Mach number (Eq. 10.1.8)

$\dot{m}$ - Mass flow rate (Fig. 10.1.1)

p - Pressure (Eq. 10.1.6)

R - Tip to hub ratio (Eq. 10.3.11)

- Gas constant (Sect. 2.12)

$^{\circ}R$ - Degree of reaction (Eq. 10.1.17)

r - Radial co-ordinate (Fig. 10.0.1)

s - Distance along meridional surface (Fig. 10.0.4)

- Spacing (Fig. 10.1.7)

T - Torque (Eq. 10.1.2)

- Temperature (Eq. 10.1.6)

U_i - Group of Bessel function defined in Eq. 10.3.23

u - Radial velocity component (Fig. 10.0.1)

$\bar{u}$ - Vector velocity (Eq. 10.3.1)

V - Velocity (Fig. 10.1.3)

- Dimensionless tangential velocity (Eq. 10.3.11)

v - Tangential velocity component (Fig. 10.0.1)

W - Dimensionless axial velocity (Eq. 10.3.11)

W_i - Group of Bessel functions defined in Eq. 10.3.24

w - Axial velocity component (Fig. 10.0.1)

- Work interaction (Eq. 10.1.1)

Y_i - Bessel function of second kind, order i (Eq. 10.3.20)

y - Dimensionless radial co-ordinate (Eq. 10.3.11)

z - Axial co-ordinate (Fig. 10.0.1)

α - Constant defined in Eq 10.3.17

- Angle of swirl (Fig. 10.4.1)

β - Relative flow angle (Fig. 10.1.4)

- Constant defined in Eq. 10.3.17

γ - Ratio of specific heats (Sect. 2.6)

δ - Constant defined in Eq. 10.3.17

η - Efficiency (Eq. 10.4.1)

θ - Cylindrical co-ordinate (Fig. 10.0.1)

- Flow angle (Fig. 10.1.4)

ρ - Density (Eq. 10.1.11)

σ - Solidity (Eq. 10.1.23)

Ψ - Dimensionless stream function (Eq. 10.3.11)

ψ - Stream function (Eq. 10.3.3)

Ω - Dimensionless angular velocity (Eq. 10.3.27)

ω - Angular velocity (Fig. 10.1.1)

Subscripts

e - Exit (Eq. 10.1.23)

h - Hub (Fig. 10.0.2)

i - Inlet (Eq. 10.1.23)

m - Mean (Eq. 10.2.26)

p - Constant pressure (Sect. 2.6)

t - Tip (Fig. 10.0.2)

- Stagnation quantity (Sect. 2.16)

0 - Reference quantity (Eqs. 10.1.8, 10.3.16), also station (Fig. 10.1.2)

1 - Upstream (Fig. 10.1.1), also station (Fig. 10.1.2), also stream surface (Fig. 10.3.2)

2 - Downstream (Fig. 10.1.1), also station (Fig. 10.1.2), also stream surface (Fig. 10.3.2)

rel - Relative (Fig. 10.1.4)

CHAPTER 10

ELEMENTARY THEORY OF BLADE AERODYNAMICS

10.0 INTRODUCTION

In this chapter the relationships of the desired performance parameters to the related compressor or turbine blade loadings (and resultant fluid flow angles) will be investigated. It is apparent that the flow field within an actual turbine or compressor is enormously complex, and it is desirable to create simplified models of the flowfields if any understanding of the physics of the flow processes is to be attained, or if any analytical prediction techniques are to be formulated.

Though several extensive efforts to model the flow through an entire compressor or turbine, in its entirety, (including transonic effects, boundary layers, wakes, etc.) have been attempted, and have met with some partial preliminary success, it is more common to model the flow field as a "sum" of less complicated parts. We will briefly describe relatively simple flow fields, and will then consider the various separate pieces.

In order to analyze what appears at first to be an almost incomprehensibly complicated flow field, it is customary to model the full three dimensional flow field as a compilation of three two-dimensional fields. These fields may be termed the "throughflow field", the "cascade field" (or blade to blade field), and the "secondary flow field". Each of these fields is described in the following paragraphs.

THE THROUGHFLOW FIELD

This flow field is considered to arise because of the influence of all the blades in a row (or rows). The effects of individual blades are not considered, and hence the combined effects of all the blades in the row are obtained by assuming the blade forces to be "smeared out" in the azimuthal direction. Mathematically, this process is accomplished by replacing the blade surface pressures by volumetric (and continuous) body forces. As a result of the simplifications contained in this model, no θ variations occur, and the throughflow flow field is hence two-dimensional with variations occurring in the radial (r), and axial (z) directions.

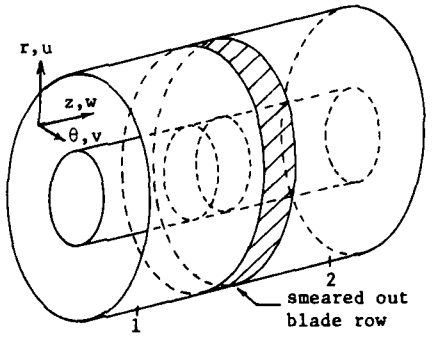

Figure 10.0.1 Coordinate System and Throughflow Representation

Figure 10.0.1 shows the coordinate system and the throughflow representation of the flow field. It can be noted that the flow field identified with this approximation would be that approached if the blade row had a very large number of very thin blades.

The solution to such a flow field would give the axial and tangential velocities throughout. Figure 10.0.2 shows typical axial velocity profiles that could occur at stations 1 and 2 of Fig. 10.0.1.

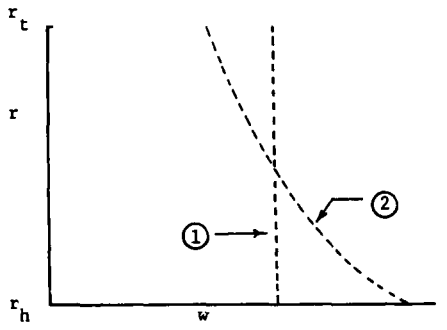

Figure 10.0.2 Typical Axial Velocity Profiles

When axial velocity profiles of the form indicated in Fig. 10.0.2 at station 2 develop, it is apparent from continuity that a downward flow of fluid must occur. Thus a typical "streamsurface" (to be more carefully defined in Sec. 10.3.1) could appear as depicted in Fig. 10.0.3.

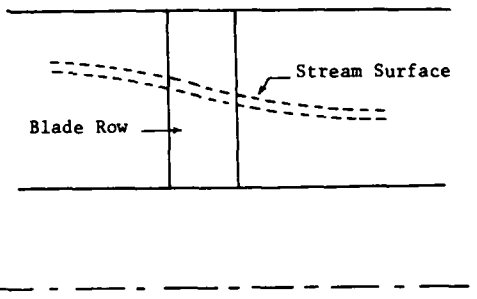

Figure 10.0.3 Typical Streamsurface

The throughflow field can be considered the parent flow field of the cascade and secondary flow fields, and because of this should be calculated with considerable accuracy. For this reason, a somewhat extensive description of throughflow calculation techniques is given in Chapter 11.

THE CASCADE FIELD

In order to estimate the flow behavior in the neighborhood of individual blades, a meridional surface such as that indicated in Fig. 10.0.3 would be expanded ("unwrapped") and the individual blade profiles considered. (Fig. 10.0.4)

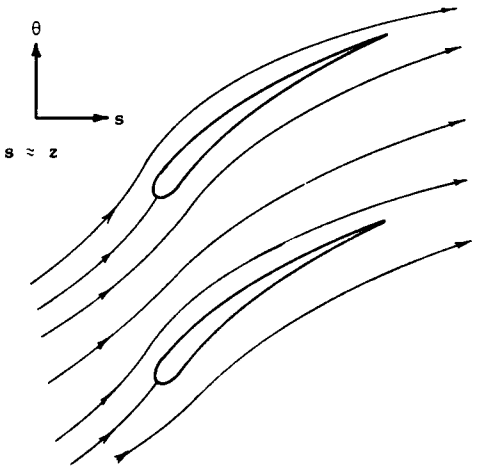

Figure 10.0.4 Meridional Projections of Blade Profiles

When the meridional surface of Fig. 10.0.3 is unwrapped in this way, a two-dimensional flowfield in the θ and meridional (almost z) coordinates is obtained. If the curvature of the streamsurfaces in the throughflow field (Fig. 10.0.3) is not too great, the pressure gradients across such streamsurfaces need not be considered, and hence the individual "strips" may be considered separately. (Hence the term "strip theory"). By considering a number of such strips, suitable blade profiles can be determined for a selected number of radial stations on the blade, and the complete blade shape necessary to describe the full three dimensional blade can be obtained by fairing in the desired profile shape.

Numerical methods may be utilized to calculate the flow field in this plane (including the boundary layers), but classically the most widely used method is to run cascade tests to obtain the blade performance data. It is to be noted that in general the flow between an example pair of streamsurfaces in the throughflow field encounters a change in cross-sectional area. As a result great care must be taken when the corresponding cascade test is conducted, to include the effects of the axial variation in flow cross-section and its related effect upon the streamwise pressure variation. It is to be further noted that the effect of the cascade sidewall boundary layer build up must also be accounted for in order to properly simulate the streamwise pressure variations. The cascade flowfield is more fully described in Chapter 12.

THE SECONDARY FLOW FIELD

The third of the three two-dimensional flow fields considered to comprise the full three-dimensional flow field of an axial turbomachine is the secondary flow field. This field exists because the fluid near the solid surfaces will have a lower velocity with respect to those surfaces than does the fluid in the "free stream" (external to the boundary layer). As a result the imposed pressure gradients (created because of the curvature of the free stream) will deflect the fluid within the boundary layers from regions of high pressure to regions of low pressure. Figure 10.0.5 indicates the possible secondary flows existing within a stator row. (Note that the blade boundary layers on a rotor would tend to be centrifuged outward, whereas the excess pressure existing at the outer annulus tends to deflect the stator blade boundary layer inward.)

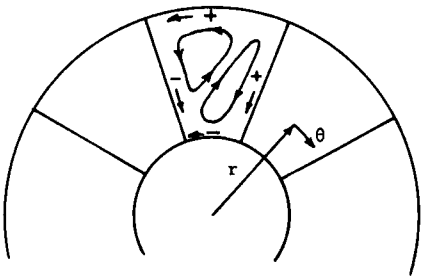

Figure 10.0.5 Secondary Flows Within a Stator Row

Secondary flows are notoriously difficult to analyze, but in spite of this, considerable progress has been made in the analysis of secondary flows in both compressors and turbines. The techniques of analysis for compressors are substantially different than those for turbines. This is because in compressors, the adverse pressure gradient leads to low wall shears, so the flows can be analyzed fairly accurately ignoring the viscous shearing terms. (The presence of the viscous shearing terms is included implicitly in the assumed entrance velocity profile.) The literature of this class of secondary flows is quite extensive, and the interested reader is encouraged to obtain several excellent recent studies (Refs. 10.1, 10.2, 10.3).

When secondary flows in turbines are to be considered, the large favorable pressure gradients existing over much of the blade surface and annulus walls leads to thin boundary layers with high shearing rates and consequently high shear stresses. As a result (three dimensional) boundary layer calculation techniques must be employed. These techniques are further discussed in Chapter 18.

10.1 TWO-DIMENSIONAL INCOMPRESSIBLE FLOW THROUGH BLADE ROWS

In this section we will relate the changes in fluid velocity, induced by blade rows, to the changes in fluid thermodynamic properties. The discussion pertains to the cascade field, but for the present, only the far upstream and far downstream conditions will be considered. In this way, description of the details of the flow in the vicinity of the blades will not be necessary, but

rather only the changes in fluid properties will be required. The more difficult problem of obtaining the necessary blade geometries to efficiently induce the assumed velocity fields will be addressed in later sections.

10.1.1 THE EULER EQUATION

We now consider the behavior of a single streamtube as it passes through a rotor row. The geometry and nomenclature of the interaction are indicated in Fig. 10.1.1. For the purposes of this section, it is not necessary to know the details of the interaction within the volume indicated by the dotted lines in the figure. Rather we require only stations 1 and 2 be sufficently far removed from the region of rotor interaction that the flow may be considered time independent and in addition it is assumed that the entire process is adiabatic.

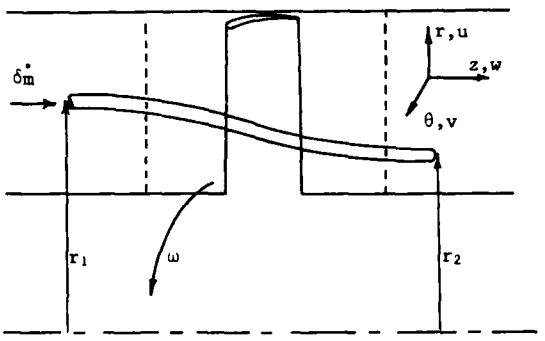

Figure 10.1.1 Streamtube Geometry and Nomenclature

We define Δw as the work interaction per unit mass that the streamtube undergoes as it passes through the rotor, and for convenience define Δw to be positive for a work "input". The first law of thermodynamics then gives (for this adiabatic flow)

$$\Delta w = h_{t_2} - h_{t_1} \tag{10.1.1}$$

The work interaction from the rotor is transmitted to the streamtube from the input shaft by the torque of the blades. Denoting that portion of the torque identified with the streamtube as δT, and the angular velocity of the shaft as ω, we have the power input to the streamtube given by

$$\text{power input} = \omega \delta T \tag{10.1.2}$$

The torque on the streamtube, itself, is equal to the rate of production of angular momentum, so that with the mass flow rate through the streamtube denoted $\dot{\delta m}$, we may write

$$\delta T = [(rv)_2 - (rv)_1]\dot{\delta m} \tag{10.1.3}$$

The work interaction per unit mass is just the power input divided by the mass flow rate, so from Eqs. 10.1.2 and 10.1.3

$$\Delta w = \omega \frac{\delta T}{\dot{\delta m}} = \omega[(rv)_2 - (rv)_1] \tag{10.1.4}$$

Combination of Eqs. 10.1.1 and 10.1.4 then gives the famous Euler momentum equation.

$$h_{t_2} - h_{t_1} = \omega[(rv)_2 - (rv)_1] \tag{10.1.5}$$

It is to be noted that no restriction to ideal flow was implied in the development of this equation, the only restriction being that the flow be adiabatic. It would, of course, be hoped that in a compressor the work interaction would occur in a primarily non-viscous manner so that after diffusion (in a stator row) the effects of the work interaction would appear primarily as a pressure increase rather than as a (static) temperature increase. Equation 10.1.5, however, is applicable no matter what the compressor efficiency.

THE PERFECT FLUID APPROXIMATION

When the flow of a perfect fluid is considered, we may relate the stagnation pressure ratio to the stagnation enthalpy ratio because the entropy remains constant. Thus, utilizing Eq. 2.16.6 we find

$$\frac{p_{t_2}}{p_{t_1}} = \left(\frac{T_{t_2}}{T_{t_1}}\right)^{\frac{\gamma}{\gamma-1}} = \left(\frac{h_{t_2}}{h_{t_1}}\right)^{\frac{\gamma}{\gamma-1}} \tag{10.1.6}$$

These forms follow because we are considering a calorically perfect gas. Thus, with Eqs. 10.1.5 and 10.1.6 there follows

$$\frac{p_{t_2}}{p_{t_1}} = \left[1 + \frac{\omega}{h_{t_1}}\{(rv)_2 - (rv)_1\}\right]^{\frac{\gamma}{\gamma-1}} \quad \text{perfect fluid} \tag{10.1.7}$$

We now introduce reference quantities denoted by a subscript, o, where such quantities are assumed to be the uniform values of the given quantities found in the approaching flow far upstream. The stagnation enthalpy does not change prior to the blade row so we may write

$$h_{t_1} = h_{to} = \gamma R T_o \frac{C_p}{\gamma R}\frac{T_{to}}{T_o} = \gamma R T_o \left(\frac{1}{\gamma-1}\right)\left(1 + \frac{\gamma-1}{2} M_o^2\right)$$

or

$$h_{t_1} = w_o^2 \frac{1}{M_o^2}\left(\frac{1}{\gamma-1}\right)\left(1 + \frac{\gamma-1}{2} M_o^2\right) \tag{10.1.8}$$

Equations 10.1.7 and 10.1.8 then give

$$\frac{p_{t_2}}{p_{t_1}} = \left[1 + \frac{(\gamma-1)M_o^2}{1 + \frac{\gamma-1}{2} M_o^2}\frac{\omega}{w_o^2}\{(rv)_2 - (rv)_1\}\right]^{\frac{\gamma}{\gamma-1}} \quad \text{perfect fluid} \tag{10.1.9}$$

If we now restrict our attention to cases where the amount of turning is small, this expression may be approximated by retaining only the first term in the binomial expansion of the right hand side. Thus

$$\frac{p_{t_2}}{p_{t_1}} - 1 \approx \frac{\gamma M_o^2}{1 + \frac{\gamma-1}{2} M_o^2}\frac{\omega}{w_o^2}\{(rv)_2 - (rv)_1\} \quad \text{perfect fluid} \tag{10.1.10}$$

It is to be noted that Eq. 10.1.10 would also be valid in the case of small Mach numbers. In such

a case, p_{t_1} becomes an inconvenient reference quantity, and it is more appropriate to reference the "dynamic head", $\rho_o w_o^2$. Thus noting

$$\gamma M_o^2 = \frac{\rho_o w_o^2}{p_o} = \frac{\rho_o w_o^2}{p_{t_1}} \frac{p_{to}}{p_o}$$

$$= \frac{\rho_o w_o^2}{p_{t_1}} \left(1 + \frac{\gamma-1}{2} M_o^2\right)^{\frac{\gamma}{\gamma-1}}$$

it follows that

$$\frac{p_{t_2}-p_{t_1}}{\rho_o w_o^2} \approx \left(1 + \frac{\gamma-1}{2} M_o^2\right)^{\frac{1}{\gamma-1}} \frac{\omega}{w_o^2} \{(rv)_2-(rv)_1\} \qquad (10.1.11)$$

perfect fluid, small turning

In the limit as M_o approaches zero we obtain the relationship for incompressible perfect flow which may be written

$$\frac{p_{t_2}-p_{t_1}}{\rho_o w_o^2} = \frac{\omega}{w_o^2} [(rv)_2-(rv)_1] \qquad (10.1.12)$$

perfect, incompressible fluid

The expressions represented by Eqs. (10.1.5 - 10.1.12) allow us to calculate the changes in stagnation enthalpy or in stagnation pressure, in terms of the imposed changes in swirl velocities. Each form of the equations should be used only in the regime for which it is valid, as indicated beside each expression. It is to be noted from Eq. (10.1.5) that no change in stagnation enthalpy can occur unless the blade row is moving. This situation is quite obvious when it is realized that without a moving surface, no work interaction with the fluid would occur. (Eq. 10.1.4)

A similar result to that for the stagnation enthalpy occurs in the case of the stagnation pressure of a perfect fluid. When losses are present, however, the accompanying entropy gains will superimpose a stagnation pressure decrease upon the flow processes in rotor and stator. (Eq. 2.16.6) Thus, the stagnation pressure rise through the rotor will not be as large as it would be if the fluid was perfect, and there will be a decrease in stagnation pressure as the fluid passes through the stator.

10.1.2 VELOCITY TRIANGLES

It was seen in the previous section that desired property changes are brought about by inducing swirl velocities with the rotors and stators. In this section we consider the resulting vector triangles of the fluid velocities in order to gain an appreciation for the fluid field the blades and vanes must create. The blade and vane angles will, of course, be closely related to the fluid flow angles. The flow is considered to be two-dimensional only, and is considered to be approaching the first row from afar with conditions denoted by the subscript, o. We consider the flow past three rows, an inlet guide vane row, rotor and stator. The rows and station numbering are indicated in Fig. 10.1.2.

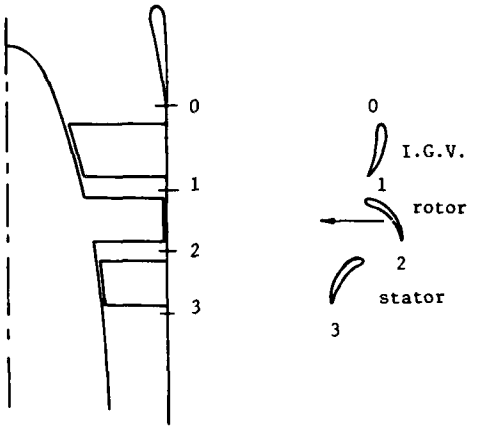

Figure 10.1.2 Blade Rows and Station Numbering

INLET GUIDE VANE (I.G.V.)

The flow approaching and following the I.G.V. row is illustrated in Fig. 10.1.3. The notation for the angle of turning, velocity components and magnitude of the velocity is indicated in the figure.

Figure 10.1.3 Flow Past an Inlet Guide Vane Row

An inlet guide vane row tends to be unique amongst all the rows in a compressor, because in all compressors with I.G.V. rows built to date, the static pressure decreases across the row. The reason for this can be inferred from Fig. 10.1.3, where it is evident that the magnitude of the velocity has increased upon passage through the row. The I.G.V. row is not moving, and hence no increase in stagnation enthalpy occurs, and for an ideal fluid, no change in stagnation pressure will occur. As a result, the increased magnitude of the velocity will have attendant with it, a decrease in static pressure. It is conceivable that a severe expansion in the annulus side walls could be incorporated, so that the axial velocity could be reduced to a sufficient extent to cause the overall velocity magnitude to reduce, but this has not been incorporated in any design to date. (There would seem to

be no reason to do so.) Because of the overall favorable pressure gradient imposed across an I.G.V. row, the tendency of the vane boundary layers to separate is much reduced, and as a result very high turning can be introduced by a single I.G.V. stage.

ROTOR

When the air departs the I.G.V. it has a velocity $V_1 = \sqrt{v_1^2+w_1^2}$, which is directed at an angle θ_1 from the axial direction. The rotor itself, has a velocity $\omega r\bar{e}_\theta$, and hence sees a relative velocity at inlet given by

$$\bar{V}_{rel_1} = \bar{V}_1 - \omega r\bar{e}_\theta \qquad (10.1.13)$$

The air is then turned within the rotor to the relative velocity $\bar{V}_{rel_2}$, so that the velocity in the absolute frame (the laboratory system of coordinates), $\bar{V}_2$, is given by

$$\bar{V}_2 = \bar{V}_{rel_2} + \omega r\bar{e}_\theta \qquad (10.1.14)$$

These velocity relationships are indicated in Fig. 10.1.4.

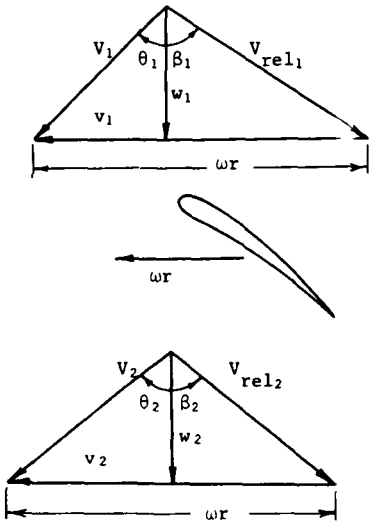

Figure 10.1.4 Flow Past a Rotor Row

The information displayed in Fig. 10.1.4 can be more compactly displayed by utilizing a composite diagram wherein both entering and leaving velocity diagrams are shown superimposed. Such a diagram is indicated in Fig. 10.1.5

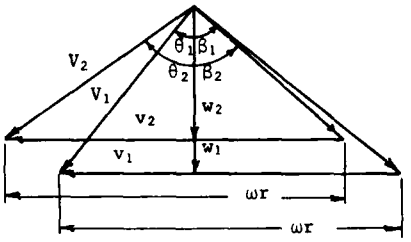

Figure 10.1.5 Rotor Row Composite Diagram

STATOR

The stator accepts the flow departing from the rotor and turns it to a more axial direction. By reducing the swirl velocity in this way the magnitude of the total velocity is also reduced, and the static pressure increases across the vane row. In those designs where the stator returns the velocity vector to that found at entrance to the rotor, the stage is said to be a repeating stage. The stator velocity relationships are indicated in Fig. 10.1.6.

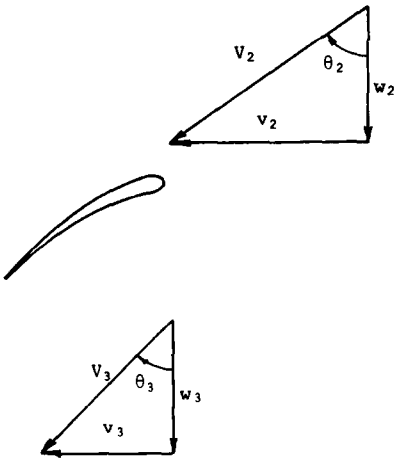

Figure 10.1.6 Flow Past a Stator Row

10.1.3 PRESSURE RELATIONSHIPS ACROSS BLADE ROWS - THE DEGREE OF REACTION AND THE DIFFUSION FACTOR

The change in stagnation properties across blade rows was investigated for various limiting conditions in Sec. (10.1.1). It is the purpose of a compressor stage to raise the stagnation pressure as much as possible and as efficiently as possible. In addition it would be desirable to have the mass flow rate per cross sectional area be as large as possible so as to reduce the required compressor cross sectional area to the minimum

possible. These desired design goals create several conflicting requirements and limitations.

It is evident from Sec. (10.1.1) that a large stagnation pressure rise would require a large amount of turning in the rotor, and hence also in the stator to return the velocity vector to (approximately) that entering the rotor. This large turning introduces two related deleterious effects. Firstly, the large stagnation pressure change introduces a related large adverse static pressure gradient. This imposed static pressure gradient enchances the probability of boundary layer separation on the blade. Secondly, the large required blade curvature leads to high blade aerodynamic loading with related very low values of minimum static pressure on the blade suction side. As a result the suction side boundary layer must surmount a local severe adverse pressure gradient which has already been made worse by the superimposed static pressure gradient due to all other blades in the row, as just described above.

It is apparent (Eq. 10.1.9) that the attainment of high pressure ratios will be aided by the use of high blade speeds and high axial Mach numbers, but each of these techniques has its own limitations. It is obvious that the blade speed will be limited by mechanical stressing considerations, though it is notable that great strides in this direction have been made in the last two decades. (Blade speeds have increased from approximately 300 m/s to approximately 500 m/s.) Both increasing the blade speed and increasing the axial Mach number lead to large relative Mach numbers on the blades, and if carried to excess can lead to large shock losses in the stage.

It is the function of a designer to make as optimal a choice as possible of the various conflicting requirements, and some simplified design aids have been developed to help in the various choices. Two coefficients often utilized in the design of axial compressors or turbines, the degree of reaction and the diffusion factor, are defined in the following. Each coefficient is related to the behavior of the static pressure change across the blade rows, so prior to defining the coefficients, we first investigate the behavior of the static pressure. For simplicity we consider the incompressible perfect fluid case.

We have from Eq. (10.1.12), for the two-dimensional case, (with $\rho_o \equiv \rho$)

$$p_2 + \frac{1}{2}\rho(v_2^2+w_2^2)-\rho\omega(rv)_2 = p_1 + \frac{1}{2}\rho(v_1^2+w_1^2)-\rho\omega(rv)_1 \tag{10.1.15}$$

Straightforward manipulation of this equation leads to the alternate form

$$p_{t_{2_{rel}}} - \frac{1}{2}\rho(\omega r_2)^2 = p_{t_{1_{rel}}} - \frac{1}{2}\rho(\omega r_1)^2 \tag{10.1.16}$$

Here we have introduced the relative stagnation pressure as seen by the rotor, $p_{t_{rel}}$, which is defined by

$$p_{t_{rel}} \equiv p + \frac{1}{2}\rho\{w^2 + (v-\omega r)^2\}$$

It can be seen that in an axial compressor, where $r_1 \approx r_2$, the relative stagnation pressure across the (ideal) rotor does not change. This, of course, is simply Bernoulli's equation for the relative coordinate system. The terms involving the square of the blade speed are related to the accounting of "energy" stored against the centrifugal forces, and can be of dominant importance in centrifugal compressors with their large change in radius from inlet to outlet. Equation 10.1.16 is equally valid for stators as well as rotors, where of course, in the case of a stator the equation simply degenerates to the statement that the stagnation pressure does not change across an ideal stator row.

Equation 10.1.16 is in a useful form for design purposes, because it makes evident that we may estimate the change in static pressure across an axial compressor rotor row, simply by observing the fluid behavior in the relative coordinate system. (Fig. 10.1.15) As was evident in the discussion introducing this section, the effect of static pressure increase is of paramount importance upon the operating limit of a blade row, and it is evident that it would be desirable to have such a static pressure increase across a stage nearly evenly divided between the rotor and the stator. A measure of this static pressure split is the degree of reaction, °R, defined in the following.

DEGREE OF REACTION °R

The degree of reaction, °R, is defined as the static pressure rise across the rotor divided by the static pressure rise across the stage. Thus,

$$^\circ R = \frac{\Delta p_{rotor}}{\Delta p_{stage}} = 1 - \frac{\Delta p_{stator}}{\Delta p_{stage}} \tag{10.1.17}$$

In the case of incompressible perfect fluid flow and nearly axial flow, we may write (utilizing the station numbering of Fig. 10.1.2)

$$\frac{1}{\rho}\Delta p_{stage} = \frac{1}{\rho}\Delta p_{t\,stage} - \frac{1}{2}\Delta\bar{V}^2_{stage}$$

or

$$\frac{1}{\rho}\Delta p_{stage} = \omega\{(rv)_2-(rv)_1\} - \frac{1}{2}(\bar{V}_3^2-\bar{V}_1^2) \tag{10.1.18}$$

and

$$\frac{1}{\rho}\Delta p_{stator} = \frac{1}{2}(\bar{V}_2^2-\bar{V}_3^2) \tag{10.1.19}$$

It follows that

$$^\circ R = 1 - \frac{\bar{V}_2^2-\bar{V}_3^2}{\bar{V}_1^2-\bar{V}_3^2+2\omega\{(rv)_2-(rv)_1\}} \quad \text{incompressible, perfect flow, small radius changes} \tag{10.1.20}$$

A repeating stage is one for which, by definition, $\bar{V}_1 = \bar{V}_3$, so that noting $w_1 = w_3$,

$$^\circ R = 1 - \frac{v_2^2-v_1^2}{2\omega\{(rv)_2-(rv)_1\}} \quad \text{incompressible, perfect flow, small radius changes, repeating stages, } w_1 = w_2 \tag{10.1.21}$$

An even simpler form results if the radius change is so small that it does not effect the angular momentum difference. In this case, we have with $r_1 = r_2 = r$,

$$^{\circ}R = 1 - \frac{v_2+v_1}{2\omega r} \quad \text{incompressible, perfect flow, no radius change, repeating stages} \qquad (10.1.22)$$

DIFFUSION FACTOR, D

This factor was developed in an attempt to describe both the effects of imposed axial pressure gradient and of blade turning angle. (It is more fully developed in Ref. 10.4 and in Sec. 17.5.3.1.) It is intended to be a measure of how highly loaded a single blade row may be considered to be. It is defined by

$$D = (1 - \frac{V_e}{V_i}) + \frac{\Delta v}{2\sigma V_i} \qquad (10.1.23)$$

here V_e = magnitude of the relative velocity at exit to the blade row

V_i = magnitude of the relative velocity at inlet to the blade row

Δv = magnitude of the change in tangential component of velocity across the blade row

σ = solidity $\equiv \frac{\text{chord}}{\text{spacing}} = \frac{c}{s}$

These relationships are shown in Fig. 10.1.7.

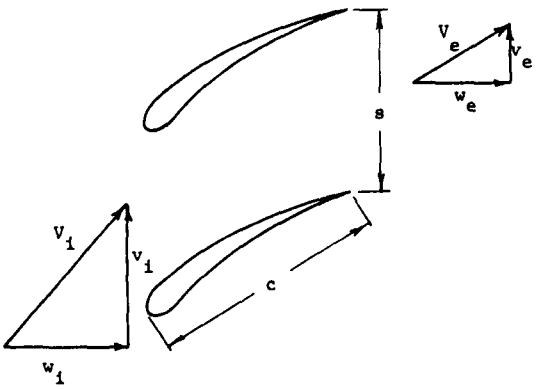

Figure 10.1.7 Geometry and Velocity Changes Across Blade Row

A typical maximum value of D obtainable for a given family of blade profiles is about 0.6. This value should not be exceeded substantially or it can be expected that flow separation will occur. Such limiting values of the diffusion factor are usually obtained from cascade tests (Chapt. 12). Such limiting values can vary substantially in some cases (for blades with extremely long chords for example), but the factor is very convenient to utilize so that possible problem areas can be pinpointed.

10.1.4 RELATIONSHIPS IN TERMS OF FLOW ANGLES

The geometry of the flow through the blade rows was discussed in Sec. 10.1.2. It is often of use to obtain expressions for the pressure change, degree of reaction and diffusion factor in terms of the fluid flow angles, because the flow angles themselves can be fairly directly related to the blade angles. In particular, the relative velocity departing each row will have a relative angle not far from the blade geometric angle. In fact relatively simple empirical rules are available to estimate the difference of the relative flow angle and blade angle at exit to the blade row (Chapt. 12), so in the following we obtain the desired relationships in terms of angles θ_1, β_2 and θ_3 .

For simplicity of presentation we consider the incompressible perfect fluid case. Thus Eq. (10.1.12) may be utilized to give with the relationships apparent from Fig. 10.1.5, namely

$$v_1 = w_1 \tan \theta_1 \qquad (10.1.24)$$

$$v_2 = \omega r_2 - w_2 \tan \beta_2 \qquad (10.1.25)$$

and hence

$$\frac{\Delta p_t}{\rho_o w_o^2} = \left(\frac{\omega r_2}{w_o}\right)^2 - \left[\frac{\omega r_2}{w_o}\frac{w_2}{w_o} \tan \beta_2 + \frac{\omega r_1}{w_o}\frac{w_1}{w_o} \tan \theta_1\right]$$

incompressible, perfect fluid (10.1.26)

In the special case where no change in axial velocity or radius occurs, this form reduces to

$$\frac{\Delta p_t}{\rho_o w_o^2} = \left(\frac{\omega r}{w_o}\right)^2 \left[1 - \frac{w_o}{\omega r}(\tan \beta_2 + \tan \theta_1)\right] \qquad (10.1.27)$$

incompressible, perfect fluid, $r_1 = r_2 = r$, $w_1 = w_2 = w_o$

In Sec. 8.4.2, it was pointed out that when a compressor is operated at low rotational speeds (during starting, for example) the front blades tend to operate with a low axial velocity to blade speed ratio, as compared to the design speed ratio. It can be seen from Eq. (10.1.27) then, that a further complication will arise, in that the stagnation pressure rise near the tip of a finite length blade will tend to be larger than that near the hub. This is because the flow angles β_2 and θ_1 tend to be relatively insensitive to flow velocity, and because β_2 and θ_1 , at all radii, would be chosen to be appropriate for the design condition, at off-design when $w_o/\omega r$ decreases, so does the effect of the second term in the brackets of Eq. (10.1.27). As a result of the larger work interaction at the tip of the blades, the static pressures can become so excessive that a region of reverse flow can possibly exist. (Fig. 10.1.8) The fluid contained within such a region of reverse flow can rapidly have its temperature raised (by the work interaction with the blades) to such an extent that blade melting can occur! This is yet another reason why the techniques mentioned in Sec. 8.4.2 for preventing excessively low axial velocities must be employed.

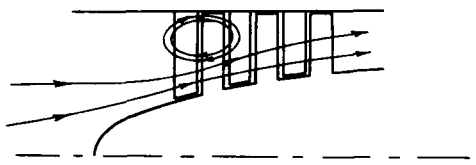

Figure 10.1.8 Recirculating Flow Region

We may obtain from Fig. 10.1.5 the relationships

$$V_1^2 = w_1^2 \sec^2\theta_1 \tag{10.1.28}$$

$$V_2^2 = w_2^2 + (\omega r_2 - w_2 \tan \beta_2)^2 \tag{10.1.29}$$

$$V_3^2 = w_3^2 \sec^2 \theta_3 \tag{10.1.30}$$

Equations (10.1.20), (10.1.24), (10.1.25) and (10.1.28 - 10.1.30) may then be combined to give

$$^{\circ}R = 1 - \{w_2^2[1+(\frac{\omega r}{w_2} - \tan \beta_2)^2] - w_3^2 \sec^2\theta_3\} \div$$

$$\{w_1^2 \sec^2 \theta_1 - w_3^2 \sec^2 \theta_3 + 2w_2^2[(\frac{\omega r_2}{w_2})^2 - (\frac{\omega r_2}{w_2} \tan \beta_2 + \frac{\omega r_1}{w_2}\frac{w}{w_2} \tan \theta_1)]\} \tag{10.1.31}$$

In the special case where no change in axial velocity or radius occurs, and the stage is repeating, this form reduces to

$$^{\circ}R = 1 - \frac{\frac{\omega r}{w_o} - \tan \beta_2 + \tan \theta_1}{2\frac{\omega r}{w_o}} \tag{10.1.32}$$

(incompressible, perfect flow, small radius changes, $r_1 = r_2 = r$, $w_1 = w_2 = w_o$, $V_1 = V_3$)

Again utilizing Fig. 10.1.5 we obtain for the rotor

$$(V_e)_{rotor} = w_2 \sec \beta_2 \tag{10.1.33}$$

$$(V_i)_{rotor} = w_1\{1+[\frac{\omega r}{w_o} - \tan \theta_1]^2\}^{1/2} \tag{10.1.34}$$

$$\Delta v_{rotor} = \omega r_2 - w_2 \tan \beta_2 - w_1 \tan \theta_1 \tag{10.1.35}$$

Equations (10.1.33 - 10.1.35) may then be substituted into Eq. (10.1.20) to give an expression for the rotor diffusion factor. In the special case where no change in axial velocity or radius occurs, there is obtained

$$D_{rotor} = 1 - \frac{\sec \beta_2 - \frac{1}{2\sigma}[\frac{\omega r}{w_o} - (\tan \beta_2 + \tan \theta_1)]}{\{1+[\frac{\omega r}{w_o} - \tan \theta_1]^2\}^{1/2}} \tag{10.1.36}$$

incompressible perfect flow, small radius changes $r_1 = r_2 = r$, $w_1 = w_2 = w_o$

Finally, we obtain an expression for the stator diffusion factor by first noting

$$(V_e)_{stator} = w_3 \sec \theta_3 \tag{10.1.37}$$

$$(V_i)_{stator} = w_2\{1 + [\frac{\omega r_2}{w_2} - \tan \beta_2]^2\}^{1/2} \tag{10.1.38}$$

$$\Delta v_{stator} = \omega r_2 - w_2 \tan \beta_2 - w_3 \tan \theta_3 \tag{10.1.39}$$

These equations may then be substituted into Eq. (10.1.23) to given an expression for the stator diffusion factor. In the special case where no change in axial velocity or radius occurs, there is obtained

$$D_{stator} = 1 - \frac{\sec \theta_3 - \frac{1}{2\sigma}[\frac{\omega r}{w_o} - (\tan \beta_2 + \tan \theta_3)]}{\{1+[\frac{\omega r}{w_o} - \tan \beta_2]^2\}^{1/2}} \tag{10.1.40}$$

(incompressible, perfect flow, small radius changes $r_1 = r_2 = r$, $w_1 = w_2 = w_o$)

Several tendencies for the degree of reaction and diffusion factor become evident in these expressions. We note from Eq. (10.1.32), for example, that in the case of a repeating stage with "symmetric blading" ($\beta_2 = \theta_1$), the degree of reaction is one half, no matter what the ratio of blade speed to axial velocity. This means, for such a stage, that the static pressure rise would remain equally split between rotor and stator as the compressor was "throttled". When the compressor is throttled (outlet flow decreased leading to an outlet pressure increase), an increased pressure rise must occur across the stage. The effect of such an increase in pressure rise is seen in D_{rotor} and D_{stator} which both increase as $\omega r/w_o$ increases. This, of course, means that the compressor is moving towards its design limit.

10.2 FREE VORTEX FLOW

We now consider the effects of finite blade height upon the required fluid flow angles. It is apparent from the preceding sections that the variation in fluid properties across blade rows is a function of the blade velocity. Thus, when we consider a blade of finite length, the blade velocity will change substantially with radius, and the corresponding effects upon the flow field should be determined. In most compressor designs it is desirable to obtain the same stagnation pressure rise across a stage, at all radii. (Note if this was consistently violated in a multistage machine, very large static pressure mismatches could occur with consequent recirculation regimes.)

We shall consider the case where the change in stagnation enthalpy across the rotor is a constant with radius, so that from Eq. (10.1.5) we have

$$h_{t_2} - h_{t_1} = \omega[(rv)_2 - (rv)_1] = \text{const.} \qquad (10.2.1)$$

Thus, a "constant work stage", that is one for which the work interaction per mass is independent of radius, requires that the change in angular momentum be the same for all streamtubes. There are many types of flows that could satisfy this requirement, but the simplest such flow would seem to be that for which (for perfect, incompressible flow) the axial velocity remains a constant with radius. (We assume a parallel walled annulus.) It is apparent from the requirement of mass continuity that if no change in axial velocity occurs, no radial flows will be induced. The radial momentum equation then reduces to the statement that the radial pressure gradient is balanced by the centrifugal forces. That is

$$\frac{\partial p}{\partial r} = \rho \frac{v^2}{r} \qquad (10.2.2)$$

The requirement that the stagnation pressure be constant with radius gives

$$p + \frac{\rho}{2}(w^2+v^2) = p_t = \text{const.}$$

$$\text{So that} \quad \frac{\partial p}{\partial r} = -\rho v \frac{\partial v}{\partial r} \qquad (10.2.3)$$

Equations (10.2.2) and (12.2.3) may be combined to given an equation for v in terms of r. Thus noting that no changes in properties occur in the axial direction (except within blade rows), we may write

$$\frac{dv}{v} + \frac{dr}{r} = 0 \text{ , or } rv = \text{const.} \qquad (10.2.4)$$

It can hence be seen that a constant work machine that has a constant axial velocity throughout, not only has the jump in angular momentum across blade rows, Δrv, equal to a constant, but also must have rv itself a constant in all regimes. Note, of course, that the "constant" that rv is equal to, changes with passage through each blade row. A machine utilizing blade rows that induce this type of flow field is termed a "free vortex" machine, and is said to be in radial equilibrium throughout. We will consider an example free vortex calculation in the next section, and will consider flows of a more general form in Sec. 10.3 and Chapt. 11.

10.2.1 EXAMPLE FREE VORTEX CALCULATION

We now consider that several design variables will be prescribed, and we wish to obtain expressions for hub and tip values of the design limit parameters D_{rotor} and D_{stator}, as well as for $^{\circ}R$. In generating these expressions, all the velocity components and relative velocity components necessary to determine the flow vector diagrams will be obtained so that the velocity triangles could be constructed if desired.

We consider a repeating stage, and assume we have the following variables prescribed:

$$\underline{1}\ \frac{\omega r_h}{w_o} \qquad \underline{3}\ r_t/r_h \qquad \underline{5}\ \sigma_{r_m}$$

$$\underline{2}\ \frac{\Delta p_t}{\rho_o w_o^2} \qquad \underline{4}\ {}^{\circ}R_{r_m} \qquad (10.2.5)$$

Here $^{\circ}R_{r_m}$ and σ_{r_m} refer to the degree of reaction and solidity at the "mass average radius", r_m. The mass average radius is that radius that has half the mass flowing within it and the hub, and half flowing within it and the tip. In this case of uniform axial velocity, we have

$$r_m = \sqrt{\frac{r_t^2 + r_h^2}{2}} \qquad (10.2.6)$$

DEGREE OF REACTION

Equation (10.1.22) is valid for this case, so that with Eq. (10.2.4) we have

$$^{\circ}R = 1 - \frac{\text{const.}}{r^2}$$

here

$$\text{Const.} = r_m^2(1-{}^{\circ}R_{r_m}) = r_h^2\left(\frac{(r_t/r_h)^2+1}{2}\right)(1-{}^{\circ}R_{r_m})$$

thus

$$^{\circ}R = 1 - \frac{1}{(r/r_h)^2}\left(\frac{(r_t/r_h)^2+1}{2}\right)(1-{}^{\circ}R_{r_m}) \qquad (10.2.7)$$

Denoting the value of $^{\circ}R$ at the hub by $^{\circ}R_h$, we note also

$$^{\circ}R_h = 1 - \frac{(v_2+v_1)_h}{2\omega r_h}$$

$$\text{hence} \quad \frac{v_{2h}}{w_o} + \frac{v_{1h}}{w_o} = 2\frac{\omega r_h}{w_o}(1 - {}^{\circ}R_h) \qquad (10.2.8)$$

TANGENTIAL VELOCITIES

An expression for the difference in angular velocities follows from Eq. (10.1.12) to give

$$\frac{v_{2h}}{w_o} - \frac{v_{1h}}{w_o} = \frac{1}{\frac{\omega r_h}{w_o}}\frac{\Delta p_t}{\rho_o w_o^2} \qquad (10.2.9)$$

and from Eqs. (10.2.8) and (10.2.9) there follows

$$\frac{v_{2h}}{w_o} = \frac{1}{2}\left[2\frac{\omega r_h}{w_o}(1-{}^{\circ}R_h) + \frac{1}{\frac{\omega r_h}{w_o}}\frac{\Delta p_t}{\rho_o w_o^2}\right] \qquad (10.2.10)$$

$$\frac{v_{1h}}{w_o} = \frac{1}{2}\left[2\frac{\omega r_h}{w_o}(1-{}^{\circ}R_h) - \frac{1}{\frac{\omega r_h}{w_o}}\frac{\Delta p_t}{\rho_o w_o^2}\right] \qquad (10.2.11)$$

Equation (10.2.4) then gives

$$\frac{v_2}{w_o} = \frac{v_{2h}}{w_o}\frac{r_h}{r} \quad \text{and} \quad \frac{v_1}{w_o} = \frac{v_{1h}}{w_o}\frac{r_h}{r} \qquad (10.2.12)$$

DIFFUSION FACTORS

In order to obtain values for the diffusion factors, some assumption must be made with regard to the behavior of the solidity. It is clear that the spacing s will be proportional to the radius. The chord length can be tapered in a variety of ways, but for illustrative purposes it is sufficient to consider the chord length constant. In such a case we obtain

$$\frac{\Delta v}{2\sigma V_i} = \frac{(\frac{v_{2h}}{w_o} - \frac{v_{1h}}{w_o})\frac{r_h}{r}}{2\sigma_{r_m}\frac{r_m}{r}\frac{V_i}{w_o}} = \frac{(\frac{v_{2h}}{w_o} - \frac{v_{1h}}{w_o})}{2\sigma_{r_m}\frac{r_m}{r_h}\frac{V_i}{w_o}} \quad \text{(constant chord length)} \tag{10.2.13}$$

and with Eq. (10.1.23)

$$D = (1 - \frac{V_e}{V_i}) + \frac{(\frac{v_{2h}}{w_o} - \frac{v_{1h}}{w_o})}{2\sigma_{r_m}\frac{r_m}{r_h}\frac{V_i}{w_o}} \quad \text{(constant chord length)} \tag{10.2.14}$$

The relative velocities for use in this expression follow by reference to Fig. 10.1.5 and may be written

$$V_{i\,rotor} = [(\omega r - v_1)^2 + w_o^2]^{1/2} = w_o[(\frac{\omega r_h}{w_o}\frac{r}{r_h} - \frac{v_{1h}}{w_o}\frac{r_h}{r})^2 + 1]^{1/2}$$

$$V_{e\,rotor} = [(\omega r - v_2)^2 + w_o^2]^{1/2} = w_o[(\frac{\omega r_h}{w_o}\frac{r}{r_h} - \frac{v_{2h}}{w_o}\frac{r_h}{r})^2 + 1]^{1/2}$$

$$V_{i\,stator} = [w_o^2 + v_2^2]^{1/2} = w_o[1 + (\frac{v_{2h}}{w_o}\frac{r_h}{r})^2]^{1/2}$$

$$V_{e\,stator} = [w_o^2 + v_3^2]^{1/2} = w_o[1 + (\frac{v_{1h}}{w_o}\frac{r_h}{r})^2]^{1/2} \tag{10.2.15}$$

Equations (10.2.6) through (10.2.15) give the desired design limit parameters in terms of the design input variables listed in Eq. (10.2.5). As an example we consider the values

$$\frac{\Delta p_t}{\rho_o w_o^2} = 0.9, \quad \frac{r_t}{r_h} = \sqrt{7}, \quad {}^\circ R_{r_m} = 0.5 \quad \text{and} \quad \sigma_{r_m} = 1 .$$

We consider two values of the blade speed, namely $\omega r_h/w_o = 0.5$ and 0.7 . Direct calculation leads to the results shown in Table 10.2.1 .

	$D_{rotor,\ hub}$	$D_{rotor,\ tip}$	$D_{stator,\ hub}$	$D_{stator,\ tip}$
$\frac{\omega r_h}{w_o} = 0.5$	-.179	.558	.741	.552
$\frac{\omega r_h}{w_o} = 0.7$	-.350	.381	.590	.431

$^\circ R_t = 5/7$, $^\circ R_h = -1$, both cases.

Table 10.2.1 Example Results, Free Vortex Design

Several important trends are evident in this example calculation. Thus, for example, it is apparent that the large value for the diffusion factor found at the hub of the stator for the low blade speed case indicates that such a blade row is too heavily loaded. The designer of such a row would have several options open to him. Perhaps the most obvious change should be to increase the degree of reaction so that the rotor tip will become as highly loaded as the stator hub. A rather peculiar result appears to occur when the degree of reaction $^\circ R_{r_m}$ is raised to 0.7 . As expected the stator hub diffusion factor is reduced (to .670), but the rotor tip diffusion factor is also reduced (to .540)! The explanation for this unexpected behavior lies in the fact that the introduction of a degree of reaction $^\circ R_{r_m}$ (for this geometry) in excess of 0.55 leads to values of v_1 that are negative. As a result large relative velocities with the rotor occur, so that in spite of the increased static pressure rise, the diffusion factor reduces. This result is not without physical credence, because the larger relative dynamic pressure would help to transfer momentum to the fluid in the boundary layers and hence reduce the tendency to separate. The use of such negative swirl in actual aircraft engines would, however, introduce possible shock losses because of the large relative Mach numbers. It might be noted parenthetically, however, that the use of such negative swirl could hold promise in helium compressors (for use in gas cooled nuclear reactors) where the Mach numbers are extremely low.

It is obvious that if the designer could utilize materials that allowed a higher blade speed, he could decrease the diffusion factor, as indicated by the result for the higher blade speed case. If this option was not available to him he might choose to reduce the tip to hub ratio, thereby preventing the large negative degree of reaction near the hub. This option carries with it the undesirable side effect of reducing the mass flow per cross sectional area capability of the compressor. Another option available would be to decrease the stagnation pressure rise per stage, but this of course would lead to the requirement of more stages for a given compressor pressure rise.

It is apparent that the free vortex design carries with it some unpleasant design restrictions. Thus the related rapid change with radius of the degree of reaction causes the blades to be loaded so that the stator hub requires very high diffusion as does the rotor tip. Note that the very large turning required in the rotor at the hub leads to such an acceleration that the static pressure actually decreases across the rotor at the hub, for this example. (Note $^{\circ}R_h = -1$) This means that the stator must undergo an extreme pressure rise in order to return the fluid velocities to those entering the stage (as required for a repeating stage). A design of this sort that places the design limit so strongly at the limits of the blades is quite undesirable because, in effect, the remaining portions of the blades are relatively lightly loaded even when the stator hub and rotor tip are loaded to their limit.

In the following sections we consider alternate flow swirl distributions that reduce the disparity in loading along the blade length, but it should be noted that the tendency for the rotor tip and stator hub to be diffusion limited remains to some extent in all designs. As a result, the allowable stage loading is a function of the tip to hub ratio, with the smaller tip to hub ratio allowing the attainment of larger stage pressure ratios. A designer, then, can be faced with the choice of providing a large cross sectional area compressor of fewer stages, versus a small cross sectional compressor of many stages. The appropriate choice often depends on the selected airplane mission. (Chapt. 26)

10.3 RADIAL EQUILIBRIUM FLOWS

In the preceding section, it was seen that the very simple free vortex theory led to large variations with radius of the degree of reaction. As a result, the free vortex distribution led to blades with excessive diffusion factors at the rotor tip and at the stator hub. Other swirl distributions must hence be investigated, and as a result, the effects of radial flows must be considered.

A very simple limiting case of flows in which radial flows exist, is obtained by considering conditions very far from the blade rows. We again assume perfect incompressible flow, and consider conditions in a parallel walled annulus, as shown in Fig. 10.3.1 .

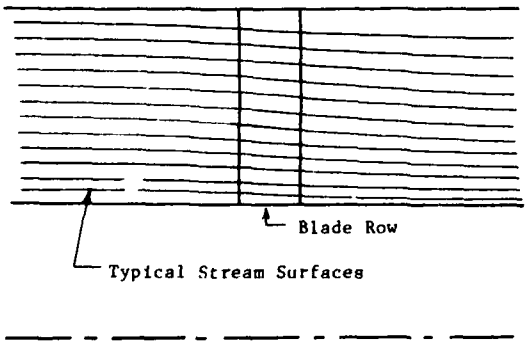

Figure 10.3.1 Parallel Walled Annulus

The virtue of considering conditions far from the blade rows, is that any radial flows will have ceased, because the flow will have become parallel to the containing annulus. In this way we obtain ordinary differential equations for the flow properties. At this stage we will not be able to estimate how long it takes the flow to approach this condition of "radial equilibrium", but good estimates do follow from the results of the through-flow theory, Chapt. 11.

10.3.1 THE STREAM FUNCTION

We here introduce the stream function, ψ , and include for future convenience, the possibility of axial variations in fluid properties. We still consider incompressible flow, only, so that the continuity equation may be written

$$\nabla \cdot \bar{u} = 0 \tag{10.3.1}$$

In cylindrical coordinates this becomes

$$\frac{1}{r}\frac{\partial ru}{\partial r} + \frac{\partial w}{\partial z} = 0 \tag{10.3.2}$$

This latter equation is identically satisfied if we introduce the stream function, ψ , defined by

$$w = -\frac{1}{r}\frac{\partial \psi}{\partial r} \qquad u = \frac{1}{r}\frac{\partial \psi}{\partial z} \tag{10.3.3}$$

An equation for ψ follows by considering the normal derivative of the momentum equation (Chapt. 11 and Sec. 10.3.2), but before developing such an equation, let us first consider a physical interpretation of the quantity ψ .

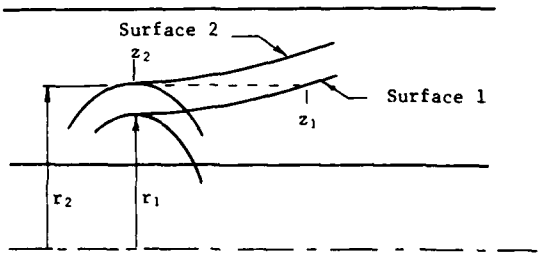

Figure 10.3.2 Flow in an Annulus

Figure 10.3.2 shows an annulus bounded by two "meridional surfaces". A meridional surface is defined as a surface through which no fluid passes. We may calculate the mass flow rate convected between the two meridional surfaces in either of the alternate ways

$$\dot{m} = \rho\int_{r_1}^{r_2} w(2\pi r dr) = -\rho\int_{\psi_1}^{\psi_2} 2\pi d\psi = -2\pi\rho(\psi_2-\psi_1)$$

$$\text{or} \quad \dot{m} = -\rho\int_{z_1}^{z_2} u(2\pi r dz) = -2\pi\rho(\psi_2-\psi_1) \tag{10.3.4}$$

Thus the mass flow rate between the surfaces is proportional to the difference in streamfunctions of the surfaces. It follows then that if $\psi_2 = \psi_1$, there is no (net) flow through the surface, so that a constant ψ denotes a "streamsurface". If the equations of the streamsurface are known, the velocity components follow from Eq. (10.3.3).

10.3.2 THE EQUATIONS FOR RADIAL EQUILIBRIUM FLOWS

It is apparent from the Euler equation (Eq. 10.1.5), that the stagnation enthalpy does not vary along streamlines that are external to the blade rows. Similarly, it is apparent from Eq. (10.1.3) that the angular momentum also does not vary along streamlines that are external to blade rows. Because of this, it is convenient (particularly in throughflow theory, Chapt. 11) to consider the stagnation enthalpy and angular momentum to be prescribed functions of the streamfunction, ψ. The prescribed function will, of course, be determined by the history of blade loading that the streamtube has encountered.

We note from Eq. (10.3.3), that for the case of no axial variations, we may write

$$w = -\frac{1}{r}\frac{d\psi}{dr}, \text{ or } \frac{d(\ )}{d\psi} = -\frac{1}{wr}\frac{d(\ )}{dr} \qquad (10.3.5)$$

This transformation is of particular utility when we consider variations in the stagnation enthalpy and angular momentum, because as previously described, these quantities will be given as functions of the streamfunction.

For this case of perfect flow, there is no change in entropy throughout, so the Gibbs equation, Eq. (2.8.2), gives

$$dh = \frac{1}{\rho}dp \qquad (10.3.6)$$

The differential change in stagnation enthalpy may be written

$$dh_t = dh + wdw + vdv \qquad (10.3.7)$$

so
$$\frac{1}{\rho}dp = dh_t - wdw - vdv \qquad (10.3.8)$$

Because the flow is in radial equilibrium, the radial momentum equation remains as in Eq. (10.2.2), so that we find

$$\frac{1}{\rho}\frac{dp}{dr} = \frac{v^2}{r} = \frac{dh_t}{dr} - w\frac{dw}{dr} - v\frac{dv}{dr}$$

$$\text{or } -\frac{1}{r}\frac{dw}{dr} = -\frac{1}{rw}\frac{dh_t}{dr} - \frac{v}{r}\left\{\frac{-1}{rw}\frac{drv}{dr}\right\} \qquad (10.3.9)$$

Utilizing Eq. (10.3.5) we then obtain

$$\frac{1}{r}\frac{d}{dr}\left(\frac{1}{r}\frac{d\psi}{dr}\right) = \frac{dh_t}{d\psi} - \frac{v}{r}\frac{drv}{d\psi} \qquad (10.3.10)$$

This is a second order differential equation for the streamfunction ψ, in terms of the prescribed stagnation enthalpy and angular momentum. It is, in general, non-linear. There are several linear solutions of the equations corresponding to blade loadings of design interest, however, and such special cases will be considered in the next section. It is most convenient to consider a non-dimensional form of Eq. (10.3.10), so we introduce (see Fig. 10.3.3)

$$W = \frac{w}{w_o}, \quad V = \frac{v}{w_o}, \quad \Psi = \frac{\psi}{w_o r_h^2}, \quad H = \frac{h_t}{w_o^2},$$

$$y = \frac{r}{r_h}, \quad R = \frac{r_t}{r_h} \qquad (10.3.11)$$

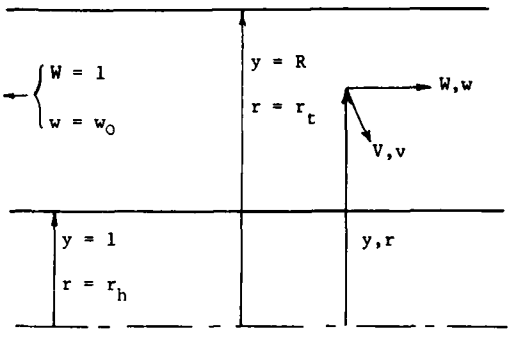

Figure 10.3.3 Nomenclature for Radial Equilibrium Flow

Routine substitution of the variables of Eq. (10.3.11) into Eq. (10.3.10) leads to

$$\frac{1}{y}\frac{d}{dy}\left(\frac{1}{y}\frac{d\Psi}{dy}\right) = \frac{dH}{d\Psi} - \frac{V}{y}\frac{dyV}{d\psi} \qquad (10.3.12)$$

The related boundary conditions are obtained by first noting that we may prescribe the streamfunction within a constant. Thus, for future convenience we assign the streamfunction on the hub, Ψ_h,

$$\Psi_h = -\frac{1}{2} \text{ on } y = 1 \ (r = r_h) \qquad (10.3.13)$$

We note also

$$W = -\frac{1}{y}\frac{d\Psi}{dy} \qquad (10.3.14)$$

so obtain (noting that $W = 1$ far upstream)

$$\Psi_t = -\int_1^R yWdy - \frac{1}{2} = -\frac{R^2}{2} \text{ on } y = R \ (r = r_t) \qquad (10.3.15)$$

Equations (10.3.12 - 10.3.15) prescribe the mathematical problem.

10.3.3 SOLUTION OF THE RADIAL EQUILIBRIUM EQUATIONS

Equation (10.3.12) may be integrated for any arbitrary prescription of H and yV (as a function of Ψ), but particularly simple forms arise if we consider forms for which H and $(yV)^2$ are quadratic in Ψ. Thus, for such flows, Eq. (10.3.12) reduces to a linear equation in Ψ and a solution can be obtained in terms of known functions. We thus consider H and $(yV)^2$ to be given by

$$H = A\Psi + H_o \tag{10.3.16}$$

$$(yV)^2 = (-\alpha\Psi+\beta)^2-\delta\Psi \tag{10.3.17}$$

In these expressions, A, H_o, α, β and δ are constants which may be selected at the designers discretion. We note

$$\frac{dH}{d\Psi} = A$$

$$V\frac{dyV}{d\Psi} = \frac{1}{2y}\frac{d(yV)^2}{d\Psi} = \frac{1}{y}\left[\alpha^2\Psi-(\alpha\beta+\frac{\delta}{2})\right]$$

$$\frac{d}{dy}\left(\frac{1}{y}\frac{d\Psi}{dy}\right) = \frac{d}{dy}\left(\frac{1}{y}\frac{d}{dy}\left[y\left(\frac{\Psi}{y}\right)\right]\right) = \frac{d^2(\Psi/y)}{dy^2}+\frac{1}{y}\frac{d(\Psi/y)}{dy} - \frac{1}{y^2}\left(\frac{\Psi}{y}\right)$$

With these expressions we obtain from Eq. (10.3.12)

$$\frac{d^2(\Psi/y)}{dy^2}+\frac{1}{y}\frac{d(\Psi/y)}{dy}+(\alpha^2-\frac{1}{y^2})(\frac{\Psi}{y}) = yA+\frac{1}{y}(\alpha\beta+\frac{\delta}{2}) \tag{10.3.18}$$

We note that the inhomogeneous portion of this equation may be integrated immediately to give

$$\left(\frac{\Psi}{y}\right)_{\text{inhom.}} = \frac{A}{\alpha^2}y+\frac{1}{y}(\frac{\beta}{\alpha}+\frac{\delta}{2\alpha^2}) \tag{10.3.19}$$

The homogeneous portion of the solution can be recognized as consisting of a linear combination of Bessel functions of the first and second kinds, and of order one. Thus

$$\left(\frac{\Psi}{y}\right)_{\text{hom.}} = C_1J_1(\alpha y)+C_2Y_1(\alpha y) \tag{10.3.20}$$

and hence

$$\Psi = C_1yJ_1(\alpha y)+C_2yY_1(\alpha y)+\frac{A}{\alpha^2}y^2+\frac{\beta}{\alpha}+\frac{\delta}{2\alpha^2} \tag{10.3.21}$$

The constants C_1 and C_2 are now determined by applying the boundary conditions, Eqs. (10.3.13) and (10.3.15). After straightforward but tedious manipulation we find

$$\Psi = -[\frac{A}{\alpha^2}+\frac{\beta}{\alpha}+\frac{\delta}{2\alpha^2}+\frac{1}{2}]\frac{yU_1(\alpha y)}{U_1(\alpha)} -[\frac{A}{\alpha^2}R^2+\frac{\beta}{\alpha}+\frac{\delta}{2\alpha^2}+\frac{R^2}{2}]\frac{yW_1(\alpha y)}{R\,U_1(\alpha)} + \frac{A}{\alpha^2}y^2+\frac{\beta}{\alpha}+\frac{\delta}{2\alpha^2} \tag{10.3.22}$$

Here we have introduced the notation

$$U_i(\alpha y) \equiv J_i(\alpha y)Y_1(\alpha R)-J_1(\alpha R)Y_i(\alpha y) \tag{10.3.23}$$

$$W_i(\alpha y) \equiv J_1(\alpha)\,Y_i(\alpha y)-Y_1(\alpha)\,J_i(\alpha y) \tag{10.3.24}$$

here i is an integer

It is convenient to note that

$$U_1(\alpha R) = 0 = W_1(\alpha), \text{ and } U_1(\alpha) = W_1(\alpha R) \tag{10.3.25}$$

With these relationships it can be easily checked that Eq. (10.3.22) satisfies the boundary conditions, $\Psi = -1/2$ on $y = 1$ and $\Psi = -R^2/2$ on $y = R$.

When the parameter α is equal to zero, the expression Eq. (10.3.22) becomes indeterminate. For this case, rather than taking the mathematical limit of the expression, it is simpler to return to Eq. (10.3.12), which for the case $\alpha = 0$ becomes

$$\frac{d}{dy}\left(\frac{1}{y}\frac{d\Psi}{dy}\right) = yA+\frac{\delta}{2y} \tag{10.3.26}$$

Successive integration gives

$$\Psi = C_1\frac{y^2}{2}+C_2+\frac{y^4}{8}A+\frac{\delta}{8}\{2y^2\ell n\ y-y^2\} \tag{10.3.27}$$

The constant C_1 and C_2 are again determined through application of the boundary conditions Eq. (10.3.13) and (10.3.15). The solution may be written in the form

$$\Psi = -\frac{y^2}{2}-\frac{A}{8}(y^2-1)(R^2-y^2)+\frac{\delta}{4(R^2-1)}\times [(R^2-1)y^2\ell n\ y-(y^2-1)R^2\ell n\ R] \quad (\alpha = 0) \tag{10.3.28}$$

INTERPRETATION OF THE PARAMETERS

Equations (10.3.22) and (10.3.28) provide the solution to the equilibrium flow for a rather general swirl and enthalpy distribution leading to linear solutions of the governing equation. It is of interest to interpret each of the parameters α, β, δ, and A, individually, however. To do so we consider the flows prescribed for the cases where all parameters but one are zero.

FREE VORTEX FLOW (β)

When A, α and δ are all zero, we see from Eq. (10.3.17) that the angular momentum is constant with y, ($yV = \beta$), which is of course a free vortex distribution. Equation (10.3.28) then reduces to

$$\Psi = -\frac{y^2}{2}$$

$$\text{hence } W = -\frac{1}{y}\frac{d\Psi}{dy} = 1, \text{ (free vortex)} \tag{10.3.29}$$

Thus, for a free vortex distribution, the axial velocity remains unperturbed, just as previously established in Sec. 10.2.

SOLID-BODY-LIKE ROTATION (α)

When A, β and δ are all zero, Eq. (10.3.17) reduces to

$$yV = -\alpha\Psi \text{ (solid body like)} \tag{10.3.30}$$

It is evident from Eq. (10.3.22) that a perturbation in axial velocity will be present for this case. If we investigate the case where very little swirl is introduced (α small), we may say that the variation of axial velocity with radius will itself be small. (This may be verified by calculation from Eq. (10.3.22).) In such a case we have

$$\Psi = -\int_1^y y dy - \frac{1}{2} \approx -\frac{y^2}{2} \quad \text{(small swirl)} \qquad (10.3.31)$$

We then have

$$V \approx \frac{\alpha y}{2} \quad \text{(small swirl)} \qquad (10.3.32)$$

Thus, for small swirl this swirl distribution approximates that corresponding to a "solid body" swirl. Such a distribution is sometimes termed a forced vortex.

APPROXIMATELY CONSTANT SWIRL (δ)

When A, α and β are zero, Eq. (10.3.17) reduces to

$$yV = (-\delta\Psi)^{1/2} \quad \text{(approximately constant swirl)} \qquad (10.3.33)$$

We may again argue that for small swirl, the perturbation in axial velocity may be expected to be small (see Eq. (10.3.28)), so that Ψ will be given approximately by $\Psi = -y^2/2$. Hence

$$V \approx \sqrt{\frac{\delta}{2}} \qquad (10.3.34)$$

Thus for small swirl, this swirl distribution approximates a constant swirl velocity.

VARIABLE STAGNATION ENTHALPY (A)

When α, β and δ are zero, there is no swirl in the flow, and because the flow is in radial equilibrium, no static pressure variation with y will be present. Thus, we note from the Gibbs equation $dh = Tds + 1/\rho\ dp = 0$, and hence

$$dH = d\left(\frac{h}{w_o^2}\right) + WdW = WdW \qquad (10.3.35)$$

Thus with $dH = Ad\Psi = -AyWdy$, it follows that

$$\frac{dW}{dy} = -Ay \qquad (10.3.36)$$

This result is consistent with Eq. (10.3.28), which simply emphasizes that for this case, any change in stagnation enthalpy must be supplied by a variation in the axial velocity.

The stagnation enthalpy will be changed only across rotor rows, so we see from the Euler momentum equation, Eq. (10.1.5), together with Eq. (10.3.11) and the definition $\Omega = \omega r_h/w_o$,

$$H_2 - H_1 = \Omega[(yV)_2 - (yV)_1] \qquad (10.3.37)$$

Thus, in terms of the parameters introduced in Eqs. (10.3.16) and (10.3.17), we find

$$H_2 - H_1 = \Omega[\{-\alpha_2\Psi+\beta_2)^2 - \delta_2\Psi\}^{1/2} - \{(-\alpha_1\Psi+\beta_1)^2 - \delta_1\Psi\}^{1/2}] \qquad (10.3.38)$$

It thus follows that if all terms in the expression for angular momentum are to be included, when flow across a rotor is considered, the desired linear form for the stagnation enthalpy cannot be utilized. If the "approximately constant swirl" term is excluded, however we may write

$$H_2 - H_1 = H_{O_2} - H_{O_1} + (A_2 - A_1)\psi =$$

$$\Omega[-\alpha_2\Psi+\beta_2-(-\alpha_1\Psi+\beta_1)] \quad (\delta = 0) \qquad (10.3.39)$$

and hence

$$H_{O_2} = H_{O_1} + (\beta_2 - \beta_1)\Omega \qquad (10.3.40)$$

and

$$A_2 = A_1 - (\alpha_2 - \alpha_1)\Omega \qquad (10.3.41)$$

In a compressor, we generally desire little, if any, variation of stagnation enthalpy with radius, so it is usually appropriate to exclude variation of the parameter α across a rotor row. We note, however, that the solid-body-like component of swirl may be introduced by the stator (or inlet guide vane row), which hence gives us another parameter to utilize for design purposes. In the next section a detailed example solution is considered.

10.3.4 EXAMPLE RADIAL EQUILIBRIUM CALCULATION

In this section we consider an example calculation for a rotor-stator pair. The pair will be a repeating stage, with constant work interaction with radius (A = 0) and with no "approximately constant swirl" term (δ = 0). For this special case, the solution of Eq. (10.3.22) reduces to

$$\Psi = -(\beta + \frac{\alpha}{2})\frac{yU_1(\alpha y)}{\alpha U_1(\alpha)} - (\frac{\beta}{R} + \frac{\alpha R}{2})\frac{yW_1(\alpha y)}{\alpha U_1(\alpha)} + \frac{\beta}{\alpha} \qquad (10.3.42)$$

The derivatives of Bessel functions may be obtained from any standard mathematics book (ref. 10.5 for example). We note here the general relationship

$$\frac{d}{dx}[x\{C_1J_1(\alpha x) + C_2Y_1(\alpha x)\}] =$$

$$\alpha x\{C_1J_0(\alpha x) + C_2Y_0(\alpha x)\} \qquad (10.3.43)$$

Hence in our notation

$$\frac{d}{dy}\left(yU_1(\alpha y)\right) = \alpha y U_0(\alpha y) \quad \text{and}$$

$$\frac{d}{dy}\left(yW_1(\alpha y)\right) = \alpha y W_0(\alpha y) \qquad (10.3.44)$$

Thus

$$-\frac{1}{y}\frac{d\Psi}{dy} = W = (\beta + \frac{\alpha}{2})\frac{U_0(\alpha y)}{U_1(\alpha)} + (\frac{\beta}{R} + \frac{\alpha R}{2})\frac{W_0(\alpha y)}{U_1(\alpha)} \qquad (10.3.45)$$

We now consider $\Delta H = H_2 - H_1$, Ω, β_1, R and σ_{r_h} to be prescribed, and arrange the equations in order to calculate the various velocity components as well as the diffusion factor at stator hub and rotor tip, and the degree of reaction at hub and tip.

SUMMARY

Inputs: ΔH, Ω, α, β_1, R, σ_{r_h}, y

Outputs: $V_1(y)$, $V_2(y)$, $W_1(y)$, $W_2(y)$, $D_{STAT.,HUB}$, $D_{ROT.,TIP}$, ${}^{\circ}R_h$, ${}^{\circ}R_t$

Equations:

$$\beta_2 = \beta_1 + \frac{\Delta H}{\Omega} \tag{10.3.46}$$

$$\Psi = -(\beta + \frac{\alpha}{2}) \frac{yU_1(\alpha y)}{\alpha\, U_1(\alpha)} - (\frac{\beta}{R} + \frac{\alpha R}{2}) \frac{yW_1(\alpha y)}{\alpha\, U_1(\alpha)} + \frac{\beta}{\alpha} \tag{10.3.47}$$

$$W = (\beta + \frac{\alpha}{2}) \frac{U_o(\alpha y)}{U_1(\alpha)} + (\frac{\beta}{R} + \frac{\alpha R}{2}) \frac{W_o(\alpha y)}{U_1(\alpha)} \tag{10.3.48}$$

$$V = \frac{1}{y} [-\alpha\Psi + \beta] \tag{10.3.49}$$

(Note Eqs. (10.3.47 - 10.3.49) may be used for any value of y and stations 1 and 2 (with $\beta = \beta_1$ or β_2). It is convenient also to employ the relationships of Eq. (10.3.25) as well as the relationships (Ref. 10.5) .)

$$U_o(\alpha R) = -\frac{2}{\pi\alpha R}\,, \quad W_o(\alpha) = \frac{2}{\pi\alpha} \tag{10.3.50}$$

$$V_{iSTAT,HUB} = [W_{h_2}^2 + V_{h_2}^2]^{1/2} \tag{10.3.51}$$

$$V_{eSTAT,HUB} = [W_{h_1}^2 + V_{h_1}^2]^{1/2} \tag{10.3.52}$$

$$V_{iROT,TIP} = [W_{t_1}^2 + (\Omega R - V_{t_1})^2]^{1/2} \tag{10.3.53}$$

$$V_{eROT,TIP} = [W_{t_2}^2 + (\Omega R - V_{t_2})^2]^{1/2} \tag{10.3.54}$$

$$D = (1 - \frac{V_e}{V_i}) + \frac{\Delta H/\Omega}{2\sigma_{r_h} V_i} \tag{10.3.55}$$

(Note Eq. (10.3.55) may be used for both stator hub and rotor tip. The appropriate values for V_e and V_i follow from Eqs. (10.3.51 - 10.3.54). Note, also, it has again been assumed that the solidity is inversely proportional to the radius.)

$${}^{\circ}R_h = 1 + \frac{1}{2\Delta H} [V_{eSTAT,HUB}^2 - V_{iSTAT,HUB}^2] \tag{10.3.56}$$

$${}^{\circ}R_t = 1 + \frac{1}{2\Delta H} [W_{t_1}^2 + V_{t_1}^2 - W_{t_2}^2 - V_{t_2}^2] \tag{10.3.57}$$

As an example calculation, the case $\Delta H = 0.9$, $\Omega = 0.5$, $\alpha = 0.15$, $\beta_1 = -0.4$, $R = \sqrt{7}$, $\sigma_{r_h} = 2$ was considered. This case is closely comparable to the first case considered in Sec. (10.2.1). Thus, the geometry and "stage loading" considered are the same, and the tip swirl velocity at inlet to the rotor is very nearly the same (.0472) here, compared to .0378). This configuration then does not acquire an advantage because of increased relative velocity at the rotor tip (where Mach losses could be important). Straightforward calculation gives.

$$D_{STAT,HUB} = .689(.741) \quad {}^{\circ}R_h = -.352\ (-1)$$

$$D_{ROT,TIP} = .606(.558) \quad {}^{\circ}R_t = .803\ (.714)$$

The comparative values for the free vortex case are shown in parentheses. It can be seen that the introduction of a rather small amount of solid-body-like swirl has helped to reduce the stator hub diffusion factor substantially (even though the value is still rather large). Figure 10.3.4 shows the related equilibrium velocity profiles.

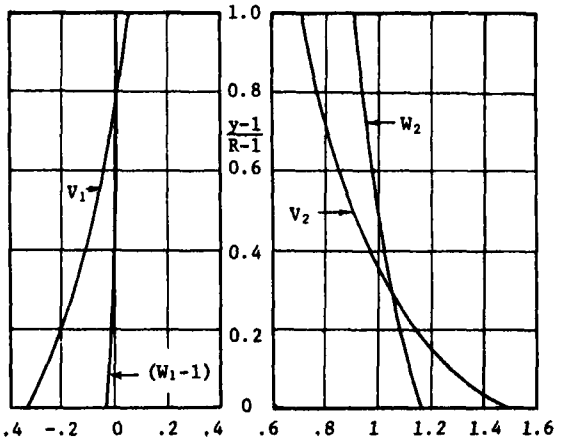

Figure 10.3.4 Radial Equilibrium Velocity Profiles

These results give a relatively quick estimate of the flow profiles to be expected between blade rows and may be utilized for simple approximate design calculations. The behavior of the through-flow flow field (which includes the axial variation of the fluid properties) will be investigated in Chapter 11.

10.4 THE EFFECTS OF COMPRESSIBILITY

In modern axial flow turbomachinery, the pressure ratios found across typical stages, particularly across turbine stages, are so large that the effects of variation in fluid density cannot be ignored. In order to consider such compressibility effects, we again consider the pseudo two-dimensional flow of a perfect gas across a blade row. The Euler equation, Eq. (10.1.5) relates the change in stagnation enthalpy across a rotor row to the blade angular velocity and change in fluid angular momentum. This change in stagnation enthalpy is, of course, the total change in stagnation enthalpy for the stage, so we may write from Eqs. (6.3.7), (6.5.4) and (10.1.5) with the stage efficiency written η_{c_j}, for the compressor and η_{t_j} for the turbine

$$\frac{p_{t_2}}{p_{t_1}} = [1 + \frac{\eta_{c_j}\omega}{h_{t_1}} \{(rv)_2 - (rv)_1\}]^{\frac{\gamma_c}{\gamma_c - 1}} \quad \text{(compressor)} \tag{10.4.1}$$

$$\frac{p_{t2}}{p_{t1}} = \left[1 - \frac{\omega}{\eta_{tj} h_{t_1}} \{(rv)_1 - (rv)_2\}\right]^{\frac{\gamma_t}{\gamma_t - 1}} \quad \text{(turbine)} \tag{10.4.2}$$

In these expressions, in each case conditions at 1 are those at entry to the rotor and conditions at 2 are those at exit from the rotor. Eq. (10.4.1) is different from the previously obtained Eq. (10.1.7) only in that the effect of the stage efficiency has been included. We may again introduce the upstream reference quantities denoted by a subscript o , and obtain in a similar manner to Sec. (10.1).

$$\frac{p_{t_2}}{p_{t_1}} = \left[1 + \frac{(\gamma_c - 1) M_o^2 \eta_{cj}}{1 + \frac{\gamma - 1}{2} M_o^2} \frac{\omega}{w_o^2} \{(rv)_2 - (rv)_1\}\right]^{\frac{\gamma_c}{\gamma_c - 1}} \quad \text{(compressor)} \tag{10.4.3}$$

$$\frac{p_{t_2}}{p_{t_1}} = \left[1 - \frac{(\gamma_t - 1) M_o^2}{\eta_{tj}(1 + \frac{\gamma_t - 1}{2} M_o^2)} \frac{\omega}{w_o^2} \{(rv)_1 - (rv)_2\}\right]^{\frac{\gamma_t}{\gamma_t - 1}} \quad \text{(turbine)} \tag{10.4.4}$$

Simple approximate forms follow from these equations for the case of small turning or small Mach number by simply expanding the bracketed terms to only the first term in their binomial expansions.

10.4.1 TURBINE AERODYNAMICS

The aerodynamic and engineering limitations of turbines are of a substantially different nature than those of compressors. Firstly, the extreme favorable pressure gradients allow very high blade loadings before the local adverse pressure gradients on the blades approach values leading to boundary layer separation. The expansion ratio can, in fact, be limited by choking of the downstream flow. The materials problem will clearly be aggravated as the blades are submerged in a high temperature corrosive environment. Modern blades are cooled, which in itself adds greatly to the complexity, both from the gas dynamic and stress point of view. (Chapter 19)

In turbines it is possible to be confronted with a design trade-off between mass flow capability and power output per stage. The mass flow per cross sectional area increases as the approach axial Mach number approaches unity, and the work interaction per mass increases as the nozzle outlet swirl velocity increases. It will be shown shortly that the maximum work interaction for a single stage occurs when the entire static pressure drop occurs across the stator, the function of the rotor then being to remove the kinetic energy identified with the swirl component of velocity with no further static pressure drop. There tends to be two restrictions on obtaining high swirl velocities. Thus, if the flow Mach number becomes too large severe shock losses can occur, and it also happens that a maximum possible swirl occurs because the flow will choke. This latter restriction is a function of the approach Mach number, and conflicts with the desired high mass flow capability.

To analyze the effect of this compressible limitation on the maximum attainable swirl, we consider the flow of a perfect fluid through a turbine nozzle row. (Fig. 10.4.1)

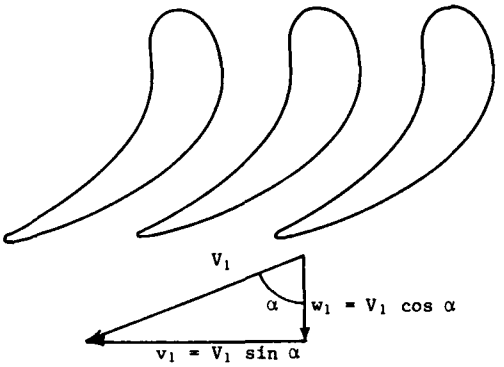

Figure 10.4.1 Turbine Nozzle Row

The approaching flow is assumed to be uniform and swirl free, and the cross-sectional areas at inlet and exit, respectively, are denoted A_o and A_1 . We then have

Continuity $$\rho_o w_o A_o = \rho_1 V_1 A_1 \cos \alpha \tag{10.4.5}$$

Isentropic $$\frac{\rho_1}{\rho_o} = \left(\frac{T_1}{T_o}\right)^{\frac{1}{\gamma - 1}} \tag{10.4.6}$$

Enthalpy $$T_o\left(1 + \frac{\gamma - 1}{2} M_o^2\right) = T_1\left(1 + \frac{\gamma - 1}{2} M_1^2\right) \tag{10.4.7}$$

These equations may be combined to give

$$\frac{M_1}{M_o} = \frac{V_1}{w_o} \sqrt{\frac{T_o}{T_1}} = \left(\frac{T_o}{T_1}\right)^{\frac{\gamma + 1}{2(\gamma - 1)}} \frac{A_o}{A_1} \frac{1}{\cos \alpha}$$

hence

$$\frac{M_1}{M_o} = \left[\frac{1 + \frac{\gamma - 1}{2} M_1^2}{1 + \frac{\gamma - 1}{2} M_o^2}\right]^{\frac{\gamma + 1}{2(\gamma - 1)}} \frac{A_o}{A_1} \frac{1}{\cos \alpha} \tag{10.4.8}$$

We wish to find the maximum value of the swirl velocity for a given approach Mach number, M_o . Thus noting

$$\left(\frac{V_1 \sin \alpha}{a_o}\right)^2 = \frac{T_1}{T_o} M_1^2 \left(1 - \cos^2 \alpha\right)$$

we find

$$\left(\frac{V_1 \sin \alpha}{a_o}\right)^2 = \frac{1 + \frac{\gamma - 1}{2} M_o^2}{1 + \frac{\gamma - 1}{2} M_1^2} M_1^2 - \left(\frac{1 + \frac{\gamma - 1}{2} M_1^2}{1 + \frac{\gamma - 1}{2} M_o^2}\right)^{2/(\gamma - 1)} M_o^2 \left(\frac{A_o}{A_1}\right)^2 \tag{10.4.9}$$

The derivative of this equation with respect to M_1^2 may now be taken and equated to zero. After some manipulation it follows that

$$M_o^2 \left(\frac{A_o}{A_1}\right)^2 \left[\frac{1 + \frac{\gamma-1}{2} M_1^2}{1 + \frac{\gamma-1}{2} M_o^2}\right]^{(\gamma+1)/(\gamma-1)} = 1 \qquad (10.4.10)$$

Equations (10.4.8) and (10.4.10) then give immediately that the maximum possible swirl occurs when

$$\cos \alpha = \frac{1}{M_1} \qquad \text{(max. swirl)} \qquad (10.4.11)$$

It is clear then that the maximum swirl occurs when the downstream axial Mach number is unity, or in other words, when the flow chokes. The maximum value of the swirl velocity follows from Eqs. (10.4.9) and (10.4.10) to give

$$\left(\frac{V_1 \sin \alpha}{a_o}\right)^2_{max} = \frac{2}{\gamma-1}\left[1 + \frac{\gamma-1}{2} M_o^2 - \frac{\gamma+1}{2}\left(M_o \frac{A_o}{A_1}\right)^{2(\gamma-1)/(\gamma+1)}\right] \qquad (10.4.12)$$

Figure 10.4.2 shows the dimensionless kinetic energy of the swirl component plotted versus incoming Mach number. ($A_o = A_1$, $\gamma = 1.4$)

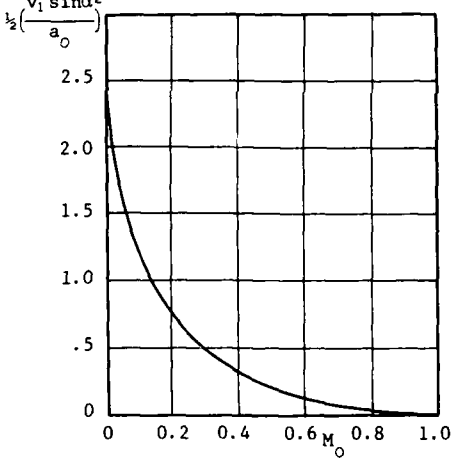

Figure 10.4.2 Maximum Swirl Kinetic Energy

The related stage pressure ratio identified with a nozzle row producing this maximum swirl may be estimated by noting that the work interaction per mass for the stage will be equal to the kinetic energy identified with the swirl. (Note that the rotor simply removes this kinetic energy with no further pressure drop.) Thus with

$$a_o^2 = \gamma R T_o = \frac{\gamma R}{C_p} \frac{T_o}{T_{to}} C_p T_{to} = \frac{\gamma-1}{1+\frac{\gamma-1}{2} M_o^2} h_{to} \qquad (10.4.13)$$

we have with Eq. (10.4.12)

$$(h_{to} - h_{t_2})_{max} = \frac{1}{2}(V_1 \sin \alpha)^2_{max} = h_{to}\left[1 - \frac{(\gamma+1)\left(M_o \frac{A_o}{A_1}\right)^{2(\gamma-1)/(\gamma+1)}}{2+(\gamma-1)M_o^2}\right]$$

hence

$$\left(\frac{h_{t_2}}{h_{to}}\right)_{to\,max} = \frac{(\gamma+1)\left(M_o \frac{A_o}{A_1}\right)^{2(\gamma-1)/(\gamma+1)}}{2+(\gamma-1)M_o^2} \qquad (10.4.14)$$

If the efficiency of the turbine stage, η_{t_j}, can be estimated, the related stage pressure ratio can be approximated by

$$\left(\frac{p_{t_2}}{p_{to}}\right)_{to\,max} = \left[1 - \frac{1}{\eta_{t_j}}\left(1 - \left(\frac{h_{t_2}}{h_{to}}\right)_{to\,max}\right)\right]^{\frac{\gamma}{\gamma-1}} \qquad (10.4.15)$$

Example results from the case $\frac{A_o}{A_1} = 1$, $\eta_{t_j} = 1$ and $\gamma = 1.3$ are shown in Fig. 10.4.3

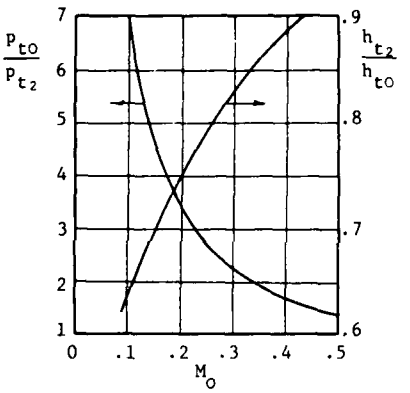

Figure 10.4.3 Stage Pressure Ratio Versus Axial Mach Number

It is apparent that the power extraction from the fluid will soon drive the axial Mach number to unity unless an axial area change is incorporated, and of course, turbines usually have increases in cross-sectional areas in the axial direction. A measure of the effectiveness of incorporating an axial area variation can be obtained by noting the increase in maximum swirl velocity attainable and decrease in enthalpy ratio identified with an axial area change. Thus, choosing $M_o = 0.5$ and $\gamma = 1.3$, the results of Fig. 10.4.4 are obtained from Eqs. (10.4.12) and (10.4.14).

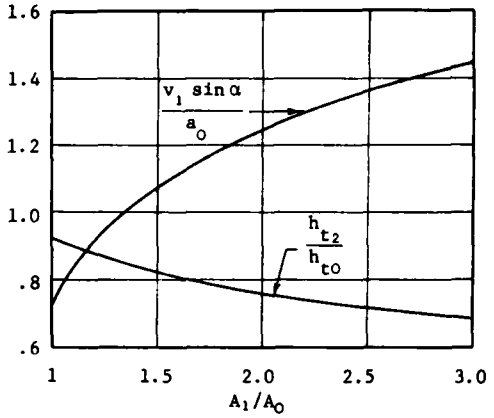

Figure 10.4.4 Enthalpy Ratio and Maximum Swirl Velocity Versus Area Ratio

10.4.2 THE IMPULSE TURBINE

An impulse turbine stage is defined as a turbine stage in which the entire static pressure drop occurs across the stator. Equivalently, of course, the impulse turbine stage is a stage with degree of reaction zero. Because no pressure drop occurs in the rotor, the relative velocity in the rotor will not change if the fluid is assumed perfect. A typical velocity diagram would hence be as indicated in Fig. 10.4.5

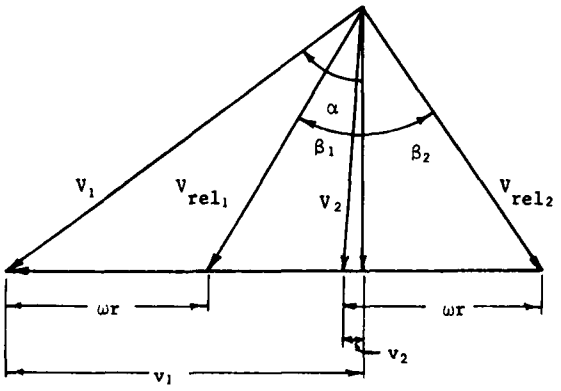

Figure 10.4.5 Velocity Diagram for an Impulse Turbine Stage

The Euler momentum equation gives

$$C_p(T_{t_1}-T_{t_2}) = \omega r(v_1-v_2)$$

It is apparent from Fig. 10.4.5, that for this case where the axial velocity has not changed across the rotor, that $\beta_1 = -\beta_2$ and hence

$$v_1 - \omega r = \omega r - v_2$$

and hence

$$C_p(T_{t_1}-T_{t_2}) = 2\omega r(v_1-\omega r) \qquad (10.4.16)$$

It is clear that the maximum work interaction per mass for the given pressure drop will occur when the rotor leaves no residual swirl ($v_2 = 0$). At this condition $v_1 = 2\omega r$, and we find from Eq. (10.4.16)

$$1 - \frac{T_{t_2}}{T_{t_1}} = \frac{2(\omega r)^2}{C_p T_{t_1}} \quad \text{max work impulse turbine} \qquad (10.4.17)$$

THE RELATIVE STAGNATION TEMPERATURE

The relative stagnation temperature, or that temperature that the gas would achieve if brought to rest adiabatically on the rotor, is of great importance because it determines what the heat transfer loading to the blade will be (Chapt. 19). Defining T_{t_r} as the relative stagnation temperature as seen by the rotor, we may write

$$C_p T_{t_r} = C_p T_1 + \frac{1}{2}[w_1^2+(v_1-\omega r)^2]$$

$$= C_p T_1 + \frac{1}{2}(w_1^2+v_1^2) + \frac{1}{2}[(v_1-\omega r)^2-v_1^2]$$

$$\text{hence} \quad \frac{T_{tr}}{T_{t_1}} = 1 - \frac{1}{2C_p T_{t_1}}[v_1^2-(v_1-\omega r)^2] \qquad (10.4.18)$$

In the max work impulse turbine case, $v_1 = 2\omega r$, so that

$$\frac{T_{tr}}{T_{t_1}} = 1 - \frac{3(\omega r)^2}{2C_p T_{t_1}} \quad \text{max work impulse turbine} \qquad (10.4.19)$$

Thus it can be seen that because the blades are retreating from the flow, the relative stagnation temperature is reduced. This effect can be quite significant, and allows the rotors to operate at higher stress levels than might at first be expected. For example, with $T_{t_1} = 1600$ K, $\omega r = 400$ m/sec, $C_p = 1250$ J/kg K it follows that $\frac{T_{tr}}{T_{t_1}} = 0.88$. Hence, the effective stagnation temperature is reduced 192 K because of the blade movement.

10.4.3 THE REACTION TURBINE

The reaction turbine stage is defined simply as a turbine stage in which the degree of reaction is other than zero. As an illustrative example we consider a stage for which the velocity triangles are those that would give °R = 0.5 if the flow was incompressible and perfect. It is to be noted that when losses are present and the Mach numbers are finite the static pressure behavior will not strictly correspond to °R = 0.5. As a further simplification we consider no change in axial velocity, and assume a symmetric diagram as illustrated in Fig. 10.4.6.

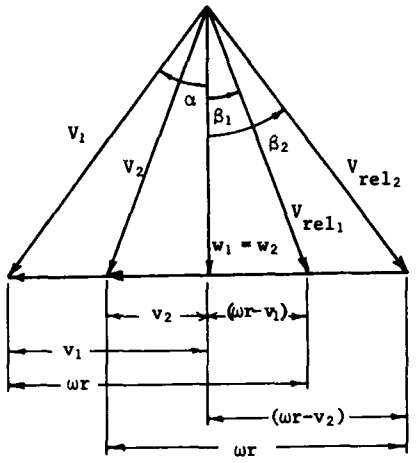

Figure 10.4.6 Velocity Diagram for a Reaction Turbine Stage

Because of the assumed symmetry of the velocity diagram, it follows that $v_2 = \omega r - v_1$, so that the Euler momentum equation becomes

$$C_p(T_{t_1}-T_{t_2}) = \omega r(v_1-v_2) = (\omega r)^2 \left(2\frac{v_1}{\omega r} - 1\right)$$

Again restricting our attention to the case where the maximum work interaction occurs, which as before corresponds to no residual swirl remaining in the flow, we note $v_1 = \omega r$, and hence

$$1 - \frac{T_{t_2}}{T_{t_1}} = \frac{(\omega r)^2}{C_p T_{t_1}} \quad \text{max work "50%" reaction turbine} \qquad (10.4.20)$$

Equation (10.4.18) is valid generally, and hence here reduces to

$$\frac{T_{tr}}{T_t} = 1 - \frac{(\omega r)^2}{2C_p T_{t_1}} \quad \text{max work "50%" reaction turbine} \qquad (10.4.21)$$

10.4.4 COMPARISON OF THE IMPULSE TURBINE AND "50%" REACTION TURBINE

It is of interest to note the comparison behavior of the impulse turbine and 50% reaction turbine. The behavior of important parameters is compared in Table 10.4.1.

It can be seen from the summary of Table 10.4.1 that for a given wheel speed, the impulse turbine has a larger work interaction and experiences a lower relative stagnation temperature on the rotor than does the 50% reaction turbine. (Note that the lower relative stagnation temperature could allow operation at a slightly higher wheel speed.) These advantages for the impulse turbine do not come without penalty however, as the stage efficiencies tend to be lower than those of the reaction turbines. This is because the Mach numbers (and hence frictional and shock losses) tend to be large in impulse turbines, and also the rotors operate without the benefit of an ambient favorable pressure gradient.

In practice, impulse turbines are often used in very high thrust to weight engines where their enormous work capability is of direct benefit in reducing the required number of stages and hence weight. In some cases, the first few stages of a turbine will have impulse blading so that the number of stages requiring cooling will be reduced. Transport aircraft, which require highly efficient engines, will usually have blading with thirty to fifty percent reaction.

10.5.1 REFERENCES

10.1 Horlock, J. H. and Lakshminarayana, B., "Secondary Flows," Ann. Rev. Fluid Mech., Vol. 5, 1973, pp. 247-279.

10.2 Hawthorne, W. R., "The Applicability of Secondary Flow Analysis to the Solution of Internal Flow Problems," in Fluid Mechanics of Internal Flow, Sovran, G., ed., Elsivier, Amsterdam, 1967, pp. 238-269.

10.3 Hawthorne, W. R., "Secondary Vorticity in Stratified Compressible Fluids in Rotating Systems," University of Cambridge, Department of Engineering, Report No. CUED/A-TURBO/TR63, 1974.

10.4 Johnsen, I. A. and Bullock, R. O., eds., "Aerodynamic Design of Axial Flow Compressors," Washington, U.S. NASA SP-36, 1965.

10.5 Gray, A. and Mathews, G. B., A Treatise on Bessel Functions and Their Applications to Physics, Dover, 1966.

Parameter	Item	Impulse	50% Reaction	Impulse	50% Reaction
$1 - \frac{T_{t_2}}{T_{t_1}}$	work interaction	$\frac{2(\omega r)^2}{C_p T_{t_1}}$	$\frac{(\omega r)^2}{C_p T_{t_1}}$	High	Low
$\frac{T_{tr}}{T_{t_2}} - 1$	increment in rotor temperature	$-\frac{3(\omega r)^2}{2C_p T_{t_1}}$	$-\frac{(\omega r)^2}{2C_p T_{t_1}}$	High	Low
	efficiency			Low	High

Table 10.4.1 Comparative Turbine Behavior

Chapter 11

THROUGHFLOW THEORY

Gordon C. Oates

University of Washington

TABLE OF CONTENTS

CHAPTER 11 THROUGHFLOW THEORY

		Page
11.0	Introduction	11-1
11.1	The Throughflow Equations	11-1
11.1.1	The Conservation Equations	11-1
11.1.2	The Convective Derivative	11-1
11.1.3	The Equation for the Tangential Momentum	11-1
11.1.4	The Euler Turbine Equation	11-2
11.1.5	The Compressible Form of the Stream Function	11-2
11.1.6	The Natural Coordinate System	11-2
11.1.7	Equation for the Tangential Vorticity	11-3
11.2	The Actuator Disc	11-4
11.3	Integral Relationships	11-4
11.4	Example Solutions	11-6
11.4.1	Solution of the Homogeneous Equation - the Natural Eigenfunctions	11-6
11.4.2	Solution of the Inhomogeneous Form of the Equation	11-7
11.4.3	The Radial Equilibrium Limit of the Solutions	11-8
11.4.4	Expressions for the Axial Force and Torque	11-9
11.4.5	Solution for a Single Row	11-9
11.5	Advanced Problems in Throughflow Theory	11-11
11.5.1	Effects of Compressibility	11-11

LIST OF FIGURES

		Page
Figure 11.1.1	*Pressure Stress on Stream-surfaces*	11-2
Figure 11.1.2	Throughflow Coordinate Systems	11-3
Figure 11.3.1	Axial Forces	11-5
Figure 11.4.1	Axial Velocity Profiles	11-11
Figure 11.4.2	Tangential Velocity Profiles	11-11

CHAPTER 11

LIST OF SYMBOLS

The symbols are listed in alphabetical order, first in the English alphabet, then in the Greek alphabet. Subscripts and superscripts are then given. The equation, figure or section in which the symbols are first introduced is indicated in parentheses. Often the symbol will be defined in the text just preceding or just following the equation or figure.

Where appropriate, the location of the introduction of the symbol is referred to in previous chapters.

A_n - Constants defined by Eq. 11.4.29

B_n - Constants defined by Eq. 11.4.31

C_p - Specific heat at constant pressure (Sect. 2.6)

E - Group of Bessel functions (Eq. 11.4.12)

E_{in} - Orthonormal group of Bessel functions of order one Eq. (11.4.23)

E_{on} - Orthonormal group of Bessel functions of order zero (Eq. 11.4.26)

$\bar{e}_r, \bar{e}_\theta, \bar{e}_z$ - Unit vectors in cylindrical co-ordinate directions (Eq. 11.1.8)

$\bar{F}$ - Vector body force (Eq. 11.1.2)

f - Component of $\bar{F}$ (Eq. 11.1.9)

H - Dimensionless enthalpy (Eq. 11.4.11)

h - Enthalpy (Eq. 11.1.3)

J_p - Bessel function of the first kind, of order p (Eq. 11.4.11)

M - Group defined by Eq. 11.3.9

$\dot{m}$ - Mass flow rate (Eq. 11.1.16)

$\bar{n}, \bar{e}_\theta, \bar{e}_\ell$ - Unit vectors in natural co-ordinate system (Fig. 11.1.2)

p - Pressure (Eq. 11.1.2)

R - Tip to hub ratio (Eq. 11.4.1)

- Gas constant (Sect. 2.12)

r, θ, z - Co-ordinates in cylindrical co-ordinate system (Eq. 11.1.5)

s - Entropy (Eq. 11.1.3)

T - Temperature (Eq. 11.1.3)

$T_n^{(i)}$ - Function defined by Eq. 11.4.34

t - Time (Eq. 11.1.1)

$\bar{u}$ - Vector velocity (Eq. 11.1.1)

U, V, W - Dimensionless velocity components (Eq. 11.4.1)

u, v, w - Velocity components (Eq. 11.1.5)

Y_p - Bessel function of the second kind, of order p (Eq. 11.4.11)

y, x - Dimensionless co-ordinates (Eq. 11.4.1)

α - Constant defined in Eq. 11.4.5

β - Constant defined in Eq. 11.4.5

γ - Ratio of specific heats (Sect. 2.6)

ϵ - Small distance (Eq. 11.2.4)

θ - Constant defined in Eq. 11.4.5

λ_n - Eigenvalue (Eq. 11.4.13)

ξ, η, ζ - Components of the vorticity (Eq. 11.1.26)

ρ - Density (Eq. 11.1.1)

τ - Torque (Eq. 11.3.1)

Φ - Transformed streamfunction (Eq. 11.4.27)

Ψ - Dimensionless streamfunction (Eq. 11.4.1)

ψ - Streamfunction (Eq. 11.1.15)

Ω - Dimensionless angular velocity (Eq. 11.4.6)

ω - Constant defined in Eq. 11.4.5

- Angular velocity (Eq. 11.1.13)

$\bar{\omega}$ - Vector vorticity (Eq. 11.1.26)

Subscripts

A - Axial (Eq. 11.3.7)

d - Conditions at (or across) the actuator disc (Eq. 11.2.2)

h - Hub (Eq. 11.3.2)

i - Region of flow (Fig. 11.4.1)

j - Number of actuator disc (Fig. 11.4.1)

ℓ - Meridional direction (Eq. 11.1.17)

N - Total number of actuator dics (Fig. 11.4.1)

r, θ, z - Component in given direction (Eq. 11.1.3)

t - Stagnation quantity (Sect. 2.16)

- Tip (Eq. 11.3.2)

o - Reference quantity (Eq. 11.1.15)

CHAPTER 11

THROUGHFLOW THEORY

11.0 INTRODUCTION

In an early paper (Ref. 11.1) Wu formulated the basic concept of representing the inviscid three-dimensional flow field as the sum of two separate two-dimensional flowfields. These two separate flow fields were composed of surfaces located in the blade to blade direction (s_1 surfaces) and surfaces lying in the hub to tip direction (s_2 surfaces). The solution to the flowfield composed of these combined two-dimensional fields would formally require an iterative solution, since the solution for either surface requires the knowledge of the shape of the other surface.

In practice (Refs. 11.2, 11.3, 11.4) the problem is simplified by taking appropriate averages for the blade to blade direction, and then assuming the flow to be axisymmetric. In this way, the s_2 planes become meridional surfaces and the expressions for the derivatives along, and normal to such surfaces are easily represented in terms of the derivatives in the radial and axial directions.

When the complete throughflow equations are considered, the variations of the fluid properties in the axial direction are included. It is to be expected then that the radial equilibrium solutions obtained in Chapter 10 will again appear as the asymptotic limits of the far upstream and far downstream flows.

The equations will be formulated in a manner that allows the inclusion of compressibility and entropy variation effects. However, the solution of the resulting rather general equation must rely upon the application of advanced computer techniques which cannot reasonably be reported in detail in this document because of space limitations. Sec. 11.6 briefly describes some of the various calculational methods available and provides references for further reading.

11.1 THE THROUGHFLOW EQUATIONS

In the following we develop equations appropriate for the description of the (axisymmetric) throughflow. The viscous stresses in the fluid will not be included explicitly, but a general "body force", $\bar{F}$, (see list of symbols, page 11-ii) will be included. It is possible to utilize this general body force to artifically introduce the effects of viscosity (Ref. 11.2), but in any case we will be primarily considering the flowfield external to the blade rows, and it is consistent with throughflow theory to consider the viscous effects to be negligible in this region. The effects of viscous stresses within the blade row will appear implicitly in the variation of entropy in the direction normal to the streamsurfaces, and also in the effective body force of the related blade forces. (Sects. 11.2 and 11.3)

11.1.1 THE CONSERVATION EQUATIONS

When vector notation is utilized the continuity, momentum and Gibb's equations may be written

$$\frac{\partial \rho}{\partial t} + \nabla\cdot(\rho\bar{u}) = 0 \qquad (11.1.1)$$

$$\frac{D\bar{u}}{Dt} = \bar{F} - \frac{1}{\rho}\nabla p \qquad (11.1.2)$$

$$\nabla h - \frac{1}{\rho}\nabla p = T\nabla s \qquad (11.1.3)$$

also

$$\frac{Dh}{Dt} - \frac{1}{\rho}\frac{Dp}{Dt} = T\frac{Ds}{Dt} \qquad (11.1.4)$$

11.1.2 THE CONVECTIVE DERIVATIVE

The convective derivative, represented by the operator $(\bar{u}\cdot\nabla)$, may be expanded as

$$(\bar{u}\cdot\nabla) = u\frac{\partial}{\partial r} + \frac{v}{r}\frac{\partial}{\partial\theta} + w\frac{\partial}{\partial z} \qquad (11.1.5)$$

It is important here to retain the partial derivative with respect to θ, because even though the fluid properties have no θ variation (because of the assumption of axial symmetry), the coordinate directions themselves change with θ. Thus we note in particular

$$\frac{\partial\bar{e}_r}{\partial\theta} = \bar{e}_\theta \qquad (11.1.6)$$

$$\frac{\partial\bar{e}_\theta}{\partial\theta} = -\bar{e}_r \qquad (11.1.7)$$

Utilizing equations 11.1.5 - 11.1.7, the convective derivative of the velocity vector may be expanded into the components:

$$(\bar{u}\cdot\nabla)\bar{u} = \{(\bar{u}\cdot\nabla)u - \frac{v^2}{r}\}\bar{e}_r + \{\frac{1}{r}(\bar{u}\cdot\nabla)(rv)\}\bar{e}_\theta + \{(\bar{u}\cdot\nabla)w\}\bar{e}_z \qquad (11.1.8)$$

11.1.3 THE EQUATION FOR THE TANGENTIAL MOMENTUM

The equation for the tangential momentum follows immediately by taking the scalar product of Eq. (11.1.2) with $\bar{e}_\theta$, and utilizing Eq. (11.1.8) to give

$$\frac{Drv}{Dt} = r\{f_\theta - \frac{1}{\rho}\frac{1}{r}\frac{\partial p}{\partial\theta}\} \qquad (11.1.9)$$

It is to be noted that the tangential body force existing in this expression may include a viscous as well as non-viscous term. The equation may be interpreted to explain the mechanism by which angular momentum is introduced into the flow. Thus, if we consider perfect flow through an actual blade row, no body forces exist, and the angular momentum is imparted by the pressure forces of the blade row. Clearly, if the contribution of such pressure forces to a control volume between repetitive streamlines of a cascade, external to the cascade is considered (Fig. 11.1.1, Case A) the streamsurfaces cannot support a pressure change, and the (net) angular momentum cannot change. Once within the blade row, however, the blade surfaces

can support the pressure change, and the angular monetum changes. (Fig. 11.1.1, Case B)

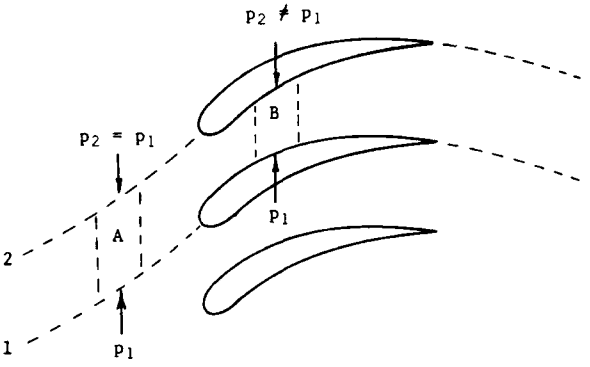

Figure 11.1.1 Pressure Stresses on Streamsurfaces

It can be noted here, that the formal mechanism for obtaining the throughflow form of the equations is to replace the term

$$\frac{1}{\rho}\frac{1}{r}\frac{\partial p}{\partial \theta}$$

in Eq. (11.1.9) by an equivalent (artificial) body force f_θ. In this way the θ dependence of the properties is removed. The relationship between this artificial body force and the torque and forces existing on the blade is further developed in Sec. 11.3.

11.1.4 THE EULER TURBINE EQUATION

The vector form of the Euler turbine equation (see also Sec. 10.1.1) may be obtained directly by taking the scalar product of Eq. (11.1.2) with $\bar{u}$ and adding the result to Eq. (11.1.4), to give

$$\frac{Dh_t}{Dt} = \frac{1}{\rho}\frac{\partial p}{\partial t} + \bar{u}\cdot\bar{F} + T\frac{Ds}{Dt} \qquad (11.1.10)$$

The velocity may be written as the sum of the velocity relative to the blade, $\bar{u}_{rel}$, and the blade velocity, $\omega r \bar{e}_\theta$ to give

$$\bar{u}\cdot\bar{F} = (\bar{u}_{rel} + \omega r\,\bar{e}_\theta)\cdot\bar{F} = \bar{u}_{rel}\cdot\bar{F} + \omega r f_\theta \qquad (11.1.11)$$

Combination of Eqs. (11.1.9), (11.1.10), and (11.1.11) then gives:

$$\frac{Dh_t}{Dt} = \frac{1}{\rho}\left\{\frac{\partial p}{\partial t} + \omega r\left(\frac{1}{r}\frac{\partial p}{\partial \theta}\right)\right\} + \left\{\bar{u}_{rel}\cdot\bar{F} + T\frac{Ds}{Dt}\right\} + \omega\frac{Drv}{Dt} \qquad (11.1.12)$$

It can be noted that the expression within the first pair of brackets represents the pressure perturbation as viewed by an observer fixed to the rotating blade. Under normal circumstances where the pressure perturbations are created by the blades themselves, this group of terms is zero.

When considering the terms in the second pair of brackets we note that because the body force term is identified with the blade forces, the product $\bar{u}_{rel}\cdot\bar{F}$ represents the effect of the frictional forces alone. (Note that if there was no frictional stress, $\bar{F}$ would be perpendicular to the relative velocity giving $\bar{u}_{rel}\cdot\bar{F} = 0$.) The term $\bar{u}_{rel}\cdot\bar{F}$ is hence the sole source of entropy generation, so we note as with Eq. (2.15.6), that the terms in the second pair of brackets also cancel. There is thus obtained the vector form of the Euler turbine equation:

$$\frac{Dh_t}{Dt} = \omega\frac{Drv}{Dt} \qquad (11.1.13)$$

11.1.5 THE COMPRESSIBLE FORM OF THE STREAM FUNCTION

When the throughflow limit of the equations is taken, the replacement of the group

$$\frac{1}{\rho}\frac{1}{r}\frac{\partial p}{\partial \theta}$$

by an equivalent body force allows consideration of not only the axisymmetric form of the equations, but in addition, the time dependent terms do not contribute. Thus the continuity equation may be written

$$\frac{1}{r}\frac{\partial(\rho r u)}{\partial r} + \frac{\partial(\rho w)}{\partial z} = 0 \qquad (11.1.14)$$

This equation is identically satisfied if we introduce the compressible form of the streamfunction, ψ, defined by

$$\rho u = \rho_o\frac{1}{r}\frac{\partial \psi}{\partial z}\ , \quad \rho w = -\rho_o\frac{1}{r}\frac{\partial \psi}{\partial r} \qquad (11.1.15)$$

In these expressions ρ_o is a suitable reference density. It follows, just as in the development of Sec. 10.3.1 for the incompressible form of the streamfunction, that the mass flow rate between two streamsurfaces, $\dot{m}$, is related to the streamfunction by

$$\dot{m} = -2\pi\rho_o(\psi_2 - \psi_1) \qquad (11.1.16)$$

11.1.6 THE NATURAL COORDINATE SYSTEM

The streamtube surfaces form natural coordinates for throughflow studies, and lead to the introduction of a coordinate system with directions $\bar{n}$ (normal to streamtube surfaces), $\bar{e}_\ell$ (meridional component) and $\bar{e}_\theta$ (tangential). This coordinate system is depicted in Fig. 11.1.2.

The velocity vector in the natural coordinate system has components given by

$$\bar{u} = (0\ ,\ v\ ,\ v_\ell) \qquad (11.1.17)$$

AD-A152 757 COST REDUCTION IN VERTICALLY RELATED INDUSTRIES: 4/9
INTEGRATION VERSUS NONLINEAR PRICING(U) RAND CORP SANTA
MONICA CA H C QUIRMBACH MAY 83 RAND/P-6839

UNCLASSIFIED F/G 5/1 NL

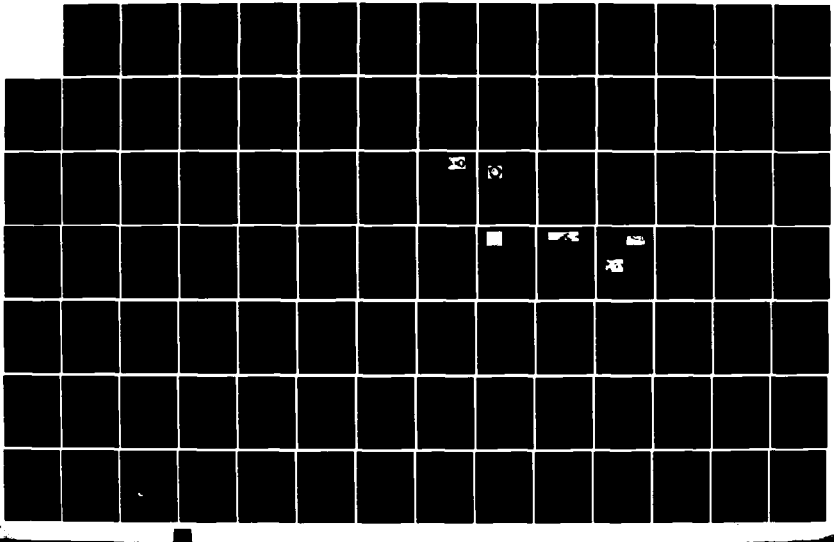

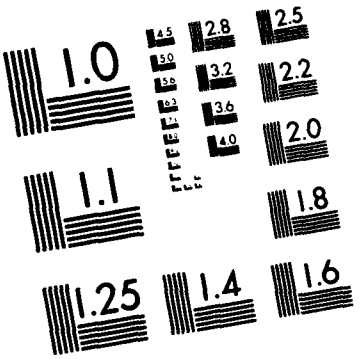

MICROCOPY RESOLUTION TEST CHART
NATIONAL BUREAU OF STANDARDS-1963-A

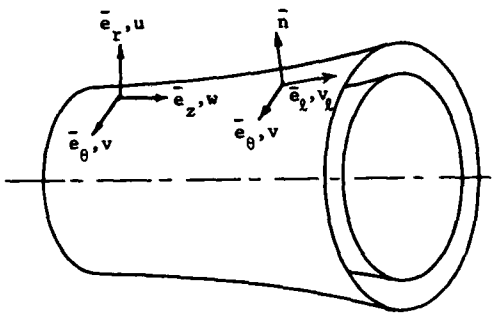

Figure 11.1.2 Throughflow Coordinate Systems

The meridional velocity, v_ℓ, is related to the cylindrical velocity components by

$$v_\ell^2 = u^2 + w^2 \tag{11.1.18}$$

and the unit vectors are given in terms of the cylindrical coordinate quantities by

$$\bar{e}_\ell = \frac{1}{v_\ell}(u\bar{e}_r + w\bar{e}_z) \tag{11.1.19}$$

$$\bar{n} = \bar{e}_\theta \times \bar{e}_\ell = \frac{1}{v_\ell}(\bar{e}_\theta \times \bar{u}) \tag{11.1.20}$$

The scalar magnitude of the differential difference dn occurring for a differential displacement $d\bar{r}$ is given by

$$dn = \bar{n}\cdot d\bar{r} = \frac{w}{v_\ell}dr - \frac{u}{v_\ell}dz \tag{11.1.21}$$

This may be related to the corresponding change in the streamfunction by utilizing Eqs. (11.1.15) to give

$$dn = -\frac{1}{rv_\ell}\frac{\rho_o}{\rho}\left\{\frac{\partial\psi}{\partial r}dr + \frac{\partial\psi}{\partial z}dz\right\} = -\frac{1}{rv_\ell}\frac{\rho_o}{\rho}d\psi \tag{11.1.22}$$

The unit derivative in the direction normal to the streamsurfaces, $(\bar{n}\cdot\nabla)$, is thus given in terms of the streamfunction as

$$(\bar{n}\cdot\nabla) \equiv \frac{\partial}{\partial n} = \frac{\partial\psi}{\partial n}\frac{\partial}{\partial\psi} = -\frac{\rho r v_\ell}{\rho_o}\frac{\partial}{\partial\psi} \tag{11.1.23}$$

This same derivative in cylindrical coordinates follows directly from Eq. (11.1.20) and the definition of the operator ∇ (in cylindrical coordinates) to give

$$(\bar{n}\cdot\nabla) = \frac{1}{v_\ell}(\bar{e}_\theta \times \bar{u})\cdot\left(\bar{e}_r\frac{\partial}{\partial r} + \bar{e}_\theta\frac{1}{r}\frac{\partial}{\partial\theta} + \bar{e}_z\frac{\partial}{\partial z}\right)$$

or $$(\bar{n}\cdot\nabla) = \frac{w}{v_\ell}\frac{\partial}{\partial r} - \frac{u}{v_\ell}\frac{\partial}{\partial z} \tag{11.1.24}$$

11.1.7 EQUATION FOR THE TANGENTIAL VORTICITY

The Euler momentum equation and the conservation of angular momentum equation describe the behavior of the angular momentum and stagnation enthalpy along stream surfaces. It can be expected that the essence of the two dimensional problem lies in the variation of properties across stream surfaces, so to this end we investigate the rate of change of properties normal to stream surfaces.

The steady state form of the momentum equation (Eq. 11.1.2) may be added to Eq. (11.1.3) to give

$$\nabla h_t + \bar{\omega}\times\bar{u} = T\nabla s + \bar{F} \tag{11.1.25}$$

In obtaining this expression the vector identity

$$(\bar{u}\cdot\nabla)\bar{u} = \nabla\frac{\bar{u}^2}{2} + \bar{\omega}\times\bar{u}$$

has been utilized. This in turn introduces the vorticity $\bar{\omega}$, defined by

$$\bar{\omega} = \xi\bar{e}_r + \eta\bar{e}_\theta + \zeta\bar{e}_z \equiv \nabla\times\bar{u} \tag{11.1.26}$$

Utilizing Eq. (11.1.20) it follows from vector expansion that

$$\bar{n}\cdot(\bar{\omega}\times\bar{u}) = \frac{1}{v_\ell}\{(\bar{e}_\theta\cdot\bar{\omega})(\bar{u}\cdot\bar{u}) - (\bar{e}_\theta\cdot\bar{u})(\bar{u}\cdot\bar{\omega})\}$$

Thus expanding the vorticity into its components there is obtained

$$\bar{n}\cdot(\bar{\omega}\times\bar{u}) = \eta v_\ell - \frac{v}{r}(\bar{n}\cdot\nabla)(rv) \tag{11.1.27}$$

An equation for the tangential vorticity, η, follows by taking the scalar product of Eq. (11.1.25) with $\bar{n}$, and utilizing Eq. (11.1.27). Thus

$$\eta = \frac{1}{v_\ell}\left[\bar{n}\cdot\bar{F} - (\bar{n}\cdot\nabla)h_t + T(\bar{n}\cdot\nabla)s + \frac{v}{r}(n\cdot\nabla)rv\right] \tag{11.1.28}$$

This expression may be written as an equation for the streamfunction ψ, density ratio ρ/ρ_o and prescribed variables (h_t, s, rv, $\bar{F}$) by utilizing

$$\eta = \frac{\partial u}{\partial z} - \frac{\partial w}{\partial r}$$

and Eqs. (11.1.15) and (11.1.23) to give

$$\frac{\partial}{\partial z}\left(\frac{\rho_o}{\rho}\frac{1}{r}\frac{\partial\psi}{\partial z}\right) + \frac{\partial}{\partial r}\left(\frac{\rho_o}{\rho}\frac{1}{r}\frac{\partial\psi}{\partial r}\right) =$$

$$\frac{1}{v_\ell}\bar{n}\cdot\bar{F} + \frac{\rho}{\rho_o}r\left[\frac{\partial h_t}{\partial\psi} - T\frac{\partial s}{\partial\psi} - \frac{v}{r}\frac{\partial rv}{\partial\psi}\right] \tag{11.1.29}$$

The density ratio follows from Eq. (2.14.10) and the perfect gas equation of state to give

$$\frac{\rho}{\rho_o} = \left(\frac{T}{T_o}\right)^{\frac{1}{\gamma-1}} e^{-\frac{s-s_o}{R}} = \left[\frac{h_t - \frac{1}{2}(w^2+u^2+v^2)}{h_{to} - \frac{1}{2}(w^2+u^2+v^2)_o}\right]^{\frac{1}{\gamma-1}} e^{-\frac{s-s_o}{R}}$$

Utilizing Eq. (11.1.15) this expression may be rearranged to give

$$\left(\frac{\rho_o}{\rho}\right)^2 \frac{1}{2}\left[\left(\frac{1}{r}\frac{\partial\psi}{\partial r}\right)^2 + \left(\frac{1}{r}\frac{\partial\psi}{\partial z}\right)^2\right]$$

$$+ \left(\frac{\rho}{\rho_o}\right)^{\gamma-1}\left[h_{to} - \frac{1}{2}(w^2+u^2+v^2)_o\right] e^{\frac{\gamma}{c_p}(s-s_o)}$$

$$- \left[h_t - \frac{1}{2r^2}(rv)^2\right] = 0 \qquad (11.1.30)$$

Equations (11.1.29) and (11.1.30) constitute two coupled, highly nonlinear, equations for the streamfunction in terms of the reference (o) conditions and the prescribed quantities $\overline{F}$, h_t, s, rv .

11.2 THE ACTUATOR DISC

The presence of the body force term, $\overline{F}$, in Eq. (11.1.29) complicates the solution for the throughflow considerably. A useful approximate solution can be obtained by considering all the forces to be concentrated in an infinitesimally thin disc, the actuator disc. The forces are chosen to have the same integral effect upon the tangential momentum, stagnation enthalpy and entropy as would the axially distributed forces of the actual blade rows. (Sec. 11.3) The result is then that the body forces themselves do not appear in the resulting equations, but the effects of the blade forces appear as matching conditions across the (infinitely thin) blade row. The approximation can be made as accurate as desired by taking a number of actuator discs to simulate a single blade row.

The equation for the streamfunction, Eq. (11.1.29), thus reduces to

$$\frac{\partial}{\partial z}\left(\frac{\rho_o}{\rho}\frac{1}{r}\frac{\partial\psi}{\partial z}\right) + \frac{\partial}{\partial r}\left(\frac{\rho_o}{\rho}\frac{1}{r}\frac{\partial\psi}{\partial r}\right) =$$

$$\frac{\rho}{\rho_o} r\left[\frac{\partial h_t}{\partial\psi} - T\frac{\partial s}{\partial\psi} - \frac{v}{r}\frac{\partial rv}{\partial\psi}\right] \qquad (11.2.1)$$

THE MATCHING CONDITIONS

Because in the actuator disc approximation the blade row is taken to be infinitely thin, the continuity of mass ensures that the value of the streamfunction on one side of the disc is identical to that at the same radial location on the other side of the disc. This simple relationship may be written

$$\left[\psi\right]_d = 0 \qquad (11.2.2)$$

where the notation $[\ ]$ refers to the jump in the value of the quantity, and the subscript d refers to conditions at the disc.

A second matching condition may be obtained by considering the radial momentum equation. Thus, noting that by the assumption of axisymmetry no θ derivatives of fluid properties are present, and combining Eqs. (11.1.2) and (11.1.8), there is obtained

$$\rho u\frac{\partial u}{\partial r} + \rho w\frac{\partial u}{\partial z} - \rho\frac{v^2}{r} + \frac{\partial p}{\partial r} = \rho f_r \qquad (11.2.3)$$

This equation is now integrated from an infinitesimal distance, ε , upstream of the disc to an infinitesimal distance downstream of the disc. It is to be noted that no terms on the left side of the equation can become infinite except, possibly, those involving an axial derivative. Thus, integration over the infinitesimal distance (noting ρw is constant) gives

$$\int_{-\varepsilon}^{\varepsilon}\frac{\partial u}{\partial z}dz \equiv \left[u\right]_d = \frac{1}{\rho w}\int_{-\varepsilon}^{\varepsilon}\rho f_r dz$$

Utilizing Eq. (11.1.15) there is then obtained

$$\left[\frac{\rho_o}{\rho}\frac{1}{r}\frac{\partial\psi}{\partial z}\right]_d = \frac{1}{\rho w}\int_{-\varepsilon}^{\varepsilon}\rho f_r dz \qquad (11.2.4)$$

The integral on the right side represents the effect of the total radial force of the blade row at the given radius of the actuator disc. In many applications the radial force of the almost radial blades is very small, and Eq. (11.2.4) is often approximated by

$$\left[\frac{1}{\rho}\frac{\partial\psi}{\partial z}\right]_d = 0 \qquad (11.2.5)$$

Equations (11.1.30), (11.2.1), (11.2.2), and (11.2.5) together with the boundary conditions that the stream function is prescribed on the containing walls (or that the pressure be constant on the bounding streamline in the case of a free streamline) constitutes the mathematical statement of the problem. In Sec. 11.4 an example solution for incompressible flow will be presented, and methods for calculating compressibility effects will be described in Sec. 11.5 . Before proceeding to the calculational examples, however, we first consider the relationships of the overall torque applied to the blade row and the overall axial force on the blade row, to the resulting changes in fluid properties.

11.3 INTEGRAL RELATIONSHIPS

An equation for the tangential momentum was developed in Sec. 11.1.3, and the equivalence of the body force field utilized in the throughflow approximation, and the pressure field existing on the actual blade surfaces was discussed. The relationship between the equivalent force field and the torque on the blade (taken about the axis) may be determined by noting that the differential contribution to the torque of an annular volume $2\pi r\,dr\,dz$ is given by:

$$d\tau = 2\pi\rho f_\theta r^2\,dr\,dz \qquad (11.3.1)$$

The torque upon the entire blade row is then obtained by integrating from the blade leading edge to trailing edge (z_1 to z_2) , and from the hub radius to tip radius (r_h to r_t) . Hence:

$$\tau_{1-2} = 2\pi \int_{z_1}^{z_2} \int_{r_h}^{r_t} \rho\, r^2\, f_\theta \, dr\, dz \qquad (11.3.2)$$

The throughflow form of the tangential momentum equation, Eq. (11.1.9) gives

$$rf_\theta = u \frac{\partial rv}{\partial r} + w \frac{\partial rv}{\partial z} \qquad (11.3.3)$$

By adding rv times the continuity equation (Eq. 11.1.14) to this expression, there is obtained

$$\rho r f_\theta = \frac{1}{r} \{ \frac{\partial (\rho u r)(rv)}{\partial r} + \frac{\partial (\rho r w)(rv)}{\partial z} \} \qquad (11.3.4)$$

When Eq. (11.3.4) is substituted into Eq. (11.3.2), the resulting expression may be integrated immediately to give with Eq. (11.1.15)

$$\tau_{1-2} = 2\pi\rho_o \int_{\psi(z_1)}^{\psi(z_2)} [(rv)_t - (rv)_h] d\psi$$

$$- 2\pi\rho_o \int_{\psi_h}^{\psi_t} [(rv)_{z_2} - (rv)_{z_1}] d\psi$$

In this expression the first integral vanishes, because the value of the streamfunction does not change along the hub or tip (i.e., $d\psi = 0$ on r_t or r_h). There is hence obtained a relationship that is itself obvious from first principles when the relationship between the streamfunction and the mass flow (Eq. 11.1.16) is recognized. Thus

$$\tau_{1-2} = -2\pi\rho_o \int_{\psi_h}^{\psi_t} [(rv)_{z_2} - (rv)_{z_1}] d\psi \qquad (11.3.5)$$

Then noting from Eq. (11.1.16) that $-2\pi\rho_o\, d\psi = d\dot{m}$, we have

$$\tau_{1-2} = \int_{hub}^{tip} [(rv)_{z_2} - (rv)_{z_1}] d\dot{m} \qquad (11.3.6)$$

When the desired angular momentum distribution with streamfunction is prescribed, the resulting torque on the blade row can be immediately determined from Eq. (11.3.5). It is to be noted that there is no need to obtain any of the detailed flow information through the blade row. The overall torque depends only upon the overall change in angular momentum through the blade row.

AXIAL FORCE IMPARTED TO THE BLADE ROW

The axial force on the blade row and containing annulus walls may be obtained by considering the control volume shown in Fig. 11.3.1 .

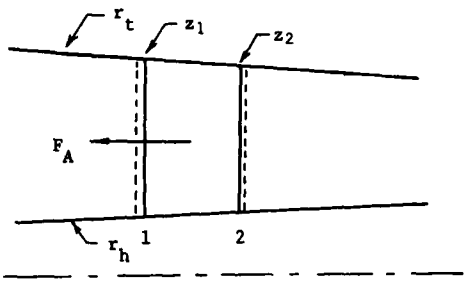

Figure 11.3.1 Axial Forces

Equating the rate of production of momentum to the force applied to the fluid, it follows that the upstream directed force on the blade row and annulus wall, F_A , is given by:

$$F_A = \{ \int_{r_h}^{r_t} (P + \rho w^2) 2\pi r dr \}_2 - \{ \int_{r_h}^{r_t} (P + \rho w^2) 2\pi r dr \}_1 \qquad (11.3.7)$$

When the actuator disc limit is considered, F_A becomes the force on the blade row alone. It is convenient to write this expression in the form

$$F_A = 2\pi\rho_o \left[M \right] \qquad (11.3.8)$$

where M is defined by

$$M = \int_{r_h}^{r_t} (\frac{p}{\rho_o} + \frac{\rho}{\rho_o} w^2) r dr \qquad (11.3.9)$$

It is clear from the way M has been defined that M will be constant with axial position if the walls are parallel and no blades are present. (Recall that the flow was assumed to be nonviscous outside the blade rows.) The quantity M is most easily evaluated by considering the radial equilibrium form of the solutions, which we may do because M would stay constant in a parallel walled annulus until all radial flows vanished. The expression for M can be manipulated in the following manner (noting $u = 0$ in radial equilibrium)

$$M = \int_{r_h}^{r_t} [\frac{p}{\rho_o} + \frac{1}{2}\frac{\rho}{\rho_o} \bar{u}^2 - \frac{1}{2}\frac{\rho}{\rho_o} (v^2 - w^2)] r dr$$

$$= \int_{r_h}^{r_t} [r(\frac{p}{\rho_o} + \frac{1}{2}\frac{\rho}{\rho_o} \bar{u}^2) - \frac{\rho}{\rho_o}\frac{(rv)^2}{2r}$$

$$+ \frac{1}{2r}\frac{\rho_o}{\rho} (\frac{\partial \psi}{\partial r})^2] dr \qquad (11.3.10)$$

Noting

$$\frac{d}{dr} \{ \frac{\rho_o}{\rho} \frac{\psi}{r} \frac{d\psi}{dr} \} = \psi \frac{d}{dr} \{ \frac{\rho_o}{\rho} \frac{1}{r} \frac{d\psi}{dr} \} + \frac{\rho_o}{\rho} \frac{1}{r} (\frac{d\psi}{dr})^2$$

and utilizing the radial equilibrium form of Eq. (11.2.1), Eq. (11.3.10) may be written

$$M = \int_{r_h}^{r_t} [r\left(\frac{p}{\rho_o} + \frac{1}{2}\frac{\rho}{\rho_o}\bar{u}^2 - \frac{\rho}{\rho_o}\frac{\psi}{2}\frac{dh_t}{d\psi}\right) - \frac{\rho}{\rho_o}\frac{(rv)}{2r}\left(rv - \psi\frac{drv}{d\psi}\right)$$
$$+ \frac{1}{2}\frac{d}{dr}\left\{\frac{\rho_o}{\rho}\frac{\psi}{r}\frac{d\psi}{dr}\right\} + \frac{\rho}{\rho_o}\frac{\psi}{2}T\frac{ds}{d\psi}]dr \qquad (11.3.11)$$

When the stagnation enthalpy, entropy and angular momentum are prescribed, all terms in this integral may be evaluated (with solution of Eqs. (11.1.30) and (11.2.1)) and the integral obtained. In the following section simple explicit solutions are obtained for special forms of the blade loading, and for these cases evaluation of the integral is very straightforward. It may be noted here that when the flow considered is perfect and incompressible, the group

$$\frac{p}{\rho_o} + \frac{1}{2}\frac{\rho}{\rho_o}\bar{u}^2$$

is identical to the stagnation enthalpy, h_t .

11.4 EXAMPLE SOLUTIONS

As an example set of solutions we consider the simple case of flow of a perfect, incompressible fluid in a parallel walled annulus. As indicated in Fig. 11.4.1, there are N actuator discs located at $x = x_j$ $(1 < j < N)$, and N+1 regions of flow in regions $i (0 \le \bar{i} \le N)$.

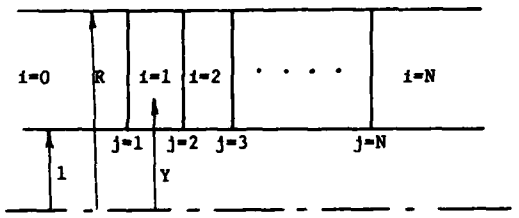

Figure 11.4.1 Actuator Discs and Nomenclature

It is most convenient to consider the non-dimensional form of the equations so we again utilize the dimensionless variables introduced in Eq. (10.3.11). Thus with the addition of a dimensionless axial variable x , we define:

$$W = \frac{w}{w_o}, \quad V = \frac{v}{w_o}, \quad \Psi = \frac{\psi}{w_o r_h^2}, \quad H = \frac{h_t}{w_o^2}$$
$$y = \frac{r}{r_h}, \quad x = \frac{z}{r_h}, \quad R = \frac{r_t}{r_h} \qquad (11.4.1)$$

With the restrictions listed above, and with the introduction of these new variables, Eq. (11.2.1) reduces to

$$\frac{1}{y}\frac{\partial^2\Psi}{\partial x^2} + \frac{\partial}{\partial y}\left(\frac{1}{y}\frac{\partial\Psi}{\partial y}\right) = y\frac{\partial H}{\partial\Psi} - V\frac{\partial yV}{\partial\Psi} \qquad (11.4.2)$$

The boundary conditions are

$$\Psi = -\frac{1}{2} \text{ on } y = 1 \text{ and } \Psi = -\frac{R^2}{2} \text{ on } y = R \qquad (11.4.3)$$

The matching conditions are

$$\left[\Psi\right]_j = 0 \text{ and } \left[\frac{\partial\Psi}{\partial x}\right]_j = 0 \qquad (11.4.4)$$

The mathematical statement of the problem is completed by prescribing the desired distribution of stagnation enthalpy and angular momentum with streamfunction. A particularly simple and instructive set of solutions is obtained when forms of H and yV leading to linear forms of the equations are considered. We thus consider (as in Sec. 10.3.3) the special forms given by

$$H = H_o - \omega_i\Psi + \theta_i \text{ and } (yV)_i = -\alpha_i\Psi + \beta_i \qquad (11.4.5)$$

It follows from the Euler momentum equation that

$$\omega_i = \omega_{i-1} + \Omega_i(\alpha_i - \alpha_{i-1}) \qquad (11.4.6)$$

$$\theta_i = \theta_{i-1} + \Omega_i(\beta_i - \beta_{i-1}) \qquad (11.4.7)$$

Here Ω_i is the nondimensional angular velocity $(\omega r_h/w_o)$ of the rotor row located at x_j where $j = i$.

Equations (11.4.2-11.4.7) constitute the mathematical statement of the problem. We begin the solution by incorporating Eq. (11.4.5) into Eq. (11.4.2) to give

$$\frac{\partial^2\Psi}{\partial x^2} + y\frac{\partial}{\partial y}\left(\frac{1}{y}\frac{\partial\Psi}{\partial y}\right) + \alpha_i^2\Psi = \alpha_i\beta_i - \omega_i y^2 \qquad (11.4.8)$$

11.4.1 SOLUTION OF THE HOMOGENEOUS EQUATION - THE NATURAL EIGENFUNCTIONS

We now consider solution of the homogeneous form of Eq. (11.4.8) by separation of variables. Thus substitute

$$\Psi = yE(y)\,\Phi(x)$$

into Eq. (11.4.8) to obtain the two ordinary differential equations

$$\frac{d^2\Phi}{dx^2} - (\lambda^2 - \alpha_i^2)\Phi = 0 \qquad (11.4.9)$$

$$\frac{d^2E}{dy^2} + \frac{1}{y}\frac{dE}{dy} + (\lambda^2 - \frac{1}{y^2})E = 0 \qquad (11.4.10)$$

here, λ^2 is the separation constant.

The solution of Eq. (11.4.10) is obtained in terms of Bessell functions of the first order, and may be written

$$E = C_1J_1(\lambda y) + C_2Y_1(\lambda y) \qquad (11.4.11)$$

In order to satisfy the boundary conditions that $\partial\Psi/\partial x$ be zero on the hub, one of the constants may be chosen such that

$$E = C_3[J_1(\lambda y)\,Y_1(\lambda) - J_1(\lambda)\,Y_1(\lambda y)] \qquad (11.4.12)$$

In order to satisfy the remaining boundary condition that $\partial\Psi/\partial x$ be zero on the tip, only selected values - the eigenvalues - of the separation constant λ can be allowed. We thus obtain a family of solutions, each solution having a corresponding eigenvalue, λ_n . These eigenvalues follow from solution of the equation

$$J_1(\lambda_n R)\,Y_1(\lambda_n) - J_1(\lambda_n)\,Y_1(\lambda_n R) = 0 \qquad (11.4.13)$$

A series approximation to the value of λ_n is given on page 261 of reference 11.5, and may be written

$$\lambda_n = \frac{n\pi}{R-1}\left[1 + \left(\frac{R-1}{n\pi}\right)^2 \frac{3}{8R} - \left(\frac{R-1}{n\pi}\right)^4 \left\{\frac{21(R^3-1)}{128R^3(R-1)} + \frac{9}{64}\frac{1}{R^2}\right\} + \ldots\right] \quad (11.4.14)$$

This series is quite accurate, the third term reaching a value of only 0.015 for the case R = 3, n = 1 . This set of values corresponds to about the largest correction expected in practice. If a higher accuracy be desired for exceptional cases, Eq. (11.4.3) is easily solved by iteration.

The constant C remains arbitrary because the functions E have yet to be multiplied by the still to be determined functions Φ . Because there is an infinite set of the functions Φ and E we now write the solution for Ψ in the form

$$\Psi = \sum_{n=1}^{\infty} \Phi_n(x)\, y\, E_{1n}(y) \quad (11.4.15)$$

here the subscript n denotes the eigenfunction corresponding to the eigenvalue λ_n , and we have introduced the added subscript 1 in the function E_{1n} to indicate that the Bessel functions with argument $\lambda_n y$ contained in E_{1n} are of first order.

It is a very useful result that the functions $E_{1n}(y)$ are orthogonal, which can be shown directly from the two integral formulae (Ref. 11.6, page 146)

$$\int y Z_p(\alpha y)\bar{Z}_p(\beta y)dy = \frac{1}{\alpha^2-\beta^2}\left[\beta y Z_p(\alpha y)\bar{Z}_{p-1}(\beta y) - \alpha y Z_{p-1}(\alpha y)\bar{Z}_p(\beta y)\right] \quad (11.4.16)$$

$$\int y[Z_p(\alpha y)]^2 dy = \frac{y^2}{2}\left[Z_p^2(\alpha y) - \frac{2p}{y} Z_{p-1}(\alpha y) Z_p(\alpha y) + Z_{p-1}^2(\alpha y)\right] \quad (11.4.17)$$

In these expressions $Z_p(\alpha y)$ and $\bar{Z}_p(\beta y)$ refer to any groups of the form $C_1 J_p(\alpha y) + C_2 Y_p(\alpha y)$ or $C_3 J_p(\beta y) + C_4 Y_p(\beta y)$. It then follows directly, with Eqs. (11.3.22) and (11.3.23), that

$$\int_1^R y E_{1n}(\lambda_n y) E_{1m}(\lambda_m y)dy = 0 \quad m \neq n \quad (11.4.18)$$

$$\int_1^R y[E_{1n}(\lambda_n y)]^2 dy = C_3^2\left\{\frac{R^2}{2}\left[J_0(\lambda_n R)Y_1(\lambda_n) - J_1(\lambda_n)Y_0(\lambda_n R)\right]^2 - \frac{1}{2}\left[J_0(\lambda_n)Y_1(\lambda_n) - J_1(\lambda_n)Y_0(\lambda_n)\right]^2\right] \quad (11.4.19)$$

Equation (11.4.19) may be greatly simplified by noting from Eq. (11.4.13)

$$\frac{Y_1(\lambda_n)}{Y_1(\lambda_n R)} = \frac{J_1(\lambda_n)}{J_1(\lambda_n R)} \quad (11.4.20)$$

and the relationship (Ref. 11.6, page 144)

$$Y_{p-1}(x)\, J_p(x) - Y_p(x)\, J_{p-1}(x) = \frac{2}{\pi x} \quad (11.4.21)$$

to obtain:

$$\int_1^R y[E_{1n}(\lambda_n y)]^2 dy = \frac{2C_3^2}{(\pi\lambda_n)^2}\left[\left\{\frac{J_1(\lambda_n)}{J_1(\lambda_n R)}\right\}^2 - 1\right] \quad (11.4.22)$$

This suggests the convenient choice for the constant C_3 as that value which will render the functions orthonormal. We thus define the orthonormal set of functions $E_{1n}(\lambda_n y)$ by:

$$E_{1n}(y) = \lambda_n \frac{\pi}{\sqrt{2}} \frac{J_1(\lambda_n y)Y_1(\lambda_n) - J_1(\lambda_n)Y_1(\lambda_n y)}{\left[\left\{\frac{J_1(\lambda_n)}{J_1(\lambda_n R)}\right\}^2 - 1\right]^{1/2}} \quad (11.4.23)$$

These functions have the property that

$$\int_1^R y E_{1n}(y)E_{1m}(y)dy = 0 \quad n \neq m$$
$$= 1 \quad n = m \quad (11.4.24)$$

In addition we may note from Eq. (11.4.10)

$$\frac{d}{dy}\left[\frac{1}{y}\frac{d}{dy}\left(yE_{1n}(y)\right)\right] = -\lambda_n^2 E_{1n}(y) \quad (11.4.25)$$

Also, it may be noted that

$$\frac{1}{y}\frac{d}{dy}\left(yE_{1n}(y)\right) = \lambda_n E_{on}(y) \quad (11.4.26)$$

11.4.2 SOLUTION OF THE INHOMOGENEOUS FORM OF THE EQUATION

The emergence of the orthonormal functions $E_{1n}(y)$ from solution of the homogeneous equation suggests we now consider the $\Phi_n(x)$ to be a transformed variable defined by

$$\Phi_n(x) = \int_1^R \Psi(y,x)E_{1n}(y)dy \quad (11.4.27)$$

Obviously the inverse of the transformation is

$$\Psi(y,x) = \sum_{n=1}^{\infty} \Phi_n(x) y E_{1n}(y) \quad (11.4.28)$$

The transformation of Eq. (11.4.8) is now taken by multiplying the equation by $E_{1n}(y)$ and integrating between y = 1 and y = R . The several terms appearing are evaluated as follows.

we define $A_n = \int_1^R y^2 E_{1n}(y)dy =$

$$\frac{1}{\lambda_n}\left[y^2\left\{\frac{2}{\lambda_n y}E_{1n} - E_{on}\right\}\right]_1^R$$

or $$A_n = \frac{1}{\lambda_n}\left[E_{on}(1) - R^2 E_{on}(R)\right] \quad (11.4.29)$$

With the definition of $E_{on}(y)$, and with Eqs. (11.4.20) and (11.4.21), this expression may be rearranged to give

$$A_n = \frac{\sqrt{2}}{\lambda_n} \frac{RJ_1(\lambda_n)-J_1(\lambda_n R)}{\{J_1^2(\lambda_n)-J_1^2(\lambda_n R)\}^{1/2}} \qquad (11.4.30)$$

Now define

$$B_n = \int_1^B E_{1n}(y)dy = \frac{1}{\lambda_n}[E_{on}(1)-E_{on}(R)]$$

With Eqs. (11.4.20) and (11.4.21) this becomes

$$B_n = \frac{2}{\lambda_n} \frac{\frac{1}{R}J_1(\lambda_n)-J_1(\lambda_n R)}{\{J_1^2(\lambda_n)-J_1^2(\lambda_n R)\}^{1/2}} \qquad (11.4.31)$$

Then

$$\int_1^R \frac{\partial^2\psi}{\partial x^2} E_{1n}(y)dy = \frac{\partial^2}{\partial x^2}\int_1^R \psi E_{1n}(y)dy = \frac{d^2\phi_n}{dx^2} \qquad (11.4.32)$$

and

$$\int_1^R y \frac{\partial}{\partial y}\left(\frac{1}{y}\frac{\partial\psi}{\partial y}\right)E_{1n}(y)dy = [E_{1n}(y)\frac{\partial\psi}{\partial y}]_1^R - \lambda_n \int_1^R \frac{\partial\psi}{\partial y} E_{on}dy$$

$$= [-\lambda_n E_{on}(y)\psi]_1^R - \lambda_n^2\int_1^R \psi E_{1n}(y)dy$$

$$= -\frac{\lambda_n}{2}[E_{on}(1)-R^2E_{on}(R)]-\lambda_n^2\phi_n$$

Thus, with Eq. (11.4.29) this may be written

$$\int_1^R y \frac{\partial}{\partial y}\left(\frac{1}{y}\frac{\partial\psi}{\partial y}\right)E_{1n}(y)dy = -\lambda_n^2\phi_n - \frac{\lambda_n^2}{2}A_n \qquad (11.4.33)$$

The last term in Eq. (11.4.8), $\alpha_i^2\psi$ transforms directly to $\alpha_i^2\phi_n$, so that combining Eqs. (11.4.8) and (11.4.30 - 11.4.33) an equation for ϕ_n is obtained.

$$\frac{d^2\phi_n}{dx^2} - (\lambda_n^2-\alpha_i^2)\phi_n = -(\lambda_n^2-\alpha_i^2)T_n^{(i)} \qquad (11.4.34)$$

where

$$T_n^{(i)} \equiv \frac{1}{\lambda_n^2-\alpha_i^2}[(\omega_i - \frac{\lambda_n^2}{2})A_n - \alpha_i\beta_i B_n]$$

The solution to Eq. (11.4.34) consists of exponentials, and is conveniently grouped in the forms

$$\phi_n = \begin{cases} \frac{D_n^{(o)}}{\eta_n^{(o)}} \exp[\eta_n^{(o)}(x-x_1)] + T_n^{(o)} & x < x_1 \\ \frac{D_n^{(i)}\cosh[\eta_n^{(i)}(x-x_i)]-C_n^{(i)}\cosh[\eta_n^{(i)}(x_{i+1}-x)]}{\eta_n^{(i)}\sinh[\eta_n^{(i)}(x_{i+1}-x_i)]} + T_n^{(i)} & x_i < x < x_{i+1} \\ -\frac{C_n^{(N)}}{\eta_n^{(N)}} \exp[\eta_n^{(N)}(x_N-x)] + T_n^{(N)} & x_N < x \end{cases} \qquad (11.4.35)$$

here there has been introduced $\eta_n^{(i)}$ defined by $\eta_n^{(i)} = \sqrt{\lambda_n^2-\alpha_i^2}$.

We note that the boundary conditions $\frac{\partial\phi}{\partial x} \to 0$ as $x \to \pm\infty$ are satisfied. The coefficients $C_n^{(i)}$ and $D_n^{(i)}$ are to be determined from the matching conditions at the discs, Eq. (11.4.4). The condition $\left[\frac{\partial\phi}{\partial x}\right]_j = 0$ gives immediately that $D_n^{(i-1)} = C_n^{(i)}$, and continuity of ϕ at each disc then gives the set of equations

$$\frac{C_n^{(1)}}{\eta_n^{(o)}} + T_n^{(o)} = \frac{C_n^{(2)}-C_n^{(1)}\cosh[\eta_n^{(1)}(x_2-x_1)]}{\eta_n^{(1)}\sinh[\eta_n^{(1)}(x_2-x_1)]} + T_n^{(1)}$$

$$\frac{C_n^{(j)}\cosh[(\eta_n^{(j-1)}(x_j-x_{j-1})]-C_n^{(j-1)}}{\eta_n^{(j-1)}\sinh[\eta_n^{(j-1)}(x_j-x_{j-1})]} + T_n^{(j-1)} =$$

$$\frac{C_n^{(j+1)}-C_n^{(j)}\cosh[\eta_n^{(j)}(x_{j+1}-x_j)]}{\eta_n^{(j)}\sinh[\eta_n^{(j)}(x_{j+1}-x_j)]} + T_n^{(j)}$$

$$\frac{C_n^{(N)}\cosh[\eta_n^{N-1}(x_N-x_{N-1})]-C_n^{(N-1)}}{\eta_n^{(N-1)}\sinh[\eta_n^{(N-1)}(x_N-x_{N-1})]} + T_n^{(N-1)} =$$

$$-\frac{C_n^{(N)}}{\eta_n^{(N)}} + T^N \qquad (11.4.36)$$

Though unwieldy in appearance, this coefficient matrix is diagonally dominant and tridiagonal, and is solved extremely rapidly on a computer. Once the coefficients have been determined, the values of ϕ_n follow from Eq. (11.4.35), and the values of $\psi(x,y)$ from Eq. (11.4.28). The tangential velocity then follows directly from

$$V = \frac{1}{y}(-\alpha_i\psi + \beta_i) \qquad (11.4.37)$$

and the axial velocity from

$$W = -\frac{1}{y}\frac{\partial\psi}{\partial y} = -\sum_{n=1}^{\infty} \lambda_n\phi_n(x)E_{on}(y) \qquad (11.4.38)$$

11.4.3 THE RADIAL EQUILIBRIUM LIMIT OF THE SOLUTIONS

Very useful summations are obtained by noting that because the $T_n^{(j)}$ are independent of x, the portions of the eigenfunction expansions with coefficients $T_n^{(j)}$ correspond to the radial equilibrium solutions already obtained in Sec. (10.3.3). Thus with A of Eq. (10.3.22) replaced by $-\omega_i$ (see Eq. 11.4.6) it follows that

$$\sum_{n=1}^{\infty} T_n^{(i)} yE_{1n}(y) = -\left[\frac{-\omega_i}{\alpha_i^2} + \frac{\beta_i}{\alpha_i} + \frac{1}{2}\right] \frac{yU_1(\alpha_i y)}{U_1(\alpha_i)} - \left[\frac{-\omega_i R^2}{\alpha_i^2} + \frac{\beta_i}{\alpha_i} + \frac{R^2}{2}\right] \frac{yW_1(\alpha_i y)}{RU_1(\alpha_i)} - \frac{\omega_i}{\alpha_i^2} y^2 + \frac{\beta_i}{\alpha_i} \qquad (11.4.39)$$

In the case where $\alpha_i = 0$, Eq. (10.3.28) gives

$$\sum_{n=1}^{\infty} T_n^{(i)} yE_{1n}(y) = -\frac{\omega_i}{8} y^4 + \left[\frac{\omega_i}{4}(R^2+1) - 1\right] \frac{y^2}{2} - \frac{\omega_i}{8} R^2 \qquad (11.4.40)$$

The summations relate principal contributions of the summations to the determination of the streamfunction. Similar summations are obtained for the axial velocity from the relationship $W = -\frac{1}{y}\frac{d\Psi}{dy}$. Thus, it follows directly from Eqs. (11.4.39) and (11.4.40) that

$$-\frac{1}{y}\frac{d}{dy}\left\{\sum_{n=1}^{\infty} T_n^{(i)} yE_{1n}(y)\right\} = -\sum_{n=1}^{\infty} \lambda_n T_n^{(i)} E_{on}(y) = \left[-\frac{\omega_i}{\alpha_i} + \beta_i + \frac{\alpha_i}{2}\right] \frac{U_o(\alpha_i y)}{U_1(\alpha_i)} + \left[-\frac{\omega_i R^2}{\alpha_i} + \beta_i + \frac{\alpha_i R^2}{2}\right] \times \frac{W_o(\alpha_i y)}{RU_1(\alpha_i)} + \frac{2\omega_i}{\alpha_i^2} \qquad (11.4.41)$$

and when $\alpha_i = 0$

$$-\frac{1}{y}\frac{d}{dy}\left\{\sum_{n=1}^{\infty} T_n^{(i)} yE_{1n}(y)\right\} = -\sum_{n=1}^{\infty} \lambda_n T_n^{(i)} E_{on}(y) = \frac{\omega_i}{2} y^2 - \frac{\omega_i}{4}(R^2+1) + 1 \qquad (\alpha_i = 0) \qquad (11.4.42)$$

11.4.4 EXPRESSIONS FOR THE AXIAL FORCE AND TORQUE

When the special forms of blade loading described by Eq. (11.4.5) are considered, particularly simple forms of the integrals of Eqs. (11.3.5) and (11.3.11) result. Thus, the dimensionless torque may be written from Eq. (11.3.5) as

$$\frac{\tau_{1-2}}{\rho_o w_o^2 r_h^3} = -2\pi \int_{-1/2}^{-R^2/2} \{(yV)_2 - (yV)_1\} d\Psi$$

hence, with Eq. (11.4.5), integration leads to

$$\frac{\tau_{1-2}}{\rho_o w_o^2 r_h^3} = \pi(R^2-1)\left[\frac{R^2+1}{4}(\alpha_2-\alpha_1) + (\beta_2-\beta_1)\right] \qquad (11.4.43)$$

The dimensionless, incompressible and perfect form of Eq. (11.3.11) may be written

$$\frac{M}{r_h^2 w_o^2} = \int_1^R \{y(H - \frac{\Psi}{2}\frac{dH}{d\Psi}) - \frac{yV}{2y}(yV - \Psi\frac{dyV}{d\Psi}) + \frac{1}{2}\frac{d}{dy}(\frac{\Psi}{y}\frac{d\Psi}{dy})\} dy \qquad (11.4.44)$$

Utilizing the dimensionless radial equilibrium form of Eq. (11.2.1) together with Eqs. (11.4.5) this expression may be manipulated to give

$$\frac{M}{r_h^2 w_o^2} = \int_1^R [y(H - \frac{\omega_i \beta_i}{2\alpha_i}) + \frac{\omega_i}{2} y\Psi + \frac{1}{2}\frac{d}{dy}\{\frac{(\Psi - \beta_i/\alpha_i)}{y}\frac{d\Psi}{dy}\}] dy$$

Integration then gives

$$\frac{M}{r_h^2 w_o^2} = (H - \frac{\omega_i \beta_i}{2\alpha i})\frac{R^2-1}{2} + \frac{1}{2}(\frac{R^2}{2} + \frac{\beta_i}{\alpha_i}) W_{eR} - \frac{1}{2}(\frac{1}{2} + \frac{\beta_i}{\alpha_i}) W_{e1} + \frac{\omega_i}{2}\int_1^R y\Psi dy \qquad (11.4.45)$$

The integral in this expression is easily obtained in terms of elementary functions when Eq. (11.4.38) (for Ψ) is used. The terms W_{eR} and W_{e1} refer to the equilibrium axial velocity at tip and hub respectively, and follow directly from Eq. (11.4.41). The dimensionless axial force across the blade row then follows from

$$\frac{F_A}{\rho_o r_h^2 w_o^2} = 2\pi\left[\frac{M}{r_h^2 w_o^2}\right] \qquad (11.4.46)$$

11.4.5 SOLUTION FOR A SINGLE ROW

The equation set (11.4.36) allows rapid computer evaluation of the fluid velocities when a large number of actuator discs exist in the annulus. For small numbers of actuator discs, however, there is some advantage to analytically inverting the matrix to obtain explicit forms for desired quantities. The simplest imaginable case is that for which only one disc is present, and for this case the solution of Eq. (11.4.35) reduces to

$$\Phi_n = \frac{C_n^{(1)}}{\eta_n^{(o)}} \exp\{\eta_n^{(o)}(x-x_1)\} + T_n^{(o)} \qquad x < x_1$$

$$= -\frac{C_n^{(1)}}{\eta_n^{(1)}} \exp\{\eta_n^{(1)}(x_1-x)\} + T_n^{(1)} \qquad x_1 < x \qquad (11.4.47)$$

The matching condition Eq. (11.4.35) becomes simply

$$\frac{C_n^{(1)}}{\eta_n^{(o)}} + T_n^{(o)} = -\frac{C_n^{(1)}}{\eta_n^{(1)}} + T_n^{(1)} \qquad (11.4.48)$$

It is thus evident that the flow adjusts in an exponential fashion from its far upstream equilibrium condition as it approaches the actuator disc, and then exponentially relaxes toward its far downstream value as it departs the disc. It is apparent from Eq. (11.4.14) that λ_n is given

approximately by $\lambda_n \approx \frac{n\pi}{R-1}$. Closer investigation of the terms (Ref. 11.7) indicates also that α_1 must be quite small compared to λ_1 if reverse flow is not to occur. Thus is can be seen that the slowest decaying harmonic of the series decays approximately as $\exp\left(\frac{-\pi|x-x_1|}{R-1}\right)$, away from the row. This can be a useful approximation when attemping to estimate upstream effects.

The final forms of the solutions will be summarized below, but before doing so it will be of value to note that when conditions at the blade row are considered, the terms may be regrouped somewhat to ensure more rapid convergence of the summational terms. This is particularly useful because the disappearance of the exponential decay terms in the summations causes a much slower convergence of the summational terms. A familiar result from linearized theories is that the stream-function at the disc would be one-half of the far upstream and far downstream value. We thus utilize this result to write

$$(\Phi_n)_{x=x_1} = \frac{T_n^{(o)} + T_n^{(1)}}{2} + \frac{T_n^{(o)} - T_n^{(1)}}{2} + \frac{C_n^{(1)}}{\eta_n^{(o)}}$$

with Eq. (11.4.48), this may be manipulated to give

$$(\Phi_n)_{x=x_1} = \frac{T_n^{(o)} + T_n^{(1)}}{2} + \frac{T_n^{(o)} - T_n^{(1)}}{2}\left\{\frac{(\eta_n^{(o)})^2 - (\eta_n^{(1)})^2}{(\eta_n^{(o)} + \eta_n^{(1)})^2}\right\} \qquad (11.4.49)$$

The second group in this expression will always be found to be very small, and further will be found to decrease with increasing n much faster than the terms $\frac{C_n}{\eta_n^{(o)}}$.

As a particular example we consider a uniform flow approaching a stator which introduces a "solid body-like" rotation. In terms of the above parameters we then have

$$\beta_o = \omega_o = \alpha_o = 0 \qquad \beta_1 = \omega_1 = 0\ ,\ \alpha_1 = \alpha$$

$$\eta_n^{(o)} = \lambda_n \qquad \eta_n^{(1)} = \sqrt{\lambda_n^2 - \alpha^2} \equiv \eta_n$$

and

$$\sum_{n=1}^{\infty} T_n^{(o)}\, y\, E_{1n}(y) = -\frac{y^2}{2} \equiv \Psi_{-\infty}$$

$$\sum_{n=1}^{\infty} T_n^{(1)}\, y\, E_{1n}(y) = -\frac{yU_1(\alpha y)}{U_1(\alpha)} - \frac{RyW_1(\alpha y)}{2U_1(\alpha)} \equiv \Psi_{\infty}$$

$$-\sum_{n=1}^{\infty} \lambda_n T_n^{(o)} E_{on}(y) = 1 = W_{-\infty}$$

$$-\sum_{n=1}^{\infty} \lambda_n T_n^{(1)} E_{on}(y) = \frac{\alpha U_o(\alpha y)}{2U_1(\alpha)} + \frac{\alpha R W_o(\alpha y)}{2U_1(\alpha)} \equiv W_{\infty}$$

then with Eq. (11.4.34)

$$T_n^{(o)} = -\frac{A_n}{2}\ ,\ T_n^{(1)} = \frac{-\lambda_n^2}{\lambda_n^2 - \alpha^2}\frac{A_n}{2}$$

so that

$$T_n^{(o)} - T_n^{(1)} = \frac{\alpha^2}{\lambda_n^2 - \alpha^2}\frac{A_n}{2} \equiv \frac{\alpha^2}{\eta_n^2}\frac{A_n}{2}$$

Thus

$$\Psi = \Psi_{-\infty} - \frac{\alpha^2}{2}\sum_{n=1}^{\infty} \frac{A_n}{\eta_n(\lambda_n + \eta_n)} \exp\left(\lambda_n(x-x_1)\right) \qquad x < x_1$$

$$\Psi = \Psi_{\infty} + \frac{\alpha^2}{2}\sum_{n=1}^{\infty} \frac{\lambda_n A_n}{\eta_n^2(\lambda_n + \eta_n)} \exp\left(\eta_n(x_1-x)\right) \qquad x > x_1$$

$$\Psi = \frac{1}{2}(\Psi_{-\infty} + \Psi_{\infty}) + \frac{\alpha^4}{4}\sum_{n=1}^{\infty} \frac{A_n}{\eta_n^2(\lambda_n + \eta_n)^2} \qquad x = x_1$$

The tangential velocity follows from Eq. (11.4.37) to give

$$V = 0 \qquad x < x_1$$

$$V = -\frac{\alpha}{y}\Psi \qquad x > x_1$$

$$V = -\frac{\alpha}{2y}(\Psi_{-\infty} + \Psi_{\infty}) - \frac{\alpha^5}{4y}\sum_{n=1}^{\infty} \frac{A_n}{\eta_n^2(\lambda_n + \eta_n)^2} \qquad x = x_1^+$$

The axial velocities follow from Eqs. (11.4.38), (11.4.41) and (11.4.42) to give

$$W = 1 + \frac{\alpha^2}{2}\sum_{n=1}^{\infty} \frac{\lambda_n A_n}{\eta_n(\lambda_n + \eta_n)} \exp\left(\lambda_n(x-x_1)\right) \qquad x < x_1$$

$$W = W_{\infty} - \frac{\alpha^2}{2}\sum_{n=1}^{\infty} \frac{\lambda_n^2 A_n}{\eta_n^2(\lambda_n + \eta_n)} \exp\left(\eta_n(x_1-x)\right) \qquad x > x_1$$

$$W = \frac{1}{2}(1 + W_{\infty}) - \frac{\alpha^4}{4}\sum_{n=1}^{\infty} \frac{\lambda_n A_n}{\eta_n^2(\lambda_n + \eta_n)^2} \qquad x = x_1$$

Example values for the dimensionless velocities have been calculated for the case where $R = 3$, $\alpha = 0.84$. The results are shown in Figs. 11.4.2 and 11.4.3 .

The results indicate that for this rather large swirl introduced by the stator, substantial perturbations to the axial velocity profile are introduced. The resulting streamsurface shapes and ambient diffusion or acceleration can now be obtained to determine the overall flow field in which the blade row is imbedded. These results in turn will allow the establishment of the correct cascade geometry to determine the cascade flow field.

Examples with more blade rows are relatively easily obtained, though if more than two blade rows are considered, the analytic inversion of the coefficient matrix, Eq. (11.4.36) becomes very messy algebraically. It is much easier to simply program the matrix and numerically invert it. More complicated example solutions are provided in Refs. 11.7 and 11.8 .

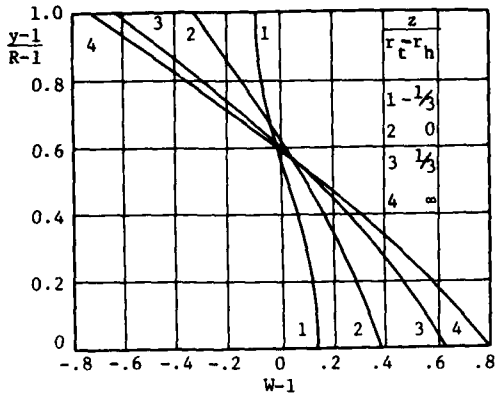

Figure 11.4.2 Axial Velocity Profiles

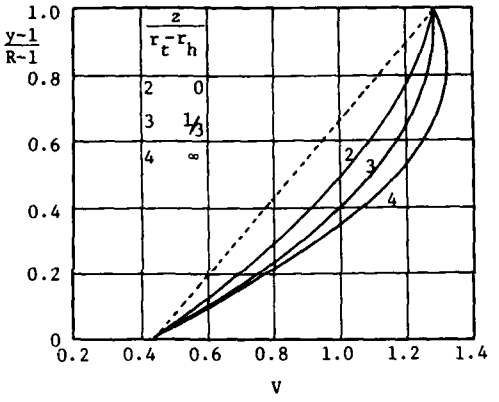

Figure 11.4.3 Tangential Velocity Profiles

11.5 ADVANCED PROBLEMS IN THROUGHFLOW THEORY

The example solutions illustrated in Sec. 11.4 allow rapid calculation of the flowfields existing in an annulus with many blade rows, but the solutions though quite instructive have incorporated into them many limitations. Thus, it was necessary to assume that the fluid was perfect and incompressible, that the blade loading (in terms of H and yV) was such as to lead to linear equations, and that the annulus had parallel walls. More advanced investigations allow some or all of these restrictions to be relaxed, so in the following sections a brief description of some of the methods available for solution of the more general forms of the throughflow equation will be outlined.

11.5.1 EFFECTS OF COMPRESSIBILITY

When the flow has substantial compressibility effects, the full coupled equations, Eqs. (11.1.30) and (11.2.1) together with the boundary conditions and matching conditions must be utilized. In virtually all calculation schemes these equations are solved in an iterative manner, with Eq. (11.2.1) first solved (by finite difference or finite element techniques) with an assumed density distribution, and then the density "updated" by utilizing the obtained values for ψ in Eq. (11.1.30). Eq. (11.1.30) is then solved (iteratively) to determine a new set of values for the density, and the coupled iteration process continued till convergence is obtained. Simple Newtonian iteration is usually used to solve Eq. (11.1.30) for the density ratio. Thus, from Eq. (11.1.30) we may write

$$F \equiv [2h_t - v^2]\left(\frac{\rho}{\rho_o}\right)^2 - 2h_o \exp\left[\frac{\gamma}{C_p}(s-s_o)\right]\left(\frac{\rho}{\rho_o}\right)^{\gamma+1} - \left[\left(\frac{1}{r}\frac{\partial\psi}{\partial r}\right)^2 + \left(\frac{1}{r}\frac{\partial\psi}{\partial z}\right)^2\right] = 0 \qquad (11.5.1)$$

Then we may write

$$\left(\frac{\rho}{\rho_o}\right)_{j+1} = \left(\frac{\rho}{\rho_o}\right)_j - \frac{F_j}{F'_j} \qquad (11.5.2)$$

where

$$F' = 2[2h_t - v^2]\frac{\rho}{\rho_o} - 2(\gamma+1)h_o \exp\left[\frac{\gamma}{C_p}(s-s_o)\right]\left(\frac{\rho}{\rho_o}\right)^{\gamma} \qquad (11.5.3)$$

We note that

$$[2h_t - v^2] = [2h + u^2 + w^2] = 2h\left[1 + \frac{\gamma-1}{2}M_m^2\right] \qquad (11.5.4)$$

here M_m is the meridional Mach number.

Equation (11.5.4) may be combined with Eq. (11.5.3) to give

$$F' = 4h\frac{\rho}{\rho_o}\left[1 + \frac{\gamma-1}{2}M_m^2 - \frac{\gamma+1}{2}\frac{h_o}{h}\left(\frac{\rho}{\rho_o}\right)^{\gamma-1} \times \exp\left\{\frac{\gamma}{C_p}(s-s_o)\right\}\right]$$

It is evident from integration of the Gibbs equation (Sec. 2.8), however, that

$$\frac{h_o}{h}\left(\frac{\rho}{\rho_o}\right)^{\gamma-1} \exp\left\{\frac{\gamma}{C_p}(s-s_o)\right\} = 1$$

and the equation for F' hence becomes

$$F' = -2(\gamma-1)h\frac{\rho}{\rho_o}(1-M_m^2) \qquad (11.5.5)$$

It is thus evident that it is the meridional Mach number (rather than the "total" Mach number) that plays the crucial role in determining the mathematical behavior of the solution. It is evident also that Newtonian iteration will fail in the vicinity of $M_m = 1$. As a result most calculation schemes are limited to the description of flows with meridional Mach numbers less than unity, even though the total Mach number may be far in excess of unity. It is to be noted that because the density ratio itself is primarily dependent on the total Mach number, very large density changes can occur for flows with modest meridional Mach numbers, so great care should be taken to properly calculate the resulting density distribution.

Hawthorne and Ringrose (Ref. 11.9) in an early paper considered the perfect flow of a calorically perfect gas through actuator discs

contained within a parallel walled annulus. The flow considered had a free vortex distribution, but was considered to be compressible. The analysis, which is one of the very few analytical treatments (as compared to numerical) of compressible flows in turbomachines, was carried out by linearizing the equations. Both the radial velocity and meridional Mach number, as well as the turning induced by the blades, were considered to be small. The results are very useful, because by restricti the study to free vortex flows in parallel walled annuli, the perturbations in axial velocity that arise must be caused by the effect of compressibility alone. Example cases can be calculated with ease because of the analytical form of the results leading to easy physical interpretation of the results.

Fully numerical methods can usually be categorized into one of three methods, i) streamline curvature, ii) finite difference, or iii) finite element. The streamline curvature method utilizes an approximate method of solving the throughflow equations (Refs. 11.10-11.13) and as such rests somewhat between the radial equilibrium method, and methods that solve the full throughflow equations. The essence of the method is that approximate forms of the streamtube curvature are assumed, so that the describing equations become quite simplified. Various "curve fits" are assumed for the several example solutions detailed in Refs. 11.10 - 11.13 .

Finite difference methods, as might be expected, incorporate finite difference approximations to the various derivatives appearing in the throughflow equation. A finite number of "nodal points" are selected, and as a result a finite set of algebraic equations results to be solved for the values of streamfunction at each point. This leads to the requirement to invert a sizable matrix, and such methods are hence often referred to as matrix methods. Wu (Ref. 11.1) in his pioneering work utilized a finite difference technique, and many investigators have utilized the method since that time. Examples are given in Refs. 11.14 and 11.15.

In common with most techniques, the finite difference methods encounter computational difficulties when the meridional Mach numbers approach unity. A further difficulty arises when curved boundaries are encountered, because very complicated computational "stenciles" are required to insure numerical stability. Davis (Ref. 11.5) considers the flow in very highly curved channels and finds a fifteen point stencil is required to adequately represent the Taylor series expansion of the derivatives of the streamfunction. A quasi-orthogonal finite difference net is introduced to aid the computation. It is to be noted that the extreme curvature of the boundaries in the Davis study are such as to render most streamline curvature techniques incapable of describing the flow field. This is because the curvature of the streamtube is very difficult to estimate in the approximate way required for streamline curvature techniques when such extreme boundary curvatures are present.

In the fairly recent past, finite element methods have been developed in the hopes of circumventing some of the difficulties found in applying finite difference techniques. Hirsch and Warzee (Ref. 11.3) describe an investigation where the finite element method is applied to the description of flows in axial turbomachines. The compressible throughflow equations are derived in the (r,z) plane and a Galerkin finite element method is applied leading to a system of equations for the unknown streamfunction. The curved hub and tip boundaries are well fit by utilizing high-order isoparametric quadrilateral elements. The method hence does not require approximation of the streamline curvature (with possible introduction of numerical instabilities or errors), nor does it require the use of complicated and extensive stencils with resultant programming difficulty and possibly increased computational times.

Oates and Carey (Ref. 11.6) and Oates, Knight and Carey (Ref. 11.7) present studies which also involve the use of a finite element approximation. In addition, a variational functional, Γ , is defined where

$$\Gamma = \int_{-\infty}^{\infty} \int_{\text{hub}}^{\text{tip}} (P-P_e + \frac{\rho}{\rho_o} \{U^2+W^2\})y \, dy \, dz \quad (11.5.6)$$

here P_e is a (dimensionless) reference pressure.

It is shown that when the formal variation of Γ , $\delta\Gamma$, is taken, and put equal to zero, the throughflow equation, boundary conditions and all matching conditions are automatically satisfied. The method developed in Refs. 11.16 and 11.17 then involves putting the discrete approximation (using finite elements) of $\delta\Gamma$ equal to zero. A further useful manipulation is introduced in that rather than solving for $\psi(y,z)$, the equations are transformed to solve for $y(\psi,z)$. By this artifice, the flow domain is mapped to a rectangular domain with $\psi = -1/2$ and $\psi = -R^2/2$ on the horizontal boundaries. These several manipulations lead to a very efficient computational scheme.

Reference 11.18 gives a fairly recent extensive review and comparison of many throughflow calculation techniques.

All the fully numerical calculation schemes described above can include the effects of variations in hub and tip radii. Several analytic studies to explore such effects have been carried out, however, and offer the advantage of relative simplicity in calculation of desired example cases. References 11.2 and 11.19 consider a study that includes the effect of variation in annulus radii when both the wall slopes and the annulus contraction or expansion are restricted to be small. A similar study is reported in Ref. 11.8, except that the restriction to small contraction or expansion is not required though the small wall slope must be retained. Finally, Ref. 11.20 describes the passage of swirling flows through conical ducts. In all the investigations into the effects of wall shape reported in Refs. 11.2, 11.8, 11.19, and 11.20, the flows are considered perfect and incompressible.

11.6.1 REFERENCES

(11.1) Wu, C. H., "A General Theory of Three-Dimensional Flow in Subsonic and Supersonic Turbomachines of Axial, Radial and Mixed Flow Type." NACA TN 2604, 1952.

(11.2) Marble, F. E., "Three-Dimensional Flow in Turbomachines." Aerodynamics of Turbines and Compressors, High Speed Aerodynamics and Jet Propulsion, Vol. X, Section F, Princeton 1954.

(11.3) Hirsch, Ch. and Warzee, G., "A Finite-Element Method for Through Flow Calculations in Turbomachines." Trans, A.S.M.E. Journal of Fluids Engineering, Vol. 98, Series I, No. 3, September 1976, pp. 403-421.

(11.4) "Throughflow Calculations in Axial Turbomachinery." AGARD Conference Proceedings, No. 195, October 1976.

(11.5) Gray, A. and Mathews, G. B., "A Treatise on Bessel Functions and Their Applications to Physics." Dover, 1966.

(11.6) Jahnke, E. and Emde, F., "Tables of Functions." Dover, 1945.

(11.7) Oates, G. C., "Actuator Disc Theory for Incompressible Highly Rotating Flows." Journal of Basic Engineering, Vol. 94, Series D, No. 3, September 1972.

(11.8) Oates, G. C. and Knight, J., "Throughflow Theory for Turbomachines." Technical Report AFAPL-TR-73-61.

(11.9) Hawthorne, W. R. and Ringrose, J., "Actuator Disc Theory of the Compressible Flow in Free-Vortex Turbomachines." Paper No. 5, Proceedings of the Institution of Mechanical Engineers, Vol. 178, Pt. 31(ii0, 1963-64, pp. 1-13.

(11.10) Smith, L. H., Traugott, S. C., and Wislicenus, G. F., "A Practical Solution of a Three-Dimensional Problem of Axial Flow Turbomachinery." Trans. A.S.M.E., Vol. 75, 1953, p. 789.

(11.11) Wu, C. H. and Wolfenstein, L., "Applications of Radial-Equilibrium Conditions to Axial Flow Compressor and Turbine Design." NACA Rept. No. 955, 1955.

(11.12) Seipell, C., "Three-Dimensional Flow in Multistage Turbines." Brown Boveri Rev., Vol. 45, No. 3, 1958, p. 99.

(11.13) Wilkinson, D. H., "Stability, Convergence and Accuracy of Two-Dimensional Streamline Curvature Methods Using Quasi-Orthogonals." Proceedings of the Institution of Mechanical Engineers, Vol. 184, 1970, p. 108.

(11.14) Marsh, H., "A Digital Computer Program for the Through-Flow Fluid Mechanics in an Arbitrary Turbomachine Using a Matrix Method." National Gas Turbine Establishment, Report No. R282, 1966.

(11.15) Davis, W. R., "A General Finite Difference Technique for the Compressible Flow in the Meridional Plane of a Centrifugal Turbomachine." A.S.M.E. Paper No. 75 GT 121, 1975.

(11.16) Oates, G. C. and Carey, G. F., "A Variational Formulation of the Compressible Throughflow Problem." AFAPL-TR-74-78, November 1974.

(11.17) Oates, G. C., Knight, C. J. and Carey, G. G., "A Variational Formulation of the Compressible Throughflow Problem." Trans. A.S.M.E., Journal of Engineering for Power, Series A, Vol. 98, No. 1, January 1976, pp. 1-8.

(11.18) "Throughflow Calculations in Axial Turbomachinery." AGARD Conference Proceedings, No. 195, October 1976.

(11.19) Oates, G. C., "Theory of Throughflow in Axial Turbomachines with Variable Wall Geometry." California Institute of Technology, Jet Propulsion Center, Technical Note No. 1, AFOSR TN 59-680, August 1959.

(11.20) Horlock, J. H. and Lewis, R. I., "Non-Uniform Three-Dimensional and Swirling Flows Through Diverging Ducts and Turbomachines." International Journal of Mechanical Science, Vol. 3, No. 3, 1961, pp. 170-196.

Chapter 12

CASCADE FLOWS

Gordon C. Oates

University of Washington

TABLE OF CONTENTS

CHAPTER 12 CASCADE FLOWS

		Page
12.0	Introduction	1
12.1	Cascade Losses	1
12.2	Cascade Notation	3
12.3	Calculational Methods	4
12.3.1	Two-Dimensional, Inviscid, Incompressible Flow	5
12.3.2	The Complex Potential	5
12.3.3	The Cascade Transformation	6
12.3.4	The Cascade Flow Field	7
12.3.5	Summary of the Equations - Cascade Transformation	10
12.3.6	Example Results - Two-Dimensional Straight Line Cascade	10
12.4	References	11

LIST OF FIGURES

		Page
Figure 12.0.1	Typical Cascade Wind Tunnel	1
Figure 12.1.1	Variation in Stagnation Pressure and Flow Deflection	1
Figure 12.1.2	Variation of Average Stagnation Pressure Loss and Turning Angle With Angle of Attack	2
Figure 12.1.3	Simplified Stagnation Pressure Profile	2
Figure 12.1.4	Secondary Flow Patterns	3
Figure 12.2.1	Cascade Notation	3
Figure 12.3.1	Cascade Coordinate System	4
Figure 12.3.2	Flow Through a Two-Dimensional Cascade	5
Figure 12.3.3	The Cascade Transformation	6
Figure 12.3.4	Location of $\zeta \to \infty$ in the z-Plane	7
Figure 12.3.5	Cascade Velocities	7
Figure 12.3.6	Incremental Velocity Relationship	8
Figure 12.3.7	Singularities in the Circle Plane	9
Figure 12.3.8	Deviation Angle Versus Angle of Attack	10
Figure 12.3.9	Cascades at Two Stagger Angles C/S = 0.5	10
Figure 12.3.10	Deviation Angle Versus Solidity	11

CHAPTER 12

LIST OF SYMBOLS

The symbols are listed in alphabetical order, first in the English alphabet, then in the Greek alphabet. Subscripts and superscripts are then given. The equation, figure or section in which the symbols are first introduced is indicated in parentheses. Often the symbol will be defined in the text just preceding or just following the equation or figure.

Where appropriate, the location of the introduction of the symbol is referred to in previous chapters.

a - Distance from blade leading edge to point of maximum camber (Eq. 12.2.1)

b - Blade depth (Fig. 12.3.1)

C - Chord (Fig. 12.2.1)

$d\ell$ - Differential length (Eq. 12.1.1)

$\bar{e}_x, \bar{e}_y$ - Unit vectors (Eq. 12.3.11)

F - Force (Eq. 12.3.9)

h - Enthalpy (Eq. 12.3.7)

m - Parameter defined in Eq. 12.2.1

p - Pressure (Fig. 12.1.1)

S - Spacing (Fig. 12.1.3)

T - Temperature (Eq. 12.3.7)

u,v,w - Velocity components (Eq. 12.1.1)

$\bar{u}$ - Vector velocity (Eq. 12.3.1)

V - Magnitude of the velocity (Fig. 12.2.1)

W - Complex potential defined by Eq. 12.3.17

z - Complex variable = $x+iy$ (Eq. 12.3.19)

α - Angle of attack (Fig. 12.1.2)

- Ratio of masses (Eq. 12.1.3)

β - Gas angle (Eq. 12.1.1 and Fig. 12.2.1)

Γ - Circulation (Eq. 12.3.14)

γ - Camber angle (Fig. 12.2.1)

γ_1 - Stagger angle (Fig. 12.2.1)

δ - Deviation angle (Fig. 12.2.1)

- Small quantity (Eq. 12.3.32)

ζ - Complex variable = $\xi+i\eta$ (Eq. 12.3.22)

η - Complex co-ordinate (Fig. 12.3.3)

θ, θ' - Angles (Fig. 12.3.2)

θ^* - Blade camber angle (Fig. 12.2.1)

ξ - Complex co-ordinate (Fig. 12.3.3)

ρ - Density (Eq. 12.3.3)

σ - Solidity (Fig. 12.2.1)

ϕ - Flow turning angle (Fig. 12.2.1)

- Velocity potential (Eq. 12.3.2)

- Angle in complex (ζ) plane (Fig. 12.3.3)

ψ - Stream function (Eq. 12.3.4)

- Parameter appearing in the transformation function (Eq. 12.3.22)

$\bar{\omega}$ - Vector vorticity (Eq. 12.3.1)

Subscripts

ℓ - Leading edge (Eq. 12.3.27)

t - Trailing edge (Eq. 12.3.27)

- Stagnation quantity (Sect. 2.16)

o - At location of the trailing edge (Eq. 12.3.25)

∞ - Average (velocity) (Fig. 12.3.2 and Eq. 12.3.12)

Superscripts

$*$ - Design condition (Eq. 12.2.1)

- Value of circulation placed at the origin (Eq. 12.3.38)

CHAPTER 12

CASCADE FLOWS

12.0 INTRODUCTION

When the throughflow flow field (Chapter 11) has been determined, the blade profiles necessary to induce the desired fluid conditions can then be (approximately) determined by consideration of the cascade flow field. As previously discussed (Sec. 10.0), a cascade flow field is obtained by "unwrapping" the desired meridional surface that has been determined from the throughflow analysis. The required blade geometries necessary to give the desired flow turning efficiently for the particular "strip" considered, are then obtained by experimental and/or theoretical consideration of a quasi-two-dimensional configuration such as that indicated in Fig. 12.0.1.

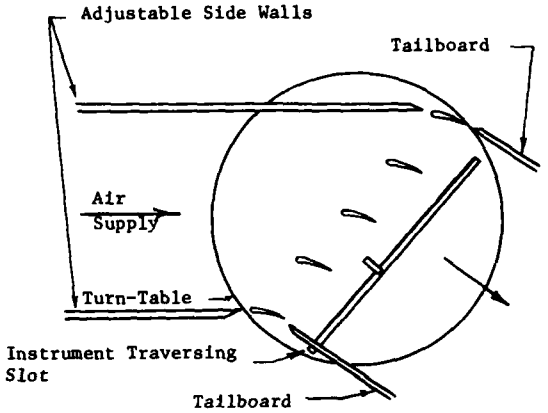

Figure 12.0.1 Typical Cascade Wind Tunnel

It should be noted that because the meridional surface will, in general, have a streamwise varying cross-sectional area (with its attendant imposed pressure gradients), the cascade wind tunnel should be constructed to impose this desired area variation. This is by no means a simple experimental task, because the upper and lower walls will have to be adjusted (in a curved fashion) to include not only the area variation actually occurring in the throughflow, but in addition corrections should be made for the growth of the wind tunnel sidewall boundary layers.

Even when the streamwise variation of the cross-sectional area is well approximated, a further problem of considerable difficulty remains. Thus, it is apparent that the flow is (very nearly) periodic in the actual (annular) blade row, so it is important that enough blades be incorporated in the two-dimensional cascade to ensure that the required periodicity occurs over the middle (test) blades. In reference 12.1, the results of considerable discussion on this matter were reported, and specialists' estimates of the minimum number of blades required ranged from five to fifteen for subsonic cascades and three to nine for supersonic cascades. The required minimum number of blades was considered to depend somewhat on the purpose of the tests, so that for example, if the surface pressure distribution only, of a blade was to be determined, relatively few blades would be required. In contrast, if an accurate estimate of the cascade losses was desired, a large number of blades would be required.

It is apparent that the approximation to exact periodicity can be aided somewhat by shaping the sidewalls to approximate the expected approach streamline shape. In practice this is rarely attempted, because the shape of the approaching streamline will, of course, vary with loading on the cascade. "Tailboards", as indicated in Fig. 12.0.1 are sometimes used to reduce the effects of external flow interaction at the sidewalls.

The number of blades utilized in a given facility cannot usually be greatly increased because of the resulting small size of the blades (if the solidity is to be maintained at the desired value). Excessively small blades create difficulties in that it becomes difficult to maintain the appropriate range of Reynolds numbers. Further, when detailed flow information such as the surface pressure distribution is desired, small blade sizes lead to great instrumentation difficulties.

In spite of these many difficulties, the results of careful cascade tests remain a most important source of information for evaluating the performance of, and determining the detailed flow behavior of the many candidate blade profiles considered for use in turbomachinery. It should be recognized, however, that even "routine" cascade tests should be carried out with a great deal of care.

12.1 CASCADE LOSSES

When a cascade has been successfully constructed to minimize the problems discussed in the preceding section, the performance can be determined by traversing stagnation pressure probes and yaw meters across the exit plane.

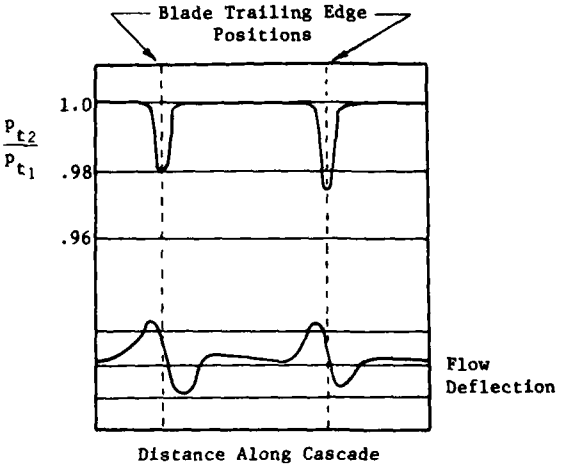

Figure 12.1.1 Variation in Stagnation Pressure and Flow Deflection

The detailed information obtained from the instrument traverses can be presented in the form indicated in Fig. 12.1.1. Each setting of inlet incidence angle and Mach number will have identified with it one such graph.

Customarily, the detailed information contained in Fig. 12.1.1 is averaged in one of several ways so that the effect of variation in angle of attack can be presented in a single graph such as that shown in Fig. 12.1.2.

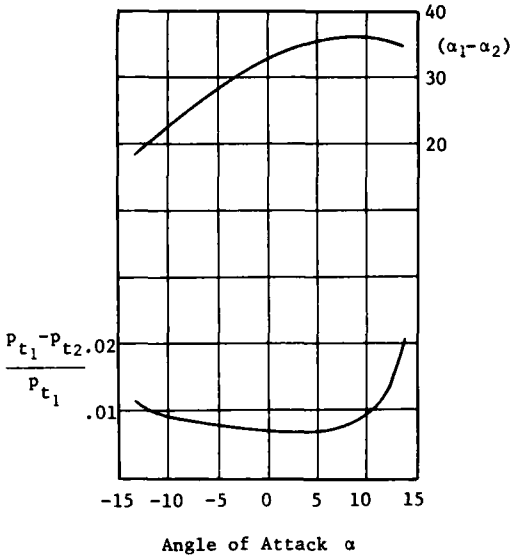

Figure 12.1.2 Variation of Average Stagnation Pressure Loss and Turning Angle With Angle of Attack

A common form of averaging is that of mass flow averaging. Thus, for example, the gas exit angle, β_2, would be obtained in terms of the mass flow averaged tangential momentum and mass averaged axial momentum. Thus:

$$\tan \beta_2 = \frac{\int_0^S \rho u v d\ell}{\int_0^S \rho u^2 d\ell} \qquad (12.1.1)$$

Similarly, the mass flow averaged pressure loss would be obtained from

$$\Delta p_t = \frac{\int_0^S \rho u (p_{t_1}-p_{t_2}) d\ell}{\int_0^S \rho u d\ell} \qquad (12.1.2)$$

It is evident, particularly in the case of the mass flow averaged pressure loss that considerable difficulty will arise when the results of different cascade measurements are to be compared. This is because ΔP_t as defined by Eq. (12.1.2) will change (for the same cascade test) with the distance from cascade exit at which the measurements are taken. This problem is present even if the cascade wall losses do not intrude into the measurement region, because the wake mixing process itself introduces further entropy gains.

As a result of the difficulty of interpreting mass flow averaged pressure losses, it has been suggested (Ref. 12.2 for example) that "mixed out" values of the pressure loss be used to compare the performance as determined from different cascades. The mixed out value corresponds to that value of the pressure loss that would exist if the fluid was allowed to fully mix in an ideal (no sidewall friction) constant area mixer (Sec. 5.15.2). It is also pointed out in Ref. 12.2 that the results will have to be carefully interpreted no matter what averaging method is used, because the blade wakes will have a substantial interaction with the following blade rows.

A measure of the expected size of the effect of averaging techniques can be obtained from a simple example. Thus, we assume a simple abrupt wake to be imbedded in a flow which otherwise has experienced no stagnation pressure decrease.

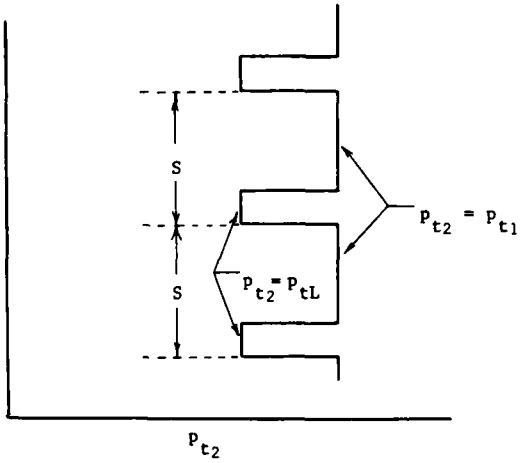

Figure 12.1.3 Simplified Stagnation Pressure Profile

Denoting the ratio of the mass flow with stagnation pressure decrement to the mass flow without stagnation pressure decrement as α (So as to directly utilize the results of Sec. 5.15.2), we may write for this simple case

$$\frac{\Delta P_{t\ \text{mass av}}}{P_{t1}} = \frac{1}{P_{t1}} \frac{\int_0^S \rho u (P_{t1}-P_{t2}) d\ell}{\int_0^S \rho u d\ell} = \frac{\alpha}{1+\alpha}\left(1-\frac{P_{tL}}{P_{t1}}\right) \qquad (12.1.3)$$

The mixed out stagnation pressure losses for this simple flow may be calculated by utilizing the results of Sec. 5.15.3 directly. As an example we consider the case with Mach number of the high pressure stream M_1 equal to 0.6, $\alpha = 0.2$, $\gamma = 1.4$ and stagnation temperature ratio of the two streams equal to unity. (Of course.) There is obtained

$\frac{P_{tL}}{P_{t1}}$	$\frac{\Delta P_{t\ \text{mixed out}}}{P_{t1}}$	$\frac{\Delta P_{t\ \text{mass av}}}{P_{t1}}$
0.95	.0090	.0083
0.9	.0197	.0167
0.85	.0336	.0250
0.8	.0625	.0333

These simple calculations indicate that it is very important indeed to be aware of which averaging technique has been utilized for a given data set, and in addition at what location was the measurement traverse taken. Note that an alternate way of looking at this problem is to realize that if two data sets were compared where one set of measurements has been taken far downstream (where conditions approach mixed out) and $\frac{\Delta P_{t\ \text{mass av}}}{P_t}$ found to be .0333, and then a second set of data taken in close proximity of the cascade exit which also had $\frac{\Delta P_{t\ \text{mass av}}}{P_t} = .0333$, the second cascade would in fact have almost double the losses of the first.

In an actual turbomachine the various loss mechanisms are quite interactive. Thus, the flow profiles departing one blade row affect the losses produced in the following row. In addition losses occurring on the annulus walls and at the blade tips affect the total losses produced within the blade row, and are themselves influenced by the blade losses. It is the hope in representing the entire flowfield as a compilation of three two-dimensional fields that knowledge of the "pure" cascade flowfield will allow accurate estimates to be made of other losses. Thus, for example, when determining the performance of a cascade, every effort is made to remove the influence of the cascade wall losses from the data. Later, however, the losses experienced in the turbomachine at the annulus walls will be estimated with the help of the cascade results.

Several major flow interactions that occur have been classified and attempts made to analyze them. An important example of such flows is termed the secondary flow. Secondary flows have been thoroughly reviewed in Ref. 12.3, where many example applications of secondary flow analyses are described. With regard to their applicability for use in the analysis of flows in turbomachines, secondary flow analyses are particularly useful in describing the flow through compressor rows. Figure 12.1.4 depicts a distorted flow profile as could be produced by the annuli walls, approaching a stator row. When fluid with such a profile enters the pressure field of the blades the low momentum air is turned more ("overturned") than the high momentum air, leading to the secondary flow patterns indicated.

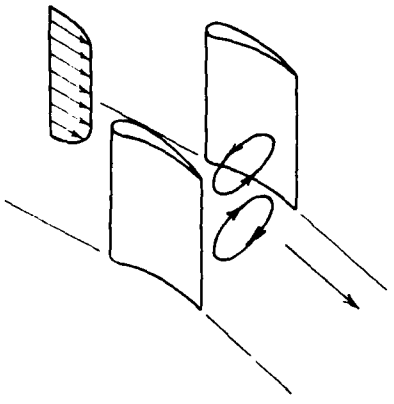

Figure 12.1.4 Secondary Flow Patterns

Secondary flow in compressors is particularly amenable to analysis because to a good approximation the viscous stresses may be ignored in the region of the blades. This is an allowable approximation because the adverse pressure gradient imposed by the blades moves the flow towards separation with consequent low viscous stresses. The effects of viscosity are, of course, implicitly present in the distorted entry profile that has been developed by the long approach flow over the annulus walls. It is to be noted that the high favorable pressure gradients found over much of the turbine blade profile leads to thin boundary layers that must be analyzed using (3-D) boundary layer techniques.

Cascade tests are necessarily conducted with single rows of blades, so the effects of upstream blade rows (particularly moving blade rows) cannot be simulated. The effects of shed blade wakes can be substantial however, and several extensive studies to describe the flow interactions have been conducted. Ref. 12.4 extends the analytical models of the early references of Refs. 12.5 and 12.6, and provides experimental verification of the analytical predictions. A more recent study is reported in Ref. 12.7 where a method of directly estimating the stagnation temperature profile following a stator in terms of the rotor blade loss factor is presented. The latter study has particular utility in the description of flow in high Mach number stages.

In summary, it should be noted that the various losses occurring in turbomachines, other than two-dimensional profile losses, described above are not those to be found in a cascade wind tunnel investigation. The cascade flowfield, however, appears as the "parent" flowfield for all these secondary flows, just as the throughflow flowfield appeared as the parent flowfield for the cascade flowfield. The results of cascade studies are hence of utility not only in determining the blade losses, but also in establishing the cascade flowfield so that the secondary losses can be estimated.

12.2 CASCADE NOTATION

Typical cascade notation is illustrated in Fig. 12.2.1.

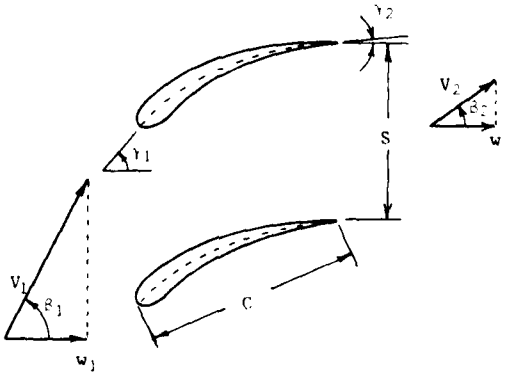

Figure 12.2.1 Cascade Notation

In Fig. 12.2.1 we have

subscript 1 = inlet condition

subscript 2 = outlet condition

β = flow angle

γ = angle of blade camber line

γ_1 = stagger angle

θ^* = blade camber angle = $\gamma_1 - \gamma_2$

ϕ = flow turning angle = $\beta_1 - \beta_2$

δ = deviation angle = $\beta_2 - \gamma_2$

α = angle of attack = $\beta_1 - \gamma_1$

w = "axial" (x) velocity

v = magnitude of the velocity

S = spacing

C = chord

σ = solidity = $\frac{C}{s}$

When presenting the data, as already depicted in Fig. 12.1.3, it is usual to depict the stagnation pressure loss in a dimensionless manner, such as

$$\frac{\Delta P_t}{\frac{1}{2}\rho_1 V_1^2}$$

It is customary to describe an airfoil shape in terms of its thickness distribution about a prescribed camber line. The camber line is often taken to be of parabolic shape (which reduces to a circular arc profile as a special case). Many attempts have been made to relate the blade camber angle and other geometric properties of the blade to the deviation angle. (See particularly Ref. 12.8, Chapt. 6.) A quite convenient approximate form has also been suggested (Refs. 12.9 and 12.10) to relate the value of the deviation angle at design conditions, δ^*, to the blade geometry and flow exit angle at design β_2^*. The suggested relationship is

$$\delta^* = \frac{m}{\sqrt{\sigma}}\theta^* \qquad (12.2.1)$$

where

$$m = 0.23\left(\frac{2a}{C}\right)^2 + 0.1\left(\frac{\beta_2^*}{50}\right)$$

in this expression a is the distance from blade leading edge to point of maximum camber and β_2^* is to be measured in degrees.

By utilizing this approximate relation, the blade turning angle necessary to introduce the desired flow turning can be easily estimated.

12.3 CALCULATIONAL METHODS

We now consider the quasi-two-dimensional flow in the cascade plane. Figure 12.3.1 illustrates the coordinate system. The flow will be assumed to be of depth b, where b is a function of x alone.

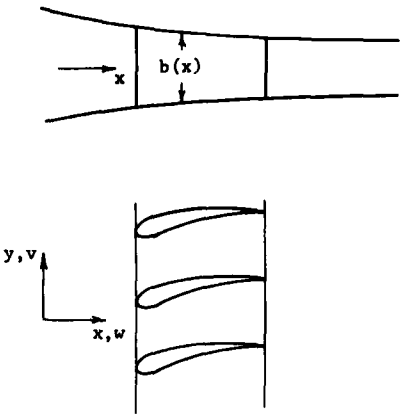

Figure 12.3.1 Cascade Coordinate System

It is apparent that if vorticity is to be present in the flow field it must be directed perpendicular to the cascade plane. With ideal (isentropic) flow assumed, with uniform properties far upstream, Eq. (11.1.25) then gives directly

$$\bar{\omega} \times \bar{u} = 0 \qquad (12.3.1)$$

but because $\bar{\omega}$ must be perpendicular to $\bar{u}$, $\bar{\omega}$ itself must be zero. It is thus possible to define a potential ϕ, such that

$$\bar{u} = \nabla\phi \qquad (12.3.2)$$

The quasi-two-dimensional form of the continuity equation may be written

$$\frac{\partial(\rho u b)}{\partial x} + \frac{\partial(\rho v b)}{\partial y} = 0 \qquad (12.3.3)$$

Utilizing this equation, a streamfunction may be defined by the relationships

$$u = \frac{1}{\rho b}\frac{\partial\psi}{\partial y}, \quad v = \frac{-1}{\rho b}\frac{\partial\psi}{\partial x} \qquad (12.3.4)$$

The condition that the vorticity is zero,

$$\frac{\partial u}{\partial y} - \frac{\partial v}{\partial x} = 0 \qquad (12.3.5)$$

then gives an equation for the streamfunction which may be written

$$\nabla^2\psi = \frac{1}{b}\frac{db}{dx}\frac{\partial\psi}{\partial x} + \frac{1}{\rho}\frac{\partial\rho}{\partial y}\frac{\partial\psi}{\partial y} + \frac{1}{\rho}\frac{\partial\rho}{\partial x}\frac{\partial\psi}{\partial x} \qquad (12.3.6)$$

As in Sec. 11.1.7, a subsidiary equation for the density may be obtained by utilizing the isentropic condition. Thus

$$\frac{\rho}{\rho_1} = \left(\frac{T}{T_1}\right)^{\frac{1}{\gamma-1}} = \left[\frac{h_t - \frac{1}{2}(u^2+v^2)}{h_t - \frac{1}{2}(u_1^2+v_1^2)}\right]^{\frac{1}{\gamma-1}}$$

and hence with Eq. (12.3.4)

$$h_t\rho^2 - \{h_t - \frac{1}{2}(u_1^2+v_1^2)\}\rho_1^2\left(\frac{\rho}{\rho_1}\right)^{\gamma+1} - \frac{1}{2b^2}\{(\frac{\partial\psi}{\partial y})^2 + (\frac{\partial\psi}{\partial x})^2\} = 0 \qquad (12.3.7)$$

Equations (12.3.6) and (12.3.7) are two coupled nonlinear equations for ψ and ρ in terms of the far upstream conditions and the prescribed area variations. When the flow can be approximated as incompressible, the equation for the streamfunction reduces to

$$\nabla^2\psi = \frac{1}{b}\frac{db}{dx}\frac{\partial\psi}{\partial x} \text{ (incompressible)} \qquad (12.3.8)$$

The solution to the above equations is usually dependent upon the application of fully numerical techniques, though analytical methods have been applied in special cases. Refs. 12.11 and 12.12 report upon a study of incompressible flow with area variation. A perturbation analysis is carried out in which it is necessary to restrict the wall slope to be small.

A method that applies conformal mapping techniques to two dimensional (db/dx = 0) transonic flows is described in Ref. 12.13. This paper represents a recent application of a highly developed analytical technique. In conformal mapping techniques, the cascade geometry is transformed to a geometry that is much more simply analyzed (either analytically or numerically), and the results of the analysis in the simple plane are then transformed back to the more complex plane. Because of the utility of such techniques, the next section considers a relatively simple example problem that leads to an exact solution for the flow field.

12.3.1 TWO-DIMENSIONAL, INVISCID, INCOMPRESSIBLE FLOW

When the case of flow of an incompressible, inviscid fluid in a strictly two dimensional channel is considered, the equations describing the flow field simplify greatly, and in fact both the velocity potential and the streamfunction satisfy Laplace's equation. As a result, the very powerful techniques of complex variable theory can be used, including the technique of conformal mapping. Before embarking upon a formal analysis of the problem, however, it is instructive to first consider the force relationships and circulation relationships for a two-dimensional cascade. Figure 12.3.2 depicts the flow through such a cascade.

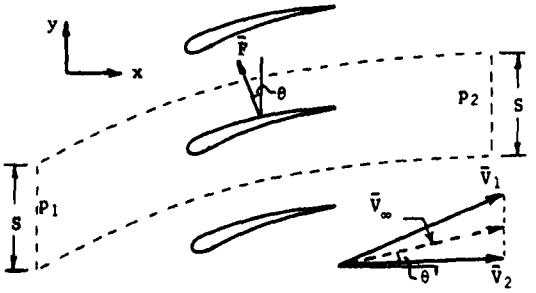

Figure 12.3.2 Flow Through a Two-Dimensional Cascade

Noting that the forces on the two streamlines depicted are equal, and that continuity ensures that the axial (x) velocity remains unchanged, the momentum equation gives

$$F_x = (p_1 - p_2)S\Delta b \qquad (12.3.9)$$

and $$F_y = \rho u(v_1 - v_2)S\Delta b \qquad (12.3.10)$$

Utilizing Bernoulli's equation to relate the pressure difference to velocity differences, the vector force may then be written

$$\bar{F} = \rho S\Delta b(v_1 - v_2)[-\frac{1}{2}(v_2+v_1)\bar{e}_x + u\bar{e}_y] \qquad (12.3.11)$$

Thus the magnitude of the force, F , is given by

$$F = \rho S\Delta b(v_1 - v_2)V_\infty$$

where

$$V_\infty = \{(\frac{v_2+v_1}{2})^2 + u^2\}^{1/2} \qquad (12.3.12)$$

Noting that

$$\tan\theta = \frac{v_2+v_1}{2u} = \tan\theta'$$

it can be seen that the force $\bar{F}$ is perpendicular to the velocity $\bar{V}_\infty$, where

$$\bar{V}_\infty = \frac{1}{2}(\bar{V}_1+\bar{V}_2) \qquad (12.3.13)$$

The circulation about the contour follows immediately to give

$$\Gamma = S(v_1 - v_2) \qquad (12.3.14)$$

so that just as with an isolated airfoil, there is obtained

$$F = \rho\Gamma V_\infty\Delta b \qquad (12.3.15)$$

12.3.2 THE COMPLEX POTENTIAL

When, as in the case of frictionless two-dimensional flow through cascades, the flow may be considered irrotational, a velocity potential may be defined as in Eq. (12.3.2). The continuity equation, Eq. (11.1.1), then gives for incompressible flow,

$$\nabla^2\phi = 0 \qquad (12.3.16)$$

The streamfunction also satisfies Laplace's equation, as may be seen directly from Eq. (12.3.6) for the case of incompressible flow with constant flow depth, b . We thus define a complex potential W , by

$$W = \phi + i\psi \qquad (12.3.17)$$

and note that

$$\nabla^2 W = 0 \qquad (12.3.18)$$

If the complex potential is to satisfy Laplace's equation, it must be a function of $z = x + iy$ only. Thus we may write

$$\frac{\partial W}{\partial x} = \frac{dW}{dz}\frac{\partial z}{\partial x} = \frac{dW}{dz} \qquad (12.3.19)$$

but from Eqs. (12.3.2) and (12.3.4):

$$u = \frac{\partial \phi}{\partial x} = \frac{\partial \psi}{\partial y} \ , \ v = \frac{\partial \phi}{\partial y} = - \frac{\partial \psi}{\partial x} \qquad (12.3.20)$$

and hence

$$\frac{dW}{dz} = u - iv \qquad (12.3.21)$$

In the following sections, a transformation function is introduced to allow solution for the complex potential, W, (for special cases of the cascade geometry), and once W is obtained, the velocity components may be obtained directly from Eq. (12.3.21).

12.3.3 THE CASCADE TRANSFORMATION

In order to illustrate the use of conformal mapping techniques, we consider a transformation that maps a cascade of straight line airfoils onto a circle. The resulting flow in the "circle plane" is relatively easy to analyze, and the cascade mapping function allows the flow in the circle plane to be mapped back into the "physical" plane. This is a relatively simple example of a highly developed analytical technique which has been extensively reported elsewhere. (See Refs. 12.14 and 12.15 for example)

The transformation function to be investigated is

$$z = \frac{S}{2\pi} \left[e^{-i\beta} \ln \frac{e^{\psi} + \zeta}{e^{\psi} - \zeta} + e^{i\beta} \ln \frac{e^{\psi} + 1/\zeta}{e^{\psi} - 1/\zeta} \right] \qquad (12.3.22)$$

We will show that this function takes a unit circle in the ζ plane and maps it into a straight line cascade in the z-plane, with geometry as indicated in Fig. 12.3.3. It is to be noted that for notational convenience, the geometry has been rotated so that the flat plate airfoils are horizontal in the z-plane.

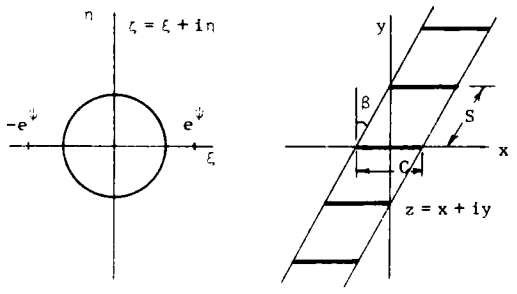

Figure 12.3.3 The Cascade Transformation

To verify that Eq. (12.3.22) has the desired transformation properties, we first note that on the unit circle (where $\zeta = e^{i\xi}$), the second term in the brackets of Eq. (12.3.22) is the complex conjugate of the first. Thus the imaginary part of the expression must be zero (or a constant), and hence the circle is mapped onto the x-axis in the z-plane.

A further property of the transformation is evident in that the points $\zeta = \pm e^{\psi}$ map into $\pm\infty$ in the z-plane. It can be seen also that the mapping is multiple valued by considering the mapping in the neighborhood of the point $\zeta = e^{\psi}$. Thus, consider the behavior of the related point z as we proceed around the point $\zeta = e^{\psi}$ in a small circle of radius r. That is, we consider

$$\zeta = e^{\psi} + re^{i\theta} \ ,$$

and change θ from 0 to 2π radians. It is evident from Eq. (12.3.22) that all the logarithmic terms return to their original value except the term containing $e^{\psi} - \zeta$. Thus denoting the difference of the final and initial values of z as $z_2 - z_1$, there is obtained

$$z_2 - z_1 = - \frac{S}{2\pi} e^{-i\beta} [\ln(-re^{i2\pi}) - \ln(-re^{i0})]$$

$$= - \frac{S}{2\pi} e^{-i\beta} \ln e^{i2\pi}$$

hence

$$z_2 - z_1 = - iSe^{-i\beta} = - S \sin\beta - is \cos\beta \qquad (12.3.23)$$

Thus, the transformation from the ζ to the z-plane is not unique, but rather a given point in the ζ-plane can be reproduced n-times in the z-plane simply by going around the point

$$\zeta = e^{\psi} \ (\text{or} \ \zeta = -e^{\psi})$$

n-times. Each point is removed from the previous by the vector $-s \sin\beta - is \cos\beta$ which leads to the geometrical relationship indicated in Fig. 12.3.3. The ζ-plane may be considered to consist of an infinite number of Riemann-sheets, each sheet mapping to a given strip in the z-plane. The z-plane itself can be considered a two sheet plane because both the inside and outside of the unit circle map into the same strip in the z-plane. We will consider only the mapping of the exterior of the circle, however.

We have shown that Eq. (12.3.22) transforms the unit circle to a series of straight line airfoils in the z-plane. The airfoils are staggered at an angle of β, and have a spacing of magnitude S. In order to determine the airfoil chord in terms of the properties of the mapping function, we locate the transformation singularities which occur at $dz/d\zeta = 0$. (It is at these singularities that the transformation is not conformal, and hence the angle of the circular profile is not conserved in transforming to the z-plane.) We thus note:

$$\frac{dz}{d\zeta} = 0 = e^{-i\beta} \left[\frac{1}{e^{\psi} + \zeta} + \frac{1}{e^{\psi} - \zeta} \right] + e^{i\beta} \left[\frac{1}{\zeta + e^{-\psi}} - \frac{1}{\zeta - e^{-\psi}} \right]$$

After some manipulation we then obtain

$$\zeta_c = \zeta_{\ell} = \frac{e^{i\beta+\psi} + e^{-(i\beta+\psi)}}{e^{-i\beta+\psi} + e^{i\beta-\psi}} \qquad (12.3.24)$$

It can be noted that the numerator and denominator are complex conjugates and hence, of course, the singularities exist on the unit circle in the ζ-plane. A more convenient form of Eq. (12.3.24) is obtained in terms of the angle to the location of the (rear) singularity, ϕ_o, where

$$\zeta_o = e^{i\phi_o} .$$

There is thus obtained

$$\frac{\zeta_o^2-1}{\zeta_o^2+1} = \frac{e^{i\beta}-e^{-i\beta}}{e^{i\beta}+e^{-i\beta}} \frac{e^{\psi}-e^{-\psi}}{e^{\psi}+e^{\psi}}$$

hence $\quad i \tan \phi_o = i \tan \beta \tanh \psi$

or $$\phi_o = \tan^{-1}[\tan \beta \tanh \psi] \qquad (12.3.25)$$

The location of the blade leading edge in the ζ-plane follows immediately by noting $\tan(\phi_o+\pi) = \tan \phi_o$, and hence the leading edge singularity occurs at $\phi_o + \pi$.

A location, x, on the blade in the ζ-plane may be determined by writing $\zeta = e^{i\phi}$. Upon sutstituting into Eq. (12.3.22), and after some manipulation, there is then obtained

$$\frac{2\pi x}{S} = \cos \beta \ln\{\frac{\cosh \psi + \cos \phi}{\cosh \psi - \cos \phi}\} + 2 \sin \beta \tan^{-1}\{\frac{\sin \phi}{\sinh \psi}\} \qquad (12.3.26)$$

The location of the blade trailing edge is then obtained by inserting the value of ϕ_o from Eq. (12.3.25) into Eq. (12.3.26), and the leading edge follows with $\phi = \phi_o + \pi$ to give $x_\ell = -x_t$. We then obtain, with $C = 2x_t$,

$$\frac{\pi C}{2s} = \cos \beta \ln\{\frac{\sqrt{\sinh^2 \psi + \cos^2 \beta} + \cos \beta}{\sinh \psi}\}$$

$$+ \sin \beta \tan^{-1}\{\frac{\sin \beta}{\sqrt{\sinh^2 \psi + \cos^2 \beta}}\} \qquad (12.3.27)$$

This expression relates the parameter ψ to the solidity $\sigma = C/S$. Thus, when the solidity is prescribed the equation may be solved (iteratively) for ψ, and the appropriate transformation function determined. Before considering the behavior of the flow field, one last characteristic of the transformation will be observed. Thus it is noted that the point $\zeta \Rightarrow \infty$ transforms to

$$z \Rightarrow \frac{S}{2\pi} e^{-i\beta} \ln(-1) = \frac{S}{2\pi} e^{-i\beta} \ln[e^{i(2n+1)\pi}]$$

hence $\quad z \Rightarrow S(n+\frac{1}{2})(\sin \beta + i \cos \beta)$

Thus $\zeta \Rightarrow \infty$ transforms into points midway between the blades.

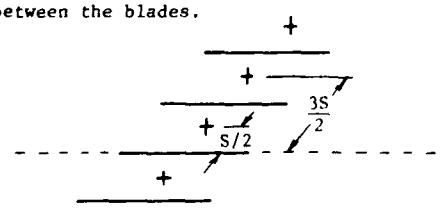

Figure 12.3.4 Location of $\zeta \Rightarrow \infty$ in the z-Plane

This concludes our investigation of the properties of the transformation. In the next section the behavior of the flow field will be considered. It can be noted here, however, that the effect of the tranformation has been to bring upstream and downstream infinity in the x-plane, into the proximity of the circle in the ζ-plane. When circulation about the circle exists, then, the angle of flow in the proximity of $\zeta = \pm e^{\psi}$ ($z = \pm\infty$) can be affected. Thus, unlike the case for an isolated two-dimensional airfoil, the angle of turning of the fluid can be made other than zero.

12.3.4 THE CASCADE FLOW FIELD

Figure (12.3.5) depicts aspects of the flow field in the coordinate system being presently considered.

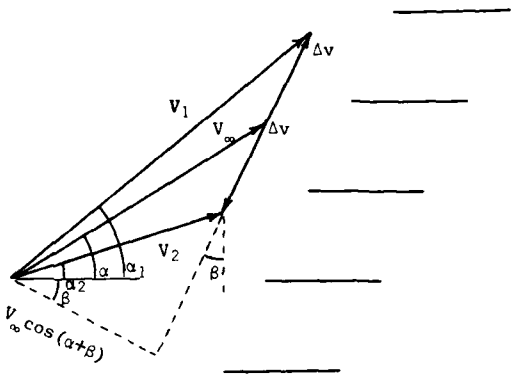

Figure 12.3.5 Cascade Velocities

The mean velocity, V_∞, was previously defined in Eq. (12.3.12), so we may write for the mean complex velocity

$$(u - iv)_\infty = V_\infty e^{-i\alpha}$$

Equation (12.3.14) gave the circulation in terms of the blade spacing change and tangential velocities, which here may be written

$$\Delta v = \frac{\Gamma}{2S} \qquad (12.3.28)$$

Thus, the desired far upstream and far downstream complex velocities may be written

$$\left.\frac{dW}{dz}\right|_{-\infty} = V_\infty e^{-i\alpha} - i \frac{\Gamma}{2S} e^{i\beta} \qquad (12.3.29)$$

$$\left.\frac{dW}{dz}\right|_{+\infty} = V_\infty e^{-i\alpha} + i \frac{\Gamma}{2S} e^{i\beta} \qquad (12.3.30)$$

Figure 12.3.6 indicates these incremental velocity relationships.

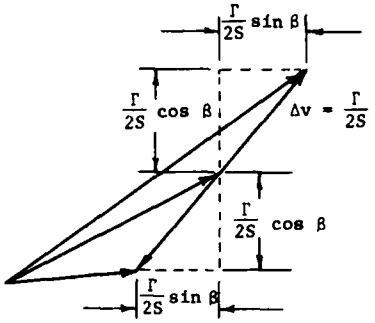

Figure 12.3.6 Incremental Velocity Relationships

In order to create the desired velocities at upstream and downstream infinity, as prescribed in Eqs. (12.3.29) and (12.3.30), we investigate the flow behavior in the circle plane in the vicinity of the points $\pm e^{\psi}$. Thus, by placing (complex) sources at these points, the flow at $\pm\infty$ will be affected in the physical plane. It will then be necessary to adjust conditions in the vicinity of the circle in the ζ-plane in order to satisfy both the boundary condition of no flow through the circle, and the Kutta condition at the trailing edge of the blades in the z-plane. It is to be noted that the adjustments to match the boundary condition and Kutta condition can be carried out without further affecting the flow properties at $z = \pm\infty$, because $dz/d\zeta$ approaches infinity as ζ approaches $\pm e^{\psi}$ (i.e., as z approaches infinity) so the only terms that will contribute to dW/dz at $z = \pm\infty$ are those which cause $dW/d\zeta$ to also approach infinity. The only terms that lead to $dW/d\zeta$ approaching infinity as ζ approaches $\pm e^{\psi}$ arise from the complex sources located at $\zeta = \pm e^{\psi}$.

We now place a complex source of strength A at $\zeta = -e^{\psi}$, so that the complex potential in the vicinity of the source, W_{s-}, may be written

$$W_{s-} = \frac{A}{2\pi}\ln(\zeta + e^{\psi}) \tag{12.3.31}$$

To investigate the behavior near the source we write $\zeta = -e^{\psi} + \delta$, where δ is very small, and obtain

$$\frac{dW_{s-}}{d\zeta} = \frac{A}{2\pi}\frac{1}{\zeta + e^{\psi}} = \frac{A}{2\pi\delta} \tag{12.3.32}$$

From Eqs. (12.3.22) we note

$$\frac{dz}{d\zeta} = \frac{S}{\pi}\left[e^{-i\beta}\frac{e^{\psi}}{e^{2\psi}-\zeta^2} - e^{i\beta}\frac{e^{-\psi}}{\zeta^2-e^{-2\psi}}\right] \tag{12.3.33}$$

In the vicinity of $\zeta = -e^{\psi}$ (where $\delta \to 0$) this approaches

$$\frac{dz}{d\zeta} \to \frac{Se^{-i\beta}}{2\pi\delta} \tag{12.3.34}$$

Combination of Eqs. (12.3.32) and (12.3.34) then gives

$$\left.\frac{dW}{dz}\right|_{-\infty} = \left\{\left.\frac{dW_{s-}}{d\zeta}\right|_{-e^{\psi}}\right\}\left\{\left.\frac{dz}{d\zeta}\right|_{-e^{\psi}}\right\}^{-1} = \frac{A}{S}e^{i\beta}$$

then with Eq. (12.3.29),

$$A = V_{\infty}Se^{-i(\alpha+\beta)} - i\frac{\Gamma}{2} \tag{12.3.35}$$

In a similar manner, placing a source of strength B at the location $\zeta = e^{\psi}$, and satisfying Eq. (12.3.30) leads to

$$B = -V_{\infty}Se^{-i(\alpha+\beta)} - i\frac{\Gamma}{2} \tag{12.3.36}$$

With the two sources at locations $\zeta = \pm e^{\psi}$, we have a complex potential, $F(\zeta)$, in the ζ-plane given by

$$F(\zeta) = \frac{SV_{\infty}}{2\pi}e^{-i(\alpha+\beta)}\ln\frac{\zeta+e^{\psi}}{\zeta-e^{\psi}} - i\frac{\Gamma}{4\pi}\ln(\zeta^2-e^{2\psi}) \tag{12.3.37}$$

A complex potential satisfying the boundary condition for flow around the circle can now be obtained by adding a complex function of the form of Eq. (12.3.37), but with i replaced by -i (where i appears explicitly), and with ζ replaced by $1/\zeta$. This result (known as the circle theorem, Ref. 12.16) follows because the added function becomes the complex conjugate of $F(\zeta)$ when ζ is on the unit circle, and hence ψ is zero on the circle. (And, of course, the circle is hence a streamline.) Finally, a circulation Γ^* is added at $\zeta = 0$ (which does not violate the boundary conditions) to give the complex potential in the ζ-plane, W. Thus

$$W = \frac{SV_{\infty}}{2\pi}e^{-i(\alpha+\beta)}\ln\frac{e^{\zeta+\psi}}{e^{\psi}-\zeta} - i\frac{\Gamma}{4\pi}\ln(e^{2\psi}-\zeta^2)$$

$$+ \frac{SV_{\infty}}{2\pi}e^{i(\alpha+\beta)}\ln\frac{e^{\psi}+1/\zeta}{e^{\psi}-1/\zeta} + i\frac{\Gamma}{4\pi}\ln(e^{2\psi}-1/\zeta^2)$$

$$+ i\frac{\Gamma^*}{2\pi}\ln\zeta \tag{12.3.38}$$

Investigation of this expression reveals that application of the circle theorem has introduced further singularities at the conjugate points of $\pm e^{\psi}$, that is at $\zeta = \pm e^{-\psi}$. Figure 12.3.7 indicates the location and strength of all the singularities in the circle plane.

It is evident that, as must be the case, the total source strength is zero. The net circulation about the circle is Γ^*, and the net circulation about the entire field is $\Gamma^*-\Gamma$. It will be recalled that when the ζ-plane is entirely traversed at infinity, the image point in the z-plane simply traverses a point midway between the blades. Obviously the circulation about such a point must be zero, so we require $\Gamma^* = \Gamma$. The expression for the velocity potential in the circle plane may hence be written:

$$W = \frac{SV_{\infty}}{2\pi}\left[e^{-i(\alpha+\beta)}\ln\frac{e^{\psi}+\zeta}{e^{\psi}-\zeta} + e^{i(\alpha+\beta)}\ln\frac{\zeta+e^{-\psi}}{\zeta-e^{-\psi}}\right.$$

$$\left. - \frac{i\Gamma}{4\pi}\ln\frac{e^{2\psi}-\zeta^2}{e^{2\psi}\zeta^2-1}\right] \tag{12.3.39}$$

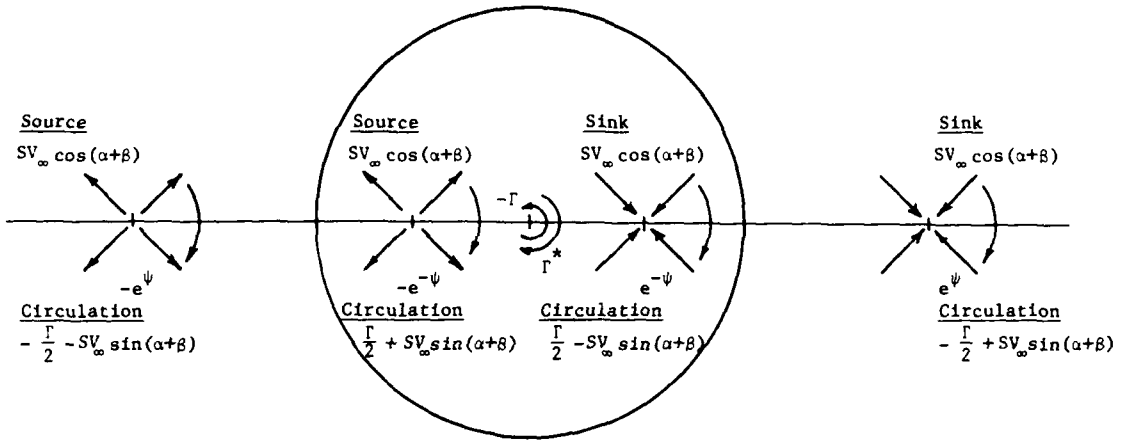

Figure 12.3.7 Singularities in the Circle Plane

The complex potential given by Eq. (12.3.39) describes a flow field that, when transformed to the z-plane, matches the upstream and downstream conditions as well as the boundary conditions for flow around the blades. To complete the description of the flow field it remains to determine an appropriate value for the circulation Γ. Such a condition is obtained by applying the Kutta condition that the velocity not be infinite at the trailing edge of the blades. At the location of the trailing edge (where $\phi = \phi_o$, Eq. (12.3.25) the derivative $dz/d\zeta$ is zero. Thus to prevent an infinite velocity at the trailing edge in the z-plane, Γ must be chosen to put $dW/d\zeta = 0$ at $\zeta = e^{i\phi_o}$.

Taking $dW/d\zeta$ from Eq. (12.3.39), and putting $\zeta = e^{i\phi}$, the complex velocity components for the flow on the circle are obtained, to give after some manipulation.

$$\left.\frac{dW}{d\zeta}\right|_{\zeta=e^{i\phi}} = e^{-i\phi}(u_r - iu_\phi)$$

$$= \frac{i}{2\pi}\frac{e^{-i\phi}}{\cosh 2\psi - \cos 2\phi}\{4SV_\infty[\sin\phi\cosh\psi\cos(\alpha+\beta) - \cos\phi\sinh\psi\sin(\alpha+\beta)] + \Gamma\sinh 2\psi\} \tag{12.3.40}$$

It can be seen that as required, $u_r = 0$. The Kutta condition requires $u_\phi = 0$ when $\phi = \phi_o$. We have from Eq. (12.3.25)

$$\sin\phi_o = \frac{\sinh\psi\sin\beta}{\sqrt{\sinh^2\psi+\cos^2\beta}}, \quad \cos\phi_o = \frac{\cosh\psi\cos\beta}{\sqrt{\sinh^2\psi+\cos^2\beta}} \tag{12.3.41}$$

The value of circulation necessary to satisfy the Kutta condition, Γ_K, then follows to give

$$\Gamma_K = \frac{2SV_\infty \sin\alpha}{\sqrt{\sinh^2\psi+\cos^2\beta}} \tag{12.3.42}$$

When this value of the circulation is substituted into Eq. (12.3.40), it follows after some manipulation that

$$\left.\frac{dW}{d\zeta}\right|_{\zeta=e^{i\phi}} = -\frac{i2SV_\infty}{\pi}\frac{e^{-i\phi}}{\sin 2\phi_o}\frac{\cosh\psi\sin\psi}{\sqrt{\sinh^2\psi+\cos^2\beta}} \times \frac{\sin(\phi_o-\phi)}{\sinh^2\psi+\sin^2\phi}[\cos\beta\sin(\alpha+\beta) - \sin\alpha\cos\phi_o\frac{\cos\left(\frac{\phi_o+\phi}{2}\right)}{\cos\left(\frac{\phi_o-\phi}{2}\right)}] \tag{12.3.43}$$

To obtain the complex velocity on the blade surface, we note that on the blade $\zeta = e^{i\phi}$, and $z = x$, so that

$$\frac{dz}{d\zeta} = -ie^{-i\phi}\frac{dx}{d\phi} \tag{12.3.44}$$

$dx/d\phi$ may be obtained directly from Eq. (12.3.26). Thus it follows that

$$\frac{dz}{d\zeta} = -\frac{i2S}{\pi}\frac{e^{-i\phi}}{\sin 2\phi_o}\frac{\cosh\psi\sinh\psi}{\sqrt{\sinh^2\psi+\cos^2\beta}} \times \frac{\sin(\phi_o-\phi)}{(\sinh^2\psi+\sin^2\phi)\sin\beta\cos\beta} \tag{12.3.45}$$

The velocity on the blade surface follows directly from Eqs. (12.3.43) and (12.3.45) to give

$$\left.\frac{dW}{dz}\right|_{\text{blade}} = \frac{dW}{d\zeta}\left[\frac{dz}{d\zeta}\right]^{-1}$$

$$= \frac{V_\infty}{\sin\beta\cos\beta}[\cos\beta\sin(\alpha+\beta) - \sin\alpha\cos\phi_o\frac{\cos\left(\frac{\phi_o+\phi}{2}\right)}{\cos\left(\frac{\phi_o-\phi}{2}\right)}] \tag{12.3.46}$$

To complete the description of the flow in the cascade plane, the various flow angles will be obtained. With reference to Fig. 12.3.5, we

note the relationships

$$\frac{\Delta v}{V_\infty \cos(\alpha+\beta)} = \tan(\alpha+\beta) - \tan(\alpha_2+\beta)$$
$$= \tan(\alpha_1+\beta) - \tan(\alpha+\beta) \qquad (12.3.47)$$

Equations (12.3.28), (12.3.42), and (12.3.47) then lead to

$$\alpha_1 = \arctan\left[\sin\alpha \frac{\sqrt{\sinh^2\psi + \cos^2\beta} + \cos\beta}{\sqrt{\sinh^2\psi + \cos^2\beta}\,(\cos\alpha) + \sin\beta\sin\alpha}\right]$$

$$\alpha_2 = \arctan\left[\sin\alpha \frac{\sqrt{\sinh^2\psi + \cos^2\beta} - \cos\beta}{\sqrt{\sinh^2\psi + \cos^2\beta}\,(\cos\alpha) - \sin\beta\sin\alpha}\right] \qquad (12.3.48)$$

These equations complete the desired description of the flow field. They are summarized in a form suitable for calculation in the next section.

12.3.5 SUMMARY OF THE EQUATIONS - CASCADE TRANSFORMATION

Inputs: β, $\frac{C}{S}$, α, ϕ

Outputs: $\frac{x}{C}$, $\frac{u}{V_\infty}$, α_1, α_2

Equations:

$$\frac{\pi C}{2S} = \cos\beta \ln \frac{\sqrt{\sinh^2\psi + \cos^2\beta} + \cos\beta}{\sinh\psi} + \sin\beta \tan^{-1} \frac{\sin\beta}{\sqrt{\sinh^2\psi + \cos^2\beta}}$$

$$\zeta = \arctan(\tan\beta \tanh\psi)$$

$$\frac{x}{C} = \frac{1}{2\pi C/S}\left[\cos\beta \ln \frac{\cosh\psi + \cos\phi}{\cosh\psi - \cos\zeta} + 2\sin\beta \tan^{-1}\frac{\sin\phi}{\sinh\psi}\right]$$

$$\frac{u}{V_\infty} = \frac{1}{\sin\zeta\cos\beta}\left[\cos\zeta\sin(\alpha+\beta) - \sin\alpha\cos\phi_o \frac{\cos\left(\frac{\phi_o+\phi}{2}\right)}{\cos\left(\frac{\phi_o-\phi}{2}\right)}\right]$$

$$\alpha_1 = \arctan\left[\sin\alpha \frac{\sqrt{\sinh^2\psi + \cos^2\beta} + \cos\beta}{\sqrt{\sinh^2\psi + \cos^2\beta}\,(\cos\alpha) + \sin\beta\sin\alpha}\right]$$

$$\alpha_2 = \arctan\left[\sin\alpha \frac{\sqrt{\sinh^2\psi + \cos^2\beta} - \cos\beta}{\sqrt{\sinh^2\psi + \cos^2\beta}\,(\cos\alpha) - \sin\beta\sin\alpha}\right]$$

12.3.6 EXAMPLE RESULTS - TWO-DIMENSIONAL STRAIGHT LINE CASCADE

The equations summarized in the preceding section lead to rapid computation of the performance variables of this ideal straight line cascade. The results are useful for detecting design trends of real cascades, and in fact techniques to relate the performance of more complicated (and more realistic) geometries to an equivalent straight line cascade have been developed. (Ref. 12.15 for example) The singularity in fluid velocity remains at the blade leading edges, but the fluid velocities at blade locations away from the leading edges exhibit the tendencies of the flow fields existing on real geometries.

As an example calculation Fig. 12.3.8 shows the deviation angle (α_2) versus angle of attack (α_1) for three values of blade stagger angle and two values of the solidity.

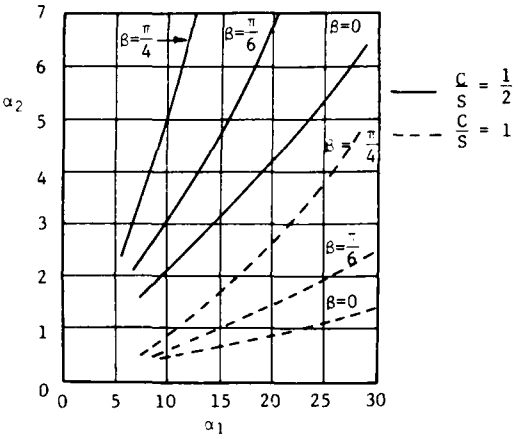

Figure 12.3.8 Deviation Angle Versus Angle of Attack

It is apparent that the reduced blade loading existing for the case of high solidity greatly reduces the tendency of the flow to depart from the angle of the blade trailing edge. The deviation angle also varies strongly with stagger angle, with large stagger angles causing increases in deviation angle. It is evident from Fig. 12.3.9 that increasing the stagger angle leads to geometrical separation of the blades, so that the pressure fields of the blades do not interact as much at higher stagger angles.

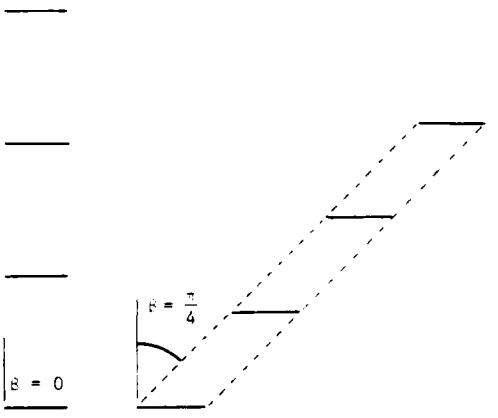

Figure 12.3.9 Cascades at Two Stagger Angles C/S = 0.5

It is of interest to note that this effect of increasing stagger angle is not as limiting at it might at first appear. Thus, the example calculations of Sections 10.2.1 and 10.3.4 indicated that

the required turning angles near the blade tips are very much reduced compared to those at the hub, for a compressor or turbine with large tip to hub ratio. Hence, even though the geometry of a compressor or turbine is such that solidity decreases and the blade stagger angle increases with increasing radius, the effects of these geometry changes is much mitigated by the large reduction in required turning angle of the cascade.

As a final calculational example, the deviation angle versus solidity has been calculated for the case of constant angle of attack. (Note that this calculation required iteration of the input variable, α_1, to obtain the desired angle of attack $\alpha_1 = 15°$.) The results shown in Fig. 12.3.10 indicate once again the sensitivity of the deviation angle to solidity.

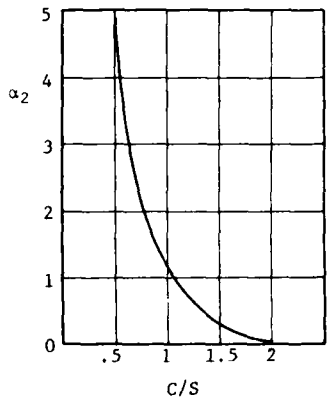

Figure 12.3.10 Deviation Angle Versus Solidity

These relatively simple results provide a method of quickly estimating the effects of design choices upon the overall cascade performance. Extensions of the method, such as those described in Refs. 12.13-12.15 lead to rapid computer solution for much of the detailed information of realistic (ideal) flow fields. As has hopefully been evident throughout this document, however, the analytical cascade results contribute only a portion of the information desired in the very complicated process of designing the optimum compressor. Careful experimental studies, in the form of cascade tests, have contributed invaluable information for researchers and designers. Finally, the effects of interactive loss mechanisms such as wake shedding and thence wake chopping by the following blade row, annulus wall boundary layer buildup and interaction with the blade pressure fields, blade boundary layer buildup and interaction with the centrifugal field etc.,etc. must all be included in a careful program to develop the best possible compressor or turbine.

12.4 REFERENCES

(12.1) Pianko, M. (ed.) Modern Methods of Testing Rotating Components of Turbomachines, AGARD-A6-167, September 1972.

(12.2) Taylor, E. S., Boundary Layers, Wakes and Losses in Turbomachines, M.I.T.G.T.L. Report No. 105, April 1971.

(12.3) Hawthorne, W. R., The Applicability of Secondary Flow Analysis to the Solution of Internal Flow Problems "in" Fluid Mechanics of Internal Flow, Sovran, G. (ed.) Elsivier, Amsterdam, 1967, pp. 238-269.

(12.4) Lefcort, M. D., Wake Induced Unsteady Blade Forces in Turbo-Machines, M.I.T.G.T.L. Report No. 70, November 1962.

(12.5) Kemp, N. H. and Sears, W. R., "The Unsteady Forces Due to Viscous Wakes in Turbomachines, Journal of Aeronautical Sciences, Vol. 22, 1955, pp. 478-483.

(12.6) Meyer, R. X., Interference Due to Viscous Wakes Between Stationary and Rotating Blades in Turbomachines, Dr. of Engr. Thesis, Johns Hopkins University, 1955.

(12.7) Kerrebrock, J. L. and Mikolajczak, A. A., Intra-Stator Transport of Rotor Wakes and Its Effect on Compressor Performance, Trans. ASME Series A, Vol. 92, Journal of Engineering for Power, October 1970, pp. 359-368.

(12.8) Johnsen, A. I. and Bullock, R. O. (ed.) Aerodynamic Design of Axial-Flow Compressors, NASA SP-36, 1965.

(12.9) Vincent, E. T., Theory and Design of Gas Turbines and Jet Engines, McGraw-Hill, 1950.

(12.10) Cohen, H., Rogers, G. F. C., Saravanamutto, H. J. H., Gas Turbine Theory, John Wiley & Sons, New York, 1973.

(12.11) Mani, Ramani and Acosta, A. J., Quasi-Two-Dimensional Flows Through a Cascade, Trans. ASME, Journal of Power, Vol. 90, No. 2, April 1968.

(12.12) Wislon, M. B., Mani, R., and Acosta, A. J., A Note on the Influence of Axial Velocity Ratio on Cascade Performance, pp. 101-133 in Fluid Mechanics, Acoustics and Design of Turbomachinery, Part I, NASA SP-304, 1974.

(12.13) Ives, David C., A Modern Look at Conformal Mapping Including Multiple Connected Regions, AIAA J., Vol. 14, Aug. 1976, pp. 1006-1011.

(12.14) Lighthill, M. J., A Mathematical Method of Cascade Design, British Aeronautical Research Council Reports and Memo No. 2104, 1945.

(12.15) Weinig, F. S., Theory of Two-Dimensional Flow Through Cascades, in Aerodynamics of Turbines and Compressors, Vol. 10 of High Speed Aerodynamics and Jet Propulsion, Princeton, 1964.

Chapter 13

CONSIDERATIONS IN INLET/ENGINE INTEGRATION

by J.L. Younghans and D.L. Paul

General Electric Company
Aircraft Engine Group
Evendale, Ohio

TABLE OF CONTENTS

CHAPTER 13 CONSIDERATIONS IN INLET/ENGINE INTEGRATION

		Page
13.0	Introduction	13-1
13.1	Elements of a Successful Inlet/ Engine Integration Program	13-1
13.1.1	Definition of Subsonic Inlet/ Engine Operational Requirements.	13-1
13.1.2	Definition of Supersonic Inlet/ Engine Operational Requirements.	13-7
13.1.3	Engine Impact on Inlet Design	13-9
13.1.4	Inlet Impact on Engine Design	13-12
13.2	Validation of Inlet/Engine System.	13-16
13.2.1	Background and Basic Considerations	13-16
13.2.2	Analytical Evaluation of Inlet and Engine Operation	13-17
13.2.3	Engine Development Test Elements for Inlet Integration	13-19
13.2.4	Inlet Development Test Elements for Engine Integration	13-22
13.2.5	Flight Testing: The Acid Test	13-23
13.3.1	References	13-23

LIST OF FIGURES

		Page
Figure 13.1.1	Specific Corrected Flow Versus Mach Number for $\gamma = 1.4$	13-2
Figure 13.1.2	Definition of Inlet Capture Area A_I and Characterization of Flow Incidence Approaching Inlet Via Mass Flow Ratio A_o/A_i	13-3
Figure 13.1.3	Schematic Illustration of Key Operating Conditions Involving Relatively Large Flow Incidence Approaching Inlet Lip.	13-3
Figure 13.1.4	Representative STOL Inlet Design Requirements, per Reference 13.1	13-4
Figure 13.1.5	Experimentally Determined STOL Inlet Separation Boundaries at Angle of Attack	13-4
Figure 13.1.6	Effect of Inlet Separation on Angle of Attack Performance for STOL Inlet, $V_o \approx 80$ kn	13-4
Figure 13.1.7	Effect of Mass Flow Ratio and Inlet Cowl Diameter Ratio on Inlet Spillage Drag Coefficient	13-5
Figure 13.1.8	Example of an Inlet Employing Four Acoustically Treated Rings for Additional Noise Suppression	13-5
Figure 13.1.9	Relationship Between Local Inlet Flow Acceleration and Noise Suppression	13-5
Figure 13.1.10	Representative Contracting Cowl Sonic Inlet Test Configuration	13-6
Figure 13.1.11	Schematic Representation of Inlet/Ground Vortex Formation	13-6
Figure 13.1.12a	Typical Tactical Fighter Placard	13-7
Figure 13.1.12b	Representative Supersonic Inlet Maneuver Design Requirements	13-7
Figure 13.1.13	Recovery Versus Mass Flow Ratio, Showing Operating Regimes for a Mixed Compression Inlet	13-8
Figure 13.1.14	Comparison of Supersonic Inlet Diffuser Types	13-8
Figure 13.1.15	Subsonic Inlet Sizing Considerations	13-10
Figure 13.1.16	Typical Engine Corrected Airflow Demand Variation with Flight Mach Number	13-10

LIST OF FIGURES Continued

		Page
Figure 13.1.17	Elements of Inlet Airflow Supply Determination . . .	13-11
Figure 13.1.18	Inlet/Engine Flow Matching for a Supersonic Cruise Sizing Point	13-11
Figure 13.1.19	Compatibility Assessment of Inlet Buzz and Minimal Flow Demand Characteristics . .	13-12
Figure 13.1.20	Predicted Hammershock Overpressure Correlation for Inlet Duct Structural Design	13-12
Figure 13.1.21	Inlet Control System Pressure Measurements and Schematic Interface Diagram	13-13
Figure 13.1.22	Schematic Representation of the Typical Need for Engine Airflow Tailoring, Transonic Inlet Sizing Point .	13-13
Figure 13.1.23	Effect of Power Setting on Installation Losses	13-14
Figure 13.1.24	Representative Installation Losses for Mach 0.9/36K ft Operation of a Mach 2.5 Aircraft with a Mixed-Flow Turbofan Engine	13-14
Figure 13.1.25	Schematic of Variable Cycle Engine Concept	13-14
Figure 13.1.26	Improvement in Maximum Supersonic Airflow Capacity with Advanced Variable Cycle Engine	13-14
Figure 13.1.27	Improvement in Subsonic Part Power Flow Matching Via Variable Cycle Engines for the Same Cycle Parameters	13-15
Figure 13.1.28	Typical Aerodynamic Performance Map for Fan or Compressor Component	13-15
Figure 13.1.29	Cumulative Representation of Degraded Surge and Operating Lines for a Compression Component, Leading to Reduced Stability Margin for Inflow Distortion . . .	13-15
Figure 13.2.1	Stability Experience of Some Operational USAF Systems, 1954-1967	13-16
Figure 13.2.2	Example of an Inlet/Engine Stability Development Test Program	13-17

LIST OF FIGURES Concluded

		Page
Figure 13.2.3	Comparison of Calculated and Measured Internal Surface Pressure Distributions for a Translating Centerbody Inlet in the Unchoked Mode . .	13-18
Figure 13.2.4	Example of Boundary Layer Separation Prediction Capability	13-18
Figure 13.2.5	Representative Engine Compression System Test Sequence for Inlet Integration	13-19
Figure 13.2.6	Circumferential (1/Rev) Distortion Screen	13-20
Figure 13.2.7	Compressor Map Showing Effect of Inlet Distortion on Surge Margin	13-20
Figure 13.2.8	F-111 Wind Tunnel Inlet Model Configuration	13-21
Figure 13.2.9	Variable Ramp Type of Unsteady Flow Generator for Engine Compression System Evaluation	13-21
Figure 13.2.10	Unsteady and Spatial Temperature Distortion Generator for Engine Compression System Evaluation	13-21
Figure 13.2.11	Peebles Facility Crosswind Test Arrangement	13-22
Figure 13.2.12	DC-10/CF6 Installation on B-52 Flying Test Bed	13-22
Figure 13.2.13	Representative Inlet Development Test Sequence for Engine Integration	13-23

NOMENCLATURE

Symbols: (The use of a consistent set of units is assumed.)

A	Area
C_D	Inlet drag coefficient, $F_D/q_o A_{MAX}$ where A_{MAX} refers here to maximum nacelle cross-sectional area
Cf_{MIN}	Minimum value of wall friction coefficient
D	Diameter
F_D	Drag force
F_{MAX}	Maximum value of boundary layer separation parameter from compressibility-adjusted Stratford and Beavers method
g	Gravitational constant
h	Pressure altitude
K	Overpressure parameter, equation 13.1.7
L	Inlet length from highlight to fan or compressor rotor leading edge
M	Mach number
$\dot{m}$	Mass flow rate
N	Fan or compressor rotational speed
ΔPNdB	An incremental change in perceived noise level in decibels
P_T	Total pressure
p	Static pressure
q	Incompressible dynamic pressure, $(1/2)\rho V^2$
R	Gas constant for air
S	Stagnation point
SFC	Specific fuel consumption
T	Static temperature
T_T	Total temperature
V	Velocity
X	Inlet forebody length
α	Angle of attack; bypass ratio
γ	Specific heat ratio for air
δ	Corrected total pressure, P_T/P_{STD}
θ	Corrected total temperature, T_T/T_{STD}
π_c	Fan or compressor (total) pressure ratio
π_d	Inlet total pressure recovery

Subscripts:

AVG	Average
CB	Cowl bleed
CW	Crosswind
EFF	Effective
F	Fan tip
HL	Highlight, the inlet nose point whose tangent is normal to the inlet centerline
i	Inlet incidence; also refers to inlet highlight or capture area
MAX	Maximum
MIN	Minimum
NS	Normal shock
net	Refers to net airflow available to satisfy engine-related demand, i.e., inlet capture flow less aircraft-related flow demands
S	Separation
SP	Spillage
STD	Standard sea level atmospheric value
T.O.	Takeoff
th	Throat
w	Wall
0	Freestream
1	Engine spinner plane
2	Plane of inlet diffuser exit and engine face

CHAPTER 13

CONSIDERATIONS IN INLET/ENGINE INTEGRATION

13.0 INTRODUCTION

The manner in which the inlet and engine designs are integrated plays a key role in determining the degree to which propulsion system and aircraft operational goals are ultimately realized in the production article. This is true for subsonic transport applications, as well as transonic and supersonic installations, although the latter's potential problems are generally more extensive. Perhaps the leading example of this situation occurred with the advent of turbofan engine installations in tactical aircraft during the 1960's, when inlet/engine operational difficulties well in excess of anticipated or tolerable levels were experienced. Resolution of this problem involved assessing the importance of time variant, or unsteady, pressure distortion produced by the inlet. This is a prime example of the multidimensional effects, mentioned in Chapter 6, associated with inlet operation that can degrade installed performance. In this particular case, the absence of one-dimensionality extends to both dimensions of space (variation of flow properties over the engine face at a given instant of time) and time (similar variation, except as a function of time). As the subject of measurement and evaluation of time variant distortion is specifically developed in Chapter 23, which deals with engine stability, it is sufficient to say here that this problem revolutionized integration of the aircraft and propulsion system, introducing a necessary complication that has continued to the present.

Lack of an effective program to integrate the aircraft inlet and engine during their development phases can result in unacceptable aircraft performance, as reflected by one or more of the following figures of merit:

- Range/Payload
- Maneuverability
- Weapons Delivery and Gun Firing
- Engine Life and/or Maintenance Costs

Since the desirability of successfully blending the inlet and engine seems self-evident, its accomplishment may appear straightforward. In practice, however, various impediments exist during the development cycles. For example, component performance may be emphasized at the expense of obtaining the best overall integrated system performance, in order to meet or exceed contract guarantees. Thus "component optimization" may result in "system suboptimization" in terms of aircraft capability. This somewhat natural tendency can be amplified by the multiorganizational structure that generally prevails during inlet and engine development - customer, airframer, and engine manufacturer. In addition, cost and time considerations may strongly shape the available development integration effort.

The ensuing discussion will develop the elements of a successful inlet/engine integration program. These elements include careful definition of the required inlet and engine operational requirements, consideration of the various ways in which the inlet and engine may interact to influence the other's design, several phases of developmental component and system testing, and frequent information exchange supplemented by formalized, periodic meetings between cognizant aircraft and engine design personnel. The potential need for modification of individual component performance goals/guarantees, based on demonstrated or projected capabilities, with the purpose of maximizing overall aircraft performance, must be kept in mind during an ongoing development program. This chapter should convince the reader that more than serendipity is required for achievement of a successful flight test demonstration. Rather, a successful flight test demonstration is characteristically the product of at least three to four years of concentrated, well-coordinated effort between aircraft and engine developers under ultimate customer cognizance.

13.1 ELEMENTS OF A SUCCESSFUL INLET/ENGINE INTEGRATION PROGRAM

The first step in embarking on the design integration of the inlet/engine combination, as with any design task, is establishment of the functional requirements to be placed upon the design. These are primarily dictated by the desired aircraft capability, toward which end all aspects of the propulsion system development must be responsive. Basic component performance levels must sometimes be compromised, when necessary and where feasible, to achieve this overriding objective. Once initiated, the individual inlet and engine design efforts must consider the interactions that will inherently exist, such that various pitfalls in achieving a harmonious installation are avoided. These factors can be increasingly investigated during the development phases, which involve various component and system tests. However, a point is generally reached, during this period but well before first flight, where the design configurations must of necessity be "frozen", to facilitate efficient fabrication. Thus, design modifications must be made under some time pressure, often without complete knowledge of all pertinent factors. Integration planning must consider this fact of life so that development activities are structured to provide a maximum of needed information to the designers at a time when configuration flexibility still exists. Provision for frequent transmittal of information and coordination between the aircraft, engine and customer organizations, together with periodically scheduled audits to review progress and adjust future plans as required, are keystones of success in this endeavor.

The following remarks will elaborate upon the considerations just set forth. Due to the complexity of the subject and the wide range of configurations with singular operational requirements, the discussion is not intended to be all-inclusive. Rather, it should serve to illustrate the kinds of factors requiring attention to produce a successful inlet/engine interface.

13.1.1 DEFINITION OF SUBSONIC INLET/ENGINE OPERATIONAL REQUIREMENTS

Specification of operational requirements for the inlet and engine is largely driven by the intended aircraft capabilities. For example, a subsonic transport will spend a dominant proportion of its flight time at cruising speed and altitude,

with the main objective being delivery of a specified payload over a certain distance or range within some allowable total fuel consumption. This is the classic example of a (primarily) single design point application. By contrast, the last decade has witnessed the emergence of military aircraft designed to multimission capability. These roles may include high speed/low altitude penetration, transonic maneuvering, and supersonic dash to fulfill the vehicle's intended objectives. Such specifications strongly impact the propulsion system's design and operating conditions. Requirements typically facing subsonic installations are discussed next. It is understood that some of these are mandatory for the basic vehicle success, while others are less crucial and may be traded to some extent in the interests of overall capability. The prioritization involved is beyond the scope of this discussion, but it must obviously be addressed in an actual development program, via figures of merit or ranking criteria appropriate to the particular application.

The areas deserving attention in developing a subsonic transport type of installation may be loosely categorized and explained as follows.

FLIGHT CONDITIONS PRODUCING HIGH INLET INFLOW INCIDENCE

There are several common flight conditions that involve large incidence of the flow approaching the inlet lip, relative to the inlet axis. Foremost among these are takeoff rotation and climb, and landing approach. Other less common but design-significant points are takeoff during crosswind and takeoff climb with a failed engine. Such conditions must be examined because they typically result in a rapid acceleration and deceleration of the flow as it proceeds around the inlet lip, raising the possibility of flow separation during the flow recompression due to the adverse pressure gradient. Flow separation can degrade vehicle performance, either through decreased inlet pressure recovery and/or increased flow distortion causing compression system surge and possibly flameout in the case of internal flow separation, or increased inlet drag for external flow separation.

The inlet mass flow ratio developed in Chapter 6 is the parameter that best describes the approaching flow pattern. For ease of computation the mass flow ratio may be expressed as

$$\frac{A_o}{A_1} = \frac{\left(\dot{m}_2\sqrt{\theta_2}/\delta_2\right)\left(\delta_2/\delta_o\right)}{\left(\dot{m}\sqrt{\theta}/\delta A\right)_o\left(A_1\right)} = \frac{\left(\dot{m}_2\sqrt{\theta_2}/\delta_2\right)\left(\pi_d\right)}{\left(\dot{m}\sqrt{\theta}/\delta A\right)_o\left(A_1\right)} \qquad (13.1.1)$$

in which there have been utilized the facts that the inlet compression is adiabatic ($\theta_2 = \theta_o$) and typically no mass transfer occurs in a subsonic inlet ($\dot{m}_2 = \dot{m}_0$). The inlet pressure recovery π_d is generally within 1% of unity for most subsonic installations and may be neglected without major effect in most preliminary studies. The specific corrected flow term in the denominator of Eq. (13.1.1) may be expressed, utilizing continuity, the perfect gas equation and the relationships for stagnation temperature and pressure in terms of Mach number, as follows:

$$\frac{\dot{m}\sqrt{\theta}}{\delta A} = p_{STD}\sqrt{\frac{\gamma g}{RT_{STD}}}\;\frac{M}{\left(1+\frac{\gamma-1}{2}M^2\right)^{\frac{\gamma+1}{2(\gamma-1)}}} \qquad (13.1.2)$$

hence for $\gamma = 1.4$, $R = 53.34$ lbf-ft/lbm-°R and inserting the standard temperature and pressure,

$$\frac{\dot{m}\sqrt{\theta}}{\delta A} = 85.386\;\frac{M}{\left(1+0.2\,M^2\right)^3}\;\;\frac{\text{lbm/sec}}{\text{ft}^2}\,, \qquad (13.1.3)$$

so that the specific corrected flow is a function only of Mach number, for a given specific heat ratio. This relationship may be tabulated or plotted to facilitate computation. A plot is shown in Figure 13.1.1; it illustrates the familiar maximization at the sonic point. For convenience,

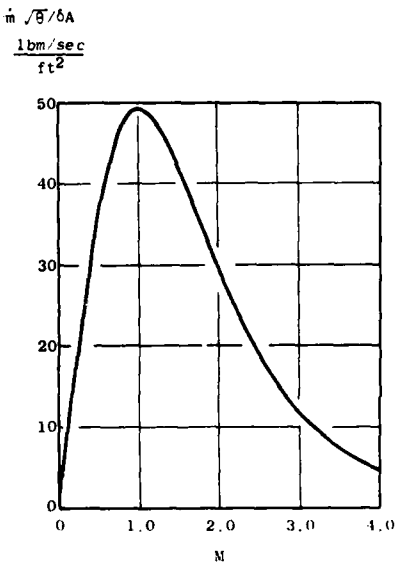

Figure 13.1.1 Specific Corrected Flow Versus Mach Number for $\gamma = 1.4$.

the subsonic inlet area A_1 is generally defined as the highlight value, i.e. the projected area at the point where a normal to the inlet axis is tangent to the inlet nose, as shown in Figure 13.1.2. This terminology eliminates the complexity of determining the stagnation point location for a variety of operating conditions, which would be impractical.

For subsonic inlets, the numerical value of A_o/A_1 is a direct indication of the general incidence of the flow approaching the inlet. Referring to Figure 13.1.2, a value of unity means that the inlet is capturing its projection in the freestream and the stagnation point will occur at the inlet highlight, for level flight. A_o/A_1 less than unity indicates flow is prediffusing in the freestream such that an outward flow incidence occurs; this is generally the case for cruise flight speeds. Conversely, A_o/A_1 will exceed unity at low flight speeds and moderate to high

power settings, such that an inward flow incidence develops with the stagnation point on the outer portion of the lip.

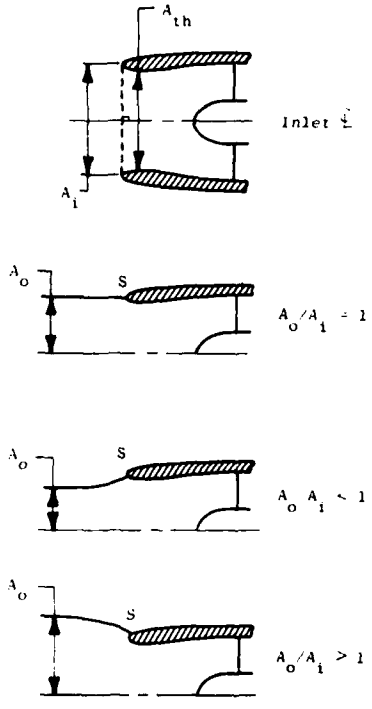

Figure 13.1.2 Definition of Inlet Capture Area, A_i, and Characterization of Flow Incidence Approaching Inlet via Mass Flow Ratio, A_o/A_i

The specific operating conditions mentioned previously are schematically represented in Figure 13.1.3 in terms of the approaching flow incidence. These situations add the effect of a velocity component normal to the freestream to the basic mass flow ratio effect. The top three conditions (takeoff rotation and climb, landing approach, and crosswind takeoff) involve a mass flow ratio greater than one that is accentuated either by a non-zero pitch attitude or a prevailing ground wind normal to the inlet axis. This introduces the possibility of internal lip flow separation with attendant performance degradation and reduction in engine stability margin that may lead to compressor surge, blade damage or life reduction, and possibly burner flameout.

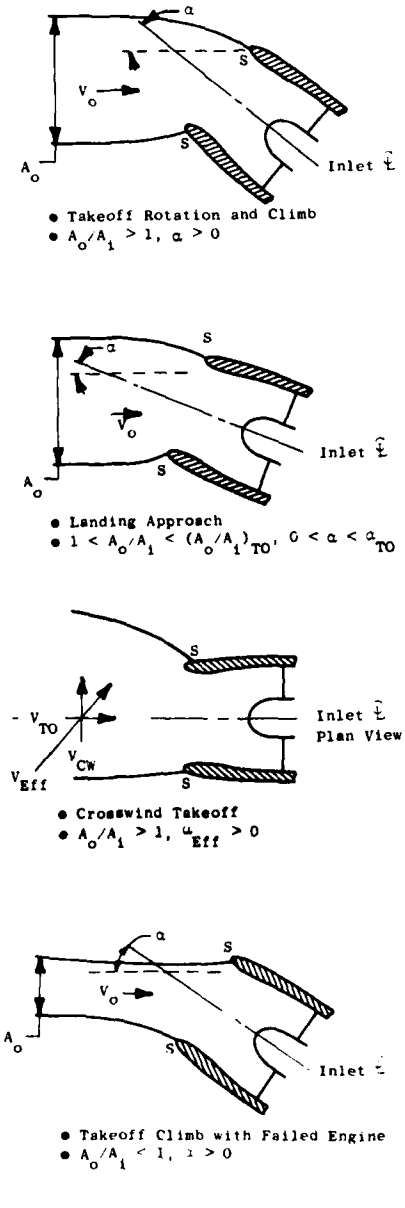

Figure 13.1.3 Schematic Illustration of Key Operating Conditions Involving Relatively Large Flow Incidence Approaching Inlet Lip

An example of low-speed flow incidence requirements for a STOL (Short Takeoff and Landing) installation, the YC-14 AMST candidate, is given in Figure 13.1.4, from Reference 13.1. It shows the manner in which measured and calculated inflow angles for several limiting flight conditions were combined to define a required incidence angle envelope in terms of airplane velocity. In addition, a line of constant total pressure distortion for the ultimately selected inlet lip shape is also included to indicate that none of the operating conditions will exceed the distortion limit, simply expressed in terms of $(P_{T_{MAX}} - P_{T_{MIN}})/P_{T_{AVG}}$. It should be noted that the YC-14 employs an upper wing surface blowing powered lift system for lift augmentation, with an over-the-wing engine installation. Other lift augmentation concepts, such as blown flap, with an under-the-wing engine location, develop a different wing circulation and attendant upwash characteristics, such that somewhat different magnitudes of inlet inflow angles are produced. However, the results of Figure 13.1.4 illustrate the general procedure involved in defining the required inflow envelope for a high incidence subsonic installation.

The STOL inlet incidence represents an extreme requirement and is considerably more severe than comparable requirements for CTOL (Conventional Takeoff and Landing) transport aircraft. For example, a CTOL maximum liftoff

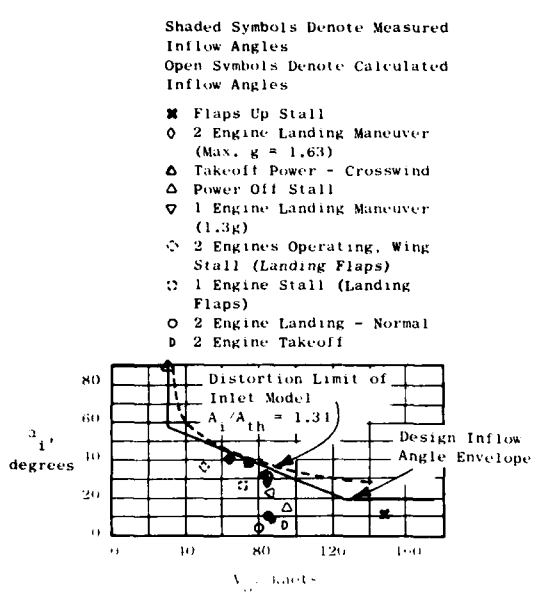

Figure 13.1.4 Representative STOL Inlet Design Requirements, per Ref 13.1

incidence is on the order of 20°, compared to the 40 to 50° characteristic of STOL applications.

Experimentally determined inlet separation boundaries for a typical STOL application from Reference 13.2 are shown in Figure 13.1.5 to illustrate the problem for low-speed, angle-of-attack operation. These data show that the unseparated angle of attack capability of a given inlet is a function of engine corrected flow demand (i.e., inlet throat Mach number) and flight speed. The selection of an inlet design must consider both

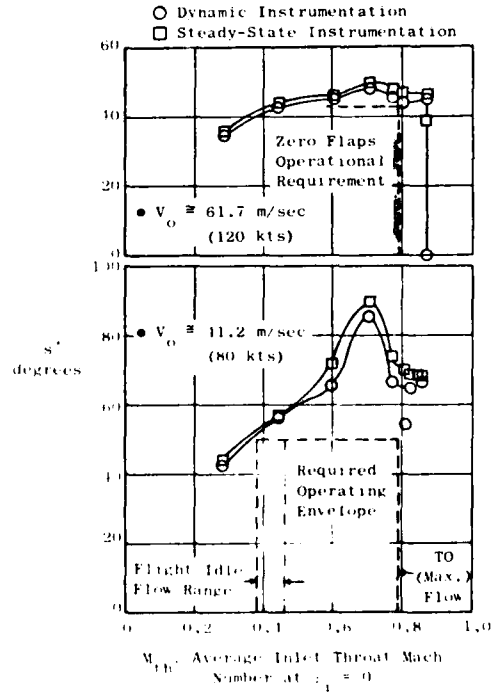

Figure 13.1.5 Experimentally Determined STOL Inlet Separation Boundaries at Angle of Attack

the projected flow incidence, including the actual pitch angle plus local flow field effects such as wing upwash, as well as the engine flow demand range, e.g. flight idle to takeoff, over which these incidence levels may be encountered. If necessary, increasing inlet nose bluntness and/or internal lip contraction (highlight-to-throat area ratio A_1/A_{th}) will extend the inlet capability, at the expense of a larger nacelle. Similar considerations apply to the crosswind takeoff condition.

The inlet performance decrements caused by flow separation for this inlet are shown in Figure 13.1.6 for a flight speed of 80 knots. Indicated pressure recovery penalty is about 5% at takeoff power, and the pressure distortion is roughly doubled from the levels obtained with maximum angle of attack (50°) takeoff.

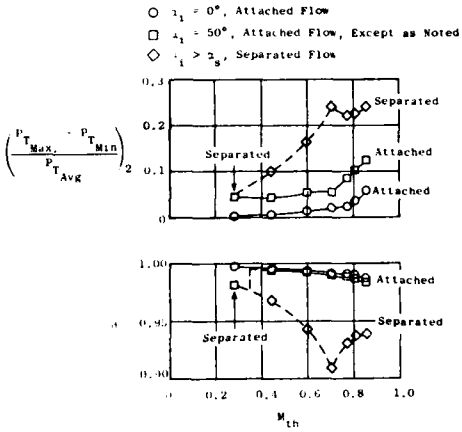

Figure 13.1.6 Effect of Inlet Separation on Angle of Attack Performance for STOL Inlet, $V_o \approx 80$ kn

The fourth condition of Figure 13.1.3, takeoff climb with an engine out, involves the possibility of external inlet surface flow separation. It is mentioned here because it can be a key constraint on sizing the external inlet cowl for a commerical transport. This situation arises because of the need to certify a minimum climb gradient capability with an engine out, in order to obtain sufficient altitude to dump fuel and return to the airfield landing pattern. The incremental drag that can result from an external inlet of insufficient thickness to maintain attached flow at the extremely low mass flow ratios characteristic of a windmilling engine, say 0.3, can preclude the attainment of this required minimum climb gradient. Data from Reference 13.3 are shown in Figure 13.1.7 to illustrate this point. While these data require extrapolation to estimate the windmilling spillage drag, in actual practice appropriate data would be acquired to facilitate this phase of the design.

OTHER OPERATING CONDITIONS AFFECTING INLET/ENGINE INTEGRATION

Depending upon the particular installation, one or more of the following conditions may impact the inlet/engine interface.

Inlet noise suppression requirements can significantly affect inlet design and installed performance characteristics. Two major suppression mechanisms have been extensively investigated: (1) placing sound absorbing material in the inlet

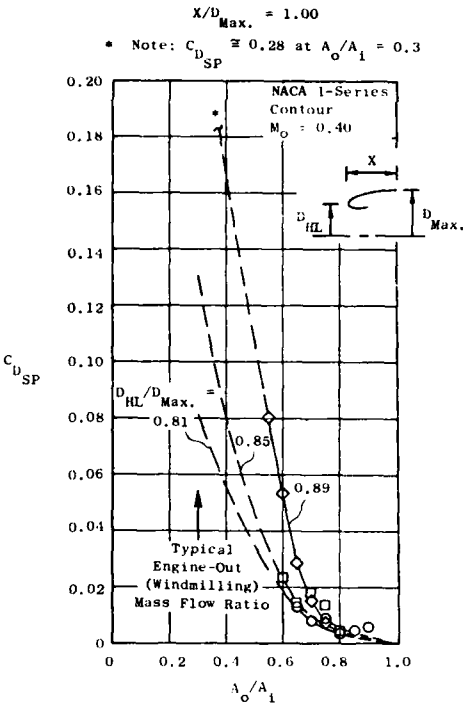

Figure 13.1.7 Effect of Mass Flow Ratio and Inlet Cowl Diameter Ratio on Inlet Spillage Drag Coefficient

and (2) accelerating the flow locally to transonic velocities to aerodynamically block the forward propagation of pressure waves generated by the engine compression component. The combination of treatment and acceleration suppression has also been employed and is termed "hybrid", to denote the dual suppression modes.

Sound absorbing material is used along the diffuser walls of the current wide-body commercial aircraft, placed outside of perforated liners. Depending upon the magnitude of suppression required, the need for acoustic absorption material may drive the inlet length beyond that required solely to fulfill its aerodynamic diffusion function. As a result, alternative means of introducing this material into the inlet have been studied, such as concentric rings, Figure 13.1.8. Naturally, such devices add inefficiency, due to the additional surface area and wakes generated, that must be traded against their acoustic merit. They may also compromise inlet flow stability at high incidence conditions, with attendant engine operational problems. Use of absorption material itself leads to an increase in wall friction, due to its inherently rougher surface, relative to smooth wall nacelle construction.

Acceleration suppression affects inlet/engine performance, via the increased diffusion resulting from the elevated throat velocity. The acoustic suppression obtained via flow acceleration may be explained by considering the radial Mach number distribution existing at the inlet throat plane. A typical profile is shown in Figure 13.1.9. Wall curvature, together with mass flow ratios greater than one (generally prevalent at the acoustically significant low flight speeds), create a zone of above average velocity adjacent to the inlet wall. Since the compressor rotor tangential velocity is

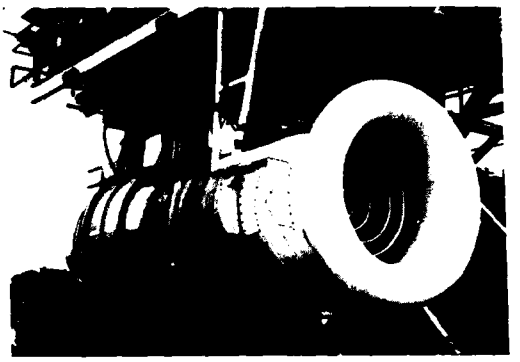

Figure 13.1.8 Example of an Inlet Employing Four Acoustically Treated Rings for Additional Noise Suppression

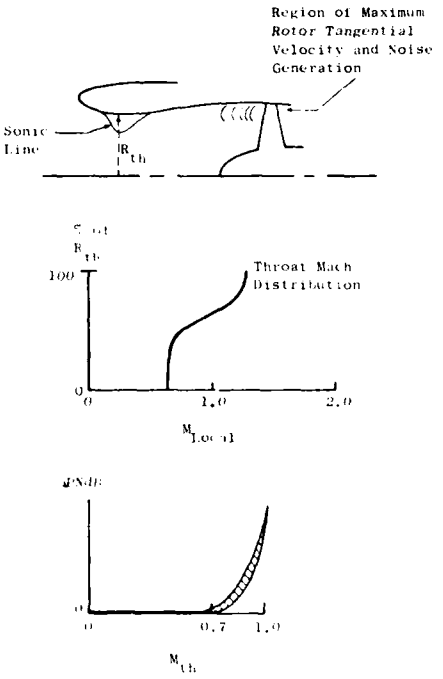

Figure 13.1.9 Relationship Between Local Inlet Flow Acceleration and Noise Suppression

obviously highest at the tip, this region of greatest noise generation is naturally suppressed most effectively by the locally supersonic inlet throat, which will not permit upstream propagation of compressor-generated waves (noise). Depending somewhat on lip shape, an average throat Mach number above 0.7 is generally required to obtain some measurable acceleration suppression, with the suppression magnitude rising at an increasing rate with M_{th}.

Some experimental investigations of variable geometry systems have been made, based on variable internal inlet contraction to provide sonic or near-sonic flow. In such cases, approach flight condition airflow demand is increased through variable exhaust geometry, using either a fan rig or engine, e.g. References 13.4 and 13.5. The sonic inlet reported in Reference 13.5 is shown in Figure 13.1.10. These tests have been restricted to static conditions and slave hardware, such that flight effects and control

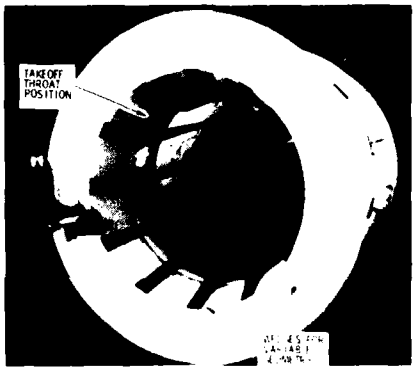

a. Takeoff Configuration Showing 12 Wedges

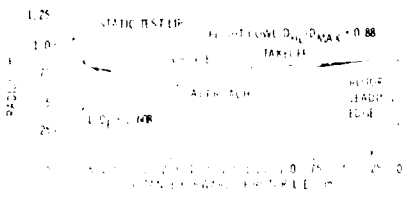

b. Flowpath

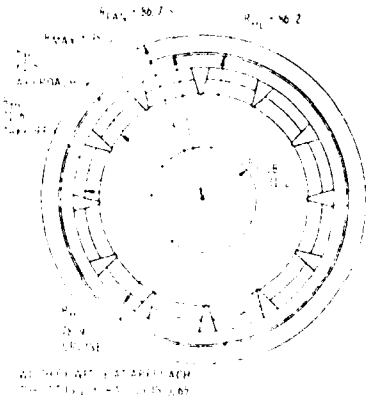

c. Front View

Figure 13.1.10 Representative Contracting Cowl Sonic Inlet Test Configuration

system requirements were not addressed. With those qualifications, the tests have shown the contracting cowl concept provides a workable means of inlet noise suppression for moderate to high bypass ratio turbofan engines. This requires that the implementation of the high diffuser area ratio at approach be carefully considered to ensure that flow distortion does not exceed engine tolerance. The additional complexity and weight of these inlets remain as development items prior to inclusion of this concept in a production installation. Similar considerations apply to the numerous other variable geometry concepts for acceleration suppression, such as expanding or translating centerbody, vanes, rings, and duct grid.

Foreign object ingestion is a topic of past and current interest that can relate to the inlet/engine installation via the need to control the inlet/ground vortex formed at low forward velocities. When present, the ground vortex can cause dust and heavy object ingestion, thereby eroding the compression system, which in turn degrades performance and component life, and increases maintenance costs. Ground vortex formation requires wind shear and is schematically represented in Figure 13.1.11. Various devices, generally involving the use of compressor bleed air directed outward from the lower inlet lip in some fashion, have been evaluated for their

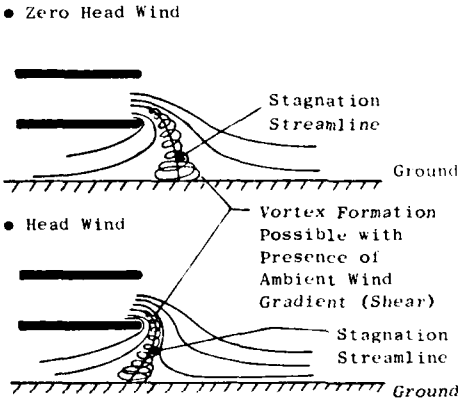

Figure 13.1.11 Schematic Representation of Inlet/Ground Vortex Formation

potential in eliminating or reducing the vortex ingestion characteristics. These devices are directed toward eliminating the stagnation point, which typically occurs on the ground, that is inherently required for vortex formation. The Boeing 737 has such a system available and in use in relatively remote areas with unimproved runways. In addition, there are indications of current interest for other existing installations, to aid in engine performance retention via controlling compressor blade contour erosion.

Inlet flow distortion occurring during thrust reverser operation on ground deceleration can be controlled to some extent by inlet/engine placement, although the reverser type and discharge flow pattern and the aircraft operating procedure, e.g. cut-off aircraft speed and engine power setting, which control the penetration characteristics of the reversed gases, are usually the primary means of avoiding excessive distortion. The flow disturbances experienced in the reverse thrust mode result from ingestion of the reversed exhaust gases, either self-ingestion or cross-ingestion from an adjacent engine, and, therefore, can include variations in total temperature as well as pressure; both of these properties can also experience fluctuations with time, owing to the chaotic, turbulent motion of the ingested flow pattern.

OTHER CONSIDERATIONS

Additional factors that are not directly associated with the functioning of the inlet/engine but must be considered in any overall installation study are cost, weight, reliability, and maintainability. The items just discussed, such as acoustic absorption material, incremental length, duct obstructions, and variable geometry with its associated control system, should readily suggest tradeoffs that must be made in those areas prior to ultimate configuration selection.

13.1.2 DEFINITION OF SUPERSONIC INLET/ENGINE OPERATIONAL REQUIREMENTS

Although, in principle, many of the subsonic applications' considerations also apply to transonic and supersonic installations, additional complexity is realized in practice by the latter, due to the more extensive flight placard and to the impact of the inlet shock structure on flow stability and inlet-engine flow matching. Additionally, the local supersonic inlet flowfield includes considerable upwash and outwash as a result of the inlet's proximity to the fuselage and wing and is considerably more sensitive to inlet placement than a typical subsonic installation. There are also some additional factors given increased importance by the generally closer integration of the inlet and engine with the aircraft itself, such as boundary layer diversion to minimize the amount of low energy airflow entering the inlet. Finally, the predominantly military nature to date of transonic/supersonic aircraft imposes other requirements on the inlet/engine combination.

INLET/ENGINE OPERATIONAL PLACARD

The flight placard dictated by the particular aircraft mission has a major effect upon inlet/engine operation. The generalized tactical fighter placard shown in Figure 13.1.12a provides a framework for discussion of the various demands that can be placed on the system. Flight along line A requires that the aircraft operate at or near peak lift coefficients, due to the low dynamic pressure (q) available to produce lift. This results in relatively large aircraft pitch and inlet lip flow incidence angles that can produce high inlet pressure distortion. Generally, the engine must be able to tolerate this distortion since the inlet lip is usually less blunt than on typical subsonic inlets to allow reasonable supersonic drag. The lip shape is a compromise between drag and distortion during maneuvering. This situation can affect compression system blade design, and may influence the ultimate selection of the engine operating line to allocate sufficient margin for surge-free operation. The intersection of lines B and C, or peak Mach number, is generally the inlet design point. Here, inlet recovery and drag as well as other determinants of engine thrust are given much emphasis, and tailored in conjunction with the aircraft drag polar, to ensure that the vehicle can meet or exceed its design speed. Lines C and D define the locus of maximum ram conditions and, therefore, are significant to the design of both the inlet and engine structure and the engine cycle, since they represent pressure and/or temperature extremes. The aircraft combat arena is denoted by the box E, which in practice may be fairly extensive. In this region, severe angle of attack and yaw can confront the inlet (Figure 13.1.12b) and produce

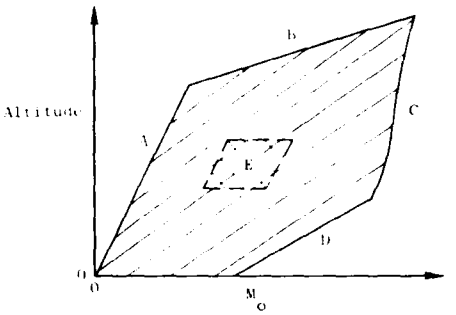

Figure 13.1.12a Typical Tactical Fighter Placard

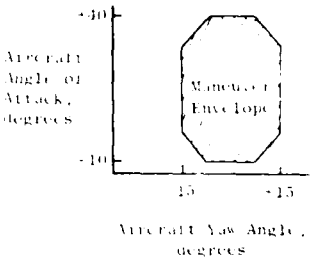

Figure 13.1.12b Representative Supersonic Inlet Maneuver Design Requirements

limiting design conditions from the standpoint of sufficient maneuverability, due to engine stability considerations. As previously mentioned, the fuselage and wing can produce local inlet flow angles which differ significantly from the aircraft measured angle of attack and yaw. For this reason, supersonic inlet tests are usually conducted with at least a partial forebody and wing simulation to produce inlet flow fields typical of the actual aircraft operation.

ADDITIONAL DEMANDS ON INLET FLOW CAPACITY

There are several potential sources of airflow demand, other than the engine requirement, that can affect inlet design and operation. These flow rates are typically small relative to the engine's and are often termed "secondary" flows for that reason and for distinction. Examples include engine periphery and/or exhaust nozzle cooling, electronic equipment cooling, and boundary layer bleed from inlet ramp or spike and internal cowl surfaces (for prevention of separation in the adverse pressure gradients and especially at shock wave impingement locations). The extent and manner in which these flows are removed from the inlet and ultimately exhausted can greatly affect the efficiency, uniformity, and stability of the engine inflow, and this subject must, therefore, receive commensurate attention during development of the propulsion system and will be discussed later in this chapter.

CONSIDERATIONS RELATED TO SHOCK STRUCTURE STABILITY

Two phenomena associated with stability of the shock structure inherently present in a supersonic inlet require consideration during inlet

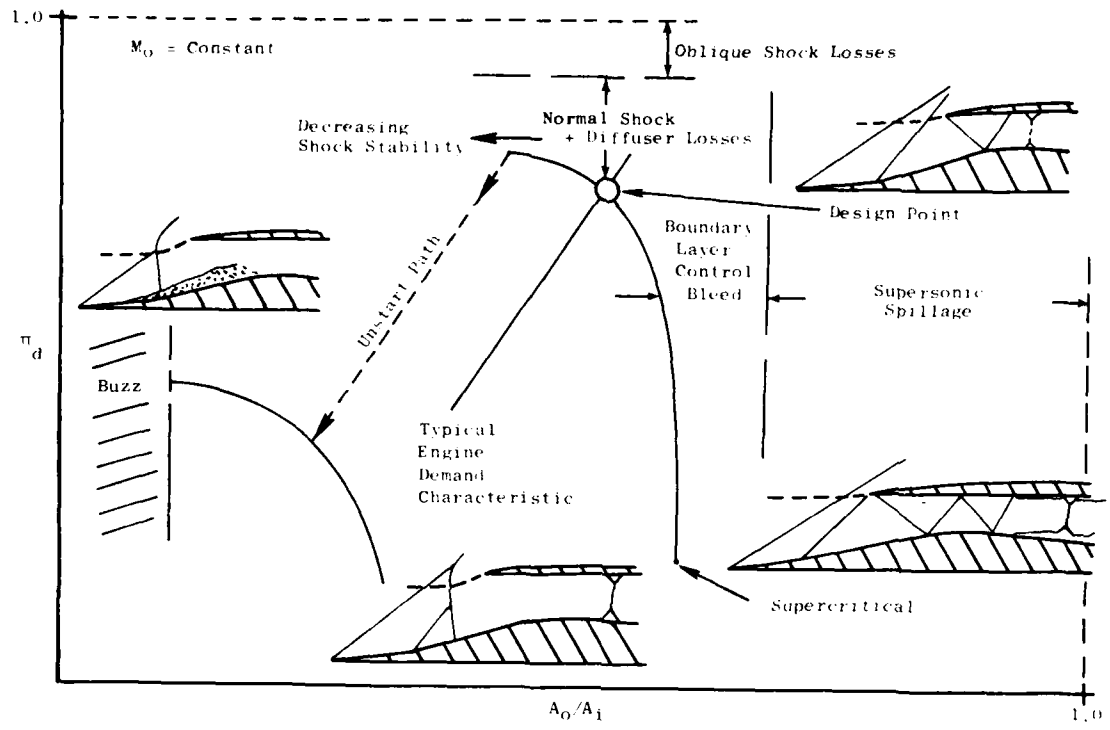

Figure 13.1.13 Recovery Versus Mass Flow Ratio, Showing Operating Regimes for a Mixed Compression Inlet

system definition. One is inlet buzz and the other involves the location of the terminal (normal) shock in a mixed compression (supersonic flow deceleration occurring both external and internal to the inlet duct) inlet. Figure 13.1.13 illustrates these situations in the framework of a pressure recovery/mass flow ratio map. Figure 13.1.14 compares the mixed compression inlet and two other possible supersonic inlet types, classified according to whether supersonic diffusion occurs external or internal to the duct or both.

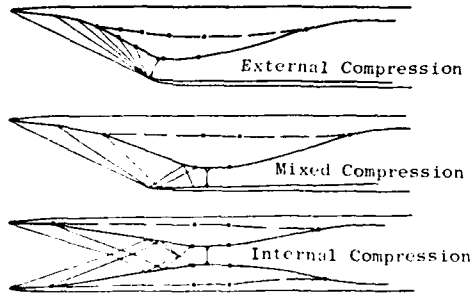

Figure 13.1.14 Comparison of Supersonic Inlet Diffuser Types

Buzz is a low-frequency, high-amplitude pressure oscillation that is linked to shock/boundary layer and/or shock/shock interaction at relatively low inlet mass flow ratio. An example flow condition leading to buzz is that wherein a shock wave impinging on the boundary layer causes the boundary layer to separate which in turn causes the (mixed compression) inlet to unstart. When unstarted, the shock that initiated the separation will be disgorged, hence allowing the boundary layer to become reestablished. As a consequence of the boundary layer reestablishment the inlet re-starts thereby beginning the cycle again. Analytical techniques have been developed that allow approximate determination of the buzz boundary, but experimental investigation for each design configuration is required for detailed definition of buzz onset and magnitude. Although the buzz region of Figure 13.1.13 is shown in the context of the unstarting (terminal shock expulsion) of a mixed compression inlet, buzz can also occur with an all-external compression inlet design. The obvious concerns here are the degraded pressure recovery and increased flow distortion, both spatial and temporal, during the buzz cycle. Typically, during development of an inlet, extensive efforts are made to preclude the buzz regime from intersecting the expected engine/aircraft operating zone.

When operation near the inlet/engine design point is considered, inlet sizing and terminal (normal) shock stability become of critical importance. The desire for peak efficiency, which would occur if a throat Mach number of one could be maintained, must be compromised in practice by operating a mixed compression inlet with the terminal shock located somewhat downstream of the throat. Typically the terminal shock Mach number will be maintained in the range of 1.2 to 1.3, whereas the throat Mach number will be in the range of 1.1 to 1.2. Operation in this mode is termed supercritical operation. Generally the percentage of total pressure loss across the shock is taken as an indication of both the inefficiency accepted and the corresponding stability margin for shock retention. The latter effect occurs because when the inlet is operated at substantial supercriticality, the terminal shock has latitude to move upstream at the impetus of a sudden externally imposed pressure pulse (e.g. reduction in total inlet flow demand or

upstream Mach number) without entering the upstream converging duct segment and then emerging from the inlet duct (unstarting). More forward terminal shock locations are impractical because of inherent lack of shock stability in a converging duct. In practice, atmospheric nonuniformities, such as wind shear and thermal gradients, are responsible for occasional variations in aircraft flight Mach number that affect the nominal terminal shock position.

An attendant penalty for inlet shock positioning with mixed compression inlets is the need for variable geometry and control systems. This need will vary deperding on the specific aircraft performance requirements, such as maximum speed, acceleration, and maneuverability. However, such features can include variable ramp angle(s) or spike position (axial or radial movement), variable cowl lip angle, variable throat area and diffuser area distribution, shock position sensor, and variable bypass system, together with the boundary layer control previously mentioned. The ultimate design will bear heavily upon the nominal inlet system efficiency and the relative likelihood of encountering situations that tax the engine's available surge margin. For these reasons, a mixed compression inlet requires mechanical complexity and a sophisticated control sytem. Both of these add weight relative to an external compression inlet.

For perspective, we should note that the bulk of supersonic inlets that have been developed have employed all external compression, with the notable exceptions of the SR-71, XB-70, and United States SST. The mixed compression inlet shows substantial performance advantages over all external compression inlets when flight at high Mach number ($M > 2$) is considered. Future mixed compression inlet development will probably be restricted to applications whose maximum Mach number and/or time at supersonic cruise can justify the additional complexity, weight and cost.

An all internal compression inlet has been excluded from practical consideration until flight Mach numbers reach 4 to 5.

MILITARY APPLICATION CONSIDERATIONS

An application of emerging military interest is the 'stealthy" type of aircraft. This designation generally connotes the suppression of all "observables", which include noise, radar cross section (RCS), and infrared radiation. The first two items concern the inlet, while all three may pertain to the exhaust system. Having already discussed inlet noise suppression in connection with subsonic inlets, only RCS reduction will be considered here. The principles involved are somewhat analogous to acoustics, in that the propagation of waves is central to the concept. When radar, rather than acoustics, is considered, however, the frequency range of interest is of the order of Gigahertz (10^9 Hertz). RCS reduction may be effected in two principal ways - by employing absorbent material and by exploiting geometrical shapes that lead to cancellation of the reflected waves, or to shielding of desired components. Significant inlet geometric variables include line of sight blockage of the inlet cavity/engine face from the observer, plus shape and size of the opening. Indications are that variations in shape can have a more pronounced effect than (allowable) variations in size. Suppression by absorption can conceivably be obtained with flowpath lining or duct obstructions. It is found, however, that the required material thicknesses are large enough to require the suppression material to be part of the duct structure, as opposed to an inserted panel. The engine compression system itself may be designed in a manner to reduce RCS, by choosing appropriate blade angles, blade numbers, and possibly blade materials (e.g. nonmetallic composites). Potential implications of the foregoing RCS suppression concepts for the inlet/engine design integration problem are obviously significant.

The possibility of inflow temperature distortion exists due to several features of some military applications. These include ingestion of exhaust gases on V/STOL installations, missile/gun gas ingestion, and steam ingestion for catapult-launched vehicles as on naval carriers. Investigation, particularly of the V/STOL situation, has shown hot gas ingestion to be highly configuration dependent, and significant variables include inlet location and shielding potential, wing design (especially vertical position and proximity to the inlet), and number and spacing of exhaust nozzles. In addition to possibly influencing these installation design features, ingestion may impact the compression system via the necessity for interstage bleed and/or reduced operating line for additional stability margin.

The subject of temperature distortion has received attention in its own right and is discussed further in Chapter 23. We note here that it can be expressed in terms of an equivalent total pressure distortion and also that it can be a significant factor in downstream compression components, depending upon its rate of attenuation and its spatial relationship with respect to any pressure distortion with which it may coexist.

OTHER CONSIDERATIONS

Factors such as cost, weight, reliability, and maintainability assume additional importance as the aircraft design speed increases, due to the increased nominal and maneuvering pressure loading, more extensive operational placard, and increased complexity due to need for geometric variability and control systems plus more intimate interaction with the adjacent vehicle flow field. Optimization of these features with those previously outlined is complex, but it must be addressed on some rational basis, consistent with the needs of the particular application, for the realization of effective mission performance.

13.1.3 ENGINE IMPACT ON INLET DESIGN

Having just discussed the major factors that may direct the design integration of the inlet and engine, let us now consider the way in which several engine characteristics impact design of the inlet component. This viewpoint will then be reversed in the following section to address the effect of the inlet on the engine design process.

INLET SIZING

One of the most fundamental considerations in the design process is selection of the inlet size, or intake area. For a subsonic installation, this is a relatively straightforward task, for a wide airflow range can be accommodated by a fixed geometry intake, since the engine compressor can propagate pressure disturbances forward into the freestream as a means of "signaling" the need for

a flow rate variation. Thus the throat, or minimum, area becomes the major determinant of inlet flow capacity. Inlet drag, weight, and cost increase with size, so the objective is to satisfy the maximum engine flow requirement with the smallest possible throat area that is consistent with the desired internal performance (recovery) and stability (pressure distortion). Several ramifications of this statement deserve discussion. First, the maximum engine flow demand is influenced not simply by the largest nominal corrected flow in the engine operating envelope, but also by engine-to-engine airflow variation, which may run 1-1/2 to 2% from nominal. Further, flow increments arising from foreseeable engine thrust growth in a particular installation must be anticipated, so that installation redesign and retooling will be avoided. Second, practical considerations preclude sizing the throat to operate at its theoretical maximum flow capacity, Mach 1. Both flowpath curvature and boundary layer growth act to reduce the maximum achievable one-dimensional throat Mach number below unity; a typical value is 0.85 to 0.90. In addition, some margin from this actual choke point is necessary because, near choking, a small variation in flow rate produces a disproportionately large change in performance. In practice, a small increase in engine flow demand will cause an abrupt drop in total pressure recovery as well as a jump in diffuser flow distortion and turbulence. For this reason, existing inlets have generally been sized for maximum throat Mach numbers of 0.75 or less. This situation is represented schematically in Figure 13.1.15. Third, even this nominal practical value may need to be reduced to satisfy operating

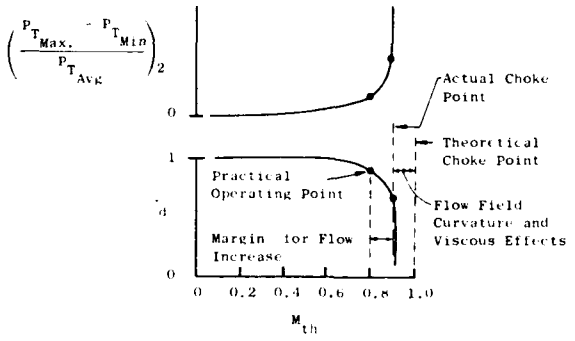

Figure 13.1.15 Subsonic Inlet Sizing Considerations

requirements, like takeoff rotation and crosswind takeoff discussed in Sec. 13.1.1, where significant local flow acceleration further reduces the inlet flow capacity, or "effective" throat area. Finally, as the throat area is reduced to achieve a higher throat Mach number, the amount of diffusion required is correspondingly increased. This necessitates a longer diffuser section for a given allowable diffusion rate. Thus, there is a tradeoff between inlet diameter and length.

Once the foregoing considerations have been resolved, the required throat area is obtained from the following relation:

$$A_{th} = \frac{(\dot{m}_2\sqrt{\theta_2}/\delta_2)(\delta_2/\delta_{th})}{(\dot{m}\sqrt{\theta}/\delta A)_{M_{th}}} \qquad (13.1.4)$$

where δ_2/δ_{th} is the reciprocal of the diffuser pressure recovery and may be considered unity for preliminary sizing studies. The throat specific corrected flow $\dot{m}\sqrt{\theta}/\delta A$ is a function of the desired throat Mach number, as developed in Sec. 13.1.1, and may be obtained from Eqs. (13.1.2) or (13.1.3) or from a plot of these, such as Figure 13.1.1.

For a supersonic application, inlet sizing is more complex. The inlet shock structure prohibits operation at a mass flow ratio greater than one. Indeed, variable geometry is required even to approach unity mass flow ratio across the supersonic range, due to the variation in oblique shock angle with Mach number. Therefore either the shock structure or throat area can limit the airflow in a supersonic inlet. The supersonic inlet must be able to pass the largest flow demanded by the engine throughout the flight envelope. Engine flow versus flight Mach number will typically behave as shown in Figure 13.1.16, decreasing at higher M_o due to achievable corrected speed ($N/\sqrt{\theta_2}$) reduction for a given mechanical speed (N) limit as corrected ram temperature ($\theta_2 = \theta_o$) rises with increasing Mach number. Again, the total engine flow demand should include engine tolerance and secondary demands such as engine cooling and nozzle flow.

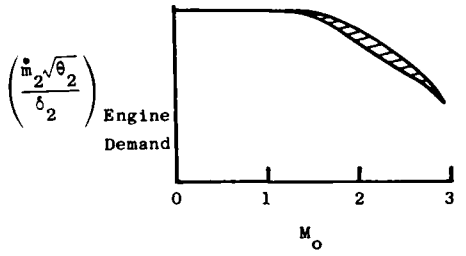

Figure 13.1.16 Typical Engine Corrected Airflow Demand Variation with Flight Mach Number

The inlet supply characteristic must then be determined for comparison with the engine demand. For this purpose, the inlet supply available to the engine should be the total inlet flow minus boundary layer bleed, subcritical spillage, and all other aircraft related flows, such as electronics and cabin cooling and engine bay purge. The factors entering into determination of the inlet airflow supply are illustrated in Figure 13.1.17. For supersonic flight, the flow ingested by the inlet will be less than that contained in the projection of its area A_1, unless the shock-generating surface(s) is oriented to place the oblique shock wave(s) on the cowl lip. Subsonically, the inlet cannot supply the full area A_1 due to the physical limitation of throat area when the ramps are collapsed to their mechanical limit. Variable ramp scheduling with flight Mach number is possible and is a feature used on many aircraft. However, the practical ramp variation is limited by considerations of shock detachment, buzz, and throat area sizing required for terminal normal shock control. Therefore, supersonic (or supercritical) flow spillage will generally occur, at least at off-design Mach numbers as shown on parts (a) and (b) of Figure 13.1.17. In addition, a certain amount of bleed will be required supersonically for boundary layer control. Removing these effects results in the net supersonic inlet supply indicated in these figures. During subsonic and transonic operation, at flight Mach numbers below the oblique shock detachment value, throat choking is the counterpart of supersonic spillage and bleed. A representative engine demand schedule is also shown in

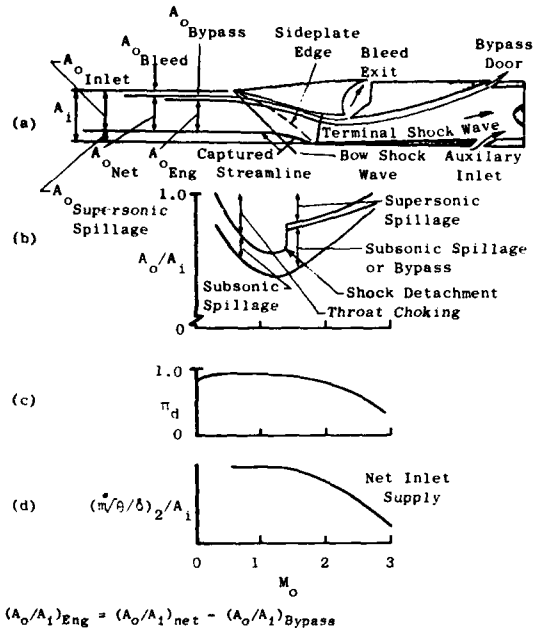

Figure 13.1.17 Elements of Inlet Airflow Supply Determination

part (b) to indicate that any excess flow must either be bypassed [as shown in (a)] or spilled subsonically (subcritically) behind the terminal shock, which will move forward of its position shown in the figure to effect this. Combining the net inlet supply mass flow ratio with a typical recovery schedule (c) results in the net specific airflow supply as follows:

$$\left(\frac{\dot{m}_2\sqrt{\theta_2}/\delta_2}{A_i}\right)_{\substack{\text{Total}\\\text{Engine}\\\text{Required}}} = \left(\frac{\dot{m}\sqrt{\theta}}{\delta A}\right)_{M_o} \times \left(\frac{\delta_o}{\delta_2}\right) \times \left(\frac{A_o}{A_i}\right)_{net} \qquad (13.1.5)$$

where the specific corrected flow $\dot{m}\sqrt{\theta}/\delta A$ has been previously discussed, and δ_o/δ_2 is the reciprocal of the overall total pressure recovery. $(A_o/A_i)_{net}$ is the mass flow ratio of the net inlet airflow available to satisfy engine-related demand, i.e. it excludes other demands such as boundary layer bleed and subcritical spillage. The resulting supply characteristic will appear similar to that of Figure 13.1.17 (d).

The inlet sizing procedure then consists of determining the required capture area as a function of flight Mach number via the following equation:

$$A_i = \frac{\dot{m}_2\sqrt{\theta_2}/\delta_2}{\left(\frac{\dot{m}_2\sqrt{\theta_2}/\delta_2}{A_i}\right)} = \frac{\text{Engine Flow Demand}}{\text{Available Inlet Specific Airflow}} \qquad (13.1.6)$$

The largest capture area required, considering all pertinent Mach number/altitude combinations, is the necessary inlet size. A comparison of the resulting inlet supply and engine demand characteristics where the inlet size is set by the maximum Mach number condition is shown in Figure 13.1.18. Depending upon the application, it may be feasible to incorporate variable inlet geometry as a way of reducing the extent (Mach number range) and magnitude of the excess flow.

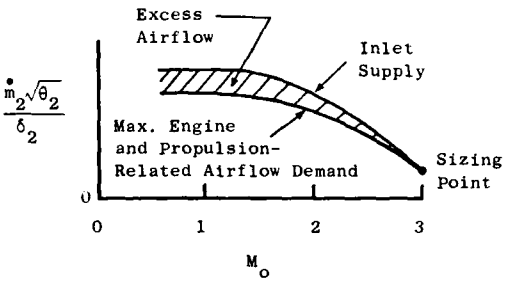

Figure 13.1.18 Inlet/Engine Flow Matching for a Supersonic Cruise Sizing Point

The excess flow must either by bypassed, via a duct leading to the engine exhaust nozzle or through overboard exits, or spilled around the inlet. Additional drag forces arise from the failure to employ the captured flow to produce thrust. These remarks also apply to the need for flow dispersal at reduced power setting conditions or in an engine out situation. Failure to size the inlet large enough to supply the engine with sufficient physical airflow is self-compensating to a certain degree. Since compressors and fans tend to be constant corrected flow devices (changing with speed), the normal shock adjusts itself to provide the desired corrected flow. This is accomplished by drawing the terminal shock to the lip and setting up another normal shock in the diffuser which lowers the pressure recovery and therefore increases the corrected flow to the required value. Two problems arise when this happens: (1) Large pressure distortion levels are usually produced and (2) A loss in net thrust can result from an undersized inlet, since engine thrust is a function of engine physical flow and inlet pressure. For these reasons, inlet sizing is undertaken with extreme care to ensure inlet/engine flow matching compatibility.

Although the supersonic inlet is usually faced with a throat area restriction on airflow capacity only while operating subsonically, the lip shapes required for good supersonic external performance can introduce significant internal losses at the high mass flow ratios characteristic of low-speed flight, Reference 13.6. If the ramps are already collapsed to their mechanical limit to provide maximum throat area, auxiliary inlets are often utilized to improve performance. These may take the form of discrete slots, located around the periphery of the nacelle slightly forward of the engine face plane, and incorporate cover doors externally and internally that are actuated, via either pressure differential or mechanically, to expose the required opening. Figure 13.1.17 indicates this feature schematically. By utilizing such cover doors, the required corrected airflow can be inducted at a higher overall efficiency, because the auxiliary inlet reduces the flow demand and associated losses for the main inlet, but does not suffer from the losses identified with flow around supersonic lips.

INLET BUZZ AVOIDANCE

Minimum engine airflow demand must also be considered in inlet design and development, in order to preclude inlet buzz occurrence. As discussed in

Sec. 13.1.2, this phenomenon occurs at low inlet mass flow ratios and is characterized by low frequency, high amplitude pressure fluctuations that are detrimental to engine stability and structural integrity. A goal of the inlet development phase is to arrive at a configuration whose buzz boundary is removed from the minimum propulsion system flow schedule by an appropriate margin, as indicated in Figure 13.1.19. To aid this achievement, the inlet

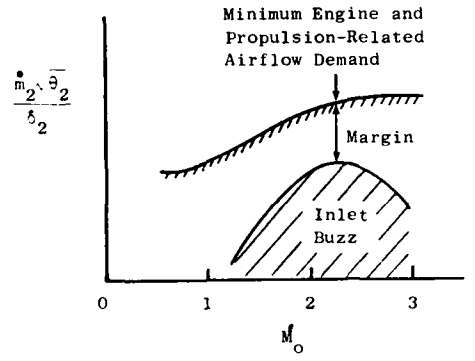

Figure 13.1.19 Compatibility Assessment of Inlet Buzz and Minimal Flow Demand

bypass system previously discussed and shown in Figure 13.1.17(a) is usually sized to pass sufficient flow to avoid inlet buzz under a failed engine situation.

Thus, an assessment must be made of the engine airflow rate that will prevail due solely to ram flight effects, when the rotor is windmilling or is locked. Then the bypass capacity must account for the remaining flow needed to preclude encountering the inlet buzz boundary and provide any desired margin.

INLET DUCT DESIGN FOR ENGINE SURGE OVERPRESSURE

The inlet duct's structural design must consider the condition providing the largest internal-to-external surface pressure differential. This situation is likely to arise during a severe engine surge at high dynamic pressure, when a transitory flow reduction occurs, followed by transmission of a strong positive pressure pulse forward from the compression system. This phenomenon is often termed hammershock overpressure, in reference to the suddenness and severity of pressure rise. The initial overpressure pulse is generally followed by successive damped pressure cycles, resulting in application of an oscillatory static pressure loading on the inlet duct surfaces.

The analytical framework presented in Reference 13.7 to describe the overpressure phenomenon indicates that it is, in general, a function of the overall compressor pressure ratio, the inlet duct static pressure and Mach number, and the engine bypass ratio. Figure 13.1.20, from Reference 13.7, shows a typical correlation obtained for the overpressure in terms of a parameter

$$P = \frac{\Delta p}{p_1 M_1^{1.26}} = f(\pi_c, \alpha) \qquad (13.1.7)$$

where

Δp = pressure rise caused by the passage of the surge-induced wave as it propagates into the inlet duct

and p_1, M_1 = duct static pressure and Mach number at engine spinner prior to surge.

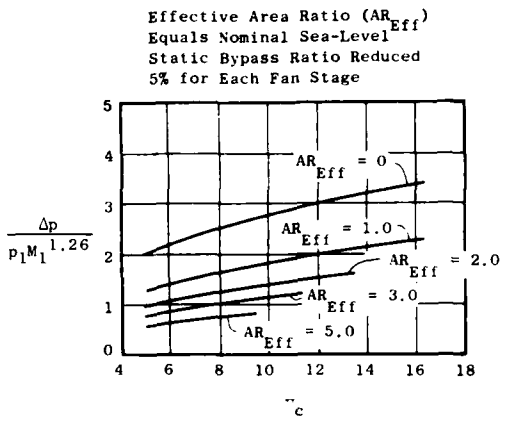

Figure 13.1.20 Predicted Hammershock Overpressure Correlation for Inlet Duct Structural Design

These characteristics are partially based on measurements for bypass ratios (α) from 0 to 1.37, with the higher bypass ratio curves based on an analytical solution to a transmitted shock wave flow model.

INLET CONTROL SYSTEMS FOR FLOW STABILITY

Several needs for a mixed compression inlet control system were noted in Sec. 13.1.2 and may be briefly summarized here. They arise primarily due to the need to maintain the terminal shock in a stable position, and to prevent boundary layer separation. Control of shock Mach number value, and hence location, is required for stable and fairly efficient inlet performance and is necessitated by such destabilizing effects as variation in engine power setting/flow demand, intended aircraft flight speed change, atmospheric nonuniformities, and aircraft maneuvers. A flow bypass system, variable inlet geometry, boundary layer bleed, and a throat Mach number sensor are elements of a general control system. Some of these elements are shown in simplified fashion in Figure 13.1.21, together with the types of interactions between the cockpit and airframe, for a translating centerbody type of inlet. Use of these particular features depends on the specific vehicle performance requirements discussed in Sec. 13.1.2, such as flight speed and maneuverability, which will strongly influence the inlet type and allowable complexity. However, even an external compression inlet generally requires control provision for inlet bleed flow, bypass flow, and ramp scheduling. The complexity of an active terminal shock positioning system is not required.

13.1.4 INLET IMPACT ON ENGINE DESIGN

Several aspects of the inlet's behavior are worthy of consideration relative to design of the engine, particularly the compression components.

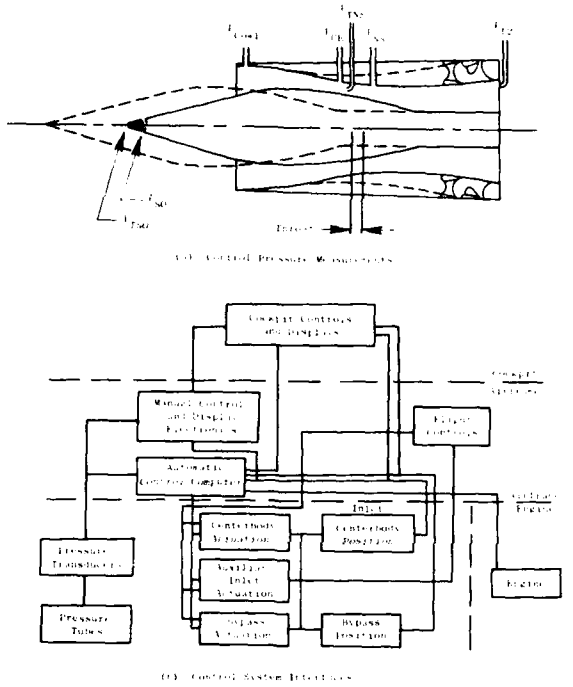

Figure 13.1.21 Inlet Control System Pressure Measurements and Schematic Interface Diagram

To an extent, they are the complement of the engine factors affecting the inlet design discussed in Sec. 13.1.3.

ENGINE AIRFLOW DEMAND TAILORING

If the inlet configuration and operating characteristics are defined early enough in the propulsion system design phase, some tailoring of the engine airflow schedule is possible. The incentive for closely matching the inlet supply and engine demand airflows is minimization of inlet spillage and/or bypass system drags, which can contribute to upgraded aircraft performance in terms of maneuverability, range, or acceleration, as desired for a particular vehicle mission.

Two possible engine/inlet flow matching situations are indicated schematically in Figure 13.1.22 for a transonic sizing point. Designated as the propulsion-related airflow requirements associated with two engines, A and B, the flow demand will typically differ from the inlet supply; the potential for either over- or under-supply exists. In this illustration, flow mismatch occurs in the supersonic regime as a result of the assumed sizing point. Depending on the aircraft mission and associated engine type (turbojet or turbofan), limited flexibility exists to shift the engine demand schedule to better fit the inlet supply, through such means as varying the turbine temperature or varying the exhaust area. As developed in Chapt. 8, if variable geometry techniques were to be employed, considerably more flexibility in airflow matching could result.

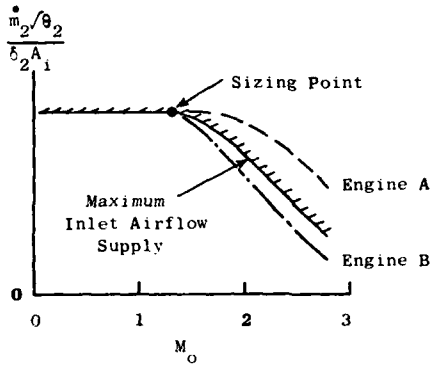

Figure 13.1.22 Schematic Representation of the Typical Need for Engine Airflow Tailoring, Transonic Inlet Sizing Point

In practice, the amount of flow mismatch reduction is constrained by considerations of cycle performance and component operational limits. For the turbofan, an additional barrier is imposed by the need to match stream static pressure at the juncture of the hot core and cool bypass flows. Accordingly, fan speed and flow must be reduced at higher Mach numbers to achieve the pressure balance, with the possibility of trading subsonic performance for some additional supersonic flow capability via modifications to the basic cycle.

An alternative to accepting the smallest achievable residual supersonic flow mismatch via the means just discussed is as follows. Referring again to Figure 13.1.22, engine A's supersonic flow could be reduced via speed cutback, as long as full thrust is not required, per the transonic sizing assumption. Engine B's flow schedule could be matched via use of an auxiliary inlet, to provide subsonic/transonic flow, together with a downsized primary inlet.

In addition to the foregoing maximum power consideration, a need exists to reduce the installation losses that arise during part power operation; this is especially important for mixed (supersonic/subsonic) mission aircraft. While the afterburning turbojet and mixed-flow augmented turbofan engines share this problem, the latter type has been selected as the best current powerplant for such applications. The part-power installation losses consist of afterbody drag, due to increased boattail angles associated with reduced variable exhaust nozzle area, as well as inlet spillage. These losses are qualitatively indicated in Figure 13.1.23 in terms of their associated descriptive parameters. The resulting typical performance decrements are shown in Figure 13.1.24 in terms of specific fuel consumption for Mach 0.9 operation of an aircraft with Mach 2.5 capability. Considering that modern fighter engines must be so oversized to meet combat maneuverability requirements that they typically operate at only 40 to 60% of maximum dry thrust for altitude cruise at Mach 0.8 to 0.9, significant inlet and nozzle drag penalties can exist. To date, these effects have prevented the fullest realization of multimission capability.

A concerted effort is currently underway in industry and government organizations to identify and develop feasible new engine concepts for the flexible, efficient performance required by future supersonic military and commercial vehicles. Inherent in the desire to combine the best features

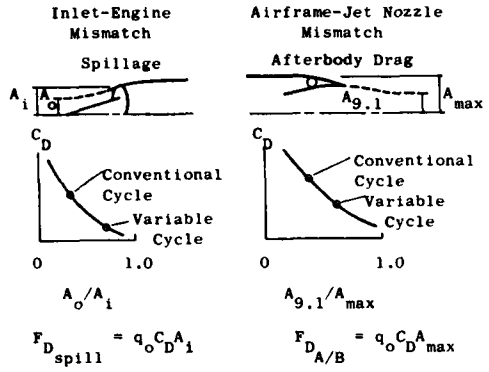

Figure 13.1.23 Effect of Power Setting on Installation Losses

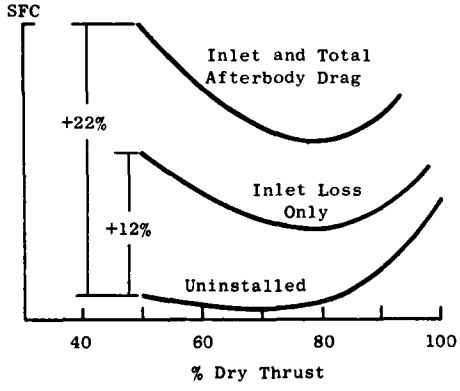

Figure 13.1.24 Representative Installation Losses for Mach 0.9/36K ft Operation of a Mach 2.5 Aircraft with a Mixed-Flow Turbofan Engine

of the current leading subsonic (turbofan) and supersonic (turbojet) single-mission powerplants is the need for a variable cycle engine (VCE), which in turn requires variable geometry and more complex component arrangement than existing engines.

Reference 13.8 discusses one ongoing VCE concept development effort, and also recounts in detail the performance characteristics of turbojet versus turbofan engines and traces various VCE developments of the past 10 to 15 years that have led to the currently pursued concepts. Some essential features of these VCEs are illustrated schematically in Figure 13.1.25; three compression components are interconnected to each other via bypass ducts, in addition to the normal transition ducts. This allows a wide range of component airflow combinations, so that the effective engine bypass ratio can range from near zero (turbojet) for good supersonic performance to the high values needed for efficient subsonic cruise. In addition, total airflow demand can be held constant at a cruise Mach number while bypass ratio and thrust are modulated so that inlet flow matching, and, hence, installed performance, are improved. Variable turbine and exhaust system geometry can also be utilized to control the flow split.

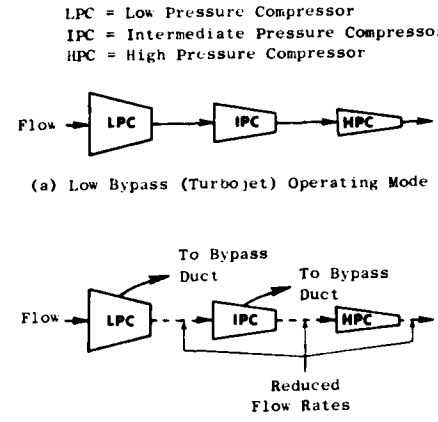

Figure 13.1.25 Schematic of Variable Cycle Engine Concept

The VCE's improvement of supersonic flow matching is shown in Figure 13.1.26, relative to

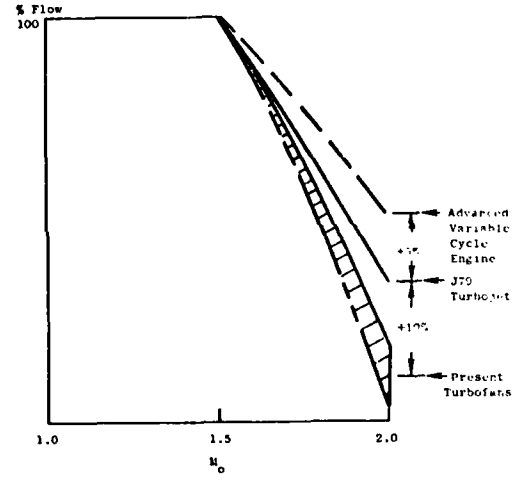

Figure 13.1.26 Improvement in Maximum Supersonic Airflow Capacity with Advanced Variable Cycle Engine

typical turbojet and turbofan engines. Since the supersonic flow increase is available while holding subsonic flow constant, it is clearly beneficial from a flow matching standpoint. The partial power matching gains described in the previous paragraph are indicated in Figure 13.1.27. Reduction of both inlet spillage and afterbody drag will result, as schematically indicated in Figure 13.1.23. With this capability, the basic cycle can be oriented toward maximum thrust requirements and yet arrive at more balanced, mixed mission performance.

SURGE MARGIN ALLOCATION FOR ANTICIPATED DISTORTION

The general topic of engine stability analysis is discussed in detail in Chapter 23. Accordingly, the objective of this section is to provide an overview of the basic effect of distorted inflow on a compression component and indicate the impact distortion may have on engine design and performance.

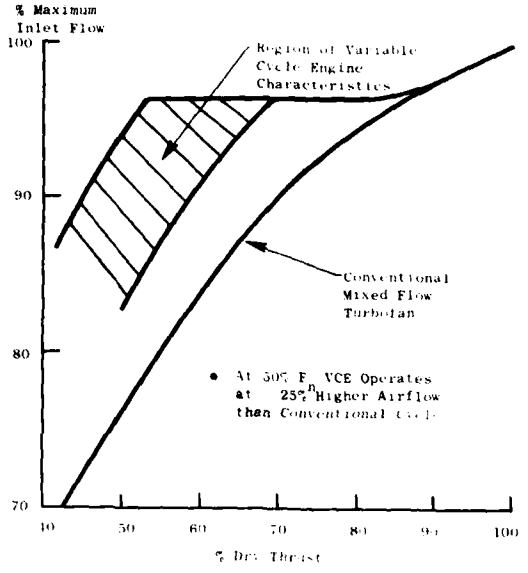

Figure 13.1.27 Improvement in Subsonic Part Power Flow Matching Via Variable Cycle Engines for the Same Cycle Parameters

A typical compression component aerodynamic performance map may be represented as shown in Figure 13.1.28. The operating line is established by back-pressure characteristics set by turbine and exhaust nozzle areas, and is selected to achieve required engine performance levels (Sects. 8.1 and 8.4). It is therefore adjustable, at the expense of performance in the case of a reduced (lowered) position. The surge line represents the limit of stable operation and is by definition fixed for a given configuration and operating condition.

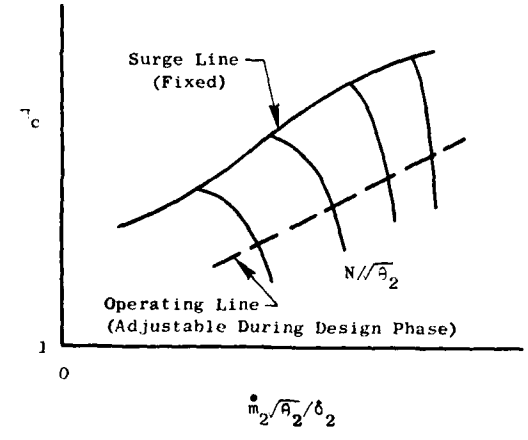

Figure 13.1.28 Typical Aerodynamic Performance Map for Fan or Compressor Component

The nominal operating and surge lines of Figure 13.1.28 are subject to various degrading effects that act to decrease available surge margin, which is related to the difference in their respective pressure ratios. Figure 13.1.29 is a simplified representation of this situation. The stall line degradation results from effects such as manufacturing tolerances, variable stator accuracy and response time, casing/blade clearance increases and airfoil contour deterioration with age, and Reynolds number at appropriate points in the flight placard. The maximum transient operating "line", or locus of maximum operating points, is elevated from the nominal steady-state operating line by engine component tolerances and by fuel control margin required for acceleration and deceleration, compressor bleed effects, afterburner lightoff transients and thrust modulation effects, and control mode effectiveness, especially for more complex engine systems.

The shaded region between the degraded surge line and the maximum transient operating line of Figure 13.1.29 represents the surge margin available to tolerate distorted inflow in the compression system. The fundamental impact of nonuniform flow entering the engine is that a change in the nominal velocity field affects the flow incidence on the blading and may lead to locally stalled

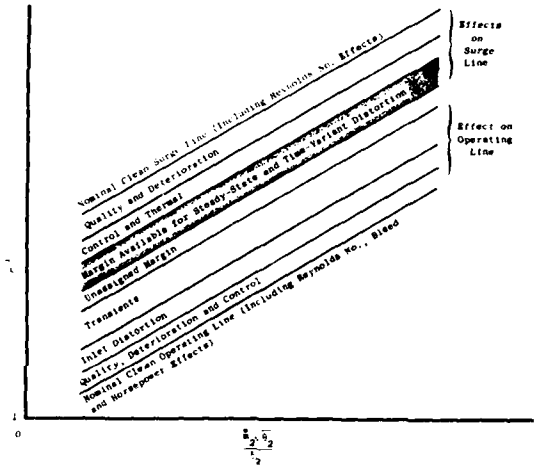

Figure 13.1.29 Cumulative Representation of Degraded Surge and Operating Lines for a Compression Component, Leading to Reduced Stability Margin for Inflow Distortion

regions or, in the limit, to complete surge of a component. Other possible undesirable effects include aeromechanical excitation that can reduce blade life or cause catastrophic failure. Depending on transmission of the inlet distortion through the compression system, creation of a turbine inlet temperature profile that locally exceeds nominal levels may occur so that either turbine component life is degraded or performance must be derated. Performance is reduced by average burner temperature reductions. Actual installed compressor inlet velocity fields can be quite complex, with axial, radial, and circumferential components superimposed on the nominal compressor velocity vector. In practice, flow distortion is expressed in terms of total pressure variation, since this is more readily measurable than velocity.

The detailed effects of pressure distortion on compressor flow stability are complex and not completely understood. They depend heavily upon the flow pattern shape, i.e. magnitude, circumferential and radial extent, and location of the distortion (hub versus tip), and upon compressor geometric and aerodynamic design features such as stage loading, aspect ratio, and solidity. However, the net result

of a distorted flow is primarily to effectively lower the undistorted surge line of a compression component; a possible secondary effect is reduction of component efficiency. If this surge line degradation exceeds the available amount, an impasse is reached at which point in the development cycle one or more of several options must be exercised. Such options include inlet distortion reduction via modified design or operating point, engine compression system design changes, reduction or reallocation of the other previously mentioned factors degrading surge margin, redefinition of aircraft operational goals, or acceptance of some type of performance penalty such as range reduction.

The essential feature, then, of surge margin allocation is determination of an amount such that the inlet/engine combination provides both adequate performance and reliability. Insufficient margin results in engine surge and power reduction that, at best, curtail the aircraft's operational envelope and, at worst, compromise vehicle safety. Alternately, excessive surge margin represents foregone propulsion potential that prevents efficient realization of the full aircraft performance capability.

EFFECTS OF INLET BUZZ, UNSTART, AND HAMMERSHOCK INTERACTION

The transient pressure characteristics of inlet buzz and engine surge-induced hammershock, mentioned in Sec. 13.1.3 in connection with inlet duct structural design, are also significant inputs to the engine mechanical design. The inlet buzz pressure frequency spectrum must be carefully defined to ensure that none of the engine's rotating or stationary structural members have resonant frequencies in the range of the predominant buzz frequencies. Similar considerations apply to the case of inlet unstart. In addition, the pressure signature resulting from interaction of the inlet and engine during a hammershock incident must be factored into the compressor design, since it affects the rotor axial force as well as bending and torsional blade loading.

13.2 VALIDATION OF INLET/ENGINE SYSTEM

Having set forth the factors that affect the inlet/engine design integration, we can now consider the manner in which integration of the inlet and engine into an effective propulsion system is undertaken and confirmed. This section discusses the basic objective of such an effort, together with a brief historical background of some problems that have arisen from lack of an effective integration program; the current and projected role of analytical methods in aiding inlet and compressor system development; and the progressive complexity and integration of the various types of test programs leading to confirmation of the production vehicle's capabilities.

13.2.1 BACKGROUND AND BASIC CONSIDERATIONS

The complexity of inlet/engine interaction is so extensive that, in the past, many unforeseen inlet/engine compatibility problems have arisen at advanced times in the development schedule. Frequently, resolution of major system compatibility shortcomings has been forced well into the flight test program. Figure 13.2.1 from Reference 13.9 indicates the difficulties and ultimate solutions for some military vehicles during the 1954-1967 period. In addition, operational problems have occasionally occurred during initial service of commercial transports. This experience has demonstrated that it is generally more cost effective to integrate design and development of the engine and its interfacing aircraft components, such as the inlet, through a formally structured series of steps, such that flight test is merely a final system demonstration built upon subscale and full-scale inlet and compressor component development. The incremental costs associated with more extensive and sophisticated development programs are more than justified by reducing the outlay that would have been created by the aftereffects of a less thorough effort. Such aftereffects may include increased development costs during flight test, delayed system availability, and derated performance capability of the final production aircraft.

An effective integration effort for a supersonic installation normally requires 5 to 6 years, beginning with analytical design studies leading to an increasingly sophisticated series of tests to evaluate inlet and compression component characteristics, singly at first and later together. A general experimental program directed at development of a stable inlet/engine system is shown in Figure 13.2.2. These test features will be discussed in more detail in subsequent sections of this chapter.

A subsonic application generally requires a shorter period of less extensive testing following the design phase, depending somewhat upon the particular application and applicability of the various design requirements discussed in Sec. 13.1.1. Experimental development and design validation techniques are currently utilized more heavily

Operational [illegible]	Instability Problem	Resolution Area
Fighter I	Engine Stall - Level Flight and Maneuver	Compressor and Inlet Configurations
II	Inlet Instability, Engine Stall During Maneuver	Compressor and Inlet Configurations
III	Engine Stall - Weapon Release, Maneuver, Inlet Crossbleed	Inlet Configuration, Engine [illegible] Plus Restart
IV	Inlet Instability - Engine Stalls During Afterburning Flight	Compressor Changes Plus Restart
V	Inlet Instability During A/B Shutdown	Inlet Control
VI	None	None
VII	Engine Stall - Weapons Release	Engine Control [illegible]
Bomber I	None	None
II	High Power at Low Inlet Flow - Inlet Crossbleed Takeoff	Inlet Configuration
III	None	None
IV	Minor Inlet Instability	Inlet Control
Reconn I	Engine Stall and Maneuver	Engine Control Changes
Cargo I	None	None
II	None	None
III	Crosswind Takeoff	Inlet Configuration

Figure 13.2.1 Stability Experience of Some Operational USAF Systems, 1954-1967

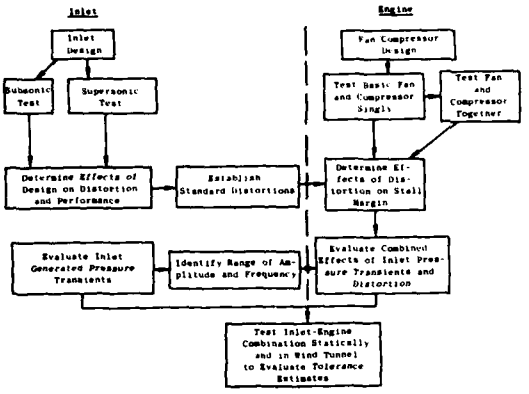

Figure 13.2.2 Example of an Inlet/Engine Stability Development Test Program

than are analytical methods. This largely reflects gaps in present day analytical capabilities, as for example, where complex inlet geometry (i.e., three-dimensional), highly vehicle-integrated, is involved. Similar shortcomings exist in detailed understanding of the interrelationship between compressor design variables and distortion sensitivity, component interdependence, and transient performance with distorted inflow. However, these and other areas are receiving attention on a broad front and it is reasonable to project that analytical methods will become a more significant factor in the inlet/engine development process during the next decade.

The structure of a program to develop and validate an effective inlet/engine subsystem will be discussed in more depth in the following sections.

13.2.2 ANALYTICAL EVALUATION OF INLET AND ENGINE OPERATION

To the extent of their capabilities, analytical methods are extremely useful, because they allow evaluation or screening of alternative concepts and facilitate determination of component performance sensitivity to various design parameters of interest. This information can usually be obtained at a lower cost than that which would be required by an analogous experimental program. The following discussion is intended to outline some current and projected capabilities in three areas: inlet aerodynamic design, modelling compression system response to distortion, and inlet/engine dynamic analysis.

INLET AERODYNAMIC DESIGN ANALYSIS

At present, analytical methods are available with the capability of providing solutions to flow about two-dimensional bodies (i.e. axisymmetric or planar), including the effects of angle of attack. The resulting (three-dimensional) solution can be improved by introducing a boundary layer analysis to determine the viscous effects. The boundary layer analysis (which is strictly valid only for2-D flows) utilizes the potential flow solution to provide the necessary "free stream conditions" required for the boundary layer solution. This process can be continued by modifying the apparent body dimensions to include the effect of the boundary layer displacement thickness to recalculate the potential solution, and, thence, a further boundary layer solution. This procedure is repeated until convergence is obtained. Convergence is assessed by some limit on local velocity changes between successive iterations. Analytical results obtained in this manner closely duplicate test measurements, provided that separation does not occur. The onset of separation can be well predicted by this technique, however, so that the range of applicability of the analytical results can be determined.

Example results are indicated in Figure 13.2.3 (from Reference 13.11) where the agreement between the analytical prediction and the experimental results is seen to be close (except at the inlet highlight, X/L = 0). Inlet flow properties are equally well predicted for circumferential locations other than the windward side, Reference 13.12. An example of the capability of boundary layer separation prediction is given by Figure 13.2.4 from Reference 13.2. Here, inlet wall pressures measured at various angles of attack in a wind tunnel test were used as input to two boundary layer analyses (Reference 13.13). Their separation parameters, F_{MAX} and Cf_{MIN} respectively, are plotted against measured proximity to separation, $\alpha_s-\alpha_i$. The critical values predicting separation, $F_{MAX} = 0.5$ and $Cf_{MIN} = 0$, are asymptotically approached in most cases as the separation point, $\alpha_s-\alpha_i = 0$, is neared.

The foregoing capability serves well for most current subsonic inlet configurations, which are axisymmetric or nearly so. Efforts are underway to develop analytical tools for general three-dimensional potential and viscous flows that will eventually include interactions between inlet and adjacent aircraft flow fields, shock waves and boundary layers, and inlet turbulence effects.

Supersonic inlet design analysis applies to both supersonic and subsonic diffuser components. The former includes the boundary layer bleed system mentioned in Sec. 13.1.2. The method of characteristics is utilized in supersonic diffuser analysis for two-dimensional configurations. Iterative viscous calculations are utilized and bleed flow effects are considered in subsequent calculations. For a detailed discussion of supersonic and subsonic diffuser design considerations, the reader is referred to Chapter 26. Current supersonic and subsonic diffuser analytical capabilities are generally limited to two-dimensional shapes for design purposes; this is somewhat restrictive considering the wide variety of supersonic inlet geometries. Effort is underway to develop the ability to analyze angle of attack effects for design of axisymmetric inlets. In addition, three-dimensional subsonic diffuser programs are being widely pursued to analytically address the general asymmetric configurations associated with buried engine installations/offset inlet ducts plus cross-sectional transition sections necessitated by non-circular inlet entrances. The flowfield complexity of typical supersonic inlets thus suggests that their dependence on experimental development methods will continue to be somewhat greater than that of subsonic inlets for the foreseeable future.

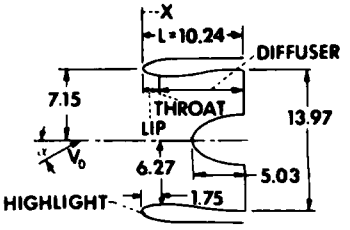

(a) Inlet Geometry, (All Dimensions in cm)

----- Incompressible Potential Flow Solution

——— Incompressible Potential Flow Solution with Compressibility Correction

——·—— Incompressible Potential Flow Solution with Compressibility and Boundary Layer Displacement Thickness

o Experiment

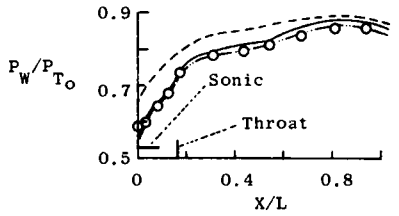

(b) Static Condition

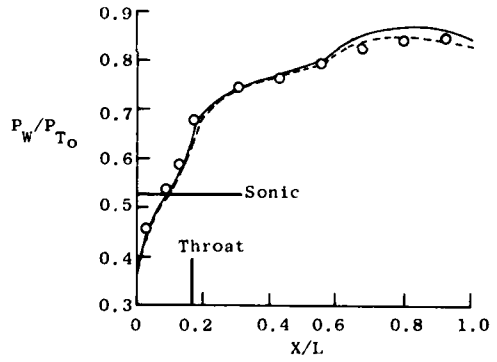

(c) Free-Stream Velocity, V_O, 24 Meters per Second; Incidence Angle, α_1, 40°; Windward Side of Inlet

Figure 13.2.3 Comparison of Calculated and Measured Internal Surface Pressure Distributions for a Translating Centerbody Inlet in the Unchoked Mode

MATHEMATICAL MODELLING OF COMPRESSOR DYNAMIC RESPONSE TO DISTORTION

Advances have been made in recent years which permit the effects of inlet distortion upon compression component stability to be estimated economically using relatively simple models. These models (Ref. 13.14, 13.15, and 13.16), which are quasi-one-dimensional pitch-line blade-row-by-blade-row or stage-by-stage, parallel-compressor representations of compression components, can predict the effects of 1/rev circumferential distortions and the effects of

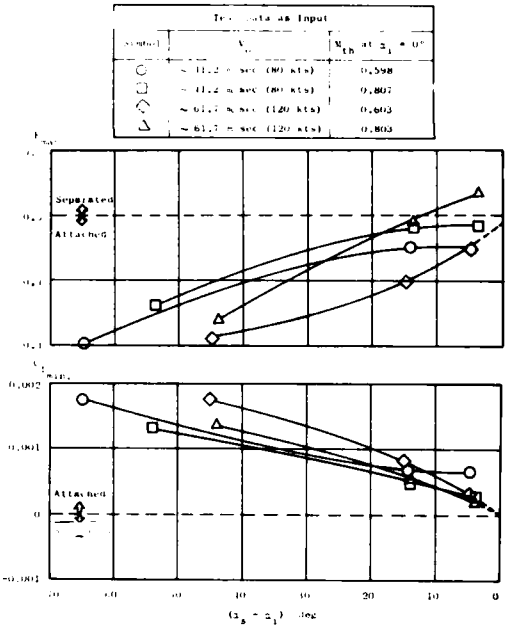

Figure 13.2.4 Example of Boundary Layer Separation Prediction Capability

planar waves upon the stability of the compression components. The parallel compressor concept is discussed more fully in Chapter 23. Distorted flow field predictions are now being made which include the pumping effect of this compression component upon the distorted flow field giving rise to tangential velocities and tangential static-pressure gradients. For both steady flow distorted and spatially undistorted planar wave flow, stability predictions are conducted accounting for the unsteady flow effects associated with the finite time required for the flow surrounding the blades to adjust to the new local flow conditions. Models with these capabilities permit accurately predicting the stability trends, and in many cases the actual levels, associated with the circumferential and unsteady components of inlet distortion. Development of models to handle radial components of distortion in as direct a manner as for the other components of distortion is currently being undertaken.

INLET/ENGINE CONTROL SYSTEM MODELS

Transient or dynamic simulation models are available for analytically assessing the stability of various propulsion system components or systems. Generally, digital models are preferable to analog because of their ease of translation/standardization among organizations concerned with the various components and their controls, and because of their flexibility in terms of user access and problem set-up. To arrive at a useful model during the propulsion system development cycle, exploratory component tests must address dynamic/time dependent characteristics as well as steady state performance trends. This facilitates subsequent integration of components into systems. The model can be used initially to roughly approximate response characteristics to other component stimuli and can then be updated as additional component and subsystem data are acquired. Engine and inlet demonstrator vehicle

testing can eventually be used to correlate and fine tune the model, to verify that the model can be used to direct subsequent demonstrator component scaling and/or minor resizing that are typically required for production hardware. The dynamic simulation model, then, is a tool that can be used in component and system stability studies as well as general performance evaluation. In terms of inlet/engine integration for example, it could encompass inlet installation, inlet geometry control, bypass system, and engine compression system. Successful application of such a tool in its early stages can lead to identification and resolution of interface problems prior to construction of actual hardware.

13.2.3 ENGINE DEVELOPMENT TEST ELEMENTS FOR INLET INTEGRATION

As indicated in Figure 13.2.2, an effective engine development program aimed at achieving compatibility with the aircraft inlet centers on the compression system and proceeds through several phases. Initially, the effort addresses basic fan and compressor operation under clean and standardized distorted flow conditions and may investigate some blading geometric variables. Then, as inlet development proceeds in parallel, the compression system development progresses to evaluating the specific inlet's distortion, both steady state and dynamic, as well as other transient behavior. Finally, the inlet and engine are often tested together in large propulsion wind tunnels, outdoor facilities, or flying test beds for direct interaction effects. This is generally the last step prior to flight testing of the actual experimental or prototype aircraft, which is discussed separately in Sec. 13.2.5. A representative engine development test sequence oriented toward integration with the inlet system is shown in Figure 13.2.5 as a framework for the following discussion of these specific test elements.

as indicated in Figure 13.2.5, the fan and compressor will be tested singly, and possibly together in a dual setup, to allow component interactions to be studied. The components are externally powered to desired speed and a variable area discharge valve is used to throttle them so that the complete operating envelope, i.e. up to surge or mechanical operating limit, can be mapped. The initial builds will be devoted largely to clean (undistorted) inlet flow conditions to obtain basic aerodynamic and mechanical performance data. Some fundamental distortion patterns, and/or selected inlet distortion patterns if available, may be examined. To produce inlet pressure distortion, local area blockage is introduced upstream of the test component via wire screens so that the desired nonuniform total pressure field exists slightly forward of the component's first stage. Fundamental, or standard, pattern types are often used so that a particular design's distortion tolerance can be directly compared with experience on other systems. These include circumferential patterns, termed "one per rev" in the case of the 180° contiguous spoiled sector shown in Figure 13.2.6, and radial distortion where a complete annulus of low pressure flow is produced, generally at the tip or hub region of the blade. Refinements of these simple screens are often used, such as variable extent, graded level (multiporosity screening, as opposed to a uniform screen), and "mixed" patterns combining circumferential and radial distortion.

Generally, a second build of the compression system will be required, as shown in Figure 13.2.5. This test will be aimed at either mechanical and/or aerodynamic design modifications, as may be required to achieve the required capability. Examples of design features, one or two of which may be perturbed at this point, include axial spacing, stage stall margin, stage work, blade solidity, blade aspect ratio, blade tip clearance, radial energy

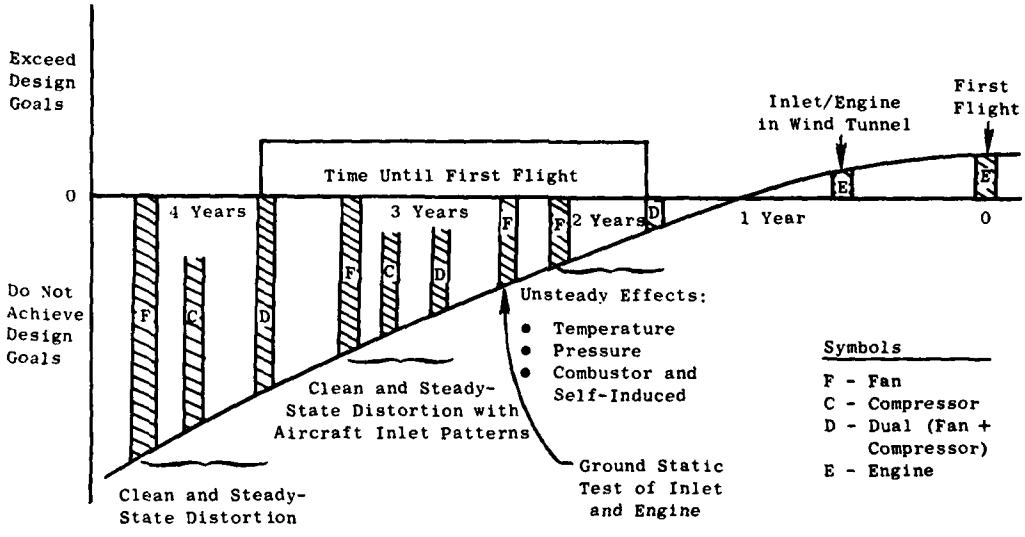

Figure 13.2.5 Representative Engine Compression System Test Sequence for Inlet Integration

COMPRESSION COMPONENT TESTING WITH DISTORTION

The test programs shown in Figure 13.2.5 typically follow the "exploratory development" or "research and development" phase, which consists of aerodynamic and mechanical design, blade tests in cascade arrangement, and perhaps a limited amount of single stage testing. At this point, distribution, variable stator scheduling, and interstage bleed. Initial or additional aircraft inlet patterns will be evaluated at this time, generally for key operating conditions like takeoff rotation, crosswind takeoff, subsonic and supersonic cruise, and extreme maneuvering conditions, as applicable.

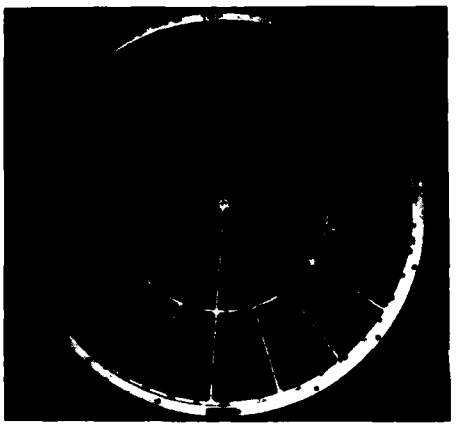

Figure 13.2.6 Circumferential (1/Rev) Distortion Screen

This type of testing defines the quantitative effect of steady-state distortion on compressor stability and efficiency. Stability or surge margin is determined from knowledge of both the clean and distorted surge line locations, as represented in Figure 13.2.7. In this manner the sensitivity, or reduction in surge margin relative to distortions of

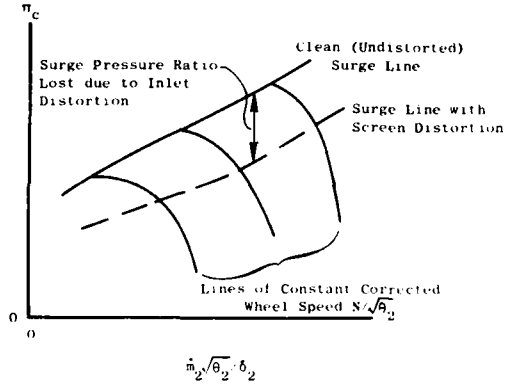

Figure 13.2.7 Compressor Map Showing Effect of Inlet Distortion on Surge Margin

various magnitudes, extents, and locations, is directly obtained.

UNSTEADY FLOW EFFECTS

Until the mid 1960's, the foregoing effort represented the major extent of assessing inlet/engine stability with distorted inflow. Time and financial constraints, as well as the more viable payoff potential of performance improvements, as opposed to the negative connotation of operational limitations, combined to temporarily orient the aircraft/propulsion system development toward the attainment of greater integration and performance levels. However, the introduction of the TF30 augmented turbofan engine into the multimission F-111 aircraft resulted in unexpected engine surges that significantly reduced its operational capabilities or usefulness. After some investigation, the real importance of unsteady pressure distortion was realized. The cause was a complex combination of vehicle flow field variation with aircraft pitch attitude, boundary layer ingestion and shock wave/boundary layer interaction. This inlet is highly integrated with the aircraft fuselage and wing (Figure 13.2.8).

Since successful engine operation is commonly achieved despite the known presence of transitory inlet flow effects such as turbulence, vorticity, and swirl, the concept of disturbance frequency is essential to determination of the significance of any unsteady flow phenomenon. Experimental evidence indicates when the period of the disturbance approaches that of one fan or compressor revolution, the engine will respond to or "see" it as a steady condition, since essentially all its blades will have experienced the same condition. Conversely, if the disturbance frequency is high enough, or its period short enough, very few of the blades will experience it and presumably there will be negligible effect. Thus we conclude that there is a critical frequency band in which time-variant inflow can significantly affect compressor flow stability.

The approach used on the TF30 was to make compressor inlet total pressure surveys with sensors capable of responding to frequencies somewhat beyond the compressor 1/rev rotational value. These data revealed the existence of "instantaneous" distortion well in excess of the corresponding steady-state conditions. When pressure signals (filtered to an appropriate frequency) were used as input to the steady-state distortion index or descriptor, the sensitivity of the TF30 to instantaneous distortion was confirmed (Reference 13.17).

While this approach facilitiated ex post facto identification and resolution of the F-111 problem, its application to the early stages of subsequent integration activities, while certainly warranted, has greatly complicated development testing. Currently, the need exists to measure unsteady pressures during inlet testing and also to determine their effect on compression system stability. While development of analytical compressor modelling techniques is underway, as described in Sec. 13.2.2, use is being made of test devices that simulate inlet dynamic behavior or introduce controlled pressure variations in order to advance understanding of this phenomenon. Such test equipment may use variable ramp or choked plug features, or a device to generate variable sinusoidal planar pressure waves. Figure 13.2.9 depicts a device that produces broad spectrum turbulence. References 13.18 and 13.19 address the quantitative assessment of unsteady pressure distortion's impact on turbomachinery, including the allocation of surge margin, in some detail. This task is quite complex, owing to the wide variety of disturbances that may be present, singly or in concert, at the inlet/engine interface. Examples of potential destabilizing transient influences include:

- Ramp-type changes in throttle setting, inlet or engine geometry, or attitude.
- Viscous effects such as shock wave/boundary layer interaction, transitory flow separation, and vortex shedding.
- Engine-generated pressure waves caused by rotating compressor stall, combustor instability, aerodynamic mismatch between compression components, and interactions between the engine and its control system.
- Acoustic wave propagation, or resonance, within the inlet cavity.

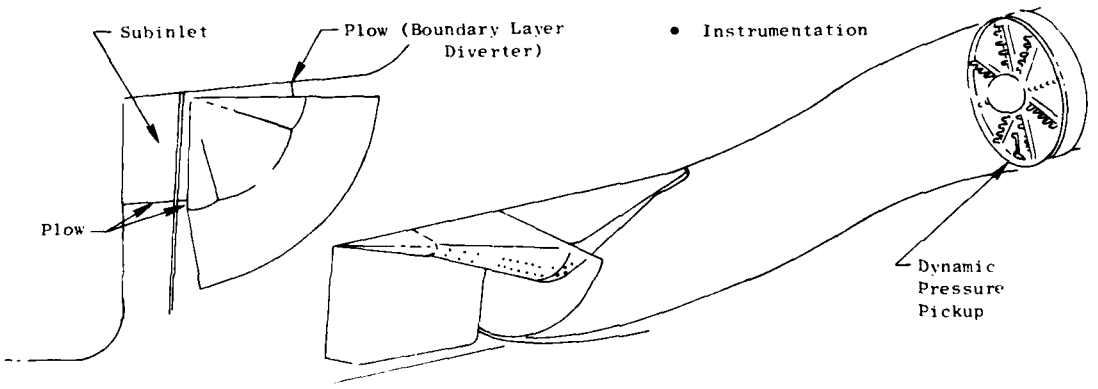

Figure 13.2.8 F-111 Wind Tunnel Inlet Model Configuration

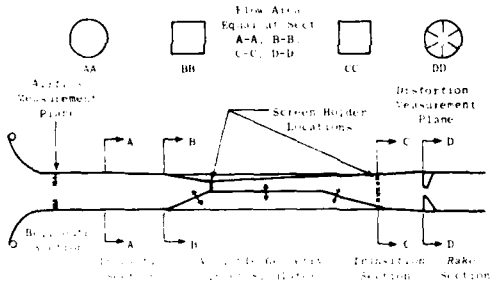

Figure 13.2.9 Variable Ramp Type of Unsteady Flow Generator for Engine Compression System Evaluation

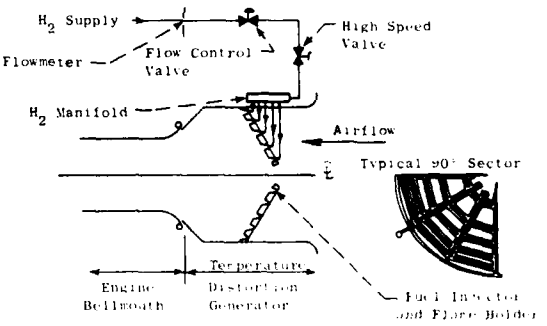

Figure 13.2.10 Unsteady and Spatial Temperature Distortion Generator for Engine Compression System Evaluation

As indicated in Sects. 13.1.1 and 13.1.2, temperature distortion produced by ingestion of hot gases from adjacent aircraft systems can also degrade engine operation. Reference 13.20 describes an investigation of spatial and unsteady temperature distortion conducted with a turbofan engine, using a hydrogen fueled burner as a temperature distortion generator. Figure 13.2.10 from this report is a sketch of this device. Results showed the high pressure compressor to be more sensitive than the fan to this type of distortion, with the primary variables affecting stability being the magnitude of spatial temperature distortion and the time-rate-of-change for unsteady distortion.

The foregoing types of compression component or engine testing with unsteady pressure and temperature distortions have been confined mainly to systems for supersonic applications, where the likelihood of occurrence and severity are generally greater than for subsonic systems. Subsonic installation operating conditions producing potentially significant unsteady distortion are generally evaluated initially by defining the inlet dynamic distortion in a model test and later by testing the inlet and engine directly, as discussed next.

INLET/ENGINE TESTING

Several means exist for evaluating inlet/engine interactions prior to flight testing the actual aircraft. They include propulsion wind tunnels, outdoor static testing, and use of a flying test bed. The role of each of these activities, with some examples, will now be briefly discussed.

Several large propulsion wind tunnels are in place at AEDC and NASA centers to test full-scale inlet and engine installations over a portion of the design flight envelope. Currently, evaluation of pitch and yaw conditions is somewhat restricted due to tunnel blockage considerations. Promising efforts are underway to develop inlet flow field simulation techniques to extend tunnel capability in this regard. However, this type of testing still provides valuable information on installed inlet/engine compatibility and, when conducted roughly one year prior to first flight as shown in the timetable of Figure 13.2.5, it allows some lead time for design modifications to resolve any problems that are evidenced. This type of facility is devoted mostly to supersonic applications.

Outdoor static facilities have been used for early evaluation of basic static operation, as well as simulated takeoff rotation, crosswind takeoffs, and compatibility with thrust reverser deployment. The Peebles facility of the General Electric Company's Aircraft Engine Group is an example of such a test site. It includes a wind generator employing an array of motor-driven fans that produces wind velocities of up to approximately 120 kts. The engine orientation relative to the wind direction is fully variable, allowing simulation of takeoff roll (0° orientation), takeoff rotation (15-20°), static crosswind (90°), and tailwind (180°) starts. Figure 13.2.11 shows a typical crosswind test arrangement for a subsonic installation in this facility.

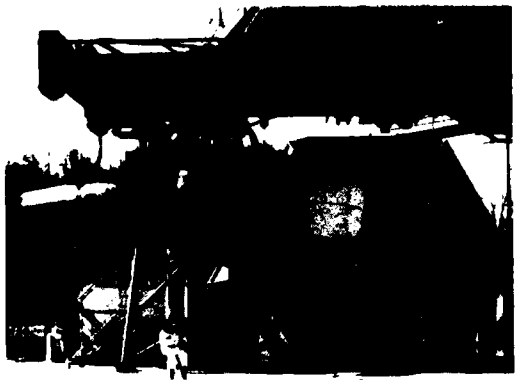

Figure 13.2.11 Peebles Facility Crosswind Test Arrangement

Flying test beds involve the use of an existing aircraft as a vehicle for mounting and flight-testing a developing engine installation, which may either replace one or more of the existing engines or be mounted elsewhere on the aircraft. This test mode has been exercised in the development of many systems, including the DC-10/CF6, C-5A/TF39, and 747/JT9D, which used a B-52; the S-3A/TF34, on a B-47; and the 727/JT8D, on a 707 aircraft. Figure 13.2.12 shows the DC-10/CF6 installation and its B-52 Flying Test Bed, in which the right inboard pair of existing engines was replaced.

13.2.4 INLET DEVELOPMENT TEST ELEMENTS FOR ENGINE INTEGRATION

A representative schedule of supersonic inlet development test programs is shown in Figure 13.2.13 as a counterpart of the Figure 13.2.5 engine test sequence. In general, two

Figure 13.2.12 DC-10/CF6 Installation on B-52 Flying Test Bed

types of testing are conducted: inlet model tests, with engine flow simulated via a vacuum system or propulsion simulator; and inlet/engine tests. The latter category was discussed in Sec. 13.2.3 and will not be further developed here, except to note that static inlet/engine tests are especially meaningful for supersonic installations due to the distortion that generally prevails during takeoff. In addition, the model test discussion in this section is restricted to the internal flow factors that directly impact engine performance and operation, such as recovery, distortion, and buzz. External performance integration is excluded here but will be discussed in Chapter 26.

Initial inlet test models are usually small scale, to minimize model and wind tunnel costs. Typical scale range is 5 to 15%, with a nominal value of 10% in Figure 13.2.13. Factors influencing the model scale besides cost and available tunnel size are minimum instrumentation size requirements and requirements for Reynolds number simulation. Both the amount and type of instrumentation desired are significant. Miniaturization of instruments is limited and expensive; therefore, installation access and inlet internal flow area blockage must be considered. Requirements for unsteady pressure sensors and associated electronic acquisition equipment are affected by the frequency range over which accurate response is needed. As discussed in Sec. 13.2.3, experience has shown that pressure fluctuation frequencies at least as high as the engine rotational speed are significant in terms of engine stability determination. Therefore, for similar geometry and Mach number, similarity requires that a model test must have a frequency response capability that is related to the full-scale value by the reciprocal of the model scale. With typical engine rotational frequencies on the order of 100 to 200 Hertz, a 10% scale model requires response on the order of 1 to 2 KHz. The trade between the foregoing factors is complex, but it must be resolved.

The first test is useful in providing an indication of inlet distortion trends that serve to "ballpark" the magnitude of the integration task ahead. Timely information interchange between airframe and engine manufacturers is necessary during this and subsequent test phases to facilitate this evaluation and direct the design modifications required to achieve compatibility between inlet distortion and engine tolerance. In terms of the Figure 13.2.13 sequence, which is oriented toward a supersonic application,

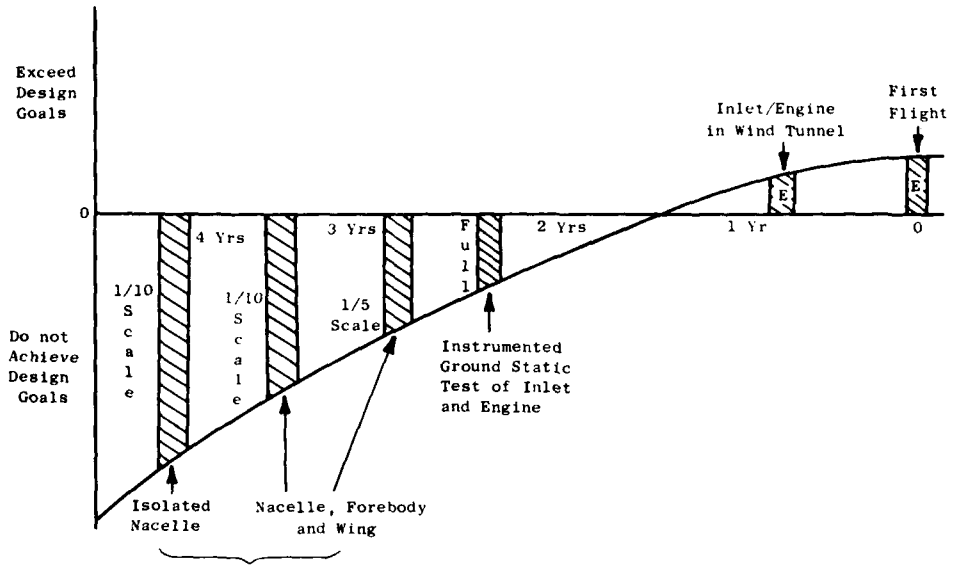

- Wind Tunnel Test
- Steady and Nonsteady Pressures for Distortion Assessment
- Range of Mach No., Angle of Attack, and Yaw
- Recovery Data
- Buzz Boundaries
- Mass Flow Ratio Variation to Define Stability Margin Characteristics

Figure 13.2.13 Representative Inlet Development Test Sequence for Engine Integration

subsequent tests increase in size and/or complexity as the inlet system becomes increasingly well-defined. More of the aircraft components adjacent to the inlet will be simulated for direct vehicle flow field interaction effects, such as fuselage forebody, wing, and adjacent nacelle, if applicable. This is crucial for evaluation at maneuvering conditions. Other inlet features such as controls, bleed, and bypass systems will be included or modelled more realistically as time progresses. Examples of other supersonic inlet variables that are characteristically evaluated during some portion of the model program include diffuser length and contouring, throat section length, duct axis offset, and auxiliary inlet placement and contouring. Corresponding subsonic inlet test variables include internal lip contraction A_i/A_{th}, leading edge bluntness, diffuser design, and the auxiliary inlet arrangement. Finally, the amount of unsteady pressure instrumentation generally increases as the model test phase proceeds.

Completion of the inlet model tests should produce a well-resolved inlet aerodynamic design with a good start on definition of distortion characteristics that will be presented to the engine. The ensuing inlet/engine ground and wind tunnel tests then serve to extend the inlet model results, within facility limits, by determining the integrated operational characteristics (including buzz) prior to flight testing the actual vehicle. At this point, the bulk of the integration effort has been completed. Achievement of most, if not all, operational and performance goals should be visible, with acceptable trades or minor design modifications already identified to resolve the most marginal area(s).

13.2.5 FLIGHT TESTING: THE ACID TEST

The evaluation of engine/inlet integration is just one of many flight test objectives. If test elements such as those described in the preceding sections have been utilized, the flight test should mainly confirm characteristics already demonstrated. Operational situations either not amenable to prior simulation, or predicted as marginal, represent the most likely problem areas. Examples of the former type of condition could include transient maneuvers and weapon firing. The actual assessment of success in inlet/engine integration is relatively simple. The main criteria are surge free operation over the complete aircraft flight placard and engine survival without structural damage following an intentional supersonic inlet buzz cycle, providing the aircraft meets its broader goals, such as range/payload and maneuverability. Generally, this entails provision of sufficient diagnostic instrumentation in at least one inlet/engine to allow resolution of any difficulties that may occur during the flight test program. Key instrumentation features include a compression system face total pressure survey as well as unsteady wall pressure sensors at several stations through the inlet and compression systems.

Following the initial flight test, production aircraft experience must be monitored, as manufacturing variations, engine deterioration with age, or altered usage may adversely affect some aspect of in-service capability.

13.3.1 REFERENCES

13.1 Grotz, C.A., "Development of the YC-14 Propulsion System," AIAA Paper No. 75-1314, September 1975.

13.2 Paul, D.L., "Quiet, Clean Short-haul Experimental Engine (QCSEE) Aerodynamic Characteristics of 30.5 cm Diameter Inlets," NASA CR-134866, August 1975.

13.3 Re, R.J., "An Investigation of Several NACA 1-Series Axisymmetric Inlets at Mach Numbers from 0.4 to 1.29," NASA TM X-2917, March 1974.

13.4 Sullivan, T.J., Silverman, I., and Little, D.R., "Single Stage, Low Noise, Advanced Technology Fan, Volume IV - Fan Aerodynamics," NASA CR-134892, February 1977.

13.5 Bloomer, H.E. and Schaefer, J.W., "Aerodynamic and Acoustic Performance of a Contracting Cowl High Throat Mach Number Inlet Installed on NASA Quiet Engine 'C'," AIAA Paper No. 76-540, July 1976.

13.6 Wyatt, D.D. and Fradenburgh, E.A., "Theoretical Performance Characteristics of Sharp-Lip Inlets at Subsonic Speeds," NACA Report 1193, 1954.

13.7 Marshall, F.L., "Prediction of Inlet Duct Overpressures Resulting from Engine Surge," AIAA Paper No. 72-1142, November 1972.

13.8 Johnson, J.E., "Variable Cycle Engines - The Next Step in Propulsion Evolution?" AIAA Paper No. 76-758, July 1976.

13.9 Tear, R.C., "Approaches to Determine and Evaluate the Stability of Propulsion Systems," AFAPL-TR-67-75, February 1968.

13.10 Gratz, H.J., "Procedures and Suggested Programming Emphasis to Obtain Criteria Essential to Attaining Propulsion System Flow Stability," AFAPL-TR-68-30, May 1968.

13.11 Albers, J.A. and Stockman, N.O., "Calculation Procedures for Potential and Viscous Flow Solutions for Engine Inlets," ASME Paper No. 74-GT-3, 1974.

13.12 Albers, J.A., "Comparison of Predicted and Measured Low-Speed Performance of Two 51-Centimeter-Diameter Inlets at Incidence Angle," NASA TM X-2937, November 1973.

13.13 Keith, J.S., Ferguson, D.R., Merkle, C.L., Heck, P.H., and Lahti, D.J., "Analytical Method for Predicting the Pressure Distribution About a Nacelle at Transonic Speeds," NASA CR-2217, July 1973.

13.14 Tesch, W.A. and Steenken, W.G., "Blade Row Dynamic Digital Compressor Program, Volume I, J85 Clean Inlet Flow and Parallel Compressor Models," NASA CR-134978, 1976.

13.15 Reynolds, G.G. and Steenken, W.G., "Dynamic Digital Blade Row Compression Component Stability Model - Model Validation and Analysis of Planar Pressure Pulse Generator and Two-Stage Fan Test Data," AFAPL-TR-76-76, August 1976.

13.16 Mazzawy, R.S. and Banks, G.A., "Circumferential Distortion Modeling of the JT-9D-7-3 Compression System," NASA CR-135124, 1977.

13.17 Plourde, G.A. and Brimelow, B., "Pressure Fluctuations Cause Compressor Instability," Airframe/Propulsion Compatibility Symposium, June 1969.

13.18 Brimelow, B., Collins, T.P., and Pfefferkorn, G.A., "Engine Testing in a Dynamic Environment," AIAA Paper No. 74-1198, October 1974.

13.19 Collins, T.P., Reynolds, G.G., and Vier, W.F., "An Experimental Evaluation of Unsteady Flow Effects on an Axial Compressor," AFAPL-TR-73-43, July 1973.

13.20 Rudey, R.A. and Antl, R.J., "The Effect of Inlet Temperature Distribution on the Performance of a Turbo-Fan Engine Compressor System," NASA TM X-52788, June 1970.

Chapter 14

VARIABLE CONVERGENT-DIVERGENT EXHAUST NOZZLE AERODYNAMICS

by A.P. Kuchar

General Electric Company
Aircraft Engine Group
Evendale, Ohio

TABLE OF CONTENTS

CHAPTER 14 VARIABLE CONVERGENT-DIVERGENT EXHAUST NOZZLE AERODYNAMICS

		Page
14.0	Introduction	14-1
14.1	Nozzle Concept	14-2
14.2	Performance Predictions	14-2
14.2.1	Flow Coefficient	14-3
14.2.2	Baseline Thrust Coefficient	14-5
14.2.2.1	Angularity Coefficient	14-6
14.2.2.2	Velocity Coefficient	14-6
14.2.2.3	Generalized Performance	14-7
14.2.3	Leakage Loss Calculations	14-8
14.2.4	Cooling Air Loss Calculations	14-10
14.2.5	Separation/Overexpansion Effects	14-11
14.3	Aerodynamic Load Predictions	14-12
14.3.1	Primary Nozzle	14-13
14.3.2	Secondary Nozzle	14-14
14.3.3	External Flaps	14-15

LIST OF FIGURES

Figure 14.1	Schematic of Typical Exhaust Systems	14-1
Figure 14.1.1	C-D Nozzle Geometric Parameters	14-2
Figure 14.1.2	C-D Nozzle Schematic	14-2
Figure 14.2.1	Total Flow Available to the Nozzle	14-3
Figure 14.2.2	Nozzle Flows	14-4
Figure 14.2.3	Conic Nozzle Flow Coefficient	14-4
Figure 14.2.4	Nozzle Maximum Flow Coefficient	14-4
Figure 14.2.5	C-D Nozzle Flow Coefficient	14-4
Figure 14.2.6	Adjusted C-D Nozzle Flow Coefficient	14-5
Figure 14.2.7	C-D Nozzle Thrust Coefficient	14-5
Figure 14.2.8	Nozzle Angularity Coefficient	14-6
Figure 14.2.9	C-D Nozzle Angularity Coefficient	14-6
Figure 14.2.10	C-D Nozzle Velocity Coefficient	14-7

LIST OF FIGURES (Concluded)

		Page
Figure 14.2.11	C-D Nozzle Area Ratio Schedule	14-7
Figure 14.2.12	Flow Chart of Calculation Procedure for Generalized Performance Curves	14-8
Figure 14.2.13	C-D Nozzle Leakage Paths	14-8
Figure 14.2.14	Nozzle Leakage Control Volume	14-8
Figure 14.2.15	Nozzle Leakage Test Setup	14-9
Figure 14.2.16	Nozzle Cooling Flowpath	14-10
Figure 14.2.17	Nozzle Cavity Flows	14-11
Figure 14.2.18	Overexpansion Effects on C-D Nozzle Aerodynamic Characteristics	14-11
Figure 14.2.19	C-D Nozzle Separation	14-12
Figure 14.2.20	Thrust Coefficient Curve Adjusted for Overexpansion Effects	14-12
Figure 14.2.21	Separation Thrust Recovery, Scale Model Data	14-12
Figure 14.3.1	One-Dimensional Static Pressure Distribution Calculation	14-13
Figure 14.3.2	Wall Turning Effect on Static Pressure	14-13
Figure 14.3.3	Afterburner Heat Addition Pressure Loss Effect on Nozzle Pressure Distribution	14-13
Figure 14.3.4	Generalized Primary Nozzle Pressure Distribution	14-14
Figure 14.3.5	Secondary Nozzle Pressure Distribution	14-14
Figure 14.3.6	Secondary Nozzle Gas Loads Correction Factor	14-14
Figure 14.3.7	Cooling Slot/Leakage Flow	14-14
Figure 14.3.8	Adjusted Secondary Nozzle Pressure Distribution	14-14
Figure 14.3.9	Specific Heat Ratio Effects on Nozzle Pressure Distribution	14-15

CHAPTER FOURTEEN

VARIABLE CONVERGENT-DIVERGENT EXHAUST NOZZLE AERODYNAMICS

14.0 INTRODUCTION

The exhaust nozzle is a very important component of the overall engine propulsion system. The sensitivity of the net thrust delivered by the engine to nozzle performance is higher than any other engine component. For this reason, it is extremely important to obtain the highest possible nozzle performance with due consideration for nozzle cost, weight, complexity, and reliability.

There is a wide variety of exhaust systems which can be utilized. These are: the category of fixed nozzles which includes the conic nozzle and the high bypass, separate flow nozzles and the category of variable nozzles which includes converging-diverging nozzles, plug nozzles, and nonaxisymmetric nozzles of all kinds and shapes. The selection of exhaust system type is determined largely by a combination of engine, aircraft, mission requirements, and trade studies. A schematic of typical exhaust systems is shown in Figure 14.1.

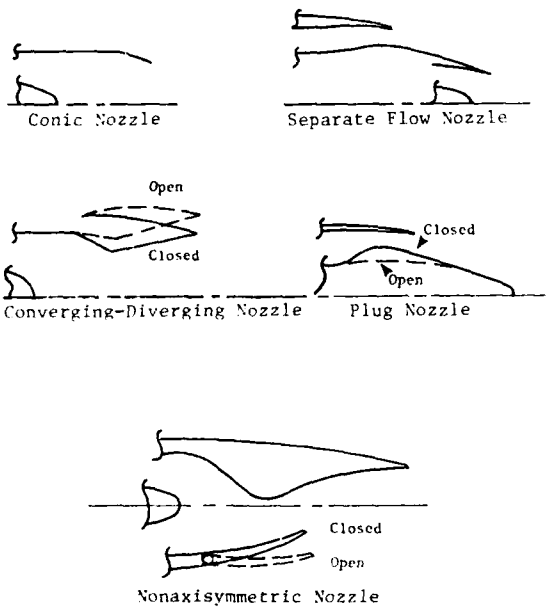

Figure 14.1 Schematic of Typical Exhaust Systems

Fixed conic nozzles are the simplest of nozzles. They have no moving parts and are used to exhaust a single engine exhaust flow in a purely converging exhaust duct. They are utilized primarily on subsonic transports, particularly on commercial applications of the older generation straight turbojet or low bypass ratio fan engines. The high bypass, separate flow, converging nozzles are also used in subsonic transport applications. However, they are compatible with the newer generation of high bypass, separate exhaust engines, in which one nozzle is used for fan bypass air discharge and one is used for core engine air discharge.

Variable nozzles are required where the engine cycle is such that large variations in nozzle exit area are necessary. In virtually all cases, this area variation is a result of afterburning engine cycles which require area increases of 60 to 150% from nonafterburning to full afterburning operation. A few variable nozzle applications employ a converging nozzle only. They are used for applications where aircraft Mach numbers are near but not much above 1.0. By far, most variable nozzle applications utilize the axisymmetric, converging-diverging (C-D) type. The C-D nozzle is most common with afterburning engines because usually, an engine that has afterburning thrust requirements is matched with an airplane that must achieve supersonic Mach numbers. Supersonic flight Mach numbers result in high engine exhaust nozzle pressure ratios and, if a C-D nozzle is not used, the engine exhaust gases cannot be expanded efficiently resulting in a severe loss in engine net thrust. The axisymmetric nozzles are structurally efficient pressure vessels and, because of their extensive use, have a tremendous technology base from which to design. Even within the class of axisymmetric C-D nozzles, there is a variety of types. The older generation turbojets still in use are characterized by requirements for bypassing varying amounts of inlet air around the engine to provide engine cooling and good inlet recovery and engine matching. This low pressure secondary air is injected back into C-D nozzles which are hence called ejector nozzles. Ejector nozzles can also take air on board from outside the nacelle directly into the nozzle for better overall nozzle matching and these are called two-stage ejector nozzles. For very high Mach number aircraft (2.7 and above), the C-D nozzles can be very long with curved diverging sections. For lower supersonic Mach numbers, the diverging section is usually conical. For the new generation high bypass augmented turbofan engine, secondary air is not utilized and the nozzles are simple C-D geometries with primarily conical sections.

In addition to the C-D nozzle, the variable plug nozzle has also been considered for afterburning engine applications. These are generally heavier than the C-D nozzles and pose more difficult cooling conditions, but because of the kinematic/structural arrangement, the nozzle actuation forces are low. Plug nozzles are characterized by a "flatter" nozzle thrust coefficient curve which gives high performance over a wider range of pressure ratios than a C-D nozzle. They are generally applied for very high Mach applications with low Mach requirements.

A final class of nozzles is that of the nonaxisymmetric variety. These are exhaust systems which can be fixed but are most often variable and are, by definition, nonaxisymmetric. Systems of this type are considered when their need is dictated by unusual requirements imposed on the installation. Examples of such requirements could include thrust vectoring, wing lift augmentation, aircraft survivability, or low drag, blended body exhaust systems. Although there are no nonaxisymmetric exhaust systems currently in use, they are becoming more important candidates for future aircraft applications because of more complex and flexible aircraft system requirements. These systems are generally heavier and less structurally efficient than axisymmetric nozzles and, because of their current state of the art, the technology base is low.

In this chapter, the aerodynamics of and design procedures for the variable axisymmetric C-D nozzle will be described in detail. This class of nozzle was selected for detailed illustration for several reasons. A prime reason is that this class of nozzle has associated with it variants of most of the design problems associated with all exhaust systems. Additionally, a substantial data base and high technology level exists for the nozzles, leading to the availability of well-understood design criteria. Finally, the fixed convergent and variable C-D nozzles probably comprise more than 95% of all exhaust systems currently in use. Because of the additional complexity of the variable C-D nozzle as compared to the fixed convergent nozzle, it was felt that considering the example of the variable C-D nozzle would prove to be the most instructive.

This chapter discusses the aerodynamic design considerations of the variable C-D nozzle which appear most prevalent for current and near future technology engines. These are bypass engines with no secondary air, and which are compatible with aircraft maximum Mach numbers of ~2.5 or less. Included in the chapter are discussions on how to predict and assess internal performance and aerodynamic gas loads. Considered in the performance aspects are nozzle flow coefficients and thrust coefficients with breakdowns in basic nozzle efficiency, leakage effects, cooling air losses, and separation effects. Procedures are provided for estimating aerodynamic loads of the primary nozzle, secondary nozzle, and external flaps. It is to be noted that the discussions are related to analysis techniques, and that specific design curves/criteria are limited.

14.1 NOZZLE CONCEPT

The analysis approaches discussed apply to (but are not necessarily restricted to) variable area C-D nozzles of the type characterized by straight flap, sharp cornered throats with little or no secondary cooling air introduced at the nozzle throat.

The nozzle flowpath geometric parameters used consistently throughout are indicated in Figure 14.1.1. Station 8 is the nozzle charging station; i.e., all nozzle losses included in the thrust coefficient (Section 14.2) are defined to occur between Station 8 and the exit, Station 9.

A cross section schematic of a typical single actuation system nozzle is shown in Figure 14.1.2. The primary nozzle is most often actuated by a cam and roller system, whereas the secondary nozzle is most often actuated by a linkage system. The linkage system shown is a very simple type, but more complex systems can be designed which provide different area ratio schedule characteristics (A_9/A_8 vs A_8). The choice of cam shape and linkage arrangement depends on the requirements of nozzle throat area in combination with the desired area ratio schedule.

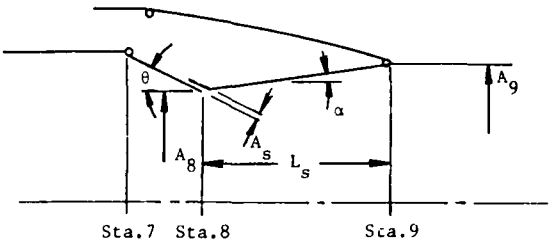

A_8 - Primary Nozzle Throat Area

A_9 - Secondary Nozzle Exit Area

A_s - Cooling Slot Flow Area (if applicable)

α - Secondary Nozzle Half Angle

θ - Primary Nozzle Half Angle

L_s - Secondary Nozzle Length, Parallel to Nozzle Centerline

Figure 14.1.1 C-D Nozzle Geometric Parameters

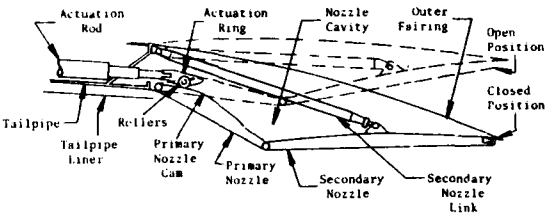

Figure 14.1.2 C-D Nozzle Schematic

14.2 PERFORMANCE PREDICTIONS

Two, dimensionless parameters are used to measure exhaust nozzle performance: the thrust coefficient and the flow coefficient. The thrust coefficient is the ratio of actual nozzle gross thrust to the ideal available gross thrust and represents the measure of nozzle efficiency.

$$C_{fg} = \frac{F_{g\ Actual}}{F_{g\ Ideal}} \qquad (14.2.1)$$

Referring to Figure 14.2.1, the ideal gross thrust available to the nozzle is based on the total airflow supplied to the nozzle, the total pressure and temperature at the nozzle throat, and the fuel-air ratio at the nozzle throat.

Thus,

$$F_{gi} = f(W_{Actual}, T_{T8}, P_{T8}, FAR8, P_0) \qquad (14.2.2)$$

$$= \frac{W_{Actual}}{g}\sqrt{2g\,J(H_8-h_0)}$$

Where:

$W_{actual} = W_7 = W_{UL} + W_L$ = Total actual flow supplied to the nozzle
T_{T8} = Total temperature of gas flow at the nozzle throat, Station 8
P_{T8} = Total pressure at the nozzle throat, Station 8
P_O = Ambient pressure
FAR8 = Overall fuel-air ratio
g = Gravitational constant = 32.174 ft/sec^2
J = Joules constant = 778.26 ft-lb/Btu
H_8 = Total enthalpy of gas at P_{T8} and T_{T8}, Btu/lb
h_o = Enthalpy of gas at fully expanded pressure and temperature, Btu/lb

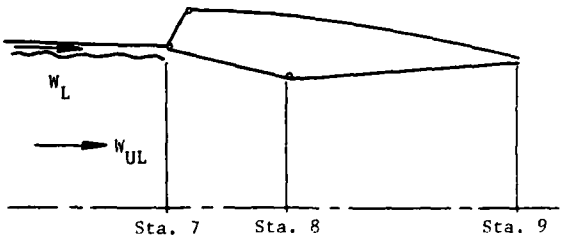

Figure 14.2.1 Total Flow Available to the Nozzle

Total pressure losses due to mixing, tailpipe friction, tailpipe liner drag, and afterburner heat addition pressure loss up to the throat are considered part of the mixer/augmentor performance. The nozzle thrust coefficient thus includes losses due to the following:

(1) friction (momentun loss due to wall friction in the nozzle)

(2) angularity (momentum loss due to non-axial flow at the exit plane of the nozzle)

(3) expansion (loss due to mismatch of the nozzle exit pressure with ambient)

(4) leakage

(5) cooling air throttling loss

The flow coefficient is the ratio of total actual nozzle flow to ideal nozzle flow.

$$C_{D8} = \frac{W_{7\ Actual}}{W_{8\ Ideal}} \qquad (14.2.3)$$

The ideal flow is calculated from the flow conditions at the nozzle throat (P_{T8}, T_{T8}, γ_8), the nozzle physical throat area (A_8), and the overall nozzle pressure ratio (P_{T8}/P_0). Using the continuity equation, this can be expressed as:

$$W_{8\ Ideal} = \frac{P_{T8}\ A_8\ \bar{m}_8}{\sqrt{T_{T8}}} \qquad (14.2.4)$$

where $\bar{m}_8 = f(\gamma_8, P_{T8}/P_0)$

This parameter is not a measure of efficiency, but rather it is a sizing parameter which allows the nozzle physical area to be matched to an engine cycle.

These parameters are used in the engine cycle analysis to complete the engine cycle performance assessment. For a given operating condition, the basic engine turbomachinery determines the flow conditions to the nozzle throat, Station 8. These flow conditions include the total flow W_7, total temperature and pressure T_{T8} and P_{T8}, and fuel-air ratio FAR8. From these conditions, the effective flow area at the nozzle throat required to pass the total flow is determined. Using the flow coefficient, the nozzle physical throat area A_8 is calculated which then "sizes" the nozzle for that operating condition. The nozzle geometry is determined from the selected nozzle geometry schedule, and the thrust coefficient is likewise determined from the geometry and the engine/nozzle operating condition. The thrust coefficient is then used to calculate the actual gross thrust produced by the engine at the operating condition of interest.

14.2.1 FLOW COEFFICIENT

As previously stated, the flow coefficient is the ratio of total actual flow through the nozzle to ideal flow. The effective flow area required to pass the actual delivered flow is given by

$$A_{e\ Actual} = \frac{W_{Actual}\sqrt{T_{T8}}}{P_{T8}\ \bar{m}_8} \qquad (14.2.5)$$

where $\bar{m}_8 = f(\gamma_8, P_{T8}/P_0)$

Combination of the preceding three equation gives

$$C_{D8} = \frac{W_{7Actual}}{W_{8Ideal}} = \frac{A_{eActual}\ P_{T8}\ \bar{m}_8/\sqrt{T_{T8}}}{A_8\ P_{T8}\ \bar{m}_8/\sqrt{T_{T8}}} = \frac{A_{eActual}}{A_8} \qquad (14.2.6)$$

Thus, the flow coefficient is identically equal to the ratio of the effective flow area required to pass the total actual nozzle flow to the nozzle physical throat area. The required effective area is determined from the engine cycle calculations and the flow coefficient is used to calculate the required nozzle physical throat area by substituting the expression for $W_{8_{ideal}}$ into the flow coefficient equation.

$$C_{D8} = \frac{W_{7Actual}}{W_{8Ideal}} = \frac{W_{7Actual}}{P_{T8}\ A_8\ \bar{m}_8/\sqrt{T_{T8}}} = \frac{W_{7Actual}\sqrt{T_{T8}}}{P_{T8}\ A_8\ \bar{m}_8}$$

Finally,

$$A_8 = \frac{W_{7Actual}\sqrt{T_{T8}}}{C_{D8}\ P_{T8}\ \bar{m}_8} \qquad (14.2.7)$$

Depending on the particular engine cycle/exhaust nozzle performance bookkeeping system selected, the actual flow in the flow coefficient can include not only the flow passing through the nozzle throat area, A_8, but it can also include primary nozzle leakage and, in some cases, bypass cooling air.

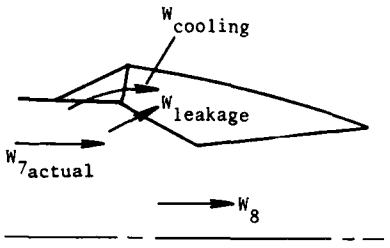

Figure 14.2.2 Nozzle Flows

Thus,

$$W_{7_{Actual}} = W_8 + W_{Leakage} + W_{Cooling}$$

The leakage and cooling flow can be estimated using methods discussed later and knowing each of these flows, a total nozzle effective area can be determined based on P_{T8}, T_{T8}, and $\bar{m}_8$ as follows:

$$A_{e_{Total\ Actual}} = A_{e_8} + A_{e_{Leakage}} + A_{e_{Cooling}}$$

$$= \frac{W_8 \sqrt{T_{T8}}}{P_{T8}\,\bar{m}_8} + \frac{W_{Leakage} \sqrt{T_{T8}}}{P_{T8}\,\bar{m}_8} + \frac{W_{Cooling} \sqrt{T_{T8}}}{P_{T8}\,\bar{m}_8} \qquad (14.2.8)$$

Thus,

$$C_{D8} = \frac{A_{e_8} + A_{e_{Leakage}} + A_{e_{Cooling}}}{A_8} \qquad (14.2.9)$$

The effective area at the nozzle throat comprises most of the total effective area. The leakage effective area is typically 1/2 to 1% of the total and the cooling effective area is typically 0 to 2% of the total. The ratio of throat effective area to physical area, A_{e8}/A_8, is less than 1.0 because of the loss of flow in the boundary layer and the contraction effect of the nozzle. A typical flow coefficient curve for an isolated conic nozzle with no leakage or cooling bypass flow will appear as follows:

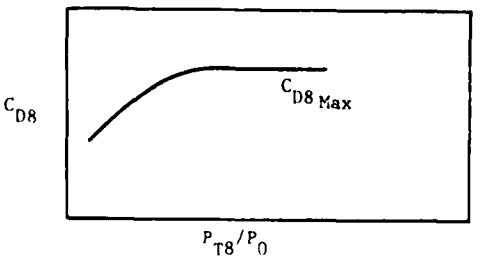

Figure 14.2.3 Conic Nozzle Flow Coefficient

When the nozzle is "hard choked," the flow coefficient will reach a maximum value and remain constant with increasing pressure ratio. The level of $C_{D8_{MAX}}$ and the pressure ratio at which it occurs is, for all practical purposes, a function of primary nozzle half angle only as shown in Figure 14.2.4. Note that at $\theta = 0$, the flow coefficient is still less than 1.0; this is the effect of the boundary layer.

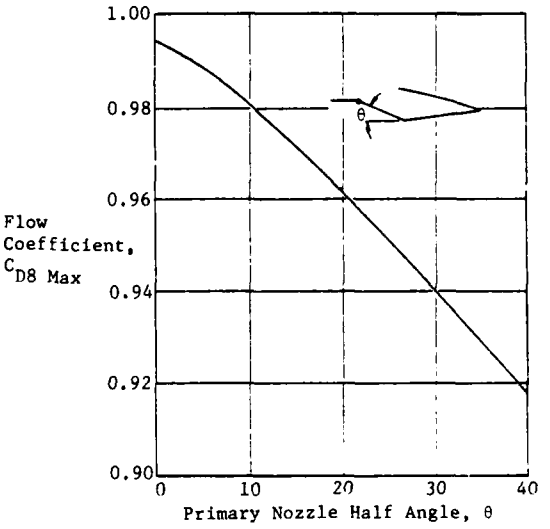

Figure 14.2.4 Nozzle Maximum Flow Coefficient

Since the C-D nozzles in consideration are assumed not to accommodate secondary air, the primary and secondary nozzles are close coupled; there is either a very small cooling slot at the nozzle throat or none at all. With this arrangement, the C-D nozzle will behave as a venturi, and the drop-off in C_{D8} as pressure ratio is reduced will not occur. The presence of the secondary nozzle will cause the throat to remain sonic at low pressure ratios (below 1.9); for example, during an engine throttle back. Since the flow coefficient is based on overall nozzle pressure ratio, recall

$$C_{D8} = \frac{W_{7_{Actual}} \sqrt{T_{T8}}}{P_{T8}\, A_8\, \bar{m}_8} \text{ and } \bar{m}_8 = f(P_{T8}/P_0,\ \gamma_8)$$

The flow coefficient will remain constant down to the sonic pressure ratio and in fact, because of the definition, will rise to higher levels at pressure ratios below sonic as sketched in Figure 14.2.5.

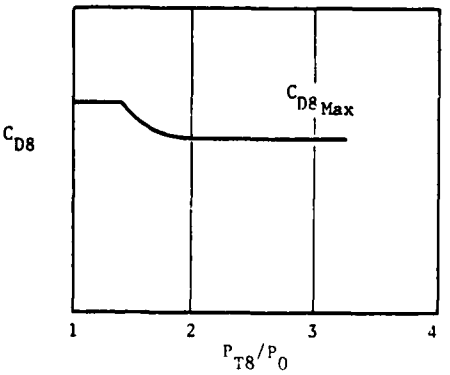

Figure 14.2.5 C-D Nozzle Flow Coefficient

This occurs because, as in the case with a venturi nozzle, the static pressure in the throat is lower than the ambient pressure. Therefore, while the flow function, m_8, is based on the overall nozzle pressure ratio P_{T8}/P_0, the actual pressure ratio at the throat, P_{T8}/P_{S8} is higher than P_{T8}/P_0 and as a result, the throat Mach number is higher than the nozzle exit Mach number and passes more flow than that calculated from P_{T8}/P_0.

The eventual peaking out at very low pressure ratios is a result of the fact that the amount of static pressure drop in the throat is limited by the nozzle area ratio. This rise characteristic in flow coefficient can be influenced by the size of the cooling slot, the separation characteristics of the nozzle, and the secondary nozzle half angle, α, all of which can affect the throat static pressure.

A baseline flow coefficient curve accounting for the throat effective area only is thus defined from Figure 14.2.4 and analytical calculations. Since the flow coefficient to be used in the cycle analysis can include the leakage and bypass cooling flows, the final flow coefficient would be that given previously:

$$C_{D8} = \frac{A_{e_8}}{A_8} + \frac{A_{e_{Leakage}}}{A_8} + \frac{A_{e_{Cooling}}}{A_8}$$

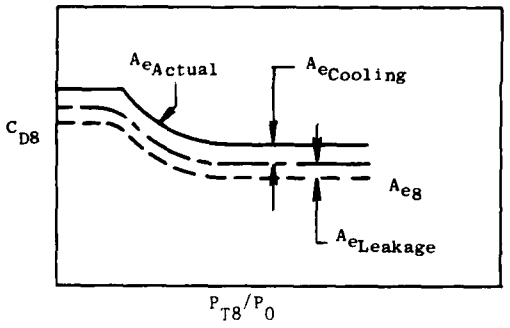

Figure 14.2.6 Adjusted C-D Nozzle Flow Coefficient

It is important to recognize that for a variable geometry nozzle, the flow coefficient is not a measure of nozzle efficiency, it is a parameter that sizes the nozzle to an engine. The flow coefficient is simply used to determine the nozzle area necessary to pass the required engine flow. For this reason, flow coefficient errors or discrepancies of 1/4 percent, which are significant for thrust coefficients, have essentially no impact on nozzle performance.

14.2.2 BASELINE THRUST COEFFICIENT

The thrust coefficient is the measure of nozzle efficiency and accounts for all nozzle losses. As described earlier, these losses include friction, angularity, expansion, leakage, and cooling air throttling. The thrust coefficient equation showing these losses can be written as follows:

$$C_{fg} = \frac{C_V C_A \frac{W_{7_{Actual}}}{g} \overbrace{V_{9i} + (P_{S9i} - P_0) A_9}^{\text{Expansion}}}{\frac{W_{7_{Actual}}}{g} V_{\textcircled{S}}} - \Delta C_{fg\ \text{Leakage Losses}} - \Delta C_{fg\ \text{Cooling Air Throttling Losses}} \qquad (14.2.10)$$

(Friction: C_V; Angularity: C_A)

where:

C_V = velocity coefficient accounting for friction losses.

C_A = angularity coefficient accounting for angularity losses.

$W_{7_{actual}}$ = actual total airflow supplied to the nozzle.

V_{9i} = ideal velocity at the nozzle exit based on A_9/A_8, C_{D8}, T_{T8}, and FAR8.

P_{S9i} = ideal static pressure at the nozzle exit consistent with V_{9i}

A_9 = nozzle physical exit area

$V_{\textcircled{S}}$ = isentropic or fully expanded jet velocity based on P_{T8}/P_0, T_{T8}, and FAR8.

Basic nozzle aerodynamic efficiency includes the effects of losses due to angularity and friction, while expansion losses are attributable to "off design" operation. These three losses establish a *baseline nozzle thrust coefficient curve* for a typical C-D nozzle.

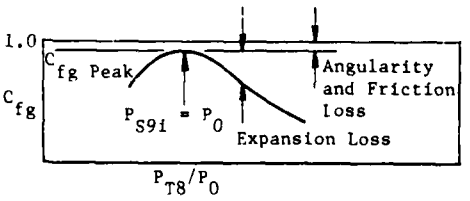

Figure 14.2.7 C-D Nozzle Thrust Coefficient

The maximum thrust coefficient is the peak thrust coefficient and occurs at a nozzle pressure ratio where the nozzle exit static pressure, P_{S9i}, equals ambient pressure, P_0. At this condition, the ideal nozzle exit velocity, V_{9i}, is equal to the fully expanded velocity, $V_{\textcircled{S}}$. Equation 14.2.10, without the leakage or throttling losses, becomes

$$C_{fg} = \frac{C_V C_A \frac{W_{7_{Actual}}}{g} V_{9i} + (P_{S9i} - P_0) A_9}{\frac{W_{7_{Actual}}}{g} V_{\textcircled{S}}} \qquad (14.2.11)$$

At the peak thrust coefficient condition, the ideal exit static pressure is equal to ambient pressure, $P_{S9i} = P_0$ and, by definition $V_{9i} = V_{\textcircled{S}}$. Therefore

$$C_{fg\ Peak} = C_V C_A \qquad (14.2.12)$$

Thus, the peak thrust coefficient is the product of the angularity and velocity coefficients. At any other pressure ratio, the difference between the C_{fg} peak and the C_{f_g} is the expansion loss.

14.2.2.1 ANGULARITY COEFFICIENT

The angularity coefficient, C_A, is the thrust loss due to the nonaxial exit of the exhaust gases from the nozzle. For a small element of flow, this coefficient is simply the cosine of the local exit flow angle α.

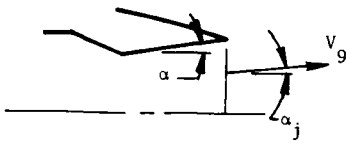

$$V_{9\ axial} = V_9 \cos \alpha_j$$

$$C_{A_j} = \frac{V_{9\ axial}}{V_9} = \cos \alpha_j$$

Figure 14.2.8 Nozzle Angularity Coefficient

Since the exit angle α_j varies from zero at the nozzle centerline to α at the outer radius, the overall nozzle angularity loss coefficient is the integral of cos α_j across the nozzle exit. For the assumption of constant mass flow per unit area;

$$C_A = \frac{1}{A_9} \int_{r=0}^{r=R_9} \cos \alpha_j \, 2\pi r_j \, dr \qquad (14.2.13)$$

For the case of a variable mass flow distribution, the equation would be adjusted to include the mass flow variation. In theory, for a nozzle of sufficient length such that the exit flow angle follows a specific pattern (point source flow), the angularity coefficient is represented by the classical equation,

$$C_A = \frac{1 + \cos \alpha}{2} \qquad (14.2.14)$$

Exhaust nozzles for practical applications, however, are relatively short and do not allow the angularity loss coefficient to follow the above equation.

Analytical studies of the supersonic C-D nozzle inviscid flow field have allowed the evaluation of the angularity coefficient for a range of practical nozzle geometries. Based on these studies, the angularity loss coefficient can be correlated with α and A_9/A_8 as in Figure 14.2.9. In real nozzle geometries, there is also a slight loss in nozzle aerodynamic efficiency because the exit static pressure is not equal to ambient pressure across the entire nozzle exit area.

For practical engineering purposes, this loss is included in the angularity coefficient; thus, the trends shown in Figure 14.2.9 represent an angularity coefficient given by the equation:

$$C_A = \frac{1}{A_9} \int_{r=0}^{r=R_9} \cos \alpha_j \, 2\pi r_j \, dr$$

$$+ \frac{1}{\frac{W_{7_{Actual}}}{g} V_{9i}} \left[\int_{r=0}^{r=R_9} (P_{S9j} - P_{S9i}) \, 2\pi r_j \, dr \right.$$

$$\left. + \int_{r=0}^{r=R_9} (V_{9j} - V_{9i}) \, \rho_{9j} \, V_{9j} \, 2\pi r_j \, dr \right] \qquad (14.2.15)$$

The second and third terms in this equation are the static pressure variation loss and velocity variation loss (due to pressure variation) and are functions of the nozzle geometry only.

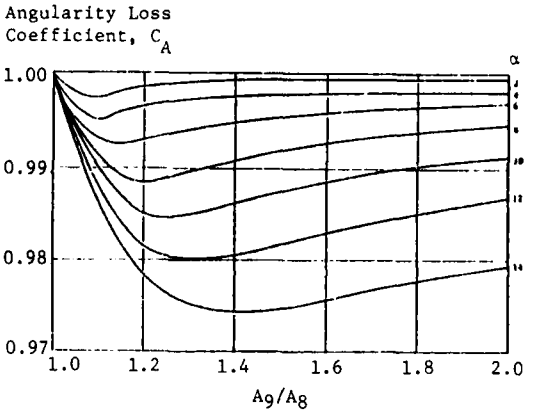

Figure 14.2.9 C-D Nozzle Angularity Coefficient

For nozzles with area ratio below 1.1, the angularity coefficient is typically 0.995 to 0.997 or higher, but for higher area ratio nozzles, the loss can be 1 or 2% such that $C_A = 0.98$ or 0.99.

14.2.2.2 VELOCITY COEFFICIENT

The velocity coefficient represents the effects of boundary layer momentum loss caused by friction in the nozzle. Because it is related to friction, this coefficient is essentially a function of the secondary nozzle surface area, Mach number near the wall, and Reynolds number. The Reynolds number effects are generally very small, less than ±0.1% for typical ranges of full scale nozzle operating conditions. Since the wall Mach number distribution is a function of nozzle geometry, the velocity coefficient can thus be expressed uniquely as a function of geometry only. Thus, the velocity coefficient, like the angularity coefficient, can be presented as in Figure 14.2.10 as a function of nozzle area ratio, A_9/A_8, and half angle, α. This characteristic has also been evaluated analytically by inviscid flow field analyses and boundary layer calculations.

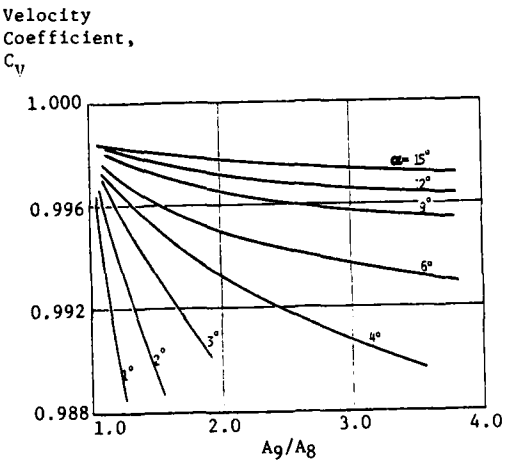

Figure 14.2.10 C-D Nozzle Velocity Coefficient

It should be recognized that while angularity and velocity coefficients can be determined separately by analytical studies, it is extremely difficult and virtually impractical to determine the individual coefficients by experimental methods. The velocity coefficients typically range from 0.992 to 0.997 and any reasonably accurate experimental analysis would require very precise pressure and flow angle measurements in a supersonic flow field. However, as stated earlier, since the peak thrust coefficient is the product of C_V and C_A, this product can be determined experimentally rather easily with a carefully controlled scale model nozzle test. Scale model tests using strain gage force balance systems to measure nozzle thrust can provide accurate measurements of thrust coefficients. Comparison of peak scale model thrust coefficients with the predicted peak coefficient using the analytical C_V C_A product has shown agreement better than ±1/4%.

14.2.2.3 GENERALIZED PERFORMANCE

The angularity and velocity coefficients define the nozzle peak efficiency or maximum thrust coefficient as discussed earlier. Once the nozzle peak thrust coefficient has been defined, either from C_V and C_A curves or from a scale model test, a baseline nozzle thrust coefficient curve is defined using basic one-dimensional fluid dynamics. The equation for thrust coefficient presented in Section 14.2.2 (less leakage and cooling air losses) may be manipulated as follows to give

$$C_{fg} = \frac{C_V C_A \frac{W_{7_{Actual}}}{g} V_{9i} + (P_{S9i} - P_0) A_9}{\frac{W_{7_{Actual}}}{g} V_{\textcircled{s}}}$$

$$= \frac{C_V C_A C_{D8} \frac{W_{8i}}{g} V_{9i} + (P_{S9i} - P_0) A_9}{C_{D8} \frac{W_{8i}}{g} V_{\textcircled{s}}}$$

$$= \frac{C_V C_A C_{D8} \frac{P_{T8} A_8 \bar{m}_8}{\sqrt{T_{T8}}} V_{9i} + (P_{S9i} - P_0) A_9}{C_{D8} \frac{P_{T8} A_8 \bar{m}_8}{\sqrt{T_{T8}}} V_{\textcircled{s}}}$$

$$= \frac{\frac{\bar{m}_8}{\sqrt{T_{T8}}} V_{9i} + \left(\frac{P_{S9i}}{P_{T8}} - \frac{P_0}{P_{T8}}\right)\frac{A_9}{A_8}}{C_{D8} \frac{\bar{m}_8}{\sqrt{T_{T8}}} V_{\textcircled{s}}} \qquad (14.2.16)$$

where we recall that, since the nozzle is assumed fully choked, $\bar{m}8 = f(\gamma_8)$, and,

$$V_{9i} = f\left(\frac{A_9}{C_{D8} A_8}, T_{T8}, \gamma_8\right)$$

$$P_{S9i}/P_{T8} = f\left(\frac{A_9}{C_{D8} A_8}, \gamma_8\right)$$

$$V_{\textcircled{s}} = f\left(\frac{P_{T8}}{P_0}, T_{T8}, \gamma_8\right)$$

Since $\gamma_8 = f(T_{T8}, FAR8)$, the thrust coefficient can be defined as a function of pressure ratio from the following six parameters:

geometry: A_9/A_8, C_V, C_A, C_{D8}

engine cycle: T_{T8}, FAR8

The resulting thrust coefficient curve, as shown in Figure 14.2.7, now includes the losses due to friction and angularity in the velocity momentum ($C_V C_A$) and the losses due to over or underexpansion in the pressure-area term (nozzle pressure ratio and gas properties) with the correct, full scale engine gas properties.

It should be obvious that the thrust coefficient curve assumes constant geometry (A_9/A_8) and constant gas flow conditions (T_{T8} and FAR8). This is a very reasonable assumption since, for variable area C-D nozzles, A_9/A_8 (which defines α and thus C_V and C_A) and C_{D8} are unique functions of A_8, and T_{T8} and FAR8 are essentially single valued functions of A_8. Thus, for a given nozzle position or A_8, all six parameters are constant. To provide nozzle performance characteristics for an engine cycle deck, a sufficient number of C_{fg} curves should be generated to cover the nozzle operating range of interest. For example, a typical area ratio schedule for a C-D nozzle is shown in Figure 14.2.11 along with the operating ranges of interest and the minimum number of geometries at which C_{fg} curves should be defined.

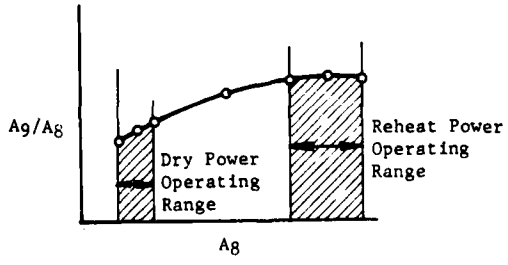

Figure 14.2.11 C-D Nozzle Area Ratio Schedule

As previously mentioned, the C_{fg} curves assume a full flowing, fully choked nozzle. The resulting curve must therefore be adjusted to account for separation at low pressure ratio, overexpanded conditions. In addition, any leakage and cooling air throttling loss adjustments must be made to these curves. These adjustments are discussed in subsequent sections. This entire procedure is summarized on the flow chart in Figure 14.2.12.

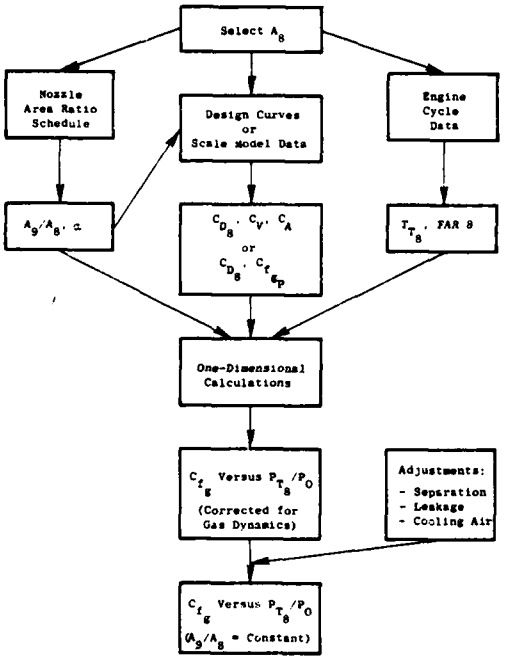

Figure 14.2.12 Flow Chart of Calculation Procedure for Generalized Performance Curves

14.2.3 *LEAKAGE LOSS CALCULATIONS*

Nozzle performance losses due to gas leakage out of the nozzle are inherent with variable nozzles and must be accounted for in performance estimates. Since it is impractical and virtually impossible to accurately simulate leakage areas in a scale model test, these thrust losses must be analytically calculated. The calculations require the use of nozzle wall pressure distributions to obtain gas pressure loading and a knowledge of the effective leakage areas in the nozzle.

Various nozzle leakage paths which can be encountered are defined in Figure 14.2.13. Note that, with the exception of the primary nozzle, the leakage flows can be in either direction; this depends on the nozzle type an the operating condition.

If a control volume is drawn inside the nozzle as shown in Figure 14.2.14, only those leakages which cross the control volume need be specifically calculated; these include leakages ① through ④. The reason for this is that for a nozzle with no cooling slot at the throat: 1) the nozzle cavity is most likely unpressurized and is essentially equal to ambient pressure and 2) the external nozzle will not be designed to seal. Thus, leakages ⑤, ⑥, and ⑦ are of no

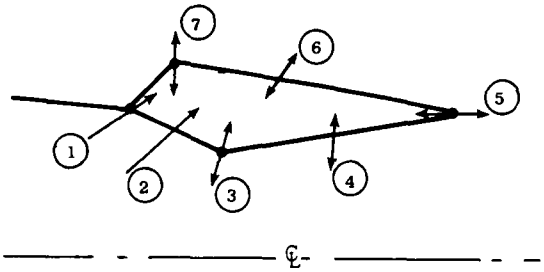

① Primary Nozzle Forward Hinge
② Primary Nozzle Flaps and Seals
③ Nozzle Throat Hinge
④ Secondary Nozzle Flaps and Seals
⑤ Nozzle Aft Hinge
⑥ External Nozzle Flaps and Seals
⑦ External Nozzle Forward Hinge

Figure 14.2.13 C-D Nozzle Leakage Paths

consequence. With a cooling slot at the throat: 1) the nozzle cavity is probably pressurized with cooling air, 2) there is no throat hinge leakage path (③) as it is substituted by a cooling slot, and 3) although only leakages ①, ②, and ④ need be specifically calculated, leakages ⑤, ⑥, ⑦ contribute to nozzle performance because they affect cavity pressure level and the fraction of total cooling air flow which comes back into the nozzle through the cooling slot as opposed to going overboard.

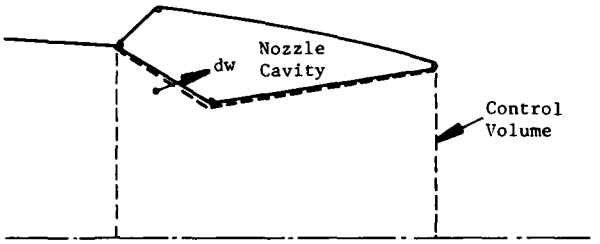

Figure 4.2.14 Nozzle Leakage Control Volume

Although leakages ③ and ④ are shown to occur in either direction, any flow leaking back into the nozzle is generally neglected. The reason for this is that, for a nozzle with no throat cooling slot, the flow will reenter the nozzle at a pressure which is at or very near ambient pressures and the thrust gain will be negligible. For a nozzle with a throat cooling slot, there will be conditions where a small amount of flow, which is significantly above ambient pressure, can leak back into the main gas stream through the secondary flaps and seals. However, since this leakage will be coming into the main stream in a circumferential direction, losses will occur in turning the flow axially. Thus, for a pressurized cavity nozzle, a theoretical thrust gain due to leakage flow from the cavity into the nozzle will be very small and can be assumed to be zero.

In order to calculate thrust losses due to leakage, the effective area of the leakage flow must be determined. Since this is extremely difficult and impractical to calculate analytically, the leakage characteristics of various sealing arrangements are obtained by tests of full scale nozzle hardware. A typical setup for a leakage test of a primary nozzle is shown in Figure 14.2.15.

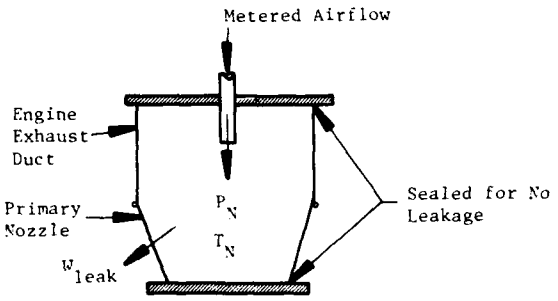

Figure 14.2.15 Nozzle Leakage Test Setup

By measuring the airflow, the pressure and temperature in the nozzle, and the ambient pressure, the effective leakage area can easily be calculated as follows;

$$A_{e_{Leak}} = \frac{W_{Leak}\sqrt{T_N}}{P_N \bar{m}} \qquad (14.2.17)$$

where $\bar{m} = f(P_N/P_{amb})$

The effective areas can be plotted as a function of the ΔP, $P_N - P_{amb}$, across the nozzle.

In general, the performance loss calculation due to leakage is handled as follows. Leakage flow, W_{leak}, which crosses the control volume, is considered to be completely lost to the nozzle with no thrust recovery. The loss in thrust coefficient is the ideal thrust of the leakage flow divided by the nozzle ideal thrust; i.e.,

$$\Delta C_{fg\ Leak} = \frac{F_{gi\ Leakage}}{F_{gi}} \qquad (14.2.18)$$

By expanding the equation for ideal thrust, it can be shown that:

$$F_{gi} = \frac{W}{g} V_i = \left(\frac{F}{W\sqrt{T_T}}\right) W\sqrt{T_T} \qquad (14.2.19)$$

$$\text{where } \left(\frac{F}{W\sqrt{T_T}}\right) = \sqrt{\frac{2\gamma R}{g(\gamma-1)}\left[1 - \left(\frac{1}{P_T/P_0}\right)^{\frac{\gamma-1}{\gamma}}\right]} = \bar{F} \qquad (14.2.19a)$$

Substituting into equation 14.2.18 and rearranging leads to the following:

$$\Delta C_{fg\ Leak} = \frac{\bar{F}_{Leakage}\, W_{Leak}\sqrt{T_{T_{Leak}}}}{\bar{F}_8\, W_{7_{Actual}}\sqrt{T_{T8}}}$$

$$= \frac{\bar{F}_{Leakage}\, \bar{m}_{Leakage}\, P_{T_{Leak}}\, A_{e_{Leak}}}{\bar{F}_8\, \bar{m}_8\, P_{T8}\, C_{D8}\, A_8}$$

$$= \left(\frac{\bar{F}_{Leakage}}{\bar{F}_8}\right)\left(\frac{\bar{m}_{Leakage}}{\bar{m}_8}\right)\left(\frac{P_{T_{Leak}}}{P_{T8}}\right)\left(\frac{A_{e_{Leak}}}{C_{D8}\, A_8}\right) \qquad (14.2.20)$$

Since leakage losses are generally less than 1% and because the flow function, $\bar{m}$, will generally be choked or near choked, assuming $\bar{m}_{leak} = \bar{m}_8$ will create an insignificant error in the calculation. Therefore,

$$\Delta C_{fg\ Leakage} \cong \left(\frac{\bar{F}_{Leak}}{\bar{F}_8}\right)\left(\frac{P_{T_{Leak}}}{P_{T8}}\right)\left(\frac{A_{e_{Leak}}}{C_{D8}\, A_8}\right) \qquad (14.2.21)$$

Since leakage flow emanates from the boundary layer, the total pressure of the leakage flow is approximately equal to the wall static pressure. The leakage thrust function, $\bar{F}_{leak}$, will be based on this pressure expanded to ambient pressure; i.e.,

$$\bar{F}_{Leak} = f\left(\frac{P_{T_{Leak}}}{P_0}\right) = f\left(\frac{P_{s_{Wall}}}{P_0}\right)$$

A typical leakage loss calculation is thus performed in the following manner:

1) For the specific operating condition of interest, nozzle pressure ratio P_{T8}/P_0, total nozzle effective area $C_{D8}A_8$, and gas constant γ can be obtained from engine cycle data.

2) A nozzle geometry is determined consistent with the cycle, and wall pressure distributions are estimated as discussed in Section 14.3.

3) From the wall pressure distribution and the cavity pressure, a pressure loading is determined, $\Delta P = P_{s_{wall}} - P_{cav}$, and a leakage pressure ratio is obtained, $P_{s_{wall}}/P_0$.

4) From the pressure loading, ΔP, and appropriate leakage test data, an effective leakage area is determined, $A_{e_{leak}}$.

5) From the nozzle pressure ratio P_{T8}/P_0 and leakage pressure ratio P_{swall}/P_0, the thrust functions $\bar{F}_8$ and $\bar{F}_{leak}$ are determined. The leakage flow γ can be estimated with negligible error.

6) The leakage loss is then calculated from equation 14.2.21.

14.2.4 COOLING AIR LOSS CALCULATIONS

Some C-D nozzles incorporate a cooling slot at the nozzle throat to provide additional film cooling air for the secondary nozzle during reheat operation. The cooling air typically is extracted from the tailpipe liner cooling flow upstream of, or at, the primary nozzle hinge, dumped into the nozzle cavity, and exhausted through the cooling slot as sketched in Figure 14.2.16.

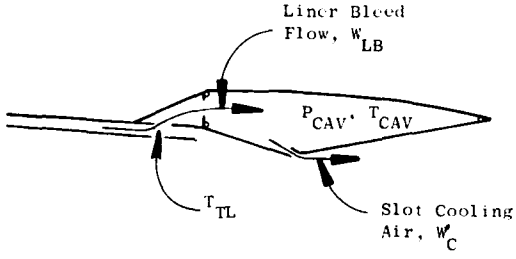

Figure 14.2.16 Nozzle Cooling Flowpath

Since the pressure level of the liner flow is significantly higher than the nozzle cavity pressure, the cooling flow which is removed from the liner experiences a pressure drop and is put back into the nozzle at a lower total pressure and, thus, lower available thrust. Note that the liner bleed, W_{LB}, will dump into the cavity and will mix with primary leakage air (and possibly secondary leakage). As mentioned in Section 14.2.3, some of the flow will leak overboard depending on the sealing qualities of the external flaps and seals. In the design of the nozzle, the cooling slot must be sized to provide the desired amount of cooling air, W_C, at the estimated cavity air conditions.

The cooling air throttling loss should be estimated as the difference in the ideal thrust of the flow between the condition where it is extracted from the liner and the condition at which it is put back into the nozzle; i.e.,

$$\Delta C_{fg\ \text{Cooling Air Throttling}} = \frac{F_{gi\ \text{Liner Bleed Flow}} - F_{gi\ \text{Slot Flow}}}{F_{gi}}$$

$$= \frac{\left(\frac{F}{W\sqrt{T_T}}\right)_{7L} W_{LB}\sqrt{T_{TL}} - \left(\frac{F}{W\sqrt{T_T}}\right)_{CAV} W_C\sqrt{T_{TC}}}{\left(\frac{F}{W\sqrt{T_T}}\right)_8 W_{7Actual}\sqrt{T_{T8}}}$$

$$-\left(\frac{\bar{F}_{7L}}{\bar{F}_8}\right)\left(\frac{W_{LB}}{W_{7Actual}}\right)\sqrt{\frac{T_{TL}}{T_{T8}}}$$

$$-\left(\frac{\bar{F}_{CAV}}{\bar{F}_8}\right)\left(\frac{W_C}{W_{7Actual}}\right)\sqrt{\frac{T_{T\ CAV}}{T_{T8}}} \qquad (14.2.22)$$

where $\bar{F} \left(\frac{F}{W\sqrt{T_T}}\right) = f(P_T, P_0, \ldots)$

Since the total pressure of the liner bleed flow is very near mainstream total pressure, it can be assumed that $\bar{F}_{7L} = \bar{F}_8$, thus,

$$\Delta C_{fg\ \text{Cooling Air Throttling}} = \left(\frac{W_{LB}}{W_{7Actual}}\right)\sqrt{\frac{T_{TL}}{T_{T8}}}$$

$$-\left(\frac{\bar{F}_{CAV}}{\bar{F}_8}\right)\left(\frac{W_C}{W_{7Actual}}\right)\sqrt{\frac{T_{T\ CAV}}{T_{T8}}} \qquad (14.2.23)$$

where:

T_{TL} is the gas temperature of the liner flow near the aft end of the liner.

$\frac{W_{LB}}{W_{7actual}}$ and $\frac{W_C}{W_{7actual}}$ are specified by design and are usually set equal to each other.

$T_{T_{CAV}}$ is an estimated cavity temperature.

$$\bar{F}_{CAV} = \left(\frac{F}{W\sqrt{T_T}}\right)_{CAV} = f\left(\frac{P_{CAV}}{P_0}, \gamma_{CAV}\right)$$

$$\gamma_{CAV} = f\left(T_{CAV}\right)$$

Note that if a scale model test has been conducted with simulation of the cooling slot geometry, A_S/A_8, cavity pressure level, P_{CAV}/P_{T8}, and corrected flow ratio, $W_C/W_{7actual}\sqrt{T_{T_{CAV}}/T_{T8}}$, the recovered thrust of the cooling flow is already included in the scale model coefficient; i.e.,

$$C_{fg\ \text{Scale Model}} = \frac{F_{g\ \text{Primary Air}} + F_{g\ \text{Cooling Air}}}{F_{gi\ \text{Primary Air}}} \qquad (14.2.24)$$

In this case, the scale model data, after being adjusted for full scale gas dynamics effects, as in Section 14.2.2.3, is corrected for cooling air throttling by the equation,

$$\Delta C_{fg\ \text{Cooling Air Throttling}} = \frac{W_{LB}}{W_{7Actual}}\sqrt{\frac{T_{TL}}{T_{T8}}} \qquad (14.2.25)$$

In the cooling air loss analysis, the nozzle cavity pressure, P_{CAV}, is the most difficult parameter to estimate primarily because an analysis to determine the pressure can be very complicated. The cavity pressure (and in fact the temperature) will be a function of the flows going into and out of the nozzle cavity.

The cavity pressure and temperature can be estimated by performing a flow and energy balance around the nozzle cavity control volume; i.e., for the flow directions shown in Figure 14.2.16,

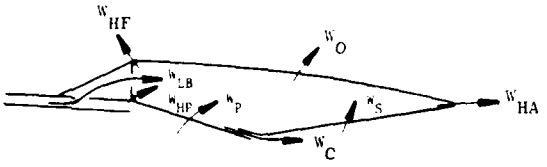

Figure 14.2.17 Nozzle Cavity Flows

Flow Balance

$$W_{LB} + W_{HP} + W_P + W_S = W_C + W_{HA} + W_O + W_{HF} \qquad (14.2.26)$$

Energy Balance

$$W_{LB}H_{LB} + W_{HP}H_{HP} + W_PH_{HP} + W_SH_S = W_CH_{CAV} + W_{HA}H_{CAV} + W_OH_{CAV} + W_{HF}H_{CAV} \qquad (14.2.27)$$

where H = total enthalpy of gas

The leakages will be a function of the individual leakage path effective area characteristics, the nozzle wall pressure and temperature distributions, and the nozzle cavity pressure and temperature.

As can be expected, the cooling slot area has a significant effect on the cavity pressure level and cooling slot flow, W_C. The cooling slot area schedule, A_S versus A_8, therefore must necessarily be determined by a proper balance of nozzle performance (thrust recovery), nozzle gas loads, and cooling requirements. This is accomplished by continued feedback and interfacing of analyses by mechanical and aero designers until an acceptable slot area schedule is established. Because of the small size of the cooling slots (1 to 3% of A_8), hardware tolerances can affect the cooling slot area by a significant percentage and should therefore be included in the analysis. It should be noted that the cooling flow, W_C, in the final analysis may not be a constant percentage of $W_{a\,total}$ because of the performance and load trade considerations. Since the additional cooling flow is usually not required for dry operation, it is advantageous to eliminate or shut off the bleed at $W_{a\,min}$ of these conditions and, hence, to design the slot with this capability.

[illegible] OVEREXPANSION EFFECTS

The generalized performance curves discussed in Section [illegible] assumed a "full flowing" nozzle with no internal separation at low pressure ratios. In reality, this condition occurs only at nozzle pressure ratios which are at or higher than the design pressure ratio corresponding to the nozzle effective area ratio; i.e.,

$$P_{T8}/P_0 \text{ Full Flowing} \geq P_{T8}/P_0 \text{ Design Point}$$

where

$$P_{T8}/P_0 \text{ Design Point} = f(A_9/C_{D8}\,A_8, \ldots)$$

At pressure ratios below the full flowing condition, the flow field within the nozzle will deviate from the design point flow field and adjust to satisfy conservation of mass, momentum, and energy consistent with the ambient pressure boundary condition. Thus, the flow field will adjust to provide a static pressure at the nozzle exit which is equal to the ambient pressure. This flow field adjustment is reflected as a static pressure distribution change on the secondary nozzle which in turn affects the nozzle gross thrust coefficient as shown in Figure 14.2.18. Thrust coefficient predictions defined from the procedure in Section 14.2.2.3 must be adjusted at lower pressure ratios to account for these pressure adjustment effects.

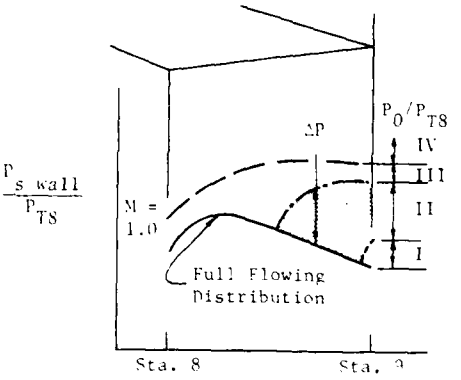

$$C_{fg} = \frac{\int_x \Delta P\, dA}{F_{gi}}$$

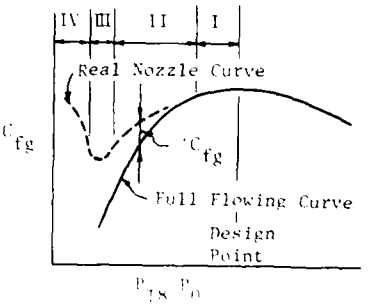

Figure 14.2.18 Overexpansion Effects on C-D Nozzle Aerodynamic Characteristics

Referring to Figure 14.2.18, as the nozzle pressure ratio is decreased below the design point, a compression wave develops in the nozzle which raises the static pressure to the ambient pressure level. As the pressure ratio is further reduced, the location of the compression wave moves forward and its strength increases, affecting more of the nozzle wall pressure distribution. This change in wall pressure distribution can be integrated as a pressure-area term to calculate the effect on C_{fg} as shown. In general, this region of overexpansion can be divided into four regions of operation which are displayed in a simplified fashion in Figure 14.2.18.

Region I - In this region, the pressure rise at the nozzle exit is very small. The resulting pressure-area integration is minuscule with virtually no impact on thrust coefficient.

Region II - In this region, the compression wave has increased in strength and has moved forward affecting a larger portion of the nozzle. The flow in the forward portion of the nozzle is still supersonic, and physical flow separation within the nozzle may or may not occur as in Figure 14.2.19.

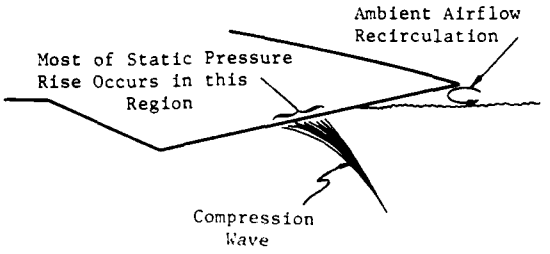

Figure 14.2.19 C-D Nozzle Separation

Region III - This is a transition region where the location of the compression wave moves rapidly to the throat region during a relatively small pressure ratio change. This region usually occurs around the minimum thrust coefficient pressure ratios. Significant separation can still occur in this band of operation.

Region IV - In this region, the flow is attached and entirely subsonic, and the nozzle is performing as a diffuser.

It is emphasized that these regions are described only in a general sense. They blend and overlap from one to another and should not be mistaken to start and end at discreet pressure ratios. Additionally, each nozzle will behave differently depending on nozzle geometry. Thrust coefficient predictions, defined from the procedure in Section 14.2.2.3, must be adjusted at lower pressure ratios to account for these separation effects as shown in Figure 14.2.20.

Unfortunately, this region of nozzle operation is the least understood and most difficult to analyze. Experience has shown that real full scale nozzle separation characteristics can be greatly influenced by nozzle leakage, quantity of slot cooling flow, wall surface quality, and probably local flow field nonuniformities and

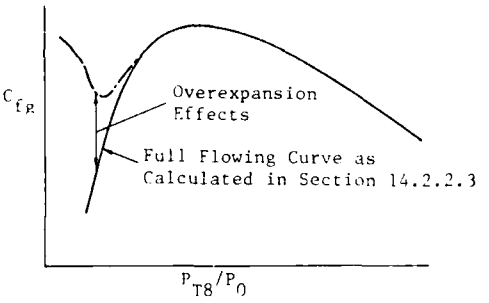

Figure 14.2.20 Thrust Coefficient Curve Adjusted for Overexpansion Effects

Reynolds number. Additionally, little reliable model test data are available for analysis primarily because nozzles normally are not designed to operate at these extremely overexpanded conditions at important design points, and little test data have been accumulated in the interest of keeping test costs down. Thus, there are no reliable analytical design methods currently available to accurately predict the real full scale effects of separation/overexpansion on nozzle performance.

Some scale model data have been analyzed and correlated as shown in Figure 14.2.21. This figure will provide a "minimum" thrust recovery estimate. In the real nozzle, the actual thrust recovery virtually will always be higher since leakage, discontinuities, profiles, etc., generally encourage more separation. These real nozzle effects will be different for each nozzle design, and no design criteria for estimating these effects are available.

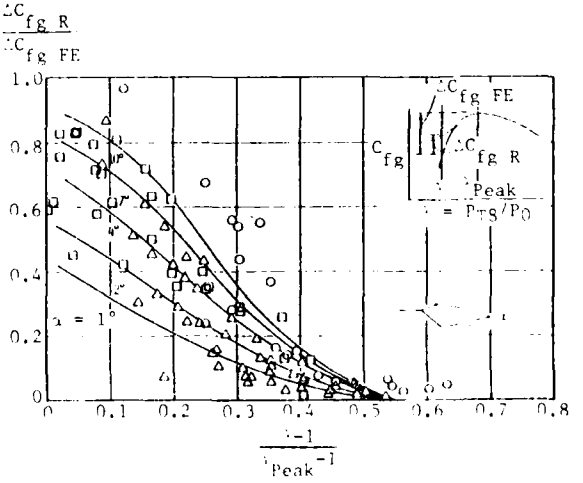

Figure 14.2.21 Separation Thrust Recovery, Scale Model Data

14.3 AERODYNAMIC LOAD PREDICTIONS

Nozzle pressure distributions are used by mechanical designers to determine hardware structural loads and actuation system loads. These loads thus effect detailed mechanical design, weight, and cost and are, therefore, very important estimates to be provided by the aero designer.

Internal pressure distributions can be estimated for the primary and secondary nozzle to cover all nozzle geometries and operating conditions. Although the external loads on the nozzle are generally much smaller than the internal loads, external pressure distributions should be provided as best possible.

Pressure distributions can be obtained either from scale model tests or from analytical methods. Scale model tests are more accurate; however, it is not always possible to obtain test data, particularly early in a development program. The following sections define procedures to analytically estimate nozzle pressure distributions.

14.3.1 PRIMARY NOZZLE

Pressure distributions on a simple conical primary nozzle can be estimated by several methods. There are a number of flow field analysis computer programs in industry which can provide quite accurate estimates of wall pressure distributions. However, since the flow consists primarily of a subsonic accelerating flow, adequate accuracy for preliminary estimates of the pressure distribution can be obtained by utilizing the assumption of one dimensional flow. From standard gas flow tables, the local static pressure to total pressure ratio can be obtained as a function of the local flow area to sonic flow area. This technique is applied to the primary nozzle as in Figure 14.3.1. Pressure distributions can be estimated using this approach over any range of A_8's using the appropriate ratio of specific heats, γ.

$$(P_S/P_{T8})_i = f\ (A_i/A^*,\ \gamma) = f\ (A_i/C_{D8}\ A_8,\ \gamma)$$

Figure 14.3.1 *One-Dimensional Static Pressure Distribution Calculation*

This approach however can produce errors in several ways. A small error will occur at the forward hinge point near the nozzle entrance, Station 7, where the local turning of the flow will not be accounted for with the one-dimensional calculation. The actual pressure near the turn will be slightly higher than that calculated assuming one-dimensional conditions, the difference being dependent on the Mach number and turn angle θ'. However, since this is close to the hinge, impact on actuator loads is usually negligible.

A second and more significant error can occur for nozzle designs with unusually long primary nozzles. The error occurs at afterburning conditions only and becomes larger at the high fuel-air ratios. If the gas volume within the primary nozzle is significant relative to the total afterburner burning volume (~20% or greater), then significant combustion can take place within the primary nozzle. Under these conditions, there is a heat addition total pressure loss (Rayleigh line

$P_{s\ actual} > P_{s\ one\text{-}dimensional}$

Figure 14.3.2 Wall Turning Effect on Static Pressure

effect, Section 2.17.2) occurring within the primary nozzle, thus, the reference choke area A^* will be continuously changing along the primary nozzle. As a result, the real static pressure distribution will be significantly higher than the calculated pressure distribution. This can cause a sizeable error as shown in Figure 14.3.3.

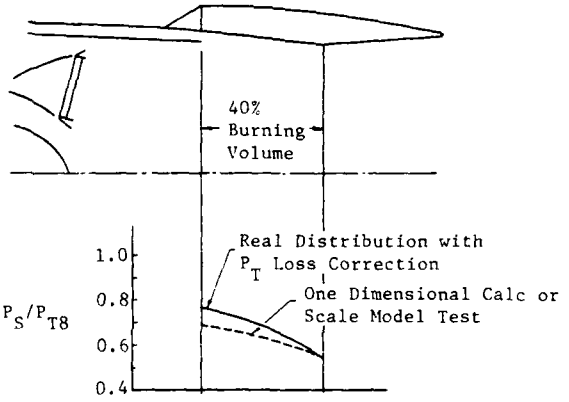

Figure 14.3.3 Afterburner Heat Addition Pressure Loss Effect on Nozzle Pressure Distribution

The correction for reheat burning effects must be applied to any analytical calculation and all scale model data. For most applications, the primary nozzle is relatively short; thus, this effect is very small, if not insignificant. However, it should always be checked. The correction is a simple Rayleigh line heat addition calculation.

Independent of the method used, pressure load estimates should be provided to the mechanical designer, as shown in Figure 14.3.4, at a sufficient number of nozzle A_8 area settings to allow easy interpolation for A_8. These curves will be independent of pressure ratio and, because of the sharp corner throat, will apply for very low pressure ratios down to 1.5 or perhaps lower.

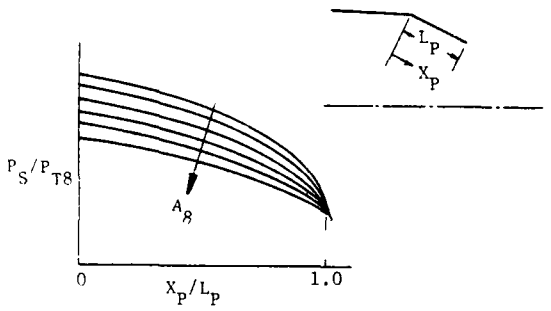

Figure 14.3.4 Generalized Primary Nozzle Pressure Distribution

14.3.2 SECONDARY NOZZLE

Prediction of the secondary nozzle gas loads is not as straightforward as for the primary. Because of the sharp corner throat, a sudden overexpansion of the flow immediately downstream of the throat causes the pressure distribution to deviate significantly from that predicted by a one-dimensional analysis as shown in Figure 14.3.5. The amount of deviation is dependent on both the primary and secondary nozzle half angles and the amount of cooling slot flow, if present. Thus, reliable analytical predictions can be done by only two methods: semiempirical using test data and theoretical using computerized flow field equations.

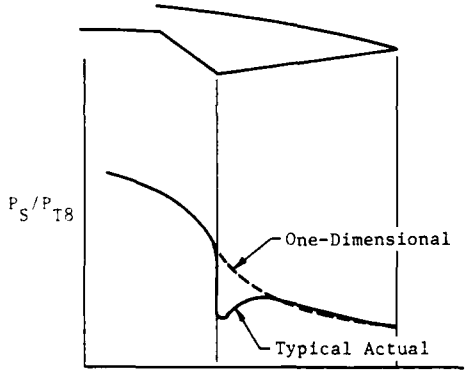

Figure 14.3.5 Secondary Nozzle Pressure Distribution

For nozzles with no throat cooling slot, scale model test data have shown a reasonable correlation with a one-dimensional calculation. This correlation is shown in Figure 14.3.6 as the difference between actual pressure minus the one-dimensional calculation versus a nondimensionalized length parameter. Note that the one-dimensional calculation includes a rough estimate of boundary layer effects in the secondary nozzle (0.995 factor) and the effect of nozzle flow coefficient, C_{D8}. Inclusion of the flow coefficient accounts for the primary nozzle half angle effect. This curve can be used for an initial estimate of full flowing nozzle gas loads.

Figure 14.3.6 can be used to estimate gas loads for full flowing nozzles with no flow at the throat. For nozzles with a throat cooling slot, the wall pressure in the forward 20% of the secondary nozzle will be higher than the no-flow case. Additionally, even nozzles with no cooling slot will have some amount of leakage flow at the

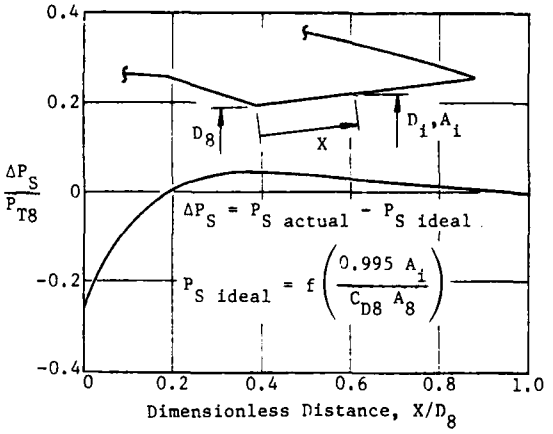

Figure 14.3.6 Secondary Nozzle Gas Loads Correction Factor

throat due to hardware stack-up tolerances. An approximate correction due to the flow effect can be made using the curve in Figure 14.3.7. This curve presents the change in throat static pressure relative to a no-flow condition based on scale model test data. The correction is applied as in Figure 14.3.8.

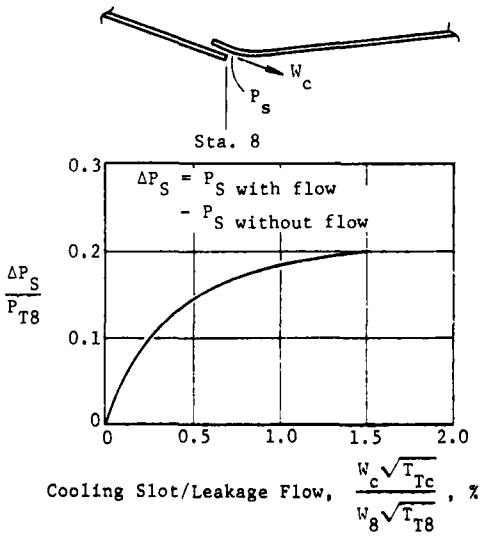

Figure 14.3.7 Cooling Slot Leakage Flow

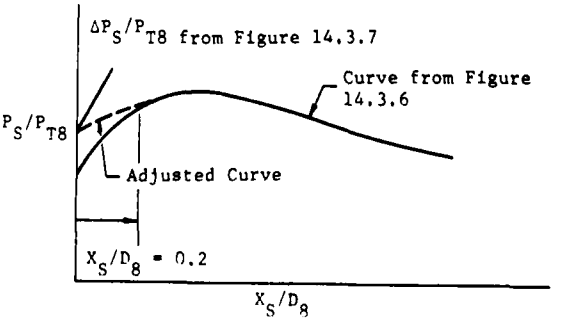

Figure 14.3.8 Adjusted Secondary Nozzle Pressure Distribution

This procedure can be used for an initial estimate of secondary nozzle, full flowing gas loads.

As with the primary nozzle gas loads, secondary nozzle gas loads should be provided at a sufficient number of geometries to allow easy interpolation by mechanical designers. Reheat total pressure loss corrections made for the primary nozzle are not necessary for the secondary nozzle, since virtually no combustion takes place within this portion of the nozzle. However, if pressure distributions are obtained on a cold flow ($\gamma = 1.4$) basis, an adjustment in secondary nozzle gas load estimates for the effects of changes in specific heat ratio should be made. The error in the trailing edge pressure for a C-D nozzle increases on a percentage basis with increasing area ratio as noted in Figure 14.3.9.

$\frac{A_9}{A_8}$	P_S/P_{T8} $\gamma = 1.4$	P_S/P_{T8} $\gamma = 1.3$	$\frac{P_{S(\gamma = 1.3)}}{P_{S(\gamma = 1.4)}}$
1.2	0.258	0.278	1.08
1.5	0.160	0.176	1.10
2.0	0.093	0.106	1.14
2.5	0.064	0.074	1.16
3.0	0.047	0.056	1.19

Figure 14.3.9 Specific Heat Ratio Effects on Nozzle Pressure Distribution

Thus, although the difference in absolute level appears small at first glance, on a percentage basis the correction can amount to nearly 20%. A mechanical designer must work with pressure differences, ΔP, and this kind of error could be 20 to 50% of the ΔP. It is therefore important to provide the most precise load possible. If analytical load predictions are made or if scale model tests are conducted, the ratio of specific heat corrections should be made along the entire secondary nozzle. The adjustment is made by 1) converting the "cold flow" pressure distribution to a Mach number and then an A/A^*, 2) assuming the "hot" A/A^* = the cold A/A^*, and finally 3) converting the hot A/A^* to a Mach number and then a pressure distribution; i.e.,

$$\frac{P_{si}}{P_{T8}}\Big/_{\gamma=\text{Cold}} \rightarrow M_i\Big/_{\gamma=\text{Cold}} \rightarrow \frac{A_i}{A^*}\Big/_{\gamma=\text{Cold}}$$

$$= \frac{A_i}{A^*}\Big/_{\gamma=\text{Hot}} \rightarrow M_i\Big/_{\gamma=\text{Hot}} \rightarrow \frac{P_{si}}{P_{T8}}\Big/_{\gamma=\text{Hot}}$$

14.3.3 EXTERNAL LOADS

Nozzle external pressure distributions will be dependent on many parameters including specific nozzle geometry, overall propulsion system installation, local aircraft configuration including control surface position, Mach number, and nozzle pressure ratio as well as Reynolds number and aircraft attitude (angle of attack, yaw). Because of the large number of variables it is virtually impossible to devise semiempirical parametric curves which could be used to provide an initial estimate. External loads are obtained either directly from a specific wind tunnel test, indirectly by interpolating previous wind tunnel test data from similar installations, or analytically by computer techniques.

By far the most accurate pressure distributions are obtained from wind tunnel tests of the exact nozzle/airplane configuration of interest at the appropriate operating conditions. Extrapolation or interpolation of this data is often necessary to provide load estimates at all the conditions of interest. In the absence of directly applicable wind tunnel data, pressure distributions can be estimated by using previous wind tunnel test data or by analytical methods. When using previous data, configurations and conditions which most closely resemble the nozzle of interest should be used for load estimates. Computerized analytical methods can also be used to predict external loads. This approach gives very good results for two-dimensional or axisymmetric configurations. However, for three-dimensional configurations, which are most usually found in practice, the local geometric variations, which are difficult to simulate in the computer, can have a significant effect on the local nozzle pressure distribution. In either case, engineering judgment will be required to properly interpret and apply the information to define load estimates.

Chapter 15

FUNDAMENTALS OF COMBUSTION

William S. Blazowski

AF Aero Propulsion Laboratory

(Currently at Exxon Research and Engineering Company)

TABLE OF CONTENTS

CHAPTER 15 FUNDAMENTALS OF COMBUSTION

		Page
15.0	INTRODUCTION	15-1
15.1	CHEMISTRY	15-1
	15.1.1 Reaction Rate	15-1
	15.1.2 Chemical Equilibrium	15-2
	15.1.3 Hydrocarbon Chemistry	15-3
15.2	THERMODYNAMICS	15-5
	15.2.1 Energy Release and Flame Temperature	15-5
	15.2.2 Important Flame Temperature Dependencies	15-7
15.3	GAS DYNAMICS AND DIFFUSION PROCESSES	15-9
	15.3.1 Premixed Laminar Flames	15-9
	15.3.2 Diffusion Controlled Combustion	15-10
	15.3.3 Turbulence Effects	15-11
	15.3.4 Perfectly Stirred Reactor	15-12
15.4	COMBUSTION PARAMETERS	15-14
	15.4.1 Combustion Efficiency	15-14
	15.4.2 Flame Stabilization	15-14
	15.4.3 Ignition	15-15
15.5	JET FUELS	15-17
	15.5.1 Combustion Characteristics	15-17
	15.5.2 Common Jet Fuels	15-17
15.6	SUMMARY	15-18
15.7	BIBLIOGRAPHY AND REFERENCES	15-19
	15.7.1 Bibliography	15-19
	15.7.2 References	15-20

LIST OF ILLUSTRATIONS

CHAPTER 15 FUNDAMENTALS OF COMBUSTION

		Page
15.0.1	The Interdisciplinary Nature of Combustion Technology	15-1
15.1.1	Concentration Variations During the Course of a Reaction	15-2
15.1.2	Equilibrium Constants for Important Dissociation Reactions	15-3
15.1.3	Equilibrium CO and H_2 Concentration Dependence on Temperature	15-4
15.1.4	Hydrocarbon Combustion Chemistry Schematic	15-4
15.2.1	Theoretical Flame Temperature Dependence on Equivalence Ratio	15-7
15.2.2	Effect of Inlet Temperature on Adiabatic Flame Temperature	15-7
15.2.3	Effect of Inlet Temperature on Stoichiometric Flame Temperature	15-8
15.2.4	Effect of Pressure on Stoichiometric Flame Temperature	15-8
15.2.5	Combustor Exit Total Temperature for Jet A Fuel and Arbitrary Pressure (Working Chart)	15-8
15.2.6	Effect of Vitiation on Stoichiometric Flame Temperature	15-9
15.3.1	Flame Velocities of Paraffin-Oxygen Mixtures at One Atmosphere Pressure and Room Temperature	15-10
15.3.2	Diffusion Flame Characteristics	15-10
15.3.3	Simplified Representation of a Turbine Combustion System	15-12
15.3.4	Perfectly Stirred Reactor Operating Conditions	15-13
15.3.5	Stirred Reactor Stability Dependence on Equivalence Ratio	15-13
15.4.1	Flammability Characteristics for a Kerosene-Type Fuel in Air at Atmospheric Pressure	15-15
15.4.2	Physical Processes in Flameholding	15-15
15.4.3	Ignition Delay Times for Practical Fuels	15-16
15.4.4	Minimum Ignition Energies	15-16
15.5.1	Distillation Characteristics of Common Jet Fuels	15-17

LIST OF TABLES

CHAPTER 15 FUNDAMENTALS OF COMBUSTION

		Page
15.1.1	Hydrocarbon Oxidation Kinetics Scheme	15-5
15.3.1	Turbulent Flame Theories	15-12
15.3.2	Importance of Turbulence to Chemical Reactions -- Values of $(E/R\bar{T})^{-2}$	15-13
15.4.1	Flammability Limits in Air at Atmospheric Pressure and Room Temperature	15-15
15.4.2	Spontaneous Ignition Temperatures	15-16
15.5.1	Heats of Combustion and Formation	15-18
15.5.2	Important Jet Fuel Properties	15-19

CHAPTER 15

FUNDAMENTALS OF COMBUSTION

15.0 INTRODUCTION

Background information necessary to the understanding of aircraft turbine engine combustion systems is distinctly different from that applying to diffusers, rotating machinery, or nozzles and a separate discussion of fundamentals is warranted. The purpose of this chapter is to review the fundamental concepts important to aeropropulsion combustion. Two additional chapters will consider the practical application of this information to mainburners (Chapter 20) and afterburners (Chapter 21).

While large volumes can be written on the subject of aeropropulsion combustion, the scope of this chapter is limited to highlighting key information. The difficult task of deciding which information to include was accomplished by adhering to the objective that the reader be provided that material necessary for understanding the combustion system's operating principles, performance parameters, and limitations. The reader contemplating aeropropulsion combustion as an area of specialization should develop a more thorough background and is referred to a number of readily available texts listed in the bibliography to this chapter (Section 15.7.1).

Studies of combustion involve interdisciplinary investigations requiring consideration of three normally separate topics: chemistry, thermodynamics, and gas dynamics. Interrelationships between these areas, shown schematically in Figure 15.0.1, require combustion engineers and scientists to develop a fundamental understanding of each topic. A number of sub-topics in each of these areas have been listed to further describe the broad scope of subject matter involved. Each of these subjects will be addressed in this chapter.

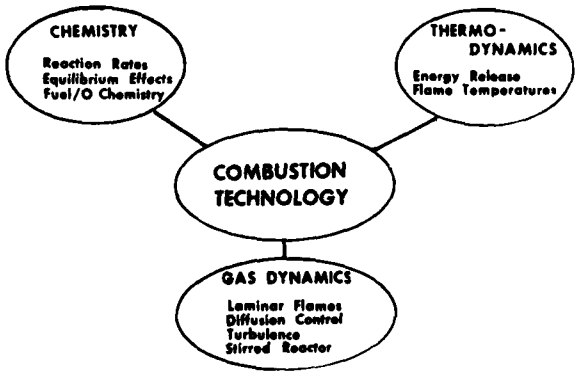

Figure 15.0.1 The Interdisciplinary Nature of Combustion Technology.

The information to be presented in this chapter is organized into five further sections. As might be expected, the first three consider chemistry, thermodynamics, and gas dynamics. The fourth involves discussion of combustion parameters of importance to the combustor designer. Finally, the combustion properties of jet fuels are briefly described.

15.1 CHEMISTRY

Three combustion chemistry topics will be discussed in this section. The first, chemical reaction rate, addresses fundamental concepts vital to all of chemical kinetics. Important dependencies of reaction rate on thermodynamic conditions, especially temperature, will be addressed. The second topic, chemical equilibrium, is of importance in relation to the understanding of and ability to analyze high temperature combustion systems. Finally, the current understanding of practical hydrocarbon fuel combustion chemistry will be reviewed. Understanding of the sequence of chemical processes leading to H_2O and CO_2 production allows the explanation of many practical combustion characteristics.

15.1.1 Reaction Rate

One of the most basic concepts of chemistry involves the law of mass action which relates the rate of a reaction, or the time rate of change of the reactant species concentration, to the concentrations of reactive species. This can be illustrated with the use of the following generalized chemical reaction:

$$aA + bB \rightarrow cC + dD \qquad (15.1.1)$$

In this example, a moles of molecule A combine with b moles of molecule B to form c and d moles of products C and D. The reactant stoichiometric coefficients of the atomic balance equation (a and b) are also called the reaction "molecularity". The law of mass action states that the rate of reaction is expected to be proportional to the product of the concentrations of reactant species raised to their respective stoichiometric coefficients. For this example, the rate of forward reaction, r_f, would be:

$$r_f = k_f[A]^a[B]^b \qquad (15.1.2)$$

The brackets, [ ], correspond to the molar concentration (moles/volume) of the molecular species indicated. k_f is the rate coefficient for the forward reaction.

Note that the rate of forward reaction, r_f, could be representative of either rate of disappearance of the reactants A and B or the rate of formation of products C and D. These four rates are interrelated by the stoichiometric coefficients a, b, c, and d. For example, if r_f were representative of the rate of disappearance of A, the following relationships would be valid:

$$r_f = -\frac{d[A]}{dt} = -\frac{b}{a}\frac{d[B]}{dt} = \frac{c}{a}\frac{d[C]}{dt} = \frac{d}{a}\frac{d[D]}{dt} \qquad (15.1.3)$$

The variable t represents time.

There is analytical justification for the observed reactant concentration dependencies of the law of mass action. An analysis based on the assumption that product formation can only occur after collision of reactant molecules predicts the same concentration dependencies as described in Equation 15.1.2. The rate coefficient in Equation 15.1.2, k_f, appropriately converts the results of collision theory to yield the units of reaction rate. In addition, k_f accounts for reaction rate dependencies due to variations in molecular energy levels and in the geometrical orientation of colliding molecules.

For many reactions of importance to combustion systems, k_f is a strong function of temperature. The temperature dependence of the molecular collision rate is minor ($T^{1/2}$) and has only a small influence on k_f. The predominant temperature dependence is a result of the necessity for molecular collisions to occur with sufficient "force" to overcome any energy barrier necessary for reactant molecules to undergo conversion to products. Physically, the formation of an activated complex is assumed to be necessary for successful conversion of colliding reactants to products. The height of the energy barrier, the energy necessary to form the activated complex, is often termed the activation energy, E_a. Not all of the colliding reactant molecules will have sufficient energy and only a fraction of the collisions will be successful. Since molecular energy distribution can be described by Boltzman statistics, the fraction of collisions which are successful is $\exp(-E_{af}/RT)$ where R is the universal gas constant and the subscript refers to the forward reaction.

The geometrical misalignment of reactant molecules during collision can also prevent conversion to products; only a fraction of the collisions occurring with sufficient energy will be successful. Consideration of the "steric factor" is a final necessary aspect in analysis of the reaction rate coefficient. This factor can be thought of as a means of compensating for collisional inefficiencies due to the peculiarities of geometrical alignment necessary for successful reaction.

An important expression for reaction rate is obtained by combining the reaction rate coefficient dependencies discussed above with Equation 15.1.2. The forward rate of the general reaction described in Equation 15.1.1 is:

$$r_f = -\frac{d[A]}{dt} = [A]^a [B]^b C_f (T)^{\frac{1}{2}} \exp(-E_{af}/RT) \qquad (15.1.4)$$

where C_f includes the steric factor and the necessary constants to convert collision rate to reaction rate. The strong exponential nature of the reaction rate dependence on temperature was first recognized by Arrhenius. Equation 15.1.4 with the pre-exponential factor taken as temperature independent (i.e., not including the $T^{\frac{1}{2}}$ dependence) is called the Arrhenius equation. Equation 15.1.4 itself is said to be the modified Arrhenius relationship.

It should be noted that the rate dependency given by Equation 15.1.4 is only correct in cases where the written stoichiometric equation represents the entire sequence of events leading to product formation. As will be discussed in Section 15.1.3, combustion of a practical hydrocarbon fuel involves many complex chemical reaction steps before formation of final products, CO_2 and H_2O. In cases where the stoichiometric equation does not describe the entire reaction sequence, the dependencies of the reaction rate on reactant concentration may not correspond to the molecularity and even fractional "reaction orders" may be observed. Nevertheless, the form of Equation 15.1.4 is valid for each individual reaction step of the complex sequence.

15.1.2 Chemical Equilibrium

As a reaction like that described in Equation 15.1.1 proceeds, changes of concentration with time occur as illustrated in Figure 15.1.1. When the concentrations of products C and D become significant, backward or reverse reaction (i.e., conversion of products back to reactants) can become important. The rate of backward reaction, r_b, may be analyzed in the same manner as in the case of forward reaction (Equation 15.1.2) to yield the following relation:

$$r_b = k_b[C]^c [D]^d \qquad (15.1.5)$$

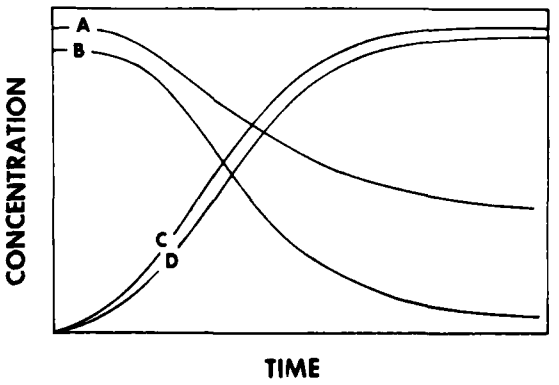

Figure 15.1.1 Concentration Variations During the Course of a Reaction.

In recognition of the existence of both forward and reverse reactions, the more appropriate convention for expressing the general chemical system described in Equation 15.1.1 is:

$$aA + bB \underset{k_b}{\overset{k_f}{\rightleftharpoons}} cC + dD \qquad (15.1.6)$$

Because reverse reactions always exist to some extent, concentrations of A and B will eventually decrease to some finite, non-zero values such that rates of forward and reverse reactions are equal. These equilibrium concentrations are the asymptotes of Figure 15.1.1. Note that the more general case where the reactants concentrations are not in exact stoichiometric proportions has been illustrated in Figure 15.1.1 which corresponds to the situation of a large excess of reactant A.

The equilibrium concentrations can be determined from Equations 15.1.2 and 15.1.5. At equilibrium, the rate of disappearance of reactant (Equation 15.1.2) will be entirely balanced by the reactant formation rate (Equation 15.1.5). Consequently, the equilibrium condition is $r_f = r_b$ or:

$$k_f[A]^a[B]^b = k_b[C]^c[D]^d \qquad (15.1.7)$$

Rearranging yields the following useful expression:

$$\frac{k_f}{k_b} = \frac{[C]^c\ [D]^d}{[A]^a\ [B]^b} \qquad (15.1.8)$$

Because k_f and k_b are functions of temperature only, Equation 15.1.8 provides a convenient means of relating equilibrium concentration to mixture temperature. The ratio k_f/k_b is known as the equilibrium constant based on concentration, K_c. An additional equilibrium constant based on mole fractions, K_x, can also be developed.

An even more familiar means of characterizing equilibrium involves the partial pressure equilibrium constant, K_p. Partial pressure is a concept in which the total mixture pressure is envisioned as a sum of pressure contributions from each of the mixture constituents. The partial pressure of each constituent is the fraction of the total pressure corresponding to the mole fraction of that compound. The equilibrium constant defined in terms of partial pressure is:

$$K_p = \frac{(P_C)^c(P_D)^d}{(P_A)^a(P_B)^b} \qquad (15.1.9)$$

where P_A, P_B, P_C, and P_D are the partial pressures of each constituent. By convention, these pressures are always expressed in atmospheres when used in equilibrium chemistry calculations.

Both K_c and K_p are functions of temperature only. The temperature dependencies can be deduced from Equations 15.1.4 and 15.1.7:

$$[A]^a\ [B]^b\ C_f\ T^{\frac{1}{2}}\exp(-E_{af}/RT) = [C]^c\ [D]^d\ C_b\ T^{\frac{1}{2}}\exp\ (-E_{ab}/RT) \qquad (15.1.10)$$

which can be reduced to:

$$K_C \text{ or } K_p \sim \exp\left(\frac{\Sigma_{ab} - E_{af}}{RT}\right) \qquad (15.1.11)$$

Consequently, the equilibrium constant may have a strong, exponential temperature dependency.

In hydrocarbon-air combustion applications, two equilibrium relations are of paramount importance. They are the dissociations of CO_2 and H_2O:

$$CO + 1/2\ O_2 \rightleftharpoons CO_2 \qquad (15.1.12)$$

$$H_2 + 1/2\ O_2 \rightleftharpoons H_2O \qquad (15.1.13)$$

Mathematical treatment of these equilibrium relationships is often simplified by the use of the water gas reaction:

$$CO + H_2O \rightleftharpoons H_2 + CO_2 \qquad (15.1.14)$$

It should be noted that this is not a third independent relationship but a linear combination of Equations 15.1.12 and 15.1.13. Partial pressure equilibrium constants for each of these three reactions are illustrated in Figure 15.1.2 (data from Reference 15.1 have been utilized). Note the relative temperature insensitivity of the water gas equilibrium constant.

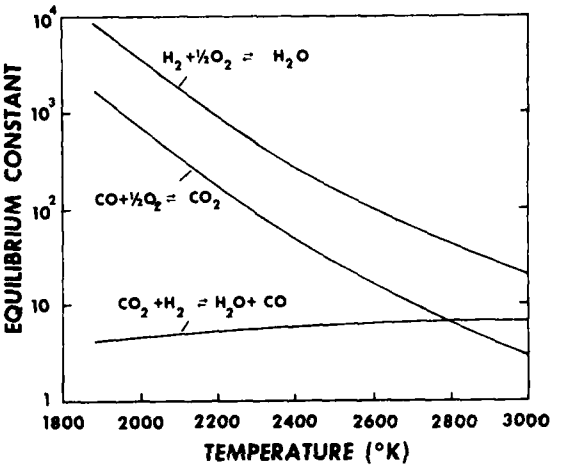

Figure 15.1.2 Equilibrium Constants for Important Dissociation Reactions.

Since the maximum chemical energy is released from a hydrocarbon fuel upon conversion to CO_2 and H_2O, dissociation of either of these products results in a decrease of energy released. As will be shown in Section 15.2, equilibrium flame temperature is strongly influenced by dissociation. Because of the temperature sensitivity of the equilibrium constants, dissociation is more pronounced at higher flame temperatures. Figure 15.1.3 illustrates the effect of final mixture temperature on dissociation using the example of stoichiometric combustion of a C_nH_{2n} type fuel with air at one atmosphere. The influence of final mixture temperature on CO and H_2 concentration in the combustion product is pronounced.

15.1.3 Hydrocarbon Chemistry

The sequence of events occurring during combustion of a practical hydrocarbon fuel is extremely complex and not understood in detail. Major aspects of hydrocarbon combustion chemistry involve hydrocarbon pyrolysis and partial oxidation to H_2 and CO, chain branching reactions resulting in H_2 consumption, and CO oxidation by radicals generated during chain branching. Each of these reaction steps is schematically illustrated in Figure 15.1.4. Note that the chronology of these processes is schematically indicated by the

flow of mass through the reaction steps. Each process is individually described below.

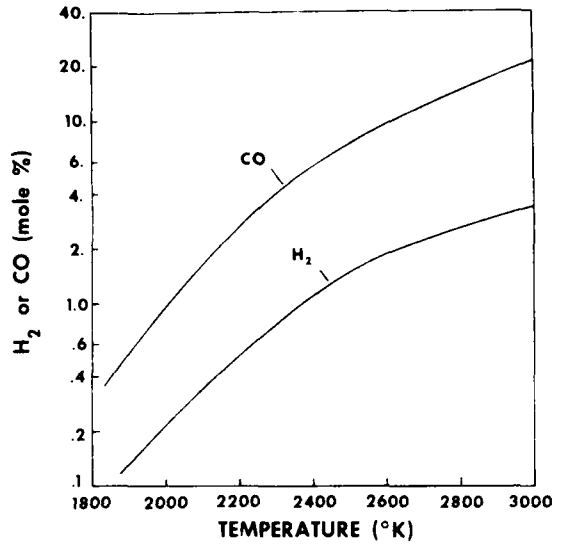

Figure 15.1.3 Equilibrium CO and H_2 Concentration Dependence on Temperature

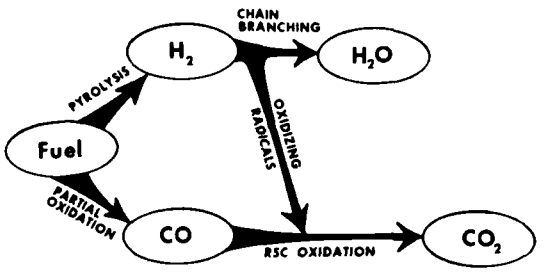

Figure 15.1.4 Hydrocarbon Combustion Chemistry Schematic.

Pyrolysis is the term given to the process by which fuel molecules are broken into smaller fragments due to excessive temperature and partial oxidation. This molecular destruction is accomplished during the first phase of the combustion process. The predominant resulting products are hydrogen and carbon monoxide. Little detailed information is available concerning the chemistry of these processes for practical fuels--large hydrocarbons with molecular weights of 50 to 200. It is well-recognized that hydrocarbon structure and its influence on the pyrolysis chemistry affects the combustion process. For example, low fuel hydrogen concentration leads to excessive carbon particle formation in the early stages of combustion.

Edelman (Ref. 15.2) has developed a single-step quasi-global model to characterize the pyrolysis and partial oxidation of any practical hydrocarbon fuel. His approach is to characterize the kinetics of the numerous complex chemical reactions resulting in production of H_2 and CO by a single reaction step. An Arrhenius type expression has been fitted to experimental data involving variations in temperature and pressure as well as fuel and oxygen concentration. Edelman's result is:

$$-\frac{d[C_nH_m]}{dt} = \frac{5.52 \times 10^8 T}{P^{.825}} [C_nH_m]^{\frac{1}{2}} \cdot [O_2]\exp(-24{,}400/RT) \qquad (15.1.15)$$

where concentrations are expressed in moles/cc, T in ^{o}K, and P in atmospheres. The activation energy of 24,400 is in the units cal/g mole^{o}K. Although this expression has proven to be useful in some combustion models, additional effort is required to determine chemical kinetic differences between hydrocarbon fuel types and to study pyrolysis mechanisms in mixtures. Further, the interface between fuel pyrolysis and carbon particulate formation requires additional study.

The products of pyrolysis are reduced state compounds (RSC). Oxidation of these species is better understood than their formation. The important oxidation reactions for the reduced-state compounds are of the general form:

$$RSC + OR = OSC + RR \qquad (15.1.16)$$

where RSC = reduced-state compound
OR = oxidizing radical
OSC = oxidized-state compound
RR = reducing radical.

The rate of oxidation of the RSC may be assumed to be given by the appropriate Arrhenius controlled mechanism.

While reactions of the nature described by Equation 15.1.16 play a role in consuming the H_2 formed during the pyrolysis process, many gross characteristics of hydrocarbon combustion are a result of other chemical reactions which involve "chain branching." This type of reaction sequence involves the production of additional radical species during the process. In the case of the H_2 oxidation process, the important chain branching reactions are:

$$H_2 + O \rightarrow H + OH \qquad (15.1.17)$$

$$H + O_2 \rightarrow OH + O \qquad (15.1.18)$$

Note that in either reaction a single radical (O or H) results in the production of two radicals (H + OH or OH + O). This type of reaction has the potential of producing large quantities of radical species. In portions of the combustion zone having high H_2 concentration, radical species can reach levels far in excess of equilibrium. During this process, OH radicals also participate in RSC reactions (Equation 15.1.16) to produce H_2O from H_2.

Carbon monoxide consumption is controlled by the following RSC reaction:

$$CO + OH \rightarrow CO_2 + H \qquad (15.1.19)$$

Since the activation energy of the reaction indicated by Equation 15.1.19 is generally low (only a few kcal/g-mole) the carbon monoxide oxidation rate is predominantly influenced by OH concentration. As previously noted, this quantity is controlled by the chain branching mechanism. Nevertheless, a common method of approximating radical concentration in a RSC reaction involves

assuming local or partial equilibrium. This type of approach has been used in CO oxidation studies by Howard et al. (Ref 15.3). Because the functional relationship between equilibrium OH concentration and temperature is exponential (Equation 15.1.11), an Arrhenius like dependence can be written for a quasi-global O_2 + CO reaction in the presence of H_2O. Howard, et al. determined:

$$-\frac{d[CO]}{dt} = k_o[CO][O_2]^{\frac{1}{2}}[H_2O]^{\frac{1}{2}}(e)^{\frac{-30,000}{RT}} \qquad (15.1.20)$$

where k_o is a constant = 1.3×10^{14} cc/mole sec. This assumption is not necessarily in conflict with the knowledge that higher-than-equilibrium free radical concentrations may be produced by the reactions of Equations 15.1.7 and 15.1.18. CO oxidation is much slower than H_2 consumption and, in non-recirculating systems, occurs predominantly after the chain branching H_2 reactions are largely complete. However, gas turbine combustion systems do employ recirculation and the suitability of this assumption for that application is not straightforward.

The production of H_2O and especially CO_2 through the RSC reactions described above results in the release of a great deal of energy. Consequently, the rate of consumption of CO and the predominant energy release rate are strongly connected. Experience has shown that combustion characteristics influenced by the principal heat release processes (e.g. flame propagation) are correlated by considerations of Equations 15.1.19 and 15.1.20. On the other hand, those characteristics dependent on fuel breakdown/pyrolysis (e.g., ignition delay) are better correlated by consideration of Equation 15.1.15.

The above discussion provides only a simplified description of the complex chemistry of hydrocarbon combustion. Additional detailed treatment has recently been undertaken in efforts to predict pollutant emissions from combustion systems. Table 15.1.1 illustrates one of the more complex schemes which has been utilized in Reference 15.4.

TABLE 15.1.1: Hydrocarbon Oxidation Kinetics Scheme (From Reference 15.4)

(1) $C_8H_{16} + O_2 \rightarrow 2C_4H_8O$

(2) $C_4H_8O + O_2 \rightarrow HO_2 + CO + CH_3 + C_2H_4$

(3) $C_8H_{16} + OH \rightarrow H_2CO + CH_3 + 3C_2H_4$

(4) $CH_3 + O \rightarrow H_2CO + H$

(5) $CH_3 + O_2 \rightarrow H_2CO + OH$

(6) $H_2CO + OH \rightarrow H_2O + CO + H$

(7) $C_2H_4 + O_2 \rightarrow 2H_2CO$

(8) $C_2H_4 + OH \rightarrow CH_3 + H_2CO$

(9) $CH_3 + H_2 \rightarrow CH_4 + H$

(10) $C_2H_4 \rightarrow C_2H_2 + H_2$

(11) $C_2H_2 + OH \rightarrow CH_3 + CO$

(12) $2H + M \rightarrow H_2 + M$

(13) $2O + M \rightarrow O_2 + M$

(14) $OH + H + M \rightarrow H_2O + M$

(15) $H + O_2 \rightarrow OH + O$

(16) $O + H_2 \rightarrow OH + H$

(17) $H + H_2O \rightarrow H_2 + OH$

(18) $O + H_2O \rightarrow 2OH$

(19) $CO + OH \rightarrow CO_2 + H$

(20) $HO_2 + M \rightarrow H + O_2 + M$

(21) $HO_2 + H \rightarrow 2OH$

15.2 THERMODYNAMICS

This section is intended to describe the thermodynamic relationships of importance in evaluating the effect of chemical energy release in combustion systems. The first subsection highlights application of the first law of thermodynamics, offers straightforward evaluations of flame temperature dependencies, and describes methodology used in calculating flame temperature. The second addresses important flame temperature dependencies in the practical situation of jet fuel/air combustion.

15.2.1 Energy Release and Flame Temperature

The first law of thermodynamics, energy conservation, is an important factor in any analysis of combustion systems. Adiabatic, flowing, constant pressure combustion systems, approximated by both main burners and afterburners of gas turbines, can be analyzed using conservation of total enthalpy. In this case, total enthalpy includes sensible (or thermal), chemical, and kinetic contributions.

$$h_t = h_s + \left(\frac{f/a}{f/a + 1}\right) \cdot + \frac{u^2}{2J} \qquad (15.2.1)$$

where: h_t = total enthalpy (Kcal/kg)

h_s = sensible enthalpy (Kcal/kg)

f/a = mass ratio of fuel to air

$\cdot$ = chemical energy (Kcal/kg fuel)

u = flow velocity (m/sec)

J = mechanical equivilent of heat = $4186 \frac{\text{joule}}{\text{Kcal}}$

Most frequently, standard heats of formation are used to determine the chemical energy released during a combustion process. The standard heat of formation, h_f, represents the energy addition necessary for constant pressure formation of a compound from its elements in their natural state at 25°C. The energy required to accomplish any reaction can be calculated by algebraically summing the heat of formation contributions of products minus reactants.

$$(\Delta h_r)_{25^oC} = \Sigma x_i (h_f)_i - \Sigma x_j (h_f)_j \quad (15.2.2)$$

where: Δh_r = heat of reaction at 25°C

x_i = stoichiometric coefficients of product compounds

x_j = stoichiometric coefficients of reactant compounds.

If Equation 15.2.2 is applied to a complete oxidation process of a hydrocarbon where all fuel hydrogen is converted to H_2O and all fuel carbon is converted to CO_2, the heat of combustion, Δh_c, will be calculated. Note that this result is normally a large negative value (i.e. the reaction is strongly exothermic).

The amount of heat required to accomplish a reaction, Δh_r, is a function of reaction temperature. Heat required at temperature T_1, rather than 25°C would be:

$$(\Delta h_r)_{T_1} - (\Delta h_r)_{25^oC} =$$

$$(h_{sp} - h_{sr})_{T_1} - (h_{sp} - h_{sr})_{25^oC} \quad (15.2.3)$$

where h_{sp} and h_{sr} are the product and reactant sensible enthalpies. Heats of combustion are generally greater (i.e. less energy is released) as temperature is increased.

With the important exception of the afterburner nozzle, the kinetic contribution to total enthalpy in gas turbine combustion systems is relatively small. In such a case, the relationship between the energy released due to combustion and the final flame temperature is:

$$-(\Delta h_c)_{T_1} = (h_{sp})_{T_2} - (h_{sp})_{T_1}$$

$$= \int_{T_1}^{T_2} C_p dT \quad (15.2.4)$$

where C_p is the temperature-dependent specific heat of the combustion products and the heat of combustion at temperature T_1 is calculated using Equation 15.2.3. In this flame temperature calculation, the heat generated in forming combustion products at temperature T_1 can be envisioned as an energy source for constant pressure heating of the combustion products from T_1 to T_2.

The term ζ in Equation 15.2.1 is a temperature invariant representation of a fuel's chemical energy. It may be calculated using the following relationship:

$$\zeta = (-\Delta h_c)_{25^oC} + (h_{sp} - h_{sr})_{25^oC} \quad (15.2.5)$$

The concept of chemical energy in conjunction with Equation 15.2.1 provides a second method for determining final flame temperature (Ref. 15.1). Conservation of total enthalpy, for the case where kinetic contributions are negligible, results in the following expression:

$$(h_{sr})_{T_1} + \left(\frac{f/a}{1 + f/a}\right)\zeta = (h_{sp})_{T_2} \quad (15.2.6)$$

It can be shown that the solutions for Equations 15.2.5 and 15.2.6 and Equations 15.2.3 and 15.2.4 are identical.

The case where a hydrocarbon fuel is completely reacted to CO_2 and H_2O results in the maximum achievable flame temperature, as the maximum energy is released upon formation of these products. Note that this can only be achieved for a lean mixture (i.e., more oxygen necessary than required for stoichiometric reaction). Conversion to H_2O, CO_2, and CO is often assumed for rich mixtures, as the conversion of H_2 to H_2O is much more rapid than CO oxidation (see Section 15.1.3). The temperature that would result if the reaction were complete is defined as the "theoretical flame temperature." Because of incomplete combustion, energy losses, and the effects of CO_2 and H_2O dissociation, the theoretical flame temperature is never achieved in real combustion systems. Nevertheless, consideration of this simplified flame temperature concept reveals important trends dictated by the first law of thermodynamics.

Equations 15.2.4 and 15.2.6 relate temperature rise to heat release due to combustion. For a given amount of energy release it is apparent that the final flame temperature will increase with initial temperature. Secondly, since for lean mixtures the heat released will be proportional to the amount of fuel burned per mass of mixture, it is implied that T_2 will increase directly with fuel-air ratio. However, when the mixture ratio exceeds stoichiometric CO, and possibly H_2 and unburned fuel, will be present in the exhaust products and a decreasing flame temperature trend will result. Consequently, this analysis indicates a maximum flame temperature for stoichiometric conditions. These trends are illustrated in Figure 15.2.1. Rather than considering fuel-air ratio, the equivalence ratio, ϕ, has been used in this illustration. Equivalence ratio is the fuel-air ratio of consideration divided by the stoichiometric fuel-air ratio:

$$\phi = \frac{f/a}{(f/a)_{stoichiometric}} \quad (15.2.7)$$

Values of ϕ less than unity correspond to lean operation while those greater than unity correspond to rich combustion.

Accurate flame temperature prediction requires consideration of dissociation effects and variable specific heats. Iterative solution of at least four simultaneous equations is involved. The equations are:

a) stoichiometric chemical equation (mass and atomic conservation)

b) energy conservation

c) CO_2 dissociation

d) H_2O dissociation.

Additional equilibrium relationships may be added to improve accuracy and predict concentrations of NO, NO_2, O, H, OH, N, etc. Note further that the water gas equilibrium equation is usually substituted for either c) or d) to simplify mathematical procedures (see Section 15.1.2).

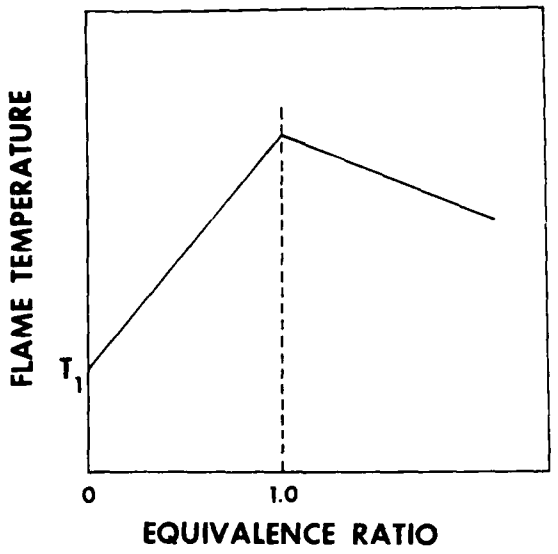

Figure 15.2.1: Theoretical Flame Temperature Dependence on Equivalence Ratio.

A number of methods of solving these equations are practical. One technique involves assuming a flame temperature and calculating species concentrations using the equilibrium relationships. The values are then used to check for balance of the energy equation. Additional guesses and iterations are made till a temperature is determined such that the conservation of energy is satisfied within acceptable limits.

Because of the involved nature of these calculations, detailed tabulated results and computer programs have been established to assist combustion scientists and engineers. Some of the early tabulated calculations are the subject of Reference 15.5 while the most popular of currently available computer programs for this purpose is described in Reference 15.6.

15.2.2 Important Flame Temperature Dependencies

This sub-section presents calculated flame temperature results of practical importance to turbine engine combustion. Important variables to be examined are fuel-air ratio, initial pressure and temperature, and mixture inert concentration.

The simplified relationship between calculated constant pressure adiabatic flame temperature and mixture ratio shown in Figure 15.2.1 is significantly altered when the detailed effects of dissociation and specific heat variations are included. This is illustrated in Figure 15.2.2 which shows results for combustion of Jet A with air at 800°K and 25 atm (representative of modern combustor inlet conditions at 100% power operation). The difference between theoretical and actual flame temperature as the mixture ratio approaches stoichiometric is due to the presence of significant CO and H_2 concentrations at the higher temperatures (see Figure 15.1.3).

In addition, note that dissociation causes the peak flame temperature to occur at slightly rich conditions.

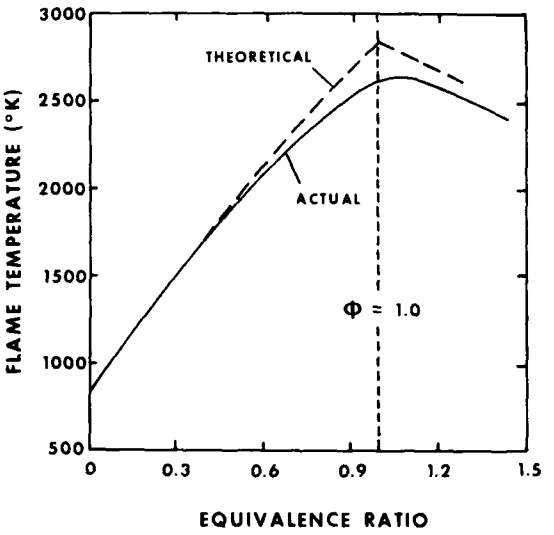

Figure 15.2.2: Effect of Equivalence Ratio on Adiabatic Flame Temperature.

An understanding of the influences of initial pressure and temperature on flame temperature is important to the combustion engineer, as testing is frequently accomplished at scaled operating conditions. Figure 15.2.3 illustrates the relationship between stoichiometric flame temperature and inlet temperature at a pressure of 25 atmospheres using Jet A fuel. Note that only one-half of an increase in inlet temperature is translated to flame temperature at these conditions. Again, the non-linearity is primarily due to the strong temperature dependence of the equilibrium constants for CO_2 and H_2O dissociation. The effect of pressure is illustrated in Figure 15.2.4. An increase in pressure at constant initial temperature results in an increase in flame temperature. This dependence can be explained by examining the form of the H_2O and CO_2 dissociation equations. In both cases, dissociation requires an increase in the total number of moles of product. The physics of the equilibrium process, as embodied in Equations 15.1.8 and 15.1.9, cause an increase in pressure to result in a shift to less total moles of product -- in this case less dissociation. The increased amounts of H_2O and CO_2 in the combustion products result in greater flame temperature.

Consideration of main combustor exit temperatures can be somewhat simplified from the complexities of the foregoing discussion. Most of the variations discussed with respect to Figures 15.2.2 - 15.2.4 occur at the highest values of flame temperature. Since main burner exit temperatures are generally below 1750°K, the inlet temperature and pressure effects of dissociation are far less pronounced. Figure 15.2.5 illustrates the relationship between fuel-air ratio and total

temperature which may be used for any pressure at flame temperatures less than 1750°K.

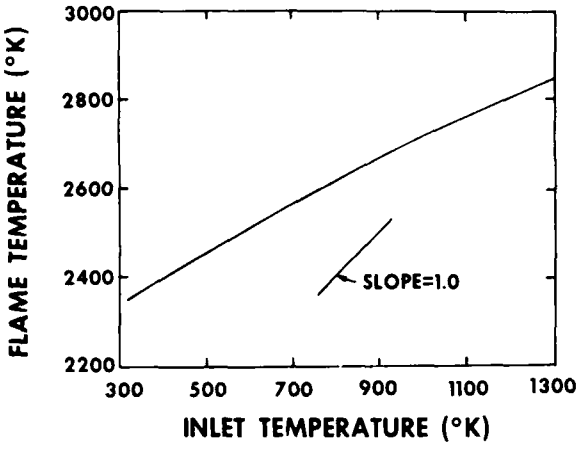

Figure 15.2.3 Effect of Inlet Temperature on Stoichiometric Flame Temperature.

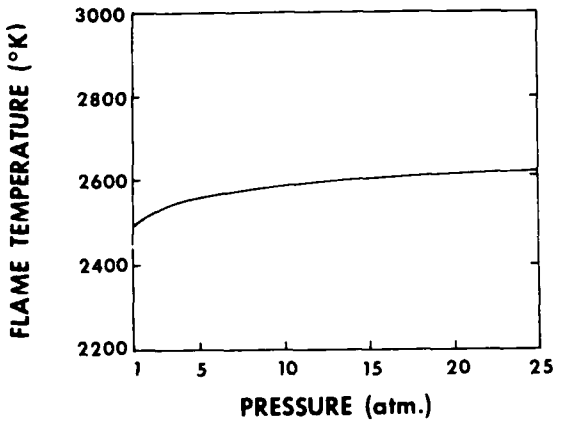

Figure 15.2.4 Effect of Pressure on Stoichiometric Flame Temperature.

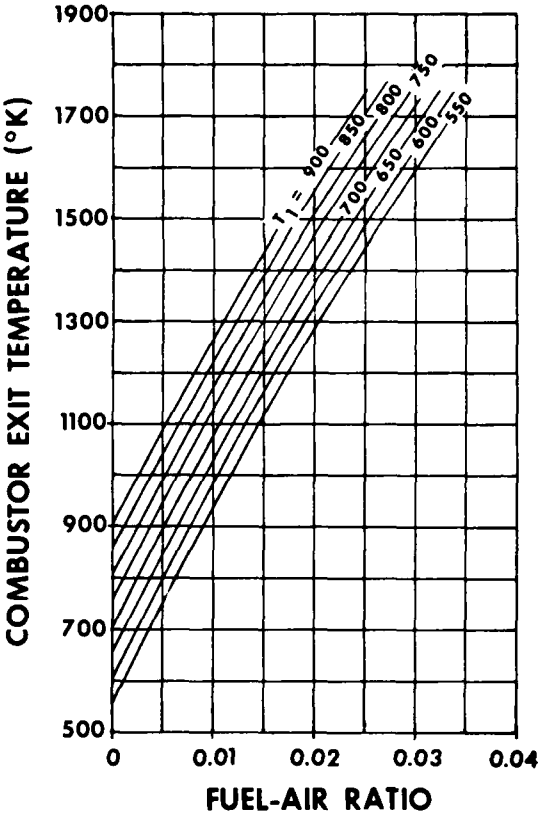

Figure 15.2.5 Combustor Exit Total Temperature for Jet A Fuel and Arbitrary Pressure (Working Chart).

Another important factor influencing flame temperature is oxygen concentration. Two very important instances of combustion with an O_2 concentration less than that of air are vital to the combustion engineer. While a gas turbine engine main burner encounters air with approximately 21% O_2 in actual operation (preheating being accomplished by the compressor), testing is sometimes conducted using vitiated air -- inlet temperature requirements are satisfied by pre-combustion rather than compression or indirect heating using a heat exchanger. The other very important example of vitiated combustion is, of course, the afterburner. In this case, some of the energy previously added by the compressor and main burner combustion has been extracted by the turbine. Consequently, temperatures in stoichiometric zones of the main combustor significantly exceed maximum achievable temperatures within the afterburner.

A means of evaluating the effect of vitiation on flame temperature is to consider oxygen availability. Vitiated combustion is characterized by abnormally high H_2O and CO_2 concentrations and lower O_2 concentrations. Therefore, the effect of vitiation is to reduce the amount of fuel per mass of mixture which can

be stoichiometrically burned; reduced final flame temperature would be predicted by Equations 15.2.4 and 15.2.6. Figure 15.2.6 illustrates the effect of reduced oxygen concentration as a function of the degree of vitiation. These calculations were performed with combustor inlet conditions of 900°K and one atmosphere pressure, values typical of turbine exit conditions. The results include the effects of dissociation.

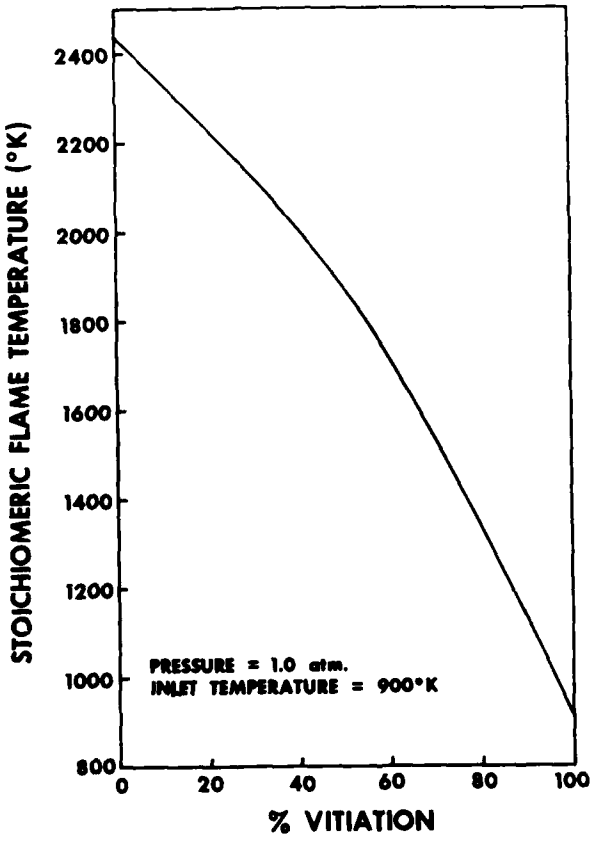

Figure 15.2.6 Effect of Vitiation on Stoichiometric Flame Temperature.

15.3 GAS DYNAMICS AND DIFFUSION PROCESSES

The influences of gas dynamics and diffusion of species and heat on combustion are extremely complex. Rather than treat these involved processes in detail, this section intends to explain the impact of these phenomenon in turbopropulsion combustion and to outline the general approaches utilized to model these processes in turbine engine combustion systems. The topics of consideration include premixed laminar flame propagation, diffusion-controlled combustion, effects of turbulence on combustion processes, and the perfectly stirred reactor.

15.3.1 Premixed Laminar Flames

The simplest situation involving simultaneous treatment of combustion and gas dynamics is the premixed laminar flame. In this case, a reaction front proceeds through a uniform mixture of gaseous fuel and air with a constant propagation speed. An analysis of the mass, momentum, and energy conservation equations governing this case (called the Rankine-Hugoniot analysis) predicts two types of solutions. First, the reaction front can proceed into the unburned gases supersonically. The velocity of the burned gases with respect to the reaction front can be either subsonic (the detonation case) or supersonic (the supersonic combustion case). Secondly, the reaction front can proceed into the unburned gases subsonically. In this case, the burned gases must also be subsonic, as the supersonic case would violate the second law of thermodynamics. Subsonic flame propagation is also called deflagration.

While the Rankine-Hugoniot equations predict the existence of deflagration and relationships between the properties of burned and unburned gases, the analysis does not allow calculation of the propagation velocity, S_L. Prediction of S_L requires consideration of heat conduction and species diffusion across the reaction front. The basic thermal theory of Mallard and LeChatelier first proposed in 1883 results in the following important temperature dependence:

$$S_L \sim \exp(-E_a/2RT_f) \qquad (15.3.1)$$

This temperature relationship is similar to that for reaction rate (Equation 15.1.4) except for the factor of 2 in the exponential denominator. Equation 15.3.1 is consistent with empirical flame propagation dependencies on fuel air ratio as shown in Figure 15.3.1; the highest propagation velocity is at approximately $\phi = 1$, where T_f is at its maximum value.

Variations in flame propagation rate with the hydrocarbon types of practical interest to turbopropulsion combustion are not substantial (Ref. 15.8). Practical jet fuels would be expected to behave in a manner similar to that of the fuels described in Figure 15.3.1. The pressure dependence of flame propagation is not straightforward. In mixtures with burning velocities below 50 cm/sec, S_L decreases with increasing pressure. Between 50 and 100 cm/sec S_L remains approximately constant. Above 100 cm/sec S_L increases with increasing pressure (Ref 15.8).

Across the reaction front a substantial decrease in gas densities occurs. Consequently, mass conservation requires a substantial increase in velocity. This acceleration results at the expense of some pressure drop across the front. The pressure drop is:

$$\frac{\Delta P}{P} = \gamma \left(1 - \frac{T_1}{T_F}\right)\left(\frac{S_L}{a}\right)^2 \qquad (15.3.2)$$

where γ is the ratio of initial gas specific heats, T_1 is the initial temperature and a is the speed of sound in the initial mixture.

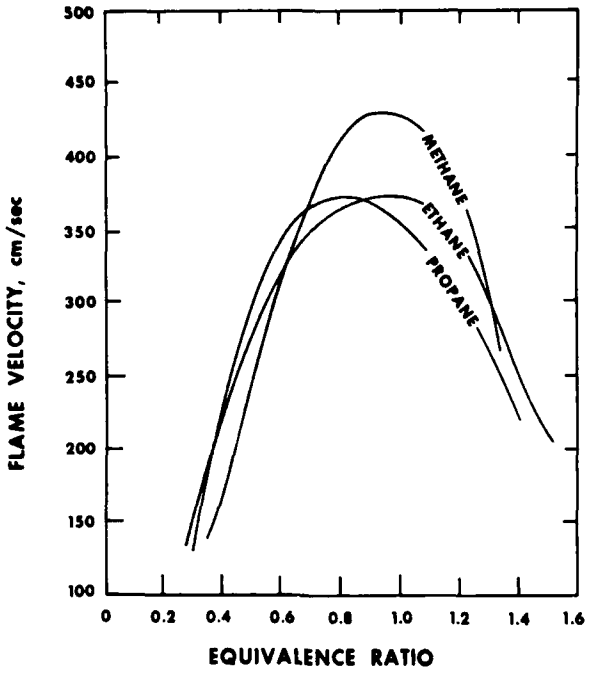

Figure 15.3.1 Flame Velocities of Paraffin-Oxygen Mixtures at One Atmosphere Pressure and Room Temperature.

This quantity represents the minimum pressure drop (usually less than 1%) a combustion system can experience in order to accomplish a given energy release.

Values of laminar flame propagation are usually no greater than 5 m/sec. Since reference velocities in modern combustion turbine engine systems are generally greater than 25 m/sec, laminar flame propagation is not considered a predominant mode of combustion. Other modes of combustion involving diffusion control, turbulent mixing, and the establishment of zones approaching perfectly stirred reactors are necessary.

15.3.2 *Diffusion Controlled Combustion*

In many practical devices the fuel and air are not entirely premixed prior to combustion. In these cases, reactions take place in flame zones where the influx of oxygen and fuel occur at a rate corresponding to the stoichiometric ratio. In laminar flows, the mechanism for transport of fuel and oxygen into these zones is molecular diffusion and these types of systems are called diffusion flames.

Common examples of laminar diffusion flames are the candle, a kerosene lamp, or a match; in each case the fuel and O_2 do not premix prior to the flame. An appreciation for the nature of diffusion flames may be gained by examining the early work of Burke and Schumann (Ref. 15.9) which was published in 1928. Experimentally, they utilized a system similar to that shown in Figure 15.3.2a. Fuel enters the combustion zone through a central tube. A laminar diffusion flame, the shape of which is governed by the ratio of fuel to air flow, is established in the combustion zone.

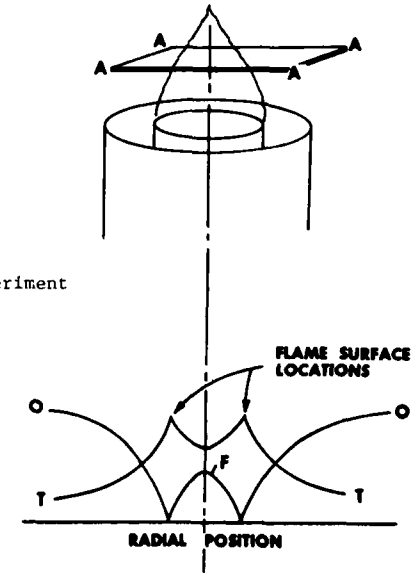

a. Experiment

b. Important Profiles at Plane A: O, Oxygen Concentration, F, Fuel Concentration, T, Temperature.

Figure 15.3.2 Diffusion Flame Characteristics.

Burke and Schumann's analysis constituted the first successful treatment of laminar diffusion flames, and it continues to represent the approach taken in modern work. They modeled the flame as an infinitely thin sheet into which fuel and oxygen flow in stoichiometric proportions. All heat release from chemical reaction occurs at this surface. This approach is equivalent to the assumption that the chemical reactions are infinitely fast compared to the diffusion processes which, therefore, control the burning rate. In order to mathematically prohibit an infinite gradient of fuel or oxygen at the flame surface (which would indicate infinite flux into the surface) it is necessary to require both fuel and oxygen concentrations to be zero at the surface. This concept of concentration and temperature profiles is illustrated in Figure 15.3.2b.

Important differences between premixed and diffusion flames center around the existence of the flame sheet. In the case of the premixed flame with no flame sheet, temperatures achieved correspond to that for contant pressure combustion at the premixture fuel-air ratio and the burning rate is controlled by the chemical kinetic rate and flame temperature (Equation 15.3.1). However, in the case of laminar diffusion flames, combustion always occurs at stoichiometric conditions at the flame sheet and the burning rate is controlled by

molecular diffusion. Moreover, the temperature at the flame does not generally correspond to the premixed constant pressure stoichiometric flame temperature. The thermodynamics at the flame sheet are strongly influenced by the rates of heat and mass transfer near the flame (i.e., mass and temperature gradients) and are not calculable through the use of a simple energy balance.

The simplifying assumption of an infinite chemical reaction rate can be eliminated through the utilization of a much more sophisticated analysis. The primary effects of including finite reaction rates are prediction of a flame of finite thickness, lesser gradients of concentration and temperature at the flame, and lower peak flame temperatures. While more accurate prediction of near-flame characteristics is achieved by the more sophisticated analysis, many important properties, notably burning rate, are predicted nearly as well with the less elaborate approach.

The instance in which the classical thin-flame theory of diffusion flames is of importance to turbine combustion systems involves fuel droplet burning. While many combustion engineers question whether droplet combustion occurs under the high temperature and turbulent conditions characteristic of high power operation, it would be likely during starting and idle operation. In this case, vaporization is caused by heat transfer from a flame surrounding the liquid droplet, assumed to be at its boiling temperature. The gaseous fuel proceeds to the flame and stoichiometrically reacts with oxygen diffusing radially inward from the surroundings. Analysis of this situation, similar to the Burke and Schumann analysis discussed above, results in the following burning rate prediction:

$$d^2 = d_o^2 - kt \qquad (15.3.3)$$

where d is the fuel droplet diameter at time t, d_o is d at t = 0, and k is a constant. This relationship, known at Godsave's law, predicts fuel efforts through variations in k (Ref. 15.10). The influence of convective velocity, air temperature, and oxygen concentration can also be included in determination of the value of k. Note that this relationship is also applicable to droplet evaporation without combustion, the difference being a smaller value of k.

The foregoing discussion addresses the simplified concept of fuel droplet combustion wherein the process of each individual droplet is assumed to be independent and the fuel is comprised of a single hydrocarbon component. In reality, the situation is far more complex; droplet interactions and complications of multi-component fuels cause significant departures from the simplified case discussed above (Ref. 15.11 and 15.12). The combustion engineer should utilize empirical information when available. Recent data are presented in Reference 15.12.

Diffusion-controlled combustion will also occur in the cases where fuel droplets have vaporized but not mixed with surrounding air, thus forming fuel-rich pockets, or where the gases from a rich primary zone mix with secondary air. Many of the performance characteristics of present day combustors confirm the existence and importance of such processes. However, the diffusion controlled reactions in practical gas turbine combustion systems cannot be simply treated by classical laminar diffusion flame theory; turbulence effects are extremely important and the effects of turbulent diffusivity must be included. These will be discussed in the following subsection.

15.3.3 Turbulence Effects

Previous discussions of both premixed and diffusion controlled combustion have concentrated on laminar systems. In practice, however, the presence of turbulence has an extremely important influence on both premixed and diffusion controlled combustion.

The rate of flame propagation in a premixed system is greatly enhanced by turbulence. Most available information on this subject has been developed to improve the understanding of turbulent flame propagation in afterburners. However, turbulent flame propagation information is currently of additional importance, as low emission combustors employ a highly turbulent fuel-air mixing and vaporization zone prior to combustion (see Chapter 20). An important consideration in such systems is the possibility of "flashback" or turbulent flame propagation upstream to the fuel injection point.

Lefebvre and Reid (Ref. 15.13) have reviewed important turbulent flame propagation literature. The relationships shown in Table 15.3.1 have been cited as representative of the understanding of turbulence effects. The important parameters influencing turbulent flame propagation, S_T are:

- u' = the fluctuating component of gas velocity.
- $\bar{y}$ = parameter describing free stream and flame generated turbulence intensity.
- ℓ = turbulence length scale.

Generally speaking, the turbulent flame velocity can be the order of the turbulent velocity, u', far exceeding S_L.

Turbulence also causes increased burning rates in diffusion flames (Ref. 15.18). Analyses for turbulent diffusion flames are similar to the laminar case but use an artificially high diffusivity constant. Physically, the increased fuel/air mixing is explained as due to forced mixing of small fuel lean or fuel rich elements of gas by turbulent forces. These small elements of gas are called eddies. The analytical adjustment, called eddy diffusivity, accounts for the enhanced mixing at the reaction front. This approach is taken as a convenience and is based on empirical correlations rather than fundamental principles.

The importance of turbulence on many practical aspects of turbine engine combustion has recently been highlighted by Mellor (Ref. 15.19). He proposes a simplified model for main burner combustion in which important processes are assumed to occur in a highly turbulent diffusion flame stabilized by a recirculation zone behind a bluff body (see Figure 15.3.3). His analysis, based on characteristic times for turbulent mixing and chemical reaction and focusing on the shear layer mixing zone, has been shown to be successful in correlating a number of combustion characteristics ranging from exhaust pollutants to stability.

TABLE 15.3.1: Turbulent Flame Theories (From Reference 15.13).

Investigator	Relationships	Conclusions
Damkohler (Ref. 15.14)	$S_T = S_L + u'$ At high velocities this approaches $S_T = u'$	S_T is independent of turbulence scale. At high velocities S_T is determined solely by turbulent velocity.
Shchelkin (Ref. 15.15)	$S_T = S_L[1 + (u'/S_L)^2]^{.5}$ At high velocities this approaches $S_T = u'$	In agreemnt with Damkohler.
Karlovitz (Ref. 15.16)	For weak turbulence $S_T = S_L + u'$ For strong turbulence: $S_T = S_L + (2S_L u')^{.5}$ Where: $u' = \frac{S_L}{\sqrt{3}}\left(\frac{\rho_u}{\rho_b} - 1\right)$	S_T is independent of turbulence scale. Laminar flame speed is most important parameter.
Scurlock (Ref. 15.17)	$S_T = S_L[1 + C_3(\bar{y}/\ell)^2]^{.5}$ Where: $\bar{y}$ is dependent on approach stream and flame generated turbulence; ℓ is the turbulence scale; C_3 is a constant.	S_T is dependent on laminar flame speed and turbulence scale.

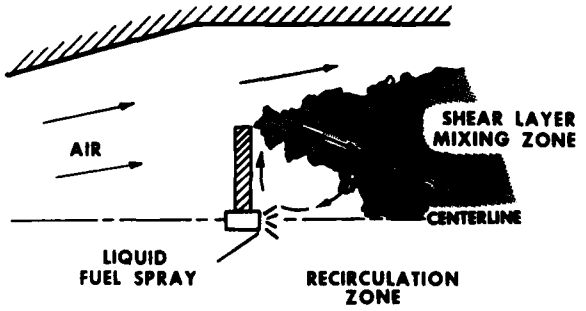

Figure 15.3.3: Simplified Representation of a Turbine Combustion System.

A final aspect of turbulence to be discussed here involves its effect on chemical reactions. During fuel-air mixing as well as in the reaction zone, the individual turbulent eddies can have widely differing values of fuel-air ratio and temperature. Because reaction rates are very sensitive to these variables (Equation 15.1.4) the turbulence characteristics can strongly influence the rates and end products of the combustion process. Gouldin (Ref. 15.20) has performed an analysis which indicates that turbulence is of importance to chemical reactions when turbulent temperature fluctuations T' are such that:

$$\frac{\overline{(T')^2}}{(\bar{T})^2} > \left(\frac{Ea}{R\bar{T}}\right)^{-2} \qquad (15.3.4)$$

where the bars indicate average values. Table 15.3.2 indicates $(E_a/R\bar{T})^{-2}$ for different values of E_a and $\bar{T}$. Turbulence can be expected to play a significant role in all cases except those involving low activation energies (<20 Kcal/g mole) and high temperatures (>2500°K). Because of the obvious difficulties in accomplishing temperature or concentration measurements on the time and length scales of interest to this subject, only limited empirical information is available to provide further explanation of this complex phenomena.

15.3.4 Perfectly Stirred Reactor

The perfectly stirred reactor (PSR) is defined as a combustion region in which reactant and product concentrations as well as temperature are completely homogeneous (Ref. 15.21, 15.22). The fuel-air mixture entering the reactor is assumed to be instantaneously mixed with the combustion products. In principle, this immediately increases the temperature of the entering reactants far beyond the initial state and provides a substantial and continuous supply of chain carriers

TABLE 15.3.2: Importance of Turbulence to Chemical Reactions -- Values of $(E_a/R\bar{T})^{-2}$

$E_a\left(\frac{Kcal}{g\text{-}mole}\right)$	T(°K)		
	1500	2000	2500
10	.09	.16	.25
20	.0225	.04	.0625
40	.0052	.01	.0156
60	.0025	.0044	.00694
80	.0014	.0025	.0039

which are of paramount importance to hydrocarbon combustion (See Section 15.1.3).

Reaction rates per unit volume are maximized in the PSR. Stabilization characteristics of practical systems -- primary zones of main combustors and regions behind flameholders of afterburners -- are often modeled using PSR analyses. A simplified version of the analysis presented in Reference 15.22 results in the following dependence of the reaction rate on key parameters:

$$\frac{m}{V} \sim \left(\frac{P}{RT_R}\right)^n \frac{(T_F - T_R)^n}{(T_F - T_u)^{n-1}(T_R - T_u)} \cdot \exp(-E_a/RT_R) \qquad (15.3.5)$$

where: V = reactor volume

m = mass flow rate into the reactor

n = total reaction order

T_F = adiabatic flame temperature for complete reaction

T_R = PSR temperature

T_u = initial temperature of entering (unburned) mixture.

Figure 15.3.4 illustrates the relationship between mass burning rate and reactor temperature. These results correspond to a case where n = 2, E_a = 40 Kcal/g mole and stoichiometric combustion of a fuel yielding T_F values of 2550, 2500 and 2400°K for T_u values of 1000, 800, and 600°K. Equation 15.3.5 yields three solutions for any value of m/VP^n -- only the two highest T_R solutions are indicated in Figure 15.3.4, as the lowest T_R solution, while stable, is not of practical interest here. The mid-T_R solution is also of academic importance, as it is unstable. Considering only the highest T_R solution, the analysis indicates that the adiabatic flame temperature for complete reaction is only achieved at flow rates approaching zero. Further, a maximum value of m/VP^n is indicated and blow out is expected if a further increase is attempted. Typically, this PSR blow out point is imminent when the temperature rise above inlet conditions is 75% of that corresponding to complete combustion.

The exponential nature of reaction rates (Equation 15.1.4) is directly reflected in Equation 15.3.5. For this reason, perfectly stirred reactors have been extensively utilized for high temperature chemical kinetic studies. Equation 15.3.5 also indicates the beneficial effect of higher values of T_R on stabilization. This can be achieved by higher initial mixture temperature (as shown in Figure 15.3.4) and/or an equivalence ratio closer to unity. Figure 15.3.5 illustrates the dependence of the well-stirred reactor stability region on equivalence ratio. Consequently, combustor designers strive to create primary zones which promote stabilization with an approximately stoichiometric fuel-air mixture ratio.

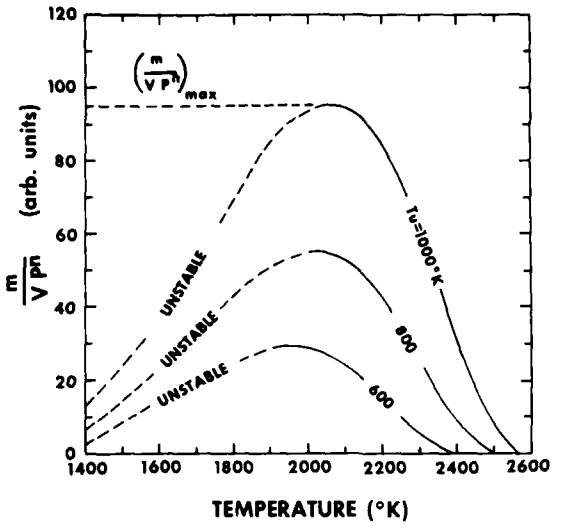

Figure 15.3.4 Perfectly Stirred Reactor Operating Conditions.

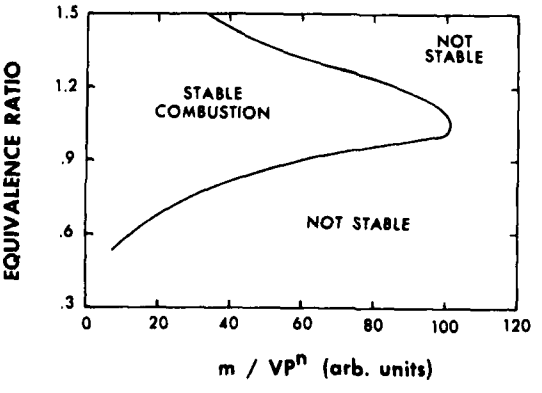

Figure 15.3.5 Stirred Reactor Stability Dependence on Equivalence Ratio.

Equation 15.3.5 can be rearranged and simplified while maintaining the most important temperature characteristics to yield the following relationship:

$$\frac{\dot{m}}{VP^n} \sim \exp^{-E_a/RT} \qquad (15.3.6)$$

This relationship provides some guidance in developing a parameter with which the volumetric heat release of practical combustion systems may be judged. Following the units of Equation 15.3.6 a specific heat release rate parameter, SHRR, has been established for aircraft gas turbine combustors with the units of energy/time-pressure-volume. This topic is discussed further in Chapter 20.

15.4 COMBUSTION PARAMETERS

Three important combustion parameters will be discussed in this section. Descriptions of combustion efficiency, flame stabilization, and ignition phenomena are included.

15.4.1 Combustion Efficiency

Perhaps the most fundamental of all combustion performance characteristics is the combustion efficiency, η_c. This parameter is defined as the fraction of the maximum possible energy which has been released during a combustion process. For the case of constant pressure combustion, η_c can be expressed as:

$$\eta_c = \frac{(h_{sp})_{T_2} - (h_{sp})_{T_1}}{(h_{sp})_{T_2\ ideal} - (h_{sp})_{T_1}} \qquad (15.4.1)$$

An excellent approximation of η_c can be made by assuming that the product specific heat is independent of temperature:

$$\eta_c = \frac{(T_2 - T_1)_{actual}}{(T_2 - T_1)_{ideal}} \qquad (15.4.2)$$

In cases where significant acceleration occurs during the combustion process, total enthalpy or temperature must be used in Equations 15.4.1 and 15.4.2. Further, the ideal value of T_2 in Equation 15.4.2 or $(h_{SP})_{T_2}$ in Equation 15.4.1 is that corresponding to the calculated equilibrium flame temperature. Consequently, the consideration of dissociation effects is vital when temperatures are in excess of 1650°K.

In cases where the temperature is below 1650°K, combustion efficiency can be related to operating and fuel parameters as follows:

$$\eta_c = \frac{C_p(T_2 - T_1)_{actual}}{\left(\frac{f/a}{1 + f/a}\right)(\Delta h_c)_f} \qquad (15.4.3)$$

where C_p is an average specific heat and $(\Delta h_c)_f$ is the fuel heat of combustion.

In practice, η_c can be determined by measuring the actual T_2. This method, however, presents some difficulty in cases where combustion efficiencies are above 90%. The objective of such testing usually involves reduction of the remaining combustion inefficiency and relatively small temperature measurement errors can cause large uncertainties in the determined inefficiency. Consequently, exhaust gas analysis has received wide acceptance as a means of more accurately determining combustion inefficiency. Exhaust concentrations of species containing chemical energy (predominantly carbon monoxide, unburned hydrocarbons, and hydrogen) must be determined. Inefficiency may then be calculated using the following equation.

$$1 - \eta_c = \frac{X_{CO}(\Delta h_c)_{CO} + X_{HC}(\Delta h_c)_{HC} + X_{H_2}(\Delta h_c)_{H_2}}{\frac{f/a}{1 + f/a}(\Delta h_c)_f} \qquad (15.4.4)$$

where X_i is the mass fraction of species i, and $(\Delta h_c)_i$ is the heat of combustion of species i. The numerator of this expression represents the unused chemical energy per mass of exhaust while the denominator represents the chemical energy per mass of the initial fuel-air mixture.

Another common means of expressing Equation 15.4.4 involves the use of the emission index, EI, which represents the mass of CO, hydrocarbons, or H_2 in the exhaust per 1000 mass units of fuel. In this case the equation reduces to:

$$1 - \eta_c = 10^{-3}(.232\ EI_{CO} + EI_{HC} + 2.76\ EI_{H_2}) \qquad (15.4.5)$$

Note that in cases where the combustion temperature exceeds 1650°K, Equation 15.4.4 and 15.4.5 must be modified to account for the amounts of CO, hydrocarbons, or H_2 which are present due to equilibrium dissociation. The calculated combustion inefficiency should correspond only to that CO, hydrocarbon, or H_2 which is present at concentrations levels in excess of equilibrium.

15.4.2 Flame Stabilization

Not all fuel-air mixtures are capable of supporting sustained combustion. The equilivalence ratio, temperature, and pressure conditions within which combustion can be sustained in a quiescent, gas-phase system are defined as the flammability limits. Figure 15.4.1 illustrates the existence of both fuel lean and fuel rich limits for a kerosene-air system. While these limits are dependent on pressure, experimental configuration, and the existence of a quiescent system, the fundamental concept of flammability limits is invaluable as it defines the widest possible regimes of combustion. Flammability limit data for some typical hydrocarbons are indicated in Table 15.4.1. It is noted that variations in the limiting equivalence ratio are not substantial for the lean limit, that of primary practical importance to the combustor designer.

Flammability limits are sensitive to mixture temperature. Correlations have indicated the following approximate relationships between the mixture equivalence ratios for the lean and rich limits (ϕ_L and ϕ_R) and initial mixture temperature (Ref. 15.23):

$$\phi_L(T_2) - \phi_L(T_1) = -9.2 \times 10^{-4}(T_2 - T_1) \qquad (15.4.6)$$

$$\phi_R(T_2) - \phi_R(T_1) = 25 \times 10^{-4}(T_2 - T_1) \qquad (15.4.7)$$

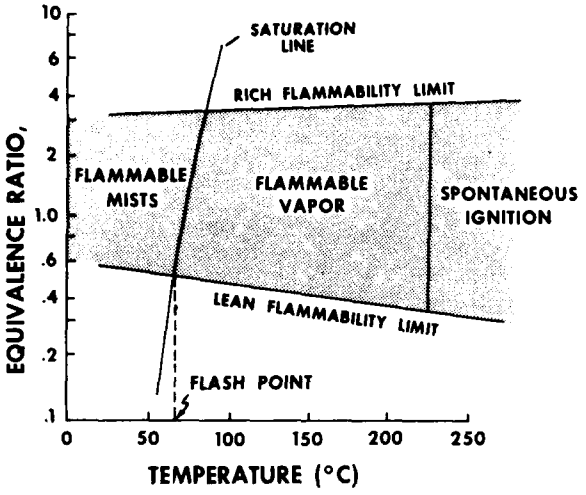

Figure 15.4.1: Flammability Characteristics for a Kerosene-Type Fuel in Air at Atmospheric Pressure.

TABLE 15.4.1: Flammability Limits in Air at Atmospheric Pressure and Room Temperature (From Ref. 15.23).

	Equivalence Ratio	
Fuel	Lean Limit	Rich Limit
n-Paraffins		
Methane	.53	1.56
Propane	.53	2.51
Butane	.60	2.88
Pentane	.58	3.23
Hexane	.55	3.68
Heptane	.63	3.78
Octane	.60	----
Isoparafins		
2,2-Dimethylpropane	.54	2.01
2-Methylpentane	.55	3.42
2,2,4-Trimethylpentane	.66	----
2,2,3,3-Tetramethylpentane	.53	3.45
Olefins		
Ethene	.45	6.76
Propene	.52	2.47
1-Butene	.46	2.94
Aromatics		
Benzene	.50	2.75
Toluene	.61	----
Ethylbenzene	.50	----

Substantial pressure differences may also be observed if the test container is sufficiently small for wall quench reactions to be of importance.

Often a flowing system will not be capable of sustained stable combustion under temperature, pressure, and equivalence ratio conditions within the flammability limits. In practical systems, the limits within which combustion will be stable are dependent on design details. An example of the onset of instability in a premixed fuel-air system is found in the stabilization process for a turbulent flame at the tip of a bunsen burner. The blow off characteristics of such a system have been successfully related to the velocity gradient near the bunsen burner rim.

To reduce the possibility of instabilities in flowing premixed systems, flameholders and primary zones are often used. In either case, the stability of the system is achieved by creating a region of violent recirculation and thorough mixing. Such a zone approximates the perfectly stirred reactor (PSR) which provides maximum stability for a flowing system. Fuel and air flow distributions are intended to provide a near-stoichiometric equivalence ratio in this region to maximize stability. In many cases, especially the flameholder, the portion of the flow intercepted by the recirculation zone is small and the predominant heat releasing combustion mechanism involves reactions within the shear layer which bounds the recirculation zone (see Figure 15.4.2). The PSR portion of the flow can be thought of as providing a continuous pilot to sustain the shear layer combustion region.

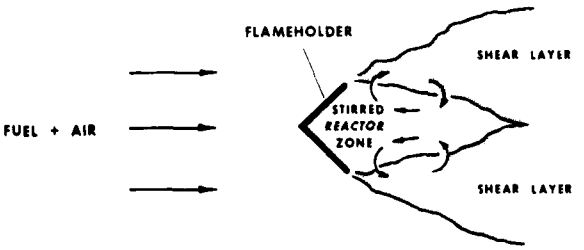

Figure 15.4.2 Physical Processes in Flameholding

Blow out of these systems can be envisioned as occurring in two phases (Refs. 15.24 and 15.25). First the less stable shear layer becomes unable to sustain itself as flow is increased and will extinguish. As previously implied, this results in the elimination of the predominant heat transfer source and causes the combustion efficiency to drop to nearly zero. The recirculation zone, being more stable, will continue to operate until $(m/VP^n)_{max}$ is reached (see Figures 15.3.4 and 15.3.5) at which time this region will also blow out. Since it represents a minor heat release factor, this final blow out point is of secondary interest.

15.4.3 Ignition

By definition, ignition is possibly only for those fuel-air mixture conditions within the flammability limits. The entire region within the flammability limits must be further

divided into two sub-regions separated by the spontaneous ignition temperature (SIT). This parameter is usually determined using a standardized test procedure where a liquid fuel is dropped into an open air container heated to a known temperature. The spontaneous ignition temperature is defined as the lowest temperature at which visible or audible evidence of combustion is observed. Typical values of SIT are listed in Table 15.4.2. Note the trend towards reduced SIT as the length of a n-paraffin chain is extended. Further the impact of side methyl groups in the case of iso-octane is to increase SIT to a level consistent with an n-paraffin of much lower molecular weight. Because these data are specific to a particular experiment, direct usage of these data as hazard criteria is not advisable. Most importantly from the combustor designer's standpoint, SIT variations due to pressure are significant. SIT decreases rapidly until approximately 2 atmospheres with apparently small changes above this pressure (15.20).

TABLE 15.4.2: Spontaneous Ignition Temperatures (From Reference 15.20).

Fuel	S.I.T. (°K)
Propane	767
Butane	678
Pentane	558
Hexane	534
Heptane	496
Octane	491
Nonane	479
Decane	481
Hexadecane	478
Iso-octane	691
Kerosene (JP-8 or Jet A)	501
JP-3	511
JP-4	515
JP-5	506

Above the spontaneous ignition temperature the key combustion characteristic is the ignition delay time. This parameter is defined as the time lag for a given fuel-air mixture to achieve significant reaction. Zero time may be defined as the incidence of initial mixing (as in a flow reactor) or of near instantaneous heating (as in a shock tube). While there are many ways to define the onset of significant reaction (dT/dt, $\Delta T/\Delta T_{max}$, etc.), the important point is that the ignition delay is exponentially related to initial temperature, T_1:

$$t_{ign} \sim \exp\ (E_a/RT_1) \qquad (15.4.8)$$

Because the ignition mechanism is not dependent on final flame temperature, t_{ign} is not strongly dependent on mixture ratio within the flammability limits. However, a strong dependence on pressure is usually observed. Ignition delay times for typical fuels are illustrated in Figure 15.4.3.

Below the spontaneous ignition temperature, an additional heat source must be utilized to allow temperatures to locally exceed the SIT. The most common method of achieving this is the spark discharge. The necessary amount of energy release to achieve ignition is called the minimum ignition energy (MIE). The quantity varies very

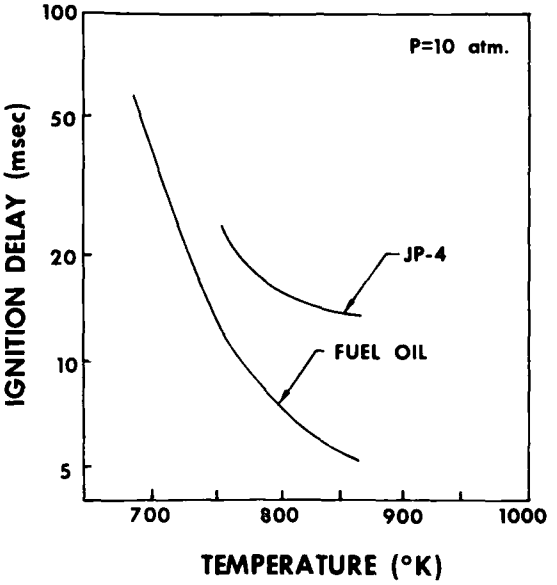

Figure 15.4.3 Ignition Delay Times for Practical Fuels.

significantly with equivalence ratio as shown in Figure 15.4.4 for the case of vapor fuel-air mixtures. It is important to note that the minimum condition is not always at a stoichiometric mixture ratio. For heavy fuels the minimum occurs closer to $\phi = 2$. Other important variables include initial mixture temperature and pressure. Finally, in the more practical case of liquid fuel spray-ignition, the extent of fuel vaporization is vital to ignition characteristics. Rao and Lefebvre (15.27) have shown that liquid fuel droplet diameter has a powerful influence on minimum ignition energy.

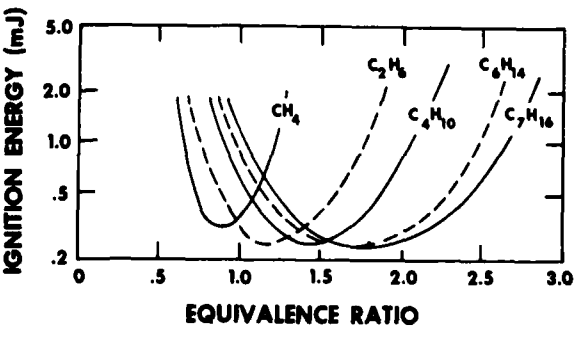

Figure 15.4.4 Minimum Ignition Energies

15.5 JET FUELS

15.5.1 Combustion Characteristics

The most fundamental of all fuel characteristics is the heat of combustion or heating value. This empirically-determined parameter represents the energy released per mass of fuel upon complete combustion when both initial and final temperatures are nearly 25°C. The actual experiment involves a combustion bomb pressurized with pure oxygen immersed in a well insulated water bath. The temperature rise of the water (usually only a few °C) is determined and the energy necessary to cause this increase for the entire system is determined. This value, which is calculated as negative for exothermic combustion reactions, is the constant volume higher heating value.

Since the experiment is performed at 25°C, condensed water from the combustion products within the bomb provides additional energy release which is included in the constant volume higher heating value. The measurement can be corrected to yield the constant volume lower heating value $(\Delta h_c)_v$ which corresponds to the energy which would have been released if the water in the combustion products had remained in the vapor phase. The constant pressure lower heating value (Δh_c), which has been previously discussed in Section 15.2.1, can then be calculated:

$$\Delta h_c - (\Delta h_c)_v = (n_p - n_R)\frac{RT}{J} \qquad (15.5.1)$$

where n_p and n_R are the number of moles of gaseous products and reactant, T is initial or final temperature (approximately 298°K), and J is the mechanical equivalent of heat. Values of Δh_c and heats of formation for typical hydrocarbons and jet fuels are shown in Table 15.5.1.

While heat of combustion differences among hydrocarbons are relatively small, changes in volatility are substantial. Fuels can range from methane (boiling point of -161°C) to heavy liquid hydrocarbons containing napthalene (boiling point of 211°C). In non-aircraft turbine applications, future fuel candidates include even residual oils (which have non-volatile components). Common aircraft turbine fuels, however, are a blend of many hydrocarbons and their volatility is usually characterized by a distillation curve as shown in Figure 15.5.1.

The chemical composition of common jet fuels is extremely complex. The hundreds of hydrocarbon types present are often categorized into three groups, paraffins, olefins, and aromatics. Paraffins are the straight chain or cyclic saturated molecules like propane, butane, or cyclohexane. These are generally very clean burning fuels (low soot formation). Olefins are characterized by the presence of a carbon-carbon double bond as occurs in ethylene. These compounds are suspected of causing gum and stability problems in jet fuels. Aromatics are molecules containing unsaturated ring structures. These may be single ring (e.g. benzene) or polycyclic (e.g. napthalene) in nature. The combustion of aromatic fuels is likely to cause problems associated with carbon particle formation, flame radiation and exhaust smoke.

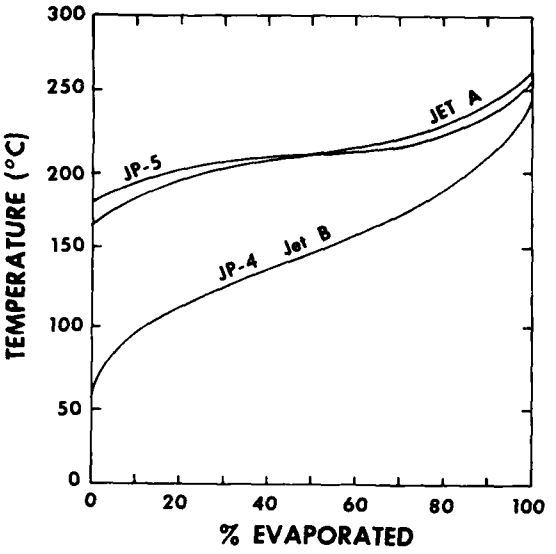

Figure 15.5.1 Distillation Characteristics of Common Jet Fuels.

A final important fuel characteristic from the handling, crash hazard, and tactical vulnerability standpoints is the flash point. This parameter is empirically determined using a controlled temperature container partially filled with fuel. A small flame is passed over the fuel/air mixture. The minimum temperature at which some evidence of ignition is observed is defined as the flash point. It has been demonstrated that this temperature corresponds to conditions where the equilibrium vapor/air mixture above the liquid fuel is at the lean flammability limit. This characteristic is illustrated in Figure 15.4.1.

15.5.2 Common Jet Fuels

Three jet fuel types are in wide use throughout the free world. JP-4 is the fuel used by the air forces of NATO, including the United States. Jet B, a fuel nearly identical to JP-4, is used by Canadian commercial airlines. These fuels can be grossly represented as a blend of kerosene and gasoline. The high volatility of JP-4 results in a vapor pressure of about 0.17 atm (2.5 psia) at 310°K (100°F), and a flash point of approximately -25°C.

Jet A is the kerosene-based fuel used by most of the world's commercial airlines, including the United States. It has a much lower volatility than JP-4 resulting in a flash point of about 52°C. Because of the reduced probability of post crash fires and the reduction of combat vulnerability, the NATO nation air forces are considering conversion to JP-8. This fuel is nearly identical to Jet A-1, a commercial fuel similar to Jet A in all respects except freeze point (-50°C versus -40°C for Jet A). The combustion characteristics of JP-8, Jet A, and Jet A-1 are virtually identical.

The unique problems associated with shipboard jet fuel use cause the U.S. Navy to use a third fuel type, JP-5, which has an even higher flash point (>63°C).

TABLE 15.5.1: Heats of Combustion and Formation
(From Reference 15.1)

Name	Formula	Molecular Weight	$-\Delta h_c$ Constant Pressure Lower Heating Value (cal/gm)	Δh_f Heat of Formation (cal/gm)
Methane	CH_4	16.04	11,946	1115
Ethane	C_2H_6	30.07	11,342	739
Propane	C_3H_8	44.09	11,072	563
n-Butane	C_4H_{10}	58.12	10,925	513
Isobutane	C_4H_{10}	58.12	10,897	541
n-Pentane	C_5H_{12}	72.15	10,744	573
n-Hexane	C_6H_{14}	86.17	10,685	551
n-Heptane	C_7H_{16}	100.20	10,643	535
n-Octane	C_8H_{18}	114.22	10,611	523
2,2,4-Trimethylpentane	C_8H_{18}	114.22	10,592	542
n-Nonane	C_9H_{20}	128.25	10,587	
n-Decane	$C_{10}H_{22}$	142.28	10,567	
n-Tetradecane	$C_{14}H_{30}$	198.38	10,515	
n-Hexadecane	$C_{16}H_{34}$	226.43	10,499	
n-Pentatriacontane	$C_{35}H_{72}$	492.93	10,573	
Ethylene	C_2H_4	28.05	11,264	-445
Propylene	C_3H_6	42.08	10,935	-116
Isobutene	C_4H_8	56.10	10,759	60
Octene	C_8H_{16}	112.21	10,556	
Cyclopentane	C_5H_{10}	70.13	10,458	
Cyclohexane	C_6H_{12}	84.16	10,376	
Benzene	C_6H_6	78.11	9,588	-150
Toluene	C_7H_8	92.13	9,680	-31
x-Xylene	C_8H_{10}	106.16	9,748	-55
Methyl alcohol	CH_3OH	32.0	4,802	
Ethyl alcohol	C_2H_5OH	46.0	6,447	
Propyl alcohol	C_3H_7OH	60.0	7,388	
Butyl alcohol	C_4H_9OH	74.1	7,936	
Acetylene	C_2H_2	26.04	11,518	-2,080
Hydrogen	H_2	2.016	28,651	0
Carbon (solid, graphite)	C	12.01	7,826	0
Carbon (coke) to CO_2	C	12.01	8,077	0
Carbon (coke) to CO	C	12.01	2,467	0
Carbon Monoxide	CO	28.01	2,413	
JP-4	$CH_{2.02}$		10,389	476
JP-5	$CH_{1.92}$		10,277	458
JP-8/Jet A/Jet A-1	$CH_{1.94}$		10,333	428

The physical and chemical properties of these fuels are illustrated in Table 15.5.2. Yearly consumption figures for 1974 have also been shown.

15.6 SUMMARY

This chapter has reviewed fundamental concepts necessary for the understanding of aeropropulsion combustion. Two additional chapters will consider the practical application of this information to mainburners (Chapter 20) and afterburners (Chapter 21). Much of this chapter has reflected the theme that the subject of combustion involves interdisciplinary study of chemistry, thermodynamics, and gas dynamics.

Key topics to the study of combustion chemistry are reaction rates, equilibrium considerations, and the mechanisms of hydrocarbon-air combustion. The Arrhenius relationship, which describes the basic dependencies of reaction rate on pressure, temperature, and concentration, has been highlighted and its impact on combustion systems has been described. CO_2 and H_2O dissociation and the water gas relationship are the primary equilibrium considerations. Current understanding of hydrocarbon combustion has been reviewed. This complex process can be envisioned as a sequence of events involving hydrocarbon pyrolysis and partial oxidation to H_2 and CO, chain branching reaction resulting in H_2 consumption, and CO oxidation by OH radicals generated during chain branching.

Combustion thermodynamics involves relating energy release from fuel consumption to combustion product effects. For constant pressure systems, the first law of thermodynamics implies conservation of total enthalpy across the reacting system. Using this relationship, definitions and methods of calculating flame temperature have been offered. Theoretical flame temperature, calculated assuming no dissociation, has been used to explain the effects of initial temperature, fuel-air ratio, fuel type, and extent of vitiation. Methods of more accurate flame temperature calculation, including dissociation effects, have been presented and the above-described effects were illustrated.

TABLE 15.5.2: Important Jet Fuel Properties

Property	JP-4 Spec Reqm't	JP-4 Typical Value	JP-8 (Jet A-1) Spec Reqm't	JP-8 (Jet A-1) Typical Value	JP-5 Spec Reqm't	JP-5 Typical Value
Vapor Pressure (atm) @ 38°C (100°F)	.13 - .2	.18	--	.007	--	.003
Initial Boiling Point (°C)	--	60.	--	169.	--	182.
End Point (°C)	--	246	288	265	288	260
Flash Point (°C)	--	-25	>49	52	>63	65
Aromatic Content (% Vol)	<25	12	<20	16	<25	16
Olefinic Content (% Vol)	< 5	1	--	1	--	1
Saturates Content (% Vol)	--	87	--	83	--	83
Net Heat of Combustion (cal/gm)	>10,222	10,388	>10,222	10,333	>10,166	10,277
Specific Gravity	0.751 - 0.802	.758	0.755 - 0.830	0.810	0.788 - 0.845	0.818
U.S. Yearly Consumption (10^9 gal)		5		12		1

Gas dynamics and diffusion processes affecting combustion have been described. Premixed laminar flames have been discussed and the dependence of propagation rate on temperature and especially fuel-air ratio have been highlighted. In the case where fuel and air are not initially mixed, rates of fuel and oxygen diffusion into the flame region control the burning rate. Key properties of diffusion flames and methods of analyzing laminar systems have been reviewed. The impact of turbulence on premixed and diffusion flames has been discussed. In the case of premixed systems, flame propagation rates are enhanced. In the case of diffusion flames, combustion zone mixing rates are increased, resulting in greater burning rates. Finally, a model of the ultimate turbulent system, the perfectly stirred reactor, has been offered. In this system, mixing rates are instantaneous relative to chemical kinetic effects and uniform temperature and species concentration exist throughout the reactor. This perfectly stirred reactor analysis has indicated important dependencies of such a system on temperature, mixture ratio, and combustion kinetics.

Combustion parameters of importance to aeropropulsion have been reviewed and explained using the fundamental information regarding chemistry, thermodynamics, and gas dynamics presented in earlier sections. Parameters which have been reviewed are combustion efficiency, flame stabilization, and ignition. Combustion efficiency has been defined and related to both exhaust temperature and species concentration. Flame stabilization has been discussed relative to the definition of flammability (which applies to a quiescent system), as well as to the basic processes occurring in flameholder or primary zone regions. In the latter case, the roles of the recirculation and shear layer zones have been highlighted. Ignition has been discussed in terms of spontaneous ignition temperature, ignition delay time, and minimum ignition energy.

Finally, the important combustion characteristics of jet fuels have been defined and discussed. These include the heats of combustion and formation, volatility and distillation characteristics, and flash point. The properties of current jet fuels, JP-4 (or Jet B), JP-8 (similar to Jet A), and JP-5, have been tabulated.

15.7 BIBLIOGRAPHY AND REFERENCES

15.7.1 Bibliography

American Chemical Society, Literature of the Combustion of Petroleum, No. 20 of the Advances in Chemistry Series, American Chemical Society, Washington, DC, 1958.

Combustion Institute, Proceedings of the International Combustion Symposia, Vols. 1-15, The Combustion Institute, Pittsburgh, PA.

Fenimore, C. P., Chemistry in Premixed Flames, Pergamon Press, New York, 1964.

Frank Kaminetskii, D. A., Diffusion and Heat Exchange in Chemical Kinetics, translated by N. Thon, Princeton University Press, Princeton.

Fristrom, R. M., and Westenberg, A. A., Flame Structure, McGraw-Hill Book Company, New York, 1965.

Gaydon, A. G., and Wolfhard, H. G., Flames, Chapman and Hall, London, 1960.

Laidler, K. J., Reaction Kinetics, Vol. I, Homogeneous Gas Reactions, Pergamon Press, New York, 1963.

Laidler, K. J., Chemical Kinetics, Second Edition, McGraw Hill Book Co., New York, 1961.

Lewis, B., and Won Elbe, G., Combustion Flames and Explosions of Gases, Academic Press, New York, 1964.

Moelwyn-Hughes, E. A., Physical Chemistry, Second Revised Edition, MacMillan, New York, 1964.

Moore, W. J., Physical Chemistry, Third Edition, Prentice-Hall Inc., Englewood Cliffs, NJ, 1962.

Propulsion Chemistry Division, Lewis Flight Propulsion Laboratory, "Basic Considerations in the Combustion of Hydrocarbon Fuels with Air," edited by H. C. Barnett and R. R. Hibbard, NACA Report 1300, 1957.

Smith, M. L., and Stinson, K. W., Fuels and Combustion, McGraw Hill Book Company Inc., 1952.

Strehlow, R. A., Fundamentals of Combustion, International Textbook Co., Scranton, PA, 1967.

Swithenbank, J., Combustion Fundamentals, Air Force Office of Scientific Research, Washington, DC, February 1970.

Williams, F. A., Combustion Theory, Addison-Wesley, Reading, MA, 1965.

15.7.2 Cited References

15.1. Smith, M. L., and Stinson, K. W., Fuels and Combustion, McGraw Hill Book Co., Inc., 1952.

15.2. Edelman, R. B., Fortune, O., and Weilerstein, G., "Some Observations on Flows Described by Coupled Mixing and Kinetics," Emissions from Continuous Combustion Systems, edited by W. Cornelius and W. Agnew, Plenum Press, New York, 1972, pp 55-90.

15.3. Howard, J. B., Williams, G. C., and Fine, D. H., "Kinetics of Carbon Monoxide Oxidation in Postflame Gases," 14th International Symposium on Combustion, the Combustion Institute, Pittsburgh, PA, 1973, pp 975-986.

15.4. Mosier, S. A., and Roberts, R., "Low Power Turbopropulsion Combustor Exhaust Emissions," AFAPL-TR-73-36, Vols. 1-3, Air Force Aero Propulsion Laboratory, Wright-Patterson AFB, OH, 1974.

15.5. Fremont, H. A., Powell, H. N., Shaffer, A., and Siecia, S. N., Properties of Combustion Gases, Vols. I and II, Aircraft Gas Turbine Development Department, General Electric Co., Cincinnati, OH, 1955.

15.6. Gordon, S., and McBride, B. J., "Computer Program for Calculation of Complex Chemical Equilibrium Compositions, Rocket Performance, Incident and Reflected Shocks, and Chapman Jouguet Detonations," NASA Special Publication 273, 1971.

15.7. Zabetakis, M. G., "Flammability Characteristics of Combustible Gases and Vapors," Bureau of Mines Bulletin 627, U.S. Dept. of Interior, 1965.

15.8. Belles, Frank E., "Flame Propagation in Premixed Gases," in Literature of the Combustion of Petroleum, No. 20 of the Advances in Chemistry Series, American Chemical Society, Washington, DC, pp 166-186, 1958.

15.9. Burke, S. P., and Schumann, T. E. W., "Diffusion Flames," Ind. Eng. Chem., Vol. 20, 1928, pp 998-1004.

15.10. Dryer, F. L., "Fundamental Concepts on the Use of Emulsified Fuels," presented at the Fall Meeting of the Western States Section of the Combustion Institute, Palo Alto, California, 1975.

15.11. Brokaw, R. S., and Gerstein, M., "Diffusion Flames" Chapter VII of Basic Considerations in the Combustion of Hydrocarbon Fuels with Air, NACA Report 1300, 1957.

15.12. Rao, K. V. L., and Lefebvre, A. H., "Evaporation Characteristics of Kerosene Sprays Injected into a Flowing Air Stream," Combustion and Flame, Vol. 26, No. 3, June 1976, pp 303-310.

15.13. Lefebvre, A. H., and Reid, R., "The Influence of Turbulence on the Structure and Propagation of Enclosed Flames," Combustion and Flame, Vol. 10, pp 355-366.

15.14. Damkohler, G., Z. Elektrochem, 46, 1949, p 601.

15.15. Shchelkin, K. I., Soviet Phys-Tech Phys., 13, Nos. 9-10, 1943.

15.16. Karlovitz, B., Denniston, D. W., and Wells, F. E., J. Chem Phys., Vol. 19, 1951, p 541.

15.17. Scurlock, A. C., and Grover, J. J., Fourth Symposium (International) on Combustion, the Combustion Institute, Pittsburgh, PA, 1953, p 645.

15.18. Gerstein, J. and Dugger, G. L., "Turbulent Flames," Chapter V of Basic Considerations in the Combustion of Hydrocarbon Fuels with Air, NACA Report 1300, 1957.

15.19. Mellor, A. M., "Gas Turbine Engine Pollution," in Pollution Formation and Destruction in Flames, Vol. 1 of Progress in Combustion Science and Energy, N. A. Chigier Editor, 1975.

15.20. Gouldin, F. C., "Controlling Emmissions from Gas Turbines - The Importance of Chemical Kinetics and Turbulent Mixing," Combustion Science and Technology, Vol. 7, 1973.

15.21. Woodward, E. C., "Application of Chemical Reactor Theory to Combustion Processes," in Literature of the Combustion of Petroleum, No. 20 of the American Chemical Society Advances in Chemistry Series, 1958, pp 22-38.

15.22. Longwell, J. P., Frost, E. E., and Weiss, M. A., "Flame Stability in Bluff Body Recirculation Zones," Industrial and Engineering Chemistry, Vol. 45, 1953, pp 1629-1633.

15.23. Dynamic Science Corp., "Fire Protection Research Program for Supersonic Transport," Report No. APL-TDR-64-105, AF Aero Propulsion Laboratory, Wright-Patterson AFB, OH, 1964.

15.24. Zukoski, E. E., and Marble, F. E., Proceedings Gas Dynamics Symposium on Aerothermochemistry, p 205, Northwestern University, 1956.

15.25. Altenkirch, R. A., and Mellor, A. M., "Emissions and Performance of Continuous Flow Combustors," Fifteenth International Symposium on Combustion, the Combustion Institute, Pittsburgh, PA., 1974, pp 1181-1189.

15.26. Spadaccini, L. J., "Autoignition Characteristics of Hydrocarbon Fuels at Elevated Temperatures and Pressuees," ASME Paper 76-GT-3, 1976.

15.27. Rao, K. V. L., and Lefebvre, A. H., "Minimum Ignition Energies in Flowing Kerosene-Air Mixtures," Combustion and Flame, Vol 27, No. 1, August 1976, pp. 1-20.

15.28. Lewis, B., and Von Elbe, G., Combustion Flames and Explosions of Gases, Academic Press, New York, 1961.

15.29. Exxon Company, USA, Data Book for Designers: Fuels, Lubricants, and Hydraulic Fluids used in Aerospace Applications, Houston, TX, 1973.

Chapter 16

COMPUTATION OF TURBOMACHINERY BOUNDARY LAYERS

by H. McDonald

United Technologies Research Center
currently at Scientific Research Associates, Inc.

TABLE OF CONTENTS

CHAPTER 16 COMPUTATION OF TURBOMACHINERY BOUNDARY LAYERS

		Page
16.0	Introduction	16-1
16.1	Two-Dimensional or Axisymmetric Boundary Layers	16-2
16.1.1	Integral Methods for Predicting the Blade Boundary Layers	16-2
16.1.1.1	The Momentum Integral Equation	16-3
16.1.1.2	Skin Friction Laws and the Mean Velocity Profiles	16-4
16.1.1.3	The Temperature Profile	16-7
16.1.1.4	The Integral Thermal Energy Equation	16-12
16.1.1.5	Moment of Momentum Equation	16-12
16.1.1.6	The Turbulence Model	16-13
16.1.1.7	Concluding Remarks on Two-Dimensional Integral Methods for Blade Boundary Layers	16-17
16.1.2	Numerical Procedures for Solving the Boundary Layer Partial Differential Equations	16-18
16.1.2.1	Motivation	16-18
16.1.2.2	General Comments	16-18
16.1.2.3	Order Accuracy	16-19
16.1.2.4	Explicit and Implicit Methods	16-20
16.1.2.5	Some Factors Influencing the Choice of Numerical Method	16-21
16.1.2.6	Non-Linear Aspects	16-22
16.1.2.7	The Coupled System of Equations	16-25
16.1.2.8	Coordinate Systems and Finite Difference Grids	16-25
16.1.2.9	Starting Profiles	16-27
16.1.2.10	The Current Status of Finite Difference Boundary Layer Procedures	16-28
16.1.3	Axisymmetric (Pitch-Averaged) Boundary Layers	16-29
16.1.3.1	Motivation	16-29
16.1.3.2	The Governing Equations	16-30
16.1.3.3	The Momentum Integral Approach	16-32
16.1.3.4	The Finite Difference Approach	16-33
16.1.3.5	Concluding Remarks on the Pitch-Averaged Procedures	16-34
16.2	Three-Dimensional Boundary Layers	16-34
16.2.1	The Momentum Integral Approach.	16-35
16.2.2	The Finite Difference Approach.	16-37
16.2.3	The Extended Three-Dimensional Boundary Layer Equations	16-38
16.3	Boundary Layer Separation	16-42
16.3.1	Motivation and Background	16-42
16.3.2	The Governing Equations	16-44
16.3.3	Concluding Remarks	16-47
16.4	Turbulence Models	16-48
16.4.1	Special Problems of Flow in Turbomachinery	16-48
16.4.2	Categories of Turbulence Models	16-49
16.4.3	Algebraic Stress Models	16-50
16.4.3.1	The Outer Wake-Like Region	16-50
16.4.3.2	The Near Wall Region	16-52
16.4.3.3	The Viscous Sublayer	16-53
16.4.3.4	The Heat Transfer Coefficient	16-55
16.4.3.5	Extensions to Three Dimensions.	16-56
16.4.3.6	Summary of Algebraic Stress Models.	16-57
16.4.4	One Equation Turbulence Models.	16-57
16.4.5	Two Equation Turbulence Models.	16-60
16.5	Concluding Remarks	16-60
	References.	16-62

LIST OF FIGURES

		Page
Figure 16.1	Compressible Turbulent Velocity Defect Profiles on a Rough Surface with Heat Transfer	16-70
Figure 16.2	Temperature Law of the Wall.	16-71
Figure 16.3	Temperature Wake Component	16-72
Figure 16.4	Calculated and Measured Total Temperature Distributions	16-73
Figure 16.5	Comparison Between Computed and Measured Axial Velocity Profiles for Square Duct on the Midplane with Laminar Flow	16-74
Figure 16.6	Velocity Profiles at Selected Streamline Locations in a Separation Bubble	16-74

AD-A152 757 COST REDUCTION IN VERTICALLY RELATED INDUSTRIES: INTEGRATION VERSUS NONLINEAR PRICING(U) RAND CORP SANTA MONICA CA H C QUIRMBACH MAY 83 RAND/P-6839 5/9

UNCLASSIFIED F/G 5/1 NL

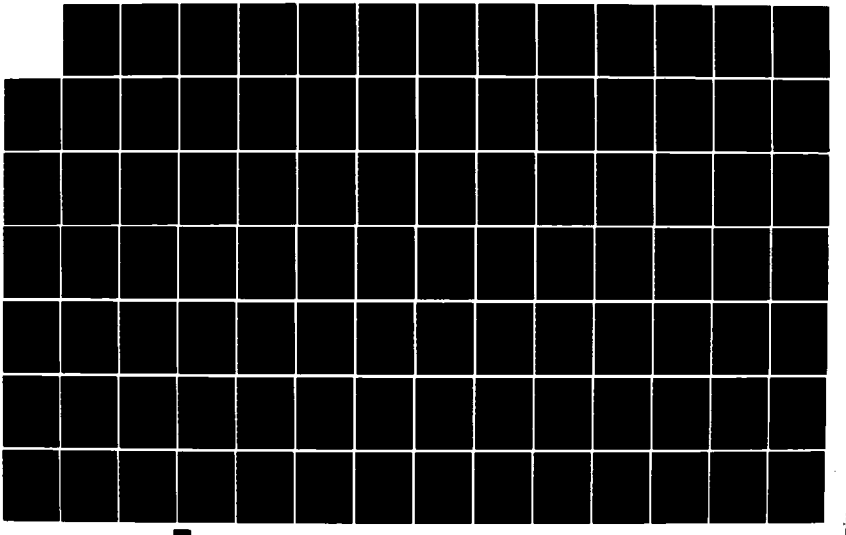

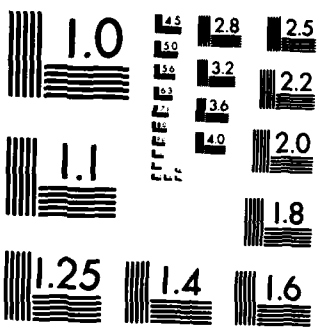

MICROCOPY RESOLUTION TEST CHART
NATIONAL BUREAU OF STANDARDS-1963-A

LIST OF FIGURES
(Continued)

		Page
Figure 16.7	Surface Pressure Distributions	16-75
Figure 16.8	Comparison Between Measured and Computed Velocity Profiles Along the Midplane of a Rectangular Duct Turning Through 90°	16-75
Figure 16.9	Selected Streamline for Duct Flow with Moving Walls	16-76
Figure 16.10	Effect of Free Stream Turbulence on the Boundary Layer Mean Velocity Profile	16-76
Figure 16.11	Heat Transfer Coefficient on the Suction Side of a Turbine Airfoil	16-77

16.0 Introduction

In this chapter the term "boundary layer" is applied very loosely in the generic sense of a shear layer which is not necessarily thin, rather than the quite precise terminology usually implied in classical external aerodynamics. Excluded from this very broad category of flows are shear layers whose behavior can be adequately described by assuming the transport of momentum or energy across streamlines of the mean flow is quite negligible. The present chapter is devoted to describing the concepts and procedures which are available to allow the prediction of the behavior of these "boundary layers" in the diverse and special circumstances found in turbomachinery.

In view of the crucial role of boundary layers in setting loss levels, heat transfer rates and operating limits, there can be no doubting the desire of the turbomachinery designer to understand and predict the behavior of these boundary layers as they are influenced by flow and geometric changes. Despite this desire, boundary layer prediction schemes are not, with minor exceptions, at present in extensive use in practical design systems. Real engines have been found to introduce complexities which cannot be allowed for in the prediction schemes and which subsequently dominate the flow behavior. Fortunately, it appears that in the near future this rather sad state of affairs will be changed, due to the combined development of efficient methods for solving multi-dimensional nonlinear systems of partial differential equations together with recent advances in the modeling of turbulent transport processes. In the subsequent sections a hierarchy of techniques will be evolved all based on using modern computers to effect the solution. The particular turbomachinery application of the various techniques will be introduced together with their current status and shortcomings and, since many of the techniques are still being evolved, a prognosis for their eventual success will be given.

In developing the solution hierarchy it is first convenient to divide the problem into its two major constituents, firstly the problem of developing then solving the set of equations purporting to describe the problem at hand and secondly the problem of describing the turbulent transport of momentum and energy to some reasonable degree of accuracy for that problem. The first part of the problem can be broken down further on the basis that certain physical approximations greatly simplify the numerical process of solving the set of equations. In particular the neglect of streamwise diffusion in the equations is usually a very good approximation. When this is followed by the assumption that the pressure forces can be approximated either locally by mass conservation, i.e., a blockage correction, and/or without an a priori knowledge of the boundary layer behavior, the governing equations for time averaged steady flow are greatly simplified, and can be solved relatively easily by forward marching procedures. Thus a solution hierarchy is developed based first of all on one, two, and three dimensional marching schemes followed by techniques in one, two, and three space dimensions which cover problems which do not permit the aforementioned simplification and require both upstream and downstream boundary conditions to be satisfied. Turbulence models are treated separately, although in the literature often a given model is associated with a particular scheme. As a practical matter the various turbulence models are usually interchangeable.

Turning to the special problems which arise as a consequence of the operating mode of the gas turbine, it turns out that the inlet conditions to many components of interest are often unsteady and more often than not contain total pressure and total temperature variations, usually distributed in a highly three dimensional manner. In a time averaged frame which could either be rotating with the blades or stationary on a stator or vane, such unsteadiness can be viewed as "inlet turbulence" with, in some instances, both ordered and random components in the motion. It is to be expected that the response of the flow to this "inlet turbulence" would vary depending on the composition of the turbulence. Primary measures of turbulence such as rms intensity and/or some spatial scale would only be expected to give some sort of zeroth order estimate of its effect. Within the device itself blades and vanes are noticeably more cambered than is usual with conventional wing sections (see Fig. 19.2.1). This camber leads to the possibility of curvature effects on the turbulence structure within the boundary layer itself, but fortunately in all but film cooled turbine blades the effect of curvature on the turbulence structure may probably be of secondary importance when compared to other unknowns. However, the camber and the consequent large amounts of flow turning, such as occurs in the turbine, can cause the annulus wall (hub and casing) boundary layers to overturn within the blade or vane passageway leading to pronounced boundary layer migrational effects which can eventually result in streamwise vortices of considerable strength (see Fig. 19.3.2). Streamwise vortices can also be produced in the region of vane or blade intersection with the annulus wall boundary layers, the so-called horse shoe vortices. The appearance and the subsequent fate of such streamwise vortices appear to have a considerable impact on the aerodynamics and heat transfer rates within the device and their presence usually signifies that conventional boundary layer concepts are no longer valid. These and related problems are discussed in Chapters 18 and 19.

Insofar as the operating conditions of the compressor and turbine are concerned it appears that in modern compressor technology the aim is to obtain higher loadings, leading to the airfoils working closer and closer to a catastrophic flow breakdown (stall) somewhere in the machine. It turns out that the operating limits of highly loaded stages are very difficult to predict and stage performance appears only loosely related to the two dimensional airfoil boundary layer characteristics. These facts have led compressor designers to place comparatively little reliance on boundary layer calculations and to develop a correlation approach based on rig tests. Turbines, on the other hand, accelerate the flow and consequently the problem of operating close to stage stall is mitigated. However, as is pointed out in Chapter 18, separation can still be a problem even in turbines. Further, the local heat transfer on the vanes or blades are of considerable design interest and dominated by the boundary layer. In view of the relative success of two dimensional boundary layer analyses in predicting the heat transfer rates in the turbine, turbine designers have come to place a greater reliance on boundary layer analyses. More recent developments in turbine technology such as even higher turbine inlet temperatures, film cooling, and higher work extraction levels per stage have led to a commensurate interest by designers in developing and using appropriate analyses. In particular the higher work extraction levels and the accompanying

high levels of flow acceleration cause extended regions of transition from laminar to turbulent flow (and vice versa) which are discussed in Chapters 18 and 19. The various practical film cooling schemes introduce three-dimensional effects and the higher turbine inlet temperatures make it necessary to know with some precision the intra-blade hub and casing heat transfer distributions.

The foregoing problems are in many ways much more difficult to treat than the boundary layer problems encountered in external aircraft aerodynamics. The wide variety of possible configurations open to the turbomachinery designer and the probable impact of the boundary layer on any selected configuration, leads one to suspect that the correlation, i.e., extrapolation approach, would be both uncertain and expensive. Further development of boundary layer analyses seems entirely justified even if it only results in an improvement in the correlation approach to the design of turbomachinery.

In the subsequent sections attention is first of all devoted to both integral and finite difference procedures for predicting the two-dimensional blade or vane boundary layers. Here the aim is to provide the means of estimating the airfoil section loss coefficient and the detailed distribution of heat transfer coefficient around the airfoil. This is followed by a discussion of the axisymmetric pitch averaged equations and the procedures available for solving this set of equations and their role in predicting the pitch averaged, i.e., circumferentially averaged hub and casing boundary layer behavior. Next the rather limited role played by conventional three-dimensional boundary layers in turbomachinery will be introduced and the available schemes, both integral and finite difference, discussed. The much enlarged capability of what is here termed the extended three dimensional boundary layer procedures, sometimes termed (rather euphemistically) the parabolized Navier-Stokes equations, will then be described and the problems of this concept discussed. The difficulties arising from boundary layer separation are then introduced and the status of the very limited number of schemes for treating this problem as rigorously as possible reviewed. Finally the problems of turbulence modeling and the current approaches to this most difficult of topics will be reviewed. Each topic is discussed from the point of view of the special problems of turbomachinery applications and the aim is to give the reader guidance in selecting an approach, concept or procedure which would be suitable for his particular problem.

16.1 Two-Dimensional or Axisymmetric Boundary Layers

The turbomachinery designer has a very profound interest in vane and blade boundary layers from heat transfer and loss point of view, as is emphasized in Chapters 18 and 19. Further, the flow in the various ducts and the resulting total pressure losses are of a similar considerable interest. In spite of the often very noticeable three-dimensional variations present in both of the foregoing instances and largely as a result of the absence up until now of better simulations, two-dimensional and axially symmetric boundary layer analyses have been applied to these problems. In the present section both integral and finite difference techniques for predicting the two-dimensional vane boundary layer behavior will be discussed. Finally the additions required to describe axisymmetric flow, both swirling and non-swirling, will be introduced.

16.1.1 Integral Methods for Predicting the Blade Boundary Layers

In view of the highly satisfactory status of methods which directly and numerically integrate the boundary layer partial differential equations of motion, it seems at first sight incongruous at this point in time to dwell upon the so-called integral procedures for predicting boundary layer development. The arguments against the further development or application of integral methods seem very persuasive. Direct numerical treatment of the governing partial differential equations of motion can now be performed routinely, and, in view of the general availability and comparatively low cost of modern computers, quite cheaply compared to, say, the cost of engineering man hours. The potential cost savings of integral procedures are dependent upon utilization and code construction and in some applications an order of magnitude reduction in an already small computing cost is not a significant factor. Ease of use is not usually a deciding factor either, since a number of the direct numerical procedures have been made to operate, upon user request, with the same identical input as integral procedures usually demand, together with such features as optional automatic grid selection. The direct procedures, by virtue of their not requiring the a priori adoption of velocity, temperature and turbulence profile families, certainly contain less empiricism than the integral methods, and, thereby focus attention upon the essential problem of the turbulent boundary layer, that is adequate specification of the turbulent transport mechanism. Finally, it is claimed by their protagonists that the direct procedures are much more general and flexible with regard to such items as boundary conditions and inlet profiles, so that such features as heat transfer, wall transpiration, rough walls and film cooling, for instance, may be readily incorporated into the procedure, subject solely to the accuracy of the boundary layer approximations and the turbulent transport model.

In spite of the foregoing, however, a case for the continued development and application of integral methods for predicting boundary layer behavior in some instances does exist. It is now becoming apparent, for example, that a whole category of flow problems arise where a rapid and often iterative estimate of the boundary layer growth is required as a sub-task in a procedure for predicting, say, the pressure field in or around a body. In such instances, provided the required degree of accuracy is attainable, the potential cost savings of the integral procedure might be very considerable and hence desirable. Although the cost savings attributed to the integral procedures are usually thought of as arising from the reduced use of the computer, the engineering labor required to code and debug an integral procedure can be one or more orders of magnitude smaller than that required by the better direct numerical procedures. However, since detailed listings of a number of satisfactory direct procedures are available in the open literature, the code construction cost savings may not be realized. Also, it does not follow that the use of empirical information, such as velocity profile families, necessarily degrades a prediction, and this is only the case when the empirical input is inaccurate or inappropriate and parameters of interest depend on the empirical input. It is true, however, that the necessity of supplying this additional empirical information does limit integral techniques to those problems where such empirical information exists

and has been suitably correlated. Here the degree of collapse to which the empirical correlations must adhere is dictated solely by the user's overall required predictive accuracy, and this, of course, is the user's perogative to decide. It does seem clear, however, that, for instance, the displacement thickness over a smooth shock-free two-dimensional unseparated airfoil without heat transfer at high Reynolds numbers may be predicted quite satisfactorily by a number of simple integral procedures. If now the problem is changed to estimate the heat transfer to the same airfoil with a rapidly varying wall temperature distribution typical of those encountered in gas turbine operations, few, if any, of the currently available integral procedures could be relied upon to provide an acceptable prediction of the heat transfer rate. The reason for the failure in the presence of heat transfer is the inadequacy of the presently available temperature profile families when the wall temperature varies rapidly.

In the subsequent discussion an attempt will be made to delineate those areas where integral methods at present might be expected to be inaccurate as a result of the inadequate additional empirical information required, relative to direct procedures. At the same time, some integral procedures possess characteristic features which are of considerable importance in the convenient application of the procedure and these desirable features will also be emphasized. Also certain integral procedures can be fashioned to permit incorporation of turbulence models of the same type as are currently being developed for the direct numerical procedures. Such features are obviously attractive and they, too, will be emphasized in the subsequent development.

16.1.1.1 The Momentum Integral Equation

As is well known, the basic technique of deriving an infinite family of integral momentum equations from the partial differential equations of motion consists of multiplying the partial differential equations by a factor $y^n u^m$ and integrating the equations in the coordinate direction normal to the wall. When n = m = 0 the von Karman momentum integral equation is obtained, and if the external flow is varying slowing in time compared to the typical turbulent velocity fluctuations (McDonald and Shamroth, Ref. 16.1) this equation can be written for compressible flow neglecting the Reynold; normal stresses as

$$\frac{\partial \theta}{\partial x} + \frac{\theta}{u_e}\frac{\partial u_e}{\partial x}(2+H) + \frac{\theta}{\rho_e}\frac{\partial \rho_e}{\partial x} + \frac{1}{u_e}\frac{\partial \delta^*}{\partial t} + \frac{\delta^*}{u_e^2}\frac{\partial u_e}{\partial t}$$

$$+ \frac{\delta^*}{\rho_e u_e}\frac{\partial \rho_e}{\partial t} - \frac{1}{\rho_e u_e}\frac{\partial \rho_e}{\partial t}\theta_\rho - \frac{1}{u_e}\frac{\partial \theta_\rho}{\partial t} = \frac{C_f}{2} + C_Q$$

16.1 (1)

where

$$\rho_e \frac{\partial u_e}{\partial t} + \rho_e u_e \frac{\partial u_e}{\partial x} = -\frac{\partial p}{\partial x}$$

$$\theta = \int_0^\delta \frac{\rho u}{\rho_e u_e}\left(1 - \frac{u}{u_e}\right) dy$$

$$\delta^* = \int_0^\delta \left(1 - \frac{\rho u}{\rho_e u_e}\right) dy$$

$$\theta_\rho = \int_0^\delta \left(1 - \frac{\rho}{\rho_e}\right) dy$$

16.1 (2)

and H is the shape factor given by δ^*/θ and

$$C_f = \frac{\tau_w}{\frac{1}{2}\rho_e u_e^2}$$

$$C_Q = \frac{(\overline{\rho v})_w}{\rho_e u_e}$$

16.1 (3)

Given the external velocity distribution $U_e(x,t)$ and external density field $\rho_e(x,t)$ from an inviscid calculation of the flow round the body displacement surface, the momentum integral equation relates the three thickness parameters and the skin friction. Obviously additional relationships must be supplied to form a determinate system. Before proceeding to develop the required additional equations some observations seem appropriate. Firstly, the axial momentum integral equation is not particularly controversial and most investigators have made it a point to base their analysis upon this foundation. Some authors include the Reynolds normal stress terms but this seems to be quite optional and to date has not proven to be a particularly crucial item, except possibly near separation where, in any event, the conventional boundary layer analysis is in difficulties. Evans and Horlock (Ref. 16.2) have pointed out that unless the integration is carried out far enough into the free stream, the fact must be taken into account that the skin friction term on the right hand side of the momentum integral equation is actually the net result of the wall stress minus the apparent Reynolds shear stress $-\overline{u'v'}$ at the $y = \delta$ point where the integration is terminated. In principle this does not cause any difficulty with the momentum integral equation since it is evident from Eq. (2) that the upper limit on the integration can be arbitrarily large for the defect thicknesses defined there. Problems can arise however with the auxiliary relationships if they involve integral thickness parameters which do depend on the location of the boundary layer edge. The problem manifests itself principally in flows where the velocity profile tails off very gradually into the free stream, such that there might be a factor in excess of 1.25 between the point at which the local velocity equaled .99 of the external stream ($y = \delta_{.99}$) and the point at which the local velocity equaled .995 of the free stream ($y = \delta_{.995}$). This long tail seems to be a characteristic of flows with a significant amount of free stream turbulence present, i.e., $T_u = (\overline{u'^2})^{1/2}/ue > .03$. The implication here is that boundary layers with this characteristic long tail should integrate out to where the Reynolds apparent shear stress is negligible compared to the wall stress. This was the approach adopted by McDonald and Kreskovsky (Ref. 16.3). As an alternative an estimate of the Reynolds stress at some convenient thickness can be made and this approach was adopted by Evans and Horlock (Ref. 16.2)

Finally it is observed that the momentum integral equation is independent of any assumption about the form of the mean velocity or temperature profile and is equally valid for laminar, transitional or fully turbulent flow. This fact is convenient in applying the momentum integral equation and leads one to seek, where possible, auxiliary equations with this same formal detail profile independence property. Detail profile independence permits the overall technique to be constructed so as to be valid for any type boundary layer flow and places the flow distinction mechanism in the more easily isolated region of turbulence model and profile specification.

16.1.1.2 Skin Friction Laws and the Mean Velocity Profiles

Turning to the auxiliary relationships to be supplied, the great majority of methods specify, often explicitly, a skin friction law which relates the integral thickness parameters θ, δ^* etc., to the skin friction coefficient c_f. Typical forms of these explicit relationships are discussed by Nash (Ref. 16.4) for incompressible turbulent flow and an apparently quite satisfactory relationship is derived by Nash and Macdonald (Ref. 16.5) for turbulent compressible adiabatic flow. Several other similar quite satisfactory explicit relationships are available in the literature for compressible unseparated flow in a pressure gradient on a smooth wall without heat transfer. Less satisfactory, however, are the skin friction laws for flows with heat transfer when either the free stream or the wall temperature is varying rapidly. As an alternative but equivalent process to assuming an explicit skin friction law, and as a result of the near wall dependence of velocity on wall friction, a skin friction law may be obtained as a by-product of the assumed velocity profile family, to be discussed in detail subsequently. This latter practice is much more consistent with the overall analysis, although not necessarily any more accurate and, of course, it does demand a velocity profile be adopted which depends on the wall friction. Certainly obtaining the skin friction from the assumed velocity profile makes a mechanical process of the extrapolation of the skin friction law into compressible flows with pressure gradients, or any other flow where the skin friction measurements to correlate are sparse, and is the procedure recommended by the present author at this time.

Turning now to the question of mean velocity profile correlations, first of all in turbulent incompressible flow, three broad classifications of approaches can be discerned. In the first of these, now largely abandoned for turbulent flows, a simple polynomial representation of the mean velocity profile is proposed, usually of the type velocity proportional to $y^{1/n}$ where n is some exponent, perhaps even an integer, which could vary with the boundary layer condition. Experience has shown that for all but the crudest of estimates the simple polynomial is inadequate. Fortunately much better representations are possible and this leads us to the second category where the correlations are based on the law of wall with an allowance for a departure from the logarithmic region in the far wall region. The best known formulation of this type is that due to Coles, and experience has shown his correlation to be remarkably accurate for a wide range of unseparated low speed flows in both favorable and adverse pressure gradients (Coles and Hirst, Ref. 16.6). Coles (Ref. 16.7) suggests a profile of the form given here for flows with surface transpiration as

$$\frac{2}{v_w^+}\left[(1+u^+v_w^+)^{1/2}-1\right] = \frac{1}{\kappa}\ln y^+ + C + \frac{\Pi}{\kappa}2(1-\cos\pi y/\delta)$$

where 16.1 (4)

$$\rho u_\tau^2 = \tau_w \qquad v_w^+ = v_w/u_\tau$$

$$u^+ = u/u_\tau \qquad y^+ = yu_\tau/\nu$$

$$C = C_o + \frac{2}{v_w^+}\left[(1+B_o v_w^+)^{1/2}-1\right] - B_o$$

16.1 (5)

B_o is Simpson's (Ref. 16.8) blowing intercept taken as 10.805 and κ is the well-known von Karman constant and C_o is the additive constant in the law of the wall, taken as .41 and 5.0, respectively by Coles for smooth walls. Π is the wake strength parameter (Coles, Ref. 16.9) and Eq. 16.1.(4) may be integrated to give the desired integral profile thickness parameters. It is also clear that if the profile is evaluated at $y = \delta$ where $u = u_e$, a skin friction law is obtained. The strength of the wake component, Π, may be eliminated from a knowledge of the integral thickness parameters. The skin friction relationship is apparently quite an awkward transcendental formulation; however, if necessary, it is easily and very efficiently solved by a Newton-Raphson scheme. Another shortcoming of the Coles profile as presented is that it is not continuous all the way to wall and is only valid outside the viscous sublayer, say for $y^+ > 50$. Coles does however present corrections to the various integral formulae to account for the neglect of the sublayer and, if needed, Waltz (Ref. 16.10) has constructed a version of Coles' profile which is continuous, all the way down to the wall. Also it should be noted that Coles' profile does not have zero gradient at the point where $y = \delta$, although this discrepancy is usually not significant in normal profile usage.

In the third and final category considerable emphasis is placed on the local equilibrium hypothesis to obtain velocity profiles. To understand this concept it is necessary to recall that an equilibrium boundary layer is a boundary layer which in a normalized sense exhibits velocity profile similarity as it develops downstream. These normalized and similar (self-preserving) profiles are functions only of a non-dimensional pressure gradient parameter β, where $\beta = \delta^*(dp/dx)/\tau_w$ and their existence in an equilibrium turbulent flow where β is constant was demonstrated by Clauser (Ref. 16.11). (A slight Reynolds number effect is to be expected for these turbulent equilibrium profiles as a result of the viscous sublayer and superlayer, but it generally may be safely neglected.) The local equilibrium hypothesis simply asserts that non-equilibrium boundary layers, characterized by non-constant values of the pressure gradient parameter β, have velocity profiles that may be described by some, as yet undetermined, equilibrium boundary layer velocity profile, regardless of the streamwise rate of change of the pressure gradient parameter. To determine the appropriate equilibrium boundary layer it is necessary to note that, as Clauser observed, equilibrium velocity defect profiles are of the form

$$\frac{u_e-u}{u_\tau} = f(y/\delta) \quad , \quad \beta = \text{const.}$$

16.1 (6)

Clauser further suggested useful integral parameters G and I for instance, where

$$G = \int_0^1 f^2 d(y/\delta) \Big/ \int_0^1 f\, d(y/\delta) = \sqrt{\frac{2}{C_f}}\,(1-1/H)$$

$$I = \int_0^1 f\, d(y/\delta) = \left(\frac{2}{C_f}\right)^{1/2}\frac{\delta^*}{\delta} \qquad 16.1\ (7)$$

and obviously an infinite sequence of integral shape parameters can be defined to relate the various commonly used integral parameters arising from the integral moment equations to equilibrium parameters. It follows that in an equilibrium boundary layer specification of the pressure gradient parameter β immediately determined the profile shape $f(y/\delta)$ and the sequence of shape parameters G, I, etc. follow. Indeed Nash (Ref. 16.12), for example, has correlated the available experimental and theoretical equilibrium profile information to obtain the relationship between the shape parameter G and the

parameter β in the form

$$G = 6.1(\beta + 1.81)^{1/2} - 1.7 \qquad 16.1\ (8)$$

and of course a similar relationship may be developed for the other parameters, I, etc. The local equilibrium hypothesis then suggests that given any one of the infinite sequence of shape parameters G, I, etc., all the others in the sequence are determined as belonging to that particular equilibrium boundary layer. The β parameter thus is no longer to be interpreted as the pressure gradient parameter but merely as a characterizing independent parameter of the velocity profile. The actual shape of the profiles may be obtained from several sources, such as the calculations of Mellor and Gibson (Ref. 16.13) or by examining the measured equilibrium flows. Usually the detailed definition of the velocity profile is not required in the prediction scheme and the velocity profile only serves to provide a relationship between the various integral thickness parameters. The user therefore can evaluate the required integral relationships in advance and express the results in simple look-up tables or in polynomials with G or β as the independent variable.

In normal usage it is much more convenient to omit the β parameter altogether and evaluate the required profile relationships with the shape parameter G as the dependent variable, as did Michel, Quemard and Durant (Ref. 16.14) for instance. Nash's skin friction law (Ref. 16.4), previously mentioned, was evolved in the foregoing spirit from equilibrium concepts proposed initially by Clauser (Ref. 16.11) and later developed by Rotta (Ref. 16.15). The general technique is closely related to the well accepted technique for predicting laminar boundary development where the appropriate equilibrium information is obtained from the Falkner-Skan solutions.

In the practical matter of accuracy there seems little to choose between the Coles' profiles and the local equilibrium profiles. Both representations have been used with considerable success by differing authors; however, on balance this author has found the Coles' representation more convenient in view of its analytic profile specification.

Insofar as the effect of compressibility is concerned the satisfactory development of two parameter incompressible velocity profile families has led to the search for a transformation technique which will reduce the compressible problem to an equivalent incompressible problem for which the existing correlations would be adequate. Two broad categories of approach have been pursued in this area and the first of these exploits the fact that since the integral approaches usually only demand a relationship between integral thickness parameters, the detailed profiles can be ignored and essentially empirical correlation techniques developed to map integral thickness relationships from incompressible to compressible flow. The well-known reference temperature methods (see for instance Rubesin and Johnson- Ref. 16.16, or the Appendix to the paper by Coles- Ref. 16.17) provide a very simple mapping of this type which might be useful in certain restricted applications. The second broad category of approach is much more ambitious and here attempts are made to define a point by point mapping of the velocity profile and develop the required integral thickness relationships and skin friction law as a consequence of the pointwise mapping. Two techniques have emerged from these efforts, both of which seem to have been sufficiently successful to justify their consideration for use in calculation schemes. The first mapping is one based on the observation of a number of investigators, for instance Waltz (Ref. 16.10), that when expressed in coordinates not containing local density (or equivalently local temperature) either implicitly or explicitly, the velocity profiles become fairly insensitive to Mach number. Winter, Smith and Gaudet (Ref. 16.18) show this to be true in the usual logarithmic region for their measurements at Mach 2.2 when they used the kinematic viscosity and density evaluated at the wall temperature in the usual law of the wall formulation for velocity. Subsequently Winter and Gaudet (Ref. 16.19) showed the wake component for their conditions also to have a Mach number independent shape. The results of this very simple mapping are quite encouraging particularly for low Mach numbers, but at the present time caution must be advocated since to date little in the way of detailed evaluation of this concept in flows with pressure gradient has been carried out.

The second mapping has been more thoroughly evaluated and is based on a transformation originally developed by Van Driest (Ref. 16.20) from mixing length arguments for the law of the wall region of the flow and subsequently found by Maise and McDonald (Ref. 16.21), following an observation by Coles (Ref. 16.22), to yield a surprisingly accurate collapse of a wide range of compressible adiabatic constant pressure boundary layer profiles including the wake region of the boundary layer. More recently Mathews, Paynter and Childs (Ref. 16.23) demonstrated that this same profile formulation gave reasonable results in adiabatic compressible flow in adverse gradients. The transformation was derived by Van Driest from the mixing length hypothesis together with the Crocco temperature profile assumption. Using the usual assumption that in a transpired boundary layer the local shear stress τ is given by

$$\tau = \tau_w + \rho v v_w \qquad 16.1\ (9)$$

the suggested form of the velocity profile for the compressible transpired boundary layer may be readily derived as

$$u^* = \frac{1}{\tilde{A}} \sin^{-1}\left[\frac{2\tilde{A}^2 u^* - \tilde{B}}{(\tilde{B}^2 + 4\tilde{A}^2)^{1/2}}\right] = \frac{1}{\kappa} \ln y^+ + \tilde{C} + \frac{\Pi}{\kappa} 2\left(1 - \cos \pi \frac{y}{\delta}\right) \qquad 16.1\ (10)$$

Π is the conventional wake component and $\tilde{C}$ is an additive constant. With negligible transpiration, i.e., $v_w^+ << \tilde{B}$ their is no ambiguity and ensuring that at low Mach numbers the conventional law of the wall is returned requires that

$$\tilde{C} = -\frac{1}{\tilde{A}} \sin^{-1}\left[\frac{\tilde{B}}{(\tilde{B}^2 + 4\tilde{A}^2)^{1/2}}\right] + C_o \quad , \quad v_w^* << \tilde{B}$$

where C_o is as defined in Eq. 16.1(5). However with significant transpiration present determining the additive constant $\tilde{C}$ becomes quite involved and in view of the uncertainty of the effect of compressibility on Simpson's blowing intercept B_o the topic is best left for future investigation.

$$\tilde{A}^2 = \frac{(\gamma-1)}{2} M_e^2 \frac{C_f}{2}$$

$$\tilde{B} = \left[\left(1 + \frac{\gamma-1}{2} M_e^2\right) \frac{T_e}{T_w} - 1\right]\left(\frac{C_f}{2} \frac{T_w}{T_e}\right)^{1/2} + v_w^* \qquad 16.1\ (11)$$

In the definition of y^+ and u_τ the kinematic viscosity and density are evaluated at the wall temperature which, although it gives reasonable results, it still is a fairly arbitrary choice of temperature. The consequent skin friction law follows immediately by evaluating the profile at $y = \delta$, just as in incompressible flow.

Recently a number of investigators have investigated the various suggested forms for the compressible velocity profile and skin friction law at hypersonic Mach number, where of course the compressibility effect is accentuated. Hopkins et al., (Ref. 16.24) and Owen and Horstman (Ref. 16.25) for instance found the Van Driest relationship given above performed acceptably for adiabatic flow and better on average than the wall temperature procedure mentioned earlier. Finally it is noted that quite satisfactory mean velocity profile predictions have been made by the numerical procedures using turbulence models which reduce to the same mixing length model that Van Driest adopted in developing his transformation. It seems plausible that provided the actual temperature profile is reasonably close to the Crocco distribution assumed by Van Driest, then the Van Driest mapping would be satisfactory, and in view of the more recent confirmatory experimental evidence, the Van Driest mapping is the recommended procedure to obtain the compressibility effect on the mean velocity profile and skin friction in turbulent adiabatic flow at the present time. In view of the poor predictions of the velocity profiles in the presence of heat transfer, noted by Maise and McDonald (Ref. 16.21) and others, the application of the Van Driest transformation to flows with heat transfer must be viewed with caution for the present and here the temperature profile may well be the culprit.

Before leaving the topic of compressibility effects on the mean velocity profile however, mention must be made of those transformations that have their roots in the Stewartson-Illingworth transformations which have proven so useful for laminar flow. This latter type of transformation seeks to obtain a rigorous mapping of the governing partial differential equations into an equivalent constant density system. The Van Driest transformation introduced earlier is of course also a transformation, but not in the same sense as implied here, since no attempt is made in the Van Driest formulation to reduce the governing partial differential equations to an equivalent constant density form. The velocity profiles in the Van Driest sense could also be regarded simply as empirical correlations. Coles (Ref. 16.26) has reviewed the status of the rigorous transformation approaches for turbulent flow and suggested some improvements. However, even Coles' improved formulation suffers from observable defects (Maise & McDonald, Ref. 16.21). The central problem is that these rigorous transformations imply a relationship between the apparent Reynolds stresses in the two fields. At one time it was felt that when a transformation was obtained which could properly relate the mean profiles in the two fields, the resulting Reynolds stress mapping would, as a consequence, be valid. Unfortunately for this approach it turned out, because of the apparent validity of Morkovin's hypothesis (Ref. 16.27) much easier to determine the effect of compressibility on the Reynolds stress than to obtain a rigorous reduction of the compressible equations of motion to an equivalent incompressible form. Indeed a satisfactory rigorous transformation technique for the turbulent boundary layer apparently does not yet exist.

Turning now to wall roughness, it turns out that with a little effort profile families based on the law of the wall generalize readily to account for wall roughness effects. The generalization follows since the direct effect of surface roughness is felt only in the vicinity of the wall and that further from the wall the flow is independent of viscosity and scales on the wall stress, but is relatively independent of how that wall stress is generated. Indeed, as Coles (Ref. 7) points out, it is virtually impossible to determine whether the wall was smooth or rough by examination of a velocity profile given in the defect form of $(u_e-u)/u_\tau = f(y/\delta)$. Similarity considerations lead to a roughness scale $k^+ = ku_\tau/\nu_w$ and the observed roughness effects are contained in the additive constant of the velocity profile C which is now symbolically written $C(k^+) = C_0-\Delta u_r^+$. The constant $C(k^+)$ is a function of the geometry of the roughness and data for various geometries has been correlated by a number of investigators. For the time being it is necessary to restrict attention to the case of zero transpiration and here following the suggestion of Clauser (Refs. 16.11, 16.28), for instance, the incompressible Coles' profile may be written

$$u^+ = \frac{1}{\kappa}\ln y^+ + C_0 + \frac{\Pi}{\kappa}\,2(1.-\cos \pi y/\delta) - \Delta u_r^+ \qquad 16.1\ (12)$$

and as a result of the observation that the fully rough wall profile scales on u^+ vs. $f(y^+/k^+)$, there results for $k^+ > 70$ say

$$\Delta u_r^+ = C_r + \frac{1}{\kappa}\ln k^+ \qquad 16.1\ (13)$$

where C_r is a constant for a particular geometry of roughness and on the basis of experimental investigations Dvorak (Ref. 16.29) suggests the correlation

$$C_r = \alpha(\log_{10}\lambda^\beta - 1) \qquad 16.1\ (14)$$

with

$$\alpha = 17.35 \quad \beta = 1.625 \quad 1 < \lambda < 4.68$$
$$= 5.95 \quad = 1.103 \quad \lambda \geq 4.68 \qquad 16.1\ (15)$$

where λ is the ratio of the total surface area to the roughness (wetted) surface area. Typically for Nikuradse's sand grain roughness C_r is near -3.4. For roughness heights in the intermediate (transitional) range of $5 < k^+ < 70$ it is necessary to fair the Δu_r^+ parameter down to zero in some reasonable manner as k^+ is reduced below 70. Note that Δu_r^+ is always positive. As before in dealing with the additive constant C it is supposed that wall temperature effects are allowed for by evaluating any of the temperature dependent parameters appearing in the roughness relations, at the wall temperature. The assumption that the compressible defect profile remains unaltered by the wall roughness appears very logical based on the incompressible arguments, and indeed Chen (Ref. 16.30) has found this to be the case using Young's (Ref. 16.31) measurements, as can be seen in Fig. 16.1. Lastly, it is observed that Simpson's (Ref. 16.8) blowing intercept B_o which determined the additive constant C for smooth wall transpiration would not be expected to hold for rough walls and to date this problem has not been resolved.

16.1.1.3 The Temperature Profile

In developing the governing integral equations the local density appears under the integral sign. Excepting the case of incompressible flow with small temperature differences it becomes necessary to determine the variation of density across the boundary layer. Since to the boundary layer approximations the static pressure is constant across the boundary layer, the gas law gives the product of local density and local temperature as constant, and so the problem becomes one of specifying the local temperature. There is little doubt however that the specification of the temperature profile across the boundary layer has been and is, the least satisfactory area of the overall problem of predicting the boundary layer behavior by an integral technique. It seems clear that if the mean velocity profile had been as poorly characterized as the mean temperature profile, investigators would have long since abandoned simple integral procedures in even greater numbers than have done so at present. The difficulty is implicit in the solution to the problem adopted by Dvorak and Head (Ref. 16.32), who, for heat transfer in low speed flow, computed the development of the velocity profile sufficiently accurately for their purposes via the very compact simple integral scheme due to Head (Ref. 16.33). However, in order to obtain a commensurately accurate solution of the energy equation Dvorak and Head felt obliged to resort to a finite difference technique with an assumed turbulent effective Prandtl number and they performed the integration of the energy equation with velocities and turbulent shear stress obtained from the momentum integral calculation. Clearly Dvorak and Head did not consider any temperature profile family known to them at that time adequate for the purpose of predicting heat transfer in the presence of a pressure gradient. However, the overall prognosis now is not quite as bleak as the preceding remarks might lead one to believe. For instance, Green (Ref. 16.34) was able to successfully extend Head's scheme to compressible flow with adiabatic walls. It follows therefore that the required and actual accuracy of the temperature profile is dependent on the flow situation and in order to clarify the areas of application and the various computational strategies it is necessary to review the entire question of determining the boundary layer temperature.

Starting with the energy equation in the form

$$\bar{\rho}\frac{\partial \bar{H}}{\partial t} - \frac{\partial \bar{p}}{\partial t} + \bar{\rho}\bar{u}\frac{\partial \bar{H}}{\partial x} + \bar{\rho}\bar{v}\frac{\partial \bar{H}}{\partial y} = \frac{\partial}{\partial y}(Q + u\tau) \qquad 16.1\ (16)$$

where H is the stagnation enthalpy defined in the usual manner as

$$\bar{H} = \bar{h} + \bar{u}^2/2$$

$$\bar{h} = \int c_p d\bar{T} \simeq c_p \bar{T} \qquad 16.1\ (17)$$

since for the usual gas turbine applications the specific heat at constant pressure may be taken as constant. The total apparent heat flux Q is defined as

$$Q = k\frac{\partial \bar{T}}{\partial y} - \bar{\rho}\,\overline{v'h'}$$

$$= (k + k_t)\frac{\partial \bar{T}}{\partial y} \qquad 16.1\ (18)$$

Where in spite of its shortcomings an effective conductivity k_t times the temperature gradient has been used to represent the velocity enthalpy transport correlation. Recalling the definition of the effective viscosity ν_t, the energy equation may be rewritten as

$$\bar{\rho}\frac{\partial \bar{H}}{\partial t} - \frac{\partial \bar{p}}{\partial t} + \bar{\rho}\bar{u}\frac{\partial \bar{H}}{\partial x} + \bar{\rho}\bar{v}\frac{\partial \bar{H}}{\partial y}$$

$$= \frac{\partial}{\partial y}\bar{\rho}\left[\left(\frac{\nu_l}{P_{rl}} + \frac{\nu}{P_r}\right)\frac{\partial \bar{h}}{\partial y} + (\nu_t + \cdot)\frac{\partial}{\partial y}\bar{u}^2/2\right] \qquad 16.1\ (19)$$

and the laminar and turbulent effective Prandtl number have been introduced where

$$P_r = \bar{\rho} c_p \nu/k \quad , \quad P_{rl} = \bar{\rho} c_p \nu_t/k_t \qquad 16.1\ (20)$$

Note that the introduction of the turbulent effective Prandtl number is not in itself controversial if the relationship given above is simply regarded as a definition of the turbulent Prandtl number. As will become evident, the usual mode of operation is, of course, quite the inverse and in a calculation scheme a turbulent Prandtl number distribution is often specified and the above relationship interpreted as a definition of the turbulent effective conductivity k_t. Viewed as a method of determining the turbulent effective conductivity the concept of a well-behaved turbulent Prandtl number is best regarded for the time being as an acceptable working hypothesis subject to very similar limitations as the mixing length hypothesis undoubtedly is for determining the turbulent momentum transport. Various definitions of the turbulent Prandtl number can be adopted for instance based upon whether the transport of static or stagnation enthalpy is used. Here static enthalpy has been adopted and Owen and Horstman (Ref. 16.25) found that this Prandtl number was much less sensitive to Mach number than that based on stagnation enthalpy. The usual arguments for the similarity of the transport mechanism for heat and momentum for a gas in both laminar the turbulent flow leads to the assumption of unit laminar and turbulent Prandtl number. If this is done the energy equation further simplifies and as Crocco pointed out for laminar flow and later Young for turbulent flow, by inspection it can be seen that the condition of constant stagnation enthalpy, $\bar{H} = \bar{H}_e = \bar{H}_w$ satisfies the energy equation. Constant stagnation enthalpy cannot allow for wall heat transfer but it does give perhaps the simplest temperature profile for an insulated wall. Actually as Crocco pointed out a more general profile can readily be determined from the energy equation by assuming that the stagnation enthalpy $\bar{H}$ is some undetermined function of local velocity alone, i.e., $\bar{H} = f(u)$. If this (similarity) assumption is introduced into the energy equation and the result compared with the momentum equation it can be seen that if the axial pressure gradient is negligible, solutions of the assumed form can be obtained if $d^2f/du^2 = 0$. Integrating twice and introducing the wall and free stream boundary conditions gives the profile

$$\bar{H}^* = \bar{H}_w + (\bar{H}_e^* - \bar{H}_w)\,\bar{u}/\bar{u}_e$$

$$= c_p\bar{T} + \bar{u}^2/2 \qquad 16.1\ (21)$$

which is the well-known Crocco quadratic temperature profile. The Crocco profile allows for wall heat transfer and it has been widely used in calculation schemes and its limitations will be discussed in

detail in a moment. Note that if the Crocco profile is differentiated to give the temperature gradient at the wall the skin friction C_f and Stanton numbers S_t can be introduced to give the relationship

$$\frac{2S_t}{C_f} = \frac{1}{P_r} \qquad 16.1\ (22)$$

where the Stanton number is defined as

$$S_t = \frac{Q_w}{\rho_e u_e (\bar{H}_e^* - \bar{H}_w)} \qquad 16.1\ (23)$$

but since it was assumed that $P_r = P_{rt} = 1$ in deriving the temperature profile, the Stanton number-skin friction relationship given by Eq.16.1(22) should have the Prandtl numbers set to unity. Normally this is not done, but in any event the ratio $2S_t/C_f$ is termed the Reynolds analogy factor.

Now having covered the preliminaries the various commonly adopted profile strategies can be reviewed. The first observation is that the assumption of constant stagnation temperature, although very convenient, can only be valid for insulated wall, if at all. Secondly the wall temperature is generally observed to fall below the free stream stagnation temperature so that if a wall recovery factor r is defined as

$$r = \frac{T_w - T_e}{T_e^* - T_e} \qquad 16.1\ (24)$$

experimentally the recovery factor in turbulent flow over an insulated wall is generally found to lie between .8 and .9, This fact obviously cannot be allowed for within the framework of a constant stagnation enthalpy.

The next level of sophistication is obviously the Crocco quadratic temperature profile, and this profile has been used extensively in calculation schemes. The Crocco profile does at least allow the wall temperature to reach its recovery value, but it will be recalled that the derivation would appear to restrict its use to boundary layers in thermal equilibrium ($T = f(u)$ alone will suffice for a definition of thermal equilibrium at this time) in the absence of streamwise pressure gradients. In view of the lack of suitable alternatives various authors have used the Crocco profile outside the region where it was observed to be a reasonable approximation to the temperature within the boundary layer. For insulated walls the results were not too unreasonable but there seems little justification for the use of the Crocco relationship in flows with heat transfer and pressure gradients. The observed results show the Reynolds analogy factor to vary widely from the value near unity deduced from the Crocco relationship and observed in constant pressure boundary layers in thermal equilibrium. In light of this there have been a number of attempts to derive modified Reynolds analogy factors but none seem at this point to be satisfactory. The search for a modified Reynolds analogy factor is motivated to a considerable degree by its convenience in application. If such a factor could be found, it would allow the heat transfer to be computed after the fact from a knowledge of skin friction. In this manner the heat transfer may be computed without overt solution of the energy equation, although of course the solution is implied in the statement that the enthalpy is a function of local velocity alone. While one might overlook measured turbulent Prandtl number being slightly different from unity, the requirement of negligible axial pressure gradient gives cause for concern and the assumption of enthalpy-velocity similarity is positively alarming. The latter assumption is obviously violated when the wall temperature varies in an arbitrary manner, such as on a cooled turbine blade. The high accelerations present on the suction side of a turbine blade jeopardize the axial pressure gradient restriction. The more recent experimental evidence is quite unambivalent. Boundary layers developing in the absence of heat transfer or pressure gradients eventually reach an equilibrium state where the temperature distribution is adequately described by a Crocco type relation. However, even in the absence of pressure gradients boundary layers which are, or have been, subjected to severe temperature variations possess temperature profiles which do not agree well with the Crocco relation until after a recovery length which could take many boundary layer thicknesses of development. The controversy over the temperature profile on a wind tunnel nozzle wall vis-à-vis the same profile measurement on a boundary layer grown in an essentially insulated flat plate (see Ref. 16.35 for discussions on this point) is a clear indication of the combined effect of favorable pressure gradients and wall temperature. The nozzle temperature profile is markedly different from the Crocco distribution and recovers very slowly even when the wall is maintained at its adiabatic temperature. Rotta (Ref. 16.26) has reviewed a number of the measurements and suggested that in spite of the measurement difficulties there were many instances where he felt it could be concluded that the Crocco distribution performed poorly, particularly in the presence of heat transfer. As a corollary, obviously the simple Reynolds analogy factor in many cases failed to predict the heat transfer. Dvorak and Head (Ref. 16.32) evidently agreed with Rotta and were led to the numerical scheme discussed earlier to obtain their temperature profile. The only positive counters that can be made to date to the preceding are the observations that first of all a Van Driest type relationship obtained using mixing length arguments and a Crocco temperature relationship correlates well with the skin friction measurements on insulated and hot or cold walls over a wide Mach number, wall temperature, and Reynolds number range (Hopkins, Ref. 16.37). Secondly, calculation methods which use a Crocco temperature relationship usually perform quite as well on insulated nonhypersonic wall boundary layer growing in an arbitrary pressure gradient as those techniques which solve the energy equation directly. Here again the users subjective judgment on acceptable accuracy enters and the existing evaluations have not normally proceeded much beyond the usual integral thickness parameter comparisons. Little in the way of evaluation has been done in similar flows with heat transfer but it seems abundantly clear that while integral thickness parameters may or may not be adequately predicted by an integral technique, the heat transfer will not be acceptable if obtained from a simple Crocco temperature profile, especially for gas turbine applications.

As a result of the dissatisfaction with the Crocco distribution for certain applications (for which it really was never meant to apply), remedies have been sought by a number of investigators. Of particular note, Cousteix, Houdeville and Michel (Ref. 16.38) developed an analogous treatment for

the temperature field to the local equilibrium concepts previously introduced for the mean velocity profile. In their treatment Cousteix et al., developed profile families of temperature (enthalpy) and velocity from predicted equilibrium boundary layers over a range of Mach numbers, wall temperature ratios and pressure gradient parameters. As with the velocity profiles in incompressible flow, the shape factor G is used to replace the pressure gradient parameter, β. Although here Cousteix et al., base the friction velocity u_τ appearing in the definition of G upon a transformed (i.e., 'incompressible') skin friction coefficient $\bar{C}_f$ and express $\bar{C}_f$ as a function of Mach number, wall temperature ratio, local Reynolds number based on a boundary layer integral thickness and shape parameter G. The formulation is, therfore, somewhat awkward but as with the Coles' incompressible skin friction law, solutions can readily be obtained by a Newton-Raphson process. Reynolds analogy factors are similarly expressed and consequently the formulation of Cousteix et al., does allow for the direct effect of pressure gradient upon the Stanton number in a reasonable manner. The principle shortcoming of this procedure is that the equilibrium solutions are, of necessity, obtained with a specified variation of wall temperature. The pathological case of a rapid variation in wall temperature, such as might occur on a turbine blade in passing over a cooling labyrinth, is still not properly accounted for in this procedure. The interested reader can refer to the original work for the detailed formulae.

The last technique which will be discussed here, although not completely developed at the present time, is very promising and apparently works well in simple flows. The basic idea involved is to develop a temperature profile analogous to the law of the wall - law of the wake profile for velocity. The idea has considerable merit both from similarity and/or mixing length arguments if the concept of a well-behaved turbulent Prandtl number is tenable. A few preliminaries are involved and in view of the fact that this approach has probably the best chance of success, these preliminaries will be explained in detail. First of all a temperature law of the wall can be obtained using mixing length or similarity arguments using the previously introduced relationships

$$Q = k_T \frac{\partial T}{\partial y} \quad , \quad P_{rt} = \frac{\bar{\rho} C_p \nu_t}{k_t}$$

16.1 (25)

and defining heat flux parameter Q_T analogous to the friction velocity u_τ as

$$Q_w = \bar{\rho}_w C_p u_\tau Q_T$$

16.1 (26)

If it is now assumed that across the wall region of the flow the local total stress τ does not vary ($\approx \tau_w$), the static temperature gradient outside the viscous sublayer but within the fully turbulent wall region of the flow is written after a little manipulation as

$$\frac{1}{P_{rt}} \left(\frac{\rho}{\rho_w}\right)^{1/2} \frac{dT^+}{dy^+} = \frac{1}{\kappa y^+} (1 - A_Q u^+)$$

16.1 (27)

where it has been assumed that

$$Q = Q_w - u\tau_w$$

$$T^+ = T/Q_T$$

$$A_Q = \tau_w / (\bar{\rho}_w C_p Q_T)$$

16.1 (28)

and the relationship $\nu_t = \ell u_\tau (\bar{\rho}_w/\bar{\rho})^{1/2}$ has been introduced. Using now the definition of stagnation temperature and differentiating one obtains

$$\frac{dT^+}{dy^+} = \frac{dT^{0+}}{dy^+} - A_Q u^+ \frac{du^+}{dy^+}$$

16.1 (29)

and recalling the compressible law of the wall, one can write

$$\left(\frac{\rho}{\rho_w}\right)^{1/2} \frac{du^+}{dy^+} = \frac{1}{\ell^+}$$

16.1 (30)

and consequently the stagnation temperature can be used to reduce the thermal equation to

$$\left(\frac{\rho}{\rho_w}\right)^{1/2} \frac{dT^{0+}}{dy^+} = \frac{P_{rt}}{\ell^+} \left[1 - A_Q u^+ (1 - 1/P_{rt})\right]$$

16.1 (31)

with the consequent simplification when $P_{rt} = 1.0$ of

$$\left(\frac{\rho}{\rho_w}\right)^{1/2} \frac{dT^{0+}}{dy^+} = \frac{1}{\ell^+}$$

16.1 (32)

and by comparison with the compressible velocity law of the wall there results

$$T^{0+} = u^+ + C_0$$

16.1 (33)

The linear stagnation temperature - velocity profile relationship thus derived is quite intriguing. It follows immediately that the Van Driest compressible velocity law of the wall can be used to describe the stagnation temperature. However, for the record, we can proceed and integrate to obtain the stagnation temperature law of the wall directly. First of all, the density ratio can be expressed in terms of the stagnation temperature using the linear velocity-stagnation temperature relationship developed previously together with the assumption of a negligible static pressure gradient normal to the wall and this results in

$$\frac{\rho}{\rho_w} = \frac{T_w}{a_0 (T^{0+})^2 + a_1 (T^{0+}) + a_2}$$

16.1 (34)

where

$$a_0 = -A_Q Q_T / 2 = u_\tau^2 / 2C_p$$

$$a_1 = Q_T (1 + A_Q C_0)$$

$$a_2 = -C_0^2 A_Q Q_T / 2 = -C_0^2 u_\tau^2 / 2C_p$$

16.1 (35)

Now using a mixing length $\ell^+ = \kappa y^+$ the temperature profiles integrate out to give

$$\frac{-T_w^{1/2}}{(-a_0)^{1/2}} \sin^{-1}\frac{2a_0T^{**}+a_1}{(a_1^2-4a_0a_2)^{1/2}} = \frac{1}{\kappa}\ln y^* + B_Q$$

16.1 (36)

As with the compressible velocity law of the wall the profile given above can be reinterpreted as a temperature transformation of the form

$$\frac{T^*}{Q_T} = \frac{-T_w^{1/2}}{(-a_0)^{1/2}} \sin^{-1}\frac{2a_0T^{**}+a_1}{(a_1^2-4a_0a_2)^{1/2}} + \frac{T_w^{1/2}}{(-a_0)^{1/2}} \sin^{-1}\frac{a_1}{(a_1^2-4a_0a_2)^{1/2}}$$

16.1 (37)

where T^* is the transformed, i.e., "incompressible" value of stagnation temperature. Insofar as the constants C_Q and B_Q are concerned, Rotta (Ref. 16.36) previously suggested an intercept relationship, while not for precisely the same linear profile as is given by Eq. 16.1 (33), nevertheless sufficiently close that it could be used herein, of the form

$$C_Q = \beta_Q(1 + 3.4\beta_Q - 0.2M_\tau)$$

16.1 (38)

where

$$M_\tau = M_e\sqrt{\frac{C_f}{2}}$$

$$\beta_Q = Q_w/(\rho_w C_p u_\tau T_w) = 1/T_w^*$$

16.1 (39)

The remaining constant B_Q takes on values identical to the same constant in the mean velocity profile, that is about 5.0, according to McDonald and Owen (Ref. 16.39). A comparison of this temperature profile to data is given in Fig. 16.2 and in this zero pressure gradient flow the results are very satisfactory. The similarity of the transformed temperature profile to the mean velocity prompts the hypothesis that a wake component of temperature might exist such that

$$B_Q = \frac{2\Pi}{\kappa}\left(1 - \cos\frac{\pi y}{\delta_T}\right)$$

16.1 (40)

where δ_T is the thickness of the thermal boundary layer. Although the initial results are encouraging (as can be seen in Fig. 16.3) further evaluation of this hypothesized profile is required. Initial unpublished results by McDonald and Owen in pressure gradient flows indicate that apart from an apparent variation of C_Q with pressure gradient the proposed log law holds up quite well.

The compressible temperature law of the wall given by Eq. 16.1 (36) is apparently not widely known or used. Before going on, it should be noted that the temperature profile given by Eq. 16.1 (36) has been derived somewhat obliquely by assuming a unit turbulent Prandtl number. An alternate derivation can be made by neglecting A_Q in Eq. 16.1 (27) and simplifying for small temperature differences. The central point is that in the alternate derivation the assumption is made that the local apparent heat flux Q is constant in the near wall region and equal to the wall heat flux Q_w whereas in the derivation given here leading to Eq. 16.1 (36) the local apparent heat flux is given by $Q = Q_w - u\tau_w$. Certainly the experimental evidence cited by Meir and Rotta (Ref. 16.40) clearly favors the $Q = Q_w - u\tau_w$ assumption used here.

Rotta (Ref. 16.41) developed a similarly motivated but slightly different thermal law of the wall starting from the relationship

$$T^* - T_w = \Delta T^* = \frac{\kappa}{\kappa_T}(u^* - C_Q) + C_T$$

16.1 (41)

Taking the accepted values .4 for κ, .5 for κ_T, a value of 5.0 for C_Q smooth wall and a value of 4.0 for C_T gives a net additive constant of zero, although for the moment this fact will not be used. If now Rotta's previously used parameter β_Q is introduced, the static temperature profile at low speeds in the region of the wall can now be written

$$\frac{T}{T_w} = 1 + \beta_Q u^* \frac{\kappa}{\kappa_T} + \beta_Q\left(C_T - C_Q\frac{\kappa}{\kappa_T}\right)$$

16.1 (42)

In developing his thermal profiles Rotta added a wake contribution to the above profile of strength B' and distribution $(e^{-3F_D})^{3/4}$ where

$$F_D = \frac{u_e - u}{u_\tau}\left(\frac{T_w}{T_e}\right)^{1/2}$$

16.1 (43)

The strength of the temperature wake component B' may be determined by evaluating the profile at the boundary layer edge, that is

$$B' = \frac{T_e}{T_w} - 1 - \frac{\kappa}{\kappa_T}\beta_Q\left(\frac{T_e}{T_w}\frac{2}{C_f}\right)^{1/2} - \beta_Q\left(C_T - C_Q\frac{\kappa}{\kappa_T}\right)$$

16.1 (44)

The resulting profile was shown by Rotta to be in very good agreement with some low speed data. Actually Rotta was a little more general in his derivation than implied by the above and he generated a temperature profile which did not necessarily require the velocity and temperature to have the same (logarithmic) functional dependence on y^+. Note that as given by Rotta the temperature profile thickness cannot exceed the velocity profile thickness, and this might prove an embarrassment in a highly accelerated flow.

Rotta has yet to apply this same concept to high speed flow but several points do seem appropriate. Firstly Eq. 16.1 (42) does give rise to a logarithmic stagnation temperature profile for moderate to small stagnation temperature ratios, of the form

$$T^{**} - T_w^* = \frac{1}{\kappa_T}\ln y^* + C_T$$

16.1 (45)

or, if Rotta's wake contribution is added

$$\frac{T^*}{T_w} = 1 + \frac{\beta_Q}{\kappa_T}\ln y^* + \beta_Q C_T + B'e^{-3F_D^{3/4}}$$

16.1 (46)

and as before one could now replace the $\ln y^+$ term in the temperature profile by the compressible law of

the wall derived earlier. This poses an additional minor problem however, since the compressible law of the wall, it will be recalled, was obtained by introducing the Crocco temperature profile to enable the velocity profile to be obtained by integration via the mixing length hypothesis. In more general terms the mixing length analysis gives the velocity profile as

$$\int_{ref}\left(\frac{\rho}{\rho_w}\right)^{1/2} du^* = \frac{1}{\kappa}\ln y^* + C$$

16.1 (47)

and the Van Driest law of the wall emerges when it is assumed that the static pressure is constant across the wall region and the temperature is given in accordance with the Crocco profile. For modest heat transfer rates and Mach number, Rotta suggested that the density ratio would vary less than the velocity in the law of the wall region, leading him to suggest a compressible law of the wall of the form

$$\left(\frac{\rho}{\rho_w}\right)^{1/2} u^* = \frac{1}{\kappa}\ln y^* + C$$

16.1 (48)

and the experimental evidence leads one to believe that this is quite a reasonable approximation. If Rotta's form of the compressible law of the wall is inserted into the stagnation temperature law of the wall - law of the wake profile there results the relationship

$$\frac{T^*}{T_w} = 1 + \beta_q\frac{\kappa}{\kappa_T}\left(\frac{\rho}{\rho_w}\right)^{1/2} u^* + \beta_q\left(C_T - \frac{\kappa}{\kappa_T}C\right) + B' e^{-3r_D^{3/4}}$$

16.1 (49)

and as with the low speed static temperature profile, the wake contribution B' is readily evaluated from the assumed profile value at the edge of the layer. Note that for an insulated wall the wake contribution B' is related to the recovery factor r defined earlier. Meir and Rotta (Ref. 16.40) present a number of measured stagnation temperature profiles plotted against $M_T = u^+(\rho/\rho_w)^{1/2}$ in the Mach number range 2.5 - 4.5 and the resulting linear behavior is quite remarkable, as can be seen in Fig. 16.4. A similar plot at low speed (Ref. 16.41) also demonstrated the same linear behavior and, as mentioned previously, the intercept (additive constant) was close to zero. However, not surprisingly, in view of the kinematic viscosity temperature dependence, the additive constant appears to exhibit a local temperature dependence so that at high speeds

$$\beta_q\left(C_T - \frac{\kappa}{\kappa_T}C\right) \sim .03\ ,\ \beta_q \sim -1.\times 10^{-3}$$

16.1 (50)

The implication of the additive constant being nonzero is twofold. First of all, the absolute magnitude is small but significant, it being apparent that if the linear behavior were extrapolated back to zero velocity the temperature intercept would give a temperature value of 0.97 as opposed to unity for zero additive constant. Secondly, the velocity profile evidence would lead one to believe that C_T is exhibiting the dependence on β_q as opposed to C, the velocity profile intercept, although the evidence is not at all conclusive. If it is the temperature intercept C_T that is varying, its variation is certainly very large, going from a value of 4.0 to a value of 35.0 in the Meir-Rotta experiments. Rotta's calculations at low speed indicate a modest variation of the temperature intercept with β_q the heat transfer parameter, giving a value of C_T near 9 for a value of β_q of -.03. It would appear that C_T was also varying with some Mach number parameter to give rise to the value of 35.0 when β_q was in the region of -.001 at a free stream Mach number of between 2.5 and 4.5. Obviously, this point must be clarified before extensive use of the temperature law of the wall - law of the wake is to be recommended.

Several additional points should also be made concerning the stagnation temperature law of the wall. The first of these points concerns the relationship to the Crocco distribution, which many investigators have shown to be valid in certain restricted classes of boundary layer. A cursory examination of the stagnation temperature law of wall shows that the replacement of $\ln y^+$ by Rotta's suggested compressible law of the wall velocity gives rise to a term in $u^+(\rho/\rho_w)^{1/2}$ which is implicitly a non-linear u velocity term and is in conflict with the simple u^+ dependence which would arise from the Crocco distribution. It should be recalled from the section of the compressible velocity profile, however, that Winter, Smith and Gaudet (Ref. 16.18) have shown a very simple law of the wall not containing the $(\rho/\rho_w)^{1/2}$ term gives a reasonable representation of the insulated wall compressible profiles in the low to moderate supersonic Mach number range. It is further recalled that Maise and McDonald (Ref. 16.21) obtained a satisfactory collapse of the insulated wall velocity profile data using the Van Driest compressible coordinates which again differs from both the Winter, Smith and Gaudet and Rotta suggestions. The foregoing would seem to indicate that the $(\rho/\rho_w)^{1/2}$ term was not causing a first order effect in the insulated wall velocity profiles and hence for non-hypersonic boundary layers with low heat transfer rates it could be expected that the stagnation temperature law of the wall profile would exhibit a near linear velocity dependence, consistent both with observation and the Crocco relationship.

To conclude, although a logarithmic temperature profile is observed in many cases in both the slope $1/\kappa_T$ and the additive constant C_T show considerable scatter even within a given experiment. Even though the experiment is not easy to perform the question must arise then as the validity of the hypothesis on which the profile has been derived and/or the departure from equilibrium arising from the thermal history of the flow. To date neither of these questions have been satisfactorily explored or answered. It must be noted, however, that the success of direct numerical schemes using mixing length and turbulent Prandtl number concepts leads one to suspect the other approximations should the logarithmic profile not be observed. Obviously a great deal of additional work remains to be performed so that the temperature profile may be placed on the same footing as the mean velocity profile. In the interim the stagnation temperature law of the wall using wake component, Eq. 16.1 (33), would seem the procedure of choice, with perhaps a wake component added. Of course the introduction of an additional parameter, the wall heat transfer parameter β_q, in both this profile and the profile of Coustelx et al., requires the introduction of an additional determining relationship, and for this the integral thermal energy equation will be introduced.

16.1.1.4 The Integral Thermal Energy Equation

The integral thermal energy equation in determining heat transfer plays an analogous role to the von Karman momentum integral equation and its role in determining the skin friction. In the skin friction case, the von Karman equation could be used to determine the magnitude of the skin friction after the fact if the streamwise behavior of the various integral thicknesses together with the axial pressure were known. In practice the equation is not used in this manner, even if it were possible, in view of the known inaccuracies inherent in this approach, and instead the various integral thicknesses are related one to another and to the skin friction by means of the assumed velocity profile or equivalently by the skin friction law. In this fashion the von Karman equation can be recast either implicitly or explicitly as a differential equation for the skin friction and the local skin friction obtained accurately by streamwise integration. A precisely equivalent treatment of the integral thermal energy equation can be adopted and Cousteix et al., (Ref. 16.38) provide a heat transfer (Stanton number) relationship which depends on the local flow and the various integral thickness parameters. Use of the relationship of Cousteix et al., reduces the integral thermal energy equation to implicit differential equation for the wall heat transfer. On the other hand a stagnation temperature law of the wall with a Rotta type wake component allows the integral thermal energy equation to be reduced to an explicit differential equation for the heat transfer.

The integral thermal energy equation is readily derived by integrating the energy equation, Eq. 16.1 (16), from the wall to the free stream to give

$$\frac{1}{\rho_e u_e}\frac{\partial}{\partial t}\rho_e\delta^*_H + \frac{\delta}{\rho_e u_e}\frac{\partial p}{\partial t} + \frac{1}{\rho_e u_e}\frac{\partial}{\partial x}\rho_e u_e \theta_H = C_Q \frac{\bar{H}_e - \bar{H}_w}{\bar{H}_e - \bar{H}_{ref}} + S_t$$

16.1 (51)

where

$$\delta^*_H = \int_0^\delta \frac{\bar{\rho}}{\bar{\rho}_e}\frac{\bar{H}_e - \bar{H}}{\bar{H}_e - \bar{H}_{ref}}\,dy$$

$$\theta_H = \int_0^\delta \frac{\bar{\rho}\bar{u}}{\bar{\rho}_e u_e}\frac{\bar{H}_e - \bar{H}}{\bar{H}_e - \bar{H}_{ref}}\,dy$$

16.1 (52)

where θ_H is termed the enthalpy thickness and the Stanton number definition has been generalized to

$$S_t = \frac{Q_w}{\rho_e u_e (\bar{H}_e - \bar{H}_{ref})}$$

16.1 (53)

In the above derivation the free stream stagnation enthalpy is assumed constant although this assumption can readily be relaxed. Rotta's heat transfer parameter (Ref. 16.41) introduced earlier is related to the above defined Stanton number by

$$\beta_q = \frac{Q_w}{\rho_w \bar{H}_w u_\tau} = \left(\frac{\bar{\rho}_e}{\bar{\rho}_w}\frac{2}{C_f}\right)^{1/2} \cdot \frac{\bar{H}_e - \bar{H}_{ref}}{\bar{H}_w} \cdot S_t$$

16.1 (54)

The implementation of the energy equation is best visualized from a predictor-corrector point of view. At a given streamwise location with a steady external flow the current values of the problem parameters such as skin friction coefficient, Stanton number, momentum thickness, etc., can be used to integrate the momentum and energy integral equations, to yield the values of the dependent integral thicknesses at the next streamwise station. These new level thicknesses can be used in collaboration with the mean velocity and temperature profiles to yield new level skin friction, Stanton number and all the other integral thickness parameters. Thus a corrector step can be taken where the required information can now be taken as the average of the new and current station values.

16.1.1.5 Moment of Momentum Equation

It is quite clear that the use of a two parameter velocity profile, either that based on Coles' profile or that obtained from the local equilibrium hypothesis, demands one more relationship in addition to the momentum integral equation in order to specify the second profile parameter, provided of course that one of the velocity profile parameters does contain the skin friction. Various forms of auxiliary relationships have been employed and a number are discussed by Rotta (Ref. 16.15) and many examples are to be found in the Stanford Conference Proceedings. The entirely empirical auxiliary relationships will not be considered further herein, mainly because they have been largely abandoned by the research community as a consequence of their inherent limitations which are liable to be very severe in gas turbine applications. The remaining auxiliary relationships are usually derived by taking integral moments of the axial momentum equation. As mentioned earlier this process is formalized by multiplying the boundary layer partial differential equations of motion by $y^n u^m$ and integrating, either partially or entirely across the boundary layer. When $n = 1$, $m = 0$ the y-moment of momentum equation is obtained and this equation has been used by a number of authors quite successfully. When $n = 0$, $m = 1$ the kinetic energy integral equation is obtained and again this equation has found favor with a number of investigators. At one time it was felt by a number of individuals that the y-moment equation was to be preferred to the kinetic energy equation in spite of the fact that the y-moment equation does not integrate out neatly in terms of the accepted integral thickness parameters until a velocity profile is specified. Even then in incompressible flow with a two parameter velocity profile such as Coles', the resulting differential equation is quite clumsy. The argument against the use of the kinetic energy integral equation was simply that for many turbulent flows the velocity varies slowly above the sublayer so that the u-momentum equation has a tendency to approach a constant times the momentum equation, which ultimately would lead to indeterminacy when the momentum and kinetic energy equations were solved simultaneously to predict boundary layer behavior. In view of the apparent lack of difficulty experienced by users of the kinetic energy integral equation it would appear that these fears are unfounded.

It turns out, however, that linear dependence within the system of equations can and does occur; that is, for some set of conditions, one of the equations turns out to be a simple linear combination of other equations and the determinant of

the coefficients of the system goes to zero. The difficulty is not restricted to systems containing the kinetic energy integral equation but it does in fact also arise with the y-momentum equation under very similar conditions, notably near, but not at, separation or reattachment. The problem of linear dependence is explained in detail by Shamroth (Ref. 16.42), who points out that no physical significance should be ascribed to such singular points since they pose no difficulty to the direct numerical procedures. Shamroth also suggests ways of dealing with the problem, which almost certainly as a result of occurring close to the region where the predictions would be expected to be in considerable error, has long gone unrecognized. Certainly the most powerful remedy to the problem is Shamroth's suggested least squares technique, which is probably best viewed as an alternate system to be used only when the existing system in the region of a singular point, as determined by monitoring the determinant of the coefficients of the system. When the determinant becomes small, in a normalized sense, one can develop N moment equation by integration from the wall to the point Ly/N, L = 1, N. A weighted least squares averaging can then be performed to reduce the N equations to one to replace the offending linearly dependent equation. Obviously if N is taken large there would be little chance of encountering a system singularity, but at the expense of greatly increasing the computer run time. Certainly a less expensive answer and possibly quite effective one would be to integrate the appropriate moment of the momentum equation out to say $y = \delta^*$ and use it to replace the linearly dependent $y = \delta$ moment equation. Other less expensive techniques could also be investigated.

One additional moment equation, the u^{-2} equation, also integrates out quite easily and after some manipulation can give a differential equation for the displacement thickness. Weinbaum and Garvine (Ref. 16.43) derived this equation and obtained some very interesting conclusions from it regarding the viscous analogue of the sonic throat. Bradshaw and Ferriss (Ref. 16.44) also present a version of this equation; however, they did not attempt to use it in a calculation scheme. Although not singular at the wall, care must be taken with the u^{-2} moment equation to ensure the proper limiting behavior as the wall is approached and since it offers no clear advantage for normal boundary layer computation, it cannot be recommended over the kinetic energy equation at this time.

In summary then, if for no other reason than the kinetic energy integral equation integrates out to a convenient form without the introduction of a specific velocity or temperature profile, the kinetic energy integral equation is to be recommended for use, bearing in mind that linear dependence may occur and must be guarded against. The kinetic energy integral equation can be written for a slowly varying time dependent external flow as

$$\frac{\partial \theta_\xi}{\partial x} + 3\frac{\theta_\xi}{u_e}\frac{\partial u_e}{\partial x} + \frac{2}{u_e}\frac{\partial u_e}{\partial x}(\delta^* - \delta_u^*) + \frac{\theta_\xi}{\rho_e}\frac{\partial \rho_e}{\partial x} + \frac{1}{u_e}\frac{\partial}{\partial t}(\delta^* + \theta)$$
$$+ \frac{\theta}{\rho_e u_e^3}\frac{\partial \rho_e u_e^2}{\partial t} + \frac{2}{u_e^2}\frac{\partial u_e}{\partial t}(\delta^* - \delta_u^*) - \frac{1}{u_e}\frac{\partial \theta_\rho}{\partial t} - \frac{1}{\rho_e u_e}\frac{\partial \rho_e}{\partial t}\theta_\rho$$
$$+ \frac{\delta^*}{\rho_e u_e}\frac{\partial \rho_e}{\partial t} = \frac{2}{\rho_e u_e^3}\int_0^\delta \tau \frac{\partial u}{\partial y}\,dy + C_e$$

16.1 (55)

where the various thicknesses are as previously defined but in addition

$$\delta_u^* = \int_0^\delta \left(1 - \frac{u}{u_e}\right) dy$$

16.1 (56)

and

$$\theta_\xi = \int_0^\delta \frac{\rho u}{\rho_e u_e}\left[1 - \left(\frac{u}{u_e}\right)^2\right] dy$$

16.1 (57)

16.1.1.6 The Turbulence Model

At this point it is worth recalling that the appearance of turbulent correlation coefficients in the time averaged momentum equations represents the contribution to the momentum transport by the turbulent motion. While not appearing directly in the von Karman momentum integral equation, various integral moments of these turbulent correlation coefficients appear in the auxiliary equations introduced earlier. For example, in the kinetic energy integral equation, the term C_D is called the dissipation integral (more properly the production integral), where $\rho_e u_e^3 C_D = \int_0^\delta \tau \partial u/\partial y\, dy$. In general the specification of the dissipation integral, or some other integral moment of the turbulent stress, is crucial to the overall accuracy of the more general methods. There are specific flows, however, where simplification is possible, for instance when the turbulent transport is negligible compared to the inertial effects, and in such flows very poor estimates of the turbulent transport can still result in acceptable predictions and consequently a degree of over-optimism concerning the general predictive capabilities of a number of schemes. Also turbulence information is, in fact, introduced into the system of equations by two means, firstly via the various aforementioned integral moments of the Reynolds stress and secondly by means of the assumed velocity profile family. Indeed, if it were possible to define an accurate one parameter velocity profile with skin friction as that parameter, the von Karman equation could be integrated without introduction of any turbulence model. After the fact the implied dissipation integral could be recovered directly from the computed solution and the kinetic energy integral equation. Higher moment equations would eventually allow the complete implied Reynolds stress distribution to be reconstructed. White (Ref. 16.45) has in fact suggested such a one parameter velocity family and his suggestion may be recast slightly and the hypothesized profile interpreted as a Coles' profile with an assumed wake parameter Π - pressure gradient parameter β relationship. White justifies the one parameter profile on the grounds of expediency in deriving a prediction scheme feasible for hand computation. The defects of the one parameter profile can have major consequences and in cases where the assumed $\Pi - \beta$ relationship is inappropriate, White's method would be expected to give overall poor predictions. A case in point, for instance, is the constant pressure recovery from separation or near separation. Here the observed wake component is initially very large yet the pressure gradient is zero, a fact completely inconsistent with the assumed $\Pi - \beta$ relationship. Such a recovering flow places a strong emphasis upon the adequacy of the turbulence information as it is clear that without a pressure gradient to drive the flow, the rate of recovery is entirely

dictated by the extent of the turbulent momentum transport and its ability to energize the flow near the wall. Thus, restricted procedures which either rely on an inertial effect dominating the turbulent transport in some region of the boundary layer (Stratford, Ref. 16.46, develops this concept very clearly) or rely upon the assumed one parameter mean velocity profile to furnish a sufficient description of the turbulent transport (such as White's, Ref. 16.45, procedure) will not be considered further as the restriction may in fact result in quite misleading predictions for general vane or blade boundary layers.

The simplest method of obtaining the necessary turbulent stress integrals is to correlate the measured distributions and in this manner, for example, Escudier and Nicoll (Ref. 16.47) developed for incompressible flow the relationship

$$C_0 = \int_0^\delta \frac{\tau}{\rho_e u_e^3} \frac{\partial \bar{u}}{\partial y}\, dy = \frac{1}{6}(2\zeta+1)C_f + C_1 |1-\zeta|^n \qquad 16.1\ (58)$$

where

$$\zeta = (3-H)/2H \qquad 16.1\ (59)$$

and

$$C_1 = .00565 \quad n = 2.715 \quad \zeta < 1.$$

$$C_1 = .01 \quad n = 3 \quad \zeta \geq 1. \qquad 16.1\ (60)$$

which for many applications they found quite satisfactory. Interestingly, Escudier and Nicoll also showed that over a fairly wide range of conditions pertaining to attached boundary layers, the dissipation integral could equally well be deduced by assuming the turbulent Reynolds stress was related to the local mean velocity gradient by a simple mixing length hypothesis, so that, for instance, differentiation of the Coles' profile and specification of the mixing length could yield the dissipation integral directly

$$C_0 \approx \int_0^\delta \frac{-\bar{\rho}\overline{u'v'}}{\rho_e u_e^3} \frac{\partial \bar{u}}{\partial y}\, dy \qquad 16.1\ (61)$$

where

$$-\overline{u'v'} = \ell^2 \left(\frac{\partial \bar{u}}{\partial y}\right) \left|\frac{\partial \bar{u}}{\partial y}\right| \qquad 16.1\ (62)$$

and

$$\ell = \kappa y \quad , \ y < \ell_\infty/\kappa$$

$$\ell = \ell_\infty = .0758 \quad , \ y \geq \ell_\infty/\kappa \qquad 16.1\ (63)$$

This latter means of obtaining the required turbulence structural information by making the same detailed postulates as do the direct numerical schemes, goes some way to countering the claim that the direct numerical schemes are to be preferred since they introduce the turbulence information in a much more direct and easily identifiable manner. To continue, rather than perform the differentiation and integration demanded by the mixing length formulation, the correlation given in Eq. 16.1 (58) is equivalent in incompressible flow and less time-consuming in a calculation scheme. The mixing length formulation, however, provides a straightforward, if laborious, means of obtaining the effect of compressibility upon the dissipation integral. This extension to compressible flow follows immediately since the compressible velocity profile is already supposedly available and Maise and McDonald (Ref. 16.21) have shown that the mixing length profile is not sensitive to compressibility effects. Similarly, other features which can effect the turbulence structure such as wall curvature, that have been expressed effectively as a change in the mixing length (Bradshaw, Ref. 16.48) can readily be incorporated into the evaluation of the shear integrals.

The next stage in the development of a more general stress integral relationship follows from the observation that the simple mixing length profile used by Escudier and Nicoll (Ref. 16.47) and the equivalent eddy viscosity profile used by Mellor and Gibson (Ref. 16.13) is really only valid for equilibrium turbulent flows in the sense previously introduced by Clauser (Refs. 16.11, 16.28). A number of investigators, for instance Goldberg (Ref. 16.49) and Bradshaw and Ferris (Ref. 16.44) have measured in varying degrees the failure of the invariant normalized mixing length or eddy viscosity profile. The fact remains that equilibrium assumptions give reasonable results for a large number of measured non-equilibrium boundary layers and this observation testifies to the validity of the local equilibrium hypothesis (introduced earlier) for these particular flows, even to the extent of determining the various turbulent stress integrals solely on the basis of some profile shape parameter such as G. In order to decide when a local equilibrium procedure such as that presented by Escudier and Nicoll might or might not suffice, and here the subjective criteria of the individual user must be acknowledged, it is necessary to obtain some yardstick to warn of the failure of the local equilibrium hypothesis. An appealing technique would of course be some parameter characterizing the state of the turbulent transport relative to the equilibrium transport but obviously no local equilibrium prediction procedure could return this information. One plausible hypothesis which fits within the framework of a local equilibrium prediction scheme is the suggestion that the further the boundary layer is from actual equilibrium the less likely it will be that the local equilibrium hypothesis would be valid. Thus, as the calculation proceeds, the computed value of say, the shape factor G(X) could be compared to the equilibrium value of $G(=\hat{G})$ which would result from the local pressure parameter $\beta(X)$. The value of $\hat{G}$ could readily be evaluated for correlations of equilibrium boundary layers such as that given by Nash (Ref. 16.12) and reproduced here as Eq. 16.1 (8). Again, it depends upon the user's criteria of accuracy, but based on the Stanford Proceedings (Ref. 16.50) results, if in a local equilibrium calculation $(G - \hat{G})/\hat{G}$ exceeded 0.5 at some location, as a rough guide, an improvement in the predictions might be expected in going to a better, non-equilibrium, turbulence model.

Early attempts to improve the turbulence transport description to allow for non-equilibrium effects for use in integral methods centered on developing empirical rate expressions for the integral moments of the turbulent stress, such as the dissipation integral or the stress integral, of the general form

$$\frac{dC_D}{dx} = k(C_D - C_{De})$$

16.1 (64)

where C_{De} is the local equilibrium value of the dissipation integral which would result from a $C_D - G$ relationship such as that of Escudier and Nicoll (Ref. 16.49) given by Eq. 16.1 (59), and k is an empirically determined constant of approximate value $.013/\delta^*$. Relationships of the foregoing type were suggested by Goldberg for the dissipation integral, who incidentally proposed C_D should be used rather than C_{De}, but C_{De} does seem the appropriate choice, and for the stress integral by Nash and Hicks (Ref. 16.51). Such relationships are obviously very convenient to use, add so little in the way of computer logic or run time, and in view of both the aesthetics and observed improvements, their use would appear almost mandatory with any of the existing incompressible local equilibrium procedures. With an entirely empirical expression such as Eq. 16.1 (64), the extension to say, compressible flow or flows with free stream turbulence does pose possible problems which to date have not been addressed.

As a further development, McDonald (Ref. 16.5) was able to show that rate expressions quite similar to the type suggested intuitively by Goldberg and Nash could be developed from the turbulence kinetic energy equation using turbulence structural similarity concepts advanced by Townsend (Ref. 16.53). The turbulence kinetic energy equation is an exact conservation equation governing the kinetic energy residing in the turbulent fluctuations and its derivation from the Navier-Stokes equations is given by Favre for compressible flow. As a result of the exact formulation of the turbulence kinetic energy equation and the approximate validity of the turbulence similarity concepts invoked, it has become a popular method of developing non-equilibrium turbulence models with the potential for allowing for some of the observed effects particularly significant in gas turbine applications. To observe how the turbulence kinetic energy equation may be used in the integral boundary layer procedures this equation can be integrated across the boundary layer for non-hypersonic flows and flows where the mean flow varies slowly with time compared to the turbulent motion, to yield

$$\frac{1}{2}\frac{\partial}{\partial t}\int_0^\delta \bar{\rho}\,\overline{q^2}\,dy + \frac{1}{2}\frac{\partial}{\partial x}\int_0^\delta \bar{\rho}\bar{u}\,\overline{q^2}\,dy = \int_0^\delta -\bar{\rho}\,\overline{u'v'}\,\frac{\partial \bar{u}}{\partial y}\,dy - \int_0^\delta \bar{\rho}\,\epsilon\,dy$$
$$-\int_0^\delta \bar{\rho}\left(\overline{u'^2} - \overline{v'^2}\right)\frac{\partial \bar{u}}{\partial x}\,dy + \int_0^\delta \overline{p'\frac{\partial u_i'}{\partial x_i}}\,dy + E + w$$

16.1 (65)

where

$$w = \left(\overline{q^2}\,\overline{\rho v}\right)_w$$

$$E = \left[\frac{1}{2}\overline{q^2}\left(\bar{\rho}\bar{u}\frac{\partial \delta}{\partial x} - \overline{\rho v}\right) - \overline{\rho' v'} + \frac{1}{2}\overline{(\rho v)' q^2} + \frac{1}{2}\rho q^2\frac{\partial \delta}{\partial t}\right]_e$$

16.1 (66)

The resulting equation is, like the von Karman momentum equation, quite uncontroversial; however, it is also quite unhelpful in fashioning a calculation scheme without the introduction of further approximations. It can be seen, for instance, that although the previously introduced dissipation integral appears explicitly in the integral turbulence kinetic energy equation, it serves in part simply to determine the rate of change of yet another turbulence quantity, an integral of the turbulence kinetic energy flux.

There are, of course, a large number of ways in which simplifications and approximations can be introduced in the turbulence kinetic energy equation to convert it into an equation which would control the development of the Reynolds shear stress either implicitly or explicitly. As mentioned earlier, McDonald (Ref. 16.52) and later Green, Weeks and Brooman (Ref. 16.54) applied the turbulence kinetic energy equation along the locus of the maximum stress occurring within the boundary layer. After the introduction of Townsend's structural similarity arguments, McDonald (Ref. 16.52) developed a rate expression for the stress integral appearing in the y-moment of momentum equation while, on the other hand, Green et al., constructed an equation for the streamwise rate of change of an entrainment coefficient. The principle difficulty with these approaches, which follows the locus of the maximum shear stress, is that this locus may be difficult to determine with the necessary precision.

Hirst and Reynolds (Ref. 16.55) introduce a series of intuitive suggestions to reduce the integral turbulence kinetic energy equation given above to a differential equation governing the streamwise development of the entrainment rate M, where M is defined as

$$M = \frac{d}{dx}\int_0^\delta u\,dy = \frac{d}{dx}\,u_e(\delta - \delta^*)$$

16.1 (67)

but as with the entirely empirical rate equations of Goldberg (Ref. 16.49) and Nash (Ref. 16.51), although satisfactory for conventional low speed boundary layers, difficulties arise in attempting to introduce compressibility and curvature effects, for instance, into the Hirst-Reynolds scheme.

A less intuitive analysis than those described above has been developed by McDonald and Camarata (Ref. 16.56), who followed Townsend (Ref. 16.53) and Bradshaw, Ferris and Atwell (Ref. 16.57) and defined structural parameters a_n, L together with a mixing length ℓ where

$$-\overline{u'v'} = a_1\overline{q^2},\ \overline{u'^2} = a_2\overline{q^2},\ \overline{v'^2} = a_3\overline{q^2}$$

$$\overline{w'^2} = (1 - a_2 - a_3)\,\overline{q^2}$$

$$\epsilon = (-\overline{u'v'})^{3/2}/L,\ (-\overline{u'v'}) = \ell^2\left|\frac{\partial \bar{u}}{\partial y}\right|\frac{\partial \bar{u}}{\partial y}$$

16.1 (68)

and this permits the turbulence kinetic energy equation to be written as

$$\frac{1}{2}\frac{\partial}{\partial t}\int_0^\delta \bar{\rho}\,\overline{q^2}\,dy + \frac{\partial}{\partial x}\left(\frac{\phi_1 \rho_e u_e^3 \delta^*}{2a_1}\right)$$
$$= \rho_e u_e^3\left(\phi_2 - \phi_3 + \frac{E}{\rho_e u_e^3}\right) + \int_0^\delta \overline{p'\frac{\partial u_i'}{\partial x_i}}\,dy + w$$

16.1 (69)

where

$$\phi_1 = \int_0^{\delta/\delta^+} \frac{\bar\rho\bar u}{\rho_e u_e}\left(\frac{\ell}{\delta^+}\frac{\partial \bar u/u_e}{\partial\eta}\right)^2 d\eta$$

$$\phi_2 = \int_0^{\delta/\delta^+} \frac{\bar\rho}{\rho_e}\left(\frac{\ell}{\delta^+}\right)^2\left(\frac{\partial \bar u/u_e}{\partial\eta}\right)^3\left(1-\frac{\ell}{L}\right) d\eta$$

$$\phi_3 = \int_0^{\delta/\delta^+} \frac{\bar\rho}{\rho_e}\left(\frac{a_2-a_3}{a_1}\right)\left(\frac{\ell}{\delta^+}\frac{\partial \bar u/u_e}{\partial\eta}\right)^2 \frac{\delta^+}{u_e}\left(\frac{\partial \bar u}{\partial x}\right)_{y=\text{const.}} d\eta$$

16.1 (70)

and where η is a nondimensional transverse distance y/δ^+, δ^+ is arbitrary. Now on the basis of the experimental evidence a dissipation length profile and a one parameter mixing length profile are assumed to be of the general form

$$\frac{L}{L_\infty} = \tanh\left[\kappa y/L_\infty\right]$$

$$\frac{\ell}{L_\infty} = \tanh\left[\kappa y/L_\infty\right] \qquad 16.1\ (71)$$

and the value of L_∞ can be taken to be 0.1δ on the basis of Bradshaw's measurements. For fully developed turbulence the structural parameters a_1, a_2, and a_3 are assumed to have reached a condition of structural equilibrium characterized by constant values of 0.15, 0.5, and 0.2 respectively, chosen on the basis of the available evidence. In accordance with Morkovin's (Ref. 16.27) hypothesis the aforementioned structural parameters are assumed to be independent of the direct effects of compressibility for non-hypersonic boundary layers. If the normal stress terms are neglected, Eq. 16.1(69) becomes an integro-differential equation for wake value of the mixing length ℓ_∞. This integro-differential equation can be integrated in the streamwise direction along with the other momentum integral equation and the wake value of the mixing length derived by a Newton-Raphson iterative scheme once a value of ϕ_1, at the streamwise location in question is obtained. The process is described in detail by McDonald and Fish (Ref. 16.58) who have quite successfully used the scheme in conjunction with a direct numerical procedure which solved the boundary layer partial differential equations of motion. Once a value of the wake mixing length ℓ_∞ is obtained the various stress integrals can be obtained directly from the assumed velocity profile family and the mixing length hypothesis.

As formulated above, the integral turbulence kinetic energy scheme has the disadvantage that the dependent variable ℓ_∞ appears in the kernel of an integro-differential equation. The latter disadvantage is quite troublesome in an integral procedure which must execute rapidly or lose to the generality of the direct numerical procedures. If implementation of this type of scheme is contemplated, some consideration should be given to ways of simplifying the integro-differential equation even further and with this in mind it is observed that the piecewise linear mixing length family used by Escudier and Nicoll (Ref. 16.47) could also be used in the integral turbulence kinetic energy equation with a resulting major simplification. The join point between the inner region of the boundary layer where $\ell = y$ and the outer region where $\ell = \ell_\infty$ is designated by δ_j. Note that

$$\eta_j = \delta_j/\delta^+ = L_\infty/(\kappa\delta^+)$$

16.1 (72)

It is then further supposed that the dissipation length L can also be represented by a similar piecewise linear distribution as the mixing length. Since usually the mixing length is not too dissimilar from the dissipation length L in value, the turbulence integral thickness parameters appearing in the turbulence kinetic energy equation can be written to a reasonable degree of approximation as

$$\phi_1 = \left(\frac{L_\infty}{\delta^+}\right)^2\int_{\eta_j}^{\eta_e}\frac{\bar\rho\bar u}{\rho_e u_e}\left(\frac{\partial \bar u/u_e}{\partial\eta}\right)^2 d\eta + \kappa^2\int_0^{\eta_j}\left(\eta\frac{\partial \bar u/u_e}{\partial\eta}\right)^2\frac{\bar\rho\bar u}{\rho_e u_e}\, d\eta$$

$$\phi_2 = \left(\frac{L_\infty}{\delta^+}\right)^2\left(1-\frac{L_\infty}{L_\infty}\right)\int_{\eta_j}^{\eta_e}\left(\frac{\partial \bar u/u_e}{\partial\eta}\right)^3\frac{\bar\rho}{\rho_e}\, d\eta$$

16.1 (73)

In this simplified system the wake mixing length no longer appears under the integral sign, and the interpretation now of the integral turbulence kinetic energy equation as a differential equation for the wake mixing length greatly simplified the implementation of the concept. The resulting scheme is still appreciably more complicated than the simple rate expressions of Goldberg (Ref. 16.49) or Nash (Ref. 16.51). However, the effects of time dependency, compressibility, free stream turbulence, wall transpiration and curvature are all accounted for within a relatively simple framework (presuming Bradshaw's (Ref. 16.48) correction to the dissipation length L for the effect of curvature is accepted). In view of the demands of the turbomachinery environment, schemes such as the foregoing, based on the turbulence kinetic energy equation or other equations in the double velocity fluctuation set, have much to recommend them.

The disadvantages of schemes based on the turbulence kinetic energy equation are mainly that a profile family for the turbulent shear stress usually must be adopted, although if the assumed profile is reasonable then little is lost. In the foregoing scheme, by means of the mixing length assumption the shear stress profile is related to the mean velocity profile in a manner which does appropriately recover the observed equilibrium state. However, at the same time the assumed profile does suffer from the discrepancy that the Reynolds stress will disappear precisely at the same point the velocity gradient does. Boundary layers with velocity profile overshoots, such as film-cooled boundary layers, would probably therefore be subject to error, but almost certainly other factors will be involved such that the errors from the stress profile assumption might be insignificant. A problem also can arise with the assumed invariance of the relationship between the kinetic energy and the Reynolds shear stress, for instance when the shear stress changes sign but of course the energy does not. Such consideratons give impetus to the development of better turbulence models but for the more conventional boundary layers the assumptions given above are probably as accurate as the assumed mean velocity profile.

Additional moments of the turbulence kinetic energy equation could also be introduced to allow a more complex stress profile to be used but it must be acknowledged that at the present time there is neither motivation nor information to proceed in

this direction. A much more promising avenue for future development would be to integrate the equations governing the individual components of the turbulence kinetic energy, that is the $\overline{u'^2}$, $\overline{v'^2}$, and $\overline{w'^2}$ equations, in conjunction with the Reynolds shear stress equation which governs the production of $-\overline{u'v'}$. Such a strategy alleviates some of the more restrictive aspects of the structural similarity hypothesis previously invoked. A preliminary evaluation by the present author of a four integral equation scheme which used Rotta's hypothesis for the partitioning of dissipation yielded very favorable results.

As a final observation at this point it should be clear, if it has not become so earlier, that it should be possible to take integral moments of any of the current model partial differential equations that describe the spatial development of the time averaged Reynolds stress tensor. In this manner eventually it should be possible to construct versions of these model systems suited for use with the integral procedures for solving the boundary layer equations. The additional capability attributable to these newer turbulence models would therefore become available within the framework of the integral procedure, subject of course to the limitations of the profile families, both of velocity and turbulence.

16.1.1.7 Concluding Remarks on Two-Dimensional Integral Methods for Blade Boundary Layers

In arriving at certain recommendations it seems appropriate to mention briefly those particular methods which demonstrate the various recommended characteristic properties. To some degree this has already been done in the previous discussion but certainly it can bear repeating and re-emphasizing here. A great deal of the work done on integral methods for predicting turbulent two-dimensional or axially symmetric boundary layers is summarized in the 1967 Stanford Conference Proceedings (Ref. 16.50) and only a comparatively small number of additional contributions have been made since that time. It is not the purpose of this section to exhaustively review these various contributions but merely to point out certain desirable features and to cite examples where these desirable features have been employed.

A convenient starting point is probably the method due to Head (Ref. 16.33), since this particular method seems to mark the beginning of the present era of more accurate boundary layer predictions. Head's procedure is, in the previously introduced terminology, a local equilibrium procedure in that the implied Reynolds apparent shear stress is uniquely determined by the local mean velocity. The technique is sufficiently simple as to be suitable for use with a programmable pocket calculator and its accuracy quite acceptable for a surprisingly wide range of flows. The procedure was incorporated into a heat transfer prediction scheme by Dvorak and Head (Ref. 16.32), although in this case the resulting scheme was a hybrid since the energy equation was solved by a finite difference procedure after the mean flow was obtained by Head's integral scheme. Later Head's scheme was extended to compressible flow over insulated walls by Green (Ref. 16.34) and for transpired flow by Thompson (Ref. 16.59). Perhaps with the exception of the heat transfer scheme, any potential user would be well advised to inquire whether or not Head's scheme or an existing development of it, might be adequate for their purposes. Insofar as the heat transfer version of Head's scheme is concerned, it seems, at least to this author, that the hybrid heat transfer scheme really does not have such a great deal to offer to warrant its use compared to a full finite difference scheme.

Most well constructed local equilibrium procedures do perform, or could probably be made to perform, about as well as Head's method. However, methods which use the integral kinetic energy equation are particularly convenient in that they have a simple form independent of the assumed form of the boundary layer mean profile. A good example of this type of method is to be found in the work of Escudier and Nicoll (Ref. 16.47). As an additional feature, methods such as that due to Escudier and Nicoll can permit the direct use of the same type of turbulence models as are being developed for the direct numerical procedures. It follows then that once the mean velocity and temperature profile families are specified, variables such as wall transpiration, wall roughness, free stream turbulence and streamwise curvature can eventually be allowed for in this type of method. Compared to the direct numerical procedures all the constraints of the integral procedures lie in the adopted velocity and temperature profile families. To continue, Lubard and Fernandez (Ref. 16.60) developed a local equilibrium procedure which used the integral kinetic energy equation for transpired flows. Alber (Ref. 16.61) has developed an impermeable wall procedure similar to the Lubard and Fernandez scheme but for compressible flow. Based on these precedents and the suggestions and development given earlier in the present work, it would be a simple matter to construct a compressible, transpired, rough wall, integral procedure based on local equilibrium concepts using the von Karman momentum equation and the integral kinetic energy equation. In view of good results previously obtained with the various individual procedures, such as synthesis of methods, would be expected to be quite successful for boundary layers in near equilibrium, with perhaps the compressible law of the wall additive constant with transpiration being the only questionable parameter over and above the mean velocity and temperature profiles at the present time.

The next step in the hierarchy would be to consider the departure from local equilibrium and here an expression for the rate of change of the appropriate integral of the turbulent stress, in the spirit of Goldberg (Ref. 16.49) or Nash and Hicks (Ref. 16.51) for instance, is very convenient and would result in a trivial amount of coding and increased computation. Turbulent lag equations of the foregoing type, although presently only developed for incompressible flow, do seem, at least conceptually, to result in an improvement over the local equilibrium procedures. Less empirical but more laborious are the schemes which use lag equations developed from the turbulence kinetic energy equation. The simplified version of the lag equation developed by McDonald and Camarata (Ref. 16.56) from the integral form of the turbulence kinetic energy equation which was presented earlier, allows for compressibility, free stream turbulence and, using Bradshaw's (Ref. 16.48) suggestion, for streamwise curvature. In collaboration with what could be termed the synthesized procedure described in the previous paragraph, the simplified integral turbulence kinetic energy equation would certainly typify the state of the

art of integral procedures for predicting turbulent boundary layer development in 1975.

The final stage in the hierarchy of problems which will be considered here is the problem of heat transfer. It is clear from the literature that for insulated wall boundary layers, a Crocco type temperature profile suffices to predict the effects of compressibility on the integral thickness parameters. It is also clear from work such as Rotta's (Ref. 16.36) that really none of the convenient so-called Reynolds analogy factors, modified or otherwise, can adequately predict the heat transfer with a variable wall temperature in the presence of streamwise pressure gradients. These rather demanding conditions are unfortunately precisely those normally encountered in turbine blade design. The preliminary indications are that a stagnation temperature law of the wall with a wake component such as that originally suggested by Rotta (Ref. 16.41) when used in conjunction with the integral thermal energy equation might improve the current poor status of heat transfer predictions by integral methods. Lastly, while it is very possible that heat transfer prediction for internally convectively cooled turbine blades or vanes might relatively easily be made acceptable, it seems less likely that film cooled components will be adequately treated within the framework of integral boundary layer prediction schemes. Even for the idealized case of parallel slot injection of the coolant film, the resulting velocity profiles are not well described by the existing law of the wall - law of the wake concepts. At this point the research effort required to further enlarge the mean velocity and temperature profile families to encompass film cooling taken together with the estimated success probability, would seem to outweigh the increased cost of the present day direct numerical schemes which already have shown their capability to handle at least simple film cooling configurations. Thus film cooled boundary layers almost certainly lie outside the scope of present integral procedures and will probably remain there for some time to come.

16.1.2 Numerical Procedures for Solving the Boundary Layer Partial Differential Equations

16.1.2.1 Motivation

In the light of the preceding discussion caution must be advocated when using integral procedures for solving the boundary layer equations whenever profile families for the dependent variables are either inadequately verified or known to be inaccurate. It may well be that, in spite of the known profile shortcomings, as a consequence of the averaging out of the integral schemes, some of the flow properties will be predicted adequately for certain purposes. Unfortunately heat transfer is usually a very demanding property to predict accurately and one of very keen interest to turbine designers. The problems which arise with two and three-dimensional profile families in highly accelerated flows when the laminar and turbulent transport of heat and momentum are of a similar order (or in a film cooled boundary layer developing on a curved surface) can be euphemistically termed "difficult". Numerical procedures which directly solve the partial differential equations and hence do not require this profile information therefore become much more attractive when these particular "difficult" problems must be treated.

Another very valid reason for using a numerical procedure for solving the partial differential equations lies in the flexibility of the resulting scheme. Changes in boundary conditions, higher order terms, generalizations to include chemical reactions, magneto-hydrodynamic forces may all be incorporated with surprisingly little additional work. In some instances, such as the flow in a duct, the merging of shear layers causes perhaps only a re-assessment and readjustment within the turbulence model being used within the numerical procedure; whereas, in the integral scheme it calls for major reconstruction. Such developments are not simply mere possibilities but even at this present time, clearly demonstrate the advantages of the numerical procedures.

16.1.2.2 General Comments

In the course of the subsequent development, frequent reference will be made to existing or potential numerical procedures which could be used to obtain solutions to the problem under discussion. At this point it is worth observing that in the present context a potential numerical procedure is considered to be a technique which has shown promise on simple problems, such as the transient heat conduction problem in one space dimension. Since the real problems are generally non-linear, coupled and multi-dimensional with initial and boundary conditions to be specified, there is a considerable difference between a potential and demonstrated capability and it is necessary to keep this distinction firmly in mind. In some instances, certain of the candidate procedures have clear advantages over others, provided the procedures can, in fact, return the solution to the degree of numerical accuracy required by the user. The potential advantages in practice might be quite unrelated to the relative cost of running the computer to obtain the solution. To evaluate the relative advantages it is first recognized that the engineer user has the choice of constructing a scheme based upon one of the more promising potential procedures to solve his problem or, of adapting an existing available procedure for this purpose. The engineer user must therefore on an ad hoc basis evaluate the relative economics of the projected utilization of the possibly less than optimum existing procedures weighed against the engineering effort required to develop a new procedure embodying the better suited technique for his particular problem. Since computer costs even for the same computer vary from installation to installation dependent upon the computer configuration, the degree to which the computer is utilized, the accounting procedures used to obtain a charge rate and to the actual charge algorithm itself which weights the various internal processes and resources within the computer, the relative computing economics can change dramatically from institution to institution. While computing costs at a given site may usually be projected with relative certainty, the task of the engineer user in making the economic evaluation is often plagued with major uncertainties. In particular, the engineer user and more often than not, the computational expert also, may not be sufficiently knowledgeable of the problem or of candidate techniques to accurately assess the labor required to cast them into a working procedure, or of their possible operational idiosyncrasies once ready for use. Since the more complex techniques can take many months of engineering effort to develop into operational procedures, a judgment error by either the computational expert or the engineer user in the evaluation phase can have a catastrophic economic impact.

In addition, it is sometimes the case that both the existing and the prospective procedures might not behave in an acceptable manner for the particular application the user has in mind, and this fact might not be widely known or apparent to the user in advance. Similarly, certain procedures are user sensitive in operation and considerable skill might be necessary with these procedures to obtain satisfactory solutions. In seeking information upon which to base a reasonable evaluation of the risk factors involved, the diligent engineer is often further confounded by the conflicting claims and observations made by different authors regarding the operational characteristics of certain of the procedures. Several factors contribute to the generation of these conflicting claims. Principal among these factors is the user sensitivity mentioned earlier and this leads to a successful computation being dependent on such user selected items such as the computational mesh distribution and density or the initial and boundary conditions. Also a factor is a sensitivity of many of the procedures to computational detail and here the precise treatment of such items as non-linearities, boundary conditions, or simply the ordering of the computation can have a major impact on the eventual outcome of the computation. Precise details such as this are often not given in archival journal publications, for among others, the obvious reason of space limitation.

Naturally, such real and prospective pathological difficulties demand that the engineer be thoroughly familiar with the existing candidate procedures and that very powerful reasons must exist to justify the development cost of any new and relatively untried procedure. There are, of course, valid reasons for embarking upon the prolonged development of a new procedure embodying more appropriate techniques for solving the particular problem. Unavailability or the general unsuitability of the existing procedures would be key factors in such a decision. Here again, however, conflicting claims of suitability or unsuitability are frequently to be found in the literature, often simply as a result of different authors having differing constraints and standards. The need to use the procedure on a computer with very small high speed memory might, for instance, sway judgment one way whereas the need for a locally refined mesh, say to define the viscous sublayer of a turbulent boundary layer, might be a critical factor in another user's estimation. Less tangible, but not trivial, is the consideration that, should the engineer decide to develop the relatively untried procedure himself, he then is fully aware of the numerous approximations and prejudices incorporated into the procedure and is then well equipped to further extend the procedure into other problem areas.

The foregoing is in part designed to caution the engineer against a precipitous adoption of a promising but relatively untried numerical scheme for solving his particular problem. It is also aimed in part at answering the oft heard question of the computational expert who feels that he has the most efficient algorithm for solving the particular problem under study, and who questions why the engineering public continues to use what is to him a non-optimum method.

Before going on to discuss the actual methods available for treating the boundary layer equations it is necessary to develop some basic concepts about numerical methods in general. However, it is not the purpose here to provide a broad introduction into general numerical methods for solving partial differential equations as there are some fine textbooks available on this subject. Only those topics which would be appropriate to aid a potential user in evaluating the numerical aspects of the candidate procedure will be discussed here. In this regard, three broad categories of methods exist for numerically solving the equations of fluid mechanics. These being the finite difference, the finite element and the spectral methods. In the main, the subsequent discussion concerns finite difference methods simply because at the present time finite difference methods are the furthest advanced in terms of fluid mechanics applications. Hybrid techniques also have made their appearance, for instance, finite difference methods may be viewed as a collocation technique with the dependent variable represented by a polynomial. If now the dependent variable in one or more coordinate directions instead is represented by some trigonometric expansion such as a Fourier series, the resulting scheme is termed a pseudo-spectral method or hybrid pseudo-spectral method, depending on the degree of finite differencing employed. Indeed other related methods can readily be formulated using orthogonal polynomials or piecewise polynomial splines to represent the dependent variables in one or more directions. In the usual spectral methods the trigonometric series used to represent the dependent variable is introduced into the governing equations by means of the Galerkin technique, but at present the pseudo-spectral methods seem about a factor two more efficient than the spectral methods. Finite element methods have been very successful in structural problems where they have proven especially useful with irregular boundaries. At the present time the application of the finite element procedure to fluid mechanics problems is sparse and inconclusive. Certainly in many applications the matrix inversion problem obtained from the finite element technique is identical to that arising from implicit finite difference formulations so that such schemes must have comparable computational costs. The claimed attribute of finite element methods of ease of treatment of irregular boundaries is obtained at the expense of a non-trivial element construction process. To this must be added the observation that element shape and size variations can have a detrimental effect on accuracy so that it does not at this point appear that the finite element approach will be quite the hoped-for panacea for geometric complexity. Lastly, in the present work the usual Eulerian body fixed coordinate systems will be considered as opposed to the Lagrangian system where the coordinates move with fluid. Lagrangian coordinate systems have considerable utility for relatively uncomplicated time dependent flows containing discontinuities but in the steady distorted flow, at present, the mesh interpolation problem [illegible] prohibitive.

16.1.2.3 Order Accuracy

The simplest way to discuss order accuracy is in terms of a truncated Taylor series. In setting up a finite difference molecule the function value at adjacent grid points can be related to conditions at the grid point in question by means of a Taylor series. The Taylor series may then be appropriately truncated and an expression for the derivative at the point obtained. The truncation term in the Taylor series then determines the formal order accuracy of the difference scheme. For example, consider the three point scheme with a mesh spacing

of h and the continuous function f with single valued finite derivatives

$$f(x+h) = f(x)+hf'(x)+h^2/2\,f''(x)+h^3/6\,f'''(x)+\cdots$$

$$f(x-h) = f(x)-hf'(x)+h^2/2\,f''(x)-h^3/6\,f'''(x)+\cdots$$

so by subtraction we have

$$f'(x) = \frac{f(x+h)-f(x-h)}{2h} + \frac{h^2}{6}f'''(x)+\cdots$$

and hence the terminology that if in the above equation the terms in h^2 and higher are neglected the resulting finite difference representation of the derivative is termed second order. A fourth order representation would be one where the first neglected term was h^4, and so on. The second order finite difference representation given above is usually termed the first derivative second order central difference formula. A one-sided derivative is sometimes of use and from the foregoing in simplest form is written for a forward difference first derivative as

$$f'(x) = \frac{f(x+h)-f(x)}{h} - \frac{h}{2}f''(x)+\cdots$$

and clearly this is a first order approximation.

Frequently and erroneously the order accuracy of a finite difference formula for the derivative as defined above is appended to the solution procedure for the governing system of equations as a whole. Clearly other factors can contribute to the errors in the solution to the system of equations. Three obvious sources of error which can swamp the errors arising from the derivative formula are (1) linearization errors arising from the non-linear nature of the governing equations, (2) errors arising from the treatment of the coupling between the equations within the system, including the boundary conditions, and (3) machine roundoff The first two of these three sources of error will be discussed further later. In the subsequent development, order accuracy will be appended only to the difference formula and not to the overall procedure. Machine roundoff cannot be ignored as a possible source of error but usually this problem manifests itself catastrophically during the initial development of the procedure, where appropriate remedies must be developed or the procedure abandoned.

It is observed that higher order difference formulae are desirable in principle, and in some cases represent the only reasonable alternative to reducing the mesh to an absurd degree to obtain accuracy. Several points must be noted, the first being that to obtain the increased order accuracy there has usually been an increase in labor. The question must now be asked if it is not more economic to use a lower order difference with a more refined mesh. A number of authors for instance have argued against methods of order greater than fourth on this basis. Various ad hoc particularities can affect this judgment however, for instance, in performing reacting boundary layer calculations the chemistry computation could greatly overshadow the fluid mechanics, thus driving one towards the use of as few grid points as possible regardless of the cost per grid point of the fluid mechanics calculation.

Additional difficulties can be associated with higher order methods, the obvious one being the application of boundary conditions since more extensive spatial differencing in the region of the boundaries would almost certainly be needed. Further, it has been observed that higher order schemes tend to be difficult to work with in practice due to their propensity to develop solutions with undesirable features such as "wiggles". Without doubt, improved higher order schemes will appear in the future and will alleviate these problems.

It should be clear from the above that higher order methods are not necessarily to be preferred over lower order schemes. Accuracy can always be obtained from the consistent lower order schemes, computer willing, by mesh refinement. The question is then simply the cost to the user of the required mesh. Should this cost be prohibitive then a higher order method or an alternative more efficient lower order scheme might be the answer. In the subsequent discussion of the various methods, order accuracy, including the more subtle errors which might arise from linearization and decoupling, will be touched upon but hopefully will not be overstressed.

16.1.2.4 Explicit and Implicit Methods

In the usual steady turbulent boundary layer equations, if the laminar transport is not neglected with respect to the turbulent transport, the governing equations are everywhere parabolic and upon specification of a turbulence model form a well posed initial-boundary value problem. In certain cases the neglect of the laminar transport can result in a hyperbolic set of equations but this depends on the precise nature of the model of the turbulence transport. In either event the equations may be solved by a forward marching technique, since one coordinate direction will possess a time-like property. In the subsequent discussion this marching direction will frequently be termed the time coordinate for obvious reasons. The numerical methods for solving parabolic or hyperbolic equations which form a well posed initial-boundary value problem are usually termed either explicit or implicit methods. In an explicit technique the unknown variables are expressed at the advanced "time" level entirely in terms of the known values at the current time level together with the appropriate boundary conditions. Explicit schemes on the whole tend to be conditionally stable. That is, a stable calculation can only be obtained provided certain limitations on the time step are adhered to. In an implicit procedure the finite difference representation introduces unknown variables at both the advanced and the current time level. Generally speaking, a procedure of this type necessitates the solution of a set of simultaneous equations and this usually results in a complex and time consuming procedure on a per grid point per time step basis. Implicit methods are usually stable for large time steps (although not necessarily unconditionally stable) and are therefore competitive with conditionally stable explicit procedures when the physical processes are changing on a time scale much greater than the marching step permissible with the conditionally stable explicit schemes. It turns out that the stability limits of the better known explicit schemes can be very restrictive in performing turbulent boundary layer calculations, and consequently implicit schemes have found considerable favor. Unconditionally stable explicit schemes such as the DuFort-Frankel scheme are available, but to date these schemes have all been inconsistent. That is to say that in the limit as the mesh is refined the truncation error in the Taylor series expansion does not disappear for an aribtrary mesh spacing. In such a scheme even given an unlimited computer the user no longer has the ability to make the error as

small as he wishes simply by mesh refinement. Inconsistent schemes therefore have not been widely used, although Pletcher (Ref. 16.62) for instance, has not had any apparent difficulty in using a DuFort-Frankel scheme on the boundary layer equations.

Predictor-corrector procedures have been developed and these can be either of the explicit or the implicit type, or of some hybrid of the two types. Predictor-corrector schemes have become quite attractive for three-dimensional boundary layers and the prospect for treating aspects of the non-linearities in the governing equations within the predictor-corrector framework is appealing.

Lastly, the so-called shooting methods defy description by the simple explicit-implicit terminology. In this and related techniques, the marching direction is discretized first, resulting in a non-linear ordinary differential equation which poses a two-point boundary value problem. After linearization the ordinary differential equation can be treated by a number of different schemes as an initial value problem, for instance, in perhaps the most successful version of the shooting technique a particular integral and a complimentary function are generated by numerical integration. The outer boundary condition then serves to determine the arbitrary constant in the complimentary function, and the solution of the linearized equation obtained by adding the particular integral to the complimentary function. Unfortunately, iteration is required if more than one outer boundary condition is to be applied, as is usually the case in boundary layer flows. Although successfully used for laminar flows and some turbulent flows, the convergence of the iteration involved in the shooting technique is not particularly reliable for arbitrary boundary layer flows and has now been largely abandoned in favor of implicit methods. More recent developments of the shooting process such as parallel shooting have apparently not been evaluated on the boundary layer equations.

In assessing the candidate methods for suitability for one's own particular problem a definite screening process can be suggested based on the foregoing discussion. This process will now be discussed in detail in view of its importance in practice. Particular emphasis will of course be given to the special problems which arise from turbomachinery considerations.

16.1.2.5 Some Factors Influencing the Choice of Numerical Method

On the basis of the preceding discussion the choice of the most suitable numerical method for a given problem is an ad hoc one. Perhaps the most critical item is to estimate the rate at which physical processes of interest can change in the marching (or iteration) direction. This leads to an estimate of the maximum step in the marching direction that the changing physical processes permit. This maximum physical step can then be compared to the maximum computational marching step that the various candidate procedures allow. The number of computational steps required to march the maximum physical step is thus estimated. To now compare the various schemes an estimate must be made of the computational effort required to take one computational step. With this latter piece of information the computational cost of marching the maximum physical step can be estimated and used to eliminate some of the candidate schemes. Finally, computer storage requirements and coding complexity together with estimated reliability and prior experience may be factored in to complete the choice of method.

To see how this process works in practice, consider the simple incompressible turbulent boundary layer momentum equation.

$$(\rho u)u_x + (\rho v)u_y = -p_x + (\mu_e u_y)_y \qquad 16.1\ (74)$$

where the turbulent transport of momentum has been represented by an eddy viscosity coefficient μ_e. Now, based on experience with the simple transient heat conduction equation

$$\frac{\partial T}{\partial t} = K\frac{\partial^2 T}{\partial y^2} \qquad 16.1\ (75)$$

where t is the time (marching) coordinate and K is the thermal conductivity and T the temperature, it is well known that most conditionally stable schemes when applied to the simple heat conduction equation given above exhibit a step size restriction of the form

$$R_{VSL} = \frac{K\Delta t}{\Delta y^2} \le 1/2 \qquad 16.1\ (76)$$

In the linearized boundary layer problem the above restriction approximately transforms into

$$\frac{\mu_e \Delta x}{\rho u \Delta y^2} \le 1/2 \qquad 16.1\ (77)$$

and it is found in practice that this type of restriction does indeed hold when these same methods are applied to the boundary equations. Now, Clauser has suggested that in the outer region of an equilibrium incompressible turbulent boundary layer

$$\mu_e \simeq .016\rho_e u_e \delta^* \qquad 16.1\ (78)$$

and this suggestion is in good accord with measurement. If now an equally spaced mesh normal to the wall is introduced

$$\Delta y = \delta/N \qquad 16.1\ (79)$$

where N is as yet the undefined number of intervals, the viscous stability requirement reduces to

$$R_{VSL} \simeq .016N^2\delta^*\Delta x/\delta^2 \le 1/2 \qquad 16.1\ (80)$$

and typically in a turbulent incompressible boundary layer, $\delta/\delta^* \sim 6$ so that there results in round figures

$$\frac{\Delta x}{\delta} \le \frac{200}{N^2} \qquad 16.1\ (81)$$

It is observed that unfortunately the computational marching step decreases as the square of the number of grid points and this of course aggravates the problem of having to add grid points for increased accuracy. Further, based on observation, the physical processes change such that axial steps of greater than or equal to the boundary layer thickness would be desirable in a computational scheme. It then follows that for more than about 14 grid points normal to the wall in the boundary layer the viscous stability restriction would force an axial step size of less than the desired boundary layer thickness. This would not necessarily rule out schemes governed by a viscous stability criterion if the computational cost per axial step or accuracy were sufficiently better than competitive schemes taking a larger axial step. Now, a significant portion of the cost of marching one axial step goes into forming the coefficients for the integration scheme and is roughly independent of the type of integration, be it an explicit or implicit formulation. Further, very efficient matrix elimination schemes are available to treat the system of linear equations resulting from the implicit formulation. Thus on balance, in practice, the implicit schemes generally tend to be only a factor of two or three times more costly per axial step than the explicit schemes. Thus, superficially, the break-even point between conditionally stable explicit schemes and the (nominally) unconditionally stable implicit schemes for the usual boundary layer equations occurs at roughly 20 grid points normal to the wall.

The axial step restriction can actually be a great deal more severe than the foregoing simplified arguments indicate. Firstly, accuracy studies have indicated that 40 or more grid points normal to the wall might be required with a second order difference scheme to accurately define the boundary layer in many circumstances, particularly when skin friction (or heat transfer) is important. (This figure could be reduced in some cases by fine tuning the mesh distribution.) Secondly, the previous arguments were based upon an equal mesh spacing normal to the wall and the viscous stability restriction is greatly aggravated if it becomes necessary to try and define the viscous sublayer of the turbulent boundary layer. The only alternative to defining the viscous sublayer by means of mesh points is to assume the validity of the law of the wall between the first grid point away from the wall and the wall proper. However, although the viscous sublayer is very thin, approximately 50% of the velocity change in the entire boundary layer occurs across it, so it is a comparatively important region. Thus to date only the remarkably wide validity of the law of the wall has made the fitting of the profiles a viable alternative to adding more grid points. Unfortunately, in a number of instances of critical importance in gas turbine applications the law of the wall is influenced by severe favorable pressure gradients and heat transfer (amongst other factors) and such influences cannot readily be accounted for as a simple correction to the law of the wall. Indeed as was discussed in the section on integral prediction schemes the whole topic of the thermal law of the wall is much less secure than the velocity law of the wall. Hence, in certain cases much better success has been obtained using assumptions concerning the turbulence structure than assuming velocity or thermal profile similarity in the viscous sublayer. Thus in gas turbine heat transfer applications the desire to place grid points deep within the viscous sublayer is present and virtually precludes the use of any conditionally stable procedure with a viscous stability limit near ½. With only a few exceptions computer central memory storage requirements are not normally a problem with implicit schemes and if required out of core storage can usually be obtained and the cost factored into the evaluation. Coding complexity, sometimes raised as a factor against implicit methods, turns out to be quite mythical, as that portion of the complete prediction procedure dealing with the actual integration can comprise less than 15% of the overall coding. For this reason nominally unconditionally stable methods such as implicit schemes have found favor in boundary layer prediction methods.

A second commonly encountered stability restriction is termed the Courant-Fredericks-Lewy (CFL) criterion and considering the simple advection equation

$$\frac{\partial u}{\partial t} = a\frac{\partial u}{\partial x} \qquad 16.1\ (82)$$

the CFL criterion generally requires that

$$\frac{a\Delta t}{\Delta x} \leq 1. \qquad 16.1\ (83)$$

which when interpreted in the boundary layer frame of reference requires

$$\frac{v\Delta x}{u\Delta y} \leq 1 \qquad 16.1\ (84)$$

and since v is small within a boundary layer the CFL requirement generally does not pose as severe a restriction as the viscous stability condition discussed previously.

16.1.2.6 Non-Linear Aspects

As has been observed earlier the boundary layer equations are non-linear when expressed in terms of the velocity variables, and some discussion of the particular problems arising from this complication is required. A change of variables can alleviate the non-linearities somewhat but with a temperature dependent viscosity, compressible flow or a turbulent effective viscosity, no completely linear system can be achieved by a change of variable. As a general rule implicit methods with their eventual goal of a system of linear algebraic equations make a formal linearization at some point inevitable if the governing equations are non-linear. The key point here is that inadequate treatment of the non-linear terms can seriously degrade the overall accuracy of the method. Two popular methods of dealing with the non-linearities are to be found in the literature In the first method finite difference operators are applied to the governing equations and a non-linear set of algebraic equations obtained. The non-linear set of algebraic equations can then be solved, for instance, by a Newton-Raphson technique. As an alternative, the governing equations can be linearized by some procedure and the finite difference operators then produce a linear algebraic system without further ado. Explicit procedures can, of course, be applied to exactly the same set of linearized governing equations, however as a class they do permit a simpler process of linearization as a result of the extensive use of the known level

solution. In the explicit schemes it is usual to formulate the problem in the so-called conservative form of the governing equations, that is, as many as possible of the dependent variables are placed within the derivative operator. For example, by use of the continuity equation the streamwise momentum equation given by Eq. 16.1 (74) can be rewritten as

$$(\rho u^2)_x + (\rho uv)_y = -p_x + (\mu_e u_y)_y$$

16.1 (85)

and denoting X marching locations by the subscript 'j' and y locations by the subscript 'i' the momentum equation can give, for instance, the explicit formula

$$(\rho u^2)_{j+1} = (\rho u^2)_j + (x_{j+1}-x_j)\left[-\left\{\frac{(\rho uv)_{i+1}-(\rho uv)_{i-1}}{y_{i+1}-y_{i-1}}\right\}_j - \left\{\frac{p_{j+1}-p_j}{x_{j+1}-x_j}\right\}_i + \left\{\frac{(\mu_e u_y)_{i+1/2}-(\mu_e u_y)_{i-1/2}}{(y_{i+1}-y_{i-1})/2}\right\}_j\right]$$

16.1 (86)

and clearly the only remaining problem, since everything at the j location is known and p(x) given, is the determination of ρ and v and this is accomplished by similar integration of the continuity and energy equations. The linearization problem has been effectively circumvented by the explicit integration of the conservative form of the governing equations. However, the conditional stability problem of explicit methods remains.

There are, of course, other advantages to using a conservative form of the governing equations and their use is not restricted to explicit schemes (see Roache, Ref. 16.63). Here it is not proposed to discuss this particular aspect in depth. Clearly if the two forms of the governing equations are equivalent, then for a properly resolved flow the same answer should be obtained from the conservative as the non-conservative system, to within the truncation error. The preference for a particular form, usually the conservative form, stems either from the linearization simplification or from the case where the flow is only marginally or poorly resolved and here the truncation errors are large and are often more palatably disguised within the conservative scheme. For this reason when either form can be used without prejudice, the conservative form is usually selected. Some procedures, such as the Lax-Wendroff scheme, require governing equations written in a conservative form.

Returning to the question of linearization with implicit schemes in addition to the two previously mentioned approaches at least one other strategy has been evolved. This third approach is an ad hoc process which examines an expression and in each term the highest derivative for the dependent variable is taken as the implicit term and all others evaluated as a known coefficient using either a previous station's information or an estimate. For example, in the streamwise momentum equation, considering incompressible flow for the moment, the streamwise convective term would be linearized

$$(\rho u)u_x = (\rho u)_{j,i}\left[\frac{u_{j+1}-u_j}{x_{j+1}-x_j}\right]_i$$

16.1 (87)

Now obviously such a linearization is quite crude and introduces a first order error in the solution. A second and considerable improvement is to use a Newton-Raphson process to obtain

$$u^2_{n+1} = 2u_n u_{n+1} - u_n^2 + O(u_{n+1}-u_n)^2$$

16.1 (88)

and so obtain

$$uu_x = \frac{1}{2}(u^2)_x = \frac{1}{2}(2u_n u_{n+1} - u_n^2)_x$$

16.1 (89)

where n is an iteration index. The concept here is that starting from an initial guess, perhaps the previous x-station solution, a sequence of linear problems can be solved until the non-linear terms are adequately represented. The point to note with this process is that it can be time-consuming and unrewarding in fact, to iteratively reduce the errors arising from the linearization approximation below the basic truncation error of the difference scheme; for instance, why represent u^2 much better than the streamwise derivative? This point is the basis of noniterative linearization which will now be developed in detail in view of the importance of implicit methods in boundary layer theory and the critical role of linearization in implicit methods.

In a recent study Briley and McDonald (Ref. 16.64) and McDonald and Briley (Ref. 16.65) applied a noniterative linearization technique in developing implicit procedures for solving the multi-dimensional compressible Navier-Stokes and reduced Navier-Stokes equations. The linearization was based on a Taylor expansion of the nonlinear terms about the known level solution. In order to illustrate this technique and introduce the concepts of the relationship of truncation error arising from linearization to truncation errors arising from spatial discretization, consider the nonlinear ordinary differential equation

$$\frac{d\phi}{dx} = f(\phi)$$

16.1 (90)

with exact solution $\phi = \phi(x)$. A centered difference between levels n+1 and n leads to

$$\frac{\phi^{n+1}-\phi^n}{\Delta x} = \frac{1}{2}(f^{n+1}+f^n) - \frac{\Delta x^2}{12}\phi'''(x_i)$$

16.1 (91)

The central problem of the linearization now is to obtain a satisfactory representation of f^{n+1} which contains only linear contributions from ϕ^{n+1}. This can be done by expanding about the n level, as follows,

$$f^{n+1} = f^n + \left(\frac{df}{d\phi}\right)^n \Delta\phi + \left(\frac{d^2 f}{d\phi^2}\right)^n \frac{\Delta\phi^2}{2} + O(\Delta\phi^3)$$

16.1 (92)

and again by expansion about the n level,

$$\phi^{n+1} = \phi^n + \Delta x\left(\frac{d\phi}{dx}\right)^n + \frac{\Delta x^2}{2}\left(\frac{d^2\phi}{dx^2}\right)^n + O(\Delta x^3)$$

16.1 (93)

Thus from Eq. 16.1 (93), the error in Eq. 16.1 (91) arising from retaining only linear terms in the representation of f^{n+1} given by Eq. 16.1 (92),

termed the nonlinear truncation error (NLTE), is of the order

$$\frac{1}{4}\left(\frac{d^2 f}{d\phi^2}\right)^n\left[\Delta x\left(\frac{d\phi}{dx}\right)^n+\frac{\Delta x^2}{2}\left(\frac{d^2\phi}{dx^2}\right)^n\right]^2$$

$$+\frac{1}{4}\left(\frac{d}{dx}\left\{\frac{df}{d\phi}\Big/\frac{d\phi}{dx}\right\}\Big/\frac{d\phi}{dx}\right)^n\left[\Delta x^2\left(\frac{d\phi}{dx}\right)^{2n}+\cdots O(\Delta x^3)\right]$$

$$\approx\frac{1}{4}\Delta x^2\left[\Phi'''(x_i)-\Phi''^2(x_i)/\Phi'(x_i)\right]\quad\text{where } f=\Phi'(x)\neq 0$$

16.1 (94)

whereas the spatial truncation error (STE) in Eq. 16.1 (91) is of order $(\Delta x^2/12)\,\phi'''(x_i)$. Both truncation errors are of the same formal order so that in this example it is obviously inappropriate in general to proceed to improve only the NLTE by say, a Newton-Raphson technique or a predictor-corrector procedure, since the effort involved is more effectively expended by decreasing the step size Δx which would, consequently, decrease <u>both</u> the NLTE and the STE.

Based on the results of the simple example shown above, several additional points are suggested, notably that the <u>ad hoc</u> linearizations mentioned previously could effectively reduce the order of the truncation error of the overall method. Furthermore, an optimum situation is where the NLTE and the STE are of the same order. Since the overall truncation error is determined by the lowest order error, the effort required to obtain the higher order truncation error, be it NLTE or STE, must be carefully weighed against the lack of improvement in the overall method truncation error. Should a case arise where the NLTE is the determining factor, this error can be reduced in the present linearization by taking additional terms into account in the expansion about the known time level. These additional terms may be evaluated in a number of different ways, by iteration across a step, for instance, but once again care must be taken to ensure that the result is worth the effort. In this regard, the degree of iteration consistent with the spatial truncation error in the above linearization is quite evident, unlike, for instance, some of the techniques for solving the nonlinear difference equations where careful establishment of the convergence criterion (or number of allowable iterations) is necessary.

The procedure may be formalized for a typical system with ϕ a function of x,y

$$\frac{\partial}{\partial x}H(\phi)=F(\phi)\frac{\partial}{\partial y}G(\phi)$$

16.1 (95)

Centering between the n+1 and n pseudo time levels and proceeding as in Eqs. 16.1 (90), (91), (92) and (93) yields

$$\frac{H(\phi_i^{n+1})-H(\phi_i^n)}{\Delta x}=F(\phi_i^n)\,\delta_y G(\phi_i^n)+\frac{1}{2}\left\{F(\phi_i^n)\,\delta_y\left[\left(\frac{dG(\phi)}{d\phi}\right)_i^n(\phi_i^{n+1}-\phi_i^n)\right]\right.$$

$$\left.+\left(\frac{dF(\phi)}{d\phi}\right)_i^n(\phi_i^{n+1}-\phi_i^n)\,\delta_y G(\phi_i^n)\right\}+O(\Delta x^2,\Delta y^2)$$

16.1 (96)

If $H(\phi)$ were simply equal to ϕ, the expansion given by Eq. 16.1 (96) is both linear and second order, and could then be utilized in the implicit elimination without further manipulation. If further, $F(\phi)$ were unity and $G(\phi)$ were equal to ϕ, the conventional Crank-Nicolson scheme is recovered. It is apparent from Eq. 16.1 (96) that if the pseudo-time derivatives are themselves linear, then second-order accuracy requires no more than a simple Crank-Nicolson averaging of the transverse spatial derivatives followed by linearization in the manner of Ref. 64. If the pseudo-time derivatives are nonlinear, such as occur in the conventional boundary layer equations, then care is required to maintain second-order accuracy. The problem becomes apparent if, for the moment, attention is devoted to the simple problem of Eq. 16.1 (90). Here it can easily be shown that even with the simplest of linearizations, i.e., that f^{n+1} is equal to f^n, first-order accuracy in the pseudo-time direction is obtained. Thus it is intuitively reasonable to expect even a modest linearization (approximation) to f^{n+1} to do better than first-order accuracy. Turning now to Eq. 16.1 (96), where pseudo-time derivatives contain nonlinearities, it is obvious here that the simplest of linearizations, $H(\phi^{n+1})$ equal to $H(\phi^n)$, completely destroys the solution. Thus considerable care is required in the case of nonlinear pseudo-time derivatives. In these circumstances, an advantage is obtained by basing the linearization on an expansion about the (n+1/2) level, as outlined below, and this yields

$$\frac{H(\phi^{n+1})-H(\phi^n)}{\Delta x}=\left(\frac{dH}{d\phi}\;\frac{\partial\phi}{\partial x}\right)^{n+1/2}+O(\Delta x^2)$$

16.1 (97)

further,

$$\left(\frac{dH}{d\phi}\right)^{n+1/2}=\left(\frac{dH}{d\phi}\right)^n+\left(\frac{d^2H}{d\phi^2}\;\frac{\partial\phi}{\partial x}\right)^n\frac{\Delta x}{2}+O(\Delta x^2)$$

16.1 (98)

and, of course, in Eq. 16.1 (97) $(\partial\phi/\partial x)^{n+1/2}$ is readily represented by a second-order accurate finite-difference operator. The critical term in the linearization is then $(\partial\phi/\partial x)^n$ appearing in the expression for $(dH/d\phi)^{n+1/2}$, and this term must be represented <u>without</u> a (n+1) level term in the finite-difference operator, otherwise linearity would be lost. However, it is clear that in Eq. 16.1 (98) a first order representation of $(\partial\phi/\partial x)^n$ is adequate to preserve overall second-order accuracy and so with a central difference for $(\partial\phi/\partial x)^{n+1/2}$ and a backward difference for $(\partial\phi/\partial x)^n$, there results

$$\frac{H^{n+1}(\phi)-H^n(\phi)}{\Delta x}=\frac{\phi^{n+1}-\phi^n}{\Delta x}\left[\left(\frac{dH}{d\phi}\right)^n\right.$$

$$\left.+\left(\frac{d^2H}{d\phi^2}\right)^n\left(\frac{\phi^n-\phi^{n-1}}{\Delta x_b}\right)\frac{\Delta x}{2}\right]+O(\Delta x^2)$$

16.1 (99)

which is the desired expansion. The combination of Eqs. 16.1 (96) and (99) then provides the linear difference representation of the model equation, Eq. 16.1 (95), to second-order accuracy.

The foregoing linearization is readily applied to the boundary layer equations using chain rule differentiation and interpreting H, for instance, as ρu^2 and ϕ as $\rho u v$. In combination with either a multi-level difference scheme or by use of iteration, any order non-linear truncation error can be obtained if desired. Again, it must be clearly stated that the marching linearization as presented above is conceptually quite different from the Newton-Raphson linearized system developed as part of the solution of the nonlinear equation. In the marching

case, by linearizing about the previous station's known solution the spatial discretization error and non-linear truncation errors go hand-in-hand and improvements in both are obtained by reducing the marching direction step. Iteration, which only improves the non-linear error (and perhaps stability), costs roughly the same as one marching step and if possible should be avoided. Newton-Raphson (or quasi-linearization, as it is sometimes called) is a technique for solving a non-linear equation, which as a by-product produces a linear system for iteration. If one identified the first (known) iterant as the previous marching direction solution and the second (unknown) iterant as the current marching direction solution, then in many cases identical formulae to the marching linearization are obtained. As a result, many investigators have not discriminated between marching linearization and Newton-Raphson (quasi-linearization) but without this discrimination the critical relationship between spatial and non-linear error is lost.

16.1.2.7 The Coupled System of Equations

In the usual boundary layer system of equations the transverse momentum equation reduces to the requirement that the static pressure be constant across the boundary layer and this leaves the streamwise momentum equation, the continuity equation and the thermal energy equation to determine the velocity components, u, v and the density ρ. Further it is clear that these three remaining equations are coupled together in that all three of the dependent variables appear in each of the governing equations. The inadequate treatment of this coupling can seriously degrade the quality of the solution (Blottner, Ref. 16.66). Perhaps the simplest coupling treatment is a Picard type of iteration with the streamwise momentum equation generally being regarded as an equation for u, the energy equation giving ρ, and the continuity equation yielding v. The three equations are then solved sequentially using the most recent values of the dependent variables. Iteration then serves to couple the equations together. Blottner was able to show that a very large number of such iterations (greater than 10) was often required to obtain overall second-order accuracy with second-order spatial difference formulae with iterative coupling.

A much more attractive method is to introduce a stream function ψ which identically satisfies the continuity equation and the coupling remains only between the energy and streamwise momentum equation. This residual coupling is often handled in the sequential Picard manner outlined previously and certainly in cases of high heat transfer rates or at high Mach numbers one would expect a similar large number of iterations would be necessary in this scheme for overall second-order accuracy. Finally, of course, the system can be treated directly as a coupled system and the matrix enlarged to form a block banded system, see for instance the pioneering work of Flugge-Lotz and Blottner (Ref. 16.85), (see Ref. 16.66 for a bibliography). The cost of solving the complete coupled system is quite high compared to solving each of the equations individually. However, considering the number of iterations required in the sequential process and possible convergence problems, the direct coupled system becomes very attractive. In two dimensions there does seem quite a lot to be gained from eliminating the continuity equation by some means or other, although the resulting complication of the streamwise momentum equation might be significant. The continuity equation is a first order equation with the momentum equations being at least second-order and boundary conditions on the continuity equation can pose a problem, so that its elimination from the system can be advantageous from this point of view also. Unfortunately, in three space dimensions the utility of the stream function is greatly diminished since at least two stream functions must be introduced to eliminate the continuity equation.

16.1.2.8 Coordinate Systems and Finite Difference Grids

For a numerical solution of the boundary layer equations the finite differencing could be applied directly to the governing equations in primitive variable form in physical coordinates. Clearly, however, difficulty would be experienced as the boundary layer grew in the streamwise direction and stagnation points would require special treatment. At first sight it might appear that stagnation regions could be dispersed with in talking about turbulent boundary layers. However, the stated aim here is to perform airfoil type boundary layer calculations so that some treatment of the stagnation region is called for. One major attribute of finite difference methods which it is hoped to retain, is that the discrimination between the boundary layer states can all reside in the turbulence model and that one single scheme can (conceptually) integrate the governing equations from the stagnation point into the wake.

The problem is further compounded in turbulent flow by having at least two length scales in the direction normal to the wall, y^+ and y/δ, where y^+ is the previously defined law of the wall coordinate $y(\tau_w/\rho_w)^{1/2}/\nu_w$ and δ is some outer region thickness scale such as the boundary layer thickness. The problems of boundary layer growth and stagnation points are generally treated by means of a transformation of the governing equations while the problem of multiple length scales is usually treated by means of a non-uniform finite difference grid. Both topics will be briefly reviewed.

Insofar as transformations of the governing equations are concerned, much of the early work in laminar flow used the Crocco variables x and u as independent variables with the shear stress τ as dependent variable. This scheme has several valuable properties, among them is the combining of the continuity equation and streamwise momentum equation, and this has distinct advantages from the equation coupling viewpoint discussed previously. In addition, by choosing equal increments in u, the problem of the multi-length scale boundary layer is treated without the need for a non-uniform mesh. Unfortunately, this transformation does not countenance double-valued velocities such as might occur with a velocity profile overshoot, a common occurrence in a film-cooled boundary layer. Consequently this transformation is not widely used in turbulent boundary layer procedures.

As was mentioned previously, many authors introduce the stream function and this can be done as an independent variable in the von Mises form of the equations. Here the advantages are similar to the use of the Crocco variables but the double-valued stream function problem is not permissible in any event in the steady boundary layer system of equations as it implies reverse flow. In the von Mises system a singularity at the wall requires

careful handling; however, in many circumstances the governing equations need not be solved at the wall proper but can be structured such that the first point away from the wall is the first location the governing equations are used. Thus the von Mises form is quite attractive although it does not remove the problem of leading edge singularities nor grid growth. Patankar and Spalding (Ref. 16.67), for instance, use this formulation in their widely used turbulent boundary layer prediction scheme.

Other authors have used transformations of the Dorodnitsyn-Howarth-Stewartson-Illingworth variety which introduced a new normal coordinate stretched by the local density. Use of this transformation reduces the resolution problem with severe density gradients; however, it does nothing for the stagnation point problem. This transformation is in fact incorporated into the Levy-Lees transformation which does have the property of removing the leading edge starting point difficulty. The Levy-Lees transformation is quite straightforward and is particularly well suited to laminar flow due to its close relationship to the laminar flow similarity coordinates. This relationship obviously is of less importance in turbulent flow where the laminar flow similarity coordinates are not relevant and such a formulation may even be at some disadvantage. Be this as it may, the Levy-Lees transformation has been used quite successfully by Cebeci and Smith (Ref. 16.68) for both laminar and turbulent flow.

Now in all of the foregoing transformations use may be made of known edge quantities to nondimensionalize variables. As an extension of this process some authors use a transformation where the distance normal to the wall is normalized by some local boundary layer thickness parameter, usually the "incompressible" displacement thickness δ^*. Such a transformation has the advantage that it can remove the leading edge starting problem and also ease the nonlinear problem since, for instance, the stream function ψ/ψ_e as a function of y/δ^* does not change rapidly in the marching direction, thus a prior station's solution provides a very good approximation for treating the nonlinear process. Grid growth is also more easily treated in this frame. The principle disadvantage of this transformation is that the unknown thickness δ^* at the location where the solution is being sought is required and this can be accomplished either iteratively (as part of a nonlinear iterative process) or directly as part of the elimination process in the solution of the banded matrix. This δ^* transformation has been used successfully by Herring and Mellor (Ref. 16.69) and McDonald and Fish (Ref. 16.58).

In summary then, given the basic desire to have one formulation which can encompass the entire turbine airfoil boundary layer starting at the leading edge stagnation point and ending in the airfoil wake, the choice would seem to lie between the Levy-Lees or δ^* transformation (or indeed a combination of them both) with the use of a streamfunction in either case. Apart from the stagnation region problem, (which has been circumvented by a number of authors who simply start from a very thin initial boundary layer of some assumed shape) the von Mises transformation is also very attractive.

Turning now to the problem of distributing the mesh points across the boundary layer, two complicating factors in what would otherwise be a straightforward process are observed. The aim here is to have a grid which allows roughly equal increments in the variables ρ, u or ρu, whichever is the most demanding. As was mentioned earlier, use of the von Mises transformation greatly simplifies this process in all but a few instances. However, in general the first complication is the a priori determination of what will be an adequate grid for a given problem. The second complication concerns the structure of the finite difference formulation with a nonuniform mesh. Each of these factors will be discussed in turn.

Taking the easier factor first, that of considering the effect of the nonuniform mesh on the finite difference structure itself, it is noted that this problem only arises when the finite difference molecule requires more than two grid points. The Keller box method (Ref. 16.70), which centers the solution between grid points, thus very neatly circumvents the unequal mesh problem since it is essentially a two point method. The Keller box method does have certain other less attractive features so that in general other treatments of the unequal mesh problem might be required. The very straightforward method of simply devising unequally spaced difference formulae by Taylor expansion or equivalently by Lagrange interpolation does have the problem that unless the mesh eccentricity, i.e., ratio of adjacent grid step size, is near unity, a reduction in order accuracy of the calculation will result. Blottner (Ref. 16.71) has discussed this problem in detail and advocates use of a transformation to determine the unequal mesh difference formulae where

$$y = f(y') \qquad 16.1\ (100)$$

and in the y' space an equally spaced mesh is used. Difference formulae are then constructed by the chain rule

$$\frac{\partial}{\partial y} = \frac{\partial}{\partial y'}\frac{dy'}{dy} = \left(\frac{df}{dy'}\right)^{-1}\frac{\partial}{\partial y'}$$

$$\frac{\partial^2}{\partial y^2} = \left(\frac{df}{dy'}\right)^{-2}\left[\frac{\partial^2}{\partial y'^2} - \frac{d^2f}{dy'^2}\left(\frac{df}{dy'}\right)^{-1}\frac{\partial}{\partial y'}\right] \qquad 16.1\ (101)$$

and Blottner (Ref. 16.71) advocates a finite difference approximation to the derivatives of the stretching function f, with the second derivative evaluated in conservative form, e.g.,

$$\left(\frac{df}{dy'}\right)_i^{-1} = \frac{\Delta y^+(\Delta y^{+2} + \Delta y^{-2})}{\Delta y^+\Delta y^-(\Delta y^+ + \Delta y^-)}$$

and $$\Delta y^+ = y_{i+1} - y_i\ ,\ \Delta y^- = y_i - y_{i-1} \qquad 16.1\ (102)$$

whereas Briley and McDonald (Ref. 16.64) have preferred with some success to differentiate an analytic stretching function, notably the one suggested by Roberts (Ref. 16.72). Similar analytic differentiation of the geometric progression form of the distribution function used by Smith and Cebeci (Ref. 16.73) and McDonald and Fish (Ref. 16.58) is readily accomplished. In practice given the choice, the transformation process is to be preferred for determining unequally spaced difference formulae, if for no other reason than to ensure a smooth distribution of truncation error.

Turning now to the second factor, that of determining a suitable mesh distribution for a given problem, here the various approaches exhibit little unanimity. The problem is greatly simplified if it is not desired to define the

sublayer, a course of action previously deemed unacceptable in regions of high heat transfer or highly accelerated flows. Above the sublayer a very nearly equal mesh suffices for the turbulent boundary layer and the only problem is the growth of the boundary layer. The growth problem may be treated by periodic re-interpolation of the solution and is particularly simple with an explicit scheme (Nash, Ref. 16.74). Two stretching techniques in use to define the sublayer are the previously mentioned geometric progression and the Roberts' technique. In using either technique a minimum step size normal to the wall is estimated, usually on the basis of requiring a y^+_{MIN} to be in the region of two to four. In the geometric progression scheme the number of grid points felt appropriate to define the boundary layer thickness serve to define the required constant grid eccentricity. This selection process usually assures a good grid for turbulent flow provided the eccentricity is less than about 1.1. However, for laminar flow the grid is almost certainly too refined, but overall this rather conservative selection works quite well in practice in performing airfoil boundary layer calculations. Even so, McDonald and Fish found it convenient to have a re-interpolation scheme available so that if necessary the grid can be restructured during the course of a calculation.

In using the Roberts' technique two or more domains of uniform but differing mesh sizes are identified. Obviously in the boundary layer the two regions are the wall and wake regions. The Roberts' scheme then distributes the grid points to smoothly blend the various regions. Again the desire to place say, three or four grid points, below a y^+ of 15 determines the inner scale while the total number of available grid points and the overall maximum boundary layer thickness provide the necessary information to prescribe the transformation. Again in practice the laminar region of a typical airfoil is probably overly described but the overall problem does not usually lend itself to optimizing the normal grid for the axial flow development. The most feasible approach at this point is to monitor the axial development and should the mesh become too badly distributed, perform a reinterpolation of the grid. Excepting very high Mach number flows where the density gradients near the outer edge of the boundary layer can be appreciable, either the geometric progression or the Roberts' scheme can lead to an acceptable grid. Use of a non-dimensional y-coordinate with a localized boundary layer thickness scale as the normalizing agent does greatly simplify the problem of having an adequate grid for the entire airfoil surface.

Lastly, it remains to define the term "adequate grid" used previously and here only very general guidelines can be given. It should be clear at this point that the onus of determining whether or not a grid is acceptable must lie with the user, in view of the ad hoc nature of the grid selection process. It is quite unrealistic to expect the originators of the procedure to provide a default mesh selection scheme which will be adequate for all boundary layer problems. The user must select a mesh, both normal and axial, and determine the variation of some critical parameter, such as skin friction, with mesh refinement on a typical problem case. Only when the critical parameter does not change to some acceptable degree of tolerance (user defined) can the mesh be considered adequate. Subsequent cases must still be examined to see that the solution remains similarly distributed to the mesh refinement case. For airfoil calculation an approximate guide might be to take axial step sizes in the region of the boundary layer thickness and this translates roughly into fifty to sixty axial locations per surface. Normal to the wall prior experience suggests something in excess of forty grid points in a second or lower order scheme with the first grid point placed at a y^+ or between two and four. Subsequently it does not seem advisable to allow the velocity to change from grid point to grid point by more than $.05\ u_e$ without redistributing the mesh. Given a mesh of this degree of refinement it might be expected that changes in heat transfer rates could be held to less than approximately two percent upon mesh refinement.

16.1.2.9 Starting Profiles

For an initial value problem of the boundary layer type, information must be supplied which either directly or indirectly allows starting profiles of the dependent variables to be prescribed. The velocity and temperature profile families for both laminar and turbulent flow discussed in the section on integral methods have been widely used in this regard. Without difficulty these profiles can be used to specify the density and axial velocity at some initial location. Difficulty, however, can be experienced in determining the variation of transverse (or spanwise) velocity across the boundary layer. Examination of the continuity equation reveals that this transverse velocity is a function of the axial rate of change of the axial velocity. Thus for consistency this transverse velocity really should be obtained from some suggestion as to the axial variation of the axial velocity profile. The various methods used in this regard will now be reviewed briefly.

Firstly, the problem can be resolved by setting the transverse velocity to zero at the initial station, since indeed boundary layer theory requires the transverse velocity to be small in any event. Subsequently, quite rapid changes in the predicted boundary layer behavior can occur and this starting technique cannot be recommended unless in the region of interest the predictions can be shown to be insensitive to the starting conditions. When predictions are being compared with measurements, often it is desired (and the information known) to match the initial rate of change of, say, the displacement thickness to the observed value. By integrating the continuity equation, one obtains

$$\left(\frac{v}{u}\right)_e = \frac{d\delta^*}{dx} - \frac{(\delta-\delta^*)}{\rho_e u_e}\frac{d}{dx}(\rho_e u_e) \qquad 16.1\ (103)$$

so that the desired transverse velocity v_e the edge of the boundary layer at the initial location is known and by a simple axial iteration the transverse velocity profile shape at the first computed axial location in terms of, for instance, v/v_e vs y/δ^* could be used at the initial location with the v_e obtained from Eq. 16.1 (103). Further, in cases where the measured axial rate of change of displacement thickness is not known, some approximation (such as the flat plate value) for this rate of change could be adopted.

As a straightforward development of the foregoing technique it is often assumed that in terms of certain similarity coordinates the axial derivatives are negligible, i.e., a local equilibrium is assumed. Special forms of the governing equations independent of the axial coordinate are then obtained and

the equilibrium values of all the velocity components found usually iteratively by integration. This is in essence the treatment used at stagnation points for, although the stream function ψ or the velocities u and v might be zero, ψ/ψ_e, u/u_e and v/v_e are still well behaved and can be derived from assumptions of the type

$$\psi/\psi_e = f(y/h) \qquad 16.1\ (104)$$

and

$$\frac{\partial f}{\partial x} = 0 \qquad 16.1\ (105)$$

By use of the local equilibrium hypothesis both axial and transverse velocity profiles can be obtained at the starting location. The iterative solution of the similarity equations can be started from the laminar or turbulent profile families described earlier. In this mode of operation no additional information is required by the finite difference procedures that would be required to start the integral methods. This local equilibrium starting technique has been used very successfully in both laminar and turbulent flows by Mellor and Herring (Ref. 16.69), Cebeci and Smith (Ref. 16.73) and McDonald and Fish (Ref. 16.58).

Lastly, some finite difference schemes, notably some of the Russian methods of splitting described by Yanenko (Ref. 16.75) offer the prospect by careful structuring of not requiring an initial profile of transverse velocity when applied to the boundary layer equations. Such methods are multi-level in that several intermediate level solutions are obtained in the process of marching one axial step. While the user might not wish to use such a scheme once the solutions were started, as a starting technique they are very intriguing.

16.1.2.10 The Current Status of Finite Difference Boundary Layer Procedures

Unlike integral procedures for predicting boundary layer development, the status of finite difference schemes for solving parabolic and hyperbolic equations is changing rapidly at the present time. For this reason it is not proposed to review the available schemes with a view to recommending some "best" procedure for the turbine problem. Such a recommendation would doubtless soon be outdated. Nor is it intended to describe any one scheme in detail, for to do justice considerably more space would be required than is available here. Instead some of the better known current schemes will be reviewed in the light of the topics discussed in earlier paragraphs. Hopefully, by following this same process the reader will be better able to evaluate the suitability of the newer schemes that will become available in the future. Again the pitfalls of the relatively untried scheme must be cautioned against and anyone contemplating such an application should read the charming little essay on this subject by Moretti (Ref. 16.76). Finally little comment at this point will be made on the various turbulence models incorporated into the various procedures. Almost certainly the various models are interchangeable and best reviewed separately as a class.

If a start is made by ruling out any scheme that cannot treat both laminar and turbulent boundary layers for the simple reason that extensive regions of both types of boundary layers are found on turbine blades, curiously enough the highly regarded scheme of Bradshaw-Ferriss (Ref. 16.77) must be discarded. Doubtless an implicit version of the Bradshaw-Ferriss procedure which retained the laminar viscosity could be constructed (and at this point probably has) and in this state it would be a much more practical procedure for gas turbine applications. In any event, the original Bradshaw-Ferriss code is probably best viewed as a vehicle for implementing a turbulence model and not as a general purpose boundary layer code. Nash (Ref. 16.74) uses a modified version of Bradshaw's turbulence model in an explicit three-dimensional turbulent procedure but with the same scheme he has performed a number of laminar two-dimensional calculations without difficulty. The major objection that one would have to Nash's scheme for gas turbine applications would be that the conditional stability arising from the explicit integration would not allow the viscous sublayer to be defined efficiently. Using the DuFort-Frankel scheme, Pletcher (Ref. 16.62) developed an apparently unconditionally stable explicit procedure (in the usual linear sense) in which the sublayer was defined without difficulty. Pletcher has successfully tested his procedure on a wide variety of flows and the usual objection to inconsistent schemes, that of not being able to reduce the truncation error beyond some point for an aribitrary mesh, although disquieting, apparently did greatly influence his results as far as can be determined. Coupling and nonlinear truncation errors might be expected to affect the aforementioned procedures in gas turbine applications however.

Turning to the implicit schemes, attention still is restricted to procedures with a demonstrated capability for treating turbulent as well as laminar flow. Thus, highly regarded schemes such as the Davis coupled scheme (Blottner, Ref. 16.78) and the fourth order scheme of Peters (Ref. 16.79) will not be discussed. Such schemes may well be the fabric of the future but further discussion at this point is probably premature. Rapidly becoming one of the most widely used schemes, the procedure of Spalding and Patankar has much to recommend it. In its original form only the lack of a sublayer or stagnation point could seriously be held against the procedure for gas turbine applications. The lack of the sublayer has been removed by a number of people, for instance Launder and Jones (Ref. 16.80) and a highly developed version widely available from Kays et al. (Ref. 16.81) in a form well suited for gas turbine use, with the exception of the stagnation point treatment. In this regard it is claimed by Becko (Ref. 16.82) that starting the Patankar and Spalding (Ref. 16.67) scheme for some arbitrary and small boundary layer thickness is an adequate treatment of the stagnation region. However, should this fail to be satisfactory in some instances, an acceptable alternative stagnation point treatment might be very costly to develop.

Three widely available, highly developed, and extensively tested schemes of quite similar construction have been developed by Herring and Mellor (Ref. 16.69), Cebeci and Smith (Ref. 16.73) and McDonald and Fish (Ref. 16.58). In all three cases the procedure of Hartree and Womersly is followed where the streamwise direction is discretized first. Originally Mellor and Herring then treated the resulting two point boundary value problem by a shooting technique but subsequently abandoned this technique in favor of an implicit Gaussian elimination process very similar to that developed by McDonald and Fish (Ref. 16.58). Cebeci

and Smith (Ref. 16.73) used the Choleski process to treat their implicit system of equations. All three methods treat both the sublayer and stagnation points and have optional equilibrium starting procedures. As a result of their structure this type of method requires the non-linear two point boundary value system be iterated out to a fair degree of convergence to retain spatial stability. During this non-linear processing, grid growth and equation coupling can be taken care of.

More recently in an effort to improve the efficiency of performing routine boundary layer calculations, presumably with the three-dimensional problem in mind, Keller and Cebeci (Ref. 16.83) have applied Keller's so-called box scheme. In this scheme the boundary layer equations are written as a nonlinear set of coupled first order equations which are treated directly by a Newton-Raphson process which gives rise to a block tridiagonal matrix for elimination. Only four grid points are used in this scheme, hence the box terminology. Although with the passing of time the first wave of enthusiasm for this technique has diminished somewhat (Blottner, Ref. 16.66), it does seem to be a very neat scheme for the boundary layer equations and is marred really only by its storage requirements. The technique has apparently no problem at stagnation points and can treat the sublayer. At the present time it is being extensively tested and developed.

Although not so widely known as the foregoing schemes, Harris (Ref. 16.84) has developed a turbulent version of the laminar scheme originally developed by Flugge-Lotz and Blottner (Ref. 16.85) which apparently worked well but is not widely used. Adams (Ref. 16.86) developed a scheme of quite remarkable similarity to that constructed by Harris. Finally the strip scheme of Kendall (Ref. 16.87) has fallen into widespread use for performing reacting boundary layer calculations, for which purpose it has been highly developed. Given the ready availability of other schemes with well documented capabilities, there has not been any great incentive to pursue the application of Kendall's scheme for turbomachinery problems.

A number of the foregoing schemes are very widely available and of quite similar nominal capability. In certain cases the choice would appear to reduce to evaluating the relative economics of the competing schemes, since the schemes mentioned earlier all seem quite robust in operation. Order accuracy considerations, which might be expected to provide some guidance, are such that in most of the schemes formal second order accuracy is relatively easily attained by proper centering of the scheme. However, in many schemes routinely a first order difference in the axial direction is used to avoid spatial wiggles which can remain undamped in some cases. Thus the demonstrated ability to routinely use a second order axial scheme and consequently use fewer axial steps in a computation would be an attractive feature of the selected scheme, but one which has not yet been clearly attributed to any developed procedure. Hence, given that the schemes all require about the same number of mesh points, the point can be made that a large portion of the cost of marching one axial step is made up of forming coefficients of the discretized governing equations and is roughly independent of the precise details of the integration scheme. Thus the great variations in quoted run times among the various procedures, even given the difficulty of establishing a common base for comparison, must reside in the treatment of the nonlinearities and coupling between equations. Rigorous treatments like that in the Keller box scheme or the one used in the Hartree-Womersly based schemes are obviously time-consuming and very conservative in comparison to say, the scheme of Patankar and Spalding (Ref. 16.67) with its almost pathological avoidance of iteration. The question of adequacy and accuracy can only be answered on an ad hoc basis and it must therefore be the onus of the potential user to satisfy himself that the solutions to his problem are mesh independent to his required degree of accuracy. Clearly in the eyes of some experts it will be necessary to use a much more refined axial mesh, either that, or iterate at given axial locations for some demanding problems with a method like Spalding and Patankar with its cursory treatment of non-linearities and coupling, than with the Keller or Hartree-Womersly schemes. The ideal situation is one in which the treatment of the coupling, non-linearities and spatial differencing are all accurate to the same degree, and Anderson (Ref. 16.88) has tried to implement this concept in developing a modified version of the Keller box scheme. However, the key point is that as obtained "off the shelf" so to speak, the various suitable and similar schemes might exhibit markedly differing run times for a given problem. This run time variation would be related to the degree of conservatism (or lack of it) of the originator. Further, many of the quoted run times are times required to achieve a level of comparison with experiment, not necessarily some degree of mesh independence of solution.

At this point discussion of the finite difference procedures for predicting the boundary layer behavior will be terminated. Several good robust schemes are widely available and the prospects are excellent for the development of even more efficient schemes.

16.1.3 Axisymmetric (Pitch-Averaged) Boundary Layers

16.1.3.1 Motivation

In the turbomachine, the hub and casing boundary layers, commonly called the "annulus wall boundary layers" can, in a very simple minded view, be thought of as swirling axially symmetric boundary layers and as such the study of this type of boundary layer would obviously seem worthwhile. That such a simplified viewpoint necessitates a high degree of compromise is well known. The hub and casing surfaces are often not continuous and frequently stationary surfaces lie adjacent to rotating components. Leakage and coolant flow often occurs through gaps in the surface, but all these difficulties shrink to insignificance when compared to the effect of blade or stator rows. Here the overturning of the annulus wall boundary layers within the blade or stator row due to the mainstream deflection and the periodic shedding of these large wakes into the subsequent stages causes major effects which cannot be rigorously taken into account in any axially symmetric boundary layer analyses. The difficulties involved in any more rigorous approach are of course quite daunting and this has led to the development of the concept of "pitch averaging". In the pitch averaging approach the azimuthal variations are expressed as a mean value plus a small perturbation and the equations of motion averaged in the azimuthal direction. The resulting equations are quite as rigorous as the original unaveraged set and, as in the similarly treated turbulence problem, the unknowns are now the mean values and the correlation of the perturbations or "fluctuation". The pitch

averaged approach has obvious value if the mean values and correlations can be approximated such that the resulting averaged flow is reasonably well predicted. The current indications are that indeed this pitch averaging could be a very useful tool and this concept will now be developed. Much of the original work on this topic has been carried out by Horlock and his co-workers with independent contributions by Mellor and its application in an integral formulation described in detail by Horlock and Perkins (Ref. 16.89) and Mellor and Wood (Ref. 16.92).

16.1.3.2 The Governing Equations

Implicit in the form of the governing equations is a coordinate system. In developing integral moments of the governing equations it has long been recognized that certain coordinate systems possess major advantages over others. In particular streamline coordinates based on the local direction of the inviscid flow at the edge of the boundary layer greatly simplify the momentum integral equations. This advantage disappears when the partial differential equations themselves are treated directly by numerical methods and in this case the effort has been to develop coordinate systems which allow the solution to be obtained in some logical manner. Anderson (Ref. 16.88) has pointed out that use of streamline coordinates or approximations to them on a local basis allows the governing equations to be simplified since the velocities normal to the approximate streamlines may be small, particularly in internal flow where the flow is constrained between two boundary surfaces. For his finite difference scheme Anderson used the potential flow streamlines as an approximation to the real flow. Most authors have also used orthogonal coordinate systems although this is by no means necessary and in the numerical schemes orthogonality can readily be abandoned if a more convenient coordinate system results. Starting then from the orthogonal system of curvilinear coordinates originally due to Hayes (Ref. 16.90) for the three-dimensional boundary layer one has:

Continuity

$$\frac{\partial \rho}{\partial t} + \frac{1}{h_1 h_2 h_3}\left[\frac{\partial}{\partial x} h_2 h_3 \rho u + \frac{\partial}{\partial y} h_1 h_3 \rho v + \frac{\partial}{\partial z} h_1 h_2 \rho w\right] = 0$$

16.1 (106)

Streamwise-Momentum

$$\frac{\partial}{\partial t}\rho u + \frac{1}{h_1 h_2 h_3}\left[\frac{\partial}{\partial x} h_2 h_3 \rho u^2 + \frac{\partial}{\partial y} h_1 h_3 \rho u v + \frac{\partial}{\partial z} h_1 h_2 \rho u w\right]$$
$$+ \frac{1}{h_1 h_2 h_3}\left[\rho u v h_3 \frac{\partial h_1}{\partial y} + \rho u w h_2 \frac{\partial h_1}{\partial z} - \rho v^2 h_3 \frac{\partial h_2}{\partial x} - \rho w^2 h_2 \frac{\partial h_2}{\partial x}\right]$$
$$= \frac{1}{h_2}\left[\frac{\partial}{\partial y}\frac{\mu}{h_2}\frac{\partial u}{\partial y}\right] - \frac{1}{h_1}\frac{\partial p}{\partial x}$$

16.1 (107)

Normal-Momentum

$$\frac{\partial}{\partial t}\rho v + \frac{1}{h_1 h_2 h_3}\left[\frac{\partial}{\partial x} h_2 h_3 \rho u v + \frac{\partial}{\partial y} h_1 h_3 \rho v^2 + \frac{\partial}{\partial z} h_1 h_2 \rho v w\right]$$
$$+ \frac{1}{h_1 h_2 h_3}\left[\rho v w h_1 \frac{\partial h_2}{\partial z} + \rho u v h_3 \frac{\partial h_2}{\partial x} - \rho w^2 h_1 \frac{\partial h_3}{\partial y} - \rho u^2 h_3 \frac{\partial h_1}{\partial y}\right] = -\frac{1}{h_2}\frac{\partial p}{\partial y}$$

16.1 (108)

Spanwise-Momentum

$$\frac{\partial}{\partial t}\rho w + \frac{1}{h_1 h_2 h_3}\left[\frac{\partial}{\partial x} h_2 h_3 \rho u w + \frac{\partial}{\partial y} h_1 h_3 \rho v w + \frac{\partial}{\partial z} h_1 h_2 \rho w^2\right]$$
$$+ \frac{1}{h_1 h_2 h_3}\left[\rho u w h_2 \frac{\partial h_3}{\partial x} + \rho v w h_1 \frac{\partial h_3}{\partial y} - \rho u^2 h_2 \frac{\partial h_1}{\partial z} - \rho v^2 h_1 \frac{\partial h_2}{\partial z}\right]$$
$$= \frac{1}{h_2}\left[\frac{\partial}{\partial y}\frac{\mu}{h_2}\frac{\partial w}{\partial y}\right] - \frac{1}{h_3}\frac{\partial p}{\partial z}$$

16.1 (109)

with the metric coefficients h_1, h_2, and h_3 giving the arc length ds by

$$ds^2 = h_1^2 dx^2 + h_2^2 dy^2 + h_3^2 dz^2$$

16.1 (110)

and it is in essence assuming that the local boundary layer thickness is small compared with the principle radius of curvature of the surface. Of the two possibilities, either to Reynolds time average first then pitch average, or vice versa, the usual precedent of time averaging first is adopted. With the accepted boundary layer approximations, the Reynolds time averaging of the equations results in

Continuity

$$\frac{\partial \bar{\rho}}{\partial t} + \frac{1}{h_1 h_2 h_3}\left[\frac{\partial}{\partial x} h_2 h_3 \bar{\rho}\bar{u} + \frac{\partial}{\partial y} h_1 h_3 \overline{\rho v} + \frac{\partial}{\partial z} h_2 h_1 \overline{\rho w}\right]$$

16.1(111)

Streamwise-Momentum

$$\frac{\partial}{\partial t}\bar{\rho}\bar{u} + \frac{1}{h_1 h_2 h_3}\left[\frac{\partial}{\partial x} h_2 h_3 \bar{\rho}\bar{u}^2 + \frac{\partial}{\partial y} h_1 h_3 \overline{\rho v}\,\bar{u} + \frac{\partial}{\partial z} h_2 h_1 \overline{\rho u w}\right]$$
$$+ \frac{\bar{\rho}\bar{u}\bar{w}}{h_1 h_3}\frac{\partial h_1}{\partial z} - \frac{\bar{\rho}\bar{w}^2}{h_1 h_3}\frac{\partial h_3}{\partial x} = -\frac{1}{h_1}\frac{\partial \bar{p}}{\partial x} + \frac{1}{h_2}\frac{\partial}{\partial y}\left(\frac{\bar{\mu}}{h_2}\frac{\partial \bar{u}}{\partial y} - \overline{\rho u' v'}\right)$$

16.1 (112)

Normal-Momentum

$$-\frac{1}{h_2}\frac{\partial \bar{p}}{\partial y} = \frac{1}{h_1 h_2 h_3}\frac{\partial}{\partial y} h_1 h_3 \overline{\rho v^2}$$

16.1 (113)

Spanwise-Momentum

$$\frac{\partial}{\partial t}\bar{\rho}\bar{w} + \frac{1}{h_1 h_2 h_3}\left[\frac{\partial}{\partial x} h_2 h_3 \bar{\rho}\bar{u}\bar{w} + \frac{\partial}{\partial y} h_1 h_3 \overline{\rho v}\,\bar{w} + \frac{\partial}{\partial z} h_2 h_1 \overline{\rho w^2}\right]$$
$$- \frac{\bar{\rho}\bar{u}^2}{h_1 h_3}\frac{\partial h_1}{\partial z} + \frac{\bar{\rho}\bar{u}\bar{w}}{h_1 h_3}\frac{\partial h_3}{\partial x} = -\frac{1}{h_3}\frac{\partial \bar{p}}{\partial z} + \frac{1}{h_2}\frac{\partial}{\partial y}\left(\frac{\bar{\mu}}{h_2}\frac{\partial \bar{w}}{\partial y} - \overline{\rho v' w'}\right)$$

16.1 (114)

where the Reynolds normal stresses have been neglected. Subsequently the stress terms $\bar{\mu}\,\partial\bar{u}/\partial y - \bar{\rho}\,\overline{u'v'}$ are written τ_x, τ_y etc. The time derivatives are retained on the supposition that the mean motion can still be allowed to vary in time provided the variation does not occur on a time scale approaching that of the turbulence. It has also been assumed that $\bar{\rho}\bar{w} >> \overline{\rho' w'}$.

Anderson (Ref. 16.88) retains the h_2 metric in his derivation of the averaged equations. Such a development might well be important in certain applications but for the moment the usual precedent of setting the h_2 metric to unity is followed (the thin shear layer approximation). The pitch averaged equations can now be derived by introducing

the dependent variable f as being the sum of some pitch averaged quantity $\bar{f}$ and a perturbation f'. Subsequently f' will be assumed small relative to $\bar{f}$. By definition

$$\bar{f} = \frac{1}{z_a - z_b}\int_{z_a}^{z_b} f\,dz$$

$$\int_{z_a}^{z_b} f'\,dz = 0$$

16.1 (115)

Now for the typical variable f an integral average of the derivative of f is

$$\int_{z_a}^{z_b} \frac{\partial f}{\partial \bar{x}}\,dz = \frac{\partial}{\partial \bar{x}}(z_a - z_b)\bar{f} - f_b\frac{\partial z_a}{\partial \bar{x}} + f_a\frac{\partial z_b}{\partial \bar{x}}$$

16.1 (116)

where $\bar{x}$ could be any coordinate direction except z. Now the governing equations are pitch averaged dropping the Reynolds averaged overbars on all but the Reynolds shear stress term. Now the single overbar signifies the pitch averaged value of some time mean quantity. The double overbar denotes the pitch averaged value of a turbulent correlation. The single overbar over a primed quantity denotes correlation between perturbations from the pitch averaged mean of some time averaged quantity. Taking the streamwise momentum equation as an example and writing $g = z_a - z_b$ their results

$$\frac{\partial}{\partial t}g\bar{\rho}\bar{u} + \frac{1}{h_1h_3}\frac{\partial}{\partial x}h_3 g\,\overline{\rho u^2} + \frac{1}{h_1h_3}\frac{\partial}{\partial y}h_1h_3\,\overline{\rho u v}\,g$$

$$+ g\,\overline{\rho u w}K_1 - g\,\overline{\rho w^2}K_3 = -\frac{1}{h_1}\frac{\partial \bar{p}}{\partial x}g + p_b\frac{\partial z_b}{\partial x} - p_a\frac{\partial z_a}{\partial x}$$

$$+ \frac{\partial}{\partial y}\bar{\tau}_x g - \tau_{xb}\frac{\partial z_b}{\partial x} + \tau_{xa}\frac{\partial z_b}{\partial x}$$

16.1 (117)

and in the usual manner the pitch averaged terms can be expressed as

$$\overline{\rho u} = \bar{\rho}\bar{u}$$

$$\overline{\rho u^2} = \bar{\rho}\bar{u}^2 + 2\bar{\rho}\bar{u} + \bar{\rho}\overline{u'^2}$$

$$\frac{\overline{\rho u v}}{\bar{u}\bar{\rho}\bar{v}} = \bar{\rho}\bar{u}\bar{v} + \bar{u} + \bar{v} + \bar{\rho}\overline{u'v'} + \bar{u}\overline{\rho v} + \overline{u'\rho v'}$$

16.1 (118)

and so on. Clearly for low speed flow it seems reasonable to neglect the density perturbation and certainly the triple correlations will normally be negligible in comparison with the double correlations. This leaves the pitch averated equivalent of the usual Reynolds shear and normal stresses. At this point in the development little is known of the behavior of these correlations and in applications these terms are usually neglected or crudely approximated. It is to be hoped that the description of these terms will be improved upon in the future since it is by no means clear at this stage that they can be neglected. The remaining additional terms due to pitch averaging arise from the forces on the blade surface and these too, although perhaps less controversial, are still the subject of some debate. The inviscid (but not necessarily irrotational) pressures could be used for the blade surfaces. The stresses on the blades τ_a and τ_b emerge as part of a separate blade boundary layer calculation but in many instances their difference may be quite negligible. Finally of course the gradients of the pitch averaged quantities in the azimuthal direction are dropped. Additional simplifications such as assuming the blades are thin allow the gap g to cancel everywhere except the effective blade force terms. The assumption of the thin blade also allows the upper and lower surface gap coordinate rates of change to be set equal, however for the moment this simplification is not applied. The governing equations are now expressed

Continuity

$$\frac{\partial \bar{\rho}}{\partial t} + \frac{1}{g h_1 h_3}\left[\frac{\partial}{\partial x}g h_3\bar{\rho}\bar{u} + \frac{\partial}{\partial y}g h_1 h_3\overline{\rho v}\right] = 0$$

16.1 (119)

Streamwise-Momentum

$$\frac{\partial}{\partial t}\bar{\rho}\bar{u} + \frac{1}{g h_1 h_3}\frac{\partial}{\partial x}g h_3\bar{\rho}(\bar{u}^2 + \overline{u'^2}) + \frac{1}{g h_1 h_3}\frac{\partial}{\partial y}g h_1 h_3(\bar{u}\overline{\rho v} + \overline{u'\rho v'})$$

$$+ K_1\bar{\rho}(\bar{u}\bar{w} + \overline{u'w'}) - K_3\bar{\rho}(\bar{w}^2 + \overline{w'^2}) = -\frac{1}{g h_1}\frac{\partial}{\partial x}g\bar{p} + \frac{1}{g}\frac{\partial}{\partial y}\bar{\tau}_x g$$

$$+ p_b\frac{\partial z_b}{\partial x} - p_a\frac{\partial z_a}{\partial x} - \tau_{xb}\frac{\partial z_b}{\partial y} + \tau_{xa}\frac{\partial z_b}{\partial y}$$

16.1 (120)

Normal-Momentum

$$-\frac{1}{h_2}\frac{\partial \bar{p}}{\partial y} = -\overline{\overline{\rho v^2}}K_2$$

16.1 (121)

Spanwise-Momentum

$$\frac{\partial}{\partial t}\bar{\rho}\bar{w} + \frac{1}{g h_1 h_3}\frac{\partial}{\partial x}g h_3\bar{\rho}(\bar{u}\bar{w} + \overline{u'w'}) + \frac{1}{g h_1 h_3}\frac{\partial}{\partial y}g h_1 h_3\bar{w}\overline{\rho v}$$

$$+ \overline{w'\rho v'} - K_1\bar{\rho}(\bar{u}^2 - \overline{u'^2}) + K_3\bar{\rho}(\bar{u}\bar{w} + \overline{u'w'}) + \frac{1}{g}\frac{\partial}{\partial y}\bar{\tau}_z g$$

$$-\frac{1}{h_3}(p_b - p_a) - \tau_{zb}\frac{\partial z_b}{\partial y} + \tau_{za}\frac{\partial z_a}{\partial y}$$

16.1 (122)

and for example

$$\bar{\tau}_x = \bar{\mu}\frac{\partial \bar{w}}{\partial y} - \bar{\rho}\,\overline{v'w'}$$

16.1 (123)

To recap, the single overbar signifies the pitch averaged value of some time mean quantity. The double overbar denotes the pitch averaged value of a turbulent correlation. The single overbar over a primed quantity denotes correlation between perturbations from the pitch averaged mean of some time averaged quantity.

Having derived the pitch averaged equations, as usual the choice of further integrating the governing equations or of treating the partial differential equations directly remains open. During the initial stages of the development of this concept, the various authors wisely chose to use the simple integral approach (see Horlock and Perkins, Ref. 16.89, for a discussion of the development of this approach). Encouraged by their success Anderson (Ref. 16.88) developed a finite difference scheme for solving the basic partial differential equations of motion. Both approaches will be briefly reviewed. Again it is not the purpose here to present in detail the various approaches and the reader intent in performing calculations should consult the original references. Here the aim is to outline the approach and detail its strengths and weaknesses.

16.1.3.3 The Momentum Integral Approach

A straightforward integral normal to the annulus wall of Eqs. 16.1 (120) and 16.1 (122) gives the pitch averaged momentum integral equations. The derivation is given in detail by Daneshyar (Ref. 16.91) for instance. Various integral thickness parameters can be introduced and the equations recast and, with certain coordinate systems, simplified somewhat. Here the analysis will not be specialized to that extent and it serves the present purposes sufficiently well to present the integral equation in a comparatively primitive form.

Continuity

$$\overline{\rho v}_e = \overline{\rho v}_w - \frac{1}{g h_1 h_3}\left[\frac{\partial}{\partial x}\int_0^\delta \bar{\rho}\bar{u}\,dy\right] g h_3 + \frac{\rho_e u_e}{h_1}\frac{\partial \delta}{\partial x} - \frac{\partial}{\partial t}\int_0^\delta \bar{\rho}\,dy + \bar{\rho}_e \frac{\partial \delta}{\partial t} \qquad 16.1\,(124)$$

Streamwise-Momentum

$$\frac{\partial}{\partial t}\int_0^\delta \bar{\rho}\bar{u}\,dy - \overline{\rho_e u_e}\frac{\partial \delta}{\partial t} + \frac{1}{g h_1 h_3}\frac{\partial}{\partial x} g h_3 \int_0^\delta \bar{\rho}(\bar{u}^2 + \overline{u'^2})\,dy$$

$$- \frac{\rho_e}{h_1}(\bar{u}^2 + \overline{u_e'^2})\frac{\partial \delta}{\partial x} + \bar{u}_e \overline{\rho v}_e + \overline{u'\rho v_e'} + K_1 \int_0^\delta \bar{\rho}(\bar{w}\bar{u} + \overline{u'w'})\,dy$$

$$- K_3 \int_0^\delta \bar{\rho}(\bar{w}^2 + \overline{w'^2})\,dy = \frac{1}{g h_1}\int_0^\delta \frac{\partial}{\partial x} g \bar{p}\,dy + \bar{\tau}_{xw} + \tilde{D}_{x1} \qquad 16.1\,(125)$$

Spanwise-Momentum

$$\frac{\partial}{\partial t}\int_0^\delta \bar{\rho}\bar{w}\,dy - \tilde{\rho}_e \bar{w}_e \frac{\partial \delta}{\partial t} + \frac{1}{g h_1 h_3}\frac{\partial}{\partial x} g h_3 \int_0^\delta \bar{\rho}(\bar{u}\bar{w} + \overline{u'w'})\,dy$$

$$- \frac{\rho_e}{h_1}(\bar{u}_e \bar{w}_e + \overline{u'w_e'})\frac{\partial \delta}{\partial x} + \bar{w}_e \overline{\rho v}_e + \overline{w'\rho v_e'}$$

$$- K_1 \int_0^\delta \bar{\rho}(\bar{u}^2 + \overline{u'^2})\,dy + K_3 \int_0^\delta \bar{\rho}(\bar{u}\bar{w} + \overline{u'w'})\,dy = \tau_{zw} + \tilde{D}_{z1} \qquad 16.1\,(126)$$

and

$$\tilde{D}_{x1} = \int_0^\delta \left(\frac{p_b}{h_1}\frac{\partial z_b}{\partial x} - \frac{p_a}{h_1}\frac{\partial z_a}{\partial x} - \tau_{xb}\frac{\partial z_b}{\partial y} + \tau_{xa}\frac{\partial z_a}{\partial y}\right) dy$$

$$\tilde{D}_{z1} = -\int_0^\delta \left(\frac{p_b}{h_3} - \frac{p_a}{h_3} - \tau_{zb}\frac{\partial z_b}{\partial y} + \tau_{za}\frac{\partial z_a}{\partial y}\right) dy \qquad 16.1\,(127)$$

If now the original governing equations are evaluated at the edge of the boundary layer and then nominally integrated normal to the wall the resulting set of equations can, by subtraction, be used to recast the integral equations in integral defect form. Following Horlock and Perkins (Ref. 16.89) and Mellor and Wood (Ref. 16.92) all of the contributions from pitch averaging can be lumped together into force defects of the type,

$$D_x = \sum D_{xn}$$

$$D_{x1} = \tilde{D}_{x1e} - \tilde{D}_{x1}$$

$$D_{x2} = \frac{\partial}{\partial x} g h_3 \int_0^\delta \bar{\rho}(\overline{u_e'^2} - \overline{u'^2})\,dy$$

$$D_{x3} = \int_0^\delta \left[\frac{\partial \bar{p}_e}{\partial x} - \frac{\partial \bar{p}}{\partial x}\right] dy$$

etc.

$$D_z = \sum D_{zn}$$

$$D_{z1} = \tilde{D}_{z1e} - \tilde{D}_{z1}$$

$$D_{z2} = \frac{\partial}{\partial x}\int_0^\delta \bar{\rho}(\overline{u'w_e'} - \overline{u'w'})\,dy \qquad 16.1\,(128)$$

and so on. In this form the pitch averaged momentum equations can now be made to look exactly like the usual axisymmetric swirling momentum integral equations with the addition of force defect terms D_x and D_z. Adequate specifications of the force defects is therefore the key to the eventual success of this type of analysis and this point will be returned to in a moment. For the time being it is observed that in addition to the problem of determining the streamwise velocity $\bar{u}$ there now arises the problem of determining the swirl component $\bar{w}$, commonly termed the cross flow velocity, for which one additional equation, the spanwise momentum equation, has already become available (the continuity equation can be thought of as eliminating $\overline{\rho v_e}$ from the system). In the usual integral manner, profiles of $\bar{u}$ and $\bar{w}$ must be specified and additional momentum equations constructed until the number of equations is equal to the number of parameters describing the profiles.

Considering now the velocity profile family problem, the strategy commonly adopted has been to consider a streamwise velocity component aligned with the direction of the edge inviscid streamline and a cross-flow component normal to this inviscid streamline direction. For small cross flows it is argued that any of the accepted two-dimensional profiles, such as that due to Coles (Ref. 16.9) suffices for a streamwise profile, thereby also specifying wall stress. Coles' profile, as discussed at length earlier, is a two parameter family so that immediately an additional integral equation is required. Cumpsty and Head (Ref. 16.93) in the related problem of the infinite yawed wing, for instance, generalized Head's very simple entrainment concept into three dimensions, and subsequently Horlock (Ref. 16.94) has applied an entrainment equation in the present problem. For the cross-flow profile a variety of suggestions has been made, such as the variation of Prandtl's profile made by Mager (Ref. 16.95) or the well known polar profile due to Johnson (Ref. 16.96). The Prandtl-Mager profile is a very simple one parameter family of the form

$$\frac{w}{u} = \tan\beta_w (1 - y/\delta)^2 \qquad 16.1\,(129)$$

where β_w is nominally the angle between the wall streamline and the edge streamline. Being a one parameter family (β_w) the Prandtl-Mager profile requires that no additional equations need be generated, probably explaining its widespread use. Johnson's two parameter polar profile has been shown to be an improvement over the Prandtl-Mager profile. Wheeler and Johnson (Ref. 16.97) however, noted in review of this cross-flow profile problem that none of the cross-flow profiles available at that time, including some developments of the Johnson profile, were entirely satisfactory for their purposes. For this reason Wheeler and Johnson (Ref. 16.97) went on to develop a direct numerical scheme for the three-dimensional turbulent boundary layer equation. Horlock and Perkins (Ref. 16.89) argue against Wheeler and Johnson's pessimism concerning the cross-flow profile for the present problem citing the reason that in the passage a reasonable form for the cross flow can be obtained from secondary flow theory (Horlock, Ref. 16.94).

Horlock's profile is similar in many respects to Johnson's profile and the necessary integrals are given by Lindsay (Ref. 16.98). For flows where the force defects D_x and D_z are absent the set of equations including Head's entrainment equation can be solved without particular difficulty. Lindsay (Ref. 16.98) for instance, has compared predictions made using the Johnson profiles with the swirling axisymmetric flow without blades or body forces, measured by Hoadley (Ref. 16.99) and achieved moderate success. Earlier calculations by Hoadley using the Prandtl-Mager profile, probably fortuitously, achieved slightly better agreement.

Turning now to flows with azimuthal variations the critical problem of the force defect integrals D_x and D_z arises. The pressure on the blade surfaces can obviously be determined from some inviscid (but not necessarily irrotational) analyses. Estimates of the gapwise variations in u and w can be made from the same type of analyses and correlation coefficients constructed using the mean flow averaged variables as the normalizing scale. The problem with this approach is that the variations within the endwall boundary layers are likely to be significant and possibly not well predicted by the preceding type of approach. By trial and error Horlock and his co-workers have found that fair estimates of axial blockage can be made by setting $D_x = 0$, presumably as a result of the individual components cancelling out (Daneshyar, Ref. 16.100). Horlock and Perkins (Ref. 16.89) cite two different methods for determining D_z. The first is based on a secondary flow analysis (which also results in $D_x = 0$) and the second, due to Daneshyar, is semi-empirical. At this point it seems clear that a very careful evaluation of the accuracy and generality of the presently available suggestions for the force defects D_x and D_z must be made. If satisfactory forms for D_x and D_z can or have been developed it would appear that even in spite of the known profile limitations a very useful tool would exist where none is presently available. Obviously endwall loss levels are important and any means of estimating their level and behavior are of keen interest to designers.

16.1.3.4 The Finite Difference Approach

Given the generally accepted difficulty of adequately specifying the cross-flow velocity profile, a number of investigators, for instance Nash (Ref. 16.74), Wheeler and Johnson (Ref. 16.97), Harris and Morris (Ref. 16.101), Cebeci et al., (Ref. 16.102), have been led to develop finite difference techniques for solving the three-dimensional turbulent boundary layer equations. The governing equations in the pitch averaged problem are in fact the simplest nontrivial form of these same three-dimensional boundary layer equations, that is the axisymmetric swirling boundary layer equations, with the addition of (given) source terms D_x and D_z. No new numerical difficulties over and above those normally encountered with the three-dimensional boundary layer equations would therefore be expected with the pitch averaged equations of motion. Furthermore, the presence of the large cross flow, often found in practice, leads to potential difficulty with an adequate specification of even the streamwise velocity profile family. Finally compressibility and heat transfer, features of interest to the designer, lead to a general concern about all the profile assumptions, thus paving the way for a numerical approach. Naturally the direct numerical approach would not have been embarked upon had not the simpler integral methods been encouragingly successful within their limited sphere of applicability.

It follows immediately that all of the available schemes for solving the three-dimensional boundary layer equations could be used in the simplified situation considered here. Alternatively, the two-dimensional schemes discussed earlier could be extended to incorporate a swirl equation. In either event almost all of the previous discussion on numerical methods for the boundary layer equations applies in the present instance with almost certainly there being less interest in laminar flow or regions of extended transition, both forward and reverse.

Anderson (Ref. 16.88) appears to have been the first to apply a finite difference scheme to the pitch averaged equations of motion. In Anderson's case the approach was an extension of a two-dimensional scheme rather than a cut down version of a three-dimensional scheme. Three-dimensional schemes will be discussed later in a separate section so no discussion of the merits or demerits of various three-dimensional schemes will be given here. Initially, Anderson used a straightforward explicit integration scheme with a law of the wall fit to cover the region below the first grid point. Difficulty with the law of the wall in swirling flow together with the desire to have a large number of grid points for accuracy led to the abandonment of the explicit scheme and the adoption of an implicit formulation. In view of its many attractive features, the Keller box scheme, (Ref. 16.70), was finally selected. The inclusion of the swirl and energy equations, however, led to a very large demand for storage with this technique, the problem mentioned earlier in connection with the Keller scheme. Also Anderson followed the linearization concepts developed by McDonald and Briley (Ref. 16.65) and linearized the governing equations to second order, consistent with the spatial differencing, without any iteration such as that in the scheme used by Keller and Cebeci (Ref. 16.83), thus effecting a substantial savings in already modest computer run times. The Richardson extrapolation, also recommended by the originators, was not employed in Anderson's modified version of the box scheme since in general accuracy in skin friction below 1% was not sought. Blottner (Ref. 16.66) recently demonstrated with the box scheme the inadvisability of using the Richardson extrapolation unless extreme accuracy was being sought.

Turning to the question of the turbulence model the penalty for use of the detailed numerical approach is the requirement of specifying the x-y variation of the turbulent correlations $\overline{u'v'}$ and $\overline{u'w'}$. As was mentioned earlier, Horlock and co-workers were able to circumvent this problem by the use of a generalized version of Head's entrainment law. At a later stage the problem of three-dimensional turbulence models will be examined in detail. For the moment it is noted that for $\overline{u'v'}$ Anderson (Ref. 16.88) used scalar eddy viscosity with Van Driest's suggestion for the sublayer followed by Prandtl's mixing length for the wall region and finally he used Clauser's suggestion for the outer wake like region. In this concept, the extension to three dimensions

of essentially a two-dimensional model is achieved by defining the eddy viscosity as

$$\epsilon = \ell^2 \left| \frac{\partial \vec{Q}}{\partial y} \right|$$

16.1 (130)

where $\vec{Q}$ is the velocity parallel to the wall and ℓ is the scalar mixing length. Consequently,

$$\left| \frac{\partial \vec{Q}}{\partial y} \right| = \left[\left(\frac{\partial u}{\partial y} \right)^2 + \left(\frac{\partial w}{\partial y} \right)^2 \right]^{1/2}$$

16.1 (131)

The stresses $\bar{\tau}_x$ and $\bar{\tau}_z$ incorporate $\overline{u'v'}$ and $\overline{v'w'}$ and are defined by

$$\bar{\tau}_x = \rho \epsilon \frac{\partial \bar{u}}{\partial y}$$

$$\bar{\tau}_z = \rho \epsilon \frac{\partial \bar{w}}{\partial y}$$

16.1 (132)

The scalar mixing length, here, takes on the appropriate two-dimensional form in accordance with the Van Driest-Prandtl-Clauser suggestion discussed previously. Aside from a need to take a four point y averaged value of the eddy viscosity ϵ, the resulting scheme worked quite well in practice. Averaging of the eddy viscosity compromises either the claimed second order accuracy of the scheme or the turbulence model, but was necessary to obtain stability with the scheme. A similar problem was treated in a like manner by Keller and Cebeci (Ref. 16.83).

In dealing with the force defects Anderson now had to contend with the detailed specification of these quantities across the annulus wall boundary layers. Here Anderson utilized strip theory with each blade or stator element treated two-dimensionally as a plane cascade. The cascade performance was then estimated either theoretically or from one of the accepted correlations, both methods being available in the code. In this way the hub to tip variations could be obtained by stacking the two-dimensional strips. Obviously alternative more complex schemes to obtain the hub to tip variations can be developed and incorporated into Anderson's scheme. Given the encouraging results already obtained, such developments might be very rewarding and at the present time a thorough evaluation of the force defect problem is appropriate.

16.1.3.5 Concluding Remarks on the Pitch-Averaged Procedures

Insofar as formal pitch averaging is concerned it must be emphasized that the resulting equations are quite as rigorous as the three-dimensional equations from which they were obtained. The simplification resulting from the decrease in dimensionality of the problem has been obtained at the expense of the loss of information on the details of the flow in the eliminated dimension. No approximations have as yet been introduced concerning the nature of this flow. The situation is identical to the Reynolds averaged equations of motion but almost certainly much more tractable due to the less random nature of the flow in the azimuth compared to the complex nature of the time variations in a turbulent flow. The expectations are therefore, that given reasonable estimates of the azimuthal variations and hence the correlation terms in the equations, accurate predictions of the pitch averaged flow can be made if the vane or blade forces are known.

In spite of the foregoing difficulties the pitch averaged approach has a great deal to recommend it, particularly when the alternative of either giving up or treating the complete three-dimensional problem is considered. Much work remains to be done at this point; however, the design needs are pressing. The approach clearly provides a bridge between the simple through flow analyses and the more exotic but at present incomplete three-dimensional intra-vane or blade analyses.

16.2 Three-Dimensional Boundary Layers

Within turbomachinery three-dimensional flows are encountered with unfortunate regularity, both within the boundary layers and the free stream. The term "free stream" being used here to denote a region where little diffusion, dissipation, or production of turbulence occurs but a region in which vorticity and turbulence might still well exist by convection. Simple three-dimensional flows such as that encountered on conventional moderate and high aspect ratio wings (the so-called boundary sheets) are not usually found in turbomachinery applications. End effects, such as the strut or rotor endwall interaction, are the flows of critical concern. Such flows cannot be treated properly within the framework of conventional three-dimensional boundary layer analyses. This failure of the conventional analyses may be seen in the previously introduced three-dimensional boundary layer equations, due originally to Hayes (Ref. 16.90). In the derivation it has obviously been assumed that diffusion of momentum in one direction only (in this notation, in the y direction) is important. Clearly this assumption breaks down for instance in the vicinity of a right-angled corner where diffusion normal to both walls is significant. Fortunately, the extra diffusion terms do not change the basic nature of the problem from an initial boundary value problem treatable by means of a forward marching procedure, providing that diffusion in the marching direction is still negligible and that the elliptic character of the pressure can still be largely suppressed or determined a priori. The extra complexity of the corner flow does, however, make solution of the system by an integral moment technique an exercise with a very low probability of success. The equations embodying diffusion in both coordinate directions are here termed the extended boundary layer equations.

An additional feature of the extended boundary layer equations concerns the absence of zones of influence. To discuss this problem it is necessary to recall the work of Raetz (Ref. 16.103) who first investigated the properties of the conventional three-dimensional laminar boundary layer equation. Raetz pointed out that diffusion only occurred in the direction normal to the wall in the conventional system and that in the other directions the equations were essentially hyperbolic and therefore characteristic surface would exist. As a result Raetz suggested an "influence principle" would hold and that the influence of the solution at any point would be transferred to other points firstly by diffusion in the direction of the surface normal

through the point and then by convection along all the streamlines passing through this surface normal. The zone of influence is then the region bounded by the body surface, the boundary layer edge, and a pair of characteristic surfaces: one, the surface normal envelope passing through the external streamline, the other the surface normal envelope passing through the limiting surface streamline. As a companion to the zone of influence Raetz also suggested a "zone of dependence" which is bounded by the upstream edges of the normal to the wall passing through the free stream and limiting wall streamline which intersect at the point in question. Only conditions within the zone of dependence influence the solution at the point in question and in turn only the flow in the subsequent zone of influence would be affected by the flow at the point.

Wesseling (Ref. 16.104) considered the zone of influence problem from the point of view of the conventional three-dimensional turbulent boundary layer equations and concluded that within this system Raetz's influence principle would hold but the possibility of a smaller zone in turbulent flow than in laminar flow could not be ruled out. The smaller zone would arise from the nearly hyperbolic nature of turbulent transport normal to surface outside of the viscous sublayer, (Bradshaw et al., Ref. 16.57). The zone of influence problem has also been discussed by Wang (Ref. 16.105).

The zone of influence has obvious attributes when boundary conditions are being applied. For the conventional system, conditions on the initial surface and subsequently on the edges of the domain must be prescribed. The initial surface conditions are discussed by Ting (Ref. 16.106) and it follows that only a limited number of dependent variables can be arbitrarily assigned starting values in view of the need to have starting values of the dependent variables which also satisfy the governing equations. The usual course of action is to specify the streamwise velocity and either by implication or directly, its axial rate of change. The Reynolds shear stress, the cross-flow velocity and the corresponding cross-flow Reynolds stress, and the density must also be specified: one, the surface normal to the wall passing through the external flow streamline, the other, the surface normal to the wall passing through the limiting wall streamline. The transverse velocity is derived from the continuity equation and the variables specified everywhere on the inlet surface. Edge conditions pose a particular problem; but intuitively, outflow along the edge requires no boundary conditions as it is completely determined by the known interior flow field. Wall surface and free stream edge condition are assumed given. The central problem rests with the unknown inflow edge conditions. Here the zone of dependence principle becomes invaluable for it clearly requires the effect of the unknown inflow boundary information to remain within the zone of influence of the inlet plane edges. Thus if the region of interest is outside the inlet edge zone of influence, little concern for the unknown inflow boundary information need be expressed. The conventional three-dimensional boundary layer equations therefore can be very useful for describing the boundary layer flow on a wing surface where the inflow regions near the wing root or tip have a limited zone of influence. Unfortunately the converse is also true and that is if the region of interest lies within the zone of influence of the edge, then the appropriate boundary condition information must be supplied. By the usual law of perversity of circumstances, the root and tip regions of wings, for instance, are regions of great boundary layer interest in view of their major contribution to losses and to stall. Physically then within these important regions the zone of influence principle is of little immediate help and it is of no great concern that when diffusion in the spanwise direction is allowed for, as it is within the extended boundary layer equations, the dependence principle is no longer obtained. The extended boundary layer equations can also have difficulty with inflow boundary conditions but they do possess the major attribute of being able to "turn the corner" and proceed to close the domain, as in a duct, or to proceed to a plane of symmetry where known information is available for boundary conditions. Given the type of problem normally encountered in turbomachinery applications, the attributes of the extended boundary layer equations are very impressive.

In the subsequent section a very brief discussion of some of the better known methods of predicting the conventional three-dimensional boundary layer equations will be given, mainly from the point of view of introducing some of the major difficulties involved with performing three-dimensional calculations. A more complete discussion of three-dimensional boundary layers has been given recently by Nash and Patel (Ref. 16.107) and from the computational point of view by Blottner (Ref. 16.78). In view of the limited utility of the conventional boundary layer equations much more emphasis will be placed upon the development of the extended three-dimensional boundary layer equations and techniques for their solution. Although major subjects in their own right, the problem of determining the free stream and the geometric information will not be discussed here.

16.2.1 The Momentum Integral Approach

The conventional three-dimensional boundary layer equations have been presented earlier during the development of the pitch averaged equations. These boundary sheet equations were also integrated in the effectively normal direction y and can be cast into a number of different forms depending on the integral defect thickness parameters introduced. Regardless of the precise form of the equations if an n-parameter profile family for the streamwise velocity u is introduced and an m-parameter profile for the cross-flow velocity w is introduced then, since the transverse mass flux ρv can be determined from the continuity equation, at least $m + n + 3$ independent equations must be provided to render the system determinate. The number 3 in the above expression arises from the need to define the density ρ and the skin friction components τ_{wx} and τ_{wz}. The problem of compressibility will not be directly addressed at this point and it will be assumed that some energy relationship exists to specify the local density. The skin friction relationships will be addressed later. Of the required remaining $m+n$ equations arising from the adopted mean profile families the first integral moment of the momentum equations provide two equations and, as has already been discussed at length in two dimensions, additional moment equations are readily obtained at the expense of introducing more information on the turbulent transport mechanisms. The problem of generating the additional moments of the turbulence will be deferred until turbulence models are discussed. Alternatively additional equations may be derived by introducing plausible physical arguments such as Head's entrainment hypothesis. With the foregoing as background the various procedures will be evaluated.

Consider the streamwise profile first of all. Although not mandatory, frequently in integral methods the direction for this velocity has been chosen to be that of the external streamline in a plane locally parallel to the surface. In this Cartesian coordinate system the cross-flow component at the edge of the boundary layer w_e, disappears, thus simplifying matters. If now the simple power law profile is supposed valid for the streamwise direction of the cross flow, the Prandtl-Mager profile is used. To recap, these are written by

$$u = u_e(y/\delta)^{1/n}$$

$$w = u(1-y/\delta)^2 \tan\beta$$

16.2 (1)

Now since u_e is given, these profile families introduce three parameters n, δ and β, the angle between the wall and free-stream streamline directions. Note that since the limiting streamline angle β is a problem parameter, the skin friction determination is simplified since

$$\tau_w = (\cos\beta)^{-1}\tau_{wx}$$

$$\tau_{wz} = \tau_{wx}\tan\beta \quad ,$$

16.2 (2)

and thus, only one skin friction relationship need be specified, usually the streamwise component τ_{wx}. Perhaps the simplest use of the foregoing set was by Mager (Ref. 16.95) who assumed that the streamwise component of wall shear was given by the very simple Prandtl-von Karman Law for two dimensional flow. Since the formulation now only uses three independent profile parameters, one more than the number of equations already on hand, Mager closed the set by specifying that the power law exponent n was a constant for some particular flow, and usually ascribed a value around 7. For a simple flow Mager achieved a very creditable degree of accuracy with his prediction, due almost certainly to his use of a value of n taken from the experiment. The assumption of a constant power law exponent is now widely regarded as being an oversimplification and as information on two-dimensional boundary layer behavior increased over the years a number of investigators have incorporated these developments into the three dimensional framework following Mager's lead. Dring (Ref. 16.126) later refined and developed Mager's technique and applied his scheme to the turbine endwall problem. Perhaps the next major development occurred when Cumpsty and Head (Ref. 16.93) introduced Thompson's two parameter profile family (Ref. 16.116) for the streamwise velocity profile. Thompson's profile is in effect very similar to Coles' law of the wall - law of the wake profile family introduced earlier. Retaining the Prandtl-Mager profile for the cross-flow component left Cumpsty and Head with one auxiliary equation to specify, since the streamwise skin friction was one of the parameters of the streamwise velocity profile. For the auxiliary equation Cumpsty and Head chose to postulate that the rate of entrainment of free stream fluid into the boundary layer was uniquely related to the shape of the streamwise velocity profile in the same way as in two-dimensional flow. To obtain the actual auxiliary equation, the continuity equation is integrated, (Eq. 16.1(124)), and the terms representing the free-stream entrainment rate collected and replaced by the assumed relationship to the streamwise profile. It is to be expected that Cumpsty and Head's procedure would perform much more satisfactory with (vanishingly) small cross flow than would Mager's procedure, as a general observation, in view of the close relationship of the Cumpsty-Head scheme to Head's simple and very effective two-dimensional boundary layer prediction scheme. The relative behavior at higher cross flows is not so apparent however, since it is by no means certain that for these flows the power law profile and other assumptions are inferior to law of the wall - law of the wake concepts for the streamwise velocity profile under these particular conditions. In any event the predictions shown by Cumpsty and Head agree moderately well with their measurements for certain integral parameters on an infinite yawed wing.

In spite of the well understood techniques for generating integral moment equations and the tolerance of the concept of an isotropic eddy viscosity even in some finite difference schemes (to generate the integral moments of the Reynolds stresses), there has been little attempt so far to generate three-dimensional multi-parameter integral schemes. Eichelbrenner and Penke (Ref. 16.112) used a polynomial cross-flow profile and essentially the u-moment of the streamwise momentum equation, simplified somewhat. Horlock (Ref. 16.94) and Lindsay (Ref. 16.98) used developments of Johnson's profiles together with Head's entrainment concept. Smith (Ref. 16.114) followed a similar course to Cumpsty and Head and used either the Prandtl-Mager profile or a simplified version of Johnson's profile (the simplification being that the apex of the Johnson's triangle is assumed to fall at some fixed value of u^+). Smith treated compressibility by assuming that the incompressible profile families hold in a 'y' coordinate stretched by the local density,

$$u/u_e = f(y'/\delta)$$

$$y' = \int_0^y \rho/\rho_e \, dy \qquad 16.2\ (3)$$

and the density evaluated by a quadratic temperature profile and, following Myring's (Ref. 16.111) lead, abandoned external streamline coordinates. A very similar study was subsequently undertaken by Thompson and Macdonald (Ref. 16.113).

While not as demanding as the more complete numerical approaches, solution of the coupled nonlinear integral equations is not trivial. Most people have tended to use a variant of the scheme used by Mager (Ref. 16.95) who solved the coupled integral momentum equations iteratively and sequentially starting with the streamwise momentum equation and lagging the cross flow information. Once again, unless the number of iterations is small then the principle attribute of integral methods, that of speed, is being squandered. Thompson and Macdonald (Ref. 16.113) encountered severe numerical problems with the sequential iterative solution technique near separation and in some regions of favorable pressure gradient. Thompson and Macdonald (Ref. 16.113) thereupon solved the problem by means of a coupled implicit technique treating the nonlinear coefficients by iteration. While no details of the Thompson-Macdonald algorithm are given, it would seem on the surface to be a very appropriate solution technique.

Two observations can be made on the work done to date. The first is that in general the level of agreement between prediction and measurement is poorer than that which is achieved by integral

techniques in two dimensions. The second is that none of the existing three-dimensional schemes when applied in two dimensions are more advanced than say Green's version (Ref. 16.115) of Head's simple entrainment method. Clearly then for three dimensions there is much room for improvement since the existing level of agreement is in general not adequate even for loss level estimates. In restricted classes of three-dimensional problems it would seem feasible to modify the various assumptions such that for that particular class of problem good agreement with measurement could be obtained. The question that any user must answer for his particular projected use, is the investment of effort best spent in developing an integral scheme further or are the mean profile problems such that the effort is better invested in a finite difference scheme? Insofar as the profile assumptions are concerned Wheeler and Johnson (Ref. 16.97) and Nash and Patel (Ref. 16.107) show the limitations of the existing suggestions and, while improvements can be made, it must be remembered that each additional profile parameter introduced to improve the profile description requires an additional equation be added to the system. Only if the number of profile parameters is kept small do integral schemes retain an attractive speed advantage over the completely numerical treatment of the basic three-dimensional boundary layer equations of motion. It must also be recalled that with the existing integral schemes compressibility is at best given a rather cursory treatment, the application envisaged for these schemes usually being the subsonic wing problem where compressibility effects are not large. Significant heat transfer effects, such as might occur on turbine blades, are as yet not allowed for within the existing integral schemes. As a consequence of these problems with integral procedures a number of investigators have been led to develop finite difference methods for solving the three-dimensional boundary layer equations. These finite difference schemes would appear better suited for general turbomachinery applications than existing integral schemes, although still limited by the boundary sheet approximations.

16.2.2 The Finite Difference Approach

Largely evaded in the treatment by existing integral methods is the question of the two Reynolds stress components. This problem is inescapable when the finite difference approach is considered, and the problem will be discussed and current solution techniques described in the section on turbulence models. The remaining problems are the variety of choices for the form of the equations and the coordinate system, the stability and accuracy of the numerical methods, the starting problem and the previously mentioned inflow boundary conditions. As in the discussion of integral schemes both the boundary layer edge conditions and the metrical information are assumed known. In actuality determination of both of these latter items might well involve more work than the determination of the boundary layer behavior itself, but discussion of them is inappropriate here.

Historically work on the three-dimensional boundary layer equations has been concerned either with the development of some innovative numerical scheme or with the description of the turbulent transport in three dimensions. In the former case much progress has already been made and in the latter instance fairly simple numerical schemes were adopted to expedite the description and evaluation of the critical features of the turbulent flow, again with an encouraging degree of success. Presently second generation turbulent boundary layer schemes are being evolved embodying aspects of the more recent numerical developments.

In discussing the numerical problem of treating the three-dimensional boundary layer equations the previous section on numerical methods for the boundary layer partial differential equations is relevant. In the present section the additional special features arising in the case of the three-dimensional boundary layer will be discussed in the same order of presentation as was adopted in the earlier numerical section. Starting with the choice of numerical method, yet another stability parameter arises. Frequently, due to the cross-flow velocity w, it is of the form

$$\gamma = \frac{h_1 w \Delta x}{h_3 u \Delta z} \qquad 16.2\ (4)$$

with Δx and Δz being the marching and spanwise directions and h_1 and h_3, the appropriate metric. Krause et al., (Ref. 16.109) have shown the stability parameter γ must satisfy certain restrictions for many schemes. Perhaps the most common restriction is that for a number of schemes γ must never be negative. The implication being that, for these schemes, the cross flow velocity w cannot be allowed to change sign (the spanwise marching direction chosen to give w positive). Certainly the cross-flow velocity can change sign in flows of real interest, as evidenced by the measurements of Klinksiek and Pierce (Ref. 16.108) in an S-shaped duct. Indeed much of the criticism of Johnson's profile family (Ref. 16.96) was directed at its inability to treat cross-over profiles where the cross flow changed sign. It would seem then that the cross flow stability parameter could prove catastrophically restrictive in some applications. Much less dangerous is the other restriction sometimes encountered that $-1<\gamma$, for here at least the prospect exists of reducing the axial step to satisfy the stability requirement and on average -1 is not a particularly small value of the parameter. Difficulties could be expected when a small spanwise mesh was desired simultaneously with a large axial step, a not uncommon set of circumstances. Also it is possible to have local flow angles in excess of 45° so that w/u can exceed unity and this again might require the axial step be reduced. Unfortunately, there is as yet no unconditionally stable scheme available for the usual three-dimensional boundary layer equations, (this observation will be qualified in a moment) even implicit methods suffering in this regard. In the extended boundary layer equations, diffusion in the spanwise direction is retained and several unconditionally stable schemes for the linearized system of equations are available. The converse is also true in that one of the unconditionally stable implicit techniques for treating the extended boundary layer equations could be reduced by neglecting spanwise diffusion. When applied to the conventional boundary layer equations, it is indeed hardly best to think of the procedure of Kendall et al., (Ref. 16.125) in this light. This brings into focus the essential difference of the extended implicit schemes and the conventional implicit schemes. In the former, both the spanwise direction and the normal direction are considered implicitly and boundary conditions at either end of the spanwise sweep

are satisfied. In the latter case of the conventional boundary layer equations, only the normal direction is considered implicitly; an embarassment if the initial value behavior of the spanwise sweep is not obtained. In line with the foregoing, it seems appropriate to term the case, where only the normal direction is considered implicitly, a semi-implicit method and when both directions are taken implicitly, a fully implicit method.

Insofar as the linearization process is concerned no additional problems arise in three dimensions. The problems of ad hoc linearizations and coupling are emphasized however since non-negligible product terms ρuw, for instance, appear in the equations, calling attention to the coupled nonlinear nature of the problem. The cross-flow velocity w is of course not necessarily small and indeed a great deal of the difficulty with obtaining even integral solutions has been traced by Thompson and Macdonald (Ref. 16.113) to the linearized sequential treatment of the equations. Aside from the explicit formulations (which retain all of their two-dimensional problems), the process of a formal linearization followed by a coupled solution of the governing equation would seem to be a very powerful method of treating the problem. Indeed a number of techniques of this type, usually embodying a Newton-Raphson treatment of the nonlinearities, are described in the review by Blottner (Ref. 16.78).

In the early work on the turbulent equations Nash (Ref. 16.74) worked with the primitive variables uvw, $u'v'$ and $v'w'$ and treated the growth of the boundary layer within the computational domain by periodic reinterpolation. Stream function approaches lose some of their attractiveness in three dimensions in view of the need to introduce two such functions; however, a number of investigators, for instance Cebeci (Ref. 16.110), have favored this approach again to achieve the simplification which arises from the elimination of the continuity equation. In another approach Harris and Morris (Ref. 16.101) used the square of the normalized velocity defect to replace the normal coordinate y; and, while obtaining some advantage from this type of transformation, clearly the double value problem of streamwise velocity profile overshoot would be a major difficulty for gas turbine applications. Apparently the addition of the third dimension has not introduced new major problems (or remedies), insofar as the dependent variables are concerned, the problem is much the same as in two dimensions. Grid stretching functions also have a major role to play; although, they have not yet been widely used since a great deal of the effort to date has been on laminar flows where their use is not nearly so critical as it is in turbulent flow. Again, in three-dimensional turbulent problems the desire to place grid points in the sublayer still exists particularly for highly accelerated flows with heat transfer. The viscous sublayer problem becomes even more accute since the three-dimensional version of the law of the wall is not nearly as secure as in two dimensions. Counter-balancing the desire to place grid points in the sublayer is the increased cost of doing so in three dimensions but, be that as it may, an inadequate sublayer treatment is castle building on a bed of sand.

Finally, insofar as coordinate systems are concerned, these to date have been quite specifically tuned to the problem at hand. As a rule the body surface is taken as one coordinate with the other two taken as convenient. The body surface not lying on a coordinate can lead to difficult computer logic and interpolation inaccuracies and hence is not to be recommended. Orthogonal systems have in the past often been selected but nonorthogonal systems are quite readily accommodated in finite difference schemes and can be recommended should their use simplify the computation significantly. More general coordinate systems, not so specifically tuned to one particular geometry, are being developed. The overall problem is reviewed in detail by Eiseman and McDonald (Ref. 16.117). The least that can be done at present, is in constructing or modifying a computer code, the metric information should be left arbitrary in the main body of the code and set in some easily accessible subroutine.

16.2.3 The Extended Three-Dimensional Boundary Layer Equations

As was mentioned earlier the conventional "boundary sheet" form of the three-dimensional boundary layer equations only takes into account diffusive effects in one coordinate direction. The thin boundary sheet approximations have proven very valuable but in a number of critical turbomachinery problems some of the boundary sheet approximations are not valid, for instance, the assumption that spanwise rates of change are negligible when compared to gradients normal to a wall is often violated. In the extended boundary layer equations the spanwise and normal velocities and their rates of change are assumed to be of the same order. The usual boundary sheet approximation is retained that the streamwise rates of change are small when compared to the normal and spanwise rates of change. Finally, it is assumed, almost as a matter of definition, that in the "boundary layer" the pressure field (or at least the major portion of it) is determined either without an a priori knowledge of the boundary layer behavior or locally by means of mass conservation without upstream propagation.

The extended boundary layer equations first seem to have become popular in studies of hypersonic boundary layers on finite flat plates. In view of the flow complexity the approaches have, to date, all been entirely numerical. Nardo and Cresci (Ref. 16.124) treated the extended three-dimensional laminar boundary layer equations at hypersonic speeds and assumed that the pressure gradients were negligible. In subsequent work Rubin and Lin (Ref. 16.123) were able to retain the pressure terms and still treat the problem by forward marching in view of the hypersonic speeds involved. No problems seem to have arisen as a result of the locally subsonic region of flow immediately adjacent to the wall. McDonald and Briley (Ref. 16.65) treated a viscous supersonic jet using essentially the extended boundary layer equations while rigorously retaining the pressure terms. The aim of the work of McDonald and Briley was mainly to investigate the numerical properties of their scheme without the complication of pressure assumptions necessary in subsonic flow. Subsequently Briley and McDonald (Ref. 16.118) applied their scheme to compute the flow in a subsonic rectangular curved duct which was in fact a model of the turbine vane passage.

In a separate development Caretto, Curr and Spalding (Ref. 16.122) devised a technique for solving the extended boundary layer equations in incompressible flow. Subsequently Patankar and Spalding (Ref. 16.121) produced a simplified version of the procedure of Caretto et al., and later Patankar, Pratap and Spalding (Ref. 16.120) and Bergeles,

Gosman and Launder (Ref. 16.119) have applied versions of this simplified scheme to practical problems of turbomachinery interest. Neglecting turbulent triple correlations Briley and McDonald (Ref. 16.118) write the extended turbulent compressible three-dimensional boundary layer equations in an orthogonal coordinate system as

Continuity

$$\frac{\partial}{\partial x} h_2 h_3 \bar{\rho}\bar{u} + \frac{\partial}{\partial y} h_1 h_3 \bar{\rho}\bar{v} + \frac{\partial}{\partial z} h_1 h_2 \bar{\rho}\bar{w} = 0$$

16.2 (5)

Streamwise-Momentum

$$\frac{\partial}{\partial x} h_2 h_3 \left(\bar{\rho}\bar{u}^2 + \bar{\rho}\overline{u'^2}\right) + \left[\frac{\partial}{\partial y} + \frac{1}{h_1}\frac{\partial h_1}{\partial y}\right](h_1 h_3 \bar{\rho}\bar{v}\cdot\bar{u})$$
$$+\left[\frac{\partial}{\partial z} + \frac{1}{h_1}\frac{\partial h_1}{\partial z}\right](h_1 h_2 \bar{\rho}\bar{w}\bar{u}) - h_3 \bar{\rho}\bar{v}^2 \frac{\partial h_2}{\partial x} - h_2 \bar{\rho}\bar{w}^2 \frac{\partial h_3}{\partial x} + h_2 h_3 \frac{\partial p}{\partial x}$$
$$= h_1 h_3 \frac{\partial}{\partial y}\left[\frac{\mu}{h_2}\frac{\partial \bar{u}}{\partial y} - \bar{\rho}\overline{u'v'}\right] + h_1 h_2 \frac{\partial}{\partial z}\left[\frac{\mu}{h_3}\frac{\partial \bar{u}}{\partial z} - \bar{\rho}\overline{w'u'}\right]$$

16.2 (6)

Normal-Momentum

$$\left[\frac{\partial}{\partial x} + \frac{1}{h_2}\frac{\partial h_2}{\partial x}\right](h_2 h_3 \bar{\rho}\bar{u}\bar{v}) + \frac{\partial}{\partial y} h_1 h_3 \left(\bar{\rho}\bar{v}\cdot\bar{v} + \bar{\rho}\overline{v'^2}\right)$$
$$+\left[\frac{\partial}{\partial z} + \frac{1}{h_2}\frac{\partial h_2}{\partial z}\right] h_1 h_2 \bar{\rho}\bar{w}\bar{v} - h_3 \bar{\rho}\bar{u}^2 \frac{\partial h_1}{\partial y} - h_1 \bar{\rho}\bar{w}^2 \frac{\partial h_3}{\partial y}$$
$$+ h_1 h_3 \frac{\partial p}{\partial y} = h_1 h_2 \frac{\partial}{\partial z}\left[\frac{\mu}{h_3}\frac{\partial \bar{v}}{\partial z} - \bar{\rho}\overline{v'w'}\right]$$

16.2 (7)

Spanwise-Momentum

$$\left[\frac{\partial}{\partial x} + \frac{1}{h_3}\frac{\partial h_3}{\partial x}\right](h_2 h_3 \bar{\rho}\bar{u}\bar{w}) + \frac{\partial}{\partial z} h_1 h_2 \left(\bar{\rho}\bar{w}\cdot\bar{w} + \bar{\rho}\overline{w'^2}\right)$$
$$+\left[\frac{\partial}{\partial y} + \frac{1}{h_3}\frac{\partial h_3}{\partial y}\right](h_1 h_3 \bar{\rho}\bar{v}\bar{w}) - h_2 \bar{\rho}\bar{u}^2 \frac{\partial h_1}{\partial z}$$
$$- h_1 \bar{\rho}\bar{v}^2 \frac{\partial h_2}{\partial z} + h_1 h_2 \frac{\partial p}{\partial z} = h_1 h_3 \frac{\partial}{\partial y}\left[\frac{\mu}{h_2}\frac{\partial \bar{w}}{\partial y} - \bar{\rho}\overline{v'w'}\right]$$

16.2 (8)

In this form the governing equations can be seen to introduce two additional aspects relative to the conventional boundary layer equations. The first aspect is that additional Reynolds stress information is now required and the second is, as has been commented upon earlier, diffusive fluxes in both the normal and spanwise directions now appear. Deferring discussion of the Reynolds stress information until the section on turbulence modeling, it appears at first sight that little in the way of complexity has been introduced by retaining the second derivatives with respect to the spanwise direction z, since first derivatives with respect to z were already present and indeed with explicit schemes this is obviously true. The complexity mainly occurs with implicit schemes (provided the stability of the explicit scheme is not degraded) and is quite subtle and is best explained by referring to the appropriate finite difference molecule. The complexity also needs to be explained so that the correct relationship between the conventional and the extended boundary layer equations can be established. The molecule is structured with the y-direction out of the plane of the page and j the running subscript in that direction. The y-direction integration is essentially that of the normal to the wall of conventional boundary sheet flows. The molecule is written

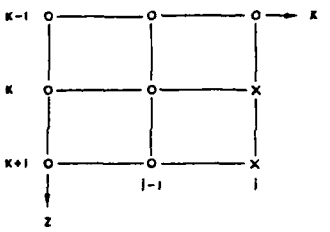

Presuming that the scheme is started and the pressure given (this point will be returned to), the streamwise marching direction is x and the solution is desired at the i, j, k^{th} point with the entire solution already obtained at the i-1 and i-2 and k-1 planes. The accepted techniques advance in x all the y grid points at each z station. The process is repeated in the direction of increasing z. Since only first derivatives in the z-direction appear in the conventional boundary layer equations it is possible to structure a z-direction first derivative at the i, j, k-1/2 point of second order accuracy involving only one unknown, the desired i, j, k^{th} point. It follows that if the scheme is centered on the k-1/2 plane the x and z marching step are accomplished simultaneously without significant complexity. Indeed centering on k-1/2 has been used to good effect even with explicit integration schemes. The problem of negative cross flows can at least be intuitively explained by observing that as the scheme is marched in z, a negative cross flow velocity w implies information being *transferred upstream against* the direction of integration, a situation well known to be fraught with danger and not alleviated by any implicit formulation unless this implicit direction is in the direction of information transfer. This thought is discussed in detail by Kendall et al., (Ref. 16.125), but for the moment the problem with the conventional normal direction implicit formulation arises if a second derivative in the z-direction occurs, since such a derivative requires three points in the z-direction as a minimum and in an implicit scheme this introduces two unknown values, the values at k and k+1, complicating the z-step considerably. The z-step difficulty now resembles the problem of advancing a y-step and indeed this resemblance can be used in an intuitive manner to structure an algorithm. First of all it can be imagined that in some instances an explicit evaluation of the 2nd derivative in z might suffice. If this proved inadequate either from the stability or accuracy viewpoint (as it would in general), one could conceive of either repeating the axial step this time retaining the z derivative implicitly and treating the v direction explicitly. With an explicit scheme the two-level process also can be used to good effect and it seems on an intuitive basis that the extended boundary layer equations need only take at most about a factor two in central processor computing time more than the conventional equations. Storage may be increased in the two step process but peripheral mass storage devices can be used to good effect in this problem since only a limited number of z stations need be in the central memory at any one time. The question concerning the role of the pressure complicates matters and it will be discussed further.

The foregoing very intuitive suggestions are in fact central to the very powerful Alternating Direction Implicit schemes first proposed by Peaceman and Rachford, of which more is said, for instance by Yanenko (Ref. 16.75).

There are two major problems with the numerical treatment of the extended boundary layer equations, the first being the treatment of the pressure and the second the problem of starting the integration. The pressure problem is considered first and for convenience incompressible laminar flow is assumed. The continuity equation and the three momentum equations then provide four equations in four unknowns, u, v, w, and p. If now it is desired to specify the pressure field p, it is necessary to drop one equation or make some other approximation. Within the usual boundary layer framework the transverse momentum equation is favored and the pressure field consistent with a negligibly small transverse velocity is imposed upon the system. After the fact, the known velocity field could be used to obtain a modified pressure but if the boundary layer approximations are valid the corrected pressure would be negligibly different from that imposed. The problem is now evident that in the present case it is desired to impose a pressure field yet retain all of the momentum equations so that some sort of further approximation is required. From the foregoing it is not immediately evident why in the present case it is necessary to impose a pressure field upon the problem; to explain this the problem must be viewed slightly differently. If each of the momentum equations is differentiated in turn with respect to the direction of the pressure gradient and the three equations added, an expression for pressure can be constructed in the form

$$\nabla^2 p = f(u,v,w) \qquad 16.2\ (9)$$

where ∇^2 is the usual three dimensional Laplacian operator. The pressure equation as it stands is then governed by a three-dimensional elliptic partial differential equation even given the velocity field, a fact inconsistent with the forward marching nature of the proposed solution. It will be recalled that in developing the extended boundary layer equations in order to produce a problem which could be forward marched, it was necessary to introduce the assumption that second derivatives with respect to the marching direction were negligible; however, it is apparent that this approximation has not been introduced into the pressure behavior, nor indeed is it desirable to do so. Previously it has been observed that in the normal two-dimensional boundary layer it was more appropriate to neglect pressure gradients normal to the wall rather than in the axial direction, and for many reasons it is desirable to have the present system reduce to the well established two-dimensional system in the limit. The dilemma is resolved when it is realized that in generating a system of equations that can be forward marched it is not necessary to assume that second derivatives with respect to the streamwise direction are negligible but only necessary to assume that they are known a priori. This observation leads to the assumption of a split pressure

$$p = p_I + p_C + p_M = p_I(x,y,z) + p_C(y,z) + p_M(x) \qquad 16.2\ (10)$$

where p_I is the imposed pressure, supposed known in advance throughout the domain, and p_C is a small additional pressure assumed to vary negligibly slowly in the axial direction and determined by the cross-flow momentum equations. The pressure p_M is a cross-sectionally averaged pressure including, in internal flow, any blockage correction to the pressure determined by the need to globally conserve mass in the duct. Although such a formulation achieves the desired goal of rendering the system amenable to treatment by a forward marching integration scheme several new problems have been introduced. The imposed pressure p_I is clearly of no more of a numerical problem than any other known source term and need not be considered further at this point, although of course the problem of determining p_I may be very significant. The first and obvious difficulty is that in turning the problem into an initial-boundary value problem an extra unknown parameter $p_M(X)$ has been introduced. In unbounded flows p_M is usually not assumed to vary throughout the domain or, as in internal flows, an estimate of its value can be made using the local condition of the boundary layer which would either be of the displacement surface type or, in internal flows, the usual blockage type of correction. Such an estimating process has the salient feature that it does not allow the pressure to propagate back upstream and preserves the forward marching capability. A second difficulty emerges when it is realized that since no axial derivative of the cross-flow pressure appears, the cross-flow momentum equations determine the cross-flow pressure p_C only to within an arbitrary function of X. The arbitrary function may be evaluated at each streamwise station by the corrolary to the definition of p_M, which is that

$$\frac{1}{A}\iint p_C\,dy\,dz = 0 \qquad 16.2\ (11)$$

and this definition may be applied to eliminate the uniqueness problem by allowing rather arbitrary function boundary conditions to be applied at one end for the cross-flow pressure. If the solution thus obtained for some assigned value of dp_M/dx is denoted by a prime the additive constant 'a' required to set the correct cross-flow pressure level is obtained by

$$\frac{1}{A}\iint p_C\,dy\,dz = \frac{1}{A}\iint (p_C' + a)\,dy\,dz = 0$$

$$a = -\frac{1}{A}\iint p_C'\,dy\,dz \qquad 16.2\ (12)$$

Returning now to the problem of determining the mean pressure gradient dp_M/dx, it is to be borne in mind that the pressure gradient in the streamwise momentum equation has been approximated

$$\frac{\partial p}{\partial x} = \frac{\partial p_I}{\partial x} + \frac{\partial p_M}{\partial x} + \cancel{\frac{\partial p_C}{\partial x}}^{\,=0} \qquad 16.2\ (13)$$

and the problem is to determine the appropriate value of the mean pressure gradient, dp_M/dx.

As has been pointed out by Briley, if the local continuity equation is satisfied everywhere in the cross-section and the no slip velocity boundary conditions are applied all around, then global continuity must of necessity be satisfied. Thus in schemes of this aforementioned type, global continuity cannot then be applied to determine the mean pressure gradient. Indeed it is quite clear that in any scheme, global continuity can only be used to determine the mean pressure gradient in lieu of the

zero cross-flow velocity boundary condition, presuming of course, that no one would care to have a solution which violated the local continuity equation. As a matter of definition the *local continuity equation in cartesian coordinates is*

$$\frac{\partial}{\partial x}\bar{\rho}\bar{u} + \frac{\partial}{\partial y}\overline{\rho v} + \frac{\partial}{\partial w}\overline{\rho w} = 0$$

16.2 (14)

and the global equation obtained by integration over the cross section and application of the no slip conditions is

$$\frac{d}{dx}\iint_A \bar{\rho}\bar{u}\, dy dz = 0$$

16.2 (15)

At the present time, three schemes have been suggested for treating this problem and all center around iteratively satisfying the local continuity equation by correcting the pressure field. That is, to date, the solution strategies have usually been to obtain a solution to the momentum equations at the expense of the local continuity equation then subsequently correct the pressure to ensure local satisfaction of the continuity equation to within some tolerance. The three schemes are those of Briley (Ref. 16.135), Patankar and Spalding (Ref. 16.121) and Dodge (Ref. 16.182). The very interesting duct flow analysis of Rubin, Khosla and Saari (Ref. 16.186), although it will not be discussed further here since it has not yet been developed to the point to where it can be applied to turbulent curved duct flow, is mandatory reading for anyone seriously interested in this problem and gives yet another method of correcting the pressure field.

In the work of Briley (Ref. 16.135) the axial momentum equation is solved assuming a known cross-flow velocity field and the mean axial pressure gradient to satisfy global continuity determined by a secant iteration. Using the upstream cross-flow pressures, the cross-flow momentum equations are solved to yield improved cross-flow velocities. Small corrections to these cross-flow velocities are computed to enable local continuity to be satisfied. The corrections are assumed to satisfy a potential function. Finally an improved cross-flow pressure is determined from a Poisson equation obtained from the differentiated cross-flow momentum equations. With this scheme it turns out to be impossible to set the no slip conditions on the corrections which allow the local continuity equation to be satisfied so that the global continuity equation serves to ensure the satisfaction of zero normal velocity on average and the uniqueness problem is not encountered. The principle difficulty with this scheme lies in the uncoupled sequential nature of the calculation, leading one to suspect problems in compressible flow or if the cross flows became large. Also the assumption of an irrotational form of the correction to the cross-flow velocities to ensure satisfaction of the local continuity equation is quite speculative. In Fig. 16.5 some predictions using Briley's scheme are compared to measurements. For this particular flow the secondary velocities are small and very good agreement with data is obtained.

The scheme of Patankar and Spalding (Ref. 16.121) is conceptually quite similarly structured but whereas Briley (Ref. 16.135) iterates around the full axial momentum equation, Patankar and Spalding simply correct the first trial pressure gradient and velocity field using an inviscid and approximate form for the appropriate momentum equation. The approximate technique involves balancing the streamwise convective derivative by the appropriate pressure gradient. Diffusive effects and the convective terms in the cross section are neglected in this approximation and close to and at a wall the approximation is obviously incorrect. At this point it is not clear to what extent these assumptions and resulting approximations prejudice the solutions; however, as with Briley's scheme, difficulties would be expected in treating compressible flow with strong secondary flow as a result of the coupled sequential nature of the calculation.

In the work of Dodge (Ref. 16.182) the entire pressure field is supposed known and the momentum equations marched through the duct to produce a flow field. This process of course leaves the local continuity equation unsatisfied so now a new three-dimensional potential flow, i.e. pressure field, for the duct is computed which results in an inviscid velocity correction which permits local continuity to be satisfied. The inviscid and three-dimensional pressure field is computed on a very coarse mesh to obtain reasonable computational run times. The whole process is repeated iteratively until the solution of the momentum equations also satisfy local continuity to some tolerance. The somewhat arbitrary equation splitting technique used by Dodge, together with the coarse mesh inviscid pressure field used, also give one the impression that a great deal remains to be done by way of formalizing this particular solution technique.

The preceding discussion has centered on the low speed problem and in going to flows with significant compressibility effects and heat transfer both the energy equation and the equation of state become available. At supersonic speeds the pressure and all its attendant problems can be removed by eliminating the pressure in favor of the density and temperature, the temperature being specified by the energy equation. At subsonic speeds the same elimination process can be carried out but the elliptic pressure problem still manifests itself in the inability to impose a condition of negligible or specified second derivative of density in the streamwise direction. No benefit thus accrues at subsonic speeds to eliminating the pressure via the density and temperature.

Before leaving the pressure problem it should be stated that at the present time none of the solution strategies developed so far seem adequate for flows with significant viscous effects on the pressure field. Clearly none of the present proposals give a good representation of nearly inviscid rotational flow and thus, as yet cannot provide a bridge between boundary theory and secondary flow analyses. Repeated sweeping through the duct to obtain the partially parabolic approach squanders the economic advantage of the parabolic approach vis à vis a solution of the full Navier-Stokes equations unless an improved pressure field is obtained in a few global sweeps through the duct. Indeed it is a presumption which has to be proven valid that an iteration sequence for solving the full Navier-Stokes equations will provide a sequence of physically more realistic pressure fields, except of course, close to convergence. It is to be hoped that further effort on the pressure problem will result in much improved analyses.

Turning now to the starting problem it can be seen that the starting problem is quite similar to the problem of starting a conventional three-dimensional boundary layer with only the addition

of the cross-flow pressure gradient in the spanwise direction. The tempting proposition of neglecting this cross-flow gradient, strictly valid for a collateral inflow, has not been fully explored to date. Similarity solutions, which have proven so helpful in both the conventional two and three-dimensional boundary layer problem, still retain a great deal of attraction for starting the extended boundary layer equations but again have not yet been evaluated in this problem. Also it follows from the observations concerning the simplifications which arose from equation splitting that the precise numerical formulation can have an impact on the starting problem. Indeed Briley et al., (Ref. 16.185) noted that with the Russian method of splitting (Yanenko, Ref. 16.75) as opposed to a Peaceman-Rachford ADI split, the system no longer required a starting value for the spanwise cross-flow component w (except as a consequence of the linearization process, which can be circumvented). Obviously, a great deal remains to be done by way of exploring starting procedures. Indeed it is clear that whilst full of promise, the existing techniques for solving the extended three-dimensional boundary layer equations at low speeds have a long way to go even before they can be applied with confidence even to those flows where the flow approximations embodied in the overall concept might be expected to be valid.

16.3 Boundary Layer Separation

Separation is the rather loose term given to the flow when it forms a region within itself which is inaccessible by convection to the flow coming from upstream. Usually a wall forms one of the bounding surfaces of this region but for instance the recirculating region formed by the release of a swirling axial jet is an example of separation where a wall is not involved.

16.3.1 Motivation and Background

In several instances of very great concern to turbomachinery designers the occurrence of significant regions of separated flow is termed 'stall' and determines the boundary of the operating envelope of the device. Compressor stall is a very obvious example which springs to mind. Diffuser stall is a further example and in both these examples the significant regions of flow separation cause major changes in the pressure distribution around the body as well as greatly increasing the drag of the system. Stall is often accompanied by an increased flow unsteadiness. The separation prediction problem is compounded by the observation that catastrophic flow separation (stall) is a very sensitive phenomenon and that small local separation regions can occur without significant deterioration in the flow. For a number of subtle reasons arising from both upstream and downstream conditions, these small and well-behaved local separations can suddenly degenerate into the large separation zones characterizing stall. It follows that it is often not enough simply to predict the onset of separation, difficult enough as that may be, but it can also be important to be able to predict at what point the small separation undergoes its metamorphosis into stall. The problem is quite acute in both compressor and diffuser stall since to obtain optimum performance it is often desired to operate the device on the verge of stall. Frequently in this optimum condition small local separation regions occur in the flow and a knowledge of the factors influencing this behavior would be very valuable.

In the absence of any reliable theoretical stall prediction procedure the empirical approach has had to be adopted by the design engineers. In this empirical approach, maps of stall zones are built up by observation as the device is operated over a range of critical performance parameters. The resulting correlations are then attributed a more general significance and applied to other similar devices. Unfortunately the sensitivity of stall to a myriad of factors has caused a great deal of concern, difficulty and expense with the empirical approach in view of the ad hoc nature of the stall correlations. In an effort to improve the above type of stall correlation, the stall has been supposed determined by boundary layer separation and criteria for boundary layer separation occurring within the components of the devices developed. Sanborn (Ref. 16.136) for instance has recently discussed some of these separation criteria and generally they relate the condition of the boundary layer at separation to the applied pressure gradient, in the general form

$$(\delta^*/\theta)_{sep} = f\left(-\frac{\theta^2}{\nu}\frac{du_e}{dx}\right) \qquad 16.3\ (1)$$

where f is some function determined by observation and δ^* and θ and the usual boundary layer displacement and momentum thicknesses. The ratio of displacement to momentum thickness is usually termed the shape parameter, H, and the problem of determining the streamwise variation of the shape parameter H is left open at this point. The obvious suggestion of predicting the entire boundary layer behavior and thereby determining the variation of shape parameter H is somewhat self defeating at this point since such a procedure would also either directly predict the separation point or allow an estimate of the separation point location to be made independently of the empirical correlation function f. Sanborn's view was that none of the available procedures (at that time) could give a reliable prediction of the separation location and that these empirical correlations would serve as 'correctors' to the theoretical predictions. Valid as that observation may have been it is to be expected that in the light of the rapid developments with the conventional two and three-dimensional boundary layer equations and turbulence models in the near future, efficient and accurate means of theoretically predicting the onset of separation will become available (this remark will be qualified subsequently). The crucial problem of determining at what point the separating boundary layer degenerates into stall can be solved by tracing the subsequent 'boundary layer' behavior. At this point difficulties (conceptual and/or numerical) are encountered with spatial forward marching solutions to the governing equations. Downstream effects are most evidently propagating upstream and clearly both the governing equations and the integration schemes must allow this upstream propagation. Pressure effects require special consideration since the thickening of the boundary layers as separation is approached can cause changes in the very pressure distribution which is driving the boundary layer to separate in the first place.

In recent years, with the achievement of satisfactory predictions of the mean flow behavior of many attached two-dimensional boundary layers, a number of investigators have turned their attention to the problem of not only predicting the onset of separation but of predicting also the subsequent separated flow behavior. When the external flow is supersonic the topic actually has had a long and illustrious history starting with the shock wave boundary layer interaction work of Crocco and Lees (Ref. 16.134) with integral methods playing a major role. The more recent studies have been concerned with the problems which arise both at subsonic and supersonic speeds when finite difference schemes are used to predict the behavior of the shear layers. It turns out that in using integral prediction schemes a number of difficulties which cause major problems with finite difference schemes are not immediately evident. The motivation for persevering with the finite difference scheme stems from the belief that such schemes are, or will eventually be, more accurate in view of the difficulty of accurately characterizing integral velocity and temperature profile families for separating turbulent two or three dimensional boundary layers. Another motivation for persevering with the finite difference schemes could be the belief that by glossing over some of the difficulties the integral moment equations are in fact missing some key physical processes.

Before proceeding to develop the governing equations it is convenient to introduce the concept of strong, weak and local interaction. As is well known in developing the usual Prandtl form of the boundary layer equations the assumption of nearly parallel flow to the boundary surface results in the approximation that the pressure acting on the boundary layer is that imposed by the free stream and further that, at worst, the growth of the boundary would cause only a small change in this imposed pressure which could be accounted for by a slight 'displacement surface' shift in the body contour. For obvious reasons this type of boundary layer flow is termed 'weak interaction' and this terminology refers in the main to the pressure field distortion due to the presence of the boundary layer. Strong interaction is the term applied to flows where the imposed pressure would be considerably different if the boundary layer were not present. The flow over a stalled airfoil would be one example of such a flow. Lastly the term local interaction refers to some small domain in an otherwise weak interaction flow field where it is necessary to take into account the local distortion of the pressure field due to the boundary layer. The aim here might be more to locally improve the boundary layer prediction than an interest in determining the boundary layer impact on the pressure. The softening effect of a rapidly growing boundary layer on the pressure gradient driving it has been known for some time, but to some extent disguised by the usual mode of testing boundary layer prediction schemes which uses measured pressure distributions.

The foregoing categorization into strong, weak and local interaction serves to give an indication as to the degree of approximation possible in the governing equations. Exceptions can and do arise, depending to some extent on the information being sought. For instance, supersonic shock wave boundary layer interaction is probably the origin of the term 'strong interaction' yet boundary layer momentum integral methods have an enviable prediction record in this category, at least insofar as the wall pressure distribution in laminar flow is concerned. However, it is to be expected that in a strong interaction subsonic flow, the full Navier-Stokes equations would be required to make any sort of reasonably reliable mean flow prediction, even given an adequate turbulence model. The weak interaction approximation follows from the boundary layer approximations and its use is permissible wherever the streamwise rate of change of displacement thickness is not large. At least superficially, use of the weak interaction hypothesis is not restricted to attached flows and it can in principle be applied to separated flow. Locally strong interactions have a restricted domain wherein the rate of change of displacement thickness is not small but where the flow still retains much of its boundary layer like character. Within this rather loose category one might place the supersonic shock wave boundary layer interactions which are quite well predicted by the integral moment procedures. More generally, however, the local interaction concept raises the prospect of a locally imbedded region wherein something more than the conventional boundary layer equations could be used to describe the flow and interface boundary conditions between the flow regions used to obtain the flow interaction. The benefit here would be that by restricting the region within which the flow is described by something other than the usual boundary layer equations the computational expense is similarly restricted.

There are two remaining aspects of the separation problem which merit discussion here. The first is that treatment of the problem by forward marching in space results in the inflow boundary condition problem. Here at some point fluid enters the computational domain in some amount which varies with the upstream boundary conditions but which physically also depends upon some downstream boundary conditions not yet part of the spatial marching domain. One could for instance easily bleed off a small amount of fluid from near the reattachment end of a two-dimensional separation bubble which supposedly only weakly interacted with the pressure field. This small amount of bleed would move the separation point but would not be known in advance to a spatial marching scheme unless by iteration. Clearly the problem requires that downstream conditions have an effect on the solution and insofar as forward marching in space this implies a shooting, iterative type of approach. The second problem with separation lies in the observation that the steady boundary layer equations are in fact singular at a separation point when solved in the conventional manner with an imposed free stream pressure distribution. The separation singularity has been discussed for example by Goldstein (Ref. 16.187) and more recently has been reviewed by Stewartson (Ref. 16.188) who earlier introduced 'triple deck' to treat this problem, of which more will be said later. The belief that the boundary layer equations should be able to describe weak interaction separation has led to the suggestion that the singularity results from a failure to recognize a very local interaction with the inviscid flow. Since the usual separation singularity in two dimensions is manifested by an infinite displacement thickness and an infinite gradient of wall shear at separation, efforts have been made to compute inverse solutions in which either a smooth distribution of displacement thickness or wall shear is imposed and the free

stream velocity distribution is recovered as part of the solution. Such techniques have sometimes been termed 'indirect' to differentiate them from the 'direct' approach where the pressure gradient is either imposed or determined locally. There is numerical evidence, Catherall and Mangler (Ref. 16.189), Klineberg and Steger (Ref. 16.190), and Carter (Ref. 16.191) that an inverse technique does indeed remove the singularity at separation although in some cases other difficulties have persisted downstream of separation. Inverse techniques do also have the attribute that they introduce downstream information into the problem, thus meeting the first difficulty with the steady boundary layer equations mentioned earlier. The major problem with inverse procedures, regardless of how well they remove any singularities and introduce the downstream boundary conditions, is the necessity of arranging to satisfy the free stream boundary conditions, perhaps not in the immediate locality of the separation, but certainly both upstream and downstream of separation. Inverse procedures are therefore expected to be either difficult or relatively expensive to use routinely since they would require some sort of iteration to determine the appropriate distribution of the specified variable which would allow the desired free stream conditions to be obtained.

In the literature there are at present two alternatives to shooting or inverse techniques of treating separated boundary layers in subsonic flow. The first is simply to abandon the boundary layer equations and retreat to the safety of the complete Navier-Stokes equations. This approach obviously allows for the proper influence of downstream boundary conditions and avoids the separation singularity since the Navier-Stokes equations are regular at separation. Both Briley (Ref. 16.192), Leal (Ref. 16.193) and Briley and McDonald (Ref. 16.194) have used this approach and, as well as not being limited to flows where the boundary layer approximations are valid, the techniques are not necessarily computationally much more expensive than the shooting or inverse techniques for the boundary layer equations in view of the outer global iteration required with the 'boundary layer' techniques. A second alternative is suggested by Briley and McDonald and solves the steady boundary layer equations by an asymtotic time marching integration (which is quite analogous to an iterative or relaxation solution process). At each time step (or 'iteration', if one prefers that terminology) the imposed pressure field is corrected for the displacement thickness change which occurred across the time step. In the previously introduced terminology this type of solution may be termed a 'locally interacted direct' solution. Downstream boundary conditions are allowed for, and Briley and McDonald (Ref. 16.194) were able to structure the boundary layer solution algorithm such that they obtained significant gains in efficiency relative to the solution techniques for the full Navier-Stokes equations. The Briley-McDonald suggestion is very similar in concept to the 'triple-deck' approach described by Stewartson (Ref. 16.188), indeed the Briley-McDonald technique could be thought of as a 'double-deck' version of triple deck, and more of this will be discussed later.

For thin small separation bubbles Briley and McDonald were able to show that there was very little difference between solutions to the Navier-Stokes equations and the boundary layer equations, at least for the range of flow conditions and boundary conditions they investigated. In this way the belief that the boundary layer equations would be valid in certain types of flow separation is justified.

16.3.2 The Governing Equations

Here the format of Briley and McDonald (Ref. 16.194) is followed for illustrative purposes. Subsequently this development will be related to the triple-deck approach described by Stewartson (Ref. 16.188). The analysis is for the present restricted to two-dimensional incompressible flow. The extension to compressible flow is quite straightforward if it is not desired to retain true time-dependent behavior. More skill is required if true time dependency with compressibility is required. Three-dimensional compressible flow is also amenable to treatment along similar lines but as yet very little has been accomplished. It is likely that this state of affairs will be altered in the near future. The ensemble averaged incompressible Navier-Stokes equations are written in terms of stream function and vorticity to eliminate the awkward pressure terms. This simplifies matters but similar algorithms can be constructed retaining the pressure.

The vorticity and stream function equations are written

$$\frac{\partial \zeta}{\partial t} + \bar{u}\frac{\partial \zeta}{\partial x} + \bar{v}\frac{\partial \zeta}{\partial y} = \nu\left(\frac{\partial^2 \zeta}{\partial x^2} + \frac{\partial^2 \zeta}{\partial y^2}\right)$$
$$-\left(\frac{\partial^2 \overline{u'v'}}{\partial y^2} + \frac{\partial^2 \overline{u'v'}}{\partial x^2}\right) - \frac{\partial^2}{\partial x \partial y}\left(\overline{u'^2} - \overline{v'^2}\right)$$

$$\zeta = \frac{\partial^2 \psi}{\partial x^2} + \frac{\partial^2 \psi}{\partial y^2} \qquad 16.3\ (2)$$

with the usual definitions of stream function and vorticity

$$u = \frac{\partial \psi}{\partial y} \qquad v = -\frac{\partial \psi}{\partial x}$$

$$-\zeta = \frac{\partial \bar{v}}{\partial x} - \frac{\partial \bar{u}}{\partial y} \qquad 16.3\ (3)$$

If the shear layer is thin then the Reynolds stress term in streamwise direction $\partial^2 \overline{u'v'}/\partial x^2$ may be neglected. Also based on presently available information the Reynolds normal stress term $\partial^2(\overline{u'^2} - \overline{v'^2})/\partial x^2$ may be dropped without serious loss of accuracy. Both of these stress contributions can be retained if desired or subsequent information indicates their importance in certain flows, and they cause little numerical difficulty with the Navier-Stokes procedures. Within the boundary layer framework such terms would be very awkward unless some time lagged evaluation sufficed. With all of the usual reservations the eddy viscosity concept is introduced to describe the Reynolds shear stress $-\overline{u'v'}$ and is written

$$-\overline{u'v'} = \nu_T \frac{\partial \bar{u}}{\partial y}$$
$$\simeq \nu_T \zeta \qquad 16.3\ (4)$$

where the $\partial v/\partial x$ term in the vorticity definition has been neglected. The vorticity equation then becomes

$$\frac{\partial \zeta}{\partial t} + u\frac{\partial \zeta}{\partial x} + v\frac{\partial \zeta}{\partial y} = \frac{\partial^2}{\partial y^2}(\nu + \nu_T)\zeta + \nu\frac{\partial^2 \zeta}{\partial x^2}$$

16.3 (5)

and the stream function equation retains its previously given form. If now the second derivatives with respect to the streamwise direction x are neglected, the vorticity and stream function equations reduce to a form which is equivalent to the boundary layer equations. Indeed the reduced equations can alternatively be derived from the usual time dependent boundary layer equations by differentiating with respect to the normal direction y and using the boundary layer approximation that ξ is approximately given by $\partial u/\partial y$.

The wall and free stream boundary conditions employed are

$$\bar{u} = \bar{v} = 0 \qquad y = 0$$

$$\bar{u} = \bar{u}_e + \bar{u}_I \qquad \zeta = 0 \qquad y > \delta$$

16.3 (6)

where δ is some boundary layer thickness and $\bar{u}_e$ is the specified inviscid 'free stream' velocity distribution. The term $\bar{u}_I$ represents the elliptic correction due to the local interaction between the viscous and inviscid regions via the displacement surface. This contribution can be estimated from the standard techniques of inviscid aerodynamics and Briley and McDonald (Ref. 16.194) discuss a particularly simple source-sink technique; however the topic will not be discussed further here. Stewartson (Ref. 16.188) discusses various techniques for deriving similar corrections within triple-deck theory. As initial conditions either a stagnation point similarity solution or some other boundary layer procedure could be used to specify inlet profiles of ξ, Ψ and ν_T. At the downstream boundary, provided the separated region is enclosed between the upstream and downstream stations, the boundary condition that $\partial^2\xi/\partial x^2 = 0$ can be applied. The corresponding stream function condition can be implied from the coupled nature of the solution at the boundaries but if this is not a convenient process the condition that $\partial^2\Psi/\partial x^2 = 0$ usually serves just as well. To complete the problem the turbulent viscosity ν_T must be prescribed as before this item is deferred until the section on turbulence modeling and for the time being it is simply assumed that ν_T is known.

At this point the problem is defined. In the traditional boundary layer manner the inviscid flow outside the immediate vicinity of the boundary layer is assumed known from some other source. A conventional boundary layer calculation is performed and in the vicinity of the predicted separation an embedded region is defined which would be expected to encompass the entire separated region. Inlet conditions to the region are obtained from the conventional boundary layer calculation. Outer boundary conditions are obtained from the inviscid flow calculation (note that $\bar{v}$, the transverse velocity is not matched on the interface). Surface boundary conditions are the usual no slip conditions. Exit boundary conditions are the very mild restriction that the flow should exhibit boundary-layer like characteristics on exit. Within the embedded region the governing equations, which depending on the nature of the separation could either be the full Navier-Stokes equations or the boundary layer equations, are then solved. In view of the desire to interact the embedded viscous region and the inviscid flow an iterative, or equivalently, a time marching scheme is very attractive. In this way at each time step the interaction contribution to the inviscid axial velocity at the outer edge of the viscous domain can be computed based on the computed displacement surface effect at that time. Thus both the interaction effect and the iteration process can be carried out simultaneously. Direct methods, that is non-iterative methods, of solving the steady Navier-Stokes equations are obviously at a considerable disadvantage if the solution must be subsequently corrected iteratively for the interaction process. Some results from the work of Briley and McDonald (Ref. 16.194) are shown in Fig. 16.6.

At this point, it is worthwhile to introduce Stewartson's 'triple deck' (Ref. 16.188) concept in a little more detail. In this approach Stewartson has very effectively synthesized the Stratford (Ref. 16.46) and Lighthill (Ref. 16.196) boundary layer points of view into an analysis of separation. In the direction normal to the wall three distinct layers or 'decks' are identified. The middle deck joins an outer external flow to an inner region where viscous effects are important. This middle deck follows the Stratford view of the outer region of the boundary layer inasmuch as at high Reynolds numbers and with rapid pressure changes this region is supposed adequately described by a rotational but inviscid analysis with Bernoulli's equation governing the flow along streamlines. The lower deck is supposed thin and here the boundary layer approximations are assumed valid, resulting in a layer governed by the usual (incompressible) boundary layer equations. The upper deck is the external inviscid flow containing the effects of the interaction with the middle and lower decks. Length scales appropriate to each region are introduced and the three decks matched using the pressure from the lower edge of the upper deck. By this means a very powerful analysis of considerable theoretical interest emerges. Stewartson's analysis is applicable in subsonic, supersonic and hypersonic flows and in view of the assumptions used in it, the analysis is appropriate for high Reynolds numbers, rapid pressure rises and thin separation zones. Whilst providing very valuable information as to the interaction scales, the triple deck analyses are somewhat limited for routine use in design analysis problems by virtue of its many idealized approximations introduced to allow the penetrating theoretical development which has subsequently followed.

As mentioned previously the approach of Briley and McDonald (Ref. 16.194) whilst not originally framed in the triple deck terminology can clearly be thought of as a double deck analysis where Stewartson's middle and lower decks are merged into one deck which is treated entirely numerically. This direct numerical approach allows laminar, transitional or turbulent flow with non-similar initial boundary layers to be treated. The casualty is of course that interaction scale relationships no longer emerge by analysis but by numerical experiment when the

double deck approach is used. The reward is that the direct numerical approach is less restrictive and well suited to implementation into design analyses.

One further subtlety remains and this concerns the relationship between the Navier-Stokes equations and the boundary layer equations. In performing calculations with the direct numerical approach it is quite feasible to initiate the process using the boundary layer equations and later when the system is nearly converged if desired the Navier-Stokes equations could be used. In iterative solution techniques it usually follows that the better the initial guess the more rapidly the solution will converge and obviously a nearly converged boundary layer solution is better than some arbitrary guessed initial solution. The subtlety arises in obtaining significant computational savings by using the boundary layer equations. It follows that if an algorithm has been structured to solve the Navier-Stokes equations then simply deleting the appropriate second derivatives will only reduce the amount of computation by a trivial amount. The algorithm must be restructured to take full advantage of the deleted terms. The problem is merely another variant, indeed the inverse, of the previously introduced problem of the conventional vis à vis, the extended three-dimensional boundary layer equations. It will be recalled that it was observed that the conventional three-dimensional boundary layer equations contained only diffusive fluxes normal to one wall and as a result some schemes took good advantage of the appearance of only first derivatives in the spanwise direction. However when the extended boundary layer equations were treated, the appearance of two diffusive fluxes and the consequent appearance of a second derivative in the spanwise direction required a special restructuring of the algorithm. For the present problem the analogy is complete if the streamwise coordinate of the three-dimensional problem is interpreted as the time coordinate of the present two-dimensional problem. The extended boundary layer cross-flow equations are then interpreted as the two-dimensional time-dependent Navier-Stokes equations and the conventional boundary layer cross-flow equations are interpreted as the two-dimensional time-dependent boundary layer equations. With this in mind the cross-flow stability parameter γ for the three-dimensional boundary layer equations can now be written in Cartesian coordinates as

$$\gamma = \frac{w\Delta t}{\Delta x} \qquad 16.3\ (7)$$

and as before numerical schemes which are restricted to γ positive (no reverse flow) as clearly unacceptable in the present problem. The restriction of γ greater than -1 would obviously be much more acceptable. The inference to be drawn from the foregoing remarks is, not only does it require more effort than simply dropping some terms in the governing equations to obtain benefit from solving the time-dependent boundary layer equations, but care must be taken to ensure that any modified algorithm does not suffer from unduly restrictive stability conditions. In their scheme Briley and McDonald (Ref. 16.194) obtained an unconditionally stable scheme by retaining a fully implicit treatment of the boundary layer form of the vorticity equation much as was done for the Navier-Stokes equation. The savings in computation all comes from the simplified stream function equation. Previously in solving the Navier-Stokes equations, the stream function equation was an elliptic equation of the Poisson type and required considerable computational effort to obtain a solution at each time step. In the boundary layer scheme this Poisson equation is reduced to a one-dimensional relationship which can readily be treated implicitly and simultaneously with the y-implicit sweep of the vorticity equation. Further restructuring of the algorithm could doubtlessly be undertaken particularly with a view to treating the vorticity equation in the semi-implicit manner mentioned earlier with regard to the three-dimensional boundary layer equations. Such restructuring would doubtless be at the expense of the unconditional stability of the system and at most it would only reduce the present computational effort by roughly 25%, an amount not commensurate with the cost, in the opinion of Briley and McDonald (Ref. 16.194).

As mentioned earlier, a compressible version of the previously described scheme of Briley and McDonald could be constructed relatively easily if true time dependency were not required, since no simple analogous form of the vorticity equation exists for time-dependent compressible flow. A simple time-dependent vorticity equation could be fabricated and solved with the only requirement being that at steady state the correct form of the compressible vorticity equation was obtained. Another approach would be to proceed in a similar fashion to Patel and Nash (Ref. 16.127) and convert a three-dimensional boundary layer scheme into a two-dimensional time-dependent procedure. In view of the their unconditional stability, three-dimensional implicit schemes such as that devised by Kendall et al.,(Ref. 16.125) and McDonald and Briley (Ref. 16.65) would obviously be candidates. In their present forms the schemes of Patel and Nash (Ref. 16. 127) and Kendall et al., (Ref (Ref. 16.125) are really only suitable for performing the boundary layer version of the interaction but little difficulty would be expected with the scheme of McDonald and Briley (Ref. 16.65) in treating both the compressible boundary layer and the Navier-Stokes formulation. Stewartson (Ref. 16.188) describes the application of triple deck to supersonic as well as subsonic interactions.

As was mentioned earlier, the reason for considering an embedded separation region was simply to restrict the problem domain for economy reasons. In some cases either it is not feasible to restrict the domain or the embedding is done differently to that explained here. Examples of this type are to be found mainly in the more recent work in shock wave boundary layer interaction. Baldwin and MacCormack (Ref. 16.129) and Diewert (Ref. 16.130) considered shock wave boundary layer interactions in turbulent flow using MacCormack's variant of the Lax-Wendroff scheme to solve the two-dimensional compressible time-dependent Navier-Stokes equations, see Fig. 16.7. A similar study on the separated region occurring at a compression ramp was made by Shang and Hankey (Ref. 16.131) who also used a Lax-Wendroff type of scheme. Subsequently Murphy, Presley and Rose (Ref. 16.128) evaluated both the time-dependent boundary layer and the Navier-Stokes approach to a shock wave boundary layer interaction problem. As well as showing little difference in the

predictions of the time-dependent approach to the boundary layer equations and the Navier-Stokes equations for locally strong interactions, Murphy et al., found little difference in run time since no restructuring of the Navier-Stokes algorithm was carried out in reducing the algorithm to solve the boundary layer equations. Nevertheless, all of the preceeding examples give a great deal of encouragement for the eventual success of this approach for predicting transonic and supersonic separation. Indeed the main objection to much of this work at present is the use of stability restricted finite difference schemes which, in view of the importance of the near wall region, have had of necessity very long computing times. Before leaving this particular topic it is probably worthwhile to consider briefly the spatial marching approach to supersonic separated flows and this will now be done.

As was mentioned earlier, spatial boundary layer marching with local viscous-inviscid region matching has become quite commonplace in supersonic laminar flow and to a lesser extent in supersonic turbulent flow. The Goldstein separation singularity does not manifest itself in these schemes since the interface boundary condition is usually of the type determined by integration across the boundary layer of the continuity equation, i.e.,

$$\phi_e = \left(\frac{v}{u}\right)_e = \frac{d\delta^*}{dx} - \frac{(\delta-\delta^*)}{\rho_e u_e}\frac{d}{dx}(\rho_e u_e)$$

16.3 (8)

where ϕ_e is the local flow angle and in the hyperbolic supersonic external flow the specification of the local flow angle at the interface serves to determine the local axial pressure gradient imposed on the boundary layer and hence the axial gradient of displacement thickness is determined from the integrated continuity equation. At this point the boundary layer equations can be solved with the specified gradient of displacement thickness for the pressure gradient (the inverse technique referred to before) and either directly or by iteration at an axial station, the local flow angle which will permit a matched pressure gradient to be returned by the boundary layer solution technique is determined. Such a technique clearly reduces the possibility of the solution returning an infinite gradient of displacement thickness and seems to have been the inspiration for the subsonic inverse schemes referred to earlier. The main difference with the elliptic subsonic problem resides in the spatially hyperbolic nature of the supersonic free stream which does not permit upstream propagation. Thus the global outer iteration required at subsonic speeds of repeating the entire boundary layer calculation with a new interacted pressure field is (at first sight) apparently not necessary at supersonic speeds. This very happy situation contains one major drawback in that at one or more points in the flow, usually termed the Crocco-Lees (Ref. 16.134) point, the compressible boundary layer equation becomes independent of the imposed pressure gradient. The triple deck view of the matter is that the inner layer is still subsonic and able to transmit information upstream (a very valid observation) and the emergence of the Crocco-Lees point is a manifestation of physical laxity. At the Crocco-Lees point then there is no way to arrange to vary the computed displacement thickness except by changing the initial conditions of the boundary layer. Thus a shooting technique is suggested whereby initial conditions are varied such that the flow angle varies smoothly across the Crocco-Lee point. The physical and mathematical properties of the Crocco-Lees point are discussed in detail by Weinbaum and Garvine (Ref. 16.43). In brief it emerges that the Crocco-Lees point is the viscous analogue of the sonic throat. At the Crocco-Lees point a Mach number integral defined by Weinbaum and Garvine as

$$w = \int_0^\delta \frac{M^2-1}{M^2}\,dy$$

16.3 (9)

passes through zero and from this it follows that in some mean sense the Crocco-Lees point is the point at which the average Mach number within the boundary layer passes through unity. Changing the match point from the boundary layer edge to say the displacement surface, changes the location of the critical point but not its existence.

The frequency with which the Crocco-Lees point arises in regions of interest, particularly in turbulent flows, has led to practical difficulties in performing spatial marching calculations in supersonic flow. The shooting technique for passing through the critical point is both time consuming and relatively inaccurate, since a portion of the flow in the immediate vicinity of the Crocco-Lees point is extrapolated across. Also a problem with this spatial marching approach is allowing for downstream boundary condition influence, since most assuredly information can and does propagate upstream in the subsonic separated flow region. Both of these considerations have led some investigators to consider variants of time marching or pseudo-time marching even for supersonic free streams for instance Werle and Vatsa (Ref. 16.132) and Murphy et al., (Ref. 16.128) much as is done in subsonic flow. Initial results with these techniques indicate that the performing of routine calculations of supersonic interactions where with spatial marching the Crocco-Lees point is encountered, is very much simplified with a time marching approach.

16.3.3 Concluding Remarks

The prediction of separated flows in three dimensions is in its infancy. Given the developments that have occurred in two dimensions, time or pseudo-time marching either the three-dimensional extended boundary layer equations or the full Navier-Stokes equations would appear to have the best chance of success if zone embedding were feasible using double or triple deck concepts. Naturally in view of the time consuming nature of current three-dimensional calculation schemes zone embedding becomes even more attractive in three dimensions. It seems also that the conventional three-dimensional boundary layer equations even if time marched would not be adequate in view of the possible importance of spanwise diffusive effects in separated flows. Lastly in three space dimensions the problem of ensuring a gain in computational efficiency by using boundary layer approximations becomes even more difficult. At the present time there are at least two schemes available which have performed calculations

of subsonic separated flows both of which have used the full Navier-Stokes equations. These are the scheme of Patankar and Spalding (Ref. 16.133) and the scheme of Briley and McDonald (Ref. 16.64). The scheme of Patankar and Spalding (Ref. 16.133) is also described by Patankar (Ref. 16.195). Further extensive work on these and similar schemes will of course be necessary before they can be used in turbomachinery problems. In particular the capability to perform calculations in reasonable geometries is lacking and even the evaluation of the status of the presently available procedures is bedeviled by the high computing costs of performing the calculations. A demonstration of the capabilities of these two schemes is given in Figs. 16.8 and 16.9. Work in the area of representing the more realistic geometries is going forward, see for instance, Eiseman and McDonald (Ref. 16.117), but the problem of computing times will require either a breakthrough in computational procedures or a marked reduction in the cost of performing computations. In any event it has not yet been established that the turbulence models proposed for use in this problem are either adequate or inadequate even for the predictions of the gross features of the flow. Obviously a great deal of work remains to be done but at least a plan of attack on this most difficult of problems has been formulated and the initial stage implemented.

16.4 Turbulence Models

In an earlier chapter a physical description of turbulent motion has been given. Here the emphasis is on the various prescriptions for the quantitative evaluation of the extent of the transport of heat, mass and momentum which results from this turbulent motion. The turbulent transport mechanism is evidenced by the appearance of nonzero correlations of fluctuating quantities in the averaged equations describing the conservation of heat, mass and momentum. These correlations are usually grouped together and for the momentum equations are termed the Reynolds stress tensor. The aim of the turbulence model is to provide an adequate description of the dominant terms in this Reynolds stress tensor for the flow under consideration. At the present time the relationship between the Reynolds stresses and the resulting mean motion is poorly understood and it is necessary to resort to empiricism at some point in order to proceed. In principle resorting to empiricism is not necessarily evil, indeed the coefficient of laminar viscosity is an empirical quantity. The problem arises due to the lack of generality of the various turbulent transport models and as attempts are made to formulate more general models so the complexity of application has increased as well as the speculative nature of the various closure hypothesis. In describing turbulence models then, it is still necessary to include the simple prescriptions since they will continue to be used in the foreseeable future for those flows where their predictions are known to be reasonable. It is also necessary to outline where possible the areas where the various models can, or do, fail to give reasonable predictions. As before the emphasis will be on the special problems of turbomachinery. Several good treatments giving the various points of view on turbulence models in general are to be found in the works of Launder and Spalding (Ref. 16.163) and Bradshaw (Ref. 16.198), for instance. Since detailed turbulence models are normally thought of in terms of direct numerical solutions to the governing equation, the present discussion will reflect this bias. As previously mentioned, however, the detailed prescription can usually be incorporated into integral methods, at least with conceptual ease. Lastly an extensive catalogue of the more complex multi-equation turbulence models is given in the thesis of Ng (Ref. 16.171) and critical reviews of the topic given by Bradshaw (Ref. 16.198) and Reynolds (Ref. 16.170). Further discussion and categorization is also given by Launder and Spalding (Ref. 16.163) and Mellor and Herring (Ref. 16.173). Interested readers are encouraged to read these works to get the full flavor of both the divergent and convergent views held by the various authors.

16.4.1 Special Problems of Flow in Turbomachinery

Here those aspects of the turbulent flow in turbomachinery which give rise to special problems are discussed. The order in which the problems are introduced does not imply their relative importance as this will vary from application to application. No consideration is given specifically to the very difficult problems of centrifugal compressors.

One of the most striking features of the flow in turbomachinery is its very pronounced three-dimensional nature. Annular ducts almost invariably have supporting struts whose intersection with the annulus wall boundary layers introduce regions of flow separation and regions of shear layers merging, the 'clash regions' referred to earlier. Of course this same problem occurs with compressors and turbines as well, with the added complication that the time-dependent nature of the flow within a stage introduces a further variable into the problem. Within the turbine high heat transfer rates can be obtained in conjunction with highly cambered blades. The resulting overturning of the endwall boundary layers can result in the formation of vane or rotor passage vortices and of course the direct effect of curvature on the turbulence structure is possible. The strong accelerations and low Reynolds numbers which occur in the turbine give rise to extensive regions of transition from laminar to turbulent flow and vice versa. All of this occurring in a region where large and or intense velocity fluctuations and pressure (acoustic) waves can occur in the nominal free stream and interact with the shear layers. Obviously at the present time many of these effects cannot be taken into account in making flow predictions. It follows, therefore, that predictions of internal turbulent shear flows must be viewed more tolerantly yet more skeptically than in external flow.

On the positive side two aspects of turbulence, compressibility and three-dimensionality, have been found in external flow to be less of a problem than thought at one time and of course, the hope is that this fortunate state will also occur for internal flow problems. In the case of compressibility, Morkovin's hypothesis (Ref. 16.27) that turbulence should be unaffected by fluctuations in density provided the fluctuations are small compared to the mean density, has been supported by a number of investigators, e.g., Maise and McDonald (Ref. 16.21). Indeed Morkovin's suggestion would seem to hold over a much wider

range of density fluctuations than has hitherto been suspected (Owen and Horstman, Ref. 16.25), leading one to believe that even in the presence of the high heat transfer rates found in turbomachinery, Morkovin's hypothesis might be adequate. In the case of three dimensionality it has been argued by a number of investigators, e.g., Bradshaw (Ref. 16.145) and Nash (Ref. 16.74) that, since even when the mean flow is two dimensional, turbulence is a three-dimensional phenomenon, modest three-dimensionality would not affect turbulence 'scalar' quantities. Application of this suggestion has led to quite acceptable three-dimensional boundary layer predictions in some instances. Clearly, however, the strong three-dimensional effects occurring in turbomachinery stretch this suggestion to its limit and probably beyond. For the present there is little in the way of substantiated working alternatives unfortunately.

In addition rotational effects are encountered in internal flows in both compressors and turbines. According to Johnson (Ref. 16.146) the rotating external blade boundary layers are sufficiently thin that the effects of the Coriolis and centrifugal forces both on the mean flow and turbulent structure are probably negligible. Internal or duct flows, such as might occur within a rotating cooling labyrinth, do, however, according to Johnson, exhibit significant rotational effects. At present little detailed quantitative information on duct rotational effects is available and insofar as performing calculations are concerned only the preliminary suggestions of Bradshaw (Ref. 16.147) are available and extensive evaluation and/or development will be necessary before calculations can be performed with any confidence. As a first step in this long process, Hughes and Horlock (Ref. 16.204) discuss the effect of centrifugal and Coriolis forces upon the turbulent shear stress and how these changes will affect the growth of boundary layers in turbomachines. The Hughes-Horlock paper therefore is mandatory reading for those interested in rotational effects on the boundary layer.

16.4.2 *Categories of Turbulence Models*

Turbulence models serve to define the unknown turbulent correlations which appear in the averaged conservation equations of heat, mass and momentum ultimately in terms of the mean flow variables. In recent years the practice has grown up of categorizing the turbulence model by the degree of complexity of the relationship between the correlations and the mean flow, usually by means of the number of partial differential equations which must be solved in order to obtain the Reynolds stresses. At the most elementary level the previously introduced Prandtl's mixing length require no partial differential equation to be solved in order to determine the Reynolds stress level and consequently this model might be termed a 'zero equation' model, or more accurately, an algebraic stress model. In a similar vein, for example, Donaldson (Ref. 16.143) after empirical modeling of certain turbulent correlations solves a partial differential equation for each of the three components of the Reynolds normal stress and the Reynolds shear stress and consequently this suggestion would be termed a four equation model.

The differential equations used can either be exact equations derived rigorously by taking moments of the Navier-Stokes equations or entirely empirical equations. If exact equations are employed, empirical relationships must be introduced for certain of the turbulence properties to 'close' the system. A further discrimination between the turbulence models can be made on the basis of whether or not the differential equations are for one or two point turbulence properties.

In a separate category the use of differential equations for the one or two point turbulence properties may be replaced by the schemes which solve the time-dependent Navier-Stokes equations. In view of the wide range of scales normally encountered in turbulence it is not feasible to resolve the flow at sufficiently small scale such that all of the motion contributing to the dynamics can be computed. Instead a turbulence model can be postulated for the unresolved sub-grid motion. Examples of this approach are to be found in the work of Deardorff (Ref. 16.142) but even with sub-grid modeling the computational cost of this approach is at present prohibitive for normal engineering applications.

In addition to the foregoing categorization particularly in dealing with algebraic stress models and one or two equation turbulence models, the terminology equilibrium or nonequilibrium, historic or (with apologies) prehistoric is sometimes used. Here care has to be taken to discriminate between the various uses of the term 'equilibrium'. In particular 'equilibrium' is often used as a synonym for self-preserving or similarly in the sense of the very special boundary layers whose mean profile does not change in the axial direction when expressed in certain coordinates. Clauser (Ref. 16.11) demonstrated quite dramatically that such boundary layers, previously well-known in laminar flow, also exist in turbulent flow. Further Clauser (Ref. 16.11) also deduced that in such equilibrium flows the eddy viscosity, Eq. 16.4(7), in the outer region of the boundary layer would have to be essentially constant when made nondimensional by a scale of velocity and length, in Clauser's case the free stream velocity u_e and the boundary layer displacement thickness δ^*. This constant nondimensional eddy viscosity concept belongs in the algebraic stress model category and in view of this the algebraic stress models are sometimes referred to as equilibrium turbulence models.

Algebraic stress models all possess the feature that the local turbulent shear stress is given directly in terms of the local mean velocity profile. Such models therefore cannot allow the observed lag in changes in the Reynold's shear stress when the mean motion is perturbed rapidly. Multi-equation turbulence models do allow a lag and consequently these models are sometimes termed 'nonequilibrium', 'lag' or 'historic' turbulence models. In view of the observation that equilibrium turbulence models do at least reflect the mean flow history, the claims and counter claims about turbulence history or lack of it have been abandoned in favor of the less controversial categorizations of equilibrium and nonequilibrium turbulence model.

The equilibrium terminology also arises in part due to the interpretation of mixing length and eddy viscosity advanced by Batchelor

(Ref. 16.141) and Townsend (Ref. 16.140). According to this interpretation the validity of the simple mixing length hypothesis and closely related well-behaved eddy viscosity is an expression of the local equilibrium between the production and dissipation of turbulence kinetic energy. This local equilibrium arising when convection and diffusion of turbulence kinetic energy is negligibly small. Care must therefore be taken in discriminating between the various uses of the term 'equilibrium'.

16.4.3 Algebraic Stress Models

For thin unseparated turbulent boundary layers it is generally excepted that only the Reynolds shear stress $-\overline{u'v'}$ need be retained in the mean axial momentum equation. Prandtl (Ref. 16.139) proposed that in general the turbulent diffusional flux of some property $\phi = \bar{\phi} + \phi'$ could be expressed by

$$-\overline{v'\phi'} = \frac{1}{\sigma_\phi}(\overline{q^2})^{1/2}\ell\frac{\partial\bar{\phi}}{\partial y} \qquad 16.4\ (1)$$

where v is the velocity in the y direction, normal to the mean flow and $\overline{q^2}$ is the turbulence kinetic energy

$$\overline{q^2} = \overline{u'^2} + \overline{v'^2} + \overline{w'^2} \qquad 16.4\ (2)$$

and the prime denotes a fluctuation and σ_ϕ is a constant and ℓ is a turbulent length scale. Note here the explicit postulate of a gradient transport mechanism (see Corrsin (Ref. 16.205) for a discussion on the limitations of gradient transport in turbulence). Attention is now restricted to the transport of axial velocity u and the constant σ_ϕ is incorporated into the definition of the length scale ℓ. At this point two additional relationships must be provided before the shear stress can be determined: first, some means to obtain the turbulence kinetic energy must be prescribed; second, the length scale ℓ must be specified. Indeed a number of the two-equation models of turbulence to be discussed later attempt to provide partial differential equations for precisely these quantities. For the algebraic stress model the relationship between shear stress and kinetic energy may be obtained by invoking the structural similarity concepts noted by Townsend (Ref. 16.140) for instance. In the structural similarity concept the hypothesis is made that after prolonged application of a mean strain the turbulence approaches a near equilibrium condition where the correlation coefficients are independent of the turbulent intensities and strain rate which produced them. Both theory and experiment have since indicated that structural similarity is only approximately obtained even after prolonged straining but it does provide a convenient, relationship of the form

$$-\overline{u'v'} = a\overline{q^2} \qquad 16.4\ (3)$$

where 'a' is a coefficient which would not be expected to vary by an appreciable amount. Again if 'a' is incorporated into the definition of the length scale, Prandtl's formulation for the Reynolds stress then gives

$$\left(-\overline{u'v'}\right)^{1/2} = \ell\frac{\partial\bar{u}}{\partial y} \qquad 16.4\ (4)$$

which is consistent with Prandtl's earlier mixing length formulation. In squaring both sides it is established practice to write the formula

$$-\overline{u'v'} = \ell^2\frac{\partial\bar{u}}{\partial y}\left|\frac{\partial\bar{u}}{\partial y}\right| \qquad 16.4\ (5)$$

so that the shear stress always has the opposite sign to the mean gradient. The definition of eddy viscosity is given as

$$-\overline{u'v'} = \ell^2\frac{\partial\bar{u}}{\partial y}\left|\frac{\partial\bar{u}}{\partial y}\right| = \nu_T\frac{\partial\bar{u}}{\partial y} \qquad 16.4\ (6)$$

so that from a formal viewpoint mixing length ℓ and eddy viscosity ν_T may be viewed interchangeably. Returning now to the specification of the mixing length in a boundary layer, a three layer formulation is now widely favored. In this three layer formulation a viscous sublayer, a near wall region and a wake-like region of the boundary layer is identified and various suggestions for the mixing length or equivalently for the eddy viscosity, made for each region.

16.4.3.1 The Outer Wake-Like Region

In the wake-like region of the flow two suggestions are extensively used. The first is the constant eddy viscosity formulation deduced by Clauser (Ref. 16.11) for equilibrium boundary layers which can be written

$$\frac{\nu_T}{\bar{u}_e\delta_\kappa^*} = 0.016 \qquad 16.4\ (7)$$

and slight variations in the value of the constant .016 are observed in the literature. Herring and Mellor (Ref. 16.69) apparently the first to extensively use this definition of eddy viscosity for nonequilibrium and compressible boundary layers. In compressible flow Herring and Mellor (Ref. 16.69) adopted a kinematic definition of the displacement thickness, i.e.,

$$\delta_\kappa^* = \int_0^\delta (1-\bar{u}/\bar{u}_e)dy \qquad 16.4\ (8)$$

omitting density from the usual definition of δ^*. Later Maise and McDonald (Ref. 16.21) found that use of the kinematic displacement thickness much improved the collapse of the eddy viscosities inferred from the correlated behavior of compressible constant pressure boundary layers. Subsequently Cebeci and Smith (Ref. 16.68) adopted the Mellor-Herring suggestion and used the kinematic displacement thickness in Clauser's formula for compressible boundary layers whilst adding an intermittency factor to give a variation of the eddy viscosity normal to the wall more in keeping with that observed.

As an alternative and conceptually equivalent process to specifying the eddy viscosity in the

outer region a number of people have suggested that the mixing length when expressed as some fraction of the boundary layer thickness δ would be constant in the outer wake-like region of the boundary layer, i.e.,

$$\ell = 0.09\delta$$

16.4 (9)

and again minor variations in the constant .09 are observed in the literature. Patankar and Spalding (Ref. 16.67) for instance made effective and extensive use of this hypothesis following the lead of Escudier (Ref. 16.152) who demonstrated that Eq. 16.4(9) was a reasonable approximation in many incompressible turbulent boundary layers. Maise and McDonald (Ref. 16.21) later found that Eq. 16.4(9) appeared to be a very reasonable approximation and quite insensitive to Mach number in a constant pressure compressible boundary layer.

Three major effects on the values adopted for the nondimensional outer layer mixing length or eddy viscosity have been identified. The first is a low Reynolds number effect, the second is the effect of free stream turbulence and the third the effect of streamline curvature. Herring and Mellor (Ref. 16.69) found, for instance, that in order to satisfactorily predict the behavior of a number of low Reynolds number boundary layers they had to introduce a low Reynolds number correction into the outer layer eddy viscosity and progressively increase its value as R_θ dropped below 5×10^3. These findings were in fact consistent with the observation of Coles (Ref. 16.17) who noted below R_θ of 5×10^3 the so-called wake component of the constant pressure boundary layer eventually disappeared. Taking Coles' data correlation and velocity profile family, McDonald (Ref. 16.157) deduced from the boundary layer axial momentum equation the consistent Reynolds stress profiles and the corresponding nondimensional eddy viscosity and mixing lengths. The results were in broad agreement with the Herring-Mellor (Ref. 16.69) suggestion and could be expressed as

$$(\ell/\delta) = (\ell/\delta)_\infty\left[1 + \exp(-1.63 \ln R_\theta) + 9.7\right]$$

16.4 (10)

where $(\ell/\delta)_\infty$ is the high Reynolds number value of the mixing length constant. Subsequently a very similar modification was proposed by Cebeci & Mosinskis (Ref. 16.166).

Consistent with the increase in mixing length and eddy viscosity noted at low Reynolds is Head's visual observation in his smoke tunnel that the turbulent interface with the free stream was much more contorted at low Reynolds numbers, presumably resulting in an increased entrainment of fluid into the boundary layer and the increased values of mixing length and eddy viscosity. Simpson (Ref. 16.149) suggested that these low Reynold's number effects might be explained by an increase in the near wall region turbulent transport but the data analysis of Coles (Ref. 16.17) does not support this idea and subsequently Huffman and Bradshaw (Ref. 16.150) argued against Simpson's suggestion.

Turning now to the second major effect, that of free stream turbulence, Kline, Lisin and Waitman (Ref. 16.158) demonstrated some time ago the very large effect this parameter could have on a turbulent boundary layer. More recently this effect has been experimentally studied in detail by Charnay et al., (Ref. 16.159) and Huffman et al., (Ref. 16.160) among others. These results are indeed all quite consistent and show a large increase in the outer layer mixing length or eddy viscosity as the free stream turbulence is increased. The physical mechanism at play here is thought once again to be the increased contortion of the turbulent free stream interface due to the action of the free stream turbulence on the interface. It is also intuitively obvious that the scale of the free stream turbulence should have an effect on the interaction since if the scale is large and this free stream disturbance lifetime is much longer than the boundary layer turbulence the boundary layer will tend to respond more as it would to a slowly varying time dependent free stream. Now time dependent free streams can be treated if the free stream time scales involved are much longer than the energy containing boundary layer turbulence lifetime (which usually does not exceed the convection time to travel ten boundary layer thicknesses). For the usual concepts of free stream turbulence to be valid the motion has to be characterized by scales less than the previously mentioned ten boundary layer thicknesses. Following convention, the free stream turbulence is defined by

$$T_u = (\overline{q^2}/3)^{1/2}/\bar{u}_e$$

16.4 (11)

which reduces to

$$T_u = \left(\overline{u'^2}\right)^{1/2}/\bar{u}_e$$

16.4 (12)

in the often assumed case of isotropic free stream turbulence.

A straightforward correlation of the Huffman et al. data would suggest the outer region mixing length would vary very roughly as

$$\ell/\delta = (\ell/\delta)_{T_u=0} + T_u$$

16.4 (13)

Bayley et al., (Ref. 16.161) successfully used a very simple relationship derived by trial and error in calculating the effect of free stream turbulence on the heat transfer to a turbine aerofoil. Within the mixing length framework formula of this type which are, like the low Reynolds number correction, nothing more than data fits, probably suffice and doubtless as more data is acquired it will be possible to improve the data curve fit.

The third major effect on the outer layer mixing length arises from streamline curvature and this effect also has been clearly noted in a number of experimental studies. Bradshaw (Ref. 16.147) discusses this curvature effect in detail and suggests on the basis of the Monin-Obeukhov meterological formula a first

order formula

$$\ell/\delta = (\ell/\delta)_{R_i=0}(1-\beta R_i)$$

16.4 (14)

where R_i is an equivalent to the Richardson number and defined

$$R_i = \frac{2u}{R}\left(\frac{\partial u}{\partial y}\right)^{-1}$$

16.4 (15)

with R the radius of curvature taken positive on a convex surface. The constant β takes on a value about 7 for convex (blade upper surface) curvature and takes a value of about 4 on a concave surface. Typically on a convex surface δR_i might reach a value near 30 δ/R or 40 δ/R so that for ratios of boundary layer thickness to surface radius of curvature greater than say 1/100, very substantial effects of curvature on the outer layer mixing length are to be expected. Fortunately highly cambered blades are typical of turbines rather than compressors and the high acceleration levels of the turbine ensure that the naturally occurring surface boundary layers are very thin so that except for film cooled boundary layers the ratio δ/R does not usually approach the troublesome magnitudes. Nonetheless surface i.e., streamline, curvature must be observed as a potential source of difficulty. Hughes and Horlock (Ref. 16.204) provide a discussion of this problem.

16.4.3.2 The Near Wall Region

Turning now to what has been termed the near wall region of the flow, and here almost complete unanimity in the choice of relationship is to be found among the various investigators, notably that Prandtl's mixing length should be proportional to distance from the wall, viz.,

$$\ell = \kappa y$$

16.4 (16)

where κ is termed von Karman's constant and is usually attributed a value close to .40. The crossover to the outer layer is achieved by selecting the smaller value of eddy viscosity or mixing length as computed by both the near wall formula and the outer wake-like region formula. McDonald and Camarata (Ref. 16.56) suggested the continuous relationship

$$\ell = \ell_\infty \tanh \kappa y/\ell_\infty$$

16.4 (17)

to cover both regions without the sharp break which follows from the use of two piecewise, discontinuous relationships. More recently, Galbraith and Head (Ref. 16.154) have suggested that the von Karman constant κ does in fact vary with pressure gradient, and this effect has also been noted by Glowacki and Chi (Ref. 16.155). While the effects of this variation in the von Karman constant are negligibly small on the integral thickness parameters, the effect on skin friction and presumably heat transfer is significant. Glowacki and Chi deduced the turbulent shear stress from the axial momentum equation and the mean velocity profile development and found that

$$\kappa = 0.4 + 0.1823\left\{1.0 - \exp(-0.3207\beta)\right\}$$

16.4 (18)

where

$$\beta = \frac{\delta^*}{\tau_w}\frac{dp_e}{dx}$$

16.4 (19)

which when used in conjunction with the continuous distribution of mixing length, Eq. 16.4(17), and a Van Driest sublayer model which will be described shortly, gave very good predictions when compared with measured equilibrium (self preserving) boundary layers. Unfortunately, the use of a local pressure gradient parameter (constant for equilibrium boundary layers) in the correlation for κ gives rise to doubts about the ability to properly represent nonequilibrium boundary layers. A more significant parameter for generalization to nonequilibrium layers would be the Clauser shape parameter G, and a replacement of β with G in Eq. 16.4(18) can be made using Nash's (Ref. 16.12) relationship in Eq. 16.1(8). The implication at this point is that κ is exhibiting a dependence on the local turbulence structure, which on the basis of the local equilibrium hypothesis is related to the profile shape G which in turn is caused to change by the imposition of the pressure gradient β. An even more direct link in the argument follows from the observation, implicit in all of Coles' profile development and subsequently noted by Reeves (Ref. 16.168), that the fact the logarithmic law of the wall is observed to hold in pressure gradients is inconsistent with the linear mixing length assumption. It follows that if the logarithmic law of the wall holds in a pressure gradient i.e., a flow where $\tau \neq \tau_w$ and $y^+ > 2A^+$ then the mixing length must be given by

$$\ell = \kappa y(\tau/\tau_w)^{1/2}$$

16.4 (20)

to recover the logarithmic law of the wall. This observation has of course been well known for some time and the predictors have usually responded by pointing out good agreement between prediction and measurement which results from ignoring this dependence on the ratio of local to wall stress. Further the departures from the log law as it fairs into the defect or wake formulation are subject to minor fitting variations which can have considerable impact upon the local velocity gradients which are crucial to the derived mixing length variations. Thus predictors have ignored the strict interpretation of the log law in the presence of a pressure gradient and view the log law as an approximate relationship arising from $\tau = \kappa y$ and $\tau \simeq \tau_w$ and not vice versa, as Eq. 16.4(20) suggests. Indeed a number of people have generalized the log law to account for pressure gradients e.g., Townsend (Ref. 16.167) and the resulting profile certainly has a more realistic asymptotic behavior than the log law as τ_w decreases to zero. The inference of the generalizations of the law of the

wall to account for pressure gradients is that indeed Eq. 16.4(20) does not hold. The truth probably lies somewhere in between as evidenced by the fact that Glowacki and Chi did not assume a log law in their data reduction yet their results can be conveniently expressed as

$$\ell = \kappa_0 y(\tau/\tau_w)^a$$

$$= \kappa_{eff} y \qquad 16.4\ (21)$$

and the exponent 'a' is nearer to 1/4 than 1/2 as in Eq. 16.4(20). The exponent of 1/4 is of course a middle ground between the two viewpoints and would certainly result in more of a log law being evidenced by the predictions. The half power variation given by Eq. 16.4(20) is not at all suitable for implementation in a finite difference scheme to determine the local stress τ since the local stress which is to be obtained from the mixing length relationship would then cancel out the shear stress - mixing length formula. A caution also to the use of a more general (τ/τ_w) type of correction for the von Karman constant lies in the asymptotic condition of vanishing wall shear and here obviously it is necessary to provide a limit of the type

$$\kappa_{eff} = \kappa_0(\tau/\tau_w)^{1/4}, \quad 0.5 < \tau/\tau_w \leq 15.0$$

$$= 1.968\kappa_0 \qquad \tau/\tau_w > 15.0$$

$$= 0.84\kappa_0 \qquad \tau/\tau_w < 0.5$$

16.4 (22)

Finally, it is observed that a κ_{eff} relationship such as the above or Eq. 16.4 (21) is of course inconsistent with the notion of a linear variation of mixing length i.e., κ_{eff} = const, in the wall region except in some very special cases. If a linear dependence of mixing length on wall height is demanded (and here the experimental evidence in pressure gradient is not all that definitive) then it becomes necessary to postulate a dependence of mixing length upon the stress gradient $\partial\tau/\partial y$ which in turn possesses the ability to be nearly constant across the wall layer. Further, in equilibrium boundary layers near the wall but outside the viscous sublayer one observes that the stress gradient $\partial\tau/\partial y$ is nearly constant and given by

$$\frac{\delta^*}{\tau_w}\frac{\partial\tau}{\partial y} \simeq 0.7\beta \qquad 16.4\ (23)$$

so that Glowacki and Chi's relationship Eq. 16.4(18) can easily be converted to a stress gradient rather than a pressure gradient or shape parameter relationship.

Thus in attempting to use the information deduced by Galbraith and Head, and Glowacki and Chi there are four obvious alternatives. The first is to use Glowacki and Chi's equilibrium correlation of the effective value for the von Karman constant as presented on the basis of pressure gradient for nonequilibrium flows. It is suggested that this proposal should be rejected. To follow the local equilibrium hypothesis it would be more reasonable to base the extension to nonequilibrium flows on a local mean velocity profile shape parameter G rather than the local pressure gradient parameter β. This second alternative seems quite reasonable for relatively unsophisticated turbulence models in view of the global nature of the mean velocity profile characterization. The third alternative is to take note of the widespread appearance of a logarithmic region in the mean velocity profile near the wall and characterize the effective von Karman constant by some function of the local value of the ratio of the turbulent shear to wall shear stress. This latter practice however is inconsistent with the observed near linear dependence of the mixing length on distance from the wall in the near wall region (and poses difficulty near separation). The only way to recover a much wider region of linear dependence is to base the correlation of effective von Karman constant on the local stress gradient as opposed to the local stress. Either of the latter two suggestions seem reasonable and presumably the correct choice will become obvious as more experimental evidence becomes available.

16.4.3.3 The Viscous Sublayer

Finally a variation of eddy viscosity or mixing length across the viscous sublayer must be hypothesized. Here however, the option is open of specifying this variation once and for all and integrating the so-called Couette flow approximation to the axial momentum equation

$$\tau = -\bar{\rho}\overline{u'v'} + \mu\frac{\partial u}{\partial y} = +\left[\ell^2(y)\left|\frac{\partial u}{\partial y}\right| + \mu\right]\frac{\partial u}{\partial y}$$

$$= \tau_w + y\frac{dp}{dx}$$

16.4 (24)

i.e., neglecting the convective terms in the boundary layer axial momentum equation to obtain u at the edge of the viscous sublayer as a function of τ_w, ν and dp/dx and of course any of the parameters upon which $\ell(y)$ is supposed to depend on in the sublayer. This functional dependence of u at the edge of the sublayer can be parameterized and consequently the integration of the governing equations within the sublayer need not be performed so long as the Couette flow approximation is valid. This same parametric approach can be viewed alternatively as determining from observation the variation of the additive constant B in the law of the wall mean velocity profile Eq. 16.1(10). Patankar and Spalding (Ref. 16.67) in their scheme chose to implement the once and for all integration of Jayatelleke (Ref. 16.204) while Bradshaw, Ferriss and Atwell (Ref. 16.57) prefer to view the sublayer problem as an empirical problem of determining the variation of the law of the wall additive constant. In either case the result is the same in that the governing equations are not integrated within the viscous sublayer but the solution is matched to some prescribed velocity outside the sublayer. A variety of rather neat matching techniques have been devised but will not be discussed here. A similar process is followed for the energy and species equations.

There are two attributes to the previously outlined wall function procedure for dealing with the sublayer aside from the obvious one of saving computer time by reducing the required number of grid points. The first is that if the sublayer profile is viewed simply as a problem of

determining the law of the wall additive constants, the conceptual difficulty of explicitly postulating a turbulent transport mechanism for the very low Reynolds number asymptotic wall region is avoided. Bradshaw and Ferriss (Ref. 16.77), for instance, cite this as one reason for selecting the law of the wall approach (in spite of the apparent ease with which reasonable sublayer profiles can be obtained from postulated transport models). The second attribute has been previously mentioned and derives from the absence of grid points very close to the wall as a result of matching the computed and analytic variables at some point removed from the wall. Clearly stability restricted prediction methods derive a considerable benefit in increasing the allowable axial step which follows from the increased step size normal to the wall. Indeed it is doubtful that current stability restricted methods would be at all competitive in terms of computer run times unless the wall function approach were adopted.

The problem with the wall function approach in general lies first of all with the limitations on the Couette flow approximation, for here it is observed that frequently the stress near the wall but outside the sublayer may be represented by the linear relationship

$$\tau = \tau_w + Ay\frac{dp}{dx}$$

16.4 (25)

where A can reach values as low as .2 and as high as 2.0 with relative ease. At the wall itself a value of 1.0 for A must be obtained so that a variation in A across the sublayer, not taken into account in the Couette flow assumption, is to be expected. The value of velocity at the edge of the sublayer arrived at by a once and for all integration of the Couette flow approximation, therefore, cannot be relied upon in the case of strong pressure gradients or in the vicinity of flow separation. Further there arises the question of the temperature variation in the sublayer and aside from the interest in this quantity for heat transfer, the temperature is required in the sublayer integration for the velocity profile. As was mentioned in the earlier discussion on the law of the wall, the temperature variation in the sublayer seems much more sensitive to variables such as pressure gradient than the velocity field. Consequently the adoption of the Couette flow approximation for the temperature field or equivalently assuming an additive constant for the thermal law of the wall is more suspect than for the velocity field.

In view of the foregoing it would seem reasonable that if the wall function approach were to be selected it is probably better to proceed for instance as Bradshaw and Ferriss (Ref. 16.77) do and to view the sublayer as the problem of determining the law of the wall additive constants and to correlate the variation of these constants with parameters such as pressure gradient, transpiration rate or wall roughness etc. On the other hand, viewed pragmatically, considerable success has been obtained by specifying a turbulent transport mechanism for the sublayer and not adopting the Couette flow simplification. This approach has particular merit in gas turbine applications where low Reynolds numbers combine with high acceleration levels to give extensive blending regions between laminar and turbulent flow. In such regions the law of the wall does not hold so the question of the value of the additive constant does not arise. Further since in some turbine problems the sublayer may comprise the whole boundary layer, the neglect of the convective terms in the Couette approximation is clearly unacceptable.

Of the sublayer transport models proposed, the most commonly used in calculation schemes is that due to Van Driest (Ref. 16.151) who suggested that the mixing length in the wall region be written

$$\ell = \kappa y \cdot \mathcal{D}$$

16.4 (26)

where $\mathcal{D}$ is a damping factor defined by

$$\mathcal{D} = 1.0 - \exp(-y^+/A^+)$$

16.4 (27)

and A^+ is a coefficient which could be given the physical interpretation as the thickness of the sublayer when expressed in law of the wall coordinates

$$y^+ = y\sqrt{\tau/\rho}\,/\nu_w$$

16.4 (28)

It turns out that the sublayer damping factor is a critical parameter in obtaining accurate heat transfer and wall friction predictions. Other suggestions for the sublayer damping factor have been given by Mellor (Ref. 16.156) and McDonald and Fish (Ref. 16.58). The differences in the various suggestions are i matters of detail and are not worth dwelling on here. Probably the most significant items in the damping factor are the definitions of the normal distance y^+ and the value ascribed to the Van Driest coefficient A^+. In the definition of y^+ given above the local shear stress τ has been used, as seems proper. Frequently however, this local stress is approximated by the wall value τ_w, and aside from being unnecessary in a direct numerical scheme the approximation of the local stress by the wall stress leads to obvious difficulty near separation where $\tau_w \to 0$. Some authors, for example Cebeci (Ref. 16.165) have proposed to remedy the situation by reverting to the Couette flow approximation replacing τ by

$$\tau = \tau_w + y\frac{dp}{dx}$$

16.4 (29)

As was pointed out above there is considerable experimental evidence that Eq. 16.4(29) is not particularly accurate near a wall and there is little ground (except numerical instability) for not using the total stress in the definition of y^+.

The second item of importance is the Van Driest coefficient A^+ (equivalent parameters arise in the formulations of Mellor (Ref. 16.156) and McDonald and Fish (Ref. 16.58)). For boundary layer flow over a smooth impermeable

wall the coefficient is usually given a value around 27. Unfortunately the Van Driest coefficient is known to vary. For instance Van Driest suggested that the effect of surface roughness could be modeled by varying A^+ such that when k^+, defined by

$$k^+ = k\sqrt{\tau/\rho}/\nu_w \qquad 16.4\ (30)$$

with k the rms roughness height, exceeds A^+, the sublayer would be erradicated. A simple preliminary formulation embodying this feature has been implemented by McDonald & Fish (Ref. 16.58) and Crawford and Kays (Ref. 16.201).

It is noted however that Van Driest's original suggestion of eradicating the sublayer does not account for the observed continued effect on the flow for roughness heights k^+ in excess of 27. In terms of the law of the wall additive constant, B, this continues to decrease by very significant amounts as the roughness height k^+ increases beyond 27. In order to model this effect either a shift in the effective wall location or a capacity of the roughness to enhance the turbulence production (or both) must be postulated. Although incorporated into the formula of McDonald and Fish, the turbulence production capability of wall roughness clearly merits much additional study. As given by Crawford and Kays (Ref. 16.201) there does not seem to be any mechanism to reduce B as k^+ increases beyond 27 in their formulation.

Insofar as pressure gradients and wall transpiration are concerned numerous workers have observed the need to vary A^+ in order to match the experimental results e.g., Cebeci (Ref. 16.165). It is noted however that if the local stress τ is used in the definition of y^+ as opposed to the wall value τ_w, the required variation of A^+ is lessened. Indeed both Herring and Mellor (Ref. 16.69) and Kreskovsky, Shamroth, and McDonald (Ref. 16.200) in published and unpublished studies were able to satisfactorily predict the behavior of a wide range of boundary layers in strong variable pressure gradients for both transpired and impermeable walls, without resorting to varying the equivalent of A^+ in their formulations. This capability was attributed to the use of the local stress in the definition of y^+. Huffman and Bradshaw (Ref. 16.150) found that even when the local stress was used, A^+ was observed to vary when the stress gradient $\nu_w/\rho_w u_\tau^3 \partial\tau/\partial y$ exceeded -5×10^{-3}. In any event if the wall stress is used to define y^+ then A^+ must be allowed to vary. Kays and Moffat (Ref. 16.81) suggest on the basis of the extensive studies at Stanford the empirical relationship

$$A^+ = \frac{24}{a\left[v_w^+ + b\dfrac{p^+}{1+cv_w^+}\right]+1.} \qquad 16.4\ (31)$$

where

$a = 7.1 \quad v_w^+ \geq 0.0$ otherwise $a = 9.0$
$b = 4.25 \quad p^+ \leq 0.0$ otherwise $b = 2.0$
$c = 10.0 \quad p^+ \leq 0.0$ otherwise $c = 0.0$

16.4 (32)

with a constant pressure zero transpiration value of 24 for A^+ is adopted, and where

$$p^+ = \frac{\nu_w}{\rho_w u_\tau^2}\frac{\partial p}{\partial x}$$

$$v_w^+ = \frac{v_w}{u_\tau}$$

$$u_\tau = \sqrt{\tau_w/\rho_w} \qquad 16.4\ (33)$$

The Stanford group have incorporated the foregoing suggestion into an extensively modified version of the Patankar-Spalding finite difference boundary layer scheme (Ref. 16.201) and achieved comparable results to Herring and Mellor (Ref. 16.69).

The question of relaminarizing boundary layers is also treatable within the mixing length framework if the suggestion of Launder and Jones (Ref. 16.80) is followed and A^+ obtained by integration of the differential equation

$$\frac{dA^+}{dx^+} = (A^+ - A_{eq}^+)/C \qquad 16.4\ (34)$$

and C is a constant whose value has been found by trial and error to be about 4. A_{eq}^+ is the local equilibrium value of A^+ which would be obtained from a relationship such as Eq. 16.4(31). Launder and Jones subsequently abandoned this formulation in favor of a multi-equation model of turbulence which will be discussed subsequently.

16.4.3.4 The Heat Transfer Coefficient

Turning now to the turbulent transport of heat with the usual thin boundary layer approximations only the turbulent heat transfer correlation $-\overline{v'T'}$ assumes importance. If Prandtl's formulation Eq. 16.4 (1) is retained for consistency with the momentum transfer analysis then the ratio of the turbulent heat transfer correlation to the Reynolds shear stress is simply

$$\frac{-\overline{v'T'}}{-\overline{v'u'}} = \frac{\sigma_u}{\sigma_h}\frac{\dfrac{\partial\bar{T}}{\partial y}}{\dfrac{\partial\bar{u}}{\partial y}} \qquad 16.4\ (35)$$

which from the definition of the eddy viscosity ν_T may be written

$$-\overline{v'T'} = \frac{\sigma_u}{\sigma_h}\nu_T\frac{\partial\bar{T}}{\partial y} \qquad 16.4\ (36)$$

so that if an eddy diffusivity of heat is introduced

$$-\overline{v'T'} = \nu_h\frac{\partial\bar{T}}{\partial y} = \frac{\sigma_u}{\sigma_h}\nu_T\frac{\partial\bar{T}}{\partial y} \qquad 16.4\ (37)$$

the turbulent Prandtl number is arrived at as

$$P_{rt} = \frac{\nu_T}{\nu_h} = \frac{\sigma_u}{\sigma_h} \qquad 16.4\ (38)$$

which in Prandtl's formulation would be a constant.

Although it is quite feasible to deduce a three (or more) layer model for the heat transport correlation in an analogous fashion to the algebraic Reynolds shear stress models, it has long been felt that the mechanism resulting in the turbulent transport of momentum would be the same mechanisms at play in the turbulent transport of heat so that the turbulent Prandtl number would indeed take on values close to unity. Initial boundary layer calculations performed using this assumption of unit turbulent Prandtl number resulted in very good agreement with available data. Subsequent measurements by a number of different authors e.g., Meir and Rotta (Ref. 16.40) and Simpson, Whilten and Moffat (Ref. 16.137) for instance, have all confirmed that indeed the turbulent Prandtl number takes on values close to unity in the turbulent boundary layer. Nonetheless, in spite of the experimental uncertainties involved in making such measurements at the present time, the results of the differing investigations are fairly consistent in showing values of the turbulent Prandtl number in excess of one near the wall and falling below one in the wake-like region of the boundary layer. This has led a number of authors to suggest distributions of turbulent Prandtl number for use in performing turbulent boundary calculations. For instance, Pai and Whitelaw (Ref. 16.138) used

$$P_{r_t} = 1.75 - 1.25y/\delta \qquad 16.4\ (39)$$

however they found that by a large margin best predictions of a film cooled boundary layer were obtained with the old assumption of unit turbulent Prandtl number. Kays and Moffat (Ref. 16.81) on the other hand obtained reasonable predictions with a constant turbulent Prandtl number but recommended a variation with y^+ if an accurate detailed temperature profile were to be desired. Hopefully in the future improved techniques of making time resolved temperature measurements in turbulent boundary layers will clarify this situation.

16.4.3.5 Extensions to Three Dimensions

The usual boundary sheet approximations in three dimensions result in two Reynolds stresses making their appearance in the axial and cross stream momentum equation (see for instance Nash & Patel (Ref. 16.107))

$$\tau_x/\rho = -\overline{u'v'} + \nu\frac{\partial \bar{u}}{\partial y}$$

$$\tau_z/\rho = -\overline{w'v'} + \nu\frac{\partial \bar{w}}{\partial y} \qquad 16.4\ (40)$$

The natural extension of the previously described algebraic stress models to three dimensions is to take the eddy viscosity in three dimensions as

$$\nu_T = \ell^2\left|\frac{\partial \vec{v}}{\partial y}\right| \qquad 16.4\ (41)$$

and

$$\left|\frac{\partial \vec{v}}{\partial y}\right| = \left[\left(\frac{\partial \bar{u}}{\partial y}\right)^2 + \left(\frac{\partial \bar{w}}{\partial y}\right)^2\right]^{1/2} \qquad 16.4\ (42)$$

where ℓ is assumed to be a scalar and have exactly the same form as that used in two dimensions. The closing assumption is now that the eddy viscosity is a simple isotropic scalar i.e., its magnitude is independent of direction so that one obtains for the stresses

$$\frac{\tau_x}{\rho} = (\nu_T + \nu)\frac{\partial \bar{u}}{\partial y}$$

$$\frac{\tau_z}{\rho} = (\nu_T + \nu)\frac{\partial \bar{w}}{\partial y} \qquad 16.4\ (43)$$

Thus as in two dimensions the description of the three-dimensional Reynolds stresses can be poor when the mixing length assumptions are inadequate. However, in addition, in three dimensions the assumption that the eddy viscosity is an isotropic scalar results in the shear stress direction being that of the mean rate of strain. Experimental evidence shows that in many cases this is at best a crude assumption but probably no worse than the assumption of a well-behaved mixing length or eddy viscosity and according to Nash and Patel the calculations are not overly sensitive to the direction of the shear stress. In the foregoing the generalization of mixing length formula to three dimensions has been given and the extension of the conventional two-dimensional eddy viscosity models, which usually only differ in the outer wake-like region in any event, are obtained similarly i.e.,

$$\frac{\nu_T}{\bar{v}_e\delta^*} = 0.016 \qquad 16.4\ (44)$$

where the free stream velocity u_e in two dimensions has simply been replaced by the free stream velocity vector parallel to the wall $\bar{v}_e$. As in two dimensions the wall similarity scale is based upon the resultant stress i.e.,

$$\frac{\tau}{\rho_w} = (\nu_T + \nu)\left[\left(\frac{\partial \bar{u}}{\partial y}\right)^2 + \left(\frac{\partial \bar{w}}{\partial y}\right)^2\right]^{1/2} \qquad 16.4\ (45)$$

and the three-dimensional displacement thickness is defined

$$\delta^* = \int_0^\infty\left(1 - \frac{\bar{v}}{\bar{v}_e}\right)dy \qquad 16.4\ (46)$$

Cebeci et al., (Ref. 16.102) have in fact constructed a three-dimensional boundary layer prediction scheme using an eddy viscosity formulation which has been generalized in the aforementioned manner from the two-dimensional model used by Cebeci and Smith (Refs. 16.68 and 16.73). Cebeci's initial results are quite encouraging. Wheeler and Johnson (Ref. 16.97) examined three different three-dimensional shear stress models including an eddy viscosity model similar in many respects to that used by Cebeci (only the viscous sublayer differed as Wheeler and Johnson elected to fit a three-dimensional law of the wall profile). In general Wheeler and Johnson concluded that there appeared to be a fairly large class of three-dimensional flows which could be quite well predicted by a direct numerical method using even the very simple description of the Reynolds stresses obtained from the isotropic eddy viscosity model.

16.4.3.6 Summary of Algebraic Stress Models

Even a cursory glance through the literature will show the quite remarkable accuracy and range of predictions possible with these very simple models of turbulence. Notable objections to mixing length and eddy viscosity such as the fact that different outer layer prescriptions of the mixing length are required for differing types of flow operationally causes little difficulty since the required typical value for that category of flow is known in advance. Difficulties with the transverse velocity gradient disappearing at some point other than where the shear stress goes through zero also can be circumvented, as for instance was done in the film cooling studies of Pai and Whitelaw (Ref. 16.138). Real problems arise with these models when substantial variations in the outer layer values of mixing length or eddy viscosity are required during the course of development of one particular shear layer and/or no convenient scale of length for the flow can readily be determined.

16.4.4 One Equation Turbulence Models

There are two major defects in algebraic stress models, one being that practical flows can arise where the changes in the turbulent structure cannot keep pace with the changes in mean velocity, the other being that in many turbulent flows no convenient turbulent scale of length is present. One equation turbulence models are aimed at the turbulence lag problem. In using one equation turbulence models it is usual to suppose that a well-defined length scale such as the boundary layer thickness δ is present and therefore such models are of necessity restricted to flows where such a scale exists. Turning once again to Prandtl's constitutive relationship, Eq. 16.4 (1), it will be seen that the turbulent diffusioned flux is supposed related to some turbulent scale of length ℓ and a turbulent velocity scale $\overline{q^2}$, where q^2 is the turbulence kinetic energy. A number of one equation models then have concentrated on solving a transport equation for the turbulence kinetic energy, which can be derived by manipulating the Navier-Stokes equations, whilst retaining the existing Prandtl formulation so that effectively a transport equation for the eddy diffusivity is constructed. Alternatively an entirely empirical equation for the transport of the eddy diffusivity can be formulated such as was done by Nee and Kovasney (Ref. 16.164). Lastly, as an alternative to both of the preceding, the structural equilibrium hypothesis of Townsend (Ref. 16.167) can be recalled and in this framework it is then only necessary to predict the turbulence kinetic energy to obtain the turbulent diffusional flux of interest since with this hypothesis all correlations scale, however a 'dissipation length' now enters the problem. Prandtl's constitutive relationship is bypassed in the structural equilibrium approach as is the local gradient transport hypothesis it embodies. An example of the structural equilibrium approach is to be found in the work of Bradshaw and Ferriss (Ref. 16.77). If the entirely empirical transport equation is omitted from further consideration and most investigators prefer where possible to work with a rigorously based equation, the concensus seems to be that the turbulence kinetic energy equation is the most suitable single equation characterizing the Reynolds stress. Mellor and Herring (Ref. 16.173) dispute this however, arguing that the Reynolds shear stress equation, also derived by straightforward manipulation of the Navier-Stokes equations, is the 'correct' equation, embodying as it does the transport of the Reynolds shear stress directly. However, at the outset of this particular development in turbulence modeling the turbulence kinetic energy equation on a term by term basis was much better understood than the Reynolds shear stress equation and hence the selection of the energy equation for development.

In general the various rigorous 'transport' equations are formed from the instantaneous Navier-Stokes equations written in the form of fluctuating components by subtracting out the averaged Navier-Stokes equations. The resulting set may be regarded as equations governing the fluctuating components of velocity. The various single point correlations may then be formed by taking appropriate moments of the fluctuation equations and averaging. Boundary layer approximations, if valid, may then be introduced. The turbulence kinetic energy equation derived in the foregoing manner can be written in a three-dimensional Cartesian coordinate system in incompressible 'boundary sheet' flow, (see Nash and Patel, Ref. 16.107) as

$$\frac{\partial}{\partial x}\frac{\bar{u}\overline{q^2}}{2}+\frac{\partial}{\partial y}\frac{\bar{v}\overline{q^2}}{2}+\frac{\partial}{\partial z}\frac{\bar{w}\overline{q^2}}{2}=-\overline{u'v'}\frac{\partial\bar{u}}{\partial y}-\overline{v'w'}\frac{\partial\bar{w}}{\partial y}$$
$$-\frac{\partial}{\partial y}\left(\frac{\overline{v'q^2}}{2}+\frac{\overline{v'p'}}{\bar{\rho}}\right)-\nu\overline{(u'\nabla^2u'+v'\nabla^2v'+w'\nabla^2w')} \qquad 16.4\ (47)$$

the viscous term appearing above is the sum of the dissipative and diffusive effects of viscosity and often is rewritten as such, i.e.,

$$\nu\overline{(u'\nabla^2u'+v'\nabla^2v'+w'\nabla^2w')}=\nu\sum_{i=1,3}\sum_{k=1,3}\overline{u_i'\frac{\partial^2u_i'}{\partial x_k^2}}$$
$$=-\nu\sum_{i=1,3}\sum_{k=1,3}\left(\overline{\frac{\partial u_i'}{\partial x_k}}\right)^2+\frac{\partial^2\overline{u_i'^2}}{\partial x_k^2}=-\nu\sum_{k=1}\sum_{i=1,3}\left(\left(\overline{\frac{\partial u_i'}{\partial x_k}}\right)^2-\frac{1}{2}\frac{\partial^2}{\partial x_k^2}\overline{u_i'^2}\right) \qquad 16.4\ (48)$$

where the gradients in kinetic energy are normally negligible except close to a wall when the second derivative with respect to y may be important, and can readily be retained without difficulty. Now in order to proceed further it is necessary to relate the higher order correlations appearing in Eq. 16.4(47) to the lower order correlations and/or the mean flow. This process is termed the 'closure problem', and subsequently the more commonly used strategies to effect this closure will be discussed.

Common to most approaches based on Eq. 16.4(47) is the treatment of the viscous energy dissipation terms in the energy equation and the appeal here is to the well-known observation that at high Reynolds numbers the rate of energy dissipation is controlled by the essentially inviscid turbulent motion supplying the energy which cascades to the smaller dissipative scales of the motion. Dimensional analysis then suggests that the viscous terms, represented by ε, can be written

$$\varepsilon=c_\varepsilon\frac{(\overline{q^2})^{3/2}}{L} \qquad 16.4\ (49)$$

and L once again is a turbulence length scale (prescribed) and C_ϵ is some constant. If at this point an appeal is made to Prandtl's constitutive relationship and the length scale L is prescribed as for the algebraic stress models, it only remains to set values for the various constants to close the system (normally the pressure velocity correlation gradient is neglected). Usually these constants are derived by forcing the system to return the mixing length values when the convective and diffusive terms in the kinetic energy equation can be neglected. Detailed values of the various constants are given in the book by Launder and Spalding (Ref. 16.163).

As an alternative to adopting Prandtl's constitutive relationship and the gradient transport hypothesis it embodies, Townsend's structural similarity arguments can be cited to yield

$$-\overline{u'v'} = a\overline{q^2} \qquad 16.4\ (50)$$

where 'a' could also be some prescribed function of the turbulent length scale L and hence y/δ but in application Bradshaw and Ferriss (Ref. 16.77), Nash (Ref. 16.74) and McDonald and Camarata (Ref. 16.56) all chose the simple expedient of setting 'a' to a constant value (.15). At this point two further quantities, the turbulent diffusive term and the turbulent length scale appearing in the expression for the dissipation remain to be specified. Insofar as the former is concerned Bradshaw and Ferriss (Ref. 16.77) suggested

$$\frac{\overline{v'q^2}}{2} + \frac{\overline{v'p'}}{\rho} = G\cdot\overline{q^2}\,(\overline{q^2}_{MAX})^{1/2} \qquad 16.4\ (51)$$

where $\overline{q^2}_{MAX}$ is the maximum value of the turbulence kinetic energy in the boundary layer at that particular streamwise location. This quantity $\overline{q^2}_{MAX}$ is introduced as a scale of the velocity responsible for the bulk transport (as opposed to gradient transport). G is a dimensionless function of normal distance in the boundary layer. Townsend (Ref. 16.167) postulates a slightly different form, used by Nash (Ref. 16.74).

$$\frac{\overline{v'q^2}}{2} + \frac{\overline{v'p'}}{\rho} = -k(\overline{q^2})^{3/2}\,\mathrm{sgn}\left(\frac{\partial\overline{q^2}}{\partial y}\right) \qquad 16.4\ (52)$$

thus ensuring the transport is always down the gradient of $\overline{q^2}$. It is likely that both gradient and bulk diffusion of kinetic energy are present in turbulent boundary layers and in various situations one or the other may dominate. At the present time the situation is unclear and the arguments for both forms are given by their respective advocates in the appropriate references. Future study will doubtless clarify the matter and for moment the issue is sidestepped with the observation that boundary layer predictions are not unduly sensitive to the assumptions made concerning diffusion of turbulence kinetic energy.

The other item of specifying the turbulent dissipation length scale is now taken up and here again the proposition is that this scale is a unique function of position in the boundary layer. As with the other Prandtl type formulations a convenient method of estimating this length scale is given by considering equilibrium flows where convection and diffusion are negligible in comparison to production and dissipation of turbulence kinetic energy, leading to the observation that the dissipation length should have a very similar (but invariant) form to the mixing length distribution in an equilibrium boundary layer. This led McDonald and Camarata (Ref. 16.56) to fit the dissipation length by a relationship similar to Eq. 16.4(17) notably incorporating the constant C_ϵ and defining the dissipation scale as $L = \ell/C_\epsilon$ where

$$\frac{L}{\delta} = \left\{0.1\tanh\left(\frac{\kappa}{0.1}\,y/\delta\right)\right\}\mathcal{D} \qquad 16.4\ (53)$$

and the damping factor $\mathcal{D}$ is defined as before. McDonald and Camarata further chose to integrate the turbulence kinetic energy equation normal to the wall to remove the necessity for modeling the turbulent diffusion process. The closing assumption in this case was that it was then assumed that the usually defined mixing length could be described by formulae such as Eq. 16.4(17) but now it was possible to regard the outer layer value of the mixing length, the .09 δ referred to previously, as a free parameter whose value is determined by the turbulence kinetic energy equation.

All in all the one equation models as outlined above have performed at least as well and usually better by varying degrees than the algebraic stress models described earlier. A key ingredient to their success has been the fact that they represent a very modest and in the main, physically plausible extension, (indeed perturbation might be better) to the algebraic stress models. Two powerful capabilities the one equation models do possess over the algebraic stress models of particular note in turbumachinery applications are firstly the ability to reflect the observed lag in turbulent boundary layer response to severe pressure gradients being applied or removed. Secondly use of the turbulent kinetic energy equation with a nonzero free stream value allows the free stream turbulence to enter the prediction in a natural manner (see Fig. 16.10 and Eq. 16.1.(66)). Examples of the range and power of one equation models are to be found in the predictions presented in Bradshaw and Ferriss (Ref. 16.77), Patel and Nash (Ref. 16.127), Nash (Ref. 16.74), McDonald and Kreskovsky (Ref. 16.3) and Briley and McDonald (Ref. 16.194). The ability of the Townsend structural equilibrium approach to avoid zero shear stress when the mean velocity gradient goes through zero, not possible using the Prandtl constitutive relationship is certainly attractive but in most of the boundary layer studies performed to date it has not been a crucial feature. An exception could arise in the film cooling studies where the Townsend approach would eliminate the need for the simple ad hoc modification to the algebraic stress model predictions such as that used by Pai and Whitelaw (Ref. 16.138).

One notable feature of the one equation models which has not yet been mentioned concerns the effect of low Reynolds numbers. Glushko (Ref. 16.176), McDonald and Fish (Ref. 16.58), and Jones and Launder (Ref. 16.177) suggested

that the structural coefficient used to close the turbulence kinetic energy equation would exhibit dependence on a turbulence Reynolds number

$$R_T = \frac{|-\overline{u'v'}|^{1/2} \ell}{\nu}$$

16.4 (54)

where ℓ is the previously introduced turbulence length scale. A very similar alternative Reynolds number can be obtained by using $(\overline{q^2})^{1/2}$ in place of $(-\overline{u'v'})^{1/2}$. If this length scale is supposed related to the conventional mixing length then the turbulence Reynolds number is simply the ratio of the eddy viscosity to the actual viscosity. Using only the assumption that the local conditions obtained in Townsend's structural equilibrium state would also depend on the turbulence Reynolds number, i.e.,

$$-\overline{u'v'} = a \cdot f(R_T)\overline{q^2}$$

16.4 (55)

McDonald and Fish were able to model both forward and reverse transition as it is influenced by free stream turbulence wall roughness and pressure gradients. McDonald and Fish (Ref. 16.58) argued that the mean strain effect on 'a' would for the flows of interest still be negligible compared to the R_T effect. The functional dependence of the structural coefficient 'a' on the turbulence Reynolds number R_T is given in Ref. 16.58 and was somewhat contrived being chosen to have the correct asymtotic limits of 0 and 1 but with the variation in between selected judiciously to result in good agreement with the observed dependence of forward transition Reynolds number on free stream turbulence intensity. In spite of this the selected dependence survived intact to give very reasonable predictions of boundary layer relaminarization as a function of pressure gradient, see for instance, McDonald and Fish (Ref. 16.58). Subsequently it was found that the effect of convex curvature in inhibiting the forward transition process was reasonably well accounted for in this model if Bradshaw's (Ref. 16.147) suggestion for the effect of curvature on the dissipation length L were adopted. The destabilizing effect of concave curvature was not well predicted with this model however.

Three observations are probably appropriate at this point. The first is that the heat transfer to a turbine airfoil is one of the major turbomachine boundary layer problems and this problem is dominated by low Reynolds number effect such as forward and reverse transition. Consequently unless the boundary layer analysis can account in some plausible manner for these phenomena as they are influenced by free stream turbulence and streamwise acceleration the entire analysis would be of little use to design engineers. Secondly the alternatives to the adoption of turbulence Reynolds number effect on the structural coefficient are either to abandon the problem as too difficult or to attempt to correlate the location of the initiation and extent of the transition region as it is observed to vary with Reynolds number pressure gradient and free stream disturbances. There is evidence that a unique correlation of this type would exist since it is observed that for the moderate to high levels of free stream turbulence typical of turbomachinery the overall energy level of the broad band free stream disturbances seems to characterize the transition process at a given Reynolds number. If desired, the suggested a-R_T relationship can be thought of as a particularly simple means of implementing precisely this type of empirical correlation. Thirdly a number of authors (see for instance Kays and Moffat (Ref. 16.81) for a discussion) have suggested a parameter such as R_T might at least characterize the relaminarization phenomenon such that in general when R_T fell below about 33 the turbulent motion would die out. The suggested variation of the structural coefficient 'a' with R_T reflects this concept but rather than have an on-off switch the functional relationship adopted assures a smooth transition and a rate controlled change in the structure which is quantitatively in accordance with that observed. Bearing in mind these three points, it is felt that while a contrived a-R_T relationship, such as that suggested by McDonald and Fish (Ref. 16.58), although at present unsupported by direct experimental evidence and doubtlessly a gross oversimplification of the physical phenomena at play, does introduce a degree of realism into the predictions, without which the analysis would be almost worthless for detailed turbine blade design purposes. Some ideal of the complexities involved may be obtained from Fig. 16.11.

In the context of the multi-equation models to be discussed subsequently a number of authors e.g., Jones and Launder (Ref. 16.177) and Donaldson (Ref. 16.143) have postulated a turbulence Reynolds number dependence of various parameters. In his one equation model Glushko (Ref. 16.176) proposed a series of parameters varying with the turbulence Reynolds number, again with little direct experimental support. In any event Glushko's model has not been as extensively tested or developed as that of McDonald and Fish (Ref. 16.58), which from the results of Kreskovsky, Shamroth and McDonald (Ref. 16.200) can be seen to perform quite well over a very wide range of flows. It is to be expected that the dissipation process would exhibit a very marked effect on turbulence Reynolds number such that 'L', the dissipation length, would also depend on the turbulence Reynolds number. Glushko (Ref. 16.176) and Hanjalic and Launder (Ref. 16.180) indeed make specific suggestions as to the form of this Reynolds number dependence. McDonald and Fish (Ref. 16.58) while recognizing that such an effect was probably present, pointed out that in their one equation formulation the ratio of turbulence length scale to dissipation length appears, so that unless the dissipation length scale L decreased with Reynolds number much faster than the turbulence length scale ℓ (an unlikely event) the low Reynolds number effect on dissipation would not have a significant effect on their predictions, provided that $\ell/L \ll 1.0$ at low Reynolds numbers. No matter which approach is favored, that of postulating an effect only on the structural coefficient 'a' or an effect only on the dissipative process, or both, the postulated dependence can, at present, only be obtained by the indirect process of attempting to duplicate measured flow development. Clearly experimental guidance is required.

16.4.5 Two Equation Turbulence Models

There is one major defect in the one equation models in current use, this being the need to specify a turbulent length scale. If continued use of Prandtl's constitutive relationship is made in the one equation models, the argument can also be valid that the use of the mean gradient further preserves the defect of zero correlation at the point of zero mean gradient. This point will not be pursued here but it is noted that in a number of flows of practical interest no convenient shear layer thickness can be identified, for example in can or annular combustors. In the two equation system the additional equation is aimed at providing a differential equation for some turbulence quantity which can be related to a turbulent scale of length, thus eliminating the need to directly specify some shear layer thickness upon which the turbulence length scale can be based. The idea has a great deal of merit but unfortunately at present much of this work is still relatively preliminary and cannot be confidently used by design engineers. It is to be expected that this state of affairs will be improved upon in the near future however, in view of the potential of two equation models some outline of the present status will be given.

With few exceptions the choice of one of the two equations has been the turbulence kinetic energy equation which performed so well in the single equation system. The choice of second equation has exhibited a great deal of variety, although the chosen dependent variables have generally been associated more or less directly with some turbulent length scale. Heuristic transport equations also have made their reappearance, justified persuasively on the grounds that so little is known about how to model the various correlations appearing in the rigorous equations that one might as well use a heuristic transport equation. Such arguments have led Bradshaw (Ref. 16.198) and Saffman (Ref. 16.199) to propose heuristically a dissipative length scale transport equation on the one hand and a psuedo-vorticity transport equation on the other. Criticism of the speculative nature of the various hypothesis required to convert the various rigorous equations into length scale transport equations or their equivalent is certainly justified. At this point in time little in the way of experimental support, or even insight, is available to justify many of the suggestions. Be that as it may, it seems probable that as the store of experimental information on the structure of turbulence is increased an improvement in the modeling of the terms in the rigorous equations will result. Heuristic transport equations which cannot eventually be related to some rigorous transport equation seem destined to a limited lifetime. In seeking to remedy the lack of experimental support on the detailed modeling assumptions required to close the rigorous equations, an effort is usually made to ensure that certain well-known results, usually concerning the decay of isotropic turbulence, are reproduced by the modeled equations. Again this process on the surface seems very reasonable but as argued by Bradshaw the wide disparity between isotropic and shear flow turbulence confuses this issue dramatically.

Of the two equation models proposed to date only the Jones-Launder model (Ref. 16.177) and the Saffman-Wilcox model (Ref. 16.199) have been developed to any great extent. Earlier or alternative two equation models such as those developed by Ng (Ref. 16.171) based on an even earlier proposal of Rotta (Ref. 16.179) or the suggestion of Spalding (Ref. 16.178), have not as yet demonstrated any clear superiority and according to Launder are slightly more complicated. In his critical review Reynolds (Ref. 16.170) cautions against the use of the Saffman-Wilcox model as an engineering tool at present in view of the extreme sensitivity of the predictions to both the wall and free stream boundary conditions. To date most success, measured in terms of satisfactory predictions obtained without changing the empirical constants, has been obtained using a modeled form of the equation governing the dissipation of turbulence kinetic energy. The reader then would be recommended to choose from the two equation model shopping list described by Launder and Spalding (Ref. 16.163), for instance, one model based upon the turbulence kinetic energy and the dissipation of turbulence kinetic energy. Caution must still be advocated however since clearly the use of an eddy viscosity, albeit derived from Prandtl's constitutive relationship, still suffers from the observed discrepancy of zero stress not occurring at zero mean gradient. Further the known anisotropy of the eddy viscosity, so important in three-dimensional flows, is at present missing from these models. Clearly much remains to be done on these multi-equation models before they can be used with confidence by design engineers. The extension of capability which these models offer, however, does lend encouragement to their continued development. At this point further discussion of turbulence models will be discontinued since beyond this point the topic becomes even more controversial.

16.5 Concluding Remarks

At the request of the editor I would like to conclude this section with some observations about the audience that I had hoped to reach. I would also like to add some personal comments on the contents of the section now that it has been completed; completed that is, in the sense that there is no longer any time to include additional material!

First, insofar as the hoped for audience was concerned, the model I had in mind grew out of my rather long and fruitful (at least on my part!) association with the engineers at Pratt & Whitney (Aircraft). The educational level of these engineers was generally at the masters or doctoral level in mechanical engineering. Often they were faced with the very difficult task of evaluating new or advanced fluid mechanics technology. If following the evaluation they deemed it attractive, they then had to further develop, validate and ultimately to transfer the technology into the design system, that it might usefully impact the end product. The understanding and prediction of general turbulent 'boundary layers' has the potential of greatly assisting in the turbomachinery design process, and consequently was and is a topic of considerable interest to these engineers.

The literature on the subject is not turbomachinery biased, however, and sometimes methods or approaches were explored which had hereditary traits which either precluded successful application to turbomachinery problems or preordained certain very unfortunate limitations. It was in part with the goal of helping the industrially based engineers to become 'selective shoppers' in the evaluation phase of their work that this section was initiated. It was further hoped that the section would be of assistance to new recruits to the subject to help bridge the gap between graduate level courses and the current areas of interest of those involved in evaluation, development, validation and implementation of viscous flow prediction schemes.

Concerning the actual material presented, in retrospect it seems clear that too much effort was spent on the two-dimensional integral boundary layer procedures. This occurred partly because the subject is relatively secure and partly because I poorly budgeted the time I had available to write the whole section. A much better allocation would have been to reduce the emphasis on integral procedures and include some discussion on wake flows. Although I did not intend to interpret the section I was requested to prepare as one dealing exclusively with boundary layers, over the years I had not detected any great interest by the engine manufacturers in wake flows, and hence their omission from the section. More recently it appears that there is interest in wake controlled problems and this area will grow in importance. A very encouraging contribution to this near wake problem has recently been made by Pope and Whitelaw (Ref. 16.208). Insofar as three-dimensional flows are concerned, I regret not having more time available to develop the relationship between what my colleagues and I term 'classical secondary flow theory' as described by Hawthorn and Horlock, and the extended boundary layer equations discussed in the text. Such a relationship does exist and its exploration and further development may provide the key to understanding the observed complex intra-blade or stator boundary layer flows.

Having touched on the major omissions and offering my apologies, I close by promising to try to do better with the second edition.

Acknowledgements

A major portion of the writing of this section was carried out while the author was on sabbatical leave from United Technologies Research Center. During this period of time the author was appointed Senior Research Fellow at the University of Glasgow, Department of Aeronautics. The author is deeply indebted to both institutions for their generosity and help.

The author is also indebted to his colleagues at Scientific Research Associates, Inc., for their help in the final preparation of this manuscript.

References

16.1 McDonald, H., S. J. Shamroth: An Analysis and Application of the Time-Dependent Turbulent Boundary-Layer Equations. AIAA Journal, Vol. 9, No. 8, pp. 1553-1560, August, 1971.

16.2 Evans, R. L., J. H. Horlock: Calculations of the Development of Turbulent Boundary-Layers with a Turbulent Free-Stream. ASME Paper 74-FE-24.

16.3 McDonald, H., J. P. Kreskovsky: Effect of Free Stream Turbulence on the Turbulent Boundary Layer. Int. J. Heat and Mass Transfer, Vol. 17, pp. 705-716, 1974.

16.4 Nash, J. F.: A Note on Skin-Friction Laws for the Incompressible Turbulent Boundary Layer. NPL Aero Report 1135, December 1964.

16.5 Nash, J. F., A. G. J. MacDonald: A Turbulent Skin Friction Law for Use at Subsonic and Transonic Speeds. NPL Aero Report 1206, also Aero Res. Council, CP No. 948, July, 1966.

16.6 Coles, D. E., E. A. Hirst: Proceedings: Computation of Turbulent Boundary Layers. 1968 AFOSR-IFP, Stanford Conference, Vol. II, Compiled Data.

16.7 Coles, D. E.: A Survey of Data for Turbulent Boundary Layers with Mass Transfer. AGARD Conference Proceeding No. 93, Turbulent Shear Flows, September, 1971.

16.8 Simpson, R. L.: Ph.D. Thesis, Stanford University, 1967.

16.9 Coles, D. E.: The Law of the Wake in the Turbulent Boundary Layer. J. Fluid Mech., Vol. 1, pp. 191-226, 1956.

16.10 Waltz, A.: Boundary Layers of Flow and Temperature. M.I.T. Press, 1969.

16.11 Clauser, F. H.: Turbulent Boundary Layers in Adverse Pressure Gradients. J. of Aero. Sci., Vol. 21, pp. 91-108, 1954.

16.12 Nash, J. F.: Turbulent-Boundary-Layer Behavior and the Auxiliary Equation. AGARDograph 97, Part 1, 1965.

16.13 Mellor, G. L., D. M. Gibson: Equilibrium Turbulent Boundary Layers. J. Fluid Mech., Vol. 24, Part 2, pp. 225-253, 1966.

16.14 Michel, R., C. Quemard, R. Durant: Hypothesis on the Mixing Length and Application to the Calculation of the Turbulent Boundary Layer. Proceedings: Computation of Turbulent Boundary Layers, AFOSR-IFP, Stanford Conference, Vol. 1, 1968.

16.15 Rotta, J. C.: Turbulent Boundary Layers in Incompressible Flow. Progress in Aero. Sci., Vol. 2, Pergamon Press, 1962.

16.16 Rubesin, M. W., H. Johnson: A Summary of Skin Friction and Heat Transfer Solutions of the Laminar Boundary Layer on a Flat Plate. Trans. ASME, 71, pp. 383, 1949.

16.17 Coles, D.: The Turbulent Boundary Layer in a Compressible Fluid. Rand Report R-403-PR, 1962.

16.18 Winter, K. G., K. G. Smith, L. Gaudet: Measurements of Turbulent Skin Friction at High Reynolds Numbers at Mach Numbers of .2 and 2.2. AGARDograph 97, Part I, 1965.

16.19 Winter, K. G., L. Gaudet: Some Recent Work on Compressible Turbulent Boundary Layers and Excrescence Drag. NASA SP-216, Compressible Turbulent Boundary Layers, 1968.

16.20 Van Driest, E. R.: Turbulent Boundary Layer in Compressible Fluids. J. of the Aero Sci., Vol. 18, pp. 631-638, 1951.

16.21 Maise, G., H. McDonald: Mixing Length and Kinematic Eddy Viscosity in a Compressible Boundary Layer. AIAA J., Vol. 6, p. 73, 1968.

16.22 Coles, D. E.: Measurements in the Boundary Layer on a Smooth Flat-Plate in Supersonic Flow. Ph.D. Thesis, 1953, Cal. Inst. Tech.

16.23 Mathews, D. C., G. C. Paynter, M. E. Childs: On the Use of Coles' Universal Wake Function for Compressible Turbulent Boundary Layers. J. of Aircraft, Vol. 7, No. 2, pp. 137-140, 1970.

16.24 Hopkins, E. J., E. R. Keener, T. E. Polek: Hypersonic Turbulent Skin-Friction and Boundary-Layer Profiles on Non-Adiabatic Flat Plates. AIAA J., Vol. 10, pp. 40-48, 1972.

16.25 Owen, F. K., C. C. Horstman: On the Structure of Hypersonic Turbulent Boundary Layers. J. Fluid Mech., Vol. 53, Part 4, pp. 611-636, 1972.

16.26 Coles, D. E.: The Turbulent Boundary Layer in a Compressible Fluid. Physics of Fluids, Vol. 7, No. 9, pp. 1403-1423, September 1964.

16.27 Morkovin, M. V.: Effects of Compressibility on Turbulent Flows. Collogues Internationaux du Centre National de Recherche Scientifique, No. 108, pp. 367-380, 1962.

16.28 Clauser, F. H.: The Turbulent Boundary Layer. Advances in Applied Mechanics, 4, Academic Press, 1956.

16.29 Dvorak, F. A.: Calculation of Turbulent Boundary Layers on Rough Surfaces in Pressure Gradient. AIAA J., Vol. 7, No. 9, pp. 1752-1759, 1969.

16.30 Chen, K. K.: Compressible Turbulent Boundary Layer Heat Transfer to Rough Surfaces Under Arbitrary Pressure Gradient. AIAA Paper 71-166, 1971.

16.31 Young, F. L.: Experimental Investigation of the Effects of Surface Roughness on Compressible Turbulent Boundary Layer Skin Friction and Heat Transfer. University of Texas, DRL 532, (AD621085), 1965.

16.32 Dvorak, F. A., M. R. Head: Heat Transfer in the Constant Properly Turbulent Boundary Layer. Int. J. of Heat and Mass Transfer, Vol. 10, pp. 61-81, 1967.

16.33 Head, M. R.: Entrainment in the Turbulent Boundary Layer. Aero. Res. Council, R&M 3152, 1958.

16.34 Green, J. E.: Application of Head's Entrainment Method to the Prediction of Turbulent Boundary Layers and Wakes in Compressible Flow. Royal Aircraft Establishment, TR 72231, 1973.

16.35 Compressible Turbulent Boundary Layers. NASA SP 216, Proc. Langley Sym., December 1968.

16.36 Rotta, J. C.: Heat Transfer and Temperature Distribution in Turbulent Boundary Layers at Supersonic and Hypersonic Flow. AGARDograph 97, Part 1, 1965.

16.37 Hopkins, E. J., M. W. Rubesin, M. Inouye, E. R. Keener, G. C. Mather, T. E. Polek: Summary and Correlation of Skin Friction and Heat Transfer Data for a Hypersonic Turbulent Boundary Layer on Simple Shapes. NASA TN D 5089.

16.38 Cousteix, J., R. Houdeville, R. Michel: Couches Limites Turbulentes Avec Transport de Chaleur. La Recherche Aerospatiale, No. 6, pp. 327-337, 1974.

16.39 McDonald, H., F. K. Owen: Unpublished Work.

16.40 Meier, H. U., J. C. Rotta: Experimental and Theoretical Investigation of Temperature Distributions in Supersonic Boundary Layers. AIAA Paper No. 70-744, 1970.

16.41 Rotta, J. C.: Die Turbulente Grenzschicht an Einer Stark Geheizten Ebenen Platte Bei Unterschattströmung. Warme-und Stoffubertragung, pp. 133-144, 1974.

16.42 Shamroth, S. J.: On Integral Methods for Predicting Shear Layer Behavior. J. of App. Mech., Vol. 36, December, 1969.

16.43 Weinbaum, S., R. W. Garvine: On the Two Dimensional Viscous Counterpart of the One Dimensional Sonic Throat. J. Fluid Mech., Vol. 39, Part I, pp. 57-85, 1969.

16.44 Bradshaw, P., D. H. Ferriss: The Response of a Retarded Equilibrium Turbulent Boundary Layer to the Sudden Removal of Pressure Gradient, NPL Aero Rpt., 1145, 1965.

16.45 White, F. M.: A New Integral Method for Analyzing the Turbulent Boundary Layer with Arbitrary Pressure Gradient. ASME Paper No. 68, WA/FE 22, 1968.

16.46 Stratford, B. S.: The Prediction of Separation of the Turbulent Boundary Layer. J. Fluid Mech., Vol. 5, Part I, pp. 1-16, 1959.

16.47 Escudier, M. P., W. B. Nicoll: A Shear Work Integral Method for the Calculation of Turbulent Boundary Layer Development. Proceedings: Computation of Turbulent Boundary Layers, AFOSR-IFP, Stanford Conference, Vol. 1, 1968.

16.48 Bradshaw, P.: The Analogy Between Streamline Curvature and Buoyancy in Turbulent Shear Flow. J. Fluid Mech., Vol. 36, pp. 177-191, 1969.

16.49 Goldberg, P.: Upstream History and Apparent Stress in Turbulent Boundary Layers. MIT Gas Turbine Lab. Rpt. No. 85, May, 1966.

16.50 Kline, J. J., M. V. Morkovin, G. Sovran, D. J. Cockrell: Computation of Turbulent Boundary Layers. AFOSR-IFP, Stanford Conf., Vol. 1, 1968.

16.51 Nash, J. F., J. G. Hicks: An Integral Method Including the Effect of Upstream History on the Turbulent Shear Stress. Proceedings: Computation of Turbulent Boundary Layers, AFOSR-IFP, Stanford Conf., Vol. 1, 1968.

16.52 McDonald, H.: The Departure from Equilibrium of Turbulent Boundary Layers. The Aero. Quart., Vol. XIX, Part 1, pp. 1-19, February, 1968.

16.53 Townsend, A. A.: Equilibrium Layers and Wall Turbulence. J. Fluid Mech., Vol. 1, pp. 97-120, 1961.

16.54 Green, J. E., D. J. Weeks, J. W. F. Brooman: Prediction of Turbulent Boundary Layers and Wake in Compressible Flow by a Lag-Entrainment Method. Royal Aircraft Establishment Tech. Report 72231, 1973.

16.55 Hirst, E. A. and W. C. Reynolds: An Integral Prediction Method for Turbulent Boundary Layers Using the Turbulent Kinetic Energy Equation. Proceedings: Computation of Turbulent Boundary Layers, AFOSR-EFP, Stanford Conference, Vol. 1, 1968.

16.56 McDonald, H., F. J. Camarata: An Extended Mixing Length Approach for Computing the Turbulent Boundary Layer Development. Proceedings: Computation of Turbulent Boundary Layers, AFOSR-IFP, Stanford Conference, Vol. 1, 1968.

16.57 Bradshaw, P., D. H. Ferriss, N. P. Atwell: Calculation of Boundary Layer Development Using the Turbulent Energy Equation. J. Fluid Mech., Vol. 28, Part 3, pp. 593-616, 1967.

16.58 McDonald, H., R. W. Fish: Practical Calculations of Transitional Boundary Layers. Int. J. of Heat and Mass Transfer, Vol. 16, No. 9, pp. 1729-1744, 1973.

16.59 Thompson, B. J. G.: The Calculation of Shape Factor Development in Incompressible Turbulent Boundary Layers with or without Transpiration. AGARDograph 97, Vol. 1, 1965.

16.60 Lubard, S. C., F. L. Fernandez: The Turbulent Boundary Layer with Mass Transfer and Pressure Gradient. ASME J. of Appl. Mech., Vol. 28, Part 3, 1971.

16.61 Alber, I. E.: Application of an Exact Expression for the Equilibrium Dissipation Integral to Calculation of Turbulent Nonequilibrium Flows. Proceedings: Computation of Turbulent Boundary Layers, AFOSR-IFP, Stanford Conference, Vol. 1, 1968.

16.62 Pletcher, R. H.: Calculation Method for Compressible Turbulent Boundary Flows with Heat Transfer. AIAA Journal, Vol. 10, No. 3, 1972.

16.63 Roache, P. J.: Computational Fluid Dynamics, Hermosa Publishers, 1972.

16.64 Briley, W. R., H. McDonald: Solution of the Three-Dimensional Compressible Navier-Stokes Equations by an Implicit Technique. Proc. 4th Int. Conf. on Num. Methods in Fluid Dynamics, June, 1974. See also J. Comp. Physics, 1977.

16.65 McDonald, H., W. R. Briley: Three Dimensional Supersonic Flow of a Viscous or Inviscid Gas. J. of Comp. Physics, Vol. 19, No. 2, October, 1975.

16.66 Blottner, F. G.: Investigations of Some Finite-Difference Techniques for Solving the Boundary Layer Equations. Computer Methods in Applied Mechanics and Engineering, Vol. 6, pp. 1-30, 1975.

16.67 Patankar, S. V., D. B. Spalding: Heat and Mass Transfer in Boundary Layers. Intertext, London, 2nd Ed., 1970.

16.68 Cebeci, T., A. M. O. Smith: A Finite Difference Method for Calculating Compressible Laminar and Turbulent Boundary Layers. J. Basic Eng., Vol. 92, No. 3, pp. 323-535, 1970.

16.69 Herring, H. J., G. L. Mellor: A Method of Calculating Compressible Turbulent Boundary Layers. NASA CR-1144, 1968.

16.70 Keller, H. B.: A New Difference Scheme for Parabolic Problems. Numerical Solutions of Partial Differential Equations, Vol. II, Academic Press, pp. 327-350, 1971.

16.71 Blottner, F. G.: Variable Grid Scheme Applied to Turbulent Boundary Layer. Computer Methods in Applied Mechanics and Engineering, Vol. 4, pp. 179-194, 1974.

16.72 Roberts, G. O.: Computational Meshes for Boundary Layer Problems. Proceedings: Second International Conference on Numerical Methods in Fluids Dynamics, Springer-Verlag, New York, p. 171, 1971.

16.73 Cebeci, T., A. M. O. Smith: Analysis of Turbulent Boundary Layers. Applied Mathematics and Mechanics, 15, Academic Press, 1974.

16.74 Nash, J. F.: The Calculation of Three Dimensional Turbulent Boundary Layers in Incompressible Flow. J. Fluid Mech., Vol. 37, Part 4, p. 625, 1969.

16.75 Yanenko, N. N.: The Method of Fractional Steps. Translation Edited by M. Holt, Springer-Verlag, New York, 1971.

16.76 Moretti, G.: A Pragmatical Analysis of Discretization Procedures for Initial and Boundary Value Problems in Gas Dynamics and Their Influence on Accuracy. Polytechnic Institute of Brooklyn, Ae/Am Report No. 74-15, September, 1974.

16.77 Bradshaw, P., D. H. Ferriss: Application of a General Method of Calculating Turbulent Shear Layers. ASME Paper No. 71-WA/FE-8.

16.78 Blottner, F. G.: Computational Techniques for Boundary Layers. AGARD Lecture Series.

16.79 Peters, N.: Boundary Layer Calculations by a Hermitian Finite Difference Method. Proceedings: Fourth International Conference on Numerical Methods in Fluid Dynamics, Springer-Verlag, 1974.

16.80 Launder, B. E., W. P. Jones: On the Prediction of Laminarization. Aero Res. Council of Great Britain, CP 1036, February, 1968.

16.81 Kays, W. M., R. J. Moffat: Behavior of Transpired Turbulent Boundary Layers. Studies in Convection Theory, Measurement and Applications, Vol. 1, ed. B. E. Launder, 1975.

16.82 Becko, Y.: Heat Transfer Analysis Along the Blades of a Gas Turbine Stator by Thermal and Kinematic Boundary Layer Theory. ASME Paper 75-GT-15, 1975.

16.83 Keller, H. B., T. Cebeci: Accurate Numerical Methods for Boundary Layer Flows, II. Two Dimensional Turbulent Flows, AIAA J., Vol. 10, No. 9, 1972.

16.84 Harris, J. E.: Numerical Solution of the Equations for Compressible, Laminar, Transitional and Turbulent Boundary Layers and Comparison with Experimental Data. NASA TR R-369, 1971.

16.85 Flugger-Lotz and F. G. Blottner: Computation of the Compressible Laminar Boundary Layer Flow Including Displacement Thickness Interaction Using Finite-Difference Methods. AFOSR-220S, 1962.

16.86 Adams, J. C.: Eddy Viscosity - Intermittency Factor Approach to Numerical Calculation of Transactional Heating on Sharp Cones in Hypersonic Flow. AEDC-TR-70-210, 1970.

16.87 Kendall, R. M., E. P. Bartlett: Non-similar Solution of the Multi-Component Laminar Boundary Layer by an Integral Matrix Method. AIAA J.,Vol. 6, No. 6, 1968.

16.88 Anderson, O. L.: Finite Difference Solution for Turbulent Swirling Compressible Flow in Axisymmetric Ducts with Struts. NASA CR-2365, February, 1974.

16.89 Horlock, J. H., H. J. Perkins: Annulus Wall Boundary Layers in Turbomachines. AGARDograph 185, 1975.

16.90 Hayes, W. D.: The Three Dimensional Boundary Layer. NAVORD Rept. 1313, 1951.

16.91 Daneshyar, M.: Annulus Wall Boundary Layer in Turbomachines. Ph.D. Thesis, Cambridge University, 1973.

16.92 Mellor, G. L., G. M. Wood: An Axial Compressor Endwall Boundary Layer Theory. ASME J. of Basic Engineering, June, 1971.

16.93 Cumpsty, N. A., M. R. Head: The Calculation of Three-Dimensional Turbulent Boundary Layers (1) Flow Over the Rear of an Infinite Swept Wing. Aero Quart., Vol. 18, 1967.

16.94 Horlock, J. H.: Cross Flows in Bounded Three Dimensional Turbulent Boundary Layers. J. of Mech. Eng. Sci., Vol. 15, No. 4, pp. 274-284, 1973.

16.95 Mager, A.: Generalization of Boundary Layer Momentum Integral Equations to Three Dimensional Flow Including Those of Rotating Systems. NASA Report No. 1067, 1952.

16.96 Johnston, J. P.: On the Three-Dimensional Turbulent Boundary Layer Generated by Secondary Flows. J. of Basic Eng., Trans. ASME, Vol. 81 (3), 1960.

16.97 Wheeler, A. J., J. P. Johnson: Three-Dimensional Turbulent Boundary Layer - An Assessment of Prediction Methods. Stanford U., Dept. of Mech. Eng., Report MD-30, July 1971, See Also ASME Paper No. 73-FE-25, 1973.

16.98 Lindsay, W. L.: Tip Clearance Effects in the Growth of Annulus Wall Boundary Layers in Turbomachines. Ph.D. Thesis, Cambridge University, 1974.

16.99 Hoadley, D.: Three-Dimensional Turbulent Boundary Layers in an Annular Diffuser. Ph.D. Thesis, Cambridge University, 1970.

16.100 Daneshyar, M.: Prediction of Annulus Wall Boundary Layers in Axial Flow Turbomachines. AGARDograph 164, 1972.

16.101 Harris, J. E., D. J. Morris: Solution of the Three-Dimensional Compressible Laminar and Turbulent Boundary Layer Equations with Comparisons to Experimental Data. Fourth International Conference on Numerical Methods in Fluid Dynamics, 1974.

16.102 Cebeci, T., K. Kamps, G. J. Mosinskis, J. Rehn: Some Problems of the Calculation of Three-Dimensional Boundary Layer Flow on General Configuration. NASA CR-2285, July, 1973.

16.103 Raetz, G. S.: A Method of Calculating Three-Dimensional Laminar Boundary Layers of Steady Compressible Flows. Northrop Corp. Report No. NAI-58-73, 1957.

16.104 Wesseling, P.: Calculations of Incompressible Three-Dimensional Turbulent Boundary Layers, Part 1: Formulation of a System of Equations. Nat. Lucht. Labs (Netherlands), Rep. No. AT-69-01, 1969.

16.105 Wang, K. C.: On the Determination of the Zones of Influence and Dependence for Three-Dimensional Boundary Layer Equations. J. Fluid Mech., Vol. 48, No. 2, pp. 397-404, 1971.

16.106 Ting, L.: On the Initial Condition for Boundary Layer Equations. J. Math. Phys., Vol. XLIV, No. 4, pp. 353-367, December, 1965.

16.107 Nash, J. F., V. C. Patel: Three-Dimensional Turbulent Boundary Layers. Scientific and Business Consultants, Inc., 1972.

16.108 Klinksiek, W., F. Pierce: Secondary Flow Reversal and Velocity Profile Models in a Three-Dimensional Turbulent Boundary Layer. Mech. Eng. Dept., Virginia Polytech Institute, 1968.

16.109 Krause, E., E. H. Hieschel, T. Bothmer: Numerical Stability of Three-Dimensional Boundary Layer Solutions. Z. angew Math. Mech., Vol. 48, No. 8, pp. T205-T208, 1968.

16.110 Cebeci, T.: A General Method for Calculating Three-Dimensional Incompressible Laminar and Turbulent Boundary Layer. II Three-Dimensional Flow in Cartesian Coordinates. Rept. No. MDC J 6517, March, 1974.

16.111 Myring, D. F.: An Integral Prediction Method for Three-Dimensional Turbulent Boundary Layers in Incompressible Flow. Royal Aircraft Establishment Tech. Rept. 70147, 1970.

16.112 Eichlbrenner, E. A., J. L. Penke: Theoretical and Experimental Investigations in Three-Dimensional (Laminar and Turbulent) Boundary Layers. Laboratories de Mechnique des Fluides Rapport, 1966.

16.113 Thompson, B. G. J., A. G. J. MacDonald: The Prediction of Boundary Layer Profile Development for Infinite Yawed Wings. Aero Res. Council CP No. 1307.

16.114 Smith, P. D.: An Integral Prediction Method for Three-Dimensional Compressible Turbulent Boundary Layers. Royal Aircraft Establishment TR 72228, December, 1972.

16.115 Green, J. E.: Applications of Head's Entrainment Method in the Prediction of Turbulent Boundary Layers and Wakes in Compressible Flow. Royal Aircraft Establishment TR 72079, 1972.

16.116 Thompson, B. G. T.: A New Two Parameter Family of Mean Velocity Profiles for Incompressible Turbulent Boundary Layers on Smooth Walls. Aero. Res. Council Paper No. 26830, 1965.

16.117 Eiseman, P., H. McDonald: A Method for Computing Three-Dimensional Flow in Ducts. Proceedings of the NASC Symposium of Aerodynamic Problems of VSTOL Aircraft, 1975.

16.118 Briley, W. R., H. McDonald: Computation of Three-Dimensional Turbulent Subsonic Flow in Curved Passages. United Aircraft Research Labs., Report R75-911596-8, 1975.

16.119 Bergeles, G., A. D. Gosman, B. E. Launder: The Prediction of Three-Dimensional Discrete Hole Cooling Processes: Part 1 - Laminar Flow. ASME Paper No. 75-WA/HT-109, November, 1975.

16.120 Patankar, S. V., V. S. Pratap, D. B. Spalding: Prediction of Turbulent Flow in Curved Pipes. J. Fluid Mech. Vol. 67, Part 3, pp. 583-595, 1975.

16.121 Patankar, S. V., D. B. Spalding: A Calculation Procedure for Heat Mass and Momentum Transfer in Three-Dimensional Parabolic Flows. Int. J. of Heat and Mass Transfer, Vol. 15, pp. 1787-1806, 1972.

16.122 Caretto, L. S., R. M. Curr, D. B. Spalding: Two Numerical Methods for Three-Dimensional Boundary Layers. Computer Methods in Applied Mechanics and Engineering, Vol. 1, pp. 39-51, 1973.

16.123 Rubin, S. G., T. C. Lin: A Numerical Method for Three-Dimensional Viscous Flows Application to the Hypersonic Leading Edge. J. of Comp. Physics, Vol. 9, No. 2, pp. 339-364, 1972.

16.124 Nardo, C. T., R. J. Cresci: An Alternating Directional Implicit Scheme for Three-Dimensional Hypersonic Flows. J. Comp. Physics, Vol. 8, pp. 268-284, 1971.

16.125 Kendall, R. M., W. S. Bonnett, C. T. Nardo, M. J. Abbett: Computational Procedure for Three-Dimensional Boundary Layers on Aircraft and Aerospace Vehicles. AIAA Paper, Hartford, CT, 1975.

16.126 Dring, R. P.: A Momentum Integral Analysis of the Three-Dimensional Turbine End Wall Boundary Layer. Transactions of the ASME Journal of Engineering for Power, October, 1971.

16.127 Patel, V. C., J. F. Nash: Some Solutions of the Unsteady Two-Dimensional Turbulent Boundary Layer Equations. Recent Research on Unsteady Boundary Layer, IUTAM Symposium, Vol. 1, Laval University Press, pp. 1106-1164, 1971.

16.128 Murphy, J. D., L. L. Presley, W. C. Rose: On the Calculation of Supersonic Separating and Reattaching Flows. AGARD-CP-168, Conference on Flow Separation, 1975.

16.129 Baldwin, B. S., R. W. MacCormack: Interaction of Strong Shock Wave with Turbulent Boundary Layer. AIAA Paper 74-558, 1974.

16.130 Deiwert, G. S.: Computation of Separated Transonic Turbulent Flows. AIAA J., Vol. 14, No. 6, 1976.

16.131 Shang, J., W. Hankey, Jr.: Numerical Solution of the Navier-Stokes Equations for Supersonic Turbulent Flow Over a Compression Ramp. AIAA Paper 75-3, January, 1975.

16.132 Werle, M. J., V. N. Vatsa: Numerical Solution of Interacting Supersonic Boundary Layer Flows Including Separation Effects. ARL TR 73-0162, December, 1973.

16.133 Patankar, S. V., D. B. Spalding: Numerical Predictions of Three-Dimensional Flows. Imperial College, Mech. Eng. Dept. Report EE/TN/A/46, June, 1972.

16.134 Crocco, L., L. Lees: A Mixing Theory for Interaction Between Dissipative Flow and Nearly Isotropic Streams. J. of the Aero. Sci., Vol. 19, No. 10, 1962.

16.135 Briley, W. R.: Numerical Method for Predicting Three-Dimensional Steady Viscous Flow in Ducts. J. of Comp. Physics, Vol. 14, No. 1, 1974.

16.136 Sanborn, V. A.: Boundary Layer Separation and Reattachment. Fluid Mechanics, Acoustics and Design of Turbomachinery, Part 1, NASA SP-304, p. 279, 1974.

16.137 Simpson, R. L., D. G. Whitten, R. J. Moffat: An Experimental Study of the Turbulent Prandtl Number of Air with Injection and Suction. Int. J. of Heat and Mass Transfer, Vol. 13, p. 125, 1970.

16.138 Pai, B. R., J. H. Whitelaw: The Prediction of Wall Temperature in the Presence of Film Cooling. Int. J. of Heat and Mass Transfer, Vol. 14, pp. 409-426, 1971.

16.139 Prandtl, L: Über ein neues formelsysterm der ausgebildeten Turbulenz. Nachr. Akad. Wiss, Göttigen, Math-Phys. Kl., p. 6, 1945.

16.140 Townsend, A. A.: The Structure of Turbulent Shear Flow. Cambridge University Press, 1956.

16.141 Batchelor, G. K.: Note on Free Turbulent Flows with Special Reference to the Two-Dimensional Wake. J. Aero Sci., Vol. 17, p. 441, 1950.

16.142 Deardorff, J. W.: Numerical Investigation of Neutral and Unstable Planetary Boundary Layers. J. Atmos. Sci., Vol. 29, p. 91, 1972.

16.143 Donaldson, C. DuP: A Computer Study of an Analytical Model of Boundary Layer Transition, AIAA J., Vol. 7, p. 271, 1969.

16.144 Morkovin, M. V.: Effects of Compressibility on Turbulent Flows. Mechanics of Turbulence, p. 24, 1964, ed. Favre, Gorden and Breach.

16.145 Bradshaw, P.: Outlook for Three Dimensional Procedures. Proceedings: Computation of Turbulent Boundary Layers, AFOSR-IFP, Stanford Conference, Vol. 1, 1968.

16.146 Johnson, J. P.: The Effects of Rotation on Boundary Layers in Turbomachine Rotors. Fluid Mech., Acoustics and Design of Turbomachinery, Part 1, NASA SP 304, 1974.

16.147 Bradshaw, P.: The Effects of Streamline Curvature on Turbulent Flow. AGARDograph 169, 1973.

16.148 Owen, F. K.: Private communication. See also Ref. 16.25.

16.149 Simpson, R. L.: Characteristics of Turbulent Boundary Layers at Low Reynolds Numbers with and without Transpiration. J. Fluid Mech. Vol. 9, No. 8, p. 1632, 1974.

16.150 Huffman, G. D., P. Bradshaw: A Note on von Karman's Constant in Low Reynolds Number Turbulent Flow. J. Fluid Mech. Vol. 53, p. 45, 1972.

16.151 Van Driest, E. R.: On Turbulent Flow Near a Wall. Heat Transfer and Fluid Mechanics Institute, 1956.

16.152 Escudier, M. P.: The Distribution of the Mixing Length in Turbulent Flows Near Walls. Imperial College, Mech. Eng. Dept. Rpt. TWF/TN/1, 1965.

16.153 Jayatelleke, C. L. V.: The Influence of Prandtl Number and Surface Roughness on the Resistance of the Laminar Sub-Layer to Momentum and Heat Transfer. Progress in Heat and Mass Transfer, Vol. 1, Pergamon Press, p. 193, 1969.

16.154 Galbraith, R. A. McD., M. R. Head: Eddy Viscosity and Mixing Length from Measured Boundary Layer Developments. Aero. Quart. Vol. XXVI, May, 1975.

16.155 Glowacki, W. J., S. W. Chi: A Study of the Effect of Pressure Gradient on the Eddy Viscosity and Mixing Length for Incompressible Equilibrium Turbulent Boundary Layers. Naval Ordnance Laboratory Report, NOLTR 74-105, May 1974. See also, AIAA Paper 72-213, 1972.

16.156 Mellor, G. L.: The Effect of Pressure Gradients on Turbulent Flow Near a Smooth Wall. J. Fluid Mechanics, Vol. 24, pp. 255-274, 1966.

16.157 McDonald, H.: Mixing Length and Kinematic Eddy Viscosity in a Low Reynolds Number Boundary Layer. United Aircraft Research Laboratories Report No. J214453-1, July, 1970.

16.158 Kline, S. J., A. V. Lisin, B. A. Waitman: Preliminary Experimental Investigation of Effect of Free Stream Turbulence on Turbulent Boundary Layer Growth. NASA TND-368, 1960.

16.159 Charnay, G., G. Comte-Bellot, J. Mathieu: Development of a Turbulent Boundary Layer on a Flat Plate in an External Flow. AGARD Conf. Proc. 93, 1972.

16.160 Huffman, G. D., D. R. Zimmerman, W. A. Bennet: The Effect of Free Stream Turbulence Level on Turbulent Boundary Layer Behavior: AGARD Specialists Meeting, Boundary Layer Effects in Turbomachines, 1972.

16.161 Bayley, F. J., W. D. Morris, J. M. Owen, A. B. Turner: Boundary-Layer Prediction Methods Applied to Cooling Problems in the Gas Turbine. Aero. Res. Council of Great Britain, Current Paper 1164, 1971.

16.162 Green, J. E.: On the Influence of Free Stream Turbulence on a Turbulent Boundary Layer as it Relates to Wind Tunnel Testing at Subsonic Speeds. R. A. E., TR 72201.

16.163 Launder B. E., D. B. Spalding: Mathematical Models of Turbulence. Academic Press, 1972.

16.164 Nee, V., L. S. G. Kovasznay: The Calculation of the Incompressible Turbulent Boundary Layers by a Simple Theory. Proceedings: Computation of Turbulent Boundary Layers, AFOSR-IFP, Stanford Conference, Vol. 1, 1968.

16.165 Cebeci, T.: Behavior of Turbulent Flow Near a Porous Wall with Pressure Gradient. AIAA J., Vol. 8, No. 12, pp. 2152-2156, 1970.

16.166 Cebeci, T., G. J. Mosinskis: Computation of Incompressible Turbulent Boundary Layers at Low Reynolds Numbers. AIAA J., Vol. 9., No. 8, pp. 1632-1634, 1971.

16.167 Townsend, A. A.: Equilibrium Layers and Wall Turbulence. J. Fluid. Mech., Vol. II, Part 1, p. 97.

16.168 Reeves, B. L.: Two Layer Model of Turbulent Boundary Layers. AIAA Journal, Vol. 12, No. 7, pp. 932-939, 1974.

16.169 Cebeci, T., K. Kamps, J. Ramsey, A. Maser: Calculation of Three-Dimensional Compressible Boundary Layers on Arbitrary Wings. B. Douglas Aircraft Company, Rpt. MDC J6866, April, 1975.

16.170 Reynolds, W. C.: Computation of Turbulent Flow Rpt. No. FT-4, Dept. of Mech. Eng., Stanford U., 1975.

16.171 Ng. H. K.: Predictions of Turbulent Boundary-Layer Developments Using a Two Equation Model of Turbulence. Ph.D. Thesis Dept. of Mech. Eng. Imperial College., TM/TN/E/12, November, 1971.

16.172 Townsend, A. A.: The Structure of Turbulent Shear Flow. Cambridge Univ. Press, 1956.

16.173 Mellor, G. L., H. J. Herring: A Survey of the Mean Turbulent Field Closure Methods. AIAA J. Vol. 11, p. 590, 1973.

16.174 Shamroth, S. J., H. McDonald: Application of a Transitional Boundary Layer Theory in the Low Hypersonic Mach Number Regime. Int. J. Heat & Mass Transfer, Vol. 18, p. 1277, 1975.

16.175 Orszag, S. A., M. Israeli: Numerical Simulation of Viscous Incompressible Flows. Annual Reviews in Fluid Mechanics Vol. 6, pp. 281-317, 1974.

16.176 Glushko, G. S.: Turbulent Boundary Layer on a Flat Plate in an Incompressible Fluid. Izv. Akad, Nank, SSSR, Seriya Mekihanika, 4, p. 13, 1964 (Transl. NASA TT F-10,080).

16.177 Jones, W. P., B. E. Launder: The Calculation of Low Reynolds Number Phenomena with a Two-Equation Model of Turbulence. Int. J. of Heat & Mass Transfer, Vol. 16, p. 1189, 1973.

16.178 Spalding, D. B.: Concentration Fluctuations in a Round Free Turbulent Jet. Chem. Eng. Sci. Vol. 26, p. 95, 1971.

16.179 Rotta, J. C.: Uber eine Methode zer Berechnung Turbulenz Scherstromungsfelder. Aerodynamische Versuchsanstalt, 69A14, 1969.

16.180 Hanjalic, K. , B. E. Launder: Contribution Towards a Reynolds Stress Closure for Low Reynolds-Number Turbulence. Imperial College, Mech. Eng. Rep. HTS/74/24. See also J. Fluid Mech., Vol. 74, Part 4, pp. 593-610, 1976.

16.181 Bradshaw, P.: The Turbulence Structure of Equilibrium Boundary Layers. J. Fluid Mech., Vol. 29, Part 4, pp. 625-645, 1967.

16.182 Dodge, P. R.: A Numerical Method for Two- and Three-Dimensional Flows. AIAA Paper No. 76-425, 1976.

16.183 Bokenbrink, D.: The Influence of Cooling, Freestream Turbulence and Surface Roughness on the Aerodynamic Behavior of Cascades. ASME Paper No. 74-WA/GT 9, 1974.

16.184 Pratap, V. S., D. B. Spalding: Numerical Computations of the Flow in Curved Ducts. Aero. Quart. Vol. 26, 1975. See also Int. J. Heat and Mass Transfer, Vol. 19, pp. 1183-1188, 1976.

16.185 Briley, W. R., J. P. Kreskovsky, H. McDonald: Computation of Three-Dimensional Viscous Flow in Straight and Curved Passages. United Technologies Research Center Report R76-911841-9, 1976.

16.186 Rubin, S. G., R. K. Khosla., S. Saari: Laminar Flow in Rectangular Channels. Numerical/Laboratory Computer Methods in Fluid Mechanics. ASME, 1976.

16.187 Goldstein, S.: On Laminar Flow Near a Position of Separation. Quart. J. Mech. App. Math., Vol. 1, pp. 43-69. 1948.

16.188 Stewartson, K.: Multistructural Boundary Layers. Advances in App. Mech., Vol. 14, pp. 145-239, 1974.

16.189 Catherall, D., K. W. Mangler: The Integration of the Two Dimensional Laminar Boundary Layer Equations Past the Point of Vanishing Skin Friction. J. Fluid Mech., Vol. 26, p. 163, 1966.

16.190 Klineberg, J. M., J. L. Steger: On Laminar Boundary Layer Separation. AIAA Paper No. 74-94, 1974.

16.191 Carter, J. E.: Solutions for Laminar Boundary Layers with Separation and Reattachment. AIAA Paper 74-583, 1974. See also NASA SP-347, 1975.

16.192 Briley, W. R.: A Numerical Study of Laminar Separation Bubbles Using the Navier-Stokes Equations. J. Fluid Mech., Vol. 47, p. 713, 1971.

16.193 Leal, L. G.: Steady Separated Flow in a Linearly Decelerated Free Stream. J. Fluid Mech., Vol. 59, p. 513, 1973.

16.194 Briley, W. R., H. McDonald: Numerical Predictions of Incompressible Separation Bubbles. J. Fluid Mech., Vol. 69, Part 4, pp. 631-656, 1975.

16.195 Patankar, S. V.: Studies in Convection Theory, Measurement and Applications. Vol. 1, ed. by B. Launder, 1975.

16.196 Lighthill, M. J.: On Boundary Layers and Upstream Influence. Proc. Roy. Soc. Ser. A, 217, pp. 478-507, 1953.

16.197 Stewartson, K., P. G. Williams: Self Induced Separation. Proc. Roy. Soc. Ser. A, 312, pp. 181-206, 1969.

16.198 Bradshaw, P.: The Understanding and Prediction of Turbulent Flow. The Aero Journal, pp. 403-418, 1972. See also Imperial College Rpt. 73-05, 1973.

16.199 Saffman, P. G.: A Model for Inhomogenius Turbulent Flow. Proc. Roy. Soc., London, Series A, Vol. 317, pp. 417-433, 1970.

16.200 Kreskovsky, J. P., S. J. Shamroth, H. McDonald: Application of a General Boundary Layer Analysis to Turbulent Boundary Layers Subjected to Strong Favorable Pressure Gradients. ASME J. of Fluids Eng., June, 1975.

16.201 Crawford, M. E., W. M. Kays: STAN5 - A Program for Numerical Computation of Two-Dimensional Internal and External Boundary Layer Flows. NASA CR 2742, December, 1976.

16.202 Saffman, P. G., Wilcox, D. C.: Turbulence-Model Predictions for Turbulent Boundary Layers. AIAA J., Vol. 12, No. 4, pp. 541-546, 1974.

16.203 Issa, R. I., F. C. Lockwood: On the Prediction of Two-Dimensional Supersonic Viscous Interactions Near Walls. AIAA J., Vol. 15, No. 2, 1977.

16.204 Hughes, D. W., J. H. Horlock: Effect of Rotation on the Development of the Turbulent Boundary Layer. Paper No. 18, Salford Conference on Internal Flows.

16.205 Corrsin, S.: Limitations of Gradient Transport Models in Random Walks and Turbulence. Advances in Geophysics, Vol. 18A, Academic Press, 1974.

16.206 McDonald, H., R. W. Fish: Practical Calculations of Transitional Boundary Layers. Int. J. of Heat & Mass Transfer, Vol. 16, No. 9, pp. 1729-1744, 1973.

16.207 Humphrey, J. A. C., A. M. K. Taylor, J. H. Whitelaw: Laminar Flow in a Square Duct of Strong Curvature. J. Fluid Mech., 1977.

16.208 Pope, S. B., J. H. Whitelaw: The Calculation of Near-Wake Flows. J. Fluid Mech., Vol. 73, Part 1, pp. 9-32, 1976.

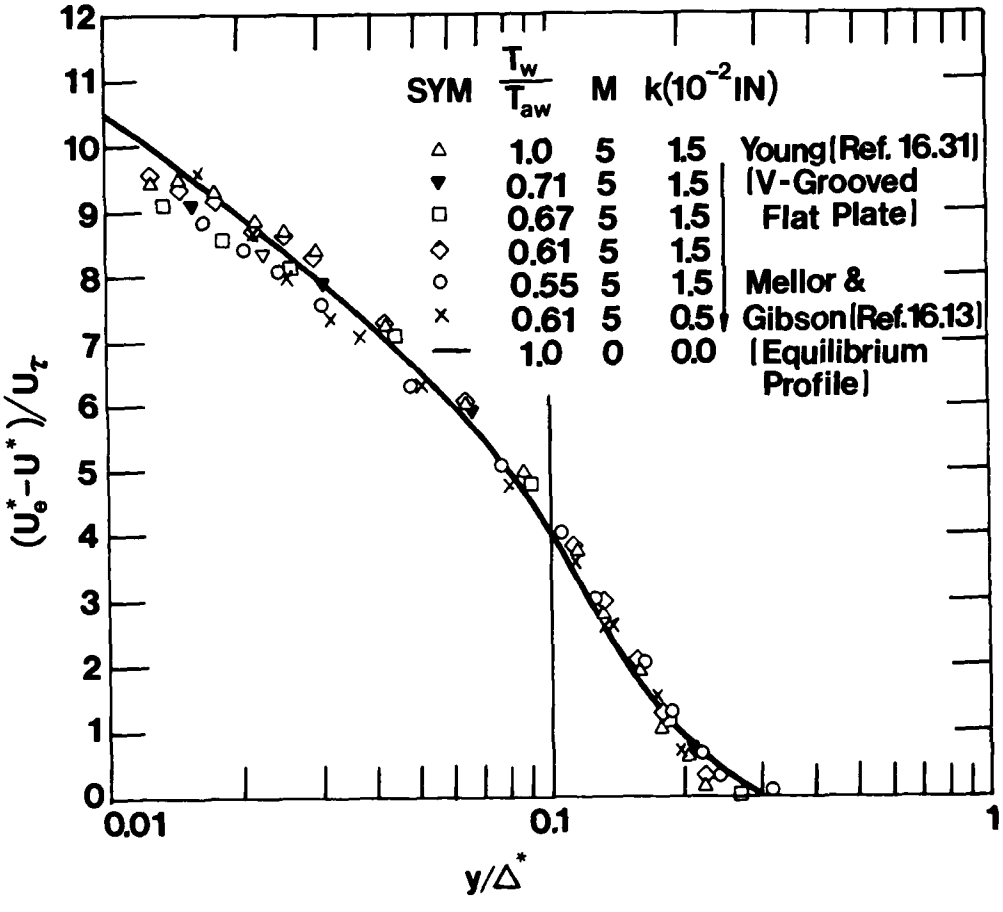

Fig. 16.1 Compressible Turbulent Velocity Defect Profiles on a Rough Surface with Heat Transfer, M is the free stream Mach number, k is the roughness height, u* is Van Driest's (Ref. 16.20) transformed velocity and Δ^* is Clauser's thickness scale, δI^*, Eq. 16.1(7).
Figure is taken from Chen (Ref. 16.30).

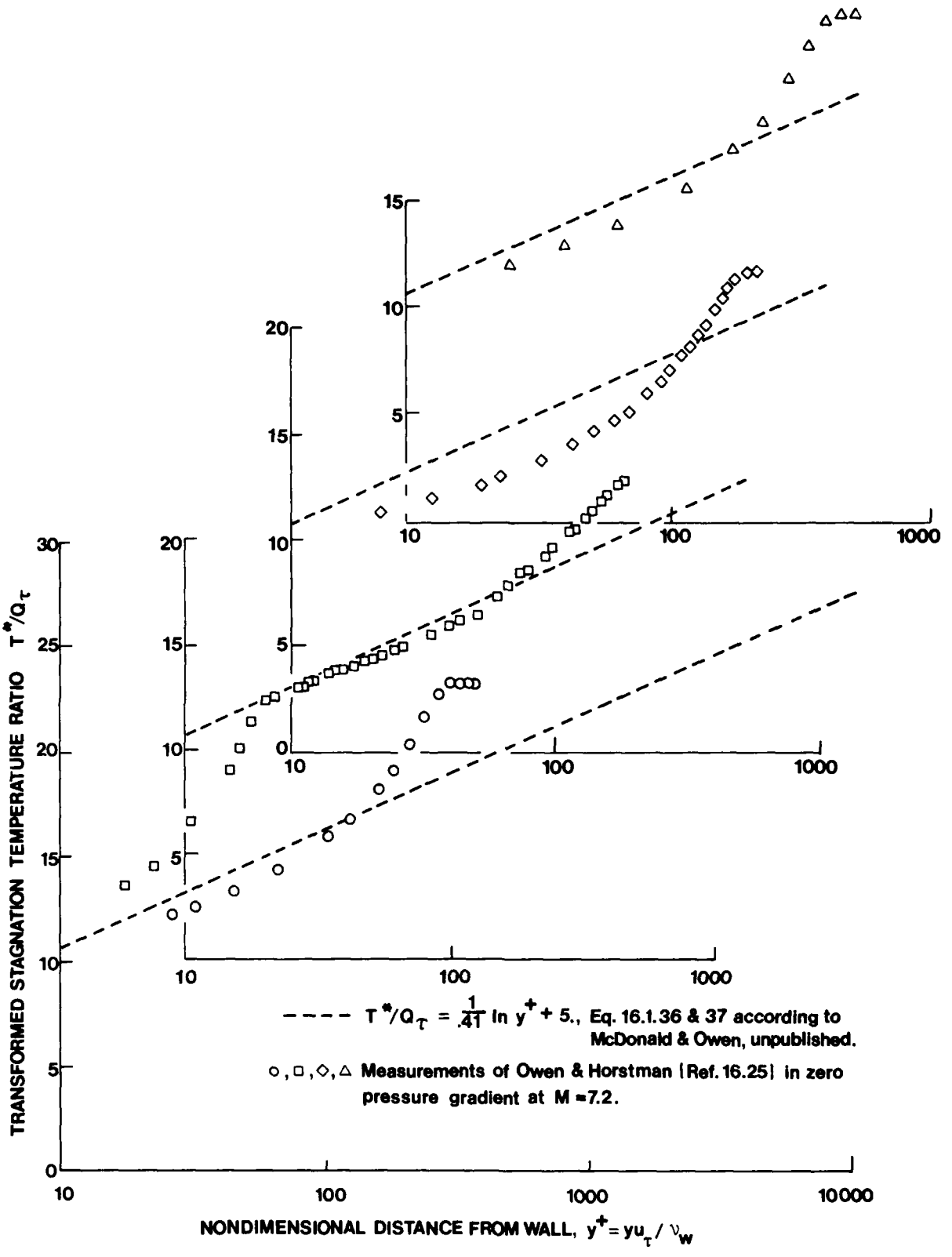

Fig. 16.2 Temperature Law of the Wall

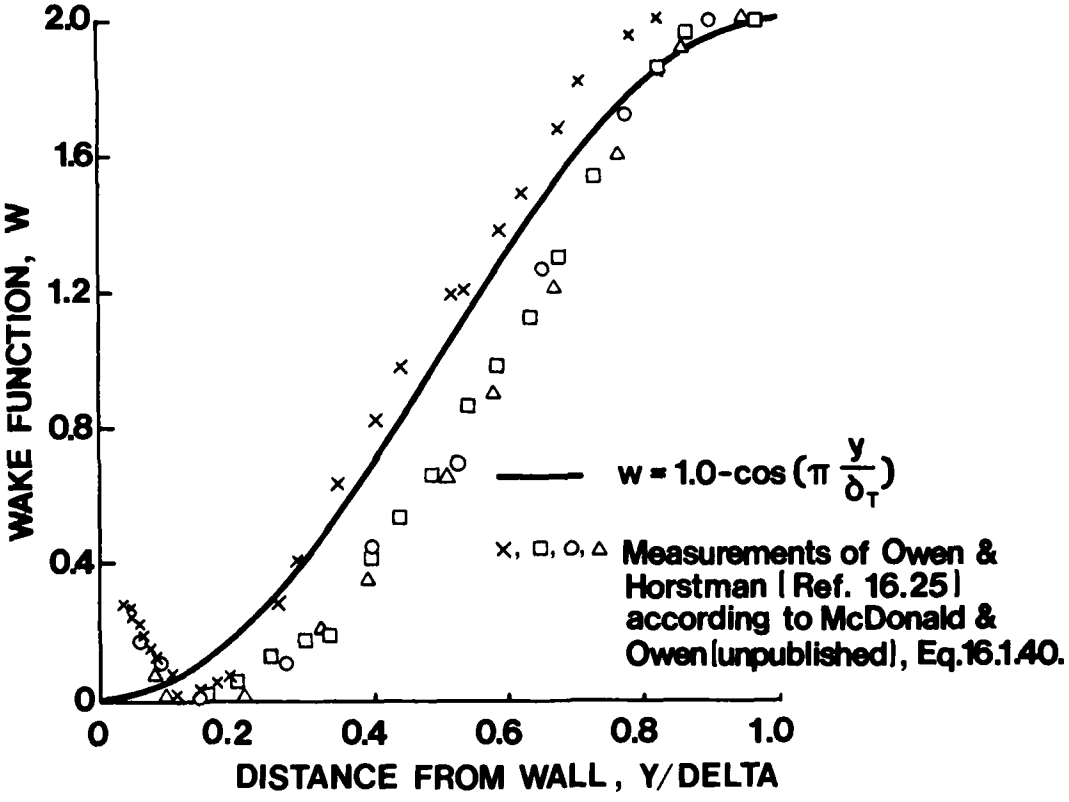

Fig. 16.3 Temperature Wake Component

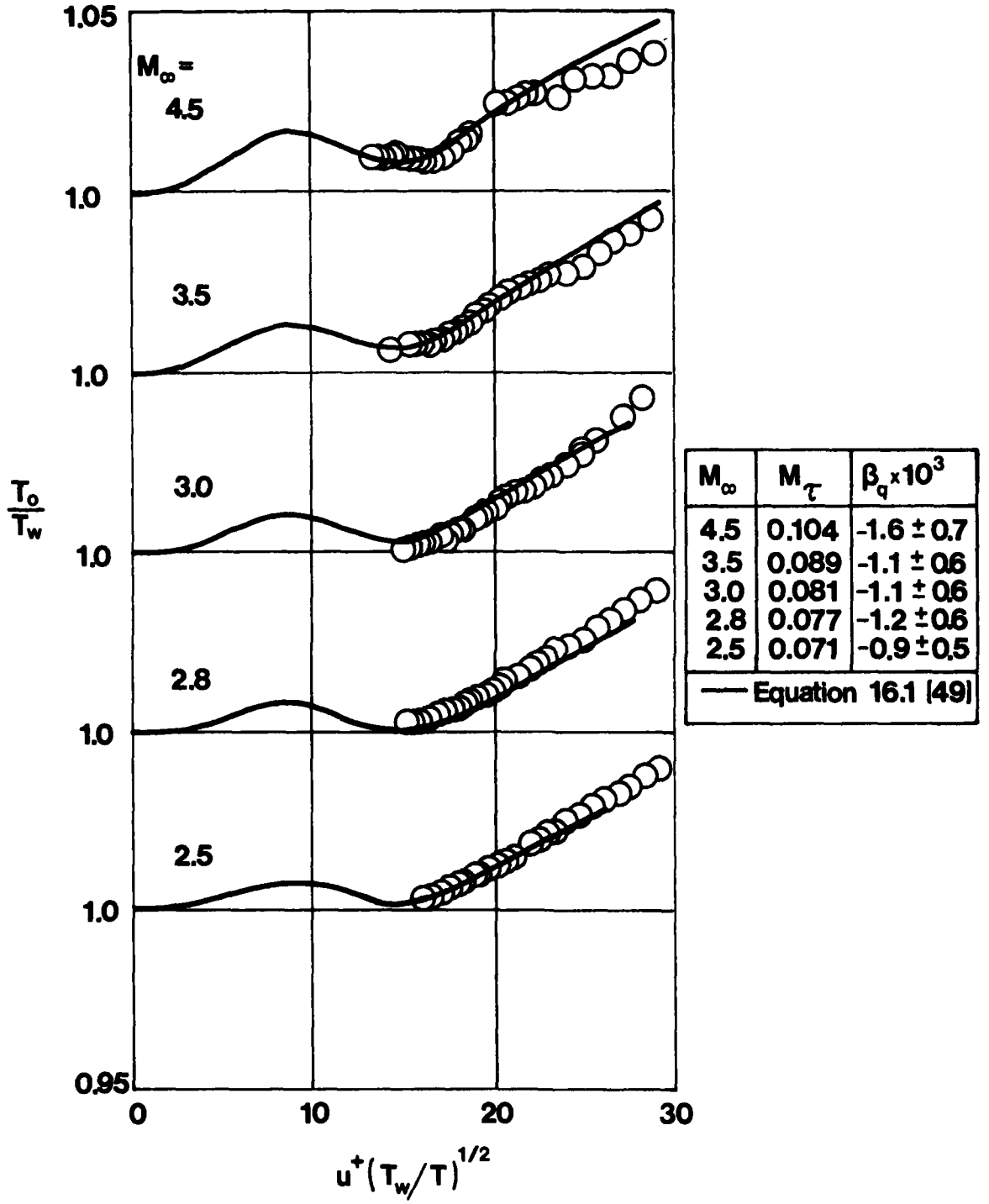

Fig. 16.4 Calculated and Measured Total Temperature Distributions According to Meier and Rotta (Ref. 16.40)

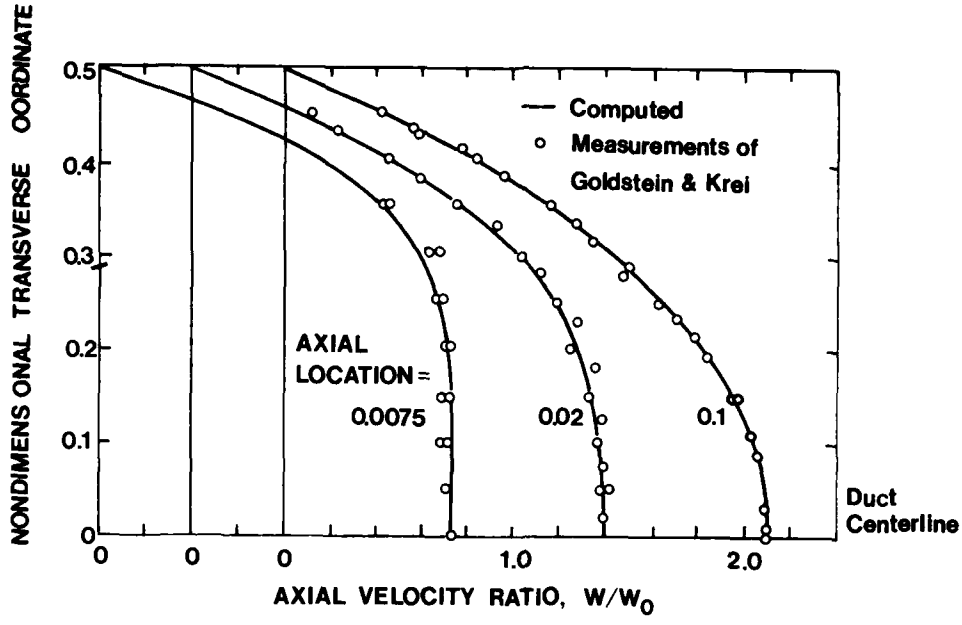

Fig. 16.5 Comparison Between Computed and Measured Axial Velocity Profiles for Square Duct on the Midplane with Laminar Flow. Taken from the work of Briley (Ref. 16.135).

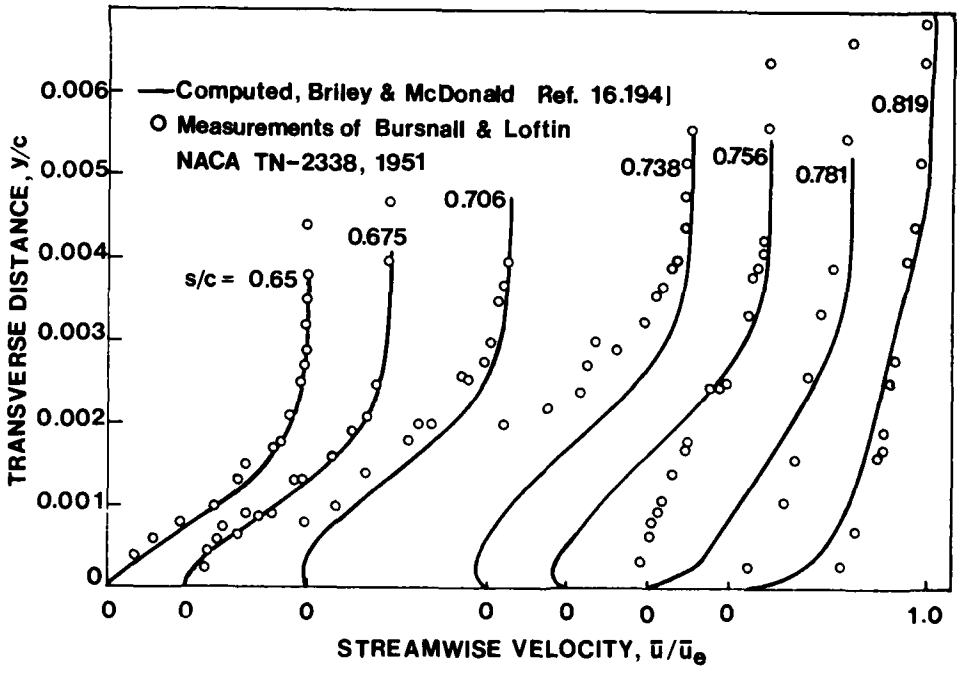

Fig. 16.6 Velocity Profiles at Selected Streamwise Locations in a Separation Bubble

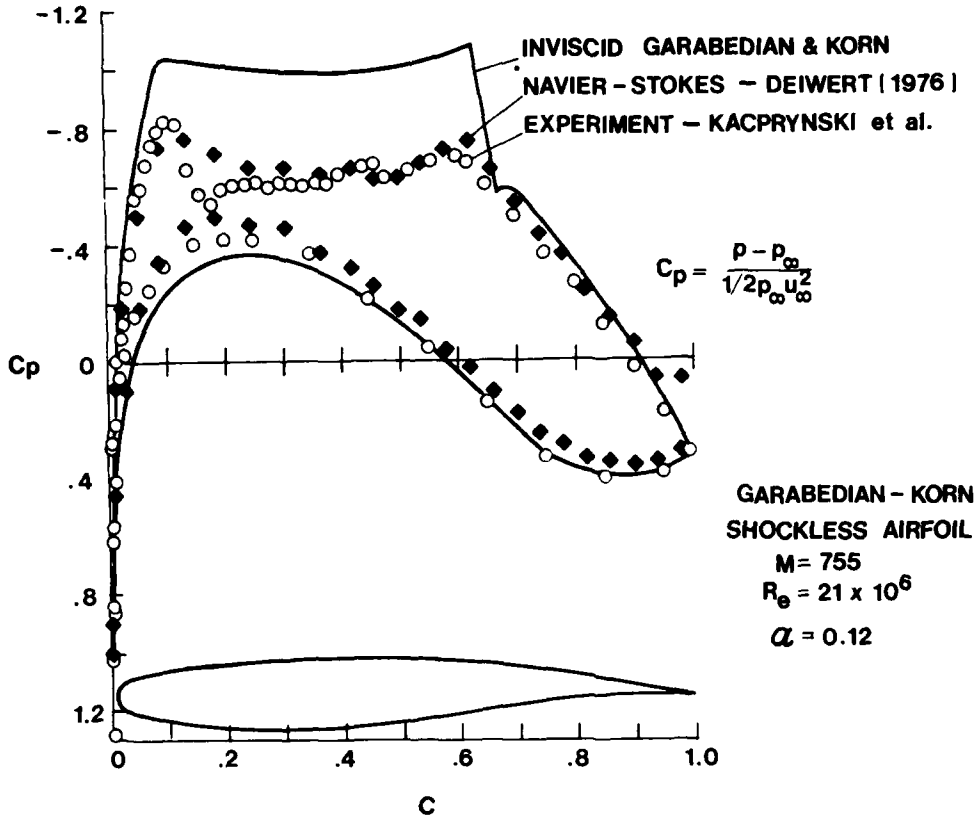

Fig. 16.7 Surface Pressure Distribution

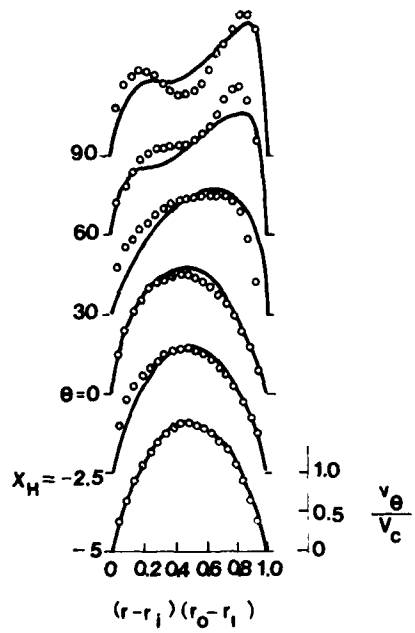

Fig. 16.8 Comparison Between Measured (Circles) and Computed Velocity Profiles Along the Midplane of a Rectangular Duct Turning Through 90°. X is the streamwise distance from the start of the bend and θ is the duct centerline turning angle, r_i is the inner wall radius, r_o is the outer wall radius. Taken from the work of J.A.C. Humphrey, A.M.K. Taylor and J.H. Whitelaw (Ref. 16.207).

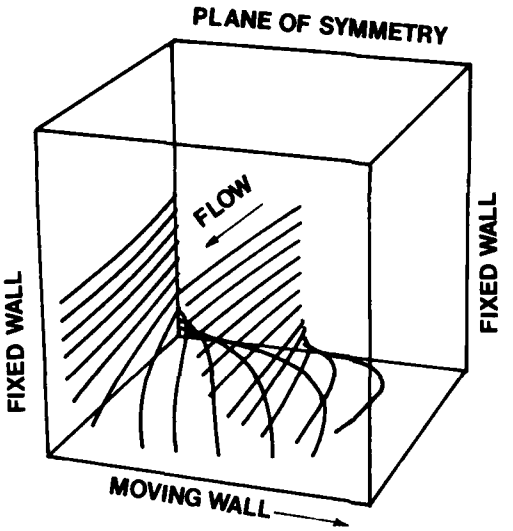

Fig. 16.9 Selected Streamlines for Duct Flow with Moving Walls, M = 0.44, Re = 60, taken from the work of Briley and McDonal (Ref. 16.64) Predictions made using the compressible time dependent Navier-Stokes equations.

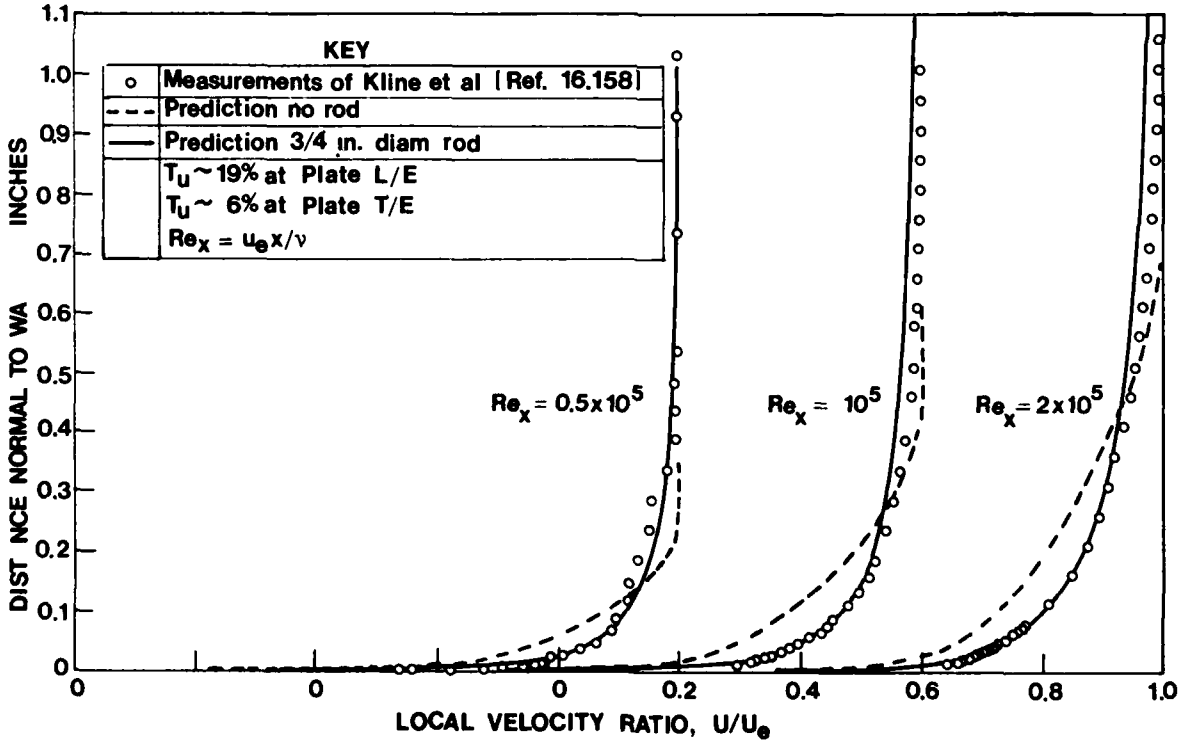

Fig. 16.10 Effect of Free Stream Turbulence on the Boundary Layer Mean Velocity Profile

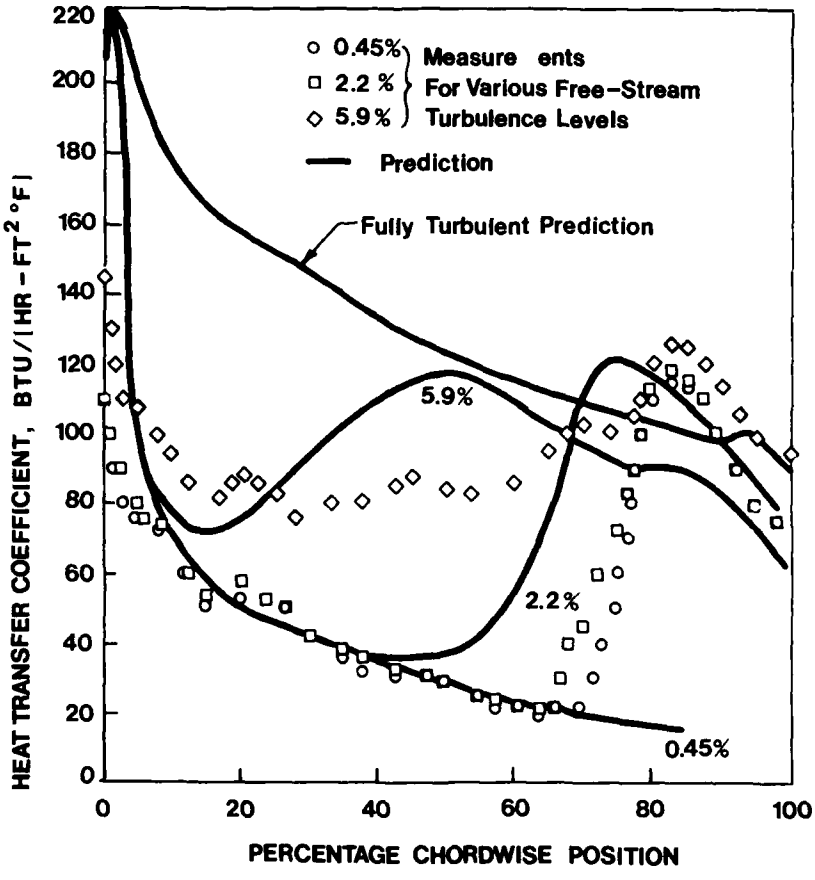

Fig. 16.11 Heat Transfer Distribution on the Suction Side of a Turbine Airfoil. Measurements of Turner (Ref. 16.206), Predictions According to McDonald and Fish (Ref. 16.58).

Chapter 17

AXIAL-FLOW COMPRESSOR AERODYNAMICS

George K. Serovy

Engineering Research Institute, Iowa State University

TABLE OF CONTENTS

CHAPTER 17 AXIAL-FLOW COMPRESSOR AERODYNAMICS

		Page
17.0	Introduction	17-1
17.1	Axial-Flow Compressor Nomenclature and Terminology	17-1
17.1.1	Meridional Plane Flow Passage Terminology	17-1
17.1.2	Blade-to-Blade Flow and Cascade Nomenclature and Terminology	17-3
17.2	Characteristics of the Flow in Axial-Flow Compressor Configurations	17-5
17.2.1	Velocity Diagrams, Energy Transfer, Path Lines and Streamlines	17-5
17.2.2	Performance of Axial-Flow Compressors	17-8
17.2.3	Variations on the Basic Performance Map	17-9
17.2.4	Individual Stage Characteristics	17-10
17.3	Aerodynamic Design Objectives for Axial-Flow Compressor Units	17-11
17.4	Elements of a Compressor Design System--Technical Requirements	17-12
17.5	Content of Current and Developing Design Systems--The Technology Base	17-13
17.5.1	General Comments on Flow Models	17-13
17.5.2	Equations	17-15
17.5.3	Performance Limiting Flow Phenomena--Design Limit Parameters	17-16
17.5.4	Preliminary Design	17-21
17.5.5	Design Analysis	17-23
17.5.6	Performance Prediction	17-23
17.5.7	Stress, Aeroelastic and Acoustic Analysis	17-24
17.6	Component and Configuration Experimental Development	17-24
17.7	Axial-Flow Compressor Performance Trends	17-26
17.8	Acknowledgments	17-27

LIST OF FIGURES

		Page
Figure 17.1.1	Meridional plane sections of turbojet engine and compressor	17-1
Figure 17.1.2	Meridional plane section of a two-spool turbofan engine	17-2
Figure 17.1.3	Meridional plane section of high bypass ratio turbofan engine	17-2
Figure 17.1.4	Schematic view of axial-flow compressor rotor blade row	17-3
Figure 17.1.5	Meridional plane section of three-stage axial-flow fan	17-3
Figure 17.1.6	Compressor stage with cascade intersection trace in developed cylindrical surface	17-4
Figure 17.1.7	Schematic layout of a plane cascade test section for transonic flow conditions	17-4
Figure 17.1.8a	Blade section geometry and cascade terminology	17-5
Figure 17.1.8b	Blade row geometry and cascade terminology	17-5
Figure 17.1.9	Example set of experimental plane cascade data	17-6
Figure 17.2.1a	Velocity diagrams for flow along path line A-B-C-D in a compressor stage	17-6
Figure 17.2.1b	Combined velocity diagram for flow along path line A-B-C-D in a compressor stage	17-7
Figure 17.2.2	Trends in stage velocity diagrams and performance with changes in flow rate	17-7
Figure 17.2.3	Equilibrium performance map for an eight-stage axial-flow compressor	17-9
Figure 17.2.4	Example of axial-flow compressor map showing effect of inlet flow distortion and rotating stall region	17-9
Figure 17.2.5	Schematic compressor map showing boundaries for four types of blade flutter	17-10
Figure 17.2.6	Example of assumed stage performance characteristics used in stage-matching study	17-11
Figure 17.2.7	Trends in stage performance for axial-flow compressor operating at off-design conditions	17-12

		Page
Figure 17.4.1	Compressor design system flow chart	17-13
Figure 17.5.1	S_1 and S_2 surfaces in blade-to-blade flow passage	17-14
Figure 17.5.2	Variation of loss parameters with diffusion factor at reference minimum-loss incidence angle computed from low-speed-cascade tests of NACA 65-(A_{10})10 cascade blades	17-18
Figure 17.5.3	Variation of loss parameters with diffusion factor for blade sections in compressors operating near minimum-loss incidence angle	17-18
Figure 17.5.4	Compressor specific flow rate as a function of axial Mach number and hub-tip ratio	17-19
Figure 17.5.5	Trends in low hub-tip ratio stage performance with rotor tip speed and loading level	17-19
Figure 17.5.6	Layout of compressor blade sections on conical surface through stream surface intersection radii at blade row leading and trailing edge	17-22
Figure 17.5.7	Meridional plane section of axial-flow compressor showing axisymmetric stream surface notation	17-24
Figure 17.5.8	Calculation control surfaces for an axial-flow compressor stage with computed stream surface shapes	17-25
Figure 17.5.9	Comparison of cascade experiments and rotor blade section data	17-25
Figure 17.6.1	Compressor test facility	17-26
Figure 17.7.1	Overall performance of single-stage axial-flow compressor designed to operate at a tip speed of 1600 feet per second (488 m/s)	17-26
Figure 17.7.2	Predicted and measured performance characteristics of three-stage axial-flow compressor	17-27
Figure 17.7.3a	Stage performance map for IGV/stator schedule 0°/0°	17-28
Figure 17.7.3b	Stage performance map for IGV/stator schedule 40°/8°	17-28
Figure 17.7.4	Schematic of one form of compressor rotor tip casing treatment	17-29
Figure 17.7.5	Design characteristics of advanced transonic compressor stages	17-29

CHAPTER 17 AXIAL-FLOW COMPRESSOR AERODYNAMICS

George K. Serovy
Department of Mechanical Engineering
Engineering Research Institute
Iowa State University of Science and Technology
Ames, Iowa 50011 U.S.A.

17.0 INTRODUCTION

This Chapter begins with qualitative descriptions of axial-flow compressor geometry and of some of the features of the flow in this form of turbomachine. The purpose of these sections is to develop a working understanding of the specialized terminology associated with compressor aerodynamics and aeromechanics. Subsequent sections discuss the elements of axial-flow compressor design, including design objectives, the requirements for a design system, and the characteristics of typical current and developing design methods. Finally, a brief outline of the quantitative status of axial-flow compressor technology is given. This is done, not to guarantee the prompt obsolescence of the Chapter, but to provide baseline data and illustrate trends.

Like most of the other subjects covered in the specialized Chapters of these volumes, the axial-flow compressor has a tremendous literary background. This Chapter should be a book, but since it is not, readers should consult the Bibliography in Sec. (17.9). These references cover a broad range of topics and points of view, and each one makes a contribution to real axial-flow compressor technology, which is the only kind worth writing about.

17.1 AXIAL-FLOW COMPRESSOR NOMENCLATURE AND TERMINOLOGY

All gas turbine propulsion systems must have a compressor component which develops some or all of the pressure rise specified by the system cycle. Shaft work for the compression process is supplied by the turbine component of the system. In some system cycles, the compressor unit is divided into sections driven by separate shafts, and identified by descriptive names such as fan, low-pressure compressor, intermediate-pressure compressor and high-pressure compressor.*

17.1.1 MERIDIONAL PLANE FLOW PASSAGE TERMINOLOGY

Three axial-flow compressor units from current aircraft gas turbine engines are shown in the sectional views of Figures 17.1.1, 17.1.2, and 17.1.3. In each case, the section shown is one intersected by a plane including the rotational axis of the engine. This section is known as a meridional plane section. The compressor units of Figures 17.1.1, 17.1.2, and 17.1.3 are described as axial-flow compressors because the through-flow direction of the working fluid is approximately parallel to the rotational axis.

Figure 17.1.1 shows a single-shaft compressor for a turbojet engine. This compressor has eight stages with each stage consisting of one rotating

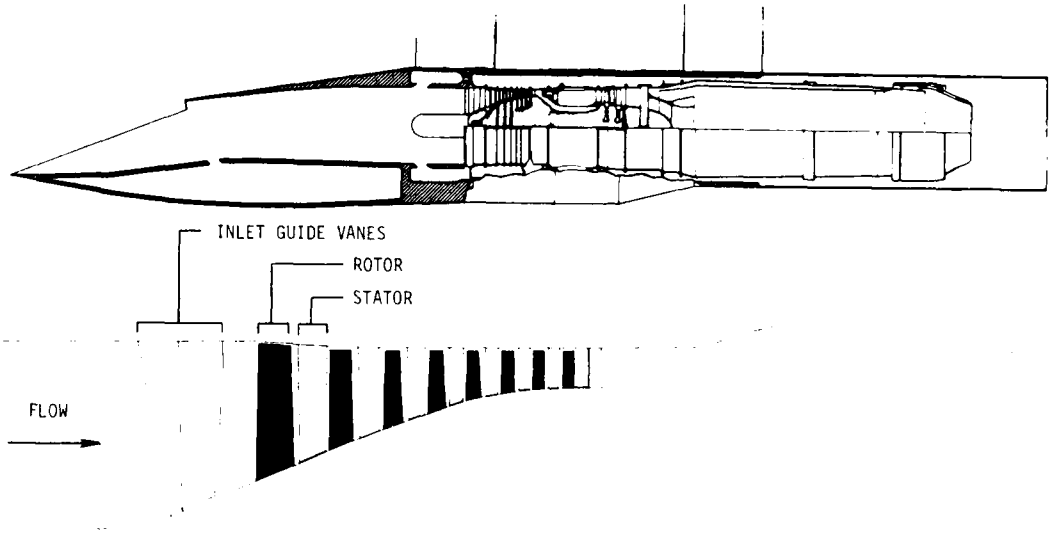

Figure 17.1.1. Meridional plane sections of turbojet engine and compressor (Ref. 17.1,17.2).

*Words or phrases underscored throughout the text are significant terms for compressor designers.

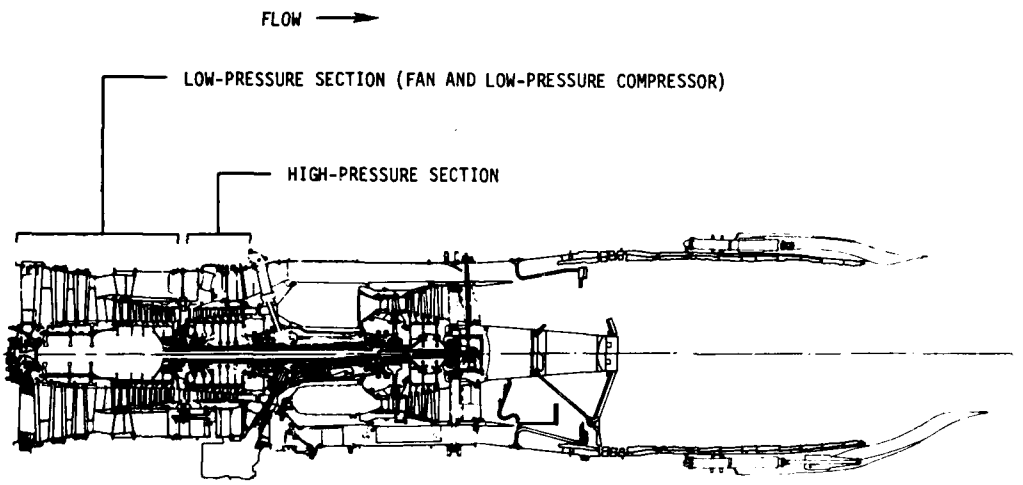

Figure 17.1.2. Meridional plane section of a two-spool turbofan engine (Ref. 17.3).

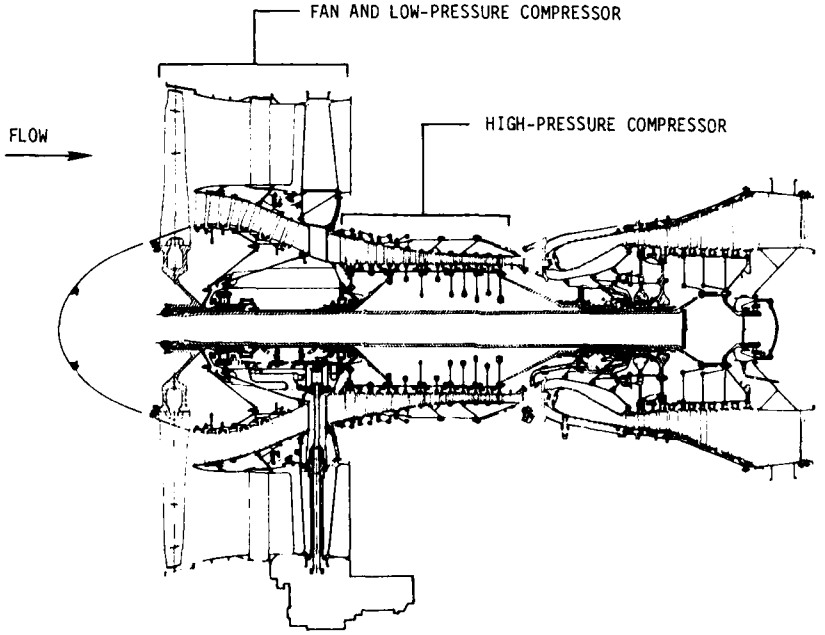

Figure 17.1.3. Meridional plane section of high bypass ratio turbofan engine (Ref. 17.4).

(rotor) row and one stationary (stator) row of blades. Each blade (Figure 17.1.4) is made up of individual airfoil sections "stacked" on an axis so as to produce a prescribed flow field. The first stage in Figure 17.1.1 has a row of inlet guide vanes. The function of this type of row is to set up a design distribution of velocity vectors at the first rotor entrance. In some compressor units one or more rows of stationary blades (exit guide vanes) may be used at the outlet of the last stator row to establish a desired flow pattern at the exit of the compressor.

Figure 17.1.2 shows a two-shaft (two-spool) compressor in a turbofan engine. In this case a three-stage fan and six-stage low pressure compressor section are driven by the low-pressure section of the turbine, while the seven-stage high-pressure compressor is driven by the high-pressure turbine section through a separate shaft. The fan has inlet guide vanes. Note that there is a splitter in the flow passage just downstream from the rotor of the third fan stage. This splitter separates the core flow into the low- and high-pressure compressor sections from the by-pass flow in the outer duct.

A two-spool compressor for a large turbofan engine is shown in Figure 17.1.3. The fan, low-pressure compressor and high-pressure compressor have one, four and eleven stages, respectively. In this case the fan has no inlet guide vanes.

In order to clarify additional compressor terminology, Figure 17.1.5 shows a meridional section of a three stage fan at a larger scale. The rotor and stator rows are installed in an annular flow passage. The outer or tip casing

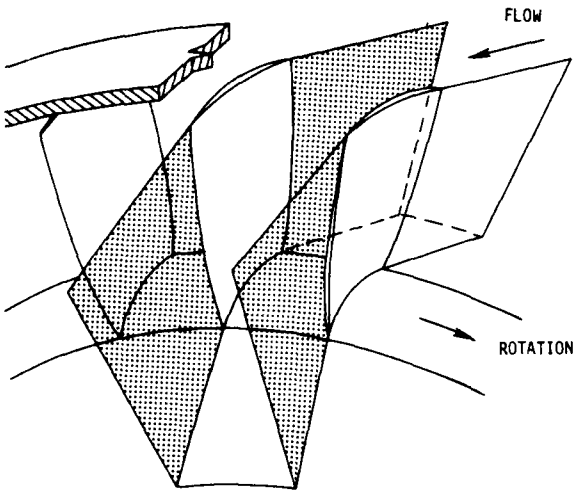

Figure 17.1.4. Schematic view of axial-flow compressor rotor blade row.

The hub-tip ratio for a specific stage is usually defined as the numerical ratio of the hub diameter to the tip casing diameter taken at the leading edge of the rotor row for the stage. The term aspect ratio is frequently used in describing compressor blade rows, but the definition may vary from one case to another. Typically, the aspect ratio might be defined as the ratio of an average blade span to an axial projection of the blade row length or chord at the hub.

17.1.2 BLADE-TO-BLADE FLOW AND CASCADE NOMENCLATURE AND TERMINOLOGY

We now recognize that the flow through an axial-flow compressor is an internal flow through an annular flow path, where the flow is influenced by both rotor and stator blade rows. The blades are generally non-uniform in the spanwise direction, and consist of stacked airfoil sections as shown in Figure 17.1.4. We might expect that these individual airfoil sections would exhibit some of the same behavioral characteristics as isolated airfoils, and they do. They are subject to lift and drag forces, they stall, they generate boundary layers,

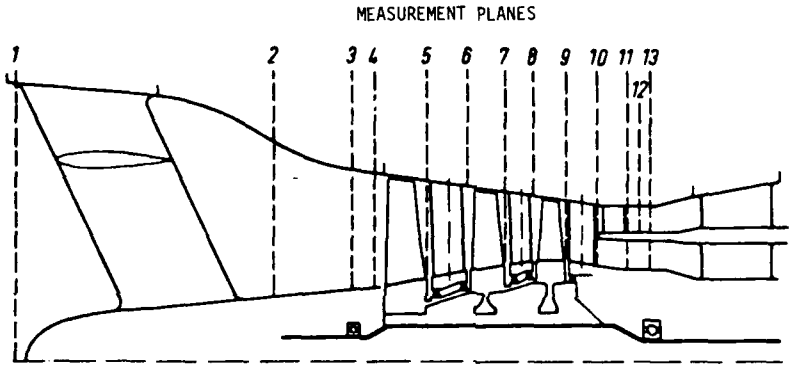

Figure 17.1.5. Meridional plane section of three-stage axial-flow fan (Ref. 17.5).

wall holds the stator blade rows. The inner or hub ends of the stator blades are joined by circumferential shrouds which make up a part of the annulus boundary at the hub. The rotor rows are in this case installed in rotor disks so that the hub profile is made up of alternate rotating and stationary wall segments. In some compressors the rotor blades are installed in a built up series of disks and rings making up a continuous rotating hub wall for the flow path. In the latter case there is a clearance between the ends of the stator blades and the hub, just as there is normally a tip clearance at the rotor outer radius. Occasionally, a rotating shroud is used at the rotor tips, but more frequently part-span shrouds or dampers are used at a location along the rotor span between the hub and tip (Figures 17.1.2 and 17.1.3). If shrouds or dampers are used, the principal function is aeromechanical, to limit the amplitude of blade vibration. They are not likely to be an asset in an aerodynamic sense. The number of blades in each rotor and stator row is specified in the aerodynamic and aeromechanical design of the unit. Each blade, just as an isolated airfoil, has a chord length and span. The chord (axial projection only is seen in the meridional plane) may vary between the hub and tip and the span normally varies between the entrance and exit of a given blade row because of design variations in fluid density and velocity levels.

wakes, and under some circumstances shock waves. They frequently possess dihedral and act as swept airfoils. However, the blades operate under conditions unlike the typical isolated airfoil case. They are located near other airfoils, both in the circumferential and axial directions, and they are influenced by these adjacent bodies. They are bounded at both ends by walls which may be stationary or moving with the blades. In all rows except the first, the airfoils operate in an unsteady flow, where both the velocity magnitude and direction fluctuate. Most important, the airfoil rows in the compressor produce a significant flow deflection and change in the thermodynamic state of the fluid. Rows are generally designed so as to behave as diffusers, with an increase in static pressure from the upstream to the downstream flow region.

To aid in the discussion of blade row characteristics, consider a cylindrical surface at constant radius r from the rotational axis of the compressor stage of Figure 17.1.6. If this surface is developed on a plane the intersection traces of the blades produce two lattices or cascades of airfoil sections. There is no reason to believe that the flow in a compressor would follow the cylindrical surface of Figure 17.1.6 and, in fact, the real paths followed by fluid particles are much more

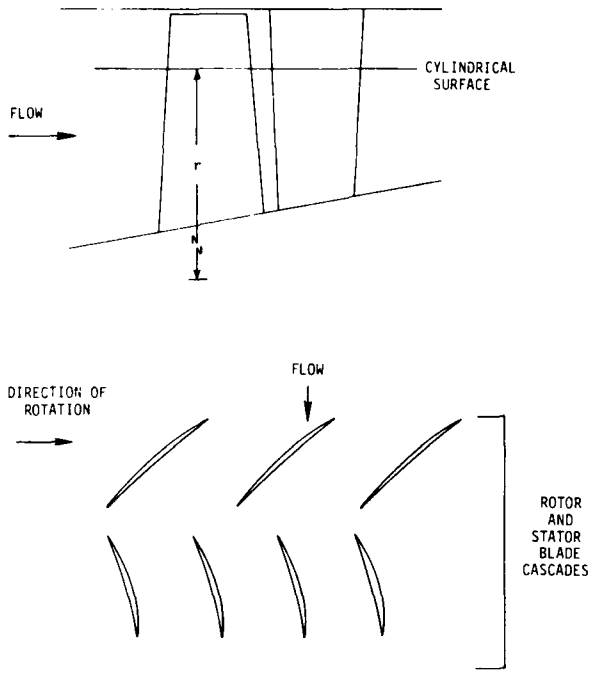

Figure 17.1.6. Compressor stage with cascade intersection trace in developed cylindrical surface.

complex. Nevertheless, the concept of an airfoil cascade is not only convenient for the purpose of introducing compressor nomenclature, but it also is the basis for historically and currently significant models of the flow in compressors and turbines.

In both computation and experimentation it has been common practice to follow the flow through axial-flow compressors as if it followed axisymmetric paths. In the earliest axial-flow configurations these paths were assumed to by cylindrical, but more recently have become more complex surfaces of revolution which change radius in an attempt to follow the flow more accurately. The validity of these paths will be discussed in more detail later, but in any case they define a cascade array of airfoil sections by their intersections with each blade row.

For many years the flows through compressor blade rows have been simulated experimentally using both annular and plane cascade test facilities. In an annular cascade facility, blades are installed in an annulus, just as in a real compressor, so that the infinite character of the blade row in a real machine is correctly modeled. In a plane or linear cascade, a finite number of blades are installed in a flow passage with a rectangular cross-section as shown in Figure 17.1.7. In both annular and plane cascades, measurements are made upstream and downstream from the blade row with the row arranged geometrically so that it is exposed to an entrance flow similar to that found in a compressor blade row. When reference is made to cascade data in the literature, the data may have been obtained in either an annular or plane cascade, but it is a fact that the vast majority of cascade data has originated in plane cascade facilities.

Figure 17.1.8 shows a plane cascade of airfoils with some important geometric and flow variables. Blades of a uniform blade section geometry are aligned at the blade setting angle or stagger angle γ with respect to the cascade axis. The cascade axis corresponds to the axial direction in the compressor. The blades are equally spaced at a distance s, called the gap or blade spacing. The cascade has a solidity σ, defined as the ratio of blade chord to blade spacing, c/s. Although the three variables--blade section geometry, blade setting angle and solidity--completely define the plane cascade geometry, there are, of course, a very large number of subsidiary variables required to describe the blade section geometry. Many of these have important effects in determining the flow field in a cascade.

The plane cascade test facility is really a special form of wind tunnel. In cascade experiments compressor blade row flow fields are simulated by varying or controlling the relative inlet flow angle β_1, the upstream Mach number M_1, the Reynolds number and/or the upstream turbulence properties. Changing the angle β_1 for a constant blade setting angle changes the angle of incidence i (or angle of attack) by an equal amount.

Downstream boundary conditions may be varied to control the axial velocity x density ratio (AVDR) or the static pressure ratio across the cascade, because these exit parameters affect the cascade blade surface pressure distributions and the two cascade performance parameters which are of most interest in design. These dependent variables are the downstream fluid flow angle β_2 and a measure of the loss in total pressure across the cascade. The parameters most commonly used to quantify these measurements are the gap-averaged deviation angle

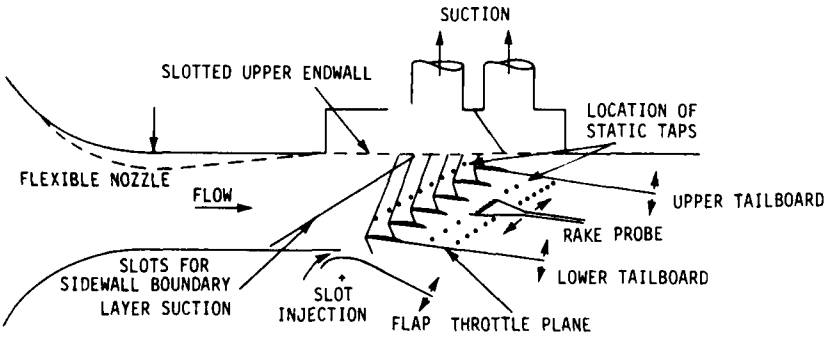

Figure 17.1.7. Schematic layout of a plane cascade test section for transonic flow conditions.

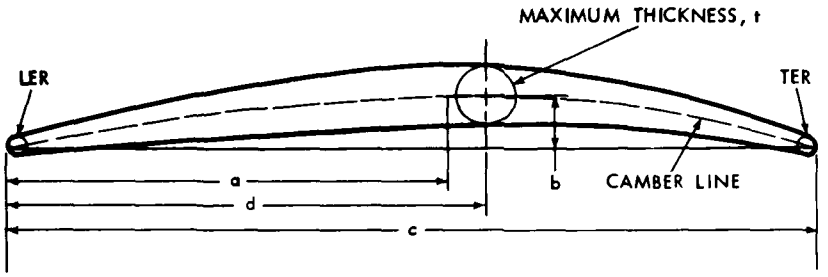

a = LOCATION OF MAXIMUM CAMBER
b = COORDINATE OF MAXIMUM CAMBER
c = CHORD LENGTH
d = LOCATION OF MAXIMUM THICKNESS
LER = LEADING EDGE RADIUS
TER = TRAILING EDGE RADIUS

Figure 17.1.8a. Blade section geometry and cascade terminology.

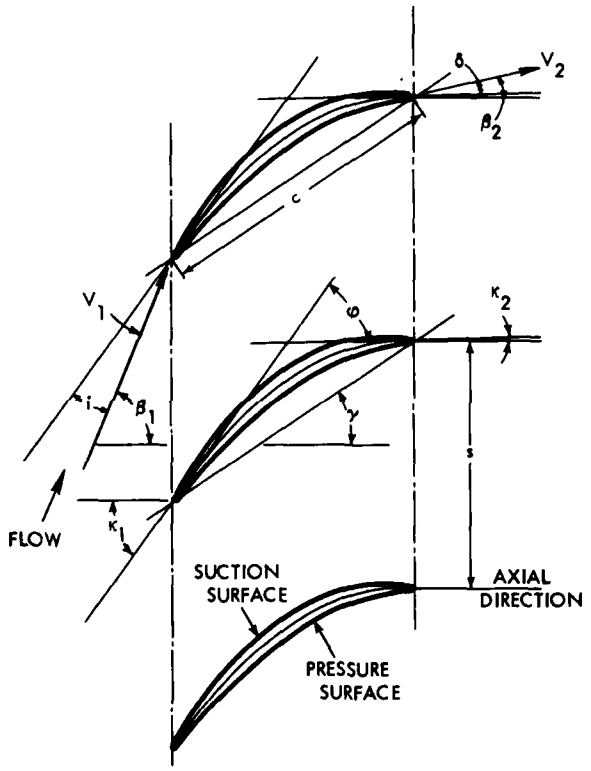

Figure 17.1.8b. Blade row geometry and cascade terminology.

δ and the gap-averaged total-pressure loss coefficient $\bar{\omega}$. Averaging methods used have an effect on measured cascade performance, as does the location of the measuring station with respect to the cascade trailing-edge line.

There is disagreement about the value of cascade data in design, and there is some factual basis for a negative view of cascade experiments. However, cascade results represent an important part of the data base in most design systems and new cascade data continue to appear in the literature on a regular basis.

Figure 17.1.9 is a typical plot representing the results of a series of subsonic plane cascade experiments. The fact that the loss coefficient rises at both ends of the incidence angle range clearly shows that flow separation and stall are present in cascade flow fields. These cascade experiments were run under two-dimensional flow conditions (AVDR = 1.0) and with a constant entrance Mach number M_1. Some additional comments on cascade results will be made later in this Chapter, especially in connection with the effects of Mach number and blade row geometry.

17.2 CHARACTERISTICS OF THE FLOW IN AXIAL-FLOW COMPRESSOR CONFIGURATIONS

17.2.1 VELOCITY DIAGRAMS, ENERGY TRANSFER, PATH LINES AND STREAMLINES

It is essential to clearly understand velocity component diagrams and their use in describing the annulus flow field. This is a good time to consider these diagrams and their relation to the complete flow field.

At each point and at each instant of time in the compressor flow field, a velocity vector $\vec{V}$ exists. We will generally use a cylindrical coordinate system with the coordinates r measured from the rotational axis, θ measured from an arbitrary meridional plane (with the positive θ direction in the direction of rotor rotation) and x measured parallel to the rotational axis from an arbitrary r, θ plane. In this coordinate system, $\vec{V}$ = function (x, r, θ, t) and for any point and time we can determine velocity components V_x, V_θ and V_r. We can also define a meridional plane velocity component as the resultant of V_x and V_r. We will call this meridional plane velocity V_m.

Because we will work with rotating blades, it is necessary to consider both absolute velocities and velocity components measured relative to points on rotating blades. For example, if we wanted to study the fluid velocity relative to the leading edge point A on the rotor of Figure 17.2.1a, we would subtract the local rotor velocity $\vec{U}$ from the absolute fluid velocity $\vec{V}$ to get the relative velocity W_A.

$$\vec{W}_A = \vec{V}_A - \vec{U}_A$$

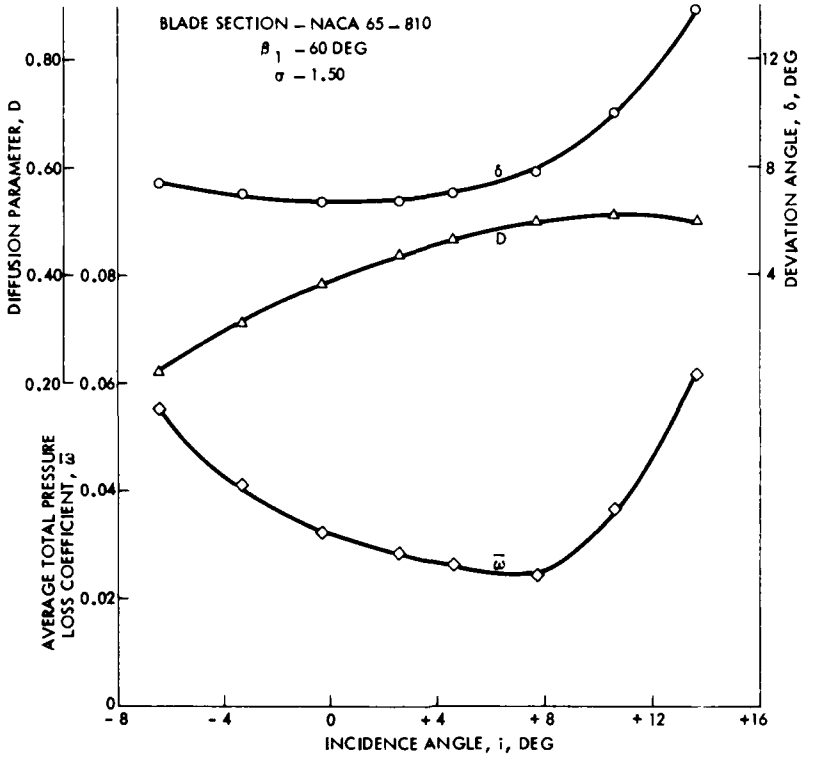

Figure 17.1.9. Example set of experimental plane cascade data.

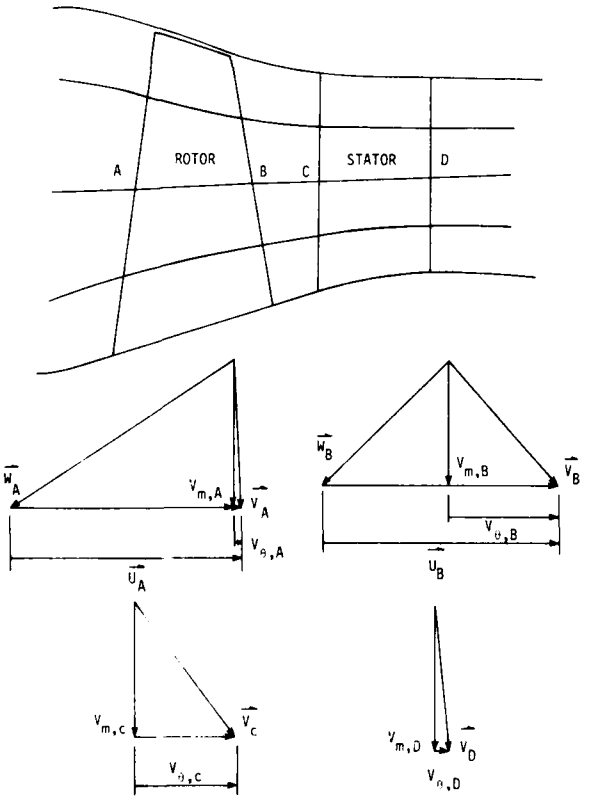

Figure 17.2.1a. Velocity diagrams for flow along path line A-B-C-D in a compressor stage.

The relative velocity at any point has components W_x, W_θ and W_r

$$W_x = V_x$$

$$W_r = V_r$$

$$W_\theta = V_\theta - U$$

A typical velocity diagram for a rotor leading edge point such as A is shown in Figure 17.2.1a as it would appear in a plane tangent to the meridional velocity component V_m at A. If a particle entering the rotor at A followed a path such that it left the rotor at B and continued through the stator row along the path C-D (for convenience all points are rotated from their actual circumferential locations into the meridional plane shown), velocity diagrams could also be constructed at B, C and D as in Figure 17.2.1a. The four diagrams are combined in a single composite stage velocity diagram in Figure 17.2.1b, showing the effect of the passage and blades on fluid particles following a path line A-B-C-D.

For a fluid particle of mass δm passing through a rotor row from A to B (see Figure 17.2.1a, the energy transferred as work done on the fluid by the blades is given by Euler's turbine equation

$$E = \delta m(\omega)[r_B V_{\theta,B} - r_A V_{\theta,A}] = \delta m[U_B V_{\theta,B} - U_A V_{\theta,A}] \qquad (17.2.1)$$

Eq. (17.2.1) is a consequence of the law of conservation of angular momentum (see Sec. 17.5). If we want to use this equation to determine energy trans-

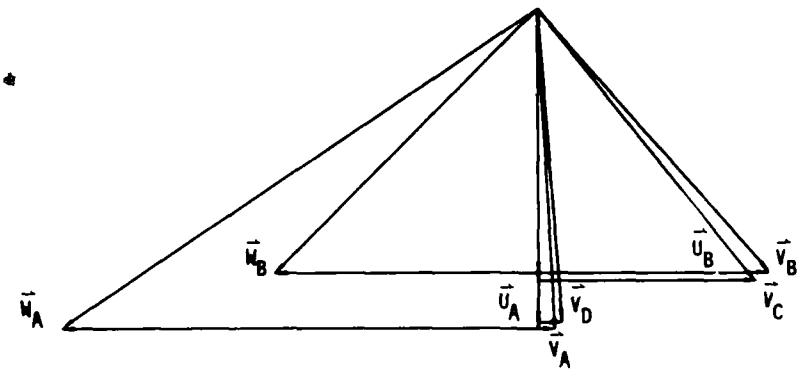

Figure 17.2.1b. Combined velocity diagram for flow along path line A-B-C-D in a compressor stage.

fer or work done on δm by the rotating blades, we must know the exit point B for δm as well as the entrance point A. Determination of this point by computation or by experiment is no trivial matter and is a part of the flow modeling problem.

In the total flow passing through a rotor, each fluid particle will experience an energy transfer governed by Eq. (17.2.1) for the points corresponding to A and B at which it enters and leaves the rotor. There is no reason why the work done on fluid passing through the rotor at the tip cannot differ from the work done on fluid particles crossing the rotor at other locations. In fact, there is no reason why subsequent particles entering the rotor at A should experience the same energy transfer rate as our original δm, because they may leave at points other than B or at different values of V_θ due to an unsteady or non-axisymmetric real flow.

In spite of our doubts about the real flow, to gain a simplified qualitative understanding of the performance of a compressor blade row or stage, let us assume that the flow A-B-C-D in the stage of Figure 17.2.1 is steady and representative of the entire flow across that stage. The airfoils encountered by the flow are represented by cascades of blades similar to those already shown in Figure 17.1.6. We will consider the rotor to have a constant angular velocity so that the rotor blade speed will be a constant at a given radius. We will vary the meridional velocity component, simulating a variation in the stage flow rate. The sequence of stage operating conditions is represented in Figure 17.2.2 by velocity diagrams and by a plot of total pressure rise against flow rate for three flows, 1, 2 and 3. For each of the three flows V_m is assumed to remain constant along A-B-C-D. Some features to note are as follows:

1. As the flow varies the angle of incidence on the rotor blade airfoils will vary, with the highest angle of incidence at the lowest flow. For excessive angles of incidence cascade airfoils will stall (unacceptable flow separation occurs). Compressor blade rows will also stall at extreme angles of attack, and, just as cascades do, they operate most effectively at moderate angles of attack and less effectively at high and low values. This was shown in Figure 17.1.9.

2. The energy transfer rate as measured by the change in V_θ across the rotor (U is nearly constant) increases with decreasing flow rate. This assumes, as Figure 17.1.9 showed, that the deviation angle for the rotor exit does not change a great deal until the losses begin to increase rapidly. The stage performance shows this effect as a higher stage total pressure rise at lower flows. However, good aerothermodynamic common sense tells us that there will be limits to this trend. If the airfoils stall, there will be large thermodynamic losses and the total pressure rise trend will be reversed.

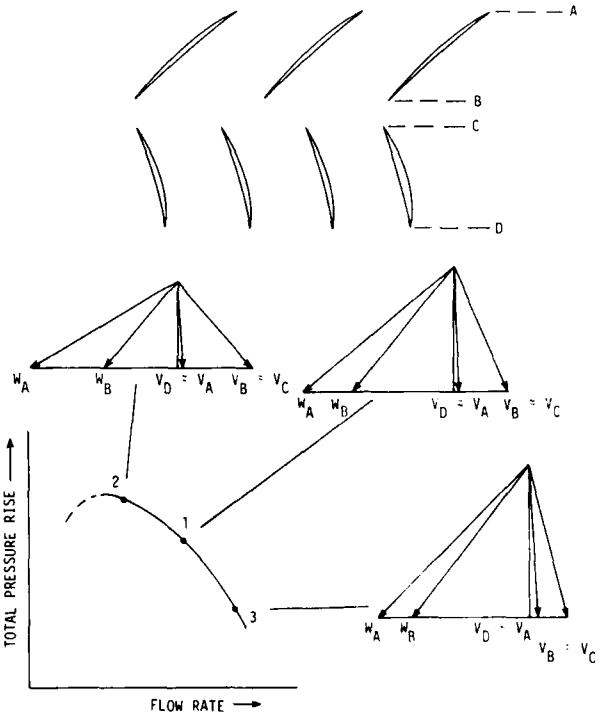

Figure 17.2.2. Trends in stage velocity diagrams and performance with changes in flow rate.

To aid in the interpretation of Figure 17.2.2, it might be helpful for readers to write some simple steady, one-dimensional energy, continuity and momentum equations for the flow A-B-C-D, considering the effect of work done by the blades on fluid total enthalpy and how this might, in turn, affect the total pressure changes from A to B and from C to D if the flow were isentropic, or if it were non-isentropic. Draw an enthalpy-entropy diagram to represent the processes.

In the axial-flow compressor, work is done on the fluid only through the action of the rotating blade rows, and this transfer of energy results in an increased level of fluid stagnation or total enthalpy. An increase of total pressure also results in each rotor row, with this increase dependent on the losses or irreversibility associated with the flow process as well as on the energy transfer. In the stator rows no energy is transferred as work and there can only be reduced values of total pressure because of irreversibility. Static pressure levels may increase or decrease in either rotor or stator row flows, but the predominant design intent is, naturally, to develop significant static pressure level increases in each stage. This aspect of blade row design is important and will receive substantial attention in later sections. It is important to observe that in constructing combined velocity diagrams like those of Figures 17.2.1b and 17.2.2 for a stage, we are beginning to think about path lines (such as A-B-C-D) as streamlines, and in layout of the blade rows as cascades, we are thinking in terms of axisymmetric stream surfaces. When this extension of terminology is made, the requirement for steady flow should be recalled and understood. Subsequent sections in this Chapter and many important referenced publications use the terms "streamline," "stream tube" and "stream surface." The assumption of a steady relative and/or absolute flow as a part of the development of a flow model is generally involved when these terms are used and it should be remembered in evaluating any analysis.

17.2.2 PERFORMANCE OF AXIAL-FLOW COMPRESSORS

17.2.2.1 DESIGN POINT FLOW FIELD CHARACTERISTICS

We will now turn to a qualitative discussion of the real flows in axial-flow compressors. At the same time we will develop further terminology and additional concepts useful in flow field analysis and in experimental research and development.

A compressor geometry is usually specified initially for operation at a design point. This means that it is configured so that it will develop a design value of exit to entrance pressure ratio with a predicted value of thermodynamic efficiency at a design value of shaft rotational speed, while a design value of mass flow rate exists in each stage. Flow rate may vary from one stage to the next bacause of by-pass arrangements or extraction of flow. All of the design requirements are associated with a particular working fluid and with design values of total pressure and total temperature distribution at the compressor section inlet. At the design point, the flow path dimensions are fixed and the blade rows are arranged so as to produce an ordered distribution of fluid velocities and properties through the compressor. In other words, the design point velocity diagrams are specified. However, the real design point flow field must be recognized as extremely complex. Every row following the first sees an entering flow which is unsteady. The flow is viscous, and in almost all modern compressors the flow is compressible with regions of both supersonic and subsonic local flow. Boundary layers develop on blade surfaces and on the hub and tip annulus walls. The annulus boundary layers are called end-wall boundary layers. Local regions of laminar, transitional and turbulent boundary layer flow may exist, accompanied by separation of flow from the blades or end walls. Both blade surface and end-wall boundary layers are generally three-dimensional in character. The flow throughout the annulus is in fact normally three-dimensional in nature. Secondary flows are generated, which have been widely discussed, but which are difficult to predict for design purposes. The real flow is by no means axisymmetric.

It must be recalled that all of the above complexities are associated with the design operating point. Away from the design point the configuration must operate in a flow field matching neither the annulus shape nor the angular settings of the stacked airfoils which form the blades.

17.2.2.2 EQUILIBRIUM PERFORMANCE MAPS

To demonstrate that axial-compressor flows are not beyond redemption in a real situation, Figure 17.2.3 shows what is called an equilibrium performance map for an eight-stage fixed-geometry compressor. The performance parameters used are discussed in Chapter 6. They are more or less traditional in nature. The experimental performance of the compressor was measured at several constant values of equivalent rotational speed (corrected to standard sea-level compressor inlet conditions).

At each rotational speed the mass flow rate was varied between two limits. The upper limit was close to the maximum obtainable at that speed. The lower limit was fixed by the existence of an aerodynamic instability common to all compressor types and known as surge. The character of surge is associated with the nature of the compressor geometry, and with aerodynamic and geometric boundary conditions imposed upon it by the installation arrangement and by the flow field (e.g., inlet geometry, downstream struts or flow control devices, inlet flow nonuniformity). Surge is manifested by large-scale flow instability, often with pulsating reversal of flow involving the entire unit. In an aircraft engine application, compressor surge may produce highly disturbing acoustic evidence (violent bangs). Individual surge points at the various rotational speeds define a surge line which is universally considered as a boundary for acceptable compressor operation in an aircraft engine.

Surge occurs only when one or more blade rows in the compressor are operating so that flow separation or stall occurs in the flow field. However, one or more blade rows may be stalled without the occurrence of surge. Stall in a blade row is unique in a number of respects, and especially in the fact that zones of flow separation propagate from blade to blade in the annulus, resulting in a phenomenon known as rotating stall.

Contours of constant adiabatic efficiency* are plotted in Figure 17.2.3. These contours show that the thermodynamic quality of compressor performance is reduced significantly when the compressor operates at flows and rotational speeds other than the design values.

The equilibrium performance map for a fixed geometry compressor is a classical example of the use of dimensional analysis and the principles of similitude. However, as plotted, it presents some possibility for misinterpretation. First, the plotting parameters $m\sqrt{\theta}/\delta$ and $N/\sqrt{\theta}$ have been inten-

*This efficiency is defined as

$$\eta_{ad} = \frac{(H_{20} - H_0)_{is}}{(H_{20} - H_0)_{act}}$$

and the subscripts 20 and 0 refer to compressor exit and inlet measuring stations, respectively.

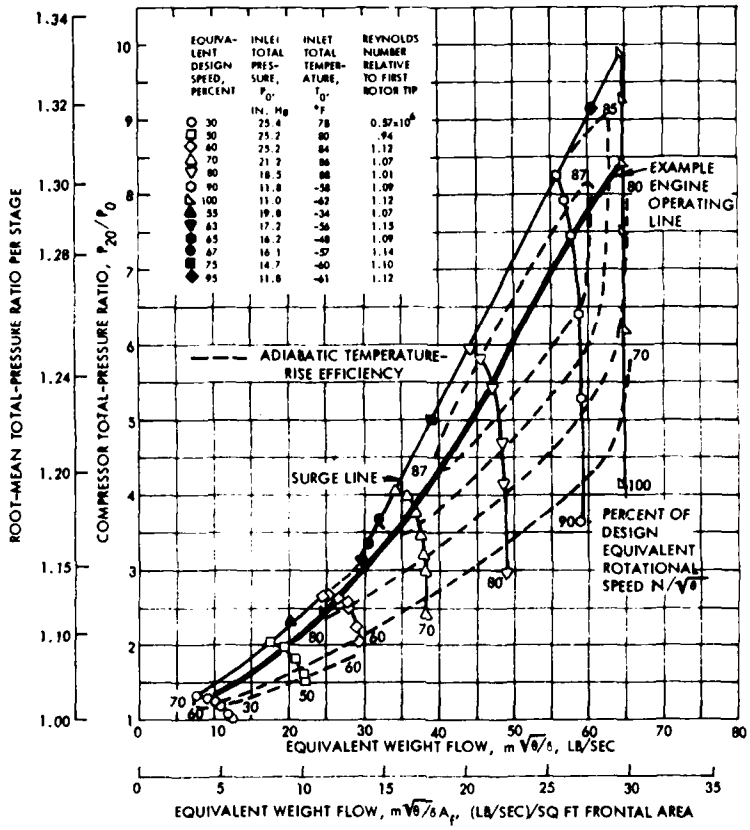

Figure 17.2.3. Equilibrium performance map for an eight-stage axial-flow compressor (Ref. 17.6).

tionally simplified to report performance of a single compressor geometry at entrance conditions corresponding to standard sea-level temperature and pressure. These modified parameters are not dimensionless. They are, respectively, proportional to Mach numbers associated with the throughflow components of velocity and with the velocities of points on the rotating blades.

Second, the map does not define the effect of Reynolds number changes or of entrance turbulence parameter changes on performance. These parameters are dynamic similarity variables and can have substantial effects on the map.

Third, the map is based on a single working fluid (air) and would be modified for other fluids with a different specific heat ratio (γ) or molecular weight. Finally, the map is based on uniform values of fluid properties and velocities at the compressor entrance. Distorted or unsteady entrance conditions change surge lines and other mapped performance values.

No one should forget that when relatively minor geometric changes in a compressor take place, for example when tip clearances change or when blade surfaces are abraded or damaged, the alterations in the compressor performance may not be minor in terms of the effect on engine specific fuel consumption or thrust.

17.2.3 VARIATIONS ON THE BASIC PERFORMANCE MAP

Figure 17.2.4 is a simplified performance map which shows two aspects of equilibrium compressor performance not included in Figure 17.2.3. First, the map shows the general effect on the compressor surge line caused by non-uniform inlet flow (inlet

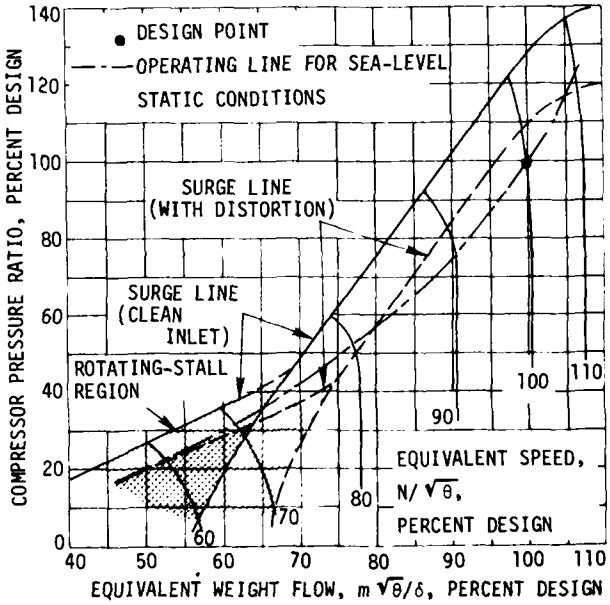

Figure 17.2.4. Example of axial-flow compressor map showing effect of inlet flow distortion and rotating stall region (Ref. 17.7).

distortion). The significance of this effect can be seen in terms of the estimated engine operating line superimposed on the map. Not shown are possible adverse effects of inlet distortion on the constant $N/\sqrt{\theta}$ lines and on compressor efficiency.

Figure 17.2.4 also defines regions at low rotational speeds in which rotating stall occurs in the entrance stages of the compressor. Although we have not yet looked into the background of rotating stall we will need to determine why any forms of stall occur in the entrance stages at low speeds and why rotating stall appears to be tolerated by aerodynamicists. We can at least see that measurements are made in the presence of rotating stall and this indicates some toleration level greater than that for surge.

Figures 17.2.3 and 17.2.4 do not show another class of performance phenomena which frequently creates problems in compressor development and operation. These are the aeromechanical or aeroelastic phenomena known as flutter. Figure 17.2.5 shows in schematic form some general regions on a compressor map in which specific varieties of flutter are encountered. Blade vibration amplitudes in flutter have frequently caused catastrophic compressor failures. We need to understand flutter so that mechanisms for its elimination can be applied where possible, or so that we can limit its occurrence to zones on the map where the compressor will not operate when installed in an engine.

each blade row are those that the designer specified. Although we do not know a great deal about the mechanics of this specification of the flow field, we do know about velocity diagrams and can understand that the designer must specify design point velocity diagrams at the entrance and exit to each blade row. Extending this line of reasoning, it is obvious that each stage must have a design point flow rate, pressure ratio and efficiency which in combination with the other stages will give the overall compressor design point performance. To describe this situation, we say that the stages are matched to function at certain operating points when the complete machine is at its design point. Studies related to changes in the operation of the individual stages in a multistage compressor are frequently called stage-matching studies.

Although individual stage performance could be plotted using the same parameter forms used for multistage maps, we generally find that these stage plots for matching purposes are plotted as shown in Figure 17.2.6. The parameters used (ϕ, ψ and η) are historically related to the parameters used for fans and blowers in which the flow is approximately at a constant density (incompressible flow). At this point we must note that a plot with single ψ-ϕ and η-ϕ curves such as in Figure 17.2.6 does not adequately represent Mach number or Reynolds number effects on stage performance.

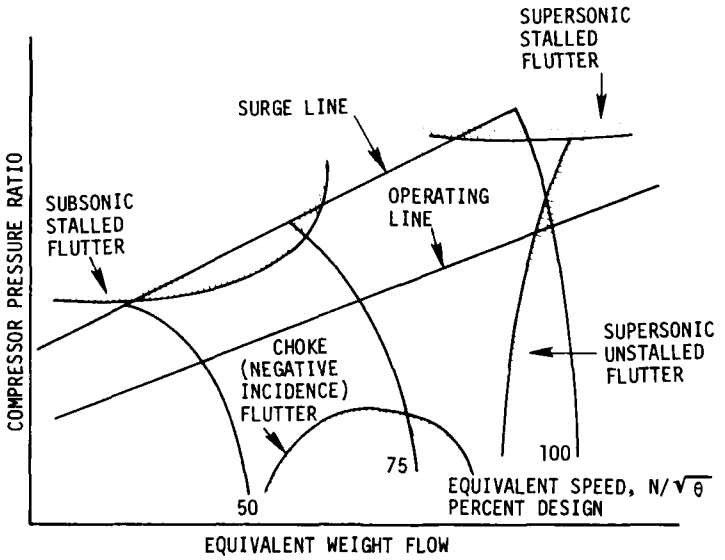

Figure 17.2.5. Schematic compressor map showing boundaries for four types of blade flutter (Ref. 17.8).

17.2.4 INDIVIDUAL STAGE CHARACTERISTICS

Recalling Figure 17.2.3 as a performance parameter plot showing some of the features of off-design operation for an eight-stage axial-flow compressor, we might examine briefly what the individual stages are doing in a multistage compressor as it runs at various locations on its overall map. Naturally we might expect or hope that when a multistage compressor operates at its design point flow rate and rotational speed, each stage would be running under favorable aerodynamic conditions. Ideally, this would mean that the velocity diagrams and properties of the fluid entering and leaving

For a fixed-geometry multistage compressor, a good qualitative understanding of off-design performance can be gained by considering the three stage plots of Figure 17.2.7. Remember that we are assuming that when confronted with a given value of ϕ, the entrance, "middle" and exit stages will each follow the curves shown, regardless of what other stages are doing. In other words, we are neglecting some elements of the interaction of stages. The three stages are assumed to be matched so as to operate at the points marked A on Figure 17.2.7 when the multistage compressor is at its design point. Under these conditions, in the fixed-geometry compressor each stage will develop exit levels of

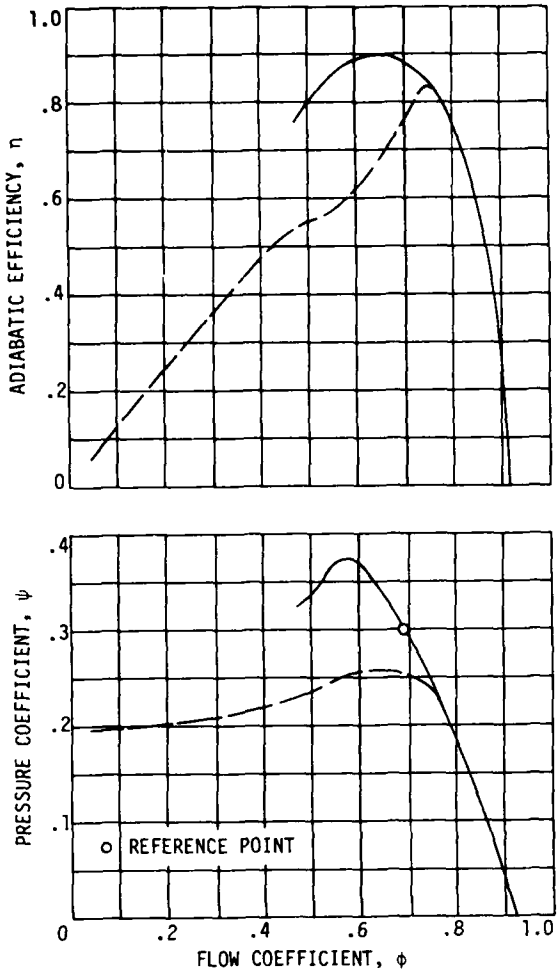

Figure 17.2.6. Example of assumed stage performance characteristics used in stage-matching study (Ref. 17.9).

pressure, density and velocity such that the downstream stage will be at its point A.

Now suppose that the compressor operates at a point B which is at a rotational speed substantially lower than the design value. It is evident that at any value of ϕ the pressure increase across any stage will be reduced because U^2 is reduced in the ψ parameter. This in turn means that no stage can develop its design density rise. However, the annulus area variation through the compressor is based on the design point rate of fluid density rise. The result will be to force the level of through-flow velocity up in the exit stages so that ϕ will be higher than design values, with a tendency toward a limiting maximum at low rotational speeds. The entrance stages will in turn be forced to operate at lower than design ϕ, with a tendency toward unstable (stalled) operation at low speeds. This is why the performance map of Figure 17.2.4 showed a rotating stall zone at low $N/\sqrt{\theta}$ values. The trends will be reversed at rotational speeds greater than design (point C, Figure 17.2.7), with the exit stages moving toward stall and the entrance stages moving toward a maximum limiting flow coefficient ϕ. This is one reason why Figure 17.2.5 shows a region of supersonic stalled flutter at high rotational speeds.

17.3 AERODYNAMIC DESIGN OBJECTIVES FOR AXIAL-FLOW COMPRESSOR UNITS

As an introduction to a discussion of design systems for axial-flow compressors, we should state some criteria for a good design. To do this in a logical way, we might look again at the equilibrium performance characteristics shown in Figure 17.2.3. The first goal of a design system should be to generate a compressor geometry which will produce the design point total pressure ratio when the design point mass flow rate exists in each stage of the compressor. These design point values are developed in the course of selection of the best propulsion system cycle parameters for the aircraft application. Because each compressor section is driven by a turbine component, the rotational speed at the compressor design point must be consistent with the aerodynamic and aeromechanical design requirements of the turbine. Design point pressure ratio, flow rate and rotational speed must be associated with an acceptable if not superior level of compressor thermodynamic efficiency and with adequate surge margin. Surge margin is a measure of the location of any operating point with respect to the surge line at a given rotational speed and should be sufficient so that no engine transient will force the compressor into surge.

However, while design point performance is a primary consideration, Figure 17.2.3 and earlier chapters remind us that the design operating point for the compressor is only reached after starting and accelerating the complete engine, and that propulsion system operation may call for extended periods of performance at locations on the equilibrium performance map which are substantially different from the design point. Furthermore, transient system operation may create additional deviation from normal compressor operating points. In terms of Figure 17.2.3, engine operation may be expected to require the compressor to run within a band of flows and pressure ratios at any rotational speed. In fact, the performance map itself will be altered by changes in parameters such as tip clearance and compressor entrance flow distribution. The compressor design process must therefore develop a compressor geometry (and possible variable compressor geometry) which demonstrates the following characteristics:

1. stable aerodynamic and aeromechanical operation, including sufficient surge margin and no excessive blade or disk vibrations for all potential operating conditions in the system installation;
2. acceptable thermodynamic efficiency for all expected operating conditions;
3. acceptable noise generation characteristics.

Subject to these constraints the compressor configuration should be designed for

4. the maximum possible mass flow rate per unit frontal area;
5. the highest possible average pressure ratio per stage; and
6. minimum values of axial stage length and number of blades specified for each row.*

*Objectives 4, 5 and 6 may not apply in a few design cases. If the compressor is very small in size, manufacturing limits on geometry (e.g. blade dimensions) may force the design of a compressor larger than the minimum that aerodynamic criteria alone would allow.

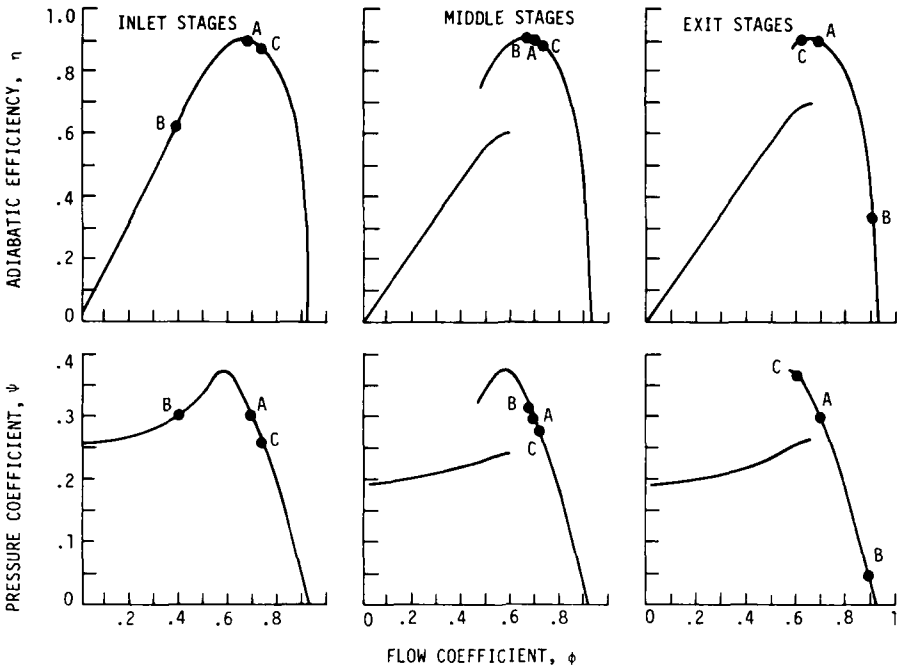

Figure 17.2.7. Trends in stage performance for axial-flow compressor operating at off-design conditions (Ref. 17.10).

These characteristics, of course, lead to the minimization of compressor unit weight and cost. Axial-flow compressor configurations for aircraft propulsion systems have demonstrated good and improving characteristics measured against the six objectives listed, but they have remained very expensive, primarily because of the complex, sometimes variable geometry required to realize the best possible performance.

17.4 ELEMENTS OF A COMPRESSOR DESIGN SYSTEM--TECHNICAL REQUIREMENTS

Consideration of the required elements of a compressor design system leads directly to the definition of more detailed requirements for flow field models and for aeromechanical models of the blading and other flow path components. Based on the objectives listed in Sec. 17.3 we can see that at a minimum the design system must include the following.

1. A procedure for determining potentially satisfactory flow path geometries capable of stable and efficient operation at the design flow rate and at a rotational speed acceptable to the turbine and mechanical system designers, with the procedure sufficiently quantitative to permit
   - specification of annulus dimensions throughout the compressor
   - selection of blade row geometric parameters such that design point velocity diagrams and fluid property distributions are realized at acceptable efficiencies (low blade row thermodynamic losses).
2. Procedures for predicting the flow field throughout the compressor at the design point, with emphasis on details of the flow within the blade rows, so that forces acting on the blades may be computed and so that potential aerodynamic problem areas may be located (e.g. blade sections with excessive adverse pressure gradients).
3. Methods for predicting compressor performance at off-design flows and rotational speeds and with non-design entrance fluid properties and flow distributions.
4. Stress analysis techniques to verify the stress-strain characteristics of blade row geometries, disks and shrouds.
5. Aeroelastic analysis methods to ensure that blades, disks and shrouds will not be subject to unexpected flutter or other vibrational effects at potential compressor operating points.

In subsequent sections we will refer to these parts of the complete design system by the following terminology:

1. preliminary design
   - hub-to-tip passage design
   - blade row geometry selection
2. design analysis
3. performance prediction
4. stress analysis
5. aeroelastic analysis

Figure 17.4.1 is a possible design system flow diagram which indicates an order of procedure and most probable iterations. However, compressor design is likely to remain in some ways an artistic endeavor for many years to come, and as a result it will be highly "specialist dependent" with "local philosophy" in each competing organization. In terms of the flow diagram, this artistic specialist activity enters the picture mainly at the preliminary design level, where past experience in compressor development--including memories of performance maps and of mechanical, fabrication and aeroelastic problems--has a large influence on the choices which produce candidate geometries for further study.

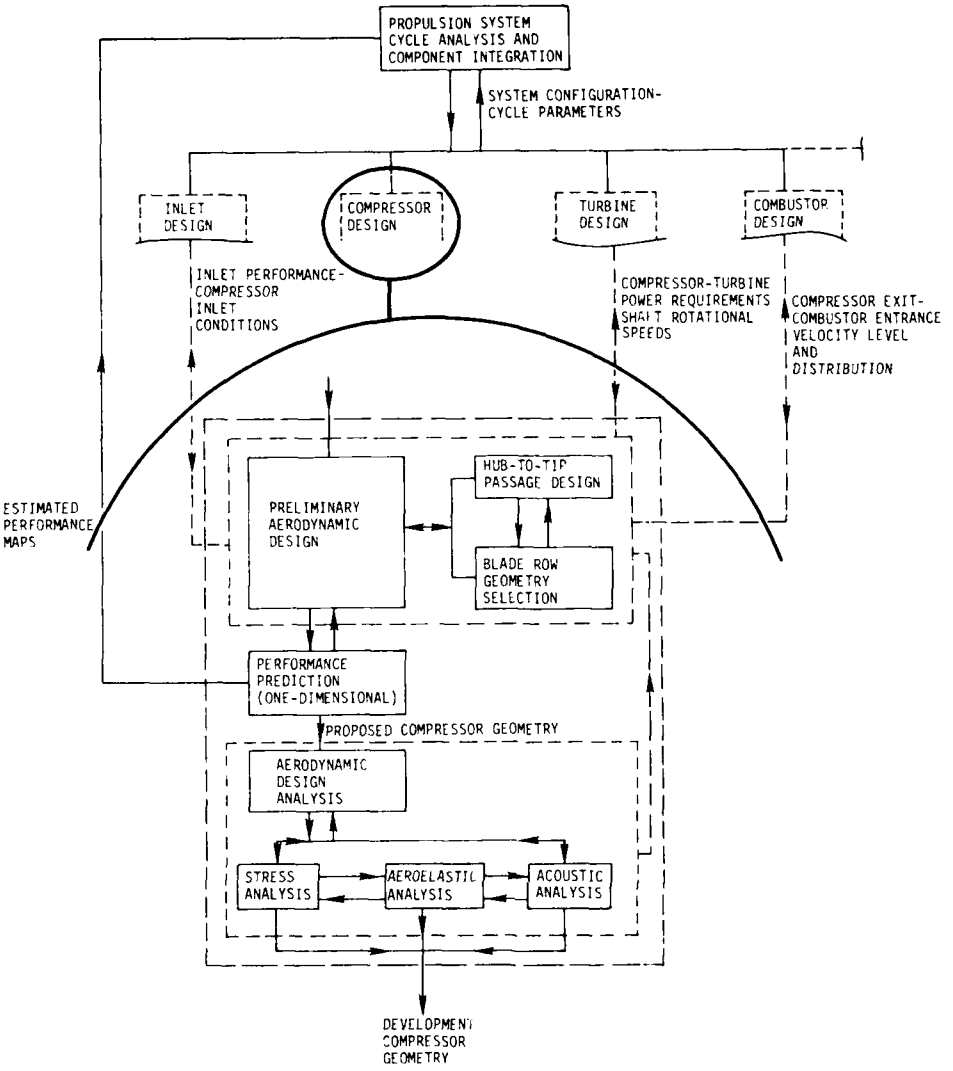

Figure 17.4.1. Compressor design system flow chart.

17.5 CONTENT OF CURRENT AND DEVELOPING DESIGN SYSTEMS--THE TECHNOLOGY BASE

The previous sections reviewed the objectives and component parts of a design system. Our next step will be to outline in more detail the strategy followed in setting up a series of computational models for the flow as required by the various phases of design. In this process the significant aerodynamic and aeromechanical problems and limits encountered in axial-flow compressor design will be described.

The design and development process is not just a matter of deriving a set of equations and a technique for solution. It requires access to a significant amount and variety of experimental data in correlated form, which will aid in the estimation of 1) the flow turning and loss characteristics of the multiple cascades of airfoils encountered in the various blade rows, 2) the growth of boundary layers on the flow passage walls, and 3) the proximity of operating conditions to possible regions of aerodynamic and aeromechanical trouble. In most cases it demands constant access to experimental installations such as plane or annular cascade tunnels, single-stage and stage group test units, and model or full-scale multistage compressor experimental facilities. While the experimental support for a design task was intentionally omitted from the discussion of the requirements for a design system, the nature of the necessary experimental base will be referred to frequently in this section.

An overwhelming array of background literature exists on the development and evaluation of flow models and associated computational methods for turbomachinery. There is no possibility of condensing the content of the literature in the present chapter. There is a possibility that we can briefly describe and compare the important technical features of the most-used models and methods.

17.5.1 GENERAL COMMENTS ON FLOW MODELS

17.5.1.1. FLOW FIELD MODELS--STEADY AND ADIABATIC FLOW, CONTINUOUS FLUID MEDIUM

In axial-flow compressor design and analysis the working fluid is almost invariably and without discussion assumed to behave as a continuous medium,

allowing us to use as sources for equations the standard texts on the subject of fluid mechanics. Existing flow field models for design and design analysis cases almost always are based on a line of reasoning which views the flow relative to each blade row as steady and adiabatic. While this assumption contradicts obvious physical facts, it has been essential in order to reach quantitative solutions, and fortunately many of these solutions have been quantitatively acceptable. Only a few design analysis studies have approached the unsteady flow model problem in a realistic way, and even fewer have seriously attacked the computational aspect of these unsteady flow models. In the following subsection we will deal almost exclusively with design system components using adiabatic, steady or time-average relative flow field assumptions.

17.5.1.2 STREAMLINES, STREAM SURFACES, STREAM TUBES

The process of development of mathematical models for the flow field in axial-flow turbomachines is often based on the concepts of streamlines, stream surfaces and/or stream tubes in the flow path. These lines, surfaces or tubes have been generally handled aerodynamically and mathematically, as if they were the paths of fluid particles or conduits through which specific fluid particles could be followed. In order for streamlines and path lines to coincide in a flow, the flow must be steady. Although we often make additional restrictive assumptions about stream lines and surfaces, the steady flow assumption is the most common.

There has been no lack of recognition in the past that the streamlines and surfaces in an axial-flow compressor or turbine would be geometrically complex even if the steady flow assumption is made. In relatively recent times the most widely-referenced recognition of this complexity is found in the analyses of C.-H. Wu. His work brought the idea of S_1 and S_2 stream surfaces into the working vocabulary of the compressor specialist. Wu formulated equations for relative flows on families of hub-to-tip (S_2) surfaces between and within blade rows and for the relative flows on families of periodic blade-to-blade (S_1) surfaces both between and inside blade rows. These intersecting families of surfaces, shown schematically in Figure 17.5.1, were proposed as a means for computation of the turbomachine flow field by an iterative process.

S_1 and S_2 surfaces have been discussed in many publications on flow modeling and in many reports and papers in which quantitative results of flow field computations have been presented. Readers, however, should be very cautious in their study of any of these analyses because the vast majority do not determine or compute on true S_1 or S_2 surfaces but only on approximations to these surfaces.

In the case of blade-to-blade (S_1) flows, frequent use is made of the idea of assumed axisymmetric stream surfaces or stream tubes. These lead to simplified but not simple equation formulation and add credibility to the thinking which justifies the use of "circumferentially-averaged" velocities and fluid properties in hub-to-tip flow model equations.

For hub-to-tip computations, the flow (when computed inside blade rows) is often handled as if it took place on a "mean stream surface" between

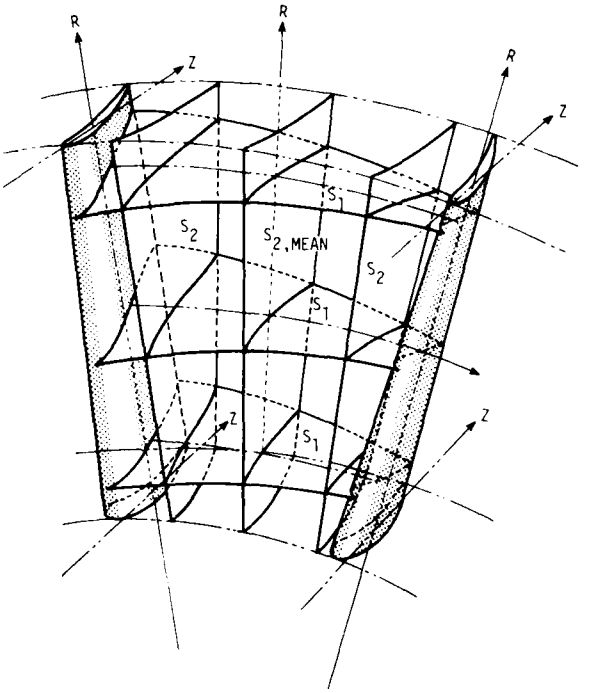

Figure 17.5.1. S_1 and S_2 surfaces in blade-to-blade flow passage (Ref. 17.11).

blades. When used, this mean surface is supposed to be representative of the family of S_2 surfaces inside the channel formed by adjacent blades.

Based on the preceding discussion, one should examine every proposed compressor flow analysis to reveal whether it is based on axisymmetric or true S_1 equation formulation, and on whether it works with a true S_2 surface, a mean surface or in a meridional plane. In the end we should remember that none of the above is more than a simulation of the real flow because of the equation forms assumed. In almost every case where the hub-to-tip and blade-to-blade solution surface idea is utilized (whether or not the surfaces are S_2 and S_1 stream surfaces), the result is what should be called a quasi-three-dimensional or pseudo-three-dimensional flow field method.

17.5.1.3 EFFECTS OF VISCOSITY AND COMPRESSIBILITY

The effects produced by fluid viscosity in real compressor flow fields are included in the flow models used for preliminary design and design analysis in a variety of ways. Because these real fluid effects are the ultimate source of irreversibility in the compression process they must be simulated or modeled in some fashion in the flow field computation process. It is essential in preliminary design to set quantitative limits on aerodynamic parameters which will guarantee that viscous and compressibility losses will not be excessive, and it is necessary in design analysis to be able to estimate these effects as a function of aerodynamic parameters associated with the flow field.

The sources of losses or thermodynamic irreversibility effects observed in compressor configurations are not different than those found in any other viscous, compressible internal flow. As already noted, three-dimensional boundary layers

form on blade surfaces and on the hub and tip and wall. Complex shear flows occur in the corners (where blades meet end walls) and at the tip radial clearances (between rotors and stators and the end wall). Wakes develop downstream of blade row trailing edges, and vorticity is generated because of circulation gradients along the blade span and unsteady flow at the entrance to most blade rows.

All of these effects of viscosity lead to continuous and cumulative increases in entropy along the paths followed by fluid particles. If we assume the existence of streamlines and stream surfaces, we should allow for entropy increases in the flow direction in a consistent way.

In most contemporary compressors absolute or relative velocities are sufficiently high so that regions of relative sonic flow occur on the surfaces of blades. In many contemporary compressors the velocities relative to rotor and/or stator blade rows are supersonic along at least a portion of the blade span. These configurations are called transonic compressors. In some compressors velocities relative to the rotor and/or stator blade rows have been supersonic along the entire span of the blade at entrance and/or exit. These configurations are called supersonic compressors. Shock wave patterns developed in all of these cases are complex in shape and are sources of losses, as are all shock waves. At the same time the shock wave field interacts with boundary layers and influences their development. Once again the situation calls for consistent accounting for entropy increase in the direction of flow.

When we study methods for modeling the flow field in a compressor flow path, we will often see a strategy for formulation which is to some extent controversial. The level of controversy is reduced somewhat by the fact that the strategy seems to work. In all real flows there are local shear stresses acting on all individual fluid particles. These shear stresses are recognized and modeled, for example, in the Navier-Stokes equations of motion. As we follow an individual particle along its path, from a blade row entrance to the exit, the shear stresses acting on it at any particular point may be quite small compared to the other influences on its motion. However, if we look at the cumulative thermodynamic effect of shear stresses along a path line between the entrance and exit of a blade row, we can measure a significant irreversibility. Readers will see evidence of a double-standard approach when viscous terms are dropped from the equation of motion, but the terms are effectively reintroduced by using entropy gradients in flows as a means of accounting for an accumulating irreversibility along path lines.

17.5.1.4 SPECIFIC EFFECTS OF BLADE ROW AND PASSAGE GEOMETRY ON THE FLOW FIELD

Another frequently misunderstood or misrepresented influence on design and design analysis flow models for turbomachines are the force terms in the equations of motion. In a typical textbook set of component equations of motion for cylindrical coordinates, x, r, and θ, one might find

$$F_r - \frac{1}{\rho}\frac{\partial p}{\partial r} = \frac{\partial V_r}{\partial t} + V_r\frac{\partial V_r}{\partial r} + \frac{V_\theta}{r}\frac{\partial V_r}{\partial \theta} + V_x\frac{\partial V_r}{\partial x} - \frac{V_\theta^2}{r} \qquad (17.5.1)$$

$$F_\theta - \frac{1}{\rho r}\frac{\partial p}{\partial \theta} = \frac{\partial V_\theta}{\partial t} + V_r\frac{\partial V_\theta}{\partial r} + \frac{V_\theta}{r}\frac{\partial V_\theta}{\partial \theta} + V_x\frac{\partial V_\theta}{\partial x} + \frac{V_r V_\theta}{r} \qquad (17.5.2)$$

$$F_x - \frac{1}{\rho}\frac{\partial p}{\partial x} = \frac{\partial V_x}{\partial t} + V_r\frac{\partial V_x}{\partial r} + \frac{V_\theta}{r}\frac{\partial V_x}{\partial \theta} + V_x\frac{\partial V_x}{\partial x} \qquad (17.5.3)$$

These equations are usually considered in fluid mechanics to model the flow of an inviscid, compressible and continuous fluid medium. The $F_{x,r,\theta}$ terms are body force components; for example, those due to the influence of a gravitational force field. In turbomachine flow models, however, an F-component term may be used to

1. simulate the viscous or "dissipation" effects in the flow field, and
2. represent a distributed force field in the flow, which accounts for the effects on the flow due to blade forces (because blades have camber and lean or dihedral there can be components in x, r and θ directions).

For hub-to-tip surface solutions inside blade rows the computation model should account for physical blockage of the flow path by the blades as well as for effective blockage by boundary layers on the blade surfaces. At the blade ends and on the passage walls between rows, effective blockage due to end-wall and corner flows should be recognized. The mechanism for accounting for effective blockage will vary with the nature of the flow model.

17.5.2 EQUATIONS

Upon the initial assumption of a continuous fluid medium, we can recognize the existence of a number of mathematical formulations of physical laws that may be the basis for models of the real flow in turbomachines, and specifically in axial-flow compressors. The physical laws are

1. conservation of mass,
2. conservation of linear and angular momentum,
3. first law of thermodynamics,
4. second law of thermodynamics.

These are supplemented for any working fluid by

5. equations of state,
6. relationships between thermodynamic properties of a pure substance,
7. relationships between the flow field velocities and velocity gradients and the shear stresses in the fluid.

Table 17.5.1 gives some equations based on these laws and other relationships. In the case of some of the differential equations, component equations are written for a cylindrical coordinate system. Table 17.5.1 will serve as a reference for subsequent sections.

The second law of thermodynamics, of course, enters into the parameters which measure irreversibility or losses in the flow field and, since in classical thermodynamics the property entropy is derived as a consequence of the second law, the law enters into the formulation of the Gibbs relation Eq. (17.5.11).

AD-A152 757 COST REDUCTION IN VERTICALLY RELATED INDUSTRIES: 6/9
INTEGRATION VERSUS NONLINEAR PRICING(U) RAND CORP SANTA
MONICA CA H C QUIRMBACH MAY 83 RAND/P-6839

UNCLASSIFIED F/G 5/1 NL

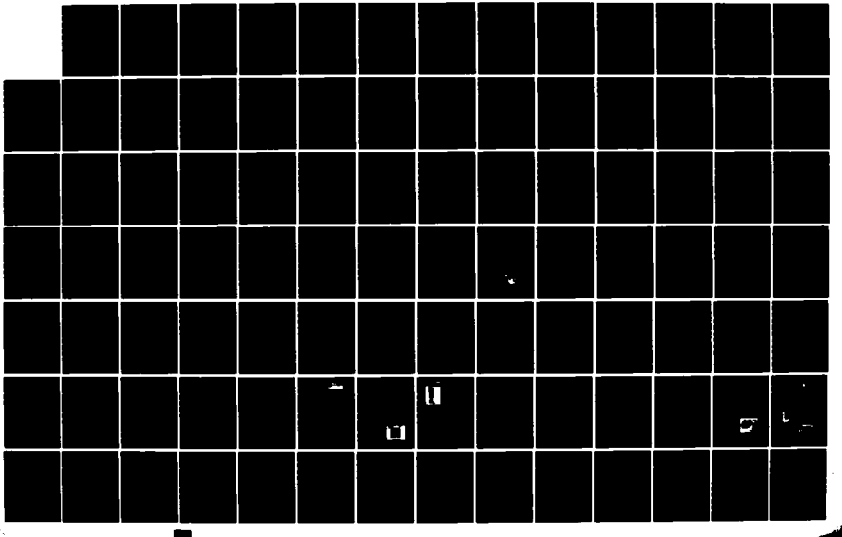

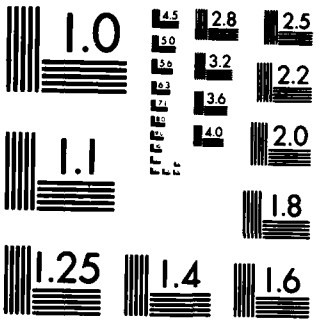

MICROCOPY RESOLUTION TEST CHART
NATIONAL BUREAU OF STANDARDS-1963-A

Table 17.5.1. Reference Equations

From the law of conservation of momentum for steady flow in an inertial, cylindrical coordinate system, local shear stresses neglected. At any point in flow field

$$F_r - \frac{1}{\rho}\frac{\partial p}{\partial r} = V_r\frac{\partial V_r}{\partial r} + \frac{V_\theta}{r}\frac{\partial V_r}{\partial \theta} + V_x\frac{\partial V_r}{\partial x} - \frac{V_\theta^2}{r}$$

$$F_\theta - \frac{1}{\rho r}\frac{\partial p}{\partial \theta} = V_r\frac{\partial V_\theta}{\partial r} + \frac{V_\theta}{r}\frac{\partial V_\theta}{\partial \theta} + V_x\frac{\partial V_\theta}{\partial x} + \frac{V_r V_\theta}{r}$$

$$F_x - \frac{1}{\rho}\frac{\partial p}{\partial x} = V_r\frac{\partial V_x}{\partial r} + \frac{V_\theta}{r}\frac{\partial V_x}{\partial \theta} + V_x\frac{\partial V_x}{\partial x} \qquad (17.5.4)$$

From the law of conservation of momentum for steady flow measured relative to a cylindrical coordinate system rotating at angular velocity ω about x axis: At any point in flow field

$$T\frac{\partial s}{\partial r} - \frac{\partial I}{\partial r} = -\frac{W_\theta}{r}\left[\frac{\partial}{\partial r}(rV_\theta) - \frac{\partial W_r}{\partial \theta}\right] + W_x\left[\frac{\partial W_r}{\partial x} - \frac{\partial W_x}{\partial r}\right]$$

$$\frac{T}{r}\frac{\partial s}{\partial \theta} - \frac{1}{r}\frac{\partial I}{\partial \theta} = \frac{W_r}{r}\left[\frac{\partial}{\partial r}(rV_\theta) - \frac{\partial W_r}{\partial \theta}\right] - W_x\left[\frac{1}{r}\frac{\partial W_x}{\partial \theta} - \frac{\partial W_\theta}{\partial x}\right]$$

$$T\frac{\partial s}{\partial x} - \frac{\partial I}{\partial x} = -W_r\left[\frac{\partial W_r}{\partial x} - \frac{\partial W_x}{\partial r}\right] + W_\theta\left[\frac{1}{r}\frac{\partial W_x}{\partial \theta} - \frac{\partial W_\theta}{\partial x}\right]$$

$$I = H - \omega(rV_\theta) = h + \frac{\overline{V}^2}{2} - \omega(rV_\theta) \qquad (17.5.5)$$

From the law of conservation of mass for steady flow in a cylindrical coordinate system: At any point in flow field

$$\frac{1}{r}\frac{\partial}{\partial r}(r\rho V_r) + \frac{1}{r}\frac{\partial}{\partial \theta}(\rho V_\theta) + \frac{\partial}{\partial x}(\rho V_x) = 0 \qquad (17.5.6)$$

or

$$\frac{1}{r}\frac{\partial}{\partial r}(r\rho W_r) + \frac{1}{r}\frac{\partial}{\partial \theta}(\rho W_\theta) + \frac{\partial}{\partial x}(\rho W_x) = 0 \qquad (17.5.7)$$

From the law of conservation of mass for a fixed control volume and steady flow:

$$\oiint_{cs}(\rho\overline{V}\cdot d\overline{A}) = 0 \qquad (17.5.8)$$

for region A_1 of control surface

$$m = \oiint_{A_1}(\rho\overline{V}\cdot d\overline{A})$$

From the first law of thermodynamics for a fixed control volume and steady flow:

$$\frac{\delta q}{dt} - \frac{\delta W_{shaft}}{dt} - \frac{\delta W_{shear}}{dt} = \oiint_{cs}\left(h + gz + \frac{\overline{V}^2}{2}\right)(\rho\overline{V}\cdot d\overline{A}) \qquad (17.5.9)$$

From the law of conservation of angular momentum for a fixed control volume and steady flow, component equation for x-axis

$$T_s + T_B = \oiint_{cs}(rV_\theta)(\rho\overline{V}\cdot d\overline{A}) \qquad (17.5.10)$$

T_S = sum of moments about x-axis of all surface forces acting on contents of control volume

T_B = sum of moments about x-axis of all body forces acting on contents of control volume

For a pure substance

$$dh = \frac{dp}{\rho} + Tds \qquad (17.5.11)$$

Equations of state for fluid media are available in the usual mathematical or tabular forms. The relationships between velocities, velocity gradients and fluid shear stresses are subjects which cannot be covered here, but which are discussed in Chapters 3, 4 and 16.

17.5.3 PERFORMANCE LIMITING FLOW PHENOMENA--DESIGN LIMIT PARAMETERS

Design limit parameters provide a quantitative basis for predicting the conditions under which unacceptable blade row or overall performance will occur. They are needed in preliminary design as arbitrary stop signs in setting up a geometry-flow field combination, and they are used in design analysis to estimate the degree of risk associated with a particular flow pattern. In terms of design system objectives we would like to establish the following:

1. whether any form of aerodynamic or aeromechanical instability will occur anywhere in the performance range of the compressor as the result of a design decision, and parameters which will permit estimation of the margin of safety between any operating point and the nearest unstable condition,
2. values of parameters influencing mass flow per unit frontal area that may be utilized in design to realize high specific mass flow rates without adversely affecting other elements of compressor performance,
3. quantitative values of parameters which will determine the maximum stage pressure ratios which can be realized at specified efficiency levels, and which will allow us to estimate the thermodynamic irreversibility associated with specified combinations of blade row geometry and flow field conditions.

These are not three unrelated problems. For example, a decision made in design which will lead to high stage pressure ratio at acceptable efficiency for a given stage may set up flow conditions which will cause that stage to have an inadequate stall (instability) margin.

Historically, limiting aerodynamic parameters in axial-flow compressors have been of four fundamental types.

1. Limits related to aerodynamic "loading," especially to the generation of unacceptable losses or flow instability by possible blade row geometries, and to the prediction of proximity of an operating condition to regions of high loss or instability.
2. Limits related to the generation of high losses or flow instability as the result of the effects of compressibility.
3. Parameters related to the limiting of flow rate through a flow path element as the result of compressibility.
4. Limits related to the aeroelastic aspects of compressor blade rows, including prediction of the occurrence of the various flutter regimes.

The first three of these will be briefly dealt with in the following subsections. The aeroelastic limits are considered in Chapter 22.

17.5.3.1 AERODYNAMIC DESIGN LIMITS RELATED TO EXCESSIVE VELOCITY DIFFUSION RATES

The velocity diagrams discussed earlier in this Chapter were used to aid in understanding the functions of blade rows in typical compressor configurations and to point out that some familiar parameters and characteristics of the flow in isolated airfoil technology are encountered again in the technology of airfoil cascades. We also noted that there were some fundamental differences in these technologies. One of these differences is that in the cascade arrangements utilized in compressors and turbines there is generally a change in static pressure level between the flow field upstream and the flow field downstream of the cascade. In compressors we expect to find rows in which static pressure rises. This is evident in typical velocity diagrams for axial flow compressors (e.g. Figure 17.2.1) where we see that the blade rows act as diffusers of the relative fluid velocity. Diffusers are flow passages in which the relative velocity decreases from entrance to exit while the static pressure level increases. Boundary layers in excessive adverse (positive) pressure gradients separate. This is the cause of stalling of isolated airfoils and of stalling and flow instability in airfoil cascades (as well as other diffusers). It might be well to recall here that in fluid mechanics there are both subsonic diffusers and supersonic diffusers. Both have the same function, but the geometries are significantly different. Both subsonic and supersonic diffusing situations are encountered in compressor blade rows.

A second look at the velocity diagram of Figure 17.2.1 shows us that some of the diffusion of relative flow takes place in these cascades because the flow is deflected (turned). Velocity diffusion is increased if we turn the flow more (while the axial velocity remains constant) or if we reduce the axial velocity across a blade row (with a constant turning).

There should now be no question about the fact that higher stage pressure ratios will be related to increased diffusion rates across blade rows and that there are quantitative limits on diffusion rates which in turn limit stage pressure ratios. What are these quantitative limits? A lot of suggestions have been made. Some are simple and direct. One used frequently is $p_2 - P_1/P_1 - P_1$, the static pressure rise coefficient. Another is the exit/entrance relative velocity ratio $(W_2/W_1)_{rotor}$ or $(V_2/V_1)_{stator}$. A slightly less direct parameter which has been widely used is the parameter D. This parameter was originally developed by Seymour Lieblein as a measure of the diffusion of velocity on the suction surfaces of cascades of blade sections in two-dimensional flow. The equation derived was

$$D = 1 - \frac{\bar{V}_2}{\bar{V}_1} + \frac{V_{\theta 1} - V_{\theta 2}}{2\sigma\bar{V}_1} \qquad (17.5.12)$$

Initial application to rotating blade rows used two defining equations

$$D = 1 - \frac{\bar{W}_2}{\bar{W}_1} + \frac{V_{\theta 2} - V_{\theta 1}}{2\sigma\bar{W}_1} \qquad (17.5.13)$$

or

$$D = 1 - \frac{\bar{W}_2}{\bar{W}_1} + \frac{W_{\theta 1} - W_{\theta 2}}{2\sigma\bar{W}_1} \qquad (17.5.14)$$

which are not equivalent unless $U_1 = U_2$.

Subsequently, for cases in which compressor blade rows were involved, a version allowing for flow on stream surfaces which change radius between row entrance and exit was developed.

$$D = 1 - \frac{\bar{W}_2}{\bar{W}_1} \pm \frac{r_1V_{\theta 1} - r_2V_{\theta 2}}{(r_1 + r_2)\sigma\bar{W}_1} \qquad \begin{matrix} + = \text{stators} \\ - = \text{rotors} \end{matrix} \qquad (17.5.15)$$

In all of these definitions the final term is a measure of blade row circulation.

The parameter D was intended to provide a quantitative limit for diffusion in cascades operating near the minimum-loss angle of incidence. It could be calculated using flow velocities readily available from design point velocity diagrams. Through the years, its application has evolved by extrapolative thinking to include situations in which it is not correct. Alternative parameters have been suggested but the final answer is not in hand and the ultimate diffusion limit remains a subject for research, just as there are not genuinely definitive design limits available for most other diffuser cases.

All of the diffusion or blade-loading limit parameters mentioned are useless without numerical values which define regimes of acceptable and unacceptable blade row performance. Such values are established by correlation of experimental blade row performance data from plane cascades or from rotor and stator blade rows in compressors. Such correlations have been published for cascades and blade rows by the National Aeronautics and Space Administration (NASA), such as Figures 17.5.2 and 17.5.3, and by others for specific compressor test data sets. Generally the correlations allow estimation of an expected profile total pressure loss coefficient for blade rows at incidence angles in the low-loss region. The loss parameters used are in forms such as $\bar{\omega}_{cos}\beta_2/2\sigma$ or θ^*/c. Although the parameter D has probably been the most widely accepted blade-loading parameter for preliminary design, others have been proposed to replace or supplement it in design analysis. These include a second Lieblein parameter, known as D_{eq}, which has been utilized in both design analysis and off-design point performance prediction.

In the regions near the hub and tip end walls, some design groups prefer to use the static pressure rise coefficient $(p_2 - p_1)/(P_1 - p_1)$ as a limit. This parameter is considered to be a useful criterion in the prediction of the onset of "wall stall."

17.5.3.2 INFLUENCE OF MACH NUMBER LEVELS ON AXIAL-FLOW COMPRESSOR DESIGN

For many years there have been continuous trends toward higher levels of Mach number in axial-flow compressor blade rows. Figure 17.5.4 shows one reason why this trend exists. The figure demonstrates how flow rate per unit frontal area (specific flow rate) for a compressor stage varies with

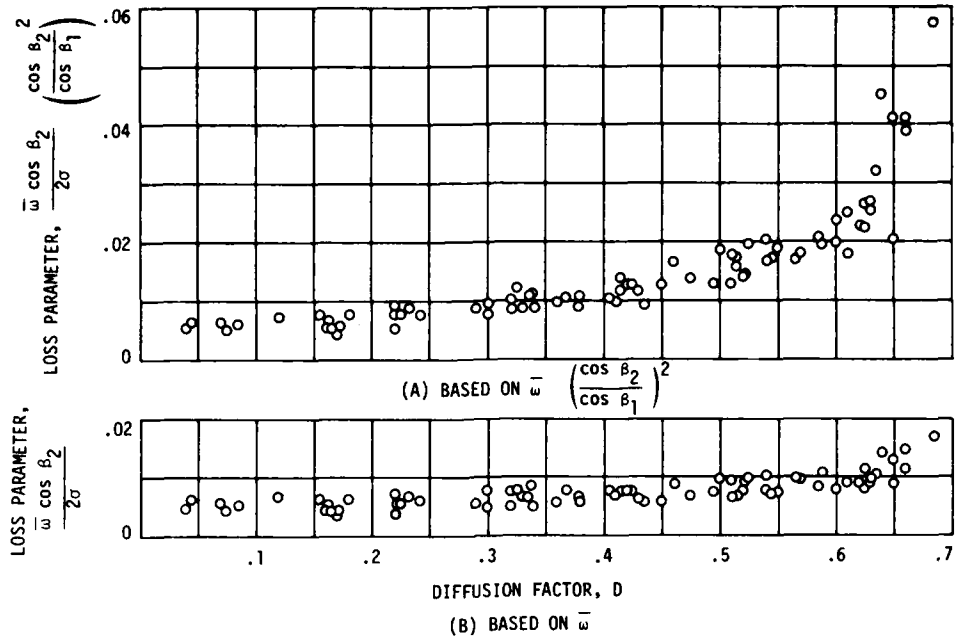

Figure 17.5.2. Variation of loss parameters with diffusion factor at reference minimum-loss incidence angle computed from low-speed-cascade tests of NACA 65-(A_{10})10 cascade blades (Ref. 17.12).

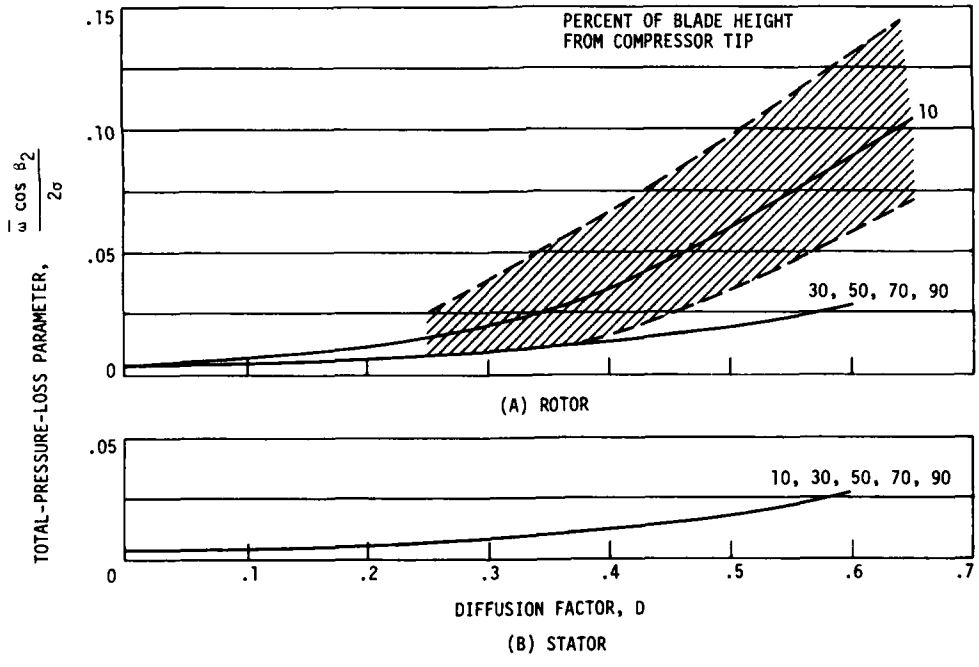

Figure 17.5.3. Variation of loss parameter with diffusion factor for blade sections in compressors operating near minimum-loss incidence angle (Ref. 17.13).

average axial Mach number and hub-tip ratio. High flow rate per unit frontal area has been designated as an important design objective because of the obvious relationship between required frontal area and component weight. The gains to be made by increased axial Mach number and by decreased hub-tip ratios are evident in Figure 17.5.4.

A second reason for the trend toward higher Mach number levels in compressor stages develops from the design objective calling for increased stage pressure ratios. As observed previously, the energy transfer in a compressor stage takes place in the rotor and is governed by the Euler turbine equation which represents an application of the law of conservation of angular momentum, Eq. (17.5.10), to a stream tube at constant radius.

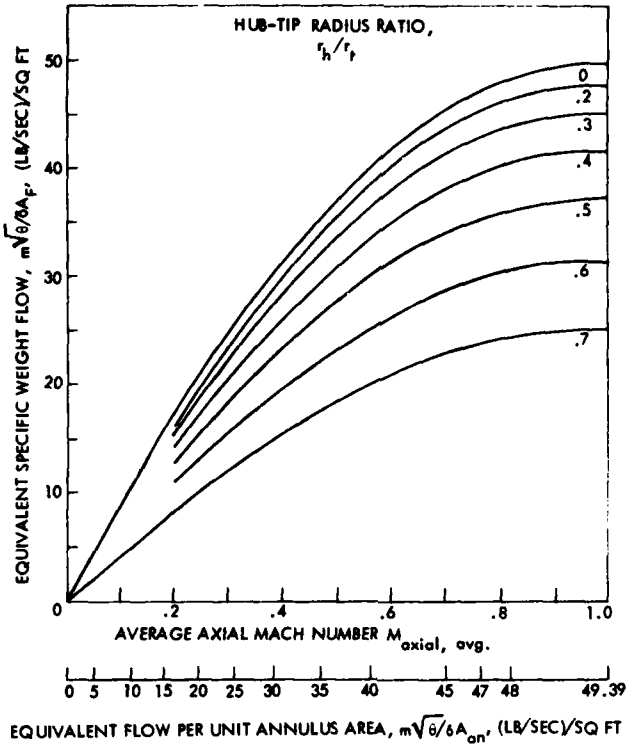

Figure 17.5.4. Compressor specific flow rate as a function of axial Mach number and hub-tip radius ratio.

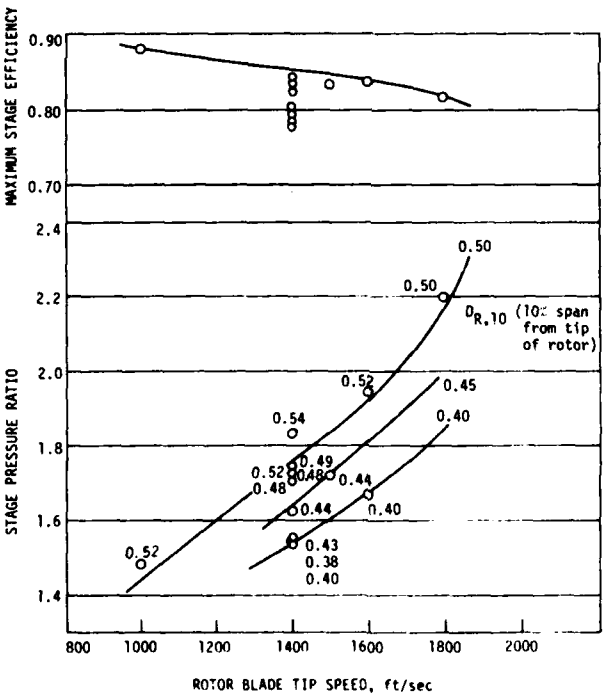

Figure 17.5.5. Trends in low hub-tip ratio stage performance with rotor tip speed and loading level.

$$\frac{E}{\delta m} = U_2 V_{\theta,2} - U_1 V_{\theta,1} \qquad (17.5.16)$$

In an axial-flow compressor stage the change in stream surface radius between the points where a fluid particle enters or leaves the blade row usually results in $U_2 \approx U_1$. For a stream surface with $U_1 = U_2$

$$\frac{E}{\delta m} = U[V_{\theta,2} - V_{\theta,1}] \qquad (17.5.17)$$

Either increased U or increased change in absolute tangential velocity is effective in increasing energy transfer. However, we have just discussed the loading limit D, which includes a term showing the direct contribution of $V_{\theta,2} - V_{\theta,1}$ to diffusion rates. Estimation of the other diffusion limits shows that the change in $V_{\theta,2} - V_{\theta,1}$ enters each limit in a similar way. Figure 17.5.5 shows how increased blade speed and increased rotor loading, as measured by Lieblein's diffusion factor, affect the pressure ratio available from a stage. The effect of increased blade speed is impressive. The data points are measured values for single stages.

The problem associated with high blade speed values has several facets. First, such values lead to high centrifugal force loadings on rotor blades. Second, there are direct relationships between blade speed and noise generation. The third and most significant aerodynamic feature of the problem is that high blade speeds are likely to result in high flow Mach numbers measured relative to the rotating blades. Suppose that we consider a rotor row with no tangential fluid velocity component at the leading edge. The relative velocity would be

$$W_1 = \sqrt{V_m^2 + U^2} \tag{17.5.18}$$

$$M_{rel,1} = \sqrt{M_m^2 + M_u^2} \tag{17.5.19}$$

$$M_u = \frac{U}{a_1} \tag{17.5.20}$$

The objectives of high mass flow per unit frontal area and high pressure ratio per stage, both, therefore, force designers to move in the direction of high rotor relative Mach numbers, and these same objectives also lead to high values of absolute Mach number at the entrance of stator blade rows.

The potential for advanced compressor performance levels associated with high average axial Mach number levels and high rotor blade speeds has been understood since the early 1940s, and since that time numerous stage configurations utilizing supersonic Mach number levels have been suggested, designed and tested. Until about 1950, the actual performance levels achieved were discouraging. Most of the rotors and stages involved were true supersonic configurations, with relatively high hub-tip ratios and supersonic relative Mach numbers along the entire blade span in rotors and/or stators at the design point. The poor performance included low, sometimes disastrous efficiencies and vertical pressure ratio-flow lines at design rotational speed. On the other hand, experimental subsonic rotors and stators were designed to operate with high blade speeds, but with inlet guide vanes to reduce the level of inlet Mach number at the tip to "advanced" subsonic values. Unfortunately, these stages generally used blade section geometries and design velocity diagrams which combined to produce excessive blade diffusion loading and poor stage performance.

Then around 1950 the observation was made simultaneously in several countries that some supersonic stages were performing very well at rotational speeds below the design value. These stages were of the shock-in-rotor type, in which the design relative Mach number at rotor inlet was supersonic and both the relative Mach number at rotor exit and the absolute Mach number approaching the stator row were subsonic. This encouraging performance was observed under flow conditions involving supersonic relative inlet Mach numbers along only part of the rotor span. Subsequently, stages were designed to operate in this transonic mode and were extremely successful.* The key features of these stages were the selection of an aerodynamically desirable blade geometry and a velocity diagram which eliminated inlet guide vanes while limiting blade diffusion loading.

The transonic compressor design concept was a dramatic breakthrough, which can be seen in proper perspective if we note that over about a two-year period, limiting relative Mach number levels for experimental rotor blade rows increased from about 0.75 to about 1.2, and a typical research inlet stage pressure ratio level increased from about 1.25 to 1.5. The transonic stage concept led directly to lower inlet stage hub-tip ratios, higher specific flow rates and higher stage pressure ratios, all at acceptable efficiencies and with acceptable stability characteristics.

While the story of the transonic compressor has a certain romantic flavor, it is a long and difficult one beyond the first "breakthrough" years. Mach number levels approaching or exceeding 1.0 at the inlet, within or at the exit of a blade row tend to be associated with increased thermodynamic losses, particularly so at incidence angles away from the minimum-loss values. Also associated with high subsonic and all supersonic Mach number levels is the problem of blade-channel "choking." As a result, it was necessary to develop models for the losses due to shock waves, and for the incorporation of both shock and profile losses into the design computation method. Furthermore, the higher stage pressure ratio levels caused more rapid passage area changes and wall curvature, again calling for changes in design procedures.

Mach number levels in axial-flow compressor designs have increased steadily during the past 25 years, so that average axial Mach number levels of 0.60 to 0.70 at the first rotor entrance are found in a number of aircraft engine applications, accompanied by compressor exit Mach numbers as high as 0.45. Rotor blade tip relative Mach numbers have been increased to levels from 1.4 to as high as 2.0 in experimental stages. This has required extensive use of special blade sections and detailed consideration of flow field control in the region of the blade row. Stator blade Mach number levels have also increased, but not as rapidly, with most design values in the high subsonic regime.

The quantitative effects of compressibility on blade row performance have been studied extensively in plane cascades and in compressor rotor and stage facilities. As a result, the computation of losses due to shock patterns has been enhanced considerably and the quantitative understanding of the effects of incidence angle, blade row geometry and downstream conditions on both losses and passage flow rate limits has been improved. Currently, we do not set absolute limits on Mach number levels in compressor design, but we do consider carefully the control of

*In the United States the early transonic compressor studies were carried out by the National Advisory Committee for Aeronautics (NACA). In the USSR the basic studies were apparently completed in the Central Institute for Aerohydrodynamics (TsAGI) and the Central Institute for Aviation Engines (TsIAM).

the flow field and the magnitude of expected losses at all required levels.

17.5.4 PRELIMINARY DESIGN

In preliminary design an immediate confrontation occurs between elegance in flow modeling and the requirement to complete the design task. Several approaches are possible. Two will be mentioned.

Suppose that you were given the task of designing and developing an axial-flow compressor for an aircraft gas turbine propulsion system. The given design point information might include only the following: the thermodynamic state of the working fluid in a duct upstream from the compressor; the total pressure increase required from this location to the compressor exit; and mass flow rates at the compressor entrance, in any by-pass ducts, at extraction points and at the exit. A table of thermodynamic properties of the working fluid should be available, and there will probably be an estimated overall efficiency used by the cycle analysts in preliminary system studies. As suggested by Figure 17.4.1, an early step should be to ensure frequent exchanges of information with the designers and developers of other components. The turbine shaft rotational speed is important to compressor designers and the fluid velocity levels and patterns at the compressor exit will be a major concern in combustor design.

All that is required of the compressor design group is a geometry meeting objectives which we have already set out. The only remaining question is how and where to start.

17.5.4.1 INPUT INFORMATION--FIRST OUTPUT

The given information suggested above was the following:

- $\dot{m}$ = compressor entrance flow rate
- $\dot{m}_a$, $\dot{m}_b$ = all flow rates by-passed or extracted from the configuration with the total pressure levels involved
- P_{ex}/P_{in} = overall total-pressure ratio for configuration
- T_{in} = total temperature at compressor entrance
- P_{in} = total pressure at compressor entrance
- η = compressor component efficiency or efficiencies used in cycle analysis

The first geometric output information needed includes general configuration dimensions and a proposed shaft rotational speed.

- $D_{tip,max}$ = maximum tip diameter
- $(D_{hub}/D_{tip})_{stage\ 1}$ = hub-to-tip diameter ratio, first stage
- N = shaft rotational speed
- N_{st} = estimated number of stages required
- L_{comp} = estimated total length of bladed compressor flow path

17.5.4.2 COMPONENT SCALING AS AN APPROACH TO PRELIMINARY DESIGN

At this point no compressor designer should overlook the possibility or underestimate the advantages of <u>scaling</u> an existing compressor geometry of known performance to meet his current design goals. Recalling the similarity parameter used in comparing performance for a given working fluid

$$\left.\begin{matrix}\frac{P_{ex}}{P_{in}} \\ \eta\end{matrix}\right\} = \text{functions of } \left[\text{GEOMETRY}, \frac{\dot{m}\sqrt{T_{in}}}{P_{in}D^2}, \frac{ND}{\sqrt{T_{in}}}, \frac{P_{in}D}{\mu\sqrt{T_{in}}}, \text{Tu}, \gamma\right]$$

it is easy to set up a procedure for predicting the geometric scale ratio required to meet any flow requirement if a specific operating point to be scaled is picked from an existing performance map. It will probably not be easy to satisfy all of the equalities needed for exact similitude, nor will it always be possible to find an existing geometry which produces the right pressure ratio at a good operating point. However, judicious scaling can often be supplemented by addition or deletion of stages at the front (e.g. adding "<u>zero</u>" <u>stages</u>) and rear of existing multistage geometries and by other geometric modifications.

There are dangers in scaling. Aerodynamic, aeroelastic and stress considerations are all involved, and numerous examples of expensive problems in compressor development testify to the need for careful analysis of all these areas of similarity.

17.5.4.3 PRELIMINARY DESIGN BY COMPUTATIONAL METHODS USING A SIMPLE FLOW MODEL

Geometric scaling and related techniques for performance modification do not add significantly to the state-of-the-art, and aside from the satisfaction of creating a genuinely superior compressor configuration there are other reasons for the decision to design "from scratch." Even though we describe flow models for preliminary design which are not very sophisticated, it should be understood that real skill is necessary in selecting parameters for a preliminary design study.

From the input and first geometric output listed in Section 17.5.3.1, as well as the design objective list of Section 17.3, we can see that a number of questions will be answered when we set target levels for mass flow per unit frontal area and pressure ratio per stage. There is no way to set these target levels except on the basis of past experience and trends.

In the case of mass flow per unit frontal area, the target level is generally set for and by the first stage. Figure 17.5.4 shows the values of equivalent specific flow rate attainable for various levels of average axial Mach number and hub-tip radius ratio for a first stage rotor. One significant point demonstrated by Figure 17.5.4 is that there are only small gains available in going below hub-tip ratios of about 0.3 and above axial Mach number values of about 0.7. While values of hub-tip ratio of 0.4 and below and $M_{axial,avg}$ greater than 0.6 are common in current compressor designs, it will become evident that there are problems created by pushing too far in either of the directions leading to higher specific flow rates.

Setting target levels for pressure ratio per stage requires the designer to make additional de-

cisions. The attainable total-pressure ratio in a given stage is a function of the energy transfer in the rotor of that stage as determined by Eq. (17.2.1) for each fluid particle, and by the thermodynamic losses in the stage which determine how much of the energy transfer is converted to an increase in total pressure. However, total-pressure ratio is not in itself a completely valid goal. The real goal should be to realize adequate static pressure rises in each stage so that excessive velocity increases across stages do not result. In gas turbine applications the compressor exit Mach number will be limited by combustor design requirements and both entrance $M_{axial,avg}$ and $M_{axial,avg}$ changes from stage to stage must be influenced by this limit.

An estimate of the pressure ratio levels which might be achieved must be made, and experience-based plots such as Figure 17.5.5 can be of help in this regard. This figure might, for example, be used to select several possible combinations of first rotor tip speed, blade-loading parameter and average stage efficiency to be studied. These selections will be only trial values, subject to change by iteration as the design process continues.

Based on the trial values of $[M_{axial}]_{avg}$, $[D_{hub}/D_{tip}]_{stage\ 1}$, U_{tip} and $D_{R,10}$, along with the given design point conditions, the size of the compressor and its rotational speed can be estimated by setting rough values for blade row aspect ratios and axial row spacing. At this level in the design, obvious misfit configurations can be eliminated by consultation with the turbine and engine configuration integration groups. If all trial configurations are misfits, some accommodation may be possible by adding inlet guide vanes or by other strategies.

Successful first output configuration combinations may be used as partial input to a less empirical second phase of preliminary design in which the first real use of our flow field model ideas takes place.

The overall design of an axial-flow compressor requires the solution of an inverse problem in aerodynamics. The problem is to determine the compressor geometry for a proposed flow field. In real compressor design the only time when we seriously work on the problem in this fashion is at the preliminary design level. We do this in a restricted way by specifying a few features of the flow field at selected calculation locations in the compressor, usually located in the spaces between blade rows.

The computation process ordinarily is based on a very simple form of the radial component of the equation of motion, Eq. (17.5.4), on the principal of conservation of mass, Eq. (17.5.8), and on the use of Euler's turbine equation, Eq. (17.5.10), with the first law of thermodynamics, Eq. (17.5.9). The flow is assumed steady, adiabatic, axisymmetric and free from radial gradients in entropy at any of the between row calculation planes. An efficiency level is assumed for each rotor and stage. Experience-based estimates are made for tip casing radius variation through the compressor, blade row loadings, solidities and stage-to-stage velocity variations. Approximate velocity diagram shapes are set. The effect of stream surface shape and curvature is omitted. Even under these much oversimplified conditions the differential euqation governing the radial variation in axial velocity in each calculation plane is

$$V_x \frac{\partial V_x}{\partial r} = \frac{\partial H}{\partial r} - \frac{V_\theta^2}{r} - V_\theta \frac{\partial V_\theta}{\partial r} \qquad (17.5.21)$$

This equation, along with conservation of mass, must be satisfied by iteration in each calculation plane throughout the compressor. This is a hub-to-tip or meridional plane solution which provides sufficient input to allow first trial blade row geometries to be determined.

At this level in design, correlated cascade and stage blade row data are generally used for blade selection. Because solidities and chord lengths

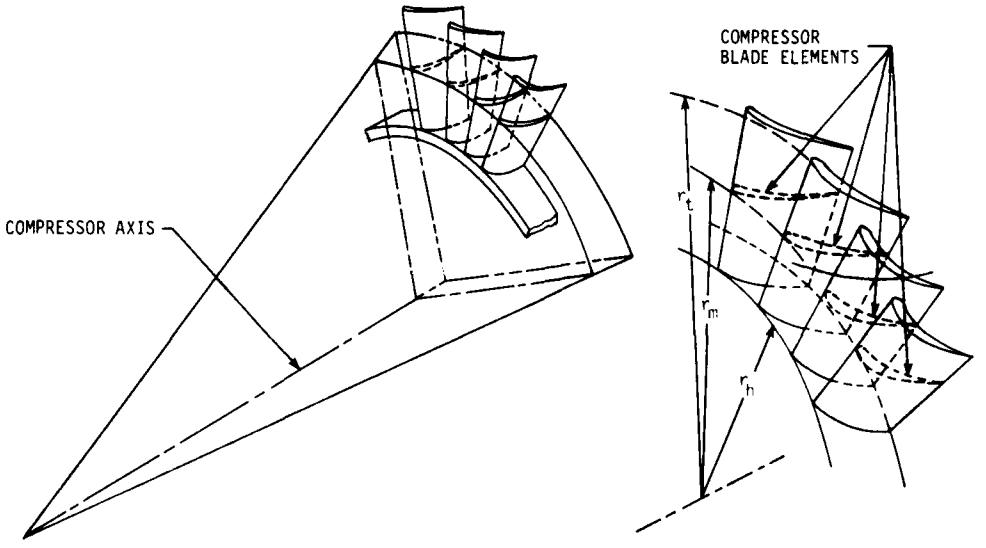

Figure 17.5.6. Layout of compressor blade sections on conical surface through stream surface intersection radii at blade row leading and trailing edge.

were estimated for the meridional plane solution some degrees of freedom of choice have been eliminated. A great many, however, have not. These include blade section geometry (profile shape, thicknesses and camber line shape) and incidence angle.

Computer programs, of course, exist for both meridional plane flow field equations and for blade selection. Blade sections are, in preliminary design, usually specified on conical stream surfaces as shown in Figure 17.5.6.

The result of the immense array of choices made and a significant amount of computation is a rough configuration geometry or series of configuration geometries which can be subjected to the initial scrutiny and criticism of stress analysts, aeroelasticians and engine layout designers. Any approval at this stage can be only tentative, because the flow field solution is almost totally incomplete within the blade rows. The next step is design analysis.

17.5.5 DESIGN ANALYSIS

17.5.5.1 INPUT AND OUTPUT INFORMATION

The inputs to the design analysis phase of overall compressor design are the configuration geometries generated in the preliminary design. This represents a complex and extensive collection of information, supplemented by the same design point flow, rotational speed, working fluid and compressor entrance condition data used in the preliminary design. Now, however, the result for each geometry will be an estimated value of overall pressure ratio and efficiency, with detailed velocity and fluid property distributions throughout the configuration, including those within the blade rows. This information is used to

1. determine whether the configuration geometry when operating at the design point will be capable of producing the correct input flow to the next cycle component,
2. locate any aerodynamically dangerous flow field conditions, such as regions of excessive diffusion rate or passage choking, and
3. provide adequate input for stress, aeroelastic and acoustic analysis.

17.5.5.2 CURRENT DESIGN ANALYSIS METHODS

The nature of design analysis output requirements calls for a much more inclusive flow model. These models are so detailed in content that the numerical structure of a solution can only be dealt with by large-scale digital computers.

Most design analysis methods are based on a loosely coupled combination of hub-to-tip flow field equations and empirically-based blade-to-blade surface row performance correlations. The hub-to-tip solution model is generally based on adiabatic, steady relative flow on axisymmetric approximations to stream surfaces. Computations are often based on equations written for quasi-S_2 surfaces. Stream surface geometry (curvature, lean, slope) are computed and subjected to iteration. Values computed are usually projected into the meridional plane. The equations of motion for fixed coordinates, Eq. (17.5.4), or relative coordinates, Eq. (17.5.5), control the distribution of velocity subject to the conservation of mass.

Calculation control surfaces may be radial as in Figures 17.5.7 and 17.5.8 or non-radial to conform to a leading or trailing edge shape. As a result, the component equations of motion become complex and difficult to interpret and compare. "Body" force field terms, as discussed in Section 17.5.1.4, are encountered inside blade rows.

Equilibrium equations of motion for a radial calculation surface such as those of Figure 17.5.7 may be as simple as

$$\frac{1}{\rho}\frac{\partial p}{\partial r} = F_r + \frac{V_\theta^2}{r} \pm \frac{V_m^2 \cos \epsilon}{r_c} \qquad (17.5.22)$$

but are much more difficult when calculation surfaces are non-radial. In any case, the solution of the equations of motion, conservation of mass and energy transfer, and of the equations resulting from conditions imposed by the second law of thermodynamics is iterative, numerical and subject to mathematical problems in convergence and stability. The iterations related to stream surface shape and curvature often must be subject to stability control by damping adjustments.

In design analysis, because the complete blade row geometries are input, both analytical and empirical procedures for estimating cascade performance are potentially useful. Whatever procedures are used must predict shock and profile (diffusion rate) losses and flow angle distributions through and downstream of each stream surface-cascade intersection. This is also an iterative process because of the dependence of both losses and downstream flow angle on the real downstream conditions (see Figure 17.5.9). A final problem in design analysis method development and application is in the treatment of end-wall flows. In this region the typical main channel flow model assumptions are not adequate, especially with regard to viscous loss accumulation. Several auxiliary end-wall models have been suggested, varying from simple empirical blockage allowances through three-dimensional boundary layer computation methods.

17.5.5.3 DEVELOPMENT OF ADVANCED METHODS FOR INTERNAL FLOW FIELD COMPUTATION

Recently, serious attempts have been made to develop three-dimensional internal flow field computation methods, all based on digital computers of large capacity and high speed. Most of these methods involve modeling of viscous effects, including turbulent shear stresses. Results have been obtained for certain geometries and flow situations, which, unfortunately, do not correspond to those which occur in axial-flow compressors. Over a time span of 20 to 50 years, it seems probable that meaningful progress will be made in realistic problem situations. However, these methods will no doubt assist in the design analysis process, and they may help to guide the correlation of data during the interim.

17.5.6 PERFORMANCE PREDICTION

Design analysis methods as defined in the previous section attempt to predict the compressor configuration flow field for the design operating point only. This is by no means easy because the flow model and numerical methods must adapt to some degree of non-optimum blade section operation. However, if in design analysis a significant region

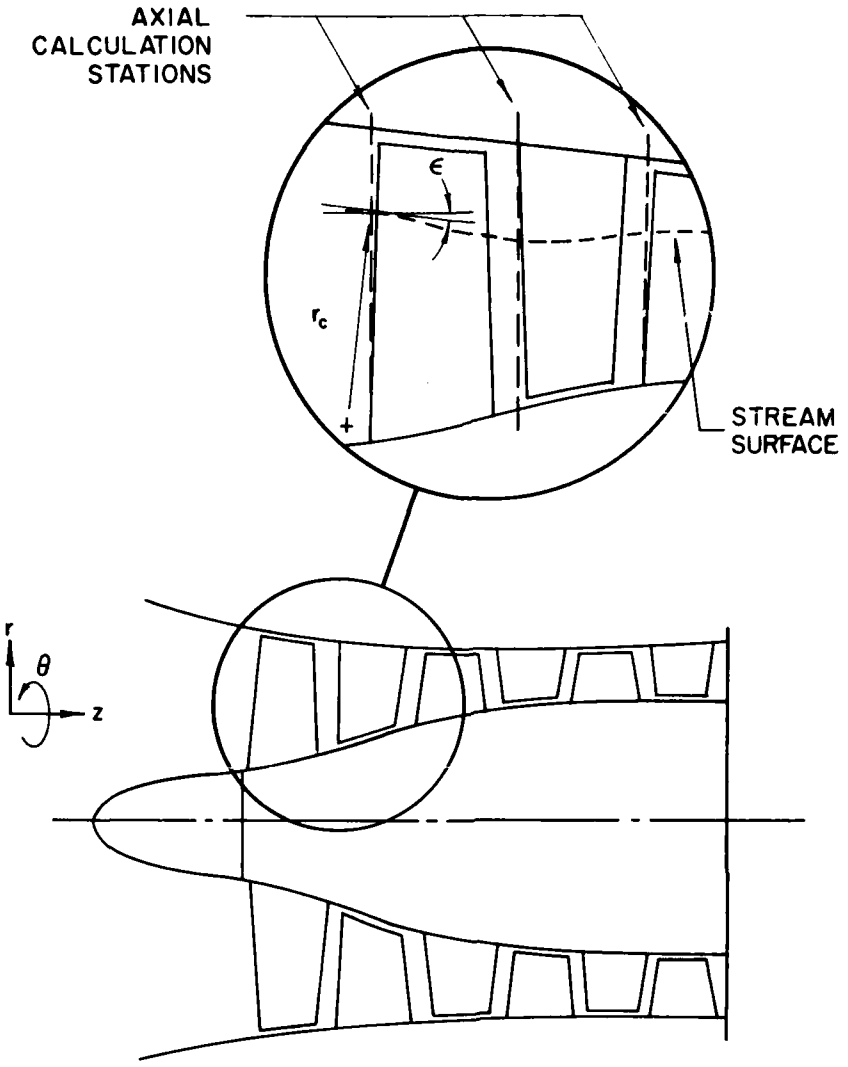

Figure 17.5.7. Meridional plane section of axial-flow compressor showing axisymmetric stream surface notation.

of separated flow was indicated, the calculation would stop until geometric adjustments were made.

In performance prediction, however, the primary objective is to estimate the overall compressor unit performance map, including the surge line, and this requires capability for accommodating flow phenomena in the computation system which are not easily modeled. Therefore, it is not easy to use a design analysis flow model and computation system for general performance prediction.

Current performance map prediction methods are normally based on one of two simplified approaches. The first is "map generalization," in which families of performance maps are correlated on a non-dimensional basis so that similarity methods can be used for proposed compressor geometries. The second is a stage characteristic "stacking" method using approximate stage or stage group performance (see Figure 17.5.7) as a starting point. Both map generalization and stage-stacking procedures are relatively easy to apply, but are inadequate for most advanced configuration applications because they are based on past experience.

Over a period of several years, some of the current design analysis methods should be developed into true performance prediction systems. This will require some adjustments to the flow model and especially improved capability in estimating cascade-stream surface flow turning and loss for nonoptimum entrance and exit conditions.

17.5.7 STRESS, AEROELASTIC AND ACOUSTIC ANALYSIS

Flow field property and velocity distributions from the design analysis phase are utilized as partial input to stress and aeroelastic evaluation methods. During recent years the interaction between "pure" aerodynamic analysis and "pure" aeroelastic predictions has become better understood and as a result genuine progress has been made. Reference should be made to Chapter 22 for more detailed comments. Compressor acoustic analysis is covered in Chapter 24.

17.6 COMPONENT AND CONFIGURATION EXPERIMENTAL DEVELOPMENT

A high-quality design system is under contin-

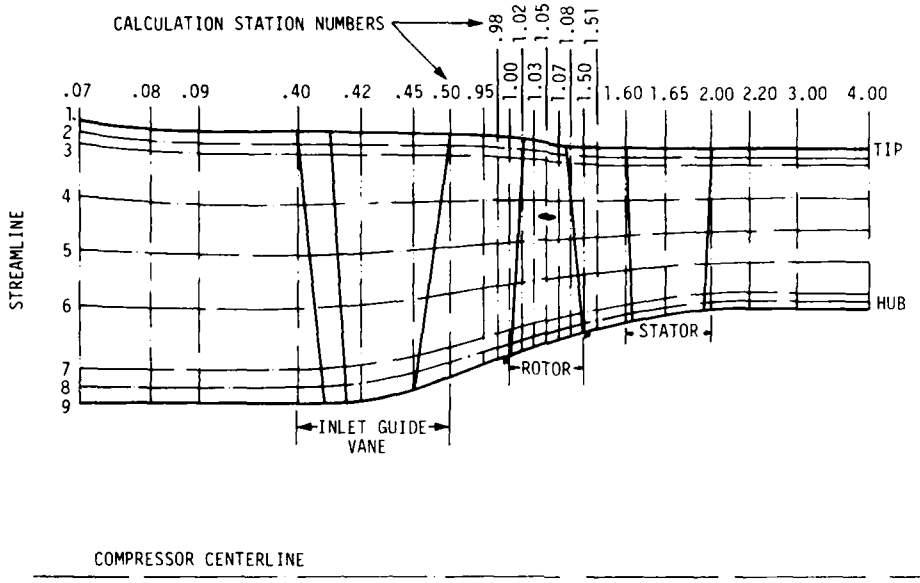

Figure 17.5.8. Calculation control surfaces for an axial-flow compressor stage with computed stream surface shapes (Ref. 17.14).

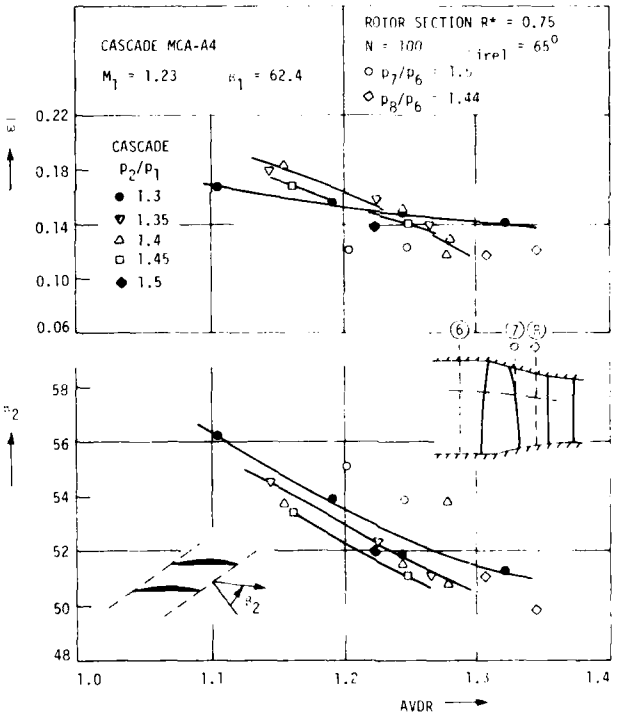

Figure 17.5.9. Comparison of cascade experiments and rotor blade section data (Ref. 17.33).

uous development and one of the primary sources of change lies in the base of experimental information supporting all elements of the system. We have briefly discussed cascade experimental results and data correlation. We have seen some evidence that rotor and stage test results supply important adjustments to cascade correlations by introducing the effects of rotation (end-wall relative motion, adjacent blade section influence and other secondary flow features). There is, in fact, an awesome accumulation of experimental design system support.

As advanced and exploratory axial-flow compressor configurations are designed and evaluated, there has been a continual requirement to upgrade test facility and measurement quality. Plane cascade test section design has been improved radically by adding new flow field control techniques as well as performance measurement strategy for both subsonic and supersonic flow regimes. Open- and closed-

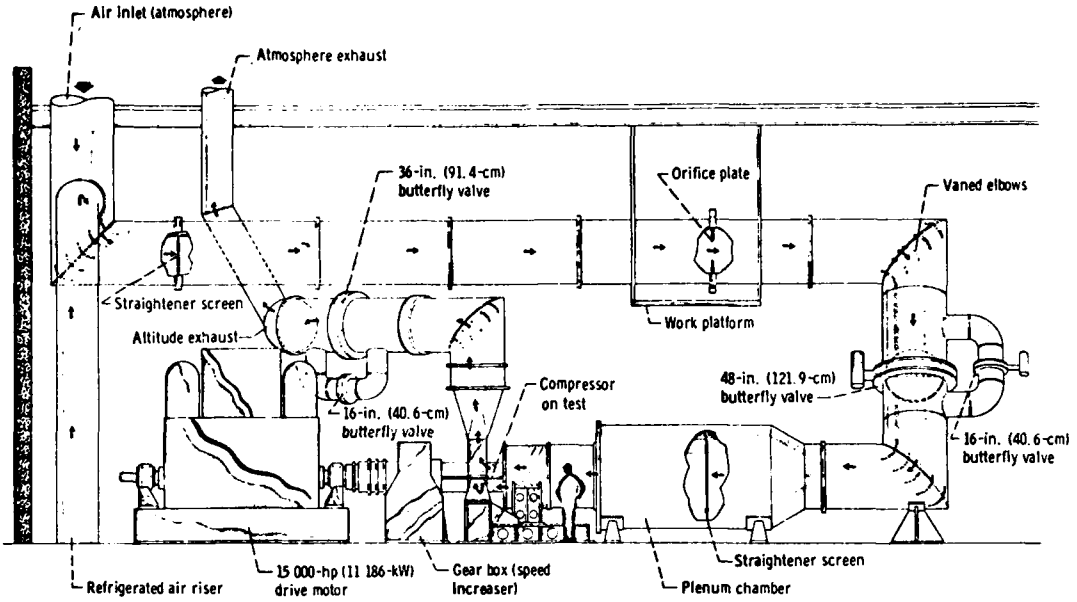

Figure 17.6.1. Compressor test facility.

loop rotor, stage, and multistage compressor facilities have been built (see Figure 17.6.1) and equipped with extensive instrumentation to reveal transient and unsteady flow phenomena.

However, the greatest direct element of support for compressor design systems comes from steady-state or time-average flow passage measurements, both between blade rows and, where possible, inside rows. Review of any preliminary design or design analysis method will quickly demonstrate the dependence of the method on correlated experimental information.

Because a compressor unit installed in an aircraft engine can operate over only a limited part of its performance map and because configuration adjustments are much more difficult in an engine installation, test facilities such as those in Figure 17.6.1 are used directly in component development programs. In these programs, only limited instrumentation may be possible, but if some characteristics of stage behavior (frequently only casing static pressure patterns) can be measured along with overall performance, significant improvements in performance maps can often be made by rematching individual stages or by alterations to specific blade row geometries.

17.7 AXIAL-FLOW COMPRESSOR PERFORMANCE TRENDS

Figures 17.7.1, 17.7.2 and 17.7.3 have been included to show in a very limited way performance results representative of recent compressor research and development activities. They also give a qualitative idea of the capabilities and limitations of compressor design systems. Reference should be made to Figures 17.5.4 and 17.5.5 as the performance is reviewed to see where the individual units fall in relation to preliminary design choices.

Figure 17.7.1 is a plot of measured overall performance for a single-stage transonic compressor design. This stage had a rotor entrance tip diameter of 33.0 in. and a hub-tip ratio at the rotor entrance of 0.5. No guide vanes were used.

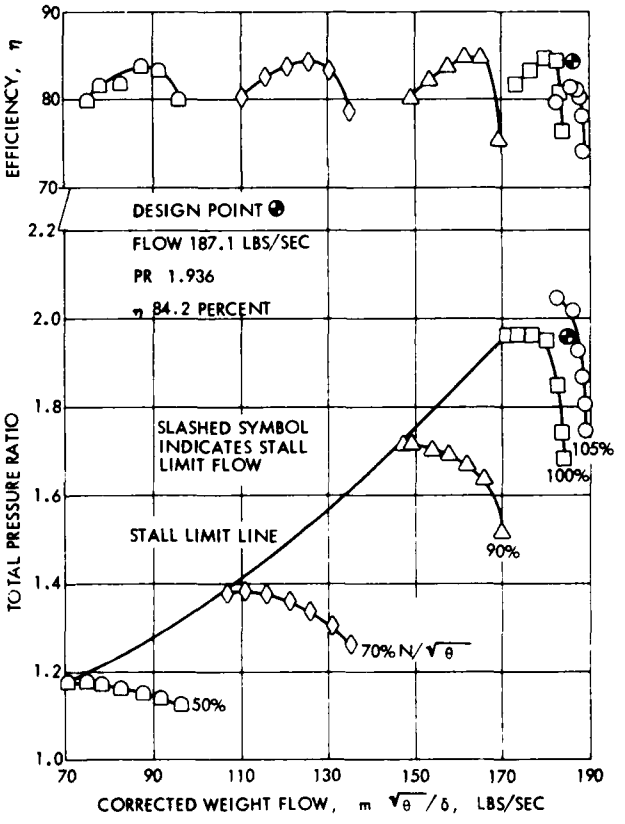

Figure 17.7.1. Overall performance of single-stage axial-flow compressor designed to operate at a tip speed of 1600 feet per second (488 m/s) (Ref. 17.15).

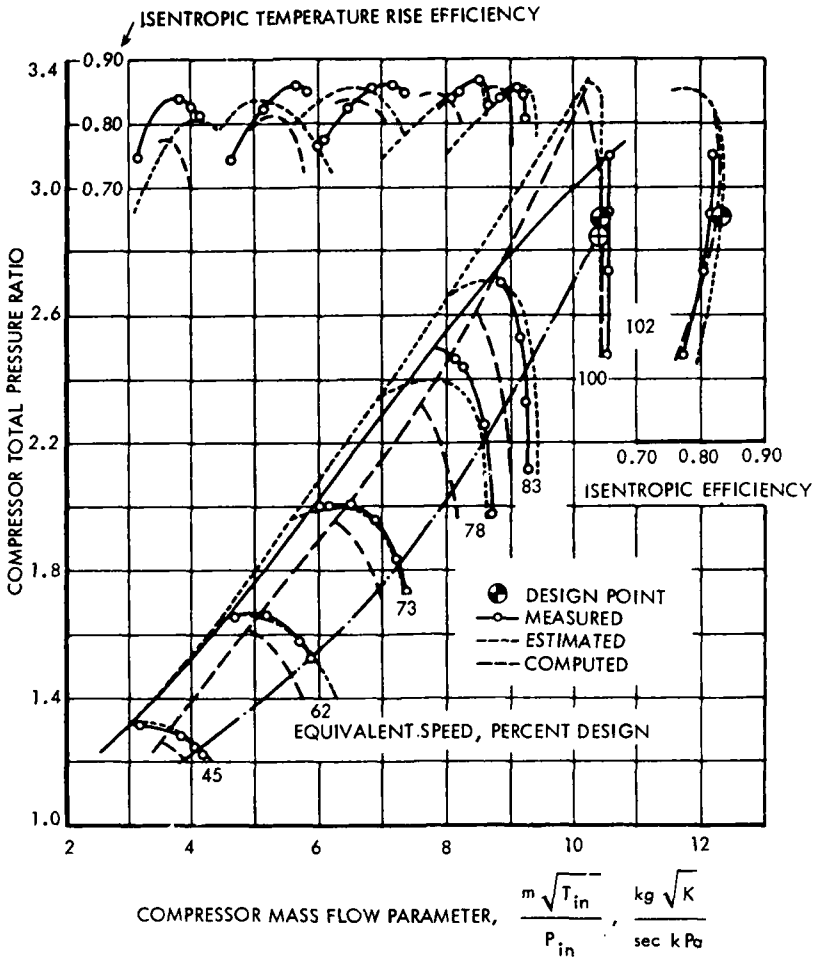

Figure 17.7.2. Predicted and measured performance characteristics of three-stage axial-flow compressor (Ref. 17.5).

Figure 17.7.2 shows the predicted and measured performance of the three-stage axial-flow compressor (fan) previously shown in the meridional plane section of Figure 17.1.5.

Figure 17.7.3 shows performance plots for a compressor stage with variable inlet guide vane geometry and variable stator blading (meridional section in Figure 17.5.9). The two maps show that significant performance changes are possible with variable blade geometry. This stage had a 0.5 hub-tip ratio and a tip diameter of 36.5 in.

In multistage compressors the trend has been and is toward higher flow rates per unit annulus area and higher stage pressure ratios. This has been true partly because the higher tip speeds associated with transonic entrance stages are also present in subsequent stages. This leads to higher stage pressure ratios for a given blade row loading level. Although general Mach number levels decrease as temperature levels rise through a compressor, transonic stage operation frequently exists in several stages at the design point.

Continual emphasis has been placed on development of broad range stable engine core compressors. Variable geometry blading has entered many configurations, and other geometric techniques such as casing treatment (see Figure 17.7.4) have been introduced into both core and fan stages. The technology of high hub-tip ratio high-pressure stages is a complex and difficult research area.

Throughout the relatively short technological history of the axial-flow compressor, the most significant overall trends have been toward reduction of size and cost by increasing average Mach number levels and stage pressure ratios. All of the configuration maps shown in this chapter have been the direct result of attempts to advance these trends. Transonic and supersonic compressor development have demonstrated that there are certain design features common to most successful stages. These are summarized in Figure 17.7.5. A good way to review the content of this chapter would be to consider these features and to justify them in terms of the flow parameters and phenomena exposed herein.

17.8 ACKNOWLEDGMENTS

Some good friends among axial-flow compressor scholars have provided information, advice and data to support the preparation of Chapter 17. Included in this list are A. W. Stubner and J. W. Wells of the Pratt and Whitney Aircraft Division, United Technologies Corporation; Robert O. Bullock of AiResearch; Arthur J. Wennerstrom of the Air Force Aero Propulsion Laboratory; Melvin J. Hartmann and

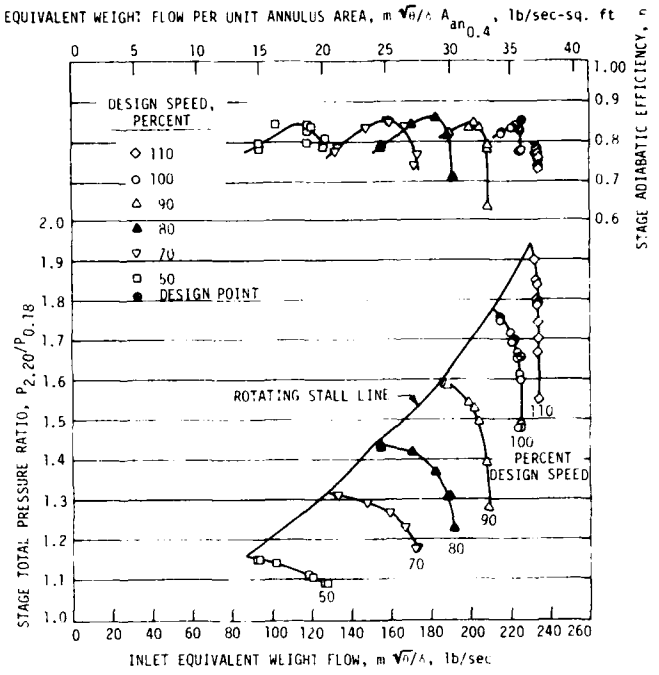

Figure 17.7.3a. Stage performance map for IGV/stator schedule $0^{o}/0^{o}$ (See Figure 17.5.8 and Ref. 17.14).

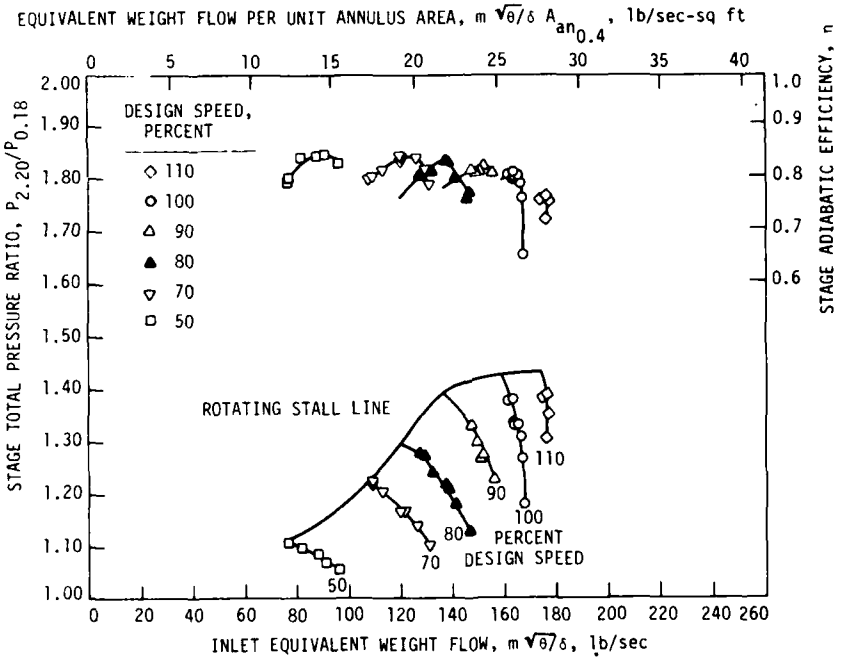

Figure 17.7.3b. Stage performance map for IGV/stator schedule $40^{o}/8^{o}$ (See Figure 17.5.8 and Ref. 17.14).

Donald M. Sandercock of the Lewis Research Center, National Aeronautics and Space Administration. The data shown in Figure 17.5.5 were assembled by D. M. Sandercock from the results of NASA research.

Errors of all kinds are the responsibility of the author. I would appreciate hearing about any that are found.

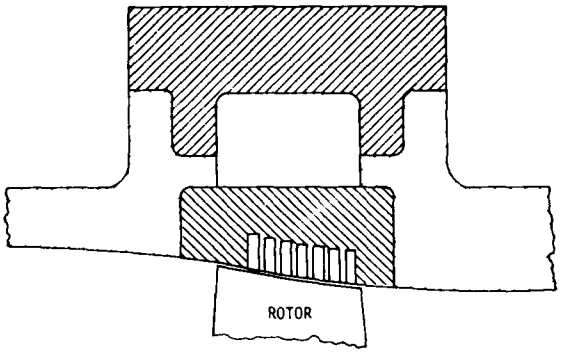

Figure 17.7.4. Schematic of one form of compressor rotor tip casing treatment.

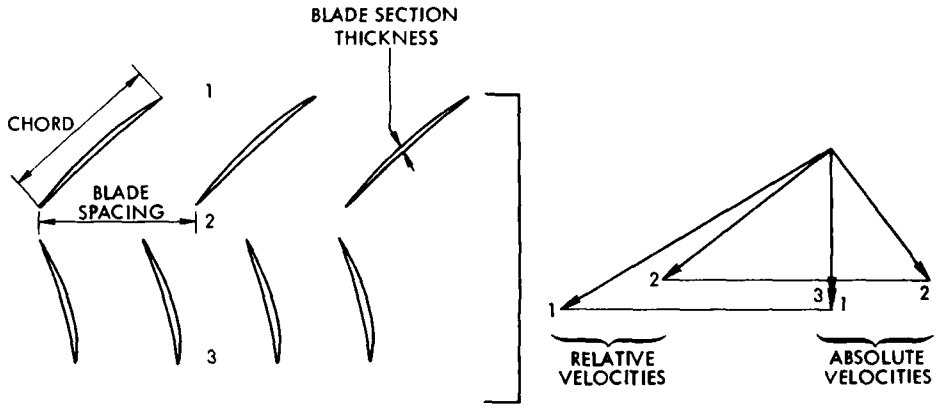

TRANSONIC STAGE DESIGN CHARACTERISTICS

VELOCITY DIAGRAMS

- AXIAL ENTRANCE FLOW
- NEAR AXIAL EXIT FLOW
- MAXIMUM RELATIVE M AND MINIMUM FLOW TURNING IN ROTOR TIP REGION
- MAXIMUM FLOW TURNING IN ROTOR HUB REGION
- MAXIMUM STATOR M IN HUB REGION

BLADE ROW GEOMETRY

- LOW RATIOS OF MAXIMUM THICKNESS/CHORD
- HIGHER LEVELS OF SOLIDITY IN MAXIMUM M REGIONS THAN WOULD BE USED FOR SUBSONIC BLADING
- BLADE CAMBER (TURNING) MOVED TOWARD REAR OF AIRFOIL IN REGIONS OF HIGH M
- REDUCED ASPECT RATIO

Figure 17.7.5. Design characteristics of advanced transonic compressor stages.

17.9 BIBLIOGRAPHIC NOTES AND GUIDE TO REFERENCE MATERIALS

Many references to technical papers and books were considered necessary to give a balanced review of axial-flow compressor aerodynamic technology. It was, therefore, decided that the main text should be presented without interruption and that all bibliographic notes should be assembled and references classified by section at the end of the Chapter.

Ref. 17.1-17.16 are sources of Figures as well as information. In some cases the Figures were redrawn or modified to illustrate a specific point.

17.1 Mitchell, G. A. Effect of Inlet Ingestion of a Wing Tip Vortex on Compressor Face Flow and Turbojet Stall Margin. NASA TM X-3246. 1975.

17.2 Tesch, W. A. and Steenken, W. G. Blade Row Dynamic Digital Compressor Program, Volume I, J85 Clean Inlet Flow and Parallel Compressor Models. NASA CR-134978. March 1976.

17.3 ---. Fact Sheet, TF30-P-412A Turbofan Engine. Pratt and Whitney Division of United Technologies Corporation. 1973.

17.4 ---. Fact Sheet, JT9D-70/-70A Turbofan Engine. Pratt and Whitney Division of United Technologies Corporation. 1974.

17.5 Volkmann, H., Föttner, L. and Scholz, N. Aerodynamische Entwicklung eines dreistufigen Transsonik-Frontgebläses. Zeitschrift für Flugwissenschaften 22:135-144. 1974.

17.6 Geye, R. P., Budinger, R. E. and Voit, C. H. Investigation of High-Pressure-Ratio Eight-Stage Axial-Flow Research Compressor with Two Transonic Inlet Stages. II - Preliminary Analysis of Over-All Performance. NACA RM E53J06. 1953.

17.7 Bullock, R. O. and Prasse, E. I. Compressor Design Requirements. In Aerodynamic Design of Axial-Flow Compressors. NASA SP-36. 1965. Chapter II.

17.8 Snyder, L. E. and Commerford, G. L. Supersonic Unstalled Flutter in Fan Rotors; Analytical and Experimental Results. J. Eng. Power. Trans. ASME, Ser. A, 96:379-386. 1974.

17.9 Benser, W. A. Analysis of Part-Speed Operation for High-Pressure-Ratio Multistage Axial-Flow Compressors. NACA RM E53I15. 1953.

17.10 Huppert, M. C. and Benser, W. A. Some Stall and Surge Phenomena in Axial Flow Compressors. J. Aero. Sci. 20:835-845. December 1953.

17.11 Herzig, H. Z. and Hansen, A. G. Three-Dimensional Compressor Flow Theory and Real Flow Effects. In Aerodynamic Design of Axial-Flow Compressors. NASA SP-36. 1965. Chapter XIV.

17.12 Lieblein, S. Experimental Flow in Two-Dimensional Cascades. In Aerodynamic Design of Axial-Flow Compressors. NASA SP-36. 1965. Chapter VI.

17.13 Robbins, W. H., Jackson, R. J. and Lieblein, S. Blade-Element Flow in Annular Cascades. In Aerodynamic Design of Axial-Flow Compressors. NASA SP-36. 1965. Chapter VII.

17.14 Doyle, V. L. and Koch, C. C. Evaluation of Range and Distortion Tolerance for High Mach Number Transonic Fan Stages. Design Report. NASA CR-72720. 1970.

17.15 Sulam, D. H., Keenan, M. J. and Flynn, J. T. Single-Stage Evaluation of Highly-Loaded High-Mach-Number Compressor Stages. II - Data and Performance Multiple-Circular-Arc Rotor. NASA CR-72694. 1970.

17.16 Bilwakesh, K. R. Evaluation of Range and Distortion Tolerance for High Mach Number Transonic Fan Stages. Task II, Stage Data and Performance Report for Undistorted Inlet Flow Testing (Volumes I and II). NASA CR-72787. January 1971.

SECTION 17.0 INTRODUCTION

SECTION 17.1 AXIAL-FLOW COMPRESSOR NOMENCLATURE AND TERMINOLOGY

Ref. 17.17-17.23 are textbooks and summary reports which have significant content on axial-flow compressors. They are historically valuable and represent several independent points of view on compressor design.

17.17 Horlock, J. H. Axial Flow Compressors. London. Butterworths. 1958. (Reprint with supplemental material, Huntington, N.Y., Krieger. 1973.)

17.18 Johnsen, I. A. and Bullock, R. O. eds. Aerodynamic Design of Axial-Flow Compressors. NASA SP-36. 1965.

17.19 Kholshchevnikov, K. V. Theory and Design of Aircraft Turbomachines. Translation of Teoriya i Raschet Aviatsionnykh Lopatochnykh Mashin, 1970. Foreign Technology Division. Wright-Patterson AFB, Ohio. FTD-HC-23-754-71. 1972.

17.20 Scholz, N. Aerodynamik der Schaufelgitter. Volume I. Karlsruhe. G. Braun. 1965.

17.21 Stechkin, B. S., Kazandzhan, P. I., Alekseev, L. P., Govorov, A. N., Nechaev, Yu. N. and Fedorov, R. M. Theory of Reaction Engines (Bladed Machines). Moscow. Oborongiz. 1956.

17.22 Traupel, W. Thermische Turbomaschinen. Volume I. Second Edition. Berlin/Heidelberg/New York. Springer-Verlag. 1966.

17.23 Vavra, M. H. Aero-Thermodynamics and Flow in Turbomachines. New York. Wiley. 1960.

Cascade test facilities and experimental techniques are described in Ref. 17.24-17.29, and some examples of systematic cascade test programs are contained and referenced in Ref. 17.30-17.34. Ref. 17.35-17.37 are thorough explanations of supersonic flows in cascades.

17.24 Schilhansl, M. J. Survey of Information on Two-Dimensional Cascades. Tech. Rep. 54-322, Wright Air Development Center, Air Research and Development Command, USAF, Wright-Patterson Air Force Base, Mar. 1955. (Aero. Res. Lab. Contract AF 33(616)-16, Proj. 3066.)

17.25 Erwin, J. R., and Emery, J. C. Effect of Tunnel Configuration and Testing Technique on Cascade Performance. NACA Report 1016. 1951.

17.26 Stubner, A. W., Case, L. F., and Blake, T. R. Supersonic Cascade Tunnel Used to Evaluate Compressor Blade Performance. J. Eng. Power. Trans. ASME, Series A. 88A:153-156. 1966.

17.27 Breugelmans, F. A. E. High Speed Cascade Testing and Its Application to Axial Flow Supersonic Compressors. ASME Paper 68-GT-10. March 1968.

17.28 Dzung, L. S. Averaging Procedure in the Theory of Blade Cascades. Brown Boveri Review 54(1):36-43. January 1967.

17.29 Sieverding, C., Starken, H., Lichtfuss, H.-J. and Schimming, P. Aerodynamic Measurements in Cascades. In Modern Methods of Testing Rotating Components for Turbomachines (Instrumentation). AGARD-AG-207. 1975. pp. 1-76.

17.30 Emery, J. C., Herrig, L. J., Erwin, J. R., and Richard, F. A. Systematic Two-Dimensional Cascade Tests of NACA 65-series Compressor Blades at Low Speeds. NACA Report 1368. 1958.

17.31 Savage, M., Boxer, E. and Erwin, J. R. Resume of Compressor Research at the NACA Langley Laboratory. J. Eng. Power., Trans. ASME, Ser. A, 83:269-285. 1961.

17.32 Schlichting, H. and Das, A. Recent Research on Cascade Flow Problems. J. Basic Eng. Trans. ASME, Ser. D, 88:221-228. 1966.

17.33 Schreiber, H. A. Comparison Between Flows in Cascades and Rotors in the Transonic Range. II - Investigation of Two Transonic Compressor Cascades and Comparison with Rotor Data. Von Karman Institute Lecture Series 84. February 1976.

17.34 Starken, H., Breugelmans, F. A. E. and Schimming, P. Investigation of the Axial Velocity Density Ratio in a High Turning Cascade. ASME Paper 75-GT-25. 1975.

17.35 Starken, H. and Lichtfuss, H.-J. Supersonic Cascade Performance. In Advanced Compressors. AGARD-LS-39-70. 1970. Paper 8.

17.36 Starken, H. and Lichtfuss, H.-J. Some Experimental Results of Two-Dimensional Compressor Cascades at Supersonic Inlet Velocities. J. Eng. Power., Trans. ASME, Ser. A, 92:267-274. 1970.

17.37 Lichtfuss, H.-J. and Starken, H. Supersonic Cascade Flow. In Progress in Aerospace Science, 15:37-149. New York. Pergamon Press Ltd. 1974.

SECTION 17.2 CHARACTERISTICS OF THE FLOW IN AXIAL-FLOW COMPRESSOR CONFIGURATIONS

Ref. 17.17 and 17.38 develop the similarity parameters used in plotting compressor performance. Performance map features and additional influences on map characteristics are discussed as follows:

Reynolds number and scaling effects	Ref. 17.39-17.41
Turbulence level effects	Ref. 17.42
Rotating stall and surge	Ref. 17.43-17.47
Unsteady flow and inlet distortion	Ref. 17.1, 17.48-17.52
Aeroelastic phenomena	Ref. 17.8, 17.53

Stage performance and stage-matching methods are covered by Ref. 17.9, 17.10 and 17.54-17.57.

17.38 Hodge, J. Cycles and Performance Estimation. New York. Academic Press. 1955.

17.39 Bullock, R. O. Analysis of Reynolds Number and Scale Effects on Performance of Turbomachinery. J. Eng. Power. Trans. ASME, Ser. A, 86:247-256. 1964.

17.40 Wassell, A. B. Reynolds Number Effects in Axial Compressors. J. Eng. Power, Trans. ASME, Ser. A, 90:149-156. 1968.

17.41 Pampreen, R. C. Small Turbomachinery Compressor and Fan Aerodynamics. J. Eng. Power. Trans. ASME, Ser. A, 95:251-256. July 1973.

17.42 Schlichting, H. and Das, A. On the Influence of Turbulence Level on the Aerodynamic Losses of Axial Turbomachines. In Flow Research on Blading, Dzung, L. S., ed. Amsterdam. Elsevier. 1969.

17.43 Emmons, H. W., Kronauer, R. E., and Rockett, J. A. A Survey of Stall Propagation-Experiment and Theory, J. Basic Eng.. Trans. ASME, Ser. D, 81:409-416. 1959.

17.44 Fabri, J. Rotating Stall in Axial Flow Compressors. In Internal Aerodynamics (Turbomachinery). Proceedings of a conference sponsored by the Royal Society at Cambridge, 19-21 July, 1967. London. The Institution of Mechanical Engineers. 1970. pp. 96-110.

17.45 Yershov, V. N. Unstable Conditions of Turbodynamics. Rotating Stall. FTD-MT-24-04-71. 12 August 1971.

17.46 Greitzer, E. M. Surge and Rotating Stall in Axial Flow Compressors. Part I: Theoretical Compressor System Model. J. Eng. Power. Trans. ASME, Ser. A, 98:190-198. 1976.

17.47 Greitzer, E. M. Surge and Rotating Stall in Axial Flow Compressors. Part II: Experimental Results and Comparison with Theory. J. Eng. Power. Trans. ASME, Ser. A, 98:199-217. 1976.

17.48 Langston, C. E. Distortion Tolerance - By Design Instead of By Accident. ASME Paper 69-GT-115. 1969.

17.49 Mikolajczak, A. A. and Pfeffer, A. M. Methods to Increase Engine Stability and Tolerance to Distortion. In Distortion Induced Engine Instability. AGARD LS-72. Paper 7. October 1974.

17.50 Greitzer, E. M. and Griswold, H. R. Compressor-Diffuser Interaction with Circumferential Flow Distortion. J. Mech. Eng. Sci. 18:25-38. 1976.

17.51 Mikolajczak, A. A. The Practical Importance of Unsteady Flow. In Unsteady Phenomena in Turbomachinery. AGARD-CP-177. Paper 1. 1976.

17.52 Hetherington, R. and Moritz, R. R. Influence of Unsteady Flow Phenomena on the Design and Operation of Aero Engines. In Unsteady Phenomena in Turbomachinery. AGARD-CP-177. Paper 2. 1976.

17.53 Mikolajczak, A. A., Arnoldi, R. A., Snyder, L. E. and Stargadter, H. Advances in Fan and Compressor Blade Flutter Analysis and Predictions. J. Aircr. 12:325-332. 1975.

17.54 Finger, H. B. and Dugan, J. F., Jr. Analysis of Stage-Matching and Off-Design Performance of Multi-Stage Axial-Flow Compressors. NACA RM E52D07. 1952.

17.55 Benser, William A. Compressor Operation with One or More Blade Rows Stalled. In Aerodynamic Design of Axial-Flow Compressors. NASA SP-36. Chapter XIII. 1965.

17.56 Doyle, M. D. C. and Dixon, S. L. The Stacking of Compressor Stage Characteristics to Give an Overall Compressor Performance Map. Aeronaut. Q. 13:349-367. 1962.

17.57 Gray, S. Stage Matching, Stall, and Surge in Multi-Stage Axial-Flow Compressors. In Thermodynamics and Fluid Mechanics Convention 1970. Volume II - Axial and Radial Turbomachinery. Proc. Inst. Mech. Eng. 184: Part 3G(II):49-56. 1970.

SECTION 17.3 AERODYNAMIC DESIGN OBJECTIVES FOR AXIAL-FLOW COMPRESSOR UNITS

SECTION 17.4 ELEMENTS OF A COMPRESSOR DESIGN SYSTEM--TECHNICAL REQUIREMENTS

Ref. 17.7 and 17.58 outline these subjects.

17.58 Bullock, R. O. and Johnsen, I. A. Compressor Design System. In Aerodynamic Design of Axial-Flow Compressors. NASA SP-36. Chapter III. 1965.

SECTION 17.5 CONTENT OF CURRENT AND DEVELOPING DESIGN SYSTEMS

The development of design systems can be best studied with an understanding of how present thinking evolved. Ref. 17.59-17.63 are some important British base points and Ref. 17.58 and 17.64-17.66 give some background on compressor design systems in the United States.

17.59 Howell, A. R. Fluid Dynamics of Axial Compressors. Proc. Inst. Mech. Eng. 153:441-452. 1945.

17.60 Howell, A. R. Design of Axial Compressors. Proc. Inst. Mech. Eng. 153:452-462. 1945.

17.61 Carter, A. D. S. Three-Dimensional-Flow Theories for Axial Compressors and Turbines. Proc. Inst. Mech. Eng. 159:255-268. 1948.

17.62 Carter, A. D. S., Turner, R. C., Sparkes, D. W. and Burrows, R. A. The Design and Testing of an Axial-Flow Compressor having Different Blade Profiles in Each Stage. Aero. Res. Council R & M 3183. 1957.

17.63 Carter, A. D. S. Blade Profiles for Axial-Flow Fans, Pumps, Compressors, Etc. Proc. Inst. Mech. Eng. 175:775-806. 1961.

17.64 Johnsen, I. A. Investigation of a 10-Stage Subsonic Axial-Flow Research Compressor. I - Aerodynamic Design. NACA RM E52B18. 1952.

17.65 Giamati, C. C., Jr. and Finger, H. B. Design Velocity Distribution in Meridional Plane. Chapter VIII of Aerodynamic Design of Axial-Flow Compressors. NASA SP-36. 1965.

17.66 Serovy, G. K. Recent Progress in Aerodynamic Design of Axial-Flow Compressors in the United States. Eng. for Power. Trans. ASME, Ser. A, 88:251-261. 1966.

The subject of flow field models for the hub-to-tip problem is brought forward from the period beginning about 1950 until very recent years in Ref. 17.67-17.89 and for the blade-to-blade problem in Ref. 17.20, 17.24 and 17.90-17.100. Important reference material on these subjects may also be found in the listed references for design analysis, beginning with Ref. 17.160.

17.67 Wu, C.-H. and Wolfenstein, L. Application of Radial-Equilibrium Condition to Axial-Flow Compressor and Turbine Design. NACA Report 955. 1950.

17.68 Hatch, J. E., Giamati, C. C. and Jackson, R. J. Application of Radial-Equilibrium Condition to Axial-Flow Turbomachine Design Including Consideration of Change of Entropy With Radius Downstream of Blade Row. NACA RM L54A20. 1954.

17.69 Holmquist, C. O. and Rannie, W. D. An Approximate Method of Calculating Three-Dimensional Compressible Flow in Axial Turbomachines. J. Aero. Sci. 23:543-556, 582. 1956.

17.70 Wu, C.-H. General Through-Flow Theory of Fluid Flow with Subsonic or Supersonic Velocity in Turbomachines of Arbitrary Hub and Casing Shapes. NACA TN 2302, 1951.

17.71 Wu. C.-H. A General Theory of Three-Dimensional Flow in Subsonic and Supersonic Turbomachines of Axial-, Radial-, and Mixed-Flow Types. NACA TN 2604. January 1952.

17.72 Hamrick, J. T., Ginsburg, A. and Osborn, W. M. Method of Analysis for Compressible Flow Through Mixed-Flow Centrifugal Impel-

lers of Arbitrary Design. NACA Report 1082. 1952.

17.73 Smith, L. H., Jr. The Radial-Equilibrium Equation of Turbomachinery. J. Eng. Power. Trans. ASME, Ser. A, 88:1-12. 1966. (Discussion in 88:282-283. 1966)

17.74 Novak, R. A. Streamline Curvature Computing Procedures for Fluid-Flow Problems. J. Eng. Power. Trans. ASME, Ser. A, 89: 478-490. 1967.

17.75 Sirotkin, Ya. A. Aerodynamic Calculation of Blades in Axial-Flow Turbomachines. FTD-MT-24-1809-72. 31 May 1973.

17.76 Silvester, M. E. and Hetherington, R. Three Dimensional Compressible Flow Through Axial Flow Turbomachines. In Numerical Analysis: An Introduction. Walsh, J. ed. Academic Press. 1966.

17.77 Horlock, J. H. On Entropy Production in Adiabatic Flow in Turbomachines. J. Basic Eng. Trans. ASME, Ser. D, 93:587-593. 1971.

17.78 Marsh, H. A Digital Computer Program for the Through-Flow Fluid Mechanics in an Arbitrary Turbomachine Using a Matrix Method. NGTE Rep. R.282. 1966.

17.79 Marsh, H. The Through-Flow Analysis of Axial Flow Compressors. In Advanced Compressors. AGARD-LS-39-70. 1970. Paper 2.

17.80 Horlock, J. H. and Marsh, H. Flow Models for Turbomachines. J. Mech. Eng. Sci. 13:358-368. 1971.

17.81 Marsh, H. The Uniqueness of Turbomachinery Flow Calculations Using the Streamline Curvature and Matrix Through-Flow Methods. J. Mech. Eng. Sci. 13:376-379. 1971.

17.82 Hearsey, R. M. and Marsh, H. Communication. J. Mech. Eng. Sci. 14: . 1972.

17.83 Katsanis, T. Use of Arbitrary Quasi-Orthogonals for Calculating Flow Distribution in the Meridional Plane of a Turbomachine. NASA TN D-2546. 1964.

17.84 Katsanis, T. Use of Arbitrary Quasi-Orthogonals for Calculating Flow Distribution in a Turbomachine. J. Eng. Power. Trans. ASME, Ser. A, 88:197-202. 1966.

17.85 Smith, D. J. L. and Barnes, J. F. Calculation of Fluid Motion in Axial Flow Turbomachines. ASME Paper 68-GT-12. 1968.

17.86 Davis, W. R. and Millar, D. A. J. A Discussion of the March Matrix Technique Applied to Fluid Flow Problems. C.A.S.I. Trans. 5(2):64-70. September 1972.

17.87 Smith, D. J. L. Computer Solutions of Wu's Equations for Compressible Flow Through Turbomachines. In Fluid Mechanics, Acoustics, and Design of Turbomachinery. NASA SP-304, Part I:43-74. 1974.

17.88 Wennerstrom, A. J. On the Treatment of Body Forces in the Radial Equilibrium Equation of Turbomachinery. In Suter, P. and Gyarmathy, G., eds., Traupel-Festschrift. Zurich. Juris-Verlag. 1974.

17.89 Wu, C.-H. Three Dimensional Turbomachine Flow Equations Expressed with Respect to Non-Orthogonal Curvilinear Coordinates and Methods of Solution. Paper presented at Third International Symposium on Air Breathing Engines. Munich. March 1976.

17.90 Wu, C.-H. and Brown, C. A., Method of Analysis for Compressible Flow Past Arbitrary Turbomachine Blades on General Surface of Revolution. NACA TN 2407. 1951.

17.91 Roudebush, W. H. Potential Flow in Two-Dimensional Cascades. In Aerodynamic Design of Axial-Flow Compressors. NASA SP-36. Chapter IV. 1965.

17.92 Roudebush, W. H. and Lieblein, S. Viscous Flow in Two-Dimensional Cascades. In Aerodynamic Design of Axial-Flow Compressors. NASA SP-36. Chapter V. 1965.

17.93 Wu. C.-H. and Brown, C. A. A Theory of Direct and Inverse Problems of Compressible Flow Past Cascade of Arbitrary Airfoils. J. Aero. Sci. 19:183-196. 1952.

17.94 Scholz, N. A Survey of the Advances in the Treatment of the Flow in Cascades. In Internal Aerodynamics (Turbomachinery). Proceedings of a conference sponsored by the Royal Society at Cambridge, 19-21 July, 1967. The Institution of Mechanical Engineers. pp. 20-31. (Discussion pp. 41-56 by K. Barsun and D. J. L. Smith). 1970.

17.95 Katsanis, T. Use of Arbitrary Quasi-Orthogonals for Calculating Flow Distribution on a Blade-to-Blade Surface in a Turbomachine. NASA TN D-2809. 1965.

17.96 Miller, M. J. and Serovy, G. K. Deviation Angle Estimation for Axial-Flow Compressors Using Inviscid Flow Solutions. J. Eng. Power. Trans. ASME, Ser. A, 97(2):163-172. 1975.

17.97 Silvester, M. E. and Fitch, C. M. Matrix Methods for the Design of Cascades to Prescribed Surface Velocity Distributions and for Fully Compressible Flow. Part I. In Lakshminarayana, B., Britsch, W. B. and Gearhart, W. S., eds. Fluid Mechanics, Acoustics and Design of Turbomachinery. NASA SP-304, pp. 75-100. 1974.

17.98 Gostelow, J. P. Review of Compressible Flow Theories for Airfoil Cascades. J. Eng. Power. Trans. ASME, Ser. A, 95:281-292. 1973. (Discussion by D. C. Prince, Jr. in J. Eng. Power. 95:77-79. 1974)

17.99 Gostelow, J. P. Trailing Edge Flows Over Turbomachine Blades and the Kutta-Joukowsky Condition. ASME Paper 75-GT-94. 1975.

17.100 Wilkinson, D. H. Stability, Convergence, and Accuracy of Two-Dimensional Streamline Curvature Methods Using Quasi-Orthogonals. Proc. of the Inst. Mech. Engr. 184:Part 3G (1):108-119. 1969-1970.

Design limit parameters are developed and discussed in Ref. 17.101-17.109.

17.101 Voit, C. L. and Thomson, A. R. An Analytical Investigation Using Aerodynamic Limitations of Several Designs of High Stage Pressure Ratio Multistage Compressors. NACA TN 2589. 1951.

17.102 Lieblein, S., Schwenk, F. C., and Broderick, R. L. Diffusion Factor for Estimating Losses and Limiting Blade Loadings in Axial-Flow-Compressor Blade Elements. NACA RM E53D01. 1953.

17.103 Lieblein, S. and Roudebush, W. H. Theoretical Loss Relations for Low-Speed Two-Dimensional-Cascade Flow. NACA TN 3662. 1956.

17.104 Lieblein, S. and Roudebush, W. H. Low-Speed Wake Characteristics of Two-Dimensional Cascade and Isolated Airfoil Sections. NACA TN 3771. 1956.

17.105 Lieblein, S. Analysis of Experimental Low-Speed Loss and Stall Characteristics of Two-Dimensional Compressor Blade Cascades. NACA RM E57A28. 1957.

17.106 Savage, M. Analysis of Aerodynamic Blade-Loading-Limit Parameters for NACA 65-(C_{20} A_{10})10 Compressor-Blade Sections at Low Speeds. NACA RM L54L02a. 1955.

17.107 Lieblein, S. Review of High-Performance Axial-Flow-Compressor Blade-Element Theory. NACA RM E53L22. 1954.

17.108 Klapproth, J. F. General Considerations of Mach Number Effects on Compressor Blade Design. NACA RM E53L23a. 1954.

17.109 Lakshminarayana, B. and Horlock, J. H. Effects of Shear Flows on the Outlet Angle in Axial Compressor Cascades--Methods of Prediction and Correlation with Experiments. J. Basic Eng. Trans. ASME, Ser. D, 89:191-200. 1967.

Supersonic and transonic compressor progress beginning in about 1945 can be followed in Ref. 17.110-17.129.

17.110 Kantrowitz, A. The Supersonic Axial Flow Compressor. NACA TR 974. 1950.

17.111 Erwin, J. R. Early Work on Supersonic Compressor. In Hawthorne, W. R., ed. Aerodynamics of Turbines and Compressors. Volume of High Speed Aerodynamic and Jet Propulsion. Princeton, N. J. Princeton Univ. Press. Section G, Chapter 1. 1964.

17.112 Ferri, A. Aerodynamic Properties of Supersonic Compressors. In Hawthorne, W. R., ed. Aerodynamics of Turbines and Compressors. Volume X of High Speed Aerodynamics and Jet Propulsion. Princeton, N. J. Princeton Univ. Press. Section G, Chapter 2. 1964.

17.113 Wilcox, W. W., Tysl, E. R. and Hartmann, M. J. Resume of the Supersonic-Compressor Research at NACA Lewis Laboratory. J. Basic Eng. Trans. ASME, Ser. D, 81:559-568. 1959.

17.114 Klapproth, J. F. A Review of Supersonic Compressor Development. J. Eng. Power. Trans. ASME, Ser. A, 83:248-268. 1961.

17.115 Conrad, O. Statistische Untersuchung von Überschallverdichtern. Jahrbuch 1965 der WGLR. pp. 374-383. 1965.

17.116 Conrad, O., Pleiss, J. and Weber, T. Study of Supersonic Compressors. FTD-HT-23-1436-68. 18 February 1969.

17.117 Chauvin, J., Breugelmans, F. and Janigro, A. Supersonic Compressors. In Chauvin, J., ed. Supersonic Turbo-Jet Propulsion Systems and Components. North Atlantic Treaty Organization. Agardograph 120. 1969.

17.118 Lieblein, S. and Johnsen, I. A. Resume of Transonic-Compressor Research at NACA Lewis Laboratory. J. Eng. Power. Trans. ASME, Ser. A, 83:219-234. 1961.

17.119 Bullock, R. O. Critical High Lights in the Development of Transonic Compressor. J. Eng. Power. Trans. ASME, Ser. A, 83:243-257. 1961.

17.120 Calmon, J. Le Developpement du Compresseur Transsonique a la SNECMA. Technique et Science Aeronautiques et Spatiales. No. 5, 431-445. 1965.

17.121 Breugelmans, F. A. E. The Supersonic Compressor Research at the von Karman Institute for Fluid Dynamics. Paper presented at the 1st International Symposium on Air Breathing Engines, Marseilles, France. 19-23 June 1972.

17.122 Thiaville, J.-M. Tassement des Compresseurs Axiaux. L'Aeronautique et l'Astronautique. 44:21-31. 1974.

17.123 Benser, W. A. Transonic Compressor Technology Advancements. In Lakshminarayana, B. et al., ed. Fluid Mechanics, Acoustics, and Design of Turbomachinery, Part II. NASA SP-304. pp. 581-602. 1974.

17.124 Simon, H. A Contribution to the Theoretical and Experimental Examination of the Flow Through Plane Supersonic Deceleration Cascades and Supersonic Compressor Rotors. J. Eng. Power. Trans. ASME, Ser. A, 95: 233-243. 1973.

17.125 Simon, H. and Bohn, D. Experimental Investigation of a Recently Developed Supersonic Compressor Stage (Rotor and Stator Performance). ASME Paper 74-GT-116. 1974.

17.126 Wennerstrom, A. J. and Hearsey, R. M. The Design of an Axial Compressor Stage for a Total Pressure Ratio of 3 to 1. ARL 71-0061. 1971.

17.127 Wennerstrom, A. J., Frost, G. R. and DeRose, R. D. Test of an Axial Compressor Stage Designed for a Total Pressure Ratio of Three to One. ARL TR 74-0001. 1974.

17.128 Wennerstrom, A. J. and Frost, G. R. Design of a Rotor Incorporating Splitter Vanes for a High Pressure Ratio Supersonic Axial Compressor Stage. ARL 74-0110. 1974.

17.129 Wennerstrom, A. J., Buzzell, W. A. and DeRose, R. D. Test of a Supersonic Axial Compressor Stage Incorporating Splitter Vanes in the Rotor. ARL TR 75-0165. 1975.

Ref. 17.130 describes a typical computer program which may be used for preliminary design of the hub-to-tip flow passage.

17.130 Bryans, A. C. and Miller, M. L. Computer Program for Design of Multistage Axial-Flow Compressors. NASA CR-54530. 1967.

For blade row geometry selection, Ref. 17.131-17.134 summarize some methods originally developed in the United Kingdom based on cascade data correlation.

17.131 Howell, A. R. The Present Basis of Axial Flow Compressor Design. Part 1. Cascade Theory and Performance. Aero. Res. Council R. & M. 2095. 1942.

17.132 Andrews, S. J. Tests Related to Profile Shape and Camber Line on Compressor Cascade Performance. Aero. Res. Council R. & M. 2743. 1949.

17.133 Carter, A. D. S. The Low Speed Performance of Related Aerofoils in Cascades. Aero. Res. Council CP 29. 1950.

17.134 Howell, A. R. Flow in Cascades. In High Speed Aerodynamics and Jet Propulsion, Hawthorne, W. R., ed. Vol. 10, Aerodynamics of Turbines and Compressors. Princeton, N. J. Princeton Univ. Press. 1964.

Ref. 17.12, 17.13 and 17.135-17.139 cover methods and considerations involved in cascade data correlation in the United States.

17.135 Lieblein, S. Incidence and Deviation-Angle Correlations for Compressor Cascades. J. Basic Eng. Trans. ASME, Ser. D, 82:575-587. 1960.

17.136 Lieblein, S. Loss and Stall Analysis of Compressor Cascades. J. Basic Eng. Trans. ASME, Ser. D, 81:387-400. 1959.

17.137 Wright, L. C. Blade Selection for a Modern Axial-Flow Compressor. In Fluid Mechanics, Acoustics, and Design of Turbomachinery, Part II. Lakshminarayana, B. et al., editors. NASA SP-304. 1974. pp. 603-626.

17.138 Serovy, G. K. Utilization of Cascade Data in Axial-Flow Compressor Design and Analysis--A Critical Review. ASME Paper 70-GT-108. 1970.

17.139 Miller, M. J. Deviation Angle Prediction Methods--A Review. Iowa State University Engineering Research Institute Report 580. 1969.

Cascade data procedures developed in the USSR are reviewed in Ref. 17.140-17.142.

17.140 Bunimovich, A. I. and Svyatogorov, A. A. Generalization of Results of Investigation of Foil Compressor Cascades at Subsonic Speed. FTD-MT-24-69-68. 1968.

17.141 Bunimovich, A. I. and Svyatogorov, A. A. Aerodynamic Characteristics of Foil Compressor Cascades at High Subsonic Speed. FTD-MT-24-69-68. 1968.

17.142 Komarov, A. P. Investigation of Flat Compressor Grids. FTD-MT-24-69-68. 1968.

Losses produced by transonic and supersonic operation are studied in Ref. 17.143-17.145.

17.143 Miller, G. R., Lewis, G. W., Jr. and Hartmann, M. J. Shock Losses in Transonic Blade Rows. J. Eng. Power. Trans. ASME, Ser. A, 83:235-242. 1961.

17.144 Mikolajczak, A. A., Morris, A. L. and Johnson, B. V. Comparison of Performance of Supersonic Blading in Cascade and in Compressor Rotors. J. Eng. Power. Trans. ASME, Ser. A, 93:42-48. 1971.

17.145 Huffman, G. D. and Tramm, P. C. Airfoil Design for High Tip Speed Compressors. J. Aircraft. 11:682-689. 1974.

Some additional paper on subjects related to blade selection are Ref. 17.109 and 17.146-17.154.

17.146 Lakshminarayana, B. and Horlock, J. H. Review - Secondary Flows and Losses in Cascades and Axial-Flow Turbomachines. Int. J. Mech. Sci. 5:287-307. 1963.

17.147 Bardon, M. F., Moffatt, W. C. and Randall, J. L. Secondary Flow Effects on Gas Exit Angles in Rectilinear Cascades. J. Eng. Power. Trans. ASME, Ser. A, 97:93-100. 1975.

17.148 Smith, L. H., Jr. Secondary Flow in Axial-Flow Turbomachinery. Trans. ASME. 77:1065-1976. 1955.

17.149 Dzung, L. S. Consistent Mean Values for Compressible Media in the Theory of Turbomachines. Brown Boveri Review. 58(10): 3-10. October 1971.

17.150 Brown, L. E. Axial Flow Compressor and Turbine Loss Coefficients: A Comparison of Several Parameters. J. Eng. Power, Trans. ASME, Ser. A, 94:193-201. 1972.

17.151 Esgar, G. M. and Sandercock, D. M. Some Observed Effects of Part-Span Dampers on Rotating Blade Row Performance Near Design Point. NASA TM X-2696. 1973.

17.152 Smith, L. H., Jr. and Yeh, H. Sweep and Dihedral Effects in Axial-Flow Turbomachinery. J. Basic Eng. Trans. ASME, Ser. D, 85:401-416. 1963.

17.153 Smith, L. H., Jr. Some Aerodynamic Design Considerations for High Bypass Ratio Fans. General Electric Company. Advanced Fan and Compressor Aerodynamic Operation, T.M. 74-131. February 1, 1974.

17.154 Koch, C. C. and Smith, L. H., Jr. Loss Sources and Magnitudes in Axial-Flow Compressors. J. Eng. Power. Trans. ASME, Ser. A, 98:411-424. 1976.

Methods for blade section and blade row computation and stacking are described in Ref. 17.155-17.157 and 17.158.

17.155 Frost, G. R., Hearsey, R. M. and Wennerstrom, A. J. A Computer Program for the Specification of Axial Compressor Airfoils. ARL 72-0171. 1972.

17.156 Frost, G. R. and Wennerstrom, A. J. The Design of Axial Compressor Airfoils Using Arbitrary Camber Lines. ARL 73-0107. 1973.

17.157 Frost, G. R. Modifications to ARL Computer Programs Used for Design of Axial Compressor Airfoils. ARL 74-0060. 1974.

17.158 Crouse, J. E. Computer Program for Definition of Transonic Axial-Flow Compressor Blade Rows. NASA TN D-7345. 1974.

A useful system for estimating compressor size and weight is given in Ref. 17.159.

17.159 Sagerser, D. A., Lieblein, S. and Krebs, R. P. Empirical Expressions for Estimating Length and Weight of Axial-Flow Components of VTOL Powerplants. NASA TM X-2406. 1971.

Programs for design analysis are the subject of Ref. 17.160-17.181.

17.160 Hetherington, R. Computer Calculations of the Flow in Axial Compressors. In Internal Aerodynamics (Turbomachinery). London. Inst. of Mech. Eng. pp. 57-63. 1970.

17.161 Marsh, H. A Digital Computer Program for the Through-Flow Fluid Mechanics in an Arbitrary Turbomachine Using a Matrix Method. Aero. Res. Council, R. & M. 3509. 1968.

17.162 Davis, W. R. A Computer Program for the Analysis and Design of Turbomachinery--Revision. Report ME/A 71-5. Division of Aerothermodynamics. Carleton University. September 1971.

17.163 Davis, W. R. A Computer Program for the Analysis and Design of the Flow in Turbomachinery. Part B - Loss and Deviation Correlations. Report ME/A 70-1. Division of Aerothermodynamics. Carleton University. July 1970.

17.164 Davis, W. R. and Millar, D. A. J. A Comparison of the Matrix and Streamline Curvature Methods of Axial Flow Turbomachinery Analysis, From a User's Point of View. J. Eng. Power, Trans. ASME, Ser. A, 97: 549-560. 1975.

17.165 Smith, D. J. L. and Frost, D. H. Calculation of the Flow Past Turbomachine Blades. In Thermodynamics and Fluid Mechanics Convention 1970. Volume II - Axial and Radial Turbomachinery. Proc. Inst. Mech. Eng. 184:Part 3G(II):72-85. 1970.

17.166 Glenny, D. E. An Application of Streamline Curvature Methods to the Calculation of Flow in a Multistage Axial Compressor. Aeronautical Research Laboratories (Australia). Note ARL/M.E. 346. 1974.

17.167 Glenny, D. E. Performance Evaluation of a Multistage Axial Compressor Using a Streamline Curvature Model. ASME Paper 75-WA/GT-10. 1975.

17.168 Hearsey, R. M. A Revised Computer Program for Axial Compressor Design. Volume I: Theory, Descriptions and User's Instructions. ARL TR 75-0001, Volume I. 1975. Volume II: Program Listing and Program Use Example. ARL TR 75-0001, Volume II. 1975.

17.169 Novak, R. A. and Hearsey, R. M. A Nearly Three-Dimensional Intrablade Computing System for Turbomachinery. J. Fluids Eng. Trans. ASME, Ser. I, 99:154-166. 1977.

17.170 Novak, R. A. Through-Flow Calculations in Axial Turbomachinery. AGARD-CP-195. 1976.

17.171 Biniaris, S. The Calculation of the Quasi-Three-Dimensional Flow in an Axial Gas Turbine. J. Eng. Power. Trans. ASME, Ser. A, 97:283-294. 1975.

17.172 Hirsch, C. and Warzee, G. A Finite Element Method for Flow Calculations in Turbomachines. Vrije Universiteit Brussel, Dienst Stromingsmechanica. Rep. VUB-STR-5. July 1974.

17.173 Katsanis, T. and McNally, W. D. Fortran Program for Calculating Velocities and Streamlines on the Hub-Shroud Mid-Channel Flow Surface of an Axial- or Mixed-Flow Turbomachine. I - User's Manual. NASA TN D-7343. 1973. II - Programmer's Manual. NASA TN D-7344. 1974.

17.174 Wilkinson, D. H. Calculation of Blade-to-Blade Flow in a Turbomachine by Streamline Curvature. Aero. Res. Council R. & M. 3704. 1972.

17.175 Katsanis, T. Fortran Program for Calculating Transonic Velocities on a Blade-to-Blade Stream Surface of a Turbomachine. NASA TN D-5427. 1969.

17.176 Katsanis, T. and McNally, W. D. Fortran Program for Calculating Velocities in a Magnified Region on a Blade-to-Blade Stream Surface of a Turbomachine. NASA TN D-5091. 1969.

17.177 Frost, D. H. A Streamline Curvature Through-Flow Computer Program for Analyzing the Flow through Axial-Flow Turbomachines. Aero. Res. Council R. & M. 3687. 1970.

17.178 McDonald, P. W. The Computation of Transonic Flow Through Two-Dimensional Gas Turbine Cascades. ASME Paper 71-GT-89. 1971.

17.179 Dodge, P. R. The Use of a Finite Differ-

ence Technique to Predict Cascade, Stator, and Rotor Deviation Angles and Optimum Angles of Attack. J. Eng. Power, Trans. ASME, Ser. A, 95:185-190. 1973.

17.180 Dodge, P. R. A Non-Orthogonal Numerical Method for Solving Transonic Cascade Flows. ASME Paper 76-GT-63. 1976.

17.181 Hantman, R. G., Mikolajczak, A. A. and Camarata, F. J. Application of a Two-Dimensional Supersonic Passage Analysis to the Design of Compressor Rotors. ASME Paper 74-GT-97. 1974.

Ref. 17.182-17.187 outline methods for end-wall boundary layer prediction.

17.182 Hanley, W. T. A Correlation of End Wall Losses in Plane Compressor Cascades. J. Eng. Power. Trans. ASME, Ser. A, 90:251-257. 1968.

17.183 Stratford, B. S. The Use of Boundary Layer Techniques to Calculate the Blockage from the Annulus Boundary Layers in a Compressor. ASME Paper 67-WA/GT-7. 1967.

17.184 Jansen, W. The Application of End-Wall Boundary Layer Effects in the Performance Analysis of Axial Compressors. ASME Paper 67-WA/GT-11. 1967.

17.185 Horlock, J. H. and Hoadley, D. Calculation of the Annulus Wall Boundary Layers in Axial Flow Turbomachines. Aero. Res. Council CP 1196. 1972.

17.186 Bradshaw, P. Prediction of Turbulent Shear Layers in Turbomachines. In Fluid Mechanics, Acoustics, and Design of Turbomachinery. NASA SP-304, Part I:251-277. 1974.

17.187 Smith, L. H., Jr. Casing Boundary Layers in Multistage Axial-Flow Compressors. In Flow Research on Blading. Amsterdam. Elsevier. 1969.

Some potentially attractive three-dimensional flow field computation methods are described in Ref. 17.188-17.191.

17.188 Stuart, A. R. and Hetherington, R. The Solution of Three-Variable Duct-Flow Equations. In Fluid Mechanics, Acoustics, and Design of Turbomachinery. NASA SP-304, Part I:135-153. 1974.

17.189 Erdos, J., Alzner, E., Kalben, P., McNally, W. and Slutsky, S. Time-Dependent Transonic Flow Solutions for Axial Turbomachinery. In Aerodynamic Analyses Requiring Advanced Computers, NASA SP-347, Part I:587-621. 1975.

17.190 Briley, W. R. and McDonald, H. Computation of Three-Dimensional Turbulent Subsonic Flow in Curved Passages. United Aircraft Research Laboratories Report R75-911596-8. March 1975.

17.191 Eiseman, P. R. and McDonald, H. A Method for Computing Three-Dimensional Flow in Ducts. In Prediction Methods for Jet V/STOL Propulsion Aerodynamics. Naval Air Systems Command Research and Technology Group. 1:83-113. July 1975.

Performance prediction by simplified methods is discussed in Ref. 17.192-17.196.

17.192 Howell, A. R. and Bonham, R. P. Overall and Stage Characteristics of Axial-Flow Compressors. Proc. Inst. Mech. Eng. 163:235-248. 1950.

17.193 Robbins, W. H. and Dugan, J. F., Jr. Prediction of Off-Design Performance of Multistage Compressors. In Aerodynamic Design of Axial-Flow Compressors. NASA SP-36. Chap. X. 1965.

17.194 Southwick, R. D. A Stage-Stacking Simulation of Axial Flow Compressors with Variable Geometry. Aeronautical Systems Division, U.S. Air Force Systems Command. ASD-TR-74-38. 1974.

17.195 Serovy, G. K. Compressor and Turbine Performance Prediction System Development--Lessons from Thirty Years of History. In Modern Prediction Methods for Turbomachine Performance. AGARD-LS-83. 1976.

17.196 Wall, R. A. Axial Flow Compressor Performance Prediction. In Modern Prediction Methods for Turbomachine Performance. AGARD-LS-83. 1976.

Performance prediction by extension of design analysis methods is discussed in Ref. 17.197-17.203, and for cases where inlet distortion is present Ref. 17.204-17.206 are suggested.

17.197 Serovy, G. K. A Method for the Prediction of the Off-Design Performance of Axial-Flow Compressors. Ph.D. Dissertation. Iowa State University. Ames, Iowa. 1958.

17.198 Serovy, G. K. and Anderson, E. W. Method for Predicting Off-Design Performance of Axial-Flow Compressor Blade Rows. NASA TN D-110. 1959.

17.199 Swan, W. C. A Practical Engineering Solution of the Three-Dimensional Flow in Transonic Type Axial Flow Compressors. WADC Technical Report 58-57. February 1958.

17.200 Swan, W. C. A Practical Method of Predicting Transonic-Compressor Performance. J. Eng. Power, Trans. ASME, Ser. A, 83:322-330. 1961.

17.201 Jansen, W. and Moffatt, W. C. The Off-Design Analysis of Axial-Flow Compressors. J. Eng. Power, Trans. ASME, Ser. A, 89: 453-462. 1967.

17.202 Grahl, K. Teillastberechnung für Axialverdichterstufen. Zeitschrift für Flugwissenschaften 20:42-51. 1972.

17.203 Novak, Richard A. Flow Field and Performance Map Computation for Axial-Flow Compressors and Turbines. In Modern Prediction Methods for Turbomachine Performance. AGARD-LS-83. 1976.

17.204 Novak, R. A. and Hearsey, R. M. The Performance Prediction of Multistage Axial Compressor of Arbitrary Geometry Operating with Combined Radial and Circumferential Distributions. In Proceed-

ings of the Air Force Airborne-Propulsion Compatibility Symposium, 24-26 June, 1969. AFAPL-TR-69-103, pp. 627-672. 1970.

17.205 Novak, R. A., Hearsey, R. M. Model for Predicting Compressor Performance with Combined Circumferential and Radial Distortion - Computer Program. APL-TR-68-142, Part VIII. December 1968.

17.206 Mazzawy, R. S. Multiple Segment Parallel Compressor Model for Circumferential Flow Distortion. Paper presented at AGARD Conference on Unsteady Phenomena in Turbomachinery. Monterey, California. 22-26 September 1975.

Aeroelastic analysis methods should be understood by the aerodynamicist. Ref. 17.53 and 17.207-17.210 will help.

17.207 Jeffers, J. D., II, and Meece, C. E., Jr. F100 Fan Stall Flutter Problem Review and Solution. J. Aircr. 12:350-357. 1975.

17.208 Danforth, C. E. Distortion-Induced Vibration in Fan and Compressor Blading. J. Aircr. 12:216-225. 1975.

17.209 Danforth, C. E. Blade Vibration: Same Key Elements in Design Verification. J. Aircr. 12:333-342. 1975.

17.210 Fleeter, S., McClure, R. B., Sinnet, G. T. and Holtman, R. L. Supersonic Inlet-Torsional Cascade Flutter. J. Aircr. 12(8): 664-669. 1975.

SECTION 17.7 COMPONENT AND CONFIGURATION EXPERIMENTAL DEVELOPMENT

SECTION 17.8 AXIAL-FLOW COMPRESSOR AND PERFORMANCE TRENDS

Some specific programs of continuing and current interest can be located and are summarized by configuration.

NACA 8-stage compressor	Ref. 17.211-17.219
NACA 5-stage compressor	Ref. 17.220-17.225
J-83 turbojet engine compressor	Ref. 17.226-17.227
CJ805-23 fan component	Ref. 17.228
NASA-GE rotor research program	Ref. 17.229-17.231
NASA-PW 1600 ft/sec tip speed stage	Ref. 17.232 and 17.15
NASA-GE 1500 ft/sec tip speed stage	Ref. 17.14-17.16
NASA-PW 1800 ft/sec tip speed stage	Ref. 17.233-17.234
NASA-AiResearch 1500 ft/sec fan stage	Ref. 17.235-17.237
NASA-PW two-stage fan	Ref. 17.238-17.240
NGTE 4-stage compressor	Ref. 17.241

17.211 Voit, C. H. Investigation of a High-Pressure-Ratio Eight-Stage Axial-Flow Research Compressor with Two Transonic Inlet Stages. I - Aerodynamic Design. NACA RM E53I24. 1953.

17.212 Geye, R. P., Budinger, R. E. and Voit, C. H. Investigation of High-Pressure-Ratio Eight-Stage Axial-Flow Research Compressor with Two Transonic Inlet Stages. II - Preliminary Analysis of Over-All Performance. NACA RM E53J06. 1953.

17.213 Voit, C. H. and Geye, R. P. Investigation of a High-Pressure-Ratio Eight-Stage Axial-Flow Research Compressor with Two Transonic Inlet Stages. III - Individual Stage Performance Characteristics. NACA RM E54H17. 1954.

17.214 Geye, R. P. and Voit, C. H. Investigation of a High-Pressure-Ratio Eight-Stage Axial-Flow Research Compressor with Two Transonic Inlet Stages. IV - Modification of Aerodynamic Design and Prediction of Performance. NACA RM E55B28. 1955.

17.215 Standahar, R. M. and Geye, R. P. Investigation of High-Pressure-Ratio Eight-Stage Axial-Flow Research Compressor with Two Transonic Inlet Stages. V - Preliminary Analysis of Over-All Performance of Modified Compressor. NACA RM E55A03. 1955.

17.216 Standahar, R. M., Hanson, M. P. and Geye, R. P. Investigation of a High-Pressure-Ratio Eight-Stage Axial-Flow Research Compressor with Two Transonic Inlet Stages. VI - Over-All Performance, Rotating Stall, and Blade Vibration at Low and Intermediate Compressor Speeds. NACA RM E55I13. 1955.

17.217 Geye, R. P. and Lucas, J. G. Investigation of Effects of Reynolds Number on Over-All Performance of an Eight-Stage Axial-Flow Research Compressor with Two Transonic Inlet Stages. NACA RM E56L11a. 1957.

17.218 Sievers, G. K., Geye, R. P. and Lucas, J. G. Preliminary Analysis of Over-All Performance of an Eight-Stage Axial-Flow Research Compressor with Two Long-Chord Transonic Inlet Stages. NACA RM E57H14. 1958.

17.219 Sievers, G. K., Geye, R. P. and Lucas, J. G. Investigation of Reynolds Number Effect on Performance of an Eight-Stage Axial-Flow Research Compressor with Long- and Medium-Chord Lengths in the Two Transonic Inlet Stages. NACA RM E57J30. 1958.

17.220 Sandercock, D. M., Kovach, K. and Lieblein, S. Experimental Investigation of a Five-Stage Axial-Flow Research Compressor with Transonic Rotors in All Stages. I - Compressor Design. NACA RM E54F24. 1954.

17.221 Kovach, K. and Sandercock, D. M. Experimental Investigation of a Five-Stage Axial-Flow Research Compressor with Transonic Rotors in All Stages. II - Compressor Over-All Performance. NACA RM E54G01. 1954.

17.222 Sandercock, D. M. and Kovach, K. Experimental Investigation of a Five-Stage Axial-Flow Research Compressor with Transonic Rotors in All Stages. III - Interstage Data and Individual Stage Performance Characteristics. NACA RM E56G24. 1956.

17.223 Sandercock, D. M. Experimental Investigation of a Five-Stage Axial-Flow Research Compressor with Transonic Rotors in All Stages. IV - Blade-Element Performance. NACA RM E57B12. 1957.

17.224 Robbins, W. H. and Glaser, F. W. Experimental Investigation of the Effect of Circumferential Inlet Flow Distortion on the Performance of a Five-Stage Axial-Flow Research Compressor with Transonic Rotors in All Stages. NACA RM E57J17. 1958.

17.225 Kovach, Karl and Sandercock, D. M. Aerodynamic Design and Performance of Five-Stage Transonic Axial-Flow Compressor. J. Eng. Power, Trans. ASME, Ser. A, 83: 303-321. 1961.

17.226 King, J. A. The J-83 Seven-Stage Transonic Compressor. J. Eng. Power, Trans. ASME, Ser. A, 83:291-302. 1961.

17.227 Swan, W. C. An Experiment with Aspect Ratio as a Means of Extending the Useful Range of a Transonic Inlet Stage of an Axial-Flow Compressor. J. Eng. Power, Trans. ASME, Ser. A, 86:243-246. 1964.

17.228 Wright, L. C. and Novak, R. A. Aerodynamic Design and Development of the General Electric CJ805-23 Aft Fan Component. *ASME* Paper 60-WA-270. 1960.

17.229 Seyler, D. R. and Smith, L. H., Jr. Single Stage Experimental Evaluation of High Mach Number Compressor Rotor Blading. Part 1 - Design of Rotor Blading. NASA CR-54581. 1967.

17.230 Gostelow, J. P., Krabacher, K. W. and Smith, L. H., Jr. Performance Comparisons of High Mach Number Compressor Rotor Blading. NASA CR-1256. 1968.

17.231 Gostelow, J. P. Design and Performance Evaluation of Four Transonic Compressor Rotors. J. Eng. Power, Trans. ASME, Ser. A, 93:33-41. 1971.

17.232 Monsarrat, N. T., Keenan, M. J. and Tramm, P. C. Design Report. Single-Stage Evaluation of Highly-Loaded High-Mach-Number Compressor Stages. NASA CR-72562. 1969.

17.233 Morris, A. L., Halle, J. E. and Kennedy, E. High-Loading, 1800 Ft/Sec Tip Speed Transonic Compressor Fan Stage. I. Aerodynamic and Mechanical Design. NASA CR-120907. 1972.

17.234 Morris, A. L. and Sulam, D. H. High-Loading, 1800 Ft/Sec Tip Speed Transonic Compressor Fan Stage. II. Final Report. NASA CR-120991. 1972.

17.235 Wright, L. C. Vitale, N. G., Ware, T. C. and Erwin, J. R. High-Tip-Speed, Low-Loading Transonic Fan Stage (Part 1 - Aerodynamic and Mechanical Design). NASA CR-121095. 1973.

17.236 Ware, T. C., Kobayashi, R. J. and Jackson, R. J. High-Tip-Speed, Low-Loading Transonic Fan Stage (Part 2 - Data Compilation). NASA CR-121262. 1974.

17.237 Ware, T. C., Kobayashi, R. J. and Jackson, R. J. High-Tip-Speed, Low-Loading Transonic Fan Stage (Part 3 - Final Report). NASA CR-121263. 1974.

17.238 Messenger, H. E. and Kennedy, E. E. Two-Stage Fan. I. Aerodynamic and Mechanical Design. NASA CR-120859. 1972.

17.239 Messenger, H. E. and Keenan, M. J. Two-Stage Fan. II. Data and Performance with Redesigned Second Stage Rotor Uniform and Distorted Inlet Flows. NASA CR-134710. 1974.

17.240 Ruggeri, R. S. and Benser, W. A. Performance of a Highly-Loaded Two-Stage Axial Flow Fan. NASA TM X-3076. 1974.

17.241 Dransfield, D. C. and Calvert, W. J. Detailed Flow Measurements in a Four Stage Axial Compressor. ASME Paper 76-GT-46. 1976.

General development reviews are available in Ref. 17.242-17.243.

17.242 Doll, W. Turbomachinery Technology at Pratt and Whitney Aircraft. In Internal Aerodynamics (Turbomachinery). Proceedings of a conference sponsored by the Royal Society at Cambridge, 19-21 July, 1967. The Institution of Mechanical Engineers. pp. 3-8. 1970.

17.243 Newton, A. G. Some Thoughts on Axial Flow Compressors. In Internal Aerodynamics (Turbomachinery). Proceedings of a conference sponsored by the Royal Society at Cambridge, 19-21 July, 1967. London. The Institution of Mechanical Engineers. pp. 9-13. 1970.

Experimental development of compressors and special methods for performance improvement are described in Ref. 17.244-17.250.

17.244 Stone, A. Effects of Stage Characteristics and Matching on Axial-Flow-Compressor Performance. Trans. ASME, 80:1273-1293. 1958.

17.245 Watkins, J. Stage Performance and Radial Matching of Axial Compressor Blade Rows. J. Eng. Power, Trans. ASME, Ser. A, 81:13-23. 1959.

17.246 Brown, L. E. and Groh, F. G. Use of Experimental Interstage Performance Data to Obtain Optimum Performance of Multistage Axial Compressors. J. Eng. Power, Trans. ASME, Ser. A, 84:187-194. 1962.

17.247 Brown, L. E. The Use of Experimental Interstate Data for Matching the Performance of Axial Compressor Stages Having

Variable-Setting-Angle Blade Rows. ASME Paper 76-GT-42. 1976.

17.248 Kovach, K. and Griffiths, P. R. Engine Compression System Surge Line Evaluation Techniques. Paper presented at Third International Symposium on Air Breathing Engines. Munich. 1976.

17.249 Prince, D. C., Jr., Wisler, D. C. and Hilvers, D. E. A Study of Casing Treatment Stall Margin Improvement Phenomena. ASME Paper 75-GT-60. 1975.

17.250 Holman, F. F. and Kidwell, J. R. Effects of Casing Treatment on a Small, Transonic Axial-Flow Compressor. ASME Paper 75-WA/GT-6. 1975.

17.10 SYMBOLS AND NOTATION

A	area
AVDR	axial velocity-density ratio, $\rho_2 V_{x_1 2} / \rho_1 V_{x_1 1}$ for blade sections in cascade or blade row
a	distance measured along chord line from leading end of section camber line to maximum camber point (Figure 17.1.7)
a	acoustic velocity
b	coordinate of maximum camber measured along perpendicular to chord line (Figure 17.1.7)
c	chord length, length of straight line connecting leading and trailing end points of camber line (Figure 17.1.7)
D	diffusion parameter (Eq. 17.5.12 to 17.5.15)
D	diameter
d	distance of maximum thickness location from leading end of section camber line (Figure 17.1.7)
E	energy transfer
F	body force
g	local gravitationa' acceleration
H	total enthalpy
h	static enthalpy
I	rothalpy (Eq. 17.5.5)
i	incidence angle, angle between inlet flow direction and line tangent to blade section camber line at leading edge
L	length
LER	leading-edge radius of blade section
M	Mach number
m	mass flow rate
N	rotational speed of shaft
P	total pressure
P	static pressure
q	heat transferred
R	radius
R^*	passage radial location, $(r - r_h)/(r_t - r_h)$
r	radial coordinate, measured from compressor axis
r_c	radius of curvature of stream surface trace in meridional plane (Figure 17.5.7)
s	entropy
s	blade spacing (Figure 17.1.8)
T	temperature
T_B, T_S	moments of forces, see Eq. (17.5.10)
T_U	turbulence parameter
TER	trailing-edge radius of blade section
t	time
t	maximum thickness of blade section (Figure 17.1.7)
U	blade section velocity
V	velocity in fixed coordinate system
W	velocity relative to coordinate system attached to rotor
x	axial coordinate
β	angle between velocity vector and axial direction
γ	stagger angle, angle between chord line and axial direction (Figure 17.1.8)
γ	fluid specific heat ratio
δ	deviation angle, angle between cascade exit fluid velocity and line tangent to section camber line at trailing edge (Figure 17.1.8)
δ	ratio of total pressure at compressor inlet to standard sea-level pressure
ϵ	angle in meridional plane between line tangent to stream surface and axial direction
η	compressor or stage efficiency
θ	circumferential coordinate
θ	ratio of total temperature at compressor inlet to standard sea-level temperature

θ^*	total boundary-layer momentum thickness at section trailing edge
κ	angle between line tangent to section camber line and axial direction (Figure 17.1.8)
μ	fluid dynamic viscosity
ρ	fluid density
σ	cascade or blade row solidity, chord length/blade spacing
ϕ	flow coefficient, $(V_x/U)_{mean}$
φ	blade section camber angle, $\kappa_1 - \kappa_2$ (Figure 17.1.8)
ψ	pressure coefficient, $\Delta H_{isentropic}/U^2_{mean}$
$\bar{\omega}$	average total pressure loss coefficient, $\overline{P}_1 - \overline{P}_2/\overline{P}_1 - p_1$ (Figure 17.1.8)

Subscript

A, B, C, D	location of computing station
a, b	measurement location
act	actual
ad	adiabatic
an	annulus
CS	control surface
ex	exit
F	frontal cross-section
h	hub
i	inlet
in	inlet
is	isentropic
m	meridional component
R	rotor
r	radial component
rel	relative
t	tip
u	blade velocity
x	axial component
θ	circumferential or tangential component
1	inlet to blade row (Figure 17.1.8)
2	exit of blade row (Figure 17.1.8)
1 to 20	measurement or computing station location

Superscript

$\rightarrow$	vector quantity
$-$	average

Chapter 18

TURBINE AERODYNAMICS

Robert P. Dring
United Technologies Research Center

and

William H. Heiser
Arnold Engineering Development Center

TURBINE AERODYNAMICS

THE AEROTHERMODYNAMICS OF AIRCRAFT GAS TURBINE ENGINES

Chapter 18

by

Robert P. Dring
United Technologies Research Center

and

William H. Heiser
Arnold Engineering Development Center

Table of Contents

		Page
Table of Contents		18-i
List of Figures		18-i
18.0	Introduction	18-1
	18.0.0 General Trends	18-1
	18.0.1 Related Disciplines	18-1
18.1	Turbine Airfoil Characteristics	18-2
	18.1.0 Introduction	18-2
	18.1.1 Mach Number	18-2
	18.1.2 Reynolds Number	18-2
	18.1.3 Endwall and Leakage Flows	18-2
	18.1.4 Conclusion	18-3
18.2	Design Considerations	18-3
	18.2.0 Introduction	18-3
	18.2.1 Design Constraints	18-3
	18.2.2 The Design System	18-4
	18.2.3 Summary	18-4
18.3	Performance	18-5
	18.3.0 Introduction	18-5
	18.3.1 Uncooled Turbine Efficiency	18-5
	18.3.2 Cooled Turbine Efficiency	18-5
	18.3.3 Total Pressure Loss Breakdown	18-6
18.4	Profile Aerodynamics	18-6
	18.4.0 Introduction	18-6
	18.4.1 Design Approach	18-6
	18.4.2 Potential Flow	18-7
	18.4.3 Boundary Layer	18-8
	18.4.4 Wake Mixing	18-9
	18.4.5 Cascade Testing	18-9
	18.4.6 Cooling Effects	18-10
	18.4.7 Conclusions	18-10
18.5	Endwall Aerodynamics	18-10
	18.5.0 Introduction	18-10
	18.5.1 Experimental Evidence	18-10
	18.5.2 Classical Secondary Flow Analysis	18-11
	18.5.3 Endwall Boundary Layer Analysis	18-12
	18.5.4 Three-Dimensional Flow Analysis	18-12
	18.5.5 Unshrouded Rotor Tip Leakage	18-12
	18.5.6 Loss Reduction Devices	18-13
	18.5.7 Conclusions	18-13
18.6	Parasitic Loss	18-13
	18.6.0 Introduction	18-13
	18.6.1 Sources and Mechanisms	18-13
	18.6.2 Conclusions	18-14
18.7	Structural Excitation	18-14
	18.7.0 Introduction	18-14
	18.7.1 Buffeting	18-14
	18.7.2 Flutter	18-15
18.8	Stage Performance	18-15
	18.8.0 Introduction	18-15
	18.8.1 The Limits of Uncooled Stage Performance	18-15
	18.8.2 Controlled-Vortex Aerodynamics	18-15
	18.8.3 Some Related Considerations	18-16
18.9	Looking Ahead	18-16
18.10	Acknowledgement	18-17
18.11	References	18-17
18.12	Nomenclature	18-19

Figures

18.1	Cascade Airfoil Pressure Distributions	18-20
18.2	Transonic Cascade Flow	18-20
18.3	Predicted and Measured Stator Pressure Distribution	18-20
18.4	Predicted and Measured Rotor Pressure Distribution	18-21
18.5	Cascade Airfoil Pressure Distribution	18-21
18.6	Effect of Reynolds Number on Cascade Loss	18-21
18.7	Cascade Profile Loss versus Reynolds Number	18-21
18.8	Cascade Endwall Limiting Streamlines	18-21
18.9	Cascade Static Pressure Distribution Showing Effect of Endwall Flow	18-22
18.10	Isobar Plot of Total Pressure Loss Coefficients at Three Axial Planes	18-22
18.11	Schematic Diagram of Turbine Sealing Arrangements	18-22
18.12	Goodman Diagram for Combined Static Load and Fatigue Life	18-22
18.13	Limits of Turbine Stage Performance	18-23
18.14	Measured Free-Vortex and Controlled-Vortex Spanwise Traverse Effiency	18-23

18.0 Introduction

Few devices have changed so drastically during the past decade as the aircraft gas turbine. The changes are the natural result of improving jet engine performance by means of new cycle parameters or configurations. We have seen in Section II - Performance that such advances are usually tied to increasingly demanding turbine operating conditions, including higher temperature, pressure and output power levels. In order to meet these requirements with acceptable cost, weight and durability, turbine cooling has been reduced to practice and the designer has sought to extract as much work as possible from each stage and, indeed, from each airfoil. Because these cycle changes spring from a fundamental thermodynamic foundation, there is every reason to expect the progression to continue into the next century.

A curious fact is that no comprehensive review of turbine aerodynamic technology has appeared since Horlock published "Axial Flow Turbines" in 1966 (Ref. (18.1)). That book still provides an excellent framework for the study of aircraft gas turbines, and we shall employ many of the concepts developed there in what follows. The main purpose of this Chapter is to describe what has happened to turbine aerodynamics during the past decade. Our remarks are largely concerned with two types of knowledge: first, improved understanding of familiar but complex phenomena (e.g. transonic flows and transitional boundary layers) and, second, information regarding areas which have received essentially new attention (e.g. cooling flows and endwall flows).

We will be seen to have a bias in favor of sophisticated analysis supported by realistic testing. Our experience has shown us that the pressures of the marketplace have made these tools not only desirable, but essential. On one hand, cooling has driven the number of design permutations to the point where correlations based on existing data cannot provide the required design information. On the other hand, building an experimental turbine has become so costly and time-consuming that a modern engine development program is under a tremendous handicap if the initial turbine design falls short of the mark. Both arguments lead to the conclusion that confident analysis and accurate model and component testing are highly desirable. As described subsequently, many important advances have already been made, and others now seem likely. Much of the chance has been removed from turbine design, and we are hopeful that this trend will continue.

18.0.0 General Trends

The leading trends in turbine technology can be illustrated by means of the information contained in Table 18.0.1, which compares the Pratt and Whitney JT3D and JT9D engines operating under sea-level, hot-day, take-off conditions. Both engines were designed for commercial usage and employ similar cycles, but were developed almost a decade apart.

The most remarkable feature of the data below is that the high pressure turbine (HPT) inlet temperature rose beyond the working temperatures of available materials during the period in question. This required the extensive use of cooling air and led to new airfoil shapes capable of providing suitable coolant passages. Meanwhile, the average stage loading coefficient (i.e. stage specific work/wheel speed squared), a direct measure of the associated aerodynamic difficulties, remained essentially constant. One is led to the conclusion that the HPT designers were well occupied with the novel problems of cooling.

Table 18.0.1

Parameter	JT3D	JT9D
Year of introduction	1961	1970
Engine bypass ratio	1.45	4.86
Engine overall pressure ratio	13.6	24.5
Core engine flow (lb/sec)	187.7	272.0
High pressure turbine		
Inlet temperature (°F)	1745	2500
Power output (HP)	24,100	71,700
Number of stages	1	2
Average stage loading coefficient	1.72	1.76
Coolant plus leakage flow (%)	2.5	16.1
Low pressure turbine		
Inlet temperature (°F)	1410	1600
Power output (HP)	31,800	61,050
Number of stages	3	4
Average stage loading coefficient	1.44	2.47
Coolant plus leakage flow (%)	0.7	1.4

The low pressure turbine (LPT) presents a completely different picture. In order to satisfy the greatly increased demand for power by the fan without either increasing the wheel speed or adding a large number of stages, the average stage loading had to be increased. In fact, if the JT9D LPT was based upon JT3D aerodynamic technology, six or seven stages would be required to replace the existing four. In order to avoid the excessive corresponding cost and weight penalties, LPT designers concentrated on applying advanced uncooled turbine aerodynamics.

The foregoing examples lead to a key point, namely that natural forces have combined to drive turbine aerodynamics into unexplored and uncertain territory. This has increased the risks being taken, and increased the demand for methods which help assure success. The remainder of this Chapter is largely devoted to an elaboration of our current understanding of the art.

18.0.1 Related Disciplines

Although this Chapter deals principally with aerodynamics, we feel that there are other aspects of turbine design of equal importance. Since turbines are expected to run for thousands of hours without major overhaul, it follows that they cannot be based upon aerodynamic considerations alone. A successful machine results only from a highly iterative series of thoughtful aerodynamic, heat transfer, materials and structural evaluations. The best solution to each design problem effectively couples respect for the important factors together in the correct proportions.

The literary history of turbines is rather out of balance in this regard, the overwhelming emphasis having been upon aerodynamics until the most recent times. It now appears that this situation is slowly changing for the better, largely because persistent development difficulties of modern machines have shown that turbine durability can make or break an engine program. References (18.2), (18.3) and

(18.4) are compilations of papers reviewing heat transfer, high temperature materials and structural integrity, respectively. They provide a good starting point for those wishing to pursue these topics further.

A deep appreciation of these sister technologies is essential to anyone seriously interested in gas turbine design. In fact several specific examples of the interaction between structures and aerodynamics will be found in Section 18.2.

18.1 Turbine Airfoil Characteristics

18.1.0 Introduction

We turn now to a somewhat closer look at the prevailing turbine aerodynamic situation. This will be done by means of well-known airfoil dimensionless parameters, some of the most revealing of which are gathered together in Table 18.1.1. The JT3D and JT9D again serve as examples because of the fair comparison they provide.

Table 18.1.1

Parameter	JT3D	JT9D
High pressure turbine		
Exit Mach number	0.7-1.0	0.6-0.9
Reynolds number (millions)	0.8-1.5	0.9-2.4
Aspect ratio (span/chord)	1.7-2.6	1.0-2.2
Turning angle (degrees)	68-110	70-111
Maximum thickness/axial chord	0.24	0.27
Low pressure turbine		
Exit Mach number	0.6-0.9	0.5-0.8
Reynolds number (millions)	0.34-0.87	0.29-0.53
Aspect ratio (span/chord)	2.0-4.8	2.7-6.0
Turning angle (degrees)	36-97	67-107
Maximum thickness/axial chord	0.15	0.15

This information should immediately convey the message that turbine airfoils have unique geometrical characteristics. In conventional terms they would be called thick, highly cambered and stubby. This means that they will exhibit a wide variety of fluid phenomena and are not especially susceptible to many classical analytical approaches.

This impression will be confirmed by the following remarks regarding aerodynamic parameters.

18.1.1 Mach Number

When high subsonic or low supersonic exit Mach numbers are found in combination with airfoils of large thickness and/or deflection, local regions of supersonic flow (sometimes called bubbles) will often be found on the suction (or convex) surface. This is evidently the case for several HPT and LPT airfoils of Table 18.1.1, and one can safely presume that the trend will be toward higher exit Mach numbers and greater turning angles in order to increase stage work. There are, in fact, several "transonic" (i.e. subsonic inlet, supersonic exit) turbine airfoils already in service, a good example being the inlet guide vane of the JT15D, and the maximum JT9D turning angles have already been exceeded.

Predicting the behavior of "mixed" (i.e. partly subsonic, partly supersonic) flows around cascaded airfoils is not any easier than it is for isolated airfoils, and the consequences of mistakes can be unacceptably severe.

18.1.2 Reynolds Number

A convenient reference point here is that natural transition occurs on a flat plate at a Reynolds number of about two million. This might lead to the conclusion that the turbine airfoils of Table 18.1.1 are dominated by laminar flow, but that would be wrong. One of the main reasons for this is that they are immersed in an extraordinarily turbulent environment, the turbulence level being in the range of 3 - 20%. The disturbances are initially generated in the combustion process, and any tendency to decay is resisted by the boundary layers and wakes produced by the successive rows of airfoils. Large pressure gradients, particularly adverse ones appearing near the trailing edge on the suction surface, also exert a strong effect on boundary layer transition.

An intense competition therefore often takes place along the suction surface between Reynolds number, turbulence level and pressure gradient over the state of the boundary layer. The result is difficult to predict in advance, but crucial to both the aerodynamic and thermal performance of the airfoil. It is even frequently found that there are long stretches which do not resemble either purely laminar or fully turbulent behavior, and are best thought of as extended transition regions.

Ample evidence of these effects exists in the open literature. For example, Hebbel (Ref. (18.5)) and Kiock (Ref. (18.6)) have carried out classical experiments which demonstrate the sensitivity of turbine airfoils to suction surface boundary layer behavior. Much of what we now know began with their fine research.

The data of Table 18.1.1 show that the Reynolds number has increased in the HPT and decreased in the LPT with time. Since these were due, respectively, to increasing engine overall pressure ratio and increasing bypass ratio, the future will probably offer more of the same.

18.1.3 Endwall and Leakage Flows

The above remarks apply to that part of the flow which can be described in two-dimensional terms. A very important part of turbine aerodynamic behavior, however, is governed by three-dimensional effects. These latter flows generally lead to lost performance or inefficiency, and therefore require special mention.

Passage endwall flows are one of the most common forms of three-dimensional flows found in turbines. They are caused by the blade-to-blade pressure difference which the mainstream flow impresses upon the endwall boundary layer, and result in an unrecoverable skewing of the exit plane velocity field. As the airfoil aspect ratio is reduced, endwall flow effects occupy an increasing portion of the span and must therefore become more significant. Table 18.1.1 reveals that higher cycle temperatures and pressures have acted to reduce the aspect ratio of HPT airfoils. The effect of increasing inlet temperature has been to require a longer airfoil chord in order to provide sufficient coolant flow passage area. The effect of increasing inlet pressure has been to reduce the necessary through-flow area and, correspondingly, the span. When the aspect ratio nears unity, as it has in the JT9D HPT, the endwall flow assumes equal importance with the mainstream flow, and the boundary layer approach breaks down.

Similar remarks can be made for leakage or clearance effects. Since clearances have minima which are independently determined by manufacturing tolerances, and are harder to maintain in the more hostile environments, they have a relatively greater impact on the shorter airfoils of high pressure ratio machines. Leakage losses have become, in fact, a determining factor in turbine engine development.

18.1.4 Conclusion

One clear message emerges from the foregoing facts; turbine design simultaneously involves most of those things that aerodynamicists have learned to dread. This includes at least transonic, transitional flow over thick, highly chambered cascaded airfoils in the presence of strong turbulence and three-dimensional effects. Contrast this with the recent comments of the authoritative A. M. O. Smith (Ref. (18.7)) regarding high-lift isolated airfoils, "That is not to say that nearly all problems have been solved, but to a certain extent the remaining problems amount to just irritating details." In this context our modern machines seem intent upon overwhelming us with irritating details.

18.2 Design Considerations

18.2.0 Introduction

At this point in our development it will be profitable to stand back and view the actual design approach and procedure so that the various advances can be appreciated in their proper context. In this regard the work by Horlock (Ref. (18.1)) is an excellent starting point. He has provided a concise derivation and description of the relationships between stage loading coefficient, flow coefficient (axial velocity/wheel speed), reaction, turning and the velocity triangles in general. In addition, he has included a discussion of structural considerations such as the centrifugal tensile stress at blade roots (blade pull stress) and the hoop stress due to centrifugal loading on rotor disks. These derivations will not be repeated here. The reader who is unfamiliar with these terms would profit greatly by examining that work.

The designer has before him the task of satisfying certain requirements and remaining within certain constraints while meeting or exceeding his performance goal. The requirements are generally specified by the cycle and they include, for example, producing a given power at given values of inlet pressure, temperature and mass flow. The constraints stem from many different sources including structural, mechanical and aerodynamic considerations. They could include limits on rotor blade pull stress, disk rim speed, airfoil maximum thickness and trailing edge thickness, flow turning and Mach number. The performance goal that must be met is efficiency. Thus, while satisfying the requirements the designer must consider a multitude of configurations in order to establish the trends which lead to maximum efficiency. When the final design emerges it is invariably true that the performance is limited as a direct result of one or more of the constraints. With this in mind we shall briefly consider several typical and commonly occurring design constraints. In particular, attention will be given to the way in which structural constraints can bring about limitations on the blade tip and disk rim speeds and hence on the stage loading coefficient. Following this a brief description of the design system itself shall be presented. Among other things the importance of the aerodynamic loss system shall be discussed.

18.2.1 Design Constraints

The material limitations of maximum allowable blade pull stress and disk stress are not difficult to appreciate. What shall become clear is that these stresses can pose severe restrictions on the aerodynamicist in his selection of a flowpath and consequently they can have a direct impact on the ability to reach the goal efficiency. As shown by Horlock (Ref. (18.1)) the blade pull stress is proportional to the product of flowpath annulus area and shaft speed squared. The disk stress is proportional to the disk rim velocity squared. Thus, three variables that the designer has at his disposal in configuring a stage consistent with these two constraints are the annulus inner and outer radii and the shaft speed. He would look at various combinations of these variables (and others, such as reaction) that lead in the direction of increasing efficiency. In the design of a high pressure turbine it is frequently true that the search for higher efficiency places the design on the limit of allowable blade pull stress. The reason for this is the desire to minimize the stage loading factors (by raising the wheel speed) and the Mach number level (by increasing the annulus area). In addition, if the shaft speed is specified by compressor requirements the designer's freedom is considerably restricted. In the ultimate case it can occur that with a specified shaft speed the highest achievable efficiency occurs when both blade pull and disk stresses are at their limiting values. In this case there is only one flowpath that can satisfy all the constraints simultaneously and the highest efficiency the turbine can reach has been limited by the structural and mechanical constraints.

Although low pressure turbine design is seldom hampered by these stress considerations, the shaft speed is frequently limited to a very low value because of restrictions on fan tip speed. Further, the maximum diameter of the turbine may be limited by restrictions on engine size and weight. The evolution of low pressure turbines with high stage loading coefficients (see Table 18.0.1) is a direct result of these constraints. The consequence is a trend toward airfoils with increased turning, decreased flow acceleration and in general a more severe aerodynamic environment.

The discussion up to this point has addressed the impact of constraints on the flowpath and the velocity triangles but there are also constraints on the airfoil design. The leading and trailing edge diameters must be large enough to allow the incorporation of cooling devices as necessary. The airfoil thickness distribution is often dictated by the necessity of allowing room for internal cooling devices and the entire spanwise layout of an airfoil may be dictated by the need to insert and withdraw these devices. It is only a slight exaggeration to say that many cooled airfoils are a result of the best aerodynamic design that could be wrapped around their internal cooling devices.

Although only a very few of the constraints on a turbine design have been mentioned here it should be clear that they can have a profound impact on the final configuration. The not uncommon misconception that turbines present few difficult aerodynamic challenges stems in part from a lack of appreciation of the constraints placed upon them. It is the constraints that have brought about the need for advanced analytical design tools.

18.2.2 The Design System

Before one can appreciate the importance of an improved analytical capability one must have some appreciation of the design system in which it is incorporated. The system is a sequence of different types of calculations with inputs and constraints from various sources. It is a sequence in that each analysis provides input to the next. It is also an iterative sequence in that the results of each analysis alter inputs used earlier. What follows here is a brief summary of this sequence. A far more in-depth discussion of a modern computer interactive turbine design system has been presented by Thomas and Piendel (Ref. (18.8)).

The initial input is in the form of cycle performance requirements. These would typically include parameters such as inlet and exit pressures and temperatures, primary and secondary (coolant) mass flows and shaft speeds. The constraints at this point might include for example, blade pull stress, airfoil chord and trailing edge thickness. These serve as input to the meanline analysis.

The meanline analysis provides midspan velocity triangles. Preliminary root and tip velocity triangles may be determined with an assumption such as free-vortex flow. The variables include the flowpath definition, blade speed, stage work and reaction. Input must include sufficient information about the airfoil geometry such that the various loss systems can be employed. This analysis may be carried out for a single turbine or for a complete system including the high and low pressure turbines and the exit guide vane. As mentioned above, the objective of the analysis is to point out the highest performance configuration (flowpath and velocity triangles) that will satisfy the cycle requirements while remaining within all the constraints.

The performance is determined by the loss system. This system is a series of calculations and correlations which determine the magnitude of the various losses (profile, endwall, parasitic and cooling loss) based on the aerodynamic and geometric input provided. The problem is, for example, to make an accurate estimate of the profile loss without having any detailed idea of the airfoil contour but only having the velocity triangles, pitch, chord and trailing edge thickness. The loss system is the most crucial feature of a meanline optimization study. An an example, the number of stages in a turbine will be dictated to a large degree by the way the predicted efficiency responds to variations in the stage loading coefficient. These efficiency variations are dictated by the loss system. Thus, a loss system with an excessive penalty for higher turning will cause the final configuration to have lower stage loading coefficients and hence more stages. For this reason improvements in loss systems can lead to significant changes to the final turbine configuration. Great care must be exercised to insure that your best aerodynamics are reflected in the loss system. Otherwise they need never appear in the final configuration. Results of the meanline analysis provide up-dated input to the cycle analysis. They also provide input to the streamline analysis.

The streamline analysis is a two-dimensional axisymmetric meridional plane solution by, for example, streamline curvature or martix inversion techniques. It brings the spanwise variations into the design. The streamline analysis may simply serve as a refinement of the results of the meanline analysis or it may be employed in place of the meanline analysis as a basic optimization tool which includes spanwise variations. An example of this approach can be seen in the work by Schlegel et al. (Ref. (18.9)). Regardless of the way it is employed, the basic virtue of the streamline analysis is that it permits one to eliminate many of the adverse effects that accompany a simple free-vortex design. The large radial variations of reaction that occur in a free-vortex design, for example, can be eliminated by "controlled-vortex" design (Ref. (18.10)). The result is that the difficulties of very low reaction (impulse) blade roots and the leakage penalties of very high reaction shrouded blade tips can be minimized. The results of the streamline analysis serve as input to further iterations with the meanline analysis and also as input to the airfoil contour design calculation.

Turbine airfoil contours are generally uniquely designed for each application. This is a major departure from the approach in many compressor designs where the airfoils are selected from standard families of contours. With the velocity triangles dictated at each radial section by the streamline analysis and a first estimate of the gap/chord ratio from lift coefficient considerations the objective is to devise a contour which will have a pressure distribution with desirable boundary layer characteristics. One aspect of turbine airfoil design that simplifies matters is that flow deviation, and hence mass flow, can be determined with sufficient accuracy from the geometry of the airfoil. Thus turbine airfoil design is a matter of defining the contour that will most efficiently provide the desired lift.

Two approaches are currently being followed in airfoil design. In the "direct" approach the contour is defined and the pressure distribution is determined. In the "indirect" approach a pressure distribution is specified and the contour is determined. The important point to be appreciated is that accurate and fast cascade flow calculations are becoming increasingly available (e.g. Ives and Liutermoza (Ref. (18.11))).

The results of the airfoil design serve as input to the meanline analysis in terms of updated profile loss estimates and to the heat transfer, structural and mechanical designers for all of their various analyses.

18.2.3 Summary

The turbine design sequence is a highly analytical procedure aimed at the objective of simultaneously satisfying a wide variety of requirements and constraints while optimizing on high performance, low weight and low cost. It is an unusual turbine which is not pressed hard against one or more of the imposed constraints. In addition the basic configuration of the turbine, for example the number of stages, will be largely defined by the nature of the aerodynamic loss system used to predict efficiency. These are but a few examples of the numerous trade-offs that occur during a turbine design. The trade-off between increased stress and higher efficiency is only one example. Other trade-offs include: (1) reductions in airfoil solidity which cause reductions in weight and the number of airfoils (cost) but bring with them the risk of flow separation and reduced efficiency and (2) increases in rotor blade cooling which can permit increased operating stress levels and higher aerodynamic performance but also bring about increased cooling losses.

The advances in technology that will be discussed in following sections are generally associated with either moving a constraint or reducing the penalty associated with a constraint. Advances in turbine aerodynamics have, for example, pushed to much higher values the historical constraints on maximum turning and exit Mach number. The result has been much higher performance in high stage loading machines than had ever been anticipated.

18.3 Performance

18.3.0 Introduction

We are now ready to examine turbine aerodynamic phenomena in detail. The attendant complexities can best be unravelled by organizing our thinking about the factors which determine performance or efficiency. This approach leads directly to a comprehensive framework for the remainder of this Chapter.

18.3.1 Uncooled Turbine Efficiency

When the engine cycle calls for turbine inlet temperatures below about 1800°F, airfoils can usually be safely manufactured from available materials which require no protective cooling. In such cases the weight flow does not change throughout the turbine. If the working fluids are taken to behave as perfect gases with constant properties, some useful results can be obtained in convenient algebraic form. Translation to real gases is, of course, required for any actual turbine design, but this is easily accomplished in practice. Effects of changing streamline radial location can also be rigorously included in these formulations. Since they are relatively minor for axial flow machines and unnecessarily complicate the resulting expressions they are omitted here.

The uncooled turbine is best thought of as an open-cycle machine working between two reservoirs of different total pressure levels. Total pressure and total temperature levels not only turn out to be the most thermodynamically meaningful, but are also far easier to measure than static properties.

Application of the first and second laws of thermodynamics leads directly to the relation

$$\eta = \frac{\text{actual power}}{\text{ideal power}} = \frac{1 - \left(\frac{P_e}{P_i}\right)^{\frac{\gamma-1}{\gamma}} \exp\left(\frac{s_e - s_i}{c_p}\right)}{1 - \left(\frac{P_e}{P_i}\right)^{\frac{\gamma-1}{\gamma}}} \leq 1 \qquad (18.3.1)$$

Even though the turbine appears to have both steady and unsteady flow processes taking place when viewed from any single frame of reference, the path traversed by each particle of fluid in passing through the machine can be thought of as consisting of a series of steady flow processes viewed from appropriate frames of reference. Each of these sequential steady flow processes, viewed in its appropriate frame of reference (alternately stationary or rotating), will be referred to here as a unit process. The special advantage of this approach is that the total entropy change for any particle of fluid is equal to the sum of the entropy changes for all the unit processes, for entropy is a state property and does not depend upon frame of reference. Since the entropy only rises in each unit process, then

$$s_e - s_i = \Sigma \Delta s \geq 0 \qquad (18.3.2)$$

This reasoning and Eq. (18.3.1) lead to the usual conclusion that unit process entropy increases must be held to a minimum in order to maximize turbine efficiency. Finally, since in each unit process the total temperature remains constant, then

$$\frac{\Delta s}{c_p} = -\left(\frac{\gamma-1}{\gamma}\right) \ln\left(1 + \frac{\Delta P}{P_i}\right) \qquad (18.3.3)$$

so that entropy increases and total pressure losses go hand-in-hand.

18.3.2 Cooled Turbine Efficiency

The same reasoning which led to a useful definition of thermodynamic efficiency for uncooled turbines can be applied to each of the individual streams entering a cooled turbine for the same purpose. Care must be taken to provide a proper control volume completely surrounding the turbine and all inlet and outlet flows must be accounted for. The resulting expression, equivalent to that of Eq. (18.3.1), is

$$\eta = \frac{\sum_j \text{actual power}}{\sum_j \text{ideal power}} = \frac{\sum_j T_{ji} \left\{1 - \left(\frac{P_{je}}{P_{ji}}\right)^{\frac{\gamma-1}{\gamma}} \exp\left(\frac{s_{je} - s_{ji}}{c_p}\right)\right\} m_j}{\sum_j T_{ji} \left\{1 - \left(\frac{P_{je}}{P_{ji}}\right)^{\frac{\gamma-1}{\gamma}}\right\} m_j} \leq 1 \qquad (18.3.4)$$

where j is the minimum number of separate streams necessary to describe the operation of the turbine. Eq. (18.3.4) shows that the thermodynamic efficiency of the machine in question is entirely dependent upon the total entropy changes experienced by the individual streams while traversing the turbine. This is a satisfying and valuable result. Among other things, it shows that the unit process reasoning still applies, and that each stream contributes to inefficiency in proportion to its mass flux and entropy rise. However, as was previously mentioned and as will be elaborated upon later, the entropy change of a unit process now also includes irreversibility due to thermal mixing.

Specifically, unit process entropy changes for each of the j separate streams are given by

$$\frac{\Delta s}{c_p} = \ln\left(1 + \frac{\Delta T}{T_i}\right) - \left(\frac{\gamma-1}{\gamma}\right) \ln\left(1 + \frac{\Delta P}{P_i}\right) \qquad (18.3.5)$$

rather than by Eq. (18.3.3).

In some cases Eq. (18.3.4) can be further simplified. These cases require that the inlet and exit total pressures are each uniform over the j streams. They occur, for example, when the exit flow is taken to be completely mixed and the inlet

flow either comes from a single source or the turbine is included as part of a full accounting of the losses which take place after the compressor discharge station. The corresponding expression for efficiency becomes

$$\eta = \frac{\sum_j T_{ji} \left\{ 1 - \left(\frac{P_e}{P_i} \right)^{\frac{\gamma-1}{\gamma}} \exp\left(\frac{s_{je} - s_{ji}}{c_p} \right) \right\} m_j}{\left\{ 1 - \left(\frac{P_e}{P_i} \right)^{\frac{\gamma-1}{\gamma}} \right\} \sum_j m_j T_{ji}} \leq 1 \qquad (18.3.6)$$

which contains some useful guidance. First, the denominator reveals that the temperature of thermodynamic significance is the mass average value, regardless of the distribution between streams. Second, it emphasizes the fact that all of the streams passing through the turbine are capable of producing work. This leads, in turn, to the conclusion that all losses experienced by all streams coming from the total pressure reservoir to the turbine must be understood and considered if maximum efficiency is to be obtained. These losses include, for example, those generated by metering holes and slots or within cooled airfoils. Although this point should be fairly obvious, it is not always honored in practice.

18.3.3 Total Pressure Loss Breakdown

By now it should be clear that increases in entropy are the root cause of inefficiency, and that they occur as a result of total pressure loss and thermal mixing (see Eq. (18.3.5)). The entropy change due to thermal mixing is both inevitable and easily calculated. The contribution of total pressure loss, on the other hand, is neither completely under our control nor easy to predict. The designer will seek to minimize total pressure losses. His most fruitful avenue of approach is through an understanding of the phenomena which generate them.

The sources of total pressure or aerodynamic losses are the same as those encountered throughout fluid mechanics. They include:

a. skin friction drag
b. pressure or form drag
c. shock losses
d. leakage
e. mixing

Of these only the first four matter in uncooled turbines. The last must be accounted for in cooled turbines, where gases of considerably different properties are irreversibly mixed together (see Eq. (18.3.5)).

It is convenient and has become customary to partition the losses into four other categories, namely:

a. profile
b. endwall
c. parasitic
d. cooling

This method associates losses with the location of their production rather than with their phenomenological origins. A rough but useful idea of the relative importance of each category can be found in the following table.

Loss Category	Percent	
	Cooled HPT	Uncooled LPT
Profile	35	60
Endwall + Parasitic	35	40
Cooling	30	0
Total	100	100

Although profile losses are evidently important, it is clear that the others cannot be disregarded. The surrounding world seems to have overlooked these simple facts, for the bulk of turbine aerodynamic research has been aimed at profile design.

The above information has been used to shape the remainder of this Chapter. Careful attention is given to each category of loss, cooling losses also being dealt with in Chapter 19.

18.4 Profile Aerodynamics

18.4.0 Introduction

Well designed airfoil contours are an essential feature of any gas turbine that is to reach its performance goals, not to mention its goals in weight and cost. The vast amount of effort that has been expended in this area in recent years is an indication of the recognition of this fact. To say that profile design is simplified by the generally accelerating nature of the flow is highly misleading. Turbine airfoils do have strong recompressions and boundary layer separation is a real and present problem that must be addressed in every design. Furthermore, the obvious advantages of reduced weight and cost that can be achieved with highly loaded (low solidity) designs brings pressure to have even stronger local recompressions. Keeping this in mind, and remembering also, as mentioned earlier, that turbine airfoils can be thick, highly cambered, transonic and can have transitional boundary layers leads one to the conclusion that the design of good turbine airfoils is a challenging and difficult task.

18.4.1 Design Approach

At the outset of an airfoil design the velocity triangles are available as a result of the streamline analysis. Included in them are the effects of the anticipated total pressure loss across the cascade and also the stream-tube thickness variations (due to meridional plane streamline curvature and/or annulus area divergence). In addition, constraints such as on leading and trailing edge diameters, the value and location of the maximum or minimum thickness and others may have already been specified. If, for example, the airfoil is a highly stressed (centrifugally) high pressure turbine rotor blade it will be necessary to taper the airfoil. This will require an airfoil with a very thin, low solidity tip and a relatively thick, high solidity root.

The first step in the airfoil design is to set the cascade throat dimension and/or the trailing edge mean camber line angle in order to provide the proper mass flow through the cascade. In subsonic flow there is no unique relationship between throat area and mass flow and one is totally dependent on correlations. The work by Ainley and Mathieson (Ref. (18.12)) is a good starting point in this area. In transonic flow, once the cascade is choked, the simple one-dimensional relationship between flow area, throat

area and Mach number can be applied with confidence. Care must be taken in both cases to properly account for things that can alter the continuity relationship between the throat and downstream. These include, for example, total pressure loss, mass addition and thermal dilution. With an estimate on the solidity based on something like the Zweifel (Ref. (18.13)) coefficient a first guess on the profile contour is made.

The potential flow calculation is then executed keeping in mind various aerodynamic requirements. There will be a need to hold down the maximum suction (convex) surface Mach number in order to reduce the adverse pressure gradient at the trailing edge. In transonic flow pains must be taken to minimize the effects of shocks both from considerations of shock loss and impact on the suction surface boundary layer. One final requirement might be related to the leading edge overspeeds and how they affect performance at incidence.

With an acceptable potential flow a boundary layer calculation may be carried out. The aerodynamic requirements here include avoidance of gross separation and possibly that the region of laminar flow be as long as possible. The boundary layer results at the trailing edge are coupled with other information (e.g. trailing edge blockage) and a wake mixing calculation is performed, as described by Stewart (Ref. (18.14)), to determine the cascade loss.

An extremely useful aspect of cascade aerodynamics is that there are several rules to which the pressure distribution around any airfoil designed for a specific purpose must conform. Portrayed on Figure 18.1 are the pressure distributions for two differently shaped cascade airfoils intended to accomplish the same purpose. The two curves will have at least the following things in common:

a. The static pressure equals the stagnation pressure on the leading edge stagnation point.

b. The areas circumscribed by the curves are equal (to the circumferential force on the airfoil).

c. The trailing edge pressure approximates the ultimate downstream static pressure (which is available from prior streamline calculations).

d. There is a minimum pressure point along the suction surface from which recompression is required to reach the trailing edge (this can be shown to be true by means of streamline curvature arguments and is due to the generally convex shape of that surface).

The last point is crucial, for it guarantees that there are regions within every turbine where the vulnerable boundary layer must "run uphill." When the adverse pressure gradient in the recompression region is sufficiently large, the boundary layer separates. The profile losses are then controlled by pressure or form drag rather than skin friction drag and are usually unexpectedly and unacceptably large.

By this time it must be obvious that the designer must sometimes reduce the trailing edge pressure rise. This is accomplished by altering the geometric shape of the airfoil and checking the results. The two pressure distributions of Figure 18.1 are intended to illustrate the beginning and end of successful iterative search process. The reader can also use Figure 18.1 to understand why increasing the number of airfoils (which reduces the circumscribed area) or increasing the airfoil reaction (by lowering the exit static pressure) are other tricks which can help reduce the strength of the recompression.

This entire process is iterative in nature and may require a large number of passes before a suitable contour is defined satisfying all (or most) of the aerodynamic requirements. It should be noted here that this iteration could be altered significantly by a "synthesis" or "indirect" analysis. In this case the pressure distribution is specified and the contour is computed from it. The discussion in the following section will be limited to the "direct" approach since it has been the main focus of attention in the literature.

18.4.2 Potential Flow

The progress during the past decade in the area of potential flow in cascades has been remarkable. For flows which are compressible but subsonic a large number of fast, versatile and accurate calculations are now available. The works by Katsanis and McNally (Ref. (18.15)) and Van den Braembussche (Ref. (18.16)) give ample evidence of this progress. The state-of-the-art today is such that one is even able to perform detailed analysis on the leading edge flow (Katsanis and McNally (Ref. (18.17))) to determine the impact of incidence on the leading edge overspeed.

In the area of transonic cascade flow progress has been equally remarkable. The complicated nature of these flows is illustrated in Figure 18.2. The pressure distribution and the locations of the sonic lines and shocks are shown schematically for several Mach numbers. At an exit Mach number of 0.7 the flow is everywhere subsonic. As the back pressure is lowered (holding the inlet flow angle and total pressure fixed) the area within the pressure distribution (i.e. the work producing tangential force) increases until at an exit Mach number of 0.9 there is a thin supersonic region with a sonic line extending from 35 to 75% axial chord. This type of flow is typical of a large number of existing gas turbines. As the back pressure is further lowered the exit Mach number passes through 1.0. Near this condition several things happen. The inlet Mach number, which has been increasing up to this point, reaches an asymptotic upper limit and will not respond to further reductions in back pressure. In addition, the sonic line, which has expanded across the throat and moved forward on the suction surface, also reaches an asymptotic position. At this condition the sonic line is highly curved. This is a result of the relatively high loading on this airfoil. With lower loading on the airfoil (higher solidity) the area within the pressure distribution would be reduced. The suction surface would have gone through sonic velocity further aft and the sonic line would have come nearly straight across the throat. As the back pressure is further reduced the pressure distribution on the pressure surface and most of the suction surface remains unchanged. What is occurring is that a shock has formed emanating from near the trailing edge and reflecting off the suction surface. As the Mach number is increased this shock moves further aft leaving the flow upstream of it unchanged. The condition when the shock reaches the trailing edge is referred to as "limit loading" since the force on the airfoil has reached a maximum. This condition corresponds to an exit axial Mach number of 1.0 and hence the back pressure can be reduced no further.

As one would expect, the prediction of transonic cascade flows has lagged behind that of subsonic flows. Presently, however, there are a number of analyses which are available. A time marching approach has been followed by McDonald (Ref. (18.18))

and by Delaney and Kavanagh (Ref. (18.19)). The results often seem too good to be true, as the portions of McDonald's work contained in Figures 18.3 and 18.4 will attest. As a matter of fact, these flows can be so complex that the experimental data shown there was considered suspect until later verified and clarified by the analysis. In recent work, such as Ref. (18.11) and Ref. (18.20), conformal mapping and relaxation techniques have been applied to achieve equally remarkable results.

The present status of turbine cascade potential flow analysis is that the problems that existed ten years ago have been for the most part solved. Although there are still a number of areas being worked in transonic cascade flow, they are in the detail, or quality, of the results and not in the basic computational capability. Unfortunately, many of the missing details are intimately tied to the near wake flow and can therefore only be predicted by a viscous analysis.

18.4.3 Boundary Layer

Another area of aerodynamics that has seen great advances during the past ten years has been boundary layer theory. The gains in understanding of the various phenomena and the analytical modeling of them has drawn together into a rational system what had earlier been a large quantity of unexplained and confusing data. It is becoming increasingly clear that the wide variations in cascade performance which had been previously attributed to the basic nature of the velocity triangles and overall cascade parameters (e.g. solidity) can now be explained in detail by boundary layer analysis. The very large losses conventionally associated with high turning can to a great extent be avoided by proper airfoil design and boundary layer analysis. In order to understand this more clearly let us consider the phenomena occurring in a cascade profile boundary layer.

The pressure distribution in Figure 18.5 is not necessarily a good one from a performance point of view but it will serve as an example. Let us consider the suction surface boundary layer. It starts at the stagnation point (0) as laminar and begins to accelerate strongly around the leading edge circle. Leaving the circle the flow goes into a strong recompression as a result of the leading edge overspeed. This recompression may cause the boundary layer to separate at (1) and to form a bubble which may undergo transition and reattach fully turbulent. The very large penalties associated with large incidences occur when this overspeed is sufficiently strong such that the bubble cannot reattach. Assuming that the bubble has reattached (fully turbulent) the boundary layer accelerates strongly at (2) and may undergo relaminarization, or reverse transition, by point (3). The boundary layer continues to accelerate down to the minimum pressure (4) and there the final recompression begins. At this point several things may occur. The boundary layer may undergo transition. It may separate to form a bubble which reattaches fully turbulent or it may not reattach at all. If the boundary layer does reattach it will proceed all the way to the trailing edge (6) or will undergo turbulent separation (without reattachment) at point (5) before it reaches the trailing edge. A similar story can easily be imagined for the pressure surface boundary layer but without the final recompression. For a given cascade of airfoils this sequence of events can be altered greatly by variations in Reynolds number, Mach number, free stream turbulence and incidence. Also, for a given set of flow conditions, the sequence of events can be altered by relatively small variations in the airfoil design. It is this latter point which makes it difficult to construct a truly universal loss system. In a meanline analysis the detailed contour does not exist yet and hence some assumptions must be made in the construction of the loss system. An analytical loss system might, for example, be based on the assumption of boundary layers which are fully turbulent at all points. An experimentally based loss system can be misleading unless the tests are carefully controlled and the results properly analyzed and generalized. The significance of this latter point cannot be overemphasized. In Figure 18.6 the variations with Reynolds number of the normalized performance of a number of cascades from various sources is illustrated. As would be expected from the complicated sequence of events that can occur in a cascade boundary layer as described above, no single scaling rule appears to apply. It is upon application of the analyses that are now available that the situation begins to become clear.

The cascade designer has at his disposal two basically different approaches to the boundary layer calculation. The first is based on a simplified set of equations, correlations and criteria. The second is based on a more fundamental approach which, although more complicated and time consuming, will provide a more definitive result. As an example of the first type of approach the closed form integral boundary layer analysis by Dring (Ref. (18.24)) is typical. Although it is presented in the context of a turbulent boundary layer it can also be used for laminar flows with an appropriate choice of constants. Typical of the many conditions used in the literature to correlate the occurrence of boundary layer separation is the following:

$$\Gamma = \delta_2 \left(\frac{U\delta_2}{\nu} \right)^{1/n} \left(\frac{1}{U} \frac{dU}{dS} \right) \qquad (18.4.1)$$

For laminar flow n = 1 and $\Gamma_{sep} = -0.1567$ correspond to the Karman-Pohlhausen solution and for turbulent flow n = 4 and $\Gamma_{sep} = -0.06$ correspond to the Buri solution (Ref. (18.25)). Similar conditions for the occurrence of transition and relaminarization have been published by Dunham (Ref. (18.26)) and by Launder (Ref. (18.27)) respectively. Finally, the work of Horton (Ref. (18.28)) and Roberts (Ref. (18.29)) provides empirical criteria for determining the onset and size of separation bubbles as well as the nature of the boundary layer upon reattachment, if it occurs. With an analytical arsenal such as this even the complicated boundary layer situation described above can be attacked.

The second, more fundamental, approach to the analysis of turbine airfoil boundary layers is composed of various sophisticated solutions of the boundary layer equations and the Navier-Stokes equations. An exhaustive discussion of this entire area of computational fluid dynamics is presented in Chapter 16. Only brief mention of some typical work that relates to the prediction of airfoil boundary layers shall be related here. The prediction procedure of McDonald and Fish (Ref. (18.30)) and Kreskovsky et al. (Ref. (18.31)) is an excellent example of the high quality techniques that have been perfected in recent years. This single computational tool provides accurate prediction of laminar, transitional and fully turbulent boundary layer flow as well as relaminarization. The effects of compressibility, Reynolds number, pressure

It can be shown from the references cited above that there is a reduction in turbine stage efficiency of approximately 1½% for every percent of relative clearance. Thus it is an unusual unshrouded turbine stage which is not giving up at least two percent in performance to this mechanism. This powerful impact has led turbine designers to strive for minimal clearances as well as to minimize the penalty occurring for a given clearance. This and other endwall loss reduction schemes are discussed in the following section.

18.5.6 Loss Reduction Devices

As a result of the powerful impact endwall loss mechanisms have on turbine performance a number of attempts have been made to reduce these penalties. Some success has been seen in these attempts but it is difficult to extrapolate a successful device from one turbine configuration to another. There is the distinct risk that a loss reduction scheme, if improperly executed, may result in a significant loss increase. With this in mind let us consider a few of the successes that have been reported.

A method of contouring the annulus of a first vane to reduce endwall loss has been presented by Deich et al. (Ref. (18.63)). Incorporation of this scheme into turbine designs has produced conflicting results. Ewen et al. (Ref. (18.64)) applied the scheme to a small axial turbine and saw a remarkable improvement in performance. The results of Okapuu (Ref. (18.65)), however, indicate no effect on performance at the design point but some improvement at lower pressure ratios.

Another trial-and-error approach to the reduction of endwall loss has been followed by Prumper (Ref. (18.66)). He employed boundary layer fences of varying size, shape and location in an attempt to reduce the endwall loss in an annular cascade of first vanes. The result was that after testing over four hundred configurations, an optimum was established which gave a significant improvement in performance. The underlying physics and its universality, however, remain to be determined.

The area of unshrouded rotor tips and rubstrips has also received considerable attention. Grooves and recesses have been cut into the airfoil tips in an attempt to make them behave as labyrinth seals. Rubstrips have been recessed radially in an attempt to keep them in a low flow, separated, environment. Rubstrips have also been made out of honeycomb in an effort to reduce the running clearance as well as to reduce the loss for a given clearance.

Turbine endwall loss reduction is at this point a black art and without any real design discipline. It is at best a trial-and-error approach with no guarantee that success in one application can be extrapolated to another application. The underlying problem is the basic lack of understanding of the composite of the numerous mechanisms that go into producing endwall loss.

18.5.7 Conclusions

At this point the conclusions with regard to the state-of-the-art of endwall aerodynamics relative to that of profile aerodynamics must be obvious. Although the mechanisms by which one can lose total pressure can be counted on the fingers of one hand, these individual effects have not been tied together into a meaningful, unified picture.

The loss correlations that have been derived are at best inadequate. Scatter on the order of 100% is not uncommon. This is not surprising considering the questions of net and gross loss and the large increase in endwall loss downstream of a cascade. Accurate endwall loss correlations may eventually become available but there is little evidence of it today. One notable exception is unshrouded rotor tip clearance loss which appears to be well within the realm of correlation.

Analytical attacks on the problem stem from a number of different approaches. Those based on conventional secondary flow and three-dimensional boundary layer arguments are at present inadequate. These approaches have and probably will continue to contribute to our understanding of the situation but the ultimate answer is probably to be found in the fully, or quasi, three-dimensional numerical approach. Although still in its infancy this approach has the potential to be ultimately successful.

The situation today is that design control does not exist and that the trends of endwall loss with only a few gross parameters can be predicted with any confidence.

18.6 Parasitic Loss

18.6.0 Introduction

In the present context the term "parasitic loss" is used to include all the numerous losses arising from flows that leave and/or enter the mainstream flowpath as a direct result of gaps or clearances between adjacent pieces of hardware. One distinguishing feature of parasitic loss relative to endwall loss is the paucity of work on the subject. Relative to all other sources of aerodynamic loss parasitic loss has received the least attention and yet, as shall be seen, it can have a powerful impact on turbine performance.

18.6.1 Sources and Mechanisms

Even a casual inspection of any typical turbine will reveal a surprisingly large number of gaps and clearances that can produce parasitic loss. The only type to receive any attention at all in the literature is the tip clearances that occur on shrouded rotors (e.g. Dunham and Came (Ref. (18.42))). As illustrated in Figure 18.11(a), mainstream air can leave the flowpath, flow through the tip (or labyrinth) clearance and re-enter the flowpath. The loss mechanisms include the throttling as the flow passes through the tip seal and the momentum mixing that occurs as the leakage flow re-enters the mainstream flowpath. The driving potential for the leakage flow is the static pressure drop that occurs in the mainstream between the inlet and exit to the rotor tip. An aerodynamic approach to minimizing the leakage flow can be found in controlled-vortex meridional plane streamline design. The reduction in tip reaction from the level produced by free-vortex design results in a reduced rotor tip static pressure drop. Thus the driving potential for the leakage flow is reduced. Exotic sealing devices are also employed in practice to minimize the leakage flow.

An identical and equally important situation occurs at the roots of stator vanes. The presence of the rotor shaft beneath them necessitates clearances and sealing devices like those at shrouded rotor tips (Figure 18.11(b)). The losses produced by vane root leakage have the same impact on

turbine performance as rotor tip leakage losses. It is worthy of note that controlled-vortexing can also reduce the static pressure drop across the vane root which in turn reduces these leakage flows.

Another type of leakage flow occurs as a result of the gaps between the platforms of adjacent airfoils in a row (Figure 18.11(c)). Mainstream flow can enter these gaps in the high static pressure region toward the front of an airfoil row and then re-enter the mainstream flowpath in the low static pressure region at the aft end of the row. Attempts to minimize these flows have included bonding adjacent platforms, mechanical sealing devices and also conforming the mechanical design of the gap to the pressure gradients in the flow above it in such a way as to minimize leakage. The problem has upon occasion been completely eliminated by making the endwall platforms out of continuous hoops and then inserting the airfoil profiles.

The examples of parasitic loss discussed above all had in common the fact that they were driven by mainstream flowpath pressure differences. This is not always the case. For example, the cavities surrounding the rotor disks (Figure 18.11(d)) are linked to the mainstream by clearances on the flowpath hub. These clearances are governed by the minimum gap necessary to prevent a rub between rotating and stationary hardware during transient operation. The rotating disk acts like a pump on the air in the cavity as a result of surface shear forces. This in itself causes a not insignificant dissipation of power. In addition, however, this higher energy air is forced out of the cavity into the flowpath where [illegible] mixing losses occur. The effect is to [illegible] the endwall boundary layer entering the downstream row of airfoils and hence increase the endwall [illegible] at that row. The situation is further complicated by the presence of cooling air deliberately [illegible] through the cavity in order to protect the [illegible].

[illegible] that should be mentioned here is that [illegible] for this reason it is difficult to calibrate an [illegible] loss system on turbine rotating rig results [illegible] that it is difficult to isolate the true endwall [illegible] from the frequently unavoidable parasitic loss. As an example of this the turbine loss system calibration by Dunham and Came (Ref. (18.42)) only considers the effects of what we have referred to here as endwall loss and the parasitic loss produced by [illegible] blade tip clearance. One must conclude that the loss contributions of all the other types of parasitic loss have been lumped in with these two. [illegible] analysis of rotating rig turbine [illegible] requires careful documentation of the flow characteristics of all the various leakage paths and [illegible] of the loss produced by each. Thus [illegible] must be understood but so also must be the mechanical [illegible] of the specific test hardware being analyzed. [illegible] to appreciate the difficulty of [illegible].

[illegible] the losses requires a predic[illegible] flow through the gap and then [illegible] unit leakage flow. The amount of [illegible] by various orifice flow calcu[illegible]. There exist disc pumping useful analyses [illegible] are available (e.g. Kott and [illegible]), the various loss mecha[illegible] analytically. For example, [illegible] that occur as the leakage [illegible] the flowpath may be estimated [illegible] type of analysis is used to [illegible] airfoil cooling losses (see Section 19.2.4).

As mentioned above, however, this problem is complicated by interaction of the thickened endwall boundary layer with the downstream row of airfoils.

18.6.2 Conclusions

The most significant advance in the area of parasitic loss is that the nature and importance of the problem is becoming appreciated. Once the mechanical designer has done his best to minimize clearances it is up to the aerodynamicist to do the best he can with what remains. The potential for success in this regard is clearly evident in the work of Deich et al. (Ref. (18.68)). In this example large improvements in turbine efficiency were gained by using endwall platform extensions. They had the effect of forcing the air entering the flowpath at the hub to have an axial rather than a radial direction. The point is that even with the clearances and gaps specified there are often aerodynamic means by which one can reduce both the amount of leakage flow and the loss per unit leakage flow.

18.7 Structural Excitation

18.7.0 Introduction

The useful life of a turbine airfoil is greatly affected by the flow in which it is immersed. Both the thermal stresses (see Chapter 19) and the steady-state gas loadings, for example, have aerodynamic origins. The flow is also responsible for airfoil vibratory stresses, the least publicized consumer of structural endurance.

Turbine airfoils ordinarily fail as a combined result of steady-state and cyclic stresses. Their interaction can be quickly appreciated by means of the Goodman diagram (Figure 18.12), a commonly used structural design device. The design point must lie within the safe region in order to be found acceptable.

It is interesting to note that no methods now exist to predict the magnitude of the aerodynamically induced vibratory stresses. Most designers simply assume that they will not exceed values they have previously experienced because they have no other choice. The fact that many engines have had to employ dampers, inserts and other fixes in order to reduce cyclic stresses to tolerable levels shows that this approach is not entirely satisfactory. Premature turbine airfoil failure is an expensive and dangerous problem, and deserves our most serious attention.

Another interesting aspect of aerodynamic vibrations is that they can be caused in two entirely different ways, as described below.

18.7.1 Buffeting

An airfoil will experience buffet stresses when exposed to any unsteadiness in the surrounding flow. The unsteadiness may be due to an axially propagating disturbance (e.g. combustor turbulence or afterburner transients), but the most important effects are usually obtained when the row of airfoils cuts through the spatial disturbances (e.g. wakes, vortices or potential flow field) of its neighboring rows. Because of the latter, designers carefully avoid tuning any natural airfoil vibratory mode to at least the first ten orders of blade passing frequency at all operating conditions.

The principal problem here is the almost complete lack of relevant research. It would seem that the high stakes would justify a concerted attack.

gradients and freestream turbulence are included in the analysis. The calculation is a solution of a finite difference model of the boundary layer equations with an integral form of the turbulence kinetic energy equation. An equally rigorous treatment of separation bubbles is presented by Briley and McDonald (Ref. (18.32)). This consists of a time dependent solution of the Navier-Stokes equations employing the McDonald-Fish turbulence model. The intention here is not to summarize all of the work in the computational area but simply to point out that the analytical power does exist for the problems at hand.

As an example of the type of analytical results that have been produced consider Figure 18.7 from Ref. (18.23). The variation of loss with Reynolds number is shown for a cascade and the effect of the nature of the boundary layer is demonstrated. The transitional boundary layer case has a loss level over much of the range 30% below the fully turbulent level. The incentive is clear for designing airfoils with pressure distributions that encourage as much laminar and transitional flow as possible.

The conclusion regarding the present level of understanding and predictability of the boundary layers on gas turbine airfoils is that the tools are now available to do reasonably accurate predictions. There are, however, still a number of areas in need of further work. One of the examples pointed out by Brown and Martin (Ref. (18.33)) in their review of heat transfer predictions is that of the relatively subtle and competing influences of free-stream turbulence and favorable pressure gradient on the onset of transition.

18.4.4 Wake Mixing

The final step in computing cascade performance is the wake mixing analysis. This is a conceptually straight-forward control volume calculation which establishes the uniform, far downstream conditions once the conditions have been specified at the cascade trailing edge plane. Having specified the gapwise variation of flow properties (static pressure, speed and direction) in the potential flow region between the airfoils, the boundary layer displacement and momentum thicknesses at the trailing edge, and finally the trailing edge blockage and base pressure one can compute exactly the far downstream Mach number, flow direction and ultimate total pressure loss (Ref. (18.14)). This type of analysis can be generalized to include the effects of trailing edge discharge of cooling air (Ref. (18.34)). The feature of wake flow which is presently not at all well understood is the base pressure. This influence may be thought of as a form drag. For most cases the trailing edge base pressure is very nearly equal to the downstream static pressure. Prust and Helon (Ref. (18.35)), however, demonstrated that trailing edge shape can have a pronounced effect on airfoil performance. The fundamental reason for the effect was that the base pressure was varying with trailing edge shape. The conclusion from their work is that a sharply squared-off trailing edge can degrade performance significantly by lowering base pressure. The advantages of rounded trailing edges becomes apparent. Another, far more serious, situation that can cause a lower base pressure (increased loss) is high exit Mach number. MacMartin and Norbury (Ref. (18.36)) report base pressures 40 to 50% below the downstream static pressure for exit Mach numbers between 1.0 and 1.3. Base pressure levels as low as this have a major impact on the transonic performance of turbine cascades. Until a basic analysis is devised or sufficient experimental data is amassed the uncertainty of base pressure is going to plague the design of transonic turbine airfoils. Evidence of such difficulty can even now be seen in the literature. In the work of Waterman (Ref. (18.37)) a surprisingly large increase in base pressure contributed to an equally significant improvement in cascade performance. The source of the change was a relatively subtle change in the airfoil contour.

The conclusion is that the major area of wake mixing requiring study is the base pressure excursions that occur in transonic flow. The problem is further complicated by the fact that most transonic airfoils are in high pressure turbines and hence are likely to have trailing edge discharge of cooling air. The present situation is simply that there is no design control.

18.4.5 Cascade Testing

During the years prior to the development of the analytical capabilities discussed in the preceding sections the most powerful research and development tool available to the turbine aerodynamicist was the cascade test. The types of information that could be produced in such testing include the airfoil pressure distribution, loss, surface flow visualization (to indicate separation and the nature of the boundary layer) and schlieren photographs (to indicate shock locations). A large amount of parametric testing was carried out with the goal of improving airfoil performance and developing general profile loss systems. Cascade testing is still used today as a basic profile aerodynamic research tool. The value of the results, however, have been greatly enhanced by the analysis that now accompanies them. The analysis has helped to point out the importance of running a truly controlled test. The misleading conclusions that can be drawn from data taken without proper simulation of variables such as Reynolds number, free-stream turbulence and spanwise streamtube divergence can be made clear by analysis where there is a far greater degree of control over the individual variables.

Cascade testing today focuses on those areas on the fringes of aerodynamics technology where analyses are either being developed or are nonexistent. Transonic aerodynamics is receiving much attention as a result of the need for efficient high work HPT stages. The specific areas include the trailing edge shock system and the impact of the shock on the suction surface pressure distribution and boundary layer. Trailing edge base pressure is also receiving attention in that it has direct effects on both the performance and the shock system. Interest in the area of low Reynolds number LPT performance has been on the rise as a result of trends in this direction caused by higher by-pass ratio engines. In this regime the rather subtle interactions of Reynolds number, free-stream turbulence and pressure gradient are under study. As a final example there is the area of spanwise streamtube divergence. Virtually all turbines have diverging flow paths. The effect of this divergence on a high turning low reaction airfoil can be very large. There are implications on both the potential flow and the boundary layer. It is not difficult to imagine that accurate simulation of these effects is extremely difficult to achieve.

The successful execution of a cascade test program has a number of key ingredients. The phenomenon under study and the important parameters must be defined as well as possible. The actual cascade

test situation should be analyzed to make sure it provides an adequate simulation. Before the test is carried out analytical predictions of the expected measured results should be available for immediate comparison with test results as they become available. In terms of the test facility, its characteristics should be well understood ahead of time. For example, inlet distortions not only in the total pressure but also in the flow direction must be documented before one can begin to evaluate airfoil performance. Simple flow visualization at an early stage of the testing can provide some early and frequently startling insight. Finally, the importance of a high accuracy, dependable data system with rapid reduction of the results to an intelligible form cannot be overemphasized. The best check on data is an immediate comparison with the best prediction available.

The conclusion is that cascade testing continues to be a valuable research tool. An intimate marriage between testing and analytical prediction only serves to mutually enhance both.

18.4.6 Cooling Effects

As turbine inlet temperatures have risen the need for increasingly effective airfoil cooling configurations has driven the turbine designer to what are referred to as film cooling and multi-hole cooling schemes. Both are discussed at length in Chapter 19. The only point to be made here is that these cooling schemes have a first order effect on airfoil profile performance. In both schemes cooling air is brought into the flow field through arrays of discharge holes in the airfoil surface. When 5 to 10% of the flow passing through a cascade is being discharged through the airfoil surface it is not surprising that performance is affected. Progress in understanding these effects would be facilitated if cascade loss data were reported in their entirety, rather than being reduced to a single elusive parameter (Ref. (18.34)).

The impact of coolant discharge on pressure distributions under most circumstances is not very significant. As a result there has been no major analytical effort in this area. It would not be difficult, however, to modify any one of the numerous existing potential flow calculations to include the effect of mass addition.

Far and away the major influence of coolant discharge on cascade performance is as a result of total pressure losses due to mixing of the coolant and mainstream flows and alterations to the nature of the boundary layer. Both effects are described in more detail in Chapter 19. The point to remember is, however, that cooling losses can equal or exceed all other contributions to the profile loss of highly cooled airfoils.

18.4.7 Conclusions

During the past ten years turbine profile aerodynamics has passed from a state of being almost entirely dependent on a relatively small body of experimental data, to its present condition of being based almost totally on a fundamental analytical sequence of design procedures. Although there are a number of areas still badly in need of attention, the majority of the former problem areas are now subject to a high degree of analytical design control.

18.5 Endwall Aerodynamics

18.5.0 Introduction

In the context used here the term endwall aerodynamics will refer to all the complex three-dimensional flow phenomena occurring in the hub and tip regions of a turbine flowpath. The endwall loss relating to leakage and other such flows that leave and/or enter the flowpath is referred to separately as parasitic loss and shall be discussed in section 18.6. The concern of the present section is the large concentration of loss and flow distortion that occurs near the endwalls of both shrouded and unshrouded turbine airfoils.

The state-of-the-art of understanding and predicting endwall aerodynamics is extremely primitive relative to that of profile aerodynamics. Strongly three-dimensional endwall flows occur as a result of the interacting effects of inviscid and viscous flow mechanisms. In addition, whereas profile loss is purely a function of the row of airfoils in question, the endwall loss will depend on the nature of the endwall flow entering the row and hence it depends on the endwall region performance of all of the upstream rows. Thus the endwall performance of each row cannot be uniquely related to the geometry of that row. For this reason one is in the position of having to consider net (that generated within the airfoil row) versus gross (the total appearing at the exit plane) loss. With this rather challenging situation in mind we shall now consider some of the developments that have occurred in the area of endwall aerodynamics during the past ten years.

18.5.1 Experimental Evidence

The evolution of the manner in which investigators have studied endwall aerodynamics reflects an increasing degree of respect for the complexity of the problem. At the outset endwall loss was measured downstream of cascades in much the same manner as profile loss, that is, with little or no regard for the incoming endwall boundary layer. Concern then began to expand toward what was entering the cascade on the endwall as well as what was exiting from it. An extremely fine example of this can be seen in the work by Armstrong (Ref. (18.38)) where the exit plane loss was shown to depend strongly on the nature of the inlet boundary layer. A review of cascade data, especially that including the effect of inlet boundary layer, has been given by Dunham (Ref. (18.39)). He presented a composite gross loss correlation of the available data with an inlet boundary layer thickness dependence in the form

$$f(\delta_1/c) = 0.0055 + 0.078\sqrt{\delta_1/c} \qquad (18.5.1)$$

The scatter in the data, however, is rather large. Subsequent work by Came (Ref. (18.40)) and by Morris and Hoare (Ref. (18.41)) lead them to a function in the form

$$f(\delta_1/c) = 0.011 + 0.294\ (\delta_1/c) \qquad (18.5.2)$$

Both forms lead to roughly similar conclusions over the range of the bulk of the data ($0 \leq \delta_1/c \leq 0.07$). Two other important points are mentioned in these papers. The first is that the loss continues to rise for a distance downstream of the cascade. This rise cannot be explained by endwall skin friction alone. The second point is that far more success was had in correlating the cascade gross loss (including the inlet endwall loss) than in correlating

the net loss (inlet loss subtracted out). Both observations severely aggravate the problem of trying to develop a reliable endwall loss correlation for design purposes. As an example of this, when Dunham and Came (Ref. (18.42)) examined the performance of a number of turbine rigs they were forced to correlate the data with a single constant instead of a function of inlet boundary layer thickness. Such boundary layer data is rarely available in a turbine environment. The constant, f = 0.0334, corresponds to a correlation for net loss since it is based on turbine performance. Hence it is not comparable, even in magnitude, to either of the above correlations for gross loss.

The trend toward more highly detailed testing is proceeding to its logical next step in that now careful studies are being conducted within the cascade passage. Examples of this approach are the fine works by Langston et al. (Ref. (18.43)), Carrick (Ref. (18.44)) and Sjolander (Ref. (18.45)). With these studies a far more complete appreciation of the truly complex nature of the flow has been achieved. As an example, consider the flow visualization of the endwall limiting streamlines taken by Langston et al. (Ref. (18.43)), presented in Figure 18.8. As the boundary layer ($\delta/c \approx 0.1$) approaches the cascade a horse-shoe vortex is formed on the endwall. It is similar to that which the boundary layer forms in front of a circular cylinder but displaced away from the extension of the mean camber line toward the pressure (concave) surface. This displacement is a result of the potential flow around the airfoil. This vortex is a feature peculiar to cascades. It would not be found, for example, in a simple turning duct. One leg of the vortex preceeds down the channel while the other is wrapped around the leading edge and is carried down the adjacent channel. The result is that in some areas the limiting streamlines at the wall are flowing in the opposite direction of the mainstream potential flow above them. This is particularly true in the region near the pressure surface just behind the leading edge circle. Most of the fluid in the inlet boundary layer is carried to the suction surface in the vortex. It reaches the suction surface approximately halfway (axially) through the cascade. The endwall region in the channel between the airfoils downstream of this vortex is virtually void of fluid coming from the inlet boundary layer. The boundary layer in this region is extremely thin ($\delta/c \approx .002$) and skewed toward the suction surface. The fluid swept to the suction surface forms an intense vortex which has a first order effect on the pressure distributions both on the endwall and on the airfoil suction surface. The unloading that occurred in work by Langston et al. (Ref. (18.43)) is shown in Figure 18.9. The flow into the suction surface - endwall corner is so strong that the occurrence of corner stall (back flow) in turbine cascades is highly unlikely. The entire process can be seen clearly in Figure 18.10. At a station just downstream of the leading edge the distortion of the inlet boundary layer due to the legs of the horse-shoe vortex is visible (Figure 18.10a). By midchord the bulk of the inlet boundary layer has been swept over to the suction surface leaving an extremely thin endwall boundary layer behind it (Fig. 18.10b). Near the trailing edge plane the flow has moved up the suction surface and a vortical motion is apparent (Fig. 18.10c). As the vortex proceeds downstream of the cascade it decays slowly (relative to a two-dimensional wake) and in the process produces significant additional loss.

This is a description of what has been observed in a plane cascade with a collateral (unskewed) inlet boundary layer. In a turbine environment, however, the inlet boundary layer could be highly skewed. As pointed out by Moore and Richardson (Ref. (18.46)) inlet skew can have a favorable effect in compressors where it tends to drive the low momentum boundary layer fluid away from the suction surface and toward the pressure surface (opposing the endwall flow). In a turbine just the opposite occurs. The inlet skewing drives the inlet boundary layer fluid toward the suction surface and as a result enhances the endwall flow. The data taken by Carrick (Ref. (18.44)) demonstrates that inlet skewing can cause a significant increase in cascade endwall loss.

Another troublesome feature of endwall flows is the spanwise mixing they produce. The streamwise vortices produced near the endwalls cause strong mixing of incident radial profiles of total pressure and total temperature. This causes problems both in the axisymmetric meridional plane streamline analysis where the conventional assumption is that there is no transport between stream tubes, and also in designing rotor blades where it is desirable to have a particular spanwise temperature distribution so that the highly stressed sections are not in the highest temperature flow region.

The spanwise mixing is very intense close to the endwall due to the vortices discussed above. Even well above the endwall, however, there can also be relatively strong streamwise vorticity. The source of this is the streamwise vorticity produced by putting relatively weak shear flows through high deflection cascades. This phenomenon is discussed in the following section.

18.5.2 Classical Secondary Flow Analysis

The aspect of endwall aerodynamics to first receive analytical attention was secondary flow. Inviscid rotational flows produce a streamwise component of vorticity when they are put through a deflection. The original work by Squire and Winter (Ref. (18.47)) and the classic by Hawthorne (Ref. (18.48)) provide ample clear evidence of the nature of this phenomenon. The theory of secondary flow has been generalized by Hawthorne (Ref. (18.49)) to include the effects of stratified, compressible fluids in a rotating frame of reference. This is an essential feature when considering secondary flow effects in turbine rotor blade passages. The recent work by Came and Marsh (Ref. (18.50)) presents a simple derivation not only of the distributed secondary vorticity but also of the trailing filament and shed vorticity. Taking the normal assumptions of secondary flow, most notably that it doesn't alter the primary flow, Belik (Ref. (18.51)) performed a very thorough parametric analysis of secondary flow losses. In this inviscid analysis the kinetic energy of the relative secondary motion was taken to be lost. His analysis included variations in the inlet velocity profile shape, velocity triangles, aspect ratio and solidity. The results showed remarkably good qualitative agreement with endwall loss data from a number of sources. In an effort to provide a more generally applicable analysis Stuart and Hetherington (Ref. (18.52)) devised a method which permitted a strong coupling between the primary and secondary flows. The result was that severe distortions of the Bernoulli surfaces could be accounted for.

Classical secondary flow analysis has the potential of being helpful in understanding spanwise mixing in that viscosity may not necessarily have a strong role away from the endwalls. In light of the complex viscous nature of the endwall flow described earlier it would seem optimistic to expect this mechanism to make anything more than a relatively small contribution to the total endwall loss picture.

18.5.3 Endwall Boundary Layer Analysis

The application of boundary layer theory to the endwall problem in turbomachinery has followed two distinctly different paths. The first consists of tangentially averaging the annulus boundary layer equations, and then, with additional approximations, following the growth of the boundary layer axially through the machine. The work by Mellor and Wood (Ref. (18.53)) is an example of this approach. This method has met with some success in compressor applications where the solidity is high and the turning is low relative to turbines. Owing to the very strong cross-flows and the large gapwise variation in the endwall boundary layer in a turbine cascade, it would appear that the gap-averaged approach offers little hope.

The second approach consists of solving the three-dimensional boundary layer equations over the cascade endwall. Mager (Ref. (18.54)) presented a study of the momentum-integral form of the equations which was not limited to weak cross-flows. This work was applied to the case of a turbine cascade endwall boundary layer by Dring (Ref. (18.55)). The flowpath between the cascade airfoils was treated as a duct. In this way the complexity of the leading edge flow, most notably the horse-shoe vortex, was avoided. The solution gave qualitatively reasonable predictions of the endwall flow in that for the case presented the incoming limiting streamlines (on the endwall surface) reached the suction surface at an axial location approximately halfway through the cascade. The predicted losses, however, were generally well below the measured values. Booth (Ref. (18.56)) extended this approach to include the effects of compressibility. His loss calculation included an additional effect due to the displaced inviscid flow. For several first vane test cases his predictions were also significantly below measured loss values. Carrick (Ref. (18.44)) applied the general integral method of Smith (Ref. (18.57)) to the cascade endwall problem. Steps were taken to include a degree of periodicity in the boundary layer ahead of the cascade leading edge but not to the extent necessary to account for the complex nature of the flow observed by Langston et al. (Ref. (18.43)). Even more powerful three-dimensional boundary layer analyses are available (e.g. Nash and Patel (Ref. (18.58))) but one must keep in mind that many aspects of the turbine endwall flow do not satisfy the basic boundary layer approximations. The horse-shoe vortex, the back-flow region behind it and the alterations to the two-dimensional pressure distribution are features beyond the scope of boundary layer analysis.

18.5.4 Three-Dimensional Flow Analysis

The recent availability of larger and faster computational facilities has made possible the fully three-dimensional flow analysis. This area of computational fluid dynamics is described at length in Chapter 16. Attention here shall be restricted to an example of such a calculation as it has been applied to the turbine cascade endwall flow problem. The calculation by Waterman (Ref. (18.37)) and by Waterman and Tall (Ref. (18.59)) is a fully viscous solution of the three-dimensional, incompressible fluid flow equations. The calculation was executed for several geometrically complex first vane annular cascades. The full equations were "split" into separate equations containing the viscous and pressure effects. The viscous equation was made parabolic by the assumption that the streamwise diffusion terms are negligible. This permitted a standard marching solution with each step containing a solution of the elliptic in-plane equation. The equation containing the pressure effects is fully elliptic and is solved by relaxation. It includes a displacement effect due to the viscous equation. By this means a coupling has been achieved between the viscous and inviscid phenomena. The advantages over the inviscid secondary flow and viscous boundary layer analyses become clear. Although there are many features of the analysis that one might argue about, the fact remains that this approach has the potential to account for more of the observed features of turbine endwall flows than any other approach currently available.

18.5.5 Unshrouded Rotor Tip Leakage

The clearance between the tip of a turbine blade and the outer air seal, or rubstrip, has long been recognized as a source of large turbine inefficiencies. Every effort is made to reduce this clearance mechanically. However, as a result of mechanical and thermal transients, eccentricities and other reasons the running clearance on most gas turbine rotor tips is between 1 and 5% of the blade span. In turbines where, for cycle reasons, the flow area is to be varied a similar situation occurs. A relatively simple means of varying flow area is to rotate the vanes about a radial axis. The resulting mechanical configuration can have clearances between the airfoil and the flowpath annulus at both the root and the tip. Thus, as many as three clearances can be present in a single turbine stage. The topic of clearance losses in shrouded rotors is discussed in Section 18.6. This mechanism is included under parasitic loss since it involves flow which leaves and re-enters the flowpath.

The impact of these clearances on turbine performance has been under continuous study for years. This source of endwall loss has a unique feature which makes it relatively easy to study experimentally. That is, that the clearance in a rig or cascade test can usually be easily varied and the impact of clearance on performance can be isolated. The result is that there is a large body of cascade and rotating rig data available (e.g. Refs. (18.60), (18.61), and (18.62)) which permits one to construct a relatively accurate correlation of performance penalty as a function of relative clearance and other variables. A simple order-of-magnitude study will indicate that, except for very small clearances, the flow in a clearance gap is dominated by the pressure difference across an airfoil and not by the viscous effects in the gap. For this reason the effects of relative wall motion, as in the case of a rotor tip, are usually weak. Hence a correlation based on rotor tip data would be expected to be adequate for the prediction of variable area vane clearance losses where there is no relative wall motion.

18.7.2 Flutter

Under some conditions a row of airfoils operating in a completely uniform flow can enter into a spontaneous (or self-excited) oscillation known as flutter. The motion is sustained by net energy extracted from the uniform flow during each vibratory cycle, the observed frequency generally corresponding to one of the lower blade or coupled blade/disk natural frequencies.

The outstanding feature of flutter is that the accompanying stresses are usually much higher than was allowed for in the design, and the life correspondingly reduced.

Very little is said or written about turbine flutter, leaving the impression that it never occurs. Perhaps the thick, heavy turbine parts do not seem capable of responding to the wind in that manner. These impressions are, however, incorrect, and turbines can and do flutter. Our experience indicates, in fact, that turbines behave much like compressors in the sense that flutter should be anticipated whenever the reduced natural frequency (flow velocity/axial chord x blade natural frequency) approaches unity. If that is the case, we may immediately conclude that the trend towards higher flow velocities may also increase the probability of flutter. We would also conclude that this source of airfoil structural excitation is worthy of study.

18.8 Stage Performance

18.8.0 Introduction

The time has come for us to face the crucial questions about turbine aerodynamic design. Have reliable means been found for increasing efficiency? If so, what approaches have been most fruitful, and have they been fully exploited? What are the most promising future directions?

One solid measure of our control over turbine aerodynamics is stage performance. Since each stage is affected by many of the phenomena previously discussed, it challenges the totality of the knowledge of the designer.

18.8.1 The Limits of Uncooled Stage Performance

We are indeed fortunate that Smith (Ref. (18.69)) provided a 1965 benchmark against which uncooled turbine efficiency progress can be gauged. Smith used existing single stage data to establish efficiency contours on a stage loading coefficient - flow coefficient chart, based on mean flow conditions and mean wheel speed. The chart reveals that there is a maximum efficiency that can be obtained at any given stage loading. When the locus of these points is plotted on an efficiency - stage loading coefficient chart (see the lower curve on Figure 18.13), the upper bound for possible turbine performance is established. Please note that Smith's data were corrected to zero tip leakage and that most of his stages had axial entry, which gives them the somewhat artificial benefit of about 2% in efficiency.

A particularly interesting aspect of the Smith contour in Figure 18.13 is the rapid decrease of stage efficiency with increasing stage loading coefficient. With data like this in hand it is small wonder that designers hesitated to venture much beyond a stage loading coefficient of 2.

The upper curve in Figure 18.13 represents our best estimate as to where the boundary stands today. It is based primarily upon data, yet supported by considerable analysis and experience. Special note should be taken of the fact that the data are from stages with non-axial inlet flows and realistic clearances, trailing edge thicknesses, platforms, and sealing arrangements. Comparison of these curves leads to two major conclusions. First, earlier methods are perfectly adequate for designing lightly loaded stages (stage loading coefficient < 2). Second, the penalty associated with highly loaded stages (stage loading coefficient > 2) is considerably less than previously thought. Special note should be taken of the apparent flatness of the presently recognized boundary. This has made it possible, in fan-drive turbines for example, to trade several stages for only a few points of efficiency, as was done in the case of the JT9D. These improvements are neither accidental nor beyond the grasp of any serious designer, and open the door to many possibilities once considered forbidden. We will describe below some of the methods which have contributed to these advances.

18.8.2 Controlled-Vortex Aerodynamics

Turbine aerodynamic design systems originally used a free-vortex calculation procedure largely because of its mathematical simplicity. Unfortunately, free-vortex designs exhibit an undesirable radial distribution of rotor reaction. Rotor reaction decreases from tip to root in such a turbine and can even become negative at the root. Small root reactions can make it extremely difficult to contour a passage which remains attached. Large blade tip reactions lead to excessive leakage losses in shrouded machines.

During the mid-sixties it became abundantly clear that a fundamental barrier to designing efficient, highly loaded stages was flow separation in the low reaction region of the rotor blade root. Not only did this cause large localized losses, but the unexpected blockage upset the intended flow pattern across much of the airfoil span. In this manner additional losses appear away from the wall, as well as in subsequent rows of a multi-stage machine.

This led to a search for flow patterns which would alleviate the problem. Fortunately, streamline calculation procedures were already available to permit the design of turbines with carefully tailored radial distributions of reaction. Systematic analytical studies showed that the best solutions increased root reaction by altering the spanwise work distribution. By reducing the work done at the root, less turning is required. The opposite situation holds true at the tip, where additional work can be done without difficulty. Such non-constant work machines have come to be known as controlled-vortex turbines.

The success of this approach has been well documented by Dorman et al. (Ref. (18.70)). In one program they demonstrated a highly loaded, controlled-vortex turbine stage which considerably raised the efficiency standard to 89.5% at a stage loading coefficient of 3.46 (Figure 18.14). In another program they compared controlled-vortex and free-vortex stages under exactly the same conditions and realized a 1.6% gain in efficiency at a stage loading coefficient of 1.51. They repeatedly found that controlled-vortex design lead to better performance across the entire span (Figure 18.14). There was no indication that an unusually distorted exit

condition will be produced in a multistage controlled-vortex turbine due to the stacking up of nonuniform work profile effects. This is due to the relatively small change in each stage, relative to a free-vortex design, and the improved efficiency near the endwalls which actually results in an improved temperature distribution. In addition, an analysis of the actual flow distribution has shown that the controlled-vortex stage has less tendency to force the flow away from the endwalls, and measurements have shown that the flow per unit area is more uniform than for the free-vortex stages.

18.8.3 Some Related Considerations

The above remarks are not intended to imply that the rest is now easy. On the contrary, many other techniques must be brought to bear in order to insure continuing progress. Some of them will be discussed in this Section.

Correct airfoil contouring has already been mentioned frequently, and certainly affects achievable stage performance. As loading increases, even the midspan airfoil section becomes more and more difficult to design. Once gross separation occurs, the aerodynamic losses become prohibitively high, and nothing approaching the upper stage efficiency limit can be reached. Successful design of highly loaded stages is best accomplished with the combined help of controlled-vortex flow patterns and good airfoil contouring methods.

Small gas turbines have special problems of their own, one of the outstanding being the excessive endwall flow losses which accompany their low aspect ratio airfoils. In fact, as cycle temperatures and pressures increase, this situation is spreading to bigger machines. As we have seen so often, the large disturbances near the endwalls upset the entire flow field and strip the designer of his ability to control the outcome. One method for dealing with this situation might be to reduce the endwall loss and cross-flows at the walls by reducing the turning and work done there. This can be thought of as controlled-vortex aerodynamics of a different sort. Midspan turning must, of course, be slightly increased in order to maintain constant work extraction. In this way performance would be improved both by doing more of the work in the more efficient region of the airfoil and by unloading the endwalls. This notion was put to the test by Schlegel et al. (Ref. (18.9)) with excellent results. The design-point performance of a research turbine stage revealed a 1.2% efficiency improvement over the baseline stage which it directly replaced. Furthermore, the flow field behaved much more in accordance with the design intent in the research stage.

One may freely speculate that the very best turbines of the future will contain all of the ideas described above. This was distinctly the case of Welna and Dahlberg (Ref. (18.70) and Figure 18.13), in which these approaches were combined and applied in a straight-forward way to their turbine. It should be particularly borne in mind that they exceeded the ambitious goal of their program on the first try. Better testimony on behalf of modern methods can hardly be expected.

Not all ideas are good ones, however. Many tricks have been proposed and tried through the years with no success. Among these are various schemes which tilt, lean, sweep, bow, serrate, place in tandem, or slit turbine airfoils, none of which has demonstrated superior performance.

It is difficult if not hopeless to attempt to define an efficiency boundary for cooled stages because the number of degrees of freedom is so large. Furthermore, the lack of completeness and consistency of reported results has made it difficult to establish an adequate data base. Suffice it to say that the best aerodynamics are applied to maintain cooled stage performance, and yet a stage efficiency of even less than 85% might be adequate in some high temperature applications.

18.9 Looking Ahead

It is already clear that the future holds many opportunities and challenges for gas turbine technology. We shall briefly outline some of the outstanding expected developments in this section, as well as their meaning to turbine aerodynamics.

The most exciting new concept in propulsion technology is the variable cycle engine (VCE). Providing sufficient flexibility to flowpath geometry will enable the VCE to continuously match its characteristics to the needs of the airframe while in flight. The large gains of system performance offered by the VCE make its development within this century almost certain. In fact, several propulsion companies have already modified existing engines in order to gain early experience with the VCE concept.

An essential ingredient of the VCE is the variable area turbine (VAT). As presently conceived, the VAT will replace one or more rows of fixed airfoils with rows of airfoils which can be adjusted by rotation about a radial axis. In this manner, the turbine operating map can be continuously altered to suit the immediate needs of the engine. Although the early attempts to capitalize on this concept are likely to be confined to uncooled turbine stages, progression into the cooled stages seems inevitable.

The reader can well imagine what these new degrees of freedom mean to the turbine designer. Each VAT will have to meet its aerodynamic and heat transfer goals over a wide range of flow conditions. Continuously changing cascade geometry, as well as marked increases in incidence angle and Reynolds number variation, will make great demands upon our design systems.

We may also rest assured that the progression to higher temperature and bypass ratio engines will continue throughout the century. During this period we can expect the stoichiometric limit for hydrocarbon fuels (about 3600°F) to be reached and bypass ratios to double or triple. As far as the turbine is concerned, this continues the trends already discussed in this Chapter. A thorough understanding of all facets of turbine aerodynamics will be essential to the orderly and successful development of such machines.

The turbine will ultimately become involved in the movement towards quieter engines. As the other components are made more and more silent, the noise floor of the engine will tend to become set by turbine noise, and acoustical tools tailored specifically for turbines will be required.

The turbine exit guide vane (EGV) diffuses and removes the swirl from the turbine exit flow. Since the EGV must often carry structural loads or contain fuel and oil lines, it can resemble a very low aspect-ratio compressor airfoil. Because exit swirl increases with stage loading, the EGV will become a limiting design factor and attract increased attention.

As fuel consumption becomes an increasingly critical item, performance will increase in importance relative to engine cost and weight. To the turbine designer this means pushing the limits of aerodynamics and reaching efficiencies near 95%.

The above remarks lead to a rather simple conclusion. Our appetite for reliable turbine aerodynamic prediction techniques will only grow as the years go by. There is every reason to concentrate on their successful development and to exploit them as they become available.

The gas turbine is one of the most demanding machines we know. It embodies a combination of power, precision and endurance which is at least awesome. But our modern devices are not the result of a single technological leap or revolutionary breakthrough. They are the product of simultaneous application of many small advances, and a lot of hard work. Research has played an important role in this unfolding drama, and has much to offer in the future.

Rather than being the docile, well-behaved devices of our mythology, turbines have become the bête noir of many recent development programs. Our course is inextricably set so that this will continue to occur. But the struggle against former limits has brought success again and again, and the future holds more of the same. For turbine designers, these are the good old days.

18.10 Acknowledgement

The authors wish to acknowledge the generous and valuable support and cooperation of the Pratt & Whitney Aircraft Group, Commercial Products Division, of United Technologies Corporation in the preparation of this Chapter.

18.11 References

18.1 Horlock, J. H. Axial Flow Turbines, Butterworths, London, 1966.

18.2 High Temperature Turbines, AGARD Conference Proceedings No. 73, Jan. 1971.

18.3 Sahn, P. R. and Speidel, M. O. (ed) High-Temperature Materials in Gas Turbines, Elsevier, New York, 1974.

18.4 Special Issue: Propulsion System Structural Integration and Engine Integrity, Journal of Aircraft, Vol. 12, No. 4, Apr. 1975.

18.5 Hebbel, H. The Influence of the Mach Number and the Reynolds Number on the Aerodynamic Coefficients of Turbine Cascades at Various Turbulence Intensities of the Flow, Forsch. Ing. Wis.: 30: 65-77, 1964.

18.6 Kiock, R. Influence of the Degree of Turbulence on the Aerodynamic Coefficients of Cascades, AGARD-AG-164, Dec. 1972.

18.7 Smith, A. M. O. High-Lift Aerodynamics, Journal of Aircraft, Vol. 12, No. 6, June 1975.

18.8 Thomas, K. M. and Piendel, J. J. An Automated Interactive Design System for Advanced Gas Turbines, ASME Paper No. 74-GT-82, 1974.

18.9 Schlegel, J. C., Liu, H. C. and Waterman, W. F. Reduction of End-Wall Effects in a Small Low-Aspect-Ratio Turbine by Radial Work Redistribution, Trans. ASME, J. Eng. for Power, Jan. 1976.

18.10 Dorman, T. E., Welna, H. and Lindlauf, R. W. The Application of Controlled-Vortex Aerodynamics to Advanced Axial Flow Turbines, Trans. ASME, J. Eng. for Power, July 1968.

18.11 Ives, D. C. and Liutermoza, J. F. Analysis of Transonic Cascade Flow Using Conformal Mapping and Relaxation Techniques, AIAA Paper No. 76-370, 1976.

18.12 Ainley, D. G. and Mathieson, G. C. R. A Method of Performance Estimation for Axial Flow Turbines, A.R.C., R&M 2974, 1957.

18.13 Zweifel, O. The Spacing of Turbomachine Blading, Especially with Large Angular Deflection, Brown Boveri Rev., Vol. 32, Dec. 1945.

18.14 Stewart, W. L. Analysis of Two-Dimensional Compressible Flow Loss Characteristics Downstream of Turbomachine Blade Rows in Terms of Basic Boundary Layer Characteristics, NACA TN-3515, July 1959.

18.15 Katsanis, T. and McNally, W. D. Revised FORTRAN Program for Calculating Velocities and Streamlines on a Blade-to-Blade Stream Surface of a Turbomachine, NASA TM X-1764, 1969.

18.16 Van den Braembussche, R. A. Calculation of Compressible Subsonic Flow in Cascades with Varying Blade Height, ASME Paper No. 73-GT-59, 1973.

18.17 Katsanis, T. and McNally, W. D. FORTRAN Program for Calculating Velocities in a Magnified Region on a Blade-to-Blade Stream Surface of a Turbomachine, NASA TN D-5091, 1969.

18.18 McDonald, P. W. The Computation of Transonic Flow Through Two-Dimensional Gas Turbine Cascades, ASME Paper No. 71-GT-89, 1971.

18.19 Delaney, R. A. and Kavanagh, P. Transonic Flow Analysis in Axial-Flow Turbomachinery Cascades by a Time-Dependent Method of Characteristics, Trans. ASME, J. Eng. for Power, July 1976.

18.20 Luu, T. S. and Coulmy, G. Relaxation Solution for the Transonic Flow Through a Cascade, Symposium Transsonicum II, Ed. Oswatitsch, K. and Rues, D., Springer-Verlag New York Inc., 1976.

18.21 Jaumotte, A. L. and Devienne, P. Influence du Nombre de Reynolds sur les Pertes dans les Grilles D'Aubes, Technique et Science Aeronautiques, No. 5, 1956.

18.22 Mukhtarov, M. K. An Experimental Study of Losses in Turbine Cascades at Low Reynolds Numbers, Teploenergetika, 1968, 15 (9), 56-68.

18.23 Webster, P. Design of a 4½ Stage Turbine with a Stage Loading Factor of 4.66 and High Specific Work Output, NASA CR-2659, Aug. 1975.

18.24 Dring, R. P. A Closed Form Solution for Compressible Turbulent Boundary Layer Problems, Z. Flugwiss., 19, Heft 5, 1971.

18.25 Schlichting, H. Boundary Layer Theory, 6th ed., McGraw-Hill Book Co., New York, 1968.

18.26 Dunham, J. Predictions of Boundary Layer Transition on Turbomachine Blades, AGARD-AG-164, Dec. 1972.

18.27 Launder, B. E. Laminarization of Turbulent Boundary Layer by Acceleration, MIT Gas Turb. Lab. Report No. 77, Nov. 1964.

18.28 Horton, H. P. A Semi-Empirical Theory for the Growth and Bursting of Laminar Separation Bubbles, A.R.C., CP No. 1073, June 1967.

18.29 Roberts, W. B. The Effect of Reynolds Number and Laminar Separation on Axial Cascade Performance, Trans. ASME, J. Eng. for Power, July 1975.

18.30 McDonald, H. and Fish, R. W. Practical Calculations of Transitional Boundary Layers, Int. J. Heat Mass Transfer, Vol. 16, No. 9, 1973.

18.31 Kreskofsky, J. P., Shamroth, S. J. and McDonald, H. Application of a General Boundary Layer Analysis to Turbulent Boundary Layers Subjected to Strong Favorable Pressure Gradients, Trans. ASME, Jour. Fluids Eng., June 1975.

18.32 Briley, R. W. and McDonald, H. Numerical Prediction of Incompressible Separation Bubbles, Jour. Fluid Mech., Vol. 69, Pt. 4, 1975.

18.33 Brown, A. and Martin, B. W. A Review of the Bases of Predicting Heat Transfer to Gas Turbine Rotor Blades, ASME Paper No. 74-GT-27, 1974.

18.34 Anderson, L. R. and Heiser, W. H. Systematic Evaluation of Cooled Turbine Efficiency, ASME Paper No. 69-GT-63, 1969.

18.35 Prust, H. W. and Helon, R. M. Effect of Trailing Edge Geometry and Thickness on the Performance of Certain Turbine Stator Blading, NASA TN D-6637, Jan. 1972.

18.36 MacMartin, I. P. and Norbury, J. F. The Aerodynamics of a Turbine Cascade with Supersonic Discharge and Trailing Edge Blowing, ASME Paper No. 74-GT-120, 1974.

18.37 Waterman, W. F. Low-Aspect-Ratio Turbine Technology Program, Garrett Airesearch, Report 75-211701 (1), Aug. 1975.

18.38 Armstrong, W. D. The Secondary Flow in a Cascade of Turbine Blades, A.R.C., R&M 2979, Mar. 1955.

18.39 Dunham, J. A Review of Cascade Data on Secondary Losses in Turbines, Jour. Mech. Eng. Sci., Vol. 12, No. 1, 1970.

18.40 Came, P. M. Secondary Loss Measurements in a Cascade of Turbine Blades, Inst. Mech. Eng., Conf. Publ. No. 3, 1973.

18.41 Morris, A. W. H. and Hoare, R. G. Secondary Loss Measurements in a Cascade of Turbine Blades with Meridional Wall Profile, ASME Paper No. 75-WA/GT-13, 1975.

18.42 Dunham, J. and Came, P. M. Improvements to the Ainley-Mathieson Method of Turbine Performance Prediction, Trans. ASME, J. Eng. for Power, July 1970.

18.43 Langston, L. S., Nice, M. S. and Hooper, R. M. Three-Dimensional Flow Within a Turbine Cascade Passage, Trans. ASME, J. Eng. for Power, Jan. 1977.

18.44 Carrick, H. B. Secondary Flow and Losses in Turbine Cascades with Inlet Skew, Ph.D. Thesis, Cambridge University, Oct. 1975.

18.45 Sjolander, S. A. The Endwall Boundary Layer in an Annular Cascade of Turbine Nozzle Guide Vanes, Tech. Rep. No. ME/A 75-4, Dept. Mech/Aero. Eng., Carleton University, Dec. 1975.

18.46 Moore, R. W. and Richardson, D. L. Skewed Boundary Layer Flow Near the End Walls of a Compressor Cascade, Trans. ASME, Vol. 79, Nov. 1957.

18.47 Squire, H. B. and Winter, K. G. The Secondary Flow in a Cascade of Airfoils in a Nonuniform Stream, J. Aero. Sci., Vol. 18, 1951.

18.48 Hawthorne, W. R. Secondary Circulation in Fluid Flow, Proc. Roy. Soc., London, Ser. A, Vol. 206, A 1086, 1951.

18.49 Hawthorne, W. R. Secondary Vorticity in Stratified Compressible Flow in Rotating Systems, Cambridge University, CUED/A - Turbo/TR 63, 1974.

18.50 Came, P. M. and Marsh, H. Secondary Flow in Cascades: Two Simple Derivations for the Components of Vorticity, Jour. Mech. Eng. Sci., Vol. 16, No. 6, 1974.

18.51 Belik, L. An Approximate Solution for Kinetic Energy of Secondary Flow in Blade Cascades, Int. J. Mech. Sci., Pergamon Press Inc., New York, Vol. 10, 1968.

18.52 Stuart, A. R. and Hetherington, R. The Solution of Three Variable Duct Flow Equations, NASA SP-304, Fluid Mechanics, Acoustics and Design of Turbomachinery, Pt. I, 1974.

18.53 Mellor, G. L. and Wood, G. M. An Axial Compressor Endwall Boundary Layer Theory, Trans. ASME, J. Eng. for Power, June 1971.

18.54 Mager, A. Generalization of Boundary-Layer Momentum-Integral Equations to Three-Dimensional Flows Including Those of Rotating System, NACA Report 1067, 1952.

18.55 Dring, R. P. A Momentum-Integral Analysis of the Three-Dimensional Turbine End-Wall Boundary Layer, Trans. ASME, J. Eng. for Power, Oct. 1971.

18.56 Booth, T. C. An Analysis of the Turbine Endwall Boundary Layer and Aerodynamic Losses, ASME Paper No. 75-GT-23, 1975.

18.57 Smith, P. D. An Integral Prediction Method for Three-Dimensional Compressible Turbulent Boundary Layers, A.R.C., R&M 3739, 1974.

18.58 Nash, J. F. and Patel, V. C. Three-Dimensional Turbulent Boundary Layers, SBC Technical Books, Atlanta, 1972.

18.59 Waterman, W. F. and Hall, W. A. Measurement and Prediction of 3-D Viscous Flows in Low-Aspect-Ratio Turbine Nozzles, ASME Paper No. 76-GT-73, 1976.

18.60 Szanca, E. Research Turbine for High-Temperature Core Engine Application; Part II - Effect of Rotor Tip Clearance on Overall Performance, NASA TN D-7639, Apr. 1974.

18.61 Marshall, R. and Rogo, C. Experimental Investigation of Low Aspect Ratio and Tip Clearance on Turbine Performance and Aerodynamic Design, Continental Aviation and Engineering Corp., Report 1043, May 1968.

18.62 Kofskey, M. and Nussbaum, W. Performance Evaluation of a Two-Stage Axial-Flow Turbine For Two Values of Tip Clearance, NASA TN D-4388, Jan. 1968.

18.63 Deich, M. E., Zaryankin, A. E., Filippov, G. A. and Zatsepin, M. F. Method of Increasing Efficiency of Turbine Stages With Short Blades, Teploenergetika, 1960, 7(2), 18-24.

18.64 Ewen, J. S., Huber, F. W. and Mitchell, J. P. Investigation of Aerodynamic Performance of Small Axial Turbines, ASME Paper No. 73-GT-3, 1973.

18.65 Okapuu, U. Some Results From Tests on a High Work Axial Gas Generator Turbine, ASME Paper No. 74-GT-81, 1974.

18.66 Prumper, H. Application of Boundary Layer Fences in Turbomachinery, AGARD-AG-164, Dec. 1972.

18.67 Rott, N. and Lewellen, W. S. Boundary Layers in Rotating Flows, Aerospace Corporation, General Research, Report No. ATN-64 (9227) -6, 1964.

18.68 Deich, M. E., Frolov, V. V., Krugleukov, G. A. and Kustov, O. P. Influence of the Pattern of Leakage of the Medium Through the Root Clearance on the Stage Efficiency, Teploenergetika, 1972, 19(6), 81-83.

18.69 Smith, S. F. A Simple Correlation of Turbine Efficiency, J. R. Aeronaut. Soc., Vol. 69, 1965.

18.70 Welna, H. and Dahlberg, D. E. Investigation of a Highly Loaded Two-Stage Fan-Drive Turbine, Volume VI, Final Technical Report, AFAPL-TR-69-92, Nov. 1971.

18.71 Whitney, W. J., Behning, F. P., Moffitt, T. P. and Holtz, G. M. Investigation of a 4½ Stage Turbine with a Stage Loading Factor of 4.66 and High Specific Work Output, I - Overall Performance, NASA TMX-3498, 1977.

18.12 Nomenclature

18.12.0 Symbols

c	true airfoil chord
c_p	specific heat at constant pressure
f	function
m	mass flow
n	exponent
P	total pressure
q	dynamic head
s	specific entropy
S	airfoil surface distance
T	total temperature
U	freestream velocity
γ	ratio of specific heats
Γ	boundary layer dimensionless parameter
δ	boundary layer thickness
δ_1	boundary layer displacement thickness
δ_2	boundary layer momentum thickness
Δ	unit process change (exit-inlet)
η	thermodynamic efficiency
ν	kinematic viscosity
Σ	summation

18.12.1 Subscripts

e	exit
i	inlet
j	stream number
sep	separation

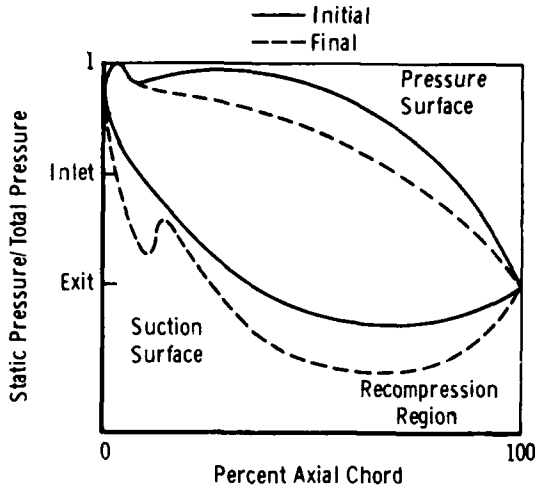

Figure 18.1 Cascade Airfoil Pressure Distributions

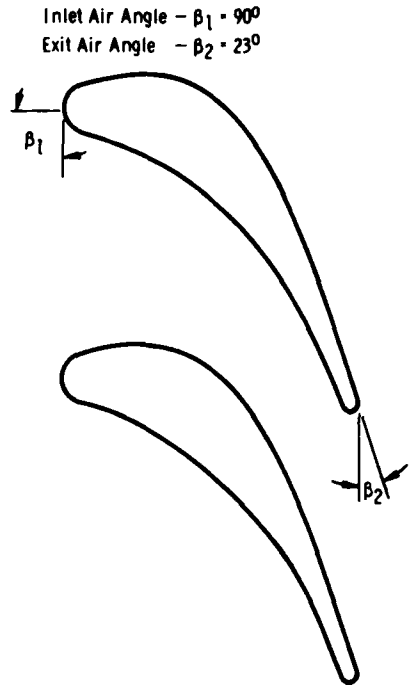

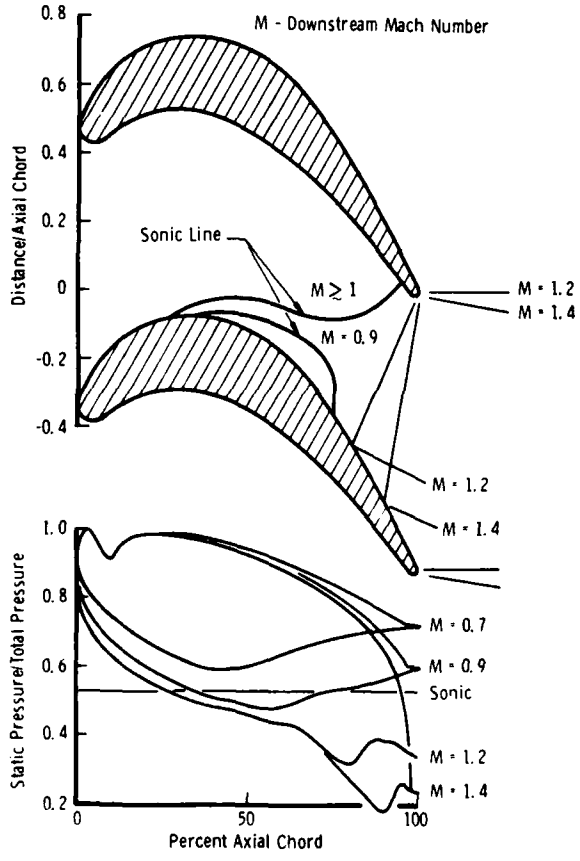

Figure 18.2 Transonic Cascade Flow

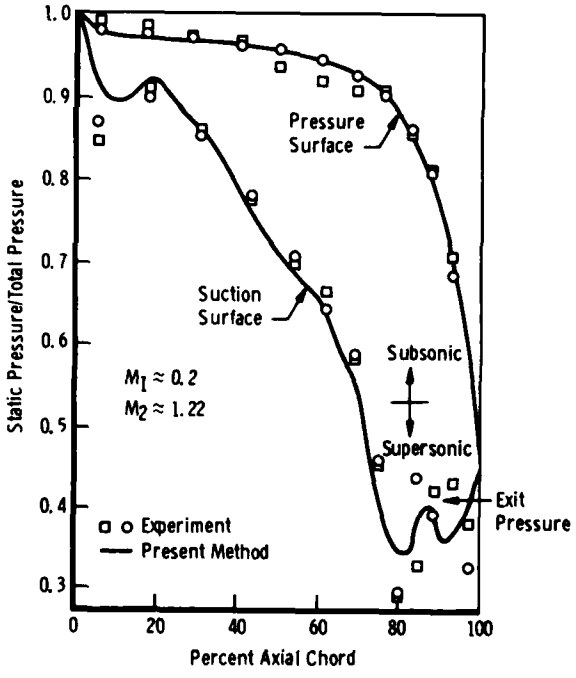

Figure 18.3 Predicted and Measured Stator Pressure Distribution

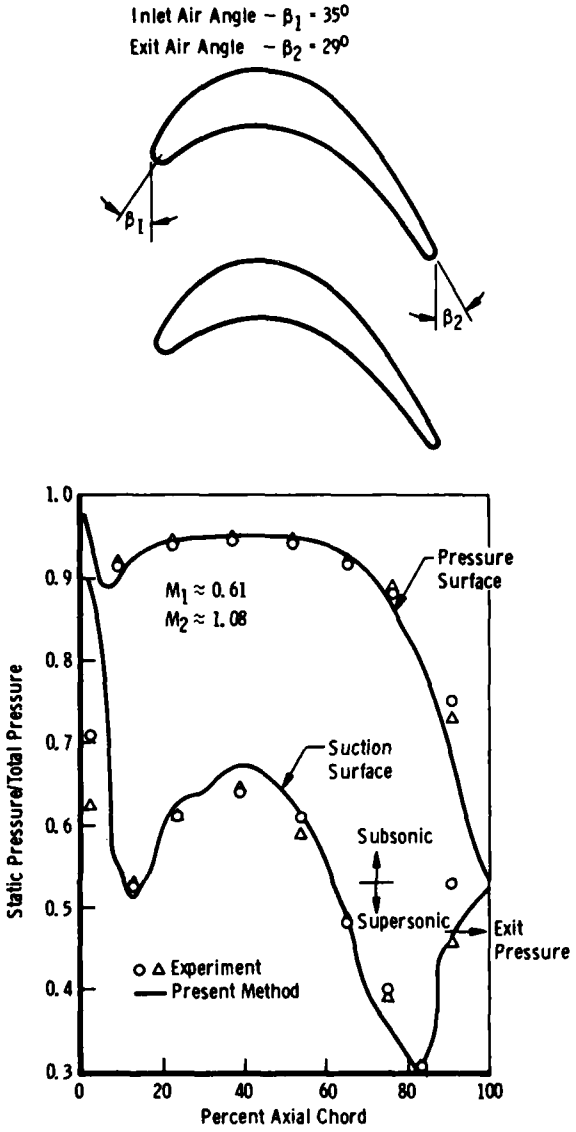

Figure 18.4 Predicted and Measured Rotor Pressure Distribution

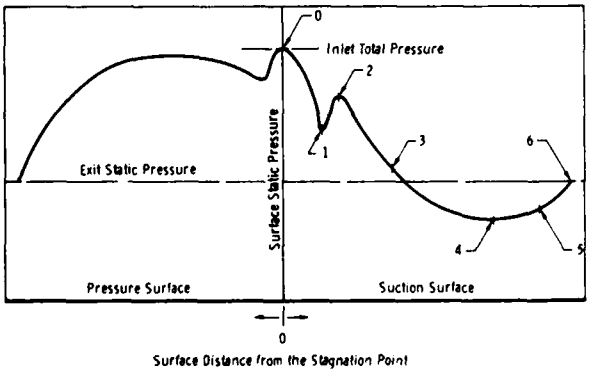

Figure 18.5 Cascade Airfoil Pressure Distribution

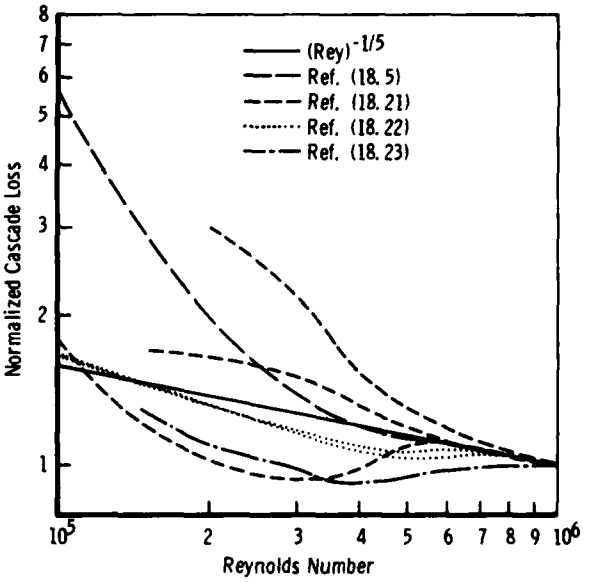

Figure 18.6 Effect of Reynolds Number on Cascade Loss

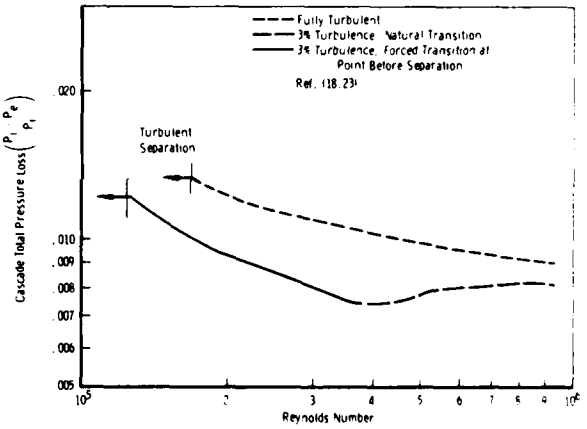

Figure 18.7 Cascade Profile Loss versus Reynolds Number

Figure 18.8 Cascade Endwall Limiting Streamlines

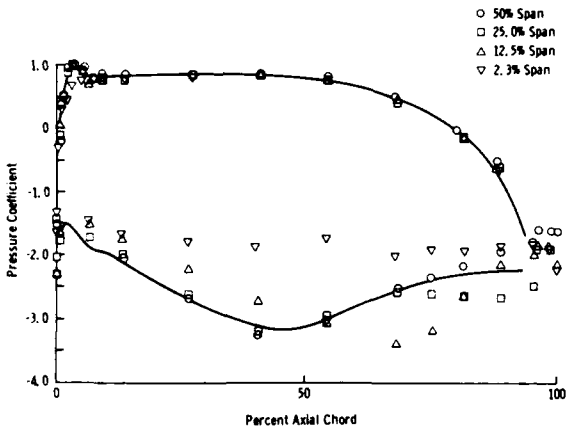

Figure 18.9 Cascade Static Pressure Distribution Showing Effect of Endwall Flow

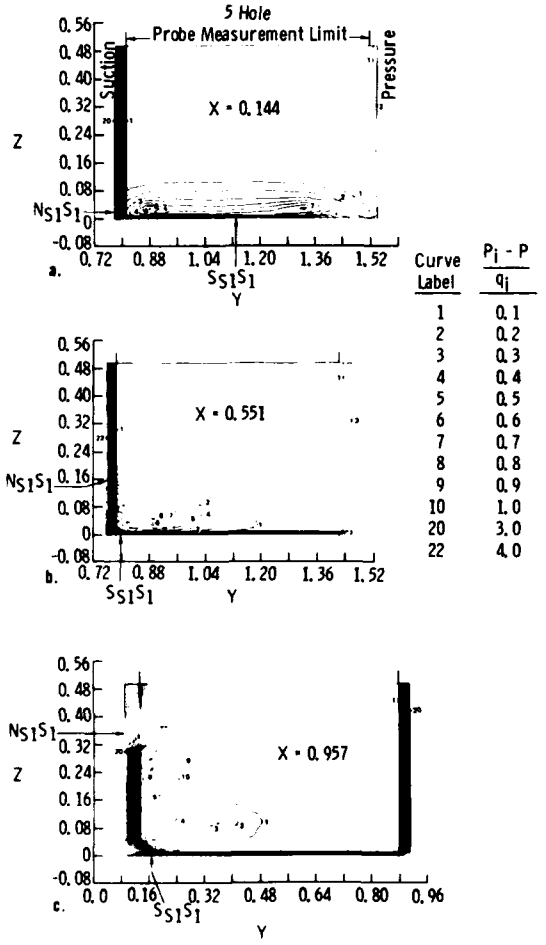

Curve Label	$P_i - P / q_i$
1	0.1
2	0.2
3	0.3
4	0.4
5	0.5
6	0.6
7	0.7
8	0.8
9	0.9
10	1.0
20	3.0
22	4.0

Figure 18.10 Isobar Plot of Total Pressure Loss Coefficients at Three Axial Planes

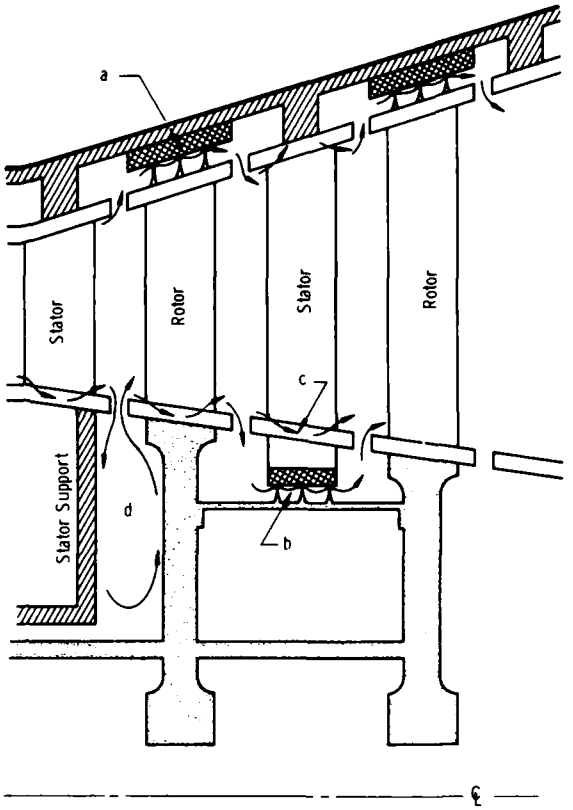

Figure 18.11 Schematic Diagram of Turbine Sealing Arrangements

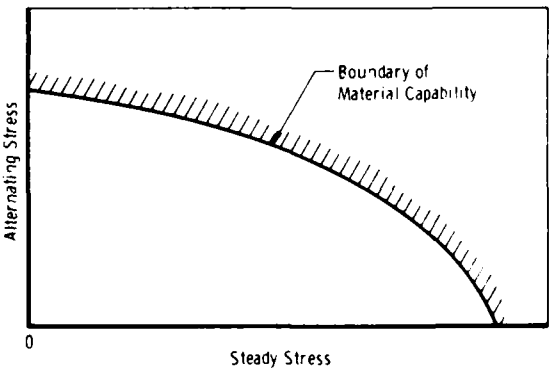

Figure 18.12 Goodman Diagram for Combined Static Load and Fatigue Life

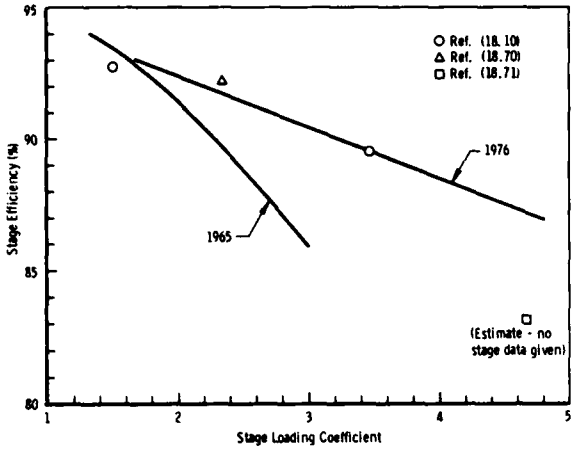

Figure 18.13 Limits of Turbine Stage Performance

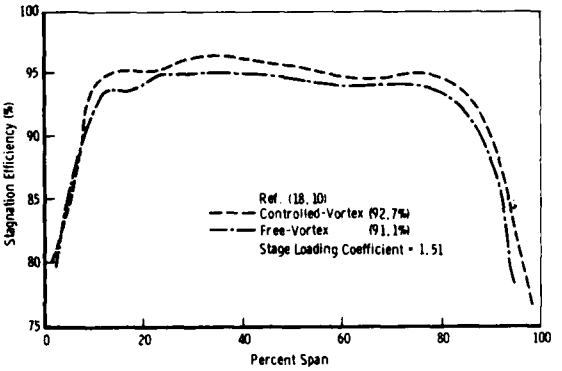

Figure 18.14 Measured Free-Vortex and Controlled-Vortex Spanwise Traverse Efficiency

Chapter 19

TURBINE COOLING

Mikio Suo

United Technologies Research Center

Turbine Cooling

The Aerothermodynamics of Aircraft Gas Turbine Engines

Chapter 19

by
Mikio Suo
United Technologies Research Center

August 1976

Table of Contents

Section		Page
Table of Contents		19-i
List of Figures		19-i
19.0	Introduction	19-1
19.1	Cooling Design Problem	19-1
19.1.1	Modes of Thermal Failure	19-1
19.1.2	Thermal Environment	19-2
19.1.3	Cooling Air Supply	19-2
19.1.4	Cooling Design Methodology	19-2
19.2	Airfoil Cooling	19-3
19.2.1	Convective Cooling	19-3
19.2.2	Film Cooling	19-6
19.2.3	Leading Edge Film Cooling	19-11
19.2.4	Aerodynamic Losses of Film Cooling	19-11
19.2.5	Transpiration Cooling	19-12
19.3	Endwall Cooling	19-13
19.3.0	*Introduction*	19-13
19.3.1	Stator Platforms	19-13
19.3.2	Stationary Shrouds	19-13
19.3.3	Rotating Platforms and Shrouds	19-14
19.4	Conclusions	19-14
19.5	References	19-14
19.6	Nomenclature	19-16
Figures		19-18

List of Figures

Figure		Page
19.0.1	Turbine Inlet Temperature History and Projection	19-18
19.0.2	Blade Material Temperature Capability History and Projection	19-18
19.1.1	Typical Radial and Circumferential Temperature Distribution for an Annular Burner @ 2500 F	19-18
19.1.2	Burner Average Radial Temperature Profile	19-18
19.1.3	Cooling Air Supply System	19-18
19.2.1	Convestively Cooled Blades	19-18
19.2.2	Airfoil Heat Transfer Coefficient Distribution	19-18
19.2.3	Typical Pressure and Heat Transfer Coefficient Distribution	19-18
19.2.4	Leading Edge Impingement Cooling	19-19
19.2.5	Leading Edge Impingement Cooling Model (Ref. 19.3)	19-19
19.2.6	Heat Transfer Distribution From Impingement Cooling (Ref. 19.3)	19-19
19.2.7	Leading Edge Impingement Cooling Model (Ref. 19.4)	19-19
19.2.8	Midchord Impingement Cooling	19-19
19.2.9	Roughened Walls in Airfoils	19-20
19.2.10	Roughened Wall Model (Ref. 19.7)	19-20
19.2.11	Film Cooling	19-20
19.2.12	Entrainment Model for Film Cooling	19-20
19.2.13	Oil Traces of Film Cooling From a Row of Holes (Ref. 19.14)	19-20
19.2.14	Spanwise Film Effectiveness From a Row of Holes (Ref. 19.15)	19-20
19.2.15	Film Cooling Geometry	19-20
19.2.16	Effect of Blowing Rate on Centerline Film Cooling Effectiveness (Ref. 19.16)	19-21
19.2.17	Effect of Coolant Density on Film Effectiveness (Ref. 19.17)	19-21
19.2.18	Correlation of Film Effectiveness with Coolant to Mainstream Momentum Flux Ratio (Ref. 19.17)	19-21

Figure		Page
19.2.19	Film Cooling Effectiveness on an Airfoil with a Double Row of Holes (Ref. 19.20)	19-21
19.2.20	Heat Transfer Coefficient Under Film Cooling (Ref. 19.20)	19-21
19.2.21	Film Cooled Airfoil With Mutliple Rows of Holes	19-21
19.2.22	Airfoil With Multihole Film Cooling	19-22
19.2.23	One-Dimensional Model for Multihole Cooling	19-22
19.2.24	Effects of Convective and Film Effectiveness on Overall Effectiveness	19-22
19.2.25	Multihole Cooling Geometry (Ref. 19.25)	19-22
19.2.26	Film Effectiveness From Multihole Cooling (Ref. 19.25)	19-22
19.2.27	Overall Effectiveness of Leading Edge Film Cooling (Ref. 19.32)	19-23
19.2.28	Comparison of Data For Cooled Cascade Efficiency with Mixing Analysis of Eq. 19.2.24	19-23
19.3.1	Endwall Regions	19-23
19.3.2	Endwall Film Cooling Data (Ref. 19.36)	19-23
19.3.3	Endwall Heat Transfer Distribution (Ref. 19.36)	19-23

19.0 Introduction

High turbine inlet temperatures have significant advantages for aircraft gas turbine engines. The reasons for these advantages have been discussed in Ch. 7. Engine manufacturers have recognized this for some time and have been continuously increasing turbine inlet temperature, especially during the last fifteen years. Figure 19.0.1 illustrates this trend.

A vital part of going to high turbine inlet temperatures is the technology of turbine cooling. This was recognized by some almost from the inception of the first turbojet engine. Cooling studies were first performed in the 40's and many investigations were carried on in the 50's. Around 1960, turbine cooling was first used in a commercial aircraft engine (Ref. 19.1). Since that time, there has been a very rapid rise in turbine inlet temperatures, which has placed an even greater emphasis on turbine cooling.

The turbine inlet temperature trend shown in Fig. 19.0.1 has been made possible not only by turbine cooling but also by continuous improvements in high temperature materials. Figure 19.0.2 shows the trend in improvements in rotor blade materials. As can be seen, materials improvements have played and will continue to play an important part in the increasing turbine inlet temperature trend. The materials shown in Fig. 19.0.2 are nickel-based alloys used for stators and rotors. A similar figure could be shown for cobalt-based alloys which are used to a more limited extent in stator vanes and uncooled rotor blades. Many other types of materials have been proposed for use in turbines. Examples of these are refractory-metal alloys and ceramics. Although much research has been performed on these materials, they have yet to receive widespread utilization. In this chapter on turbine cooling the nickel- or cobalt-based alloys are presumed to be used.

The cooling flows currently required on new aircraft engines are very large, of the order of 20% of the compressor discharge flow. This large quantity of flow has two effects which tend to reduce the advantages of high turbine inlet temperature. The first is that the air used for cooling reduces the capability of the turbine to drive the compressor because of the lower temperature at which it enters the turbine. The second is that the cooling air mixes with the mainstream turbine air and causes aerodynamic losses. Both these effects are strong, and, therefore, vigorous steps are taken to minimize them by minimizing both the quantity of cooling air and the aerodynamic penalty associated with that quantity of cooling air which is used. The technical question addressed in this chapter is: how to maintain turbine durability while minimizing the quantity of cooling air and the aerodynamic losses associated with it.

In the above discussion reference was made to turbine inlet temperature. There appears to be some disagreement on the definition of this term in the industry, but in this chapter, consistent with the other chapters, the turbine inlet temperature will always refer to the average combustor exit temperature into the first stator vane.

19.1 Cooling Design Problem

19.1.1 Modes of Thermal Failure

There are several modes of turbine failure which are associated with turbine cooling. These are oxidation/corrosion/erosion, creep, and thermal fatigue. Oxidation/corrosion/erosion occurs because of chemical and particulate attack from the hot turbine gases. The materials used for parts exposed to turbine gases, when used at a temperature commensurate with the other modes of failure, cannot survive this mode of attack for very long unless coated with special high temperature coatings. These coatings, in general, provide a layer of aluminum oxide on the surface to prevent chemical attack. Beyond this the method of control is to limit the maximum surface temperature on the part.

Creep occurs as a result of prolonged exposure of materials to high stresses at high temperatures. This is a particularly acute problem on rotating turbine blades which are highly stressed. This mode of failure is, in general, controlled by limiting the average temperature of a turbine blade and thus the average creep. Creep also occurs as a local problem in airfoils, and this mode of failure is controlled by limiting the local temperature within an airfoil.

Thermal fatigue occurs as a consequence of repeated cycling through high thermal stresses. These stresses are large enough to cause local plastic deformation in each cycle. As a result, failure can result in relatively few cycles (of the order of thousands rather than hundreds of thousands). The problem is the most severe in highly-cooled airfoils, which must operate through rapid transients of the order of several seconds. The different parts of the airfoils respond at different rates to the transients and suffer large thermal stresses as a result. Thermal stresses are minimized by consideration of the overall cooling distribution, mass distribution within the airfoil (which sets thermal response), and the interior geometrical configuration.

In addition to creep and thermal stress as separate entities, there is a combined effect of the two acting together. Airfoils which incur high cyclic thermal stresses as well as prolonged exposure at high temperatures and high stresses fail before failure would occur if each mode were to act alone. This is called creep/thermal fatigue failure and is a mode of failure receiving increasing attention in turbine design.

19.1.2 Thermal Environment

The combustion gases enter the turbine in a nonuniform manner. A typical distribution of temperature coming out of an annular burner is shown in Fig. 19.1.1. The distribution is random in a circumferential direction but has some degree of order in the radial direction. The randomness of the temperature distribution causes the design of first stator vanes to be designed for the maximum temperature (hot spot) coming out of the burner. This maximum temperature is generally a specified burner design parameter. Typically, in a 2500 F turbine inlet temperature engine the hot spot may be 3000 F. The rotating structure may be designed for an average temperature in the circumferential direction. The radial distribution of the circumferentially-averaged temperature is typically as shown in Fig. 19.1.2. This profile tends to occur naturally because burner cooling air reduces temperatures at the endwalls. In addition to this natural tendency, the burner is generally specifically designed to produce such a profile to ease the turbine cooling problem by reducing blade root and endwall cooling requirements. This profile is also the feature which causes the small degree of order in temperature out of the annular burner in the radial direction.

The first stator vanes are exposed to the highest turbine temperatures (including the hot spot from the burner). The first rotating blade row is exposed to a somewhat lower temperature because of circumferential averaging, dilution of turbine gases with first stator vane cooling air, and relative velocity effects. The second stator vane is exposed to a lower temperature because of cooling air dilution, work extraction from the turbine gases and a small amount of radial mixing, which dilutes the hot spots. The turbine temperature decreases in a like manner through each airfoil row.

19.1.3 Cooling Air Supply

The cooling air to cool the turbine is bleed air from the compressor. A typical cooling system is shown in Fig. 19.1.3. The first stator vane is fed by compressor discharge air which has bypassed the combustor. This is because the first stator vane requires a very high supply pressure. The first rotor blade is also fed by compressor discharge air. However, this air is accelerated through a row of nozzles pointed in the direction of rotation. The effect of this is to reduce the amount of work to pump the cooling air and to reduce the cooling air temperature within the blade. The second stator vane and second rotor blade are also cooled by compressor discharge air in this case, but in general these airfoils can be fed from compressor bleed air further up the compressor. This helps engine performance because of reduced compressor work requirements and reduced cooling air temperature.

Many variations on this delivery system are in use today. The basic principle is to deliver the required cooling air pressure at the minimum temperature possible. By clever design there is great potential in this area for improving engine performance. For example, it has been proposed in some applications to cool the cooling air with fan air through a heat exchanger. This would reduce the requirement for cooling flow but would add complexity and weight.

The cooling air delivery system also performs another function. The cavities adjacent to the gas path are not directly cooled, but are kept at low temperatures by being surrounded by cool air. This air is furnished by the cooling air delivery system through controlled leakages from the delivery system. An interesting thought is that the cooling air is often around 1000 F. One does not normally think of cooling with air which is that hot.

In this chapter, only air cooling of turbines will be considered. There are obviously many other ways to cool turbines such as heat pipes, water, fuel, etc. These are of some interest for aircraft applications but by far the greatest practical interest is in air cooling. Since air cooling is the method of greatest interest, this chapter will not address other methods of cooling.

19.1.4 Cooling Design Methodology

The cooling design process is by necessity an iterative one. The designer starts by either being given or assuming certain life requirements on oxidation/corrosion/erosion, creep, thermal fatigue, and creep/thermal fatigue. Simultaneously he is given a mission under which these life requirements must be met. An initial aerodynamic design up to and including airfoil contours and cooling air flows and temperatures is also given. The last two quantities are generally closely estimated from past design practices. The designer can usually decide from past experience what type of cooling will be necessary, convective or film cooling, on each surface to be cooled. At this point the detailed design problem begins. The process is one of analysis and not one of synthesis, so the designer must first lay out a configuration. Having done this, he must then analyze it to determine life and cooling penalties, and, in general, he must do this several times, modifying the design each time.

To determine metal temperature and thus life he must consider three aspects of the problem. The first is the heat load to the surface from the mainstream gas. This will be convection through a viscous boundary layer or through a film cooling layer. The second is the convective cooling of the part by the coolant within the interior of the part. The third is the thermal conduction and absorption within the part. The designer calculates the metal temperatures taking account of each of the above considerations, utilizing whatever tools he has available. In going through this he generally finds that he must request relief from some of the initial constraints on airfoil shape or cooling flows because of practical fabrication considerations, or because he simply cannot cool the part adequately under the

given conditions. During this time, a continuous re-evaluation of the penalties caused by the cooling air is also made. After several configurations are laid out and analyzed, the designer generally can 'home in' on a design which meets most or all of the original criteria.

In the following sections the required information to calculate heat loads, internal convective cooling, and cooling penalties are discussed. They are discussed in a way that, hopefully, a designer new to the field might see what information is available in the literature and, perhaps more important, determine what additional information is required to execute successful designs.

19.2 Airfoil Cooling

19.2.1 Convective Cooling

19.2.1.0 Introduction

The simplest way to cool airfoils is by convective cooling. In this process the air is brought in at the root or tip of the airfoil then discharged at the other end of the airfoil or through the trailing edge. This method of cooling is quite efficient and is always used where it is adequate to cool the airfoils. Cutaway views of two convectively cooled airfoils are shown in Fig. 19.2.1.

At this point it is useful to introduce a definition. The average cooling effectiveness for an airfoil is defined by

$$\bar{\phi} \equiv \frac{T_{tg} - T_m}{T_{tg} - T_c} \qquad (19.2.1)$$

where T_m is the average temperature of the airfoil. A value of cooling effectiveness of one is the maximum possible and a value near zero represents little or no cooling. The required average cooling effectiveness is the strongest parameter determining methods of cooling and quantities of cooling air.

Convective cooling is used where average cooling effectiveness levels required are less than about 0.5. This limitation exists for two reasons. The first is that the air supply pressure is limited and much higher effectiveness would only be possible with higher supply pressures. The second is that with high effectiveness levels and convective cooling the temperature gradients tend to get very large and aggravate thermal stress problems.

19.2.1.1 Airfoil Heat Transfer Coefficients

In gas turbines the heat transfer coefficients to the airfoils are very high and the conductivities of the materials are fairly low. This combination makes it imperative that the heat transfer coefficient distribution over a whole airfoil be known in great detail. One cannot depend upon conductivity to smooth out errors in distribution.

The heat transfer coefficient distribution to an airfoil is typified in Fig. 19.2.2. At the stagnation point the heat transfer coefficient is very high. Its level can be correlated as the heat transfer coefficient to the stagnation point of a cylinder in cross flow with an effect of free stream turbulence, which raises its level. On the concave or pressure side of the airfoil the boundary layer almost always trips to turbulent flow and attains a heat transfer coefficient level corresponding to a low Reynolds number turbulent flow. On the convex or suction side of the airfoil the boundary layer often is first laminar with an effect of free stream turbulence, then goes through a gradual transition from laminar to turbulent flow. The gradual transition appears to occur because of very high pressure gradients, which tend to force the boundary layer to stay laminar. The curvature of the airfoil also tends to maintain laminar flow.

The heat transfer coefficient distribution to an airfoil is calculated utilizing two-dimensional boundary layer theory. The pressure distribution within the cascade is first calculated using an inviscid, two-dimensional, compressible, numerical solution. Such solutions have become readily available within the past few years. The boundary layer is then calculated in a manner described in Ch. 16. The pressure distribution and heat transfer coefficient distribution calculated from boundary layer theory for a typical airfoil are shown on Fig. 19.2.3. The heat transfer coefficient distribution thus calculated, although by no means exact, is reasonably valid except for the stagnation point and the laminar region on the suction side. There the heat transfer coefficient distribution must be increased by a factor of 1.2 to 1.8 to account for the effects of free stream turbulence mentioned above. The very high levels of the heat transfer coefficient distribution in this example are typical of modern turbines.

The two-dimensional calculations have inherent drawbacks because of three-dimensional effects, which are present to varying degrees of importance. For example, the two-dimensional calculation assumes that the gas is at a constant total temperature. Because of secondary flows and consequent radial mixing the gas temperature at a given radial location tends to change as it goes through an airfoil row. This effect is fairly strong and is generally not calculable to any degree of accuracy. There are also radial flows in boundary layers caused by the radial pressure gradients. However, there is some theoretical evidence (Huile, Ref. 19.2) that radial boundary layer flows do not significantly affect heat transfer. Near the tips of unshrouded airfoils a significant amount of radial flow occurs because of leakage over the tip. This effect is strong and not well quantified.

In addition to three-dimensional flow effects, radiation plays a part in the heat transfer. This effect is generally limited to the leading edge of the first stator vanes. Beyond that, convection effects far outweigh radiation effects.

19.2.1.2 Impingement Cooling at the Leading Edge

The airfoil external heat transfer coefficient distribution discussed in the last section must be counterbalanced with a comparable heat transfer coefficient distribution on the inside of the airfoil. At the leading edge the high heat transfer coefficient is often counterbalanced with impingement cooling. Figure 19.2.4 shows how this is achieved in an airfoil. This method of cooling has been recognized for some time as being highly effective and, therefore, has received much attention from researchers. As a result, a large quantity of data and correlations are available in the literature. Of the rather large quantity of literature, only two works will be discussed here. Chupp, et al. (Ref. 19.3) measured and correlated the heat transfer in the geometry shown in Fig. 19.2.5. They correlated the heat transfer coefficient over the leading edge radius region. They also obtained information on the distribution of the heat transfer coefficient. The average and stagnation point Nusselt numbers were correlated by:

$$Nu_{ave} = 0.63\ Re^{0.7}\ (d/p)^{0.5}\ (d/L)^{0.6} \exp\left[-1.27\ (\ell/d)(d/p)^{0.5}\ (d/L)^{1.2}\right] \quad (19.2.2)$$

$$Nu_{stag} = 0.44\ Re^{0.7}\ (d/p)^{0.8} \exp\left[-0.85\ (\ell/d)\ (d/p)\ (d/L)^{0.4}\right] \quad (19.2.3)$$

where d is the characteristic dimension in the Nusselt numbers and Reynolds number and the impingement hole velocity is the characteristic velocity in the Reynolds number. The thermal conductivity is evaluated at the average of wall and coolant temperature and the viscosity is evaluated at the coolant temperature. The range of variables tested were:

$3{,}000 < Re < 15{,}000$
$0.006 \text{ in.} < d < 0.026 \text{ in.}$
$0.0312 \text{ in.} < p < 0.125 \text{ in.}$
$0.040 \text{ in.} < L < 0.094 \text{ in.}$
$0.006 \text{ in.} < \ell < 0.160 \text{ in.}$

The distribution away from the stagnation point is shown on Fig. 19.2.6. This distribution was found to be relatively independent of (d/p) and Re.

Metzger, et al. (Ref. 19.4) performed a more complete investigation in that they correlated more geometric variables. Their geometry is shown in Fig. 19.2.7, which in a gross way approximates most of the geometric variables in an airfoil design. Of particular interest in the work of Ref. 19.4 are the effects of a small leading edge radius. Small internal leading edge radii tend to occur in airfoils because of requirements to design small external leading edge radii to give good aerodynamic performance and thick leading edge walls to prevent overly rapid thermal response to transients. Their correlations, unfortunately, are not easily put into a simple form. Their correlations have the functional form of

$$St_{ave} = St_{ave}(Re, p/d, r/b, \ell/b, 2H/L, 2r/L) \quad (19.2.4)$$

where St_{ave} is based on impingement hole velocity and where Re is a Reynolds number based on twice an equivalent slot b and on impingement hole velocity. The reader is referred to the original work for the correlations. This work measured only average heat transfer coefficients over the region 2f rather than local heat transfer coefficients, but fortunately these are generally adequate for airfoil design.

19.2.1.3 Impingement Cooling at Midchord

High levels of heat transfer coefficients are desirable in the midchord region, as well as the leading edge. This is often accomplished with impingement cooling, as shown in Fig. 19.2.8. This is similar in some respects to impingement cooling at the leading edge, but is different in two major aspects. The radius of curvature of the impingement surface approaches infinity, and the spent impingement air causes a strong cross flow.

Kercher and Tabakoff (Ref. 19.5) performed experiments on impingement with cross flow on a flat plate. They correlated the data with the relationship

$$Nu_x = \xi_1 \xi_2 Re^m Pr^{1/3} (\ell/d)^{0.091} \quad (19.2.5)$$

where

Nu_x = local Nusselt number with the impingement hole diameter d as the characteristic length

Re = Reynolds number based on the mass velocity through the hole and on impingement hole diameter

Pr = Prandtl number

ℓ = length from impingement hole to wall

r = hole pitch (square arrays)

ξ_1, ξ_2, m are empirically determined parameters.

All properties are evaluated at the average temperature of wall and coolant. The range of variables tested was:

$1 < \ell/d < 4.8$

$332 < Re < 3.7 \times 10^4$

$3.1 < p/d < 12.5$

Colladay (Ref. 19.6) has taken the correlations of Ref. 19.5 for ξ_1, ξ_2, and m and presented them in the following form:

$$m = a_1(p/d)^2 + b_1(p/d) + c_1 \qquad (19.2.6)$$

$$\xi_1 = \exp[a_2(p/d)^2 + b_2(p/d) + c_2] \qquad (19.2.7)$$

$$\xi_2 = \frac{1}{1 + a_3[(G_{cf}/G_h)(p/d)]^{b_3}} \qquad (19.2.8)$$

where a_1, a_2, a_3, b_1, b_2, b_3, c_1, and c_2 are given in TABLE 19.2.1 and

G_{Cf} = cross flow mass velocity

G_h = impingement hole mass velocity

TABLE 19.2.1

IMPINGEMENT COOLING CORRELATION (Ref. 19.6)

Coefficient	Reynolds Number 300 to 3000	Reynolds Number 3000 to 30000
a_1	-0.0015	-0.0025
b_1	0.0428	0.0685
c_1	0.5165	0.5070
a_2	0.0126	0.0260
b_2	-0.5106	-0.8259
c_2	-0.2057	0.3985
a_3	0.4215	0.4696
b_3	0.580	0.965

19.2.1.4 Roughened Walls

Another technique which is commonly used to obtain high heat transfer coefficients is to place fins normal to the coolant flow path. Such a cooling scheme is shown in Fig. 19.2.9. Little data are available in the literature for the exact geometries used in airfoils, but data for circular pipes are available and may be applied utilizing the concept of a hydraulic diameter. For example, Webb, Eckert, and Goldstein (Ref. 19.7) investigated the geometry shown in Fig. 19.2.10 with the range of parameters

$0.01 < e/d < 0.04$

$10 < p/e < 40$

and obtained heat transfer and friction factor correlations. The reader is referred to the original work for the correlations.

19.2.1.5 Trailing Edges

The aerodynamic requirement for thin trailing edges makes it very difficult to cool the trailing edge by convective cooling unless the coolant air ejects through the trailing edge. One way in which this is accomplished is shown in the airfoils of Fig. 19.2.1. In these airfoils the two halves of the trailing edge are held together with pins which are commonly called pedestals. These pins serve two purposes. They structurally hold the airfoil together, and they augment the heat transfer. Halls (Ref. 19.8) reports the use of the correlation from Grimison (Ref. 19.9) for tube banks

$$Nu_{ave} = Fa\ 0.284\ Re^{0.61} \qquad (19.2.9)$$

where

$0.7 < Fa < 1.2$

and where the reference velocity is on the minimum flow area and the reference dimension is the pedestal diameter. Coolant properties are evaluated at the average temperature of wall and coolant. In Ref. 19.9, F_a is correlated as well as the friction factor for in-line and staggered tube banks.

Another way to get the coolant out of the trailing edge is to use drilled holes. These are normally calculated using standard pipe heat transfer correlations and an entry length correction term. This technique cannot achieve as high effectiveness as pedestals can, but nevertheless is often used where a high degree of trailing edge cooling is not required.

19.2.1.6 Flow Distribution

In airfoil internal cooling design one of the most important parameters is the flow distribution. The calculation of flow distribution is generally performed through the use of one-dimensional branched circuits. These circuits account for friction, expansion-contraction losses, area change, heating and rotation. The necessary correlations for each of the pressure loss mechanisms come from the data and correlations discussed above.

A quick look at airfoils such as in Fig. 19.2.1 will lead one to question the acceptability of such a simple model of the flow. In a complex flow situation (which seems to be almost every airfoil) it is found to be useful to back-up the one-dimensional flow calculations with model testing. Two types of models are often used. The first is a large-scale (10X) plastic model of the airfoil to determine regions of low flow through the use of water flow and dye injection. The

second is also a large-scale model but made of sheet metal. The model is placed in a steam bath and instrumented with heat flux sensors. Cooling air is passed through the model at low velocity and local heat transfer coefficients are measured. Neither of these two modeling techniques is completely satisfactory because they do not account for rotation and compressibility. Yet, they are found to be useful in that they often point out local problem areas which would undoubtedly fail had they not been detected and corrected. The one-dimensional branched circuit analysis, when used with physical model testing, gives a reasonably good account of itself. Airfoils designed using these techniques tend to behave adequately close to design.

19.2.1.7 General

In the above discussions the general types of convection cooling have been discussed. There are, of course, many variations on the detailed geometries and no attempt has been made to cover them all. The correlations which have been presented are from the open literature. In most cases, manufacturers of gas turbines have further proprietary data from which airfoils are designed. These data are generally more directly focused on the range of geometries and flow variables required for airfoils.

Improvements in computational methods for viscous, turbulent, compressible, three-dimensional flows are being made at a rapid pace. It is conceivable that these will some day replace the one-dimensional branched circuit analyses currently used. However, because of the geometric complexity of the internal flows, it is thought that the one-dimensional branched circuit analyses will be used for some time to come.

19.2.2 Film Cooling

19.2.2.0 Introduction

With the levels of cooling supply pressures generally available in turbines it becomes very difficult to convectively cool airfoils at average cooling effectiveness values greater than about 0.5. When the turbine gas temperature, coolant temperature, and allowable metal temperature require a higher effectiveness level, film cooling is utilized.

The general concept of film cooling is shown in Fig. 19.2.11. A layer of coolant air is placed over the airfoil, which serves to insulate the airfoil from the hot turbine gases. Because the coolant mixes with the turbine gases, the film is not a very effective method of cooling by itself. However, when it is combined with convective cooling from the inside of the airfoil, it is a very effective method of cooling airfoils.

In the discussions which follow, the problem of film cooling will, for the most part, be divided into two parts. The first will be to determine the adiabatic wall temperature in the presence of a film but without convective cooling. This will be called film temperature. Film temperature is correlated in terms of film effectiveness. In general, two types of film effectiveness definitions are useful, local and lateral-average. Local film effectiveness is defined by

$$\eta_f \equiv \frac{T_g - T_f(z,x)}{T_g - T_c} \qquad (19.2.10)$$

and lateral average film effectiveness by

$$\bar{\eta}_f \equiv \frac{T_g - \bar{T}_f(x)}{T_g - T_c} \qquad (19.2.11)$$

The second part will be to determine the heat transfer coefficient based on the film and airfoil temperature difference as the driving potential. Some workers have chosen to utilize instead an overall heat transfer coefficient with the difference between the mainstream gas temperature and the airfoil temperature as the driving potential. This method of describing film cooling will also be discussed, but only for one type of film cooling, multihole film cooling.

19.2.2.1 Slot Cooling

Research in film cooling started at least thirty years ago. Wieghardt (Ref. 19.10) measured film temperature from a two-dimensional slot on a flat plate during the Second World War. Since that time many others have measured film temperature. Goldstein (Ref. 19.11) gives an excellent review of the work up to 1971.

An approach used by many workers to correlate slot film cooling is the heat sink or entrainment model. This model is shown in Fig. 19.2.12. In this model the mainstream air is assumed to be entrained into a film layer. In the simplest form of the model, which is described here, the entrainment W_{ge} is assumed to progress as in a boundary layer without film cooling. Furthermore, the air in the boundary layer is assumed to be at a uniform temperature corresponding to the mixed mean temperature of the entrained air and film cooling air. A seventh power velocity profile is normally used to calculate the entrained flow. In each of the different versions of the model a choice must be made for the origin of the boundary layer. This is an important variable near the slot but becomes less so further downstream. A typical result is given in Ref. 19.11 for a flat plate low velocity boundary layer starting at such a location that W_{ge} equals W_c at the injection point. The result is

$$\bar{\eta}_f = \frac{1}{1 + 0.249\,\zeta^{0.8}} \qquad (19.2.12)$$

where

$$\zeta = (x/M_s)\,[\,(\mu_c/\mu_g)\,R_e\,]^{-0.25} \qquad (19.2.13)$$

and Re is based on coolant mass velocity, viscosity, and slot height. This simple model compares favorably with a lot of data as is shown in Ref. 19.11. Other workers such as Goldstein and Haji-Sheikh (Ref. 19.12) have proposed more sophisticated models which account for the effects of the blowing on the entrainment and the distribution of temperature within the boundary layer.

The heat transfer coefficient under a slot film has been shown by Hartnett, Birkebak, and Eckert (Ref. 19.13) to be very close to that which would occur without blowing except near the slot at high blowing rates. This feature, which is found to be common in many applications of film cooling, is one of the reasons dividing the problem into an adiabatic wall temperature and heat transfer coefficient is useful.

19.2.2.2 Rows of Holes

Slots are not often used on airfoils because of thermal stress and mechanical design considerations. High thermal stresses are caused by the fact that the airfoil just upstream of a slot becomes very hot while just downstream of a slot it becomes very cold. The mechanical design problem of slots is caused by the difficulty in holding the airfoil together at the slot, especially in the presence of the high thermal stresses. An approach which is commonly used is to substitute rows of holes for slots. These tend to solve both problems because the metal between holes relieves thermal gradients and stresses and holds the airfoil together.

Rows of holes tend to solve some problems but they do so at the expense of others. The film effectiveness is lower in general than from a slot and the flow fields are more difficult to predict or correlate. Much of the film cooling work in the literature in recent years has addressed these problems. Some of this work will be discussed here.

The flow from a row of holes is very much three-dimensional. This can be seen in Figs. 19.2.13 and 19.2.14. Liess (Ref. 19.14) obtained the oil trace flow visualization of Fig. 19.2.13. It can be seen that the flow from each cooling hole maintains its identity for a long way downstream as it goes from left to right. Ericksen (Ref. 19.15) obtained the film effectiveness data in Fig. 19.2.14 for the same geometry (details shown on Fig. 19.2.15). It can be seen that the film does not become uniform until a distance somewhat greater than 40 diameters downstream.

The three-dimensionality of the flow field causes some questions in calculating heat fluxes to airfoils. Normally one wishes to calculate the lateral-average heat flux where the wall temperature is uniform in the lateral direction. To do this one should calculate

$$\bar{q}(x) = \frac{1}{p}\int_0^p h(z,x)\,[T_f(z,x) - T_m(x)]\,dz \qquad (19.2.14)$$

where $h(z,x)$ and $T_f(z,x)$ are local values of heat transfer coefficient and film temperature. This would, of course, necessitate a rather extensive data base which is expensive and time consuming to obtain. Fortunately, the problem is minimal in practice, because $h(z,x)$ is generally a weak function of z and may be taken out of the integral. Then, Eq. (19.2.14) reduces to

$$\bar{q}(x) = h(x)\,[\,\bar{T}_f(x) - T_m(x)\,] \qquad (19.2.15)$$

From Eq. (19.2.15) it can be seen that the lateral-average heat flux may be calculated from correlations for lateral-average rather than local film temperature.

A great deal of understanding of rows of holes film cooling has been gained by Eckert and coworkers (Refs. 19.15-19.18) at the University of Minnesota. They worked extensively on the geometry shown in Fig. 19.2.15 on a flat plate at low velocities. Because of the large amount of information generated by them on this geometry, rows of holes film cooling will be discussed largely from their work and from the work of Liess (Ref. 19.14) who tested the same geometry. This will eliminate the geometric variables of hole spacing and orientation and, hopefully, provide clearer insight into the film cooling process. With the exception of Ref. 19.17, all of the work in Refs. 19.14-19.18 was performed at coolant to mainstream density ratios close to one. For brevity, this will not be mentioned again, but this parameter is an important one as is shown in Ref. 19.17.

Figure 19.2.16, showing data from Goldstein, et al. (Ref. 19.16), illustrates one of the common features of film cooling from rows of holes. As the coolant to mainstream mass flux ratio M increases the effectiveness first increases, reaches a maximum at a mass flux ratio of 0.5, and then decreases. This maximum is attributed to penetration of the jet into the mainstream as opposed to laying down on the surface. The effect is strongest near the row of holes and very weak far downstream.

Pedersen (Ref. 19.17) investigated the effect of coolant density in this same geometry. His data for lateral-average effectiveness at a downstream location of 10 diameters is shown in Fig. 19.2.17. The same general shape of the effectiveness curve can be seen here as in Fig. 19.2.16. As the

coolant to mainstream density ratio increases, however, the maximum effectiveness increases. Reference 19.17 interprets the data to give maximum effectiveness at a value of coolant to mainstream velocity ratio (U_c/U_g) of approximately 0.4. Ericksen, Eckert, and Goldstein (Ref. 19.18) proposed a model for film effectiveness based on a point heat sink located at some distance above the surface. Reference 19.17 used the argument that the distance above the surface of the heat sink should be a function of the coolant to mainstream momentum flux ratio I and, using the above model, proposed a correlation of the form

$$\bar{\eta}_f/M = f(I) \qquad (19.2.16)$$

for its data at constant U_g and hole diameter. His data at a distance 10 diameters downstream are shown in Fig. 19.2.18. The correlation is reasonable except at large (ρ_c/ρ_g). This may be related to the fact noted in Ref. 19.17 that at values of (U_c/U_g) below 0.45 a change in the character of the flow seems to occur. At values of (U_c/U_g) below 0.45 the jet has the characteristic of appearing to remain attached to the wall and being independent of I, whereas above that value of (U_c/U_g) the jet appears to penetrate the mainstream further and appears controlled by I. This is about the same velocity ratio mentioned above for penetration to occur. It does appear somewhat surprising that the penetration condition should be controlled by velocity,but this effect also appears in data of others. As of this time, no further generalization on the effect of (ρ_c/ρ_g) has appeared in the literature.

The variables of coolant to mainstream mass flux, density, and momentum flux ratios appear to be the strongest parameter affecting film cooling. However, there are other variables of varying degrees of importance and levels of confirmation. Ericksen (Ref. 19.15) and Liess (Ref. 19.14) have measured the effect of the ratio of the displacement thickness of the inlet boundary layer to the hole diameter. They agree that there is a significant effect and that the thinner boundary layer has a higher film effectiveness. They differ in that Ref. 19.15 finds that effectiveness on the hole centerline increases with decreasing boundary layer thickness to a value of δ^*/D as low as 0.06, whereas Ref. 19.14 finds that lateral-average effectiveness reaches a maximum value at δ^*/D around 0.2. References 19.14 and 19.15 both indicate that free stream Reynolds number U_gD/ν_g appears at most to be a weak variable. Reference 19.14 indicates that free stream Mach number is not an important variable either. It also finds that an accelerating pressure gradient reduces film effectiveness at low coolant to mainstream mass flux ratios (< 1.0) but does not have as strong an effect at high mass flux ratios (> 1.0).

The heat transfer coefficient does not differ greatly from that which would occur without film cooling. In the same geometry discussed above, Ericksen (Ref. 19.15) shows that the heat transfer coefficient does not vary hardly at all up to a coolant to mainstream mass flux ratio of 0.5 and at 2.0 differs by only 27 percent from the no blowing case. Other than at the leading edge of an airfoil the coolant to mainstream mass flux ratio is generally below 2.0.

The geometry discussed above is useful because of the many features of film cooling which have been demonstrated for it. However, it is seldom, if ever, used in actual practice for film cooling. The reason that it is not widely used is that the overall effectiveness is too low. In general, closer hole spacing and/or multiple rows of holes are utilized to obtain the high levels of film effectiveness required. Metzger and Fletcher (Ref. 19.19) measured high effectiveness values with close spacing of holes (pitch to diameter ratio equal 1.55) on a flat plate at low velocities. Lander, Fish, and Suo (Ref. 19.20) also measured high film effectiveness from a double row of holes on an airfoil in a cascade, as shown in Fig. 19.2.19. It should be noted that the coolant to mainstream total temperature ratio T_c/T_{tg} was 0.53 to give coolant to mainstream density ratio similarity with engines in the experiments of Ref. 19.20. Muska, Fish, and Suo (Ref. 19.21) also showed very high effectiveness on a flat plate from double rows of holes at pitch to diameter ratios of 2.0 and low blowing rates. Goldstein, Eckert, and Burggraf (Ref. 19.22) showed that by flaring the holes of the single row of holes geometry of Fig. 19.2.15 a significant increase in film effectiveness can be achieved.

In addition to film effectiveness data, Ref. 19.20 obtained heat transfer coefficient data for the double row of holes geometry as shown in Fig. 19.2.20. These data lead to two conclusions. First, the presence of holes in the airfoil will likely lead to rapid transition of the boundary layer to turbulent flow. Second, the effect of blowing on the heat transfer coefficient is not large. This latter conclusion reinforces the results from flat plates.

Total airfoils generally cannot be adequately cooled with just a single or double row of holes. Additional film cooling is required from another row or double row of holes. An example of this is shown on Fig. 19.2.21 where there is film cooling at the leading edge plus additional film cooling from two additional sets of double rows of holes. Reference 19.21 shows that the effect of multiple rows of holes may be determined in an additive manner first suggested by Sellers (Ref. 19.23) for slots. In this method the mainstream temperature downstream of the first set of rows of holes is taken to be the film temperature from the film cooling at the leading edge. The mainstream temperature for all subsequent downstream rows is calculated in a similar manner. Then behind the nth set of holes

$$\bar{\eta}_f = \sum_{i=1}^{n} \bar{\eta}_{f_i} \prod_{j=0}^{i-1} (1-\bar{\eta}_{f_j}) \qquad (19.2.17)$$

where $\bar{\eta}_{f_0}$ is equal to zero and

where $\bar{\eta}_{f_i}$ is the lateral-averagefilm effectiveness from the i^{th} set of film cooling holes. This has been shown to be valid down to spacings of 16.7 hole diameters.

The thermal design of film cooled airfoils must account for both the effects of film cooling and the effects of convective cooling. Fortunately for the designer, the convective cooling information developed for purely convectively-cooled airfoils is directly applicable and is, therefore, somewhat straightforward. However, the data in the literature for film effectiveness are not anywhere near being adequate. At the present time, in addition to the data in the literature, one must obtain data in cascades for geometries very close to that which will be used. In performing these tests one must simulate Reynolds number, Mach number, coolant to mainstream density ratio, and coolant to mainstream flow ratio. Turbulence effects must also be simulated in some manner. The literature discussed above can be used for guidance in these tests.

This procedure to obtain information for film cooling assumes, as in convective cooling, that a two-dimensional solution is valid. The shortcomings of a two-dimensional approach have already been discussed for convectively-cooled airfoils and those arguments can be equally applied to film cooling. There may be a difference in that the effects of rotation may be different in film-cooled airfoils because of the thickness of the film cooling layers. In spite of the shortcomings of the two-dimensional approach, it has been successfully applied to airfoil design. This is evidenced by the successful design of film-cooled turbines in the 2500 F class.

19.2.2.3 Multihole Film Cooling

In regions where very high effectiveness is required (>0.60) multihole film cooling becomes desirable. Multihole film cooling differs from rows of holes film cooling in that the geometry is one of a uniform array of holes rather than of rows of holes and the holes tend to be smaller. An example of multihole film cooling can be seen in Fig. 19.2.22. This type of film cooling is treated separately from rows of holes film cooling because the analytical modeling for it is rather different and, in fact, is more similar to that for transpiration cooling discussed later in 19.2.5.

Both the film effectiveness and the overall heat transfer coefficient approaches will be discussed for multihole film cooling. Both methods have their adherents and the available literature is somewhat evenly divided between them. The literature will first be discussed from the film effectiveness viewpoint.

As in all methods of film cooling, convective cooling is an important part of multihole film cooling. A simple one-dimensional model by Mayle and Camarata (Ref. 19.24) has been found very useful to demonstrate this and to show the relative effects of film cooling and convective cooling for multihole film cooling. This model considers a small chordwise region where the film effectiveness, gas side heat transfer coefficient, and metal temperature take on lateral-average values. The model is shown in Fig. 19.2.23. It can be shown that a local cooling effectiveness ϕ defined below can be calculated from

$$\phi \equiv \frac{T_g - T_m}{T_g - T_c} = \frac{\bar{\eta}_f + \eta_c(F/St - \bar{\eta}_f)}{1 + \eta_c(F/St + \bar{\eta}_f)} \qquad (19.2.18)$$

where

$$\eta_c = 1-\exp\left[\frac{A_h h_h + A_i h_i}{W_c c_p}\right] \quad \text{(Convective effectiveness)} \qquad (19.2.19)$$

$$\bar{\eta}_f = \frac{T_g - \bar{T}_f(x)}{T_g - T_{ce}} \quad \text{(Lateral-average film effectiveness)} \qquad (19.2.20)$$

$$St = \frac{\bar{h}_g}{\rho_g U_g c_{pg}} \quad \text{(External Stanton number based on } \bar{T}_f \text{ and } T_m) \qquad (19.2.21)$$

$$F = \frac{W_c}{A_g \rho_g U_g}\left(\frac{c_{pc}}{c_{pg}}\right) \quad \text{(Coolant mass flux parameter)} \qquad (19.2.22)$$

In airfoils it is usually found that

$$0.2 < \eta_c < 0.6$$

and where the unblown heat transfer coefficient is used in the Stanton number

$$1 < F/St < 5$$

The results of Eq. (19.2.18) are shown on Fig. 19.2.24 for two values of F/St. The significant contribution of convective cooling in both these cases can be readily seen. Furthermore, it can be seen that convection is more important when F/St is larger.

As in rows of holes film cooling, the film effectiveness part of the model is the more difficult problem. Figure 19.2.25 shows a geometry tested at low speeds on a flat plate by Mayle and Camarata (Ref. 19.25). They have reported local as well as lateral average film effectiveness data for this geometry. Lebrocq, Launder, and Pridden (Ref. 19.26) and Launder and York (Ref. 19.27) have also reported film effectiveness data for similar arrays of holes on a flat plate at low velocities, but in their work the holes were normal to the surface or angled directly to the rear. In Ref. 19.26 a non-staggered array was also tested. The work in Ref. 19.25 was performed at a coolant to mainstream density ratio near one, while the work in Refs. 19.26 and 19.27 was performed at several values of this density ratio.

Several interesting features of the flow for this type of film cooling are shown in Fig. 19.2.26. The figure on the top indicates a strong spanwise variation in film effectiveness even at a far downstream location. The figure on the bottom indicates a strong chordwise buildup in lateral-average film effectiveness in the downstream direction. At a chordwise distance of 100 the buildup of film effectiveness flattens. This is interpreted in Ref. 19.25 as the region where mixing of the jets with the mainstream just balances the replenishment of cooling air in the film. This feature is more prominent at lower values of M and less at higher values of M. Another feature is the slow drop off in effectiveness at the end of the hole array. This can add significantly to airfoil cooling, especially near the trailing edge where it is difficult to place film cooling holes.

Limited success was achieved in Ref. 19.25 in modeling the film effectiveness utilizing a heat sink model proposed by Ramsey, Goldstein, and Eckert (Ref. 19.28) for single holes and the additive film model of Ref. 19.23. In this case the model of Ref. 19.23 was applied on a spanwise local basis rather than on an average basis as described above for rows of holes film cooling.

It was also found in Ref. 19.25 that there appeared to be an optimum hole density. Decreases in the pitch to diameter ratio from 14 to 10 to 8 formed a small but definite optimum for film effectiveness at a pitch to diameter ratio of 10. This is very important to the manufacturers of turbines, who do not wish to drill a very large number of holes.

References 19.26 and 19.27 show similar results for holes normal to the surface and angled directly to the rear. In Ref. 19.26 it is argued from velocity profile measurements that staggered arrays of holes are superior to in-line arrays and from direct data that holes angled to the rear are superior to normal holes. In Refs. 19.26 and 19.27 effects of coolant density were also measured. The effects of coolant density were found to be similar to that for rows of holes film cooling. The higher density coolant caused higher film effectiveness with maximum effectiveness at levels of coolant to mainstream velocity ratio similar to that for rows of holes film cooling. In Ref. 19.27 it was found that accelerating the flow increased the film effectiveness locally behind the holes but tended to decrease the effectiveness in the lateral direction. They also found that free stream turbulence decreased film effectiveness in accelerating flows but did not in constant velocity flows. These latter two phenomena were explained in terms of transition of the coolant jet flow from laminar to turbulent flow. In practice, the Reynolds number of the coolant holes is such that the coolant jets are generally already turbulent. Thus any effects of acceleration and turbulence which might be found on a turbine airfoil would require further rationalization.

Heat transfer coefficients were also measured and reported in Ref. 19.25. It was found there that the effects of blowing were stronger than for a similar value of M in rows of holes film cooling. The effects were to increase the heat transfer coefficients with increasing mass flux of coolant and decreasing hole pitch. The levels were as high as 2.5 times greater than for a flow without blowing at a pitch to diameter ratio of 8 and a value of M of 1.5. Furthermore, the Stanton number for a given geometry reached a value independent of streamwise location when the blowing parameter F was greater than 0.007. In this region they correlated the Stanton number of Eq. (19.2.21) with

$$St = 0.038\ (D/p)\ M^{0.28} \qquad (19.2.23)$$

At lower values of F the Stanton number monatonically approached the unblown Stanton number.

The heat transfer data of Ref. 19.25 are for the lateral-average case with the coolant and mainstream temperatures equal. The use of a lateral average may well be questioned when the effect of blowing on the heat transfer coefficient is so strong, but at the present time there is little else in the literature.

Choe, Kays, and Moffat (Ref. 19.29) have taken the approach of a reduced heat transfer coefficient concept. They have defined a parameter

$$\theta \equiv \frac{T_g - T_{ce}}{T_g - T_m} \qquad (19.2.24)$$

where T_m is a lateral-average metal temperature. For the case of low velocity flows and small temperature differences and thus small property variations, Ref. 19.29 shows that the linearity of the energy equation gives

$$St = St(\theta=0) - \theta\ \left[St(\theta=0) - St(\theta=1)\right] \qquad (19.2.25)$$

Where St is based on $(T_g - T_m)$.
Then, since the Stanton number is linear with θ, the Stanton number can be measured at two values of θ, and all values of Stanton numbers can then be calculated. Furthermore, the adiabatic wall temperature can be found from the relationship

$$\bar{\eta}_f = \frac{1}{\theta(St=0)} \qquad (19.2.26)$$

where $\bar{\eta}_f$ is the lateral-average film effectiveness of a good conductor. Metzger, Takeuchi, and Kuenstler (Ref. 19.30) have defined a similar parameter but in their work the metal temperature is a lateral and chordwise-average temperature.

This viewpoint on the problem of multihole cooling is quite interesting in that heat transfer coefficients to an airfoil may be generalized from limited data. The major drawback, however, is the required linearity of the energy equation. It is not at all clear how one calculates the film effectiveness when the coolant to mainstream density ratio is around two (creating nonlinearity in the energy equation) as it often is in airfoil design.

Choe, Kays, and Moffat (Ref. 19.31) have shown how the reduced heat transfer concept might reach greater application. They have shown that a two-dimensional boundary layer-type analysis is capable of calculating the Stanton number in the presence of multihole cooling. Some empirical input is required but certainly no more than correlations for multihole adiabatic wall temperature.

The current status of multihole film cooling in engines is somewhat behind rows of holes film cooling. There is much fundamental data available in the literature but there is little application in service engine design. Much the same recommendations must be made here as for rows of holes film cooling, if one wishes a multihole film-cooled airfoil. An airfoil close to the actual design must be tested in a cascade with Reynolds number, Mach number, and coolant to mainstream density ratio, and coolant to mainstream flow ratio similarity to engine conditions. The effect of engine turbulence must also be modeled in some way. Questions raised because of rotating effects are the same as for rows of holes film cooling.

Special design problems appear on this type of airfoil because of the multiplicity of small holes in the surface. The large number of holes cause an especially difficult flow distribution problem which must be solved for each design. Also there is a high cost associated with the large number of holes. Another problem is that the small holes are suspected to be more prone to plugging from dirt in the cooling air. In spite of these problems, the relatively high cooling effectiveness achievable with multihole cooling makes it an attractive cooling scheme for very high temperature engines.

19.2.3 Leading Edge Film Cooling

Airfoils which require film cooling generally require it over the whole airfoil including the leading edge. The leading edge region is especially difficult to cover with a film because the film must be established at the stagnation point, the exact location of which is not known. To cover the leading edge, large quantities of cooling air are introduced through rather densely packed holes. Examples of leading edge film cooling holes are shown in Figs. 19.2.21 and 19.2.22. Because of the large quantities of cooling air it might be thought that the cooling mechanism is purely film effectiveness. However, this is not necessarily so. The one-dimensional model of 19.2.2 is equally valid here and can be used to determine the relative importance of film and convective effectiveness. At the leading edge the parameter F/St is calculated to be large if $\overline{h}_g$ is assumed to be of the same order as without blowing. Then from the arguments of 19.2.2 the convective effectiveness is seen to be very important. The exact levels of $\overline{h}_g$ in the region of leading edge film cooling are not known, but some results reported in the literature, discussed in the next paragraph, confirm that convective cooling is very important in leading edge film cooling.

Hiroki and Katsumata (Ref. 19.32) obtained data on a four row leading edge geometry. They tested a leading edge where they had impingement on the inside as well as film cooling holes and a leading edge where they had just the film cooling holes. They performed these tests on models made of conductive materials. Their results are shown in Fig. 19.2.27. It can be seen that the leading edge with impingement is definitely superior to that without impingement. Because of the use of conductive models, a large amount of convective cooling must have occurred in both models because of convective cooling within the holes. The additional effect of impingement convective cooling, as shown in Fig. 19.2.27, is indicative of the importance of convective cooling in leading edge film cooling. Unfortunately, there is very little other data published in the literature on leading edge film cooling. Thus a designer without unpublished information must rely again on testing to gain design data.

One other feature of leading edge film cooling should be noted. The film formed at the leading edge persists to the trailing edge of the airfoil. This is shown in Ref. 19.21. The level of film effectiveness decreases from the leading to the trailing edge as one might expect. However, its presence is important to airfoil design and should not be discounted.

19.2.4 Aerodynamic Losses of Film Cooling

The efficiency of a cooled turbine can be thought to be determined by a series of entropy production processes (called unit processes) as is pointed out in Ch. 18. Eq. 18.3.5 shows that there are two contributions to entropy production in a unit process, the changes in the total temperatures and the changes in the total pressures of the coolant and mainstream flows. In a unit process each of these properties, total temperature and total pressure, are defined in terms of the appropriate reference frame, rotating or stationary. If one considers a unit process to be across a row of airfoils, the total temperature changes can be readily calculated from the energy equation. However, the total pressure changes cannot be so readily calculated. Thus, to calculate cooled turbine performance a method is required to calculate the total pressure changes. This is generally reported in terms of the decrease in the total pressure of the mainstream which is herein called the total pressure loss.

There is a significant total pressure loss associated with injecting cooling air into the hot turbine flow. The present state of the art is that the loss cannot be completely calculated from first principles. However, a simple mixing model has been shown to be reasonably accurate by Hartsel (Ref. 19.33). In this model it is assumed that the coolant does not in any way affect the pressure distribution on the airfoil. Furthermore, it does not interact with the boundary layer, and thus the skin friction, on the airfoil. The model is one where the coolant mixes with some portion of the mainstream, called the mixing layer, in a one-dimensional manner. The losses are calculated within the mixing layer from the leading to the trailing edge, being accumulated to the trailing edge. At the trailing edge plane the two mixing layers (suction and pressure side) are mixed with the mainstream unaffected flow at the average trailing edge static pressure. This flow is then mixed with the viscous boundary layers and any trailing edge coolant flow in a one-dimensional manner which also accounts for trailing edge blockage. Each of the mixing calculations are performed using simple control volume arguments. In addition the losses within the mixing layer for each coolant flow W_c are calculated using the one dimensional linearized relationship

$$\frac{\Delta P_{tg}}{P_{tg}} = \frac{\gamma}{2} M^2 \frac{W_c}{W_g} \left[1 + \frac{T_{ce}}{T_{tg}} - 2 \frac{U_c}{U_g} \cos \beta \right] \qquad (19.2.27)$$

where all quantities are evaluated at the point of injection. It is not at all obvious what fraction of the total mainstream flow W_g should be. However, in Ref. 19.33 W_g was varied from 3 to 30 percent of the total mainstream flow and very little effect on loss was found. Figure 19.2.28 from Ref. 19.33 shows the results of this analysis compared to the data of Prust, Schum, and Szanca (Ref. 19.34). The comparison is made on the basis of airfoil efficiency, which is defined in Ref. 19.33 as the ratio of the actual kinetic energy of the total flow to that which would occur if the coolant and the mainstream air each isentropically expanded to the same downstream static pressure. The corroboration is good especially at coolant flow rates equal to or greater than design conditions. One might question the data and the analysis at coolant flow rates below design conditions where the airfoil efficiency does not approach the uncooled airfoil efficiency. The data is exemplary of cascade data where the coolant flow is supplied from a single source to several regions of different static pressures on an airfoil. At flow rates and thus supply pressures below design conditions, mainstream flow enters into the airfoil in regions of high airfoil static pressures, while coolant continues to flow out in regions of low airfoil static pressures. The outflow of coolant can cause total pressure loss even when the net coolant flow is zero.

The analysis of Ref. 19.33 is similar to others in the industry. At this point, it does not appear that the effect of film cooling on skin friction can be properly taken into account but the mixing effect seems to account for much of the loss. The important end result of this is that it gives guidance to the designer on the optimum location for film cooling holes. It is apparent from Eq. (19.2.27) that film cooling near the stagnation point and on the pressure side of airfoils where the Mach numbers are low will give small total pressure losses, whereas film cooling on the suction side near the throat where Mach numbers are high will give high total pressure losses.

It is quite often argued that trailing edge ejection of coolant flow will reduce aerodynamic losses by filling in the wake. The works of Anderson, Heiser, and Jackson (Ref. 19.35) and Anderson and Heiser (Ref. 19.36) have shown analytically and experimentally that Eq. 19.2.27 can be used to approximate the behavior of trailing edge ejection in the absence of gross changes in the mainstream flow (e.g., base pressure) by the coolant flow. Close examination of Eq. 19.2.27 will show that with fixed geometry and temperatures the total pressure loss caused by the coolant flow will first rise with coolant flow rate, reach a maximum, then decrease with coolant flow rate to zero and become negative (total pressure gain). This occurs because the velocity (and thus the total pressure) of the coolant must continually increase with coolant flow rate. The characteristic of reducing total pressure loss with high coolant flow rates is, unfortunately, of little practical value. Although the total pressure loss of the mainstream may be reduced to zero or negative values in this way, the entropy generation of the coolant and the mainstream considered together as in Eq. 18.3.4 causes losses in efficiency because of the high coolant total pressures required for high coolant flow rates. It is, of course, possible that the mainstream flow might be affected by the trailing edge ejection, especially the base pressure. As discussed in Ch. 18, any changes in base pressure would have a strong effect on total pressure losses. However, there have been no reports in the literature showing variations in base pressure caused by trailing edge ejection of coolant flow. From these arguments, it appears at the present time that trailing edge ejection of coolant flow causes a net loss in overall turbine performance. Similar arguments can be applied to all other film cooling flows.

19.2.5 Transpiration Cooling

Transpiration cooling is considered by many to be the ideal cooling method. In this method coolant is introduced through a porous wall, so that it convectively cools the porous wall to the maximum theoretical limit and also film cools it with well distributed low velocity coolant. This type of cooling is amenable to analysis and has received much attention from a theoretical boundary layer approach. As a result, transpiration cooling can be considered calculable by the boundary layer methods of Ch. 16.

Transpiration cooled airfoils have reached the stage of having been extensively tested in turbines. Most of the tests on transpiration-cooled turbine airfoils have been conducted on airfoils fabricated from woven wire cloth which simulates a transpiration surface. Moskowitz and Lombardo (Ref. 19.37) have run such airfoils for several hours at 2750 F turbine inlet temperature.

In spite of the desirability of the cooling method, transpiration-cooled airfoils have not received widespread acceptance and utilization. The reasons for this are mostly structural in nature. Porous metals are generally not strong enough to make viable airfoils. The woven wire described above is stronger but is still difficult to manufacture into good aerodynamic shapes with adequate smoothness. There is also a large amount of surface area on the metal which causes oxidation to be a problem,which must be offset with lower metal temperatures. In spite of these problems, there are still strong proponents of transpiration-cooled airfoils, and with effort they may yet prove their case.

19.3 Endwall Cooling

19.3.0 Introduction

The endwall regions shown on Fig. 19.3.1 are generally exposed to a lower gas temperature than the corresponding airfoils, as was discussed in 19.1.2. In the past when the turbine inlet temperature levels were low enough, the temperature profile could be so shaped that no endwall cooling was required. However, as gas temperatures have increased, cooling has become required on the endwalls. This is a particularly difficult area to cool because of the complex flow fields near the endwalls.

The environment for each of the endwall regions is somewhat different. The stator platforms must accept a random temperature distribution, just as stator vanes must. The stationary shroud around blade tips is exposed to a similarly random temperature field, which is further described by blade tip passing. In addition the stationary shroud is exposed to a gas with a decreasing total temperature because of work being performed on the rotor. The rotor platform receives the benefit of an average temperature because of the rotation.

Much of the literature on turbine cooling has consisted of work on turbine airfoils. That which has appeared on the endwall region is very limited. There are some data available in engine manufacturing companies, but again less so than on airfoils. At the present time, the state of the art is such that an endwall cooling configuration is designed by some relatively crude design process, after which the configuration must be tested and modified.

19.3.1 Stator Platforms

The stator platforms are subjected to strong secondary cross flows. These cross flows are caused by vorticity in the mainstream inlet flow and by viscous effects within the passage. Blair (Ref. 19.38) has published what is probably the most detailed experimental data on stator endwalls. He measured film effectiveness and heat transfer coefficients for a first stator vane passage. The tests were run on a single passage at large-scale low-velocity flow conditions. The results are shown in Figs. 19.3.2 and 19.3.3.

The effect of film cooling from an upstream slot is shown on Fig. 19.3.2. The most interesting feature of Fig. 19.3.2 is that the cross channel flow drives the film away from the pressure surface so strongly that little of the upstream slot film goes very far down the channel near the pressure surface. For this reason film cooling of stator platforms must utilize further replenishment within the channel.

The heat transfer coefficient distribution is shown in Fig. 19.3.3. As one might expect the heat transfer coefficient is highest where the velocity is the highest. In Ref. 19.38 an attempt was made to rationalize the heat transfer coefficient distribution in terms of the airfoil heat transfer coefficient distribution. The results indicated that the level of the heat transfer coefficient distribution on the endwall is close to that on the airfoil forming the passage. Louis (Ref. 19.39) obtained heat transfer coefficient data on stator platforms in a turbine operating under transient blowdown conditions. His data were less detailed than that in Ref. 19.38 because of the small size of his turbine, but he did measure heat transfer coefficients at several locations on a stator platform. His data had similar trends to that of Ref. 19.38. He also made an attempt at an analysis of the heat transfer coefficient. In spite of his efforts and that of Ref. 19.36, the problem of heat transfer to the endwalls must be considered beyond analysis at this time.

Little other data exist in the literature on stator platforms. Hopefully, more is forthcoming to clarify the heat transfer picture in this complex flow region.

19.3.2 Stationary Shrouds

Very little data have been published on stationary shroud heat transfer. Reference 19.39 has reported data from the same blowdown turbine facility mentioned in the previous section. Very high heat transfer coefficients near the leading edge of the blade row which then tapered off rapidly in the axial direction were measured. The data did not appear amenable to analysis. The reported heat transfer coefficients were based on the temperature into the blade row. Therefore, at least some of the drop in the reported heat transfer coefficients might be attributed to work being performed by the blade.

Stationary shrouds may require film cooling at high turbine inlet temperatures. Little data are available in the literature on this type of cooling. The data required are very difficult to obtain because credible data must be obtained in a rotating turbine. Reference 19.39 has obtained a limited amount of data for this cooling problem but it is difficult to ascertain the generality of the information.

19.3.3 Rotating Platforms and Shrouds

At lower temperatures most turbines have rotating shrouds for aerodynamic performance reasons. At higher temperatures where shroud cooling might be required, however, the designer generally chooses to relieve blade stress problems caused by rotating shrouds by eliminating them. Thus rotating shroud heat transfer is only of small interest. The platforms at the blade roots, however, require some cooling. This problem has received the least attention because of several factors which tend to diminish the problem.

The first is that, like the stator, the gas temperature has a profile such that the platform sees a lower temperature than the rotor blade. The second is that, like the rotor blade, the rotor blade platform tends to see an average temperature rather than a local temperature. The third factor is that, the relative total temperatures incident on a given rotor platform are lower than that incident on the corresponding vane platform because of vane cooling air dilution and relative velocity effects. Thus only at very high turbine inlet temperatures is rotor platform cooling required. At present, there appears to be no published data on this cooling problem. The only recourse appears to be to apply stator vane-type data and analyses to design rotor blade platforms. Since only meager data are available in the literature for stator vane platforms, this is not all that easy to do. There is, of course, the remaining question of whether the effects of rotation are significant on the endwalls.

19.4 Conclusions

The state of the art in turbine cooling is that turbines with inlet temperatures of the order of 2500 F can be successfuly designed. This is seen most dramatically by observing that gas turbine engines in this temperature class are operating successfully in commercial operation. In the above, the open literature data and analyses which form the background for the design of such engines have been discussed. A point which has been mentioned several times but is worth repeating is that, in addition to open literature, much data and analyses exist which are proprietary to engine companies. Without this additional information, it is questionable whether these engines could have been successfully built.

The state of the art in airfoil profile convective cooling is probably the most advanced with relatively accurate designs currently possible. Much of the information for this appears in the open literature. The state of the art in film cooling is not as far advanced. Enough design information exists so that successful turbines can be built utilizing film cooling, but a certain amount of testing after design is required to assure adequate airfoil life. The actual design data for this do not appear in the open literature, although much background information does appear. Transpiration cooling, which intuitively appears to be the most efficient means of cooling, has not achieved great success. This appears to be more because of structural reasons than for cooling reasons. The endwalls, which fortunately require less cooling, are several years behind airfoils in cooling technology. Because of the complexity of endwall flows, this will probably always be so.

19.5 References

19.1 Holland, M. J.: Olympus 593 Turbine Cooling, AGARD Conf. Proc. No. 73, 1970.

19.2 Huile, K. R.: A Theoretical Study of Three-Dimensional Compressible Turbulent Boundary Layers on Rotating Surfaces in Turbomachinery, PhD Thesis, M.I.T., 1970.

19.3 Chupp, R. E., Helms, H. E., McFadden, P. W., and Brown, T. R.: Evaluation of Internal Heat Transfer Coefficients for Impingement Cooled Turbine Airfoils, J. of Aircraft, Vol. 6, No. 3, May-June 1969, pp. 203-208.

19.4 Metzger, D. E., Baltzer, R. T., and Jenkins, C. W.: Impingement Cooling Performance in Gas Turbine Airfoils Including Effects of Leading Edge Sharpness, ASME J. of Eng. for Power, July 1972, pp. 219-225.

19.5 Kercher, D. M. and Tabakoff, W.: Heat Transfer by a Square Array of Round Air Jets Impinging Perpendicular to a Flat Surface Including the Effect of Spent Air, ASME J. of Eng. for Power, Jan. 1970, pp. 73-82.

19.6 Colladay, R. S.: Turbine Cooling, NASA SP-290, Vol. 3, 1975, Ch. 11.

19.7 Webb, R. L., Eckert, E. R. G., and Goldstein, R. J.: Heat Transfer and Friction in Tubes with Repeated-Rib Roughness, Int. J. of Heat and Mass Trans., Vol. 14, Pergamon Press, 1971, pp. 601-617.

19.8 Halls, G. A.: Nozzle Guide Vane Cooling - The State of the Art, AGARD Conf. Proc. No. 73, 1970.

19.9 Grimison, E. C.: Correlation and Utilization of New Data on Flow Resistance and Heat Transfer for Cross Flow of Gases over Tube Banks, Trans. ASME, Vol. 59, 1937, pp. 583-594.

19.10 Wieghardt, K.: AAF Translation No. F-TS-919-RE, 1946.

19.11 Goldstein, R. J.: Film Cooling Advances in Heat Trans., Vol. 7, Academic Press, 1970, pp. 321-379.

19.12 Goldstein, R. J. and Haji-Sheikh, A.: Prediction of Film Cooling Effectiveness, ASME 1967 Semi-Int'l. Symp., Tokyo, 1967, pp. 213-218.

19.13 Hartnett, J. P., Birkebak, R. C., and Eckert, E. R. G.: International Developments in Heat Transfer, Part IV, ASME, New York, 1961, p. 682.

19.14 Liess, C.: Film Cooling with Ejection from a Row of Inclined Circular Holes, An Experimental Study for the Application to Gas Turbine Blades, Tech. Note 97, von Karman Institute for Fluid Dynamics, Mar. 1973.

19.15 Ericksen, V. L.: Film Cooling Effectiveness and Heat Transfer with Injection Through Holes, NASA CR-72991, Aug. 1971.

19.16 Goldstein, R. J., Eckert, E. R. G., Ericksen, V. L., and Ramsey, J. W.: Film Cooling Following Injection Through Inclined Circular Tubes, NASA CR-72612, 1969.

19.17 Pedersen, D. R.: Effect of Density Ratio on Film Cooling Effectiveness for Injection Through a Row of Holes and for a Porous Slot, PhD Thesis, Univ. of Minn., Mar. 1972.

19.18 Ericksen, V. L., Eckert, E. R. G., and Goldstein, R. J.: A Model for the Analysis of the Temperature Field Downstream of a Heated Jet Injected into an Isothermal Crossflow at an Angle of 90°, NASA CR-72999, 1971.

19.19 Metzger, D. E. and Fletcher, D. D.: Surface Heat Transfer Immediately Downstream of Flush, Non-Tangential Injection Holes and Slots, J. of Aircraft, Vol. 8, No. 1, Jan. 1971, pp. 33-38.

19.20 Lander, R. E., Fish, R. W., and Suo, M.: External Heat Transfer Distribution on Film Cooled Turbine Vanes, J. of Aircraft, Vol. 9, No. 10, Oct. 1972, pp. 707-714.

19.21 Muska, J. W., Fish, R. W., and Suo, M: The Additive Nature of Film Cooling, ASME J. Eng. for Power, Vol. 98, Oct. 1976, pp. 457-464.

19.22 Goldstein, R. J., Eckert, E. R. G., and Burggraf, F.: Effects of Hole Geometry and Density on Three Dimensional Film Cooling, Int. J. of Heat and Mass Trans., Vol. 17, Pergamon Press, 1974, pp. 595-607.

19.23 Sellers, J. P.: Gaseous Film Cooling with Multiple Injection Stations, AIAA J., Vol. 1, No. 9, Dec. 1963, pp. 2154-2156.

19.24 Mayle, R. E. and Camarata, F. J.: Heat Transfer Investigation for Multihole Aircraft Turbine Blade Cooling, AFAPL-TR-73-30, June 1973.

19.25 Mayle, R. E. and Camarata, F. J.: Multihole Cooling Film Effectiveness and Heat Transfer, ASME J. of Heat Trans., Nov. 1975, pp. 534-538.

19.26 LeBrocq, P., Launder, B. E. and Priddin, C. H.: Discrete Hole Injection as a Means of Transpiration Cooling, Proc. Inst. of Mech. Engrs., Vol. 187, 1973, pp. 17-75.

19.27 Launder, B. E. and York, J.: Discrete-Hole Cooling in the Presence of Free-Stream Turbulence and Strong Favorable Pressure Gradient, Int. J. of Heat and Mass Trans., Vol. 17, Pergamon Press, 1974, pp. 1403-1409.

19.28 Ramsey, J. W., Goldstein, R. J., and Eckert, E. R. G.: A Model for Analysis of the Temperature Distribution with Injection of a Heated Jet into an Isothermal Flow, Heat Trans. 1970, Elseuiar Pub., Amsterdam, 1970.

19.29 Choe, H., Kays, W. M., and Moffat, R. J.: The Superposition Approach to Film Cooling, ASME Paper 74-WA/HT-27, 1974.

19.30 Metzger, D. E., Takeuchi, D. I., and Kuenstler, P. A.: Effectiveness and Heat Transfer with Full-Coverage Film Cooling, ASME Paper 73-GT-18, 1973.

19.31 Choe, H., Kays, W. M., and Moffat, R. J.: The Turbulent Boundary Layer on a Full-Coverage Film-Cooled Surface: An Experimental Heat Transfer Study with Normal Injection, Report No. HMT-22, Thermosciences Div., Dept. of Mech. Eng., Stanford Univ., May 1975.

19.32 Hiroki, T. and Katsumata, I.: Design and Experimental Studies of Turbine Cooling, ASME Paper 74-GT-30, 1974.

19.33 Hartsel, J. E.: Prediction of Effects of Mass Transfer Cooling on the Blade Row Efficiency of Turbine Airfoils, AIAA Paper 72-11, Jan. 1972.

19.34 Prust, H. W., Schum, H. J., and Szanca, E. M.: Cold Air Investigation of a Turbine with Transpiration-Cooled Stator Blades, I. Performance of Stator with Discrete Hole Blading, NASA TM X-2094, 1970.

19.35 Anderson, L. R., Heiser, W. H., and Jackson, J. C.: Axisymmetric One-Dimensional Compressible Flow Theory and Applications, ASME Paper 70-GT-82, May 1970.

19.36 Anderson, L. R. and Heiser, W. H.: Systematic Evaluation of Cooled Turbine Efficiency, ASME Paper 69-GT-63, Mar. 1969.

19.37 Moskowitz, S. L. and Lombardo, S.: 2750 Degree F Engine Test of a Transpiration Air-Cooled Turbine, ASME J. of Eng. for Power, April 1971, pp. 238-248.

19.38 Blair, M. F.: An Experimental Study of Heat Transfer and Film Cooling on Large Scale Turbine Endwalls, ASME J. of Heat Trans., Nov. 1974, pp. 524-529.

19.39 Louis, J. F.: Heat Transfer in Turbines, AFAPL-TR-75-107, Sept. 1975.

19.6 Nomenclature

a_1, a_2, a_3	constants given in TABLE 19.2.1
A_g	gas side surface area
A_i	inside surface area
A_h	coolant hole surface area
b	equivalent slot width, $\frac{\pi}{4}\frac{d^2}{p}$ or $\frac{\pi}{4}\frac{D^2}{p}$
b_1, b_2, b_3	constants given in TABLE 19.2.1
c	axial chord
c_{p_c}	coolant specific heat
c_{p_e}	approach gas specific heat
c_{p_g}	mainstream gas specific heat
c_1, c_2	constants given in TABLE 19.2.1
d	impingement coolant hole diameter or internal coolant hole diameter
D	film cooling hole diameter
e	roughness height in Fig. 19.2.10
f	half the heat transfer region in Fig. 19.2.7
F	coolant mass flux parameter of Eq. (19.2.22)
F_a	empirical parameter of Eq. (19.2.9)
G_{cf}	cross flow mass velocity
G_h	impingement hole mass velocity
h(z,x)	local heat transfer coefficient
h(x)	heat transfer coefficient (independent of z)
h_g	local gas side heat transfer coefficient in Fig. 19.3.3
$\overline{h}_g$	lateral-average gas side heat transfer coefficient in Eq. (19.2.21)
h_h	coolant hole heat transfer coefficient
h_i	inside heat transfer coefficient
H	leading edge dimension in Fig. 19.2.7
I	coolant to mainstream momentum flux ratio
ℓ	impingement hole to impingement point distance
L	leading edge impingement dimension in Figs. 19.2.5 and 19.2.7
m	empirically determined parameter of Eq. (19.2.5)
M	coolant to mainstream mass flux ratio
η	Mach number
n	wall roughness ring spacing in Fig. 19.2.10
Nu_{ave}	average Nusselt number based on characteristic dimension as used

Nu_{stag}	stagnation point Nusselt number based on characteristic dimension as used
Nu_x	local Nusselt number based on characteristic dimension as used
p	center-to-center hole spacing
P_{tg}	mainstream total pressure
ΔP_{tg}	mainstream total pressure loss
Pr	Prandtl number
q	heat flux
$\bar{q}(x)$	lateral-average heat flux
r	leading edge radius in Fig. 19.2.7
Re	Reynolds number with characteristic dimension and velocity defined as used
s	slot height
St	Stanton number defined as used
St_{ave}	average Stanton number defined as used
T_c	coolant supply total temperature
T_{ce}	coolant total temperature at exit of coolant hole
$T_f(z,x)$	local film temperature
$\bar{T}_f(x)$	lateral-average film temperature
T_e	mainstream gas total temperature
T_g	mainstream gas adiabatic wall temperature (also low velocity gas static and total temperature)
T_m	temperature of metal defined as used
$T_m(x)$	temperature of metal (independent of z)
T_{tg}	mainstream gas total temperature
$\bar{T}$	film layer average total temperature
U_c	coolant velocity
U_e	cascade approach velocity
U_g	mainstream gas velocity
W_c	coolant flow rate
W_g	mainstream mass flow mixed with film cooling air for aerodynamic losses
W_{ge}	mainstream mass flow entrained in film cooling boundary layer
x	surface distance in streamwise direction
x'	surface distance in streamwise direction from effective starting point for boundary layer
z	surface distance in lateral or spanwise direction
β	angle of coolant flow from mainstream flow
γ	ratio of specific heats
δ^*	boundary layer displacement thickness
ζ	defined by Eq. (19.2.13)
η_c	convective effectiveness defined by Eq. (19.2.19)
η_f	local film effectiveness
$\bar{\eta}_f$	lateral-average film effectiveness
θ	defined by Eq. (19.2.24)
μ_c	coolant viscosity
μ_e	approach gas viscosity
μ_g	mainstream viscosity
ν_g	mainstream kinematic viscosity
ξ_1	empirically determined parameter of Eq. (19.2.5)
ξ_2	empirically determined parameter of Eq. (19.2.5)
ρ_c	coolant density
ρ_e	approach gas density
ρ_g	mainstream gas density
ϕ	local cooling effectiveness defined by Eq. (19.2.18)
$\bar{\phi}$	average cooling effectiveness defined by Eq. (19.2.1)

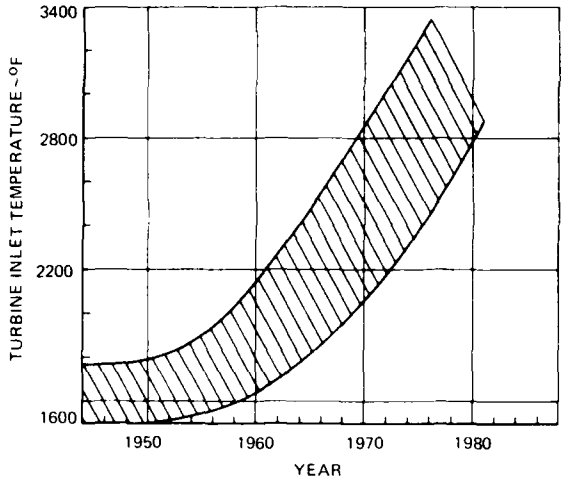

Figure 19.0.1 Turbine Inlet Temperature History and Projection

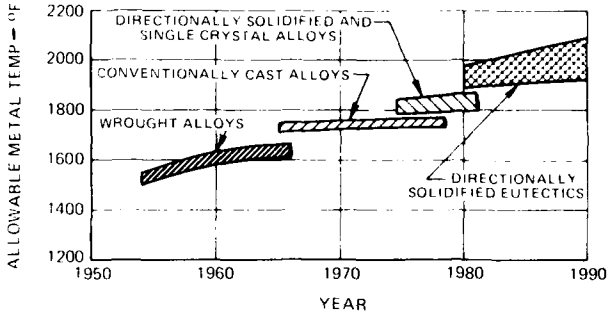

Figure 19.0.2 Blade Material Temperature Capability History and Projection

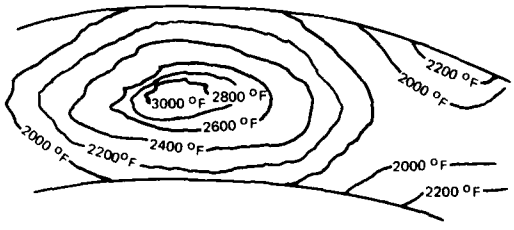

Figure 19.1.1 Typical Radial and Circumferential Temperature Distribution for an Annular Burner @ 2500 F

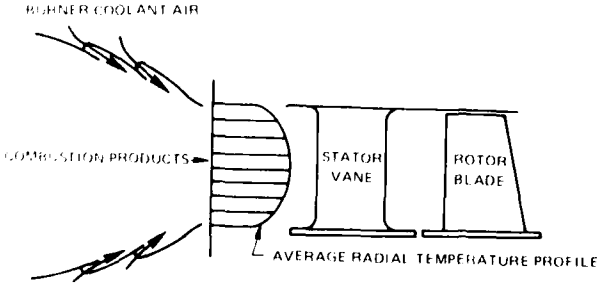

Figure 19.1.2 Burner Average Radial Temperature Profile

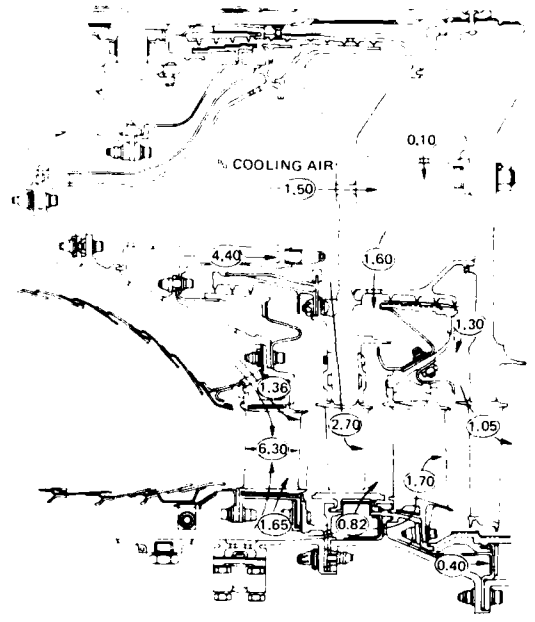

Figure 19.1.3 Cooling Air Supply System

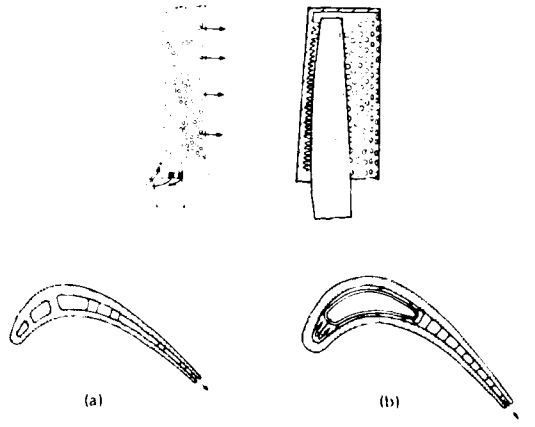

Figure 19.2.1 Convectively Cooled Blades

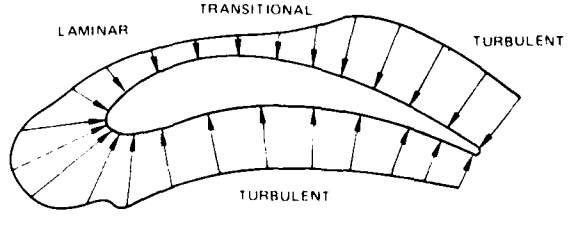

Figure 19.2.2 Airfoil Heat Transfer Coefficient Distribution

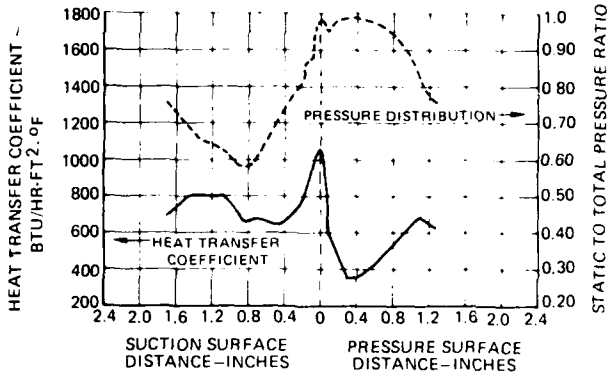

Figure 19.2.3 Typical Pressure and Heat Transfer Coefficient Distribution

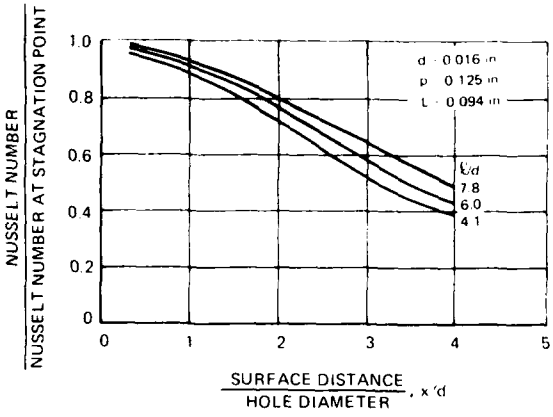

Figure 19.2.6 Heat Transfer Distribution from Impingement Cooling (Ref. 19.3)

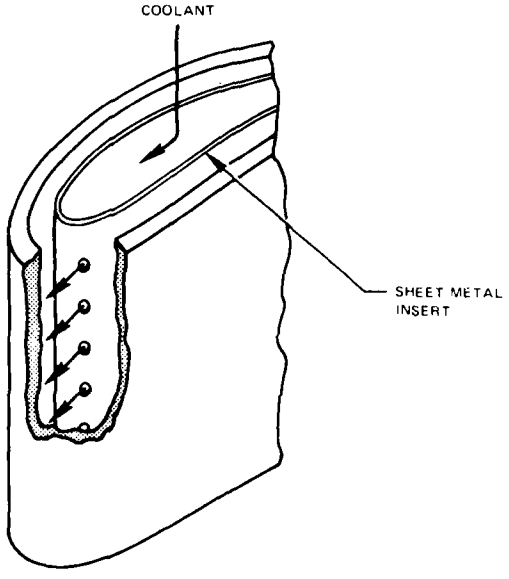

Figure 19.2.4 Leading Edge Impingement Cooling

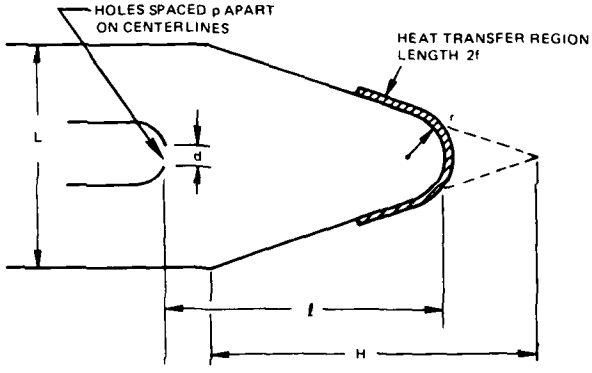

Figure 19.2.7 Leading Edge Impingement Cooling Model (Ref. 19.4)

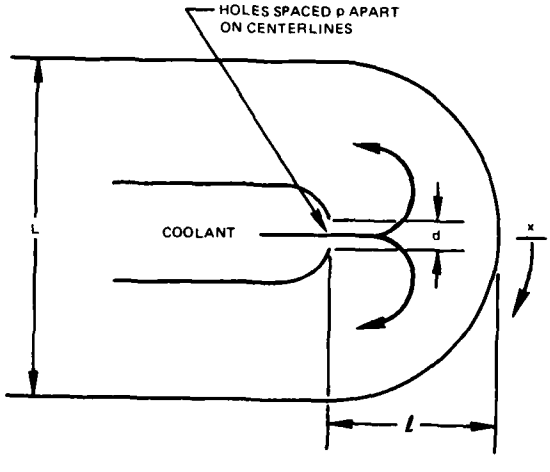

Figure 19.2.5 Leading Edge Impingement Cooling Model (Ref. 19.3)

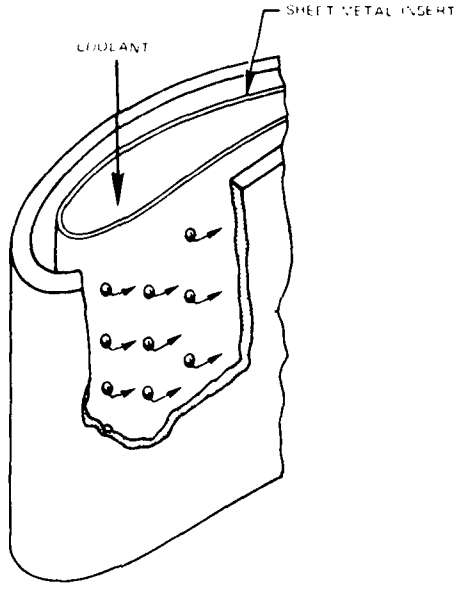

Figure 19.2.8 Midchord Impingement Cooling

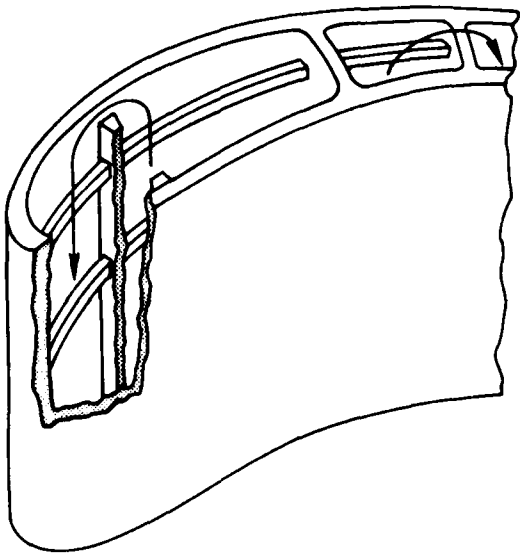

Figure 19.2.10 Roughened Walls in Airfoils

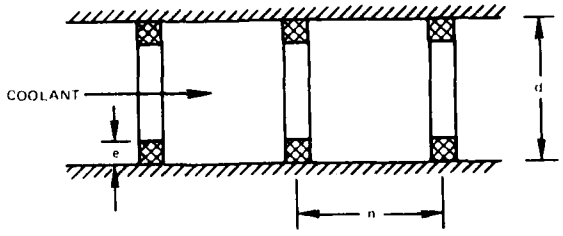

Figure 19.2.10 Roughened Wall Model (Ref. 19.7)

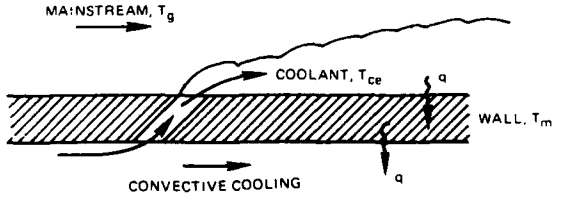

Figure 19.2.11 Film Cooling

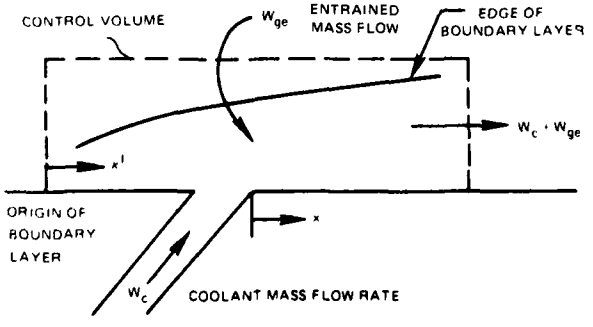

Figure 19.2.12 Entrainment Model for Film Cooling

Figure 19.2.13 Oil Traces of Film Cooling from a Row of Holes (Ref. 19.14)

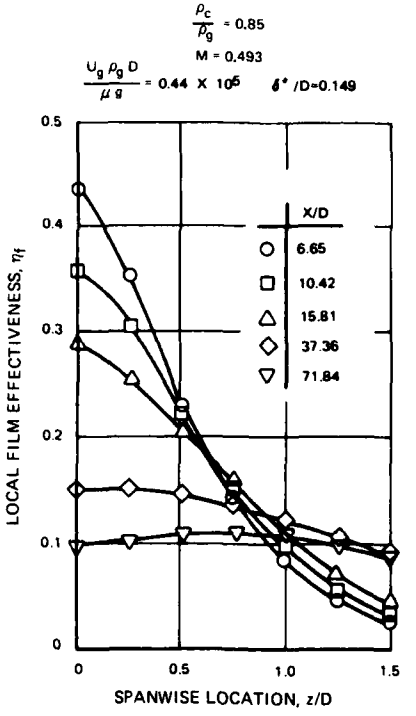

Figure 19.2.14 Spanwise Film Effectiveness from a Row of Holes (Ref. 19.15)

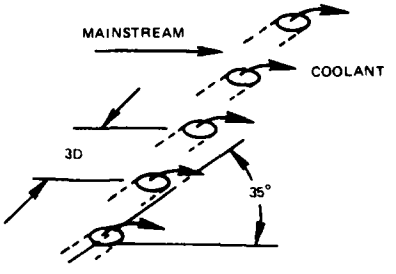

Figure 19.2.15 Film Cooling Geometry

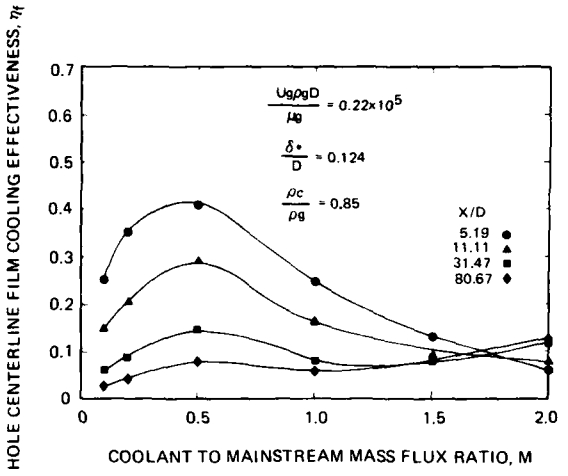

Figure 19.2.16 Effect of Blowing Rate on Centerline Film Cooling Effectiveness (Ref.19.16)

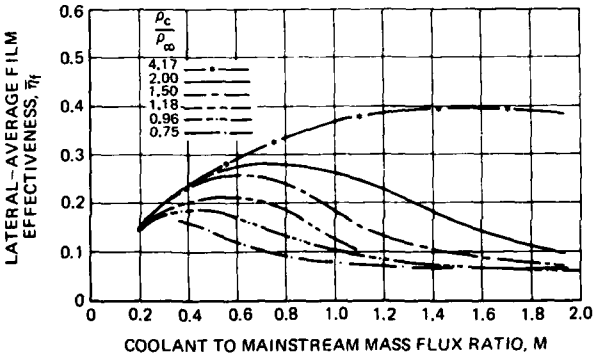

Figure 19.2.17 Effect of Coolant Density on Film Effectiveness (Ref. 19.17)

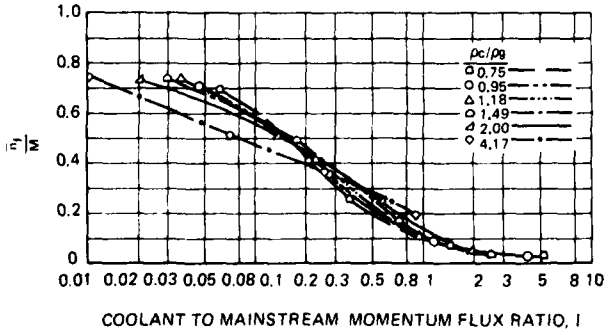

Figure 19.2.18 Correlation of Film Effectiveness with Coolant to Mainstream Momentum Flux Ratio (Ref. 19.17)

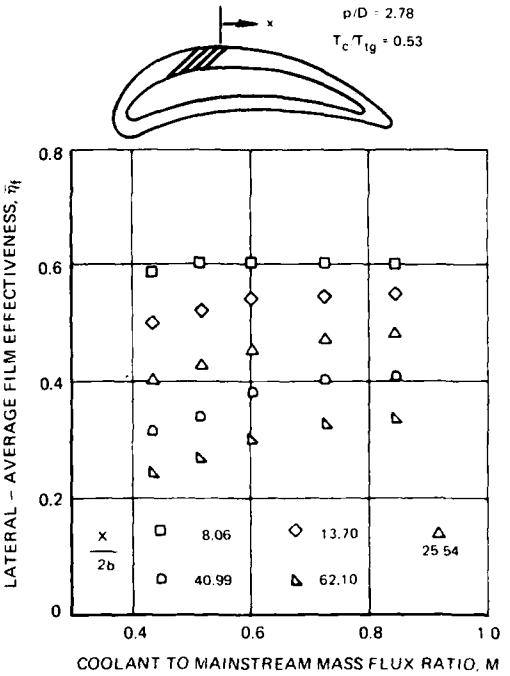

Figure 19.2.19 Film Cooling Effectiveness on an Airfoil with a Double Row of Holes (Ref. 19.20)

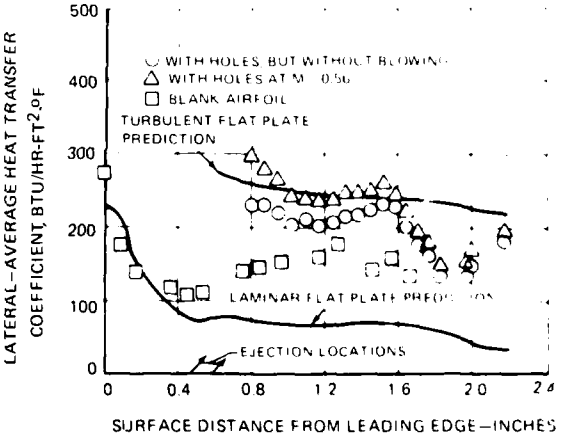

Figure 19.2.20 Heat Transfer Coefficient under Film Cooling (Ref. 19.20)

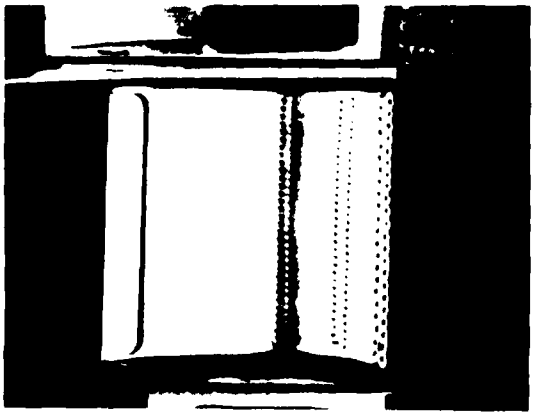

Figure 19.2.21 Film Cooled Airfoil with Multiple Rows of Holes

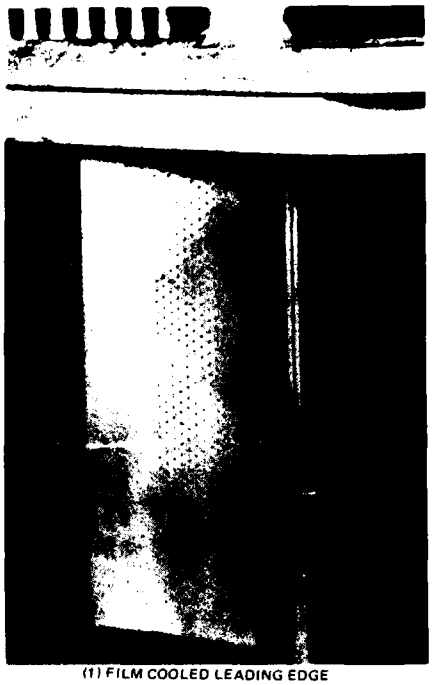

(1) FILM COOLED LEADING EDGE

(2) MULTI-HOLE PATTERN ON PRESSURE SIDE OF VANE

Figure 19.2.22 Airfoil with Multihole Film Cooling

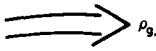

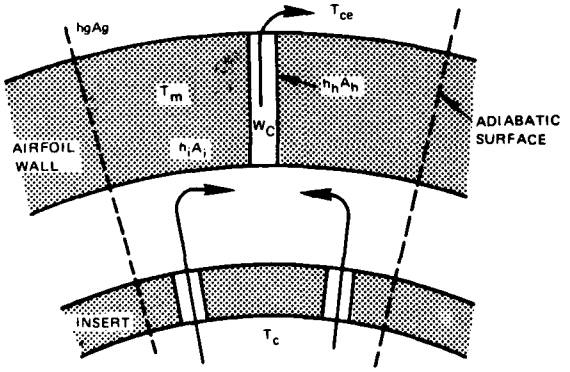

Figure 19.2.23 One Dimensional Model for Multihole Cooling

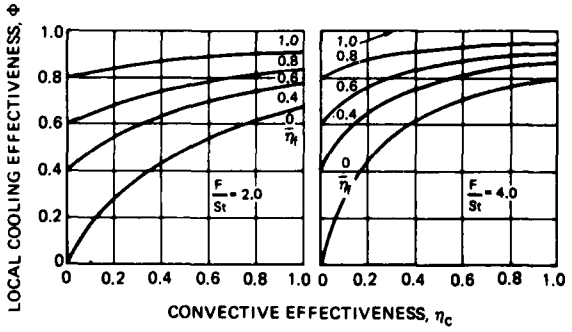

Figure 19.2.24 Effects of Convective and Film Effectiveness on Cooling Effectiveness

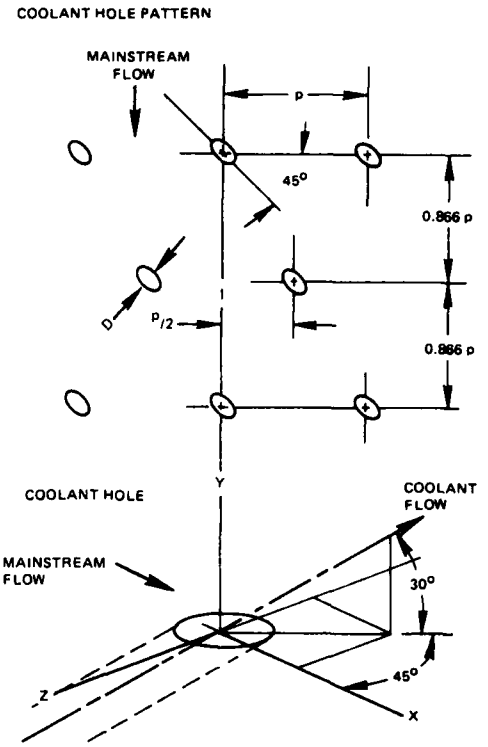

Figure 19.2.25 Multihole Cooling Geometry (Ref. 19.25)

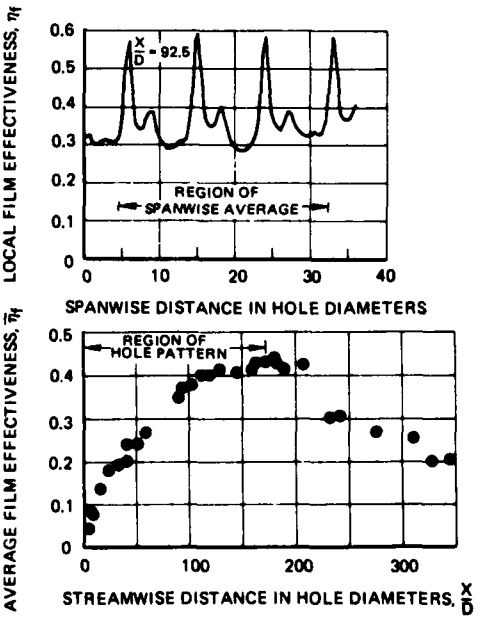

Figure 19.2.26 Film Effectiveness from Multihole Cooling (Ref. 19.25)

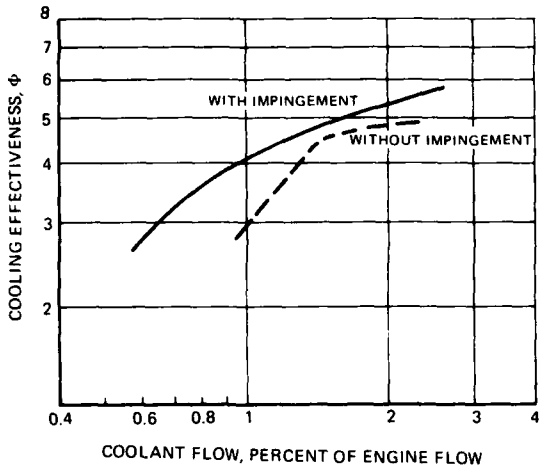

Figure 19.2.27 Cooling Effectiveness of Leading Edge Film Cooling (Ref. 19.32)

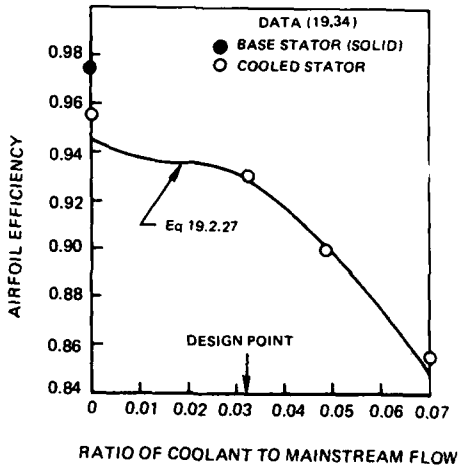

Figure 19.2.28 Comparison of Data For Cooled Cascade Efficiency with Mixing Analysis of Eq. 19.2.27

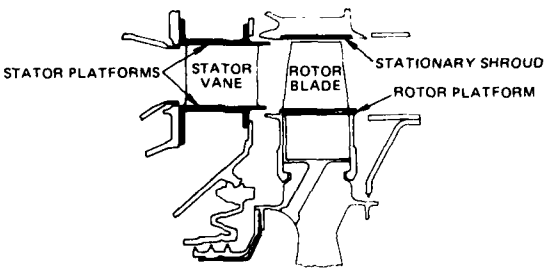

Figure 19.3.1 Endwall Regions

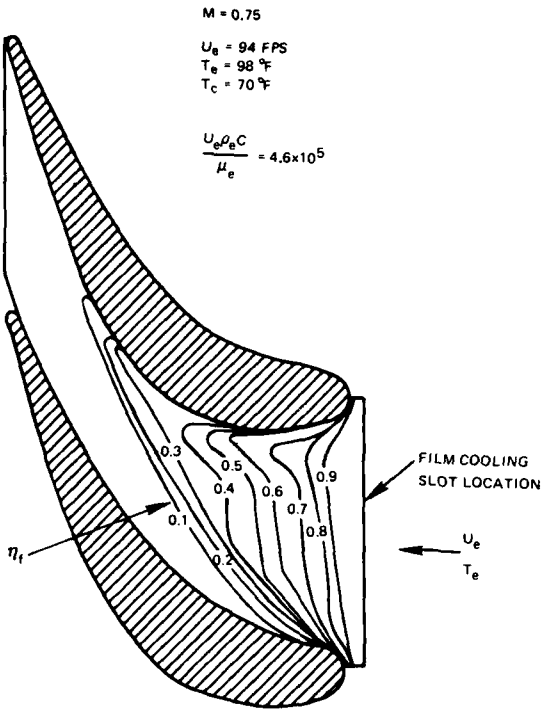

Figure 19.3.2 Endwall Film Cooling Data (Ref. 19.38)

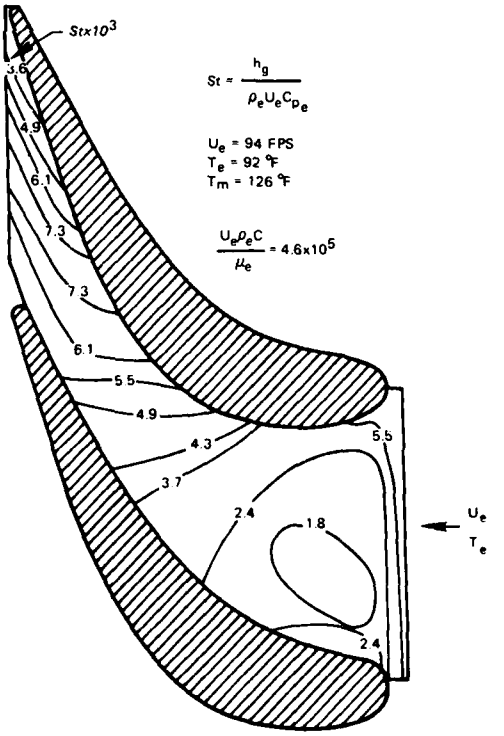

Figure 19.3.3 Endwall Heat Transfer Distribution (Ref. 19.38)

Chapter 20

TURBOPROPULSION COMBUSTION TECHNOLOGY

Robert E. Henderson
AF Aero Propulsion Laboratory

and

William S. Blazowski
AF Aero Propulsion Laboratory
(Currently at Exxon Research and Engineering Company)

TABLE OF CONTENTS

CHAPTER 20 TURBOPROPULSION COMBUSTION

		Page
20.0	INTRODUCTION	20-1
20.1	COMBUSTION SYSTEM DESCRIPTION/DEFINITIONS	20-1
20.1.1	Types	20-1
20.1.2	Size	20-2
20.1.3	Combustor Configurations	20-3
20.1.4	Flowpath Terminology	20-3
20.2	COMPONENT CONSIDERATIONS	20-3
20.2.1	Combustion System Demands	20-3
20.2.1.1	Combustion Efficiency	20-4
20.2.1.2	Overall Pressure Loss	20-4
20.2.1.3	Exit Temperature Profile	20-5
20.2.1.4	Combustion Stability	20-6
20.2.1.5	Ignition	20-6
20.2.1.6	Size/Weight/Cost	20-6
20.2.1.7	Durability/ Reliability/ Maintainability	20-7
20.2.1.8	Exhaust Emissions	20-7
20.2.2	Design Factors	20-7
20.2.2.1	Inlet Diffuser	20-8
20.2.2.2	Dome and Snout	20-9
20.2.2.3	Liner	20-9
20.2.2.4	Fuel Injection	20-10
20.2.2.5	Ignition	20-12
20.2.2.6	Materials	20-12
20.3	DESIGN TOOLS	20-13
20.3.1	Combustor Modeling	20-13
20.3.1.1	Empirical	20-13
20.3.1.2	Combined Empirical/ Theoretical	20-14
20.3.1.3	Theoretical	20-14
20.3.2	Combustion Diagnostics	20-14
20.4	FUTURE REQUIREMENTS	20-15
20.4.1	Exhaust Emissions	20-15
20.4.1.1	Problem Definition	20-15
20.4.1.2	Exhaust Content	20-15
20.4.1.3	Emission Characteristics	20-17
20.4.1.4	Minimization of Emissions	20-19
20.4.2	Future Jet Fuels	20-21
20.4.2.1	Fuel Effects on Combustion Systems	20-21
20.4.2.2	Combustion System Design Impact	20-23
20.4.3	Design and Performance Advancements	20-23
20.4.3.1	High Mach Combustor (HMC)	20-23
20.4.3.2	Advanced Diffusion Techniques	20-24
20.4.3.3	Shingle Liner	20-24
20.5	CONCLUSIONS	20-24
20.6	REFERENCES	20-26

LIST OF ILLUSTRATIONS

CHAPTER 20 TURBOPROPULSION COMBUSTION

		Page
20.1.1	Combustor Types	20-1
20.1.2	T63 Turboprop Engine with Can Combustor	20-1
20.1.3	J33 Turbojet Engine with Can Combustors	20-2
20.1.4	J79 Cannular Combustor	20-2
20.1.5	TF39 Annular Combustor	20-2
20.1.6	WR19 Turbofan Engine	20-2
20.1.7	JT9D Annular Combustor	20-2
20.1.8	TFE 731 Turbofan Engine With Reverse-Flow Combustor	20-3
20.1.9	Main Combustor Airflow Distribution	20-3
20.2.1	Pressure Loss Correlation	20-5
20.2.2	Radial Temperature Profile at Combustor Exit	20-6
20.2.3	Combustion Stability Characteristics	20-6
20.2.4	Ignition/Relight Envelope	20-6
20.2.5	Component Identification	20-7
20.2.6	Diffuser Design and Performance Characteristics	20-8
20.2.7	Contemporary Diffuser Designs	20-9
20.2.8	Combustor Dome Types	20-9
20.2.9	Combustor Cooling Techniques	20-10
20.2.10	Liner Cooling Characteristics	20-11
20.2.11	Fuel Injection Methods	20-11
20.2.12	Pressure Atomizing Fuel Injector	20-11
20.2.13	Spark Ignitor	20-12
20.3.1	Empirical Combustion Efficiency Correlation	20-13
20.3.2	Prediction of Combustion Efficiency Using θ-Parameter	20-14
20.3.3	Effect of Primary Zone ϕ on Inlet Temperature Factor	20-14
20.3.4	Combustor Model Computational Schematic	20-14
20.4.1	CO and HC Idle Emissions	20-17
20.4.2	Correlation of Current Engine NO_x Emissions with Combustor Inlet Temperature	20-18
20.4.3	Dependence of Sea Level Standard Day NO_x Emissions on Compressor Pressure Ratio of Current Engines	20-18
20.4.4	Dependence of NO_x Emission on Flight Mach Number	20-19
20.4.5	Staged Premix Combustor, JT9D Engine	20-19
20.4.6	Ideal Effectiveness of Water Injection for NO_x Control	20-20
20.4.7	Effect of Residence Time and ϕ on Nitrogen Oxide Emissions	20-20
20.4.8	Overall Scheme for Alternate Jet Fuel Development Program	20-21
20.4.9	Liner Temperature Correlation for Many Combustor Types	20-22
20.4.10	Smoke Emission Dependence on Hydrogen Content	20-22
20.4.11	Fuel Bound Nitrogen Conversion to NO_x in an Aircraft Gas Turbine Combustor	20-23
20.4.12	Effect of Lean Operation on Combustor Fuel Sensitivity	20-23
20.4.13	HMC With Advanced Bleed Diffuser	20-23
20.4.14	Swirl Burning HMC	20-24
20.4.15	Vortex Controlled Diffuser	20-24
20.4.16	Shingle Liner Combustor	20-24
20.5.1	Annular Combustor Development Trends	20-25
20.5.2	F101 Annular Combustor	20-25
20.5.3	Catalytic Combustor Efficiency	20-25

LIST OF TABLES

CHAPTER 20 TURBOPROPULSION COMBUSTION

		Page
20.2.1	Contemporary Combustor Size, Weight and Cost	20-7
20.4.1	Engine Combustion Products	20-16

CHAPTER 20

TURBOPROPULSION COMBUSTION

20.0 INTRODUCTION

The evolution of aircraft gas turbine combustor technology over the past forty years has been extremely impressive. While the combustion system was the primary limitation in development of the first aircraft gas turbine in 1939 (Ref 20.1), the complexity and hardware costs associated with current rotating engine components (compressor and turbine) now far exceed that of the combustion system. Recent developments, however, have once again caused significant shifts in development emphasis toward combustion technology. New concepts and technology improvements will be necessary to satisfy recently legislated exhaust pollutant regulations. Moreover, future emphasis on engines which can utilize fuels with a broader range of characteristics are expected to require additional combustor technology development.

Beyond these externally imposed requirements are the combustion system performance improvements necessary to keep pace with new engine developments. Further reductions in combustor physical size and weight are expected to continue as firm requirements. Performance improvements, especially with respect to engine thrust/weight ratio and specific fuel consumption, will require higher combustor temperature rise, greater average turbine inlet temperatures, and closer adherence to the design temperature profile at the turbine inlet. High performance designs must also permit greater Mach number operation within and around the combustor to reduce pressure drop and minimize the physical size of compressor exit diffuser hardware. Costs (both initial and operating) must be minimized, as recent experiences with high temperature engines have confirmed the necessity to consider reliability and maintenance aspects of life cycle cost as well as performance and fuel consumption.

The purpose of this chapter is to introduce the reader to the hardware aspects of aircraft gas turbine main burners; fundamental aspects have been addressed in Chapter 15, and afterburners are to be discussed in Chapter 21. A number of reference texts (Ref 20.2 - 20.6) have been published which address various aspects of turbopropulsion combustion in a detailed manner. In particular, reference 20.6 cites more than 700 reports and technical articles on the topic of turbopropulsion combustion. The balance of this chapter will discuss the following four topics: a) description of various hardware types and definition of all terms of importance, b) review of parameters pertinent to performance, c) discussion of tools available to the combustor designer, and d) review of the future requirements of exhaust emission reduction, achievement of greater fuel flexibility, and advancement of burner performance.

20.1 COMBUSTION SYSTEM DESCRIPTION/DEFINITIONS

In order to fully appreciate and comprehend contemporary turbopropulsion combustor design philosophy, a number of general design and performance terms must be understood. The purpose of this section is to acquaint the reader with commonly used combustion nomenclature which will be utilized throughout this chapter. A brief description and/or definition of combustion system types, sizes, configurations, and flow-path terminology is given in the following subsections.

20.1.1 Types

Turbine engine combustors have undergone continuing development over the past 40 years resulting in the evolution of a variety of basic combustor configurations. Contemporary combustion systems may be broadly classified into one of the three types schematically illustrated in Figure 20.1.1.

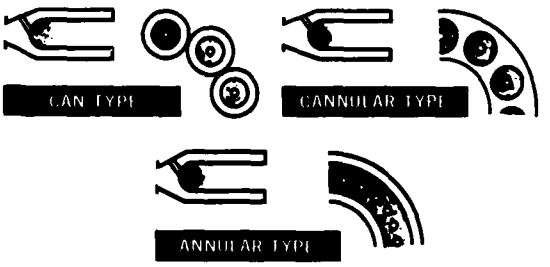

Figure 20.1.1 Combustor Types

a. Can: A can combustion system consists of one or more cylindrical combustors each contained in a combustor case. In the small T-63 turboshaft engine of Figure 20.1.2, a single combustor can is used while larger propulsion systems use a multican assembly in an arrangement designed to provide a continuous annular gas flow to the turbine section. The combustion system of the J33 engine illustrated in Figure 20.1.3 is representative of such multican systems.

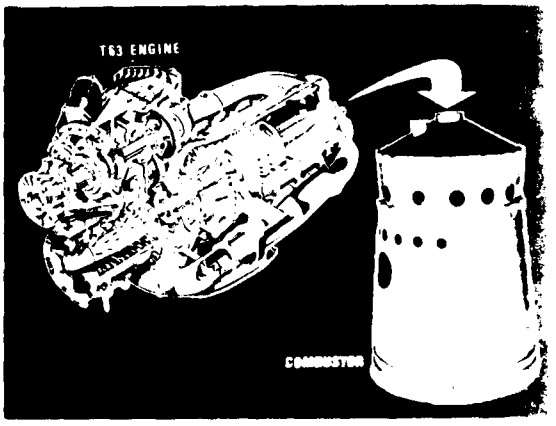

Figure 20.1.2 T63 Turboprop Engine With Can Combustor

Figure 20.1.3 J33 Turbojet Engine With Can Combustors

b. Cannular: This combustion system consists of a series of cylindrical-combustors arranged within a common annulus--hence, the cannular name. This combustor type is the most common in the current aircraft turbine engine population, but is rapidly being replaced with the annular type as more modern engines comprise larger portions of the fleet. The J79 turbojet engine main combustor, illustrated in Figure 20.1.4, exemplifies cannular systems.

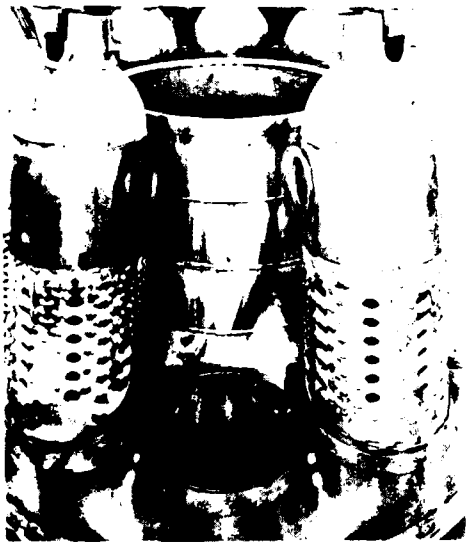

Figure 20.1.4 J79 Cannular Combustor

c. Annular: Most modern combustion systems employ the annular design wherein a single combustor of toroidal annular cross-section supplies gas to the turbine. An example of this combustor type, the CF6, is illustrated in Figure 20.1.5. The improved combustion zone uniformity, design simplicity, reduced liner surface area, and shorter system length provided by the annular combustion chamber are major reasons for its popularity in advanced turbofan propulsion systems.

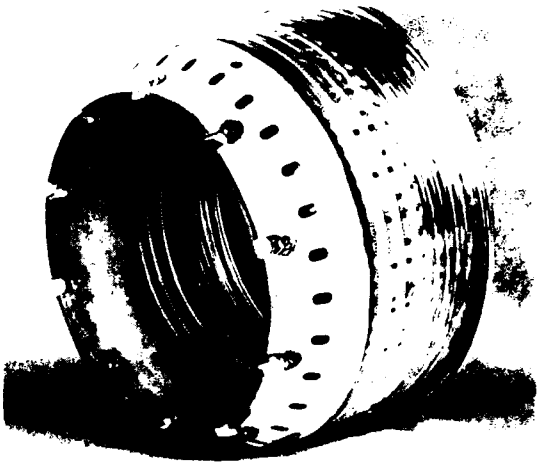

Figure 20.1.5 CF6 Annular Combustor

20.1.2 Size

Contemporary combustion systems may come in a variety of sizes ranging from the small 2.3 Kg/sec (5 lbm/sec) annular burner of the WR-19 engine (Figure 20.1.6) to the large 110 Kg/sec [illegible] annular combustor of the JT9D engine (Figure 20.1.7). The WR-19 combustor is approximately 25.4 cm (10 in) in diameter and intended principally for missile and remotely-piloted vehicle engine application while the JT9D combustor is approximately 91 cm (36 in) in diameter and is used in engines to power the wide-body 747 and DC-10 class aircraft.

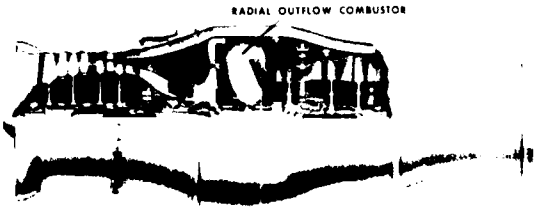

Figure 20.1.6 WR19 Turbofan Engine

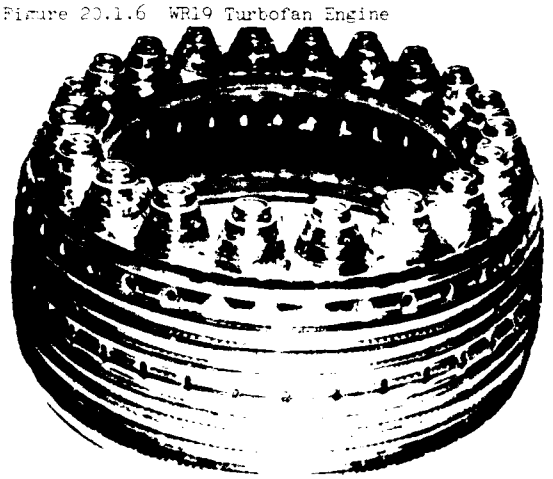

Figure 20.1.7 JT9D Annular Combustor

... Combustor Configurations

... system configuration may also be ... to airflow direction through ... engine.

a. Axial Thru-Flow: The most common configuration is the axial thru-flow design where combustion flow is in a direction approximately ... to the axis of the engine. The JT9D ... illustrated in Figure 20.1.7 is ... axial thru-flow configuration.

b. Reverse-Flow, Folded: Engines with ... compressors often employ compact, reverse-flow combustors. In these combustion systems, ... flows on the outside of the burner and ... flow through the combustion chamber. ... gases are then turned once again to ... the turbine. Hence, the air is reversed ... reversals in moving from ... the turbine. The reverse flow ... is often employed to minimize engine ... especially in small turboshaft and turboprop ... propulsion system length is an ... Figure 20.1.8 illustrates ... a typical reverse flow con-...

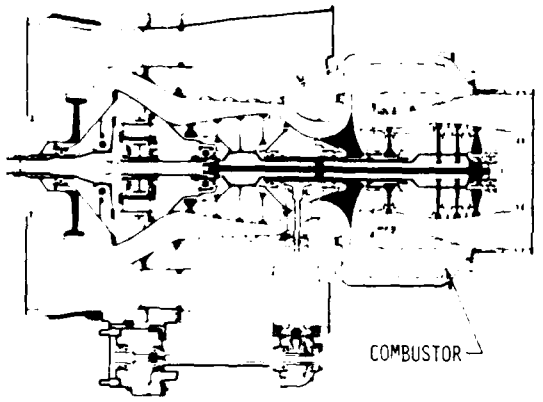

... CFE TF Turbofan Engine with Reverse-Flow Combustor

c. Radial-Inflow or Radial-Outflow: The radial-inflow and radial-outflow combustor configurations are ... well suited to centrifugal compressor propulsion systems. The radial-inflow combustor has an outward-oriented dome or headplate with combustion gas flow directed toward the engine centerline, while the radial-outflow configuration has an inward-oriented dome with the primary flow direction being away from the engine centerline. For example, the WP-19 combustor illustrated in Figure 20.1.6 is typical of compact radial-outflow designs.

20.1.4 Flowpath Terminology

This subsection will identify and briefly describe basic airflow distribution terminology for a conventional combustor. Distribution of air in, around, and through the combustor results in ... basic airflow regions illustrated in ... Figure 20.1.9. Effective control of this air ... is vital to the attainment of complete ..., stable operation, correct combustor exit ... profile, and acceptable liner temperatures for long life.

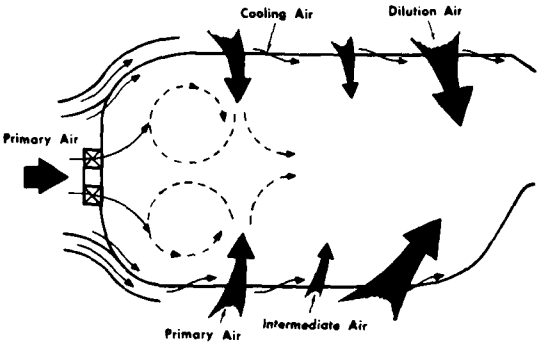

Figure 20.1.9 Main Combustor Airflow Distribution

a. Primary Air: This is the combustion air introduced through the dome or headplate of the combustor and through the first row of liner air holes. This air mixes with incoming fuel producing the approximately stoichiometric mixture necessary for optimum flame stabilization and operation (see discussion on combustion stabilization in Section 15.4 of Chapter 15).

b. Intermediate Air: To complete the reaction process and consume the high levels of primary zone CO, H_2, and unburned fuel, intermediate air is introduced through a second row of liner holes. The reduced temperature and excess air cause CO and H_2 concentrations to decrease (see the chemical kinetic and equilibrium relationships presented in Section 15.1 of Chapter 15).

c. Dilution Air: In contemporary systems, a large quantity of dilution air is introduced at the rear of the combustor to cool the high temperature gases to levels consistent with turbine design limitations. The air is carefully used to tailor exit temperature radial profile to ensure acceptable turbine durability and performance. This requires minimum temperatures at the turbine root (where stresses are highest) and at the turbine tip (to protect seal materials). However, modern and future combustor exit temperature requirements are necessitating increased combustion air in the primary and intermediate zones; thus, dilution zone air flow is necessarily reduced or eliminated to permit these increases.

d. Cooling Air: Cooling air must be used to protect the combustor liner and dome from the high radiative and convective heat loads produced within the combustor. This air is normally introduced through the liner such that a protective blanket or film of air is formed between the combustion gases and the liner hardware. Consequently, this airflow should not directly affect the combustion process. A detailed discussion of the various design techniques employed to cool the combustor liner is given in 20.2.2.3.

20.2 COMPONENT CONSIDERATIONS

20.2.1 Combustion System Demands

During the past several years, significant engine performance gains have required advancements in turbopropulsion combustion. Advanced strategic

and tactical aircraft propulsion systems utilize main burners with the operational flexibility to accept broad variations in compressor discharge pressure, temperature and airflow while providing an acceptable exit temperature profile with minimum pressure loss and near-perfect combustion efficiency. Furthermore, heat release rates and combustor temperature rise capabilities have significantly increased and will continue to progress toward stoichiometric exit temperature conditions.

A broad list of combustion system performance and design objectives is required of all new combustors as they enter development. Although this list can be quite lengthy, the more important requirements, some of which were alluded to above, are given below:

Performance Objectives

- High combustion efficiency (100%) at all operating conditions.
- Low overall system total pressure loss.
- Stable combustion at all operating conditions.
- Reliable ground-level ignition and altitude relight capability.

Design Objectives

- Minimum size, weight, and cost.
- Combustor exit temperature profile consistent with turbine design requirements.
- Low stressed structures.
- Effective hot parts cooling for long life.
- Good maintainability and reliability.
- Minimum exhaust emissions consistent with current specified limitations and regulations.

A number of these demands will be discussed in more detail in the following subsections.

20.2.1.1 Combustion Efficiency: In that propulsion system fuel consumption has a direct effect on aircraft system range, payload and operating cost, it is imperative that design point combustor efficiency be as close to 100% as possible. Combustion efficiency at the high power/high fuel consumption conditions of take-off and cruise is always near 100% (usually greater than 99.5%). However, off-design efficiency, particularly at idle, can be in the low nineties. With the advent of chemical emission controls and limitations, this parameter becomes of particular significance during low power operation. For example, combustion efficiencies at off-design conditions, such as idle, must now exceed 98.5% to satisfy limitations on exhaust carbon monoxide and unburned hydrocarbons.

As discussed in Chapter 15, combustion efficiency can be defined in a number of equation forms:

$$\eta_c = \frac{\text{Enthalpy Rise (Actual)}}{\text{Enthalpy Rise (Ideal)}} = \frac{(h_4 - h_3)_a}{(h_4 - h_3)_i} \qquad (20.2.1)$$

$$= \frac{\text{Temperature Rise (Actual)}}{\text{Temperature Rise (Ideal)}} = \frac{(T_4 - T_3)_a}{(T_4 - T_3)_i} \qquad (20.2.2)$$

where: Subscript 4 represents the combustor exit condition

Subscript 3 represents the combustor entrance condition

Combustion efficiency (η_c) can also be determined from the concentration levels of the various exhaust products. A description of the combustion efficiency calculation based on exhaust product chemistry is given in Section 15.4 of Chapter 15.

Combustion efficiency can be empirically correlated with several aerothermodynamic parameters such as system pressure, temperature, reference velocity (V_R)*, and temperature rise. Two examples of such correlations will be discussed in 20.3.1.1.

20.2.1.2 Overall Pressure Loss: The combustion system total pressure loss from the compressor discharge to the turbine inlet is normally expressed as a percent of compressor discharge pressure. Losses of 5 - 8% are typically encountered in contemporary systems. Combustion system pressure loss is recognized as necessary to achieve certain design objectives (pattern factor, effective cooling, etc.), and can also provide a stabilizing effect on combustor aerodynamics. However, pressure loss also impacts engine thrust and specific fuel consumption. A 1% increase in pressure loss will result in approximately a 1% decrease in thrust and a .5 - .75% increase in specific fuel consumption. Consequently, design goals for pressure loss represent a compromise among the above factors.

Overall pressure loss is the sum of inlet diffuser loss, combustor dome and liner loss, and momentum loss resulting from combustor flow acceleration attendant with increased gas temperature (see Chapter 15, Section 15.3). Since many aspects of combustor performance are dependent on airflow turbulence generated within the combustor (which in turn depends on liner pressure drop), rapid and complete burning of the fuel and air is strongly influenced by the extent of pressure drop experienced as air is introduced into the combustion zone.

Combustion system pressure drop can be expressed in terms of three different loss parameters: fractional pressure loss, inlet velocity head loss and reference velocity head loss.

* That velocity at the reference plane, or plane of maximum cross section, within the combustor under flow conditions corresponding to T_4. Values of reference velocity range from 15-30 meters per second for contemporary combustor designs.

a. Fractional Loss--Overall combustor/diffuser pressure loss is most commonly expressed as the fractional loss defined as:

$$\frac{\Delta P}{P_3} = \frac{P_3 - P_4}{P_3} \qquad (20.2.3)$$

where $\Delta P = P_3 - P_4$ = Pressure Drop

P_3 = Compressor discharge total pressure

P_4 = Turbine nozzle inlet or combustor exit total pressure

This loss generally increases with the square of the diffuser inlet Mach number.

b. Inlet Velocity Head Loss--This loss coefficient is given in terms of inlet velocity head. It expresses losses in a manner which accounts for the additional difficulties in designing for minimum pressure loss as inlet velocities are increased. Inlet velocity head loss is defined as:

$$\frac{\Delta P}{q_3} = \frac{P_3 - P_4}{q_3} \qquad (20.2.4)$$

where: P_3 = Compressor discharge total pressure

P_4 = Combustor exit total pressure

q_3 = Dynamic pressure at the compressor discharge

c. Reference Velocity Head Loss--This loss coefficient is expressed in terms of reference velocity. It represents a measure of the pressure loss normalized by a term which accounts for difficulties associated with high combustor volumetric flow rates. Reference velocity head loss is defined as:

$$\frac{\Delta P}{q_r} = \frac{P_3 - P_4}{q_r} \qquad (20.2.5)$$

where: P_3 = Compressor discharge total pressure

P_4 = Combustor exit total pressure

q_r = Dynamic pressure corresponding to V_R

The relationship between fractional pressure loss (or overall pressure loss) and reference velocity head loss is shown in Figure 20.2.1 as a function of reference Mach number.

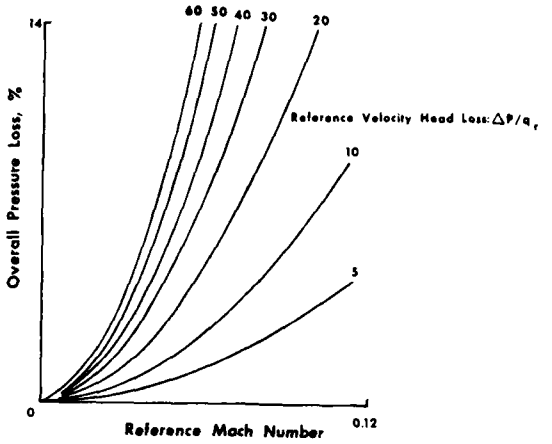

Figure 20.2.1 Pressure Loss Correlation

20.2.1.3 Exit Temperature Profile: A third performance parameter relates to the temperature uniformity of the combustion gases as they enter the turbine. In order to ensure that the proper temperature profile has been established at the combustor exit, combustion gas temperatures are often measured by means of high temperature thermocouples or via gas sampling techniques employed at the combustor exit plane. A detailed description of the thermal field entering the turbine both radially and circumferentially can be determined from this data. A simplified expression called pattern factor or peak temperature factor may be calculated from this exit temperature data. Pattern factor is defined as:

$$\text{Pattern Factor} = \frac{T_{max} - T_{avg}}{T_{avg} - T_{in}} \qquad (20.2.6)$$

where: T_{max} = Maximum measured exit temperature (local)

T_{avg} = Average of all temperatures at exit plane

T_{in} = Compressor discharge average temperature

Contemporary combustors exhibit pattern factors ranging from 0.25 to 0.45. Pattern factor goals are based primarily on the design requirements of the turbine first-stage vane which requires low gas temperatures at both the hub and tip of the turbine -- areas where high stresses and protective seals require cooler gas temperatures. Consequently, a pattern factor of 0.0 is not required. Durability considerations require high temperature rise combustors to provide combustor exit temperature profiles corresponding to pattern factors in the 0.15 to 0.25 range. One will note that although pattern factor is an important combustor design parameter, it describes the possible thermal impact on the turbine and is an important factor in matching the combustor and turbine components.

Although pattern factor defines the peak turbine vane inlet gas temperature, the shape of the combustor exit temperature radial profile is the critical factor controlling turbine blade life. Figure 20.2.2 illustrates typical

radial profile characteristics and their attendant relationship with pattern factor. By proper control of dilution air, the combustor exit temperature field is tailored to give the design pattern factor and radial profile consistent with turbine requirements.

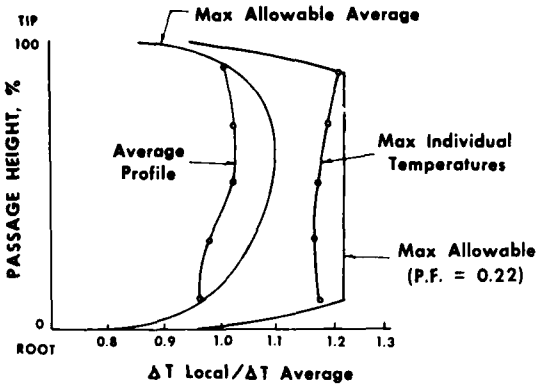

Figure 20.2.2 Radial Temperature Profile at Combustor Exit

20.2.1.4 Combustion Stability: Combustion stability is defined as the ability of the combustion process to sustain itself in a continuous manner. Stable, efficient combustion can be upset by the fuel-air mixture becoming too lean such that temperatures and reaction rates drop below the level necessary to effectively heat and vaporize the incoming fuel and air. Such a situation causes blowout of the combustion process. An illustration of stability sensitivity to mass flow, velocity and pressure characteristics as a function of equivalence ratio is given in Figure 20.2.3. These trends can be correlated with the perfectly stirred reactor theory described in Section 15.3 of Chapter 15.

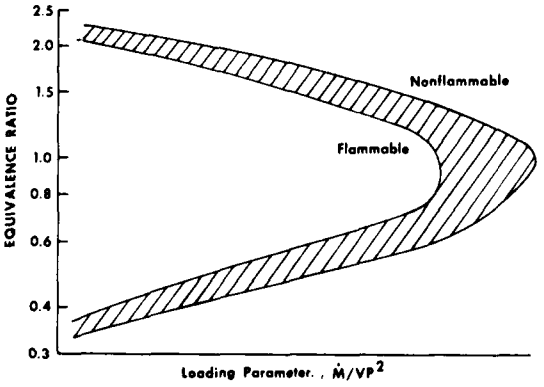

Figure 20.2.3 Combustion Stability Characteristics

20.2.1.5 Ignition: Ignition of a fuel-air mixture in a turbine engine combustor requires inlet air and fuel conditions within flammability limits, sufficient residence time of the potentially burnable mixture, and the location of an effective ignition source in the vicinity of the burnable mixture. Each of these factors has been discussed from a fundamental standpoint in Section 15.4 of Chapter 15. Reliable ignition in the combustion system is required during ground-level startup and for relighting during altitude windmilling. The broad range of combustor inlet temperature and pressure conditions encompassed by a typical ignition/relight envelope is illustrated in Figure 20.2.4. It is well known that ignition performance is improved by increases in combustor pressure, temperature, fuel-air ratio, and ignition-source energy. In general, ignition is impaired by increases in reference velocity, poor fuel atomization, and low fuel volatility. A more extensive discussion of the ignition source itself is deferred to 20.2.2.5.

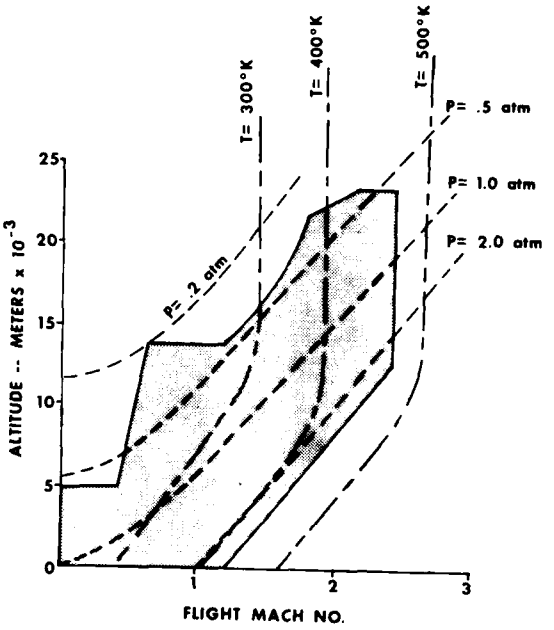

Figure 20.2.4 Ignition/Relight Envelope

20.2.1.6 Size, Weight, Cost: The main combustor of a turbine engine, like all other main components must be designed within constraints of size, weight, and cost. The combustor diameter is usually dictated by the engine casing envelope provided between the compressor and turbine and is never allowed to exceed the limiting diameter defined for the engine. Minimization of combustor length allows reduction of engine bearing requirements and permits substantial reductions in weight and cost. Advancements in design technology have permitted major reductions in combustor length. With the advent of the annular combustor design, length has been reduced by at least 50% when compared to contemporary cannular systems.

While reductions in both size and weight have been realized in recent combustor developments, the requirement for higher operating temperatures has demanded the use of stronger, higher temperature and more costly combustor materials (to be discussed in 20.2.2.6). Nevertheless, the cost of contemporary combustion systems including ignition and fuel injection assemblies remains at approximately 2 - 4 percent of the total engine cost. A tabulation of the approximate size, weight, cost and capacity of some contemporary combustion systems is given in Table 20.2.1.

Naturally, the final cost of any component is significantly affected by the level of production.

TABLE 20.2.1 Contemporary Combustor Size, Weight, and Cost

	TF39	TF41	J79	JT9D	T63
Type	Annular	Cannular	Cannular	Annular	Can
Mass Flow (Design Point)					
Air Flow, lb/sec	178.	135.	162.	242.	3.3
Kg/sec	81.	61.	74.	110.	1.5
Fuel Flow, lb/hr	12,850.	9,965.	8,350.	16,100.	235.
Kg/hr	5,829.	4,520.	3,788.	7,303.	107.
Size					
Length, in	20.7	16.6	19.0	17.3	9.5
cm	52.6	42.2	48.3	43.9	24.1
Diameter, in	33.3	5.3/24.1*	6.5/32.0*	38.0	5.4
cm	84.6	13.5/61.2	16.5/81.3	96.5	13.7
Weight, lb	202.	64.	92.	217.	2.2
kg	92.	29.	42.	98.	1.0
Cost, $	42,000.	17,000.	11,300.	80,000.	710.

* Can Diameter/Annulus Diameter

20.2.1.7 Durability, Maintainability, Reliability: A principal combustor design objective is to provide a system with sufficient durability to permit continuous operation until a scheduled major engine overhaul, at which time it becomes cost effective to make necessary repairs and/or replacements. In the case of the main burner, durability is predominantly related to the structural and thermal integrity of the dome and liner. The combustor must exhibit good oxidation resistance and low stress levels at all operating conditions if durability is to be achieved.

A maintainable component is one that is easily accessible, repairable and/or replaceable with a minimum of time, cost, and labor. While most combustor liners can be weld repaired, if damaged or burned, turbine removal is required for replacement of combustors in many cases. Consequently, a burner life consistent with the planned engine overhaul schedule is a primary objective. Combustor cases and diffuser sections require minimal maintenance and fuel nozzles and ignitors can generally be replaced and/or cleaned with minimal effort.

Reliability can be defined as the probability that a system or subsystem will perform satisfactorily between scheduled maintenance and overhaul periods. Component reliability is highly dependent on the aircraft mission, geographical location, and pilot operation since these factors strongly affect the actual combustor temperature-pressure environment and cyclic history of the components. In that the combustor has virtually no moving parts, its reliability is strongly related to fuel nozzle and ignitor performance. While Fouling and carboning of these subcomponents are common causes for engine rejection, these problems are relatively easy to correct through normal inspect and replace field maintenance procedures.

20.2.1.8 Exhaust Emissions: With the advent of environmental regulations for aircraft propulsion systems, the levels of carbon monoxide, unburned hydrocarbons, oxides of nitrogen, and smoke in the engine exhaust become important. Naturally, the environmental constraints directly impact the combustion system--the principal source of nearly all pollutants emitted by the engine. Major changes to combustor design philosophy have evolved in recent years to provide cleaner operation at all conditions without serious compromise to engine performance. A detailed discussion of the exhaust emissions area is offered in Section 20.4.1.

20.2.2 Design Factors

The turbine engine combustion system consists of three principal elements--the inlet diffuser, the dome and snout, and the inner and outer liners. In addition, two important subcomponents are necessary--the fuel injector and the ignitor. These elements are illustrated in Figure 20.2.5. This section will describe each of these items and will conclude with a materials summary.

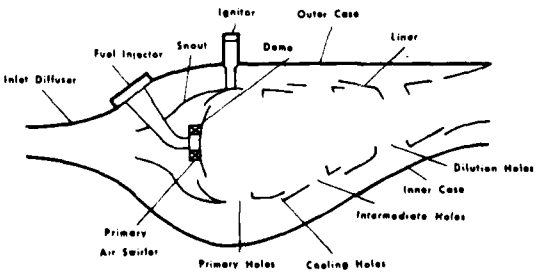

Figure 20.2.5 Component Identification

20.2.2.1 Inlet Diffuser: The purpose of the combustor inlet diffuser is to reduce the mean velocity of the air exiting the compressor and deliver it to the combustion chamber as a stable, uniform flow field recovering as much of the dynamic pressure as possible. Compressor discharge air velocities range from 90-180 meters per second; consequently, before this high velocity air is allowed to enter the combustor, it must be diffused to levels consistent with the stable, low pressure loss, high efficiency requirements of contemporary combustors. Additionally, this resulting flow field must be introduced in a relatively non-distorted manner to ensure uniform flow distribution to the combustion chamber. The diffuser must accomplish this by effectively controlling boundary layer growth and avoiding flow separation along the diffuser walls while minimizing length and overall size. A balance must be found between (a) designs with increased size and complexity and their attendant performance penalties, and (b) short-length, rapid divergence designs which have inherent flow non-uniformity and separation problems. Hence, the inlet diffuser represents a design and performance compromise relative to required compactness, low pressure loss and good flow uniformity.

A number of performance parameters are commonly used to describe a diffuser and its operation.

a. Pressure Recovery Coefficient (Cp)--This is a measure of the pressure recovery efficiency of the diffuser reflecting its ability to recover dynamic pressure. The coefficient is defined as the ratio of static pressure rise to inlet dynamic head:

$$C_p = \frac{P_{S2} - P_{S1}}{\frac{\rho V_1^2}{2g}} \qquad (20.2.7)$$

Where: P_{S2} = Exit static pressure

P_{S1} = Inlet static pressure

$\frac{\rho V_1^2}{2g}$ = Inlet dynamic pressure

For the ideal flow situation; i.e., full dynamic pressure recovery, C_p can be expressed in terms of area ratio:

$$C_p = 1 - \left(\frac{A_1}{A_2}\right)^2 \qquad (20.2.8)$$

where: A_1 = Inlet cross sectional area

A_2 = Exit cross sectional area

b. Pressure Recovery Effectiveness--This parameter describes the ability of a diffuser design to achieve ideal recovery characteristics. Hence, it is the ratio of the actual to the ideal pressure recovery coefficient:

$$\eta = \frac{C_p}{C_{p_{Ideal}}} = \frac{P_{S2} - P_{S1}}{\frac{\rho V_1^2}{2g}\left[1 - \left(\frac{A_1}{A_2}\right)^2\right]} \qquad (20.2.9)$$

c. Kinetic Energy Distortion Factor (α)--This factor is a measure of the radial non-uniformity of the axial flow velocity profile. The distortion factor is defined as:

$$\alpha = \frac{\int_a (u^2/2)u\rho dA}{(V^2/2)V\rho A} \qquad (20.2.10)$$

where: V = Mean flow velocity

u = Local axial velocity

ρ = Density

A = Cross-sectional area of duct

A factor of 1.0 is equivalent to a flat one-dimensional velocity profile (i.e. plug flow); turbulent pipe flow has a factor of approximately 1.1.

In addition, a number of design parameters are often utilized to predict diffuser performance.

a. Area Ratio (A_R)--This is the ratio of the exit to inlet areas of the diffuser and defines the degree of area change for a particular design.

b. Length-to-Height Ratio (L/H)--This is the ratio of diffuser length (entrance to exit) to the entrance or throat height and serves as a sizing parameter.

c. Divergence Half-Angle (θ)--This is equivalent to one-half the equivalent cone angle of the diffuser and describes the geometric divergence characteristics of the diffuser walls.

Figure 20.2.6 relates area ratio, length-to-height ratio and divergence half-angle to pressure recovery effectiveness.

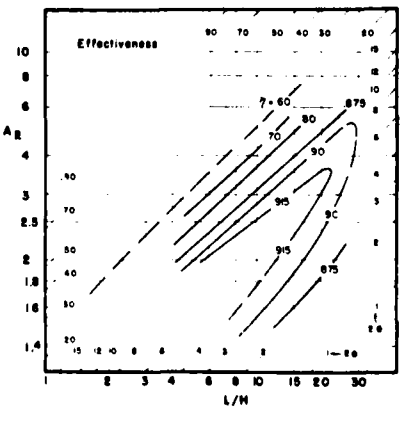

Figure 20.2.6 Diffuser Design and Performance Characteristics

Early inlet diffuser designs were of the smooth curved wall or contoured wall designs. Because of the wide variations in flow-field characteristics exiting the compressor, however, the curved wall diffuser cannot always provide uniform, non-separated flow at all operating conditions. This can become a critical problem in the short length diffusers required of many current systems. Consequently, a trend toward dump or combination curved wall and dump diffuser designs is occurring. Although this design results in somewhat higher pressure losses, it provides a known and constant point of flow separation, the dump plane, which prevents stalled operation at all diffuser entrance conditions. Figure 20.2.7 illustrates these contemporary designs.

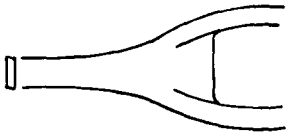

CURVED WALL DIFFUSER

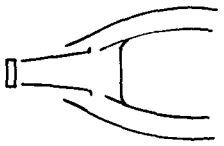

DUMP DIFFUSER

Figure 20.2.7 Contemporary Diffuser Designs

The design procedures commonly employed to develop a specific diffuser configuration involve the use of a combination of experimentally generated performance maps, empirical equations, and analytical models. Most available performance maps were generated for two -dimensional straight wall and conical diffusers, the most notable source being the work of Klein and his associates (Ref. 20.7). Until recent years, empirical results such as those illustrated in Figure 20.2.6 have been used in the development of annular diffusers. However, with the advent of improved numerical methods and high speed computers, a number of improved two-dimensional and three-dimensional analytical models are now being developed which more accurately describe the flow-field characteristics of the annular diffuser design. Such programs will provide improved analysis of pressure loss characteristics inlet velocity profile effects and the influence of turbulence level on diffuser performance.

The need for high performance in short compact diffusers takes on increasing importance as future engine operating conditions become more and more severe. An advanced compact diffuser design which provides improved boundary layer control and greater pressure recovery is described in 20.4.3.2.

20.2.2.2 Dome and Snout--At the front of the combustion chamber is the snout and dome where air and fuel are initially introduced. The snout is actually a forward extension to the dome dividing the incoming air into two streams--one directly entering the primary zone of the combustor through air passages in the dome. the other entering the annulus around the combustor. The snout also improves diffusion by streamlining the combustor dome, permitting a larger diffuser divergence angle and providing reduced overall diffuser length. The dome plate contains provisions for receiving the fuel injector and maintains its alignment during operation. Combustor domes are of two basic types--bluff-body and swirl stabilized as illustrated in Figure 20.2.8. Early combustors like the J79 (Figure 20.1.4) generally fall into the bluff-body class wherein the high blockage dome plate establishes a strong wake region providing primary zone recirculation. In effect, the bluff-body dome interacts with the first row of primary zone air holes to establish this strong recirculation region. Most contemporary combustors, however, utilize the swirl-stabilized dome. With this design, the fuel-injector is surrounded by a primary air swirler. The air swirler sets up a strong swirling flow field around the fuel nozzle generating a centralized low pressure zone which draws or recirculates hot combustion products into the dome region. As a result, an area of high turbulence and flow shear is established in the vicinity of the fuel nozzle finely atomizing the fuel spray and promoting rapid fuel-air mixing.

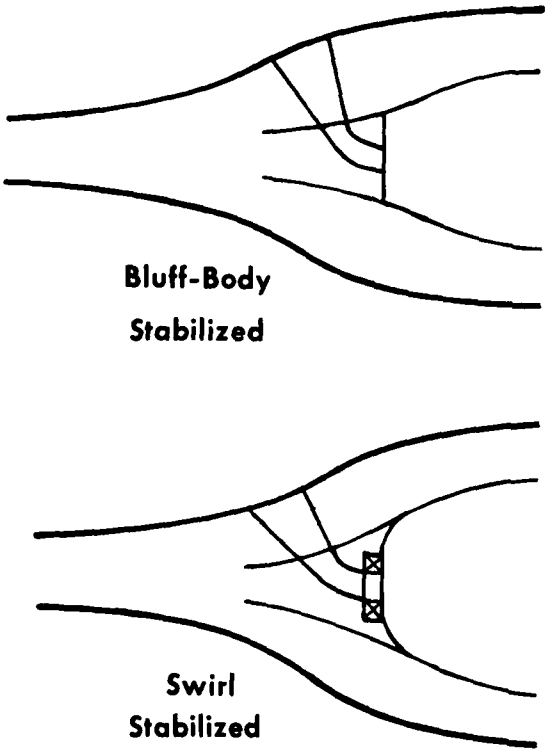

Figure 20.2.8 Combustor Dome Types

20.2.2.3 Liner: The liner provides containment of the combustion process and allows introduction of intermediate and dilution air flow. Contemporary liners are typically of sheet-metal braze and welded construction. The liner is mounted to the combustor dome and generally suspended by a support and seal system at the turbine nozzle entrance plane. Its surface is often a system of holes of varying sizes which direct

primary, intermediate, dilution, and liner cooling air into the combustion chamber. While combustion gas temperatures may be in excess of 2500°K, the liner is protected by a continuous flow of cool air (at approximately compressor exit temperature levels) and maintained at temperatures less than 1200°K.

The liner must be designed with high structural integrity to support forces resulting from pressure drop and must have high thermal resistance capable of continuous and cyclic high temperature operation. This is accomplished through utilization of high strength, high temperature oxidation-resistant materials and effective use of cooling air. Depending upon the temperature rise requirements of the combustor, 20-50 percent of the inlet airflow may be utilized in liner cooling. A number of cooling techniques are illustrated in Figure 20.2.9.

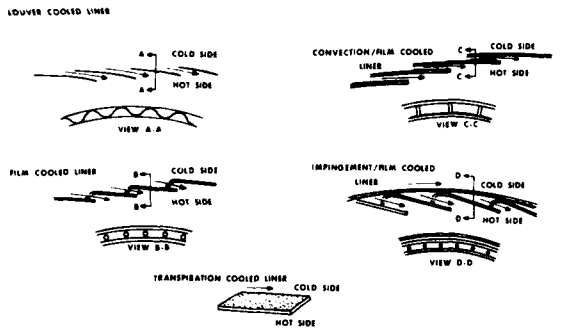

Figure 20.2.9 Combustor Cooling Techniques

a. Louver Cooling--Many of the early jet engine combustors used a louver cooling technique in which the liner was fabricated into a number of cylindrical panels. When assembled, the liner contained a series of annular air passages at the panel intersection points, the gap heights of which were maintained by simple wiggle-strip louvers. This permitted a film of air to be injected along the hot side of each panel wall providing a protective thermal barrier. Subsequent injection downstream through remaining panels permitted replenishment of this cooling air boundary layer. Unfortunately, the louver cooling technique did not provide accurate metering of the cooling air which resulted in considerable cooling flow nonuniformity with attendant variations in combustor exit profiles and severe metal temperature gradients along the liner.

b. Film Cooling--This technique is an extension of the louver cooling technique but with machined injection holes instead of louvers. Consequently, airflow metering is more accurate and uniform throughout the combustion chamber. Most current combustors use this cooling technique. However, increased operating gas temperatures of future combustors will result in less air for cooling and more advanced cooling techniques/materials will be required.

c. Convection/Film Cooling--This relatively new technique* permits much reduced cooling air flow (15 - 25 percent) while providing high cooling effectiveness and uniform metal temperatures. It is particularly suited to high temperature rise combustion systems where cooling air is at a premium. The convection/film cooled liner takes advantage of simple but controlled convection cooling enhanced by roughened walls while providing the protective boundary layer of cool air at each cooling panel discharge plane. Although somewhat similar in appearance to the louver cooled liner, the confection/film coolant passage is several times greater; more accurate coolant metering is provided and a more stable coolant film is established at the panel exit. Principal disadvantages of this design are somewhat heaver construction, increased manufacturing complexity and repairability difficulties.

d. Impingement/Film Cooling--This cooling technique is also well suited to high temperature rise combustors. When combined with the additional film cooling feature, impingement cooling provides for excellent thermal protection of a high temperature liner. Its disadvantages, however, are similar to those of the film/convection liner--heavier construction, manufacturing complexity and repairability difficulties.

e. Transpiration Cooling-- This is the most advanced cooling scheme available and is particularly well-suited to future high temperature applications. Cooling air flows through a porous liner material, uniformly removing heat from the liners while providing an excellent thermal barrier to high combustion gas temperatures. Both porous (regimesh and porolloy) and fabricated porous transpiring materials (Lamilloy**) have been examined experimentally. Fabricated porous materials tend to alleviate plugging and contamination problems, inherent disadvantages of the more conventional porous materials.

Figure 20.2.10 shows the axial thermal gradient characteristics of each of the liner designs discussed above as a function of relative liner length. As can be seen, transpiration cooling offers better temperature control and uniformity than any other cooling technique.

20.2.2.4 Fuel Injection--Basically four methods of fuel introduction are currently used or proposed for future use. These techniques--pressure atomizing, air blast, vaporizing, and premix/prevaporizing--are discussed below in increasing order of complexity. Each of these is illustrated in Figure 20.2.11.

a. Pressure Atomizing--Most contemporary combustion systems use pressure atomizing fuel injectors. They are relatively simple in construction, provide a broad flow range and can provide excellent fuel atomization when fuel system pressures are high. A typical pressure atomizing fuel injector is illustrated in Figure 20.2.12. At least five different design concepts or variations are included in this category: simplex, duplex, dual

* Patent Pending--Patent Application Numbers SN 876,264 & SN 298,434, titled "Combustion Liner"

**Developed by Detroit Diesel Allison, Div of GMC, Patent Number 3,584,972, titled "Laminated Porous Material," 15 June 1971.

orifice, variable area, and slinger. These devices typically utilize high fuel pressure (about 500 psi above combustor pressure) to achieve fine fuel atomization. The slinger design, although a pressure atomizing type, is very different from the conventional fuel nozzle in that the fuel is injected through small holes in the rotating turbine shaft. The high centrifugal forces imparted to the fuel provide atomization. Slinger systems are used in several small engine combustors--the WR19 of Figure 20.1.6 is one such system. The principal disadvantages of the pressure atomizing systems are the propensity for fuel system leaks due to the inherently high fuel pressures required, potential plugging of the small fuel orifices by contaminants entrained in the fuel, and increased difficulty in achieving low smoke levels when fuel system pressures are low.

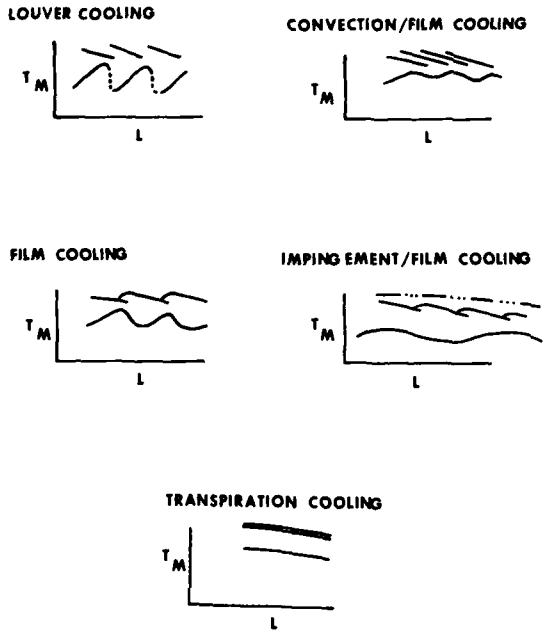

Figure 20.2.10 Liner Cooling Characteristics

b. Airblast--A number of modern combustor designs achieve fuel atomization and mixing through use of primary zone air momentum. Strong swirling motion, often accompanied by a second counter swirl, causes high gas dynamic shear forces to atomize liquid fuel and promote mixing. Low fuel injection pressures (50 - 200 psi above combustor pressure) are utilized in these schemes. Rizkalla and Lefebvre (Ref 20.8, 20.9) describe airblast atomizer spray characteristics relative to air and liquid property influences. In addition, the development of a specific airblast atomizer for gas turbine application is discussed in Reference 20.10.

c. Vaporizing: A number of vaporizing fuel injection systems have been developed; perhaps the most common is the "candy-cane" vaporizer. In this design, fuel and air are introduced into a cane-shaped tube immersed in the combustion zone. During operation, the heat transferred from the combustion region partially vaporizes the incoming fuel, while the liquid/vapor fuel within the tube provides thermal protection for the tube. It is generally agreed, however, that fuel vaporization is very much incomplete in this type vaporizer and is considered by many to be merely an extension of the airblast principles described above. This design is simple in construction, inexpensive, and can operate with low fuel injection pressures. The resultant fuel-air mixture burns with low flame radiation reducing liner heat loads. This design, however, has certain serious shortcomings: poor ignition and lean blowout characteristics, vaporizer tube durability problems during low fuel flows, and slow system response time.

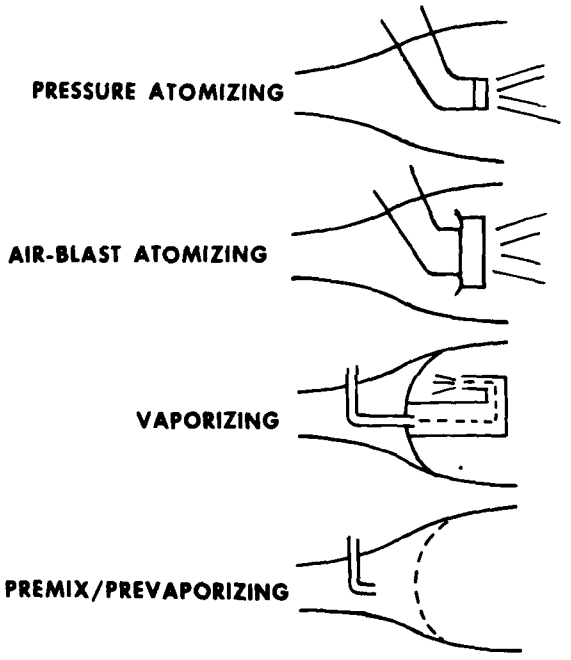

Figure 20.2.11 Fuel Injection Methods

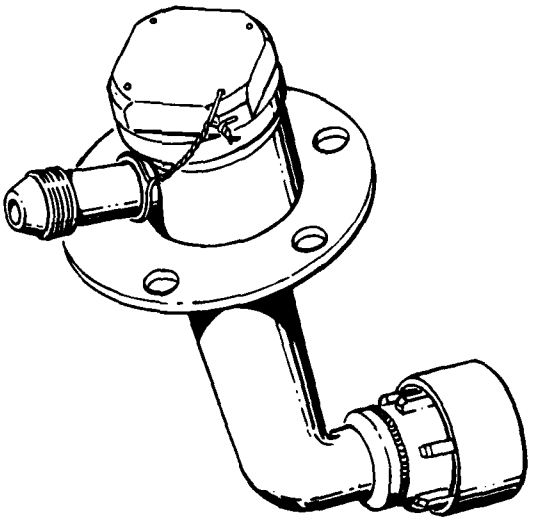

Figure 20.2.12 Pressure Atomizing Fuel Injector

d. Premix/Prevaporizing--The advent of gas turbine emission regulations has resulted in increased interest in premix/prevaporizing fuel injection. In this technique, fuel is introduced and premixed with the incoming air prior to introduction to the combustion zone. The design intent is to provide a uniform, low equivalence ratio, fully mixed field of vaporized fuel in the combustion region. As a result, low smoke and chemical emissions, low flame radiation, improved fuel-air uniformity in the combustion region and virtual elimination of hot-spot burning occurs. Potential problem areas with this system include incomplete fuel vaporization, danger of flashback through or auto ignition of the fuel-air premixture upstream of the combustor dome plate with resulting damage to the combustor hardware, poor lean blowout characteristics, and difficulty with ignition and altitude relight. Staged combustion, utilizing a pilot zone with a relatively conventional stoichiometric design, is often proposed as a method of overcoming stability and ignition difficulties.

20.2.2.5 Ignition: Ignition of the cold flowing fuel-air mixture can be a major combustor design problem. Nearly all conventional combustors are ignited by a simple spark-type igniter similar to the automotive spark plug. Turbine engine ignition energies are typically 4 to 12 joules with several thousand volts at the plug tip. Figure 20.2.13 illustrates a typical spark type igniter.

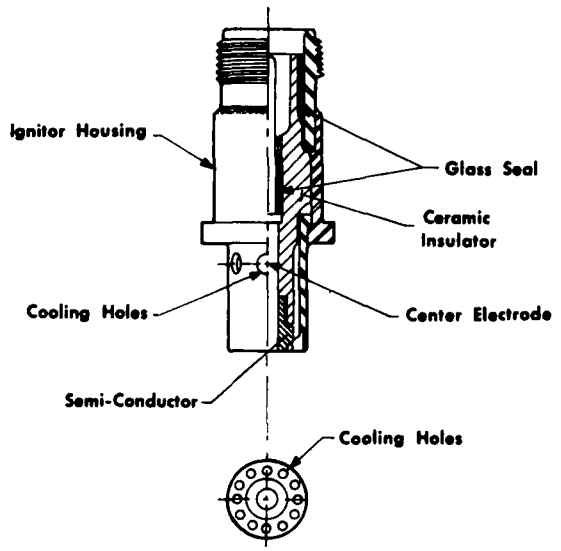

Figure 20.2.13 Spark Igniter

Each combustion system is generally fitted with two spark igniters to provide system redundancy. Potential ignition system problems include spark plug fouling with carbon or fuel, plug tip burn-off, electrode erosion with time and corona-discharge losses along the ignition system transmission lines under high altitude, low pressure conditions.

During engine start-up, the flame must propagate from can-to-can in a cannular combustion system via cross-fire or inter-connector tubes located near the dome of each can. The large cross-fire ports of the J79 are readily visible in Figure 20.1.4. The cross-fire region must be designed to insure rapid and complete flame propagation around the combustion system. Without proper cross-firing, a "hung start" can occur wherein only one or two combustors are ignited. This condition of poor flame propagation can also occur in annular combustors. In either case, severe local gas temperatures (high pattern factor) are generated which can thermally distress the turbine.

Although the spark igniter is the most common ignition source in use today, a number of other ignition or ignition-assist techniques have been employed: the torch igniter, oxygen injection, and the use of pyrophoric fuels. The torch ignitor, a device combining the functions of fuel injection and spark ignition, is extremely reliable and permits a wide ignition envelope. However, it is more complex and costly and increases maintainability problems relative to conventional ignition systems. Oxygen injection assists ignition by lowering minimum ignition energy requirements. It is especially applicable to facilitating altitude relight. The use of pyrophoric fuels provides perhaps the most positive ignition source available. Pyrophorics will react spontaneously in the presence of oxygen and provide excellent altitude relight capability. Unfortunately, pyrophoric fuels are extremely toxic and create special handling and logistics problems. Consequently, these factors have limited its use as a viable ignition technique.

20.2.2.6 Materials: The selection of proper materials is a critical element in combustion system design for component structural integrity. Materials which possess high stress tolerance, good oxidation and corrosion resistance, and the ability to withstand the broad cyclic aero-thermal loads imposed by the engine during its operation are required. Several high strength alloy materials are used in combustors today, the selection of which is generally based on the projected operating environment of the propulsion system. This section will highlight a few of the more common combustor materials in use today.

a. Hastelloy X--Hastelloy X is a nickel-base alloy strengthened in solid solution by chromium and molybdenum. It is the most common combustor liner material in use today. Its formability is good, its machinability is difficult but not impractical and its weldability and brazing characteristics are good. Hastelloy X exhibits good strength and oxidation properties in the 1040°K to 1140°K metal temperature range. Most combustors with Hastelloy X liners are designed to operate at metal temperatures of 1090°K to 1120°K.

b. Haynes 188: Haynes Alloy 188 is a wrought solid, solution strengthened, cobalt-base alloy applicable to static parts operating at temperatures up to 1370°K. It can be readily formed and welded, its oxidation resistance is good although protective coatings are required for applications above 1250°K, and like Hastelloy X, its machinability is difficult but not impractical. It is finding increased applicability in the newer combustion systems where liner metal temperatures of 1140°K to 1230°K are necessary.

c. TD Nickel: This super alloy is a non-heat-treatable, high nickel alloy strengthened by dispersion of fine ThO_2 particles in a nickel matrix. This alloy maintains useful strengths at temperatures up to 1420°K. Its oxidation-erosion resistance is inferior to

Hastelloy X or Haynes 188 and requires protective coatings for applications above 1220°K. Its machinability and formability are good. Fusion and resistance welding of this material can be difficult; however, its brazeability is considered good. TD Nickel offers considerable promise in future high temperature liner applications where metal temperatures greater than 1250°K may be common. Current material costs and the need for protective coatings, however, have generally precluded serious consideration of TD Nickel in contemporary combustion systems. Further, advanced liner cooling techniques have succeeded in maintaining metal temperatures at levels consistent with the Hastelloy X/Haynes 188 material capabilities.

Significant advancements in super alloy technology are required to meet future high temperature rise combustor requirements. New materials well beyond the capability of TD Nickel will be necessary. Improved coatings may provide part of the solution if developed with long life and improved high and low cycle fatigue capabilities. Ceramics and advanced thermal barrier and coating materials may also find a role in future combustor design.

20.3 DESIGN TOOLS

The complexity of the aerothermodynamic and chemical processes occurring simultaneously in the combustor prevent a purely analytical approach to component design and performance prediction. Insufficient capability to accomplish measurements of importance within the combustor has precluded all but the most basic understanding of practical gas turbine combustion processes. As a result, one has had little choice but to formulate new designs largely on the basis of personal or organizational experience. Continuation of this approach to combustor design for high temperature sophisticated systems under development today and in the future would be extremely costly and time consuming. The turbine engine industry can no longer afford to conduct component development activities on a generally empirical basis. Hence, significant R&D programs are now being directed toward developing improved analytical design procedures reinforced by more powerful measurement diagnostics.

20.3.1 Combustor Modeling

The principal objective of the combustion system model is to analytically describe and predict the performance characteristics of a specific system design based on definable aerodynamic, chemical, and thermodynamic parameters. Many modeling approaches describing the flow field and characteristics of a particular combustion system have evolved over the past twenty years. Early models were almost entirely empirical while the newest models currently under development are based more on fundamental principles. Improved computer availability and capability as well as more efficient numerical techniques have had a significant impact on combustion modeling by permitting the more complex, theoretically-based approaches to be considered.

20.3.1.1 Empirical: The empirical model utilizes a large body of experimental data to develop a correlation often using multiple-regression analysis techniques. Such an approach involves a selection of the appropriate design and aerothermodynamic parameters which have been empirically found to influence the performance (e.g., combustion efficiency) of a particular combustor design. Each of the non-dimensionalized parameters or ratios are acted upon by appropriate "influence" coefficients or exponents, the value of which reflects the degree of importance of a particular parameter. Since these influence terms are usually derived from test data obtained from combustors which generally represent the same basic design family, a major change in design philosophy can require the definition of a new set of influence factors. Consequently, this modeling approach works well on specific combustor designs for which there is a broad base of technical data. Unfortunately, it cannot be arbitrarily used as a general design tool. One example of an empirical correlation model is illustrated in Figure 20.3.1. In this model, combustion system efficiency is defined as a function of the more important combustor design and performance parameters. As can be seen, the model is written in general form and a tabulated listing of appropriate coefficients and exponents is provided to permit the computation of combustion efficiency. Again, these influence terms are empirically based and were derived from a bank of combustor data representative of a particular class of combustors.

$$E.C. = C \left(\frac{W_3\sqrt{P_3A}}{4.7}\right)^A \left(\frac{T_3}{1000}\right)^B \left(\frac{\Delta T}{1000}\right)^C \left(\frac{L_c}{12}\right)^D \left(\frac{\Delta P/Q_R}{10}\right)^E \left(\frac{N_r/A_R}{10}\right)^F \left(\frac{W_1/W_3}{0.5}\right)^G \left(\frac{N_R}{6}\right)^H$$

DETERMINE: COMBUSTION EFFICIENCY

	ΔT: 600° to 1600°F	ΔT: 1600° to 2500°F
C	0.88	0.79
A	0.0	0.04
B	0.22	-0.04
C	0.11	-0.09
D	0.14	0.16
E	0.07	0.07
F	-0.07	0.0
G	-0.10	0.23
H	0.0	0.0

Figure 20.3.1 Empirical Combustion Efficiency Correlation

A second empirical correlation employed by some combustor designers today defines a reaction rate parameter (θ) based on the "burning velocity" theory of Lefebvre (Ref 20.11). The θ-parameter is given in Figure 20.3.2. The resulting correlation establishes the relationship between combustor efficiency, operating condition and geometric size. One can see that efficiency is not only a function of airflow, inlet pressure, and inlet temperature, but also is strongly dependent on combustion zone fuel-air ratio. Herbert (Ref 20.12) estimated the effect of equivalence ratio on reaction rate by the following equation:

$$b = 220\ (\sqrt{2} + \ln \phi/1.03), \qquad (20.3.1)$$

where ϕ is primary zone equivalence ratio. A graphic illustration of the above expression (Figure 20.3.3) describes the variation of b with primary zone equivalence ratio. Hence, to achieve maximum efficiency, a primary zone fuel-air ratio of 0.067 (ϕ = 1) should be used.

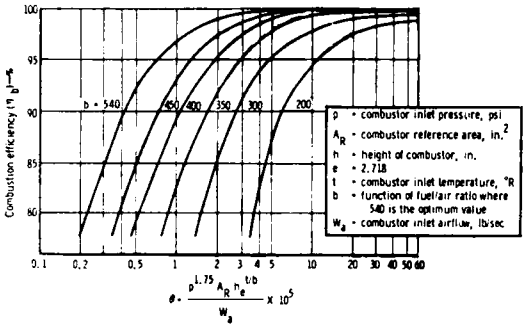

Figure 20.3.2 Prediction of Combustion Efficiency Using θ--Parameter

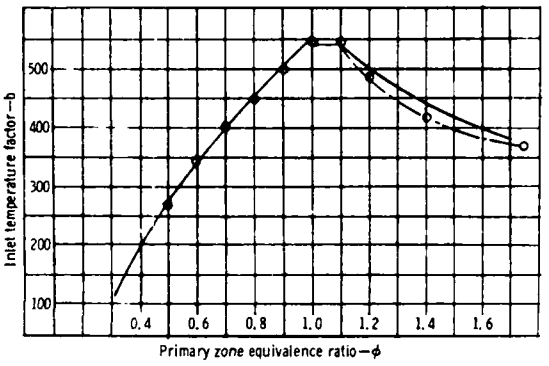

Figure 20.3.3 Effect of Primary Zone ϕ on Inlet Temperature Factor

20.3.1.2 Combined Empirical/Theoretical: More complex theoretical descriptions of combustion must be incorporated into combustor models to allow predictions based on hardware design details. Physical models of important combustion processes (i.e., a "perfectly stirred reactor" primary zone) combined with available empirical analyses result in hybrid models. A number of two-dimensional models have been developed in recent years ranging from the perfectly-stirred reactor plug flow models (Ref 20.13) to the more complex axisymmetric combustor flow-field calculations which account for heat, mass, and momentum transfer between fluid streams and include chemical reaction kinetic effects (Ref 20.14, 20.15). One such axisymmetric stream tube model was developed by Pratt & Whitney Aircraft in support of an Air Force-sponsored combustor program (Ref 20.16). Figure 20.3.4 is the flow chart of computational steps for this analytical model illustrating the increased complexity of this procedure wherein both theory and experiment have been integrated. It is currently being used as an engineering tool for both current and advanced combustor design and exhaust emission analyses.

Another more recently developed model leans even more heavily on combustion theory and advanced numerical procedures. Anasoulis et al (Ref 20.17) developed a two-dimensional computational procedure for calculating the coupled flow and chemistry within both cannular and annular combustors. A field relaxation method is used to solve the time-average Navier-Stokes equations with coupled chemistry including the effects of turbulence, droplet vaporization and burning. Extensions to the three-dimensional case are also under development permitting more accurate descriptions of the recirculation and mixing zones of the combustor.

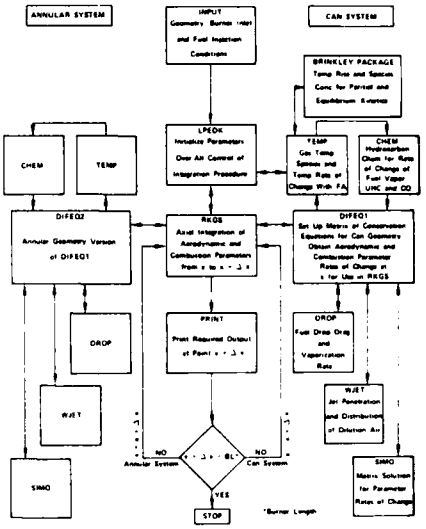

Figure 20.3.4 Combustor Model Computational Schematic

20.3.1.3 Theoretical: While Reference 20.17 represents a significant advancement, the fully theoretical computerized design procedure has not yet evolved. A building block approach, however, has been envisioned wherein a number of submodels (e.g., chemistry, turbulence, droplet vaporization, mixing, etc.) are developed independently, verified experimentally and then coupled with the other submodels. Each coupled submodel set would undergo an experimental validation process before the next submodel is added to the overall analytical procedure. The ultimate is a fully theoretical description of all reacting flow processes enabling prediction of overall combustor performance as a function of basic design parameters. Hence, prior to any hardware fabrication, the model will serve to evaluate the proposed combustion system design such that desired objectives will be met with a minimum of subsequent hardware iterations and fine tuning.

20.3.2 Combustion Diagnostics

Development of valid combustor models is hampered by difficulty in acquiring data for use in comparing and refining analytical solutions. Different types of measurements are required to validate various aspects of the important submodels; i.e., droplet size distribution, turbulence intensity, etc. In addition, improved instrumentation will be required to aid the combustor development process. Such equipment would provide the information on which the engineer will base subsequent design improvements and eventually the final version.

The rapidly growing field of combustion diagnostics will play an increasingly important role in satisfying the above objectives. Conventional thermocouple and sampling problems have been previously utilized to study combustion processes in practical systems. However, additional application and technique refinements are

necessary. Further, new, laser-based combustion diagnostic measurement equipment can be expected to play an important role in the future. Techniques such as laser Raman scattering and coherent anti-Stokes Raman scattering hold new promise for fundamental studies of combustion processes requiring real-time "point" (≈ 1 mm^3) measurements of temperature, concentration, and velocity. Other simpler methods may find application in measurement of combustor exit temperature profiles during combustion system development.

20.4 FUTURE REQUIREMENTS

The aero-propulsion combustion community is currently confronted with two new and difficult challenges: reduction of exhaust pollutant emissions and accommodation of new fuels which will reduce cost while increasing availability. The first two of the following three subsections summarize the problems and current state-of-the-art in each of these two areas. Further, projected engine technology requirements necessitate advancements in combustion system design techniques and performance. Section 20.4.3 addresses the combustion engineer's task in this area.

20.4.1 Exhaust Emissions

20.4.1.1 Problem Definition: In recent years, increased citizen concern over environmental issues coupled with the obvious visible smoke emissions from jet aircraft has brought substantial public attention to aircraft-contributed pollution. As airport traffic increased, it became evident that at least the possibility existed that pollutant emissions, when concentrated in the local airport environment, could result in ambient levels which exceed allowable limits. Concern within the United States culminated in the inclusion of exhaust emissions from aircraft engines in the considerations of the Clean Air Act Amendments of 1970 (Ref 20.18). This legislation requires that the Environmental Protection Agency (EPA) assess the extent to which aircraft emissions affect air quality, determine the technological feasibility of controlling such emissions and establish aircraft emissions standards, if necessary.

The resulting EPA assessment (Ref 20.19) has indicated the necessity to regulate commercial aircraft emissions. Currently, EPA standards (Ref 20.20) apply to commercial and general aviation but not to military aircraft. The following excerpt from EPA's discussion accompanying the final announcement of the aircraft emissions standards (Ref 20.20) summarizes this policy.

> In judging the need for the regulations, the Administrator has determined:
>
> (1) that the public health and welfare is endangered in several air quality control regions by violation of one or more of the national ambient air quality standards for carbon monoxide, hydrocarbons, nitrogen oxides, and photochemical oxidants, and that the public welfare is likely to be endangered by smoke emissions; (2) that airports and aircraft are now, or are projected to be significant sources of emissions of carbon monoxide, hydrocarbons, and nitrogen oxides in some of the air quality control regions in which the national ambient air quality standards are being violated, as well as being significant sources of smoke, and therefore (3) that maintenance of the national ambient air quality standards and reduced impact of smoke emissions requires that aircraft and aircraft engines be subject to a program of control compatible with their significance as pollution sources. Accordingly, the Administrator has determined that emissions from aircraft and aircraft engines should be reduced to the extent practicable with present and developing technology. The standards proposed herein are not quantitatively derived from the air quality considerations ... but, instead, reflect EPA's judgment as to what reduced emission levels are or will be practicable to achieve for turbine and piston engines.

Current EPA regulations are based on reducing aircraft engine emissions during their operation below 3000 feet. However, an additional potential problem has been associated with aircraft--the possible environmental impact of high altitude emissions (Ref 20.21). There are many mechanisms by which this might arise: (a) emission of water vapor and carbon dioxide into the stratosphere may cause a "greenhouse effect." (b) sulphur compound emissions can cause particulate formation which would cause solar radiation to be diverted away from the earth's surface reducing the equilibrium atmospheric temperature, and (c) increased concentrations of water vapor and oxides of nitrogen due to emissions into the stratosphere might deplete the ozone layer and allow increased penetration of solar ultraviolet radiation. Potential problem (a) has been shown not to be significant. Much more investigation is needed concerning (b) and (c), however, before the extent of potential stratospheric environmental problems can be suitably defined.

The discussion which follows defines the exhaust gas content, presents engine emission characteristics, and reviews emissions control technology.

20.4.1.2 Exhaust Content: Aircraft engine exhaust constituents usually considered to be pollutants are smoke, carbon monoxide (CO), hydrocarbons (HC), and oxides of nitrogen (NO_x)*. The magnitude of emissions depends on operating mode and engine type. The combustion products are conveniently organized into five groups, as listed in Table 20.4.1. More than 99 percent of the exhaust products are in the first two categories, which include those species not generally considered to be objectionable. The last three categories contain small quantities of constituents and are dominated by the principal pollutants: hydrocarbons (HC), carbon monoxide (CO), oxides of nitrogen (NO_x), and smoke. Because emissions characteristics at engine idle, nonafterburning high power, and afterburning operation vary substantially, columns listing composition for each of these operating modes are given. Note that levels given in Table 20.4.1 correspond to the turbojet case or to the core flow only in the case of a turbofan.

* Exhaust nitrogen oxides are in the form of both NO and NO_2. Collectively, they are expressed as NO_x

TABLE 20.4.1 Engine Combustion Products

Group	Type	Species	Approximate Concentration: Low Power (Idle) Concentration	High-Power (non AB) Concentration	Cruise (With Afterburner) Concentration
1.	Air	N_2	77%	77%	73-76%
		O_2	17.3-19%	13-16.3%	0-13%
		Ar	.9%	.9%	.9%
2.	Products of Complete Combustion	H_2O	1.4-2.4%	3-5%	5-13%
		CO_2	1.4-2.4%	3-5%	5-13%
3.	Products of Incomplete Combustion	CO	50-2000 ppmv	1-50 ppmv	100-7000 ppmv
		Total HC	50-1000 ppmC	1-20 ppmC	100-1000 ppmC
		Partially Oxidized HC	25-500 ppmC	1-20 ppmC	?
		H_2	5-50 ppmv	5-100 ppmv	100-1000 ppmv
		Soot	.5-25 ppmw	.5-50 ppmw	.50-50 ppmw
4.	Non-hydrocarbon Fuel Components	SO_2, SO_3	1-5 ppmw	1-10 ppmw	1-30 ppmw
		Metals, Metal Oxides	5-20 ppbw	5-20 ppbw	5-20 ppbw
5.	Oxides of Nitrogen	NO, NO_2	5-50 ppmv	50-500 ppmv	100-600 ppmv

a. Group 1, Air: These species pass through the engine unaffected by the combustion process and unchanged in chemical composition, except for oxygen depletion due to fuel oxidation. Argon is clearly inert. Although molecular nitrogen is nearly inert, the less than 0.01 percent that undergoes "fixation" to its oxide form (Group 5) is, of course, extremely important.

b. Group 2, Products of Complete Combustion: Water and carbon dioxide are the dominant combustion products and the fully oxidized forms of primary fuel elements, hydrogen and carbon. It is the formation of these species that releases maximum energy from the fuel. H_2O and CO_2 are not generally considered to be air pollutants.

c. Group 3, Products of Incomplete Combustion: Hydrogen and carbon not converted to water or carbon dioxide are found in compounds categorized as products of incomplete combustion. The important species in this group are carbon monoxide, unburned and partially oxidized hydrocarbons, molecular hydrogen, and soot.

CO and HC emissions contain the largest portion of unused chemical energy within the exhaust during idle operation. Combustion efficiency at this operating condition may be calculated from exhaust CO and HC concentration data. At higher power settings, especially with afterburner operation, H_2 levels may also significantly contribute to inefficiency. Exhaust hydrocarbons are usually measured as total hydrocarbons as specified by the SAE ARP 1256 (Ref 20.22). Although it is well known that the toxicological and smog-producing potential of different hydrocarbon types varies widely, little work has been done to characterize the distribution of hydrocarbon types in the exhaust.* Presently available analytical techniques to accomplish such a characterization are complex, time consuming, expensive, and of unconfirmed accuracy.

A similar problem exists in quantifying soot emissions. The measurement technique that has evolved, ARP 1179 (Ref 20.23), does not directly relate to exhaust visibility or soot concentration. However, Champagne (Ref 20.24) has developed a correlation between measured ARP 1179 smoke number (SN) dry and particulate emissions. Efforts to measure and characterize particulate emissions directly are currently in progress. Complications have developed because the contribution of condensed hydrocarbons in the exhaust to the particulate measurement varies greatly with sampling conditions. Although a technique to determine exhaust soot concentrations may eventually be developed, characterization of size distribution appears to require a longer range effort.

d. Group 4, Non-Hydrocarbon Fuel Components: The elemental composition of petroleum-based fuel is predominantly hydrogen and carbon. Of its trace components, sulfur is the most abundant. Most of the sulfur in the exhaust is in an oxidized form, probably as sulfur dioxide. Giovanni and Hilt (Ref 20.30) and Glasser (Ref 20.31) have found that the ratio of SO_3 to SO_2 is from 0.02 to 0.14 in the case of heavy-duty stationary and aircraft gas turbines. The total amount of sulfur in exhaust compounds is directly related to, and calculable from, fuel sulfur content. The second most abundant

*Existing data can be found in Boudon and McAdams (Ref 20.25), Groth and Robertson (Ref 20.26), Kendall and Levins (Ref 20.27), Price and Kendall (Ref 20.28), and Katzman and Libby (Ref 20.29).

AD-A152 757 COST REDUCTION IN VERTICALLY RELATED INDUSTRIES: INTEGRATION VERSUS NONLINEAR PRICING(U) RAND CORP SANTA MONICA CA H C QUIRMBACH MAY 83 RAND/P-6839 7/9

UNCLASSIFIED F/G 5/1 NL

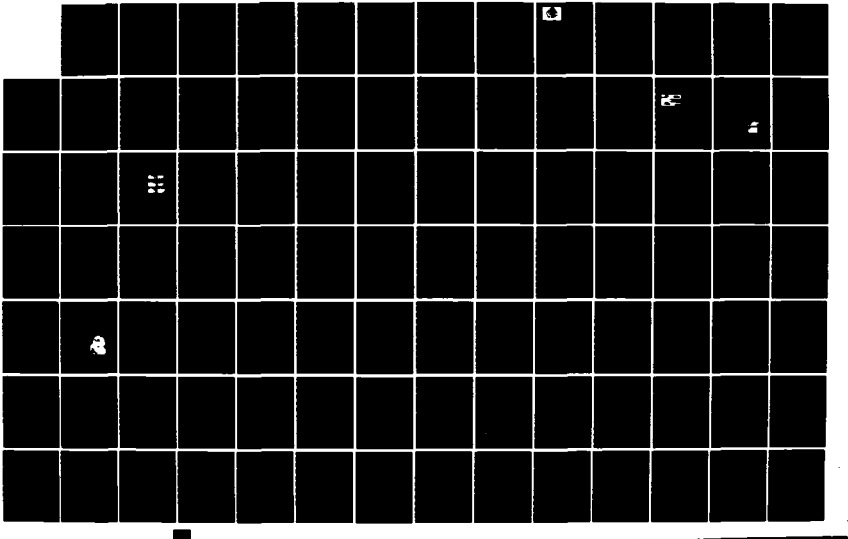

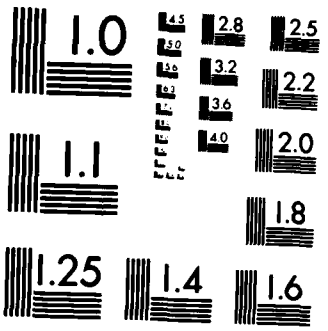

MICROCOPY RESOLUTION TEST CHART
NATIONAL BUREAU OF STANDARDS-1963-A

trace component of non-hydrocarbon fuel involves metals. It is expected that these elements, which may be either natural components of the fuel or additions to it, appear in the exhaust as metal oxides. Further, it is generally expected that these species are particulates and often found with the soot.

e. Group 5, Oxides of Nitrogen: Although the ratio of NO to NO_2 emitted by aircraft gas turbines may shift with operating conditions, NO will eventually be converted to NO_2 in the atmosphere and subsequently participate in smog formation chemistry. Some attention, however, must be paid to the influence of time delay required for atmospheric NO_2 formation and the subsequent effect on smog formation. Stratospheric NO and NO_2 emissions are generally thought to have equally detrimental effects.

As stated above, product species are usually measured in terms of their volume (or sometimes mass, especially for condensed phases) fraction in the product sample. Occasionally, the suffix "dry" or 'wet" is appended, according to whether or not the water is removed before analysis. A more useful and unambiguous method of reporting exhaust emissions from gas turbines has proved to be the use of an emission index which represents the ratio of the pollutant mass to the fuel consumption. A commonly used dimension is grams of pollutant per kilogram of fuel. Conversion of volume fraction measurements to emission indices requires assignment of molecular weights, which is not difficult for a single compound category, but may lead to confusion for categories consisting of more than one compound. It is conventional to report oxides of nitrogen (NO_x) as though they were entirely NO_2. Similarly, the oxides of sulfur (SO_x) are usually reported as SO_2. Hydrocarbon measurements usually lead to a volumetric fraction related to a single hydrocarbon compound; e.g., parts per million equivalent hexane (or methane, propane, carbon atom, etc.). In reducing these measurements to an emission index, a hydrogen-carbon ratio of two is usually assumed.

20.4.1.3 Engine Emissions Chracteristics: Processes that influence pollutant formation occur within both the main burner and afterburner. Conditions under which combustion occurs in these two systems are extremely different, and studies of emissions from the main burner and augmentor are generally treated separately.

a. Main Burner Emissions: Carbon monoxide and hydrocarbon emissions are a strong function of engine power setting. As thrust is increased, the combustion system experiences greater inlet temperature and pressure, as well as higher fuel-air ratio. The increased fuel flow results in improved fuel atomization and higher combustor inlet temperature provides more rapid vaporization. Chemical reaction rates responsible for CO and HC consumption are sharply increased by higher flame temperatures resulting from the greater fuel-air ratio (See Section 15.1 of Chapter 15). Each of these changes tends to decrease the rates at which HC and CO are emitted. Consequently, the relationship between an engine's emission of HC and CO (or combustion inefficiency) and power setting indicates a sharply decreasing trend. Idle CO and HC emissions far exceed that at other engine conditions. A correlation of idle CO and hydrocarbon emissions for a number of engines can be established by plotting these values as a function of combustor inlet temperature. Figure 20.4.1 illustrates the trends that can be obtained.

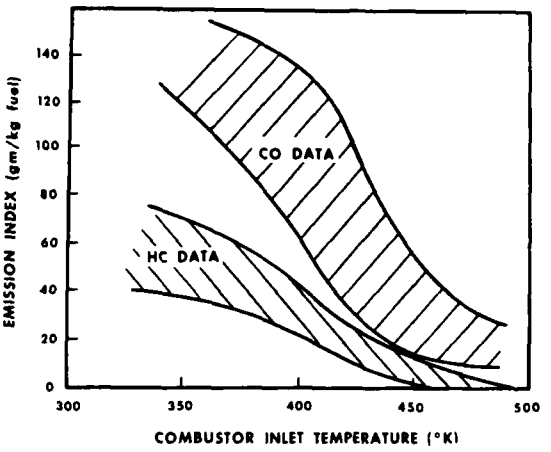

Figure 20.4.1 CO and HC Idle Emissions

As discussed in Chapter 15, combustion efficiency can be related to exhaust content. In the case of idle operation, the inefficiency is predominantly due to CO and HC. The idle CO and HC emission index values can be related to combustion inefficiency by the following equation:

$$1 - \eta_b = [0.232\ (EI)_{CO} + (EI)_{HC}] \times 10^{-3} \qquad (20.4.1)$$

where: η_b = Combustion efficiency

$1 - \eta_b$ = Combustion inefficiency

$(EI)_i$ = Emission index of species i.

Oxides of nitrogen emission levels are greatest at high-power operating conditions. The predominant NO forming chemical reaction is:

$$N_2 + O \rightarrow NO + N \qquad (20.4.2)$$

It is usually assumed that NO formation takes place in regions of the combustor where oxygen atoms are present at their equilibrium concentration. Reaction 20.4.2 and the oxygen atom concentration are extremely temperature sensitive; NO is produced only in the highest temperature (near-stoichiometric) combustion zones. Since the stoichiometric flame temperature is dependent on combustor inlet temperature (a function of compressor pressure ratio and flight speed) oxides of nitrogen emissions can be expected to increase substantially with power setting.

An excellent correlation of NO_x emissions from a large number of engines has been established by Lipfert [Ref 20.4]. This correlation, reproduced in Figure 20.4.2, relates NO_x emission index to combustor inlet temperature and the stoichiometric temperature rise of the fuel burned. However, the data base used to

design has little apparent effect on NO_x emission is noteworthy. This implies that mixing and quenching processes within combustors operating with rich (ϕ>1.0) primary zones are strikingly similar; the temperature effect alone controls the NO_x emission rate. No strong fuel effects are apparent from existing data. However, it has been shown that fuel-bound nitrogen is readily converted (50 to 100 percent) to NO_x in both stationary and aircraft turbine combustors (Ref 20.33 - 20.36). Should aircraft fuel-bound nitrogen levels be increased in the future because of changing fuel requirements, fuel-bound nitrogen could become a significant problem (See Section 20.4.2).

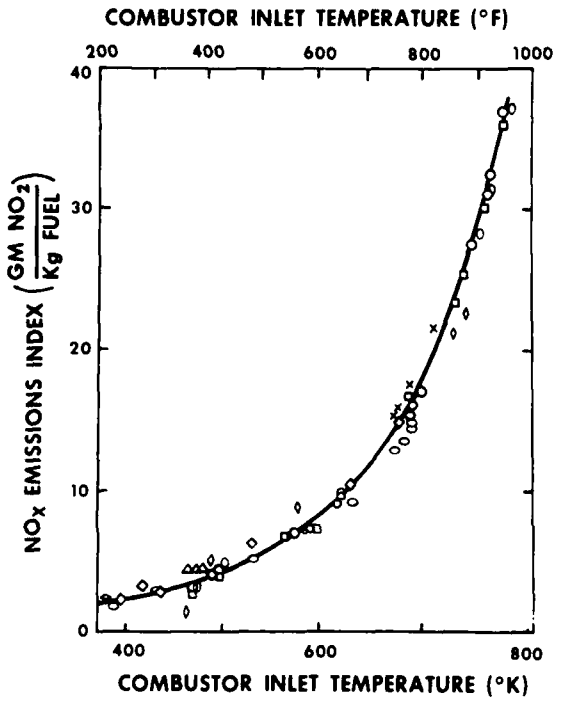

Figure 20.4.2 Correlation of Current Engine NO_x Emissions with Combustor Inlet Temperature

The dependence of NO_x emission on combustor inlet temperature is reflected in a strong relationship with cycle pressure ratio at sea level conditions and with cycle pressure ratio and flight Mach number at altitude. Figure 20.4.3 illustrates the relationship between NO_x emission and cycle pressure ratio at sea level static conditions. Figure 20.4.4 presents the dependence of NO_x emission on cycle pressure ratio and flight Mach number. Since the optimum pressure ratio increases with flight Mach number which, in turn, is dictated by economic considerations, a higher temperature operating condition at the high flight Mach number sea level condition is indicated in Figure 20.4.4.

Smoke formation is governed by local fuel-air ratio and pressure. In a lean combustion, the heavy molecular weight fuel molecules are subjected to intense heating and pyrolysis (breakdown of fuel molecules). If this process occurs in the absence of sufficient oxygen (i.e., high fuel-air ratio), the small hydrogen fragments can form carbon particulates which eventually result in smoke emission. The process by which carbon particulates are formed is known to be very pressure sensitive. Combustor designers have been successful in tailoring the burner to avoid fuel-rich zones, thus substantially reducing smoke levels. The current generation of engines (JT9D, CF6, RB211) has nearly invisible exhaust trails. The techniques resulting in these improvements will be highlighted in a subsequent subsection.

b. Afterburning Engines: Relatively little information is available regarding emission during afterburner operation. General trends in existing data indicate possible significant levels of CO and HC at the exhaust plane, especially at the lower afterburner power settings (Ref 20.37 - 20.41). However, Lyon (Ref 20.41) has confirmed that, at sea level, much of the CO and HC is chemically reacted to CO_2 and H_2O in the exhaust plume downstream of the exhaust plane. These downstream reactions have been shown to consume up to 93% of the pollutants present at the exhaust plane. The extent of these plume reactions at altitude is uncertain. Although lower ambient pressures tend to reduce chemical reaction rates, reduced viscous mixing and the exhaust plume shock field tend to increase exhaust gas time at high temperature and thus reduce the final emission of incomplete combustion products.

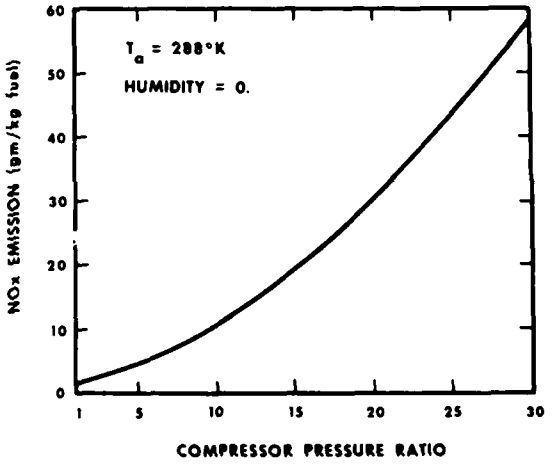

Figure 20.4.3 Dependence of Sea Level Standard Day NO_x Emissions on Compressor Pressure Ratio of Current Engines

NO_x emission during afterburner operation expressed on an EI basis is lower than during non-afterburning operation because of reduced peak flame temperatures in the afterburner. The value, under sea-level conditions, is approximately 2 - 5 g/kg fuel (Ref 20.42). At altitude, it is expected that the emission index would be 3.0 or less. Duct burners are expected to have an NO_x EI of about 5.0 during altitude operation (Ref 20.42). While the total NO_x emission is not significantly influenced by plume reactions, there is speculation that conversion of NO to NO_2 occurs both within the afterburner and in the plume (Ref 20.41).

Smoke or carbon particle emissions are reduced by the use of an afterburner (Ref 20.41). Conditions within an afterburner are not conducive to carbon particle formation, but soot from the

main burner may be oxidized in the afterburner, thus resulting in a net reduction.

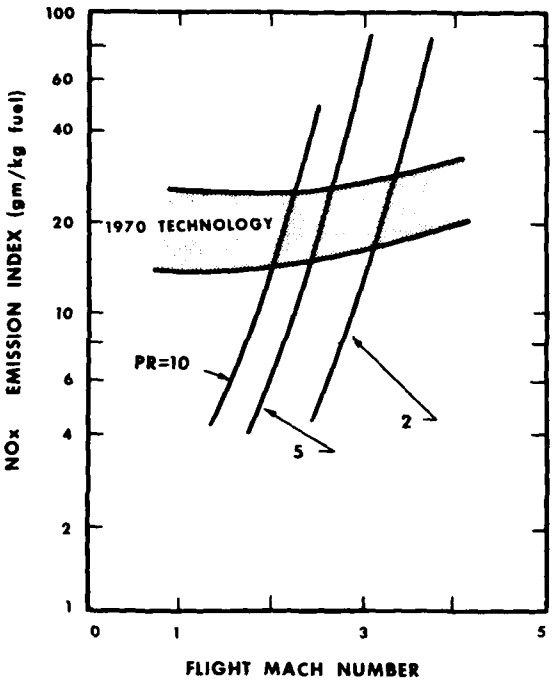

Figure 20.4.4 Dependence of NO_x Emission on Flight Mach Number

20.4.1.4 *Minimization of Emissions:* Previous discussions of emissions levels concerned existing engines. Control technology may reduce emissions from these baseline levels by varying degrees. The fundamental means by which emissions may be reduced are discussed in this section.

a. *Smoke Emission:* Technology to control smoke emission is well in hand and it would appear that future engines will continue to be capable of satisfying the future requirement of exhaust invisibility. The main design approach used is to reduce the primary zone equivalence ratio to a level where particulate formation will be minimized. Thorough mixing must be accomplished to prevent fuel-rich pockets which would otherwise preserve the smoke problem, even with overall lean primary zone operation. This must be done while maintaining other combustor performance characteristics. Airflow modification to allow leaner operation and airblast fuel atomization and mixing have been employed to accomplish these objectives. However, ignition and flame stabilization are the most sensitive parameters affected by leaning the primary zone and must be closely observed during the development of low smoke combustors.

b. *HC and CO Emission:* To prevent smoke formation, the primary zone equivalence ratio of conventional combustors at higher power operation must not be much above stoichiometric--this leads to much lower than stoichiometric operation at idle where overall fuel-air ratios are roughly one-third of the full-power value. Inefficient idle operation may be improved by numerous methods. The objectives in each technique are to provide a near-stoichiometric zone for maximum consumption of hydrocarbons while allowing sufficient time within the intermediate zone (Where ϕ = 0.5) to allow for CO consumption.

To achieve increased localized fuel-air ratio, dual orifice nozzles are frequently applied to modify fuel spray patterns at idle. Attempts to improve fuel atomization also provide decreased idle HC and CO through more rapid vaporization (Ref 20.43). Greater local fuel-air ratios at idle can also be achieved by increased compressor air bleed or fuel nozzle sectoring. In this latter case, a limited number of nozzles are fueled at a greater fuel flow rate. Schemes where two 90° or one 180° sector is fueled have shown significant HC and CO reduction (Ref 20.44).

Advanced approaches make use of staged combustion. The first stage, being the only one fueled at idle, is designed for peak idle combustion efficiency. The second stage is only utilized at higher power conditions. This main combustion zone is designed with a primary motivation toward NO_x reduction. Significant HC and CO reductions have been demonstrated using the staged approach (Ref 20.45 - 20.50). An example of such a design is shown in Figure 20.4.5.

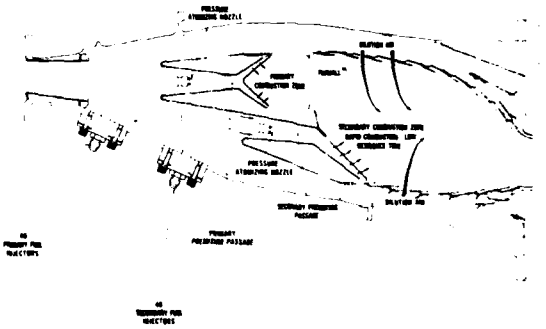

Figure 20.4.5 Staged Premix Combustor, JT9D Engine

c. *NO_x Emission:* NO_x has been the most difficult aircraft engine pollutant to reduce in an acceptable manner. Currently available technology for reducing NO_x emissions consists of two techniques discussed briefly below.

Water injection into the combustor primary zone has been found to reduce oxide-of-nitrogen emissions significantly (up to 80%). Peak flame temperatures are substantially reduced by the water injection resulting in a sharp reduction in NO_x formation rate. In a number of cases where this technique has been attempted, however, CO emissions have increased, although not prohibitively. Figure 20.4.6 shows the relation between water injection rate and NO_x reduction (Ref 20.51). This method is not feasible for reducing cruise NO_x because the water flow required to attain significant abatement is of the order of the fuel-flow rate. In addition, there are difficulties with engine durability, performance, logistics, and economic problems associated with the cost of providing necessary demineralized water. Consequently, these factors have caused this technique to receive negative evaluation as an approach toward universal reduction of ground level NO_x.

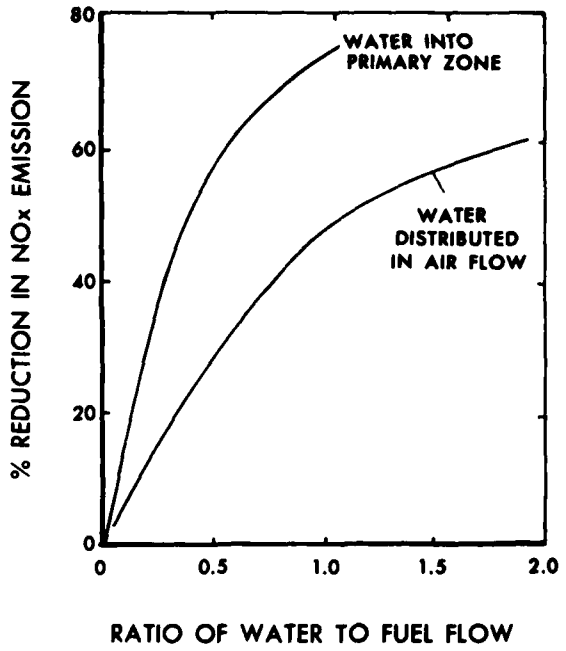

Figure 20.4.6 Ideal Effectiveness of Water Injection for NO_x Control

A second method that has been used to reduce NO_x emissions involves airblast atomization and rapid mixing of the fuel with the primary-zone air flow. Much literature has been generated on this technique (notably the NASA swirl-can technology, References 20.52 - 20.54). One engine, the F101, used in the B-1 aircraft, employs this principle. In the case of the F101, the overall combustor length was shortened from typical designs because of improved fuel-air mixture preparation. As a result, this method reduced both ground-level and altitude NO_x emissions. Reductions of approximately 50 percent below the uncontrolled case (Figure 20.4.3) have been measured.

Advanced approaches to the reduction of NO_x can be divided into two levels of sophistication. The first level involves staged combustors like that shown in Figure 20.4.5. In this case, fuel is injected upstream of the main combustion zone, which may be stabilized by a system of struts (or flameholders). Residence time in the premixing zone is short (i.e., high velocity and short length) because of the possibility of pre-ignition or flame propagation upstream. It is known that these designs provide a fuel-air mixture far from ideal premix/prevaporization. In fact, the turbulence and nonuniformity characteristics of this system are probably not unlike those of conventional combustors. However, since the mixture ratio is only 0.6 stoichiometric, reduced NO_x levels result. Reductions of up to a factor of 3 have been achieved (Ref 20.45 - 20.50).

Testing the advanced techniques of the second level--combustors utilizing premixing and prevaporization operating at equivalence ratios below 0.6--has aimed at ultra low NO_x emission levels. These fundamental studies have been motiviated by efforts to reduce automotive gas turbine emissions, as well as those to reduce stratospheric aircraft gas turbine emissions--the pressure ratio of the automotive engine is low with the absolute pressure level being similar to the aircraft case at altitude. Nevertheless, inlet temperatures are high in the automotive case because of the use of regenerators. Ferri (Ref 20.55), Verkamp, et al. (Ref 20.56), Anderson (Ref 20.57), Wade, et al. (Ref 20.58), Azelborn, et al. (Ref 20.59), Collman, et al. (Ref 20.60), and Roberts, et al. (Ref 20.61) have published results that indicate that levels below 1 g NO_2/kg fuel can be approached. Anderson's work is particularly thorough in discussing fundamental tradeoffs with combustion efficiency. His results are shown in Figure 20.4.7. Good agreement with analytical model results indicates that useful conclusions may be drawn from the model predictions. These predictions all indicate that an "emissions floor" of approximately 0.3 to 0.5 g/kg fuel is the limit of NO_x emissions reduction.

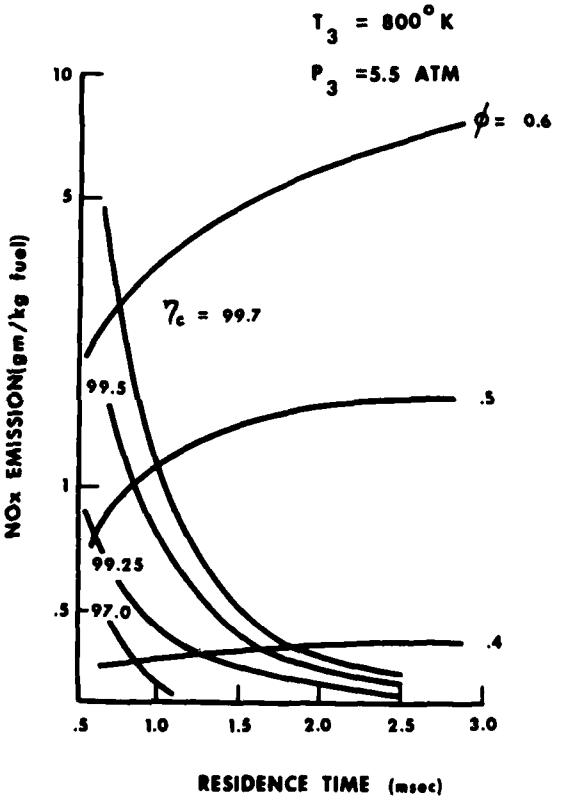

Figure 20.4.7 Effect of Residence Time and ϕ on Nitrogen Oxide Emissions

A number of difficulties associated with the combustion of premixed/prevaporized lean mixtures can be alleviated by the use of a solid catalyst in the reaction zone. Recent developments to construct catalytic convertors to eliminate automotive CO and HC emissions have increased the temperature range within which such a device might operate. Test results have now been published that apply the concept of catalytic combustion to aircraft gas turbine combustors (Ref 20.62 - 20.69). The presence of the catalyst in the combustion region provides stability at lower equivalence ratios than possible in gas-phase combustion. This is due to the combined effect of

heterogeneous chemical reactions and the thermal inertia of the solid mass within the combustion zone. The thermal inertia of the catalytic combustor system has been calculated to be more than two orders of magnitude greater than in the gas-phase combustion system. NO_x reductions up to factors of 100 seem to be possible using the catalytic combustor approach.

20.4.2 Future Jet Fuels.

Between 1973 and 1976, the cost and availability of aircraft jet fuels have drastically changed. Per-gallon jet fuel costs have more than tripled for both commercial and military consumers. In addition, fuel procurement actions have encountered difficulties in obtaining desired quantities of fuel, even though significantly reduced from 1972 consumption levels. These developments have encouraged initial examinations of the feasibility of producing jet fuels from non-petroleum resources (Ref 20.70 - 20.72).

Although economics and supply are primarily responsible for this recent interest in new fuel sources, projections of available world-wide petroleum resources also indicate the necessity for seeking new means of obtaining jet fuel. Regardless of current problems, the dependence on petroleum as the primary source of jet fuel can be expected to cease sometime within the next half century (Ref 20.73).

If the general nature of future aircraft (size, weight, flight speed, etc.) is to remain similar to today's designs, liquid hydrocarbons can be expected to continue as the primary propulsion fuel. Liquified hydrogen and methane have been extensively studied as alternatives but seem to be practical only for very large aircraft. The basic non-petroleum resources from which future liquid hydrocarbon fuels might be produced are numerous. They range from the more familiar energy sources of coal, oil shale, and tar sands to possible future organic materials derived from energy farming. Some of the basic synthetic crudes, especially those produced from coal, will be appreciably different than petroleum crude. Reduced fuel hydrogen content would be anticipated in jet fuels produced from these alternate sources.

Because of the global nature of aircraft operations, jet fuels of the future are likely to be produced from a combination of these basic sources. Production of fuels from blends of synthetic crudes and natural crudes may also be expected. In light of the wide variations in materials from which world-wide jet fuel production can draw, it is anticipated that economics will dictate the acceptance of future fuels with properties other than those of currently used JP-4, JP-5, and Jet A. Much additional technical information will be required to identify the fuel characteristics which meet the following objectives:

a) Allow usage of key world-wide resources to assure availability.

b) Minimize the total cost of aircraft system operation.

c) Avoid major sacrifice of engine performance, flight safety, or environmental impact.

A complex program is necessary to establish the information base from which future fuel specifications can be derived. Figure 20.4.8 depicts the overall nature of the required effort. Fuel processing technology will naturally be of primary importance to per gallon fuel costs. The impact of reduced levels of refining (lower fuel costs) on all aircraft system components must be determined. These include fuel system (pumps, filters, heat exchangers, seals, etc.), and airframe (fuel tank size and design, impact on range, etc.) considerations as well as main burner and afterburner impacts. In addition, handling difficulties (fuel toxicity) and environmental impact (exhaust emissions) require evaluation. The overall program must be integrated by a system optimization study intended to identify the best solution to the stated objective.

20.4.2.1 Fuel Effects on Combustion Systems: Future fuels may affect combustion system/engine performance through changes in hydrogen content, volatility, viscosity, olefin content, fuel nitrogen, sulfur, and trace metal content.

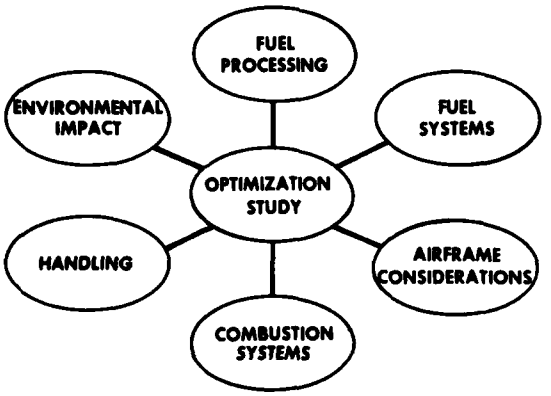

Figure 20.4.8 Overall Scheme for Alternate Jet Fuel Development Program

Fuel hydrogen content is the most important parameter anticipated to change significantly with the use of alternate fuels. In particular, fuels produced from coal would be expected to have significantly reduced hydrogen content. In most cases, reduction in fuel hydrogen content would be due to increased concentrations of aromatic-type hydrocarbons in the fuel. These may be either single ring or polycyclic in structure. Experience has shown that decreased hydrogen content significantly influences the fuel pyrolysis process in a manner which results in increased rates of carbon particle formation. In addition to increased smoke emission, the particulates are responsible for formation of a luminous flame where blackbody radiation from the particles is a predominant mode of heat transfer.

Significantly increased radiative loading on combustor liners can result from decreased fuel hydrogen content. Increases in liner temperature translate into decreases in hardware life and durability. Figure 20.4.9 illustrates the sensitivity of combustor liner temperature to hydrogen content. The following non-dimensional temperature parameter is used to correlate these data (Ref 20.34, 20.74 - 20.77) representative of older engine designs.

$$\frac{T_L - T_{LO}}{T_{LO} - T_3}$$

The numerator of this expression represents the increase in combustor liner temperature, T_L, over that obtained using the baseline fuel (14.5% hydrogen JP-4), T_{LO}. This is normalized by the difference between T_{LO} and combustor inlet temperature, T_3. It was found that data obtained using different combustors could be correlated using this parameter. It should also be noted that the parameter is representative of the fractional increase (over the baseline fuel) in heat transfer to the combustor liner.

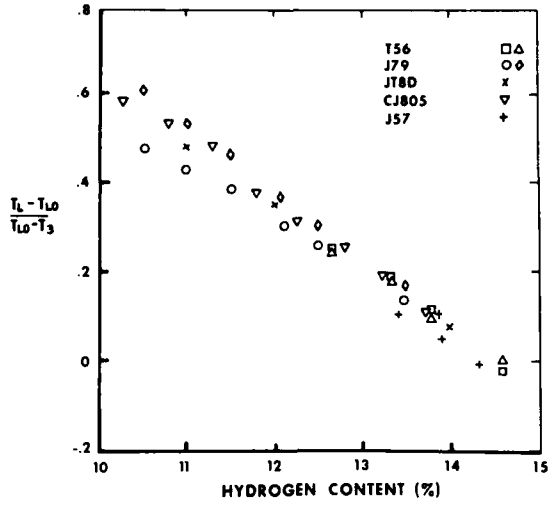

Figure 20.4.9 Liner Temperature Correlation for Many Combustor Types

Because combustor design differences play an important part in determining engine smoke characteristics, differences in emission are not correlatable in the same manner as combustor liner temperature. However, results obtained using a T56 single combustor rig (Ref 20.34) are illustrative of the important trends (see Figure 20.4.10). Significantly increased smoke emission was determined with decreased hydrogen content for each condition tested. Trends between smoke emission and hydrogen content are similar for each combustion condition. Increased absolute smoke emission between the 394°K and 644°K combustor inlet temperature conditions is attributable to increased pressure and fuel-air ratio. Although a further small increase might be expected for the 756°K condition because of higher pressure, the lower fuel-air ratio required to maintain the 1200°K exhaust temperature results in a lower absolute smoke emission.

Volatility affects the rate at which liquid fuel introduced into the combustor can vaporize. Since important heat release processes do not occur until gas phase reactions take place, reduction of volatility shortens the time for chemical reaction within the combustion system. In the aircraft engine this can result in difficulty in ground or altitude ignition capability, reduced combustor stability, increased emissions of carbon monoxide (CO) and hydrocarbons (HC), and the associated loss in combustion efficiency. Moreover, carbon particle formation is aided by the formation and maintenance of fuel-rich pockets in the hot combustion zone. Low volatility allows rich pockets to persist because of the reduced vaporization rate. Again, increased particulates can cause additional radiative loading to combustor liners and more substantial smoke emissions.

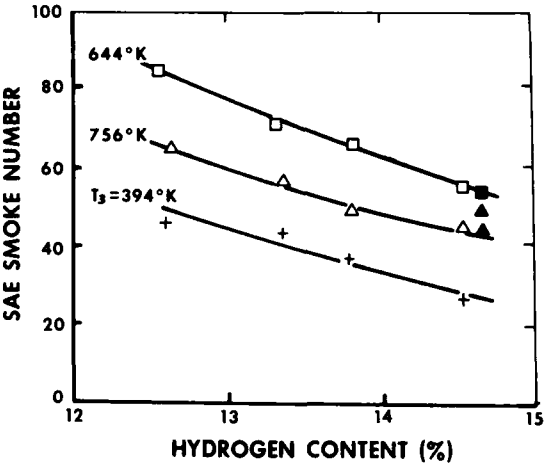

Figure 20.4.10 Smoke Emission Dependence on Hydrogen Content

The desired formation of a finely dispersed spray of small fuel droplets is adversely affected by viscosity. Consequently, the shortened time for gas phase combustion reactions and prolonging of fuel-rich pockets experienced with low volatility can also occur with increased viscosity. The ignition, stability, emissions, and smoke problems previously mentioned also increase for higher viscosity fuels.

Olefin content is known to influence fuel thermal stability. Potential problems resulting from reduced thermal stability include fouling of oil-fuel heat exchangers and filters, and plugging of fuel metering valves and nozzles. No negative effect of fuel olefin content on gas phase combustion processes would be expected.

The effect of increased fuel-bound nitrogen is evaluated by determining the additional NO_x emission occurring when nitrogen is present in the fuel and calculating the percent of fuel nitrogen conversion to NO_x necessary to cause this increase. The baseline petroleum fuels used in this study had near zero (<10 ppmw) fuel-bound nitrogen. Results presented in Figure 20.4.11 indicate the importance of two variables. First, as combustor inlet temperature is increased, conversion is reduced. Secondly, as fuel-bound nitrogen concentrations are increased, conversion decreases. This second trend is consistent with available results for oil shale fuels which had less than .05% nitrogen. Synfuel results are shown as a band in Figure 20.4.11 because of difficulties in accurately measuring small NO_x increases.

Both sulfur and trace metals are at very low concentrations in current jet fuels. Sulfur is typically less than 0.1% because the

petroleum fraction used for jet fuel production is nearly void of sulfur-containing compounds. Although syncrudes from coal or oil shale would be expected to contain higher sulfur levels, it is not likely that the current specification limit of 0.4% would be exceeded with the processed jet fuel. Because of the way in which future jet fuels are expected to be produced, trace metals are also expected to continue to be present at low concentrations (less than 1 ppmw). Should higher levels appear possible, the serious consequences (deleterious effects on turbine blades) would justify additional expense for removal.

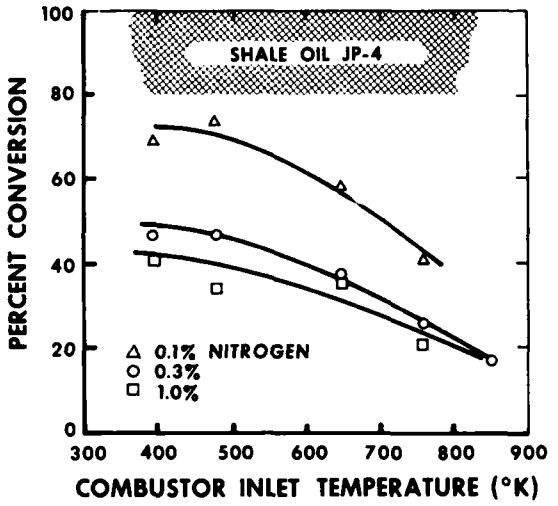

Figure 20.4.11 Fuel-Bound Nitrogen Conversion to NO_x in an Aircraft Gas Turbine Combustor

20.4.2.2 Combustion System Design Impact: Although in the early stages of assessment, it appears certain that future combustion system designs will be significantly influenced by the changing character of fuel properties as alternate energy sources are tapped. Designs that accommodate lower hydrogen content fuels with good combustor liner durability and low smoke emission while maintaining the customary level of combustion system performance must be developed.

Lean primary zone combustion systems, which are much less sensitive to fuel hydrogen content, will comprise a major approach to utilizing new fuels. Low smoke combustor designs have been shown to be much less sensitive to fuel hydrogen content variations. Figure 20.4.12 compares the correlation for older designs (Figure 20.4.9) with results for a newer, smokeless combustor design, the CF6 (Ref 20.78). Current research on staged combustion systems (See 20.4.1.4) will further contribute toward achieving the goal of leaner burning while maintaining desired system performance. Some of these designs have demonstrated very low sensitivity to fuel type (Ref 20.78). These extremely important developments provide encouragement that future fuels of lower hydrogen content can be accommodated while maintaining acceptable emissions characteristics.

20.4.3 Design and Performance Advancements

The following subsection briefly addresses three new design concepts currently under consideration intended to address future turbopropulsion performance requirements. The High Mach Combustor (HMC) is an advanced system design concept for substantially increased performance relative to contemporary systems. The Vortex Controlled Diffuser (VCD) is an improved, low-loss boundary-layer bleed diffuser which supports the needs of both current and future combustion systems. The shingle liner is an advanced concept combining new design features for both improved structural and thermal durability.

20.4.3.1 High Mach Combustor (HMC): The HMC is an advanced combustor design concept required to meet the needs of the High Thru-Flow Propulsion System (HTFPS). The HTFPS is an advanced technology engine designed for high performance, light-weight and low cost. It will utilize a variable-geometry compressor, a high entrance Mach number, high temperature rise combustor and a variable-geometry turbine and exhaust nozzle. As a result, the combustor must be capable of accepting entrance flow fields at Mach numbers nearly twice that of contemporary systems but at virtually the same pressure loss levels. Two approaches may be taken to meet these technology requirements: (1) slow the combustor entrance Mach number to conventional levels by an advanced diffusion system (bleed, dump, or staged diffuser) and utilize contemporary combustor technology; or (2) design the combustor to accept the high velocity flow field by use of swirl combustion techniques. A cross-section of a bleed HMC is illustrated in Figure 20.4.13 while a high velocity swirl burning concept is illustrated in Figure 20.4.14.

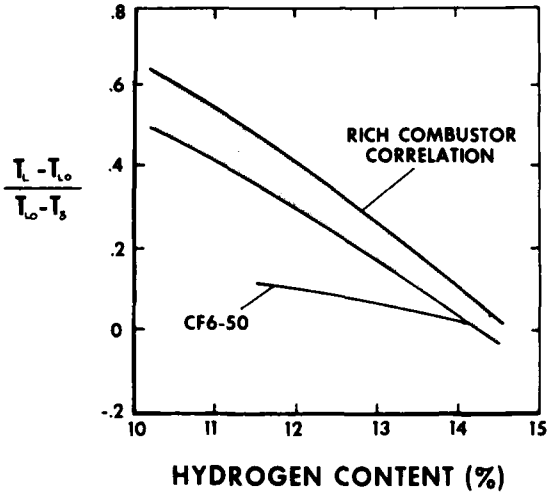

Figure 20.4.12 Effect of Lean Operation on Combustor Fuel Sensitivity

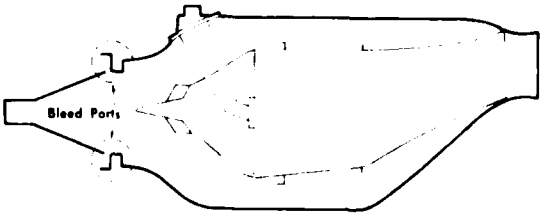

Figure 20.4.13 HMC with Advanced Bleed Diffuser

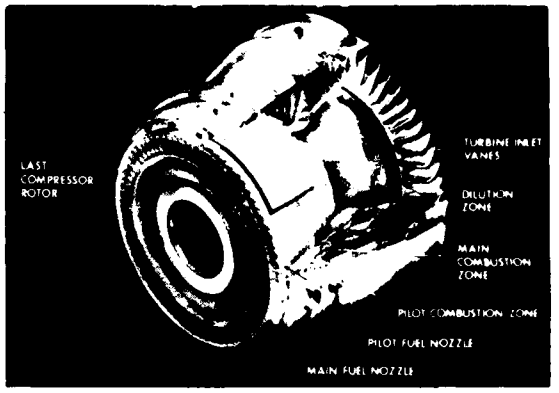

Figure 20.4.14 Swirl Burning HMC

20.4.3.2 Vortex Controlled Diffuser (VCD): The VCD is a compact boundary-layer-bleed combustor inlet diffuser designed to effectively diffuse both conventional and high Mach number flow fields while providing good pressure loss and flow stability in a very short length (relative to contemporary diffusion systems). The VCD was initially investigated at Cranfield Institute of Technology by Adkins (Ref 20.79). The basic VCD geometry and nomenclature are defined in Figure 20.4.15. Inner and outer VCD bleeds flow from the primary duct exit providing high pressure recovery and low pressure loss. The VCD advantages are principally (1) short diffuser length, (2) high pressure recovery, (3) design simplicity and (4) stable flow provided by the vortex retaining fences. This concept offers considerable promise and is expected to find its way into a wide range of future propulsion system applications. Extended development of the VCD has been sponsored by the Air Force and conducted at the Detroit Diesel Allison Division of GMC.

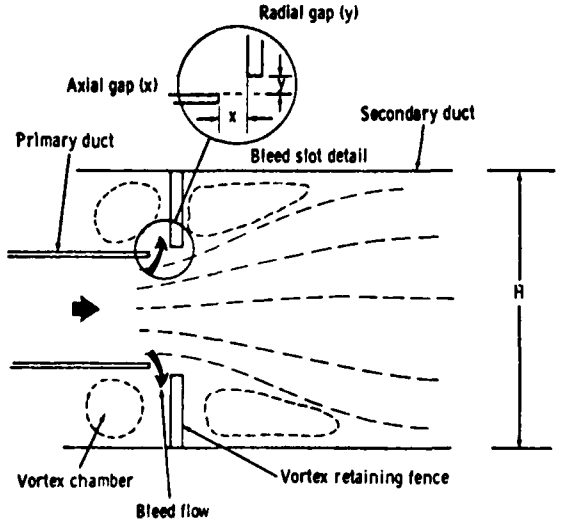

Figure 20.4.15 Vortex Controlled Diffuser

20.4.3.3 Shingle Liner: The Shingle Liner design concept is an advanced combustor cooling technique featuring a new liner version wherein the thermal and mechanical stress loads of the combustor are isolated and controlled by independent means. The liner is basically an impingement cooled segmented design as illustrated in Figure 20.4.16. The outer shell serves as the structural or load carrying portion of the combustion system and provides impingement cooling for the inner segments or shingles. As a result, the shingles provide an effective thermal barrier, protecting the highly-stressed outer shell. The shingle liner is particularly well suited to high temperature rise combustor operation where cooling airflow is at a premium. Additionally, the shingle concept offers improved liner life due to its thermally relieved mechanical design aspect and the possibility of improved maintainability, as low-cost "throw-away" segments may be employed. The Shingle Liner development was sponsored by the Navy and conducted by the General Electric Company. It is presently being considered for both near-term and future propulsion system application.

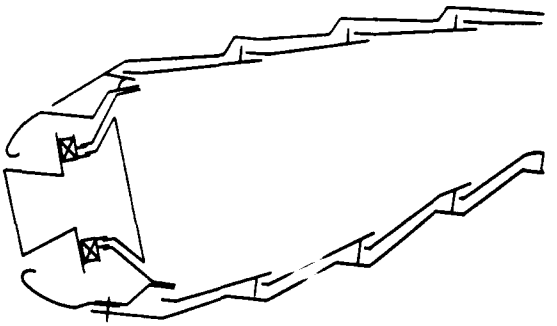

Figure 20.4.16 Shingle Liner Combustor

20.5 CONCLUSIONS

As discussed earlier, the turbine engine combustion system has undergone an evolutionary development process over the past forty years beginning with long, bulky, can-type combustors (i.e., the J33 shown in Figure 20.1.3) and progressing to the compact, high temperature rise annular combustors of today's newest turbopropulsion systems. In recent years, significant technological advancements have been realized in both combustion system design and performance. With respect to the important design parameters of combustion efficiency and stability, pressure loss, combustor size, and pattern factor, the annular combustors recently developed have provided substantial improvements. Further improvements in these parameters will be required, however, if propulsion system demands of the future are to be met.

In the vital area of durability, improvements in liner design and cooling have added substantially to the maintainability and durability aspects of the combustor at a time when system operating pressures and temperatures are on the rise. Figure 20.5.1 illustrates the technological improvements realized in the 10 - 15 years since annular combustors where introduced. For example, the continued drive for reduced cost, improved fuel economy and design compactness and simplicity has led to the compact, high temperature combustor of the F101 engine (developed for the B-1 Bomber) illustrated in Figure 20.5.2. This combustor is a low pressure loss (5.1%), high heat release (7.5×10^6 BTU/hr/atm/ft^3) design

employing an improved low pressure fuel injection system, a machined-ring high durability liner and a simple, cast, low-loss inlet dump diffuser. Relative to other contemporary combustion systems, the F101 is the most advanced annular design developed to date and introduces a new family of compact, high temperature systems for fighter, bomber, and transport applications.

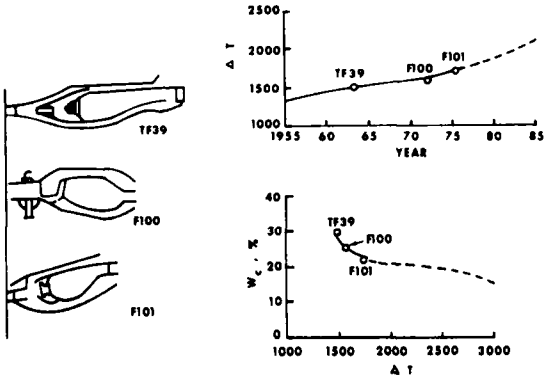

Figure 20.5.1 Annular Combustor Development Trends

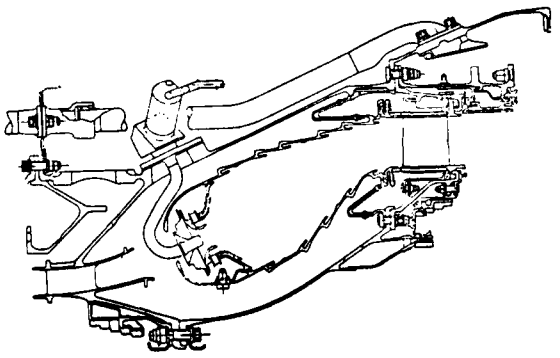

Figure 20.5.2 F101 Annular Combustor

Future aircraft propulsion requirements call for primary combustors capable of: (1) accepting greater variations in compressor discharge pressure, temperature and airflow, (2) producing heat release rates and temperature rise which will ultimately approach stoichiometric levels, and (3) providing high operational reliability and improved component durability, maintainability, and repairability. In addition, the new requirements discussed in Section 20.4--exhaust emissions and fuel flexibility--must be addressed.

It is only possible to speculate on new concepts which might be employed in the next quarter century in aero-propulsion combustion. Nevertheless, such an effort is worthwhile as the reader may gain an appreciation for the wide range of opportunity and flexibility which remains available to the combustion system designer. Two new concepts, catalytic combustion and photochemically-assisted combustion, will be highlighted below.

Catalytic combustion involves the use of a heterogeneous catalyst within the combustion zone to increase the energy release rate (Ref 20.62 - 20.69). Fuel and air are premixed at low equivalence ratios, often below the lean flammability limit, and passed through a catalytically-coated, ceramic honeycomb structure. Due to the combined effect of heterogeneous chemical reactions and the thermal inertia of the solid structure, this concept can be utilized to achieve stable, efficient combustion outside the normal flammability limits of gas-phase systems (Ref 20.62 - 20.69). Typical experimental results are shown in Figure 20.5.3. The benefits of lean combustion (low radiative emission, decreased tendency for turbine inlet temperature non-uniformities, reduced smoke and NO_x formation) provide significant potential payoff. Applications in both main burners and afterburners are likely. The promising concept of a porous flameholder with low pressure drop is under investigation. Such a device would provide a means of stabilizing combustion flows that reach final flame temperatures in excess of flameholder material limitations.

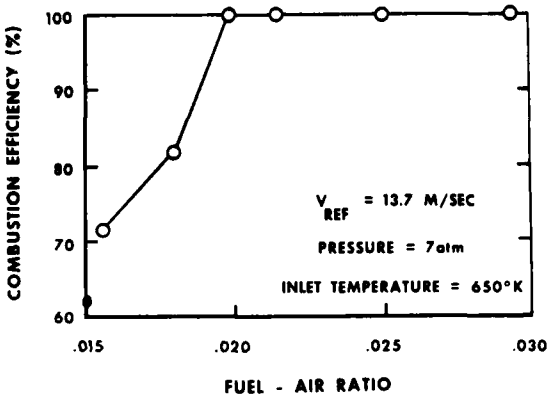

Figure 20.5.3 Catalytic Combustor Efficiency

A second new concept utilizes either ultraviolet light sources or plasmas to stabilize or promote combustion processes. Recent studies have confirmed the possibility of photochemical ignition where a pulse of ultraviolet light (from an arc discharge) is used to dissociate molecular oxygen and provide ignition at lower temperatures and with lower energy input than in the case of a spark ignition source (Ref 20.80, 20.81). Other investigations have confirmed the capability of plasma jets in supplying reactive species to stabilize and improve the efficiency of combustion flows (Ref 20.82). The payoff of these two concepts can be flame stabilization without flameholding devices--an "optical flameholder" with zero pressure drop. Such a device would further promote the feasibility of practical lean combustion.

While the example concepts described above are in their infancy and may not find eventual practical application in the turbopropulsion field, they are illustrative of future combustion technology developments. As the combustor designer is confronted with the new requirements of the future, especially exhaust emissions and fuel flexibility, new concepts like these will play an important role in problem solution. Engineers in the aero-propulsion combustion community will certainly enjoy challenges with the possibility for imaginative

solutions as the next quarter century unfolds.

20.6 REFERENCES

20.1 Whittle, Sir Frank, Jet, The Story of a Pioneer, Frederich Muller Ltd, London, 1953.

20.2 Smith, I. E., Combustion in Advanced Gas Turbine Systems, Pergamon Press, New York, 1967.

20.3 Cornelius, W., and Agnew, W. G., Emissions From Continuous Combustion Systems, Plenum Press, New York, 1972.

20.4 Swithenbank, J., Combustion Fundamentals, Air Force Office of Scientific Research, Washington DC, February, 1970.

20.5 Propulsion Chemistry Division, Lewis Flight Propulsion Laboratory, "Basic Consideration in the Combustion of Hydrocarbon Fuels with Air", edited by H. C. Barnett and R. R. Hibbard, NACA Report 1300, 1957.

20.6 "The Design and Performance Analysis of Gas-Turbine Combustion Chambers," Vol I, Northern Research and Engineering Corporation, 1964.

20.7 Reneau, L. R., Johnston, J. P., and Kline, S. J., "Performance and Design of Straight Two-Dimensional Diffusers, Report PD-8, Thermosciences Division, Department of Mechanical Engineering, Stanford University, Stanford CA, 1964.

20.8 Rizkalla, A. A., and Lefebvre, A. H., "The Influence of Air and Liquid Properties on Airblast Atomization," Journal of Fluids Engineering, Vol 97, Series I, Number 3, PP 316-320, September 1975.

20.9 Rizkalla, A. A., and Lefebvre, A. H., "Influence of Liquid Droplets on Airblast Atomizer Spray Characteristics," Journal of Engineering for Power, Series A of ASME Transactions, Volume 97, April 1975.

20.10 Lefebvre, A. H., and Miller, D., "The Development of Airblast Atomizer for Gas Turbine Application, College of Aero. Rep., Aero No. 193, 1967.

20.11 Lefebvre, A. H., Theoretical Aspects of Gas Turbine Combustion Performance, College of Aeronautics, Cranfield, Co. A., Note Aero No 163, August 1966.

20.12 Herbert, J. D., "Theoretical Analysis of Reaction Rate Controlled Systems - Part I", AGARD Combustion Research and Reviews, Chapter 6, 1957.

20.13 Swithenbank, J., Poll, I., Wright, D. D., and Vincent M. W., "Combustion Design Fundamentals," 14th Symposium (International) on Combustion, The Combustion Institute, Pittsburgh, PA, August 1972.

20.14 Spaulding, D. B., "Mathematical Models of Continuous Combustion," in Emissions From Continuous Combustion Systems, Edited by W. Correlius and W. G. Agnew, Plenum Publishing Corporation, New York, 1972.

20.15 Gosman, A. O., Pun, W. M., Runchal, A. K., Spaulding, D. B., and Wolfshtein, M., Heat and Mass Transfer in Recirculating Flows, Academic Press, New York, New York, 1969.

20.16 Mosier, S. A., and Roberts, R. "Low Lower Turbopropulsion Combustor Exhaust Emissions," Vol I, II and III, Air Force Aero-Propulsion Laboratory Report AFAPL-TR-73-36, June 1973.

20.17 Anasoulis, R. F., McDonald, H., and Buggelin, R. C., "Development of a Combustor Flow Analysis," Vol I and II, Air Force Aero-Propulsion Laboratory Report AFAPL-TR-73-98, January 1974.

20.18 Clean Air Act Amendments of 1970, 40 USC 1857 as amended by PL 91-604.

20.19 U.S. Environmental Protection Agency, "Aircraft Emissions: Impact on Air Quality and Feasibility of Control," February 1972.

20.20 U.S. Environmental Protection Agency "Control of Air Pollution from Aircraft and Aircraft Engines," Federal Register, Vol 38, No 136, 17 July 1973.

20.21 Grobecker, A. J., Coroniti, S. C., and Cannon, R. H. Jr., "Report of Findings--Executive Summary, The Effects of Stratospheric Pollution by Aircraft," Department of Transportation Climatic Impact Assessment Program, Washington DC, December, 1974.

20.22 Society of Automotive Engineers, "Procedure for the Continuous Sampling and Measurement of Gaseous Emissions From Aircraft Turbine Engines," Aerospace Recommended Practice 1256, New York, 1971.

20.23 Society of Automotive Engineers, "Aircraft Gas Turbine Engine Exhaust Smoke Measurement," Aerospace Recommended Practice 1179, New York, 1970.

20.24 Champagne, D. L., "Standard Measurement of Aircraft Gas Turbine Exhaust Smoke," ASME Paper No. 71-GT-88, Paper presented at the Gas Turbine Conference and Products Show, Houston, TX, March-April 1971.

20.25 Bogdan, L., and McAdams, H. T., "Analysis of Aircraft Exhaust Emissions Measurements," Rep No. NA-5007-K-1, Cornell Aeronautical Labs, Buffalo NY, 1971.

20.26 Groth, R. H., and Robertson, D. J., "Reactive and Unreactive Hydrocarbon Emissions from Gas Turbine Engines," APCA Paper No. 74-89, Paper presented at the 67th Meeting of the Air Pollution Control Association, Denver, CO, June 1974.

20.27 Kendall, D. A., and Levins, P. L., "Odor Intensity and Characterization of Jet Exhaust and Chemical Analytical Measurements," NASA CR-12-159, 1973.

20.28 Butze, H. F., and Kendall, D. A., "Odor Intensity and Characterization Studies of Exhaust from a Turbojet Engine Combustor," AIAA Paper No. 73-1278, Paper presented at the AIAA/SAE 9th Propulsion Conference, Las Vegas, NV, November 1973.

20.29 Katzman, H., and Libby, W. F., "Hydrocarbon Emissions from Jet Engines Operated at Simulated High-Altitude Flight Conditions," Paper presented at the AIAA/AMS Second International Conference on the Environmental Impact of Aerospace Operations in the High Atmosphere, San Diego, CA, July 1974.

20.30 Giovanni, D. V., and Hilt, M. B., "Particulate Matter Emission Measurements from Stationary Gas Turbines," ASME Paper No. 73-PWR-17, September 1973.

20.31 Slusher, G. R., "Sulfur Oxide Measurement in Aircraft Turbine Engine Exhaust " FAA-RD-75-101, September 1975.

20.32 Lipfert, F. W., "Correlations of Gas Turbine Emissions Data," ASME Paper 72-GT-60, Paper presented at the 17th International Gas Turbine Conference and Products Show, San Francisco, CA, March 1972.

20.33 Blazowski, W. S., Fahrenbruck, F. S., and Tackett, L. P., "Combustion Characteristics of Oil Shale Derived Jet Fuels," Paper 75-13 presented at the 1975 WSS/CI Fall Technical Meeting, Palo Alto, CA, October 20-21, 1975.

20.34 Blazowski, W. S., "Combustion Considerations for Future Jet Fuels," 16th International Symposium on Combustion, the Combustion Institute, Pittsburgh, PA, 1976.

20.35 Butze, H. F., and Ehlers, R. C., "Effect of Fuel Properties on Performance of a Single Aircraft Turbojet Combustor," NASA-TM-X-71789. Presented at the 1975 WSS/CI Fall Technical Meeting, Palo Alto, CA, October 1975.

20.36 Wilkes, C. A., and Johnson, R. H., "Fuel Property Effects on Gas Turbine Emissions Control," Paper presented at the ASME Joint Power Conference, Miami, FL, September 1974.

20.37 Lazalier, G. R., and Gearhart, J. W., "Measurement of Pollution Emissions from an Afterburning Turbojet Engine at Ground Level, Part 2, Gaseous Emissions," AEDC-TR-72-70, Arnold Engineering Development Center, Tullahoma, TN, 1972.

20.38 Palcza, J. L., "Study of Altitude and Mach Number Effects on Exhaust Gas Emissions of an Afterburning Turbofan Engine," Rep No FAA-RD-72-31, Federal Aviation Administration, 1971.

20.39 German, R. C., High, J. D., and Robinson, C. E., "Measurement of Exhaust Emissions from a J85-GE-5B Engine at Simulated High-Altitude, Supersonic, Free-Stream Flight Conditions," AEDC-TR-73-103, Arnold Engineering Development Center, Tullahoma, TN 1973.

20.40 Diehl, L. A., "Measurement of Gaseous Emissions from an Afterburning Turbojet Engine at Simulated Altitude Conditions, NASA-TM-X-2726, 1973.

20.41 Lyon, T. F., Colley, W. C., Kenworthy, M. J., and Bahr, D. W., "Development of Emissions Measurement Techniques for Afterburning Turbine Engines," AFAPL-TR-75-52, October 1975.

20.42 Grobman, J., and Ingebo, R. D., "Forecast of Jet Engine Exhaust Emissions of High Altitude Commercial Aircraft Projected to 1990", In CIAP Monograph 2, Propulsion Effluents in the Stratosphere, DOT-TST-75-52, September 1975.

20.43 Norgren, C. T., and Ingebo, R. D., "Effect of Fuel Vapor Concentrations on Combustor Emissions and Performance," NASA-TM-X-2800, 1973.

20.44 Bahr, D. W., "Control and Reduction of Aircraft Turbine Engine Exhaust Emissions," In Emissions from Continuous Combustion Systems, pp 345-373, Plenum, New York, 1972.

20.45 Mularz, E., "Results of the Pollution Reduction Technology Program for Turboprop Engines," AIAA Paper 76-760, July 1976.

20.46 Roberts, R., Fiorentino, A., and Diehl, L., "Pollution Reduction Technology for Turbofan Engine Can Annular Combustors," AIAA Paper No. 76-761, July 1976.

20.47 Niedzwiecki, R., and Roberts, R., "Low Pollution Combustors for CTOL Engines - Experimental Clean Combustor Program (JT9D)," AIAA Paper No. 76-762, July 1976.

20.48 Niedzwiecki, R., and Gleason, C., "Low Pollution Combustor for CTOL Engines - Experimental Clean Combustor Program (CF6)," AIAA Paper No. 76-763, July 1976.

20.49 Roberts, P. B., White, D. J., Shekleton, J. R., and Butze, H. F., "Advanced Low NO_x Combustors for Aircraft Gas Turbines," AIAA Paper No. 76-764, July 1976.

20.50 Verdouw, A. J., "Evaluation of a Staged Fuel Combustor for Turboprop Engines," ASME Paper No. 76-WA/GT-5, July 1976.

20.51 Blazowski, W. S., and Henderson, R. E., "Aircraft Exhaust Pollution and Its Effects on the U.S. Air Force," AFAPL-TR-74-64, Air Force Aero-Propulsion Lab, Wright-Patterson Air Force Base, OH, 1974.

20.52 Niedzwiecki, R. W., and Jones, R. E., "Parametric Test Results of Swirl Can Combustor," NASA-TM-X-68247, June 1973.

20.53 Jones, R. E., "Advanced Technology for Reducing Aircraft Engine Pollution," NASA-TM-X-68256, November 1973.

20.54 Mularz, E. J., Wear, I. D., and Verbulecy, P. W., "Pollution Emissions from Single Swirl Can Combustor Modules at Parametric Test Conditions," NASA-TM-X-3167, January 1975.

20.55 Ferri, A., "Reduction of NO Formation by Premixing in Atmospheric Pollution by Aircraft Engines," AGARD Conf. Proc. No. 125, April 1973.

20.56 Verkamp, F. J., Verdouw, A. J., and Tomlinson, J. G., "Impact of Emissions Regulations on Future Gas Turbine Engine Combustors, AIAA Paper No. 73-1277, Paper presented at the AIAA/SAE 9th Propulsion Conference, Las Vegas, NV, November 1973.

20.57 Anderson, D. N., "Effects of Equivalence Ratio and Dwell Time on Exhaust Emissions from an Experimental Premixing Prevaporizing Burner," NASA-TM-X-71592, 1974.

20.58 Wade, W. R., Shen, P. I., Owens, C. W., and McLean, A. F., "Low Emissions Combustion for the Regenerative Gas Turbine, Part I - Theoretical and Design Considerations," ASME Paer No. 73-GT-11, December 1972.

20.59 Azelborn, N. A., Wade, W. R., Seeord, J. R., McLean, A. F., "Low Emissions Combustion for the Regnerative Gas Turbine, Part II - Experimental Techniques, Results, and Assessment," ASME Paper No. 73-GT-12, Dec 1972.

20.60 Collman, J. S., Amann, C. A., Mathews, C. C., Stettler, R. J., and Verkamp, F. J., "The GT-255-- An Engine for Passenger Car Gas Turbine Research," SAE Paper No. 750167, February 1975.

20.61 Roberts, P. B., Shekleton, J. R., White, D. J., and Butze, H. F., "Advanced Low NO_x Combustor for Supersonic High-Altitude Aircraft Gas Turbines," ASME Paper No. 76-GT-12.

20.62 Blazowski, W. S., and Bresowar, G. E., "Preliminary Study of the Catalytic Combustor Concept as Applied to Aircraft Gas Turbines," AFAPL-TR-74-32, Air Force Aero-Propulsion Laboratory, Wright-Patterson AFB, Ohio, 1974.

20.63 Wampler, F. P., Clark, D. W., and Gaines, F. A., "Catalytic Combustion of C_3H_8 on Pt Coated Monolith," Western States Section of the Combustion Institute, Paper No. 74-36, October 1974.

20.64 Blazowski, W. S., and Walsh, D. E., "Catalytic Combustion: An Important Consideration for Future Applications," Comb. Sci. and Tech. Vol 10, pp 233-244, 1975.

20.65 Rosfjord, T. J., "Catalytic Combustors for Gas Turbine Engines," AIAA Paper 76-46, January 1976.

20.66 Anderson, D. N., Tacina, R. R., and Mroz, T. S., "Performance of a Catalytic Reactor at Simulated Gas Turbine Operating Conditions," NASA-TM-X-71747, 1975.

20.67 Pfefferle, W. C., et al, "Catathermal Combustion: A New Process for Low Emissions Fuel Conversion," ASME Paper 75-WA/Fu-1, December 1975.

20.68 DeCorso, S. M., et al., "Catalysts for Gas Turbine Combustors - Experimental Test Results," ASME Paper 76-GT-4, March 1976.

20.69 Anderson, D. N., "Preliminary Results from Screening Tests of Commercial Catalysts with Potential Use in Gas Turbine Combustors, Part I. Furnace Studies of Catalyst Activity," NASA-TM-X-73410, and "Preliminary Results from Screening Tests of Commercial Catalysts with Potential Use in Gas Turbine Combustos, Part II. Combustion Test Rig Evaluation," NASA-TM-X-73412, May 1976.

20.70 Goen, R. L., Clark, C. F., and Moore, M. A., "Synthetic Petroleum for Department of Defense Use," AFAPL-TR-74-115, November 1974.

20.71 Shaw, H., Kalfadelis, C. D., and Jahnig, C. E., "Evaluation of Methods to Produce Aviation Turbine Fuels from Synthetic Crude Oils, Phase I,.," AFAPL-TR-75-10, March 1975.

20.72 Bartick, H., Kunchal, K., Switzer, D., Bowen, R., and Edwards, R., "The Production and Refining of Crude Shale Oil into Military Fuels," Final Report for Contract N00014-75-C-0055, Office of Naval Research, Arlington VA, August 1975.

20.73 Pinkel, I. I., "Future Fuels for Aviation," AGARD Advisory Report No. 93, January 1976.

20.74 McClelland, C. C., "Effects of Jet Fuel Constituents on Combustor Durability," Naval Air Propulsion Test Center Report NAPC-AEL-1736, May 1963.

20.75 Butze, H. F., and Ehlers, R. C., "Effect of Fuel Properties on Performance of A Single Aircraft Turbojet Combustor," NASA-TM-X-71789, October 1975.

20.76 Macaulay, R. W., and Shayeson, M. W., "Effects of Fuel Properties on Liner Temperatures and Carbon Deposition in the CJ805 Combustor for Long Life Applications," ASME Paper 61-WA-304, October 1961.

20.77 Schirmer, R. M., McReynolds, L. A., and Daley, J. A., "Radiation from Flames in Gas Turbine Combustors," SAE Transactions, Vol 68, pp 554-561, 1960.

20.78 Gleason, C. C., and Bahr, D. W., "Experimental Clean Combustor Program Alternate Fuels Addendum Phase II Final Report," NASA-CR-134972, January 1976.

20.79 Adkins, R. C., "A Short Diffuser with Low Pressure Loss," ASME/CSME Fluids Engineering Conference, Montreal, Canada, 13-15 May 1974.

20.80 Cerkanowicz, A. E., Levy, M. E., and McAlevy, R. F., "The Photochemical Ignition Mechanism of Unsensitized Fuel-Air Mixtures," AIAA Paper No. 70-149, January 1970.

20.81 Cerkanowicz, A. E., "Photochemical Enhancement of Combustion and Mixing in Supersonic Flows," AFOSR-TR-74-0153, November 1973.

20.82 Weinberg, F. J., "The First Half Million Years of Combustion Research and Today's Burning Problems," 15th International Symposium on Combustion, the Combustion Institute, Pittsburgh PA, 1975.

AFTERBURNERS

THE AEROTHERMODYNAMICS OF GAS TURBINE ENGINES

Chapter 21

by

E. E. Zukoski

California Institute of Technology
Pasadena, California

Table of Contents

		Page
21.0	INTRODUCTION	21-2
21.1	DIFFUSER	21-4
21.2	FUEL INJECTION, ATOMIZATION AND VAPORIZATION	21-4
21.3	IGNITION	21-7
21.4	STABILIZATION PROCESS	21-8
21.4.1	Flame Stabilization By Bluff Bodies In Premixed Flow	21-9
21.4.1.1	Fluid Dynamic Parameters	21-12
21.4.1.2	Chemical Parameters	21-16
21.4.1.3	Alternate Schemes	21-17
21.4.2	Flame Stabilization By Jets In A Homogeneous Stream	21-17
21.4.3	Flame Stabilization In A Heterogeneous Fuel-Air Mixture	21-19
21.4.4	Discussion	21-20
21.5	FLAME SPREAD IN PREMIXED AND HOMOGENEOUS FUEL-AIR MIXTURES	21-21
21.5.1	Spreading Rates Of Turbulent Flames	21-22
21.5.2	One-Dimensional Heat Release	21-27
21.5.3	Two-Dimensional Heat Addition Calculations	21-31
21.6	NOZZLE AND FUEL CONTROL SYSTEMS	21-39
21.8	COMPLETE AFTERBURNER SYSTEMS	21-42
21.8	COMBUSTION INSTABILITIES	21-45
21.9	REFERENCES	21-48
21.10	FURTHER READING	21-50

List of Figures

Figure		Page
21.0.1	Sketch of General Electric J-79 Afterburner	21-2
21.0.2	Pratt and Whitney F100-PW-100 Augmented Turbofan Engine	21-3
21.0.3	Afterburner Performance Characteristics for the TF30-P-3 Engine	21-3
21.2.1	Schematic for Estimate of Penetration Distance	21-5
21.3.1	Flight Envelope for an Afterburner	21-8
21.4.1	Flame Stabilization Schemes for Mixtures of Fuel Vapor and Air	21-8
21.4.2	Stability Limit Curves for Circular Cylinders	21-9
21.4.3	Photograph and Sketch of the Flame Stabilization Region of a Circular Cylinder	21-10
21.4.4	Spark Schlieren Photographs of Stabilized Flames	21-11
21.4.5	Sketch of Notation Used in Analysis of Stabilization	21-12

Chapter 21

AFTERBURNERS

E. E. Zukoski

California Institute of Technology

Figure		Page
21.4.6	Dependence of Recirculation Zone Length and Wake Width on Flame Holder Blockage Ratio	21-12
21.4.7	Dependence of Stability Parameter on Blockage Ratio and Flame Holder Geometry	21-14
21.4.8	Transition to Turbulence in Recirculation Zone of Cooled Circular Cylinder	21-15
21.4.9	Variation of Characteristic Ignition Time with the Equivalence Ratio	21-16
21.4.10	Effect of Fuel Properties on Characteristic Time	21-16
21.4.11	Schematic for Discussion of Flame Stabilization by a Jet	21-18
21.5.1	Flame Stabilized on a Two-Dimensional Wedge Flame Holder	21-22
21.5.2	Sketch for Calculation of Stream Line Angle at Flame Front	21-23
21.5.3	Dependence of Flame Width on Fuel-Air Ratio, Approach Stream Temperatures and Fuel Type	21-24
21.5.4	Flame Shapes for Flame Holders of Several Sizes in a Duct of Fixed Size	21-25
21.5.5	Sketch of Flame Edge and Temperature Profiles for a Three Flame Holder Array	21-25
21.5.6	One-Dimensional Flow of Gas with Infinitesimal Heat Addition	21-27
21.5.7	Sketch of Velocity Change Across an Infinitely Thin Flame	21-31
21.5.8	Notation for Ideal Flame Spread Calculation	21-32
21.5.9	Dependence of Normalized Pressure on Fraction Burned	21-33
21.5.10	Dependence of Normalized Width of Flame on Fraction Burned	21-34
21.5.11	Dependence of Cold Stream Velocity Ratio on Fraction Burned	21-34
21.5.12	Dependence of Hot Stream Central Velocity on Fraction Burned	21-34
21.5.13	Dependence of Hot Stream Central Velocity on Fraction Burned	21-35
21.5.14	Sketch of Spreading Flame with Flame Holding Region	21-35
21.5.15	Dependence of $\bar{u}$ on Fraction Burned and Flame Width at Recirculation Zone	21-35
21.5.16	Dependence of Flame Width on Fraction Burned and Flame Width at Recirculation Zone	21-36
21.5.17	Dependence of Combustion Efficiency on Combustion Chamber Length	21-38
21.6.1	Ejector Nozzle Configuration	21-41
21.6.2	Sketch of Nozzle for Pratt and Whitney F-100-PW-100 Augmented Turbofan Engine	21-42
21.7.1	Photograph of Afterburner Flame Holders and Fuel Spray Rings	21-42
21.7.2	Sketch of Afterburner for TF30-P-3 Turbofan Engine	21-43
21.7.3	Time History of Engine and Afterburner Parameters During Afterburner Starting Transient	21-44
21.7.4	Effect of Fuel-Air Ratio and Pressure on Steady State Performance Parameters	21-44
21.8.1	Sketches Illustrating the Flame Front Geometry During Unstable and Stable Combustion	21-47

21.0 INTRODUCTION

The simple gas turbine cycle can be designed to have good performance characteristics at a particular operating or design point. However, a particular engine does not have the capability of producing a good performance for large ranges of thrust, and this inflexibility can lead to problems when the flight program for a particular vehicle is considered. For example, many airplanes require a larger thrust during take-off and acceleration than they do at a cruise condition. Thus, if the engine is sized for take-off and has its design point at this condition, the engine will be too large at cruise. The vehicle performance will be penalized at cruise for the poor off design point operation of the engine components and for the larger weight of the engine. Similar problems arise when supersonic cruise vehicles are considered.

The afterburning gas turbine cycle was an early attempt to avoid some of these problems and afterburners or augmentation devices were first added to aircraft gas turbine engines to increase their thrust during take-off or for brief periods of acceleration and supersonic flight. The devices make use of the fact that the maximum gas temperature at the turbine inlet, in a gas turbine engine, is limited by structural considerations to values less than half the adiabatic flame temperature at the stoichiometric fuel-air ratio. As a result, the gas leaving the turbine contains most of its original concentration of oxygen. This oxygen can be burned with additional fuel in a secondary combustion chamber located downstream of the turbine where temperature constraints are relaxed. The increased total temperature produced at the nozzle by this additional heat addition results in an increased exit velocity and thrust.

The advantage of using the afterburning gas turbine engine cycle is that the weight of the augmented engine is much less than the weight of a turbojet engine which can produce the same maximum thrust. This advantage is partially offset by the low thermal efficiency of the augmented turbojet cycle which is characterized by values of specific fuel consumption which are much higher than those for the gas turbine cycle. However, when the afterburner is used for a small part of a flight, the weight reduction is more important than the increase in fuel consumption.

In the middle 1960's, an augmented gas turbine engine, the General Electric GE4, was selected as the cycle to be used on the Boeing supersonic transport. It was an afterburning turbojet engine and the afterburner was used not only during take-off or transonic acceleration but also during the Mach 2.7 cruise. At these speeds, afterburning is required even during cruise to obtain a reasonable air-specific thrust.

Finally, with the advent of the turbofan engines in the late 1960's, and the Variable Cycle Engines in the 1970's, the afterburner must be viewed as one of an increasing number of devices which can be used to enhance the flexibility of the basic gas turbine cycle. The aim of these systems is to optimize engine performance over the widest possible range of operating conditions. Augmentation can be used in both fan and core streams. In some flight regimes afterburning in the bypass air stream alone is advantageous and in others, where maximum augmentation is required, afterburning in both bypass and core engine exhaust streams is desirable. Under some circumstances mixing fan and core engine exhaust streams prior to afterburning may produce a large enough performance gain to more than offset total pressure losses and increased engine weight associated with the mixing process.

An afterburner for the gas turbine engine cycle is very similar to a ramjet engine. Gas leaving the turbine is diffused, liquid fuel is added through fuel injection tubes or rings, the combustion process is initiated in the wakes of a number of flame stabilizers, and heat is added along flame surfaces spreading from these stabilization positions. Nozzles with variable area throats are necessary to accommodate the large total temperature changes produced by afterburning.

These elements of the afterburner are illustrated in Figure 21.0.1 for the turbojet cycle and in Figure 21.0.2 for the turbofan cycle. The turbojet engine is a sketch of the General Electric J79 engine and the turbofan engine is a sketch of the Pratt and Whitney F100 engine. In the latter case, afterburning is accomplished without mixing core and fan streams and the inner contour of the nozzle is shown in closed (11) and open (12) positions. In both engines, a combustion chamber liner with an air cooling passage is used to protect the outer, pressure vessel wall from heat transfer by convection and radiation.

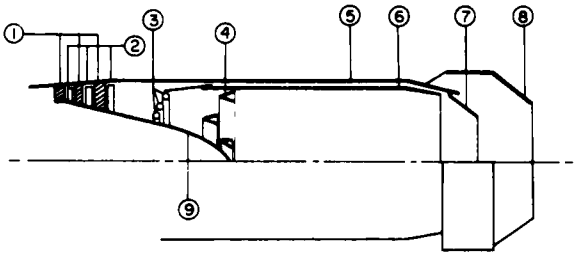

Figure 21.0.1 Sketch of General Electric J-79 afterburner. (1) Turbine nozzles, (2) Turbine blades, (3) fuel injection rings, (4) three annular V-gutter flame holders, (5) afterburner case, (6) perforated liner, (7) and (8) primary and secondary nozzle flaps, and (9) diffuser inner cone.

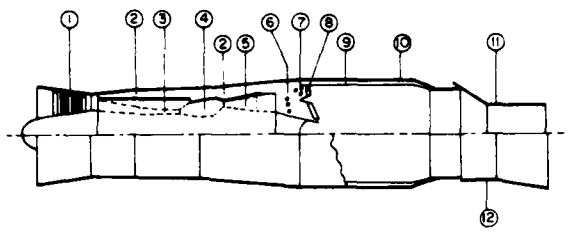

Figure 21.0.2 Pratt and Whitney F100-PW-100 augmented turbofan engine. (1) Three stage fan; (2) bypass air duct; core engine compressor (3), burner (4), and turbine (5); (6) fuel injectors for core engine gas stream; (7) fuel injectors for bypass air stream; (8) flame stabilizer for afterburner; (9) perforated afterburner liner; (10) afterburner case; nozzle closed to minimum area (11) and opened to maximum area (12).

To illustrate typical afterburner operating conditions, performance curves are shown in Figure 21.0.3 for a turbofan engine, the Pratt and Whitney TF30 engine. This engine is similar to that shown in Figure 21.0.2 and the core and turbine gas streams are not mixed. The specific fuel consumption SFC and thrust F are shown as ratios of their values to their values with no afterburning and as a function of afterburner fuel-air ratio. Afterburner total pressure ratio π_{ab} and combustion efficiency η_{ab} are also given. The two curves on each plot correspond to operating altitudes of about 12 km and 14.6 km and a flight Mach number of 1.4. Flow conditions at afterburner entrance for the core stream and for the two altitudes were for the core stream: Total pressure of 1.05 and 0.69 atm, total temperatures of about 900° k for both, inlet velocities of 180 and 230 meter/sec; for the fan stream: Total temperature was about 400° k. At these conditions, thrust augmentation of about 60 percent can be achieved at a cost of an increase of 120 percent in specific fuel consumption. Performance decreases as altitude is increased. Note that the afterburner total pressure ratio with no heat addition is about 0.94; the 6 percent loss represented by this ratio accounts for some diffusion loss in addition to the flame holder drag losses.

For this engine, fuel is injected through orifaces with diameters of about 0.15 cm in a number of concentric rings of fuel injection tubes which are similar to those shown in Figure 21.0.2. Afterburner fuel-air ratio is increased by adding fuel first to the core flow near the interface between the core flow and fan air stream, then to the fan air, and finally to the rest of the core flow. Because the fan air contains the most oxygen and the lowest temperature, afterburning in the stream produces the largest performance gain. However, the low temperature of this stream makes

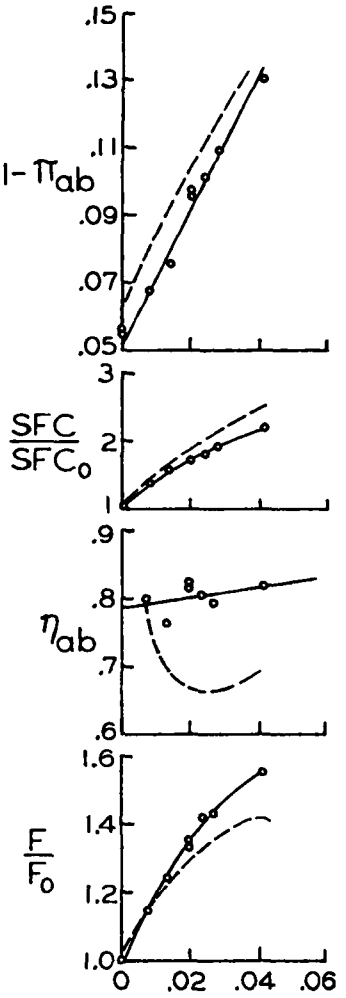

Figure 21.0.3 Afterburner performance characteristics for the TF30-P-3 engine. Engine characteristics: $\pi_c = 17$, $\pi_c' = 2.1$, bypass ratio $\alpha = 1.0$, flame holder blockage 0.38. Flight Mach number 1.4. Solid curves are for an altitude of 12 km and dashed curves for 14.6 km. Data from Reference 21.1.

vaporization of the fuel and hence afterburning most difficult. The addition of fuel in the order suggested here first produces a high temperature at the outer edge of the core stream where it can act as a pilot for the fan air combustion process. The rapid fall in combustion efficiency at 14.6 km and for low fuel-air ratios is due to the problem of burning in the cold fan streams where vaporization of the fuel is very poor.

The purpose of this chapter is to discuss the engineering information available concerning afterburner components and to indicate some

current design practices. Because of the author's interests, some problem areas will be more thoroughly described than others. Section 21.10 contains references to review articles which discuss a number of subjects concerning afterburners which are omitted here.

21.1 DIFFUSER

The heat which can be added to a compressible flow in a constant area duct before choking occurs and the pressure loss which accompanies this heat addition depend on the Mach number of the flow entering the burner. As the inlet Mach number decreases, the maximum heat addition increases and the total pressure loss decreases. In addition, the flame stabilization process becomes more difficult as gas speed increases. Hence, it is desirable to use as low a value as possible for the burner inlet Mach number and a diffuser is used between the turbine exit plane and the afterburner itself.

The minimum Mach number at the burner inlet is usually fixed by the requirement that the diameter of the afterburner section of the engine not exceed that of the engine components located upstream of the afterburner. This limitation arises from the desire to minimize the drag of the engine due to frontal area and nozzle exit area, and the desire to minimize the weight of the afterburner itself.

The desire to minimize weight also results in the requirement that the diffuser be kept as short as possible without producing flow separation from the inner body. Relatively large divergence angles can be used because the blockage of the flow, produced by the flame holder and fuel injection systems, reduces the tendency of the flow to separate from the diffuser cone. Finally, the general problem of producing a steady, uniform and unseparated flow at the diffuser outlet is often complicated by the presence of a large swirl component in the gas leaving the turbine (15 - 20 percent tangential component) and the interaction of this swirling flow with struts required to support the rear engine bearing.

In augmented turbofan engines in which the two gas streams are to be mixed before afterburning is initiated, the diffuser is usually combined with the mixer. For example, the fan stream and core streams can be ducted together to form a series of adjacent radial slots with fan air and core air in alternate slots. This geometry has the advantage that mixing will occur in a distance much smaller than required with the undisturbed annular geometry shown in Figure 21.0.2. By keeping cross section areas of each stream almost constant, pressure losses in mixers of this type can be minimized.

21.2 FUEL INJECTION, ATOMIZATION AND VAPORIZATION

The goal of the fuel injection system is to produce a specified distribution of fuel vapor in the gas stream entering the afterburner. In most engines, fuel is introduced in a staged manner so that heat addition rate can be increased gradually from zero to the desired value. Because ignition, flame stabilization and flame spreading are easiest to achieve when the fuel-air ratio is close to the stoichiometric value, staging is usually produced by adding fuel to successive annular stream tubes so that the mixture ratio in each tube is nearly stoichiometric. Each stream tube has its own set of fuel injectors and control system which can be activated independently. For example, see the six injectors used in the F100 engine shown in Figure 21.0.2.

The most remarkable fact concerning the fuel system for afterburners is their simplicity. In many engine systems, fuel is supplied to a circular tube which lies with its axis perpendicular to the gas stream. Fuel is injected into the gas through small diameter holes located in the sides of the tube such that the liquid jet enters the gas stream in a direction perpendicular to the undisturbed flow direction. The liquid jet penetrates some distance into the gas stream before its momentum is dissipated. During this penetration process, the air stream tears the jet apart and produces droplets with diameters of micron size. Heat transfer from the hot gas stream then vaporizes the droplets.

Given the wide range of values of mass flows of fuel required, it is remarkable that reasonably thorough mixing of the fuel with the air can be achieved with this simple injection system. In some recent engines efforts are being made to use simple variable area injection ports which may possibly give better preparation of the fuel-air mixture.

The whole area of fuel penetration, atomization and vaporization is not well understood from first principals and one of the time consuming parts of an afterburner development program is to determine the optimum distribution of locations for injector tubes, injector ports and port diameters. In the following paragraphs a very brief analysis is made of several aspects of the fuel injection problem with the aim of illustrating some of the important scaling parameters rather than of furnishing design procedures.

Penetration. The trajectory of a fluid jet injected into a high speed air stream can be crudely analyzed by treating the boundaries of the jet and resulting droplet stream as a solid body and applying continuity and momentum conservation laws. The force applied to the surface of the stream tube in the direction of the flow, see sketch of Figure 21.2.1, will be proportional to the dynamic pressure of the gas, $\rho_\infty v_\infty^2/2$, and some cross sectional area, say $\overline{w} \times h$. Here $\overline{w}$ is an average width and h is the penetration distance. This force must be balanced by the momentum flux of the injectant stream with mass flux $\dot{m}_j$. If we assume that the fluid is accelerated to a velocity v_∞ at the exit of the control volume and that it enters with no momentum flux in the direction of flow, the force balance gives:

$$\rho_\infty v_\infty^2 (w\ h) \propto \dot{m}_j v_\infty$$

so that

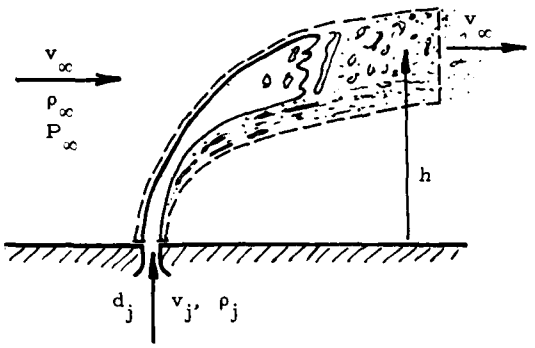

Figure 21.2.1 Schematic for Estimate of Penetration Distance.

$$\left(\frac{\dot{m}_j}{\rho_\infty v_\infty (w\ h)}\right) = \text{constant} \quad (21.2.1)$$

The actual penetration distance is obtained by assuming $w \propto d_j$ and $\dot{m}_j \propto (\pi d_j^2/4)\rho_j v_j$; it is given by:

$$\frac{h}{d_j} \propto \sqrt{\frac{\rho_j}{\rho_\infty}} \left(\frac{\rho_j v_j^2}{\rho_\infty v_\infty^2}\right)^{1/2}$$

Note that the denominator of Equation 21.2.1 is proportional to the mass flux of air through the region fed by the injector. Thus, if the injector flow rate is changed in order to keep h fixed (as some other parameter such as flight altitude is varied), the overall fuel-air ratio in the stream tube fed by the injector will be held fixed.

Recent experimental work by Schetz and Padhye, Reference 21.2, suggests that an analysis of this type does predict a reasonable dependence of penetration distance h on the dynamic pressure ratio $\rho_j v_j^2/\rho_\infty v_\infty^2$. Penetration distances of 10's of diameters can be achieved with dynamic pressure ratios between one and two.

Atomization. The breakup of the injected fuel stream, into small droplets depends on the dynamic pressure parameters listed above, and in addition on the viscosities of the fuel and gas streams, and on the interfacial tension of the fuel-gas system. The physical process of atomization of the fluid jet probably involves the production of waves on the fluid-gas interface, the shedding of long ligaments of fluid as the waves break and then the breakup of the ligaments into droplets. The overall process is sufficiently complex that no model or set of scaling parameters has been generally accepted. The problem is complicated by the necessity for measuring and describing a distribution of drop sizes rather than a single drop diameter.

To give the flavor of the results obtained in experiments, we describe the results of Ingebo and Foster (Reference 21.3). They worked with the volume-median droplet diameter defined as

$$D_{30} = \left(\sum_i n_i D_i^3 / \sum_i n_i\right)^{1/3}$$

where n_i is the number of particles with diameter D_i. They found that D_{30} depended on the injector diameter d_j and two dimensionless parameters, a Reynolds number,

$$Re \equiv \rho_\ell v_\infty d_j/\mu_\ell$$

based on the gas stream velocity v_∞, the injector diameter d_j and the liquid density and viscosity ρ_ℓ and μ_ℓ; and a Weber number,

$$We \equiv \sigma_j/\rho_\infty v_\infty^2 d_j$$

based on fuel surface tension σ_j and dynamic pressure of the gas. The relationship for D_{30} found by these authors was

$$\frac{D_{30}}{d_j} = 4\left(\frac{We}{Re}\right)^{1/4} \quad (21.2.2)$$

For a gas stream with a speed of about 200 m/sec., temperature of 900°k and pressure of 3 atm., and a gasoline like fuel jet, the Reynolds and Weber numbers for a millimeter diameter injector port are about 2×10^5 and 10^{-3} respectively. Using these values in the above equation we find $D_{30} \approx 40$ microns.

The equation given above indicates that there is no dependence of atomization on the injection velocity v_j but there is an inverse 1/4 power dependence of D_{30} on gas stream density and, hence, pressure. Thus, as the pressure decreases, droplet diameter will increase slowly. Finally, D_{30} is proportional to the square root of port diameter d_j.

Evaporation. The evaporation rate of the droplets formed in the injection process is a strong function of gas and droplet temperature, and the relative velocity of the droplets with respect to the air. For most conditions of interest to us, the pressure of the vapor at the surface of the drop will be close to the equilibrium value fixed by the surface temperature of the drop. Vapor is removed from this region by diffusion and forced convection; and the heat required to produce the evaporation is transferred to the surface by conduction from within the drop, and by conduction and forced convection from the gas stream. The drop radius and the temperature distribution within the drop will be functions of the time. Transport of vapor and heat occur by diffusion and by forced convection, and both processes may be either laminar or turbulent.

The most simple situation to analyze for this complex problem is the case in which

molecular transport processes for mass and heat are dominant, and for which we can ignore temperature changes within the drop. This quasisteady situation is most likely to occur for small (e.g., 10μ diameter) drops moving with a small velocity with respect to the gas stream. Under these conditions we can show that the rate of change of mass M of a droplet is given by

$$\dot{M} = -4\pi r(\rho_v \mathcal{D}) \qquad (21.2.3)$$

where r is the droplet radius, and ρ_v and $\mathcal{D}$ are vapor density and diffusion coefficient at the particle surface. Since the particle mass is $(4/3)\pi r^3 \rho_\ell$,

$$\frac{r dr}{dt} = \frac{\rho_v \mathcal{D}}{\rho_\ell}$$

and the time required t_e for complete evaporation of a particle of initial radius r_o is

$$t_e = r_o^2 / (\overline{\rho_v \mathcal{D}/\rho_\ell}) \qquad (21.2.4)$$

Here, the denominator is the value averaged over the evaporation time of the droplet. Clearly, the time for complete evaporation will be much longer for large drops.

The term in the denominator of the above equation is a strong function of the temperature and in order to determine its value, an energy balance for the droplet must also be used. The vapor density at the droplet surface ρ_v is only a function of temperature and since $\mathcal{D} \propto 1/P$ holds roughly, we find that $\overline{\rho_v \mathcal{D}}$ will be proportional to 1/P, the inverse of the local static pressure. Thus, as the pressure in the region of injection falls, the time required for evaporation of small droplets of a <u>fixed</u> temperature will decrease.

For the simple situation under investigation here, the energy balance reduces to

$$-\dot{M}L = \dot{q}$$

where L is the heat of vaporization, $(-\dot{M})$ is the rate of generation of vapor and $\dot{q}$ is the heat transferred by conduction to the drop. We can show that $\dot{q}$ is given by $4\pi r k(T_\infty - T_p)$ where k is coefficient of thermal conductivity, and T_∞ and T_p are the temperatures of the gas far from the drop, and the temperature of the drop. Given these results, the energy balance given above reduces to:

$$\frac{T_\infty - T_p}{T_\infty} = \left(\frac{\rho_v}{\rho_g}\right)\left(\frac{\rho_g \mathcal{D} C_{pg}}{k_g}\right)\left(\frac{L}{C_{pg} T_\infty}\right) \qquad (21.2.5)$$

Note, ρ_v is an exponential function of T_p. Here the vapor density at the particle surface has been normalized by ρ_g, the density of the gas stream evaluated at T_p. The second and third terms on the right hand side of Equation 21.2.5 are almost independent of pressure and temperature. (The second term is the Lewis number.) However, the first term is a very strong function of temperature and is inversely proportional to pressure because the gas density is proportional to P/T_p. Hence, the above equation can be written in the form

$$(T_\infty - T_p) = f\{T_p\}/P_\infty \qquad (21.2.6)$$

where f increases exponentially with T_p.

If P_∞ is reduced, e.g., by increasing the altitude at which the engine is flying, the droplet temperature must adjust to satisfy this equality. Two regimes of interest can be defined. In the first, let the gas temperature be much greater than the particle temperature. Then a drop in P_∞ must be accompanied by a drop in T_p. Because of the strong dependence of f on T_p, a small change in T_p will be required to satisfy the equation. Hence, the temperature difference $(T_\infty - T_p)$ will not change appreciably, and, consequently, the conduction term and thus the evaporation rate will not change appreciably. For this example, the increase in diffusion coefficient due to a reduction in pressure is offset by a reduction in vapor pressure (due to reduced T_p) so that the vapor diffusion and evaporation rates are held almost constant. For this case then, the evaporation time t_e of Equation 21.2.4 will not be affected directly by the pressure.

In the second regime, assume that T_∞ is almost equal to T_p. Then, when P_∞ is caused to drop, the small change in T_p needed to balance Equation 21.2.6 will make an appreciable difference in the temperature difference $(T_\infty - T_p)$. Thus, the heat transfer rate and consequently the evaporation rate will increase as the pressure falls.

If we combine the simplified results presented above, we find that as the pressure in the afterburner falls, say as a result of the increase in altitude of an engine operating at a fixed Mach number, the simple injector discussed here is capable of supplying the required fuel flow to the appropriate volume of space. However, as pressure decreases, the droplet diameter will increase. In addition, for the first vaporization regime discussed above, the evaporation rate will be independent of pressure but will decrease rapidly as the drop radius increases. Hence, the effect of the reduction in pressure will be to increase the initial diameter of the droplets and to decrease the evaporation rate. In the second regime the effect of increase in the initial radius of the drops will be offset by the increase in diffusion rates.

Also note that the evaporation rate depends on the diameter of the injector part d_j. It is

clear from Equation 21.2.2 that D_{30} is proportional to $\sqrt{d_j}$ and consequently that the evaporation time given in Equation 21.2.4 is directly proportional to d_j. Hence, more rapid evaporation could be achieved by using injection ports of a smaller diameter. However, the number and location of the injector ports would need to be changed to keep the fuel distribution unchanged. In addition, the smaller holes would be more subject to blockage by dirt and pyrolized fuel.

In real systems, the observed effect of a pressure decrease is that combustion efficiency falls off badly when the pressure is reduced below some limiting value which is often of the order of one atmosphere. This pressure limit is a major limitation on the operating range for an afterburner.

21.3 IGNITION

The fuel-air mixture produced by the injection process has a flame propagation velocity which is much less than the gas speed in the combustion chamber. Hence, unless sources of continuous ignition are present in the chamber, the burning gas ignited by a temporary process would be blown out of the engine as soon as ignition stopped. In most afterburner systems, the continuous source of ignition is the wake of a bluff body, (called the flame holder), held with its axis perpendicular to the flow. Hot gas, trapped in the first few diameters of the flame holder wake, mixes with the combustible mixture flowing over the wake and acts as the source of ignition. The process of flame stabilization is the subject of the next section; here we will describe the process of initiation of the stabilization process. This ignition process need only start the stabilization process and may then be turned off. Furthermore, it has been found that once the stabilization process has been established in a relatively short length of flame holder, say five diameters, the process will spread to the rest of the stabilizer system if the wakes of the stabilizers form a continuous pathway. Finally, fuel is usually added in sequence to a number of annular stream tubes to prevent pressure surges during afterburner ignition and to allow modulation of the afterburner thrust. Hence, once one region is "lit", it can act as a source of ignition for adjacent regions when fuel is added to them. Thus, the purpose of the ignition system is to establish a stabilized flame in a relatively small part of the flame stabilizer system. The bluff body flame holder system will then furnish a path for further spreading of the stabilized flame as additional fuel is added.

Three general systems have been used. There are the hot streak technique, spark or arc ignition and the pilot burner technique. In the hot streak system, fuel is injected for a short period into the gas stream of the core engine just upstream of the turbine. The combustible flow formed by this process produces a very hot stream of burning gas which is positioned radially to coincide with the primary fuel-air injection stream-tube for the afterburner. Combustion occurs in this stream by auto ignition (because of the high temperatures present upstream of the turbine) and the flame stabilization process is initiated when the hot burning gas fills the initial wake-region of the flame holders. The hot streak can only be maintained for a brief period to prevent thermal damage to the turbine.

Ignition and initiation of the flame stabilization process can also be initiated by producing a high energy electric arc in the primary stream tube. Ignition in this case is usually produced by placing the arc in a region of the wake of the flame holder system which is particularly sheltered and which may have its own fuel supply system. Stabilization is initiated locally by the heat from the arc and spreads by the mechanism described above.

The pilot burner system is similar to the arc system and may use an arc to initiate combustion. In this system, a small can-burner similar to that used in the core-engine primary-burner, is located in the primary stream tube. This system furnishes a continuous source of hot combustion products which act in a manner similar to the hot streak system to start the stabilization process once fuel injection is started.

The energy required to initiate the flame stabilization process comes primarily from chemical reactions which are initiated in the premixed fuel-air stream by the ignition system. At present, the amount of energy required (e.g., joules supplied to the arc discharge or total mass of fuel injected into the hot streak) to achieve ignition cannot be calculated for a particular design. However, some trends can probably be determined by examination of experimental results concerned with ignition of flowing streams of fuel-air mixtures.

Studies with various sources of ignition such as arcs, hot surfaces and hot gas streams indicate that the energy required is a strong function of fuel-air ratio, fuel properties, the local pressure and temperature, and the residence time of the combustible gas in the system. The energy required is smallest for mixture ratios near the stoichiometric value and increases very rapidly as the mixture ratio is decreased below 0.5 to 0.7 of the stoichiometric ratio. Also, it decreases as pressure, temperature, the oxygen mole fraction and residence time of the flow in the ignition region increase. The exact values required are very sensitive to the particular device being studied and the calculation of conditions required to produce ignition for a particular system cannot yet be carried out even for very idealized experimental conditions.

Based on these results, one expects ignition in afterburner systems to be easiest to achieve in gas with a fuel-air ratio close to the stoichiometric value, in the most sheltered regions of the stabilization system where residence times are longest, and when pressures and temperatures are highest.

Ignition is usually harder to achieve than stabilization. Because velocities and temperatures do not change a great deal at the afterburner inlet, the primary problem for afterburner ignition systems is the high altitude relight problem. The difficulty here is associated with low pressure in the afterburner which effects both the preparation of the fuel (by the

injector system) and the ignition process directly. The operating regime for the engine is often plotted, as shown in Figure 21.3.1, on an altitude versus Mach number map. The boundary called the Ignition curve is the altitude (i.e., the pressure) limit above which ignition is no longer possible. Afterburner operation above this altitude is possible (for this example) if the afterburner is ignited at a lower altitude.

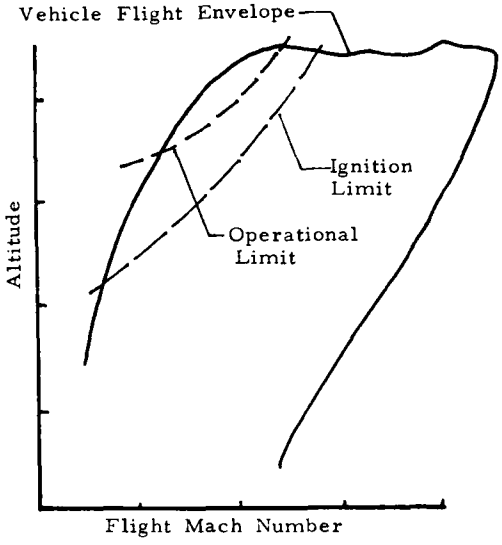

Figure 21.3.1 Flight Envelope for an Afterburner.

21.4 STABILIZATION PROCESS

The purpose of the flame stabilization process is to establish a continuous source of ignition in a fuel-air mixture whose velocity is much greater than the turbulent flame speed for the mixture. Laminar flame speeds in mixtures of typical hydrocarbon fuels with air heated by partial combustion are in the range of a few meters per second. If the flow is turbulent, this speed may be as large as a few tens of meters per second although the meaning of the term, turbulent flame speed, is poorly defined. These turbulent speeds are still much less than the gas speeds encountered in the flame stabilization region of afterburner systems where gas speeds of hundreds of meters per second are typically encountered. Hence, a continuous source of ignition is required to start the combustion process. Once started, the combustion wave can spread from its point of ignition across the fuel-air mixture produced by the injection system in a wave like manner similar to the propogation of an oblique shock wave across a supersonic flow.

One of the most important parameters of the stabilization process is the state of the fuel in the fuel-air mixture. In the core flow, temperatures are high enough to insure that most of the fuel is vaporized. However, in the fan stream, temperatures can be so low that only a small fraction of the fuel will be vaporized and the stabilization mechanism will have the additional job of vaporising the fuel used in producing a stable flame. In existing systems this problem is usually avoided by starting the afterburning process in the core stream. The hot gas generated in the core is then used to stabilize the flame in the fan stream. In the first part of the following discussion we will restrict ourselves to the vaporized fuel example.

The ignition process, usually called flame stabilization in afterburner systems, is typically achieved in a mixture of fuel vapor and air by allowing hot products of combustion to mix with the unburnt fuel-air mixture. The steady flow of hot gas required for this process is usually obtained by setting up a recirculating flow of burnt material. When a bluff body flame holder is used, see Figure 21.4.1a, hot gas, generated by the recirculation of burning material in the wake of the bluff body, supplies the energy and the mass of products of combustion required to ignite the unburnt material flowing past the wake. This process is described and analyzed in detail in the following sections.

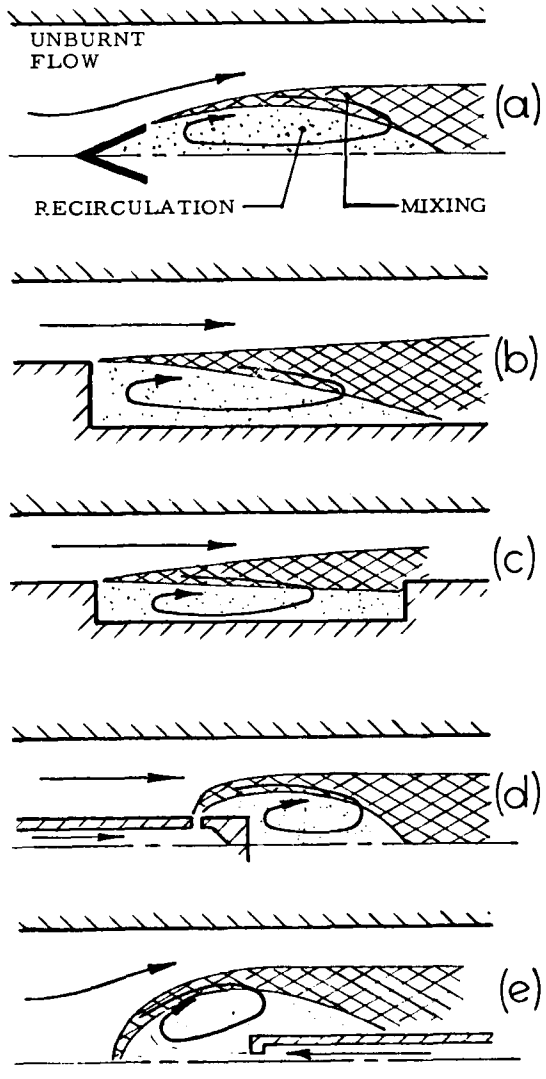

Figure 21.4.1 Flame Stabilization Schemes for Mixtures of Fuel Vapor and Air.

The processes occuring in the wake of the bluff body also occur in the wake of a step or in a wall recess, see Figure 21.4.1b and c. In these examples heat transfer from the gas to walls of the cavity reduces the gas temperature in the recirculation zone and makes stabilization more difficult.

The wake region required to produce the recirculation zone described above, can also be produced by injecting a secondary gas stream into the unburnt flow, see Figure 21.4.1d and e. Again, a wake region with strong recirculation is formed by the interaction of the two streams. In these examples the fluid which enters the recirculating wake is made up in part of the injected fluid. Hence, the fuel-air ratio of the recirculation zone gas can be changed by changing the fuel-air ratio of the injectant. We shall see later that this process can give us a powerful control over the stabilization process.

The configurations shown schematically in Figure 21.4.1 can be used in either axisymmetric or two-dimensional geometries. The latter configuration is the most common.

The performance of a flame stabilization system is usually presented in the form of a map on which the boundaries of a stabilization parameter are given as a function of fuel-air ratio. An elementary map of this type is shown in Figure 21.4.2 where the velocity at which the stabilization process fails (called here the blowoff velocity) is presented as a function of the fuel-air ratio with the flame holder scale as a parameter. The experimental data of Haddock, Reference 21.4 were obtained in a mixture of vaporized gasoline and air, and with circular cylinders used as flame holders. For each flame holder, flame stabilization was found to be possible for the range of values of fuel-air ratio within the curves shown in the Figure. For example, stabilization was possible with the 1/2 inch (1.3 cm) diameter cylinder for fuel-air ratios between 0.70 and 1.15 times the stoichiometric value when the gas speed approaching the cylinder was about 600 ft./sec. (183 m/sec.). As the gas speed increased, the fuel-air ratio range for which stabilization could be achieved decreased and the peak value, about 740 ft./sec. (226 m/sec.) occurred for values close to stoichiometric. Flame holders with diameters between 1/2 inch (1.27 cm) and 1/8 inch (0.32 cm) had clearly turbulent wakes and exhibited similar behavior. The blowoff velocities increase regularly as holder scale increases.

The three remaining curves are for holders with laminar wakes. The peak blowoff velocity for these examples is progressively shifted toward fuel-air ratios greater than stoichiometric as the flame holder scale is reduced. This behavior is a result of a molecular diffusion process which usually is of no importance in flame holder systems operating in gas turbine engines. However, note that even for the largest flame holder, the lean stability limit is well above 0.5 of stoichiometric and that values above 0.8 are required to stabilize flames in high speed flows.

It is clear from these data that the velocity at which stabilization can be maintained

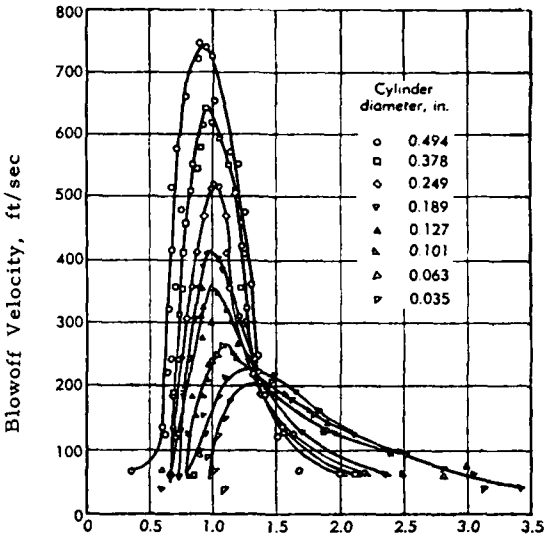

Figure 21.4.2 Stability Limit Curves for Circular Cylinders. Data from Haddock (Reference 21.4). Vaporized Hydrocarbon Fuel-Air Mixture at One Atmosphere and 60° C.

is a strong function of flame holder scale, fuel-air ratio and wake condition (laminar or turbulent). Other experiments show that it also depends on fuel characteristics; the temperature, pressure and oxygen content of the unburnt gas stream, and on a number of geometric factors which describe the flame holder-duct system. The nature of these dependences and their origin will be discussed in later paragraphs of this section. Stability limits obtained with the other systems shown in Figure 21.4.1 follow a pattern similar to that described above when mixtures of fuel vapor and air are used. However, when a large fraction of the fuel is not vaporized the picture is quite different.

The bluff body flame stabilization process which occurs in fuel vapor-air mixtures will be treated in detail in Section 21.4.1. Briefer descriptions will also be given of scaling parameters for stabilization by secondary injection (illustrated in Figure 21.4.1d) and of bluff body stabilizers operating in unvaporized fuel-air mixtures.

21.4.1 FLAME STABILIZATION BY BLUFF BODIES IN PREMIXED FLOW

The mechanism of flame stabilization by bluff body flame holders is still a subject of some contention and the mechanism described here is that developed at California Institute of Technology by F. E. Marble, E. E. Zukoski, and a number of co-workers at the Jet Propulsion Laboratory, C.I.T. (E.g., see References 21.5 to 21.8.)

This approach is based on a picture of the wake of a two-dimensional flame holder shown in Figure 21.4.3. Figure 21.4.3a is a photograph taken in the light of the flame of the flame stabilization region of a circular

cylinder. The line of sight is along the cylinder. The sketch of Figure 21.4.3b is a highly simplified drawing of the velocity field for the same region. The mixing zones are illuminated in (a) by light from the combustion process occuring there. Chemiluminescence and, hence, chemical reaction is almost absent in the recirculation zone.

We divide the wake of the flame holder into two regions: The recirculation zone, a region characterized by strongly recirculating flow and the mixing zone which separates the recirculation zone from the unburnt mixture.

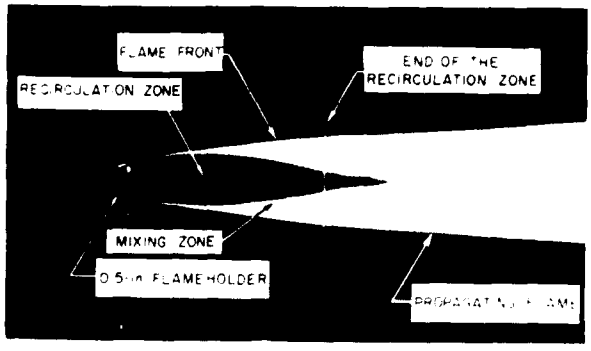

(a)

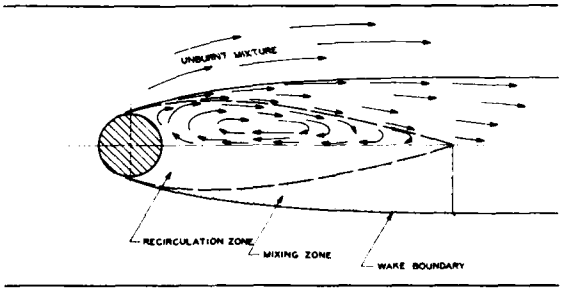

(b)

Figure 21.4.3 Photograph and Sketch of the Flame Stabilization Region of a Circular Cylinder Used as a Bluff Body Flame Holder.

The temperature of the recirculation zone gas is typically within 5 to 10 percent of the adiabatic flame temperature corresponding to the mixture ratio of the approach stream and is independent of gas speed, and the flame holder-duct geometry. Chemical reaction appears to be almost complete in this volume, and the residence of gas is 5 to 10 times the time required by the flow at the cold side of the mixing region to pass over the recirculation zone. This long residence time insures that if any chemical reaction takes place in the wake at all, it will be most nearly complete in the recirculation zone.

The mixing zones on either side of the recirculation zone are turbulent regions of very strong shear, steep temperature gradients and vigorous chemical reaction. These regions thicken almost linearly and their junction forms the downstream end of the recirculation zone.

The process which leads to the formation of a self propagating chemical reaction takes place in the mixing zone. This region is fed by turbulent mixing processes with cool combustible gas from the approach stream and with very hot burnt material, from the recirculation zone. Thus, if no chemical reaction were present, the mixing zone gas would still be at a high temperature at the inner edge (or recirculation zone side) of the region. Downstream of the end of the recirculation zone, the cool, unburnt gas continues to be entrained into the wake, but no more hot gas is added; hence, if no chemical reaction were present, the temperature would fall.

Chemical reaction is initiated in the mixing zone by heat and species transfer from the hot burnt gases to the unburnt material. The total heat and species transferred to any particle of unburnt gas, and its reaction rate, will largely depend on the time this particle spends in contact with hot burnt gas. Thus, the temperature, species concentration, and consequently the local chemical reaction rate of unreacted material will depend strongly on the residence time of this unburnt material in the mixing zone.

For a sufficiently long residence time, a chemical reaction will be started in the mixing zone flow and will continue as this gas moves on downstream to form the wake. If this reaction is vigorous enough in the wake region, then the quenching action of the continuing entrainment of cool unburnt gas will be overcome and a propagating flame will be produced.

It is reasonable to suppose that the residence time of unburnt gas in the mixing zone will be proportional to $L_e / \bar{v}$ where $\bar{v}$ is a suitably chosen average speed in the mixing zone, and L_e is the scale of the recirculation zone. Hence, when the velocity of the flow increases, $\bar{v}$, will increase proportionately and the residence time will decrease. When the residence time is too short, the chemical reaction in the wake will be quenched and no propagating flame will be stabilized. Thus, flame extinction or blowoff occurs due to failure of the ignition process and not as a direct result of cooling of the recirculation zone gas.

The important parameters of the system as indicated by this discussion are: $\bar{v}$, an average gas in the mixing zone; τ, a time which characterises the period required to achieve ignition in the mixing zone; and L_e, the length of the recirculation zone which is effective in igniting the mixing zone. The dimensionless stability parameter of interest is then $(\bar{v}\,\tau / L_e)$. There is good evidence that mixing layer flow fields are roughly similar, i.e., have similar velocity, composition and temperature fields. Thus, if we compare similar systems with the same chemical parameters but under different

fluid dynamic conditions, our stability parameter must take on a particular value at blowoff condition, i.e.,

$$\left.\frac{\bar{v}\tau}{L_e}\right]_{\text{blowoff}} = \beta_c$$

Because of the similarity of the turbulent mixing zones of bluff body flame holders, the parameters L_e and $\bar{v}$ used in this expression can be replaced without loss of generality by the maximum length of the recirculating flow, L, and the unburnt gas speed at the edge of the mixing zone V_2. Then the blowoff condition given above can be rewritten as:

$$\frac{\bar{v}\tau}{L_e} = \left(\frac{\bar{v}}{V_2}\,\frac{L}{L_e}\right)\left(\frac{V_2\tau}{L}\right) = \beta_c$$

When $\bar{v}/V_2$ and L/L_e can be assumed to be constants (for similar turbulent mixing regions), the stability criterion becomes:

$$\frac{V_2\tau}{L} = \text{constant}$$

at the flame extinction or blowoff condition.

A number of experiments have verified the usefulness of this relationship. However, an independent calculation of the characteristic chemical time τ has not been developed and consequently it is necessary to experimentally determine τ from a set of flame blowoff experiments. In these experiments, V_{2c} and L are determined at the blowoff state and τ is obtained from $\tau_c \equiv L/V_{2c}$. Given this definition the flame blowoff criteria is

$$\left.\frac{V_{2c}\tau_c}{L}\right]_{\text{blowoff}} = 1 \qquad (21.4.1)$$

In this formulation the unknown constant β_c has been absorbed in the measured quantity τ_c. One of the great advantages of this approach is that all dependence on chemical parameters is naturally lumped in τ_c and all dependence on fluid dynamic parameters, in (L/V_{2c}).

When τ_c has been determined experimentally for a single duct-flame holder configuration, and for the desired ranges of the chemical parameters, it can be used to predict stability limits for any other duct-flame holder configuration and the same range of chemical parameters. Thus, τ_c is a scaling parameter.

A number of experiments with a wide range of flame holder-duct configurations have shown that the values of τ_c do depend on a number of chemical parameters such as fuel type, fuel-air ratio, gas temperatures, and degree of vitiation, but are substantially independent of the geometry and scale of flame holder-duct configuration and of gas speed so long as the flow in the mixing region is turbulent. A few typical results are summarized in Table 21.4.1. The top two flame holders are circular cylinders with their axis held perpendicular to the flow and the latter three had cylindric bodies with their axis parallel to the flow and several types of axisymmetric noses. The third body is the two-dimensional analog of the fourth. The large differences in the flow field produced by these bodies is illustrated by the Schlieren photographs shown in Figure 21.4.4. Note that values of the critical times evaluated at the stoichiometric ratios are about the same regardless of geometry.

Flame Holder Geometry	D or d	τ_c
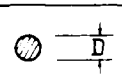	1/4 and 3/16 3/8 1/4	3.00 x 10⁻⁴ sec 2.35 2.3
1/4 mesh screen	1/4	3.0
	1/4 3/8 1/2 3/4	2.33 2.70 2.45 2.53
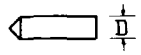	1/4 3/8 1/2 3/4	3.43 3.44 3.7 3.3
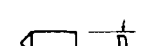	3/4	3.45
	3/4	3.20

Table 21.4.1 Dependence of Ignition Time τ_c Obtained at the Stoichiometric Fuel-Air Ratio on Flame Holder Geometry and Gas Speed.

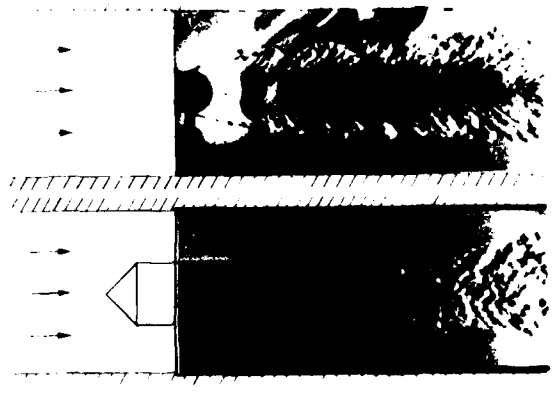

Figure 21.4.4 Spark Schlieren Photographs of Flames Stabilized on: (Upper) Circular Cylinder Received from the Side and (Lower) on Axisymmetric Body With Axis Parallel to Flow. The Recirculation Zone, Clearly Outlined in Upper Photograph, Is Not Visible in the Lower.

In addition, for flames in which mixing length similarity does not hold, values of τ_c determined by integration of local velocity measurements along a path in the mixing zones again confirmed the validity of this approach. For example, see the work of Broman, Reference 21.8.

The fluid dynamic and chemical aspects of the stability criterion will be discussed separately in the following paragraphs.

21.4.1.1 FLUID DYNAMIC PARAMETERS

The flame stabilization criterion given above in Equation 21.4.1 is not immediately useful even when the characteristic τ_c is known as a function of the chemical parameters because the recirculation zone length L and the gas speed in the flow over the wake V_2 are not simply related to the scale of the flame holder and the velocity far upstream. To illustrate the dependence of these parameters on other fluid dynamic variables we will discuss the case of a two-dimensional flame holder of height d located on the center line of a rectangular duct of height H and subject to a flow with an upstream velocity V_1. We need to connect the fluid dynamic parameters used in our model with these parameters which are the ones usually specified. These two sets of parameters are illustrated in Figure 21.4.5. In a formal way the stability criterion can be written as:

$$\frac{V_{2c}\,\tau_c}{L} = 1 \quad \text{or} \quad \frac{V_{1c}\,\tau_c}{H} = \left(\frac{V_1}{V_2}\right)\left(\frac{L}{W}\right)\left(\frac{W}{H}\right) \tag{21.4.2}$$

Here W is the width of the wake near the downstream and of the recirculation zone. Its introduction in Equation 21.4.2 will lead to a useful simplification which is described below. Also V_{1c} and V_{2c} are the values of velocity of the approach stream and the flow past the wake evaluated at blowoff condition.

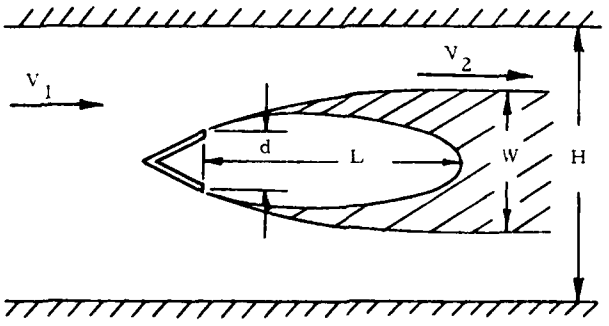

Figure 21.4.5 Sketch of Notation Used in Analysis of Stabilization.

In order to apply the criterion we need to know V_1/V_2, L/W and W/H as functions of the blockage ratio d/H, the flame holder geometry and the usual parameters of compressible and viscous flows, the Reynolds and Mach numbers. In addition, we must consider the flame holder temperature which affects the boundary layer on the holder and the turbulence level in the approach stream. In the following paragraphs, the effects of changing d/H, called the blockage ratio, and the flame holder geometry will be considered first, and later the effects of Reynolds number, Mach number, flame holder temperature, and turbulence will be described. Note in some Figures D replaces d.

Blockage and Flame Holder Geometry. Consider again the flow described schematically in Figure 21.4.5. Note that the flow separates from either side of the flame holder and that the wake continues to spread downstream of the holder and asymptotically approaches a width W. (We will find later that W rather than d is the most useful characteristic scale for the holder in this problem.) The flame holder and its burning wake block an appreciable part of the cross section area of the duct and causes the unburnt flow to accelerate to a higher velocity, V_2.

The wake width is a critical parameter since it not only affects the ratio V_2/V_1 but also fixes the recirculation zone length L. For example, the width of the mixing zone increases almost linearly with distance along its length. This spreading rate is similar to that of many other two-dimensional turbulent shear layers and has a constant width-to-length ratio of roughly 1/8. At the downstream end of the zone, the two mixing layers occupy the entire width of the wake and consequently we expect that the ratio of recirculation length to wake width L/W should be close to 4. For a wide range of flame holder shapes experimental data lie in the range:

$$3.6 \le (L/W) \le 4$$

Data for a number of circular cylinders which illustrate this result are shown in Figure 21.4.6. Despite the strong dependence of

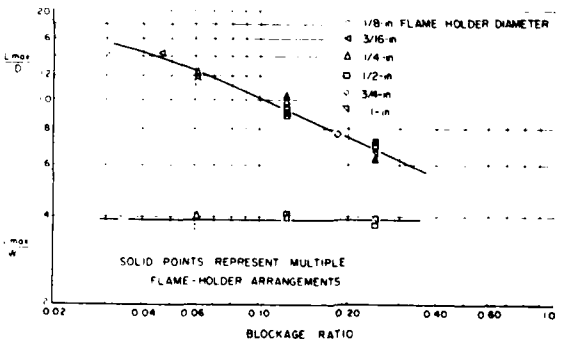

Figure 21.4.6 Dependence of Recirculation Zone Length and Wake Width on Flame Holder Blockage Ratio, d/H.

L/d on the blockage ratio, values of L/W are almost constant for the whole range. The dependence of L/d on blockage, shown here, is for circular cylinders; and in general, the dependence of L/d on blockage is a strong function of flame holder geometry. However, the spreading of the mixing zones and presumably, the entrainment in the mixing zones is remarkably independent of the shape of the wake region and flame holder. This simple dependence of recirculation zone length on wake width indicates that in this problem (as in many fluid dynamic problems involving flows over bluff bodies), the wake width rather than flame holder scale is the most useful measure of bluff body scale.

The ratios V_2/V_1 and W/H which appear in Equation 21.4.2 depend on flame holder geometry and the blockage ratio. A simple continuity argument for incompressible flow can be used to estimate the velocity change if we neglect entrainment in the mixing layer. Conservation of mass gives:

$$\rho V_1 H = \rho V_2 (H - W)$$

or

$$(V_2/V_1) = 1/(1 - W/H) \qquad (21.4.3)$$

An approximate calculation is also available which allows W/H to be calculated as a function of geometry and blockage ratio for a "V" gutter or wedge flame holder geometry. Consider again the flow shown in the sketch of Figure 21.4.5. We examine an incompressible and inviscid flow over a wedge shaped body of half angle α and treat the outer boundary of the wake as a streamline which separates the unburnt flow from a stagnant and constant pressure wake. The wake spreads asymptotically to reach a width W. In the region where W is constant, the unburnt flow speed reaches a value V_2 given by Equation 21.4.3 and the pressure will be uniform across the wake and the unburnt flow. Application of the Bernoulli equation shows that the velocity along the dividing streamline must be constant and be equal to V_2. Values of W/H can be computed from this model by a simple hodograph transformation. Calculations of this type are given by Cornell (Reference 2.9) for the "V" gutter flame holder geometry with $0 \leq \alpha \leq 90^\circ$. Values of W/H, V_2/V_1 and the parameter (WV_1/HV_2) which appears in Equation 21.4.2 are given in Table 21.4.2 for wedge half angles of 15° and 90° (a flat plate) and a range of blockage ratios. Note that values of W/d decrease and values of V_2/V_1 increase as flame holder blockage is increased. The net result is that the parameter $(W/H)(V_1/V_2)$ has a rather broad maximum around blockage ratios of 0.5 for the 30° wedge (half angle) and 0.3 for the 90° wedge or flat plate.

Wake widths and velocity ratios determined from this simple model are in reasonable agreement with values obtained experimentally for stabilized flames. The excellent measurements obtained by Wright (Reference 21.7),

	$\alpha = 15^\circ$			$\alpha = 90^\circ$		
$\frac{d}{H}$	$\frac{W}{d}$	$\frac{V_2}{V_1}$	$\frac{W}{H} \times \frac{V_1}{V_2}$	$\frac{W}{d}$	$\frac{V_2}{V_1}$	$\frac{W}{H} \times \frac{V_1}{V_2}$
.05	2.6	1.15	.11	4.0	1.25	.16
.10	1.9	1.23	.15	3.0	1.43	.21
.20	1.5	1.42	.20	2.2	1.75	.248
.30	1.3	1.62	.23	1.7	2.09	.250
.40	1.2	1.90	.25	1.6	2.50	.248
.50	1.2	2.3	.25	1.4	3.16	.22

Table 21.4.2 Dependence of Wake Width W, Edge Velocity V_2, and a Stability Parameter on Blockage Ratio d/H, and Wedge Half Angle α.

for flat plate holder, $\alpha = 90^\circ$, and 30° are available for comparison. Differences in values of W/H are no more than 20 percent and those for the ratio V_2/V_1 are less than 6 percent.

Given data or calculations of this type and assuming that $L/W = 4$, all of the parameters given in Equation 21.4.2 can be evaluated. The experimental results of Wright and values calculated by the method described above are presented in Figure 21.4.7 as a plot of $\tau_c V_{1c}/H$ versus the blockage ratio B. The agreement between the data and calculated values is good and suggests that the model discussed here is correct.

The material presented above in Table 21.4.2 and Figure 21.4.7 shows that the maximum values of the stability parameter $(V_{1c}\tau_c/H)$ are close to one for the 15°, 30° and 90° half angle wedges. We can show that this value is a reasonable estimate for all two dimensional flame holders. For example, if we use the continuity argument presented above for V_1/V_2, and our rule of thumb $L/W = 4$ we can rewrite Equation 21.4.2 in terms of W/H and then find for the blowoff criteria, the relationship:

$$(V_{1c}\tau_c/H) = 4(W/H)(1 - W/H) \qquad (21.4.4)$$

Note that flame holder shape does not appear here explicitly. However, both flame holder geometry and blockage ratio enter in the determination of (W/H). Equation 21.4.4 is a particularly useful and interesting result because it shows the importance of the wake width as the critical parameter (independent of flame holder-duct geometry) and because it allows a most simple starting point for the determination of the holder scale which maximizes the stabilization velocity V_{1c}. The function $(W/H) \times (1 - W/H)$ clearly has a maximum at $W/H = 1/2$. For small (W/H),

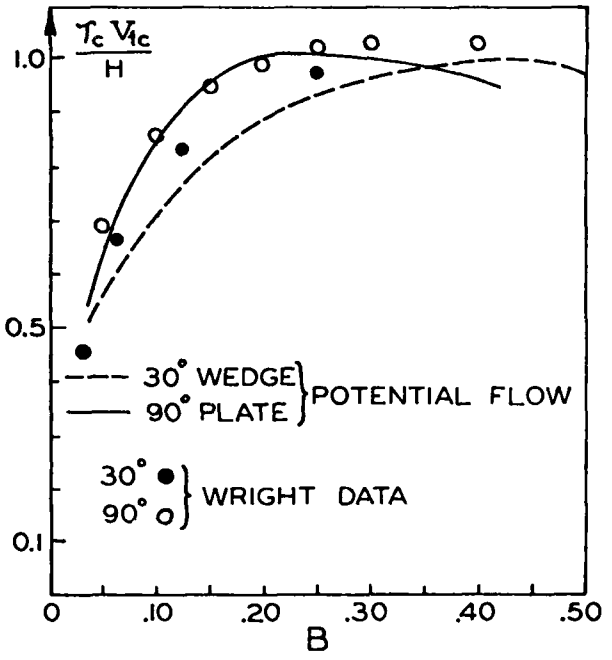

Figure 21.4.7 Dependence of Stability Parameter on Blockage Ratio B and Flame Holder Geometry for Wedges With Half Angles of 30° and 90°.

V_{1c} increases almost linearly with W. However, as W/H approaches 1/2, the effect of increasing W is offset by the increase in V_2 produced by the wake-blockage effect. For W/H > 1/2, the blockage effect dominates and blowoff speed decreases.

The optimum wake width in this simple model is exactly one half the duct height and consequently the maximum value of blowoff velocity which can be achieved for any flame holder geometry, V_{1m}, is given by

$$\frac{V_{1m}\tau_c}{H} = 1 \quad . \qquad (21.4.5)$$

Note that this result is independent of flame holder geometry and is corroborated by the experiments described above.

We can also examine flows over axisymmetric bodies such as the flame holder shown in the lower half of Figure 21.4.3. For this geometry, the wake width W and body diameter d are equal and consequently the recirculation zone length is 4W or 4d. If this holder is placed on the axis of a circular duct of diameter D, and the blockage is defined as $B = (d/D)^2$, the stabilization criterion given in Equation 21.4.2 becomes

$$\frac{V_{1c}\tau_c}{D} = 4\sqrt{B}(1 - B) \quad .$$

For this example the value of B which maximizes V_1 is 1/3 and

$$\frac{V_{1m}\tau_c}{D} = 1.54 \quad . \qquad (21.4.6)$$

The above result holds for <u>any</u> axisymmetric flame holder-duct geometry. In the general axisymmetric case, V_{1m} is attained when the wake width to duct diameter ratio, W/D is $1/\sqrt{3} = 0.57$. It is interesting to note that the analysis indicates that the axisymmetric holders will allow about a 50 percent greater value of approach stream velocity than the two-dimensional holders.

In summary, for the two-dimensional case, the effects of blockage and flame holder geometry can be predicted from a simple model. Results obtained from the model and experimental work show that blockage effects are very important, that a maximum in blowoff velocity exists as flame holder scale is increased in a duct of fixed size, and that this maximum occurs when the flame wake width is about 50 percent of the duct height for all two-dimensional flame holder shapes. Similar conclusions hold for axisymmetric shapes except that for this case the optimum wake width is 1/3 of the duct diameter. The flame holder scale and blockage ratio required to produce the optimum wake width depend strongly on flame holder geometry.

<u>Temperature, Fuel-Air Ratio and Vitiation</u>. Temperature changes have little observable effects on wake width or velocity. However, a large increase in temperature does result in a reduction in recirculation length. For example, doubling the unburned mixture temperature can decrease recirculation zone length by 15 to 20 percent. Similar changes are observed when fuel-air mixture ratios are changed to values far from the stoichiometric value.

In both cases, the length of the zone decreases when the ratio of burned to unburned gas density λ increases. This trend is in agreement with trends recently observed in spreading rates of turbulent mixing regions formed between parallel flows with different velocities and densities. Experimental investigation of this simpler problem shows that if the high speed stream is also the high density stream, an increase in the density of the low speed and low density stream will increase the spreading rate. In our case, increasing spreading rates of the mixing layers will decrease the length of the recirculation zone.

For a given temperature, vitiation of the approach stream produces a reduction in oxygen content, which results in a reduction in heat release and consequently an increase in λ. Again the effect is qualitatively similar to an increase in approach stream temperature.

<u>Multiple Flame Holder Arrays</u>. The previous discussion was restricted to a single flame holder placed on the center line of a duct of constant height. In most practical situations, a number of flame holders must be used. When these are arranged in a single plane perpendicular

to the flow direction and when they are spaced so that each holder lies on the center line of equivalent ducts of equal height, the above analysis can be used directly to estimate stability limits and spreading characteristics. For this case, each holder is treated as if it were in an isolated duct. E.g., see Figure 21.4.6 and blowoff data of Reference 21.10.

This approach gives reasonable results for laboratory scale experiments but interactions do occur which may change stability limits by 5 - 10 percent. One effect results when flame stabilization fails on one holder in a multi-flame holder array slightly before the others. Failure of one stream to ignite has the effect of reducing the acceleration of the flow over the wake and hence of reducing the velocity of the flow past the wakes of the other holders. Thus, a partial blowoff can occur which leaves the remaining holders in a more stable configuration.

When holders are spaced irregularly in either lateral dimension, or fore and aft, prediction of the wake geometry from results of tests on isolated flame holders is no longer possible. However, our modeling ideas are still useful in a qualitative way. For example, we would expect that if flame holders are not arranged in a plane, the disturbance produced by flow over the downstream flame holders will pinch off the circulation zone of the upstream holder unless the spacing along the duct axis is greater than the recirculation zone length. Similarly, the burning wake of the upstream holder will increase the effective blockage of the downstream holders and hence reduce their stability limits.

Reynolds Number and Mach Number Effects. When the Reynolds number is so low that the mixing layers in the wake of the flame holder become laminar or transitional the transport processes in the wake change drastically. Molecular diffusion becomes important and the rule of thumb for L / W is no longer applicable.

Measurements made in systems with low approach stream turbulence levels have shown that the transition Reynolds number for circular cylinder-flame holders is in the range 1 to 4 x 10^4 (see Reference 21.6). This result is for flame holders cooled to approach stream temperature, and the Reynolds number is based on upstream flow properties; $R_e = \rho_1 V_1 d / \mu_1$. When the flame holder is allowed to reach temperatures hotter than the approach stream, gas properties based on holder temperatures should be used. Some effects of the geometrical shape of the holder on transition is expected.

Transition occurs when the separated flame holder boundary layers become turbulent very close to the separation point, and upstream of the location in the mixing zone where mixing effects or combustion can heat the gas in the separated layers. Any heating will increase the kinematic viscosity (which is roughly proportional to temperatures to the 1.75 power) and reduce the effective Reynolds number. When the flow in the separated boundary layers remains laminar up to the point of appreciable heat addition, it remains laminar throughout the whole recirculation zone and region of flame spread. The development of a turbulent boundary layer on the flame holder upstream of separation and high levels of approach stream turbulence will also insure that the mixing zone will be turbulent.

Transition to turbulence in the wake of a circular cylinder used as a flame holder is shown in Figure 21.4.8. The Schlieren photographs are taken along a line of sight looking down on the plane containing the undisturbed velocity vector and the flame holder axis. At the lowest Reynolds number (top pair of photographs) large scale vortices are present and these show up as vertical lines in the left hand picture. However, at the highest Reynolds number these regular features are hidden by small scale disturbances which we assume to be evidence of turbulent flow. The Reynolds numbers examined here differ by a factor of less than two and the change in the appearance is quite striking.

Reynolds Number 2.45 X 10^4

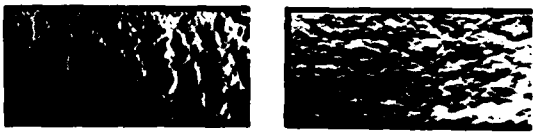

Reynolds Number 3.35 X 10^4

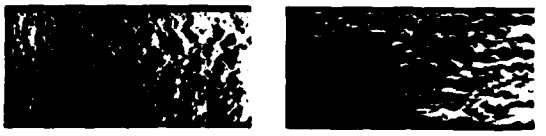

Reynolds Number 4.60 X 10^4

Schlieren Sensitive to Horizontal Density Gradients

Schlieren Sensitive to Vertical Density Gradients

Figure 21.4.8 Transition to Turbulence in Recirculation Zone of 1.3 cm Cooled Circular Cylinder.

Because the Reynolds number is directly proportional to the pressure level in the engine (through the density dependence) the Reynolds number will decrease as the altitude increases. Hence, the Reynolds number should be evaluated at high altitudes to insure that the transition to laminar flow described here does not occur.

When appreciable heat is to be added in a burner of constant cross section area, inlet Mach numbers of about 0.15 to 0.25 must be used to prevent choking due to heat addition. Thus, compressibility effects usually are not important near the flame holder and recirculation zone.

However, note that the near optimum wake width of 1/2 (for the two-dimensional case), the flow area is reduced by a factor of two. Consequently for approach stream Mach numbers as low as $M_1 = 0.3$ we would get sonic speed past the recirculation zone. Measurements of Wright, (Reference 21.7) bear out this prediction and further show that the W/H correlation discussed above fails when the Mach number past the recirculation zone, M_2, is greater than 0.8.

Free Stream Turbulence. The effects of free stream turbulence can be described only in a qualitative manner. As the intensity of turbulence increases, the recirculation zone shortens but the stabilization criterion in its most direct form, $V_{2c}\tau_c / L = 1$, remains valid even when recirculation zone length is reduced by factors of 2. Thus, turbulence appears to effect the rate of spread of the mixing layers without changing the mechanism of stabilization.

21.4.1.2 CHEMICAL PARAMETERS

The dependence of τ_c on chemical parameters is very strong and unfortunately much less well understood than the influence of the fluid dynamic parameters. Hence, the chief use of the scaling scheme discussed here is to predict the effect of changes in fluid dynamic parameters for fixed chemical parameters. However, it is still interesting to list the important chemical parameters and to indicate the nature of their effects. The principal parameters are: Fuel properties, fuel-air mixture ratio, approach stream temperature and oxygen concentration, and approach stream pressure.

The dependence of the critical time on fuel-air ratio and fuel type is illustrated in Figures 21.4.9 and 21.4.10. In both, τ_c is plotted as a function of the equivalence ratio which is the fuel-air ratio divided by the stoichiometric fuel-air ratio. In Figure 21.4.9, values are presented for a hydrocarbon fuel vapor with a molecular weight of about 100. A number of flame holder geometries were used to obtain this data. In the second Figure, a number of fuels were used which were made up of this hydrocarbon plus various mass fractions of hydrogen. Values of τ_c decrease dramatically as the fraction of hydrogen increases. Also note that τ_c increases very rapidly for both high and low values of the equivalence ratio.

The characteristic time is also a sensitive function of approach stream temperature and oxygen concentration. In general, τ_c decreases rapidly as temperatures increase even when this increase is due to vitiation; (i.e., preburning at a fuel-air ratio below stoichiometric). However, for a given temperature, τ_c increases as the oxygen mass fraction decreases due to increasing vitiation.

The critical time increases as pressure decreases roughly as $\tau_c \propto 1/P$ for hydrocarbon fuels of high molecular weight. E.g., see Reference 21.11. A similar result was obtained in small scale experiments carried out with hydrogen.

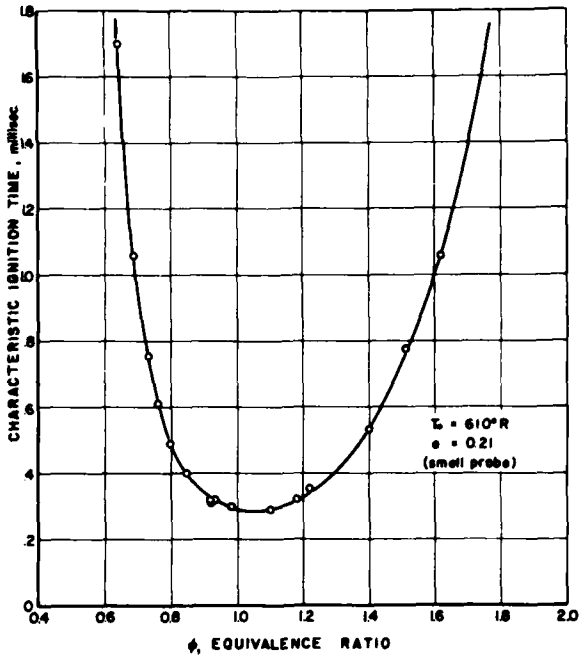

Figure 21.4.9 Variation of Characteristic Ignition Time τ_c with the Equivalence Ratio.

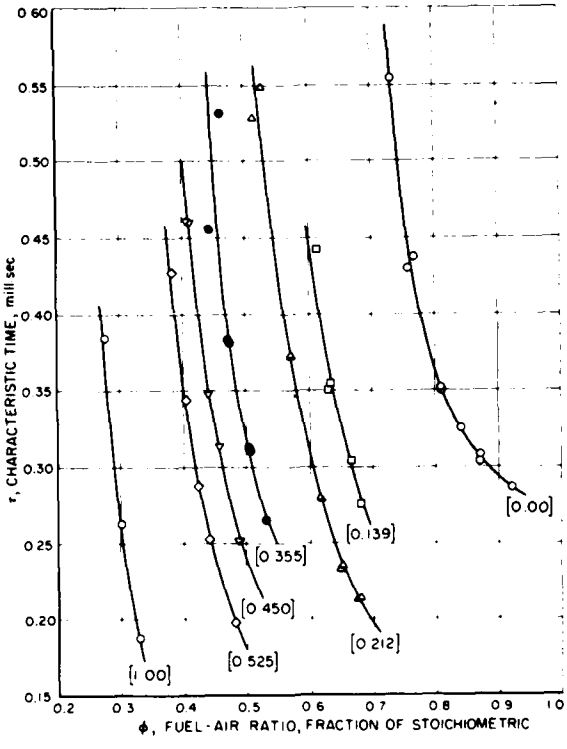

Figure 21.4.10 Effect of Fuel Properties on Characteristic Time. The Parameter is Mass Fraction of Hydrogen in the Fuel.

In attempting to obtain an independent estimate of values of τ_c or some other experimentally determined quantity which is proportional to τ_c, we have examined the dependence of a time based on the ratio of the laminar flame thickness δ to laminar flame speed, S. In the single case for which comparable data were available values of $\delta / S\tau_c$ for methane were computed for stoichiometric fuel-air ratio of one and approach stream temperature between 300 and 400°K. The ratio had a value close to one for the whole range of temperature examined. Similarly, values of the ratios of δ / S and τ_c for hydrocarbon and hydrogen fuels are about 10. Thus, δ / S may be a useful predictor for the dependence of τ_c on various chemical parameters.

Finally, there is a persistent attempt to relate the characteristic stabilization time to a thermal ignition time (e.g., Reference 21.12) or a global reaction rate (e.g., References 21.13 and 21.14). These efforts often lead to a representation for τ which is similar to the reciprocal of a reaction rate:

$$\tau_c \propto T^m P^{-n} e^{+(A / RT_f)} / \emptyset$$

where m and n are numbers of the order of one or two, A is an activation energy determined empirically, R is the universal gas constant, T_f is an ignition temperature or the gas temperature in the recirculation zone, and $\emptyset$ is the equivalence ratio which is less than one, the stoichiometric value. In the works of Solokhin and Mironenko (Reference 21.13 and 21.14), where a more complex expression is used, the effective values of the parameters are

$$n = 1 \quad m = 2.5 \quad \frac{A}{R} = 2 \times 10^4 {}^oK$$

Although the dependence on temperature and pressure by this approach is plausible, the use of global reaction rates and the application of this approach to processes which involve chemical reactions in turbulent mixing regions does not have a sound physical basis and should be viewed as a sophisticated form of curve fitting.

Because of our lack of understanding of the chemical parameters, the stabilization criterion is only useful when τ_c values have been determined for the range of chemical parameters expected in practice. However, small scale experiments can be used to make the required determinations and some physical feel is given by the flame speed correlation suggested above.

21.4.1.3 ALTERNATE SCHEMES

One popular alternate scheme for scaling stabilization phenomena is based on the arbitrary use of a dimensional parameter group of the form

$$V_{1c} / P^a d^b T^c = F\{f\}$$

to correlate a body of experimental results. Here f is the fuel-air ratio, d is the flame holder scale, P and T are the pressure and temperature of the approach flow, and F is a function of the fuel-air ratio. (For example, see the work of Reference 21.15.) The values for the exponents selected by various authors to correlate their data have the ranges,

$$0.8 \leq a \leq 2$$

$$1/2 \leq b \leq 1$$

$$1/2 \leq c \leq 2.5$$

and F must be determined experimentally.

At the beginning of the study of bluff body flame stabilizers, there was great confusion concerning the exponent for d which arose because the influence on the recirculation zone region of flame holder and duct geometry, described above, was not fully appreciated. For example, when a circular cylinder held with its axis perpendicular to the gas stream is used as a flame holder, the duct walls have a large effect on the flame holder wake width even when the ratio of holder diameter to duct height is as small as 1/50. In the range $1/20 \leq d/H \leq 1/4$ and in a duct of fixed size, the wake width and hence the recirculation zone length scale approximately as $L \propto W \propto \sqrt{d}$ rather than as $L \propto d$. This square root dependence leads to a value of the exponent b of 1/2. Similarly, if cylinders with their axis parallel to the flow are used as flame holders, the wake width grows linearly when d is increased in a duct of fixed size. There is an effect of blockage in this example too, since the ratio V_2 / V_1 will increase with d due to blockage changes but this increase depends on $(1 - (d/D)^2)^{-1}$ and hence is hard to detect when $d/D < 1/4$. Hence, in this example the exponent b would be close to one. Further confusion arose because data in the laminar and turbulent regimes were used together to determine these exponents.

A value of the pressure exponent near one is a typical choice and for the temperature, values still range between 1/2 and 2.5. Thus, a scaling parameter of the form V_{1c} / Pd is often used for fixed inlet temperature. When d is changed by scaling the entire flame holder-duct system this parameter gives an excellent correlation - as we would expect from our previous analysis. A correlation of this type is given by Hottel et al (Reference 21.15). However, note that this correlation is only useful in general if d characterizes the scale of the system; if d is changed and the duct height is held fixed, the correlation will fail because of the effect of changes in blockage on recirculation zone length and the velocity ratio V_2 / V_1.

21.4.2 FLAME STABILIZATION BY JETS IN A HOMOGENEOUS STREAM

The process of flame stabilization in the wake of a gas jet is similar to the processes, described above, which occur in the wake of a

bluff body. In either example, a region of strong recirculating flow is created by a physical obstacle or in the wake of interacting jets in which hot products of combustion can be trapped. This hot gas then acts as a steady source of ignition for the oncoming stream. In the case of flame stabilization by gas jets, two new features are added. First, the size of the recirculation zone can be changed by changing the rate of gas injection. Second, the fuel-air ratio and hence the temperature of the gas in the recirculation zone can be changed by changing the fuel-air ratio of the injectant. Because the stabilization process is very strongly affected by changes in the temperature of the recirculation zone gas, having an independent control on this parameter will allow stabilization at fuel-air ratios far below which could be achieved with bluff body holders which produced the same sized recirculation zone. The advantages of these two features are offset in part by the performance losses and the mechanical problems associated with supplying the gas flow required for flame stabilization, and, if a fuel-air mixture is to be used, the problems involved with the production of the vaporized fuel and the preparation of a homogeneous mixture prior to injection.

We will develope a crude scaling law for one example of this type of system and will give a few experimental results to illustrate the general features of the stabilization process.

The flow field produced by axisymmetric injection of a jet into a cross flow is shown in the sketch of Figure 21.4.11. The jet is injected through an annular slot of width b in the

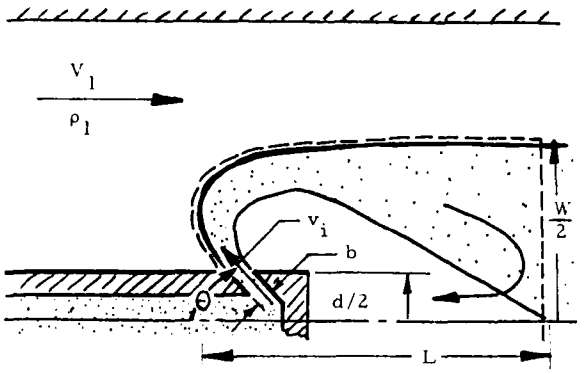

Figure 21.4.11 Schematic for Discussion of Flame Stabilization by a Jet.

wall of a center body of diameter d and at an angle $(\theta - \frac{\pi}{2})$ with respect to the oncoming flow. In this model, we make a momentum balance on the injectant and make the approximation that the drag of the effective body produced by injection, see dotted contour in Figure 21.4.11, is balanced by the momentum change of the injectant. Thus

$$\tfrac{1}{2}\rho_1 V_1^2 C_d \left(\frac{\pi W^2}{4}\right) = (\rho_i v_i \pi d b) v_i (1 + \cos\theta)$$

Here, the drag is characterized by a drag coefficient C_d which has a value around one, and we we have assumed that the injected mass flow $(\rho_i v_i \pi d b)$ enters and leaves the control volume with its velocity of injection v_i. (The assumption that the exit velocity is v_i and not a value closer to V_1 is certainly questionable.) Given this crude balance, we find that

$$\frac{W}{b} = \left[\left(\frac{d}{b}\right)\left(\frac{8(1 + \cos\theta)}{C_d}\right) q\right]^{\frac{1}{2}}$$

where

$$q = (\tfrac{1}{2}\rho_i v_i^2) / (\tfrac{1}{2}\rho_1 V_1^2)$$

When W is much larger than the thickness of the boundary layer on the center body, and when W is much smaller than the duct diameter (so that blockage effects can be ignored), we expect C_d to be constant. Consequently the above equation indicates that W will scale as $q^{\frac{1}{2}}$ and when ρ_i/ρ_1 and the geometric parameters are constant, this equation reduces to

$$W \propto \rho_i v_i \propto \dot{m}_i$$

where $\dot{m}_i$ is the mass flow of injectant.

Experiments have shown, (E.g., Reference 21.16) that the length of the recirculation zone formed by this injection process is between one and two times the width of the region and that the value of L/W is independent of q but does depend on the injection angle θ. Hence, $L \propto \dot{m}_i$ will hold for this system and $L \propto \sqrt{q}$, for the more general case. When we combine the latter results with the scaling law for W and the blowoff criterion, $\tau_c V_{1c}/L = 1$, we get an equation for the blowoff velocity:

$$V_{1c} \propto L/\tau_c \propto (L/W)(W/\tau_c)$$

or

$$V_{1c} = \left[\left(\frac{L}{W}\right)^2 \frac{8(1 + \cos\theta)}{C_d}\right]^{1/4}\left[\frac{v_i\sqrt{bd}}{\tau_c}\right]^{1/2}$$

when the densities of injectant and the approaching stream are equal. The terms in the first square bracket on the right hand side of this equation depend on the angle of injection, and those in the second, on the velocity and area of the injector. If the geometry and chemical parameters are held fixed we find that the blowoff velocity is proportional to the square root of the injector velocity and the injector mass flow rate.

As an example, the experiments of Kosterin et al (Reference 21.16) indicate that flame stabilization in a stream with approach stream speeds of about 100 m/sec. and a fuel-air ratio near 1/2 of stoichiometric could be achieved with values of q near 50. Mass flows in the injector were less than 1 percent of the approach stream flow for this example. In addition, the data are roughly correlated by

$V_{lc} \propto \sqrt{q}$ which agrees with the above analysis.

The gas which enters the recirculation zone is made up from the approach stream as well as the injectant stream and the ratio of these two mass flow rates has been found to be independent of q and strongly dependent on the injectant angle. For example, Kosterin et al (Reference 21.16) find that the ratio of approach stream to injectant entrainment rates, E_r, is about 6.5 at $\theta = 135^\circ$, 4.0 at 90° and 2.5 at 180° and 70°. Thus, the mixture ratio and hence temperature of the recirculation zone can be strongly influenced by the injectant.

The magnitude of this effect is shown below in Table 21.4.3 where equivalence ratio (the fuel-air ratio, fraction of stoichiometric), in the approaching stream at the blowoff condition ϕ_{lc} is shown as a function of the equivalence ratio in the injectant stream ϕ_i when the gas speed of the approach stream was 100 m/sec. In this example, the lean blowoff limit of the approach stream was reduced from 60 percent of the stoichiometric fuel-air ratio to 40 percent when the fuel-air ratio of the injectant fluid was increased from zero to 120 percent of stoichiometric. The quantity ϕ_e is the calculated value of the equivalence ratio in the recirculation zone based on a measured value of entrainment ratio E_r. Note that ϕ_e is almost constant. Hence, we are again led to believe that the recirculation zone temperature which is presumably also almost constant is a critical feature in the ignition process.

ϕ_i	ϕ_{lc}	ϕ_e	Flame holder characteristics
0	0.60	.52	b ≈ .5 mm d ≈ 15 mm
0.54	0.54	.54	q ≈ 45
1.0	0.43	.51	Kerosene fuel
1.2	0.40	.51	$\theta \approx 135^\circ$

Table 21.4.3 Effect of Injectant Equivalence Ratio on Equivalence Ratio of Main Stream at Blowoff.

Note that using injectant angles with smaller values of E_r will increase the sensitivity of the equivalence ratio at the blowoff condition to changes in ϕ_i but at the same time will change the relationship between wake width, recirculation zone length and injectant parameter q.

Large scale tests of a complete afterburner system which used two-dimensional arrays of jets, of the type discussed here, as flame stabilizers are reported in Reference 21.17. Good stabilization characteristics and afterburner combustion efficiency were achieved with a total injectant flow rate of between 2 and 4 percent of the total flow to the afterburner. Total pressure losses associated with jet-flame holder systems were found to be 3 to 4 percent lower than corresponding values for bluff body systems when the augmentation was zero. The possibility that gains can be made in reducing the non-afterburning total pressure loss is another reason for pursuing the investigation of this system.

21.4.3 FLAME STABILIZATION IN A HETEROGENEOUS FUEL-AIR MIXTURE

In almost any afterburner configuration the weight savings to be made by reducing all length scales in the system will insure that the fuel injection system will be located so close to the flame stabilizers that some of the liquid fuel will arrive at the plane of the flame holders in an unvaporized state. When afterburners are to be used in the air stream of a fan engine, the low temperatures of these streams will greatly increase the fraction of fuel which is not evaporated. For example, in low pressure ratio fan engines operating at high altitudes, present day jet fuels will be almost completely in the liquid state. In such streams, the flame stabilization system must produce some vaporization of the fuel in addition to acting as a continuous source of ignition.

In addition to these low temperature problems, special requirements are placed on the fan stream augmentation system (often called a duct burner) by the operating characteristics of the fan. The fan is typically a low pressure ratio device and a relatively weak pressure disturbance propagating upstream from the augmentor can push the fan into a strong surge or stall. Hence, ignition of the fan stream augmentor must be achieved at a very low overall fuel-air ratio so that the sudden increase in total temperature (due to the start of afterburning) will not interact with the choked nozzle to produce a pressure pulse which will cause the fan to stall.

Common Duct System. Under conditions such that the fuel in the fan stream is poorly vaporized, the simplest system is the engine in which afterburning takes place in a common duct with fuel injection system modulated so that combustion starts in the afterburner in the core stream where high temperatures insure good vaporization. Some of the hot gas produced by afterburning in the homogeneous core stream can then serve to support the flame stabilization process in the fan-air stream and to produce vaporization in regions where the fan and core streams mix. The fan engines described in the introduction of this chapter (e.g., Figure 21.0.2 on page 21-3) uses this system.

If fan air is to be burned in a separate duct where this support is not available, the flame holder must operate alone. In the following paragraphs we will give a qualitative picture of several flame stabilization schemes for this second and most extreme example. Few experimental data are available and because the process is complex, systematic experimental or theoretical treatment of this important problem is lacking.

Bluff Body Flame Holders. There is evidence that the picture of the bluff body stabilization process, described above, applies in most respects to bluff body stabilization in a heterogeneous flow. The principal difference is that

in heterogeneous flows, fuel vaporization must take place during the stabilization process itself. This can occur in two ways: first when liquid fuel drops impinge on the hot flame holder and second when fuel drops enter the mixing zone. In either case the fuel-air ratio in the wake will be fixed by local conditions in a manner similar to that described above for the gas jets when a fuel-air mixture is used as the injectant. In this case, as there, the fuel-air ratio of the gas entering the wake appears to be the dominant factor and maximum blowoff velocity occurs for the injection conditions which supply the recirculation zone with a stoichiometric fuel-air mixture. Proper design and control of the fuel injection system can be used to get the best conditions for stabilization regardless of the overall fuel flow requirements.

The process of fuel vaporization by the flame holder involves a number of steps. First the fuel droplets must be captured by the flame holder. Capture results because the droplets cannot exactly follow the gas stream lines; as the gas flows over the flame holder the droplets will first be accelerated toward the holder (region (a) of the sketch shown below)

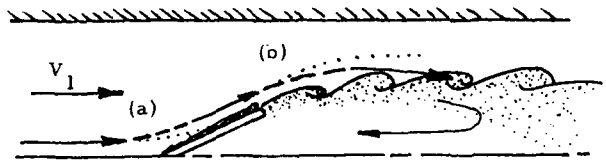

and then away from the mixing zone at region (b). The drift rate across streamlines will depend strongly on particle size, the flame holder shape and the velocity, density and viscosity of the gas. After the fluid is captured on the holder its residence time there will be fixed by a balance between shear forces produced by the gas stream, and the shear and surface tension forces acting between the liquid film and the flame holder. If too thick a film is formed ablation of liquid drops from the downstream edge of the holder will result. If vaporization rates are high the holder may operate in a dry state. Heat transferred between the recirculation zone gas and the liquid film will depend on the usual convective parameters, and hence will increase with the speed, temperature, and pressure of the gas in the recirculation zone, and again will depend on flame holder geometry.

Given the capture and heat transfer processes, the properties of the fuel will then fix the rate of production of the fuel vapor at the flame holder, and the entrainment of vapor and air in the mixing zones will fix the fuel-air ratio of the recirculation zone gas. Additional vaporization of fuel droplets entrained in the mixing and recirculation zones will further increase the fuel-air ratio.

When the capture, heat transfer and evaporation rates are high, the fuel-air ratio in the recirculation zone can be much higher than in the stream approaching the flame holder. This difference would make possible ignition and stabilization when the overall fuel-air ratio is far below stoichiometric and hence would be advantageous during start-up of the augmentation process. However, when the overall fuel-air ratio is increased toward the stoichiometric value (as it must be to achieve maximum augmentation), the fuel-air ratio in the recirculation zone could increase to values far above stoichiometric and a flame blowoff on the fuel rich side would occur. Hence, having the fuel-air ratio in the wake larger than that in the flow is not always advantageous.

It is clear from this brief qualitative description that the fuel injection system and the fuel capture and heat transfer rates of the flame holder must be carefully controlled over a wide range of operating conditions if the simple bluff body flame holder is to be used successfully. In general, such control is not possible with existing injection systems over wide operating ranges.

Flame Stabilization by Jets. A second system which has shown promise in heterogeneous systems is the aerodynamic flame holder or gas-jet holder described in a previous section. For duct burners, this system is perhaps the best of the three discussed here as far as its flame stabilization properties are concerned. However, losses and mechanical problems associated with the system may make its use impractical. (For example, see Reference 21.17.)

Pilot Burner. A third system suggested for use in heterogeneous fuel-air mixtures is a piloted burner. A small part of the afterburner flow, say 5 to 10 percent, is burned in a can-like pilot burner (or a number of burners) at the stoichiometric fuel-air ratio. The hot gas from this source is then used to support stabilization by a system of conventional flame holders. The pilot burners require separate fuel injection and control systems to maintain fuel-air ratios different from those in the main flow. Systems of this type can be ignited at very low overall fuel-air ratios (e.g., Reference 21.17) and low pressure levels. However, larger total pressure losses are produced by this system both with and without augmentation.

In summary, a number of schemes are available to produce flame stabilization in heterogeneous flows under conditions suitable for fan engine applications. Although, the common burner scheme is the most well developed, the aerodynamic and pilot burner schemes offer advantages which are worth further exploration.

21.4.4 DISCUSSION

The model used above to describe flame stabilization in homogeneous fuel-air streams by bluff bodies has the advantage of cleanly separating aerodynamic and chemical features of the process. The influence of various aerodynamic parameters is well understood from a qualitative point of view and many features can be treated in a quantitative manner. In particular, the dependence of stability limits on the geometry and scale of the flame holder-duct system is now clear.

The influence of the various chemical parameters of the problem are much less well understood. The use of an ignition time delay as suggested by Mullins, Solokhin and Kosterin to describe ignition in a turbulent mixing zone

is not correct, in the opinion of the author.

In one typical version of this approach (Solokhin, Reference 21.14), the ignition time is calculated from a global model of the chemical reaction rate, and the chemical concentrations and temperature used in the calcu ation are taken from a mathematical model of the mixing zone which is based on time averaged measurements of these parameters. There are three problems here. Global models for reaction rates have been used in calculations of laminar flame speeds and have led to qualitatively useful results. However, in order to obtain quantitatively accurate predictions it has been found necessary to consider detailed chemical analyses which usually involve a large number of reaction steps, reaction rates and activation energies.

A second and perhaps more serious problem arises from the treatment of the mixing layer. The model used by Solokhin pictures the layer as a region in which the temperature and concentrations change smoothly from values corresponding to the unburnt mixture on one side to values corresponding to the products of combustion on the other. This is the result obtained experimentally with instrumentation which produces time averaged values. However, recent experimental developments (e.g., Roshko and Brown, Reference 21.18) suggest that the conditions in the shear or mixing layer are quite different. Experimental results indicate that large scale structures predominate in the mixing layer and consequently that gas in the layer, at a given instant and at a given point has a high probability of being either completely burned or unburned. The probability of finding gas with a temperature or concentration of an intermediate value is small even at the center of the layer. In this picture of the flow, chemical reactions will start at boundaries between fully burnt and unburnt masses of gas and not in a uniform mixture of burnt and unburnt material. Thus, if the new model of the mixing layer is correct, the use of the time averaged values of temperature and composition in the calculation of chemical reaction rates is inappropriate.

Finally, flame stabilization involves more than the simple ignition process. In order to stabilize a flame, gas ignited in the mixing layer must continue to burn after it moves past the downstream end of the recirculation zone. Thus, the heat release rate in the mixing zone gas must be high enough to overcome the quenching effects of the entrainment of unburnt gas in the region downstream of the recirculation zone. A simple ignition model is probably not sufficient to describe this process.

21.5 FLAME SPREAD IN PREMIXED AND HOMOGENEOUS FUEL-AIR MIXTURES

In this section, the process of heat addition after flame stabilization has been achieved is discussed. Processes occuring in a premixed and homogeneous fuel-air mixture are considered. The term homogeneous is used here to denote mixtures of fuel vapor and air as contrasted with heterogeneous mixtures by which we mean mixtures of fuel droplets and perhaps some fuel vapor with air. The combustion in the latter fuel-air system is important in duct-burner systems for fans but will not be discussed here. (See References cited in Section 21.10.)

Given the flame stabilized in a duct, we would like to be able to calculate the distance downstream of the stabilizer which is required to achieve a selected value of the heat release or combustion efficiency. The parameters which may influence the required length are: (a) Flow properties (such as the pressure, temperature, and oxygen concentration; the fuel-air ratio and fuel properties; and the Mach number, velocity and turbulence level of the unburned stream). And, (b) Duct parameters (such as duct height, flame holder geometry and blockage, and cross-section area changes with axial distance).

Unfortunately, at the present time, we cannot predict the dependence of heat release rate in a combustion changer of fixed size on any of these parameters from basic principles. Indeed, our understanding is so poor that the appropriate dimensionless parameters have not been identified or agreed upon. However, several fluid dynamic parameters, the Reynolds number and Mach number, are used to characterize the flow.

Although a great deal of experience is available which can serve as a guide for a new combustion chamber design, a large and expensive development effort is usually required to produce a satisfactory configuration. Conventional wisdom is in agreement, for example, that an increase in pressure, temperature, oxygen concentration, and turbulence level will increase the heat release rate and reduce the combustion chamber length required for high combustion efficiency. However, quantitative measures of the effects to be expected, given a particular change in a parameter, are not available. The reason for this is that the combustion process is turbulent and occurs in a region of strong shear and large axial pressure gradient.

General features of the flow field of a typical flame are shown in Figure 21.5.1. In this example the flame is stabilized by a bluff body placed on the centerline of a constant area duct. The downstream end of the recirculation zone is about one tunnel height H downstream of the flame holder. The fuel is a hydrocarbon which produces a highly visible flame and the outer boundaries, shown in Figure 21.5.1a, are based on time exposure photographs taken in the light of the flame itself.

Temperature profiles shown in the lower-half of Figure 21.5.1a at a number of positions exhibit a sharp initial rise from the cold gas temperature which is followed by a very small and more gradual further increase. The maximum values, reached at the centerline of the duct, are close to the adiabatic flame temperature. The two boundaries based on the positions at which the initial temperature rise starts and stops are also shown in the lower half of Figure 21.5.1b and they contain the region of strong chemiluminescence (shown here as a dotted region).

Values of temperature shown here are averaged over long periods of time. Time resolved temperature measurements suggest that

the rapid initial rise is produced by averaging in time over temperatures which fluctuate rapidly between values close to the unburnt and burnt gas temperatures.

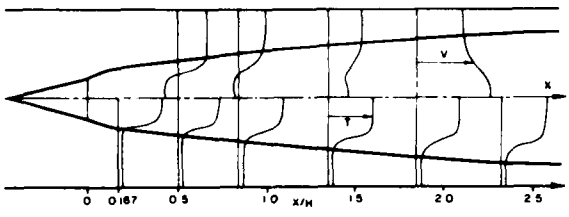

(a)

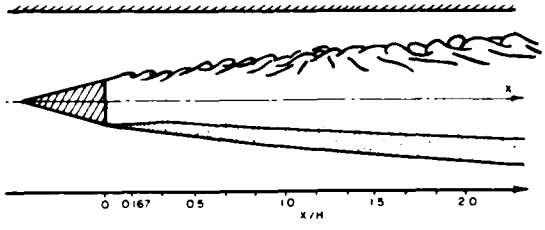

(b)

Figure 21.5.1 Flame Stabilized on a Two-Dimensional Wedge Flame Holder. (a) Temperature and Velocity Profiles (b) Schlieren and Chemiluminescence Boundaries.

Spark Schlieren photographs, similar to the sketch at the top half of Figure 21.5.1b, support this picture. They indicate that the edge of the flame contains distinct vortex-like structures which produce a strongly corrugated surface. See photographs shown in Figures 21.4.4 and 21.4.8. Hence, a probe located in this region would alternately observe hot and cold fluid. The scale of these structures grows slowly with increasing distance from the flame holder and typically occupies between 30 to 40 percent of the width of the flame W. That is, regions of strong temperature gradients penetrate far into the flame front.

Concentration profiles for products of combustion are similar to the temperature profiles; and regions of the strong chemiluminescence produced by combustion, (the dotted region in Figure 21.5.1b), and of strong ionization, concentration and temperature gradients almost exactly coincide. This result suggests that the sharp boundaries shown in the Schlieren photographs are flame fronts and that their positions are restricted to the region of sharp temperature rise.

The velocity profiles (shown in Figure 21.5.1a) are also averaged over long periods of time, and they show less steep gradients than the temperature profiles. Near the flame holder and in the recirculation zone, the time averaged velocity is reversed. The centerline velocity increases rapidly for positions farther downstream and exceed the unburnt gas speed at positions farther downstream than 1-1/2 duct heights. This acceleration of the burnt gas is a result of the action of the axial pressure gradient, produced by heat addition, on the high density unburnt gas and the lower density burnt material. The axial gradient, which is uniform across the duct, causes the lower density fluid to accelerate more rapidly than the high density stream and thus produces the hat shaped profile.

In summary, the flame front appears to be made up of thin regions of chemical reaction which are rolled up into vortex-like structures. The size of these structures grows slowly as the axial distance increases and they occupy between 30 to 40 percent of the "flame" width. Strong chemical reaction and large heat release occur in the shear layers which form the boundaries between streams with large density and velocity differences.

The vortex-like structures lie in the region of strong average velocity gradient. This suggests that they are related to the large scale structures observed in two-dimensional shear layers. However, the vortex pairing observed without combustion has not been observed in spreading flames.

This picture of the spreading flame suggests that the rate of consumption of unburnt fluid in the spreading flame is fixed by an entrainment process rather than by a simple flame propagation process which might be expected to depend at least weakly on molecular transport properties. Much of the experimental data presented later support this view. The primary problem concerned with the prediction of flame spreading rates is the determination of this entrainment process. At the present time, no satisfactory physical model has been developed to describe it.

In the remainder of this section, we first review experimental information concerning flame spreading rates and discuss the implications of this data for turbulent entrainment rates or flame speed. We then describe several simple models which allow a reasonable description of the dependence of some of the fluid dynamic parameters on the heat addition from the flame. However, even these restricted models remain incomplete because we cannot yet prescribe the entrainment rate of the turbulent flame.

21.5.1 SPREADING RATES OF TURBULENT FLAMES

The quantity which the afterburner designer needs to know is the manner in which the combustion efficiency of a burner varies with the parameters described in the previous paragraph. Unfortunately, combustion efficiency is difficult to measure accurately and has not been the subject of detailed investigations under conditions in which the effects of changing combustion chamber parameters were clearly isolated. Instead, a number of investigations have been made of the spreading rate of the flame front and then conclusions regarding the more applied problem of

combustion efficiency have been drawn based on these results. See, for example, Williams et al (Reference 21.19), Wright and Zukoski (Reference 21.20), and Solntsev (Reference 21.21).

There are a number of problems with this approach. First, the flame is observed to have a finite thickness, which may be as great as 20 percent of the duct height (e.g., see Figure 21.5.1). The spreading rate and conclusions drawn from it will depend strongly on which surface is defined as the flame front. Further, since the combustion process presumably takes place within this thickness any interpretation of combustion efficiency which is based on a single boundary will be suspect.

Secondly, there is a strong interaction of the flow with the heat addition process. The strong axial pressure gradient produced by heat addition produces acceleration in the unburnt fluid which produces an appreciable curvature of stream lines near the flame front. The acceleration and curvature can have important effects on the interpretation of the flame width data.

This process is illustrated by the two-dimensional flow shown in the sketch of Figure 21.5.2. We simplify the problem by assuming that the unburnt flow is isentropic, incompressible, and has a velocity vector which is almost

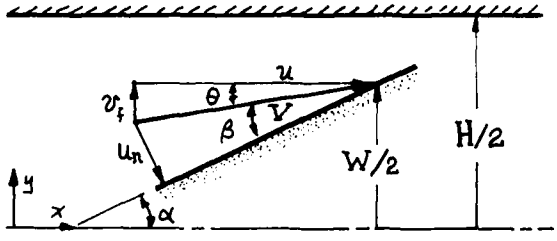

Figure 21.5.2 Sketch for Calculation of Stream Line Angle at Flame Front.

axial and almost uniform. Under these assumptions the continuity and axial momentum equations can be written for the unburnt flow as:

$$\frac{\partial u}{\partial x} + \frac{\partial v}{\partial y} = 0 \quad \text{and} \quad \rho u \frac{\partial u}{\partial x} + \frac{\partial P}{\partial x} = 0$$

If we combine these and make use of the approximation that ρ, u, $\partial u / \partial x$ and P are independent of vertical position y, we can solve for the small angle which the velocity vector V makes with respect to the axis at the flame front:

$$\theta \approx \frac{v_f}{V} = \left(\frac{V_1}{V}\right)^2 \left(\frac{H - W}{4}\right) \left(\frac{\partial Cp}{\partial x}\right) \qquad (25.1.1)$$

Here V_1 is the gas speed far upstream of the flame holder, v_f is the y component of the velocity at the flame front and Cp is the pressure coefficient defined as:

$$C_p = (P_1 - P) / \tfrac{1}{2} \rho_1 V_1^2$$

The ratio (V / V_1) is different from one because of the velocity change produced by acceleration of the flow around the flame holder and then by heat addition.

The angle α is the angle made between the flame front at the point of interest and the axis of the duct. It can be obtained from the shape of the flame front and is just

$$\alpha = \tfrac{1}{2} \frac{dW}{dx} \qquad (25.1.2)$$

The velocity of the gas normal to the flame front, u_n, some times called the turbulent entrainment velocity, or flame speed is given by $V \sin\beta$ and β can be obtained from the difference between angles θ and α. That is,

$$u_n / V = \sin(\alpha - \theta) \qquad (25.1.3)$$

Thus, to calculate u_n consistent with any choice of the flame front, we must know V / V_1 and both angles α and θ. In many situations in which turbulent flame spreading is considered, the ratio V / V_1 can be as large as 2 to 3 and the angles α and θ are often nearly equal. Hence, neither of these effects can be ignored a priori.

In the present section we will describe the dependence of the wake width on a number of parameters which describe the combustion chamber and will then comment on the implications of these results with regard to combustion efficiency and the turbulent entrainment velocity.

Flame Spreading. The spreading rate of the flame is a very strong function of the condition of the flame. When the flame is laminar, the flame width is a strong function of laminar flame speed and turbulence level in the approach stream. E.g., Lefebvre (Reference 21.22), and Wohl et al (Reference 21.23). However, at higher speeds and Reynolds numbers, the flame becomes turbulent under the same conditions that the mixing layers become turbulent and the dependence of flame shape on molecular transport processes becomes negligible.

This transition is illustrated by the Schlieren photographs of Figure 21.4.8 and by the data shown in Table 21.5.1, taken from Thurston (Reference 21.24). He examined flame spreading in a rectangular duct (about 15 cm by 7.5 cm in cross section) and used several cooled circular cylinders as flame holders. The data of this table show the wake width and velocity ratios measured near the downstream end of the recirculation zone (Subscript 2) at about 4 cm and at a station 37 cm downstream of the holder (Subscript 37). The outer edge of the flame defined in schlieren

V_1 m/sec	$\frac{V_2}{V_1}$	$\frac{W_2}{H}$	$\frac{V_{37}}{V_1}$	$\frac{W_{37}}{H}$
30	1.09	.23	1.55	.40
60	1.06	.22	1.34	.34
80	1.06	.21	1.31	.33
100	1.05	.21	1.29	.33
120	1.04	.21	1.27	.33
140	1.04	.21	1.27	.33

Table 21.5.1 Variation With Approach Speed of Velocity Ratio and Wake Width at the Downstream End of Recirculation Zone (Sub 2), and at 37 cm (Sub 37) from Flame Holder. Duct About 15 cm by 7.5 cm With 0.32 cm Diameter Cylinder Spanning the 7.5 cm Dimension. Stoichiometric Fuel-Air Ratio.

photographs, and averaged through its bumpy surface was used to determine the wake width. Total and static pressure measurements were made as a function of axial position and the velocity in the unburnt flow was determined from the pressure measurements.

Note in Table 21.5.1 that as the approach speed V_1 is increased from 30 m/sec (at the beginning of the transition to turbulence) to 60 m/sec, the wake width at the 37 cm station decreases by about 15 percent. A similar doubling of speeds to 120 m/sec produces a much smaller change. Similarly, at x = 37 cm, the ratio of the velocity to the approach stream speed decreases rapidly at first and then approaches a constant value. Further, of the 6 percent velocity reduction which occurs as the approach speed is changed from 60 to 120 m/sec, 2 percent is evidently caused by changes which occur in the neighborhood of the recirculation zone, e.g., see the V_2 / V_1 column. The small changes in wake width and velocity ratio observed here for the turbulent flow condition are typical of measurements obtained in the turbulent regime for holder sizes in the range 0.32 to 2.54 cm. A similar transition was also reported in Reference 21.19.

The spreading rates of flames stabilized on bluff body flame holders operating in constant area ducts and in the turbulent regime have been determined by Wright and Zukoski (Reference 21.20), as a function of the approach stream speed, fuel-air ratio, temperature, fuel type and flame holder-duct geometry. Fortunately for the designer of afterburners, the observed spreading rates have been found to be almost independent of these parameters. Typical results are shown in Figure 21.5.3 taken from (Reference 21.20).

In Figure 21.5.3a, the dependence of wake width on fuel-air ratio is shown. In this range of equivalence ratios, the laminar flame speed for a typical hydrocarbon fuel has a maximum near an equivalence ratio of 1.10 and would decrease to about 60 percent of the maximum value for $\phi \approx 0.75$. Similarly for the temperature increase shown in Figure 21.5.3b, the laminar flame speed would increase by factors of about 2 or more. Finally, the laminar flame speed for hydrogen-air mixtures is of the order of 10 times that of the hydrocarbon fuel used in these tests. Despite these changes in parameters which produce large changes in laminar flame speed, little change is observed in flame geometry. The lack of change in Figure 21.5.3c is particularly interesting.

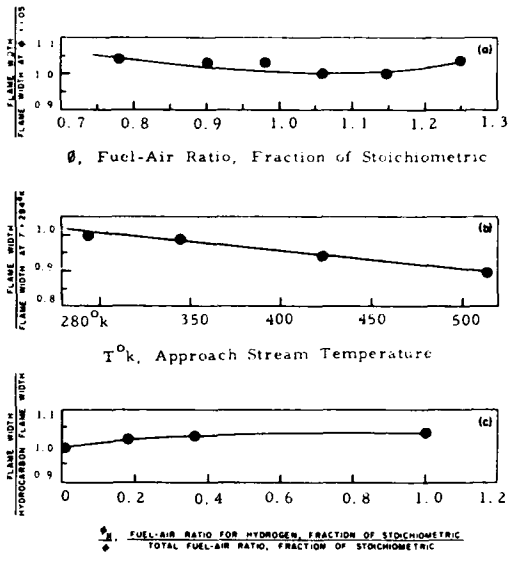

Figure 21.5.3 Dependence of Flame Width on Fuel-Air Ratio, Approach Stream Temperatures and Fuel Type. Holder is a 1/8 Inch Circular Cylinder and Width is Measured 15 Inches From Holder.

Similar results concerning the very weak dependence of flame geometry on approach stream speed and fuel-air ratio are reported by Williams et al (Reference 21.19), and also by Solntsev (Reference 21.21) who carried out experiments in much larger scale apparatus. The former measurements were made from schlieren photographs and Solntsev used photographs, and also temperature, oxygen concentration and ion density profiles to determine the widths. Thus, it is clear that the measurements described above are general and that the laminar flame speed and presumably other molecular transport processes are <u>not</u> important in fixing the geometry of the spreading turbulent flame.

The dependence of flame geometry on the turbulence level of the unburnt mixture is less clear. The experiments of Williams et al showed a very weak dependence in small scale experiments where as Solntsev found a somewhat larger dependence and he suggested that the entrainment rate of the turbulent flame is proportional to the turbulence level in the unburnt flow.

Experiments carried out by Wright (Reference 21.7) in which high subsonic speeds were observed in the flow past the wake indicate that the Mach number does not have a large effect on flame geometry as long as the local Mach number is below 0.8.

No experiments have been reported which deal directly with the pressure dependence of the flame spreading phenomena. A number of experiments have been made of complete afterburner systems in which pressure effects were examined and were found to have strong effects on combustion efficiency when the pressure fell below a limiting value. (See Reference 21.15.) However, since the complete system was involved, it is not clear which process, injection, flame stabilization or flame spreading, was responsible for the drop in efficiency as the pressure was reduced. The Reynolds number is reduced when the pressure falls and the velocity is held fixed. Such a reduction could cause a transition from turbulent to laminar flow which would hava a very adverse effect on flame spreading and combustion efficiency as well as on the flame stabilization process. In addition, Hottel et al (Reference 21.15) suggest that a pressure reduction would also reduce the turbulence level of the approach stream and that this will result in a reduction of the flame spreading rate.

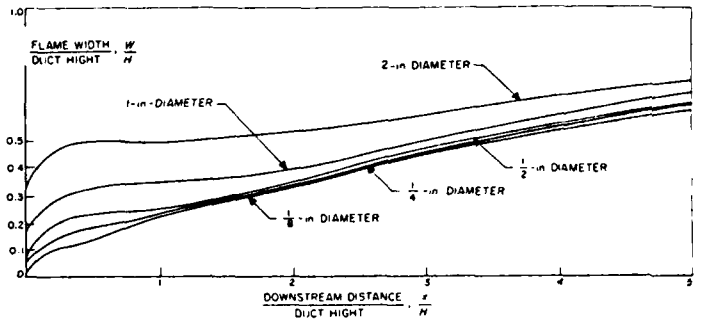

Figure 21.5.4 Flame Shapes for Flame Holders of Several Sizes in a Duct of Fixed Size, V = 300 ft/sec, Ø = 1.0, H = 15 cm.

The dependence of flame geometry on flame holder-duct geometry is weak and complicated. The wake width at a given distance downstream from flame holder in a duct of fixed size does increase slowly as the flame holder scale is increased. However, at distances greater than several recirculation zone lengths of the larger holder, wake widths are almost independent of holder scale. Thus, an increase in blockage for a flame holder of fixed size will cause a slight decrease in the flame spreading rate.

Data which illustrate this result are shown in Figure 21.5.4 and are taken from Reference 21.20. Flame boundaries are shown for flames stabilized in a rectangular duct (15 cm high by 7.5 cm wide) for five cooled circular cylinders with diameters of 0.32, 0.63, 1.27, 2.54, and 5 cm. The outer edge of the flame, determined from schlieren photographs and normalized by the duct height H of 15 cm, is given as a function of axial position which is also normalized by the duct height. The large initial differences are due to differences in the width of the recirculation zone, discussed earlier. However, farther downstream the boundaries begin to merge and at x/H of 5 the differences in wake width are small despite the change in blockage ratio from 1/48 to 1/3.

If we compare the flame geometry of a single flame holder in a duct with the flames produced by two holders of the same scale located in the same duct, each flame width of the latter configuration will be slightly smaller than that of the single holder. However, the fraction burned will be greatly increased at a given distance downstream of the holder. Hence, if stabilization problems are not a limiting constraint, increasing the number of holders would always improve combustion efficiency.

This situation is illustrated by the data of Solntsev (Reference 21.21) which are shown in the sketches of Figures 21.5.1 and 21.5.5, and in Table 21.5.2. The sketches show flame boundaries and temperature profiles for two flame holder configurations placed in the same 300 cm high duct. In Figure 21.5.1, the holder is a 30° half angle wedge with a 70 mm base height; in Figure 21.5.5, three 30° half angle wedges are used. Wake widths are presented as a fraction of the duct height and for a number of axial positions in Table 21.5.2. The duct height used in presenting the 3 flame holder data is divided by 3 so that each holder is charged with its equivalent duct height. The flame fronts, for the three holder configurations begin to merge near x/H of 1.3 and combustion is complete before the x/H = 2.8 station at which the flame width of the single holder configuration is less than 75 percent of the duct height. If we normalize the wakes widths and axial positions by the height of the duct occupied by each holder, i.e., by 300 mm for the single holder and 100 mm for the three holder configuration, the systems look more similar. Thus, the flames occupy about 65 percent

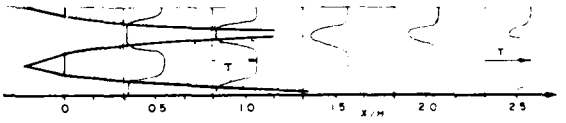

Figure 21.5.5 Sketch of Flame Edge and Temperature Profiles for a Three Flame Holder Array. Reference 21.21.

x cm	$\frac{x}{H}$	$\frac{W_1}{H}$	$\frac{W_3}{\frac{1}{3}H}$	$\frac{x}{\frac{1}{3}H}$
100	.33	.31	.68	1.0
250	.83	.48	.89	2.5
400	1.33	.60	1.00	4.0
850	2.83	.71	1.00	8.5

Table 21.5.2 Comparison of Flame Widths for 30° Half Angle Wedge Holders in a Duct of 300 mm Height, H. Subscript (1): One Single 70 mm Holder; Subscript (3): Three 30 mm Holders.

of their ducts at a station one equivalent duct height downstream of the holder.

Entrainment Rates. The entrainment rate of the flame can be determined from knowledge of the flame geometry and the pressure and velocity field produced by the flame. However, the entrainment rates determined by this method are very strongly dependent on the definition used for selection of the flame front position and on a number of corrections. To illustrate the process, we show a set of calculations made from the data of Thurston (Reference 21.24).

Consider the sketch shown above in Figure 21.5.2 and the data presented in Table 21.5.3. Values of experimental parameters and the angles α, β and θ calculated from Equations 21.5.1 and 21.5.2 are presented in the table for three flame holders of diameter, D and a range of approach stream speeds, V_1. Calculated values of the entrainment speed are given in the last column.

The entrainment rate per unit area of the flame is ρu_n which we showed earlier, see Equation 21.5.3, was given by

$$\text{Entrainment Rate} = \rho u_n = \rho V \sin\beta$$

and when β is small

$$\text{Entrainment Rate} = \rho V \cdot \beta$$

One interesting result shown below in Table 21.5.2 is that the entrainment angle β is almost independent of approach stream speed and flame holder blockage when the flame is turbulent. The values of β lie around 0.02 with a scatter of at least .005 or 25 percent. Some of the data used to calculate values of $\beta = \alpha - \theta$ are also shown in the table. Examination of the quantities shows that β is constant despite substantial changes in these quantities which result from changes in flame holder diameter D. Note also that β changes only slightly when the speed of the approaching stream V_1 is increased by a factor of 2.

The large scatter is due to the rather arbitrary definition of the flame width W and uncertainties in estimation of the slopes for W and Cp which appear in calculation of α and θ. Notice that in most cases the velocity vector V is turned away from the axis through an angle θ which is roughly half of α, the angle between the spreading flame front and the axis of the duct. Because θ is greater than the angle β for many of the conditions presented here, we must expect large errors in β from this source. In addition, the boundary layers growing on the walls of the combustion chamber will also produce an acceleration of the flow by reducing the effective cross section area of the duct and hence must be taken into account in calculating the angle θ. For the data presented in Table 21.5.2, the growth of the displacement thickness on the top wall of the duct would decrease θ and hence increase β by about .002 radians. Side wall boundary layers will have a similar effect. Hence, we expect the entrainment velocity for those experiments is about .025 $\pm$ .007 of the local unburnt gas speed.

The entrainment rate can also be obtained directly from the flame width and velocity data by a different mass balance technique. The idea here is to measure the mass flow of the unburnt gas outside the flame as a function of axial position. The rate of change of this flow rate $\dot{m}_c$ with axial position can then be used to determine the entrainment rate. When α is small, the entrainment rate per unit area at one side of the flame is $(-1/2)(d\dot{m}_c/dx)$ and it can be expressed in terms of the total mass flow $\dot{m}_1 = \rho_1 V_1 H$ as:

$$\beta = \frac{u_n}{V} = -\frac{H}{2}\left[\frac{d}{dx}\left(\frac{\dot{m}_c}{\dot{m}_1}\right)\right]\left(\frac{V_1}{V}\right)$$

Measurements of $\dot{m}_c$ of the type required were carried out by Thurston (Reference 21.24) for one of the experiments reported in Table 21.5.2. An estimate of β based on the above equation and Thurston's data was 0.027 for the 0.32 cm flame holder. The agreement of the two methods is close considering all the uncertainties.

The entrainment rate of a turbulent flame will certainly depend on a number of parameters not changed in the experiments described here and hence this value for β cannot be viewed as having any general applicability. However, the small rate of entrainment is of general interest and probably represents the lower bound of values for entrainment in a low turbulence experiment.

D cm	V_1 m/sec	C_{p37}	$\frac{\partial C_p}{\partial x}$ 1/cm	$\frac{(H-W)}{2}$ cm	$\frac{\partial W}{\partial x}$	α	θ	β u_n/V	u_n m/sec
.32	30	1.40	.040	4.6	.140	.070	.040	.030	1.4
.32	60	.80	.020	5.0	.086	.043	.028	.015	1.2
.32	120	.62	.016	5.1	.090	.045	.025	.020	3.1
.32	140	.62	.016	5.1	.090	.045	.025	.020	3.6
.64	60	.87	.015	4.9	.076	.038	.019	.019	1.6
.64	120	.70	.013	5.0	.062	.031	.011	.020	3.1
1.27	60	1.10	.014	4.6	.066	.033	.015	.018	1.6
1.27	120	.96	.010	4.6	.065	.033	.012	.021	3.5

Table 21.5.3 Parameters Used in the Calculation of Entrainment Velocity u_n for Stoichiometric Fuel-Air Ratio. Data from Thurston (Reference 21.24). Note, No Boundary Layer Correction Has Been Made for β.

21.5.2 ONE-DIMENSIONAL HEAT RELEASE

As a first crude approximation for the processes occurring in the combustion chamber of an afterburner, it is convenient to investigate the process of heat addition in simple, one-dimensional channel flow. The calculation will be carried out with the assumption that the heat is added uniformly across the channel.

Differential Relations. The aim of the calculations is to illustrate the variation of the variables as heat is added; of particular interest are the dependence of stagnation pressure and Mach number on the stagnation enthalpy or temperature. We will first consider the process when the assumption of constant channel area is made; later, expressions including the variation of area will be derived.

Referring to Figure 21.5.2.3, a quantity of heat dH is added between two control planes separated by a distance dx. It is assumed that no change in the initial conditions, u, ρ, p, T, M is invoked by this addition of heat. Therefore, the flow process may be described by the laws of continuity, momentum, and energy transport

$$d(\rho u) = 0$$

$$(\rho u)du + dp = 0$$

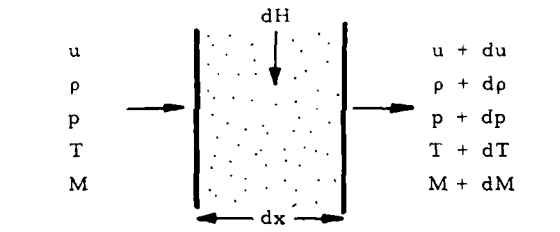

Figure 21.5.6 One-dimensional flow of gas with infinitesimal heat addition.

$$C_p dT + udu = dH = C_p dT_t \qquad (21.5.4)$$

and the equation of state for a perfect gas,

$$p = \rho RT \quad .$$

The change of gas velocity accompanying an addition of heat may be found by eliminating the temperature variation from the energy equation, using the equation of state:

$$udu + C_p T\left(\frac{dp}{p} - \frac{d\rho}{\rho}\right) = dH \quad . \qquad (21.5.5)$$

Now computing $dp/p = -udu/RT$ and $d\rho/\rho = -du/u$ from the momentum and continuity equations, respectively, it follows, upon collecting and rearranging terms, that

$$\frac{du}{u} = -\frac{1}{M^2-1}\frac{dH}{C_p T} \quad . \qquad (21.5.6)$$

The result indicates that the variation of gas velocity with heat addition depends critically upon the Mach number of the flow at the point of heat addition. The velocity increases with heat addition for subsonic flow and decreases with heat addition for supersonic flow. This distiction between the behavior of flow at subsonic and supersonic velocities is somewhat reminiscent of that which occurs in the behavior of the velocity during a contraction of the channel cross-section in isentropic flow.

The pressure variation may be computed directly from the momentum relation as,

$$udu = -\frac{1}{\gamma}a^2\frac{dp}{p} \quad , \qquad (21.5.7)$$

and employing the equation (21.5.6) for the velocity variation,

$$\frac{dp}{p} = +\frac{\gamma M^2}{M^2-1}\left(\frac{dH}{C_p T}\right) . \qquad (21.5.8)$$

The addition of heat causes a drop in gas pressure for subsonic velocities which becomes progressively more severe as the Mach number approaches unity.

The static temperature is found by writing the logarithmic derivative of the equation of state as:

$$\frac{dT}{T} = \frac{dp}{p} - \frac{d\rho}{\rho} \quad ,$$

and substituting for terms on the right from continuity and momentum equations, this gives

$$\frac{dT}{T} = 1 - \left(\frac{u^2}{RT}\right)\frac{du}{u} \quad ,$$

or, substituting from (21.5.6) for the velocity variation,

$$\frac{dT}{T} = \left(\frac{\gamma M^2 - 1}{M^2 - 1}\right)\left(\frac{dH}{C_p T}\right) . \qquad (21.5.9)$$

The factor $(\gamma M^2-1)/(M^2-1)$ exhibits two changes of sign because the numerator and denominator pass through zero at $M^2 = 1/\gamma$ and $M^2 = 1$, respectively. So long as $M^2 < 1/\gamma$, the temperature rises with the addition of heat, which is the trend naturally to be expected. However, as the Mach number increases, but remains in the range $1/\gamma < M^2 < 1$, the temperature decreases as heat is added to the gas, a result which is not at all obvious physically and requires a bit closer investigation. Finally, when $M > 1$, the static temperature again increases with dH, as would be expected.

The energy equation (21.5.4), indicates the proportion of a heat increment dH which appears as gas enthalpy, $C_p dT$, and that which appears as kinetic energy of mean motion, udu. Expressing the differentials du and dT in terms of dH and simplifying the result, it is found that

$$\underbrace{\frac{(\gamma-1)M^2}{1-M^2}\frac{dH}{C_p T}}_{\text{increment of kinetic energy}} + \underbrace{\frac{1-\gamma M^2}{1-M^2}\frac{dH}{C_p T}}_{\text{increment of gas enthalpy}} = \frac{dH}{C_p T} \qquad (21.5.10)$$

so that a portion $\left(\frac{(\gamma-1)M^2}{1-M^2}\right)$ of the added energy dH is devoted to increasing the kinetic energy of the gas, while a portion $\left(\frac{1-\gamma M^2}{1-M^2}\right)$ appears as the enthalpy of the gas. Now clearly, as the Mach number increases, the amount of heat required to supply the kinetic energy increases until, at $M^2 = 1/\gamma$, the entire heat addition is required to supply the kinetic energy alone, with the result that the gas enthalpy cannot change. Further increase of Mach number increases the kinetic energy requirement even more, so that a portion of it must be furnished by the gas enthalpy itself. As a consequence, the gas temperature decreases.

The situation is clear for supersonic flow. Here, the gas velocity decreases as heat is added, with the result that all of the heat which is added, plus that resulting from kinetic energy reduction, is available to increase the gas enthalpy. The enthalpy increase is

$$\left[1 + \frac{(\gamma-1)M^2}{M^2-1}\right]dH ,$$

and hence is in excess of the amount supplied. Note that the ratio of the quantity of heat passing to kinetic energy, to that passing to gas enthalpy, is given by

$$\frac{\text{kinetic energy increment}}{\text{gas enthalpy increment}} = \left[\frac{(\gamma-1)M^2}{1-\gamma M^2}\right], \qquad (21.5.11)$$

and hence is a function of the Mach number alone.

It is a simple matter now to compute the change of Mach number with heat addition; logarithmic differentation indicates that

$$\frac{dM}{M} = \frac{du}{u} - \frac{1}{2}\frac{dT}{T} .$$

Combining the known values of du/u and dT/T from eqs. (21.5.6) and (21.5.9), the formula for dM/M is simply

$$\frac{dM}{M} = \frac{1}{2}\left(\frac{1+\gamma M^2}{1-M^2}\right)\frac{dH}{c_p T} . \qquad (21.5.12)$$

It is clear from eq. (21.5.12) that heat addition always brings the flow toward a Mach number of unity, that is, heat addition results in a Mach number increase for subsonic flow and a Mach number decrease for supersonic flow.

The variation of stagnation pressure can now be simply determined by taking the logarithmic derivative of:

$$p_t = p\left(1 + \frac{\gamma-1}{2}M^2\right)^{\gamma/\gamma-1}$$

and substituting for the appropriate results given above. Then it is found that

$$\frac{dp_t}{p_t} = \left(\frac{(-\gamma/2)M^2}{1+\frac{\gamma-1}{2}M^2}\right)\frac{dH}{c_p T} ,$$

or, more simply,

$$\frac{dp_t}{p_t} = -\left(\frac{\gamma}{2}M^2\right)\left(\frac{dH}{c_p T_t}\right) . \qquad (21.5.13)$$

It is evident that stagnation pressure drops with heat addition and that the rate depends very strongly on the Mach number at which the heat is added.

The results derived in the previous paragraphs concern heat addition in a constant area channel. The effect of simultaneous changes in area and total gas enthalpy are also of interest and may be simply derived on the basis of the following considerations. Let the Mach number, for example, be considered to be a function of both area and stagnation temperature. Then,

$$dM = \left(\frac{\partial M}{\partial T_t}\right)_A dT_t + \left(\frac{\partial M}{\partial A}\right)_{T_t} dA .$$

However, the quantity $(\partial M/\partial T_t)$ is obtained from (21.5.12) since the derivative given in the latter equation was obtained with the area held fixed. Thus,

$$\left(\frac{\partial M}{\partial T_t}\right)_A = \left(\frac{M}{T}\right)\left(\frac{1}{2}\right)\left(\frac{1+\gamma M^2}{1-M^2}\right) .$$

Similarly, the quantity $(\partial M/\partial A)_{T_t}$ was previously obtained during study of isentropic channel flow, and is given by:

$$\left(\frac{\partial M}{\partial A}\right)_{T_t} = \left(\frac{M}{A}\right)\left(-\frac{1+\frac{\gamma-1}{2}M^2}{1-M^2}\right) .$$

Therefore,

$$\frac{dM}{M} = \left(\frac{1}{2}\frac{(1+\gamma M^2)}{(1-M^2)}\right)\left(\frac{dH}{c_p T}\right) + \left(-\frac{1+\gamma-1}{1-M^2}M^2\right)\frac{dA}{A} .$$

The results for other parameters of interest are:

$$\frac{du}{u} = \left(\frac{1}{1-M^2}\right)\frac{dH}{c_p T} + \left(-\frac{1}{1-M^2}\right)\frac{dA}{A}$$

$$\frac{dp}{p} = \left(\frac{-\gamma M^2}{1-M^2}\right)\frac{dH}{c_p T} + \left(\frac{\gamma M^2}{1-M^2}\right)\frac{dA}{A}$$

$$\frac{dT}{T} = \left(\frac{1-\gamma M^2}{1-M^2}\right)\frac{dH}{c_p T} + \left(\frac{(\gamma-1)M^2}{1-M^2}\right)\frac{dA}{A}$$

$$\frac{d\rho}{\rho} = \left(\frac{-1}{1-M^2}\right)\frac{dH}{c_p T} + \left(\frac{M^2}{1-M^2}\right)\frac{dA}{A}$$

$$\frac{dp_t}{p_t} = \left(\frac{-(\gamma/2)M^2}{1+\frac{\gamma-1}{2}M^2}\right)\frac{dH}{c_p T} = \left(-\frac{\gamma}{2}M^2\right)\frac{dH}{c_p T_t}$$

and

$$\frac{dT_t}{T_t} = \left(\frac{1}{1+\frac{\gamma-1}{2}M^2}\right)\frac{dH}{c_p T} = \frac{dH}{c_p T_t} .$$

(21.5.14)

Use of these equations makes possible a determination of the local rate of changes of the various parameters when both heat addition, dH, and area change, dA, are made. Note, although, that dM/M, dp/p, dT/T, dρ/ρ may be held constant by appropriate matching of the variation of dH/c_pT and dA/A. For example, if $dH/c_pT = dA/A$, then the static pressure and velocity remain constant. However, the ratio dp_t/p_t is always finite and negative.

The equations cannot be used in general to abstain algebraic solutions for the flow field in a duct of specified area variation and heat addition. However, they can be used in numerical calculations.

Integrated Relations. The equations for heat addition in constant area channel flows can be integrated to give the changes in the variables of interest which occur when heat is added or the equations for conservation of energy momentum and mass can be applied directly across the heat addition zone. The results are:

$$\frac{T_{2t}}{T_{1t}} = \left(1 + \frac{\Delta H}{c_p T_{1t}}\right) = \left(\frac{1+\gamma M_1^2}{1+\gamma M_2^2}\right)^2 \left(\frac{1+\frac{\gamma-1}{2}M_2^2}{1+\frac{\gamma-1}{2}M_1^2}\right)\left(\frac{M_2^2}{M_1^2}\right)$$

$$\frac{p_{2t}}{p_{1t}} = \left(\frac{1+\gamma M_1^2}{1+\gamma M_2^2}\right)\left(\frac{1+\frac{\gamma-1}{2}M_2^2}{1+\frac{\gamma-1}{2}M_1^2}\right)^{\gamma/\gamma-1}$$

$$\frac{u_2}{u_1} = \frac{\rho_1}{\rho_2} = \left(\frac{1+\gamma M_1^2}{1+\gamma M_2^2}\right)\left(\frac{M_2}{M_1}\right)^2$$

$$\frac{p_2}{p_1} = \left(\frac{1+\gamma M_1^2}{1+\gamma M_2^2}\right)$$

$$\frac{T_2}{T_1} = \left(\frac{1+\gamma M_1^2}{1+\gamma M_2^2}\right)^2 \left(\frac{M_2}{M_1}\right)^2 \qquad (21.5.15)$$

These equations are also discussed in Section 2.17.3. They are given in terms of M_1 and M_2, whereas in most problems of interest, the heat addition $(\Delta H/c_pT_{1t})$ and M_1 will be the specified quantities. Since elimination of M_2 from the above equations is algebraically complicated, we need to express the results numerically in order to obtain a directly useful form.

Pick state (1) as the initial condition corresponding to a Mach number M at the start of heat addition in a constant area duct. Define a second state, denoted by a super *, at which heat addition has been sufficient to drive the Mach number to one. This state is to be used as a reference condition in a manner analogous to the A* state (of Section 2.18) of one-dimensional, isentropic, channel flow.

In the above equations, P_{1t}, for example, becomes P_t, P_{2t} becomes P_t*; M_1 becomes M and M_2 becomes 1.0. Values of p_t/p_t*, p/p*, T/T*, and T_t/T_t* are given in Table (21.5.4) as a function of initial Mach number M, and for $\gamma = 1.40$. The variation with γ is small in subsonic regions, but becomes important when $M > 1.5$. Also note the rapid increase in p_t/p_t* for supersonic speeds.

The table or a plot may be used to obtain solutions of problems involving uniform heat addition in a channel of constant cross-section. Note that the starred quantities are functions of the initial conditions, e.g., $T_t^* = T_t^*\{M_o, T_{ot}, \gamma\}$, and hence vary in magnitude as M_o and T_{ot} are changed. The tabulated values can be used in the following manner. Assume conditions at the inlet and total temperature ratio across the burner τ_b are given. Then:

$$\tau_b = \frac{T_{3t}}{T_{2t}} = \frac{T_{3t}}{T_{3t}^*}\,\frac{T_{3t}^*}{T_{2t}^*}\,\frac{T_{2t}^*}{T_{2t}}$$

Since a constant mass flow, constant area burner is used,

$$T_{3t}^* = T_{2t}^* = T_t^*$$

and

$$\frac{T_{3t}}{T_t^*} = \tau_b\,\frac{T_{2t}}{T_t^*}$$

But if M_2 is specified, T_{2t}/T_t* can be found from the table and consequently T_{3t}/T_t* can be evaluated. Given this result, the other properties at (3) can be determined. Consider a few examples:

Example 1: Let $M_1 = 0.2$; we ask how much heat can be added to the flow if heat addition is limited by choking the flow. Since the final Mach number is one, $T_{t\,max} = T_t^*$, and from Table 21.5.1,

$$\left(\frac{T_t^*}{T_t}\right) = \left(\frac{1}{0.17355}\right) = 5.8 \ .$$

Thus, the total temperature of the flow may be increased by a factor of 5.8. The total pressure ratio across the area of heat addition is:

$$\left(\frac{P_t^*}{P_t}\right) = \left(\frac{1}{1.2346}\right) = 0.81 \ .$$

Example 2: We wish to determine Mach number change and stagnation pressure ratio across a combustion chamber when $M_2 = 0.2$ and $T_{3t}/T_{2t} = 4$. Then

$$\frac{T_{3t}}{T_{2t}} = \frac{T_{3t}}{T_t^*} \times \left(\frac{T_t^*}{T_{2t}}\right) = 4$$

TABLE (21.5.4) FRICTIONLESS, CONSTANT-AREA FLOW WITH CHANGE IN STAGNATION TEMPERATURE (perfect Gas, $\gamma = 1.4$ exactly)

M	T_t/T_t^*	T/T^*	p/p^*	p_t/p_t^*	M	T_t/T_t^*	T/T^*	p/p^*	p_t/p_t^*
.02	.00192	.00230	2.3987	1.2675	.62	.83982	.93585	1.5603	1.06821
.04	.00765	.00917	2.3946	1.2665	.64	.86920	.95298	1.5253	1.06146
.06	.01712	.02053	2.3880	1.2647	.66	.87709	.96816	1.4908	1.05502
.08	.03021	.03621	2.3787	1.2623	.68	.89350	.98144	1.4569	1.04890
.10	.04678	.05602	2.3669	1.2591	.70	.90850	.99289	1.4235	1.04310
.12	.06661	.07970	2.3526	1.2554	.72	.92212	1.00260	1.3907	1.03764
.14	.08947	.10695	2.3359	1.2510	.74	.93442	1.01062	1.3585	1.03253
.16	.11511	.13843	2.3170	1.2461	.76	.94546	1.01706	1.3270	1.02776
.18	.14324	.17078	2.2959	1.2406	.78	.95528	1.02198	1.2961	1.02337
.20	.17355	.20661	2.2727	1.2346	.80	.96394	1.02548	1.2658	1.01934
.22	.20574	.24452	2.2477	1.2281	.82	.97152	1.02763	1.2362	1.01569
.24	.23948	.28411	2.2209	1.2213	.84	.97807	1.02853	1.2073	1.01240
.26	.27446	.32496	2.1925	1.2140	.86	.98363	1.02826	1.1791	1.00951
.28	.31035	.36667	2.1626	1.2064	.88	.98828	1.02690	1.1515	1.00698
.30	.34686	.40887	2.1314	1.1985	.90	.99207	1.02451	1.1246	1.00485
.32	.38369	.45119	2.0991	1.1904	.92	.99506	1.02120	1.09842	1.00310
.34	.42057	.49327	2.0647	1.1821	.94	.99729	1.01702	1.07285	1.00174
.36	.45723	.53482	2.0314	1.1737	.96	.99883	1.01205	1.04792	1.00077
.38	.49346	.57553	1.9964	1.1652	.98	.99972	1.00636	1.02364	1.00019
.40	.52903	.61515	1.9608	1.1566	1.00	1.00000	1.00000	1.00000	1.00000
.42	.56376	.65345	1.9247	1.1480	1.10	.99392	.96031	.89086	1.00486
.44	.59748	.69025	1.8882	1.1394	1.20	.97872	.91185	.79576	1.01941
.46	.63007	.72538	1.8515	1.1308	1.30	.95798	.85917	.71301	1.04365
.48	.66139	.75871	1.8147	1.1224	1.40	.93425	.80540	.64102	1.07765
.50	.69136	.79012	1.7778	1.1140	1.50	.90928	.75250	.57831	1.1215
.52	.71990	.81955	1.7410	1.1059	2.00	.79339	.52893	.36364	1.5031
.54	.74695	.84695	1.7043	1.0979	2.50	.71005	.37870	.24616	2.2218
.56	.77248	.87227	1.6678	1.09010	3.00	.65398	.28028	.17647	3.4244
.58	.79647	.89552	1.6316	1.08255	3.50	.61580	.21419	.13223	5.3280
.60	.81892	.91670	1.5957	1.07525	4.00	.58909	.16831	.10256	8.2268
					4.50	.56983	.13540	.08277	12.502
					5.00	.55555	.11111	.06667	18.634

and

$$\frac{T_{3t}}{T_t^*} = \frac{T_{2t}}{T_t^*} \times 4 = 0.17355 \times 4 = 0.695 .$$

The Mach number corresponding to this value of T_t/T_t^* is 0.50. Consequently, $M_3 = 0.50$, and

$$\frac{p_{3t}}{p_{2t}} = \frac{p_{3t}}{p_t^*} \times \frac{p_t^*}{p_{2t}} = \frac{1.114}{1.235} = 0.90 .$$

Example 3: The total temperature of a stream is to be increased by 50 percent. We wish to compare the total pressure loss if the heat is added at Mach 3.0 and 0.3. For the high Mach number case,

$$T_{3t}/T_{2t} = 1.5 ;$$

therefore

$$T_{3t}/T_t^* = 1.5 \times 0.654 = 0.98 ,$$

and

$$M_3 = 1.15 .$$

Then,

$$\frac{p_{3t}}{p_{2t}} = \frac{p_{3t}/p_t^*}{p_{2t}/p_t^*} = \frac{1.01}{3.42} = 0.296 .$$

For the low Mach number case,

$$M_3 = 0.40 ,$$

and

$$\frac{p_{3t}}{p_{2t}} = \frac{1.16}{1.20} = 0.97 .$$

Obviously, supersonic heat addition causes a much greater reduction in total pressure.

Thermal Choking. If the heat addition for Example 1 had been greater than $(4.8\, T_{1t})$, the

tables give no solution. This is a result of the fact that as heat is added to a subsonic flow of constant cross-sectional area, the Mach number approaches unity. If more heat is added, the Mach number at the channel exit will remain at the value unity, but the upstream boundary condition must change so that the ratio $[T_{1t}/T_t^*\{M_1\}]$ corresponds to the actual heat addition. For example, if heat addition in Example 1 had been $(5.32)T_{1t}$, then $T_t^* = T_{1t} + (5.32)T_{1t}$, or $T_{1t}/T_t^* = 1/6.32 = 0.158$, and the value of M_1 would drop from 0.2 to 0.19.

21.5.3 TWO-DIMENSIONAL HEAT ADDITION CALCULATIONS

In this section we want to calculate the effect on the flow parameters of heat addition from a spreading flame in a constant cross section duct. Although the calculations are idealized they give a more realistic picture of heat addition than the one-dimensional calculation described above. We start with a brief description of flow across a flame sheet and proceed to a discussion of heat addition at a thin flame which is spreading across a constant area duct. Following this analysis, a brief description is given of the effects of the flame holder and of compressibility. Finally, problems involved with calculation of the flame geometry are described briefly.

Flow Across a Flame Sheet. Before examining the geometric spreading of a flame in a duct it is interesting to examine the processes occuring at a flame front. Consider the sketch of Figure 21.5.7. Unburnt gas with velocity V_c approaches the flame front which makes a small angle α with respect to the axis of the combustion chamber. After passing through the flame, the velocity is V_h and the density is ρ_h.

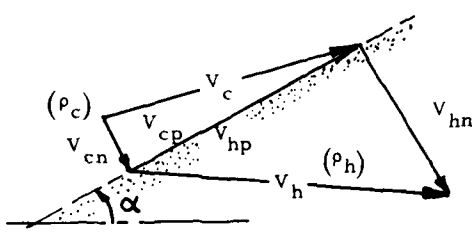

Figure 21.5.7 Sketch of Velocity Change Across an Infinitely Thin Flame.

Subscripts n and p denote components of velocity normal and parallel to the flame. We can apply the continuity equation and the two momentum equations to determine the relationship of the vector components and the static pressure. We consider an incompressible flow and replace the energy equation with the statement that the density ratio $\lambda = \rho_h / \rho_c$ is a given quantity. The three equations are:

$$\rho_c V_{cn} = \rho_h V_{hn}$$

$$\rho_c V_{cn}^2 + P_c = \rho_h V_{hn}^2 + P_h$$

$$(\rho_c V_{cn}) V_{cp} = (\rho_h V_{hn}) V_{hp}$$

These equations can be manipulated to give:

$$\left.\begin{aligned} \frac{V_{hn}}{V_{cn}} &= \frac{\rho_c}{\rho_h} = \frac{1}{\lambda} \\ V_{cp} &= V_{hp} \\ \frac{P_c - P_h}{\rho_c V_c^2} &= \left(\frac{V_{cn}}{V_c}\right)^2 \left[\frac{1}{\lambda} - 1\right] \end{aligned}\right\} \quad (21.5.16)$$

The total pressure loss can be written as:

$$\frac{P_{ct} - P_{ht}}{\frac{1}{2}\rho_c V_c^2} = \left(\frac{V_p}{V_c}\right)^2 (1-\lambda) + \left(\frac{V_{cn}}{V_c}\right)^2 \left(\frac{1}{\lambda} - 1\right) \quad (21.5.17)$$

The major problem which arises in computing flame spreading is that values of the normal velocity of the cold stream cannot be predicted accurately. However, some idea of the order of magnitude of the static pressure difference can be obtained if we select a value for λ, say 0.25, and use the value of 0.025 for V_{cn}/V_c. (The latter value is that determined from experimental data in Section 21.5.1 where the velocity ratio was called β or u_n/V). With these assumptions the pressure jump is less than 2×10^{-3} of the dynamic pressure in the cold gas. If a laminar flame speed were used, V_{cn}/V_c would be even smaller for conditions of interest. Hence, we are justified in ignoring the effects of the pressure rise on the flow field and can assume that the static pressure across the entire duct is constant for the afterburner flow field. (However, if one is interested in laminar flame shapes $(V_{cn}/V_c)^2$ may be made as large as we wish and the pressure difference clearly cannot be ignored.)

In addition, when $V_{cn} << V_c$, the magnitudes of the velocity vectors V_c and V_h will be approximately equal to the parallel velocity component and hence they will be equal. That is: $V_c \approx V_{cp} \equiv V_{ch} \approx V_h$. The total pressure change (see Equation 21.5.17) reduces to $(1 - \lambda)$ or $(1 - \rho_h/\rho_c)$ and is produced by the change in the density due to heat addition. Hence, the velocity and pressure jumps which occur at the flame front are often negligibly small. Given these results, the velocity profile chosen for the following study and the assumption that pressure only depends on axial position are reasonable.

Idealized Flame Spread. The effects of adding heat to a one-dimensional, compressible flow in a constant area duct have been discussed above. In this section we will investigate the effect on the flow of heat addition by a flame spreading from the center of a constant area duct.

To simplify the analysis, first consider a flame developing in a two-dimensional flow of an incompressible gas. Because the entrainment rate of a turbulent flame is not known, we are interested in describing the pressure drop, velocity profile and width between flame fronts as a function of the fraction of the gas which has been burned. Even though the distance required to obtain complete combustion cannot be obtained from this analysis, the total pressure loss, flow acceleration and a rough idea of the resulting velocity profile can be obtained. The approach used here is taken from that of Tsien (Reference 21.25) whose work was based on profiles suggested by the experiments and calculations of Scurlock (Reference 21.19).

Tsien proceeded by using an integral approach. He specified the shape of the velocity profile in terms of the width of the burned region W and two velocity parameters. These unknown parameters and a pressure parameter were found as functions of the fraction of the mass flow which is burned at any station by use of integrated forms of the continuity equation, and the Bernoulli relationship applied to the burned and unburned streams. We use a similar approach but apply a momentum equation instead of the Bernoulli equations for the burned gas, and use a slightly more complex velocity distribution. Since the burned gas flow is rotational this appears to be a more satisfactory approximation. Notation and velocity distribution are identified in Figure 21.5.8.

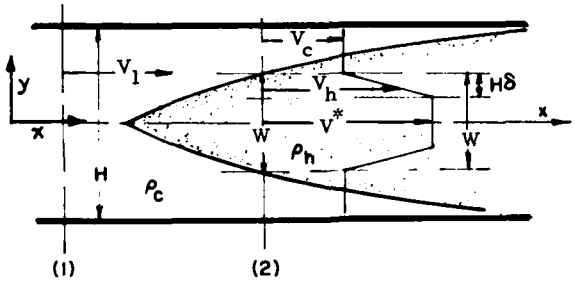

Figure 21.5.8 Notation for Ideal Flame Spread Calculation.

We have chosen to use the trapezoidal velocity profile shown in this Figure. The axial velocity in the unburnt gas is constant at any x station and is V_c; the velocity in the burnt gas rises linearly from V_c to V^* over a distance $H\delta$ at the edge of the flame and is constant with value V^* over the central region of the burnt gas. The static pressure P is assumed to be a function of axial position, x, alone and heat addition at the flame is taken into account by specifying that the burnt stream density ρ_h is constant and is given by $\lambda\rho_c$. The y component of velocity is ignored.

Continuity and momentum equations are:

$$\rho_c V_1 H = 2\left(\int_o^{H/2} (\rho V dy)\right) = \dot{m}_1 \qquad (21.5.18)$$

$$(P_1 - P)H = 2\left(\int_o^{H/2} \rho V^2 dy\right) - \dot{m}_1 V_1 \qquad (21.5.19)$$

Here the subscript (1) refers to conditions for upstream of the flame. The Bernoulli equation for the unburnt stream is:

$$\tfrac{1}{2}\rho_c V_1^2 + P_1 = \tfrac{1}{2}\rho_c V^2 + P \qquad (21.5.20)$$

The fraction burned,

$$f \equiv \left(2\int_o^{W/2} \rho V dy\right) \Big/ \dot{m}_1 \qquad (21.5.21)$$

where $\dot{m}$ is total mass flow rate, $\rho_1 V_1 H$.
The trapezoidal velocity profile is:

$$\left.\begin{aligned} V &= V_c, \quad W/2 \le y \le H/2 \\ V &= \left[V_c + (V^* - V_c)\left(\frac{W}{2} - y\right)/H\delta\right], \\ &\qquad (W/2 - H\delta) \le y \le (W/2) \\ V &= V^*, \quad 0 \le y \le (W/2 - H\delta) \end{aligned}\right\} \qquad (21.5.22)$$

The unknowns are f, W, V_c, V^*, and P, and since there are four equations we can solve for four of them, say V_c, V^*, f, and P as a function of the fifth, the width, W. The parameter δ is treated as a fixed fraction of duct height H and must be specified. It is included here so that the effect of the velocity profile shape on the other parameters can be examined.

The solution of the four algebraic equations which result from the substitution of the velocity profiles assumed here in Equations 21.5.18 to 21.5.21 is straightforward and can be expressed in terms of dimensionless parameters defined as:

$$\left.\begin{aligned} \psi &\equiv (P_1 - P)/\tfrac{1}{2}\rho_c V_1^2 \\ \bar{u} &\equiv V_c/V_1 \end{aligned}\right\} \qquad (21.5.23)$$

$$\left.\begin{aligned} \bar{u}^* &\equiv V^*/V_1 \\ \eta &= W/H \\ \lambda &= \rho_h/\rho_c \\ f &= \text{fraction burned.} \end{aligned}\right\} \quad (21.5.23)$$

The solutions are:

$$\psi = (\bar{u}^2 - 1)$$

$$f = [1 - \bar{u}(1 - \eta)]$$

and a pair of equations for $\bar{u}$ and $\bar{u}^*$:

$$\bar{u}(1 + \lambda\delta - \eta) + \bar{u}^*(\eta - \delta)\lambda - 1 = 0$$

$$\bar{u}^2(1/2 + 2/3\,\lambda\delta - \eta) + \bar{u}^*(\eta - (4/3)\delta)\lambda + (2/3)\bar{u}^*\bar{u}(\delta\lambda) - 1/2 = 0$$

Numerical solutions are found by specifying values for δ and λ, and calculating values of $\bar{u}$, $\bar{u}^*$ and f from the above equations for various values of η. The following table presents numerical examples to illustrate the variation of the parameters for the conditions that ρ_h/ρ_c = 0.25 and δ = 0.1.

η	f	ψ	$\bar{u}$	$\bar{u}^*$
.2	.07	.36	1.17	1.55
.3	.12	.59	1.26	1.69
.4	.18	.89	1.37	1.88
.5	.25	1.3	1.50	2.11
.6	.34	1.7	1.65	2.38
.7	.45	2.4	1.83	2.70
.8	.59	3.2	2.05	3.08
.9	.76	4.4	2.31	3.55
1.0	1.0	6.1	2.66	4.15

Table 21.5.5 Dependence of Flame Spread Parameters on Dimensionless Flame Width, η, for λ = .25 and δ = 0.1.

Note that the fraction burned does not reach 50 percent until the flame width is about 75 percent of the duct height, and that both cold and hot streams have large velocity changes. The velocity increase for the simple one-dimensional case is just $1/\lambda$ or 4.0 for the incompressible when δ = 0. The total pressure change along the central stream line for this incompressible case is:

$$\Delta P_t/\tfrac{1}{2}\rho_c V_1^2 = -\left(1 + \psi - \lambda(\bar{u}^*)^2\right)$$

The dependence of the parameters on f is shown in Figures 21.5.9 to 21.5.13 with λ and δ as parameters. Consider first the effect of changing the profile parameter δ. Remember that δ = 0 corresponds to a square velocity profile with all the burned fluid moving with speed V*, and the $\delta = \eta/2$ corresponds to a triangular profile with a linear change from velocity V_c at the flame front to V* on the axis.

The dependence of the pressure drop on fraction burned is shown in Figure 21.5.9 with δ as a parameter. The pressure drop is almost independent of δ for this example and similar results were obtained for values of the density ratio λ between 1/8 and 1/2. A similar result is obtained for the cold stream velocity $\bar{u}$ and wake width η, and the examples

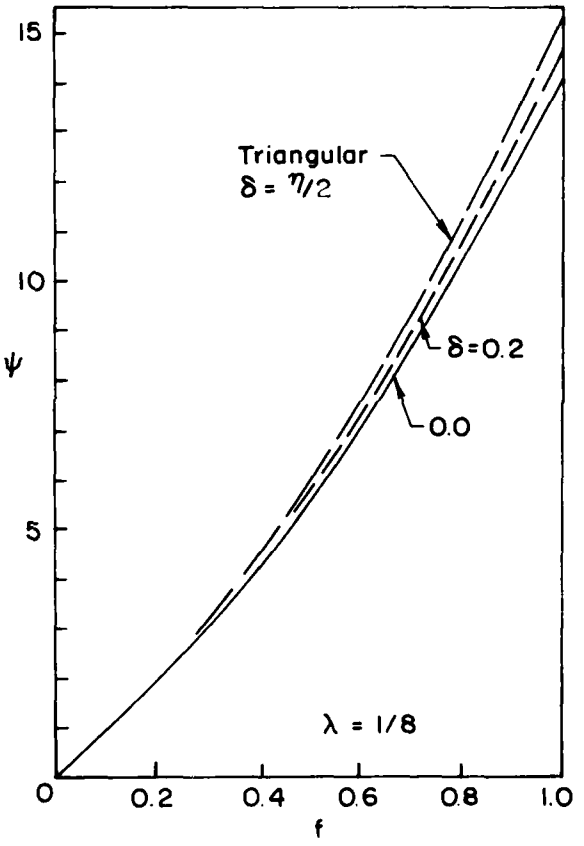

Figure 21.5.9 Dependence of Normalized Pressure ψ on Fraction Burned and Hot Steam Profile Parameter.

shown in Figures 21.5.10 and 21.5.11 on the following page for δ = 0.1 are representative for all δ values. The velocity profile shape factor δ was found to have very little effect on these parameters and we can conclude that the predicted relationships between burned gas wake width (ηH), the cold stream velocity (V_c/V_1) and the fraction burned f will be reasonably accurate regardless of the real velocity

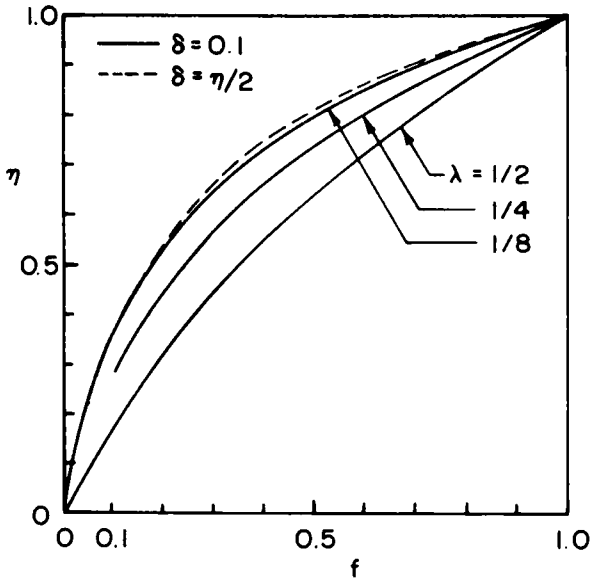

Figure 21.5.10 Dependence of Normalized Width of Flame on Fraction Burned with Density Ratio as a Parameter.

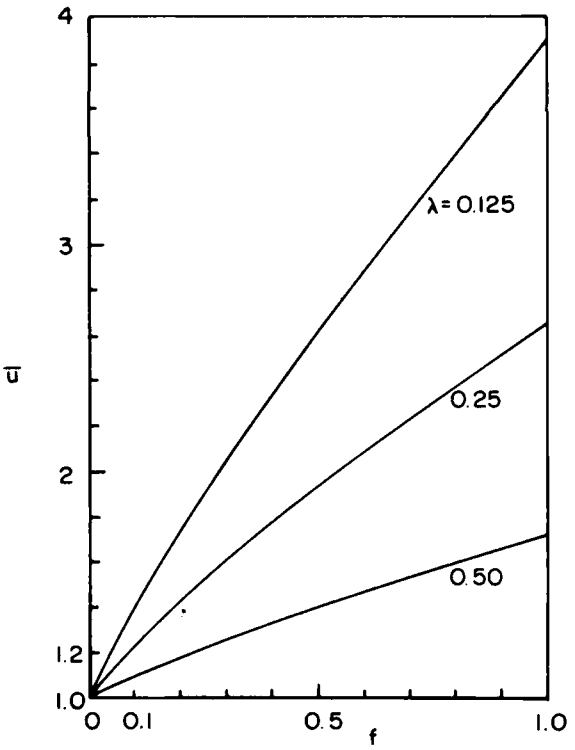

Figure 21.5.11 Dependence of Cold Stream Velocity Ratio on Fraction Burned with Density Ratio as a Parameter.

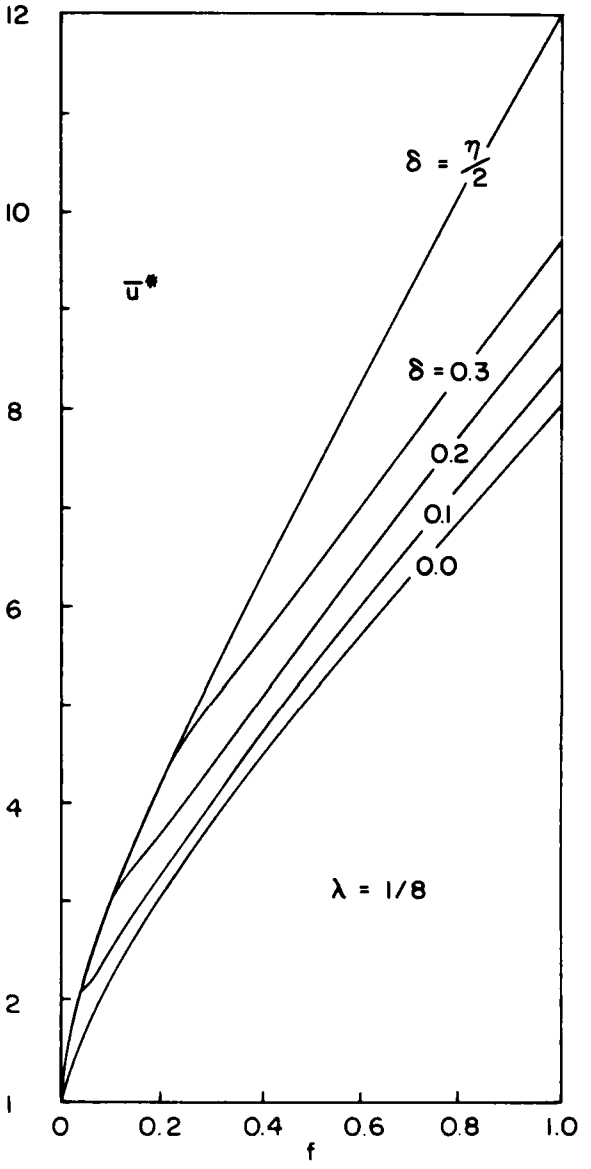

Figure 21.5.12 Dependence of Hot Stream Central Velocity on Fraction Burned and Velocity Profile Parameter.

profile in the burned stream. Of course, the choice of profile parameter will have a large effect on the value of maximum velocity in the hot stream. An example of this dependence is shown in Figures 21.5.12 for $\lambda = 1/8$ and in 21.5.13 for all λ's and small δ values.

The strong dependence of ψ and $\bar{u}$ on density ratio is to be expected because the density change fixes the fluid acceleration. The weak dependence of $\eta\{f\}$ on λ is more surprising. An appreciable change in λ, see Figure 21.5.10, would produce only a few percent change in the fraction burned. For example, when λ is changed from 1/8 to 1/6, values of f corresponding to $\eta = 0.4$ change from 0.12 to 0.15 and values of f corresponding to $\eta = 0.7$ change from 0.37 to 0.39.

Comparison of Figures 21.5.11 and 21.5.12 for $\lambda = 8$ and $\delta = .1$ shows the rapid acceleration of the hot gas as compared with the unburnt stream. The gas speed on the centerline is always greater than the cold flow.

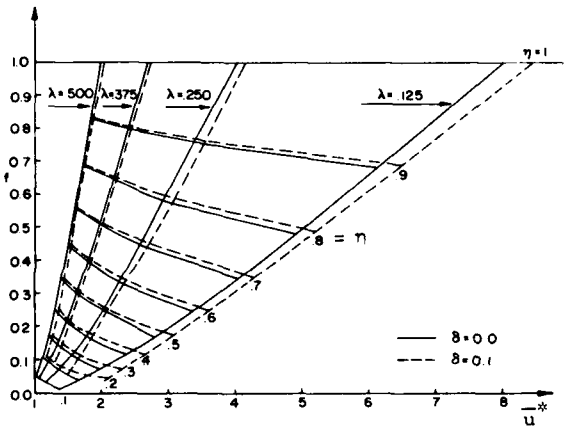

Figure 21.5.13 Dependence of Hot Stream Central Velocity on Fraction Burned with Density Ratio λ and Velocity Profile Factor δ as Parameters.

Effect of Flame Holder. We can easily extend this type of calculation to include the effects of the flame holder and recirculation zone on the flame spreading calculation. For example, consider the flow shown schematically in Figure 21.5.14. The simple triangular velocity profile will be used with the additional assumption that the velocity on the centerline of the flow and at the downstream end of the recirculation zone, station (2) of the sketch, is zero. This approximation is a reasonable one since this point corresponds to the rear stagnation point of the recirculation zone.

Conditions at station (2) are specified when the wake width there, $\eta_2 H$, and density ratio λ are chosen. Combining the continuity equation and Bernouilli equation for the unburnt flow, we find that:

$$\bar{u}_2 = 1/[1 - \eta_2(1 - \lambda/2)]$$

$$f_2 = (\tfrac{1}{2}\lambda)\eta_2\bar{u}_2$$

$$\frac{P_1 - P_2}{\frac{1}{2}\rho_c V_1^2} = (\bar{u}_2)^2 - 1 = \psi_2$$

Conditions at an arbitrary point downstream of (2) can be calculated by an analysis which is identical to that described above. Tabulated values are shown in Table 21.5.6 for $\lambda = 0.25$ and as a function of η_2, the flame width at station (2). Here f_2, $\bar{u}_2$ and ψ_2 are the fraction burned, the cold stream velocity ratio and the normalized pressure difference at station (2), and $\bar{u}_3$ and $\bar{u}_3{}^*$ are the cold stream and centerline values of gas speeds at station (3) where the fraction burned is one. When $\eta_2 \equiv 0$, this solution reduces to that described above for the triangular velocity profile. Values of $\bar{u}$ and η are presented in Figures 21.5.15 and 21.5.16 as functions of the fraction burned and with $\lambda = 0.25$.

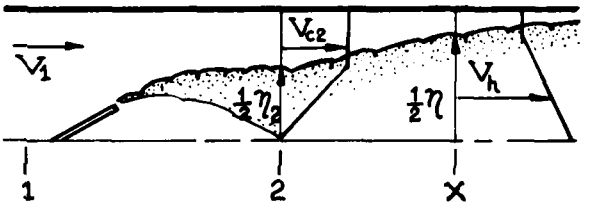

Figure 21.5.14 Sketch of Spreading Flame with Flame Holding Region.

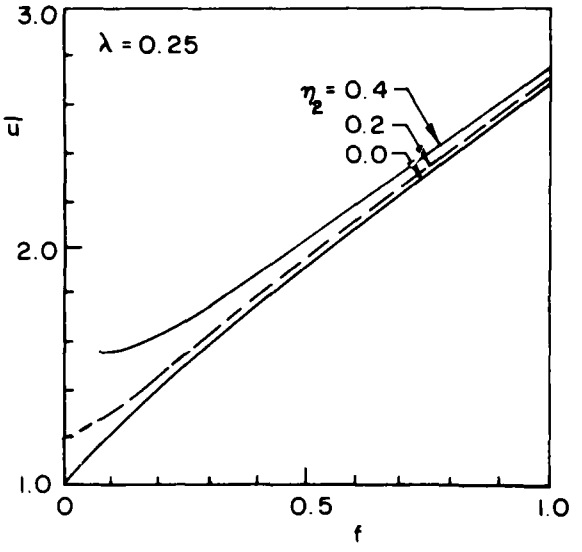

Figure 21.5.15 Dependence of $\bar{u} \equiv V_c/V_1$ on Fraction Burned f and Flame Width at Recirculation Zone.

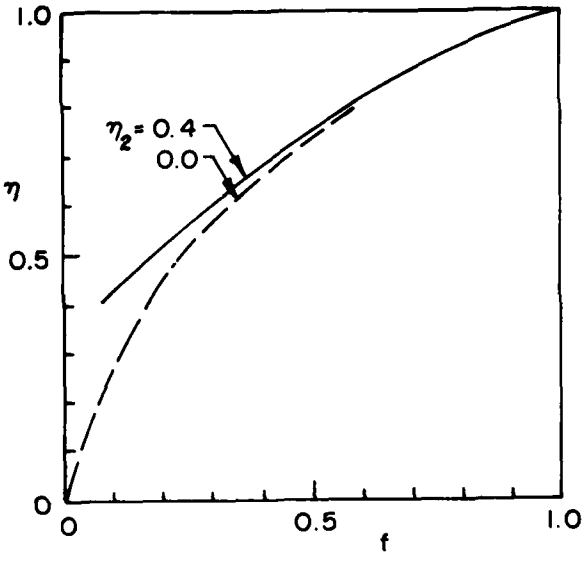

Figure 21.5.16 Dependence of Flame Width η on Fraction Burned f and Flame Width at Recirculation Zone, η_2.

At low values of f, the present solutions differ appreciably from the simple $\eta_2 = 0$ case. However, for values of the fraction burned greater than about 1/3 the solutions are insensitive to η_2. Hence, the overall pressure drop and

η_2	f_2	$\bar{u}_2$	ψ_2	$\bar{u}_3$	$\bar{u}_3$*	ψ_3
0	0	1.00	0	2.69	5.30	6.28
.2	.04	1.21	0.46	2.70	5.28	6.32
.4	.08	1.54	1.37	2.75	5.24	6.64
.5	.11	1.78	2.17	2.82	5.18	6.99

Table 21.5.6 Dependence of Conditions at Station (3), Where f = 1, on Recirculation Zone Width η_2. For $\delta = \eta/2$ and $\lambda = 1/4$.

acceleration of the burnt stream at station (3) where the flow is completely burned, can be estimated with reasonable accuracy from the simple $\eta_2 = 0$ case. Changing η_2 in this example corresponds to changing the wake width and hence, to increasing the flame holder size in a duct of constant height. This calculation suggests that flame holder size or blockage effects will not be very strong when η is greater than $(1.5\ \eta_2)$. Also note in Table 21.5.6 that despite very large differences in the pressure coefficient at station (2), ψ_2, differences in values of ψ_3 are no more than 10 percent. The dependence in $\eta\{f\}$ on η_2 is even weaker.

This analysis indicates that flame holder blockage effects will not be large.

Effect of Compressibility. Tsien (Reference 21.25) earlier carried out this calculation for the triangular velocity profile discussed above. He also extended the calculation to include compressible flows in which density changes in the unburnt flow must be considered. The assumption is made that the density in the burnt region at position x, $\rho_h\{x\}$ is uniform and equal to $\lambda(\rho_c\{x\})$ where λ is a constant.

Values of the parameters for the spreading flame discussed above were calculated for the triangular velocity profile. The dependence of the width of the burnt region η on the fraction burnt f is almost identical to that obtained here for the incompressible case as long as no choking occurred.

For large enough values of the approach stream Mach number M_1, Tsien's solutions do not reach $\eta = f = 1$ but reverse themselves. These solutions are inadmissible and we assume that the smallest value of M_1 at which this behavior is observed corresponds to the "choking" limit. Values of the critical inlet Mach number for the "choked" flow, M_{1c}, were calculated by this technique and are compared with values found in Section 21.5.2 for inlet Mach number required to choke the flow for one-dimensional heat addition in Table 21.5.7

$1/\lambda$	$M_{1c})_{2\text{-dim}}$* ($\lambda \equiv T_1/T_2$)	$M_{1c})_{1\text{-dim}}$* ($\lambda \equiv T_1/T_2$)	$M_{1c})_{1\text{-dim}}$* ($\lambda \equiv T_{1t}/T_{2t}$)
2	.36	.34	.38
2.67	.29	.29	.32
4	.22	.22	.25
8	.13	.15	.17

*Air with $\gamma = 1.40$

Table 21.5.7 Comparison of Critical Mach Numbers Calculated by One-Dimensional and Two-Dimensional Techniques.

The density ratio λ in the two-dimensional treatment presented here is the density ratio across the flame (or the temperature ratio since the static pressure change across the flame front is small). Critical Mach numbers are given in the Table for both static and total temperature ratios across the one-dimensional heat addition region described earlier. There is little difference between these two, and also between the one- and two-dimensional results. Hence, the one-dimensional calculation gives as good an approximation for calculation of choking as the more complex two-dimensional calculation.

A number of other calculations of this type have been made (e.g., Fabri et al (Reference 21.26) and they also lead to predicted values of the critical Mach numbers which are close to the one-dimensional values.

Another parameter of interest is the total pressure loss associated with heat addition. Calculations based on the two-dimensional and incompressible model discussed above, predict mass averaged values of the total pressure ratio across the burner which are a few percent higher than the one-dimensional values when the triangular velocity profile was used in the calculation. Again, the simple one-dimensional heat addition calculation appears to give satisfactory estimates.

Burning Rate. We can use the ideas developed in several of the preceeding paragraphs to illustrate the problems associated with calculating the position of the flame front in a duct. Consider the flow shown earlier in Figure 21.5.7 to be a small part of the spreading flame shown in Figure 21.5.8. Let the mass flux in the burnt flow be $\dot{m}_b$ and total mass flux be $m_1 = \rho_c V_1 H$. Then continuity of mass requires that:

$$\frac{d(\dot{m}_b)}{dx} = 2\left(\frac{\rho_c V_{cn}}{\cos \alpha}\right)$$

Here, the $(1/\cos \alpha)$ term enters because the flame front length corresponding to the length dx is $dx/\cos \alpha$ and the factor 2 because there are two flame fronts. We have defined the fraction burned f as $\dot{m}_b/\dot{m}_1$, (see Equation 21.5.23) and thus the previous equation becomes:

$$\frac{df}{dx} = \left(\frac{V_{cn}}{V_1}\right)\left(\frac{2}{\cos \alpha}\right)\left(\frac{1}{H}\right) \qquad (21.5.24)$$

In order to proceed further in a simple way, some other approximations must be used. One reasonable one is that α is small enough that $\cos \alpha$ is approximately one. With this approximation the effects of flame shape on f are removed from the calculation.

In addition, information concerning the normal velocity component must be supplied. If the flow is laminar, (an unlikely event for afterburners), then V_{cn} = laminar flame speed = S, is a reasonable supposition. Then

$$\frac{df}{dx} = \frac{2S}{V_1 H}$$

and integration with the assumption that S is constant gives:

$$f = \left(\frac{2S}{V_1 H}\right) x\{f\}$$

If we define the position at which the combustion is complete, i.e., at f = 1, as $x\{1\}$ we get:

$$\frac{x\{1\}}{H} = \frac{V_1}{2S}$$

Thus as the initial velocity V_1 increases or the flame speed S decreases, the length required for complete combustion will increase. Also, the fraction burned at any station x will decrease under these same circumstances.

If the flow is turbulent other approaches to describe V_{cn} must be developed. As an illustrative example, consider the following analysis. We start by considering the combustion region at the edge of the flame as a turbulent mixing layer with unburnt gas, density ρ_c and velocity V_c, on one side, and hot combustion products, density ρ_h and velocity V_h, on the other. Entrainment rates in shear layers have been the subject of considerable study and the conventional wisdom is that entrainment rates scale as the velocity difference or as $(V_h - V_c)$ in this example. Recent studies by Brown (Reference 21.27), and Brown and Roshko (Reference 21.18) of shear layers with large density differences, e.g., large differences in ρ_h and ρ_c, have led to an appreciation of the importance of large scale structures in the mixing region and the influence of the density ratio in fixing entrainment rates. Brown suggests that the entrainment velocity from the cold stream could be expressed as:

$$\frac{V_{cn}}{V_c} \approx 0.18\left(\frac{\bar{u}^*}{\bar{u}} - 1\right)\left(1 + \left(\frac{1}{\lambda}\right)^{1/2}\right)$$

Direct use of Brown's suggestion leads to entrainment rates which are within a factor of two to three of those presented above in Table 21.5.7 for mixing layer experiments in which the density and velocity ratios are similar to those in the combustion experiments discussed above.

The axial pressure gradients and the complicated flow at the duct centerline are certainly not anticipated by Brown's model and may be responsible for the differences. Errors in determination of experimental values for entrainment rates may also be responsible.

Finally, part of this difference may also be associated with the definition used to determine the flame front and with the effects of combustion on the mixing process. The similarities of the processes of entrainment with and without combustion appear to be large and indicate that approaching the determination of turbulent flame speeds or entrainment rates from this point of view will be useful.

Despite differences, it is interesting to calculate spreading rates when entrainment rates are given by an ad hoc expression of the form:

$$\beta = \frac{V_{cn}}{V_c} = (.03)\left(\frac{\bar{u}^*}{\bar{u}} - 1\right) \qquad (21.5.25)$$

where

$$\bar{u}^* = \left(V_h^*/V_1\right) \text{ and } \bar{u} = \left(V_c/V_1\right)$$

The dependence on density is ignored here and the constant .03 was picked to give values of β of .025 which were observed experimentally for $\lambda = 1/8$. If this suggestion is followed, Equation 21.5.24 can be usefully rewritten as:

$$\frac{df}{dx} = 2\left(\frac{V_{cn}}{V_c}\right)\left(\frac{V_c}{V_1}\right)\left(\frac{1}{H}\right) = 2\left(\frac{V_{cn}}{V_c}\right)\frac{\bar{u}}{H}$$

where $\bar{u} = (V_c/V_1)$ is the function of f and the density parameter λ determined in preceeding paragraphs. Integration gives:

$$\frac{2\,x\{f\}}{H} = \int_0^f \frac{df}{\left(\beta\,\{\bar{u}^*/\bar{u}\}\right)\bar{u}\,\{f,\ \lambda\}} \qquad (21.5.26)$$

This form is convenient since the ratio $(\bar{u}^*/\bar{u})$ which appears in the expression for β is a very weak function of f.

The results of carrying out the integration are presented in Table 21.5.8 where the changes in several parameters are shown as $\eta = W/H$ increases from .2 to 1.0 for $\lambda = 1/8$ and $\delta = 0.10$. The orders of magnitude for values of x determined here agree roughly with experimental values for $0 \le \eta \le 0.4$. When we examine the influence on solutions of this type of changes in values of the density ratio, we find a strong dependence on density ratio. This dependence arises because both $\bar{u}^*/\bar{u}$ and $\bar{u}$ decrease as the density ratio increases. We can see from Equations 21.5.25 and 21.5.26 that these changes cause $x\{f\}/H$ and $x\{W/H\}/H$ to increase. However, experimental results indicate that for the range of values of W/H and f examined experimentally, the dependence of flame geometry on density ratio is very small.

We can eliminate this discrepancy by replacing the constant .03 which appears in our definition for β (Equation 21.5.25) by a function of λ. However, we currently have no rational explanation for this dependence although the work of Brown (Reference 21.27) indicates that β does depend on λ in a mixing layer.

The preceding calculation is indicative of the types of simple approaches used in calculation of the geometric features of turbulent flames. Calculations of this type cannot be taken very seriously until the dependence of V_{cn} or β on density ratio, turbulence level, flame width, etc., has been established.

Other more ambitious schemes have been developed to calculate the complete flow field. For example, the calculations of Spalding are based on a general model for computing turbulent flows. A set of differential equations is developed in an ad hoc manner from which turbulent transport parameters can be determined as part of the general solution of the equations of motion. Combustion phenomena are included by assuming infinitely fast reaction rates when the premixed fuel-air gas is mixed with the burnt gas at the flame front. The results of one set of calculations made by Spalding are reported in Reference 21.28, and they do agree with the picture reported here of the dependence of flame spreading rates on approach stream parameters. However, the infinite reaction rate assumption and the ad hoc nature of the treatment of the turbulent transport phenomena suggest that great care must be exercised in using the results of this type of calculation outside of the range of the parameters used in fixing the constants which appear in the model and which were used in checking the accuracy of the results.

η	f	$\frac{\bar{u}^*}{\bar{u}}$	β	x/H
0.2	.04	1.73	.022	0.9
0.4	.12	1.80	.023	2.2
0.6	.25	1.93	.024	2.7
0.8	.49	2.05	.027	5.4
1.0	1.00	2.16	.029	7.8

Table 21.5.8 Variation of Spreading Parameters with Dimensionless Flame Width, η for $\lambda = 1/8$ and $\delta = 0.1$

Combustion Efficiency in Full Scale Tests. The previous discussion has concerned flame spreading rather than combustion efficiency. A large number of experiments have been carried out on full scale systems, in which combustion efficiency has been measured as a function of parameters such as the inlet temperature, pressure, velocity and fuel-air ratio, the flame holder geometry, and, in at least one case, the combustion chamber length. Typical results are presented in Reference 21.29, Reference 21.30, and Reference 21.1. Because the injection and vaporization processes as well as stabilization and spreading processes are affected by changing the inlet conditions, we cannot distinguish which process is affected by the changes.

However, Useller (Reference 21.30) has measured the effects of changing combustor length while holding the other parameters constant. Some of his results are shown in Figure 21.5.17 where combustion efficiency η_{ab} is plotted as a function of combustion chamber length downstream of the plane of the flame holder. The flame holders were 1.5 inch high V-gutters arranged in two concentric rings and with two crossed gutters on diameters serving as supports. Each flame holder occupied a part of

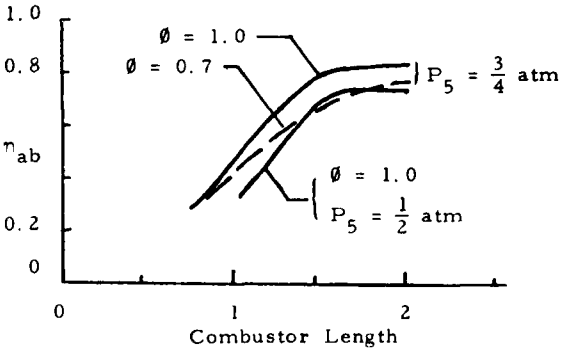

Figure 21.5.17 Dependence of Combustion Efficiency on Combustion Chamber Length. Data from Reference 21.30.

duct with an equivalent duct height of very roughly 10 cm. The actual duct diameter was 62 cm and the inlet velocity was 170 m/sec. Note that all three curves of Figure 21.5.17 have a well defined knee for chamber lengths of about 150 cm and that a further increase in combustor length has little effect on efficiency. Thus, the length to height ratios of roughly 15 are required to approach the maximum efficiency and this ratio is unchanged as pressure is dropped. This length ratio is slightly larger than one would expect from the smaller scale flame spreading experiments discussed above. However, the complex flame holder shape makes direct comparison impossible. As noted above the effects of pressure and fuel-air ratio may not be due to the influence of these parameters on the spreading process.

Summary. Simple one and two-dimensional calculations are available which allow reasonably accurate predictions for the changes in static and total pressure, and velocity across a region of heat addition in a constant area duct. The inlet conditions leading to "choking" can also be predicted with reasonable accuracy. However, predictions cannot be made of the combustion chamber length required to produce a given level of combustion efficiency because the entrainment rate at a turbulent flame front is presently not understood.

A number of full scale tests are available but because all components are subject to the same changes in operating parameters it is not possible to determine whether or not changes in the spreading process produce the observed performance changes.

21.6 NOZZLE AND FUEL CONTROL SYSTEMS

The afterburner control system has the primary function of controlling the flow of fuel to the afterburner and of keeping the pressure level in the afterburner at the desired value by controlling the nozzle throat area. The control system is also responsible for carrying out the ignition process and supplying the various zones of the afterburner injection system with fuel in the proper sequence and at the proper rate during the starting sequence, and later, during steady operation and termination of thrust. The control must be able to receive data from the core engine control system from which it can determine the air flow rate to the afterburner and then set the required fuel flow rate to each injector zone. Although inlet temperature and velocity do not change a great deal, pressure levels may vary by factors of 10, and thus a wide range of fuel injection rates must be accommodated.

In addition to this control function, the control system must carry out a number of other functions. For example, the fuel lines and injector rings which are within the afterburner are heated to high temperatures when the afterburner is turned off by convective heat transfer from the high temperature flow from the engine. If any jet fuel is left in these tubes, the high wall temperatures may cause the fuel to decompose and produce tar-like deposits. These deposits can clog the tubes and the small diameter injector ports in the tube walls. This problem is usually avoided by venting the lines to a region at lower pressure than the combustion chamber when afterburner thrust is terminated. The resultant flow of gas cleans out the lines and leaves them empty. However, during the afterburner start-up process, these lines must be filled again before the ignition process is initiated. The problem here is that in order to reduce the pressure pulse associated with ignition, the initial fuel flow rate is usually set at a value far below that required to fill the injector rings and supply lines in a reasonable length of time, i.e., in several seconds. Thus, the control system must be designed to fill the lines at a high flow rate and then to stop the flow so that no fuel is allowed to spill into the combustion chamber where the high temperatures in the core stream could cause auto ignition.

Another important function of the afterburner control system is to maintain conditions at the turbine and fan outlets in an unchanged state so that the operation of these components will not be affected by the afterburner. This control function is particularly difficult to perform during the starting and stopping transients. To understand this problem, examine the mass flux equation for the afterburner nozzle under steady state conditions and for a simple turbojet cycle. The mass flux at the throat of the nozzle throat can be written in terms of the total pressure and temperature, P_{7t} and T_{7t}, the nozzle throat area A_n, and the gas constant and specific heat ratio R and γ. (E.g., see Section 2.18 and 5.11.) The result is:

$$\dot{m}_7 = \frac{P_{7t}}{\sqrt{T_{6t}}} A_n \left(\sqrt{\frac{\gamma}{R}} \left[\frac{2}{\gamma+1} \right]^{\frac{1}{2}\frac{\gamma+1}{\gamma-1}} \right) \tag{21.6.1}$$

If we call the fuel-air ratio f_{ab}, we can relate the mass flow at the inlet (Station (5)) to that at the nozzle (Station (7)) by:

$$\dot{m}_7 = \dot{m}_5 + \dot{m}_{fuel} = (1 + f_{ab})(\dot{m}_5) \tag{21.6.2}$$

When we rewrite Equation 21.6.1 in terms of conditions at (5), and use the definitions $\pi_{ab} = P_{7t}/P_{5t}$ and $\tau_{ab} = T_{7t}/T_{5t}$, Equation 21.6.1 can be stated as:

$$\dot{m}_7 = \left(\frac{\pi_{ab}}{\sqrt{\tau_{ab}}} A_n \right) \left[\frac{P_{5t}}{\sqrt{T_{5t}}} \left(\sqrt{\frac{\gamma}{R}} \left[\frac{2}{\gamma+1} \right]^{\frac{1}{2}\frac{\gamma+1}{\gamma-1}} \right) \right] \tag{21.6.3}$$

Let the condition for which the afterburner fuel-air ratio is zero be designated by a sub zero suffix. Then, if conditions at Station (5) are held fixed by the control system, $\dot{m}_5$ will be a constant and we can show from 21.6.2 and 21.6.3 that:

$$\frac{\dot{m}_7}{\dot{m}_7)_o} = \frac{\dot{m}_7}{\dot{m}_5} = (1 + f_{ab}) \frac{\pi_{ab}}{\tau_{ab}} A_n \Big/ \frac{\pi_{ab})_o}{\tau_{ab})_o} A_{no}$$

Consequently,

$$\frac{A_n}{A_n)_o} \approx \left(\frac{\pi_{ab})_o}{\pi_{ab}} \right) (\tau_{ab}) (1 + f_{ab}) \qquad (21.6.4)$$

Where $\tau_{ab})_o \equiv 1.0$ since fuel flow and consequently heat addition is zero when the afterburner is turned off. However, $\pi_{ab})_o$ is not one since flame holder drag and wall losses will always reduce the total pressure. The nozzle throat area required to keep conditions at Station (5) unchanged, when f_{ab}, π_{ab} and τ_{ab} are changed due to afterburning, can be obtained from Equation 21.6.4. This equation is only approximate because we have ignored changes in γ and R due to heat addition, non-uniform velocity, etc.

A similar analysis can be used for a fan engine but account must be taken of differing conditions in the fan and core streams. To illustrate the changes required in nozzle throat area, data (taken from Reference 21.29) are shown in Table 21.6.1 for a TF30-P-3 afterburner with an inlet pressure of about one atmosphere. Equation 21.6.4 is applied to this fan cycle and averaged values of π_{ab} and τ_{ab} are used to evaluate the area changes. For an afterburner fuel-air ratio of 0.005, (typical of values used for ignition) the nozzle area must be still increased by about 13 percent and for f = 0.04, the increase is nearly 80 percent. The change is almost totally the result of large changes in τ_{ab}. Nozzle area changes of this magnitude must be effected within 5 to 10 seconds to keep the duration of the starting transient within reasonable limits. The nozzle actuation rate is usually the slowest and hence limiting rate in the control process.

f_{ab}	τ_{ab}	$\pi_{ab}/\pi_{ab})_o$	$A_{nt}/A_{nt})_o$
0.0	1.0	1.0	1.0
.01	1.5	.98	1.26
.02	1.90	.96	1.46
.03	2.30	.94	1.57
.04	2.50	.93	1.77

Table 21.6.1 Variation of Nozzle Throat Area A_{nt}, and Afterburner Total Pressure and Temperature Ratios with Afterburner Fuel-Air Ratio, f_{ab}. Data from the TF30-P-3 Afterburner (Reference 21.29).

This example shows that large changes in the nozzle area must be controlled in order to maintain unchanged flow conditions at the turbine and fan exit stations. High precision is also required. For example, it is clear from Equation 21.6.1 that under steady conditions, a 10 percent error in area A_n must be balanced by a 10 percent error of opposite sign in P_{7t} when $\dot{m}_7$ and T_{7t} are held fixed. A 10 percent increase in P_{7t} and P_{5t} would often be sufficient to stall the fan stages and later the core compressor of the TF30 engine examined here. Hence, control of the exit area must be precise during both starting transients and steady state operation of the afterburner.

The afterburner control system can be organized in a number of ways concerning the primary functions of fuel flow rate and nozzle throat area. One common technique is the double open-loop system. In this system movement of the power lever by the pilot, produces a demand in the control unit for a fuel flow rate and nozzle exit area. The control system changes fuel flow rates and nozzle area according to specified schedules which must be very accurately matched and timed to avoid an excursion in burner pressure levels far from the desired values. As the term "open loop" implies, no feedback control is used, and thus dynamic interaction between the two control functions and any chance for control system instabilities are eliminated.

A large number of alternate schemes are possible including systems involving feedback. A number of existing systems are based on hydraulic control systems and digital systems are currently being studied. The use of closed loop systems have been delayed by the lack of fast response transducers which can perform well in the high temperature environment of the afterburner.

In the selection of a control system, the designer must choose a device from a range bounded on one side by the very complicated systems which attempt to get the highest possible performance with the shortest delay times in all engine operating modes, and on the other by very simple systems with reduced average performance and with longer delay times. See Reference 21.31 for a detailed discussion of control systems and control system hardware.

A detailed design of the afterburner or any variable area jet engine exhaust nozzle for supersonic flight is also beyond the scope of this chapter. A general discussion of this subject is given in References 21.32 and 21.33. However, a few general remarks are made below concerning several important nozzle design problems.

The afterburner is often used during takeoff and at supersonic speeds. In the first regime, a high subsonic or sonic exit velocity may be desired and in the second, a supersonic exhaust velocity will be necessary. Thus, the exhaust nozzle must be capable of operating both as a convergent and as a convergent-divergent nozzle. This can be achieved in a simple design by several techniques. Consider first the system illustrated in the three sketches of Figure 21.6.1 and described in detail in the caption. The nozzle consists of two basically coaxial convergent nozzles which are designed to have variable exit areas. The primary nozzle

(e.g., number (3)) is made up of a large number of overlapping leaves hinged at their upstream end and sealed against each other to prevent leaks. Exit area variations by factors of 1.5 to 2 can be accomplished with this type of nozzle. The secondary nozzle (numbers 5, 10 or 16) is a variable area design of the same type. In the example shown here, it has a contoured inner surface. In other designs it may be the same type of design as the primary nozzle.

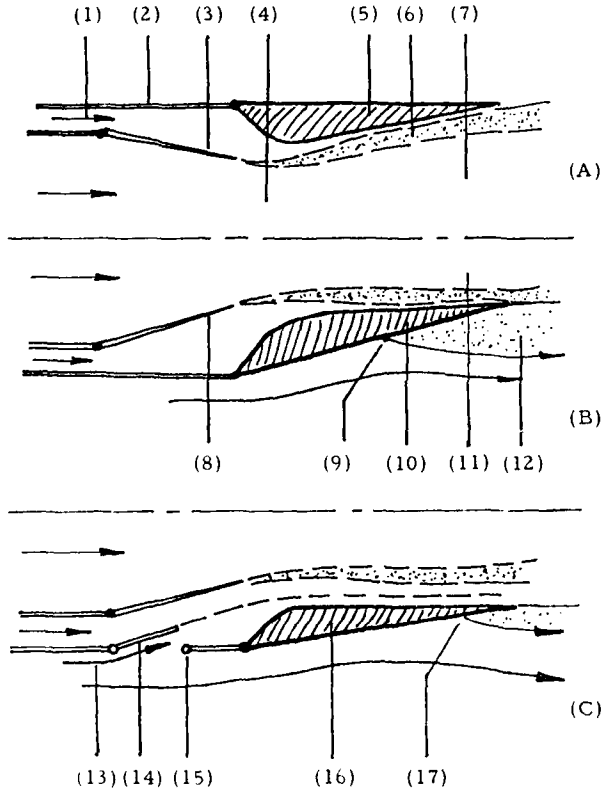

Figure 21.6.1 Ejector Nozzle Configuration.

(A) Supersonic nozzle configuration with afterburning: (1) Secondary flow, (2) Outer case of engine, (3) Moveable primary nozzle shown at maximum area, (4) Primary flow, effective throat, (5) Moveable secondary nozzle shown at maximum exit area, (6) Mixing layer between primary and secondary streams, and (7) Supersonic primary flow.

(B) Subsonic nozzle configuration with no afterburning: (8) Primary nozzle at minimum area, (9) Separation point of external flow, (10) Secondary nozzle at minimum area, (11) Sonic primary stream, and (12) Region of separated flow in external flow.

(C) Subsonic nozzle configuration, no afterburning and blow in door in use: (13) Tertiary flow of ambient gas into nozzle, (14) Blow in door, inflow configuration, (15) Reversible hinge/latch, (16) Moveable secondary nozzle, and (17) Separation point of external flow.

The primary nozzle is responsible for fixing the throat area which controls the primary or afterburner mass flow rate and the secondary nozzle is used to fix the expansion ratio for the nozzle. The primary flow separates from the downstream lip of the primary nozzle and usually reattaches to the secondary nozzle. Reattachment is not necessary in the subsonic case (see B) but is necessary in the supersonic case (see A) if the secondary nozzle is to be effective in fixing the exit area.

A supersonic nozzle configuration with maximum primary throat area is shown in Figure 21.6.1A and a sonic jet with minimum throat area is shown in B. The primary nozzle area changes between examples (A) and (B) by a factor of about two and the expansion ratio for case (A) is about 1.5.

In both examples (A) and (B), a secondary gas stream (number 1) flows between the outer and inner cases of the engine. This flow serves several purposes in the nozzle. First the secondary gas is usually much cooler than the primary and hence this stream can act as a film coolant for the secondary nozzle. Second, the secondary flow occupies a coaxial region about the primary flow and hence can be used to determine and control the exit area of the primary flow. For example if the secondary flow of Figure B were turned off the effective exit area of the primary stream would be increased. Finally, the entrainment of fluid by the shear layer, (e.g., see number (6)), removes fluid from the cavity between the secondary and primary nozzles. If no secondary flow were supplied to compensate for this effect, a strong recirculating flow would be set up to supply this entrained material. This flow would reduce the nozzle thrust coefficient, increase heat transfer rates and contribute to the unsteadiness of the exhaust flow.

The motion required by the secondary nozzle flaps (numbers (5) and (10)) to accommodate the area changes necessary to produce optimum expansion ratios are large when both afterburning and supersonic flight speeds are contemplated. Some of this motion can be avoided by use of the "blow in" doors shown in Figure 21.6.1C as number (14). When doors of this type are opened, a tertiary flow of ambient gas can enter the nozzle and form a stream coaxial with the secondary and primary flows. Control of the secondary and tertiary streams can again change the throat area of the primary stream and hence reduce the motion required of the secondary nozzle flaps. The "blow in" doors can also be used as blow out doors, i.e., can be used as part of the control system to dump some of the secondary flow around the nozzle.

The secondary flow is usually made up of air used to cool the afterburner walls and it may also be drawn from the combustion chamber inlet flow or as far forward as the engine inlet. This nozzle is called an ejector nozzle because the primary stream can be used to pump a low total pressure secondary stream, just as the primary stream of an ejector pump is used to actuate a secondary flow.

A second nozzle type, shown in Figure 21.6.2, does not use the ejector to minimize the motion of the secondary nozzle. In this

case a single flap (numbers (6) and (8)) with two hinged joints (numbers (5) and (7)) forms the nozzle contour. In case (A) of Figure 21.6.2, a subsonic outlet is formed by maximum inward rotation of both members; in (B), outward rotation of both, produces a larger throat area and a diverging nozzle at the exit. The nozzle is again constructed of overlapping leaves which must be sealed against each other. The throat area for this example changes by a factor of about 2 and the exit area ratio for the supersonic nozzle is about 1.5.

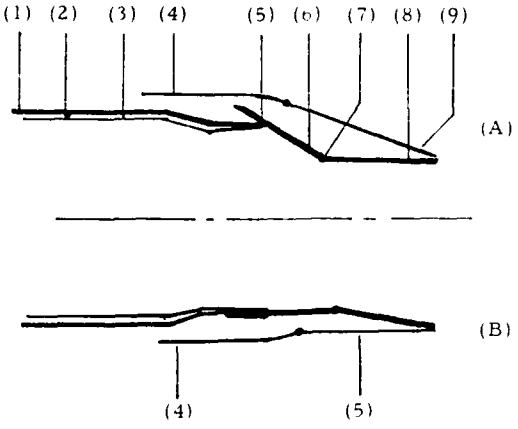

Figure 21.6.2 Sketch of Nozzle for Pratt and Whitney F-100-PW-100 Augmented Turbofan Engine.

(A) Subsonic nozzle configuration: (1) Engine case, (2) Cooling passage, (3) Perforated cooling liner, (4) Fixed outer cowl, (5) Hinge for nozzle contraction, (6) Nozzle contraction member, (7) Hinge for nozzle expansion, (8) Nozzle expansion member, and (9) Moveable outer cowl.

(B) Supersonic nozzle configuration.

Another major area of concern for nozzle designers is the external drag of the nozzle and aft end of the propulsion pod or vehicle. Large nozzle exit area changes are required to accommodate afterburner operation and, consequently, it is difficult to make an aerodynamic design for the aft end of the engine which will not result in excessive drag during either afterburning or non-afterburning operation. For an example, if the external surface is fixed to accommodate the maximum nozzle exit area, see Figure 21.6.1A, a large base drag will occur because of flow separation on the "boat tail" of the nozzle when a smaller exit area is actually used, see Figure 21.6.1B. The flow separation shown in (B) produces a significant increase in drag. Use of "blow in" doors of Figure (C) reduce the required motion of the secondary nozzle, and hence decrease the boat tail angle, and the size and importance of the separated region. E.g., compare (B) and (C). A similar problem arises for the nozzle shown in Figure 21.6.2. Drag from this source and other sources associated with the installation of engines in vehicles or pods is an important problem for the nozzle designer.

Ejector nozzles are used on a number of engines in operational use in the 1970's. Examples are the General Electric TF30-P-3 augmented turbofan engine used in the United States Air Force F111 airplane and the Olympus engine used in the Concord. In the latter case the secondary nozzle flaps are also used as part of the thrust reverser system. (See Reference 21.34.)

The system illustrated in Figure 21.6.2 is used on the Pratt and Whitney F100-PW-100 augmented turbofan engine used in the United States Air Force F-15 and F-16 fighter airplanes.

21.7 COMPLETE AFTERBURNER SYSTEMS

In this section we will describe design details and performance for a typical afterburner system. The afterburner selected for examination, the standard TF30-P-3 afterburner, is shown in the photograph of Figure 21.7.1 and the sketch of Figure 21.7.2. The material discussed here is taken directly from Reference 21.29. This is the same system that was described briefly in the introduction. Conditions in the fan stream at the afterburner inlet were a velocity of about 95 m/sec and a temperature of about 390° k, and conditions in the core or gas generator stream, were about 220 m/sec and 875° k respectively. The bypass ratio was about one for these tests.

Figure 21.7.1 Photograph of Afterburner Flame Holders and Fuel Spray Rings, from Reference 21.29.

The flame holder system consists of three rings of V-gutters and a number of short radial segments of V-gutters. The gutters all have an included angle of 45°; the outer gutter ring and the radial gutters attached to it have a height of 5.1 cm and the inner two gutter rings have a height of 3.6 cm. The outer ring is held in place by a rod assembly, shown in the

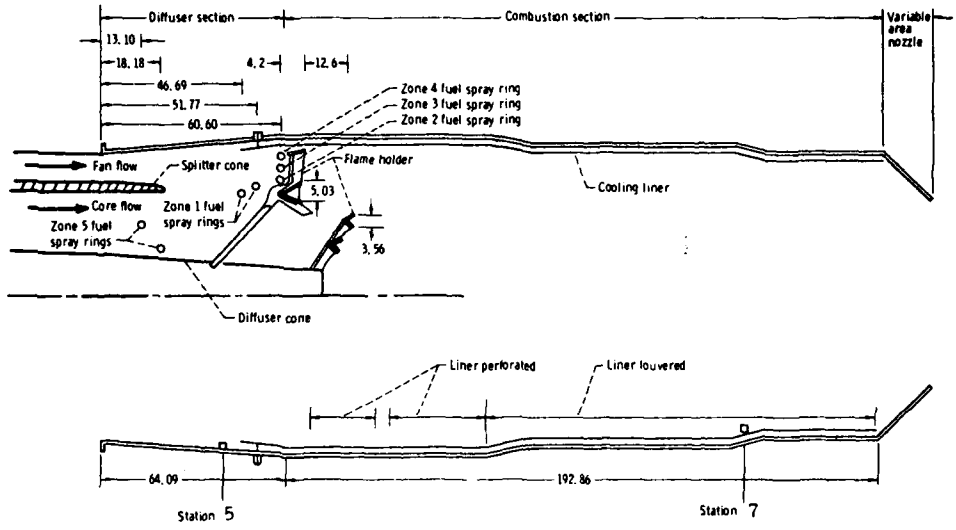

Figure 21.7.2 Sketch of Afterburner for TF30-P-3 Augmented Turbofan Engine. (All Dimensions in cm.; Taken Directly From Reference 21.29.)

sketch, and the ring supports 18 radial V-gutters (which have their axis lying along a radius). The inner two rings are supported by six V-gutters, which are attached to the diffuser cone and are visible in Figure 21.7.1. The projected area of all the flame holders was about 38 percent of the duct cross-section area although the holders do not lie in a single plane. The combustion chamber is made up of an outer shell, which is the pressure vessel and an inner shell which is part of the cooling system. The inner shell is perforated at its upstream end and louvered at its downstream end. The narrow space between the shells acts as a cooling passage; the pressure at the upstream end of this passage is high enough compared to that in the combustion chamber to produce a flow of cool fan air through the passage and out into the combustion chamber through the holes and louvers. Flow in the passage cools by forced convection, and flow through the holes and louvers cools by a film cooling effect. The holes in the upstream section also have been designed to produce maximum damping of acoustic disturbances at frequencies for which combustion instabilities have been observed in the chamber.

Fuel is injected into the flow through seven fuel spray rings, shown in both Figures 21.7.1 and 21.7.2, and they are arranged in five zones. Modulation of the fuel injection system is accomplished by an integrated afterburner-nozzle control system which simultaneously opens the nozzle and increases the fuel flow. These two operations are controlled by an open loop hydraulic control mechanism which has no feedback information concerning afterburner ignition or pressure level. In the present engine, fuel is first introduced to zone 1. Under low pressure (i.e., high altitude) operation fuel is injected through one of the rings, and when the pressure level is above 124 N/cm^2 the second ring is also used. These fuel spray rings lie close to the interface between the fan and core gas streams and the fuel is primarily injected into the core or gas generator stream. If Maximum Power is required, the control system will start fuel flowing to the other 4 zones at intervals of about 1-1/2 seconds.

Zones 2, 3 and 4 are single ring injectors which feed fuel to the fan stream. They are placed close to the radial flame holders to insure a supply of liquid fuel to the flame holders which is then evaporated and fed to the recirculation in the manner suggested in Section 21.4.3, page 21-19.

Zone 5 is a double ring which supplies the core engine exhaust stream. These rings are placed about 65 cm upstream of the flame holders to give the fuel time (about 3 m/sec) to vaporize before reaching the flame stabilization region.

Each of the three flame holder rings occupy an equivalent duct with a height of about 15 cm and a length of about 175 cm. Thus, the length to height ratio is very roughly 12 but this interpretation is complicated by the presence of numerous radial gutters. Thus, in the outer region which has many radial holders, this ratio is much larger.

The transient processes which occur during a rapid advance of the throttle from Military Power setting to Maximum Power setting are shown on the next page in Figure 21.7.3 which is taken directly from Figure 9 of Reference 21.29. (The horizontal axes on these diagrams is the time in seconds.) The position of the power lever controlled by the pilot is shown in Figure 21.7.3a, the upper diagram, as a function of the time. It is moved forward from a Military Power level at time zero to Maximum Power at about 1.4 seconds. The nozzle control system opens the nozzle throat area according to the schedule shown in Figure 21.7.3b.

The total fuel flow rate to the afterburner system is shown in Figure 21.7.3c. Fuel flow starts at about 0.3 seconds after the power lever is moved to Maximum Power and ignition of the zone 1 system occurs at about 1.6 seconds. The time for ignition is deduced from the first rapid increase in static pressure at the nozzle exit (P_7) shown in the sketch of Figure 21.7.3d. As fuel injection into each zone is started the overall injection rate, shown in (c), increases. The particularly large excursion in flow which peaks at about 2.6 seconds is an artifact of the measuring system and does not represent an increase in fuel delivered to the combustion chamber. It is caused by a change in fuel

pumps from the afterburner hydraulic pump, used at very low fuel flow rates, to the main afterburner fuel pump. Note that the maximum fuel flow of the afterburner system is about 6000 kg/hr whereas that of the core engine is only about 1200 kg/hr at the condition discussed here. Ignition of each zone is indicated by the pressure cusps which appear in the nozzle inlet pressure, see line (d). The schedule for nozzle area changes, shown in line (b), lags these ignition events by about 0.2 seconds and this mismatch produces the observed pressure disturbances.

For this particular throttle excursion the only pressure pulse which could cause any trouble at the fan or compressor is the first pulse which starts at 1.6 seconds. The large rise in nozzle inlet pressure, line (d), also appears at the fan exit station, line (e). This excursion increases the fan exit pressure above the steady state stall line for the fan. In this example, the transient nature of the disturbance kept the fan from stalling. However, the disturbance was observed throughout the complete compressor system as a 5-10 percent excursion in pressure.

The steady state characteristics for this afterburner are shown in Figure 21.7.4 as a function of afterburner fuel-air ratio and with inlet pressure as a parameter. Afterburner total temperature τ_{ab} and pressure π_{ab} ratios are shown in (A) and (B), and the specific fuel consumption SFC and thrust F are shown as ratios of their values with and without afterburning in (C) and (D). Finally, the combustion efficiency is shown in

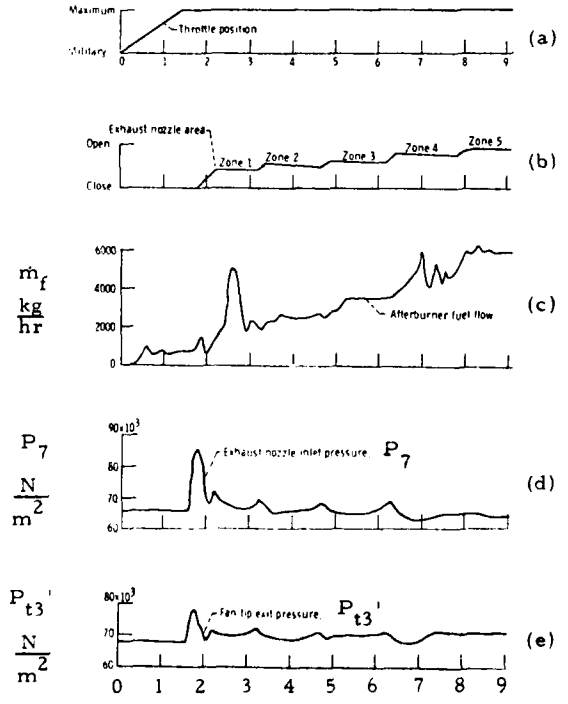

Figure 21.7.3 Time History of Engine and Afterburner Parameters During Afterburner Starting Transient. Data from Reference 21.29.

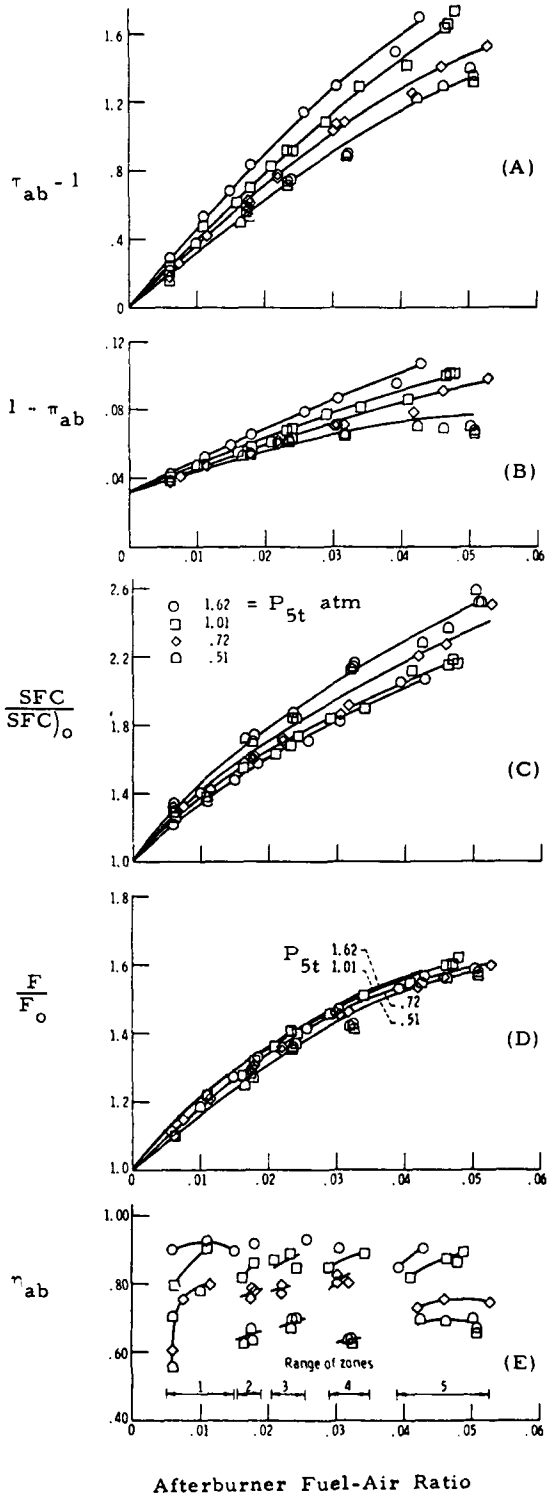

Figure 21.7.4 Effect of Fuel-Air Ratio and Pressure on Steady State Performance Parameters. Reference 21.29

Figure 21.7.4(E). The values presented here are based on measurements of static pressure at Stations (8) and (9) of Figure 21.7.1, total temperatures at Station (8) and the measured thrust of the engine. Hence, the values are reasonable estimates but they are not the result of detailed measurements made in the flow.

The latter figure also shows the relationship between the five zones and the afterburner fuel-air ratios which can be achieved when each is activated. Thus, when zones 1 to 3 are operating, fuel-air ratios between 0.020 and 0.026 can be used. However, the value $\eta_{ab} = 0.80$ obtained for an inlet total pressure of 0.72 atm and a fuel-air ratio of 0.022 is the overall efficiency and is not associated with any particular zone. For inlet pressures greater than one atmosphere, combustion efficiency is uniform and greater than 85 percent.

Note that all the steady state parameters except the thrust drop off rapidly when the inlet pressure falls below about one atmosphere.

It is comforting to find that relatively effective augmentation systems can be developed despite our lack of understanding of many very important features of the fuel preparation, stabilization and flame spreading processes. However, the cost of developing these systems is greatly increased by our ignorance.

21.8 COMBUSTION INSTABILITIES

One of the principal problems associated with the development of high performance augmentation systems is the suppression of large amplitude pressure oscillations which often accompany the combustion process. Disturbances of this type are called combustion instabilities and most appear to be driven by a coupling between an acoustic oscillation at one of the many resonant modes of the system and some step in the heat addition process.

The range of frequencies is very wide. Longitudinal modes with frequencies as low as 50 to 100 hz have been identified, and frequencies for radial or tangential modes can be as high as 5000 hz. The frequency spectra of strong oscillations often exhibit 5 to 10 harmonics with amplitudes within 10 db of the fundamental frequency. Also peak to peak amplitudes of oscillations as large as 50 percent of the average pressure are observed and many systems regularly operate with oscillations with an amplitude of 5-10 percent of the average pressure.

In a typical situation, the amplitude of the oscillation at low fuel-air ratios is small and grows slowly as the fuel-air ratio is increased. Finally, near some critical fuel-air ratio, the amplitude grows very rapidly to a much larger value. The fuel-air ratio at the critical threshold and the rapidity with which the amplitude of the disturbance grows after the threshold has been passed often depend on the combustor inlet velocity, pressure and temperature.

The oscillations reduce the life of combustion chamber apparatus or force an increase in weight to obtain a given life expectancy. Life of components is decreased because of fatigue produced by high frequency oscillating forces and by increased heat transfer which often accompanies the oscillations.

In analyzing problems of this type it is helpful to consider the energy stored in a mode of oscillation of the gas in the afterburner system. This energy can be increased by a number of driving mechanisms and it can be decreased by a number of damping or attenuation mechanisms. In order to tune the driving processes to the natural resonant frequencies for acoustic disturbances, a feedback or coupling mechanism is required. A steady amplitude is reached when the attenuation and driving processes are in balance. In the following discussion, we will describe several of these damping, driving and coupling processes but will not attempt to give an overall description of a stability calculation.

Damping. There are a number of damping terms which arise at the inlet or inlets and outlet to the cavity. For example, when a traveling acoustic wave impinges on a nozzle, reflected and transmitted waves are generated. The energy carried through the nozzle by the transmitted wave is lost from the cavity and represents a loss. Similar losses can occur at the inlet. However, interactions at the inlet to the afterburner occur at interfaces defined by turbine blades (in the case of the core stream) and by compressor blades (in the case of the fan stream). Interaction between the gas flowing through these components and the acoustic disturbances can produce either a loss or gain for the disturbance.

Additional sources of acoustic damping arise due to viscous interactions involving boundary layers on the walls and the drag forces on bluff bodies such as flame stabilizers, fuel injection rings and support struts.

In addition, resonators built into combustion chamber walls can be used to greatly increase damping rates. The cooling liner shown in Figure 21.7.2 is an example of the application of this technique and it will be described briefly here because this technique is commonly used to control high frequency disturbances. The liner has been perforated in the region close to the flame stabilizers. When there is no mean flow across these holes, a pressure oscillation in the combustor and close to the liner will produce a pressure difference across the holes which will drive gas from the combustion chamber into the cooling passage when the combustor pressure is high, and suck gas back into the combustion chamber when the pressure is low. This process feeds energy from the acoustic mode into the kinetic energy of the gas, which flows through the openings, and which is subsequently dissipated. This process removes energy from the acoustic mode and hence represents a damping of the oscillation.

The rate at which energy is removed from a particular mode of oscillation can be maximized by selecting the proper hole size and volume for the cooling passage associated with each hole so that the natural frequency for the cavity is close to that of the acoustic mode. For example, Helmholtz showed that a cavity with a narrow neck had a natural frequency which could be

analyzed approximately by treating the compressible gas in the cavity as the spring, and the mass of gas in the narrow throat as the mass in a spring-mass system. The natural frequency for the cavity is approximately $\left(a\sqrt{A/L_e V_e}\right)$ where (a) is the speed of sound, A is the cross section area of the neck, L_e is the effective length of the narrow neck (which in our thin wall case is roughly the hole diameter), and V_e is the volume of the cavity associated with each hole. By proper selection of A, L_e and V_e we can design the cavity so that its natural frequency is close to the frequency of the combustion instability, and thus, maximize the energy loss rate or the damping. Damping can be further increased by allowing fluid to flow from the liner cooling passage into the combustion chamber. Fortunately, this flow direction is in agreement with that required to produce the best cooling effect.

Perforated cooling liners are often used successfully to suppress high frequency oscillations. However, the effectiveness decreases for frequencies below 1000 hz, and devices of this type are almost impossible to implement for the lowest frequencies encountered in augmented turbofan systems because of constraints on the allowable volume of the cavity.

A number of numerical computer codes have been developed to analyze acoustic fields inside cavities of arbitrary shapes. Resonant frequencies and damping due to wall friction effects can be calculated by these codes. However, the effects of regions with large temperature differences and high Mach numbers have not been included in the codes yet. A discussion of calculations of this type is given in Reference 21.35 which deals primarily with combustion instabilities in solid and liquid propellant rockets.

The physical principals required to formulate the description of the acoustic field in a cavity, which contains a gas with large temperature and mean flow variations, are well understood and the properties of the acoustic field can be calculated as accurately as required (given sufficient effort and funds). Most of the damping characteristics can also be treated with reasonable accuracy for simple modes and combustor configurations, and the physical processes are well understood. The same statement cannot be made for the driving and coupling mechanisms discussed in the following paragraphs.

Driving Mechanisms. Consider a one-dimensional compressible gas stream flowing in a constant area duct and let heat be added uniformly at a rate $\dot{Q}$ over some finite length of the duct. The heat addition process will produce an acceleration of the gas and a drop in the pressure according to the relationships derived in Section 21.5.2. However, as long as $\dot{Q}$ is independent of time, no acoustic field will be produced.

When $\dot{Q}$ has a periodic component, say $\dot{Q} = (\dot{Q}_o + \epsilon \sin \omega t)$ and $\epsilon << \dot{Q}_o$, a pair of traveling acoustic waves will be generated, and one will propagate upstream and the other downstream. The strength of the waves will depend on ϵ, $\dot{Q}_o$ and the Mach number at the heat addition station. If these waves are in phase with an acoustic disturbance already present in the duct, the fluctuating heat addition will drive the disturbance, i.e., will put energy into the acoustic mode.

The fluctuating heat input rate also produces a fluctuating entropy or total temperature in the gas flowing through the heater which is convected downstream with the flow. Marble and Candel (see the review in Reference 21.36) have pointed out that acoustic disturbances are created when a flow which contains periodic entropy variations of this type passes through a region which contains pressure gradients. Thus, if we place a nozzle at the downstream end of the duct discussed above, acoustic disturbances will be generated at the nozzle by the entropy fluctuations produced farther upstream by the periodic variations in heat input. In the present example, the nozzle will generate a second pair of traveling waves, one of which will move upstream and the other, downstream. The nozzle will also act as a partial reflector of the traveling waves produced directly in the heat addition process and the reflected wave will also move back upstream. Note that the acoustic disturbances travel downstream to the nozzle at a velocity which is the sum of the local speed of sound (a) and the flow speed (u), i.e., (u + a), where as the entropy fluctuations are carried by the flowing gas and travel at a speed (u). Hence, the phase difference in the two traveling waves which move upstream from the nozzle will depend on the distance between the heat addition region and the nozzle, and also on the Mach number of the flow. If the phase difference is close to a multiple of 2π, the waves originating at the nozzle will reinforce each other.

In summary, any fluctuation in heat input rate to a gas flow will produce acoustic disturbances directly and also variations in the entropy of the flowing gas. When these entropy variations are convected through a pressure gradient a second acoustic disturbance is produced. The interaction of the traveling waves produced in this process will depend on the geometry and Mach number of the flow.

Coupling. The most difficult step in stability calculations for afterburner systems is the description of the process by which acoustic disturbances interact with the combustion process to produce fluctuations in the heat input rate. This coupling process must be understood before any meaningful stability calculations can be made.

A large number of coupling mechanisms are present in the afterburner system. These may be conveniently grouped under the heading of fuel preparation, flame stabilization, and flame spreading mechanisms. We will discuss briefly a few of these processes.

Acoustic disturbances can interact with each step in the fuel preparation process. Thus, the rates of fuel injection, atomization and vaporization processes can each be affected by local pressure and velocity fluctuations. For example, the rate of fuel flow at the injector orifice is proportional to the square root of the

pressure drop across the orifice and hence will be affected by fluctuations in gas pressure at the injector due to an acoustic disturbance in the duct. The fluctuations in mass flow and pressure at the upstream side of the orifice produced by this interaction must be treated as matching conditions which will specify the non-steady operation of the whole fuel feed system. (A system which will also have a set of resonant frequencies.) If for simplicity we examine a system with perfect atomization and vaporization, the resulting fluctuation in fuel injection rate at the injector will produce a fluctuation in fuel-air ratio at the flame front after a time delay which is fixed by the time required for the fuel to be carried from the injector to the flame front. The variation in fuel-air ratio will produce a fluctuation in the heat release rate at the flame front and when the acoustic disturbance in the duct is in phase with this variation of heat release, it will be driven by this process. If the two disturbances are sufficiently out of phase, the disturbance in the duct will be damped. Analysis of the reaction of feed systems to pressure oscillations of the type described here are presented in detail in Reference 21.35.

Several coupling mechanisms associated with the flame stabilization region have been suggested and we will describe one of these mechanisms in some detail to illustrate this class of coupling processes. This discussion is drawn from the work of Marble, Rogers and Barker presented in References 21.37 and 21.38. Consider the two-dimensional flow shown in Figure 21.8.1 and assume that a strong transverse oscillation is present downstream of the flame holder. The smallest resonant frequency for a transverse mode is that corresponding to a plane wave moving vertically, and with a pressure node at the axis and a maximum pressure amplitude at the walls. (E.g., Figure 21.8.1C.) The corresponding fluctuation amplitude for the vertical velocity is also shown in this Figure. The frequency f of this oscillation will be $f = \overline{(a)}/2H$, where H is the height of the channel and $\overline{(a)}$ is an average speed of sound in the gas.

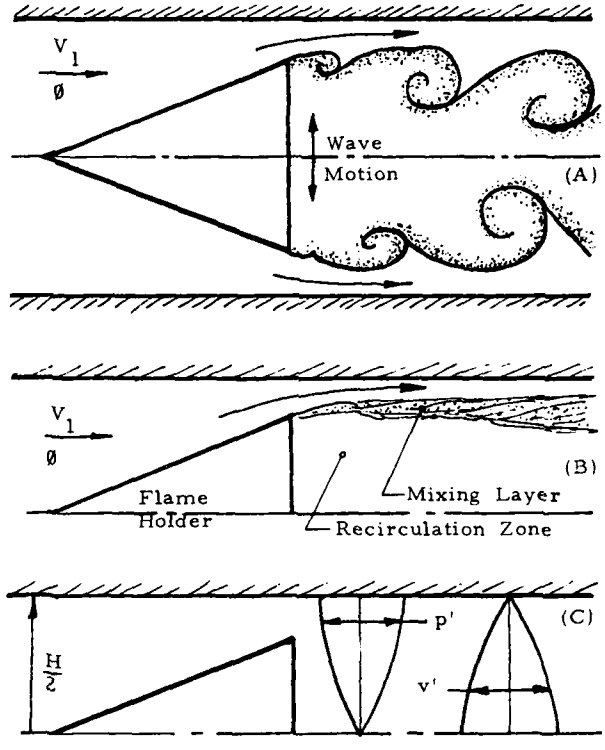

Figure 21.8.1 Sketches Illustrating the Flame Front Geometry During (A) Unstable and (B) Stable Combustion. (C) Mode Shapes for Perturbations in Pressure (p') and Transverse Velocity (v').

In this flow, the strong transverse wave interacts with the shear layers on either side of the flame holder to produce a regular train of vortices which are shed alternately from each lip of the flame holder in the manner suggested in the sketch of Figure 21.8.1A. Vortices are shed in an antisymmetric mode in keeping with the antisymmetric shape of the velocity and pressure perturbations, and they grow rapidly as they convect downstream.

The coupling mechanism in this example appears to be the triggering of these vortices which in turn are responsible for the unsteady heat addition which drives the oscillations. Marble (Reference 21.37) suggested that the vortices sweep unburnt gas deep within the recirculation zone and that this combustible material will burn rapidly after a short time delay. In this situation, the time delay associated with the entrainment of combustible fluid is short, and the delay is primarily fixed by the chemical reaction. The entrained material will start to react τ_d seconds after the vortex is shed, and the heat addition rate will receive a sharp pulse at that time. When τ_d is close to an integral multiple of the period of the resonant frequency for the acoustic disturbance, $2H/\overline{(a)} = 1/f$, the oscillation will be driven. In the present case, driving at the frequency of the first mode was strong enough to produce a large amplitude oscillation. However, oscillations at higher harmonics were not observed.

In this example, the instability was not present at low values of the fuel-air ratio and started at a well defined value when the fuel-air ratio was increased. This threshold value $\emptyset_s$ was found to vary with mixture temperature and fuel type. In both instances, the authors were able to predict the observed variations in $\emptyset_s$ by using the model suggested above. In making these predictions, values of the delay time τ_d were found by using the assumption that τ_d scaled with τ_c, the characteristic time described in the flame stabilization discussion in Section 21.4.1.2, page 21-16. Some of the experimental values of τ_c used in this process are shown in Figure 21.4.10. The sharp boundary for $\emptyset_s$ is a result of the very rapid change of τ_d with fuel-air ratio which is inferred from the variation of τ_c shown by

the data of this figure. In their example the resonant frequency was about 4000 hz which suggests that τ_d should be close to 0.25 msec (if the heat release rate rises after the first cycle of the oscillation). Thus, values of τ_d and of τ_c (see Figure 21.4.10) are almost equal.

The successful application of perforated liners for the suppression of high frequency combustion instabilities has very often involved the use of liner perforations in the immediate neighborhood of the flame stabilization region. This suggests that the flame stabilization region is very important in coupling high frequency disturbances to the heat addition process and that one important mechanism is that described above.

Because of the large scale inhomogenities which are present in the flame spreading region, one would expect that coupling between heat release and acoustic disturbances would be possible in this region too. However, no experimental evidence for such processes has been developed yet.

Finally, any non-steady heat release which occurs in the combustor will react with the nozzle to produce longitudinal disturbances. Note that the amplitude of these disturbances can be very large. For example, for wave lengths which are long compared to the nozzle inlet length and an inlet Mach number of 0.8, a total temperature fluctuation with an amplitude of 10 percent will produce an upstream propagating wave with an amplitude of about 5 percent of the mean pressure.

In summary, we have described some of the aspects of the combustion instability problem and a few of the many possible driving, damping and coupling mechanisms. Given the many resonant acoustic modes, the many possibilities for coupling, the high rate of heat release per unit volume and the small energy required to drive a large amplitude oscillation, it is surprising that any afterburner system operates without acoustic disturbances.

21.9 REFERENCES

(21.1) Johnson, R.L. and Cullom, R.R. "Altitude Test of Several Afterburner Configurations on a Turbofan Engine With a Hydrogen Heater to Simulate an Elevated Turbine Discharge Temperature." NASA Technical Paper 1068. Lewis Research Center, Cleveland, Ohio, 1977.

(21.2) Schetz, J. and Padhye, A. "Penetration and Breakup of Liquids in Subsonic Airstreams." AIAA Journal, Vol. 15, No. 10, pp. 1385-1390. New York, N.Y., October 1977.

(21.3) Ingebo, R.D. and Foster, H.H. "National Advisory Committee for Aeronautics." NACA Technical Note 4087. Lewis Flight Propulsion Laboratory, Cleveland, Ohio, October 1957.

(21.4) Haddock, G.H. "Flame-Blowoff Studies of Cylindrical Flame Holders in Channeled Flow," Progress Report No. 3-24, Pasadena Jet Propulsion Laboratory, May 14, 1951.

(21.5) Zukoski, E.E. and Marble, F.E. "The Role of Wake Transition in the Process of Flame Stabilization on Bluff Bodies." Combustion Researches and Reviews 1955. Butterworths Scientific Publications, London, 1955.

(21.6) Zukoski, E.E. and Marble, F.E. "Experiments Concerning the Mechanism of Flame Blowoff from Bluff Bodies," in Proceedings of the Gas Dynamics Symposium on Aerothermochemistry, Northwest University Press, 1955.

(21.7) Wright, F.H. "Bluff Body Flame Stabilization: Blockage Effects." Combustion and Flame, Vol. 3, p. 319, 1959.

(21.8) Broman, G.E. and Zukoski, E.E. "Experimental Investigation of Flame Stabilization in a Deflected Jet." Eighth Symposium (International) on Combustion, p. 944. The Williams and Williams Company, Baltimore, 1960.

(21.9) Cornell, W.G. "The Flow in a Vee-Gutter Cascade." Trans. Amer. Soc. Mech. Engrs., 1956, 78, p. 573.

(21.10) Wright, F.H. "Multiple Flame Holder Arrays: Flame Interactions," American Rocket Society Journal, February 1959.

(21.11) Potter, A.E., Jr. and Wong, E.L. "Effect of Pressure and Duct Geometry on Bluff Body Flame Stabilization." National Advisory Committee for Aeronautics. Technical Note 4381, Lewis Flight Propulsion Laboratory, Cleveland, Ohio, September 1958.

(21.12) Mullins, B.P. "A Spontaneous Ignition Theory of Combustion Intensity and Combustion Stability Behind a Baffle." Combustion Researches and Reviews 1955. Butterworths Scientific Publications, London, 1955.

(21.13) Mironenko, V.A. "The Use of Thermal Ignition Theory to Determine General Conditions for Flame Stabilization by Means of a Bluff Body." Izvestiya VUZ. Aviatsionnaya Tekhnika, No. 1, pp. 140-145, 1966 (Translated).

(21.14) Solokhin, E.L. and Mironenko, V.A. "Stable Combustion Limits in GTE Reheat Combustion Chambers." Izvestiya VUZ. Aviatsionnaya Tekhnika, Vol. 15, No. 1, pp. 135-141, 1972 (Translated).

(21.15) Hottel, H.C., Williams, G.C., Jensen, W.P., Tobey, A.C. and Burrage, P.M.R. "Modeling Studies of Baffle-Type Combustors." Ninth Symposium (International) on Combustion, p. 923. Academic Press, 1963.

(21.16) Kosterin, V.A., Dudin, L.A., Motylinskii, I.P., Khismatullin, A. Ya. and Gilyazov, M. Sh. "Correlation of Experimental Data on the Limits of Flame Stabilization." Izvestiya VUZ. Aviatsionnaya Tekhnika, Vol. 11, No. 3, pp. 59-66, 1968 (Translated).

(21.17) Marshall, R.L., Canuel, G.E. and Sullivan, D.J. "Augmentation Systems for Turbofan Engines." Cranfield International Symposium Series, Vol. 10, p. 129, Pergamon Press, Ltd., 1968.

(21.18) Brown, G.L. and Roshko, A. "On Density Effects and Large Structure in Turbulent Mixing Layers." J. Fluid Mech., Vol. 64, Part 4, pp. 775-816, Great Britain, 1974.

(21.19) Williams, G.C., Hottel, H.C., and Scurlock, A.C. "Flame Stabilization and Propagation in High Velocity Gas Streams." Third Symposium on Combustion and Flame and Explosion Phenomena, p. 21. Williams and Wilkins Company, Baltimore, Maryland, 1949.

(21.20) Wright, F.H. and Zukoski, E.E. "Flame Spreading from Bluff Body Flame Holders." Eighth Symposium (International) on Combustion, p. 933. The Williams and Williams Company, Baltimore, 1960.

(21.21) Solntsev, V.P.: Stabilization of a Flame and Development of the Process of Combustion in a Turbulent Stream, (G.M. Gorbunov, Ed.), p. 75, Oborongiz, Moscow, 1961.

(21.22) Lefebvre, A.H. and Reid, R. "The Influence of Turbulence on the Structure and Propagation of Enclosed Flames." Combustion and Flame, Vol. 10, p. 355, 1966.

(21.23) Wohl, K., Shore, L., Von Rosenberg, H., and Weil, C.W. "The Burning Velocity of Turbulent Flames." Fourth Symposium (International) on Combustion, p. 620. Williams and Wilkins Company, Baltimore, Maryland, 1953.

(21.24) Thurston, D.W. "An Experimental Investigation of Flame Spreading from Bluff Body Flameholders." Thesis. California Institute of Technology, Pasadena, California, 1958.

(21.25) Tsien, H.S. "Influence of Flame Front on the Flow Field." Journal of Applied Mechanics, p. 188, June 1955.

(21.26) Fabri, J., Siestrunck, R. and Foure, C. "On the Aerodynamic Field of Stabilized Flames." Fourth Symposium (International) on Combustion, p. 443. Williams and Wilkins Company, Baltimore, Maryland, 1953.

(21.27) Brown, G.L. "The Entrainment and Large Structure in Turbulent Mixing Layers." Fifth Australasian Conference on Hydraulics and Fluid Mechanics at the University of Canterbury, Christchurch, New Zealand, 1974 December 9 to December 13, p. 352.

(21.28) Spalding, D.B. "The Spread of Turbulent Flames Confined in Ducts." Eleventh Symposium (International) on Combustion, p. 807. The Combustion Institute, Pittsburgh, Pennsylvania, 1967.

(21.29) McAulay, J.E. and Abdelwahab, M. "Experimental Evaluation of a TF30-P-3 Turbofan Engine in an Altitude Facility: Afterburner Performance and Engine-Afterburner Operating Limits." NASA Technical Note D-6839. Lewis Research Center, Cleveland, Ohio, July 1972.

(21.30) Useller, J.W. "Effect of Combustor Length on Afterburner Combustion." Combustion and Flame, Vol. 3 p. 339, 1959.

(21.31) Robinson, K. "Afterburning Regulation Concepts." AGARD Conference Proceedings No. 151 on Power Plant Controls for Aero-Gas Turbine Engines. Presented at the 44th Meeting of the AGARD Propulsion and Energetics Panel held at the Høyfjellshotell, Ustaoset, Norway, 9-13 September 1074. February 1975.

(21.32) Carrierre, P. "Exhaust Nozzles." Supersonic Turbo-Jet Propulsion Systems and Components. Pelham, New York, Circa Publications, 1969. AGARDograph No. 120, pp. 287-379.

(21.33) Beheim, M.A. et al "VIII. Supersonic Exhaust Nozzles." Aircraft Propulsion. NASA SP-259, p. 233. Conference Held at Lewis Research Center, Cleveland, Ohio. November 18-19, 1970.

(21.34) Devriese, J. and Young, P.H. "Olympus in Concorde." Aeronautical Journal, Vol. 76, No. 774, pp. 683-694. December 1972.

(21.35) Harrje, D.T., Ed. Liquid Propellant Rocket Combustion Instability. National Aeronautics and Space Adminiatration, Washington, D.C., 1972. NASA SP-194.

(21.36) Marble, F.E. and Candel, S.M. "Acoustic Disturbance from Gas Non-Uniformities Convected Through a Nozzle." Journal of Sound and Vibration. 1977. 55(2), pp. 225-243.

(21.37) Rogers, D.E. and Marble, F.E. "A Mechanism for High-Frequency Oscillation in Ramjet Combustors and Afterburners." Jet Propulsion, June 1956. Volume 26, pp. 456-462.

(21.38) Barker, C.L.R "Experiments Concerning the Occurrence and Mechanism of High Frequency Combustion Instability." Thesis. California Institute of Technology, Pasadena, Calif., 1958.

21.10 FURTHER READING

The purpose of this section is to call attention to a few reference works which will give the reader a different perspective on some of the material covered in this chapter and, in several cases to provide a source of more detailed information. The reference material discussed here is listed at the end of this section.

A number of general reviews of jet propulsion systems appeared in the late 1950's and early 1960's. The material presented in these volumes is dated, but in many cases is still of interest today and still covers many topics as adequately as they can be covered now. Two volumes from the High Speed Aerodynamics and Jet Propulsion series are of interest. Volume 12, edited by Lancaster contains information on augmentation systems and also ramjet systems which are pertinent. Volume 11, edited by Hawthorne and Olson contains a series of articles which cover all the engine components and includes a discussion of flame stabilization in heterogeneous flows. A brief introduction to the Soviet work on combustion problems in gas turbines is given in the translation of the book by Zuyev and Skubachevskii. Material relevant to afterburners is discussed in the chapters on ramjet engines and reheat combustion chambers.

A good report on current diffuser research work is that of Dolan and Rundstadler. They present a large body of data on conical diffusers which covers the effects of inlet Mach number for the whole subsonic range, a wide range of inlet boundary layer thickness, and diffuser geometry including area ratio, length and divergence angle.

The specific problems concerning ignition in afterburner systems are not treated in detail in any combustion texts. A detailed treatment of a number of experiments concerned with ignition are presented by Lewis and von Elbe who also discuss other material concerning flame stabilization and flame spreading.

The generation of fuel sprays and their vaporization and combustion is still a topic of vigorous research. Analytic treatments are available in the text by Williams, and the Fourteenth and Fifteenth Symposia (International) on Combustion contain interesting collections of recent papers given at Sessions on Heterogeneous Combustion. Beer and Chigier also discuss relevant material although their chief interest is in industrial furnaces rather than aircraft engines.

Alternate views of the flame stabilization process are presented by Lewis and von Elbe, and by Beer and Chigier.

Finally, five journals are particularly useful sources of information. These are the AIAA Journal of the American Institute of Aeronautics and Astronautics; Combustion and Flame, (published by Elsevier, New York); and Combustion Science and Technology, (published by Gordon and Breach, New York); and translations of two Soviet journals: Combustion, Explosion and Shock Waves, (translated and published by Consultants Bureau, New York); and Soviet Aeronautics (translated and published by Elsevier, New York).

Beer, J.M. and Chigier, N.A. Combustion Aerodynamics, Halsted Press Division, John Wiley and Sons, Inc., New York, 1972.

Dolan, F.X. and Runstadler, P.W. Jr., "Pressure Recovery Performance of Conical Diffusers at High Subsonic Mach Numbers." NASA Contractor Report CR-2299, August 1973.

Fifteenth Symposium (International) on Combustion. Held at The Toshi Center Hall, Tokyo, Japan, August 25-31, 1974. The Combustion Institute, Pittsburgh, Pennsylvania, 1974.

Fourteenth Symposium (International) on Combustion. Held at The Pennsylvania State University, University Park, Pennsylvania, August 20-25, 1972. The Combustion Institute, Pittsburgh, Pennsylvania, 1973.

Hawthorne, W.R. and Olson, W.T. (Eds.) Design and Performance of Gas Turbine Power Plants. Princeton University Press, Princeton, New Jersey, 1960.

Lancaster, O.E. (Ed.) Jet Propulsion Engines. Princeton University Press, Princeton, New Jersey, 1959. (Volume XII High Speed Aerodynamics and Jet Propulsion.

Lewis, B. and von Elbe, G. Combustion Flames and Explosions of Gases. Second Edition. Academic Press, Inc., New York, 1961.

Williams, F.A. Combustion Theory. Addison-Wesley Publishing Company, Inc., Reading, Massachusetts, 1965.

Zuyev, V.S. and Skubachevskii, L.S. Combustion Chambers for Jet Propulsion Engines. (Translated) The MacMillan Company, New York, 1964.

Chapter 22

AEROELASTICITY AND UNSTEADY AERODYNAMICS

Franklin O. Carta

United Technologies Research Center

CHAPTER 22 AEROELASTICITY AND UNSTEADY AERODYNAMICS

Franklin O. Carta
United Technologies Research Center
East Hartford, Conn.

TABLE OF CONTENTS

		Page
22.0	INTRODUCTION	22-1
22.1	OVERVIEW OF TURBOMACHINERY FLUTTER	22-1
22.1.1	DEFINITIONS AND CONCEPTS	22-1
22.1.2	HISTORICAL SKETCH.	22-2
22.1.3	BRIEF SURVEY OF TURBOMACHINERY FLUTTER REGIMES	22-2
22.1.4	ELEMENTARY CONSIDERATIONS OF AIRCRAFT WING FLUTTER.	22-4
22.1.4.1	Equations of Motion	22-4
22.1.4.2	Theodorsen Theory	22-5
22.1.4.3	Simplified Approach to Flutter . .	22-7
22.1.5	FUNDAMENTAL DIFFERENCES BETWEEN TURBOMACHINERY FLUTTER AND WING FLUTTER	22-10
22.1.5.1	Elementary Vibration Concepts for Rotating Systems	22-10
22.1.5.2	Mass Ratio, Stiffness, and Frequency Differences	22-11
22.2	UNSTEADY AERODYNAMICS	22-13
22.2.1	FUNDAMENTALS OF UNSTEADY THEORY FOR ISOLATED AIRFOILS.	22-13
22.2.1.1	Incompressible Flow.	22-13
22.2.1.2	Compressible Subsonic Flow	22-15
22.2.1.3	Compressible Supersonic Flow . . .	22-17
22.2.2	UNSTEADY THEORY FOR CASCADED AIRFOILS	22-18
22.2.2.1	Incompressible Flow	22-18
22.2.2.2	Compressible Subsonic Flow	22-22
22.2.2.3	Compressible Supersonic Flow . . .	22-23
22.2.2.4	Acoustical Resonance	22-27
22.2.3	DYNAMIC STALL - EMPIRICISM AND EXPERIMENT	22-29
22.2.3.1	Historical Background for Torsional Stall Flutter.	22-29
22.2.3.2	Two-Dimensional Work Per Cycle and Aerodynamic Damping	22-31
22.2.3.3	Dynamic Stall and Stall Flutter of a Pitching Isolated Airfoil . .	22-33
22.2.3.4	Unsteady Cascade Aerodynamics at High Incidence	22-35
22.3	STABILITY THEORY AND APPLICATIONS	22-37
22.3.1	COUPLED BLADE-DISK-SHROUD THEORY .	22-38
22.3.2	ROTOR APPLICATIONS	22-42
22.4	LIST OF SYMBOLS	22-45
22.5	REFERENCES	22-48
22.6	BIBLIOGRAPHY	22-51

CHAPTER 22 AEROELASTICITY AND UNSTEADY AERODYNAMICS

Franklin O. Carta
United Technologies Research Center
East Hartford, Conn.

22.0 INTRODUCTION

The object of this chapter is to acquaint the reader with several turbomachinery flutter problems confronting the design engineer and to suggest some of the ways in which the designer can cope with these problems. It is obvious that an in-depth examination of the problem is beyond the scope of this single chapter, and the reader will be directed to the available literature for more details. Nevertheless, an attempt will be made to approach this exposition from the point of view of the designer, and the application of theoretical or empirical methods to overcome design barriers will be stressed wherever possible. To achieve this end the problem area will first be defined, and following this the reader will be exposed to the basic differences between wing flutter and turbomachinery blade flutter. This will be helpful in establishing the areas in which elementary theories can be used to explain basic principles, and will also point up the need for advanced theories. Next, a brief discussion of the unsteady aerodynamics of isolated airfoils will lead into the more complicated problems involving cascaded airfoils, and some time will be spent dealing with the dynamic stall problem. Finally, in the section devoted to stability theory, the design methodology for avoiding flutter will be discussed. Here the introduction of advanced unsteady aerodynamic theories into a basic stability theory involving energy balance will be shown to provide the designer with some of the necessary constraints for flutter-free operation.

It should be emphasized that flutter has never been a "trivial" problem. Several instances of aircraft flutter have been documented in the first chapter of Ref. 22.1, with the earliest known instance occurring during World War I, indicating that flutter is not a newcomer to the hierarchy of aerodynamic problems. Nor should its severity be underestimated, in view of two known instances of catastrophic wing failures due to flutter on passenger aircraft (c.1960). Turbomachinery flutter is not so well documented as aircraft lifting surface flutter, but as noted in the following historical overview, has been known to exist since the initial development of the turbomachine. Furthermore, the potential for damage to aircraft and/or engine is very real, and ranges from individual blade failures, to the destruction of several stages (if the blades can be contained within the case), and to the ultimate destruction of the engine support structure or the aircraft itself (if the blades cannot be contained or if the unbalanced rotating mass cannot be restrained by the surrounding structure). Clearly, then, this is a problem to be avoided at all cost, and it is to this end that the following sections are directed.

22.1 OVERVIEW OF TURBOMACHINERY FLUTTER

22.1.1 DEFINITIONS AND CONCEPTS

In general, flutter is the name given to any self-excited oscillation of an aerodynamically lifting surface. The phenomenon is characterized by two necessary requirements: 1) an available energy supply (e.g., the moving airstream) and 2) a zero or negatively damped system. Here the word "system" applies to the combination of the lifting surface and the airstream. By itself the lifting surface is a system with positive damping. The inclusion of the airstream will either increase or decrease the damping. The mechanism whereby the airstream changes the damping will be discussed in detail below.

First, however, it should be noted that there are many different types of flutter which affect the many different types of lifting surfaces. To name but a few, there are: 1) classical coupled flutter of an aircraft wing or of a wing-aileron combination; 2) single degree of freedom stall flutter of compressor blades, of propeller blades, or of helicopter rotor blades; 3) coupled flutter of shrouded compressor blades. These few examples, plus all of the other possible types of flutter, share one thing in common -- the joint requirement of an available energy supply and a zero or negatively damped system. However, there are many more differences than similarities, and a different technique is often required to deal with each of the various types of flutter.

Also shared by all flutter phenomena is a dimensionless parameter called the reduced frequency,

$$k = \frac{b\omega}{V} \qquad (22.1.1)$$

or its inverse, the reduced velocity, $V/b\omega$. Here b is the blade semichord, ω is the frequency of the oscillation, and V is the free stream velocity. As will be seen in the work that follows, this parameter appears both explicitly and implicitly in the governing equations for unsteady aerodynamics of oscillating airfoils, and also plays an extremely important role in the empirical relationships associated with dynamic stall and stall flutter. Therefore, it is appropriate to begin this chapter with a brief discussion of the physical meaning of

k. Consider an airfoil of chordlength 2b oscillating at a frequency of $\omega = 2\pi f = 2\pi/T$ in a stream moving past it at a velocity V, as shown in Fig. 22.1.1 below. A sinusoidal wake will

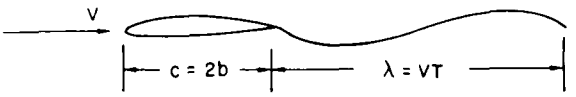

Fig. 22.1.1 Disturbance Wavelength of an Oscillating Airfoil

be formed which is imbedded in the free stream and hence also moves relative to the airfoil at a velocity V, with wavelength

$$\lambda = VT = \frac{2\pi V}{\omega} \qquad (22.1.2)$$

If we divide the airfoil chord by this wavelength we obtain

$$\frac{2b}{\lambda} = \frac{2b\omega}{2\pi V} = \frac{k}{\pi}$$

or

$$k = \pi\left(\frac{2b}{\lambda}\right) = \frac{\pi C}{\lambda} \qquad (22.1.3)$$

Thus, at low reduced frequency ($k \cong 0.05$) the wavelength is very large relative to the chord while at high reduced frequency ($k \cong 1$) the wavelength is not so large relative to the chord. (Here we cannot talk about the wavelength small relative to the chord because even at the largest values of reduced frequency encountered in practice the wavelength is still three times the blade chord.)

22.1.2 HISTORICAL SKETCH

In the early days of compressor technology, bending flutter near the surge line was a primary design problem. Because it occurred near stall it was universally referred to as stalling flutter and it was understood that the phenomenon occurred in the first bending or flexural mode of vibration. Pearson (Ref. 22.2) specifically states that stalling flutter in the torsion mode was not a problem. A great deal of time and effort was devoted to this problem and a large number of reports were written by British authors and others (cf. Bibliography). Most of these studies dealt with the problem phenomenologically although a few attempted to explain the physical nature of stalling flutter.

As early as 1945, Shannon (Ref. 22.3) found that torsional stall flutter of compressor blades could occur for values of the reduced frequency $k = b\omega_\alpha/V < 0.75$, based on blade semichord. (This is equivalent to a reduced velocity $V/b\omega_\alpha > 1.33$.) However, as stated above, the primary flutter problem in these early days of compressor technology occurred in the bending mode. More recently, though, the problem of flutter near stall has shifted from the bending mode to the torsion mode. Most of this newer work has been done privately and hence has gone largely unreported. In 1960, Armstrong and Stevenson (Ref. 22.4) corroborated Shannon's results and cited a critical value of $k < 0.8$ for torsional stall flutter; i.e., if $k < 0.8$, or if $V/b\omega_\alpha > 1.25$, then torsional stall flutter is possible. Sisto, in Ref. 22.5, attributes this shift from bending flutter to torsion flutter to the progressive changes which have occurred in the mechanical and aerodynamic design of compressor and fan blades. He states that "the trend toward transonic stages and supersonic blade tips has been at the expense of blade thickness and has been accompanied by a rearward movement of the center of twist along a typical blade chordline. For example, double circular arc airfoil profiles have the elastic axis and center of twist both at midchord as opposed to more forward locations for the earlier 65-series profiles. Supersonic sections of the so-called parabolic or 'J section' variety have even more rearward twist centers. Higher stagger angles and increased solidities have been other concomitant parametric trends that may have aggravated the current susceptibility to severe torsional stalling flutter."

The several flutter phenomena that are most likely to occur in turbomachines are discussed below.

22.1.3 BRIEF SURVEY OF TURBOMACHINERY FLUTTER REGIMES

A typical plot showing the flutter regions on a compressor performance map is shown in Fig. 22.1.2. The subsonic stall flutter region, schematically shown near the surge line at part speed, can be regarded as representing either the bending mode or

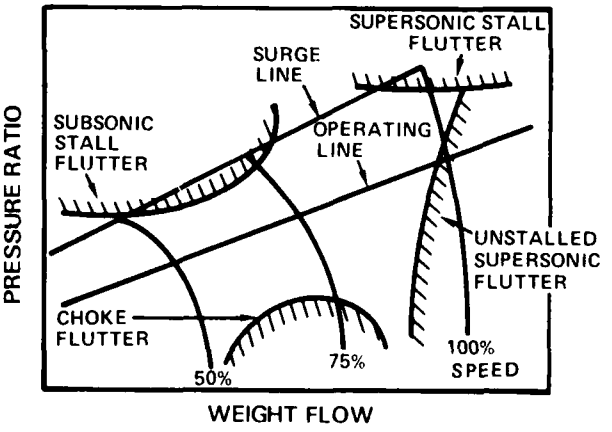

Fig. 22.1.. Schematic Compressor Performance Map Showing Flutter Boundaries for Four Types of Flutter

the torsion mode. An equivalent plot of the flutter region on an incidence, Mach number diagram is shown in Fig. 22.1.3. Superimposed on this plot are two possible operating lines for the compressor. At idle the incidence angle is high and the relative Mach number is low, while at full speed the incidence angle is low and the Mach number is high. Thus, the operating line traverses the plot from lower right to upper left. It is seen that operating line no. 1 passes

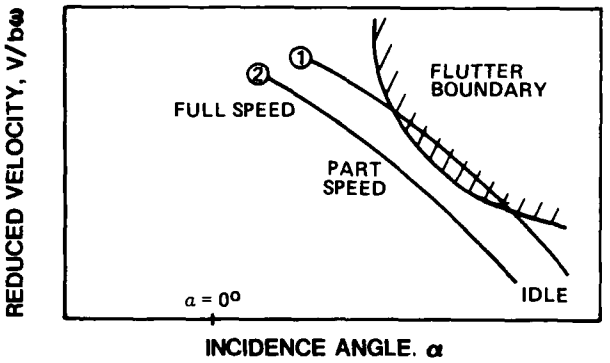

Fig. 22.1.3 Schematic Stall Flutter Map with Hypothetical Operating Lines

through the flutter region at part speed. A redesign, either by stiffening the blades (increasing bω) or reducing the incidence, has the effect of moving the operating line down and/or to the left relative to the flutter region, and operating line no. 2 is seen to be flutter free.

Choking flutter in the bending mode is a phenomenon which has received relatively little attention in the published literature. It is mentioned briefly in Refs. 22.6 and 22.7 and its position on the performance map is also shown schematically in Fig. 22.1.2. It usually occurs at negative incidence angles at a part speed condition. The difference in the flow conditions for stall and choke are shown schematically in Fig. 22.1.4. It is seen that in the stall condition the inlet flow can expand through a larger in-passage stream area, but in the choked condition the inlet flow is constrained to pass through a smaller

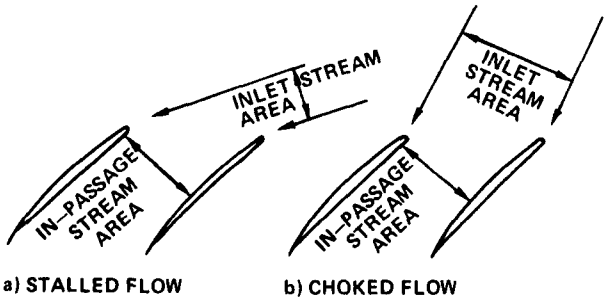

Fig. 22.1.4 Differences Between Stalled Flow and Choked Flow Through a Cascade (Schematic)

in-passage stream area. Thus it is possible to produce higher in-passage Mach numbers, sometimes exceeding local critical values, than the external velocities would indicate. When this happens, in-passage shocks can form which can either cause flow separation or can directly couple adjacent blades. In either case, large amplitude oscillations are then possible.

In Ref. 22.6, Carter states that choking flutter in compressors is not likely to be a problem because the operating line will not approach the choke region. This statement was written in the early 1950's, prior to the use of variable geometry (i.e., movable stators) in modern compressors. Thus, although one would not deliberately run an engine into the choke region, it is possible that an inadvertant malfunction of the stator control might cause such an encounter. It is also possible that choking flutter might be experienced during prototype testing, when the effects of various stator positions were being explored.

In view of the meager information available on this subject, it will not be discussed at length in any subsequent section of this chapter.

It will be shown below that a single compressor blade with well-separated frequencies in the fundamental torsion and bending modes will not be susceptible to the classical coupled flutter sometimes encountered on aircraft wings. This has always been true for practical, unshrouded compressor blades mounted on reasonably stiff disks. However, with the advent of fan stages and necessarily longer blades, frequencies in the two fundamental modes were decreased. This had the effect of increasing the reduced velocity parameter, $V/b\omega$, which is equivalent to shifting from operating line no. 2 to operating line no. 1 in Fig. 22.1.3. Part span shrouds were then employed in the United States (snubbers or lacing wires in Great Britain) to introduce additional bending and torsion restraints, which increased the single-degree-of-freedom mode frequencies. Thus the system was stiffened and the operating line was again shifted from position 1 to position 2, away from single-degree-of-freedom flutter.

Unfortunately, the additional part span constraint also provided an additional degree of freedom to the structure, and a pseudo-disk mode was introduced which carried the blades in a combined bending-torsion mode, automatically coupled, which could extract energy from the airstream and sustain a self-excited flutter. This phenomenon was first described in Ref. 22.8, and a detailed analysis will be presented in a later section of this chapter. A description of the structural dynamics of the blade-disk-shroud modes will be found in Ref. 22.9. Fundamental information on the structural dynamics problem can be found in the pioneering work of Campbell or in the later analyses of Ehrich, Tobias and Arnold, and Ewins (cf. Bibliography). The region of occurrence of this phenomenon cannot be precisely defined on the compressor map, and hence is not indicated on Fig. 22.1.2.

In recent years supersonic unstalled flutter has become an increasingly important factor in the design of high performance turbomachinery fan blades. This flutter occurs at a supersonic relative flow but at a subsonic axial flow; i.e., the vector sum of the subsonic axial velocity and the rotational velocity is a supersonic relative velocity (see Fig. 22.1.5). Only a small portion of the blade row has been schematically shown in Fig. 22.1.5 to illustrate the complexity of the flow geometry.

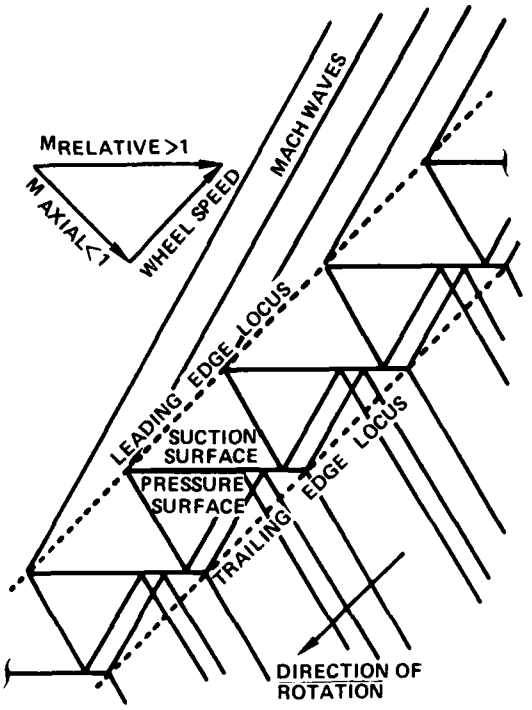

Fig. 22.1.5 Supersonic Relative Flow Past a Blade Row with Subsonic Leading Edge Locus

It is seen that because the axial flow Mach number is less than 1, Mach waves can propagate forward of the plane of rotation (referred to here as the leading edge locus). If the blades are fluttering, the Mach wave positions and strengths will become variable, and constitute an unsteady energy path ahead of the adjacent blades in the rotor. It is seen that the internal flow geometry is also very complicated, involving several internal Mach wave reflections and also involving the influence of a portion of the unsteady wake of any blade on the upper adjacent blade near the trailing edge.

The problem has manifested itself largely in thin fan blades operating at supersonic relative flow velocities at the tip. It generally occurs in the vicinity of the operating line or below, so it is not generally categorized as a stall flutter. Furthermore, its intensity, which can be catastrophically high, diminishes rapidly as one traverses a constant speed line towards higher pressure ratio, as shown in the boundary of Fig. 22.1.2. A more comprehensive description of this phenomenon can be found in Ref. 22.10. Here it is further noted that the flutter boundary sets a real limit on high speed operation, and that at high stress levels all blades tend to flutter at a common frequency with a constant interblade phase angle between blades. Thus, the phenomenon is amenable to analysis, using the coupled flutter energy method of Ref. 22.8 and the more advanced supersonic aerodynamic analysis of Refs. 22.11 and/or 22.12. This has been successfully implemented as part of the design system, and as stated in Ref. 22.10, has provided an accurate flutter prediction of the unstalled supersonic flutter boundary for high speed rotor blades.

It was stated earlier that supersonic unstalled flutter can be diminished and even eliminated by increasing the pressure ratio while traversing a constant speed line. However, this relief has its limitations because high speed operation near the surge line can lead to a supersonic stalled flutter, as shown by the boundary in Fig. 22.1.2. Because this flutter is associated with high pressure ratios, there can be strong shocks present within the blade passages, and in some circumstances, ahead of the blade row. Hence, supersonic stalled flutter is not amenable to analysis, and no headway has been made to provide a reliable prediction technique for use in a compressor design system. To date, only limited data are available for empirical predictions.

22.1.4 ELEMENTARY CONSIDERATIONS OF AIRCRAFT WING FLUTTER

In pursuing our objective here of dealing with turbomachinery flutter, it is advantageous to discuss first the elementary flutter theory for aircraft wings developed by Theodorsen (Ref. 22.13). Once these elementary considerations are understood it will be possible to point out the similarities where they exist, and to identify the origins of the differences between aircraft wing flutter and the various types of turbomachinery flutter to be discussed below.

22.1.4.1 Equations of Motion

Before launching into the discussion of the equations of motion of an oscillating airfoil, it is useful to review briefly the method of approach to be used in this section. We shall begin with the generalized equations of motion, using unsteady aerodynamic forcing functions on the right hand side that have not yet been derived (but which will be derived in a subsequent section). The utility of this approach will lie in the use of specific aerodynamic functions to show the general form of the right hand side, and to use this general form to investigate the underlying physics of the problem at a relatively early point in the development. Later, in subsequent sections, the several relevant unsteady aerodynamic theories will be derived and their use in solving turbomachinery-related flutter problems will be discussed.

The equations of motion of a classical, two-dimensional aircraft wing which is executing a combined plunging and pitching motion in a moving airstream (cf. Fig. 22.1.6) are given by

$$mb\ddot{h} + S_\alpha \ddot{\alpha} + K_h bh = Q_h \qquad (22.1.4)$$

$$S_\alpha b\ddot{h} + I_\alpha \ddot{\alpha} + K_\alpha \alpha = Q_\alpha \qquad (22.1.5)$$

where h and α are the dimensionless displacements in plunge and pitch. (See the List of Symbols for the definitions of the quantities used herein, and refer to Ref. 22.1 or the texts listed in the Bibliography for further details of the concepts discussed here.)

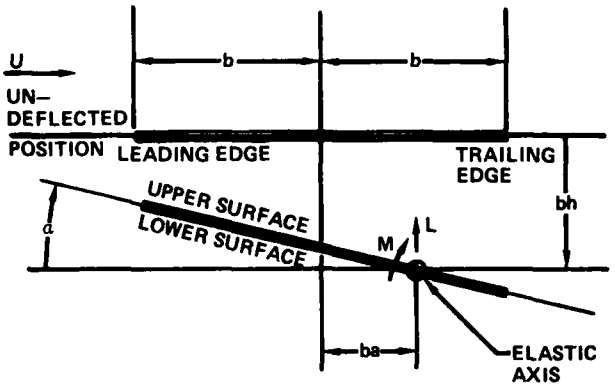

Fig. 22.1.6 Airfoil Coordinate System

There are many possible ways to express the quantities Q_h and Q_α on the right hand sides of Eqs. (22.1.4) and (22.1.5). For the simple case being considered here, it is easily shown (Ref. 22.13) that the generalized forces Q_h and Q_α are simply the two-dimensional aerodynamic lift and moment, and are expressed as follows:

$$Q_h = L = -\pi\rho b^3 \left\{ -\ddot{h} - \frac{2V}{b} C(k)\dot{h} + a\ddot{\alpha} - \left[1 - 2\left(a - \frac{1}{2}\right)C(k)\right]\frac{V}{b}\dot{\alpha} - \frac{2V^2}{b^2} C(k)\alpha \right\} \qquad (22.1.6)$$

$$Q_\alpha = M = \pi\rho b^4 \left\{ a\ddot{h} + 2\left(\frac{1}{2} + a\right)C(k)\frac{V}{b}\dot{h} - \left(\frac{1}{8} + a^2\right)\ddot{\alpha} + \left[a - \frac{1}{2} + 2\left(\frac{1}{4} - a^2\right)\right] \times C(k)\frac{V}{b}\dot{\alpha} + 2\left(\frac{1}{2} + a\right)C(k)\frac{V^2}{b^2}\alpha \right\} \qquad (22.1.7)$$

Thus it is seen that the right hand sides of Eqs. (22.1.4) and (22.1.5) are also dependent on the displacements and their derivatives. As a first approximation, it is possible to identify the coefficients of the second derivatives as aerodynamic inertia or mass terms, the coefficients of the first derivatives as aerodynamic damping terms, and the coefficient of the angular displacement as an aerodynamic stiffness term. Actually, this is not strictly true because the complex Theodorsen function

$$C(k) = F(k) + iG(k) \qquad (22.1.8)$$

enters into certain terms of the right hand side and complicates the situation. Nevertheless, the unsteady aerodynamic terms directly affect virtually all of the terms in the equations of motion. It will be shown below that this is accomplished through changes in the frequencies of the natural system modes that permit the two modes to couple, producing flutter.

22.1.4.2 Theodorsen Theory

In 1935 Theodorsen published his now famous theory (Ref. 22.13) which laid the foundations for modern flutter theory. The key to this theoretical development lay in the way in which vorticity was shed into the moving wake to account for changes in the bound vorticity caused by a sinusoidal variation in either plunging or pitching displacement. In the course of his mathematical development (later verified rigorously by Schwarz in Ref. 22.14) Theodorsen derived a complex circulation function, C(k), which is defined above in Eq. 22.1.8 in terms of its real and imaginary parts, and which is expressable as a ratio of Hankel functions.

$$C(k) = \frac{H_1^{(2)}(k)}{H_1^{(2)}(k) + iH_0^{(2)}(k)} \qquad (22.1.9)$$

The real and imaginary parts, F(k) and G(k) are plotted versus k in Fig. 22.1.7, and a phase plane diagram of the entire function is shown in Fig. 22.1.8.

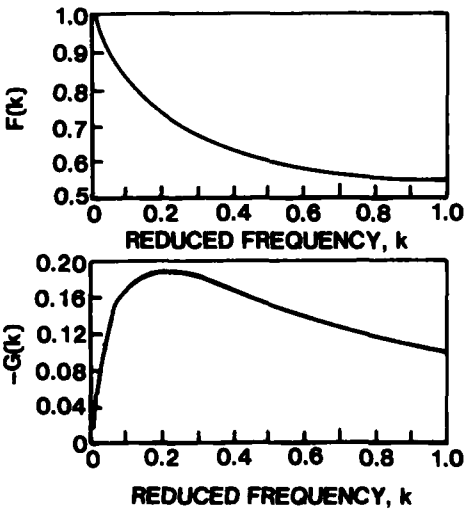

Fig. 22.1.7 Real and Imaginary Parts of the Theodorsen Circulation Function

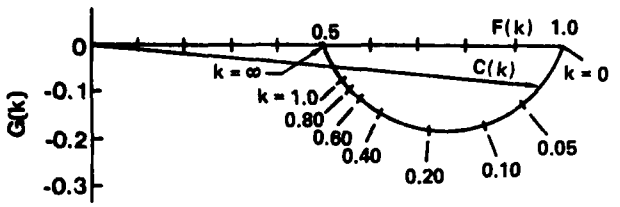

Fig. 22.1.8 Complex Phase Plane Diagram of Theodorsen Circulation Function

Theodorsen's method of solution was to assume a coupled sinusoidal motion of the system at a common (but unknown) frequency, say ω, and then seek the values of V and ω that satisfied the equations of motion, Eqs. (22.1.4) and (22.1.5). Specifically, he assumed that

$$h = \bar{h} e^{i\omega t} \tag{22.1.10}$$

and

$$\alpha = \bar{\alpha} e^{i(\omega t + \theta)} \tag{22.1.11}$$

where θ is the phase angle between the motions. When these quantities were inserted into the left hand sides of Eqs. (22.1.4) and (22.1.5) he obtained

$$-\omega^2 mbh - \omega^2 S_\alpha \alpha + \omega_h^2 mbh = Q_h = L \tag{22.1.12}$$

$$-\omega^2 S_\alpha bh - \omega^2 I_\alpha \alpha + \omega_\alpha^2 I_\alpha \alpha = Q_\alpha = M \tag{22.1.13}$$

after previously relating the stiffness to the natural frequencies of the separate modes,

$$K_h = \omega_h^2 m \tag{22.1.14}$$

$$K_\alpha = \omega_\alpha^2 I_\alpha \tag{22.1.15}$$

A similar substitution of Eqs. (22.1.10) and (22.1.11) into the right hand sides, Eqs. (22.1.6) and (22.1.7), and a great deal of algebraic manipulation yields the following results.

$$L = -\pi\rho b^3 \omega^2 \left\{ L_h h + \left[L_\alpha - \left(\tfrac{1}{2} + a\right) L_h \right] \alpha \right\} \tag{22.1.16}$$

$$M = \pi\rho b^4 \omega^2 \left\{ \left[M_h - \left(\tfrac{1}{2} + a\right) L_h \right] h + \left[M_\alpha - \left(\tfrac{1}{2} + a\right)\left(M_h + L_\alpha\right) + \left(\tfrac{1}{2} + a\right)^2 L_h \right] \alpha \right\} \tag{22.1.17}$$

where

$$\left.\begin{aligned} L_h &= 1 - \frac{2i}{k} C(k) \\ L_\alpha &= \frac{1}{2} - \frac{i}{k}\left[1 + 2C(k)\right] - \frac{2}{k^2} C(k) \\ M_h &= \frac{1}{2} \\ M_\alpha &= \frac{3}{8} - \frac{1}{k} \end{aligned}\right\} \tag{22.1.18}$$

The quantities L_h, L_α, M_h and M_α are taken from the report by Smilg and Wasserman (Ref. 22.15) in which the unsteady aerodynamic quantities are referred to the aerodynamic center of the airfoil at the quarter chord. When the pivot axis is also at this point, then a = -1/2 and Eqs. (22.1.16) and (22.1.17) are greatly simplified. Note that in Ref. 22.15 the positive lift and vertical translation are both directed downward, whereas in the present instance only the vertical displacement is positive downward. This accounts for the negative algebraic sign on the right hand side of Eq. (22.1.16)

For simplicity in the present application, rewrite Eqs. (22.1.16) and (22.1.17) in influence coefficient form,

$$L = \pi\rho b^3 \omega^2 \left[A_h h + A_\alpha \alpha \right] \tag{22.1.19}$$

$$M = \pi\rho b^4 \omega^2 \left[B_h h + B_\alpha \alpha \right] \tag{22.1.20}$$

where all of the unsteady quantities have been gathered together into four quantities,

$$\left.\begin{aligned} A_h &= -L_h \\ A_\alpha &= -L_\alpha + \left(\tfrac{1}{2} + a\right) L_h \\ B_h &= M_h - \left(\tfrac{1}{2} + a\right) L_h \\ B_\alpha &= M_\alpha - \left(\tfrac{1}{2} + a\right)\left(M_h + L_\alpha\right) + \left(\tfrac{1}{2} + a\right)^2 L_h \end{aligned}\right\} \tag{22.1.21}$$

When Eqs. (22.1.19) and (22.1.20) are substituted into Eqs. (22.1.12) and (22.1.13), then after considerable algebraic manipulation we obtain

$$\left\{ \frac{m}{\pi\rho b^2}\left(1 - \frac{\omega_h^2}{\omega^2}\right) + A_h \right\} h + \left\{ \frac{S_\alpha}{\pi\rho b^3} + A_\alpha \right\} \alpha = 0 \tag{22.1.22}$$

$$\left\{ \frac{S_\alpha}{\pi\rho b^3} + B_h \right\} h + \left\{ \frac{I_\alpha}{\pi\rho b^4}\left(1 - \frac{\omega_\alpha^2}{\omega^2}\right) + B_\alpha \right\} \alpha = 0 \tag{22.1.23}$$

or, more simply, using the notation of Ref. 22.16,

$$\left.\begin{aligned} \bar{A} h + \bar{B} \alpha &= 0 \\ \bar{D} h + \bar{E} \alpha &= 0 \end{aligned}\right\} \tag{22.1.24}$$

where

$$\left.\begin{aligned} \bar{A} &= \mu\left[1 - \left(\frac{\omega_h}{\omega_\alpha}\right)^2 \left(\frac{\omega_\alpha}{\omega}\right)^2\right] + A_h \\ \bar{B} &= \mu X_\alpha + A_\alpha \\ \bar{D} &= \mu X_\alpha + B_h \\ \bar{E} &= \mu r_\alpha^2 \left[1 - \left(\frac{\omega_\alpha}{\omega}\right)^2\right] + B_\alpha \end{aligned}\right\} \tag{22.1.25}$$

and where μ is the mass parameter,

$$\mu = \frac{m}{\pi \rho b^2} \tag{22.1.26}$$

X_α is the c.g. position aft of the elastic axis,

$$x_\alpha = \frac{S_\alpha}{mb} \tag{22.1.27}$$

and r_α is the radius of gyration of the airfoil about the elastic axis,

$$r_\alpha^2 = \frac{I_\alpha}{mb^2} \tag{22.1.28}$$

Coupled flutter occurs when the determinant of the complex coefficients in Eq. (22.1.24) vanishes,

$$\begin{vmatrix} \bar{A} & \bar{B} \\ \bar{D} & \bar{E} \end{vmatrix} = 0 \tag{22.1.29}$$

This equation must be separately satisfied by the vanishing of the real and imaginary parts. These two equations are all that are needed to form a determinate set because the only unknowns in the system are the reduced frequency, $k = b\omega/V$, and the frequency ratio, $\sqrt{X} = \omega_\alpha/\omega$. The procedure used by Theodorsen was to select a series of values of k, substitute them into the real and imaginary solutions of Eq. (22.1.29) and solve for the values of $\sqrt{X}$ which constituted the real and imaginary roots of the determinant. The intersection of the real and imaginary branches of the curves was the flutter point. This is schematically shown in Fig. 22.1.9.

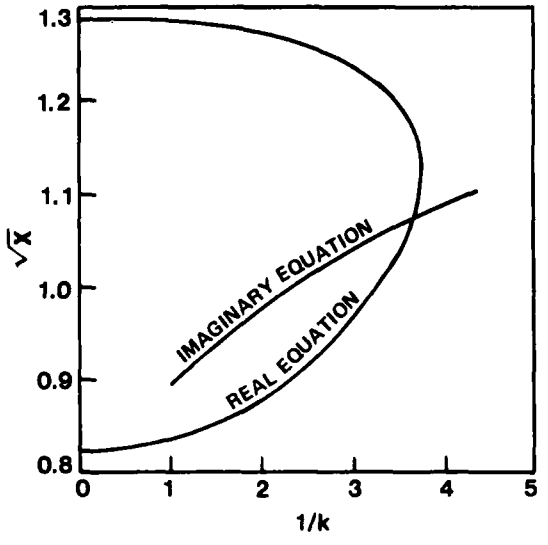

Fig. 22.1.9 Typical Flutter Solution Using Theodorsen's Method

22.1.4.3 Simplified Approach to Flutter

Theodorsen's theory has been in use now for approximately forty years and it has proved to be a very durable theory that has spawned many modifications and extensions. Within the limits of the assumptions made by Theodorsen, it has proved to be reasonably accurate. It has been found to be amenable to solution with a desk calculator, although moderately time-consuming, and it has been possible to automate it without difficulty for solution on high-speed digital computers. However, one overriding fact becomes apparent to anyone who uses this theory. It is virtually impossible to derive any physical insight into the flutter mechanism from its direct application.

Fortunately, it is possible to simplify the unsteady aerodynamic quantities to varying degrees and obtain flutter solutions which, although somewhat inaccurate, possess sufficient simplicity to reveal much of the underlying physics of the instability. A particularly lucid survey of a number of simple applications is found on pp. 258-277 of Ref. 22.17. In the present discussion we shall take the simplest possible approach in an effort to focus on the specific items which constitute the major differences between aircraft wing flutter and compressor blade flutter. In this section, we shall concentrate on developing the necessary formulas and facts, while the comparison between wing and compressor flutter will be deferred to a subsequent section.

In this very simple approach, consider a single degree of freedom system capable of torsional motion only. Actually, this is equivalent to a study of the torsional mode of a binary system with well separated modes. To this end, combine Eqs. (22.1.5) and (22.1.7) and suppress the bending mode. The resulting equation is given by:

$$I_\alpha \ddot{\alpha} + K_\alpha \alpha = M_1 \ddot{\alpha} + M_2 \dot{\alpha} + M_3 \alpha \tag{22.1.30}$$

where

$$M_1 = -\pi \rho b^4 \left(\frac{1}{8} + a^2 \right) \tag{22.1.31}$$

$$M_2 = \pi \rho b^4 \left[a - \frac{1}{2} + 2\left(\frac{1}{4} - a^2 \right) C(k) \right] \frac{V}{b} \tag{22.1.32}$$

$$M_3 = 2\pi \rho b^4 \left(\frac{1}{2} + a \right) C(k) \frac{V^2}{b^2} \tag{22.1.33}$$

We shall continue to simplify by assuming that k is very small and therefore the system can be represented by the quasi-steady approximation in which the normally complex circulation function goes asymptotically to

$$\lim_{k\to 0} C(k) = 1 + i \times 0 \qquad (22.1.34)$$

With this additional simplification, M_1 remains the same, but M_2 and M_3 are approximated by

$$M_2 \cong \pi\rho b^4 a\,(1-2a)\frac{V}{b} \qquad (22.1.35)$$

$$M_3 \cong 2\pi\rho b^4\left(\frac{1}{2}+a\right)\frac{V^2}{b^2} \qquad (22.1.36)$$

which are both real. Thus, Eq. (22.1.30) becomes a simple, second order differential equation with constant coefficients

$$\left(I_\alpha - M_1\right)\ddot{\alpha} - M_2\dot{\alpha} + \left(K_\alpha - M_3\right)\alpha = 0 \qquad (22.1.37)$$

whose solution is

$$\alpha = \bar{\alpha}e^{\lambda t} \qquad (22.1.38)$$

where

$$\lambda = \frac{M_2}{2(I_\alpha - M_1)} \pm i\sqrt{\frac{K_\alpha - M_3}{I_\alpha - M_1} - \left(\frac{M_2}{2(I_\alpha - M_1)}\right)^2} \qquad (22.1.39)$$

First consider the zero velocity limit. (Strictly speaking, this is an invalid limit for this equation since we have already assumed that $k = b\omega/V$ is vanishingly small. It is obvious that this assumption is incompatible with the zero velocity limit. However, our physical understanding will not be altered in this limit because the same terms will vanish here as would vanish in the case of nonvanishing k.) When $V \to 0$, both M_2 and M_3 vanish, so Eq. (22.1.39) reduces to

$$\lambda_0 = \pm i\sqrt{\frac{K_\alpha}{I_\alpha - M_1}} = \pm i\omega_{\alpha_0} \qquad (22.1.40)$$

where $\omega_{\alpha 0}$ is the natural torsional frequency of the system in still air. When $V \neq 0$, Eq. (22.1.39) can be rewritten as

$$\lambda = -\frac{C_\alpha}{2(I_\alpha - M_1)} \pm i\sqrt{\omega_\alpha^2 - \left(\frac{C_\alpha}{2(I_\alpha - M_1)}\right)^2} \qquad (22.1.41)$$

where

$$C_\alpha = -M_2 = \pi\rho b^4 a(2a-1)\frac{V}{b} \qquad (22.1.42)$$

is the aerodynamic damping, and where

$$\omega_\alpha^2 = \frac{K_\alpha - M_3}{I_\alpha - M_1} = \omega_{\alpha_0}^2 - \frac{M_3}{I_\alpha - M_1} \qquad (22.1.43)$$

is the square of the natural wind-on frequency of the system. In the second form of Eq. (22.1.43) $\omega_{\alpha 0}$ has been taken from Eq. (22.1.40), and in Eq. (22.1.42) the new definition of aerodynamic damping, C_α, has been introduced as a positive quantity for convenience. Actually, the value of C_α is unimportant here in our attempt to gain physical understanding. The more exact value of the aerodynamic damping in torsion would be a strong function of the circulation function, C(k), which has been neglected in the present analysis. Furthermore, the system damping for the coupled modes would be all-important in determining the instability point, and this is beyond the scope of the present simplified analysis.

In the equations just derived, $I_\alpha - M_1$ is the effective inertia in pitch, including virtual mass effects. It is customary (cf., Ref. 22.16, p. 69) to define critical damping in terms of system mass or inertia as

$$C_c = 2(I_\alpha - M_1)\omega_\alpha \qquad (22.1.44)$$

and to define the damping ratio as

$$\gamma = \frac{C_\alpha}{C_c} = \frac{C_\alpha}{2(I_\alpha - M_1)\omega_\alpha} \qquad (22.1.45)$$

Then Eq. (22.1.41) becomes

$$\lambda = -\gamma\omega_\alpha \pm i\omega_\alpha\sqrt{1-\gamma^2} \qquad (22.1.46)$$

which, when substituted into Eq. (22.1.38) represents a damped, oscillatory pitching motion.

The most important thing here is the definition of ω_α given above in Eq. (22.1.43). When M_1 and M_3 are inserted from Eqs. (22.1.31) and (22.1.36) this becomes

$$\omega_\alpha^2 = \omega_{\alpha_0}^2 - \frac{2\pi\rho b^4\left(\frac{1}{2}+a\right)V^2/b^2}{I_\alpha + \pi\rho b^4\left(\frac{1}{8}+a^2\right)} \qquad (22.1.47)$$

For our purposes, it will be convenient to select a midchord pivot axis, a = 0, and when Eqs. (22.1.26) and (22.1.28) are used this equation simplifies to

$$\omega_\alpha = \omega_{\alpha_0}\sqrt{1-\frac{(V/b\omega_{\alpha_0})^2}{\mu r_\alpha^2+0.125}} \qquad (22.1.48)$$

Thus, it is seen that as the velocity increases from zero, the square of the frequency decreases monotonically as the square of the velocity. To put this in simpler terms, the presence of a moving airstream introduces an aerodynamic spring term, M_2, into Eq. (22.1.43) which is proportional to the pitch displacement, and which reduces the torsional stiffness of the system. Thus, the torsional frequency initially decreases as the velocity increases.

A similar but slightly more elaborate analysis of the bending mode will now be performed. A combination of Eqs. (22.1.4) and (22.1.6) with the torsion mode suppressed yields the result

$$mb\ddot{h}+K_h bh = L_1\ddot{h}+L_2\dot{h} \qquad (22.1.49)$$

where

$$L_1 = -\pi\rho b^3 \qquad (22.1.50)$$

$$L_2 = -2\pi\rho b^3\frac{V}{b}C(k) \qquad (22.1.51)$$

Here there is no direct aerodynamic stiffness term proportional to h in Eq. (22.1.6). Instead, an aerodynamic stiffness effect will be obtained by retaining the complex C(k) function in the analysis. Rewrite Eq. (22.1.49) as

$$(mb-L_1)\ddot{h}-L_2\dot{h}+K_h bh = 0 \qquad (22.1.52)$$

assume a solution having the form

$$h = \bar{h}e^{i\omega_h t} \qquad (22.1.53)$$

and upon introducing Eqs. (22.1.8), (22.1.50), and (22.1.51), Eq. (22.1.52) becomes

$$-\omega_h^2\left(m+\pi\rho b^2\right)-2\pi\rho b\omega_h\frac{V}{b}G+K_h = 0 \qquad (22.1.54)$$

Note that for the no-flow condition, V and G both vanish and $\omega_h \to \omega_{ho}$, where

$$\omega_{ho} = \sqrt{\frac{K_h}{m+\pi\rho b^2}} \qquad (22.1.55)$$

is the natural bending frequency of the system in still air. After dividing through by mω² and using Eq. (22.1.26), these equations yield the result

$$\omega_h = \omega_{ho}\left[\sqrt{1+\left(\frac{(V/b\omega_{ho})G}{\mu+1}\right)^2}-\frac{(V/b\omega_{ho})G}{\mu+1}\right] \qquad (22.1.56)$$

In this equation G is the imaginary part of the Theodorsen function which is negative for all values of k, and it is seen that the bending frequency tends to increase with increasing velocity from its still air value. Thus, as the velocity increases, the originally well-separated torsion and bending frequencies approach one another, as shown in Fig. 22.1.10, in which the frequency is plotted versus

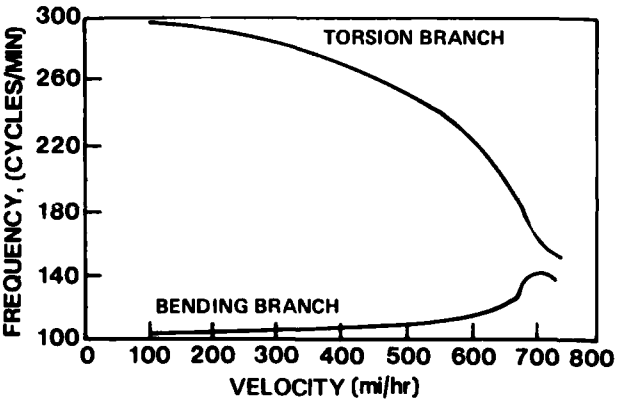

Fig. 22.1.10 Example of Frequency Coalescence at the Flutter Point

velocity. A comparable plot of the frequency versus the modal damping, taken from the Pines analysis of Ref. 22.18 (see also pp. 269-274 of Ref. 22.17), is shown in Fig. 22.1.11. Here it is seen that as the frequencies first depart from their no-flow values the system damping in each mode initially increases. However, when the frequencies become close enough the damping in one of the modes suddenly decreases, passes through zero, and the system becomes unstable. Another interpretation is that when the two frequencies are sufficiently close an energy exchange between the two modes can take place and if the conditions are favorable, a coupled flutter will occur.

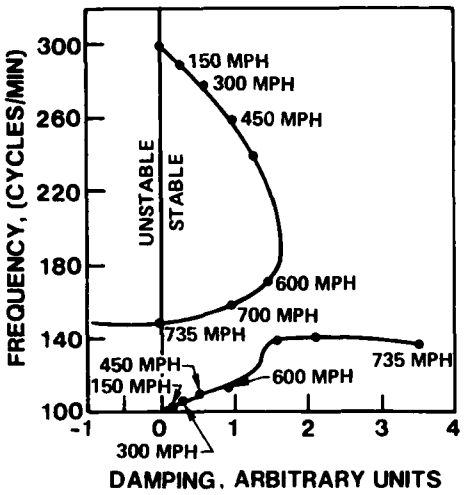

Fig. 22.1.11 Effect of Frequency Coalescence on Modal Damping

Before going on to the discussion of turbomachinery flutter, it should be reemphasized that this section has used extremely simple concepts and does not purport to be accurate. Instead, its primary purpose has been to attempt to introduce physical meaning into an otherwise complicated and sometimes bewildering mathematical exercise.

22.1.5 FUNDAMENTAL DIFFERENCES BETWEEN TURBOMACHINERY FLUTTER AND WING FLUTTER

In this section we shall attempt to point out the differences between aircraft wings and turbomachinery blades, particularly as these differences affect the flutter experienced by these configurations. Certain of these differences will be related to the fundamental discussions in the previous section while other differences will be newly developed. To begin with, the discussion will center on some pertinent characteristics of the vibrations of rotating systems. Following this, the concept of the frequency shifts in both the bending and torsion modes will be amplified and extended.

22.1.5.1 Elementary Vibration Concepts for Rotating Systems

The object of this discussion is not to expound on vibration theory. It is assumed that the reader already has an adequate grasp of the fundamentals of vibration theory, or that he can refer to one or more of the excellent texts on the subject (e.g., Refs. 22.19 or 22.20). Instead, the object here is to concentrate on one or two specific concepts that are unique to rotating machinery, and hence are germaine to the turbomachinery flutter problem.

As in many other flexible systems involving continuously distributed mass and stiffness, a turbomachine blade can vibrate in an infinity of discrete, natural modes, although practically, only the lowest several modes are of any interest. However, even here there will be an added complication relative to a fixed-base vibrating system because the rotation of the turbomachine causes variations in both mode shape and frequency. Only the latter will be considered herein, and the discussion will be further restricted to the relatively simple concept of centrifugal stiffening. To understand this concept as it applies to turbomachinery blades, consider first the rotation of a chain possessing no inherent (or at-rest) stiffness. At zero rotational speed the chain will hang limply from its support, but under rotation (say, about a vertical axis) the chain will be raised from its limp position and will approach the plane of rotation as the rotational speed increases (cf. Fig. 22.1.12)

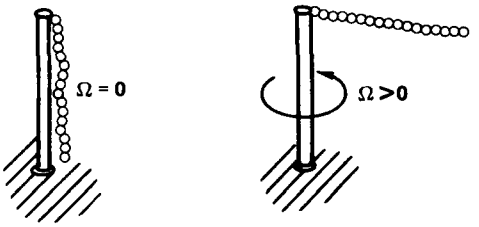

Fig. 22.1.12 Schematic of Rotating Chain

This centrifugal stiffening effect will also cause changes in the frequency of vibration of the chain. If the system is displaced from equilibrium a restoring force, equivalent to a spring force, will be imposed on each element of the chain and will tend to return the chain to its equilibrium position. This force is caused by the lateral displacement of the radial tension vector, and is proportional to the square of the rotation speed, Ω (cf. Ref. 22.19). It is easily shown in Ref. 22.19 that the frequency of such a chain is equal to Ω. (See curve labled $\omega_1 = 0$ in Fig. 22.1.13.)

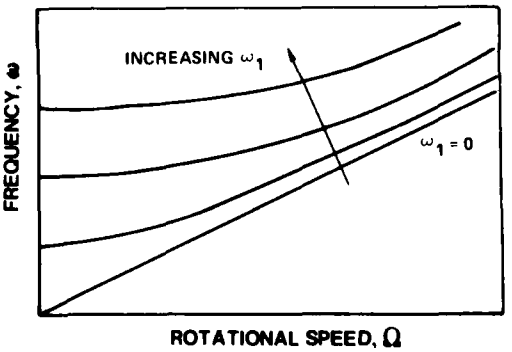

Fig. 22.1.13 Effect of Rotation on Frequency of a Flexible Cantilever Beam (Southwell's Theorem)

For a cantilever blade having inherent stiffness and hence having an at-rest frequency of ω_1, the result is similar, although somewhat more complicated. A simplification is afforded by Southwell's Theorem (cf. p. 270 of Ref. 22.19) which states that the natural frequency of the system is approximately equal to

$$\omega = \sqrt{\omega_1^2 + \omega_2^2} \qquad (22.1.57)$$

where ω_1 is the at-rest frequency and ω_2 is the frequency due solely to rotation. For the general case of a rotating, flexible beam this is equivalent to

$$\omega = \sqrt{\omega_1^2 + \beta\Omega^2} \qquad (22.1.58)$$

which yields a hyperbolic relationship between ω and Ω for $\omega_1 \neq 0$, as shown in the family of curves in Fig. 22.1.13. In Eq. (22.1.58) β is of order 1 for the lowest mode, and increases in magnitude as the mode number increases. It should be noted that this phenomenon manifests itself primarily in the bending (or flatwise) modes and has virtually no effect on the torsion mode frequency under rotational conditions.

The importance of this type of behavior lies in the multiple sources of excitation for any rotating system. This is illustrated in Fig. 22.1.14, in which frequency of excitation or vibration is plotted versus rotational speed. First consider the radial lines from the origin labeled 1E, 2E, 3E, ... These lines represent the loci of available excitation energy at any rotational speed for 1 excitation per revolution, 2 excitations per revolution, 3 excitations per revolution, etc. (Note the coordinate intersection of the 1E line at 6000 rpm and 100 cps.) Superimposed on this diagram are three lines labeled 1B, 1T and 2B which are hypothetical plots of the first bending, first torsion, and second bending frequencies, respectively. In this hypothetical plot, the designer has managed to keep the first bending frequency high enough so that it never intersects the 2E line, which is usually the source of most forced vibration energy. If such an intersection had occurred, the rotor blades could be subjected to a severe 2-per-rev bending vibration at the rpm of intersection, sufficiently strong to cause fatigue failures of the blades. Also in the diagram, the designer has permitted an intersection of the first bending mode line with the 3E line at approximately 2600 rpm. If this rotor is designed to idle at 3000 rpm and has a maximum speed of 7000 rpm, then the designer has succeeded in avoiding all integral order vibrations over the entire operating range.

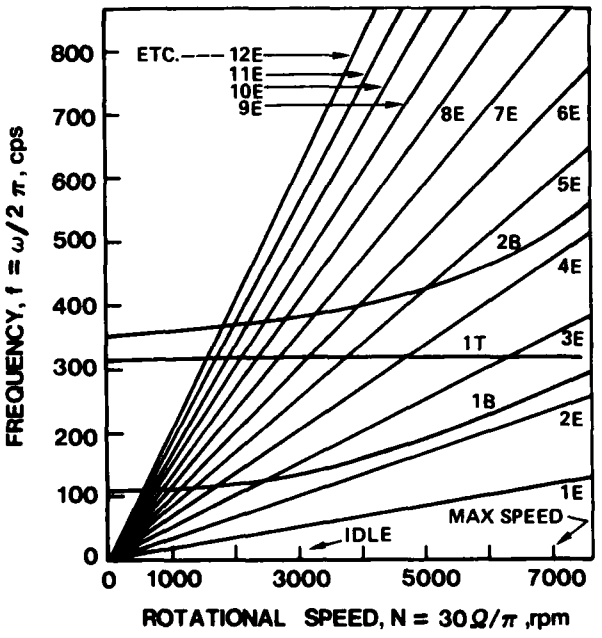

Fig. 22.1.14 Excitation Diagram for Rotating System

Note further in this diagram that the first torsion mode which is unaffected by Southwell stiffening and is therefore a horizontal line, will intersect the 6E, 5E, 4E and 3E lines as rotor rpm is increased from idle to full speed. This could conceivably cause trouble for a rotor blade operating at high aerodynamic load at part speed (4E) or near full speed (3E) rpm. Under such conditions a stall flutter could occur (cf. Section 22.3.2), aggravated by an integral order excitation in the vicinity of the intersection with the integral order line. Thus, the designer must be aware of the existence of these problems and must be in a position to redesign his blading to eliminate the problem.

Finally, the second bending mode, 2B, will encounter excitations at all integral orders from 8-per-rev to 5-per-rev as rpm is increased. However, the 4-per-rev excitation will be avoided over the operating range of the rotor.

The reader should be aware that only a simple example has been demonstrated here. An actual rotor blade system, particularly one with a flexible disk or a part-span shroud, will also experience coupled blade-disk or blade-shroud modes which are not characterized here, and which are beyond the scope of the present discussion. However, these concepts are covered adequately in the advanced literature dealing with such coupled motions.

22.1.5.2 Mass Ratio, Stiffness, and Frequency Differences

In Section 22.1.4.3 we described the coupled flutter phenomenon in terms of frequency coalescence of the two fundamental bending and torsion

modes. It was shown that the torsional frequency would decrease with increasing velocity (Eq. (22.1.48)), and that the bending frequency would increase with increasing velocity (Eq. (22.1.56)). However, the extent of the frequency change over the operational range was not discussed. This is of extreme importance in deciding whether or not a given system will be susceptible to classical coupled flutter. (Note that these frequency changes are aerodynamically induced and are not caused by rpm changes.)

Refer now to Eqs. (22.1.48) and (22.1.56). It is seen here that the structural and geometric parameters governing the frequency changes for the two modes are the mass and inertia ratios, μ and μr_α^2, and the stiffness parameters, $b\omega_{oh}$ and $b\omega_{o\alpha}$. Before we can examine the orders of magnitudes of these parameters we must first consider the differences in the structural makeup of aircraft wings and compressor blades.

The traditional subsonic aircraft wing has a built-up section consisting of a box beam or spar which supports a stressed skin and stringer shell. It is usually made of aluminum. Hence, much of the wing consists of empty space, and what little metal there is, is relatively lightweight. Typical values of the mass and inertia ratios for aircraft wings lie in the ranges

$$5 < \mu < 20$$

$$1 < \mu r_\alpha^2 < 15$$

(Of course, these values would change if the empty space was replaced by fuel.)

The traditional compressor blade is a solid forged and machined blade made of titanium or steel. It may have a cambered, double circular arc profile, and an average thickness-to-chord ratio of 5 percent. If it is made of titanium, the blade described above will have mass and inertia ratios of approximately

$$\mu \cong 190$$

$$\mu r_\alpha^2 \cong 3$$

If it is made of steel, this same blade will have mass and inertia ratios 1.7 times larger than the values just cited.

To a first approximation, then, the inertia parameter, μr_α^2, for a compressor blade is of the same order of magnitude as that for an aircraft wing. However, the mass parameter, μ, for a compressor blade is an order of magnitude (or more) greater than that for an aircraft wing. Thus, with everything else held the same in Eqs. (22.1.48) and (22.1.56), we would expect roughly the same change in ω_α with V, but a much smaller change in ω_h with V. Under these circumstances, frequency coalescence and coupled flutter would take place at a higher value of V for a compressor blade than it would for an aircraft wing.

Another factor which enters into the situation here is the inherent stiffness of compressor blades versus the inherent flexibility of aircraft wings. Although the wing chord is many times the compressor blade chord, the compressor blade frequencies are often many more times the wing frequencies. Thus the stiffness parameters $b\omega_{o\alpha}$ and $b\omega_{oh}$ are at least the same for blade and wing, and quite often are larger for the blade than for the wing. This is another way in which the blade frequency change with velocity is smaller than that of the wing.

There are many additional reasons for the observed differences between wing flutter and blade flutter. Most of these are subtle and contribute to the differences in minor ways. However, one additional difference exists which makes a major contribution. This is related to the Pines criteria (cf. Fig. 22.1.15, taken from Ref. 22.18) that (a) no flutter exists for center of gravity (c.g.) positions forward of the elastic axis (e.a.), and (b) if the c.g. is aft of the e.a. and if the aerodynamic center (a.c.) is forward of the e.a., flutter is possible only if the frequency ratio ω_h/ω_α is less than some specified amount involving these locations and the radius of gyration. In most aircraft wings the e.a. is quite often in the neighborhood of the spar, between 25 and 40 percent of the chord, the c.g. is in the neighborhood of the 50 percent chord location, and the a.c. is at the 25 percent chord location for subsonic flows. Hence, the c.g. is aft of the e.a., the a.c. is forward of the e.a.,

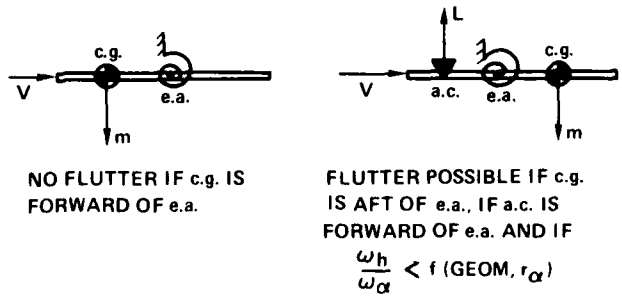

Fig. 22.1.15 Pines Criteria Applied to Compressor Blade and Aircraft Wing

and flutter is possible if the frequency criterion is met. In contrast to this, the solid compressor blade usually has a circular arc profile which is symmetric fore and aft. Hence the c.g. and the e.a. are coincident or very nearly so at the 50 percent chord location. According to Pines, no coupled flutter is possible if the c.g. is forward of the e.a., no matter how small the distance. Thus, the compressor blade with coincident c.g. and e.a. would constitute a borderline case between flutter and no flutter, and we would expect much less susceptibility to coupled flutter in such a configuration than we would in an aircraft wing with conventional separation between the e.a. and the c.g.

22.2 UNSTEADY AERODYNAMICS

Before we examine the unsteady aerodynamics of multiblade systems we shall look briefly into the theory for isolated airfoils. We shall proceed from the simpler, more physical view, into the more complicated analysis, and thereby establish some groundwork for further study. As stated earlier, the scope of this single chapter limits us to an exposition of concepts with a minimum of mathematical derivations, and the reader will be directed to the appropriate sources for further study. The notation and the dimensionality of the variables will usually remain consistent with the primary source used for the derivations.

22.2.1 FUNDAMENTALS OF UNSTEADY THEORY FOR ISOLATED AIRFOILS

22.2.1.1 Incompressible Flow

Although Theodorsen is generally credited with the first comprehensive analysis of airfoil flutter (Ref. 22.13), the simpler and more rigorous version by Schwarz (Ref. 22.14) will be discussed here. In addition to the basic reference, a detailed analysis of this version of the theory is available in Ref. 22.1 (pp. 272-278), and only the highlights will be of concern to us.

In the analysis of the isolated airfoil the coordinate system of Fig. 22.1.6 will be used, together with the physical picture shown below in Fig. 22.2.1. All lengths in this derivation have been made dimensionless with respect to the semichord, b, and the coordinate system has been located at the midchord of the airfoil. It is assumed that the airfoil is executing small timewise displacements relative to its mean position ($z = 0$), and that its vertical velocity is given by

$$\left.\begin{aligned} w_a(x,t) &= b\frac{\partial Z_a}{\partial t} + U\frac{\partial Z_a}{\partial x} \\ Z &= 0, \quad -1 \le x \le 1 \end{aligned}\right\} \qquad (22.2.1)$$

(where the subscript a denotes the region over the airfoil). It should be noted that this equation is used in all unsteady aerodynamic derivations to define the interfacial condition between the fluid and the body in motion. For a prescribed mode of oscillation Eq. (22.2.1) defines the known vertical velocity (or downwash) over the extent of the airfoil chord.

The quantities γ_a and γ_w in Fig. 22.2.1 are the vorticity per unit chord in the vortex sheet over the airfoil chord and the wake, respectively. Use of the Biot-Savart law yields the relationship

$$w_a(x,t) = -\frac{1}{2\pi}\oint_{-1}^{1}\frac{\gamma_a(\xi,t)}{x-\xi}\,d\xi - \frac{1}{2\pi}\int_{1}^{\infty}\frac{\gamma_w(\xi,t)}{x-\xi}\,d\xi \qquad (22.2.2)$$

in which the known downwash is equal to an integral of the unknown chordwise vorticity distribution. However, from potential flow theory it can be shown that the chordwise pressure difference distribution is given by

$$\frac{\Delta P(x,t)}{\rho U} = -\gamma_a(x,t) - ik\int_{-1}^{x}\gamma_a(\xi,t)\,d\xi \qquad (22.2.3)$$

Hence, the determination of the unsteady loads on an oscillating airfoil requires the successful inversion of the integral equation (22.2.2).

The assumption will now be made that the airfoil is oscillating in simple harmonic motion, with frequency ω such that all time-dependent quantities in the forgoing equations can be rewritten in the typical form

$$w_a(x,t) = \bar{w}_a(x)e^{i\omega t} \qquad (22.2.4)$$

whereupon Eq. (22.2.2) becomes

$$\bar{w}_a(x) = -\frac{1}{2\pi}\oint_{-1}^{1}\frac{\bar{\gamma}_a(\xi)}{x-\xi}\,d\xi - \frac{1}{2\pi}\int_{1}^{\infty}\frac{\bar{\gamma}_w(\xi)}{x-\xi}\,d\xi \qquad (22.2.5)$$

At this point in the analysis Schwarz makes the key assumption that any circulation change on the airfoil appears as shed vorticity in the wake having equal magnitude and opposite sign, or

$$d\Gamma(t) = -b\gamma_w(1,t)\,dx \qquad (22.2.6)$$

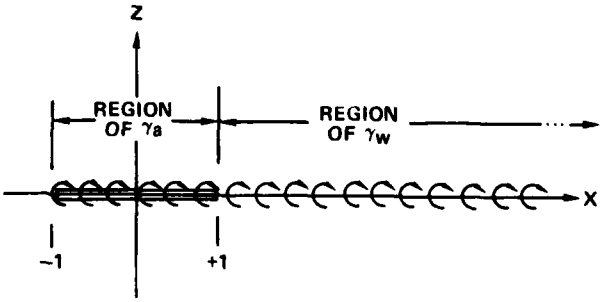

Fig. 22.2.1 Vortex Sheet Representation of Isolated Airfoil

where

$$\Gamma(t) \equiv b\int_{-1}^{1} \gamma_a(x,t)\,dx \qquad (22.2.7)$$

Equation (22.2.6) can be rewritten as

$$\frac{d\Gamma(t)}{dt} = -b\gamma_w(1,t)\frac{dx}{dt} = -U\gamma_w(1,t) \qquad (22.2.8)$$

Schwarz now makes the further assumption that this shed vorticity is convected downstream at freestream velocity, U, and after a series of logical manipulations, arrives at the formula

$$U\gamma_w\left(\xi, t + \frac{b(\xi-1)}{U}\right) = -\frac{d\Gamma(t)}{dt} \qquad (22.2.9)$$

With the assumption of simple harmonic motion all variables are proportional to $e^{i\omega t}$ so this becomes

$$U\bar{\gamma}_w(\xi)e^{i\omega\left(t+\frac{b(\xi-1)}{U}\right)} = -i\omega\bar{\Gamma}e^{i\omega t} \qquad (22.2.10)$$

which further reduces to

$$\bar{\gamma}_w(\xi) = -\frac{i\omega}{U}\bar{\Gamma}e^{ik}e^{-ik\xi} \qquad (22.2.11)$$

Following Reissner (Ref. 22.21), we introduce a reduced circulation function (which is unknown but constant, and can be evaluated at the conclusion of the analysis)

$$\bar{\Omega} = \frac{\bar{\Gamma}}{b}e^{ik} \qquad (22.2.12)$$

so Eq. (22.2.11) becomes

$$\bar{\gamma}_w(\xi) = -ik\bar{\Omega}e^{-ik\xi} \qquad (22.2.13)$$

and when this is substituted into Eq. (22.2.5) the result is

$$\bar{w}_a(x) = -\frac{1}{2\pi}\oint_{-1}^{1}\frac{\bar{\gamma}_a(\xi)}{x-\xi}\,d\xi + \frac{ik\bar{\Omega}}{2\pi}\int_{1}^{\infty}\frac{e^{-ik\xi}}{x-\xi}\,d\xi \qquad (22.2.14)$$

Now only one unknown, $\bar{\gamma}_a(\xi)$, is under the integral and the remaining unknown, $\bar{\Omega}$, is a constant. Thus, the integral equation can be inverted by Söhngen's method (Ref. 22.22) and the resulting equation now yields the unknown $\bar{\gamma}_a(x)$ in terms of an integral of the known downwash, $\bar{w}_a(\xi)$,

$$\bar{\gamma}_a(x) = -\frac{2}{\pi}\sqrt{\frac{1-x}{1+x}}\left\{-\oint_{-1}^{1}\sqrt{\frac{1+\xi}{1-\xi}}\,\frac{\bar{w}_a(\xi)}{x-\xi}\,d\xi + \frac{ik\bar{\Omega}}{2\pi}\oint_{-1}^{1}\sqrt{\frac{1+\xi}{1-\xi}}\left[\int_{1}^{\infty}\frac{e^{-ik\lambda}}{\xi-\lambda}\,d\lambda\right]\frac{d\xi}{x-\xi}\right. \qquad (22.2.15)$$

Once this crucial step has been performed, the remainder of the problem, although formidable in appearance, involves nothing more than a sequence of complicated algebraic manipulations and integrations to yield the final desired results. (Note that this solution for $\bar{\gamma}_a(x)$ yields $\bar{\Omega}$ by integration, via Eqs. (22.2.7) and (22.2.12).) Specifically, substitution of Eq. (22.2.15) into the time-independent form of Eq. (22.2.3) yields the pressure difference distribution

$$-\frac{\Delta\bar{p}(x)}{\rho U} = \frac{2}{\pi}\left[1-C(k)\right]\sqrt{\frac{1-x}{1+x}}\int_{-1}^{1}\sqrt{\frac{1+\xi}{1-\xi}}\,\bar{w}_a(\xi)\,d\xi + \frac{2}{\pi}\oint_{-1}^{1}\left[\sqrt{\frac{1-x}{1+x}}\sqrt{\frac{1+\xi}{1-\xi}}\,\frac{1}{x-\xi} - ik\Lambda_1(x,\xi)\right]\bar{w}_a(\xi)\,d\xi \qquad (22.2.16)$$

where

$$\Lambda_1(x,\xi) = \frac{1}{2}\log\left[\frac{1-x\xi+\sqrt{1-\xi^2}\sqrt{1-x^2}}{1-x\xi-\sqrt{1-\xi^2}\sqrt{1-x^2}}\right] \qquad (22.2.17)$$

Further integration of Eq. (22.2.16) yields the unsteady lift and moment per unit span,

$$L(t) = -b\int_{-1}^{1}\Delta p(x,t)\,dx \qquad (22.2.18)$$

$$M(t) = b^2\int_{-1}^{1}(x-a)\Delta p(x,t)\,dx \qquad (22.2.19)$$

Actual values for these integrals can be obtained by introducing the generalized dimensionless motion

$$z = -h - a(x-a) \qquad (22.2.20)$$

into Eq. (22.2.1) for the downwash

$$w_a(x,t) = -b\dot{h} - b\dot{a}(x-a) - Ua \qquad (22.2.21)$$

and thence into the equations given above. It can be shown (cf. Ref. 22.1) that this procedure will yield the time-independent versions of Eqs. (22.1.6) and (22.1.7). Furthermore, if the bars are removed from the quantities in Eq. (22.2.16) the resulting lift and moment formulas are identical to Eqs. (22.1.6) and (22.1.7) although it should be clearly understood that these are to be regarded as the time-dependent loads due to simple harmonic motions. (The reader should be cautioned that the symbol h in the present document is equivalent to h/b in Ref. 22.1.)

Although this chapter is devoted primarily to the unsteady aerodynamics of cascaded airfoils, it would appear that an undue degree of attention has been placed on the isolated airfoil solution.

However, it will be seen below in Section 22.2.2.1 that this method is partially extendable to the study of cascaded airfoils in incompressible flow. Although not all of the mathematical techniques (such as the Söhngen inversion of the integral equation) can be used, the fundamental approach is still based on the vortex sheet concept, which makes the Schwarz method particularly valuable as a basic reference.

22.2.1.2 Compressible Subsonic Flow

There are two basic approaches to the solution of the unsteady aerodynamic problem of an isolated airfoil oscillating in a subsonic compressible flow. The first, historically, involves a solution of an integral equation for a distribution of acceleration potential doublets. It was solved by Possio (Ref. 22.23) with subsequent refinements and computations by Dietze (Ref. 22.24) and Fettis (Ref. 22.25). The second approach by Timman, van de Vooren, and Greidanus (Ref. 22.26) involves a transformation of the differential equation for the acceleration potential into elliptical coordinates and expanding the solution as an infinite series of Mathieu functions. Although the Mathieu function approach leads to a mathematically exact solution, it is necessary to compute several infinite sums, even for uncoupled, simple harmonic motions. Furthermore, these sums converge slowly at rates that depend on both reduced frequency and Mach number. Finally, no serious effort has yet been made to extend this method to a solution of the subsonic oscillating cascade problem. *Hence it will not be considered herein.*

Conversely, Possio's method, although tedious, is relatively straightforward, and has been the basis for several solutions to the unsteady cascade problem. Hence it will be described briefly below. The reader should be aware that the notation of this section is dimensional and the equations outlined below are a condensation of the discussion in Ref. 22.1, pp. 318-325.

The starting point for this analysis is the differential equation for the acceleration potential, ψ,

$$\nabla^2\psi - \left(\frac{1}{a_\infty^2}\frac{\partial^2\psi}{\partial t^2} + \frac{2M}{a_\infty}\frac{\partial^2\psi}{\partial x\,\partial t} + M^2\frac{\partial^2\psi}{\partial x^2}\right) = 0 \qquad (22.2.22)$$

where ψ is defined in terms of the disturbance pressure

$$p - p_\infty = -\rho_\infty\psi \qquad (22.2.23)$$

It is shown in Ref. 22.1 that the substantial derivative of the downwash, w, is given by

$$Dw = \frac{\partial\psi}{\partial z}\,dt \qquad (22.2.24)$$

and that integration along the trajectory of a fluid particle leads to the useful result

$$w(x,z,t) = \int_{-\infty}^{x} \frac{\partial\psi\left(\xi', z, t - \frac{x-\xi'}{U}\right)}{\partial z}\,\frac{d\xi'}{U} \qquad (22.2.25)$$

where U is the freestream velocity. As in the previous section, w on the airfoil surface is regarded as the prescribed quantity

$$\left.\begin{aligned} w_a(x,t) &= \frac{\partial z_a}{\partial t} + U\frac{\partial z_a}{\partial x} \\ &\text{for } z = 0, -b \le x \le b \end{aligned}\right\} \qquad (22.2.26)$$

(Note that the length variables used herein are dimensional quantities.) We shall assume simple harmonic motion such that a common time dependence factor $e^{i\omega t}$ can be removed, and we shall prescribe the additional boundary conditions:

1) There is zero pressure discontinuity across the x axis both ahead of and in the wake of the blade, or

$$\psi = 0 \text{ for } |x| > b,$$

2) All signals must propagate outward from the blade without reflection;

3) The Kutta condition must be satisfied, so ψ is not discontinuous at x = b.

The method used in Ref. 22.1 to obtain Posso's integral equation is to represent the airfoil with a sheet of acceleration potential doublets along the projection of the airfoil. Each elementary doublet is the mathematically derived superposition of a source-sink pair, and each source (or sink) is a solution of the differential equation (22.2.22), and is referred to as a source pulse,

$$\psi_{SP} = \frac{A(\xi,\zeta,T)}{R} \qquad (22.2.27)$$

where

$$R^2 = a_\infty^2(t-T)^2 - \left[(x-\xi) - U(t-T)\right]^2 - (z-\zeta)^2 \qquad (22.2.28)$$

and where ψ_{sp} is a two-dimensional pressure disturbance originating at ξ, ζ at time T which propagates outward in a cylindrical fluid region while being carried downstream at the freestream velocity U. $A(\xi, \zeta, T)$ is a time dependent amplitude function of the disturbance which will be evaluated later by means of the boundary conditions. Both ψ_{sp} and A in Eq. (22.2.27) can be regarded as infintesimal quantities since they represent a single source pulse out of a continuous sheet, and in Ref. 22.1 it is stated that for simple harmonic

motion we can write

$$A(\xi,\zeta,T) = -\frac{\bar{A}(\xi,\zeta)U^2 a_\infty e^{i\omega T}dT}{2\pi} \qquad (22.2.29)$$

which allows us to integrate Eq. (22.2.27) over T and obtain

$$\psi_S(x,z,t) = -\frac{\bar{A}(\xi,\zeta)U^2 a_\infty}{2\pi}\int_{-\infty}^{g}\frac{e^{i\omega T}dT}{R} \qquad (22.2.30)$$

In this equation ψ_S is related to the pressure disturbance at x,z due to a disturbance with complex amplitude $\bar{A}$ located at ξ, ζ. The upper limit of integration

$$g = t - \frac{\sqrt{(x-\xi)^2+(z-\zeta)^2(1-M^2)} - M(x-\xi)}{a_\infty(1-M^2)} \qquad (22.2.31)$$

is the most recent value of T for which a disturbance at ξ, ζ can be felt at x, z at time t. After some manipulations of the integrand Eq. (22.2.30) may be integrated to yield

$$\psi_S(x,z,t) = \frac{\bar{A}(\xi,\zeta)U^2 e^{i(\omega t+\bar{k})}}{4\sqrt{1-M^2}}\, iH_0^{(2)}(w') \qquad (22.2.32)$$

where

$$\left.\begin{aligned} w' &= \frac{kM}{1-M^2}\sqrt{\left(\frac{x-\xi}{b}\right)^2+(1-M^2)\left(\frac{z-\zeta}{b}\right)^2} \\ \bar{k} &= \frac{kM^2(x-\xi)}{(1-M^2)b} \end{aligned}\right\} \qquad (22.2.33)$$

A sinusoidally pulsating doublet is now obtained by differentiating the source solution with respect to the vertical coordinate, with the result

$$\psi_D(x,z,t) = \left(\frac{\partial\psi_S}{\partial\zeta}\right)_{\zeta=0} = \frac{\bar{A}(\xi)\omega^2M^2z}{4(1-M^2)^{3/2}}\, i\,\frac{H_1^{(2)}(w')}{w'}\, e^{i(\omega t+\bar{k})} \qquad (22.2.34)$$

Finally, the acceleration potential of the entire sheet of doublets is obtained by integrating over the chord,

$$\psi(x,z,t) = \int_{-b}^{b}\psi_D\,d\xi = \frac{\omega^2M^2e^{i\omega t}}{4(1-M^2)^{3/2}}\, iz\int_{-b}^{b}\bar{A}(\xi)\,\frac{H_1^{(2)}(w')}{w'}\, e^{i\bar{k}}\,d\xi \qquad (22.2.35)$$

Use is now made of the singular behavior of the intergrand. Note that the integral is multiplied by z. Hence the imposition of the limit $z \to 0$ as the airfoil surface is approached causes the right hand side to vanish everywhere except in the neighborhood of $\zeta = x$ where the integrand becomes large without bound in the limit. Use of appropriate limiting techniques as z is allowed to vanish from above (approaching the suction surface) and from below (approaching the pressure surface) yields the results

$$\left.\begin{aligned} \psi(x,0^+,t) &= -\frac{U^2\bar{A}(x)}{2}\, e^{i\omega t} \\ \psi(x,0^-,t) &= \frac{U^2\bar{A}(x)}{2}\, e^{i\omega t} \end{aligned}\right\} \qquad (22.2.36)$$

and from Eq. (22.2.23) we can identify the quantity $\bar{A}(x)$ as

$$\bar{A}(x) = \frac{\Delta\bar{p}_a(x)}{\rho_\infty U^2} \qquad (22.2.37)$$

where $\Delta\bar{p}_a(x)$ is the desired but as yet unknown pressure difference across the airfoil. When this is substituted into Eq. (22.2.35) the result is

$$\psi(x,z,t) = \frac{\omega^2M^2\,iz\,e^{i\omega t}}{4\rho_\infty U^2(1-M^2)^{3/2}}\int_{-b}^{b}\frac{H_1^{(2)}(w')}{w'}\, e^{i\bar{k}}\,\Delta\bar{p}_a(\xi)\,d\xi = \frac{-ie^{i\omega t}}{4\rho_\infty\sqrt{1-M^2}}\int_{-b}^{b}\left[\frac{\partial H_0^{(2)}(w')}{\partial z}\right]_{\zeta=0} e^{i\bar{k}}\,\Delta\bar{p}_a(\xi)\,d\xi \qquad (22.2.38)$$

Use is now made of Eq. (22.2.25) relating downwash to the disturbance potential. When this is evaluated along the x-axis for a simple harmonic motion, we obtain

$$w(x,0,t) = \frac{1}{U}e^{-\frac{i\omega x}{U}}\int_{-\infty}^{x}\left[\frac{\partial\psi}{\partial z}\right]_{z\to0^+} e^{\frac{i\omega\xi'}{U}}\,d\xi' \qquad (22.2.39)$$

and substitution of Eq. (22.2.38) yields the result

$$\bar{w}_a(x) = \frac{-ie^{\frac{-ikx}{b}}}{4\rho_\infty U\sqrt{1-M^2}}\int_{-b}^{b}\Delta\bar{p}_a(\xi)e^{\frac{ik\xi}{b}}\int_{-\infty}^{x}\left[\frac{\partial^2H_0^{(2)}(w')}{\partial z^2}\right]_{\substack{z\to0^+\\ \zeta\to0}} e^{i\bar{k}}\,d\xi'\,d\xi \qquad (22.2.40)$$

This is still an inconvenient form, and considerably more manipulation must be performed (as shown in Ref. 22.1) before the final solution is obtained

$$\bar{w}_a(x) = -\frac{\omega}{\rho_\infty U^2} \int_{-b}^{b} \Delta\bar{p}_a(\xi)\, K\left(M, \frac{k(x-\xi)}{b}\right) d\xi \qquad \text{for } -b \le x \le b \tag{22.2.41}$$

where the kernel function is given by

$$K\left(M, \frac{k(x-\xi)}{b}\right) = \frac{1}{4\sqrt{1-M^2}} \left\{ e^{i\bar{k}\left[iM \frac{|x-\xi|}{x-\xi} H_1^{(2)}(M\lambda) - H_0^{(2)}(M\lambda)\right]} + i(1-M^2)\, e^{\frac{-ik(x-\xi)}{b}} \left[\frac{2}{\pi\sqrt{1-M^2}} \log \frac{1+\sqrt{1-M^2}}{M} + \int_0^{\bar{k}/M^2} e^{iu} H_0^{(2)}(M|u|)\, du \right] \right\} \tag{22.2.42}$$

and where

$$\left.\begin{aligned} \lambda &= \frac{k|x-\xi|}{(1-M^2)b} \\ u &= \frac{k(\xi-\xi')}{(1-M^2)b} \end{aligned}\right\} \tag{22.2.43}$$

Equation (22.2.41) is Possio's integral equation in which the known downwash is written in terms of an integral of the unknown pressure difference distribution. Unlike the Schwarz integral equation (22.2.14), there is no convenient inversion formula available, and it has been necessary for the several authors working on this problem to resort to approximate iterative techniques. Tabulations of the unsteady aerodynamic coefficients are found in Refs. 22.24, 22.27, and 22.28.

As in the case of incompressible flow, the form of this solution will be important in our discussion of compressible subsonic flow past cascades (Section 22.2.2.2) and of acoustical resonance (Section 22.2.2.4).

22.2.1.3 Compressible Supersonic Flow

Although several researchers attacked the problem of compressible supersonic flow past an oscillating airfoil, the first systematic and straightforward approach was that of Garrick and Rubinow (Ref. 22.29) who extended some of Possio's early work and used the method of distributed source pulses. However, this solution has little or no relevance to the cascade problem except for its extensive tabulated values which are used later to provide isolated airfoil reference values. It is mentioned here primarily for its historical significance, and will not be studied in any detail.

More relevant to the work on cascades which follows is the use of the Laplace transform (cf. Refs. 22.1, pp. 364-367, and 22.30, pp. 37, 38, 50). Our starting point is the wave equation (22.2.22) with Ψ replaced by the disturbance potential Φ and with the assumption of simple harmonic motion

$$\Phi(x,z,t) = \bar{\Phi}(x,z)\, e^{i\omega t} \tag{22.2.44}$$

such that

$$\nabla^2\bar{\Phi} = M^2 \frac{\partial^2\bar{\Phi}}{\partial x^2} + \frac{2Mi\omega}{a_\infty} \frac{\partial\bar{\Phi}}{\partial x} - \frac{\omega^2}{a_\infty^2}\bar{\Phi} \tag{22.2.45}$$

with boundary condition

$$\frac{\partial\bar{\Phi}}{\partial z} = \bar{w}_a(x) \quad \text{for } z=0 \text{ over } 0 \le x \le 2b \tag{22.2.46}$$

where the origin of the dimensional coordinates is now at the leading edge. A straightforward use of Laplace transform technique, defined by

$$\bar{\Phi}^*(s,z) = \mathcal{L}\left\{\bar{\Phi}(x,z)\right\} = \int_0^\infty e^{-sx}\bar{\Phi}(x,z)\, dx \tag{22.2.47}$$

leads ultimately to the solution

$$\bar{\Phi}(x^*,0^*) = -\frac{b}{\sqrt{M^2-1}} \int_0^{x^*} \bar{w}_a(\xi^*)\, e^{-\frac{i\bar{\omega}}{2}(x^*-\xi^*)} J_0\left(\frac{\bar{\omega}}{2M}(x^*-\xi^*)\right) d\xi^* \tag{22.2.48}$$

where

$$\bar{\omega} = \frac{2kM^2}{M^2-1} \tag{22.2.49}$$

and where the starred coordinates are dimensionless with respect to b. Equation (22.2.48) can be substituted into the pressure relationship (cf. p. 357 of Ref. 22.1)

$$\Delta\bar{p}_a(x^*) = -2\rho_\infty \frac{U}{b}\left(ik\bar{\Phi} + \frac{\partial\bar{\Phi}}{\partial x^*}\right)\Bigg|_{z^*=0^+} \tag{22.2.50}$$

and use of Eqs. (22.2.18) and (22.2.19) yields the desired values of the unsteady lift and pitching moment.

22.2.2 UNSTEADY THEORY FOR CASCADED AIRFOILS

22.2.2.1 Incompressible Flow

Several attempts were made to extend isolated unsteady theories to solve the unsteady cascade problem in the early 1950's, most notably the efforts of Lilley (Ref. 22.31), Sisto (Ref. 22.32) and Lane (Ref. 22.33). As with any early work on a difficult technical problem, these pioneering efforts were hampered by lack of precedent to serve as a mathematical guide, and by a lack of adequate and efficient computational equipment to cope with the need to account for a doubly-infinite array of airfoils in the flow field. In contrast to the isolated airfoil in potential flow, in which the reduced frequency was the only explicit parameter (for incompressible flow), the unsteady cascade analysis had the additional parametric influence of blade gap, leading edge locus stagger angle, and interblade phase angle. Nevertheless, the solutions obtained in the cited works represented valid approaches and the few available tabulated values clearly indicated the differences between cascades and isolated airfoils, and pointed up the need for additional work.

In the early 1960's Whitehead published his theoretical analysis of the incompressible unsteady cascade problem (Ref. 22.34), based largely on his earlier dissertation (Ref. 22.35). In it he used a standard vortex sheet approach similar to that described earlier (Section 22.2.1.1) in connection with the theory of Schwarz. However, the integral inversion technique of Söhngen has no counterpart in the cascade problem and Whitehead resorted to a matrix formulation and a subsequent matrix inversion technique. By virtue of an ingeneous use of the Multhopp cosine transformation he showed that a trapezoidal integration would yield exact results for certain key integrals, and an analytical removal of the leading edge logarithmic singularity produced a tractable result that was relatively easy to tabulate. In the following summary of Ref. 22.34 only a few of the key steps in Whitehead's derivation can be included, and an effort will be made to bridge the gap between these steps with verbal references to his report. Use will be made of the notation of the report throughout.

The cascade geometry is shown below in Fig. 22.2.2 in which c is the chord, s is the slant gap and ξ is the stagger angle of the leading edge locus relative to the vertical coordinate axis, which passes through the leading edge of the reference blade. In addition to the usual assumptions of two-dimensional, incompressible, inviscid potential flow past flat plate airfoils at zero incidence angle, it is further assumed that all blades vibrate with the same amplitude and with constant phase angle between the motions of any pair of adjacent blades.

To begin with, Whitehead assumes a vortex sheet distribution on the blades and defines the strength of one element of bound vorticity located at a distance x behind the leading edge of the reference blade to be $\gamma(x)e^{i\omega t}$ to account for periodic motions. If the motion of the upper adjacent blade (m = 1) leads the motion of the reference blade, then blade no. 1 has a corresponding element of vorticity of strength $\gamma(x + s \sin \xi, s \cos \xi)\, e^{i(\omega t+\beta)}$ located at the point $(x + s \sin \xi, s \cos \xi)$, and in general, for the m^{th} blade in the array we have $\gamma\, e^{i(\omega t+m\beta)}$ at $(x+ms \sin \xi, ms \cos \xi)$ which establishes the periodicity condition over the array of blades. Because the motion is assumed to be sinusoidal, any change in γ appears in the wake as free vorticity. As in the Schwarz theory, we can relate the elementary free vorticity $\epsilon(x_1,x)$ at x_1 in the wake to a bound vortex element at x by the formula

$$\epsilon(x_1,x) = -\frac{i\omega}{U}\gamma(x)e^{\frac{i\omega}{U}(x-x_1)} \qquad (22.2.51)$$

The total free vorticity at x_1 in the wake due to the entire bound vorticity sheet is obtained from an integration of Eq. (22.2.51),

$$\epsilon(x_1)e^{\frac{i\omega x_1}{U}} = -\frac{i\omega}{U}\int_0^{x_1}\gamma(x)e^{\frac{i\omega x}{U}}dx \qquad (22.2.52)$$

After differentiating this with respect to x_1 and rearranging, the result is

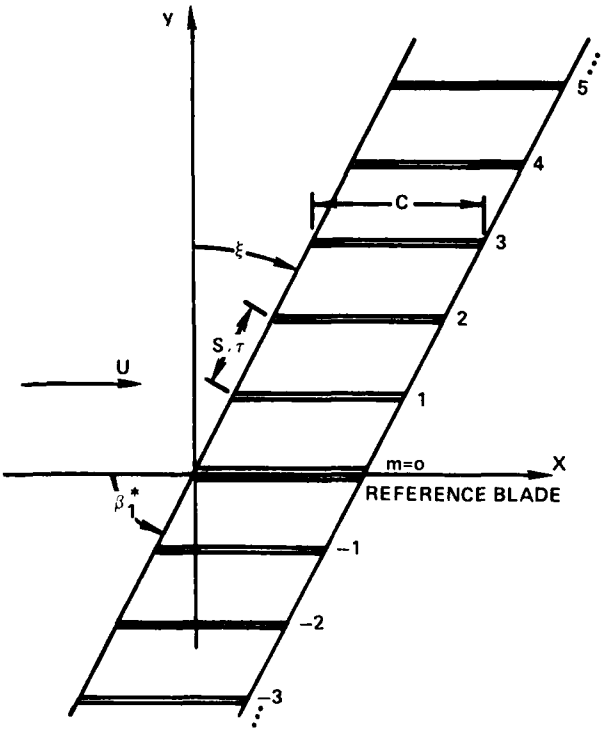

Fig. 22.2.2 Cascade Geometry

$$\frac{d\epsilon}{dx} + \frac{i\omega}{U}(\epsilon+\gamma)=0 \qquad (22.2.53)$$

which will be useful below.

Next the bound vorticity is related to the pressure difference across the blade. Since the theory is to be used in situationsin which the whole flow contains vorticity (i.e., the wake vorticity of adjacent blades) the velocity potential concept eannot be used. Instead we use the equation of motion in tne x-direction, linearized to read

$$\left(\frac{\partial}{\partial t} + U\frac{\partial}{\partial x}\right)\left(u e^{i\omega t}\right) = -\frac{1}{\rho}\frac{\partial p}{\partial x} \qquad (22.2.54)$$

where u is the horizontal perturbation velocity. When this equation is written for points just above (+) and just below (-) the plane of the airfoil and the difference is taken we have

$$\left(\frac{\partial}{\partial t}+U\frac{\partial}{\partial x}\right)\left\{(u_- - u_+)e^{i\omega t}\right\} = -\frac{1}{\rho}\frac{\partial}{\partial x}(p_- - p_+) \qquad (22.2.55)$$

but the difference between the perturbation velocity yields the total vorticity of the system,

$$u_- - u_+ = \gamma + \epsilon \qquad (22.2.56)$$

When this is substituted into Eq. (22.2.55) and manipulated the result is

$$-\frac{1}{\rho}\frac{\partial}{\partial x}(p_- - p_+) = U\left[\left\{\frac{i\omega}{U}(\gamma+\epsilon)+\frac{d\epsilon}{dx}\right\}+\frac{d\gamma}{dx}\right]e^{i\omega t} \qquad (22.2.57)$$

and substitution of Eq. (22.2.53) simplifies this to

$$-\frac{1}{\rho}\frac{\partial}{\partial x}(p_- - p_+) = U\frac{d\gamma}{dx}e^{i\omega t} \qquad (22.2.58)$$

This can be directly integrated to yield

$$p_- - p_+ = -\rho U\gamma e^{i\omega t} \qquad (22.2.59)$$

whereupon the lift and pitching moment (about the leading edge) are obtained by the further integration of Eq. (22.2.59),

$$F = -\rho U\int_0^c \gamma\,dx \qquad (22.2.60)$$

$$M = -\rho U\int_0^c \gamma x\,dx \qquad (22.2.61)$$

Note, however, that up to this point in the analysis the blade motion has not yet been prescribed, and γ is an unknown function of x.

The next step in the analysis is to relate the vorticity distribution γ to the motion-induced vertical velocity on the reference blade. We begin by postulating a single, staggered row of vortices, each one being located on a separate blade of the cascade, and each one at the same distance behind the leading edge of its respective blade. If the vortex on the reference blade at (x,0) has strength Γ_0, then the vortex on the m^{th} blade will have a strength

$$\Gamma_m = \Gamma_0 e^{im\beta} \qquad (22.2.62)$$

(assuming the existence of an interblade phase angle β), and will be located at

$$\left.\begin{aligned} x_m &= x + ms\sin\xi \\ y_m &= ms\cos\xi \end{aligned}\right\} \qquad (22.2.63)$$

For this one vortex Γ_m at (x_m, y_m) the velocity induced on the reference blade at $(\eta,0)$ is, by the Biot-Savart law,

$$v = \frac{\Gamma_m}{2\pi}\frac{\eta - x_m}{(\eta-x_m)^2 + y_m^2} \qquad (22.2.64)$$

Hence the velocity for the entire array of vortices is obtained from the doubly infinite sum

$$v = \frac{\Gamma_0}{2\pi}\sum_{m=-\infty}^{\infty}\frac{e^{im\beta}(\eta - x - ms\sin\xi)}{(\eta - x - ms\sin\xi)^2 + (ms\cos\xi)^2} \qquad (22.2.65)$$

or, symbolically,

$$v = \frac{\Gamma_0}{c}V(z) \qquad (22.2.66)$$

where $z = (\eta - x)/c$ and where

$$V(z) = \frac{1}{2\pi}\sum_{m=-\infty}^{\infty}\frac{e^{im\beta}\left(z - m\frac{s}{c}\sin\xi\right)}{\left(z - m\frac{s}{c}\sin\xi\right)^2 + \left(m\frac{s}{c}\cos\xi\right)^2} \qquad (22.2.67)$$

This can be summed, using the methods described on pp. 364-370 of Bromwich (Ref. 22.36) to yield the closed form result

$$V(z) = \frac{(a+ib)e^{-(\pi-\beta)z(a+ib)}}{4\sinh\left[\pi z(a+ib)\right]} + \frac{(a-ib)e^{(\pi-\beta)z(a-ib)}}{4\sinh\left[\pi z(a-ib)\right]} \qquad (22.2.68)$$

where

$$\left.\begin{aligned} a &= \frac{c}{s}\cos\xi \\ b &= \frac{c}{s}\sin\xi \end{aligned}\right\} \qquad (22.2.69)$$

There are some subtleties associated with the values of V for the end-point values of β, but Whitehead disposes of this problem by showing that the function V(z) will only appear as a difference in the subsequent steps.

Once the form of Eq. (22.2.66) has been established we can rewrite it for a similar row of elements of bound vorticity on the oscillating blades. Specifically, the normal velocity induced at a point $(\eta,0)$ by a set of bound vorticity elements $\gamma(x)e^{i(\omega t+m\beta)}$ is obtained by writing v'_γ in place of v and $\gamma(x)$ in place of Γ_o/c in Eq. (22.2.66)

$$v'_\gamma(\eta,x) = \gamma(x)\,V(\eta-x) \qquad (22.2.70)$$

(At this point in the analysis Whitehead assumes that x and y are now dimensionless quantities with respect to c.) The strength of an element of free vorticity at some point $(x_1,0)$ due to the element of bound vorticity at $(x,0)$ is given by Eq. (22.2.51) as

$$\epsilon(x_1,x) = -i\lambda\gamma(x)\,e^{i\lambda(x-x_1)} \qquad (22.2.71)$$

where λ is the reduced frequency relative to the full blade chord,

$$\lambda = \frac{c\omega}{U}\ \left(= 2k = \frac{2b\omega}{U}\right) \qquad (22.2.72)$$

The velocity induced at $(\eta,0)$ by a single element of this free vorticity is obtained, as in Eq. (22.2.70) by writing

$$v'_{\delta\epsilon}(\eta,x,x_1) = \epsilon(x_1,x)\,V(\eta-x_1) \qquad (22.2.73)$$

Now, for each element of bound vorticity $\gamma(x)$ at $(x,0)$ there is a sheet of free vorticity represented by $\epsilon(x_1,0)$ where the elements are located at points $(x_1,0)$ extending over the range $x \le x_1 < \infty$ and each element of ϵ is caused by the element γ. Thus the velocity induced at $(\eta,0)$ by all the free vorticity associated with $\gamma(x)$ is obtained by integrating Eq. (22.2.73) over all x_1 in the range $x \le x_1 < \infty$,

$$v'_\epsilon(\eta,x) = \int_x^\infty \epsilon(x_1,x)\,V(\eta-x_1)\,dx_1 \qquad (22.2.74)$$

The sum of Eqs. (22.2.70) and (22.2.74) yields the velocity induced at $(\eta,0)$ as a result of a single element of bound vorticity and its associated free vortex sheet. However, as Whitehead points out, when $\beta = 0$ the integral of Eq. (22.2.74) remains finite at the upper limit and the integral fails to converge. If the assumption is made that the system started from rest, then the total vorticity on each blade and its wake is zero, or

$$\int_0^\infty (\gamma+\epsilon)\,dx = 0 \qquad (22.2.75)$$

and if this integral is rewritten for a single bound vortex element and is multiplied by the limiting value $V(-\infty)$ and subtracted from the sum of Eqs. (22.2.70) and (22.2.74), a convergent result is obtained. Ultimately this can be written in the form

$$v'(\eta,x) = \gamma(x)\,K(x-\eta) \qquad (22.2.76)$$

where K is the kernel function

$$K(z) = V(-z) - V(-\infty)$$
$$-i\lambda e^{i\lambda z}\int_z^\infty \left[V(-z_1) - V(-\infty)\right] e^{-i\lambda z_1}\,dz_1 \qquad (22.2.77)$$

Finally, the velocity at η due to all vorticity elements is given by the integral of Eq. (22.2.76) over the blade chord,

$$v(\eta) = \int_0^1 v'(\eta,x)\,dx = \int_0^1 K(x-\eta)\,\gamma(x)\,dx \qquad (22.2.78)$$

As in previous analyses of this sort, $v(\eta)$ is prescribed by the motion and is known, and $\gamma(x)$, which is needed for load calculations, is unknown.

This is the essence of the physical portion of Whitehead's analysis. Three possible vertical velocities, associated with vertical translation, pitch about the blade leading edge, and an imposed sinusoidal vertical gust velocity imbedded in the free stream, are postulated as

$$v = q + \alpha U(1+i\lambda\eta) - w e^{-i\lambda\eta} \qquad (22.2.79)$$

An influence function approach, in which each component of vorticity is defined as the vorticity per unit vertical velocity amplitude, yields the total strength of the bound vorticity sheet as

$$\gamma = q\gamma_q + \alpha U\gamma_\alpha - w\gamma_w \qquad (22.2.80)$$

where the γ's are solutions of the following three integral equations, expressed in a single matrix equation as

$$\int_0^1 \left[\gamma_q, \gamma_\alpha, \gamma_w\right] K(x-\eta)\,dx = \qquad (22.2.81)$$
$$= \left[1, (1+i\lambda\eta), e^{-i\lambda\eta}\right]$$

where the notation $[\cdots]$ represents a 1 x 3 row matrix.

Space does not permit a detailed account of Whitehead's solution procedure. In essence, he used a Multhopp transformation for the two variables, $x = \frac{1}{2}(1 - \cos\theta)$ and $\eta = \frac{1}{2}(1 - \cos\phi)$ over n stations along the blade chord, and found that the trapezoidal rule yielded exact results for several of the integral equations in the transformed notation. Although the process was tedious and painstaking, the inversion of the integral equations written in matrix form was relatively straightforward, the only exception being the leading edge logarithmic singularity,

which was analytically accounted for. Specifically, Eq. (22.2.81) was written in matrix form as

$$A\Gamma = B \qquad (22.2.82)$$

where A is an n x n matrix of kernel function elements, Γ is an n x 3 matrix of bound vorticity elements, and B is also an n x 3 matrix representing the right hand side of Eq. (22.2.81). Here it is seen that A and B are known and Γ is unknown, and the report details the steps necessary to yield the formal solution

$$\Gamma = A^{-1} B \qquad (22.2.83)$$

Substitution of this solution for each component of Γ into Eqs. (22.2.60) and (22.2.61) rewritten in matrix form as

$$C = -\frac{1}{\pi} X\Gamma = -\frac{1}{\pi} X A^{-1} B \qquad (22.2.84)$$

yields the desired values of normal force coefficient and moment coefficient for each component of imposed vertical velocity. The 2 x n matrix X in Eq. (22.2.84) contains a factor 1 in its first row and a sequence of moment arm weighting functions in its second row such that the C matrix consists of normal force components in its first row and moment components in its second row.

$$C = \begin{bmatrix} C_{F_q} & C_{F_\alpha} & C_{F_w} \\ C_{M_q} & C_{M_\alpha} & C_{M_w} \end{bmatrix} \qquad (22.2.85)$$

(It should be noted that the force and moment for vertical translation are defined per unit vertical velocity rather than the customary vertical displacement. This is discussed further by Whitehead in Ref. 22.34.)

Whitehead's report contains tabulated values of all of his coefficients for a variety of parameter values. Although it is not the purpose of this document to examine these tabulations in detail, it is instructive to note the effect of cascading on two of the unsteady coefficients, the unsteady force due to plunging, C_{F_q}, and the unsteady moment due to pitch, C_{M_α}. These two coefficients are important determinants of the flow of energy in single degree of motion oscillations, as will be seen presently. In Figs. 22.2.3 and 22.2.4 are found phase plane plots of C_{F_q} and C_{M_α}, respectively; i.e., the real part of each quantity is plotted along the abscissa and the imaginary part along the ordinate. Both plots are for s/c = 1 and ξ = 60 deg, and each plot contains three connected curves for λ = 0.5, 1.0, and 2.0 (κ = 0.25, 0.5, and 1.0). On each curve the point β = 0 is noted, and subsequent points, in the direction of the arrows, are

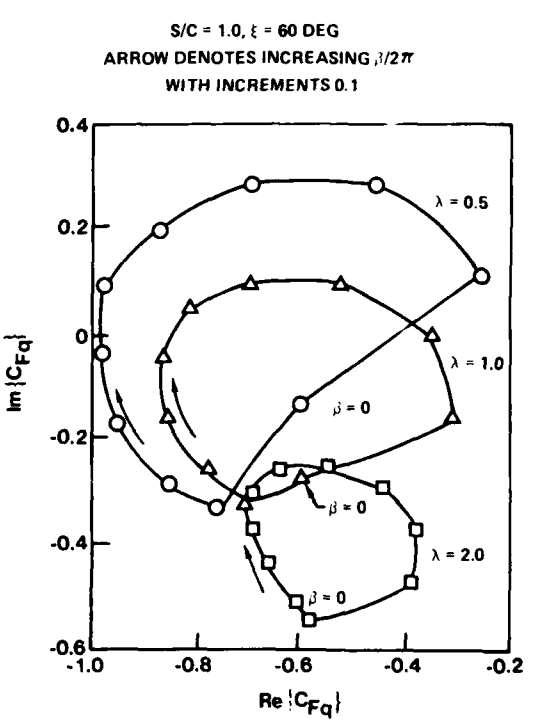

Fig. 22.2.3 Phase Plane Diagram of Lift due to Plunge

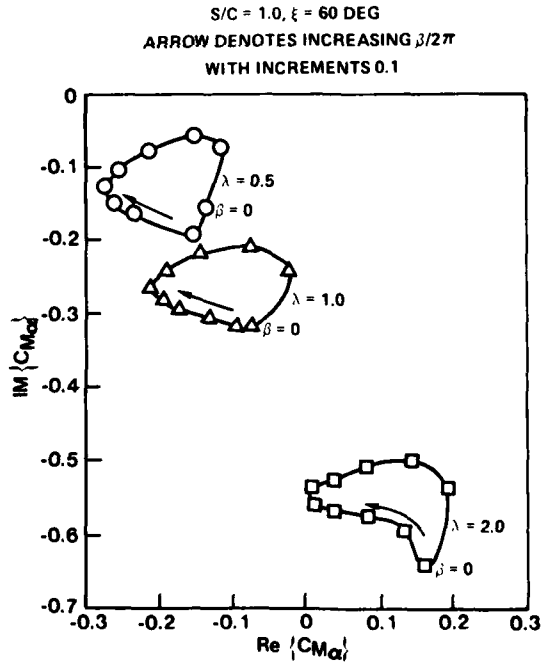

Fig. 22.2.4 Phase Plane Diagram of Moment due to Pitch

for incremental increases of $\beta/2\pi = 0.1$. A dominant effect in each plot is that of reduced frequency, but this is not particularly surprising since comparable changes occur for isolated airfoils. What is of importance here is the large change that occurs from point to point as interblade phase angle is varied. This is uniquely associated with the presence of neighboring blades, and is indicative of the importance of these cascade parameters on the ultimate determination of blade stability.

22.2.2.2 Compressible Subsonic Flow

Several authors have attacked the problem of cascaded flat plate airfoils oscillating in a compressible stream (Refs. 22.37-22.41 to name a few). In almost every case the acceleration potential method of Possio was extended to account for the presence of neighboring blades. In Ref. 22.37 the present author extended the method to the point of writing the formal solution in integral equation form but was unable to obtain numerical values because of the limitations of the available computing equipment in the mid-1950's. Similarly, Lane and Friedman employed a Fourier transform approach but they too were stymied by inadequate computer facilities to a few calculations for an unstaggered cascade oscillating at an interblade phase angle of $\sigma = 180$ deg. This case was specifically chosen by the authors because it represented the cascade equivalent of compressible wind tunnel wall interference (Ref. 22.42), and they were able to show good agreement with previous theory for the few cases they calculated.

The three later analyses concentrate primarily on the acoustical properties of the oscillating cascade in a compressible flow. This is especially true of the Kaji analysis (Ref. 22.40) in which the results are confined to an equation for the acceleration potential function and to plots of acoustical transmission coefficients. More to the point are the analyses of Whitehead (Ref. 22.39) and Smith (Ref. 22.41) who both seek primarily for acoustical answers, but who also discuss the results for unsteady lift and moment. Of the two it appears that the Smith calculation procedure is somewhat more straightforward and easier to implement. Unfortunately, although the analysis is completely general, the only coefficients tabulated are either for incompressible flow or for zero stagger with antiphase motion, in both instances for comparison of Smith's limiting cases with the work of previous authors.

In retrospect, much of this subsonic compressible work has remained unused by designers. As stated earlier (Section 22.1.3) the most critical design problem appears to be supersonic flutter, which cannot be attacked by the methods of this section. Another almost equally critical problem is that of part speed flutter under loaded conditions. Although the flow in this problem is often in the high subsonic range, the additional characteristic of the problem is non-zero blade load, with the problem becoming more acute as the surge line is approached. This implies blades with non-zero incidence angle, non-zero camber angle, and non-zero thickness distribution, all of which are specifically excluded by the assumptions of the analyses in Refs. 22.37-22.41. Therefore, in view of the diminished relevance of these analyses to the designer's needs, the reader will be spared any detailed overview of these theories, and only a cursory description of the form of the final solution will be given at the end of this section.

One additional analytical study to examine the effects of subsonic compressible flow past a cascade of oscillating airfoils bears mentioning (Ref. 22.43). In it Verdon and his coauthors formulate a set of basic equations which govern the subsonic flow in a single extended blade passage of a high-deflection, two-dimensional, oscillating cascade. This derivation is based on a perturbation expansion of the velocity potential leading to a nonlinear boundary value problem for the zeroth order or steady potential, and a linear, time-independent, variable coefficient boundary value problem for the first order or unsteady potential. In lieu of explicit boundary conditions at finite distances upstream and downstream of the blade row, analytic far field solutions are determined which can be matched to near field numerical solutions. The variable coefficients in the unsteady boundary value problem depend on the steady flow potential and represent the effects of finite steady-state loading on the unsteady aerodynamics. At present the numerical procedures for solving the steady and unsteady boundary value problems for realistic blade profiles are still under development. However, unsteady predictions, based on this model, have been found to be in excellent agreement with predictions based on Smith's solution (Ref. 22.41) for subresonant and superresonant motions (cf. Section 22.2.2.4) of flat plate cascades at zero mean incidence relative to a uniform stream.

Finally, it is instructive to look at the form of the flat plate cascade integral equation, for comparison with isolated airfoil results, and for use in explaining the significance of the acoustical resonance phenomenon, described later in Section 22.2.2.4. One version of this solution, taken from Ref. 22.37, is

$$\bar{w}(x) = -\frac{1}{4\rho V\beta}\int_{-b}^{b} \Delta\bar{p}(x_0)\left[K_0(M,x-x_0) + K_1(M,x-x_0,\tau)\right]dx_0 \tag{22.2.86}$$

where $\beta = \sqrt{1-M^2}$, τ is the slant gap between blades, $\bar{w}(x)$ is the known prescribed downwash on the blade at x, and $\Delta\bar{p}(x_0)$ is the unknown pressure difference at x_0. In this equation

$$K_0(M,x-x_0) = -e^{\frac{-i\omega}{V}(x-x_0)} \lim_{\eta\to 0}\int_{-\infty}^{x-x_0} e^{\frac{i\omega\xi}{V\beta^2}} \times\left(\frac{\partial^2}{\partial\xi^2} + \frac{\omega^2}{a^2\beta^2}\right) H_0^{(2)}\left(\frac{\omega r_0}{a\beta^2}\right) d\xi \tag{22.2.87}$$

is the Possio kernel function for an isolated airfoil (cf. a different form of this function in Eq. (22.2.42)) and where

$$K_1(M,x-x_0,\tau) = -e^{\frac{-i\omega}{V}(x-x_0)} \lim_{\eta\to 0} \int_{-\infty}^{x-x_0} e^{\frac{i\omega\xi}{V\beta^2}} \times \sum_{\substack{n=-\infty \\ n\neq 0}}^{\infty} e^{2i\pi Rn} \left(\frac{\partial^2}{\partial\xi^2} + \frac{\omega^2}{a^2\beta^2}\right) H_0^{(2)}\left(\frac{\omega r}{a\beta^2}\right) d\xi \qquad (22.2.88)$$

is the kernel function associated with the cascaded blades. In these equations,

$$r = \sqrt{(\xi - n\tau\sin\theta)^2 + \beta^2(\eta - n\tau\cos\theta)^2} \qquad (22.2.89)$$

$$r_0 = \sqrt{\xi^2 + \beta^2\eta^2} \qquad (22.2.90)$$

$$R = \frac{\sigma}{\pi} - \frac{\omega M}{2\pi a\beta^2}\tau\sin\theta \qquad (22.2.91)$$

where, in addition, θ is the stagger angle and σ is the interblade phase angle.

It was found in Ref. 22.37 that for certain values of the cascade parameters (to be discussed in Section 22.2.2.4) the cascade kernel function K_1 became unbounded. This was determined upon integrating Eq. (22.2.88) by parts, applying some well-known Hankel function identities, and taking the limit as $\eta \to 0$. The resulting series of Hankel functions were examined for convergence and were found to diverge at these resonance points. The implications of this series divergence is quite profound, as can be seen from an examination of Eq. (22.2.86). By virtue of the assumption of small displacements, $\bar{w}(x)$ must represent a bounded amplitude, and experience has shown that K_0 is always bounded. If K_1 is unbounded for certain values of the cascade parameters, then the only way this equation can be satisfied is for $\Delta\bar{p}$ to vanish identically. However, by Eqs. (22.2.18) and (22.2.19), both the unsteady lift and moment must also vanish, and hence the naturally occurring aerodynamic damping, associated with the quadrature components of these quantities, will also vanish. Under these conditions, if an external oscillatory energy source imparts energy to the blades at a frequency at or near the natural blade frequency, there is no aerodynamic dissipation of this energy. Consequently the amplitude of the blade motion is limited only by the structural damping of the system, and under conditions of extreme excitation, such as an integral order encounter (cf. Fig. 22.1.14), large and damaging blade response can occur.

22.2.2.3 Compressible Supersonic Flow

Supersonic unsteady aerodynamics of multiblade systems was first discussed by Lane in 1957 (Ref.22.44) who analyzed the problem in which the axial velocity into the blade row is supersonic. As seen in the sketch of Fig. 22.2.5, all velocities relative to the plane of the leading edge are supersonic, and accordingly this is referred to as the supersonic leading edge locus condition. Although such a configuration

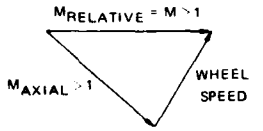

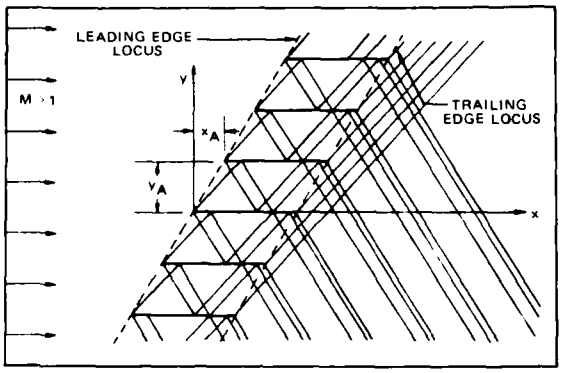

Fig. 22.2.5 Supersonic Cascade with Supersonic Leading Edge Locus

has several reflected waves within any blade passage, no disturbances exist upstream of the blade passages and further, the unsteady wakes cannot influence the flow adjacent to neighboring blade surfaces. Hence, this problem was amenable to Laplace transform techniques, as demonstrated by Lane in his paper. However, it soon became evident that this solution was of academic interest only because no practical high-speed design, either within the current state of the art at that time or for the foreseeable future, would have a supersonic axial through flow. Instead, all high speed engines were to be configured with a subsonic axial flow and a supersonic relative flow, as pictured in Fig. 22.1.5 above and repeated in Fig. 22.2.6 for use in the analytical description that follows. In this case, referred to as the subsonic leading edge locus condition, unsteady disturbances exist infinitely far upstream of each blade passage and the unsteady wakes influence the flow field adjacent to the lower surfaces of the blades above them.

The first practical solution to this problem was obtained by Verdon in the late 1960's and subsequently published as Ref. 22.11 in 1973. This was a numerical solution for a cascade consisting of a finite number of blades. It was found that in such a finite cascade approximation the number of blades in the cascade had to be chosen sufficiently large so that a limiting behavior for the aerodynamic

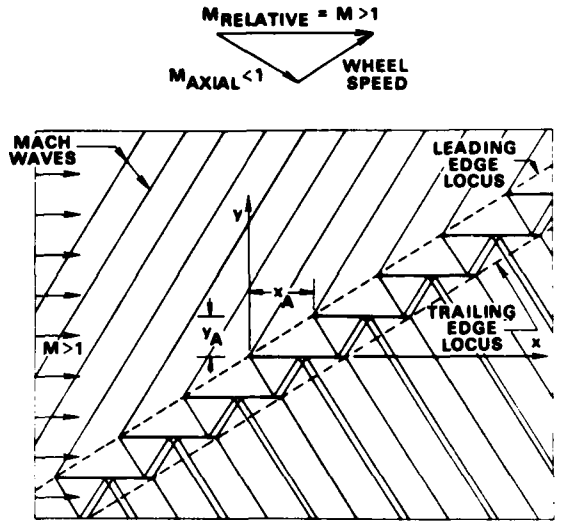

Fig. 22.2.6 Supersonic Cascade with Subsonic Leading Edge Locus

forces and moments could be estimated. It was then assumed that these limit values were representative of the baldes of an infinite array. However, there were no mathematical proofs to validate this reasoning, and further, it was recognized, by virtue of the slow convergence of the series in the solution, that the numerical process was inefficient computationally. In addition, its use did not reveal the physics of the phenomena as well as an analytic solution would. Nevertheless, it was shown by Mikolajczak, et al (Ref. 22.10) and by Snyder and Commerford (Ref. 22.45) that the results of this finite cascade approximation yielded predictions which are in agreement with rotor fan experience.

Despite the apparent success of this method it was seen that, in addition to the shortcomings cited above, the necessity to build a solution by successively adding blades to the cascade yielded a procedure that lacked computational efficiency. Consequently, an improved "closed form" solution was developed by Verdon and McCune (Ref. 22.12) which eliminated most of the objections raised by the previous solution, but which largely confirmed the approximations to be valid. This method is described in summary form below.

In this discussion all quantities are dimensionless. The fluid is assumed to be an inviscid, nonconducting, ideal gas with constant specific heats, and the flow is assumed to be irrotational and isentropic. Disturbances in the supersonic stream are caused by an infinite array of thin, slightly cambered, lifting surfaces or blades which are performing rapid harmonic motions of small amplitude. These motions are generally normal to the blade chord lines which are aligned parallel to the free stream direction. Based on these flow field assumptions, the differential equation governing the disturbed flow field is

$$\frac{\partial^2 \psi}{\partial y^2} - \mu^2 \frac{\partial^2 \psi}{\partial x^2} - \mu^2 k^2 \psi = 0 \qquad (22.2.92)$$

where

$$\left.\begin{aligned} \mu^2 &= M^2 - 1 \\ k &= \frac{\omega M}{\mu^2} \end{aligned}\right\} \qquad (22.2.93)$$

and

$$\psi(x, y) = \phi(x, y, t) e^{i(kMx - \omega t)} \qquad (22.2.94)$$

Here M is the free stream Mach number, ω is the reduced frequency of the blade motion (based on full chord), ψ is the modified velocity potential of the unsteady flowfield, and ϕ is the velocity potential defined in the usual manner. The pressure, p, at a point in the flowfield is given by

$$\begin{aligned} (p - p_\infty)\, e^{i(kMx - \omega t)} &= P(x,y) \\ &= -2\left(\frac{\partial}{\partial x} - \frac{i\omega}{\mu^2}\right) \psi(x,y) \end{aligned} \qquad (22.2.95)$$

where p_∞ is the freestream pressure and P(x,y) is the modified relative pressure. In addition, a blade-to-blade periodicity condition

$$\psi(x + nx_A, ny_A)\, e^{-in\Omega} = \psi(x,y), \qquad n = 0, \pm 1, \pm 2, \ldots \qquad (22.2.96)$$

must be satisfied, where

$$\Omega = \sigma + kMx_A \qquad (22.2.97)$$

and where σ is the interblade phase angle. With this periodicity condition it is sufficient to determine ψ in a single extended blade passage region, defined in Ref. 22.12 by $|x| < \infty$, $0 < y < y_A$. The boundary conditions applied to the upper and lower boundaries of this region are:

1. Modified potential and normal velocity components are continuous in y along the upstream extensions of the blade chordlines.

2. Normal velocity component is continuous across blade and wake surfaces.

3. Flow must be tangent to blade surfaces.

4. Pressure must be continuous across wake surfaces.

Furthermore, there can be no upstream propagation of disturbances in supersonic flow, unsteady disturbances must be bounded at an infinite distance from their origin, disturbance waves impinging on blade surfaces must be reflected, and disturbance waves impinging on wake surfaces must be transmitted through the wake.

In the analysis of Ref. 22.12 the expression for the modified potential in the reference region

is developed in terms of component potentials which account for disturbances originating from different sources. Component potential functions are then superposed to obtain the complete expression for the modified potential which satisfies the conditions listed above. There then follows in Ref. 22.12 a long and rather complicated analysis in which the isolated airfoil solution of Miles (Ref. 22.30) is generalized to represent the potential due to the reference blade and wake, and in which the supersonic leading edge locus solution of Lane (Ref. 22.44) is generalized to account for interference effects of neighboring blades. Although the complete solution is too involved to be repeated here, its salient features will now be reviewed.

To begin with, two cascade geometries are considered, as shown in Fig. 22.2.7. In the upper part, referred to as cascade A, a parameter defined as

$$D = x_A + \mu y_A > 1$$

and the lower leading edge Mach wave from any blade passes behind the lower blades. Here there is a single Mach wave intersection on each blade, denoted by point 1 on the pressure surface of the reference blade. In the lower part of the figure, referred to as cascade B, we have

$$D = x_A + \mu y_A < 1 < x_A + 3\mu y_A \qquad (22.2.98)$$

and the leading edge Mach waves are reflected once by the adjacent blades below. Here there are three Mach wave intersections on each blade, denoted by points 1 and 2 on the pressure surface and by point 3 on the suction surface of the reference blade. Discontinuities occur in the reference blade pressure distributions at these points.

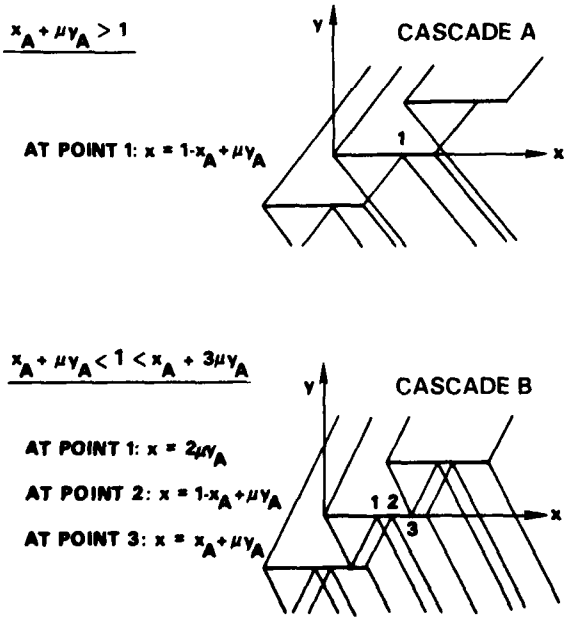

Fig. 22.2.7 Two Supersonic Cascade Flow Geometries of Current Interest

Verdon chooses to begin his analysis with the construction of the modified potential for cascade B, and shows that the result for the simpler flow geometry of cascade A is readily obtained by neglecting the terms for the additional reflections. Without going into mathematical detail, the analysis proceeds as follows. The Miles modified normal velocity distribution, $V(x,ny_A)$ is replaced by the disturbance function distributions $A_n(x)$, which are not known a priori, but are determined from relations derived from the boundary conditions on the unsteady flow. Five different potential functions, $\psi_i(x,y)$, $i = 1, 2, \ldots, 5$, can be written to represent the various disturbance sources, including those originating on the reference blade and its wake, and the adjacent upper blade and its wake. These potential functions also account for those disturbance sources which cause a propagation into the reference passage from both upstream and downstream locations. Each of the five is an integral expression, typified by that for the fourth component potential,

$$\mu\psi_4(x,y) = -\sum_{n=-\infty}^{-1} \int_{1+\mu n y_A}^{\infty} A_n(\xi)\, I^{-}_{0,n}(x-\xi,y)\,d\xi$$

$$-\sum_{n=-\infty}^{-1} \int_{1+\mu n y_A}^{1+B+\mu n y_A} A_n(\xi)\, I^{+}_{0,2-n}(x-\xi,y)\,d\xi \qquad (0<y<y_A) \qquad (22.2.99)$$

where the influence functions, $I^{\pm}_{0,n}$, are algebraic combinations of Bessel functions and unit step functions. (A complete definition of these quantities is found in Ref. 22.12.) Then the modified potential distribution in the reference passage region is obtained by a summation of the component terms,

$$\psi(x,y) = \sum_{i=1}^{5} \psi_i(x,y) \qquad 0<y<y_A \qquad (22.2.100)$$

which satisfies all of the boundary conditions cited above. Verdon then uses the flow tangency and pressure continuity conditions and specifies an unknown disturbance function distribution, $A(x)$, which now appears in the several integrals on the right hand side of Eq. (22.2.100). (This function for the reference blade is obtained from each of the more general terms, $A_n(x)$, on the nth blade by virtue of the blade motion periodicity condition, (Eq. 22.2.96) which involves the interblade phase angle, σ.)

Ultimately, all of this analysis must be directed toward computing the unsteady load on the reference blade, and to accomplish this Eq. (22.2.100) is substituted into Eq. (22.2.95) whereupon the reference blade pressure distribution can be expressed in terms of several integrals and summations of the unknown disturbance function, $A(x)$. This is determined by using the boundary conditions of flow

tangency at the upper surface of the reference blade,

$$A(x) = V(x,0) - \int_0^{x_A - \mu y_A} A(\xi) K(x-\xi)\, d\xi \qquad (22.2.101)$$
$$(0 \le x \le 1)$$

and of continuity of pressure across the reference wake,

$$A(x) - \int_1^x A(\xi) K_{0,0}(x-\xi)\, d\xi = F(x) - G\left[A(x), x\right] \qquad (22.2.102)$$
$$(x > 1)$$

where $K(x)$ is a semi-infinite series involving Bessel functions, $V(x,o)$ is the prescribed vertical velocity on the airfoil surface due to blade motion, and where F and G are functionals defined by Verdon in Ref. 22.12. For $0 \le x \le x_A - \mu y_A$ Eq. (22.2.102) is a Fredholm integral equation with unknown function $A(x)$. The solutions of these equations were obtained numerically. Substitution into the potential function equations and thence into Eq. (22.2.101) yields the pressure, and subsequent integrals of $P(x,y)$ yield the unsteady normal force and moment on the reference blade.

It is beyond both the scope and the purpose of this chapter to go any deeper into the details of this theory, which is adequately covered in Ref. 22.12. However, it is instructive to look at some of the results of the theory and to examine the implications of these results. To this end, consider Fig. 22.2.8,

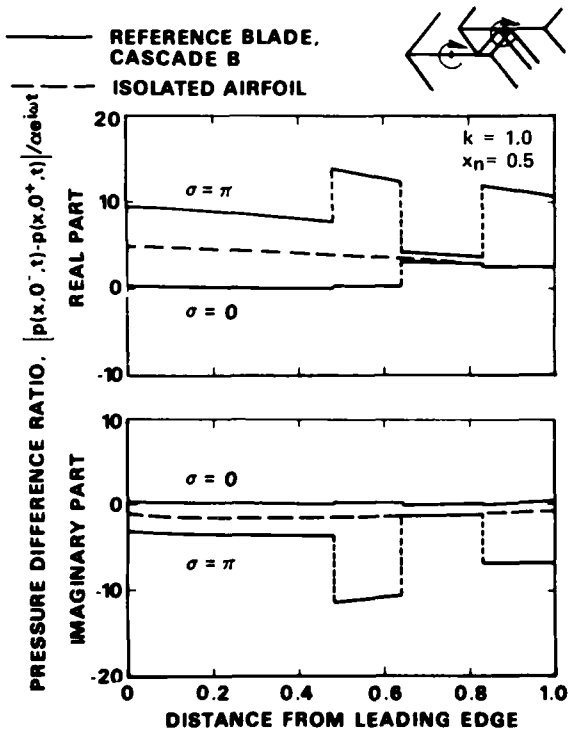

Fig. 22.2.8 Pressure Difference Distributions for Pitching Motions of Cascade B and Isolated Airfoil

in which the real and imaginary parts of the unsteady chordwise pressure difference distribution due to pitch are plotted for cascade B (cf. Fig. 22.2.7). The results for two interblade phase angles, $\sigma = o$ and $\sigma = \pi$, representing in phase and antiphase motions of adjacent blades, are presented here, and are compared to the results from isolated airfoil theory (e.g., Ref. 22.29 or 22.30). The several discontinuities that occur in the cascade results are directly related to the various primary and reflected waves impinging on the reference blade. This is discussed in detail in Ref. 22.12. It is clear that significant differences exist between isolated airfoil theory and cascade theory, and this is borne out in an examination of the predicted stability of the blade row.

It will be shown presently (cf. Section 22.3.1) that a convenient measure of blade stability can be obtained from the exchange of energy between the blade and the surrounding airstream (Ref. 22.8). For single-degree-of-freedom pitching motions of the supersonic cascade the work done by the airstream over one cycle of blade motion is

$$W_{\text{per cycle}} = \pi \omega \alpha \, \text{Im}\left\{C_M\right\} \qquad (22.2.103)$$

where the moment coefficient is obtained by direct integration of the chordwise pressure difference distribution,

$$C_M e^{i\omega t} = -\int_0^1 (x - x_n)\left[p(x,0^-) - p(x,0^+)\right] dx \qquad (22.2.104)$$

For positive work per cycle the flow of energy is from the airstream into the airfoil. Hence, from Eq. (22.2.103) $\text{Im}\left\{C_m\right\} > 0$ implies instability. The usefulness of this concept is illustrated in Figs. 22.2.9 and 22.2.10 in which moment phase plane diagrams are presented for cascades A and B, respectively. Each continuous curve is for a specific value of k, and the points along each curve denote variations in interblade phase angle. Also included in each diagram is a set of comparable values of C_m for an isolated airfoil.

It is seen from both figures that an increase in k is beneficial in stabilizing the system. However, it is also seen that use of isolated airfoil theory is significantly unconservative, that a dominant stability parameter is σ, and that changes in blade-to-blade interference strongly affect the stability of the system (compare cascade A with cascade B). In general, unstable cascade pitching motions are possible over a broad range of frequencies and interblade phase angles, and experience has shown that these parameter ranges are relevant to current state-of-the-art turbomachines (Ref. 22.10). This aerodynamic theory together with the coupled blade-disk-shroud stability theory of Ref. 22.8 (to be discussed in Section 22.3.2) has provided the designer with an essential tool to avoid serious rotor blade instabilities within the flight envelope of modern aircraft.

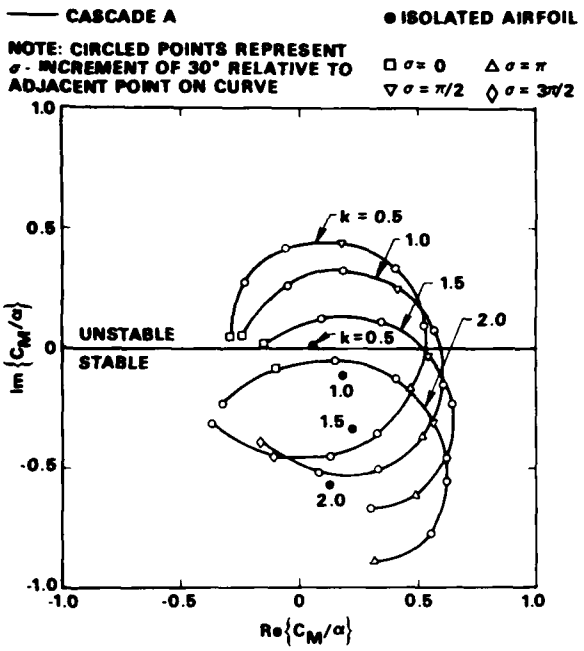

Fig. 22.2.9 Phase Plane Diagram of Moment due to Pitch for Cascade A and Isolated Airfoil

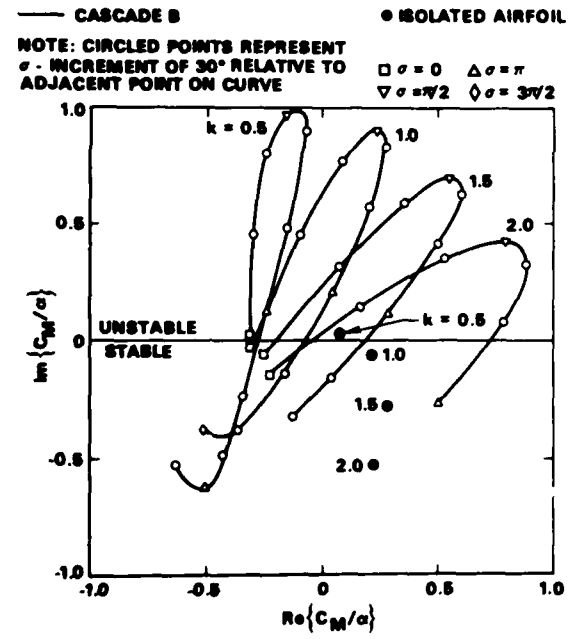

Fig. 22.2.10 Phase Plane Diagram of Moment due to Pitch for Cascade B and Isolated Airfoil

It should be noted that the phase plane diagrams in Figs. 22.2.9 and 22.2.10 appear to be incomplete. As noted in Ref. 22.12, this was related to the failure of the wake iteration procedure to converge for certain combinations of the cascade parameters. The condition for this convergence failure is referred to as "acoustical resonance" and is discussed in the next section. At this writing, the convergence difficulties have been overcome and solutions have now been obtained over the missing values of σ (Ref. 22.46), excluding the immediate neighborhood of the resonance points themselves.

In closing this section it should be noted that, commensurate with the importance of this problem, a large number of investigators have worked on it, using a variety of techniques and with various constraints on their parameter ranges (e.g. Kurosaka in Ref. 22.47 and Platzer in Ref. 22.48). However, it is believed that Verdon's work is the most complete, and this factor governed its choice for this chapter.

22.2.2.4 Acoustical Resonance

The implications of the acoustical resonance phenomenon, in terms of the vanishing of unsteady aerodynamic damping for subsonic compressible flow, has already been discussed in Section 22.2.2.2. Its effect on the convergence of solutions for supersonic flow was noted in the previous section. The analysis of the present section will be restricted only to the evaluation of the specific flow and configuration parameter values which lead to resonance, and will be based strictly on the geometric construction of the phenomenon.

First consider the cascade geometry of Fig. 22.2.11, which has an approach velocity, V, at zero incidence in the relative frame of reference. The object will be to determine the conditions under which a signal emanating from point O on the reference blade will travel to either point P or point Q on the adjacent blades in time to be in phase with the production of the same signal on the neighboring blade. The line connecting points Q, O, and P must be parallel to the leading edge locus.

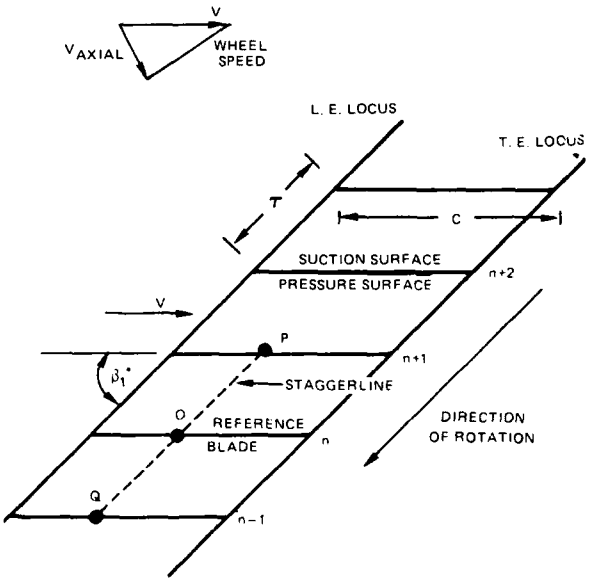

Fig. 22.2.11 Cascade Geometry for Resonance Calculations

and will be referred to as a stagger line. The signal will be assumed to be propagated outward as a cylindrical wave from O at the speed of sound, a, and returned to either point P or Q as the vector sum of a and V. The resonance condition will be satisfied when the time required to propagate the signal along the stagger line to a neighboring blade is equal to the time lag between the motions of adjacent blades. The latter is concerned with the interblade phase angle, σ, which will be defined here to be positive for blade n leading blade n-1 (forward traveling wave).

Assume all blades to be executing an unsteady motion at frequency ω, and assume further that blade n performs this motion before blade n-1 so σ is a positive number. The time lag between the motions of blades n and n-1 will be any of the following quantities,

$$t_{L(+)} = \frac{\sigma}{\omega}, \frac{2\pi+\sigma}{\omega}, \ldots, \frac{2\pi\nu+\sigma}{\omega} \qquad (22.2.105)$$

$$(\nu = 0,1,2,\ldots.)$$

depending on the harmonic being considered. The time lag between the motions of blades n and n+1 will be

$$t_{L(-)} = \frac{2\pi-\sigma}{\omega}, \frac{4\pi-\sigma}{\omega}, \ldots, \frac{2\pi\nu-\sigma}{\omega}$$

$$(\nu = 1,2,3\ldots.) \qquad (22.2.106)$$

(The plus and minus subscripts have no bearing on the algebraic signs and are merely used to designate the apparent direction of propagation, with (+) associated with propagation in the direction of rotation.)

To determine the time of propgation, t_p, first consider Fig. 22.2.12. This diagram in velocity coordinates shows a sonic circle centered about the point O on the reference blade, and shows several possible vector constructs, all of which terminate on the stagger line. Thus, for example, propagation from point O to point P in Fig. 22.2.11 could take place by virtue of the vector sum of the sonic velocity $\overline{OC}$ = a and the free stream velocity $\overline{CM}$ = V. In this case a propagation velocity $\overline{OM} = V_P$ would carry the signal from point O on the reference blade to point P on the upper adjacent blade and would be associated with the time lag of Eq. (22.2.106). To reduce the apparent complexity of this situation, two specific cases will be extracted from Fig. 22.2.12 and will be treated separately.

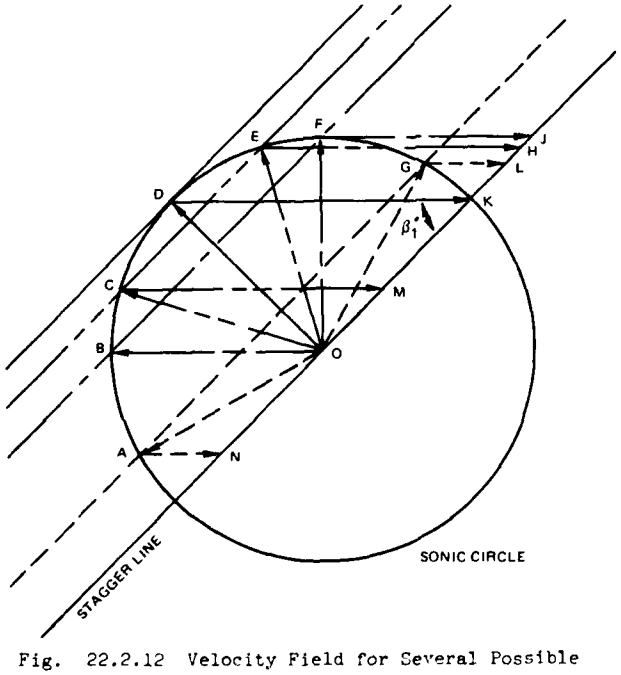

Fig. 22.2.12 Velocity Field for Several Possible Resonance Conditions

First consider the case of subsonic relative flow, shown in Fig. 22.2.13, in which V < a. The two possible propagation velocities have been subscripted in accordance with the direction of propagation and are consistent with the time lag notation used earlier. (Note that these are not physical velocities so the propagation velocity, V_P, can be greater than a.) Use of the law of cosines on triangle OAN yields

$$a^2 = V_{P(+)}^2 + V^2 - 2V V_{P(+)} \cos(\pi - \beta_1^*) \qquad (22.2.107)$$

and after some algebraic manipulations it can be shown that

$$V_{P(+)} = \sqrt{a^2 - V^2 \sin^2\beta_1^*} - V\cos\beta_1^* \qquad (22.2.108)$$

for propagation in the direction of rotation. Similarly, for triangle OGL,

$$V_{P(-)} = \sqrt{a^2 - V^2 \sin^2\beta_1^*} + V\cos\beta_1^* \qquad (22.2.109)$$

The time required for the signal to propagate from point O to point Q will be

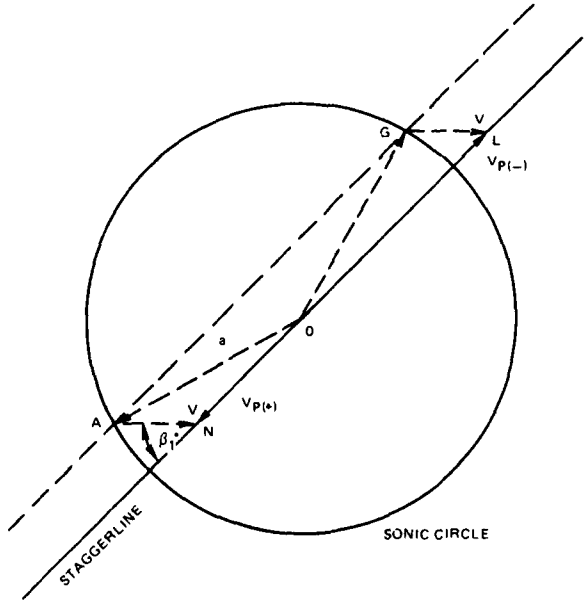

Fig. 22.2.13 Velocity Field for Subsonic Flow

$$t_{P(+)} = \tau / V_{P(+)} \qquad (22.2.110)$$

and similarly the time of propagation from 0 to P will be

$$t_{P(-)} = \tau / V_{P(-)} \qquad (22.2.111)$$

The resonance condition occurs when propagation time equals lag time, and after equating $t_{P(+)} = t_{L(+)}$ and $t_{P(-)} = t_{L(-)}$ and performing some intermediate steps, a general formula for resonance can be written as

$$\left.\begin{aligned} &2\pi\nu \pm \sigma = \frac{2kM(\tau/c)}{\sqrt{1-M^2\sin^2\beta_1^*} \mp M\cos\beta_1^*} \\ &\text{forward, upper sign, } \nu = 0,1,2,\ldots, M<1 \\ &\text{backward, lower sign, } \nu = 1,2,3,\ldots, M\le 1 \end{aligned}\right\} \qquad (22.2.112)$$

where $M = V/a$ and $k = c\omega/2V$. The conditions under Eq. (22.2.112) indicate the direction of propagation and the valid ranges of parameter applicability. Note that there is a limiting case as $M \to 1$. As this case is approached, the appropriate vectors in Fig. 22.2.12 will be $\overline{OB}$ and $\overline{OF}$, and it is seen that the time required for forward propagation becomes arbitrarily large without bound. Hence, only backward propagation is possible for sonic and supersonic speeds.

Next consider the case of supersonic relative flow, shown in Fig. 22.2.14, in which $V > a$. This *time only backward propagation* is possible, so the velocities along the stagger line are defined simply as V_{P_1} and V_{P_2}. Once again, use of the law of cosines yields the two solutions

$$V_{P_{1,2}} = V\cos\beta_1^* \pm \sqrt{a^2 - V^2\sin^2\beta_1^*} \qquad (22.2.113)$$

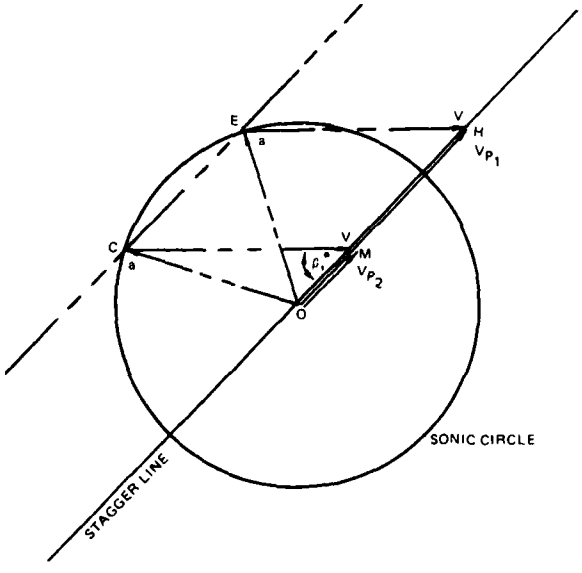

Fig. 22.2.14 Velocity Field for Supersonic Flow

where the subscripts 1,2 are associated with the upper and lower sign, respectively. When the time for propagation, $t_{L(-)}$, from Eq. (22.2.106) is set equal to $t_{P(-)} = t_{P_{1,2}} = \tau/V_{P_{1,2}}$ the result is

$$\left.\begin{aligned} &2\pi\nu - \sigma = \frac{2kM(\tau/c)}{M\cos\beta_1^* \pm \sqrt{1-M^2\sin^2\beta_1^*}} \\ &\text{backward only, } \nu = 1,2,3,\ldots \\ &1 \le M \le \csc\beta_1^* \end{aligned}\right\} \qquad (22.2.114)$$

which can be shown to agree with the result obtained in Refs. 22.12 and 22.46.

The sonic Mach number limit has already been discussed. The upper limit represents the condition under which the axial Mach number becomes unity, and is denoted in Fig. 22.2.12 by the single vector $\overline{OD}$. For any $M > \csc\beta_1^*$ the axial Mach number will be greater than unity and the Mach wave from point 0 on the reference blade (Fig. 22.2.11) will lie behind point P on blade n+1. Hence, no resonance condition (as defined herein) can occur for a supersonic throughflow blade row. For further discussions of the resonance phenomenon the reader is referred to the several articles listed in the bibliography.

22.2.3 DYNAMIC STALL - EMPIRICISM AND EXPERIMENT

22.2.3.1 Historical Background for Torsional Stall Flutter

Of all the flutter problems confronting the turbomachinery designer the most persistent has been that associated with single-degree-of-freedom torsional motion under high load conditions. For many years the designer had little choice in his approach to this problem. He either applied empirical "laws" obtained by the correlation and consclidation of previous flutter experiences on rotors, or he attempted to use predictions based on the growing body of isolated airfoil experience which was then modified to fit cascade experience. Either choice was unsatisfactory and progress was ultimately made by encountering problems and overcoming them. This, at best, was a time-consuming and costly procedure.

Recently, considerable progress has been made (and continues to be made) in a direct attack on the multiblade flutter problem. In addition to the theoretical approaches cited in previous sections, the determination of empirical data for realistic multiblade configurations has also enhanced the ability of the designer to provide flutter-free operation over the flight envelope of the turbomachine. It is interesting to note, however, that current techniques still rely heavily on past practice, and in particular on the considerable effort devoted to isolated airfoil stall flutter. Thus, it is instructive to review this field and to determine where its results are still applicable, and where new discoveries indicate that large differences exist.

As early as 1938, Bratt and Scruton (Ref. 22.49) were conducting tests to measure moment hysteresis in pitch, and were using the concept of work per cycle around the moment loop to determine the stability derivatives. More will be said about this in a subsequent section. In 1943, Mary Victory published a definitive and comprehensive study of torsional stall flutter (Ref. 22.50). In this experiment she measured the quadrature, or out-of-phase, component of the moment to determine the aerodynamic damping derivative. This was found to decrease with increasing angle of attack. Victory used these empirical variations of aerodynamic damping in the classical theory and was able to calculate the critical flutter speed at stall with reasonable accuracy.

In the United States, Mendelson attempted to derive an analysis for stall flutter (Ref. 22.51). This work was only partially successful in that it required some rather arbitrary assumptions on the vector amplitudes of the unsteady forces and moments to make the analysis agree with the experiment. A critique of Mendelson's paper will be found in Ref. 22.52.

A significant contribution to stall flutter literature was published by Halfman and his colleagues in Ref. 22.53. This was an extensive study of the lift and moment responses of three symmetric profiles oscillating separately in both pure pitching and pure plunging motions. A balance was used to measure both the in-phase and out-of-phase components of lift and moment. The data are presented in tabular form and in hysteresis loop form, and the aerodynamic stability of the airfoil is discussed using damping derivatives.

Baker (Refs. 22.54 and 22.55) measured the stall flutter stress response as a function of velocity and incidence angle. A crossplot of these results at constant stress yielded the familiar stall flutter contour shown in Fig. 22.2.15. This figure is particularly interesting in that it shows the transition from classical flutter at low incidence and very high $V/b\omega$ to stall flutter at high incidence and moderate $V/b\omega$. In both of these reports the lower limit of

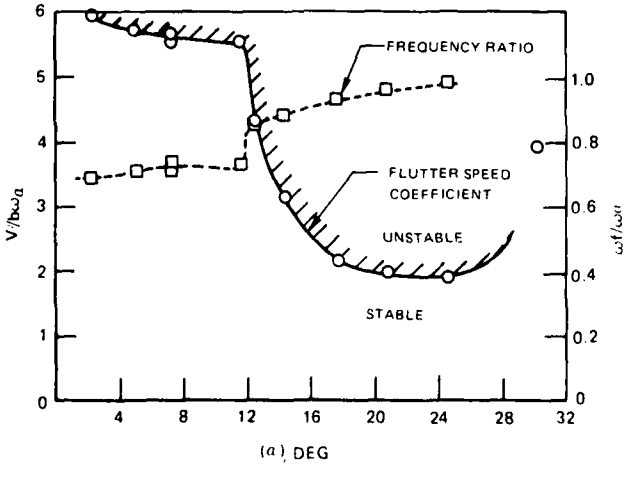

Fig. 22.2.15 Transition from Classical Flutter to Stall Flutter

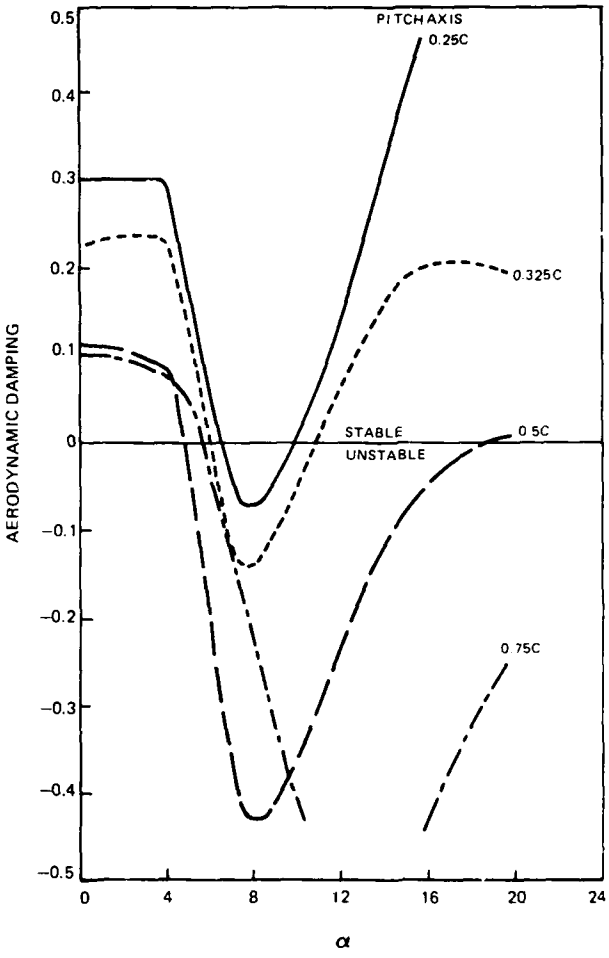

Fig. 22.2.16 Effect of Rearward Movement of Pivot Axis in Stall Flutter

$V/b\omega$ for flutter seems to be $V/b\omega \cong 1.0$ for large values of incidence angle. Further work was done by Rainey on a variety of planforms with different pitching axes (Ref. 22.56). This report clearly showed the detrimental effect of a rearward movement of the pitching axis on stall flutter response. A crossplot of these results was published in Ref. 22.57 and is presented herein in Fig. 22.2.16.

In all of the work cited above, the measurements were made either with a dynamic balance or with strain gage beams or flexures. These devices permitted gross measurements of force, moment, or damping to be made, but the details of the unsteady flow over the blade could not be determined. In 1957, Rainey published a report describing the use of miniature pressure transducers distributed chordwise over the airfoil to measure unsteady load distribution (Ref. 22.58). Although Rainey did not discuss this detailed pressure data and confined his analysis to the integrated lift and moment responses, his technique paved the way for more elaborate pressure tests which have been and still are seeking to explain the underlying mechanism of stall flutter. A few of these subsequent investigations are reported in Refs. 22.59, 22.60 and 22.61.

AD-A152 757 COST REDUCTION IN VERTICALLY RELATED INDUSTRIES: 8/9
INTEGRATION VERSUS NONLINEAR PRICING(U) RAND CORP SANTA
MONICA CA H C QUIRMBACH MAY 83 RAND/P-6839

UNCLASSIFIED F/G 5/1 NL

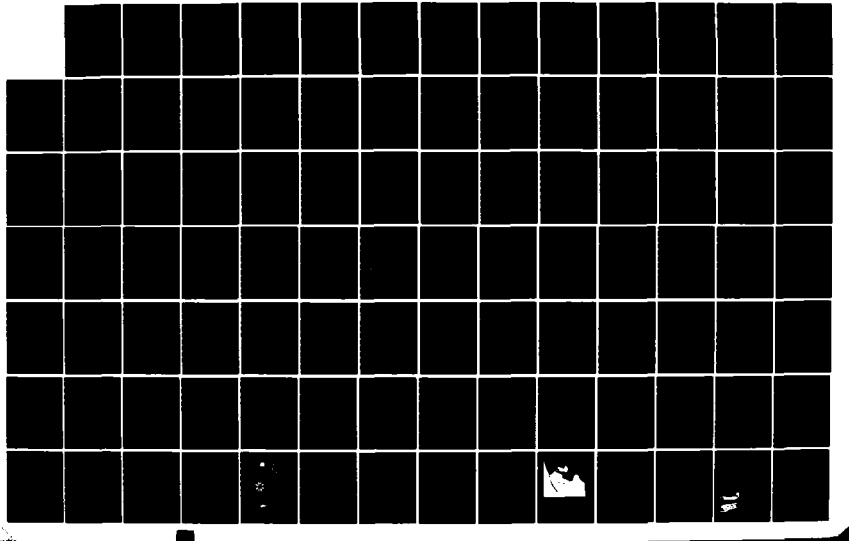

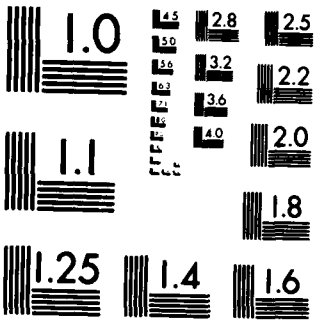

MICROCOPY RESOLUTION TEST CHART
NATIONAL BUREAU OF STANDARDS-1963-A

Consideration will now be given to these recent experiments and to some modern theoretical approaches.

22.2.3.2 Two-Dimensional Work Per Cycle and Aerodynamic Damping

In this section the method of Ref. 22.62 will be followed, but the basic derivation will be equally applicable to both multiblade systems and to isolated airfoils. To begin with, the work per cycle of torsional motion is given by the cyclic integral of the product of the real parts of the moment and differential pitch angle,

$$W = \oint M_R \, d\alpha_R \tag{22.2.115}$$

With the assumption of sinusoidal torsional motion,

$$\alpha = \bar{\alpha} e^{i\omega t} \tag{22.2.116}$$

where α is complex and $\bar{\alpha}$ is a real amplitude. Similarly, the unsteady moment can be written as

$$M = \bar{M} e^{i\omega t} = (\bar{M}_R + i\bar{M}_I) e^{i\omega t} \tag{22.2.117}$$

but here both M and $\bar{M}$ are complex. This is because $\bar{M}$ is generally not in phase with α. Note that the $\bar{M}_R$ in Eq. (22.2.117) is the real part of only the moment amplitude, and is not the real part of the entire moment, $\bar{M}_R$, that is needed for Eq. (22.2.115). To obtain this, expand the exponential in Eq. (22.2.117) and extract the real part,

$$M_R = \bar{M}_R \cos\omega t - \bar{M}_I \sin\omega t \tag{22.2.118}$$

A similar expansion and differentiation of Eq. (22.2.116) yields the real part of the differential

$$d\alpha_R = -\bar{\alpha} \sin\omega t \; d(\omega t) \tag{22.2.119}$$

Substitute Eqs. (22.2.118) and (22.2.119) into Eq. (22.2.115)

$$W = \int_0^{2\pi} (\bar{M}_R \cos\omega t - \bar{M}_I \sin\omega t)(-\bar{\alpha} \sin\omega t) \, d(\omega t) \tag{22.2.120}$$

and by orthogonality, we have

$$W = \pi \bar{\alpha} \bar{M}_I \tag{22.2.121}$$

which says that the aerodynamic work per cycle is directly proportional to the quadrature, or out-of-phase, component of the moment. This is the work done by the air on the airfoil; hence, a positive value of W will indicate an unstable motion, since this implies a net energy exchange from the air to the airfoil, whereas a negative value of W will indicate a stable, or damped, motion. Equations (22.2.115) and (22.2.121) may be rewritten in coefficient form by dividing through by $(1/2)\rho V^2 (2b)^2$, with the result

$$c_\omega = \oint c_{M_R} \, d\alpha_R = \pi \bar{\alpha} \bar{c}_{M_I} \tag{22.2.122}$$

Next we shall consider the aerodynamic damping of the airfoil, but first it is useful to review briefly the behavior of a linear, damped, torsional system such as the one described by the differential equation,

$$I\ddot{\alpha} + C\dot{\alpha} + K\alpha = 0 \tag{22.2.123}$$

where I is the inertia, C is the damping, and K is the stiffness. If the motion is essentially sinusoidal (i.e., only slightly damped and hence very nearly a constant amplitude sinusoid), then Eq. (22.2.116) is a solution. The equation then becomes

$$(-\omega^2 I + i\omega C + K)\bar{\alpha} = 0 \tag{22.2.124}$$

It is seen that the damping coefficient is contained in the imaginary part of this expression, and we can assume that the equivalent damping terms for any similar linear system will also be contained in the imaginary part of the differential equation solution.

Equation (22.2.123) represents a system oscillating in torsion in a vacuum. If the same system were to oscillate in torsion in a moving airstream, the right-hand side would be replaced by the unsteady aerodynamic moment as in Eq. (22.1.30),

$$I\ddot{\alpha} + C\dot{\alpha} + K\alpha = M_1\ddot{\alpha} + M_2\dot{\alpha} + M_3\alpha \tag{22.2.125}$$

From Eqs. (22.1.31), (22.1.32), and (22.1.33) we see that M_1 is a pure real quantity whereas M_2 and M_3 are complex,

$$M_2 = M_{2R} + iM_{2I} \tag{22.2.126}$$

$$M_3 = M_{3R} + iM_{3I} \tag{22.2.127}$$

When these are substituted into Eq. (22.2.125) and the terms are rearranged, the result is

$$(I - M_1)\ddot{\alpha} + (C - M_{2R} - iM_{2I})\dot{\alpha} + (K - M_{3R} - iM_{3I})\alpha = 0 \tag{22.2.128}$$

Once again, if the damping is sufficiently small, the motion will be nearly sinusoidal and Eq. (22.2.116) represents a solution, so Eq. (22.2.128) becomes

$$\left[-\omega^2(I - M_1) + i\omega(C - M_{2R} - iM_{2I}) + (K - M_{3R} - iM_{3I})\right]\bar{\alpha} = 0 \tag{22.2.129}$$

After collecting real and imaginary parts,

$$\left[\left\{-\omega^2(I - M_1) + \omega M_{2I} + K - M_{3R}\right\} + i\left\{\omega(C - M_{2R}) - M_{3I}\right\}\right]\bar{\alpha} = 0 \tag{22.2.130}$$

As in the case of the system oscillating in vacuum, the imaginary part of Eq. (22.2.130) will be the total damping of the system,

$$\text{total damping} = \omega(C - M_{2R}) - M_{3I} \qquad (22.2.131)$$

The quantity ωC is the system damping in vacuum; therefore, the remainder of Eq. (22.2.131) must be the aerodynamic damping of the system, defined by

$$\xi = -\omega M_{2R} - M_{3I} \qquad (22.2.132)$$

The symbol ξ denotes the (dimensional) aerodynamic damping parameter of a system executing a single-degree-of-freedom torsional motion.

Now, the right-hand side of Eq. (22.2.125) is the unsteady aerodynamic moment acting on the airfoil, which is the same as the right-hand side of Eq. (22.2.117). If the two right-hand sides are equated, Eq. (22.2.116) is substituted for α, and the exponential factor $e^{i\omega t}$ is cancelled, the result is

$$\bar{M}_R + i\bar{M}_I = \qquad (22.2.133)$$
$$\left[\left\{-\omega^2 M_1 - \omega M_{2I} + M_{3R}\right\} + i\left\{\omega M_{2R} + M_{3I}\right\}\right]\bar{\alpha}$$

After equating real and imaginary parts, it is seen that

$$\bar{M}_I = \left[\omega M_{2R} + M_{3I}\right]\bar{\alpha} \qquad (22.2.134)$$

A comparison of Eqs. (22.2.132) and (22.2.134) shows that the aerodynamic damping parameter, ξ, is equal to the negative of the derivative of the imaginary component of the unsteady moment with respect to the amplitude of motion,

$$\xi = -\frac{d\bar{M}_I}{d\bar{\alpha}} = -(\omega M_{2R} + M_{3I}) \qquad (22.2.135)$$

This may be rewritten in dimensionless form by dividing through by $(1/2)\rho V^2(2b)^2$,

$$\Xi \equiv \frac{\xi}{(1/2)\rho V^2(2b)^2} = -\frac{\omega M_{2R} + M_{3I}}{(1/2)\rho V^2(2b)^2} \qquad (22.2.136)$$

and hence

$$\Xi = -\frac{d\bar{C}_{MI}}{d\bar{\alpha}} \qquad (22.2.137)$$

In the ultimate formulation to be obtained herein, it will be useful to express the aerodynamic damping parameter in terms of the work per cycle of motion, since the latter is a quantity which is usually easy to measure or to calculate. To accomplish this, a few manipulations are necessary since both $\bar{C}_{MI}$ and C_W are implicit functions of $\bar{\alpha}$. First return to the influence coefficient form of the moment equation in Eq. (22.1.20), and rewrite this for α-motion only. If both M and α are put in amplitude-exponential form, the exponential can be cancelled and the result is

$$\bar{M} = \pi\rho b^4 \omega^2 B_\alpha \bar{\alpha} \qquad (22.2.138)$$

After dividing through by $(1/2)\rho V^2(2b)^2$ and using the reduced frequency, $k = b\omega/V$, this becomes

$$\bar{C}_M = \frac{\pi k^2}{2} B_\alpha \bar{\alpha} \qquad (22.2.139)$$

which has an imaginary part written simply as

$$\bar{C}_{M_I} = \frac{\pi k^2}{2} B_{\alpha I} \bar{\alpha} \qquad (22.2.140)$$

Note that the influence coefficient $B_{\alpha I}$ is independent of $\bar{\alpha}$, so Eq. (22.2.140) may be substituted into Eq. (22.2.137) to obtain

$$\Xi = -\frac{\pi k^2}{2} B_{\alpha I} \qquad (22.2.141)$$

Also, Eq. (22.2.140) can be substituted into (22.2.122) to yield

$$C_W = \pi\left(\frac{\pi k^2}{2} B_{\alpha I}\right)\bar{\alpha}^2 \qquad (22.2.142)$$

and a comparison of Eqs. (22.2.141) and (22.2.142) yields the useful formula

$$\Xi = -\frac{C_W}{\pi\bar{\alpha}^2} \qquad (22.2.143)$$

To this point in the analysis there is no restriction on the number of blades or the flow velocity.

Additional insight can be gained if we specialize the equations for the specific case of an isolated airfoil oscillating about its quarter chord ($a = -1/2$) in an incompressible potential flow. Although this is not the axis of rotation for compressor blades, a great deal of oscillatory data were obtained with this pivot axis (Refs. 22.59, 22.60 and 22.61), and further, the equations for potential flow past an isolated airfoil reduce to an extremely simple form. With the substitution $a = -1/2$, Eq. (22.1.21) for B_α reduces to

$$B_\alpha = M_\alpha \qquad (22.2.144)$$

and from Eq. (22.1.18), the imaginary part of this is

$$B_{\alpha I} = M_{\alpha I} = -\frac{1}{k} \qquad (22.2.145)$$

When this is substituted into Eqs. (22.2.140), (22.2.141) and (22.2.142), we obtain

$$\bar{C}_{M_I} = -\frac{\pi k}{2}\bar{\alpha} \qquad (22.2.146)$$

$$\mathcal{H} = \frac{\pi k}{2} \qquad (22.2.147)$$

$$C_W = -\frac{\pi^2 k}{2}\bar{\alpha}^2 \qquad (22.2.148)$$

Thus, we see from Eq. (22.2.148) that, for these ideal conditions of potential flow and pivot axis at the quarter chord, the work coefficient will always be negative, which means the net work flowing from the airstream into the airfoil is negative. In other words, the airfoil is dissipating energy, and the system is stable. Furthermore, the work coefficient is directly dependent on k and $\bar{\alpha}$. Similarly, Eq. (22.2.147) shows that the aerodynamic damping is always positive and is independent of amplitude.

22.2.3.3 Dynamic Stall and Stall Flutter of a Pitching Isolated Airfoil

The process of dynamic stall is extremely complicated and has been treated phenomenologically by most investigators, as it will be in this section. To begin with, let us assume that an airfoil is oscillating in pitch and that a time history of the aerodynamic response shows that the normal force or moment is not in phase with the pitching motion, as shown in the two upper panels of Fig. 22.2.17. When these two time histories are combined and the time parameter is eliminated, the result will be a closed curve of normal force or moment versus angle of attack as shown in the bottom panel of Fig. 22.2.17. The arrows denote the direction of increasing time. The enclosed area, in the case of the moment, represents the energy absorbed or dissipated (i.e., the work per cycle) as discussed in the previous section. This is found to be the case in both classical and separated flows. In the former, the closed contour will be elliptical whereas in the latter the contour will be distorted.

A few representative unsteady normal force coefficient loops for an isolated airfoil taken from Ref. 22.62 are presented in Fig. 22.2.18. The solid lines represent the unsteady data, and the dashed lines represent the steady-state characteristics. Three of the inset figures are for a constant reduced frequency of k = .075 and show the effects of varying mean incidence angle, from α_M = 6 to 12 to 18 deg. The two right-hand inset figures are for α_M = 12 deg and illustrate the effect of a change in frequency from k = .075 to k = .3. It is clear that the increase in α_M to values greater than the steady-state stall angle has a profound effect on the dynamic force response of the oscillating airfoil. It is also clear that an

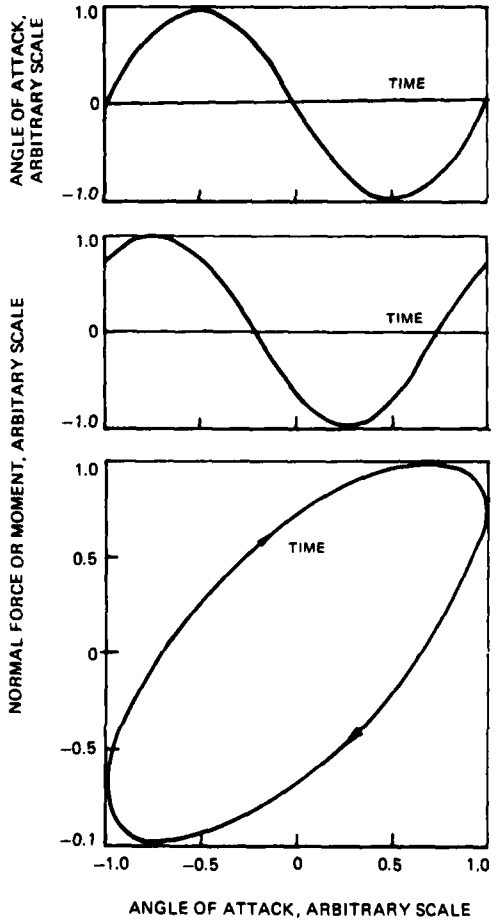

Fig. 22.2.17 Hypothetical Normal Force or Moment - Angle of Attack Hysteresis Loops

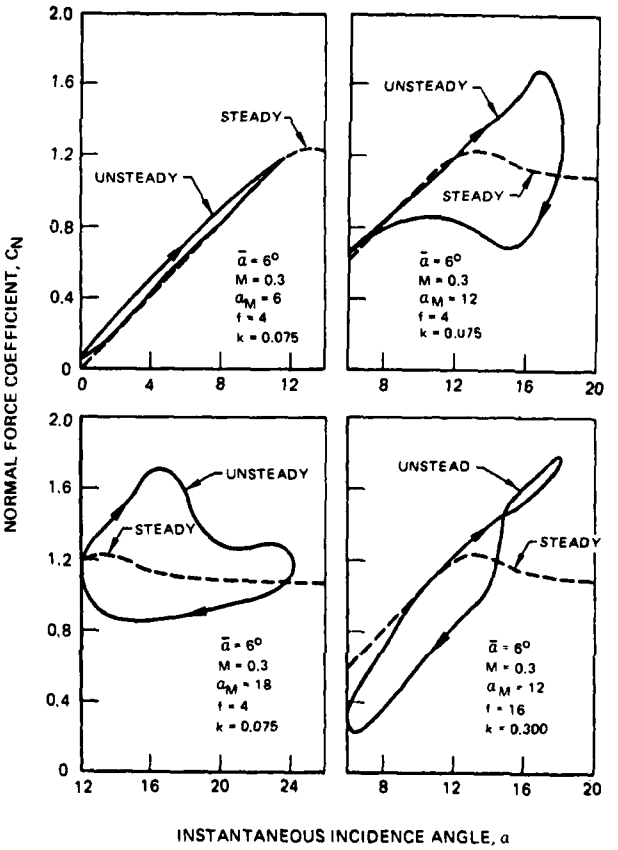

Fig. 22.2.18 Normal Force Hysteresis Loops

increase in k produces a radical change in the dynamic stalling behavior of the airfoil. Specifically, at low frequency the dynamic force response reaches its peak value just before the maximum incidence angle is reached; it then drops precipitously to a value far below the steady-state stall value and remains there for almost the entire region of decreasing incidence. In contrast to this behavior, the effect of high frequency is to maintain a nearly elliptical response loop, even for incidence angles beyond stall, over the entire angle-of-attack range.

Until recently, very little work had been done to examine in detail the fluid dynamics of dynamic stall of isolated airfoils. Even with some of the fundamental studies now being conducted or newly completed (Refs. 22.63 through 22.67), a great deal of speculation remains on the nature of dynamic stall. We know that stall is produced in association with separation of flow from the airfoil surface, and that separation is the disruption of the boundary layer on the airfoil. This disruption is invariably associated with an unfavorable pressure gradient (i.e., increasing pressure on the suction surface) which exceeds some unknown (for dynamic processes) critical amount. We would expect that two time-dependent effects would be present in the boundary layer: (1) a direct time lag associated with the inertia or mass of the fluid contained in the boundary layer, and (2) a pressure time lag on the airfoil due to dynamic motion which changes the severity of the unfavorable pressure gradient. From these concepts we can speculate that at low frequency there is ample time for the boundary layer to respond to the motion, and separation can occur. Once the separation has taken place, recovery can occur only when the unfavorable conditions have been removed by a sufficiently large margin. Conversely, at high frequency, the time lag effects suppress the unfavorable effects and either no separation or only partial separation occurs. In other words, the separation doesn't have a chance to occur at the top of the motion before the airfoil has returned to lower angles of attack.

We now turn our attention to some representative unsteady moment loops taken from Ref. 22.62 which are presented in Fig. 22.2.19. This figure shows the effects of increasing the reduced frequency from k = .112 to k = .450 for two mean angles of attack, α_M = 0 deg and α_M = 15 deg. The solid curves are from the experiment, and the potential flow theory predictions are shown as dashed curves for α_M = 0 deg. At this low mean angle of attack the theory and experiment are in good agreement, and all of the loops, from low frequency to high frequency, exhibit the same general behavior. However, at α_M = 15 deg, the low frequency loops are badly distorted and exhibit a crossover behavior, while the high frequency loops behave more like the theoretical loops. This crossover generally occurs at or above the static stall condition, and it will now be shown that this behavior is the key to the stall flutter phenomenon for isolated airfoils.

It was stated in the previous section that system stability is related to work per cycle of motion, and from Eqs. 22.2.115 or 22.2.122, this is given by the cyclic integral around the loop, which is equivalent to the area enclosed by the loop. From elementary considerations, a counterclockwise enclosure of the area represents negative work, which is equivalent to positive damping and hence a stable motion. Conversely, a clockwise enclosure of the area represents positive work, negative damping, and hence an unstable system. It is seen from Fig. 22.2.19 that all the α_M = 0 deg loops as well as the two highest frequency loops for α_M = 15 deg have counterclockwise enclosures and hence are stable. However, the two lowest frequency loops for α_M = 15 deg have crossover or figure-8 characteristics in which the low-α portion is counterclockwise, implying stability, but the high-α portion is clockwise, implying instability. In other words, these crossover loops indicate an energy balance in which negative work done in the left-hand side of the loop is balanced by positive work done in the right-hand side of the loop. Actually, there is no actual balance of energy in the loops shown here because the airfoil was rigidly driven through its motion. If the airfoil had been free to oscillate, it would have reached an equilibrium amplitude, known as a limit cycle, in which a true energy balance could have been achieved.

It should be emphasized that this discussion is primarily applicable to isolated airfoils at high incidence angle. For many years it was believed that these arguments could be applied to multiblade systems as well, provided that the right scaling factor or transformation variable could be found. To this end

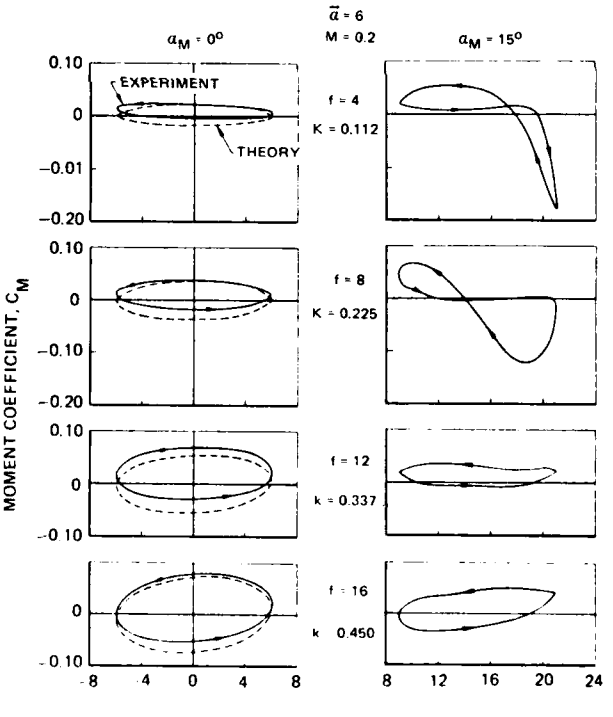

Fig. 22.2.19 Effect of Frequency and Mean Incidence Angle on Moment Hysteresis Loops

a considerable amount of time and effort were expended in searching for these quantities. However, it has now been determined that other mechanisms involving strong interblade interactions appear to be dominant in the flutter of compressor blades under high aerodynamic loading. This will now be discussed in the next section.

22.2.3.4 Unsteady Cascade Aerodynamics at High Incidence

The very early efforts to employ empiricism in the prediction of rotor blade flutter have already been described above, and will not be referred to again. Instead, the purpose of this section is to document the recent and current efforts to develop a more rational approach to the problem. To date these efforts still involve some degree of empiricism in their implementation, but they represent a significant improvement over the stress rise-flutter boundary approach of twenty years ago.

One approach that has yielded promising results is that of Ref. 22.68. In this analysis the aerodynamic damping of a rotor blade is calculated on the basis of an algorithm incorporating (at present) isolated airfoil experimental data for separated flow to modify otherwise unseparated analytical predictions based on the best available cascade theoretical analyses. Although this method has obvious limitations in its present form the general procedure is sufficiently flexible to employ any valid aerodynamic input as, for example, the unsteady loaded theory under development by Verdon, et al. (Ref. 22.43), or the data being produced by the test program described below.

Unsteady aerodynamic tests have been conducted by the present author and his coworker in a linear, subsonic Oscillating Cascade Wind Tunnel (OCWT) which is shown schematically in Fig. 22.2.20. The general characteristics of this facility are fully discussed in Ref. 22.69 and only a brief description will be given here.

The test section of the OCWT is 10 inches wide and 25 inches high, and is presently configured to have 11 shaft-mounted blades in cascade, equally placed along a line making a 30-degree angle with respect to the tunnel floor. Hence, the sidewall stagger of the OCWT is nominally 30 degrees.

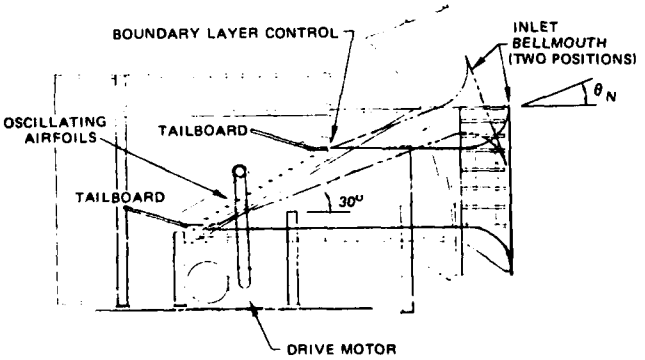

Fig. 22.2.20 Schematic of Subsonic Oscillating Cascade Wind Tunnel

Boundary layer slots are located ahead of the test section on both sidewalls and on the tunnel ceiling and floor. The boundary layer air is evacuated by means of an auxiliary vacuum pump. The main 10- by 25-inch test section receives its air from atmosphere through an upstream bellmouth and discharges downstream through two Allis-Chalmers centrifugal compressors. Inlet angle variations into the test section are obtained by rotating the floor and ceiling nozzle blocks about a pair of pivots whose centers lie along the locus of blade leading edges.

The cascade configuration under test consists of eleven blades, each of which has a chord of C = 6 inches and a span of L = 10 inches. The airfoil has a NACA 65 series profile with 10 degree camber and a thickness-to-chord ratio of 0.06. The slant gap, measured along the blade-to-blade stagger line is τ = 4.5 inches so the gap-to-chord ratio is τ/c = 0.75. The blade stagger angle, β_1^*, is measured between the tangent to the blade mean camber line at the leading edge and the leading edge locus line. Note that this angle is the complement of NASA definition of blade angle. Finally, the blade inlet angle, β_1, is measured between the inlet velocity V and the leading edge locus line.

The center airfoil of the cascade is heavily instrumented with both miniature high response pressure transducers and with hot film transducers. Figure 22.2.21 shows the permanent locations of all pressure orifices and the array of hot films at the leading edge region used in the first series of tests. The entire set of airfoils is driven coherently in a sinusoidal pitching motion with an amplitude of $\alpha = \pm 2$ degrees. The system is driven by an electric motor through a series of timing belts and pulleys. The direct drive to each blade culminates in a four bar linkage which provides a sinusoidal motion with low harmonic distortion.

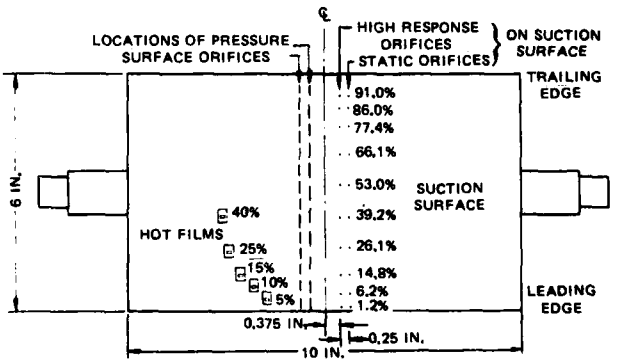

Fig. 22.2.21 Schematic Plan View of Instrumented Airfoil

An initial experimental program was performed at a free stream velocity of 200 ft/sec and an incidence angle of α_{MCL} = 8 deg (relative to the mean camber line) at frequencies of 4.5, 11.0 and 17.1 cps, over a range in interblade phase angles from σ = -60 deg to +60 deg. The equivalent reduced frequencies were k = .035, .086 and .134.

At this incidence angle the blades were heavily loaded but no actual stall was observed that was comparable to the stall customarily experienced on isolated airfoils. Indeed, the steady state pressure distribution was devoid of any obvious signs of stall, as seen in Fig. 22.2.22. Nevertheless, a strong instability was found to exist

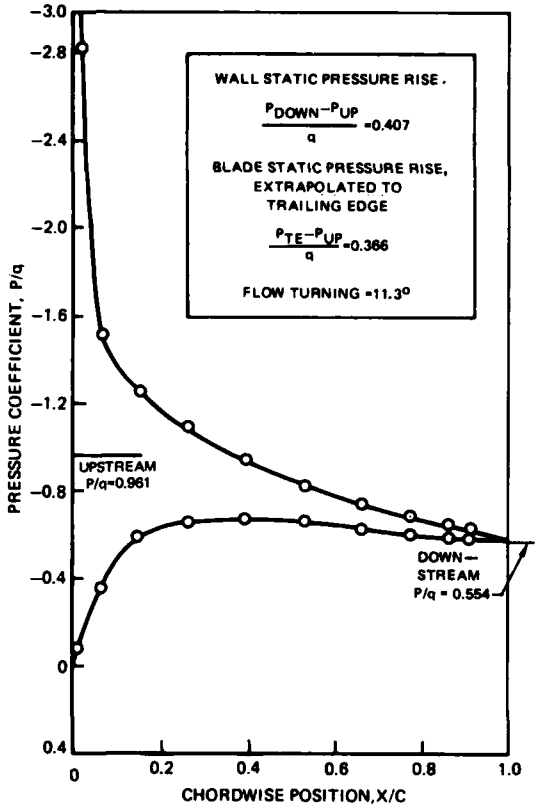

Fig. 22.2.22 Steady State Chordwise Pressure Distribution

on examination of the imaginary part of the moment coefficient (cf. Eq. (22.2.122)) or of the integrated aerodynamic damping coefficient (cf. Eq. (22.2.137)). Typical phase plane plots for the three frequencies are shown in Fig. 22.2.23, and the aerodynamic damping variation with interblade phase angle is shown in Fig. 22.2.24. It is seen here that the dominant parameter affecting stability is σ, the interblade phase angle. This is reminiscent of the theoretical results for supersonic torsional flutter described in Figs. 22.2.9 and 22.2.10. In both cases the comparable isolated airfoil results are found to be almost completely inadequate.

Some insight into the mechanism of this interaction effect may be gained by a brief study of the pressure time histories near the leading edge, which are shown in Fig. 22.2.25 over a range of interblade phase angles. The most revealing evidence here is found in the right half of this figure for the 6.2 percent chord location. A comparison with Fig. 22.2.23 shows that the system is stable for $\sigma < -5^\circ$ and unstable for $\sigma > -5^\circ$, and an examination of

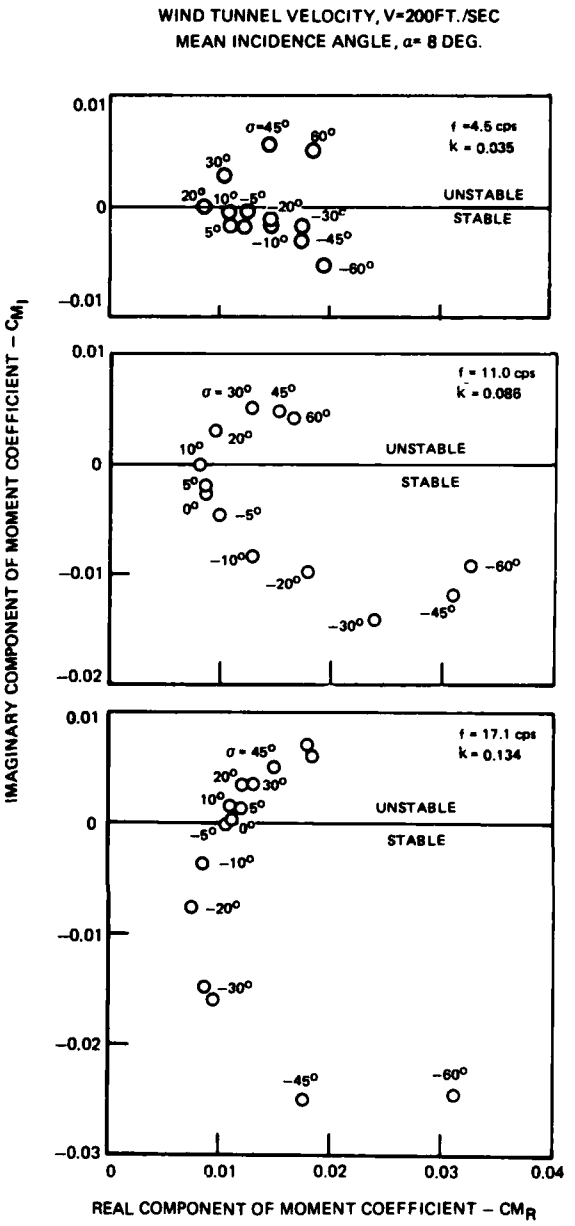

Fig. 22.2.23 Phase Plane Diagram of Moment due to Pitch from Cascade Experiment

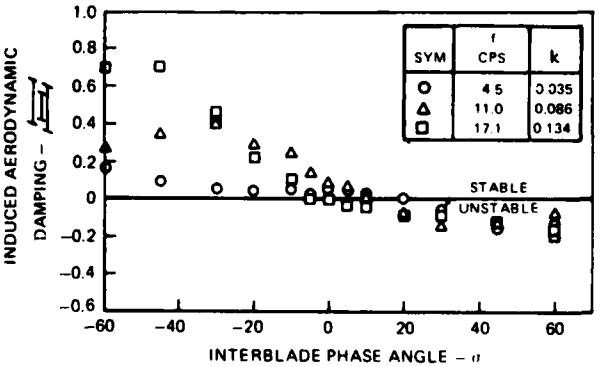

Fig. 22.2.24 Variation of Aerodynamic Damping with Interblade Phase Angle

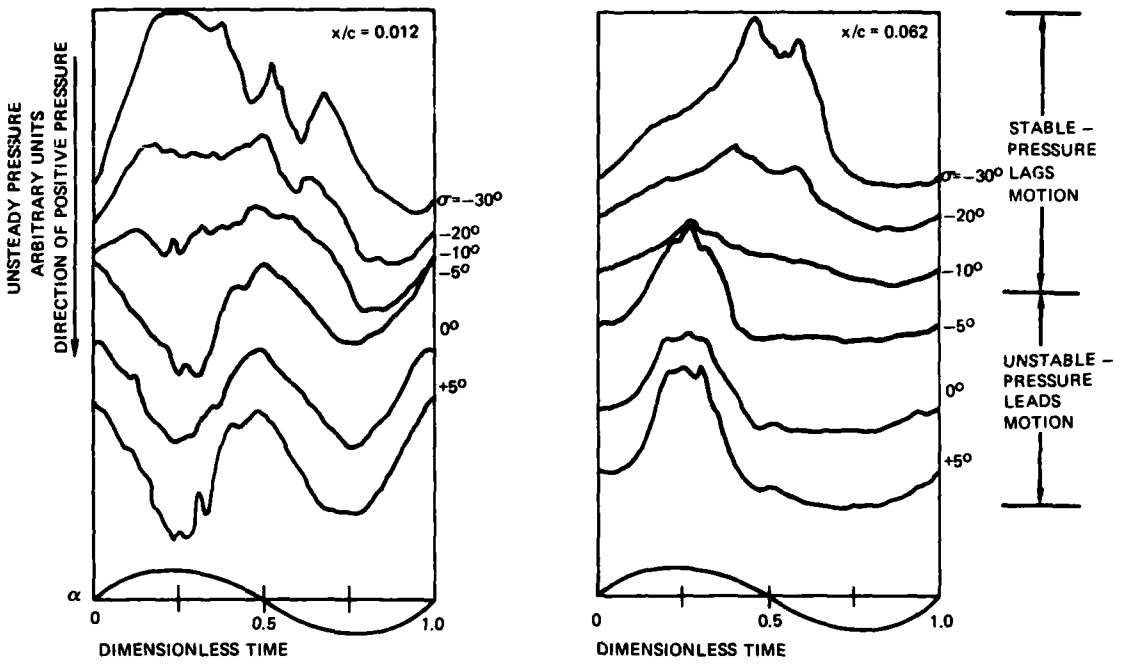

Fig. 22.2.25 Time-Averaged Pressure Wave Forms from Airfoil Suction Surface for Several Interblade Phase Angles

Fig. 22.2.25 shows that the pressure lags the motion for $\sigma < -5^\circ$ and leads the motion for $\sigma > -5^\circ$. Thus, the pressure lead or lag, caused by interblade phase angle variations, plays a key role in the system stability. An even more interesting observation may be made of the left half of Fig. 22.2.25 for the 1.2 percent chord location. Here the dominant effect of interblade phase angle variation appears to be the transition *from* a *predominantly first* harmonic response for $\sigma \approx -30^\circ$ to a strong second harmonic response for $\sigma \geq -5^\circ$. The pressure deficit in these latter cases occurs at peak incidence angle and has all of the outward appearances of the loss in suction peak associated with dynamic stall. Some additional details of these and other results will be found in Ref. 22.70. Additional tests are currently underway as this document is being written and a comprehensive report on all of these experimental results is expected to be published by Project SQUID in the next year.

It is obvious that the work cited above represents only a small portion of the empirical investigations currently underway (e.g., Refs. 22.71, 22.72, 22.73 and the Bibliography). It was chosen for examination here primarily because of the present author's intimate knowledge of this work, but also because it represents an approach that, while empirical, will be of use to the theoretician. The direct measurement of unsteady aerodynamic surface pressures or other load variables is of immediate use in the modification and implementation of existing aerodynamic theories. Furthermore, the observations made in such experimental studies provide the necessary information for the development of new and advanced theoretical work.

22.3 STABILITY THEORY AND APPLICATIONS

The ultimate objective of any theoretical (or experimental) study is generally to put its results into practice. In the present instance the turbomachinery design system is the beneficiary of the several flutter studies undertaken over the past two decades. This section will focus on a single fundamental paper (Ref. 22.8) which has made a significant impact on the design system and which has provided the design engineer with sufficient constraints to prevent the occurrence of flutter and its attendant fatigue failures on both prototype hardware and flight hardware. This first paper is now 10 years old, and the genesis of the underlying theory is approximately 20 years old. It represents the summary of a theoretical study undertaken by the present author, first to identify a type of flutter that was unknown on stiff, low-speed blade-disk assemblies, and second, after identifying the problem as one of coupled flutter, to provide the designer with the necessary tools to avoid this flutter in the future. The key to identification of the phenomenon lay in the way in which it manifested itself. Specifically, the observed flutter occurred as a system mode involving participation of all flexible parts of the rotor-disk-shroud combination, but it did not occur as an integral order excitation. In other words, with reference to Fig. 22.1.14, the observed behavior on the frequency-rpm plot would cut across the radial order lines and follow the natural frequency plots of the coupled system modes. As seen in the first paper, discussed below, the unsteady aerodynamics used was Theodorsen's incompressible, flat plate, isolated airfoil theory, largely because it was the only theory

available that could be implemented easily and at low computer cost. Furthermore, it worked well enough to both identify and predict the phenomenon, at least at first, to warrant its continued use.

In the last section of this chapter a design applications paper (Ref. 22.10) will be surveyed. Here it is shown that use of this coupled-blade-disk-shroud theory together with advanced unsteady aerodynamic analyses has provided the designer with the necessary analytical tools to create a design system that prevents flutter at supersonic speeds and at the design condition. Many more problems remain to be solved, including supersonic stall flutter in the bending mode, and subsonic and transonic stall flutter in the torsion mode. It is hoped that advances can continue to be made and that ultimately these problems can also be removed from the engine operating range by design.

22.3.1 COUPLED BLADE-DISK-SHROUD THEORY

The vibratory mode shapes which can exist on a rotor consisting of a flexible blade-disk-shroud system are well known to structural dynamicists in the turbomachinery field and a detailed discussion of these modes is beyond the scope and purpose of this section. Although both concentric and diametric modes can occur, the latter are the only system modes which are of interest. These diametric modes are characterized by node lines lying along the diameters of the wheel and having a constant angular spacing. Thus, for example, a two-nodal-diameter mode would have two node lines intersecting normally at the center of the disk, and a three-nodal-diameter mode would have three node lines intersecting at the disk center with an angular spacing of 60 deg between adjacent node lines (see Fig. 22.3.1). These diameteric modes are the physical embodiment of the eigensolutions of the system, and it can be shown, using standard structural dynamics techniques, that the system frequency for each mode is primarily a function of the physical distribution of the system mass and stiffness and is only slightly affected by the rotation of the system. Thus the system frequencies do not necessarily coincide with integral multiples of the rotor speed, and in fact, such coincidences of frequency are avoided for the lower frequencies if possible.

With the advent of the turbofan engine in the early 1960's a number of instances of nonintegral order vibrations at high stress occurred in both engine and test rig compressor rotors. The stage affected was invariably the front fan which consisted of high aspect ratio blades having part-span shroud supports. The stress levels reached in a number of these cases were sufficiently high to severely limit the safe operating range of the compressor. Attempts to relate these vibrations to the stall flutter phenomenon or to rotating stall essentially failed, largely because the vibrations often occurred on or near the engine operating line. Subsequent analysis of these cases

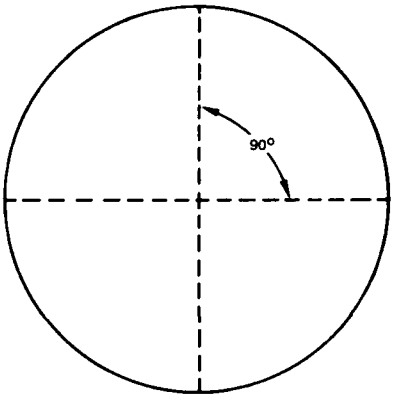

a) TWO NODAL DIAMETER PATTERN

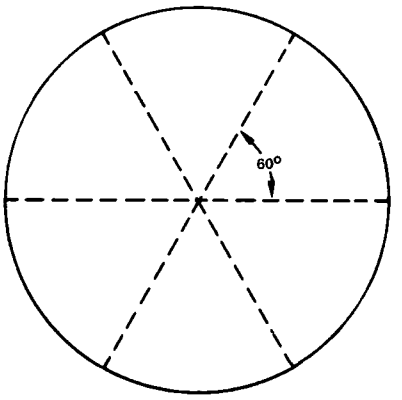

b) THREE NODAL DIAMETER PATTERN

Fig. 22.3.1 Typical Diametric Node Configurations

revealed that the observed frequencies of these instabilities correlated well with the predicted frequencies of the coupled blade-disk-shroud motion described previously. In view of the available information, it appeared likely that the coupled motion resulted in a system instability, even under potential flow conditions.

The object of this study is to explore the underlying mechanism of this instability and to show that under certain conditions of airflow and rotor geometry this coupled oscillation is capable of extracting energy from the airstream in sufficient quantities to produce an unstable vibratory motion. To do this, reference is first made to Fig. 22.1.6 which shows the coordinate system of the airfoil under consideration. Once again use will be made of Eqs. (22.1.19) and (22.1.20) to represent the complex, time-dependent unsteady lift and moment per unit span, which are repeated

$$L = L_R + iL_I = \pi\rho b^3\omega^2\left[A_h h + A_\alpha \alpha\right] \qquad (22.3.1)$$

$$M = M_R + iM_I = \pi\rho b^4\omega^2\left[B_h h + B_\alpha \alpha\right] \qquad (22.3.2)$$

here for completeness. In these equations the quantities A_h, A_α, B_h, B_α represent the lift due to bending, the lift due to pitch, the moment due to bending and the moment due to pitch, respectively. They may be taken from any valid aerodynamic theory from the incompressible isolated airfoil results of Theodorsen (Ref. 22.13) to the supersonic cascade results of Verdon (Ref. 22.12). In the paper being reviewed here (Ref. 22.8), it was expedient to use Theodorsen's theory whereas in the next section it is shown that application to the design system requires the more complete theoretical representation of Verdon. At present, though, the development will use the notation A_h, A_α, B_h, B_α and consequently will be completely general.

It is well known from unsteady aerodynamic theory that the forces and moments acting on an oscillating airfoil are not in phase with the motions producing these forces and moments. A convenient representation of this phenomenon is obtained on writing the unsteady coefficients in complex form as $A_h = A_{hR} + iA_{hI}$, etc., and the time dependent displacements as

$$\left.\begin{aligned} h &= \\ & h_R + ih_I = \bar{h}e^{i\omega t} = \bar{h}\cos\omega t + i\bar{h}\sin\omega t \\ \alpha &= \\ & \alpha_R + i\alpha_I = \bar{\alpha}e^{i(\omega t+\theta)} = \bar{\alpha}\cos(\omega t+\theta) \\ & \qquad + i\bar{\alpha}\sin(\omega t+\theta) \end{aligned}\right\} \quad (22.3.3)$$

where, in general, it has been assumed that the torsional motion leads the bending motion by a phase angle, θ. In this equation $\bar{h}$ and $\bar{\alpha}$ are the dimensionless amplitudes of the motion in bending and torsion, respectively.

The differential work done by the aerodynamic forces and moments in the course of this motion is obtained by computing the product of the in-phase components of force and differential vertical displacement and moment and differential twist. Accordingly, the work done per cycle of motion in each mode is obtained by integrating the differential work in each mode over one cycle. The total work done per cycle of coupled motion is given by the sum

$$W_{TOT} = -b\oint L_R dh_R + \oint M_R d\alpha_R \qquad (22.3.4)$$

where the minus sign is required because L and h are defined to be positive in opposite directions. It is important to note that in Eq. (22.3.4), positive work implies instability since these equations represent work done by the air forces on the system.

To compute these integrals, L_R and M_R are obtained from Eqs. (22.3.1) and (22.3.2), the real parts of Eqs. (22.3.3) are differentiated, and these quantities are substituted into Eq. (22.3.4) to yield

$$\begin{aligned} W_{TOT} = & \\ & -\pi\rho b^4\omega^2\left\{\bar{h}\oint\left[A_{hR}\bar{h}\cos\omega t - A_{hI}\bar{h}\sin\omega t\right.\right. \\ & + A_{\alpha R}\bar{\alpha}\cos(\omega t+\theta) - A_{\alpha I}\bar{\alpha}\sin(\omega t+\theta)\Big]\sin\omega t\, d(\omega t) \\ & + \bar{\alpha}\oint\Big[B_{hR}\bar{h}\cos\omega t - B_{hI}\bar{h}\sin\omega t + B_{\alpha R}\bar{\alpha}\cos(\omega t+\theta) \\ & \left.\left. - B_{\alpha I}\bar{\alpha}\sin(\omega t+\theta)\Big]\sin(\omega t+\theta)\, d(\omega t)\right\} \end{aligned} \qquad (22.3.5)$$

The line integrals over one cycle of motion are equivalent to an integration over the range $0 \le \omega t \le 2\pi$; after the indicated integrations in Eq. (22.3.5) are performed and the equation is simplified the total work done on the system is given by

$$W_{TOT} = \pi^2\rho b^4\omega^2\left\{A_{hI}\bar{h}^2 + \left[(A_{\alpha R} - B_{hR})\sin\theta + (A_{\alpha I} + B_{hI})\cos\theta\right]\bar{\alpha}\bar{h} + B_{\alpha I}\bar{\alpha}^2\right\} \qquad (22.3.6)$$

In this equation, the quantities $A_{\alpha I}$ and $B_{\alpha I}$ represent the damping in bending and the damping in pitch, respectively. For an isolated airfoil oscillating at zero incidence in an incompressible flow, both of these damping terms will be negative and hence will contribute to the stability of the system. For cases involving aerodynamic inputs other than those for an isolated airfoil at zero incidence in incompressible flow, the situation may be considerably altered.

The sign of the cross-coupling term in Eq. (22.3.6) (the term enclosed by the square brackets and multiplied by the product $\bar{\alpha}\bar{h}$) is strongly dependent on the phase angle between the motions, θ. In the usual classical flutter analysis, the phase angle remains an unknown until the end of the calculation, at which time it may be evaluated as an output quantity. For the configuration presently under consideration, however, the physical constraint of the structure on the mode shape fixes θ to be a specific input quantity, as will be shown below. This quantity within the square brackets is dominant in specifying regions of unstable operation.

It is shown in Ref. 22.8 that for the specific case analyzed therein the bending motion leads the torsion motion by 90 deg, so $\theta = -\pi/2$. An intuitive demonstration of this result is presented in Fig. 22.3.2. Here it is shown that at the nodal points in the disk or shroud rim the blade will experience maximum twist with no normal displacement, whereas at antinodes in the rim the blade will have no twist, but will experience maximum normal displacement.

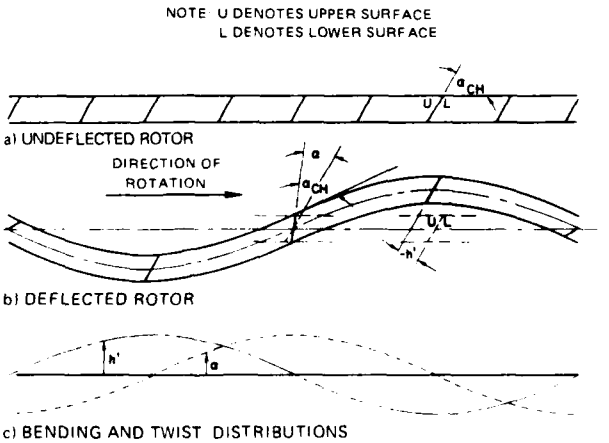

Fig. 22.3.2 Torsion and Bending Motions Caused by Coupled Blade-Disk-Shroud Interaction

The value of the phase angle, $\theta = -\pi/2$, may now be substituted into Eq. (22.3.6) and the resulting two-dimensional aerodynamic work per cycle at each spanwise station reduces to

$$W_{TOT} = \pi^2 \rho b^2 U^2 \left[k^2 A_{hI} \bar{h}^2 - (k^2 A_{\alpha R} - k^2 B_{hR}) \bar{\alpha} \bar{h} + k^2 B_{\alpha I} \bar{\alpha}^2 \right] \quad (22.3.7)$$

where $k = b\omega/U$ is the reduced frequency parameter. The use of the combinations $k^2 A_{hI}$, $k^2 A_{\alpha R}$, $k^2 B_{hR}$, and $k^2 B_{\alpha I}$ is dictated by convenience and by the availability of the aerodynamic coefficients in this form.

Equation (22.3.7) is an expression for the two-dimensional aerodynamic work per cycle at any arbitrary span station, say at radius r, as measured from the engine centerline. The work done on the entire blade is obtained by integrating Eq. (22.3.7) over the blade span, from the root, at $r = r_o$, to the tip, at $r = r_T$, and after normalizing the deformations, $\bar{h}$ and $\bar{\alpha}$, with respect to the tip bending deflection, $\bar{h}_T$, this gives

$$\frac{W}{\bar{h}_T^2} = \pi^2 \int_{r_o}^{r_T} \rho b^2 U^2 \left[k^2 A_{hI} \left(\frac{\bar{h}}{\bar{h}_T} \right)^2 - (k^2 A_{\alpha R} - k^2 B_{hR}) \frac{\bar{\alpha}}{\bar{h}_T} \frac{\bar{h}}{\bar{h}_T} + k^2 B_{\alpha I} \left(\frac{\bar{\alpha}}{\bar{h}_T} \right)^2 \right] dr \quad (22.3.8)$$

It was stated earlier that the stability of the system was related to the algebraic sign of the work expression; i.e., positive aerodynamic work implies instability and negative aerodynamic work implies stability. As shown in Eq. (22.3.8), the aerodynamic work done on the system is a direct function of the squares and products of the oscillatory amplitudes which are ordinarily obtained from a numerical solution of the characteristic equation for the vibratory system. It is well known from elementary vibration theory that the results of such a calculation are given in the form of relative amplitudes rather than absolute amplitudes. Therefore, the aerodynamic work can only be calculated on a relative basis and in its present form it cannot be used to predict either the absolute stability level of a particular configuration or the relative stability levels between two configurations. Since one of the objects of this analysis is to devise a prediction technique that will permit the evaluation of alternative rotor designs from the standpoint of system stability, the theoretical development must now be extended to overcome this deficiency.

In addition to the relative amplitudes of motion, the structural dynamics computer program also calculates the average kinetic energy of vibration of the entire blade-disk system, based on the relative amplitudes of motion. It is shown in Ref. 22.8 that for a simple, linear, spring-mass-dashpot system, the ratio of damping work per cycle to average kinetic energy is proportional to the logarithmic decrement of the system, which is independent of the absolute amplitudes of the system. A comparable ratio of the aerodynamic work done per cycle on the entire blade-disk-shroud system to the average kinetic energy of vibration of the system may be made and this will be equal to the logarithmic decrement of the system. First, however, the normalized aerodynamic work per cycle obtained for one blade in Eq. (22.3.8) must be multiplied by the number of blades on the entire disk, n, and then by the proportionality factor, 1/4, from Eq. (26) in Ref. 22.8. The result is

$$\delta = - \frac{nW/\bar{h}_T^2}{4\bar{K}_E/\bar{h}_T^2} \quad (22.3.9)$$

where $\bar{K}_E/\bar{h}_T^2$ is the average kinetic energy of the system, also normalized with respect to $\bar{h}_T^2$, and where a positive value of δ represents stable operation. Equation (22.3.9) yields an absolute measure of system stability which is independent of relative amplitudes. Hence the results obtained may be used to evaluate both the absolute stability of a particular configuration and the relative stability between two or more configurations.

To illustrate the use of this theory the stability characteristics of a typical rotor were investigated. The input quantities for use in Eq. (22.3.8) were obtained both from experiments and analytical studies conducted on an actual rotor at a given rpm. These data consisted of: (a) the geometric parameters for the configuration, α_{CH}, b, r_o, r_T, and n; (b) the steady-state aerodynamic parameters, ρ and U; and (c) for each prescribed disk nodal diameter pattern and blade mode, the relative amplitudes of the blade deformation components, $\bar{h}$, $\bar{\alpha}$, the average system kinetic energy, $\bar{K}_E$, and the system natural frequency, ω_o. For each nodal diameter both $\bar{h}$ and $\bar{\alpha}$ were then normalized with respect to the tip bending deflection, $\bar{h}_T$, and are plotted in Figs. 22.3.3 and 22.3.4 as functions of the dimensionless spanwise variable η, defined by

$$\eta = \frac{r - r_o}{r_T - r_o} \quad (22.3.10)$$

In both of these figures the shroud location at $\eta = 0.653$ is indicated by short tic-marks on each curve.

The dynamic system chosen for analysis in Ref. 22.8 consisted of a blade-disk-shroud configuration in which the blade oscillates in its first bending and first torsion modes, and the overall system vibration modes encompass 2 through 8 nodal diameters. Figures 22.3.3 and 22.3.4 contain the spanwise variations of bending deflection and blade twist, both normalized with respect to the bending deflection at the blade tip for the specific nodal diameter under consideration. Figure 22.3.3 shows that as the number of nodal diameters increases, the bending mode shape undergoes a consistent change in which the deformation of the tip region, outboard of the shroud, increases relative to the inboard region. In Fig. 22.3.4, however, it is seen that the torsional content of the vibration (relative to the tip bending) first

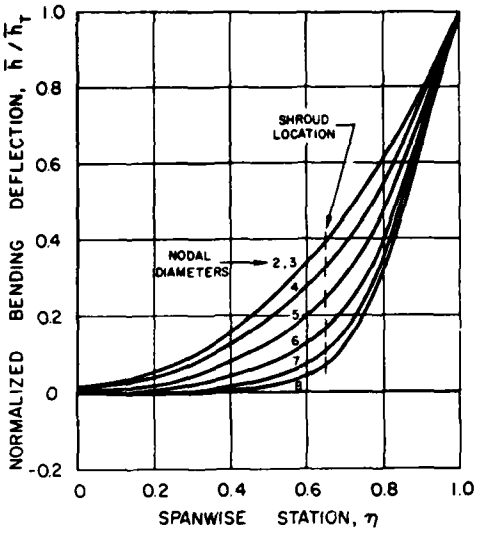

Fig. 22.3.3 Spanwise Variation of Bending Deflection Normalized with Respect to Tip Bending Deflection for Each Nodal Diameter

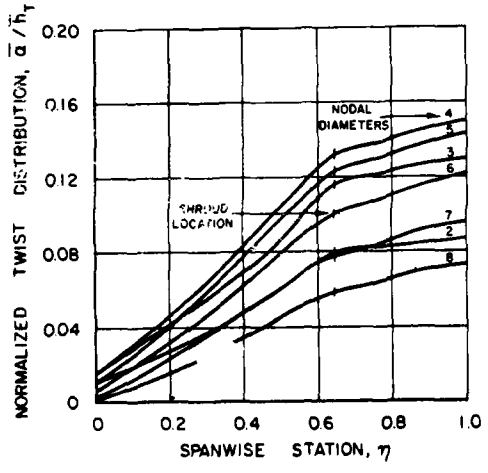

Fig. 22.3.4 Spanwise Variation of Twist Distribution Normalized with Respect to Tip Bending Deflection for Each Nodal Diameter

increases and then decreases with increasing number of nodal diameters. This suggests a variable amount of coupling between bending and torsion as the system mode changes from one nodal diameter to another. Furthermore, the major change in twist distribution for each curve occurs over the portion of the blade inboard of the deformed shroud, which imposes a twisting moment on the blade as a result of this deformation. Hence, the presence of a deformed shroud produces the coupling between blade twist and bending, and the degree of this coupling is modified by the diametric modal pattern.

A very revealing and informative plot is shown in Fig. 22.3.5, in which only the tip value of the normalized deformation ratio, $(\bar{\alpha}/\bar{h}_T)_T$, has been plotted as a function of frequency. This figure indicates a very strong variation of $(\bar{\alpha}/\bar{h}_T)_T$ with the number of nodal diameters (i.e., with natural frequency); it is relatively small at both small and large nodal diameters and reaches a maximum value at approximately 4 or 5 nodal diameters. Thus, it appears that torsion-bending coupling is a maximum for intermediate nodal diameters, with a predominantly bending motion occurring at either extreme. This increase in coupling for intermediate nodal diameters may be regarded as either a relative increase in blade twist or a relative decrease in blade bending. The absolute deformations are unimportant since the stability equations (22.3.8) or (22.3.9) are expressed solely in terms of the normalized deformations $\bar{h}/\bar{h}_T$ and $\bar{\alpha}/\bar{h}_T$.

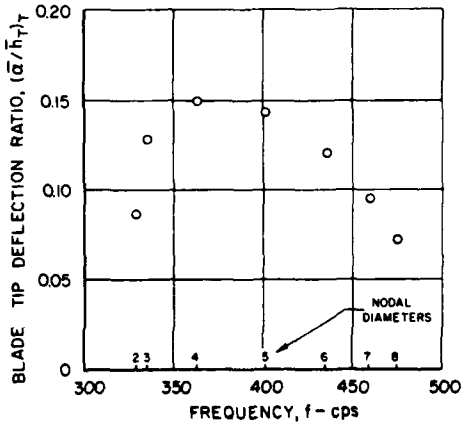

Fig. 22.3.5 Variation of Blade Tip Deflection Ratio with Frequency

It is noted in Ref. 22.8 that the measured velocities in the region of the rotor blade tip are generally in excess of 1000 ft/sec. Although these velocities are rather large, the unsteady incompressible flow theory from Ref. 22.13 was used to make the analysis amenable to parametric variation. As stated earlier, the purpose of the analysis in Ref. 22.8 was to understand the mechanism of this coupled flutter phenomenon, and to achieve that end, only the simplest of aerodynamic inputs are considered herein.

The stability analysis of the rotor system for any given nodal pattern was performed by calculating the spanwise variation of the reduced frequency parameter, k, and using this to obtain the spanwise variations in the unsteady aerodynamic coefficients, k^2A_{1r}, k^2A_{1p}, k^2B_{1r}, k^2B_{1i}, which are functions of k. These quantities were then

inserted into Eq. (22.3.8) together with the normalized mode shapes and other spanwise variables and integrated numerically. Finally, the logarithmic decrement, δ, was computed from Eq. (22.3.9) for each nodal diameter (2 through 8) at the resonant frequencies appropriate for each case. Results of these stability calculations are found in Fig. 22.3.6. The natural frequency in each case is denoted by the circled point. System stability is indicated by positive values of δ and instability is indicated by negative values of δ. It is seen from this figure that the system is stable for the 2, 6, 7, and 8-nodal-diameter modes and is unstable for the 3, 4, and 5-nodal-diameter modes, with minimum stability (i.e., maximum instability) occurring at four nodal diameters. A comparison of Fig. 22.3.6 with Fig. 22.3.5 reveals a strong correlation between maximum system instability and maximum torsion-bending coupling, represented in Fig. 22.3.5 by the maximum values of $(\bar{\alpha}/\bar{h}_T)_T$ at 4 nodal diameters. Similar results have been obtained for a number of rotor configurations which were analyzed using these procedures. Thus it was tentatively concluded that the greater the degree of coupling between torsion and bending in a shrouded rotor, the greater is the likelihood of a coupled flutter instability. The ability of this theory to predict the flutter boundary of actual turbomachine rotors is discussed in the next section.

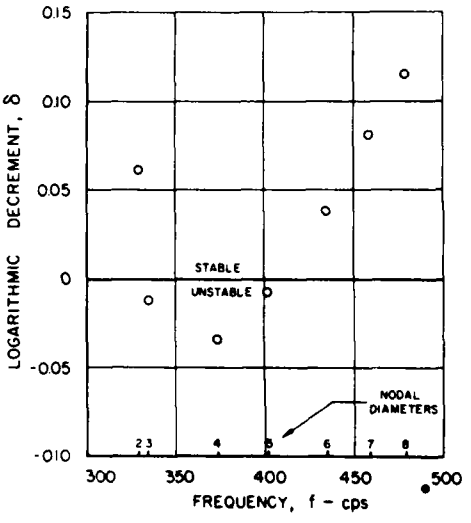

Fig. 22.3.6 Variation of Logarithmic Decrement with Frequency using Isolated Airfoil Theory from Ref. 22.13

22.3.2 ROTOR APPLICATIONS

A Symposium on Propulsion System Structural Integration and Engine Integrity was held in September 1974 at the Naval Postgraduate School, Monterey, California. The proceedings of this meeting appeared as a collection of papers published in the April 1975 issue of the Journal of Aircraft (Ref. 22.74). It is interesting to note that of the 39 papers presented at the meeting, no more than 3 or 4 dealt with the design aspects of flutter prevention. This is indicative of two facets of the flutter design procedure currently employed. The first is that it is limited in its usefulness to only those problems that are amenable to direct analysis, as will be seen presently. The second is that it remains a proprietary item to virtually all of the large engine manufacturers. Therefore, the discussion of this section will be limited by these constraints to material available only in the open literature.

To begin with, it is useful to review briefly the scope of the paper by Mikolajczak and his coworkers (Ref. 22.10) that was presented at the Monterey Symposium. The paper first discusses the flutter prediction model which utilizes the energy method of Ref. 22.8 (examined in the previous section). The work per cycle is extended somewhat by the inclusion of the material and structural dynamic damping of the system, by noting that flutter occurs when

$$\delta_{total} = \delta_{aero} + \delta_{mechanical} < 0 \qquad (22.3.11)$$

where δ represents the logarithmic decrement for each damping source. However, for a conservative prediction it is customary to assume that $\delta_{mechanical} = 0$. Next the paper examines the various possible mode shapes and frequencies. It is noted that for a rotor with n blades vibrating in a N nodal diameter pattern, the interblade phase angle will be

$$\sigma = \pm 2\pi N/n \qquad (22.3.12)$$

with the algebraic sign dependent on whether the wave is traveling forward or backward on the rotor. It is further stated that both forward and backward waves must be analyzed for flutter prediction to determine the least stable mode. The paper then goes into various methods to predict and to measure the system mode shapes and frequencies to ensure accuracy in the final analysis.

In a section on unsteady aerodynamics, the paper discusses the characteristics and symptoms of the several flutter problems illustrated by Fig. 22.1.2. However, the emphasis here is placed on supersonic unstalled flutter and most of the remainder of the paper is devoted to this problem. This situation is defined to exist if a self-excited vibration of the blades in a rotor occurs when the rotor inlet flow relative to the blades is supersonic over a significant portion of the blade span and the internal passage flow is unstalled. This flutter exhibits the following characteristics:

1) The boundary is a limit on high-speed operation as shown in Fig. 22.1.2.

2) Supersonic unstalled flutter is not related to an off-design aerodynamic condition but can occur at the design point.

3) Strain-gage records show that prior to flutter each blade in a rotor may be vibrating at a low stress level at its own natural frequency, but when flutter is encountered and the stress level becomes significant, all blades flutter at the same frequency with a constant interblade phase angle between the blades. Thus, there is a traveling wave which rotates with respect to the rotor.

4) The onset of the flutter is characterized by a sudden increase in blade stress at a natural mode frequency. It has been observed that the stress boundary is very steep; however, because of mechanical damping and nonlinearities in the system, a catastrophic failure does not occur and it is possible to obtain some data during flutter.

5) Flutter stress is reduced as the fan pressure ratio is increased at a constant speed. Hence, the most critical requirement is to predict the onset of flutter at the low pressure ratios.

The unsteady aerodynamic forces calculated using the linearized supersonic and compressible subsonic analyses of Refs. 22.12 and 22.41 can be used for the prediction of the unstalled supersonic flutter boundary for high speed fans with part-span shrouds. Vibrational mode shape calculations show that for such fans only the outer 50 to 60 percent of the blade contributes significantly to the unsteady aerodynamic work. This is the portion of the rotor blade where the relative inlet flow is supersonic, blade camber is low, blades are thin, and at low pressure ratio the steady state shocks are weak.

The supersonic unsteady analysis and a coupled blade-disk-shroud vibration analysis have been used successfully to calculate the aerodynamic damping and hence the susceptibility to flutter of high tip speed fan rotors. Detailed comparisons of predictions with experimental data were given for two fan rotors (Rotors A and B) and an overall comparison was made for four additional rotors.

Rotor A was designed to experience supersonic unstalled flutter in the second mode when the relative inlet Mach number was greater than 1.4. Rotor B was an 1800 ft/sec tip speed NASA fan stage which was designed to be flutter free. The aerodynamic damping of both rotors was calculated using the equations developed in Ref. 22.8 and subsequently modified for actual use in the design applications. Spanwise integration of the work term was carried out over the portion of the blade where the relative inlet Mach number was greater than 1.1. For both rotors, the first three vibrational modes were analyzed to identify the least stable mode.

Rotor A

The rotor design is summarized in Table 1. The blade aspect ratio, part-span shroud location and thickness distribution were chosen so that unstalled supersonic flutter would occur in the second mode.

TABLE 1 DESIGN PARAMETERS

	Rotor A	Rotor B
Tip Speed	1800 ft/sec @ 15,000 rpm	1800 ft/sec @ 12,464 rpm
Hub to tip ratio	0.38	0.50
Aspect ratio based on root chord	4.00	2.87
Part-span shroud position	50%	65%

The rotor experienced supersonic unstalled flutter at 13,290 rpm while accelerating along a low pressure ratio operating line. Flutter occurred in the second mode with a four-nodal diameter vibrational pattern.

The predicted aerodynamic damping for the least stable nodal diameters of the first three vibrational modes of the rotor is given in Fig. 22.3.7. The calculated values show that, for low pressure ratio operation at this rotor speed, the second coupled mode is the least stable mode. The aerodynamic damping of the least stable vibrational mode is negative. Since flutter occurs when the sum of the aerodynamic damping and mechanical damping equals zero, a negative value of aerodynamic damping is necessary before flutter will occur in a rotor where mechanical damping is present.

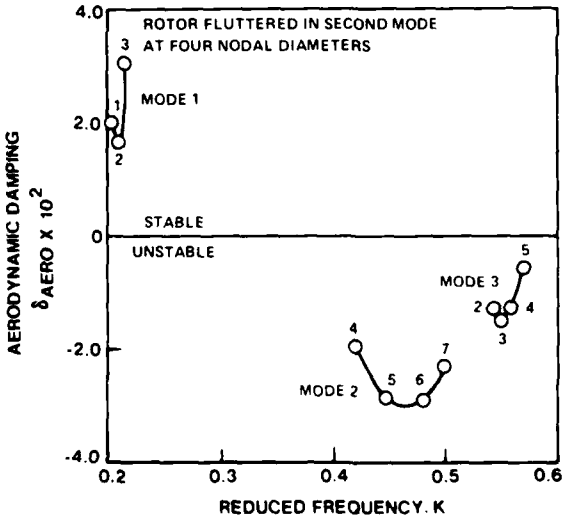

Fig. 22.3.7 Damping Predictions for Research Rotor at Flutter Speed

The sensitivity of aerodynamic damping to rotor speed is shown in Fig. 22.3.8. The rotor has been analyzed at three different rotor speeds, the lowest being where the least stable nodal diameter in the second mode has nearly zero aerodynamic damping. It can be seen that susceptibility of the rotor to flutter is reduced when speeds are lowered. The amount of mechanical damping in this rotor has not

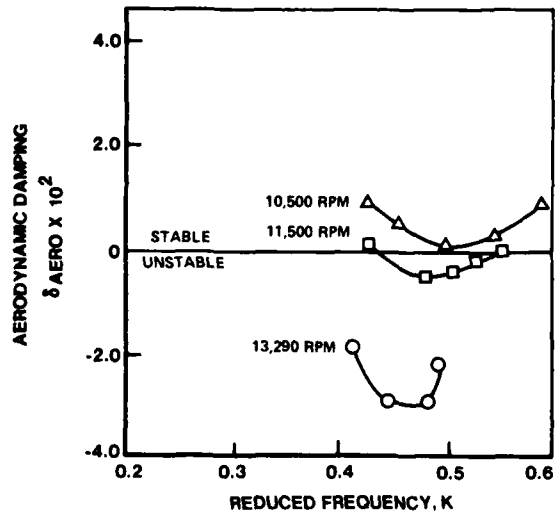

Fig. 22.3.8 Second Mode Damping as a Function of Rotor Speed

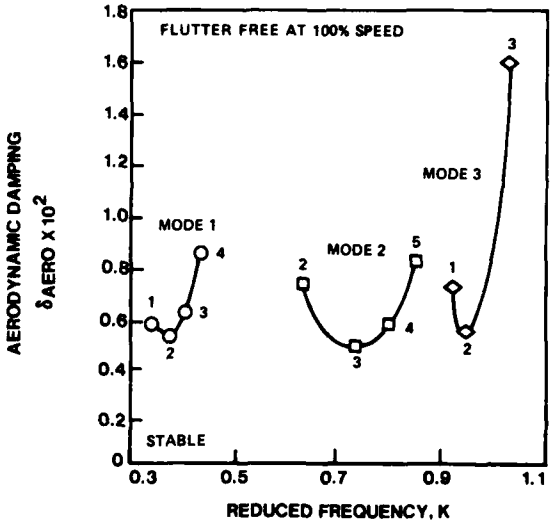

Fig. 22.3.9 Damping Prediction for NASA 1800 ft/sec Rotor at 100% Speed

been measured, but estimates based on material damping alone indicate that it could be as high as 0.02. At this level of damping, the predicted rotor flutter speed would be 5 percent lower than the actual speed at which flutter occurred. If we assume that the total mechanical damping (material damping and frictional damping at part-span shrouds and rotor root attachments) is approximately 0.03, then the predicted and the actual rotor speed at which flutter occurred match exactly. These comparisons show that the analysis predicts accurately the least stable flutter mode. However, it is conservative in predicting the rotor speed at which flutter occurs if the mechanical damping is assumed to be no greater than that due to the material hysteresis damping alone.

ROTOR B

Rotor B was designed to be flutter-free; its design is also summarized in Table 1. This rotor was tested successfully to 12,464 rpm and no supersonic unstalled flutter was observed. Figure 22.3.9 shows the results of analyzing the rotor at the maximum speed condition. All modes are calculated to have positive aerodynamic damping at this most severe condition. It can be seen that the design is optimized insofar as all the vibrational modes exhibit the same aerodynamic damping at this rotor speed. The high positive aerodynamic damping shows this fan to have been conservatively designed.

Other rotors were also analyzed using the procedures described above with comparable success. These included both shroudless and single and double shrouded fan stages, and the results are summarized in Ref. 22.10.

A comparable but somewhat more limited discussion of design applications in the supersonic regime is presented by Halliwell in Ref. 22.75. In general, he shows results that are similar in most respects to those of Ref. 22.10, even to the extent that the correct system mode is predicted to be unstable, but that the instability usually occurs at a lower nodal diameter value than is usually predicted (cf., Fig. 22.3.7). This particular reference is interesting in that it examines the spanwise distribution of energy in the various components of the work integral and clearly shows that: 1) the dominant contribution to instability is from the coupling term, 2) the dominant contribution to stability is from the bending term, and 3) the bulk of the energy in all three terms is concentrated in the outer 15 percent of the span.

Finally, we return to Ref. 22.10 to summarize its discussion of stalled flutter. This phenomenon usually occurs near the compressor surge line, and is identified by an increase in flutter stress (usually in the torsion mode for subsonic flow and in the bending mode for supersonic flow) as pressure ratio is increased along a constant speed line (cf., Fig. 22.1.2).

There are no experimental data available to indicate whether at the onset of flutter the flow is fully attached along the blade suction surface or is separated during part of the blade oscillation or is separated during the entire blade oscillation. Time-averaged flow measurements taken recently in a research fan stage during stall flutter have shown that aerodynamic losses behind the rotor did not increase measurably as the flutter boundary was crossed. Hence, it does not appear that a large portion of the blade was stalled during flutter. Furthermore in some instances the stall flutter boundary has been observed to occur near maximum

compressor efficiency indicating that stalling is not an essential condition for "stalled" flutter, although it could be the most severe condition. Indeed, it appears that a more accurate terminology to describe this phenomenon would be loaded cascade flutter.

Some efforts have been made to include the effects of blade loading on cascade aerodynamic stability. One of these, described more fully in Ref. 22.10, is an incompressible, unsteady flow analysis for small turning which was used in combination with the coupled blade-disk-shroud stability analysis to calculate the predicted aerodynamic damping for the first three vibrational modes of a number of shrouded fan stages operating at part speed. The second mode was predicted to be the least stable, and flutter was observed to occur in the second mode in all cases. However, no instability was actually predicted because the aerodynamic damping in the least stable mode, although small, remained positive even when the incidence was increased past the measured values. Hence, it does not appear that an incompressible, unsteady analysis for cascades with low flow turning can be used to accurately model the unsteady flowfield present during the "stalled" type of flutter.

At this writing, the loaded subsonic theory of Ref. 22.43 has not yet been completed and its use in a design analysis must necessarily take place at some time in the future. It is felt that this approach ultimately offers some hope in providing the designer with an analytical prediction technique that is sorely needed. In the interim he must rely on a combination of empiricism and approximation. Also at this writing, no progress is known to have been made in an analysis of the supersonic stalled flutter instability in the bending mode. The conditions to be modeled in this problem include high back pressure and strong, curved shocks both within and ahead of the blade passages, a combination that is much too formidible for the current state of the art.

22.4 LIST OF SYMBOLS

Note: Equation numbers refer to the defining relationship or to the first use of the given symbol. Multiple definitions are given for multiple use of symbols.

A	Disturbance amplitude function, Eqs. (22.2.27) and (22.2.101)
A_h, A_α	Influence coefficients, aerodynamic lift per unit deflection, Eq. (22.1.21)
$\bar{A},\bar{B},\bar{D},\bar{E}$,	Coefficients in the equation of motion, Eq. (22.1.25)
A,B	Matrices in Eq. (22.2.82)
a	Dimensionless distance of elastic axis aft of midchord, in semichords, Eq. (22.1.6) or speed of sound, ft/sec, Eq. (22.2.22)
a,b	Cascade parameters, Eq. (22.2.69)
B_h,B_α	Influence coefficients, aerodynamic moment per unit deflection, Eq. (22.1.21)
b	Airfoil semichord, ft, Eq. (22.1.1)
C	Damping coefficient, lb-sec, Eq. (22.2.123), or force coefficient matrix, Eq. (22.2.85)
C_c	Critical damping, lb-sec, Eq. (22.1.44)
C_{Fq},C_{F_α},C_{F_w}	Force coefficient due to given motion, Eq. (22.2.85)
C_M	Moment coefficient, Eq. (22.2.104)
C_{Mq},C_{M_α},C_{M_w}	Moment coefficient due to given motion, Eq. (22.2.85)
C_N	Normal force coefficient, Fig. 22.2.18
C_w	Work coefficient, Eq. (22.2.122)
C_α	Aerodynamic damping, lb-sec, Eq. (22.1.42)
C(k)	Theodorsen circulation function, Eq. (22.1.8)
c	Chord length, ft, Eq. (22.1.3)
D	Cascade parameter, Eq. (22.2.98)
F	Aerodynamic force per unit span, lb/ft, Eq. (22.2.60)
F(k)	Real part of Theodorsen function, Eq. (22.1.8)
F,G	Compressible cascade functionals, Eq. (22.2.102)
f	Frequency, cycles/sec, Fig. 22.1.14
G(k)	Imaginary part of Theodorsen function, Eq. (22.1.8)
g	Upper limit of integration, Eq. (22.2.31)
$Ho^{(2)}$,$H_1^{(2)}$	Hankel functions, Eq. (22.1.9)
h	Dimensionless bending deflection of elastic axis (or rotation point) in semichords, positive downward, Eq. (22.1.4)

$I_\alpha = \int r^2 dm$	Mass moment of inertia about elastic axis, slug ft^2, Eq. (22.1.5)
$I^{\pm}_{o,n}$	Influence functions, Eq. (22.2.99)
K	Kernel function, Eqs. (22.2.42) and (22.2.77), or semi-infinite series, Eq. (22.2.101)
K_o	Possio Kernel function, Eq. (22.2.87)
K_1	Kernel function, Eq. (22.2.88)
$\bar{K}_E$	Average system kinetic energy, ft-lb, Eq. (22.3.9)
K_h	Bending spring stiffness, lb/ft, Eq. (22.1.4)
K_α	Torsion spring stiffness, ft-lb, Eq. (22.1.5)
$k=b\omega/V$	Reduced frequency, Eq. (22.1.1)
k	Compressible reduced frequency, Eq. (22.2.93)
$\bar{k}$	Function defined by Eq. (22.2.33)
L	Lift, positive up, lb, Eq. (22.1.6)
L_h, L_α	Lift influence functions, Eq. (22.1.18)
L_1, L_2	Lift functions, Eq. (22.1.4))
M	Moment about elastic axis, positive nose up, ft-lb, Eq. (22.1.7), or Mach number, Eq. (22.2.22)
M_h, M_α	Moment influence function, Eq. (22.1.18)
M_1, M_2, M_3	Moment functions, Eq. (22.1.30)
m	Wing mass per unit span, slug, Eq. (22.1.4), or blade number, Eq. (22.2.62)
N	Rotor speed, rpm, Fig. 22.1.14, or number of nodal diameters, Eq. (22.3.12)
n	Blade number, Eq. (22.2.88) or number of blades in rotor, Eq. (22.3.12)
P	Modified relative pressure, Eq. (22.2.95)
p	Pressure, lb/ft^2. Eq. (22.2.3)
Q_h	Generalized force in bending mode per unit span, lb, Eq. (22.1.4)
Q_α	Generalized force in torsion mode per unit span, ft-lb, Eq. (22.1.5)
q	Dynamic pressure, lb/ft^2, Fig. 22.2.23, or blade vertical translation, ft/sec, Eq. (22.3.79)
R	Radius function, ft, Eq. (22.2.28), or dimensionless function, Eq. (22.2.91)
r	Chordwise coordinate relative to elastic axis, positive aft, ft (used in definition of S_α below), or radius, ft, Eq. (22.3.10)
r, r_o	Radius functions, ft, Eqs. (22.2.89), (22.2.90)
r_α	Radius of gyration about elastic axis, ft, Eq. (22.1.28)
$S_\alpha = \int r dm$	Static moment about elastic axis, slug ft, Eq. (22.1.4)
s	Cascade gap, ft, Fig. 22.2.2, or Laplace transform variable, Eq. (22.2.47)
T	Disturbance period, sec, Eq. (22.1.2), or time, sec, Eq. (22.2.27)
t	Time, sec, Eq. (22.1.10)
U	Free stream velocity, ft/sec, Eq. (22.2.1)
u	Perturbation velocity, ft/sec, Eq. (22.2.54), or function defined by Eq. (22.2.43)
V	Free stream velocity, ft/sec, Eq. (22.2.1), or auxiliary function, Eq. (22.2.67), or normal velocity distribution, Eq. (22.2.101)
V_P	Propagation velocity, ft/sec, Eq. (22.2.107)
v	Induced vertical velocity, ft/sec, Eq. (22.2.64)
W	Work per cycle, ft-lb, Eq. (22.2.103)
w	Downwash velocity, ft/sec, Eq. (22.2.1) or transverse gust velocity, ft/sec, Eq. (22.2.79)
w'	Function defined by Eq. (22.2.33)
$X=(\omega_\alpha/\omega)^2$	Frequency ratio used in flutter solution, Fig. 22.1.9
X_α	Location of center of gravity relative to elastic axis, positive aft, ft, Eq. (22.1.27)

x Dimensionless chordwise position in semichords, positive aft, Eq. (22.2.1)

x_A, y_A Cascade parameters, Eq. (22.2.96)

x_n Distance from blade l.e. to pitching axis, Fig. (22.2.8)

z Vertical coordinate, positive up, ft, Eq. (22.2.1)

α Angular deflection about elastic axis (or rotation point), positive nose up, rad or deg, Eq. (22.1.4)

β Southwell stiffness parameter, Eq. (22.1.58) or interblade phase angle, positive forward, deg or rad, Eq. (22.2.62), or compressible function $= \sqrt{1-M^2}$, Eq. (22.2.86)

β_1^* Cascade stagger angle, deg or rad, Fig. 22.2.11

Γ Airfoil bound circulation, ft^2/sec, Eq. (22.2.7), or circulation matrix, Eq. (22.2.82)

γ Damping ratio, Eq. (22.1.45), or vorticity distribution, ft/sec, Eq. (22.2.2)

δ Logarithmic decrement, Eq. (22.3.9)

ε Free vorticity, ft/sec, Eq. (22.2.51)

ζ Vertical coordinate, ft, Eq. (22.2.27)

η Chordwise coordinate, Eq. (22.2.64) or dimensionless spanwise station, Eq. (22.3.10)

θ Phase angle between torsion and bending, rad, Eq. (22.1.11), or cascade stagger angle, deg or rad, Eq. (22.2.91)

Λ_1 Auxiliary function, Eq. (22.2.17)

λ Disturbance wavelength, ft, Eq. (22.1.2), or reduced frequency based on full chord, Eq. (22.2.72), or function defined by Eq. (22.2.43)

λ, λ_o Characteristic value of equation of motion and no flow value, sec^{-1}, Eqs. (22.1.39), (22.1.40)

μ Mass parameter, Eq. (22.1.26), or compressible function, $= \sqrt{M^2-1}$, Eq. (22.2.93)

ν Integer, Eq. (22.2.112)

Ξ Dimensionless aerodynamic damping, Eq. (22.2.136)

ξ Aerodynamic damping, ft lb, Eq. (22.2.132), or cascade stagger angle, deg or rad, Fig. 22.2.2, or dimensionless chordwise coordinate in semichords, positive aft, Eq. (22.2.2)

ρ Air Density, $slug/ft^3$, Eq. (22.1.6)

σ Interblade phase angle, positive forward, deg or rad, Eq. (22.2.91)

τ Cascade gap, ft, Eq. (22.2.86)

ϕ Disturbance potential, ft^2/sec, Eq. (22.2.44), or velocity potential, Eq. (22.2.92)

ψ Acceleration potential, $(ft/sec)^2$, Eq. (22.2.22), or modified velocity potential, Eq. (22.2.94)

Ω Rotor angular velocity, rad/sec, Eq. (22.1.58), or interblade function, Eq. (22.2.97)

ϖ Auxiliary function, Eq. (22.2.12)

ω Oscillatory frequency, rad/sec, Eq. (22.1.1), or reduced frequency based on full chord, Eq. (22.2.93)

$\omega_h \quad \omega_\alpha$ Natural modal frequencies, rad/sec, Eqs. (22.1.14), (22.1.15)

ω_o No flow frequency, rad/sec, Eq. (22.1.40)

ω_1, ω_2 Frequencies used in Southwell Theorem, rad/sec, Eq. (22.1.57)

$\bar{\omega}$ Compressible reduced frequency, Eq. (22.2.49)

Subscripts, superscripts, and operators

$( )_a$ On airfoil, Eq. (22.2.2)

$( )_D$ Doublet, Eq. (22.2.34)

$( )_I$ Imaginary part, Eq. (22.2.117)

$( )_m$ Pertaining to mth blade, Eq. (22.2.62)

$( )_{MCL}$ Referred to mean camber line, Fig. 22.2.22

$( )_o$	Root value, Eq. (22.3.10)
$( )_q$	Due to blade vertical translation, Eq. (22.2.80)
$( )_R$	Real part, Eq. (22.2.115)
$( )_S$	Source, Eq. (22.2.30)
$( )_{SP}$	Source pulse, Eq. (22.2.27)
$( )_T$	Tip Value, Eq. (22.3.8)
$( )_w$	In wake, Eq. (22.2.2), or due to transverse gust, Eq. (22.2.80)
$( )_\alpha$	Due to pitch, Eq. (22.2.80)
$( )_+$	Just above plane of airfoil, Eq. (22.2.55)
$( )_-$	Just below plane of airfoil, Eq. (22.2.55)
$( )_\infty$	Free stream value, Eq. (22.2.23)
$( )^*$	Transformed quantity, Eq. (22.2.47), or dimensionless coordinate, Eq. (22.2.48)
$(\cdot)$, $(\cdot\cdot)$	First and second derivative with respect to time, Eq. (22.1.4)
$(\bar{\ })$	Amplitude, Eq. (22.1.10)
$D( )$	Substantial derivative, Eq. (22.2.24)
$\Delta( )$	Difference, upper minus lower, Eq. (22.2.3)
∇^2	Laplacian operator, Eq. (22.2.45)
$\mathcal{L}$	Laplace transform operator, Eq. (22.2.47)
$\oint$	Cyclic integral, Eq. (22.2.115)
$\int$	Cauchy principal value, Eq. (22.2.2)

22.5 REFERENCES

1. Bisplinghoff, R. L., H. Ashley, and R. L. Halfman: Aeroelasticity. Addison-Wesley Publishing Company, Reading, Mass., 1955.

2. Pearson, H.: The Aerodynamics of Compressor Blade Vibration. Fourth Angle-American Aeronautical Conference, London, September 15-17, 1953, pp. 127-162.

3. Shannon, J. F.: Vibration Problems in Gas Turbines, Centrifugal and Axial-Flow Compressors. A.R.C. R.&M. No. 2226, 1945.

4. Armstrong, E. K. and R. E. Stevenson: Some Practical Aspects of Compressor Blade Vibration. Journ. Royal Aero. Soc., Vol. 64, No. 591, March 1960, pp. 117-130.

5. Sisto F. and Ron Ho Ni: Research on the Flutter of Axial-Turbomachine Blading. Stevens Institute of Technology, Technical Report ME-RT 70004, June 1970.

6. Carter, A. D. S.: Some Preliminary Notes on the Flutter of Axial Compressor Blades. N.G.T.E. Memorandum No. M. 181, November 1953.

7. Carter, A. D. S. and D. A. Kilpatrick: Self-Excited Vibration of Axial-Flow Compressor Blades. Proceedings of the Institution of Mechanical Engineers, Vol. 171, 1957, pp. 245-281.

8. Carta, F. O.: Coupled Blade-Disk-Shroud Flutter Instabilities in Turbojet Engine Rotors. Trans. ASME, Journ. Engineering for Power, Vol. 89(A), No. 3, July 1967, pp. 419-426.

9. Stargardter, H.: Dynamic Models of Vibrating Rotor States. Presented at ASME Winter Annual Meeting, November 1966, Paper No. 66-WA/GT-8.

10. Mikolajczak, A. A., L. E. Snyder, R. A. Arnoldi, and H. Stargardter: Advances in Fan and Compressor Blade Flutter Analysis and Predictions. AIAA Journal of Aircraft, Vol. 12, No. 4, April 1975, pp. 325-332.

11. Verdon, J. M.: The Unsteady Aerodynamics of a Finite Supersonic Cascade With Subsonic Axial Flow. Transactions of the ASME, Journal of Applied Mechanics, Ser. E., Vol. 40, No. 3, Sept. 1973, pp. 667-671.

12. Verdon, J. M. and J. E. McCune: Unsteady Supersonic Cascade in Subsonic Axial Flow. AIAA Journal, Vol. 13, No. 2, February 1975, pp. 193-201.

13. Theordorsen, T.: General Theory of Aerodynamic Instability and the Mechanism of Flutter. NACA Report 496, 1935.

14. Schwarz, L.: Berechnung der Druckverteilung einer Harmonisch sich Verformenden Tragfläche in ebener Strömung. Luftfahrt forschung, Vol. 17, 1940, p. 379.

15. Smilg, B. and L. S. Wasserman: Application of Three-Dimensional Flutter Theory to Aircraft Structures. U. S. Air Force Technical Report 4798, 1942.

16. Scanlan, R. H. and R. Rosenbaum: Introduction to the Study of Aircraft Vibration and Flutter. The MacMillan Co., New York, 1951.

17. Bisplinghoff, R. L. and H. Ashley: Principles of Aeroelasticity. John Wiley and Sons, New York, 1962.

18. Pines, S.: An Elementary Explanation of the Flutter Mechanism. Proc. National Specialists Meeting on Dynamics and Aeroelasticity, Inst. of the Aeronautical Sciences, Ft. Worth, Texas, November 1958, pp. 52-58.

19. Den Hartog, J. P.: Mechanical Vibrations, McGraw-Hill Book Company, Inc., New York, 1956.

20. Timoshenko, S., D. H. Young and W. Weaver: Vibration Problems in Engineering, Fourth Edition. John Wiley and Sons, New York, 1974.

21. Reissner, E.: Effect of Finite Span on the Airload Distributions for Oscillating Wings, I - Aerodynamic Theory of Oscillating Wings of Finite Span. NACA TN 1194, 1947.

22. Söhngen, H.: Die Lösungen der Integralgleichung und deren Anwendung in der Tragflügeltheorie. Math. Z., Band 45, 1939, pp. 245-264.

23. Possio, C.: L'Azione Aerodinamica sul Profilo Oscillante in un Fluido Compressibile a Velocità Iposonora. L'Aerotecnica, t. XVIII, fasc. 4, April 1938. (see also British Ministry of Aircraft Production R.T.P. translation 987)

24. Dietze, F.: The Air Forces of the Harmonically Vibrating Wing at Subsonic Velocity (Plane Problem), Parts I and II. U. S. Air Force Translations F-TS-506-RE and F-TS-948-RE, 1947. (Originally, Luftfahrt forschung, Bd. 16, Lfg. 2, 1939, S. 84-96.)

25. Fettis, H. E.: An Approximate Method for the Calculation of Nonstationary Air Forces at Subsonic Speeds. U. S. Air Force, Wright Air Development Center Technical Report 52-56, 1952.

26. Timman, R., A. I. van de Vooren, and J. H. Griedanus: Aerodynamic Coefficients of an Oscillating Airfoil in Two-Dimensional Subsonic Flow. Journal of the Aeronautical Sciences, Vol. 18, No. 12, December 1951, pp. 797-802. (Corrected tabulations appear in Journal of the Aeronautical Sciences, Vol. 21, No. 7, July 1954, pp. 499-500.)

27. Fettis, H. H.: Tables of Lift and Moment Coefficients for an Oscillating Wing Aileron Combination in Two-Dimensional Subsonic Flow. Air Force Technical Report 6688, 1951.

28. Luke, Y. L.: Tables of Coefficients for Compressible Flutter Calculations. Air Force Technical Report 6200, 1950.

29. Garrick, I. E. and S. I. Rubinow: Flutter and Oscillating Air Force Calculations for an Airfoil in Two-Dimensional Supersonic Flow. NACA Report 846, 1946.

30. Miles, J. W.: The Potential Theory of Unsteady Supersonic Flow. Cambridge University Press, Cambridge, England, 1959.

31. Lilley, G. M.: An Investigation of the Flexure-Torsion Flutter Characteristics of Aerofoils in Cascade. College of Aeronautics, Cranfield Report No. 60, 1952.

32. Sisto, F.: Unsteady Aerodynamic Reactions on Airfoils in Cascade. Journal of the Aeronautical Sciences, Vol. 22, No. 5, May 1955, pp. 297-302.

33. Lane, R. and C. T. Wang: A Theoretical Investigation of the Flutter Characteristis of Compressor and Turbine Blade Systems. Wright Air Development Center Technical Report 54-449, 1954.

34. Whitehead, D. S.: Force and Moment Coefficients for Vibrating Aerofoils in Cascade. Great Britain A.R.C. R.&M. No. 3254, 1962.

35. Whitehead, D. S.: The Aerodynamics of Axial Compressor and Turbine Blade Vibration. PhD. Thesis, Cambridge University, Cambridge, England, 1957.

36. Bromwich, T. J.: An Introduction to the Theory of Infinite Series. 2nd ed., McMillan & Co., Ltd., London, 1955.

37. Carta, F.O.: Unsteady Aerodynamic Theory of a Staggered Cascade of Oscillating Airfoils in Compressible Flow. United Aircraft Research Department Report R-0582-19, August 1957.

38. Lane, F. and M. Friedman: A Theoretical Investigation of Subsonic Oscillatory Blade-Row Aerodynamics. NACA Technical Note 4136, February 1958.

39. Whitehead, D. S.: Vibration and Sound Generation in a Cascade of Flat Plates in Subsonic Flow. Great Britain A.R.C. R.&M. No. 3865, February 1970.

40. Kaji, S. and T. Okazaki: Propagation of Sound Waves Through a Blade Row, II. Analysis Based on the Acceleration Potential Method. Journal of Sound and Vibration, Vol. 11, No. 3, March 1970, pp. 355-375.

41. Smith. S. N.: Discrete Frequency Sound Generation in Axial Flow Turbomachines. Great Britain A.R.C. R.&M. 3709, 1971.

42. Runyan, H. L., D. S. Woolston and A. G. Rainey: Theoretical and Experimental Investigation of

the Effect of Tunnel Walls on the Forces on an Oscillating Airfoil in Two-Dimensional Subsonic Compressible Flow. NACA Report 1262, 1956.

43. Verdon, J. M., J. J. Adamczyk, and J. R. Caspar: Subsonic Flow Past an Oscillating Cascade with Steady Blade Loading -- Basic Formulation. United Aircraft Research Laboratories Report R75-214185-1, April 1975. (Also presented at a Symposium on Unsteady Aerodynamics, sponsored by the University of Arizona and the United States Air Force Office of Scientific Research, March 18-20, 1975.)

44. Lane, F.: Supersonic Flow Past an Oscillating Cascade With Supersonic Leading-Edge Locus. Journal of the Aeronautical Sciences, Vol. 24, No. 1, January 1957, pp. 65-66.

45. Snyder, L. E. and G. L. Commerford: Supersonic Unstalled Flutter in Fan Rotors; Analytical and Experimental Results. Transactions of the ASME, Journal of Engineering for Power, Series A, Vol 96, No. 4, October 1974, pp. 379-386.

46. Verdon, J. M.: Further Developments in the Aerodynamic Analysis of Unsteady Supersonic Cascades, Part 1: The Unsteady Pressure Field; Part 2: Aerodynamic Response Predictions. Presented at ASME Gas Turbine Conference, March 1977, Paper Nos. 77-GT-44 and 77-GT-45. Also to be published in Trans. ASME, Journal of Engineering for Power.

47. Kurosaka, M.: On the Unsteady Supersonic Cascade with a Subsonic Leading Edge - An Exact First Order Theory: Parts 1 and 2. Transactions of the ASME, Journal of Engineering for Power, Ser. A., Vol. 96, No. 1, January 1974, pp. 13-31.

48. Brix, C. W. and M. F. Platzer: Theoretical Investigation of Supersonic Flow Past Oscillating Cascades with Subsonic Leading Edge Locus. AIAA Paper 74-14, Washington, D. C., 1974.

49. Bratt, J. B. and C. Scruton: Measurements of Pitching Moment Derivatives for an Aerofoil Oscillating About the Half-Chord Axis. A.R.C. R.& M. No.1921, November 1938.

50. Victory, M.: Flutter at High Incidence. A.R.C. R.& M. No. 2048, January 1943.

51. Mendelson, A.: Aerodynamic Hysteresis as a Factor in Critical Flutter Speed of Compressor Blades at Stalling Conditions. Journal Aero. Sci., Vol. 16, No. 11, November 1949, pp. 645-652.

52. Wang, C. T., R. J. Vaccaro and D. F. DeSanto: A Practical Approach to the Problem of Stall Flutter. Paper presented at the ASME Semi-Annual Meeting, June 1955, Paper No. 55-SA-69.

53. Halfman, R. L., H. C. Johnson and S. M. Haley: Evaluation of High-Angle-of-Attack Aerodynamic-Derivative Data and Stall-Flutter Prediction Techniques. NACA TN 2533, November 1951.

54. Baker, J. E.: The Effects of Various Parameters, Including Mach Number, on Propeller-Blade Flutter with Emphasis on Stall Flutter. NACA TN 3357, January 1955.

55. Brooks, G. W. and J. E. Baker: An Experimental Investigation of the Effect of Various Parameters, Including Tip Mach Number, on the Flutter of Some Model Helicopter Rotor Blades. NACA TN 4005, September 1958.

56. Rainey, A. G.: Preliminary Study of Some Factors Which Affect the Stall-Flutter Characteristics of Thin Wings. NACA TN 3622, March 1956.

57. Regier, A. A. and A. G. Rainey: Effect of Mean Incidence on Flutter. Paper presented at Seventh Meeting, Structures and Materials Panel, AGARD, Rome, Italy, March-April 1958.

58. Rainey, A. G.: Measurement of Aerodynamic Forces for Various Mean Angles of Attack on an Airfoil Oscillating in Pitch and on Two Finite-Span Wings Oscillating in Bending with Emphasis on Damping in the Stall. NACA Report 1305, 1957.

59. Carta, F. O.: Experimental Investigation of the Unsteady Aerodynamic Characteristics of an NACA 0012 Airfoil. United Aircraft Research Lab., Report M-1283-1, August 1960.

60. Liiva, J., et al.: Two-Dimensional Tests of Airfoils Oscillating Near Stall, Vol. I, Summary and Evaluation of Results. USAAVLABS TR 68-13A, April 1968, AD 670957.

61. Carta, F. O., G. L. Commerford, R. G. Carlson, and R. H. Blackwell: Investigation of Airfoil Dynamic Stall and Its Influence on Helicopter Control Loads. USAAMRDL Technical Report 72-51, September 1972.

62. Carta, F. O. and C. F. Niebanck: Prediction of Rotor Instability at High Forward Speeds. Vol. III, Stall Flutter. USAAVLABS TR 68-18C, February 1969.

63. Ham, N. D.: Aerodynamic Loading on a Two-Dimensional Airfoil During Dynamic Stall. AIAA Journal, Vol. 6, No. 10, October 1968, pp. 1927-1934.

64. McCroskey, W. J. and R. K. Fisher: Detailed Aerodynamic Measurements on a Model Rotor in the Blade Stall Regime. Journal of the American Helicopter Society, Vol. 17, No. 1, January 1972, pp. 20-30.

65. Carta, F. O.: Effect of Unsteady Pressure Gradient Reduction on Dynamic Stall Delay. AIAA Journal of Aircraft, Vol. 8, No. 10, October 1971, pp. 839-841.

66. Carta, F. O.: Analysis of Oscillatory Pressure Data Including Dynamic Stall Effects. NASA CR-2394, May 1974.

67. McCroskey, W. J., L. W. Carr, and K. W. McAlister: Dynamic Stall Measurements on Oscillating Airfoils. AIAA Paper 75-125, Pasadena, California, January 1975.

68. Jeffers, J. D.,II and C. E. Meece, Jr.: F100 Fan Stall Flutter Problem. Review and Solution. AIAA Journal of Aircraft, April 1975, pp. 350-356.

69. Carta, F. O. and A. O. St. Hilaire; An Experimental Study on the Aeordynamic Response of a Subsonic Cascade Oscillating Near Stall. Project SQUID Technical Report UTRC-2-PU, July 1976.

70. Arnoldi, R. A., F. O. Carta, R. H. Ni, W. N. Dalton, and A. O. St. Hilaire: Analytical and Experimental Study of Subsonic Stalled Flutter. Air Force Office of Scientific Research Technical Report AFOSR-TR-77-0854, July 1977.

71. Fleeter, S., A. S. Novick, and R. E. Riffel: Supersonic Unsteady Aerodynamic Phenomena in Airfoil Cascades. Office of Naval Research Report EDR 8617, October 1975.

72. Fleeter, S., A. S. Novick, R. E. Riffel, and J. E. Caruthers: An Experimental Determination of the Unsteady Aerodynamics in a Controlled Oscillating Cascade. ASME Paper No. 76-GT-17, March 1976.

73. Triebstein, H., V. Carstens, and J. Wagener: Unsteady Pressures on a Harmonically Oscillating, Staggered Cascade. Part I: Incompressible Flow, Part II: Compressible Flow. DFVLR Reports DLR-FB 75-57 and DLR-FB 75-58, Göttingen, West Germany, October 1974. (English translations available from ESA, Paris, TT272 and TT273).

74. Many authors: Papers from a Symposium on Propulsion System Structural Integration and Engine Integrity, September 1974, Monterey, California. AIAA Journal of Aircraft, Vol. 12, No. 4, April 1975, pp. 193-436.

75. Halliwell, D. G.: Fan Supersonic Flutter: Prediction and Test Analysis. Great Britain A.R.C., R.& M. No. 3789, 1977.

22.6 BIBLIOGRAPHY

Abramson, H. N.: An Introduction To The Dynamics of Airplanes. The Ronald Press Company, New York, 1958.

Arnoldi, R. A., F. O. Carta, A. O. St. Hilaire, and W. N. Dalton: Supersonic Chordwise Bending Flutter in Cascades. Naval Air Systems Command Report No. PWA-5271, 31 May 1975.

Ashley, H., and G. Zartarian: Piston Theory - A New New Aerodynamic Tool for The Aeroelastician. Jour. Aero. Sciences, Vol. 23, No. 12, December 1976, pp. 1109-1118.

Ashley, H., and M. Landahl: Aerodynamics of Wings and Bodies. Addison-Wesley, Reading, Mass., 1965, pp. 97, 248-249.

Bell, J. K.: Theoretical Investigation of the Flutter Characteristics of Supersonic Cascades with Subsonic Leading-Edge Locus. Aeronautical Engineering Thesis, Naval Postgraduate School, Monterey, California, June 1975.

Bratt, J. B., K. C. Wight and A. Chinneck: Free Oscillations of an Aerofoil About the Half-Chord Axis at High Incidences, and Pitching Moment Derivatives for Decaying Oscillations. A.R.C. R.&M. No. 2214, September 1940.

Bratt, J. B. and K. C. Wight: The Effect of Mean Incidence, Amplitude of Oscillation, Profile and Aspect Ratio on Pitching Moment Derivatives. A.R.C. R.&M. No. 2064, 4 June 1945.

Campbell, W.: Protection of Steam Turbine Disc Wheels from Axial Vibration. ASME Paper No. 1920, May 26, 1924.

Campbell, W. and W. C. Heckman: Tangential Vibration of Steam Turbine Buckets. ASME Paper No. 1925, May 26, 1924.

Carter, A. D. S.: A Theoretical Investigation of the Factors Affecting Stalling Flutter of Compressor Blades. N.G.T.E., A.R.C. Technical Report No. R. 172, C.P. No. 265, April 1955.

Carter, A. D. S., D. A. Kilpatrick, C. E. Moss and J. Ritchie: An Experimental Investigation of the Blade Vibratory Stresses in a Single-Stage Compressor. N.G.T.E., A.R.C. Technical Report No. R. 174, C.P. No. 266, April 1955.

Cavaille, Y.: Aerodynamic Damping in Turbomachinery. ASME Paper No. 72-GT-8, March 1972.

Chadwick, W. R., J. K. Bell and M. F. Platzer: Analysis of Supersonic Flow Past Oscillating Cascades. In Unsteady Flow in Turbomachinery, AGARD-CP-177, Papers presented at the 46th Meeting of the AGARD Propulsion and Energetics Panel held at the Naval Postgraduate School, Monterey, California, September 22-26, 1975.

Cottney, D. J. and D. J. Ewins: Towards the Efficient Vibration Analysis of Shrouded Bladed Disk Assemblies. Transactions of the ASME, Journal of Engineering in Industry, Vol. 96, No. 3, August 1974, pp. 1054-1059.

Dye, R. C. F. and T. A. Henry: Vibration Amplitudes of Compressor Blades Resulting from Scatter in Blade Natural Frequencies. ASME Paper No. 68-WA/GT-3, December 1968.

Ehrich, F. F.: A Matrix Solution for the Vibration Modes of Nonuniform Disks. Journ. Appl. Mech., Vol. 23, No. 1, March 1956, pp. 1-7.

Ewins, D. J.: Vibration Characteristics of Bladed Disc Assemblies. Journal of Mechanical Engineering Science, Vol. 15, No. 3, 1973, pp. 165-186.

Fanti, R., and F. O. Carta: Aerodynamic Interaction Effects on a Staggered Cascade of Airfoils Oscillating in Two-Dimensional Compressible Flow. United Aircraft Corporation Research Department Report R-0582-17, August 1957.

Fleeter, S.: Fluctuating Lift and Moment Coefficients for Cascaded Airfoils in a Nonuniform Compressible Flow. AIAA Journ. of Aircraft, Vol. 10, No. 2, February 1973, pp. 93-98.

Fleeter, S., R. B. McClure, G. T. Sinnet and R. L. Holtman: The Torsional Flutter Characteristics of a Cantilevered Airfoil Cascade in a Supersonic Inlet Flow Field with a Subsonic Axial Component. AIAA Paper 74-530, Palo Alto, California, June 1974.

Fung, Y. C.: An Introduction to the Theory of Aeroelasticity. John Wiley and Sons, New York, 1955.

Garelick, M. S.: Nonsteady Airloads on Dynamically Stalling Two-Dimensional Wings. S. M. Thesis, M. I. T., June 1967.

Goldstein, M. E.: Cascade with Subsonic Leading-Edge Locus. AIAA Journal, Vol. 13, No. 8, August 1975, pp. 1117-1118.

Gorelov, D. N.: Lattices of Plates in an Unsteady Supersonic Flow. Fluid Dynamics, Vol. 1, No. 4, July-August 1966, Faraday Press, pp. 34-39 (Translation of Izv. AN SSSR. Mekhanika, Zhidkosti i Gaza, Vol. 1, No. 4, pp. 50-58, 1966).

Graham, R. W. and E. L. Costilow: Compressor Stall and Blade Vibration. (Chapter XI in Vol. III of Aerodynamic Design of Axial-Flow Compressors) NACA RM E56B03b, August 1, 1956, pp. 1-52.

Ham, N. D.: Stall Flutter of Helicopter Rotor Blades: A Special Case of the Dynamic Stall Phenomenon. Jour. American Helicopter Soc., Vol. 12, No. 4, October 1967, pp. 19-21.

Hamamoto, I.: Minute Harmonic Oscillations of a Flat Plate Cascade in Transonic Flow. Japanese 2nd Applied Mathematics and Mechanics General Meeting, Preprint, 1957.

Hawthorne, W. R.: Flow Through Moving Cascades of Lifting Lines With Fluctuating Lift. Journ. of Mechanical Engineering Science, Vol. 15, No. 1, 1973, pp. 1-10.

Henderson, R. E. and J. H. Horlock: An Approximate Analysis of the Unsteady Lift on Airfoils in Cascade. Trans. ASME, Journal of Engineering for Power, October 1972, pp. 233-240.

Huppert, M. C., H. F. Calvert and A. J. Meyer: Experimental Investigation of Rotating Stall and Blade Vibration in the Axial-Flow Compressor of a Turbojet Engine. NACA RM E54A08, April 26, 1954.

Ikui, T., M. Inoue and M. Kuromaru: Researches on the Two-Dimensional Retarded Cascade. Parts 1 and 2, Bulletim of JSME, Vol. 15, No. 84, 1972, pp. 705-720. Parts 3 and 4, Bulletin of JSME, Vol. 16, No. 92, February 1973, pp. 252-271.

Isogai, K.: An Experimental Study on the Unsteady Behavior of a Short Bubble on an Airfoil During Dynamic Stall with Special Reference to the Mechanism of the Stall Overshoot Effect. M. I. T. Aeroelastic and Structures Research Lab. Report, ASRL TR 130-2, June 1970.

Kemp, N. H. and W. R. Sears: Aerodynamic Interference Between Moving Blade Rows. Journ. of the Aeronautical Sciences, Vol. 20, No. 9, 1953, pp. 585-598.

Kilpatrick, D. A. and J. Ritchie: Compressor Cascade Flutter Tests - 20° Camber Blades, Medium and High Stagger Cascades. N.G.T.E., A.R.C. Technical Report No. R. 133, C. P. No. 197, December 1953.

Kilpatrick, D. A. and J. Ritchie: Compressor Cascade Flutter Tests - Part II. 40° Camber Blades, Low and Medium Stagger Cascades. N.G.T.E., A.R.C. Technical Report No. R. 163, C.P. No. 296, October 1954.

Kilpatrick, D. A. and R. A. Burrows: Aspect-Ratio Effects on Compressor Cascade Blade Flutter. A.R.C. R.&M. No. 3103, July 1956.

Kilpatrick, D. A., A. D. S. Carter and L. O'Neill: Blade Vibratory Stresses in a Multistage Axial-Flow Compressor. A.R.C. R.&M. No. 3181, January 1958.

Kurosaka, M. and J. M. Verdon: Discussion and Author's Closure - Unsteady Aerodynamics of a Finite Supersonic Cascade with Subsonic Axial Flow. Transactions of the ASME: Journal of Applied Mechanics, Ser. E, Vol. 41, No. 1, June 1974, pp. 539-541.

Kurosaka, M.: On the Issue of Resonance in an Unsteady Supersonic Cascade. AIAA Journal, Vol. 13, No. 11, November 1975, pp. 1514-1516.

Lane, F.: System Mode Shapes in the Flutter of Compressor Blade Rows. Journal of the Aeronautical Sciences, Vol. 23, No. 1, January 1956, pp. 54-66.

Lang, J. D.: A Model for the Dynamics of a Separation Bubble Used to Analyze Control-Surface Buzz and Dynamic Stall. AIAA Paper 75-867, Hartford, Connecticut, June 1975.

Lefcort, M. D.: An Investigation into Unsteady Blade Forces in Turbomechanics. ASME Paper No. 64-WA/GTP-3, November 1964.

Lotz, M. and J. Raabe: Blade Oscillations in One-

Stage Axial Turbomachinery. ASME Paper No. 68-FE-7, May 1968.

McCroskey, W. J.: Inviscid Flow Field of an Unsteady Airfoil. AIAA Journal, Vol. 11, No. 8, August 1973, pp. 1130-1137.

Miles, J. W.: The Compressible Flow Past an Oscillating Airfoil in a Wind Tunnel. Journal of the Aeronautical Sciences, Vol. 23, July 1956, pp. 671-678.

Nagashima, T. and D. S. Whitehead: Aerodynamic Forces and Moments for Vibrating Supersonic Cascade Blades. University of Cambridge Department of Engineering Report CUED/A - Turbo/TR59, 1974.

Namba, M.: Subsonic Cascade Flutter with Finite Mean Lift. AIAA Journal, Vol. 13, No. 5, May 1975, pp. 586-593.

Naumann, H. and H. Yeh: Lift and Pressure Fluctuations of a Cambered Airfoil under Periodic Gusts and Applications in Turbomachinery. ASME Paper No. 72-GT-30, March 1972.

Ni, R. H.: Nonstationary Aerodynamics of Arbitrary Cascades in Compressible Flow. Ph.D. Dissertation, Stevens Institute of Technology, Hoboken, N. J., June 1974.

Ni. R. H. and F. Sisto: Numerical Computation of Nonstationary Aerodynamics of Flat Plate Cascades in Compressible Flow. Paper No. 75-GT-5, ASME Int. Gas Turbine Conference, Houston, Texas, 1975.

Nishiyama, T. and H. Kobayashi: Theoretical Analysis for Unsteady Characteristics of Oscillating Cascade Airfoils in Subsonic Flows. Technology Reports, Tohoku University, Vol. 38, No. 1, July 1973, pp. 287-314.

Parker, R. and J. F. Watson: Interaction Effects Between Blade Rows in Turbomachines. Proceedings of the Institution of Mechanical Engineers, Vol. 186, 1972, pp. 331-340.

Platzer, M. F. and H. G. Chalkley: Theoretical Investigation of Supersonic Cascade Flutter and Related Interference Problems. AIAA Paper 72-377, San Antonio, Texas, 1972.

Platzer, M. F.: Unsteady Flows in Turbomachines - A Review of Current Developments. Presented at the AGARD Symposium on Unsteady Aerodynamics, Ottawa, Canada, 26-28 September, 1977. (To be published in AGARD - CPP - 227).

Rowe, J. R. and A. Mendelson: Experimental Investigation of Blade Flutter in an Annular Cascade. NACA TN 3581, November 1955.

Samoilovich, G. S.: Resonance Phenomena in Sub- and Supersonic Flow Through an Aerodynamic Cascade. Mekhanika Zhidkosti i Gaza, Vol. 2, No. 3, May-June 1967, pp. 143-144.

Samoilovich, G. S.: Unsteady Flow Around and Aeroelastic Vibration in Turbomachine Cascades. (Translated from Russian), Report FTD-HT-23-242-70, Foreign Technology Division, WPAFB, Ohio, February 1971.

Schnittger, J. R.: Single Degree of Freedom Flutter of Compressor Blades in Separated Flow. Journal Aero. Sci., Vol. 21, No. 1, January 1954, pp. 27-36.

Schnittger, J. R.: The Stress Problem of Vibrating Compressor Blades. Journ. Appl. Mech., Vol. 22, No. 1, 1955, pp. 57-64.

Shinohara, K., H. Tanaka and Y. Hanamura: Stall Flutter of a Thin Aerofoil with Leading Edge Separation. Bulletins of JSME, Vol. 17, No. 107, May 1974, pp. 578-586.

Sisto, F.: Flutter of Airfoils in Cascade. Sc.D. Dissertation, MIT, August 1952.

Sisto, F.: Stall Flutter in Cascades. Journ. Aero. Sci., Vol. 20, No. 9, September 1953, pp. 598-604.

Sisto, F.: Linearized Theory of Nonstationary Cascades at Fully Stalled or Supercaviated Conditions. ZAMM, Vol. 47, Part 8, 1967, pp-531-542.

Sisto, F.: Aeroelasticity of Fans and Compressors. Paper No. 9, AGARD-CP-34, Part 1, September 1968.

Sisto, F. and P. V. K. Perumal: Lift and Moment Predictions for an Oscillating Airfoil with a Moving Separation Point. ASME Paper 74-GT-28, 1974.

Sisto, F. and R. Ni: Research on the Flutter of Axial Turbomachine Blading. ONR Tech. Rept. ME-RT 74-008, May 1974, Stevens Institute of Technology, Hoboken, N. J.

Snyder, L. E.: Supersonic Unstalled Torsional Flutter. Aeroelasticity in Turbomachinery, Fleeter, S. ed., Proceedings of a Project SQUID Workshop held at Detroit Diesel Allison, Indianapolis, Ind., June 1-2, 1973, Project SQUID, Office of Naval Research, pp. 164-195.

Stargardter, H.: Optical Determination of Rotating Fan Blade Deflections. Trans. ASME, Journ. of Engineering for Power, Vol. 99, No. 2, April 1977, pp. 204-210.

Studer, H. L.: Experimentelle Untersuchunger über Flügelschwingungen. Mitt. aus dem Institute fur Aerod., Eidgenossiche Tech. H. S., Zürich, No. 4/5, 1936. (Experimental Study of Wing Flutter. A.R.C. Oscill. Paper No. 60.)

Tanida, Y., K. Hatta, and T. Asanuma; Experimental Study on Flutter in Cascading Blades. Bulletin of JSME, Vol. 6, No. 24, 1963, pp. 736-743.

Tanida, Y., and T. Okazaki: Stall Flutter in Cascade,

Parker, R.: Resonance Effects in Wake Shedding from Parallel Plates: Some Experimental Observations. Journal of Sound and Vibration, Vol. 4, No. 1, 1966, pp. 62-72.

Parker, R. and S. A. Awal: The Influence of Upstream Unsteadiness on the Vibration of Rotating Blades. Proceedings of the Institution of Mechanical Engineers, Vol. 189, 1975, pp. 461-469.

Verdon, J. M.: The Unsteady Supersonic Flow Downstream of an Oscillating Airfoil. In Unsteady Flows in Jet Engines, Hawthorne, F. O. and H. D. Thomas, Jr. (eds.), Proceedings of a Symposium held at United Aircraft Research Laboratories, East Hartford, Connecticut, August 1-2, 1974, Princeton University Press, Office of Naval Research, pp. 135-150.

Verdon, J. M.: The Unsteady Flow Downstream of an Airfoil Oscillating in a Supersonic Stream. AIAA Journal of Aircraft, Vol. 12, No. 7, July 1975, pp. 636-643.

Verdon, J. M.: Comment on the Issue of Resonance in an Unsteady Supersonic Cascade. AIAA Journal, Vol. 13, No. 11, November 1975, pp. 1542-1543.

Whitehead, D. S.: Aerodynamic Aspects of Blade Vibration. Proceedings of the Institution of Mechanical Engineers, Vol. 180, Pt. 3I, 1965-66, pp. 42-53.

Whitehead, D. S.: Effect of Mistuning on the Vibration of Turbomachine Blades Induced by Wakes. Journal of Mechanical Engineering Science, Vol. 8, No. 1, 1966, pp. 15-21.

Wieselsberger, C.: Electric Measurement of Forces by Varying an Inductivity. Forsch. Ber. 266, 1935. (see p. 452 of Fung).

Woods, L. C.: Aerodynamics Forces on an Oscillating Airfoil Fitted with a Spoiler. Proceedings of the Royal Society (London), Series A. Vol. 239, 1957, pp. 388-397.

Yashima, S. and H. Tanaka: Stall Flutter in Cascade with Leading Edge Separation, Part 1. Theory, Part 2 Experiment. Trans. JSME, Vol. 40, No. 340, December 1974, pp. 3349-3375.

Anon: The Calculation of Aerodynamic Forces and Moments on Airfoils Vibrating in Cascade. Rept. 1084-1, prepared for Pratt & Whitney Aircraft, June 1974, Northern Research and Engineering, Cambridge, Massachusetts.

Many authors: Aerodynamic Flutter. Vol. V of AIAA Selected Reprint Series. I. E. Garrick, ed., March 1969.

Many authors: AGARD Conference on Unsteady Phenomena in Turbomachinery, CP No. 177, September 1975.

Chapter 23

ENGINE STABILITY CONSIDERATIONS

by T.P. Collins

General Electric Company
Aircraft Engine Group
Evendale, Ohio

TABLE OF CONTENTS

CHAPTER 23 ENGINE STABILITY CONSIDERATIONS

		Page
23.0	Introduction	23-1
23.1	Engine Stability Factors	23-1
23.1.1	External Factors	23-1
23.1.1.1	Total-Pressure Distortion	23-1
23.1.1.2	Total-Temperature and Combined-Total-Temperature/Pressure Distortion	23-5
23.1.2	Internal Factors	23-5
23.1.2.1	Engine Transients	23-5
23.1.2.2	Engine and Control Tolerances	23-6
23.1.2.3	Clearances and Bleeds	23-6
23.1.3	Analytical Models	23-7
23.1.4	Stability Stackups	23-7
23.2	Stability and Performance Tradeoffs	23-8
23.3	References	23-8

LIST OF ILLUSTRATIONS

		Page
23.1	Surge Margin Definitions	23-1
23.2	Pressure Distortion Methodology	23-2
23.3	Ring Circumferential Distortion for a One-per-Rev Pattern	23-3
23.4	Ring Circumferential Distortion for a Multiple-per-Rev Pattern	23-4
23.5	Radial Distortion Pattern	23-4
23.6	Typical Screen Test Configurations	23-4
23.7	Two Compressor Analogy	23-5
23.8	Acceleration Path on Compressor Map	23-6
23.9	Acceleration Surge Margin	23-6
23.10	Typical Stability Stackup	23-7
23.11	Stackup Statistical Interpretation	23-8

CHAPTER 23

ENGINE STABILITY CONSIDERATIONS

23.0 INTRODUCTION

Engine stability, for the purposes of this discussion, is concerned with the engine side of inlet/engine compatibility. The inlet side of this interface was discussed in Chapter 13. The subject of inlet/engine compatibility was addressed early in the development of the jet engine; however, it was not until the mid-sixties that the subject received extensive attention. This increased interest was due to severe aircraft restrictions and other problems encountered because of engine surges. Engine surge is the loss of engine control resulting from an engine compression flow instability which manifests itself as a complete flow breakdown and possible turbine inlet overtemperature. This chapter will concentrate on the primary facet of engine stability - surge free operation. Engine surge can result in mechanical damage to the inlet and/or engine as well as loss of engine thrust. For this reason, it is a safety as well as an operational consideration. Since the mid-sixties, much attention has been paid to, and definite improvements achieved in, understanding the factors affecting engine stability. Some of the more significant publications which track the development of this subject are contained in the reference list at the end of this chapter.

The problem of providing sufficient surge margin to ensure stable engine operation within the flight envelope is difficult and imposes a significant dilemma on the engine designer, i.e., how to optimally satisfy conflicting requirements of high thrust levels, low fuel consumption, low weight, long life, low cost, and adequate engine stability. This chapter deals primarily with engine stability; however, some of the design tradeoffs are discussed.

A portion of the material contained herein is based on the work being done by the SAE Committee S-16 relative to the proposed SAE Aerospace Recommended Practice 1420 - Gas Turbine Engine Inlet Flow Distortion Methodology.

23.1 ENGINE STABILITY FACTORS

The elements comprising the two basic factors of engine stability - external and internal surge margin usage - are combined in what is called a "Stability Stackup or Audit." The "Stability Stackup" is an orderly accounting or audit procedure used to establish required surge margins and to monitor the engine development program. It is based on the basic stability equation which in its most simple form is:

STABILITY = AVAILABLE SURGE MARGIN - (EXTERNAL + INTERNAL) SURGE MARGIN USAGE

≥ 0 - STABLE ENGINE OPERATION

< 0 - POTENTIAL ENGINE SURGE

where, the available surge margin (ΔSM) illustrated in Figure 23.1 is defined as:

$$\Delta SM = \frac{PR_{CLEAN\ SURGE\ LINE} - PR_{OPERATING\ LINE}}{PR_{OPERATING\ LINE}}$$

Alternatively, another measure of stability, loss in surge pressure ratio (ΔPRS) is defined as:

$$\Delta PRS = \frac{PR_{CLEAN\ SURGE\ LINE} - PR_{OPERATING\ LINE}}{PR_{CLEAN\ SURGE\ LINE}}$$

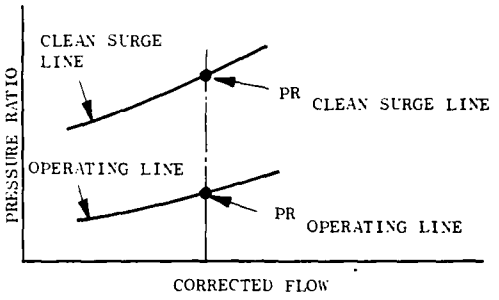

Figure 23.1 Surge Margin Definitions

EXTERNAL SURGE MARGIN USAGE is the surge margin lost due to distortion (pressure and/or temperature) imposed at the engine/aircraft interfaces.

INTERNAL SURGE MARGIN USAGE is the surge margin lost due to engine and control tolerances, deterioration, transients, etc.

These two destabilizing factors are discussed in this section.

23.1.1 EXTERNAL FACTORS

In most applications, the external factor of primary importance is inlet total-pressure distortion. This type of distortion is generated in many ways: flow separation (in the inlet diffuser or at the inlet lip), shock wave/boundary layer interaction, vortex or boundary layer ingestion, etc. In some applications, total-temperature or combined total-pressure/temperature distortion must be considered. Total-temperature distortion can be generated by: missile or gun gas ingestion, hot gas reingestion during thrust reverser operation, hot gas ingestion due to ground effects in VTOL or helicopter applications, etc. The aerodynamic response of turbomachinery to steady and time-variant total-pressure and total-temperature distortion is covered in some detail in Reference 23.1.

The advances made in the development of methods or descriptors for defining the effects of total-pressure, -temperature, and/or combined total-pressure/temperature distortion on engine stability have been primarily empirical in nature. However, recent developments in analytical techniques or models show significant promise. These models are discussed briefly in Section 23.1.3.

23.1.1.1 TOTAL-PRESSURE DISTORTION

Inlet total-pressure distortion is generated in many ways; it is primarily the responsibility of the inlet designer to minimize this distortion. The

engine designer must be cognizant of the total-pressure distortion characteristics to which the engine will be subjected and must assess and develop the compression components to operate stably with this distortion. Total-pressure distortion affects both the engine surge and operating lines. The former effect normally is of predominant importance and will be discussed in some detail.

The problem of defining the effects of pressure distortion on engine stability resulted in the development of descriptors or indices. Each of these descriptors had as its objective a procedure for transforming a given inlet pattern into a numerical value which would accurately correlate the loss in surge pressure ratio (ΔPRS). The problem was compounded further by the time-variant nature of the pressure distortion. The deleterious effects of pressure distortion were recognized early in the development of the jet engine (Reference 23.2). However, it was not until the mid-sixties that the time-variant (unsteady) nature of total-pressure distortion was evaluated qualitatively (Reference 23.3). Since that time, significant advances have been made in unsteady total-pressure measurements, data acquisition, and analysis techniques.

The first quantitative data, reported in Reference 23.4, supported the theory that the compression component would respond to total-pressure distortion patterns which persist for a period of time on the order of one rotor revolution. A more recent investigation (Reference 23.5) provided a significant step forward in quantifying the effects of unsteady total-pressure distortion. The development of high response instrumentation and data acquisition systems had provided the capability of defining "peak" inlet distortion patterns at sufficiently high frequencies (on the order of one to one-half rotor revolution). The accepted practice was to duplicate these peak patterns with screens to evaluate engine stability. There was reason for concern that the difference in distortion character between the inlet dynamic peak pattern and a screen-generated simulated peak pattern could have an effect on the compression system response. Results of the aforementioned test program, Reference 23.5, led to the following conclusion:

> An "averaging time" equivalent to the time for one revolution of the compression unit provided the best correlation between measured and predicted loss in surge pressure ratio. The high degree of correlation indicates that screen-generated distortion test results can be used to accurately assess inlet distortion patterns provided the proper "averaging time" is used. In this test, the difference in results obtained using times between those required for one-half and one-and-one-half rotor revolutions was small. Outside this time interval, the correlation decreases significantly for small changes in averaging time.

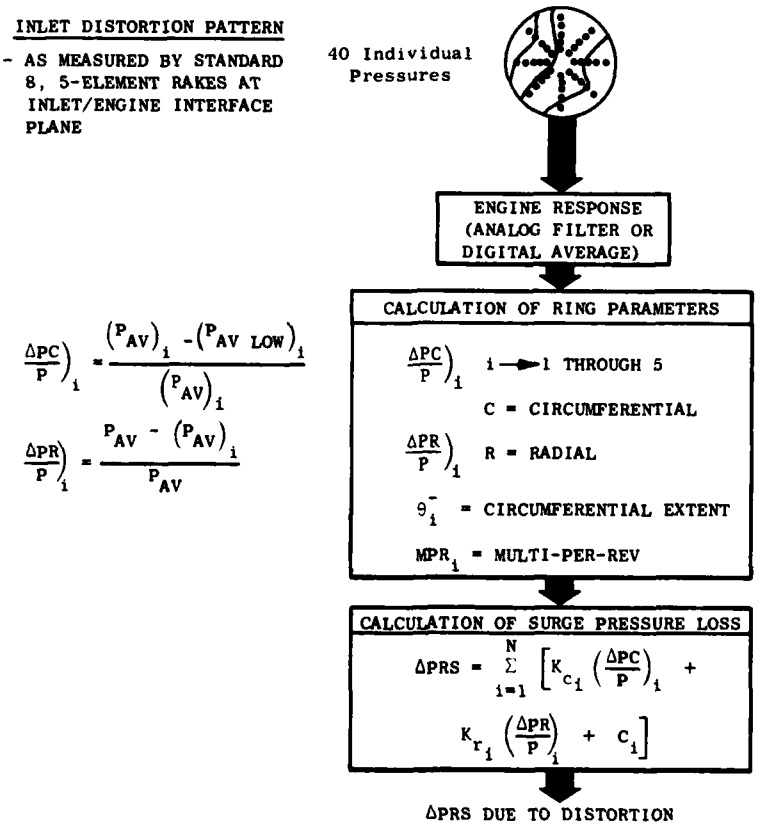

$$\left(\frac{\Delta PC}{P}\right)_i = \frac{(P_{AV})_i - (P_{AV\ LOW})_i}{(P_{AV})_i}$$

$$\left(\frac{\Delta PR}{P}\right)_i = \frac{P_{AV} - (P_{AV})_i}{P_{AV}}$$

$$\Delta PRS = \sum_{i=1}^{N} \left[K_{c_i} \left(\frac{\Delta PC}{P}\right)_i + K_{r_i} \left(\frac{\Delta PR}{P}\right)_i + C_i \right]$$

Figure 23.2 Pressure Distortion Methodology

The numerical description of turbine engine inlet-flow pressure distortion is defined through the use of both inlet-distortion and engine-stability descriptors. Inlet-distortion descriptors are used to quantify inlet distortion data to identify the relative severity of the inlet flow distortion. Engine-stability and -performance descriptors are used to quantify the effect of the inlet distortion on engine stability and performance. The descriptors defined herein are based on the SAE S-16 Committee Aerospace Recommended Practice. The pressure distortion methodology is summarized schematically in Figure 23.2.

The purpose of the inlet-distortion computation procedure is to reduce the aerodynamic-interface-plane (AIP) individual pressure readings to a standard set of numerical values which describe the inlet-distortion pattern. The inlet-distortion descriptors define the complex (aircraft) inlet pattern in terms of circumferential and radial pressure defects. These distortion descriptors are combined with engine sensitivities to determine surge pressure ratio loss.

While it is desired to use one standard expression to relate the distortion descriptors to the loss of compressor surge pressure ratio, there does not appear to be any formula that can meet the requirements of every compressor; the following equation, general in nature, can be expanded to form nearly any distortion descriptor used to date:

$$\Delta PRS = \sum_{i=1}^{N}\left[K_{c_i}\left(\frac{\Delta PC}{P}\right)_i + K_{r_i}\left(\frac{\Delta PR}{P}\right)_i + C_i\right]$$

where:

ΔPRS is the loss of surge pressure ratio due to distortion, expressed as a fraction of the undistorted surge pressure ratio.

N is the number of instrumentation rings.

K is the generalized distortion sensitivities (empirically determined).

$\frac{\Delta PC}{P}$ is the circumferential distortion intensity.

$\frac{\Delta PR}{P}$ is the radial distortion intensity.

C is an empirically defined constant.

Subscript c refers to circumferential distortion.

Subscript r refers to radial distortion.

Subscript i refers to a particular instrumentation ring.

The sensitivity terms and constant C can vary with distortion (extent, multiple-per-rev, etc.) and with compression system. They are derived from test data and can be of sufficient accuracy to correlate the effect of distortion patterns to within approximately ±2 percent surge pressure ratio.

CIRCUMFERENTIAL DISTORTION ELEMENTS

Circumferential distortion is described on a ring-by-ring basis in terms of intensity, extent, and multiple-per-revolution elements. The intensity or level of distortion is a numerical indication of the magnitude of the pressure distortion. The extent element is a numerical indication of the circumferential size of the low pressure region. The multiple-per-rev element is a numerical indication of the effective number of circumferential regions of low pressure.

The "intensity" and "extent" elements of circumferential distortion are obtained by linear interpolation of the pressures in a given ring. Figure 23.3 shows typical pressures in the i^{th} ring

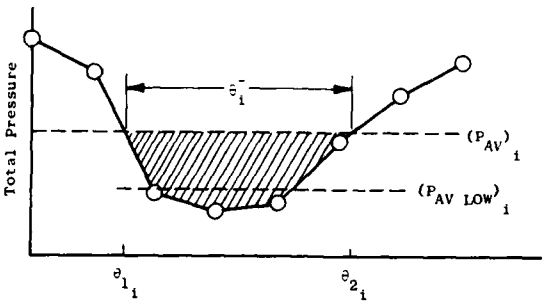

Figure 23.3 Ring Circumferential Distortion for a One-per-Rev Pattern

for a one-per-revolution pattern (one pressure defect in 360°). Theta minus, $\bar{\theta}$, is the circumferential extent of the low pressure region. It is defined by the intersection between the ring average pressure and the linear interpolation which subtends the low pressure region, as shown in Figure 23.3.

$$\text{Extent} = (\bar{\theta})_i = \theta_{2_i} - \theta_{1_i}$$

$$\text{Intensity} = \left(\frac{\Delta PC}{P}\right)_i = \frac{(P_{AV})_i - (P_{AV\ LOW})_i}{(P_{AV})_i}$$

$$(P_{AV})_i = \frac{1}{360}\int_0^{360} P(\theta)_i\, d\theta$$

$P(\theta)_i$ is a function resulting from a linear fit through the data points, as shown in Figure 23.3.

$$(P_{AV\ LOW})_i = \left(\frac{1}{\bar{\theta}_i}\right)\int_{\theta_{1_i}}^{\theta_{2_i}} P(\theta)_i\, d\theta$$

$$\text{Multiple-Per-Rev} = (MPR)_i = 1$$

The circumferential distortion intensity and extent elements for multiple-per-revolution distortion patterns also are determined by a linear interpolation procedure. Figure 23.4 shows a pattern with two low pressure regions separated by two high pressure regions of extents θ^+_1 and θ^+_2. In the general case, there can be any number of separated low pressure regions. If either θ^+_1 or θ^+_2 is less than some minimum extent ($\leq 25°$), the pattern is considered an equivalent one-per-rev pattern.

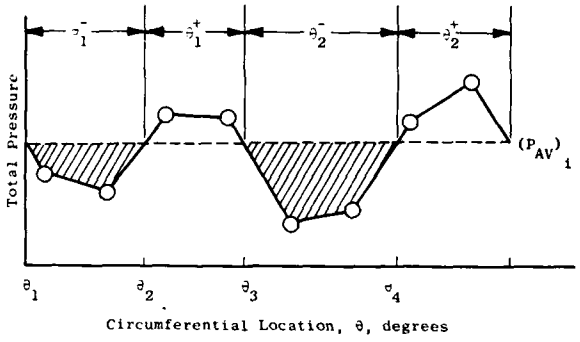

Figure 23.4 Ring Circumferential Distortion for a Multiple-per-Rev Pattern

RADIAL DISTORTION ELEMENTS

The radial distortion intensity of a ring is defined as the difference between the face-average pressure and the ring-average pressure, divided by the face-average pressure. Both positive and negative values of radial intensity are considered; however, since positive values reflect a ring-average pressure that is below the face average, it is the basic distortion indicator. A typical tip-radial distortion pattern is shown in Figure 23.5. The arrows indicate the difference in radial pressure for ring 5. For the general ring, i, the radial intensity is:

$$\left(\frac{\Delta PR}{P}\right)_i = \frac{(P_{FACE\ AV}) - (P_{AV})_i}{(P_{FACE\ AV})}$$

where,

$$(P_{FACE\ AV}) = \frac{1}{N} \sum_{i=1}^{N} (P_{AV})_i$$

ENGINE PRESSURE DISTORTION SENSITIVITIES

The definition of the inlet dynamic total-pressure pattern in terms of a set of distortion descriptors is but the first step in achieving the primary objective of determining the sensitivity of the engine to this distortion. The vast majority of the component and engine testing to determine distortion sensitivity has been done using distortion screens. These screens are designed to permit determination of the basic circumferential and radial sensitivities as well as the superposition factors required for complex distortion patterns. A typical screen test setup (including basic screen designs) is shown in Figure 23.6. To provide a comprehensive distortion descriptor, a rather large number of screens is required to generate various pattern shapes and levels.

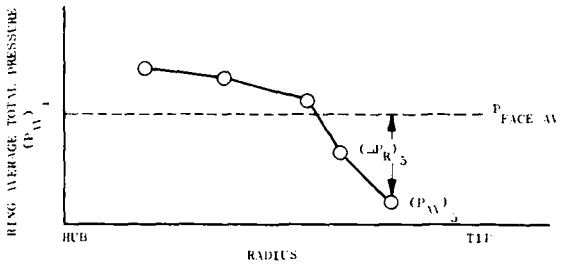

Figure 23.5 Radial Distortion Pattern

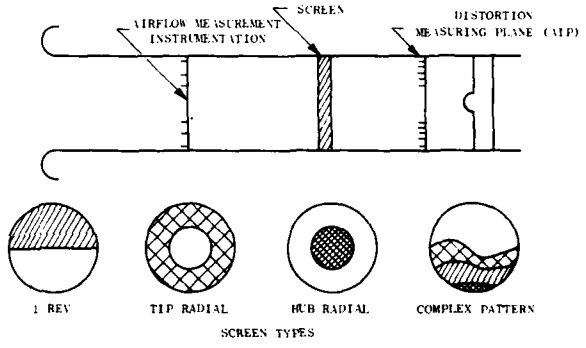

Figure 23.6 Typical Screen Test Configurations

It should be noted that screens produce basically steady-state distortion, whereas inlet distortion has a large dynamic content. However, as mentioned previously, the results of the investigation of Reference 23.5 indicated that the screens can be used to accurately assess the effects of time-variant distortion provided proper "averaging" or filter frequency characteristics are considered.

The large number of screens required to develop a comprehensive methodology results in a considerable amount of test time. This is due, to a large extent, to the relatively limited useful flow range of a given screen (reasonable distortion levels can only be obtained over a small airflow range), the time required to install a screen, and the test time lost in shutting down and restarting the engine or compression component for a screen replacement. In order to improve test efficiency, alternate distortion-generating devices are being developed (References 23.6 and 23.7).

A number of other distortion-generating devices has been developed for specific test purposes. Various systems developed to produce dynamic "inlet-type" distortion are described in References 23.3, .4, and .5. Other devices developed for the purpose of investigating the dynamic response of the compression

system are described in References 23.6, .8, and .9. The system described in Reference 23.8 provided data of significant value to the analytical studies described in Section 23.1.3.

23.1.1.2 TOTAL-TEMPERATURE AND COMBINED-TOTAL-TEMPERATURE/PRESSURE DISTORTION

Total-temperature distortion into a compression unit can be due to either external factors (rocket, missile or gun firing, catapult launch, thrust reverser operation, hover in ground effects, etc.) or internal generation resulting from the attenuation of pressure distortion by an upstream compression unit. Regardless of the source of the total-temperature distortion, it is accompanied by some level of total-pressure distortion. The problem then is to determine not only the effect of total-temperature distortion but also the combined effect of total-temperature and -pressure distortion.

The subject of total-temperature distortion has not received the attention afforded pressure distortion. The primary reasons for this are twofold: first, the severity of the problem is closely related to the specific aircraft design/requirements; and, second, the state of the art of reliable high response instrumentation has hampered the experimental effort.

The SAE S-16 Committee has stated that sufficient experience does not currently exist to permit recommending procedures for assessing total-temperature distortion. It does seem quite logical, however, that the form of the total-temperature-distortion descriptor should be quite similar to the pressure-distortion descriptor. A potential approach for this type of formulation is discussed in Reference 23.10.

Some degree of success in correlating pure total-temperature as well as pure total-pressure and combined total-pressure/temperature distortion with the loss in surge pressure ratio has been obtained in using a parallel compressor model technique (References 23.11, .12, and .13). The basic concept of the parallel compressor, illustrated in Figure 23.7, assumes that the overall compressor operates as independent sectors with individually defined inlet conditions and a common exhaust pressure.

23.1.2 INTERNAL FACTORS

Internal engine destabilizing factors comprise a major part of the stability stackup and affect both the compression unit surge and operating lines. In general, engine transients are the primary single internal destabilizing factor. However, the combined effects of tolerances and deterioration are equally important and must be assessed carefully. Another destabilizing factor can be attributed to Reynolds number effects, which are reflected in both the surge and operating lines and are quite significant at reduced Reynolds number. Effects of Reynolds number on compressor airflow, efficiency, and surge line are included in the engine cycle deck and are reflected in the clean available surge margin. For this reason, Reynolds number will not be considered as a specific internal destabilizing item in the stackup.

23.1.2.1 ENGINE TRANSIENTS

Two types of transients are of primary importance: (1) dry engine power transients which affect the compressor on a turbojet or the high pressure compressor on a turbofan; and, (2) augmentor transients which primarily affect the low pressure compressor on a turbofan. There are other transients to be considered in specific applications; however, they will not be considered here.

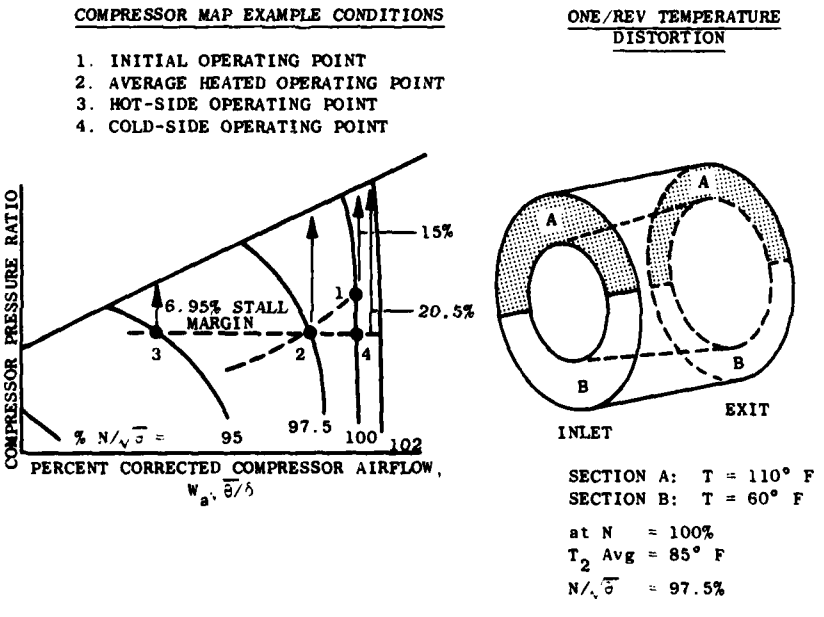

Figure 23.7 Two Compressor Analogy

DRY ENGINE POWER TRANSIENTS

Dry engine power changes require an increase (decrease) in engine fuel flow producing an increase (decrease) in turbine torque above (below) the steady-state level to accelerate (decelerate) engine speed and increase (decrease) thrust. The increased fuel flow required for acceleration produces a higher compressor discharge pressure than steady-state and, therefore, results in a loss in surge margin. From the standpoint of the turbojet compressor or high pressure turbofan compressor, the acceleration is the destabilizing factor of concern.

The engine acceleration path on the compressor map is illustrated in Figure 23.8.

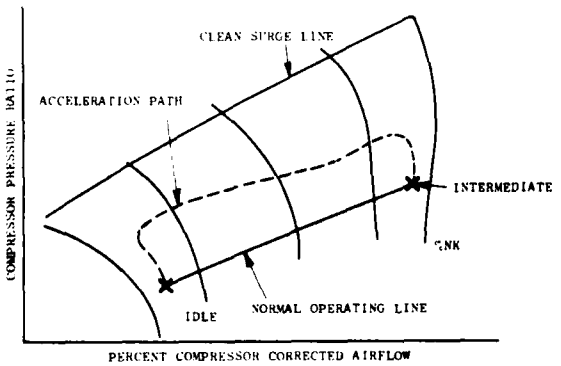

Figure 23.8 Acceleration Path on Compressor Map

The area between the steady-state operating and acceleration lines is related to the acceleration. The faster the acceleration time, the more margin (higher acceleration line) that is required. The acceleration schedule is designed to apportion the margin usage throughout the engine speed range. Typical margin versus corrected engine speed characteristics for two acceleration time requirements are shown in Figure 23.9.

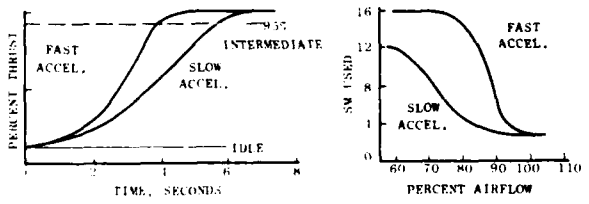

Figure 23.9 Accel ration Surge Margin

Engine decelerations on high bypass turbofans, especially those with "T compressors," have caused stability problems because of back pressure effects on the booster stages. This results from a speed mismatch between the low and high pressure compressors. The lower inertia high pressure compressor decelerates rapidly resulting in a reduced flow capacity and an increased back pressure on the low pressure compressor. Bypass valves between the spools now are being used to eliminate this problem.

Dry engine power changes also result in surge margin losses due to control system lags resulting in off-schedule stator tracking and thermal effects on compressor tip clearances. In some cases, these effects are quite significant and must be considered in the overall stability assessment.

AUGMENTOR TRANSIENTS

The effect of augmentor transients is a primary engine destabilizing item on the fan of an augmented turbofan application. The direct flow path between the fan and the augmentor/nozzle permits propagation of disturbances resulting from such transients as lightoffs and augmentor zone changes. The matching of the augmentor fuel flow and nozzle controls during augmentor transients is an area of significant concern.

Augmentor lightoff results in a very rapid rise in augmentor discharge temperature. This "step" rise in temperature is translated approximately into a "step" increase in required nozzle total pressure which, if unattenuated, results in a direct increase in the fan operating line. If the augmentor fuel flow is not limited to and held at the lightoff level, much harder lightoffs and, hence, much larger surge margin losses will occur.

During augmentor transients, it is quite important that augmentor fuel flow and exhaust nozzle area rates be matched closely. If the transient nozzle area position is too far closed for the transient level of fuel flow, the fan operating line will be increased. This situation can occur during either increases or decreases in augmentation level.

23.1.2.2 ENGINE AND CONTROL TOLERANCES

Manufacturing tolerances have a definite impact on engine stability. Surge margin checks on new production engines indicate a measurable variation about the nominal value. These variations are due to both surge-line variations arising from compression unit blade quality, buildup tolerances, etc., as well as variations in the engine operating line arising from turbine nozzle area variations, component efficiencies, etc. The problem is complicated further when the effects of control tolerances are added.

In general, the engine and control tolerances are combined in a statistical procedure. However, transient control tracking errors, such as variable stator position, which are one-sided and measurable, must be included as a direct additive item.

23.1.2.3 CLEARANCES AND BLEEDS

Rotor-blade-tip and cantilevered-stator-root clearances play an important part in the stability characteristics of the compression system. The loss of pressure rise capability and, hence, the loss of stability margin is discussed in detail in Reference 23.14. Modern engine designs contain extremely sophisticated techniques to maintain tight tip clearances. Computer simulations, material selection, casing construction, and other studies are conducted to arrive at a design which permits running with proper clearances during all phases of engine operation including transients. The effect of transient operation on compression system clearances and the resulting loss in surge margin must be accounted for in the stability assessment.

The importance of compressor clearances in establishing stability margin has been recognized for a long time; however, the effects of turbine clearances are not well recognized. An increase in turbine tip clearance results in a decrease in turbine efficiency. This loss in efficiency impacts the operating line and/or transient characteristics.

Compressor bleed (interstage or discharge), in general, is a stabilizing factor and has been used successfully to increase stability margin during extreme external disturbances such as missile firing, thrust reverser operation, etc. Interstage bleed also has been used to improve overall performance by providing a means to better match stability requirements over the complete engine speed range. The stability improvement is due to a reduced overall compressor operating line and/or reduced stage(s) loading resulting from a properly designed bleed system. However, compressor bleed can result in significant losses in engine stability if the bleed cavities are not properly designed. Significant cross-flows and/or cavity resonances (resulting in stability margin losses) have been experienced during distorted inlet operation. Normally, compressor bleed is not a specific stability stackup item; however, it is reflected in the available margin and other included items.

23.1.3 ANALYTICAL MODELS

Prime tools in engine stability studies are transient engine and compression unit mathematical models. The former has been in use for many years. The model consists basically of the steady-state thermodynamic cycle coupled with complete dynamic simulation of the engine controls and various levels of sophistication in simulating internal engine dynamics. The degree of sophistication in simulating internal engine dynamics determines the valid frequency response limit of the model. The transient engine model is used primarily for analyzing and defining transient control schedules and provides information for the stability stackup relative to surge margin usage for transients and tolerances.

The development of detailed, validated, compression-unit modeling techniques has progressed significantly in the last five years. The techniques being developed include both steady- and unsteady-flow systems based on stage-by-stage or individual blade-row models. Two of the techniques are discussed in detail in References 23.12, 23.13, 23.15, 23.16, and 23.17. The compression unit model permits a detailed evaluation of the internal stage or blade behavior as well as the overall performance. Continued development of these models will provide additional benefit early in the design, maximize test effectiveness, and provide a firm basis for potentially required design modifications.

23.1.4 STABILITY STACKUPS

The external and internal destabilizing factors discussed in the previous sections are combined in the stability stackup. Stackups are made for specific flight conditions (Mach number, altitude, distortion level, and inlet pressure recovery) and engine operating conditions (power setting, transient, and bleed and power extraction) to determine margin throughout the flight envelope.

The upper left hand corner of the flight envelope, in general, is the most critical for fighter aircraft. This is due to the combination of aircraft maneuver requirements (high distortion) and low Reynolds number (reduced available clean surge margin). Subsonic aircraft generally have minimum margin at rotation or during reverser operation. Sea-level-static operation at maximum power has been a problem on both types of aircraft.

A typical stackup format illustrating the destabilizing effects previously discussed and typical allocations are shown in Figure 23.10.

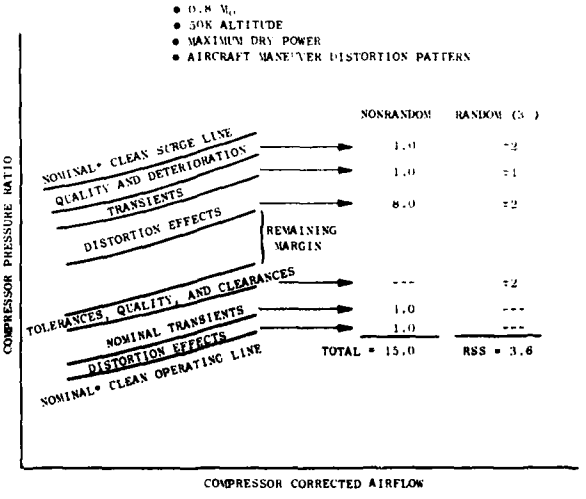

* NOMINAL OPERATING AND SURGE LINES CONTAIN REYNOLDS NUMBER EFFECTS.

Figure 23.10 Typical Stability Stackup

A number of the destabilizing effects is directly added, while others are statistical in nature and are combined in a "Root Sum Squared" (RSS) method. The presently accepted method of interpreting the stackup is to add directly the totals of the direct additive and the RSS items and subtract this total from the available margin. This is called a net stability margin stackup. The stability stackup is statistical in nature as mentioned previously; therefore, it truly represents a probability of the occurrence of surge for a set of specified conditions. A statistical interpretation of the stackup shown in Figure 23.10 is summarized in Figure 23.11, where the random destabilizing effects are assumed to follow a Gaussian distribution. In the example net stability stackup (Figure 23.11), the result would be a 1.5% deficit in surge margin. Using the statistical method, the probability of surge is 4% (4 surges per 100 occurrences of the conditions of the stackup).

These stability stackups should be an integral part of the phased engine development program as illustrated below.

PRELIMINARY DESIGN PHASE

During this phase, the stability stackup must be based on anticipated requirements and previous experience with related components. The results of the stackup are used to define preliminary surge margin requirements.

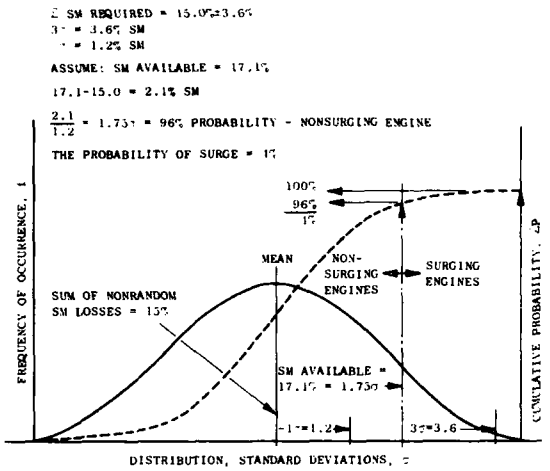

Figure 23.11 Stackup Statistical Interpretation

DEVELOPMENT PHASE

During this phase, the stackups are revised to reflect component and engine test information on distortion sensitivity, transient margins, etc. In addition, inlet data from model testing are factored into the stackups. As more information becomes available, it is factored into the stability stackup to define critical stability conditions.

PRODUCTION PHASE

During this phase, attention is focused on deterioration and quality items in the stackup. In addition, any inlet/engine modifications or control changes must be assessed relative to their impact on stability.

23.2 STABILITY AND PERFORMANCE TRADEOFFS

A simple approach to achieve engine stability would be to increase available surge margin by merely lowering the engine operating line. This, however, would lead to serious performance losses because the resulting match point on the compression unit would be moved from its peak efficiency. In the majority of cases, the compression unit peak efficiency occurs at a point above the operating line dictated by minimum surge margin requirements. The engine design must be such that adequate stability margin is provided with a minimum performance loss. The real challenge in the future will be to reduce the required level of adequate stability margin. Some approaches for achieving this goal are outlined in Reference 23.18.

This chapter has dealt with current state-of-the-art engine stability requirements, procedures, techniques, etc. Future developments will be aimed at achieving adequate stability margin with reduced impact on engine installed performance.

23.3 REFERENCES

23.1 Hercock, R.G. and Williams, D.D., "Aerodynamic Response," AGARD Lecture Series No. 72 on Distortion Induced Engine Instability, AGARD Report AGARD-LS-72, 1974.

23.2 Alford, J.S., "Inlet Duct - Engine Flow Compatibility," Fifth Aeronautical Conference, June 1955.

23.3 Kimzey, W.F. and Lewis, R., "An Experimental Investigation of the Effects of Shock-Induced Turbulent In-Flow on a Turbojet Engine," AIAA 2nd Propulsion Specialist Conference, June 1966.

23.4 Plourde, G.A. and Brimelow, B., "Pressure Fluctuations Cause Compressor Instability," Proceedings of the Air Force Airframe-Propulsion Compatibility Symposium, Air Force Aero Propulsion Laboratory, Technical Report AFAPL-TR-69-103, June 1970.

23.5 Brimelow, B., Collins, T.P., and Pfefferkorn, G.A., "Engine Testing in a Dynamic Environment," presented at the AIAA/SAE 10th Propulsion Conference, San Diego, California, October 21-23, 1974 as AIAA Paper No. 74-1198.

23.6 Meyer, C.L., McAuley, J.E., and Busiadany, T.J., "Technique for Inducing Controlled Steady-State and Dynamic Inlet Pressure Disturbances for Jet Engine Tests," National Aeronautics and Space Administration, Report NASA TMX-1949, January 1970.

23.7 Stevenson, C.W and Rakowski, W.G., "Evaluation of an Airjet System for Producing Steady-State Total Pressure Distortion at the Inlet of Turbine Engines," Arnold Engineering and Development Center, Technical Report AEDC-TR-73-68.

23.8 Kutschenreuter, P.H.,Jr., Collins, T.P., and Vier, W.F., "The P^3G - A New Dynamic Distortion Generator," presented at the AIAA/SAE 9th Propulsion Conference, Las Vegas, Nevada, November 5-7, 1973 as AIAA Paper 73-1317.

23.9 Lazalier, G.R. and Parker, J.R., "Performance of a Prototype Discrete Frequency Total Pressure Fluctuation Generator for Jet Engine Inlet Compatibility Investigations," Arnold Engineering and Development Center, Technical Report AEDC-TR-69-139, October, 1969.

23.10 Brimelow, B. and Steenken, W.G., "Compatibility Technology Requirements," presented at the Project SQUID Workshop on Engine-Airframe Integrations (Short-haul Aircraft) held at the Naval Academy, Annapolis, Maryland on May 11-12, 1977.

23.11 Braithwaite, W.M., Graber, E.J., Jr., and Mehalic, C.M., "The Effect of Inlet Temperature and Pressure Distortion on Turbojet Performance," presented at the AIAA/SAE 9th Propulsion Conference, Las Vegas, Nevada, November 5-7, 1973 as AIAA Paper No. 73-1316.

23.12 Tesch, W.A. and Steenken, W.G., "Blade Row Dynamic Digital Compressor Program, Volume 1, J85 Clean Inlet Flow and Parallel Compressor Models," National Aeronautics and Space Administration, Report NASA CR-134978, March 1976.

23.13 Mazzaway, R.S., "Multi-Segment Parallel Compressor Model for Circumferential Flow Distortion," presented at the 46th AGARD Propulsion and Energetics Panel Meeting, Unsteady Phenomena in Turbomachinery, Monterey, California, September 1975.

23.14 Smith, L.H., Jr., "The Effect of Tip Clearance on the Peak Pressure Rise of Axial Flow Fans and Compressors," ASME Symposium on Stall, New York, December, 1958.

23.15 Tesch, W.A. and Steenken, W.G., "Dynamic Blade Row Compression Component Model for Stability Studies," presented at the AIAA 14th Aerospace Sciences Meeting, Washington, D.C., January 26-28, 1976 as AIAA Paper No. 76-203.

23.16 Reynolds, G.G. and Steenken, W.G., "Dynamic Digital Blade Row Compression Component Stability Model, Model Validation and Analysis of Planar Pressure Pulse Generator and Two-Stage Fan Test Data," Air Force Aero Propulsion Laboratory, Technical Report AFAPL-TR-76-76.

23.17 Mazzaway, R.S. and Banks, G.A., "Modeling and Analysis of the TF30-P-3 Compressor System with Inlet Pressure Distortion," National Aeronautics and Space Administration, Report NASA CR-134996, April 1976.

23.18 Mikolojczak, A.A. and Pfeffer, A.M., "Methods to Increase Engine Stability and Tolerance to Distortion," AGARD Lecture Series No. 72 on Distortion-Induced Engine Instability, AGARD Report AGARD-LS-72, 1974.

Chapter 24

ENGINE NOISE

N. A. Cumpsty

University of Cambridge

TABLE OF CONTENTS

CHAPTER 24 ENGINE NOISE

		Page
24.1	Introduction	24.1
24.2	Scales and Ratings for Noise	24.2
24.3	Introduction to Acoustics of Ducts	24.4
24.4	Compressor and Fan Noise	24.7
24.4.1	Interaction Tone Noise	24.8
24.4.1.1	Kinematics	24.8
24.4.1.2	Rotor-Stator Interaction Experiments	24.9
24.4.1.3	Analysis for Interaction Tone Noise	24.11
24.4.1.4	Rotor-Inflow Distortion Interactions	24.13
24.4.2	Multiple Pure Tone Noise	24.14
24.4.3	Broad Band Noise	24.16
24.5	Turbine Noise	24.18
24.6	Core Noise	24.21
24.7	Acoustic Treatment	24.25
24.8	Concluding Remarks and Future Prospects	24.29
24.9	References	24.30

LIST OF FIGURES

		Page
Figure 24.1	The changes in 90 EPNdB footprint area over fifty years	24.1
Figure 24.2	The comparative noise sources for low and high bypass ratio engines	24.1
Figure 24.3	The change in dominant noise source and the variation in noise level during aircraft flyover	24.1
Figure 24.4	Three flyovers for an aircraft with high bypass ratio	24.1
Figure 24.5	A single noise signal analysed by a constant bandwidth and a third-octave filter	24.3
Figure 24.6	Perceived noise levels for representative situations	24.3
Figure 24.7	Take-off and approach noise levels - regulations and typical measurements	24.4
Figure 24.8	Measurement, analysis and correction procedures for in-flight noise measurement leading to certification	24.4
Figure 24.9	The radial variation in pressure amplitude in a cylindrical duct with 0.5 hub tip ratio. Circumferential and radial orders of mode denoted by m and μ respectively	24.5
Figure 24.10	A comparison of measured and predicted (broken line) decay ahead of subsonic fan	24.6
Figure 24.11	Decay rates for modes of zero radial order in ducts of hub-tip ratio 0.5	24.6
Figure 24.12	Radiated field shapes predicted by three models; Lowson's theory is for unducted source	24.7
Figure 24.13	Typical forward arc spectra of noise from a fan or compressor with subsonic and supersonic tip speeds	24.8
Figure 24.14	Schematic representation of rotor-stator interaction; B = 4, V = 3	24.9
Figure 24.15	Schematic representation of wave fronts for rotor-stator interaction above and below cut-off	24.9
Figure 24.16	Forward arc field shapes of tones at second harmonic of blade passing frequency	24.10
Figure 24.17	Correlations of the change in tone level with the ratio of axial gap between rotor and stator to the chord	24.10

LIST OF FIGURES

Page

Figure 24.18 Forward radiated tone level at blade passing frequency fundamental (Blade tip speed sonic at approx. 5000 RPM) 24.10

Figure 24.19 Rearward radiated tone level at blade passing frequency fundamental (Blade tip speed sonic at approx. 5000 RPM)..... 24.10

Figure 24.20 Comparison of prediction and measurement of rearward acoustic power at blade passing frequency from 54 bladed fan in closed cycle Freon rig 24.10

Figure 24.21 Comparison between predicted and measured acoustic pressure fluctuation at blade passing frequency, downstream of 23 bladed rotor with 24 upstream wakes. (Pressure non-dimensionalised with relative dynamic pressure into rotor)...24.12

Figure 24.22 Comparison between compact and non-compact representation of rotor interacting with distortion.(Stagger, $\theta = 45^{\circ}$, pitch chord ratio $\frac{s}{c} = 1$).....24.12

Figure 24.23 The level of the transmitted and reflected pressure waves from a cascade of uncambered blades staggered at 60°. Incident pressure wave from downstream..... 24.12

Figure 24.24 Predicted spectra of acoustic power produced by a rotor interacting with isotropic, homogeneous turbulence.....24.13

Figure 24.25 Comparison of in-duct tone levels, static and in-flight....24.13

Figure 24.26 Schematic representation of streamline patterns into an intake, static and inflight.....24.14

Figure 24.27 Schematic representation of shock waves ahead of a supersonic rotor.....24.14

Figure 24.28 Decay rates of the average amplitude of shocks ahead of a supersonic rotor. (Blade pitch approx. 2.7 inch).....24.15

Figure 24.29 Measured evolution of time histories and spectra ahead of supersonic fan. (Blade pitch approx. 2.7 inch).....24.15

Figure 24.30 Idealised shock and expansion system around leading edge of a two-dimensional supersonic cascade.....24.15

Page

Figure 24.31 Predicted spectra ahead of supersonic cascade of uncambered blades for small variations in stagger angle.....24.15

Figure 24.32 Spectra of forward arc broad band noise from a fan at two operational speeds.....24.16

Figure 24.33 The broad band noise spectrum of high speed fans.....24.17

Figure 24.34 Variation of broad band noise level with incidence (effect of Mach number removed).....24.17

Figure 24.35 Broadband noise radiated from a small plate held in a jet of diameter D.....24.18

Figure 24.36 Typical rear arc spectra from low and high bypass ratio engines at low jet velocity.....24.19

Figure 24.37 The effect of duct geometry on the spectral shape of turbine tones perceived in far field....24.19

Figure 24.38 Changes in turbine BPF tone power with increase in nozzle-rotor spacing; tip axial gap/chord equal 0.29 (baseline), 0.89 (spaced).....24.20

Figure 24.39 Changes in spectrum and field shape (SPL and PNL) with changes in combustion chamber.....24.20

Figure 24.40 Turbine BPF tone power; effect of pressure ratio and speed.....24.20

Figure 24.41 Comparison of measured turbine noise with predictions.....24.21

Figure 24.42 Definition of core noise.....24.21

Figure 24.43 Spectra, using Strouhal number as abscissa, of jet noise with and without pure tone excitation 24.22

Figure 24.44 Variation in acoustic power from an isolated combustion can as a function of air flow rate 24.23

Figure 24.45 Variation in acoustic power from an isolated combustion can as a function of fuel/air ratio.....24.23

Figure 24.46 The effect of temperature rise on the noise of a fullscale, isolated, annular combustor.....24.24

Figure 24.47 The spectrum of temperature fluctuation measured at outlet from a can-annular combustion chamber.....24.24

Figure 24.48 Measured and predicted spectra of rear arc acoustic power from a JT8D engine at low jet velocity 24.24

LIST OF FIGURES

Page

Figure 24.49 Schematic Illustration of Installation of Linings in a High Bypass-Ratio Engine.....24.25

Figure 24.50 Schematic of Various Lining Types.....24.25

Figure 24.51 Schematic of Impedance Components of a Perforate Plate-Honeycomb Backing Acoustic Lining.....24.26

Figure 24.52 Comparison of Predicted and Measured Attenuation Spectrum in a Rectangular Duct showing Importance of Flow and Shear (i.e. Boundary Layer).....24.27

Figure 24.53 Variation in Predicted Attenuation Spectrum with Boundary Layer Thickness δ in a Cylindrical Duct of Diameter D.....24.28

Figure 24.54 Variation in Predicted Attenuation Spectrum with Flow Mach Number in a Cylindrical Duct of Diameter D.....24.28

Figure 24.55 Variation in Predicted Attenuation Spectrum with Lining Backing Depth d in a Cylindrical Duct of Diameter D.(Propagation Upstream).....24.28

Figure 24.56 Variation in Predicted Attenuation Spectrum with Specific Resistance $R/\rho c$ of Lining in a Cylindrical Duct of Diameter D. (Propagation Upstream).....24.29

CHAPTER TWENTY-FOUR
ENGINE NOISE

24.1 INTRODUCTION

The advent of the jet engine brought a new noise nuisance and its introduction into civil airline use was a major disaster for communities living near airports. This is indicated by Fig. 24.1, taken from Interavia, which shows how the area at a given level of subjective noisiness, the so-called noise footprint, has changed over the years. (More will be said about the subjective assessment of noise in section 24.2).

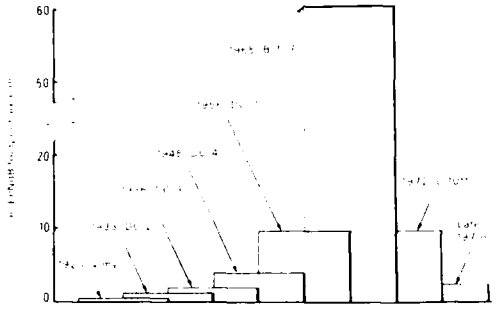

Figure 24.1 The changes in 90 EPNdB footprint area over fifty years.

The jets in the 1960's brought about a sixfold increase in the footprint area, but the more recent engines in civil aviation service with high bypass ratios are restoring conditions back to where they were with propeller aircraft. Where for particular duties the propulsive efficiency requires a low bypass ratio and high jet velocity the noise levels remain very high.

At first the predominant source of noise was produced by high speed jet mixing, but with the introduction of low bypass engines the compressor rapidly became every bit as irritating in some circumstances. In the more recent high bypass ratio engines the fan is usually the predominant noise nuisance, but this is mitigated to some extent by the incorporation of noise reducing features. The changes in the sources with bypass ratio are indicated by the sketches in Figure 24.2. The size of the lobes gives an indication of the strength of the source and the direction indicates the direction in which radiation occurs.

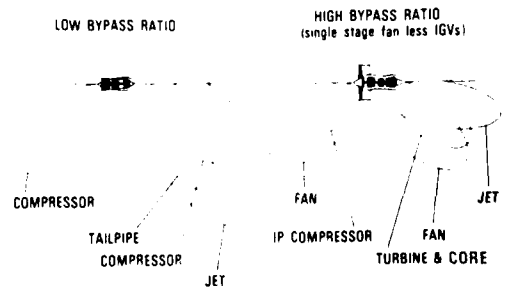

Figure 24.2 The comparative noise sources for low and high bypass ratio engines.

The direction of sound radiation may be as important as the intensity of radiation; if radiation can occur away from the ground no community complaints are likely to be received.

As an aircraft flies overhead the sound changes with time, of course. The levels change both because of the variation in distance between aircraft and observer, but also because of the angle changes. Fig. 24.3 gives some idea of how the various sources contribute as the aircraft passes overhead.

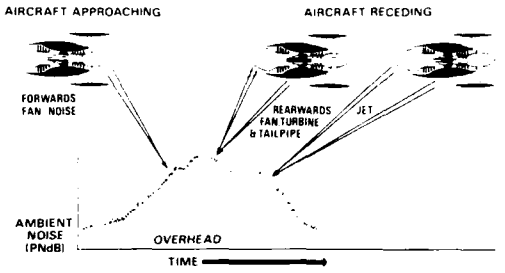

Figure 24.3 The change in dominant noise source and the variation in noise level during aircraft flyover.

The precise variation in noise with time depends on the engine, the installation, the aircraft and the mode of operation, but nevertheless the salient features are shown up by Fig. 24.3. The noise time histories of flyovers of one aircraft with a high bypass ratio engine at approach, take-off and with throttled take-off power are shown in Fig. 24.4.

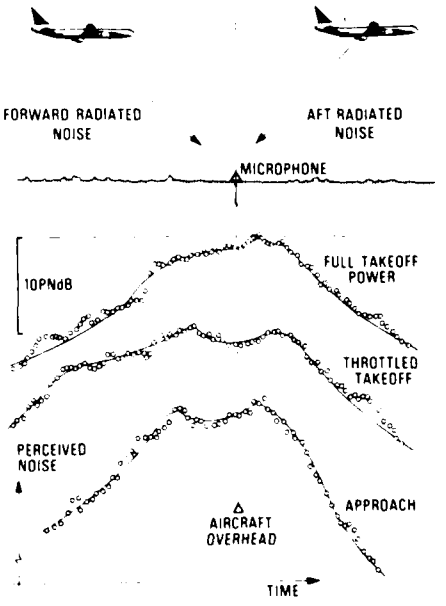

Figure 24.4 Three flyovers for an aircraft with high bypass ratio.

It should be noted that the throttled take-off extends the period of high noise level so that in certain cases its use may be found to increase the noise nuisance.

The aircraft type influences the noise sensed on the ground directly through the time for which the noise persists and the nearness of the aircraft. Since two engine aircraft climb faster than three and three faster than four, the take-off noise experienced tends to be lower with fewer engines. Wing design affects drag and power at approach; aircraft with low drag tend to have lower noise at approach. Mounting engines on top of the wings can also be highly beneficial for engine noise since the the wing can shield the ground. Naturally there are endless permutations for different aircraft designs and engine installations and it is inappropriate to consider this topic in any detail here. The over-riding effect is, of course, the aircraft duty and the bypass ratio and jet velocities that this determines.

The experimental study of noise is difficult in general, but in the case of the high speed machinery normal for aircraft engines it is both very difficult and very expensive. The machinery in aircraft engines typically operates with velocities close to sonic and it also turns out that the acoustic wavelengths are normally of the same order as the blade chords. This latter tendency makes the localisation of sound sources by ray techniques inapplicable. The high Mach number flows refract the sound and this further complicates the study. The insertion of a probe into the flow can itself initiate the generation of sound by adjacent moving blades. A picture for the noise generation has gradually been built up by noting the changes occurring as parameters are altered, but this remains an erratic means of progress.

The theoretical study of noise, or acoustics, in the case of aircraft engines presents special problems because of the same two factors. First the flow Mach numbers are generally not far from unity, and this complicates the analytic description of acoustic processes enormously. Second, the wavelength of the sound is typically comparable to the physical dimensions of the machine, such as blade chord, and this also greatly complicates any analysis. For both those reasons classical acoustics found in textbooks has not contributed very much to the growth of understanding of the subject.

A different theoretical approach to the problem known as the aero-acoustic approach and described by Goldstein Ref. (24.1), began with the work of Lighthill Ref. (24.2) towards the understanding of noise from the turbulence of jets. Over the last twenty years or so this has been extended and generalised to cover even the noise from arbitrarily moving surfaces, Ffowcs Williams and Hawkings Ref. (24.3). Despite its generality this approach leads to what an engineer might regard as a mathematical statement of the problem rather than a solution. To provide a solution requires a range of information which is unfortunately unavailable and quantitative results are obtainable only by incorporating the most sweeping assumptions. The aero-acoustic approach therefore provides less help than one might expect, and the growth of understanding is dependent on a more ad hoc approach.

Having drawn attention to the difficulties of theoretical studies of noise it is proper to point out one ameliorating factor. This is that the amplitudes of the fluctuations normally of concern as noise are very small, and that a linear analytic treatment is almost always justified. It is therefore a field which attracts considerable interest from theoreticians.

The development of high bypass engines for transport aircraft in the late 1960's and the international recognition of the need to limit or reduce noise led to a surge of interest in noise research. The literature grew accordingly and it would be out of place to reference all of it in this Chapter; instead some excellent review articles will be referenced as well as works which are of particular importance to anyone wishing to study the subject further.

Before considering noise sources from particular components of engines in this chapter there are two more general sections which bear on what follows. In Sec. 24.2 the methods of rating noise are described, the essential problem being to find objective measures of a subjective annoyance. In Sec. (24.3) the elements of duct acoustics are treated, since this bears on all aspects of noise generation and attenuation due to liners.

The largest section of the Chapter, 24.4, is concerned with compressor and fan noise. As well as being the most studied aspect it is also probably the most serious noise nuisance after jet noise. The noise from turbines is in some ways similar to that of compressors and it is convenient to examine it next in 24.5. Except for jet noise, considered separately in Chapter 25, all the other noise sources, sometimes lumped together as core-noise, are considered in 24.6. The use of acoustic treatment on the walls of the ducting around the engines is now common. This is an area where the designer can exercise a very large beneficial effect and where design is both relatively subtle and precise. Some aspects of this are described in Sec. (24.7). Prospects for the future and an over-view of achievements are briefly considered in Sec. (24.8).

24.2 SCALES AND RATINGS FOR NOISE

Because acoustic signals vary by such large amounts it is the almost invariable practice to use logarithmic scales, expressing the level in terms of decibels (dB). Acoustic signals levels may either refer to the local level of pressure fluctuation or to the acoustic power generated. In the former it is known as the sound pressure level (SPL) defined by

$$SPL = 20 \log_{10} \frac{p}{p_{ref}} \quad dB$$

where p is the RMS pressure fluctuation and p_{ref} is the reference RMS pressure fluctuation equal to 20 $\mu N/m^2$ or 2.10^{-5} dyne/cm^2.

The acoustic power, or power watt level (PWL) is defined by

$$PWL = 10 \log_{10} \frac{W}{W_{ref}} \quad dB$$

where W is the acoustic power in watts and W_{ref} is the reference acoustic power equal to 10^{-12}W. (In some work 10^{-13}W is used as the reference).

The acoustic power carried by unit area of wavefront is known as the intensity. Generally this is not a convenient quantity to use and either the pressure amplitude (or SPL) or else the total acoustic power (or PWL) are more common.

For a plane wave, the intensity, power and pressure level are conveniently related; a plane wave being one in which the wavefront is flat and perpendicular to the direction of travel. For the plane wave the intensity, or power per unity area, is given by $w = pu$ (units Watt/m^2) u being the RMS velocity associated with the RMS pressure p. For the plane wave $u = \frac{p}{\rho c}$, ρ and c being the density and velocity of sound in the medium. For air at STP (0°C and 101 kN/m^2) ρc = 428 kg $m^{-2}s^{-1}$. The acoustic intensity corresponding to the reference RMS pressure, p_{ref} = 20 μN/m^2 is therefore given by

$$w = p^2_{ref}/\rho c \quad W/m^2$$

$$= \frac{4.10^{-10}}{428} \approx 10^{-12} \quad W/m^2$$

$$\approx W_{ref} \text{ the reference power per unit area.}$$

In other words for a plane wave the level expressed in terms of intensity or sound pressure are sufficiently nearly equal to be regarded as equivalent. For more complicated waves, such as spiraling waves in ducts or in the near-field close to sources, the connection between power, intensity and sound pressure is no longer simple.

The signals of pressure or power will have a frequency spectrum, and the level referred to may either be the total signal (i.e. the spectrum integrated over frequency) or else components of the spectrum at particular frequencies. If the overall signal is used to obtain the RMS pressure or power the levels are generally known as the overall sound pressure level (OASPL) or overall power watt level (OAPWL) respectively. Very frequently the signal is broken down into its spectral components and in this case it is necessary to specify the bandwidth over which the signal is summed. Mathematically the process is a fourier transform. Fourier transforms produce power-spectral density, for which the bandwidth is 1Hz, but electrical analogue filters or computer algorithms usually have a different bandwidth. The bandwidth may be constant regardless of the frequency being examined or it may vary with frequency, usually so that the bandwidth is proportional to frequency. The most common bandwidths of this type are the octave and third-octave bandwidths. An octave corresponds to a doubling of frequency, a third-octave bandwidth is therefore one where the upper frequency is equal to $\sqrt[3]{2}$ times the lower frequency. Depending on the choice of bandwidth very large differences in the displayed spectrum can be obtained. This is illustrated by Fig. (24.5) in which the same signal was analysed with a constant bandwidth and with a third-octave filter. Evidently quite different information is emphasised in the two traces. The narrow, constant bandwidth filter is useful for study and diagnosis, whilst the third-octave filter is more similar in its discernment to the human ear.

So far the discussion has referred to objective measures, but noise is inherently subjective. To assess noise one requires an assessment of the annoyance produced on a person or, to be more reliable, a large group of people, since no two people will be affected in quite the same way. The different ratings used throughout the world have been collected and described by Pearsons and Bennett Ref. (24.4). The simplest ratings weight the overall sound pressure level in a manner related to the sensitivity of the human ear. The most common of these, the A-weighted sound pressure level, finds wide use in non-aeronautical as well as aeronautical applications throughout the World and the levels are seen expressed as dBA or dB(A). Though less common there are also B,C and D scales intended for different levels and conditions. A great advantage of the A,B, C and D weighted levels is that they can be produced by an electrical circuit to provide immediate direct readings.

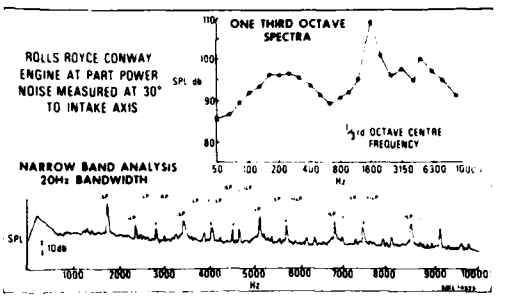

Figure 24.5 A single noise signal analysed by a constant bandwidth and a third-octave filter.

A more complicated noise rating, which is also described in detail by Pearson and Bennett, is the perceived noise level (PNL) for which the units are PNdB. The numerical value of PNL was intended to represent the sound pressure level of the octave band of "white noise" centred at 1kHz which would be judged equally noisy as the sound to be rated. A sound is judged equally noisy to another when one would just as soon have or not have it in ones home during the night or day. This definition emphasises the essentially subjective nature of the scale. Unfortunately the calculation of PNL is more complicated and cannot be produced by an electrical circuit. The noise must first be analysed into third octaves sound pressure levels (SPL) before appropriate corrections for amplitude and frequency are applied. To make the values of PNL more tangible Fig. (24.6), taken from Interavia, compares levels of representative situations. This figure also emphasises that with modest reductions in aircraft noise the prime nuisance for most of the population shifts to other sources.

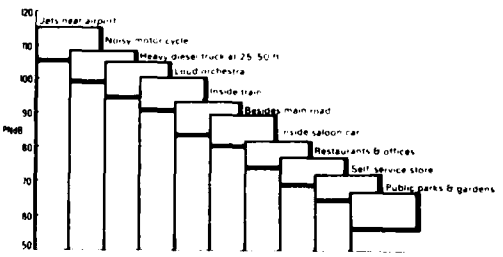

Figure 24.6 Perceived noise levels for representative situations.

The perceived noise level was found to be less reliable as an indicator of annoyance when the spectrum was no longer broad-band but contained a strong tone. A tone corrected perceived noise level (PNLT) was therefore produced. The third octave spectrum is first examined to determine if tones are present, evident by the protrusion of one band

above its neighbours by a prescribed ratio. If a tone is present a correction is added to the PNL calculated in the normal way, the amount of the correction depending on frequency and on the extent of the protrusion.

The noise from aircraft is of short duration, and the annoyance caused is related to the time over which the noise level is high. To take this into account the Effective Perceived Noise Level (EPNL) was evolved. The tone corrected perceived noise level is calculated at half second intervals and these are summed according to the following expression to yield EPNL:

$$EPNL = 10 \log \sum_{i=0}^{d} \text{antilog} \frac{PNLT_i}{10} - 13$$

where $PNLT_i$ is the tone corrected perceived noise level after the i-th 0.5 s interval. The summation is over the time for which the PNLT is within 10 dB of the peak level, levels outside this being ignored.

The Effective Perceived Noise Level provides the basis for the recent noise regulations. The regulations specify maximum EPNL as a function of all-up weight for sideline, take-off (flyover) and approach. The sideline noise is the maximum anywhere along a line parallel to and at a fixed distance from the runway. The take-off noise is prescribed at a fixed distance from the start of roll and the approach noise is at a fixed distance from the threshhold along a prescribed glide path. It turns out that it is meeting the take-off and approach noise limits which has created the greatest challenge.

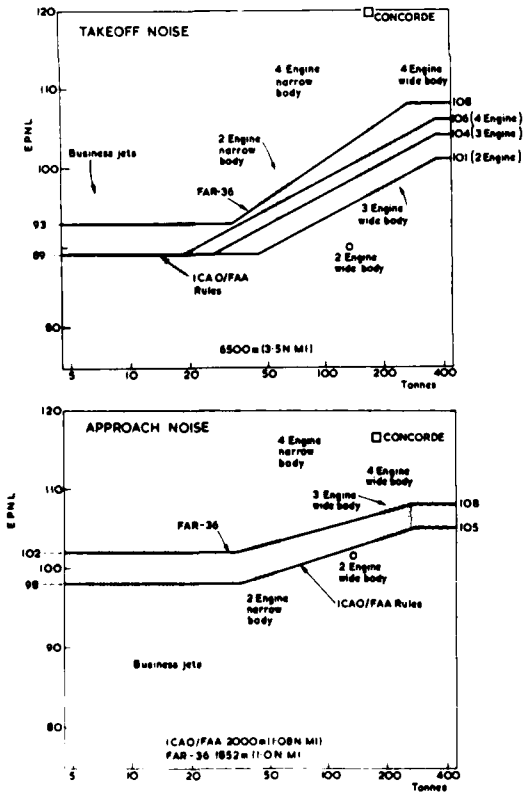

Figure 24.7 Take-off and approach noise levels - regulations and typical measurements, abscissa shows all-up-weight.

Fig.(24.7) shows the levels of the regulations at take-off and approach. The highest line on each corresponds to the United States FAR Part 36 regulations which first put compelling pressure on manufacturers to reduce noise of civil aircraft. The lower lines are the more recent and internationally agreed ICAO/FAA rules; the distances on the bottom of each part of Fig. (24.7) show the distances at which the criteria are laid down. To take account of the reduced rate of climb with larger numbers of engines the rules allow differing take-off levels depending on the number of engines.

The importance of aircraft type is borne out by the measured levels superimposed on Fig. (24.7). The hatched regions contain a wide range of results. The older jets are described as "narrow body" to distinguish them from the more recent "wide-body" aircraft. Essentially it is the engines, and not the aircraft, which have brought about the noise change.

The accurate measurement of noise from aircraft in flight is difficult and costly. A practical scheme for doing this is illustrated in Fig. (24.8). In this the second, third and fourth steps are those which evaluate the level of EPNL, the later steps are corrections for atmospheric absorbtion and non-standard aircraft conditions.

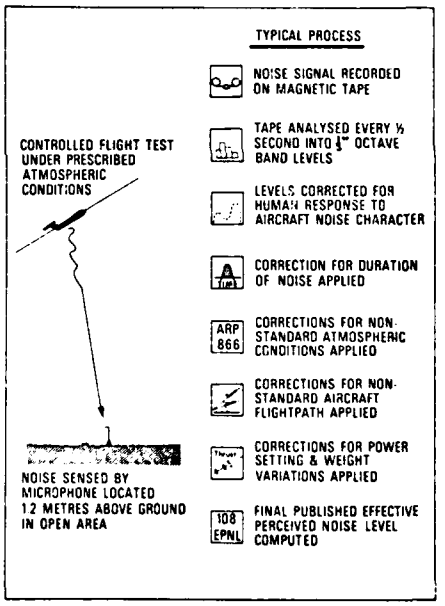

Figure 24.8 Measurement, analysis and correction procedures for in-flight noise measurement leading to certification.

24.3 INTRODUCTION TO ACOUSTICS OF DUCTS

To understand the noise of turbomachinery it is first essential to understand the propagation processes of acoustic waves in the ducts upstream and downstream. The need for this consideration arises because the pressure waves are not all uniform across the annulus or duct and do not propagate in the purely axial direction. In fact the pressure

varies circumferentially and radially in amplitude and phase, and the wave fronts spiral along the duct. The consideration of acoustic linings also requires an understanding of duct acoustics, but the presence of acoustically soft walls (i.e. walls where the normal velocity perturbations do not vanish) introduces great complications.

Downstream of a fan or compressor the duct is almost always annular, but upstream it is generally a circular cylinder. The circular nature of the problem determines the equation describing the propagation and the type of functions obtained. When the hub-tip ratio, σ, becomes sufficiently high it is often possible to unwrap the circular annulus into an equivalent rectangular duct, thereby simplifying the problem somewhat.

The first comprehensive treatment of the properties of the pressure field in both rectangular and circular ducts was given by Tyler and Sofrin Ref. (24.5). Not long after another account was given by Morfey, Ref. (24.6). These are clear and complete and it would be inappropriate to consider the details here. Because of its importance it is worthwhile to summarise the most important points to remind readers of the subject, but a more serious study should include reading more detailed accounts. For a circular duct with no mean flow the homogeneous wave equation can be written

$$\frac{\partial^2 p}{\partial r^2} + \frac{1}{r}\cdot\frac{\partial p}{\partial r} + \frac{1}{r^2}\cdot\frac{\partial \rho}{\partial \theta^2} + \frac{\partial p}{\partial x^2} - \frac{1}{c^2}\cdot\frac{\partial p}{\partial t^2} = 0$$

The homogeneous equation is used, i.e. acoustic sources are not considered, because the propagation is so important in its own right.

This equation can be solved by separating the variables so that the pressure fluctuation p is written

$$p = \Theta(\theta).\, R(r).X(x).T(t)$$

where each function is a function only of the variable shown. Four separate equations are then produced for Θ, R, X and T, with constants interrelating them. The variation with respect to time, T(t), is given by $e^{i\omega t}$ and the requirement that Θ repeat around the circumference determines that $\Theta = e^{im\theta}$ in which m is any integer including zero. The circumferential variation is therefore generally sinusoidal in form. By substituting for m in the equation for R, the familiar Bessel ordinary differential equation is produced for which the solutions are of the form

$$R(r) = J_m(k_{m\mu} r) + Q_{m\mu} Y_m(k_{m\mu} r)$$

where J_m and Y_m are Bessel functions of the first and second kind of order m respectively. $k_{m\mu}$ and $Q_{m\mu}$ are eigenvalues for the particular mode and particular hub-tip ratio. The mode consists of circumferential order m (i.e. m cycles or lobes around the circumference) and radial order μ (i.e. μ nodes or zero-crossings in the radial sense). When the hub-tip ratio is zero, that is to say the duct is a circular cylinder, $Q_{m\mu}$ is equal to zero and only Bessel functions of the first kind are involved. In the case of ducts with hard walls the boundary condition that there can be no velocity normal to the wall gives

$$\frac{\partial p}{\partial r} = \frac{\partial R}{\partial r} = 0$$

and this makes it possible to calculate $k_{m\mu}$ and $Q_{m\mu}$.

Tyler and Sofrin have tabulated $k_{m\mu}$ and $Q_{m\mu}$ for a range of cases. Fig. (24.9) shows some of the radial patterns presented by Tyler and Sofrin for a hub-tip ratio of 0.5 D for various values of circumferential and radial orders m and μ respectively. In this figure the amplitude of pressure is shown upwards with radial direction outwards to the right.

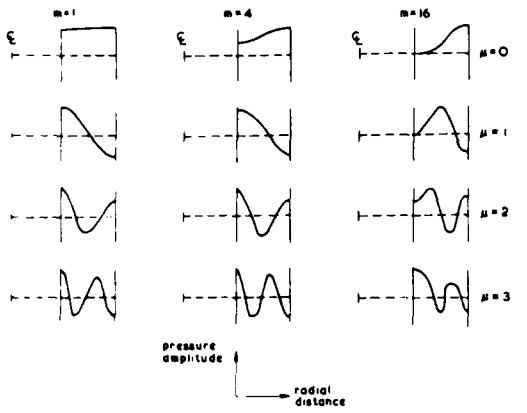

Figure 24.9 The radial variation in pressure amplitude in a cylindrical duct with 0.5 hub-tip ratio. Circumferential and radial orders of mode denoted by m and μ respectively.

Negative pressure corresponds to perturbations in *anti-phase* to that at the outer wall; note that the radial order denotes the number of zero-crossings. As the circumferential order becomes large the region of high amplitude tends to collect near the outer wall.

The radial eigenvalue, $k_{m\mu}$, appears in the equation for the axial variation X(x). Writing X(x) in the form $\exp(ik_x X)$, the axial wave number is then given by

$$k_x = \frac{1}{r}\sqrt{\frac{\omega^2}{c^2} - k_{m\mu}^2}$$

Thus when $\frac{\omega}{c} > k_{m\mu}$ the axial variation is harmonic with no decrease in amplitude. When $\frac{\omega}{c} < k_{m\mu}$, however, the axial variation becomes one of exponential axial decay and the wave is said to be cut-off. When $\frac{\omega}{c} = k_{m\mu}$, however, the axial wavenumber, k_x, is zero and this is referred to the cut-off condition. A comparison of predicted and measured decay, taken from Ref. (24.7), is shown in Fig.(24.10).

The form of the equation for k_x can be given more physical significance for turbomachinery by realising that the frequency sensed by a stationary observer will be related to the circumferential speed with which the pattern sweeps the circumference. If Ω is the pattern speed in radian/s, and r_o is the outer radius, then Ωr_o is the speed at the wall. If m is the circumferential order $\omega = m\Omega$. Denoting

the wall Mach number $\frac{\Omega r_o}{c}$ by M the expression for axial wave number becomes:

$$k_x = \frac{1}{r}\sqrt{M^2m^2 - k_{m\mu}^2}$$

and the condition for unattenuated propagation can be expressed as $M > \frac{k_{m\mu}}{m}$. Fig. (24.11), taken from Ref. (24.5) shows how the decay rate varies with the pattern wall Mach number for a hub-tip ratio of 0.5 and a radial order of zero. For large circumferential orders, i.e. large m, the decay rates below cut-off are enormous, so large in fact that for most purposes it is possible to ignore such modes altogether. The cut-off Mach number is slightly greater than one for large values of m, and significantly greater than one for low values of m. When the hub-tip ratio becomes very nearly equal to one the propagation in duct can be treated as if it were in a rectangular duct; the cut-off Mach number then tends to unity for all the zero radial-order modes. The corresponding Mach numbers for the cut-off of the higher radial orders are all higher. Thus for the 16th circumferential order in a duct of hub-tip ratio 0.5, the cut-off Mach numbers are 1.13, 1.46, 1.71 and 1.95 for radial orders of 0,1,2 and 3 respectively. In other words if the zero radial-order mode is cut-off all the higher radial order modes will be as well; in fact the rise in cut-off Mach number with radial order is even more rapid for small values of m.

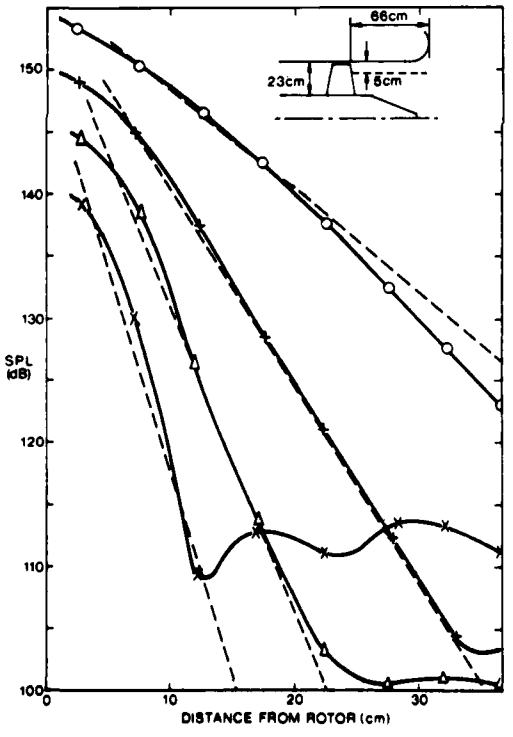

Figure 24.10 A comparison of measured and predicted (broken line) decay ahead of subsonic fan.

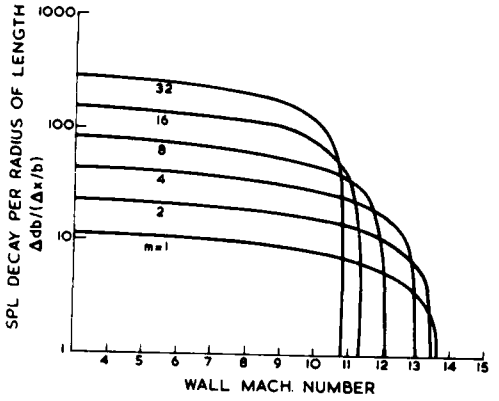

Figure 24.11 Decay rates for modes of zero radial order in ducts of hub-tip ratio 0.5.

The axial wavelength, λ_x, is equal to $2\pi/k_x$, k_x being the axial wave number, and the circumferential wavelength, λ_θ, is equal to $2\pi/m$. The angle between the direction in which a wave front propagates along the duct (i.e. at constant radius) and the axial direction is equal to $\tan^{-1}\frac{\lambda_x}{\lambda_\theta}$ or $\tan^{-1}\frac{m}{k_x}$. Thus at the point of cut-off, when $k_x = 0$, the wave fronts, or surfaces of constant phase, are axial and move in a circumferential direction. With k_x real and non-zero the wave fronts spiral along the duct so that in the limit when $\frac{k_x}{m} \to \infty$ the wave fronts are normal to the axis of the duct and propagation is purely axial.

In the ducts of aircraft engines flow Mach numbers are generally not negligible, being typically between 0.2 and 0.5. Sofrin and McCann Ref. (24.8) extended the analysis to include the effect of uniform axial flow, such a flow being an idealisation to that in ducts upstream and downstream of compressors, fans and turbines. The circumferential and radial form of the solution is unchanged by this mean flow and it is only the axial variation which is altered. In this case the axial wavenumber can be written:

$$k_x = \frac{1}{1-M_x^2}\left[M_x\frac{\omega}{c} \pm \sqrt{\left(\frac{\omega}{c}\right)^2 - 1(1-M_x^2)k_{m\mu}^2}\right]$$

M_x is the axial mean flow Mach number and x is taken positive in the direction of M_x. The ± signs refer to the downstream and upstream directions of propagation respectively. The effect of the axial flow is to reduce the frequency (or pattern wall Mach number) for cut-off. At the point of cut-off the argument inside the square root vanishes but in the case with a mean flow the axial wave number is not equal to zero, but to $\frac{M_x}{1-M_x^2}\frac{\omega}{c}$. The wave fronts (or constant phase surfaces) are then convected downstream and are not aligned in the axial direction. In fact with axial flow it is

possible for both the upstream and downstream propagating waves to be travelling upstream relative to the flow. Only when the mean convection speed is included does one of the waves move downstream in a frame of reference stationary with respect to the duct.

The axial mean flow is a convenient idealisation for the situation upstream and downstream of turbomachines. Sometimes the behaviour is required between blade rows and these may be quite a significant distance apart. Between blade rows the flow is usually swirling and in general this makes it impossible to separate the variables. For certain special distributions of swirl, such as forced or free vortex distributions, it is possible to handle pressure wave propagation after some restriction to small swirl, Kerrebrock, Ref.(24.9). The general distribution is, however, beyond present capabilities. Indeed with swirl in the flow inhomogeneities (like entropy or vorticity) also give rise to pressure fluctuations and the problem becomes most complicated.

The idealisation adopted so far has been the constant diameter circular or annular duct. In practically all cases this is fulfilled for only a short distance, and the diameter or shape of the duct is changed. Some methods have been produced for considering propagation in ducts of varying shape, this aspect is considered in the review by Nayfeh, Kaiser and Telionis, Ref. (24.10). In many cases the principal effects can be uncovered without considering the change of shape because if cut-off occurs the attenuation is generally so rapid that the amplitudes are very small before the change of shape is significant.

The modal structure in a duct is ultimately of less interest than the radiated field outside it. The most common approach to this is that adopted originally by Tyler and Sofrin, Ref. (24.5). The mean flow is ignored and the duct exit is surrounded by a large baffle. This baffle is merely a mathematical convenience but it appears that it does not seriously distort the radiation field or total acoustic power. Lansing, Ref. (25.11) has calculated the radiation field from an intake represented rather more realistically by an unflanged pipe and has shown very close agreement with the Tyler and Sofrin flanged method, Fig.(24.12). Towards 90° to the intake axis there is also a discrepancy apparent in Fig. (24.12) because the bounday conditions on the flange begin to be evident. Lansing, Drischler and Pusey, Ref.(25.12) considered this in greater detail and showed that only for modes in the duct close to cut-off is the calculation using flanged exits significantly in error using the flanged model.

Fig. (24.12) is dominated by the results of the Lowson, Ref. (24.22) which treats components such as fans as if they were unducted, i.e. it ignores the constraint of the duct on propagation and radiation. This is discussed further in Sec. (24.3), but this Figure does show the discrepancy, compared with Lansing's theory, that it implies.

The radiation method of Tyler and Sofrin does not include the effect of mean flow and although the formulation used by Lansing includes it, the calculated results shown do not. Candel, Ref.(24.13) considered a two dimensional (unflanged) case to examine specifically the effects of flow and soft duct walls. The boundary condition at duct ends are different for an inlet and an exhaust duct; specifically there is a Kutta condition to be satisfied at the nozzle exit. The radiation patterns obtained are very little affected at frequencies significantly above cut-off, with just a slight change in the field around 90° to the axis. The changes which occur close to cut-off are probably related to the change in the duct cut-off frequency produced by the mean flow. The lobes in the pattern towards 90° appear always to be those most affected, and as Candel shows it is also these lobes which are significantly reduced by having soft lining to the duct.

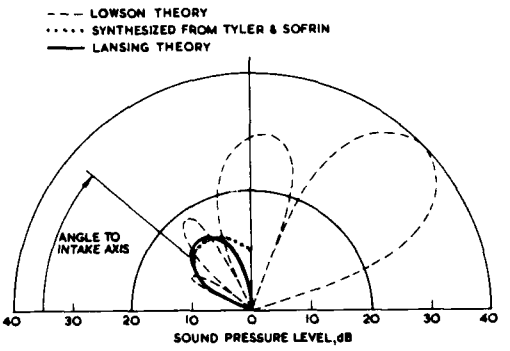

Figure 24.12. Radiated field shapes predicted by three models; Lowson's theory is for unducted source.

The analyses of radiation referred to have omitted at least two important effects. On the inlet side there are frequently strong refraction effects; the use of flared intakes reduces the velocity gradients and refraction effects and, as will be seen in the next section, with flared intakes the radiated field is accurately predicted. Flight type intakes frequently produce very severe velocity gradients, including local supersonic patches, and any prediction of field shape from this is suspect, particularly in the forward arc. On the exhaust side the radiated field shape is, in practice, radically altered by the refraction produced by the velocity and temperature gradients in the exhaust. The effect here is to move the field away from the exhaust axis and has recently been calculated by Savkar, Ref.(24.14). In fact the turbulence in the jet very frequently disturbs the field shape so that the distinctly lobed pattern is lost.

24.4 COMPRESSOR AND FAN NOISE

Having laid the basis of duct acoustics it is possible to consider the noise from compressors and fans. This in turn will lead naturally into consideration of noise from turbines.

The earliest work was concerned with noise from the multistage compressors used with low (or zero) bypass ratio engines. The compressors for these engines were designed with no regard for noise whatsoever, and almost invariably used inlet guide vanes. When it was recognised that the compressor noise could be as disturbing as the jet noise the mechanical constraints of these existing engines prevented very much being done to ameliorate matters. The advent of the high bypass-ratio fan allowed, for the first time, noise to be considered from design inception, but introduced a new type of noise

from the supersonic blade tips. The engine is dominated by a large fan on the front, the inlet guide vanes (IGV) have disappeared, the fan tip speeds are normally supersonic at high-power conditions, and the fan flow is split into core and bypass streams with very different geometries for each. Very importantly fan noise from the rear may be as significant or more significant than that from the front, often known as inlet noise. The new fans therefore introduce a marked change in emphasis and it was upon these that the largest amount of work was expended. It took some time for it to be realised how important the rearwards radiated noise is, and for it to receive equal attention.

The field of axial turbomachinery noise has been thoroughly reviewed, with excellent and readable accounts by Morfey, Refs.(25.15) and(24.16) and one from a different point of view by Cumpsty, Ref.(24.17). Morfey, Ref.(24.15) referenced no fewer than 180 papers in 1973, since when the number has increased, and it is obviously impractical to repeat that here.

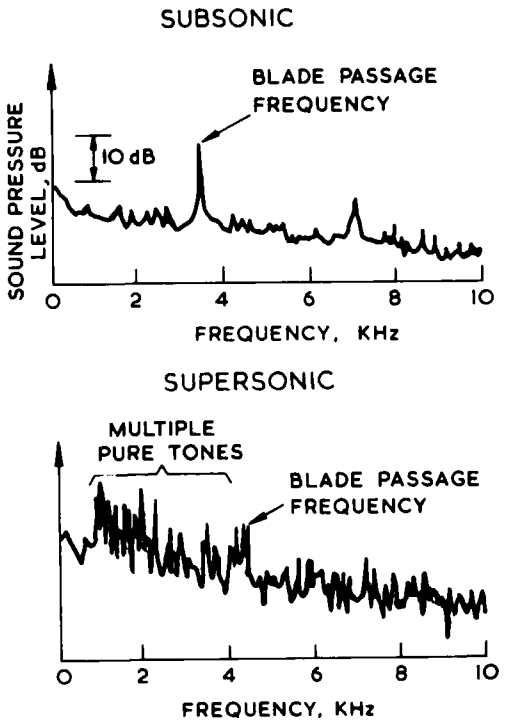

Figure 24.13 Typical forward arc spectra of noise from a fan or compressor with subsonic and supersonic tip speeds.

Fig. 24.13 shows typical spectra of the noise radiated from the inlet(i.e. forward arc) of a fan. The subsonic tip speed case shows tones at blade passing frequency and its harmonics and broadband noise, of lower level, elsewhere. The supersonic spectrum shows tones at multiples of shaft passing frequency with rather ill-defined broadband noise between them. These tones at shaft frequency are known as multiple pure tones, combination tones, or "buzz-saw" noise after the subjective impression gained by listening to this supersonic phenomenon. In the rear arc the spectrum at both subsonic and supersonic tip speeds is generally like the forward arc subsonic spectrum.

The radiated field shape was discussed in the section on duct acoustics. The spectra illustrated in Fig. (24.13) correspond to a particular angle to the axis of the machine and, since the field shape of each element of the spectrum is different, a different spectrum could be found at another angle. A"complete" picture requires spectra at a wide range of angles, but very rapidly the amount of data becomes too large to assimilate. The normal approach is to consider the spectrum at one angle and to look at the field shape of particular spectral components, such as the blade passing frequency tone.

The discussion of compressor and fan noise will be under the headings: Interaction tone noise (producing the forward radiated tones from subsonic machines and the rearward radiated tones from all machines), Multiple pure tone noise (a supersonic phenomenon) and Broad Band Noise.

24.4.1 INTERACTION TONE NOISE

Interaction tone noise has been the most widely studied aspect of compressor noise, and relates to the forward and rearward arc of subsonic machines, as well as to the rear arc of supersonic machines. The kinematics of the process are first examined. After this the experiments relating to rotor stator interaction are considered,and this leads naturally into the analytic studies. The theory has attracted many workers and there is a perhaps disproportionate amount to describe here. Finally, the effect of inlet flow distortion is considered.

24.4.1.1 KINEMATICS

From the discussion of duct acoustics it will be recalled that the pressure field which is rotating with a wall Mach number less than unity decays rapidly in the axial direction, i.e. is cut-off. It is therefore at first sight remarkable that tones are produced by machines with subsonic tip speeds. The essential explanation was presented by Tyler and Sofrin, Ref. (24.5) and is that the rotors interact with stationary non-uniformities, such as the wakes or potential field of stators, to set up an interference pattern for which the circumferential Mach number of a point on the wave is greater than the cut-off value. They showed that for B rotor blades and V stator vanes an interaction pattern is set up with a circumferential order m given by

$$m = nB \pm KV$$

where n is the harmonic of blade passing frequency and k is the spatial harmonic of the distortion produced by the stators. It follows that the angular velocity of the interaction pattern, Ω_p, is given by

$$\Omega_p = \Omega \frac{nB}{nB \pm kV}$$

where Ω is the rotor shaft angular velocity. Although formulated in terms of rotors and stators interacting, it is equally valid for inflow distortion where V would denote the circumferential order of distortion.

This expression is purely kinematic, and takes no account of the interaction process involved. The effect is illustrated schematically in Fig.(24.14) where a four bladed rotor interacts with a three bladed stator (B = 4, V = 3). The fundamental blade passing frequency interaction, n = 1, would therefore be expected to rotate at

$\frac{4}{4 \pm k}$ times the rotor speed. The largest value

is achieved taking k = 1 and the negative sign to give a ratio of 4. Fig. (24.14), taken from a recent article on fan noise by Lowrie, Ref.(24.18), shows that after the rotor moves 30° from the top interaction the next interaction moves round by 120° or four times as far. This is continued so that after moving 90° the pattern has rotated a full 360°. If there had been five stators, V = 5, the same situation would be achieved again when k = 1. In this case the value of m is equal to -1 and the pattern would again rotate at four times the rotor speed but in the opposite sense to the rotation of the rotor.

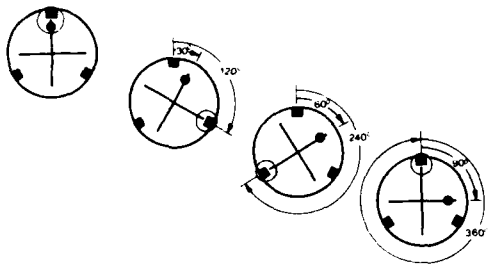

Figure 24.14. Schematic representation of rotor-stator interaction; B = 4, V = 3.

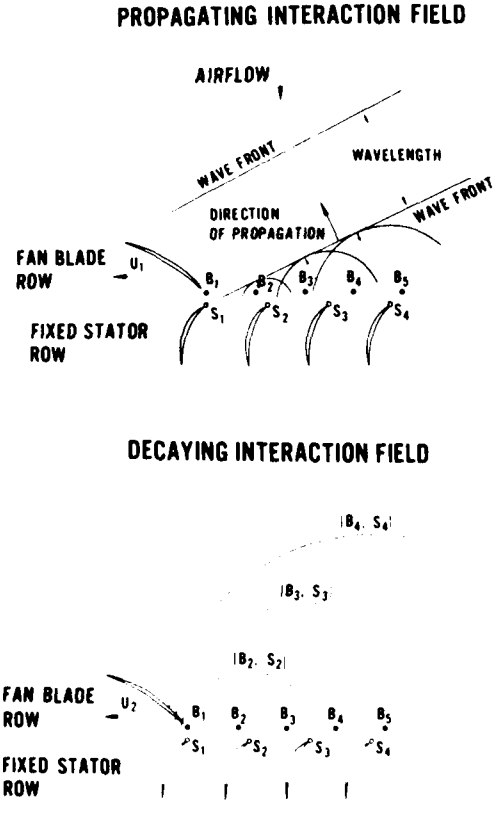

Figure 24.15 Schematic representation of wave fronts for rotor-stator interaction above and below cut-off

A schematic representation of the way in which the waves from interactions which are above cut-off add to produce wave fronts, whereas below cut-off they overlap and cancel, is given in Fig. (24.15). The analogy can be drawn between supersonic and subsonic projectiles, the former producing disturbances which coalesce, the latter waves which interact and cancel.

24.4.1.2. ROTOR-STATOR INTERACTION EXPERIMENTS

Some insight into aspects of interaction processes can be obtained from Fig. (24.16) which shows forward arc field shapes of the second harmonic of blade passing frequency from a high-speed fan. These field shapes were obtained by slowly traversing a microphone along the arc of a circle drawn about a point in the inlet plane. The fan in this case had no inlet guide vanes, 25 rotor blades and 39 outlet guide vanes placed very close behind the rotor. From the blade numbers it will be noted that at blade passing frequency a mode of order m = 14 will be set up rotating in the opposite sense to the rotor at $\frac{25}{14}$ times rotor speed, whilst at the second harmonic an m = 11 mode is produced rotating $\frac{50}{11}$ times faster than the rotor. Even at the lower speed shown in Fig. (24.16) the second-harmonic will be well above cut-off. The strong zero-radial order (μ = 0) mode is shown at the lower speed, identified by overlaying the field shape predicted by the flanged model (after Tyler and Sofrin). The good agreement is apparent. At the lower speed the field is dominated by the μ = 0 mode, even though higher radial orders are above cut-off, but at the higher speed the higher radial order modes become much more important. Further increases in speed actually led to a drop in the level and to an increase in the random fuzziness visible in the traces presented.

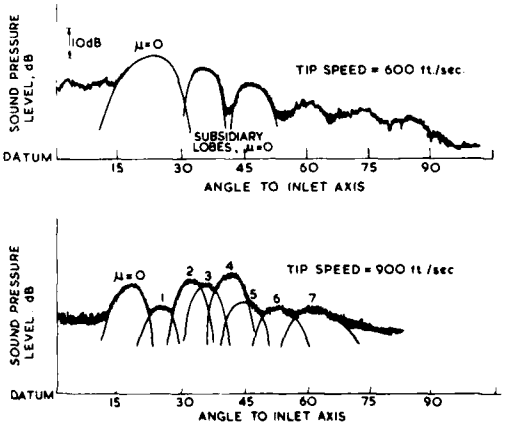

Figure 24.16 Forward arc field shapes of tones at second harmonic of blade passing frequency.

The second harmonic field shapes have been shown here because field shapes at the blade passing frequency fundamental were smooth in overall shape, with no evidence of lobes due to rotor-stator interaction, but a large level of fuzziness. This fuzziness, or unsteadiness of the tone is characteristic of the traces obtained when a rotor is run without stators and the tone produced under these

circumstances is sometimes misleadingly called the rotor-alone tone. In fact it is the result of interaction of the rotor with random, turbulent distortions drawn into the machine and will be discussed below in Sec. 24.4.1.4. The absence of the rotor-stator interaction at the blade passing frequency fundamental, even when this is above cut-off and the rotor and stator are close together, and reduction in level noted for the second harmonic as the speed is increased are a result of the rotor blocking the sound generated on the outlet guide vanes. This, too, will be discussed below.

There have been a large number of tests run to determine the level of the tones produced by the interaction of rotors and stators. In the early tests, using multistage compressors, the principal interaction was produced between the inlet guide vanes and the rotor, and correlations were obtained from these. An example is shown in Fig. 24.17, taken from the discussion of Ref. (24.19). Considerable variation in the details of the trends with axial gap-chord ratio due to different companies can be seen, but each shows the rapid rise in level at small axial gaps between rows associated with the interaction of the potential fields around the blades. At larger spacings it is the wake which interacts with the downstream row, and the viscous decay is much slower. The true complexity of the situation was illustrated by the tests of Kilpatrick and Reid, Ref. (24.20), where in some cases the radiated tone level from a two-stage transonic compressor actually increased with increase in spacing.

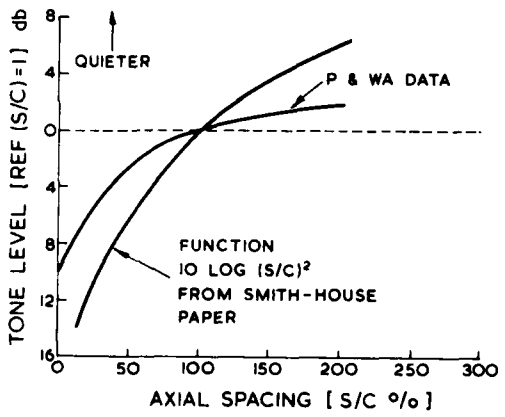

Figure 24.17 Correlations of the change in tone level with the ratio of axial gap between rotor and stator to the chord.

The generation by high bypass ratio fans is rather different from most multistage compressors, both because of the absence of inlet guide vanes and the low hub-tip ratio, but also because large spacing is usually included between rotor and bypass section outlet guide vanes to reduce the interaction. Fig. (24.18) shows forward radiated power and Fig. (24.19) the rearward power from tests of a high bypass fan reported by Burdsall and Urban, Ref. (24.21). The reference case shown is one where sufficient outlet guide vanes have been fitted to ensure that the rotor-stator interaction is cut off; these results show the blade passing frequency tone from an aerodynamically equivalent fan with the rotor-stator interaction effectively eliminated from the acoustic point of view. Any tone produced in this reference case must be related to other sources of distortion, almost certainly the atmosphere. At 4 chords spacing the tone can be therefore seen to be due to the interaction with atmospheric distortion, with the rotor-stator interaction playing no part. At higher speeds this is also true for the forward arc noise at 2 chord spacings, and this reflects the tendency of the rotor to block the forward propagation of the sound generated on the outlet guide vanes. The same blocking is not evident in the rear arc since the sound is being generated on the furthest downstream blade row. Although the tone levels do increase rapidly with speed, particularly close to cut-off, it may be seen from these results that the trend is not so simple at higher speeds.

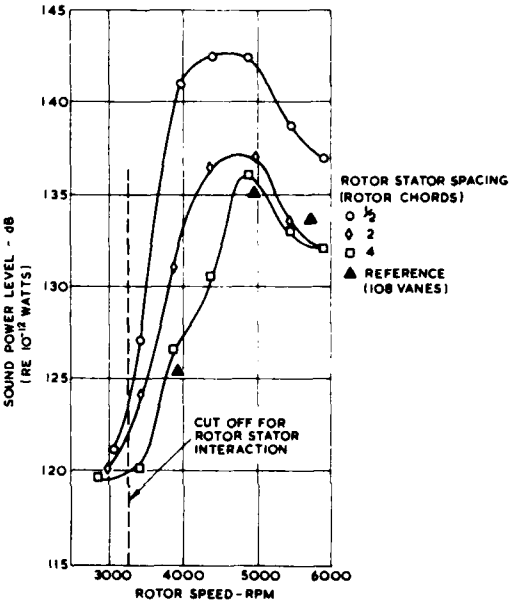

Figure 24.18 Forward radiated tone level at blade passing frequency fundamental (Blade tip speed sonic at approx. 5000 RPM).

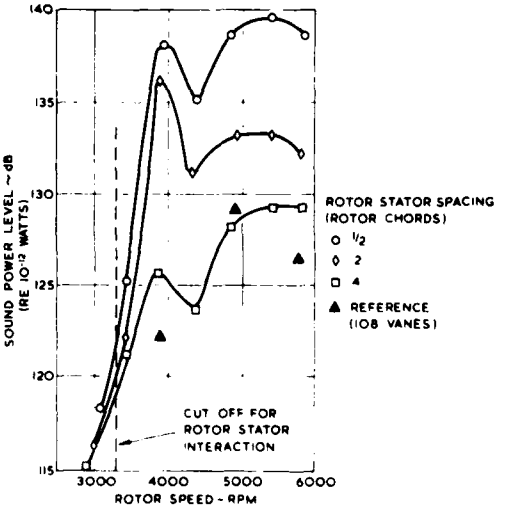

Figure 24.19 Rearward radiated tone level at blade passing frequency fundamental (Blade tip speed sonic at approx. 5000 RPM).

24.4.1.3 ANALYSIS FOR INTERACTION TONE NOISE

The rotor-stator interaction in a high-speed, low hub-tip ratio machine is highly complex. The blade rows are normally highly loaded, so that as well as significant pressure changes across the blades, large deflections are normally encountered, particularly near the root. The wakes from rotors are distinctly different from those behind isolated aerofoils, and in addition the wakes in turbomachines twist because of the radial variation in the swirl velocity. Thus the interaction will not take place simultaneously along the whole span but the wake will sweep along it. The wake also tends to collect at the hub or tip and become confused with the secondary flows, which will themselves produce an interaction with the downstream row. As already mentioned the blade rows are able to block the transmission of sound, and this is just one example of the more general interaction where the two blade rows should really be seen as a coupled pair.

There have been a large number of analytical models for the interaction between blade rows. Basically, they may be divided into those which treat the problem as a two-dimensional cascade (i.e. ignoring radial effects) and those which treat blade rows as if they were unducted propellers. The unducted methods are often associated with Lowson, Ref. (24.22) and more recently, Hanson, Ref. (24.23). Kinematically both the cascade and the unducted propeller are similar, with the interaction between moving blades and stationary disturbances (or vice versa) setting up a pattern rotating much faster. In the two-dimensional case the criterion for unattenuated propagation is that the cut-off Mach number should be exceeded, whilst for the unducted propeller radiation becomes efficient only when the disturbance is supersonic, and the two criteria are very similar. At least two major disadvantages may be associated with the unducted models, one is that the field shapes are very different from those predicted by other methods which have themselves been shown to agree quite well with measurement, Figs. (24.12) and (24.16). A second disadvantage is that the blockage of sound by blade rows may be as important as the generation itself, and the unducted models do not lend themselves to predicting this.

Directing attention to two-dimensional cascade methods two basic approaches to calculating the interaction of blade rows with inlet velocity or sound waves can be found. Conveniently these can be designated the compact and distributed approaches.

If the blade chords are assumed to be sufficiently short in relation to the wavelength they may be regarded as acoustically compact sources. By treating the sources as compact it is a simple application of classical acoustics to relate the dipole source strength to the fluctuation in lift (or drag) of the blades. The lift fluctuation is normally much larger than the drag and is generally obtained by one of Sears, Ref.(24.24) or Kemp and Sears, Ref.(24.25 and 24.26) methods for incompressible flow about uncambered blades. Probably the first example of this was applied by Hetherington, Ref. (24.27) who obtained quite good estimates for the power produce by IGV-rotor interaction. Another compact source method is due to Mani, Ref. (24.28) and this was used to predict acoustic power produced by a small rotor running in the wake of a number of rods in a Freon tunnel, Lipstein and Mani, Ref. (24.29). The theory predicted that when the wavefronts generated are nearly parallel to the blade chord the power would be much higher than when the wavefronts are normal to the chord. With 82 rods the wave fronts were very nearly normal to the blade chords whereas with 41 the wave fronts were nearly parallel. As Fig.(24.20) shows the theory accurately prediced the levels in each case and, in particular, the higher levels for 41 rods.

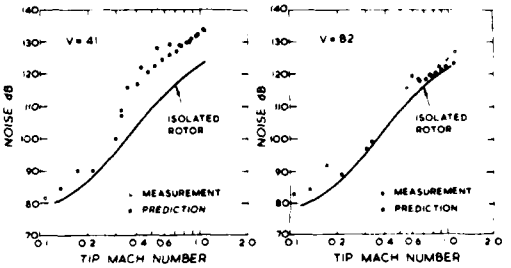

Figure 24.20 Comparison of prediction and measurement of rearward acoustic power at blade passing frequency from 54 bladed fan in closed cycle Freon rig.

Despite these successes one is nevertheless concerned about many of the steps in compact source models such as this; the calculation of lift fluctuation makes many restrictions which are not satisfied but, perhaps more seriously, the blade chord and the sound wavelength turn out to be very nearly equal. In calculating rotor-stator wake interactions a very simple model is used for the wake, and this too is open to the most serious doubt.

The more interesting methods for two-dimensional cascades use the distributed source approach and do not make restrictions about chord length, but match incident upwash with source strength along the chord. They are, nevertheless, restricted to cascades of uncambered blades at zero incidence (flat plates) and become less accurate at Mach numbers approaching unity. The method due to Kaji and Okazaki, Ref.(24.30) is presented only for the calculation of the effects of incident pressure waves (although it may be generalised) whilst methods by Whitehead, Ref. (24.31) and Smith, Ref. (24.32) admit both this and vorticity distortion as inputs. Fig. (24.21) compares measurements with predictions produced by Smith in a special low speed test, and the agreement is evidently excellent. The rapid rise in the magnitude of the pressure fluctuation rotor tip relative Mach numbers close to 0.1 occurs as cut-off is approached. At Mach numbers below cut-off the levels fall precipitously.

Quite recently, Kaji, Ref. (24.33) has compared the predictions obtained using a distributed, i.e. non-compact, source model with that obtained for a compact source. The results for relative inlet and rotational Mach numbers of 0.8, Fig. (24.22) indicate that large errors may be produced by the compact source methods, particularly for the upstream going wave.

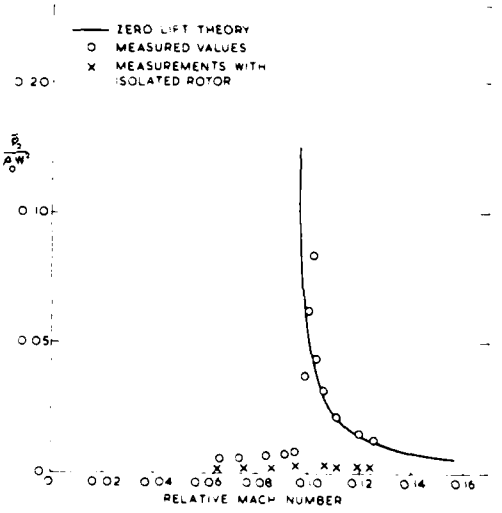

Figure 24.21 Comparison between predicted and measured acoustic pressure fluctuation at blade passing frequency, downstream of 23 bladed rotor with 24 upstream wakes. (Pressure non-dimensionalised with relative dynamic pressure into rotor).

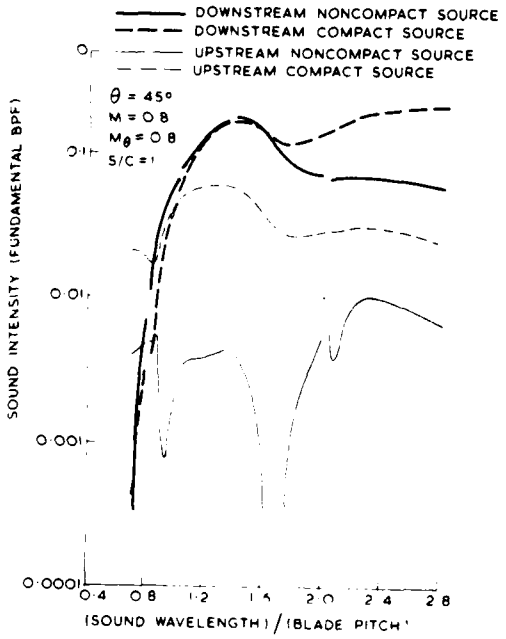

Figure 24.22 Comparison between compact and non-compact representation of rotor interacting with distortion. (Stagger, $\theta = 45^{\circ}$, pitch chord ratio $\frac{s}{c} = 1$).

The discrepancy found between the compact and distributed source methods for predicting the interaction of blade rows with flow distortion is not found for the interaction of blade rows with sound waves. Methods where the blade chords have been vanishingly short or very long produce results for the transmission and reflection agreeing closely with those calculated using a distributed source method for a chord comparable to a wavelength. Fig. (24.23) shows results calculated by Kaji and Okazaki, Ref. (24.30) for the transmission and reflection of a sound wave approaching a cascade of uncambered blades from downstream. The stagger angle is 60°, the flow Mach number 0.5 and the pitch-chord ratio is 1.0. The angle $(\theta-\alpha)$ is the angle between the incident wave propagation direction and the chord of the blades; $(\theta-\alpha) = 0$ corresponds to the direction of propagation of the waves being parallel to the chordline of the blades. For $(\theta-\alpha) = 0$ propagation occurs with no reduction in transmitted level and no reflected wave. The product of wavenumber and chord is denoted by K; the small effect of changes in this, particularly on the transmitted wave, are apparent. The reasons for this are not understood but it appears that it is the inclination of the wave propagation direction to the chord line which is crucial (the "venetian blind effect"). This makes for convenient modeling and using this Cumpsty, Ref. (24.34) was able to explain some aspects of the blocking of sound already referred to. In general it would appear that modes generated on outlet guide vanes which are rotating in the opposite sense to the rotor (i.e. $m = nB \pm kV$ negative) have an orientation relative to the rotor blades such that the amplitude of the wave transmitted through the rotor is low.

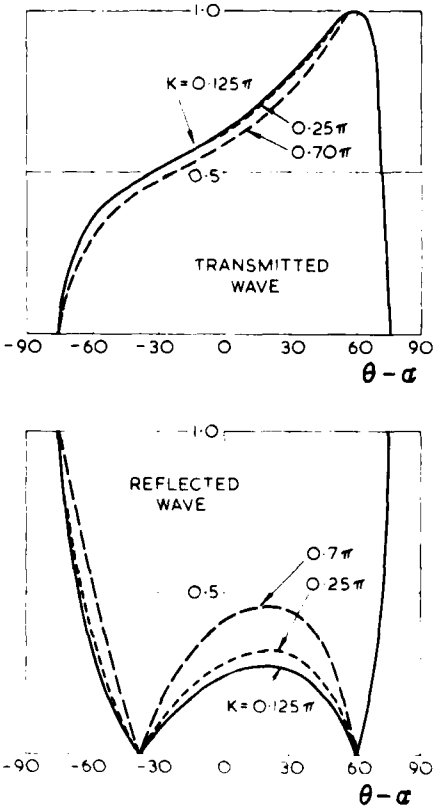

Figure 24.23 The level of the transmitted and reflected pressure waves from a cascade of uncambered blades staggered at 60°. Incident pressure wave from downstream.

There have only been two attempts at calculating the coupled interaction between rotor and stator blade rows. Kaji and Okazaki, Ref. (24.35) used their distributed source method and Osborne, Ref. (24.36) used a compact source method. The effect of spacing on sound generated is shown by these and the rapid rise of the potential interaction at small spacings is emphasised. In calculating the potential interaction steady blade loading is an essential factor, and for this analysis it is assumed small.

In the preceding paragraphs it has been assumed that the principal mechanism for the generation of sound is the pressure fluctuation on the blades when they pass through a distorted flow. This is frequently referred to as dipole noise, and in suitably idealised conditions gives acoustic power proportional to the sixth power of inlet Mach number. Quite a different mechanism was pointed out by Ffowcs Williams and Hawkings, Ref. (24.37), in which the velocity perturbation v_i interacts with the steady velocity field, V_j, surrounding the blades to produce noise proportional to $(\rho v_i V_j)$. This is generally known as quadrupole noise and the acoustic power is proportional to the eighth power of incident Mach number. Quadrupole noise may therefore be expected to become important at higher speeds than dipole noise, but it is not yet known where the crossover will occur. Experimentally the two are virtually indistinguisable because in practice it is impossible to obtain the idealised situation in which the noise varies as the sixth or eighth powers. Theoretical investigations have been tried, but these are so limited by the assumptions required that they only really indicate that the quadrupole noise probably dominates at very high subsonic speeds.

24.4.1.4 ROTOR-INFLOW DISTORTION INTERACTION

At the beginning of this section on interaction tone noise attention was drawn to the unsteady tone levels, which were sometimes of higher mean amplitude than the steady tones attributable to rotor-stator interaction. It was mentioned there that this tone is due to the interaction of the rotor with unsteady, turbulent distortions in the inlet flow. It may be added that steady inlet distortions can be present, particularly in bad test rigs, and these can produce steady tones of high level.

At one time it began to seem that the noise of high bypass engines on approach (when the tips are subsonic) would be dominated by the blade passing frequency tone attributable to this interaction. It was not, however, understood why the turbulence in the calm conditions normally used for noise testing could give rise to the high levels of distortion needed to produce the high tone levels. Mani, Ref. (24.38) applied a compact source method to the interaction of a rotor with homogeneous, isotropic turbulence and an example of the power spectrum produced is shown in Fig. (24.24). Even with large scale turbulence the spectrum does not contain peaks of comparable sharpness to the tones (or, more correctly, narrow band noise) normally measured.

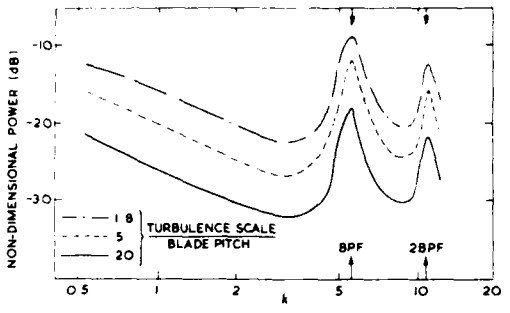

Figure 24.24 Predicted spectra of acoustic power produced by a rotor interacting with isotropic, homogeneous turbulence.

The explanation appeared indirectly by comparing the tone levels in the intake of an engine mounted on an aircraft. With the aircraft stationary on the ground a high blade passing tone level was produced, exhibiting the familiar unsteadiness. In flight, or with appreciable forward speed, the level of the tone dropped dramatically. This is shown by Fig.(24.25) presented by Cumpsty and Lowrie, Ref. (24.39) where the large reduction persists until the tips are supersonic. The change with forward speed demonstrated the essential feature of the turbulence drawn into a stationary intake, that it is not isotropic, but is strongly elongated in the axial direction. Hanson, Ref. (24.40) has measured the length scales and finds that in the axial direction they are typically 100 to 200 times that in transverse directions. The long, axial eddies are necessary for the production of narrow band noise which is recognisable as a tone. The contraction of the eddies in the lateral sense leads to an enormous increase in the lateral velocities (explaining why turbulent distortion remains important in even very calm conditions) and also allows the larger atmospheric eddies to be compressed into the intake. When the intake possesses a significant forward speed this effect is decreased, and the two conditions are illustrated by the sketch in Fig.(24.26). Tests with large screens designed to remove turbulence placed in front of the contraction of the intake have been shown by Lowrie, Ref. (24.41) and Roundhill and Schaut Ref. (24.42) to reduce the tone level due to interaction of the rotor with the flow distortion.

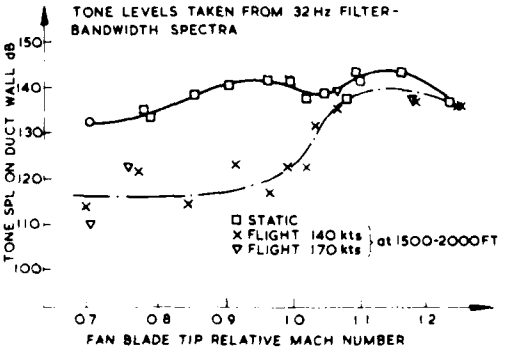

Figure 24.25 Comparison of in-duct tone levels, static and in-flight.

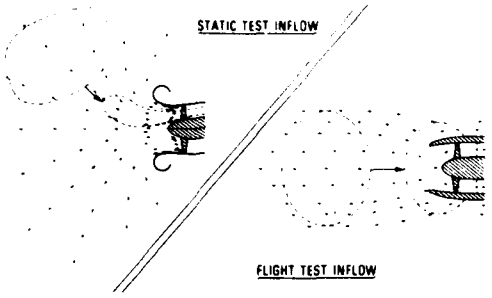

Figure 24.26 Schematic representation of streamline patterns into an intake, static and inflight.

Cumpsty and Lowrie, Ref. (24.39) however reported a strong correlation between the unsteady tone level and the intake boundary layer momentum thickness at tip Mach numbers up to about 0.85. Moore, Ref. (24.43) has observed reductions in the tone from a low speed fan when the annulus boundary layer was removed, and Lowrie, Ref. (24.41) reports similar results on a high speed machine. It has not yet been clearly demonstrated how atmospheric distortion and the boundary layer both play a part in producing the tone at lower tip Mach numbers.

Because this particular noise nuisance disappears for propulsion engines in flight, at least for good installations, the emphasis now must be on how to reproduce in-flight conditions for static tests. It is unfortunate that contamination by this noise source has irrevocably compromised data obtained from so many costly tests.

24.4.2 MULTIPLE PURE TONE NOISE

When it was first decided to build engines with tip Mach numbers of around 1.4 it was widely expected that the steady pressure field around the rotor would propagate unattenuated along the intake, being above cut-off, to produce an unparalleled noise nuisance. In the event the situation was considerably less serious than this primarily because the steady pattern towards the tip consists of shock waves and these attenuate non-linearly as they propagate. The essential processes are demonstrated schematically in Fig. (24.27); the upper sketch shows the situation for perfectly uniform shocks ahead of the rotor whilst the lower one shows the more realistic case of slightly differing shocks.

The noise produced by supersonic rotors is now perhaps better understood than that from any other source, probably because it is inherently more simple, being steady with respect to the moving blades. Multiple pure tone noise is also well understood because of an unusual meshing of theory and experiment.

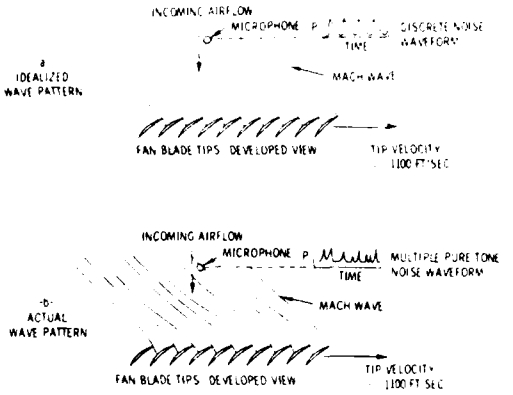

Figure 24.27 Schematic representation of shock waves ahead of a supersonic rotor.

In the development of knowledge about noise from supersonic blades a crucial experiment was reported by Sofrin and Pickett, Ref. (24.44) in which a sleeve was inserted ahead of a supersonic rotor to produce a narrow outer annulus. The shock pattern and evolution were essentially unchanged by the sleeve, indicating that for most purposes the process may be adequately modeled two-dimensionally. Sofrin and Pickett dramatically demonstrated the process of decay and evolution ahead of several rotors. Fig. (24.28) shows results obtained with the narrow annulus for the decay of the average shock wave amplitude; initially it is proportional to

$$\frac{1}{\sqrt{x}} \quad \text{and then further from the rotor as} \quad \frac{1}{x},$$

where x is the axial distance.
These two rates of decay are shown by Sofrin and Pickett to be predictable by one-dimensional shock theory. The prediction of the average rate of decay says nothing, however, about the spectral evolution. The changes in the pressure-time traces and in the spectrum at small distances ahead of the rotor are clearly demonstrated in Fig. (24.29) taken from Burdsall and Urban, Ref. (24.21). The evolution is essentially non-linear, and occurs because the stronger shocks travel faster than the weaker, eventually overtaking and absorbing them. As Fig. (24.29) shows just ahead of the rotor the shock strengths are nearly equal giving a spectrum with a dominant tone at blade passing frequency. Only a few pitches upstream the number of shocks is decreased and the spectrum altered to be dominated by tones at shaft rotating frequency.

The decay of shocks of uniform strength has also been analysed by Morfey and Fisher, Ref. (24.45). Although uniform shock strength is not the case of principal interest they have emphasised that there is a worst Mach number at which decay is least. The decay of a train of shocks (more precisely N waves) with random initial amplitudes has been calculated by Hawkings, Ref. (24.48), with the interesting conclusion that the decay becomes slower as the irregularity becomes greater. The most interesting theoretical work is due to Kurosaka, Ref. (24.47) who considered a rather idealised system of shocks and expansions around the leading edge of a cascade of uncambered blades, Fig. (24.30), restricting attention to shocks attached to the leading edges. Random variations in both blade spacing and stagger

were considered. With quite small variations in stagger the spectrum only a short distance ahead of the rotor closely resembles those measured, Fig. (24.31). Similar variations in blade pitch produced nowhere near the correct spectrum. Whilst this points very clearly to variations in the inclination of the forward part of the blade as being the principal cause of the spectral evolution, it must be borne in mind that fans usually operate with the shocks somewhat detached.

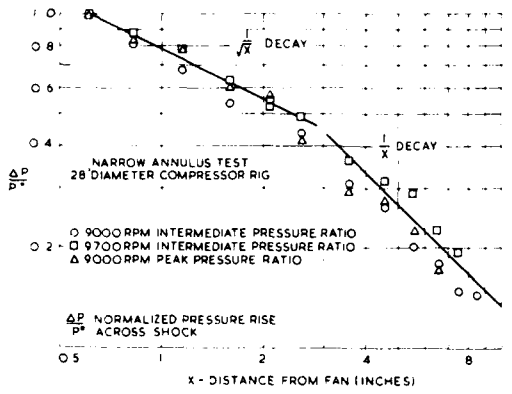

Figure 24.28 Decay rates of the average amplitude of shocks ahead of a supersonic rotor. (Blade pitch approx. 2.7 inch).

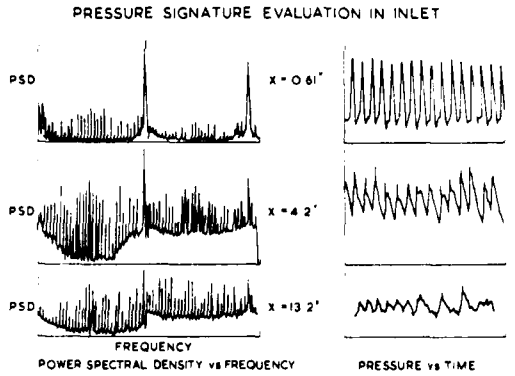

Figure 24.29 Measured evolution of time histories and spectra ahead of supersonic fan. (Blade pitch approx. 2.7 inch).

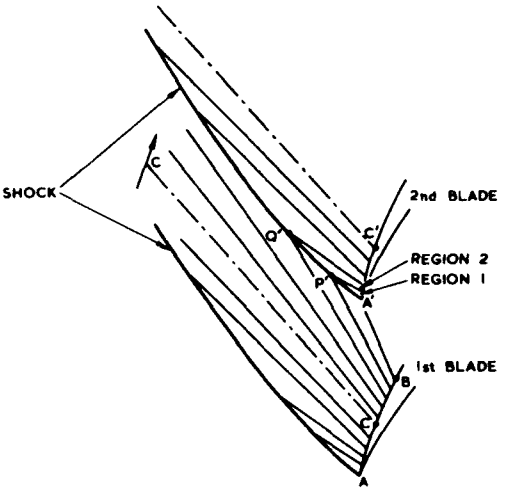

Figure 24.30 Idealised shock and expansion system around leading edge of a two-dimensional supersonic cascade.

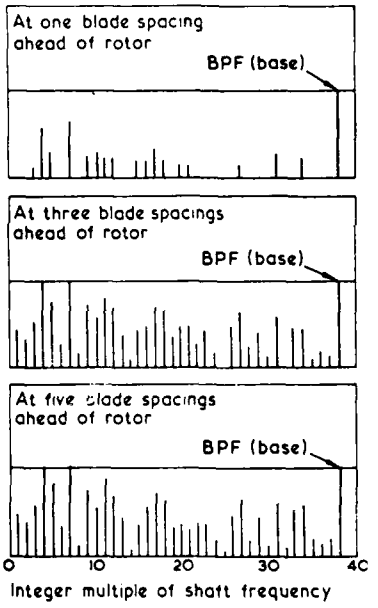

Figure 24.31 Predicted spectra ahead of supersonic cascade of uncambered blades for small variations in stagger angle.

A large number of tests have been run to try and reduce the multiple pure tone noise by altering blade profile. It will be appreciated that subjectively a change in spectrum may be as important as a change in level. One school of thought favours camber over the forward part to reduce the influence of the turning around the leading edge which is believed to produce the shock strength variations. Another school favours a flat forward part to minimise the shock strength, and hence the

propensity for the non-linear evolution. Since only small variations are needed to produce the evolution it is now known whether the special blades will survive the rigours of operation. In any case the success of acoustic treatment in intakes at attenuating multiple pure tone noise has reduced the impact in this noise and with it the interest in eliminating it at source.

24.4.3 BROAD BAND NOISE

Whereas the multiple pure tone noise is fairly well understood, the situation for broad band noise is most unsatisfactory. One of the problems is the difficulty of pin-poining this source experimentally. Unlike the blade passing tones, which are easily identified in the spectrum, and from which something can be learnt of the source by the time history and field shape, almost nothing can be said unequivocally about the broad band noise. The broad band noise forms the spectral background between the tones, as in Fig. (24.13); frequently what was believed to be broad band noise in the past has found to contain a large number of tones when analysed with a narrower band-width filter. There is in general no way of knowing whether the noise originates in the rotors or stators, whether it is produced by incident turbulence interacting with the blade rows, or whether it is random unsteadiness produced in the blade rows themselves. It is the random character of broad band noise which makes this so difficult to unravel. What understanding there is comes from observation of changes in the noise with changes such as removing a stator row or altering the pressure ratio by throttling. Unfortunately removing a downstream stator row has aerodynamic effects on the rotor which are frequently overlooked, but which are quite likely to alter the noise from it. Moreover, changing the pressure ratio by throttling also affects transmission of sound through blade rows.

Separated flow is well-known for the high level of broad band noise generated, and Sharland, Ref. (24.48), for example, compared noise from a stalled rotor with the rotor unstalled. Gordon, Ref. (24.49) has looked in detail at the noise from fully stalled bluff bodies in pipes. The broad band noise power appears to be approximately proportional to the cube of the steady pressure drop across the obstruction. One of the difficulties in turbomachines is that only one part of the machine needs to be stalled for it to dominate the broad band noise. A partially stalled set of stators or a bad rotor hub could give results which would be quite misleading if treated as general.

The two main hypotheses for broad band noise generation are the interaction of the blades with turbulence and the self-generated unsteadiness of the flow in the blades themselves. To this must be added the model proposed originally by Smith and House, Ref. (24.19), where the turbulence in the wakes of one blade row interacts with the next row downstream. An order of magnitude argument shows that the length scale of turbulence in the blade wakes is too short to correspond with noise generation at the frequencies observed. It is possible, however, that the wakes from heavily loaded blades are rather different to those normally envisaged and used in theoretical models and that they do contain significant components in the appropriate range. This hypothesis was also used in more sophisticated form by Morfey, Ref. (24.50), who used results from a number of different fans and compressors to infer the magnitude of parameters implicit in his formulation. One of the techniques used by Morfey, which is extremely common in aero-acoustics is to plot acoustic power against Mach number, in this case inlet relative Mach number. Single stage compressors change their incidence and loading relatively little as the rotational speed is changed, providing the throttle is constant. This is certainly not the case for multistage machines (some of those used by Morfey had 7 and 8 stages) and as the compressor speed is reduced the front stages move rapidly towards stall.

It has frequently been observed that on throttling a fan or compressor at constant speed there is an increase in the broad band noise level. This is illustrated for a fan by Fig. (24.32) from Burdsall and Urban, Ref.(24.21). The changes with throttling normally correspond to moving away from the condition for which the blades were designed, but Burdsall and Urban also present tests when the design tip speed has been altered but the design pressure ratio kept constant. The broad band noise is markedly higher at a given tip speed for the more highly loaded fan, but for a given pressure rise the lowest speed machine seems to be the quietest in terms of broad band noise.

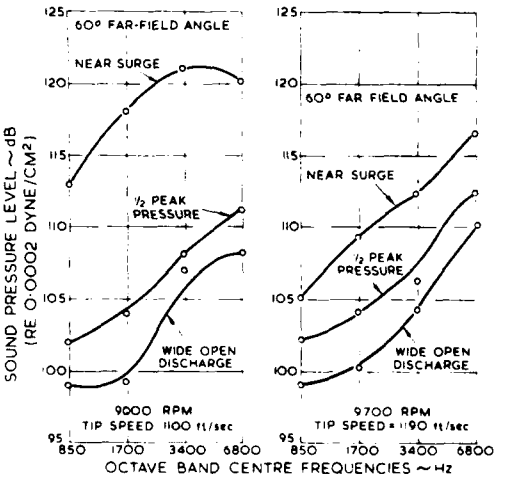

Figure 24.32 Spectra of forward arc broad band noise from a fan at two operational speeds.

The blades of compressors and fan are diffusers optimised to produce the largest pressure rise with least loss and it will be recalled that the studies of conventional diffusers reveal that peak performance occurs in the transitory stall region. It is not therefore surprising if the blade rows also exhibit unsteady behaviour leading to radiation, with increased noise as the pressure rise is raised, and that heavily loaded rows tend to produce generally higher levels of unsteadiness.

Burdsall and Urban concluded from their tests that rotor diffusion factor, approximately the ratio of the maximum change of velocity on the suction side to the velocity at inlet, was the best correlating parameter and they chose to use the value at 70% of the span. Despite the rationale

behind this approach it has not been widely adopted.

A recent correlation by Ginder and Newby, Ref. (24.51), is based on a total of nine single stage fans with design tip speeds ranging from 900 to 1450 ft/s. The correlation uses rotor incidence and tip relative Mach number as the primary correlating parameters. In fact Ginder and Newby found rotor loading at design to be a poor indicator of broad band noise and one of the quieter fans for a given tip speed was also the most heavily loaded. The broad band noise was found to vary by up to 20 dB at a given tip speed for the whole range of machines considered. If the forward arc at transonic and supersonic tip speeds is ignored (and at this condition multiple pure tone noise is dominant) the standard deviation of measured levels from the correlation curve is reduced to within ± 2 dB. Fig. (24.33) gives the measured spectra together with the correlation curve inferred. Fig.(24.34) shows the variation with incidence deduced by Ginder and Newby, approximately 1.7 dB per degree. To arrive at this data the effect of tip Mach number has been removed by assuming that the sum of the forward and rearward radiated acoustic power will be proportional to the sixth power of relative Mach number, which is equivalent to assuming a simple dipole source for the broad band noise. The collapse of the data around the correlation is encouraging.

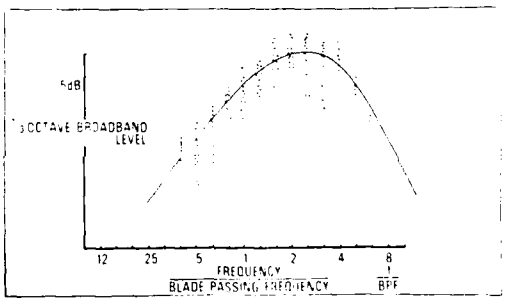

Fig. 24.33 The broad band noise spectrum of high speed fans.

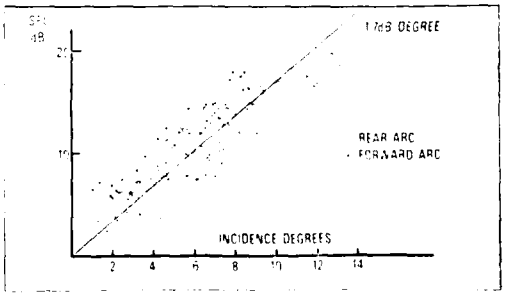

Figure 24.34 Variation of broad band noise level with incidence (effect of Mach number removed).

The correlation described above does not postulate a mechanism although it implies that incidence onto the tip is a special concern. The tip region of the rotor can be identified as a likely trouble spot, and the annulus boundary layer interacting with the tip is known to be very singificant to the tone generation. Nevertheless generalizing results can clearly be misleading when the basic noise producing mechanism is not understood. Lowson et al, Ref. (24.52) identified the tips of their low speed ducted fan as being important and were able to modify the noise by clipping the trailing edge near the tip. The explanation for the reduction with tip change given by Lowson et al for the unducted rotor is that there is less blade area for the tip vortex to act on. The presence of the vortex unsteadiness is seen as the source of noise, worsened by the proximity of the blade surfaces. For the ducted rotor (and possibly the unducted rotor too) an equally plausible explanation is that the loading near the blade tip will be reduced by clipping the tips. Changes in the tip loading also imply changes elsewhere on the blade to satisfy radial equilibrium. Mugridge and Morfey, Ref. (24.53) have also looked at the effects of the tips on ducted rotors, considering the vortex strengths due to secondary flow and tip clearance flow. The vorticity in these is of opposite sign, and Mugridge and Morfey hypothesise that the noise will be least when these cancel, leading to an optimum tip clearance. Flow visualisation studies and measurements rather belie this tidy division into discrete vortices.

For some time there has been an interest in the noise generated by unsteadiness in the flow on each blade, rather than in the diffusing combination of a cascade or the interaction with the wall at the tip. Sharland, Ref. (24.48) was probably the first to investigate this. He considered noise due to the interaction with incident turbulence carried by the flow (discussed below) and what he called "vortex noise" which is the noise produced by the aerofoil in laminar flow. This is believed to be due to the random shedding of vortices, analogous to the non-random Karman vortex street, produced by imbalance of boundary layer thickness towards the aerofoil trailing edge. Using plausible assumptions Sharland estimated the fluctuating lift and thence the compact dipole strength; the prediction agreed quite well with measurements made with an isolated aerofoil held in the potential region of a jet, see Fig. 24.35. Inherent in such a prediction are estimates for the pressures associated with the vortex shedding and the correlation area over which it extends. This led to the pressure amplitude and correlation measurements by Mugridge, Ref. (24.54) on an isolated aerfoil of unfortunately rather untypical design, having a fairly blunt trailing edge. The surface pressure fluctuations were quite different to those measured on wind tunnel walls, with much larger amplitudes at low frequencies, just as one would expect if vortex shedding were important. The boundary layer pressure fluctuations on the single aerofoil were found to give significant cross-correlation with a microphone signal well upstream. Moreover, the predicted spectral shape for the broad band noise agreed well with the measurements from two low speed fans.

More extensive tests have also been carried out more recently on an isolated aerofoil in a jet, and several results are shown by Burdsall and Urban, Ref. (24.21). In the non-turbulent region of the jet there is a significant influence of incidence; for a symmetric aerofoil the overall noise rises by about 5 dB to peak at around ± 20° incidence, but within ± 10° the effect is small. The spectra at

10° show that the frequency scales with reduced frequency $\frac{fc}{U}$, c being the chord length, and the amplitude as $U^{3.6}$, a lower index than expected. The amplitude was also found to be approximately proportional to drag coefficient. A comparison between the spectrum of broad band noise from the isolated aerofoil and from a few fans given by Burdsall and Urban using reduced frequency as abscissa is fairly good, particularly at low frequencies. Ginder and Newby, Ref. (24.51) showed, however, that the drag is not sufficient to account for the very large variations in broad band noise level obtained from fans; a variation in drag of approximately 300 would be required in their comparisons.

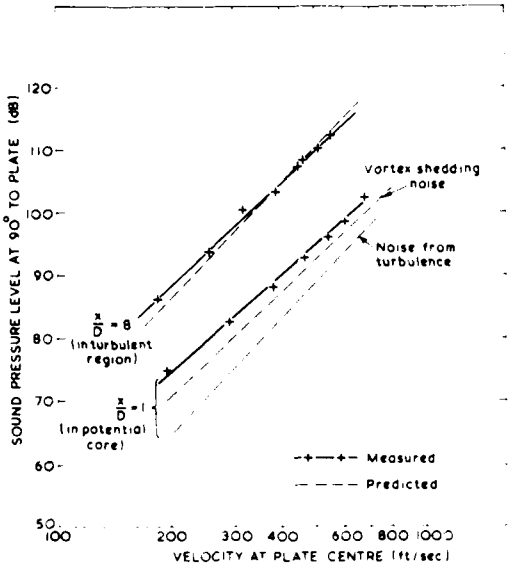

Figure 24.35 Broad band noise radiated from a small plate held in a jet of diameter D.

So far the discussion of broad band noise has been restricted to generation of unsteadiness produced by the blades themselves. The evidence from this suggests that under some conditions, such as when the blades are at high incidence, even locally, the "self-generated" noise dominates. When the blades are not in this condition it is not clear whether "self-generation" or interaction with ingested turbulence is what matters.

Sharland, Ref. (24.48) was also probably the first to investigate the noise generated by an aerofoil in a turbulent jet in experiments linked to his tests in non-turbulent flow. By application of unsteady aerofoil theory and some plausible assumptions about scale, and by treating the aerofoil as a compact acoustic dipole, Sharland was able to predict the sound pressure level. The agreement be obtained with measurements over a range of conditions was remarkably good, Fig. (24.35). By putting a ring upstream of a fan rotor he also increased the ingested turbulence to the rotor and again had some success at predicting the rise in noise. Smith and House, Ref. (24.19) also report a rise in broad band noise when a ring was placed upstream of a rotor.

Theoretical considerations of broad band noise by blades interacting with turbulence has frequently been an adjunct to the calculation of tones. Mani, Ref. (24.38), in considering the effect of homegeneous isotropic turbulence interacting with a rotor, calculated broad band noise with peaks at blade passing frequency. Pickett, Ref. (24.55) considering anisotropic turbulence found the same type of spectrum although with sharper tones. More recently Hansen, Ref. (24.56) has calculated tones and broad band noise by representing the eddies as a modulated train of pulses, and obtained rather good agreement representing the sources as compact dipoles and deriving the fluctuating lift from an incompressible unsteady method. The objections raised above to this procedure for tones apply for the broad band noise as well,and it is usually found that the broad band noise peaks at a frequency where the wavelength is comparable to the chord. In discussing tones the possible importance of the quadrupole component was considered. The same considerations apply to the broad band noise.

Up to now there has been no explicit distinction between broad band noise from subsonic and supersonic tip speed compressors. In the forward arc of a supersonic compressor it seems highly probable that the broad band noise will contain a different mechanism due to the random time variations in the bow shocks, but it must also be remembered that the flow towards the hub is subsonic and the noise from this may in some cases prevail. In fact in the foward arc noise spectra from many supersonic fans and compressors in which the multiple pure tones are dominant it is difficult to decide what is broad band noise. In the rear arc the considerations for supersonic fans are more akin to the subsonic fans, but the aerodynamic behaviour in the supersonic parts of the blades may give rise to quite different characteristics; the Ginder and Newby results appear to show that in the rear arc of fans the mechanism and dependence is similar at both subsonic and supersonic tip speeds.

The overall position with broad band noise from compressors and fans can only bs summarized as very badly understood. It must be recognised that the dominant source can change with the design, with the overall type of machine and with the mode of operation. A bad or a heavily loaded design may have a region of separation as the dominant source, whilst for a good design the interaction with the turbulence ingested may be more important. The effects of tip speed are not fully appreciated, although higher speeds for the same pressure rise seem to lead to higher levels and so frequently do higher pressure rises at the same speed. Finally, the mode of operation can radically alter the broad band noise, with a rapid rise in broad band level being normal as the machine is throttled.

24.5 TURBINE NOISE

Turbine noise is considered here separately from other sources radiating from the jet pipe, which are generally grouped under core noise, because of its resemblance to fans and compressors. Interest in turbine noise began far later than compressor noise, and it is with the high-bypass engines, producing relatively little jet noise, that it began to be very important. The spectra are rather different for low and high bypass ratios, and examples of these are shown in Fig. (24.36). To date very much less work has been devoted to turbine noise than fan or compressor noise, and because so little work has been concerned with turbine broad band

noise it is not appropriate to separate this section into subsections on tone and broad band noise. In any case the broad band noise is included implicitly in the core noise.

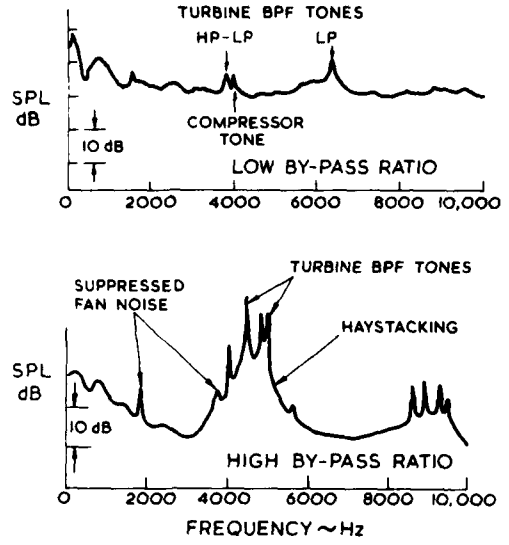

Figure 24.36 Typical rear arc spectra from low and high bypass ratio engines at low jet velocity.

Turbine testing tends to be even more difficult and costly than compressor testing, particularly when an attempt is made to run at appropriate pressure ratios and temperatures. A significant number of tests have been performed on cold models, whilst still more have used the turbines of engines, but very little indeed has been done hot using special test installations. The obvious disadvantage with using an engine is that the pressure ratio adjusts with the speed, so as to maintain the turbine close to its design condition, and it is therefore only possible to vary speed and pressure ratio independently over a fairly small range.

The measurement of noise from turbines is generally more difficult than from compressors or fans. The jets, particularly when hot, cause the field shape to be changed because of shear layer refraction so that the sound always peaks towards 60° or more from the axis. The propagation through the jet also brings about a change in the spectral shape of the tones. Instead of appearing as sharp spikes they frequently become so "haystacked" that they are no longer recognisable as anything but spectral humps, Fig.(24.36). The tones inside the duct do tend to be sharp, unless there is a region of large aerodynamic loss (and hence turbulence) when the "haystacking" can occur in the duct, Fletcher and Smith, Ref. (24.57). The thickness of the jet shear layer compared with the acoustic wavelength appears to play a crucial part in the haystacking, and changes in bypass exhaust geometry can have a striking effect as Fig.(24.37) from Mathews, Nagel and Kester, Ref.(24.58) shows. Kazin and Matta, Ref. (24.59) report that the acoustic power is about equal for the "unhaystacked" tone in the duct and "haystacked" far-field tone.

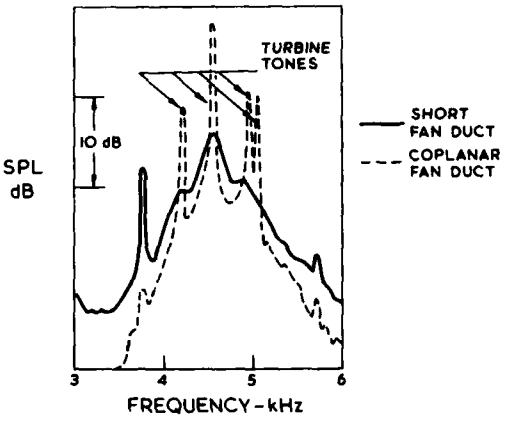

Figure 24.37 The effect of duct geometry on the spectral shape of turbine tones perceived in far field.

Almost all the published data has been concerned with turbine tone noise. Because of the jet and core noise and the "haystacked" tones it is often difficult to identify turbine broad band noise, but the first papers to consider turbine noise, Smith and Bushell, Ref. (24.60) did consider broad band noise from cold model and engine turbines. They showed an increase in this for the cold turbines according to the third power of inlet relative velocity (not the 6th power as the simple dipole analysis would suggest). There was very large scatter, for which no explanation was available, nor was the pressure ratio considered as a separate parameter. It would seem that there is still considerable uncertainty about the cause of broad band noise, and the influence of velocity, Mach number and pressure ratio on the level or spectrum. Broad band noise is, nevertheless, included in some prediction methods.

Tone noise in turbines, just like in compressors, is susceptible to cut-off and subsonic rotors produce tones which can propagate without attenuation only by interacting with non-uniformities in the flow. By choosing the rotor and stator numbers appropriately it is possible to arrange for turbine tones due to their interaction to be cut-off. This is generally easier than in fans or compressors because of the much lower tip speeds than the fan and the higher speed of sound; it can usually be achieved with less than twice as many stator blades as rotor blades. Nevertheless until recently it has not been customary to include this in turbine designs.

The effect of increased axial spacing between rotors and stators is, just like in compressors, to reduce the tone noise. The large blade loading of turbines would seem to point to the potential field interaction being relatively more important in turbines. However, many turbine blades have thick trailing edges and the wake thickness may be large. Tests have shown the large benefits to be obtained with increased spacing both in the last stage of an engine turbine and on a model 3 stage turbine with a clean intake. An example of the reduction measured with increased spacing and the predictions

of this, described below published by Kazin and Matta, Ref. (24.59) are illustrated in Fig. (24.38).

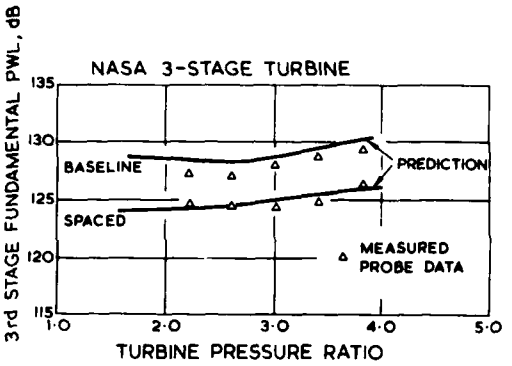

Figure 24.38 Changes in turbine BPF tone power with increase in nozzle-rotor spacing; tip axial gap/chord equal 0.29 (baseline), 0.89 (spaced).

It is not clear that all turbine stages will show the same reduction when the axial gap is increased because of the circumferential variation in velocity and temperature (entropy) out of the combustion system. Hoch and Hawkins, Ref. (24.61) compared the rear noise from a development engine when the combustion chamber was changed from can-annular to annular. Fig. (24.39). Not only was the low frequency reduced, but the turbine tones were increased. At first sight the more circumferentially uniform design of an annular combustor would be expected to be a route to lower tone noise, but it would seem that the temperature or velocity variation (perhaps unsteady) must be worse. The main point here is to show that the combustion system was a strong source of tone-generating distortion. Kazin and Matta, Ref. (24.59) did try putting a turbulence producer upstream of a single stage turbine, but found no effect. This, however, is unlikely to have reproduced the longitudinal correlation expected of turbulence out of the combustor. The production of tones by interaction of the rotor blades with circumferential variation in entropy out of the combustor is a problem not encountered in compressors, of course. It is not known how significant this is, but a characteristic of entropy variations is to diffuse rather slowly, and it seems likely that this source will provide a floor level for all stages.

Fig. (24.40) shows the results presented by Kazin and Matta, Ref. (24.59) for the effect on the blade passing frequency tone power of systematic changes in speed at constant pressure ratio, and pressure ratio at constant speed. It can be seen that at constant speed there is a general tendency for the power to rise with pressure ratio, whilst at constant pressure ratio the tone power generally falls with increase in rotational speed. This data, of course, refers to noise changes when the speed or pressure ratio are altered about the design value. The variation of noise as the design values are changed is much more difficult and expensive to obtain. Furthermore the trends illustrated in Fig. (24.40) may be rather different to those for turbines producing larger pressure drops.

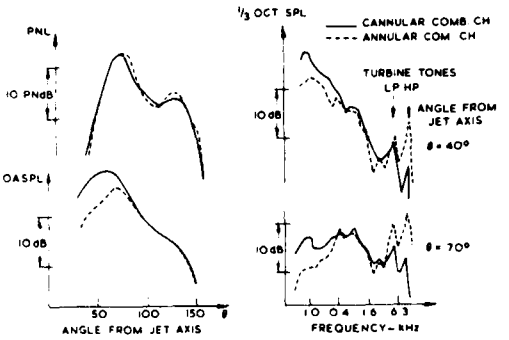

Figure 24.39 Changes in spectrum and field shape (SPL and PNL) with changes in combustion chamber.

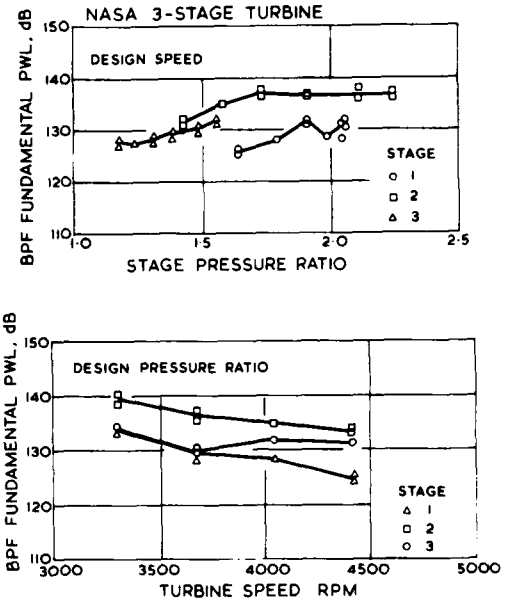

Figure 24.40 Turbine BPF tone power; effect of pressure ratio and speed.

Most data is presented in a way related to the way in which it is used in the company's correlation procedure. How unsatisfactory this is can be seen from Fig. (24.41) taken from Ref.(24.58) which is a comparison of proprietary correlation schemes (some which have since been superceded) attempting to calculate the peak sound pressure level from a new engine at a range of jet speeds. None of the methods predict even the trend with turbine speed correctly, not even that by Pratt and Whitney whose engine this is, and this must surely point to the weakness of much of the correlation that takes place. The field shape predictions are a little better, but just as varied and only one method, based on the turbines of the same company, is able to get anything like the

correct power spectrum for engine conditions corresponding to approach.

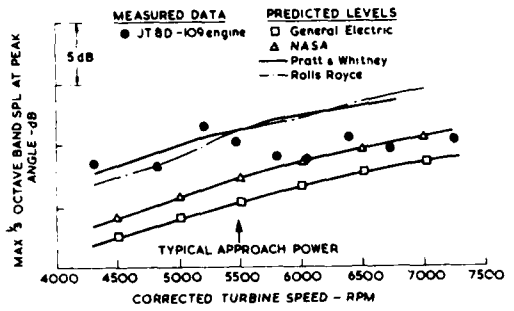

Figure 24.41 Comparison of measured turbine noise with predictions.

In discussing fans and compressors it was pointed out that the theoretical models all require the blade camber to be small. In turbines the camber is normally large and the models are even less appropriate. Nevertheless Kazin and Matta, Ref. (24.59), working on the assumption that the rotor-stator interaction will be predominantly from the wake, have predicted the level of tone power for a single stage turbine at the last stage of a three stage turbine. The method is similar to one proposed for compressors using the Kemp and Sears, Ref. (24.26) method of calculating fluctuating lift and treating the sources as compact. Despite the apparent unsuitability of the method, surprisingly satisfactory predictions of power, and change in power with change in spacing, have been obtained, Fig. (24.38). Only the last stage was considered because they had no method for calculating the transmission of sound through blade rows. In fact an actuator disc method such as Cumpsty and Marble, Ref.(24.62) is very suitable for this because the transmission and reflection are not much affected by the ratio blade chord to wavelength, as will be recalled from section 24.4.1.3.

24.6 CORE NOISE

A definition of core noise is rather arbitrary but it is taken here to mean the rear arc noise originating with the hot stream of the engine other than that due to the jet and to the turbine. This is illustrated by Fig. (24.42) taken from Mathews and Perrachio, Ref. (24.63). Whilst it is often difficult in practice to distinguish the core noise from the jet, because both are broad band, it is conceptually possible to separate the turbine noise and core noise and some authors, Hoch et al, Ref. (24.64) include the turbine noise with the core. The study of core noise has recently gathered considerable momentum and an up-to-date review is given by Bushell, Ref. (24.66).

The discovery of core noise was held back for a long time by the use of unsatisfactory jet noise rigs in which upstream valves and obstructions produced more noise than the jet mixing itself when the velocities were low. With the advent of really good rigs it was apparent that the jet noise really does follow V_j^8 right down to very low speeds. It was then clear that the noise level from engines was distinctly higher at low velocities than the noise of pure jets, Bushell, Ref.(24.65). It also became clear that the spectrum from engines with low jet velocities contained more high frequency noise than the corresponding jet, and that the angle for peak noise was near to 80° from the jet axis, whereas for pure jet noise the peak occurs around 30°. One of the main problems with this has been removing the effects of jet noise so that the behaviour of core noise can be studied in detail. Although for a given jet velocity (relative to the engine) core noise may be barely perceptible on a static test bed, it may be very important with a forward speed of, say, 200 knots, and the consequent drop in pure jet mixing noise. To overcome this there have been tests with oversize nozzles so that for a given engine speed the jet velocity is reduced. Unfortunately this changes the engine operating conditions and only when appropriate inlet throttling is included, Hoch et al, Ref. (24.64) are engine conditions maintained. Even then the acoustic conditions are altered by the changes in nozzle shape and impedance although the significance of this is not known.

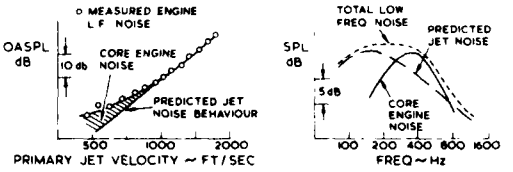

Figure 24.42 Definition of core noise

As well as reducing the jet noise, flight has also been found in some cases to lead to an absolute rise in the level of the noise in the forward arc from some engines, as well as a model jet mounted on a rotating arm, Bushell, Ref.(24.67) There is at the present time no satisfactory explanation for this.

The earliest ideas on the core noise originate with Bushell, Ref. (24.65) noting that low frequency noise was generated by a turbine rig when conditions were such that there was high incidence onto the downstream struts. Bryce and Stevens, Ref. (24.68) have followed this by a very thorough investigation of strut noise in a small model of a turbojet exhaust. The swirl was produced by vanes instead of the turbine of the real engine. They were able to correlate the extra noise with strut incidence and flow velocity onto the struts, obtaining a correlation to the sixth power of velocity. This correlation is consistant with the results of Gordon, Ref. (24.49) who carried out an extensive set of tests on bluff bodies in ducts and, as noted in Sec. 24.4.3, found that the noise appears to scale as the cube of pressure drop introduced (roughly the sixth power of velocity).

No clear evidence has emerged that strut noise is a significant source from engines, where designs usually have low incidence and avoid, so far as possible, bluff bodies to reduce aerodynamic losses. On the other hand deficiencies do occur, a separated region on the centre body downstream of the turbine is quite usual, and at low thrust conditions swirl may be large. There is, moreover, evidence that the system used in some engines to mix the bypass and primary flow before the final nozzle does not increase core noise.

These mixers are one of the most drastic ways of introducing turbulent mixing into the flow; if these do not produce a large increase in noise it would seem that other aerodynamic loss-makers are likely to be fairly insignificant in comparison with the real core noise too.

Considerable theoretical activity has recently been devoted to the "excess" noise of the jet, that is to say noise which would once have been taken to be jet noise but which is generated at the nozzle lip or upstream. Crighton, Ref. (24.69) has examined these and the reader will find the subject carefully discussed there. Three mechanisms stand out. One is the generation of sound at the nozzle lip itself because of the sudden change in boundary layer conditions. Upstream of the lip the radial component of turbulent velocity must vanish at the wall, but this is relaxed at the lip. There have been several suggestions for the boundary condition at the lip, one of which is the Kutta condition. The analysis shows this mechanism to radiate preferentially at large angles to the jet axis. Crighton also discusses the interaction of jet shear layer instabilities with the nozzle to produce unsteady outlet flow, and thus noise. Also, from a different point of view, the turbulent shear layer provides a possible amplification of sound propagating down the jet pipe. This approach is usually associated with Crow, Ref. (24.70) who demonstrated this experimentally as well as theoretically. Recent model experiments by Gerend et al, Ref. (24.71) and Bechert and Pfizenmaier (Ref.(24.72) have confirmed that tones in the upstream flow can lead to large increases in the broad band noise. A result by Bechert and Pfizenmaier is shown in Fig. 24.43.

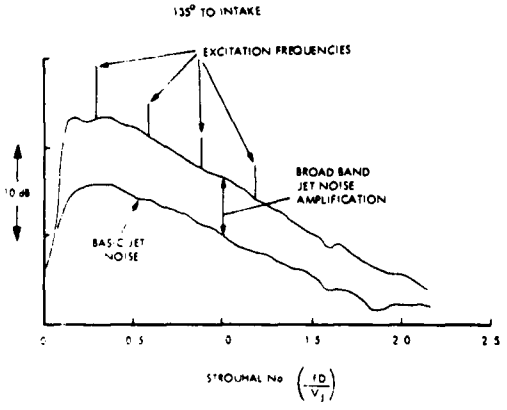

Figure 24.43 Spectra, using Strouhal number as abscissa, of jet noise with and without pure tone excitation.

Whilst these mechanisms may indeed occur in engines there have, as yet, been no definitive experiments which have established their importance there where the Reynolds numbers are at least an order of magnitude larger. It is a feature of the theories that the intensity predicted always includes an unknown constant of proportionality.

Much of the experimental evidence has linked the core noise, or at least part of it, with the combustion system. A clear example of this is the reduction in low frequency noise when an annular combustor was installed in place of a can-annular one, Fig. 24.37. More recently Mathews and Peracchio, Ref. (24.68) cross-correlated the far field noise (from where the peak of the core noise is expected) with a pressure transducer just inside the nozzle and also with a transducer in one of the eight combustion cans. The cross-correlation was filtered and in each case found to peak at around 400 Hz, which had been deduced to be the peak of the core noise spectrum by substracting the "true" jet noise from the overall measured noise. The peak cross-correlation between the nozzle lip and the far field was 0.17 which has been cited as evidence that lip noise is dominant. Between the combustion chamber and the far field the cross correlation was 0.05. This latter value appears rather low, but since there are eight combustion chambers, each of which is almost certainly wholly uncorrelated with the others, the maximum that could possibly have been achieved is 0.125. The cross correlation between the combustor and the far field is thus about 0.4 of the maximum possible, which is quite high. The hypothesis that pressure fluctuations from the jet pipe propagate upstream to the combustion chamber is quite implausible, and the dependence of the core noise on the combustion systems is well established for this engine.

Although combustion appears to be responsible for much of the core noise there are two conflicting views on how this comes about. The more familiar view is that combustion is a strong noise producing mechanism, particularly in the highly turbulent conditions necessary in a gas turbine combustor. This is often referred to as direct combustion noise.

The other approach to combustion related noise presumes that it is fluctuations in temperature (more correctly, entropy) leaving the combustion chambers which then interact with downstream components, principally the turbine, to produce noise. This is often referred to as indirect combustion noise. Because it is more familiar, however, the direct combustion noise will be discussed first.

Turbulent flames are well known for their roar, and have received quite wide study over the last few years. The flame may be regarded as a simple monopole source of low frequencies (so that the flame is acoustically compact, or in phase) and the sound generation is then related to the rate of change of the volume of the flame. A very clear demonstration of this was given by Hurle et al, Ref. (24.73) who cross-correlated light (a measure of instantaneous flame size) and sound emission. At higher frequencies the phase varies over the flame surface, and prediction is more complex. The methods thus divide into the more intuitive approach of Bragg, Ref. (24.74) and the more analytical following the aeroacoustic approach for turbulent noise of non-reacting fluids initiated by Lighthill, Ref. (24.2). Examples of this latter approach are due to Chiu and Summerfield, Ref.(24.75) and Strahle, Ref. (24.76). With combustion present the difficulty in converting the "solution", consisting of an integral, into a practical estimate are considerably greater than in non-reacting cases and only by the most drastic simplifying assumptions is this possible, see Ref. (24.76) for example.

Experimentally the combustion in an open turbulent flame introduces several variables in addition to those found in, for instance, jet noise. As an example an empirically developed expression for the acoustic power, P, from lean premixed hydrocarbon flame given by Strahle, Ref.(24.77) is

$P = 4.89.10^{-5}\ U^{2.68} D^{2.84}\ S_L^{1.35}\ F^{0.41}$ Watts, where U and S_L are mean air velocity and laminar flame speed in feet/sec. D is the diameter in feet and F is the fuel mass fraction. Such non-integer indices make it seem likely that important parameters are being overlooked. To cover the lean to rich variation with premixed and diffusion flames for a range of fuel types clearly involves extensive test programs, particularly when the spectrum and field shape must also be found.

The difficulty in applying this information on open flame to gas turbines has been summarised by Strahle, Ref. (24.77). "The main problems in application of current research results to turbopropulsion systems appear to be (a) actual combustors employ different stabilisation methods and geometrical configurations than research burners so the scaling rates and absolute power output may be different, (b) the turbulence structure is undoubtedly different, (c) enclosure effects introduce sound power augmentation over free field behaviour and feedback effects upon the combustion process may be important and (d) the sound propagation problem through turbines, ducts and compressors is a difficult one to address". It might be concluded that the noise of open flames bears little relation to combustion chambers.

A considerable number of tests have now been performed to measure noise from combustion cans tested in isolation for example Strahle and Shivashankara, Ref. (24.78). These are tested without downstream nozzles so as to minimise jet noise, but the pressures inside the can are unrepresentatively low. Furthermore, the downstream boundary conditions represented by the first turbine nozzle row is not correctly modeled. Nevertheless, some very interesting results are obtained including the strong dependence of overall power on air mass flow, Fig. (24.44) and the weak dependence on fuel flow from weak to stochiometric in the primary zone, Fig. (24.45) taken from Ref. (24.78). Curiously the noise spectra were found to be essentially unchanged over large excursions in air and fuel flow rate.

Kazin and Emmerling, Ref. (24.79) report on measurements of noise from a full scale annular combustion chamber and Fig. (24.46) is taken from this. These tests used a downstream acoustic horn, which might be expected to confuse matters, but in fact appears to have had very little effect. The acoustic power spectrum rises markedly as the temperature rise of the combustor is increased, equivalent to raising the ratio of fuel to air. Kazin and Emmerling also report tests where an acoustic absorber was placed downstream of the combustor. Large reductions in the noise were produced, proving the origin of the noise to be upstream in the combustion region itself.

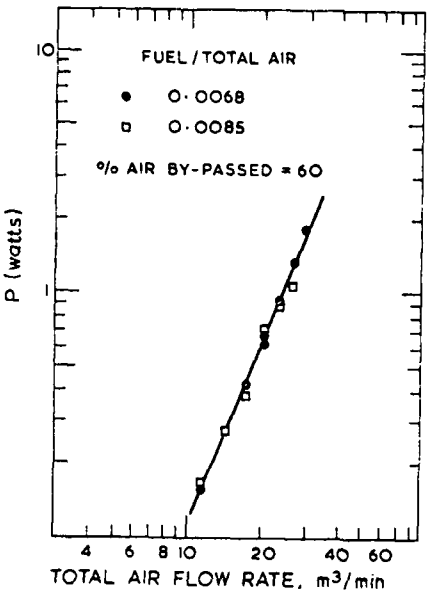

Figure 24.44 Variation in acoustic power from an isolated combustion can as a function of air flow rate.

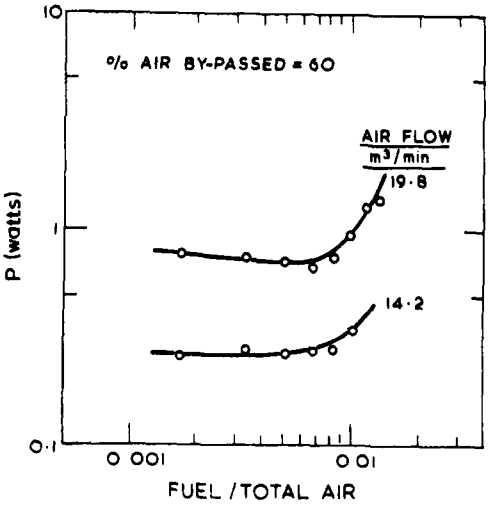

Figure 24.45 Variation in acoustic power from an isolated combustion can as a function of fuel/air ratio.

Ho and Tedrick, Ref. (24.80) examined the combustion related noise from eight small gas turbines with a range of very different types of combustion chamber, and from a combustor tested on its own with an open exit. The noise from the engines was found to collapse well when plotted against an empirically determined noise factor, F, which was modified in the light of dimensional analysis and included the temperature rise. It appeared that for engines the power is proportional to F^4 whereas for rigs it is proportional to F^2. This does suggest tha. the presence of downstream components, mainly the turbine

is highly significant.

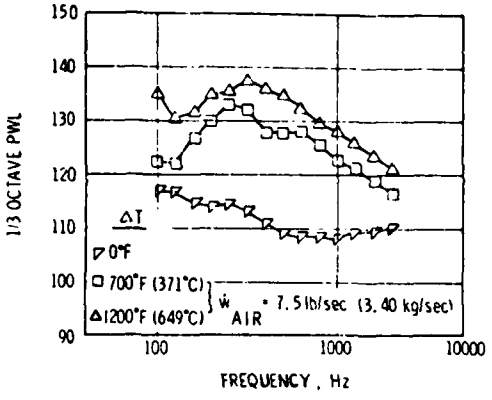

Figure 24.46 The effect of temperature rise on the noise of a full-scale isolated annular combustor.

Grande, Ref. (24.81) assumed that combustion noise is proportional to flame speed and that this varies linearly with temperature. Using a crude model for the effect of the nozzle and turbine on the propagation of noise from the combustor, Grande was able to predict the overall noise from two engines with considerable success.

Results of a very extensive program on combustion noise have recently been published by Mathews and Rekos, Ref. (24.82). Extensive tests were conducted using isolated combustors of differing design and engines for which the combustion noise was deduced by subtracting the pure jet noise from the far field spectra. The correlation, which is based on simple models for the noise generation and sweeping assumptions, provides a very satisfactory correlation of both the overall sound power and the spectrum, including combustor size, pressure, temperature, calorific value and air fuel ratio. Apart from some differences in the constants, annular and can-annular combustors appear to produce very similar noise.

The indirection combustion noise is produced by the interaction of entropy fluctuations (i.e. hot spots) with downstream components, in particular the turbine, but also the final nozzle, which was considered by Candel , Ref. (24.83). The two methods proposed for turbines by Cumpsty and Marble, Ref. (24.62) and Pickett, Ref. (24.84) both treat the turbine blade rows as two-dimensional actuator discs, assuming blades of infinitesimal chord and pitch and neglecting radial variations. The essential feature of both methods is that the changes in mean properties across the blade row are large, but perturbations in the unsteady properties (entropy, pressure, vorticity) are small. If the change in mean properties is small entropy gives rise to only second order perturbations in pressure. Cumpsty and Marble were able to examine the combined effect of many rows whilst Pickett considered rows one at a time.

As well as representative turbine flow Mach numbers and angles, the indirect calculations require as input the magnitude of the entropy fluctuation. At constant pressure the entropy perturbation is given by:

$$\frac{s'}{c_p} = \frac{T'}{T}$$

the prime denoting perturbation. The temperature perturbation has been measured and a spectrum, taken from Ref. (24.84) is shown in Fig. (24.47).

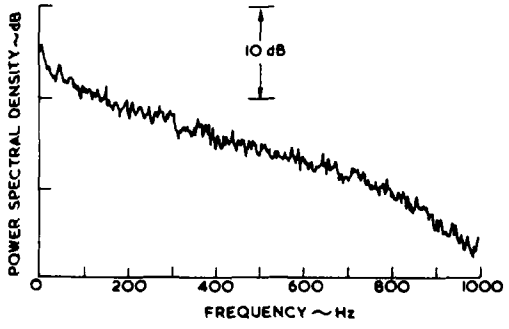

Figure 24.47 The spectrum of temperature fluctuation measured at outlet from a can-annular combustion chamber.

The overall magnitude of $\frac{T'}{T}$ in the range of audible frequencies is about 2%. The indirect combustion model predicts that the acoustic power rises rapidly with pressure drop through the whole turbine, and, in particular, the drop across each stage. With some idealisation Pickett has shown that the power is proportional to the square of the stage pressure drop. Thus for a given overall pressure drop the noise will be less with a larger number of stages. The noise is also proportional to the magnitude of the entropy perturbation. Figure (24.48) from Cumpsty and Marble, Ref. (24.85) compares the predicted and measured spctra of rear arc acoustic power for a Pratt and Whitney JT8D engine assuming $\frac{T'}{T}$ = 2%. The agreement in level and in spectrum shape is satisfactory in view of the number of assumptions necessary.

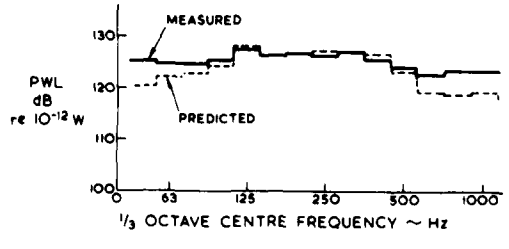

Figure 24.48 Measured and predicted spectra of rear arc acoustic power from a JT8D engine at low jet velocity.

The situation with regard to combustion noise is far from clear, with the possibility of direct or

indirect noise being most important. Experimental tests to establish which is the more important are not easy. Removing the turbine removes the prime generator of indirect noise but at the same time it alters the conditions in the combustion chamber both acoustically and from a more overall point of view. Measurements of pressure fluctuation in the combustion chamber show large amplitudes, but these are attenuated by passage through the turbine (which may be calculated). On the other hand the generation of pressure and entropy fluctuations is intimately related, and the existence of one does not mean the absence or unimportance of the other.

It would seem that very careful experiments will be needed to finally resolve whether direct or indirect combustion noise is predominant, and it is quite possible that it will be found that both may be important in differing circumstances. It seems very probable that combustion noise of one sort or other will be the prime source of core noise under most conditions at low frequencies.

24.7 ACOUSTIC TREATMENT

The character of this aspect of engine noise is quite different from those set out in earlier sections. Here the emphasis is on the design, achieving the optimum configuration of acoustic treatment for the least cost and weight with least effort and greatest confidence. There is not the same uncertainty surrounding the subject, that there is, for example, regarding the broad band noise from compressors or the cause of core noise. The strong position is partly the result of strenuous efforts over a number of years, and an excellent review of the whole field of aircraft engine duct acoustics has been provided by Mayfeh et al, Ref. (24.10).

Fig. (24.49) shows where treatment can be applied in a bypass engine and a schematic of the type of treatment used. Most impressive attenuations have been shown to be possible in this way even without the introduction of additional surfaces, such as splitters, into the ducts. The crucial quantity is the ratio of length of the lined surface to the duct height or diameter. At the present time, with linings in the inlet extending over an axial length equal to about one radius, it is possible to reduce the multiple pure tones until they essentially vanish into the background, giving an overall reduction of the intake noise of perhaps 5 PNdB in the case of a large, high bypass ratio engine. Linings in the bypass duct of a similar engine may reduce the rear arc peak noise level by about 8 PNdB and linings in the jet-pipe by about 3 PNdB.

Operation in service has demonstrated that these linings can withstand the rigous of flight and, in particular, the rigours of maintenance engineers. The need for strength, lightness and the retention of very little liquid has meant, however, that virtually all linings installed in aircraft are of one type of construction. This consists of a perforated or porous sheet over a honeycomb structure with a solid backing and is shown in the two upper drawings of Fig. (24.50). The honeycomb combines a structural role with dividing the region behind the perforate into small cavities so that the liner response depends only on local conditions. Although mechanically less suitable the bulk absorber, Fig. (24.50), has acoustic advantages. Certain special advantages can be achieved using double layers, essentially one over the other, as in Fig. (24.50), and these are now being tried experimentally.

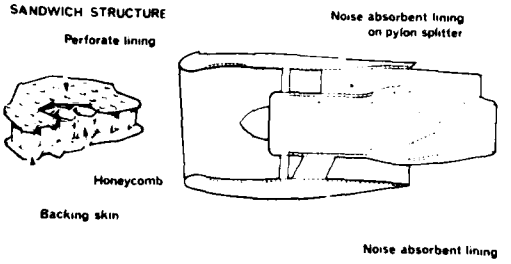

Figure 24.49 Schematic Illustration of Installation of Linings in a High Bypass-Ratio Engine.

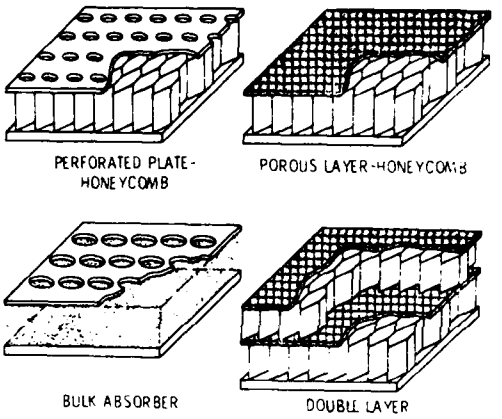

Figure 24.50 Schematic of Various Linings Types.

The special feature of acoustic liners is their finite impedance defined by $Z = \frac{p}{u}$, where p and u are the acoustic pressure and velocity normal to the surface. For a hard wall u vanishes at the wall and $|z| \to \infty$. For a perforate-honeycomb liner, with thin perforate sheet, the impedance may be represented by

$Z = R + i\left(\frac{\omega m}{c} - \cot \frac{\omega d}{c}\right)$. The resistance, R, is the ratio of in-phase pressure and velocity. In the imaginary or out-of-phase part, the reactance, the most important term is $\cot\frac{\omega d}{c}$. Here ω is the radian frequency, c is the velocity of sound and d is the honeycomb backing depth, the distance between the perforate and the solid back. The liner is essentially an array of resonators and varying d is the principal means of tuning the liner. The other imaginary term is usually small and is related to the inertia of flow through the perforate; it is affected by hole size. The various impedance terms for a perforate-honeycomb liner are shown schematically in Fig. (24.51).

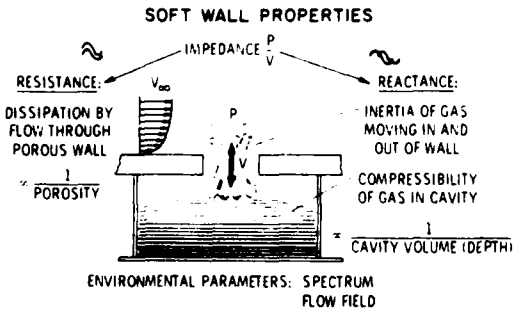

Figure 24. 51 Schematic of Impedance Components of a Perforate Plate-Honeycomb Backing Acoustic Lining.

It may be recalled from 24.1 that for a plane wave the velocity and pressure perturbations are related by $p = (\rho c)u$; ρ is the mean density of the medium and ρc is then referred to as the resistance. It is usual and convenient to non-dimensionalise the lining impedances with respect to the plane wave value, ρc, to give what are called specific impedances.

The liner resistance is determined primarily by the porosity of the facing material, and this can be obtained approximately by measuring the pressure drop through it with a steady flow of air. It does, however, increase at high flow rates due to non-linear effects and allowance must be made for this at high sound pressure levels. There is also very marked increase in resistance with the Mach number of the grazing flow past the liner and for the flow conditions typical in engine ducts this will normally override the effect due to sound pressure level. Quite typically the resistance will be increased two or three-fold by the grazing flow and companies have proprietary methods for predicting this. The porosities of perforates typically used are from 5 to 10%; at 5% porosity the resistance would be in the range $1.0\rho c$ to $3.0\rho c$, depending mainly on Mach number. The boundary layer thickness is also said to be significant to the resistance, but this is not freely documented.

The appropriate resistance is therefore not readily obtainable from laboratory bench tests, and the specification of the porosity requires a fairly accurate knowledge of conditions in service. In the past estimates of resistance in service have been inferred from the difference between predicted and measured attenuation. It is only fairly recently that methods of measuring impedance in situ have been developed, Ref. (24.86).

Whereas the resistance is almost unaffected by frequency, the reactive components are strongly frequency dependent. On the other hand the reactance is only weakly affected by grazing flow and sound pressure level and may be reasonably obtained from laboratory experiments.

The noise from the aircraft engine components propagates in ducts whose geometry varies and where the flow Mach number is significant, typically from 0.2 to 0.5. This would provide a quite intractable problem were it not for the restrictions put on the geometry by the need to keep the mean flow attached and reasonably uniform. It is therefore generally true that changes in area are smooth, gradual and relatively small. The boundary layers are generally thin and regions of separated flow small enough to be neglected. Finally, the propagation is either directly against the flow as in an inlet (negative Mach number) or with the flow as in a jet-pipe or bypass duct (positive Mach number). In the early work the effect of flow Mach number was included by assuming a uniform flow and only more recently has the boundary layer been included. In general the effect of the boundary layer on downstream propagating sound is small, whilst it can be very significant for upstream propagation. The effect of temperature gradients and swirl may also be important in some cases, but this is beyond the scope of this present section and the reader should consult Nayfeh et al, Ref. (24.10).

In predicting attenuations or designing linings the geometry of the ducts is normally greatly simplified so that only two classes of geometry are considered, the annular duct (of which the circular cylinder is a special case) and the rectangular duct. The latter is often used for narrow annuli, where radial effects are negligible, and for the rather curious and complicated passages often found in the bypass ducting; provided the duct is long in relation to its transverse dimensions this is probably reasonabl .

Most of the analyses of acoustic attenuation in ducts have used normal (i.e. independent) modes which allow the wave equation to be separated in a manner analogous to that outlined in Section 24.3. Viscosity and shear stresses are always ignored, and the boundary layer is modeled by an inviscid shear. The presence of uniform flow does not seriously alter the modes, but shear flow brought the existence of normal modes into question. Shankar Ref. (24.87) considered acoustic propagation with a mean flow which is perturbed about a uniform flow without assuming the existence of normal modes, and was able to show that the results were indeed consistent with the approach using such modes.

In the simple circular cylinder case considered in Section 24.3 with rigid walls (infinite impedance) and uniform flow, the specification of inner/outer radii ratio, circumferential order, m, and radial order, μ, are sufficient to define the radial eigenvalues $k_{m\mu}$ and $Q_{m\mu}$ and eigenfunction

$$J(k_{m\mu}r) + Q_{m\mu}Y(k_{m\mu}r).$$

(For rectangular ducts the eigenfunction is a sum of sine and cosines in place of Bessel functions). When the wall impedance is finite the values of $k_{m\mu}$ and $Q_{m\mu}$ depend on the values of resistance and reactance, but once these are specified the eigenvalues can be calculated analytically. This is not in general straightforward and it is usual to first calculate hard wall values of $k_{m\mu}$ and $Q_{m\mu}$ and proceed by numerical methods from there. From the eigenvalue $k_{m\mu}$, the axial attenuation can be immediately calculated.

Uniform flow does not affect the radial equation or the eigenfunction but it does change the boundary condition. Uniform flow is, of course, an analytic model, not realisable in practice, which implies slip between the wall and the fluid immediately adjacent to it. The acoustic pressure

is continuous across this discontinuity at the wall, but a controversy arose as to whether the acoustic velocity or displacement perturbations normal to the wall should be equated across it. It has gradually become accepted that it is the displacement which is to be used; in consequence the velocity changes abruptly.

The presence of shear means that unless resectrictions are made to small perturbations from uniform flow an analytic procedure cannot be used to calculate $k_{m\mu}$ and $Q_{m\mu}$. Different numerical methods are available for finding these eigenvalues. Mariano, Ref. (24.88) and Ko, Ref. (24.89) split the flow into a uniform core and a boundary layer, using analytic results for the core and matching this at the edge of the boundary layer where a numerical method is used. Mungar and Plumblee, Ref. (24.90) and Kaiser, Ref. (24.91) use numerical approaches across the entire annulus. Because the inviscid shear represents the mean flow boundary layer there is no slip at the wall and the velocity and displacement are both continuous.

Partly for historical reasons and partly because the calculations are so much easier, much of the published work to date considers only uniform flow and neglects the shear in the wall boundary layers. The theory is sufficiently well based and the mechanisms understood that it can be definitely shown that the neglect of the boundary layers is not in general justified. For this reason the results shown here will normally include the boundary layer.

In comparing liners and their effects certain assumptions about the input sound field must be made. In some work the attenuation of a particular mode is considered, whilst in others the sum of radial modes making a radially constant wave at entry is chosen. Most work has considered that at inlet the acoustic energy is spread into all the modes propagating (i.e. above cut-off) in an equivalent hard wall duct, either assuming equal amplitude or equal energy transmission in each mode. The observed differences in attenuation calculated for these latter two assumptions is usually too small to be significant. Indeed one of the principal and most fundamental limitations to the accuracy in predicting the attenuation from engines is the specification of the input to the calculation, that is specifying the strengths of all the modes generated by the engine, or its dominant component.

The assumption that all modes are propagating and that no mode is preferred in terms of amplitude matches the common method of testing linings between two reverberant chambers. With any input other than a single mode the apparent attenuation decreases with distance from the entry. This is because the rapidly attenuated modes are quickly reduced leaving only those modes which are least affected by the lining; finally the least attenuated mode is all that remains. Although the lowest order radial mode (in a circular duct) or its equivalent in a rectangular duct is often the least attenuated mode, it is by no means always the case. This was demonstrated in calculations performed by Ko, Ref. (24.89) in which high frequency sound in the inlet was attenuated less in the second radial order.

The attenuation upstream and downstream is affected by too many parameters for a simple demonstration of all effects to be possible. It is usual therefore to illustrate the effects with one or two cases, taking particular values of geometry (hub-tip ratio for a circular duct, aspect ratio for a rectangular duct), lining length, Mach number, boundary layer thickness and liner properties. It is more natural to consider the effect of boundary layer first, although this was the most recent effect to be included.

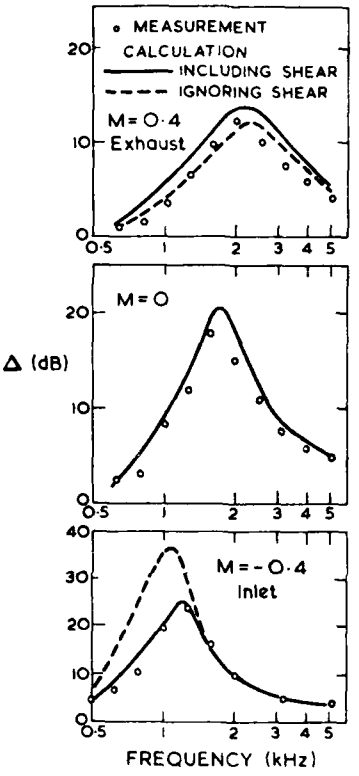

Figure 24.52 Comparison of Predicted and Measured attenuation Spectrum in a Rectangular Duct showing Importance of Flow and Shear (i.e. Boundary Layer).

Figure 24.52, taken from Ref. (24.88) compares measurement with prediction of attenuation in a rectangular duct. The comparison is shown for downstream propagation, as in an exhaust duct, (M = + 0.4) for upstream propagation, as in an inlet, (M = - 0.4), and also for the case of no flow. The predictions are shown both including and neglecting the boundary layer. These attenuations assume equal SPL for all propagating modes and growth in the boundary layers along the length of the lining is neglected. The no flow case is well predicted. So, too, is the downstream attenuation, with or without the inclusion of the shear layer. For downstream propagation shear has very little effect. In the case of upstream propagation the effect of shear can be seen to be large, and when it is included the prediction matches the measurements very well.

It is apparent from Fig. 24.52 that the mean

flow alters the peak frequency of attenuation in a given duct, as well as changing the magnitude. Propagating with the flow (M + ve) the frequency is increased, against the flow the peak frequency is reduced. The effect of the shear on the upstream propagating sound is to increase the peak frequency of attenuation, but to reduce the amount of attenuation. All these effects appear to be general for a wide range of duct geometries, wall impedances and Mach numbers. The satisfactory agreement between prediction and measurement provides confirmation that the propagation and attenuation processes are being adequately modelled. This allows the effects of parameter changes to be demonstrated usefully with the analytic methods.

Mariano, Ref. (24.92) has found that the loss in attenuation for upstream propagation with shear can be recovered by reducing lining resistance and increasing the backing depth. In Mariano's calculations the turbulent boundary layer has been found to be adequately represented by a linear profile given by $\frac{u}{U} = \frac{y}{\delta_1}$ where δ_1 is equal to half the true thickness. Mayfeh et al Ref. (24.93) have shown that it is the displacement thickness which is most important in determining the effect of the boundary layer and that the attenuation calculated assuming different types of laminar and turbulent profile are similar if compared on this basis.

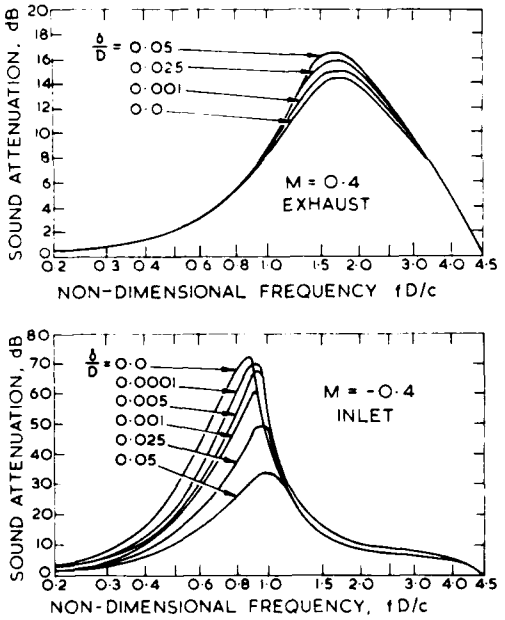

Figure 24.53 Variation in Predicted Attenuation Spectrum with Boundary Layer Thickness δ in a Cylindrical Duct of Diameter D.

Ko, Ref. (24.89) has carried out an extensive parametric study of attenuation in a circular cylindrical duct and these are shown in Figs.(24.53) to (24.56). The effect of boundary layer shear is included, although boundary layer growth in the test section is neglected. Fig. (24.53) shows the effect of boundary layer thickness on the attenuation for the upstream and downstream propagation with the same flow Mach number. The boundary layer thickness is non-dimensionalised with respect to duct diameter, D. As in the rectangular duct the effect for downstream propagation is small, whereas for upstream propagation it is large, affecting both the peak frequency and peak attenuation. Fig.(24.54) demonstrates the effect of Mach number at constant boundary layer thickness; because of the small effect of theboundary layer on downstream propagating sound (Mach number positive) the downstream attenuations have been evaluated assuming the flow to be uniform. The attenuation for sound propagating against the flow is clearly very much greater than in stationary conditions (but calculations ignoring the boundary layer then predict even larger attenuations) and the peak frequency is lower. The effect of flow for downstream propagation is to reduce the level of attenuation and to raise the frequency at which the peak occurs, but to a lesser extent than for upstream propagation.

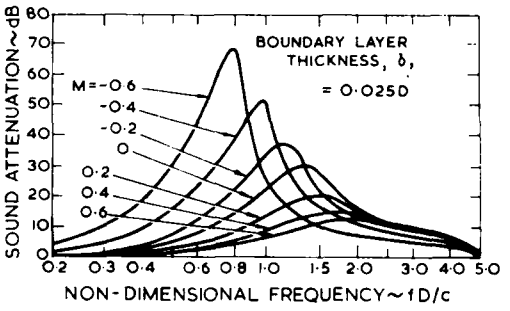

Figure 24.54. Variation in Predicted Attenuation Spectrum with Flow Mach Number in a Cylindrical Duct of Diameter D.

The parameter which primarily determines the frequency of the peak attenuation is the lining depth, d. The effect of this is shown in Fig.(24.55) from Ref. (24.89). Over a wide range of lining thickness the peak level of attenuation is more or less unchanged, only the frequency.

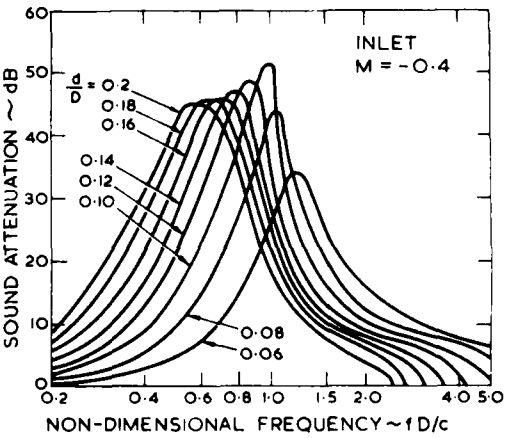

Figure 24.55 Variation in Predicted Attenuation Spectrum with Lining Backing Depth d in a Cylindrical Duct of Diameter D. (Propagation Upstream).

If the lining depth were to become comparable to the passage height, the peak frequency would be influenced by passage height as well. It has already been shown that the peak is also affected by the flow Mach number and by the boundary layer thickness. Nevertheless the largest effect, and the one over which control can be readily exercised, is the backing depth and for a design this would be arrived at by a combination of experience and test calculation.

The other main parameter of the linings over which control is exercised is the resistance, depending on porosity but also Mach number and SPL. Increasing resistance lowers the peak but broadens it, Fig. (24.56); the optimum value for a particular noise problem, geometry and flow is in general the result of calculation for a number of possible values. The complex part of the impedenace associated with the facing sheet $\frac{\omega m}{c}$, has a relatively small effect on the overall attenuation.

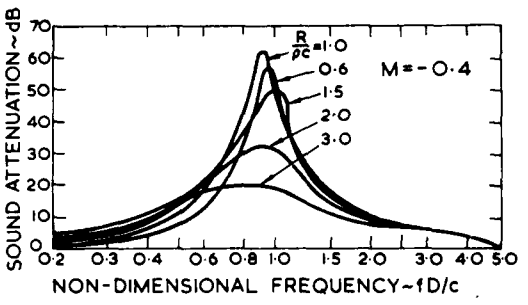

Figure 24.56 Variation in Predicted Attenuation Spectrum with Specific Resistance R/ρc of Lining in a Cylindrical Duct of Diameter D. (Propagation Upstream).

The position with regard to the design and prediction of acoustic liner performance is relatively very satisfactory. It remains, however, a relatively costly procedure whenever numerical calculations are performed to choose optimum liner resistance and cavity depth. This is because the attenuation of all the propagating modes must be found, and in general there are very many of these. For example in an intake with an internal diameter 2.4 m (8 ft) there will be approximately 812 modes propagating above cut-off at a frequency of 4 kHz. For each of these the complex radial wavenumber or eigenvalues must be found. As already indicated the calculation of the eigenvalues in the direction normal to the surface is not straightforward for non-rigid walls and it is finding these which is most time consuming. This has led to authors attaching the problem without the resolution into modes. Whether these methods will supplant the modal methods, or whether a fully satisfactory quick algorithm for calculating eigenvalues will be found, remains to be seen.

Most of the work to date has treated the problem as if the lining extended to infinity so that no waves are reflected back along the duct from the change in liner impedance. In practice this is never realised and some reflection will occur at the start and the end of the lining. Recently interest has grown in exploiting this effect by deliberately changing the liner characteristics at an axial station, Zorumski, Ref. (24.94). The possibility of further significant attenuation from this and from more complicated liners (such as double layers) appears to be real.

24.8 CONCLUDING REMARKS AND FUTURE PROSPECTS

The upsurge in research on aircraft noise over the last few years has coincided with the introduction of engines with high bypass ratios, typically about 5. Most of the research, which has been directed at civil air transport, has therefore centered on the problem of these high bypass engines.

The introduction of the high bypass ratio engines has brought an enormous reduction in noise from the newer aircraft and has stimulated the manufacturers to silence many of the older, smaller types. Whilst it is true that all the potential fan quietness could have been lost by careless design, it is nevertheless also true that it was the decision to have high bypass ratio which has made it possible to reduce the noise so far. The basic reason for this is no more subtle than the reduction in jet velocity which is implicit in the higher bypass ratio and increased propulsive efficiency. This is the intractable obstacle in the way of reducing noise from high speed aircraft where bypass ratios are necessarily low and jet velocities are high. The research into noise from supersonic transport aircraft is, as yet, nowhere near offering a solution with conventional engines. Only with such refinements as variable bypass ratio (high for take-off and landing, low for high speed operation) does a real possibility exist for quiet high speed aircraft.

The returns on noise research have been surprisingly small over the last few years. For example little more is known about compressor or fan rotor-stator interaction noise now than a decade ago. It was known then that the correct choice of rotor and stator blade numbers could make the interaction tone cut-off, and if this was impractical it was realised that a large axial gap was essential. (Interestingly, these 'rules' were ignored on a high bypass ratio engine for a military transport. The noise levels were so high that structural damage was incurred). In terms of broad band noise from fans, compressors or the engine core the basic mechanisms have yet to be identified conclusively and the control of noise - except for obvious things like avoiding regions of separation - is a long way off.

The area which continues to offer scope for hope is in the use of acoustic liners. Remarkably good results have been obtained with very simple, single layer perforate-honeycomb layers. It is probable that over the next few years the introduction of double layers and/or the use of bulk absorber types of lining will lead to a further marked increase in attenuation.

A feature of lining design is its comparative precision - it is possible to specify what is required and obtain a wall treatment attenuation which closely approximates this. The basic reason for this is that the processes are well modeled and the analytic tools are strong. In the case of noise generation the analysis has been of relatively very little use. As mentioned in the introduction the reason for this is the complexity of the mechanisms in high speed machinery; the Mach numbers are typically not far from unity and the

physical dimensions are comparable with the acoustic wavelength. In addition the flow is frequently highly three-dimensional. Without wishing to be unduly pessimistic it does not appear to be very likely that analytical methods for accurately describing and predicting engine noise generation will be sufficiently developed to be of real assistance for the next decade.

ACKNOWLEDGMENT

The author has been helped in preparing this chapter by many friends and colleagues in the aircraft and aircraft engine industries, too many for them all to be named. It is, however, a great pleasure to acknowledge the particular help and constructive criticism given by Dr. K.W. Bushell of Rolls-Royce.

24.9 REFERENCES

1. Goldstein, M.E. Aeroacoustics, NASA SP-346, 1974.

2. Lighthill, M. On sound generated aerodynamically, I. General Theory, Proc. Royal Society of London, Ser. A., vol 211, 1952, pp 564 - 587.

3. Ffowcs Williams, J.E., and Hawkings, D.L., Sound Generation by Turbulence and Sources in Arbitrary Motion, Phil. Trans. Royal Society of London, Series A, Vol. 264, 1969, pp 331-342.

4. Pearsons, K.S. and Bennett, R. Handbook of noise ratings. NASA CR-2376, 1974.

5. Tyler, J.M. and Sofrin, T.G., Axial Compressor Noise Studies, SAE Trans. Vol. 70, 1962, pp 309-332.

6. Morfey, C.L., Rotating Pressure Patterns in Ducts: Their Generation and Transmission, Journal of Sound and Vibration, Vol. 1, 1964, pp 60-87

7. Moore, C.J., In Duct Investigation of Subsonic Fan "Rotor Alone" Noise. Journal of the Acoustical Society of America, Vol. 51, No. 1., 1972, pp 1471 - 1481.

8. Sofrin, T.G., and McCann, J.C., Pratt & Whitney Experience in Compressor Noise Reduction. Paper presented at 72nd Meeting of the Acoustical Society of America, 1966.

9. Kerrebrock, J.L., Waves and Wakes in Turbomachine Annuli with Swirl, AIAA 12th Aerospace Sciences Meeting, 1974, AIAA Paper 74-87.

10. Nayfeh, A.H., Kaiser, J.E., and Telionis, D.P., The Acoustics of Aircraft Engine-Duct Systems AIAA Journal, Vol. 13, No. 2, 1975 pp 130-153.

11. Lansing, D.L., Exact Solution for Radiation of Sound from a Semi-Infinite Circular Duct with Application to Fan and Compressor Noise, Proceedings of a symposium held at NASA Ames, NASA SP-228, 1970.

12. Lansing, D.L.Drischler, J.A., and Pusey, C.G., Radiation of Sound from an Unflanged Circular Duct with Flow. Paper presented at 79th Meeting of the Acoustical Society of America, 1970.

13. Candel, S., Acoustic Radiation from the End of a Two-dimensional Duct, Effects of Uniform Flow and Duct Lining. Journal of Sound and Vibration, Vol. 28, No. 1, 1973, pp 1 - 13.

14. Savkar, S.D., Radiation of Cylindrical Duct Acoustic Modes with Flow Mismatch. Journal of Sound and Vibration, Vol. 42, No. 3, 1975, pp 363-386.

15. Morfey, C.L., The Acoustics of Axial Flow Machines, Journal of Sound and Vibration, Vol. 22, No. 4, 1972, pp 445-466.

16. Morfey, C.L., Rotating Blades and Aerodynamic Sound, Journal of Sound and Vibration, Vol. 28, No. 3, 1973, pp 587-617.

17. Cumpsty, N.A., Critical Review of Turbomachinery Noise, Trans. ASME Journal of Fluids Engineering, Vol. 99, Series 1, No. 2, 1977 pp 278-293.

18. Lowrie, B.W., Fan Noise. Paper Reprinted from AGARD Lecture Series, No. 80 on Aerodynamic Noise, 1976.

19. Smith, M.J.T., and House, M.E., Internally Generated Noise from Gas Turbine Engines. Measurement and Prediction, Trans. ASME, Journal of Engineering for Power, Vol. 89, 1967, pp 177-190.

20. Kilpatrick, D.A., and Reid, D.T., Transonic Compressor Noise, The Effect of Inlet Guide Vane/Rotor Spacing, ARC, R. & M., No. 3412, 1965.

21. Burdsall, E.A., and Urban, R.H., Fan-compressor Noise: Prediction, Research and Reduction Studies, Final Report to Dept. of Transportation, Federal Aviation Agency, 1971. Report No. FAA-RD-71-73.

22. Lowson, M.V., Theoretical Analysis of Compressor Noise, Journal of the Acoustical Society of America, Vol. 47, No. 1, 1970, pp 371-385.

23. Hanson, B., Unified Analysis of Fan Stator Noise, Journal of the Acoustical Society of America, Vol. 54, No. 6., 1973, pp 1571-1591.

24. Sears, W.R., Some Aspects of Non-stationary Airfoil Theory and its Practical Applications Journal of Aeronautical Sciences, Vol. 8, 1941, pp 104-108.

25. Kemp, N.H., and Sears, W.R., Aerodynamic Interference Between Moving Blade Rows, Journal of Aeronautical Sciences, Vol. 20, No. 9., 1953, pp 585-597.

26. Kemp, N.H., and Sears, W.R., The Unsteady Forces due to Viscous Wakes in Turbomachines, Journal of the Aeronautical Sciences, Vol. 22, No. 7., 1955, pp 478-483.

27. Hetherington, R., Compressor Noise Generated by Fluctuating Lift Resulting from Rotor-Stator Interaction, AIAA Journal, Vol. 1, No. 2., 1963, pp 473-474.

28. Mani, R., Discrete Frequency Noise Generation from an Axial Flow Fan Blade Row, Trans. ASME, Journal of Basic Engineering, Series D., Vol. 92, 1970, pp 37-43.

29. Lipstein, N.J., and Mani, R., Experimental Investigation of Discrete Frequency Noise Generated by Unsteady Blade Forces, Trans. ASME, Journal of Basic Engineering, Series D., Vol. 92, 1972, pp 155-164.

30. Kaji, S., and Okazaki, T., Propagation of Sound Waves through a Blade Row, Journal of Sound and Vibration, Vol. 11, No. 3, 1970, pp 355-375.

31 Whitehead, D.S., Vibration and Sound Generation in a Cascade of Flat Plates in Subsonic Flow, Aeronautical Research Council, R. & M. No. 3685, 1972.

32. Smith, S.N., Discrete Frequency Sound Generation in Axial Flow Turbomachines, Aeronautical Research Council, R. & M. No. 3709, 1973.

33. Kaji, S., Noncompact source effect on the prediction of Tone Noise from a Fan Rotor, AIAA 2nd Aero-Acoustics Conference 1975, AIAA Paper 75-446.

34. Cumpsty, N.A., Tone Noise from Rotor/Stator Interactions in High Speed Fans, Journal of Sound and Vibration, Vol. 24, No. 3, 1972, pp 393-409.

35. Kaji, S., and Okazaki, T., Generation of Sound by Rotor-Stator Interaction, Journal of Sound and Vibration, Vol. 13, No. 3, 1970, pp 281-307.

36. Osborne, C., Compressible Unsteady Interactions between Blade Rows, AIAA Journal, Vol. 11, No. 3, 1973, pp 340-346.

37. Ffowcs Williams, J.E., and Hawkings, D.L. Theory Relating to the Noise of Rotating Machinery, Journal of Sound and Vibration, Vol. 10, No. 1, 1969, pp 10-21.

38. Mani, R., Noise due to Interaction of Inlet Turbulence with Isolated Stators and Rotors, Journal of Sound and Vibration, Vol. 17, No. 2, 1971, pp 251-260.

39. Cumpsty, N.A., and Lowrie, B.W., The Cause of Tone Generation by Aero-Engine Fans at High Subsonic Speeds and the Effect of Forward Speed, Trans. ASME, Journal of Engineering for Power, Vol. 96, No. 3, 1974, pp 228-234.

40. Hanson, D.B., Measurements of Static Inlet Turbulence, Hamilton Standard Report 6558, 1974.

41. Lowrie, B.W., Simulation of Flight Effects on Aero Engine Fan Noise, AIAA 2nd Aero-Acoustics Conference, 1975, AIAA Paper 75-463.

42. Roundhill, J.P., and Schaut, L.A., Model and Full Scale Test Results Relating to Fan Noise In-Flight Effects, AIAA 2nd Aero-Acoustics Conference, 1975, AIAA Paper 75-465.

43. Moore, C.J. Reduction of Fan Noise by Annulus Boundary Layer Removal, Journal of Sound and Vibration Vol. 43, No. 4. 1975, pp 671-681.

44. Sofrin, T.G., and Picket, G.F., Multiple Pure Tone Noise Generated by Fans at Supersonic Tip Speeds, International Symposium on the Fluid Mechanics and Design of Turbomachinery, Penn., State University, 1970, NASA SP-304, Part II.

45. Morfey, C.L., and Fisher, M.J., Shock-Wave Radiation from a Supersonic Ducted Rotor, Aeronautical Journal, Vol. 74, 1970, pp 579-585.

46. Hawkings, D., Multiple Tone Generation by Transonic Compressors, Journal of Sound and Vibration, Vol. 17, No. 2, 1971, pp 241-250.

47. Kurosaka, M., A Note on Multiple Pure Tone Noise Journal of Sound and Vibration, Vol. 19, No. 4, 1971, pp 453-462.

48. Sharland, I.J., Sources of Noise in Axial Flow Fans, Journal of Sound and Vibration, Vol. 1, No.3, 1964, pp 302-322.

49. Gordon, C.G., Spoiler-Generated Flow Noise, II Results, Journal of the Acoustical Society of America, Vol. 45, No. 1, 1969, pp 214-223.

50. Morfey, C.L., Broadband Sound Radiated from Subsonic Rotors, International Symposium on the Fluid Mechanics and Design of Turbomachinery, Penn. State University, 1970, NASA SP-304, Part II.

51. Ginder, R.B., and Newby, D.R., An Improved Correlation for the Broadband Noise of High Speed Fans. To be published AIAA Journal of Aircraft August 1977.

52. Lowson, M.V., Whatmore, A.R., and Whitfield, C.E., Source Mechanisms for Rotor Noise Radiation NASA CR-2077, 1973.

53. Mugridge, B.D., and Morfey, C.L., Sources of Noise in Axial Flow Fans, Journal of Acoustical Society of America, Vol. 5, No. 5, Part I, 1975.

54. Mugridge, B.D., Acoustic Radiation from Aerofoils with Turbulent Boundary Layers, Journal of Sound and Vibration, Vol. 16, No. 4, 1971.

55. Pickett, G.F., Effects of Non-Uniform Inflow on Fan Noise, Presented at the Spring Meeting of the Acoustical Society of America, 1974.

56. Hanson, D.B., Spectrum of Rotor Noise Caused by Atmospheric Turbulence, Journal of the Acoustical Society of America, Vol., 56, No. 1, 1974, pp 110-126.

57. Fletcher, J.J. and Smith, P.H., The Noise Behaviour of Aero Engine Turbine Tones, AIAA 2nd Aero-Acoustic Conference, 1975, AIAA Paper 75-466.

58. Mathews, D.C., Nagel, R.T., and Kester, J.D., Review of Theory and Methods for Turbine Noise Prediction, AIAA 2nd Aero-Acoustics Conference, 1975 AIAA, Paper 75-540.

59. Kazin, S.B., and Matta, R.K., Turbine Noise Generation, Reduction and Prediction, AIAA 2nd Aero-Acoustics Conference 1975, AIAA Paper 75-449.

60. Smith, M.J.T., and Bushell, K.W., Turbine Noise - Its significance in the Civil Aircraft Noise Problem, Paper presented at ASME Winter Annual Meeting, 1969, Paper No. 69-WA/GT-12.

61. Hoch, R., and Hawkins, R., Recent Studies into Concorde Noise Reduction, AGARD Conference Proceedings on Noise Mechanisms, 1973, AGARD-CP-131.

62. Cumpsty, N.A., and Marble, F.E., The Interaction of Entropy Fluctuations with Turbine Blade Rows; A Mechanism of Turbojet Engine Noise. Proc. Royal Society of London, Series A, 1977. (To be published).

63. Mathews, D.C., and Peracchio, A.A., Progress in Core Engine and Turbine Noise Technology, 6th Aircraft Design Flight Test and Operations Meeting, 1974, AIAA Paper No. 74-948.

64. Hoch, R.G., Thomas, P., and Weiss, E., An Experimental Investigation of the Core Engine Noise of a Turbofan Engine. AIAA 2nd Aero-Acoustics Conference 1975, AIAA Paper 75-526.

65. Bushell, K.W. A Survey of Low Velocity and Coaxial Jet Noise with Application to Prediction, Journal of Sound and Vibration, Vol. 17, No. 2, 1971, pp 271-282.

66. Bushell, K.W., Gas Turbine Exhaust Noise, Paper reprinted from AGARD Lecture Series on Aerodynamic Noise, 1976.

67. Bushell, K.W., Measurement and Prediction of Jet Noise in Flight, Progress in Astronautics and Aeronautics, Vol. 43, Aeroacoustics: Jet Noise, Combustion and Core Engine Noise, 1976.

68. Bryce, W.D., and Stevens, R.C.K., An Investigation of the Noise from a Scale Model of an Engine Exhaust System, AIAA 2nd Aero-Acoustics Conference, 1975, AIAA Paper 75-459.

69. Crighton, D.G., Mechanisms of Excess Jet Noise, AGARD Conference on Noise Mechanisms, 1973, AGARD-CP-131.

70. Crow, S.C., Acoustic Gain of a Turbulent Jet, Paper presented at American Physical Society Meeting, Univ. of Colorado, 1972.

71. Gerend, R.P., Kumasaka, H.P., and Roundhill, J.P., Core Engine Noise. AIAA Aero-Acoustics Conference, 1973, AIAA Paper No. 73-1027.

72. Bechert, D., and Pfizenmaier, E., On the Amplification of Broadband Jet noise by a Pure Tone Excitation, AIAA 3rd Aero-Acoustics Conference, 1976, AIAA Paper 76-489.

73. Hurle, I.R., Price, R.B., Sugden, T.M. and Thomas, A., Sound Emission from Open Turbulent Premixed Flames. Proc. Royal Society of London, Series A, Vol. 303, 1968, pp 409-427.

74. Bragg, S.L., Combustion Noise, Journal of the Institute of Fuel, Vol. 36, 1963, pp 12-16.

75. Chiu, H.H., and Summerfield, M., Theory of Combustion Noise, Acta Astronautica, Vol. 1, 1974, pp 967-984.

76. Strahle, W.C., Some Results in Combustion Generated Noise, Journal of Sound and Vibration, Vol. 23, No.1, 1972, pp 113-125.

77. Strahle, W.C., A Review of Combustion Generated Noise. AIAA Aero-Acoustics Conference, 1973, AIAA Paper 73-1023.

78. Strahle, W.C., and Shivashankara, B.N., Combustion Generated Noise in Gas Turbine Combustors, Trans. ASME, Journal of Engineering for Power, Vol. 98, 1976, pp 242-246.

79. Kazin, S.B., and Emmerling, J.J. Low Frequency Core Engine Noise. Paper presented at the ASME Winter Annual Meeting, Paper No. 74-WA/Aero. 2, 1974.

80. Ho, P.Y., and Tedrick, R.N. Combustion Noise Prediction Techniques for Small Gas Turbine Engines, Inter-Noise Proceedings, Washington, D.C., 1972.

81. Grande, E., Core Engine Noise, AIAA Aero-Acoustics Conference, 1973, AIAA Paper 73-1026.

82. Mathews, D.C., and Rekos, N.F., Direct Combustion Generated Noise in Turbopropulsion Systems - Prediction and Measurement. AIAA 3rd Aero-Acoustics Conference 1976, AIAA Paper 76-579.

83. Candel, S.M., Analytical Studies of Some Acoustic Problems of Jet Engines, Ph.D. Dissertation, California Institute of Technology, 1972.

84. Pickett, G.F., Core Engine Noise due to Temperature Fluctuations Convecting through Turbine Blade Rows. AIAA 2nd Aero-Acoustics Conference, 1975, AIAA Paper 75-528.

85. Cumpsty, N.A., and Marble, F.E., Core Noise from Jet Engines, Journal of Sound and Vibration, Vol. 54, No. 3, 1977. (To be published).

86. Plumblee, H.E., Dean, P.D., Wymore, G.A., and Burrin, R.H., Sound Propagation in and Radiation from Acoustically Lined Flow Ducts; A Comparison of Experiment with Theory. NASA CR-2306, 1973.

87. Shankar, P.N., On Acoustic Refraction by Duct Shear Layers. Journal of Fluid Mechanics, Vol. 46, No. 1, 1971, pp 81-91.

88. Mariano, S., Effect of Wall Shear Layers on the Sound Attenuation in Acoustically Lined Rectangular Ducts. Journal of Sound and Vibration Vol. 19, No. 3, 1971, pp 261-275.

89. Ko, S-H., Sound Attenuation in Acoustically Lined Circular Ducts in the Presence of Uniform Flow and Shear Flow. Journal of Sound and Vibration Vol. 22, No. 2, 1972, pp 193-210.

90. Mungar, P., and Plumblee, H.E., Propagation and Attenuation of Sound in a Soft-Walled Annular Duct ontaining Shear Flow. NASA Basic Aerodynamic Noise Research Conference, Washington 1969, NASA SP-207, pp 305-327.

91. Kaiser, J.E., Comparison of Central Difference and Forward Integration Techniques for Sound Propagation in Lined Ducts. Report E-73-30., 1973, Virginia Polytechnic Inst., and State University.

92. Mariano, S., Optimisation of Acoustic Linings in Presence of Wall Shear Layers. Journal of Sound and Vibration, Vol. 23, No. 2, 1972, pp 229-235.

93. Nayfeh, A.H., Kaiser, J.E., and Shakar, B.S., Effect of Mean-Velocity Profile Shapes on Sound Transmission through Two-Dimensional Ducts, Journal of Sound and Vibration, Vol. 34, No. 3, 1974, pp 413-423.

94. Zorumski, W.E., Acoustic Theory of Axisymmetric Multisectioned Ducts. NASA Technical Report TR R-419, 1974.

Chapter 25

JET NOISE

R. Mani

General Electric Company

CHAPTER 25 - JET NOISE

R. Mani
General Electric Company
Corporate Research and Development
Schenectady, New York 12301

Contents

25.1 Introduction
25.2 Lighthill Theory
25.3 Results of Lighthill Theory and Comparison with Experiments
25.4 Acoustic-Mean Flow Interaction
25.5 The Prediction of Jet Noise from Nozzles with Arbitrary Upstream Stagnation Pressures and Temperatures
25.6 Excess Noise in Jet Flows
25.7 Effects of Forward Flight on Jet Noise
25.8 Acknowledgments
25.9 References
25.10 Figures

25.1 Introduction

The problem of jet noise in gas turbine exhaust systems arises from the mixing of the jet exhaust stream with the ambient. The mixing process is extremely unsteady at the high Reynold's numbers characteristic of gas turbine engines so that one is inevitably dealing with a noisy flow. From a fundamental point of view, one may say that noise is a consequence of a flow being both unsteady and compressible. Jet flows are unsteady because the mixing of two streams at different velocities is inherently unstable and hence a continuous source of turbulence.

The basis for the understanding of jet noise was laid in the early fifties in two papers of Lighthill (References 1 and 2) and since then several authoritative review articles on jet noise have appeared (References 3, 4, 5, and 6). The purpose of the present chapter is therefore much more restricted and would even strike some readers as pedestrain. It is strictly tailored to the industrial user who needs to glean from the research literature ideas, equations, etc., that enable the prediction and hopefully the achievement of some measure of control of jet noise for specific nozzle geometries with given stagnation pressure and temperature. The ideas contained in References 1-6 will first be summarized especially with regard to what they imply for jet noise estimation and prediction. This summary is followed by citation of careful experiments with both heated and room temperature jet flows that have revealed inadequacies of prior work (such as summarized in References 1-5) in predicting the results of these experiments in detail. The three experimental papers, in particular, that are most valuable are the papers of Lush (Reference 7), Ahuja and Bushell (Reference 8), and Hoch et al (Reference 9). Some new ideas that have been advanced in recent years to resolve some of the discrepancies between the Lighthill theory and data are next described. We also give a brief account of a type of combined turbulent mixing/acoustic analysis that is currently gaining acceptance as a rational way of proceeding to estimate jet noise. Finally, we deal with the "excess" jet noise problem (the only aspect of which we consider in detail is the "shock noise" problem for underexpanded supersonic jets) and briefly describe some of the puzzles that are encountered in the area of jet noise in flight (as opposed to the static case).

The gas turbine power plant designer is very often interested in a wide variety of nozzle shapes (Figure 1). The round convergent nozzle is, of course, the simplest possible shape for turbojet engines. Sometimes (in fact to reduce jet noise), turbojet engines employ noncircular nozzles of the "daisy" type. Multitube and other multielement exhaust nozzles have been proposed though they are not yet used in any flying airplane. Dual flow systems (wherein the stagnation pressure, temperature of the two streams are different) are characteristic of turbofan cycles. (Although not shown in Figure 1, dual flow systems are often characterized by noncoplanar exit planes). Even with round convergent nozzles, a central plug is frequently employed.

The present chapter will not address at all the problems with experimental techniques used to measure jet noise. Some of the more important of these will be briefly mentioned. Outdoor testing very often produces confusing effects due to ground reflections. When scale model tests are carried out (often in anechoic chambers), it is common practice to strive for geometric similarity, same working fluid (air) at the same stagnation pressure and temperature. The inevitable mismatch in Reynold's number is accepted as of little consequence in view of the high Reynold's numbers involved. Frequencies are scaled simply on the basis that $f\ell \approx$ constant (where f is the frequency in cycles per second and ℓ is a characteristic length of the nozzle) and then the scaling principle is just that the noise per unit area is the same for both model and prototype in the appropriate third octave bands. Provided proper precautions are

taken to ensure the dominance of jet noise over internally generated noise, etc., the above scaling principle works reasonably well. Reference 10 provides evidence, e.g., that the above scaling principle works well for three nozzle types; namely a round nozzle, a multitube nozzle and a daisy nozzle. One disadvantage of scale model work is the need to measure to high frequencies (as high as 40 kc). Atmospheric absorption effects are an area of controversy above 10 kc. Engine tests on the other hand are often vitiated by internally generated noise sources especially for jet velocities below 1400 feet per second or so.

It should be reiterated that from a practical point of view we do not know enough about the scaling of jet noise for complex nozzle shapes except with regard to the geometric size effect. Thus every effort is made in practical model scale studies to preserve the working fluid, stagnation temperature and stagnation pressure. As will be seen shortly, the celebrated Lighthill theory is, in essence, viewed from a strictly utilitarian point of view, an attempt to predict the scaling of jet noise with jet temperature, jet velocity and angle to the jet axis.

In Figure 2 we show, in schematic form, a layout depicting the quantities that are measured in a typical jet noise experiment. One is normally interested in sound pressure level (abbreviated as SPL) spectra (for full scale engine sizes) from about 100 Hz to 10,000 Hz (for model scale, the frequencies would obviously be higher), angles θ (in Figure 2) from 20° to 150°. Jet velocities ranging from 600 fps to 3000 fps with upstream stagnation temperatures ranging from room temperature to 3000°R are commonly of interest. When flight noise is of interest, flight speeds from 0 to 400 fps are of interest.

We now proceed to a description of the Lighthill theory of jet noise and its consequences.

25.2 Lighthill Theory

Lighthill himself introduced his theory of jet noise (References 1, 2) as follows. The exact equations of continuity and motion can be written as:

$$\frac{\partial \rho}{\partial t} + \frac{\partial}{\partial x_j}(\rho v_j) = 0 \qquad (1)$$

$$\frac{\partial}{\partial t}(\rho v_i) + \frac{\partial}{\partial x_j}(\rho v_i v_j + p_{ij}) = 0 \qquad (2)$$

$$p_{ij} = p\delta_{ij} - \tau_{ij} \qquad (3)$$

In (1), (2), and (3), ρ denotes density, v_i denotes the i^{th} component of velocity (Cartesian components), x_i the corresponding space coordinate, p_{ij} the compressive stress tensor consisting of a pressure term $p\delta_{ij}$ (δ_{ij} is the Kronecker delta function), τ_{ij} the viscous stress tensor. It is characteristic of Lighthill's development of the jet noise problem that he used the momentum equation in Reynold's form and that he made no use of the energy equation (which for an inviscid, non heat conducting gas of specific heat ratio γ would be

$$\frac{Dp}{Dt} = \frac{\gamma p}{\rho}\frac{D\rho}{Dt}$$

with D/Dt denoting a differentiation following the fluid). It should be noted that equations (1) and (2) assume the absence of any explicit mass or force sources in the fluid and are thus tailored to reveal noise sources in the absence of any obvious sources such as unsteady combustion, struts (which may induce fluctuating forces), etc. This development is certainly pertinent to jet noise since we hope that the burning, etc., is complete by the time the flow leaves the nozzle and struts, etc., are usually absent in the exhaust plume.

By taking $\partial/\partial t$ of (1) and $\partial/\partial x_i$ of (2) and subtracting the latter from the former one arrives at the Lighthill equation (which is an <u>exact</u> equation) namely

$$\frac{\partial^2 \rho}{\partial t^2} - a_0^2 \nabla^2 \rho = \frac{\partial^2}{\partial x_i \partial x_j}(T_{ij}) \qquad (4)$$

where $T_{ij} = \rho v_i v_j + (p - a_0^2 \rho)\delta_{ij} - \tau_{ij}$. a_0 so far is any constant velocity but at least for low Mach number, unheated flows it will be convenient to take it as the undisturbed speed of sound thus eliminating (approximately) the term $(p - a_0^2 \rho)\delta_{ij}$ in T_{ij}. In (4) and in what follows, the usual convention that repeated indices imply summation over the repeated index going from 1 to 3 is followed.

The ingenuity of Lighthill's manipulating (1), (2) to lead to (4) notwithstanding, it is important to note (Reference 6) that a somewhat deeper idea than mere manipulation is involved in the development of (4). Source free linear acoustics of a uniform, homogeneous medium is governed by the equation:

$$L_0\rho = \frac{\partial^2 \rho}{\partial t^2} - a_0^2 \nabla^2 \rho = 0 \qquad (5)$$

On the other hand, if sources, say $s(\bar{x}, t)$, are present (5) would be modified to

$$L_0\rho = s(\bar{x}, t) \qquad (6)$$

Based on (5) and (6), we may say that in attempting to cast the jet noise problem in the framework of classical, linear acoustics of a stationary, uniform, homogeneous medium, Lighthill saw that noise sources arise in this analogy to the extent that in a fluid flow $\partial^2 \rho / \partial t^2$ is <u>not</u> balanced by $a_0^2 \nabla^2 \rho$.

In other words, if one wishes to draw an analogy to the linear acoustics of a stationary, uniform, homogeneous medium, the sources are precisely the extent to which the pertinent wave equation for such a flow ($L_0\rho = 0$) is not satisfied. The ingenuity of Lighthill is, of course, in showing that this residual or imbalance was exactly $\partial^2/\partial x_i \partial x_j \ (T_{ij})$.

Retarded time solutions to (4) can be written down formally but they show immediately that no further progress can be made unless intuitive assessments are made of the "source" term T_{ij}. Lighthill argued that with a_0 taken as the speed of sound in the undisturbed medium and neglecting viscous stresses, the dominant part of T_{ij} would be $\rho v_i v_j$. To make further progress, he assumed that $(\delta \rho v_i v_j)$ could be approximated by $\rho_j v_{ti} v_{tj}$, where ρ_j is the mean jet density and v_{ti} the nonacoustic portion of the fluid velocities. If we accept these arguments, we can then estimate the source terms at least on a similarity basis. (In addition, hot film measurements, e.g., see Reference 11, do give us a good picture of the velocity field in jet flows.)

The second key idea that Lighthill advanced relates to the consequences of the source term appearing in (4) as a double divergence. The physical result that he deduced was that jet noise was due to a large number of small, statistically independent volumes (called eddies) with each of these eddies contributing noise of a quadrupole character. To understand this, we need to first note that if the spatial extent over which the $\rho v_i v_j$ term of T_{ij} is correlated is small compared to the wavelength of the emitted sound, the source region is what is termed "compact" in acoustic terminology and can be treated essentially as a point source. (Mathematically, at a given frequency, one would approximate $\rho_j v_{ti} v_{tj}$ by a three-dimensional delta function representation as $\rho_j Q \delta(\bar{x}) \exp(j\omega t)$). To decide when the source regions are indeed compact we need to resort to a dimensional argument as follows.

If ℓ denotes a length scale of the eddies and u the value of the velocity, Lighthill points out that the associated frequency will be proportional to (u/ℓ) so that the ratio (ℓ/λ) (λ being the wavelength of the emitted sound) will be proportional to (u/a_0). Based on this, we may say that if the flow Mach numbers are small, the eddies are likely to be compact. The condition of low Mach number flows by itself is too restrictive and not very interesting because jet flows are not noisy at low Mach numbers.

To cope with the high Mach number jet noise problem, Lighthill points out that the eddies that create jet noise are convected with the flow and in their own frame of reference are actually decaying rather slowly. (Hot film measurements of Reference 11 with two spatially separated probes confirm this.) The reader is referred to Lighthill's papers for a fuller exposition of these ideas and the end result is that, if eddy convection is accounted for, the source compactness condition becomes that the turbulent (fluctuating velocity) Mach number (M_t) be small. The reasons for this modified condition are that a frozen, subsonically convecting pattern generates no sound and hence only the time variations (frequencies) in the eddy's own (convected) frame of reference create sound. These frequencies (in the eddy's own frame of reference) are proportional to (u'/ℓ) where u' is the fluctuating velocity. The condition that M_t be small is likely to be met even for high speed jets since turbulence levels (referenced to the jet exit velocity) rarely exceed 15% or so. Even for a Mach 2.0 jet, thus M_t will not exceed 0.3.

There is a small price to be paid for this ability to cope with high jet Mach numbers which is that the linear acoustic theory has to be developed to handle the problem of radiation from convected quadrupoles and the usual Doppler type effects on frequency, pressure amplitudes, directivity, etc., have to be considered. This is the essence of Lighthill's analysis, namely that it develops the consequences of convection of the quadrupoles.

25.3 Results of Lighthill Theory and Comparison with Experiments

Analytical details of how to solve the problem of radiation from convected quadrupoles (within the framework of classical, linear acoustics of a uniform, stationary, homogeneous medium) are given in References 1, 2, 3, and 4, so that we will not repeat the details of the procedure. The purpose here is to summarize broadly the predicted results.

The results can be classified into: a) those associated with nonconvective aspects and b) those associated with the convection of the eddies. The principal result of type (a) is based on the fact that the acoustic power radiated by a point quadrupole of strength Q and frequency ω is proportional to $\omega^4 Q^2$. Since the frequency itself scales as (u/ℓ) and for a given nozzle geometry we expect ℓ to be insensitive to jet velocity, jet temperature (at least as a first approximation), we arrive at a famous prediction of Lighthill that jet noise power at low jet Mach numbers (and the mean square pressure at any given far field angle) would scale as $\rho_j^2 U^8$ when jet velocity U and jet density are varied. (Note that the quadrupole strength Q itself would vary as $\rho_j U^2$.) It is worth repeating that the eighth power velocity law is crucially related to the quadrupole nature of the jet noise radiation. The quadrupole nature of the sources in turn is not only because we can manipulate (1) and (2) to yield (4), but also because we estimate the most important part of T_{ij} to be $\rho v_i v_j$ and further assume (confirmed

by the experimental observations of Reference 11) that the Reynold's stresses $(v_i v_j)$ are correlated over lengths small compared to the acoustic wavelength corresponding to the frequency at which the eddies radiate.

The convective aspects of Lighthill's results will now be stated. The result for the acoustic pressure of a convected point quadrupole is that its pressure is modified from that of a stationary point quadrupole as

$$p_M = \frac{p_S}{(1 - M_c \cos\theta)^3} \qquad (7)$$

where p_M is the pressure of the moving quadrupole, M_c is its convection Mach number (referenced to the speed of sound of the uniform, homogeneous, stationary medium through which it moves). The angle θ in (7) is the angle made between the source-observer direction and the line of source motion with the source position taken at the instant where the source was when it emitted the radiation reaching the observer at current time (see Figure 3). p_S is the pressure that a stationary source located at the retarded position in Figure 3) would produce at the same far field location. The restrictions on (7) are that it is valid only for point quadrupoles convecting at a uniform velocity.

In applying (7) to the jet noise problem, Lighthill himself (References 1, 2) suggested that the mean square pressure would vary as

$$\langle p'^2_M \rangle \sim \frac{\langle p'^2_S \rangle}{(1 - M_c \cos\theta)^6} \qquad (8)$$

Ffowcs Williams and Ribner (References 12, 13) showed however, that two changes need to be made to (8) before it can be applied to the jet noise problem. First they showed that when the integration over a finite jet volume of a large number of statistically independent eddies is carried out, the proper factor in the denominator of (8) ought to be $(1 - M_c \cos\theta)^5$ rather than $(1 - M_c \cos\theta)^6$. The eddy convection velocity by measurement for round nozzle flows is found to be roughly 65% of the ideal jet exit velocity.

The second modification introduced by Ffowcs Williams and Ribner is of considerable importance. We note first that, if the frequency of the eddy in its own frame of reference is ω_0, the frequency of the emitted sound in the far field is given by the Doppler shift formula $\omega_0/(1 - M_c \cos\theta)$. This means that however small ω_0 might be, for supersonic eddy convection ($M_c > 1$), the observed frequency along the direction $\theta_c = \cos^{-1}(1/M_c)$ is infinite and the associated wavelength is zero. This means that however small the correlated source region, it cannot be regarded as compact along the direction θ_c. This difficulty with the original Lighthill result (a foretaste of which is that (8) "blows up" or is singular at $M_c \cos\theta = 1$) led Ffowcs Williams and Ribner to develop a more generally valid result than (8) and they concluded that this result is that

$$\langle p^2 \rangle \sim \frac{\rho_J^2 U^8 \text{ (intrinsic directionality)}}{[(1 - M_c \cos\theta)^2 + \alpha^2 M_c^2]^{5/2}} \qquad (9)$$

where α^2 is a semi-empirical constant (noncompactness parameter) allowing for finite eddy correlation volumes. We will shortly discuss the term "intrinsic directionality" that appears in the numerator of (9). For round circular nozzles, both the far field acoustic data and the hot film measurements in jets suggest that α is roughly somewhere between 0.3 and 0.55. Apart from obtaining an expression for $\langle p^2 \rangle$ valid for all angles and convection Mach numbers, (9) also points out another important feature of jet noise. Consider first angles θ and convection Mach numbers M_c such that $|M_c \cos\theta| \gg 1$ and $|1 - M_c \cos\theta| \gg \alpha M_c$. (9) shows that the acoustic mean square pressure will now vary as U^3 (since M_c itself varies as U). Similarly for angles (near θ_c) such that $|(1 - M_c \cos\theta)| \ll \alpha M_c$, $\langle p^2 \rangle$ again varies as U^3. Thus the Ribner-Ffowcs Williams development is of paramount importance in showing that for high velocities (in the supersonic eddy convection regime), the far field acoustic mean square pressure and total acoustic power will ultimately vary as U^3. Since at low velocities these quantities vary as U^8 and the flux of kinetic energy through the exhaust nozzle varies as U^3, we may say that the efficiency of noise generation (ratio of acoustic power to jet flow power) varies as M_j^5 at the lower velocities and finally (at high velocities) levels off to a constant value.

One last remark needs to be made related to the fact (9) is in terms of the "retarded" position angle θ (Figure 3) whereas jet noise measurements are made with reference to the center of the nozzle exhaust plane. Jet noise eddies obviously do not have an infinite lifetime and, in fact, have a coherent lifetime (time between the "birth" and "death" of an eddy) corresponding to a travel through several nozzle diameters. (The coherent length is greater for low frequencies as compared to high frequencies but, even for the lowest frequency eddies, does not exceed about twenty nozzle diameters). Thus, if the far field measurements are made at a distance of greater than say 150 nozzle diameters, the distinction between the angle measured from the center of the nozzle and the "retarded" position angle need not be made. If, however, the radius of measurement is significantly less than about 150 nozzle diameters, some accounting of the coherent length of the eddy may be needed especially for the low frequency sound.

An expression "intrinsic directionality" appears in (9). The most comprehensive development of this idea is due to Ribner and is summarized in Reference 14. The idea is as follows. Consider even the Lighthill approximation to T_{ij} namely, $\rho v_i v_j$. In a jet flow, to a first approximation, we may consider the velocity field as one composed of a transversely sheared axial mean flow U(r) (r denotes the transverse radial coordinate) and a fluctuating part u'_i. Then the term $\partial^2/\partial x_i \partial x_j (v_i v_j)$ appears as composed of a part

$$\frac{\partial^2 [U(x_2, x_3)\, u'_i}{\partial x_1 \partial x_i}$$

(with 1 denoting the axial direction) and a part $\partial^2/\partial x_i \partial x_j (u'_i u'_j)$. If the turbulence is assumed to be isotropic in its own frame of reference, the above decomposition shows that there are mean flow shear dependent axial quadrupoles $\partial^2/\partial x_1 \partial x_i [U(x_2, x_3)\, u'_i]$ and an omnidirectional mix of quadrupoles $\partial^2 (u'_i u'_j)/\partial x_i \partial x_j$. The mean flow shear dependent source terms (said to produce "shear" noise) and the more or less omnidirectional group of terms (said to produce "self" noise) differ from each other in three respects. Firstly, the shear noise terms have an axial orientation unlike the self noise terms which are omnidirectional. Secondly, since the shear noise involves only one power of the fluctuating velocity while the self noise involves two powers of the fluctuating velocity, shear noise would be expected to account for lower frequency noise emission than self noise. Finally, since fluctuating velocities will be smaller than mean velocities, shear noise would be expected to be more important in an absolute sense than self noise. It should be pointed out that these remarks concerning self noise and shear noise are, strictly speaking, true only for the development of jet noise theory based on Lighthill's equation (4). At any rate, Reference 14 points out that this development of Lighthill's equation leads to an intrinsic directionality of jet noise as $[A(f) + B(f) \cos^2(\theta)]$ for the mean square pressure with f the frequency (more properly a Strouhal number) and θ the angle from the jet exhaust axis. Based on the previous reasoning, one would expect B(f) to peak at a frequency one-half of that at which A(f) peaks and also expect the peak value of B(f) to be higher than that of A(f).

Essentially, the picture of jet noise prediction that emerged in the early sixties or so is shown in Figure 4. The total acoustic power was predicted and measured to vary as U^8 at low jet velocities transitioning to a U^3 law at high jet velocities. The directionality was predicted to be basically as $[(1 - M_c \cos\theta)^2 + \alpha^2 M_c^2]^{-5/2}$ with Ribner's development predicting an additional $\cos^2\theta$ type dependence at low frequencies. The spectral distribution for geometrically similar nozzles was predicted to scale such that $f\ell/V_j$ was constant. This last result was not so much an insight from the Lighthill equation as simply based on dimensional reasoning. When jet temperature was changed (keeping jet velocity constant), by virtue of the fact that jets are essentially constant pressure flows, jet density will also be changed and the theory suggests that noise power and mean squared pressure would vary as ρ_j^2. In Reference 3, Lighthill suggests that because jet noise arises from the mixing of the jet with the ambient, the strength of the quadrupoles ought to be taken as proportional to $(\rho_j + \rho_0)/2$ where ρ_0 is the density of the ambient fluid rather than just to ρ_j. Hence, he suggested that the variation with jet density might be expressible as a power law ρ_j^ω where ω lies between 1 and 2.

Apart from the source aspects (such as low frequency shear noise), the predictions of the Lighthill theory whether for the U^8 law, the ρ_j 1 to 2 dependence or the $[(1 - M_c \cos\theta)^2 + \alpha^2 M_j^2]^{-5/2}$ directivity are not noticeably frequency dependent.

The Lighthill theory led to at least two notable ideas for jet noise suppression. Since the thrust of a jet varies as $A_j V_j^2$ (where A_j is the jet exhaust area) and its acoustic power as $A_j V_j^8$, it is easily demonstrable that jet noise could be reduced at constant area by raising exhaust area and lowering jet velocity. The high bypass ratio fan engine is an embodiment of this concept and indeed by and large the noise of these engines (especially the ones that power the wide bodied transports averaging bypass ratios of 5:1) is not dominated by jet mixing noise at all. Even with straight turbojet cycles, ideas due to Greatrex and others led to the notions of "mixer" nozzles such as the daisy nozzles shown in Figure 1. The exact basis by which such nozzles serve to reduce noise is not completely understood but it seems clear that at least one ingredient in the reduction is the tendency for these nozzles to produce enhanced jet mixing by allowing for greater entrainment (as compared to a circular nozzle) and thus reducing the integrated value of the Lighthill stress tensor ($\rho v_i v_j$).

The experimental data in the early sixties tended to confirm several of the Lighthill predictions in the gross aggregate. Peak overall sound pressure levels, overall power levels (abbreviated as OAPWL), etc., showed the U^8 - U^3 behavior. The directivity of the overall sound pressure levels tended to follow roughly a $(1 - M_c \cos\theta)^{-5}$ type variation with M_c taken as $0.65 M_j$. The predicted density dependence was, however, never checked out carefully. When nozzle size was varied (other things being kept equal), frequencies do scale inversely as the length ratio but when jet velocity is varied (other things being held fixed), the measured far field frequencies do not appear to scale linearly with velocity as would be expected from the notion the ($f\ell/V$) stays constant.

One of the first measured discrepancies from the Lighthill theory was the fact that with jets with subsonic eddy convection velocities, the directivity of the high frequency noise often does not follow the predicted $(1 - M_c \cos\theta)^{-5}$ directivity but exhibits a heart shaped dip near the jet axis (Figure 5). Another significant discrepancy is what has been picturesquely termed the "reverse" Doppler shift by Ribner. If one measured jet noise from $\theta = 0$ to $\theta = 90^o$ (again for convenience restricting oneself to jets with subsonic eddy convection velocities), one would expect from the Lighthill theory that the sound field at shallow angles would be dominated by higher frequencies while that at the more broadside angles by lower frequencies. This is because, by the Doppler shift formula, the emitted frequency is related to the source frequency ω_0 by the expression $\omega_0/(1 - M_c\cos\theta)$. Actual measurements exhibit the reverse tendency with the sound pressure level at 90^o to the jet axis often being peaked at a frequency three times higher than that at $\theta = 30^o$. Ribner has explained this "reverse" Doppler shift as due to two features. Firstly, the self noise-shear noise decomposition itself shows that the low frequency noise will be biased towards the jet axis, whereas the high frequency noise is omnidirectional. Secondly, Ribner points out that the mean flow velocity and temperature profiles would refract away the high frequency sound from the jet axis. Indeed, Ribner and his students performed several experiments in the mid sixties with artificial sound sources (discrete frequency point sources) in jet flows which exhibit heart shaped dips close to the jet axis in the far field quite similar to jet noise data itself (Reference 14).

Lush's experiments (Reference 7) were notable for the fact that for subsonic, unheated jets over a range of velocities (300-1000 fps), an attempt was made to make a fairly detailed theory data comparison with the Lighthill theory.

Lush begins (in terms of theory data comparison) by noting that from the Lighthill theory, one would expect the far field acoustic pressure on a given arc (for a given nozzle exhausting into a given ambient) to vary as:

$$\left\langle p^2 \right\rangle (\theta, \omega) \sim \frac{\rho_j^2 V_j^8 F_I(\theta, \omega_0) G(\omega_0)}{(1 - M_c\cos\theta)^5}$$

where $\omega = \omega_0/(1 - M_c\cos\theta)$ (10)

In (10), $F_I(\theta, \omega_0)$ would be the intrinsic directionality of the sound at a source frequency ω_0 and $G(\omega_0)$ the intrinsic source spectrum (not predicted at all by the Lighthill theory but determined in principle by knowledge of the turbulent dynamics of the eddy in its own frame of reference). Lush assumes (unlike Ribner) that $F_I(\theta, \omega_0)$ is essentially unity (i.e., he takes the intrinsic directionality to be omnidirectional) and also neglects the $(\alpha^2 M_c^2)$ type correction in the denominator of (10). (His experiments being with subsonic jets involved $M_c < 0.65$ so that the $(\alpha^2 M_c^2)$ term was always small compared to $(1 - M_c\cos\theta)^2$. Further, to avoid the need to know $G(\omega_0)$, Lush examined the variation of $\left\langle p^2 \right\rangle (\theta, \omega_0/(1 - M_c\cos\theta))$ with fixed ω_0 and varying θ. Finally, in seeking to collapse data from different nozzle sizes and at different velocities from a given nozzle size, Lush examined the directivity at fixed values of $[\omega_0 d/2\pi U]$ where U is the jet velocity. This last procedure is sometimes called determining the directivity at fixed source Strouhal numbers and note that it entails examining the far field acoustic pressures at a frequency dependent on the angle, namely at $[\omega_0/(1 - M_c\cos\theta)]$. Also a suitable value of M_c must be assumed and Lush chose the usual estimate of $M_c = .65\, M_j$. Since Lush was working with room temperature air jets operated at subcritical pressure ratios, the variation of ρ_j^2 in his experiments was quite small and negligible. Consistent with his assumption of an omnidirectional $F_I(\theta, \omega_0)$, Lush expected to obtain (from Lighthill's theory) that the variation of $\left\langle p^2 \right\rangle [\theta, (\omega_0/1 - M_c\cos\theta)]$ at fixed ω_0, U with θ would be as $(1 - M_c\cos\theta)^{-5}$ with $M_c = 0.65 M_j$. and at fixed θ, ω ... variation with U would be as $U^8/(1 - M\cos\theta)^5$. Examining the data for $\omega(1 - M_c\cos\theta)d/2\pi U$ from 0.03 to 1.00 (which brackets the range of frequencies occurring in jet noise quite well), Lush found the following. With regard to the directivity at fixed source Strouhal numbers, he found that an expression of type $(1 - M_c\cos\theta)^{-5}$ overestimates the variation with angle of the measured data at high source Strouhal numbers and conversely at low source Strouhal numbers, the variation is underestimated. Similarly at shallow angles to the jet axis and at high frequencies, $U^8/(1 - M_c\cos\theta)^5$ overestimates the variation with U of the measured data and conversely at shallow angles and low frequencies the measured variation with U is underestimated by the expression $U^8/(1 - M_c\cos\theta)^5$. At large angles to the jet axis, Lighthill's theory and ideas work fairly well. For example at $\theta = 90^o$, the pressures scale very well as U^8 and the peak frequency scales extremely well as U/d. (Correspondingly at shallow angles, e.g., at $\theta = 30^o$, the peak frequency appears almost insensitive to jet velocity.) These results of Lush are summarized in Figure 6 schematically.

Ahuja and Bushell (Reference 8) obtained very similar results with room temperature jets over roughly the same velocity range as Lush. Developing the same idea, they point out that if the acoustic data from a given nozzle geometry is plotted such that we plot the quantity

(Sound pressure level) (SPL in dB) - $20 \log_{10}$ (D/R) - $80 \log_{10} V_j + 50 \log_{10} (1 - M_c\cos\theta)$ (11)

for fixed values of $\{fD(1 - M_c\cos\theta)/V_j\}$ where f is the observed frequency in cycles per second, V_j the jet velocity, D the nozzle size and R the radius of measurement one ought to obtain a universal curve which is really a measure of $G(\omega_0)$. This statement of Ahuja and Bushell (for room temperature jets) is what one has in mind in saying that Lighthill's theory asserts, in a strictly utilitarian sense, a powerful scaling principle. In fact, if we proceeded to subtract from (11) an additional term $10\omega\log_{10}(\rho_j)$ where ω lies between 1 and 2, the scaling principle would allow for density effects also. In principle the desired universal curve could be obtained by just one measurement (for a given nozzle type) of the far field acoustic pressure spectrum at one angle, one jet velocity/density combination. Using (11) (modified by subtracting $10\omega\log_{10}(\rho_j)$), one could then predict the complete far field acoustic pressure spectrum at any other angle, any other velocity and temperature and for any nozzle with the same geometry as the baseline nozzle.

When Ahuja and Bushell (Reference 8) attempted a collapse of this type, they failed to obtain one universal curve. Rather as shown in Figure 7 and explained earlier with regard to the Lush data, if one draws the curve of the reduced quantity in (11) for $\theta = 90^o$ (since Lighthill's theory works very well at $\theta = 90^o$), the problem is that for shallow angles the high source Strouhal number data is overpredicted and the low Strouhal number data is underpredicted.

Related to these discrepancies observed by Ahuja and Bushell and by Lush is one with regard to the scaling of the peak frequencies of the spectrum with jet velocity (Reference 15 and Figure 8). This is that whereas the peak frequency of the SPL spectrum at $\theta = 90^o$ varies linearly with jet velocity, the peak frequency of the integrated power level or PWL spectrum (which tends to be dominated for subsonic jet noise by the shallow angle levels) is often quite insensitive to jet velocity.

Last but not least, we must mention the rather significant discrepancies from the Lighthill theory in the area of heated jet noise found by Hoch et al, (Reference 16). As mentioned earlier, the Lighthill theory leads one to expect that the mean square pressures (as well as the acoustic power) would vary as ρ_j^ω where ω lies between 1 and 2 when jet density alone is varied. Measurements by Hoch and colleagues of this "jet density exponent," ω are shown in Figure 9 as a function of $\log_{10}(V_j/C_0)$ where V_j is the jet velocity and C_0 the speed of sound of the ambient. (The ratio V_j/C_0 is sometimes called the "acoustic Mach number M_0" in the literature.) The expected values from the Lighthill theory are also shown in Figure 9. Notice the rather substantial discrepancy especially at low jet velocities. As the bottom of Figure 9 shows, the effects of heating also cause the frequency spectrum to be biased progressively towards the lower frequencies. A simple explanation of all these heating effects based only on changes of jet turbulence structure due to heating is difficult to envisage since the effects of heating vary with (V_j/C_0).

Before concluding this section, we wish to point out some of the experimental advances that occurred in the late sixties - early seventies that really enabled the selective pinpointing of discrepancies between measured data and the predictions of the Lighthill theory. Firstly, especially with scale model work, the use of anechoic chambers to measure jet noise came into vogue in this period thus avoiding ground reflections, etc. Secondly, it became recognized that non jet mixing noise sources chiefly internally generated noise sources need to be suppressed very carefully in order to acquire good jet noise data. These internal noise sources are usually equivalent to lower order acoustic sources of the monopole or dipole type and hence by the usual dimensional reasoning, one would expect their contributions to the far field acoustic power to vary as U^4 and U^6 as opposed to the U^8 contribution of jet noise (at the lower jet velocities) (see Reference 17). Indeed as shown in Figure 10, the test of the "goodness" of a facility for jet noise measurements has now come to be evaluated by the lowest velocity to which the OASPL at 90^o to the jet axis exhibits an eighth power law. We also expect a good facility to yield SPL spectra at 90^o to the jet axis (for the unheated case) scaling on a proper Strouhal basis, i.e., peak frequency varying linearly with jet velocity. For the effects of heating, a good facility is currently required to produce jet density exponents similar in values (as a function of V_j/C_0) to those measured by Hoch, et al (Reference 16). Thirdly our understanding of jet noise has greatly improved because (even for simple nozzle geometries such as a round convergent nozzle), jet noise data is now available from good facilities over a wide range of velocities and temperatures. In the supercritical case, some experiments (Reference 18) are even available where the nozzle is carefully contoured to avoid underexpanded flows and associated shocks in the jet plume. (Such nozzles are often termed C-D nozzles for "convergent divergent nozzles" or as Laval nozzles.) Finally, the emphasis placed by the Lush and Ahuja-Bushell work on examining the data on a constant source Strouhal number basis is also significant inasmuch as it is a simple but effective way of checking out the acoustic implications of any jet noise theory without confusion of turbulence source spectrum effects. (In other words, we need not be stymied in terms of theory-data comparisons due to our ignorance of $G(\omega_0)$ in (10)).

25.4 Acoustic-Mean Flow Interaction

The estimation by Lighthill of $(\rho v_i v_j)$ as the most important part of T_{ij} and his subsequently approximating it by $(\rho_t v_{ti} v_{tj})$ has certainly proved most valuable in providing key insights into the jet noise problem as evidenced by the previous section. However, it is also true that this approximation essentially suppresses all effects associated with the fact that the mean flow and mean temperature environment of the jet convect, refract, and shield the radiation from the moving eddies.

This neglect of mean flow effects in the Lighthill development was pointed out by several writers in the sixties, notably Ribner, Powell, Phillips and Csanady (References 19, 20, 21 and 22). The refraction effect alluded to earlier is, of course, one example of this. Powell pointed this out by stressing the following. The convection of the elementary quadrupole generators was an important effect recognized by Lighthill. However, this very convection effect leads to the following difficulty with the theory. Since the mean square pressure of a moving quadrupole is different from that of a stationary one by the factor $(1 - M_c \cos\theta)^{-5}$, by integrating this factor weighted by $\sin\theta$ (to account for the solid angle) from $\theta = 0$ to $\theta = \pi$, one can show that the acoustic power of the moving quadrupole ought to be greater than that for a stationary one by a factor $(1 + M_c^2)/(1 - M_c^2)^2$. This means that from the Lighthill theory, one would expect, say the overall power level to vary not just as U^8 but as $U^8 (1 + M_c^2)/(1 - M_c^2)^2$ with M_c taken as $0.65 M_j$. As Powell points out, based on this one can expect not just an eighth power law but a power law with a velocity exponent ranging from 9 to 16. Experiments, of course, show a faithful adherence to an eighth power law. Lighthill himself was aware of this difficulty but felt that the turbulence intensity of jet flows (as a fraction of the jet velocity) diminished with increasing jet Mach number in a manner sufficient to restore the eighth power law. The faithful adherence to an eighth power law of the OASPL at 90° to the jet axis, however, fails to support this contention. Ribner, Powell and Csanady (References 19, 20, 22) suggested a much more reasonable resolution (see Figure 11). Figure 11 shows a schematic of an eddy moving in a jet flow. The reason that the eddy moves is, of course, that the jet fluid moves and relative to its immediate environment, the eddy is actually not moving at all. Especially at high frequencies, one would expect the power radiation of the eddy to be governed by its immediate environment and since the eddy has no velocity relative to this environment, one would expect no "convective amplification" at all at high frequencies. (The enhancement of power in the Lighthill theory by the factor $(1 + M_c^2)/(1 - M_c^2)^2$ is often referred to as "convective amplification".)

A highly simplified model problem of a simple point mass source (i.e., not a point quadrupole) convecting along the axis of a round plug flow jet was worked out by the present author (Reference 23) to examine this question in more detail. The source oscillates at a frequency ω_0 in its own frame of reference and the principle result calculated was the ratio of the power emitted by the source in the jet flow to that which it would emit if there was just a source convecting through a stationary, ambient medium (the latter situation corresponding to the Lighthill model). The results are a function of the jet and eddy convection Mach number M and the frequency parameter $\omega_0 a/c$ (where c is the ambient speed of sound). The problem and key results are shown in Figure 12. At high $(k_0 a)$ the problem does yield the result of no convective amplification but at low $(k_0 a)$ a somewhat unexpected result that convective amplification may be underestimated by Lighthill type models was obtained. (We shall not discuss this last result in any detail here except to note that the experimental work of Lush and Ahuja-Bushell also showed that Lighthill's theory tends to underestimate convective amplification at low frequencies.) Furthermore, as the result in Figure 12 shows the flowing jet column provides a natural (acoustic) mechanism for the enhancement of low frequency radiation relative to high frequency radiation. It was argued in Reference 23 that this effect more or less completely explains why the peak frequency of the PWL spectrum is so insensitive to jet velocity (Figure 8).

This idea of systematically accounting for the effect of the jet flow on the radiation by the quadrupoles was pursued intensively first by Phillips (Reference 21) and subsequently somewhat more completely by Lilley (Reference 24). To explain this idea, we revert to the notion of Lighthill that jet noise sources arise to the extent to which some standard source free wave equation is <u>not</u> satisfied (Reference 6). In Lilley's development, the standard equation chosen is not the equation governing wave propagation in a stationary, uniform, homogeneous medium. Lilley notes that to a rough, first approximation, we may treat the jet flow as a constant pressure, parallel sheared flow. The equation governing wave propagation in this type of flow is the Orr-Sommerfield equation often used to study the stability of such flows. Symbolically denoting this by $L_{OS} p' = 0$, Lilley attempts to determine by using the full equations of motion the extent to which $L_{OS} p' \neq 0$. We may symbolically summarize this exercise by saying that

$$L_{OS} p' = S_{\text{Lilley}} (\bar{x}, t) \qquad (12)$$

The problem with (12), however, is that it is not so easy to estimate S_{Lilley} from the full equations

of motion. Lilley however, does show the following. Assume: (i) that the mean flow is at constant static pressure, (ii) that we are dealing with an inviscid, non heat conducting gas of constant specific heat ratio γ without any externally imposed heat, mass or momentum sources, (iii) that we decompose all field variables into a steady and fluctuating part, e.g., $u_i = \bar{u}_i + u'_i$, where an overbar denotes a time average or steady part (also let r denote log (p/p_0) where p_0 is a reference pressure and c the local speed of sound), (iv) that the mean flow is unidirectional and depends only on one transverse coordinate x_2, i.e., $\bar{u}_i = V(x_2)\,\delta_{1i}$, (v) that whenever second order products of fluctuating quantities such as $r'u'_i$, r'^2, $(c^2)'u'_i$, $(c^2)'r'$ appear they are neglected (however second order velocity products scch as $u'_i u'_j$ are retained), (vi) that $\bar{c}^2$ is only a function of x_2. Then subtracting the time averaged portions of the equations of motion from the full equations of motion (using the six assumptions previously listed) and letting $\bar{D}/\bar{D}t$ stand for the operator

$$\left\{ \frac{\partial}{\partial t} + V(x_2)\,\frac{\partial}{\partial x_1} \right\}$$

Lilley shows that one can develop an equation of type (12) as under:

$$\frac{\bar{D}^3(r')}{Dt^3} + 2\,\frac{dV}{dx_2}\,\frac{\partial}{\partial x_1}\left(\bar{c}^2\,\frac{\partial r'}{\partial x_2}\right) - \frac{\bar{D}}{\bar{D}t}\,\frac{\partial}{\partial x_i}\left(\bar{c}^2\,\frac{\partial r'}{\partial x_i}\right) = -2\nu\,\frac{dV}{dx_2}\,\frac{\partial^2(u'_2 u'_k)}{\partial x_1 \partial x_k} + \gamma\,\frac{\bar{D}}{\bar{D}t}\,\frac{\partial^2(u'_i u'_j)}{\partial x_i \partial x_j} \qquad (13)$$

From this point on, Lilley's equation (13) is followed through in terms of application to jet noise in a manner similar to Lighthill's equation. The quantity r' for small values of p' relative to p_0 may be shown to be equal to (p'/p_0) and taking u'_i on the righthand side of (13) to be the known, solenoidal, turbulent velocity fluctuations, (13) provides an inhomogeneous Orr-Sommerfield equation for (p'/p_0) much as Lighthill's theory provides an inhomogeneous uniform, homogeneous, stationary medium wave equation. (13) may also be written in a form slightly more convenient for the hot jet noise problem as (taking r' to be p'/p_0 and taking p_0 to be the ambient pressure):

$$\frac{1}{\bar{c}^2}\,\frac{\bar{D}^3 p'}{\bar{D}t^3} - \frac{\bar{D}}{\bar{D}t}\,\nabla^2(p') - \frac{d}{dx_2}\log(\bar{c}^2)\,\frac{\bar{D}}{\bar{D}t}\left(\frac{\partial p'}{\partial x_2}\right) + 2\,\frac{dV}{dx_2}\,\frac{\partial^2 p'}{\partial x_1 \partial x_2} = \overline{\rho}\,c^2(x_2)\left\{\frac{\bar{D}}{\bar{D}t}\,\frac{\partial^2(u'_i u'_j)}{\partial x_i \partial x_j} - 2\,\frac{dV}{dx_2}\,\frac{\partial^2(u'_2 u'_k)}{\partial x_1 \partial x_k}\right\} \qquad (14)$$

It is clear that Lilley's equation (14) also exhibits "self noise" and "shear noise" (proportional to dV/dx_2 in (14)) terms on the righthand side. But (as discussed in more detail in Reference 27), the relationship between the "shear" and "self" noise terms in (14) is quite different than that in the case Lighthill's equation (4) and, as a result, it turns out to be far less profitable or necessary to differentiate between them for a development based on Lilley's equation (14) than for one based on Lighthill's equation (4).

It is true that several assumptions have to be made in arriving at (14). But granting the validity of these assumptions, a source term is obtained in (14) which is purely quadratic in the fluctuating velocities, unlike Lighthill's equation (or Phillip's equation - Reference 21 - which was a predecessor to Lilley's equation). While there is no doubt that Lighthill's equation is exact and thus contains, in principle, all the physics of jet noise (but then so do the full equations of motion), it also seems that precisely because intuitive estimates of source terms are ultimately involved, Lilley's development is better tailored to the high speed, high temperature jet noise problem. It is, however, only proper to note its limitations. It neglects jet spread by assuming a parallel, sheared flow. It assumes the jet flow to be at constant static pressure. With multielement suppressors under static conditions significant variations of "base" pressure occur thus making the constant static pressure assumption questionable. Despite the fact that the neglect of terms is carried out systematically (assumption (iv)), it is true that Lilley's development assumes fundamentally that jet mixing and jet noise is a process that can be regarded as a small perturbation about a parallel, sheared flow. Since fluctuating velocities as high as 40% of the local mean velocity are common and even local flow reversals can occur in jet flows, a "small perturbation" assumption can clearly be questioned. It is not as easy to solve Lilley's equation as it is to solve Lighthill's equation. Especially we must note that it is almost impossible to solve Lilley's equation when the jet cross section is not axially symmetric (as.e.g., would be the case for a rectangular jet or a daisy nozzle, etc.)

A final objection to Lilley's equation arises from the fact that it is an inhomogeneous Orr-Sommerfield equation. Since there are unstable solutions to the homogeneous Orr-Sommerfield

equation, it is clear that even without any "sources" (12) can yield solutions that yield acoustic radiation in the far field. (This is one advantage of Lighthill's equation (4), namely that the only solution to the homogeneous equation $\partial^2\rho/\partial t^2 - a_0^2\nabla^2\rho = 0$ satisfying the radiation condition of outgoing waves in the far field is the trivial solution $\rho \equiv 0$.)

While this difficulty with Lilley's equation is still a matter of controversy, the present author believes (along with several others to be mentioned shortly) that since Lilley's approach could be regarded as a passive analogy approach similar to Lighthill's, there is no need to avoid using it on the basis of the possibility of unstable solutions to the homogeneous Orr-Sommerfield equation.

The motivation to use an equation of the Lilley type is that several authors (References 25-28) have shown that practically all the previously cited discrepancies between the Lighthill theory and experimental data can be resolved if we systematically account for acoustic-mean flow interactions on the basis of an equation of Lilley's type. Indeed exactly how one accounts for the acoustic mean flow interaction seems less important than recognizing the need to account for it. For example, in Reference 27 the accounting was carried out in the crudest possible manner by taking the jet to be a plug flow and yet reasonable agreement was obtained with the data of Lush, Ahuja-Bushell, except at high frequencies and shallow angles to the jet axis. In Part II of Reference 27, it was pointed out that per equation (14) compact velocity quadrupoles can couple with mean density gradients (which exist in heated jet flows) to produce lower order singularities (whose power scales as U^4 and U^6 and which are hence important only at low jet velocities). With some rough estimates of these density gradient terms, good agreement was obtained with the heated jet data of Hoch, et al not only for density exponents for the OAPWL but also for those for the OASPL at various angles to the jet axis including agreement on the feature of the measured data that the relative power spectrum is biased towards lower and lower frequencies as one heats the jet.

In concluding this section, it is hard for the present author to suppress the feeling that inclusion of acoustic-mean flow interactions has proved to be a major step in bringing jet noise theory into much closer agreement with reality. It seems to be a step that completes and complements the Lighthill picture. The relative success of these studies (References 25-28) suggests that one need not necessarily invoke substantial jet Mach number, jet temperature effects on the dynamics of the turbulence structure to explain the changes in jet noise with velocity and temperature. It should be reiterated that the developments of References 24-28 have in fact retained all the key ideas of the Lighthill theory. The two most important of these ideas are the idea of identifying the "residual" from a standard wave equation as the source term for jet noise and the recognition of the convected, compact, quadrupole nature of the eddies.

25.5 The Prediction of Jet Noise from Nozzles with Arbitrary Upstream Stagnation Pressures and Temperatures

The procedure that is currently favored by several groups is indicated in Figure 13. Some scheme of mixing analysis (almost invariably based on an eddy viscosity type model) is used to derive the evolution of the mean velocity and temperature of the jet plume downstream of the nozzle exit plume. A scheme that is favored by the group that the present author is associated with is based on Reichardt's inductive theory of free turbulence (Reference 29). Reichardt's theory is undoubtedly considered simplistic by many workers in the turbulence modeling area but we have found that because the governing equation in Reichardt's theory is linear (for the axial momentum and enthalpy fluxes), it is the only technique that allows construction of quite complex jet flow fields with relatively simple mathematics. This capability is rather important since we need a capability to handle flow fields from complex nozzle shapes such as dual flow systems, lobed nozzles, etc.

Having mapped the jet plume in terms of the mean velocity and mean temperature, the jet is broken up into a large number of elemental volumes. Similarity arguments essentially derived from relationships suggested in Reference 11 are next used to associate a quadrupole strength, quadrupole convection velocity, quadrupole self oscilla- frequency ω_0 and a source spectrum (peaked at ω_0) with each such volume. As an example, Reference 11 shows by measurement that ω_0 is proportional to dV/dr for round jets (where r is a radial coordinate). The local mean velocity and mean temperature profile at the axial station where the elemental volume is located are used in the acoustic theory of Reference 28 (based on Lilley's equation (14)) to obtain the far field SPL spectrum generated by each elemental volume. Summing up all the elemental volume contributions in a mean square sense (i.e., treating the jet, as suggested by Lighthill, as a large assemblage of uncorrelated elemental generators), the total far field SPL spectrum is obtained. Note that the method considers analytically all aspects of the jet noise problem known to be important viz evolution of the mean properties of the plume, relevant quadrupole parameters such as convection velocities, source frequencies, etc., and the influence of the jet flow and temperature profiles on the radiation by the eddies. Some empirical constants are undeniably involved, especially in the mixing analysis and relation of quadrupole

parameters to the mean flow properties but the end result is a prediction of absolute sound pressure levels in various third octave bands at any angle and radius in the far field given the nozzle exhaust geometry and distribution of temperature and velocity at the nozzle exit plane. A block diagram of how such a calculation would proceed is shown in Figure 14.

In Reference 30, absolute predictions of noise for coaxial jets with both streams cold and for velocity ratios (secondary or fan stream to primary or core stream) ranging from 0 to 1 and area ratios ranging from 2.1 to 43.5 were carried out by a simpler version of the above scheme and good agreement with data was obtained. (One example of a case of a hot core stream was also predicted well.) A more sophisticated version of Reference 30 is scheduled to appear in Reference 31 with extensive theory data comparisons for conical nozzles, dual flow systems of the duct burning turbofan type (with fan stream temperatures and velocities greater than those of the core stream) conical nozzles with central plugs, variations of the above with noncoplanar exit planes. Certainly there are discrepancies here and there between theory and data but on the whole, the physics of jet noise seems to be well modified by the procedures outlined in Figures 13 and 14.

25.6 Excess Noise in Jet Flows

The term "excess" noise in the present context clearly has no precise definition. Loosely speaking, it may perhaps be defined as a mechanism that is not in accord with the Lighthill picture of jet noise as due to the mixing of a high velocity stream with the ambient generating convected eddies whose birth and decay produces noise. The present author at least would not include under the heading "excess" noise sources which are completely upstream of the nozzle exit plane such as combustor or turbine noise. The latter are perhaps best described as core noise.

The two most important excess noise mechanisms that have been identified are shock associated noise and lip noise.

Shock associated noise arises with supercritical operation and associated underexpansion of the flow (unless, as previously noted, carefully contoured nozzles are used to avoid underexpansion) leading to shock waves in the flow field aft of the nozzle plane. To avoid confusion, we are not interested here in a notorious shock noise phenomenon known as "screech" discussed by Powell (Reference 32). Screech involves a feedback mechanism and can indeed result in pure tones of very high intensity but fortunately a very high degree of nozzle symmetry and upstream smoothness seems necessary to produce screech. Practical jet configurations especially heated engine flows seem to be free from any significant screech phenomena.

The mechanism by which shocks can produce noise has been known for several years (Reference 33). In a uniformly flowing, homogeneous medium, three linearized unsteady modes of motion can be identified, namely sound waves, shear waves and entropy waves. To first order of smallness, such modes propagate independently of each other but if the flow has very steep gradients in localized areas, even to first order, mode scattering or mode conversion can occur whereby for example a shear wave produces sound and entropy waves, etc. Shocks in the flow obviously create such localized steep gradients in the flow and since turbulence in a flow can be thought of as a superposition of shear waves, it is easy to see that there is a situation of shear wave-shock interaction leading to sound production. (In this context, it is briefly worth noting that Lighthill's theory of jet noise is an example of a second order or nonlinear interaction of a shear wave with itself leading to the generation of sound (see Reference 34). This second order nature of jet noise generation partially helps to explain why jet noise production is by and large such an inefficient process. Objectionable as the noise of jets is, it is worth remembering that the efficiency of jet noise generation for a Mach one jet defined as the ratio of acoustic power to the mean flow kinetic energy power is about 10^{-5}.)

A semi-empirical model for shock associated noise based on shock-turbulence interaction has been developed by Harper-Bourne and Fisher (Reference 35) for round convergent nozzles and has been found to be extremely useful in predicting this component of noise. The physical picture employed by Harper-Bourne/Fisher is shown in Figure 15. As the turbulent eddies convect through the shocks, they generate broad band noise at each encounter. In addition, however, to the extent that the eddy is coherent between two encounters an "interference" spectrum (see Figure 15) will be produced corresponding to a fundamental frequency governed by

$$\frac{L}{V_c} - \frac{L\cos\theta}{c_a} = \frac{2\pi}{\omega}$$

or

$$\frac{\omega}{2\pi} = \frac{V_c}{L\,(1 - M_c\cos\theta)} \qquad (15)$$

where L is the shock cell spacing in Figure 15, V_c is the eddy convection velocity, c_a the ambient speed of sound and $M_c = V_c/c_a$. (Harmonics of the above frequency can also occur but experimental data show a peaking of the shock noise spectrum only at the above fundamental frequency.) For round nozzles, the shock cell spacing actually varies (decreasing as one proceeds downstream) but a good average value to use is $L_{avg} = 1.1\sqrt{M_j^2 - 1}\;D$ where M_j is the ideal jet Mach

number corresponding to the supercritical pressure ratio across the nozzle. Reference 15 also discusses by a combination of physical insight and data examination several remarkable simplifying features of shock associated noise such as:

(1) The overall level (OASPL) is independent of jet temperature and depends only on the shock strength parameter $\beta = \sqrt{M_j^2 - 1}$. In fact, the dependence on β is as β^4.

(2) The OASPL is relatively omnidirectional and a good equation for the OASPL that fits the data quite well is

$$OASPL = 158.5 + 40 \log_{10}(\beta) + 20 \log(D/R)$$

in dB where D is the nozzle size and R the radius of measurement.

(3) The peak frequency of the spectrum is a function of eddy convection velocity, ambient speed of sound, β and D and should be deduced from (15) using $L = 1.1 \beta D$. In Reference 35, a value of $0.7 U_j$ is suggested for U_c.

It only remains (for the static round nozzle shock noise problem) to discuss the spectrum of shock noise. The author's colleague, Mr. P. R. Gliebe has found that a suggestion of Reference 36 that the third octave pressure levels vary as $(\omega/\omega_p)^{-1}$ for $\omega > \omega_p$ (ω_p being the peak frequency already discussed) and as $(\omega/\omega_p)^7$ for $\omega < \omega_p$ works quite well in matching the data.

The prediction procedure outlined previously can then be modified to add on (in a mean square sense) a shock-noise component (as discussed above) to the previously discussed "turbulent mixing" noise.

Lengthy as this discussion of shock noise may seem to the reader, the problem of a generalized shock noise prediction procedure valid for arbitrary nozzles (other than the round convergent nozzle) is as yet unsolved. It should be added that when the above suggested synthesis of "turbulent mixing" and shock noise prediction is carried for round convergent nozzles, not only do we get good agreement with data (Reference 31) but one also finds that for supercritical pressure ratios, shock noise often dominates "turbulent mixing" noise for angles $\theta \geq 90^o$.

Lip noise is a term used to describe a high frequency noise source arising from an unsteady interaction of the flow with the nozzle lip. It has been described at length in Reference 37 but other than the facts that it is high frequency (its length scale being related to thin boundary layers at the nozzle exit plane rather than to the nozzle diameter) and that the baffling effect of the tailpipe causes the directivity of this source to vary as $\sin^2(\theta/2)$ (thus causing it to peak well in the forward arc) not much can be said quantitatively at the present time about how to predict this source.

25.7 Effects of Forward Flight on Jet Noise

The effects of forward flight on jet noise are, at the present time, the least understood area of this subject. Indeed the situation is so unclear that by and large the technical debate at the current time centers much less on what causes the flight effect and much more on questions such as what is the flight effect and how it should be experimentally evaluated.

An extension of the Lighthill theory of convected point quadrupoles through a stationary ambient to account for flight effects was given by Ribner (Reference 13) and Ffowcs Williams (Reference 38). This theory gave a result that the flight noise for a jet moving forward at a Mach number (referenced to the ambient speed of sound) of M_F would differ in three respects from the equivalent static problem. First of all, the velocity dependence of the "source" contribution would be as $V_r^7 V_j$ where V_j denotes the jet exhaust velocity relative to the nozzle and V_r the absolute velocity relative to the ambient ($V_r = V_j - V_F$ where V_F is the flight velocity). The dependence is not quite as V_r^8 because while the turbulent velocities would vary as V_r rather than V_j, a lengthening of the jet plume due to forward motion partially offsets the reduction of turbulent velocities. It should be emphasized that issues such as the above involving source changes can only be ultimately resolved by measurement and credible turbulent mixing analyses. (By different assumptions, for example, some have argued that the velocity dependence ought to be $V_r^{5.5} V_j^{2.5}$, etc.) Secondly, the convection factor $(1 - M_c \cos\theta)^{-5}$ (or its corrected version including the $\alpha^2 M_c^2$ term) ought to be the same provided M_c is based on V_r rather than V_j. Thirdly, an additional "dynamic" correction factor $(1 + M_F \cos\theta)^{-1}$ needs to be applied to the mean square pressure.

These results have been applied to the static to flight comparison in the following manner. Examining say the OASPL, an exponent $n(\theta)$ as a function of θ is derived on the basis of fitting the noise change flight/static as $(V_r/V_j)^{n(\theta)}$. The sort of comparison that has been obtained for the noise levels themselves (i.e., the OASPL) is shown in Figure 16. There is some measure of agreement in the exhaust arc but for $\theta \geq 90^o$, the agreement is poor. For example, the theory predicts a reduction of noise with flight at all angles whereas the data show no change at 90^o and even an increase of noise for $\theta > 90^o$ (sometimes called a "forward arc lift"). The reasons for this lift are too controversial at the present time to discuss without misleading the reader. There seems to be some agreement (Reference 39) based on careful

measurements of the noise in flight from jets with shocks and from shock free jets that the previously mentioned shock noise prediction for the static noise should be modified in flight by a factor $(1 + M_F\cos\theta)^{-4}$ and such a procedure certainly reconciles some of the problems shown in Figure 16. (Note that the Ribner-Ffowcs Williams development of References 13 and 38 was carried out for "turbulent mixing" noise.) The only broad comment that one can make presently is that many people currently believe the forward arc lift to be due to non "turbulent mixing," nozzle fixed noise sources such as shock noise, lip noise and perhaps even core noise which are not subject to a "source reduction" due to forward flight and are convectively amplified in flight by factors stronger than the $(1 + M_F\cos\theta)^{-1}$ associated with the Ribner-Ffowcs Williams theory for "turbulent mixing" noise.

There is even the question of how one ought to measure flight noise. Of the truly moving frame facilities, the Bertin Aerotrain used in Reference 39 appears to be the "cleanest" but it lacks flexibility being tied to specific engine operating cycle points in terms of jet exhaust velocity, temperature and flight speed. Anechoic wind tunnels such as the 40' by 80' tunnel at NASA, Ames, U.S.A., have been proposed but their acoustics leaves something to be desired. (See Reference 40 for an evaluation of suitable techniques for jet noise measurement in flight.) A fixed frame facility which is a compromise between a fully wetted wind tunnel (such as the Ames tunnel) and a static anechoic chamber is what has been called a free jet facility or open throat wind tunnel. How to relate data taken in such a facility to the flight case is still controversial.

The flight noise problem is of paramount importance principally because a jet noise suppressor is often rated on the basis of the noise reduction it achieves relative to say a baseline round nozzle and also on the aerodynamic performance degradation that it inevitably causes. Unfortunately, it appears that on both these counts many suppressors perform worse in flight than statically. Indeed, this is the principal reason why while aircraft employing engines not dominated by jet noise (such as the DC-10, L1011 and Boeing 747) have made significant progress in noise reduction, one is unable to report similar progress in the jet noise dominated engine area.

It must indeed seem disappointing to the reader that the present chapter has not been able to be as conclusive in the flight noise problem as it was on the static noise problem. Even in the static case, a grave omission exists in the present review in that no mention has been made so far of a topic of great current interest, namely the role of large scale, coherent structures observed in jet flows in jet noise generation. The principal reason is again that, from the point of view of the industrial user, it is not yet clear what the role of these structures is and how their contribution can be quantitatively assessed. The reader is urged to consult Reference 41 for several interesting papers, discussion, etc., on this subject.

Despite the pessimistic tone of the discussion of flight effects, the present author is optimistic that the physics of jet noise outlined in this review for the static case involving "turbulent mixing" noise, shock noise, excess noise, etc., will carry over ultimately into the flight case (with prediction procedures comparable to the static case) though the "mix" or relevance of the various physical features may be quite different for the flight case. In one respect, the void is hardly surprising. Inasmuch as it took the good quality static jet noise data obtained in the early seventies (References 7, 8, 9) to advance the state-of-the-art from Lighthill's early work, we must, it seems, await similar good quality data over wide parameter ranges in the flight case before the next advance can occur.

25.8 Acknowledgments

I am very deeply indebted to my associates T. F. Balsa and P. R. Gliebe of the General Electric Company, U.S.A., for the benefit of innumerable discussions, joint activities, etc., in the area of jet noise. P. R. Gliebe provided me with an invaluable summary of the Harper-Bourne/Fisher procedure of shock noise prediction. Over the years my participation in two U.S. government sponsored programs, contracts F33615-73-C-2031 (USAF/DOT) and DOT/FAA OS-30034, have greatly aided my understanding of jet noise. I have been privileged to discuss the matters discussed in this chapter with several authorities in jet noise many of whom have been cited herein. No one, it need hardly be said, agrees with or endorses all my views in an area as intricate as jet noise.

25.9 References

1. Lighthill, M. J., 1952, Proc. Roy. Soc. A, 211, p. 564.

2. Lighthill, M. J., 1954, Proc. Roy. Soc. A, 222, p. 1.

3. Lighthill, M. J., 1963, AIAA Journal, 1 (7), p. 1507.

4. Ribner, H. S., 1964, Adv. Appl. Mech., 8, p. 103.

5. Ffowcs Williams, J. E., 1969, Ann. Rev. Fluid Mech., 1, p. 197.

6. Ffowcs Williams, J. E., 1975, Lectures on Aerodynamic Noise, AIAA Short Course, Hampton, Virginia, U.S.A.

7. Lush, P. A., 1971, J. Fluid Mech., 46, p. 477.

8. Ahuja, K. K. and Bushell, K. W., 1973, J. Sound Vib., 30, p. 317.

9. Hoch, R. G., et al, 1972, J. Sound Vib., 28, p. 649.

10. Clapper, W. S., et al, 1976, AIAA Paper 76-532.

11. Davies, P.O.A.L., et al, 1963, J. Fluid Mech., 15, p. 337.

12. Ffowcs Williams, J. E., 1963, Phil. Trans. Roy. Soc., London A, 255, p. 469.

13. Ribner, H. S., 1962, UTIAS Report No. 86.

14. MacGregor, G. R. et al, 1973, J. Sound Vib., 27(4), p. 437.

15. Olsen, W., 1974, AIAA Paper 74-43.

16. Hoch, R. G., et al, 1972, J. Sound Vib., 28, p. 649.

17. Bushell, K. W., 1971, J. Sound Vib., 17, p. 271.

18. Tanna, H. K., 1973, AIAA Paper No. 73-991.

19. Ribner, H. S., 1960, JASA, 32, p. 1159.

20. Powell, A., 1960, JASA, 32, p. 1609.

21. Phillips, O. M., 1960, J. Fluid Mech., 9, p. 1.

22. Csanady, G. T., 1966, J. Fluid Mech., 26, p. 183.

23. Mani, R., 1972, J. Sound Vib., 25, p. 337.

24. Lilley, G. M., 1972, AFAPL-TR-72-53, Vol. 4.

25. Berman, C. H., 1974, AIAA Paper 74-2.

26. Tester, B. J., et al, 1974, AIAA Paper 74-57.

27. Mani, R., 1976, J. Fluid Mech., 73, pp. 753 and 779.

28. Balsa, T. F., 1976, J. Fluid Mech., 74, p. 193.

29. Reichardt, H., June 1943, J. Roy. Aero. Soc., pp. 167-196.

30. Gliebe, P. R. and Balsa, T. F., 1976, AIAA Paper 76-492.

31. Gliebe, P. R. and Balsa, T. F., 1977, paper entitled, "Aeroacoustics of Axisymmetric Single and Dual Flow Exhaust Nozzles," to be presented at the forthcoming AIAA/SAE 13th Joint Propulsion Conference, July 11-13, 1977, at Orlando, Florida.

32. Powell, A., 1953, Proc. Phys. Soc. B, 66, p. 1039.

33. Ribner, H. S., 1955, NACA Report No. 1233.

34. Chu, B. T., et al, 1958, J. Fluid Mech., 3, p. 494.

35. Harper-Bourne, M. and Fisher, M. J., 1973, AGARD CP-131, p. 1973.

36. SNECMA Report YKA No. 5982/76, October 11, 1976.

37. Crighton, D. G., 1973, AGARD CP-131, p. 1973.

38. Ffowcs Williams, J. E., 1963, Phil. Trans. Roy. Soc. London A, 255, p. 469.

39. Drevet, P., et al, 1976, AIAA Paper 76-557.

40. Clapper, W. S. (Editor), 1976, Task 4 Final Report under Contract DOT-OS-30034, prepared for the U.S. DOT, FAA.

41. AGARD CP-131, 1973.

25.10 Figures (Over)

25.10 Figures

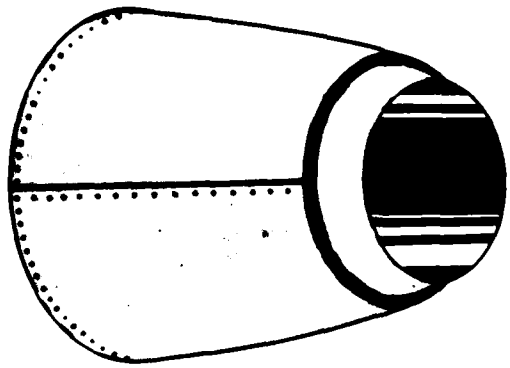

CONICAL
NOZZLE

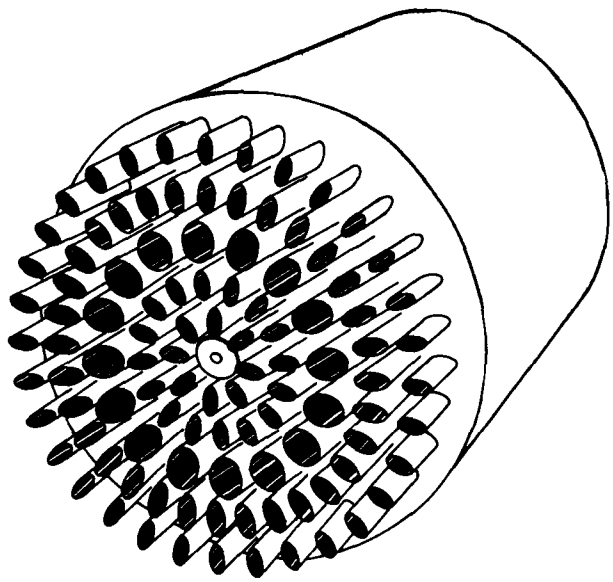

MULTITUBE
NOZZLE

Figure 1: Types of Exhaust Nozzles of Interest

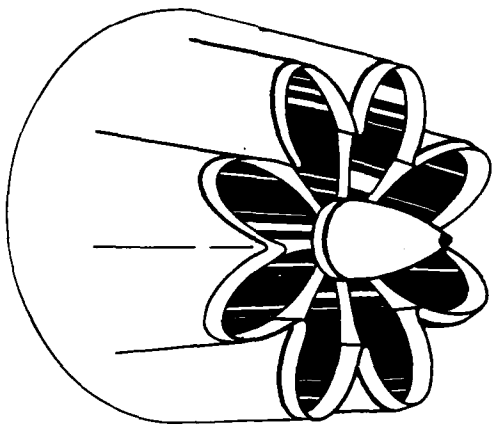

DAISY NOZZLE

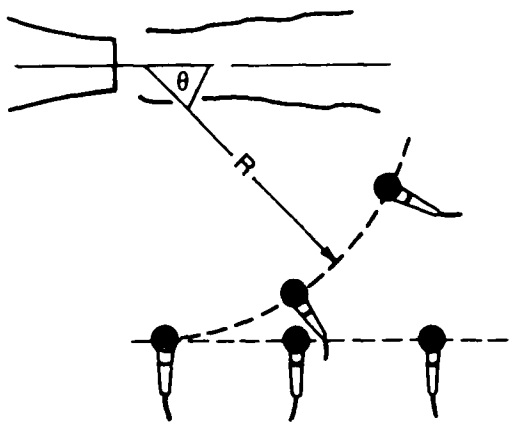

MICROPHONES
ON ARC OR
SIDELINE

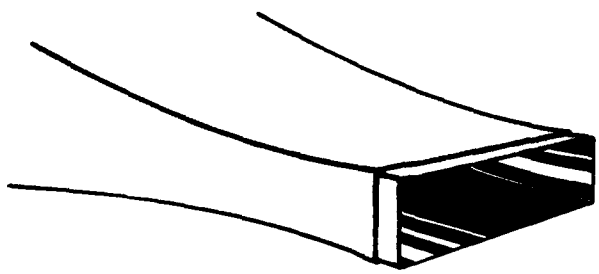

SLOT
NOZZLE

Figure 2: Layout of a Jet Noise Test

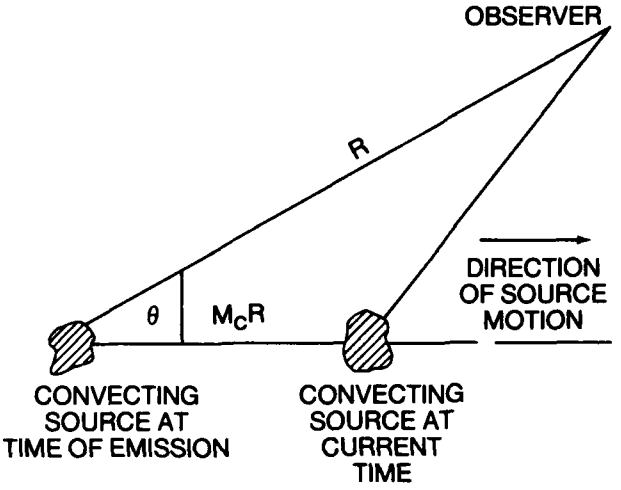

Figure 3: Geometry for "Retarded" Coordinates

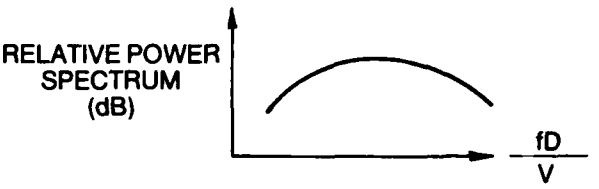

Figure 4: Predictions of Lighthill Theory

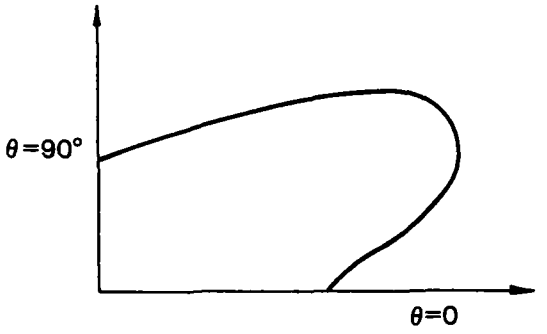

Figure 5: High Frequency Polar Directivity in dB: Subsonic Eddy Convection Velocity

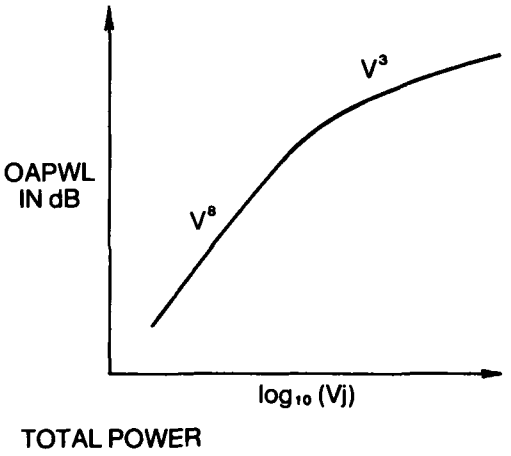

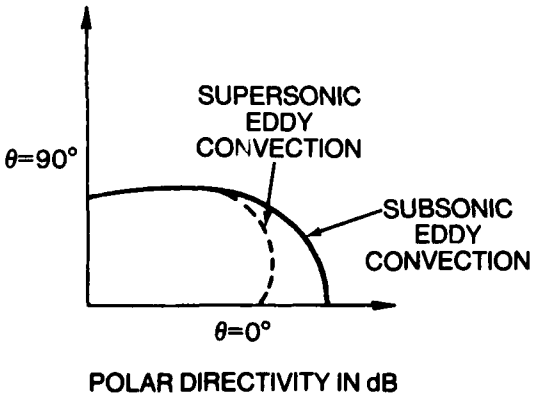

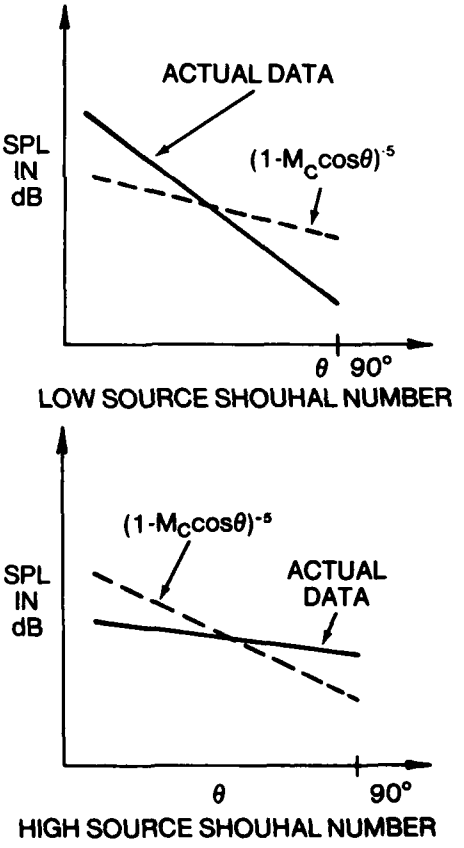

Figure 6: Schematic of Lush's Results

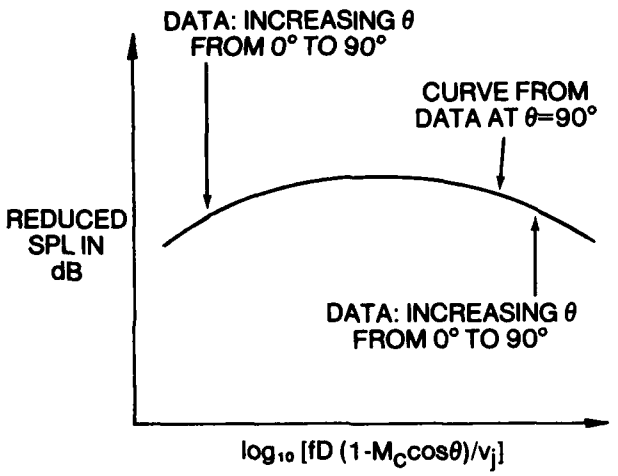

Figure 7: Schematic of Ahuja-Bushell Results

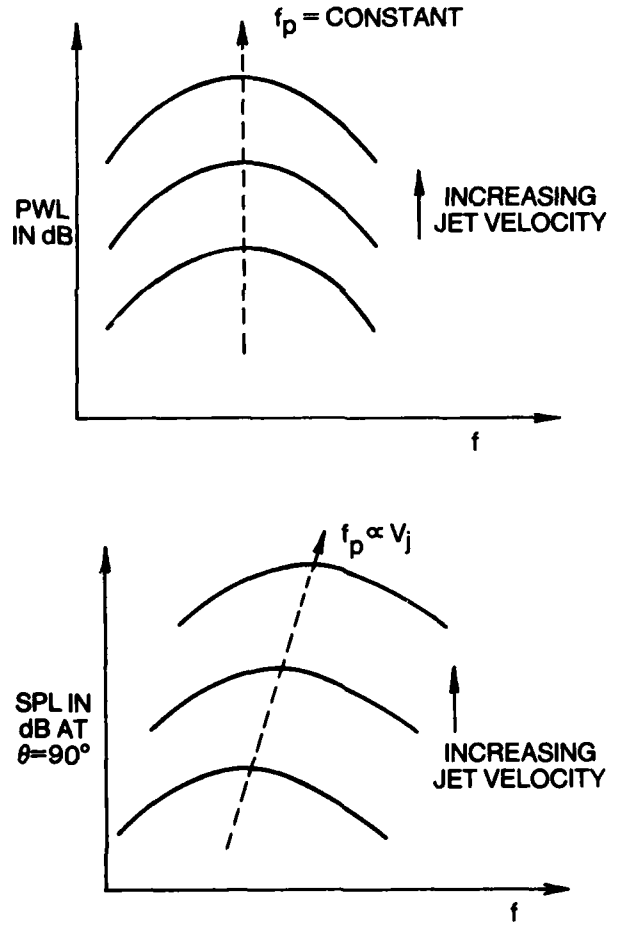

Figure 8: Results of Olsen on Effect of Jet Velocity on PWL and SPL ($\theta = 90^{o}$) Spectra

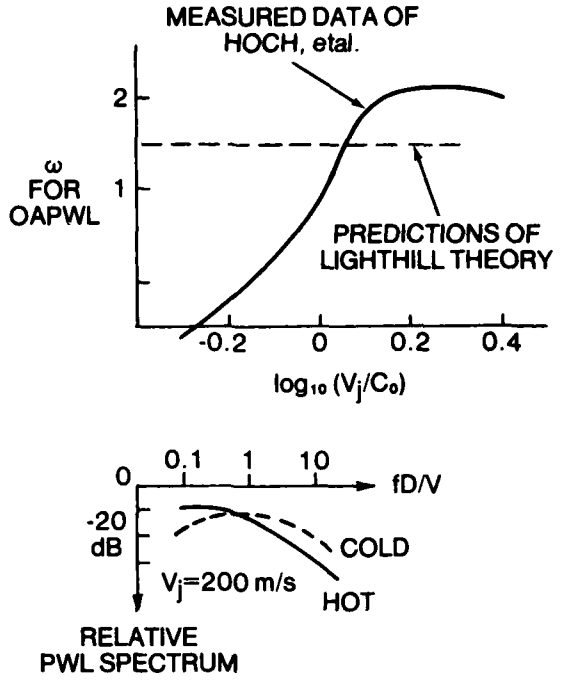

Figure 9: Results of Hoch, et al, on Heated Jet Noise

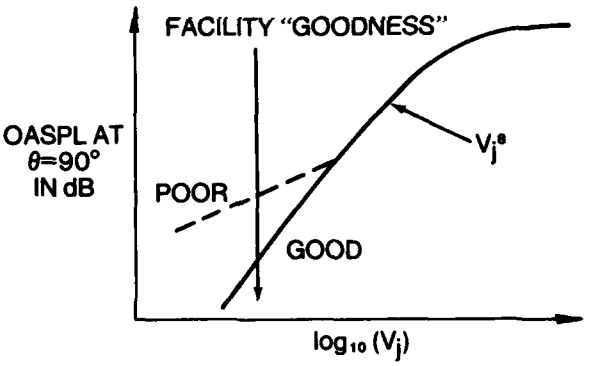

Figure 10: Test of Quality of a Jet Noise Facility

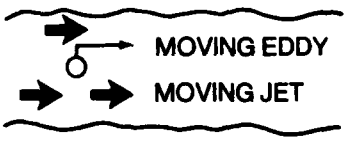

Figure 11: A Moving Eddy in a Moving Jet

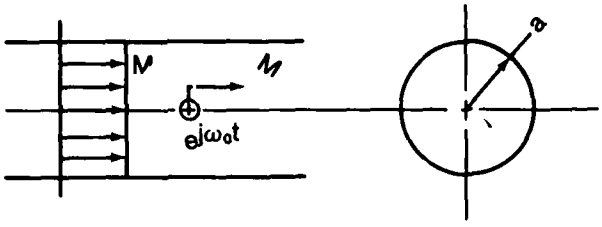

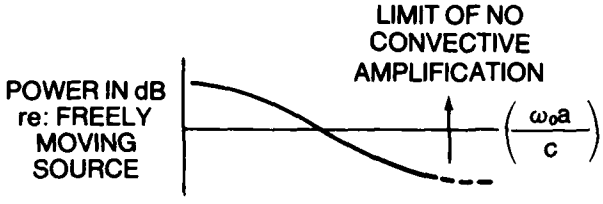

Figure 12: Effect of Jet Flow on Power of a Moving Source

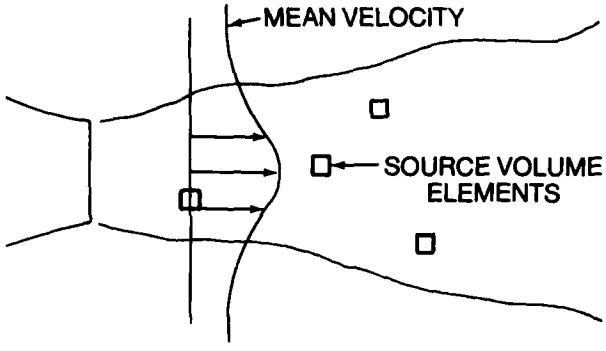

Figure 13: Aero-Acoustic Prediction Method

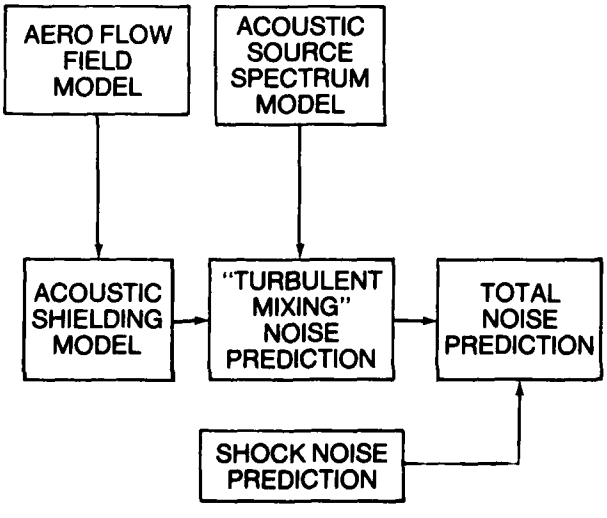

Figure 14: Block Diagram for Noise Prediction

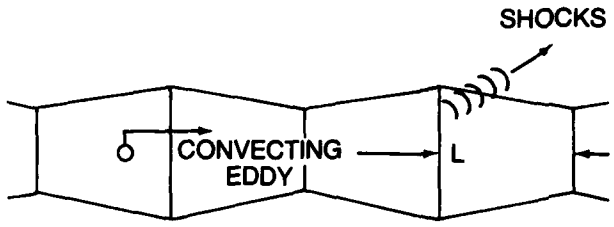

Figure 15: Shock Cell Noise

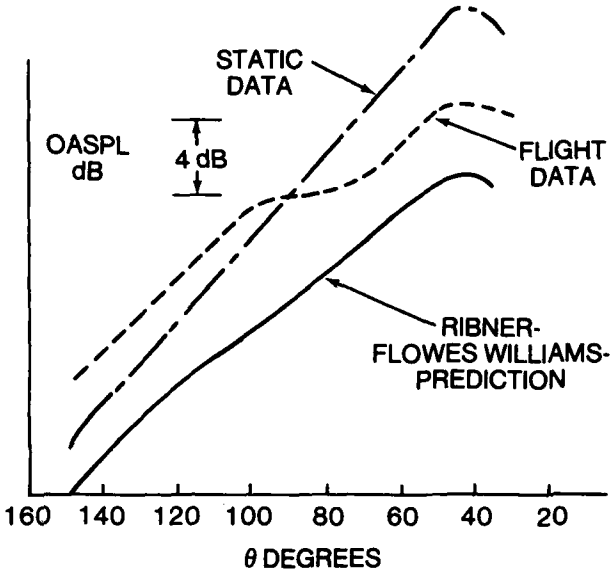

Figure 16: Flight Effects on Jet Noise

Chapter 26

SYSTEMS ASPECTS OF ENGINE INSTALLATION

R. Decher
W. Gillette
J. Koncsek
F. Marshall
R. Ridgeway
V. Salemann

The Boeing Company

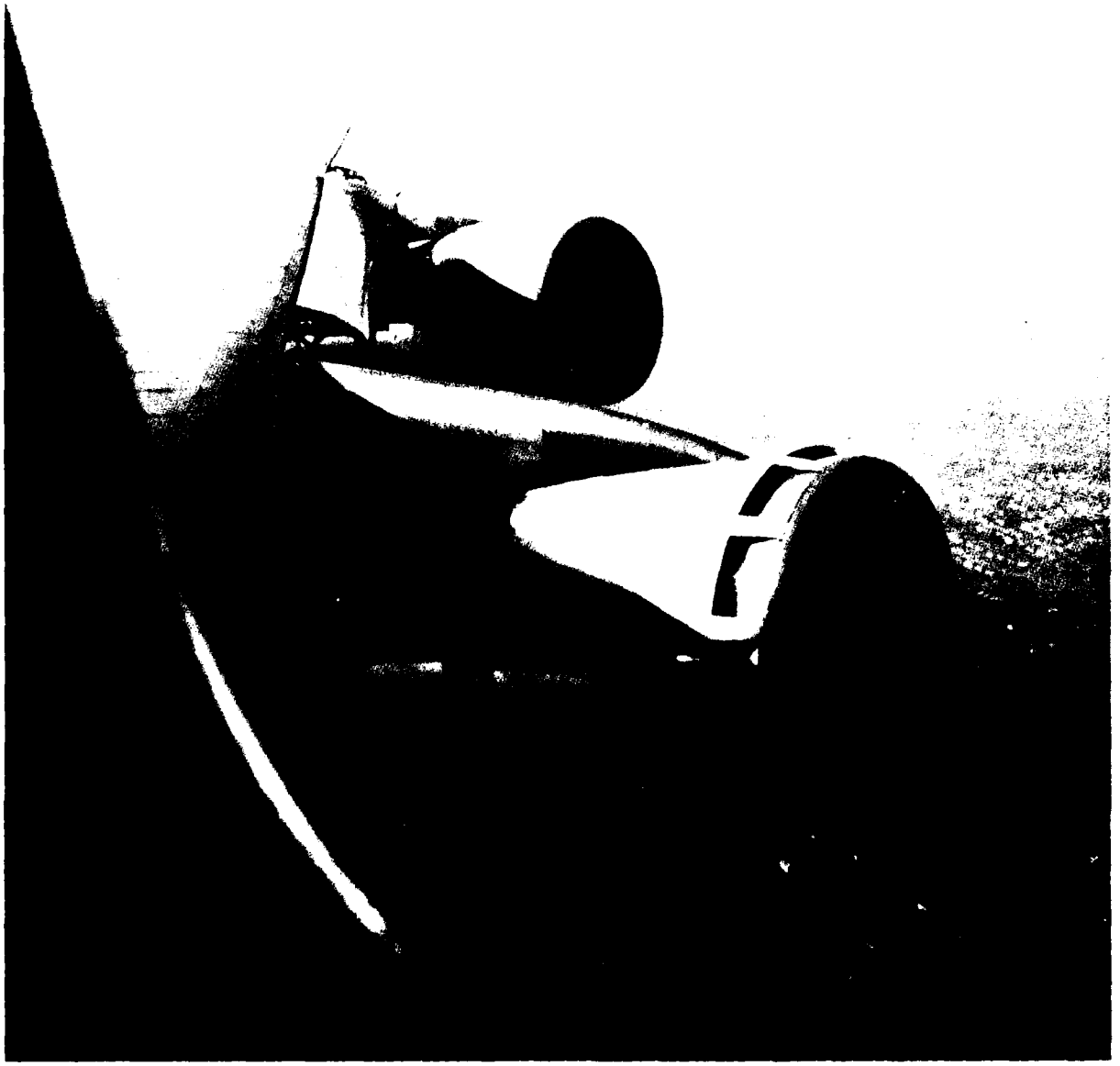

26. SYSTEM ASPECTS OF ENGINE INSTALLATION

This chapter is the work of the propulsion staff of the Boeing Company. The principal contributors were:

R. Decher
W. Gillette
J. Koncsek
F. Marshall
R. Ridgeway
V. Salemann

The chapter was edited by R. Decher. Appreciation is hereby expressed to the many contributors including E. Tjonneland, A.D. Welliver and W.C. Swan who critically reviewed the manuscript.

26. SYSTEM ASPECTS OF ENGINE INSTALLATION

26.0.1 TABLE OF CONTENTS

26.1 INTRODUCTION

1.1 The Airplane Development Problem
1.2 Engine Airframe Interactions
1.3 General Definition of Terms
1.3.1 Time Phasing
1.3.2 Performance
1.3.3 Test Techniques

26.2 ENGINE - AIRFRAME INTEGRATION: INLET AND EXHAUST DESIGN CONSIDERATIONS

2.1 Inlets
2.1.1 Subsonic Inlets
(a) Inlet Sizing
(b) Cruise Aerodynamic Performance
(c) Low Speed Performance
(d) Low Speed Noise Suppression
2.1.2 Supersonic Inlets
(a) Inlet Types
(b) Inlet Engine Airflow Matching
(c) Inlet Sizing
(d) Supersonic Diffuser Design
(e) Boundary Layer Control
(f) Subsonic Diffuser Design
(g) Supersonic Inlet Drag
(h) Concluding Remarks

2.2 Exhaust System
2.2.1 Functional Requirements of the Nozzle
(a) Engine Back Pressure Control
(b) Expansion of Engine Flow
(c) Airframe Related Considerations: Reversers
(d) Control of IR Radiation and Radar Cross-section
2.2.2 Nozzle Internal Performance
(a) Direct Flow Performance
(b) Nozzle Performance Prediction from Empirical Correlations
2.2.3 Airplane/Nozzle External Performance
(a) Analytic Methods
(b) Empirical Methods
(c) External Effects on Internal Performance
2.2.4 Concluding Remarks

26.3 PREDICTION OF AIRPLANE PERFORMANCE

3.1 Wind Tunnel Airplane Modeling
3.2 Force Measurement
3.3 Wind Tunnel Environment
3.4 Specific Test Techniques
3.5 Concluding Remarks

26.4 PERFORMANCE INTEGRATION METHODS

4.1 Element Performance Map Formats
4.1.1 Inlet Performance
4.1.2 Aft End Performance
4.1.3 Airframe and Turbo Machinery Performance: Isolated Components

4.2 Force Accounting Methodology
4.2.1 Summary of Recommended System
(a) General Features
(b) Force Equation
(c) Engine Net Thrust
(d) Inlet Force Increments and Reference Aerosynamic Drag
(e) Exhaust System Force Increments
4.2.2 Reference Exhaust System Conditions
4.2.3 Operating Reference Exhaust System Conditions
4.2.4 Determination of Exhaust System "External Forces"
4.2.5 External Metric Breaks
4.2.6 Element Performance Visibility
4.2.7 Applicability Over Entire Development Program

4.3 Turbopowered Simulator Testing

4.4 Concluding Remarks

26.5 PERFORMANCE VERIFICATION

5.1 Introduction

5.2 Performance Verification Methodology
5.2.1 Thrust Definition
5.2.2 Extrapolation of the Full Scale Engine Data to Flight

5.3 Static Test Facilities
5.3.1 Static Outdoor Test Facilities
5.3.2 Indoor Sea-Level Test Facilities
5.3.3 Indoor Altitude Facilities

5.4 Force Accounting in Static Facilities

5.5 Accuracy

5.6 Wind Tunnel Facilities

5.7 Flight Testing

26.6 UNCERTAINTIES IN THRUST AND DRAG

6.1 Random Error

6.2 Bias Uncertainty

6.3 Concluding Remarks

26.0.2 NOMENCLATURE

The symbols used in this chapter are defined in the text where they are used. Commonly accepted usage of such symbols is made whenever possible.

26.1 INTRODUCTION

A jet propelled airplane is generally developed for the achievement of a specified mission with varying consideration of performance and cost. For military fighter and bomber types of aircraft, achievement of the design mission is often most important. This mission generally consists of elements which include maximum speed or altitude capability, requirements for matching thrust lapse rate with drag and/or requirements for excess thrust for maneuverability over the mission duration. Cost and efficiency considerations generally play a major role during the definition and design of engine and airframe, and a secondary role for the acquisition and operation of the aircraft, where cost is controlled simply by number of aircraft ordered and amount of flying with aircraft on hand. Military and commercial transports require emphasis on efficiency to guide the design of the engine/airplane. The military transport can trade payload for fuel requirements whereas the commercial transport can reduce operating costs when an efficiency improvement is considered. Acquisition and operating cost are of great importance in commercial transports as they control sales relative to competitive designs.

Engine thrust is usually defined in terms of the effective velocity rise of the stream tube captured by the engine. The remaining forces in the flight direction are drag. This division between thrust and drag is made in recognition of the fact that thrust defined this way can be measured in outdoor and altitude facilities and the velocity rise can be "measured" in flight. Drag can be "measured" on a scale model of the airplane. At a particular flight condition, model drag includes adjustments to account for inlet and nozzle effects not properly reproduced on the model and a Reynolds number correction for the airplane drag. The flow field interactions between inlet and airframe, nozzle and airframe or all three for multimission aircraft can introduce large uncertainties beyond those associated with uninstalled inlet and nozzle performance and scale model airplane drag. Thus, engine/airframe interactions introduce performance risk and/or cost penalties and should guide the design of many airplane types. Errors in early estimates of engine-airframe interactions, particularly when insufficient development time was planned, have seriously reduced the effectiveness of certain airplanes.

Early engines were pure turbojets with high specific thrust and small engine capture streamtubes. In addition, the relatively low maximum speed airplanes used inlets with low spillage drag and fixed geometry exhaust nozzles with low boattail angles and little weight penalties.

In modern airplanes, the airframe and engine should be designed simultaneously because of the close matching required. Installation effects may play such a large role that the "right" engine cannot even be identified before the installation effects are understood. The performance predictions for many modern aircraft where insufficient attention was paid to engine installation effects have been generally quite poor when compared to flight test performance.

Another reason for poor performance of initial models of some airplanes is insufficient thrust to compensate for higher weight or drag of the airplane than originally predicted.

At part-power some engine cycles are penalized more than others. This is true because some losses are a function of airflow, others are a function of engine diameter and nozzle exit area and still others a function of gross thrust. At equal net thrust, the airflow, engine size, nozzle exit area and gross thrust of engines of various cycles can cause differing installation losses. It is therefore likely that if installation losses had been known earlier in the program, a different engine cycle might have been selected.

26.1.1 The Airplane Development Problem

From the time mission requirements are specified to the time of production, the uncertainty associated with airplane weight and drag decreases. The engine design may be frozen at times where these uncertainties remain sizable in order to meet the system development time goals. Figure 26.1.1-1 shows an example of the airplane and engine development timing. The most significant engine milestones are shown in relation to airplane development milestones. The drag and weight uncertainties are shown at the bottom of the figure. It is important to plan the development schedule so that when the engine design freeze occurs, a pessimistic interpretation of the uncertainties is acceptable.

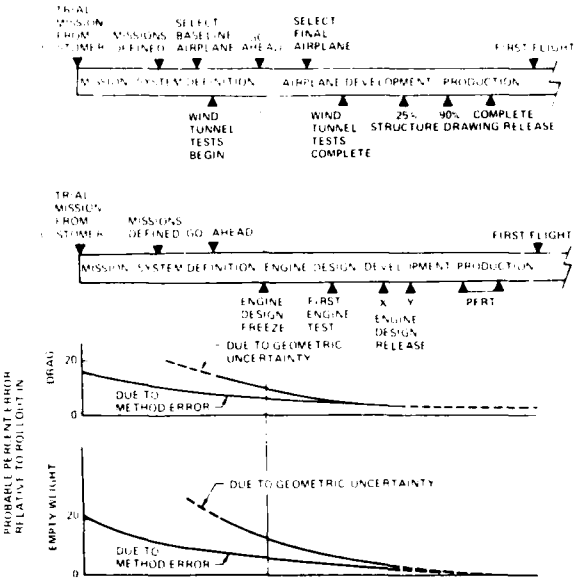

Figure 26.1.1-1. Typical Engine/Airframe Development Schedule

26.1.2 Engine Airframe Interactions

For purposes of analysis and discussion of the flow field interactions which may occur in the engine-airframe integration problem the airplane system is broken into four major elements and two subsystems as shown in Figure 26.1.2-1.

In the sketch, the interactions are shown as arrows, indicating that a change in the inlet, for example, influences both engine thrust and airplane drag.

Inlet Characteristics

For the airplane, the inlet's external performance is important in that the mass flow rate demanded by the engine may vary, effecting the pressure distribution on the body, and thus drag. For the engine the inlet should provide uniform flow at as high a stagnation pressure as possible. Excessive turbulence level and distortion at the fan or compressor face usually demand an increased surge margin which translates into a heavier engine for a desired thrust level. Stability of the flow through the inlet in the presence of flow changes is necessary within the operating envelope of the airplane.

Secondary factors which may influence the design of specific inlets have to do with radar

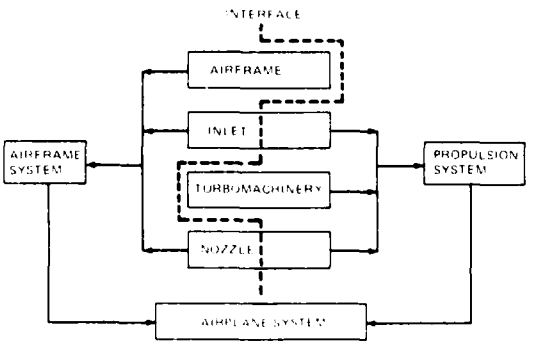

Figure 26.1.2-1. Airplane System Elements and Subsystems

reflection characteristics of the airplane as a whole.

Nozzle Characteristics

The nozzle's function is to expand the engine's exhaust air to a lower pressure to produce a high momentum jet for thrust. The nozzle, like the inlet, has internal and external surfaces. The nozzle's flow area and exit area are generally tailored to maximize the net installed thrust. Some of the conditions which may be of interest for thrust will demand excessive closure rates on the flow around the afterbody or boattail, leading to flow separation and a drag increase. The danger of flow separation is particularly severe and sensitive to operating parameters in the case of twin engine airplanes with side by side nozzles. The flow in the channel between the engines is sensitive to the airplane body's boundary layer, which, in turn, depends on airplane attitude and speed.

Engine performance may not be sensitive to the external flow for engines operating with choked nozzles. For low pressure ratio jet flows like that from turbofan engines, the interactions are greater but important primarily during take-off and climb. The challenge to achieve a successful turbofan installation is to locate the nacelle by means of struts so that a minimum interference drag penalty at cruise is incurred.

For such engine installations, the drag associated with the transonic flow between wing/strut and nacelle must be clearly discernible from external-flow-induced changes in thrust so that proper corrective action can be taken. Furthermore, in any airplane system, the performance shortfall should be assignable to engine or airframe performance deficits.

A more severe interaction situation arises in the design of STOL aircraft where thrust is used for lift as in upper surface blowing and blownflap nacelles (Figure 26.1.2-2). Wind tunnel testing of such airplanes requires modeling of the airframe flow field as well as propulsion flow. The large flow deflections of lifting propulsion systems require a large wind tunnel cross sectional area to model-size ratio and perhaps a moving ground plane for adequate simulation. This requirement has forced the testing to small model sizes where the scale mismatch is severe or to testing in large costly facilities. Integration effects are therefore not understood with great accuracy at present (Reference 26.1.2-1).

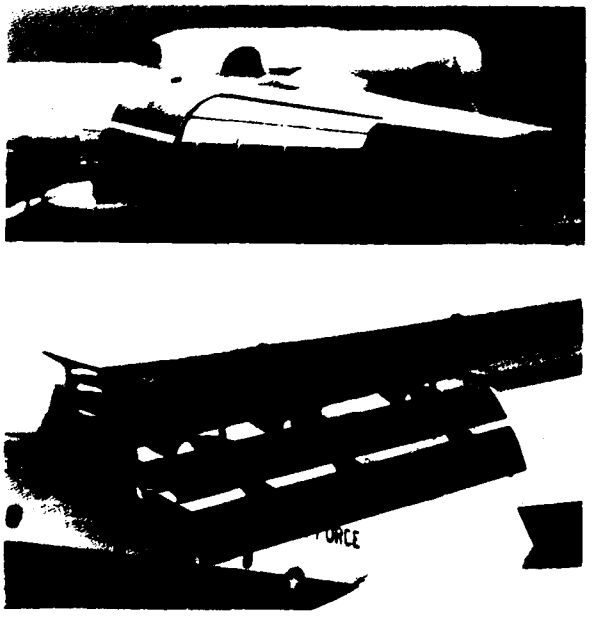

Figure 26.1.2-2. Propulsion Nozzles Integrated Into Airframe Boeing YC-14 (Top), McDonnell-Douglas YC-15 (Bottom)

The uncertainty characteristics of thrust and drag of transonic and supersonic airplanes tend to be as shown in Figure 26.1.2-3.

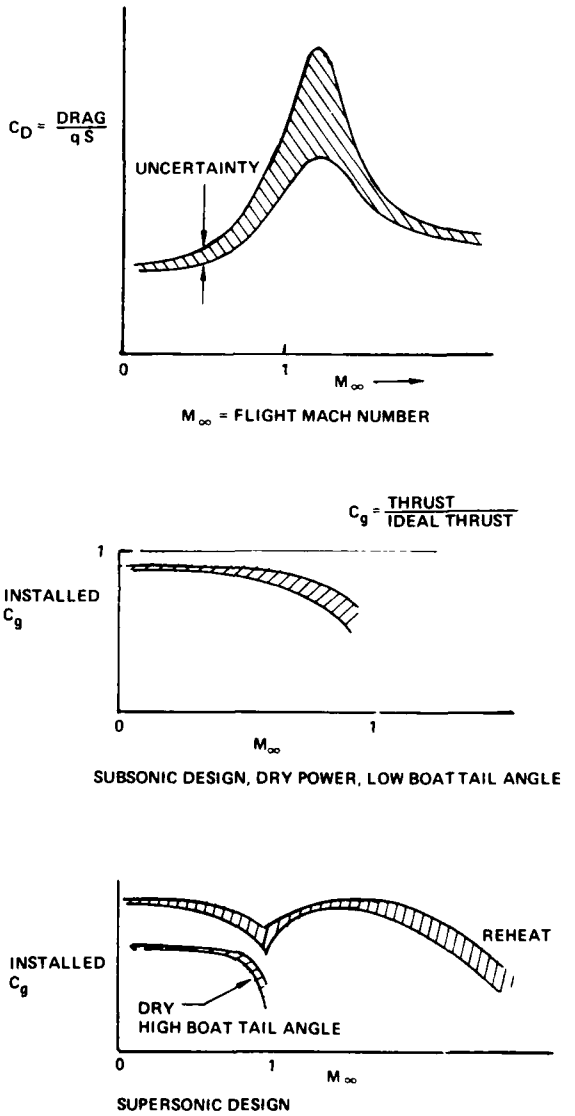

Figure 26.1.2-3. Uncertainty of Thrust and Drag in Transonic and Supersonic Flight

For VSTOL aircraft, the uncertainty bands are even larger throughout their speed range.

In the following sections, the design and characteristics of inlets and nozzles, the airplane drag buildup technique, and performance verification techniques are discussed. The sources of uncertainty in thrust and drag and methods for minimizing their impact are described in the last section.

26.1.3 General Definition of Terms

The following definitions or descriptions of many of the major terms used in this chapter are necessary for an understanding of the integration and cycle selection process. For convenience, the terms are grouped under several general headings to which they best apply.

26.1.3.1 Time Phasing

- Phase - A time sequence in an aircraft development process characterized by specific types of requirements and activities.
- Conceptual Design Phase - The earliest portion of the development process, beginning with the Required Operational Capability (ROC) definition, and proceeding up to the point of selection a general aircraft and propulsion system to satisfy the general ROC requirements.
- Preliminary Design Phase - The period where the general concepts are narrowed to a specific configuration.
- System Development Phase - The period where the design of the selected aircraft configuration is validated, the propulsion system component tests are run, and the engine testing is conducted. A system flight test program is also included in this phase.

26.1.3.2 Performance

- Levels - The state of the technology or degree of sophistication for determining system performance at the various stages of the development process representative of data accuracy.

  Level I - Historical data and analysis; little geometric data needed. The most elemental of performance prediction techniques used for conceptual design.

  Level II - Semiempirical and analytical predictions using a representative (though not necessarily exact) configuration of the system. Final aircraft guarantees are based on such predictions.

  Level III - Scale model or component rig data of the actual configuration being developed. This is a verification of the Level II predictions used in the aircraft guarantees.

  Level IV - Flight test and engine test data of the configuration being developed.

- Elements - Key portions of the overall system for which individual performance maps are obtained. The elements are: airframe, inlet system, exhaust system, and turbomachinery.
- Maps - Plots of the performance of the various elements over the full operating range.

  (1) Aircraft - usually in the form of drag polars (C_L versus C_D).

  (2) Inlet - examples are inlet drag versus mass flow ratio and Mach number; pressure recovery versus mass flow and Mach number.

  (3) Exhaust Nozzle - an example is aft-end drag coefficient versus aft-end area ratio and Mach number, possibly modified for plume shape effects.

  (4) Turbomachinery - examples are thrust and specific fuel consumption as a function of Mach number, altitude, and power setting.

- Target Performance - Performance which may not have been demonstrated, but is deemed achievable.
- Demonstrated Performance - Performance which has been verified by test.
- Figures of Merit - Those parameters used to assess the performance or usefulness of one system relative to another. Examples are takeoff gross weight, range for a given payload, life cycle cost, etc.

26.1.3.3 Model Testing

- Aero Force and Moment Model - A wind tunnel model that defines the basic airframe aerodyanmic information.
- Inlet Effects Model - The wind tunnel model used to measure inlet drags to correct the force and moment model performance to operating inlet flight conditions.
- Jet Effects Model - The wind tunnel model used to measure aft-end performance to correct the force and moment model performance to operating aft-end flight conditions.
- Metric Splitlines - Model boundaries which separate those portions of the model which have forces measured on force balance (metric) from those not measured (nonmetric).
- Aerodynamic Reference Condition - A full-scale aircraft configuration and the propulsion flow conditions to which all $-C_D$'s are related during the drag buildup. In general, this condition is chosen either for the ease with which the drag may be calculated in an analytic buildup or for the ease with which it may be measured in an experimental buildup. If an experimental buildup is used, corrections should be applied for Reynolds number effects and model mount interference.
- Operating Reference Condition - A full-scale aircraft configuration and propulsion flow conditions to which all drag increments are related when calculating aircraft performance. At this condition all drag is charged to the airframe and none to the propulsion system.
- Operating Condition - Any full-scale configuration or condition at which the aircraft may operate.
- Drag Polar - Lift coefficient versus drag coefficient for the aircraft.
- Trimmed Drag Polar - A drag polar with modifiers accounting for such effects as angle-of-attack, tail angle, surface roughness, skin friction, etc.

AD-A152 757 COST REDUCTION IN VERTICALLY RELATED INDUSTRIES: INTEGRATION VERSUS NONLINEAR PRICING(U) RAND CORP SANTA MONICA CA H C QUIRMBACH MAY 83 RAND/P-6839 9/9

UNCLASSIFIED F/G 5/1 NL

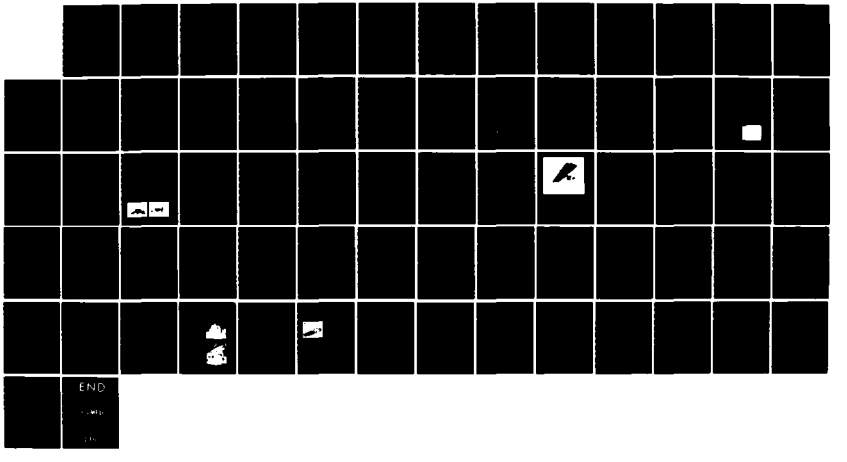

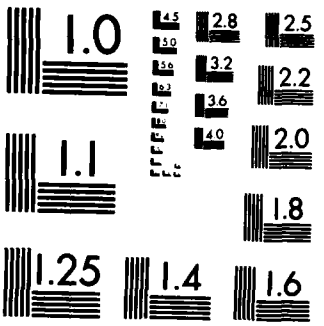

MICROCOPY RESOLUTION TEST CHART
NATIONAL BUREAU OF STANDARDS-1963-A

- Drag Buildup - The process of obtaining and adding the performance of the various elements to the basic drag polar (using the thrust/drag accounting procedure) and obtaining installed performance.

- Throttle Dependent Drags - Those drags resulting from changes in engine power level settings which cause inlet and nozzle operating conditions to change relative to the operating reference condition.

26.2 ENGINE-AIRFRAME INTEGRATION: INLET AND EXHAUST DESIGN CONSIDERATIONS

26.2.1 Inlets

A jet propulsion system generates thrust by increasing the velocity of the fluid passing through it. The thrust is the sum of the local static pressure integrated over the flow area and the momentum flux through the area. The function of the inlet is to capture the fluid and reduce its velocity so that the engine can work efficiently. The total pressure recovery of the fluid entering the engine should be as high as possible to minimize the work of the compressor. The inlet should also produce a relatively uniform velocity profile to avoid excessive blade vibration or compressor stall. Finally the inlet should be integrated with the rest of the nacelle or airframe so that the drag increment due to the presence of the inlet is minimized.

The airplane speed, angle of attack, and thrust requirements vary significantly over the flight envelope. Thus the inlet must operate efficiently over a range of freestream Mach numbers, angles of incidence and flow rates. The design of the inlet is usually constrained by limits on size, weight, mechanical complexity and sometimes by requirements of engine noise suppression. In all, the design of modern inlets calls for sophisticated design techniques.

The broadest classification of inlets is determined by whether its maximum operating speed is below or above the local speed of sound. The engine face to freestream (P_2) static pressure ratio of subsonic inlets can vary from less than 1:1 during ground static operation to about 1.7:1 near sonic flight. For subsonic applications the inlet can usually be designed with a fixed geometry. Supersonic inlets operate with higher maximum pressure ratios; typically 7:1 at Mach 2, 30:1 at Mach 3, and 60:1 at Mach 3.5. To achieve these high compression ratios supersonic inlets are generally designed with variable geometry and require a control system. Active boundary layer control also becomes necessary to prevent flow separation in the strong adverse pressure gradients.

26.2.1.1 Subsonic Inlets

a) Inlet Sizing

Some convenient terms commonly used to describe subsonic inlet geometry and performance are defined schematically in Figure 26.2.1-1. The highlight is the area bounded by the points most forward on the inlet lip. Inlet weight, drag, and cost increase with size; thus it is desirable to design the inlet to be as small as possible. A point of departure in the first design iteration is often the selection of the maximum average throat Mach number. Assuming the inlet losses to be negligible at this point, the required throat area can

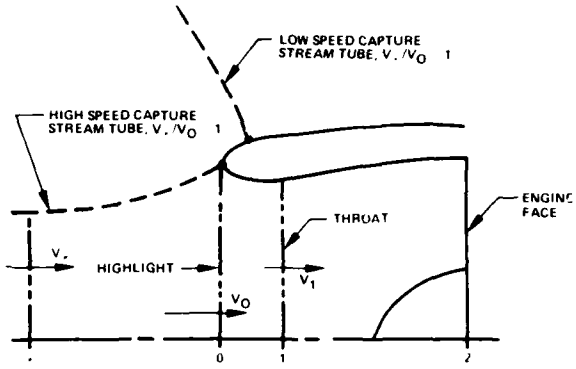

Figure 26.2.1-1. Subsonic Inlet Nomenclature

be calculated from the maximum corrected airflow of the engine from the simple relationship

$$A_1 = \frac{W_{K_2}}{(\rho u)^*} \frac{A}{A^*}_1$$

where W_{K2} is the corrected flow $W_2(\sqrt{\theta_2}/\delta_2)$ and $(\rho u)^* = 49.4\ lb_m\ air/ft^2/sec$.

With the diffuser area ratio, A_2/A_1 and the maximum entry Mach number (M_1) given (A_2 having been set by the requirement for a design engine face Mach number), the required diffuser length can be estimated using conventional diffuser design criteria. A preliminary estimate of the required contraction ratio and fineness ratio can be obtained from a comparison of the low speed and cruise performance requirements of the inlet with the performance of existing designs. After obtaining preliminary values for these parameters the analytic design of the inlet can commence.

b) Cruise Aerodynamic Performance

Subsonic inlets generally operate with an inlet velocity ratio below unity ($V_\infty/V_\infty < 1$) at cruise, as illustrated in Figure 26.2.1-1. At these conditions most designs provide high total pressure recovery and low distortion and the critical aerodynamic parameter is the external drag.

If we model the inlet as indicated in Figure 26.2.1-2 we see that the external forces acting on the inlet are: the "additive drag" (or "pre-entry

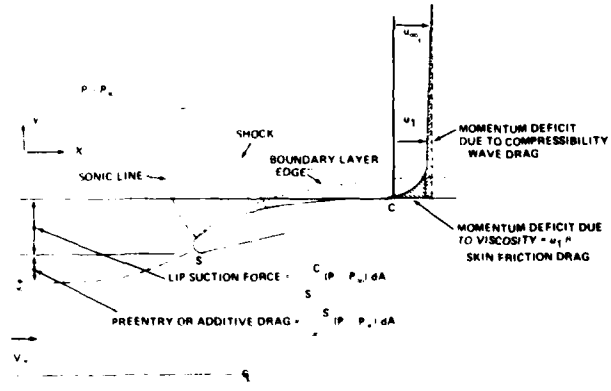

Figure 26.2.1-2. Subsonic Inlet at Cruise

drag") due to external diffusion, "lip suction" due to overspeeding the flow on the forebody, and "skin friction forces" arising from the shear stress on the surface. In an inviscid fluid friction forces are absent, and if the flow is everywhere subsonic, the lip suction force exactly cancels the additive drag so that the inlet experiences no drag. If the flow is accelerated to supersonic velocities locally on the forebody, the transition back to subsonic flow usually occurs through a normal shock. The momentum loss across the shock is sensed on the downstream surface through an alteration in the pressure distribution, and the lip suction no longer cancels the additive drag completely. The residual force is called "wave drag."

In a real fluid, friction due to viscosity is always present. The skin friction drag is defined as the surface integral of the shear stress and is a function of wetted area and velocity distribution. The boundary layer also alters the effective inviscid flow boundary by the virtue of its displacement thickness. The real pressure distribution is developed by the displaced boundary, but is applied to the real body so that the ideal lip suction force is not realized. This loss of lip suction is "pressure drag." Experimentally the pressure drag may be determined by subtracting the calculated skin friction drag from the measured total drag, if no shocks are present.

The freestream Mach number where supersonic flow first appears on the forebody is called the "critical Mach number" of the inlet. A further increase in the freestream Mach number results in wave drag which can be aggrevated by the appearance of flow separation at the shock/boundary layer intersection, if the shock strength is sufficient. The rapid rise in drag is called the "drag divergence" or "transonic drag rise." The critical Mach number is a function of the inlet velocity ratio and forebody contours, a specific case is illustrated in Figure 26.2.1-3.

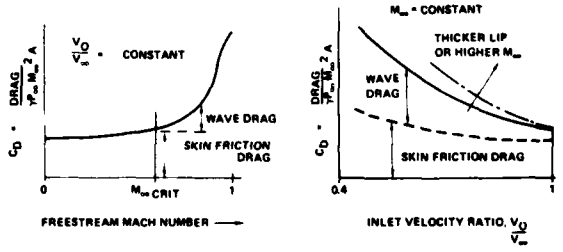

Figure 26.2.1-3. Inlet Drag Characteristics

The designer's objective is to minimize the boundary layer growth and skin friction by properly contouring the forebody surface. Over the past few years valuable analytic tools have been developed to this end. Various computer programs are available that combine solutions from inviscid and viscous flow calculations to evaluate the design. The compressible flow field, including shocks, is first computed for the inlet contours. The surface boundary layer development is then computed from the inviscid velocity distribution. The surface contours can then be modified to account for the boundary layer displacement thickness and the inviscid field can be recomputed. This procedure can be iterated until the solutions converge. The computed Mach number distribution is compared with wind tunnel test results for an inlet in Figure 26.2.1-4 illustrating the accuracy of the analysis. Subroutines can be incorporated into the program

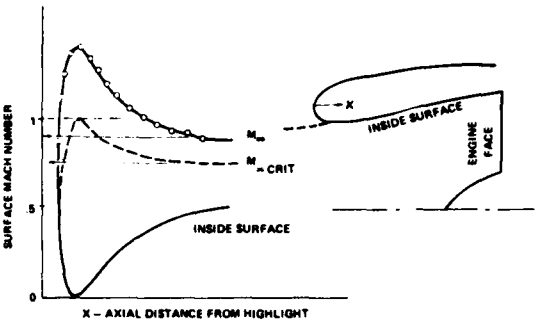

Figure 26.2.1-4. Inlet Surface Mach Number Distribution at Cruise, $M_\infty \geq M_{\infty\,CRIT}$

to calculate the inlet drag. A method was developed by Steger and Baldwin (Reference 26.2.1-1) to determine the wave drag from the characteristics of the normal shock. The total viscous drag on a body was shown to be a function of boundary layer properties at its trailing edge by Granville (Reference 26.2.1-2). The skin friction drag can be calculated separately by integrating the local skin friction along the surface. Near sonic speeds, most practical designs will have supersonic flow. A wave drag equal to about 10% of the total inlet drag is usually considered acceptable. The contours should be designed such that the drag divergence occurs above the maximum operating Mach number of the inlet.

c) Low Speed Aerodynamic Performance

During takeoff and landing maneuvers inlet drag is not significant because of the low flight speed. The inlet total pressure recovery and distortion are the critical aerodynamic parameters since the lip and diffuser are usually operating near their design limits. At takeoff the inlet velocity ratio is much greater than one (tending toward infinity at zero forward speed) and the flow stagnates on the outside of the cowl. As a result, part of the captured flow experiences a rapid acceleration (to supersonic speeds at the most severe conditions) approaching the highly curved highlight. The recompression on the inside of the lip thickens the boundary layer, and the boundary layer profile may deteriorate sufficiently to separate immediately or further downstream in the diffuser. On conventional airplanes the most severe conditions usually occur during takeoff rotation when the inlet angle of attack is maximum or on the ground while operating with a crosswind. In both cases the windward side of the inlet is affected as the stagnation line moves further aft on the outside of the nacelle effectively increasing the capture stream tube area on the side of the inlet. Figure 26.2.1-5 shows the surface Mach number distribution on an inlet at low speed at two angles of attack.

Low speed operation of V/STOL airplanes pose the most challenging design problem. Takeoff and landing generally take place at very high angles of attack with respect to the inlet. The requirement for acceptable performance is usally compensated for by increasing the inlet contraction ratio. The larger area contraction allows a reduction of the wall curvature near the highlight, thereby reducing the peak velocity and the adverse pressure gradient in the flow. At the same time, however, the cruise velocity ratio is also reduced which results in a reduction of the inlet's critical Mach number. Generally an inlet designed to tolerate high angles of attack and crosswind

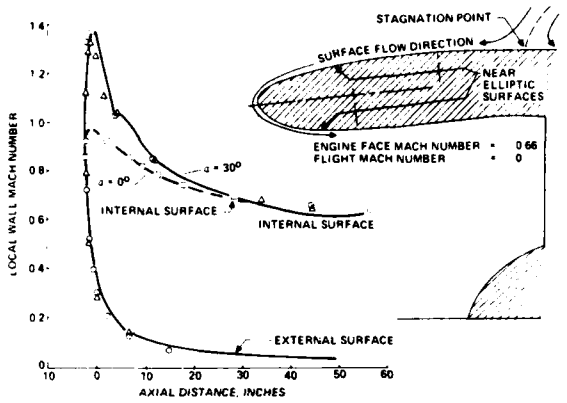

Figure 26.2.1-5. Inlet Surface Mach Number Distribution at Low Speed and At Two Angles of Attack

during low speed operation will experience the drag divergence at a relatively low freestream Mach number, thereby limiting the cruise speed.

On some airplanes, attempts have been made to achieve good performance at low speed without compromising the cruise Mach number by varying the inlet geometry. The usual approach is to provide hinged panels in the cowl (blow-in doors). The panels are free floating or lightly spring loaded and require no powered actuation. During low speed operation when the internal static pressure is lower than the external pressure, the panels open to allow additional flow to enter the inlet, thereby reducing the aerodynamic loading on the lip. At high speed when the internal pressure exceeds the external pressure, the panels are held closed and provide a streamlined configuration. Designs of this type, shown schematically in Figure 26.2.1-6, have been used with success. The primary drawbacks of variable geometry are the weight of the mechanism and the fan noise associated with the interaction between the fan and the wakes of the support structure between the doors. These drawbacks must be weighed against the higher drag of a competing fixed geometry design.

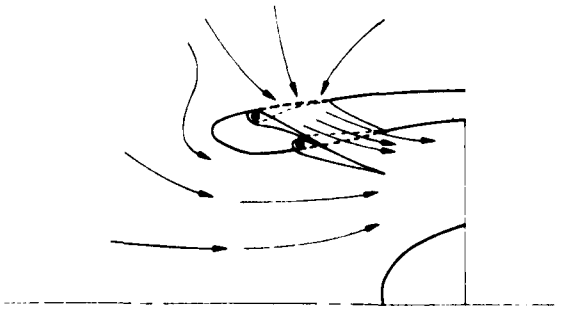

Figure 26.2.1-6. Blow In Door Inlet

Typical performance characteristics of subsonic inlets are shown in Figure 26.2.1-7 showing pressure recovery and distortion as functions of airflow and angle of attack (or crosswind) for a specific geometric configuration. A comparison of two inlets with different contraction ratios (A_0/A_1) is shown in Figure 26.2.1-8. The operational requirements of a particular airplane are shown on this plot of speed versus angle of attack showing that the inlet with the larger contraction ratio will not experience internal flow separation.

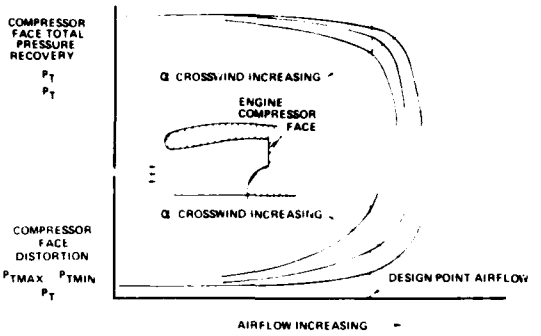

Figure 26.2.1-7. Subsonic Inlet Performance Characteristics

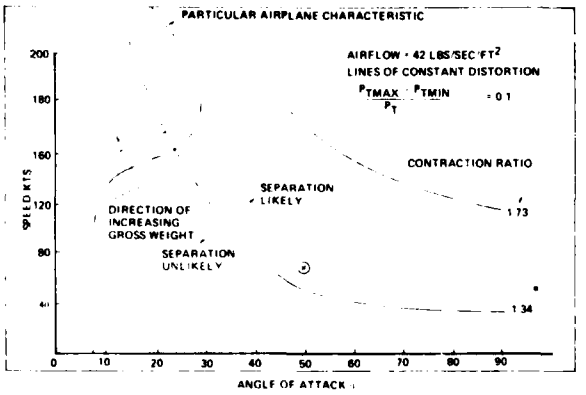

Figure 26.2.1-8. Effect of Contraction Ratio on Separation

The analytic tools used in developing the external contours for high speed operation are available to aid the designer. In analyzing the high speed cases, assumptions of two dimensional or axisymmetric flow can be made with validity, and various existing computer programs are capable of solving such problems (Reference 26.2.1-3). As noted earlier, the critical design points during low speed operation occur at angles of attack when the flowfield is three dimensional. Computer programs for solving three dimensional mixed flows (subsonic and supersonic) are only now emerging. Until these programs become operational, the low speed performance of inlets must be substantiated by the traditional wind tunnel tests.

Experience has shown that the best internal lip contours resemble elliptic shapes (see Figure 26.2.1-5) with major to minor axis ratios of between 2 and 3. Trends in test data also indicate that it is desirable to avoid discontinuities in the wall curvature that appear on some designs at the highlight and the throat.

Designing the subsonic diffuser is an easier problem since three dimensional flow effects tend to be much less significant downstream of the throat, as indicated in Figure 26.2.1-9. The diffuser contours can be developed by carrying out the analysis at zero angle of attack. This is usually accomplished using the standard iterative analysis procedure between potential flow and boundary layer analysis. For a converged solution, the boundary layer shape factor should be such that separation does not occur within some margin of the worst design point. Figure 26.2.1-9 shows surface Mach number profiles for a flow with sufficiently high inlet angle of attack to result in separation.

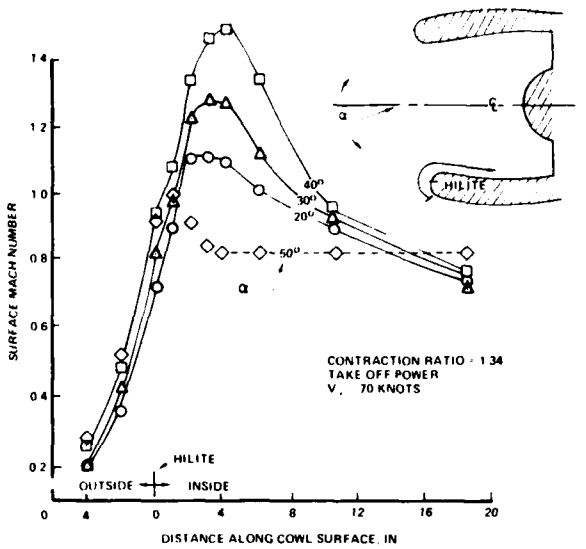

Figure 26.2.1-9. Mach Number Distribution Along the Surface of An Inlet At Low Speed Inferred From Surface Static Pressure Measurements

d) Low Speed Noise Suppression

Several concepts have been proposed to suppress or attentuate the engine noise that escapes through the inlet during near-airport operation. The two concepts that have received most attention are: a) lining the inlet with sound absorbing material, and b) setting up an aerodynamic barrier against noise propagation by accelerating the flow to transonic speeds at the throat. Designs of both types have been shown to be effective in reducing noise.

When acoustic waves impinge on a smooth hard surface they are reflected undiminished. Various materials containing small cavities have been developed that tend to absorb noise at certain frequencies. The internal surfaces of "lined inlets" are treated with material chosen for good absorption characteristics in the most annoying frequency band of the particular engine's noise spectrum. Since the lining can only absorb waves that are incident on the surface, it is necessary to provide a large lined surface to achieve effective noise attenuation. To obtain sufficient surface area the length of the inlet may need to be increased beyond what is required for good aerodynamic performance. Acoustically treated (lined) rings or grids may also be placed in the flow passage for similar reasons. These devices also make the flow passages narrower which appears to be beneficial for noise reduction. The viscous losses in lined inlets tend to be much higher than in similar hardwall designs, since the skin friction coefficient for typical lining materials is greater than for polished aluminum. This effect may be aggrevated by the increased wetted area. The increased engine pressure ratio and fuel consumption required to operate with a lined inlet must be weighed against the noise suppression benefits.

The high throat Mach number, or "sonic inlet," operates on the principle of the choked convergent-divergent nozzle. The fluid is accelerated to approximately Mach 1 at the throat, and the resulting surface of transonic flow acts as an aerodynamic barrier to the forward propagation of acoustic waves. A dramatic reduction in noise level can be perceived experimentally when the engine airflow is increased to the point where the inlet chokes. Since noise attenuation is desired during landing approach, when the engine airflow is near idle setting, as well as during takeoff at maximum power, sonic inlets generally require a variable area throat. The transition from the small to the large throat must be quick to allow for a go-around in case of a missed approach. A further complication in the diffuser design is that while the entry area (throat) varies, the exit area (engine face) remains fixed. The design difficulties have thus far discouraged the use of sonic inlets on transport airplanes. Reference 26.2.1-4 summarizes the results of an experimental program designed to explore the potential of sonic inlets.

26.2.1.2 Supersonic Inlets

a) Inlet Types

The design procedure as well as the inlet configuration becomes increasingly complex as the design Mach number of the inlet increases. For a subsonic inlet the cruise problem is essentially one of low external drag since nearly isentropic internal diffusion can be achieved with relative ease and the inlet flow rate is self regulating in the sense that the capture area adjusts to the mass demand. For supersonic inlets the internal aerodynamic performance is also a crucial problem since efficient supersonic diffusion over a wide range of Mach numbers is difficult to achieve, and the inlet must have an actively controlled flow metering capability.

The simplest design is the normal shock inlet illustrated in Figure 26.2.1-10a. This is basically a subsonic inlet with a sharper lip, and its use is limited to very low supersonic Mach numbers since the shock losses rapidly become prohibitive as the freestream Mach number is increased (Figure 26.2.1-10b). The inlet must also be equipped with a bypass system to control the flow into the inlet such that the shock remains attached to the lip

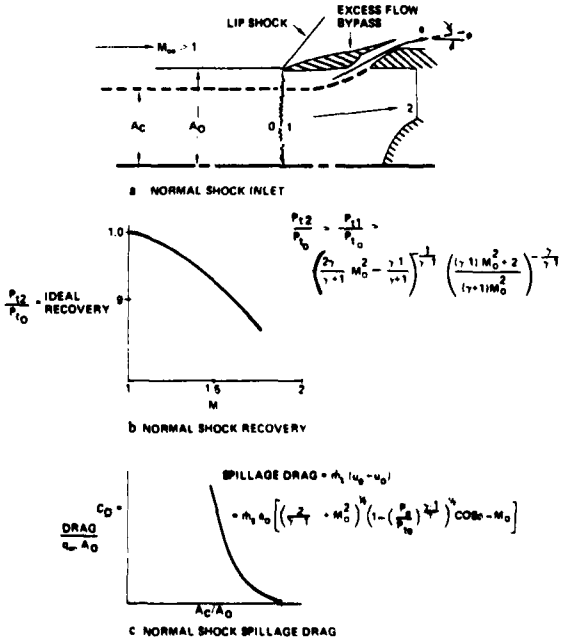

Figure 26.2.1-10.

regardless of the engine airflow demand. Flow spillage around the lip usually cannot be tolerated because of a high drag penalty, as shown in Figure 26.2.1-10c. Due to the limits of its applicability, this design is more properly a transonic flight inlet.

Supersonic inlets designs in common use may be broadly classified on the basis of how they perform supersonic diffusion. The three basic types are shown schematically in Figure 26.2.1-11. As the name implies, with the "external compression inlet" all supersonic diffusion takes place on an unopposed external body and the flow inside the inlet is subsonic throughout the diverging duct. With "mixed compression inlets" the supersonic diffusion is partially carried out on the external body, and is continued internally to a throat well downstream of the cowl lip. With "internal compression inlets" the flow is captured at the freestream Mach number, and all supersonic diffusion takes place inside the inlet duct. For all three inlet types the transition from supersonic to subsonic flow is shown to occur through a normal shock. In theory, an isentropic transition is possible but the precise control required to maintain sonic flow is difficult to achieve in practice. The normal shock design Mach number is the minimum value compatible with the control system capabilities, as will be discussed later.

The necessity of geometry variation in a supersonic inlet will be developed in the following sections. The relative ease of implementing the geometry variation can have a bearing on the selection of the inlet shape. The entry plane cross section can be axisymmetric, rectangular, or some odd shape to suit the local body or wing contours. Axisymmetric designs tend to be the shortest and lightest and have the best performance, particularly at the higher Mach numbers. However, it is difficult to design axisymmetric inlets to

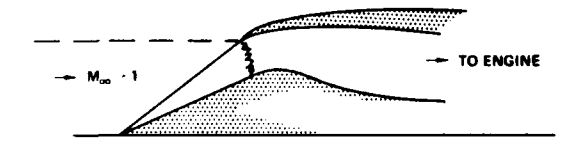

A. EXTERNAL COMPRESSION INLET

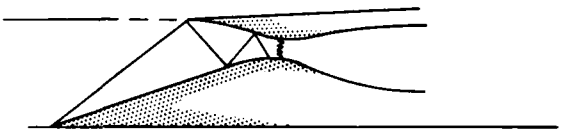

B. MIXED COMPRESSION INLET

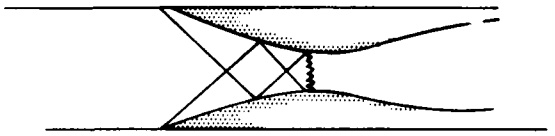

C. INTERNAL COMPRESSION INLET

Figure 26.2.1-11. Supersonic Inlet Types

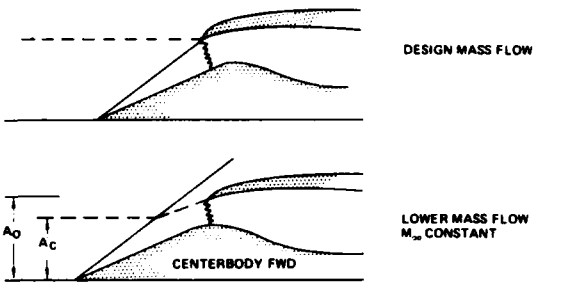

(A) EXTERNAL COMPRESSION INLET

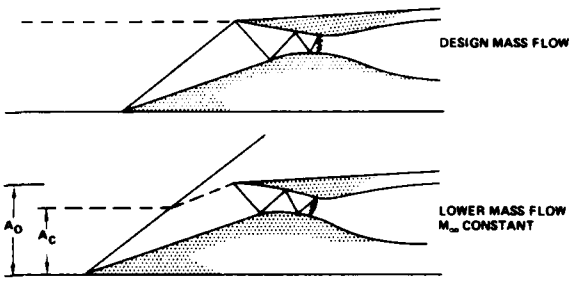

(B) MIXED COMPRESSION INLET

Figure 26.2.1-12. Design Off-Design Operation of Supersonic Inlets

operate efficiently over a wide Mach number range, and they cannot be integrated easily with certain airframes. Two-dimensional designs provide the easiest means of area variation required for operation over a wide Mach number range. Installation is usually less of a problem; however, the transition from the rectangular duct to the annular engine involves aerodynamic losses and adds to the length and weight of the inlet. Half round, quarter round, D shape, and other designs are sometimes used on airplanes where externally mounted nacelles are not feasible. These designs tend to combine the undesirable aerodynamic features of the axisymmetric and two-dimensional geometries, but may still be the best compromise. In general, the optimum inlet design is specific to the airframe, engine, and mission requirements.

b) Inlet/Engine Airflow Matching

During supersonic flight the maximum ideal capture flow rate of the inlet is equal to the flowrate in the freestream through the projected area of the inlet entry plane. The capture flow cannot be increased above this value regardless of the type of supersonic diffusion employed, however, it can be decreased with external or mixed compression inlets by deflecting the flow further upstream of the entry plane as indicated in Figure 26.2.1-12. We define A_O as the maximum capture area and A_C as the capture area, the quantity A_C/A_O is identical to the mass flow ratio $\dot{m}_C/\dot{m}_O$ and the two may be used interchangeably.

Figure 26.2.1-13 illustrates the capture area needed to satisfy the airflow demand of a typical jet engine over the flight placard. Ideally the inlet capture area should follow the same schedule. As we shall discuss later, we require that the normal shock be kept at the throat for the mixed compression inlet, thus subsonic spillage is not allowed. It follows, then, that during supersonic operation the inlet capture area is completely determined by the freestream Mach number and the inlet geometry. It also follows that the Mach

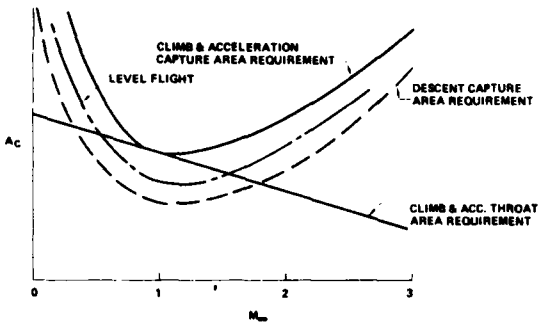

Figure 26.2.1-13. Inlet Capture Area Requirements

number and capture area determine the thoat area required for efficient operation. As indicated in Figure 26.2.1-13, the capture area demand of the engine at a given Mach number varies with the mode of operation, e.g. climb and acceleration, level flight, or descent. Smaller variations in engine airflow-demand result from changes in ambient temperature, airplane gross weight, etc. The combination of these factors make the matching of the inlet to the engine a challenging problem.

c) Inlet Sizing

The inlet must be sized so that it can capture the maximum flow required by the engine at any Mach number. The inlet is generally designed to operate with a capture ratio of unity at cruise to minimize the cruise drag. If the inlet geometry is unchanged the capture ratio will decrease with decreasing Mach number because of the increase in the bow shock angle. This decrease may not coincide with the maximum airflow schedule of the engine. The capture flow can be further reduced by a forward translation of the external body. In any case, the throat area must be changed simultaneously to maintain the upstream Mach number of the normal shock close to one. With the capture area schedule designed for the maximum airflow demand, the inlet supply exceeds the engine requirements during reduced power operation, e.g., descent. The excess flow is generally vented overboard through a bypass system. It is desirable to design the inlet to require no bypass during climb.

Supersonic inlets share with subsonic inlets the problem of insufficient flow area at takeoff. The sharp leading edges of supersonic inlets produce much higher losses when operating with velocity ratios (V_o/V_∞) above one (Reference 26.2.1-5). To allow the airplane to take off, supersonic inlets are generally equipped with auxiliary flow passages to increase the inlet supply. See for example Figure 26.2.1-14 showing an SST type inlet.

A variety of devices have been developed to achieve proper matching of the inlet supply flow to the engine demand. During low speed operation the blow-in door, introduced in Section 26.2.1.1, or some similar concept can be used. The supersonic capture area is most easily controlled by means of a translating center body as suggested in Figure 26.2.1-12. The aft part of the translating body is often shaped such that it provides the required internal area distribution at each operating position. For some applications this simple approach is not feasible, and hinged panels are used to achieve the required area variation. With axisymmetric designs, the latter approach demands relatively complex mechanisms since the compression surfaces must move in umbrella-like fashion.

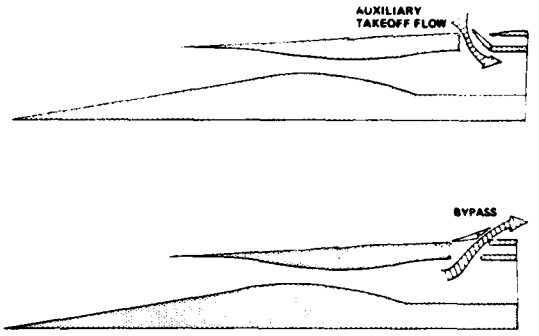

Figure 26.2.1-14. SST-Type Inlet Showing Blow-In and Bypass Doors

As we noted earlier, supersonic inlets generally require a bypass system. Flow must be bypassed while operating with reduced thrust, including engine failure modes. Part of the bypass flow can be routed through the nozzle cooling ducts if extra capacity is available; the remainder must be vented overboard through separate exits.

External Compression

Because of their relative simplicity, external compression inlets are ideally suited to lower supersonic applications, say below Mach 2. Figure 26.2.1-15 shows the three operating modes of the external compression inlet. During "critical" operation the flow passing through the supersonic capture area is equal to the inlet flow demand, the oblique and normal shocks impinge on the cowl lip, and the external flow is everywhere supersonic, while the internal flow is subsonic. If the inlet cannot pass all of the capture flow, the normal shock will move forward from the cowl lip to allow spillage of the excess flow. This mode is called "subcritical" operation. If the inlet demand exceeds the available capture flow the normal shock will be drawn further inside the inlet duct,

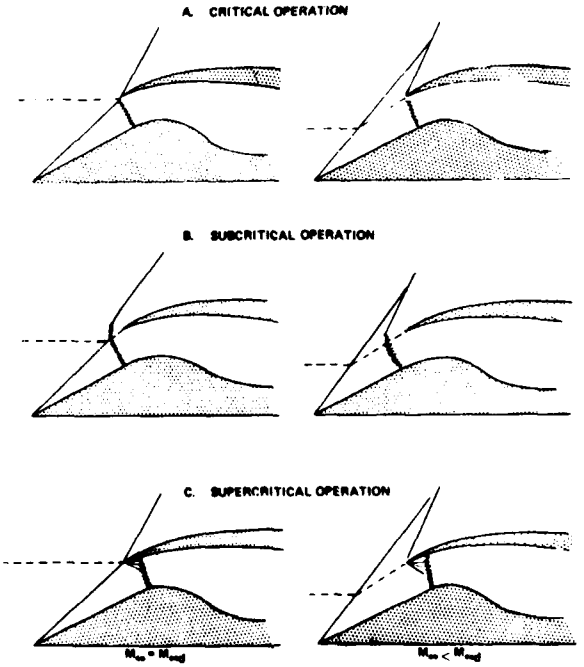

Figure 26.2.1-15. External Compression Inlet Operating Modes

a mode called "supercritical." The minimum duct area is at the lip station for an external compression inlet, therefore supersonic flow entering the inlet tends to re-expand. Because of the expansion, the normal shock will be stronger, resulting in a larger total pressure loss. The inlet characteristics, usually plotted as total pressure recovery as a function of inlet mass flow, are plotted in Figure 26.2.1-16 for an ideal, fixed geometry, external (or mixed) compression inlet. In this plot the inlet mass flow is normalized to the design value at $M_{\infty d}$. At lower M_∞, the recovery increases and the maximum capture mass flow decreases. Clearly, a variable geometry inlet should be designed to join the corner points as indicated, to minimize external drag and maximize the recovery.

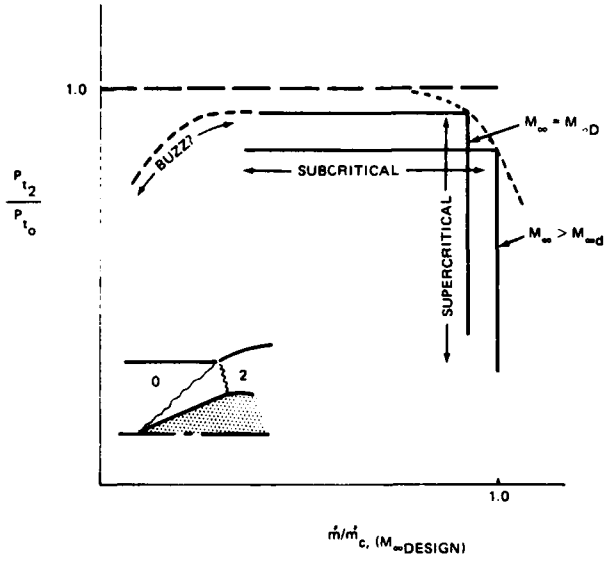

Figure 26.2.1-16. External Compression Inlet Performance Characteristics

Supercritical operation should be avoided because the total pressure loss reduces the engine thrust. Furthermore, it is usually accompanied by a flow profile distortion which could cause excessive blade vibration or compressor stall. Subcritical operation is also undesirable since subsonic spillage causes a rapid increase in the external drag which can be aggravated by flow separation on the cowl. Further, in a certain range of their subcritical operation, inlets generally experience a dynamic flow phenomenon called "buzz." The most obvious manifestations of buzz are a rapid fore-and-aft fluctuation of the external normal shock and a corresponding instability of the local pressure field. The pressure pulses can have sufficient amplitude to cause structural failure.

Inlet Buzz

It has been suggested that the inlet flow field becomes unstable against small disturbances when the slope of the pressure recovery is positive with respect to mass flow ratio, see Figure 26.2.1-16. The ingestion of vortex sheets has been proposed by Ferri (Reference 26.2.1-6) as a mechanism triggering buzz. In this scheme a vortex sheet originates from the velocity discontinuity at the intersection of the bow shock with the external normal shock. The low kinetic energy wake chokes the inlet and moves the normal shock further forward, resulting in increased flow spillage around the cowl lip. The increased spillage may divert part of the wake overboard, thereby unchoking the inlet and allowing the normal shock to move aft toward its initial position, and the cycle is repeated. Since the inlet/engine installation has a resonant frequency (flow speed/inlet length), buzz may persist even after the disturbance causing the initial flow decrease has disappeared.

Another mechanism for buzz can arise under the conditions illustrated in Figure 26.2.1-17. In normal operation of an external or mixed compression inlet, a shock terminates the supersonic flow region. This shock may separate the flow from the wall, causing choking downstream which requires spillage. When the spillage changes the conditions which result in the existence of the shock and the reason for separation, the flow is re-established and the cycle may start again.

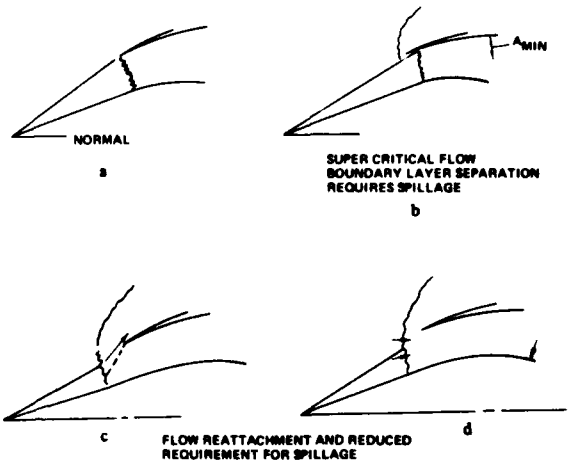

Figure 26.2.1-17. Buzz Flow Sequence

The buzz characteristics of an inlet must be evaluated experimentally, since the phenomenon does not lend itself easily to analysis. Buzz conditions can usually be avoided by increasing the bypass flow when the engine cannot accept all of the corrected flow supplied by the inlet.

The foregoing discussion indicates the desirability of operating the inlet at the critical point; i.e., the capture flow as determined by the external geometry should equal the flow requirements of the inlet. The flow demand of the inlet is the sum of the engine flow and bypass flow (and boundary layer bleed flow, if used).

External compression is achieved by turning the flow away from the freestream direction so as to reduce the flow area. The turning can be accomplished in a single step by a straight wedge or cone as indicated in Figure 26.2.1-18a or in several steps as illustrated in Figure 26.2.1-18b. The total pressure recovery of the flow ahead of the normal shock is higher for a multiple shock inlet than for a single shock inlet operating at the same compression ratio. This becomes evident when considering the isentropic compression inlet illustrated in Figure 26.2.1-18c. In this concept the supersonic diffusion is accomplished without shocks. (In reality a weak shock is present at the beginning of the compression since the leading edge angle must be finite, and there is a weak normal stock terminating the supersonic diffusion process.) The inlet is said to be "on-design" when

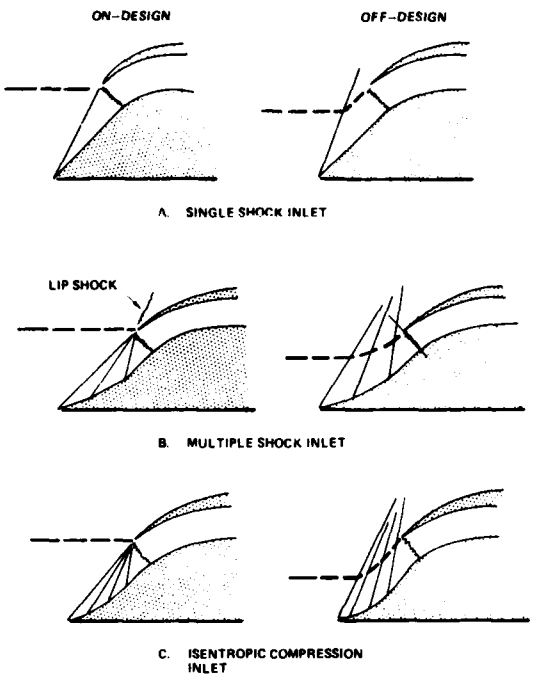

Figure 26.2.1-18. External Compression Surface Configuration

the capture ratio is unity. This condition occurs when the bow shock impinges on the cowl lip. When the capture ratio is less than one, the inlet is "off-design." To maintain efficient operation during off-design conditions, the normal shock Mach number should be kept relatively constant. This can be achieved by varying the deflection angle as a function of the freestream Mach number. The entry area must also vary with the supersonic capture area to keep the inlet critical.

The upstream Mach number of the normal shock on-design is slightly over one. (In the interest of stability the value is usually 1.2 or 1.3.) To maintain this value the deflection angle must be increased with increasing Mach number. As an example, consider a two-dimensional inlet with one oblique and a normal shock Mach number of 1.3. At a freestream Mach number of 2 the required deflection angle is about 18.5°, while at Mach 3 it is about 31.5°. The total Prandle-Meyer turning required for isentropic compression (to M=1 or 1.3) is about 20° and 40°, respectively. Since the minimum duct area is at the cowl lip, it follows that the initial slope of the internal cowl wall must be somewhat higher than the final deflection angle for two dimensional designs (see Figure 26.2.1-18). For axisymmetric designs the cowl lip slope is lower than that of a 2-D inlet due to the characteristics of conical flow. Obviously the external lip slope must be still higher. The drag penalty associated with the cowl lip shock prohibits the use of external compression inlets at high Mach numbers. For transport airplanes, where cruise efficiency is of utmost importance, the limit may be taken as approximately Mach 2. If high speed maneuverability is important and abundant thrust is available, the limit can be increased to about Mach 2.5.

Mixed Compression Inlets

The design of mixed compression inlets is not restricted by the requirement of a predetermined internal cowl lip angle. Supersonic diffusion takes place on two opposing surfaces. A typical mixed-compression inlet is shown schematically in Figure 26.2.1-12b. Since the throat is located well downstream of the entry plane, the initial cowl slope is not constrained and may be chosen to be upstream flow direction. The external cowl can be closely aligned with the freestream direction to minimize the drag during high speed flight. The inlet is generally configured to operate with a capture ratio of unity (minimum drag) at the design point, and the throat is sized for an average Mach number of between 1.2 and 1.3. Since diffusion to Mach 1 is not practical because of stability considerations. The terminal normal shock is positioned at the beginning of the diverging flow area. (Normal shocks cannot maintain a stable position in a converging duct.) During off-design operation the throat area must be varied with the capture area so as to keep the throat Mach number within the design limits.

When the normal shock first appears at the throat the inlet is said to "start." The term "started" refers to operating in the mixed compression mode. A "self-starting" inlet naturally transitions to the mixed compression mode at a particular point as the geometry is varied along the normal Mach number schedule. More commonly, inlet start is initiated by the control system. In any event, the inlet initially operates in the external compression mode during passing transonic acceleration. The engine thrust margin is generally critical during the transonic drag rise. It follows that the inlet capture flow should be maximized and normal shock spillage must be avoided while operating near sonic speeds. These requirements dictate that the throat be positioned just inside the entry plane.

External compression is generally maintained up to a specified freestream Mach number. Starting is accomplished by increasing the downstream flow demand. In this procedure care must be taken to keep the normal shock from becoming supercritical as it enters the inlet duct. Once the inlet is started, the throat area must be varied as a function of the freestream Mach number and capture area. In the started mode the inlet is said to be "critical" when the throat Mach number is one, or when the normal shock is positioned just aft of the converging area. Since the shock position is not stable in the converging duct, a reduction in the upstream Mach number or the downstream flow demand, while the inlet is critical, causes the normal shock to be expelled from the inlet in a sudden surge. This phenomenon is referred to as an "unstart." Once the shock leaves the duct it may reach a stable position or it may buzz. The unstart is accompanied by a sudden reduction in the inlet total pressure recovery and flow rate, and a large increase in the inlet drag. The internal disturbances have a high potential for surging the compressor and losing all thrust. Unstarts should obviously be avoided, and if they occur, the inlet must be "restarted" immediately. The restart sequence is similar to the starting procedure and must be available at all operating speeds.

Internal Compression Inlet

An obvious extention of the supersonic diffusion concept is the internal compression inlet. As the name implies, this device captures the flow at freestream conditions, and all supersonic diffusion is done internally. Although internal compression is conceptually feasible, it suffers from several practical handicaps. Among these

are: excessive supersonic diffuser length, difficulty in varying the capture area, and the need for external and mixed compression modes for starting the inlet.

Inlet Starting

During the starting process the terminal normal shock moves from a position upstream of the cowl lip to a position downstream of the internal throat. If we assume that the supersonic diffusion is accomplished isentropically, we can calculate, from continuity, the ratio of the throat area to the entry area that will result in sonic flow at the throat. The solid curve in Figure 26.2.1-19 shows the required supersonic diffuser area ratio

$$\frac{A_1^*}{A_1} = \frac{(\rho u)_1}{(\rho u)_1^*} = \frac{1}{M_1}\left(1 + \frac{\gamma-1}{2} M_1^2\right)^{\frac{\gamma+1}{2(\gamma-1)}}$$

as a function of entry Mach number which may be considered to be the ideal operating schedule of the inlet. When a normal shock is present at the entry plane, the throat area calculated above cannot pass the entering flow because of the reduced total pressure in the stream behind the external shock. To prevent the subsonic flow from spilling around the cowl lip, the diffuser area ratio must be increased to a value above the broken curve in Figure 26.2.1-19. This curve is obtained by calculating the area ratio required to achieve sonic flow conditions behind a normal shock at the entrance to the supersonic diffusion section. Thus

$$\frac{A_2^*}{A_1} = \frac{A_1^*}{A_1}\frac{A_2^*}{A_1} = \frac{A_1^*}{A_1}\frac{(\rho u)_1^*}{(\rho u)_2^*} = \frac{A_1^*}{A_1}\frac{P_{t1}}{P_{t2}} > \frac{A_1^*}{A_1}$$

This ratio change may be accomplished by increasing the throat area to A_2^* or by decreasing the entry area A_1. In either case the engine is usually constrained to run at constant corrected airflow which is equivalent to running at constant axial Mach number at the engine face.

If A_1 is fixed, the throat area must be equal to or greater than A_2^*, which means that A/A* at the engine face is smaller than it would be in the started condition and the Mach number at the engine is larger. this flow Mach number can be reduced by effectively increasing the flow tube area at the engine face, i.e., by providing for flow to bypass the engine through doors between A_{2*} and the engine.

If, on the other hand, A_1 is reduced to achieve a starting area ratio, the bypass door will not be necessary since the flow Mach number distribution from the throat rearward does not depend on whether the inlet is started or not. In practice, both inlet area variation and bypass are often used. The area ratio change may be accomplished by either increasing the throat area or decreasing the entry area, or both. The corrected airflow demand downstream of the throat may be adjusted to satisfy continuity, generally by varying the bypass exit area which can be better controlled than the engine-corrected airflow.

When the starting area ratio is achieved, a further increase in the downstream flow demand causes the shock to enter the inlet and will stabilize at a position downstream of the throat. At this point the inlet geometry can be restored to the high recovery (operating) configuration (solid curve in Figure 26.2.1-19). For a real

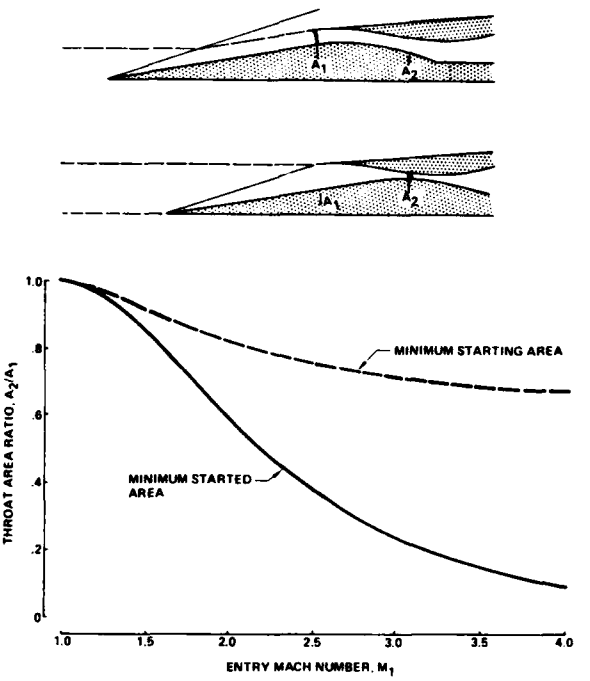

Figure 26.2.1-19. Area Ratio Variation in Starting Inlet At M_1

inlet the calculation of diffuser and bypass area ratios must include the effects of internal losses, boundary layer bleed, and operating throat Mach number (>1). Referring to Figure 26.2.1-19, we may write the continuity equation as an equation for:

$$\frac{A_2}{A_1} = \frac{(A/A_*)_2}{(A/A_*)_1}\frac{1-W_{Bleed}/W_1}{P_{T2}/P_{T1}} .$$

At the operating condition $(A/A_*)_2$ is the sonic area ratio corresponding to the operating throat Mach number, while at the initiation of the starting transient $(A/A_*)_2 = 1$.

Figure 26.2.1-20 shows the operational modes at various flight Mach numbers of a mixed compression inlet designed for $M_\infty = 2.2$.

In designing the diffuser wall contours, viscosity as well as compressibility must be taken into account. To simplify matters, the flow is initially assumed inviscid. The throat Mach number is determined from stability requirements, as will be discussed later, and is kept relatively constant throughout the started regime. The throat area schedule can then be calculated from the maximum airflow requirement schedule of the

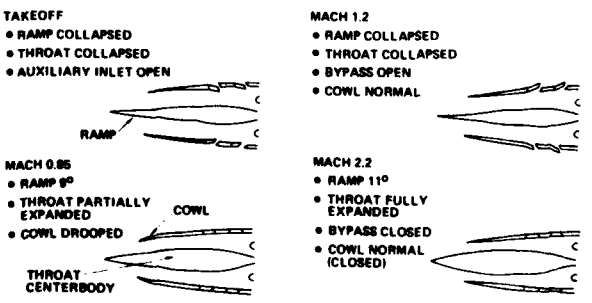

Figure 26.2.1-20. Operational Modes of a Mixed Compression Inlet

engine. We can similarly compute the capture area requirement as a function of freestream Mach number. Since the supersonic capture area is a function of the freestream Mach number and the external geometry, the external diffusion surface must be designed such that sufficient capture flow is always available. Strong shocks and severe pressure gradients should be avoided on the internal diffuser surfaces to prevent the flow from becoming subsonic upstream of the throat. The basic design tool in this effort is a supersonic flow computer program of which several are available; see Section 26.3.1.

e) Boundary Layer Control

The central problem of supersonic inlet design is efficient boundary layer control. If the inlet is made short the adverse pressure gradients become high, leading to rapid thickening and deterioration of the boundary layer profile. If, on the other hand, the length of the inlet is increased to relieve the pressure gradients, the increased wetted area may make matters worse than they were at the outset. The flow must remain attached in the supersonic diffuser since a separation can easily unstart the inlet. At the throat the boundary layer must have sufficient energy to withstand the pressure rise associated with the normal shock; the displacement thickness should be small since the performance of the subsonic diffuser is strongly dependent on the entry blockage. Supersonic diffusers in general require active boundary layer control.

The traditional approach to controlling the boundary layer is to remove, or "bleed," part of the low velocity flow near the surface through holes, slots, or scoops (Figure 26.2.1-21) (Ref. 26.2.1-7, 8). The bleed flow is often vented overboard from the inlet cowl, but a smaller drag penalty is incurred if the bleed can be routed to the nozzle when an ejector nozzle is used. In designing the bleed system we are concerned with maximizing the internal performance of the inlet and minimizing the bleed drag.

Although viscosity is present throughout the flowfield, its effect is only important in the boundary layer. For convenience we treat the flow outside of the boundary layer as though it were inviscid. The boundary layer parameters having most importance for the inlet designer are the displayement thickness and the profile shape factor. Various definitions of the shape factor are currently in use, and any one is acceptable as long as it gives a good indication of the likelihood of flow separation. The value of the displacement thickness must be known since it influences the inviscid flow boundaries.

If the inviscid flowfield contains oblique shocks, bleed is generally required at the locations where the shocks reflect from the diffuser surfaces. A generalized shock/boundary layer interaction is depicted schematically in Figure 26.2.1-22. The purpose of the bleed is to remove the low velocity portion of the boundary layer so that it will not separate in the pressure gradient produced by the shock reflection. Isentropic compressions also distort the boundary layer profile and bleed is often required in shock free pressure gradient regions. The inviscid and viscous portions of the flowfield are generally analyzed by separate computer programs, or separate subroutines of the same program. As a first approximation, the inviscid flowfield may be computed neglecting viscous effects. The surface velocity distributions thus obtained can then be used as inputs for the boundary layer program.

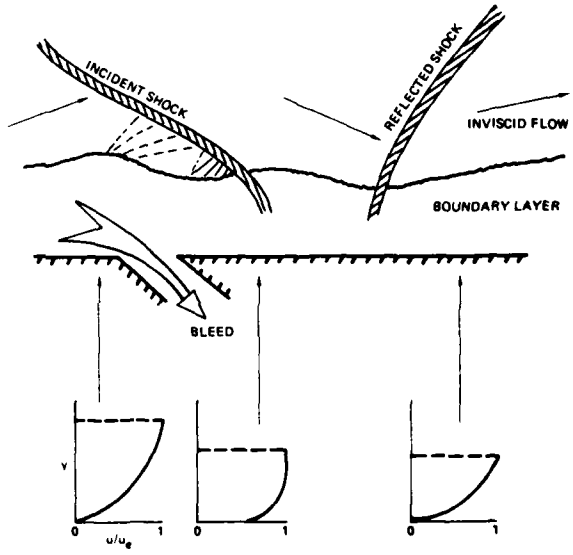

Figure 26.2.1-22. Oblique Shock/Boundary Layer Interaction

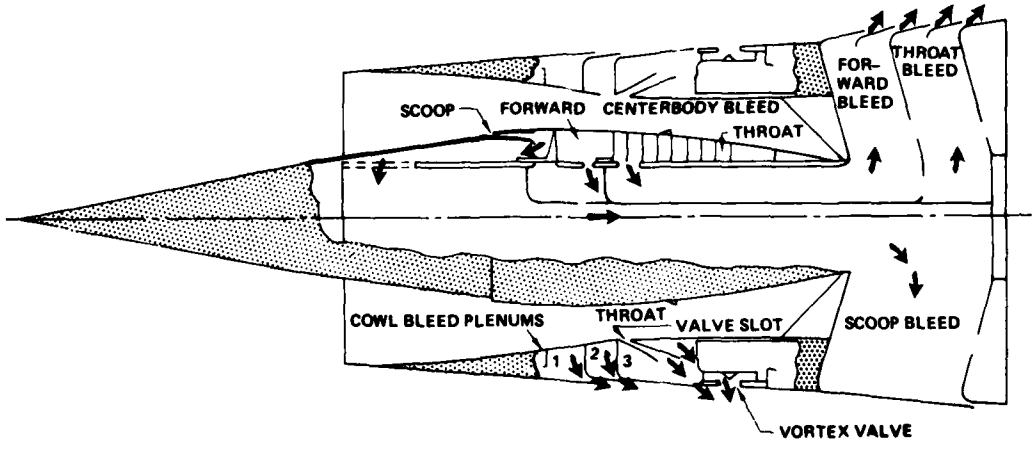

Figure 26.2.1-21. Bleed System Design Schematic

The surface contours should be modified by calculated displacement thickness when recomputing the inviscid field. For a high Mach number inlet several iterations of this procedure may be required to obtain convergence. If at any point in the calculation the boundary layer shape factor indicates incipient separation, bleed must be provided to improve the profile or the original surface contours must be changed to obtain a more favorable boundary layer development. The effects of bleed must be included in subsequent calculations.

The severe pressure gradient produced by the normal shock requires boundary layer control in the throat region. Again bleed is a common method used for providing the control. In addition to keeping the flow attached, a properly designed throat bleed system reduces the additional flow area required to pass the low velocity air and provides a margin of stability for the normal shock, as will be discussed later.

The work of Reference 26.2.1-9 gives some insight into the general problem of shock-boundary layer interactions. From an inlet design point of view, the questions which must be addressed are; 1) is the shock strong enough to separate the boundary layer flow and 2) how little bleed flow can be used to change the boundary layer characteristics so that the flow remains well behaved? Typically the bleed flow reached 10% of the inlet flow at $M_\infty = 3$, increasing linearly from $M = 1$. Roughly 50% of this flow is bled at the throat and the remainder on the compression ramps. Reference 26.2.2-8 describes a numerical procedure for calculating changes in boundary layer characteristics through shock waves.

The bleed flow prior to its removal from the boundary layer has suffered significant momentum losses which must be added to the external drag when the flow is vented overboard. This drag increment constitutes a large fraction of the total drag force acting on a high speed inlet. Therefore it is important to minimize the bleed flow as well as any additional losses in the flow that is necessary. Figure 26.2.1-23 illustrates typical discharge coefficients for bleed holes. Slots or scoops can also be used for bleeding. The bleed flow is generally collected in a plenum chamber prior to being discharged through a nozzle designed for this purpose or into the engine nozzle ejector.

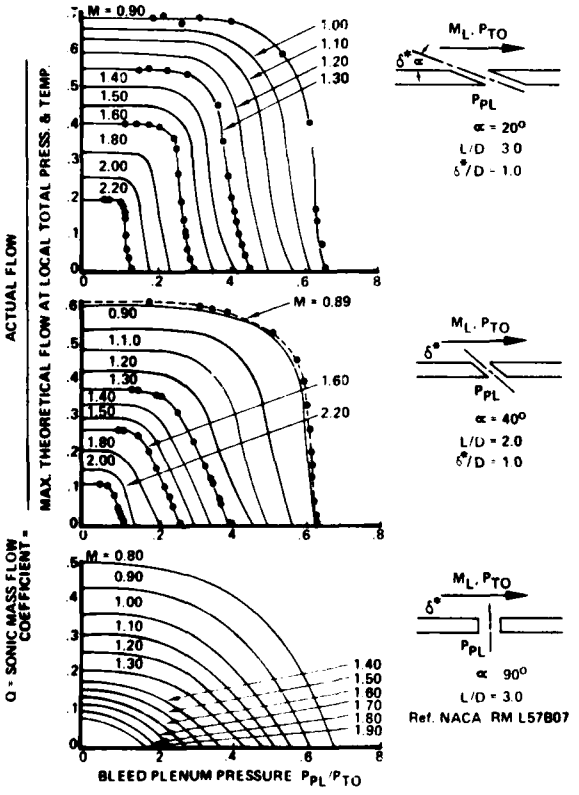

Figure 26.2.1-23. Bleed Hole Characteristics

For a given flowrate the bleed drag is a function of the plenum pressure and nozzle efficiency. If cowl exits are used, the discharge angle and wave drag produced by the discharged flow must also be considered. Since the boundary layer flow possesses low momentum, the maximum pressure in the plenum can be only slightly higher than the local surface static pressure. Thus, if a single plenum is used for collecting flow from several bleed regions, the plenum pressure must be kept below the value of the minimum static pressure region. Otherwise the flow will tend to recirculate through the bleed holes from the higher pressure bleed regions. For minimum drag, each bleed region should have its separate plenum and exit so that the individual plenum pressures can be maximized.

Alternately, the boundary layer can be energized by injection of high pressure fluid at the surface (blowing), or in hypersonic inlets the boundary layer profile can be improved by cooling the surface. To date, neither of these concepts have been widely applied.

f) Subsonic Diffuser Design

Downstream of the normal shock, the flow is at a high subsonic Mach number and needs to be further decelerated to be acceptable to the engine. This function is performed by the subsonic diffuser. Mismatches between the supersonic diffuser flow supply and the engine demand are resolved by removing excess flow from the subsonic diffuser via a bypass system. The engine face area (diffuser exit) remains constant while the throat area (diffuser entry) varies with Mach number. A versatile design, with efficient operation over a wide range of conditions, is required. The problem is further complicated by requirements of varying cross sectional shape if the supersonic diffuser is not axisymmetric.

The diffuser performance is basically a function of the flow profile at the entry plane, the diffuser length, area distribution, and overall area ratio. These parameters all influence the development of the boundary layer on the walls that governs the diffuser losses. If a thin and full boundary layer profile can be maintained throughout the diffuser, the losses will be minimal, whereas thick, distorted profiles can lead to flow separation and result in significant total pressure losses and velocity distortion at the engine face.

By the nature of its operation, the diffuser imposes a continuous adverse pressure gradient on the boundary layer. Therefore it is important that the boundary layer profile at entry be thin and full. This condition is usually measured in terms of throat "blockage," where blockage is defined as the circumferential area covered by the boundary layer displacement thickness as a percentage of the local geometric area. For most applications, efficient diffusion can only be obtained if the throat blockage does not exceed a few percent. Low blockage values are generally obtained by

relatively heavy bleeding near the normal shock. In optimizing the design, the recovery improvements must be weighed against the excess throat bleed drag. The diffuser duct area distribution and wall contours should be designed to minimize the local adverse pressure gradients without unduly increasing the diffuser length. This is an obviously difficult task and boundary layer control often is necessary in the subsonic diffuser.

Because of the high drag penalty associated with bleed, "vortex generators" (Figure 26.2.1-24) can generally be used profitably in the subsonic diffuser. These devices shed axial vorticity near the surface and increase the average axial velocity in the boundary layer by entraining fluid from the core flow into the boundary layer. The fluid transfer involves mixing losses, but the price is often justified by the avoidance of flow separation. The vortex generators are usually triangular or rectangular plates placed normal to the surface at some angle of attack with respect to the local flow direction. Vortex generators with heights on the order of the local boundary layer thickness have been found to be most beneficial.

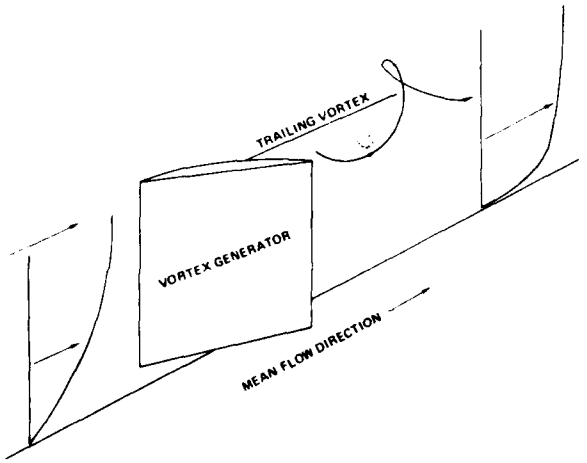

Figure 26.2.1-24. Boundary Layer Profiles Ahead and Behind Vortex Generator

g) Inlet Stability and Control

In this section we consider the external influences that tend to reduce the efficiency or to break down the process of mixed compression, and the control required to maintain efficient operation. We are primarily concerned with the location of the normal shock. If the shock moves downstream of its design position it becomes increasingly "supercritical" and occurs at a higher Mach number, increasing the total pressure loss of the flow. If the shock moves upstream to its critical position, the inlet will unstart.

The primary function of the inlet control system is to vary the supersonic diffuser geometry and bypass flowrate such that a relatively constant throat Mach number is maintained, and the normal shock is positioned just downstream of the aerodynamic throat. The throat Mach number is a function of the throat area, the capture area and the freestream Mach number. The throat area could thus be scheduled against the flight Mach number. A more convenient signal is obtained by monitoring the local pressure from which throat Mach number may be calculated. For instance, the control system may be programmed to maintain a reference value of the static to total pressure ratio in the throat by increasing or decreasing the area. The normal shock position may be controlled in like manner by programming the bypass control to maintain a fixed local static to total pressure ratio at some point downstream of the design position of the normal shock. These systems can cope with relatively slow but substantial changes in the freestream Mach number, and flowrate, respectively, and thus have a finite response time. The normal shock is also subject to small amplitude transient disturbances and it must have an inherent margin of stability. For example, a sudden reduction in upstream Mach number (commonly referred to as a tail gust) may occur when crossing the boundaries of a jet stream. If the design throat Mach number were one, the gust would unstart the inlet. Limited stability against this type of disturbance Mach tolerance is obtained by using a reference throat Mach number greater than one. The required tolerance can be determined from statistical analysis of atmospheric conditions at the operating altitudes. Increasing the Mach tolerance in this manner reduces the total pressure recovery potential of the inlet. We may note that a gust causing an increase in M_∞ results in a temporary reduction of recovery.

The normal shock must also have stability against downstream transient disturbances. Limited normal shock stability is provided by two natural flow characteristics if the reference position of the shock is chosen to be slightly supercritical. First, a reduction in the corrected airflow demand of the engine causes the shock to move upstream, but since the shock is moving toward its critical position, the downstream recovery is increasing, thereby reducing the downstream corrected flow without changing the absolute flow rate. Second, an increase in throat bleed generally accompanies the forward motion of the normal shock, which reduces the primary flowrate of the inlet. This occurs since, as mentioned, the boundary layer is usually bled near the operating position of the normal shock; as the shock travels upstream it increases the static pressure acting on the bleed region, thereby increasing the bleed flowrate. For some applications the natural stability of the normal shock must be augmented with a fast response valve system to vent excess airflow which the throat cannot handle overboard.

The same built-in stability characteristics of the inlet provide limited tolerance to variations in the inlet angle of attack. However, if high speed maneuverability is a design requirement this may be insufficient. At higher angles of attack, mixed compression inlets generally require powered control.

h) Supersonic Inlet Drag

A generalized schematic of the external forces acting on a supersonic inlet is shown in Figure 26.2.1-25. The internal forces are a part of the thrust expression and we shall not be concerned with them here. The additive drag is equal to the streamwise component of the pressure force acting on the surface of the capture stream tube. When the bow shock impinges on the cowl lip, the capture stream tube surface becomes parallel to the freestream direction, and the additive drag vanishes. If the normal shock is positioned upstream of the inlet duct, part of the supersonic capture flow will be spilled around the cowl lip. The force associated with the spilled flow and the resulting change in the axial pressure force on the external cowl are combined in the

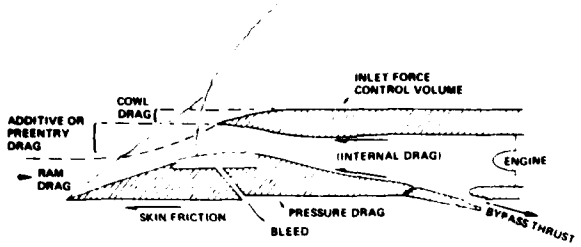

Figure 26.2.1-25. Forces Acting on a Supersonic Inlet

normal shock spillage drag term. When bleed or bypass flow is vented overboard, three aspects of the resulting force must be recognized. These are, first, the momentum deficiency of the fluid; second, the flow discharge angle and of the thrust vector is lost; third, the shock generated by the discharge flow which increases the cowl pressure force. Spillage and discharge flows may alter the cowl boundary layer development, the associated spillage drag change is difficult to isolate. Unless the external cowl is parallel to the freestream direction, the pressure force acting on it will have a streamwise component in the drag direction. Minimizing the external cowl angle is an important part of the inlet design. Typically, for an inlet of a specific design, the sum of drags due to spillage and due to bypass minimize at some combination where both are present. Figure 26.2.1-26 shows the variation of bypass drag and spillage drag and their sum which minimizes at some value of the inlet mass flow ratio.

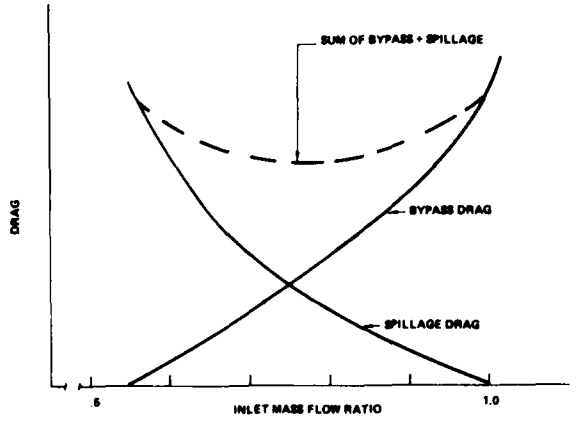

Figure 26.2.1-26. Bypass and Spillage Drag Variation at Instant M_N

The pressure drag is the force in the external flow direction which results from pressure forces acting on the body surface. Skin friction drag is a function of the wetted surface area and velocity distribution. The cowl drag and additive drag forces can be traded against each other for a minimum total drag configuration for a supersonic inlet like that shown in Figure 26.2.1-12 in a critical operation mode, i.e., with the first shock generating ramp pulled back so that it contacts the inlet lip at inlet mass flow ratio equal to unity we have the variations of cowl and pre-entry drag shown in Figure 26.2.1-27. In constrast, for well-designed subsonic inlets, the sum of these two drag components are very small, because the cowl drag is actually negative (lip suction).

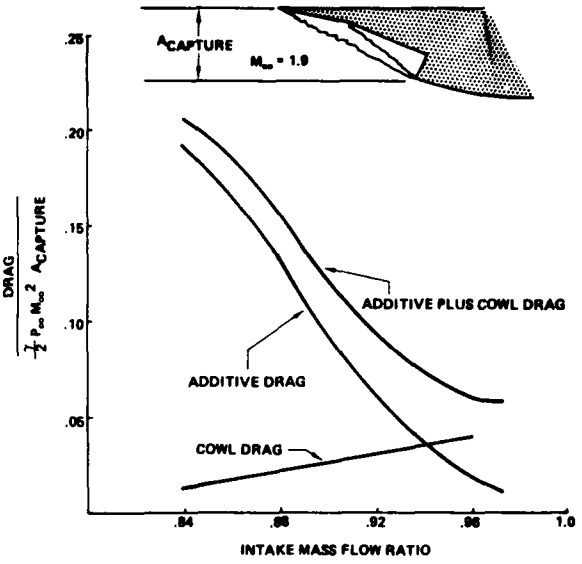

Figure 26.2.1-27. Additive and Cowl Drag Variation

All of these external forces interact with airplane drag. Propulsion and aerodynamic forces must be separated by carefully designed accounting techniques which minimize uncertainty in the performance within the constraint of work division and timeliness. The problem of force testing methodology is discussed in Sections 26.3 and 26.4.

2.1.3 Concluding Remarks

The inlet must perform the tasks of diffusing the high speed external flow to a speed that is acceptable to the engine with a minimum of total pressure loss. For minimum surge margin requirement and vibratory stress level in the blades, the diffuser should be devoid of temporal and spatial flow non-uniformities. The inlet's performance is usually given as a map of the (1) total pressure recovery, (2) distortion, and (3) turbulence, as a function of some imposed flow condition. This is usually corrected airflow (for engine cycle calculations), Mach number, or angle of attack (of interest for maneuvering flights). Figures 26.2.1-28 and 26.2.1-29 from Reference 26.2.1-10 allows a comparison of an axisymmetric and a two-dimensional inlet under varying Mach number and angle of attack conditions.

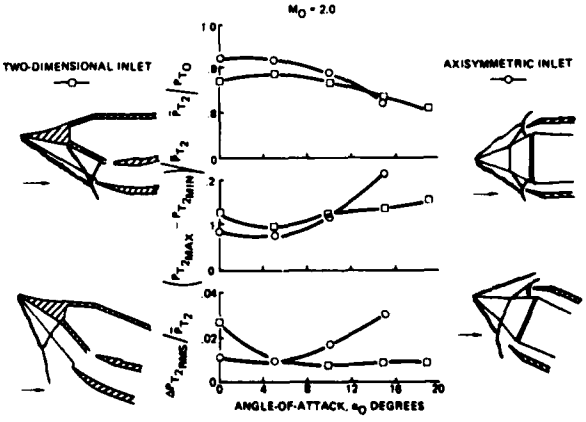

Figure 26.2.1-28. Isolated Two-Dimensional Versus Axisymmetric Inlet Performance in Maneuvering Flight

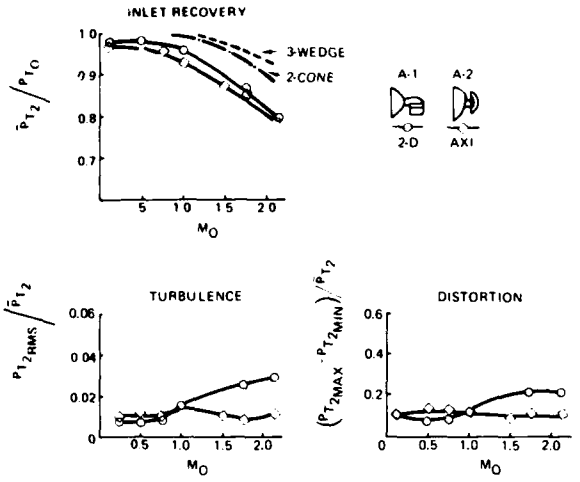

Figure 26.2.1-29. Two-Dimensional and Axisymmetric Inlet Installed Performance Variation with Mach Number

The third dimension of 2-D inlets presents a further design problem in that the side plates which bound the flow introduce the possibility of losses. For example the impingement of shocks on the boundary layer on the side plates gives rise to streamwise vorticity which may reduce the available flow area or may separate the flow along that wall. Boundary layer bleed systems to improve this situation are awkward to install because of the lack of space available in these thin plates. A means to reduce the need for bleed is to reduce the side plate area. Figure 26.2.1-30 shows the total pressure recovery characteristics for various configurations with varying degrees of "cutback" (expressed as a percentage of the normal distance from the ramp to the opposite lip). Note that zero cutback (full side plate) gives lower recovery. This configuration also shows a positive slope on the recovery map, indicating the possibility of instability or "buzz." With increasing cutback, the maximum air flow capability drops and recovery increases. The improved recovery is balanced by increased spillage drag associated with the air flow which can spill between the first shock and the cutback edge.

Modern computer methods allow the simulation of various operating conditions to aid in optimizing the inlet design. Under some circumstances experimental work is required to check out the results of the calculation or to obtain data for wide ranging conditions quickly and easily. While the problem of Reynolds number simulation is not of concern for the simulation of the major portions of the flow (see Figure 26.2.1-31 from Reference 26.2.1-11), for controlling shock boundary layer interactions, and for the design of bleed systems, the boundary layer characteristics must be understood.

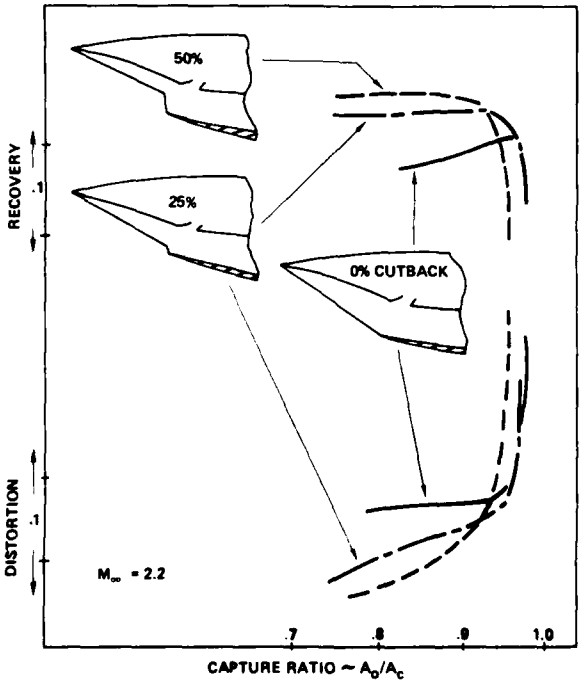

Figure 26.2.1-30. Two-Dimensional Characteristics With Varying Amounts of Sideplate Cutback

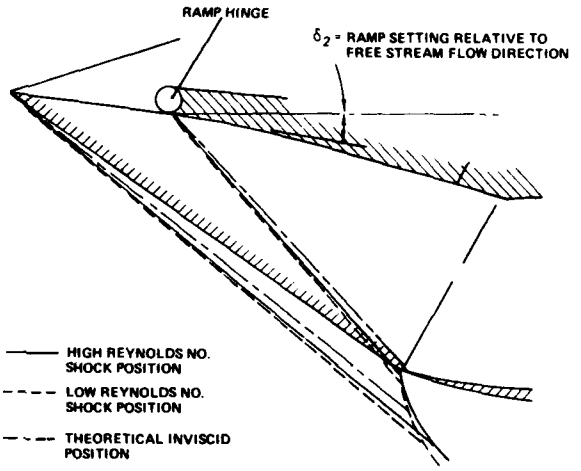

Figure 26.2.1-31. Effect of Reynolds Number on Critical Shock Pattern ($\delta_2 = 9.6^o$, $M_\infty = 1.9$)

The design of the inlet thus revolves around the problem of managing the behavior of the boundary layer. For subsonic applications this can be usually achieved by properly sizing and contouring the inlet surfaces. Supersonic inlets generally require active control, i.e., surface suction or blowing.

26.2.2 Exhaust System

26.2.2.1 Functional requirements of the nozzle.

The primary function of an aircraft engine propulsion nozzle is to divide the power available from the combustor exit gas between the requirements of the turbine and the jet power. The nozzle thus serves as:

a) a back pressure control mechanism for the engine, and as
b) a gas acceleration device to convert the available thermal energy of the gas to jet kinetic energy.

Secondary design considerations for the nozzle are requirements for:

c) thrust reversal and vectoring,

d) control of infrared (IR) radiation and rear radar cross section, and
e) matching the external contours of the airplane aft-body.

a) Engine Back Pressure Control

The nozzle throat size is the primary means available to the airframe designer to control the thrust or fuel consumption characteristics of the engine. A particular design choice of the nozzle area determines the thrust at takeoff and cruise. Within the constraints of the turbo machinery, performance at one of these conditions may be maximized at some expense to other operating conditions. The choice of size, and perhaps variability, is thus made on the basis of the propulsion requirements of the engine.

For a specific nozzle throat area, the ability to pass the desired engine mass flow is usually measured in terms of discharge (or flow) coefficient:

$$C_D = \frac{\dot{m}\ (\text{actual})}{\dot{m}\ (\text{ideal})} .$$

At nozzle pressure ratios near or below that required for choked flow, the discharge coefficient may be influenced by external flow effects as well as by nozzle shape. These external effects may be associated with the local pressure due to the flow around the aft body, or local pressure variations due to the presence of wakes from control surfaces. In the case of a primary nozzle of a bypass engine, the external flow is that of the fan stream. When the threat velocity is sonic all of the external flow determines the aerodynamic throat size for the nozzle and thus controls its mass flow carrying capability. Figure 26.2.2-1 shows the magnitude of the effect on a 3/4 length fan cowl nacelle operating statically.

In afterburning engines, large changes in nozzle throat area are necessary to compensate for the large changes in density due to changes in temperature. If a variable area nozzle is required for afterburning, it can also be used for back pressure control at non-afterburning power settings.

b) Expansion of Engine Flow

Ideally, maximum thrust is realized when the compressed engine flow is fully expanded to ambient pressure. For nozzle pressure ratios above choking, supersonic expansion must be realized along aft-facing internal or external surfaces. A small amount of underexpansion does not produce significant thrust losses; overexpansion, however, is more harmful. Figure 26.2.2-2 shows these thrust losses for isentropic, hot flow, and the nozzle expansion area ratio needed for full expansion, as a function of nozzle pressure ratio. Here C_V is the ratio of thrust obtained by expansion to area A to thrust obtained by expansion to the area where the exit pressure matches ambient pressure.

The nozzle pressure ratio is a function of ram pressure ratio, inlet recovery, and engine pressure ratio. Even at low engine pressure ratios, the nozzle pressure ratio and required area ratio rise quickly at supersonic airspeeds and convergent-divergent nozzles (or equivalent plug nozzles) are usually required for supersonic airplanes. When engine operation with variable augmentation is required, complex variable-geometry nozzles must be employed. To date, these are convergent-divergent nozzles with variable throat and exit areas. The throat area is controlled to satisfy engine back-

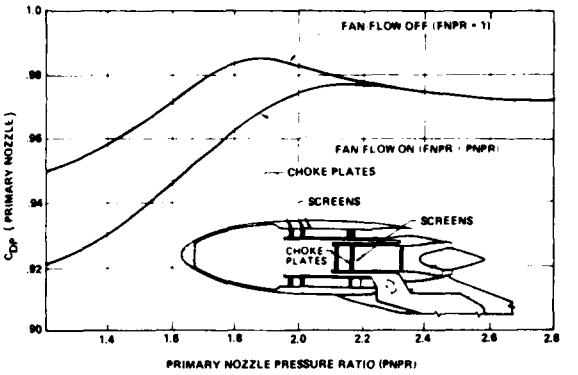

Figure 26.2.2-1. Fan Flow Suppression of Primary Nozzle Flow on a Blown 3/4 Length Fan Cowl Nacelle

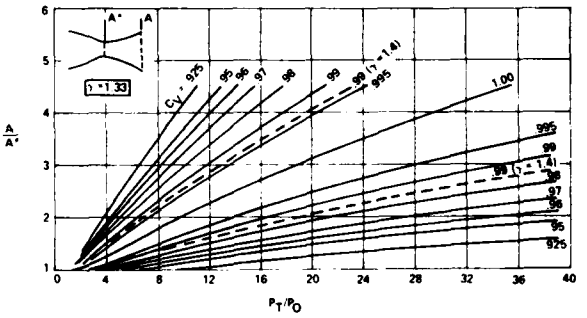

Figure 26.2.2-2. Nozzle Non-Ideal Expansion Loss $\gamma = 1.33$

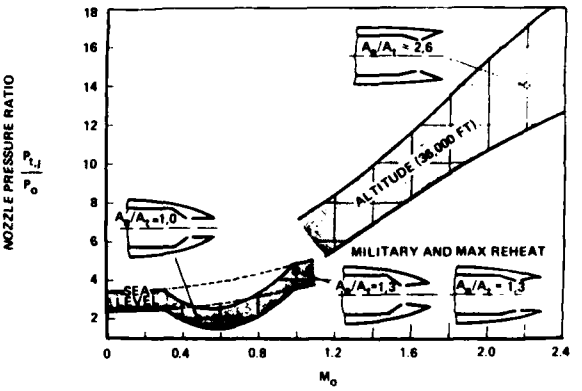

Figure 26.2.2-3. Required Variation of Nozzle Geometry of a High Performance Fighter Aircraft

pressure requirements. The exit area is scheduled with throat area. The most sophisticated nozzles, such as those on the F-15 and B-1, have two schedules, a low speed mode and a high speed mode. Figure 26.2.2-3 shows the magnitude of the required area variation for a high performance fighter aircraft throughout its flight speed regime. Various nozzle designs which achieve to some extent the objectives of exit and throat area variability are shown in Figure 26.2.2-4. In this figure the short arrows indicate the presence and flow direction of cooling air which is usually engine bypass (inlet bleed) or compressor bleed air.

c) Airframe Related Considerations: Reversers and Vectoring

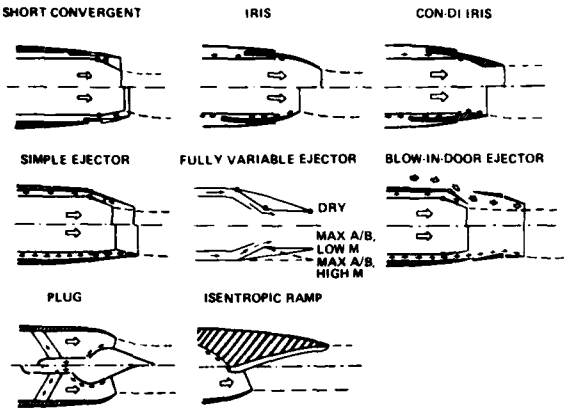

Figure 26.2.2-4. Typical Nozzle Concepts for Afterburner Engines

Thrust reversers are commonly used to supplement brakes on commercial transports to aid in stopping when brake effectiveness is reduced. In-flight thrust reversal has also been shown to enhance combat effectiveness of fighters, although no current operational fighters have reversers.

Basically, there are two types of reversers. In the blocker and cascade concept, the normal nozzle exit is blocked off and cascades are opened in the duct upstream to reverse the flow. The other concept moves the blockers downstream of the nozzle exit, such that the jet stagnates against them and then spills in the reverse direction (see Figure 26.5.5a). Combinations of concepts have also been investigated.

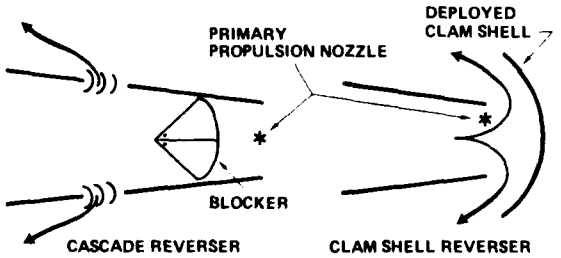

Figure 26.2.2-5a. Thrust Reversers

Thrust reversing mechanisms usually produce a change in effective nozzle area during deployment or when deployed. Reversers are designed, with an area to match the engine, within the specified limits at takeoff power. This match is usually verified by tests using the actual hardware because the impact on the complex nonlinear engine characteristics, such as stall and blade vibration, cannot be obtained analytically. Typically, exit area tolerances range from ±.5% for the gas generator (or primary) to as much as -1 to +10% on separate flow fan nozzles.

Because exit area mismatch cannot be accepted until the engine's tolerance to mismatch has been determined, a substantial risk is involved in the reverser design in that it may not turn out to be internally compatible with the engine. A new reverser must have sufficient design flexibility in exit area to cover this contingency and must be as efficient as possible to minimize the flow turning losses that cause mismatch conditions at intermediate power settings. The need for model and full scale tests must be anticipated on some reverser configurations, in addition to early coordination with the engine manufacturer. The reverser should also accept a limited engine growth (up rating) where internal pressures, temperatures and airflow may be increased (assuming no major change in hardware size).

Transient area mismatch during reverser deployment or stowage often grossly exceeds the steady state limits on some installations. Fortunately, the exit area of most reversers is increased rather than decreased during the brief transition period. A sudden reduction in exit area during reverser transition may cause engine stall and thus must be investigated carefully before the reverser design is committed to production.

The successful match between reverser (usually designed and built by the airframe manufacturer) and engine is achieved with the timely establishment of matching requirements between the respective manufacturers. This matching problem usually increases in severity with increasing nozzle pressure ratio.

Aside from back pressure problems, reversers can lose their effectiveness or create side effects when improperly installed. Reingestion and cross-ingestion of reversed hot flow may cause engine thrust losses and surging, thus reducing installed reverse thrust. The danger is reduced by limiting the turning angle of the reverser and by judicious selection of direction into which the reversed gases are exhausted. Care must also be taken not to create stagnation areas between free stream flow and engine flow under the wing, as this decreases the downward load on wheels and reduces braking effectiveness. Down-and-forward pointed jets stir up dust, gravel and "foreign objects" off the runway which may be ingested by the engine, causing accelerated wear and damage.

Thrust vectoring by means of nozzles is used on VTOL airplane and has been proposed for improved maneuvering and lift augmentation in combat. Thrust vectoring, like reversing, may be accomplished by internal turning (e.g., "lobstertail" duct or external turning) such as deflection by a target or coanda effect along a curved surface. Examples are shown in Figure 26.2.2-5.

Control of nozzle effective area may pose problems as it does for reversers. For VTOL and combat airplanes, it is desirable to vector the thrust at augmented engine power settings. However, cooling of structure in contact with turning or stagnating flows is very difficult, as film cooling becomes impractical in such cases. The only operational VTOL combat airplane, the AV-8 or Harrier, does not use augmentation.

d) Control of IR Radiation and Rear Radar Cross Section

Infrared-guided missiles have caused signifi-

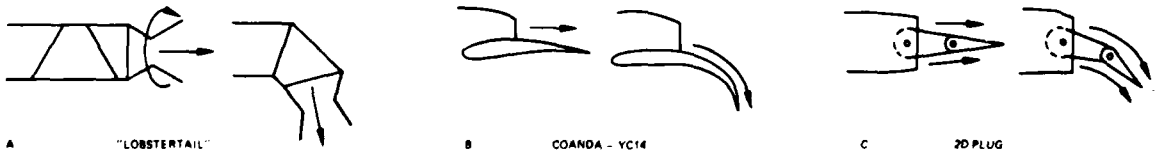

Figure 26.2.2-5b. Thrust Vectoring Nozzle Concepts

cant aircraft losses in 1973 in the Middle East war. Aft facing, visible hot engine and nozzle parts provide an excellent source of radiation. The last stage of the turbine is plainly visible through the exit area of an axisymmetric, convergent-divergent nozzle. It also serves as a good reflector of incoming radar signals.

Control of radiation is accomplished by concealing hot metal from direct view as in a plug nozzle cooled by unaugmented fan flow or ram air. Similarly, an external plug will scatter incoming radar energy and return a much weaker signal than a short conventional nozzle.

e) The matches of external airplane contours to the nozzle is discussed in detail in section 26.2.2.3

26.2.2.2 Nozzle Internal Performance

The efficiency of converting enthalpy available at the turbine exit to jet kinetic energy depends on losses ahead of the nozzle and losses associated directly with the nozzle. These losses are discussed for each of the common nozzle types.

a) Duct Flow Performance

The flow leaving the engine is generally ducted at low Mach number from the engine to the nozzle. When the flow arrives at the nozzle for expansion to lower pressure, the velocity field is three dimensional and unsteady because of imperfect mixing, nonuniform combustion (for instability suppression), and of drag on any surfaces between the engine and the nozzle.

The nonuniform flow through the nozzle may be described using approximate theories for several limiting cases. The simplest approach for determining thrust and mass flow is to obtain area or mass flow averages of the total pressure and temperature and calculate the one-dimensional values of these quantities. A better approach (which is particularly appropriate in cases where the distance between the nozzle station pressure and temperature profiles are known, and where the nozzle exit is short) is to assume that the flow consists of layers which are separated by contact surfaces that prevent mixing but allow pressure communication across the flow. Thus the flow is modelled as a set of parallel flows which can each expand to the exit pressure and contribute to the total exit momentum. The method of Reference 26.2.2-1 can be used for this calculation.

On the other extreme, if mixing is permitted by a long duct (L/D ~ 10) or is promoted through the use of an internal mixer, jet characteristics may be calculated using one-dimensional flow theory for a constant area mixer (if appropriate). For such cases, the conservation statements for mass, momentum and enthalpy can be used to calculate conditions at mixer exit or nozzle entrance which are then used for calculating average total temperature and pressure.

For most conditions of interest, the spread in thrust using the various models described above is quite small. Assuming that the real flow behavior lies between these extremes, there is a good probability that thrust uncertainty due to nonuniform flow effects is less than the spread between mixed and unmixed cases.

It is of interest to note that under many circumstances, the profiles or averages of total pressure and temperature are difficult to obtain. Often, insufficient instrumentation is used to prevent excessive losses due to the presence of these instrumentation probes. Furthermore, the flow behind the turbomachinery is rarely sufficiently steady and uniform to enable the measurement of desired flow quantities at all power settings (RPM) with fixed geometry instrumentation. The approach generally taken to circumvent this problem is to develop instrumentation correlations between flight nozzles and so-called "reference nozzles" whose behavior is well understood. Such correlations are usually carried out for easily measured average pressures and temperatures. A discussion of the steps necessary to minimize thrust determination error is described in Reference 26.2.2-2 relative to a turbo-powered propulsion simulator (TPS). In real engines, this calibration is more difficult in that the facilities, the equivalent of which were developed for the small scale TPS, do not exist or cost too much to run.

Drag on items in the flow duct is usually treated by calculating the equivalent one dimensional average total pressure reduction associated with the drag forces. In this way struts, coolers, splitters, reverser links, turning vanes and instrumentation may be accounted for. The increments are usually assumed independent so that the total pressure drop is the sum of all the invidual contributions. The fractional total pressure drop of an item with wetted area A_w, where the local friction coefficient due to flow at Mach number M_L is C_f, can be calculated from

$$\frac{\Delta P_t}{P_t} = -\frac{1}{2} M_L \frac{A_w}{A} C_f$$

or from (Reference 26.2.2-3):

$$\frac{\Delta P_t}{P_t} = -\frac{1}{2} M_L C_D \frac{A_{Ref}}{A},$$

under circumstances where the drag coefficient C_D based on the reference area A_{Ref} is known. Here A is the flow cross sectional area. The friction coefficient C_f is determined from empirical correlations appropriate to the geometry in question.

The boundary layer on the side walls grows thicker because of the frictional retarding force. This force may be larger than the flat plate shear force because of the roughness of walls due to acoustic treatment and because of steps and gaps resulting from assembly and the necessity for access doors, etc. For acoustic liners, values of the friction coefficient determined experimentally are generally used. Steps and gaps are handled as described in Reference 26.2.2-4, 5 if accuracy of this level is warranted.

Boundary layer buildup on the inside of the nozzle causes an effective reduction in internal flow area, as well as a thrust penalty due to skin friction. The thrust loss may be found from the boundary layer momentum loss as follows:

Consider the convergent nozzle shown in Figure 26.2.2-6. Assume incompressible fully expanded flow. The gross thrust is the integral of the exit momentum, viz:

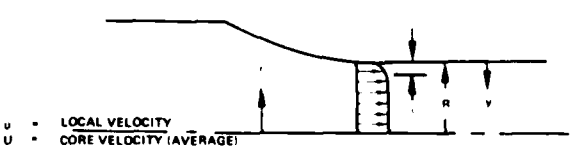

Figure 26.2.2-6. Nomenclature Definition

THRUST =

$$F = 2\pi\int_o^R \rho u^2 r dr = 2\pi\int_o^{R-\delta}\rho u^2 r dr + 2\pi\int_{R-\delta}^R \rho u^2 r dr$$

$$= \pi\rho U^2(R-\delta)^2 + 2\pi R\int_o^\delta \rho u^2 dy \text{ for } \delta << R.$$

This can be written as

$$F = \pi\rho U^2 (R-\delta)^2 + 2\pi R\rho U^2 \left[-\int^\delta(\frac{u}{U} - \frac{u^2}{U^2})dy - \int_o^\delta(1 - \frac{u}{U})dy + \int_o^\delta dy\right]$$

with the definitions

$$\int^\delta(\frac{u}{U} - \frac{u^2}{U^2})dy = \theta = \text{incompressible momentum thickness,}$$

$$\int^\delta(1 - \frac{u}{U})dy = \delta^* = \text{incompressible displacement thickness,}$$

we have for the total momentum leaving the exit plane

$$= F = \pi\rho U^2(R^2 - 2\theta R - 2\delta^* R), \text{ again using } \delta << R.$$

The air mass flow rate is

$$\dot{m} = 2\pi\int_o^R \rho u r dr = 2\pi\int_o^{R-\delta}\rho u r dr + 2\pi\int_{R-\delta}^R \rho u r dr$$

$$= \rho\pi(R-\delta)^2 U + 2\pi\int_{R-\delta}^R \rho u r dr \approx \pi\rho U(R-\delta)^2$$

$$+ 2\pi R\rho U\left[\int_o^\delta dy - \int_o^\delta(1 - \frac{u}{U})dy\right]$$

with $\delta << R$

$$\dot{m} = \rho\pi(R^2 - 2\delta R + \delta^2)U + 2\pi R\rho U\delta - \rho 2\pi R U\delta^*$$

$$= \pi\rho U\left[R^2 - R\delta^*\right]$$

Then defining

$$C_D = \frac{\dot{m}}{\dot{m}(\text{ideal, } \delta=0)}$$

$$= \frac{\rho\pi R^2 U - 2\pi R\rho U\delta^*}{\rho\pi R^2 U}$$

$$= 1 - \frac{2\delta^*}{R} \text{ where the last term represents}$$

the loss in discharge coefficient due to the presence of the boundary layer.

Similarly, defining

$$C_v = \frac{F}{F(\text{ideal, } \delta=0)} = \frac{F}{\dot{m}U}$$

$$C_v = \frac{R^2 - 2R(\theta + \delta^*)}{R^2 - 2R\delta^*} = 1 - \frac{2\theta}{R}.$$

Boundary layer calculations such as these may be useful for smooth-walled model nozzles with large wetted areas. Even there, due to the highly accelerated flow, flat-plate (zero pressure gradient) equations for δ, δ^* and θ vs Reynolds number will not produce accurate results. In real nozzles, internal steps, leaking, secondary and cooling flow preclude the application of elementary boundary layer theory.

b) Nozzle Performance Prediction from Empirical Correlations

Convergent-Divergent Nozzles

Each U.S. aircraft engine company has established its own methods for estimating full scale internal performance for convergent-divergent nozzles. In regions of attached internal flow, these methods are similar in theory and account for performance losses resulting from viscous effects, flow angularity, underexpansion, and flap seal losses.

In one method three operating regions are recognized:

Region 1 unchoked and separated at throat (approximately constant thrust coefficient) with varying nozzle-pressure ratios;

Region 2 choked throat, separated within the divergent section; and

Region 3 flowing full (choked throat and attached supersonic flow throughout divergent section).

The GE and P&WA formulations are very similar in Region 3:

P&WA	GE
$F = C_v \times$ Ideal Thrust	$F = C_{fg} \times$ Ideal Thrust

$$C_v \text{ (P\&WA)} = C_{fg} \text{ (GE)}$$

P&WA

$$C_v = \frac{C_s(\dot{m}_9 V_9 + P_9 A_9) - P_o A_9}{F_i}$$

GE

$$C_{fg} = \frac{C_v C_\theta \dot{m}_9 V_9 + (P_9 - P_o)A_9}{F_i}$$

Here F is the nozzle gross thrust. Figure 26.2.2-7 illustrates the nomenclature.

The similarities between the two expressions are quite evident in this form. Note that $C_s \neq C_v C_\theta$ because $C_v C_\theta$ multiplies only the momentum term, while C_s also multiplies a pressure term. Both C_s and $C_v C_\theta$ are described to be composed of the same three parts:

1) A loss due to angularity of the exhaust velocity vector at the exit plane.
2) A loss in the magnitude of the velocity vector due to friction in the boundary layers.
3) A loss of mass flow between the nozzle charging station and exit plane due to leakage through the nozzle walls.

The coefficients C_s and $C_v C_\theta$ are obtained from model data where leakage is usually absent. For such models, the friction portion of the thrust loss increment can be calculated and the angularity portion is obtained by subtracting this calculated

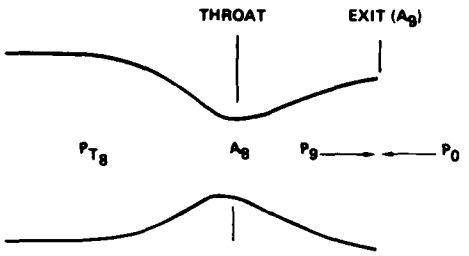

Figure 26.2.2-7. Convergent-Divergent Nozzle Nomenclature

increment from that measured on the model. For estimating full scale coefficients, the frictional portion is again calculated, with the increased Reynolds numbers and perhaps altered geometry upstream of the nozzle. This is added to the angularity component from model data and a full scale leakage estimate to obtain full scale C_s and $C_V C_\theta$.

The angularity stream thrust correction factor for full-flowing convergent and convergent-divergent nozzles is primarily a function of nozzle area ratio and divergence angle, and are independent of pressure ratio, specific heat ratio or external flow effects. C_s factors were determined for these nozzles from data correlations summarized in Figure 26.2.2-8.

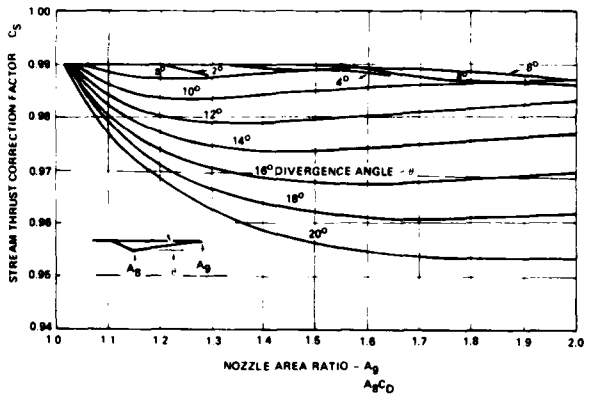

Figure 26.2.2-8. Convergent and Convergent – Divergent Nozzle Stream Thrust Correction Factor

Convergent Nozzles

The convergent nozzle has the advantage of simplicity and light-weight. Its performance is also good in the pressure ratio range of 1.0 to 5.0, making it a strong contender for use on subsonic airplanes or multimission aircraft that do not require long supersonic mission legs.

The simplest prediction methods for convergent nozzle performance are sufficient for preliminary airplane performance estimates. Results of parametric performance data from analytic studies and experimental tests of convergent nozzles are used for more accurate estimates of underexpansion losses. Such parametric studies are discussed in this section.

Experimentally determined sonic line locations for a typical convergent nozzle are shown in Figures 26.2.2-9A. These data, taken from Reference 26.2.2-6, show the variation of sonic line shape and location with nozzle pressure ratio. The nozzle discharge coefficient curves (Figure 26.2.2-9B), show that the discharge coefficient becomes constant at the same pressure ratio at which the sonic line position becomes fixed. Note that this pressure ratio for "hard choking" (i.e., mass flow independent of pressure ratio), does not correspond to the critical pressure ratio where a one-dimensional sonic line spans the nozzle exit. This results from the two-dimensional nature of the flow field. It will be evident from the following discussion that the pressure ratio for choked flow is one that allows a Prandtl-Meyer expansion approximately equal to the nozzle half angle.

Consider the nozzle in Figure 26.2-10(A) showing a 2-D supercritical but unchoked nozzle of half angle α. The sonic line and flow streamlines are shown. From point Q, a centered Prandtl-Meyer expansion expands the flow to p_0. If P_0 is not low enough (i.e., if the Mach number behind the expansion is not high enough), characteristics from points on the boundary, such as A, C, and E, intersect the sonic line at B, D, F; thus the pressure p_0 is felt upstream of the nozzle affecting the nozzle mass flow rate. The point E is the origin of the last characteristic which intersects the sonic line (at F) and is thus the limit line. When this limit line originates from the nozzle lip and fails to intersect the sonic line, the nozzle is choked. This flow configuration is shown in Figure 26.2.2-10(B). Note that the flow area is a minimum at the

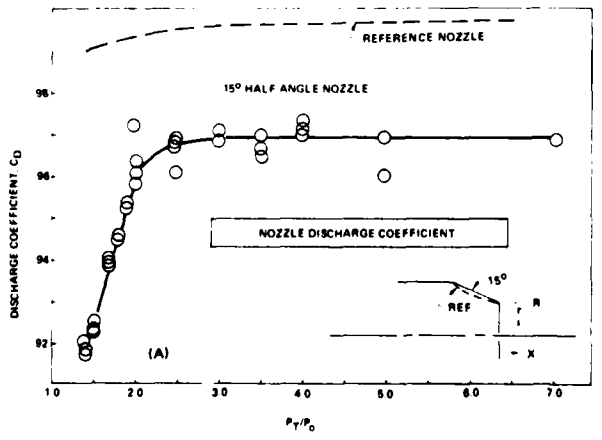

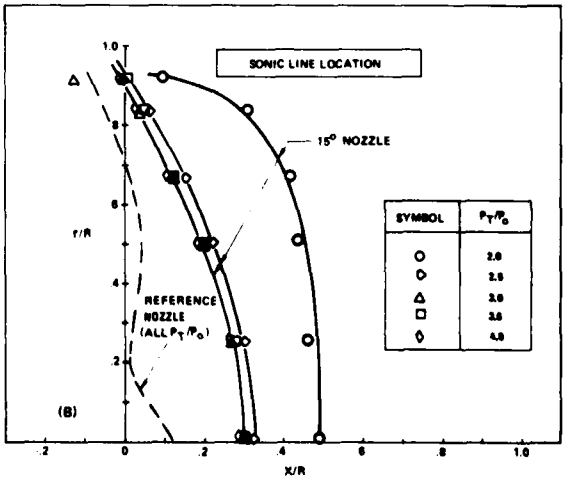

Figure 26.2.2-9. Sonic Line Location and Discharge Coefficient for 15° Convergent and Reference Nozzle

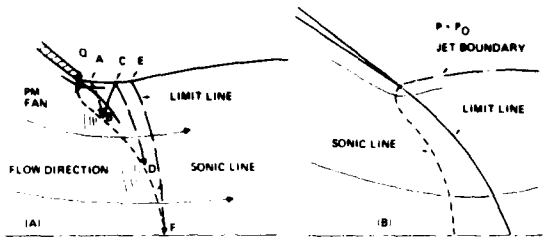

Figure 26.2.2-10. Flow in Convergent Nozzles (a) Supercritical and Unchoked, (b) Supercritical and Choked

nozzle exit plane at this choked condition, and the average Mach number at the exit plane is less than unity.

In the unchoked flow case, the identified points are located in the hodograph plane in Figure 26.2.2-11(a). The inviscid flow stream line along the wall is initially inclined at an angle α. Around the point Q, from Q to Q', the flow turns through the Prandtl-Meyer angle, ν, consistent with the pressure ratio. Since the static pressure on the jet boundary is constant and equal to ambient pressure, the velocity on the jet boundary (assuming inviscid flow) is everywhere equal to that at point Q'. Thus the jet boundary is represented on the hodograph diagram by a circle of radius $M^* = |Q'|$. The sonic line is represented by the circle $M^* = 1.0$ in the hodograph plane.

The hodograph plane is shown for the "just" choked flow situation in Figure 26.2.2-11(b). In this case, the limit line EF originates from the Point Q; i.e., points E and Q' on the hodograph plane coincide. Thus, the Prandtl-Meyer turning angle $\nu = \alpha/2$ as shown because, for two-dimensional flow, the characteristics in the hodograph plane are independent of the geometry of the physical plane and are identical to or are reflections of one another. In axisymmetric flow, the shape of the characteristics depends on the geometry of the flow and, therefore, are not symmetrical. Consequently, the choked pressure ratio for an axisymmetric nozzle is slightly higher than that for the two-dimensional nozzle of the same half angle.

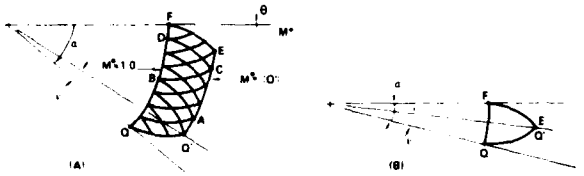

Figure 26.2.2-11. Holograph Plane Representation of the Critical Flow Though a Convergent Nozzle at Unchoked (a) and "Just" Choked Conditions (b)

Sonic line shapes and locations for other convergent nozzles may be computed for pressure ratios above 2 using the method of Reference 26.2.2-7. This has been done for a series of convergent nozzles applicable to aircraft use. Using these distributions, the inviscid nozzle discharge and velocity coefficients for non-one-dimensional flow of a perfect gas with $\gamma = 1.4$ were then computed by integration of flow properties over the exit plane as follows:

$$C_D = \frac{\int_0^{A_9} \rho u dA}{\text{Ideal one-dimensional mass flow}}$$

$$C_V = \frac{\int_0^{A_9} [\rho u^2 + (p - p_0)]dA}{\text{Ideal one-dimensional thrust}}$$

A_9 = Exit plane area

The resultant inviscid discharge coefficients are given in Figure 26.2.2-12 and the inviscid velocity coefficients are given in Figure 26.2.2-13. Note that highly convergent nozzles have a slightly higher velocity coefficient than indicated by one-dimensional calculations. This is due to the fact that values of $(\rho u^2 + P)dA$ are a minimum at M = 1.0; but for increasing convergence angle the sonic line bulges further out of the throat, as shown in Figure 26.2.2-9, changing the exit Mach number to local values greater than one.

For smooth-walled nozzles, boundary layer contributions to discharge and velocity coefficient losses may be computed as indicated in Section 26.2.2.2a. The accuracy of the method of correcting for boundary layer effects, when these are calculated by the technique described in Reference 26.2.2-8, has been checked with test data at pressure ratio 2.2. The discharge coefficient was predicted to within $\pm 1/2$ percent of measured values as shown in Figure 26.2.2-14, while the velocity coefficient was predicted to within ± 0.2 percent of measured values as shown in Figure 26.2.2-15.

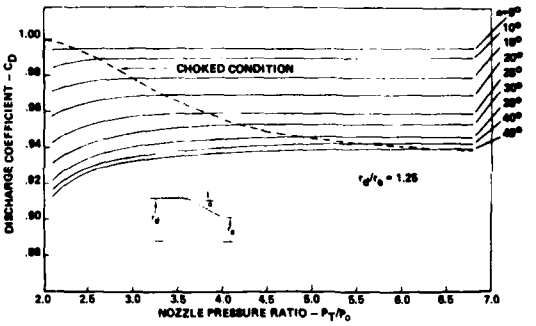

Figure 26.2.2-12. Inviscid Flow Discharge Coefficient of Convergent Conical Nozzles

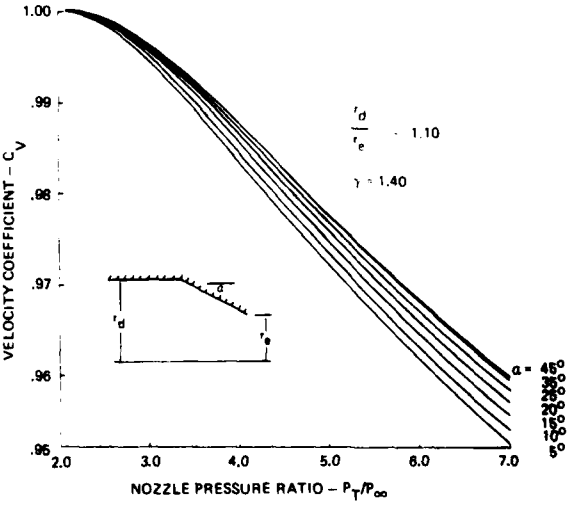

Figure 26.2.2-13. Velocity Coefficients of Convergent Conical Nozzles – No Viscous Losses

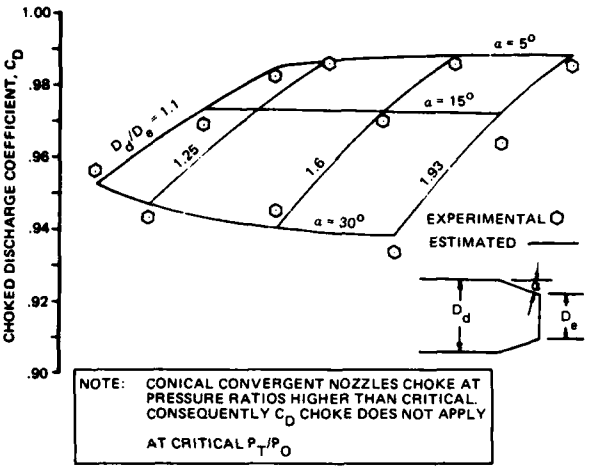

Figure 26.2.2-14. Parametric Variation of Conical Convergent Nozzle Choked Discharge Coefficient

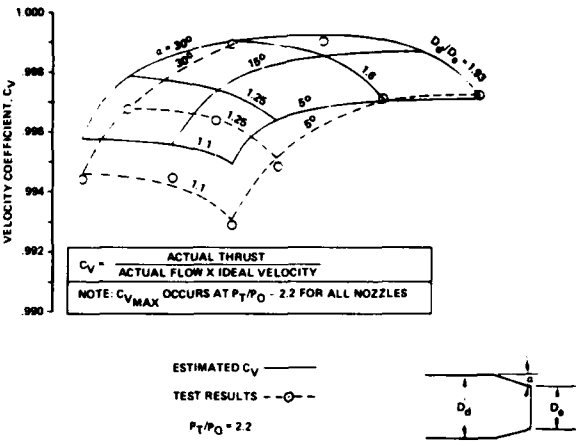

Figure 26.2.2-15. Parametric Variation of Conical Convergent Nozzle Velocity Coefficient

Multi-Element Nozzles

A multi-element nozzle differs from a conventional convergent nozzle in that the jet is broken into a series of smaller jets or into a jet with a longer perimeter (daisy petal design). The general purpose of such nozzles is to decrease the exhaust noise level by increasing the mixing of exhaust gases with the external air. A series of multi-element nozzle designs are shown in Figure 26.2.2-16. A mixing nozzle has a reduced maximum velocity coefficient when compared to a simple convergent nozzle. This performance reduction has been correlated in Reference 26.2.2-9 as a function of nozzle exit hydraulic diameter and is shown in Figure 26.2.2-16. This figure shows that the correlation method agrees quite well with test data from a wide range of nozzle designs equivalent to hydraulic diameters. The characteristics of multi-element C-D nozzles for SST-type aircraft are described in Reference 26.2.2-10, 11, 12.

Plug Nozzles

The plug nozzle is a form of convergent-divergent nozzle in which the flow expansion is guided partially by a nozzle centerbody, or plug, and partially by the surrounding external airflow.

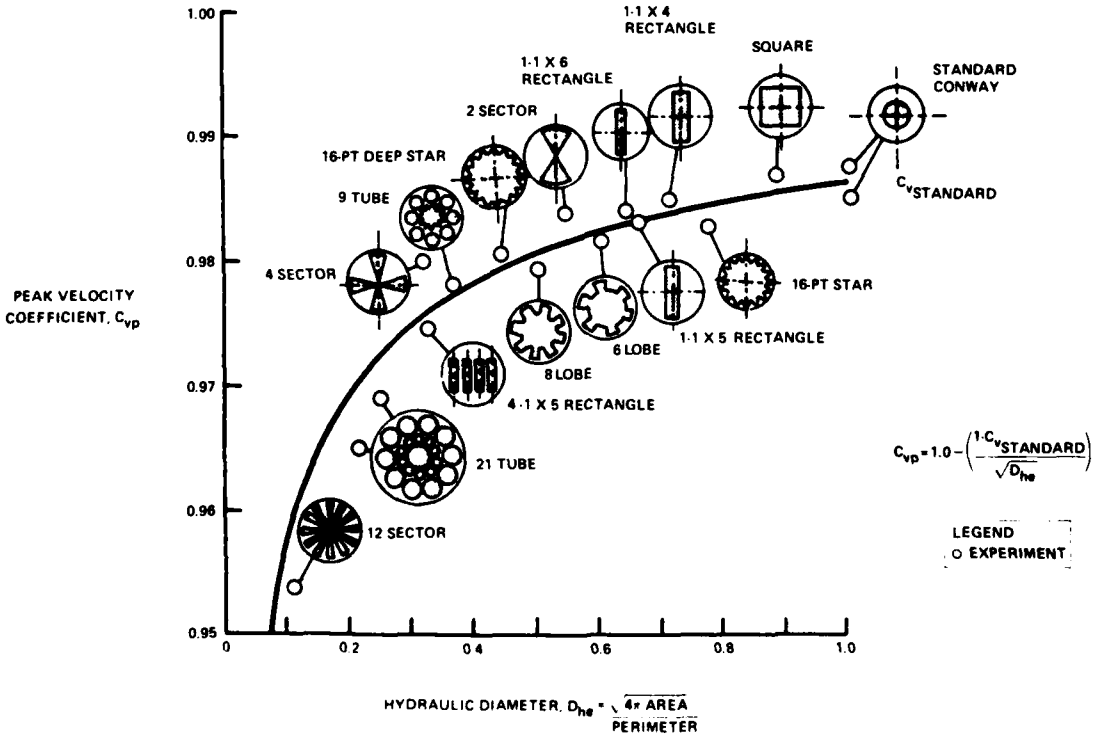

Figure 26.2.2-16. Convergent Nozzle Performance Maximum Velocity Coefficient for Noise Suppressor and Jet Mixing Configuration

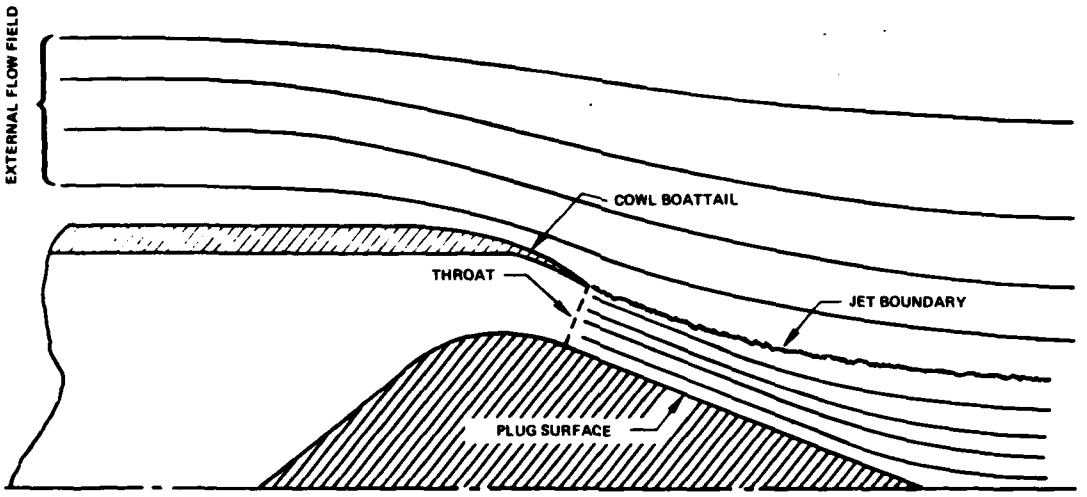

Figure 26.2.2-17. The Basic Plug Nozzle

Its performance is therefore slightly different from that of either a convergent or convergent-divergent nozzle. The basic plug nozzle concept is sketched in Figure 26.2.2-17.

The static performance of a simple conical plug nozzle as reported in Reference 26.2.2-13 is shown in Figure 26.2.2-18 along with a sketch of the nozzle geometry. Also shown in Figure 26.2.2-18 is the static performance of a convergent-divergent nozzle. The plug and C-D nozzle performance curves peak at their design pressure ratio and fall off above design pressure ratio. Below design pressure ratio the plug nozzle static performance exceeds that of the C-D nozzle. This higher performance has inspired development of plug nozzles.

The thrust-minus-drag of the nozzle of Figure 26.2.2-17 is low because of the steep boattail angle of the plug cowl. The worst drag problem is at low nozzle pressure ratios when the flow field around the nozzle is similar to that sketched. The external flow must turn to follow the outer boundary of the jet flow, thus causing low pressures along the plug and high drag. At higher pressure ratios, the jet expands more and only the cowl experiences a drag force.

Plug nozzles designed for low drag incorporate a low angle plug, generally a half angle of 12 degrees or less. The low plug half-angle tends to reduce nozzle internal performance so a shroud is generally provided to increase nozzle-guided internal expansion and consequently reduce total internal viscous drag and nozzle length. A shrouded plug nozzle of this type is shown in Figure 26.2.2-19.

Important design variables for these types of nozzles for subsonic nonafterburning aircraft are plug angle, cowl internal angle, plug truncation length, cowl exit to throat area ratio, throat inclination angle, and boattail angle. In the afterburning mode, the important design variables are shroud trailing edge position, internal area ratio, plug angle, plug truncation length, and boattail angle. The final nozzle design is usually a compromise to maximize total mission performance.

Geometry variations required of a plug nozzle for a multimission aircraft include changes in throat area and in the amount of internal expansion. Several methods of achieving each of these geometry variations are described in the following paragraphs.

Plug nozzle throat area can be varied by any combination of three basic methods. The plug can be expanded and collapsed, or translated fore and aft. The third method of throat area variation is to open or close the cowl to achieve the necessary area variation. Each method has some undesirable features.

Collapsing plugs require high temperature seals between moving plug leaves. They also require a large plug diameter to contain the necessary actuating machinery. These large plug diameters lead to either a steep plug and high drag or a long, heavy plug.

A translating plug with a low plug angle needed for high performance may require excessive plug lateral travel for adequate area variation. Further, the translating plug is cantilevered out from its actuator and may require heavy support structure.

A hinged cowl may form a steep boattail during nonafterburning operation.

A major problem of plug nozzles is the necessity for cooling the large expanse of plug surface during afterburning operation. This cooling, which is required for nozzle structural integrity, is complicated by the problems of ducting cooling air into the plug. The cooling air must be at high pressures, which means that compressor or fan bleed air must be ducted from the periphery of the engine into the plug. Losses in the ducting may be high, thus reducing engine installed performance.

Another plug nozzle design problem is the vibration of the plug which is cantilevered from its support struts. This poses structural and stability problems which must be considered in plug nozzle evaluation.

The plug weight can be reduced by plug truncation with resultant small performance penalties.

Two-Dimensional Nozzles

In recent years two-dimensional nozzles have aroused interest due to expectations that they can reduce the drag of rectangular fuselages with outboard twin vertical tails, and because they lend themselves more easily to thrust vectoring and thrust reversal. A number of designs have been tested with good results. Data for specific configurations are shown in Reference 26.2.2-14.

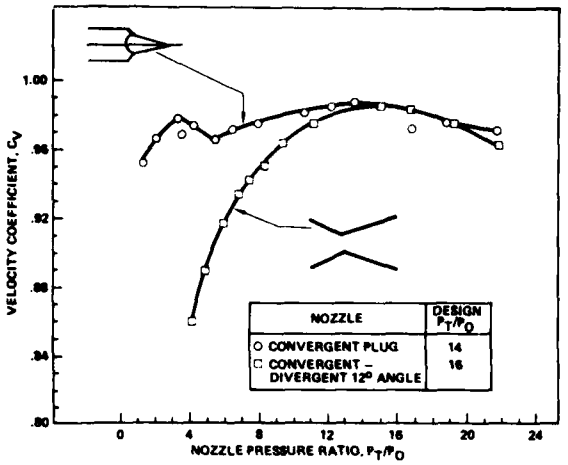

Figure 26.2.2-18. Plug Nozzle and Convergent – Divergent Nozzle Performance Comparison

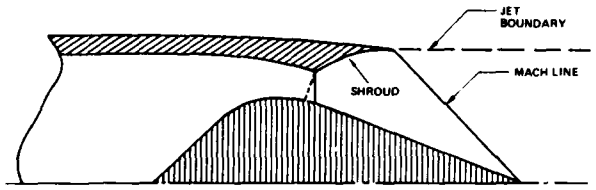

Figure 26.2.2-19. Shrouded Plug Nozzle

26.2.2-3 Airplane/Nozzle External Performance

Propulsive flows impact the behavior of the external aircraft flow because they meet at the nozzle exit. The flow field depends on the characteristics of the external flow. Thus, the proper determination of thrust and drag forces involves understanding the external flow near the nozzle. This flow is complex in that compressibility and viscous effects are important because the aftbody's role is to smoothly recompress the flow around the aircraft. The region is characterized by local Mach number greater than freestream, thick boundary layer, and an adverse pressure gradient.

In the following, the analytic and empirical tools used for the design of aftbodies are described.

a) Analytical Methods

Although exact equations may be written for some inviscid cases, solutions on digital computers are always approximate to some degree. Some solutions are based on exact equations, others on linearized equations. Solutions have also been coupled with boundary layer solutions in an iterative manner. Pressure force integrations in the drag direction are very sensitive to the number and location of sources, sinks, vortices, etc., used to represent boundary conditions and body surfaces. Errors in the evaluation of pressure integrals in the axial direction are easily as large as measured pressure drags because of large opposing pressure forces. No pressure integrations in the drag direction should be accepted without checking for insensitivity to variations in the way the problem is formulated and checking the result against a known case, such as a pressure integral around a semi-infinite body in incompressible, potential flow.

Real flows at high Reynolds numbers, subcritical Mach numbers, and without separation, will behave much like incompressible, inviscid flow. Thus, inviscid analysis may be used to estimate interactions between forebody and afterbody, support system and model, and model and tunnel walls.

In the aerospace industry, many types of computer programs are available for solving flow problems. These vary in cost and accuracy and may be detailed as follows:

1) Incompressible, inviscid flow using distributed sources, sinks, and vortex lattices to represent bodies; two-dimensional and three-dimensional
2) Compressible subcritical inviscid flow about bodies of revolution using relaxation methods or linearized equations
3) Transonic flow analysis using streamline coordinate transformation and relaxation (handles shocks)
4) Method-of-characteristics analysis of 2-D and 3-D axisymmetric, supersonic flows, including oblique shocks and reflected shocks coupled to boundary layer solutions and shock-boundary layer interactions
5) Linearized supersonic 2-D and axisymmetric solutions
6) Linearized compressibility correction to #1.
7) Boundary layer solutions coupled to #2 and #3 in an iterative manner
8) Quasi-time dependent methods

Of these the axisymmetric flow programs and three-dimensional flow programs are most relevant for airplane configuration design. These two "classes" of analysis programs will be discussed below.

Axisymmetric Geometries, Subsonic Freestream, Flow Field Without Jet

This important class of analytical capability is generally directed toward nacelle inlet and nozzle design. The analytical prediction of the axisymmetric nacelle performance provides a basis for measuring the success of the installation process, for both external drag and for nozzle efficiency. The extent to which analysis can support the nacelle design is determined by Mach number.

The greatest success is found for nacelles which have entirely subsonic flow on the external surfaces and are free from large viscous effects. Incompressible, inviscid methods using distributed sources, sinks and vortices have been in use for some time. These basic solutions are corrected for compressibility and iteratively corrected for the displacement effect of the boundary-layer to yield predictions which are very accurate for surface pressures and drag. Recently these solutions have been extended to conditions where the nacelle boattail is separated. Figure 26.2.2-20 from Reference 26.2.2-15 shows the degree of success that has been enjoyed to date.

Recent developments have been successful in analyzing flows where M_∞ is less than unity, but with locally supersonic flows. These programs most frequently employ a transonic relaxation potential flow technique which is iteratively corrected by a boundary layer solution, until the converged flow field with imbedded shock waves is found. These solutions provide both the surface pressure distribution (Figure 26.2.2-21) and the drag.

In the absence of separation and at subsonic free stream Mach numbers, boattail drag consists of shear forces due to friction, pressure drag due to

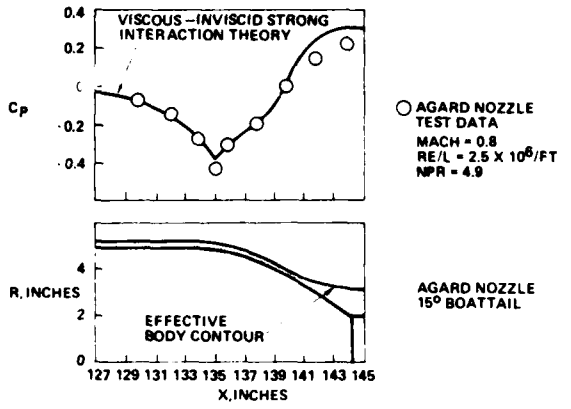

Figure 26.2.2-20. Analytical Prediction of Nacelle Boattail Pressures

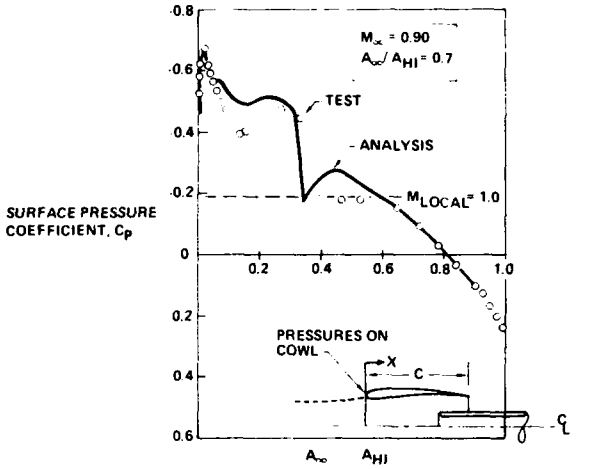

Figure 26.2.2-21. Transonic Cowl Pressures Comparison of Analysis and Test

displacement thickness growth (also due to friction), and shock losses when local supersonic flow pockets appear. Pressure drag due to displacement thickness is small (as long as separation does not occur). Therefore, the pressure drag of such boattails is generally very low up to a critical Mach number when shock losses appear. At this point a steep drag rise occurs. The new transonic analysis methods (Reference 26.2.1-3) can predict shock losses, but generally the appearance of shocks is soon followed by shock-induced separation, at which point the analysis becomes invalid.

Typical data for boattails are shown on Figure 26.2.2-22. It is seen that the drag rise is extremely steep for all boattails shown, and that below the drag rise, all longer boattails have very low pressure drags. The shortest boattail (L/D = .8) suffers from separation at all Mach numbers.

Generalizing from data of this type for various classes of boattails, we have:

1) Boattails with large radii of curvature have low pressure drags below the drag rise,
2) The drag rise Mach number is a function of boattail curvature and length
3) The drag rise is very steep for all boattails

These observations permit using subsonic and transonic analysis as a tool to avoid or recognize potentially high-drag boattails, i.e., those subject to subsonic separation and those which exhibit a drag rise below the expected flight Mach number.

Axisymmetric Geometries, Supersonic Freestream, Flow Field Without Jet

Supersonic boattail drag prediction is controlled by combinations of boattail curvature or angle and free stream Mach number. At higher Mach numbers and for lower boattail angles, when the shocks are weak and do not cause boundary layer separation, method-of-characteristics and streamline curvature methods can produce good results.

In supersonic flow, viscous effects are only part of the causes of pressure drag. Additional losses occur outside the boundary layer due to shock losses and wave drag. Wave drag is due to the flow acceleration over the afterbody and recompression at the trailing edge which cannot cancel the effect of expansion. Boundary layer effects tend to reduce the drag by reducing the initial expansion and allowing the pressure behind the trailing shock to propagate some distance upstream. Thus, inviscid results are generally pessimistic depending on boundary layer thickness. Shock-induced separation further reduces afterbody drag. A large body of experimental data is available for boattail drag at supersonic Mach numbers (see References 26.2.2-16 to 21). In addition, method-of-characteristics solutions have been obtained for conical, circular-arc and ogive boattails of various lengths and exit-to-maximum area ratios. Examples are shown on Figures 26.2.2-23 and 26.2.2-24.

Research activity in support of supersonic cruise airplane programs has also produced reliable flow field analysis methods for supersonic freestream Mach numbers ($1<M_\infty<5$). A modified version of the Lighthill method (Reference 26.2.2-22) is frequently employed. Another class of solutions predicts the wave drag of the nacelle from its equivalent area distribution (see Reference 26.2.2-23). Methods to handle the oblique shock-boundary layer interaction are being reported (Reference 26.2.2-24).

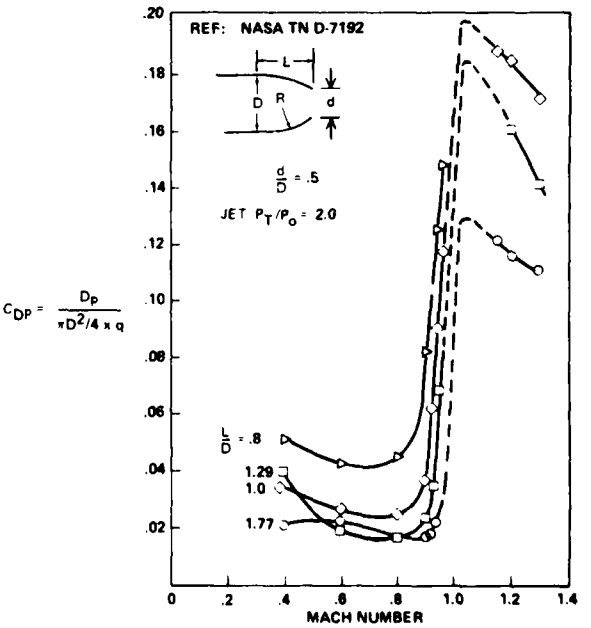

Figure 26.2.2-22. Experimental Pressure Drag Coefficients of Some Circular – Arc Boattails (Reference 26.2.2-20)

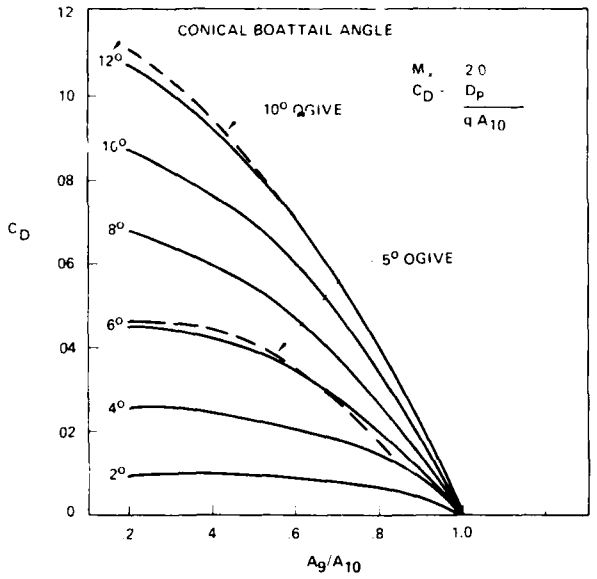

Figure 26.2.2-23. Method-of-Characteristics Prediction of Boattail Wave Drag (Ref 26.2.2-21)

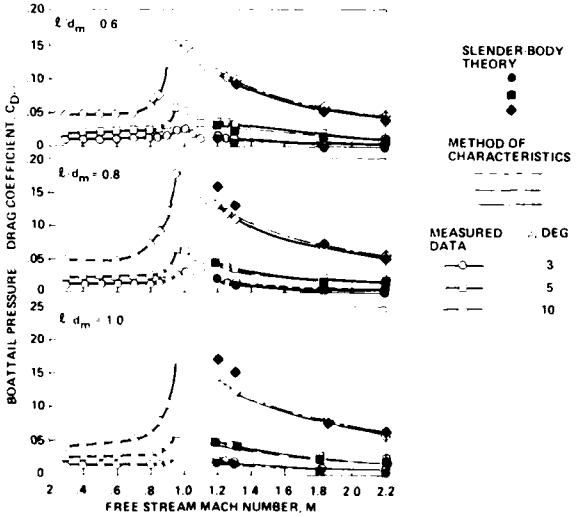

Figure 26.2.2-24. Variation of Jet – Off Boattail Pressure-Drag Coefficient with Mach Number

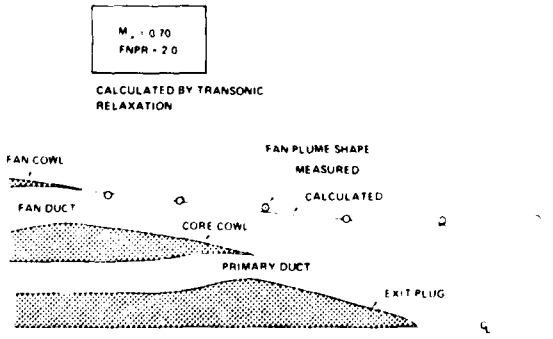

Figure 26.2.2-25. Plume Shape by Transonic Relaxation Method

Hypersonic flow, where the freestream Mach number is greater than five, is handled by several analytical methods (Reference 26.2.2-25) which give a good representation of the inviscid flow field about the configuration and are useful for design purposes.

Axisymmetric Geometries, Flows With Jets

The previous discussion has been about wall geometries with no exhaust jet. However, the exhaust jet can play a very important role in determining the overall flow field around the body, especially in the case of the nacelle. Current analytical capability for the exhaust jet characteristics is not as advanced as for the nacelle geometry and is divided into two classes, those with and those without mixing.

Jet Without Mixing

The first class of analysis methods assumes an inviscid, nonmixing jet. For subsonic external flow, there are three types of solutions. The first developed was the streamtube curvature technique, where the curvature of stream tubes within the jet and the external flow field are related by continuity and transverse static pressure balance. This method is not reliable when the exhaust jet becomes supersonic, because large local slope changes in the outer jet boundary begin to appear and drive the stream tube curvature to large values and the solution consequently diverges.

Better success is shown for the transonic relaxation technique, a method similar to that used for transonic cowl analysis. This method can represent subsonic and supersonic local flows in both the exhaust and external flow field. A measure of the accuracy of this kind of exhaust flow calculation technique is shown on Figure 26.2.2-25 (Reference 26.2.2-26). The transonic relaxation technique cannot predict the fine structure of the supersonic flow field. The method-of-characteristics (M-O-C) solution is used to calculate the flow field by finding the position of characteristic lines, which implies that the flow must be entirely supersonic (Figure 26.2.2-26). This means that use of M-O-C for the nacelle aft flow field must be an iterative solution with a potential flow technique, such as the transonic relaxation technique for the exterior flow, for the flow along the boundary of the plume, and for the subsonic flow in the plume.

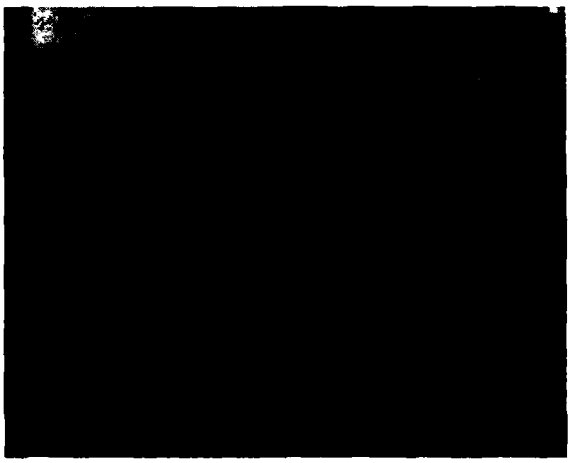

Figure 26.2.2-26. Nozzle Flow with Superimposed Methods of Characteristic Solutions

For the imbedded supersonic cells the M-O-C must be patched into the subsonic flow; this is a costly, tedious process which is not often used. Where the exterior flow is entirely supersonic, the M-O-C technique can easily be used for both the plume and exterior flow fields.

Jet With Mixing

The second class of jet modelling analyses is for plume shapes with the effect of mixing included. This analysis is not well established and is limited to the modeling of the mixed plume for subsonic exterior flow, as shown in Figure 26.2.2-27 (Reference 26.2.2-27). The mixed jet shape far downstream of the exit is well matched by analysis, but usually not near the exit plane.

Because they are still in the development stage, mixing analyses do not yet play a large role in analytical design capabilities. This is because at conditions where mixing is not important (attached flow boattails, nozzle pressure ratio <2, M_∞ <1), the mixing analyses do well; where mixing is important, for example M_∞ = 0 or large-angle boattails which have separated flow, mixing analyses are not yet reliable.

Three-Dimensional Geometries

Analytic method to support the design process for three-dimensional geometries (including axisymmetric geometries at angle-of-attack) is well developed for subsonic conditions, but are less accurate with increasing Mach number. The accuracy analysis also depends on whether the exhaust jet and remaining flow field are independent of each other or whether they strongly interact. Figure 26.2.2-28 summarizes the important jet-freestream flow interactions usually dealt with in aft body design.

Considering the independent flow situation first, the ability to analyze arbitrary configurations at subsonic speeds where the effects of viscosity are small but not necessarily negligible is well established. Figure 26.2.2-29 shows predicted versus measured surface pressures on a model flow-through nacelle at 0.7 Mach number; the surface pressures, drag and mass flow rate all compare very favorably with experiment. Similar results are obtained on full scale nacelles. The powered nacelle can be similarly represented by adding the isolated plume shape as a hard-wall geometry; Figure 26.2.2-30 shows this result. These calcula-

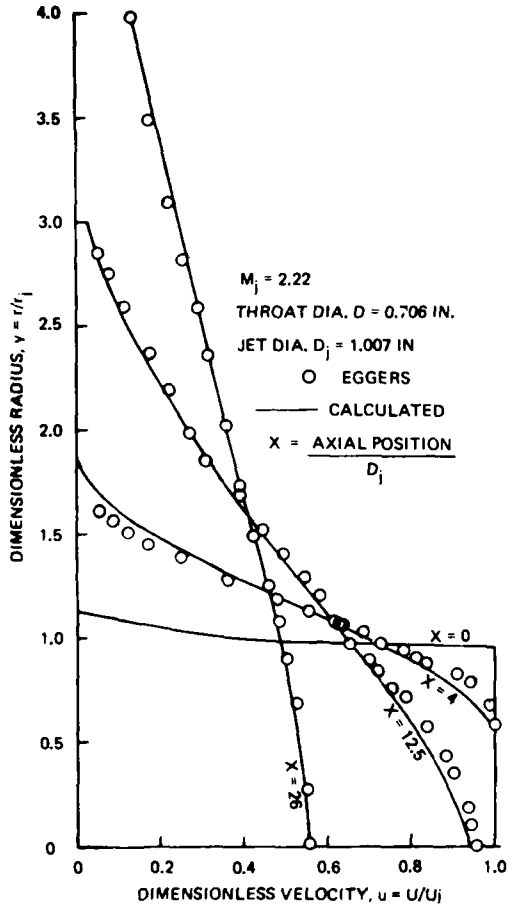

Figure 26.2.2-27. Mixing Analysis of a Single Round Jet, Mach 2.22

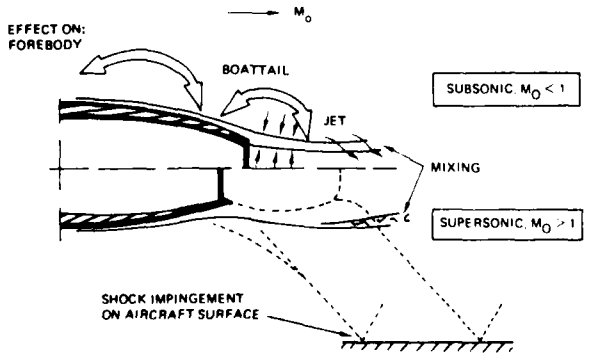

Figure 26.2.2-28. Jet-Airframe Interactions in Subsonic and Supersonic Flight

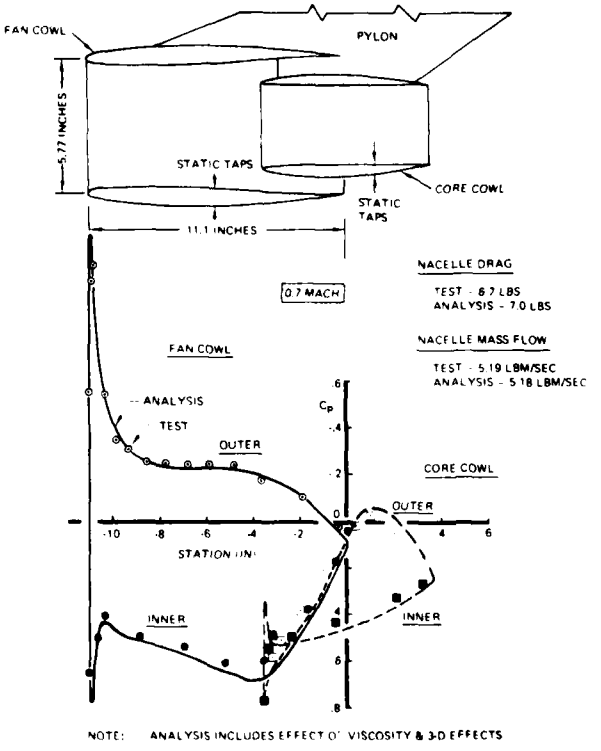

Figure 26.2.2-29. Analytical vs. Experimental Determination of Flow Nacelle Properties

tions are typical of compressibility-corrected, linearized solutions with boundary conditions applied as sources, sinks, and vortices in the flow field (Reference 26.2.2-28). In the general three-dimensional case, the effect of viscosity cannot yet be reliably determined.

Extensive examinations of various potential flow analysis methods with boundary layer corrections have been conducted by Lockheed and Pratt & Whitney under the program titled, "Experimental and Analytical Determination of Integrated Airframe Nozzle Performance," and are reported in References 26.2.2-29, 30.

Because many aircraft cruise under conditions of subsonic free stream Mach number with local regions of imbedded supersonic flow, analytic capability in this flight region is important. These methods are just becoming established for wing-body geometries (Figure 26.2.2-31, Reference 26.2.2-31), and continued research will soon allow these calculations to be done for the installed nacelle as well.

For supersonic Mach numbers, slender body theory has seen wide application to three-dimensional geometries. The nacelle plume is modeled as a solid body, and surface pressures and wave drag can be calculated to perform optimization trades. Figure 26.2.2-32 from Reference 26.2.2-32 shows the nacelle drag variation on the Boeing SST as a function of nacelle position.

Recent analyses have also emerged for hypersonic flow, especially for the wing-body-fin configuration. Figure 26.2.2-33 from Reference 26.2.2-25 shows the quality of the method by allowing comparison of measured and computed wing pressures on a M_∞=10 vehicle.

A far more difficult class of flows involve conditions where the exhaust plume interacts strongly with the pressure field resulting from flow around

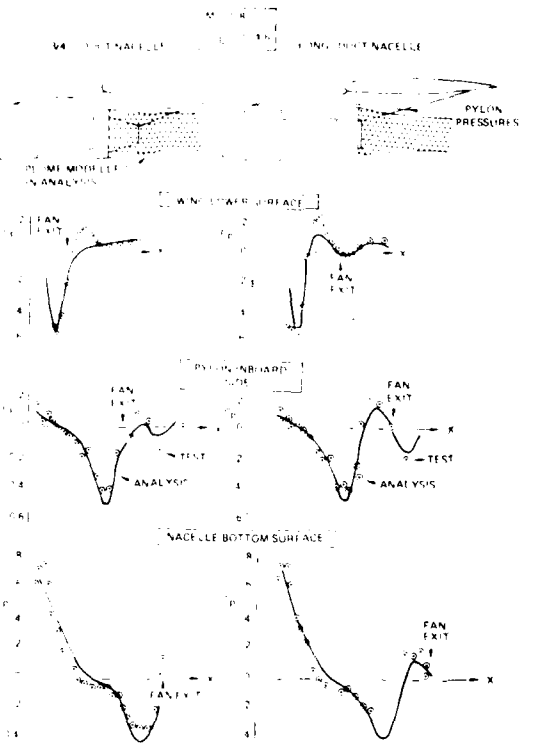

Figure 26.2.2-30. Comparison of Analytical vs Measured Pressures for Installed Powered Nacelle

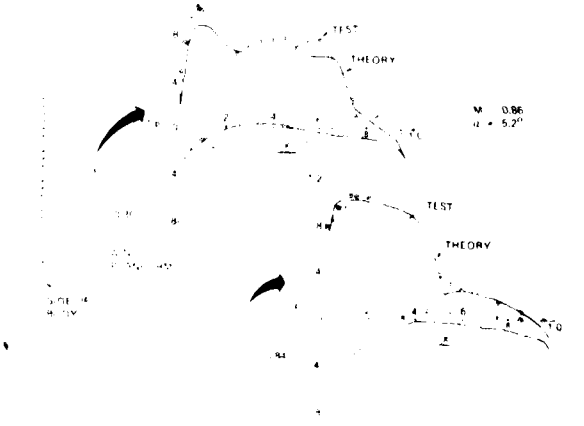

Figure 26.2.2-31. Analytical vs Experimental Wing Pressures for B 747

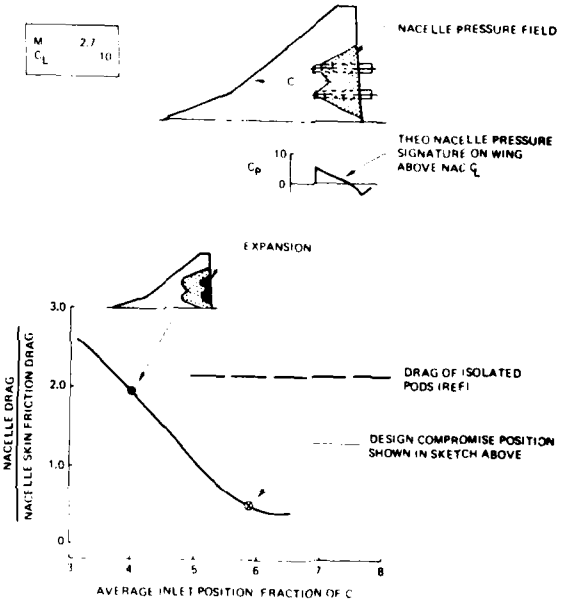

Figure 26.2.2-32. Supersonic Nacelle Optimization by Analysis

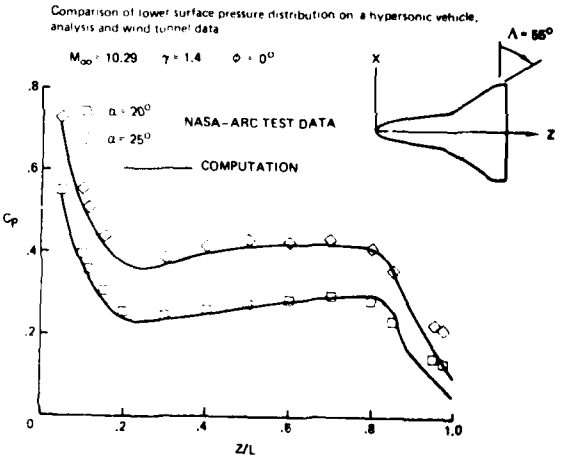

Figure 26.2.2-33. Analysis vs Experimental for Hypersonic Vehicle

the airframe to the extent where the shape of the exhaust plume is substantially altered. A typical subsonic case is the overwing D-nozzle nacelle such as found on the Boeing YC-14 (Figure 26.1.2-3) or the Quiet Short Haul research aircraft (QSRA). For these installations, three-dimensional subsonic analyses are invaluable in providing a design guide for the nacelle external contours (Reference 26.2.2-33); but the effect of the exhaust jet, its true shape, and any mixing between it and the external flow field cannot yet be reliably predicted. The over-wing pylon-mounted nacelle is slightly easier to handle from the analytical point of view since the jet is not attached to the wing surface.

At the far end of the Mach number scale, future hypersonic cruise vehicles may represent the extreme case of nacelle-airframe interaction, where the airframe forms half the nozzle and the bow shock wave forms the other (Figure 26.2.2-34). This kind of design is not accurately analyzed at the present time.

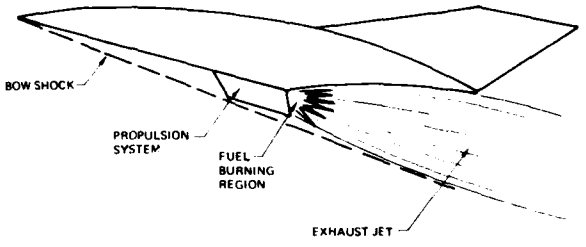

Figure 26.2.2-34. Conceptual Propulsion – Airframe Integration for Hypersonic Flight

In summary, inviscid analytical solutions are available for axisymmetric and three-dimensional nozzle/afterbody geometries for both subsonic and supersonic flows. In engine installations that include three-dimensional features such as support struts, wing pressure field, twin nacelles on integrated fuselage-taile-nozzle, the flow regions affected by these features are driven into operation with shocks and separation by trades between drag and weight. Under these circumstances theoretical methods are usually inadequate to calculate installation losses. However, in cases when the jet shape is independent of the aircraft pressure field, jet effects can be adequately predicted. Since fully three-dimensional viscous-transonic flow analysis techniques are likely to become available, reliance on prediction by correlation and wind tunnel test may be de-emphasized. Even short of the ultimate capability, these evolving analytical tools would be invaluable aids to the design process and in the interpretation of wind tunnel data.

b) Empirical Methods

Skin friction is usually the largest single drag component of nozzle/afterbodies at subsonic Mach numbers. Skin friction prediction methods are numerous. Flat plate coefficients versus Reynolds number and roughness are often used on body surfaces with slight inclination to the freestream. The effects of accelerations over bodies of revolution are accounted for by empirical factors or by "stretching" of the wetted area as a function of the local velocity. Various integral solutions for turbulent boundary layers are also used to compute skin friction losses with pressure gradient and to predict separation.

In most performance estimates, flat plate skin friction is applied to the wetted area. The effect of body thickness is approximated using the following formula:

$$C_{\Delta_f} = (1 + K)\, C_f$$

where: $K = 0.5 \frac{D}{L}$ for bodies of revolution,

$= 2 \frac{t}{c}$ for plane surfaces.

For configuration definition studies, the drag due to roughness of the aerodynamic surfaces is lumped together with the drag due to discrete excrescences which cannot be precisely defined, such as mismatched butt joints, leaks, oil-canning of skin panels, etc., by increasing the skin friction drag by 10%. When the design is defined to the point that these items can be identified they are accounted for individually.

Roughness and excrescence effects are generally as large as effects due to thickness and much larger than the differences between various popular skin friction formulae. Therefore, sophisticated methods to compute skin friction in the presence of accelerating and decelerating flows over bodies of revolution appear unwarranted until skin material, paint, gaps, excrescences, and leakage are defined. Hence, reliance on empirical methods should be exercised until the geometry is well defined.

Pressure Drag

Empirical correlations are available for isolated single and twin boattails. Single afterbody data are available through NACA and NASA reports for a variety of geometries. Data for correlated in Reference 26.2.2-34. Subsequently, correlations were developed based on a function of correlations were developed based on a function of the area variation as described in the next section. The correlations are applicable to afterbodies with smooth area variations, subject to separation due to excessive slopes. The effect of separation due to base areas, sharp corners, or divergent surfaces between twin boattails may not be properly predicted. The correlations are valid for those cases where external flow conditions do not influence the internal flow conditions, i.e., for afterbodies with choked convergent nozzles, convergent-divergent nozzles which are not excessively overexpanded, and plug nozzles when the plug is within the Mach cone of the internal flow (see Figure 26.2.2-35).

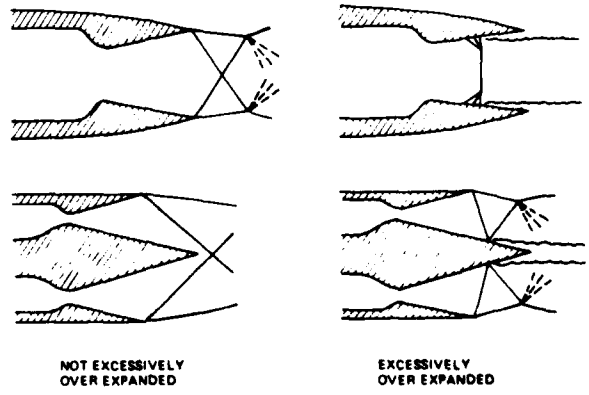

Figure 26.2.2-35. Flow Configuration for Convergent – Divergent and Plug Nozzles

Integral Mean Slope Correlations - Subsonic

This correlation method has been developed by Pratt & Whitney Aircraft (Reference 26.2.2-35) and modified by the Boeing Company to extend its usefulness for afterbodies with steep slopes. It was developed for twin nozzle afterbodies behind a long (L/D_{eq} = 8) forebody with a long (L/D_{eq} = 4) cylindrical section. Afterbody shape variations included slenderness from 1.3 to 3.6, exit to maximum area ratio of 0.1 to 0.4, spacing ratios of 0.67 and 1.28 of equivalent maximum diameter and area plots were varied to yield values of integral mean slope from 0.34 to 1.1. The integral mean slope is defined by the following equation:

$$IMS = -\frac{1}{\left(1 - \frac{A_9}{A_{10}}\right)} \int_{A_9/A_{10}}^{1} \frac{d\,(A/A_{10})}{d(X/D_{eq})}\, d\,A/A_{10}$$

IMS represents the area-weighted average slope of the non-dimensional area plot and is proportional to the ideal pressure area integral of the aft body. Here A_{10} is the maximum fuselage cross sectional area.

For afterbodies with locally steep slopes in the area plots, the integration is terminated at a maximum slope instead of the real final slope to improve the correlation. This final slope depends on freestream Mach number. The resulting parameter is called IMS_T. Data from convergent and convergent-divergent nozzles operating at design pressure ratios (1.89 for convergent nozzles) correlates with the IMS_T parameter raised to the 2.77 power. This correlation, the plot of IMS_T versus Mach number, and the area plot are sufficient to predict the pressure drag of any configuration falling into the class of those tested. Figure 26.2.2-36 summarizes the method.

Note that the IMS_T twin correlation does not cover configurations with vertical tails tangent to or outboard of the nozzles, like those illustrated in Figure 26.2.2-37.

Afterbody drags for such configurations are a strong function of vertical tail position and are as much as two or three times higher than drags of after bodies with tails on axes of symmetry. Since IMS_T is only a function of the area plot, it cannot correlate losses to strong tail interference - or any other effects such as excessively close spacing, lack of fairings, etc. which cause local losses independently of the area distribution.

Although the IMS_T correlation was developed from twin aft-end data at two spacings, no spacing effect was detected. Therefore, the correlation should be applicable to single engine aft-ends as well. Figure 26.2.2-38 shows a correlation developed from isolated boattail data at M_∞ = 0.7. The IMS correlation for twin afterbodies is shown for comparison. Isolated boattail data do not include tail effects, nor are localized losses between boattails and interfairings present, which may explain the lower level.

The effect of sharp corners between boattail and forebody is also shown. These data are very sensitive to boundary layer thickness and Reynolds number.

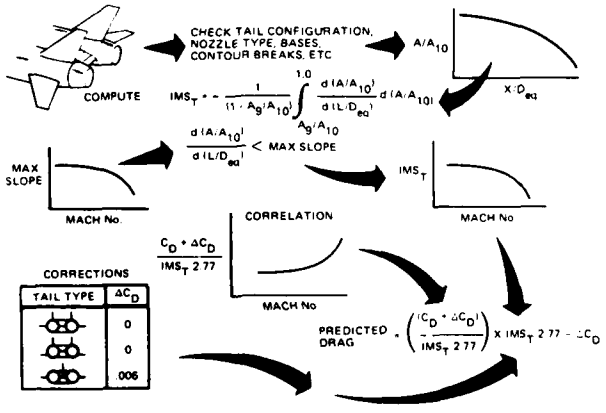

Figure 26.2.2-36. Drag Prediction Procedure

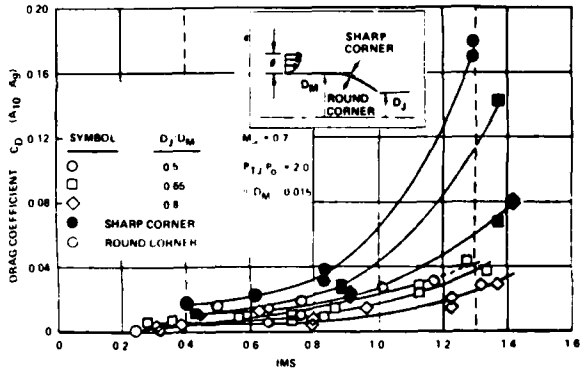

Figure 26.2.2-38. Convergent Nozzle Boattail Pressure Drag Coefficient

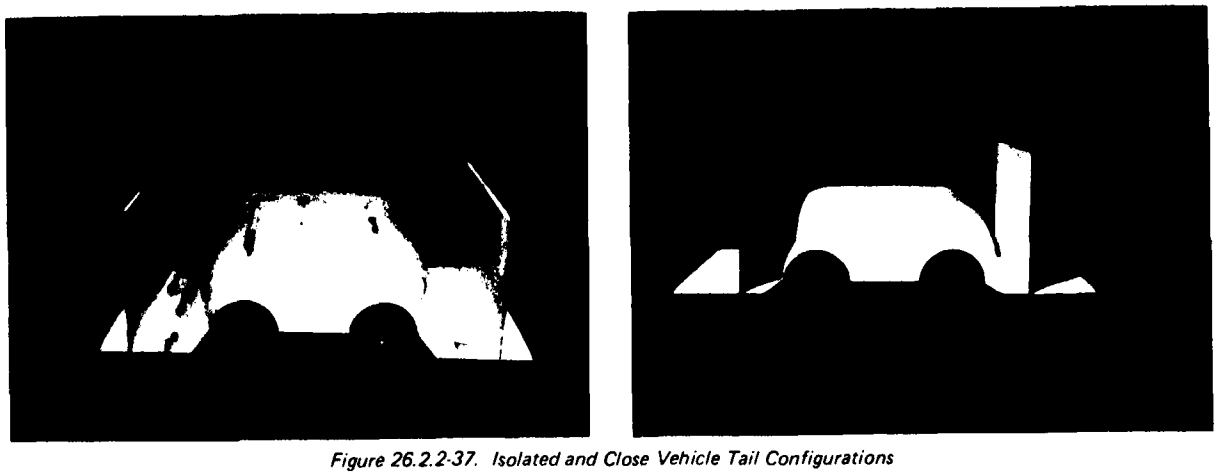

Figure 26.2.2-37. Isolated and Close Vehicle Tail Configurations

Reynolds Number Effects - Subsonic

The IMS_T afterbody pressure drag correlation is based on model data at a unit Reynolds number of 3.5 to 4 x 10^7 per foot, and a model scale resulting in 4.6 feet of forebody length and an equivalent maximum diameter of 0.6 feet for the narrower spacing. The Reynolds number based on length at the end of the forebody was 1.6 to 1.85 x 10^8.

Data from References 26.2.2-30 and 26.2.2-36 indicate that subsonic pressure drags on bodies without sharp corners and bases are not strongly affected by Reynolds number at unit Reynolds numbers above 2.5 x 10^7 per foot. The data were obtained with models whose forebody length were 9.5 feet and 4.25 feet, respectively. The equivalent diameters were 1.35 feet and 0.54 feet. The Reynolds number effect seems to flatten out at the same unit Reynolds number for both model sizes. Measured pressure coefficients reported in Reference 26.2.2-37 are more negative in the expansion region and more positive in the recompression region as Reynolds number is increased. These two effects were compensating and, and a result, there is little or no effect of Reynolds number on the pressure drag of the isolated boattails. A comparison with analysis indicated that these results were caused by the thinning of the boundary layer as Reynolds number increased; the analysis is based on an inviscid solution of Hess and Smith (Ref. 26.2.2-38) with a boundary-layer displacement thickness from a modified Reshotko-Tucker (Ref. 26.2.2-39) solution, and a separation model based on the work of Presz (Ref. 26.2.2-40).

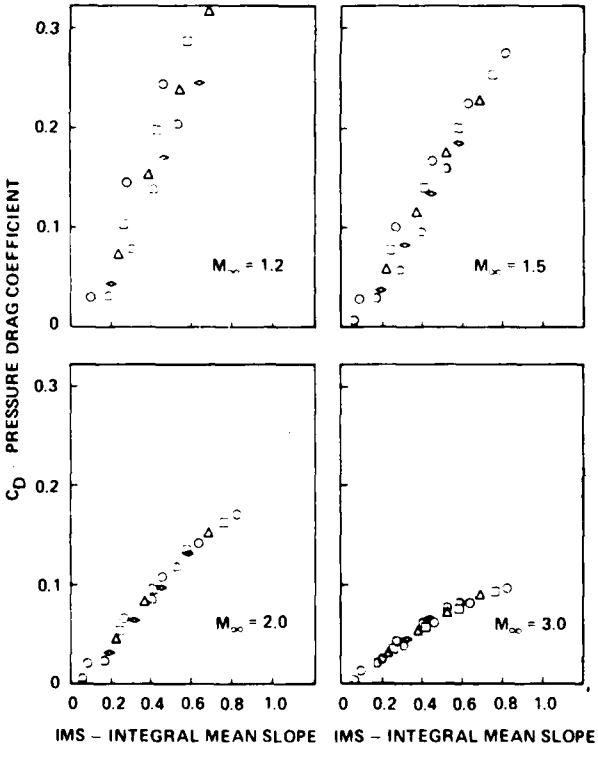

Figure 26.2.2-39. IMS Correlation of Pressure Drag on Axisymmetric Circular Arc Boattails Using the Method of Characteristics

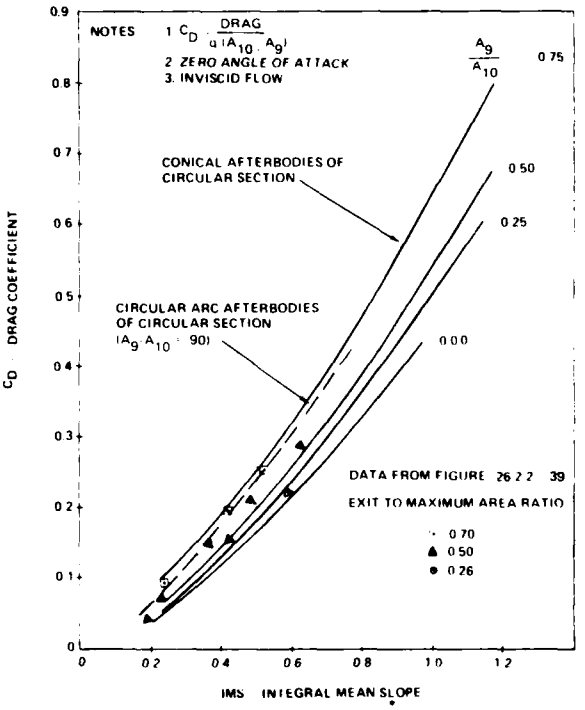

Figure 26.2.2-40. Comparison of IMS Correlation and Theoretical Wave Drag for Isolated Axisymmetric Afterbodies – Mach 1.2

Integral Mean Slope Correlations, Transonic and Supersonic

In linearized, two-dimensional, supersonic flow the pressure drag is directly proportional to the integral mean slope. Therefore, it is expected that IMS might provide a good correlation at supersonic Mach numbers. The correlation is illustrated on Figure 26.2.2-39 from Reference 26.2.2-30, where pressure drag coefficients computed using a method-of-characteristics program are plotted against IMS for circular arc boattails. Figure 26.2.2-40 shows external wave drag versus IMS for conical and circular arc afterbodies. These curves were obtained by the application of similarity laws to solutions derived by the use of second-order theory and the method-of-characteristics/quasi-cylinder theory for the truncated cone and circular arc afterbodies respectively (Reference 26.2.2-41). The data from Figure 26.2.2-39 is replotted on Figure 26.2.2-40 for comparison.

Data for isolated and twin boattails from Reference 26.2.2-30, 26.2.2-42 are as much as 50% lower than the results of a method of characteristics. Slender body wave drag calculation programs tend to give better predictions, although also on the high side.

Pressure drag coefficients have been obtained experimentally at M_∞=1.2 for equivalent bodies of revolution (EBOR) and twin jet models. These are shown in Figure 26.2.2-41. The EBOR data were obtained from an integration of measured pressure distributions. The twin jet data are obtained from balance force measurements from which calculated skin friction drag was subtracted. The data are therefore presented in drag coefficient form based on the projected area A_{10}-A_9.

These pressure drag coefficients provide the basis for the M_∞=1.2, P_9/P_∞=1.0 for the correlation shown in Figure 26.2.2-41. The drag correlation is

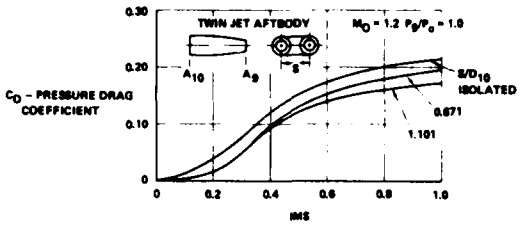

Figure 26.2.2-41. Afterbody Drag Correlation

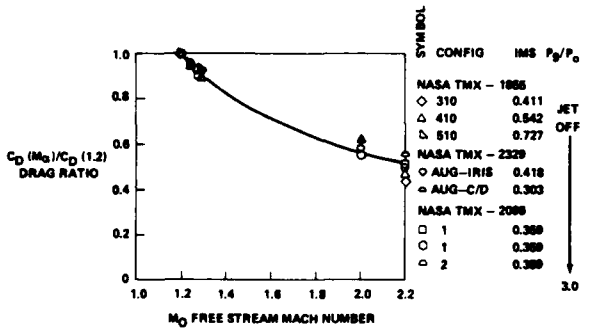

Figure 26.2.2-42. Supersonic Twin-Jet Drag Modified Similarity Solution for Pressure Drag

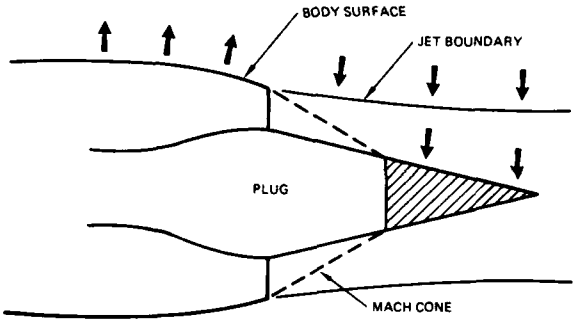

Figure 26.2.2-43. Plug Nozzle with Strong External Flow Effects

presented as a function of IMS rather than IMS_T since the IMS_T afterbody slope limits are not presently available for supersonic flows. Notice also that the correlation has been written only for P_9/P_∞=1.0. The Mach 1.2 correlation can be extended to other operating conditions by using the plume correlation presented in Reference 26.2.2-42.

Additional supersonic (M_∞ = 1.2-2.2) aft fuselage drag data have been compiled from industrial and government wind tunnel test programs. From the data, a method of extrapolating the Mach 1.2 drag to higher Mach numbers was formulated. The M_∞=1.2 drag can be extrapolated to higher Mach numbers using the following empirical Mach number similarity relation:

$$\frac{C_D(M_\infty)}{C_D(1.2)} = [1-1.4 \exp(-M_\infty^2)][M_\infty^2-1]^{-0.5}$$

A comparison of this similarity method with twin-jet data is shown in Figure 26.2.2-42. The data have been presented for jet-off conditions (p_9/p_0 = 1.0) since more data was available at high Mach numbers for this condition than for any nozzle pressure ratio. The drag trend with Mach number is not expected to be significantly different for other pressure ratios.

Plug Nozzles

The empirical methods described in the previous section do not apply to plug nozzles when the flow conditions on the plug can be affected by freestream flow conditions, i.e., when the nozzle flow is subsonic or at low supersonic exit Mach numbers such that a Mach line drawn from the shroud towards the plug intersects the plug (see Figure 26.2.2-43).

In such cases, forces on the shroud due to flow expansion are often counteracted by recompression forces on the plug acting through the jet. Boattail forces are then large in the drag direction, while thrust-minus drag measurements indicate internal and plug forces are exceeding values for loss-free expansion (C_V > 1.0).

A certain amount of success has been enjoyed by treating an isolated axisymmetric plug nozzle as an "equivalent boattail," see Figure 26.2.2-44. The overall thrust-minus drag of the plug nozzle is approximated by the thrust-minus drag of the equivalent boattail with a convergent or convergent-divergent nozzle.

IMS or IMS_T type correlations have not worked well on axisymmetric plug nozzles using the fully expanded jet diameter at the end of the plug with various assumptions for the plume shape to that point. When the thrust is computed, using the assumption that only skin friction losses on the plug are significant and that the internal flow is fully expanded, the sum of computed thrust and IMS_T-derived drag does not correlate well with experimental data. Apparently, significant variations in thrust recovery on the plug occur with

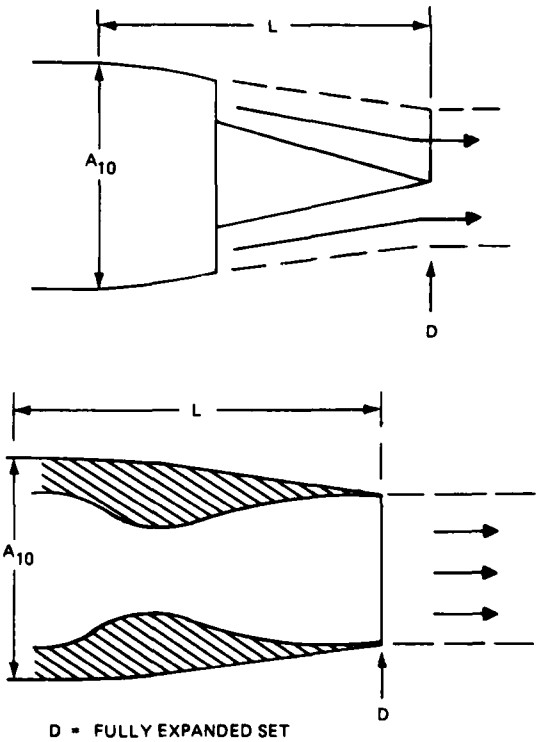

Figure 26.2.2-44. Comparison of Plug and Con-Di Nozzles Showing Comparable Equivalent Boattail Lengths.

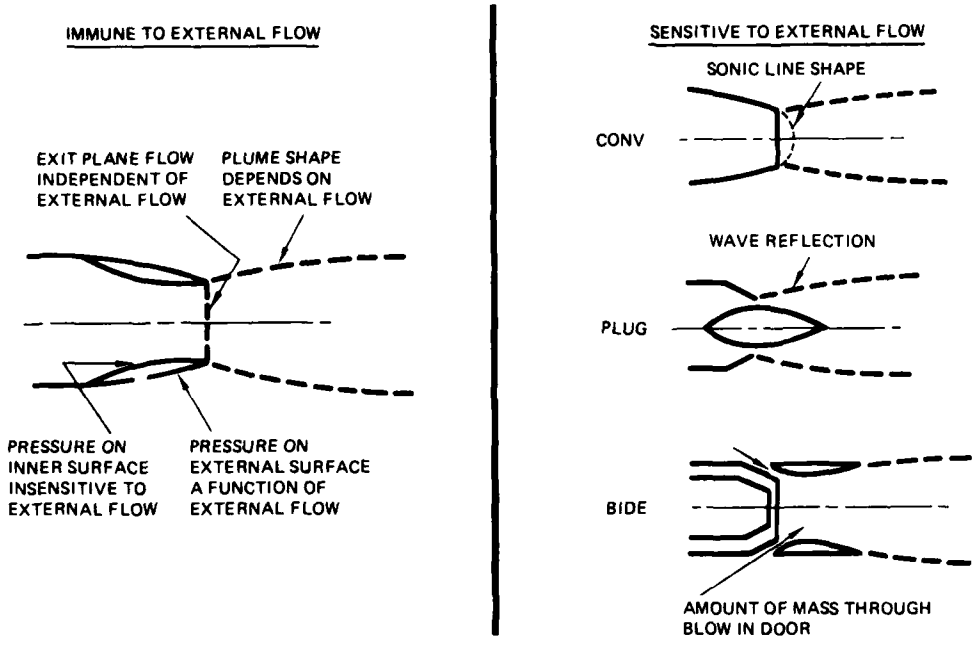

Figure 26.2.2-45. Nozzle Configurations and Sensitivity Mechanism to External Flow

minor design changes to which the value of IMS_T or calculated thrust is not sensitive.

c) External Effects on Internal Nozzle Performance

The external flow has an effect on the mass flow of an unchoked nozzle. The effects can persist at pressure ratios above those for one-dimensional choking when the velocity distribution is non-uniform and parts of the nozzle exit are not choked (see Figure 26.2.2-9.) These effects can be significant for high bypass ratio engines, which generally operate at low nozzle pressure ratios. "Suppression" of the primary flow due to fan flow, and "Suppression" of both flows due to converging free-stream flows over boattails, or due to the pressure field of the wing, must be considered.

Figure 26.2.2-45 shows examples of nozzle configurations whose performance is sensitive to external flow effects. In the case of the convergent and plug nozzles, the sonic line shape and hence C_D and C_V are influenced by the shear flow boundary. Plug pressures are affected by the wave reflection characteristics of the boundary. The tertiary mass flow through the blow-in door ejector (BIDE) nozzle is governed by local boattail pressures and flow configuration. The nozzle/airframe interactions are therefore large and depend on viscous flow effects which make small scale modeling of such configurations very difficult. Further, three-dimensional flow effects arising from wakes due to wing and tail surfaces can affect BIDE nozzle performance.

The external flow can have a significant effect on the thrust performance of highly over-expanded convergent-divergent nozzles. In such nozzles, overexpansion is followed by a normal shock and separation within the nozzle. The static pressure in the separated flow is slightly below ambient due to jet entrainment. With an external flow, the internal pressure in the separated region will be slightly above or below base pressure, depending on the boattail shape and boundary layer thickness just upstream of the base. These changes in internal pressure level will also cause the normal shock to stabilize in different positions in the nozzle. Thus, if thrust is defined as a pressure and momentum integral is at the nozzle exit, free stream conditions will influence the value. This effect is difficult to predict or measure. Fortunately, it is generally not important to predict the magnitude of this effect as such severe over-expansion usually occurs at very low power settings where thrust is not critical.

26.2.2.4 Concluding Remarks

The design of the exhaust system involves minimizing total pressure losses between the turbomachinery and the nozzle exit with consideration of the aerodynamic forces acting on the aftbody or boattail of the airplane. The latter is usually very important because of the role the propulsive jet plays on the local static pressure near the nozzle exit. In design, large body curvature is used to shorten the aftbody on an airplane or nacelle as much as possible to minimize weight. Hence, the flow is generally close to separation and may be easily influenced by the jet.

The measure of efficiency with which the nozzle converts thermal energy into jet kinetic energy for thrust is the nozzle velocity coefficient. The performance of the nozzle depends primarily on the nozzle pressure ratio and on afterburn employment. At high nozzle pressure ratio and with afterburning, variable nozzle area is usually required for aircraft with multiple design point capability such as many military combat aircraft. For subsonic aircraft, particularly transports, the nacelle nozzles are designed to achieve best thrust minus drag at cruise and adequate performance in particular corners of the flight envelope.

The difficult design areas are those with strong internal/external flow interactions, particularly where the effect of viscous forces causes large scale flow separation. The use of subscale experiments and similarity correlations to infer performance constitutes an area of risk, which may not be avoided.

26.3 PREDICTION OF AIRPLANE PERFORMANCE

The success of an airplane design depends on achieving the expected performance of the engine/airplane in flight. The problem of reconciling expected and actual performance requires a detailed understanding of airplane drag. The available analytic tools and their capabilities were described in Section 2.6.2.2 in connection with the external flow characteristics of inlets and aft ends.

The capabilities of large computers and the use of sophisticated aerodynamic theories have resulted in an improved ability to predict a major portion of the aircraft flow field at subsonic and supersonic speeds. During the design, the analytic methods can provide far more information than does the typical wind tunnel test, and usually at a much reduced cost. For example, analysis can describe the flow field off the aircraft as well as on its surface. Analysis also readily provides the force distribution on the configuration for performance and structural design.

However, the current state of the analytical art does not reliably predict drag or other forces associated with the complex flow field interactions of a viscous nature. Thus wind tunnel testing remains a fundamental step in the aircraft design sequence.

26.3.1 Wind Tunnel Measurements

There are two principal areas where wind tunnel testing is required. First, it can provide data on complex flow phenomena which analysis cannot. Examples include inlet distortion stability at high angles of pitch and yaw, at transonic speeds, and in the presence of vortex interaction. Second, wind tunnel testing provides the opportunity to observe unusual flow fields visually.

26.3.2 Drag Coefficients

This discussion deals with drag data on unpowered models, and or subsonic and supersonic flows. As in the case of analytical computer programs, each aerospace company has its own process for bookkeeping the components of drag. The coefficients used, which are listed below, are only one of a number of ways of dealing with these forces. For brevity, this discussion is not detailed to expose wind tunnel drag bookkeeping methodology. Such methodology varies somewhat with each company and the product involved.

For subsonic conditions, the drag may be defined as (see Figure 26.3.2-1)

$$C_D = C_{D_{MIN}} + C_{D_p} + C_{D_i} + C_{D_{MACH}} + C_{D_{TRIM}}$$

where:

$C_{D_{MIN}}$ = Minimum drag of the configuration, free of Mach number effects, with C_{D_i} removed. This is a calculated value.

C_{D_i} = Induced drag due to lift which is calculated assuming an elliptical lift distribution.

$C_{D_{MACH}}$ = Drag rise due to compressibility. This is measured in the wind tunnel and varies with C_L.

$C_{D_{TRIM}}$ = Drag due to changes in aircraft center of gravity (C.G.) location. This is measured in the wind tunnel and varies with C_L and C.G. location when control surfaces are deflected.

The remaining term is ΔC_{D_p} which is one of the main results of the wind tunnel test:

$$\Delta C_{D_p} = C_{D_{measured}} - C_{D_{min}} - C_{D_i}$$

and is acquired at subcritical speeds with no control surface deflections ($C_{DMACH} = 0$, $C_{DTRIM} = 0$). It represents the drag due to corner flows, non-elliptic loading interference pressure fields, and, unfortunately, the quality of the model.

The wind tunnel model experiences two kinds of forces: frictional (tangent to surface) and pressure (normal to surface) forces. Both forces are dependent on Reynolds number, although the dependence of the pressure forces on Reynolds number is much less than that of the frictional forces. This consideration is important to the scaling of the wind tunnel drag forces to full scale conditions. A customary assumption is that only $C_{D_{min}}$ is a function of Reynolds number. Since $C_{D_{min}}$ and C_{D_i} make up over half the drag and are calculated values, less than half the full scale drag is determined from wind tunnel testing.

An alternate form of the drag equation is usually employed for supersonic corditions, because of the appearance of wave drag:

$$C_D = K_1 C_{D_f} + C_{D_W} + K_2 C_L^2 + C_{D_{camber}}$$

where:

C_{D_f} = Skin friction drag, a calculated value.

K_1 = Multiplier for roughness.

C_{D_W} = Wave drag due to volume of individual components and interferences; a calculated value.

$K_2 C_L^2$ = Drag due to lift.

$C_{D_{camber}}$ = Drag at off-design C_L due to camber; a calculated value.

Paralleling the subsonic flow case, the purpose of the wind tunnel testing is to establish the size of the K_1 and K_2 coefficients. Reynolds number scaling is similar to that for the subsonic case; that is, only C_{D_f} is scaled.

26.3.3 Wind Tunnel Modeling

Unfortunately for the experimentalist, the wind tunnel has three fundamental limits. These

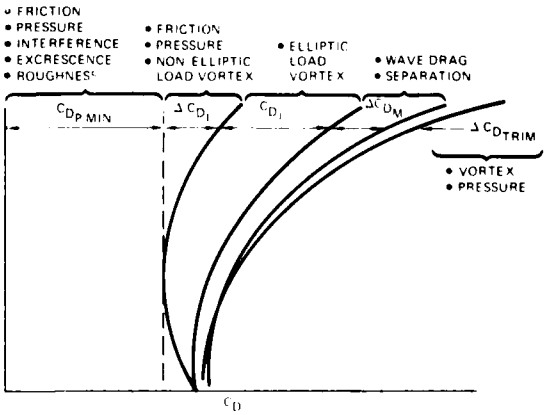

Figure 26.3.2-1. Components of Subsonic Drag Polar

are problems of parameter matching, differences in flow field from the free-flight condition, and the inevitable requirement that the model be attached to some physical restraint if forces are to be measured.

The most difficult of the three is the requirement for parameter matching. Three variables are of the most interest: Mach number, dynamic pressure, q, and Reynolds number. Mach number is important since the flow field characteristics are dominated by its magnitude. Many subsonic configurations are influenced by compressibility effects near their design points. Fortunately, Mach number can be matched exactly in model testing.

The dynamic pressure is important at low speed in powered-lift models, and at high speed because of aeroelastic effects on the model shape. Full scale dynamic pressure cannot usually be matched at high speed, but the aeroelastic properties can be duplicated by appropriate changes to the model structural properties.

The last variable is Reynolds number and is the most difficult to match in the wind tunnel. An extensive testing art has evolved to use wind tunnel techniques that evoke model characteristics which will allow reliable predictions of full scale Reynolds number. Although the outer flow field around a configuration is not strongly dependent on Reynolds number when the flow is attached, the near field frictional drag is a strong function of this parameter.

Since most test facilities provide Reynolds numbers that are one to two orders of magnitude lower than that required at full scale, a procedure using trip strips has evolved in an attempt to produce a boundary layer similar to the full scale article while closely modeling dynamic pressure and Mach number. The wind tunnel forces are then extrapolated to full scale conditions. Figure 26.3.3-1 (Reference 26.3.3-1) shows a typical variation of drag with Reynolds number. Often the modeling is inadequate, and serious errors in predicting the nature of the full scale flow field occur at transonic speed. Figure 26.3.3-2 (Reference 26.3.3-2) shows the sensitivity of the wing aerodynamic characteristics (wing upper surface shock position) to Reynolds number. In addition, the role played by the use of boundary layer tripping mechanisms on the model is illustrated. Note that the shape of the drag curve with Reynolds number does not follow that of the flat plate skin friction line. In the example shown, model data were obtained at a Reynolds number sufficiently high to allow a good prediction of the flight drag level. But if only the low Reynolds number data

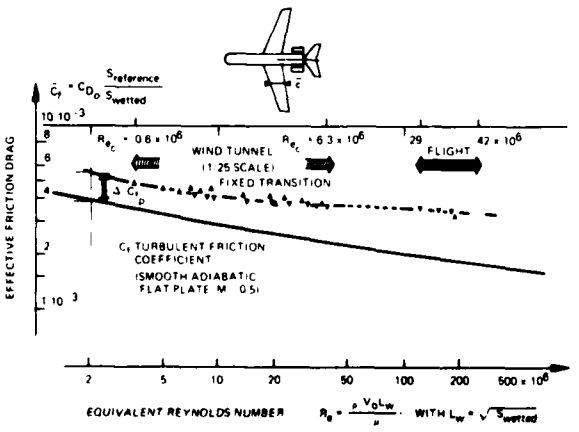

Figure 26.3.3-1. Wind Tunnel Correlation of Minimum Drag Flight for "Caravelle"

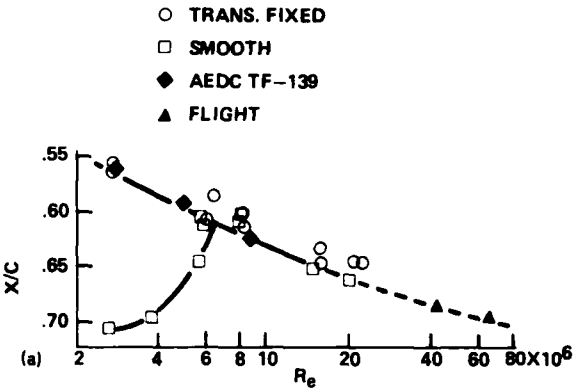

Figure 26.3.3-2. Wing Shock Position as a Function Reynolds Number (Angle of Attack = 2°, Fractional Span Position = .389, M_∞ = .825)

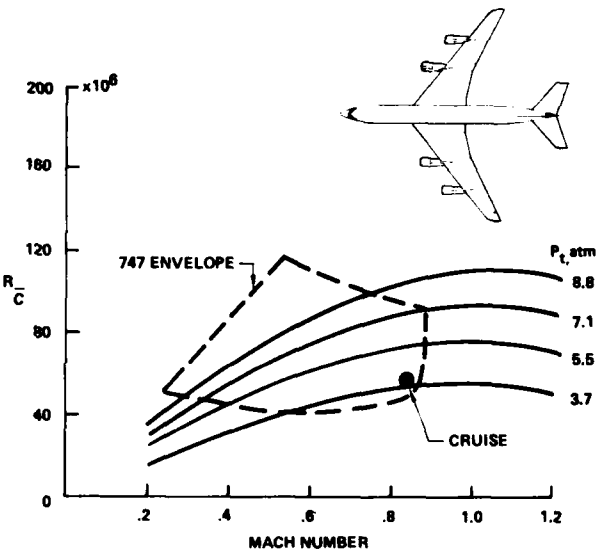

Figure 26.3.3-3. National Transonic Facility Operating Envelope, Mean Chord $\bar{c}$ = .08 x (Test Section Area) ½

had been available, a substantial error may have occurred unless proper trip techniques were used.

An alternate procedure would be to change the wind tunnel flow characteristics so that the model would experience the same Reynolds number as does the full scale geometry. Some facilities ve attempted to raise the Reynolds number by increasing density, but model forces usually limit these facilities to about five atmospheres, whereas ten to fifteen would be necessary for Reynolds number simulation. Another way to increase Reynolds number is to reduce the viscosity by lowering temperature.

A combination of cryogenic temperature and increased pressure can produce full scale Reynolds numbers on a typically sized wind tunnel model while not exceeding allowable model forces. The NASA is constructing such a facility. When operational in the 1980's, this facility will provide Reynolds number simulation for the B-747 at cruise conditions (Figure 26.3.3-3, Reference 26.3.3-3).

The quality of the tunnel flow field is a lesser problem than parametric matching, since the tunnel flow quality depends on the funds available to improve it. In general, the test section flow

field where the model is to be placed will show timewise and spatial variations in velocity, pressure and temperature. These are often referred to as crossflow and upflow, bouyancy and turbulence levels. These effects can be important in that they may lead to an uncorrectible error in the model force data.

When the model is installed, further changes in the tunnel flow arise because of tunnel wall effects. Corrections are applied for blockage, circulation produced by lift, and for model volume effects at transonic speeds. At supersonic speeds, shock wave reflection limits the size of the model.

These factors are all unique to some degree, and a combination of techniques and corrections can minimize their effect.

Finally, there are a variety of model mounting techniques (Figure 26.3.3-4), each of which possesses advantages, but also introduces mounting effects which must be carefully assessed.

Such mounting effects play a special role in propulsion wind tunnel testing of isolated inlet, nozzles, or nacelles in that the techniques are devised to allow detailed examination of a particular part of the flow field. A mount strut from the tunnel floor is usually employed. For the installed nacelle, the half-model arrangement is often used for wing mounted designs, since a model size twice that of the typical model can be obtained.

26.3.4 Specific Test Techniques

Besides the usual force data, the wind tunnel allows special data to be taken which often adds to the understanding of the flow field.

Most often, instrumentation in the form of static pressure taps on the surface of the nacelle is used. Less often employed because of the time and expense involved are wake or plume surveys. These can reveal jet plume problems or regions of poor pressure recovery due to the presence of a thick boundary layer.

An instructive but qualitative test technique is the use of a surface film preparation to reveal the nature of the boundary layer flow. Experienced observers can detect boundary layer transition, separation, shock waves and the presence of vortex flows by observing these surface films. A typical fluorescent oil visualization test is shown on Figure 26.3.4-1.

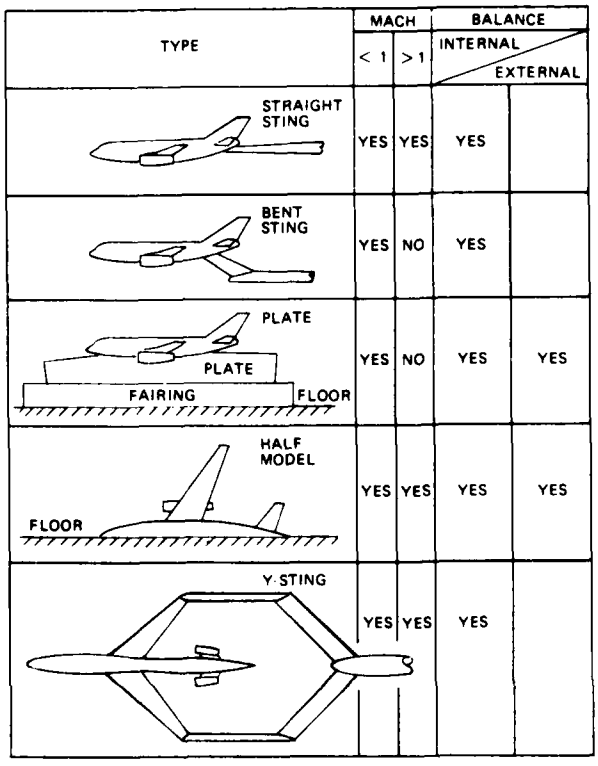

Figure 26.3.3-4. Examples of Wind Tunnel Model Mounting Techniques

26.3.5 Concluding Remarks

Airplane drag is determined to the maximum extent by analytic means; the more expensive wind tunnel is reserved for determining that part of the total drag which cannot be obtained analytically. Serious modeling problems, associated with scale effects and the wind tunnel environment, still cast into uncertainty the ability of the airplane to achieve its design objectives or performance guarantees. Much work remains to be done on both analytic and experimental fronts to reduce this uncertainty.

The need for an element performance integration method in an airplane development program arises largely from the inability to determine the performance of the complete airplane system (with simultaneous real inlet and exhaust system operation) in one test or one calculation. Furthermore, it is often desirable to optimize the inlet and exhaust system in separate tests which are independent of the general aerodynamic drag testing of the basic airplane configuration. Thus, a well-defined performance integration system is required to ensure that the performance estimates for the various elements (i.e., inlet, exhaust system, airframe, turbomachinery) of the airplane system are properly integrated to yield an accurate prediction of overall system performance.

26.4 PERFORMANCE INTEGRATION METHODS

26.4.1 Element Performance Map Formats

Airplane performance is predicted from the airframe aerodynamics, propulsion system performance, and estimates of the system weights. The performance of the airframe and propulsion systems are described by elements which interact, such as inlet, turbomachinery, exhaust system, etc. (Figure 26.4.1-1). The performance of each element can be divided into a portion that is integrated into the propulsion system and a portion integrated into the airframe system. Traditionally, the propulsion system performance contains the turbomachinery performance, inlet recovery, and internal nozzle performance, and may contain power sensitive inlet and nozzle drag increments. The remainder of the inlet and nozzle drags, as well as the airframe drag, is lumped with the airframe system drag.

The inlet and nozzle drags contained in the airframe drag polar generally correspond to a specific geometry and internal flow condition as a function of Mach number. In the past, the conditions were chosen with regard to the ease with which analytical predictions of airframe system drag could be made. Thus, the inlet flow condition corresponded to zero spillage (Mass flow ratio = MFR = 1.0) and with a cylindrical jet. An alternative reference condition was one that utilized the inlet and exhaust system geometry and flow conditions of a wind tunnel model. Most recently, an operating reference condition has been used where inlet and nozzle geometry and flow conditions are those existing on the airplane at a specified power setting, Mach number, and altitude.

Figure 26.3.4-1. Flow Visualization

Coefficients, curves or tables that describe the performance of these elements are called element performance maps. The maps provide the information actually utilized in the airplane performance prediction process. The basic requirements to be satisfied by the element performance maps are:

a) The maps must provide the information required for the airplane performance prediction over the complete range of flight and operating conditions.
b) They must be consistent with the element performance integration system; and
c) They should be presented in such a manner that the performance characteristics of each element are visible.

This section describes a format to represent the performance of each element and a method to define thrust and drag forces on external and internal surfaces of the airplane while providing maximum visibility of the performance of the elements.

26.4.1.1 Inlet Performance

Inlet performance maps give inlet recovery and total inlet drag coefficient (the sum of bleed drag, bypass drag, and spillage drag increments) as a function of engine corrected airflow demand per unit inlet lip area. A sample recovery map is given in Figure 26.4.1-1. A drag map is given in Figure 26.4.1-2. These maps provide a complete description of the inlet's installation losses. The dramatic change in performance between operation at [illegible] and [illegible] (Figure 26.4.1-1) arises when the external [illegible] of the inlet started.

These maps [illegible] inlet recovery characteristics, [illegible] with the engine characteristics, at the [illegible] pressure. Using the [illegible] interface performance [illegible] determine the nozzle area [illegible] overall installed thrust-[illegible].

Although [illegible] account for [illegible]

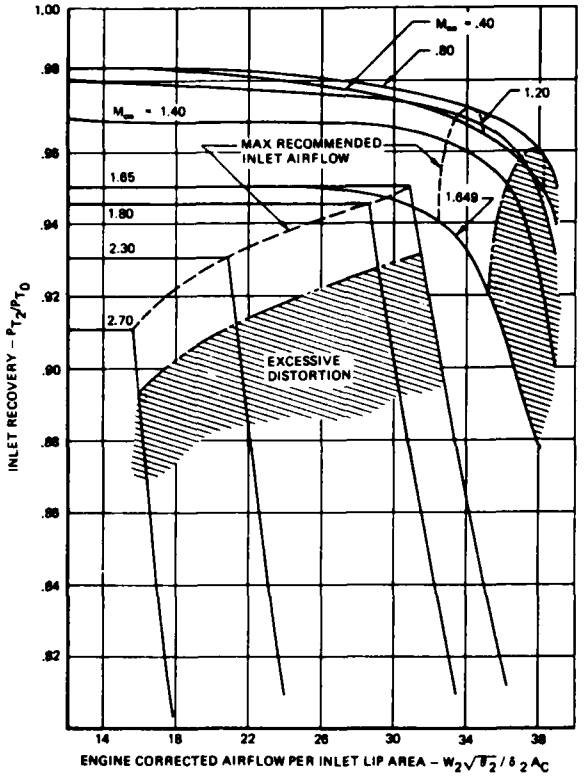

Figure 26.4.1-1. Inlet Drag Map Mach 2.72-D Mixed Compression Inlet

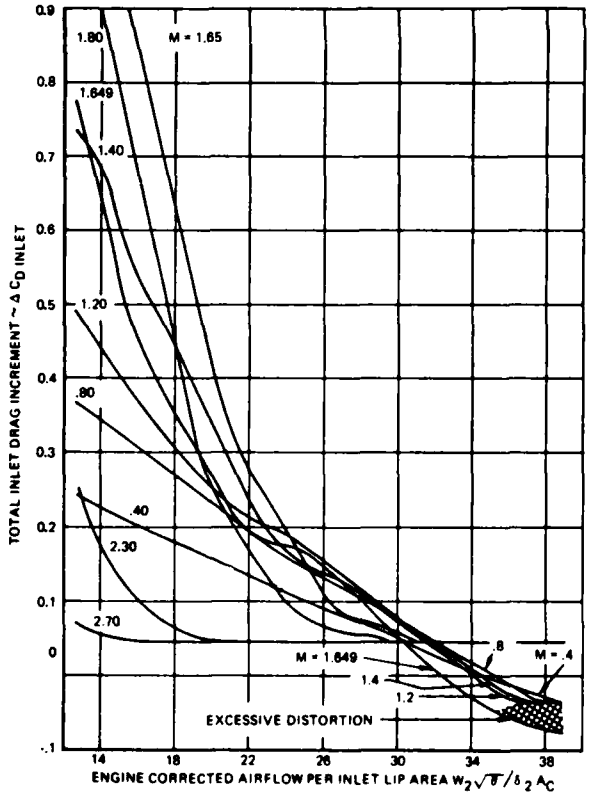

Figure 26.4.1-2. Inlet Recovery Map, Mach 2.72-D Mixed Compression Inlet

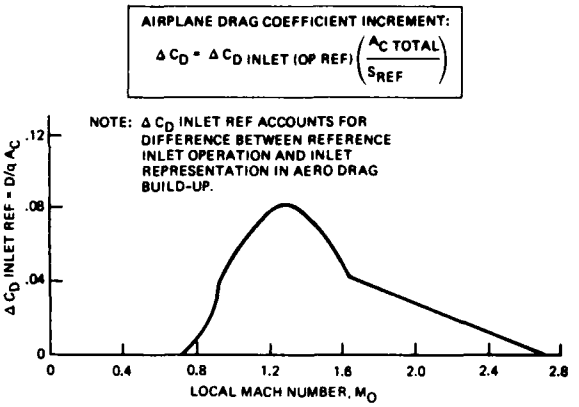

Figure 26.4.1-3. Drag Due to Inlet Spillage at Baseline Conditions

on wave drag and skin friction drag, they assume a cylindrical capture streamtube. Thus, a drag increment is required to correct the drag polars from these conditions to the actual operating mass flow ratios. These drag increments are shown for a sample inlet in Figure 26.4.1-3. In this plot, a particular variation of mass flow ratio (MFR) with Mach number is assumed.

If the drag polar is a result of a wind tunnel test, it includes the drag of the inlet at the mass flow ratio obtained in the wind tunnel. In a well-designed model, this mass flow ratio will be near the critical value. However, the model inlet may not be an exact scale model of the inlet intended for the airplane, both because of model scaling difficulties and because of design configuration changes incorporated after model fabrication. The drag differences due to these effects must be estimated and displayed as in Figure 26.4.1-3.

26.4.1.2 Aft-End Performance

Aft-end Drag Map Formats

A typical aft-end incremental drag map is shown in Figure 26.4.1-4. The parameter A_9/A_{10} is the ratio of total nozzle exit area to maximum fuselage cross-sectional area (for a fuselage buried engine). The parameter P_9/P_∞ is the ratio of the nozzle exit static pressure to freestream static pressure. The map gives the incremental aft-end pressure drag relative to the drag polar at an $A9/A_{10}$ value of 0.470. The drag increments found in this map define the exhaust system installation loss charged against the engine net thrust. The absolute drag level at the operating reference condition (A_9/A_{10} = 0.470) would be included in the airframe system drag polar.

The aft-end drag map can also be presented in the form of total drag Figure 26.4.1-5. This map gives absolute pressure drag, rather than incremental drag, as a function of A_9/A_{10}. This kind of map provides much greater visibility for the aft-end performance, provided a reasonable plan of separation between the airframe and aft-end can be defined. In potential subsonic flow around slender bodies, the pressure integral may be shown to be near zero around the forebody and afterbody individually, as well as around the total body. Therefore, afterbody pressure drags integrated to the maximum cross sectional area may be compared to values obtained from other slender afterbodies with different area variations. The differences will hence reflect drag changes due to real flow effects

rather than differences. When this form of map is used, the drag polar operating reference value of A_9/A_{10} (0.470 in this case) must be specified, as also must the absolute value for the drag of the afterbody of the analytical or wind tunnel model. When this aft body drag is subtracted from the airframe drag and the drag value from the aft body map evaluated at the operating reference is added to this difference, the airframe drag at the operating reference condition is obtained. The appropriate installation loss increments can then be calculated and the airplane drag polars can be adjusted to reflect the appropriate absolute aft-end drag levels.

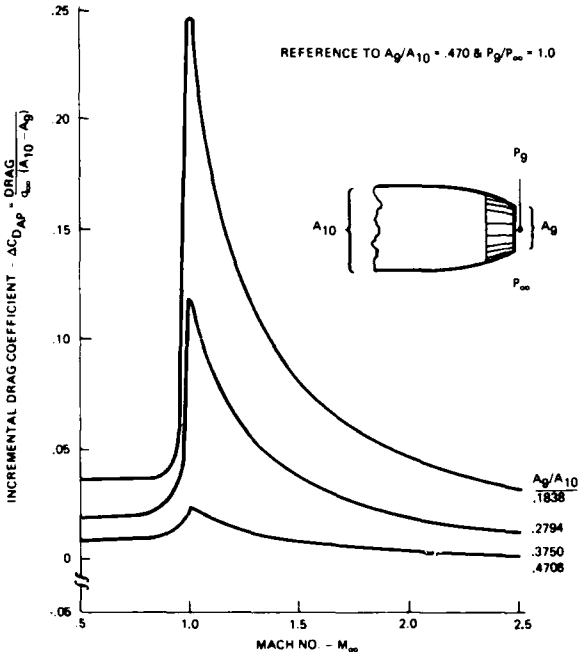

Figure 26.4.1-4. Aft End Incremental Drag Map

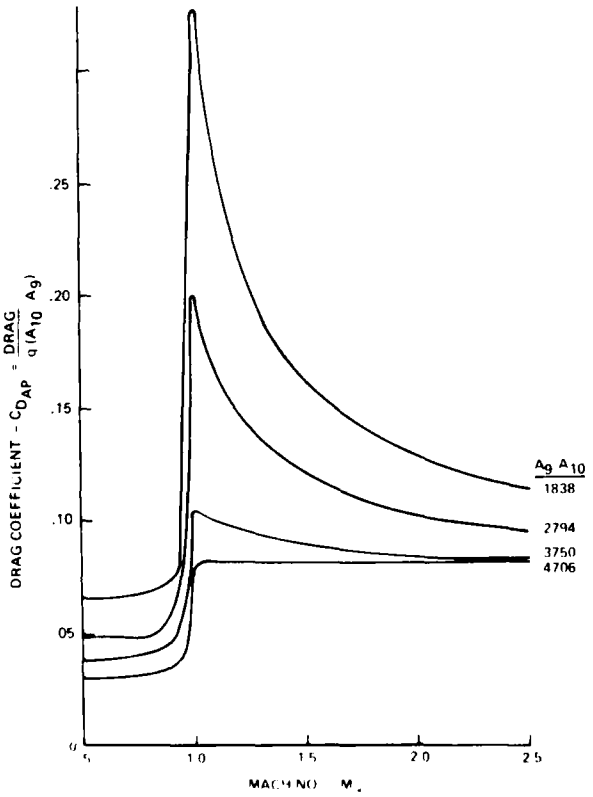

Figure 26.4.1-5. Aft End Drag Map

These pressure drag maps are presented with no altitude dependence indicated. It is recognized that, in reality, pressure drag is a function of altitude through the variation of the Reynolds number. However, for most configurations of interest, the Reynolds number dependence on drag is difficult to assess because of the complex nature of the flow resulting from the shock/boundary layer interactions in that region, and formal methods of estimating such Reynolds number effects have yet to be developed.

Nozzle Internal Performance Map Format

A typical nozzle internal performance map is shown in Figure 26.4.1-6 for the case of a convergent-divergent nozzle. The map gives the nozzle velocity coefficient C_V as a function of nozzle pressure ratio p_{t8}/p_∞, and nozzle exit-to-throat area ratio A_9/A_8. Nozzle maps for separate flow bypass engines require additional parameters.

26.4.1.3 Airframe and Turbomachinery Performance: Isolated Components

a) Airframe System Drag Map Format

The airframe drag polars themselves, of course, constitute the performance maps for the airframe system. The data for such drag polars can be generated by means of a wind tunnel test and scaling equations, or by being built up from analytical and experimental increments as discussed in Section 26.3.

The airframe system drag includes all external forces on the airplane at one designated inlet and exhaust operating condition, called the operating reference condition.

b) Turbomachinery Performance Maps

The turbomachinery performance maps are given in tabular form and provide thrust, fuel flow, and airflow of a hypothetical propulsion system having a specified internal inlet and nozzle performance schedule and having no external losses, as a function of Mach number, altitude, and power setting.

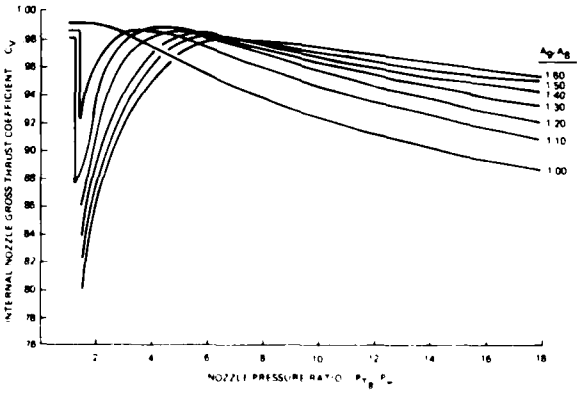

Figure 26.4.1-6. Nozzle Internal Performance Map = 1.35

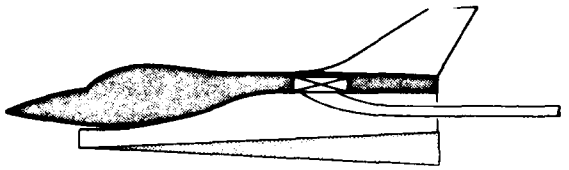

Figure 26.4.2-1. Flow-Through Aerodynamic Force-and-Moment Model

In order to facilitate the calculation of exhaust system installation losses the turbomachinery maps usually give such additional information as nozzle pressure ratio, nozzle exit area, nozzle throat area as a function of Mach number, altitude, and power setting.

26.4.2 Force Accounting Methodology

The approaches taken by the major airframe contractors (References 26.4.2-1 through 26.4.2-5) to performance integration are quite similar. The aerodynamic drag testing of the basic airplane configuration is done with some reference inlet and exhaust system conditions. Most commonly this testing is done with the propulsion system represented by a flow-through duct (Figure 26.4.2-1), in which case the reference inlet and exhaust system conditions are those achievable with such a flow-through duct.

In separate inlet and exhaust system tests the model geometry and flow properties are reproduced in the vicinity of the airplane element (inlet or exhaust system) being studied. Then as conditions are changed to simulate the real conditions (e.g., by blowing high pressure air through the exhaust system to produce the real operating pressure ratio) drag increments are taken with respect to the drag levels associated with the reference conditions. The drag levels are determined using techniques that exclude the thrust or drag forces on the surfaces of the internal ducting of the models.

The inlet and exhaust system drag increments are then combined with the internal propulsion system thrust and the airplane drag (at reference conditions) to obtain a prediction of overall thrust-minus-drag performance of the airplane system.

Fundamental to these performance integration methods is the definition of thrust and drag forces. All the forces in the flight direction which act on an aircraft in level flight are divided into one of the two groups. The way in which the split is made, of course, has little direct impact as long as all forces exerted on the airplane are considered. This split, however, has an effect on the visibility afforded the propulsion system elements.

In virtually all systems currently in use, the inclusion of internal propulsion system performance in thrust and of external forces on the airframe at reference conditions in drag are standard. For the remaining inlet and exhaust system force increments that bridge the gap between these two major force components, there is somewhat more leeway (see Figure 26.4.2-2) in the division between installed engine performance and in the airplane drag polar.

An approach is to charge these remaining force increments entirely to the engine performance (Figure 26.4.2-3), since they are functions of engine throttle setting. The airplane drag polar is then by definition, the drag polar corresponding to reference inlet and reference exhaust system conditions.

This approach can make it difficult to compare airframe system or propulsion system performance of competing airplane configurations. Airframe system drag, for example, can be a strong function of the somewhat arbitrary choice of reference exhaust-system/aft-end geometry. In addition, wind tunnel drag polars, corresponding to unrealistic reference exhaust system conditions, are not directly comparable to drag polars based on flight test results. Such a comparison would play a useful role by highlighting the need for improvements in obtaining thrust and drag forces.

The purpose of this section is to recommend a more flexible approach to the formulation of a performance integration. Because the impact of the configuration details on the performance integration system requirements may be substantial, a single element performance integration system will not be applicable to all airplane systems.

Here, the emphasis is on problems associated with airplane configurations with body-integrated propulsion system installations. For such configurations the interactions between the propulsion system and the airframe can be the dominant factors influencing overall airplane system performance.

The discussion applies specifically to performance integration systems utilizing flow-through propulsion simulation for the general aerodynamic drag testing. The application to testing with turbopowered simulators is discussed in Section 26.4.3. Most important is the requirement for accuracy in predicting the overall thrust-minus-drag performance of an airplane system.

The performance integration procedures recommended here are summarized in Section 26.4.2.1. It is shown that by using the concept of operating reference conditions, the techniques recommended here will produce airplane drag polars and installed propulsion system performance with which meaningful comparisons can be made between competing airplane configurations.

The use of static thrust measurements to isolate the external force on blowing models, combined with the use of operating reference exhaust and inlet system conditions, renders the recommended techniques applicable over an entire airplane development program. Thus, drag polar predictions based on theoretical calculations, wind tunnel measurements, or flight test results may all be developed on a common basis and meaningfully compared.

26.4.2.1 Summary of Recommended System

a) General Features

The approach recommended is based on the premise that the wind-tunnel reference propulsion system conditions (inlet mass flow ratio and configuration and exhaust system pressure ratio and geometry) is to minimize the probability of aft-end flow separation by using small boattail angles. The objective here is to obtain reference exhaust system flow conditions for in an exhaust system blowing test with faired-over, plugged inlets.

The drag polar so obtained may differ considerably from that associated with more realistic exhaust system operating conditions. Thus, it is required that a non-throttle-dependent portion, $\Delta D_{EXH.\ SYS.}$, of the drag increments measured in the blowing tests be used to correct the wind tunnel drag polar to a realistic "operating reference" exhaust system condition. This operating reference geometry and this pressure ratio combination correspond to a specified engine throttle setting, usually maximum power. All remaining drag increments associated with throttle setting changes

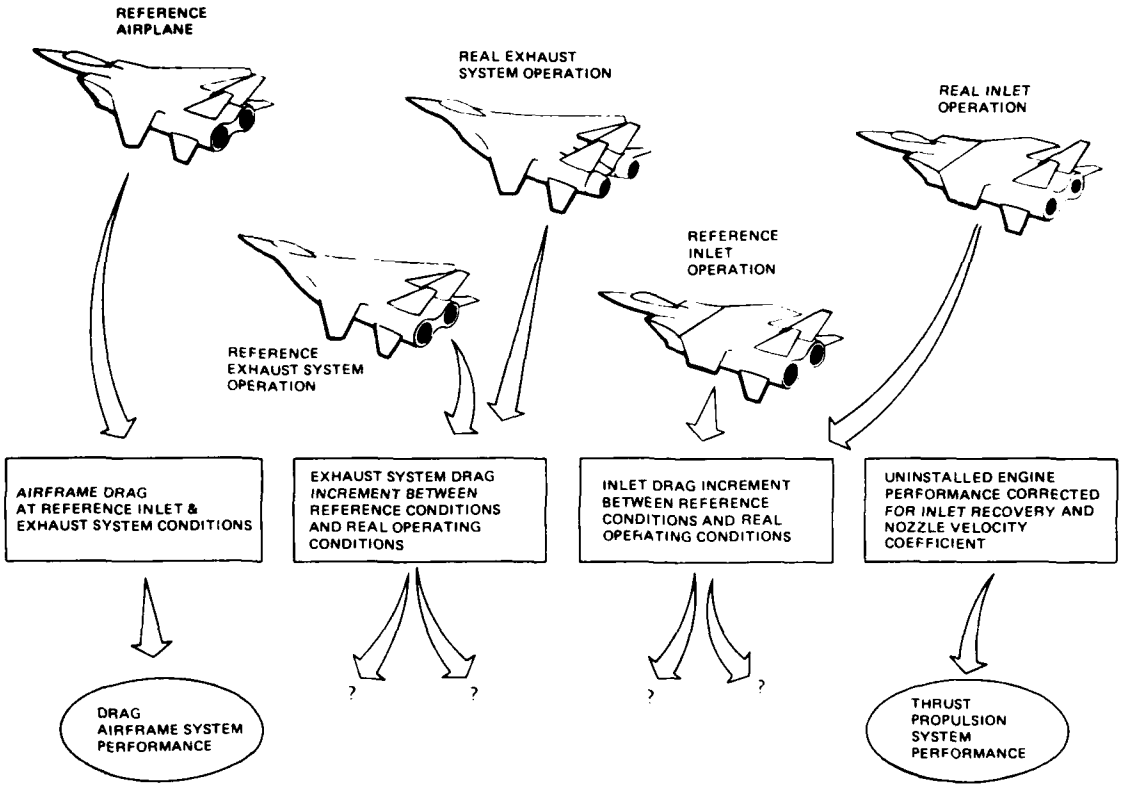

Figure 26.4.2-2. Defining the Split Between Thrust and Drag

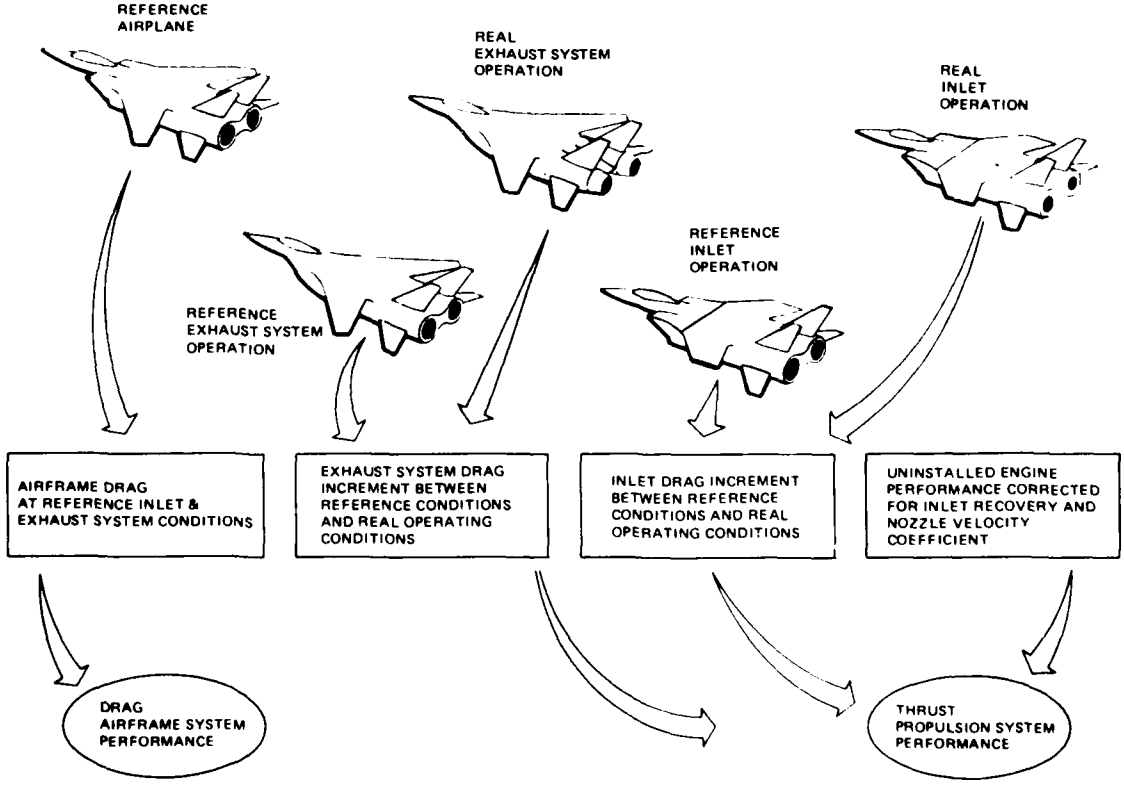

Figure 26.4.2-3. Conventional Definition of Thrust and Drag

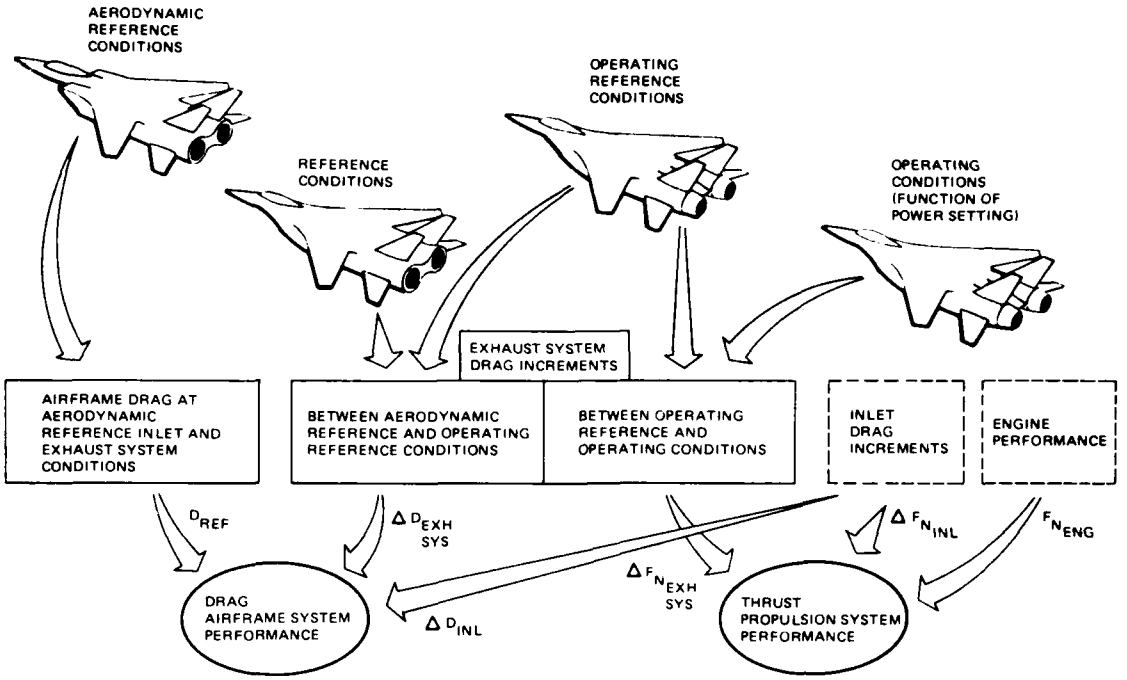

Figure 26.4.2-4. Recommended Definition of Thrust and Drag

relative to the operating reference conditions are then charged to engine net thrust, and do not affect the drag polar (Figure 26.4.2-4). This approach requires no additional testing beyond that required for conventional performance integration schemes.

It is also recommended that the thrust-minus-drag force build-up not deal with the absolute force acting on some arbitrarily specified section of the external surfaces. Such a procedure can make it difficult to account properly for the forces between the surfaces on balance (metric) and the adjacent non-metric surfaces. It also impairs accuracy by including the need to subtract large tare forces from the measured forces.

The present approach does not preclude the use of auxiliary "piggyback" balances (Figure 26.4.2-5). Such a balance may be used as a development tool to guide modifications of the airplane geometry or to verify analytical performance build-up procedure. However, such balances are generally inadequate for the build-up of total system performance.

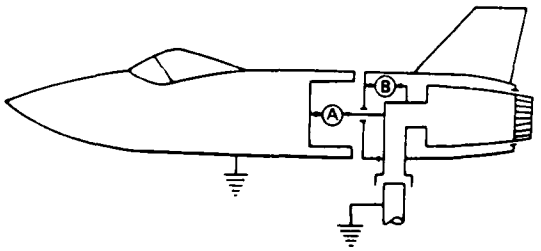

TANDEM BALANCES

BALANCE (A) READS $F_g - D_a - D_b$.

BALANCE (B) READS $D_a + D_b$.

D_a = AFT BODY DRAG

D_b = BASE DRAG

Figure 26.4.2-5. Piggy Back Balance

To determine the external force on a wind tunnel model using a force balance, it is necessary to estimate the internal force of any simulated propulsion system in order to eliminate it from the balance reading. The method used to do this, with flow-through ducts or with a blowing model simulating flow-through (reference) conditions, will depend on the experimental facilities available, the kind of model being used, and the details of the model geometry. An exit wake momentum survey, a static thrust measurement, a "piggyback" internal balance, and a static pressure integration corrected for skin friction are a few of the possibilities.

When real exhaust system operation is being simulated using a blowing model, producing realistic nozzle pressure ratios with realistic exhaust system geometry, other considerations become important. The effect, if any, of external flow on nozzle internal performance must be properly accounted for in the overall thrust-minus-drag build-up. The definition of external drag should be one that is applicable throughout an entire airplane development program. These objectives are most easily met if the internal forces are determined using a static thrust calibration, as recommended in Section 26.4.2.4.

In all of the discussion that follows unless stated otherwise, any reference to a "measured" drag is meant to describe a prediction of a full-scale airplane drag based on a particular measurement. Thus, for example, the "measured" drag of a scale model in a wind tunnel is the drag which results after correcting for flow angularity or upflow in the test section, model support interference effects, wall interference effects, longitudinal test section pressure gradients (buoyancy), and Reynolds number effects on skin friction. Furthermore, if base areas are artificially introduced on the reference exhaust system to control nozzle exit areas or to reduce boattail angles, the base drag

is subtracted from the balance reading along with the internal forces, and is specifically excluded from "measured" external drags.

b) Force Equation

All forces in the flight direction on an aircraft in level flight have been divided into the propulsion system thrust and airframe system drag. The total force in the flight direction, F_{TOTAL}, is given by the following equation:

$$F_{TOTAL} = F_{N_{ENG}} + \Delta F_{N_{INL}} + \Delta F_{N_{EXH\ SYS}} - D_{REF} - \Delta D_{INL} - \Delta D_{EXH\ SYS} + \Delta F_{N_{TRIM}} - \Delta D_{TRIM} \qquad (26.4.2\text{-}1)$$

All of the terms on the right side of equation 26.4.2-1 are defined in Figure 26.4.2-6.

The first three terms on the right side of equation (26.4.2-1) is, by definition, the propulsion system net thrust when summed over the number of engines on the airplane. The three remaining terms subtracted at the end combine to form the airframe system drag, which by definition is independent of engine throttle setting. All drag variations associated with changes in throttle setting are included in the inlet and exhaust system force increments, $\Delta F_{N_{INL}}$ and $\Delta F_{N_{EXH.\ SYS.}}$, respectively.

c) Engine Net Thrust $F_{N_{ENG}}$

The engine net thrust $F_{N_{ENG}}$ is defined to be the difference between the gross thrust of the exhaust system in quiescent air at a specified pressure ratio, and the ram drag on the engine streamtube at the specified flight conditions.

The term "gross thrust" used in this definition is the force that would be measured on the balance in a blowing test, in quiescent air, if the inlet air were introduced in a direction normal to the thrust direction. For most exhaust systems the gross thrust equals the integral of total momentum (axial momentum flux plus pressure increment above ambient) across the nozzle exit plane. For a plug nozzle it also includes the force (in quiescent air) on the part of the plug extending beyond the exit plane.

The "ram drag" used in this definition of engine net thrust is the product of the mass flow in the engine streamtube and the flight velocity. The engine streamtube includes, by definition, all of the airflow demand at the engine face as well as any secondary airflow captured by the engine inlet and ducted around the engine to the exhaust system. Any additional airflow captured by the inlet and ducted overboard through bleed or bypass systems, or simply lost by leakage, is not part of the engine stream-tube.

The effects of inlet internal performance, i.e., inlet total pressure recovery, steady-state, and dynamic distortion, are accounted for in the engine net thrust. Thus, identical engines in a multi-engine airplane might produce different engine net thrusts because of different inlets.

The effects of engine bleed, engine power extraction, and exhaust system internal performance (at static conditions) are also accounted for in the engine net thrust.

Thus, the engine net thrust $F_{N_{ENG}}$ can be determined in an altitude chamber with an available engine using conventional techniques. The effects of inlet internal performance would be simulated, and the measured thrust would be corrected for the

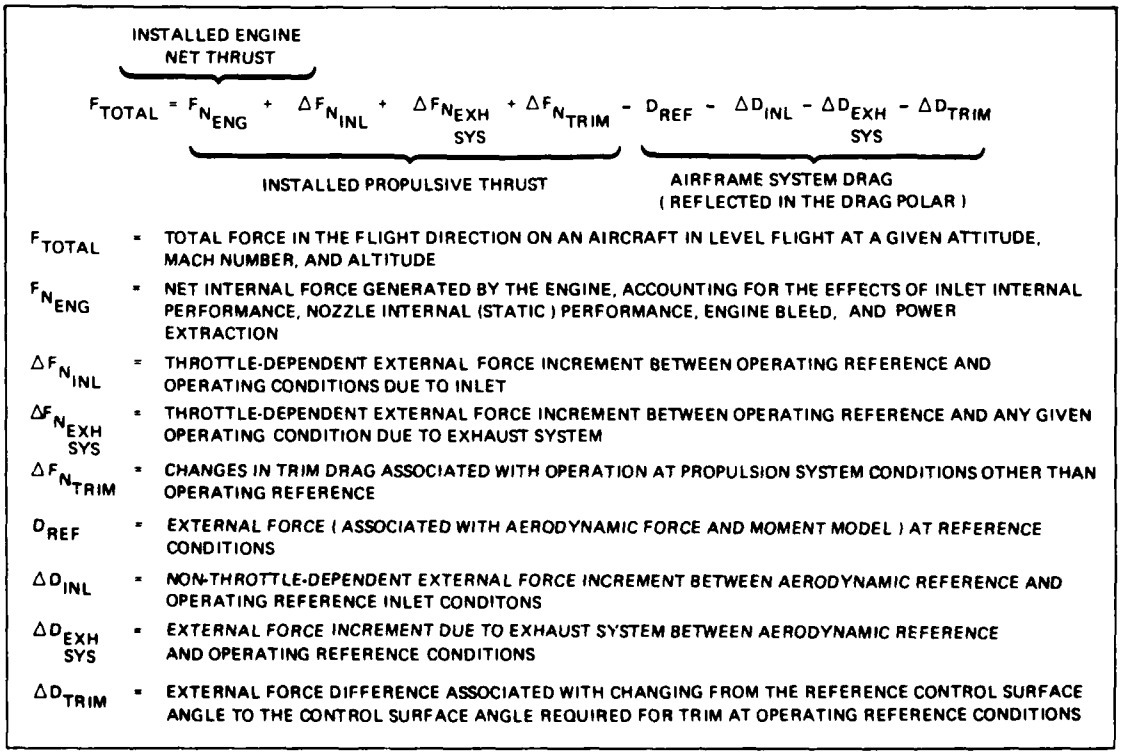

Figure 26.4.2-6. Definitions of Installed Thrust and Drag Quantities

proper ram drag for the flight conditions being simulated.

d) Inlet Force Increments $\Delta F_{N_{INL}}$ and ΔD_{INL} and Reference Aerodynamic Drag D_{REF}

The inlet force increments (as well as exhaust system force increments) are keyed to the concepts of operating reference dragpolar conditions and wind tunnel reference conditions. The expression "operating reference conditions" is used here to distinguish the wind tunnel "reference" conditions which are: (a) used on the basic aerodynamic drag model; and (b) reproduced on the propulsion models to obtain zero-points for propulsion drag increments. The operating reference conditions are those to which the drag polar corresponds by definition, whether the drag polar results from analytical build-up procedures or wind tunnel test results.

The definitions of the inlet force increments $\Delta F_{N_{INL}}$ and ΔD_{INL} and of the reference aerodynamic drag D_{REF} are based specifically on the key definitions given below:

i) Reference Inlet Configuration--The reference inlet configuration, used in the aerodynamic drag testing of the basic airplane configuration, is specified as a function of flight Mach number. It should represent a realistic inlet geometry, subject to the condition that the external flow field associated with it must be precisely reproducible on the inlet drag model. Since the inlet drag model is typically larger scale and thus is tested at different model Reynolds numbers, bleed and bypass system characteristics will be difficult to reproduce. Thus, bleed and bypass doors should be closed on the reference inlet configuration. The rest of the reference inlet geometry can usually be specified to correspond to the real inlet configuration at each flight Mach number and at the reference mass flow ratio (see definition (ii) below).

At the low Reynolds numbers typical of wind tunnel model tests a problem in operating supersonically at a desired reference mass flow ratio without using the inlet bleed system can sometimes arise. Shock-boundary layer interactions can reduce the effective inlet throat area enough that the inlet throat becomes choked at an inlet mass flow ratio less than the desired reference mass flow ratio. When this occurs, or is expected to occur, it is recommended that the inlet ramp angles or centerbody angles (for two-dimensional or axisymmetric inlets, respectively) be sufficiently reduced for the reference inlet configuration to guarantee adequate throat areas.

ii) Reference Inlet Mass Flow Ratio--The reference inlet mass flow ratio, used in the aerodynamic drag testing of the basic airplane configuration, is specified as a function of flight Mach number.

At subsonic and transonic Mach numbers, the selection of a reference mass flow ratio near the realistic operating reference mass flow ratio (defined below) is, in general, desirable. However, the external flow field associated with the reference mass flow ratio must also be precisely reproducible on the inlet drag model. Large spillage drags are generally associated with lip flow separation, which is likely to be affected by changes in Reynolds numbers. The primary criterion for selecting the reference mass flow ratio at subsonic and transonic conditions should be that it must represent a low spillage drag condition for the reference inlet configuration.

At supersonic flight Mach numbers, realistic operating mass flow ratios will normally be close to the critical mass flow ratio of the inlet for an external-compression inlet. (For a mixed-compression inlet, when the inlet is operating above the starting Mach number the normal operating condition will be precisely at the critical inlet mass flow ratio.) Critical inlet flow, however, can be reproduced from test to test far more reliably than a specified mass flow ratio slightly less than critical. For this reason it is recommended that the critical inlet mass flow ratio be used as the reference inlet mass flow for inlets operating supersonically.

iii) Operating Reference Inlet Configuration--The operating reference inlet configuration, which is reflected in the airplane drag polar, is specified as a function of flight Mach number. It is selected to correspond closely to the real inlet configuration at the same engine power setting (generally maximum power) as that used to define operating reference exhaust system conditions. The operating reference configuration should reflect the same bleed and bypass system configurations as the real inlet at the corresponding conditions.

iv) Operating Reference Inlet Mass Flow Ratio--The operating reference inlet mass flow ratio, reflected in the airplane drag polar, is specified as a function of flight Mach number. It too is selected to correspond closely to the real inlet mass flow ratio at the same engine power setting used to define other operating reference conditions.

v) Internal Force--The internal force on a flow-through duct model is equal to the difference in total momentum between free-stream conditions and nozzle exit conditions for the streamtube that passes through the nozzle. If a base area is artifically introduced to the reference exhaust system configuration in order to control nozzle exit area or to reduce afterbody boattail angles, the pressure drag associated with this base should also be included in the internal force.

vi) External Force--The external force on a flow-through duct model is the measured drag force of the model minus the internal force.

vii) Auxiliary Air Drag--The auxiliary air

drag is the drag associated with removing auxiliary air from the inlet for miscellaneous purposes, such as for use as a heat exchanger coolant. The amount of airflow involved is usually quite small and this flow would not typically be simulated on a wind tunnel model. The drag penalty is specifically defined to be the difference in total momentum (in the flight direction) between freestream and exit conditions for the streamtubes involved.

viii) Leakage Drag Increment--This increment is intended to account for the relative leakage characteristics of the inlet models and the real inlet. Drag due to leakage is defined as the difference in momentum (in the flight direction) between freestream and exit conditions of all the streamtubes that are captured by the inlet and that leave via leaks. This quantity is usually estimated for both the models and the real inlet.

The reference aerodynamic drag, D_{REF}, is then the measured external force on a flow-through duct airplane model, operating at the reference mass flow ratio with the reference inlet configuration. It must also be operating at the reference exhaust system conditions described below and in Section 26.4.2.2.

When D_{REF} is determined experimentally for those Mach numbers for which the reference inlet mass flow ratio is less than critical, it is usually very difficult to operate precisely at the desired reference mass flow ratio. In those cases it is preferable to test at several mass-flow ratios near the reference value and interpolate to the desired value. This procedure is illustrated in Figure 26.4.2-7.

The inlet drag increment, ΔD_{INL}, is the difference in the inlet drag increment, ΔD_{INL}, is the difference between the external force measured on the inlet drag model at "operating reference conditions," and that measured at "reference conditions," corrected auxiliary air drag, and leakage drag. It may be appropriate, under conditions where the model scale is large enough, to operate the inlet of the drag model at the operating reference conditions, so that ΔD_{INL} is chosen as zero.

The throttle-dependent drag increment, $\Delta F_{N_{INL}}$, is obtained from the inlet drag model and consists of the difference in the force measured at the "operating reference" condition and that measured at the desired condition. It is charged against engine net thrust, along with $\Delta F_{N_{EXH.\ SYS.}}$, in order to obtain the installed propulsion system performance.

At subsonic flight Mach numbers ΔD_{INL} and ΔF_{INL} vary primarily due to changes in inlet mass flow ratio. A typical experimental determination of these two force increments is illustrated in Figure 26.4.2-8. As is the case when measuring D_{REF}, interpolation between two or three curves obtained experimentally may be appropriate to determine these forces at reference or operating reference mass flow ratio.

At supersonic Mach numbers ΔD_{INL} and $\Delta F_{N_{INL}}$ include the effects of bleed and bypass flows. In addition, ΔD_{INL} may also account for any geometry changes which may be required to achieve adequate throat area at reference conditions. A typical experimental determination of ΔD_{INL} and $\Delta F_{N_{INL}}$ for a supersonic Mach number is illustrated in Figure 26.4.2-9.

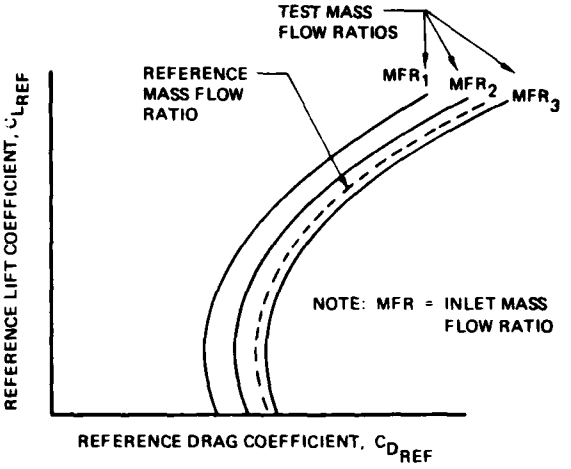

Figure 26.4.2-7. Drag Polar Generation at Reference Conditions

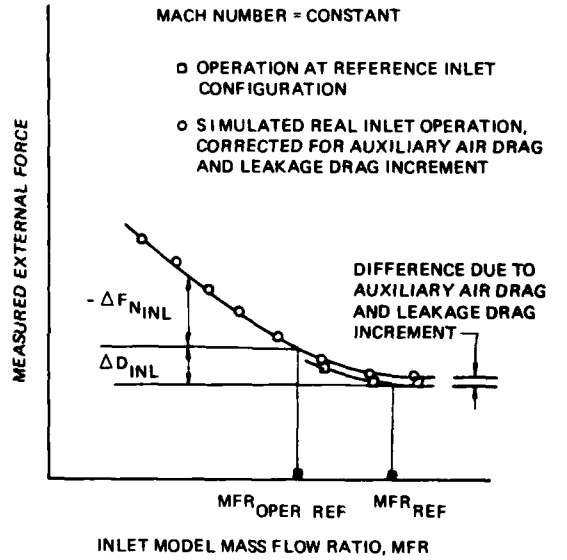

Figure 26.4.2-8. Measurements of Inlet Force Increments at a Subsonic Mach Number

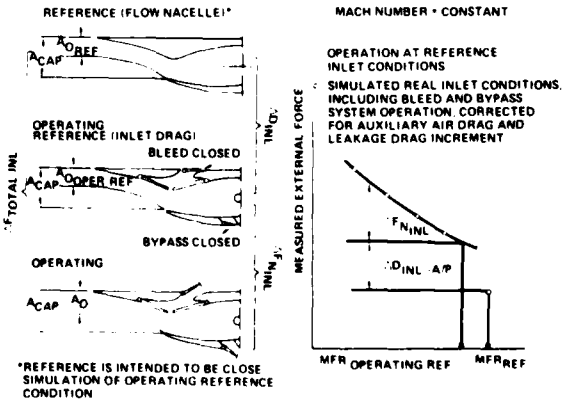

Figure 26.4.2-9. Measurement of Trilet Force Increments at Supersonic Mach Number

In the case of a theoretical build-up of airplane system performance, $\Delta F_{N_{INL}}$ and ΔD_{INL} must also be calculated theoretically. A typical calculation procedure is illustrated in Figure 26.4.2-10. Here D_I is intended to include the additive drag on the inlet capture streamtube and the pressure and friction drag on all external surfaces directly effected by inlet flow conditions.

The bleed and bypass drag D_B, for purposes of the theoretical build-up, are defined as the differences in total momentum (in the flight direction) between freestream and exit conditions for their respective streamtubes.

The theoretical build-up described here is consistent in every detail with the experimental buildup. The predicted "external force" (on the real airplane) that results from either approach includes the additive drag on the engine streamtube, as well as the forces on all internal surfaces which are wetted by streamtubes other than the engine streamtube (i.e., bleed, bypass, auxiliary air, and leakage streamtubes).

e) Exhaust System Thrust Increment $\Delta F_{N_{EXH.\ SYS.}}$ and Exhaust System Drag Increment $\Delta D_{EXH.\ SYS.}$

In an experimental performance build-up, both of the exhaust system force increments $\Delta F_{N_{EXH.\ SYS.}}$ and $\Delta D_{EXH.\ SYS.}$ would result from the same test. They represent the splitting of the conventional exhaust system force increment (one bridging the gap between reference exhaust system drag and real exhaust system drag) into two parts. The non-throttle-dependent part, $\Delta D_{EXH.\ SYS.}$, is considered a drag increment rather than a thrust increment, and thus corrects the airplane drag polar to some realistic operating reference exhaust system conditions. The other part, $\Delta F_{N_{EXH.\ SYS.}}$, is used in the conventional way to correct the engine thrust for drag changes resulting from throttle setting changes.

The word "operating reference" is used here to distinguish these exhaust system conditions (geometry and pressure ratio) from the reference conditions represented in the reference aerodynamic drag D_{REF}. The operating reference conditions actually correspond to a reference throttle setting on the real airplane.

Figure 26.4.2-11 compares this approach to the conventional approach. The main effect is to make the drag polar correspond to a realistic exhaust system geometry and pressure ratio rather than to a possibly unrealistic aft-end geometry and the low pressure ratio associated with a flow-through duct.

In an experimental build-up of exhaust system force increments, using a model with faired-over inlets and with exhaust system air ducted through the mounting strut, it is necessary to simulate both the reference conditions associated with the reference aerodynamic drag model and the real operating conditions of the real exhaust system. As explained in detail in Section 26.4.2.3, no unconventional extra testing is required to accommodate the concept of a set of operating reference conditions, since the operating reference conditions merely represent one of the many throttle settings of the real airplane system which would normally be simulated.

When a real exhaust system condition is being simulated, the present approach calls for subtracting the thrust corresponding to the measured mass flow, temperature, and pressure ratio from the measured thrust-minus-drag to obtain the external drag force. Note here the velocity coefficient used is determined from a blowing model without external flow effects. As discussed further in Section 26.4.2.4, this means the "external drag" force includes the difference ΔF_G between static and wind on internal nozzle performance, which (in the case of a plug nozzle, for example) could be significant.

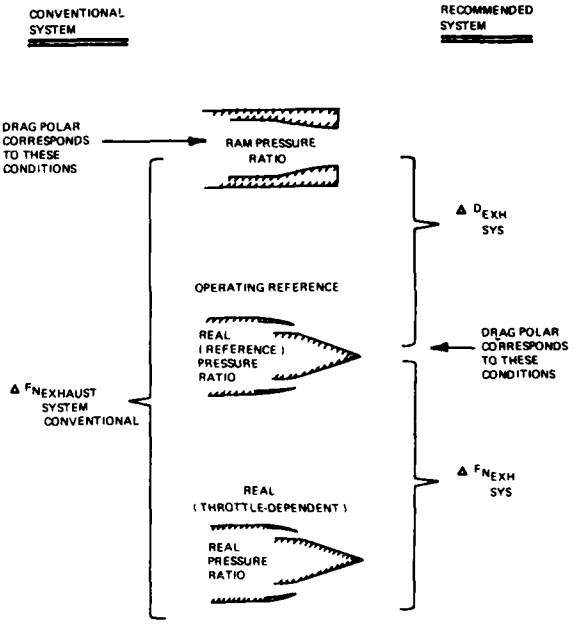

Figure 26.4.2-11. Comparison of Exhaust System Force Increments

THEORETICAL BUILDUP: $\Delta D_{INL} = \underbrace{[D_I + D_{AP} + D_B]}_{OPER\ REF}{}^{*} - \underbrace{[D_I + D_{AP}]}_{REF}{}^{*}$

EXPERIMENTAL BUILDUP: ΔD_{INL} = EXTERNAL FORCE AT OPER REF − EXTERNAL FORCE AT REF CONDITIONS

THEORETICAL BUILDUP: $\Delta F_{INL} = \underbrace{[D_I + D_{AP} + D_B]}_{OPER\ REF}{}^{*} - \underbrace{[D_I + D_{AP} + D_B]}_{REAL}{}^{*}$

EXPERIMENTAL BUILDUP: ΔF_{INL} = EXTERNAL FORCE AT OPER. REF. − EXTERNAL FORCE AT REAL CONDITIONS

D_I = DRAG ON SURFACES AFFECTED BY INLET FLOW

D_{AP} = REMAINING AIRPLANE SURFACES, DRAG OF WHICH CANCELS IN THEORETICAL BUILDUP

D_B = BLEED AND BYPASS DRAG

* CONDITIONS ADJUSTED FOR AUXILIARY AIR AND LEAKAGE DRAG

Figure 26.4.2-10. Example of Buildup of Inlet Force Increments

THEORETICAL BUILDUP $\Delta D_{EXH} = \underbrace{\left[D_N + \Sigma\Delta F_G\right]}_{\text{OPER REF}} - \underbrace{\left[D_N\right]}_{\text{REF}}$

EXPERIMENTAL BUILDUP ΔD_{EXH} = EXTERNAL FORCE AT OPER REF − EXTERNAL FORCE AT REF CONDITIONS

THEORETICAL BUILDUP $\Delta F_{N,EXH} = \underbrace{\left[D_N - \Sigma\Delta F_G\right]}_{\text{OPER REF}} - \underbrace{\left[D_N - \Sigma\Delta F_G\right]}_{\text{REAL}}$

EXPERIMENTAL BUILDUP $\Delta F_{N,EXH}$ = EXTERNAL FORCE AT OPER REF − EXTERNAL FORCE AT REAL CONDITIONS

D_N = SUM OF ISOLATED BOAT TAIL DRAGS, INTERFERENCE DRAG AND DRAG ON REMAINING AIRPLANE SURFACES, WHICH CANCELS IN THEORETICAL BUILDUP.

ALL CONDITIONS ARE EVALUATED AT APPROPRIATE NOZZLE PRESSURE RATIO AND CONFIGURATION.

Figure 26.4.2-12. Example of Exhaust System Force Increments

Figure 26.4.2-12 defines $\Delta F_{N_{EXH.\ SYS.}}$ and $\Delta D_{EXH.\ SYS.}$ and demonstrates both a theoretical and an experimental build-up of these force increments using the present system. The interference drag represents the difference between the drag of all external surfaces affected by exhaust system conditions and the calculated sum of the drags of the individual nozzle boattails. This figure illustrates the correspondence between a theoretical and an experimental build-up of these force increments.

Changes in trim drag increments associated with operation at propulsion system conditions other than operating reference conditions are likely to be very small in most cases. If not, however, they should be included as $\Delta F_{N_{TRIM}}$, which becomes one of the throttle-dependent force increments accounted for in the installed propulsion system performance.

The definitions and criteria for selection of wind tunnel reference conditions and drag-polar operating reference conditions are summarized in Figure 26.4.2-13 for both the inlet and the exhaust system.

26.4.2.2 Reference Exhaust System Conditions

One fundamental assumption underlies all performance integration systems which utilize flow-through propulsion simulation for the general aerodynamic drag testing, inlet drag testing, and blowing models for the exhaust system drag testing. The assumption is that drag increments due to changes in exhaust system conditions are independent of drag increments due to changes in inlet conditions. Specifically, it is assumed that the drag increment associated with changing from a reference exhaust system to a real exhaust system can be obtained with nonrepresentative inlet conditions (i.e., a capped, faired-over inlet for blowing tests), and then applied to an airplane with real inlet conditions. Since changes in inlet spillage and the dumping of inlet boundary layer bleed air can significantly affect the boundary layer conditions approaching the aft-end, this assumption could be invalid for many configurations.

The magnitude of the resulting errors in the build-up of airplane system performance will, in general, be a function of the reference exhaust system conditions selected for the flow-through models. Ways to minimize these errors through a prudent selection of reference exhaust system conditions can be found in the following way.

If we let D represent the total external force (as defined in Section 26.4.2.1) on an airplane or on a scale model of an airplane, then D is clearly a function of the inlet conditions, symbolically represented by the letter i, and the exhaust system conditions, e:

$$D = D(i, e)$$

(The symbols i and e represent both the physical geometry of the inlet and exhaust system, respectively, as well as the flow conditions, e.g., inlet mass flow ratio and exhaust system pressure ratio.)

For the purposes of evaluating the drag effects of the inlet and exhaust system, the drag D may be

	INLET	EXHAUST SYSTEM
REFERENCE CONDITIONS	AERO MODEL TESTED AT THESE CONDITIONS. CRITERIA FOR SELECTION INCLUDE: 1. CAN BE RELIABLY REPRODUCED IN THE SEPARATE INLET AND NOZZLE TESTS. 2. FACILITATES ACCURATE MEASUREMENT OF BOTH AERO MODEL DRAG AND ASSOCIATED PROPULSION INCREMENTS FROM THE SEPARATE TESTS. 3. REPRESENTS REALISTIC CONDITIONS MODIFIED AS NECESSARY TO SATISFY ABOVE CRITERIA. AIRPLANE SYSTEM DRAG POLAR NEED NOT CORRESPOND TO THESE REFERENCE CONDITIONS	GENERALLY REALISTIC GEOMETRY. NO BLEED OR BYPASS FLOW (WHICH ARE DIFFICULT TO REPRODUCE AT DIFFERENT SCALES). MASS FLOW RATIO SELECTED TO MINIMIZE AERO MODEL LIP SEPARATION, WHICH IS MORE ACCURATELY SIMULATED ON THE LARGER SCALE INLET SPILLAGE DRAG MODEL. THUS THERE WILL BE MINIMAL SPILLAGE DRAG AT THIS MASS FLOW RATIO.	REALISTIC GEOMETRY, IF FEASIBLE, BUT MODIFIED WHERE NECESSARY TO AVOID LIKELY REGIONS OF SEPARATED FLOW (WHICH ARE DIFFICULT TO REPRODUCE ON DIFFERENT MODELS). ANY REDUCED BOATTAIL ANGLES WOULD IMPLY EXTRA NOZZLE BASE AREA. RAM PRESSURE RATIO (SINCE AERO MODEL USES FLOW-THROUGH PROPULSION SIMULATION).
OPERATING REFERENCE CONDITIONS	THE CONDITIONS TO WHICH THE AIRPLANE SYSTEM DRAG POLAR CORRESPONDS, BY DEFINITION. THESE CONDITIONS CORRESPOND APPROXIMATELY TO A SPECIFIED ENGINE POWER SETTING, USUALLY MAXIMUM POWER, BUT WOULD NOT BE CHANGED FOR MINOR ENGINE VARIATIONS.	REALISTIC GEOMETRY, BLEED FLOW, BYPASS FLOW AND INLET MASS FLOW RATIO, CORRESPONDING TO SPECIFIED ENGINE POWER SETTING AND ACTUAL INLET OPERATING CHARACTERISTIC.	REALISTIC AFT-END GEOMETRY AND PRESSURE RATIO (BOTH P_T / P_∞ AND P_e / P_∞) CORRESPONDING TO SPECIFIED POWER SETTING.

Figure 26.4.2-13. Summary of Reference Conditions and Operating Reference Conditions

considered to be composed of three parts: D_i, the drag of the inlet-related parts of the airplane, including all surfaces directly affected by inlet flow conditions; D_e, the drag of the exhaust system of the airplane, including all surfaces directly affected by the exhaust system conditions; and D_a, the drag of the remaining surfaces of the airplane, which are not directly affected by inlet or exhaust system conditions. Thus,

$$D(i, e) = D_i + D_e + D_a.$$

The fundamental assumption identified above is that $D_i = D_i(i)$ and $D_e = D_e(e)$, that is, D_i is not a function of exhaust system conditions and D_e is not a function of inlet conditions. Thus,

$$D(i, e) = D_i(i) + D_e(e)_a + D . \qquad 26.4.2\text{-}2$$

Since inlet conditions can affect boundary layer conditions approaching the aft-end, the separation characteristics of the aft-end could be strongly influenced by inlet conditions. Even without separation, changes in displacement thickness characteristics could also affect pressure drag or wave drag. Thus, equation (26.4.2-2) may not be strictly true, and a better representation would be:

$$D(i, e) = D_i(i) + D_e(i, e) + D_a. \qquad 26.4.2\text{-}3$$

There are three sets of inlet conditions i, and three sets of exhaust system conditions e, which are relevant to the performance integration system. First, there are the real inlet and exhaust system conditions, to be represented symbolically by i_r and e_r, respectively, to which the final airplane system performance prediction applies. Secondly, there are the reference inlet and exhaust system conditions, called i_o and e_o, respectively, which correspond to the flow-through duct conditions of the reference aerodynamic drag model. Finally, there are the conditions used for one element (inlet and exhaust system) while drag increments are being measured for changes in the other element. Thus, i_c represents the capped inlet conditions used in obtaining exhaust system force increments. Similarly, e_i represents the exhaust system conditions used while measuring inlet force increments.

Neglecting for the moment any splitting of the external forces into thrust components and drag components, all performance integration schemes of the type considered develop a prediction $D_{PR}(i_r,e_r)$ for the total external force on the real airplane from three parts as follows. The first part is the measured drag $D(i_o, e_o)$ from a flow-through duct model with reference inlet and exhaust system conditions. The second part, the inlet force increment, is the difference in external drag between real and reference inlet conditions with specified exhaust system conditions e_i:

$$D(i_r, e_i) - D(i_o, e_i)$$

The third part, the exhaust system force increment, is the difference in external drag between real and reference exhaust system conditions with a capped inlet i_c:

$$D(i_c, e_r) - D(i_c, e_o)$$

Thus, the predicted external force is:

$$D_{PR}(i_R,e_R)=D(i_o,e_o)+[D(i_r,e_i)- \qquad 26.4.2\text{-}4$$

$$D(i_o,e_i)]+[D(i_o,e_i)-D(i_c,e_o)]$$

The error ϵ in the prediction is:

$$\epsilon = D_{PR}(i_r,e_r) - D(i_r,e_r) \qquad 26.4.2\text{-}5$$

If we substitute equation (-4) into equation (-5), and then use equation (-3) to express the results in terms of inlet related forces D_i's, exhaust system related forces D_e's, and other forces D_a's, we find the error ϵ is a function of only the exhaust system related forces:

$$\epsilon = [D_e(i_c,e_r) - D_e(i_r,e_r)]_1$$

$$- [D_e(i_c,e_o) - D_e(i_o,e_o)]_2$$

$$+ [D_e(i_r,e_i) - D_e(i_o,e_i)]_3 \qquad 26.4.2\text{-}6$$

Thus the error can be divided into the three bracketed components numbered 1, 2, and 3 in equation (-6), each of which has physical significance.

Bracket #1, the change in drag of the real exhaust system when the real inlet is replaced by a capped inlet, is the obvious error resulting from testing the real aft end with a capped inlet.

Similarly, bracket #2 is the error obtained in trying to reproduce the reference back end drag of the reference aerodynamic drag model on the exhaust system blowing model, using a capped inlet instead of the actual reference inlet conditions.

Bracket #3 is the error in the inlet drag tests which results if the drag of the aft-end is included in the balance measurement and changes when the inlet is changed from reference to real conditions.

There are two approaches which can be taken to minimize the error shown in equation (-6).

Method I--Method I takes advantage of the fact that brackets #2 and #3 in equation (-6) can be very small and the remaining bracket #1 is the residual error in predicted drag. This may be done when the following conditions apply:

1) The error contribution from bracket #2 is a strong function of reference exhaust system conditions. It can be essentially eliminated if the reference exhaust system is allowed to deviate enough from the real exhaust system to guarantee that no separation occurs on the reference exhaust system and to provide a minimal amount of aft-facing projected area (exclusive of base area). This means that all significant boattail angles will be reduced or eliminated for the reference exhaust system. In their place would be well-defined base areas, whose drag would be subtracted from external force measurements. For a configuration with engines buried in the fuselage, this same principle should be applied to all closing surfaces, e.g., interfairings between engines that could be influenced by inlet flow conditions.

2) The error contribution from bracket #3 can be eliminated in exactly the same way by using this same reference aft-end configuration for the inlet drag testing. This error contribution can also be eliminated by using a non-metric aft-end

in the inlet drag tests. Some potential disadvantages to this latter approach, however, are discussed in Section 26.4.2.5.

Method II--Method II is based on the following observation: if e_i,e_r, and e_o conditions (i.e., exhaust conditions for inlet testing, real and reference exhaust conditions) were identical, say e, then equation (-6) would become

$$\varepsilon = \underbrace{\{D_e(i_c,e) - D_e(i_r,e)\}}_{1} - \underbrace{\{D_e(i_c,e) - D_e(i_o,e)\}}_{2} + \underbrace{\{D_e(i_r,e) - D_e(i_o,e)\}}_{3}$$

or combining brackets #1 and #2,

$$\varepsilon = \underbrace{-\{D_e(i_r,e) - D_e(i_o,e)\}}_{1+2} + \underbrace{\{D_e(i_r,e) - D_e(i_o,e)\}}_{3} = 0$$

Bracket #3 would then cancel the rest of the error, and no error would result. In other words, the change in aft-end drag, reflected in the measured inlet drag increments when changing from reference to real inlet conditions, would represent real aft-end characteristics and would exactly cancel the errors which occur in the aft-end tests with the capped inlet.

Obviously in practice the reference exhaust system conditions must differ from the real conditions since the real nozzle pressure ratio cannot be simulated under reference conditions with a flow-through duct. However, for any configuration for which there is reason to believe that the effect of inlet conditions on aft-end drag is insensitive to nozzle pressure ratio (i.e., is sensitive only to aft-end geometry), Method II would be preferable to Method I, and would require the following:

1) The reference back end geometry should have the same external contours as the real back end geometry.

2) The inlet drag testing should be done with the reference aft-end configuration installed and on balance.

For most configurations of practical interest, the exhaust system drag characteristics are sensitive to the exhaust system pressure ratio. For this reason, Method I is generally recommended as the best way to minimize the errors in the performance build-up resulting from the influence of inlet conditions on the exhaust system performance.

26.4.2.3 Operating Reference Exhaust System Conditions

The use of a set of operating reference exhaust system conditions as recommended here is closely tied to the recommendations of Section 26.4.2.2. The use of Method I would allow the reference exhaust system geometry to deviate significantly from the real geometry for the sake of overall system accuracy. (Even if the reference exhaust system geometry corresponded to the real geometry, reference exhaust system pressure ratios would, in general, have to be unrealistically low.) Thus, if the airplane drag polar were defined to correspond to reference exhaust system conditions, meaningful comparisons between predicted and flight test drag polars would be difficult to make. Comparisons of drag polars of two competing airplane configurations would be equally difficult to make.

The concept of operating reference conditions provides a way to correct the drag polar to realistic exhaust system conditions. At each external flow Mach number the operating reference conditions would be selected to correspond to a specific throttle setting for the real airplane.

The use of these operating reference conditions does not require any additional testing or modified test techniques relative to conventional performance integration schemes. This fact is illustrated in Figure 26.4.2-14, which shows how the results of the same exhaust system performance test would be analyzed both in a conventional performance integration scheme and in the proposed scheme. The curve labeled "real exhaust system conditions" gives the measured external force corresponding to the full range of engine power settings. It is typically obtained by cross-plotting the results of tests with several exhaust system geometries, each tested over a range of pressure ratios. The resulting curve thus includes the effects of both nozzle geometry and pressure ratio associated with throttle changes. This curve is also based on the use of a static-thrust measurement in isolating the "external force" from the thrust-minus-drag balance measurement.

The exhaust system drag increment $\Delta D_{EXH.\ SYS.}$, as defined here, is independent of throttle setting. All throttle-dependent effects, as in a conventional system, would still be reflected in a net thrust penalty, $\Delta F_{N_{EXH.\ SYS.}}$.

It should be noted that lift increments would be handled much like drag increments in the proposed

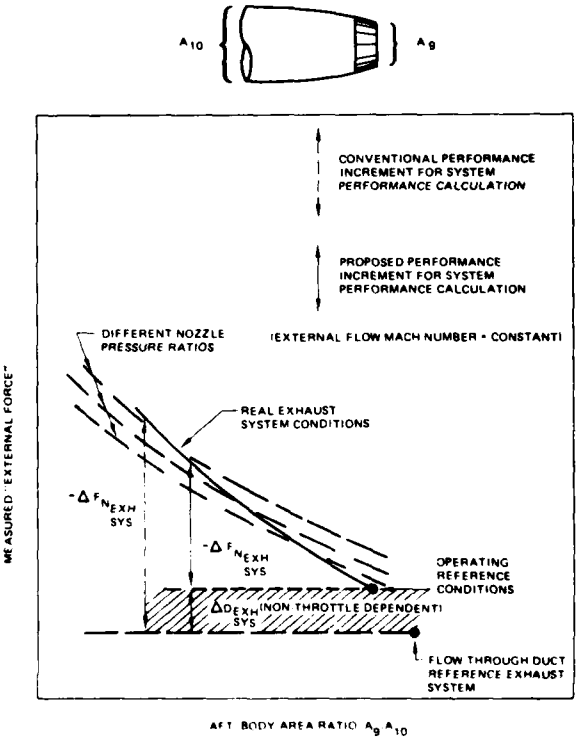

Figure 26.4.2-14. Two Ways to Analyze Exhaust System Performance Data

system. At each airplane angle of attack any lift increment associated with changing from reference to operating reference exhaust system conditions would be added to the corresponding lift measured with the reference aerodynamic drag model. In this way, at each test Mach number, the entire airplane drag polar can be constructed to correspond to baseline conditions.

26.4.2.4 Determination of Exhaust System "External Forces"

The element performance integration system recommended here does not explicitly deal with nozzle internal performance under the influence of the external flow field of the airplane. The increment between static and "wind-on" gross thrust is neither easily measured nor necessary for an accurate airplane performance build-up. The approach recommended here automatically leaves this increment in the exhaust system "external force." The resulting wind tunnel drag polars will be consistent with conventional flight test drag polars, which also include this increment.

When simulating real exhaust system operation in a blowing test, the approach recommended here is to subtract the thrust corresponding to the static performance of the same model (at the same pressure ratio) from the balance reading to determine the external force on the model.

Figure 26.4.2-15 illustrates how this leads to an accurate accounting of all forces on the airplane. The upper left box of the figure illustrates a conventional determination of the external force $D_{EXT\ REF}$ when reference conditions are being simulated. Here F_{REF} represents the total gross thrust of the reference nozzles and D_{BASE}, the drag of the base area introduced in accordance with the recommendations of Section 26.4.2.2. F_{REF}, however, includes the effects of the external flow. When the jet flow is supersonic, the reference nozzle internal performance is usually insensitive to external flow and a static thrust measurement will suffice to determine F_{REF}. When the jet flow is subsonic, however, the nozzles will be unchoked and other methods (e.g., a static thrust measurement corrected by the ratio of wind-on to static discharge coefficients) will be required to determine F_{REF}. (The nomenclature for the drag components identified in Figure 26.4.2-15 is the same as that used in Section 26.4.2.2.)

The upper right box in Figure 26.4.2-15 illustrates the determination of the external force $D_{EXT\ REAL}$ for real exhaust system operation according to the procedures recommended. Here F_{REAL} and $F_{REAL\ STATIC}$ represent the total gross thrust of the real exhaust systems under wind-on and static conditions, respectively.

Although the internal performance of the model exhaust systems will, in general, not represent the performance of the real full-scale nozzles, the difference between $F_{REAL\ STATIC}$ and F_{REAL} should produce the correct increment corresponding to the real nozzles. This occurs because the parts of the real nozzles affected by the external flow, i.e., plug surfaces extending beyond the nozzle exit planes, will in general be quite accurately represented on the model.

Equation (-7) in the figure shows the formation of the total exhaust system force increment by subtracting $D_{EXT\ REAL}$ from $D_{EXT\ REF}$. Equation (-8) restates the total engine net thrust defined in Section 26.4.2.1c in terms of $F_{REAL\ STATIC}$ and D_{RAM}, the total ram drag on the engine streamtubes.

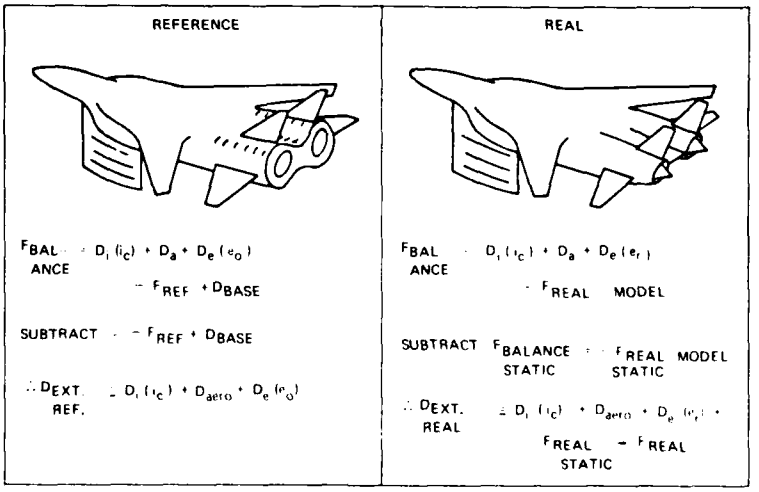

TOTAL EXHAUST SYSTEM FORCE INCREMENT

$$\Delta F_{N_{EXH.\ SYS.}} = \Delta D_{EXH.\ SYS.} = D_{EXT.\ REF.} - D_{EXT.\ REAL} = D_e(e_o) - D_e(e_r) - (F_{REAL} - F_{REAL\ STATIC}) \quad (26.4.2\text{-}7)$$

TOTAL "ENGINE NET THRUST"

$$\sum_{1}^{n} F_{N_{ENG_i}} = F_{REAL\ STATIC} - D_{RAM} \quad (26.4.2\text{-}8)$$

SUM

$$\sum F_{N_{ENG_i}} + \Delta F_{N_{EXH.\ SYS.}} = \Delta D_{EXH.\ SYS.} \quad F_{REAL} - D_{RAM} + D_e(e_o) - D_e(e_r) \quad (26.4.2\text{-}9)$$

Figure 26.4.2-15 Development of Exhaust System Force Increments

Equation (-9) is the result of adding equations (-7) and (-8) to obtain three of the five terms required for the fundamental force equation, equation (-1). What results is the true total net thrust of the engines operating in the real airplane flow field, plus the force increment required to bridge the gap between the real exhaust system drag and the reference exhaust system drag that is reflected in D_{REF}. The key here is that both the engine manufacturer and the airframe contractor are measuring thrust under identical static conditions, for which it is most easily done.

A potential problem can arise with this procedure when the airplane configuration involves closely spaced nozzles, particularly plug nozzles. The nozzles may be interfering with one another under static conditions, producing different static thrusts than if they were tested isolated. Yet, full scale rig or altitude chamber thrust measurements would normally be done with a single, isolated engine. Thus, drag (external force) estimates from model tests and from flight tests would still not be directly comparable.

When this is felt to be a potential problem for a specific configuration, there are two approaches which can be taken. First, the blowing model can be designed so that it is possible to blow one nozzle at a time, with the others plugged.

The other, less desirable, approach is to build another model to the same scale with a single nozzle and none of the upstream airplane details of the original blowing model reproduced. The isolated nozzle model would then be tested only statically to determine the static performance of the nozzles on the regular blowing model. Any discrepancies between the static model internal performance and the (wind tunnel) blowing model internal performance would, of course, become errors in the overall performance build-up of the airplane system.

A key consequence of the procedures recommended here is that the airplane drag polar includes the gross thrust increment between static and wind-on operation for the operating reference conditions. This, plus the operating reference concept, means, for example, that if two different candidate nozzle designs are being considered for a given airplane then two different airplane drag polars must be considered as well. This merely reflects a feeling that it is altogether proper for the drag polar to reflect the interactions between the airplane flow field and the exhaust system flow fields.

26.4.2.5 External Metric Breaks

The recommendation has been made here that inlet and exhaust system force measurements be made with as much of the airplane model on balance as possible, instead of using metric breaks to isolate parts of the external surfaces on the balance. This recommendation is based on several considerations.

First, particularly at subsonic conditions, the regions influenced by changes in, say, exhaust system conditions for a buried engine configuration can be so extensive that a major portion of the airplane model would have to be metric anyway to determine accurately the total force increment resulting from the changes. In general, isolating smaller parts of the airplane on balance to measure inlet or exhaust system force increments represents a dangerous gamble, unless costly preliminary testing is done with a pressure model to verify the adequacy of the metric break location.

The use of a metric break to isolate the smallest acceptable piece of the model on balance often appears, in principle, to offer an advantage in accuracy. Since smaller balances can be used, the balance accuracy in absolute terms should be better. However, if the metric break involves a significant projected area in the flight direction, internal cavity pressures produce an important tare force. The balance must be sized for this force, reducing the potential payoff. The tare must be measured independently and subtracted from the balance reading. Experience has shown that the limitations in the accuracy with which this tare force can be determined usually destroy the potential improvement in the drag accuracy inherent in the smaller balance.

2.6.4.2.6 Element Performance Visibility

Three objectives related to element visibility have been identified:

1) Compare element performance of competing airplane configurations. This is often attempted in the preliminary design period of an airplane development program.

2) Identify the source of drag problems on a given configuration. Thus, for example, one may attempt to determine whether a given exhaust system installation is "good" or "bad" from a drag standpoint.

3) Trace element performance evolution with time.

The impact of performance integration methods on the ability to achieve these objectives will be discussed below.

Most of the element performance integration systems in use in the industry today follow the general procedures schematically illustrated in Figure 26.4.2-3. Usually, the airplane drag polar is defined to be that corresponding to the reference configuration of the flow-through duct reference aerodynamic drag model. The entire exhaust system force increment obtained with the blowing model, being throttle-dependent, is charged to the engine net thrust.

The reference exhaust system configuration is often modified relative to the real geometry in order to avoid separation, as suggested in Section 26.4.2.2, or to accommodate a support sting.

The amount of configuration tailoring required to avoid separation will vary considerably for different types of airplane configurations. The amount of tailoring of the reference configuration, however, has a major impact on the split between the airplane drag and the exhaust system force increment with a conventional performance integration system.

It is nevertheless possible to salvage a modicum of element visibility, for purposes of comparison between different types of configurations, by using the element performance integration procedures suggested here.

Since the operating reference conditions can be defined at or near the engine power setting required to fly at a given point of the mission, the drag polars of two different configurations can be directly overlaid and compared on a common basis. Thus, a configuration which appears to have more airplane drag than another (using the same engines) on an acceleration leg, for example, will indeed have a smaller excess thrust margin. This is not necessarily true with conventional performance integration procedures.

Similarly, the thrust increments, $\Delta F_{N_{EXH.\ SYS.}}$, obtained with the proposed procedures will now also

be directly comparable and will accurately reflect the performance increments associated with changing the throttle setting, and nothing more.

It must be emphasized, however, that the drag increments, $\Delta D_{EXH.\ SYS.}$ still cannot be compared for two different configuration types, for the same fundamental reasons outlined earlier. The arbitrary nature of the selected reference configurations generally makes it impossible to compare the external performance to two competing but different configurations on an element-to-element basis. Only the integrated external performance of each airplane system can be made comparable.

The second objective for element visibility, the ability to rate an exhaust system drag as "good" or "bad" can be met only by comparing the $\Delta D_{EXH.\ SYS.}$ to others for the same type of airplane configuration, based on the same type of reference configuration.

The third objective, the ability to trace the element performance evolution with time, can usually be accomplished. As long as the reference configuration is fixed, $\Delta D_{EXH.\ SYS.}$ can be tracked as an indicator of the changes in the exhaust system drag in the drag polar, and $\Delta F_{N_{EXH.\ SYS.}}$ can always be used to monitor the throttle-dependent drag effects.

It should be noted that internal performance definitions do not require the definition of airplane reference configurations and are not made in terms of forces acting on parts of a body. Thus, comparisons, evaluation and tracking can readily be accomplished to provide complete visibility for internal element performance.

26.4.2.7 Applicability Over Entire Development Program

The element performance integration techniques recommended here are generally applicable over an entire airplane development program. Thus, for example, with only minor corrections (discussed below), the drag polars generated theoretically in the earliest phases of a program, those generated experimentally in wind tunnel programs, and those generated in flight test programs can all be based on the same element performance integration rules and thus can be meaningfully compared with each other.

The ability to compare flight test drag polars with those generated in a wind tunnel program, rarely found in conventional performance integration schemes, stems from two key parts of the present system. First, the concept of correcting the drag polar to a set of "operating reference" conditions eliminates the correspondence of the wind tunnel drag polar to an arbitrary reference configuration. It should perhaps be noted that this approach assumes a great deal of cooperation between aerodynamic and propulsion staffs within an airframe company, since part of the drag polar, $\Delta D_{EXH.\ SYS.}$ and ΔD_{INL}, is to be generated in what has traditionally been a propulsion man's test.

The second key part affecting the comparison of wind tunnel and flight test drag polars is the use of a static thrust measurement to isolate the external force on a blowing model simulating real exhaust system operation. The increment between static and wind-on gross thrust is thus included in the wind tunnel drag polar in exactly the same way it is conventionally included in a flight test drag polar.

The only corrections required in the present system to compare flight test and wind tunnel polars stem from a desire to avoid a "floating" definition of operating reference conditions. Thus, the operating reference conditions would not be changed for minor engine changes at the throttle settings used to define operating reference conditions. If, for example, nozzle exit areas were rescheduled at a maximum-power operating reference condition, the operating reference geometry would be held fixed and would no longer correspond exactly to the real maximum-power geometry. Changes in inlet ramp schedules would be handled in the same way.

For major engine changes, on the other hand, operating reference conditions would be redefined. The philosophy here would be that any engine changes which effectively define a new engine would justify a redefinition of drag-polar operating reference conditions.

26.4.3 Turbopowered Simulator Testing

Considerable effort has been devoted to the understanding of power plant installation effects since the advent of the gas turbine engine and the consequent encounter with important drag effects due to compressibility (References 26.4.3-1,-2). In this section, the problem of model testing using turbopowered simulators (TPS) is addressed. The problem of thrust-drag accounting procedure is described so that the thrust and the installation drag can be identified in an accurate manner consistent with full-scale and drag accounting procedures. This will be followed by a few comments on unique aspects of testing with turbopowered simulators for the development of supersonic aircraft.

The ideal engine simulator for model testing would be a miniature jet engine capable of simultaneously representing the full-scale nacelle's inlet mass flow and the exhaust plume pressure and temperature profiles. For large models (one-third scale or larger) small jet engines are sometimes used, but most model testing is done at scales of about one-twentieth for which miniature jet engines are not available. The procedure used to simulate the full-scale geometry becomes difficult, and an improper choice in modeling technique can result in a procedural bias so large that results accurately representing the full-scale installation cannot be obtained, regardless of the accuracy with which the test data may be acquired. The turbopowered simulator has been in use as a testing tool for the past decade (References 26.4.3-3 through -9) because of the aerodynamic advantage over other nacelle simulations where jet and inlet effects must be modeled simultaneously. Its principal disadvantage has been mechanical complexity and the consequent difficulties with operational reliability over purely gas dynamic simulators such as the ejector and blown jet nozzle. In addition, test techniques had not been developed where reliable results with understood accuracies could routinely be obtained.

The turbopowered simulator uses high pressure air brought to the model through the support system to drive a turbine which, in turn, drives a fan or compressor. The compressor air may then be mixed with the turbine exhaust air to simulate a jet engine or the fan air may be exhausted separately. Figure 26.4.3-1 shows a model of a high bypass TPS.

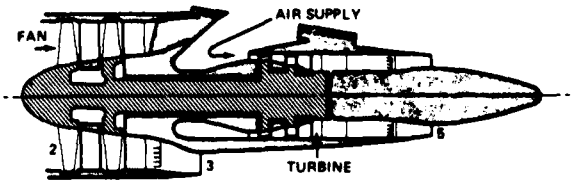

Figure 26.4.3-1. Cross Section View of a Turbopowered High Bypass Fan Engine Simulator

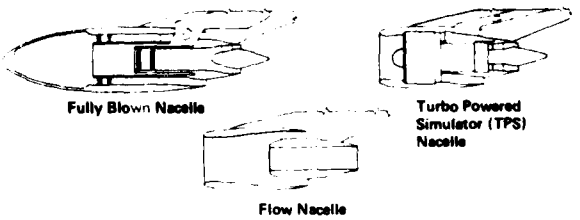

Figure 26.4.3-2. Schematic of Flow, Blown, and TPS Nacelles

Because the turbine drive air is brought to the model, the inlet airflow rate will be less than that of the exhaust. This difference may not be large or detrimental but the deficit in inlet flow must be accounted for. The turbofan nacelle shown in Figure 26.4.3-2 can represent 80% to 90% of the real engine's inlet flow. The pressure ratio of the fan and core flow jets can be simulated as well as the fan flow temperature, but the core flow temperature cannot be duplicated. This may not be too serious if there is a weak dependence of jet and freestream flow characteristics on temperature effects (Reference 26.4.3-10). Lee (Reference 26.4.3-11) notes that besides the jet pressure ratio, the specific heat ratio rather than the temperature plays a role in the modelling of the jet/air frame flow field. Thus the TPS nacelle currently provides the best simulation technique where coupling between the inlet and exhaust flow field may occur and where air displaced by the fully blown nacelle (Figure 26.4.3-2) affects installation drag.

Although many specialized test techniques are involved in testing with turbopowered engine simulators, a consistent element performance integration system is still required to: (1) separate internal and external forces; and (2) split the external force into an airframe system drag, reflected in the drag polar, and an installation loss, charged against engine net thrust. The procedures recommended in Section 26.4.2 for accomplishing these tasks are, in general, directly applicable to the case of turbopowered simulators and offer the same advantages discussed in connection with flow-nacelle/blown-model simulation.

Thus, the internal force for a model with a turbopowered simulator would be defined as the difference between nozzle gross thrust, based on velocity coefficient, and the ram drag of the streamtube captured by the simulator. This definition is convenient to use for simulator testing for the same reasons that the analogous engine net thrust definition is convenient for a flight test program.

The external force would then be defined as the difference between the measured thrust-minus-drag and the internal force. (The assumption here is that any forces associated with externally supplied turbine drive air or with bleed air removed from the model would be calibrated out of the thrust-minus-drag measurement.)

As a result of these definitions:

1) Additive drag on the simulator capture streamtube is included in the external force.
2) If an inlet bleed or bypass system is operating, the associated drag is included in the external force.
3) If the external flow influences the flow of the exhaust streamtube over nozzle surfaces, such as over a plug, the resulting force increments are by definition part of the external force.

These definitions, as in the case of flow-nacelle/ blown-model testing, lead to external force numbers which can easily be combined with the engine company's net thrust predictions to yield a consistent prediction for overall system thrust-minus-drag. Furthermore, the use of the realistic operating reference drag polar conditions discussed above would be equally applicable to a turbopowered simulator program. As before, drag polars could then be defined on a consistent basis throughout an entire development program.

In a typical application, the turbopowered simulator model would be used to supplement flow-nacelle testing. In this case the simulator model would replace the conventional inlet drag and exhaust system drag models. The selection of the reference conditions used to relate the simulator testing and the flow-nacelle testing would involve considerations of the operating characteristics of the simulator. Specifically, two inlet models or flow nacelles (Figure 26.4.3-2) are required to establish the force increments involved between the inlets of the TPS model and the real engine with its larger inlet mass flow. This increment is usually obtained at common values of the inlet velocity ratio. Typically, the exit area of the flow-through nacelle is enlarged to pass the proper inlet flow and then reduced by a plug to reproduce the turbopowered nacelle flow. Thus, aft end flow condition and geometry changes are introduced along with the intended inlet flow condition changes.

While the aft end geometry and flow conditions of flow-through models can be reproduced in a blown model (but rarely are), the large exit area, high through-flow and low nozzle-pressure ratio cannot be reproduced in a turbopowered model without extensive internal changes which have not been attempted to date. In practice, turbopowered and blown nacelle data are corrected for inlet effects using flow-through models which differ in exhaust geometry. This leaves a gap in the performance buildup. The gap is bridged by making an assumption that the exhaust system drag does not vary with geometry for the flow-through models.

Thrust Determination for Turbopowered Nacelles

The best calibration method used for the determination of thrust consists of determining the engine nozzle velocity coefficient (Reference 26.2.2-2). For pure turbojets or engines with a single nozzle, a single velocity coefficient is appropriate. For fan engines with separate nozzles for the primary and fan airstream two velocity coefficients are required. The air mass flow rate for the primary stream is easily measured using appropriate instrumentation in the model air supply line. The fan or inlet flow rate must be determined either by static pressure calibration of the inlet or, if possible, as in the case of the high bypass turbofan, by the use of a nozzle discharge coefficient. All of these nozzle coefficients should be determined as functions of the nozzle pressure ratio in the range where it is going to be used in the wind tunnel. Using the separate flow high bypass turbofan TPS as an example, the net thrust is obtained from:

$$F_N = \frac{1}{g} C_{DF} W_{IF}(C_{VF} V_{IF} - V_\infty) + \frac{1}{g} C_{VP} W_{AP} V_{IP} \qquad (26.4.3\text{-}1)$$

where:

C_{VF}, C_{VP} = fan and primary velocity coefficients

V_{IF}, V_{IP} = ideal velocities of the fan and primary nozzle based on convergent-divergent theory and nozzle charging conditions (Sta. 8)

W_{IF} = ideal weight flow of the fan nozzle based on nozzle charging station conditions and throat area of nozzle

C_{DF} = fan nozzle discharge coefficient

W_{AP} = measured primary weight flow

V_x = freestream velocity

g = gravitational acceleration

A simple and accurate thrust calculation procedure requires an accurate calibration facility. The nozzle coefficients as well as the relationship between real and measured thermodynamic pressures and temperatures are best determined using a flight simulation chamber (FSC) with an internal balance which is not unlike that in use or being developed for testing of full-scale engines (Reference 26.4.3-12).

Calibration

The static calibration is carried out to relate TPS instrumentation system readings to measurements of thrust and weight flows, using the following definition of nozzle coefficients:

$$C_{GF} = \frac{F_{Gt} - F_{GP}}{F_{GFI}} \text{ ; fan gross thrust coefficient} \quad (26.4.3\text{-}2)$$

$$C_{DF} = \frac{W_{At} - W_{AP}}{W_{IF}} \text{ ; fan discharge coefficient} \quad (26.4.3\text{-}3)$$

$$C_{VF} = C_{GF}/C_{DF} \text{; fan velocity coefficient} \quad (26.4.3\text{-}4)$$

where

$F_{GP} = W_{AP} \times C_{VP} V_{PI}/g$ is the primary thrust and C_{VP} is the indendently determined primary nozzle velocity coefficient. F_{Gt}, W_{At}, W_{AP} are the measured total thrust, total air weight flow rate, and primary nozzle weight flow rate. F_{GFI} is the ideal value of fan gross thrust.

Nozzle coefficients, used to relate the indication system readings and calculated net thrust, must reflect any changes in bias of the indicating system resulting from power setting or Mach number (see Section 26.6). This necessitates using nozzle coefficient levels that depend on power setting as well as nozzle pressure ratio.

Inlet/Exhaust Interactions

Engines with high average exhaust temperatures can be better simulated in terms of inlet and exhaust geometry, inlet flow, and exhaust pressure ratio than the turbofan. The following discussion pertains to simulation of such engines which, in contrast to high bypass turbofans, usually require the capability for multimode operation. For such engines then, the TPS will be shown to have a unique capability for identifying the existence of inlet exhaust interactions.

Figure 26.4.3-3 illustrates the resulting determination of installation loss drag with a turbopowered simulator model. The simulator model would first be used to reproduce the reference inlet and nozzle conditions of the flow-through nacelle model. If the mounting systems are different for the two models, the absolute level of external forces may not agree. The level obtained with the simulator representing flow-through nacelle conditions provides a zero point from which to take external force increments when real engine operation is simulated. The resulting increments may then be divided, as shown, into the installation loss drags charged to engine net thrust and a drag polar increment used with the flow-through nacelle results to obtain the airplane drag polar.

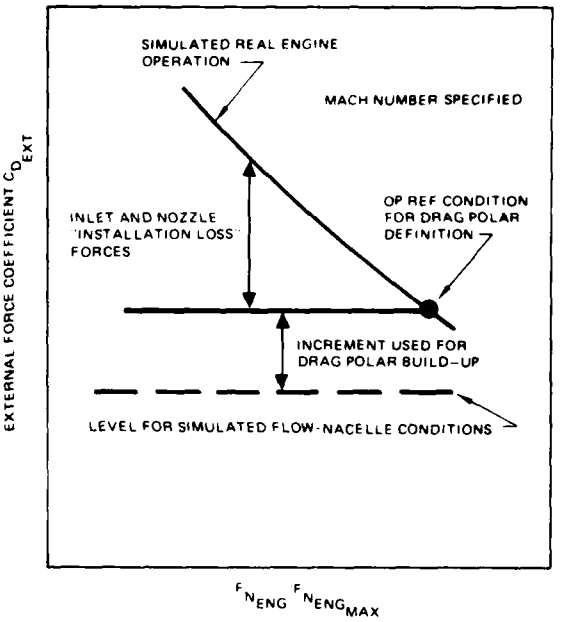

Figure 26.4.3-3. Determination of "Installation Losses" with a Turbopowered Simulation

If a simulator model were used in this way to simulate only real engine operation, much of its value as a diagnostic tool could be lost. In this kind of test the inlet drag increments, exhaust system drag increments, and any interactions between them would all be measured simultaneously. The simulator could also be used, however, to separate these effects, as described below.

For a high thrust-to-weight airplane designed to cruise subsonically at a power setting well below military power, the powered simulator may be used to check for interactions between the inlet flow field involving high spillage rates and the exhaust plume effects at relatively low nozzle pressure ratios.

Instead of only simulating real engine operation the simulator would explore the effects of independent variations of inlet and nozzle conditions, within its capabilities. The variation of external force with nozzle pressure ratio could then be obtained at several inlet mass flow ratios, as shown in Figure 26.4.3-4. The "engine operating line" represents those combinations of inlet and nozzle conditions obtained by the real engine and corresponds to curve in Figure 26.4.3-3.

In the absence of any inlet and nozzle interaction effects, all of the force-versus-nozzle-pressure-ratio curves for the given constant values of inlet mass flow ratio would be parallel to each other, displaced vertically with respect to each other.

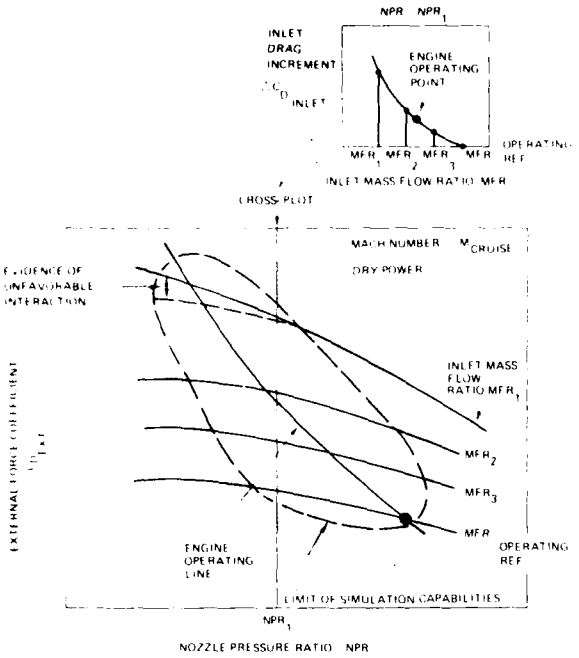

Figure 26.4.3-4. Inlet/Exhaust-System Interaction Effects

The lines of constant nozzle pressure ratio can be used as shown to obtain the inlet spillage drag increments. In the absence of an interaction, the resulting spillage drag curve would be independent of the nozzle pressure ratio to which it corresponds.

Figure 26.4.3-4 illustrates the case of an unfavorable interaction between inlet and nozzle flow fields. At the high spillage rate associated with inlet mass flow ratio MFR_1, the drag penalty resulting from reducing nozzle pressure ratio is much greater than at the higher mass flow ratios. Conversely, the cross-plotted spillage drag curves show a larger increment for operating at MFR_1 at low pressure ratios than at high pressure ratios. Thus, if the intersection of the engine operating line with the MFR_1 line represented a cruise power setting, the simulator data could be used to show that an unfavorable inlet-nozzle interaction was penalizing cruise performance and to estimate the magnitude of the penalty. (Other information, however, such as static pressure distributions, boundary layer measurements, and flow field visualization results, would likely be required to determine the exact physical mechanism responsible for the interaction.)

The absence of such interactions, of course, is the underlying assumption on which flow-nacelle/blown-model test procedures are based. When such interactions exist, the use of Methods I or II recommended here will help minimize, but not eliminate, the associated error. Only with the capability for independent inlet and nozzle flow variations, inherent in the turbopowered simulator, can this error be, first, evaluated and, secondly, eliminated.

26.4.4 Concluding Remarks

The need for an element performance integration system in an airplane development program arises largely from the inability to determine the performance of the complete airplane system in a single test or computation.

Three criteria are used to judge the effectiveness of a performance integration system. First, and most important, is the requirement for accuracy in predicting the overall thrust-minus-drag performance of an airplane system. Secondly, the performance integration procedures should afford as much visibility as feasible to the performance of the individual elements of the airplane system. Finally, the element performance integration system should be applicable throughout an entire airplane development program.

The approach recommended here is based on the premise that the reference propulsion system conditions (inlet mass flow ratio and geometry and exhaust system pressure ratio and geometry) of the flow-through wind tunnel models used for the general aerodynamic drag testing should be selected solely on the basis of overall experimental accuracy. Thus, small (often unrealistic) aft-end bottail angles are recommended for the reference exhaust system configuration to minimize the probability of aft-end flow separation. The objective here is to obtain reference flow conditions which can be precisely reproduced in an exhaust system blowing test with faired-over, plugged inlets.

A consequence of the above procedure is that the wind tunnel drag polar corresponding to reference exhaust system conditions may differ considerably from that associated with any realistic exhaust system operating conditions. However, it is also recommended that part of the drag increments measured in the blowing tests be used to correct the wind tunnel drag polar to a realistic exhaust system geometry and pressure ratio. This geometry and pressure ratio combination would correspond to a specified engine throttle setting. All remaining drag increments due to throttle setting changes relative to the baseline conditions would be charged to engine net thrust, not affecting the drag polar. This approach does not require additional testing relative to conventional performance integration schemes.

The use of a static thrust measurement to define the internal force and thereby isolate the external force on a blowing model, when real exhaust system operation is being simulated, is also recommended.

It is also suggested that the element performance integration system not deal with the absolute force acting on any arbitrarily specified (metric) section of the external surfaces.

The approach recommended here satisfies all the previously described criteria for evaluating element performance integration systems. It allows for an accurate evaluation of airplane system performance, ensuring that all force components acting on an airplane are counted only once in the overall thrust-minus-drag build-up.

Meaningful element-to-element performance comparisons between airplanes of different types are generally not physically possible (except for internal performance parameters). However, using the concept of reference exhaust system conditions, the techniques recommended here will produce airplane drag polars with which meaningful comparisons can be made between competing airplane configurations.

The use of static thrust measurements to isolate the external force on blowing models, combined with the use of exhaust system conditions, renders the recommended techniques applicable over an entire airplane development program. Thus, drag polar predictions based on theoretical calculations, wind tunnel measurements, or flight test results, may all be developed and compared on a common basis.

The turbopowered simulator gives the best measure of propulsion system effects on drag that

may be obtained for aircraft using turbojets or turbofans. The flow field modeling is accurate when corrected for the scale deficit, as long as the flow fields are attached on model and full scale aircraft. For turbofans, a compromise must be accepted either in terms of inlet mass flow or in exhaust nozzle pressure ratio because of the airflow supplied through the model support. For turbojet simulators, part of this simulator drive air may have to be returned through the model support. In comparison to models that use blown nozzles with faired-over inlets, the force increments necessary to determine thrust and drag are usually smaller with the result that decreased dependence on the validity of force superposition is realized.

26.5 PERFORMANCE VERIFICATION

26.5.1 Introduction

Engine performance verification is needed: 1) to validate the engineering estimates and guarantees made during the engine design and development phase and, 2) to identify the absolute in-flight thrust levels to assist in the determination of airplane drag. Validation is particularly important as airframe manufacturers turn toward comprehensive airplane guarantees.

Comprehensive airplane guarantees usually require the airframe manufacturer to guarantee airplane drag and engine specific fuel consumption as well as fuel mileage. As a result of this type of guarantee, the airframe and engine manufacturer must jointly conduct analyses and tests to determine the installed engine performance on the airplane in flight and correlate this performance with "referee" engine performance under guarantee conditions.

26.5.2 Performance Verification Methodology

In its simplest form, engine performance verification is accomplished as shown in the flow chart of Figure 26.5.2-1. Engine performance requirements are identified as a result of airplane performance requirements over the flight envelope. A number of critical points are selected at which thrust or specific fuel consumption or both are to be guaranteed. Guarantee conditions are further specified to include installation (inlet and exhaust system) losses incurred with a defined set of "referee" hardware and with specified bleed and power extraction. Measurements and calculations which define thrust are selected and the demonstration method (static, altitude facility, flight) is agreed upon.

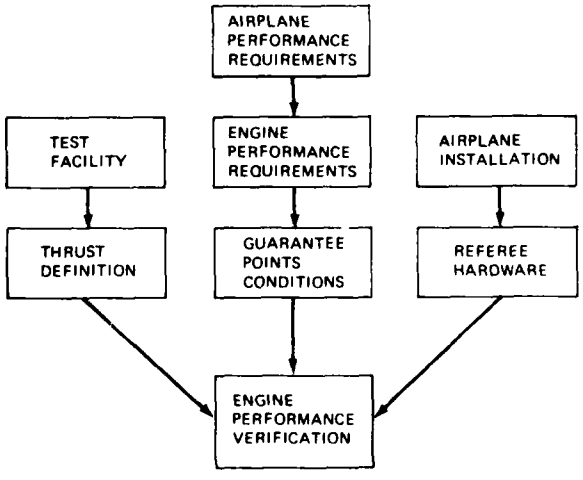

Figure 26.5.2-1. Considerations Impacting Engine Performance V Verification Procedure

26.5.2.1 Thrust Definition

Engine thrust may be measured in several ways. Gross thrust is measured directly as a restraining force on the engine in a static thrust stand as shown and described in Section 26.5.3. In a direct-connect altitude facility, thrust is obtained partly from pressure and flow measurements to define the inlet momentum. In flight, thrust is calculated from pressure and temperature measurements made in the exhaust system, from inlet and exhaust system airflow rates, and from flight velocity, Figure 26.5.2-2.

The installation force increments associated with inlet and aftbody/exhaust, which are necessary for the determination of drag, are rarely determined in flight tests and are thus handled as adjustments from subscale tests, assuming that analytic scale adjustments are valid.

There are two common ways of establishing net thrust of an engine from calibrations. It can be obtained by the so-called "brochure" method or the "gas generator" method.

The brochure method is a simple correlation of thrust to the measurements made in flight. For example, ram pressure ratio and engine shaft speed may be used to develop nondimensional thrust and mass flow functions such as

Thrust function =

$$\left(\frac{F_G}{A_9 p_\infty} + 1\right)\frac{p_\infty}{p_{t2}} = f_1\left[\frac{N}{\sqrt{\theta_2}}, \frac{p_{t2}}{p_\infty}\right], \quad \theta_2 = \frac{T_{t2}}{519°R}$$

Mass Flow Function =

$$\frac{W_2\sqrt{T_{t2}}}{p_{t2}} = f_2\left[\frac{N}{\sqrt{\theta_2}}, \frac{p_{t2}}{p_\infty}\right]$$

Here the corrected shaft speed $N/\sqrt{\theta_2}$ is related to engine pressure ratio, EPR = p_{t7}/p_{t2} and corrected fuel flow rate = $W_f/(p_{t2}\sqrt{T_t})$. Shaft speed, EPR, and fuel flow rate are therefore equally valid as correlation parameters and the choice between them is made primarily on the basis of tradition as well as consideration of relative sensitivity. For the brochure method to be valid, calibration over the entire flight regime must be available and similarity in total pressure profiles between calibration and flight is assumed.

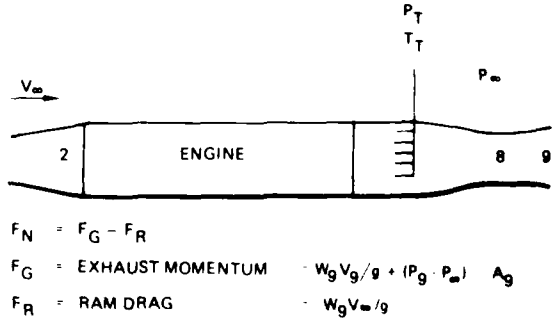

Figure 26.5.2-2. Station Number Schematic and Nomenclature Definition

"Gas generator" methods for gross thrust determination rely on the measurement of nozzle entrance conditions and the calibration characteristics of the nozzle. These methods avoid the problems associated with flow nonuniformities at the engine inlet but, in turn, demand accurate determination of flow conditions in the nozzle. Thus nozzle gas flow rate, nozzle total pressure, p_{t7}, and temperature, T_{t7}, must be determined. These measurements together with nozzle throat area (A_8), appropriate external static pressure, and calibrations of the nozzle coefficient allow the calculation of F_G.

There are two basic approaches to the employment of nozzle coefficients, these involve the use of thrust-per-unit weight flow rate and the thrust-per-unit nozzle exit area. In the former, a measurement of gas weight rate is required, whereas in the latter neither gas flow rate nor total temperature is required. No uniformly accepted description of these two methods is in use and they shall be described here by the principal measurement required for each method: area (A), and weight flow rate (W).

Thus, in the W method a nozzle coefficient is defined by

$$C = \frac{F_G}{W_9\sqrt{T_{t9}}} \quad / \text{ (ideal)}$$

and in the A method

$$C_G = \frac{F_G}{p_\infty A_9} \quad / \text{ (ideal)}$$

The ideal quantities shown may be those associated with a fictitious convergent nozzle or with a fictitious flexible convergent-divergent nozzle which adjusts A_9 to match $p_9 = p_\infty$. In the latter case, the coefficient C defined in the W method becomes the velocity coefficient discussed in Section 26.4.2.

Table 26.5-1. Ideal Weight Flow and Thrust Expressions, Here $\Gamma = (\gamma-1)/\gamma$ and $Z = P_T/P_\infty$

Ideal group	$Z \gtrless \left(\frac{\gamma+1}{2}\right)^{\frac{1}{\Gamma}}$	Convergent nozzle ($A_9 = A_8$)	Variable convergent–divergent nozzle
$\frac{W\sqrt{RT_{t7}}}{P_{t7}A_8}$	Subcritical $<$	$Z - \frac{1}{\gamma}\left[\frac{2}{\Gamma}\left(1 - Z^{\Gamma}\right)\right]^{1/2}$	$Z - \frac{1}{\gamma}\left[\frac{2}{\Gamma}\left(1 - Z^{\Gamma}\right)\cdot\frac{A_9}{A_8}\right]^{1/2}$
	Critical $=$	$\left[\gamma\left(\frac{2}{\gamma+1}\right)^{\frac{\gamma+1}{\gamma-1}}\right]^{1/2}$	
	Supercritical $>$		
$\left(\frac{F_G}{W\sqrt{RT_t}}\right)$	Subcritical	$\left[\frac{2}{\Gamma}\left(1 - Z^{\Gamma}\right)\right]^{1/2}$	
	Critical	$\left[\frac{2\gamma}{\gamma+1}\right]^{1/2}$	
	Supercritical	$\left[\frac{2(\gamma+1)}{\gamma} - \frac{1}{Z}\left[\frac{1}{\gamma}\left(\frac{\gamma+1}{2}\right)^{\frac{\gamma+1}{\gamma-1}}\right]^{1/2}\right]$	$\left[\frac{2\gamma}{\gamma-1}\left(1 - Z^{-\Gamma}\right)\right]^{1/2}$
$\frac{F_G}{P_\infty A_9}$	Subcritical	$\frac{2\gamma}{\gamma-1}\left[Z^{\Gamma} - 1\right]$	
	Critical	γ	
	Supercritical	$\left[2\left(\frac{2}{\gamma+1}\right)^{\frac{1}{\gamma-1}}\right] Z \quad 1$	$\frac{2\gamma}{\gamma-1}\left[Z^{\Gamma} \quad 1\right]$
$\frac{F_G}{P_\infty A_8}$	Supercritical		$\frac{2\gamma}{\sqrt{\gamma Z_{-1}}}\left(\frac{2}{\gamma+1}\right)^{\frac{1}{\gamma-1}} Z\left(1 - Z^{-1}\right)^{1/2}$

Table 26.5.2-1, adapted and modified from Ref. 26.5.2-1, gives the functional form of the ideal thrust, weight flow function is associated with the definition of the discharge coefficient (Section 26.4.2)

$$C_D = \frac{W_8\sqrt{T_{t8}}}{A_8 P_{t8}} \quad / \text{ (ideal, convergent nozzle)}$$

Note that $C_{G,con} = C_D \times C_{con}$.

It is therefore evident that in-flight thrust measurement depends on in-flight measurement of engine flow conditions and perhaps on previously determined nozzle coefficients.

Nozzle coefficients are a function of nozzle geometry, nozzle pressure ratio, exhaust gas temperature, Reynolds number and last, but not least, the manner in which average gas properties at the nozzle entrance (Station 8) are determined. Thus, the "art" of in-flight thrust measurement revolves largely around the proper determination of full-scale in-flight nozzle coefficients from model scale data, full-scale altitude facility data, and static full-scale data.

The following procedure is typical of those used to extrapolate model nozzle coefficients to full-scale for turbofans or turbojets that utilize a single exhaust or for turbofans with separate exhaust nozzles. For simplicity of description, a mixed-flow, single-nozzle engine will be used in the following example. Extension of the methodology to dual flow nozzle is straightforward, although it requires the additional consideration of flow interaction effects such as those illustrated in Figure 26.2.2-1.

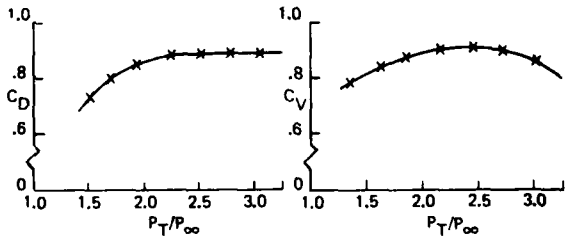

Figure 26.5.2-3. Model Nozzle Coefficients Determined Over the Nozzle Pressure Ratio Range of Interest for the Full Scale Article

The nozzle model tests are generally conducted over a range of nozzle pressure ratios (p_T/p_∞) consistent with mission requirements. Nozzle velocity coefficients (C_V) and discharge coefficients (C_D) as shown on Figure 26.5.2-3 are obtained from the model test data. Here, and in the following discussion, attention will be restricted to "flexible" ideal nozzles satisfying $p_9 = p_\infty$. Hence, attention will be focused on coefficients C_V and C_D such that $C_G = C_V C_D$.

These nozzle coefficients are used in the equation for gross thrust which can be written as follows (with $p_9 - p_\infty = 0$):

$$F_G = \frac{W_I \times C_D}{g} \quad (V_I \times C_V) \quad C_V C_D P_\infty A_9.$$

Below critical pressure nozzle pressure ratios,

$$\Psi = \frac{2}{\gamma-1}\left[\left(\frac{p_T}{p_\infty}\right)^{\frac{\gamma-1}{\gamma}} - 1\right], \quad \frac{p_T}{p_\infty} < \left(\frac{\gamma+1}{2}\right)^{\frac{\gamma}{\gamma-1}}, \; p_T = p_{t8}$$

and at choking pressure ratios and above,

$$\Psi = 2\,\frac{p_T}{p_\infty}\left(\frac{2}{\gamma+1}\right)^{\frac{1}{\gamma-1}} - 1, \quad \frac{p_T}{p_\infty} \geq \left(\frac{\gamma+1}{2}\right)^{\frac{\gamma}{\gamma-1}}$$

The symbols are defined in Section 26.4.3.

The thrust function Ψ in the basic gross thrust equation depends on nozzle pressure ratio only. In the model tests, densely spaced total pressure rakes are used to determine the entrance station total pressure distribution. The average effective nozzle total pressure is then calculated: the entrance area is divided into a number of constant total pressure stream-tubes each of which is expanded to ambient pressure, their thrust contributions are summed; effective total pressure at the entrance station is defined to be that which would ideally produce an equal thrust. This type of averaging tends to minimize the difference in nozzle coefficients due to slightly different total pressure profiles at the entrance. On this basis, the assumption is made that nozzle coefficients are a function of nozzle geometry, pressure ratio, and Reynolds number for equivalent effective total pressures. However, when the full-scale nozzle is attached to the engine, it is not practical to obtain as dense a survey and as flat a profile as in model tests due to the characteristics of the engine flow discharge into the nozzle. The engine flow includes swirl, total pressure depressions due to struts, and the possibility of combinations of radial and circumferential pressure gradients--not at all the ideal type flow provided by the carefully designed choke plates and screens upstream of model scale nozzles. Comparable nozzle pressure ratios between model and full-scale data are derived from static or altitude cell full-scale test data and model data by correcting the latter for known scale effects and then forcing agreement between model and full-scale C_V and C_D used in the thrust equation.

26.5.2.2 Extrapolation of the Full-Scale Engine Data to Flight

Model nozzle coefficients are adjusted for full-scale Reynolds number effects and estimated effects of geometric differences due to struts, roughness, steps, gaps, etc., of production nozzle hardware. Boundary layer theory, skin friction data, data on losses due to steps on flat plates (Ref. 26.2.2-5), and in-house data on model and full-scale nozzles are used to estimate the correction.

On full-scale engines, it is not practical to determine C_V and C_D separately. The thrust equation is therefore rewritten as:

$$F_G = p_\infty A_9 C_g \Psi$$

The non-dimensional term $F_G/p_\infty A_9 = \Psi C_g$ is a function of pressure ratio only and can be shown as in Figure 26.5.2-4a which is calculated from adjusted model data of Figure 26.5.2-4b. Similarly Figure 26.5.2-4c shows the data as measured directly on a full-scale engine static rig.

Since the nozzle pressure ratio determined from full-scale testing is subject to uncertainties in pressure measurements and the model results have

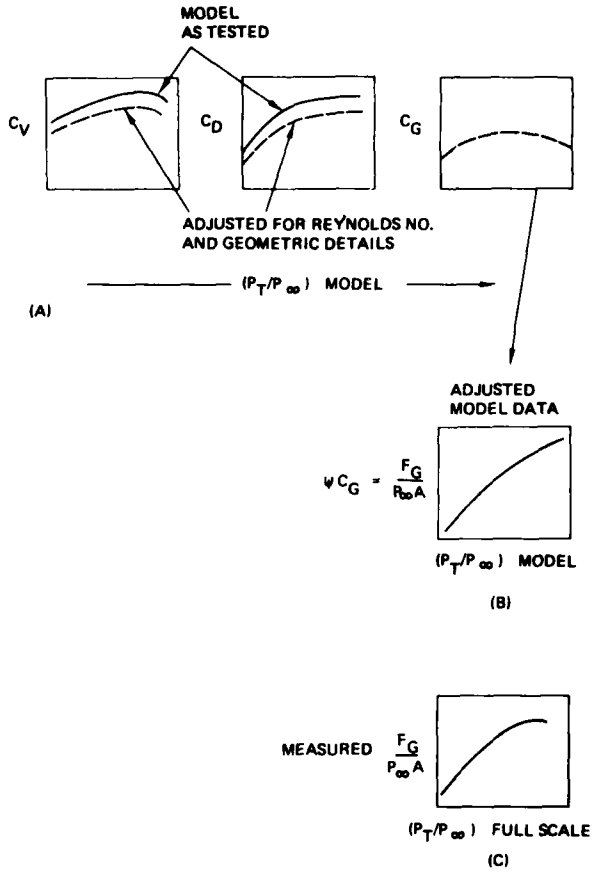

Figure 26.5.2-4. Development of Correlation Between Thrust Function of Model Scale and Full Scale Nozzles

been corrected for known scale effects, the model curve of $F_G/p_\infty A_9$ is considered correct and the discrepancy between predicted and measured $F_G/p_\infty A_9$ is assigned to the full-scale pressure ratio; the pressure correction is then obtained from Figure 26.5.2-5. A curve of $\Delta p_T/p_\infty$ can be generated as shown on Figure 26.5.2-6 for each engine tested. Thus, the pressure ratio needed on the model to calculate the same thrust on the full-scale engine can be found:

$$(p_T/p_\infty) = (p_T/p_\infty) + [(p_T/p_\infty) - (p_T/p_\infty)]$$

correlation to full-scale	model corrected	full-scale measured	model corrected
		$= \Delta P_T/p_\infty$ correction.	

The new pressure ratio is then the value that, when used in the thrust equation, will yield the same thrust as measured on a ground test rig for the engine when using model nozzle coefficients. Thus, the thrust measured on a test stand can be correlated with model nozzle data, and guarantees from the standpoint of the nozzle performance and fuel flow can be measured to determine SFC compliance. The question of whether the gas generator (engine) produces flow with the total pressure indicated for a given fuel flow rate remains open. For example, if the engine meets thrust requirements but is high on fuel flow, is the full-scale nozzle deficient or is the engine deficient in total pressure? The answer to this question can be obtained from measured engine parameters, but

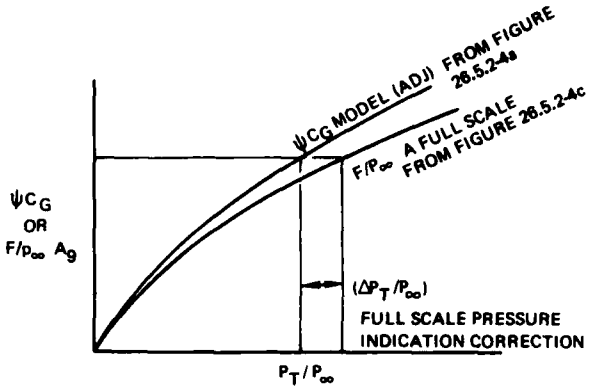

Figure 26.5.2-5. Corrections Required to Correlate Model and Full Scale Nozzle Performance for Particular Pressure Measurement Schemes

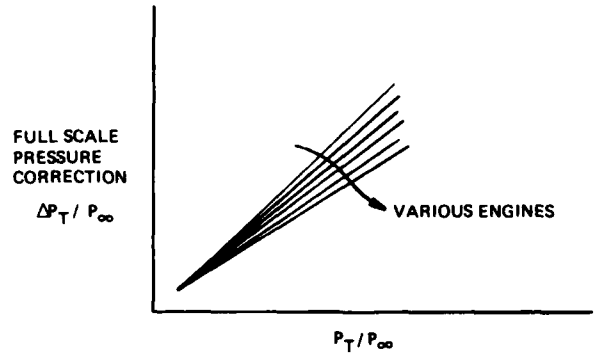

Figure 26.5.2-6. Plot of Pressure Corrections Obtained from Figure 26.5.2-5

additional testing is necessary to verify full-scale engine performance in addition to that described above. These additional tests are discussed in the following section.

26.5.3 Static Test Facilities

There are essentially three types of engine test facilities. Airframe manufacturers generally use outdoor test facilities for the evaluation of sea level static performance and acoustic characteristics. Engine manufacturers utilize both outdoor and indoor test facilities since the indoor facilities provide an altitude test capability. Government facilities also include wind tunnels wherein small engines can be run on an airplane model and full-scale engines on partial airplane models. This section is a brief examination of the characteristics of these types of facilities.

In addition to the gas property measurements usually made to determine the relation between ideal and measured thrust, static facilities are used to measure fuel flow and airflow, all to varying degrees of accuracy. Thrust measurements on engine test stands are usually obtained from a strain gage on a nearly frictionless flexure mount. Accuracy levels of these measurements can be quite high and representative values will be quoted below in connection with a specific facility. Fuel flow rates can usually be determined quite accurately, using calibrated orifices. Airflow is determined using standard (ASME, bellmouth, etc.) subsonic venturi or choked orifices; the accuracy varies with the type of device used, but the largest errors are generally associated with effects which are not or cannot be controlled, particularly environmental effects.

Thus, for facilities such as those to be described below, the potential exists for correlating propulsion forces with thermodynamic and flow measurements. In this way the thermodynamic and flow measurements made in flight may be used to infer in-flight thrust. The problem centers on achieving this while minimizing testing time and cost.

26.5.3.1 Static Outdoor Test Facilities

Figures 26.5.3-1 and 26.5.3-2 show typical outdoor test stands. Figure 26.5.3-1 shows a stand capable of measuring performance of large high-bypass turbofan engines. In the facility shown in

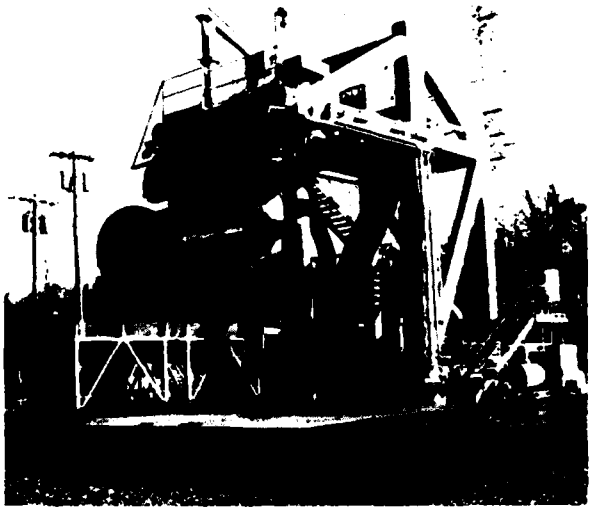

Figure 26.5.3-1. Large Outdoor Test Facility The Boeing Company Tulalip Site, Marysville, Washington

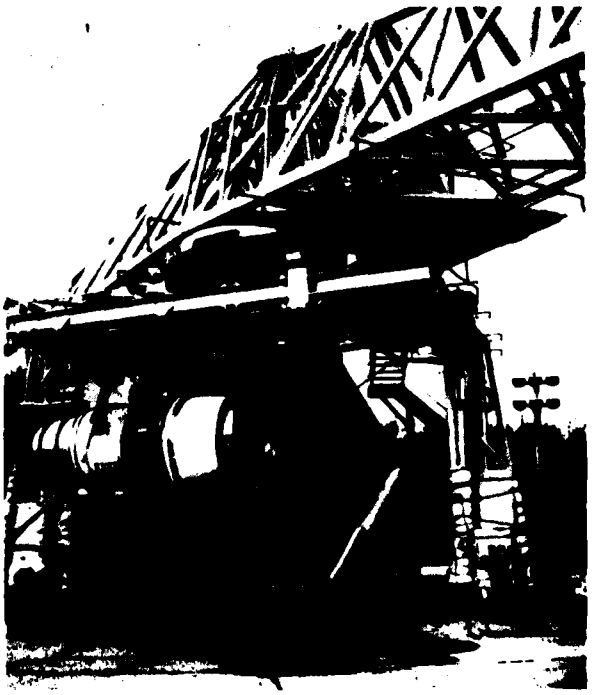

Figure 26.5.3-2. G.E. Peebles Crosswind Test Facility, Evansdale, Ohio

Figure 26.5.2, the engine/nacelle can be oriented at angles to a wind machine. The turntable on which the engine is mounted can rotate to provide crosswind tests.

Testing on outdoor facilities may be carried out with bellmouth or flight-inlet, reference or flight nozzle. Operation with bellmouth and reference nozzle is usually carried out to determine mass flow or thrust characteristics because of those component's well-understood performance. Flight hardware is used for testing for design weaknesses (inlet lip flow separation, structural failures, etc.). Since aircraft noise is primarily a low speed flight problem, static evaluation of nacelle noise treatment, as well as basic engine noise characteristics, is determined on outdoor test stands.

When altitude facilities are not available, the outdoor test facility is used to estimate flight performance of the nacelle. Typically, nozzle velocity coefficients (C_V) are developed up to the maximum nozzle pressure ratio of the nozzle. Model nozzle coefficients are then used to estimate the C_V level at cruise where the nozzle pressure ratio is higher by:

$$\frac{P_{t2}}{P_\infty} = \left(1 + \frac{\gamma-1}{2} M_\infty^2\right)^{\gamma/(\gamma-1)}$$

Figure 26.5.3-3 illustrates the overall procedure.

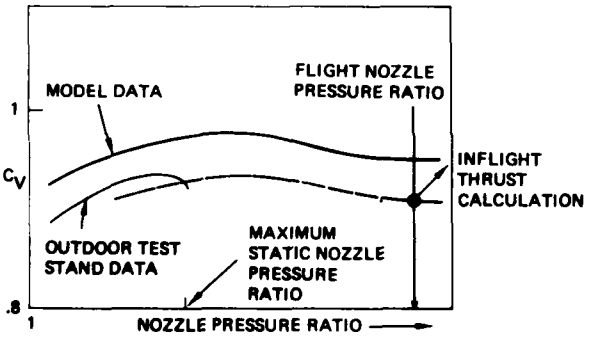

Figure 26.5.3-3. Plot of Nozzle Performance Data as Obtained from Model and Static Tests, Showing the Extrapolation Required to Flight Conditions

26.5.3.2 Indoor Sea Level Test Facilities

Indoor sea level test facilities are used primarily for climatic control of the engine inlet air as in engine icing tests. In such facilities air temperature, pressure and humidity can be adjusted to the needs of the test. Figure 26.5.3-4 is a sketch of a typical indoor engine test facility. Engines may be run with flight hardware but more often inlets and nozzles which are mass flow calibrated are used. Advantages of such a test cell over outdoor test stands may be the ease with which instrumentation may be handled by personnel. Environmental noise is rather easily reduced by acoustic treatment of inlet and exhaust stacks. The primary disadvantage of indoor facilities is that airflow around the engine, if not controlled, may result in pressure forces on the external surfaces of the engine. These forces, as well as pressure drops across the inlet and exhaust stacks of the cell, depend on the engine throttle setting and, hence, must be known over the operating range of the engine. The lack of knowledge concerning

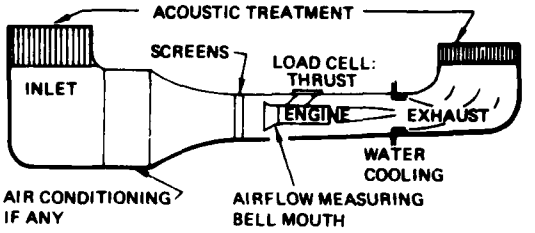

Figure 26.5.3-4. Sea Level Static Facility

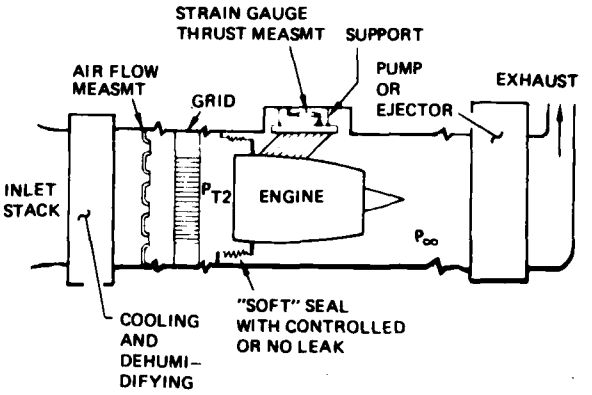

Figure 26.5.3-5. Indoor Altitude Facility Schematic (Not to Scale)

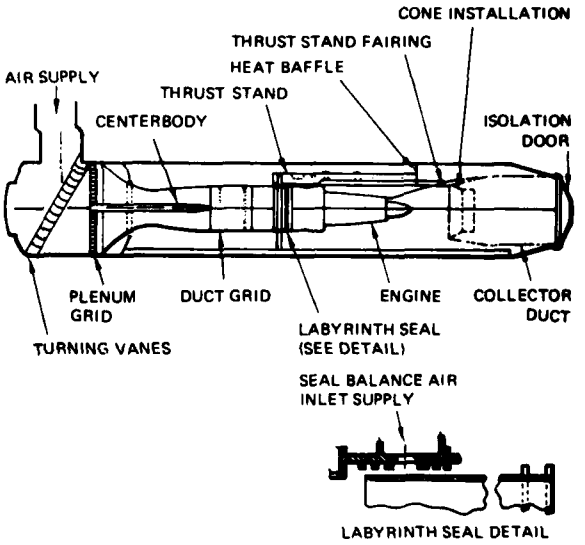

Figure 26.5.3-6. Engine Installed in the J-1 Test Cell

such forces may lead to a significant bias uncertainty.

26.5.3.3 Indoor Altitude Facilities

Figure 26.5.3-5 shows a schematic of an indoor facility where the ram pressure ratio of flight can be duplicated in a test cell. To achieve this a pump or ejector reduces the pressure in the aft portion of the test cell space to the desired value, p_∞. The forward portion is maintained at pressure p_{t2} (atmospheric less pressure losses through the air conditioning and the venturi system) by a barrier connected to the engine in a way which introduces small known mechanical forces in the thrust direction. Thus soft bellows (Figure 26.5.3-5) or controlled leakage labyrinth seals (Figure 26.5.3-6) are commonly used. The pressure barrier

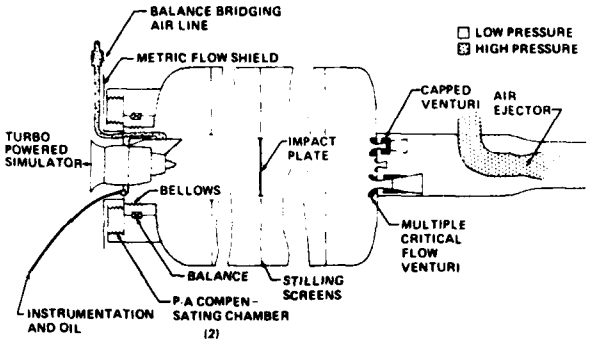

Figure 26.5.3-7. Flight Simulation Chamber

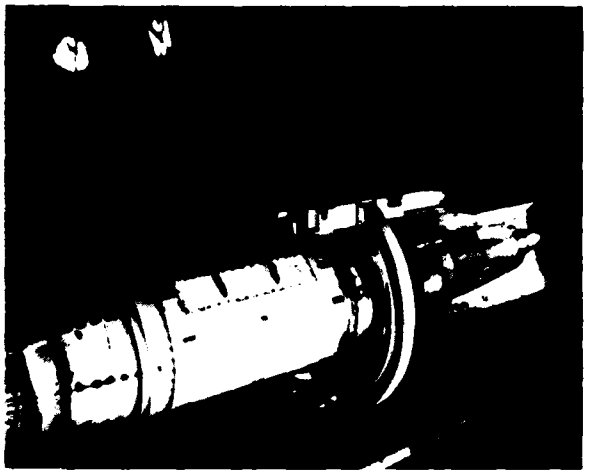

Figure 26.5.3-8. AEDC-RTF Cell J-1

can make a significant contribution to the thrust force measurement made by the load cell. This force equals approximately $(p_{t2}-p_\infty)$ times the barrier area. This force is minimized by reducing the size of the barrier to the engine cross sectional area. A mechanism for nulling the barrier pressure force is shown in Figure 26.5.3-7 where an indoor altitude facility for turbopowered simulators is shown (labeled p-A Compensation Chamber). In that facility, surface areas are provided so that the pressure forces cancel, resulting in only thrust being measured by the balance.

A large altitude test cell is shown in Figures 26.5.3-6 and 26.5.3-8 (U.S. Air Force Arnold Engineering Development Center, Tennessee). The figure shows most of the major features of test cell J-1.

The labyrinth seal shown in Figure 26.5.3-6 is used to provide a frictionless coupling device between the engine and the connected air supply. Air, conditioned to the pressure and temperature required to simulate an altitude and Mach number, enters the plenum at the front of the facility. The airflow rate is determined with either a single large venturi or with multiple venturi systems and enters a large duct where flow straighteners are located. The air passes through the engine and is captured by the collector duct. The collector duct is driven by an ejector to match the ambient pressure in the vicinity of the engine exhaust nozzle. Flight conditions can be set to $\pm$0.1 Mach and $\pm$100 ft. in altitude.

This Arnold J-1 test facility is 16 ft. in diameter and 92 ft. long. It can accommodate subsonic or supersonic airbreathing propulsion systems at Mach numbers from 0 to 3.3 at true temperature simulation. Airflow rates can be obtained up to 1300 lb/sec and temperatures can range from +750°F to -30°F for the various airflows. A TF-39 is shown installed in the test section with the door open.

The pump or ejector used to reduce the exit static pressure can allow replacement of subsonic venturis with choked venturis for airflow measurement (if sufficient power is available) because the choked venturi characteristically demands a larger total pressure drop. This enhances the airflow measurement accuracy considerably which is particularly desirable for (high bypass) turbofan engines.

Indoor facilities of the sea level and altitude type are both used to examine compressor tolerance to inlet distortion. Thus screens with nonuniform grid are mounted in the engine inlet duct to simulate nonuniform airflow of the real inlet in flight.

The cost of running indoor facilities is large because of the heavy power demand of the airconditioning and pump systems. Alternative means, such as flying test beds, usually do not allow the careful instrumentation and operational choice offered by altitude facilities. The cost can be justified if the risk associated with the uncertainty when such testing is not carried out is intolerable.

26.5.4 Force Accounting in Static Facilities

Figure 26.5.4-1 shows the control volume configurations used most commonly to evaluate the forces that interact with those recorded on the force balance for the three types of static test facilities. The force recorded on balance through the strut consists of the momenta of the fluid entering and leaving the volume plus the pressure area integrals over the various surfaces. Thus

$$F_{BAL} = \dot{m}V_9 - \dot{m}V_0 + (p_9-p_\infty)\,A + \int(p-p_\infty)dA$$

where the integral is the pressure force acting on the engine's external surface. This term is minimized by minimizing the surface area subject to pressures other than p_∞. The inlet momentum term is associated with the wind and is therefore important primarily in outdoor test stands. Specifying

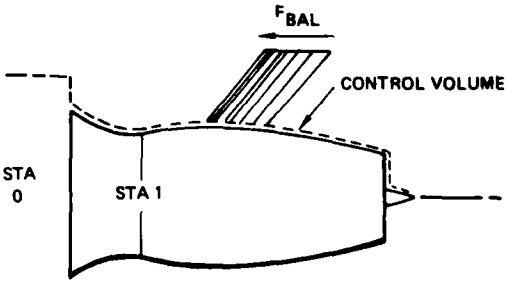

(A) OUTDOOR AND SEA LEVEL STATIC INDOOR CONTROL VOLUME DEFINITION

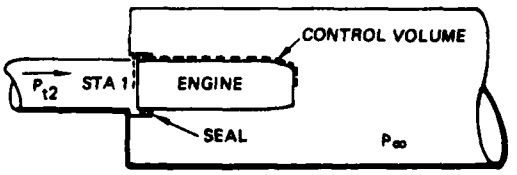

(B) INDOOR ALTITUDE FACILITY CONTROL VOLUME DEFINITION

Figure 26.5.4-1. Test Facility Control Volume Definitions

zero wind, one may write the zero term for a well-designed bellmouth inlet with little friction as

$$\dot{m}V_0 = \dot{m}V_1 - F_{INL} = 0$$

This equation shows how the pressure area integral on the inlet, F_{INL}, appears in the sum of forces impacting the balance reading. Thus, one may write

$$F_{BAL} = \dot{m}V_9 + (p_9 - p_\infty)\, A_9 + (F_{INL} - \dot{m}V_1) + \int (p - p_\infty) dA$$

If the inlet is on balance as it is in Figure 26.5.4-1a, F_{INL} is only of interest for the designer of the inlet attachment. If the inlet is off balance as in 25.5.4-1b, $F_{INL} = 0$ and the momentum at station 1 must be determined accurately.

The integral of pressure over the nacelle external surface is small enough to be negligible under most situations of interest in outdoor facilities. For sea level indoor, this term may give rise to a significant (buoyancy) force. In altitude indoor facilities, it is obviously large as discussed above.

Calculated force increments are often applied to the measured thrust which are used to adjust for items like bleed and horsepower extraction, improper condition setting, and scrubbing drag if there are geometric differences between the configuration tested and that desired.

26.5.5 Accuracy

The accuracy of outdoor test rig data used to determine engine thrust is a function of: 1) the instrumentation used to measure the force, 2) the calibration of the measuring device, and 3) the ambient conditions. Typical accuracies of measurements made on a modern high bypass ratio engine are shown on Table 26.5-2.

The total random error associated with any particular parameter is therefore determined by combining all the appropriate accuracies shown on Table 26.5-2 in a root-sum-square (R.S.S.) method for that parameter (see Section 26.6). For example, the accuracy by which primary nozzle C_V could be determined is a function of nozzle pressure (PT7) and temperature (TT7F), ambient pressure (PBAR) and temperature (DATF), compressor inlet static pressure (PS2) and gross thrust (FG) accuracies shown on Table 26.5-2. The resulting R.S.S. accuracy for primary nozzle C_V calculated from ground test data is 0.7%.

The accuracy of indoor sea-level static test facilities should be better (no wind) than outdoor test facilities. In actual fact, however, the magnitude of corrections applied to the test data to give comparable results to outdoor data may be as large as the configuration effects or engine changes being evaluated. As a result, indoor test facilities are not as accurate as outdoor cells when used with an engine which is large relative to the test cell.

Comparison of A and W Methods

The approach to a determination of random error due to uncertainty in the measurements used for obtaining net thrust described in Section 26.6 may be used to compare the A and W methods of gas generator thrust calculation. Reference 26.5.5-1 is a detailed analysis of these methods as applied to the afterburning turbofan engine used in the F-111A. The influence coefficients of net thrust on particular measurements are shown in Figure 26.6.5-1 for each of the methods. These influence coefficients show the sensitivity of the data groups characterizing flight conditions, engine power conditions, and engine/afterburner performance indexes. Note that below a power level angle of 65° the afterburner is off. Further, when afterburning, T_{t7} cannot be determined directly and must be inferred from an energy balance; hence the dependence of net thrust on afterburner efficiency using the W method. These influence coefficients may be combined with the measurement uncertainties to arrive at an expected uncertainty in net thrust. Figure 26.5.5-2 shows the results together with thrust measurements made statically with both engines operating.

The conclusions of Reference 26.5.5-1 (from which Figure 26.5.5-2 is adapted) are that the W method tends to be superior to the A method at midrange power. At low and high power the two methods tend to be comparable and both should be used whenever possible. The difference between calculated and measured static thrust lies in the 2 to 5% range.

Table 26.5-2. Measured Parameters

The steady-state performance parameters are listed below. Accuracies are to a 95% confidence level.

Item no.	Sym	Description	Range Min	Range Max	Estimated accuracy
1	N1	Low pressure compressor rotor speed	0	3600 rpm	±5 rpm
2	N2	High pressure compressor rotor speed	0	8000 rpm	±12 rpm
3	FG	Gross thrust	0	50K lbs	±.25% f.s.
4	PBAR	Ambient pressure	14.0	15.3 psia	±.07% f.s.
5	PT2.5	Fan discharge total pressure	0	8 psig	±.25% f.s.
6	PS4	High pressure compressor discharge static pressure	0	300 psig	±.25% f.s.
7	PT7	Low pressure turbine discharge total pressure	0	8 psig	±.25% f.s.
8	PW2-1 PW2-8	8 separate wall statics Engine inlet static pressure (Calibrated for Bellmouth inlet)	0	-5 psig	±.25% f.s.
9	OATF	Ambient temperature	0	100°F	±.5°F
10	TT6F	High pressure turbine discharge total temperature	0	1650°F	±.5% of rdg (530°F to 1650°F)
11	TF	Fuel sample temperature	0	100°F	±1°F
12	SG	Fuel sample specific gravity	0.77	0.83	±.15% of rdg
13	TFI	Fuel inlet temperature	0	100°F	±1°F
14	WF-1	Fuel flow	20	50 GPM	±.5% of rdg
15	SVA	Stator vane angle	-40°	+10°	±1° rot.
16	WINDV	Wind speed	0	10 MPH	±.5 mph
17	WINDD	Wind direction	-180	+180	±5°
18	R.H.	Relative humidity	0	100%	±5% f.s.
19	TT7F	Turbine exhaust temperature	0	1400°F	±.5% of rdg (530°F to 1100°F)
20	WIF	Water injection flow	0	55 GPM	±.5% of rdg
21	TT2F	Compressor inlet total temperature	0	100°F	±.5°F
23	PT2	Compressor inlet total pressure	0	-5" H20	±5% f.s.
24	PS2	Compressor inlet static pressure	0	-100" H20	±.25% f.s.
25	PT3	Low pressure compressor discharge total pressure	0	25 psig	±.25% f.s.
26	PS3	Low pressure compressor discharge static pressure	0	20 psig	±.25% f.s.
27	PS51	Combustion chamber discharge static pressure	0	300 psig	±.25% f.s.
28	TT3	Low pressure compressor discharge total temperature	0	1400°F	±2°F
29	TT4	High pressure compressor discharge total temperature	0	1400°F	±.5% of rdg (530°F to 1400°F)
30	PLA	Power lever angle	55°	127°	±1°

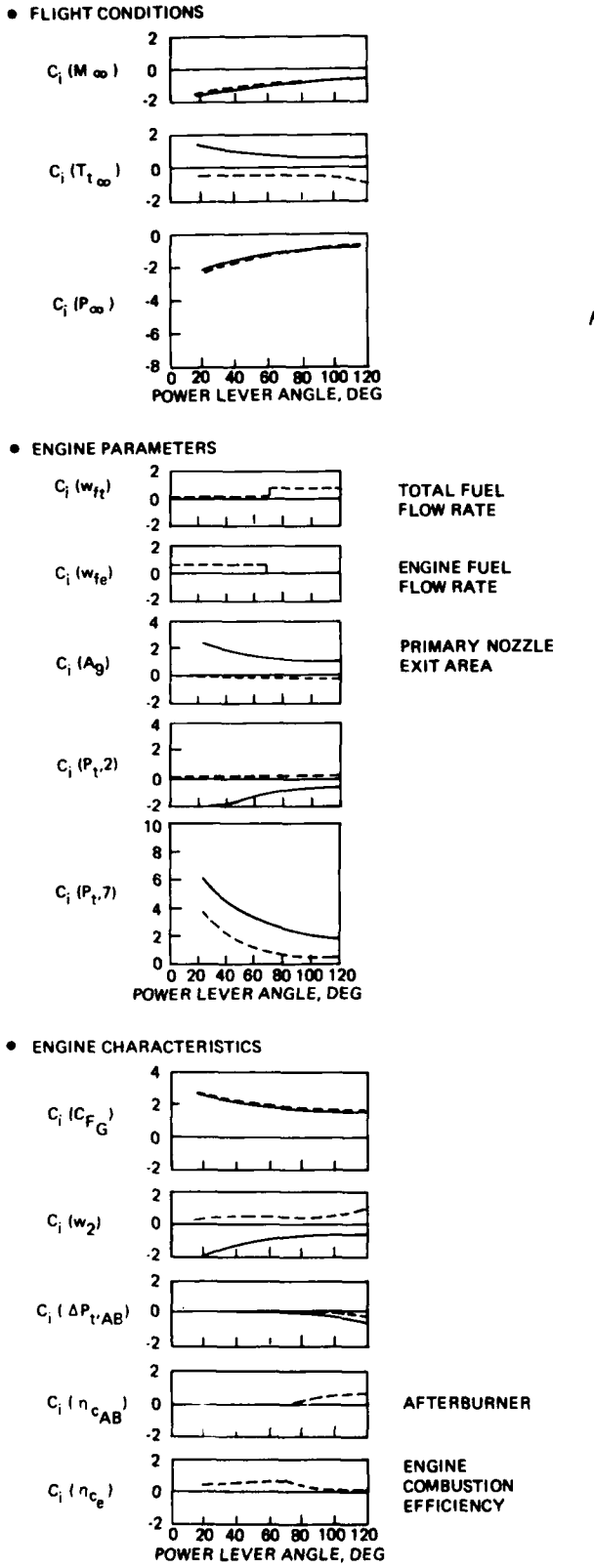

Figure 26.5.5-1. Net Thrust Influence Coefficients on a Full Scale Afterburning Turbofan Engine at .85> M > 2.2 (From Reference 26.5.5-1) Dashed Line: "A" Method, Solid Line "W" Method

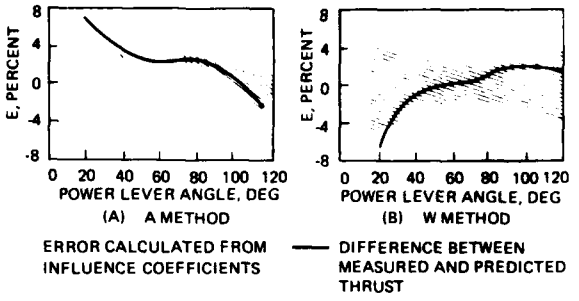

Figure 26.5.5-2. Comparison of Root Sum Square Thrust Uncertainty and Measured for a Static Run, Two Engines Operating (Reference 26.5.3)

26.5.6 Wind-Tunnel Facilities

Engine tests in wind tunnels are carried out at the aerodynamics/propulsion oriented laboratories of the NASA and military facilities. The useful testing carried out with small engines in such facilities is related primarily to the understanding of propulsive flow interactions with the aerodynamic flow around the airplane. Such flows are interactive under circumstances where the propulsive jet is large in size and small in pressure ratio or velocity. Further, such interactions are interesting at low speed on VSTOL types of airplanes. Thus, for the most part, engines for such purposes are turboshaft or high bypass turbofan engines where the engine core performance is determined primarily in the sea level facilities described earlier.

26.5.7 Flight Testing

Flight testing is carried out to determine fuel consumption, drag, and thrust-minus-drag characteristics of the completed airplane. The relative importance of each of these performance characteristics depends on the type of airplane and its primary design mission. For example on a new fighter aircraft, thrust minus drag is a measure of combat effectiveness. On new transports or bombers, the payload-range characteristics (estimated in the design process) can be determined precisely. The measurement of drag alone may be useful for new aircraft designs which are to be operated in environments which cannot be simulated.

In the flight test, the "real" environment is thus encountered for the first time, particularly for the inlet and exhaust/aft body whose performance may be Mach- and Reynolds-number dependent. Unfortunately the flight test environment rarely affords the luxury of extensive instrumentation that is required for the accurate determination of quantities like mass flows, engine face total pressure and nozzle exit ambient pressure. Thus to the extent that such instrumentation is not available and use is made of correlation techniques, uncertainty exists. This uncertainty may play an important role in preventing flight test data from being useful for the improvement of design methods.

The determination of thrust in flight is the inversion of the nozzle coefficient definition procedure. Using the "A" method, gross thrust is

$$F_G = C_G\, A_9\, P_\infty \left(\frac{F_G}{P_\infty A}\right)_{ideal}$$

Here the nozzle thrust coefficient and the ideal thrust function may be for the convergent or for

the convergent-divergent nozzle, but consistency must be maintained. The air flow may be determined from the discharge coefficient or from independent measurements made in the engine or inlet.

Gross thrust may be obtained with the "W" method using the appropriate nozzle coefficient and any of the possible measurements of mass flow. Thus

$$F_G = C\, W_9\sqrt{T_{t9}}\left(\frac{F_G}{W\sqrt{T}_t}\right)_{ideal}$$

[$C = C_V$ if convergent-divergent theory is used]

The advantage of the W method is the reduction of error associated with the fact that gross thrust and ram drag are determined using common measures of air flow rate. Thus the net thrust is not the difference of two large, independently uncertain measurements.

26.6 UNCERTAINTIES IN THRUST AND DRAG

A quantity like thrust or drag is usually determined from a complex calculation procedure using measured quantities, experimentally or analytically obtained increments, and a reliance on the concept of modeling similarity to minimize the number of independent variables.

26.6.1 Random Error

The random variation of measured data around a true mean value constitutes the simplest form of error estimation. It can be shown that the difference between true value and the mean of a series of measurements is proportional to a factor which varies as $N^{1/2}$ where N is the number of data points taken. Hence it is always possible to reduce measurement error by increasing the number of measurements.

A common problem related to the reduction of random error is to determine how much repeat data to obtain and how small the random uncertainty of the transducer should be to achieve a chosen level of result uncertainty from a particular experiment. The usual approach in the analysis of random errors is to obtain the logarithmic derivative of the desired quantity (dependent variable) with respect to the independent variables or, in the case of a data reduction program, the input quantities. This derivative, or influence coefficient, when multiplied by the fractional uncertainty of the measured input quantity, $\Delta x_i/x_i$, gives the uncertainty of the dependent variable, $\Delta Y_j/Y_j$. Specifically the total uncertainty in the output Y_j is

$$\frac{\Delta Y_j}{Y_j}_m = \left\{\sum_{i=1}^{N}\left[\frac{\partial \ell n y_j}{\partial \ell n x_i}\right]^2\left[\frac{\Delta x_i}{x_i}\right]^2\right\}^{1/2}$$

The process of obtaining the various influence coefficients in complex computations or data reduction programs requires automation. An approach is to use a complete set of input data and sequentially perturb each of the input quantities so that three values of Y_j are obtained for three nearby values of x_i. The quantity $Y_j(x_i)$ is fitted with a parabolic arc, and the slope at x_i is determined. The influence coefficients can be obtained in this way, either with test data or with dummy input data judged as representative, to determine the appropriateness of transducer sensitivities and to determine whether the overall accuracy objectives can be achieved.

Although this sum square addition procedure applies only to independent ramdom uncertainties, it is convenient to combine instrumentation bias and random uncertainties so that the large number of errors may be "added." The uncertainty of the combined measurements can then be determined in addition to the major contributors. Should the uncertainty thus obtained fall outside the uncertainty goals, additional test points may be obtained or better transducers should be chosen for the important measurements.

The power of the numerical error analysis technique lies in the ease of adapting it to new calculation procedures. Furthermore, the program perturbs each of the measured quantities, some of which may be differential measurements. These kinds of measurements are awkward to handle analytically, using conventional differentiation of the governing equations.

Since transducer uncertainties such as those for pressure and force are generally quoted as percent of full scale, the influence coefficients should be adjusted to reflect the fact that they may be used at low or mid-range. In the matrix printed out for each test condition, the influence coefficient should be multiplied by the ratio of full-scale reading to actual reading.

Table 26.6-1 shows the table output (abbreviated to save space) from an error analysis on the static calibration of a flight simulation chamber with balance for calibrating a turbopowered nacelle. The run condition is shown at the top of the table. The resulting nozzle coefficients are listed across the top of the table. Other column headings are as indicated: the transducer full-scale value in conventional dimensional units, the transducer uncertainty (given in percent of full-scale or dimensioned units if scale indicated is zero), the nominal value of the transducer reading, and the symbol (and name) of the transducer reading.

Inspection of the computer output version of this matrix shows the significant contributions to the total uncertainty quoted at the bottom of the table. The transducers not actually used show zero influence coefficients. The important measurements for the determination of fan nozzle coefficients are ambient and chamber pressures, fan flow parameters, and the axial force balance reading. For the determination of the primary nozzle discharge coefficient, the air supply line multiple critical flow venturi readings and primary flow parameters have the largest influence coefficients. It is seen that the fan nozzle coefficients' uncertainties are in the 0.5% size range.

Table 26.6-2 shows a similar result for a wind-on run in a transonic wind tunnel during an isolated nacelle test. Note that the random error net thrust uncertainty at this condition is on the order of 0.6%.

Figure 26.6.1-1 is an expanded view of the data shown in Table 26.6-2. The total uncertainty because of measured quantity uncertainties is shown for the airflow rate and components of the net thrust. To illustrate the effect of power setting and the need for making sure that the most appropriate instrumentation is used, the net thrust uncertainty is shown at M = 0.85 for reduced power setting.

26.6.2 Bias Uncertainty

The uncertainty introduced by the procedures involved in measurement is generally referred to as bias error. This error could be eliminated by

Table 26.6-1. Flight Simulation Chamber Test Influence Coefficients

INFLUENCE COEFFICIENTS AT P_{T3}/P_a = 2.4423 FPR = 1.50							
SCALE	UNCERTAINTY,* %	NOMINAL VALUES		MEASURED VARIABLE	CDF3	CVF3	CDP
					0.9805	0.9620	0.8855
3200.0	0.1000	-7.330	PM	PITCH M	0.0000	.0268	0.0001
1600.0	0.1000	5.901	YM	YAW M	0.0000	.0400	-0.0000
1200.0	0.1000	4.00666	RM	ROLL M	0.0000	.0040	0.0000
130.0	0.1000	215.46	AF	AXIAL F	0.0000	1.4368	0.0000
1500.0	0.1000	3.884	NF	NORMAL F	0.0000	.1549	0.0000
1000.0	0.1000	- .053	SF	SIDE F	0.0000	.0113	0.0000
1000.0	0.1000	380.92	P1FN3	MCV	-0.9433	0.4181	2.6535
0.0	0.0467	535.43	TTFN	MCV	0.1906	-0.0845	-0.5363
1000.0	0.1000	296.24	PBEL	AIRLINE	0.0000	-0.0026	-0.0000
15.0	0.1000	14.661	PA	AMBIENT	1.5414	-1.6190	-0.7892
7.5	0.1000	5.6697	DPVC1	CHAMBER	-1.1135	0.5743	-0.1068
0.0	0.6642	602.18	TT3	FAN EXIT	0.5013	-0.5006	-0.0000
0.0	1.4035	285.01	TT5	PRIMARY	0.0000	-0.0993	0.5060
15.0	0.1000	7.3400	PT3	FAN EXIT	-6.250	-0.3310	0.0000
15.0	0.1000	1.2707	PT5.1	PRIMARY	-0.0000	-0.1616	-1.0424
0.0	0.7614	525.33	TTVC1	CHAMBER	-0.0052	0.0052	0.0000
0.0	0.7618	525.04	TTVC16	MCV	-0.0754	0.0754	0.0000
0.0	0.7625	524.62	TTVC32	MCV	0.0000	-0.0000	0.0000
0.0	0.7625	524.58	TTVC64.1	MCV	-0.2990	0.2990	-0.0000
0.0	0.7625	524.58	TTVC64.2	MCV	-0.2990	0.2990	-0.0000
				TOTAL PERCENT UNCERTAINTY	0.5140	0.5286	0.7644

*Note: Uncertainties are based on instrument manufactures guaranteed accuracies.

Table 26.6-2. Isolated TPS Test Influence Coefficients

INFLUENCE COEFFICIENTS AT FNPR3 = 2.4062 MACH = 0.85									
SCALE	UNCERTAINTY, %	NOMINAL VALUES			FN	FGF	FGP	WAP	WAF
					86.120	181.09	35.403	1.6303	4.3935
2160.0	0.0500	1333.2	PS	TUNNEL STATIC	0.1073	0.2077	- 0.6502	-0.0298	0.6595
2160.0	0.0230	807.28	PT-PS	TUNNEL Q	- 0.0472	1.0267	0.7897	-0.0298	0.6706
0.0	0.6620	604.27	TT	TUNNEL TOTAL	- 0.7720	0.0000	- 0.0000	0.0000	0.0000
0.0	0.0365	548.69	TTFN	MCV INLET	0.2080	0.0000	- 0.5000	-0.5000	0.0000
10.0	0.1000	5.6984	PT31	FAN EXIT	0.6382	0.6430	0.0000	0.0000	0.4540
0.0	0.5812	688.19	TT31	FAN EXIT	0.7720	- 0.0006	- 0.0000	0.0000	0.5010
15.0	0.1700	1.5687	PT51	TURB EXIT	0.3200	0.0000	0.7704	0.0298	-0.0000
0.0	1.3895	287.87	TT51	TURB EXIT	0.2040	0.0000	0.4910	-0.0000	-0.0000
1000.0	0.0300	270.72	PT4	TURB INLET	1.5040	0.0000	3.6160	3.6160	-0.0000
				TOTAL PERCENT UNCERTAINTY	0.5703	0.0386	0.4161	0.1100	0.1258
NULL INFLUENCE COEFFICIENTS ARE NOTED FOR: LIFT, DRAG, SF, P1FN, PS2, TT4, PAL, RPM									

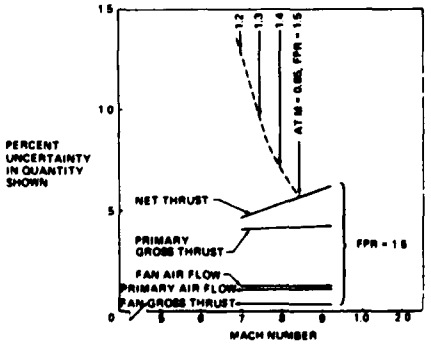

Figure 26.6.1-1.

identifying and improving the method used.

Bias error includes improper calibration, static friction, and electrical hysteresis. Most calibration procedures are sufficiently accurate that this error is quite small. For purposes of error analysis discussed above, it is possible to add bias and random instrument uncertainties into a single equivalent random uncertainty so that a large number of uncertainties can be added as described above. This leads to a conservative estimate of result uncertainty. The bias component of uncertainty can be larger than cited for an instrument if the environment in which it is used (temperature, temperature gradient, pressure) is outside the calibration range.

The measurement of average total pressure and temperature with a finite number of probes in a flow is compromised by nonuniform distribution.

The ability of the probes to sense these changes is limited by the number of probes employed, otherwise the probes will influence the experiment.

Modeling to obtain scale effects and increments for losses due to struts or rakes in the flow usually lead to bias error because the relevant similarity parameter is incorrect. While the most commonly violated parameter is the Reynolds number, the procedure may still be valid if the flow is not separated and if secondary flows are known to be small. In that case, the procedures described in Section 26.3 are appropriate and can do much to minimize this uncertainty.

An important case of bias error is that introduced by similarity arguments where the flow is three dimensional, separated and, to some extent, controlled by viscous flow effects. This is often the case in determining afterbody boattail performance on an airframe when dissimilar, improperly scaled data is used due to lack of testing time or money.

These last two components of bias generally introduce the largest risk that a performance shortfall will be experienced when the full scale article is tested.

Problems arise in the wind tunnel where bias and nonrepeatability may occur in the construction of the model and in the wind tunnel flow. Bias level shifts can be caused by model assemblies that require the use of aerodynamic filler for contour buildup and fairings. Uncertainty also arises in the wind tunnel because of upflow and crossflow, wall and mounting effects, buoyancy effects, and, in some cases, tunnel flow temperature gradients. To the extent that they are known, corrections can be made during the data reduction procedure, and the effect can be assessed from the magnitude of these correction factors.

The inability to scale small models geometrically has forced testing of larger scale portions of the airframe. In such cases the poor quality of the full model is traded against the risk of errors due to the establishment of force increments between models of varying scale. The geometric configuration of the airframe near the larger component model is often modeled by an oversimplified surface which introduces some unknown error. Careful design of such surfaces can, however, be utilized to establish appropriate boundary layer characteristics, minimizing to some extent the Reynolds number mismatch problem.

Support systems introduce unknown errors which are often minimized by utilizing two mounting systems which are "independent" of each other. For example, sting mounts from the rear of an aircraft model often alter the flow locally, and front or bottom mounts may be needed to obtain aft end "jet" effects. Considerable "art" has evolved to reduce errors to manageable levels.

26.6.3 Concluding Remarks

When insufficient time or budget is available for developing model forces, data from "similar" configurations is often used. The errors in modeling thus introduced or the failure to verify the performance of components which have been altered or "improved" as development progresses have historically led to the largest differences between predicted and actual performance. These differences are rarely resolved once the configuration is frozen and the development budget is dry. This unfortunately prevents the design problems from being resolved and little learning results which could lead to better procedures.

This chapter was assembled with the aim of illustrating the notion that an aircraft engine cannot be designed without considering the airplane and its mission. To this end, the methodologies used for the determination of the required thrust, unambiguous force accounting during the development process, and verification of flight performance are presented together with a description of the thrust or drag force increments associated with the propulsive flow. Described below is an example to illustrate the extent to which a design mismatch between engine and airplane may be experienced.

An Example

Although aircraft are designed to carry out many types of missions, a common and very important one is the ability to deliver a payload over a certain range. The payload-range problem is central to the successful design of commercial and military transports as well as bombers. Using it as an example, how uncertainties in thrust, drag, and aircraft gross weight impact the ability to fly the desired range can be shown.

Assume that there is an uncertainty in aircraft gross weight which stems from a lack of detail design information. Since lift equals weight, this uncertainty in weight results in uncertainty in lift required. The drag polar, or a relationship like that shown in Figure 26.6.3-1, gives the drag associated with a given lift. Since the drag is itself uncertain, there results a total uncertainty in estimated drag:

$$D_e = \frac{\bar{D}}{L}\ \bar{W}\ (1 \pm U_D)\ (1 \pm U_W) \qquad 26.6\text{-}1$$

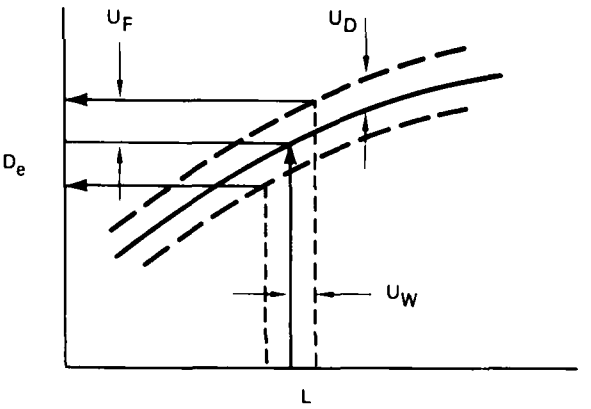

Figure 26.6.3-1. Variation of Drag With Lift Showing Uncertainty in Thrust Required

Here U is an unsigned uncertainty wherein the subscripts refer to the drag and to the weight. $\bar{W}$ and $(\frac{\bar{L}}{D})$ are the best estimates of the gross weight and lift-to-drag ratio. This estimated drag is transmitted as a thrust requirement together with its uncertainty, U_D.

To determine range, the actual weight of the airplane, W, which always equals lift, L, is required. Hence, the thrust required is:

$$D_a = (\frac{D}{L})L\ (1 + U_D) \qquad 26.6\text{-}2$$

This actual drag is uncertain only because of the uncertainty associated with the drag determina-

tion procedure. The fuel flow rate required by the engine to provide a thrust equal to drag is:

$$W_f = D_a \, (\overline{SFC}) \, (1 \pm U_s) =$$

$$(\frac{\overline{D}}{L})L \, (1 \pm U_s) \, (1 \pm U_D) \qquad 26.6\text{-}3$$

where U_s is the SFC uncertainty shown in Figure 26.6.3-2.

The Breguet range equation may be integrated with constant $\overline{SFC}$ and $(\frac{\overline{L}}{D})$ and W = L to give:

$$\text{Range, } R = u_o \frac{1}{\overline{SFC}} (\frac{\overline{L}}{D}) \ln \frac{W_o + W_f}{W_o} \qquad 26.6\text{-}4$$

where W_O is the airplane weight at the mission end, i.e., empty weight, payload, reserves, crew, etc. The range factor,

$$u_o \frac{1}{\overline{SFC}} (\frac{\overline{L}}{D}) \, ,$$

is uncertain by U_s, U_D. The range suffers further uncertainty for a given fuel load, because W_o may not be known precisely at the time range is calculated. Letting $W_o = \overline{W}_o \, (1 \pm U_w)$ and expanding for $U_w << 1$, the logarithmic term becomes:

$$\left[\ln \, (1 + \frac{W_f}{\overline{W}_o})\right] \times \left(1 \pm \alpha U_w\right)$$

$$\text{where } \alpha = \frac{W_f/\overline{W}_o}{1 + W_f/\overline{W}_o} \left[\ln \, (1 + \frac{W_f}{\overline{W}_o})\right]^{-1}$$

The α parameter is plotted in Figure 26.6.3-3

The uncertainty in range and thrust required are obtained by the combination of independent uncertainties, viz:

$$U_R^2 = U_S^2 + U_D^2 + \alpha^2 U_W^2 \quad \text{(range)} \qquad 26.6\text{-}5$$

$$U_{FR}^2 = U_D^2 + U_W^2 \quad \text{(required thrust)}$$

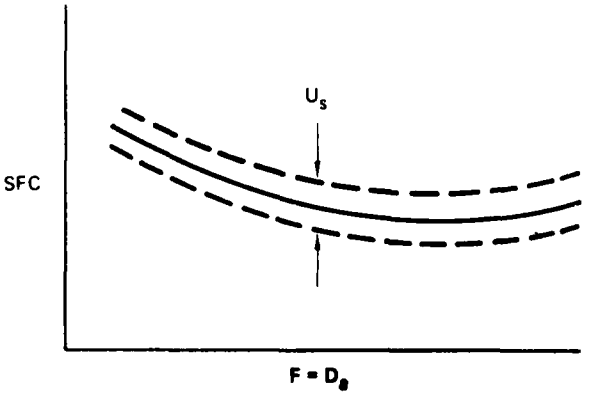

Figure 26.6.3-2. Variation of SFC With Thrust From an Engine Test

Since a fuel flow rate measurement, $W_f(1 \pm U_{FF})$, and thrust measurement, U_{FM}), determine SFC,

$$U_S^2 = U_{FF}^2 + U_{FM}^2 \qquad 26.6\text{-}6$$

combining these,

$$U_R^2 = U_{FF}^2 + U_D^2 + \alpha^2 U_W^2 + U_{FM}^2 \qquad 26.5\text{-}7$$

Here U_{FF} may be quite small. We note that range uncertainty depends on measured engine thrust, drag, and weight uncertainties.

The errors in the items described above arise, in part, from the following items:

Thrust (and SFC)

1) incomplete knowledge of component performance (turbomachinery as well as inlet and exhaust),
2) increment in component performance at cruise conditions,
3) improper engine cycle for the final airplane configuration,
4) incorrect engine size,
5) engine deterioration in service.

Drag (and L/D)

1) calculation of model and full-scale skin friction drags,
2) Reynolds number scale-up of wind tunnel data for 3-D, nonuniformity, compressibility effects,
3) wind tunnel environment for determining items (2),
4) geometric uncertainty.

Thrust and Drag

1) inlet spillage effects,
2) inlet boundary layer bleeds,
3) boundary layer bypass ramp characteristics,
4) jet/freestream interaction effects,
5) jet modeling techniques.

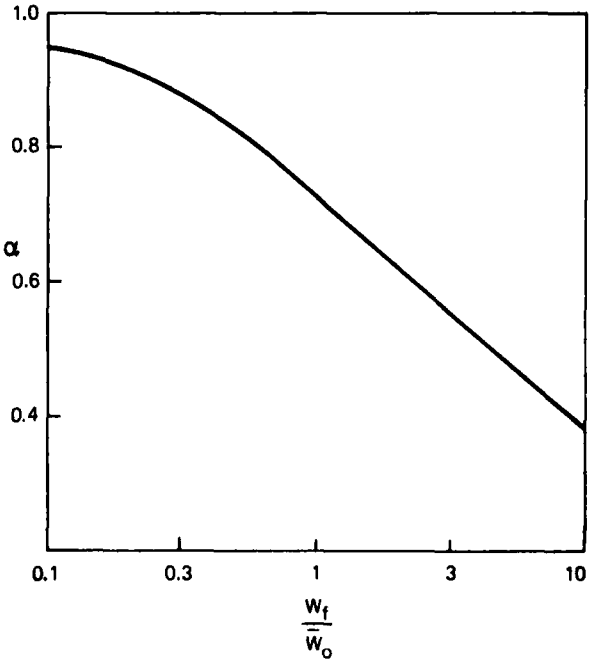

Figure 26.6.3-3. Variation of α With Ratio of Fuel Weight to Airplane Weight at Mission End

Weight

1) structural empty weight,
2) engine weight.

For design purposes the least predictable items are weights until the aircraft and engine are actually built and refined. A decrease in weight can always be traded for payload, which may not be desirable, but the most serious possibility of error is that due to the interaction between engine cycle choice and engine weight.

The discussion throughout this chapter has focused on the airplane components which impact the ability of the engine and the airplane to achieve the mission. Some of the development techniques which play a role in the iterative design procedure necessary to identify an optimum engine/airplane system are discussed from the viewpoint of highlighting their capabilities and limitations. The magnitude of potential performance shortfall between prediction and flight and the extent to which the airplane is "successful" is illustrated.

Remaining Problems

The techniques described in this chapter are adequate to predict the performance of the airplane or isolated inlets and nozzles, particularly under conditions for which a point design is appropriate. The problems which remain are those of calculating the compressible viscous flow field in three dimensions. This lack has motivated much empirical work as well as the development of new computational methods.

A second source of design risk is the customary limitation of time and money which limit the number of cycles through which a design may be iterated. Techniques are needed to reduce the time required to identify an optimum configuration. For example, if efficient calculation methods could be substituted for traditional wind tunnel tests, considerable time and money could be saved. Future propulsion simulation devices may make it possible to model simultaneously inlet and jet effects, at the right Mach and Reynolds numbers in a single test!

REFERENCES

26.1.2-1 Jaarsma, F., "Experimental Determination of Nozzle Characteristics and Nozzle Airframe Interference:" AGARD Lecture Series No. 53 on Airframe/Engine Integration, May 1972.

26.2.1-1 Steger, J. L., Baldwin, B. S., "Shock Waves and Drag in the Numerical Calculation of Isentropic Transonic Flow," NASA TN-D-6997, October 1972.

26.2.1-2 Granville, P. S., "The Calculation of the Viscous Drag of Bodies of Revolution," David Taylor Report 849, 1953.

26.2.1-3 Colehour, J. L., "Transonic Flow Analysis Using a Streamline Coordinate Transformation Procedure," AIAA 73-657, July 1973.

26.2.1-4 Klujber, F., "Results of an Experimental Program for the Development of Sonic Inlets for Turbofan Engines," AIAA 73-222, January 1973.

26.2.1-5 Wyatt, D. D., Fradenburgh, E. A., "Theoretical Performance Characteristics of Sharp-Lip Inlets at Subsonic Speeds," NACA Report 1193, 1954.

26.2.1-6 Ferri, A., Nucci, L. M., "The Origin of Aerodynamic Instability of Supersonic Inlets at Subcritical Conditions," NACA RM L50K30, January 1951.

26.2.1-7 Syberg, J., Hickcox, T. E., "Design of a Bleed System for a Mach 3.5 Inlet," NASA CR-2563, January 1973.

26.2.1-8 Syberg, J., Koncsek, J. L., "Experimental Evaluation of a Mach 3.5 Axisymmetric Inlet," NASA CR-2563, July 1975.

26.2.1-9 Seebaugh, W. R., Paynter, G. C., Childs, J. A., "Shock-Wave Reflection from a Turbulent Boundary Layer with Mass Bleed," J. Aircraft 5, 5, p 461-467, 1968.

26.2.1-10 Antonatos, P. P., "Inlet/Airframe Interference and Integration," AGARD Lecture Series No. 53, May 1972.

26.2.1-11 Neale, M. C., Armstrong, F. W., "Some Recent Research on Supersonic Intakes at NGTE," AGARD Conference on Inlets and Nozzles for Aerospace Engines, CP-91-71, September 1971.

26.2.2-1 Bernstein, A., Heiser, W. H., Hevenor, C., "Compound Compressible Nozzle Flow," Transactions ASME Series E, J. Appl. Mech., 34, 3, September 1967, pp. 54854.

26.2.2-2 Decher, R., Tegeler, D. C., "High Accuracy Force Accounting Procedures for Turbopowered Simulator Testing," AIAA 75-1324, 1975.

26.2.2-3 Shapiro, A. H., "Dynamics and Thermodynamics of Compressible Fluid Flow," Ronald Press 1954.

26.2.2-4 Schlichting, H., Boundary Layer Theory, McGraw-Hill, 1960.

26.2.2-5 Hoerner, S., Fluid Dynamic Drag, Hoerner, 1965.

26.2.2-6 Thornock, R. L., "Experimental Investigation of the Flow Through Convergent Conical Nozzles," D6-20375, The Boeing Company, 1968. (NTIS number AD 841-418)

26.2.2-7 Thornock, R. L., "Inviscid Flow Performance Coefficients for Convergent Conical Nozzles," ME-RES-851, The Boeing Company, 1970.

26.2.2-8 Paynter, G. C., Schuehle, A. L., "A Computer Program for Turbulent Boundary Layer Characteristics Through Regions of Pressure Gradient and Oblique Shock Reflection," D3-23250, The Boeing Company, 1969.

26.2.2-9 Postlewaite, J. E., "Thrust Performance of Suppressor Nozzles," J. Aircraft, 3, 6, 1966.

26.2.2-10 Morden, D. B., Armstrong, R. S., "A Guide To Multitube Suppressor Nozzle Static Performance:" Trends and Trades, Report No. FAA-SS-73-11-7, March 1975.

26.2.2-11 Morden, D. B., Armstrong, R. S., "Performance Technology - Analysis of the Low Speed Performance of Multitube Suppressor/ Ejector Nozzles (0-167 KN)," Report No. FAA-SS-73-11-9, March 1975.

26.2.2-12 Simcox, C. D., Armstrong, R. S., Atvais, Y., "Recent Advances in Exhaust Systems for Jet Suppression of High Speed Aircraft," J. Aircraft, 13, 6, June 1976.

26.2.2-13 Krull, H. G., Beal, W. T., Schmiedlin, R. F., "Effect of Several Design Variables on Internal Performance of Convergent-Plug Exhaust Nozzles," NACA RM E56G20, October 1956.

26.2.2-14 Maiden, D. L., Petit, J. E., "Investigation of Two-Dimensional Wedge Exhaust Nozzles for Advanced Aircraft," AIAA Paper 75-1317, September 1975.

26.2.2-15 Bower, W. W., "An Analytical Procedure for the Calculation of Attached and Separated Diffuser Flows," AIAA paper 74- 1173, 1973.

26.2.2-16 Compton, W. B., "Jet Effects on the Drag of Conical Afterbodies at Supersonic Speeds," NASA TN D-6789, July 1972.

26.2.2-17 Harrington, D. E., "Jet Effects on Boattail Pressure Drag of Isolated Ejector Nozzles at Mach numbers from .6 to 1.47," NASA TMX 1785, 1969.

26.2.2-18 Reubush, D. E., "Effects of Fineness and Dome Ratios on Boattail Drag of Circular Arc Afterbody Models with Jet Exhaust at Mach Number up to 1.30," *NASA TN D-7163*, May 1973.

26.2.2-19 Blaha, B. J., Mikkelson, D. C., "Wind Tunnel Investigation of Airframe Installation Effects On Underwing Engine Nacelles at Mach numbers from .56 to 1.46," NASA TMX-1683, November 1968.

26.2.2-20 Reubush, D. E., Runckel, J., "Effect of Fineness Ratio on Boattail Drag of Circular Arc Afterbodies Having Closure Ratios of .5 with Jet Exhaust at Mach Numbers up to 1.30," NASA TN D-7192, May 1973.

26.2.2-21 Benson, J. L., Miller, L. D., Horie, G., "Theoretical Study of Engine Exhaust Nozzle - Airframe Integration," AEDC TR 67-214, October 1967. (NTIS No. AD 822 024)

26.2.2-22 Lighthill, M. J., "Supersonic Flow Past Slender Bodies of Revolution, The Slope of Whose Meridian Section is Discontinuous," Quart, J. of Mech. and Appl. Math., Vol. I, Part 1, 1948.

26.2.2-23 Emington, E., Lord, W. T., "Note on the Numerical Evaluation of the Wave Drag of Smooth Slender Bodies Using Optimum Area Distributions for Minimum Wave Drag," JRAeS Technical Note, 60, 1 January 1956.

26.2.2-24 Baldwin, B. S., Rose, W. C., "Calculation of Shock-Separated Turbulent Boundary Layers," NASA SP-347, 1975.

26.2.2-25 Marconi, F., Yaeger, L., Hamilton, H. H., "Computation of High-Speed Inviscid Flows *about Real Configurations*," NASA SP-347, 1975.

26.2.2-26 Ehlers, F. E., "A Numerical Method for Computing the Transonic Fan Duct Flow over a Centerbody into an Exterior Free-stream," Boeing D6-41078, September 1974.

26.2.2-27 Lu, H. Y., "Calculation of Axisymmetric Compressible Turbulent Jet Flows," Boeing D6-40611, November 1972.

26.2.2-28 Rubbert, P. E., Saaris, G. R., "Review and Evaluation of a Three-Dimensional Lifting Potential Flow Analysis Method for Arbitrary Configurations," AIAA 72-188, 1972.

26.2.2-29 Pratt & Whitney Aircraft Report, "Experimental and Analytical Determination of Integrated Airframe Nozzle Performance."

26.2.2-30 Lockheed, LR 24830, "Program for Experimental and Analytical Determination of Integrated Airframe Nozzle Performance."

26.2.2-31 Schmidt, W., Vanino, R., "The Analysis of Arbitrary Wingbody Combinations in Transonic Flow Using a Relaxation Method," Symposium Transonium II, Gottingen, September 1975.

26.2.2-32 Kane, E. J., Middleton, W. D., "Considerations of Aerodynamic Interference in Supersonic Airplane Design," AGARD CP-71-71, January 1971.

26.2.2-33 Margason, R. J., Yip, L. P., Gainer, T. G., "Recent Developments in Propulsive Lift *Aerodynamic Theory*," *NASA SP-347*, 1975.

26.2.2-34 McDonald, H., Hughes, P. F., "A Correlation of High Subsonic Afterbody Drag in the Presence of a Propulsive Jet or Support Sting," J. Aircraft 2, 3, 1965.

26.2.2-35 Swavely, C. E., Soileau, J. F., "Aircraft Aftbody/Propulsion System Integration for Low Drag," AIAA paper 72-1101, 1972.

26.2.2-36 Castells, O. T., et al, "Twin Jet Exhaust System Interaction Test," Vol. I, R72AEG235, October 15, 1972.

26.2.2-37 Reubush, D. E., "Effect of Reynolds Number on Boattail Drag," J. Aircraft, 13, 5, May 1976.

26.2.2-38 Hess, J. L. and Smith, A. M. O., "Calculation of Potential Flow About Arbitrary Bodies," Progress in Aeronautical Sciences, edited by D. Kuchemann, Vol., 18 Pergamon Press, London, 1967, pp 1-138.

26.2.2-39 "Users Manual for the External Drag and Internal Nozzle Performance Decdeck XI - Supersonic Flow Analysis (Applicable to Deck VI)," PWA-3465, Suppl. F. Pt. I (Contract No. AF33(615)-3128), September 1, 1968, Pratt and Whitney Aircraft, East Hartford, CT.

26.2.2-40 Presz, W. M. Jr., and Pitkin, E. T., "Flow Separation Over Axisymmetric Afterbody Models," Aircraft, 11, 11, November 1974, pp. 677-682.

26.2.2-41 Royal Aeronautical Society Aerodynamics Data Sheets 5.02.03.04 and 5.02.03.05, issued March 1954, Reprinted July 1958.

26.2.2-42 Mercer, E., and Berrier, B. L., "Effect of Afterbody Shape Nozzle Type, and Engine Lateral Spacing on the Installed Performance of a Twin Jet Afterbody Model," Langley Research Center, NASA TMX-1855, September 1969.

26.2.2-43 Wynoski, T. A., Spurrell, R. M., Usab, W. S., "Final Progress Report - Exhaust System Interaction Program," Pratt & Whitney Aircraft, PWA 4745, June 1973.

26.3.3-1 Poisson-Quinton, P., "From Wind Tunnel to Flight, the Role of the Laboratory in Aerospace Design," 30th Wright Brothers Lecture, J. Aircraft, 5, 3, 1968.

26.3.3-2 Muhlstein, L., Steinle, F. W., "Fluid Dynamic Research at NASA-Ames Research Center Related to Transonic Wind Tunnel Design and Testing Techniques," AGARD CPP-174, 1975.

26.3.3-3 Kolgore, R. A., Adcock, J. B., Ray, E. J., "The Cryogenic Transonic Wind Tunnel for High Reynolds Number Research," AGARD CPP-174, 1975.

26.4.2-1 Johnson, R. H. et al., "Propulsion System Integration and Test Program (steady state) Summary: Part I. Integration Technique and Test Activities," AFAPL-TR-69-36, Part I, June 1969.

26.4.2-2 Armstrong, R. S. and Miller, S. R., "Sub-Sonic Aerodynamic Performance of Nozzle Installations in Supersonic Airplanes," AIAA 67-452, July 1967.

26.4.2-3 Migdal, D., Miller, E. H., Schnell, W. C., "An Experimental Evaluation of Exhaust Nozzle/Airframe Interference," AIAA 69-430, 1969.

26.4.2-4 Chamberlain, D., "Measurement of Drag from Interaction of Jet Exhaust and Airframe," Journal of Aircraft, 6, 2, 1969.

26.4.2-5 Migdal, D. and Greathouse, W. K., "Optimizing Exhaust-Nozzle/Airframe Thrust Minus Drag," SAE 680294, 1968.

26.4.3-1 AGARD Conference No. 150, "Airframe Propulsion Interference," Rome, Italy, September 1974.

26.4.3-2 AGARD Lecture Series No. 53, "Airframe/Engine Integration," May 1972.

26.4.3-3 Decher, R., Gillette, W. B., and Tegeler, D. C., "Nacelle-Airframe Integration: Model Testing for Nacelle Simulation and Measurement Accuracy," AGARD Specialists' Meeting on Wind Tunnel Design and Testing Techniques, London, U. K., October 1975.

26.4.3-4 Ramsay, J. W., Propulsion System Simulation with a Turbopowered Nacelle, Boeing Document D6-22772, August 1969.

26.4.3-5 Motycka, D. L., DiSabato, V. J., and Andersen, L. O., "The Use of a Powered Model for Subsonic Nacelle Optimization," ASME 72-GT-14.

26.4.3-6 Motycka, D. L., DiSabato, V. J., and McCall, J. E. Sr., "Powered Model Wing Tunnel Investigation to Determine Performance Trends with Nacelle Location," AIAA paper 72-1114.

26.4.3-7 Welge, H. R. and Ongarato, J. R., "Powered Engine Simulator Procedures and Experience for the DC-10 Wing Engine," J. Aircraft, 8, 7, July 1971.

26.4.3-8 Kutney, J. T., U.S. Patent 3,434,679, May 9, 1966.

26.4.3-9 Kutney, J. T., "Airframe/Propulsion System Analysis Using the Propulsion Simulator Technique," AGARD CP 71-71.

26.4.3-10 Robinson, C. E., High, M. D., and Thompson, E. R., "Exhaust Plume Temperature Effects on Nozzle Afterbody Performance Over the Transonic Mach Number Range," AGARD CPP-150, Rome, Italy. September 1974.

26.4.3-11 Lee, G., "An Investigation of Transonic Flow Fields Surrounding Hot and Cold Sonic Jets." NASA TN-D 853, 1961.

26.4.3-12 Yarker, A. and Stanhope, F., "Altitude Testing of High Bypass Ratio Fan Engines," SAE paper 690655, 1969.

26.5.2-1 Ascough, J. C., "Procedures for the Measurement of Engine Thrust in Flight," AGARD FMP Symposium on Flight Test Techniques, Cologne, October 1976.

26.5.5-1 Ascough, J. C., "The Accuracy of Thrust in Flight Derived from Engine Calibrations in an Altitude Test Facility," 10th ICAS Congress, Ottawa, Canada, October 1976.

26.5.5-2 Burcham, F. W., "An Investigation of Two Variations of the Gas Generator Method to Calculate the Thrust of the Afterburning Engines Installed in an F-111A." NASAS TN-D 6297, April 1971.

26.6.2-1 Abernathy, R. B., Thompson, J. W., "Uncertainty in Gas Turbine Measurements," AIAA paper 73-1230, 1973.

☆ U.S. GOVERNMENT PRINTING OFFICE: 1978-760-316

END

FILMED

7-85

DTIC